2017 IEEE International Ultrasonics Symposium

Washington, D.C., USA

September 6-9, 2017

ABSTRACT BOOK

IEEE Ultrasonics, Ferroelectrics, and Frequency Control Society

1A - MEL: Cardiac Elasticity Imaging

Regency Ballroom

Thursday, September 7, 2017, 10:30 am - 12:00 pm

Chair: **Emad Ebbini**
Univ. of Minnesota

1A-1

10:30 am Clinical Feasibility of a Noninvasive Method to Interrogate Myocardial Function via Strain and Acoustic Radiation Force-Derived Stiffness

Vaibhav Kakkad[1], Harrison Ferlauto[1], **David Bradway[1]**, Brecht Heyde[2], Joseph Kisslo[3], Gregg Trahey[1]; [1]*Department of Biomedical Engineering, Duke University, Durham, NC, USA,* [2]*Cardiovascular Imaging and Dynamics, KU Leuven, Leuven, Belgium,* [3]*Cardiology, Duke University Medical Center, Durham, NC, USA*

Background, Motivation and Objective

Myocardial elastance, derived from pressure-volume (PV) loops in the left ventricle (LV), can be used to assess LV function and myocardial performance. This method requires an invasive intracardiac pressure-volume catheter to be inserted in the LV, limiting the method's utility in clinical screening and monitoring.

Strain echocardiography and cardiac acoustic radiation force impulse (ARFI) imaging are ultrasonic techniques to noninvasively assess myocardial function by tracking the deformation through the cardiac cycle and the tissue response to repeated impulsive acoustic radiation force, respectively. Strain and ARFI imaging have largely been used in separate contexts. Our group has previously demonstrated the use of cardiac ARFI and strain in an invasive open-chest animal study, but this is the first work to examine the relationship between ARFI-derived stiffness and strain in a noninvasive in vivo clinical study.

Statement of Contribution/Methods

Patients at the Duke University Medical Center's cardiac diagnostic unit were enrolled in a institutional review board-approved study. After informed consent was obtained, a sonographer captured parasternal long axis (PLAX) and short axis (PSAX) views of the LV using a Siemens Acuson SC2000 scanner and 4V1c transducer. Custom-written beam sequences saved up to six heartbeats of data in each 5-sec acquisition for off-line analysis. ARFI displacement and strain were calculated for a region of interest in the interventricular septum.

Results/Discussion

Data from the first six patients have been examined, with a representative example shown below. In this small sample size, somewhat large variability was observed across heartbeats and patients. As more patient data are analyzed with improved methods, beat-to-beat repeatability and inter-patient reproducibility will be used to assess the clinical viability of this noninvasive cardiac imaging method.

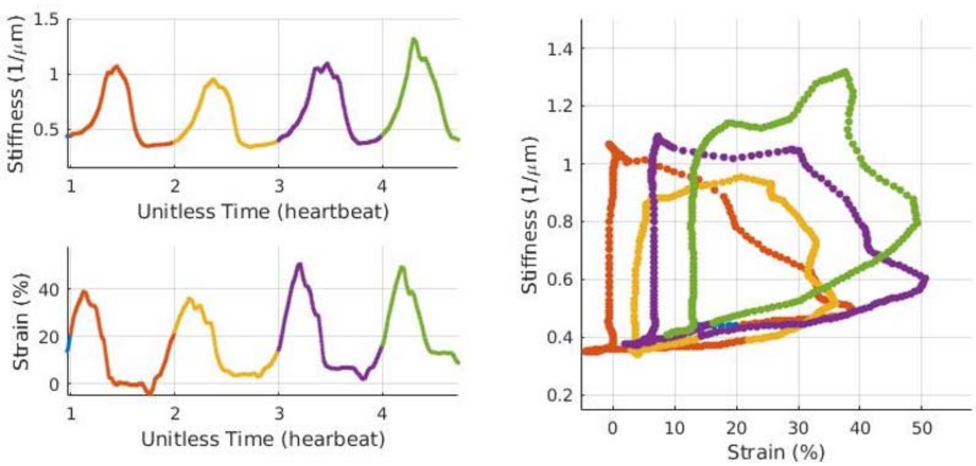

1A-2

10:45 am Spatio-Temporal Consistency of Transthoracic ARFI-Derived Metrics of Myocardial Function

Vaibhav Kakkad[1], Peter Hollender[1], Joseph Kisslo[2], Gregg Trahey[1]; [1]*Biomedical Engineering, Duke University, Durham, North Carolina, USA,* [2]*Cardiology, Duke University Hospital, Durham, North Carolina, USA*

Background, Motivation and Objective

Cardiac function has traditionally been studied using pressure-volume (PV) loop analysis. PV loops can be used to derive functional indices such as end-systolic pressure volume relationship (ESPVR) - a measure of myocardial contractility, end-diastolic pressure volume relationship (EDPVR) - a measure of myocardial compliance and relaxation time constant (τ) - a measure of left ventricular relaxation. However, PV loop analysis is largely an invasive proedure; it requires catherization and only provides a global assessment of cardiac function.

Transthoracic ARFI (TTE ARFI) has been shown to capture the dynamic trends of myocardial stiffness over the cardiac cycle in a noninvasive manner. In this work we explore the potential of using myocardial stiffness measurements made using TTE ARFI to derive functional indices similar to the ones measured using PV loops. We studied parameters impacting the spatio-temporal stability and reliability of TTE ARFI-derived measures of myocardial function.

Statement of Contribution/Methods

11 healthy volunteers were imaged at the Duke out-patient cardiology clinic through an IRB approved protocol. TTE ARFI sequences to capture stiffness data over a 2 mm lateral extent and over 4-5 consecutive cardiac cycles at 35 Hz (within FDA limits) were implemented on the Siemens SC2000 using the 4V1c (cardiac phased array probe). Dynamic

myocardial stiffness trends were measured in the interventricular septum (IVS) (as shown in Fig) through parasternal long axis and short axis views. These measurements and simultaneously acquired ECG signals were used to compute ARFI-derived indices of myocardial function such as: diastolic-to-systolic stiffness ratios and relaxation time constants.

Results/Discussion

Acoustic clutter (quantified by the contrast between the IVS and cardiac chambers), tissue motion (quantified by the temporal coherence of speckle) and systolic displacement magnitude (post motion filtering) were found to be the primary factors affecting the reliability of TTE ARFI measurements. For datasets with reliable TTE ARFI measurements, the diastolic-to-systolic ratio was found to be 2.95 ± 0.61. Relaxation time constants for the same were computed to be 69.29 ± 14.05 µs. These results demonstrate the potential of TTE ARFI as a tool for noninvasive, real-time measurement of regional myocardial function.

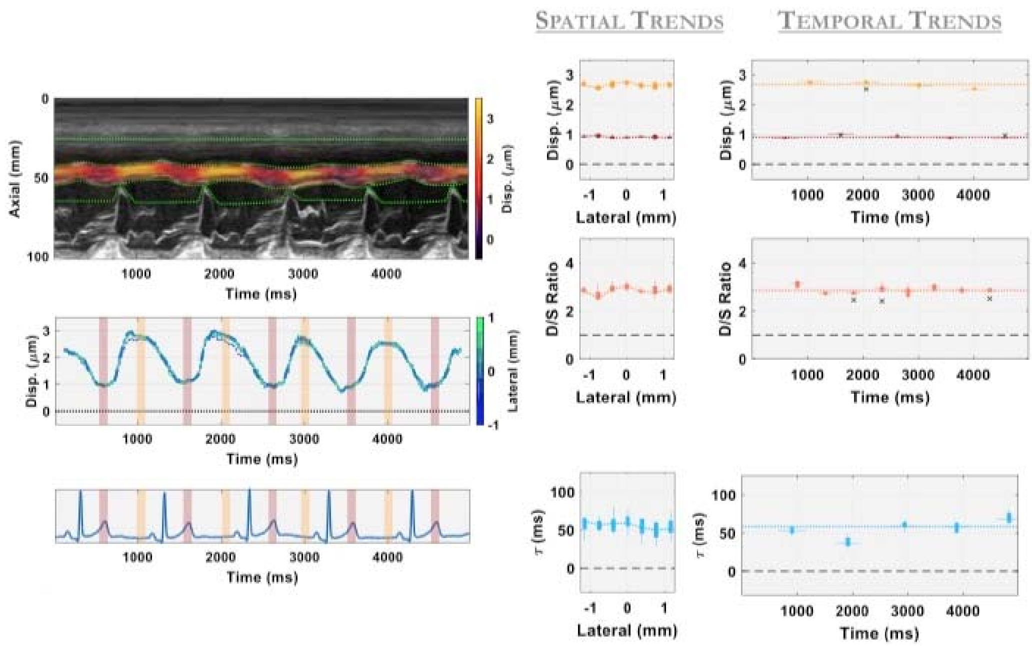

1A-3

11:00 am Calibration of ARFI Displacements Using Diastolic Shear Wave Speeds for Estimating Systolic Elasticity

Peter Hollender[1], Vaibhav Kakkad[2], Gregg Trahey[1,3]; [1]*Biomedical Engineering, Duke University, Durham, NC, USA,* [2]*Biomedical Engineering, Duke University, Durham, North Carolina, USA,* [3]*Radiology, Duke University Medical Center, Durham, North Carolina, USA*

Background, Motivation and Objective

ARFI displacements have been shown to share an inverse relationship with shear wave speed - based estimates of tissue elasticity. Both ARFI and shear wave elasticity imaging (SWEI) have been used to track the stiffening and softening of myocardium through the cardiac cycle in open-chest, intracardiac, and Langendorff preparations. In transthoracic imaging, induced shear waves have been observed during diastole, but only ARFI displacements have been accurately measured through both diastole and systole. Because ARFI displacements only map relative elasticity, they cannot be directly used to characterize absolute properties. We propose here a method for using diastolic shear wave speeds to calibrate ARFI displacement magnitudes, allowing ARFI displacements to be independently used to quantify shear wave speed throughout the cardiac cycle.

Statement of Contribution/Methods

Using Finite Element Method (FEM) techniques and FIELD II, we simulated on- and off-axis displacements in response to focused acoustic radiation force at different elasticities, mimicking the imaging configurations for both intracardiac and transthoracic imaging setups. For each setup, a calibration table of shear wave speed to the relative ARFI displacement was built. Dogs and Langendorff-perfused rabbit hearts were imaged with a Siemens AcuNav10F intracardiac phased array on a Siemens SC2000 scanner, and patients were imaged transthoracically with a Siemens 4v1c phased array. Using the calibration tables, the diastolic displacements were fit to the diastolic shear wave speeds, and the fit was extrapolated to estimate systolic shear wave speeds from systolic displacements only.

Results/Discussion

The simulations show that the selection of ARFI timestep influences the calibration curve between displacement and shear wave speed. In the Langendorff and intracardiac experiments, good agreement is seen between the estimated shear wave speeds using the extrapolated diastolic fit and the directly measured shear wave speeds. In the transthoracic imaging cases where systolic shear waves are not available, ARFI displacements can be calibrated by the diastolic shear wave speeds to estimate shear wave speed throughout the entire cardiac cycle. This method may be valuable for estimating contractility, contraction and relaxation rates, and the absolute elastic properties of myocardium.

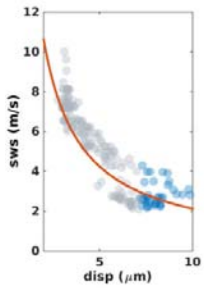

Left: Shear wave speed and ARFI displacement pairs (grey dots) throughout the cardiac cycle in a Langendorff-perfused rabbit heart. The simultation-derived model fit (red line) is scaled to fit the diastolic shear waves and displacements (blue dots). Good agreement is seen across all points.

Below: The ARFI-displacement-derived shear wave speeds (red) fit the directly-measured shear wave speeds well throughout the cardiac cycle.

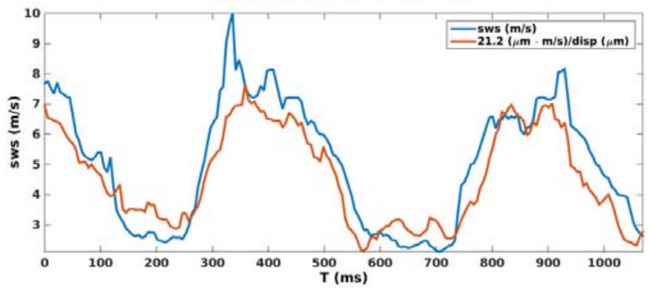

1A-4

11:15 am The Effect of Stretching on Transmural Shear Wave Anisotropy in Cardiac Shear Wave Elastography: an Ex Vivo and In Silico Study

Annette Caenen[1], Abdullah Thabit[1], Mathieu Pernot[2], Darya Shcherbakova[1], Luc Mertens[3], Abigail Swillens[1], Patrick Segers[1]; *[1]IBiTech - bioMMeda, Ghent University, Ghent, Belgium, [2]Langevin Institute, Ecole Supérieure de Physique et de Chimie Industrielles, Paris, France, [3]Hospital of Sick Children, University of Toronto, Toronto, Canada*

Background, Motivation and Objective

The feasibility of Shear Wave Elastography (SWE) for assessing fiber organization in anisotropic tissues based on the 3D spatial anisotropy in shear wave (SW) propagation has been demonstrated. In this work, we investigated the performance of SWE in mapping myocardial anisotropy of the left ventricular (LV) wall while increasing the uniaxial stretch. Additionally, a profound study of the occurring SW physics will be realized through finite element (FE) simulations.

Statement of Contribution/Methods

Ex-vivo: Pig hearts (n=4) were obtained from the slaughter house. Their LV's were cut open along the septum, put in a warm water bath (36 - 38°C) and stretched in the circumferential direction (5% - 10% - 15%), cfr. fig. a. SW measurements were done with the Aixplorer system, while rotating the SL15-4 probe from 0° to 180° in steps of 10°. Data were processed with a time-of-flight method to estimate the depth-varying group speed. By assuming an orthotropic planar fiber orientation parallel to the wall, the fiber angle could be extracted at every depth based on the major axis' angle of the fitted tilted ellipse to the group speed data. For validation purposes, the fiber orientation was determined with the naked eye on 3 samples of the sliced myocardium (fig. b).

In silico: SWs were generated in the FE software Abaqus by applying a body force, derived from simulated acoustic pressures in Field II, representing the experimental push. An orthotropic material law was implemented (Holzapfel, 2009), and the simulated specimen was subjected to uniaxial stretch to mimic the experiments.

Results/Discussion

Ex-vivo: The SWE-derived myocardial fiber orientation varied from 134.7° (epi) to 208.2° (endo) at 5% stretch (fig. c), corresponding well with image analysis (fig. d). This range in fiber angles decreased when increasing the uniaxial stretch, aligning the fibers more to the circumferential direction (fig. d). Additionally, the ellipse fitting of the group speed front in the lateral-elevational plane provided a more robust method to assess fiber orientation than tracking maximal wave speed.

In silico: Preliminary results of the simulations showed the ability to simulate myocardial anisotropy in SW propagation during stretching (fig. e). These simulations will provide additional insights in SW anisotropy maps during complex cardiac dynamics, as the actual fiber orientation is known.

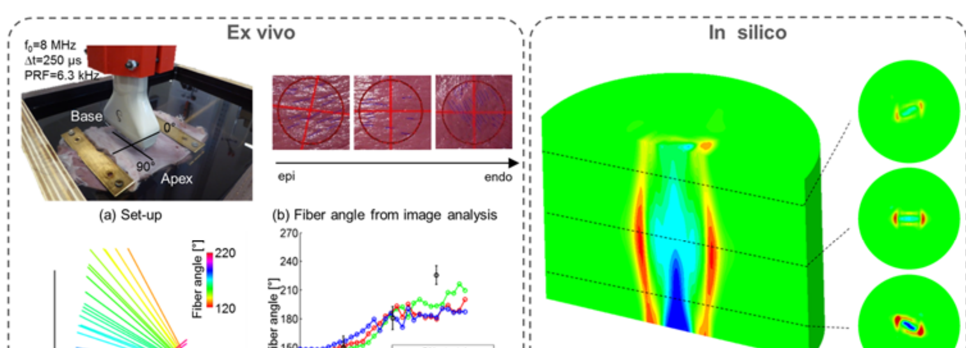

1A-5

11:30 am Cardiac Atrial Kick Shear Wave Elastography with Ultrafast Diverging Wave Imaging: An In Vivo Pilot Study

Aaron Engel[1], Hao Hsu[2], Pengfei Song[3], Gregory Bashford[1]; [1]*Department of Biological Systems Engineering, University of Nebraska-Lincoln, Lincoln, Nebraska, USA,* [2]*Department of Pediatric Cardiology, Children's Hospital and Medical Center, Omaha, Nebraska, USA,* [3]*Department of Radiology, Mayo Clinic College of Medicine, Rochester, Minnesota, USA*

Background, Motivation and Objective

Increased myocardial stiffness is characteristic of many diseases, leads to a loss of diastolic function, and is a cause of diastolic heart failure (DHF). Methods to estimate myocardial stiffness include Shear Wave Elastography (SWE). Currently, ultrasound-based cardiac SWE includes acoustic radiation force (ARF)-based methods; however, the in vivo generation and detection of the shear waves in myocardium is significantly degraded due to limited ARF penetration and clutter noise. Consistently successful cardiac SWE is limited to low BMI patients. The objective of this research is to develop an ultrafast cardiac SWE technique where the shear wave is generated by the mechanical stimulus of the diastolic atrial kick. The amplitude of this wave is at least one order of magnitude higher than ARF-induced shear waves and thus more easily visualized, having a higher chance of success in a broader patient population.

Statement of Contribution/Methods

Cardiac atrial kick SWE was performed on 14 healthy adults (ages: 24.7 ± 3.0). Data collection of the atrial kick shear wave was done on a Verasonics Vantage using an ultrafast diverging wave imaging technique. This imaging method was capable of covering the entire heart at frame rates needed to track shear waves. The shear wave speed (SWS) was estimated (Fig. 1) and correlated to common health measures in the clinic and in echocardiography, including peak tissue velocities in early diastole (E’), late diastole (A’), and isovolumetric relaxation time (IVRT’). This research is the first to investigate the in vivo atrial kick SWS in humans using an ultrafast diverging wave imaging technique.

Results/Discussion

For all subjects, the SWS was 1.78 ± 0.34 m/s, similar to other SWE results for late diastole. Peak tissue velocities were 152 ± 19 mm/s for E’, and 94 ± 16 mm/s for A’. E’/A’ was 1.68 ± 0.43 and IVRT’ was 70 ± 11 ms. The atrial kick SWS was correlated to diastolic pressure ($r = -0.75$, $p = 0.002$), E’ ($r = 0.6$, $p = 0.02$), IVRT’ ($r = -0.60$, $p = 0.02$), and E’/A’ ($r = 0.58$, $p = 0.03$). This suggests it can be a measure of diastolic function and myocardial stiffness. These results established the range of normal values of atrial kick SWS that may be used as reference values when studying myocardial pathologies such as DHF. The results also show that other factors such as blood pressure may be needed to better assess deviations of atrial kick SWS caused by disease.

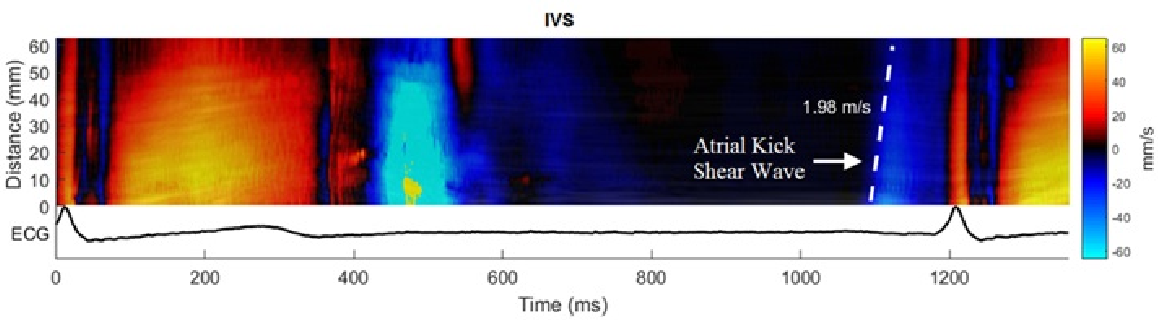

Figure 1: Tissue velocity and estimated SWS in the interventricular septum.

1A-6

11:45 am 3D Myocardial Mechanical Wave Measurements Using High Frame Rate Ultrasound Imaging and Clutter Filter Wave Imaging: Towards a 3D Myocardial Elasticity Mapping

Sebastien salles[1], Alfonso Rodriguez-Molares[1], Asbjørn Støylen[1], Tore Bjastad[2], Svein Arne Aase[2], Lasse Løvstakken[1], Hans Torp[1];[1]*Norwegian University of Science and Technology, Department of Circulation and Medical Imaging, Norwegian University of Science and Technology, Norway,* [2]*GE Vingmed Ultrasound, Norway*

Background, Motivation and Objective

Myocardial fibrosis is recognized as a physio-pathologic substrate of main cardiovascular syndromes such as myocardial infraction or heart failure. Knowing that fibrosis leads to increased myocardial stiffness, elastography techniques, such as shear wave imaging, has been showed to detect for the detection Fibrotic Tissue (FT) (Liver, arteries, ...). However, its application on the heart still remain challenging. In this work we want to estimate the velocity of Mechanical Waves (MW) produced by natural cardiac events such as the aortic valve closure, propagating along the left ventricle (LV) wall. The two main objective are to visualize the propagation of MW in 3D and achieve a 3D elasticity map of the LV.

Statement of Contribution/Methods

In order to detect 3D MW propagating along the LV wall, 3D high frame rate imaging was implemented on a modified GE Vivid E95, by transmitting 20 planes waves to cover a sector of 60°, resulting in 820 volumes/s when stitching over 4 cardiac cycles. The LV was segmented using a high quality 3D B-mode acquisition setup, to create a 3D LV surface model. Five healthy volunteers were investigated during 8 cardiac cycles for each subject.

The MW were detected using clutter filter wave imaging (see abstract 1386). By taking the time gradient of the resulting 3D B-mode image, the 3D spatiotemporal map is extracted. The wave propagation velocity is estimated with linear regression of the maxima of the waves slop in the longitudinal direction, along each arch of the 3D surface from the AV plane to the Apex. Finally, the corresponding Shear Modulus was estimated and mapped onto the 3D surface model.

Results/Discussion

For all the subjects, 2 different MW, corresponding to the late peak diastolic a’ (Fig a.) and aortic valve closure, were detected. We noticed that the a’ waves propagate from the AV plane to the Apex, while the second wave seems to follow a more complex 3D propagation path. The average velocities and the corresponding Shear Modulus are depicted in Tab. 1, and are in agreement with values in literature. Using the locally estimated Shear Modulus a 3D elasticity map was produced (Fig b.)

In this study, 3D left ventricle MW were visualized and their velocities measured. This study allowed to achieve a 3D elasticity map of the LV using ultrasound. Moreover, the visualization of MW could allow a better understanding of normal and pathologic myocardial function.

a. Mechanical waves propagation on the left ventricule at the peak late diastolic a'

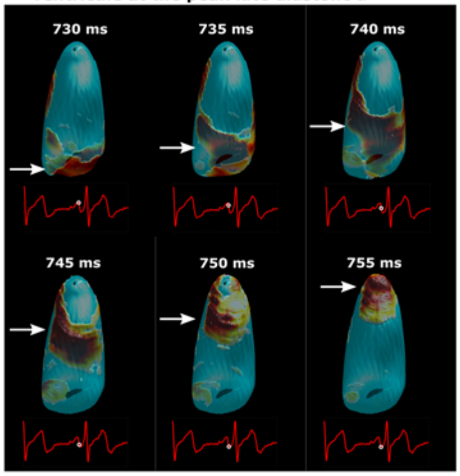

b. 3D left ventricul Shear elasticity map

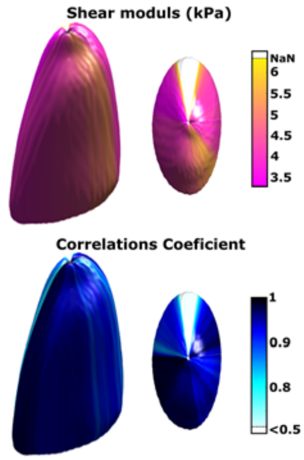

Estimated Mechanical waves velocity and shear modulus		
Subject	Wave Velocity (m.s-1)	
	a'	AVC
1	2.48 ± 0.33	5.53 ± 0.49
2	2.23 ± 0.28	5.67 ± 0.47
3	2.15 ± 0.45	5.22 ± 0.24
4	2.92 ± 0.57	6.05 ± 0.69
5	2.51 ± 0.32	5.89 ± 0.32
Subject	Wave Velocity (kPa, rho=1)	
	a'	AVC
1	6.15 ± 1.64	30.58 ± 5.42
2	4.97 ± 1.25	32.15 ± 5.33
3	4.62 ± 1.94	27.25 ± 2.51
4	8.53 ± 3.33	36.6 ± 8.35
5	6.3 ± 1.61	34.69 ± 3.77

Figure a : The colormap correspond to the positive acceleration of the wall. The white arrow indicate the propagation of the wave.
Figure b : The Shear modulus and the correlation coefficient of the linear regression are shown. The withe part correspond to a correlation coefficient less than 0.5. This part is not taking into account.

2A - MBB: Coherence and Adaptive Beamforming

Ambassador Ballroom

Thursday, September 7, 2017, 10:30 am - 12:00 pm

Chair: **Hideyuki Hasegawa**
University of Toyama

2A-1

10:30 am Enhanced Ultrasound Harmonic Imaging Using the Filtered-Delay Multiply and Sum Beamformer

Giulia Matrone[1], Alessandro Ramalli[2], Piero Tortoli[2], Giovanni Magenes[1]; [1]*Department of Electrical, Computer and Biomedical Engineering, University of Pavia, Pavia, Italy,* [2]*Department of Information Engineering, University of Florence, Firenze, Italy*

Background, Motivation and Objective

Ultrasound Harmonic Imaging (HI) exploits the second harmonic component of backscattered signals generated by non-linear propagation in tissues. HI provides images with improved resolution and contrast, but with lower signal-to-noise ratio, compared to standard fundamental imaging (FI) mode.

The Filtered-Delay Multiply And Sum (F-DMAS) non-linear beamformer (doi: 10.1109/TMI.2014.2371235) was recently demonstrated able to achieve significantly superior contrast resolution and noise rejection than the conventional Delay And Sum (DAS) beamformer. Thus, in this work we experimentally investigate whether the combination of HI with F-DMAS can further suppress beam side lobes and noise to provide an enhanced image quality.

Statement of Contribution/Methods

Experimental acquisitions were carried out with the ULA-OP256 system and an Esaote 192–element linear array probe, driven at 5 MHz. The transmit focus was set at 33 mm and a linear scan was performed using 64-element apertures. Pre-beamforming signals, collected while scanning a set of nylon wires in water and a Gammex tissue-mimicking phantom, respectively, were processed in Matlab. They were first dynamically focused, band-pass filtered around 5 MHz or 10 MHz (to perform FI or HI, respectively) and then DAS or F-DMAS beamformed. Since F-DMAS basically consists in cross-multiplying and summing the received echoes, such non-linear operations generate a second harmonic component in the beamformed signals; hence, a final band-pass filter applied to the FDMAS beamformed signals allows selecting either the second (in FI mode) or the fourth harmonics (in HI mode), respectively. Lateral resolution (LR), contrast ratio (CR) and contrast-to-noise ratio (CNR) were finally measured on the obtained images.

Results/Discussion

The experimental images (see figure) show that in HI better resolution and clarity are achieved than in FI. When F-DMAS is applied to HI, resolution is higher than with DAS (0.32 mm vs. 0.44 mm), as shown by measurements on wire targets; besides, the cyst borders are sharper and better defined (the CR is ~12 dB higher). On the other hand, the CNR decreases with F-DMAS, due to the better contrast resolution of speckle pattern.

F-DMAS thus represents a promising beamforming method that, jointly used with HI, produces images with a superior quality and improved noise suppression.

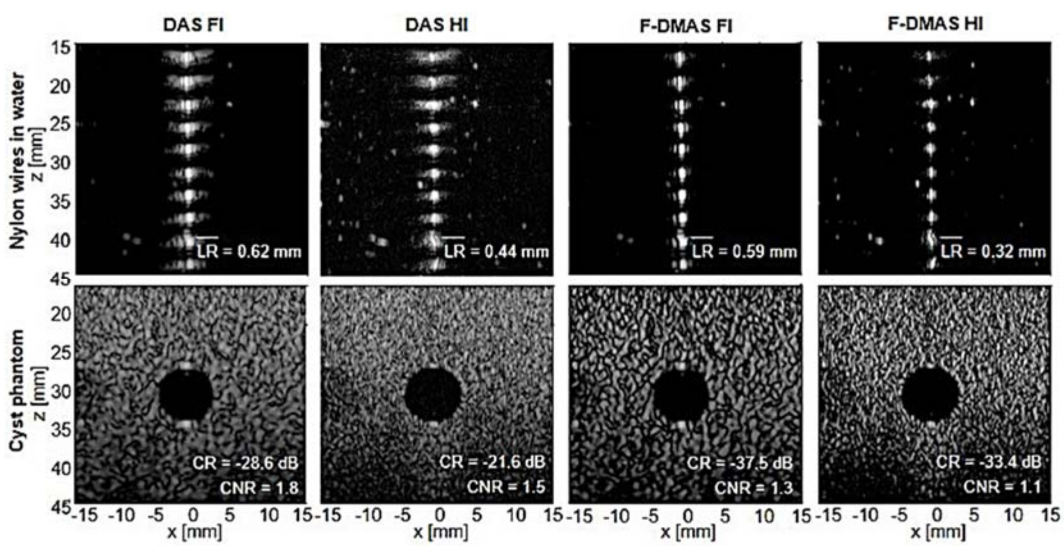

2A-2

10:45 am Adaptive Beamforming Applied to Transverse Oscillation

Hideyuki Hasegawa[1]; [1]*Graduate School of Science and Engineering, University of Toyama, Toyama, Japan*

Background, Motivation and Objective

In ultrasonic tissue motion estimation, the accuracy in the lateral motion estimate is worse than the axial estimate. For improvement of the accuracy in the lateral motion estimate, the transverse oscillation (TO) was introduced to increase the lateral spatial frequency of the ultrasonic field. In the present study, adaptive beamforming was introduced to the TO method to further improve the accuracy in motion estimation.

Statement of Contribution/Methods

TO is realized by the apodization scheme in delay-and-sum (DAS) beamforming. However, the apodization scheme has not yet been introduced in adaptive beamforming, i.e., rectangular apodization is used. In the present study, the apodization scheme was introduced to an adaptive beamformer proposed by our group [Hasegawa and Kanai, IEEE Trans. UFFC, 2015]. In the present study, TO was done by DAS and adaptive beamforming both with apodization composed of two Hanning functions. A phase-sensitive 2D motion estimator developed by our group [Hasegawa, Appl. Sci., 2016] was used for investigation of the effect of adaptive TO on the accuracy in motion estimation.

Results/Discussion

Figures (a), (b), and (c) show B-mode images of a phantom obtained with DAS beamforming with Hanning apodization, TO realized by DAS beamforming, and TO realized by adaptive beamforming, respectively. All images were obtained by ultrafast plane wave imaging (1302 fps) without compounding. As can be seen in Figs. (a) and (b), the lateral spatial frequency was increased by TO. Furthermore, a sharper oscillation in the lateral direction is realized by adaptive beamforming in Fig. (c) than the DAS beamforming in Fig. (b). Relative motion velocities of 2 mm/s (lateral) and 1 mm/s (axial) between the ultrasonic probe and phantom were produced by moving the probe by an automatic stage. The bias errors and standard deviations in the lateral velocities estimated by the phase-sensitive motion estimator with DAS-based and adaptive TOs were (4.5±21.4)% and (4.4±14.1)%, respectively. Those in the estimated axial velocities were (7.6±26.4)% and (7.4±27.0)%, respectively. With respect to the lateral velocity estimates, the adaptive TO improved the bias error slightly and reduced the standard deviation significantly. In addition, the proposed adaptive beamformer required computation time of only 3.5 times of the conventional DAS beamformer.

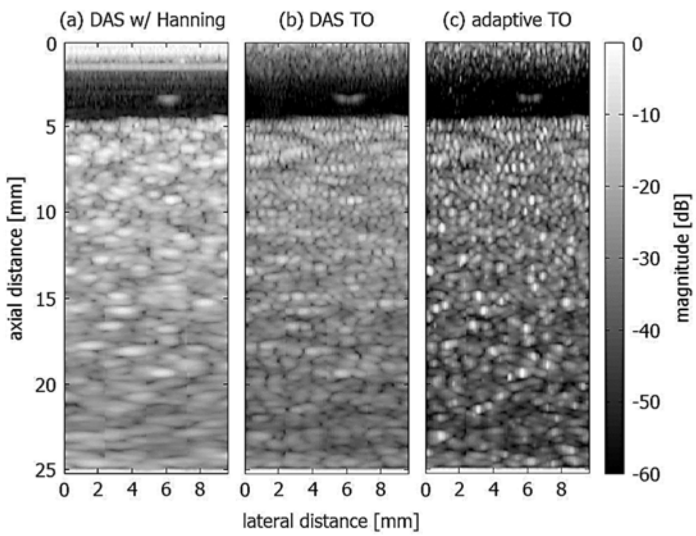

2A-3

11:00 am Influence of the Delay-Multiply-And-Sum Beamformer on the Ultrasound Image Amplitude.

Fabrice Prieur[1], Ole Marius Hoel Rindal[1], Sverre Holm[1], Andreas Austeng[1]; *[1]Department of Informatics, University of Oslo, Oslo, Norway*

Background, Motivation and Objective

Recently a new beamformer called the Delay-Multiply-And-Sum (DMAS) beamformer was introduced in the field of medical ultrasound imaging (Matrone et al IEEE Trans. Med. Imag. 2015). Instead of summing the signals recorded by each transducer element as with the Delay-And-Sum (DAS) beamformer, the DMAS algorithm multiplies the signals pairwise before summing them. This multiplication creates an "artificial second harmonic signal" around twice the transmitted pulse center frequency which is subsequently filtered.

Studies of the DMAS beamformer have shown advantageous image properties such as improved contrast and image resolution. But the nonlinearity of the DMAS beamformer leads to a different amplitude distribution in the obtained images compared to the DAS beamformer.

There is a need to precisely understand the causes of these differences and in which case the image amplitude differs the most. This work is a theoretical study of how the DMAS beamformer influences the image amplitude.

Statement of Contribution/Methods

We first study theoretically the statistics of the envelope signal used to build an image with the DMAS beamformer. It can be seen as a geometric mean of the signals recorded by each transducer element.

We then simulate B-mode images in Field II of homogeneous and heterogeneous speckle of varying amplitude obtained from a linear array. We study the amplitude of the obtained image and compare it to an image obtained by the DAS beamformer.

Results/Discussion

Our study shows that the mean amplitude of an area with homogeneous speckle obtained with the DMAS algorithm is proportional to the standard deviation of the speckle distribution as with the DAS algorithm. Although the obtained statistics differs from a Rayleigh distribution with a larger standard deviation leading to a grainier image, the mean amplitude is comparable to that obtained with the DAS beamformer.

In the case of a heterogeneous speckle with areas of different amplitude, the image obtained with the DMAS beamformer has a lower amplitude than with the DAS beamformer. This can be explained by comparing the geometric and arithmetic means of two signals (Fig. 1). This means that the image amplitude of a heterogeneous region tends to be lower with the DMAS beamformer (Fig. 1) and hypoechoic region may look "nicer" without necessarily being closer to the ground truth.

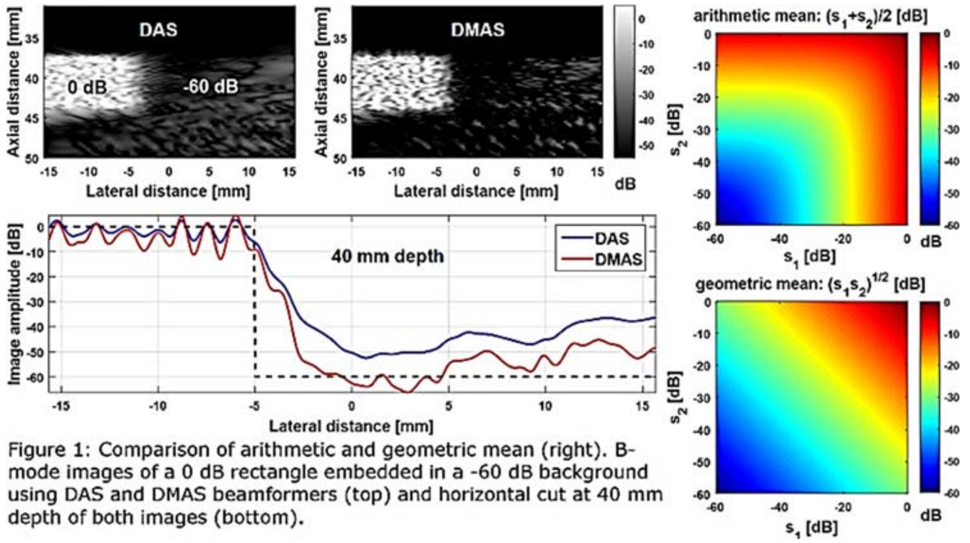

Figure 1: Comparison of arithmetic and geometric mean (right). B-mode images of a 0 dB rectangle embedded in a -60 dB background using DAS and DMAS beamformers (top) and horizontal cut at 40 mm depth of both images (bottom).

2A-4

11:15 am Phase Coherence Beamforming to Enhance Myocardial Speckle Tracking Performance

Pedro Santos[1], Nadezhda Koriakina[1], Bidisha Chakraborty[1], João Pedrosa[1], Vangjush Komini[1], Jan D'hooge[1]; [1]*Department of Cardiovascular Sciences, KU Leuven, Belgium*

Background, Motivation and Objective

Coherence-based methods have been shown to improve image quality by suppressing spurious lobes. However, when imaging a diffuse medium, such methods lead to a high variance of speckle amplitudes (i.e. granular appearance) which could limit their applicability for direct clinical imaging. The granular pattern may however be beneficial for speckle tracking echocardiography (STE), given the higher contrast inside the matching kernel. Accordingly, this study investigated the use of phase coherence methods as a pre-processing stage for STE, aiming at improving tracking performance and thereby, accuracy of myocardial function quantification.

Statement of Contribution/Methods

The hypothesis was tested in silico by imaging an ultrasound phantom constructed from a cardiac biomechanical model – thus granting ground truth motion. A full cardiac cycle (80 frames) was simulated in Field II using a typical cardiac phased array (2.5 MHz, 64 elements, 220 µm pitch). Four beamforming methods were used: delay-and-sum (DAS), phase coherence factor (PCF), sign coherence factor (SCF) and generalized coherence factor (GCF).

A set of 21 points were manually annotated and automatically tracked along the cycle using a validated non-rigid registration algorithm. The displacement estimates for all methods were compared against the ground truth and the tracking performance was assessed by the Euclidean distance error.

To further investigate the validity of the method, apical images were acquired using a clinical phased array in vivo (same geometry as in silico). Both DAS and SCF (which performed best in simulations) images were tracked during two heart cycles. The septal velocity traces were compared.

Results/Discussion

Pre-processing the channel data using all coherence methods improved STE performance in silico both in mean error and its variance (Fig A). As expected, errors accumulated along the cardiac cycle for all methods and reached its maximum at end systole. Noticeably, the cumulative displacement error decreased from 1.4 mm in DAS to 0.8 mm in SCF.

The in vivo velocity traces for both DAS and SCF were found similar and physiologically plausible (Fig C). A normalized cross-correlation of 0.96 was found, indicating that SCF preserves the anatomically relevant information on the ultrasound image while potentially improving STE. Further experimental quantification is on-going.

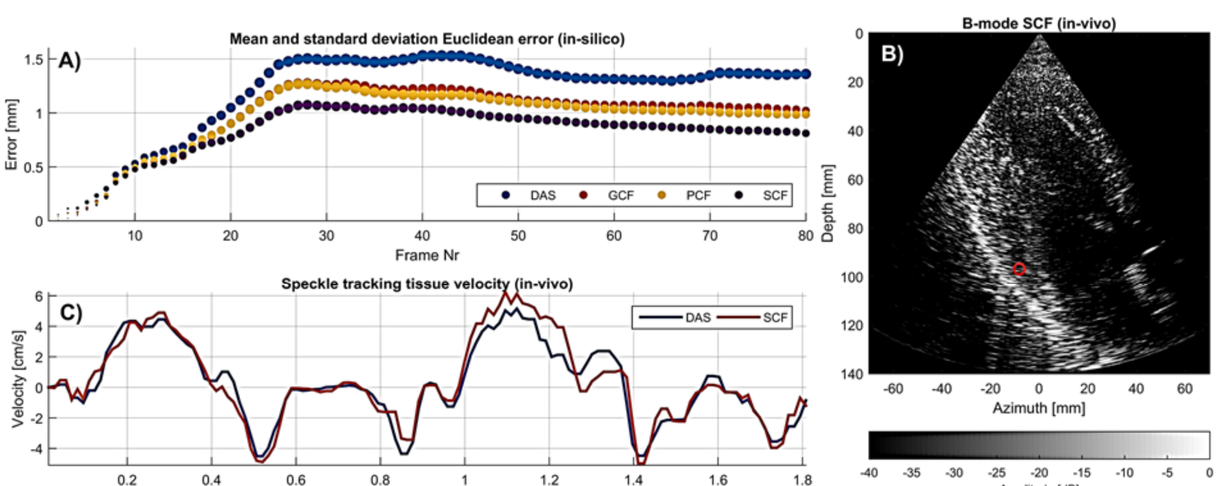

Figure - A) Euclidean error between ground truth and the displacements computed from all beamforming methods. The marker size indicates the standard deviation error per frame. B) In-vivo B-mode image reconstructed using the SCF. C) In-vivo velocity traces from the DAS and PCF methods for a point located at the red mark in panel B.

11:30 am Coherence Beamforming and its Applications to the Difficult-to-Image Patient

Jeremy Dahl[1]; [1]*Radiology, Stanford University, Stanford, CA, USA*

Background, Motivation and Objective

Poor quality ultrasound images and inadequate or suboptimal visualization of imaging targets is a common problem in individuals that are overweight or obese. The overweight and obese population in the United States has reached staggering proportions, with nearly 2 out of every 3 individuals overweight or obese. Despite advances in ultrasound imaging technology, techniques for these difficult-to-image patients are lacking. Acoustic reverberation is a common factor in these individuals and is a significant contributor to the poor image quality. Specifically, diffuse acoustic reverberation is problematic because it appears similar to common tissue texture in ultrasound images, thereby exacerbating the inadequate and suboptimal visualization.

Statement of Contribution/Methods

We discuss the coherence imaging technique called the short-lag spatial coherence (SLSC) beamformer and its related imaging methods as potential solutions to the inadequate and suboptimal visualization problem. The SLSC beamformer detects the spatial similarity of the backscattered ultrasound waves. Because diffuse reverberation is spatially incoherent in the wavefield, noise can be differentiated from tissue and other desired imaging targets, including blood and contrast agents, which display greater spatial coherence. The SLSC beamformer places a greater emphasis on the spatial similarity at closely-spaced positions, where there is greater differentiation between noise and tissue signals.

Results/Discussion

We introduce the applicability of the SLSC beamformer to other imaging techniques such as tissue harmonic imaging, flow imaging, and contrast-enhanced ultrasound. Clinical and pre-clinical applications of the technique are demonstrated in cardiac, fetal, liver, flow, and molecular imaging. Although computationally more intensive than conventional delay-and-sum beamforming, we show several techniques for fast computation of coherence, which enable real-time imaging. We demonstrate a GPU-based software beamformer and that can produce stable, high-quality, real-time in vivo imaging of SLSC images that show significantly reduced noise compared to matched B-mode images. We further discuss the challenges and criticisms of spatial coherence beamforming, including the loss in phase information and the nonlinear behavior of the technique.

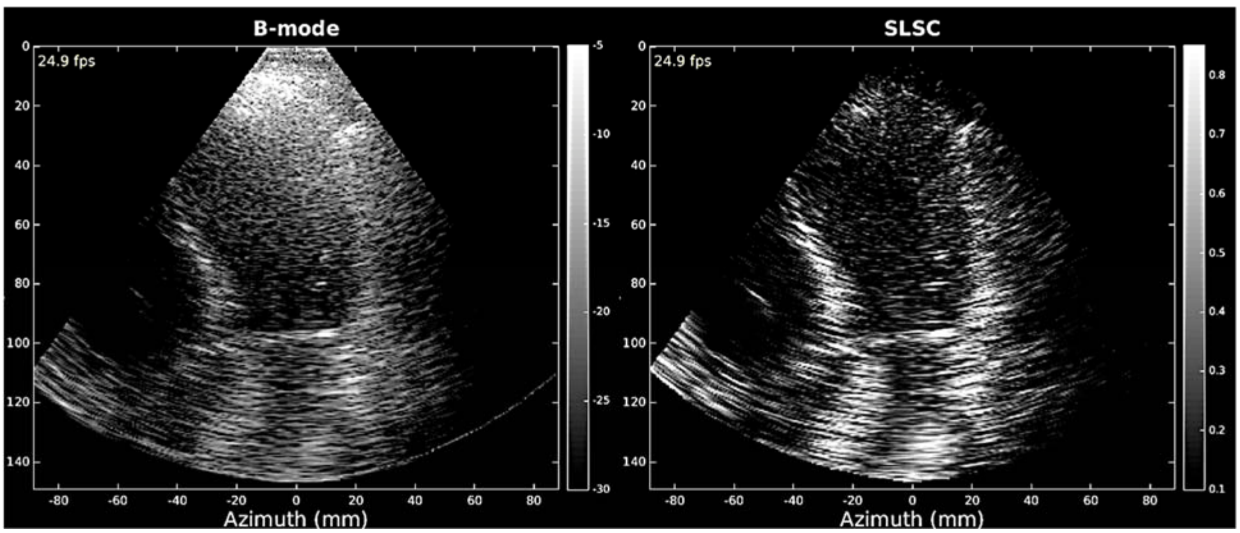

3A - MTH: Histotripsy, Lithotripsy, Thrombotripsy

Palladian Room

Thursday, September 7, 2017, 10:30 am - 12:00 pm

Chair: **Zhen Xu**
University of Michigan

3A-1

10:30 am **Rapid Liquefaction of Blood Clots Using Histotripsy in an In Vivo Porcine Intracerebral Hemorrhage (ICH) Model**

Jonathan Sukovich[1], Aditya Pandey[2], Tyler Gerhardson[1], Timothy Hall[1], Charles Cain[1], Zhen Xu[1]; [1]*Biomedical Engineering, University of Michigan, Ann Arbor, MI, USA,* [2]*Neurosurgery, University of Michigan, Ann Arbor, MI, USA*

Background, Motivation and Objective

Histotripsy is a noninvasive ultrasound therapy that fractionates target tissues via cavitation. Our group has previously demonstrated that histotripsy can be delivered transcranially through excised human skulls to rapidly liquefy large volume clots for catheter aspiration using electronic focal steering (up to 40mL in 20 min) in an ex vivo ICH model. Transcranial MRgFUS has been investigated for ICH treatment, but is much slower (40mL in 3 hours), and limited to deep targets due to prefocal skull heating. The objective of this study was to demonstrate the feasibility of using histotripsy to liquefy clots for catheter aspiration in an in vivo porcine ICH model.

Statement of Contribution/Methods

Utilizing an accepted porcine ICH model, 2mL clots were formed in the frontal lobes of nine 60-80lb pigs via pressure-controlled infusion of autologous blood. As the pig skull is not amenable to ultrasound propagation, a 5cm craniectomy was performed to allow for ICH formation as well as histotripsy delivery to the clot. Under ultrasound image guidance, histotripsy was delivered to the clot using a hand-held histotripsy transducer placed outside the brain. The therapy focus was moved through the clot to liquefy it, leaving a ~1mm untreated margin at the boundary to avoid damage to the surrounding tissues. Six clots were treated using histotripsy pulses delivered at 20Hz with estimated focal pressures of up to 40MPa. Three clots were left untreated as control. After euthanasia, MR images of the treated and untreated clots were acquired and the brains were fixed for histology.

Results/Discussion

Histotripsy was able to successfully liquefy all targeted clots in ≤20 minutes, with volumetric MR analyses indicating clot lysis/liquefaction throughout volumes measuring up to 1.25mL. MR evaluation of the treated clots showed damage to be well confined within the boundaries of the targeted clots, with minimal damage to the surrounding/overlying tissues. Histology showed lysed red blood cells within the treated clot regions and intact blood cells near the untreated peripheries. Minor extraneous lesioning was seen in tissues around some clots, however, it was generally confined to regions <1mm from the clot near irregularly shaped boundaries which were non-differentiable in US imaging.

These results demonstrated the initial feasibility and safety of using histotripsy to rapidly liquefy clots in an in vivo ICH model. MR and histological evaluation showed that histotripsy can be accurately applied within clots. While minor damage to surrounding tissues was observed, it seems to have been primarily due to limits of the US imaging system used to guide treatment and is likely avoidable. In a clinical setting real time acoustic emission feedback coupled with MR or CT images of the brain could be used to more accurately plan and guide treatment. This study is the first in vivo work indicating the potential of histotripsy as a minimally invasive method for rapid and safe treatment of ICH.

3A-2

10:45 am **Stress Waves in Model Kidney Stones Exposed to Burst Wave Lithotripsy**

Adam Maxwell[1], Brian MacConaghy[2], Michael Bailey[1,2], Oleg Sapozhnikov[2,3]; [1]*Department of Urology, University of Washington School of Medicine, Seattle, WA, USA,* [2]*Center for Industrial and Medical Ultrasound, Applied Physics Laboratory, University of Washington, Seattle, WA, USA,* [3]*Department of Acoustics, Physics Faculty, Moscow State University, Moscow, Russian Federation*

Background, Motivation and Objective

Burst wave lithotripsy (BWL) is an experimental method to noninvasively fragment urinary calculi using low-frequency focused bursts of ultrasound. To optimize many of the acoustic parameters for this technology, it is necessary to understand the physical interactions between ultrasound bursts and stones. In this study, the interaction of elastic waves with model stones was simulated and experimentally visualized by photoelastography, a technique using polarized light to spatially and temporally visualize stress patterns.

Statement of Contribution/Methods

An axisymmetric finite-difference time domain simulation based on Hooke's law and an equation of motion was used to simulate the propagation of ultrasound bursts of frequencies between 170 – 800 kHz through a cylindrical stone made from epoxy or glass. For experiments, a high speed camera was used to capture images in the model stones. A circular polariscope was placed on either side of a degassed water bath and a narrowband LED was used for backlighting. The model stones were submerged in a chamber of index-matching fluid and aligned to the focus of a BWL transducer in the water bath. The stone models were exposed to a single burst, and a series of photographs was captured during propagation through the stone at frame rates between 0.1 to 5 MHz.

Results/Discussion

Simulations and photoelastic images indicated that the greatest stress was created as the incident burst passed through the stone model, followed by reverberation of waves after the burst. The simulated and experimental photoelastic fields showed similar spatially periodic fringe zones, with smaller spacing at higher frequencies (Figure, left). Based on the measured wavelengths, shear wave propagation appears to dominate over longitudinal waves in epoxy, while the opposite was observed in glass (Figure, center and right). This effect may be due to similarity of shear wave speed in epoxy ($c_t \sim 1295$ m/s) vs. glass ($c_t \sim 3300$ m/s) compared to the sound speed in the fluid ($c_l \sim 1490$ m/s). The results show good agreement between simulations and experiment, and suggest stone material and ultrasound parameters can emphasize in different mechanisms of stress production. This effect may contribute to variation in fragmentation efficiency observed between stone types for lithotripsy. Work supported by NIH NIDDK K01 DK104854 and P01 DK043881 and NSBRI through NASA NCC 9-58.

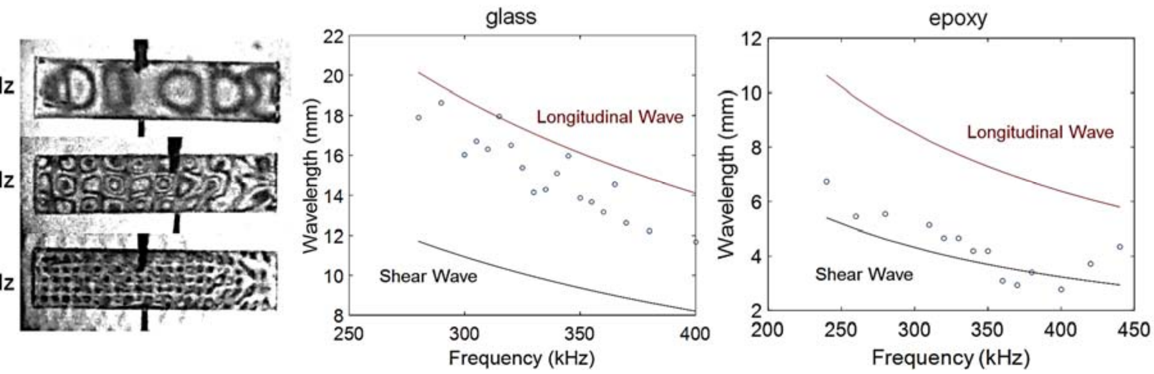

3A-3

11:00 am Non-Invasive Liver Cancer Ablation Using Histotripsy in an In Vivo Murine Hepatocellular Carcinoma (HCC) Model

Tejaswi Worlikar[1], Eli Vlaisavljevich[1], Tyler Gerhardson[1], Joan Greve[1], Shanshan Wan[1], Kimberly Ives[1], Timothy Hall[1], Theodore Welling[1], Zhen Xu[1]; [1]*University of Michigan, Ann Arbor, Michigan, USA*

Background, Motivation and Objective

Current liver cancer ablation methods are mainly thermal-based and inherently exhibit inconsistent tissue ablation due to irregular heat dissipation. Histotripsy is a non-thermal ultrasound (US) ablation method that fractionates tissue through the precise control of acoustic cavitation. This paper studies the feasibility and chronic effects of non-invasive histotripsy for liver cancer ablation in an in vivo murine HCC model.

Statement of Contribution/Methods

Liver cancer xenografts were generated by subcutaneous injection of human HCC cell line Hep3B into 28 NSG mice, divided into 3 study groups: A (partial tumor treatment, n=10), B (entire tumor treatment, n=11) and C (control - untreated, n=7). A custom 1 MHz histotripsy system equipped with a robotic positioner and real-time US imaging feedback was used to deliver 1-2 cycle histotripsy pulses with a PRF of 100 Hz (estimated p- >30 MPa). Groups A and B were treated when tumors reached ~1 cm. MR images were obtained pre and post histotripsy for assessment of treated volume. Within 3 days post treatment, a subset of mice from A and B; A1 (n=5) and B1 (n=9) were sacrificed for pathology. The remaining mice in subsets A2 (n=5), B2 (n=2), and group C were survived and monitored weekly using caliper measurements and MRI for 3 months or until tumors reached ~1.8cm.

Results/Discussion

In all treatments, histotripsy generated a bubble cloud and fractionated the targeted tumor regions guided by real-time ultrasound image (Fig.1a/b). Pathology revealed that the treated region was completely fractionated into acellular debris with a sharp boundary. In partially targeted tumors in A, some tumor cells remained at the original site, though no metastasis was observed in the distant organs in the chronic subset A2. In completely targeted tumors in subset B1, pathology revealed no intact tumor cells in the original sites at Day 3 post treatment. Follow-up monitoring of the chronic subset B2 has shown that the homogenized tumor volume and surrounding edema were mostly resorbed by Day 28 (Fig.1c). At the time of this submission, B2 has been survived for >1 month. Results indicate the potential of histotripsy therapy for non-invasive liver tumor ablation. Future work is ongoing to explore its long-term safety and biological response.

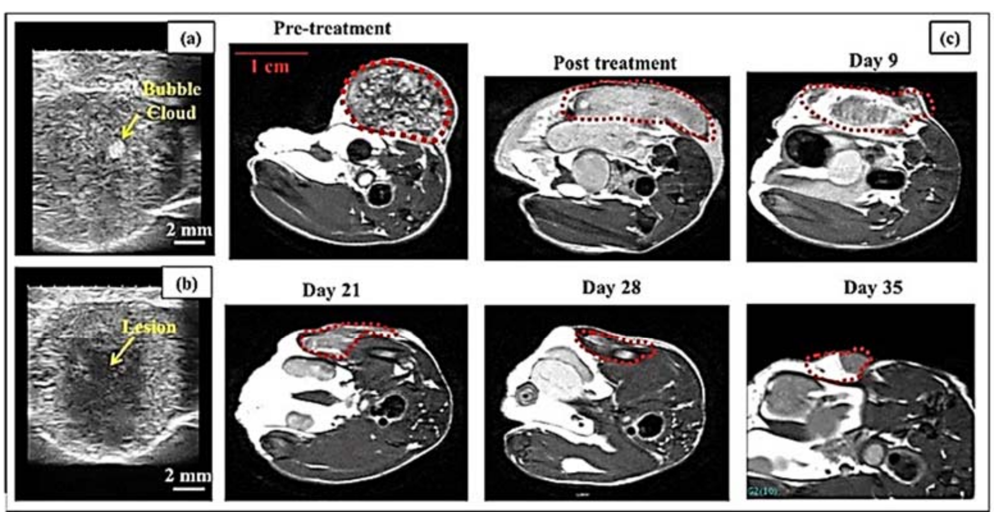

Figure 1. During treatment, the (a) bubble cloud and (b) tissue fractionation are visualized in real-time as hyperechoic and hypoechoic zones respectively on US imaging. (c) On T2-weighted MR images, the treated volume appears as a homogeneous, bright area compared to the heterogeneous tumor volume with mottled signal, providing assessment of the treated region. The homogenized tumor volume and edema resulting from the treatment were mostly reabsorbed by Day 28 post treatment in a B2 mouse. The tumor and treated region are outlined with red dashed line.

3A-4

11:15 am Evaluation of a New Non-invasive Ultrasonic Device for Venous Recanalization: Assessment of Feasibility and Safety of Thrombotripsy at 2.25 MHz in an In Vitro Model of Recent Venous Thrombosis

Guillaume Goudot[1], Bastien Arnal[1], Tristan Mirault[2], Catherine Boisson-Vidal[3], Bernard Le Bonniec[3], Mickaël Tanter[1], Emmanuel Messas[2], Mathieu Pernot[1]; *[1]Institut Langevin, INSERM U979, Paris, France, [2]PARCC, INSERM U970, Paris, France, [3]UMRS_1140, INSERM, Paris, France*

Background, Motivation and Objective

Persistent occlusion following venous thrombosis is associated with an increased risk of post-thrombotic syndrome. Venous recanalization may prevent this complication. Ultrasonic histotripsy has been shown to fractionate thrombus through a cavitation cloud generated by an external transducer and restore the flow [1]. In this study, we aimed at demonstrating that thrombotrispy can be performed with high accuracy using a 2.25 MHz transducer in vitro in a recent human blood clot

Statement of Contribution/Methods

Venous thrombosis conditions were reproduced in vitro, using human blood clotting by stasis in silicone tubes (6 mm internal diameter), in a 37°C water-bath, then mounted on a saline solution at a 25 mmHg constant pressure. All thrombi were initially occlusive. Thrombus stiffness was assessed by ultrafast ultrasound elastography. We engineered an ultrasound device composed of dual 2.25MHz transducers centred by a 10-2MHz linear probe. The size of the focal spot evaluated at -6 dB in the plane of the 2 transducers X, Z is 0.45x1.25 mm, measured by a calibrated system. The subsequent single cavitation cloud was generated at a 3.2cm depth from the device (mean femoral vein depth). Thrombotripsy was performed by longitudinal scanning of the whole thrombus at 3 pre-specified speeds (1; 2; 3mm/s). Restored outflow was assessed every 4 passages.

Results/Discussion

We evaluated 24 successive thrombi of 2.5cm mean length. Mean clot Young modulus was 4.4kPa, consistent with a recent thrombosis. Successful recanalization was systematically obtained by the succession of 3 sequences of 4 passages along the thrombus. Efficient flow restoration was carried out in 6min maximum. Within 120s, the flow restoration was of 80, 62 and 74% at respectively 1, 2 and 3mm/s. By varying the device's speed, we found an optimal speed of 1mm/s to be rapidly efficient for a complete recanalization with only one sequence of 2min. The cavitation cloud drilled a circular channel of 1.7mm mean diameter throughout the clot. End experiment examination revealed a residual thrombus coating the tube inner wall of 1.5mm mean thickness. This testifies that the cavitation cloud was far from the tube's wall. There was no macroscopic debris in the perfusion outflow. Debris analysis by filtration found 17±10 debris of 40-100μm diameter, 1.6±1.7 of 100-200μm, none>200μm. Evaluation of small fragments by a Coulter counter showed 92% of debris<10μm, thus predicting a very low risk of pulmonary embolism.

Properties of our dual transducers thrombotripsy device, high frequency with a small focal spot, allowed us to perform a fast and complete recanalization without any parietal alteration or bulky debris formation. We thus achieved a drug-free, non-invasive, localized thrombolysis technique and animal testing is currently ongoing.

1. Maxwell AD et al. Non-invasive treatment of deep venous thrombosis using pulsed ultrasound cavitation therapy (histotripsy) in a porcine model, JVIR 2011.

3A-5

11:30 am Preclinical safety and effectiveness of a longer beam and burst duration for ultrasonic repositioning of urinary stones

Barbrina Dunmire[1], Karmon M. Janssen[2], Timothy C. Brand[2], Bryan W. Cunitz[1], Yak-Nam Wang[1], Julianna C. Simon[3], Frank Starr[1], H.Denny Liggitt[4], Jeff Thiel[5], Jonathan D. Harper[6], Mathew D. Sorensen[6], **Michael R. Bailey**[6,7]; *[1]Applied Physics Laboratory, University of Washington, USA, [2]Department of Urology, Madigan Army Medical Center, USA, [3]Department of Acoustics, Pennsylvania State University, USA, [4]Department of Comparative Medicine, University of Washington, USA, [5]Department of Radiology, University of Washington, USA, [6]Department of Urology, University of Washington, USA, [7]Applied Physics Laboratory, University of Washington, Seattle, WA, USA*

Background, Motivation and Objective

In the first-in-human trial of ultrasonic propulsion, subjects passed collections of residual stone fragments after repositioning with a C5-2 probe. Here, effectiveness and safety in moving multiple fragments is compared between the C5-2 and a custom SC-50 probe that produces a longer beam and burst duration.

Statement of Contribution/Methods

In the original ultrasonic propulsion configuration, the C5-2 probe operates as both the imaging transducer and the therapy transducer. The second generation uses the SC-50, which requires a second, integrated, transducer for image guidance, in this case, a P4-2 phased array (Philips, Ultrasound). The -6dB focal beam of the C5-2 is 1.0 mm wide in the image plane, 3.5 mm wide in the elevational plane and 1 cm in depth. To spread the energy over a larger region, the beam is electronically steered in width by 0.5 mm increments creating a strobing effect over 3.5 mm x 5.0 mm beam cross section. The C5-2 allows for the stone to be targeted anywhere in the visible image plane, but requires the operator to select the location of each burst. The SC-50 insonifies a similar focal cross section, but without strobing, and extends 8 cm in depth. The SC-50 has a fixed focus and the operator must align the stone within the target region and step on a footswitch to apply the propulsion burst. The burst duration for the C5-2 probe is capped at 50 ms because of limitations in hardware and probe surface heating. The burst duration for the SC-50 was tested here at 3 s, and probe heating was measured.

Effectiveness was quantified by the number of stones expelled from a calyx phantom consisting of a 30-mm deep, water-filled well in a block of tissue-mimicking material. Each probe was positioned below the phantom to move stones against gravity. Single propulsion bursts (50 ms or 3 s) were applied to three separate targets: ten fragments of two different sizes (1-2 mm, 2-3 mm) and a single 4 mm x 7 mm human stone. Safety studies consisted of porcine kidneys exposed to 10-minute bursts and evaluated histologically in a 7-day survival study and acute studies with surgically implanted stones.

Results/Discussion

Although successful in the clinical trial, the shorter focal beam and 50-ms bursts of the C5-2 probe did not expel any stones from the phantom's 30-mm deep calyx. The longer bursts of the SC-50 probe expelled all stones at both 4.5-cm and 9.5-cm "skin-to-stone" depths with lower probe heating compared to the C5-2. No treatment-related kidney injury was observed for burst durations of 10 minutes. A longer beam and burst duration improved expulsion of a stone and multiple stone fragments from a phantom over a broad range of clinically relevant penetration depths and did not cause kidney injury in animal studies. Work support by NIH NIDDK grant DK043881 and the National Space Biomedical Research Institute through NASA NCC 9-58.

3A-6

11:45 am Integrated Histotripsy and Bubble Coalescence Transducer for Rapid Tissue Ablation

Aiwei Shi[1], Timothy Hall[1], Tejaswi Worlikar[1], Zhen Xu[1]; *[1]Department of Biomedical Engineering, University of Michigan, Ann Arbor, MI, USA*

Background, Motivation and Objective

Histotripsy uses high-pressure, microsecond-length pulses to generate cavitation microbubbles to fractionate targeted tissue. After the collapse of a cavitation cloud, remnant microbubbles can persist for a second or longer before passively dissolving. These bubbles can act as seed nuclei for subsequent cavitation events reducing treatment efficiency because the nuclei are not well distributed through the entire volume. It has been shown that this memory effect can be reduced using a second transducer to generate a long low amplitude burst to stimulate coalescence of remnant bubbles. This study presents an integrated transducer system to deliver both the high amplitude ($p_- \geq 30$ MPa) histotripsy pulses and lower-amplitude (~ 1 MPa) coalescence sequences to achieve rapid, homogenous ablation.

Statement of Contribution/Methods

The integrated system consisted of an array of 15 modules each 2 cm diameter operating at 1MHz made via rapid prototyping. The overall aperture was 9 cm wide with a 6.5 cm focal distance (Fig 1a). For histotripsy pulses, all 15 elements were excited simultaneously. For bubble coalescence, each module was excited individually in sequence. Histotripsy pulses of 1-cycle were applied at 100-Hz PRF with an estimated peak negative pressure of 43 MPa. Bubble coalescence sequence consisted of 150 1-cycle pulses at 1.1 MPa and 140 kHz PRF following each histotripsy pulse. The focus was mechanically scanned over a 10 × 10 mm region at a speed of 1, 2, or 3 mm/s in a red blood cell gel phantom, and resulting lesions were compared between with and without the bubble coalescence sequence.

Results/Discussion

The total propagated energy increase by the coalescence sequence was estimated to be 10%. Homogenous, complete fractionation of the 10 × 10 mm region was achieved using histotripsy with coalescence at all scan speed tested. At 3 mm/s scan speed, histotripsy without coalescence only achieved 76% ablation of the target volume. These results suggest that an integrated device has the potential to significantly increase the ablation speed and efficacy while maintaining homogenous volume ablation.

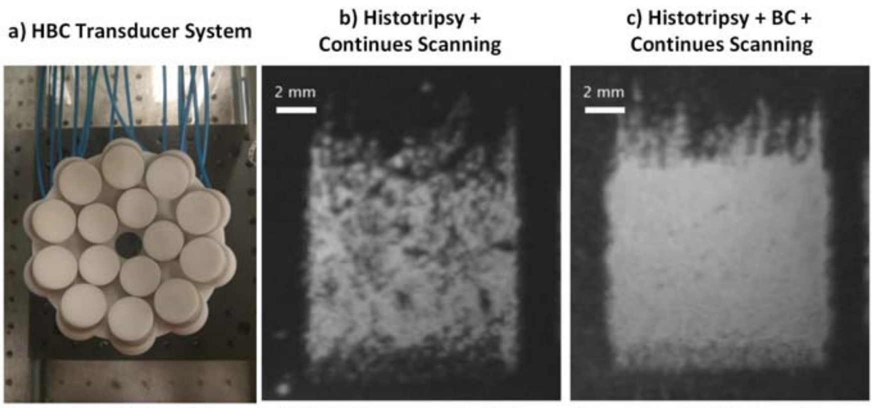

Fig 1: a) The integrated histotripsy and bubble coalescence (HBC) transducer system. The cubic lesions generated in the red blood cell phantom using b) histotripsy only and c) with bubble coalescence (BC) by continuously scanning the transducer focus at 3 mm/s.

4A - MBF: 3D Flow Imaging

Diplomat Room

Thursday, September 7, 2017, 10:30 am - 12:00 pm

Chair: **Stefano Ricci**
Florence University

4A-1

10:30 am In-Vivo 3D Cardiac Vector Flow Imaging – A Comparison between Ultrasound and Phase-Contrast MRI

Morten Wigen[1], Alfonso Rodríguez-Molares[1], Tore Bjåstad[1], Marius Eriksen[2], Knut Håkon Stensæth[2], Lasse Lovstakken[1]; [1]*Department of circulation and medical imaging, Norwegian University of Science and Technology, Norway,* [2]*Department of Radiology and Nuclear Medicine, St. Olavs Hospital, Norway*

Background, Motivation and Objective

Phase-Contrast MRI (PC-MRI) is capable of 4D flow imaging and considered a gold standard for blood velocity measurements, but is currently cumbersome and time consuming. Ultrasound is bedside applicable, but is typically limited to a 1D velocity measurement. In this work we measure 3D blood flow velocity fields using high frame rate 3D ultrasound blood speckle tracking (BST) without contrast and compare to PC-MRI in a healthy volunteer.

Statement of Contribution/Methods

A university-owned Vivid E95 scanner with research modifications was setup with a 4V 2D-matrix array probe and ECG-gated acquisition (4-7 beats) to obtain 3D volumes (35x35 degrees) at high frame rates (50-100 FPS). Conventional focused B-mode was acquired from one (or more) heart cycle(s), while plane wave color-Doppler IQ data (packet size=8-12, PRF=4kHz, f0=2.9MHz) was acquired from subsequent cardiac cycles. A FIR clutter filter was applied before 3D velocity estimation using a GPU-optimized tracking algorithm combining Doppler and a forward-backward BST. Gaussian smoothing was further applied to reduce variance (7x7x7 mm^3, 40e-3 msec).

A Siemens Avanto (Syngo B19 software) was setup for PC-MRI with a 6-point velocity measurement, and encoding velocities of 100 cm/s. Breath-holding with retrospective ECG gating was used to acquire a volume of 36x25 cm consisting of 17 6mm thick slices, resulting in 23 FPS.

Results/Discussion

Qualitative assessment of the two methods showed comparable flow features in the cardiac cycle. However, US estimates were at times partly influenced by dropouts and bias due to tissue motion and filter limitations. Further, variance of the lateral velocity components required smoothing which resulted in increased underestimation of the blood.

Quantitative analysis of velocity traces resulted in r^2 correlation coefficients of 0.89 and 0.85 with an average deviation of 1 cm/s and 8 cm/s in the central lumen and over the mitral valve respectively, but a very low r^2 of 0.03 in the aortic outflow, the latter attributed mainly to signal loss during diastole and tracking error during systole, and differences in image crossections and timing. Both estimates had the same spatiotemporal averaging in this comparison. Work is needed to improve clutter reduction and BST accuracy, but this preliminary comparison shows promising results for US. Further in vitro/vivo validation will follow.

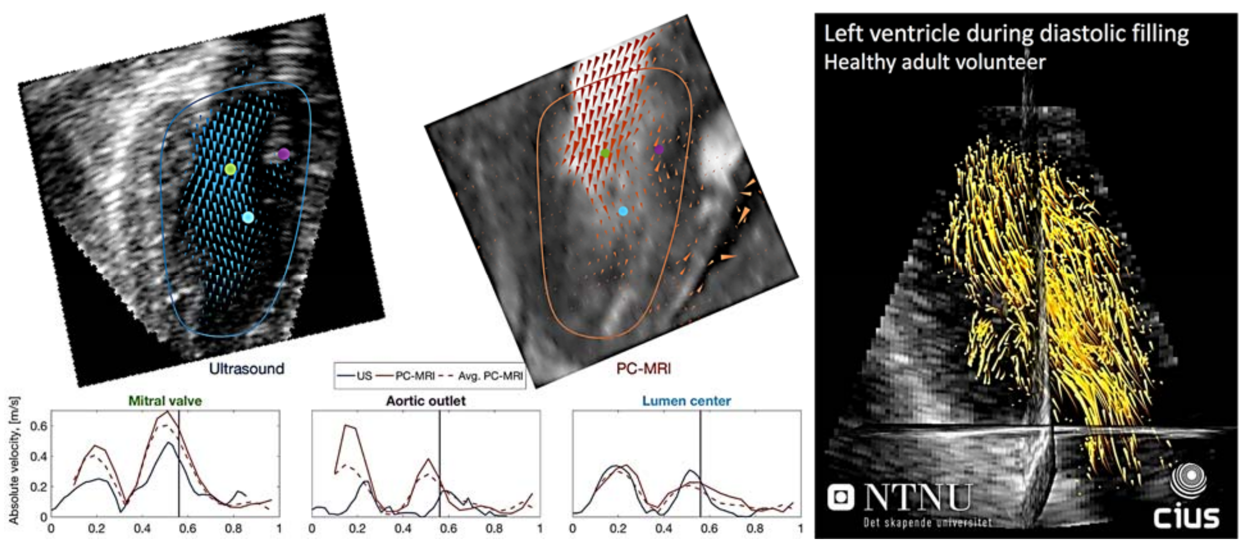

4A-2

10:45 am Validation of High Frame Rate Echo-PIV with Optical PIV in a Realistic Left Ventricular Phantom

Jason Voorneveld[1], Aswin Muralidharan[2], Timothy Hope[1], Hendrik Vos[1], Pieter Kruizinga[1], Antonius F.W. van der Steen[1], Nico de Jong[1], Frank Gijsen[1], Sasa Kenjeres[2], Johan Bosch[1]; [1]*Thorax Center, Erasmus MC, Rotterdam, Netherlands,* [2]*Transport Phenomena Section, Chemical Engineering, Delft University of Technology, Netherlands*

Background, Motivation and Objective

Investigation of the complex intra-ventricular flow patterns in the left ventricle (LV) remains a challenge in clinical ultrasound. Echo-particle image velocimetry (ePIV) is able to estimate 2D flow from 2D images, but it is known to underestimate the high velocity flows present during the filling and ejection periods of the cardiac cycle[1], [2]. High frame rate (HFR) ultrasound imaging has been shown to improve the dynamic range of velocities resolvable by ePIV[3]. However, HFR ePIV has yet to be verified in the complex flow environment of the LV. In this study we compare HFR ePIV against the gold standard optical PIV (oPIV) in a realistic geometry dynamic LV phantom.

Statement of Contribution/Methods

A compliant, optically and acoustically transparent silicone LV chamber (Figure 1A), encased in a rigid acrylic box, was fitted with mitral and aortic Björk-Shiley valves, each connected to atrial and compliance chambers, respectively (Fig 1B). A programmable piston pump driving the LV external chamber controlled the stroke volume of the LV (64ml at 1Hz, sinusoidal pattern).

Spherical wave imaging at 1000 fps was applied with a C5-2 probe (3.1 MHz) using a Verasonics Vantage-256 system. Ultrasound contrast agent (SonoVue, 90µl/l concentration) was used as an ePIV tracer. PIVlab (V1.41, [4]) was used with iteratively reducing kernel sizes (9x9 mm2 -> 9x9 mm^2 -> 4.5x4.5 mm^2 -> 2.3x2.3 mm^2) using spline interpolated image deformation.

oPIV was obtained at 1000 fps (time synchronized to ePIV) using a time resolved digital PIV system (LaVision) with a 1mm thick vertical plane aligned to the ultrasound plane. Hollow glass spheres (8-12 µm) were used as tracer particles. oPIV analysis was performed using the DaVis 8.3 (LaVision) software.

Results/Discussion

Pulsatile flow patterns in the LV phantom were captured with oPIV (Figure 1C). Very similar flow patterns were captured with ePIV, with the main vortex (Fig 1D-'V') matching almost exactly. However, the maximum velocity in the narrow inflow jet was slightly underestimated (Fig 1D-'J'), since the PSF of the system led to lateral smoothing of the axially oriented jet. Further optimization of important ePIV parameters (bubble concentration, frame rate, probe, etc.) can be achieved with this LV phantom.

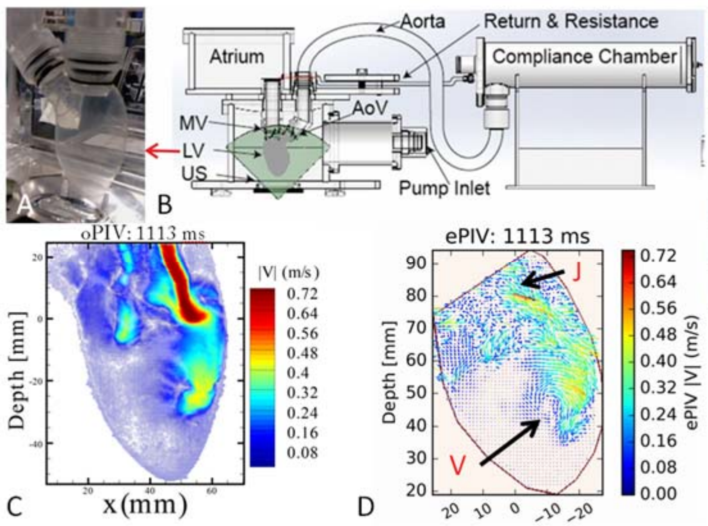

Figure 1: A) silicone LV phantom. B) LV phantom pump system: C) oPIV high-density vector map result during the high velocity filling period. D) HFR ePIV of the same frame as in C)

[1]H. Gao, *et al., Ultras Med. Biol.*, 2015.;
[2]J. Voorneveld, *et al., IEEE IUS*, 2016,
[3]W. Thielicke *et al., J. Open Res. Softw.*, 2014.

4A-3

11:00 am 3D Tracking Doppler for Quantitative Blood Flow Assessment of Coronary Arteries

Stefano Fiorentini[1], Lars Saxhaug[1], Tore Bjåstad[1], Espen Holte[1], Hans Torp[1], Jørgen Avdal[1]; [1]*Department of Circulation and Medical Imaging, Norwegian University of Science and Technology, Norway*

Background, Motivation and Objective

Several challenges limit the use of Pulsed Wave (PW) Doppler to assess coronary blood flow: 1) Transit time effect causes spectral broadening in regions with high blood flow such as stenoses, leading to overestimation of maximum velocities. 2) High beam to flow angles (>60°) and out of plane components often occur, making manual positioning of the sample volume and angle correction difficult. 2D tracking Doppler (2D TD) is a previously presented method that can reduce transit time effect by tracking blood scatterers along the flow direction and improve spectral resolution [Fredriksen, 2013]. In this work, we perform 3D high frame rate imaging of the coronaries to enable easier retrospective Doppler estimation. We also extend the previously proposed algorithm to track along any 3D direction, enabling us to measure out of plane components which could not be otherwise estimated.

Statement of Contribution/Methods

A non compounded, 3D plane wave acquisition scheme was implemented in a locally modified, commercial US system owned by the university (GE 4V probe and GE Vivid E95 scanner). Beamforming was performed offline, using a delay and sum algorithm and expanding aperture with Hamming apodization. For each packet, the power spectrum was estimated by summing phase corrected IQ samples in slow-time. For each velocity of interest, the slow-time samples were interpolated at different spatial positions along a manually defined straight trajectory.

Results/Discussion

(A) Shows a 3D CFI rendering of the left anterior descending coronary at diastasis from a healthy volunteer, proving the ability to perform retrospective Doppler estimation using 3D high frame rate imaging. (B) Shows a 3D TD spectrum estimated at the green trajectory displayed in (A). The results were generated with a packet size of 45 samples, PRF 4.5 kHz, center frequency 3.1 MHz, pulse length 3.5 cycles. In (B) spatial averaging was performed along a 1.5cm region in the defined trajectory.

Velocity overestimation in both 3D TD and PW was quantified by measuring the onesided -6dB spectral width from a thread phantom at 60° beam to flow angle and 6.5 kHz PRF. The measured overestimation was 21.4% and 13.6% for PW and 3D TD respectively at 40 cm/s thread velocity, and 15.5% and 7.31% at 80 cm/s. Tracking Doppler is therefore expected to reduce velocity overestimation in cases of clinical interest such as coronary stenoses.

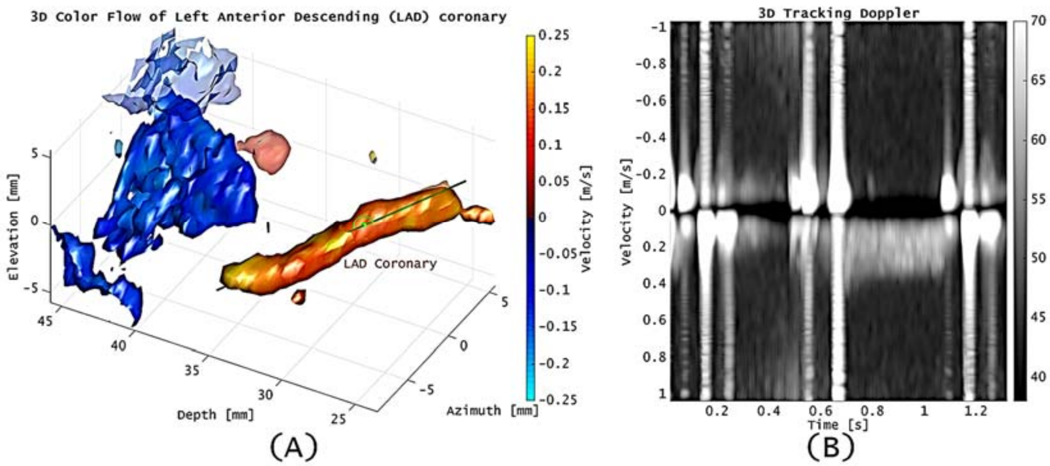

4A-4

11:15 am Doppler Velocity Estimation in 3d Cardiac Ultrafast Ultrasound Imaging: An In Vitro Study

Emilia Badescu[1], Lorena Petrusca[1], Damien Garcia[1], Denis Friboulet[1], Hervé Liebgott[1]; *[1]Univ.Lyon, INSA-Lyon, UCBL1, UJM-Saint Etienne, CNRS, Inserm, CREATIS UMR 5220, U1206, Lyon, France*

Background, Motivation and Objective

The emergence of ultrafast imaging allowed new insights into cardiac deformation/motion analysis that enabled new advancements in clinical diagnosis. Several studies showed that a good compromise between the temporal and the spatial resolution can be obtained by transmitting multiple focused beams (MLT) simultaneously. However, the current implementation of MLT in 3D cannot be used in dynamic conditions as it was obtained synthetically, by summing the Single Line Transmit (SLT) events before beamforming [Ortega et al., TUFFC, 2016]. The objective of this study is to evaluate for the first time the performance of MLT in 3D ultrasound under dynamic conditions.

Statement of Contribution/Methods

The 3D images were acquired by using four Verasonics research scanners, each of them controlling 8-by-32 elements of a 32-by-32, 3 MHz, Vermon ultrasound transducer. The scan volume was created by stitching 30 triangular sectors (each of angular width = 40°) along the azimuth angular direction. For each triangular sector, 9 transmission events were used for insonifying a full sector by sending simultaneously three focused beams. Thus, the total number of transmissions was 270 corresponding to 27 (elevational) x 30 (azimuthal) focal beams. The Pulse Repetition Frequency (PRF) was set to 2250. Our in vitro model was a tissue mimicking spinning disc having a diameter of 11 cm whose speed could be controlled by a step motor. The disk was placed at approximately 3 cm away from transducer and the image depth was 6.8 cm. Doppler velocities were estimated from the IQ signals using a 2D auto-correlator and a packet length of 7.

Results/Discussion

This study demonstrates the feasibility of Doppler velocity estimation for 3D MLT images. The estimated values presented in the image were in agreement with the expected velocities since the relative mean error was 3.5%. We obtained a three-fold increase in volume rate compared with focus imaging. Analyzing further different MLT/MLA configurations would allow increasing the frequency of volumes and obtaining the optimal compromise between high volume rate and quality color Doppler.

Experimental set-up

Estimated Doppler velocities for multiple XZ planes

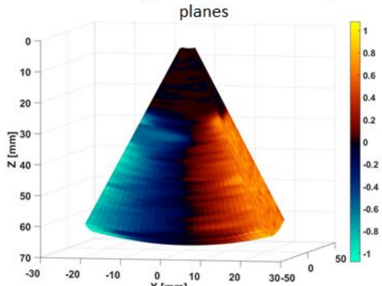

4A-5

11:30 am **3D Blood Vessel Mapping of Adult Zebrafish Using High Frequency Ultrasound Ultrafast Doppler Imaging**

Chao-Chuan Chang[1], Pei-Yu Chen[1], Chih-Chung Huang[1]; [1]*Department of Biomedical Engineering, National Cheng Kung University, Taiwan*

Background, Motivation and Objective

Zebrafish is an ideal vertebrate for studying developmental biology and genetics due to its rapid generation rate and genetic accessibility. However, once the zebrafish has fully matured, especially wild-type lines, it develops stripes that run along the body and thus lose transparency. Owing to that, conventional optical imaging techniques will have difficulty in imaging the internal anatomy and vasculature. High frequency ultrasound imaging has been used to monitor the adult zebrafish heart blood flow. However, it is still difficult to observe the dorsal blood circulation due to its resolution. Hence, the purpose of this study is to utilize ultrafast ultrasound imaging with high frequency transducer to reconstruct the 3D blood vessel mapping of adult zebrafish.

Statement of Contribution/Methods

In this study, adult zebrafishes were anesthetized in 7% Tricaine solution and then embedded in the sponge for dorsal blood circulation imaging. An ultrafast ultrasound imaging system (Vantage 256) with a 256-element high frequency array transducer (MS550D) were used to acquire the IQ signals from zebrafish, as shown in Figure 1(a). The operational frequency of transducer is 40 MHz. Five plane wave angles were transmitted to zebrafish for acquiring the compounding image of dorsal blood vessel at a high frame rate of 300 Hz for 0.5 s at each sagittal plane. Then, the transducer was moved (100 μm) to next scanning plane by motor to obtained image from different sagittal planes for 3D imaging. After all data were obtained, a high-pass spatiotemporal filtering was implemented on data processing of each sagittal plane for distinguishing blood signals from noise or tissue signals.

Results/Discussion

Figure 1(b) shows the typical 40 MHz B-mode plane wave compounding image of zebrafish at a sagittal plane view. The bone structure was observed clearly in this image. The 2D blood vessel mapping and 3D vessel structure were also obtained clearly by using 40 MHz ultrafast Doppler imaging. The measured resolution for vessel imaging is about 50 μm in diameter without micro-bubble. All the results show the feasibility of using high frequency ultrafast Doppler imaging to reconstruct the 2D and 3D blood vessel mapping for zebrafish, which are useful for modeling and observing tumorigenesis and its neighboring changes of vasculature map in zebrafish model.

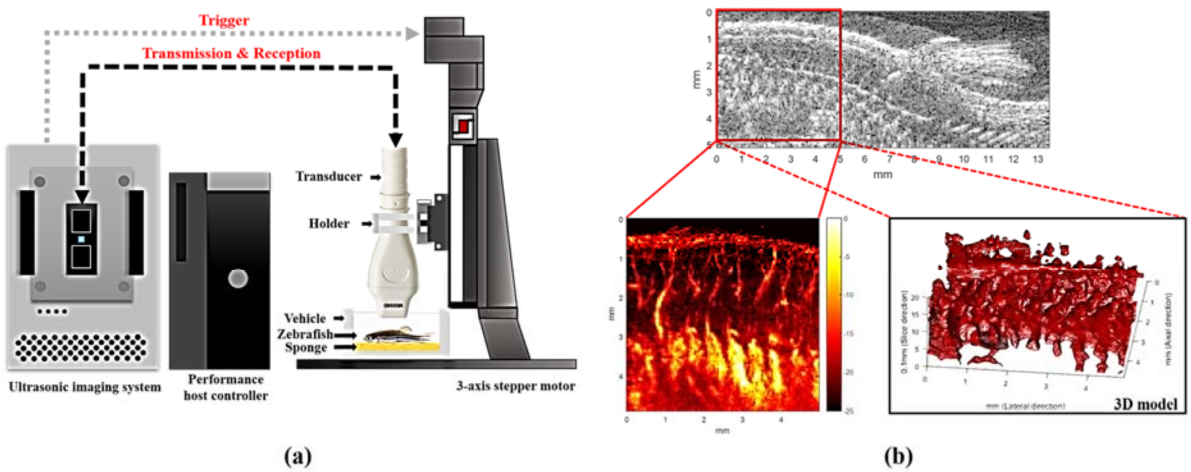

Figure 1

4A-6

11:45 am **Volumetric 3-D Vector Flow Measurements Using a 62+62 Row-Column Addressed Array**

Simon Holbek[1,2], Matthias Bo Stuart[2], Hamed Bouzari[2], Jørgen Arendt Jensen[2]; [1]*BK Ultrasound, Herlev, Denmark,* [2]*Technical University of Denmark, Lyngby, Denmark*

Background, Motivation and Objective

Today, 3-D vector flow imaging (VFI) in a full volume requires a fully populated NxN 2-D matrix array if a sufficient frame rate should be maintained. Such arrays require an expensive ultrasound system, which can handle the enormous data stream created by the N^2 channels. As an alternative to the matrix array, N+N 2-D row-column addressed (RCA) arrays were introduced, which reduce the channel count by a factor N/2. The aim of this work is to demonstrate that an RCA array with only 124 channels can provide 3-D VFI in a volume.

Statement of Contribution/Methods

A 62+62 element λ/2 pitch 2-D RCA array with a 3 MHz center frequency was connected to the experimental scanner SARUS. Measurements were made in a flow-rig where a laminar parabolic flow was present. The flow rate was 13.7 mL/s, giving a peak velocity of 24.1 cm/s. The focused transmit sequence consisted of 11 row emissions and 9 column emission. The row emissions were steered from -15° to +15° in steps of 3° and the column emissions from -8° to 8° in steps of 2°, effectively resulting in nine cross-sectional scan planes. At 3 cm depth, this corresponded to a C-plane spanning 16.1mm x 8.4 mm. The pulse repetition frequency was 10.5 kHz and 4.3 s of data were acquired. The center of the vessel (Ø = 12mm) was located at 2.9 cm depth from the transducer's surface. 3-D VFI was obtained with a conventional axial autocorrelation estimator and a 3-D RC transverse oscillation method. Each velocity estimate was found from 32 transmit events translating to 26 volumes per second.

Results/Discussion

A volumetric representation of the mean out-of-plane velocity estimates for all nine planes is shown in Fig. a), which captures the expected parabolic flow behaviour. The mean flow rate for each plane was calculated based on the velocity component perpendicular to the cross-sectional area (Fig. b). A positive bias was found for all of the steering angles, with the smallest bias at 2° (6.5 %) and the largest bias at -8° (21.2 %). Similarly, the smallest standard deviation was found for the plane steered by 8° (± 3.0 %) and the largest standard deviation was at a steering of 0° (± 3.8 %). The overall mean flow rate, based on the estimated value for each plane was 15.2 ± 0.7 mL/s. The results demonstrate that a 2-D RCA array with a channel count similar to conventional 1-D transducers can be applied to obtain 3-D vector flow estimates in a full volume with a precision bellow ± 5.0 %.

a)

b)

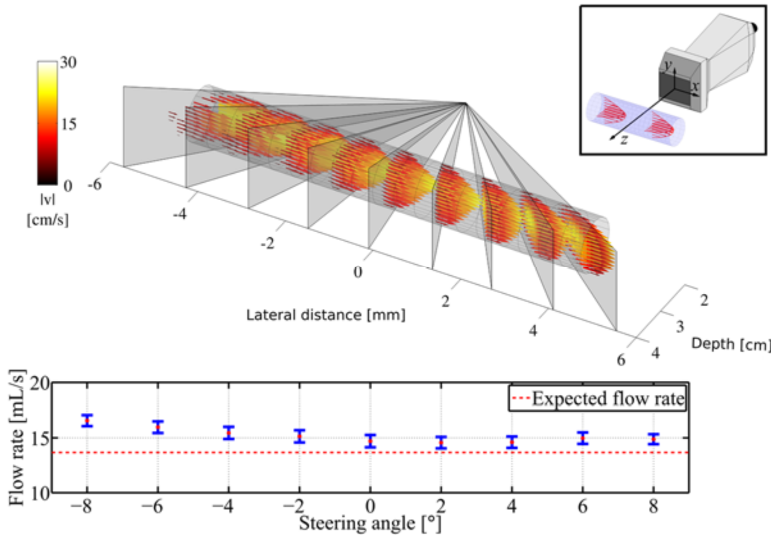
30
15
0
|v|
[cm/s]
-6
-4
-2
0
2
4
6
Lateral distance [mm]
2
3
4
Depth [cm]
y
x
z
Flow rate [mL/s]
20
15
10
Expected flow rate
−8
−6
−4
−2
0
2
4
6
8
Steering angle [°]

5A - Transducers

Blue Room

Thursday, September 7, 2017, 10:30 am - 12:00 pm

Chair: **Mario Kupnik**
Technische Universität Darmstadt

5A-1

10:30 am Transducers for Harsh Environments in Nuclear Applications

Bernhard Tittmann[1]; [1]*Engineering Science and Mechanics, Penn State University, University Park, Pennsylvania, USA*

Background, Motivation and Objective

Ultrasound offers measurements of parameters encountered in harsh environments such as steam generators, heat exchangers and nuclear reactor primary and secondary systems. But there is a lack of piezo-materials tolerant of high temperatures and nuclear irradiation.

Another issue is that transducers are needed that can be left in place on curved surfaces such as pipes and valves. The transducers should capable of providing structural health monitoring for extend periods of time. Both active and passive monitoring are necessary. The goal is a transducer that provides a leave-in-place solution to structural health monitoring where plant shutdown and an operating technician are not required. This method will significantly decrease the cost of inspection which usually requires facility shut-down.

Statement of Contribution/Methods

Pennsylvania State University was awarded an Advanced Test Reactor National Scientific User Facility (ATR NSUF) project to evaluate promising magnetostrictive and piezoelectric transducers in the Massachusetts Institute of Technology Research Reactor (MITR) for 18 months.

The transducers experienced an integrated neutron fluence of about 8.68 E+20 n/cm^2 for n >1 MeV, temperatures over 420 °C, and a gamma fluence of 7.23 Gy/cm2. Three piezoelectrics were chosen with Aluminum Nitride (AlN), Zinc Oxide (ZnO), and Bismuth Titanate (BiTi) and two magnetostrictive transducers with Remendur and Galfenol as the active elements.

Results/Discussion

Although most sensors performed well in this environment, it was not without some troubles. This is demonstrated and explained in the context of pulse-echo signals. Overall, this is the longest exposure experiment conducted to the researchers' knowledge on the chosen sensor materials and the first instrumented lead test for many of these materials. Thus,the potential usefulness of ultrasonic transducers in a nuclear reactor environment has been demonstrated. In addition, BiTi in powder form lends itself readily for the spray-on technology which allows transducers to be placed on curved surfaces with good adhesion. The advances of this technology is gaining momentum and will be described. This opens the door to leave-in-place sensors for harsh environments.

5A-2

11:00 am High Temperature Ultrasonic Transducers by $CaBi_2Ta_2O_9/Pb(Zr,Ti)O_3$ Sol-Gel Composite

Tomoya yamamoto[1], Masaki Yugawa[1], Hajime Nagata[2], Makiko Kobayashi[1]; [1]*Kumamoto University, Japan,* [2]*Tokyo University of Science, Japan*

Background, Motivation and Objective

Off-line ultrasonic non-destructive testing (NDT) is used to inspect defects in thermal power plants. However, for new-generation thermal power plants, off-line NDT is not sufficient and long-term monitoring at high temperature is desired. In the previous study, ultrasonic transducers made by $CaBi_4Ti_4O_{15}$ (CBT)/$Pb(Zr,Ti)O_3$ (PZT) were investigated and maximum operation temperature was estimated as ~600°C. Since operation temperature of new-generation thermal power plant will be ~700°C, it is necessary to develop new sol-gel composite which has higher operation temperature than 700°C.

Statement of Contribution/Methods

New sol-gel composite, $CaBi_2Ta_2O_9$/PZT was developed. CBTa was chosen as ferroelectric powder phase material because Curie temperature is sufficiently high such as 923°C, which is higher than that of CBT. PZT was chosen as dielectric sol-gel phase because of high dielectric constant. 50µm thick film was fabricated on 3mm thick titanium substrate by sol-gel spray technique. A platinum paste top electrode was manufactured and polarization process was carried out at 400°C.

Results/Discussion

CBT/PZT sample was placed in an electric furnace and ultrasonic measurement in pulse-echo mode was demonstrated between room temperature and 800°C. Platinum wires were used for electrical cables and a mechanical steel clamp was used to fix electrical connection. Figure 1 shows the ultrasonic response of the CBTa/PZT film on 3mm thick titanium substrate at 800°C. Sensitivity and signal-to-noise ratio (SNR) was high enough for thickness measurement even at 800°C. It is noted that signal amplitude and SNR were stable throughout the experiment. Long-term monitoring test at high temperature will be carried out to verify long-term operation temperature above 700°C.

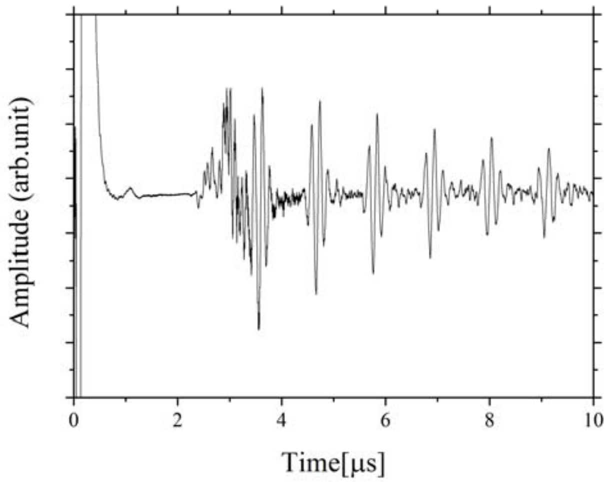

5A-3

11:15 am Design of High-Intensity Ultrasound Reactor

Örjan Johansson[1], Torbjorn Lofqvist[2], Taraka Rama Krishna Pamidi[1]; [1]*Department of Civil, Environmental and Natural Resources Engineering, Luleå tekniska universitet, Luleå, Sweden,* [2]*Department of Computer Science, Electrical and Space Engineering, Luleå tekniska universitet, Luleå, Sweden*

Background, Motivation and Objective

Design and optmiziation of ultrasonic reactors are important objectives in sonochemical processing. The recent expansion of the use of ultrasonic reactors in various research projects all faces the problem of scaling up laboratory results for industrial use. A traditional ultrasonic reactor usually has several issues, such as low effectiveness and complex and unstable system performance, which all are unfavorable for efficient sonochemical processing. This study adresses these issues and investigates a new flow type ultrasonic reactor designed to generate transient cavitation as the main source for ultrasound for sonochemical processing. This study proposes the principle of the flow type ultrasonic reactor design to generate transient cavitation. The objective of this work is to design an ultrasonic reactor with a new geometry. The idea is to improve process efficiency based on resonance enhanced ultrasound controlled cavitation.

Statement of Contribution/Methods

A high-intensity tube type ultrasound reactor was designed and developed to evaluate its energy efficiency. Some of the important factors like pressure, material, flow and geometry is considered in the design. Maximum coupling between structural vibration and a sound wave in water is obtained at the critical frequency. In this case, the reactor vibrates in a stretching and flexural mode. The perfect coupling occurs when the wavelengths in the tube structure and the water volume inside the reactor are same. Numerical optimization as well as experimental investigation are performed to reach an optimized, energy-efficient and controlled ultrsound reactor.

Results/Discussion

Results from numerical modeling is used to design an ultrasound reactor. The reactor is driven with three transducers that were mounted radially in the reactor wall with 120° spacing. The reactor is excited with sine sweep with electric power of 120 Watt. While the reactor is filled with water, T = 20°C. Figure (a) shows the vibration mode at 21.8 kHz and figure(b) shows the sound pressure distribution of water-filled tube at 21.8 kHz and same kind of sound pressure distribution modes were occurring at 37.1 kHz and 53.8 kHz. Figure(c) shows aluminum foil erosion from 20 seconds immersion in the centre of the reactor at 50° C

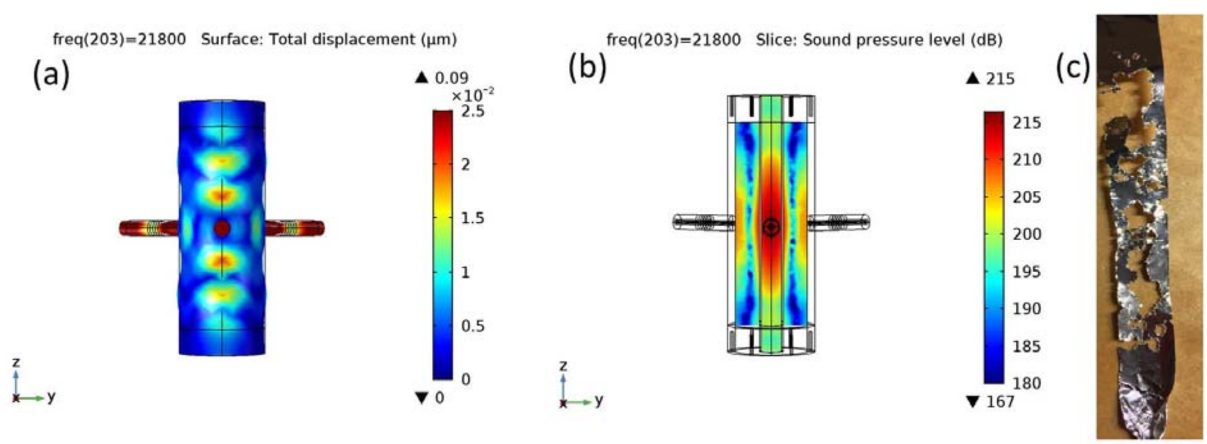

5A-4

11:30 am An Effect at the Source Creates Ringing in a Thick Plate

David Greve[1,2], Jaime Parra[3], Mario Bergés[3], Joel Harley[4], Warren Junker[5], Irving oppenheim[3], Zitian Zhang[3]; [1]Electrical and Computer Engineering, Carnegie Mellon University, USA, [2]DWGreve Consulting, Sedona, AZ, USA, [3]Department of Civil and Environmental Engineering, Carnegie Mellon University, Pittsburgh, PA, USA, [4]Department of Electrical and Computer Engineering, University of Utah, Salt Lake City, UT, USA, [5]Consultant, Pittsburgh, PA, USA

Background, Motivation and Objective

Piezoceramic discs bonded to structures have often been used as broadband transducers. We observed that a 2 mm thick, 10 mm dia. disc bonded to a 27 mm thick steel plate exhibits pronounced ringing near 250 kHz when driven by a broadband chirp. Lamb wave and defect localization studies using an array of such transducers are degraded by the ringing, which is not observed on thin plates. Our objectives are to identify the physical source of the ringing, to confirm the behavior by comparing laboratory data to simulation results, and to determine how the frequency of maximum conductance (denoted f_R) and quality factor (Q) change with transducer diameter, transducer thickness, and plate thickness.

Statement of Contribution/Methods

The simulation domain for FEM analysis is a cylindrical region of the thick plate with the transducer at the pole and a perfectly matched layer on its outer annulus. Sinusoidal steady state simulations show a narrow peak in the conductance near 260 kHz and a three-dimensional volume of high strain forming within the thickness of the plate. Laboratory admittance (C-G) measurements provide data from which f_R and Q are extracted for direct comparison to FEM simulation results.

Results/Discussion

Laboratory data for the base case show f_R = 230 kHz and Q = 18.2, comparing reasonably well with simulation results. FEM studies show f_R to increase and Q to decrease as transducer thickness decreases from the base case; also, f_R decreases with transducer diameter, Q displays a maximum for transducer thickness near 2.5 mm, and Q decreases with plate thickness. Laboratory measurements from transducers of different sizes confirm those trends. We conclude that piezoceramic transducers bonded to thick plates can

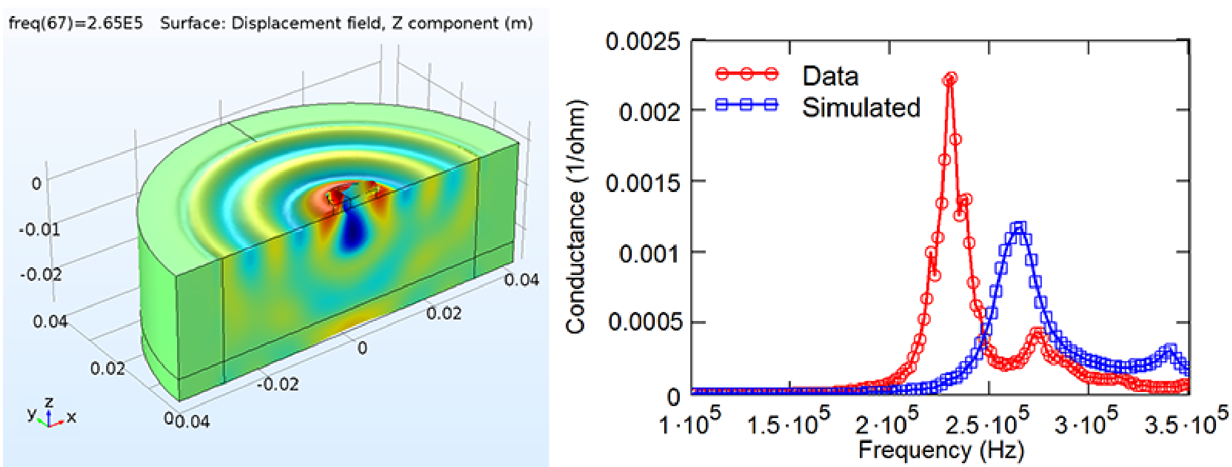

5A-5

11:45 am Flexible Ultrasonic Transducers by Automatic Spray Coating for Non-Destructive Testing

Yuto Kiyota[1], Kei Nakatsuma[1], Makiko Kobayashi[1]; [1]*Kumamoto University, Japan*

Background, Motivation and Objective

Development of flexible ultrasonic transducers for non-destructive testing (NDT) application has been desired since many infrastructures were consist of complex geometry. Sol-gel spray technique realized flexible ultrasonic transducers, however, it is difficult for manual spray coating to make quality assurance. In addition, manual spray coating is not suitable for mass production. Therefore, automatic spray coating method is desired for flexible ultrasonic transducer fabrication.

Statement of Contribution/Methods

~100μm thick PZT/PZT films were fabricated onto 30μm thickness stainless steel substrates by an automatic spray coating machine. Mixture of PZT powders and PZT sol-gel was sprayed by automatic spray coating. Spray coating process and thermal process, drying at 150°C on a hot plate for 5min and firing at 650°C in a furnace for 5 min, were repeated 14 times. Corona poling was operated at room temperature. A silver top electrode with 8mm diameter was fabricated on each film with 10mm diameter. Electrical cables were bonded with the top electrode and the substrate as ground.

Results/Discussion

Ultrasonic measurement in pulse-echo mode was operated for a steel pipe with 40mm outer diameter and 5mm thickness. Measurement result is shown in Fig.1. Multiple reflected echoes are clearly observed. Center frequency and 6dB bandwidth were ~7.0MHz and ~6.4MHz, respectively. Fabrication process and sensor design should be further optimized for NDT application.

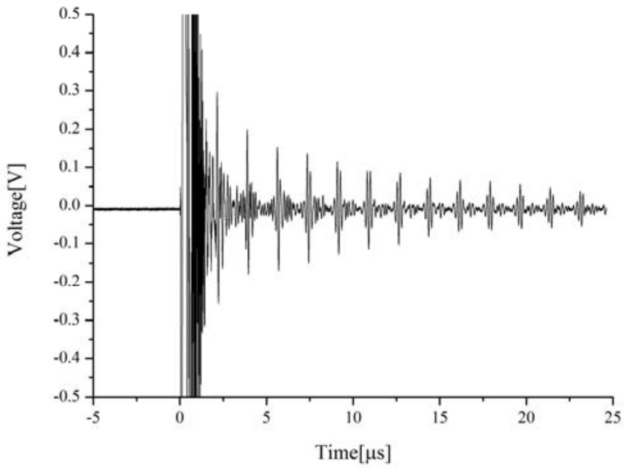

Voltage[V]
0.5
0.4
0.3
0.2
0.1
0.0
-0.1
-0.2
-0.3
-0.4
-0.5
-5
0
5
10
15
20
25
Time[μs]

6A - PNL - Nonlinear Acoustics

Hampton Room

Thursday, September 7, 2017, 10:30 am - 12:00 pm

Chair: **Dave Feld**
Broadcom Ltd

6A-1

10:30 am **Through Transmission Measurement of the Nonlinear Viscoelastic Memory of Rocks by Co-propagating Longitudinal Ultrasonic Pulses**

Xuan Feng[1], MIchael Fehler[2], Stephen Brown[2], Daniel Burns[2], **Thomas Szabo[3]**; *[1]College of Geo-Exploration Science and Technology, Jilin University, Changchun, China, People's Republic of, [2]Earth Resources Laboratory, Massachusetts Institute of Technology, Cambridge, MA, USA, [3]Biomedical Engineering, Boston University, Boston, MA, USA*

Background, Motivation and Objective

Because conventional geophysical measurements cannot directly measure the microstructure or pore fluids of rocks, new measurement approaches are needed as well as one that can select regions of interest. The aim of this study is to utilize the nonlinear interaction of two co-propagating longitudinal waves to characterize induced viscoelastic changes occurring in the rock microstructure. Our experimental technique utilizes a strong longitudinal wave pump that changes (minutely) the viscoelastic properties of the sample with dynamically applied strain and a weaker longitudinal wave probe that senses those changes.

Statement of Contribution/Methods

The interaction of the low-amplitude wave (the probe) and a high-amplitude wave (the pump) is inherently nonlinear. The turning on of the pump causes a traveltime delay that is proportional to the induced change in the elastic constant. We find evidence for viscoelastic effects in our data. We demonstrate the method on a sample of Crab Orchard sandstone, with moderate porosity and permeability and a sample of Lucite. A longitudinal wave is sent along the sample length to a receiver in a through transmission setup. The pump wave signal propagates in the same direction and overlaps the probe beam and is slowly varying compared to that of the probe; therefore, we use a 620 kHz longitudinal probe wave and a 74 kHz pump. We then vary the delay between the two signals through several periods of the pump wave to observe the induced changes on the probe signal. Particle velocities are measured on the surface of the sample with the laser vibrometer to calibrate the experiment.

Results/Discussion

Our method allows us to evaluate time dependent nonlinear effects and we find strong evidence that rocks have a short period nonlinear viscoelastic memory that is a function of the time history of the loaded strain. We develop a phenomenological model to describe the short period nonlinear viscoelastic memory and the nonlinear elastic behavior of rock. Our model describes the nonlinear elastic behavior of the sandstone and shows that the short period nonlinear viscoelastic memory is controlled by both the traditional nonlinear elastic coefficients and a memory strength parameter. Data indicate the nonlinear coefficients of Crab Orchard sandstone are two orders of magnitude greater than those of Lucite samples We evaluate the time history of modulus change with strain and find hysteresis loops in the data. The nonlinearity causes the compressional half cycle hysteresis loops to be several times greater than the loops corresponding to tension half cycles. Both half cycles cause the material to soften slightly. Our new acoustic method can measure and quantify both the nonlinear and viscoelastic properties of materials as a function of different stain amplitudes directly in the time domain.

6A-2

10:45 am **Characterizing Micro-Crack Distributions with Nonlinear Acoustic Surface and Wedge Waves**

Marek Rjelka[1], Bernd Koehler[1], Pavel Pupyrev[2], Andreas Mayer[3]; *[1]Fraunhofer IKTS, Dresden, Germany, [2]Prokhorov General Physics Institute, Moscow, Russian Federation, [3]HS Offenburg - University of Applied Sciences, Gengenbach, Germany*

Background, Motivation and Objective

Pre-fatigue damage can have drastic effects on the elastic nonlinearity of solid materials, offering the possibility of extracting spatially resolved information on the pre-fatigue state from nonlinear effects on guided waves, like harmonic generation [1]. Of particular interest are surface and wedge acoustic waves. They are sensitive to surfaces and edges and are non-dispersive in homogeneous media, at planar surfaces and – in the case of wedge waves – perfect wedge tips on the scale of the wavelength. This favors nonlinear effects.

Our current investigations focus on the nonlinearity generated by micro-cracks with the goal of extracting information about their spatial and orientational distribution from the efficiency of second harmonic generation and its dependence on amplitude and frequency of the input wave [2]. The linear dispersion arising from a spatially inhomogeneous distribution of the micro-cracks is accounted for in the propagation of the second harmonic.

Statement of Contribution/Methods

Finite element simulations have been carried out for a model system of randomly oriented micro-cracks containing a Hertzian contact. Nonlinear stress-strain relations have been computed for this system and second-order and third-order elastic constants have been extracted. A simple micro-mechanical model has been fitted to the simulation results and allows for an extension to textured orientations of the micro-cracks.

On the basis of the nonlinear stress-strain relations, the efficiency of second harmonic generation is calculated for Rayleigh waves and for wedge acoustic waves.

Results/Discussion

Results of calculations are presented and discussed for the acoustic nonlinearity parameter (ANP) of wedge acoustic waves in wedges with textured distributions of micro-cracks. An example is shown in the Figure. Consequences of non-analytical behavior (a kink or a kink of the derivative) of the stress-strain relations on second-harmonic generation of surface and wedge waves are analyzed in detail. An inversion method is introduced for the determination of the depth profile of the distribution of micro-cracks from the ANP of surface waves.

[1] Matlack, K., Kim, J.-Y., Jacobs, L., Qu, J., J. NDE, Springer US, 2014, 34, 273

[2] Rjelka, M., Koehler, B., Mayer, A., 43rd Ann. Rev. Prog. QNDE, AIP Publishing, 2017

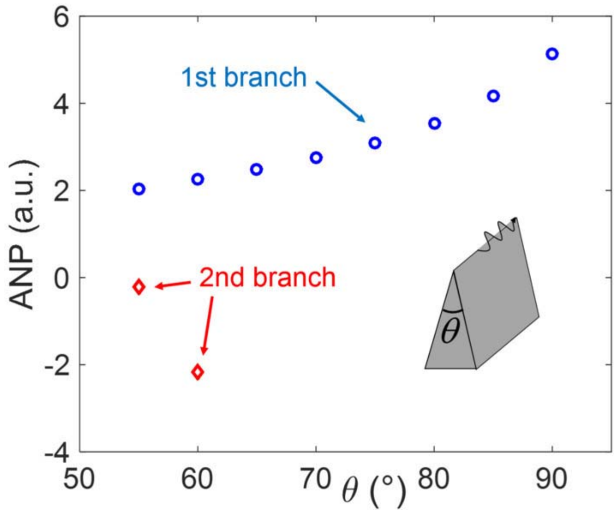

6A-3

11:00 am Nonlinear Effects in NEMS - Improving Frequency Stability

Luis Guillermo Villanueva[1], Rassul Karabalin[2], Mathew Matheny[2], Michael Cross[2], Eyal Kenig[2], Ron Lifshitz[3], Michael Lee Roukes[2]; *[1]EPFL, Switzerland, [2]Caltech, USA, [3]Tel Aviv University, Israel*

Background, Motivation and Objective

Resonant Nanoelectromechanical Systems (NEMS) have generated an enormous interest over the last 15 years, driven by a combination of fundamental questions and practical needs. The combination of relatively high frequencies, high quality factors and small masses make them ideal for a plethora of sensing applications. As an example, it has been possible to detect from a single atom landing on a carbon nanotube till single nuclear spin rotations.

Statement of Contribution/Methods

However, NEMS have failed to made an impact in the field of oscillators or frequency sources. The main reason is that noise is larger for these small devices, since nonlinearity becomes readily accessible at small vibration amplitudes.

Over the past few years we have focused our efforts in bypassing this limitation that comes from nonlinearity.

In this talk, we will analyze all the contributions to the phase noise in an oscillator based on a nonlinear resonator. We will show the existence of a special region in the parameter space, above the nonlinear threshold, where the dominant contributions to the phase noise are suppressed.

This theory has been combined with experimental work and we will show a nonlinear NEMS-based oscillator, using a nanomechanical doubly-clamped beam resonator, for which we characterized its phase noise. The agreement of experimental data with our theoretical model is good, and unequivocally confirm experimentally the existence of the special region described above, where the phase noise performance is improved beyond the limitations of the linear regime. Our findings contravene conventional phenomenological wisdom, which assumes that operation beyond the threshold of nonlinearity necessarily degrades phase noise. Indeed by operating the oscillator in this region, the signal level can be increased to large values without the conventionally expected performance degradation. It is therefore possible to overcome fundamental limitations of oscillator performance due to thermodynamic noise.

Results/Discussion

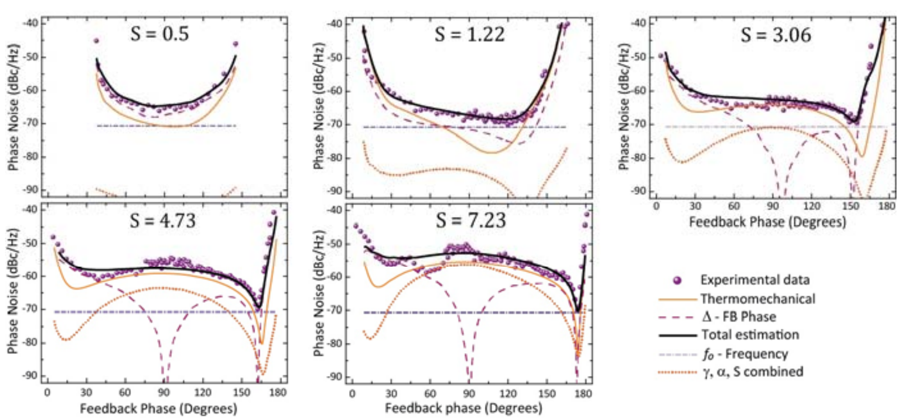

6A-4

11:30 am Force-Frequency Effects in Third Overtone Thickness Shear Quartz Resonators.

Yook-Kong Yong[1], Jianfeng Chen[1]; [1]*Civil and Environmental Engineering, Rutgers University, Piscataway, NJ, USA*

Background, Motivation and Objective

Third overtone and higher overtone thickness shear quartz resonators are used as a frequency source in ultra-stable oscillators. The governing equations for the force-frequency effect and the related acceleration sensitivity of these resonators are well established. The force exerted on the resonator causes initial stress and strain that in turn changes the resonator frequency. However, we have found recently that for accurate force-frequency effects, the calculation of initial stress and strain must include nonlinear material constants and nonlinear geometric displacements. There is a good set of experimental data by Mingins, et. al., and Fletcher, et. al. on third overtone resonators for which until now no analytical models were accurate enough. We present and demonstrate in this paper our finite element models for acceleration sensitivity with nonlinear initial stress and strain that yielded results which compared well with these experimental data.

Statement of Contribution/Methods

Finite element models were developed using theory of small deformation superposed on finite initial deformation in Lagrangian formulation. The governing equations were implemented in COMSOL with a stationary module for the initial stress/strain, and an eigenvalue module that incorporated the initial stress/strain for the force-frequency effect.

Results/Discussion

When the initial deformation included nonlinear material constants and nonlinear geometric displacements, the model results compared well with the experimental results by Mingins et al., and Fletcher et. al. For example, Fig. 1 show a third overtone thickness shear (25.2 MHz) quartz resonator subjected to clamped cantilever bending, and good comparison of model results with Mingins et. al. experimental data were obtained (Fig. 2)

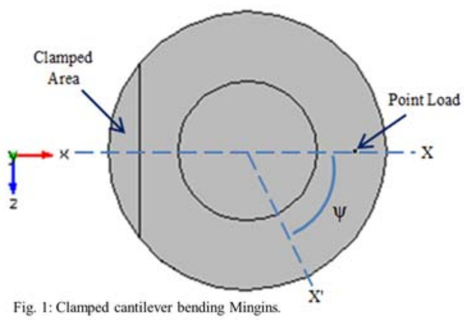

Fig. 1: Clamped cantilever bending Mingins.

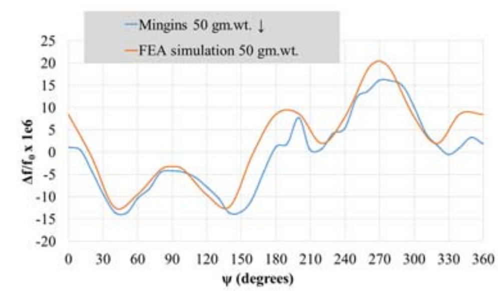

Fig.2: Frequency change as a function of azimuth angle ψ for cantilever bending at 3rd overtone frequency of 25.2 MHz by Mingins.

6A-5

11:45 am Nonlinear Ultrasound Simulations using a Time-Explicit Discontinuous Galerkin (DG) Method

James Kelly[1], Xiaofeng Zhao[2], Drew Murray[3], Simone Marras[4], Robert McGough[5]; [1]*Probability and Statistics, Michigan State University, USA,* [2]*Electrical and Computer Engineering, Michigan State University, USA,* [3]*Computer Science and Engineering, Michigan State University, USA,* [4]*Geophysics, Stanford University, USA,* [5]*Electrical and Computer Engineering, Michigan State University, East Lansing, MI, USA*

Background, Motivation and Objective

Histotripsy with ultrasound is an emerging noninvasive therapeutic modality that uses cavitation to precisely destroy diseased soft tissue. Accurate simulations of histotripsy are needed for treatment planning and device design. These simulations are performed in the time-domain, span hundreds of wavelengths, and must handle strong shocks and discontinuities between materials, such as the brain and the skull. The discontinuous Galerkin (DG) method is an outstanding candidate for such simulations. DG methods possess the following qualities: 1) high order accuracy, 2) geometric flexibility, 3) excellent dissipation properties, and 4) excellent scalability on massively parallel machines. The objective of this work is to develop a massively parallel DG method for histotripsy simulations in the brain.

Statement of Contribution/Methods

We have developed a 3D nonlinear wave equation solver using a time-explicit DG method [1]. The governing equations are expressed in first-order flux form and model the effects of diffraction, attenuation, and nonlinearity. A Rusanov numerical flux is formulated and the eigenvalues of the flux Jacobian are calculated. A third-order, strong stability preserving Runge-Kutta (RK) time-integrator is used for time-discretization. Frequency-squared attenuation is modeled via a second-order diffusion term, which is evaluated using the local DG method. To stabilize the method and guarantee a non-oscillatory solution near shocks, a parameter-free stabilization scheme is implemented [2]. We implemented our scheme in C++ using a hybrid parallelization algorithm using both shared memory threads and distributed memory MPI communication.

Results/Discussion

Full-wave 2D axisymmetric and 3D simulations are simulated for both linear and nonlinear problems. Numerical results for a planar waveguide, a pulsed circular piston, and a pulsed rectangular piston are presented and compared to existing analytical solutions and to the FOCUS software package [3]. Our nonlinear DG implementation captures strong shocks and resolves diffraction, absorption, and nonlinear for all problems considered.

References:

[1] F. X. Giraldo, J. S. Hesthaven, and T. Warburton, ``Nodal high-order discontinuous Galerkin methods for the spherical shallow water equations,'' J. Comp. Phys., 181(2):499–525, 2002.

[2] S. Marras, M. Nazarov, and F. X. Giraldo, ``Stabilized high-order Galerkin methods based on a parameter-free dynamic SGS model for LES,'' J. Comp. Phys., 301, 77-101, 2015.

[3] J. F. Kelly and R. J. McGough, ``A time-space decomposition method for calculating the nearfield pressure generated by a pulsed circular piston,'' IEEE Trans Ultrason., Ferroelect. 53(6), 1150-1159, 2006.

7A - Ultrasound Imaging Devices I

Empire Room

Thursday, September 7, 2017, 10:30 am - 12:00 pm

Chair: **Xiaoning Jiang**
North Carolina State University

7A-1

10:30 am A Magnetic Resonance Compatible E4D Ultrasound Probe for Motion Management of Radiation Therapy

Warren Lee[1], Heather Chan[1], Kwok Pong Chan[1], Timothy Fiorillo[1], Eric Fiveland[1], Thomas Foo[1], David Mills[1], James Sabatini[1], David Shoudy[1], Scott Smith[1], Bryan Bednarz[2]; [1]*GE Global Research, Niskayuna, NY, USA,* [2]*Department of Medical Physics, University of Wisconsin-Madison, WI, USA*

Background, Motivation and Objective

There is recent interest in the use of ultrasound (US) and magnetic resonance (MR) imaging modalities for motion management during radiation therapy treatments. These imaging modalities aim to improve clinical outcomes by tracking tumor motion in order to increase the therapeutic ratio. The objective of this research is to develop an MR-compatible, real-time, three-dimensional ultrasound probe (E4D) for simultaneous MR and US imaging. The probe will be used in a system which leverages the real-time capabilities of ultrasound imaging and the soft-tissue image quality of MR for image guided radiation therapy (IgRT) of moving tumors.

Statement of Contribution/Methods

We have designed a probe with an 18,000 element, 46.8 mm x 21.5 mm 2D array transducer and integrated beamforming electronics for use in our IgRT system. The probe's low-profile, side-viewing design allows it to be strapped to a patient so that abdominal images may be acquired hands-free. A custom 8.5 m cable connects the probe to the ultrasound system in a separate control room.

Results/Discussion

The ferromagnetic materials in the acoustic stack, flex interconnect and electronics boards of the E4D probe were greatly minimized for MR compatibility. In addition, the probe and cable were shielded to minimize the impact of RF noise on both the ultrasound and MRI images. Experiments using an early prototype successfully demonstrate the ability to operate the E4D probe in a 3T MRI scanner (GE MR750) with minimal artifacts in both ultrasound and MR images.

Figure 1: Photograph of the low-profile, side-viewing probe design

Figure 2: Ultrasound image of an agar sheet with probe in the MR bore and gradients on.

Partial Support by NCI/NIBIB R01CA190298

7A-2

10:45 am PIN-PMN--PT Single Crystal Composite and 3D Printed Interposer Backing for ASIC Integration of Large Aperture 2D Array

Robert Wodnicki[1], Haochen Kang[1], Rui Zhang[2], Nestor Cabrera Munoz[1], Ruimin Chen[1], Chi Tat Chiu[1], Qifa Zhou[1,3], Douglas N. Stephens[2], Katherine W. Ferrara[2]; [1]*Biomedical Engineering, University of Southern California, Los Angeles, California, USA,* [2]*Biomedical Engineering, University of California, Davis, Davis, California, USA,* [3]*Roski Eye Institute, Department of Ophthalmology, University of Southern California, Los Angeles, California, USA*

Background, Motivation and Objective

High channel count, large area ultrasound arrays at fine pitch require close integration of transducer elements and ASIC electronics. Composites of single crystal material and non-conducting epoxy filler can be used to increase bandwidth. Direct bonding of the composite to the ASIC leads to acoustic mismatch and excessive ringing.

A collimated connection block (i.e. an interposer) between the array elements and their respective ASIC connections can provide both acoustic attenuation and electrical interconnection. Here we present the implementation of an interposer backing using additive manufacturing processes and demonstrate integration of the interposer with a PIN-PMN-PT single crystal composite transducer array.

Statement of Contribution/Methods

Previous implementations of interposer backing blocks consist of non-conducting absorber material along with embedded wires. Here we present a novel methodology using a filled, 3D printed interposer frame which serves the purpose of both electrical conduction and acoustic absorption. The frame is processed using a commercial high resolution 3D printer which prints acrylic by stereo-lithography (SLA) and creates tubes which are filled with a conducting backing material. The advantage of this method of fabricating the interposer is the possibility of volume production of the frame through low cost additive manufacturing.

Results/Discussion

Fabrication of the composite and backing assembly is illustrated in Figure 1. An example of a 3D printed acrylic frame with tubes for the interposer backing is shown in (a). A frame filled by a conducting absorber (E-Solder 3022) that has been cured is shown in (b). The E-Solder forms pillars spaced at the array pitch (340 µm in azimuth and, 550 µm in elevation), and electrically isolated by acrylic walls. The completed interposer backing is 3.5 mm tall with minimum wall thickness of ~30 µm. PIN-PMN-PT composite was fabricated in our lab using EPOTEK-301 kerf filler. This was bonded to the interposer backing using a thin layer of E-Solder (c). A silver loaded epoxy provides first layer acoustic matching, and ABS plastic acts as the second matching layer (d). Pulse/echo results are shown in (e), demonstrating 60% fractional BW. This may be improved by optimized matching. In future work, individual connections will be formed to an ASIC to implement a 2D transducer array.

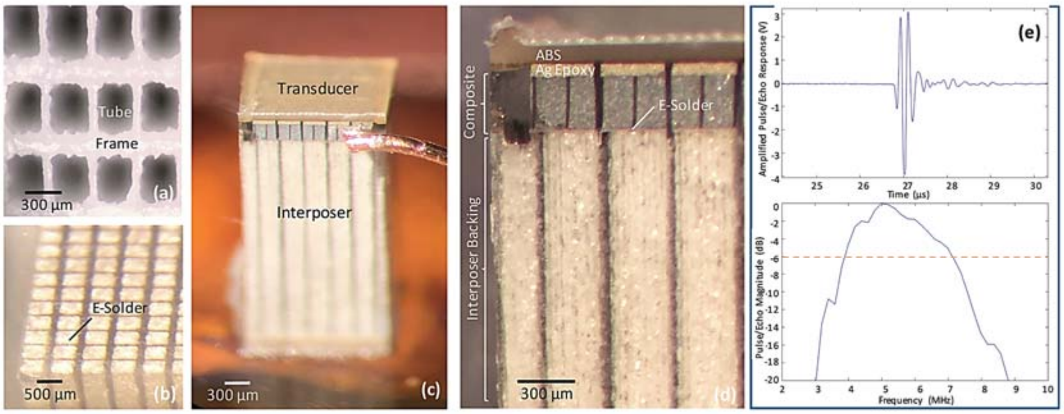

Figure 1: (a) Example 3D printed frame structure, (b) Cured E-Solder pillars, (c) PIN-PMN-PT transducer composite assembled to interposer, (d) Side view of the interposer/composite assembly illustrating the two matching layers and assembly bond line, (e) Pulse/echo response of the transducer assembly with 60% fractional bandwidth.

7A-3

11:00 am A Handheld 1D Transparent CMUT Array Probe for Photoacoustic Imaging

Jean L. Sanders[1], Xiao Zhang[1], Xun Wu[1], Oluwafemi Joel Adelegan[1], F. Yalcin Yamaner[1], Michael Kudenov[1], Ömer Oralkan[1]; [1]*Department of Electrical and Computer Engineering, North Carolina State University, Raleigh, NC, USA*

Background, Motivation and Objective

A transparent transducer array is desired in backward-mode photoacoustic imaging (PAI). CMUT technology is especially suitable for this application because of its wide bandwidth and a wide selection of processing materials. We have previously demonstrated a single-element CMUT with an ITO bottom electrode for improved transparency. The device showed 40% to 70% optical transmission from 700 nm to 900 nm, which is the wavelength range commonly used for in-vivo PAI. In this work, we will make a 1D PAI probe that integrates a fully packaged 1D CMUT array with improved transparency, a fiber bundle, in-probe optics, and low-noise amplifiers which will interface with a real-time imaging system.

Statement of Contribution/Methods

We have recently demonstrated the PAI capability of a single transparent CMUT element. The phantom was a polyethylene tube filled with indocyanine green (ICG) solution embedded in a tissue-mimicking material. In this setup, the light introduced through the back side of the CMUT enabled direct illumination of the imaging field.

We are currently developing 1D arrays for use in PAI with high Vis-NIR transmission. As a proof of principle we are building a 128-channel handheld probe which will integrate light from the back side and allow for in-probe front-end amplifiers. The center of the probe will house a compact optical design for the illuminator based on cylindrical lenses. The probe electronics will consist of two printed circuit boards, each with 64 channels of low-noise amplifiers with integrated transmit/receive switching and biasing circuitry.

Results/Discussion

The experimental setup in Fig. 1a allows direct illumination of the imaging field. The CMUT was mounted on a PCB with biasing circuitry and switches for element selection. The PCB and fiber were suspended using a custom holder to allow integration with a 3D linear stage. The ultrasound signals resulting from the 790-nm 4.5-ns laser pulses were received by an 18-V dc biased CMUT and then amplified at 40 dB and low-pass filtered at 10 MHz. The resulting maximum intensity projection image in Fig. 1b matches well with the phantom (Fig. 1c). The 3D image was reconstructed using delay-and-sum beamforming with coherence factor weighting and log-compressed with 40-dB dynamic range. The in-progress handheld probe will allow for both ultrasound and PAI to test these 1D arrays (Fig. 1d).

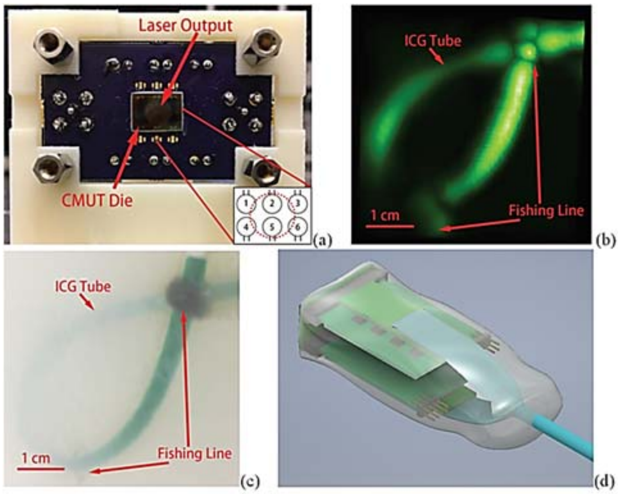

Fig 1. (a) The experimental PAI setup, (b) the resulting PAI, (c) the ICG phantom, and (d) 3D model of the in-progress handheld probe

7A-4

11:15 am Imaging Performance Analysis of a Foldable Large Aperture 2-D ICE Array

Bernard Shieh[1], Karim Sabra[1], F. Levent Degertekin[1]; [1]*Georgia Institute of Technology, USA*

Background, Motivation and Objective

Image quality of volumetric intracardiac echocardiography (ICE) catheters is severely limited, especially in the elevation direction, restricted by the catheter diameter. A natural idea is to design a foldable transducer with multiple panes which can be expanded in the heart mechanically to form a large and symmetric 2-D aperture 2-3 times the size of the catheter diameter. Here, the imaging performance of such an array is investigated and predicted to provide resolution comparable to that of transesophageal echography, imaging depth up to 12 cm in the cardiac environment, and robust performance in the presence of potential orientation misalignment of the panes while keeping total channel count within limitations imposed by a 10F catheter.

Statement of Contribution/Methods

Microfabricated transducers with integrated electronics (e.g. CMUT-on-CMOS) are strong candidates for such a design due to anticipated complexities in array layout and beamformation scheme. A 2-D sparse CMUT array based on a Lockwood Vernier design with 517 transmit and 517 and receive elements is chosen as a potential candidate[1], where each element is composed of a 2 by 2 grid of CMUT membranes (Fig 1-a). Image resolution and SNR are assessed via calculated point spread functions (PSFs) and clutter energy to total energy ratio (CTR). The array is simulated (to first order) in Field II with the assumption of uniform piston motion of the membranes. Element factor is corrected for by simulation of the CMUT directivity function. To determine the susceptibility of array performance on misalignment error, PSFs are calculated for increasing folding angle up to 5° while the beamformation delays are determined assuming a flat array.

Results/Discussion

For the proposed CMUT array operating at 7 MHz with 80% fractional bandwidth, the PSF indicates a lateral resolution of 1.7 mm at 5 cm depth with maximum side-lobe levels 69 dB below the peak sensitivity and a CTR of -27.5 dB (Fig. 1-b). Misalignment error is found to decrease peak sensitivity by up to 9 dB, to degrade resolution down to 4 mm, to increase side-lobes by up to 5 dB, and to increase CTR by up to 13 dB at 5°. It is determined that a folding mechanism with 1° tolerance, which is feasible to measure with integrated magnetic sensors on electrophysiology (EP) catheters, is sufficient to maintain adequate imaging performance (Fig. 1-c).

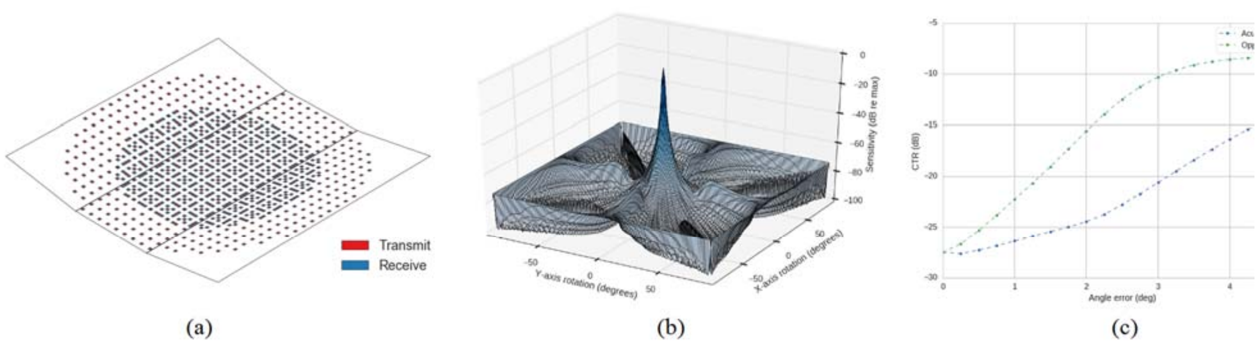

Figure 1: (a) sparse array layout, (b) point spread function, (c) CTR as a function of folding error.

[1] G. R. Lockwood et. al., "Optimizing sparse two-dimensional transducer arrays using an effective aperture approach," *IEEE Int. Ultrason. Symp. 1994.*

7A-5

11:30 am Validation of Optimal 2D Sparse Arrays in Focused Mode: Phantom Experiments

Emmanuel Roux[1], Emilia Badescu[2], Lorena Petrusca[2], François Varray[2], Alessandro Ramalli[1], Christian Cachard[2], Marc Robini[2], Hervé Liebgott[2], Piero Tortoli[1]; *[1]Department of Information Engineering, Università Degli Studi di Firenze, Firenze, Italy, [2]Univ.Lyon, INSA-Lyon, UCBL1, UJM-Saint Etienne, CNRS, Inserm, CREATIS UMR 5220, U1206, F-69100, Villeurbanne, France*

Background, Motivation and Objective

In parallel with the increasing interest for 3D ultrasound imaging, different design techniques have been investigated to find the best configurations of 2D sparse arrays to scan an entire volume of interest [Trucco, IEEE UFFC99], [Diarra, IEEE TBME13]. In particular, we recently addressed the issue of driving a full 2D array of 1024 elements with a reduced number of channels (128, 192 or 256): the optimal arrays (opti128, opti192 and opti256) were obtained using simulated annealing to sculpt the radiated wideband pressure field at multiple depths [Roux, IEEE UFFC17]. The aim of the present work is to experimentally validate these optimal configurations by performing 3D focused imaging on phantoms.

Statement of Contribution/Methods

The 1024 elements of a 3 MHz array made by Vermon were individually driven by four synchronized Verasonics Vantage 256 systems. The systems were programmed to transmit 3-cycle sine bursts at 3 MHz focused at 25 mm and to scan a 3D sector with span ±30° in 31×29 steered beams in azimuth and elevation, respectively. Six arrays were compared: the optimal arrays (opti128, opti192 and opti256), an array whose active elements where randomly selected (rand256) and two references (REF716 and REF1024). The circular dense array REF716 corresponds to the full array REF1024 array without the corner elements. The comparison criteria were the lateral resolution (full width at half maximum - FWHM) and the contrast to noise ratio (CNR), measured on the images obtained by scanning a Gammex (Sono410 SCG) and CIRS (054GS) phantoms respectively.

Results/Discussion

The results are reported in Table 1. The opti256 performs the best among all the compared sparse arrays because it presents the same resolution performance as the REF1024 and an acceptable loss of CNR while using only 25% of the active elements of REF1024. The REF716 array is very competitive with only 70% of the active elements of REF1024.

TABLE I: FULL WIDTH AT HALF MAXIMUM - FWHM (AVERAGED OVER THREE SCATTERERS LOCATED AT DEPTHS 20, 40, 60 MM) AND CONTRAST-TO-NOISE RATIO (CNR) EVALUATED ON IMAGES OF FIGURE 1.

	opti128	opti192	opti256	rand256	REF716	REF1024
FWHM (mm)	2.4	3.2	1.9	1.7	1.9	1.9
CNR (dB)	-4.1	2.4	2.1	-0.7	8.9	9.1

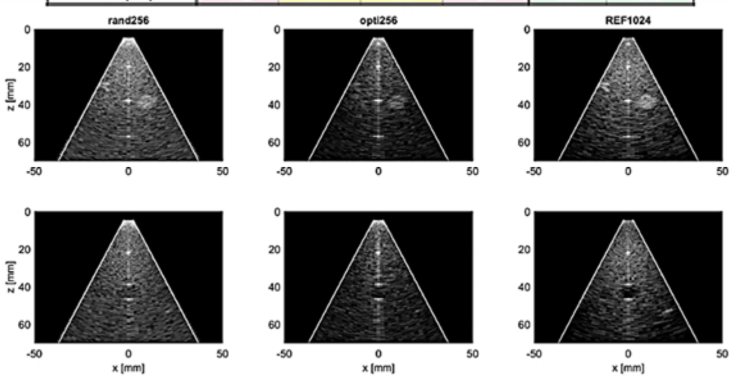

Figure 1 *In vitro* 3D image slices for resolution (top line) and contrast (bottom line) evaluation comparison between the optimal sparse array (opti256), the random sparse array (rand256) and the reference array (REF1024). The dynamic range is 60 dB.

7A-6

11:45 am Computer Aided Detection of Lumbar Spine Landmarks for Ultrasound Guided Lumbar Punctures and Epidurals

Adam Dixon[1], Kevin Owen[1], Mohamed Tiouririne[2], Will Mauldin[1]; *[1]Rivanna Medical, LLC, Charlottesville, VA, USA, [2]Anesthesiology, University of Virginia Health System, Charlottesville, VA, USA*

Background, Motivation and Objective

Lumbar puncture (LP) procedures are facilitated by palpation-based techniques in which the needle insertion location is determined by palpating spinous processes to identify the vertebral level and midline. Not surprisingly, the efficacy of this technique decreases in obese patients and in patients with spinal deformities. Ultrasound imaging significantly improves LP success rates in these difficult patients, but clinical adoption has been limited by poor image quality of bone anatomy and practical difficulties associated with acquiring and interpreting ultrasound images of the spine. In this work, we designed a handheld ultrasound system with enhanced bone image quality and automated spine landmark detection as a means to circumvent technical and practical limitations of neuraxial ultrasound. We present the first clinical evaluation of bone image quality and accuracy of automated spine landmark detection to establish feasibility of the technique.

Statement of Contribution/Methods

The handheld ultrasound system employed an application-optimized transducer plus dedicated beamforming and image processing methods that enhanced bone image quality and automatically detected the spine midline, the spinous process, and interlaminar spaces in ultrasound images. Bone image quality and accuracy of the real-time computer-aided anatomical detection system was evaluated by imaging the lumbar spines of 68 volunteers (BMI up to 40). Images were analyzed by three radiologists who determined the location of spine landmarks, which served as a ground-truth measure for evaluating the performance of the computer-aided detection system.

Results/Discussion

The bone enhancement algorithm produced images with 5.1 to 10-fold enhanced contrast when compared to a comparable handheld ultrasound imaging system. The computer-aided detection algorithm detected the interlaminar space with a sensitivity of 94.2% and specificity of 85.5% and measured its depth with an error of ± 0.5 cm. The spine midline was detected with a sensitivity of 93.9% and specificity of 91.3%, and its position within the ultrasound image was measured with an error of approximately ± 0.3 cm. The results of this study demonstrate the feasibility of enhanced bone image quality and real-time, automated detection of spine landmarks for assisting with interpretation of ultrasound images of the lumbar spine.

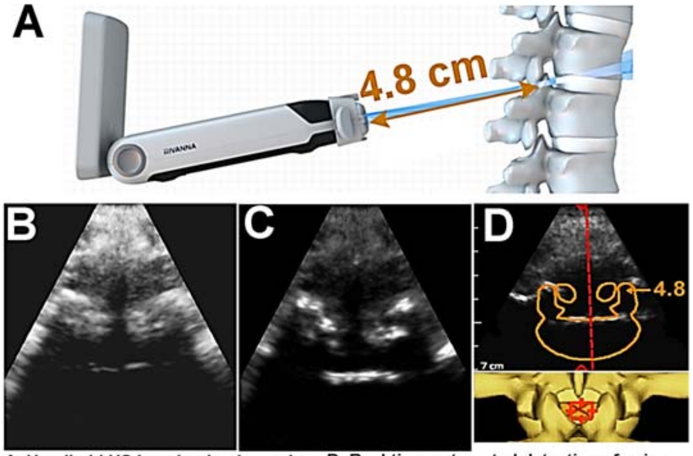

A. Handheld US imaging lumbar spine
B. B-mode mage of interlaminar space
C. Image shown in (B) after bone-enhancement processing
D. Real-time automated detection of spine midline (red) and interlaminar space (orange). 3D spine graphic shown to aid image interpretation.

1B - Clinical: Clinical Ultrasound

Regency Ballroom

Thursday, September 7, 2017, 1:30 pm - 3:00 pm

Chair: **Keith Wear**
U.S. Food and Drug Administration

1B-1

1:30 pm Shear Wave Speed: Becoming a Clinically Valuable Biomarker

Mark Palmeri[1]; [1]*Duke University, USA*

Background, Motivation and Objective

Shear Wave Elasticity Imaging (SWEI) utilizes acoustic radiation force excitations to generate transient shear waves in soft tissues. The speed of these propagating shear waves can be used to characterize the viscoelastic properties of soft tissues. Multiple manufacturers have introduced shear wave-based imaging modes on their scanners, with a variety of clinical applications, including characterizing liver stiffness and breast masses. The clinical literature, however, has highlighted an unacceptable level of variability in shear wave speed measurements between different commercial systems that could limit their future integration into clinical diagnostic workflows as a valuable biomarker. The RSNA Quantitative Imaging Biomarker Alliance (QIBA) has established a working group to evaluate the performance of current shear wave imaging systems from different manufacturers and define sources of variability when making shear wave measurements at different clinical sites.

Statement of Contribution/Methods

The RSNA QIBA workgroup has undertaken two phases of phantom studies across different commercial systems: (Phase I) elastic phantoms, and (Phase II) viscoelastic phantoms. All phantoms were fabricated by CIRS, Inc. Two different elastic phantoms were studied in Phase I, representing healthy and moderately fibrotic liver stiffnesses, while 3 different viscoelastic phantoms were studied in Phase II, again, representing health through moderately fibrotic livers. Multiple commercial systems were used at several different international sites to perform measurements at 3 focal depths (3, 4.5 and 7 cm) using multiple appraisers. Comparative measurements with Magnetic Resonance Elastography (MRE) were also made on both sets of phantoms.

Results/Discussion

Replicated elastic phantoms were able to be fabricated within 5-7% of target stiffness for use in these calibration studies. ANCOVA analysis of the elastic phantom data across 6 different systems determined that (a) system, (b) measurement site, and (c) focal depth with the primary sources of variability in shear wave speed measurements. System and site variability was with ±10%. In the viscoelastic phantoms, an ANCOVA analysis across 9 different systems yielded the same three primary sources of variability, with system variability ranging from ±10-15% depending on the viscoelastic properties phantom. MRE data acquired with a 140 Hz excitation agreed well with the aggregated ultrasound system data in both elastic and viscoelastic phantoms.

The RSNA QIBA effort will yield calibrated phantoms for manufacturers to use for validation and quality assurance of shear wave elasticity imaging systems. Open-source shear wave sequences and processing code, along with digital phantoms, have been made available to the shear wave imaging community for future development and calibration, which should allow shear wave speed measurements to become more consistent and clinically valuable.

1B-2

1:45 pm Frontiers in Elastography Including Ultrasound and Other Modalities

Brian Garra[1]; [1]*Division of Imaging and Applied Mathematics/OSEL, Food and Drug Administration, Silver Spring, Maryland, USA*

Background, Motivation and Objective

Statement of Contribution/Methods

Results/Discussion

1B-3

2:00 pm High Intensity Therapeutic Ultrasound in the Brain

Jeff Elias[1]; [1]*Neurological Surgery, University of Virginia, Charlottesville, Virginia, USA*

Background, Motivation and Objective

Statement of Contribution/Methods

Results/Discussion

1B-4

2:30 pm Frontiers in Image-Guided Intervention Including Ultrasound and Other Modalities

Keyvan Farahani[1]; [1]*National Cancer Institute, Rockville, Maryland, USA*

Background, Motivation and Objective

Statement of Contribution/Methods

Results/Discussion

2B - MSP: Improving Resolution and Detection

Ambassador Ballroom

Thursday, September 7, 2017, 1:30 pm - 00 pm

Chair: **Adrian Basarab**
University of Toulouse, Université Paul Sabatier

2B-1

1:30 pm In-Vitro Detection of Micro Calcifications using Dual Band Ultrasound

Even Flørenæs[1], Stian Solberg[2], Ola Finneng Myhre[3,4], Johannes Kvam[3,5], Ole Martin Brende[2], Bjørn Atle J. Angelsen[3]; [1]*Department of Electronic Systems, Norwegian University of Science and Technology, Trondheim, Norway,* [2]*SURF Technology AS, Trondheim, Norway,* [3]*Department of Circulation and Medical Imaging, Norwegian University of Science and Technology, Trondheim, Norway,* [4]*Klinikk for bildediagnostikk, St. Olavs Hospital HF, Trondheim, Norway,* [5]*Norsvin SA, Hamar, Norway*

Background, Motivation and Objective

Irregular patterns of micro calcifications in the breast may indicate a malignant cancer tumor. Today early detection is done with x-ray mammography. However, in some women the high density of connective tissue of the breast can limit detection using X-ray imaging. With ultrasound, improved suppression of the connective tissue can be achieved. During breast tissue biopsy ultrasound can also provide real-time guidance of the biopsy needle.

Statement of Contribution/Methods

In a dual band imaging technique called Second Order Ultrasound field (SURF) imaging, a high frequency imaging pulse (HF) and a low frequency manipulation pulse (LF) are transmitted simultaneously through a common aperture. The LF manipulates the nonlinear elasticity of the tissue by either compressing or expanding the material. Micro calcifications, due to their stiffness, seem to exhibit a non-linear response dependent on the LF pulse, which is not present in the response from soft tissue. By transmitting 3 or 4 different pulse complexes where the magnitude and polarity of the LF is varied efficient enhancement of micro calcification and suppression of scattering from tissue is possible.

Results/Discussion

In-vitro experiments performed on a commercially available breast phantom using a modified Sonix MDP scanner have shown the feasibility of the method, producing results which is coherent with mammography data of the same phantom. In the figure results of in-vitro experiment are shown where three micro calcifications are placed inside an echoic mass. The method obtains enhanced calcification-to-tissue ratio by on average 20 dB compared to ordinary B-mode. Further contrast is obtained by applying a developed image segmentation technique.

Figure 1: Comparison of B-mode (left) and new method (right). Processed image can be superimposed on B-mode image

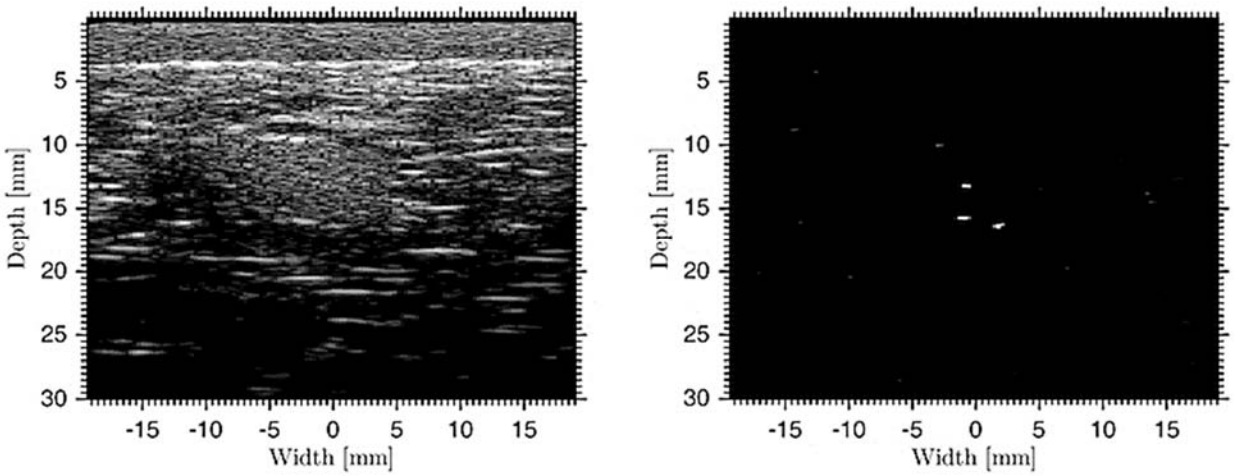

2B-2

1:45 pm Point Scatterer Enhancement in Ultrasound by Wavelet Coefficient Shrinkage

Stine M. Hverven[1], Ole Marius Hoel Rindal[1], Alan J. Hunter[2], Andreas Austeng[1]; [1]*Department of Informatics, University of Oslo, Oslo, Norway,* [2]*University of Bath, Bath, United Kingdom*

Background, Motivation and Objective

The size, distribution and morphology of microcalcifications (MCs) in breasts can for some cases be considered an early indicator of breast cancer. MCs are small, hard calcium deposits in soft breast tissue and appear as point scatterers in an ultrasound image. However, detection of MCs in ultrasound images is challenging. Background speckle often obscure the MCs and thus highly affect the probability of detection and classification. The proposed algorithm uses a coherence-based wavelet shrinkage method to suppress speckle background in order to enhance point scatterers.

Statement of Contribution/Methods

The method consists of first creating multiple images or looks from the original image with statistically independent noise realizations and retained wavenumber resolution. The algorithm then utilizes a coherence metric to determine the similarity of the wavelet coefficients between these looks. The wavelet coefficients with low coherence are attenuated to produce a de-noised image. The method has previously been applied on sonar images to separate coherent targets from incoherent background reverberation noise.

The wavelet shrinkage algorithm was applied to an ultrasound image of a tissue-mimicking phantom with several point scatterers mimicking MCs and a hyperechoic area. A coherently compounded plane wave ultrasound image was recorded with the Verasonics Vantage system using a linear probe (Philips L7-4, 128 elements, 75 angles, 5.2 MHz, f# = 1.75). To test the algorithm's ability to suppress speckle background, an image of only speckle was also recorded. The channel data of the image with point scatterers and the image with only speckle were combined to create images with varying speckle percentage and amplitude levels.

Results/Discussion

The figure shows the original ultrasound image in comparison to the wavelet shrunk image, showing that the suggested technique suppresses speckle background and retains point scatterers. For the images below, the conspicuity of the wavelet shrinkage method is around 14-17 times higher, with conspicuity defined as the mean value of background intensity subtracted from the maximum intensity of the point target at same depth, divided by the standard deviation of background. The results using the tissue-phantom are promising for further testing on real ultrasound images of breasts with MCs.

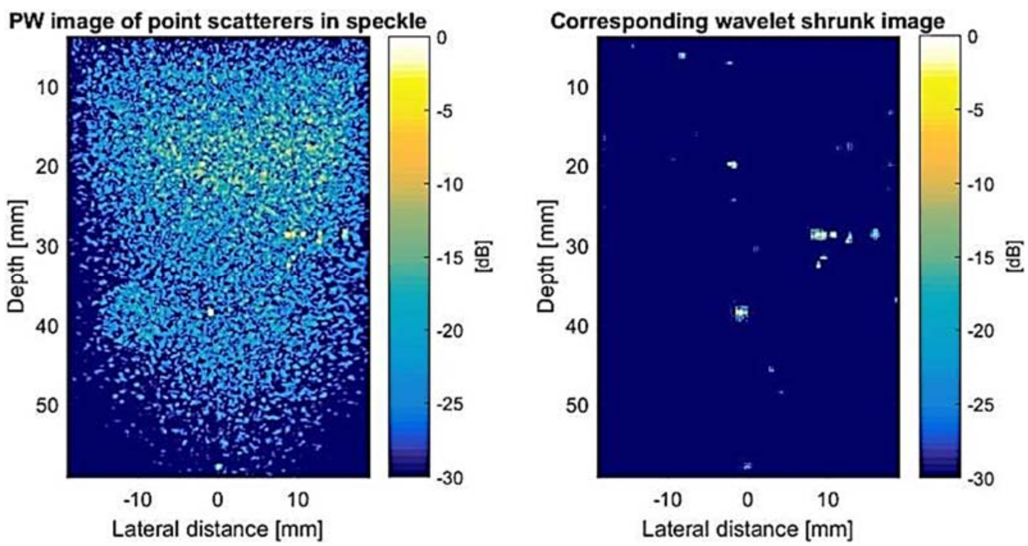

2B-3

2:00 pm Maximum Likelihood Estimation of Scattering Strength for High Range Resolution Ultrasound Imaging

Hideyuki Hasegawa[1], Michiya Mozumi[1]; [1]*University of Toyama, Toyama, Japan*

Background, Motivation and Objective

The range spatial resolution in ultrasound imaging is an important index determining the image quality and basically determined by the frequency band width of the ultrasonic transducer. In the present study, a new element-domain signal processing technique based on the maximum likelihood method was developed for improvement of the range spatial resolution in ultrasonic imaging.

Statement of Contribution/Methods

In the present study, the point spread function (PSF) of the ultrasonic system employed was suppressed to estimate the scattering strength of a target. An echo from a 15-micron stainless wire in water was used as the range PSF. An echo signal from a target, which is received by a transducer element, can be modelled as the sum of noise and convolution of the scattering strength of a target and PSF. The likelihood of an element echo signal can be obtained by assuming that noise is Gaussian. The scattering strength of a target was estimated so that the likelihood was maximized.

Results/Discussion

Figure (1-a) shows a conventional B-mode image of a 15-micron fine wire in water, which was obtained by ultrafast plane wave imaging without compounding (1302 fps). By filtering the element signals using the proposed method, the B-mode image in Fig. (1-b) was obtained. The range spatial resolution, which was determined by the width at half maximum of an echo from the wire, was improved significantly from 0.212 mm to 0.081 mm. For evaluation of the feasibility of the proposed method under an attenuation condition, which was different from water, a wire target in a tissue mimicking phantom (040GSE, CIRS) was measured. The range spatial resolution was also improved significantly from 0.209 mm to 0.086 mm under a different attenuation condition. Finally, the proposed method was applied to in vivo imaging of a human carotid artery. In the B-mode image obtained by the proposed method (Fig. (2-b)), echoes from the lumen-intima interfaces became sharper than those in the conventional B-mode image in Fig. (2-a). Also, the speckle pattern was suppressed because the interference among echoes was reduced by shortening the ultrasonic pulse length. As a result, the lateral continuity of the image was improved as indicated by the red arrow in Fig. (2-a). Furthermore, undesirable echoes in the lumen (cyan arrow in Fig. (2-a)), which were considered to be generated from sidelobes, were also suppressed.

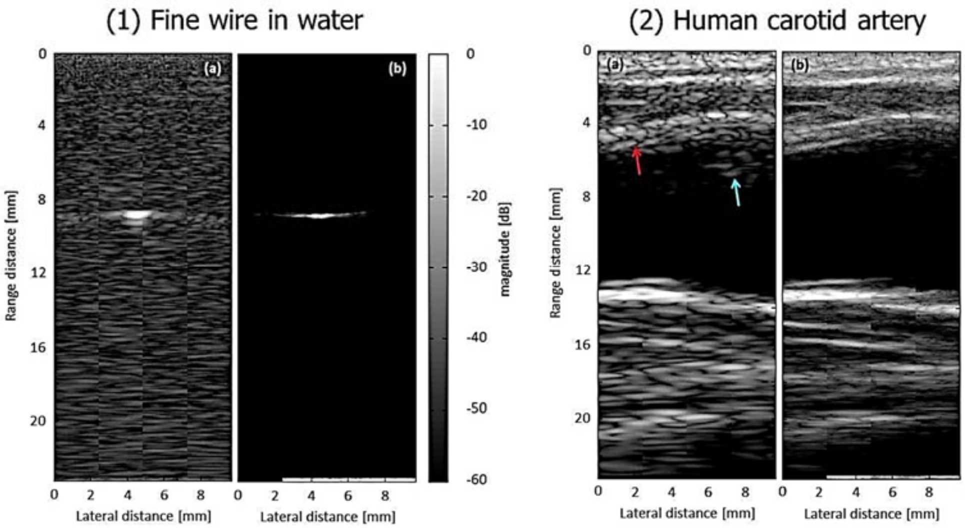

2B-4

2:15 pm **Velocity Resolution Improvement for High Temporal Resolution Ultrasonic Transducer**

Thuy Thu Nguyen[1], Andreas W. Espinoza[2], Stefan Hyler[2], Espen W. Remme[2], Jan D'hooge[3], Lars Hoff[1] ; [1]*University College of Southeast Norway, Norway,* [2]*Oslo University Hospital, Rikshospitalet, Norway,* [3]*Catholic University of Leuven, Belgium*

Background, Motivation and Objective

Time delay estimation using cross correlation between successive RF lines is an established method to estimate tissue velocity. We have applied this method on our system using 10 MHz transducers sutured to the epicardium to measure the myocardial contraction pattern at high spatial and temporal resolution. In this setup, the myocardial tissue velocity will generally increase with the depth, as the endocardial tissue usually moves at higher velocity than the epicardial tissue. Higher velocity resolution is therefore required in the epicardial region, while a higher maximum detectable velocity is needed in the endocardial region. The aim of this study is to introduce a method to balance this requirement, processing the lines slightly differently at epi- and endo-cardium

Statement of Contribution/Methods

Two custom-build 10 MHz single element 3 mm-diameter transducers were sutured on the epicardium of the anterior wall of a pig. The pulse repetition rate was 2.5 kHz, and echoes were sampled at 40 MS/s. On the M-mode images, the endocardial border was manually defined at end-diastole, and the myocardial wall was divided into 4 equally sized layers. RF signals were up-sampled by a factor of 10. Tissue velocities were estimated using a cross correlation time delay estimator, with a 616 µm kernel size and 50% window overlap. Two velocity estimates were calculated: Velocity V1 from the cross-correlation between successive scanlines, and V2 from the cross-correlation between every second scanline. The tissue velocity V was assigned to V1 and V2 at endo- and epi-cardial region, respectively. In the transition region, V was calculated as weighted average between V1 and V2 along the depth

Results/Discussion

Fig. 1a shows the results of tissue tracking using V2 and V1 separately. The result shows how V2 is better at tracking the motion near the epicardium, but misses the higher velocities near the endocardium. Fig. 1b shows the change when using the proposed method. In this figure, V2 is used for depths z < 9mm, while V1 is used for z > 10mm. This method combines the good resolution of V2 at the epicardium with the higher maximum detectable velocity of V1 at the endocardium. Hence, the layer motion is tracked more correctly both at the epi- and endo-cardial layers. For very slow motion, the method may be extended to include a velocity V4, estimating cross-correlation between every fourth scanline.

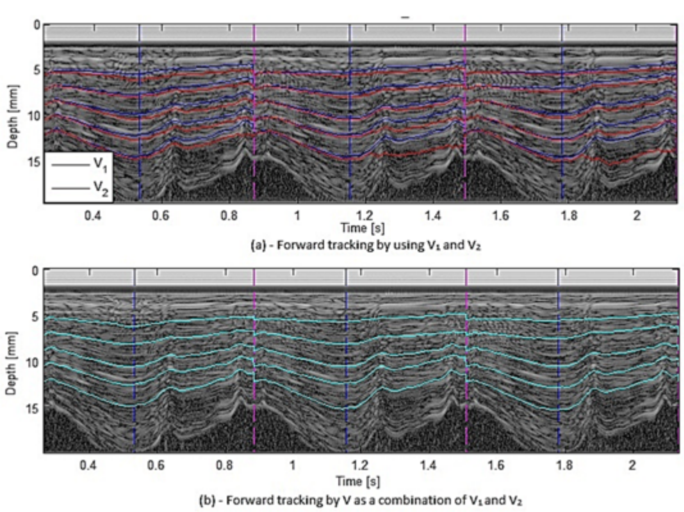

Fig. 1 Effect of V on layer tracking

2B-5

2:30 pm **Enhanced Axial and Lateral Resolution Using Stabilized Pulses**

Shujie Chen[1], Kevin Parker[2]; [1]*Electrical & Computer Engineering, University of Rochester, Rochester, NY, USA,* [2]*Electrical & Computer Engineering, University of Rochester, Rochester, New York, USA*

Background, Motivation and Objective

Ultrasound B-scan imaging systems operate under some well known resolution limits. To improve resolution, the concept of stable pulses, having bounded inverse filters, were described for lateral deconvolution (Chen and Parker, Enhanced resolution, J Med Imaging, 2016). This framework has been extended to the axial direction, enabling two-dimensional deconvolution.

Statement of Contribution/Methods

We extend our previous work to 2D (axial and lateral) resolution enhancement where stabilized beampatterns can be produced and sampled so as to have stable and useful inverse filters. We also explicitly treat the problem of scatterers positioned at sub-integer shifts, between the nominally sampled locations. Coherent deconvolution, introduced previously, may be performed in the two dimensions sequentially. Examples are provided from Field II and ultrasound B-scans. We demonstrate that axial deconvolution can be treated within the same general framework as lateral resolution, and robust 2D resolution enhancement is possible.

Results/Discussion

Examples from both Field II simulation and the Verasonics scanner have shown enhanced resolution in both dimensions by resolving individual scatterers, clarifying the anechoic cyst, and sharpening the carotid artery images. The resolution is enhanced by up to 8 and 20 times in the lateral and the axial directions, respectively, evaluating the -6 dB width of the autocorrelation of the envelope images. Figure: Two-dimensional deconvolution of an image from a conventional in vivo scan which contains the carotid artery and the thyroid. (a) The original image, and (b) the image after deconvolution.

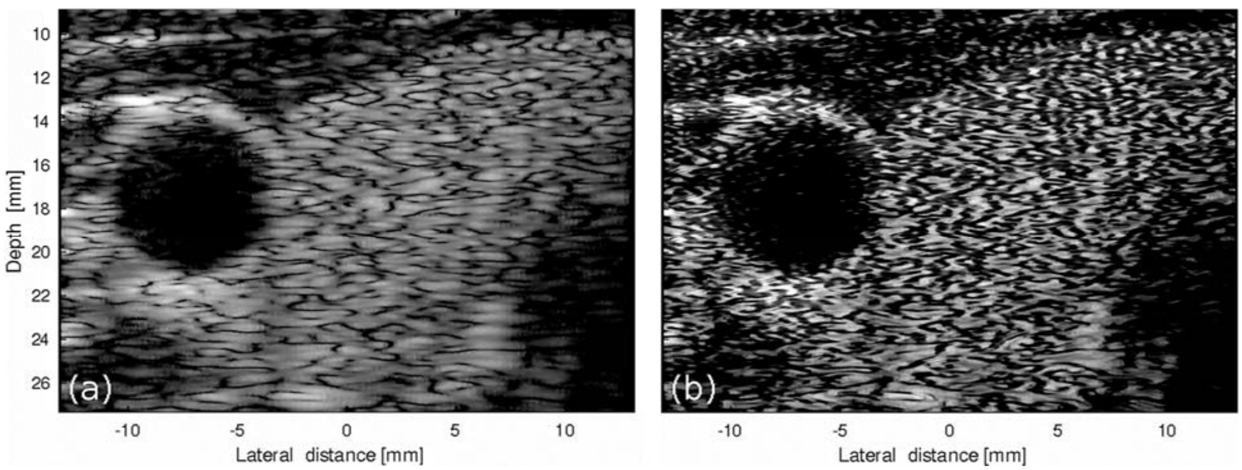

2B-6

2:45 pm **B-Mode Subwavelength Vibration Imaging**

Tzu-Min Yeh[1], Meng-Lin Li[1]; [1]*National Tsing Hua University, Taiwan*

Background, Motivation and Objective

Shear wave elastography relies on acoustic radiation force to generate shear wave vibration. In magnetomotive ultrasound (MMUS), magnetic excitation along with magnetic nanoparticles (MNPs) induces magneto-vibration. Both types of tissue vibrations are in the range of few micrometers and not observable in conventional B-mode imaging. Computationally intensive sub-wavelength motion tracking is required to visualize shear wave propagation for shear wave speed estimation and to localize magneto-vibration sources for mapping MNP distribution. Our goal is to reveal such invisible vibrations in B-mode with lower computational complexity, which, we believe, would be beneficial to the two imaging modalities.

Statement of Contribution/Methods

Toward this goal, we propose a novel vibration visualization technique – B-mode subwavelength vibration (B-SV) imaging, which magnifies the invisible few-micrometer vibrations to a level visible in B-mode without the need of sub-wavelength motion estimation. Leveraging sub-wavelength vibrations and lower spatial frequencies of beamformed baseband images, we derive the link between temporal processing and spatial vibration magnification. Accordingly, subtle motions with specific vibration frequency can be exaggerated over beamformed baseband image sequence. Unlike B-flow imaging, B-SV imaging not only highlights but also magnifies subtle vibrations in B-mode.

Results/Discussion

Simulations and MMUS experimental data (not shown here) are used to verify the proposed technique. Figure (a) shows the simulated time series of 7.5-MHz plane wave B-mode imaging with the maximum vibration = 0.5 um and figure (b) is the lateral M-mode image at the position indicated by the dashed line. The vibration is invisible. Via magnifying the vibration, the proposed B-SV imaging localizes the vibration source and presents the shear wave propagation (see figure (c)). In addition, the shear wave speed can be estimated using the derived M-mode (figure (d)). The results prove the capability of the proposed B-SV imaging technique, providing straightforward B-mode visualization of the originally invisible vibrations by exaggerating them to a visible level via temporal processing. It does not require computationally intensive motion tracking and is applicable to shear wave elastography and MMUS (vibration source localization).

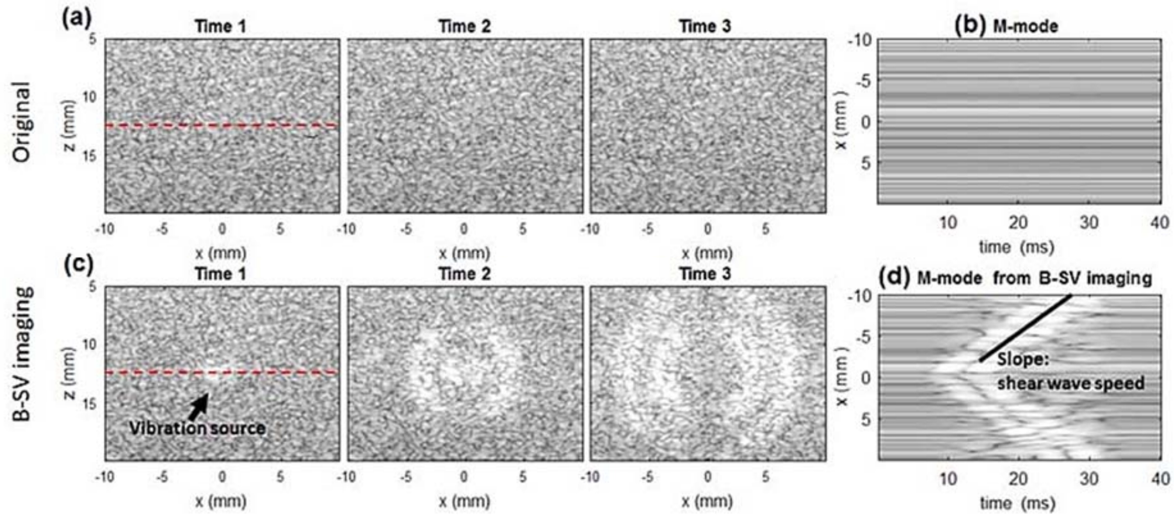

(a)
Time 1
Time 2
Time 3
Original
z (mm)
x (mm)
(b) M-mode
x (mm)
time (ms)
(c)
B-SV imaging
Vibration source
(d) M-mode from B-SV imaging
Slope:
shear wave speed

3B - MTH: Cavitation

Palladian Room

Thursday, September 7, 2017, 1:30 pm - 3:00 pm

Chair: **Brian Fowlkes**
Univ. of Michigan

3B-1

1:30 pm **Pulsed Cavitational Ultrasound Softening: A New Non-Invasive Therapeutic Approach of Calcified Valve Stenosis**

Olivier Villemain[1], Justine Robin[1], Alain Bel[2], wojciech Kwiecinski[1], Patrick Bruneval[2], Bastien Arnal[1], Mathieu Rémond[3], Mickael Tanter[1], Emmanuel Messas[2], **Mathieu Pernot[1]**; [1]*Institut Langevin, INSERM, ESPCI, Paris, France,* [2]*APHP, Paris, France,* [3]*Cardiawave, Paris, France*

Background, Motivation and Objective

Non-invasive therapy of calcified valve stenosis remains a major goal in cardiology. To date, no drug has demonstrated therapeutic efficacy on calcified valves. Valve replacement by surgery or minimally invasive techniques remain the only solutions available, despite the risks and the known side effects. We propose a novel non-invasive therapeutic approach based on the use of pulsed cavitational ultrasound (PCU) softening to improve valve opening by softening the calcified stiff cusp.

Statement of Contribution/Methods

We investigated the efficacy of PCU softening in vitro and in vivo on a large animal model. All the experiments were performed on calcified bioprosthetic valves explanted from human patients. PCU was performed in vitro on calcified bioprosthesis mounted on a hydraulic bench with pulsatile flow (n=8) and in vivo on an ovine model with implanted calcified bioprosthesis (n=7). We used echocardiography, pressure and flow sensors, quantitative stiffness evaluation using shear wave elastography, micro-CT imaging and histology to evaluate in vitro and in vivo the effect of PCU.

Results/Discussion

The transvalvular gradient was found to decrease after PCU in both in vitro (from 21.1±3.9 to 9.6±1.7 mmHg, $p<0.01$) and in vivo setup (from 16.2±3.2 to 8.2±1.3 mmHg, $p<0.01$), with a decrease of valve stiffness (in vitro: from 105.8±9 to 46.6±4 kPa, $p<0.01$; in vivo: from 82.6±10 to 41.7±7 kPa, $p<0.01$) and an increase of valve area (from 1.10±0.1 to 1.58±0.1 cm2, $p<0.01$). Histology and micro-CT imaging showed modifications of calcification structure without loss of calcification volume or alteration of the leaflet superficial structures. We have demonstrated in vitro and in vivo that PCU can decrease a calcified bioprosthesis stenosis by softening the leaflets remotely. This new non-invasive approach has the potential to improve the outcome of patients with severe bioprosthesis stenosis.

3B-2

1:45 pm **Acoustic Cavitation Emission Feedback to Monitor Tissue Fractionation During Histotripsy Therapy**

Jonathan Macoskey[1], Jonathan Sukovich[1], Timothy Hall[1], Charles Cain[1], Zhen Xu[1]; [1]*Biomedical Engineering, University of Michigan, USA*

Background, Motivation and Objective

Histotripsy uses high-pressure, microsecond-long ultrasound pulses to generate a cloud of cavitation to fractionate cells in target tissues such as tumors, blood clots and brain applications. B-mode ultrasound has been used to detect the cavitation and tissue fractionation generated by histotripsy, but it requires a separate imaging probe and can only detect substantial amounts of tissue fractionation. In this study, a specialized circuit and digitizer was designed to allow all the elements of a 112-element array to transmit extremely high-pressure (>40MPa) histotripsy pulses and receive the low-pressure Acoustic Cavitation Emission (ACE) signals. ACE feedback can be achieved via the histotripsy array itself and may have a high sensitivity to detect tissue fractionation.

Statement of Contribution/Methods

For initial validation, an 8-channel nonlinear voltage compressor circuit was constructed and tested to allow up to 3kV input signals to transmit the histotripsy pulses while compressing all the received signals to within 3V for the digitizer to collect the ACE signals. Using a 112-element, 500 kHz histotripsy array with a 15 cm focus, ex vivo bovine liver samples were treated at dosages of 30, 60, 100, 200, 300, 500, and 1000 pulses-per-location with a 219-location, 6 mm-cubed treatment region. The ACE signal was acquired during treatment and processed to correlate with the level of tissue fractionation identified histologically. After validation of the prototype 8-channel system, a 112-channel, parallelized, and digitized version of the compressor was built and is now being evaluated to add receive capability to the entire array.

Results/Discussion

Of the several methods investigated for analyzing the ACE signal, it was found that the peak absolute pressure arrival time of the ACE signal correlates well with cellular destruction and tissue fractionation identified histologically at the early stage of treatment, indicating a high sensitivity (Fig 1). This ACE metric was determined by finding the peak of a moving RMS envelope applied to each ACE signal. All elements were normalized to a mean arrival time to correct for tissue inhomogeneities. These results suggest that the ACE signal could be used to provide non-invasive and real-time quantitative feedback of tissue fractionation using the histotripsy array itself.

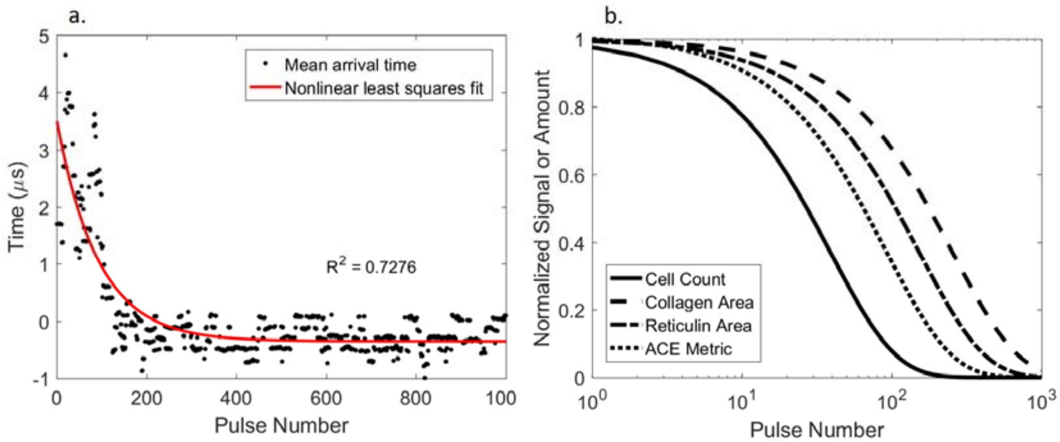

Fig 1. (a) ACE peak pressure arrival during 1000 pulse treatment and (b) correlation of ACE with histological analysis.

3B-3

2:00 pm Estimation of Size Distribution for Cavitation Bubbles Combining Time Intensity Curve and Bubble Dissolution Kinetics in Tissue

Shanshan Xu[1], Runna Liu[1], Shukuan Lu[1], Supin Wang[1], Mingxi Wan[1]; [1]*Department of Biomedical Engineering, Xi'an JiaotongUniversity, China, People's Republic of*

Background, Motivation and Objective

It has been known that cavitation is the primary mechanism to accelerate ultrasound induced thermal ablation and lesion formation. In order to increase the treatment efficiency, it is useful to know the size of existing cavitation bubbles so as to maximum the bubble oscillation using a frequency corresponds to the bubble resonant frequency at a lower acoustic pressure. In our previous work, a cavitation bubble size estimation method using the time intensity curve and bubble dissolution kinetics in liquid has been developed. In this work, we develop a method to investigate the cavitation bubble size distribution in different sorts of tissue using the bubble dissolution equation in tissue and the time intensity curve for dissolution.

Statement of Contribution/Methods

A 1.6 MHz HIFU burst lasting 600 ms at an acoustic power of 150 W was used to generate cavitation bubbles in a gel phantom with a shear modulus of 0.07 atm and an ex vivo liver with a shear modulus of 0.10 atm, respectively. Both of the gel phantom and the liver were considered as undersaturated medium (f=0.75). A scanner was used to collect the signal backscattered from samples in B-mode imaging at a frame rate of 50 Hz during the dissolution process. The amplitude of the echo from the bubbles was calculated as the intensity at the time instant on which the imaging was acquired. Different from the Epstein and Plesset's work on the rate of gas bubble dissolution in a simple liquid, a generalization for bubble dissolution rate equations that take into account the influence of a non-zero shear modulus in the medium was used to render it applicable to a gas bubble embedded in a soft elastic medium. The parameters used in the dissolution equation were: T=298.15 K, P_e =1 atm, D^*=2900 μ^2/s, γ=70 dynes/cm and K_H =161400 J/mol.

Results/Discussion

The bubbles dissolution curve in these two sorts of undersaturated soft medium was obtained using the bubble dissolution rate equationin in soft medium. The dissolution time will extend with increasing the shear modulus. Also, the estimated cavitation bubble size will be larger in the soft medium with a larger shear modulus, with a mean radius of 1.4 µm for gel and 1.8 µm for liver. To our knowledge, this is the first study on the size of cavitation bubbles embedded in tissue. It may be useful for parameter settings in the ultrasound induced treatment.

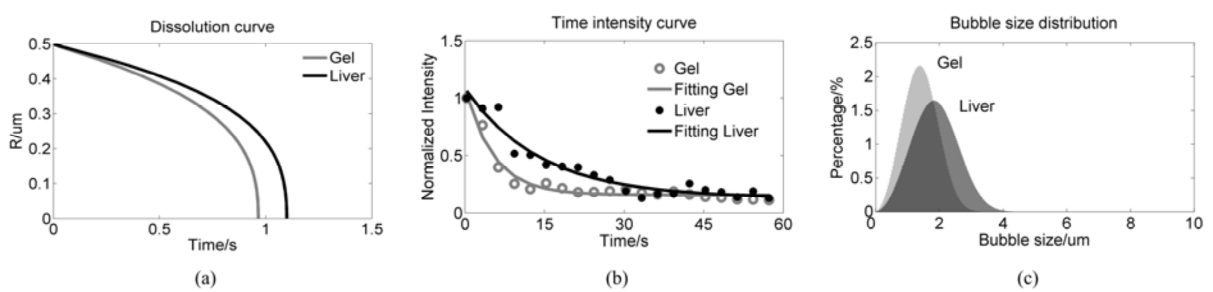

Figure (a) The dissolution curves (b) The time intensity curves and (c) bubble size distribution for gel phantom with a modulus of 0.07 atm and a liver with a modulus of 0.1 atm, respectively.

3B-4

2:15 pm Laser-Generated Focused Ultrasound for Micro-cavitation and its Application to High-Precision Cavitation Treatment

Taehwa Lee[1], Wei Luo[2], Qiaochu Li[3], Hakan Demirci[4], L Jay Guo[1]; [1]*Mechanical Engineering, University of Michigan, Michigan, USA,* [2]*School of Optical and Electrical Information, Huazhong University of Science and Technology, China, People's Republic of,* [3]*Electrical Engineering and Computer science, University of Michigan, Michigan, USA,* [4]*Kellogg Eye Center, University of Michigan, Michigan, USA*

Background, Motivation and Objective

Histotripsy is considered a non-invasive therapeutic modality capable of mechanically fractionating tissue using cavitation bubbles induced by high intensity focused ultrasound pulses. Histotripsy-induced cavitation region over relatively large focal volume is effective in treating sizable lesion, while compromising its treatment precision. We demonstrate high-precision cavitation treatment using laser-generated focused ultrasound.

Statement of Contribution/Methods

Laser-generated focused ultrasound was produced by irradiating pulse laser beam (Nd:YAG laser, 6 ns pulse duration) into a photoacoustic (PA) conversion layer coated on the concave surface of a plano-concave optical lens (namely, PA lens), as shown in Fig.1(A). The photoacoustic coating was made of a carbon nanotube (CNT)-polymer composite. Focused ultrasound pulses generated by the CNT PA lens were found to be strong enough to cause micro-cavitation in water (> 30 MPa), which was controllably regulated by the focal volume (< 100 μm). Micro-cavitation was visualized by a high-speed shadowgraph imaging technique. By moving samples mounted on a 3D motorized stage, controlled micro-cavitation was used to cut or ablate tissue-mimicking gel (agarose gel) in a high-precision targeted manner.

Results/Discussion

Figure 1(B) shows cutting results of three primitive shapes in agarose gel, each having a width of 1 mm. The inner parts were preserved while leaving the penetrating holes in the gel. The kerf was measured to be approximately 50 μm, which corresponds to cavitation regions visualized in Fig.1(C). We will also show cutting for more complex shapes and applications to tissue. Such high-precision cavitation treatment together with image guidance could open new possibility to treat tissue while sparing healthy surrounding, especially for early-diagnosed small lesion close to critical nerves.

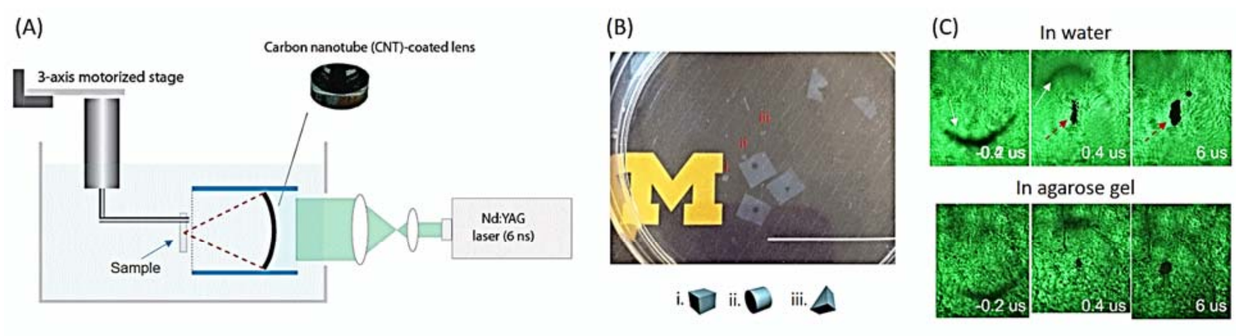

Figure 1. (A) Experimental setup for laser-generated focused ultrasound. Samples are mounted on a motorized stage. (B) High-precision cutting of agarose gel into primitive shapes with a width of 1 mm. (C) High-speed shadowgraph images of micro-cavitation in water (top) and agarose gel (bottom). Each image frame has a width of 1 mm. The white arrow indicates focused ultrasound wavefronts, while the red dashed arrow indicates micro-bubbles.

3B-5

2:30 pm Prediction of Thermal Coagulation by Short-Pulse Pre-Exposure for Cavitation-Enhanced Ultrasonic Heating

Ryosuke Iwasaki[1], Ryo Takagi[2], Shin Yoshizawa[2], Shin-ichiro Umemura[1]; [1]*Graduate School of Biomedical Engineering, Tohoku University, Sendai, Japan,* [2]*Graduate School of Engineering, Tohoku University, Sendai, Japan*

Background, Motivation and Objective

Targeting the ultrasound beam and predicting the thermal coagulation in advance are important for high-intensity focused ultrasound (HIFU) treatment. Cavitation bubbles are known to enhance ultrasonic heating, however, temporal and spatial control of their generation is not simple. In our previous study, a method utilizing acoustic radiation force to predict thermal coagulation was suggested. In this study, it was investigated whether the proposed method works effectively even for the cavitation-enhanced ultrasonic heating and can be used to ensure both safety and efficiency of the treatment.

Statement of Contribution/Methods

A high-intensity pulse called trigger pulse with a duration of 0.1 ms for generating cavitation bubbles and an immediately following moderate-intensity HIFU burst with a duration of 1.9 ms were transmitted to induce displacement for focal zone visualization. Before and immediately after this push pulse exposure, RF data were acquired via high-speed ultrasound imaging. The distribution of the axial displacement between before and after exposure was calculated from the phase shift in 1D cross-correlation. The distribution during push pulse exposure was estimated by linear extrapolation at each pixel in time domain to improve the accuracy of visualization. A chicken breast and a porcine liver were selected as the ex-vivo samples to test the proposed method.

Results/Discussion

The induced spatial peak displacement is plotted against the push pulse energy in Fig. (a), where a value of 1 on the horizontal axis corresponds to the case that both trigger pulse and burst the push pulse had the same intensity of 3 kW/cm^2. Only the intensity of trigger pulse was changed in the cases with trigger. The observed sharp increase in the peak displacement suggests the effect of cavitation to enhance ultrasonic absorption and/or back scattering. Figs. (b) and (c) show the typical distributions of displacements induced by the push pulse without and with trigger, respectively. Fig. (d) shows the slice of a coagulated porcine liver sample after treatment. The proposed method reflects the shift of the center position of ultrasonic absorption enhanced by cavitation.

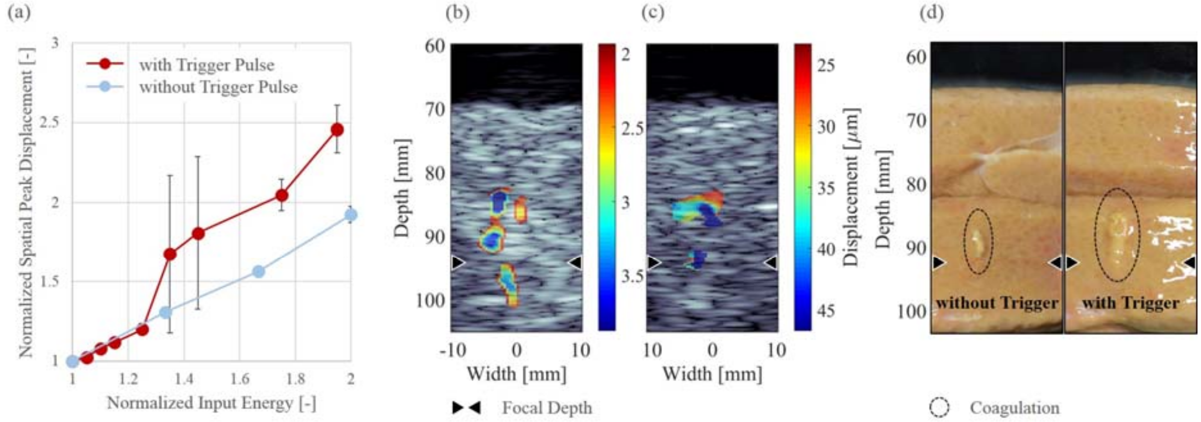

Figures (a): Induced spatial peak displacements inside chicken breast sample relative to input energy.
(b): Distributions of displacements induced by push pulse without trigger, (c): with trigger for cavitation.
(d): Tissue coagulation of porcine liver sample.

3B-6

2:45 pm Image-guided Ultrasound/Microbubble-Mediated Drug Delivery Platform with Passive Cavitation Mapping

Taehwa Lee[1], Dongwoon Hyun[1], Sayan M. Chowdhury[1], Sunitha Bachawal[1], Carl D. Herickhoff[1], Jeremy Dahl[1], Juergen K. Willmann[1]; [1]*Radiology, Stanford University, Stanford, California, USA*

Background, Motivation and Objective

Ultrasound/microbubble (US/MB)-mediated drug delivery is a promising approach to effectively deliver therapeutic agents to target tumors by increasing vascular permeability through sonoporation. Equipped with focused ultrasound, drug delivery platforms can increase site-specificity. To move toward clinical translation, such a platform requires both image guidance for accurate location of tumor targets and quantitative mapping of the therapeutic dose for effective treatment.

Statement of Contribution/Methods

We have constructed a drug delivery platform based on two linear array transducers that enables ultrasound image guidance for active and accurate targeting and passive cavitation mapping based on a newly-developed algorithm having improved spatial resolution for monitoring of therapeutic ultrasound dose. The two transducers, a 1.8 MHz transducer for cavitation induction and a 7.5 MHz transducer for imaging, are mounted in a custom-made holder with their median planes aligned and validated with a hydrophone (Fig. A). The two transducers were connected to and simultaneously controlled by a Verasonics Vantage 256 research ultrasound system. This platform allows for electronic steering of the therapy focus and imaging with both B-mode and passive cavitation maps. The system was tested by injecting lipid-shelled gas-filled MB mixed with fluorescent nanoparticles (SPN) into a mouse model of HCC tumors. Tumors were treated with 5 cycles of 1.8-MHz ultrasound pulses at pulse repetition rate of 100 Hz. The tumors were extracted and processed for quantifying SPN distribution using a fluorescent microscope.

Results/Discussion

Planned treatment regions were precisely marked on the B-mode images of the imaging transducer, allowing image guidance for accurate targeting of tumors of interest (Fig. C). Histological images showed that the SPN, which models our desired drug to be delivered, was delivered precisely to the targeted regions (Fig. B). The cavitation emissions from the treatment regions are shown to be confined within the tumor region (Fig. D), permitting accurate real-time monitoring of therapeutic ultrasound doses. Based on the developed drug delivery platform, the treatment resulted in successful delivery of the model drug over the entire tumor.

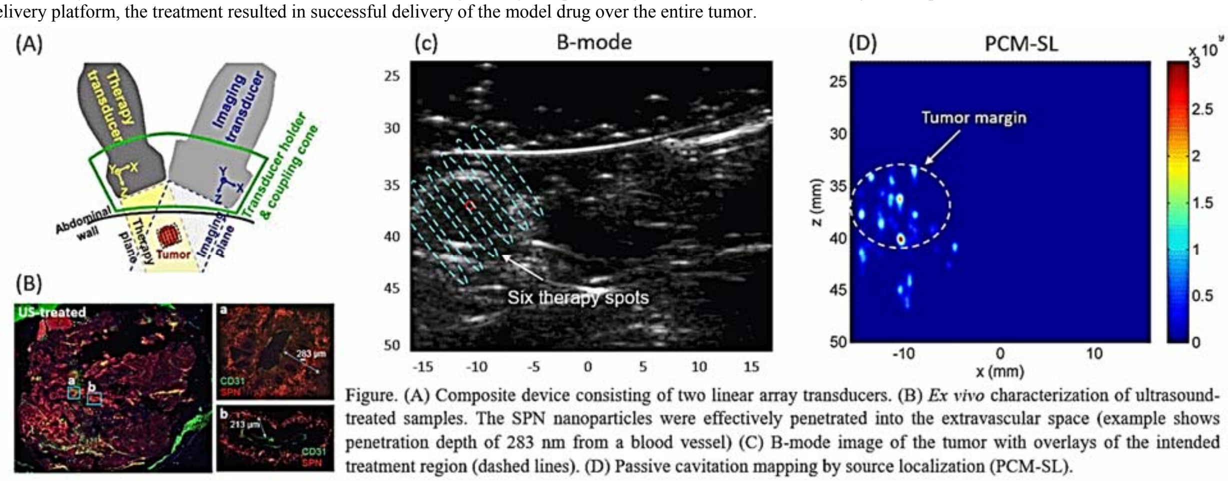

Figure. (A) Composite device consisting of two linear array transducers. (B) *Ex vivo* characterization of ultrasound-treated samples. The SPN nanoparticles were effectively penetrated into the extravascular space (example shows penetration depth of 283 nm from a blood vessel) (C) B-mode image of the tumor with overlays of the intended treatment region (dashed lines). (D) Passive cavitation mapping by source localization (PCM-SL).

4B - MPA: Endoscopic / Intravascular Photoacoustic Imaging and New Approaches

Diplomat Room

Thursday, September 7, 2017, 1:30 pm - 3:00 pm

Chair: **Stas Emelianov**
Georgia Institute of Technology and Emory University School of Medicine

4B-1

1:30 pm **Characterization of Intestinal Strictures by Photoacoustics In Vivo: Endoscopic and Transcutaneous Approaches**

Guan Xu[1], Hao Lei[2], Yunhao Zhu[3], Laura Johnson[4], Jonathan Rubin[1], Peter Higgins[4], Jun Ni[5], Xueding Wang[3]; [1]*Radiology, University of Michigan, Ann Arbor, Michigan, USA,* [2]*Mechanical Engineering, University of Michigan, Ann Arbor, Michigan, USA,* [3]*Biomedical Engineering, University of Michigan, Ann Arbor, Michigan, USA,* [4]*Internal Medicine, University of Michigan, Ann Arbor, Michigan, USA,* [5]*Mechanical Enigineering, University of Michigan, Ann Arbor, Michigan, USA*

Background, Motivation and Objective

Crohn's disease is a chronic autoimmune disease of the intestinal tract affecting 700,000 people in the United States. The pathology of Crohn's disease is characterized by obstructing intestinal strictures due to inflammation, fibrosis, or a combination of both. The identification of fibrosis in intestinal strictures is critical, as the fibrotic strictures are irreversible and have to be removed surgically. Fibrotic strictures are characterized by the increased collagen content in the submucosa below the inner surface of the intestine. The standard diagnostic procedure for the strictures is the endoscopic biopsy, which has limited diagnostic accuracy due to the superficial sampling. Conventional imaging modalities can identify intestinal strictures but cannot assess the molecular components within the strictures. In our previous studies, photoacoustic imaging (PAI) has demonstrated the capability to identify fibrosis in intestinal strictures by increased collagen content. The objective of this research is to further investigate the feasibility of identifying fibrosis in intestinal strictures using PAI in vivo.

Statement of Contribution/Methods

The proposed imaging approaches were examined by animal models in vivo. An endoscopic PA-US probe has been validated in rabbits. The transcutaneous imaging approaches by delivering the illumination endoscopically and through the skin were examined in rats.

Results/Discussion

Fig. 1 shows the result resolving the layered structure in intestinal stricture in a rabbit. Fig. 2 shows the representative results of transcutaneous imaging in rat using endoscopic illumination. Two times signal intensity increase corresponding to the collagen content has been observed (p=0.016) in the fibrotic strictures.

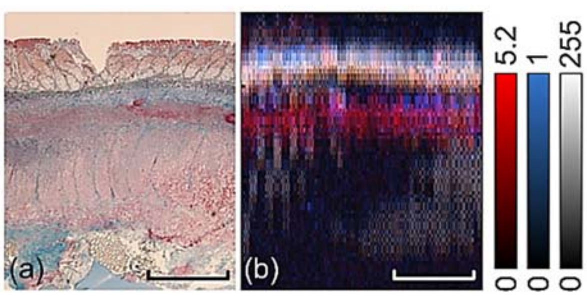

Fig. 1 Representative endoscopic PA+US images. (a) Histology. Collagen content was stained in blue. (b) PA+US coregistered image. US: Gray scale. PA@720 nm (hemoglobin): red. PA@1310 nm (collagen) : blue. Scalebars: 500 μm. Colorbars are in arbitrary units.

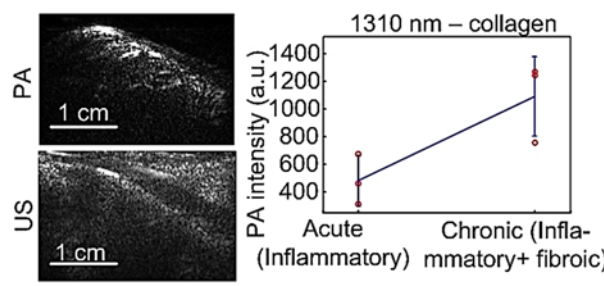

Fig. 2 Representative PA and US images of trasncutaneous imaging of intestinal stricture in rats with endoscopic illumination. The fiber optics diffuser was positioned against the inner wall of the colon of a rat to ensure that the signals are from the colon wall.

4B-2

1:45 pm **Determining the Laser Damage Threshold of Tissues for the Design of a Clinical IVPA Imaging Protocol**.

Timothy Sowers[1,2], Andrei Karpiouk[3], Don VanderLaan[3], Giji Joseph[4], Eleanor Donnelly[5], Robert Taylor[4,5], Stanislav Emelianov[3,5]; [1]*Parker H. Petit Institute for Bioengineering and Bioscience, Georgia Institute of Technology, Atlanta, GA, USA,* [2]*George W. Woodruff School of Mechanical Engineering, Georgia Institute of Technology, Atlanta, GA, USA,* [3]*School of Electrical and Computer Engineering, Georgia Institute of Technology, Atlanta, GA, USA,* [4]*Division of Cardiology, Department of Medicine, Emory University, Atlanta, GA, USA,* [5]*Wallace H. Coulter Department of Biomedical Engineering, Georgia Institute of Technology and Emory University School of Medicine, Atlanta, GA, USA*

Background, Motivation and Objective

Depth-resolved intravascular photoacoustic imaging has been shown to successfully image lipid in atherosclerotic plaques. During IVPA imaging, the level of laser irradiation and corresponding thermal dose depends on the imaging parameters (number of A-lines per frame, frame rate, pullback speed, pulse energy). It is unclear what level of laser irradiation will cause inadvertent tissue damage – the laser safety of IVPA imaging in relationship to imaging parameters has not been demonstrated. We investigated the safety of IVPA imaging by ascertaining the threshold beyond which tissue damage occurs. This will determine how parameters of IVPA imaging can be varied in order to achieve optimal image quality without damaging tissue.

Statement of Contribution/Methods

Human coronary artery endothelial cells, mouse macrophages, and human aortic smooth muscle cells were irradiated at 1064 nm (stent imaging) and 1197 nm (lipid imaging). A clinically relevant laser PRF of 7,860 Hz was used. The fraction of live cells remaining after irradiation at 8 different fluences up to 4000 J/cm^2 was evaluated using MTT, a live/dead cell assay. Next, initial ex vivo studies were conducted. The lumen of porcine aortic vessels was irradiated at 1064 nm, and heat shock protein 70 (HSP70) was used to assess damage. The energy dosage at which damage was observed for each study was then compared to the magnitude of expected irradiation in a clinical IVUS/IVPA system.

Results/Discussion

There was little variation in the damage threshold between cell types in vitro. At 1064 nm, damage occurred at dosages several times higher than what is expected for clinical imaging (0.4 mJ/pulse, 256 A-lines/frame, 30 fps, 0.5 mm/s pullback). The safety margin decreased to 50% at 1197 nm (Panel A). In excised tissue samples, HSP70 expression increased only at energy dosages many times higher than those expected to be necessary for a clinical real time system (Panel B-D). Our in vitro and ex vivo studies indicate that IVPA imaging can be performed safely. Further studies in vitro and ex vivo using other lipid wavelengths and damage markers, as well as studies in vivo, are necessary to confirm these results and elucidate the boundary of laser damage. Within this threshold, researchers will be able to optimize the parameters of IVPA imaging for lipid contrast with confidence that those parameters will be viable in a clinical system.

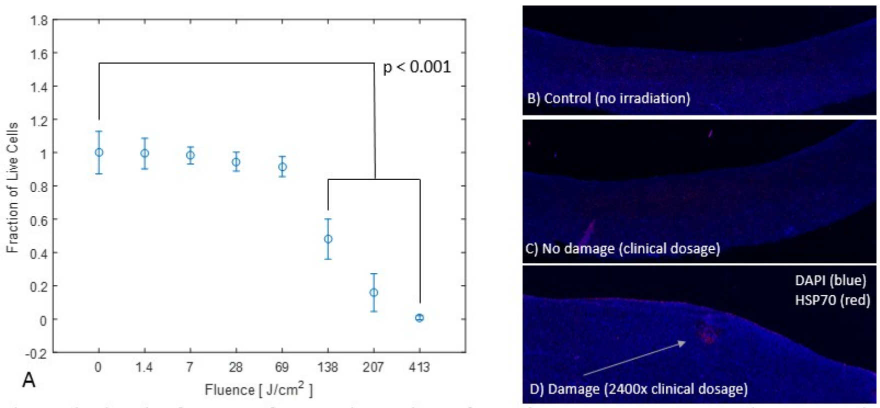

A) Normalized results of MTT assay for macrophages 6 hours after irradiation at 1197 nm in vitro B-D) porcine vessels with endothelial layer irradiated ex vivo at 1064 nm. Includes a control condition with no irradiation (A), tissue irradiated with the equivalent dosage of a vessel imaged at 128 A-lines per frame with 3 mm/s pullback and 0.4 mJ per pulse (C), and tissue irradiated with 2400x the equivalent dosage of a vessel imaged at 256 A-lines per frame with a 0.5 mm/s pullback and 0.8 mJ per pulse (D). Damage in the form of HSP70 and displaced tissue is present at the lasing region of (D). DAPI stain in blue and HSP70 in red. Endothelial layer oriented upwards in all images.

4B-3

2:00 pm Characterization of Human Carotid Plaques Sing Multi-Wavelength Photoacoustic Imaging

Mustafa Umit Arabul[1], Maarten Heres[1], Marcel Rutten[1], Marc van Sambeek[2], Frans van de Vosse[1], Richard Lopata[1]; [1]*Biomedical Engineering, Eindhoven University of Technology, Netherlands,* [2]*Vascular Surgery, Catharina Hospital Eindhoven, Netherlands*

Background, Motivation and Objective

Recently, multi-spectral photoacoustic (PA) imaging has been explored to aid in the diagnosis of atherosclerosis in carotid arteries. Using multiple wavelengths, PA has the potential to reveal vital morphological information in plaques, such as intraplaque hemorrhages, lipid pools, and the fibrous cap. In this study, we used multispectral PA and plane wave ultrasound (US) hybrid-imaging to reveal the composition of human plaques ex-vivo.

Statement of Contribution/Methods

A fully-integrated, hand-held photoacoustic probe was used, consisting of four stack of diode lasers (Ep = 1 mJ, tp = 130 ns, λ = 808, 915, 940, 980 nm, QUANTEL, FR) and a linear array transducer (fc = 7.5 MHz, ESAOTE, NL). Two intact endarterectomy samples, obtained at the local hospital, was immersed in phosphate-buffered-saline (PBS) solution and tissue mimicking fluid at approximately 9 mm depth. The probe was positioned in the cross-section of the transverse plane of each plaque sample. Next, the sample was rotated by 10° steps and the measurements were repeated for 36 angles. After acquiring data for all rotational positions, the probe was moved to the next transverse plane with 0.5 mm step and acquisition protocol was repeated for each cross-sectional position along the sample. Finally, the data were processed offline to reconstruct and spatially compound all the acquisitions into single 3D volume image of overlaid PA/PUS images.

Results/Discussion

The results revealed the presence of different absorbers in distinct cross-sections of plaques. At several positions, a high PA response was obtained at 808 nm (Fig. 1b), corresponding to intraplaque hemorrhage [1]. However, different absorbers were observed that were responsive to all 4 wavelengths, including signals at 940 nm, which is near to an absorption peak of lipid and could possibly indicate the presence of lipid.

Current ongoing work includes a quantitative analysis of multispectral PA vs histology and the ongoing inclusion of new patient samples.

[1] M. U. Arabul, M. Heres, M. C. M. Rutten, M. R. van Sambeek, F. N. van de Vosse, and R. G. P. Lopata, “Toward the detection of intraplaque hemorrhage in carotid artery lesions using photoacoustic imaging,” J. Biomed. Opt., vol. 22, no. 4, p. 41010, 2016.

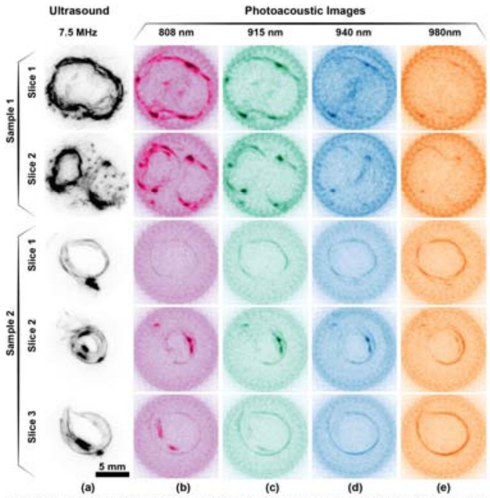

Figure 1: Spatially compounded ultrasound (a) and multi-wavelength photoacoustic images (b to e) of the 5 distinct cross-sections of two human carotid samples. Dark color in ultrasound images represents high echogenicity and corresponds to calcifications in the plaques. Darker colors at each PA column represent higher PA signal and corresponds to different absorbers.

4B-4

2:15 pm Real-Time Recording of Neuronal Voltage Membrane Variation during Seizure using Transcranial Photoacoustic Voltage-Sensitive Dye Imaging

Jeeun Kang[1], Shilpa Kadam[2], Haichong Zhang[1], Heather Valentine[2], Julie Fedorko[2], Dean Wong[2], Emad Boctor[1,2]; [1]*Johns Hopkins University, USA,* [2]*Johns Hopkins University School of Medicine, USA*

Background, Motivation and Objective

A great need exists to non-invasively quantify the neurotransmitter activity in real-time to build a comprehensive functional map of a brain. In this paper, we present real-time recording of neuronal membrane potential change in vivo using transcranial photoacoustic (PA) voltage-sensitive dye (VSD) imaging on a rat in seizure.

Statement of Contribution/Methods

For transcranial PA VSD imaging in real-time, a catheterized rat was stably fixed on a stereotaxic instrument to prevent any motion artifact during seizure. PA data were collected by an array transducer connected to a research data acquisition package (SonixDAQ, Ultrasonix Corp., Canada), and pulsed laser was generated by a second-harmonic Nd:YAG laser pumping an optical parametric oscillator (Phocus Inline, Opotek Inc., USA). The wavelength was at 790 nm to prevent undesired bias due to blood oxygenation change during the experiment, while being close to the absorbance peak of VSD used, IR780 (i.e., 780 nm). In vivo experimental protocol consists of (1) baseline acquisition, (2) VSD and Lexiscan administration through the intravenous catheter for rats in both control and seizure groups, and (3) PA recording on motor cortexes. Each PA recording was continued for 10 minutes since the half-life of Lexiscan is around 2-3 minutes for blood brain barrier (BBB) opening. Note that Pentylenetetrazol (PTZ) was used for seizure group after the baseline acquisition to induce global seizure. The EEG signals in each sequence were recorded in the separated session following precisely the same protocol used in PA recording.

Results/Discussion

We found that the VSD imaging during seizure produced a significant difference compared to those in the control group; Figure 1a indicates the temporally analyzed PA response in left and right motor cortexes for each group in 5% scale. The results are well correlated with the EEG signal shown in Figure 1b presenting significant difference before and after inducing seizure. Figure 1c shows the time-averaged image on motor cortexes over 9 minutes, and indicates there is an obvious increase around of brain activity on the motor cortex showing up to 2.5% more signal change. We believe that these results strongly imply that the PA imaging can non-invasively quantify the VSD response representing the real-time brain activity.

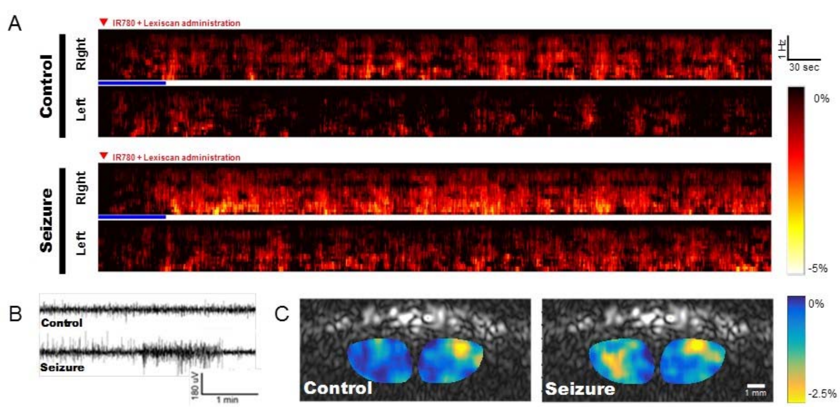

Figure 1. Real-time recording of neuronal membrane potential change during seizure using transcranial photoacoustic voltage sensitive dye; (a) normalized PA response at left and right motor cortexes for control and seizure case, and (b) corresponding EEG recording and (c) time averaged image on motor cortex of rat during 9 minutes. Note that temporal data analysis was applied, and temporally normalized using the initial intensity measure at blue indicator in (a).

4B-5

2:30 pm

Sophinese Iskander-Rizk[1], Pieter Kruizinga[1,2], Antonius F.W. Van der Steen[1,3], Gijs Van Soest[1]; [1]*Biomedical Engineering, Erasmus MC, Rotterdam, Netherlands,* [2]*Delft University of Technology, Netherlands,* [3]*Shenzhen Institutes of Advanced Technology, China, People's Republic of*

Background, Motivation and Objective

Atrial fibrillation (AF) is the most common sustained cardiac arrhythmia in clinical practice, with increasing incidence globally. RF ablation is a common treatment for AF, attempting to interrupt aberrant electrical patterns. The success rate of this procedure is suboptimal (~60%), with a substantial amount of patients needing reintervention [1]. Providing the surgeon with real time feedback on lesion formation could increase the efficacy of this procedure [2]. We consider visible contrast in the lesion and routine intracardiac echography (ICE) guidance, to put forward photoacoustic/ultrasound imaging (PAUS) as a means to visualize the lesion. The objective of this study is to identify the optimum illumination wavelengths for lesion contrast and imaging depth [3].

Statement of Contribution/Methods

We characterize porcine left atrium tissue (0-14h post mortem) using a transmission mode PAUS setup with broad illumination. We use an ultrasound transducer with center frequency matching that of ICE probes (L12-3v, with Vantage 256; Verasonics). The illumination is from the endocardial side, the transducer at the epicardium side and we sweep the laser source (Vibrant B 355II, Opotek) from 410 to 1000 nm in steps of 2 nm. We perform 2 measurements, one on fresh tissue, and one on ablated tissue (using EPT 1000XP APM, Boston Scientific, settings P <= 30W, T <= 93C, t<= 35s) . Light source, tissue and transducer alignment are preserved during ablation for optimum comparison of the signals pre/post ablation.

Results/Discussion

Ablation of atrial wall tissue affected its optical and acoustic properties; this is visible in PAUS (Fig.1-a,b). The ablated tissue was optically more attenuating than healthy atrial wall. We also observed instances of increased acoustic scattering post ablation. Visible/near-infrared wavelengths (~660-960 nm) allowed visualization of the entire depth (up to ~6 mm), at a reasonable SNR (10-30dB) for both healthy and ablated tissue at laser fluences of 2-3mJ/cm2. The lesion's signal is 4 to 12dB higher than the surrounding intact tissue throughout this wavelength range. Moreover, imaging at 820 and 900 nm is potentially sufficient to visualize lesions (Fig.1-c). In conclusion PAUS can be used to visualize RF ablation lesions (Fig.1-b). Future work targets studying the echo characteristics of lesions as well as the effect of fiber probe illumination.

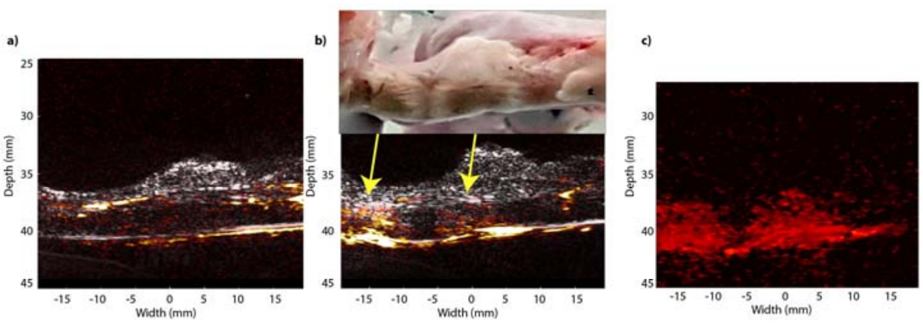

Figure 1-Images of left atrium tissue. a) Ultrasound (in gray, 40dB) overlaid on photoacoustic image at 860 nm (in orange/yellow scale, 30dB) of left atrium tissue prior to ablation;and, b) after ablation. Note the tissue expansion after treatment. Two lesions were made as is shown by the arrows on the picture above the figure in (b). c) Ratio of photoacoustic image at 820 nm to that acquired at 900 nm after ablation. The lesions are now clearly delineated.

References

[1] Ganjehei, L., Razavi, M. & Rasekh, "A. Catheter-based ablation of atrial fibrillation: a brief overview," Tex. Heart Inst. J. 38, 361–3 (2011)

[2]Haissaguerre, M. et al. "Electrophysiological End Point for Catheter Ablation of Atrial Fibrillation Initiated From Multiple Pulmonary Venous Foci", Circulation 101, 1409–1417 (2000).

[3]G. A. Pang, E. Bay, X. DeÁN-Ben, and D. Razansky, "Three-Dimensional Optoacoustic Monitoring of Lesion Formation in Real Time During Radiofrequency Catheter Ablation," Journal of cardiovascular electrophysiology, vol. 26, pp. 339-345 (2015).

4B-6

2:45 pm **Using Ultrasound and Photoacoustics to Monitor in Situ Forming Implant Structure and Drug Release**

Elizabeth Berndl[1], Eno Hysi[1], Christopher Hernandez[2], Agata Exner[2], Michael Kolios[1]; [1]*Department of Medical Physics, Ryerson University, Toronto, Ontario, Canada,* [2]*Department of Radiology, Case Western University, Cleaveland, Ohio, USA*

Background, Motivation and Objective

Most chemotherapeutics (CTs) are delivered systemically, causing nausea, hair loss, fatigue and a compromised immune system. Biocompatible in situ forming implants (ISFIs) are drug delivery vehicles which are injected as a liquid before solidifying in tissues and ultimately breaking down. By dissolving CTs in an ISFI solution, they can be injected directly to the tumour site and released in a controllable manner. ISFIs can provide localized, continuous release of CT, reducing side effects.

The complex phase change of ISFIs cause variable release rate of CT. For the first time, photoacoustic (PA) imaging was used to monitor a dye (mimicking CT) diffusing into a tissue mimicking phantom while quantitative ultrasound (QUS) was used to monitor the changes in the ISFI structure.

Statement of Contribution/Methods

ISFIs made of poly(lactic-co-glycolic acid) and Janus Green B dye dissolved in N-Methyl-2-pyrrolidone in a 39:1:60 ratio were injected in polyacrylamide phantoms containing titanium oxide and monitored over 72 hours at 11 different time points. At each time point, 31 planes of the phantoms were imaged using both PA (700nm) and US using the VevoLAZR system (21 MHz linear array transducer, Fujifilm-Visualsonics, Toronto, Canada).

Regions of interest within and proximal to the ISFI were selected, and average PA and QUS parameters were determined for each plane as a function of time post-implantation.

Results/Discussion

PA signal surrounding the ISFI increases after injection (Fig 1A) as the dye diffuses out. This is visible by the increased amplitude of the speckle pattern at 4, 24 and 48 h. PA amplitude increases by 250% in the first 24 hours before decreasing slightly at by 72 h (Fig 1B). Such changes in the PA signal amplitude correlate well with the diffusion of the dye into the area surrounding the ISFI. The US midband fit (MBF) within the ISFI drops by 3.8 dB in the first 20 minutes before recovering over the next 4 hours, with a sustained net increase of 3 dB after 24 h (Fig 1C).The changes in the US MBF suggest that the ISFI solidifies over time as it releases dye into the surrounding medium. It is postulated that the increased backscatter is due to the change the acoustical properties, namely the density of the ISFU implant.

This study shows that PA and QUS monitoring have potential as non-invasive methods of monitoring phase changes and the release of light absorbing molecules from ISFIs.

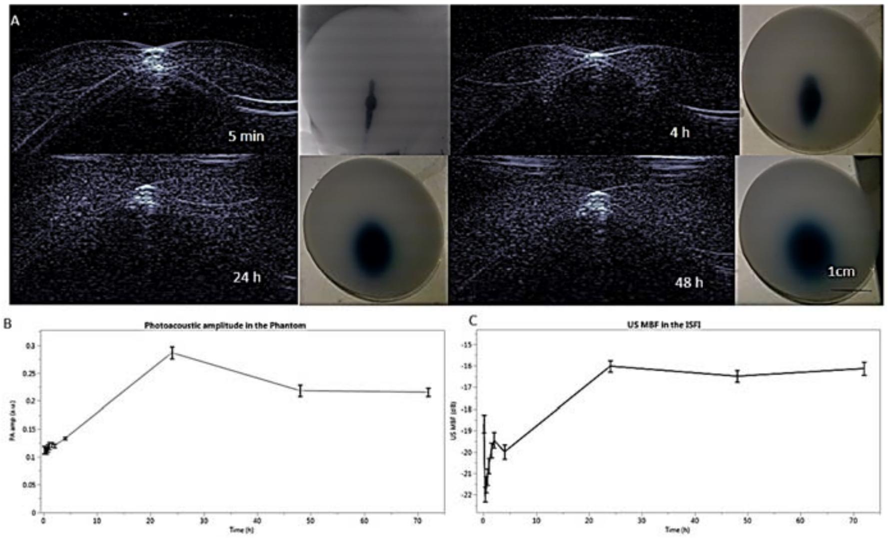

5B - Imaging and Photoacoustics

Blue Room

Thursday, September 7, 2017, 1:30 pm - 3:00 pm

Chair: **Jafar Saniie**
Illinois Institute of Technology

5B-1

1:30 pm Introducing a New Method for Efficient Visualization of Complex Shape 3D Ultrasonic Phased-Array C-Scans

Carmelo Mineo[1], Rahul Summan[1], Jonathan Riise[1], Charles MacLeod[1], Gareth Pierce[1] ; [1]*Department of Electronic & Electrical Engineering, University of Strathclyde, Glasgow, Scotland, United Kingdom*

Background, Motivation and Objective

Automated robotic inspection systems are a way of speeding up the inspection of large components with complex geometries and reducing production bottlenecks during the non-destructive evaluation of critical parts. Such systems allow the collection of large data volumes, compared to existing inspection systems. To maximise the throughput of the non-destructive evaluation phase, it is crucial that the inspection data-sets are processed and examined rapidly without a loss of detail. Traditional approaches for this task are slow and not suitable to represent large data-sets collected from complex parts. Data analysis often becomes the bottleneck of automated NDT inspections. Therefore, new data visualisation tools are urgently required.

Statement of Contribution/Methods

This paper presents a new approach, for the generation of 3D ultrasonic C-scans of large and complex parts, suitable for application to high data throughput ultrasonic phased array inspection. An intrinsic characteristic of the A-scans collected to create a C-scan map is the sequential way they are acquired along the scanning trajectory. The level of orderliness is even higher when the ultrasonic inspection is carried out through a phased array probe. The ordered spatial distribution of the A-scans locations, inspired the development of an efficient triangular mesh generation algorithm targeted to such structured point distribution. This approach is named as the Index Based Triangulation (IBT) algorithm. Existing reconstruction approaches are discussed and compared with the new IBT method.

Results/Discussion

The IBT method produces 3D C-scans presented as coloured tessellated surfaces. The approach works efficiently on challenging geometry, with concave and convex regions. An additional characteristic of the IBT method is that it allows easy detection of lack of coverage (an essential feature to ensure that inspection coverage can be guaranteed on safety critical components). Qualitative and quantitative results are presented and it is demonstrated that the IBT C-scan generation approach runs over 60 times faster than a C-scan display based on Delaunay triangulation and over 500 times faster than surface reconstruction C-scans. The method is potentially extensible to other ordered data-sets, for example in laser-based geometry mapping of curved surfaces.

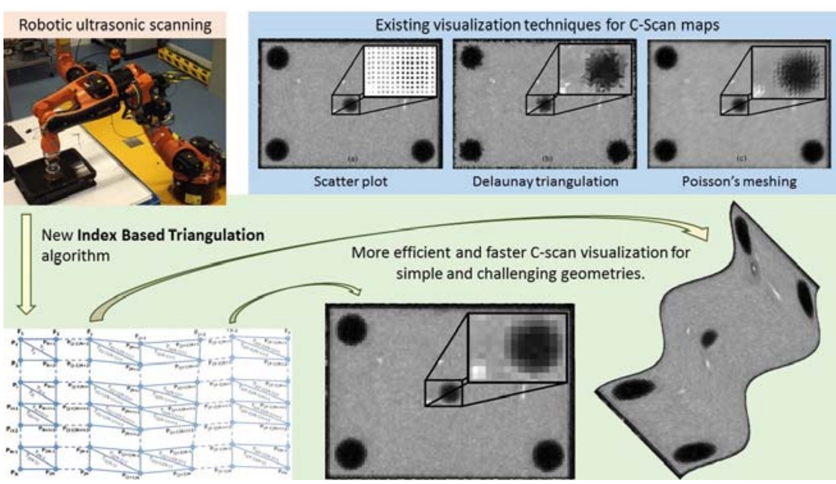

5B-2

1:45 pm NDE Application of Air-Coupled Ultrasonic Array System and f-k Domain Analysis for Delamination-Like Defect Detection in Bridge Deck

Hajin Choi[1], Sadegh Shams[1], Michael Grissom[1], Hoda Azari[1]; [1]*FAST NDE Laboratory, Federal Highway Administration, Mclean, VA, USA*

Background, Motivation and Objective

Recent development of the air-coupled sensing technique provides great potential for practical data measurement in the field; however, an improved data analysis method and careful design of test configuration are required to inspect structures appropriately.

Impact-echo (IE) is an efficient method to evaluate delamination-like defects in concrete bridge decks. However, practical application of air-coupled IE is limited due to direct impact and ambient noises. Another practical problem is the difficultly in data interpretation associated with the dominant flexural mode frequency. Although IE analysis is able to estimate a depth of delamination-like defect from the thickness mode frequency, it is well known that the flexural mode frequency is dominant for shallow delaminations but cannot provide the depth information.

The structural inspection needs of many data and conventional IE schemes possibly mislead data interpretation. New concepts for IE data measurement and analysis are needed to evaluate full-scale infrastructure in the field.

Statement of Contribution/Methods

Our newly developed air-coupled array system includes an ultrasonic transducer and Microelectromechanical systems (MEMS) array. Because an ultrasonic transducer generates much higher frequency than conventional impactors, it is possible to excite the thickness mode of shallow delaminations. Furthermore, a linearly positioned MEMS array accurately collects high resolution data.

Frequency-wave number (f-k) domain analysis separates dispersive wave modes as well as direct impact noise. The thickness mode is a portion of the first symmetric mode in Lamb waves, especially at zero-group velocity (S1-ZGV). The proposed f-k domain analysis clearly shows the S1-ZGV portion from the data obtained through the air-coupled ultrasonic array system without direct impact noise. Because noise components have significantly large wave numbers compared to the S1-ZGV portion, f-k domain analysis successfully detects the thickness mode frequency from measured data.

Results/Discussion

The developed air-coupled ultrasonic array system provides high-quality signal data acquisition, enabling fast and practical application in civil infrastructure. The system and applied f-k domain analysis significantly improve the detection of the thickness mode frequency from shallow delaminations from the S1-ZGV portion, which is limited from conventional IE scheme.

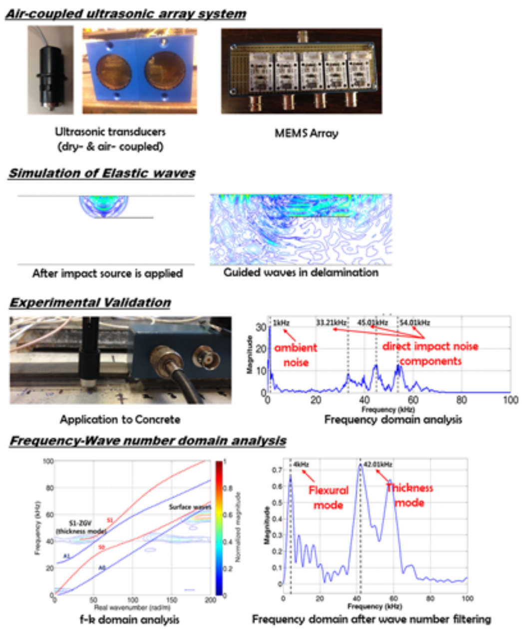

5B-3

2:00 pm Automatic Segmentation and Object Classification with Neural Network for an Airborne Ultrasound Imaging System

Wei Yap Tan[1], Grischan Erbacher[1], Till Steiner[2], Nicole V. Ruiter[1]; [1]*Karlsruhe Institute of Technology, Germany*, [2]*Pepperl+Fuchs GmbH, Germany*

Background, Motivation and Objective

An airborne ultrasound imaging system using 16 ultrasonic sensors surrounding a region of interest (ROI) was introduced in previous work. It allows reconstructing reflectivity images of multiple objects in 2D using a synthetic aperture focusing technique. The aim of this work is to automatically segment objects from these images to determine their positioning and allow classification.

Statement of Contribution/Methods

Image preprocessing is done by contrast enhancement, binarization and denoising using mathematical morphology. Connected-component labeling was applied to detect regions with objects. Centroids and other features such as major axis of these regions are used for classification of positioning and orientation. For known objects, the generalized Hough transform is used. Features such as major and minor axis length, eccentricity, convex area and perimeter of the segmented regions were used as inputs for the neural network for classification. The neural network was trained with supervised leaning and has three layers with ten hidden neurons and two outputs.

Results/Discussion

Performance of automatic detection of position and angular orientation was investigated with 20 reconstructed images of an asymmetrical object randomly placed in the ROI, see figure left and center. The images were reconstructed with 1 mm resolution with an optimal pulse with center frequency of 56 kHz and bandwidth of 64 kHz, i.e. the maximum full width half maximum is 1.7 mm. We achieved a mean position error of 2.5 mm with a standard deviation of 1.3 mm and orientation error of 0.5° with standard deviation of 7.4° using generalized Hough transform. The classification performance was tested with two objects (cylinder and square cuboid) of similar diameter. A total of 39 images were reconstructed of single object recordings at random positions in the ROI, see confusion matrix in figure right. The neural network was trained with 70% of the data set. We achieved a confidence of 96.3% in the training phase, 100% in the validation phase and 100% in the test phase.

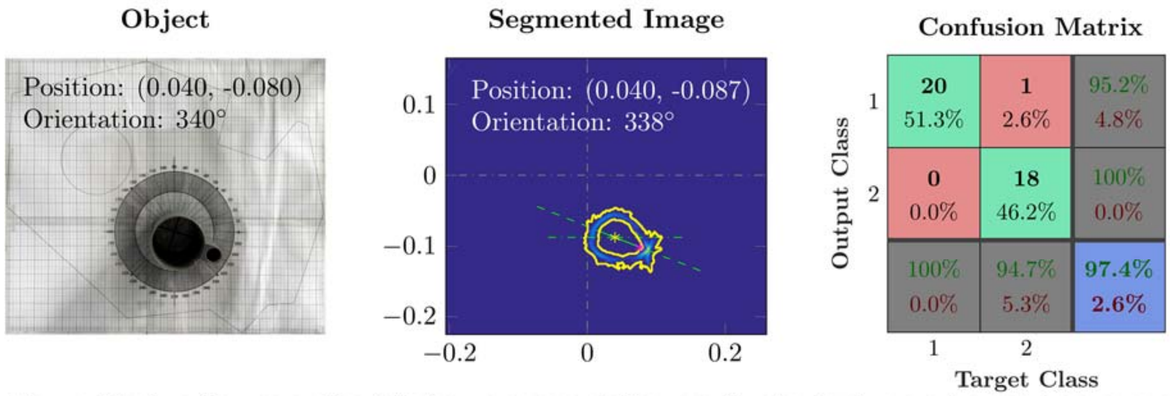

Figure: The two figures on the left show a segmentation result using features extracted from connected-component labeling of the binarized image. The position and orientation of the object were accurately detected. The right figure shows the overall confusion matrix for the classification of the cylinder and cuboid.

5B-4

2:15 pm **Isolation and Direct Imaging of Polycrystalline Backscatter Waves**

James Blackshire[1]; [1]*AFRL/RXCA, Air Force Research Laboratory, WPAFB, Ohio, USA*

Background, Motivation and Objective

The nondestructive quantification of grain feature information in polycrystalline aerospace materials is an important area of recent research, where information related to mean grain size, grain size distribution, and crystallographic orientation is needed for engineering analysis and remaining life predictions in aerospace engine components.

Statement of Contribution/Methods

In the present effort, the interaction of surface acoustic waves (SAW) with a dual-microstructure nickel polycrystalline material is studied, where the isolation and direct imaging of backscatter processes is made possible using time-gated wavefield imaging methods. The methods provide a means for studying the time-evolving nature of the backscatter energy fields, which suggest radially-expanding waves are generated by the individual and collective grain scattering events. This basic observation is consistent with long-standing backscatter theory considerations and is being used to understand the root-cause backscatter conditions that contribute to far-field ultrasonic signal capture.

Results/Discussion

Representative wavefield imaging results are presented in the accompanying figure, which depict the interaction of a 5MHz, 1-cycle SAW with large grain features (100 micron mean diameter sizes) for time-evolving (left images), and time-integrated (right image) conditions. The radially-expanding nature of the backscatter process is evident in both instances.

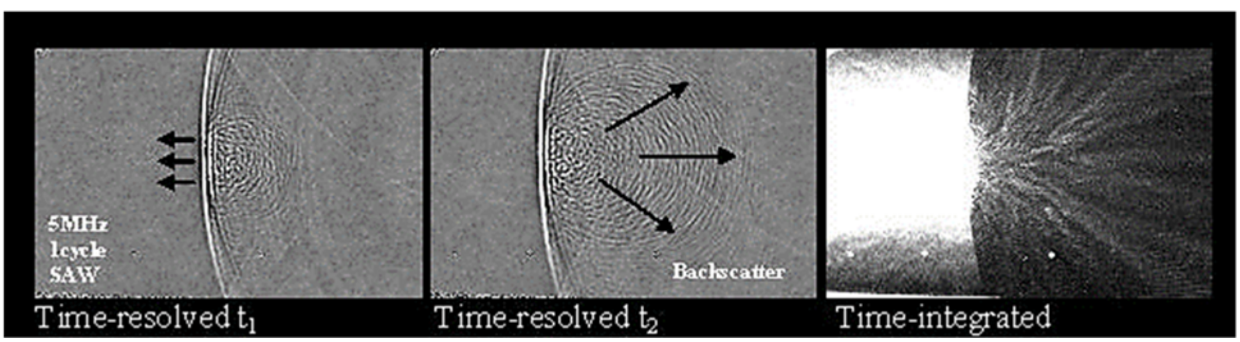

5B-5

2:30 pm **Feasibility Study of Photo Thermal Acoustic Imaging of Buried Nanowires in Gate-All-Around (GAA) Nanowire FETs**

Paul van Neer[1], Daniele Piras[2], Wouter Koek[3], Erwin van Zwet[3], Hamed Sadeghian Marnani[2]; [1]*Acoustics and Sonar, TNO, The Hague, Netherlands,* [2]*Optomechatronics, TNO, Delft, Netherlands,* [3]*Optics, TNO, Delft, Netherlands*

Background, Motivation and Objective

With the ongoing drive to integrate more functionality and processing power on the same semiconductor area, the device structures have become 3D. Such structures, like FinFETs and their successors GAA nanowire FETs, bring on new challenges to measure their geometry and material properties non-destructively at the nanometer scale. Photo Thermal Acoustic Imaging (PTAI) is a potential inspection method. Here, the sample is heated locally by a pulsed optical pump beam. This generates a propagating elastic wave in the sample, which is scattered by inclusions in the sample. Part of the scattered energy travels to the sample surface, where the surface deformations are sensed by an optical probe beam using interferometric detection. Thus, no physical contact for actuation or sensing is required. This work investigates the feasibility of PTAI for the detection and imaging of nanowires.

Statement of Contribution/Methods

The pulsed pump beam locally heated up a volume of the material – the absorption of optical energy and its conversion into heat were calculated analytically. The temperature distribution generated by the heat, the creation of a stress wave due to thermal expansion and the propagation and scattering of the resulting elastic waves were calculated using finite element modeling. The pulsed laser beam had a 400 nm optical wavelength, a 140 nm radius, an 8 pJ pulse energy and a 100 fs pulse length. The probe beam was modeled by spatially averaging the sample surface displacement. The datasets were imaged using a wavenumber frequency domain mapping. The modeled sample was a SiO_2 slab with a 15 nm thick aluminum layer on top to serve as the optically absorbing layer (case 1). In case 2 a nanoshell (tantalum, radius 12 nm) at a depth of 120 nm was added. In case 3 a nanowire (silicon, radius 4 nm) was added in the nanoshell.

Results/Discussion

The absorption depth in aluminum was ~6 nm. The 228 dB maximum intensity of the elastic wave occurred at 147 GHz. Using a 'point' probe beam the (case 2 - case 1), and (case 3 - case 1) maximum surface displacement differences were -35 pm and -5 pm, respectively (see figure). For a realistic 280 nm probe beam width, those differences reduced to -17 pm and -2 pm, respectively. This is considered measurable (detection limit from literature 0.2 pm). Detection of nanowires is feasible using PTAI, however the imaging of nanowires is limited by the optical probe beam width.

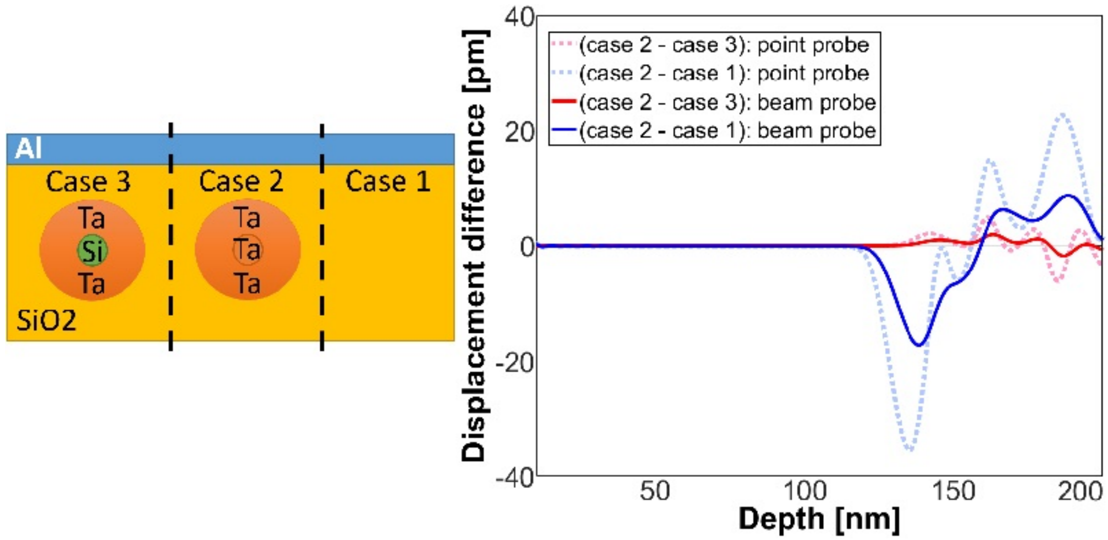

5B-6

2:45 pm Laser Generated Ultrasound Sources using Carbon-Polymer Nanocomposites for High Frequency Metrology

Srinath Rajagopal[1,2], Ben Cox[1], Bradley Treeby[1], Toby Sainsbury[3]; [1]*Department of Medical Physics and Biomedical Engineering, University College London, London, United Kingdom,* [2]*Ultrasound and Underwater Acoustics, National Physical Laboratory, Teddington, United Kingdom,* [3]*KAUST Catalysis Center and Division of Physical Sciences and Engineering, King Abdullah University of Science and Technology, Thuwal, Saudi Arabia*

Background, Motivation and Objective

Accurate characterisation of ultrasound fields generated by diagnostic and therapeutic transducers is critical for patient safety. This requires hydrophones calibrated to a traceable standard. The existing implementation of the primary standard at the National Measurement Institutes, e.g., NPL and PTB, can provide accurate calibration to a maximum frequency of 40MHz. However, the increasing use of high frequencies for both imaging and therapy necessitates calibrations to frequencies well beyond this range. For this to be possible, a source of high amplitude, broadband, quasi-planar and stable ultrasound fields is required. This is difficult to achieve using conventional piezoelectric sources, but laser generated ultrasound is a promising technique in this regard. In this study various polymer-carbon nanotube nanocomposites (PNC) were fabricated and tested for their suitability for such an application.

Statement of Contribution/Methods

A range of PNC ultrasound sources was fabricated, with varying (i) polymer type: epoxy, polyurethane (PU) or polydimethylsiloxane (PDMS), (ii) weight percentage of carbon nanotubes: 1.25, 2.5 or 3.5 %, and (iii) thickness: 10 – 85 µm. Each source was backed by a glass substrate and illuminated with a 4 ns pulsed laser operating at 1064 nm. The optical fluence was varied between 10 and 40 mJ.cm-2. A broadband hydrophone was used to measure the peak pressure and bandwidth of the laser generated ultrasound pressure pulse.

Results/Discussion

These sources were shown to generate high peak pressures (Fig. 1a) and broad bandwidths (Fig. 1b). Furthermore, (1) there is a nonlinear dependence of the peak pressure on the fluence (Fig. 1a), and (2) the bandwidth scales inversely proportionally to the peak pressure (Fig. 1b). There are two mechanisms which may contribute to the nonlinear behaviour: the saturable absorption of carbon nanotubes and nonlinear acoustic propagation. The measurements were compared to a model (k-Wave) which included the saturable absorption. These preliminary results show that laser generated ultrasound sources are a promising technique for high frequency calibration of hydrophones on the primary standard.

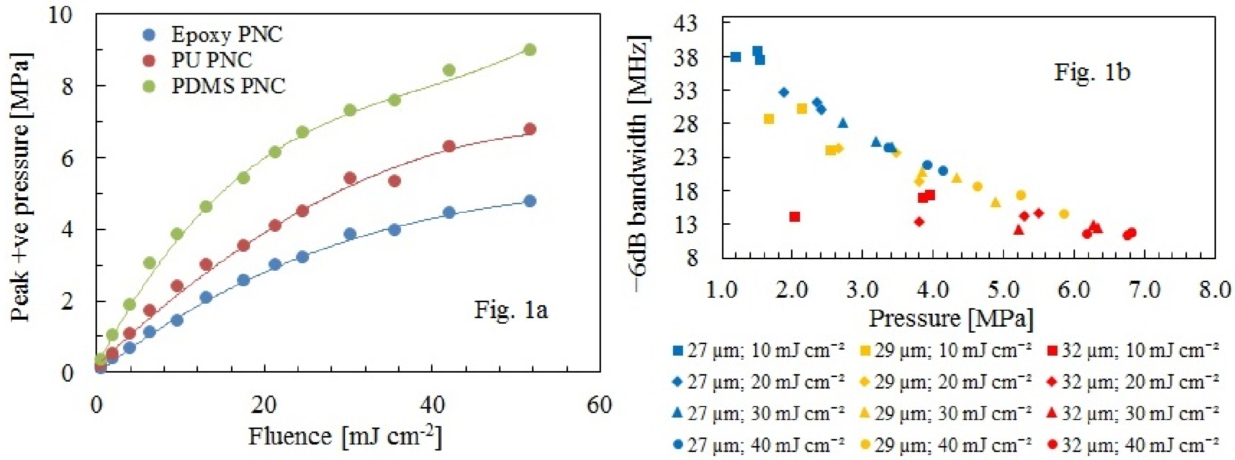

Fig. 1a
Peak +ve pressure [MPa]
Fluence [mJ cm-2]
Epoxy PNC
PU PNC
PDMS PNC
0
2
4
6
8
10
0
20
40
60
Fig. 1b
−6dB bandwidth [MHz]
Pressure [MPa]
43
38
33
28
23
18
13
8
1.0
2.0
3.0
4.0
5.0
6.0
7.0
8.0
27 µm; 10 mJ cm⁻²
29 µm; 10 mJ cm⁻²
32 µm; 10 mJ cm⁻²
27 µm; 20 mJ cm⁻²
29 µm; 20 mJ cm⁻²
32 µm; 20 mJ cm⁻²
27 µm; 30 mJ cm⁻²
29 µm; 30 mJ cm⁻²
32 µm; 30 mJ cm⁻²
27 µm; 40 mJ cm⁻²
29 µm; 40 mJ cm⁻²
32 µm; 40 mJ cm⁻²

6B - Materials for Microacoustics

Hampton Room

Thursday, September 7, 2017, 1:30 pm - 3:00 pm

Chair: **Rich Ruby**
Wireless Semiconductor Division

6B-1

1:30 pm **Dependence of the Different Elastic Constants of ScAlN Films on Sc Content: A Brillouin Scattering Study with Polarization Analysis**

Giovanni Carlotti[1], Jyothi Sadhu[2], Fabien Dumont[2]; [1]*Dept Physics and Geology, University of Perugia, Perugia, Italy,* [2]*QORVO, Apopka, FL, USA*

Background, Motivation and Objective

The production and the characterization of high-quality ScAlN films, whose electromechanical coupling and bandwidth are larger than those of traditional AlN films, is attracting interest to develop the next generation of bulk acoustic wave resonators for telecommunication devices operating above 5 GHz.

Statement of Contribution/Methods

We have exploited the Brillouin light scattering technique (BLS) to achieve a detailed elastic characterization of both AlN and ScAlN films with Sc concentration of 6% and 9.5%.

Results/Discussion

By use of different polarization states of the incoming light, either p or s, and accurate polarization analysis of the scattered light, we were able to detect and identify several distinct acoustic modes. In Fig. 1, left panel, one can see the comparison between two Brillouin spectra, relative to a 1.7 micron thick AlN film, corresponding to polarized and depolarized scattered light (labelled p-p and p-s, respectively). It is seen that in the former case one can detect the peaks corresponding to the surface Rayleigh wave (RW) and to the longitudinal guided mode (LGM), while in the latter case, only the peak relative to shear horizontal mode (SHM) is detected. The angle of incidence of light is 60°. Moreover, the peak relative to the longitudinal bulk wave (LB), was observed at larger frequency. Measurement of the phase velocities of the above modes for different values of the angle of incidence of light enabled us to determine the set of independent elastic constants of each film. In Fig. 1, right panel, we show the comparison between the experimental values of the elastic constants of ScAlN films (full circles) and those predicted by theory (dotted curves, from S. Zhang et al, J. Appl Phys. 114, 243516 (2013)) for various Sc concentrations.

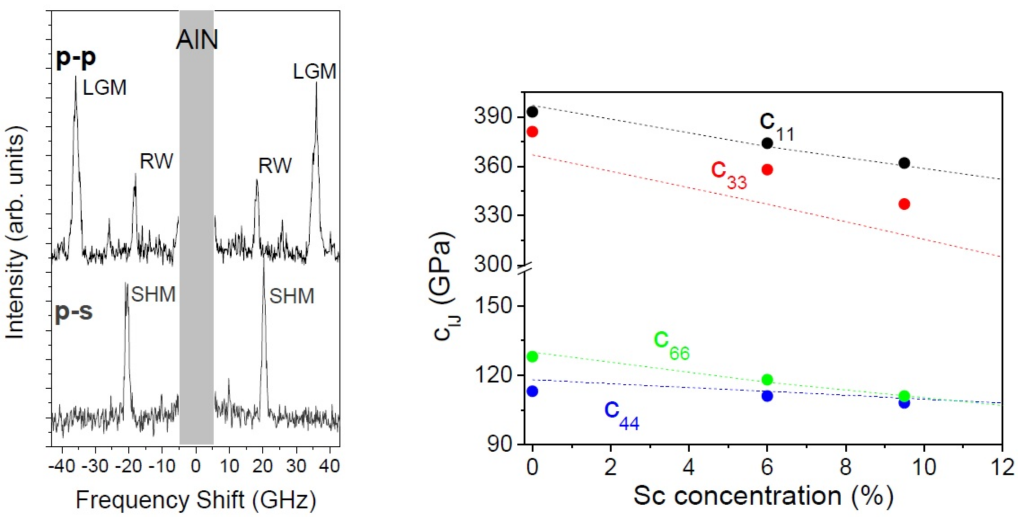

6B-2

1:45 pm **Investigation of 20% Scandium-Doped Aluminum Nitride Films for MEMS Laterally Vibrating Resonators**

Luca Colombo[1], Abhay Kochhar[1], Changting Xu[1], Gianluca Piazza[1], Sergey Mishin[2], Yury Oshmyansky[2]; [1]*ECE, Carnegie Mellon University, Pittsburgh, Pennsylvania, USA,* [2]*Advanced Modular Systems, Inc., Goleta, California, USA*

Background, Motivation and Objective

RF filtering technologies based on piezoelectric MEMS resonators have been successfully developed and commercialized in the past decade thanks to their size and outstanding performance. The challenge to enhance filter's performance in terms of lower insertion losses and wider bandwidth still makes for an active research topic, especially spurring the interest for new classes of materials such as doped-AlN [1] and thin films of lithium niobate [2]. In this work, we investigate the use of 20% Scandium-doped Aluminum Nitride (ScAlN) thin films for the making of laterally vibrating MEMS resonators (LVRs). The main goals of our work are to demonstrate: 1) a higher k_t^2 (~ 2x) compared to non-doped AlN, 2) ease of fabrication process compared to lithium niobate thin films [3], 3) fabrication of multi-frequency devices (250 MHz – 1 GHz) on the same wafer.

Statement of Contribution/Methods

We have measured the most important material properties of 20% Sc-doped AlN films and demonstrated LVRs exhibiting k_t^2 in the range of 3.7-4.5%, and Qs in excess of 1,000 in air at around 250 and 500 MHz. Equivalent Young's modulus (E=430 GPa), dielectric permittivity (ε_r=9) and average mass density (ρ=4 g·cm-3) were extracted. The etching characteristics of ScAlN films under different flows rates and gas concentrations in a Cl_2/BCl_3 chemistry were characterized to yield high selectivity with an SiO_2 hard mask and straight sidewall.

Results/Discussion

20% ScAlN-based MEMS LVR were fabricated (Fig. 1a) and measured. One-port and two-port devices at 250 and 500 MHz with Qs higher than 1000 (maximum Q of 1,500 for one-port and 1,350 for two-ports) have been tested (Fig. 1b-c). A k_t^2 as high as 4.5% (more than 2X that of AlN counterparts) has been measured for two-port devices. We believe that our Qs are currently limited by etch byproduct redeposition during the removal of the oxide mask. We expect that higher Qs approaching those we measured in identical AlN devices (2,000-3,000) can be attained from these devices once the fabrication is improved. Improved fabrication, device design and the use of 40% Sc-doped films could revolutionize the design space for RF filters, piezoelectric transformers and oscillators.

[1] Q. Wang, Hilton Head Workshop 2016

[2] S. Gong, IEEE Transaction on Electron Devices 2013

[3] A. Kochhar, MEMS 2017

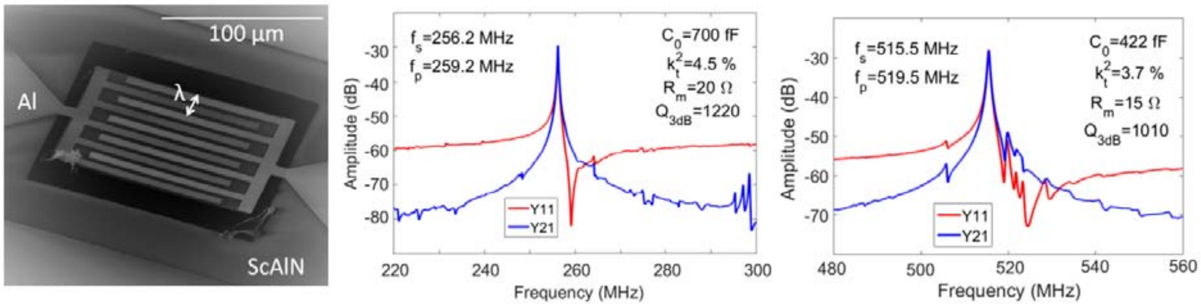

Fig. 1. 20% Sc-doped aluminum nitride (ScAlN) laterally vibrating resonator (a) SEM image of 500 MHz device, (b) Y11and Y21 admittance response of 250Mhz resonator and (c) Y11 and Y21 admittance response of 500MHz resonator.

6B-3

2:00 pm Which is the Best Thin Film Piezoelectric Material?

Paul Muralt[1]; [1]*Electroceramic Thin Films Group, EPFL, Lausanne, Switzerland*

Background, Motivation and Objective

Electro-mechanical devices for sensing, actuation, and communication are necessary ingredients for the ongoing 4th industrial revolution. Piezoelectricity plays an important role in electro-mechanical conversion, and is e.g. used in ultrasonic imaging and mobile phone communication. The drive for miniaturization will result in a strong demand for piezoelectric thin films, with improved, optimized properties. By now, we have two material families: Ferroelectric perovskites with solid solutions containing PbTiO3, like PZT and PMN-PT, and the non-ferroelectric, but polar wurztite structure AlN. The first one exhibits unbeatably high piezoelectric e and d coefficients, and thus leader in force and current generation, the second one excels by its stability, low dielectric constant, mechanical and dielectric losses, and is best in voltage generation, signal-to-noise, and high Q applications, particularly for application frequencies above about 100 MHz. Since the appearance of Al(1-x)Sc(x)N alloy thin films (Akiyama et al, 2010), the choice between the two families became less evident in all cases where charge and voltage response play a role at the same time, as in power generation, and electro-mechanical coupling. The goal of this contribution is to present critically reviewed property data as hitherto known from own work and literature sources.

Statement of Contribution/Methods

Properties are discussed in terms of figure of merits for the different applications, including as well particular issues of the ferroelectric films. A comparison with density functional theory predictions is made in case of AlScN.

Results/Discussion

Today, transverse piezoelectric coefficients e31,f of -15 to -20 C/m2 are routinely obtained by sol-gel as well as sputter techniques. PMN-PT shows even higher values of up to -26 C/m2 (Baek et. al, 2011). This is far more than can be achieved by AlScN. Inkjet printing heads and other micro actuators are thus preferentially operated by PZT thin films. When considering energy harvesting from vibrations, the ferroelectrics look less brilliant as they exhibit very high dielectric constants. A comparison of the figures of merit of the different materials is show in the figure. The talk will extend the study on longitudinal and transverse coupling coefficients.

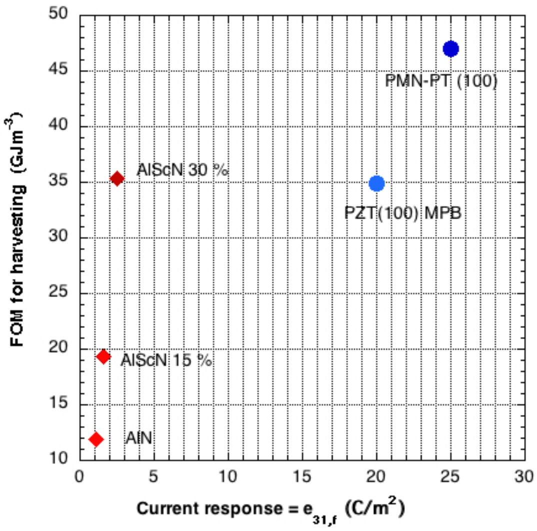

6B-4

2:30 pm **Characterization of Graphene Electrodes as Piezoresistive SAW Transducers**

Benyamin Davaji[1], Alexander Ruyack[1], Amit Lal[1]; [1]*SonicMEMS, Cornell University, Ithaca, NY, USA*

Background, Motivation and Objective

SAW sensors offer a mechanical motion in MHz to GHz range and can be immune to effects from boundary loss through the bulk and edges. SAW based gyroscopes have been implemented by added masses which impose an effect on wave prorogation fronts through the Coriolis force. A key challenge in implementing SAW based gyroscopes is to improve the sensitivity owing to small forces and SAW signals. Significant problem is that the small signal pickup using IDTs results in very small source capacitance, making parasitic capacitances a great burden reducing the SNR. In this paper, we explore the use of graphene piezoresistance to pick up SAW signals, using changes in graphene resistance due to SAWs We demonstrate 20% change in strain (displacement of 311.6 pm) at 194.4MHz. The graphene electrodes can be chosen to have an output impedance of 50-ohms leading to distinct advantages of both high sensitivity and high SNR.

Statement of Contribution/Methods

A SAW delay line devices was fabricated on a 500um thick 128º Y-cut lithium niobate crystal substrate, compensated for pyroelectric effect (black lithium niobate). The Au/Ti (100nm/10nm) electrodes are patterned on the surface using the lift-off method (Fig 1A). A commercially grown graphene monolayer is transferred onto the wafer using the wet PMMA transfer technique and defined using photolithography and O_2 plasma The Raman spectra was used to confirm graphene quality (I_{2D}/I_G >2) and the sheet resistance of transferred graphene at room temperature is 3kΩ/square (Fig 1B).

Results/Discussion

The delay line was swept in frequency and power applied to the transmitting IDT pair and measured across the receive IDT pair. A laser doppler microscope (Polytec-UHF) was used to measure the SAW displacement over the graphene resistor. The change in graphene resistance was measured as a function of transmitting SAW frequency. The graphene resistance was measured as a function of the applied RF power at the fixed SAW frequency (Fig. 1C) and then measured as a function of frequency with fixed amplitude (Fig. 1D). In the latter case, we could replicate the SAW impedance versus frequency in the graphene resistance change over the frequency with high SNR. The ΔR/R was measured to be ~20% for the drive power of 20mW which is a very large sensitivity owing to the band splitting in graphene due to strain and SAW electric field.

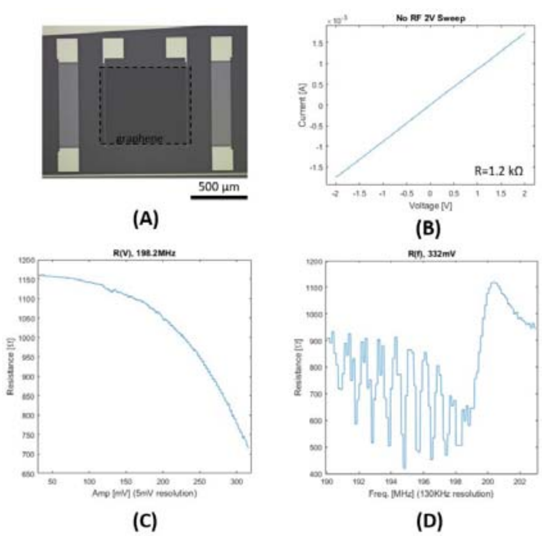

2:45 pm Comparison between Ir, $Ir_{0.85}Rh_{0.15}$ and $Ir_{0.7}Rh_{0.3}$ Thin Films as Electrodes for Surface Acoustic Waves Applications above 800°C in Air Atmosphere

Amine Taguett[1,2], Thierry Aubert[1,2], Omar Elmazria[3], Florian Bartoli[1], Marc Lomello[2], Michel Hehn[3], Stéphane Mangin[3], Yong Xu[3]; *[1]lmops, CentraleSupélec - Université de Lorraine, 57070 Metz, France, France, [2]SYMME, Université Savoie Mont Blanc, 74940 Annecy-le-Vieux, France, France, [3]Institut Jean Lamour, UMR 7198 Université de Lorraine-CNRS, 54506 Vandoeuvre-lès-Nancy, France, France*

Background, Motivation and Objective

We previously demonstrated the potential of Ir_xRh_{1-x} thin films ($x \leq 0.5$) as electrodes for high-temperature surface acoustic waves (SAW) applications [1]. To remind, we observed that after a 4-days annealing period at 800°C under air atmosphere, these films oxidize to form $Ir_xRh_{1-x}O_2$ films, which exhibit a resistivity suitable for the targeted application, especially as the Ir rate is high ($\rho \approx 180$ µΩ·cm for $x = 0.5$). Consequently, the first aim of this work is to study the most promising Ir-rich compositions ($0.7 \leq x \leq 1$). Moreover, as it is well know that pure Ir transforms into volatile IrO_3 in the vicinity of 800°C [2], we also investigate the interest of alloying Ir with Rh regarding this degradation effect. Finally, we examine the reliability of SAW devices based on Ir_xRh_{1-x} electrodes and Langasite (LGS) substrate during a 20-days annealing period between 800 and 950°C.

Statement of Contribution/Methods

Pure Ir thin films, as well as $Ir_{0.85}Rh_{0.15}$ and $Ir_{0.7}Rh_{0.3}$ multilayers thin films were deposited on LGS substrates by sputtering method. All films were 120 nm-thick. Some samples were then processed to carry out SAW delay lines with a wavelength of 24 µm. The samples underwent various annealing treatments at temperatures ranging between 800 and 950°C for periods lasting from 1 to 20 days. The morphology, the microstructure and the electrical properties of the thin films were investigated by optical and scanning electron microscopy (SEM), X-ray diffraction (XRD) and 4-points probe method respectively. The S_{21} response of the investigated SAW devices was monitored during the high-temperature exposure.

Results/Discussion

Electrical resistivity measurements, coupled to XRD and SEM analyses evidence that Ir films cannot be considered for long-term applications at 800°C (Fig.1) as a slow and gradual evaporation was detected (complete evaporation would take weeks). No evaporation effect was observed in the case of $Ir_{0.85}Rh_{0.15}$ and $Ir_{0.7}Rh_{0.3}$ thin films. The interest of alloying Ir with Rh is even more spectacular at 900°C as the evaporation effect undergone by pure Ir films is much stronger, while $Ir_{0.85}Rh_{0.15}$ and $Ir_{0.7}Rh_{0.3}$ films remain stable. The SAW devices exhibit an extremely stable signal all along the 15-days annealing period between 800 and 900°C. Some signs of degradation appear at 950°C.

[1] Taguett, Sensors & Actuators A, 2016

[2] Richter, Procedia Engineering, 2011

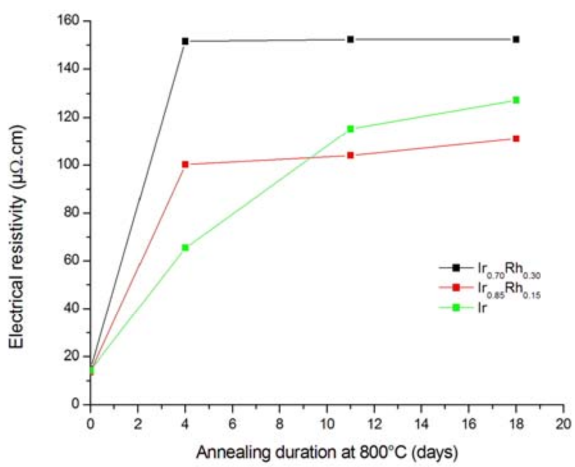

7B - High-Frequency Imaging Devices and Systems

Empire Room

Thursday, September 7, 2017, 1:30 pm - 3:00 pm

Chair: **Franck Levassort**
Francois-Rabelais University of Tours

7B-1

1:30 pm **High-Frequency Arrays and Applications**

Jeremy Brown[1,2]; [1]*Biomedical and Electrical Engineering, Dalhousie University, Halifax, Nova Scotia, Canada,* [2]*Surgery, Nova Scotia Health Authority, Halifax, Nova Scotia, Canada*

Background, Motivation and Objective

Typical high-frequency ultrasound resolution of 30-100 µm can be achieved in soft tissue over a penetration depth of 10-20 mm. The short penetration depth and high resolution, make high-frequency ultrasound particularly suitable for use in guided endoscopic surgery. In these minimally invasive procedures, a set of surgical instruments are inserted into a small incision site along with a set of imaging tools, typically endoscopic optical cameras and light sources. The entire surgical procedure is done solely under image guidance. Such an approach has become standard of care for a very large number of surgical procedures including those of the brain, colon, pancreas, uterus, bowel, etc.. Recently, our group has developed a high-frequency array-based forward-looking ultrasound endoscope, that is suitable for guiding endoscopic procedures and providing depth resolved information. The packaged form factor for this imaging array has been miniaturized down to just a few millimetres, and the imaging performance has been characterized on ex-vivo and in-vivo tissues. A summary of the latest high frequency technology will be first be presented followed by a detailed performance characterization of our group's endoscope in combination with our high frame-rate high-frequency electronic beamformer. Future and prototype versions of high-frequency array transducers in-development will be discussed that incorporate 3D volumetric imaging, shear wave elastography, and co-registered histotripsy.

Statement of Contribution/Methods

We have developed a fully sampled forward looking 64-element phased array, operating at a frequency of 45 MHz. The array is packaged into a 3 mm x 2.8 mm endoscopic form factor, and we have developed two different endoscope lengths of 5 cm, and 9 cm, targeting two applications: 1) Auditory imaging, and 2) Neuro-Imaging. We have developed a fully parallel 64-channel high-frequency beamformer that uses a variable sub-Nyquist sampling technique. We have also developed proof-of-concept variations on these prototype endoscopes for co-registered histotripsy, shear wave elastography, and 3D volumetric imaging.

Results/Discussion

The performance of the phased array endoscope was very close to the theoretical simulations. The beam profiles match impulse response simulations, with secondary lobe levels suppressed close to -60 dB. Interestingly, we have found little difference in beam-steered directivity between Kerfless and kerfed arrays, both reaching steering angles of over +/-35 degrees without significant sensitivity loss. A mass-spring vacuum deposited matching layer design provides a bandwidth greater than 60%, and the axial and lateral resolution was measured to be 40 and 85 microns respectively. Cadaveric and small animal soft tissue images have been generated showing a system penetration depth can easily reach 10 mm in soft tissue. Preliminary results for future variations of this endoscope will also be discussed.

7B-2

2:00 pm **High Frequency Row Column Addressed Matrix Array for Volumetric Ultrafast Ultrasound Imaging**

Guillaume Ferin[1], Martin Flesch[1,2], Thomas Deffieux[2], Claire Bantignies[1], Marie-Coline Dumoux[1], Tony Mateo[1], Agnes Lejeune[1], Bogdan Rosinski[1], Mickael Tanter[2], Mathieu Pernot[2], An Nguyen-Dinh[1]; [1]*Advanced Research Dpt., VERMON, Tours, France,* [2]*Institut Langevin, ESPCI Paris, PSL Research University, CNRS UMR7587, INSERM U979, Paris VII, France*

Background, Motivation and Objective

Volumetric "ultrafast" imaging is one of the major trends in ultrasound imaging techniques. It indeed paves the way for novel modalities when combined with Doppler, elastography and contrast imaging [1]. Unfortunately, due to the complexity and the inherently unaffordable costs, fully populated matrix-based systems are facing to pricing problems that limit their commercial development. Recently, row-column addressed (RCA) matrix transducer approaches have been proposed to overcome both complexity and costs issues but in a limited frequency range, i.e. below 10MHz.

However, there is also a tremendous need to deploy this solution to higher frequencies, typically 15MHz and above, mainly for brain functional ultrasound imaging investigation.

Statement of Contribution/Methods

We present in this paper the design and development of a high frequency, 2X128 elements row-column addressed transducer operating at 15MHz. With a 15x15 square millimeter footprint and a pitch of 110µm. Beyond the array topology, several piezoelectric materials, (piezoelectric 1-3 composite, bulk piezoceramic and bulk single crystal) have been tested and benchmarked with regards to transducer requirements and reliability. A suitable process flow has been proposed to overcome the manufacturability challenges. A full acoustic characterization is also shown to demonstrate the capabilities of high frequency RCA imaging device.

Results/Discussion

An original design and manufacturing process flow are presented and key aspects of RCA transducer design are described and discussed. The final transducer configuration is based on piezocomposite material as a results of the detailed benchmark between different active materials. The manufactured transducer exhibits a central frequency of 14MHz with a fractional bandwidth of 58% and an acceptable cross coupling. A preliminary implementation on research VERASONICS platform is presented as well.

[1]: J. Provost, C. Papadacci, J. E. Arango, M. Imbault, M. Fink, J.-L. Gennisson, M. Tanter, and M. Pernot, "3D ultrafast ultrasound imaging in vivo.," Phys. Med. Biol., vol. 59, no. 19, pp. L1–L13, 2014.

This work is part of the "ultrafast4D" project supported by ANR (agence nationale pour la recherche) - ANR-15-CE19-0004.

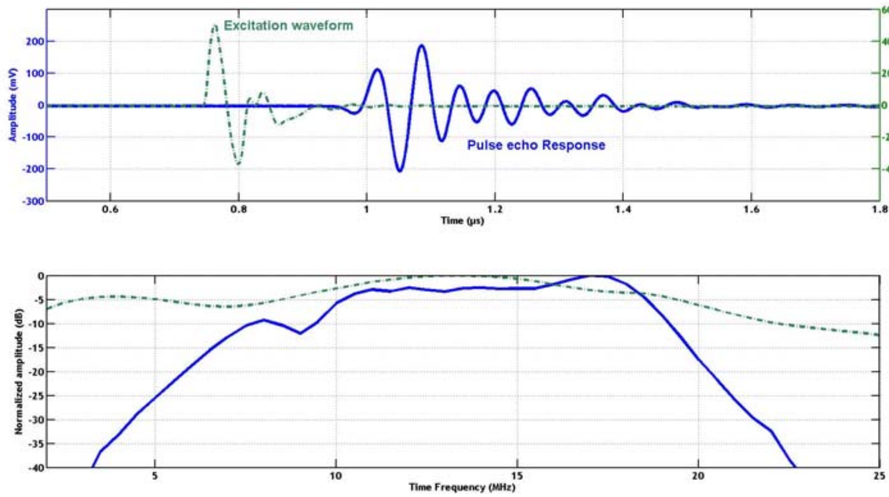

7B-3

2:15 pm Development of Multi-Frequency Intravascular Ultrasound Transducers for Tissue Harmonic Imaging

Junsu Lee[1], Eui-Ji Shin[1], Jin Ho Chang[2,3]; [1]*Electronic Engineering, Sogang University, Korea, Republic of,* [2]*Biomedical Engineering, Sogang University, Korea, Republic of,* [3]*Sogang Institute of Advanced Technology, Sogang University, Korea, Republic of*

Background, Motivation and Objective

Tissue harmonic imaging, an essential mode of ultrasound imaging scanners, can provide images with high spatial and contrast resolutions. However, it is difficult to use this imaging mode in intravascular ultrasound (IVUS) imaging. This is so because typical IVUS transducers are operated at high frequency (>20 MHz) and have a narrow fractional bandwidth (about 50%). Due to its small aperture (about 0.5 mm in diameter), additionally, the strength of signal obtained with an IVUS transducer is relatively weak. For these reasons, it may be impractical to generate the second harmonic signal, and even if the second harmonic signal is generated, the signal strength is too weak to construct a high quality second harmonic image. To solve this problem, we designed and fabricated a multi-frequency IVUS transducer for second harmonic IVUS imaging.

Statement of Contribution/Methods

The multi-frequency IVUS transducer developed has three elements as shown in Fig. 1(a): one center element operating at 35 MHz and two outer elements at 70 MHz. The center element is responsible for ultrasound transmission and the outer elements for reception of the second harmonic signal produced by the 35 MHz ultrasound. Each element has a square shape of which size is 0.5 mm X 0.5 mm. The aperture has a spherical shape in both lateral and elevation directions for geometric focusing at 3 mm. These elements are laid out the elevation direction. The IVUS transducer consists of PZT-5H as an active layer, two matching layers (2-3 silver epoxy and parylene), and a backing block (E-Solder 3022). The ability to construct the second harmonic image of the developed IVUS transducer was evaluated in tissue-mimicking phantom experiments.

Results/Discussion

In the pulse-echo test, it was found that the center and outer elements has center frequencies of 38 MHz and 68 MHz, respectively. In visual assessment of the tissue-mimicking phantom images, it was learned that the second harmonic image (Fig. 1(c)) produced by the developed transducer has higher spatial resolution and border sharpness than the fundamental image solely by the 35 MHz center element (Fig. 1(b)). We believe that the developed multi-frequency IVUS transducer can be useful for evaluating vulnerable plaques due to its ability to provide clear delineation of the intra-plaque region with different compositions that is required for accurate virtual histology.

7B-4

2:30 pm Thin Film PZT-Based PMUT Arays for Microultrasound Capsule Endoscopy

Yongqiang Qiu[1], **Christopher Cheng[2]**, Holly Lay[1], Aaron Welsh[2], Margeaux Wallace[2], Susan Trolier-McKinstry[2], Sandy Cochran[1]; *[1]University of Glasgow, United Kingdom, [2]Pennsylvania State University, USA*

Background, Motivation and Objective

Gastrointestinal (GI) disease is one of the most common causes of death. Capsule endoscopy (CE) may contribute to early detection of disease and pathological classification. Current CE relies on optical images of the internal luminal surface of the GI tract to aid diagnosis. With the addition of microultrasound, the imaging capability can be extended within the wall of the GI tract, with the potential to improve detection and classification. However, many challenges in fabrication and integration remain in the development of microultrasound transducer arrays to match CE geometry.

Statement of Contribution/Methods

These challenges can potentially be overcome with piezoelectric micromachined ultrasonic transducers (PMUTs). The resonant frequency of the PMUTs is closely related to the dimensions and mechanical stiffness of the PMUT membranes. In the present work, silicon (Si) on insulator (SOI) wafers were used as substrates. The relationship between PMUT resonant frequency and layer configuration and membrane diameter were studied with analytical techniques and finite element analysis (FEA). The PMUT diaphragms were constructed through a series of nanofabrication steps. The deposition pressure and crystallisation temperature were studied to achieve high-quality PZT. Three different diaphragm diameters, 30, 40 and 50 µm, were defined via backside Si deep reactive ion etching for different resonant frequencies. In addition, three array geometries were investigated: annular arrays, 1D linear arrays and 2D matrix arrays. The element pitch of the linear arrays was designed to be less than one wavelength to avoid grating lobes during ultrasound imaging.

Results/Discussion

High-quality phase pure PZT thin films with 1% niobium on SOI wafers were grown to a thickness of ~ 1 micron. They had high dielectric constant (> 1000), high remanent polarisation (> 20 µC/cm2) and low dielectric loss (< 4%). Each PMUT array had elements with a narrow distribution of capacitance, permittivity, and loss tangent (within 5% of one another). Electrical characterisation and acoustic measurements were performed to confirm resonant frequencies of 15 MHz – 55 MHz for the devices. Relatively good agreement between analytical results, FEA and experimental measurements has been confirmed. The acoustic performance and applications of these PMUT devices will be reported.

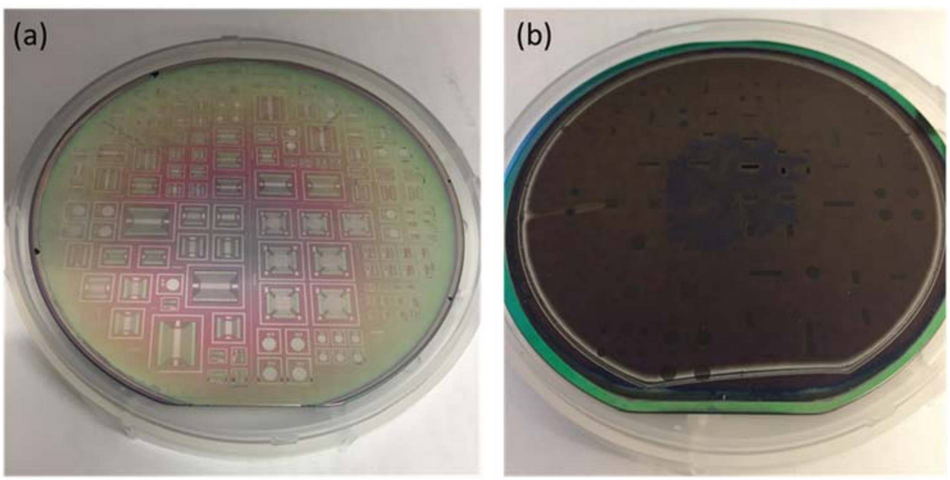

(a) Front and (b) back sides of a 4-inch wafer with PMUT array dies

7B-5

2:45 pm An Endoscope for Micro-Ultrasound and Photoacoustic Imaging of Barrett's Esophagus

Aaron Boyes[1], Jungik (Jay) Son[1], Jianhua Yin[1], Brian C. Wilson[2,3], Christine Démoré[1,3], F. Stuart Foster[1,3]; *[1]Sunnybrook Research Institute, Toronto, Ontario, Canada, [2]Princess Margaret Cancer Centre, Toronto, Ontario, Canada, [3]Medical Biophysics, University of Toronto, Toronto, Ontario, Canada*

Background, Motivation and Objective

Treatment outcomes for esophageal cancer can be significantly improved through early detection. Endoscopy, with or without fluorescence, as well as micro-ultrasound (µUS) have been explored as methods to detect the epithelial cell patterns associated with Barrett's esophagus (BE), a precursor to esophageal cancer. In addition, a characteristic microvascular pattern is associated with high grade dysplasia in BE. Photoacoustic imaging (PAI) has the added potential to visualize the microvasculature in the esophageal wall, and provide a high resolution overlay of microvessel structure and neovascularity. This is expected to provide valuable diagnostic information to complement knowledge of the tissue morphology, but requires a combined PAI and µUS probe for in vivo imaging of the esophageal wall.

Statement of Contribution/Methods

We have designed a miniature probe with a 50 MHz array for co-localized PAI and B-mode µUS suitable for connecting to a commercial PAI/µUS imaging system. The 64-element PZT array has element pitch below the imaging wavelength for sector scan imaging. Laser micromachining, using a high precision 193 nm Ar-F excimer laser system, has been investigated for definition of the high resolution features on the array and flexible circuit electrical interconnect. Strip line cabling >40 cm long is required for endoscopic applications. A biocompatible housing has been designed and prototyped with 3D printing to allow passage through a 6 mm endoscopic instrument channel for imaging the esophageal wall. The housing is equipped with passages for light fibres, and positions the fibre tips adjacent to the transducer's imaging window.

Results/Discussion

The high frequency array is bonded to a flexible circuit interposer with fan-out for connecting to strip-line cabling. The electrode tracks on the flex circuit, electrical bond layer and array elements are patterned with the laser (Fig. 1a). Array elements with 22 µm pitch and 5 µm kerf width have been achieved (Fig. 1b,c). Laser ablation parameters have been tuned to maximize cutting depth into the PZT, while maintaining edge quality on the gold electrode. Electrical impedance testing reveals 200Ω / - 50° at the anti-resonant frequency for laser machined array elements (Fig. 1d). Finite element simulations of kerf depth and element taper variation are compared to experimental results for optimisation.

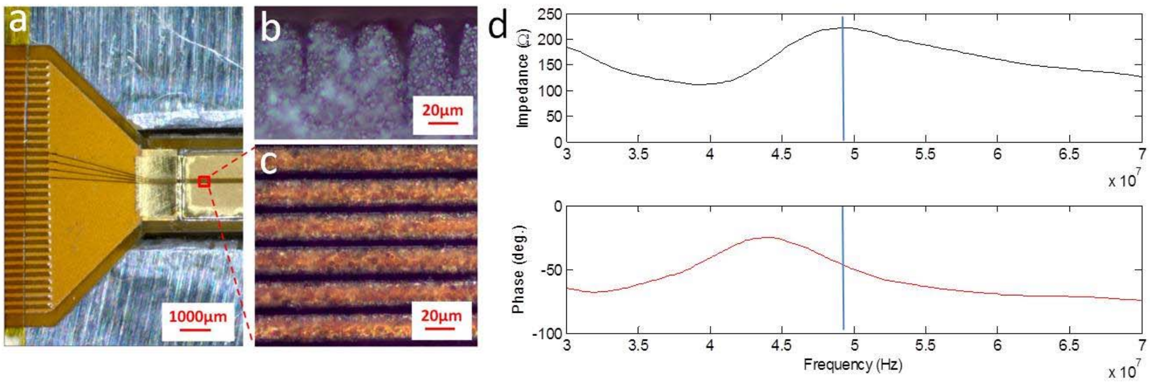

Figure 1: 50 MHz linear array. a) Low magnification view of the 50 MHz transducer bonded to a flex PCB, which expands the 22 µm pitch channels to pads with 200 µm pitch. b) Cross sectional and c) surface view of the array elements . d) Electrical impedance magnitude and phase plots for a representative element.

1C - MTH: HIFU and Ablation

Regency Ballroom

Thursday, September 7, 2017, 4:00 pm - 5:30 pm

Chair: **Kullervo Hynynen**
University of Toronto

1C-1

4:00 pm **Extracorporeal High Intensity Focused Ultrasound Treatment of the Placental Unit: In Vivo Study Using a Monkey Model of Pregnancy**

David Melodelima[1], Jonathan Caloone[1], Anthony Kocot[1], Cyril Huissoud[2]; [1]*LabTAU, INSERM, France,* [2]*CHU Croix-Rousse, France*

Background, Motivation and Objective

The last 20 years have seen the development of fetal surgery, particularly for the treatment of twin-to-twin transfusion syndrome (TTTS). Although fetoscopy increases survival rate, it is also invasive and responsible for fetal and maternal complications affecting the neonatal outcome. A completely non-invasive treatment that could occlude deep anastomoses would prevent the risks of invasive fetoscopy while offering the potential for more effective therapy. We previously developed a toroidal HIFU transducer that enables the destruction of large tissue volumes. The effectiveness of this HIFU device applied to the perfused placental unit must now be studied in a preclinical animal study under conditions similar to those in humans before starting a clinical trial. We report here the first use of a completely non-invasive treatment of the placenta in pregnant animals.

Statement of Contribution/Methods

A toroidal HIFU transducer working at 2.5 MHz and composed of 32 ring-shaped emitters was used. An ultrasound probe working at 7.5 MHz was placed in the center of the HIFU transducer. In vivo experiments were performed in eight pregnant monkeys. Lesions on placental tissues were performed non-invasively by placing the HIFU probe on the skin. Fetal and maternal parameters, such as maternal heart rate, fetal heart rate, and subcutaneous and intra-amniotic fluid temperature were recorded. A C-section was performed immediately after insonification to extract the placenta, inspect the fetus and inspect the maternal abdominal cavity. Placental HIFU lesions were studied using ultrasound images, gross pathology and histology.

Results/Discussion

Thirteen HIFU exposures were performed on placentas. The parameters used in this study were acoustic powers of 65, 80, 110 and 120 W applied for 30, 15, 20 and 20 seconds, respectively. This gradual increase in the total energy delivered was used to determine a set of parameters to create reproducible lesions in the placentas without any complications. The dimensions of the placental lesions were average diameters of 6.4 ± 0.5 mm and 7.8 ± 0.7 mm and an average depth of 3.8 ± 1.5 mm. Ultrasound images revealed a hyperechoic region that was correlated with the macroscopic analyses of the HIFU lesions. Necrosis of placental tissues exposed to HIFU was confirmed with histology. No significant variation in maternal and fetal parameters was observed during HIFU exposure. This study demonstrates in a monkey model of pregnancy the feasibility of HIFU treatment applied to the placenta for potential application to treat twin-to-twin transfusion syndrome.

1C-2

4:15 pm **Design and In-Vivo Evaluation of Next-Generation Laparoscopic HIFU Kidney Probe**

Ralf Seip[1], Adam Morris[1], Rodrigo Chaluisan[1], Jesse Clanton[1], Roy Carlson[1], Jacob Carr[1], Christie Johnson[1], Narendra Sanghvi[1], Jennifer Smith[1], Mahesh Matam[1], Jay Morris[1], Sameer Chopra[2], Inderbir Gill[2], Cheuk Fan Shum[3], Chandru Sundaram[3], Liang Cheng[3], Mark Carol[1]; [1]*Sonacare Medical, USA,* [2]*University of Southern California, USA,* [3]*Indiana University, USA*

Background, Motivation and Objective

Previously, we reported on the development and clinical evaluation of an ultrasound image-guided laparoscopic high-intensity focused ultrasound (HIFU) probe for kidney tumor ablation compatible with an 18mm trocar. Since then, the relentless march towards miniaturization of laparoscopic tools has led to the obsolescence of this trocar size, prompting a re-design of the probe to accommodate market realities and user expectations. Reducing the probe to be compatible with a 15mm trocar proved challenging, as simply scaling the existing design would have resulted in clinically unacceptable ablation performance.

Statement of Contribution/Methods

A 15mm diameter laparoscopic HIFU probe for kidney ablation was thus developed with similar ablation performance as the 18mm diameter probe. This was achieved by designing a 4MHz single-element truncated therapy 35x11mm aperture spherical shell transducer (35mm focal length) complemented by a 6.5MHz 8mm diameter imaging transducer mounted opposite of the therapy transducer. This arrangement saves space without compromising ablation aperture and focal intensity. Linear and rotational motion within a single-use probe tip allows this assembly to cover a field of view exceeding 45mm x 50mm x 90°, sufficient for its intended application of ablating solid renal masses ≤3cm in diameter. Sonication parameters to achieve consistent necrosis across varying depths and kidney target locations were optimized using a porcine kidney model (N=19, 2-3 ablations/kidney typical), and validated histologically, in preparation for follow-up clinical studies.

Results/Discussion

HIFU applied via a combination of elementary focal lesions followed by a continuous-ON delivery scheme while mechanically sweeping the therapy transducer's focal zone across the target volume produced the most consistent volumetric ablation, while protecting post-focal zone tissue from thermal ablation. Total acoustic power levels of 48W were required at the transducer face to reach target depths exceeding 30mm, with a 10mm water standoff needed to provide good tissue coupling, adequate transducer cooling, and sufficient freedom of movement of the transducer assembly within the probe tip. The developed design proved capable of delivering these power levels. The probe design effort provided further opportunities to improve on aspects of the device that simplified workflow, reduced setup time, and increased positioning flexibility as well, simplifying system use in this sterile procedure.

1C-3

4:30 pm **A HIFU Excitation Scheme to Reduce Switching-induced Grating Lobes and Hard Tissue Interface Heating**

Chris Adams[1], David Cowell[1], Luzhen Nie[1], James McLaughlan[1], Thomas Carpenter[1], Steven Freear[1]; [1]*University of Leeds, United Kingdom*

Background, Motivation and Objective

Arbitrary excitation waveforms are desirable in HIFU array systems. In trans-skull therapy this is necessary to compensate for phase aberrations and achieve even heating of the skull. To facilitate this, wave form generators and large, costly class A RF amplifiers are used. High element counts are commonplace and so the portability of these systems is greatly reduced. We propose using switched mode excitation to miniaturise these systems. Unfortunately, the curvature of therapeutic arrays and the inherent harmonic content of switched circuits induces harmful grating lobes into the therapeutic field of view. The advent of higher bandwidth transducers makes harmonic cancellation imperative. 3rd harmonic reduction (3HR) PWM can be used to negate these grating lobes but cannot implement amplitude control. We propose the use of the HRPWM technique to negate switching induced grating lobes and modulate output power to reduce hard tissue heating.

Statement of Contribution/Methods

A concave therapeutic array is tested. The electronic focus is set to 40 mm laterally and -50 mm axially. A bone layer is placed in front of the transducer with non-uniform attenuation. In the model, attenuation is considered to contribute entirely to absorbency and temperature rise is considered to be proportional to power intensity. In addition to ideal analog excitation, bipolar, 3HR and HRPWM switched mode excitation schemes are tested. The pressure profiles produced by each excitation scheme are compared with that of the ideal, analog excitation. The temperature rise at the hard tissue boundary under each array element is measured. The ratio of the local temperature rise to maximum temperature rise is calculated and plotted across the array.

Results/Discussion

Analog excitation results in the most energy at the focal point and guarantees uniform heating. Bipolar excitation induces grating lobes into the field of therapy and heats the tissue unevenly (~15% variation). 3HR is able to negate harmful grating lobes but also heats the tissue unevenly (~15% variation). 3HR and bipolar excitations also broaden the focal region, whereas HRPWM does not. The presented HRPWM excitation scheme is the only switched scheme that is able to both reduce grating lobes and hard tissue heating variation (~5%) to a satisfactory level.

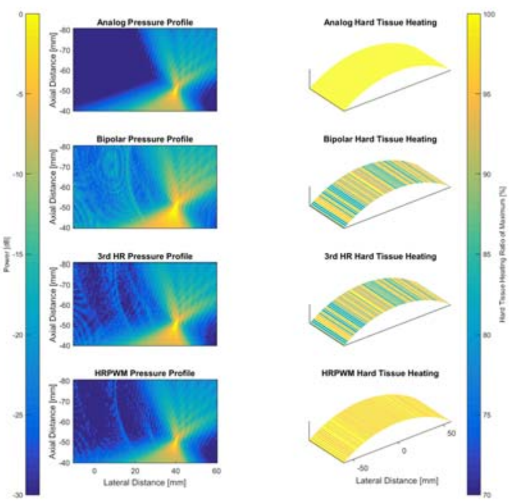

1C-4

4:45 pm **Transoesophageal HIFU for Cardiac Ablation: Experiments on Beating Hearts**

Paul Greillier[1], Bénédicte Ankou[2], Francis Bessière[2], Ali Zorgani[1], Fabrice Marquet[3], Julie Magat[3], Sandrine Melot-Dusseau[4], Romain Lacoste [4], Bruno Quesson[3], Mathieu Pernot[5], Stefan Catheline [1], Philippe Chevalier[2], Cyril Lafon[1,6]; [1]*LabTau - INSERM U1032, France,* [2]*Hôpital Louis-Pradel, France,* [3]*IHU-LIRYC - CHU Bordeaux, France,* [4]*Station de primatologie - CNRS- UPS846, France,* [5]*Institut Langevin - Ondes et Images - ESPCI ParisTech, CNRS UMR 7587, France,* [6]*University of Virginia, USA*

Background, Motivation and Objective

Atrial fibrillation and ventricular tachycardia are currently treated with catheter ablation using radiofrequency or cryoenergy. These endocardiac approaches are invasive and not fully satisfactory as the treatments are often incomplete and can be associated with side effects. HIFU were proposed as an alternative strategy, by using the excellent acoustic window between heart and esophagus. The present work described feasibility of trans-oesophageal thermal ablation on *ex-vivo* beating heart and non-human primates.

Statement of Contribution/Methods

For that purpose, an endoscope integrating a 5MHz 64-element commercial transesophageal echocardiography (TEE) probe and a HIFU transducer was built (8 elements, 3 MHz and 40mm focal length). The focus could be steered electronically over a 17 to 55 mm range from the transducer with a focal intensity (Ispta) from 3000 to 5200 W/cm^2. Circulation of water at 5°C ensured cooling of the front face of the HIFU transducer and acoustic coupling with oesophagus.

In-vivo experiments were done on three 30-kg baboons. TEE and CT-scanner demonstrated the acoustic access from the esophagus to the heart of this model. HIFU were delivered in the left atrium (LA) and the left ventricles (LV), with continuous shots of 16s, repeated 4-15 times. B-mode, shear-wave (SWE) and passive elastography were performed before and after HIFU with an ultrafast scanner. MR imaging (T1 mapping and contrast) was performed one day after HIFU treatments.

To improve *in-vivo* success rate, ultrasound parameters were adjusted on a perfused functional ex-vivo model, during a Langendorff procedure. The hearts were sonicated during diastolic period (50% of the cycle). Similar MRI procedures and elastography methods were used.

Results/Discussion

In-vivo, clinical states of the subjects during and after the treatment were positive. HIFU could be delivered at the locations identified on the CT scans. In one subject, passive elastography and SWE showed a stiffening of the LV myocardial wall after ablation (two-fold increase of the myocardial stiffness). A hypersignal zone was evidenced on T1 maps in the same area. Contrast MRI did not show local fibrosis in the heart. No lesions were evidenced in the two other subjects.

Ex-vivo, Langendorff procedure was achieved properly and the five ex-vivo hearts beat properly for 2 hours. No lesion was evidenced with in-vivo parameters when no gating was used. Gross pathology revealed three well-defined lesions at intensity of 3000 W/cm^2. Larger ultrasounds intensities (~5200 W/cm^2) resulted in systematic lesions (10x10mm) in ventricles walls, clearly visible with MRI.

Those experiments demonstrated the ability of a transoesophageal HIFU probe to produce thermal lesion in beating hearts, in *ex-vivo* Langendorff hearts and in-vivo non-human primates. Ex-vivo proved that non-ECG gated are less capable of thermal lesions production on beating and perfused heart. In-vivo experiments are still in process.

1C-5

5:00 pm **Real-Time Control of Bulk Ultrasound Thermal Ablation Using Echo Decorrelation Imaging Feedback**

Mohamed A. Abbass[1], Allison-Joy Garbo[1], Neeraja Mahalingam[1], Jakob K. Killin[1], T. Douglas Mast[1]; [1]*Biomedical Engineering, University of Cincinnati, Cincinnati, Ohio, USA*

Background, Motivation and Objective

Bulk thermal ablation, including radiofrequency ablation (RFA) as well as microwave and ultrasound (US) ablation, is an important approach to tumor treatment. To avoid incomplete treatments and cancer recurrence while reducing morbidity, a real-time monitoring and control approach, capable of providing consistent thermal ablation in minimum time, is needed. Echo decorrelation imaging has been successfully employed to monitor bulk US thermal ablation and RFA both *ex vivo* and in vivo and is investigated here for control of bulk US ablation.

Statement of Contribution/Methods

In this study the feasibility of controlling bulk US ablation using echo decorrelation imaging feedback was assessed in *ex vivo* bovine liver. US exposures (5-5.4 MHz, 8.2-8.5 s/cycle, 70-73% duty, 31-41 W/cm^2 spatial-peak, temporal-peak intensity) and echo decorrelation imaging were performed by a linear image-ablate array. Preliminary experiments (N=86) were carried out to optimize a control region of interest (ROI) and threshold Δ_{th}. In controlled trials (N=13), 9 cycles at 31.5 W/cm^2 were followed by up to 9 cycles at 35.3 W/cm^2, with treatments ending when the average cumulative echo decorrelation Δ_{cum} within the ROI exceeded Δ_{th}. Controlled trials were compared with uncontrolled trials employing 9 (N=10) or 18 (N=10) cycles of the same sonication sequence. Resulting lesion dimensions and areas under receiver operating characteristic (ROC) curves (AUC) were statistically compared.

Results/Discussion

The control threshold Δ_{th} was selected as −1.576 ($\log_{10}$-scaled decorrelation per ms). Successful control (Δ_{cum} exceeding Δ_{th}) was achieved in 10 of the 13 controlled trials. Successfully controlled trials showed significantly greater average lesion area (365.6 mm^2) and depth (14.7 mm) than 9-cycle (213.5 mm^2, $p=3\times10^{-4}$; 8.3 mm, $p=2\times10^{-4}$) uncontrolled trials, less treatment time (113.1 s) than 18-cycle (147.6 s, $p=2\times10^{-5}$) uncontrolled trials and greater prediction capability (AUC=0.858) than the combined 20 uncontrolled trials (AUC=0.628). These results indicate that echo decorrelation imaging is an effective approach to bulk US ablation control.

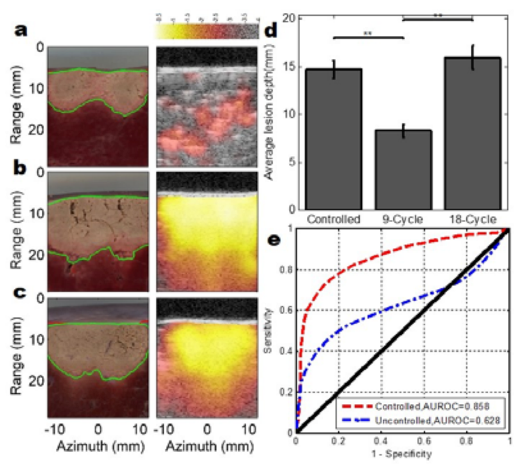

Fig.1. Comparison of controlled vs. uncontrolled results: representative histologic and US images for (a) 9-cycle, (b) 18-cycle, and (c) controlled trials with segmentation of tissue boundaries and ablated regions; (d) means and standard errors of lesion depth; (e) ROC curves for controlled trials and for all uncontrolled (9-cycle and 18-cycle) trials.

1C-6

5:15 pm **Development of a Toroidal High-intensity Focused Ultrasound Transducer for the Treatment of Pancreatic Tumors. In Vivo Study of the Safety and Efficacy in a Porcine Model**

David Melodelima[1], Aurelien Dupre[2], Anthony Kocot[1], Jeremy Vincenot[1], Yao Chen[2], Stefan Langonnet[2], Hannah Pflieger[2], Michel Rivoire[2]; [1]*LabTAU, INSERM, France,* [2]*Centre Leon Berard, France*

Background, Motivation and Objective

Pancreatic ductal adenocarcinoma (PDA) is the most frequent primary malignancy of the pancréas. PDA has increased in incidence during the last decade and now constitutes the fourth leading cause of cancer mortality. New focal destruction technologies such as high-intensity focused ultrasound (HIFU) may improve the prognosis of pancreatic ductal adenocarcinoma. Given the inconvenience and disadvantages of extracorporeal HIFU, we developed an intraoperative HIFU probe, initially designed for the treatment of colorectal liver metastasis, with encouraging results. The principal interest lies in the possibility of treating hepatic parenchyma in a short period. The intraoperative HIFU probe designed for the treatment of liver tumors could be used for pancreatic tumors. The aim of this preclinical study was to determine the safety and efficacy of intraoperative HIFU in vivo on pancreatic tissue in a porcine model.

Statement of Contribution/Methods

The HIFU transducer has a toroidal shape and was divided into 32 concentric rings of equal surface (0.13 cm2). The diameter of the transducer and its radius of curvature were 70 mm. The operating frequency was 2.5 MHz. A 7.5 MHz ultrasound imaging probe was placed in the center of the device. The imaging plane was aligned with the HIFU acoustic axis. In a porcine model (N=12) HIFU ablations were performed in either the body or tail of the pancreas, distant to superior mesenteric vessels. The user interface displayed the position of the HIFU focal region superimposed on the sonogram obtained by the integrated US imaging probe. We could therefore visualize in real time the treated zone created during US exposure. All animals were sacrificed on the eighth day. The primary objective was to obtain an HIFU ablation measuring at least 1 cm in diameter without premature death. HIFU lesions were studied using ultrasound images, gross pathology and histology.

Results/Discussion

In total, 12 HIFU ablations were carried out. These ablations were performed within 160 seconds. Every ablation could be identified by both palpation and visualization (as a greying on the pancreas surface). Ablations had a median length of 20 (15–27) mm and a median width of 16 (8–26) mm, with an interquartile coefficient of 0.16 and 0.23 mm, respectively. The primary objective was fulfilled in all but 1 pig. The clinical course was uneventful for all animals. No cases of severe pancreatitis were found at sacrifice. High-intensity focused ultrasound treatment was associated with a transitory increase in amylase and lipase levels, and pseudocysts were observed in half of the pigs without being clinically apparent. All ablations were well delimited at both gross and histological examinations. Intraoperative thermal destruction of porcine pancreas with HIFU is feasible. Reproducibility and safety have to be confirmed when applied close to mesenteric vessels and in long-term preclinical studies.

2C - MBB: Novel Imaging Methods

Ambassador Ballroom

Thursday, September 7, 2017, 4:00 pm - 5:30 pm

Chair: **Andreas Austeng**
University of Oslo

2C-1

4:00 pm **Delay-Encoded Harmonic Imaging (DE-HI) in Multiplane-Wave Compounding**

Ping Gong[1], Pengfei Song[1], Shigao Chen[1]; [1]*Department of Radiology, Mayo clinic, Rochester, MN, USA*

Background, Motivation and Objective

Ultrafast ultrasound imaging offers great opportunities to new imaging technologies such as shear wave elastography and ultrafast Doppler. Multiplane wave (MW) imaging is a new technique in which multiple positively or negatively encoded plane waves are emitted successively with short interleaved time during ***one*** transmission event (i.e. pulse-echo event), aiming at increasing the signal-to-noise ratio (SNR) of ultrafast imaging. However, the long transmit pulses of MW imaging also increase the reverberation artifacts. Here we propose a delay-encoded harmonic imaging (DE-HI) technique to enable HI for MW imaging to reduce reverberation. DE-HI encodes the 2^{nd} harmonic signals with transmit delays rather than reversing the pulse polarities, thus addressing the MW encoding challenge that the 2^{nd} harmonic polarity is independent of transmit pulse. DE-HI improves the ultrafast imaging by reducing the reverberation with HI and increasing SNR by emitting multiplane waves.

Statement of Contribution/Methods

In DE-HI, a ¼ period delay calculated at the transmit center frequency is applied on the transmit pulses of multiplane wave emissions during ***one*** transmission event, rather than reversing the pulse polarities as in standard MW imaging. The received DE-HI signals are first decoded in the frequency domain to recover the signals as those from single plane wave emissions (with improved SNR primarily at the 2^{nd} harmonic component instead of the fundamental component). The decoded signals are then aligned in the fast time direction to compensate the interleaved time introduced by MW emissions, followed by beamforming and spatial compounding to form the final image.

Results/Discussion

Fig. 1 shows images of an *in-vivo* human liver obtained from (a) plane wave fundamental imaging, (b) MW, (c) plane wave HI, and (d) DE-HI, respectively, with contrast-to-noise-ratio (CNR) values shown in the titles. DE-HI provides enhanced CNR between vessel (solid box) and tissue (dashed box) as compared to other methods. The vessels indicated by the white arrows in (d) are also more discernible under DE-HI thanks to the reduced reverberation clutters and improved image resolution and CNR. These properties of DE-HI show great potential for enhancing many emerging ultrafast imaging applications such as functional ultrasound and super-resolution imaging.

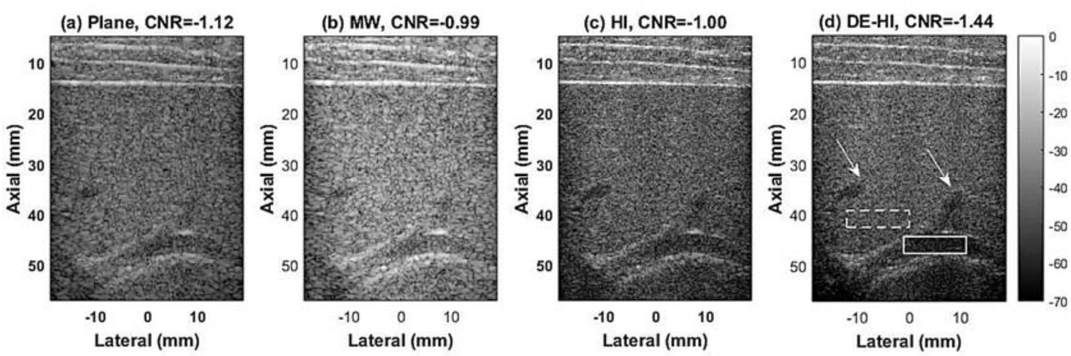

2C-2

4:15 pm **Spatial-Temporal Plane-Wave Image Formation with Sparse Uniform ReSampling**

Tanya Chernyakova[1], Aviad Aberdam[1], Eliav Bar-Ilan[1], Yonina Eldar[1]; [1]*The Technion, IIT, Israel*

Background, Motivation and Objective

Ultrafast imaging based on coherent plane-wave compounding improves image quality and allows for much faster acquisition. This method, however, is limited by severe computational loads stemming from delay-and-sum beamforming (DAS BF) that creates a major bottleneck for real-time implementation.

Spatial-temporal (ST) processing yields the entire frame without a need for DAS BF of each image line. First, the 2D Fourier transform (FT) of the non-delayed aperture data yields the non-uniform samples of 2D Fourier spectrum of the underlying image. The points of the non-uniform grid are defined by the relationship between the temporal frequency of the aperture data and the spatial frequencies of the image. The core step is then to remap the spectrum of the image to a uniform grid prior to applying an inverse 2D FT yielding the image in space. We propose implementing this interpolation step using the recently developed Sparse Uniform ReSampling (SPURS) algorithm which results in small approximation error and low computational cost.

Statement of Contribution/Methods

The remapping of the image spectrum to a uniform grid is the core step defining both the quality of the resulting image and the computational load. It can be done by either computationally efficient linear interpolation or accurate but computationally heavy non-uniform FT.

Our contribution is to perform the remapping using SPURS obtained in two steps. First, the non-uniform samples are projected to an intermediate subspace, spanned by a compactly supported kernel. The representation of the signal in the chosen subspace is found by efficiently solving a sparse system of equations with available sparse equations solvers. The result is next projected to a subspace of images with finite support, where the image of interest is known to belong. This is done efficiently through linear shift invariant filtering, yielding a uniformly sampled spectrum of the image.

Results/Discussion

The method is applied on data provided at the PICMUS Challenge 2016.

Figure 1 (a) shows an image obtained by DAS BF. Figures 1 (b) and (c) show the images obtained by ST with linear interpolation and SPURS spectrum resampling respectively, while the computational complexity is 360 times lower compared to DAS.

SPURS allows for efficient implementation of the remapping step of ST processing with improved image quality and at a low computational cost.

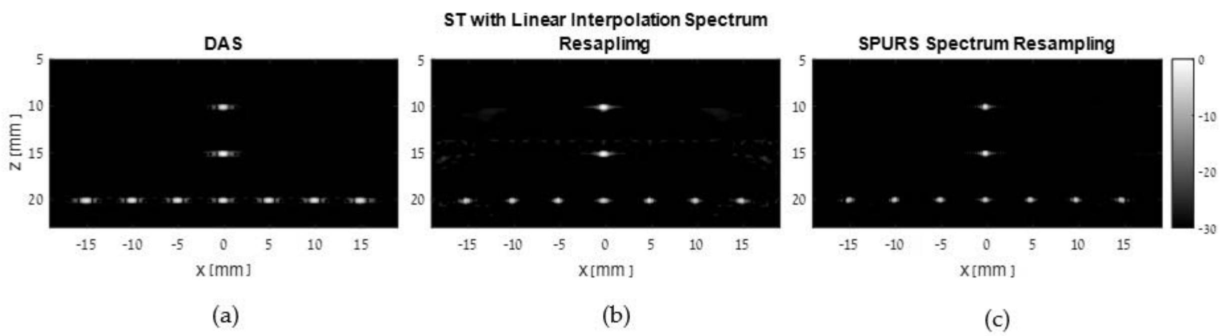

Fig.1. Images obtained by (a) DAS; (b) ST with linear interpolation; (c) ST with SPURS. The computational complexity in multiplications per frame of (b) and (c) is approximately equal and is 360 times lower compared to (a).

2C-3

4:30 pm Deep Neural Networks for Ultrasound Beamforming

Adam Luchies[1], Brett Byram[1]; [1]*Department of Biomedical Engineering, Vanderbilt University, Nashville, TN, USA*

Background, Motivation and Objective

In the past, members of our group developed a model based beamforming method called aperture domain model image reconstruction (ADMIRE). They tuned ADMIRE to improve ultrasound image quality by suppressing sources of image degradation such as off-axis scattering, reverberation, and phase aberration. In addition, the development of ADMIRE demonstrated that beamforming could be posed as a regularized nonlinear regression problem, which suggests that a deep neural network (DNN) might be used to accomplish the same task. Compared to regularized regression methods, DNNs are fast, adaptive, and fault tolerant.

Statement of Contribution/Methods

We trained feed-forward DNNs to suppress off-axis scattering. We employed FIELD II to construct the required training and validation data sets. Point scatterers were placed in the field of a simulated linear array transducer and their responses recorded. Similar to ADMIRE, we defined acceptance and rejection regions based on the characteristics of the array transducer. Backpropagation was used to train the DNNs and an extensive hyperparameter search was conducted to locate the best performing DNNs.

Results/Discussion

Our initial results showed that we can train DNNs to suppress off-axis scattering. When creating beam profile plots using a single frequency, we were able to achieve maximum side-lobe levels below -100 dB without sacrificing main lobe width as shown in the included figure. A comparison between delay and sum (DAS) and our DNN approach for a resolution target and an anechoic cyst can be seen in the included figure. For the anechoic cyst, the contrast ratio was 33.1 dB and 43.5 dB and the contrast-to-noise ratio was 4.2 dB and 4.1 dB for the DAS and DNN approaches, respectively. Although the initial hyperparameter search took weeks on an 8-GPU computing cluster to find the best performing DNN, we were able to use transfer learning to find new DNNs for different frequencies in a matter of hours. Our results suggest that DNNs have the potential to be trained to improve ultrasound image quality.

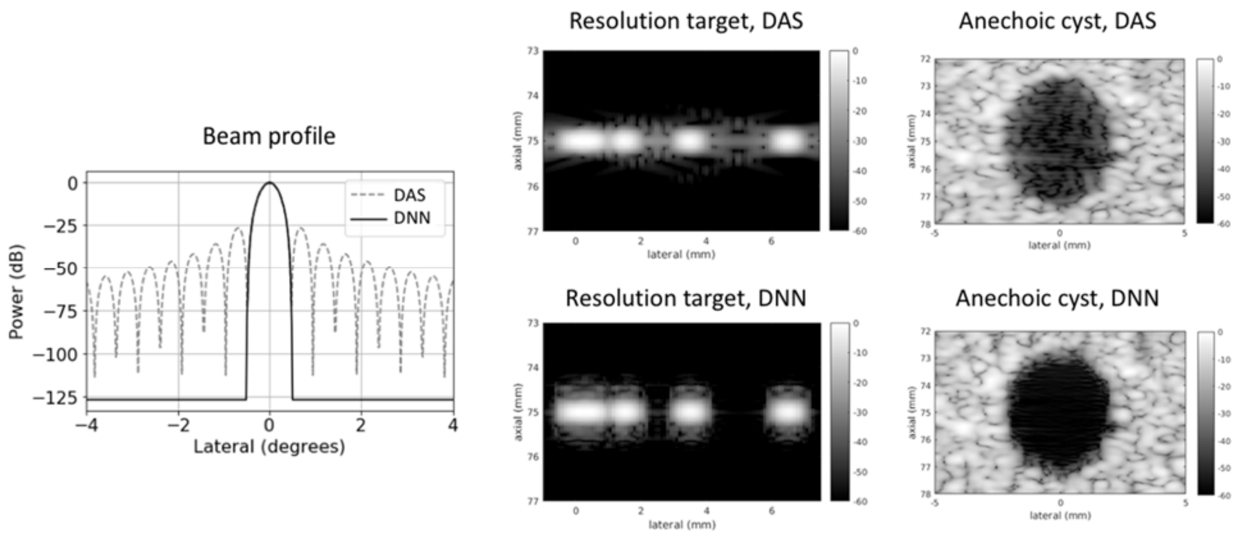

2C-4

4:45 pm High-Resolution Passive Cavitation Mapping by Source Localization from Aperture-Domain Signals

Taehwa Lee[1], Dongwoon Hyun[1], Sayan M. Chowdhury[1], Marko Jakovljevic[1], Juergen K. Willmann[1], Jeremy Dahl[1]; [1]*Radiology, Stanford University, Stanford, California, USA*

Background, Motivation and Objective

Monitoring cavitation is important for therapeutic applications relying on cavitation of microbubbles. Passive cavitation mapping (PCM) can provide quantitative and spatial information of cavitation activities; however, PCM based on time exposure acoustics (PCM-TEA) suffers from poor axial resolution. We propose a novel cavitation mapping algorithm with improved axial resolution based on localization of cavitation events from the individual element signals of the transducer array, even when the timing of the cavitation event is unknown.

Statement of Contribution/Methods

Our proposed PCM technique estimates the lateral and axial location of inertial cavitation from a microbubble or groups of microbubbles by applying a parabolic fit to the arrival-time profile of the acoustic signals from a cavitation event. The element signals are further time-window gated along the time-sampled dimension to improve spatial localization of the cavitation event, so that a parabolic fit is computed for every time-window gate. Cavitation magnitude at each PCM image point is determined by integrating the beamformed signals from each cavitation event where its spatial falls within a 0.6 mm-radius of the PCM image point. Experiments were performed in a vessel phantom containing a 2-mm diameter tube filled with a 3.5×108 MBs/ml concentration of microbubbles. Destruction pulses were applied with a P4-1 transducer (ATL) and passive cavitation signals were obtained from the individual elements of an L11-4 linear array transducer (ATL). Both transducers were connected to a Verasonics Vantage 256 research ultrasound system.

Results/Discussion

Figure 1 compares PCM-TEA and our proposed PCM based on source localization (PCM-SL). PCM-SL shows improved axial resolution compared to PCM-TEA, as the cavitation signals are mostly confined to within the flow channel. At high pressure amplitudes, PCM-TEA resulted in worse axial resolution due to stronger microbubble-microbubble interactions, whereas PCM-SL still provided acceptable spatially-confined cavitation mapping. We further demonstrate our PCM-SL technique in a mouse model of hepatocellular carcinoma tumor and show that the cavitation signals are confined to the mouse tumor boundaries.

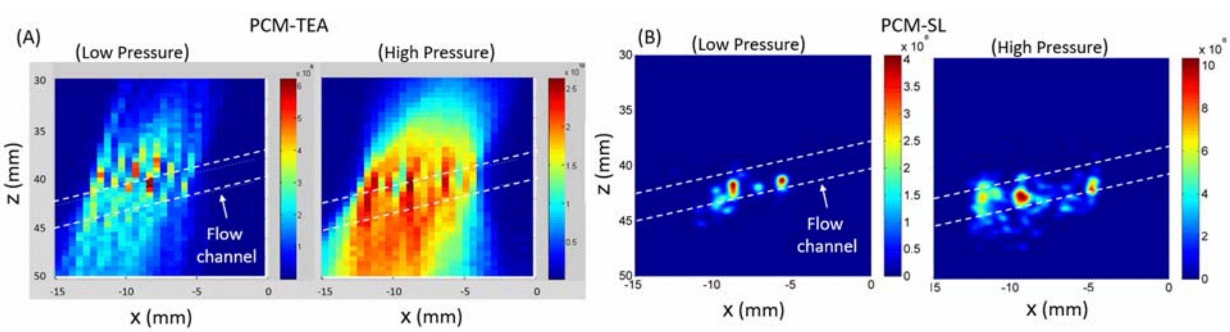

Figure 1. (A) Passive cavitation map based on time exposure acoustics (PCM-TEA) for low (left) and high pressure amplitudes (right). (B) Passive cavitation map based on source localization (PCM-SL) for low (left) and high pressure amplitudes (right). PCM-TEA showed exhibits long tail artifacts beyond actual cavitation regions due to the finite point spread function of the imaging transducer and microbubble-microbubble interactions.

2C-5

5:00 pm Contrast Ratio Dynamic Range: A New Beamformer Performance Metric

Kazuyuki Dei[1], Adam Luchies[1], Brett Byram[1]; [1]*Biomedical Engineering, Vanderbilt University, Nashville, Tennessee, USA*

Background, Motivation and Objective

The beamformer is one of the most important components of an ultrasound imaging system. Therefore, numerous beamforming algorithms have been proposed. Two well-known methods for evaluating beamformer performance include reporting the full-width at half-maximum of the lateral beam profile and the contrast ratio observed inside an anechoic cyst relative to the background. However, these metrics are easy to manipulate and are useless at predicting how well a beamformer will preserve intrinsic contrast. This has been noted by others and an effort has been made to correct for dynamic range. Here, we propose that dynamic range should be reported as a quality metric, and that is should be measured as the longest continuous duration along the true contrast line.

Statement of Contribution/Methods

We used Field II to simulate 5 mm diameter cysts with known scatterer contrast between -50 dB and +60 dB relative to the background. We included an anechoic cyst as well. We also used our pseudo non-linear simulation method to add reverberation clutter at a signal-to-clutter ratio (SCR) of 0 dB. We simulated 6 realizations of uncluttered and cluttered cases at each contrast level. We measured and quantified the dynamic range based on when the contrast curve was statistically indistinguishable from the true curve based on a two-tailed *t*-test. We applied this to several beamformers: delay-and-sum (DAS), coherence factor (CF), minimum variance (MV), short-lag spatial coherence (SLSC), and aperture domain model image reconstruction (ADMIRE). We implemented ADMIRE with different sets of regularization parameters to suggest how the anechoic cyst case can be gamed with regularized methods.

Results/Discussion

Results of measured contrast compared to intrinsic contrast are shown below; no clutter (left) and 0 dB SCR (right). The dynamic range using DAS, DAS+CF, MV, SLSC and ADMIRE with low and high degrees of freedom (*df*) are 56.3 dB, 21.0 dB, 55.5 dB, 17.1 dB, 28.5 dB and 58.1 dB, respectively, for no clutter, while the 0 dB SCR case decreases the dynamic range to 27.1 dB, 3.4 dB, 27.1dB, 3.1 dB, 3.6 dB and 36.4 dB, respectively. These findings indicate 1) clutter decreases dynamic range, 2) most methods have worse dynamic range compared to DAS, and 3) regularized approaches may outperform DAS particularly in high clutter environments, but only with deliberate selection of the tuning parameters.

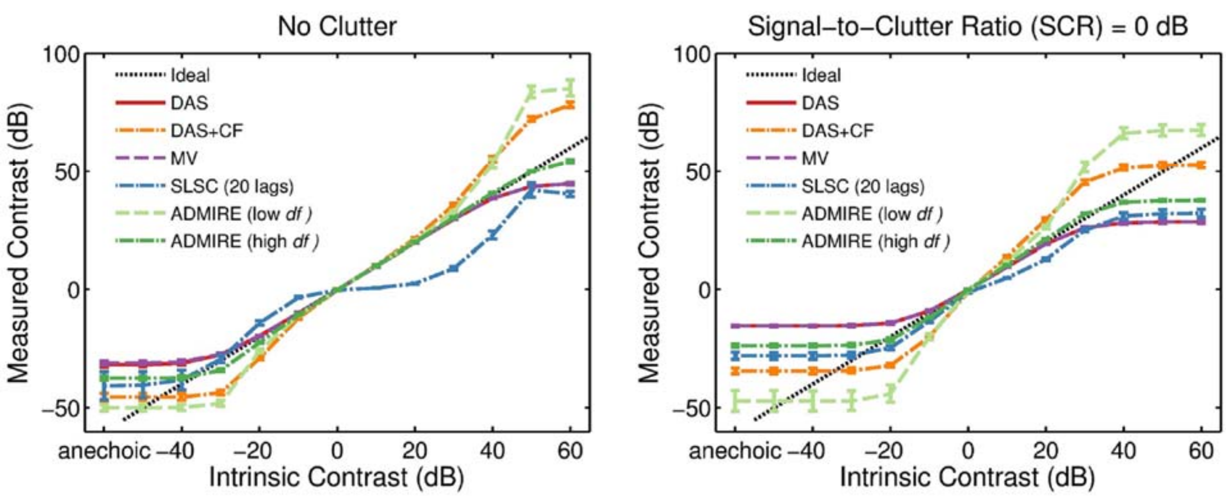

2C-6

5:15 pm The UltraSound ToolBox

Alfonso Rodriguez-Molares[1], Ole Marius Hoel Rindal[2], Olivier Bernard[3], Hervé Liebgott[3], Andreas Austeng[2], Lasse Lovstakken[1]; [1]*Norwegian University of Science and Technology, Norway,* [2]*University of Oslo, Norway,* [3]*University of Lyon, France*

Background, Motivation and Objective

In the last decade the number of beamforming methods has exploded. Many innovative ideas have been proposed, but we lack the tools to compare the different techniques efficiently. The PICMUS challenge (IUS 2016, Tours) was a pioneering step that made clear that two things are required to establish a fair comparison: a common data format, and a body of methods to process that data.

Statement of Contribution/Methods

Three universities have come together to address this problem by developing both a dedicated file format and a beamforming toolbox. We present the Ultrasound File Format (UFF): a HDF5 data format, open to any programming language, for storage of channel and beamformed data; and the UltraSound ToolBox (USTB): a MATLAB toolbox made of both native MATLAB and C++ code, with GPU support.

Together UFF and USTB provide a unified structure to share and process 2D and 3D ultrasound data. Channel data from any origin, e.g. Field II or Verasonics, and using any sequence, e.g. synthetic transmit aperture imaging (STAI) or coherent plane-wave compounding (CPWC), can be stored in UFF and beamformed with USTB.

Both UFF and USTB revolve around the concept of the General Beamformer. The wavefronts in most ultrasound sequences can be fully defined using a single point source P: in focus imaging (FI) and retrospective transmit beamforming (RTB) P is placed at the focal point, in diverging wave imaging (DWI) P is at the origin of the diverging wave, in STAI P lies on the active element, in CPWC P is at infinite in a given direction. Based on that definition we developed a data structure (Fig.1) that makes it possible to beamform all sequences with a single algorithm, or even combine them.

To illustrate this, 5 datasets have been simulated (FI, STAI, CPWC, DWI, and RTB) and reconstructed with USTB's general beamformer. It is known that CPWC is equivalent to STAI under certain circumstances. Here we use USTB to show that the same result can be extrapolated to DWI and RTB. The equivalence is demonstrated in terms of side lobe level (SLL) and full width half maximum (FWHM).

Results/Discussion

Fig.2a-e show the point spread function (PSF) of the tested sequences. The 5 methods have a nearly identical PSF with a FWHM of 369.00 ± 9.42 µm (Fig.2f) and a SLL of -26.00 ± 0.89 dB of (Fig.2g). This validates the general beamformer and supports the equivalence of the methods.

The aim of USTB is to facilitate the comparison between beamforming techniques and encourage the publication of datasets and algorithms. It is free, open source, and open to contributors. A fully functional toolbox will be released in June 2017, but an alpha version is available at http://www.ustb.no/.

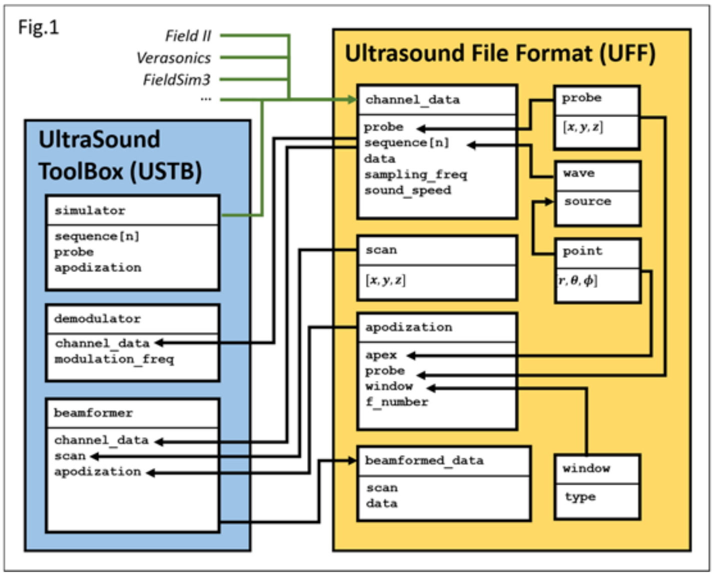

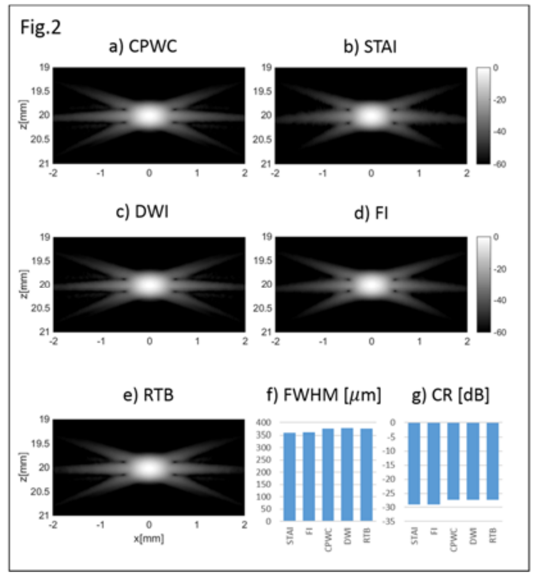

3C - MCA: Microbubbles Localization Microscopy 1

Palladian Room

Thursday, September 7, 2017, 4:00 pm - 5:30 pm

Chair: **Nico de Jong**
Erasmus Medical Centre

3C-1

4:00 pm Volumetric Ultrafast Ultrasound Localization Microscopy Using a 32x32 Matrix Array

Baptiste Heiles[1], Mafalda Correia[1], Mathieu Pernot[1], Jean Provost[1], Mickael Tanter*[1], Olivier Couture*[1]; [1]*Institut Langevin (CNRS, INSERM, ESPCI Paris, PSL Research University), Paris, France*

Background, Motivation and Objective

Ultrasound localization microscopy has first been demonstrated to overcome the penetration/resolution trade-off [Couture et al IEEE IUS 2011]. Inspired by FPALM in optics and exploiting ultrafast ultrasound imaging, it allowed the reconstruction of a full velocity map of the rat brain vasculature with a micrometric resolution (8µm) [Errico et al. Nature,2015]. Despite additional successes for tumour imaging [Lin et al, Theranostics, 2017], this plane-by-plane technique suffers from minute-long acquisitions, out-of-plane microbubbles and tissue motion which cannot be corrected for [Hingot et al. Ultrasonics 2017] and the loss of information due to the projection of a 3D vascular structure into a 2D image. We previously proposed the use of two parallel arrays to compensate part of these drawbacks [Desailly et al., APL, 2013]. We present here a method to perform super-resolution in a full volume with an isotropic 2D matrix transducer performing 3D ultrafast imaging.

Statement of Contribution/Methods

A 2D matrix array (Vermon, France) with 1024 elements arranged in a 32x32 isotropic plane was controlled by the customised, programmable 1024-channel system presented in [Provost et al. 2014]. The medium was insonified with four 2D tilted plane waves at 9-MHz and a coherent-compounded volume rate of 500 Hz. The RF data were saved for a posteriori beamforming. The medium was a custom built wall-less agar phantom. A flow of a predetermined concentration of SonoVue microbubbles - [10-80] bubbles/µL - ran through a 10-mm canal at controlled flow rates [7-50mL/s]. A 3D superlocalization process was developed to determine the position of the bubbles and render a super-resolved isotropic volume. Then, a 3D tracking algorithm was implemented to follow the microbubbles through time.

Results/Discussion

An estimate of [1E4-1E5] bubbles were recovered, depending on the concentration, and rendered a super-resolved isotropic volume with a 10x factor. These yielded velocimetry data allowing us to determine complete speed profiles of the flow within the canal. Average velocities measured ranged from 11 to 43 mm/s in magnitude and complete streamlines were reconstructed for each connected bubbles. The streamlines were super-resolved with a precision of 17µm/s which allowed to determine average speed profiles depending on the Reynolds number used [0.89-5.72]. It also proved to be a valuable tool for predicting false positive in the superlocalization process. The standard deviations of the speed profiles investigated were calculated for different acquisitions at the same flow rate and ranged from 3 to 9 mm/s depending on the flow conditions. Real volumetric super-resolution could allow for full reconstruction of the microvasculature of entire organs within one injected bolus and permit the correction of tissue motion in all directions thanks to the added dimension. The technique would also prove useful to investigate complex flow patterns in fast moving blood flow.

3C-2

4:15 pm Ultrasound Localization Microscopy to Assess the Microvasculature in Moving Tissues, Application in a Rat Kidney

Josquin Foiret[1], Hua Zhang[1], Lisa Mahakian[1], Sarah Tam[1], Tali Ilovitsh[1], Katherine W. Ferrara[1]; [1]*Department of Biomedical Engineering, UC Davis, Davis, CA, USA*

Background, Motivation and Objective

The recent development of ultrafast ultrasound localization microscopy (Errico *et al.*, Nature, 2015) provides new opportunities for imaging the vasculature with sub-diffraction resolution. However, the large number of images to be recorded requires acquisitions lasting several minutes. Therefore, physiological motion far larger than the achievable resolution presents challenges for moving tissues. In this work, single microbubbles (MB) were localized in vivo in a rat kidney using a dedicated imaging sequence allowing MB tracking and motion correction. Blood velocity in small vessels (<2 mm/s) was estimated demonstrating the potential of this technique to improve vascular characterization.

Statement of Contribution/Methods

Experiments were performed on the left kidney of a female Sprague-Dawley rat (approved by the UC Davis Institutional Animal Committee on Use and Care). A 150 µL bolus of ~7.5×10^6 house-made non-targeted MBs was injected into the tail vein of the animal and 40000 frames were recorded in 133 s (300 Hz frame rate). Each frame consisted of 3 plane waves at (-5°, 0°, 5°) with a CPS transmit scheme (½, -1, ½ with a 28.5 kHz PRF, center frequency of 6.9 MHz). Imaging was performed with the Vantage platform (Verasonics) using a CL15-7 (ATL). In recent work, the Coherence Factor (CF) was applied to CPS data to improve the signal-to-noise ratio. Translation and rotation of the kidney were determined with a least-square method. Blood velocity was estimated using a nearest neighbor method, focusing on flow velocities smaller than 2 mm/s.

Results/Discussion

Approximately 3.9 million MB positions were detected resulting in a detailed image of the kidney vasculature (Fig. 1). Vascular bundles were detected in the medulla with an average size and spacing of 126±22 µm and 470±170 µm, respectively. 4748 trajectories were recovered with a length of 500±220 µm and a velocity of 0.98±0.45 mm/s, likely as a part of the venous return. Observation of individual MBs showed coherent patterns of RF signals suggesting that MBs in small vessels can survive thousands of pulses and that the echoes themselves could be used to further characterize the vasculature based on their motion and frequency content. Current work focuses on applying this technique to other organs and superficial tumors.

Acknowledgment: NIH grants R01CA112356, R01CA210553, R01CA199658 and R01CA134659.

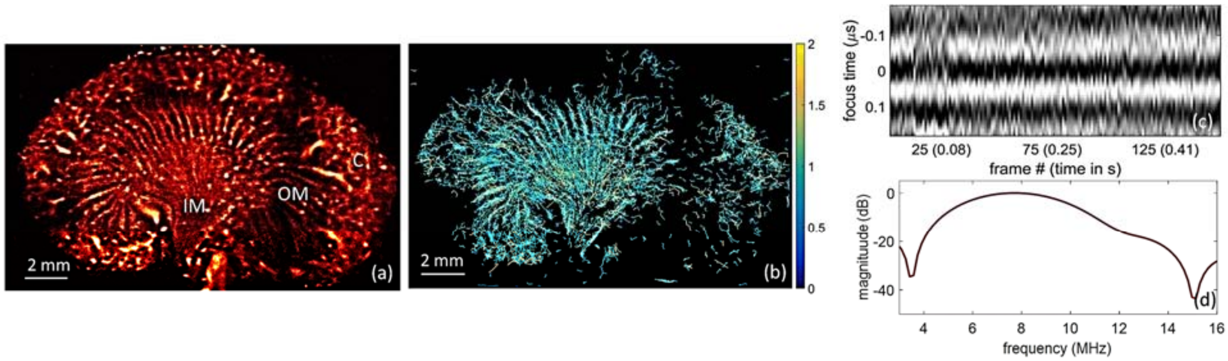

Figure 1. (a) Density map of the MB positions after motion correction showing the different vascular structures in the kidney (C: cortex, OM: outer medulla, IM: inner medulla). (b) Trajectories of individual MBs with a velocity <2 mm/s are mainly found in the medulla. (c) Slowly flowing MBs in microvessels can survive thousand of pulses and show coherence in time over hundreds of frames. (d) Access to RF signals provides supplementary ways to characterize MB oscillations.

3C-3

4:30 pm Localisation of Multiple Non-Isolated Microbubbles with Frequency Decomposition in Super-Resolution Imaging

Sevan Harput[1], Kirsten Christensen-Jeffries[2], Jemma Brown[2], Robert J. Eckersley[2], Christopher Dunsby[3], Meng-Xing Tang[1]; [1]*Department of Bioengineering, Imperial College London, London, United Kingdom,* [2]*Biomedical Engineering Department, King's College London, London, United Kingdom,* [3]*Department of Physics and Centre for Pathology, Imperial College London, London, United Kingdom*

Background, Motivation and Objective

Sub-diffraction imaging, also known as super-resolution (SR) imaging, is a novel method that can overcome the fundamental diffraction limit by localizing spatially isolated microbubbles (MBs). A low concentration of MBs is required to achieve isolated signals in microvasculature, which is especially challenging in cancerous tissue due to high vessel density and slow flow. This study proposes a frequency decomposition method that uses the polydisperse nature of commercial MB contrast agents to separate spatially non-isolated MBs with different acoustic signatures.

Statement of Contribution/Methods

Conventional methods used to decompose a signal into multiple frequency components introduce phase delays between components. Therefore, multiple zero-phase filters were implemented by bandpass filtering the signal twice and performing a time reversal operation after each filtering stage. This procedure cancels the unwanted phase shifts and hence the time delay between decomposed signals. While imaging the microvasculature, a 40 ns shift between decomposed signals can cause up to 30 µm error in the final SR image.

The proposed technique was first verified by simulation and later tested experimentally with a 200 µm cellulose tube fixed in paraffin gel. Fig A shows the contrast-mode image of two MBs in the tube. High-frame rate imaging was performed by the ULA-OP system using a 3-11 MHz probe and the acquired RF signal was decomposed into different components after beamforming.

Results/Discussion

Individual MBs cannot be localized from the contrast-mode image shown in Fig A, because their point spread functions overlap. Figs C-F show the MB signal decomposed into different frequency bands. After decomposition, two different MBs were detected in Fig C and Fig F highlighted in different colours. Fig B highlights both detected MBs after frequency decomposition overlaid on the contrast-mode image.

Similar methods based on the detection of single or multiple MBs have been previously applied to ultrasound imaging, such as bubble wavelet [1]. Our work shows the feasibility of such a decomposition technique for the first time for SR imaging by detecting two spatially overlapping MBs. The ability to separate multiple MB echoes is crucial for SR imaging since MB concentration is hard to control *in vivo*.

[1] Wang et al., Ultrasound in Med & Biol, vol 42(7), pp 1584-97, 2016.

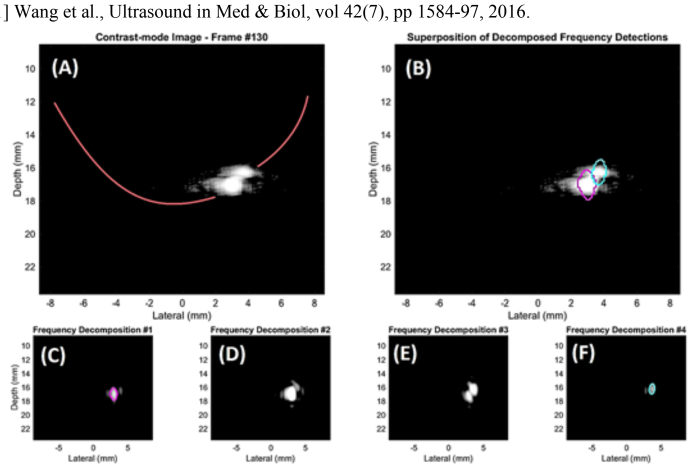

Figure (A) Contrast-mode image of two microbubbles flowing inside a 200 µm tube. Red line shows the location of the tube, where a section of the tube is intentionally missing in order to visualize the microbubble echoes clearly. **(B)** Highlights the detected MBs after frequency decomposition in light blue and purple colours overlaid on the contrast-mode image. **(C-F)** Contrast-mode image after decomposing the microbubble signal into different frequency bands. Fig C and Fig F have two different localised microbubbles highlighted with light blue and purple colours.

3C-4

4:45 pm **Determination of Adequate Measurement Times for Super-Resolution Characterization of Tumor Vascularization**

Stefanie Dencks[1], Tatjana Opacic[2], Marion Piepenbrock[1], Fabian Kiessling[2], Georg Schmitz[1]; [1]*Institute for Medical Engineering, Ruhr-University Bochum, Bochum, Germany,* [2]*Institute of Experimental Molecular Imaging, University of Aachen (RWTH), Aachen, Germany*

Background, Motivation and Objective

To implement super-resolution imaging of microvessels in clinical practice, the trade-off between the concentration of microbubbles (MB) appropriate to detect single MB and reasonable short measurement times has to be resolved. Therefore, we estimated the measurement times necessary to adequately reconstruct the microvessel trees in 3 different tumor models.

Statement of Contribution/Methods

The reconstruction of new vessels can be modeled to saturate exponentially over measurement time. The area in an US slice covered by the fully reconstructed vessel trees is expected to be proportional to the *relative blood volume* (rBV) which is used in clinical practice to characterize the vascularization. Fitting the exponential model to the covered area over measurement time, the saturation value – equivalent to rBV – as well as the percentage of the reconstruction can be estimated.

Boli (50 µL) of hard-shell MB (PBCA) were injected in murine xenograft tumors of type A431, A549, and MLS. The MB concentration of the suspension was $2x10^8$ MB/ml. 2000 US frames were acquired with a frame rate of 50 Hz using a Vevo 2100 system equipped with an MS-550D transducer (FUJIFILM Visualsonics, Toronto, ON, Canada).

To detect the MB, foreground images were generated with motion compensation followed by a temporal rank filter. From these, the positions of the MB were calculated using the intensity weighted centroids. Applying the MCMCDA algorithm [1] the tracks of the MB were estimated.

We defined a coverage *C* which was calculated via the relation of the area filled with tracks to the total area of the tumor. For this, the estimated tracks were drawn frame by frame into a matrix of 5 µm resolution and C was evaluated as a function of the acquired frame number. Then, the model $C(MB(t))=C_{final}$ $(1\text{-}exp(\text{-}\alpha \cdot MB(t))$ with the number of tracked MB(t) until time t was fitted to the computed C. We evaluated the quality of fit (R^2), the final coverage C_{final}, and the estimated final coverage eC_{final} depending on the measurement duration.

Results/Discussion

The quality of fit was high for all measurements (R^2>0.9995) demonstrating the adequacy of the model. The C_{final} were 20.6%, 5.2%, and 10.9% for the A431, A549, and MLS, respectively. These values correlate well with the characteristic rBV values of the different tumor types. After 2000 frames (40 s) 48%, 59%, and 56% of the C_{final} were reached. To reach 90% of the C_{final} 100 to 140 s would be necessary.

Evaluating shorter measurement durations, for frame numbers ≤ 1500 the eC_{final} approximated asymptotically the C_{final}. Therefore, C_{final} could already be estimated accurately for measurement times of 30 s (error of eC_{final} ≤ 0.5%).

Concluding, even if the microvessel trees are not fully reconstructed characteristic parameters can already be obtained. Thus, super-resolution characterization of tumor vascularization can be realized with commercial US-systems, by bolus injection, and within measurement times < 1 min.

[1] Ackermann, IEEE TUFFC 2016.

3C-5

5:00 pm **Subwavelength Motion-Correction for Ultrafast Ultrasound Localization Microscopy**

Vincent Hingot[1], Claudia Errico[1], Mickael Tanter[1], Olivier Couture[1]; [1]*Institut Langevin (CNRS, ESPCI, INSERM), Paris, France*

Background, Motivation and Objective

Introduced recently [Couture et al., IEEE IUS 2011], ultrasound super-resolution techniques such as ultrafast Ultrasound Localization Microscopy (uULM) surpasses the diffraction-limit and reach resolution an order of magnitude better than the diffraction limit resolution. We previously exploited uULM to achieve resolution of 8 µm over a depth of 12 mm in the rat brain vasculature [Errico et al, Nature 2015]. However, the issue of motions was addressed using physical restrain. For most applications of uULM, for example in the awake rat's brain, in soft tissues (heart, pancreas, etc.), or for imaging in humans, a tight physical restrain can't be used. The issue of subwavelength motions needs to be addressed differently. As image registration techniques are limited mainly by the SNR, subpixel displacements can be detected and corrected.

Statement of Contribution/Methods

In this study, we propose a subwavelength motion correction method on beamformed images using Singular Value Decomposition (SVD) and rigid image registration [Hingot et al, Ultrasonics 2017]. Ultrafast plane wave acquisitions are performed at 15MHz and 500fps by blocks of 400ms during 3 minutes. A spatiotemporal clutter filter based on SVD of raw data was first used to extract tissue dominated images by selecting only 2% of the singular values with the highest intensity. Rigid registration is done on tissue dominated images using 2D cross correlation on interpolated images. This way, subwavelength tissue motions are tracked and stored. SVD filter on raw data extract flowing bubbles from tissues this time excluding the 15% of the singular values with the highest intensity and the 30% with the less intensity. Individual bubbles are then localized with an 8 µm resolution and their positions are corrected with the corresponding tissue motion. Accumulation over a million bubbles creates a super-resolution image.

Results/Discussion

The method was used in a loosely restrained rat's brain for a first proof of concept with small and rigid motions. Micrometric motions could be tracked and corrected with the same resolution than uULM. We can see a clear benefit of the motion correction, especially on small vessels. If the method can be extended to non-rigid motion, out of plane motions will remain the main source of degradation of the images, which can only be addressed through 3D imaging.

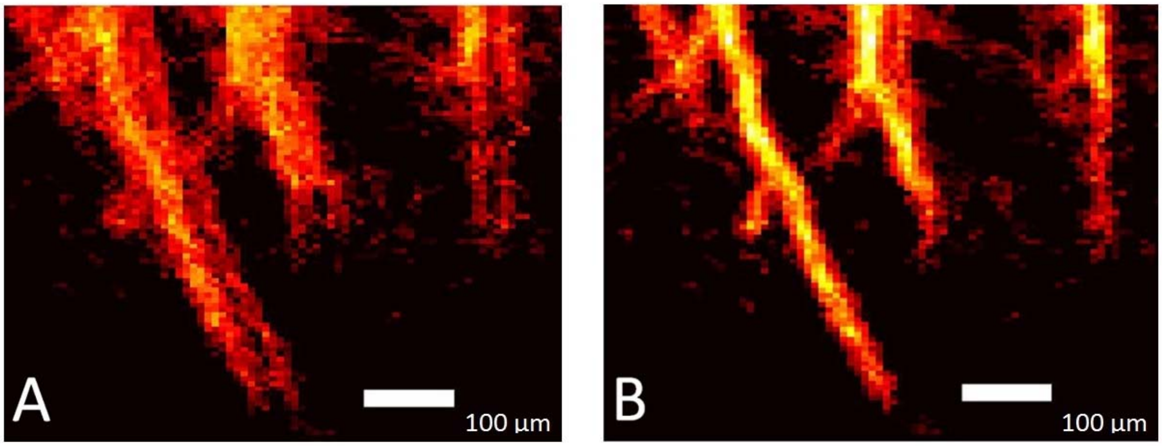

A. Uncorrected image of a 60 µm vessel **B.** Same vessel after motion correction

3C-6

5:15 pm ***In Vivo* Super-Resolution Imaging of Vasa Vasorum in Rabbit Atherosclerotic Plaque Model Using Deconvolution-Based Localization Technique**

Jaesok Yu[1,2], Linda Lavery[2], Kang Kim[1,2]; [1]*Bioengineering, University of Pittsburgh, USA,* [2]*Medicine & Heart and Vascular Institute, University of Pittsburgh, USA*

Background, Motivation and Objective

Angiogenic vasa vasorum (VV) is an important marker for atherosclerotic plaque progression and vulnerability. However, current *in vivo* imaging of tiny VV near a major vessel is limited. The super-resolution ultrasound imaging (SRI) can be a promising candidate. Microbubbles (MBs) localization technique for common SRI excludes signals from densely distributed MBs, requiring a large number of frames, which makes it impractical for assessing dynamic information. Here, we developed a SRI technique using deconvolution that allows localizing all MBs in a frame and therefore significantly reduces acquisition time, which enables dynamic SRI and evaluated it in vivo rabbit VV detection.

Statement of Contribution/Methods

Two rabbits were on high-fat diets for 4 weeks following a balloon injury in the right femoral artery. The nonsurgical left artery was considered control. At 12 weeks post-surgery, a 0.15 mL bolus of MBs (Definity, 10^{10} MBs/mL) was intravenously injected. Thirty seconds after injection, a total of 9,000 plane-wave frames compounded with 3 tilted angles were acquired at 500 Hz using a high-frequency probe (11 MHz) connected to Verasonics system. To localize each MB, RL deconvolution was applied to MBs signal extracted from beamformed data. By looking at periodic signal intensity variation in lumen, each cardiac cycle was divided into 10 steps in dynamic SRI mode. All deconvolved MBs images were relocated to corresponding each cardiac step to form a single cardiac cycle in which blood flow dynamics was characterized. VV development was evidenced by histology (H&E and vWF).

Results/Discussion

Static SRI using 3,000 frames laid over B-mode are shown in (a) diseased artery (DA) and (g) non-diseased artery (nDA). Vessel wall was thickened (410 µm) and lumen diameter was decreased (1.1 mm) in DA compared to nDA (220 µm, 1.4 mm, respectively) as shown in H&E (d) DA and (j) nDA. VVs were more populated and believed to be infiltrated into the medial area of DA, while much less populated VV were found in adventitial and connective tissue area in nDA, which were evidenced in vWF (white arrows in (e, f) DA and (k) nDA). Normalized mean signal intensity of VV in unit wall area was 0.17 for DA and 0.06 for nDA. These observations were more clearly confirmed by closely looking at blood flow through VV from adventitia into media in dynamic SRI (snapshots at diastole (b, h) and systole (c, i) peaks).

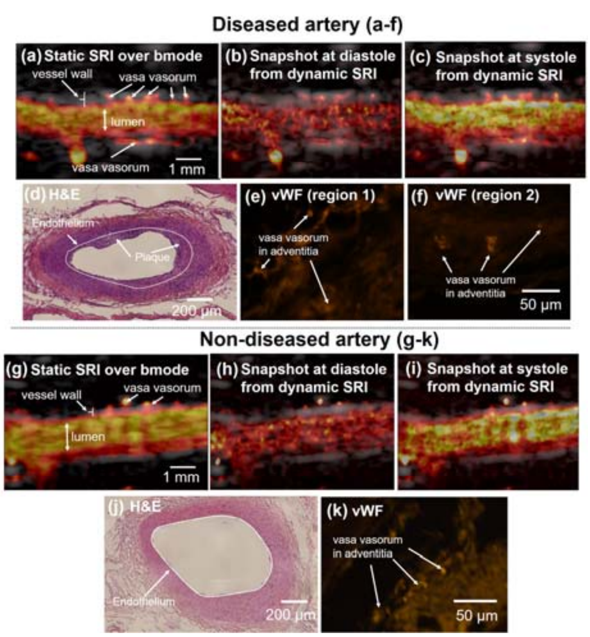

4C - MTC: Staging and Monitoring of Diseases and Tissue Physiology

Diplomat Room

Thursday, September 7, 2017, 4:00 pm - 5:30 pm

Chair: **James Miller**
Washington University

4C-1

4:00 pm **Detection of Early Tumor Response to Abraxane Using H-Scan Imaging: Preliminary Results in a Small Animal Model of Breast Cancer**

Mawia Khairalseed[1], Fangyuan Xiong[1], Robert Mattrey[2], Kevin Parker[3], Kenneth Hoyt[1]; *[1]University of Texas at Dallas, USA, [2]University of Texas Southwestern Medical Center, USA, [3]University of Rochester, USA*

Background, Motivation and Objective

H-scan is a new ultrasound (US) technique that images the relative size of acoustic scatterers. This modality relies on matching a model of pulse-echo formation to the mathematics of a class of Gaussian-weighted Hermite polynomials (GWHP). Parallel convolution filters using the second (GWH2) and eighth (GWH8) components are applied to the radio frequency US data to capture the low and high frequency signal components respectively. The relative strength from each convolution is color-coded and imaged. The purpose of this study was to evaluate the potential of H-scan imaging for characterizing tumor tissue in an animal model and any early response to systemic anticancer treatment.

Statement of Contribution/Methods

Female nude athymic mice (N = 10, Charles River Laboratories) were implanted orthotopically with 1 million breast cancer cells (MDA-MB-231/Luc, Cell Biolabs). Implanted tumors were allowed to grow for about three weeks before they were assessed using H-scan imaging. During the US imaging study, all animals were placed on a heating pad and controlled with 2% isoflurane anesthesia. Each tumor-bearing animal was imaged at baseline and before receiving an intravenous injection with the anticancer drug Abraxane via a tail vein catheter. Note that the US transducer was physically fixed over the tumor and the catheter was placed before imaging. This protocol permitted US imaging along the same tumor cross-section before and after injection of the anticancer drug in order to assess any early tumor response and cellular disruption. H-scan imaging with angular compounding (N = 5) was performed using a Vantage 256 system (Verasonics Inc) equipped with an L11-4v transducer at baseline and again every 30 min for at least 2 h after drug dosing. All animals were then humanely euthanized and tumors excised.

Results/Discussion

Preliminary experimental results revealed that there was a discernible early tumor response to therapy (within 30 min after drug dosing) that was detected using H-scan imaging. Overall, there was a significant change in the mean H-scan image intensity compared to baseline intratumoral measurements at 120 min (29.2 ± 0.8%, $p = 0.001$) which was not observed in control animals. Given Abraxane is a class of chemotherapeutic drug that disrupts cellular mitosis leading to apoptosis, we theorize that the discernible colormap shift observed in the H-scan image sequences is detection of cancer cell shrinkage as it undergoes apoptotic cell death. Both in vitro and in vivo studies have demonstrated that apoptosis occurs in cancer cells within hours after exposure to paclitaxel which is consistent with our hypothesis. This shrinkage manifests as a decrease in the scattering cross-section of the affected cells. Future work will investigate this phenomena in more detail with appropriate controls and correlate H-scan imaging results with histologic findings from excised tumor tissue sections.

4C-2

4:15 pm **Continuous Measurement of Arterial Diameter Changes Using a Wearable and Flexible Ultrasonic Sensor**

Andy Huang[1], Masayoshi Yoshida[2], Yuu Ono[1], Sreeraman Rajan[1]; *[1]Carleton University, Ottawa, Ontario, Canada, [2]Kyushu University, Japan*

Background, Motivation and Objective

Changes in the biomechanical functions of artery serve as important indicators for prediction of cardiovascular disease. Endothelial dysfunction is known to play a role to develop atherosclerosis and cardiovascular disease. Ultrasound measurement of flow-mediated dilation of the brachial artery is a method to quantify endothelial function based on changes in arterial diameter. One challenge of the ultrasonic arterial measurement is the compression of the artery due to the weight of a conventional ultrasound probe employed, resulting in the error on the diameter estimation. One approach to address this issue with low-cost is to use a wearable ultrasound sensor which is flexible and lightweight so that it does not deform the artery of interest beneath the sensor during the measurement. In this paper, the capability of the wearable sensor to measure the change in arterial diameter is investigated.

Statement of Contribution/Methods

The wearable ultrasonic sensor was constructed from an 110um-thick PVDF piezoelectric film having a top and bottom electrodes with a thickness of 6 um each. The active sensing area was 20 mm by 20 mm. The sensor was covered by aluminum foil and polyimide films for electrical noise shielding and electrical insulation. The sensor had a total thickness of 0.75 mm and weight of 2g including the electric wires. During the experiment, the sensor was secured by an adhesive tape above the brachial artery of the subject's left arm with couplant gel between sensor and skin surface. The location of the brachial artery was verified by the B-mode images using a clinical ultrasound system. An M-mode measurements was performed for 5s at a frame rate of 1 kHz and sampling rate of 125 MHz to acquire ultrasonic RF signals. The center frequency and bandwidth of the RF signals were 5.6 MHz and 4 MHz, respectively. A moving average filter with 10 frames was applied to reduce the random noises in the signals. Moreover, a stationary wavelet filter was applied to reduce the speckle noises. Then, the depths of the anterior and posterior arterial boundaries were obtained by analyzing the boundary echoes using a phase-tracking method. Finally the atrial diameter was calculated from the difference of the boundaries' depths.

Results/Discussion

The changes of the arterial diameter corresponding to a cardiac cycle were obtained. With the 4 cardiac cycles, the average arterial diameter was 3.13 mm and 3.19 mm at diastolic and systolic pressure, respectively, with a standard deviation of 2.3 µm and 2.9 µm respectively. Thus, the flexible sensor was able to capture a 60 µm arterial diameter change due to the heartbeat. Furthermore, the dicrotic notch produced by the closure of the aortic valve was observed in the measurement results. The measurement resolution was estimated about 1 µm using the noise standard deviation. Thus, it was successfully demonstrated that the wearable sensor was able to measure the arterial diameter changes corresponding to the cardiac cycle.

4C-3

4:30 pm **Staging Hepatic Steatosis in Nonalcoholic Fatty Liver Disease by Quantitative Conventional Ultrasound Imaging, Validated with Histopathology**

Gert Weijers[1], Isabelle Munsterman[2], Johan Thijssen[1], Aisha Meel - van den Abeelen[1], Joost Drenth[2], Eric Tjwa[2], Chris de Korte[1]; [1]*Medical UltraSound Imaging Center (MUSIC), department of Radiology and Nuclear Medicine, Radboud University Medical Center, Nijmegen, Nijmegen, Netherlands,* [2]*Gastroenterology and Hepatology, Radboud University Medical Center, Nijmegen, Nijmegen, Netherlands*

Background, Motivation and Objective

Nonalcoholic fatty liver disease (NAFLD) is the most common liver disorder in developed countries with a global prevalence of approximately 25%. NAFLD represents a spectrum of disorders and starts with benign steatosis (NAFL, ≥5% hepatic steatosis (HS)), but may lead to nonalcoholic steatohepatitis (NASH), inflammation with hepatocyte injury with or without fibrosis, which may lead to cirrhosis. Qualitative scoring of liver biopsies still is the gold standard for staging steatosis however, they are invasive and complications such as bleeding and infection may occur. For this reason we developed and tested a computer aided ultrasound (CAUS) protocol for the non-invasive assessment of liver HS using quantitative ultrasound (QUS) B-mode images. CAUS showed to have high predictive values (area under the curve (AUC) up to 0.95) in cows and similar correlations value with HS in a human pilot study. The current study was conducted in order to assess the predictive values of CAUS in staging hepatic steatosis in-vivo.

Statement of Contribution/Methods

Consecutive patients indicated for a liver biopsy received a simultaneous transabdominal US examination (Siemens Acuson X150; Siemens Healthcare GmbH, Erlangen, Germany, with CH5-2 transducer). Currently 205 patients with liver biopsies and QUS images are included. Biopsies were qualitatively scored using the Brunt-score for steatosis grading. Metavir, Ishak and/or Roenigk scores were used for disease specific fibrosis staging. All US images were further post-processed using the CAUS method. In CAUS corrections are applied for the: Look up table (linearization), beam-profile, and attenuation caused by the superficial tissue layers. Furthermore, segmentation of large blood vessels and bile ducts is performed automatically. Finally echo-level and texture parameters are estimated on average and as a function of depth by estimation of slope and intercept of a linear fit. CAUS parameters were correlated to the fat-score. Classification accuracy was evaluated by leave-one-out cross-validation using a multiple linear regression analysis using the CAUS parameters: average echo level (MU); Residual attenuation coefficient (RAC = slope of the MU); slope of the Signal to noise ratio. Finally receiver operating characteristic curves were constructed.

Results/Discussion

Best correlating CAUS parameter with HS severity was found to be the RAC (RAC, $R=0.79$, $p<0.01$). AUC for HS was found to be 0.95 (n=71) with a sensitivity and specificity of 86% and 85% respectively, when using a HS threshold of 5%. These results are in line with previously performed studies. 80% of the included patients were found to have NASH with fibrosis. However, no significant correlations of the CAUS parameters to a pure fibrosis-group (N=106) was found. Conclusion: CAUS is able to classify HS accurately and does not suffer from the presence of fibrosis, and thus screening with CAUS for hepatic steatosis is feasible.

4C-4

4:45 pm **In Vivo Study of Quantitative Ultrasound Parameters in Fatty Rabbit Livers**

Trong Nguyen[1], Anthony Podkowa[1], Rita Miller[1], Minh Do[1], Michael Oelze[1]; [1]*Electrical and Computer Engineering, University of Illinois at Urbana Champaign, Urbana, Illinois, USA*

Background, Motivation and Objective

Nonalcoholic fatty liver disease (NAFLD) is the most common cause of chronic liver disease and can often lead to fibrosis, cirrhosis, cancer and complete liver failure. Liver biopsy is the current standard of care to quantify hepatic steatosis but it comes with increased patient risk and only samples a small portion of the liver. Imaging approaches to assess NAFLD include proton density fat fraction (PDFF) estimated via MRI and shear wave elastography. However, MRI is expensive and shear wave elastography is not sensitive to fat content of the liver. On the other hand, ultrasonic attenuation and the backscatter coefficient (BSC) have been observed to be sensitive to levels of fat in the liver. Ultrasound evaluation offers low risk to the patient and the ability to examine the majority of the liver, as compared to liver biopsy. Therefore, a need exists to further develop ultrasonic-based techniques to quantify hepatic steatosis. In this study we explored the use of attenuation and a principal component analysis (PCA) of the BSC to detect and quantify hepatic steatosis in vivo in a rabbit model of fatty liver.

Statement of Contribution/Methods

Rabbits were maintained on a high fat diet for 0, 1, 2, 3 or 6 weeks with three rabbits per diet group (total N = 15). For analysis, rabbits were separated into three groups based on the total lipid content of the livers estimated using the Folch method: low fat (< 5%), medium fat (from 5% to 10%) and high fat (> 10%). An array transducer L9-4 with center frequency of 4 MHz connected to a SonixOne scanner was used to gather RF backscattered data in vivo from rabbits. The RF signals were used to estimate an average attenuation and BSC for each rabbit. The slope and magnitude of the attenuation, estimated by averaging the attenuation over a bandwidth (3.7 to 4.7 MHz), were used for classification by correlating attenuation estimates to total liver lipid levels. Further, the first five principal components of the PCA from the BSCs were used as input features to a support vector machine (SVM) for classification and comparison to total liver lipid levels.

Results/Discussion

The slope and magnitude of the attenuation coefficient provided statistically significant differences ($p < 0.00058$, using ANOVA) between low and high liver fat groups and between the medium and high fat groups. No statistically significant differences based on the attenuation coefficient were observed between the low and medium fat groups. The proposed PCA-SVM based classification system yielded a classification accuracy of 63.7%, 32.6% and 71.2% for the low, medium and high fat groups, respectively. PCA-derived features could not differentiate between medium and either the low or high fat groups. In the PCA analysis of the BSC, 50.6% of animals in the medium fat group were misclassified as high. The results suggest that attenuation and BSC analysis can differentiate low versus high fat content of livers in a rabbit model. This work was supported by a grant from NIH (R21EB020766).

4C-5

5:00 pm **Backscattered Power Anisotropy throughout Non-Human Primate Pregnancy**

Quinton Guerrero[1], Ivan Rosado-Mendez[1], Andrew Santoso[1], Lindsey Drehfal[1], Helen Feltovich[1,2], Timothy Hall[1]; [1]*Medical Physics Department, University of Wisconsin Madison, Madison, WI, USA,* [2]*Maternal Fetal Medicine Department, Intermountain Healthcare, Provo, UT, USA*

Background, Motivation and Objective

The non-pregnant cervix is composed of layers of pseudo-aligned collagen wrapped circumferentially around the cervical canal. Studies in rodents have shown that this structure disorganizes and breaks down throughout normal pregnancy. There is evidence to suggest that layered, pseudo-aligned collagen fibers in the non-pregnant cervix induce an angle-dependence (anisotropy) in backscattered ultrasound power. We therefore hypothesize that quantification of backscattered power anisotropy can track (ab)normal changes in the cervix collagen structure that precede (pre)term parturition. To test our hypothesis, we longitudinally measured backscattered power anisotropy throughout gestation in the cervix of a non-human primate model.

Statement of Contribution/Methods

Pregnant rhesus macaques (N=18) were recruited from the Wisconsin National Primate Research Center. All primates received a transrectal cervical ultrasound exam at 4, 10, 16, 20, and 23 weeks of gestation and at 2 weeks post-partum (normal Rhesus macaque pregnancy is 24 weeks). Cervical ultrasound exams consisted of collecting 3 sets of 15 frames of electronically beamsteered (-28° to +28°) radiofrequency echo signal data from a prototype linear array transducer operated on a Siemens S2000 ultrasound system. Backscatter power anisotropy was quantified by the difference in backscattered power between the cervix and an isotropic reference material, averaged across steering angles. This quantity, referred to as the mean Backscattered Power Difference (mBSPD), was averaged across the 3 frames of RF data.

Results/Discussion

The mBSPD monotonically and significantly decreased from week 4 to week 23 gestation ($p<0.01$; Wilcoxon Rank Sum Test). The mBSPD did not differ from week 23 gestation to 2 weeks' post-partum ($p>0.05$; Wilcoxon Rank Sum Test). Taken together, these results indicate a reduction in backscattered power anisotropy throughout gestation. This observation is consistent with the nonlinear optical microscopy images of mouse cervix demonstrating collagen structure disorganization and breakdown throughout pregnancy.

All work was approved by the IACUC at the UW-Madison. Research supported by National Institutes of Health Grants T32CA009206 from the National Cancer Institute and R01HD072077, R21HD061896, and R21HD063031 from the Eunice Kennedy Shriver National Institute of Child Health and Human Development. The content is solely the responsibility of the authors and does not necessarily represent the official views of the National Institutes of Health. We are also grateful to Siemens Healthcare Ultrasound division for an equipment loan and technical support.

4C-6

5:15 pm Ultrasonic Method for Monitoring Muscle Water Content

Colin McLeish[1], Erich Everbach[1], Sergey Tsyuryupa[2], Armen Sarvazyan[2]; *[1]Engineering, Swarthmore College, Swarthmore, PA, USA, [2]Artann Labs, West Trenton, NJ, USA*

Background, Motivation and Objective

Ultrasound velocity in soft biological tissues is defined by the molecular composition of the tissues [1]. Water is the main molecular component of soft tissues and muscle water content is typically over 70%. Ultrasound velocity in muscle is a linear function of the water content [2]. Since the muscle is the main water reservoir of human body, measurements of ultrasound velocity in muscle may serve as a means for assessment of whole-body hydration status, which is an important physiological characteristic. A compact handheld device for measuring ultrasound velocity in muscle, named "hydration monitor" (HM), was developed by Artann Laboratories to assess the water balance in muscle. The objective of this study is to test whether the HM design provides the required accuracy of ultrasound velocity measurement to estimate muscle water content variations with sensitivity on the order of 1%.

Statement of Contribution/Methods

The HM uses the pitch-catch method to measure ultrasound velocity. Because the device's C-shaped probe has a fixed acoustic base, the only variable required to evaluate sound speed is the propagation time of the ultrasound pulse between transducers in a given medium.

In vitro study—Ultrasound velocity was measured in lean beefsteak (1.5x4x6.5 cm). Water injection by a syringe was used to change the sample hydration status. Water was distributed over 20 uniformly spaced injection points in the sample. Water content changes in the sample were controlled by weighing the sample.

Human study—Subject refrained from consuming liquids for 12 hours. A baseline measurement of ultrasound velocity in the soleus (calf) muscle was established. Subject consumed 1.2 L of water. Ultrasound velocity was measured at the same position every 10 minutes over 2 hours.

Results/Discussion

Ultrasound velocity in the beef muscle linearly decreases with the increase of water content with a slope of -4.0 m/s per 1% of water content change. The dynamics of the ultrasound velocity changes in human muscle in vivo shows that the equilibration of the water content following fluid consumption has time constant of about 60 minutes. The HM is capable of tracking change in total body water, shown by the trend of ultrasound velocity. The HM design provides the required accuracy of sound velocity measurement to estimate change of the sample hydration status with resolution of better than 1%, which is sufficient for measuring physiologically meaningful variations in body hydration/dehydration.

This research was partly supported by the NIH Award Number R44AG042990.

References:

1. Sarvazyan AP, Hill CR. Physical chemistry of the ultrasound-tissue interaction. In: Physical Principles of Medical Ultrasonics. Ed. Hill CR, Bamber JC, Ter Haar GR, John Wiley & Sons, 2004; Chapter 7, 223-235.

2. Sarvazyan A, Tatarinov A, Sarvazyan N. Ultrasonic assessment of tissue hydration status. Ultrasonics 43 (2005) 661-671.

5C - Material and Defect Characterization

Blue Room

Thursday, September 7, 2017, 4:00 pm - 5:30 pm

Chair: **James Blackshire**
Air Force Research Laboratory

5C-1

4:00 pm **Ultrasonic Analysis Modifications for Imaging of Concrete Infrastructure**

James Bittner[1], John Popovics[1]; [1]*University of Illinois at Urbana/Champaign, USA*

Background, Motivation and Objective

The backbone of modern infrastructure is concrete, yet modern ultrasonic characterization techniques often fail to be accurate and repeatable. Recent advances in low frequency ultrasonic array hardware have generated a new potential for improved material and structural characterization of concrete. However, the analysis and interpretation associated with the new array based hardware is more difficult than previous ultrasonic concrete applications. In this paper we present three data analysis algorithm modifications and experimentally validate each modification for improvement over the existing commercial algorithms. Validation of each modification occurs in full scale in-service samples. After validation in this paper we present a commercially analyzed inconclusive inspection of a bridge deck, with applying the modified algorithms the results are improved and a conclusion can be safely reached.

Statement of Contribution/Methods

The work explores modifications to velocity estimation, near surface imaging and attenuation compensation algorithms of highly heterogeneous and variable concrete materials. The modifications are experimentally validated on representative material samples and display significant improvement to the proprietary commercial algorithms. The algorithms are shared with an open source license in order to encourage further cross development across specializations.

Results/Discussion

The algorithm modifications reduced the velocity estimation error by 56 percent, improved near surface identification of reflectors and normalized the amplitude of reflection of two identical reflectors at different depths inside full scale concrete elements. The algorithms are demonstrated through a field study performed on an existing concrete bridge deck. The algorithm modifications are simple in execution and display the potential opportunity for further effective application.

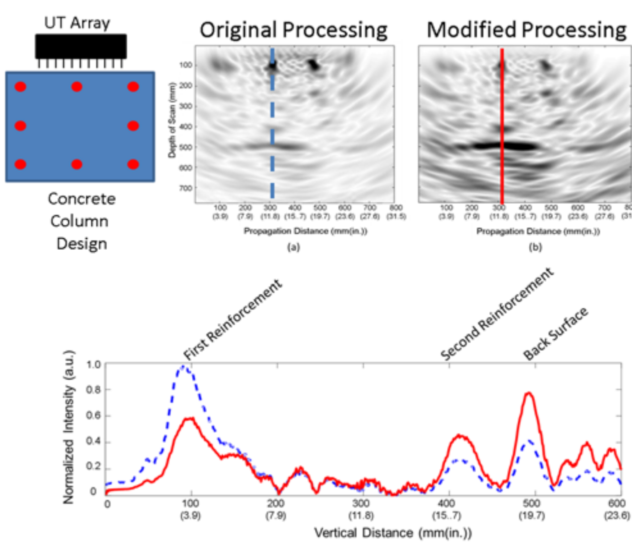

5C-2

4:15 pm **Optimized Ultrasonic Attenuation Measures for Internal Sulphate Attack Monitoring in Portland Cement Mortars**

Vicente Genovés Gómez[1], Alicia Carrión Garcia[2], Jorge Gosálbez Castillo[2], Ignacio Bosch Roig[2], Jorge Juan Payá Bernabeu[1]; [1]*Instituto de Ciencia y Tecnología del Hormigón (ICITECH), Universitat Politècnica de València, Valencia, Spain,* [2]*Instituto de Telecomunicaciones y Aplicaciones Multimedia (iTEAM), Universitat Politècnica de València, Valencia, Valencia, Spain*

Background, Motivation and Objective

Sulphate attack is considered one of the most aggressive causes of concrete degradation. Ettringite triggers expansion mechanisms that have harmful effects on the Portland cement matrix, causing micro-cracking and, consequently, a reduction in the stiffness and strength of concrete. Portland cement composites are very dispersive and heterogeneous materials that makes very challenging to do non-invasive inspections to know the intrinsic properties and integrity of such material. In this work, the degradation process due to internal sulphate attack in mortar specimens has been monitored by means of an intensive broadband frequency analysis of ultrasonic attenuation and it has been compared with mechanical and expansion analysis, and the traditional ultrasonic pulse velocity (UPV).

Statement of Contribution/Methods

The attenuative behaviour of the material implies both, intrinsic (absorption) and extrinsic (scattering) mechanisms. Particularly, it is well known that the scattering component of the global attenuation of the ultrasonic wave depends on the structure scale, and therefore, on the injected working frequency. In order to cover a wide frequency range, the frequency-dependent ultrasonic attenuation has been addressed by means of an optimal linear swept-frequency signal (chirp) which offers equivalent accuracy to narrowband signals but with a shorter measurement time.

Results/Discussion

The effect of different levels of sulphate content in mortar (addition of 0-2% of SO3 by mass of Portland cement, gypsum) were assessed along the first 150 days of the process (curing+internal attack). The expansion analysis has shown the increasing slope and the maximum expansion rate as the amount of gypsum increases. The UPV followed the trend of the stiffness of the specimens: a lower and later reached maximum value as the gypsum increases. The combination of chirp signals and the suitable signal processing reveals characteristic time-frequency attenuation diagrams which identify changes in the rate of curing process as well as the damage process. The attenuation showed similar trends to the rest of the monitored parameters for all series, but it seems to be more sensitive to the mesoscale elements in the mortar structure rather their elastic constants, constituting an interesting way to evaluate slight damage processes in non-homogeneous materials like concrete.

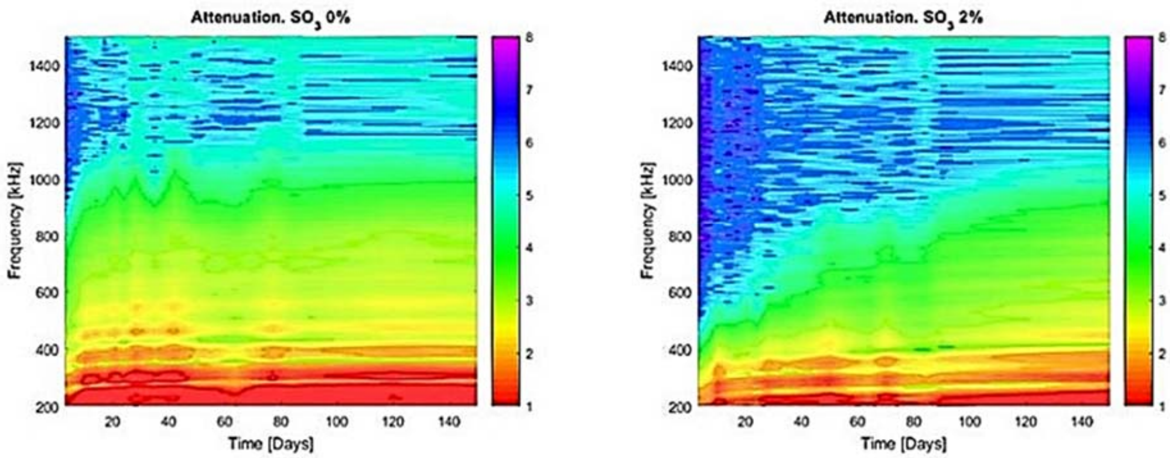

5C-3

4:30 pm Finite-Element Modelling of Elastic Wave Propagation and Scattering within Heterogeneous Media

Istvan Veres[1], Martin Ryzy[1], Tomáš Grabec[2]; [1]*RECENDT, Linz, Austria,* [2]*Laboratory of Ultrasonic Methods, IT CAS, Prag, Czech Republic*

Background, Motivation and Objective

One of the major cause for the attenuation of ultrasonic waves in polycrystalline materials is the random scattering at the grain boundaries – grain boundary scattering (GBS) -, whereby the acoustic mismatch is the result of the random orientation of the mechanical properties of the single crystals within the individual grains. Various analytical models, such as the unified theory, have been developed to describe the attenuation of the coherent wave across the different scattering regimes and recently also numerical tools have been used for the description of wave propagation in such inhomogeneous media. Comparisons of the theoretical predictions with experiments have shown, however, very little agreement and lead to theories about thermoelastic attenuation, dislocation damping or deviation in the grain size distribution as additional cause for attenuation.

Statement of Contribution/Methods

In the presented work the significance of the two point autocorrelation function (TPC) is investigated, which describes the inhomogeneity of the polycrystalline materials. We utilize a Finite Element model to investigate the attenuation of bulk and surface acoustic waves. The microstructure of the polycrystalline is described using Voronoi tessellations with 2000, 8000 or 16000 cells (grains) within a $1x2x2mm^3$ domain and meshed with $126x10^6$ elements. To achieve a better prediction of the attenuation, the theoretical models were modified with a generalized TPC which were evaluated for the corresponding Voronoi tessellations.

Results/Discussion

Numerical simulations were carried out in a frequency range where the wavelength of the propagating waves becomes shorter than the dimensions of the inhomogeneities. The model, therefore, allows the investigation of the transition between the Rayleigh and the stochastic scattering regimes. The numerical simulations for P waves show an abrupt transition between the Rayleigh and the stochastic scattering regimes compared to classical models, such as the unified theory. The modified theoretical models using TPCs from the Voronoi tessellations reproduce this sharp transition and show a good agreement with the numerical model.

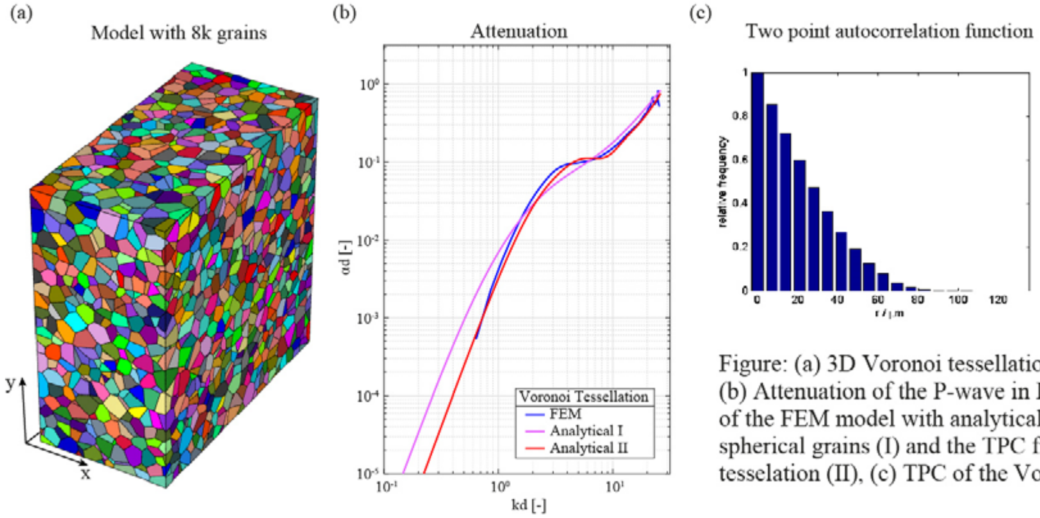

Figure: (a) 3D Voronoi tessellation with 8000 cells, (b) Attenuation of the P-wave in Inconel: comparison of the FEM model with analytical solution using spherical grains (I) and the TPC from the Voronoi tesselation (II), (c) TPC of the Voronoi tesselation.

5C-4

4:45 pm Ultrasonic Quantification of Fusion Zone in Resistance Spot Welds

Jeong Na[1]; [1]*Advanced NDI, KBRWyle, Dayton, Ohio, USA*

Background, Motivation and Objective

Resistance spot welding is one of the most widely used joining methods for sheet metals. As more advanced sheet metals are developed and used, new welding parameters need to be developed and optimized to meet a required weld strength. During this process, numerous test coupons are typically generated and examined destructively to analyze the size and microstructure character of the weld nuggets. Weld nugget sizes are commonly determined by metallurgical sectioning as well as mechanical caliper-based measurement methods. In lieu of reducing time and effort involved with weld quality analysis, a new nondestructive evaluation method has been developed to determine the size of the fusion zone quantitatively.

Statement of Contribution/Methods

A laser vibrometery system is used to detect focused ultrasonic signals in a through transmission set up in an immersion tank. Microstructural influences on the transmitted waves through the corona bond area and fusion zone are distinguishable in a high resolution ultrasonic C-scan image. The size of fusion zone can be determined quantitatively by using a newly developed ultrasonic amplitude scattering pattern recognition algorithm.

Results/Discussion

High spatial resolution C-scan images depicted in the figure were generated with a spot weld made on two sheets of an automotive grade advanced high strength steel. For a comparison purpose, the image in Figure (a) was obtained with two 20-MHz focused probes, while the image in Figure (b) was obtained using the laser detection method. The overall size and shape of the weld appear to be the same in both images, however, an additional and unique ultrasonic beam scattering pattern appears in Figure (b), which is thought to be caused by the wave interaction with the martensite within the fusion zone. Using the wave pattern recognition algorithm, the fusion zone and corona bond area were estimated to be 4.1-mm and 5.4-mm in diameter, respectively, as depicted in Figure (c). An optical image depicted in Figure (d) was taken after horizontal sectioning and the average diameters of fusion zone and corona bond area were estimated to be 4.12 mm and 5.39 mm, respectively, which were nearly identical to the nondestructive ultrasonic imaging results. In this presentation, details of the current imaging methodology, ultrasonic wave scattering phenomenon, and additional test results will be discussed.

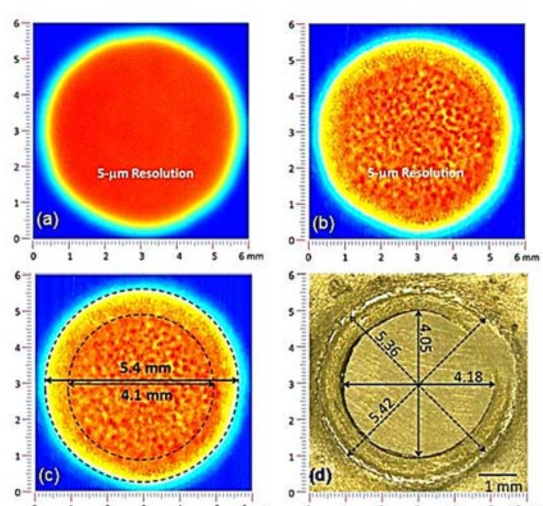

5C-5

5:00 pm **Laser Ultrasonic Assessment of the Effects of Oxidation and Microcracking on the Elastic Moduli of Nuclear Graphites**

James Spicer[1], Fan Zeng[1], Nidia Gallego[2], Cristian Contescu[2]; [1]*The Johns Hopkins University, USA,* [2]*Oak Ridge National Laboratory, USA*

Background, Motivation and Objective

Structure-property relationships in bulk materials can be important in establishing sensing methods to assess the state of material microstructure. This is particularly true for nuclear graphites since these materials can become oxidized under service conditions and the structural integrity must be confirmed during the lifetime of the material to ensure proper functioning of the reactor core. Many sensing methods might be used to assess the state of these materials, but the elastic moduli are among the physical properties that can be used to infer changes to graphite microstructure that are closely associated with loss of strength. In this work, laser ultrasonic methods were used to measure the elastic response of various graphite grades with a focus on NBG-18, NBG-25 and IG-110.

Statement of Contribution/Methods

In this work, graphite samples of NBG-18 and IG-110 were oxidized under various conditions to increase porosity with the result that samples with 5 and 10% weight loss were obtained. These samples were evaluated using laser ultrasonic methods to obtain ultrasonic transit times for longitudinal and shear waves. These results were used with mass density measurements to produce values for the elastic moduli that could be represented as a function of porosity. These results have been interpreted using effective medium models for multiphase microstructures to produce structure-property relationships as a function of oxidation-induced porosity.

In addition to porosity, microcracks have a substantial role in determining the moduli of nuclear graphites. During manufacture, microcracks can be formed that display preferred orientation and this results in elastic anisotropy of the graphite. Using laser ultrasonic methods based on shear wave birefringence, the elastic anisotropy can be quantified and interpreted using models for the texture of polycrystalline materials. To demonstrate this approach, measurements of modulus and thermal expansion in NBG-25 have been interpreted using models describing the properties polycrystalline materials composed of grains having hexagonal crystal structure. The results of this analysis provide the orientation distribution coefficients that describe crystallite orientation in this material.

Results/Discussion

Laser ultrasonic measurements in oxidized graphites show that the moduli decrease with increasing porosity. This variation can be interpreted successfully using effective medium models if the characteristics of graphite oxidation are taken into account – namely that different surfaces of graphite crystallites oxidize at different rates. Results of laser ultrasonic shear wave birefringence measurements yield values for the orientation distribution coefficients W_{400} and W_{200}. Thermal expansion coefficient measurements of anisotropy yield values for W_{200} that compare favorably to ultrasonic results if property-averaging schemes are included in the analysis of results.

5C-6

5:15 pm **Characterization of Metallic Glasses Using Ultrasound Broadband Spectroscopy**

Megha Agrawal[1], Ashwin A Seshia[1]; [1]*Nanoscience Center, Dept of Engineering, University of Cambridge, United Kingdom*

Background, Motivation and Objective

Metallic glasses (MG) are a unique class of amorphous glassy materials whose mechanical properties lie between that of metals and ceramics. Owing to their random disorganized structure, characterization of MG and ascertaining information of structure-property relationships is difficult. Ultrasonic techniques have been previously used to characterize metallic glasses either by using the time-of-flight pulse-echo technique or Resonant Ultrasound Spectroscopy (RUS). The RUS methods are however limited to certain sample types and exhaustive preparation steps.

Statement of Contribution/Methods

This paper reports a technique for characterizing a range of materials including metallic glasses with minimal sample preparation by a portable device constructed using a pair of ultrasonic transducers (Agrawal, 2015). The broadband ultrasound swept frequency spectroscopic technique works at very low input power (-15 dBm or less) and provides accurate estimation of the speed of sound for various dimensions and compositions of metallic glasses. This paper presents Ultrasound Broadband Spectroscopy technique on a range of different composition of metallic glasses and its comparison with RUS and PE technique.

Results/Discussion

The transmission acoustic response of each metallic glass is a signature response depending on the internal material properties (fig 1). The speed of sound obtained by this technique is in good general agreement with the analytical model developed in this work as well as quantitatively within 0.5- 6% error as compared to RUS (Table 1). The Ultrasound Broadband Spectroscopy technique proves to be a non -destructive, simple and effective method to enable rapid characterization material properties with results comparable to other ultrasonic characterization techniques.

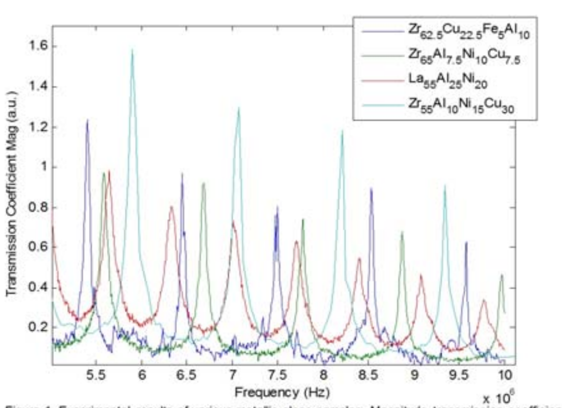

Figure 1. Experimental results of various metallic glass samples. Magnitude transmission coefficient vs sweep frequency. Peaks represent standing wave resonances generated in the medium of a given dimension which is a signature of the internal characteristic of the metallic glass

Table 1 Comparison of speed of sound for Ultrasound Broadband Spectroscopy technique with respect to RUS.

Sample	Ultrasound Broadband Spectroscopy (m/s)	Resonant Ultrasound Spectroscopy (RUS) (m/s)	% error Speed of Sound with respect to RUS
$Zr_{62.5}Cu_{22.5}Fe_5Al_{10}$	5010 ± 4.8	4989.63	0.408 %
$Zr_{65}Al_{7.5}Ni_{10}Cu_{7.5}$	5280 ± 4.2	5050*	4.55*%
$La_{55}Al_{25}Ni_{20}$	3330 ± 3.0	3531.88	-5.716%
$Zr_{55}Al_{10}Ni_{15}Cu_{30}$	4725 ± 3.7	4990.31	-5.31%

***Since RUS data was not available, the closest composition was used for comparison (Wang, 2012). $Zr_{65}Al_{10}Ni_{10}Cu_{15}$**

References:

Agrawal, M. et al., 2015. Characterization of mechanical properties of materials using ultrasound broadband spectroscopy. *Ultrasonics*.
Wang, W.H., 2012. The elastic properties, elastic models and elastic perspectives of metallic glasses. *Progress in Materials Science*, 57(3), pp.487–656.

Acknowledgements:

Thanks to Dr Yonghao Sun, Prof L Greer and Prof M Carpenter for metallic glass samples and RUS measurements.

6C - POA - Opto-Acoustics

Hampton Room

Thursday, September 7, 2017, 4:00 pm - 5:30 pm

Chair: **Vincent Laude**
Université'de Bourgogne Franche-Comté, CNRS

6C-1

4:00 pm **Generation of Acoustic Waves by an Extreme Ultra Violet Free Electron Laser in a Transient Grating Experiment**

Filippo Bencivenga[1], Andrea Canizzo[2], Flavio Capotondi[1], Riccardo Cucini[3], Ryan A, Duncan[4], Thomas Feurer[2], Laura Foglia[1], Travis Frazer[5], Hans-Martin Frey[2], Joshua Knobloch[5], Gregor Knopp[6], **Alexei A. Maznev[4]**, Riccardo Mincigrucci[1], Giulio Monaco[7], Keith A. Nelson[4], Emanuele Pedersoli[1], Alberto Simoncig[1], Alejandro Vega-Flick[8]; *[1]Elettra-Sincrotrone Trieste, Basovizza, Italy, [2]University of Bern, Bern, Switzerland, [3]IOM-CNR, Basovizza, Italy, [4]Department of Chemistry, Massachusetts Institute of Technology, Cambridge, USA, [5]University of Colorado, Boulder, USA, [6]Paul Scherrer Institute, Villigen, Switzerland, [7]Department of Physics, University of Trento, Italy, [8]Applied Physics Department, CINVESTAV-Unidad Mérida, Mexico*

Background, Motivation and Objective

The use of lasers to generate acoustic waves revolutionized the field of ultrasound and enabled numerous key developments in both fundamental research and applications. In the past decade, remarkable progress has been achieved in developing coherent sources of radiation operating in the extreme ultraviolet (EUV) and x-ray ranges, such as free electron lasers, which already yielded many breakthroughs in different fields of science. We expect that the field of ultrasonics will also greatly benefit from the availability of coherent EUV and x-ray sources. So far, a number of studies explored the use of coherent EUV and x-ray radiation for detection of acoustic waves. In this report, we describe the first experiment on the generation of surface and bulk acoustic waves in the tens of GHz range by EUV light.

Statement of Contribution/Methods

We used the transient grating (TG) geometry in which two crossed excitation EUV pulses excite acoustic waves at a wavevector defined by the period of the EUV interference pattern. The experiments were performed at the DiProI beamline at the FERMI-Elettra light source facility in Trieste. The FERMI free electron laser provided femtosecond excitation pulses at a wavelength of 13.3 nm, which were crossed in the sample to generate both longitudinal and surface acoustic waves (SAWs) at a wavelength of 280 nm. The acoustic waves were detected via diffraction of a probe 400 nm laser pulse.

Results/Discussion

We have observed bulk and surface acoustic waves in a number of materials such as diamond, silicon, SiGe, BK-7 glass, and Bi4Ge3O12. In diamond, we generated SAWs at a frequency of 39 GHz, the highest SAW frequency ever produced without periodic structures. We will discuss the frequency mixing of SAWs and bulk longitudinal waves in the TG signal and probing different acoustic modes in reflection and transmission geometries. While the use of an optical probe limited the shortest achievable acoustic wavelength, the implementation of an EUV probe will permit the generation of bulk and surface acoustic waves at wavelengths down to 10 nm and below at frequencies up to 1 THz and above, creating an ultimate source of tunable GHz-THz frequency ultrasound without the need to fabricate any transducer structures on the sample.

6C-2

4:15 pm **Adapting the Full Matrix Capture and the Total Focusing Method to Laser Ultrasonics for Remote Non Destructive Testing**

Theodosia Stratoudaki[1,2], Matt Clark[2], Paul Wilcox[3]; *[1]Electronic & Electrical Engineering, University of Strathclyde, Glasgow, United Kingdom, [2]University of Nottingham, Nottingham, United Kingdom, [3]Mechanical Engineering, University of Bristol, Bristol, United Kingdom*

Background, Motivation and Objective

Laser Induced Phased Arrays (LIPAs) use post processing to focus and steer the generated ultrasonic beam, synthesizing a phased array. Their principle is based on laser ultrasonics where lasers are used to generate and detect ultrasound. The technique is broadband, non-contact, and couplant free, making LIPAs suitable for large stand-off distances, inspection of components of complex geometries and hazardous environments. Our motivation is to demonstrate remote, non destructive testing with improved image quality, using this technique. LIPAs will be presented that are synthesized by capturing the Full Matrix (FMC), a data acquisition method where all possible transmitter receiver combinations in the array are obtained, at the nondestructive, thermoelastic regime. The Total Focusing Method (TFM) is used as the imaging algorithm, where the captured signals are summed with the appropriate time delay, in order to synthesize a focus at every point in the imaging area. The aim of our presentation is to adapt the FMC and the TFM, which have been previously developed for conventional ultrasonic transducers, to the needs of LIPAs in order to enable fast imaging and make more efficient use of the information in the data.

Statement of Contribution/Methods

The main issue of using the FMC is its lengthy data acquisition time. The theoretical and practical limits will be discussed and several steps taken to increase the data speed will be presented. Laser ultrasonics generate simultaneously longitudinal, shear and surface acoustic waves. Their directivities are different. For this reason, the TFM algorithm is adapted in order to take into account the laser generation and detection characteristics: apodization coefficients are included that weight the contribution of each waveform by the generated and detected directivity functions at each image point.

Results/Discussion

Experimental results are presented from nondestructive, laser ultrasonic inspection of aluminium samples with side drilled holes and slots at depths varying between 5 and 20 mm from the surface. The results show improved defect detectability and increased spatial resolution compared to standard laser ultrasonics. The apodization maximizes the signal to noise ratio at each point in the image, facilitating image detection.

6C-3

4:30 pm **High-Performance Lithium Niobate Quasi-Collinear Acousto-Optic Filter**

Vladimir Molchanov[1], Alexander Chizhikov[1], Sergey Chizhikov[1], Natalya Naumenko[1], Konstantin Yushkov[1]; [1]*Acousto-Optical Research Center, Natl. Univ. Sci. Technol. MISIS, Moscow, Russian Federation*

Background, Motivation and Objective

Quasi-collinear type of acousto-optic (AO) diffraction by bulk acoustic waves (BAW) is widely used for high-resolution tunable optical filters and dispersive delay lines for ultrashort laser pulse shaping. Most often, quasi-collinear paratellurite (TeO_2) AO filters are used due to high AO figure of merit of this material (V. Molchanov et al. Quant. Electron. 39:353, 2009). Lithium niobate (LN, $LiNbO_3$) collinear filters along Y-axis are known to provide a better spectral resolution or a shorter response time. A demand for higher spectral performance of AO filters is caused by progress in ultrafast laser technology and adaptive spectroscopy. The performance of a LN filter can be improved using quasicollinear diffraction. We aimed at design of a quasi-collinear AO filter in LN with maximum diffraction efficiency.

Statement of Contribution/Methods

The analysis shows that there are two maxima of AO figure of merit in YZ-plane of LN. One of the maxima, along Y+75° direction, is characterized by low resolution and hence it is not attractive for practical applications. Another maximum is along Y-30° direction. In this geometry the resolution is 20% less than in a collinear LN filter and 3 times higher than the absolute maximum in TeO_2. AO figure of merit, $M_2=10\times10^{-15}$ s^3/kg, is 2.5 times higher compared to collinear filter. Acoustic properties of this geometry look favorable for quasi-collinear diffraction: the BAW power flow angle is sufficiently high (8.4°) and diffraction coefficients are moderate, $W_1,W_2<2.5$ (N. Naumenko et al., Ultrason. 63:126, 2015).

Results/Discussion

We designed and fabricated a 35-mm long AO filter with diffraction of light by ultrasound in Y-30° direction of YZ plane. X-polarized shear BAW was excited by a LN transducer at the third harmonic. Time aperture of the AO filter was 10 µs. Transmission passband was 0.46 nm at the wavelength 1054 nm and diffraction efficiency was over 80% at 2 W driving power. As a dispersive delay line, the device was capable of processing 100 nm passband of ultrashort laser pulses. The experiments were performed with a femtosecond fiber laser (18 nm FWHM bandwidth centered at 1056 nm). The efficiency of 47% over the 20 nm bandwidth was obtained at 30 W peak ultrasonic power. The experiments proved high performance of quasicollinear AO diffraction in LN for tunable filters and femtosecond pulse shapers with a waveform update rate up to 100 kHz.

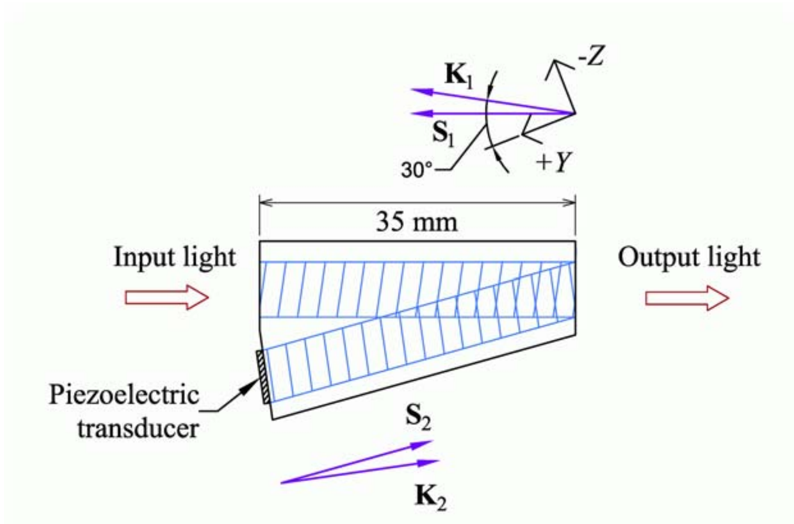

6C-4

4:45 pm **Conventional and Micro-Focused Brillouin Light Scattering for the Elastic Characterization and the Acoustic Field Mapping in SAW and BAW Resonators**

Giovanni Carlotti[1]; [1]*Dept Physics and Geology, University of Perugia, Perugia, Italy*

Background, Motivation and Objective

In order to achieve better performance of bulk and surface acoustic wave resonators operating at several GHz, it is crucial to dispose of advanced techniques and methods to provide information about the elastic constants of the constituent layered materials and to image the spatial profile of the acoustic field, both inside and outside the resonator.

Statement of Contribution/Methods

In this poster I will show how the conventional Brillouin light scattering technique (BLS), based on the inelastic scattering of photons by thermal phonons (naturally present in the materials), can be successfully exploited to achieve a selective determination of the different elastic constants of dielectric, piezoelectric and metallic films used in either BAW or SAW resonators. Moreover, I will review recent advancement in the micro-focused version of BLS, a scanning probe technique where one loses the resolution in k-space, but can achieve the imaging the spatial profile of the acoustic field with a lateral resolution of about 300 nm.

Results/Discussion

In the case of transparent (dielectric and piezoelectric) films with micrometric thickness used in resonators, by use of conventional BLS with different polarization states of the incoming light and accurate polarization analysis of the scattered light at different angles of incidence, one can detect and identify several distinct acoustic modes, such as the surface Rayleigh wave (RW), the shear horizontal mode (SHM), the longitudinal guided mode (LGM) and the longitudinal bulk (LB) mode. This provides a sufficiently large amount of information to estimate the whole set of independent elastic constants of such films (usually five). In the case of metallic layers, instead, one can attain the elastic characterization from the measurement of both the RW and several Sezawa modes at different angles of incidence.

Moreover, using the micro-focused BLS technique the spatial profile of the acoustic field of a resonator can be imaged in the real space with a submicrometric lateral resolution, investigating also the acoustic modes that spread out of the resonator, in the piezoelectric film that surrounds it. This is important in view of minimizing losses an optimizing the resonator properties, and testifies the potentiality of micro-BLS if compared to alternative and more common techniques, such as optical interferometry.

6C-5

5:00 pm **A High-Sensitivity and Wide Dynamic Range Acoustic Sensor using Multiple Mzis Micro-Opto-Mechanical Technology**

Hang Gao[1], Chih-Hsien Huang[1], **Veronique Rochus[1]**, Xavier Rottenberg[1]; *[1]LSI, imec, Leuven, Belgium*

Background, Motivation and Objective

Micro-Opto-Mechanical Pressure Sensor (MOMPS) has been demonstrated the capability of measuring acoustic waves with improved sensitivity and noise resistance compared to other methods due to its insensitivity to electromagnetic interferences and radiation hardness. It has been achieved using Mach-Zendher Interferometer (MZI) systems. However, the detection sensitivity of this standard MZI MOMPS can only be improved at the cost of a reduced dynamic range which depends on the number of loops in the MZI. To address this issue, we proposed a high sensitivity and wide dynamics range acoustic sensor by combining two different MZIs in a single wavelength system that relies on a simple readout detector.

Statement of Contribution/Methods

Traditionally, MZI MOMPS consists of a multimode interferometric splitter, two waveguide arms and a MMI combiner. The optical intensity emerging from the MZI depends on the phase difference between the arms which related to the differential pressure. As Fig. 1a shows, a new design with two different MZIs on the same membrane is presented. A multi-loop spiral pattern is fabricated on the membrane to serve as the first MZI to achieve high sensitivity. The second MZI, with low sensitivity but large linear range is used to determine which readout to use from the first one. Besides, a power tap is added to eliminate the noise introduced by the optical source. The design is implemented in a novel high quality integrated photonics platform for applications in near-infrared and visible.

Results/Discussion

A 6 kHz acoustic wave at dynamic range of 60 dB is successfully measured with a custom vacuum chamber as shown in Fig. 1b. The results are comparable to existing capacitive and piezoelectric sensors. By using low temperature PECVD SiN as waveguide core, the new MZI MOMPS can be post-processed directly on CMOS imager/detector wafers. An integrated array of acoustic sensor with embedded off-the-shelf laser diode and an imager to measure all the output would be feasible.

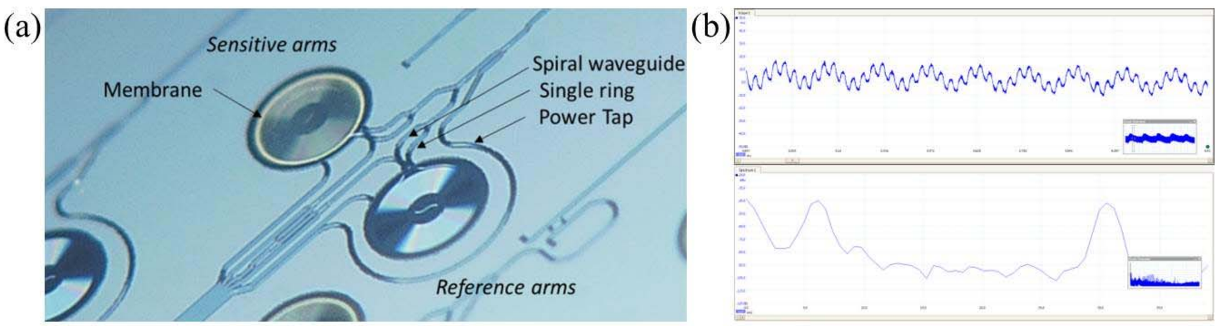

Figure 1 (a): Multiple MZIS MOMPS using outputs: the power tap, the single ring and the spiral loop
Figure 1 (b): Measurement results of a 6 kHz acoustic wave. (30kHz signal is noise of the lamp)

6C-6

5:15 pm **Optical and Acoustic Study on Phase Transition of Nanodroplets: Acoustic Droplet Vaporization versus Photoacoustic Cavitation**

Yi Feng[1], Dui Qin[1], Lei Zhang[1], Yujin Zong[1], Mingxi Wan[1]; *[1]Department of Biomedical Engineering, The Key Laboratory of Biomedical Information Engineering of Ministry of Education, Xi'an city, China, People's Republic of*

Background, Motivation and Objective

The phase transition of nanodroplet has great potential in localized therapy, e.g. gas embolotherapy, drug delivery and the extravascular tumor-targeted theranostics. To improve the temporal and spatial resolution and reduce the energy threshold of nanodroplet phase transition, photoacoustic cavitation (PAC) using synergistic laser and ultrasound was introduced and compared with acoustic droplet vaporization (ADV) in the study.

Statement of Contribution/Methods

Nanodroplet phase transition was performed in a confocal microscopic system where the ultrasound and focused laser were co-focused in a 200 µm inner diameter cellulose tube in vitro. The perfluoropentane (PFP) droplets were perfused by a syringe. The phase transition process was monitored by both high speed microphotography and acoustic detection. The acoustic signals were converted to the frequency domain and compared with ADV.

Results/Discussion

Microscopic images revealed the distinct patterns of phase transition by ADV and PAC in the cellulose tube. Acoustic signals from PAC showed distinct photoacoustic characteristics with wide-band low frequency components and harmonic components. Compared with ADV, both patterns showed the distinct advantage for predetermining the exact spatial and temporal occurrence of phase transition by the additional focused laser. The energy threshold, although relevant with droplet diameter, was also significantly reduced. ADV was also observed in micro-vessel model. It revealed the potential therapeutic applications in vessel occlusion and drug delivery.

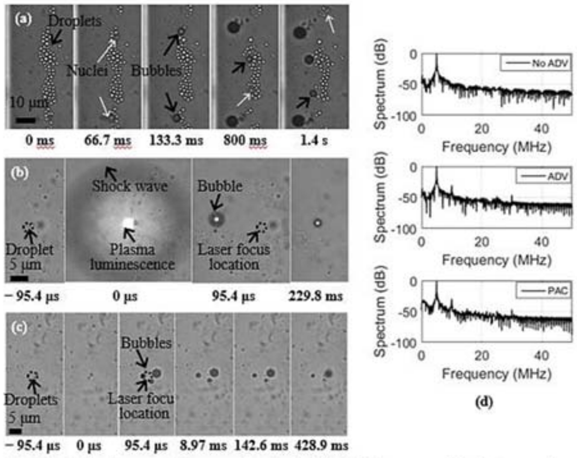

Fig.1 Optical microscopic images showing (a) the ADV process; (b) photoacoustic cavitation with single bubble formation; (c) photoacoustic cavitation with multiple bubbles formation and (d) Spectrum of acoustic signal from ADV and PAC

7C - Innovative Applications of Microacoustic Components

Empire Room

Thursday, September 7, 2017, 4:00 pm - 5:30 pm

Chair: **Shuji Tanaka**
Tohoku University

7C-1

4:00 pm AlN/GaN/Spphire as Promising Structure for Wireless, Batteryless and Packageless Acoustic Wave Sensors for High Temperature Applications

Mohammed Moutaouekkil[1], Florian Bartoli[1,2], Serguei Zhgoon[3], Thierry Aubert[2], Abdelkrim Talbi[4], Sami Hage-Ali[1], **Omar Elmazria[1]**; *[1]Institut Jean Lamour UMR 7198, Université de Lorraine - CNRS, Nancy, France, [2]LMOPS EA 4423, CentraleSupélec - Université de Lorraine, Metz, France, [3]Moscow Power Engineering Institute, National Research University, Moscow, Russian Federation, [4]LIA LEMAC/LICS - IEMN UMR CNRS 8520, ECLille -USTL, PRES Université Lille Nord de France, Villeneuve d'Ascq, France*

Background, Motivation and Objective

Waveguiding layer acoustic waves (WLAW) technology is considered as a packageless solution for extreme miniaturization of acoustic wave devices. WLAW solution is also original and suitable for high-temperature applications. Indeed, the achievement of a stable high-temperature packaging still constitutes a technological lock, in particular regarding sealing performance. In this context, we consider AlN/GaN/Sapphire as a promising WLAW structure for high-temperature applications. Indeed, the high-temperature stability of these three materials was previously demonstrated. However, in order to develop fully operational WLAW sensors based on this layered structure, it is necessary to have a better knowledge of the behaviour of each constitutive material with respect to the temperature. Consequently, the aim of this work is to experimentally validate GaN and AlN elastic constants sets in a large temperature range, which is a prerequisite to make the design of WLAW sensors according to the targeted performance.

Statement of Contribution/Methods

Several SAW devices based on AlN/Sapphire and GaN/Sapphire bilayer structures were fabricated using various wavelengths and/or various film thicknesses. The temperature coefficient of frequency (TCF) of each device was then measured and the results were compared with calculations using several thermal elastic constants C_{ij} (T) sets available in the literature (3 sets for AlN and 4 sets for GaN). Note that the available data for sapphire is reliable and was validated in various previous studies. Calculations were based on the model implemented in 2D FEM Comsol Multiphysics software using the general partial differential equations interface.

Results/Discussion

All investigated SAW devices exhibit a quasi linear dependence of the operating frequency with temperature, even up to 1000°C for the AlN/Sapphire structure. Experimental results were best fitted by calculations when using C_{ij} (T) data from reference [1] (Fig. 1-a) and [4] regarding AlN/Sapphire and GaN/Sapphire structures respectively. These sets were then used to optimize the full WLAW structure (maximization of K^2). For $\lambda = 8\mu m$, this optimization is reached when $h_{GaN} = 1\mu m$, with the following acoustic properties v = 5894m/s, $K^2 = 0.082\%$ and TCF = -48ppm/°C.

[1] J. Bjurstrom; J. Micromech. Microeng. 17, (2007) p 651.
[4] Y. Dai; J Mater Sci: 27 (2016) p 2004.

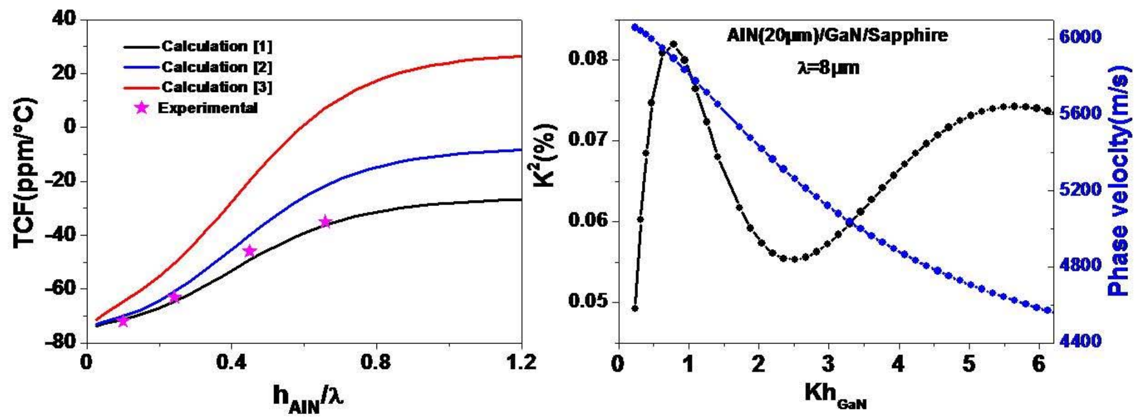

Fig. 1. (a) Dispersion curve of TFC measured and calculated using three different sets of thermal elastic constants; (b) Phase velocity and K² dispersion curves of AlN/GaN/Sapphire WLAW structure. AlN thickness being fixed to 20 µm.

7C-2

4:15 pm Design and Fabrication of Efficient Piezo-MEMS Voltage Transformers

Ventsislav Yantchev[1,2], Jeff Kriz[3], Bryan Oliver[3], Adam Weidling[3], T. Fabian[3]; [1]*Q-Arts Consulting Ltd., Sofia, Bulgaria,* [2]*Chalmers University of Technology, Goteborg, Sweden,* [3]*Advanced Sensors & Microsystems, Honeywell Inc., Plymouth, MN, USA*

Background, Motivation and Objective

RF Voltage transformers operating in one of the ISM frequency bands have recently been demanded in emerging low-power applications, such as wake-up radios in wireless networks, remotely triggered switches, stand-by units in home electronics, etc. S0 Lamb wave resonant (LWR) transformers have been first proposed. Later, SAW transformers designed as “degenerated” CRF have been proposed. Here we demonstrate a tetherless design of efficient LWR transformer and discuss the abilities to boost the voltage gain.

Statement of Contribution/Methods

High Q LWR 430MHz Transformers with edge reflectors are designed, fabricated (Fig. 1) and characterized. Optimizations of loaded and unloaded voltage gains are discussed as function of aperture, number of input (Nt) and output IDT pairs, $QxKt^2$ and Q. Design rules are deduced

Results/Discussion

Measured voltage gain of the cascaded transformer and subsequent FET detector has shown gain of about 40V/V for transformers with Q>3000 and resonated out parasitics. S-parameter measurements in environment loaded by parasitics shown gain in excess of 7.5 (Fig. 2). We found that unloaded voltage gain is better in asynchronous designs, scales primarily with $QxKt^2$, and less pronounced with the number of pairs Nt. Loaded Voltage gain scales also with aperture. Accordingly, an optimized device should employ asynchronous design, with high $QxKt^2$, aperture should be chosen as wide as possible and finally Nt should be chosen to match 50 Ohm at input.

Acknowledgement: This material is based upon work supported by the Defense Advanced Research Projects Agency (DARPA) under Contract No.: HR0011-15-C-0141. Any opinions, findings and conclusions or recommendations expressed in this material are those of the author(s) and do not necessarily reflect the views of the DARPA.

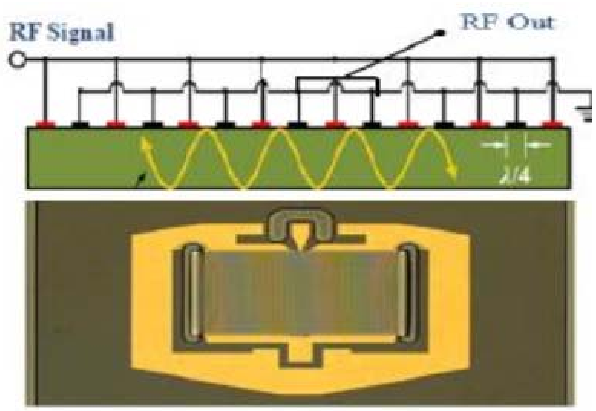

Fig 1. Cross section structure and photograph of the finished resonator

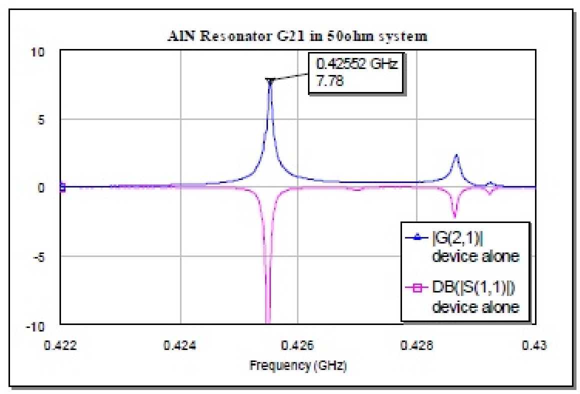

Fig 2. Measured G21 and S11 response of the resonator with its output parasitic loading

7C-3

4:30 pm Monolithic Aluminum Nitride Mems-Cmos Resonant Transformer for Wake-up Receivers

Jeronimo Segovia Fernandez[1], James Do[2], Yuhao Liu[2], Julius M. Tsai[3], Hooman Rashtian[2], Xiaoguang Liu[2], David A. Horsley[4]; [1]*Mechanical and Aerospace Engineering, University of California, Davis, Davis, California, USA,* [2]*Electrical and Computer Engineering, University of California, Davis, Davis, CA, USA,* [3]*InvenSense Inc., San Jose, California, USA,* [4]*Mechanical and Aerospace Engineering, University of California, Davis, Davis, CA, USA*

Background, Motivation and Objective

Wake-up receivers have been proposed to provide continuous sensing in a wide variety of Internet of Things applications. To achieve impedance transformation and passive amplification between the antenna and rectifier node, current wake-up receivers employ large magnetic transformers that exhibit both low *Q* and inductance per unit area in planar CMOS technology. The adoption of piezoelectric MEMS resonators to replace magnetic transformers offers an area-efficient, high-Q, monolithic solution that allows large voltage amplification for ultra-low-power applications. AlN Contour Mode Resonators (CMRs) are an emerging class of piezoelectric MEMS that offers frequency reconfiguration via lithography.

Statement of Contribution/Methods

A monolithic piezoelectric MEMS-CMOS transformer based on a 59MHz 2-port AlN CMR with Q = 900 is presented in this work (Figure 1.a). The integrated device was manufactured in a foundry-based process by conductive eutectic wafer bonding of a 0.18µm NMOS-based rectifier to the 2-port AlN CMR. When operated slightly above its resonance frequency (f_r), the AlN CMR appears as a high-Q inductor that can significantly boost the voltage swing at the rectifier input. The experimental outcome shows a ten-fold voltage boost in the rectification stage, resulting in an order of magnitude improvement in sensitivity/efficiency.

Results/Discussion

The AlN CMR is modeled as a modified Butterworth Van-Dyke (mBVD) circuit that includes the motional capacitance (C_M), resistance (R_M), and inductance (L_M) representing stiffness, damping, and mass, respectively, and a purely-electrical capacitance (C_0) that accounts for the dielectric polarization of AlN (Figure 2.b). To extract the electrical parameters of the fabricated AlN transformer, we used a Network Analyzer to measure the Y_{11}-parameter at the antenna port and fitted the admittance to the equivalent mBVD model (Figure 1.c). Thence, R_m = 112.08Ω;, L_m = 0.27mH, C_m = 27.98fF, and C_0 = 1.51pF.

To determine the maximum voltage gain of the RF-DC transformer we connected the output DC port to a 1MΩ-input impedance oscilloscope and swept the input RF signal around fr. Figure 1.d plots the voltage gain calculated as the ratio of output DC and input RF RMS voltages. Here we can see that both experimental and simulation data (assuming the equivalent circuit parameters previously fitted) show good correlation.

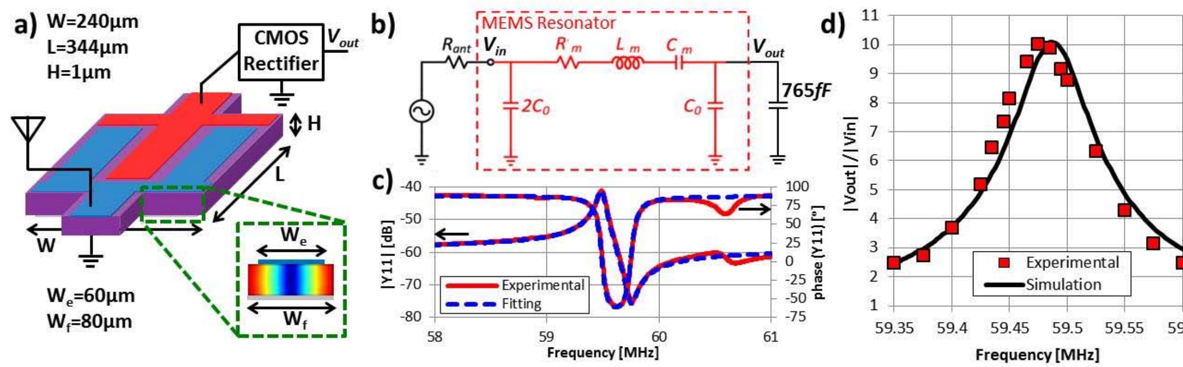

Figure 1: a) Schematic representation of the fabricated piezoelectric MEMS-CMOS transformer formed by a 2-port AlN CMR and an NMOS-based rectifier, b) mBVD model of the AlN CMR connected to a 765fF rectifier capacitance, c) fitted admittance response of piezoelectric transformer, and d) experimental and simulated voltage gain.

7C-4

4:45 pm C-Axis Zig-Zag Polarization Inverted ScAlN Multilayer for FBAR Transformer Rectifying Antenna

Rei Karasawa[1], Takahiko Yanagitani[1,2]; [1]*Fuculty of Science and Engineering, Waseda university, Tokyo, Japan,* [2]JST PRESTO, Japan

Background, Motivation and Objective

Energy harvesting from surrounding electromagnetic wave can satisfy the increasing demand of trillions of wireless sensors for IoT. RF energy harvesting is generally achieved by RF-DC conversion using a rectifying antenna (called rectenna). For weak RF signal, however, RF-DC conversion efficiency significantly decreases because weak RF signal cannot activate the diode in the rectenna. Therefore, in order to obtain high conversion efficiency for a weak signal, a Dickson charge pump[1] is generally used to increase the RF voltage. However, their low efficiency, poor impedance matching, and large size are the problem. In this study, to overcome this problem, we introduce the RF energy harvester consisting of a new type of polarization inverted FBAR transformer and rectenna. As shown in Fig.1 (a), RF input signal can be increased 7 times when 8 polarization inversion layered FBAR transformer is used. We previously reported various polarization inverted structure such as (0001)/(000-1) ScAlN films [2] and (-1-120)/(11-20) AlN films [3]. We here reports the eight layer of c-axis zig-zag polarization inverted ScAlN stack transformer resonator.

[1] A. Parks, et al. Proc. IEEE WiSNET, (2013).
[2] M. Suzuki, T. Yanagitani, and H. Odagawa, Appl. Phys. Lett. (2014)
[3] M. Suzuki, T. Yanagitani, IUS 2011, 4C-2 (2011)

Statement of Contribution/Methods

c-Axis tilted ScAlN films were grown by a glancing angle sputtering deposition. After the growth of the first ScAlN film, the substrate was rotated by 180° and the following layers were grown. The c-axis zig-zag structure was obtained by repeating this process.

Results/Discussion

c-Axis tilt angle of the layers were determined to be 35-45° by an XRD pole figure. As shown in Fig. 1 (b), monolayer ScAlN film excites fundamental shear mode of 4.0 dB at 492 MHz. In contrast, eight layer zig-zag ScAlN film clearly excites sixth-order shear mode of 1.0 dB at 576 MHz. This experimental curve shows good agreement with the theoretical curve simulated by Mason’s model considering eight polarization inversions. Comparing with the experimental and theoretical curves, average k’152 of eight layers was determined to be 6.5 %. This new type of polarization inverted FBAR transformer is promising for RF-DC conversion in the rectenna.

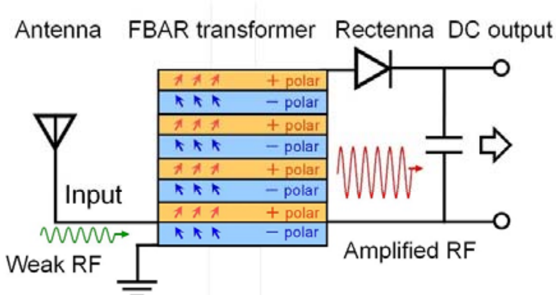

Fig. 1 (a) FBAR transformer rectifying antenna

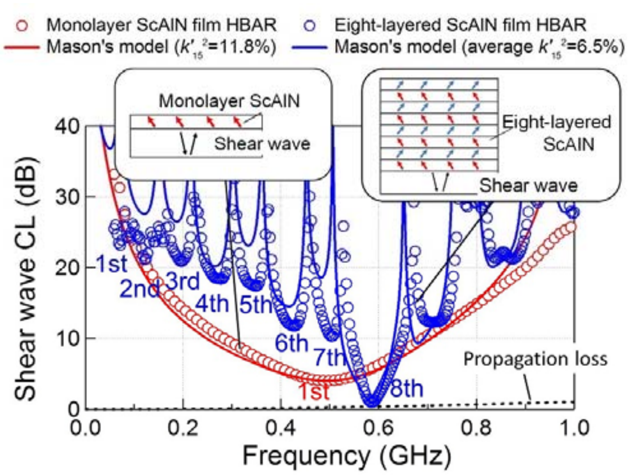

Fig. 1(b) Shear wave conversion loss of monolayer and eight-layered ScAlN film HBAR

7C-5

5:00 pm An Oven Controlled +/-1.6ppm Stable 0.32mm3 FBAR Based Transformer Coupled Colpitts Oscillator

Jabeom Koo[1,2], Kannan Sankaragomathi[1], Richard Ruby[3], Brian Otis[1]*; [1]Electrical Engineering, University of Washington, Seattle, WA, USA, [2]Intel Corporation, Hillsboro, OR, USA, [3]Avago Technologies, San Jose, California, USA*

Background, Motivation and Objective

Low power and low noise RF frequency reference is essential for radio system. Radio standards require reference frequency to be stable over a wide range of temperatures (-40 to 110oC for industrial). The state of the art radio architecture used temperature compensated resonator (ZDR), but the stability is not enough to meet the most stringent spec. for GPS application (<2ppm). The solution is here exploiting to heat and monitor the resonator temperature simultaneously

Statement of Contribution/Methods

This paper presents the first fully integrated oven-controlled ZDR version of a FBAR oscillator with temperature compensation system as shown in Fig. 1. FBAR is utilized to take advantage of its high Q-factor, and it contains heater and sensor fabricated on the top and bottom side of resonator. Temperature compensation system controls the current flowing through the heater to maintain the temperature of FBAR die. In addition, the transformer coupled Colpitts oscillator using this resonator achieves lower power consumption (250uW) and lower phase noise compared to conventional Pierce and Colpitts oscillators

Results/Discussion

Fig. 2 represents the test result of the system. It shows the frequency variation of the oscillator over the temperature. The overall frequency variation is 300ppm when the temperature changes from -5 to 90oC without temperature compensation. With compensation on, the system can be programmed to set the target temperature. The frequency variation achieved up to target temperature is ±1.6ppm with the maximum 14mW heater power. Thus, the long term and short term stability of this work is sufficient for the most stringent and ubiquitous wireless standards

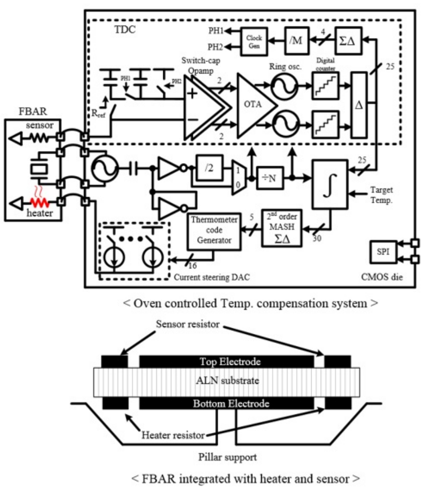

Fig. 1 Block diagram of the oven controlled temperature compensation system with FBAR die

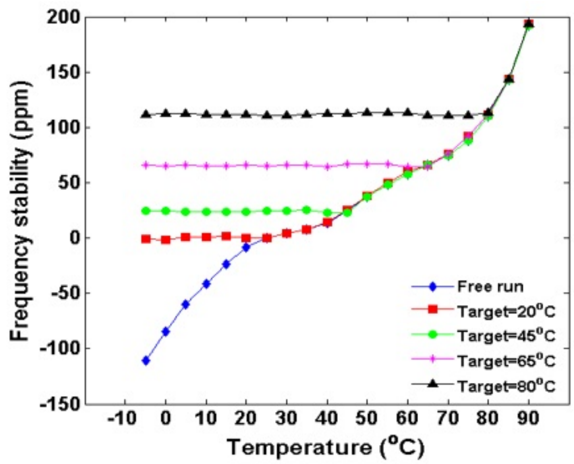

Fig. 2 Measurement results of the frequency stability with target temperatures (20°C, 45°C, 65°C and 80°C)

7C-6

5:15 pm Manipulation of Carriers in Graphene Using an On-chip Acoustic Wave Device

Ji Liang[1], Xing Yang[1], Shijun Zheng[1], Hao Zhang[1], Menglun Zhang[1], Daihua Zhang[1], Wei Pang[1]; *[1]Tianjin University, Tianjin, China, People's Republic of*

Background, Motivation and Objective

Acoustic wave devices are powerful tools for investigation of nanomaterials. For instance, acoustic waves can induce macroscopic acousto-electric (AE) current in graphene. Typically, $LiNbO_3$ is used for the acoustic wave generation. However, it is relatively inefficient in the tuning of the nanomaterials' conductivity due to its large thickness. As a solution, silicon-based acoustic transducers are potential candidates for AE current study, since the deposited thin film greatly facilitates the modulation of the graphene characteristics by gate voltage. In this work, we fabricated an on-chip SAW/GFET device to investigate the acoustic carrier transportation in graphene.

Statement of Contribution/Methods

Figure 1(a) illustrates the hybrid device. A silicon wafer with low resistivity was used as the substrate, and thus the gate voltage can be applied to the back of the wafer. AlN and Mo was deposited on silicon in turn. Mo was patterned to form the IDTs, the reflectors and the drain and source electrodes. Figure 1(b) shows the optical micrograph and the SEM image of the device. Monolayer graphene was transferred onto the device and was prepared to form the FET. Our work shed light on the AE current generated by AlN transducers and coined a new tool for investigation of various nanomaterials.

Results/Discussion

Figure 2(a) shows the electrical response of the SAW. Figure 2(b) shows the AE current induced by various RF powers. Figure 2(c) shows the transport characteristics of the GFET. Figure 2(d) demonstrates the AE current modulation by gate voltage. The AE current highly followed the frequency response of the SAW device and scales linearly with the input RF power. The on-chip device tunes the AE current efficiently, and thus opens a new avenue to explore the properties of diverse nanomaterials.

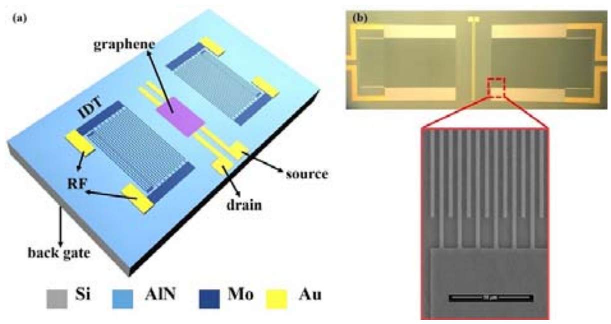

(a)
graphene
IDT
RF
source
drain
back gate
Si
AlN
Mo
Au
(b)

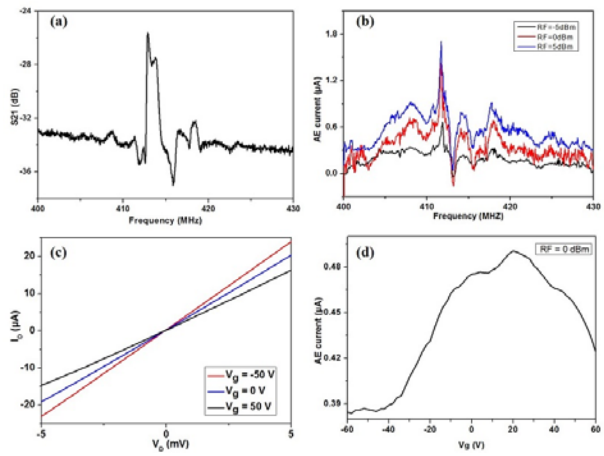

(a)
S21 (dB)
Frequency (MHz)
(b)
RF=-5dBm
RF=0dBm
RF=5dBm
AE current (μA)
Frequency (MHZ)
(c)
I_D (μA)
V_D (mV)
V_g = -50 V
V_g = 0 V
V_g = 50 V
(d)
RF = 0 dBm
AE current (μA)
Vg (V)

P1-A1 - MBB: Non Linear and Coherence Imaging

Exhibit Hall

Thursday, September 7, 2017, 9:30 am - 4:00 pm

Chair: **François Varray**
Creatis

P1-A1-1

An Improved Spatio-Temporally Smoothed Coherence Factor Combined with Eigenspace-Based Minimum Variance Beamformer for Plane-Wave Imaging in Medical Ultrasound

Xiang Wu[1], Xiao Zhang[1], **Minhua Lu[2]**; [1]*School of BIomedical Engineering, Shenzhen University, China, People's Republic of,* [2]*School of BIomedical Engineering, Shenzhen University, Shenzhen, Guangdong, China, People's Republic of*

Background, Motivation and Objective

Currently there are two main categories of adaptive beamforming applied to medical ultrasound imaging: minimum-variance-related beamforming(MV) and coherence-factor-related beamforming (CF),both of which have been applied to suppress side/granting lobe and clutter for plane-wave imaging. Unfortunately, due to low SNR/SINR, the resulting images may suffer from deficiencies: deteriorated speckle pattern, and/or black-region artifacts surrounding hyperechoic objects.

To overcome these problems above, an improved spatio-temporally smoothed coherence factor combined with eigen-space minimum variance procedure is introduced in this study.

Statement of Contribution/Methods

In our proposed method, an improved spatio-temporally smoothed coherence factor (sts-CF) beamforming was firstly used to measure the averaged signal coherence of the divided subarrys over some neighboring time samples. For those values which are lower than a predefined threshold, we cast them to the predefined threshold, so as not to excessively suppress the sidelobes . Then combing with the eigenspace-based minimum variance (ESBMV) beamforming, our proposed method could further increase the B-mode image contrast.

Results/Discussion

Simulated and experimental datasets [1] were used to evaluate performances of the proposed method. In comparison with DAS with boxcar apodization, the proposed methods improved contrast (CNR) about 2.4 dB and 2.2 dB for simulated and experimental contrast phantoms, respectively. It also significantly enhanced the lateral resolution 0.34 mm (47.2%) and 0.25 mm (30.8%) for simulated and experimental resolution phantoms, respectively. The results demonstrated that our proposed method could effectively maintain the speckle pattern and significantly remove the fore-mentioned artifacts, while the quality of resulting image still could be enhanced in a certain extent.

Reference

[1] https://www.creatis.insa-lyon.fr/Challenge/IEEE_IUS_2016/

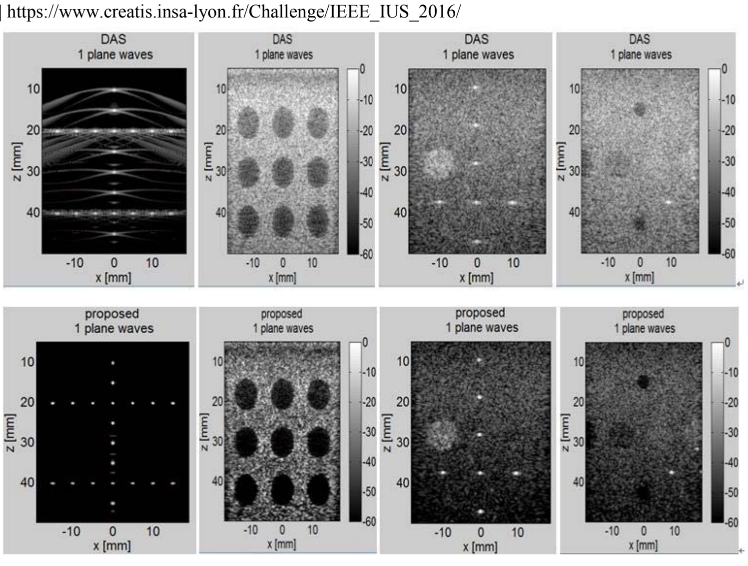

P1-A1-2

Theoretical Application of Short-Lag Spatial Coherence to Photoacoustic Imaging

Michelle Graham[1], Muyinatu Lediju Bell[1]; [1]*Electrical and Computer Engineering, Johns Hopkins University, Baltimore, MD, USA*

Background, Motivation and Objective

Short-Lag Spatial Coherence (SLSC) is a beamforming technique that was initially developed for ultrasound imaging, then applied to photoacoustic imaging with sizable improvements in contrast and signal-to-noise ratios, when compared to traditional delay-and-sum beamforming. Although the SLSC beamformer was applied to experimental photoacoustic images, the theory describing its performance in photoacoustic images was never derived. The objective of this work is to derive and evaluate spatial coherence theory for SLSC beamforming of photoacoustic images, which is critical to understanding the breadth of potential applications and their associated limitations.

Statement of Contribution/Methods

A spatial coherence equation was derived based on the van-Cittert-Zernike theorem and a linear system that describes the photoacoustic imaging process. This equation was evaluated to generate spatial covariance curves and SLSC lateral profiles for a point target and a 4 mm diameter blood vessel. The lateral resolution and contrast of the point target and vessel, respectively, were calculated as a function of lag and as a function of the theoretical ultrasound probe center frequency. Theoretical results were compared to previous experimental data and to corresponding photoacoustic k-Wave simulations.

Results/Discussion

The theoretical photoacoustic spatial covariance curves exhibited strong similarity to previous experimental data. Resolution measurements decayed exponentially as a function of lag, at a rate dependent on probe center frequency. For center frequencies of 3 to 6 MHz, when lag > 45, the average resolution remained constant at 0.75 mm. Contrast generally remained constant across all lags for both theory and simulation results. Contrast increased from 20 to 39 dB when the theoretical ultrasound probe frequency increased from 3 to 6 MHz. Lateral slices through theoretical (with no noise) and simulated (with 20 dB noise) SLSC images of a point target revealed comparable lateral resolution (see Figure 1). These results indicate that the spatial coherence of photoacoustic data is highly dependent on the ultrasound probe frequency. In general, the derived theory may be used to make inferences about the spatial coherence of photoacoustic waves, and the ultrasound probe bandwidth and lag value for SLSC image display can be optimized based on these inferences.

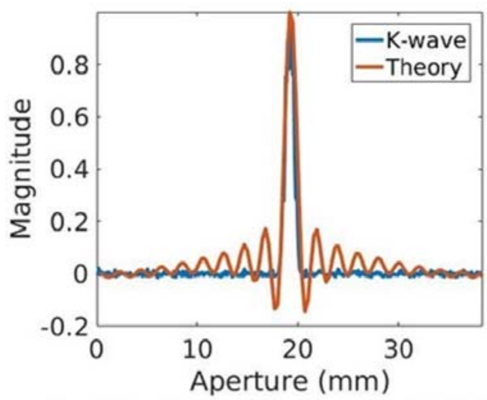

Figure1. Lateral slices through theoretical and simulated SLSC images of a point target detected by a 38.4 mm transducer aperture. Background levels fluctuate around zero for both slices and the point target is detected with comparable lateral resolution. Background noise (20 dB) was added to sensor data before SLSC beamforming in k-Wave simulations alone.

P1-A1-3

A Computationally Efficient Non-Linear Beamformer Based on p^th Root Signal Compression for Enhanced Ultrasound B-Mode Imaging

Maxime Polichetti[1], Fançois Varray[1], Giulia Matrone[2], Alessandro Stuart Savoia[3], Jean-Christophe Béra[4], Christian Cachard[1], Barbara Nicolas[1]; *[1]CREATIS, Univ Lyon, INSA-Lyon, Univ Lyon 1, UJM-Saint-Étienne, CNRS, Inserm, CREATIS UMR 5220, U1206, Lyon, France, [2]Dipartimento di Ingegneria Industriale e dell'Informazione, Università degli Studi di Pavia, Pavia, Italy, [3]Dipartimento di Ingegneria, Università degli Studi Roma Tre, Rome, Italy, [4]Université Lyon, Inserm U1032, LabTau, Université Claude Bernard Lyon 1, Lyon, France*

Background, Motivation and Objective

To improve quality of focused ultrasound images, the non-linear Filtered-Delay Multiply And Sum (F-DMAS) beamformer (DOI: 10.1109/TMI.2014.2371235) was recently proposed as an alternative to the common Delay And Sum (DAS). Given the higher computational cost as compared to DAS, in this paper we propose a simplified version of F-DMAS, which consists in applying DAS to the square root of the RF signals, followed by squaring and band-pass filtering. The lowered computational cost allows the use of the proposed beamformer in high frame-rate imaging, such as ultrafast imaging, or in 3D imaging. Besides, we generalize the method to the p^{th} root case, referred to as F-DAS$^{1/p}$.

Statement of Contribution/Methods

To reconstruct one image line, the DAS beamformer performs the sum of the N received and delayed RF signals (s_i). F-DMAS instead computes the sum of the signed square roots of the $(N^2\text{-}N)/2$ cross-products of s_i pairs. The cross-products, representing the aperture auto-correlation function, are responsible for the better resolution, while square roots preserve signal dimensionality. The F-DMAS algebraic formulation can be rearranged as the difference between the squared sum of the signed square roots of s_i, and the sum of the absolute values of s_i. The proposed F-DAS$^{1/2}$ computes the squared sum of the signed square roots of s_i, thus approximating F-DMAS by eliminating the second term of the difference, which is shown to be negligible. The same formulation is used for F-DAS$^{1/p}$, by computing the sum of the signed p^{th} roots of s_i and the p^{th} power of the resulting output.

Results/Discussion

Point Spread Functions (PSFs) and cyst phantom images were simulated using DAS, F-DMAS, F-DAS$^{1/2}$, F-DAS$^{1/3}$, and a 192-element linear array with 12 MHz excitation signals. In F-DMAS and F-DAS$^{1/p}$, RF beamformed data were band-pass filtered to select the frequency band shifted by non-linear operations. Performance equivalence between F-DAS$^{1/2}$ and F-DMAS is demonstrated by a normalized mean squared error of RF-images lower than 1%, and very similar PSF profiles and Contrast-to-Noise Ratios. Moreover, as p increases, the main lobe width decreases, side lobes are reduced (Figure 1) and the cyst Contrast Ratio is enhanced (DAS: -43.6 dB, F-DAS$^{1/2}$: -62.7 dB, F-DAS$^{1/3}$: -76.1 dB). The proposed F-DAS$^{1/p}$ has thus proved to achieve the same or better performance as F-DMAS with a lower computational cost.

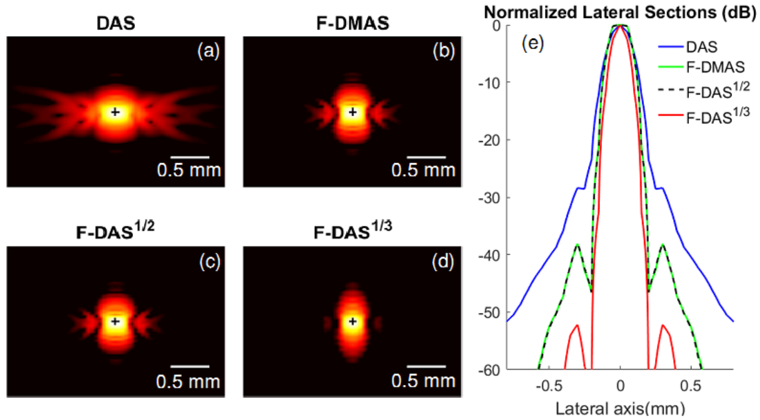

Figure 1: Simulated images of a punctual scatterer centred in front of a linear probe at 15 mm depth, on Field II. Images are displayed with a 60 dB dynamic range. Four algorithms are compared: (a) DAS, (b) F-DMAS, (c) F-DAS$^{1/2}$, proposed method to approximate F-DMAS, (d) F-DAS$^{1/3}$ proposed method, with higher order using 3rd root. The four normalized lateral profiles are presented in (e).

P1-A1-4

The Dark Region Artifact in Adaptive Ultrasound Beamforming

Ole Marius Hoel Rindal[1], Alfonso Rodriguez-Molares[2], Andreas Austeng[1]; [1]*University of Oslo, Norway,* [2]*Norwegian University of Science and Technology, Norway*

Background, Motivation and Objective

The shift to software beamforming has inspired a myriad of adaptive beamformers. Some of these overestimate which signals originate from sidelobes and which originate from the mainlobe. This results in a Dark Region Artifact (DRA) next to hyperechoic targets. We investigate this artifact for seven beamformers: Delay-And-Sum (DAS), the Coherence Factor (CF), Generalized Coherence Factor (GCF), Phase Coherence Factor (PCF), Delay-Multiply-And-Sum (DMAS), Capon's Minimum Variance (MV) and Eigenspace Based Minimum Variance (EBMV), and study how the DRA can invalidate the estimation of the contrast ratio (CR).

Statement of Contribution/Methods

The DRA is studied in both synthetic and experimental scenarios. A synthetic transmit aperture (STA) dataset was simulated in Field II containing a hyperechoic cyst and two point scatterers. A STA dataset was recorded from a CIRS phantom using a Verasonics Vantage scanner. In both datasets, a L7-4 linear probe transmitting at 5 MHz was used. The CR was measured between the cyst (region 1 in Fig. a) and three different regions for the background; region 2, region 3 and region 4.

Results/Discussion

Fig. a-g show the resulting simulated images. The DRA is observed for the CF, GCF, PCF, DMAS, and EBMV methods on both sides of the hyperechoic cyst and of the point scatterer to the right in Fig. c-g. The DRA is not observed for DAS in (Fig. a) and MV (Fig. b).

Coherence based beamformers are affected by the DRA (Fig. d-g) because next to a bright structure the strong sidelobes break the coherence across the aperture. EBMV is also affected by the DRA (Fig. c) due to the poor estimate of the signal subspace next to a bright structure, where sidelobes dominate the covariance matrix.

The CR is displayed in Fig. h. It is observed that the DRA affects the estimation of the CR. Background region 2 and 3 are both affected by the DRA. When the contrast is measured using one of these regions the CR is overestimated compared to when it is estimated using region 4. If the background region is not carefully selected when measuring contrast we end up with an invalid contrast measure for the beamformers affected by the DRA.

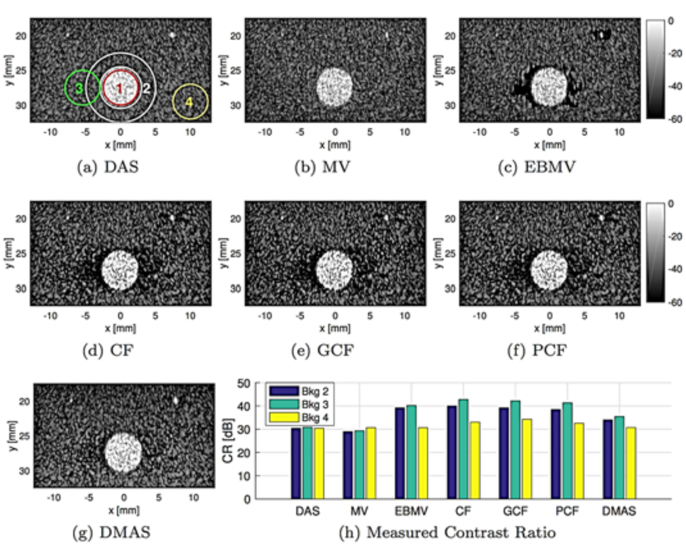

P1-A1-5

Directional Log-Gabor Filtering on the Pre-Beamformed Channel Data to Enhance Hyper Echoic Structures

Bo Zhuang[1,2], Robert Rohling[1], Purang Abolmaesumi[1]; [1]*University of British Columbia, BC, Canada,* [2]*BK Ultrasound, Canada*

Background, Motivation and Objective

One of the challenges in ultrasound bone imaging is related to the specular reflection in the soft tissue-bone interface. Since the transmit ultrasound beam is not necessarily perpendicular to the bone surface, the reflected ultrasound signals from bones are often tilted in the channel data. Even though the amount of tilting may not be large, this can still result in cancellation of the bone signals during beamforming, weakening the bone interfaces. Examples of this cancellation can be seen in Figs (a) and (c), where the spinal process (shown in the red box) in a transverse scan may disappear.

Statement of Contribution/Methods

In this paper, we have developed a novel method which applies directional Log-Gabor filtering in channel data prior to the beamforming. The channel data are first delay compensated, and then the directional Log-Gabor filter is used to enhance signals within +/-25 degrees of horizontal direction (6 dB FWHM), while suppressing signals from other directions. The filtered channel data are then masked based on the amount of energy level. Hence, weak energy is removed to highlight signals from the bones. We refer to our method as the directional Log-Gabor filtering (DLGF).

Results/Discussion

Figures below show beamformed images using delay and sum (DAS) beamforming on a vertebrae phantom (a) and from an in vivo volunteer (c). Figures (b) and (d) are the corresponding results using the proposed DLGF method. All images are shown in 40 dB range. Apart from contrast improvement and reverberation suppression, the proposed method has enhanced weak bone interfaces such as the spinal process. The average contrast ratio (CR) for the bones is improved from 0.57 in DAS to 0.91 in the proposed method.

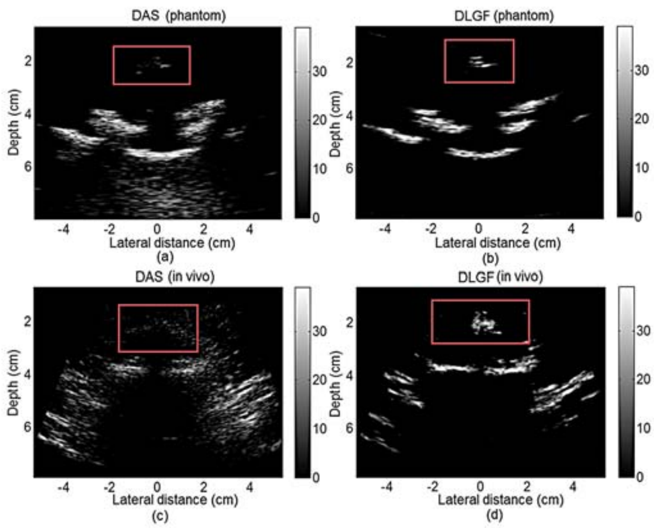

P1-A1-6

Non-Linear Beamforming Approaches for Sizing and Detecting Large Calcifications

Jaime Tierney[1], Siegfried Schlunk[1], Mark George[1], Pranav Karve[1], Ravindra Duddu[1], Ryan Hsi[1], **Brett Byram**[1]; [1]*Vanderbilt University, USA*

Background, Motivation and Objective

Standard B-mode imaging has poor sensitivity and specificity for detecting kidney stones. Additionally, B-mode imaging typically overestimates stone size. Because B-mode performs poorly, the acoustic shadow produced by the stone and twinkling artifacts seen with color Doppler have been used as substitutes for conventional imaging for stone sizing and detection. However, often neither a shadow nor a color Doppler artifact are present. In order to gain further insight into the problem of kidney stone imaging, we investigated the use of several non-linear beamforming strategies. These included plane wave synthetic aperture (PWSA), aperture domain model image reconstruction (ADMIRE), short-lag spatial coherence (SLSC) and a new coherence based method designed specifically for kidney stone detection but not sizing.

Statement of Contribution/Methods

We performed *in vitro* and ex vivo evaluations of all four methods. For the in vitro evaluation, we placed variously sized kidney stones (n=7 with width 11±5.1mm) on top of a gelatin phantom doped with graphite. The phantom served as a platform and provided a diffuse scattering background for comparisons. The phantoms were imaged 4 and 8 cm above the stone. Stones were degassed and rehydrated for at least 24 hours prior to imaging. We also performed an ex vivo evaluation where several stones were implanted into pig kidneys. The pig kidneys were immersed in water for imaging.

Results/Discussion

Below we show the qualitative results from the study in the kidneys, but here we report the results of our *in vitro* study assessing stone sizing. The distribution of stones was 11±5.1 mm. The sizing error for plane wave synthetic aperture, SLSC, ADMIRE and our custom approach were, 1.5±0.66 mm, 1.4±1.0 mm, 0.79±0.31 mm, and -1.2±4.5 mm. Based on the in vitro data ADMIRE performs best for the sizing task, although in the ex vivo example below border delineation is unclear. For detection, and based on our limited data set bolstered by combining our 4 and 8 cm depths, the custom detection method was able to achieve perfect discrimination between the stones and diffuse scattering media with a constant threshold across all data sets. We expect a planned in vivo study to serve as a more challenging and appropriate detection experiment.

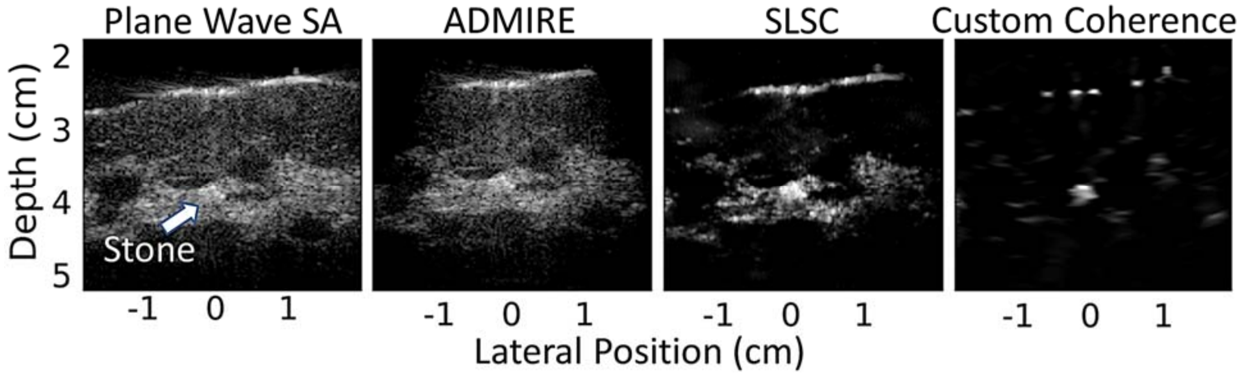

P1-A1-7

New Improved Unsharp Masking Methods Compatible with Ultrasound B-Mode Imaging

Asraf Mohamed Moubark[1], Sevan Harput[1], David M.J Cowell[1], **Steven Freear[1]**; [1]*School of Electronic and Electrical Enginnering, University of Leeds, Leeds, West Yorkshire, United Kingdom*

Background, Motivation and Objective

In medical ultrasound B-Mode imaging, increasing the image contrast, spatial and temporal resolution will improve medical diagnostic and decision making process. One of the methods used to achieve those improvement in medical imaging is unsharp masking (UM) technique. Previously UM has been successfully implemented as noise filtering and edge enhancement techniques. However the outcomes of the method is limited and influenced by the image formats conversion, lower dynamic range and high frequency noises. Furthermore the technique only enhances the image more in darker compare to lighter regions. To overcome these issues, a new improved UM methods compatible with ultrasound B-Mode imaging applied on compound plane wave imaging (CPWI) and beamformed with delay and sum (DAS) and filtered delay and sum (FDMAS).

Statement of Contribution/Methods

The proposed UM method can be represented by the following equation:

$B(x,t)_{improved}=|B(x,t)_{coherent}+\alpha\{B(x,t)_{coherent}-B(x,t)_{non\text{-}coherent}\}|$

Where $B(x,t)_{improved}$ represents a new improved B-Mode image, $B(x,t)_{coherent}$ represents coherent CPWI, $B(x,t)_{non\text{-}coherent}$ represents non-coherent CPWI and α represents weighting factor. The performance of the proposed methods was evaluated with experimental data obtained from ultrasound array research platform (UARP II) excited with 2-cycles sinusoidal signal using a 5 MHz linear ultrasound probe. The RF data was acquired from a CIRS phantom with a 4.5mm diameter anechoic target mimicking cyst located at 15 mm depth and wire of 100 µm diameter at 30 mm depth.

Results/Discussion

UM-DAS and UM-FDMAS can improve both imaging contrast and spatial resolution as compared to DAS and FDMAS, as shown in Fig.1(a-h) with 60 dB dynamic range. Fig.1(i) shows the lateral resolution measured for UM-DAS and UM-FDMAS shows improvement from DAS and FDMAS at 6 dB by 14% and 12.8 % and at 20 dB by 18.2% and 26.7 % respectively. Fig.1(j) shows beam profile in lateral direction for cyst. The contrast ratio obtained from DAS, UM-DAS, FDMAS and UM-FDMAS are -23 dB, -33.14 dB, -27 dB and -34.3 dB respectively. Since a low number of CPWI (N=9) angles have been used in the proposed technique, a higher temporal resolution can be achieved. The new techniques are also able to preserve speckle formation which is valuable for tracking tissue movement.

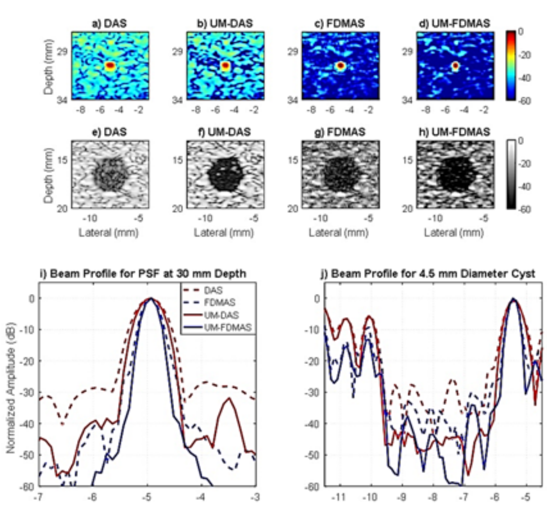

Fig. 1. B-Mode images for wire phantom representing point spread function (PSF) beamformed with (a) DAS, (b) UM-DAS, (c) FDMAS and (d) UM-FDMAS. B-Mode images for cyst phantom beamformed with (e) DAS, (f) UM-DAS, (g) FDMAS and (h) UM-FDMAS. Beam profile for (i) PSF and (j) Cyst.

P1-A1-8

Extending the Convergence Limit of Nonlinear Speed of Sound Reconstructions towards Common Ultrasonic Frequencies

Andreas Ihrig[1], Georg Schmitz[1]; [1]*Chair for Medical Engineering, Ruhr-University Bochum, Bochum, Germany*

Background, Motivation and Objective

Linear reconstruction techniques based on the Born approximation are known to be unable to reconstruct speed of sound quantitatively. Recently, it was shown that non-linear reconstructions based on the Kaczmarz method can overcome this limitation (Hesse, Salehi, and Schmitz 2013). However, a fundamental problem towards its practical application is the convergence. As described by Natterer (Natterer 2008), the maximum accumulated phase difference within the object has to be lower than π which is only fulfilled for low frequencies (10^5 Hz) in soft tissue environments. With this contribution, we present an approach to extend this limitation towards clinically relevant frequencies.

Statement of Contribution/Methods

The Kaczmarz-based reconstruction method uses an adjoint operator to update the material parameters. This operator combines forward and backward wave propagations of input signal and residuals on the border, respectively. When using high frequencies, the reconstruction does not converge due to the phase shift induced by the SoS deviations. We can estimate the objects maximal phase shift without a priori knowledge by the averaged maximal cross correlation lag between forward propagation and measured signals. With this information, we propose a modified adjoint operator suppressing high-frequency components causing divergent results. We show first results on a synthetic setup including 16 transducers in a circular arrangement surrounding the exemplary phantom (Figure (a)) with speed of sound deviations up to 50 %.

Results/Discussion

With an expected frequency limit at about 670 kHz, reconstruction at a centre frequency of 2 MHz does not converge as shown in Figure (b). In contrast, we see a successful reconstruction in Figure (c) utilizing the proposed modified operator using the same frequency. Currently, the transformation allows reconstructions with about 3 times higher frequencies, which paves the way for an experimental setup using clinically relevant US frequencies.

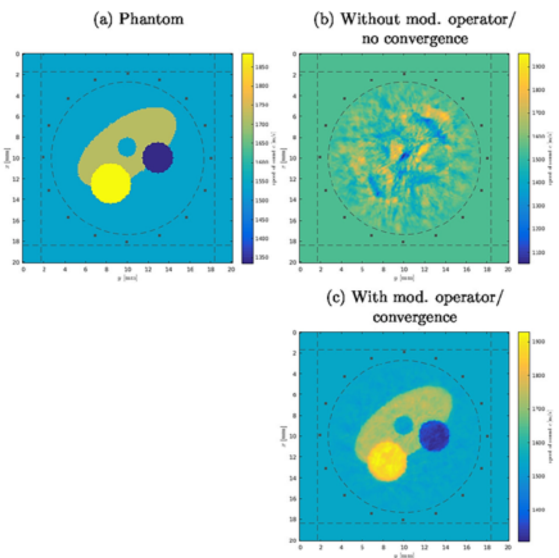

P1-A1-9

Low-Complexity Compressive Beamforming for Portable Ultrasound Imaging

Swetha George[1], Ajay Anand[2], **Jovan Mitrovic**[1], Zeljko Ignjatovic[1]; [1]*Electrical and Computer Engineering, University of Rochester, Rochester, New York, USA,* [2]*Carestream Health Inc., Rochester, New York, USA*

Background, Motivation and Objective

Compressive sensing (CS) has become a widely applied technique in ultrasound (US) so as to reduce the amount of data acquired while achieving image quality comparable or better than that of traditional delay-and-sum US (DAS). Most of the commercial US systems are bulky due to the hardware associated with each transducer channel. The need for inexpensive and easily portable US systems that can be made available to healthcare providers in rural communities and field hospitals has fueled the research presented here.

Statement of Contribution/Methods

The proposed US method is based on randomly modulating the received RF data with {0, 1} across time and space (Fig.1). This is implemented using simple analog switches controlled by a random clock sequence Φ and its complement Φ'. At each time instant 'i', the echoes from the full aperture are divided into two random and disjoint subsets, whose elements are then added together to form two vectors P and Q. This compression method spreads information across the entire available bandwidth reducing the channel count to two, while maintaining a good SNR. Next, an RF signal reconstruction is performed by a simple reshaping and interpolation of P and Q, unlike the computationally costly optimization methods in CS. The reconstructed RF signal (matrix B) is then used for beamforming and envelope detection to form a B-mode image.

Results/Discussion

Field II results of the proposed method and 64-channel DAS for a 4 mm anechoic cyst and for point scatterers (Fig. 2) show that even after applying a 1:32 compression ratio, good resolution (FWHM=0.765 mm) and contrast ratio (94%) are maintained, all while reducing the data and hardware complexity. The mean-squared-error between the DAS and compressive US images is -63dB which makes them indistinguishable on a 50dB scale.

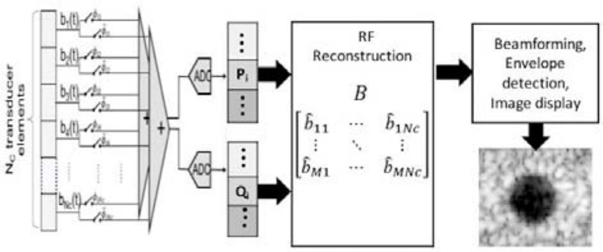

Figure 1. The proposed compressive US system showing the compression and decoding process.

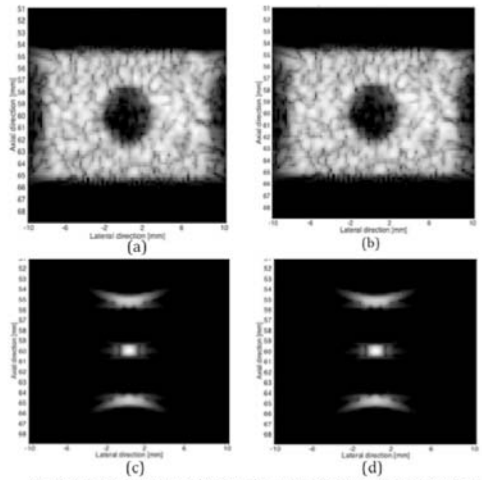

Figure 2. Example images: (a)&(c) traditional DAS beamforming approach and (b)&(d) the proposed compressive US with 1:32 compression ratio. Transducer probe is a 64-element linear array with 2.5 MHz excitation frequency with a fixed focus at 60 mm on transmit and receive.

P1-A2 - MBF: Multi-Directional and Multi-Plane Flow Imaging

Exhibit Hall

Thursday, September 7, 2017, 9:30 am - 4:00 pm

Chair: **Mengxing Tang**
Imperial College London

P1-A2-1

Plane-Wave Based Vector Flow Imaging: Beamforming and Velocity Estimation Loads in Different Processing Scenarios

Matteo Lenge[1], **Alessandro Ramalli[1]**, Stefano Ricci[1], Piero Tortoli[1]; [1]*Department of Information Engineering, University of Florence, Firenze, Italy*

Background, Motivation and Objective

Recent advancements in ultrasound vector Doppler (VD) techniques have boosted the investigation of 2D regions of interest (ROIs). Several methods have been proposed, but their implementation on commercial systems is still limited. First, the investigation of wide ROIs at high frame rate requires the transmission of plane waves (PWs) and parallel beamforming in reception. Furthermore, the extraction of vector velocities at multiple points is typically performed by computationally demanding multi-beam (MB) or speckle tracking (ST) techniques. In this work, we compare the performance of these two approaches in terms of accuracy and computational load when the vector velocities are computed along increasing numbers of velocity estimation lines.

Statement of Contribution/Methods

Two methods addressed to detect the vector velocities in N equidistant lines over the ROI, were compared by using the ULA-OP scanner and a linear array probe.

In the MB-VD method (doi:10.1109/ULTSYM.2016.7728428), unsteered PWs are transmitted and the backscattered echoes are directionally beamformed by two sub-apertures located symmetrically to each velocity estimation line. For each measurement point, the mean axial velocities, calculated through FFTs, are trigonometrically combined.

In the frequency-domain (FD) ST method (doi:10.1109/TUFFC.2014.3064), unsteered PWs are transmitted and 8 adjacent scan lines are beamformed to construct the 2D data blocks needed for ST. For each block, the velocity vectors are estimated in the frequency domain by calculating the phase shift on 3×6-point 2D-DFTs.

The methods accuracy was evaluated by using a phantom in which a steady parabolic flow (v=[5,10,15]cm/s peak velocity, θ=[60,75,90]° beam-to-flow angle) was pumped. The relative bias B_v and standard deviation σ_v were evaluated comparing the estimated and expected velocity profiles. Beamforming and velocity estimation loads were assessed for different numbers, N, of velocity estimation lines.

Results/Discussion

Experimental results demonstrate that MB-VD and FD-ST methods perform similarly in terms of accuracy (B_v<13% and σ_v<4%, Fig. A). In terms of beamforming and velocity estimation loads, FD-ST results convenient when 8 or more vector lines are processed (Fig. B). Therefore, the FD-ST method is competitive for real-time blood flow mapping over large numbers of velocity lines.

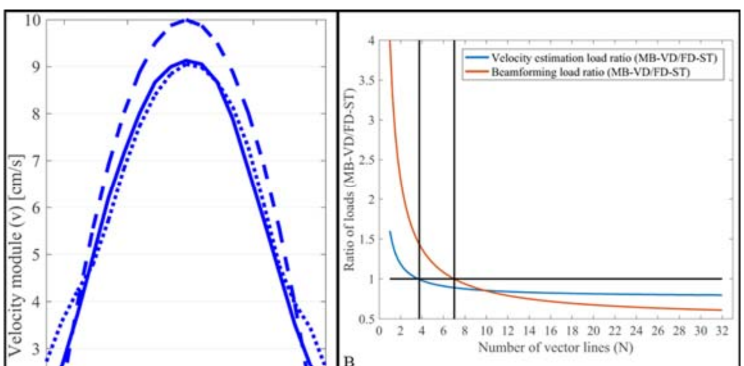

Caption. Results of the comparison between multi-beam vector Doppler (MB-VD) and frequency-domain speckle tracking (FD-ST) methods. In A, an example of the velocity modules estimated along the same line. In B, the beamforming (red) and velocity estimation (blue) load ratios for different number of processed lines. Ratios lower than 1 corresponds to a better efficiency of FD-ST.

P1-A2-2

Estimating 2D Flow Vectors in Ultrasound Plane-Wave Fourier Imaging

Shang-Ching Lin Lin[1], Pai-Chi Li[1]; [1]*National Taiwan University, Taipei, Taiwan*

Background, Motivation and Objective

Flow velocity estimation is an important feature in ultrasound imaging. However, in conventional color Doppler imaging, only parallel flow components can be estimated, the velocity information is not simultaneously measured throughout the region of interest (ROI) due to sequential firing of the ultrasound beams, and the size of the ROI is limited under frame rate concerns. On the other hand, ultrafast imaging is based on plane wave excitation, and the Fourier imaging method estimates the whole complex object function from k-space instead of the spatial delay and sum approach. Our goal is to derive the velocity vectors from the phase changes in the object function for ultrafast imaging.

Statement of Contribution/Methods

In Fourier imaging, the RF data obtained from plane wave excitation undergo 2-D Fourier Transform (FT), weighting, interpolation and inverse 2-D FT to reconstruct the object function, generating one frame per firing. In our Field II simulations, the center frequency of the 128-element array transducer is set to be 5 MHz, and the point of phase observations is 15 mm below the center of the array. Various combinations of lateral and axial velocities are used for a point scatterer initially placed at the observation point. The phase is recorded after 5 frames for 16 frames, and the slopes are calculated using linear regression.

Results/Discussion

As the figure shows, if a scatterer moves at a constant speed, the local phase varies linearly with a slope proportional to either component. If the x component is under 20 μm/frame (20 cm/s for a frame rate of 10k frames/s), R^2 of the phases vs. frames are beyond 0.97, and that of the slopes vs. velocity components are beyond 0.81, showing linearity. Directional gating may also be applied to determine the respective contributions from x and z to obtain the direction of the flow vectors. Since only a few B-mode frames are required for the calculation, the results also show potential in achieving ultrafast concurrent B-mode and flow vector imaging with a full field of view.

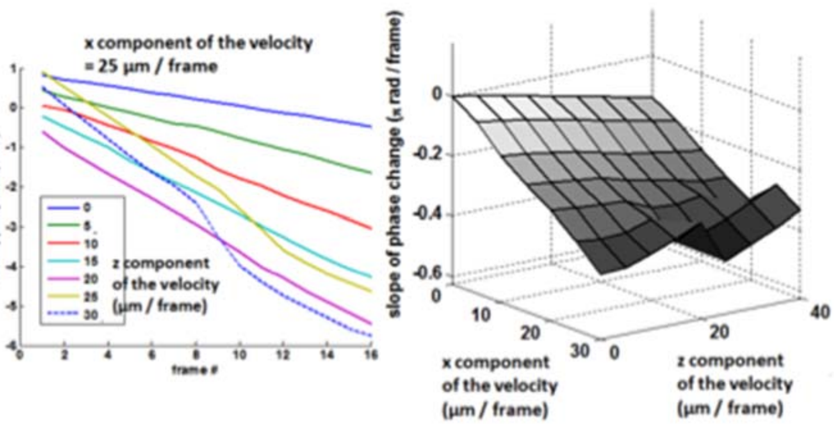

P1-A2-3 ____

Multi-Plane, Time-Synchronized Color Encoded Speckle Imaging: A New Approach for Aneurysm Flow Visualization

Billy Y. S. Yiu[1], Chung Kit Ho[1], Adrian J. Y. Chee[1], Alfred C. H. Yu[1]; [1]*Schlegel Research Institute for Aging, University of Waterloo, Waterloo, Canada*

Background, Motivation and Objective

Inside tortuous vasculatures such as aneurysms, flow patterns are inherently 3D in nature and would vary spatiotemporally in different phases of a pulse cycle. At present, it is difficult to consistently visualize such complex flow using color Doppler imaging. 4D flow imaging may be a potential solution, but existing clinical 3D scanners have hitherto yielded mediocre visualization of 3D flow volumes, and their frame rate is inadequate in tracking fast-changing flow patterns. In this work, we aim to achieve intuitive visualization of flow volumes through the design of a novel time-resolved flow visualization technique. Our new technique is a multi-plane, time-synchronized extension of a high-frame-rate flow imaging paradigm called color encoded speckle imaging (CESI) developed by our lab earlier.

Statement of Contribution/Methods

CESI was implemented on a SonixTouch scanner with pre-beamformed data acquisition capabilities, and data processing was realized in real-time on a GPU computing back-end as described earlier (UMB, 2013; 39: 1015-1025). An L14-5 array was used to perform steered plane wave pulsing (5 MHz Tx freq; 2-cycle pulse duration; 10 kHz PRF; 3 Tx angles: -10, 0, 10 deg), and the transducer was placed on multiple scan planes. For each scan plane, the effective data acquisition frame rate was 3,333 fps; between scan planes, the CESI frames were temporally synchronized by triggering the start of data acquisition with an in-house sync pulse module. Our multi-plane, time-synchronized CESI framework was applied to image the spatiotemporal evolution of pulsatile flow inside a patient-specific aneurysm phantom that we designed recently (T-UFFC, 2017; 64: 25-38). CESI cineloops were generated on different scan planes, and CESI frames from intersecting planes were stitched together for biplanar visualization.

Results/Discussion

For the aneurysm geometry shown in figure (top left), coherent biplanar CESI frame visualization can be readily achieved (figure; top right). Also, time-varying CESI flow patterns are observed in Scan Plane 1 due to the aneurysm's tortuosity and branching (figure; middle row). A persistent flow recirculation can be seen as well within the aneurysm sac, as rendered by Scan Plane 2 (figure; bottom row). These results generally confirmed that our proposed framework can consistently track the 3-D nature of flow dynamics inside an aneurysm.

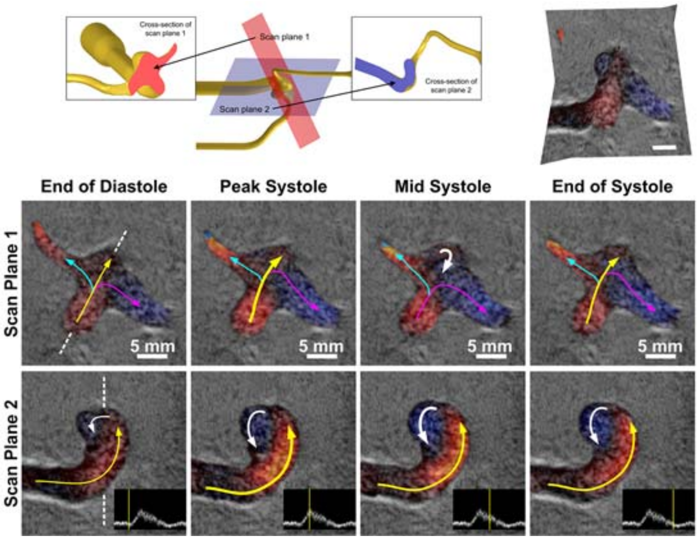

P1-A2-4

High Pulse Repetition Frequency Vector Doppler Velocity Measurements

Alessandro Dallai[1], **Alessandro Ramalli[1]**, Piero Tortoli[1]; [1]*Department of Information Engineering, University of Florence, Florence, Italy*

Background, Motivation and Objective

A dual beam vector Doppler method was proposed (DOI: 10.1016/j.ultrasmedbio.2009.11.004), in which one beam is continuously tracked perpendicular to the flow direction, and the second one is used to perform velocity measurements with known Doppler angle. Since two consecutive transmission (TX) and reception (RX) events (one for each beam) are needed, the effective Doppler pulse repetition frequency (PRF) is halved, thus facilitating the onset of aliasing when fast flow is investigated. In this work, the problem is solved by using a single TX sub-aperture and two RX sub-apertures of a linear array probe; the new approach was implemented and tested in real-time on the ULA-OP 256 open platform taking advantage of its parallel beamforming capabilities.

.

Statement of Contribution/Methods

With reference to the sample volume selected by the operator, at each pulse repetition interval ULA-OP 256 transmits an ultrasound burst from one sub-aperture of a 192-element linear array and receives the backscattered echo data by the same (reference) sub-aperture as well as by an independent (measuring) sub-aperture. The latter one is automatically set to guarantee the lowest possible Doppler angle. The echoes gathered by the two sub-apertures are beamformed in parallel by two delay and sum units, then processed to calculate the related spectra. The reference spectrum is continuously monitored to automatically steer the related beam perpendicular to the flow direction, while the mean frequency of the second beam is used to directly calculate the velocity magnitude.

.

Results/Discussion

The method has been tested both in vitro and in vivo (see Fig) at PRFs as high as 10 kHz or more, by permitting the assessment of peak velocities higher than 2 m/s. In vitro experiments based on a flow phantom confirmed the capability of repeatedly measuring velocity magnitudes irrespective of the flow direction, with a coefficient of variation equal to 2.3%. The doubling of the PRF made possible by the simultaneous use of two independent sub-apertures and parallel beamforming, may be crucial in the investigation of stenotic vessels, in which the velocities can be twice as high as in healthy vessels.

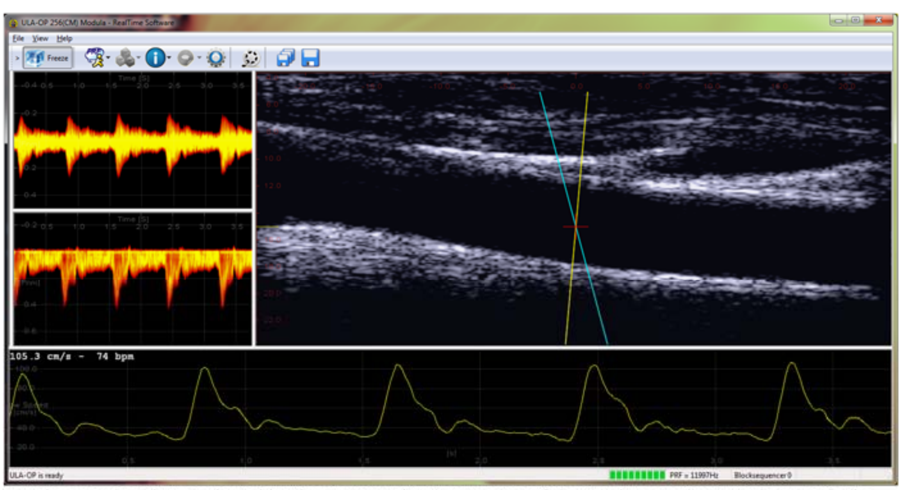

For the sample volume selected by the operator (at the crossing of the two lines in the B-Mode image), the system calculates the two spectrograms on the left, adjusts the reference beam steering to keep the related spectrum symmetrical (top left) and calculates the velocity magnitude (bottom), here higher than 1m/s.

P1-A2-5

Vector Flow Imaging using High Frequency versus Conventional Frequency Plane Wave Ultrasound

Anne Saris[1], Stein Fekkes[1], Maartje Nillesen[1], Rik Hansen[1], Chris de Korte[1,2]; [1]*Medical UltraSound Imaging Center (MUSIC), department of Radiology and Nuclear Medicine, Radboud university medical center, Nijmegen, Netherlands,* [2]*Physics of Fluids Group, University of Twente, Enschede, Netherlands*

Background, Motivation and Objective

In the Western World, the high prevalence of stenotic plaques in the carotid arteries results in many strokes and transient ischemic events. In daily clinical practice, the severity of stenosis is estimated based on the maximum velocity measured before and after the stenosis using pulsed wave Doppler. However, because of the angle dependency of Doppler techniques, novel flow imaging techniques are being developed which can quantify the local true velocity vector. Ultrafast imaging combined with speckle tracking allows for 2D vector flow imaging in the carotid. This study compares the performance of 2D vector flow imaging of a high frequency (> 20 MHz) transducer and a clinically utilized (9 MHz) transducer.

Statement of Contribution/Methods

The performance of both transducers was evaluated experimentally on a straight vessel phantom (beam-to-flow angles of 90° and 75°) with a parabolic flow profile and a peak velocity of 0.51 m/s. Furthermore, a patient-specific bifurcation phantom made of polyvinyl alcohol was used with a pulsatile flow of 60 bpm and a mean and peak flow of respectively 0.6 L/min and 1.4 L/min. A Verasonics Vantage 256 system connected with a Visualsonics MS250 transducer (f_c = 21 MHz, pitch = 88 µm, 256 elements) and a Philips L12-5 transducer (f_c = 9 MHz, pitch = 195 µm, 256 elements) acquired plane wave data at 4000 fps. After clutter removal, cross-correlation based, multi-step speckle tracking was applied on the beamformed RF-data to quantify the blood velocity magnitude and direction. Temporal averaging using an ensemble size of 40 frames resulted in an effective velocity frame rate of 100 Hz.

Results/Discussion

Straight vessel phantom results were studied quantitatively and showed a velocity bias and relative velocity standard deviation (std) of <1.94 % and <1.82 % for the L12-5 and <2.16 % and <0.81 % for the MS250. The estimated angles yielded a bias and std below 0.10° and 0.58° for the L12-5 and below 0.25° and 0.28° for the MS250. Overall, the MS250 showed a larger bias but smaller std compared to the L12-5. Qualitative comparison of the bifurcation results showed that both transducers were able to capture the presence of a vortex (Fig. 1). The MS250 was capable of quantifying low velocities close to the vessel wall (Fig. 1) that are crucial for shear stress analysis, but applicability of the MS250 is limited to shallow depths (< 2 cm).

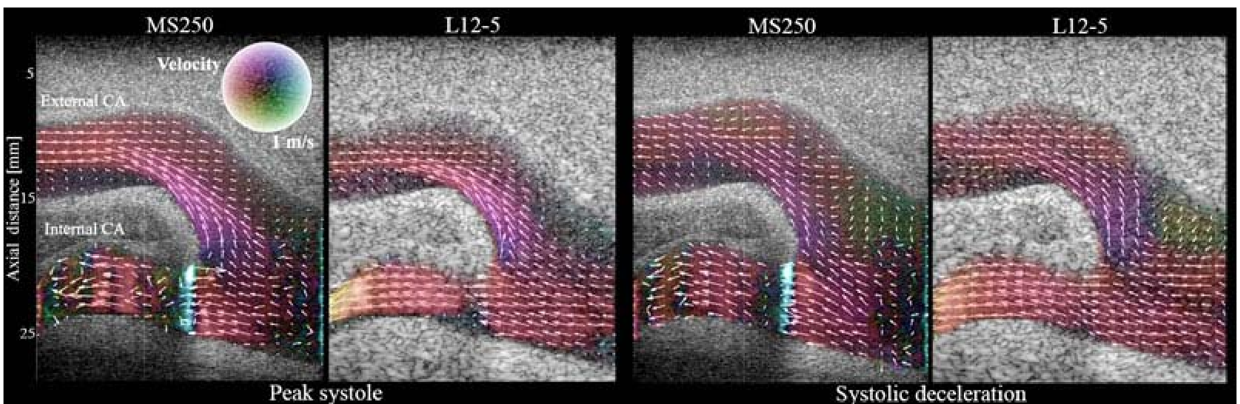

Figure 1. Bmode images of the carotid bifurcation phantom overlaid with 2D blood velocity fields. Two key time points in the cardiac cycle are visualized: a peak systolic phase, where highest velocities occur and a frame in systolic deceleration, where a vortex is present close to the upper wall of the external carotid. Both the magnitude and direction of the blood velocities are color coded using a colorwheel.

P1-A2-6

High-Frame-Rate Imaging of a Carotid Bifurcation Using a Low-Complexity Velocity Estimation Approach

Tommaso Di Ianni[1], Carlos A. Villagòmez Hoyos[1], Caroline Ewertsen[2], Michael Bachmann Nielsen[2], Jørgen A. Jensen[1]; [1]*Technical University of Denmark, Lyngby, Denmark,* [2]*Department of Radiology, Copenhagen University Hospital, Copenhagen, Denmark*

Background, Motivation and Objective

Vector flow imaging (VFI) improves the operator's workflow allowing the quantitative evaluation of blood flow with no need for manual angle corrections. Currently, commercial VFI implementations are based on a line-by-line estimation, compromising the frame rate and the possibility of imaging fast flow dynamics. High-frame-rate methods are, however, computationally demanding. The objective of this work is to demonstrate that quantitative VFI can be achieved in-vivo at high-frame-rate using only six pre-beamformed lines and with lowered requirements for the ultrasound system.

Statement of Contribution/Methods

The method is based on synthetic aperture sequential beamforming and directional transverse oscillation (TO). Six flow emissions were pre-beamformed using a fixed transmit/receive focus and used in the second-stage beamformer to obtain a high-resolution image (HRI). The focal positions were located at a depth of -15 mm and grouped in two virtual apertures, laterally separated to achieve a TO in the HRI. The lateral and axial velocities were estimated from 16 HRIs employing a 2-D phase-shift estimator. This uses signals of 16 samples in the lateral and axial directions. B-mode and flow emissions were interleaved to achieve continuous data acquisition. Data from a carotid bifurcation of a 54-year-old volunteer were acquired using SARUS and a BK Ultrasound 8L2 linear array transducer (4.1 MHz; 4 cycles flow/2 cycles B-mode; 15 kHz PRF).

Results/Discussion

In the figure below, the VFI map of the carotid bifurcation is presented on the left. Quantitative velocities are obtained in all the image points with a frame-rate of 134 fps, enabling the visualization of transient dynamics. The figure on the right shows the velocity profiles in two points (A and B in VFI plot). The red bar specifies the time of the VFI map. The mean peak systolic velocity is 0.64 +/- 0.02 m/s in A and 0.65 +/- 0.06 m/s in B.

In conclusion, in-vivo high-frame-rate VFI was successfully obtained using only six pre-beamformed lines. This effectively reduces the data rate and computational requirements of the system. Quantitative velocities are achieved everywhere in the image during the entire cardiac cycle without the need for any manual adjustment.

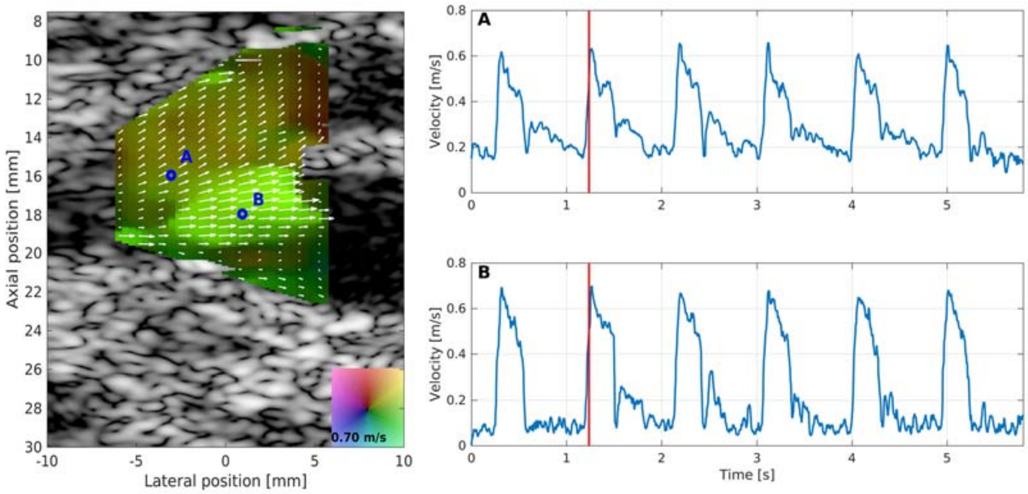

P1-A2-7

Ultrafast Cardiac 2D Vector Flow imaging

Tong Yu[1], Oudom Somphone[2], Shiying Wang[1], Sheng-Wen Huang[1], **Francois Vignon[3]**; *[1]Philips Research North America, Cambridge, MA, USA, [2]Philips Research France, Suresnes, France, [3]Philips Research North America, Andover, Massachusetts, USA*

Background, Motivation and Objective

Left intraventricular blood vortices could provide important information on cardiovascular health. However they are not explicitly measured in current-day commercial systems. Additionally, the slow frame rates (typically <30Hz) of 2D cardiac Doppler imaging do not enable adequate sampling of the intraventricular blood dynamics. Finally, current imaging modes do not allow simultaneous estimation of cardiac and blood motion.

The objective of this study was to combine ultrafast imaging and vector flow imaging to achieve fully sampled, 2D velocity vector imaging transthoracically in the left ventricle together with synchronous myocardial motion imaging. A new imaging mode based on those principles may give new insights onto the coupling between mechanical and hemodynamic cardiac function.

Statement of Contribution/Methods

Ultrafast acquisition at frame rate of 2.3kHz is achieved with diverging transmits and high order parallel receive beamforming. The 1D along-beam velocity is obtained with a conventional Doppler estimator. The second component of the velocity vector is retrieved by dynamic segmentation of the blood chamber and imposing divergence-free flow in the chamber and non-slip boundary conditions. 1D myocardial motion estimation is also performed for a simultaneous display of blood and myocardial dynamics. The technique was tested on two adult healthy volunteers with a Philips EPIQ scanner and S5-1 probe.

Results/Discussion

This technique allows visualizing temporally well-defined blood vortices and simultaneous myocardial motion (Figure).

Limitations include aliasing in early diastole and early systole, low signal-to-noise ratio, clutter signals generated by the myocardium, and the presence of the mitral valve in the middle of the region of interest during diastole. Further work will focus on improving SNR and reducing adverse clutter effects.

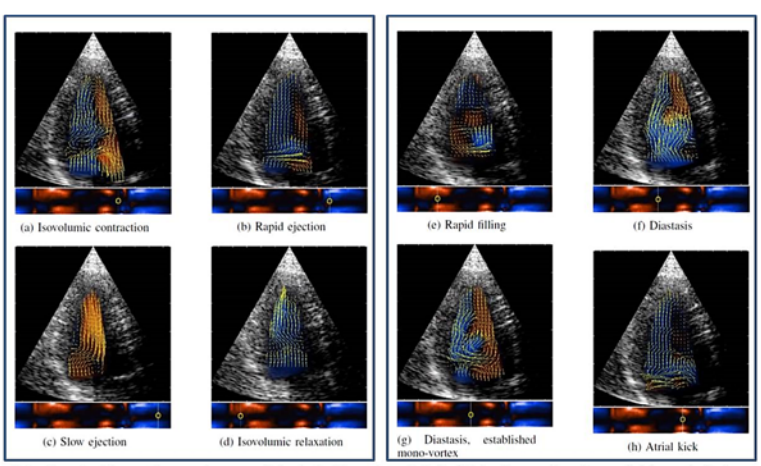

Color Doppler, Vector Flow, and myocardial velocity M-mode at 2.3kHz (Main phases of cardiac cycle). In each display, the top represents a snapshot of the Doppler velocity and velocity vectors, and the bottom trace represents the 1D velocity M-mode in the left ventricular wall on a ±10cm/s scale. The marker on the bottom trace indicates the time instant of the snapshot.

High-Speed, High-Frequency, Vector-Flow Imaging of in Utero Mouse Embryos

Jeffrey A. Ketterling[1], Orlando Aristizabal[2], Alfred C.H. Yu[3], Billy Y.S. Yiu[3], Daniel H. Turnbull[2], Colin K.L. Phoon[4], Ronald H. Silverman[5]; [1]*Lizzi Center for Biomedical Engineering, Riverside Research, New York, NY, USA,* [2]*Skirball Institute of Biomolecular Medicine and the Department of Radiology, New York University School of Medicine, New York, NY, USA,* [3]*Department of Electrical and Computer Engineering, University of Waterloo, Waterloo, Canada,* [4]*Division of Pediatric Cardiology, Hassenfeld Children's Hospital of New York at NYU Langone Medical Center, New York, NY, USA,* [5]*Department of Ophthalmology, Columbia University Medical Center, New York, NY, USA*

Background, Motivation and Objective

Plane-wave imaging has been demonstrated in humans for cardiovascular (CV) studies, but its use in mouse embryo models has received minimal attention even though the mouse is the most common experimental organism to study gene function and human disease, including CV disease (CVD). While high-frequency ultrasound Doppler modes have been used to study mouse embryo models, traditional linear-array imaging modes are limited in terms of spatial and temporal resolution which limits the amount of functional information that can be mined. The goal of this study was to obtain high-speed plane-wave data from in utero mouse embryos and then process the data to obtain vector flow information.

Statement of Contribution/Methods

A Verasonics Vantage with an 18-MHz linear-array probe was used to acquire plane-wave data at a frame rate of 20 kHz from in utero, E16.5 mouse embryos. The probe had 128 elements, a 1.5-mm elevation aperture and an 8-mm elevation focus. Batches of 5 transmissions spanning +- 10 degrees were sent out. The mother was placed supine on a heated mouse imaging platform and then a series of 2D+time data sequences coving the whole embryo cross section were captured. The data were beamformed using standard delay-and-sum methods and then vector-flow estimates were obtained at each pixel location using a least-squares, multi-angle Doppler analysis approach.

Results/Discussion

Fig. 1 shows and example of vector flow results in the embryonic heart and umbilical vessels. The spectrograms are from a region of the heart and the yellow line shows the time point of the vector image. The vector-flow analysis of the data sequence revealed the complex nature of the blood flow patterns in the embryo. Fig. 1a shows the systolic phase of the cardiac cycle just after contraction with a continuous flow, towards the embryo heart, in the umbilical vein (yellow flow vectors in the umbilical cord (UC) region). Fig. 1b shows the flow in the heart chambers while the umbilical artery revealed an increased flow 100 ms after the earlier heart contraction. Note that in each of the figures, there are flow vectors in the lateral direction. Traditional color-flow imaging would not resolve these components of the flow. These initial results indicate that plane-wave imaging and multi-angle vector-flow processing have the potential to be a useful tool to study cardiovascular function and disease in mouse embryos.

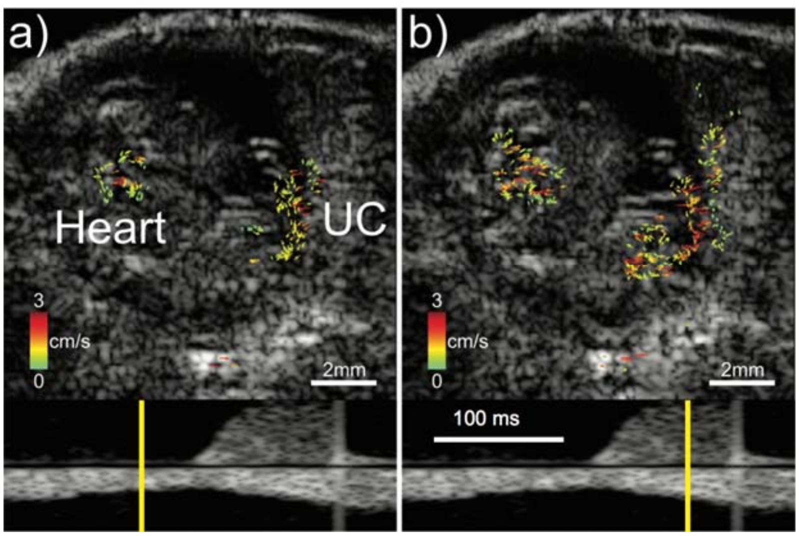

P1-A3 - MCA: Microbubbles and Therapy

Exhibit Hall

Thursday, September 7, 2017, 9:30 am - 4:00 pm

Chair: **Nico de Jong**
Erasmus Medical Centre

P1-A3-1

Tumor Hypoxia Modulation Dynamics Using Intra-tumoral, Intra-peritoneal and Intra-venous Oxygen Microbubbles Administrations – In Vivo Real-time Measurements via Spectroscopic Absorbance on a Rat Subcutaneous Fibrosarcoma Model

Virginie Papadopoulou[1], Samantha M. Fix[1,2], Hunter Velds[3], Sha Chang[4], Mark A. Borden[3], Paul A. Dayton[1]; [1]*UNC Chapel Hill, USA,* [2]*Eshelman School of Pharmacy, UNC Chapel Hill, USA,* [3]*Department of Mechanical Engineering, University of Colorado, USA,* [4]*Department of Radiation Oncology, UNC Chapel Hill, USA*

Background, Motivation and Objective

Solid tumor hypoxia is a poor outcome predictor for radiotherapy, chemotherapy and also surgical treatment options. Recently, oxygen microbubbles (OMB) have shown promise as an adjuvant therapy to relieve such tumor hypoxia. However, a key limiting factor remains the lack of available data in vivo of the dose-response and time-dynamics of this OMB-induced reoxygenation. Here we study the kinetics of OMB-induced hypoxia-modulation by continuously measuring tumor hypoxia in vivo before, during and after OMB administration.

Statement of Contribution/Methods

Six Female Fisher 344 rats with subcutaneous fibrosarcoma tumors were anesthetized (3min on oxygen + 5% isoflurane, then 2.5% isoflurane and air) and OMB were administered either directly in the tumor (IT), through intra-peritoneal (IP) or intra-venous (IV) injection. Tumor oxygenation was measured continuously using a validated optical spectroscopy absorbance technique giving oxy-hemoglobin and deoxy-hemoglobin concentrations (Zenascope, Zenalux Biomedical, Durham). The level of change was compared to that of an oxygen challenge (oxygen breathing for 3min), and also a nitrogen microbubble (NMB) administration. Each animal underwent each intervention and control over the course of the study (randomized order), and served as its own control.

Results/Discussion

Consistent measurements of tumor hypoxia were achieved in real-time, using a non-invasive spectroscopic measurement system by waiting for the baseline to stabilize after anesthesia induction and switch to air carrier gas (20min from induction start) prior to other interventions. As expected, the effects of OMB and NMB are significantly different for all administration routes, with OMB raising or keeping baseline levels of tumor oxygenation. Both IT and IV administrations of OMB increased the tumor oxygenation at least to oxygen challenge levels. To the best of our knowledge, this is the first demonstration of tumor reoxygenation with IV OMB. The 3mL IP administration of OMBs did not significantly raise the baseline oxygenation. Tumor size and baseline hypoxia significantly influence the degree of re-oxygenation (Fig.1). Finally, we propose the metric of OMB effect normalized to the maximal difference from an oxygen challenge as a way of comparing the OMB efficiency longitudinally for the same animal and between different tumors.

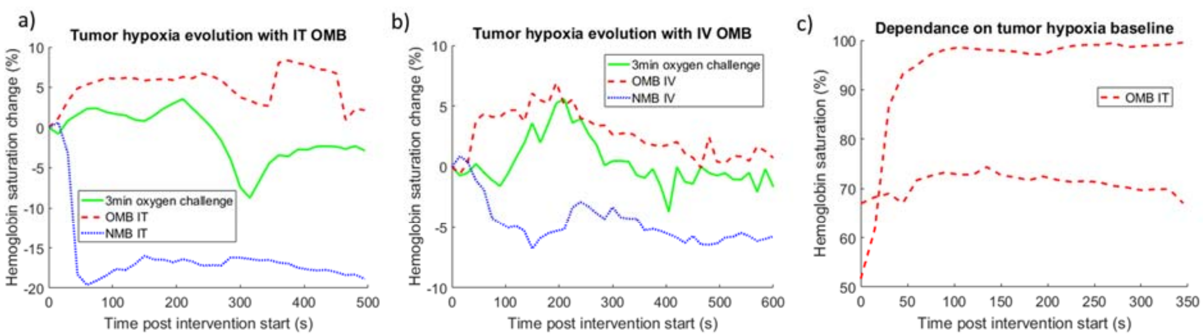

Figure 1: Hemoglobin saturation change after OMB or NMB administration compared to change with pure oxygen breathing for 180s, measured in the tumor using the Zenalux spectroscopic system in real-time, all in the same animal a) intra-tumoral injection (500µL single injection); b) intravenous administration (50µL MBs + 450µL saline, single injection); c) The change in hypoxia depends on the baseline for both the oxygen challenge and OMB administrations. For all plots, time 0 corresponds to the moment of OMB/NMB injection or to the start of the oxygen challenge.

P1-A3-2

The Effect of Pulse Length on Perfusion Kinetics Following Sonoreperfusion Therapy

Francois T.H. Yu[1], Gary Yu[1], Xucai Chen[1], Linda Lavery[1], Flordeliza S. Villanueva[1], John J. Pacella[1]; [1]*Center for Molecular Imaging and Therapeutics, University of Pittsburgh, USA*

Background, Motivation and Objective

Microembolization during PCI for acute myocardial infarction can cause microvascular obstruction (MVO). MVO severely limits the success of reperfusion therapies and is linked to worse prognosis, including death. A recent clinical trial showed that adjunct short pulse MB+US therapy prior to and following PCI in first STEMI patients, improved angiographic recanalization prior to PCI and ejection fraction at 1 month (Mathias et al. JACC. 2016;67:2506-15). This study demonstrated the clinical potential of short pulse high mechanical index MB+US as an adjunct therapy for STEMI. Based on our historical success with using long tone burst US for sonoreperfusion (SRP) therapy in a rat hindlimb model of MVO (Pacella et al. UMB. 2015;41:456-64), we sought to compare the use of short (5 cycles) and long (5000 cycles) US pulsing schemes for SRP.

Statement of Contribution/Methods

In an intact rat hindlimb, we applied therapeutic US with a single element transducer (A302S, 0.5 inch, Olympus, Waltham, MA) using long pulses (1 MHz, 1.5 MPa, 5000 cycles, 3 s pulse interval) or bursts of short pulses (1 MHz, 1.5 MPa, 5 cycles, 1 ms pulse interval, 1 s ON, 2 s OFF) with the same total number of acoustic cycles, for 2 min, during intra-femoral infusion of lipid perfluorobutane MB. Burst-replenishment imaging of the muscle was performed using a Sequoia scanner (CPS mode, 7 MHz, 0.2 MI) during jugular infusion of Definity (2 mL/hr) to monitor the kinetics of perfusion for 30 min following therapeutic US (4-5 rats/group). Image intensities of the acquired perfusion cineloops were measured to calculate the blood volume and perfusion rate in the microvasculature. Statistical analysis was performed using 2-way ANOVA.

Results/Discussion

Both US pulses affected the blood volume and perfusion rate; however the temporal responses were distinct. For the short pulses, blood volume initially increased post US (21.0±3.1 dB) but returned to baseline (BL) range (14.1±1.7 dB) starting at 6 min post US. Flow rate post US similarly increased to 9.0±4.4 dB/s but returned to BL range (4.2±2.5 dB/s) starting at 6 min. Conversely, for the long pulse, blood volume post US initially dropped to 1.7±2.6 dB but returned to BL starting at 6 min. The flow rate also initially dropped (0.1±0.1 dB/s) but started to increase at 6 min and reached 14.1±7.9 dB/s at 10 min and 10.4±4.4 dB/s at 30 min, which were both significantly higher than BL (3.1±1.2 dB/s) and higher than that with the short pulse. This increase in flow rate with the long pulse was sustained for up to 4 h.

These data strongly support that short and long pulses can both improve SRP therapy as measured using contrast burst-replenishment imaging. The short pulse increased perfusion immediately following SRP but the effect started to decrease with time. Conversely, the long pulse caused a delayed effect with a more sustained improvement in perfusion starting at 6 min and persisting for at least 4 h after therapy, suggesting potentially different pathways.

P1-A3-3

Feasibility Study of Dual-Frequency Chirp Excitation for Passive Cavitation Imaging

Hsiang-Ching Lin[1], Chih-Kuang Yeh[1]; [1]*Department of Biomedical Engineering and Environmental Sciences, National Tsing Hua University, Taiwan*

Background, Motivation and Objective

Focused ultrasound (FUS) combined with microbubbles (MBs) has been shown to locally and temporarily open the blood-brain barrier (BBB). However, concurrent opening BBB (long pulse) and mapping the location of BBB opening (short pulse) by pulsed-wave excitation always conflicts. Previously proposed passive cavitation imaging in brain suffered from degraded axial resolution because of long driving pulse and attenuation of skull in general. In this study, a coded excitation technique is combined with the dual-frequency chirp excitation (DFC excitation) method to improve these problems. The DFC excitation can generate a low-frequency chirp envelope component as the driving force of MBs cavitation by using a high-frequency pulse. The MBs cavitation was passively imaged by using chirp component with pulse compression to maintain sufficient insonation energy without any loss in the axial resolution of imaging.

Statement of Contribution/Methods

The DF excitation involves the simultaneous transmission of two sinusoids (1.25 MHz and 1.75 MHz) to produce an envelope component at the difference frequency (0.5 MHz) (Fig.1 (a)-(b)). The chirp excitation pulse was incorporated into the waveform. The details can be found in our paper (Phys. Med. Biol. 56 (2011)). In this study, a 1.5 MHz transducer transmitted DFC with envelope frequency of 0.5 MHz (60% chirp of pulse length of 50 µs) at 0.9 MPa. The transducer was fixed at a 90° angle with respect to a tube of diameter of 1.58 µm inside the graphite phantom. A 0.5 MHz transducer was used for listening the scattered signals. The 4-mm thickness pig skull was placed in front of both transducers to simulate the attenuation of skull. Herein, MBs with a mean size of 1.6 µm were injected into the tunnel at velocities of 5 mL/h.

Results/Discussion

Fig.1 (c) shows that mean spectra of signals. The CTR was 11.3±3.4 dB with respect to the cases of water in tube. The DFC excitation improved the axial resolution (FWHM) to 7.9 mm (Fig.1 (d)) after pulse compression. The preliminary results indicated that the DFC excitation improved the axial resolution of passive cavitation signal while retaining transmitting energy from skull attenuation. Next, the longer pulse with carrier frequency cascading with DFC excitation would be conducted to achieve the goal of concurrent opening BBB and mapping the location of BBB opening (passive cavitation imaging) in brain.

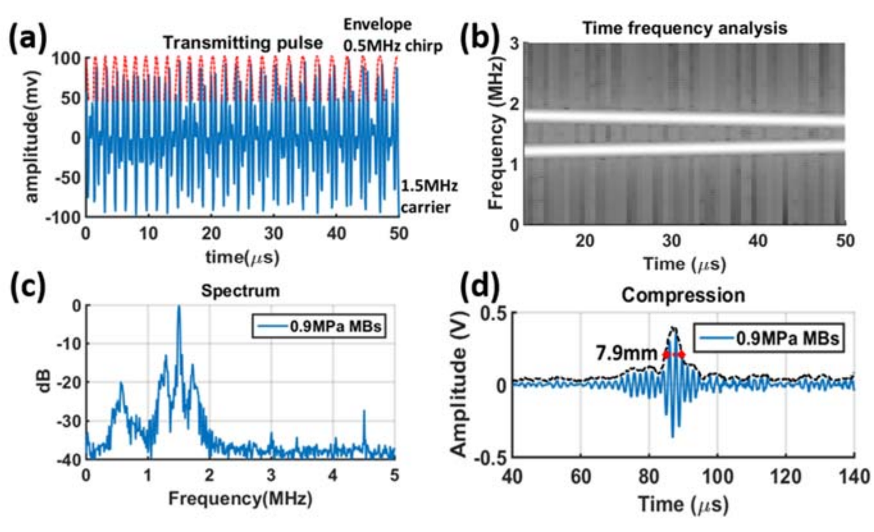

P1-A3-4

Translating Microbubbles with Millisecond Scale Ultrasound Pulses: Implications for Controlled Transport of Bubbles to a Boundary

Christopher Acconcia[1,2], **Alex Wright**[1], Dave Goertz[1,2]; [1]*Sunnybrook Research Institute, Toronto, Ontario, Canada,* [2]*University of Toronto, Toronto, Ontario, Canada*

Background, Motivation and Objective

To elicit bio-effects, ultrasound (US) stimulated microbubbles (MBs) must be in proximity to their target and this is not always the case (e.g. sonothrombolysis). Radiation forces can direct MBs to clots and our previous work suggested clot degradation patterns (Fig A) could be influenced by 'transport pulses'. However, this is a complex process involving a population of MBs, with size-dependent radiation and drag forces. We recently investigated MB accumulation at a boundary to improve exposure strategies in applications such as sonothrombolysis. The size and spatial distribution of MBs arriving at a fibrin clot (Fig B) were dependent on pressure and flow rate. The purpose of this work was to investigate the translation of individual MBs with ms pulses to constrain modeling of this process.

Statement of Contribution/Methods

Individual MBs (n=123, diameters 1.5-9 um) were isolated using in-house developed optical tweezers. Exposed to 1 ms length, 1 MHz pulses at pressures of 25, 50 100 and 150 kPa, MB translation was recorded with a fast frame camera (10 kfps). Radial oscillations were calculated with the Marmottant model with shell elasticity, viscosity, and initial surface tension as parameters. To assess displacement, radiation force, added mass, quasi-steady drag and history force were solved numerically. After empirical modification, the history force has been generalized to finite Reynolds numbers which was integrated with the numerical method of Chung et al (1982).

Results/Discussion

Reported here is the first size dependant data set MB translation with therapeutically relevant ms pulses. A pronounced feature of the displacement curves is an effective threshold size, below which there is minimal translation (Fig C). The threshold size increases with decreasing pressure and was well accounted for by the threshold dependant nature of oscillations in the encapsulated MB model. There was good agreement with data up to 100 kPa (e.g. Fig D at 25 kPa) for shell parameters within the range previously reported for phospholipid agents. Notably, the inclusion of history force was required to accurately fit the data though this is typically ignored. With these results good agreement was found when modelling our previously acquired data of size dependent MB arrivals at a surface thereby providing a tool to investigate and optimize the controlled translation of MBs to a target.

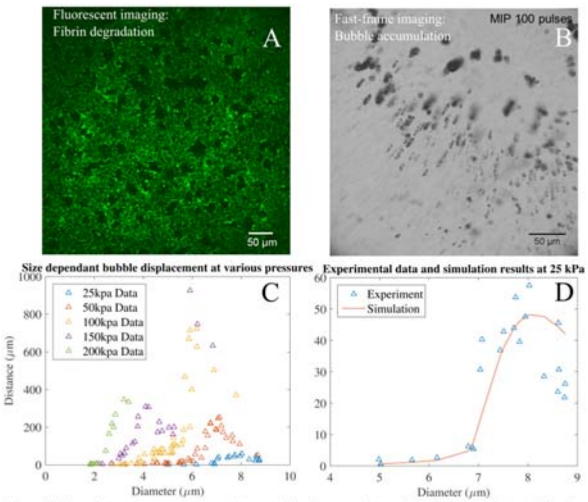

Figure. A) Two-photon microscopy of the erosion zone of the flourescently tagged fibrin network of a treated blood clot. Upon arrival, MBs penetrate and disrupt the fibrin network. B) Top view of the size dependant arrival of MBs at a planar fibrin clot boundary. A minimum intensity projection is shown over 100 US pulses. C) Size and pressure dependant displacement of MBs from a single 1 ms pulse. D) A comparison of data and modeling for the 25 kpa case with a local maximum about a peak size, approximately at the resonant size of Definity at 1 MHz.

P1-A3-5

On the Fate of Mesh-stabilized Lipid Nanobubbles after Destruction with Ultrasound

Christopher Hernandez[1], Sahil Gulati[2], Gabriella Fioravanti[1], Phoebe Stewart[2], Agata A. Exner[3]; [1]*Department of Biomedical Engineering, Case Western Reserve University, USA,* [2]*Department of Pharmacology and Cleveland Center for Membrane and Structural Bio, Case Western Reserve University, USA,* [3]*Department of Radiology, Case Western Reserve University, USA*

Background, Motivation and Objective

The dissipation of ultrasound (US) signal from microbubble contrast agents has been linked to their fragmentation, jetting or sonic cracking, leading to a loss of gas. With strong interest in the use of bubbles as drug delivery vehicles, their ultimate fate is of great importance. It has been hypothesized that remnant shells shed into the surround aqueous medium, folding into liposomes or micelles. To investigate these effects, we have applied cryogenic transmission electron microscopy (cryo-EM) to image nanoscale lipid and polymer-stabilized perfluorocarbon gas bubbles before and after their destruction with high intensity US.

Statement of Contribution/Methods

Polymer-stabilized lipid nanobubbles (NBs) were made by agitation of a lipid solution(DPPC:DPPE:DPPA), Pluronic L10, acrylamide monomers, crosslinker and irgacure 2959 in the presence of C3F8 gas, followed by crosslinking under U.V. light. Bubbles were imaged in an agarose mold in PBS using contrast harmonic imaging (Toshiba, 12 MHz, MI 0.1). Flash/replenish (20 cycles) was used to destroy bubbles. Particle size was determined by dynamic light scattering. For cryo-EM, NBs were applied to EM grids (R2/2, 400 mesh; EMS) glow-discharged for 30 sec at 15 mA and imaged on JEOL 2200FS transmission electron microscope with a total electron dose of <100 e−/A^2.

Results/Discussion

The application of the high intensity US was found to destroy all bubble contrast (Fig 1a). Mean NB diameter was significantly reduced from 172.7 ± 19.3 nm to 126.7 ± 15.0 nm suggesting a loss of gas from the particles (Fig 1b). Cryo-EM images of NBs demonstrate that particles have a monolayer shell with a dark center that is likely due to the higher density of the frozen C3F8 core relative to the surrounding water layer. Sonicated NBs appeared as amorphous and transparent lipid sheets, indicating a loss of gas (Fig 1c). While some multi-laminar vesicles were present in the NB solution prior to sonication, none could be visualized in the US disrupted solution. These results suggest that US-disrupted NBs do not reform as liposomes or micelles but rather flatten into round sheets following gas loss. This unexpected result may be due to the hydrophobic acrylamide core helping to maintain particle structure.

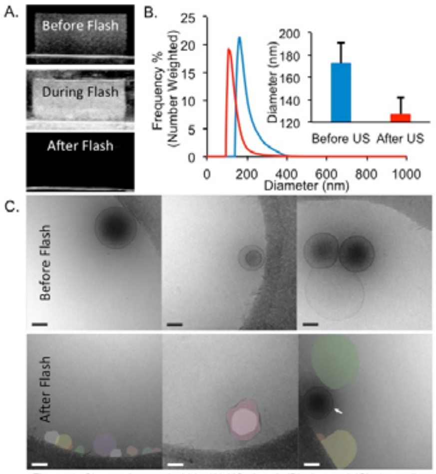

Figure 1. Change in nanobubble (A) US signal, (B) size and (C) shape (by cryo-EM) before and after destruction with high intensity US. Color added to cryoEM images for better visualization. Scale bars represent 100nm.

P1-A3-6

Destruction of Giant Cluster-like Vesicles Assisted by Contrast Agent under 2.8-MHz Ultrasound Irradiation

Kenji Yoshida[1], Ryosuke Yahagi[2], Yiting Zhang[2], Masahiko Ebata[2], Taro Toyota[3], Tadashi Yamaguchi[1], Hideki Hayashi[1]; [1]*Center for Frontier Medical Engineering, Chiba University, Japan,* [2]*Department of Medical System Engineering, Graduate School of Engineering, Chiba University, Japan,* [3]*4Department of Basic Science, Graduate School of Arts and Sciences, The University of Tokyo, Japan*

Background, Motivation and Objective

Localizing tumors and securing resection margins are sometimes difficult especially during laparoscopic surgery for malignant diseases. Therefore, we have developed a tissue marker, which is composed of giant cluster-like vesicles (GCVs) encapsulating near-infrared (NIR) fluorescent liposomes and X-ray contrast agents coated with lipids. The GCVs facilitate localizing tumors preoperatively and intraoperatively because they have superior retention effect in tissue. In addition, the GCVs can work as reservoir of a fluorescent tracer for detecting sentinel lymph nodes if they are destroyed. We propose the method to assess the destruction of GCVs using ultrasound contrast agents (UCAs) and demonstrate the effect.

Statement of Contribution/Methods

Figure 1 (a) shows the tissue marker composed of GCVs that encapsulate ICG-C18 (indocyanine green derivative) formulated liposomes and ethiodized oil (X-ray contrast agent) emulsions. The outer shell of GCVs was made of polyglycerine polyricinoleate (PGPR). In this experiment, however, no material was included in GCVs because we evaluated the destruction of PGPR shell. The optical microscopic image is shown in Fig.1(b). The diameters of the GCVs ranged from approximately 30 to 300 μm. Commercial lipid bubble with diameter of 1-4 μm was used as UCAs. A microplate with 96 wells was located on water surface in a water chamber, and a well was filled with 200 μL mixture of GCVs and UCAs. 10-cycles ultrasound with center frequency of 2.8 MHz and negative peak pressure of 1.6 MPa, which corresponded to Mechanical index (MI) = 0.96, was radiated from a concave transducer. The focus was positioned on the bottom of well. The GCVs after the irradiation were observed by optical microscope, and the amount and size were evaluated by image analysis.

Results/Discussion

Figure 1(c) shows the size and cumulative distribution of GCVs under ultrasound irradiation US(+) or no irradiation US(-) in presence or absence of UCAs i.e. UCA(+) and UCA(-). It was found that the 90% diameter of GCVs became smaller in the following order, UCA(+) and US(+),UCA(-) and US(+),UCA(+) and US(-), and UCA(-) and US(-). The results indicated that the interaction between ultrasound and UCA enhances the destruction of bigger GCVs and increased the amount of smaller GCVs. It was suggested that UCAs could assist the destruction of GCVs under safety ultrasound irradiation (MI<1).

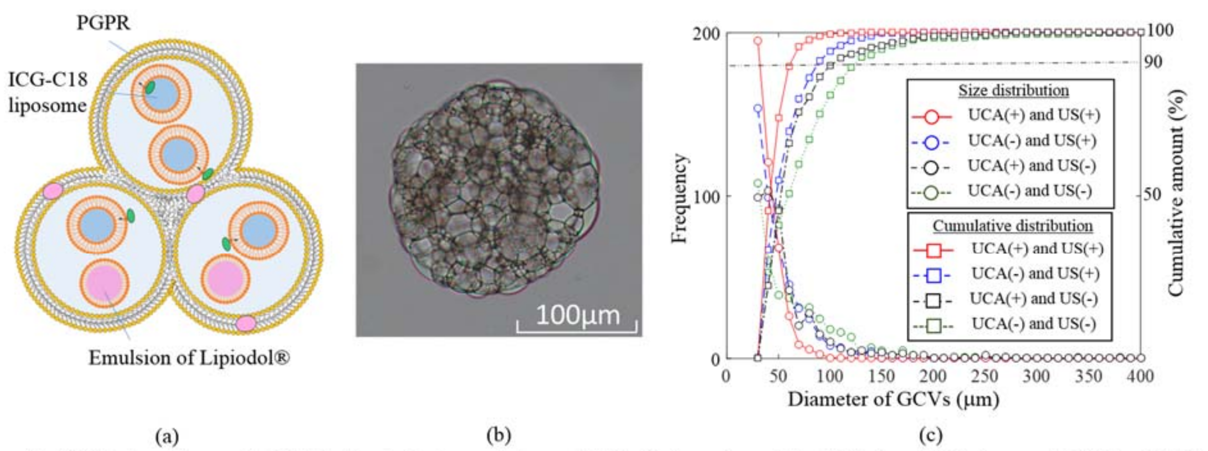

Fig. 1(a) Structure of accumulated GCVs, (b) optical microscopic image of GCVs, (c) size and cumulative distribution of GCVs in cases of UCA(+) and US(+), UCA(-) and US(+), UCA(+) and US(-) and UCA(-) and US(-).

P1-A3-7

High Resolution Ultrafast Imaging of Microbubble Destruction during Sonoporation

Sara Keller[1], Michalakis Averkiou[1]; [1]*Bioengineering, University of Washington, Seattle, Washington, USA*

Background, Motivation and Objective

Ultrasound-mediated drug delivery using microbubbles is a growing field with applications ranging from targeted chemotherapy delivery to permeating the blood brain barrier. However, the precise parameters that induce increased cellular permeability are not fully understood. For sonoporation efficiency, a high microbubble concentration is preferred, but acoustic shadowing limits the ultrasound delivery to the cells. Our hypothesis is that high-resolution ultrafast imaging will demonstrate the interaction of ultrasound with microbubbles during the sonoporation process to carefully control the ultrasound dose. This work has two aims: 1) to accurately image the ultrasound delivery to cells with high-resolution ultrafast imaging, and 2) to determine the dependence of microbubble concentration and acoustic environment on cavitation activity. This will lead to optimization of sonoporation.

Statement of Contribution/Methods

Ultrasound transmission from a 1 MHz single element transducer through a cell enclosure (Opticell-like) with increasing microbubble concentration (100-10000 bubbles/µl) was characterized at varying acoustic parameters (100-500 kPa, 20-1000 cycles) with a PVDF membrane hydrophone. A 15 MHz linear array was next used to acquire high resolution, high frame rate images of microbubble streaming and destruction patterns in the cell enclosure using the same parameters (Fig. 1a). A Philips iU22 and a Verasonics 128 system were used for imaging. HepG2 cells were seeded on the top side of the cell enclosure. Image loops were collected and analyzed to evaluate the cavitation activity near the cells and to look specifically for pulse-to-pulse destruction.

Results/Discussion

At high microbubble concentrations (7500 bubbles/µl), acoustic shadowing completely blocks ultrasound delivery to microbubbles next to cells. Attenuation through the enclosure decreases with decreasing microbubble concentration. Unique microbubble destruction patterns shown with high resolution, ultrafast imaging include streaming, vortexing, and standing waves (Fig 1b). Despite the simplicity of the cell enclosure, the complexity of the microbubble patterns during sonication as observed for the first time with ultrafast imaging reveals surprising results and gives guidance on the ultrasound parameters and concentration needed for efficient sonoporation.

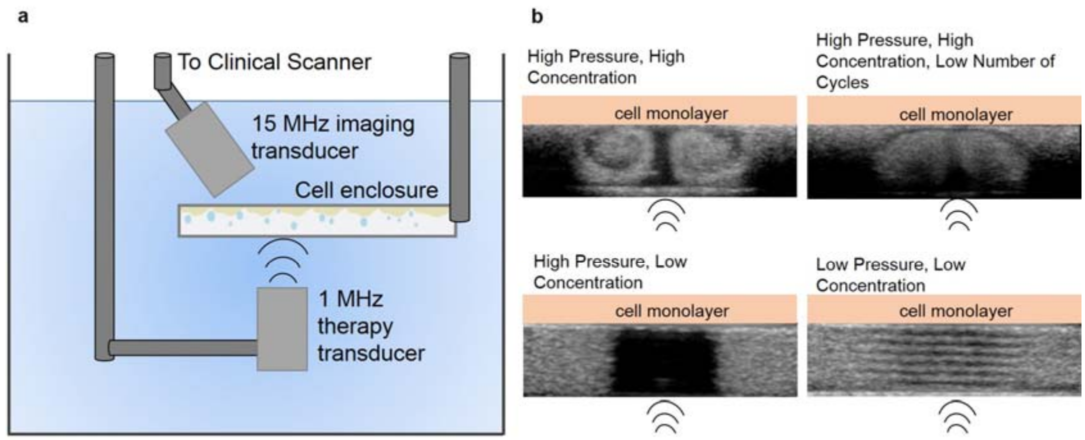

(a) Setup for imaging cavitation activity near cells. Cells are located on the top side of the enclosure. (b) Images of cavitation activity near the cells during sonoporation. Note complex destruction patterns, vortexing at high pressures and standing waves at low pressures.

P1-A3-8

Contrast-Enhanced Ultrasound Evaluation of Skeletal Muscle Perfusion in Response to Left Ventricular Assist Device (LVAD) Therapy

Lauren Jablonowski[1], Maria Stanczak[1], Priscilla Machado[1], Kathleen Fitzgerald[2], Gordon Reeves[2], Flemming Forsberg[1]; [1]*Radiology, Thomas Jefferson University, Philadelphia, PA, USA,* [2]*Cardiology, Thomas Jefferson University, Philadelphia, PA, USA*

Background, Motivation and Objective

Patients with chronic heart failure have reduced cardiac output and capacity for exercise-induced capillary vasodilation. Clinicians use left ventricular assist device (LVAD) therapy to improve physical function, but LVAD devices are designed to provide continuous blood flow and cannot increase blood flow in response to demand (i.e., exercise). Hence, this study investigated whether skeletal muscle perfusion and exercise capacity improved with LVAD therapy by quantifying muscle perfusion in heart failure patients pre- and post-LVAD implantation.

Statement of Contribution/Methods

Eight patients, enrolled in the LVAD therapy program, signed informed consent as part of an ongoing IRB-approved study to undergo contrast-enhanced ultrasound (CEUS) exams prior to implantation of the LVAD, 2 weeks post-implantation, and again at 3 months post-implantation. During each scanning session, two CEUS exams were conducted on a standardized portion of the quadriceps muscle, one scan being in a resting state and the other in a fatigue state. Muscle fatigue state was achieved by having the patient perform knee extensor exercises, while an examiner provided resistance of approximately 50% of maximum knee extensor strength until exhaustion with a handheld dynamometer (MicroFET 2, Hoggan Scientific, Salt Lake City, UT, USA). CEUS scanning was performed using Cadence Pulse Sequencing on an S3000 Helx scanner (Siemens Healthineers, Mountain View, CA, USA) with a C6 probe during 2 bolus injections of 0.3 mL of Definity (Lantheus Medical Imaging, N. Billerica, MA, USA). During each scanning session, 3 destruction-reperfusion sequences were acquired. Time-intensity curves were generated in Matlab (MathWorks, Natick, MA, USA) to estimate perfusion over the quadriceps muscle, where perfusion was calculated as the slope of the curve from the time contrast was first visualized to the peak intensity. Paired t-tests were used to compare the data through IBM SPSS statistics software (IBM Analytics, Armonk, NY, USA).

Results/Discussion

Contrast arrival times pre- and post-exercise were significantly different (38 ± 8 seconds vs. 27 ± 7 seconds; $p = 0.0025$). There were no significant differences observed in perfusion across the three time points ($p > 0.06$). CEUS-estimated muscle perfusion seems to indicate appropriate physical function in heart failure patients. However, this is an ongoing study and more data is required to bolster these preliminary results.

P1-A4 - MEL: Cardiovascular Elastography

Exhibit Hall

Thursday, September 7, 2017, 9:30 am - 4:00 pm

Chair: **Pengfei Song**
Mayo Clinic

P1-A4-1

4D Strain Imaging Using Single and Dual Probe Acquisitions of a Patient Specific Carotid Bifurcation Phantom

Stein Fekkes[1], Hendrik Hansen[1], Jan Menssen[1], Maartje Nillesen[1], Anne Saris[1], Chris de Korte[1,2]; [1]*Medical UltraSound Imaging Center (MUSIC), department of Radiology & Nuclear Medicine, Radboud university medical center, Netherlands,* [2]*Physics of Fluids Group, University of Twente, Enschede, Netherlands*

Background, Motivation and Objective

Atherosclerosis in the carotid artery (CA) elevates the risk for cerebral events. Strain imaging has demonstrated to be a technique capable of identifying plaque composition. For strain imaging of carotid cross-sections, compound techniques have been developed to solve the poor strain estimation quality perpendicular to the ultrasound beam direction. This study assesses the performance of radial and circumferential strain imaging in 4D derived from multi-plane acquisitions with a single transducer with and without compounding and using two orthogonally placed transducers.

Statement of Contribution/Methods

A phantom was created of polyvinyl alcohol resembling a stenotic CA bifurcation with surrounding tissue of a patient. A realistic pulsatile flow of 60 bpm was imposed on the phantom resulting in a fluid pressure of 150 over 100 mmHg inducing strains up to 10%. Two orthogonally aligned ATL L12-5 linear array transducers (fc = 9 MHz, pitch = 195 µm, 256 elements) were connected to two Verasonics systems (V1 / Vantage 256) and fixed in a translation stage to ensure a coinciding transversal field of view. For 120 equally spaced (0.1 mm) elevational positions, ultrasound series were acquired at 50 Hz synchronised using a trigger at the end diastole. Each series consisted of plane wave acquisitions at alternating angles (-19.5°, 19.5°, 0° for probe 1 and 0°, -19.5°, 19.5° for probe 2) at a PRF of 10 kHz. After delay-and-sum beamforming, inter-frame displacements were estimated using a cross-correlation-based, multi-step speckle tracking algorithm. Horizontal displacements were acquired using the single probe lateral estimate, the single probe compounding of axial estimates at both angles and the dual probe registered axial estimate. After tracking, an LSQ strain estimation and eigenvalue decomposition was performed to compare principal strains in 3D in radial and circumferential direction for all methods.

Results/Discussion

Figure 1 depicts the radial and circumferential median strain progression for the complete CA volume and the full pressure cycle for all three methods. The radial and circumferential median strains of the single probe method were -7.3% and 13.4% without compounding and -4.1% and 8.8% with compounding at peak systole, respectively. Taking the dual probe strains (-3.9%, 7.8%) as reference, compounding clearly outperformed the single angle method.

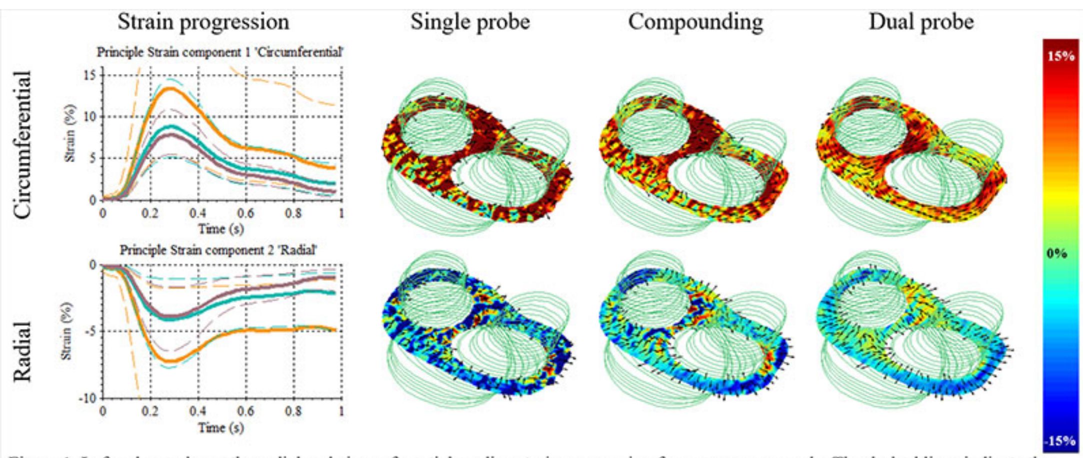

Figure 1. Left column shows the radial and circumferential median strain progression for one pressure cycle. The dashed lines indicate the 25th and 75th percentile strains for the single probe without and with compounding and dual probe. On the right, 3D representations of the lumen wall segmentations showing the radial and circumferential strain distribution at the middle elevational plane at peak systolic pressure for the single probe, compounding and dual probe methods.

P1-A4-2

3D Geometry Assessment and Wall Stress Analysis of Carotid Arteries using 2D US Segmentation during a Controlled Sweep

Joerik de Ruijter[1,2], Koen Hobelman[1], Frans van de Vosse[1], Marc van Sambeek[2], Richard Lopata[1]; [1]*Eindhoven University of Technology, Netherlands,* [2]*Catharina Hospital, Netherlands*

Background, Motivation and Objective

Patients with a 70-99% stenosed carotid artery will undergo surgery to prevent rupture of the plaque. However, the degree of stenosis does not determine the vulnerability of the plaque, since vulnerability depends on the plaque's morphology, mechanical properties and the force acting on the plaque. Mechanical models of the carotid artery can improve decision-making of the surgeon by quantifying and mapping wall stress and strain. In this study, a method was developed to obtain the 3D geometry of the carotid artery by a 'slow' sweep over the neck (5 cm) using 2D ultrasound. Rather than using a 3D ultrasound probe, the high axial and temporal resolution are maintained.

Statement of Contribution/Methods

The proposed method is tested in vivo on 5 healthy volunteers. A probe holder and translational stage was developed to control the position of the transducer in the r, θ and z direction. By applying a constant sweep speed over a known trajectory, the 2D images can be projected into a 3D space. The lumen wall is detected frame by frame on transverse acquisitions using a RF based sustain and attack filter. The initialization is based on lumen detection using the circle Hough transform. The detected wall points are filtered with a robust quadratic filter with respect to the centre point. The automatic segmentation was compared to manual segmented data of healthy volunteers.The segmented walls are converted into a volume mask and smoothened using an 3D active contour model, resulting in the 3D geometry of the carotid artery. Finite Element (FE) modeling was used to calculate the wall stress in the carotid artery wall, using the measured geometry and brachial arterial pressure as input, and assuming a population average for the material properties and wall thickness (h = 1.0 mm).

Results/Discussion

With this method we were able to obtain the 3D geometry of a healthy carotid artery non-invasively, quickly, and fully automatic with high spatial resolution. The distention caused by the pulse pressure was present in the geometries, which was removed by correcting for the blood pressure. Segmentation results were in good correspondence to the manual segmentation. FE meshing and simulation were successful in all subjects. In future work, the method proposed will be investigated in patients with a stenosis and validated using CT imaging.

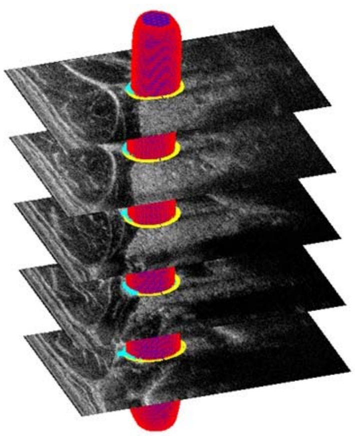

Fig 1. Automatic segmented lumen wall (yellow), 3D snake grows within the 3D mask (red).

P1-A4-3

Experimental Observations of Shear Waves in Cylindrical Phantoms and Excised Equine Carotid Artery

Darya Shcherbakova[1], Mathieu Pernot[2], Julie Vastmans[3], Mathias Kersemans[4], Annette Caenen[1], Abigail Swillens[1], Patrick Segers[1]; *[1]IBiTech - bioMMeda, Department of Electronics and Information Systems, Ghent University, Ghent, Belgium, [2]Institut Langevin, ESPCI ParisTech, CNRS UMR 7587, INSERM ERL U979, Paris Cedex 05, France, [3]Biomechanics Section, KU Leuven, Leuven, Belgium, [4]Mechanics of Materials and Structures MMS, Department of Materials, Textiles and Chemical Engineerin, Ghent University, Ghent, Belgium*

Background, Motivation and Objective

To facilitate the development and application of ultrasound shear wave elastography (SWE) in arteries, it is necessary to understand the nature of shear waves (SWs) propagating in pressurized anisotropic tubes embedded in softer surrounding tissues and blood. Phantom models are widely used to study SWE in tubular settings mimicking arterial geometry without yet considering anisotropy. To investigate SWs behavior in thin-walled structures, we performed SWE measurements in tubular phantoms (inner diameter of 6-6.5 mm; 3 mm and 1 mm wall thickness) with 2 types of boundary conditions: embedded in water or in a softer medium. Furthermore, experiments were performed on excised equine carotid arteries (diameter 5.6 mm, thickness 1 mm).

Statement of Contribution/Methods

Tubular PVA phantoms (2 freeze-thaw cycles, 10% PVA) were constructed, as well as corresponding rectangular slabs (thickness 1 mm-2.4 cm; bulk shear wave speed SWS_{Bulk} = 4.5-4.7 m/s). Two tubes were tested in water (labeled unembedded) and another two were surrounded by softer PVA medium (SWS_{Bulk}=3.9 m/s). Phantoms were pressurized under a water column with pressure values ranging from 0 to 70 mmHg with a step of 10 mmHg. The SWE measurements were repeated for an excised equine carotid artery pressurized up to 120 mmHg. The unembedded 1 mm tube was axially streched by 20%, while the 3 mm tube and carotid artery were stretched by 40%. The embedded tubes were not pre-stretched. SWS results were obtained in both longitudinal and cross-sectional views.

Results/Discussion

Contrary to our expectations, at 0 mmHg SWs in the samples with simpler setup (rectangular slab and unembedded tube) look significantly more complex than in the embedded tube or carotid artery (Fig. A), thus not allowing to obtain reliable SWS results. All samples had 1 mm wall thickness. In 3 mm phantoms such behavior was not observed. Pressurizing the 3 mm unembedded tube (Fig. B) led to an increase in SWS in the cross-sectional view, while it slightly decreased in the axial direction (Fig. B). A similar trend was observed for 1 (Fig. B) and 3 mm embedded tubes in the cross-sectional view, while the SWS in the longitudinal view remained constant upon pressurization. For the carotid artery, SWS increased in both views with applied pressure level. Numerical simulations with a known ground truth will allow to better understand SW propagation in such complex settings.

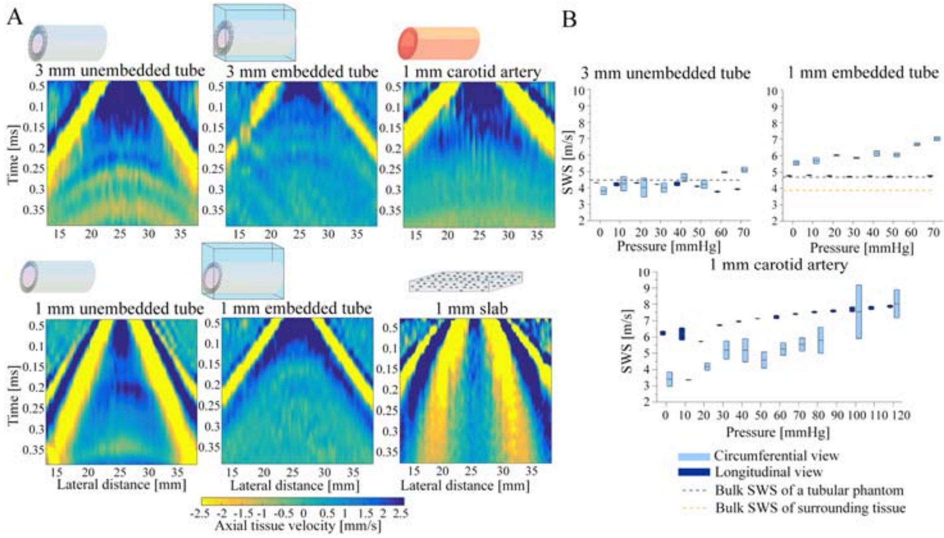

P1-A4-4

Non-Invasive Carotid Artery Elastography Using Multi-Element Synthetic Aperture and Plane Wave Imaging: Phantom and In Vivo Evaluation

Rohit Nayak[1], Giovanni Schifitto[2], Marvin Doyley[1]; [1]*Department of Electrical and Computer Engineering, University of Rochester, Rochester, NY, USA,* [2]*Department of Neurology, University of Rochester, Rochester, NY, USA*

Background, Motivation and Objective

Vascular elastography can visualize the strain distribution in the carotid artery, which governs plaque rupture. In this study, we hypothesize that multi-element synthetic aperture (MSA) imaging, which produces divergent transmit beams can produce high quality vascular strain elastograms, relative to those obtained using compounded plane wave (CPW) imaging.

Statement of Contribution/Methods

To corroborate this hypothesis, we conducted phantom and in vivo studies using both the techniques, and determined the most optimal imaging configuration for carotid elastography. The phantom studies were conducted using cryogel vessel phantoms with a plaque inclusion at ideal (0.1 dB/cm/MHz) and realistic (0.75 dB/cm/MHz) attenuations. These studies were conducted using a commercially ultrasound scanner (Sonix RP, Ultrasonix Medical Corp., Richmond, BC, Canada), operating at a transmit frequency of 5 MHz. Further, we validated the phantom study results in vivo, on a healthy volunteer of 21 years old. An electrocardiography device (Model 7600, Ivy Biomedical, CT, USA) was used to synchronize the ultrasound acquisitions with the cardiac cycle of the subject. The in vivo echo imaging was performed with a transmission frequency of 5 MHz, and frame-rate of 230 frames per second.

Results/Discussion

The results of the phantom study demonstrated that the vascular strain elastograms obtained using MSA imaging had fewer artifacts and were noticeably better than those produced using CPW imaging. Overall, the results demonstrated that the detectability and contrast of the inclusion in the MSA strain elastograms were governed by the size of the transmit sub-aperture and the number of transmit-receive events used to synthesize each RF frame. More specifically, the quality of the strain elastograms improved with increase in the size of the transmit sub-aperture, however, beyond 13 elements no significant improvement in CNRe was obtained. This was primarily because any gain in signal strength expected from using a larger transmit sub-aperture was offset by an increase in the grating lobe artifacts due to source incoherency. However, increasing the number of transmit-receive events improved the elastographic performance of MSA imaging, especially at large sub-apertures, owing to spatial compounding. The CNRe of the corresponding strain elastograms obtained using MSA imaging were approximately 9 dB higher than those obtained using MSA imaging. Beam-steering improved the elastographic performance of CPW imaging, however, only up to 8o, beyond that the grating lobe artifacts dominated. The large pitch of the L38/5-14 transducer limited the performance improvement that could be achieved with angular compounding. Further, the in vivo elastograms obtained using MSA imaging were less noisy than those obtained using CPW imaging.

It was concluded that MSA imaging performed sufficiently well enough to warrant further development and more in vivo validation.

P1-A4-5

Normalization of Carotid Plaque Based Strain Indices Using Blood Pressure Measurements

Tomy Varghese[1,2], Nirvedh Meshram[2], Carol Mitchell[3], Bruce Hermann[4], Stephanie Wilbrand[5], Daren Jackson[5], Robert Dempsey[5]; [1]*Medical Physics, University of Wisconsin School of Medicine and Public Health, Madison, Wisconsin, USA,* [2]*Electrical and Computer Engineering, University of Wisconsin-Madison, Madison, Wisconsin, USA,* [3]*Department of Medicine, University of Wisconsin School of Medicine and Public Health, Madison, Wisconsin, USA,* [4]*Neurology, University of Wisconsin School of Medicine and Public Health, Madison, Wisconsin, USA,* [5]*Neurological Surgery, University of Wisconsin School of Medicine and Public Health, Madison, Wisconsin, USA*

Background, Motivation and Objective

Ultrasound based carotid strain imaging (CSI) developed in our laboratory utilizes physiological deformation in response to arterial pressure variations. We have shown that strain indices are capable of quantifying vulnerability of carotid plaque, enhancing their validity as vascular biomarkers. However, a critique of CSI has been the lack of normalization of the maximum and peak-to-trough strain indices to the physiological stimuli, namely the blood pressure. We report on the impact of normalization of these strain indices to blood pressure measurements that are acquired immediately prior to the acquisition of radiofrequency (RF) data loops for strain imaging on human patients scheduled for a carotid endarterectomy (CEA).

Statement of Contribution/Methods

A complete clinical ultrasound examination along with RF data loops for ultrasound carotid strain imaging was performed on 44 patients (28 males and 16 females) who present with significant stenosis ≥ 60% using a S2000 system (Siemens Ultrasound, Mountain View, CA, USA) and an 18L6 transducer. All patients were scheduled for a CEA procedure based on both North American Symptomatic Carotid Endarterectomy Trial and Asymptomatic Carotid Atherosclerosis criteria. Informed consent was obtained prior to their participation under a protocol approved by the University of Wisconsin-Madison institutional review board. Patients were further identified as symptomatic or asymptomatic based on clinical symptoms. Cognition was assessed on these patients using the 60-minute neuropsychological test protocol following guidelines of the National Institute of Neurological Disorders and Canadian Stroke Network. Blood pressure measurements were utilized to normalize strain indices estimated from the axial, lateral and shear strain images over two cardiac cycles using systolic, diastolic and maximum arterial pressure (MAP) respectively.

Results/Discussion

No significant differences in the area under the curve (AUC) estimates were obtained between the maximum and peak-to-trough strain indices that were normalized to the systolic, diastolic and maximum arterial pressure when compared to the unnormalized results reported previously. Although small improvements in the correlation of the strain indices with cognition parameters and AUC values were obtained with normalization, unnormalized strain indices on their own provided a significant correlation with the reduction in executive function reported with cognitive testing. For axial strain, the correlation of peak values with cognition were -0.489, -0.470, -0.499 and -0.488 for unnormalized, systolic, diastolic and MAP normalization respectively. The corresponding AUC values for classifiers designed using logistic regression with a 10-fold cross-validation were 0.752, 0.728, 0.750, 0.731 respectively.

Acknowledgement: Funded in part by National Institutes of Health grants R21 EB010098, R01 NS064034, and 2R01 CA112192.

P1-A4-6

Update on Carotid Plaque Instability Quantification Using Strain Indices from Multiple Regions of Interest in Carotid Plaque

Nirvedh Meshram[1,2], Carol Mitchell[3], Bruce Hermann[4], Stephanie Wilbrand[5], Daren Jackson[5], Robert Dempsey[5], Tomy Varghese[1,2]; [1]*Department of Medical Physics, University of Wisconsin School of Medicine and Public Health, Univer, University of Wisconsin Madison, Madison, Wisconsin, USA,* [2]*Department of Electrical and Computer Engineering, University of Wisconsin Madison, Madison, Wisconsin, USA,* [3]*Department of Medicine, University of Wisconsin Madison, Madison, Wisconsin, USA,* [4]*Department of Neurology, University of Wisconsin Madison, Madison, Wisconsin, USA,* [5]*Department of Neurological Surgery, University of Wisconsin Madison, Madison, Wisconsin, USA*

Background, Motivation and Objective

Carotid plaque rupture is a primary cause of ischemic strokes and transient ischemic attacks (TIAs). Probability of stroke and TIAs depend on the mechanical stability of plaque. Ultrasound strain can provide a non-invasive assessment of plaque stiffness to assess mechanical stability. We report on ultrasound strain indices from multiple regions of interest (ROI) in plaque as biomarkers for plaque instability.

Statement of Contribution/Methods

The IRB approved study included 70 patients (39 symptomatic, 31 asymptomatic) scheduled for a carotid endarterectomy who participated in pre-surgical ultrasound strain imaging and cognitive testing. Patients were classified as symptomatic or asymptomatic based on clinical symptoms. We hypothesize that patients with unstable plaque are more likely to have cognitive deficits due to undetected ischemic events. Previous work evaluated strain indices from a single ROI. This work extends analysis into a multiple ROI approach. Five strain indices are identified as potentially useful biomarkers of plaque instability. These include the maximum accumulated strain indices (MASI) in the primary ROI, mean of the standard deviation of strain estimated in entire plaque (MSD), the average L1 Norm (AL1NWP), total number of unstable ROIs (NUROI), and the percent of unstable estimates in the entire plaque (PPS). We use the suffix A, L and S to identify axial, lateral and shear strain indices respectively.

Results/Discussion

The MASI, MSD and AL1NWP indices all showed a negative correlation with cognition. The highest correlation was achieved by S-AL1NWP ($r=-0.53$, $p<0.01$) and ($r=-0.60$, $p<0.01$) for all and symptomatic patients, while A-MASI ($r=-0.58$, $p<0.01$) correlated best for asymptomatic patients. NUROI and PPS showed a weak positive correlation A-NUROI ($r=0.27$, $p=0.02$) and A-PPS ($r=0.29$, $p=0.01$) for all patients. To examine combinations of strain indices for improved classification classifiers using logistic regression with 10-fold cross-validation was used. Features were restricted to four indices to avoid overfitting. Using four indices with highest correlations resulted in an Area Under Curve (AUC) of 0.80. However, since NUROI and PPS are independent and not directly related to strain a combination of the two top performing indices (S-AL1NWP, S-MSD) with S-NUROI and A-PPS provided an AUC of 0.85. Our multiple ROI approach demonstrated independent and improved indices for plaque instability quantification.

Acknowledgement: (Funded in part by National Institutes of Health grants R21 EB010098, R01 NS064034, and 2R01 CA112192.)

P1-A4-7

Assessment of Plaque Wave Velocity by Shear Wave Elastography Using a Combined Ex-Vivo and Phantom Setup

David Larsson[1,2], Elira Maksuti[1], Matthew W Urban[3], Matild Larsson[1,2]; [1]*KTH Royal Institute of Technology, Sweden,* [2]*Karolinska Institutet, Sweden,* [3]*Mayo Clinic College of Medicine, USA*

Background, Motivation and Objective

Quantifying the constitutive behavior of atherosclerotic plaques can be important in assessing plaque vulnerability. For this, acoustic radiation force-techniques such as shear wave elastography (SWE) have been applied [Ramnarine et al, UMB, 2014]. However, measurement accuracy is still uncertain due to the confined plaque geometry. The aim of this study was to create a controlled setup that would take the complexity of the arterial wall into account whilst allowing for control of plaque geometry and stiffness. Towards this aim, estimated plaque shear wave velocity was evaluated as a function of stiffness and push position.

Statement of Contribution/Methods

Poly(vinyl alcohol) (PVA) tapered plaques (10% PVA, 3% graphite) of varying stiffness were manufactured using 3D printed molds (length: 30 mm, lumen radius: 3.5 mm) and repeating 24h freeze-thaw (FT) cycles of the PVA (2–5 FT). The plaques were inserted in a porcine aorta (length: 10 cm, lumen diameter: 15 mm) and mounted on customized fixtures, with the artery subsequently embedded in agar (1% agar, 3% graphite) (Fig. 1(a-b)). SWE acquisitions were performed with a Verasonics V1 (L7-4, 4.09/5 MHz push/imaging, 85 µs push) in a longitudinal view. Pushes were placed in the anterior and posterior wall, both at the longitudinal plaque border, and 20 mm away from the plaque. Group and phase velocity in discrete intervals were extracted using in-house post-processing schemes. Velocities were compared against reference group velocities obtained from large cylindrical phantoms, manufactured from plaque PVA solutions.

Results/Discussion

Larger cumulative displacements were generated in the plaque when pushing closer to it (8–3.1 µm for 2–5 FT) compared to farther away (2.7–0.8 µm for 2–5 FT), giving higher signal-to-noise ratio. Results indicate higher accuracy for stiffer plaques, with largest deviations at 2 FT (mean deviation: 1.23 m/s). The group velocity (mean deviation: 0.54 m/s) and phase velocity around 1 kHz (mean deviation: 0.53 m/s) were closest to the reference, whereas other frequency ranges showed larger deviations. The results highlight the need for refined analysis when evaluating shear wave velocities in confined media such as plaques. With this setup, further controlled studies of shear wave propagation in plaques are enabled, aiding future development of plaque mechanical properties mapping with SWE.

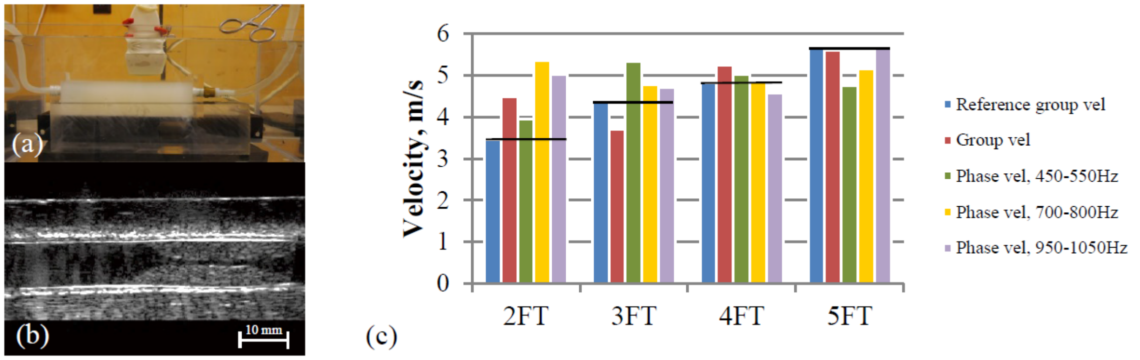

Figure 1: (a) Embedded porcine aorta with inserted phantom plaque and (b) corresponding longitudinal B-mode image of the setup. (c) Group and phase velocities in plaques of varying stiffness. Data are shown for the anterior plaque side with a push close to the plaque edge. Reference group velocities are given in the dark blue columns, with added black horizontal line for easier comparison.

P1-A4-8

Improved Ultrasound-Based Mechanical Characterization of Abdominal Aortic Aneurysms

Niels Petterson[1], Emiel van Disseldorp[1,2], Frans van de Vosse[1], Marc van Sambeek[2], Richard Lopata[1]; [1]*Cardiovascular Biomechanics, Eindhoven University of technology, Eindhoven, Netherlands,* [2]*Department of Surgery, Catharina Hospital Eindhoven, Eindhoven, Netherlands*

Background, Motivation and Objective

Novel methods for determining rupture risk in abdominal aortic aneurysms (AAAs) have focused primarily on CT-based wall stress analysis using finite element models (FEMs). Recent studies have demonstrated ultrasound (US) based FEM, and the possibility of using inverse FEM analysis: matching displacements between the models and US to find patient specific aortic stiffness. This requires an accurate representation of deformation of the FEM-based aorta, which could be highly influenced by the presence of surrounding tissue. Typically, these methods solely include the vessel, fixed on both ends. The abdominal aorta (AA) however is surrounded by other tissue including the spine, which acts as a stiff boundary. In this study, AA(A) models based on 4D US were constructed with increasing complexity. The importance of modelling surrounding tissues was investigated by comparing mechanical parameters.

Statement of Contribution/Methods

4D DICOM data of 6 healthy volunteers and 3 AAA patients were acquired with a Philips IU22 system equipped with an X6-1 matrix array. AA(A) geometry was attained by manual segmentation and 3D speckle tracking produced displacements of the wall. Three models were constructed: 1) the AA(A) geometry, 2) AA(A) including a block of generic soft tissue (G = 10 kPa), 3) the previous with a stiff rod mimicking the spine at a distance of 1mm to the AA(A) (G = 0.9 GPa). The initial guess for aortic stiffness was 150 kPa for AAs and 500 kPa for the AAAs. After applying the subject specific pressure to the FEMs, model displacements were compared to those obtained with US. The stiffness of the aorta was updated iteratively, until convergence was achieved. Final subject specific stiffness, 99-percentile and peak wall stresses were compared between the three FEM types.

Results/Discussion

Stress homogenisation was observed with the addition of surrounding tissue, which leads to a decline in estimated 99-percentile and peak wall stresses of 22-60%. When surrounded by tissue, the estimated stiffness of the aortic wall dropped from 132 ± 26 kPa to 106 ± 25 kPa for volunteers and from 638 ± 128 kPa to 572 ± 143 kPa for AAA patients. While the inclusion of the spine did not show a significant impact on stress and stiffness, the match between measured and modelled displacements did improve (see figure). In future research, the influence of patient-specific spine shape will be investigated.

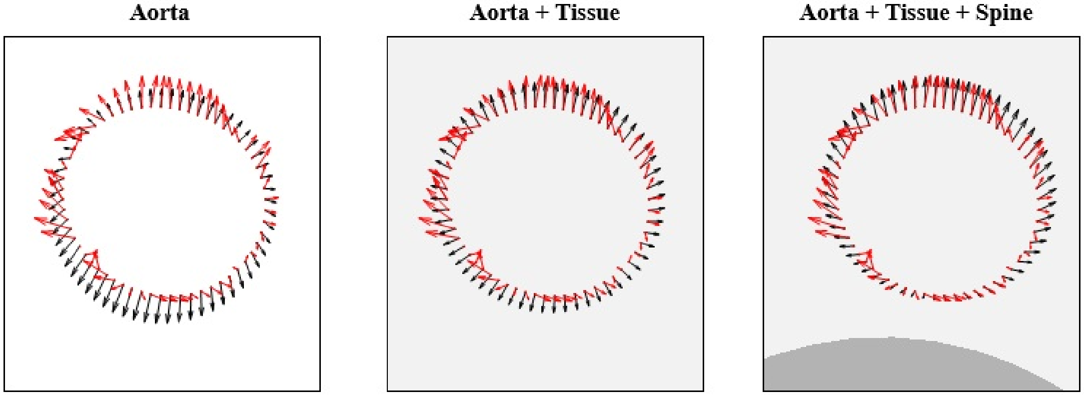

Figure: Displacements of a cross section of the aorta. Red arrows: ultrasound measured displacements; **Black** arrows: finite element model displacements

P1-A4-9

Strain and Strain Rate Generated by Shear Wave Elastography in *ex vivo* Porcine Aortas

Elira Maksuti[1], David Larsson[1,2], Matthew W. Urban[3], Kenneth Caidahl[4], Matilda Larsson[1,4]; *[1]Medical Engineering, KTH Royal Institute of Technology, Stockholm, Sweden, [2]Clinical Sciences, Karolinska Institutet, Stockholm, Sweden, [3]Radiology, Mayo Clinic, Rochester, MN, USA, [4]Molecular Medicine and Surgery, Karolinska Institutet, Stockholm, Sweden*

Background, Motivation and Objective

In shear wave elastography (SWE), acoustic radiation forces (ARF) are employed to generate shear waves within the tissue. Although the transmitted pulses are longer than those in conventional clinical ultrasound, they typically obey the mechanical and thermal regulatory limits. In arterial applications, specific safety concerns may arise, as ARF-induced stresses and strain rates could potentially affect the arterial wall. A previous simulation study (Doherty et al., J Biomech, 2013 Jan; 46(1):83-90) showed that stresses imposed by the ARF used in SWE are orders of magnitude lower than those caused by blood pressure. ARF-induced strain rates have not been investigated yet, therefore the aim of this study was to assess such strain rates in an *ex vivo* setup.

Statement of Contribution/Methods

Two porcine aortas (diameters [8.5, 12.2] mm, wall thickness [1.2, 1.2] mm) were pressurized by a saline-filled water column at 60 and 120 mmHg. A Verasonics V1 system and a L7-4 transducer were used to generate the ARF in the middle of the anterior wall (F-number = 1, push length = [100, 200, 300] µs) and to perform plane-wave imaging (10 kHz). Cumulative axial displacement was estimated using 2D auto-correlation (Fig. 1a). The axial strain rate was calculated as the time-derivative of the axial strain, obtained by spatial linear regression of the displacement inside the anterior wall. This was repeated for all lateral positions at 0-15 mm distance from the ARF focus. The *ex vivo* peak strain and strain rate were compared with peak values induced by the blood pressure changes in two healthy individuals at rest and measured by a dedicated in house speckle tracking algorithm (Larsson et al., IEEE TUFFC, 2011 Oct; 58(10):2244-51).

Results/Discussion

ARF-induced *ex vivo* peak strains were in the range 0.3-1% and strain rates in the range 6-22 s^{-1}, depending on push length and pressurization level (Fig. 1b-c). Peak values were more affected by longer push duration than pressurization level. In vivo physiological peak strain was 33% and strain rate was 2 s^{-1}. ARF-induced strain rates in the ex vivo setup were up to one order of magnitude higher than the in vivo physiological values at rest. ARF-induced strain rates in vivo are likely to be lower than those assessed in this ex vivo setup due to ultrasound attenuation and the effect of surrounding tissue. These results suggest that the use of SWE in arteries is safe.

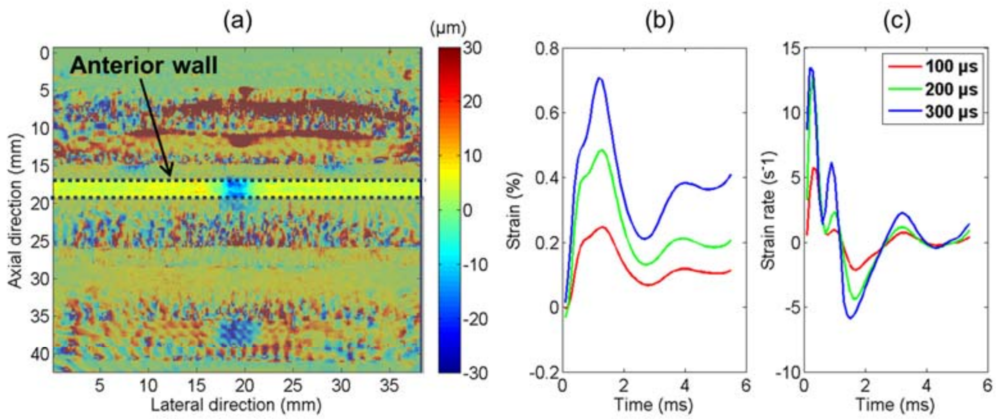

Figure 1. (a) Cumulative displacement after 5.5 ms from the acoustic radiation force (ARF) generation (push length 100 µs). Representative ARF-induced strain (b) and strain rate (c) curves over time within the arterial wall at different push lengths and at 3 mm distance from the ARF focus.

P1-A4-10

Mechanical Characterization of Vascular Tissue Using Ultrasound

Joerik de Ruijter[1,2], Frans van de Vosse[1], Marc van Sambeek[2], Richard Lopata[1]; *[1]Eindhoven University of Technology, Netherlands, [2]Catharina Hospital, Netherlands*

Background, Motivation and Objective

Rupture of carotid plaques accounts for 15 to 20% of ischemic strokes. To prevent a stroke patients undergo surgery (carotid endarterectomy). However, only one out of six patients benefits from this intervention, so there is a significant overtreatment of patients. To develop better treatment criteria, and to improve patient diagnosis and clinical decision making, patient specific information of the plaque's composition and mechanical properties is needed.

In this study, a method was developed to estimate global material properties of the vascular wall using ultrasound imaging. Here, a finite element model (FEM) is matched with the displacement field measured by US, by updating the material properties of the FEM. As a result, a measure for arterial wall stiffness is obtained non-invasively.

Statement of Contribution/Methods

This inverse FE method was tested on artificial carotid phantoms made out of polyvinyl alcohol, with increasing complexity, both in geometry (0-60% stenosis) and the number of constituents (single and two layers). An experimental set-up was used to perform US imaging during an inflation experiment. The inflation experiment is then simulated using finite element analysis: 2-D ultrasound images were segmented automatically (Fig. 1A) and converted into 3-D FE meshes (Fig. 1B). To estimate the displacements of the wall a 2-D iterative, coarse-to-fine method was used (Fig. 1C-D). The error between the measured and simulated displacements was minimized using a downhill simplex optimization method. To validate the inverse approach, the mechanical properties of PVA samples were determined using uni-axial tensile tests.

Results/Discussion

For single layer phantoms, the estimated material properties (G_{FEM} = 30 to 33 kPa) are within the range of the material properties found with the uni-axial tensile tests (G_{TT} = 29 to 36 kPa). For stenosed double layer phantoms, we were able to estimate the stiffness of the outer layer and distinguish between a weaker inner layer (G_{FEM} = 19 to 28 kPa) and a stiffer outer layer (G_{FEM} = 40 to 42 kPa).

In the present study, the material properties of a complete part of the material are estimated rather than a Young's modulus distribution. However, in future work, this methodology will be extended to an inverse method to possibly identify the presence of lipid in the arterial wall, and monitor the development of plaques over time.

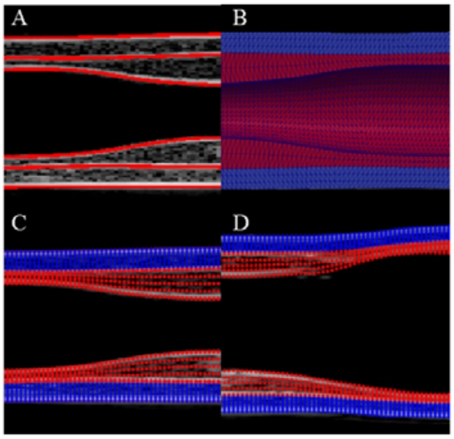

Fig. 1 Phantom (40% stenosis): automatic segmentation (A), 3-D mesh (B), and displacement estimation: tracking grid before (C) and after pressurization (D).

P1-A4-11

Comparison of Different Motion Estimation Methods for Vessel Cross-Sectional Shear Wave Imaging

Qiong He[1], Guoyang Li[2], Yanping Cao[2], Jianwen Luo[1]; [1]*Department of Biomedical Engineering, Tsinghua University, China, People's Republic of,* [2]*Department of Engineering Mechanics, Tsinghua University, China, People's Republic of*

Background, Motivation and Objective

In most studies on vascular shear wave imaging (SWI), only longitudinal section is mainly concerned, and the radial motion and reflected waves are not considered in cross section. It is important to investigate the SWI in cross section when evaluating the anisotropy of the vessel wall or the complete plaque composition. In our previous study (He et al, UMB 2017), a novel method based on coordinate transformation and directional filtering was proposed to achieve the vessel cross-sectional shear wave imaging (VCS-SWI), where the radial motion was directly estimated in polar coordinates of the vessel. The radial motion can also be calculated from the axial and lateral motions estimated in the Cartesian coordinates of the transducer, or from multiple axial motions with spatial angular compounding. In this study, a comparison of the three methods for VCS-SWI was performed.

Statement of Contribution/Methods

The shear wave motion varied with time in vessel cross section was simulated with 3D finite element analysis. A vessel phantom (12.5 scatterers /mm^3) with an inner radius of 4 mm and wall thickness of 2 mm was simulated in Field II. Plane wave imaging with a pulse repetition frequency of 10 kHz was performed by utilizing the parameters of an L12-5 probe with 3 steering angles (0° and ±10°). The radial motions were estimated from the simulated RF data with three methods (Fig. 1a), i.e., from the axial and lateral motions (no compounding), from multiple axial motions with spatial angular compounding (2 or 3 angles), and from the proposed method, respectively. 2D normalized cross-correlation was used in motion estimation, with a window size of ~1×1 mm^2 and axial/radial overlap of 80%. The root-mean-square errors (RMSEs) of the radial motions were calculated to evaluate the estimation performance.

Results/Discussion

As shown in Fig. 1, the performance of radial motion estimation without compounding is the worst due to the poor lateral motion estimation (b). With angular compounding, the radial motion can be well obtained (c), at the cost of lower frame rate. The performance of the proposed method (d) is similar to that of spatial angular compounding. The RMSEs of the radial motions estimated from different methods (e) and the corresponding dispersion curves (f) confirm the above observations. In conclusion, the proposed method could obtain good VCS-SWI without sacrificing the frame rate.

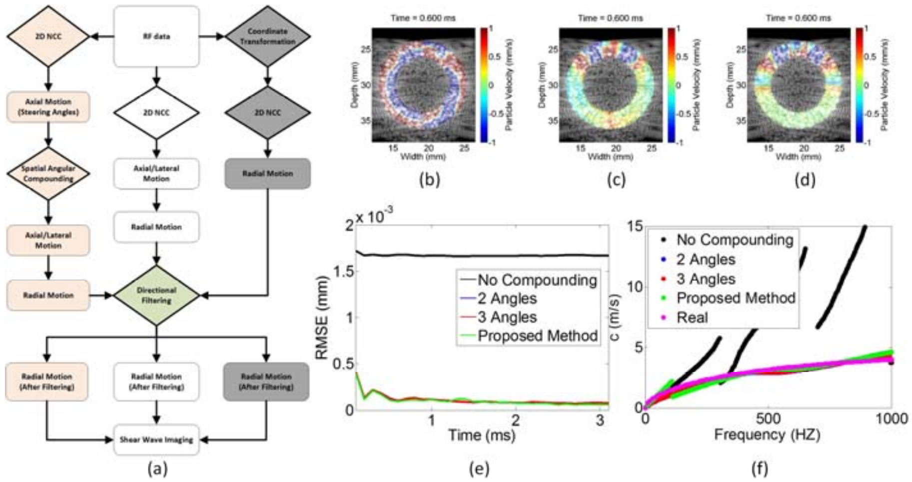

Fig. 1 (a) The three methods for comparison. The radial motion, at 0.6 ms after push, overlapped on the B-mode image with (b) no compounding, (c) spatial angular compounding with 2 steering angles, and (d) the proposed method. (e) The RMSE of the radial motion varied with time. (f) The dispersion curve derived from the radial motion.

P1-A4-12

Estimation of Arterial Transverse Stiffness Using Vascular Guided Wave Imaging (VGWI) in Comparison with Pulse Wave Imaging (PWI)

Yuexin Guo[1], Yahua Wang[1], Jing-Han Chang[1], Wei-Ning Lee[1,2]; [1]*Department of Electrical and Electronics Engineering, the University of Hong Kong, Hong Kong,* [2]*Medical Engineering Programm, the University of Hong Kong, Hong Kong*

Background, Motivation and Objective

We have recently demonstrated the feasibility of vascular guided wave imaging (VGWI) in non-invasive estimation of bi-plane (i.e., longitudinal and transverse) transmural arterial Young's modulus (E_L^V, E_T^V) in tubular phantoms using phase velocity (c_{ph}) (Guo et al., ITEC 2016). In this study, we further compare the E_T^V estimated from the circumferential Lamb type (CLT) wave by VGWI with E_T^P from the pulse wave velocity (PWV) by pulse wave imaging (PWI), *in vitro* and ex vivo, to investigate the transverse stiffness estimation from two distinct propagating waves inside the artery.

Statement of Contribution/Methods

One homogeneous and isotropic 15% polyvinyl alcohol (PVA) tubular phantom (5 freeze-thaw cycles) and one excised porcine aorta, each of which was imbedded in a 3% gelatin phantom, were studied with six repetitive measurements. A Verasonics Vantage system with an L7-4 probe (f_c = 5.2 MHz) mounted on a rotation stage was used to perform PWI with an AccuFlow-Q flow pump (Carotid flow, 15 ml/s) and bi-plane VGWI using a single focused ultrasonic push (100 us) (Fig. 1(a)). Both propagating waves were acquired by coherent plane wave compounding (-2, 0, and 2 degrees) at 4000 Hz. PWV was estimated by linearly fitting the maximum wall acceleration (Fig. 1(c)) and related to E_T^P by a modified Moens-Korteweg equation (Nichols et al., 2011). E_L^V and E_T^V were derived by fitting a simplified Lamb wave model (Bernal, et al., 2011) to the experimental c_{ph} (Fig. 1(b)). Maps of CLT-wave amplitudes in the transverse view were warped to the polar coordinates for the estimation of c_{ph}.

Results/Discussion

E_T^V was in excellent agreement with E_L^V and E_T^P in both the isotropic phantom and the aorta (Fig. 1(d)). The relative differences between E_L^V and E_T^V, E_T^P and E_T^V, were 4.0% and 0.4% in the phantom, and 5.9% and 4.9% in the aorta, respectively. Our results show that the VGWI yielded comparable transverse stiffness estimates to PWV. VGWI potentially permits reliable estimation of bi-plane arterial stiffness at an arbitrary phase in a cardiac cycle, thus complementing PWI. The mechanical anisotropy of the aorta was not observed, possibly due to the low internal pressure exerted (< 20 mmHg). Our ongoing study, hence, includes the VGWI measurement on the aorta pressurized within the physiological range for assessing the mechanical behavior of the anisotropic artery to various load conditions.

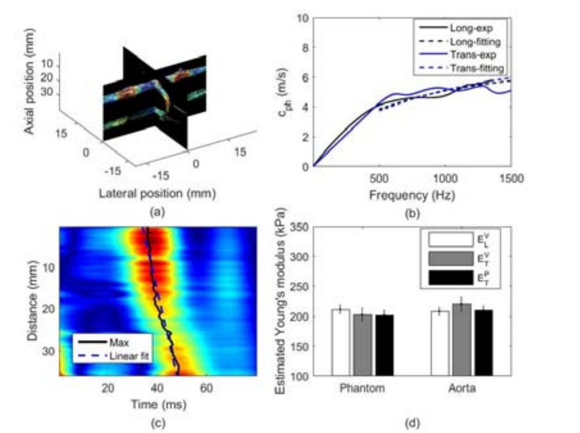

Figure 1. (a) VGWI: guided wave amplitudes overlaid on compounded images of an excised pig aorta at 1.25 ms after transmitting the focused ultrasound push beamin both the longitudinal and transverse views (b) VGWI: experimental dispersion curves and the theoretically fitted curves in the two orthogonal views (c) PWI: spatiotemporal map of the aortic wall acceleration; (d) the E_L^V, E_T^V, and E_T^P estimates in the tubular phantom and the porcine aorta.

P1-A4-13

Diffuse Shear Wave Elastography in a Thin Plate Phantom

L. Keijzer[1], A. Sabbadini[2], J.G. Bosch[1], M.D. Verweij[1,2], A.F.W. van der Steen[1,2], N. de Jong[1,2], H.J. Vos[1,2]; [1]*Biomedical Engineering, Thorax Center, Erasmus MC Rotterdam, Netherlands,* [2]*Acoustical Wavefield Imaging, ImPhys, Faculty of Applied Sciences, Delft University of Technology, Netherlands*

Background, Motivation and Objective

The diastolic functioning of the left ventricle is correlated to the stiffness of the myocardium. Shear wave (SW) elastography can be used for non-invasive stiffness measurements. These waves can have external sources such as an acoustic push, natural sources such as valve closure, or diffuse sources like breathing and flow noise. SW propagation velocities in diffuse wave fields can be analyzed after a spatio-temporal correlation technique. This technique has been applied to bulk SW [Brum et al, IEEE UFFC 2015; Parker et al, Phys Med Biol 2017] and surface waves [Sabra et al, Am Inst Phys 2007; Brum et al, JASA 2008]. However, since the myocardium is relatively thin, Lamb wave phenomena including dispersion could be expected. In this study we tested the applicability of the diffuse wave technique in a PVA thin plate phantom, and compared it to direct SW measurements and a mechanically measured shear modulus.

Statement of Contribution/Methods

To mimic in-vivo geometry, the water-immersed phantom was around 10 mm thick. Firstly, an acoustic radiation force (ARF) and secondly a mechanical push (MP) induced direct shear waves. Thirdly, finger tapping (FT) created a diffuse field, to which the correlation technique was applied – either with cross-correlation, or phase correlation [Brum et al, IEEE UFFC 2015]. Radon transforms were used in all cases to finally determine SW velocities. Moreover, dispersion curves were determined and compared with a Rayleigh and an anti-symmetric Lamb wave model for a plate submerged in fluid [Nenadic et al, Phys Med Biol 2011]. All measurements were done with an L7-4 probe connected to a Verasonics Vantage. We used a standard indentation test for reference.

Results/Discussion

For a frequency band of 100 to 200 Hz, average SW propagation speeds between 2.1 and 2.4 m/s were found with the different methods (Fig. 1A). Dispersion effects were visible (Fig. 1B). The dispersion curves of MP and FT agree well with a theoretical Rayleigh wave, while curves of ARF agree well with an anti-symmetric Lamb wave, both calculated with the mechanically measured shear modulus of 7.6 ± 0.1 kPa. Apparently the ARF induces a body force resulting in Lamb waves, while the surface forces of MP and FT induce Rayleigh waves. The similar curves for MP and FT show the potential of the correlation technique in plate structures.

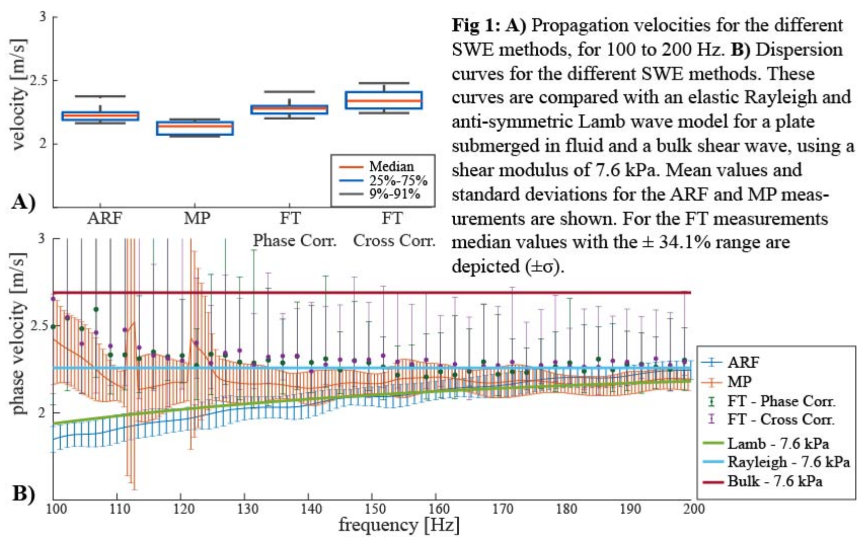

Fig 1: A) Propagation velocities for the different SWE methods, for 100 to 200 Hz. **B)** Dispersion curves for the different SWE methods. These curves are compared with an elastic Rayleigh and anti-symmetric Lamb wave model for a plate submerged in fluid and a bulk shear wave, using a shear modulus of 7.6 kPa. Mean values and standard deviations for the ARF and MP measurements are shown. For the FT measurements median values with the ± 34.1% range are depicted (±σ).

P1-A4-14

Experimental Investigation of Shear Wave Imaging in Thin Soft Media in Various Coupling Conditions

Enoch Jing-Han Chang[1], Yuexin Guo[1], **Wei-Ning Lee**[1]; [1]*Electrical and Electronic Engineering, The University of Hong Kong, Hong Kong, Hong Kong*

Background, Motivation and Objective

Ultrasound shear wave imaging has been extensively studied in thin tissues, such as the artery and cornea. The dispersion analysis of the guided wave propagating in such layered structures based on a modified Lamb wave model for homogeneous and isotropic thin soft media in water has been shown to yield accurate elasticity estimates. Nonetheless, thin soft tissues are often bounded with other tissue types. How coupling media impact the elasticity estimation in the target thin media remains to be relatively under-examined and is thus the major objective of this study.

Statement of Contribution/Methods

Homogeneous and isotropic phantoms of varying thickness (1-5 mm) and stiffness (5% and 15% polyvinyl alcohol (PVA); 1% silicone dioxide; 5 freeze-thaw cycles) were made and imaged when placed in water, 5% PVA bulk, and 15% PVA bulk. A Verasonics Vantage system with an L11-4v probe (fc = 8.9 MHz) was used to generate guided waves (Fig. 1(a)), which were acquired using coherent plane wave compounding (-4, 0, and 4 degrees) at 8000 Hz. The spatiotemporal map of the guided wave propagation at each depth of interest was obtained for velocity estimation. Group velocity (v_g) was estimated by the arrival time and position of the wave through a standard 1D cross correlation method. Phase velocity (v_p) and the corresponding shear modulus were estimated through dispersion analysis, where a simplified Lamb wave model was fitted to the experimental dispersion curve between 500 Hz and 2000 Hz (Figs. 1(b)-(d)).

Results/Discussion

Regardless of the surrounding medium, the thinner the soft media were, their stiffnesses derived from v_g were underestimated to a greater degree. For example, the v_g of 1-mm 15% PVA in water deviated from ground truth (8.72 m/s) by -88%, but the thickness of 15% PVA thin media had little effect on the v_g when surrounded in 15% PVA bulk with only a 17% increase. The v_p–based shear moduli (63.4 ±13.5 kPa) of all the examined 15% PVA thin media (Fig. 1(b)) in water agreed better with the ground truth (76.0 kPa). In the case of 15% PVA thin media on a 5% PVA bulk, the upper bound of the phase velocity of the hard thin layer was in theory the shear wave velocity of the soft bulk. Our findings show that the presented shear wave imaging framework in the guided wave regime accounted for dispersion but requires further model modification for addressing wave interference in multilayered soft media.

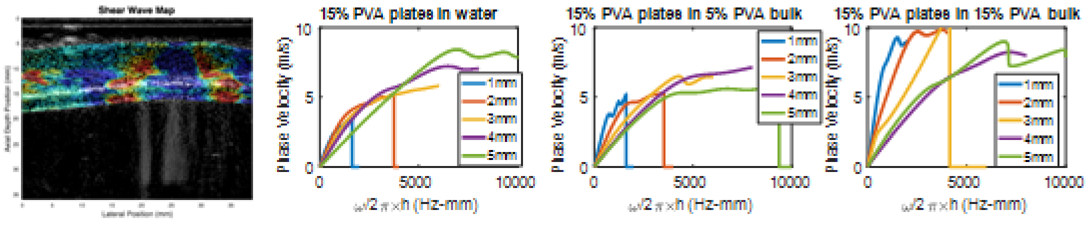

Fig. 1 (a) (b) (c) (d)

P1-A4-15 ___

Quantitative Assessment of Plate-like Tissue Viscoelastic Properties Using Ultrasonic Micro-Elsatography with Lamb Wave Model

Cho-Chiang Shih[1,2], Xuejun Qian[1], Teng Ma[1], Chih-Chung Huang[2], Qifa Zhou[1,3], K. Kirk Shung[1]; [1]*Department of Biomedical Engineering, NIH Recourse Center on Medical Ultrasonic Transducer Technolog, University of Southern California, Los Angeles, CA, USA*, [2]*Department of Biomedical Engineering, National Cheng Kung University, Tainan City, Taiwan*, [3]*Roski Eye Institute, Department of Ophthalmology, University of Southern California, Los Angeles, Los Angeles, CA, USA*

Background, Motivation and Objective

Characterization of the viscoelastic properties of tissues at the micro-level has been a challenge for many years. Recently, several micro-elastography techniques have been developed with high frequency ultrasound or optical coherence tomography to improve the spatial resolution. However, most of these techniques did not consider the medium boundary conditions and still used traditional shear wave model to evaluate the viscoelastic properties of plate-like tissues, such as artery and cornea, which might lead to estimation errors. Therefore, the aim of the study is to integrate a lamb wave model with our previously developed ultrasonic micro-elastography system for obtaining accurate viscoelastic properties in plate-like tissues.

Statement of Contribution/Methods

A 4-MHz ring transducer was used to generate acoustic radiation force for inducing tissue displacement, and the Lamb wave propagation inside the plate-like structure can be detected by a confocally aligned 40-MHz needle transducer, as shown in Fig. 1(a). The phase velocity (dispersion curve) can be obtained from the k-space transformed from the displacement mapping, as shown in Fig. 1(b). Both of impulse method and the harmonic method were used in the study. The shear elasticity and shear viscosity were evaluated by fitting the experimental data and lamb wave model equation using least linear squares. The experiments were carried out using gelatin phantoms (7% and 12%) of different thickness (2~4 mm) and a porcine cornea ex-vivo.

Results/Discussion

The phase velocities measured in the 7% and 12% gelatin phantoms with various thickness (2mm, 3mm, and 4mm) and the porcine cornea as well as their corresponding fitting curves with Lamb wave model are shown in Fig. 1(c). The shear elasticity and shear viscosity were evaluated to be 2.6±0.1 kPa and 0.1±0.05 Pa·s, 5.2±0.2 kPa and 0.31±0.16 Pa·s, in 7%- and 12%-gelatin phantom, respectively. The phantoms with different thickness were confirmed to have the same viscoelasticity. The shear elasticity and shear viscosity were estimated to be 10.6 kPa and 0.5 Pa·s in the porcine cornea. The Lamb wave model was successfully used to assess the viscoelastic properties of the plate-like tissue with two free boundaries by our ultrasonic micro-elastography system.

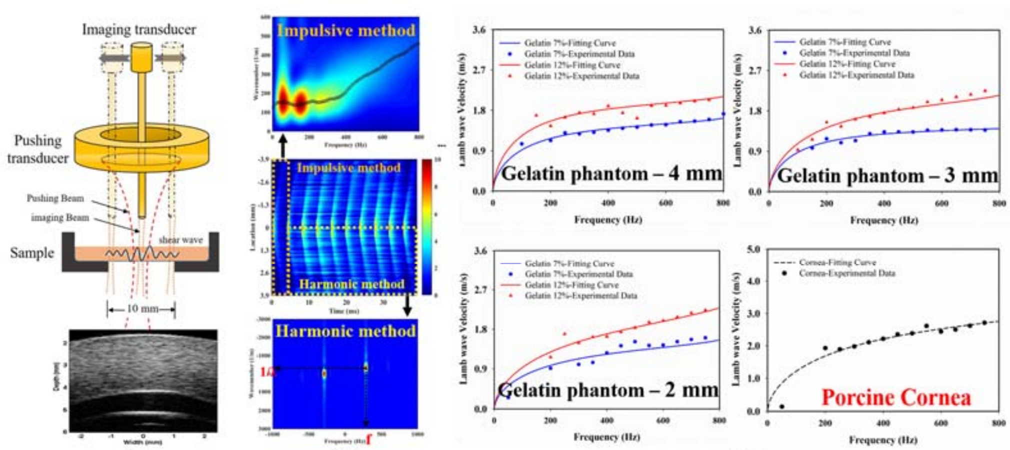

(a) (b) (c)

Fig. 1

P1-A4-16

Parameters Impacting Accuracy of ARFI-Derived Stiffness Ratios: A Simulation Study with Implications on Measurement of Dynamic Myocardial Stiffness

Vaibhav Kakkad[1], Peter Hollender[1], Mark Palmeri[1], Gregg Trahey[1]; [1]*Biomedical Engineering, Duke University, Durham, North Carolina, USA*

Background, Motivation and Objective

Measurement of myocardial stiffness using ultrasound-based transient elastography has received significant attention in recent years. The mechanical properties of myocardium not only undergo cyclic dynamic changes over the cardiac cycle but also change on a slower scale with physiological factors. They are also closely tied to several cardiovascular disorders such as heart failure, cardio-toxicity and transplant rejection.

SWEI allows for quantitative assessment of tissue mechanical properties. However, in the context of cardiac imaging it has only been shown to be feasible in diastole. ARFI, on the other hand, provides a relative estimate of tissue mechanical properties and has been shown to be viable over the entire cardiac cycle. ARFI-derived myocardial stiffness ratios have been investigated as a potential clinical metric of myocardial function. While this ratio is indicative of the change in stiffness of the myocardium over the cardiac cycle, its quantitative relationship to absolute material properties has yet to be thoroughly investigated.

Statement of Contribution/Methods

In this work, we performed finite-element simulations to study the parameters govenrning the relationship between ARFI-derived stiffness ratios and absolute material properties. ARF-excitations were simulated in elastic, isotropic materials over a range of Young's moduli relevant to myocardial mechanics (3 kPa – 36 kPa). The dynamic response to these excitations (both on-axis displacement-recovery and shear wave propagation) were tracked in Field II using focused as well as plane wave tracking configurations. ARFI-derived stiffness ratios, for each case, were compared with known material elasticity ratios for a variety of relevant parameters.

Results/Discussion

Results will be presented on the agreement of these ratios as a function of time (after the push) at which the ARFI displacement is measured (as shown in Fig), lateral offset (from push location) at which displacements are interrogated, absolute elasticity of simulated materials, motion/motion filter induced biases in displacements, tracking beam configurations (shown in Fig) and quality of displacement estimates (relative jitter). These results elucidate the inherent biases in the estimation of myocardial stiffness using ARFI and would allow for development of a more robust metric of myocardial function.

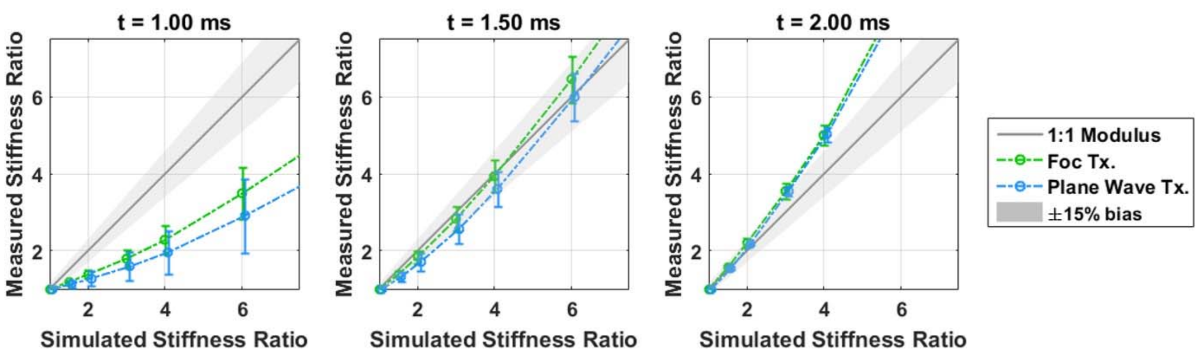

P1-A4-17

Comparison of Cardiac Displacements in a Murine model of Myocardial Ischemia Using Cardiac Elastography and Speckle Tracking Echocardiography

Rashid Al Mukaddim[1,2], Kayvan Samimi[1,2], Allison Rodgers[3], Timothy A Hacker[3], Tomy Varghese[1,2]; [1]*Department of Electrical and Computer Engineering, University of Wisconsin - Madison, Madison, Wisconsin, USA,* [2]*Department of Medical Physics, University of Wisconsin - Madison, Madison, Wisconsin, USA,* [3]*Department of Medicine, Section of Cardiovascular Medicine, University of Wisconsin School of Medicine and Public Health, Madison, Wisconsin, USA*

Background, Motivation and Objective

Investigating myocardial dynamics through the assessment of mechanical properties of heart is a challenging problem in a murine model as the heart rate is high. The objective of this study was to compare displacements estimated using radiofrequency (RF) signals with Cardiac Elastography (CE) and Speckle Tracking Echocardiography (STE) for quantifying myocardial dynamics.

Statement of Contribution/Methods

Four C57/Bl mice were intubated and ventilated with 100% O_2 and isoflurane. The left anterior descending coronary artery (LAD) was tied off with a suture assessed via a thoracotomy followed by closing of the incision. Echocardiography was performed before surgery (baseline) and 14 and 28 days later using a Vevo 2100 (FUJIFILM VisualSonics, Canada). Parasternal long and short axis images over several cardiac cycles were acquired at a frame rate of 235 fps using a MS 550D linear array transducer operated at 30 MHz. Segmental displacements over one cardiac cycle along the short axis view was generated using both CE and STE. Deformation tracking for CE was done using a Lagrangian Deformation tracking using a Polar Grid (LDPG) algorithm. Displacement estimation using STE used the Vevo Strain software. For segmental analysis, the standard AHA segmentation scheme for the left ventricle was utilized.

Results/Discussion

The cumulative radial displacement estimated in all six segments of the left ventricle was significantly reduced following ligation for estimates obtained using both methods. For LPDG, the global peak radial displacement (GPRD) reduced from 1.28 mm at baseline to 0.55 mm after 14 days and 0.43 mm after 28 days respectively. A similar trend was observed with STE with the corresponding GPRD values ranging from 0.16 mm to 0.15 mm and 0.03 mm respectively. We have previously showed with cardiac simulations and phantom experiments that CE provides accurate and precise estimation of the displacement. Note that the LPDG algorithm in this study provides global and segmental displacement estimates that are higher, however the trends are comparable to that obtained with commercial Vevo strain software.

Acknowledgment: S10 OD018505, UW Carbone Cancer Center and UW School of Medicine and Public Health (SMPH).

Figure 1 (a) provides representative accumulated radial displacement images from LPDG method, while 1 (b) depicts the trend in peak radial displacement over 30 days.

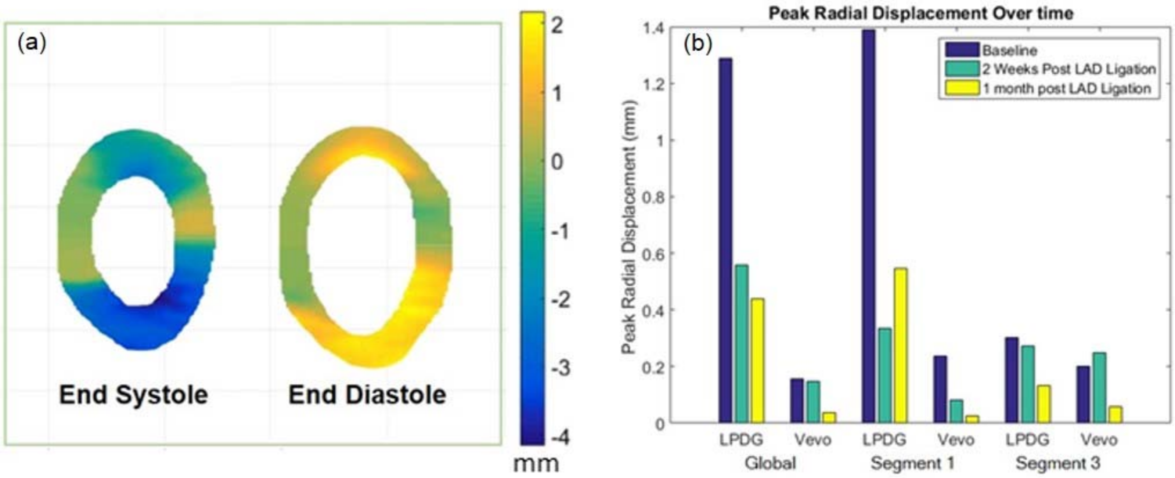
(a)
End Systole
End Diastole
2
1
0
-1
-2
-3
-4
mm
Peak Radial Displacement Over time
(b)
Baseline
2 Weeks Post LAD Ligation
1 month post LAD Ligation
Peak Radial Displacement (mm)
1.4
1.2
1
0.8
0.6
0.4
0.2
0
LPDG
Vevo
LPDG
Vevo
LPDG
Vevo
Global
Segment 1
Segment 3

P1-A5 - MIM: Ultrasound Motion/Deformation Estimation

Exhibit Hall

Thursday, September 7, 2017, 9:30 am - 4:00 pm

Chair: **Richard Lopata**
Eindhoven University of Technology

P1-A5-1

Fast Frame Rate 2D Cardiac Deformation Imaging Based on RF Data: What Do We Gain?

Francois Vignon[1], Sheng-Wen Huang[1], Shiying Wang[1], Lea Melki[1], Baptiste Blochet[1], Oudom Somphone[2], Eric Saloux[3], Patrick Rafter[4], Scott Dianis[4]; [1]*Philips Research North America, Cambridge, MA, USA,* [2]*Philips Research France, Suresnes, France,* [3]*CHU Caen, France,* [4]*Philips Healthcare, Andover, MA, USA*

Background, Motivation and Objective

Fast acquisition sequences enable >200Hz 2D cardiac B-mode imaging with little compromise in image quality. Fast imaging minimizes frame to frame decorrelation, enabling radiofrequency (RF)-based tracking for enhanced signal-to-noise ratio (SNR) in motion and deformation imaging.

Our objective was to compare the performance and clinical usefulness of Fast RF-based Tracking (FRFT) to the established modalities Tissue Doppler Imaging (TDI) and image-based speckle tracking (ST).

Statement of Contribution/Methods

We implemented and optimized 2D cardiac FRFT based on coherent compounding of diverging beams on Philips S5-1 and X5-1 probes and Epiq scanner. The RF data was tracked with a 1D cross-correlation algorithm and a 2D multi-scale optical flow algorithm. 20 healthy volunteers were scanned in apical 2, 3, and 4-chamber views, and in a parasternal long axis view. TDI and ST were also performed in a subset for comparison. The myocardial velocity and strain rate M-modes were examined to qualitatively assess performance and hypothesize on the clinical potential of the modality.

Results/Discussion

-In healthy adult volunteers at rest, 200Hz adequately samples all cardiac motion, except for the fastest frequency components related to valve closures. If valve events are excluded, 75Hz sampling is adequate.

-A nominal 5 mm spatial resolution of the velocity map was achieved with acceptable SNR and tracking success for FRFT and TDI, compared to 3 cm for ST (the dimension of a cardiac AHA segment).

-2D FRFT yields visibly higher SNR than ST (Figure). Most FRFT exams are successful in the inter-ventricular septum, but most fail in the lateral wall, presumably due to high clutter.

-The theoretical advantages of 1D FRFT over TDI did not materialize experimentally in our qualitative study.

In conclusion, high frame rate imaging enables visualization of waves related to valve closure. Improved tracking SNR promises a modality confidently displaying 2D regional strain rate. Further clutter suppression is required to improve success rate in all walls.

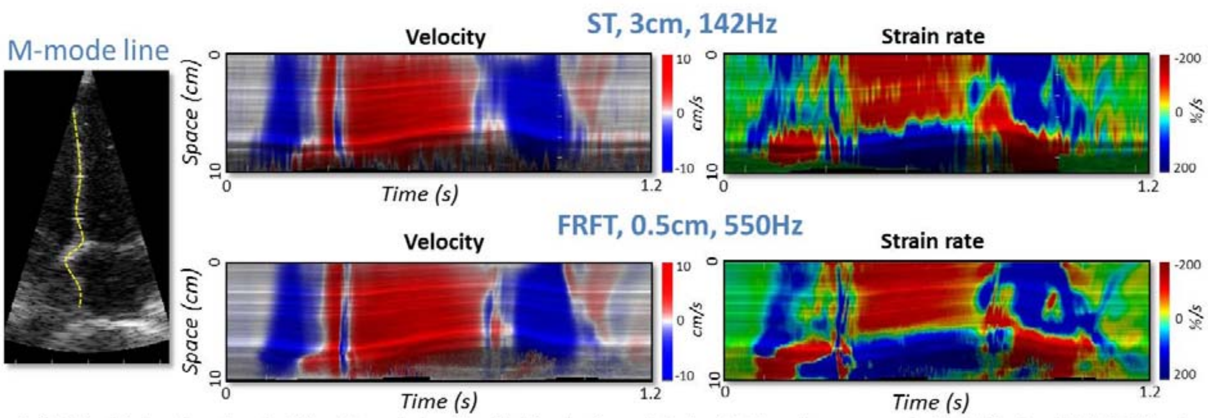

Left: Apical 4 chamber view depicting M-mode location. Right: velocity and strain rate M-modes measured with ST (top) and FRFT (Bottom).

P1-A5-2

RF-NRIR for Motion Estimation in Fast Cardiac Anatomical Imaging

Bidisha Chakraborty[1], João Pedrosa[1], Vangjush Komini[1], Brecht Heyde[1], Jan D'hooge[1]; [1]*Cardiovascular Imaging and Dynamics, KU Leuven, Leuven, Belgium*

Background, Motivation and Objective

Myocardial deformation imaging at a high frame rate (HFR) has the potential to gain new insights in cardiac mechanics by resolving short- lived mechanical events during the cardiac cycle. In order to achieve such high frame rate, our lab recently proposed to combine multi-line transmit with ‘anatomical imaging’ i.e. imaging only the anatomically relevant spatial domain (e.g. the myocardium).

Although we have previously proposed and validated a non-rigid registration (NRIR) framework for motion estimation of low frame rate (LFR) acquisitions, estimation of motion in the anatomical HFR scans poses two challenges. Firstly, since NRIR optimizes motion globally, the lack of image content outside the anatomical domain is a challenge. Secondly, HFR implies smaller inter-frame motion and therefore increases the risk of the accumulation of tracking errors. The primary aim of this study was therefore to demonstrate that NRIR tracks the myocardium in anatomically scanned HFR data with a comparable accuracy as LFR data.

Statement of Contribution/Methods

In an in-vitro setup, a univentricular PVA phantom was cyclically deformed using a flow pump (60 beats/min). The phantom was scanned using a multi-line transmit sequence using a 3.5 MHz phased array probe attached to our open ultrasound platform (HD-PULSE). For a 70-degree LFR sector, this resulted in a frame rate of 150Hz; while for the anatomical sequence it became 350Hz. Data sets were acquired by varying the stroke volume of the pump from 160ml to 180ml.

RF tracking was performed using our previously validated B-spline based NRIR which used sum-of-squared differences as a similarity measure and a fast analytical implementation of the bending energy as a regularization term.

Same set of manually annotated points in myocardium, (Figure 1, A) were tracked in both of the image sequences and compared using correlation analyses.

Results/Discussion

Figure 1. shows a correlation of r=0.97 ($p<0.01$) between the cumulative displacements of the same tracking points for the LFR vs the HFR anatomical data for two data sets over the full cardiac cycle. The high correlation indicates a comparable accumulated displacement estimates for the HFR over the cardiac cycle. Additionally, it demonstrates that the missing spatial structures in the image due to the limited field-of-view did not significantly impact the tracking accuracy.

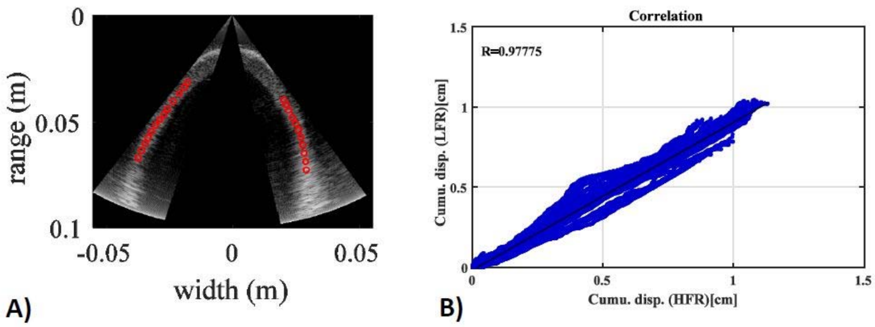

Figure 1. (A) B-mode frame from anatomically scanned data. (B) Correlation of cumulative displacements between the LFR and HFR tracking over a set of 40 points, tracked from two datasets, obtained with stroke volumes of 160 ml and 180 ml.

P1-A5-3

Improved Tendon Tracking Using Singular Value Decomposition Clutter Suppression

Raja Sekhar Bandaru[1], Stefanie Evers[2,3], Ruud W. Selles[2], Andrew R. Thoreson[3], Peter C. Amadio[3], Johan G. Bosch[1]; [1]*Biomedical Engineering, Erasmus MC, Rotterdam, Netherlands,* [2]*Department of Plastic, Reconstructive and Hand Surgery & Department of Rehabilitation Medicine, Erasmus MC, Rotterdam, Netherlands,* [3]*Biomechanics Laboratory and Tendon and Soft Tissue Biology Laboratory, Mayo Clinic, Rochester, MN, USA*

Background, Motivation and Objective

Carpal tunnel syndrome (CTS) is the most common wrist neuropathy. Ultrasound can image the tendons in real-time, enabling analysis of tendon dynamics.

We earlier developed and validated a speckle tracking algorithm [1] using Normalized Cross Correlation (NCC) on a stationary region of interest (ROI) over the tendon path (Fig 1a). However, NCC is sensitive to clutter and shadows which lead to motion underestimation. In this study, we use Singular Value Decomposition (SVD) filtering [2] to suppress clutter, compared it to previous NCC and validated it on human cadaver tendon motion studies.

Statement of Contribution/Methods

Flexor Digitorum Superficialis (FDS)3 tendons of 6 human cadaver arms were displaced mechanically at 3 speeds and with 3 excursion amplitudes, resulting in 9 unique sequences. A sequence consisted of 3 cycles of forward and backward displacement (Fig 1c). Ultrasound sequences were acquired at 75Hz (Philips iE33, L7-4). The image sequences were decomposed by SVD into individual spatio-temporal components. The lower components correspond to stationary tissue and clutter. The highest components correspond to noise. A down weighting of the lower-order components suppressed the artifacts without obstructing the tracking of semi-stationary tissue.

A multi-kernel 2D block matching method tracked the tendon motion. Outliers in the estimated kernel displacements were removed using a Tukey outlier filter (Fig 1b). The parameters of the SVD based image reconstruction and tracking were optimized for best accuracy using data from one of the cadaver.

The ground truth (GT) motion was measured by manually tracking metal markers inserted in the tendons. The displacement per sequence was found as the mean absolute displacement over 6 half cycles. The accuracy of NCC and SVD tracking methods relative to GT were calculated as relative displacement errors over all 6 studies.

Results/Discussion

For the SVD parameters, down weighting the 40 lower-order components to 20% resulted in best accuracy. A relative displacement error of 12.5(±17.1)% was observed using the SVD method vs 20.5(±20) % for NCC over all 54 sequences(Fig 1d). In conclusion, SVD improves tendon tracking by clutter suppression.

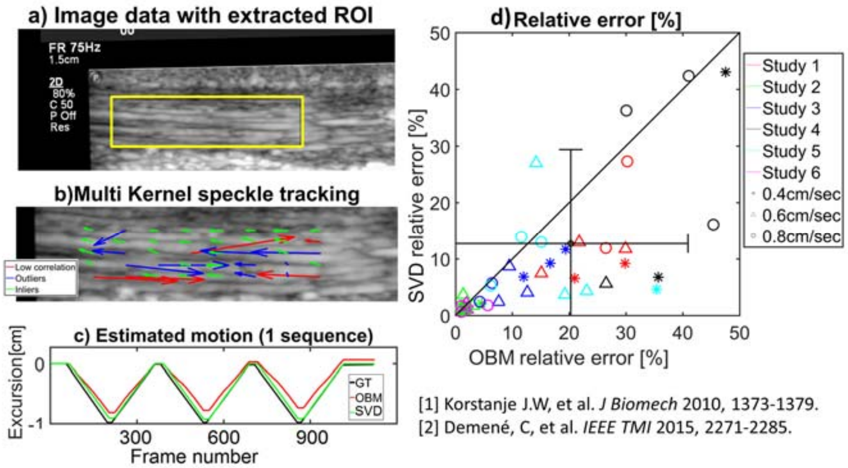

P1-A5-4

An Optical Flow Method for Elastography at Large Strains Using Three Image Frames

Zhi Liu[1], Jianwen Luo[1]; [1]*Biomedical Engineering, Tsinghua University, Beijing, China, People's Republic of*

Background, Motivation and Objective

Affine model based optical flow (OF) method has been proved to perform better in elastography than rigid model based cross-correlation method (Pan et al, TUFFC 2015). At larger applied strain (e.g., 4-5%), the performance of OF method using two image frames (OF2) is deteriorated due to signal decorrelation. However, higher compression ratios may result in some new characteristics or increase the contrast in strain image, which may be helpful for detection of the early lesion, given the fact that it has comparable stiffness with the surrounding tissues. In this study, an OF method using three image frames (OF3) is proposed for elastography at large strains.

Statement of Contribution/Methods

OF3 was achieved as follows. Three frames (F1-3) were selected from a series of ultrasound images, with a relatively low strain between F1 and F2 (0.5~1%) and high strain between F1 and F3 (1~4%). Next, the axial displacements and strains of the (F1, F2) and (F1, F3) image pairs were estimated using OF2. The ratio between the two estimates in a region with relatively high quality was also calculated. F3 was then shifted and warped according to an initial estimate of (F1, F3), obtained by multiplying the estimate of (F1, F2) by this ratio with an assumption of linear elasticity. Subsequently, a second estimation between F1 and deformed F3 was performed. The final result of (F1, F3) was obtained by combining the initial and second estimates.

A homogeneous model (25 kPa) with an inclusion (80 kPa) was compressed by 0.5~4%, and Field II was used to simulate the RF data. The root-mean-square error (RMSE) was utilized to evaluate the strain quality. Experiments were conducted on a phantom with the same elasticity contrast as in the simulations at 0.6~4.1% compression. The RF data were acquired by a Philips iU22 system. The signal-to-noise ratio (SNR) and contrast-to-noise ratio (CNR) were used to assess the strain quality.

Results/Discussion

OF3 obtains better strains than OF2 in both simulations and phantom experiments (Fig. 1). In the simulations, OF3 reduces the RMSE of axial strains by 45.6-85.0% when compared with OF2 (Fig. 1(d)). In the phantom experiments, OF3 increases the SNR and CNR of strains by 2.1-25.6 dB and 2.3-50 dB [Fig. 1(g) and (h)], respectively. Therefore, OF3 is proved to improve the performance of elastography at higher strains. Further clinical validation is still required.

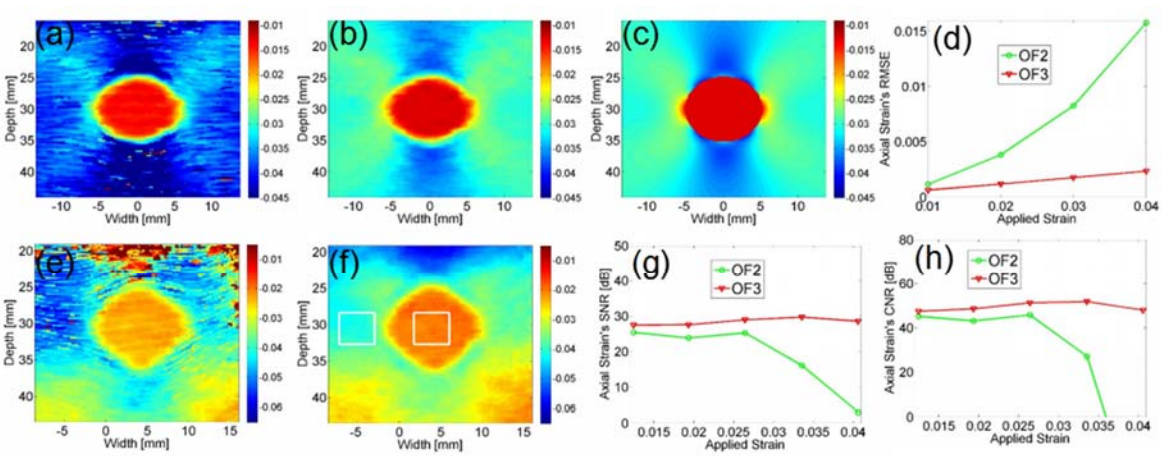

Fig 1. Axial strains estimated by (a) OF2 and (b) OF3 and (c) theoretical value at 3.0% compression, and (d) axial strain's RMSE in the simulations. Axial strains estimated by (e) OF2 and (f) OF3 at 3.4% compression, and (g) axial strain's SNR and (f) CNR in the phantom experiments. The two white ROIs in (f) were used to calculate the SNR and CNR, respectively.

P1-A5-5

A Novel Strain-based Drift Compensation Algorithm for Improved Beat-to-Beat Repeatability of Myocardial Strain Imaging: Preliminary *In Vivo* Results

Harrison Ferlauto[1], **Vaibhav Kakkad[1]**, Brecht Heyde[2], Joseph Kisslo[3], Gregg Trahey[1]; [1]*Biomedical Engineering, Duke University, Durham, North Carolina, USA,* [2]*Cardiovascular Imaging and Dynamics, KU Leuven, Leuven, Belgium,* [3]*Cardiology, Duke University Hospital, Durham, North Carolina, USA*

Background, Motivation and Objective

Strain imaging is gaining traction as a means to assess cardiac function by tracking the cyclic deformation of the myocardium. Compared to traditional measures such as ejection fraction, global myocardial strain has been shown to be an earlier and more sensitive measure of overall ventricular function. Similarly, regional myocardial strain has been shown to be useful for identifying ischemia and myocardial infarction. However, accurately quantifying myocardial strain over several cardiac cycles has proven challenging due to complications with drift and heart rate variability.

Statement of Contribution/Methods

We present a novel drift compensation scheme that improves the repeatability of myocardial strain estimates over multiple cardiac cycles. Our method uses an elastic image registration algorithm to track myocardial displacements in both axial and lateral dimensions. Displacements and strains are computed with respect to an initial frame at end-diastole (ED) of the first cardiac cycle. Subsequent ED frames are identified using local minimas of the strain curve in each following cardiac cycle. Drift compensation within each cycle is achieved by using a linearly weighted combination of forward and backward displacements between consecutive ED frames. Additionally, beat-to-beat variability in myocardial position is accounted for by tracking displacements between successive ED frames and repositioning the region-of-interest accordingly.

Results/Discussion

The performance of the drift compensation algorithm was tested on *in vivo* transthoracic cardiac images in parasternal long axis (PLAX) and short axis (PSAX) views. Images were acquired over a 5s interval so as to include 5-6 complete cardiac cycles. Drift in the ROI at beat 5 and correlation of end-diastolic radial strain distributions between beat 1 and beat 5 were the metrics used to track performance. Between the raw vs. compensated cases; drift was found to be reduced from 8.58 ± 4.96 mm to 1.73 ± 1.23 mm in PLAX and 9.11 ± 3.13 mm to 1.16 ± 0.48 mm in PSAX. Correlation of end-diastolic radial strain, for the same, was found to increase from 0.46 ± 0.21 to 0.69 ± 0.18 in PLAX and 0.43 ± 0.21 to 0.79 ± 0.05 in PSAX. These results support the hypothesis that drift compensation techniques can be implemented to improve the repeatability of myocardial strain imaging over multiple cardiac cycles (as shown in Fig).

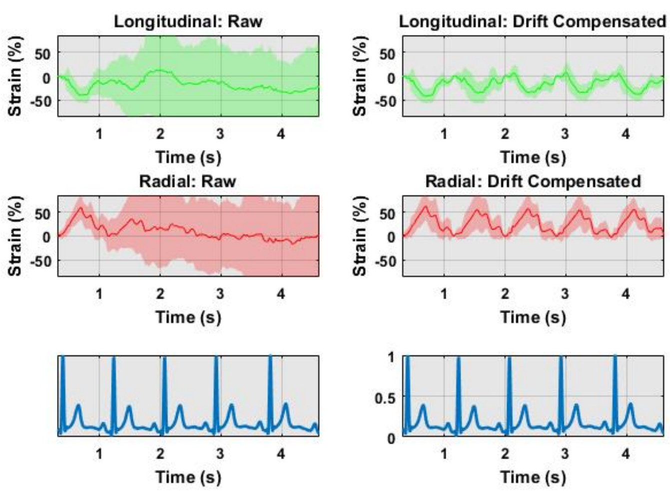

P1-A5-6

Image Registration in a Tomographic Limb Ultrasound System: Comparison between Camera-Tracking and Image-Based Motion Compensation

Bryan Ranger[1], Micha Feigin[1], Hugh Herr[1], Brian Anthony[1]; [1]*Massachusetts Institute of Technology, Cambridge, MA, USA*

Background, Motivation and Objective

Numerous recent developments in ultrasound imaging for musculoskeletal applications have emerged due to ultrasound's inherent advantages of real-time performance, high resolution, speed and relative cost compared to modalities such as MRI and CT. However, as standard ultrasound requires that the probe make contact with the imaged body segment, it is difficult to acquire an accurate representation of 3D anatomical geometry and mechanical properties due to soft tissue deformation by user-dependent applied force as well as relative motion between the probe and patient. Multiple research groups have pursued methods that involve submerging the ultrasound transducer(s) and imaged body segment into a water bath. Clinically, this method has presented several challenges; of note for this study is image distortion due to patient motion. We show that 3D optical imagery can be used to effectively track and compensate for this motion, allowing for robust stitching of circumferentially-collected ultrasound images.

Statement of Contribution/Methods

A mechanical system was constructed to circumferentially scan a body segment inside of a water bath using a clinical ultrasound probe (Fig 1). A depth camera is positioned below the tank, pointing upwards, to track the position of the imaged body segment in 3D space during the scan. Tracking is performed on the resulting point cloud using the iterative closest point (ICP) algorithm to define the transformation between frames. This method is stable over time, as opposed to image based registration which is prone to spatial drift of multiple frames. It also allows for capturing non-overlapping frames as well as compensating for motion perpendicular to the image plane.

Results/Discussion

We present comparative results of a 3D camera-based method to our previously developed image registration techniques. An example tomographic image from our system of a human arm is shown in Fig 1. We show that 3D optical imagery can effectively compensate for patient motion during a tomographic ultrasound scan. These results hold particular relevance for applications in which a volumetric dataset of an imaged body segment must be acquired rapidly, as overlapping image features are not required to stitch together an image volume.

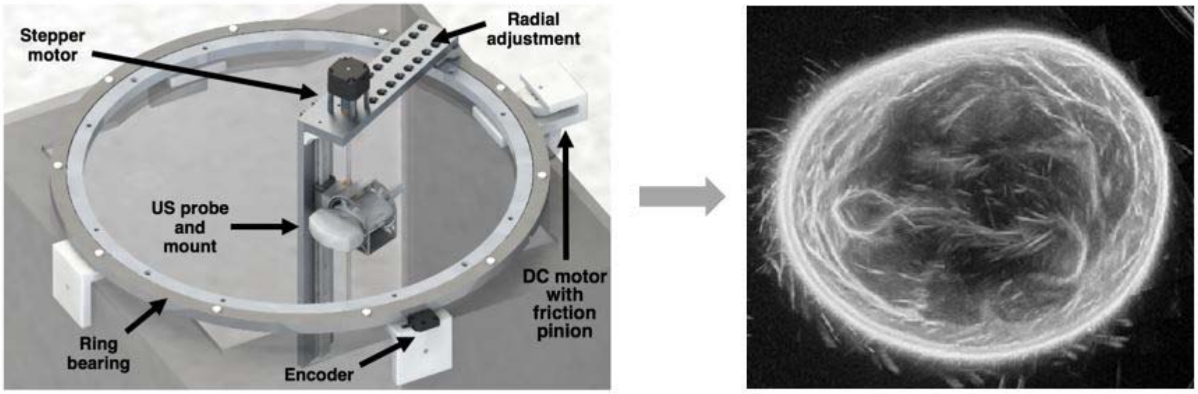
Stepper motor
Radial adjustment
US probe and mount
DC motor with friction pinion
Ring bearing
Encoder

P1-A6 - MIM: Medical Imaging

Exhibit Hall

Thursday, September 7, 2017, 9:30 am - 4:00 pm

Chair: **Massimo Mischi**
Eindhoven University of Technology

P1-A6-1

Ex-Vivo Phantom for Evaluation of Ultrasound Speckle Tracking in the Uterus

Federica Sammali[1], Celine Blank[1,2], Lin Xu[1], Dick Schoot[2,3], Massimo Mischi[1]; *[1]Eindhoven University of Technology, Netherlands, [2]Catharina Hospital Eindhoven, Netherlands, [3]University Hospital Ghent, Belgium*

Background, Motivation and Objective

Uterine peristaltic movement plays an important role for the success of embryo implantation. This is especially relevant in the context of assistive reproduction technology. Unfortunately, the lack of tools for quantitative analysis limits our understanding of the uterine activity. Recently, strain analysis by ultrasound speckle tracking has gained attention for assessment of the uterine activity. However, the absence of a ground truth hampers the optimization of this technology. This work proposes the first ex-vivo phantom able to generate controlled uterine movement, especially suitable for evaluation and optimization of ultrasound speckle tracking methods.

Statement of Contribution/Methods

A human uterus was submerged in water immediately after hysterectomy. An electromagnetic actuator generated a controlled, sinusoidal (0.05 Hz), linear displacement of a syringe piston, injecting 5-mL water through a balloon catheter inserted into the uterine cavity (Fig. 1a). This way, controlled, realistic peristaltic movement was generated while maintaining original speckle characteristics. Two needles were inserted in the uterus to realize clear markers of uterine motion. These moving markers, along with the driving signal of the actuator, represented the reference for assessing the speckle tracking accuracy. Here, block matching by normalized cross-correlation (NCC) and sum of absolute differences (SAD) were optimized and compared for their agreement with the reference signals. To this end, two blocks were positioned next to each needle (Fig. 1b). 4-min Ultrasound imaging was performed with an Accuvix 20 ultrasound scanner (Samsung-Medison) equipped with a transvaginal EC4-9IS probe.

Results/Discussion

A phantom based on an ex-vivo human uterus is proposed for simulation of realistic uterine peristaltic movement, suitable for objective evaluation of speckle-tracking techniques. The best agreement with all reference signals is obtained by SAD with block size of 3.49 x 3.49 mm^2, corresponding to twice the speckle size. Based on the proposed simulation phantom, innovations for uterine speckle tracking can be evaluated with a realistic ground truth, facilitating the development of improved methods for uterine motion analysis that enable new clinical studies aimed at expanding our knowledge on uterine activity and its influence on embryo implantation.

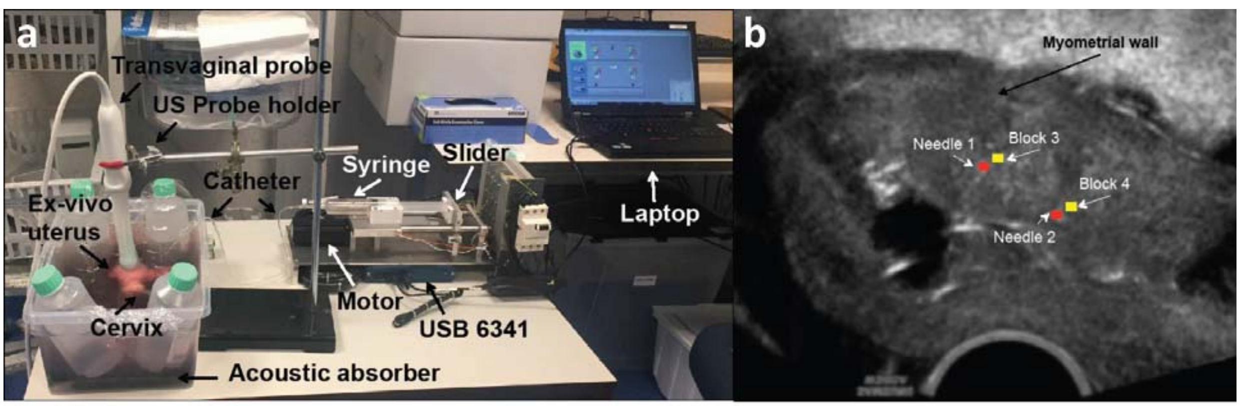

Figure 1: (a) Ex-vivo phantom for simulation of uterine peristaltic movement and (b) ultrasound image with two needle markers and two blocks positioned next to each marker for speckle tracking evaluation.

P1-A6-2

Multi-2D Reconstruction of Electromechanical Activation Maps of a Beating Heart

Pierre Nauleau[1], Lea Melki[2], Elaine Wan[3], Elisa Konofagou[2,4]; *[1]Ultrasound Elasticity Imaging Laboratory, Dpt of Biomedical Engineering, Columbia University, New York, NY, USA, [2]Ultrasound Elasticity Imaging Laboratory, Dpt of Biomedical Engineering, Columbia University, USA, [3]Department of Medicine, Division of Cardiology, College of Physicians and Surgeons, Columbia University, USA, [4]Department of Radiology, Columbia University, USA*

Background, Motivation and Objective

Arrhythmias can be treated by ablating the heart tissue in the regions of abnormal conduction, e.g. activating too early or with a different speed. The key of the treatment then lies in the location of these areas. In current clinical practice, 3-D electroanatomic maps can be created during the procedure by probing the heart with a specific catheter. However, it is a time-consuming and invasive procedure. Electromechanical wave imaging (EWI) is an ultrasound-based technique that can provide 2-D maps of the electromechanical activation of the heart. Yet, the activation follows a complex 3-D pattern. We thus propose an automated method to generate pseudo 3-D activation maps using several 2-D maps. These maps are subsequently analyzed qualitatively to locate the source of arrhythmia or quantitatively to evaluate the conduction speed in the myocardial tissue.

Statement of Contribution/Methods

Three canine models were considered to illustrate the method: one in normal sinus rhythm (NSR), one paced from the lateral part of the heart and one with an occlusion of the LAD artery. Four standard echocardiographic apical views were acquired in each dog. EWI was applied to generate four 2-D activation maps of the heart. The positions and activation timings of the walls were automatically extracted from those maps. In each short-axis slice, these values were interpolated circumferentially, resulting in a full 3-D map. This map was then used to quantify the EW speed in each point of the myocardium. The speed estimation algorithm relies on the fitting of a polynomial surface to the neighborhood of an activated point.

Results/Discussion

For each case, a 3-D activation map and a movie of the propagation of the EW were automatically generated. For the NSR, the activation starts from the atria and propagates towards the ventricles (Fig. 1-a). For the pacing case, only the left ventricle was investigated. The earliest source of activation corresponds to the location of the pacing lead (Fig.1-b). The estimated 3-D EW speeds were in the range of those previously reported from 2-D analysis ([0.1-0.6]m/s). Snapshots from the activation movie of a LAD-occluded left ventricle are shown Fig. 1-c. The proposed technique provides, automatically, a 3-D electromechanical activation map with a realistic anatomy. This represents a step towards a non-invasive tool to efficiently localize arrhythmias in 3-D.

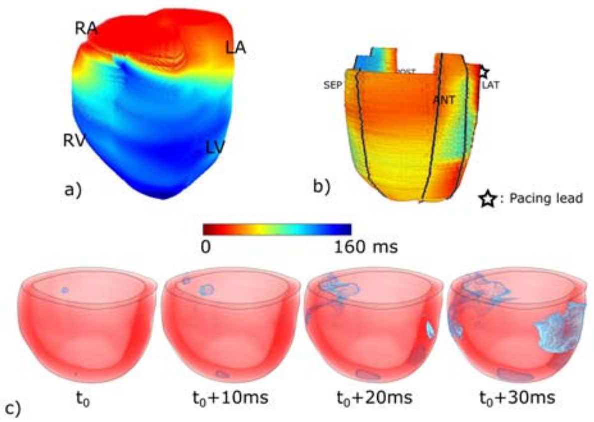

Fig. a) 3-D isochrone map of a full NSR heart (LA/RA: left/right atrium, LV/RV: left/right ventricle), b) 3-D isochrone of a canine left ventricle paced from the lateral side, c) Snapshots of the activation movie of the left ventricle of an infarct dog

P1-A6-3

An Evaluation of Microwave Diathermy Systems Using Temperature Increase Distributions Produced by Ultrasound Imaging Techniques

Yasuhiro Shindo[1], Kenji Takahashi[2], Futoshi Ikuta[3], Kazuo Kato[4], Yuya Iseki[5]; [1]*Department of Mechanical Engineering, Toyo University, Saitama, Japan,* [2]*Department of Orthopaedic Surgery, Nippon Medical School, Tokyo, Japan,* [3]*Graduate School of Medical Technology and Health Welfare Sciences, Hiroshima International University, Hiroshima, Japan,* [4]*Department of Mechanical Engineering Informatics, Meiji University, Kanagawa, Japan,* [5]*Department of Mechanical Engineering, Hachinohe National College of Technolog, Aomori, Japan*

Background, Motivation and Objective

Thermotherapy is used to inhibit the progress of osteoarthritis (OA) and to ease pain and stiffness. Effective thermotherapy occurs when heat can deeply penetrate the joint tissue, such as the cartilage and the joint cavity.

The microwave diathermy system does not contact the patient's skin; however, our previous findings show that its heat penetration depth is less than 20mm, which is not enough to heat the deep tissue for effective treatment of OA.

In this study, we developed a method using ultrasound (US) imaging techniques to calculate temperature increase distributions inside the human body. With this method, we evaluated the heating performance of current microwave diathermy systems. Finally, we compared our experimental data with computer-simulated temperature increase distributions using the finite element method (FEM).

Statement of Contribution/Methods

It is known that acoustic velocity depends on the temperature of the medium. US imaging devices reconstruct images using a specific velocity, so US images taken before thermotherapy will differ from US images taken after treatment because of temperature changes.

In this study, we accounted for the US images' movement as we conducted microwave diathermy on a live human subject's knee. We were able to estimate the heat penetration depth. Finally, for our FEM simulation, we used an anatomical knee model reconstructed from MRI.

During heating experiments, the microwave diathermy system was set at 100W and 10 minutes, matching clinical conditions. Using our own image-processing program, we compared the US images taken before and after the heating experiments.

Results/Discussion

From our simulation results, it was found that most of the electromagnetic heating energy radiating from the antenna was absorbed by the surface of the knee and did not penetrate deep into the bone cartilage or the joint cavity. A comparison between normalized temperature increase profiles inside the knee is shown in the figure. Our simulation results and our experimental results showed the same trend, and both results show little temperature increase in the deepest cartilage of the knee.

We confirmed that the microwave diathermy system could not effectively heat the deep tissue in the knee. Furthermore, we found that by using US imaging techniques, we were able to calculate the temperature increase distributions inside the human body.

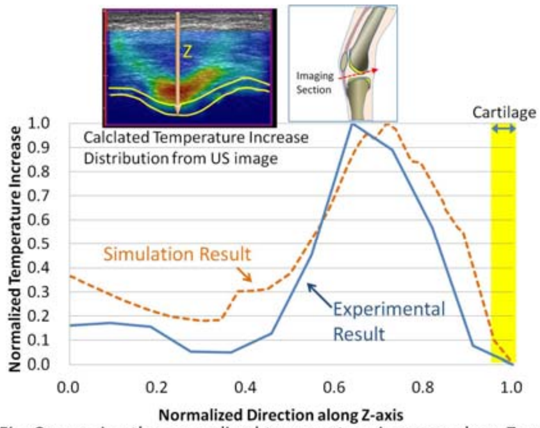

Fig. Comparing the normalized temperature increase along Z-axis (simulation result VS experimentalresult)

P1-A6-4

CT Scan Based Prostate Cancer Patient-Specific Transperineal Ultrasound Probe Setups for Image Guided Radiotherapy

Saskia Camps[1,2], Frank Verhaegen[3], Peter de With[1], Davide Fontanarosa[4]; *[1]Faculty of Electrical Engineering, University of Technology Eindhoven, Netherlands, [2]Oncology Solutions Department, Philips Research, Netherlands, [3]Department of Radiation Oncology (MAASTRO), GROW – School for Oncology and Developmental Biology, Netherlands, [4]School of Clinical Sciences, Queensland University of Technology, Australia*

Background, Motivation and Objective

Radiotherapy (RT) is a possible treatment modality for prostate cancer patients. The aim of RT is to irradiate tumor tissue, while sparing normal tissue as much as possible. Prior to treatment delivery, a CT scan is usually acquired, on which a treatment plan is prepared. Subsequently, the radiation dose is delivered to the patient in multiple fractions. The patients' setup prior to each of these fractions should replicate the setup during the CT scan, in order to deliver the dose to the correct location. This makes patient setup a crucial aspect of the RT workflow.

It has been shown that frequent imaging during the course of the treatment (image guided RT, IGRT) can allow a more accurate patient positioning. The use of 4D ultrasound (US) imaging in these IGRT workflows is not widespread, despite the many advantages (e.g. superior soft-tissue contrast, real-time volumetric organ tracking and no extra radiation). This can be mainly attributed to the high operator dependence of this image modality.

In this study, the planning CT scans of prostate cancer patients were used to calculate patient-specific transperineal US (TPUS) probe setups. The use of these setups can potentially minimize operator dependence and possibly even remove the need for a trained operator.

Statement of Contribution/Methods

The input for the workflow to obtain the probe setups (Fig. 1) were the CT scans of three prostate cancer patients. After identification of the accessible skin area (Fig. 1B-1D), a virtual X6-1 probe was positioned on this area (Fig. 1E) and translated/rotated to obtain more than 7,500 different setups for each patient (range: 7,546-11,858). After evaluation and ranking of the setups (Fig. 1F-G), the best setup could be identified (Fig. 1H).

Results/Discussion

For each of the examined patients at least 25 (range: 25-1,156) suitable US probe setups were identified, which potentially allowed visualization of all the clinically required structures. On average, the best setup of each patient potentially allowed visualization of 100% of the prostate and seminal vesicles, 84% of the bladder (range: 75-96%) and 64% of the rectum (range: 38-84%).

The results show that it is feasible to provide the operator with patient-specific probe setups, based on a CT scan, that satisfy all clinical requirements. Future steps will focus on enabling the operators to position the US probe according to the best setup.

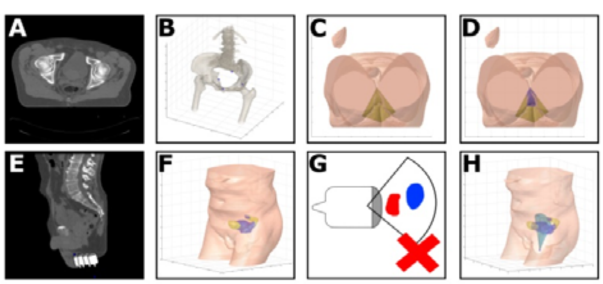

Figure 1. Workflow to obtain patient-specific US probe setups. (A) Acquire CT scan. (B) Identify internal perineum boundaries on the patients´ skeleton. (C) Project the boundaries to the perineal skin area of the patient. (D) Remove legs and the area around the anus from the accessible skin area and add the skin underneath the scrotum. (E) Identify possible US probe setups on the virtual perineum. (F) The whole prostate and seminal vesicles as well as the adjacent edges of bladder and rectum are required in the field of view (blue), while the remaining structures are optional (yellow). (G) Exclude probe setup that do not allow visualization of all clinically required structures or that have bone blockage occurrences. (H) Rank the remaining setups based on the amount of optional structures visualized and select the best setup.

P1-A6-5

A New High Definition Voxel-Based Multi-Planar Reformatting Method in 3-D Ultrasound Imaging

Sungchan KIM[1], Jinbum Kang[1], Ilseob Song[1], Yangmo Yoo[1,2]; *[1]Electronic engineering, Sogang university, seoul, Korea, Republic of, [2]Biomedical engineering, Sogang university, seoul, Korea, Republic of*

Background, Motivation and Objective

Multi-planar reformatting (MPR) in 3-D ultrasound imaging provides the viewer with planar cross-sectional images extracted from the 3-D data. To produce the MPR imaging from the acquired 3-D volume data, the 3-D scan conversion (SC), which transforms the acquired data in the 3-D polar coordinate system to the 3-D Cartesian coordinate system, is performed for display. Direct 3-D SC and separable 3-D SC method are most widely used approaches that they are followed by interpolation (e.g., trilinear or bilinear) using neighboring pixels. However, the direct 3-D SC and separable 3-D SC methods still suffer from blurring artifact; it may cause the deterioration of image quality. In this paper, we presents a new high definition MPR method using voxel based beamforming for reducing blurring artifacts.

Statement of Contribution/Methods

Fig. 1(a) illustrates the proposed voxel based MPR method in a 3-D curved transducer. Unlike the direct and separable 3-D SC, each voxel on an arbitrary imaging plane is directly reconstructed by applying the focusing delay to radio-frequency (RF) data without interpolation and the post-beamformed data corresponding to adjacent four scanlines are compounded with different weighting factor to produce a single beamformed pixel data. To evaluate the performance of the proposed method, RF channel data corresponding to 60 frames were acquired from the fetal mimicking phantom using the ultrasound data acquisition system (Ecube 11, Alpinion medical system, Seoul, Korea) with 3-D curved probe (1.0~6.0-MHz).

Results/Discussion

Fig. 1(b) represents the reconstructed MPR result (axial, sagittal and coronal view) using the proposed method and the Figs. 1(c)-(e) shows zoom-in images of a dotted box in Fig. 1(b) using the three 3-D SC methods, i.e., direct, separable and voxel beamforming, respectively. Under visual assessment, the voxel beamforming method outperformed the other 3-D SC methods in terms of conspicuity of speckle pattern and blurring artifact. Moreover, it showed the highest information entropy contrast (IEC) value compared with other 3-D SC methods, i.e., 97.02 vs. 113.60 vs. 130.22, respectively. These results indicate that the proposed MPR method effectively suppress blurring artifacts, and it also has merit to enhance spatial resolution and contrast.

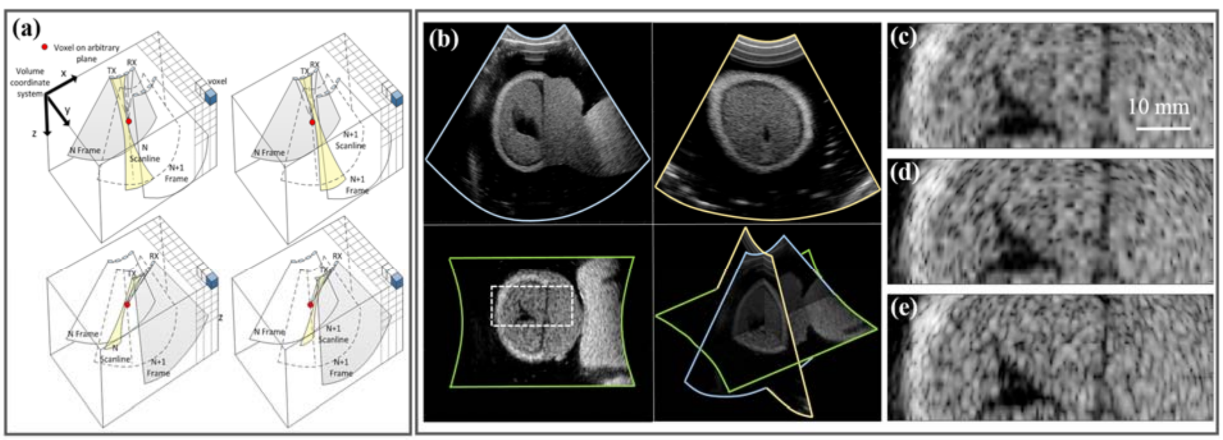

Fig. 1. (a) The proposed voxel beamforming based MPR method. (b) The reconstructed MPR imaging (Axial, sagittal and coronal view) using the proposed method. (c)-(e) The zoom-in images of a dotted box in Fig. 1(b) using the three 3-D SC methods (i.e., direct, separable and voxel).

P1-A6-6

Validation of Image Restoration Methods on 3D-Printed Ultrasound Phantoms

Krisztián Füzesi[1], Adrian Basarab[2], György Cserey[1], Denis Kouamé[2], Miklós Gyöngy[1]; *[1]Faculty of Information Tecnology and Bionics, Pázmány Péter Catholic University, Budapest, Hungary, [2]Institut de Recherche en Informatique de Toulouse, France*

Background, Motivation and Objective

The resolution of ultrasound images is limited by the bandwidth of the imaging system and the features of the propagating medium. Using certain assumptions, image restoration can recover out-of-bandwidth data and improve resolution. Several resolution improvement methods have been reported in the literature. Due to the lack of ground truth, their evaluation remains an open issue. Indeed, to evaluate the performance of such methods, knowledge of the scattering function is necessary. Usually this is achieved with numerical simulations. In the current work, a 3D-printed phantom is used to test l_p-norm-regularized deconvolution for various values of p. Knowledge of the scattering function allows comparison of the deconvolved images with the ground truth.

Statement of Contribution/Methods

A photopolymer jetting 3D printer (Objet24, Stratasys) was used to print a custom-designed phantom consisting of a propagation medium (SUP705, Stratasys; light polymerization) and 100 µm scatterers (RGD835, Stratasys). The scatterers were placed at 5 mm intervals along an outer 20x20 mm square frame, and at random positions inside a 10x10 mm square. Ultrasound images were obtained using plane wave emission from a 3-10 MHz linear array (LA522E, Esaote) connected to an ULA-OP Research US system (MSD Lab, University of Florence). Deconvolution was carried out using the recent method in [Zhao et al., IEEE TIP'15]. The outer frame was used to estimate the system point spread function *h* and the full width half maximum (FWHM). The inner frame was used to calculate the normalized root mean square error (RMSE) of the true scattering function estimates.

Results/Discussion

With the settings used in the figure, *p*=0.5 offers a higher spatial resolution gain than p=2, and also provides a higher estimation accuracy of the scattering function in terms of RMSE. With other settings, p=0.5 yields better values of FWHM than p=2 but with similar RMSE values, arguably due to increased noise. These results demonstrate the benefits of knowing the scattering function during experimental testing of image restoration methods. In summary, the current work shows an experimental method for evaluating the extent to which an image restoration method provides a faithful rendering of the underlying scattering structure.

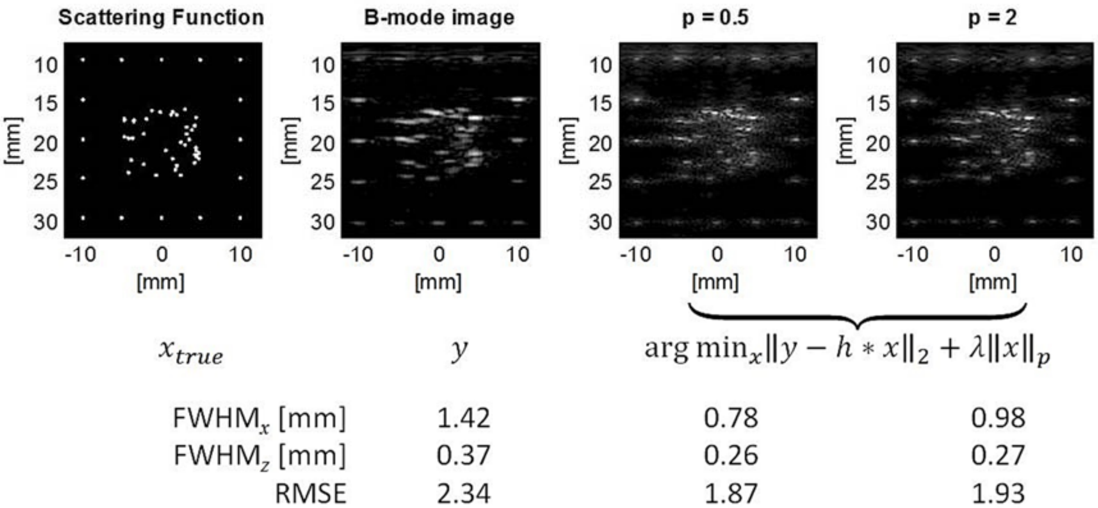

P1-A6-7

In Vivo Monitoring of Microwave Ablation in a Porcine Model Using Ultrasonic Nakagami Imaging

Siyuan Zhang[1], Shaoqiang Shang[1], Yuqiang Han[1], Ranxiang Xu[1], Sihao Liu[1], Lei Zhang[1], Mingxi Wan[1]; [1]*Department of Biomedical Engineering, Xi'an Jiaotong University, China, People's Republic of*

Background, Motivation and Objective

It is highly desirable to monitor microwave ablation (MWA) treatments noninvasively for substantially improving the clinical implementation of MWA procedures and progress toward full clinical uses worldwide. This in vivo study explored the feasibility of using ultrasonic Nakagami imaging to evaluate the thermal lesions in liver and kidney in a porcine model for the purpose of monitoring MWA.

Statement of Contribution/Methods

2-D RF data backscattered from the ablated region were captured by a modified diagnostic ultrasound scanner to estimate ultrasonic Nakagami parameters of the thermal lesions, and to reconstruct the ultrasonic B-mode and Nakagami images during HIFU and MWA. A term contrast-to-noise ratio (CNR) between the thermal lesions and the surrounding normal tissue is used to estimate the contrast resolution of the ultrasonic B-mode and ultrasonic parameter images. Receiver operating characteristic (ROC) curves were employed to assess and compare the discrimination ability of ultrasonic B-mode and Nakagami imaging to predict the thermal lesions. Area under ROC (AUC) was calculated to measure the predictability statistically.

Results/Discussion

After thermal ablation, a bright hyper-echoic region appeared in ultrasonic Nakagami parameter images as an indicator of the thermal lesion and this bright spot enlarged with lesion development during MWA exposure. The mean values of Nakagami parameter in the normal tissue were about 0.14 and 0.13 in the porcine liver and kidney, and then increased to 0.63 and 0.49 in the region of thermal lesions after MWA. During MWA exposure, the mean values of CNR calculated from the Nakagami parameter increased from 1.04 to 2.14 in the porcine liver and increased from 0.90 to 2.06 in the kidney, which were both higher than those calculated from the B-mode images. AUC values calculated from ROC curves were 0.67972 and 0.75125 for ultrasonic B-mode and Nakagami images. This in vivo study on a porcine model suggested that the Nakagami parameter may have the potential use to evaluate the formation of thermal lesions with higher accuracy and better image contrast for monitoring MWA treatment. The ultrasonic Nakagami imaging may be utilized as an alternative modality in the development of real-time monitoring systems for the image-guided MWA treatment.

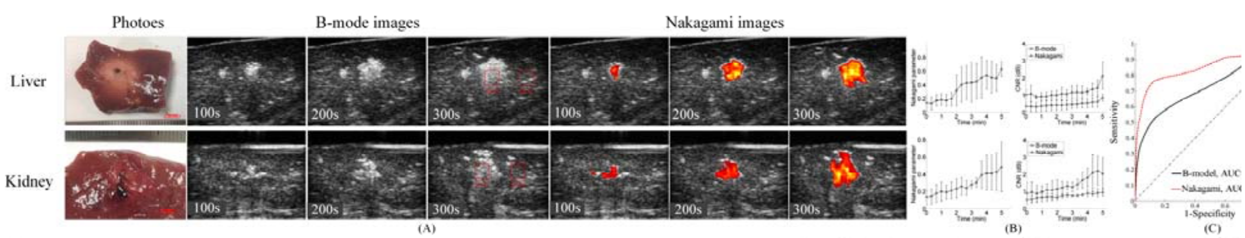

(A) Temporal evolution of ultrasonic B-mode and Nakagami images of thermal lesions in liver and kidney, as well as (B) the dynamic changes of Nakagami parameter and CNI during MWA. (C) ROC curves for accuracy of ablation prediction.

P1-A6-8

Increased Clutter Level in Echocardiography Due to Interaction between Ribs And Lungs

Ali Fatemi[1], Alfonso Rodriguez-Molares[1], Hans Torp[1], Svend Aakhus[1], Lasse Løvstakken[1], Oddveig Lyng[1], Tore Bjastad[2]; [1]*Centre for Innovative Ultrasound Solutions (CIUS), Norwegian University of Science and Technology, Trondheim, Norway,* [2]*GE Vingmed, Horten, Norway*

Background, Motivation and Objective

Some echocardiograms have limited diagnostic value due to a high-level clutter noise of unknown origin. The goal of this study is to understand the mechanism that generates this clutter.

Statement of Contribution/Methods

We propose the following theory for the clutter origin in 4-chamber view echocardiograms: In patients with short intercostal distance, the ultrasound beam can be partially blocked by the ribs in the elevation direction. Therefore, the energy can be partially deflected outside of the imaging plane towards the lung (see Fig. 1). Reverberation noise produced at the lung interface will then travel back to the transducer via a second reflection at the ribs and will be rendered as clutter on the ultrasound image.

We carried out an ex vivo experiment to verify our theory. A GE E95 scanner and a M5Sc transducer were used to take images of a PVA ventricle in a water tank. The ventricle was made of 10% polyvinyl alcohol (PVA), 2% G-25 Sephadex to increase scattering, and 88% water. Two pig ribs, mounted on a robot arm, were placed between the transducer and the ventricle (see Fig. 2a). An inflated pig lung was placed inside a net and immersed under water. Ultrasound images of the ventricle were acquired in three different scenarios: 1) with the ribs partially blocking the transducer in the elevation direction and without the lung, 2) in presence of the lung while the transducer was still partially blocked, and 3) in presence of the lung while the ribs were not blocking the transducer.

Results/Discussion

Fig. 2a-2c show photographs of the three scenarios while the corresponding ultrasound images are shown in Fig. 2d-2f. It is observed in Fig. 2e) that placing the lung close to the ventricle increases the clutter level. Unblocking the transducer, Fig. 2f), removes the clutter noise. It confirms that clutter noise is produced as a result of interaction between the ribs and the lung. This experiment supports our theory for clutter noise generation in echocardiography.

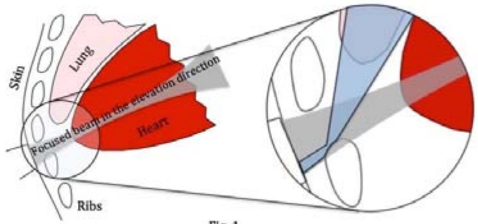

Fig. 1

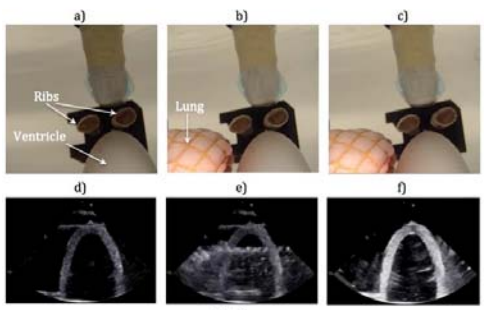

Fig. 2

P1-A7 - MPA: Applications of Photoacoustics

Exhibit Hall

Thursday, September 7, 2017, 9:30 am - 4:00 pm

Chair: **Chulhong Kim**
Pohang University of Science and Technology

P1-A7-1

Optimization of Dual Wavelength IVPA Imaging for Accurate Detection of Lipid in Atherosclerotic Plaques.

Timothy Sowers[1,2], Nicholas Dana[3], Andrei Karpiouk[4], Don VanderLaan[4], Stanislav Emelianov[4,5]; [1]*Parker H. Petit Institute for Bioengineering and Bioscience, Georgia Institute of Technology, Atlanta, GA, USA,* [2]*George W. Woodruff School of Mechanical Engineering, Georgia Institute of Technology, Atlanta, GA, USA,* [3]*Department of Biomedical Engineering, University of Texas at Austin, Atlanta, GA, USA,* [4]*School of Electrical and Computer Engineering, Georgia Institute of Technology, Atlanta, GA, USA,* [5]*Wallace H. Coulter Department of Biomedical Engineering, Georgia Institute of Technology and Emory University School of Medicine, Atlanta, GA, USA*

Background, Motivation and Objective

Intravascular photoacoustic (IVPA) imaging is being developed to improve and guide treatment of atherosclerotic vulnerable plaques. While lipid has been successfully imaged, current studies have not determined how many or which optical wavelength(s) will accurately characterize atherosclerotic plaques. We leverage Monte Carlo (MC) optical modeling to determine the optimal dual-wavelength combination for IVPA imaging. Our study will allow for enhanced lipid sensitivity and specificity while potentially reducing system costs and facilitating translation of IVPA imaging to the clinic.

Statement of Contribution/Methods

We used a 3D MC optical model to simulate IVPA excitation in coronary vessels. Four vessel geometries (see A), with plaque burdens varying from healthy to rupture prone, were simulated using IR wavelengths from 800 – 1800 nm. Cross sectional single-wavelength images were evaluated by segmentation of probable lipid-rich regions via thresholding, while dual-wavelength images were evaluated using a ratiometric image followed by thresholding (see B-C). Segmented images at different wavelength(s) were compared based on their accuracy in detecting lipid in the four vessel models. The results were validated using a 1D phantom of lipid and water.

Results/Discussion

Results indicate light penetration is best in the range of 1050 nm to 1370 nm, where 5% residual fluence can be achieved at clinically relevant depths of 2 mm or more. Analyses show that fluence may vary by over an order of magnitude across the vessel, confounding assessments of lipid content. In single-wavelength images, correlation of segmented lipid-rich regions peaked at 1210 and 1720 nm, but did not exceed 0.3. Segmented dual-wavelength images gave much better lipid identification, with several wavelength pairs reaching a near perfect correlation of 1 (see F). Experimental results and model prediction showed good agreement in the 1D phantom model (see D-E). Considerations of light penetration, fluence variation, and segmentation accuracy suggest that using a primary wavelength near 1210 nm, paired with a secondary wavelength near 1350 nm, offers the most promising clinical implementation of IVPA imaging. Pulsed laser options are available at these wavelengths, and results suggest this combination will allow for accurate differentiation of plaque from luminal blood and intimal lining.

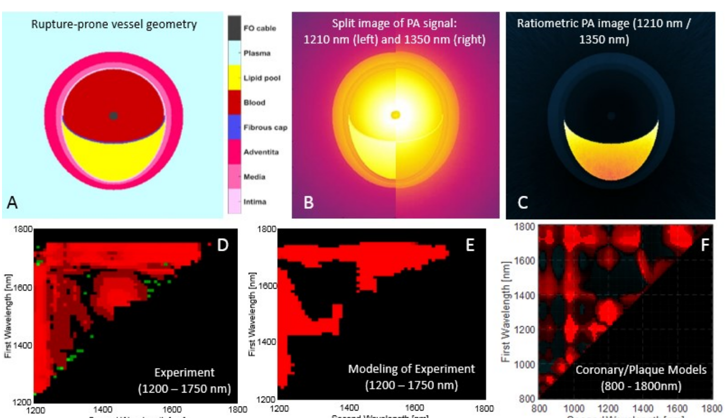

A-C) Data analysis sequence from one tissue model to a ratiometric PA image. A) one of the simulated vessel models (rupture prone plaque) with its unique tissue constituents labelled. B) split image of the simulated PA signal at 1210 nm (left) and at 1350 nm (right) C) ratiometric PA image with 1210 nm / 1350 nm. D-F) Color maps indicating the accuracy of lipid correlation for different dual wavelength pairs. In (D) and (E), experimental and modeling results on a 1D phantom of water and lipid are shown. Strong correlation bands (bright red) are present for wavelengths of 1210 nm and 1720 nm, with the experimental and simulated results showing agreement. F) results of modeling on the coronary artery models indicates that dual wavelength pairs with 1210 nm and 1720 nm give strong lipid correlation, with the strongest correlation occurring with one wavelength at 1210 nm and the other near 1350 nm.

P1-A7-2

Hemorrhages Detection in Atherosclerotic plaques using Ultrasound and Photoacoustic, Phantom Study

Louise Gouteux[1], Ümit Arabul[1], Marcel Rutten[1], Frans Van de Vosse[1], Richard Lopata[1]; [1]*Biomedical Engineering, Technische Universiteit Eindhoven, Eindhoven, Netherlands*

Background, Motivation and Objective

Rupture of an atherosclerotic plaque in the carotid artery is one of the main causes of stroke and stroke-induced death. Currently, to prevent this risk, endarterectomy is performed based on the stenosis grade assessed with Duplex ultrasound (US). However, plaque composition, e.g. presence of lipids and hemorrhages, is a more important factor of rupture risk than stenosis. The optical absorption of hemorrhages (composed of coagulated, deoxygenated blood) is different from that of oxygenated blood and allows their distinction using different wavelengths. In this study, photoacoustic (PA) imaging is used to detect intraplaque hemorrhages using contrast in optical absorption in combination with the resolution of US.

Statement of Contribution/Methods

To study the difference between hemorrhages and circulating blood in PA images, a phantom study was performed. The phantom is a thick-walled tube (d_{inner} = 3 mm, d_{outer} = 8 mm) composed of PVA gel which has no optical absorption. Blood was inserted in a 1.1 mm cylindrical hole at 0.4 mm from the lumen and coagulated. The phantom was perfused with blood-mimicking fluid, composed of a mixture of inks, resulting in the same optical absorption as oxygenated blood at each wavelength. US and PA imaging were performed, the latter at four different wavelengths (808, 915, 940 and 980 nm). During post-processing, PA signal from the lumen was removed using a US cross-correlation method.

Results/Discussion

Both thrombus and lumen are visible in the US imaging (Figure 1A), indicating their exact locations. The latter is not the case in real plaques. Absorption in the lumen is high, hence, only hemorrhages in the upper hemisphere can be detected (Figure 1B). The thrombus has a better contrast at 915 and 940nm (SNR_{915}= 1.21, SNR_{940} = 1.12, SNR_{980} = 0.57) due to optical absorption of deoxygenated blood, whereas 808 nm (SNR_{808}=1.58) is more suitable for oxygenated blood (Heres et al. 2017). Moreover, removing the PA signal from the lumen allows a major improvement in the visualization of the thrombus (Figure 1C) which can later be applied on in vivo hemorrhages detection. In future studies, this method will be applied to ex-vivo carotid plaques and in vivo. The benefit of spectral unmixing to distinguish between oxygenated blood and hemorrhages will be investigated.

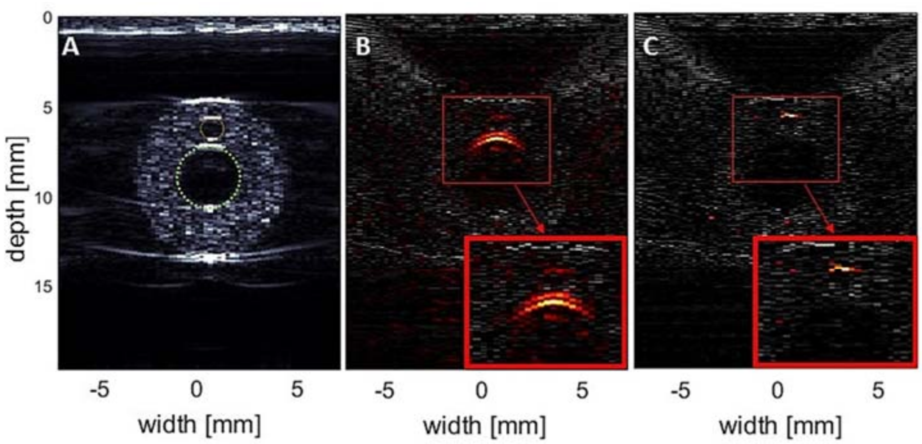

Figure 1A: US imaging of the phantom with ink in the lumen and clotted blood in the thrombus. The green circle indicates the lumen and the orange one the thrombus. **B:** PA imaging at 940nm. **C:** Post-processing PA imaging, without lumen signal. The red boxes are zooms on zones of interest.

P1-A7-3

SO_2 Quantification of Rat HCC Tumors Using Fluence-Corrected Photoacoustic Imaging

Mohamed Naser[1], Houra Taghavi[1], Nina Munoz[2], Kiersten Maldonado[1], Charles Kingsley[1], Rony Avritscher[2], Richard Bouchard[1]; *[1]Imaging Physics, The University of Texas MD Anderson Cancer Center, USA, [2]Interventional Radiology, The University of Texas MD Anderson Cancer Center, USA*

Background, Motivation and Objective

Spectroscopic photoacoustic (sPA) can estimate blood oxygen saturation (SO_2), which has been shown to correlate with hypoxia, and therefore could improve cancer diagnosis and treatment monitoring. However, accurate quantification of SO_2 is often not straightforward as local fluence varies significantly at depth due to wavelength-dependent optical scattering and absorption. Additionally, assessing the quality of an SO_2 estimate is not trivial as deep-lying (i.e., centimeter-order depth) PA data tends to be signal-limited, and SNR can vary substantially with wavelength for a particular voxel. This work implements an SNR-based thresholding approach combined with FEM-based local fluence correction to more accurately estimate SO_2 in a rat model of hepatocelluar carcinoma (HCC).

Statement of Contribution/Methods

A recursive approach to estimate the relative magnitude of HbO_2 & HHb concentrations from sPA data was employed in an orthotopic model of HCC. Volumetric sPA imaging data were acquired with the Vevo LAZR platform at 5 wavelengths with a 15-MHz array during O_2 inhalation. Fig. A shows co-registered B-mode and sPA images (tumor outline yellow) for each acquisition wavelength. Fluence maps were estimated using the diffusion approximation and FEM modeling (Fig. C). Assuming a wavelength-dependent relationship for reduced scattering, reconstructed absorber concentrations were used to calculate fluence and sPA image simulations for each iteration; convergence was achieved by minimizing the error between measured and simulated sPA values. SO_2 estimates were thresholded based on a pixel-wise SNR cut-off of 1.5 dB (Fig. B), which was measured for each TGC curve in water without an irradiation source.

Results/Discussion

Normalizing for fluence improved SO_2 estimation accuracy for deeper-lying tumors. Figs. E & D show SO_2 estimates based on umixed sPA data with and without local fluence correction, respectively. Cyan and white arrows in each denote a proximal and distal artery, respectively, which were assumed to have similar SO_2. When uncorrected (D), the proximal and distal arteries yield SO_2 estimates of 100% and 85%, respectively, while they present more similar SO_2 estimates of 100% and 97%, respectively, with fluence correction. This work demonstrates the potential of noise-based thresholding and FEM-based fluence correction for improved SO_2 assessment.

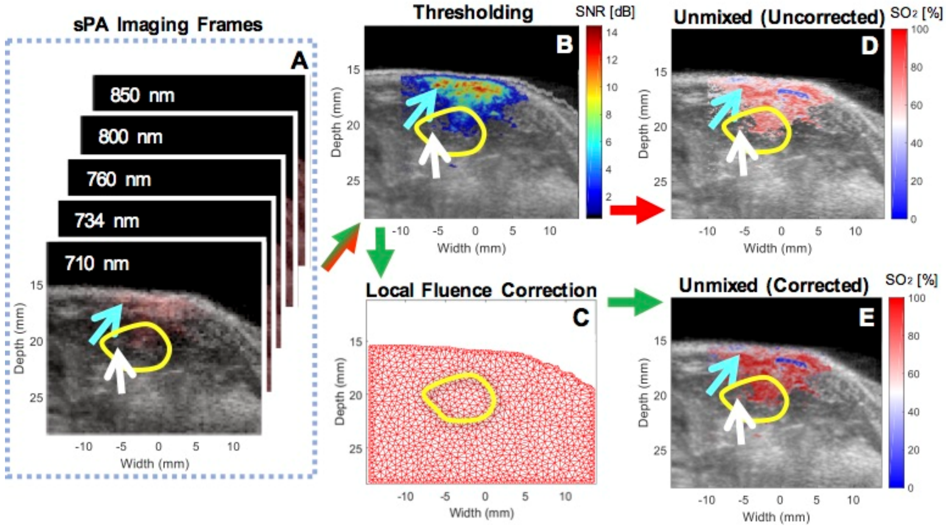

P1-A7-4

Implications of Tumor Oxygenation and Blood Flow for Cancer Treatment Monitoring using Photoacoustic Imaging and Power Doppler

Eno Hysi[1,2], Lauren A. Wirtzfeld[1,2], Azza Al-Mahrouki[3,4], Niki Law[3,4], Mai Elfarnawany[5,6], James C. Lacefield[6,7], Gregory J Czarnota[3,4], Michael C. Kolios[1,2]; [1]*Physics, Ryerson University, Toronto, ON, Canada,* [2]*Institute for Biomedical Engineering, Science and Technology, Toronto, Ontario, Canada,* [3]*Physical Sciences, Sunnybrook Research Institute, Toronto, Ontario, Canada,* [4]*Radiation Oncology, Sunnybrook Health Sciences Center, Toronto, Ontario, Canada,* [5]*Biomedical Engineering, Western University, London, Ontario, Canada,* [6]*Robarts Research Institute, London, Ontario, Canada,* [7]*Biomedical Engineering, Electrical and Computer Engineering, Medical Biophysics, Western University, London, Ontario, Canada*

Background, Motivation and Objective

Photoacoustic (PA) imaging has been proposed for cancer treatment monitoring. Tumor oxygen saturation (sO_2) should in principle be related to vascular parameters such as blood flow. In this work, in-vivo PA estimates of sO_2 were compared to power Doppler (pD) measures of vascularity hours after the administration of microbubbles (MB), radiation therapy (XRT), individually or combined (MB-XRT).

Statement of Contribution/Methods

Forty SCID mice were inoculated with subcutaneous, PC3 tumors in the left hind leg. The treatment groups consisted of: MB-XRT (N=12, 3% w/v, 550 kHz insonication, 570 kPa peak negative pressure, 8 Gy radiation), XRT only (N=10) and MB only (N=8) and untreated control (N=10). The VevoLAZR system (FujiFilm-VisualSonics) was used to acquire 3D PA (750/850 nm, 21 MHz ultrasonic frequency) and pD (16 MHz frequency, 2 kHz PRF) datasets at three timepoints: pre-treatment, 2 hours and 24 hours post-treatment. Distributions of sO_2 within the tumor were quantified at multiple planes using histograms. The Vascularization Index (VI) was estimated from the pD data for the same tumor planes as PA imaging at each timepoint.

Results/Discussion

Fig. 1a shows the sO_2 histograms and respective means for all groups. For the combined MB-XRT treatment, we observe a left shift in the histogram due to a 4% drop in the oxygenation as early as 2h post-treatment. This is attributed to the mechanical perturbations of MB on the microvessel wall leading to hemorrhaging. At 2h post-treatment, the XRT alone shows an 8% increase in tumor oxygenation. The MB group increases by 6% at 24h relative to 2h. The first significant change of the control group is at 24h. The correlation of pD metrics such as VI to the changes in tumor sO_2 is shown in Fig. 1b. In response to microvascular damage, vascular density and consequently, tumor blood flow, increases after 2 hours for the MB-XRT and MB only treatments. This suggests that the tumors respond to the PA-sensitive microvascular damage by increasing the flow within larger vessels which pD can detect flow through. The XRT only treatment exhibits a drop in VI while we speculate that an acute inflammatory response increases the tumor sO_2. This study suggests that PA imaging can be used to probe the mechanism of action of novel cancer treatments and pD can assist in interpreting vascular dynamics within the tumor.

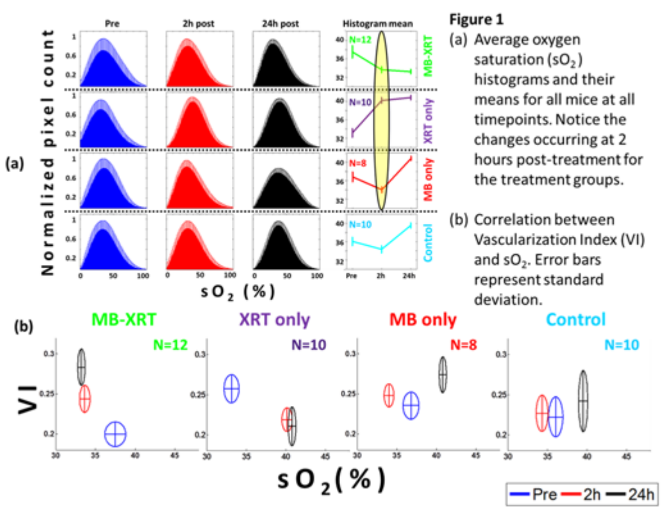

Figure 1
(a) Average oxygen saturation (sO_2) histograms and their means for all mice at all timepoints. Notice the changes occurring at 2 hours post-treatment for the treatment groups.
(b) Correlation between Vascularization Index (VI) and sO_2. Error bars represent standard deviation.

P1-A7-5

Perfusion-Rate Estimation Using Compression-Based Photoacoustic-Ultrasound Imaging

Min Choi[1], Roger Zemp[1]; [1]*Electrical and Computer Engineering, University of Alberta, Edmonton, Alberta, Canada*

Background, Motivation and Objective

The ability to measure perfusion rates of tissues in a non-invasive and label-free way could enable powerful diagnostic applications to peripheral vascular disease, ischemia, tumor hypoxia, ulcer characterization, and general tissue health. However, current medical techniques of measuring perfusion rates, which include contrast-enhanced ultrasound imaging, perfusion MR imaging require contrast agents and thus are not amenable to widespread screening procedures. A crude method of measuring net limb perfusion is measuring the capillary refill time (CRT) using a compression nail test performed in an emergency ward or a pediatric care. Yet, the test itself does not have a set standard as CRT is highly variable depending on patient status. This method also does not provide local maps of tissue perfusion. Our approach of measuring perfusion rates using combined photoacoustic and ultrasound imaging is a non-invasive method and may be suitable for high throughput mapping of perfusion rates in deep tissue (~2 mm).

Statement of Contribution/Methods

When external pressures from compression overcome internal pressures of microvessels they collapse and photoacoustic signals diminish due to blood being displaced from the compression area. The external compression is performed using an imaging transducer head. After the full compression, the transducer head is released and the recovery in PA signal is tracked. We use a commercially available system (Vevo LAZR, Fujufilm Visualsonics Inc) to perform in vivo imaging of a hand of a human subject. The system uses a 40-MHz high frequency transducer and 805-nm light. We use displacement-tracking algorithms to determine the change in shape of the tissue layer during and after each compression. To quantify the perfusion rates, the region of interest (ROI) is first chosen then an average PA signal within a small window, which is within the ROI, is calculated for each frame. The tracked PA signal is then fitted against a recovering exponential function to calculate the time constant. The perfusion rate is defined as the inverse of the time constant. Once the recovering PA signal within the window is completed, the window slides to a new location within the ROI and the PA signal tracking process is repeated until the window covers the entire ROI.

Results/Discussion

By varying the time the hand of a human subject was exposed to different temperatures, the change in perfusion rates is induced. The change is evident when the hand is submerged in a 4°C water bath: the average perfusion rates when the hand is submerged for 30s, 60s and 90s are 0.379s, 0.343s and 0.219s respectively. The opposite occurs when the hand is submerged in a 45°C water bath: the average perfusion rates are 0.561s, 0.870s and 1.28s for 0s, 30s and 60s respectively. Perfusion-rate images show significant promise for a range of clinical applications.

P1-A7-6

Quantitative Evaluation of Skin Aging with Photoacoustic Microscopy

Yuya Murata[1], Takeshi Namita[1], Kengo Kondo[1], Makoto Yamakawa[1], Tsuyoshi Shiina[1]; [1]*Graduate School of Medicine, Kyoto University, Kyoto, Japan*

Background, Motivation and Objective

In recent years, skin aging caused by ultraviolet light exposure (i.e. photoaging) has garnered attention in the fields of beauty and health care because photoaging accelerates skin aging. However, few practical techniques exist for the quantitative evaluation of such aging. Photoacoustic imaging, a novel modality, can portray differences of tissue characteristics. To verify the feasibility of quantitative evaluation of skin aging with photoacoustic technique, the effects of skin aging progress on photoacoustic signal intensity were investigated.

Statement of Contribution/Methods

Photoacoustic images of 50-µm-thick porcine skin sections were measured with acoustic resolution photoacoustic microscopy. The oxidizing reagent (i.e. acrolein) was used because it produces similar results as the photoaging. To simulate skin aging of various degrees, the concentration and processing days of acrolein were changed. Nanosecond pulses of laser light (460-600 nm wavelengths) from optical fiber passed through a conical lens to produce an annular area of illumination. Laser beams refracted by a prism irradiated a skin section. An ultrasonically focused transducer (50 MHz, 6.7 mm focal length) attached to the imaging head detected photoacoustic waves. The energy of each laser pulse was measured using a power meter to calibrate the received signal intensity. Photoacoustic signal distributions of various skin aging sections were measured at 20 µm intervals. The region of interest of each sample was 7.0×5.5 mm^2.

Results/Discussion

Figure 1 depicts maximum intensity profiles of photoacoustic signal of each sample exposed to 460 nm wavelength light. The structure of skin section is also depicted in Fig. 1. At all wavelengths, the signal intensity from the epidermis was higher than that from the dermis. Results also show higher signal intensity for light of shorter wavelengths in the region of measurement. Figure 2 portrays the relation between signal intensity and photoaging progress. Results clarified that the signal intensity from both epidermis and dermis increases as progress of photoaging.

These analyses demonstrate the feasibility of quantitative evaluation of skin aging with the photoacoustic imaging system. A quantitative evaluation method, appropriate wavelengths, *in vivo* measurements, and more practical systems must be developed and used in future studies.

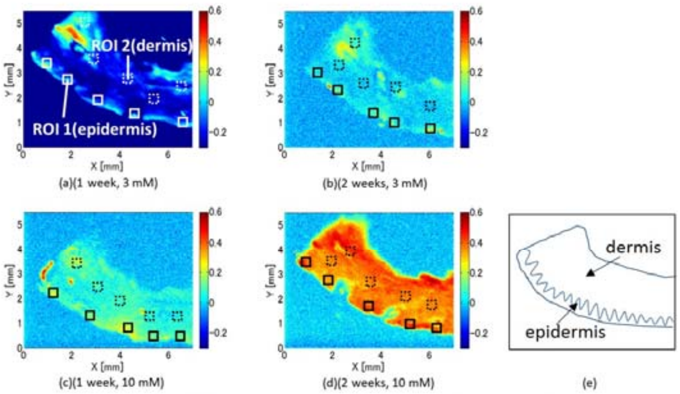

Fig. 1. (a)–(d) Maximum intensity profile of porcine skin segments in X-Y plane and ROI for skin evaluation (λ = 460 nm), and (e) skin section structure: the solid line shows ROI 1 (epidermis, 10×10 pixels), the broken line shows ROI 2 (dermis, 10×10 pixels).

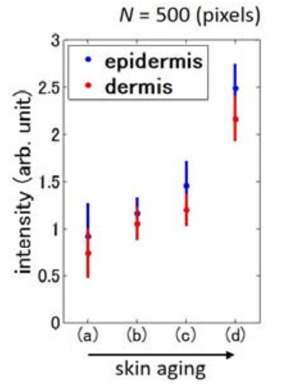

Fig. 2. Progress of skin aging effects on photoacoustic signal intensity.

P1-A7-7

Photoacoustic and High Frequency Ultrasound Imaging of Mechanical and Thermal HIFU Ablation

Khalid Daoudi[1], Martijn Hoogenboom[2], Martijn den Brok[3], Gosse Adema[3], Jurgen Futterer[4], Chris de Korte[1]; *[1]Department of Radiology and Nuclear Medicine, Medical UltraSound Imaging Centre, radboud university medical center, Nijmegen, Netherlands, [2]Radiology and Nuclear Medicine, radboud university medical center, Nijmegen, Netherlands, [3]Radiotherapy & OncoImmunology laboratory, dep. Radiation Oncology, radboud university medical center, Nijmegen, Netherlands, [4]Department of Radiology and Nuclear Medicine, radboud university medical center, Nijmegen, Netherlands*

Background, Motivation and Objective

The possibility of focusing high ultrasound intensities HIFU opened the door for promoting ultrasound as a non-invasive therapeutic method. HIFU is capable of producing both thermal and mechanical effects on tissue. The thermal effect relies on temperature increase and has been introduced to the clinic a decade ago. While mechanical effect such as boiling histotripsy induces extremely high pressures to pulverize targeted tissue and is still confined to laboratories due to the lack of adequate imaging techniques to better understand its in-vivo pathological and immunological effects. In this work, we investigate if high-frequency ultrasound (US) and photoacoustics (PA) can be a potential combination to evaluate the effect of boiling histotripsy in-vivo. Furthermore, we compare its outcome to thermal HIFU ablation.

Statement of Contribution/Methods

C57Bl/6n wild type mice were subcutaneously injected with tumor cells in the right femur. The ablation and monitoring take place in a 7T wide bore animal MR scanner. The ablation was performed using a 3MHz HIFU MR compatible system. Two different settings were used: 5 ms pulses with 230 Watts acoustic power for boiling histotripsy treatment, and 4 s pulses with 50 Watts acoustic power for thermal ablation. We utilized PA imaging with the co-registered US to non-invasively image the tumor before and after HIFU ablations. After the imaging, the tumor was resected for the evaluation of the ablated region using histopathology.

Results/Discussion

PA revealed a completely deoxygenated tumor core after mechanical treatment while mainly oxygenated vessels were detected before. Ultrasound images show a hypoechoic region in the treated area revealing a complete pulverization of the tumor cells whereas Doppler imaging (not shown) revealed the destruction of blood vessel network after the ablation. These findings were corroborated by histopathology. On the other hand, US images of thermal ablation showed no difference before and after the ablation, while PA revealed a partial deoxygenation of the tumor while leaving the remaining non treated tumor oxygenated. This result may indicate a substantial difference between both techniques in successfully treating tumors since oxygenation is known to be a key factor in tumor progression and invasiveness.

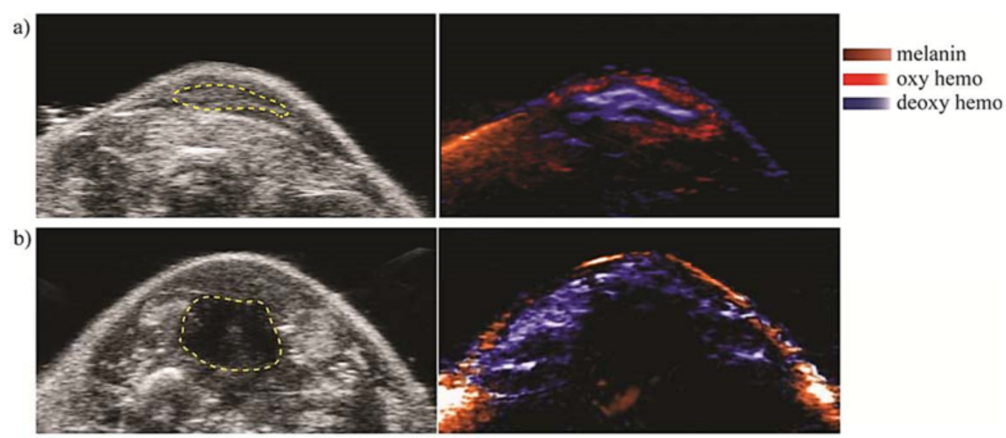

Figure1: Ultrasound (left) and photoacoustic spectroscopic images (right) of tumor treated with thermal HIFU (a) and with mechanical HIFU (b). Yellow lines delineate the treated region of the tumor

P1-A7-8

Identification of Aggressive Prostate Cancer in Ex Vivo Human Prostates by Physio-Chemical Photoacoustics

Guan Xu[1], Shengsong Huang[2], Yu Qin[3], Jing Pan[3], Qian Cheng[3], Yingna Chen[3], Xueding Wang[4], Denglong Wu[2]; *[1]Radiology, University of Michigan, Ann Arbor, MI, USA, [2]Urology, Tongji University Hospital, China, People's Republic of, [3]Tongji University, China, People's Republic of, [4]University of Michigan, USA*

Background, Motivation and Objective

Prostate cancer (PCa) is the most commonly diagnosed cancer and the second cause of cancer deaths in American men. PCa has a relatively low progression rate, yet it cannot be cured once metastasized. The accurate diagnosis of the aggressive PCa is critical for the survival of PCa patients. Prostate biopsy is the standard procedure for evaluating the presence and aggressiveness of PCa. The microarchitecture of the biopsied tissues is graded as a quantification of the PCa aggressiveness. Due to the inaccurate imaging guidance, less than 10% of the samples are clinically significant. Purposed at alleviating the complications of needle biopsy, this study investigates the feasibility of assessing the aggressiveness of PCa using interstitial photoacoustic (PA) measurements without tissue removal.

Statement of Contribution/Methods

Fig. 1 shows a prototype needle PA probe for measurements in ex vivo human prostates. Fig. 2 shows the 2D spectrograms formed by the multispectral PA measurements in the frequency domain. Such spectrograms facilitate the decomposition of the molecular components in the optical wavelength domain (x-axis) and the associated microarchitecture in the ultrasonic frequency domain (y-axis). The stripe features marked by the color contours in Fig. 2 are associated with each relevant molecular component in biological tissue. The analysis of the stripe features, namely PA physio-chemical analysis (PAPCA), could quantify the histological features in the assessed tissue. In this study, PAPCA will be implemented to the data acquired from 6 ex vivo human prostates. Measurements were acquired at 13 cancerous and 9 benign locations.

Results/Discussion

Statistically significant difference was found between the aggressive cancerous and benign regions in the prostates.

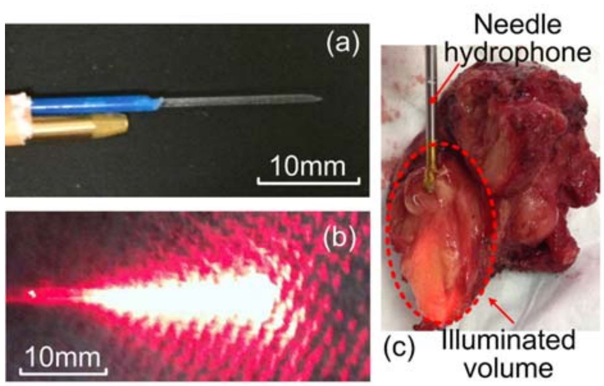

Fig. 1 (a) A prototype needle PA probe.
(b) The probe illumination pattern.
(c) Measurements in a human prostate ex vivo

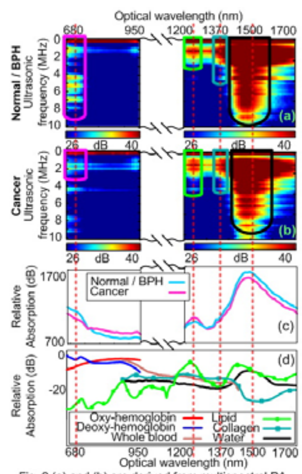

Fig. 2 (a) and (b) are derived from multispectral PA measurements of benign and cancerous regions in a human prostate, respectively. (c) Absorption spectra of benign and cancerous regions. (d) Absorption spectra of the major molecular components in prostate tissue.

P1-A7-9

In Vivo Spectroscopic Photoacoustic Imaging of Tumor Protease Activity by Using Gold Nanocage-Based Activatable Nanoprobe

Cheng LIU[1], Shiying LI[1], Yanjuan GU[2], Lei SUN[1]; *[1]Interdisciplinary Division of Biomedical Engineering, The Hong Kong Polytechnic University, China, People's Republic of, [2]Department of Applied Biology and Chemical Technology, The Hong Kong Polytechnic University, China, People's Republic of*

Background, Motivation and Objective

Malignant tumors appear to own the ability to recruit normal tissue cells that contribute to the tumorigenesis process by creating the “tumor microenvironment”. MMPs, is one of the most significant family of proteinases that are related to tumor microenvironment. Recent understanding of MMPs has recognized its role as modulators in tumor microenvironment; however, the current strategies for *in vivo* MMPs visualization are not competent to provide adequate information with high contrast-to-noise ratio, high spatial resolution and high temporal resolution. In this work, an activatable nano-probe that couples strong plasmonic gold nanocages (GNC) & chromophores to be switched by MMP-2 was selected to improve the visualization of MMP-2 activity by using spectroscopic photoacoustic Imaging (PAI).

Statement of Contribution/Methods

To synthesize the spectroscopic PA nano-probe, chromophore Alexa680 labeled peptide (chromophore-GKG*PLGV*RGC-NH2) was selected & coupled with GNC800. The final probe was named as Alexa680-peptide-GNC800. The italicized peptide sequence is the substrate specifically for MMP-2 cleavage. Once cleaved by MMP-2, the chromophore in small size could be washed out from the nano-probe. In in vitro experiment, the light absorption spectra & PA spectra of GNCs, chromophores & nano-probes (before & post enzyme cleavage) were recorded. For in vivo subcutaneous tumor model test, the distribution of nano-probes along with cleaved GNCs & chromophores were unmixed and visualized by using the PA spectra of nanoparticles & the multi-wavelength spectroscopic PAI technique.

Results/Discussion

Since the PA spectra of strong plasmonic GNCs are tunable in NIR optical window, GNC800 was selected as candidate to couple chromophore Alexa680. Classic activatable peptide structure was employed to acquire contrast information from enzyme activity *in vivo*. Distinct PA spectra of GNC, chromophore, nano-probe were used as “fingerprint” to unmix nanoparticles’s distribution in vivo & improve its visualization by using spectroscopic PAI technique. The high contrast-to-noise ratio of this strategy provide direct mapping of the enzyme activity in vivo with high suppression of endogenous contrast noise from biological tissues, such as Hb/HbO2.

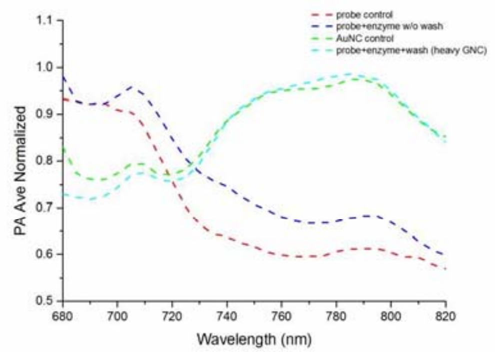

Figure 1. Photoacoustic spectra fingerprint of Probe control (Alexa680-peptide-GNC800) in red, probe+enzyme w/o wash (cleaved Alexa680-peptide-GNC800 without wash) in blue, AuNC control (GNC800) in green, probe+enzyme+wash (heavy GNC) which is cleaved probe after wash.

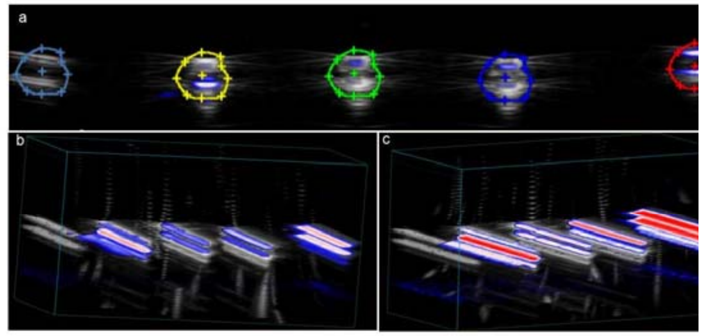

Figure 2. *In vitro* solution-based multi-wavelength PA test (680nm/800nm) with Alexa680-peptide-GNC800. a) 2D PA/US images. From left to right: DI water, probe+enzyme w/o wash, probe control, GNC control, probe+enzyme+wash (GNC); b) 3D images under 680 nm optical stimulation; c) 3D images under 800 nm optical stimulation. Samples were contained in PE tubes.

P1-A8 - MSD: Novel Medical Devices

Exhibit Hall

Thursday, September 7, 2017, 9:30 am - 4:00 pm

Chair: **Enrico Boni**
University of Florence

P1-A8-1

Simulation, Design and Implementation of External Mechanical Vibration for Shear Wave Elastography Imaging

Heng Yang[1], Man M Nguyen[2], Sheng-Wen Huang[2], Vijay Shamdasani[3], Hua Xie[2], Brian W. Anthony[1]; [1]*Massachusetts Institute of Technology, Cambridge, MA, USA;* [2]*Philips Research North America, Cambridge, MA, USA;* [3]*Philips Healthcare, Bothell, WA, USA*

Background, Motivation and Objective

Ultrasound shear wave elastography (SWE) imaging is commercially available on expensive systems. ARF-based shear wave generation requires complex electronics and may induce thermal stress to the tissue. There is need and interest to develop external mechanical vibration (EMV) as a low-cost approach to generate shear waves. Commercial development of mechanical vibration using a single-element transducer has been successful but lacks 2D imaging as guidance. Here we present the simulation, design and implementation of a new way of performing external mechanical vibration that could be adopted by commercial ultrasound probes for SWE imaging.

Statement of Contribution/Methods

Fig. 1a shows the simulation model of two solid balls vibrating on top of cylindrical deformable tissue created using ABAQUS (Dassault Systèmes, France). Due to symmetric geometry, only a quarter of the tissue needs to be analyzed, with the boundary conditions set to be symmetric. A single period of 50Hz sinusoidal vibration with 2mm peak-to-peak amplitude is applied and the following local displacements are extracted to study the propagation of shear waves. We focus on the center plane, which goes through the middle point of the connecting line of two balls perpendicularly. Displacements from 9 lines of nodes are extracted, with increasing distances from the center axis of the plane. The elasticities of the cylinder are set to be 4kPa, 12kPa and 25kPa to examine shear wave propagation inside different materials.

Results/Discussion

Fig. 1b plots local displacements of line 1 and line 5 for 4kPa and 12kPa materials. To calculate shear wave speed, first the distances from nodes to contact point B, which are shear wave travelling distances, are calculated, then the vibration time-to-peaks are found, after which a linear regression between time-to-peaks and travelling distances is performed to estimate wave speed. Results show accurate consistency between measured and real elasticities, proving spherical shear wave fronts and the speed estimation method is robust. The external mechanical vibrator with balls is custom fit to a commercial probe, as shown in Fig. 1c. Current work includes robust control of the vibrator, data collection to validate the performance, and ergonomic design refinements.

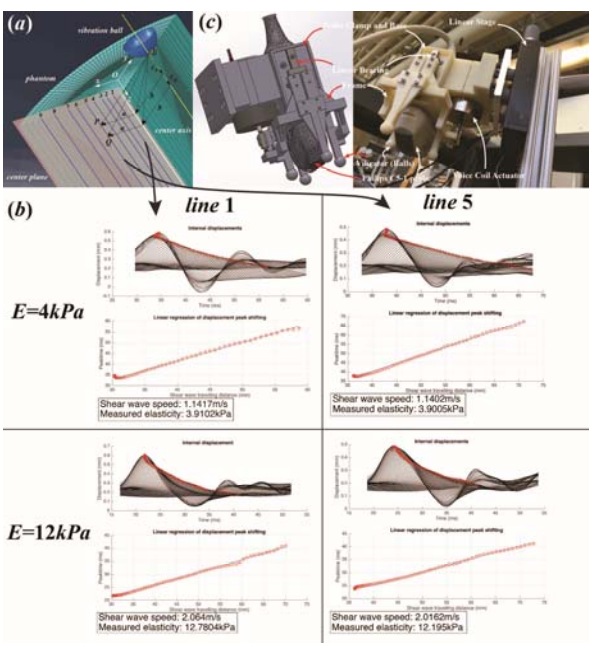

P1-A8-2

Needle Guidance Using Laser Generated Leaky Acoustic Waves

Yi-An Wang[1], U Wai Lok[1], Pai-Chi Li[1]; [1]*National Taiwan University, Taipei, Taiwan*

Background, Motivation and Objective

Needle guidance using B-mode ultrasound is performed to visualize both anatomical structures and the needle position in clinical applications such as tissue biopsy and drug delivery. However, the transducer-needle orientation is limited due to reflection of the acoustic waves. Last year, we proposed a method to exploit the use of leaky acoustic waves for needle visualization. The method uses laser pulses irradiating on the top of the needle to generate acoustic waves. These acoustic waves propagate along the needle surface which then leak into surrounding medium that can be detected by a ultrasound transducer. The needle position can be calculated based on phase velocities of two different wave modes. The objective of the current research is to further investigate performance of the proposed method and to develop improvement schemes to overcome previous limitations.

Statement of Contribution/Methods

Different needle sizes generate leaky waves of different frequencies. In addition, depending on needle positions and angles, the leaky waves that can be detected are also associated with different modes of the acoustic waves with different speeds in the needles. This has been taken into account in our scheme for robust estimation of needle orientation and position.

Results/Discussion

The proposed method was tested experimentally with an ultrasound array system (Prodigy, S-Sharp, New Taipei City, Taiwan) with a 6.4MHz linear array and a 1064 nm laser (LS-2132U, LOTIS TII, Minsk, Belarus). No optical scanning is required. We inserted different needles in a plastic phantom, observed the detectability for angles from 10 to 70 degrees and depths from 10 to 60 mm. As shown in the figure (B-mode images with red lines representing estimated needle positions) and the table (different needle sizes, angles and estimation errors), this method can achieve a maximum detectable angle of 30 degrees at a depth 30 mm. Furthermore, this method can be applied to needles with different diameters. In summary, the experiments agree with our theory with sufficient accuracy for various clinical applications.

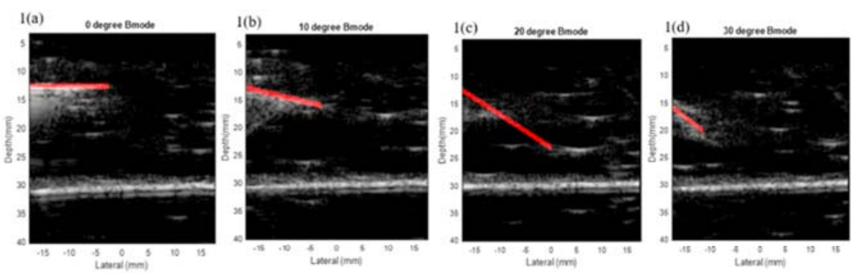

	Depth (mm)	Inserted Angle	Detected Angle	Error (%)
25G (0.5 x 25 mm)	13.5	15	17.71	18.067
24G (0.55 x 25 mm)	13.5	15	14.48	3.467
23G (0.6 x 30 mm)	13.5	15	14.73	1.800
22G (0.7 x 38 mm)	13.5	15	12.39	17.400
18G (1.2 x 38 mm)	13.5	15	14.43	3.800

P1-A8-3

A Study for Real-time B-Mode Imaging Using 100-MHz-Range Ultrasound through a Fused Quartz Fiber

Tkakasuke Irie[1,2], Masakazu Sato[1], Norio Tagawa[2], Masasumi Yosizawa[3], Tadashi Moriya[2]; [1]*Microsonic co., ltd., Tokyo, Japan,* [2]*Tokyo metropolitan university, Japan,* [3]*Tokyo metropolitan college of industrial technology, Japan*

Background, Motivation and Objective

The tissue diagnosis in the current pathological examination has two drawbacks. (1) It takes time, and (2) it gives burden on the patient. The main objective of the study is to enable an operator to observe directly microscopic image of the tissue in real time without taking out the tissue sample from the patient. To achieve the objective, we are developing a needle-type ultrasonic microscope that uses a thin fiber as an ultrasound probe.

Statement of Contribution/Methods

We have reported that the microscopic C-mode and B-mode images of the tissue samples were obtained using the focused ultrasound beam radiated from the quartz fiber. In this paper, a method to obtain the real-time B-mode image and the experimental results are described (Fig.1 and 2). The ultrasound beam is focused by lens, and is reflected at right angle by the mirror (Fig.1). The B-mode image is obtained by moving the fiber up and down. In the experiment, we measured the focal point of the ultrasound beam using the reflected echo from a stainless steel plate in water. Then, the stainless steel plate was moved to the vertical direction (Fig.2). We performed the B-mode imaging of a stainless steel mesh with 13 µm wire in diameter in order to estimate the spatial resolution. The scanning of ultrasound beams was performed with 10 µm intervals in the single direction. The stainless steel mesh was placed at the focal point of ultrasound beam in water.

Results/Discussion

The ultrasound beam was reflected at right angle by the mirror. The focal point of the ultrasound beam was approximately 1.25 mm from the end of the fiber. As the results, the B-mode image of the stainless steel mesh was obtained. The spatial resolution of the image was approximately up to 13 µm. Next, we will obtain the B-mode image of tissue samples in real time.

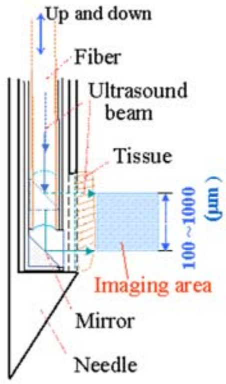

Fig. 1 Scanning system for B-mode imaging using needle-type ultrasound probe

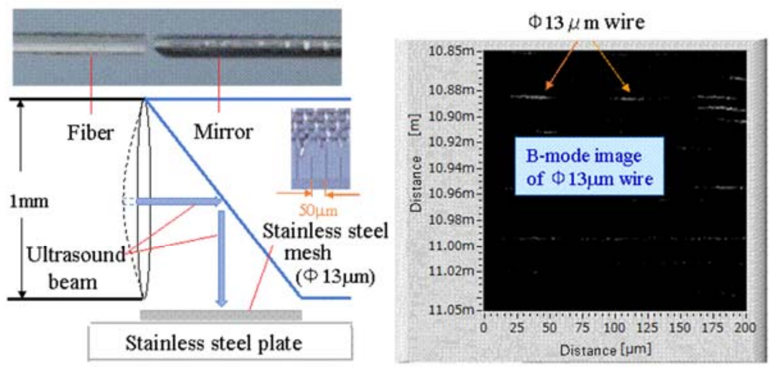

Fig. 2 Reflection of ultrasound beam at right angle (left) and B-mode image of stainless steel mesh (right)

P1-A8-4

Ultrasonic Imaging Research Platform with GPU Based Software Focusing

Chun Duck Park[1], Baek Sop Kim[1], Seong Ho Chang[2], Sung Jae Kwon[3], **Mok Kun Jeong[4]**; *[1]Computer Engineering, Hallym University, Korea, Republic of, [2]Waygence Co. Ltd., Korea, Republic of, [3]Medical IT Engineering, Daejin University, Korea, Republic of, [4]Electronic engineering, Daejin University, Korea, Republic of*

Background, Motivation and Objective

We have designed and implemented an ultrasonic imaging research platform that performs all signal processing including beamforming, using software on a GPU. Software-based approach on the GPU is expected to reduce the hardware complexity and offer the advantages of flexibility and rapid implementation even if there is any future change in the requirements for ultrasound imaging applications. An operating software was developed on a PC that can control RF data acquisition hardware to accommodate ultrasound images of various formats.

Statement of Contribution/Methods

The implemented hardware system consists of an 128-channel transmit and receive analog front-end to sample and store analog echo data, a unit using PCI Express 2 that transfers the data to a PC, a GPU (GTX980, NVIDIA) card responsible for receive focusing and image processing. The PC controls all the hardware with the software developed in C++ under the Windows operating system. The transmit and receive focusing as well as image processing was implemented using CUDA on the GPU for conventional scan line based imaging, two-way dynamic focusing in conventional scan line based imaging, multiple scan line imaging, plane wave based synthetic focusing, and color Doppler imaging.

Results/Discussion

Ultrasonic images were acquired using a 128-element linear array transducer with a 5.5-MHz center frequency (L4-7). All computations including beamforming with 128-channel RF data were performed in real time on the GPU. Conventional scan line based images and plane wave images, each consisting of 256 scan lines, can be processed at a rate of 15 fps and 200 fps, respectively. Two-way dynamic focusing in conventional scan line based images and plane wave based synthetic focusing were accomplished without a reduction in frame rate. By introducing a multiple scan line imaging technique, we obtained a frame rate of more than 60 fps. In the case of Doppler imaging using plane wave, using a PW Doppler technique resulted in cleaner color Doppler images over a full imaging area. Depending on the transmit and receive mode, a variety of experimental data acquisition conditions and various filter parameters can be changed in real time in the graphical user interface, and the RF data can be stored in a hard disk without a limit on the number of frames. Since the software for operation and signal processing can be flexibly varied, the developed system is a very useful platform for ultrasound image acquisitions.

P1-A8-5

A Micro Self-Spin Electromagnetic Actuator for Intravascular Ultrasound (IVUS) Imaging Application

Jue Peng[1,2], Lucai Ma[1,2], Hu Tang[1,2], Siping Chen[1,2]; *[1]National-Regional Key Technology Engineering Laboratory for Medical Ultrasound, Department of Biomedical Engineering, School of Medicine, Shenzhen University, Shenzhen, China, People's Republic of, [2]Guangdong Key Laboratory for Biomedical Measurements and Ultrasound Imaging, Department of Biomedical Engineering, School of Medicine, Shenzhen University, Shenzhen, China, People's Republic of*

Background, Motivation and Objective

Current IVUS probe utilizes an outer proximal motor and a flexible drive shaft transmitting rotational motion through the bending vessel segment. However, the load-bearing shaft through the long bending vessel generally rotates at unstable speed, leading to image distortions. One way to overcome the drawback is to develop a self-spin transducer driven by a micro motor inside the probe. In this study, we present an electromagnetic micro-motor with uniform rotation for minimally invasive medical applications. The schematic cross-sectional view is shown in Fig.1(a) (Detail information in independent patent PCT/CN2015/074855).

Statement of Contribution/Methods

A permanent magnet synchronous motor (PMSM) with 6 mm length and 1.2 mm outer diameter was fabricated. The micro motor consists of two staggered coils as the stator and a permanent magnet placed in a thin-wall tube as the rotor. Fig.1(b) shows a photograph of the fabricated electromagnetic motor. The two coils have the dimensions that just covers a half of the peripheral of the tube and are dislocated for 90 degrees on the thin-wall tube. When two sinusoidal currents with phase difference of $\pi/2$ are applied to the two coils, a rotating magnetic field is generated to drive the two-pole permanent magnet to rotate. We simulated the rotating magnetic field and estimated the torques at different turning speeds by a finite element method (FEM). Fig.1(c) shows the simulation result of the rotation magnetic field.

Results/Discussion

The transient motions of the motor at driving frequencies of 30 Hz, 50 Hz and 70 Hz were captured by a high speed camera with 400 FPS respectively. The initial torque of the motor was also measured as 3.2 μNm with a driving current of 0.1 A. The maximum rotation speed we were able to achieve reached 286 RPS (17160 RPM) at 0.5 A. Tab.1 shows a comparison of the proposed motor with prior arts. In conclusion, the proposed micro motor shows evident advantages in small size, relatively high torque and speed, stable rotations, and is a promising candidate for minimally invasive probe applications such as IVUS.

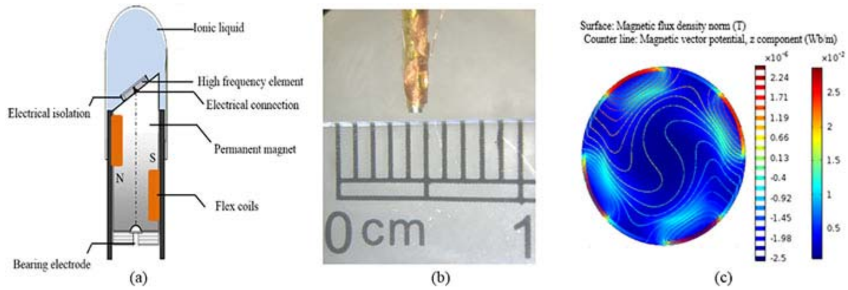

Fig. 1. (a) The schematic cross-sectional view. (b) A photograph of electromagnetic motor. (c) A simulation of rotation magnetic field by FEM.

Tab. 1 A comparison of the proposed motor with prior arts

Research Group / Parameter	Piezoelectric motor		Electromagnetic motor		
	Tomoaki Mashimo	Tanabe et al.	Proposed motor	Wang et al.	H.Lehr
Maximum speed(rpm)	1700	8000	17160	218400	100000
Size(Diameter× Length) (mm× mm)	1.0×1.0	1.4×5.0	1.2×6.0	1.0 ×2.0	1.9 ×5.0
Torque (μNm)	10	21	3.2	0.25~0.27	5

P1-A8-6

Design of a 2D Sparse Array Transducer for Integration into an Ergonomic Transcranial Ultrasound System

Xiaotong Li[1], Anthony Gachagan[1], Paul Murray[2]; [1]*Electronic and Electrical Engineering, Centre for Ultrasonic Engineering, Glasgow, United Kingdom,* [2]*Electronic and Electrical Engineering, Centre for Signal and Image Processing, Glasgow, United Kingdom*

Background, Motivation and Objective

Transcranial Doppler Ultrasound (TCD) is a non-invasive approach that has been used in both diagnosis and therapy of stroke. However, current TCD devices are highly operator dependent and a 2D sparse array transducer can help reduce the operator dependency with its improved imaging and focusing capabilities. This paper compares the potential of three aperiodic sparse array configurations: random array; sunflower spiral array; and log spiral array for application to TCD.

Statement of Contribution/Methods

Transcranial Doppler Ultrasound (TCD) is a non-invasive approach that has been used in both diagnosis and therapy of stroke. However, current TCD devices are highly operator dependent and a 2D sparse array transducer can help reduce the operator dependency with its improved imaging and focusing capabilities. This paper compares the potential of three aperiodic sparse array configurations: random array; sunflower spiral array; and log spiral array for application to TCD.

Results/Discussion

Simulation results from the parametric sweep for each array configuration demonstrate that a compromise between PSL and ISLR is required to select a transducer configuration for fabrication and further evaluation. The PSL and ISLR for the final selected array configurations are: -20.53dB/2.82dB for log spiral array; -16.17dB/1.88dB for sunflower spiral array, and -15.95dB/4.46dB for random array. These evaluation results demonstrate that the log spiral array configuration has desirably low PSL relative to the others, while the sunflower spiral array performs better in terms of ISLR. Considering this design evaluation, prototype arrays based on a log spiral layout are being manufactured, with Figure 1 illustrating the physical array element layout. Two fabrication methods are currently being pursued: electrode pattern integrated onto conventional 1-3 piezocomposite; and individual elements incorporating piezoceramic fibre bundles. Full transducer characterisation and evaluation for both array devices will be presented.

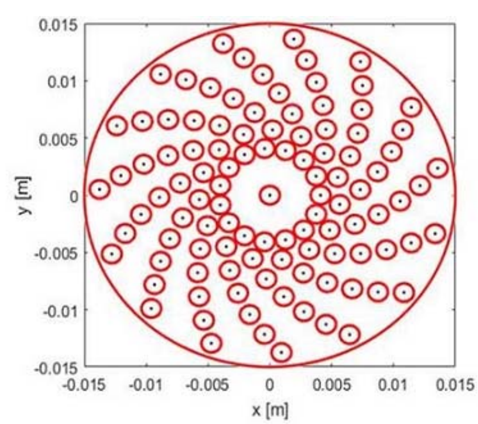

***Figure 1:** Selected Log Spiral configuration with 15 arms and 7 elements per arm. An additional element is placed in the centre for alignment purpose.*

P1-A8-7

A Delayed-Excitation Imaging Method for Micro-Ultrasound

Peitian Mu[1], Jingjing Xia[1], Xingyin Wang[1], Congzhi Wang[1], Yang Xiao[1], Ge Yang[1], Lei Sun[2], Hairong Zheng[1], Weibao Qiu[1]; [1]*Paul C. Lauterbur Research Center for Biomedical Imaging, Shenzhen Institutes of Advanced Technology, Chinese Academy of Sciences, China, People's Republic of,* [2]*Interdisciplinary Division of Biomedical Engineering, The Hong Kong Polytechnic University, Hong Kong, China, China, People's Republic of*

Background, Motivation and Objective

High-frequency ultrasound (>20 MHz) imaging has gained widespread attention due to its high spatial resolution being useful for basic cardiovascular and cancer research involving small animals. The sampling rate of the analog-to-digital converter in a high-frequency ultrasound system usually needs to be higher than 120-MHz to satisfy the Nyquist requirement. However, the sampling rate is typically within the range of 40-60 MHz in a traditional ultrasound system, which is not compatible with high-frequency ultrasound imaging. We propose a delayed-excitation method in this study for performing high-frequency ultrasound imaging with a traditional data acquisition scheme.

Statement of Contribution/Methods

In this method, the transmitted pulse is delayed by a certain time so that the ultrasound echo data are aligned into high-sampling-rate slots. The sampling clock shown in the Fig. 1 is the sampling rate of the ADC in a traditional ultrasound scanner. Fig. 1(a) shows that two excitations are used in composing one sequence of echo data. The second excitation pulse is delayed by half a cycle, which therefore results in a different sampling position for the ultrasound echo data. The echo signal is acquired at four different positions over one full clock cycle by two-times acquisition, so that the emulated high-frequency clock is two times higher than the ADC clock. Similarly, the emulated sampling rate is four times higher than the ADC clock when the delay was set to one-quarter of the ADC clock, and so four-times pulse excitation and data acquisition are employed (shown in Fig. 1(b)).

Results/Discussion

A porcine small-intestine specimen was used for *in vitro* imaging evaluations. The specimen was cut into pieces and gently unfolded by a holder. The transducer was scanned over the tissue sample immersed in a water tank to obtain the cross-sectional ultrasound images shown the right side of the figure. The images were distorted due to the low sampling rate, but all were successfully recovered by applying the delayed-excitation sampling scheme. These measurements were made with a dynamic range of 50-dB. Different layers of the lumen wall could be clearly identified when using the proposed imaging method. The test results demonstrate that the proposed method allows high-frequency ultrasound imaging to be performed by a traditional ultrasound sampling system.

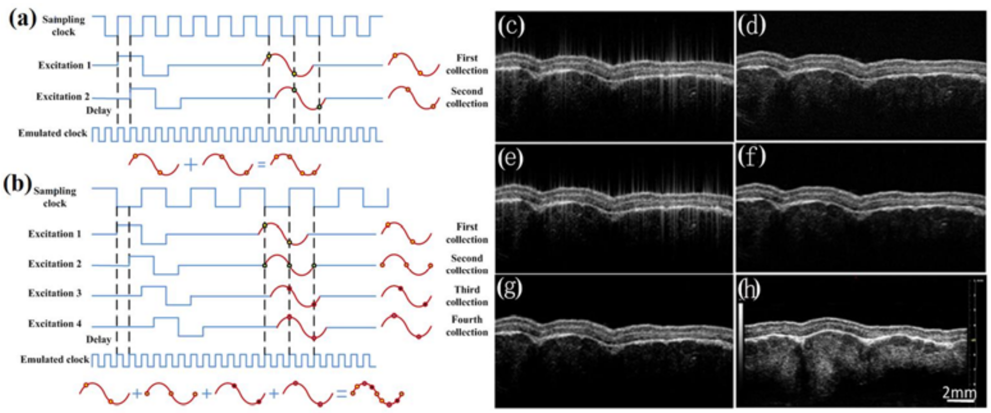

Fig. 1. Principle of delayed-excitation imaging methodology with different ADC sampling rates and imaging results. (a) An emulated sampling rate of two times higher than the sampling rate of the ADC implemented using a half-cycle pulse delay. (b) An emulated sampling rate of four times higher than the sampling rate of the ADC implemented using a quarter-cycle pulse delay.On the right is images of the porcine small-intestine specimen. (c) Image acquired using the 40-MHz ADC. (d) Combined image for four-times acquisition. (e) Image acquired using the 80-MHz ADC. (f) Combined image for two-times acquisition. (g) Image acquired using the 160-MHz ADC. (h) Image acquired using the Vevo 2100 system.

P1-A8-8

A Multi-channel Doppler Ultrasound and Near-Infrared Spectroscopic Patch for Quantitative Monitoring of Cardiopulmonary Resuscitation

Sangyeon Youn[1], Jihun Kim[1], Kijoon Lee[1], Jae Gwan Kim[2], Jae Youn Hwang[1]; [1]*DGIST, Daegu, 27 - Daegu Gwangyeogsi, Korea, Republic of,* [2]*GIST, Korea, Republic of*

Background, Motivation and Objective

When cardiac arrest occurs to patients, the emergency medical service(EMS) is a top priority for saving their life or avoiding the critical injury to the brain and internal organ. Among the EMS, cardiopulmonary resuscitation (CPR) is crucial to save their life. The implementation of CPR is usually determined by the carotid artery palpation method. However, the method has several shortcomings in the determination whether the CPR is implemented to patients as shown in the followings: 1) its detection accuracy is dependent on a person so that unnecessary CPR could be applied to a patients; 2) cerebral blood flow can be reduced by misdemeanor of a non-expert operator; 3) unnecessary CPR may damage a rib or internal organs. Therefore, a quantitative tool to determine the implementation of CPR may beneficial to save the life of patients under such emergent situation and avoid the side effects by unnecessary CPR. In this study, we thus demonstrate a multi-channel Doppler ultrasound and near-infrared spectroscopic patch which allows to obtain Doppler parameters and blood oxygen concentration (SpO2) on the carotid artery for implementing a CPR and quantitative monitoring of CPR quality for patients.

Statement of Contribution/Methods

A novel multimodal patch including the triple-pairs ultrasound transducers for ultrasound Doppler measurements and triple-pairs of diodes and photodetectors for NIRS. The center frequency of ultrasound elements were around 5MHz. For measurements of Doppler signals from carotid artery with cardiac arrest, a conventional CW Doppler method was adopted. In addition, to measure SpO2, two LEDs at 730nm and 850nm and one photodetector were incorporated into the multimodal patch. For verification of the patch, phantom study was carried out and then Doppler signals and SpO2 from the carotid artery were measured using the patch. In particular, an optimization channel selection method was applied to the patch to extract reliable Doppler signals and SpO2 in real emergence situation.

Results/Discussion

We fabricated the multimodal patch which is capable of measuring doppler signals as well as SpO2 simultaneously for determination of CPR implementation and quantitative monitoring of CPR for cardiac patients. In the phantom experiment for verification of the system's performance, both the animal blood flow and oxygen contractions were succesfully monitored. In addition, using the multimodal patch, quantitative Doppler signals and SpO2 from human carotid artery were simultnesouly measured. In particular,in the clinical test,it was found that the channel selection method applied to the patch offered the improved SNR in the measurements of Doppler signals and SpO2. The results shown in this study demonstrated that the develop multimodal patch has the potential as a novel tool for determination of CPR implementation as well as quantitative monitoring of CPR effects on patients with cardiac arrest in the uncertain medical emergency situation.

P1-A9 - MSP: Optimizing Imaging Performance

Exhibit Hall

Thursday, September 7, 2017, 9:30 am - 4:00 pm

Chair: **Jianwen Luo**
Tsinghua University

P1-A9-1

USSR: An UltraSound Sparse Regularization Framework

Adrien Besson[1], Dimitris Perdios[1], Florian Martinez[1], Marcel Arditi[1], Yves Wiaux[2], Jean-Philippe Thiran[1,3]; [1]*Signal processing laboratory (LTS5), Ecole Polytechnique Fédérale de Lausanne, Lausanne, VD, Switzerland,* [2]*Institute of sensors, signals, and systems, Heriot-Watt University, Edinburgh, United Kingdom,* [3]*Department of Radiology, University Hospital Center (CHUV) and University of Lausanne (UNIL), Lausanne, VD, Switzerland*

Background, Motivation and Objective

In pulse-echo ultrasound (US) imaging, recovering the tissue response from the element-raw data can be formulated as an ill-posed inverse problem. Standard methods rely on the delay-and-sum (DAS) which gives a fast, but rough, estimated solution of the problem. An alternative consists in using regularization approaches, which exploit a formulation of a measurement model and additional prior knowledge to leverage the ill-posedness of the problem. Among the regularization methods, sparse regularization has recently grown many interest [Besson et al. UFFC16, David et al. JASA15, Szasz et al. UFFC16]. However current methods require a tremendous amount of memory and are unachievable in realistic US imaging applications.

Statement of Contribution/Methods

The USSR framework aims at solving the problem: $m=A(\gamma)+n$, where m are the element-raw data, γ is the tissue response and A is the measurement model. It is composed of a fast, matrix-free measurement model A and its adjoint $A^\dagger$, based on the pulse-echo-spatial-impulse-response model. It consists in three different techniques which rely on sparsity of US images in well-chosen models to recover a better estimate of the tissue response. Sparse regularization (SR) is used for enhanced image reconstruction. Compressed beamforming (CB) restores high quality images from fewer raw-data. Beamforming-deconvolution solves an image reconstruction and a deconvolution problems simultaneously and recovers the tissue-reflectivity-function from the raw-data

Results/Discussion

Fig. 1(a) shows the timings corresponding to the application of A, $A^\dagger$ and the sparsifying model (8 wavelet transforms), calculated on an image of 1024x128 pixels, on a NVIDIA Titan X GPU card. One iteration of the reconstruction algorithm takes approximately 20 ms. A substantial gain may be achieved by working on acceleration strategies. As an example of USSR, an in vivo carotid, imaged with a Verasonics system (L12-5 50mm, 128 elements, 0.195 mm pitch, 5 MHz central freq., 31.2 MHz sampling freq.) with 1 plane wave (PW) insonification, is reconstructed with SR (Fig. 1(b)) and CB (Fig. 1(c)). CB is achieved with a compression ratio of 4. The compression is performed by applying a subsampled random matrix. A comparison with the DAS reconstruction with 9 PWs, displayed on Fig. 1(d), shows that USSR is able to retrieve high-quality images with 10 to 40 times less data.

	Timing [ms]	%
A	15	75
$A^\dagger$	4	19
Ψ	0.5	2.5
$\Psi^\dagger$	0.5	2.5
others	0.2	1
Total	**20,2**	**100**

(a)

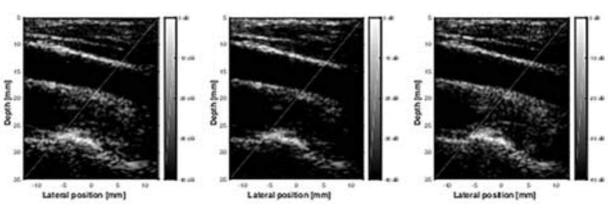

(b) (c) (d)

Figure 1: (a) Computation times of the forward and adjoint models A and $A^\dagger$ and of the Db1-8 wavelet transforms and inverse transforms Ψ and $\Psi^\dagger$; (b) Carotid reconstructed with SR for 1 PW ; (c) Carotid reconstructed with CB (compression ratio of 4) for 1 PW; (d) Carotid reconstructed with DAS algorithm for 9 PWs.

P1-A9-2

Beam Domain Adaptive Beamforming using Generalized Side Lobe Canceller with Coherent Factor for Medical Ultrasound Imaging

Acácio Zimbico[1], Diogo Granado[2], Fábio Schneider[3], Joaquim Maia[3], **Amauri Assef**[4], Daniel Pipa[5], Eduardo Costa[6]; [1]*CPGEI, UTFPR, Curitiba, PR, Brazil,* [2]*CPGEI, UTFPR, Curitiba, Brazil,* [3]*DAELN/PPGEB/CPGEI, UTFPR, Curitiba, Brazil,* [4]*DAELT/PPGSE/CPGEI, UTFPR, Curitiba, Brazil,* [5]*DAELN/CPGEI, UTFPR, Curitiba, Brazil,* [6]*DEB/FEEC/CEB, UNICAMP, Campinas, Sao Paulo, Brazil*

Background, Motivation and Objective

As the medical ultrasound signals are not stationary, the radiation pattern of the corresponding input data does not have a specific shape. Thus, their reconstruction using adaptive beamformer (BF) become indispensable in order to improve the quality of the image. Generalized Side Lobe Canceller (GSC) is a robust realization against clutter and interference, resulting from an elegant representation of Linearly Constrained Minimum Variance (LCMV) and Linearly Constrained Minimum Power (LCMP) BF. As medical ultrasound imaging uses huge arrays, we emphasize transformations in the reduced spaces in order to diminish computational complexity, while achieving similar or higher levels of signal reconstruction quality. Such as array space (AS), GSC is realized in beamspace (BS). In order to enhance the quality of the reconstructions, we apply the coherent factor (CF), defined as an index of focusing quality determined from echo channel data in which the amplitude of image pixel is weighted.

Statement of Contribution/Methods

We tested the BFGSC-CF method using experimental raw data acquired from a 84-317 Multi-purpose Tissue/Cyst Phantom (Fluke Biomedical), with the constant f-number of 0.75 and using a Verasonics ultrasound system with a 6.25 MHz central frequency 128-element linear array transducer L11-4v, 0.308 mm pitch, 60% fractional bandwidth and 40 MHz sampling rate. The performance evaluation of our proposed method was done using the lateral resolution (LR), as presented in the green box of Figure 1, Panel B (a), using Full Width at Half Maximum (FWHM) (see plots in Figure 1 Panel A) and Peak Side Lobe Level (PSL), red boxes in Panel B (a). For target/background analysis we used Contrast (CR).

Results/Discussion

For LR we found values of 1.70, 1.16, 0.94, 0.86 and 0.69 mm for Delay-and-Sum (DAS), MV, GSC, EGSC, and BEGSC-CF (7 Beams), respectively. For PSL values of -8.64, -3.51, -3.07, -0.83, -0.72 dB were observed. In similar condition, values of contrast of 11.56, 11.25, 13.03, 13.76 and 13.96 dB were found, respectively. The corresponding images following the same order are presented in Figure 1, Panel B (a)-(e). Based on these results, we can conclude that our proposed method CBGSC allows improvements in terms of array clutter suppression capabilities.

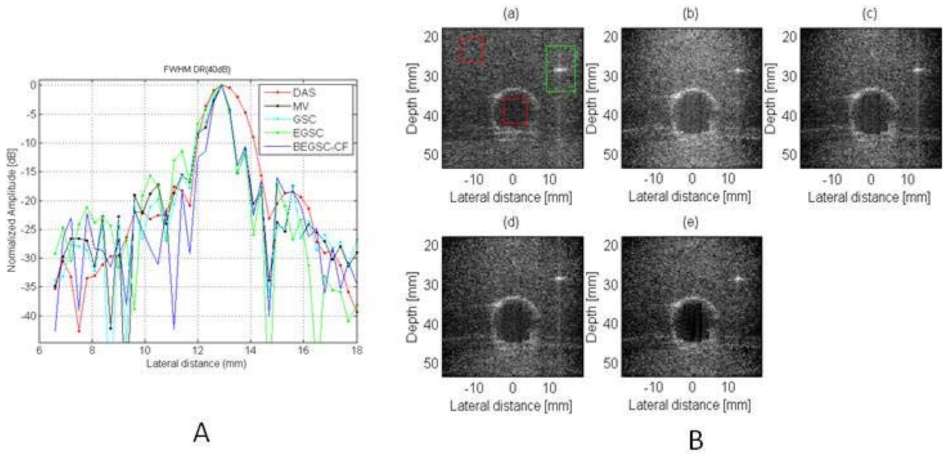

Figure 1: Panel (A) depicts the plots of LR and (B (a)-(e)) the resulting images for DAS, MV, GSC EGSC and BEGSC-CF methods, respectively. The LR was calculated with 40 dB DR while CR with 60 dB.

P1-A9-3

Estimation of Phase Velocity and Attenuation of Visco-elastic Plate with Adaptive Beamforming Technique for Cortical Bone Assessment

Shigeaki Okumura[1], Vu-Hieu Nguyen[2], Hirofumi Taki[3], Toru Sato[1]; [1]*Kyoto University, Kyoto, Japan,* [2]*Université Paris-Est, France,* [3]*Tohoku University, Japan*

Background, Motivation and Objective

The technique of non-invasive cortical bone quality assessment using ultrasound axial transmission has attracted considerable attention. Estimating the phase velocity and the attenuation of the absorbing plate will assist the assessment. Among several techniques proposed for these purposes, many employ either a thresholding process or a peak search process. The thresholding process uses the intensity of the guided wave to distinguish the noise from the signal, but may dismiss weak intensity modes. The peak search process extracts the phase velocity and attenuation from the estimated intensity in the frequency and wavenumber domains; however, this process costs a large computational load. To overcome these difficulties, we propose a novel algorithm that uses an adaptive beamforming technique.

Statement of Contribution/Methods

We expand the estimation of signal parameters via rotational invariance technique (ESPRIT) to estimate the phase velocity and attenuation. The ESPRIT algorithm is a classical high-resolution beamforming technique that can measure the phase velocity and power of arriving signals without a peak search. The original ESPRIT algorithm employs thresholding to distinguish the signal from noise. To remove this process, we situate multiple sub-arrays in the whole array and apply the ESPRIT method. We evaluate the correspondence between the results with different sub-arrays and extract reliable phase velocities. Then, we compare the estimated powers with adjacent sub-arrays to estimate the attenuation.

Results/Discussion

The proposed method is evaluated by numerical simulations. We use one transmitter, 28 receivers, and a 5-mm-thick cortical plate with P and S wave velocities of 4430 and 2120 m/s. The attenuation of the P and S waves is 320 and 400 dB/MHz/m. The figure shows the estimated phase velocity and attenuation. The estimation error of the phase velocity and attenuation is 3.6 m/s and 16 dB/m. Because the attenuation is small, we assume the phase velocity of the viscoelastic plate is very close to that of the elastic plate. As the proposed method estimates the phase velocity and attenuation accurately, we believe this method is suitable for bone quality assessments.

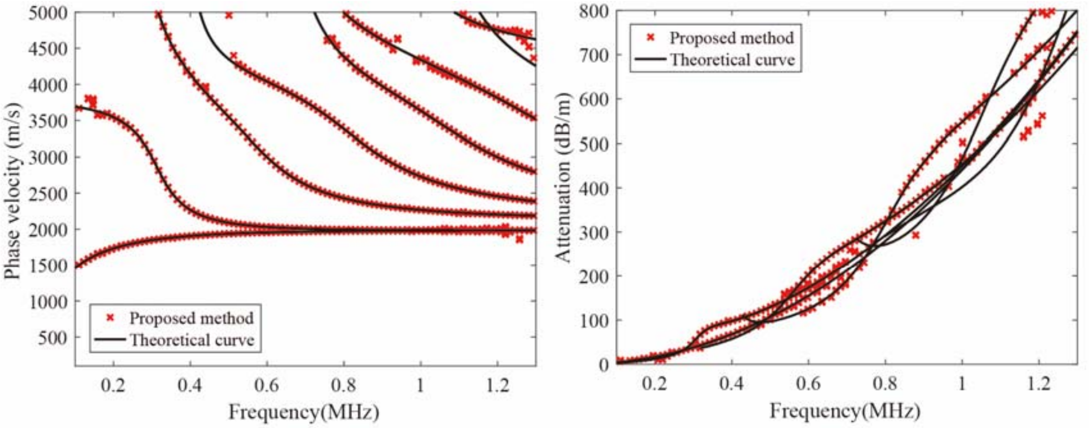

Estimated phase velocity and attenuation. The black solid lines show the theoretical curve. The red cross marks show the output of the proposed method.

P1-A9-4

Simultaneous Coded Plane Wave Imaging: Implementation on a Research Echograph

Denis Bujoreanu[1], Adeline Bernard[1], Barbara Nicolas[1], Hervé Liebgott[1], Denis Friboulet[1]; [1]*Univ.Lyon, INSA-Lyon, Université Claude Bernard Lyon 1, UJM-Saint Etienne, CNRS, Inserm, CREATIS UMR 5220, U1206, F-69100, LYON, France*

Background, Motivation and Objective

In our previous work, published in the ICASSP 2017 conference we proposed an imaging technique called Simultaneous Coded Emission (SCE) of plane waves. SCE borrows ideas from plane wave Coherent Compounding (CC) and channel estimation in telecommunication systems, and has the potential to yield similar to CC image quality at significant higher frame rates. Improving over our previous work, we address in this paper the feasibility of the SCE on a real acquisition system, and show an implementation of SCE on the Ultrasound Advanced Open Platform (Ula-OP).

Statement of Contribution/Methods

Simply put, in the concept of SCE, several plane waves are emitted simultaneously each of them carrying a pseudo-orthogonal code. In our previous work we showed that the received signal at the *i* element of the transducer can be written as $\mathbf{y}_i = Ag_i + v_i$ where A is the coding matrix and g_i are the signals that can be beamformed in order to obtain the corresponding images. Since in in-vitro acquisition the level of observation noise v_i is unknown, in this work we propose to solve the above inverse problem using an Linear Square Estimator (LSE) based on the Singular Value Decomposition (SVD) of the coding matrix A. The SVD based LSE allows decreasing the condition number of the inverse problem which implies a better stability of the solution to acquisition noise.

Results/Discussion

Experiments have been performed on a cyst phantom with two plane waves (emission angles 4° and -7°) emitted either successively (CC) or simultaneously (SCE). Figure 1 shows the results obtained using CC (Fig. 1A) and SCE (Fig. 1B). For the SCE acquisition, the SVD based solver allows reconstructing the image of the cyst (Fig. 1B) however the final image has a lower quality (CNR=6.02dB) than the corresponding CC image (Fig. 1A, CNR=7.52dB). As shown in Fig. 1C the solver has an optimal point where the tradeoff between the computational error and noise stability is optimal for a certain level of noise (here SNR≈21dB). Since no regularization is used, the overall quality of the image decreases if one wants to increase the frame rate of our method, as shown in Fig. 1D. As a consequence, future work will focus on designing an appropriate regularization technique that will allow increasing the frame rate while preserving the CNR.

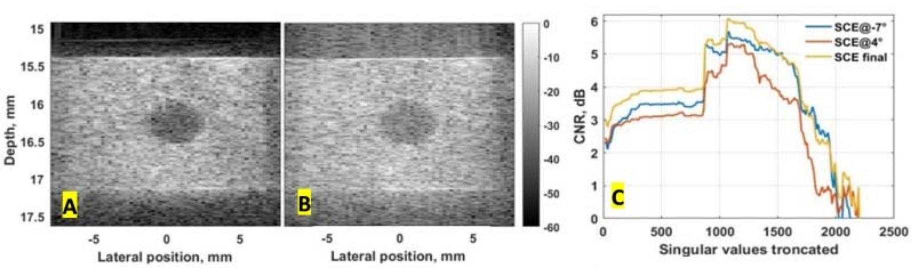

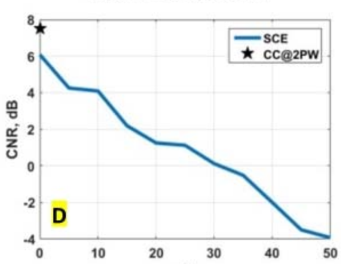

Fig.1: A – Final image obtained using CC (CNR=7.52dB); B – Final image obtained using SCE (CNR=6.02dB); C– Evolution of the CNR as a function of the SVD truncation index; D – Evolution of the CNR as a function of the time gain

P1-A9-5

Fourier-Based Ultrafast Ultrasound Imaging Based on In-phase Quadrature (IQ) Data

Miaomiao Zhang[1], Hervé Liebgott[1], François Varray[1], Denis Friboulet[1], Olivier Bernard[1]; [1]*Univ Lyon, INSA-Lyon, Université Claude Bernard Lyon 1, UJM-Saint Etienne, CNRS, Inserm, CREATIS, Villeurbanne, France*

Background, Motivation and Objective

Ultrafast imaging based on plane wave (PW) / diverging wave (DW) is an active area of research in ultrasound acquisitions because of its capacity of reaching high frame rate. Beamforming of received echoes in Fourier domain provides comparable image quality but lower computational complexity with respect to the conventional DAS approach [Zhang et al., UFFC, 2016]. However, the current state-of-the-art Fourier-based techniques only perform the reconstruction on radio frequency (RF) data. To process less data without loss of information, we adapted in this study the Fourier-based formalism of Lu [Lu et al., UFFC, 1997] to IQ data reconstruction for both PW and DW imaging.

Statement of Contribution/Methods

The original PW imaging method of Lu performs 2D FFT on the received RF signals and remaps the echoes spectrum to obtain the object spectrum, followed by a 2D IFFT to get the beamformed image. We demonstrated in this work that this method can be adapted for IQ data reconstruction by explicitly taking into account the demodulation frequency in the spectrum remapping relation. The proposed method can be easily extended to DW imaging from IQ data by using a space transformation introduced in one of our previous work [Zhang et al., UFFC, 2016]. However, the space transformation introduces time shifts that cause phase rotation and thus degrade compounding strategies. We thus integrated those time shifts into our formalism to compensate for the phase rotation during the reconstruction process.

Results/Discussion

The proposed approach is validated experimentally with an ultrasound phantom (CIRS model: 054GS) with PW / DW insonifications using a standard linear / phased array interfaced with a Verasonics system. The RF data was demodulated and downsampled 4 times to obtain the IQ data. Figure1 shows B-mode images reconstructed from RF data and IQ data using 9 PW / 15 DW in transmission. This results show the feasibility of performing IQ data reconstruction in the Fourier domain. It allows reconstructing the same image quality as from RF data but with 4 times less data samples, thus the beamforming process could be increased 4 times faster.

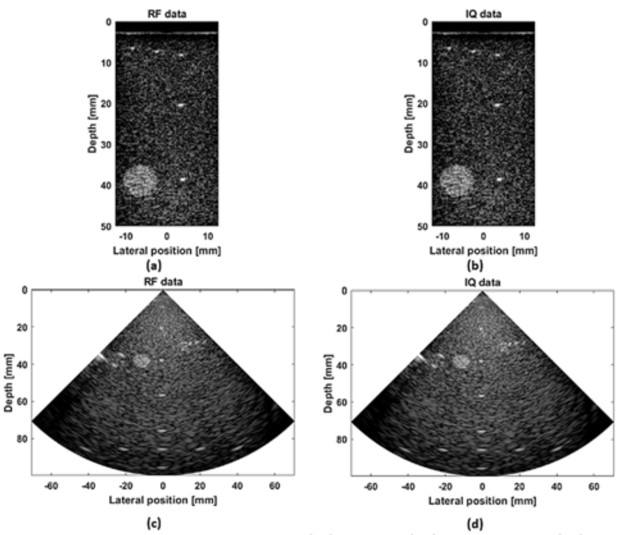

Figure1. Bmode images reconstructed from RF data (a,c) and IQ data (b,d) with 9 plane waves (a,b) and 15 diverging waves (c,d) for compounding, respectively.

P1-A9-6

On an Analytical, Spatially-varying, Formulation of the Point-spread-function with an Application to Deconvolution

Lucien Roquette[1,2], Matthieu Simeoni[1,2], Paul Hurley[1], Adrien Besson[3]; [1]*IBM, Rüschlikon, Zurich, Switzerland,* [2]*Mathematics, EPFL, Lausanne, Vaud, Switzerland,* [3]*Signal Processing Laboratory (LTS5), EPFL, Lausanne, Vaud, Switzerland*

Background, Motivation and Objective

The point spread function (PSF), namely the response of a system to a point source, is a measure of the quality of an ultrasound imager system. It highly depends on the image reconstruction algorithm, and it is usually either crudely estimated by assuming spatial-invariance, or evaluated via simulation, as proposed by Field II, coupled with reconstruction algorithms, such as delay-and-sum (DAS). The lack of an analytical formulation of the PSF inhibits many applications ranging from optimization of apodization schemes, to array-design and deconvolution algorithms.

Statement of Contribution/Methods

Based on the pulse-echo-impulse response model, we propose an analytical formulation of the PSF. This allows to directly compute the radio-frequency (RF) image, corresponding to the DAS algorithm (with or without apodization) for a given transmission scheme, from the continuous tissue reflectivity function (TRF). Formally, our PSF operator, A, acts as follows: $y = A(x)$, where x is the TRF and y is the RF image. The proposed method is compatible with any transmission schemes, such as plane waves, diverging waves, focused waves, and synthetic aperture imaging. In addition, the formulation is grid independent and equipped with fast forward and adjoint operators, making it suitable for iterative reconstructions.

Results/Discussion

A point-reflectors phantom, insonified with a phased-array probe (64 elements, 2.5 MHz central frequency, 9.6 MHz sampling frequency) is used to validate the proposed formulation. Fig. 1(b) displays the resulting image obtained by applying the proposed operator on the phantom. Fig. 1(a) shows the results of DAS beamforming applied on element-raw data simulated on Field II.

The analytical PSF image is notably similar to the one obtained from Field II simulations. Fig. 1 (c) shows an application of the proposed operator. A sparse deconvolution of Fig. 1 (c-Top) is performed, based on classical l_1-minimization with the same regularization parameter for spatially in/variant cases. For the stationary case Fig. 1 (c-Down), the considered

PSF is the one computed at the middle of the image. It cannot achieve proper reconstruction far-away from the center since the PSF rotates along the diverging wave propagation. Fig. 1(c-Middle) shows the results of the deconvolution algorithm with the proposed operator which outperforms the stationary case.

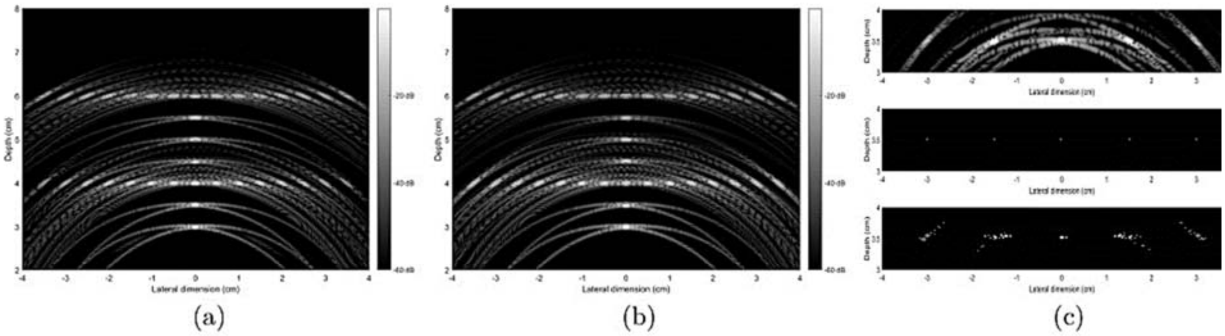

Figure 1: (a) B-mode image of the point-reflectors phantom obtained with DAS algorithn applied on element raw-data simulated with Field II; (b) B-mode image obtained with th proposed method applied on the point-reflectors phantom; (c) (Top) Radio-Frequency image (c) (Middle) Deconvolved image obtained with the proposed operator; (c) (Low) Deconvolve image obtained with the spatially invariant PSF

P1-A9-7

Improved High Axial Resolution Ultrasound Imaging Using Spectral Whitening and Minimum-Variance Based Coherence Weighting

Hong-Sheng Chen[1], Meng-Lin Li[1]; [1]*National Tsing Hua University, Taiwan*

Background, Motivation and Objective

To acquire reliable medical ultrasound images and accurately detect vascular diseases, it is inevitable to improve axial resolution and contrast facilitating clearly definition of depth and thickness of blood vessel walls.

Statement of Contribution/Methods

Here we adapt the minimum-varaince (MV) beamforming plus coherence-factor weighting (MV plus CF weighting) technique to improve axial resolution. The MV method and CF weighting technique are originally proposed to apply over aperture domain data to improve lateral resolution – reducing the mainlobe width and suppressing the sidelobes in the lateral direction. Via the help of spectral whitening, i.e, Wiener filtering here, the MV method can be adapted to be applied to the frequency components which synthesize the signal at a desired depth, minimizing the interference from other depths. In addition, the coherence factor here calculates the ratio of coherent energy to incoherent energy of the frequency components at the desired depth; the CF weighting can be used to further reduce the axial mainlobe width and suppress the axial sidelobes.

Results/Discussion

We have applied the proposed technique to simulated RF A-line data (7.5MHz center frequency, ~27-dB SNR, and two scatterers separated by 0.13 mm in the axial direction). Figure (a) compares the axial mainlobe widths of the original envelope data, the MV method, and the MV plus CF weighting method. Figure (b) shows zoom in picture of figure (a). The axial mainlobe width is greatly reduced with the MV and MV plus CF weighting methods. The MV plus CF weighting method outperforms the MV only method. Via simulation, it is explored that originally the two scatterers cannot be resolved when they are separated by 0.15 mm, whereas the proposed MV plus CF weigthing method can resolve the two scatterers with 0.077 mm apart, indicating ~46% improvement in axial resolution.

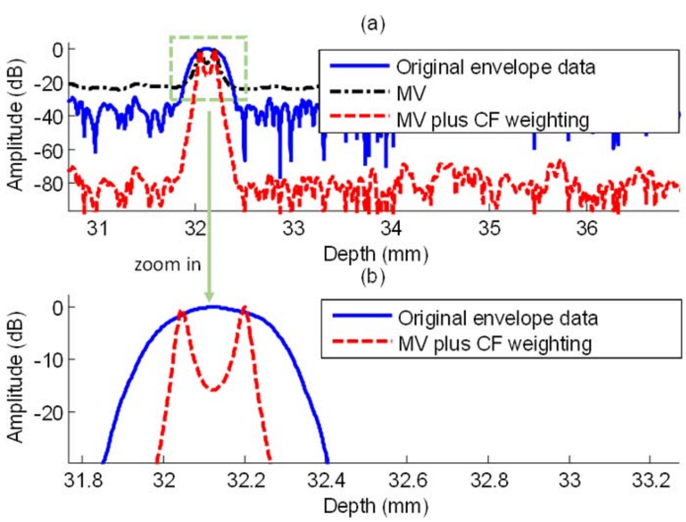

P1-A9-8

Ultrafast Ultrasound Imaging Using a Resolution and Bandwidth Enhancement Technique

Yanis BENANE[1], Roberto Lavarello[2], Christian Cachard[1], François Varray[1], Jean-Michel Escoffre[3], Anthony Novell[3], Emilie Franceschini[4], Olivier Basset[1]; [1]*Univ.Lyon, INSA-Lyon, Université Claude Bernard Lyon 1, UJM-Saint Etienne, CNRS, Inserm, CREATIS UMR 5220, U1206, F-69100, Lyon, France,* [2]*Laboratorio de Imagenes Medicas, Departamento de Ingenieria, Pontificia Universidad Catolica del Perù, Lima, Peru,* [3]*Imagerie et Cerveau, Université François-Rabelais, Inserm, Tours, France,* [4]*Aix-Marseille Université, CNRS, Centrale Marseille, Laboratoire de Mécanique et d'Acoustique, Marseille, France*

Background, Motivation and Objective

The Resolution Enhancement Compression (REC) technique is a coded excitation method developed for improving the axial resolution of ultrasound images. It consists on emitting an amplitude modulated chirp signal that transmits more energy at the frequencies where the ultrasound transducer is less efficient. The focus of this study is to elaborate a new beamforming strategy, which consists of implementing the REC technique in combination with coherent plane wave compounding. The first objective is to get a better performance in term of axial resolution than Conventional Pulse Ultrafast Imaging (CP-UI). The second objective is to demonstrate that in ultrafast imaging, REC offers a larger bandwidth than the one provided by CP-UI.

Statement of Contribution/Methods

Both simulations and experimental setups were performed. Simulations using Field II were conducted with a 128 element array of 8.5 MHz (49% bandwidth at -3 dB). The effective impulse response to be provided by the REC technique was constructed to double the fractional bandwidth (98 % at -3 dB). The linear FM chirp was tapered with a Tukey cosine window with a 20% taper and had 3 µs duration. To evaluate the performance of the Wiener filter compression, a phantom containing 2 point targets spaced 7 mm was imaged using the REC technique with coherent plane wave compounding (13 angles, 2° separation). This configuration was compared with a standard image using a single focal depth at 23 mm. To estimate the broadband performance of the REC technique, the axial resolution obtained was compared to the one given by a conventional pulse steered plane wave emission. A similar setup was experimentally used on the research open platform Ula-Op.

Results/Discussion

Simulations showed an improvement of 26% of the axial resolution with REC-UI compared to CP-UI. A broader power spectrum was also observed for REC-UI (+69%). The experimental results show that REC is capable of properly compressing the data without amplifying the noise (a). The power spectra of the reflection from the wire at a depth of 23 mm is boosted by 21% (at -6dB and -10dB) compared to the conventional approach (c). The axial resolution is also improved for this wire by 16% (i.e., 204 µm for REC-UI and 238 µm for CP-UI) (b). These results suggest that REC and plane waves can be integrated and provide enhanced resolution, boosted bandwidth and faster frame rate than focused echography.

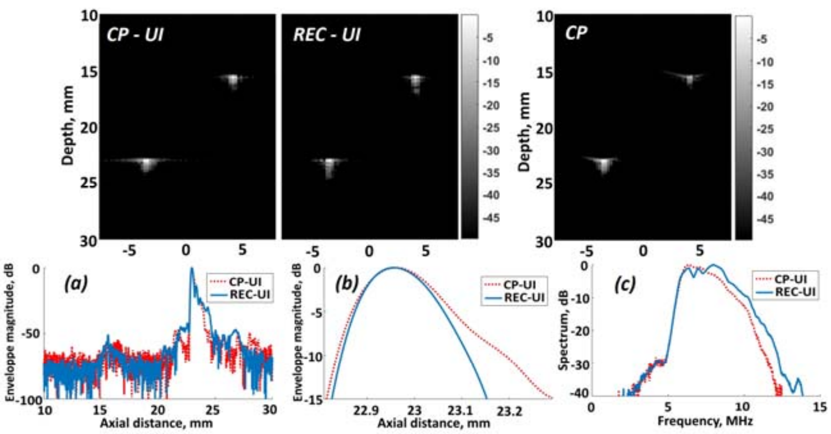

Fig. 1. **Top :** Bmode images obtained with CP and REC using Ultrafast Imaging and with CP using a single focus at 23 mm (respectively **CP-UI, REC-UI** and **CP**).
Bottom : Comparison of performance between REC-UI (solid line) and CP-UI (dashed line) using the A-line corresponding to the wire at a depth of 23 mm : **(a)** Envelope of the radiofrequency data. **(b)** Zoom of the envelope shown in (a). **(c)** Normalized spectrum derived from the radiofrequency data.

P1-A9-9

Cross-correlation Detection Improves Spatial Delineation and Enables High Resolution Tracking of Temporal Events in Magnetomotive Ultrasound Imaging

Roger Andersson[1], Maria Evertsson[2], Magnus Cinthio[2], Tomas Jansson[1,3]; [1]*Skåne University Hospital, Medical Services, Lund, Sweden,* [2]*Biomedical Engineering, Lund, Sweden,* [3]*Biomedical Engineering, Clinical Sciences, Lund, Sweden*

Background, Motivation and Objective

Magnetomotive ultrasound (MM US) imaging is a method whereby superparamagnetic iron oxide nanoparticles (SPIO NP) are used as a contrast agent. By applying an external magnetic field the particles are set in motion together with their surroundings. The induced movement is detected with ultrasound, and for the case of harmonic excitation of the magnetic source, quadrature detection (lock-in plus phase gating) can recover the magnetomotive signal (doi:10.1109/TUFFC.2013.2591). Here, we propose instead the use of cross-correlation for detection, and report the potential benefits compared to the previous approach.

Statement of Contribution/Methods

Data from previously published recordings taken on a phantom and an animal (rat), respectively, were analyzed both with quadrature detection and cross-correlation. The phantom was made from ballistic gel, had graphite as a background scattering material, and an inclusion containing SPIO NP at 0.06 mg Fe/mL. The animal recording was from a sentinel lymph node experiment, where 100 ul 3 mg Fe/mL was injected in the animal's hind paw. After 24 h MM US imaging was performed of the popliteal lymph node, where SPIOs had accumulated. The scanner was a Visualsonics VEVO2100 with a 21 MHz probe. The 5 Hz control signal for the magnetic coil was sampled at 8 kHz using the ECG-input. In the cross-correlation approach, the phase of the RF-IQ-data in each pixel in the acquired 200-image loop formed a sequence that was correlated with the control signal. Each lag was constructed by shifting the reference-signal one sample, while compensating for elapsed time as the US image was formed.

Results/Discussion

Panels A and B show the circular inclusion using the previous and proposed method, respectively, with negative correlations set to zero. Panels C and D show the corresponding animal cases. Panel E shows the correlation versus lag in two pixels exhibiting high correlation. The distinct peak at pixel (x=507, y=230) occurs at 9 ms after the reference signal transition, while at pixel (x=203, y=428) it occurs less distinct at 15-18 ms. This can be resolved since the temporal resolution of the reference signal far exceeds the frame rate of 50 Hz. Thus, aside from providing more distinct delineation of SPIO-laden areas, correlation may be used to detect temporal events with high precision, e.g. to determine differences in tissue visco-elastic parameters.

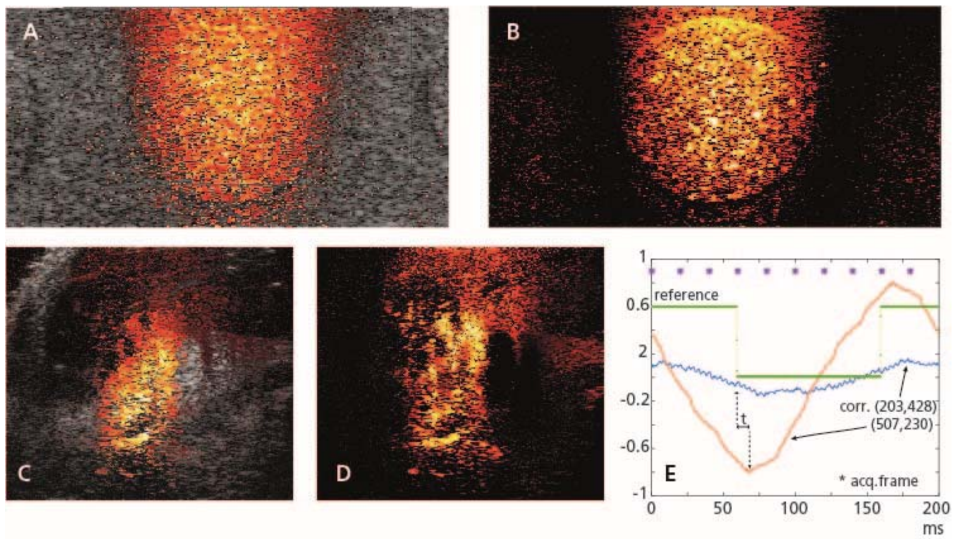

P1-A9-10 ____

The H-scan Format for Classification of Ultrasound Scattering

Kevin Parker[1]; [1]*Electrical & Computer Engineering, University of Rochester, Rochester, New York, USA*

Background, Motivation and Objective

Traditional B-Scan images show the envelope of received echoes as a grey scale image. The echoes are produced from specular reflections and scattering sites where changes in acoustic impedance occur (Cobbold, *Foundations of Biomedical Ultrasound*, Oxford Press, 2007). A long-standing area of interest concerns the frequency dependence of scatterers within different tissues, organs, and the blood.

Statement of Contribution/Methods

The H-scan is based on a simplified framework for characterizing scattering behavior, and visualizing the results as color coding of the B-scan image. The methodology begins with a standard convolution model of pulse-echo formation from typical situations, and then matches those results to the mathematics of Gaussian Weighted Hermite Functions. In this framework, echoes can be classified as returning from specific categories of scatterers, and these can be conveniently displayed as colors. Thus, some information not evident in conventional grayscale pulse-echo images can be visualized in the H-scan format.

Results/Discussion

Conventional B-scans are obtained using a Verasonics scanner with a 5 MHz ATL linear array transducer (Verasonics, Inc., Kirkland, WA, USA), with the RF sampled at 12 bits at 20 MHz and other commercial platforms. Although conventional systems do not transmit a precise $\mathbf{G}H_4$ (t) function, the transmitted pulse is sufficiently similar. An approximate analysis can be performed using the H_2 and H_8 correlation functions and then assignment of colors. Clearly identifiable changes in color are demonstrated in phantoms, liver, thyroid, and placenta resulting from changes in scattering size and structure, adding information to the assessment of soft tissues. Figure: 7 Mhz scans of ex vivo mouse livers suspended in a gelatin mold. (a) and (b) are steatotic livers (steatosis score over 50%), while the smaller normal livers (c) and (d) have negligible fat. The enhanced blue speckle in the steatotic livers is prominent and is likely related to the accumulation of small macro and microvesicles of fat that act as Rayleigh scatterers.

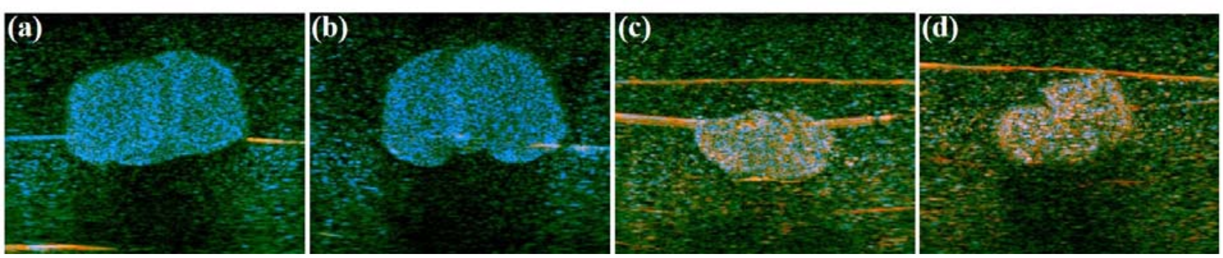

P1-A9-11 ____

Iterative Trace Reconstruction of Aliased RF Data Obtained Using Harmonic Imaging: A Feasibility Study

Paul van Neer[1], Hendrik Vos[2], Arno Volker[1]; [1]*Acoustics and Sonar, TNO, The Hague, Netherlands,* [2]*Biomedical Engineering, ErasmusMC, Rotterdam, Netherlands*

Background, Motivation and Objective

It is critical to use a proper spatial sampling, otherwise images suffer from grating lobes. However, the cost of a medical ultrasound scanner is strongly related to the channel count of the receive electronics. This has led to channel reduction using multiplexing or in-probe pre-beamforming methods at the cost of image quality or frame rate. An alternative is to reduce the receive channel count and reconstruct the non-aliased data from spatially aliased data. Last year we reported on a wavenumber frequency domain mapping (Stolt migration) based iterative trace reconstruction method developed for fundamental imaging. However, harmonic imaging is often used in medical imaging to further improve the image quality. Here, the feasibility of using the method for harmonic imaging is investigated using in-vitro and in-vivo linear array data.

Statement of Contribution/Methods

Plane wave-transmission datasets were recorded of a tissue mimicking phantom and of the right common carotid artery of a healthy volunteer using a linear array transducer (L7-4 probe – center frequency 5 MHz, 128 elements, 0.3 mm pitch –, Verasonics-256 system) emitting at 3.4 MHz. Pulse inversion was used. After removing 3 out of 4 receive traces the trace reconstruction method was applied: 1) A channel data matrix was created containing zeros at the locations where signals needed to be interpolated such that no spatial aliasing occurred. 2) Stolt migration was used to focus the wave energy. 3) Aliasing artifacts in the focused data were excluded by thresholding. 4) The channel data was reconstructed by applying an inverse Stolt migration operation. The empty traces now contained signal. 5) The original RF data was copied into the reconstructed data. 6) Steps 2 – 5 were iteratively performed with an increasingly lower threshold. The reconstructed datasets were imaged using Stolt migration.

Results/Discussion

A reconstruction example of the imaged in vivo dataset is shown in the figure: left pane – aliased (4x), middle pane – reconstructed, right pane – original. This is the first time that reconstructed in-vivo data is presented. The RMS values of a 3x3 mm^2 block at [0,11] were -45, -48 and -52 dB for the aliased (4x), reconstructed and original datasets, respectively. The imaged reconstructed dataset had higher image quality compared to the aliased (4x) dataset, but lower quality compared to the original dataset.

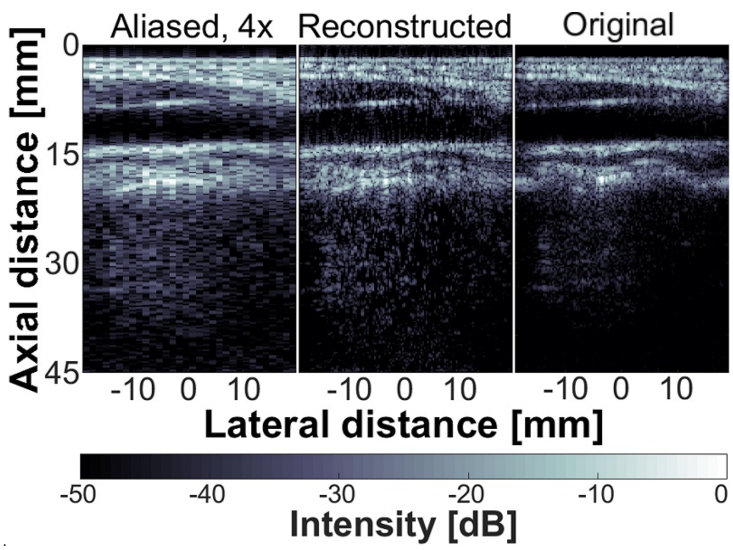

P1-A9-12

Complexity Reduction of Ultrasound Sub-Ultra-Harmonic Modeling by an Input Modified Volterra Approach

Fatima Sbeity[1], **Sebastien Menigot[2]**, Emma Kanbar[3], Jamal Charara[1], Jean-Marc Girault[2]; *[1]Department of Physics and Electronics, Faculty of Sciences I, Lebanese University, Beirut, Lebanon, [2]Polytech Tours, Université François-Rabelais de Tours, Inserm, Imagerie et Cerveau UMR U930, Tours, France, [3]Université François-Rabelais de Tours, Inserm, Imagerie et Cerveau UMR U930, Tours, France*

Background, Motivation and Objective

Contrast of echographic images has been highly improved by the injection of ultrasound contrast agents that consist of gaz microbubbles. The improvement is due to the nonlinearity of microbubbles, *i.e.* when excited with a frequency f_0, they can generate harmonics at ($2f_0$, $3f_0$, ...). However, the contrast improvement is limited by the nonlinear ultrasound propagation in tissue. To overcome this drawback, sub and ultraharmonics (SUH) contrast imaging can be used, since only microbubble can generate these components. SUH imaging consists in transmitting at f_0 and receiving at the subharmonic ($f_0/2$) and ultraharmonics ($3/2f_0$, ...) respectively.

Modeling is the main way to analyze and interpret the backscattered signal from microbubble. Volterra model has been applied in harmonic imaging to model harmonics optimally. However, it can model harmonics only, thus it cannot be directly used in SUH imaging. A multiple input single output (MISO) Volterra model has been proposed to solve this problem. The main drawback of MISO model is the large the number of coefficients to be estimated and the high computation cost. To reduce the complexity of SUH modeling process, we propose here a modified single input single output (SMISO) Volterra model based on input modulation.

Statement of Contribution/Methods

SMISO model is based on a standard Volterra model. The model input is modified by modulation to make easier the SUH modeling. Thus the modified input has to include both fundamental and subharmonic frequencies.

The model is tested using simulated and experimental signals. Simulated signals are obtained with Bubblesim software using an excitation signal at 4 MHz. Experiments are carried out by a excitation signal at 10 MHz transducer. Responses of a water-diluted solution of Sonovue were measured with a 5 MHz transducer. SUH modeling was applied using MISO and SMISO Volterra models.

Results/Discussion

Results from simulated and experimental signals showed that SUH are modeled. The number of coefficients is reduced to its half using SMISO model compared to MISO model.

The relative mean square error between the simulated signal and the modeled signal with SMISO model is -23.5 dB and it is -24 dB for experimental signals. The computational time is reduced by a factor of 6.5 and 4 in simulated and experimental cases respectively. SMISO model can make easier the SUH modeling.

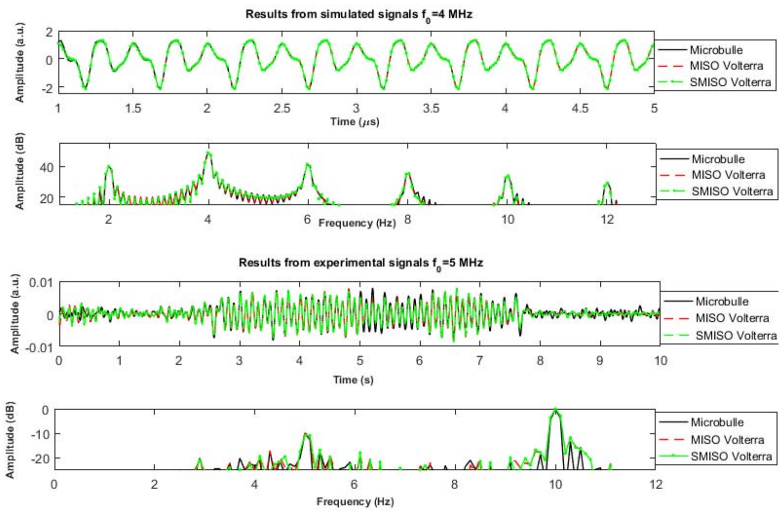

P1-A9-13

Micro-embolus Sub-band Detection based on Doppler Energy Fluctuations

Maroun Geryes[1], **Sebastien Menigot[2]**, Jamal Charara[1], Jean-Marc Girault[2]; [1]*Department of Physics and Electronics, Faculty of Sciences I, Lebanese University, Beirut, Lebanon,* [2]*Polytech Tours, Université François-Rabelais de Tours, Inserm, Imagerie et Cerveau UMR U930, Tours, France*

Background, Motivation and Objective

Robust detection of the smallest circulating cerebral microemboli is an efficient way of preventing cerebrovascular accidents (CVA). Transcranial Doppler ultrasound is widely considered as the most convenient system for the detection of microemboli. Standard detection used in commercial device is achieved through the whole Doppler energy spectrum where constant empirical thresholds are implemented. However, the nature of microembolic events is narrow band. Some microembolic detectors are thus composed of N detectors associated to N frequency sub-bands. Unfortunately employing a simple constant threshold in each sub-band is not sufficient, because the Doppler signal is heteroskedastic due to the cardiac cycle.

In this study, we propose a new type of microembolic detectors based of N frequency sub-bands. On each sub-band, a time-varying threshold is applied from energy fluctuations.

Statement of Contribution/Methods

The Doppler signals are recorded from a holter system for 25 patients. To evaluate the detector, two separate phases are introduced. The optimal number of sub-bands is determined from a training phase. Then the time-varying threshold is deduced for each signal from the Doppler fluctuations and a subband merging process counts the microembolic process. Finally, the performances are measured from a testing phase.

Results/Discussion

From the training phase, we find that 4 sub-band decomposition allows obtaining the best results considering both the detection rate and the false alarm rate. We compared our detectors to standard detection decomposed in energy sub-bands. Sub-band detection coupled with energy detectors based from negative energy fluctuations allow increasing the detection rate from 79% to 98%. Moreover, the false alarm rate is reduced by more than half of the standard values. This new type of microembolic detectors based on sub-band decomposition and energy fluctuations allows a much advanced detection of small cerebral microemboli, precursors of coming large emboli with strong CVAs risks.

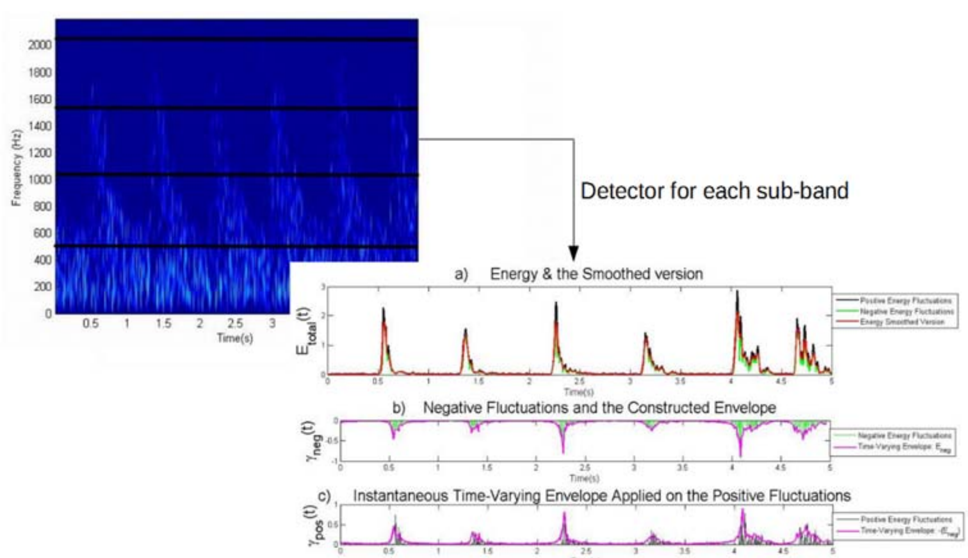

P1-A10 - MTC: Instrumentation and Processing Methods for Tissue Characterization

Exhibit Hall

Thursday, September 7, 2017, 9:30 am - 4:00 pm

Chair: **Lori Bridal**
Laboratoire d'Imagerie

P1-A10-1

Numerical Computation of Time-Domain Green's Functions for the Treeby-Cox Space-Fractional Wave Equation

Xiaofeng Zhao[1], **Robert McGough[1]**; [1]*Electrical and Computer Engineering, Michigan State University, East Lansing, MI, USA*

Background, Motivation and Objective

The attenuation of ultrasound in soft tissue follows a frequency-dependent power law. As an alternative to the time-fractional partial differential equations that describe power law attenuation and dispersion, Treeby and Cox derived a space-fractional model that accounts for both power law attenuation and dispersion. The Treeby-Cox space-fractional wave equation is convenient for simulations with the pseudo-spectral approach; however, numerical calculations of the time-domain Green's function for the Treeby-Cox wave equation are more challenging because numerical evaluation of a highly oscillatory improper integral is required. When applied to this problem, most standard numerical integration techniques perform poorly, so an alternative approach is required.

Statement of Contribution/Methods

We have recently determined that Pantis' method provides an ideal solution to this problem, where the interval of integration for the improper integral is partitioned into two subintervals. The lower subinterval then defines the limits of integration for a proper integral with an oscillatory integrand, which is evaluated with Filon's approach. The integral over the upper subinterval is then approximated by one or more terms of an asymptotic series. The effectiveness of this approach is demonstrated in calculations of the time-domain Green's function g(r, t) for the Treeby-Cox wave equation in breast with power law exponent y = 1.5, power law attenuation constant α_0 = 0.086 Np/cm/MHz^y, and sound speed constant c_0 = 1450 m/s evaluated at r = 10 cm.

Results/Discussion

We have determined that, for Green's function calculations at this distance with this combination of parameters, convergence is achieved when the result is computed with 20,000 Filon points in the lower subinterval using an upper limit of integration $k_u = 1201\pi/r$. Our experience suggests that an insufficient number of Filon points reduces the value at the peak and in nearby locations, whereas selecting an upper limit of integration for the lower subinterval that is too small introduces nonphysical oscillations in the computed time-domain Green's function. We have found that Pantis' method is an effective approach for computing the time-domain Green's functions for the Treeby-Cox wave equations at all distances, where fewer Filon points and smaller values for k_u are required at shorter distances.

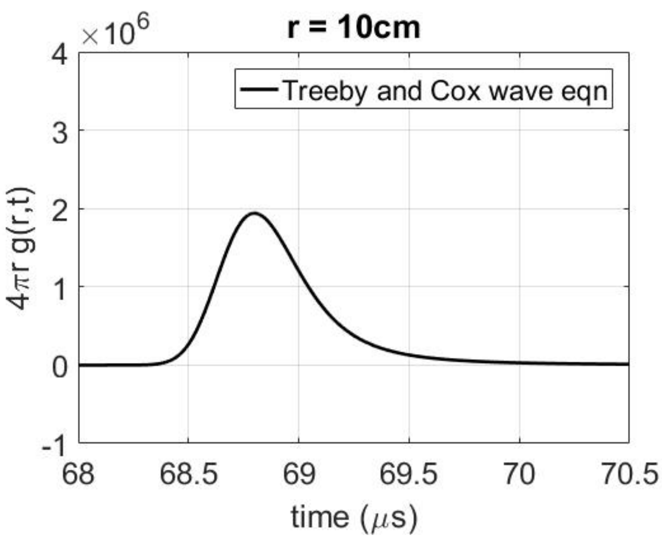

P1-A10-2

White-silicone Rubber and Copolymer-in-Oil Blend for Ultrasound Soft Tissue Mimicking Material

Felipe Grillo[1], Luciana Cabrelli[1], Letícia Ribeiro[1], Rondinelli Herculano[2], Felipe Borges[2], Theo Pavan[1], Antonio Carneiro[1]; [1]*Physics Departament, University of São Paulo, Ribeirão Preto, São Paulo, Brazil,* [2]*Departamento de Bioprocessos e Biotecnologia, UNESP, Araraquara, São Paulo, Brazil*

Background, Motivation and Objective

Phantoms are objects manufactured using a tissue mimicking material (TMM) and largely used to test protocols and mimic clinical environment for medical training. The TMM should reproduce at least one biological property to allow the association with clinical situation. The gel made by the copolymer styrene-ethylene/butylene-styrene (SEBS) in mineral oil previously reported by our group is a stable TMM to ultrasound applications. Blends of white-silicone rubber and SEBS are demonstrated to be miscible. In this study we evaluated acoustical, mechanical and chemical properties changes by white silicone rubber adding in a SEBS for tissue mimicking materials purpose to verify the miscibility of white-silicone rubber and SEBS.

Statement of Contribution/Methods

Five cylindrical samples with 7.5 cm in diameter and 2.5 cm of thickness were prepared to evaluate speed of sound and attenuation coefficient. The samples were prepared with SEBS at 10% w/w concentration, using mineral oil as solvent. White-silicone rubber was added at proportions of 0, 3, 5, 10 and 15% of solvent mass. Attenuation coefficient was evaluated using narrowband transducers with frequencies ranging from 1-10MHz at 21ºC by the substitution technique. B-Mode images were acquired to evaluate the ultrasound speckle pattern variations. Additionally, three samples with 2.5 cm in diameter and 2.0 cm of thickness, of each material with white-silicone variation, were used to estimate the Young's Modulus by compression tests. Finally, the same five white-silicone concentrations were characterized by FTIR spectroscopy to assess if there was chemical interaction between white-silicone rubber and SEBS polymer.

Results/Discussion

Speed of sound (c_m) ranged from approximately 1476 m/s to 1407 m/s, for 0% and 15% of white-silicone rubber respectively; acoustic attenuation coefficient (α_m), ranged from 0.2 to 0.55 dB/cm at 1MHz. Young's modulus had minimal variation between different percentages of white-silicone, from approximately 30kPa to 32kPa. FTIR showed white-silicone wavenumber fingerprint at approximately 1000 cm^{-1}. Adding white-silicone to the material decreased the speed of sound and increased acoustic attenuation coefficient. B-mode images revealed an increase of speckle level; therefore, we can consider white-silicone rubber as scattering agent. FTIR spectroscopy showed that transmittance for the white silicone rubber fingerprint decreased with silicone concentration. No new characteristic wavenumber was detected for the blend, suggesting that silicone is embedded by the SEBS gel. In conclusion, white-silicone rubber can be used as additive to SEBS gel as a tissue mimicking material. The next steps include the anthropomorphic phantom development using the developed material.

P1-A10-3

3D Ultrasound Imaging of Tissue Anisotropy Using Spatial Coherence: Comparison between Plane Waves and Diverging Waves

Emeline Turquin[1], François Varray[1], Lorena Petrusca[1], Magalie Viallon[1], Hervé Liebgott[1]; [1]*CREATIS, Univ.Lyon, INSA-Lyon, Univ.Lyon 1, UJM, CNRS, Inserm, UMR 5220, U1206, Villeurbanne, France*

Background, Motivation and Objective

After a myocardium infarction, cell loss is irremediable leading to a progressive local disorganization and change in the tissue structure altering heart function. An imaging method able to render the local tissue directivity would be a powerful tool to characterize the extent of the lesion. In this field, diffusion MRI is the reference. Because of its long acquisition time and the difficulty to tackle organ motion, faster imaging strategies such as ultrasound, are mandatory for such clinical applications. One of them is the spatial coherence of US waves, already developed in focused and plane waves (2D and 3D) but never in diverging waves [Papadacci, UFFC 2014]. The advantage of diverging waves is to create an image with a higher field of view, which is more appropriate to in vivo cardiac applications. The purpose of this work is to use 2D spatial coherence to determine the fibers orientation and to compare results in 3D steered plane and diverging waves.

Statement of Contribution/Methods

Spatial coherence is representative of the tissue structure. In an anisotropic medium, spatial coherence is high in that preferred local direction and the 2D coherence function exhibits an ellipsoidal shape. The main axis of this ellipse corresponds to the local main direction of the underlying tissue structure. Acquisitions have been conducted on a phantom designed from seven angled wires (ø 0.3 mm) embedded in an agar gel. The dataset was obtained using a 1024 channels ultrasound system based on the synchronization of 4 Verasonics Vantage 256 systems. A 1024 elements of a 32x32 elements 3 MHz array (Vermon) was fully controlled to transmit 2D steered plane and diverging waves on the same location. 25 transmission angles from -5° to 5° in x and y direction were used. The 2D coherence function maps were calculated on the spatial points corresponding to the centre of the seven wires and the main axis of ellipsoidal shapes are extracted to render the wires angle.

Results/Discussion

The curves representing the wires angle obtained in both plane and diverging waves are close to the reference. Using diverging waves, a RMSE of 4.8° is obtained which is better than the RMSE of 11.2° obtained with plane wave transmissions. It demonstrates the interest of 3D diverging waves to increase both the field of view and the coherence calculation accuracy. Such results must now be confirmed on heart sample acquisitions.

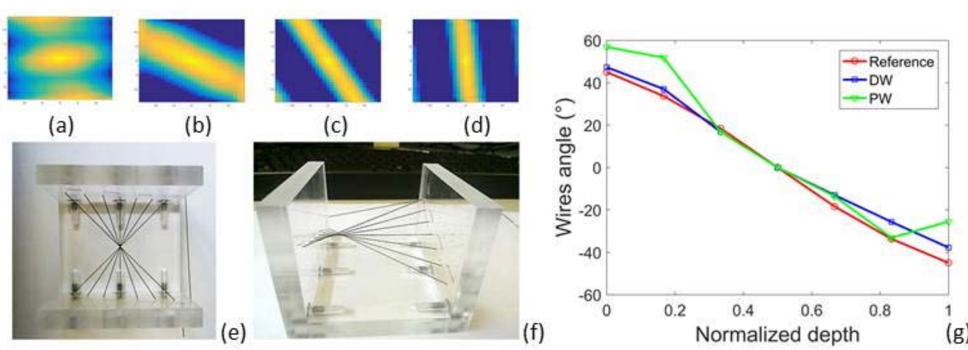

(a) – (d) Coherence function on the first, third, fifth and seventh wire respectively in the phantom using diverging waves
(e) – (f) Top and side view of the phantom consisting by seven angled wires
(g) Curves representing wires angle obtained in diverging waves (blue) and in plane waves (green) and the reference (red)

P1-A10-4

Structure Factor Model-based Approach for Analyzing Two-dimensional Impedance Map and Studying Scattering from Polydisperse Dense Media

Kazuki Tamura[1], Emilie Franceschini[2], Jonathan Mamou[3], Tadashi Yamaguchi[4]; [1]*Graduate school of Engineering, Chiba university, Chiba, Japan,* [2]*Laboratoire de Mécanique et d'Acoustique, Aix-Marseille Université, CNRS, Centrale Marseille, Marseille, France,* [3]*Lizzi Center for Biomedical Engineering, Riverside Research, New York, NY, USA,* [4]*Center for Frontier Medical Engineering, Chiba University, Chiba, Japan*

Background, Motivation and Objective

A two-dimensional (2D) computational model of acoustic impedance (Z) constructed from histological tissue images, termed 2D Z map (2DZM), was recently proposed to obtain quantitative information about tissue scattering (Luchies & Oelze 2016). However, this 2DZM approach was limited to isotropic and sparse media. The present study investigates the 2D structure factor model (SFM) in 2DZM approaches to take into account coherent scattering occurring in dense media. Studies of 2DZMs obtained from simulations of quantitative acoustic microscopy (QAM) experiments were performed to evaluate the ability of 2D SFM-based approach to accurately quantify scattering.

Statement of Contribution/Methods

Polydisperse spheres with a gamma radius distribution (mean of 6.44 µm and width factor of 45) were uniformly randomly distributed in a 3D volume to mimic a collection of whole cells (Z=1.48 MRayl) in a surrounding medium (Z_0=1.66 MRayl). 2DZMs were obtained from simulated 3D media by performing perfect cross sections. Each 2DZM was convolved with the point spread function of a 500-MHz transducer to mimic a 2DZM obtained with QAM. The 2D backscatter coefficient (BSC) was computed by averaging the magnitude squared of the 2D Fourier transforms of 100 extracted 2D relative impedance contrast maps ($(2DZM-Z_0)/Z_0$. The 2D BSC was fit to two theoretical models over the 2-100 MHz frequency range. A sparse model (fluid discs) and a concentrated model (SFM) were compared to estimate the mean scatterer size and acoustic concentration for scatterer volume fractions ranging from 0.6 % to 30 %.

Results/Discussion

Results demonstrate that in illustrative sparse and dense media the fitted BSCs obtained using the SFM modelled the 2DZM-based BSC much better than the BSC obtained with the sparse model (Fig. 1A). Acoustic concentration and scatterer radius estimates demonstrate the superiority of the 2D SFM-based approach over a wide range of volume fractions yielding maximum errors < 5.6 % (Figs. 1B and 1C). The results demonstrate the ability of the SFM-based approach to accurately estimate scatterer properties from 2DZMs even in the challenging case of dense media. The proposed methods could prove instrumental in characterizing scattering properties of a wide range of media using QAM approaches to directly obtain 2DZMs and could therefore improve QUS methods for accurate *in vivo* tissue characterization.

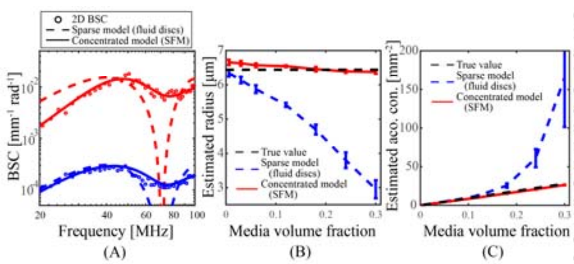

(A) Comparison between the 2D BSC obtained from 2DZMs and the BSC calculated with theoretical models (sparse and concentrated models). The blue and red curves are for the simulations at 0.6 and 30 %, respectively. (B) and (C) Mean radius and acoustic concentration estimated by the sparse and concentrated models. Mean and error bar were computed using 10 different estimations. Black dashed lines represent the true parameters.

P1-A10-5

Consistency of Echo Signal Power Spectra among Systems and Transducers

Quinton Guerrero[1], Yassin Labyed[2], Liexiang Fan[2], Shelby Brunke[2], Andy Milkowski[2], Timothy Hall[1]; [1]*Medical Physics Department, University of Wisconsin Madison, Madison, WI, USA,* [2]*Ultrasound Division, Siemens Medical Solutions USA, Issaquah, WA, USA*

Background, Motivation and Objective

The Reference Phantom Method can be used to quantify acoustic properties of tissue by compensating for system effects using the average power spectrum from a well-characterized homogeneous medium. Widespread clinical application of the Reference Phantom Method is hindered by the need to scan the reference phantom using the same transducer, system, and system settings as used for scanning the tissue each time a new study is performed. In this investigation, we questioned the need for repeat scans of the reference phantom.

Statement of Contribution/Methods

We acquired radiofrequency (RF) echo signals from a Gammex Sono403 Multi-Purpose phantom using Siemens 6C1 curved linear array transducers and S3000 systems. We used one S3000 system to acquire and compare average power spectra among eleven 6C1 transducers. We then used one 6C1 transducer to acquire and compare average power spectra among five S3000 systems. Power spectra were estimated using independent 6x6mm power spectral estimation regions (PSER) centered at the electronic focus (7 cm). We used a zeroth order discrete prolate spheroidal sequence as the spectral taper. Power spectral density (PSD) variance caused by speckle fluctuations was calculated based on the number of independent acoustic A-lines in the PSER. The number of independent A-lines in a PSER was determined by the autocorrelation length of speckle at the electronic focus. The components of variance of the PSD estimates from systems, transducers, and speckle was estimated at each frequency.

Results/Discussion

Using 750 independent A-lines, the average PSD variance due to systems, transducers, and speckle were 0.039 dB^2, 0.11 dB^2, and 0.025 dB^2, respectively. These results suggest that 6C1 transducers and S3000 systems cause a small, but measurable contribution to power spectral estimation variance. Importantly, these results suggest it is reasonable to create a calibration data set that is applicable among equivalent high-end systems and transducers in good working order.

Research supported by National Institutes of Health Grants T32CA009206 from the National Cancer Institute and R01HD072077 from the Eunice Kennedy Shriver National Institute of Child Health and Human Development. The content is solely the responsibility of the authors and does not necessarily represent the views of the National Institutes of Health.

P1-A10-6

Reflector-Based 3D Tomographic Ultrasound Reconstruction: Simulation Study

Bhaskara Rao Chintada[1], Sergio J. Sanabria[1], Wolfgang Bost[2], Orcun Goksel[1]; [1]*Computer-assisted Applications in Medicine, ETH Zurich, Switzerland,* [2]*Fraunhofer Institute for Biomedical Engineering, Sulzbach, Germany*

Background, Motivation and Objective

Ultrasound Computer Tomography (USCT) is used to map local wave propagation parameters, such as speed of sound, as potential imaging biomarkers. A reflector-based reconstruction algorithm using a conventional transducer was proposed in [1], yielding satisfactory reconstructions thanks to dynamic-programing based reflector delineation and angular-weighted total-variation regularization. In this work, we demonstrate an extension to a 2D array transducer case, where 3D reconstructions are facilitated by additional information from multiple overlapping transmits-receives wave-paths that traverse the medium. We aim to model an existing transducer and study reconstruction feasibility and resolution via numerical simulations.

Statement of Contribution/Methods

We assume multi-static data collected via each transmitter-receiver combination (see Fig. 1(a)) where the time-of-flight (TOF), t, is estimated for each path using a reflector detection algorithm. Discretizing ray-paths in each voxel as a linear system L using a ray-tracing method, the constitutive relationship Ls=t has to satisfied, where s is the vector of slowness value in each reconstructed voxel.

For a given reflector depth and orientation, from known L and measured t, s can be estimated using the regularized least-square problem:

$\hat{s}=\text{argmin}\{|Ls-t|^2+\lambda|Ds|^2\}$

Where D is the finite-difference operator for spatial regularization.

Results/Discussion

TOF values were simulated geometrically for a 32 x 16 element 2-D array transducer with a pitch of 0.75 mm for a homogeneous medium with 1540 m/s was reconstructed with mean (+-std) sound-speed of 1540(+-43) m/s. A cylindrical inclusion of 1650 m/s (compare Fig.1 (a)) within a substrate of 1515 m/s resulted in a satisfactory reconstruction with CNR 11.25 dB as shown in Fig. 1(b).

[1] Sanabria, Goksel, MICCAI: 568-576, 2016.

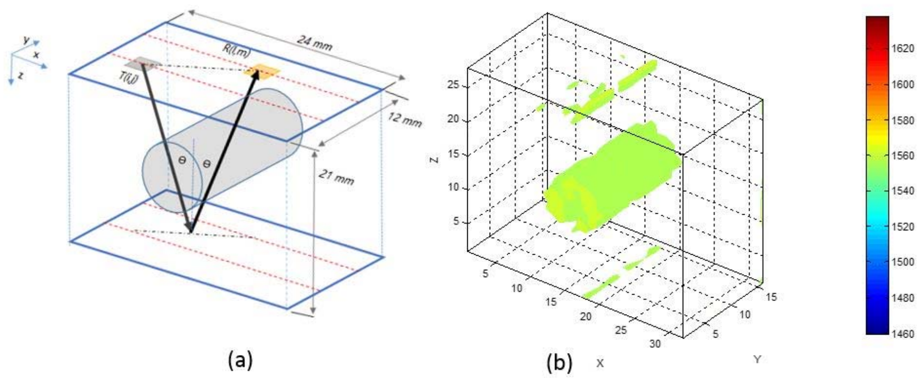

Fig. 1. (a) Imaging setup assumed in this simulation study (b) 3D speed of sound reconstruction with a cylindrical inclusion, each voxel has dimensions of 0.75 mm X 0.75 mm X 0.75mm.

P1-A10-7

Effect of Multi-Reflection on Analysis of Acoustic Impedance of Cultured Cells

Tamaki Honda[1], Kazuyo Ito[1], Kenji Yoshida[2], Hitoshi Maruyama[3], Tadashi Yamaguchi[2]; *[1]Graduate School of Engineering, Chiba University, Chiba, Japan, [2]Center for Frontier Medical Engineering, Chiba University, Chiba, Japan, [3]Graduate School of Medicine, Chiba University, Chiba, Japan*

Background, Motivation and Objective

To understand physiologic state in diseased liver e.g. non-alcoholic steatohepatitis, this study aims to analyze the acoustic impedance (Z) of hepatic cells using a scanning acoustic microscopy (SAM). Ultrasound scattering sources in cells, however, cause the multi-reflection and prevent from analyzing the precious value of Z although it provides the useful information of structure in cells (M. N. Fadhel et al. 2015). A similar effect also occurs in case of a part of cells apart from substrate. As the fundamental study, this study discusses the effect of multi-reflection on the analysis of the Z of cultured cells.

Statement of Contribution/Methods

Bovine aortic endothelial cells were cultured (BAEC) in Opticell with a DMEM + 10% FBS medium. A SAM (modified AMS-50SI, Honda Electronics Co., Ltd, Japan) equipped with a 250-MHz center-frequency transducer was employed for measuring the Z of cells. The spatial resolution of microscopy was 7 µm. High-frequency echo signals from the interface between Opticell's polystyrene film and the cells were recorded. Figure 1a shows the waveform. Z was calculated by comparing the amplitude of the target signal with the amplitude of the signal from reference material (DMEM + 10% FBS medium). In order to examine the artifact due to the multi-reflection inside the cell, the Z was evaluated by analyzing the amplitude of the first and second positive peaks.

Results/Discussion

Figures 1b and 1c show the Z obtained from the analysis of amplitude of each peaks (Z1st-peak and Z2nd-peak), respectively. The different textures inside cells were illustrated in each Z-map. The result suggested that multi-reflection occurred inside the cell. Assuming of multi-reflection effect, the recorded signal should be superposition of signal from the substrate-cytoplasm interface and signal from such as cytoplasm-nucleus interface (multi-reflected signal). Multi-reflection should give significant effect to the amplitude of 1st and 2nd peaks, leading to the difference between Z1st-peak and Z2nd-peak. To clearly confirm the effect, the impedance ratio Z1st-peak /Z2nd-peak were calculated as shown in Fig. 1d. It seemed that structure similar to cell nucleus could be found inside cells. The result implied that cell organelle could be scattering sources and made the precious analysis of Z more difficult.

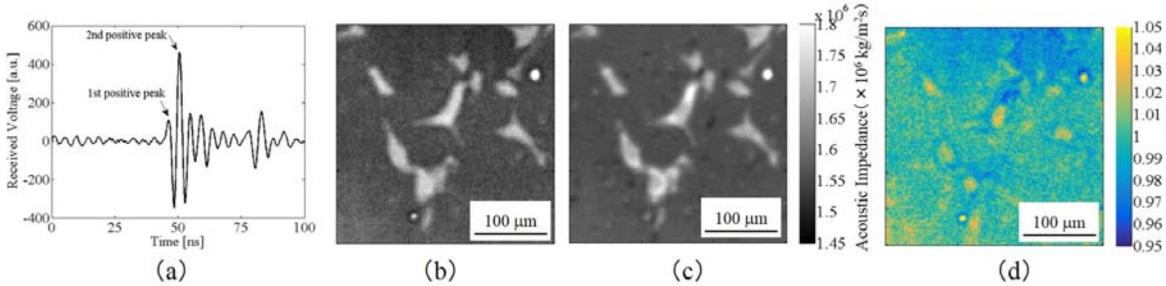

Fig. 1. (a) Typical waveform from interface between substrate and medium. (b) 2D images of $Z_{1st\text{-}peak}$ from analysis of amplitude of 1st positive peak. (c) 2D images of $Z_{2nd\text{-}peak}$ from analysis of amplitude of 2nd positive peak. (d) 2D images of the ratio of $Z_{1st\text{-}peak}$ and $Z_{2nd\text{-}peak}$.

P1-A10-8

A Model-based Approach for Estimating Local Speed of Sound in Tissue using Pulse Echo Ultrasound

Marko Jakovljevic[1], Rehman Ali[1], Dongwoon Hyun[1], Scott Hsieh[2], Jeremy Dahl[1]; [1]*Radiology, Stanford University, Palo Alto, CA, USA,* [2]*Radiology, University of California Los Angeles, Los Angeles, CA, USA*

Background, Motivation and Objective

Speed of sound (SoS) could prove useful as a biomarker for detecting and staging non-alcoholic fatty liver disease due to its dependence on fat concentration in the liver. However, current ultrasound SoS estimators yield poor accuracy and/or are difficult to implement on traditional pulse-echo scanner architectures. We propose a model and a method to estimate speed of sound in a localized region of tissue with high accuracy that can be implemented on commercial ultrasound systems.

Statement of Contribution/Methods

The proposed model relates the average speed of sound from the transducer to focus to the local sound-speed values along the wave propagation path. The average SoS values are first measured from a second-order-polynomial fit to the arrival-time profiles of ultrasound signals at each focal depth. The local SoS values are then inferred using the proposed model and the method of gradient descent. Quantitative SoS measurements were obtained from fullwave simulations of media with uniform SoS, and of two layers with different SoS (1480 m/s for the top layer; 1520, 1540, and 1570 m/s for bottom layer). Experiments were also performed in a speckle-generating phantom using a L12-3v linear array attached to a Verasonics Vantage 256 scanner. The data was acquired with and without a 4 mm thick slab of meat placed directly under the transducer.

Results/Discussion

In the homogeneous media, both average and local SoS estimators performed with high accuracy (bias < 4 m/s). Example SoS images of the two-layer media are shown in the figure below. The proposed method yielded lower bias in the estimates from the bottom layer of the two-layer media compared to the average SoS estimator. The bias of the average SoS estimates was 28.7, 41.7, and 59.4 m/s, respectively, while the proposed local estimator had bias of 7.1, 12.8, and 18.0 m/s, respectively, for the 1520, 1540, and 1570 m/s bottom layers. The standard deviation of the estimates was 4.4, 5, and 5.9 m/s for the average estimator, and 7.8, 9.5, and 8.6 m/s for the proposed local estimator, respectively. In the speckle phantom, the mean of the average SoS estimates increased by 30.2 m/s when the slab of meat was placed under the transducer, while the corresponding increase in the mean of the local estimates was 8.8 m/s. The standard deviation of the average and local SoS estimates in the presence of the meat layer was 8.5 and 17.9 m/s, respectively.

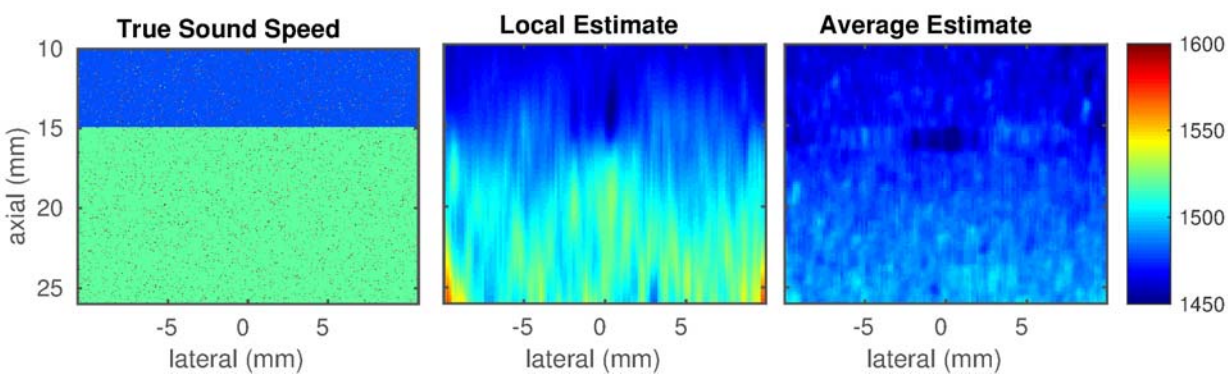

P1-A11 - MTH: Cavitation, Histotripsy, Microbubbles

Exhibit Hall

Thursday, September 7, 2017, 9:30 am - 4:00 pm

Chair: **Mingxi Wan**
Xi'an Jiaotong University

P1-A11-1

Daily Intra-Tumoral Administration of Oxygen Microbubbles Slows Tumor Growth in the Absence of other Therapy in a Rat Subcutaneous Fibrosarcoma Model

Virginie Papadopoulou[1], Samantha M. Fix[1,2], Hunter Velds[3], Mark A. Borden[3], James Tsuruta[1], Paul A. Dayton[1]; [1]*Department of Biomedical Engineering, UNC Chapel Hill, USA,* [2]*Eshelman School of Pharmacy, UNC Chapel Hill, USA,* [3]*Department of Mechanical Engineering, University of Colorado, USA*

Background, Motivation and Objective

Oxygen microbubbles (OMBs) have recently been used as adjunct treatment for solid tumors. Indeed, their ability to relieve tumor hypoxia was shown to benefit sonodynamic and other treatment outcomes in vivo. However, OMBs are often administered via intratumoral injection, and the effect of repeated OMB injections in tumors has not been investigated. Here we report on the paradoxical finding that daily OMB injections significantly reduces tumor growth rate in the absence of other therapy in vivo.

Statement of Contribution/Methods

Eight Fisher 344 rats were implanted with a fibrosarcoma (FSA) subcutaneous tumors on their right flanks from $1mm^3$ tissue transfer. After two weeks, baseline tumor volumes were measured using Bmode ultrasound (ellipsoid volume from the largest sagittal and transverse planes on Bmode ultrasound imaging of the tumor) and acoustic angiography (AA) for vessel structure and the rats were randomized into two groups. One group received daily intra-tumoral injections of 1mL OMBs for 7 days, whereas the other group had no intervention. On day 7, all rats were imaged again (Bmode and AA) for tumor volume calculation. A t-test was used to assess significant tumor volume differences between the two groups after normality test.

Results/Discussion

At the study onset, initial tumor sizes did not vary between the two groups ($p=0.89$). However, after one week of treatment, the group that received daily OMB injections showed a significantly reduced tumor volume compared to the no intervention group ($p<0.05$). We hypothesize that sustained, daily OMB administration could interfere with tumor growth, either through (1) the generation of high concentrations of reactive oxygen species that cause detrimental cell damage or (2) reduction in angiogenesis signaling resulting in slowed tumor growth. Future work will include histology assessment of resected tumor tissue, as well as an intra-tumoral saline injection control group to exclude the possibility of needle injury causing slowed growth.

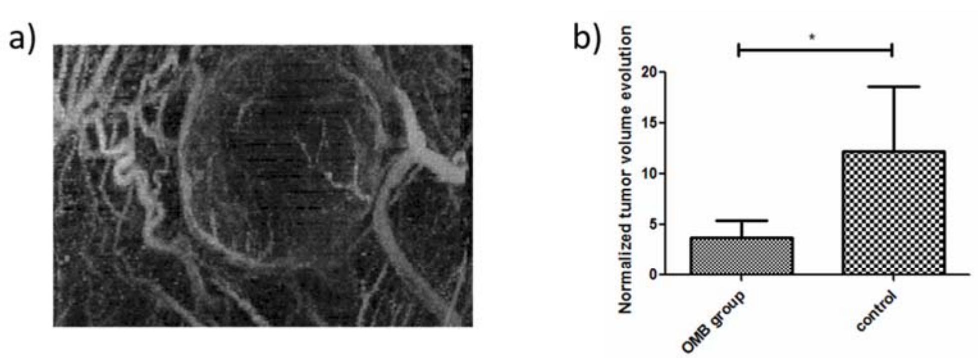

Figure 1: a) Example of baseline acoustic angiography Maximum Intensity Projection, showing vessel tortuosity around the tumor; b) Daily OMB intra-tumoral injections over one week significantly slow down tumor growth ($p<0.05$) (n=4 in each group). Normalized tumor volume was calculated as final volume (day 7) divided by initial volume (day 0).

P1-A11-2

Determining a Cavitation Threshold for Focused Ultrasound Enhanced Intranasal Drug Delivery

Robin Ji[1], Elisa Konofagou[1,2]; [1]*Biomedical Engineering, Columbia University, New York, New York, USA,* [2]*Radiology, Columbia University, USA*

Background, Motivation and Objective

Focused ultrasound enhanced intranasal drug delivery (IN+FUS) is a unique noninvasive approach that utilizes the olfactory pathway to administer drugs directly to the brain. Our group has shown that IN+FUS provides a more homogenous distribution of molecules in the targeted region than intranasal delivery alone. The underlying mechanism of IN+FUS is believed to be due to the microbubble pump effect, where microbubble cavitation causes expansion and contraction of the perivascular space. Therefore, the aim of this study is to investigate a potential cavitation threshold that is required for successful IN+FUS.

Statement of Contribution/Methods

Intranasal (IN) delivery of 3kDa dextran was administered to wild-type mice (n = 10) as 3µL droplets to alternating nostril, for a total of 48µL. Afterwards, the left caudate putamen was sonicated for 1 minute with a single element FUS transducer (center frequency: 1.5MHz, peak negative pressure: 450kPa or 650kPa, pulse repetition frequency: 5Hz), with the contralateral side used as the control case. A pulse-echo transducer confocally aligned with the FUS transducer was used for passive cavitation detection (PCD) to monitor the cavitation in the targeted region. Frequency analysis of the cavitation was quantified by integration of harmonic and ultraharmonic peaks for the first 50 pulses, yielding a summated cavitation dose (CD). T1-weighted MR contrast imaging was performed to confirm FUS targeting and fluorescence microscopy was used to quantify dextran distribution.

Results/Discussion

Our results show that there is a CD threshold that can be used to predict success of IN+FUS. Sufficient IN+FUS was characterized by diffuse distribution of fluorescence in the targeted region compared to the contralateral side (Figure 1). A CD above 11 V·s is necessary for successful dextran delivery as evidenced by an increased fluorescence homogeneity in the caudate putamen compared to the contralateral side. It is important to note that these results only apply when IN delivery was successful. IN delivery alone generates a sparse distribution of dextran throughout the brain, while applying FUS after IN further enhances the diffusivity of the dextran across the targeted region. As a result, these findings indicate that there exists a minimum cavitation response required for the microbubble pump effect to enhance IN delivery.

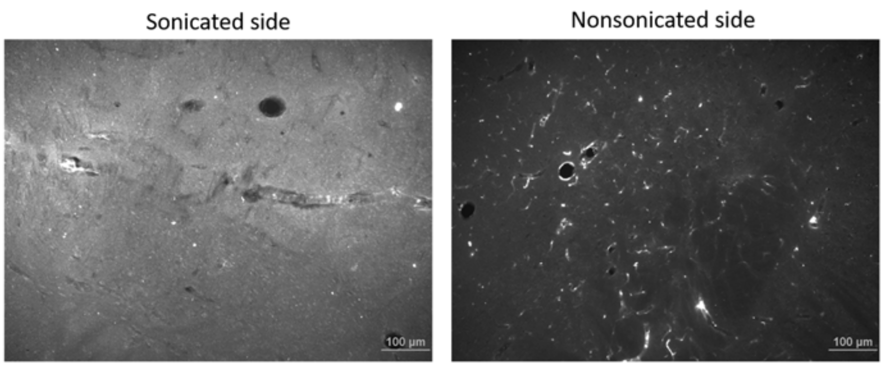

Figure 1: Horizontal sections of successful FUS+IN, comparing the sonicated caudate putamen and the contralateral nonsonicated side. Homogenous diffusion of dextran throughout the structure can be seen in the sonicated side, compared to the more heterogeneous distribution on the nonsincated side, where the dextran is trapped within the perivascular space. Images are shown at 10x magnification.

P1-A11-3

Acoustic Methods for Cavitation Threshold Modulation

Hedieh Alavi Tamaddoni[1], Timothy L. Hall[1]; [1]*Biomedical Engineering, University of Michigan, Ann Arbor, Michigan, USA*

Background, Motivation and Objective

One of the main objectives of this study is to develop active tissue protection techniques for histotripsy treatment by modulating the pressure threshold of bubble cloud initiation and focal sharpening using bubble suppressing pulses. Histotripsy is a cavitation based ultrasound therapy that can achieve tissue fractionation through a mechanical process using controlled cavitation bubble clouds. In this study, we investigate the effect of applying bubble suppressing pulses before and during shock scattering histotripsy on the cavitation initiation pressure threshold. This threshold is expected to increase by reducing the probability of having an appropriate initial nuclei presence at the focus. Bubble suppressing pulses are utilized to sharpen the focus and produce a dense bubble cloud at the focus with minimized cavitation events in the peripheral zones.

Statement of Contribution/Methods

We applied bubble suppressing pulses during histotripsy treatment with PRF of 1, 10 and 100 Hz, in three different mediums: water, agarose gel, and tissue. For experiments in tissue, cow livers were harvested and used on the day of slaughter, and then prepared by degassing under vacuum. Acoustic backscatter signals and optical imaging were used to detect and monitor initiation, maintenance and growth of resulting cavitation bubble cloud.

Results/Discussion

Results demonstrated that the use of cavitation suppressing pulses can increase the cavitation threshold by 20% in the targeted area (Figure 1). Furthermore, we showed these acoustic sequences could modify the shape and density of the bubble cloud. By applying the cavitation suppressing pulses we were able to generate a dense cavitation bubble cloud in the focus while decreasing scattered cavitation in the peripheral zone (Figure 2).

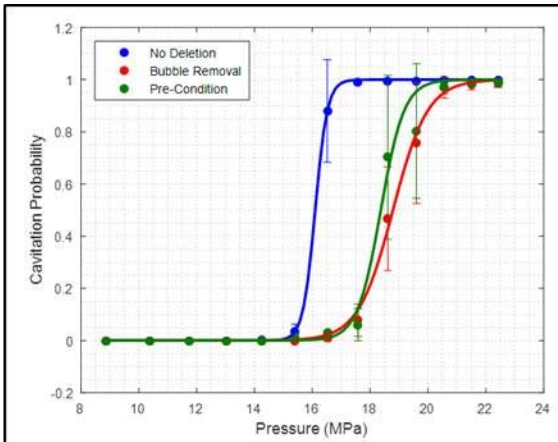

Figure 1. Cavitation probability for PRF 100 Hz (Agarose gel)

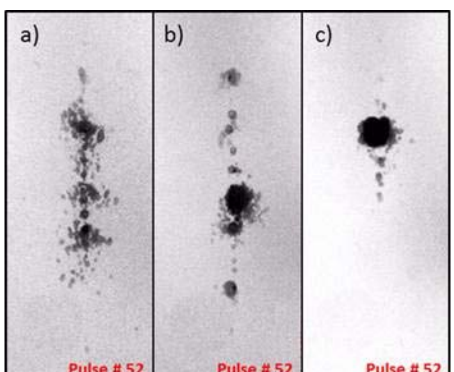

Figure 2. Cavitation bubble cloud in agarose gel generated by shock scattering at 20MPa with PRF 100Hz, a) histotripsy only, b) histotripsy with pre-conditioning, and c) histotripsy with bubble suppressing pulses.

P1-A11-4

Precisely Controlled Cavitation during the Perfluorocarbon (PFC) Nanodroplets Assisted HIFU Surgery

Nan Chang[1], Xin Wang[1], Mingzhu Lu[1], Shukuan Lu[1], Supin Wang[1], Mingxi Wan[1]; [1]*Department of Biomedical Engineering, Xi'an Jiaotong University, Xi'an, China, People's Republic of*

Background, Motivation and Objective

Previous study has demonstrated that pulsed HIFU with tens of microseconds pulse duration (PD) and 10kHz PRF is effective for cavitation generation. Meanwhile, with the assistance of PFC nanodroplets, cavitation can be further enhanced. Despite of higher efficiency, we also need cavitation to be precisely controlled and confined for sake of therapeutic safety, especially during the implementation of HIFU surgery in fine organs like brain, neuro, or blood vessel. Smaller focus is obtained by designing very large or spherical shaped transducers, which also cause some inconveniences for treatment. In our study, we propose a combinated ultrasound wave sequence to realize precisely controlled cavitation during PFC nanodroplets assisted HIFU to simultaneously achieve efficient and accurate therapy.

Statement of Contribution/Methods

All results were obtained from polyacrylamide phantoms embedded with PFC nanodroplets with mean diameter of 182.7nm. In the control group, we applied a pulsed wave with 10μs PD and 10kHz PRF sustained for 20s (Fig.1 c above). In the experimental group, we applied a combinated wave sequence composed of 2s continuous wave, then 2s pause, and finally the pulsed wave used in the control group (Fig.1 c bottom). The acoustic intensity in both groups was 19W. Sonoluminescence (SL) was employed to visualize the cavitation active spots. The luminous area and mean light intensity were measured to represent cavitation area and intensity, respectively.

Results/Discussion

Comparing the results from these two groups, cavitation distribution space is more confined and less stretched in the experimental group (Fig.1 b). The axial and lateral maximum length of the luminous region is 8.1 and 2.7mm very close to the focal size of the HIFU transducer (8x1.2mm). We measured the SL area in each image and found that the total cavitation region area decreased about 60% when irradiated by the combinated wave sequence. Meanwhile, no obvious change in the mean intensity (Fig.1 d). From the above results, we can conclude that better controlled cavitation is achieved through applying the combinated ultrasound wave sequence without any decrease in cavitation intensity. Hence, in some precise PFC nanodroplets assisted HIFU surgery, this combined wave sequence can be benefit for accurate therapy.

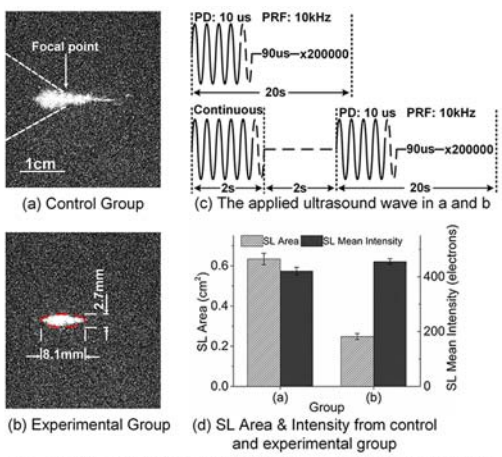

Fig.1 The SL results from the control (a) and the experimental group (b). The applied ultrasound wave (c). SL area and mean intensity (d).

P1-A11-5

Histotripsy Produced by Dual Frequency of Fundamental and Harmonic Superimposition with Protocol of Hundred-Microsecond-Length Pulses and Two Stages

Mingzhu Lu[1], Rui Wang[1], Yujiao Li[1], Linglu Zhang[1], Dan Han[1], Yanshan Liu[1], Mingxi Wan[1]; [1]*Department of Biomedical Engineering, Xi'an Jiaotong University, Xi'an, Shaanxi, China, People's Republic of*

Background, Motivation and Objective

Histotripsy is a new non-invasive therapy modality and can mechanically disintegrating target tissue for tumor treatment. In this study, we propose a strategy of dual frequency of fundamental and harmonic superimposition combined with hundred-microsecond-length pulses and two stages to get good use of the nonlinear regimes of enhanced cavitation and boiling. Confocal fundamental and harmonic superimposition can greatly lower the cavitation threshold and enhance cavitation activity via wave interference.

Statement of Contribution/Methods

Each hundred-microsecond pulse consists of 400-600 μs. Much higher 4-5% duty factor is used in stage 1 treat to induce boiling and partially homogenization tissue, and 1% duty factor is used in stage 2. The thermal effects in first stage benefits for antitumor immunity. The transducer consists of two annular elements, one is stimulated with 1.1 MHz, and the other with 3.3 or 2.2 MHz. The experiments were implemented in gel phantom with BSA, ex vivo of bovine eye lens and pig kidneys, monitored via high speed camera or PCD (Fig.1 (a) to (d)). The P+/P- pressures were 56/14 MPa in 3.3MHz, 46/12 MPa in 2.2 MHz and 26/7 MPa in 1.1MHz. The harmonic pressures in focal region appear shocks (Fig.1 (f)).

Two-frequency superimposition results in split foci, and the maximal peak intensity can reach 2 times the sum of two frequency intensities, indicating wave interference. Both negative and positive peak pressure reach the maximum with 60° phase shift in 1.1 /3.3 MHz and negative one with 135° in 1.1 /2.2 MHz.

Results/Discussion

As expected, each experiment achieves successfully a completely homogenized region (sharply demarcated from untreated tissue (Fig.1 (e))) with dimension of 7 mm×1.8 mm (axial×lateral) in ex vivo pig kidney (Fig.1 (g)). The results testify the feasibility of the dual-frequency method. Multiple boiling bubbles occurring in stage 1 from high speed imaging (Fig.1 (a) to (c)), may be the primary regimes for speed up histotripsy. The filtered-PCD mean square waveform (Fig.1 (d)) indicates the enhanced inertial cavitation energy immediately after boiling happening. In 1.1/3.3 MHz treatment, shorter pulse length and treatment time are used and formed purely disintegration tissue in focal region. In bovine lens treatment, obviously liquefied lesion occurs in stage 1, therefore efficacious disintegration also begins at the first stage.

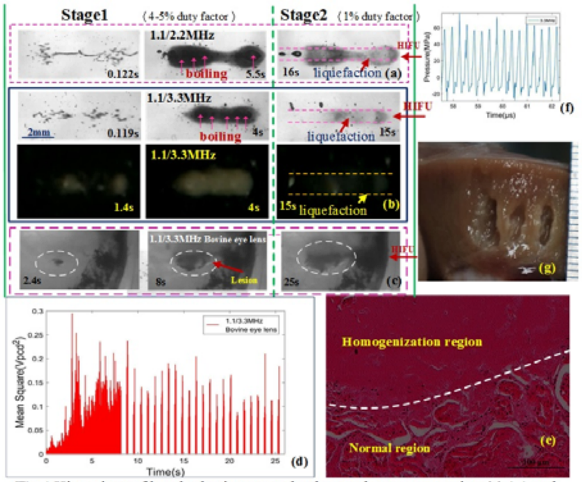

Fig.1 Histotripsy of hundred-microsecond pulses and two stages using (a) 1.1 and 2.2 MHz, (b) 1.1 and 3.3MHz in gel phantom with BSA, (c) 1.1/3.3MHz in bovine eye lens (high speed imaging, video imaging), and (g)1.1/2.2MHz in pig kidney; (d) filtered-PCD mean square waveform of 1.1/3.3MHz in bovine eye lens. (e) H&E stain slide of pig kidney. (f) Acoustic pressure using fiber optic hydrophone.

P1-A11-6

Enhanced Histotripsy Induced by Hundreds of Microsecond Pulses and Dual-Frequency Second Harmonic Superimposition: A Preliminary Study

Yujiao Li[1], Mingzhu Lu[1], Rui Wang[1], Dan Han[1], Yanshan Liu[1], Mingxi Wan[1]; [1]*Department of Biomedical Engineering, School of Life Science and Technology, Xi'an Jiaotong University, Xi'an, Shaanxi, China, People's Republic of*

Background, Motivation and Objective

Kidney cancer is a severe disease which can be treated by using a non-invasive, controllable and focused ultrasound surgery method-histotripsy. Previously, histotripsy produced by hundred-microsecond-long focused ultrasound pulses has been proposed by us, which generates mechanical homogenized lesion by employing boiling bubbles and high duty cycle compared with conventional methods. However, the efficiency of this method is not high due to single focus. In order to overcome this problem, we propose a new histotripsy method, which can produce multiple split foci along beam axial via dual-frequency second harmonic superimposition mode.

Statement of Contribution/Methods

The superimposition of two frequency pressures at confocal region can lower cavitation threshold, enhance inertial cavitation and boiling activities. There are two stages for the dual-frequency (1.1MHz/2.2MHz) second harmonic superimposition ultrasound pulse mode. The first stage is for alteration of tissue mechanical properties which is carried out by pulses with 500 µs pulse duration (PD), 100 Hz pulse repetition frequency (PRF) which is 5% duty factor. In order to enhance nucleation cavitation, the 135° phase shift in 1.1MHz/2.2MHz has been employed, which leads to the negative peak pressure reach maximum. The superimposition of two frequency pressures results in 9 split foci along beam axial within confocal region via controlling the ratio of dual-frequency acoustic powers (68W/25W), and the maximal peak intensity of split foci can reach about 2 times the sum of two frequency intensities, indicating strong wave interference. The second stage is histotripsy which is conducted by a sequence composed of 15 pulses with 500 µs PD and 100 Hz PRF followed by a 600 ms off-time which is 1% duty factor.

Results/Discussion

The final lesion exhibits long tear shape with dimensions of approximately 6.8 × 1.0 mm (axial × lateral) in BSA phantom. The high speed imaging shows the boiling bubbles occurring at split foci. The interaction of boiling bubbles between split foci speeds up the lesion formation and size enlargement. The void of 6.4 × 1.4 mm (axial × lateral) with sharp border forms in porcine kidney after enhanced histotripsy. The filtered-PCD mean square waveform reveals the strong inertial-cavitation activities. The amplitude increase in frequency domain indicates the boiling bubbles arise.

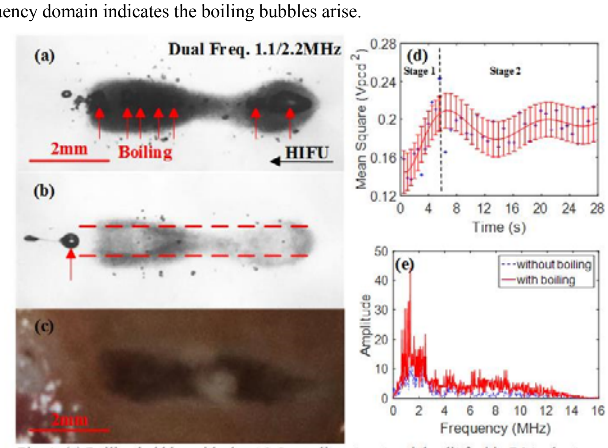

Fig .1. (a) Boiling bubbles with about 0.5 mm diameter at axial split foci in BSA phantom acquired by high-speed photography. (b) Final lesion after two-stage therapy. (c) Successive therapy in porcine kidney *ex vivo* with dimensions of approximately 6.4 × 1.4 mm (axial × lateral). (d) Mean square amplitude of the PCD signals using dual frequencies of 1.1/2.2 MHz on the phantom at different times. (e)Broadband noise amplitude in the frequency domain with/without boiling.

P1-A11-7

Impact of Step Size on Histotripsy Treatment of Staphylococcus aureus Biofilms on Surgical Mesh

Timothy Bigelow[1], Clayton Thomas[1], Huaiqing Wu[1], Kamal Itani[2,3]; [1]*Iowa State University, Ames, Iowa, USA,* [2]*VA Boston Healthcare System, USA,* [3]*Boston Medical Center, USA*

Background, Motivation and Objective

Infections on medical implants are difficult to treat because of the formation of bacteria biofilms that protect the microbes from antibiotics. Currently, infected implants must be removed, allowing for the infection to heal and a new implant inserted. The goal of our work is to develop cavitation-based ultrasound histotripsy for the noninvasive treatment of bacteria biofilms with an initial focus on the surgical mesh used for hernia repair. Based on prior results, we hypothesized that greater biofilm destruction could be achieved if we reduced the step size used for the treatment.

Statement of Contribution/Methods

Staphylococcus aureus (S. aureus) biofilms were grown on 1 cm square surgical mesh samples for 3 days. The samples were then rinsed with phosphate buffered saline prior to being inserted into Aquaflex Ultrasound Gel Pad Standoffs (Parker Laboratories Inc., Fairfield, NJ). The focus of a spherically focused transducer (1.1 MHz, 12.9 cm focal length, 12.7 cm diameter) was then aligned on the mesh samples using a low-power signal from a pulser-receiver(Panametrics 5900, Olympus Corporation, Tokyo, Japan). Once aligned, the mesh samples were exposed to either a sham exposure or histotripsy pulses (peak-compressional pressure of 150 MPa, peak rarefactional pressure of 17 MPa) with tone burst durations of 10 cycles at a pulse repetition frequency of 1000 Hz. During the treatment, the focus of the transducer was continuously scanned along one axis in the plane of the mesh at a speed of 0.8 mm/sec. Once it reached the end of the treatment zone, it was stepped down to the next scan line with a step size of either 0.35 mm or 0.7 mm. After the step, the scan direction was reversed, and the focus was moved across the next portion of the treatment zone. Once the entire mesh was treated, the focus was moved back to the initial starting location and the treatment was repeated 4 additional times for that mesh sample. After treatment, the number of colony forming units (CFUs) on the mesh and the surrounding gel was independently determined. A total of 7 repetitions were completed for each exposure condition as well as the sham exposure.

Results/Discussion

The number of CFUs on the mesh following the sham exposures was 4.2±0.8-log10 while the exposure for the 0.7 mm step had 1.1±1.4-log10 CFU. The exposure for the 0.35 mm step never had any surviving CFUs on the mesh. There was a statistically significant difference between sham and both treatment exposures for the mesh with more consistent results obtained for the smaller step size. For the gel, the sham exposures had 5.9±0.3-log10 CFUs while the 0.7 mm and 0.35 mm exposures had 5.8±0.3-log10 and 5.1±0.5-log10 CFUs respectively. The smaller step size exposure was statistically significantly different from the 0.7 mm step and the sham exposure, but the sham and 0.7 mm step were not significantly different from each other. Therefore, the smaller step size achieves better cell killing and has greater promise for clinical efficacy.

P1-A11-8

Swept Frequency Waveforms Enhance Target Specificity of Ultrasonic Neuromodulation in Mice In Vivo

Christian Aurup[1], Elisa Konofagou[1,2]; [1]*Biomedical Engineering, Columbia University, New York, NY, USA,* [2]*Radiology, Columbia University, New York, NY, USA*

Background, Motivation and Objective

Focused ultrasound (FUS) has demonstrated its ability to modulate neuronal activity in both cortical and subcortical brain regions in a noninvasive and reversible manner in mice. However, mice have very small brains relative to the size of the FUS focus. Simulations of beam profiles in rat head models have demonstrated the formation of secondary pressure peaks due to reverberations. This may explain results showing motor responses following modulation of regions not directly responsible for motor movement. Although standing wave formation decreases with increasing frequency, the success rate of neuromodulation also decreases. Our group has previously reported that the use of chirp sequences for blood-brain barrier (BBB) opening can reduce standing wave formation and decrease the region of BBB opening. In this paper, we aim to determine whether a chirped FUS sequence increases the neuromodulation selectivity.

Statement of Contribution/Methods

A 1.9-MHz single-element focused ultrasound transducer was used to sonicate the mouse cortex. Each animal was injected intraperitoneally with urethane (1500 mg/kg), which allowed for a stable plane of anesthesia and experimental window often exceeding 4 hours with minimal effects on autonomic activity. Electromyography (EMG) recordings were acquired from each limb. Heart and breathing rates were also acquired. Sonication was performed in a rectangular grid pattern and EMG responses were acquired at each location. The physiological response to stimulation with two different waveform types was evaluated: constant center frequency and linear chirp frequency swept 300 kHz about the center frequency.

Results/Discussion

Sonication with constant center frequency required lower pressure for neuromodulation than when using swept frequency waveforms. Sonication at a constant center frequency resulted in significant changes in EMG responses in 80% of trials, breathing rate in 30% of trials, and heart rate 100% of trials. Chirped sonication at the same pressures resulted in no EMG responses while significant changes in breathing and heart rates occurred in only 14% and 30% of the trials, respectively. However, the success rate of using swept frequencies increased at higher pressures. Tailored waveforms, including those utilizing swept frequencies, may be optimal for use in small animals where standing wave formation from reverberations is most exaggerated.

P2-A1 - Imaging

Exhibit Hall

Thursday, September 7, 2017, 9:30 am - 4:00 pm

Chair: **Joel Harley**
University of Utah

P2-A1-1

3D Ultrasound Palm Vein Recognition through the Centroid Method for Biometric Purposes

Michele De Santis[1], Sandro Agnelli[1], Donatella Nardiello[2], **Antonio Iula[2]**; *[1]University Niccolò Cusano, Roma, RM, Italy, [2]School of Engineering, University of Basilicata, Potenza, PZ, Italy*

Background, Motivation and Objective

A few years ago, some of the authors proposed an ultrasound technique for achieving 3D palm vein patterns for biometric recognition purposes. That technique was developed with a commercial imaging system using doppler modality. Unfortunately, even if results were promising, the acquisition time was too long for practical applications.

More recently, they proposed an effective recognition system that employs an ultrasound research scanner (ULA-OP), a CNC pantograph and a high frequency (12 MHz) commercial probe. The system is able to acquire 3D image of the human palm (38x25x15 mm3) in about 4 seconds. Successively, they developed a procedure to extract palmprint features and validated it with verification and identification experiments on a consistent ad hoc established database.

In this work, a new method for extracting palm vein pattern is proposed. The procedure uses as input the same 3D images already exploited for extracting palmprint features, as matter of fact upgrading the recognition system to a multimodal system.

Statement of Contribution/Methods

The proposed method is based on the individuation of areas in the B-mode image of lower brightness than a predefined threshold. Then, it measures a set of properties for the individuated dark areas in the binarized image and selects the vectors that specify the centers of mass of these dark regions (centroids). The same technique in applied to the successive B-mode images. Vein patterns are finally defined whenever centroids are found in the surrounding of the same coordinates for a certain number of consecutive B-mode images.

Results/Discussion

The proposed procedure has been tested on several samples. The figure below shows main steps for a single sample and a single vein pattern. As can be seen in the 8 bit gray scale B-mode (a) and C-mode images (b), the high frequency probe guarantees a sufficient resolution that allows to clearly distinguish main vein patterns of the human hand. Figure (c) shows the result of the binarization for three successive B-mode images; the threshold value was set to 64 by evaluating the experimental results. Finally, figure (d) shows the sequence of centroids (cyan color) individuated by the procedure for the selected vein pattern.

Results of a validation carried out through verification experiments on a subset of the database are finally presented and discussed.

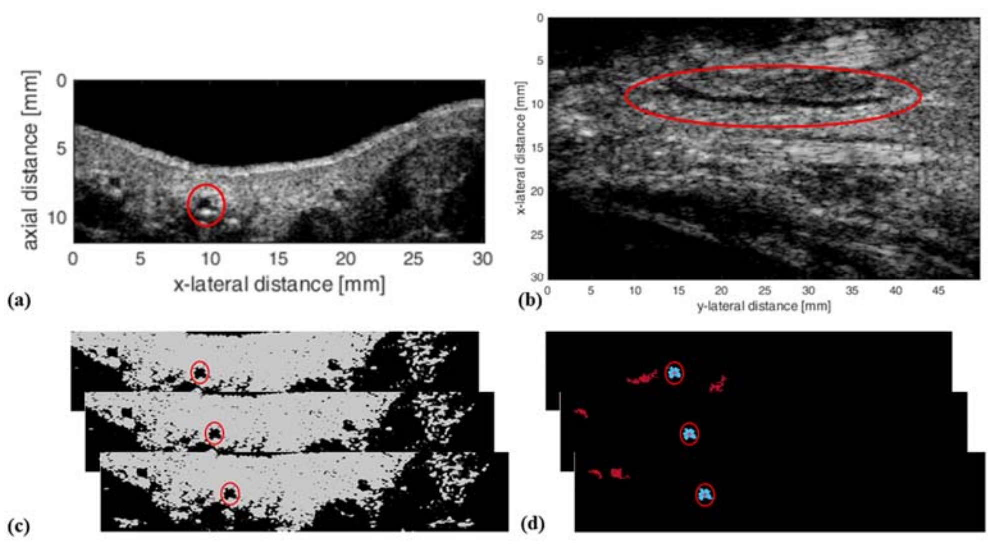

P2-A1-2

Frequency Display by Clustering Multispectral Acoustic Imaging Data

Xinhua Guo[1], Xiaodong Ye[1], Kaihua Cao[1]; *[1]School of Mechanical and Electronic Engineering, Wuhan University of Technology, China, People's Republic of*

Background, Motivation and Objective

Conventionally, images are normally displayed by amplitude or intensity information. However, acoustic images are different from optical images. The frequency information is significantly important in acoustic images since the frequency information can reflect the object characteristics (surface profiles, structures hidden under surfaces, and material properties of objects). In this study, we propose a method of displaying frequency information in acoustic images by clustering multispectral acoustic imaging data. The method for clustering, Self-Organizing Maps (SOM) is used, which effectively implements dimensional reduction of high-dimensional data.

Statement of Contribution/Methods

A rigid surface with different holes, as shown in Fig. 1(a), is illuminated by sound waves sweeping over the frequency range from 1 to 20 kHz with a 30 Hz step. Multispectral acoustic imaging data is obtained, as shown in Fig. 1(b). The three-dimensional acoustic data of the amplitude is normalized, and rearranged as a two-dimensional matrix, which is composed of 1089×635 input vectors. The matrix is input into the SOM for unsupervised training. After clustering, the fundamental frequencies are extracted from the mean value of frequency response of holes. The schematic flow of processing acoustic data by SOM method is shown in Fig. 2(a).

Results/Discussion

The results showed that the three-dimensional multispectral acoustic data was effectively reduced by the unsupervised algorithm of SOM. The profiles and depth information of the rigid model with 9 holes are easily identified by the method, as shown in Fig. 2(b). In future work, we need further to develop a systematic optimization approach to selecting classes and rapidly find the frequency characteristics of objects.

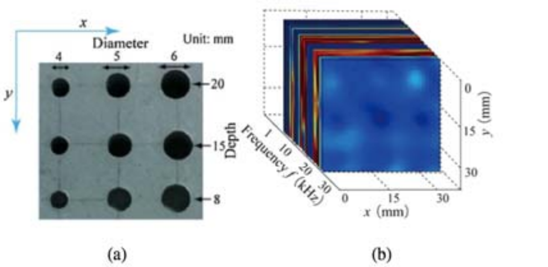

Fig. 1. (a) Photograph of imaging object with the detailed dimensions, and (b) three-dimensional acoustic data of the amplitude.

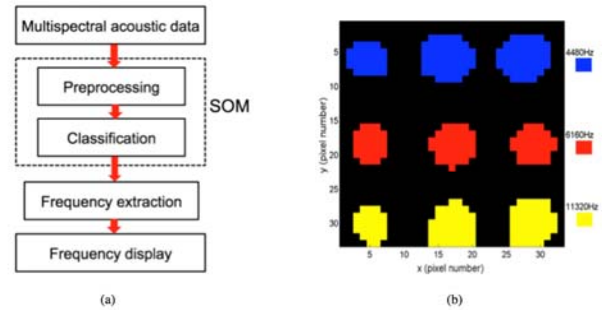

Fig. 2. (a) Schematic flow of processing acoustic data by SOM method, and (b) image of frequency display.

P2-A1-3

Evaluation of Position and Velocity Measurement for a Moving Object by Pulse Compression Using Ultrasound Coded by Preferred-Pair M-Sequences

Shinnosuke Hirata[1], Kota Yamanaka[1], Hiroyuki Hachiya[1]; [1]*Dept. of Systems and Control Engineering, Tokyo Institute of Technology, Meguro, Japan*

Background, Motivation and Objective

In pulse compression using an M-sequence, the M-sequence modulated signal is transmitted and the received signal is correlated with the transmitted signal. However, the M-sequence modulated signal reflected from a moving object is Doppler-shifted. The Doppler-shifted M-sequence modulated signal cannot be correlated with the transmitted signal. Therefore, Doppler velocity estimation from a cyclic M-sequence modulated signal and cross correlations with Doppler-shifted reference signals corresponding to the estimated Doppler velocities has been proposed. Meanwhile, in the case of measurement using multiple transducers, the B-mode image can be formed from multipath cross-correlation functions. Then, the position of the object can be measured from the B-mode image. When different ultrasound are simultaneously transmitted, preferred-pair M-sequence codes are typically used for coding to avoid the crosstalk. However, the interference of M-sequence modulated signals has the potential to degrade the proposed position and velocity measurement. In this paper, position and velocity measurement using ultrasound coded by preferred-pair M-sequences is evaluated.

Statement of Contribution/Methods

Ultrasound coded by preferred-pair M-sequences are transmitted from two loudspeaker. Then, echoes reflected from the moving object are received by three microphones. Doppler velocities in each loudspeaker are estimated and classified by the proposed Doppler velocity estimation. Then, the received signal is correlated with the Doppler-shifted reference signal corresponding to each Doppler velocity. Then, the B-mode image is formed from all cross-correlation functions by the synthetic aperture focusing technique. The position of the object is determined from this image.

Results/Discussion

The cylinder was moved by the motorized stage as the moving object. The speeds of the stage was set at 240 mm/s. Two-second measurement was repeated 10 times. Errors and standard deviations of estimated Doppler velocities of each propagation path are illustrated in the figure. Doppler velocities could be estimated within }10 mm/s. Errors and standard deviations of measured positons of the object are also illustrated in the figure. Positions could be measured within }2 mm. In this experimental configuration, position and velocity measurement was possible with high accuracy.

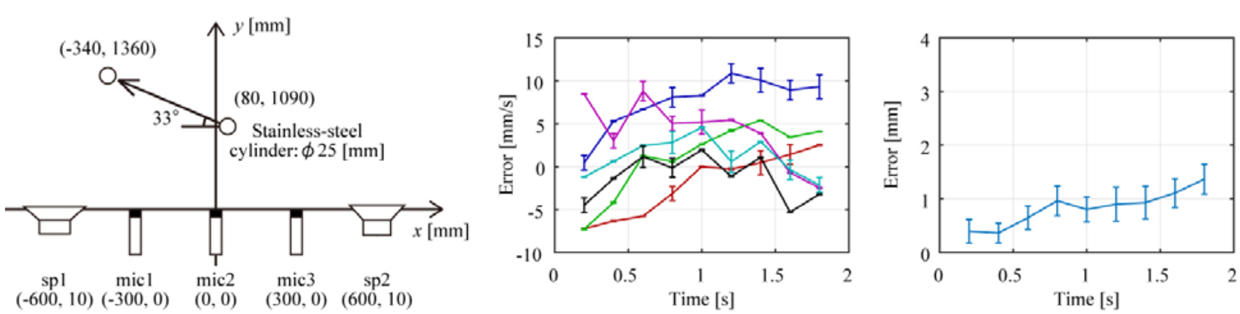

(a) Experimental configulation (b) Doppler velocity (c) Position

P2-A1-4

A Comparison of Walsh and Maximum Length Sequence Signal Coding Applied to Time Domain Beamforming

Carson Willey[1], Carlos Rentel[1]; [1]*X-wave Innovations, Inc., Gaithersburg, Maryland, USA*

Background, Motivation and Objective

Time domain beamforming is an ultrasonic method of imaging point-like scattering objects in low contrast media. This method has been widely applied in medical and industrial ultrasonic imaging modalities, but its resolution is known to be limited by pulse width and frequency. In general, high frequency components of ultrasonic signals are more heavily attenuated, and thus there is a tradeoff between resolution and the maximum distance between a transmitter and receiver of an array. This imposes an upper bound on the size of the region that can be effectively reconstructed using ultrasonic imaging. Another limitation of standard ultrasonic beamforming comes about due to the one-to-all type transmit-receive style signal acquisition. In this type of signal acquisition, one array element transmits and all elements act as receivers. This is repeated for all elements to acquire the maximum amount of information (i.e. full matrix capture) about the interrogated region. This work compares Walsh, and Maximum Length Sequence (MLS) coded ultrasound beamforming with standard beamforming to evaluate the effects on resolution, and signal strength.

Statement of Contribution/Methods

Using a numerical simulation of wave propagation in a two-dimensional acoustic medium as a framework, coded and standard ultrasonic beamforming methods are compared. Attenuation has been included in the model using a loss term that is frequency dependent. Additionally, a variable amplitude noise term is introduced in order to study its influence. A circular full-view array is used to minimize artifacts in the image due to the limited view problem. The medium under investigation contains a single circular low contrast scattering inclusion which is varied in diameter from a fraction to many multiples of a wavelength. The standard beamforming is compared with coded signal ultrasonic beamforming using both Walsh and MLS codes. The coded signals have been investigated for both the one-to-many and parallel transmit-receive (i.e. Code Division Multiple Access) communications. This approach separates the effect of the signal coding when used in each of the two modes of communication. These tests also allow for a comparison between coded signal based, and standard ultrasonic beamforming in terms of the effective resolution, and signal strength.

Results/Discussion

Results have shown that the use of coded excitation allows identification of the contribution from each transmitter within a received pulse made up of many overlapping waveforms. This result shows that parallel transmit-receive operations are possible which can reduce the total number of communications necessary by a factor equal to the number of array elements. Furthermore, it is demonstrated that signal coding increases the signal to noise ratio. Finally, the use of coded signals is shown to decrease the effective resolution length of the beamforming method.

P2-A1-5

Analytical Foundations of Multimode Focusing In Pipes

Julio Isla[1]; [1]*Mechanical Engineering, Imperial College London, London, United Kingdom*

Background, Motivation and Objective

Ultrasonic guided wave inspection has been in use for more than two decades. Its main advantage is that large sections of pipes can rapidly be screened. However, large area coverage comes at the cost of reduced resolution. Higher resolution can be achieved at higher frequencies-thickness products (> 300 kHz*mm in steel), where more wave modes are excited; however, this makes the received signals difficult to understand using current analytical techniques. In general, current techniques only work with a limited number of wave modes and array configurations. Moreover, they cannot simultaneously focus the waves on transmission and reception. All these limitations cause aliasing and therefore the loss of valuable information.

Statement of Contribution/Methods

A multimode focusing methodology that generalizes previous techniques and overcomes their limitations is presented here. The concepts of pipe impulse response function and spectrum are introduced based on linear time-invariant system theory, where the pipe spectrum is a three-dimensional representation of the conventional dispersion curves; this simplifies the analysis of the modes and the focusing algorithms. Furthermore, the methodology can be stated in a simple and compact form using the three-dimensional Fourier transform.

Results/Discussion

Using the proposed methodology, central problems in ultrasonic guided wave inspection are solved: a) any wave mode can be simultaneously controlled in any propagation direction and at any frequency subject to discretization constraints; b) any type of array can be used regardless of the number of transducers and their spatial distribution; and c) the waves can be simultaneously focused on transmission and reception. As a result, aliasing is reduced, and higher resolutions can be attained. Aliasing reduction of up to 60 dB was observed in simulations.

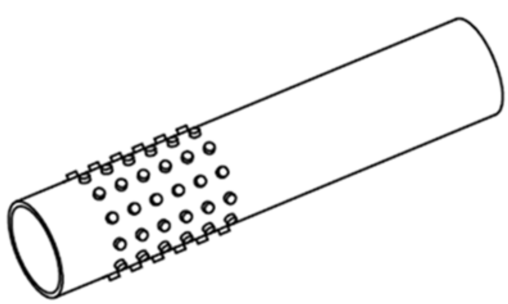

Array of M rings which have N transducers.
Transducers can be individually controlled.

P2-A2 - Sensors

Exhibit Hall

Thursday, September 7, 2017, 9:30 am - 4:00 pm

Chair: **David Greve**
Carnegie Mellon University

P2-A2-1

The influence of Surface Conductivity of Thin Layer Near the Free Side of Piezoelectric Resonator with Lateral Electric Field on Its Characteristics

Boris Zaitsev[1], Andrey Teplykh[1], Alexander Shikhabudinov[1], Irina Borodina[1]; [1]*Saratov Branch, Kotel'nikov Institute of Radio Engineering and Electronics of RAS, Saratov, Russian Federation*

Background, Motivation and Objective

Now designers of acoustic sensors pay special attention on piezoelectric resonators with lateral electric field. The advantage of such resonators is the fact that their parameters depend on the change in mechanical and electrical properties of object under study. For example, one can develop the gas sensor by placing near free side of resonator the film, properties of which are changed due to presence of analyzed gas. This paper is devoted to investigation of influence of thin layer with finite conductivity placed near free side of resonator with lateral electric field on its characteristics.

Statement of Contribution/Methods

The influence of conductivity of thin layer near free side of piezoelectric resonator with lateral electric field on its characteristics was studied theoretically and experimentally. The resonators on lithium niobate plate of X –cut (thickness of 0.5 mm) and on plate of piezoceramics PZT-19 (thickness of 3.58 mm) were studied. Two rectangular electrodes with sizes of 5×10 mm and gap of 2 mm were deposited on one side of lithium niobate plate. Resonators on piezoceramics had the shear sizes of 18×20 mm, and electrodes covered all side of plate with the gap of 4 mm. Thin conducting layer was placed near the free side of the resonators. The calculation of frequency dependencies of real and imaginary parts of electrical impedance was carried out by finite element analysis for change of surface conductivity in range 0.01 μS – 0.1 S. In experiment the influence of thin films of tin dioxide on glass substrates with various values of conductivity on the characteristics of resonators was studied. The frequency dependencies of real and imaginary parts of electrical impedance were measured by LCR meter. The dependencies of resonant frequencies for parallel and series resonances on conductivity of layer were built for different values of gap width.

Results/Discussion

Theory shows that with increase in layer conductivity frequencies of both resonances at first remain constant, then in certain range of conductivity decreases and after that remain constant. For lithium niobate resonator at zero gap changes in frequencies of parallel and series resonances are equal to 2.2% and 0.16%, respectively. The maximum change in resonant frequencies was found in conductivity range 1–1000 mkS. For piezoceramics resonator at zero gap changes in frequencies of parallel and series resonances are 13.5% and 1.57%, respectively. The maximum change in resonant frequencies was observed in conductivity range 1–100 mkS. The experimental results for given values of conductivity and gap width were in good agreement with theory. The obtained results allowed to find the ranges of change in conductivity of thin layer for resonators on lithium niobate and piezoceramics which ensure maximum change in resonant frequencies. These results will be used for development of gas sensors for choice of suitable gas sensitive film. The work is financially supported by Grant RFBR 16-07-00821.

P2-A2-2

The Influence of Viscous and Conducting Liquids on Slot Wave in the Device Based on Delay Line With Shear – Horizontal Acoustic Wave of Zero Order

Irina Borodina[1], Boris Zaitsev[1], Andrey Teplykh[1]; [1]*Saratov Branch, Kotel'nikov Institute of Radio Engineering and Electronics of Russian Academy of Sciences, Saratov, Russian Federation*

Background, Motivation and Objective

It is known that acoustic waves propagating in thin piezoelectric plates compared with wavelength have high value of electromechanical coupling coefficient. It means that electric fields accompanying such waves deeply penetrate in vacuum. Previously we have shown the possibility of the use of this property for noncontact excitation of acoustic wave in piezoelectric plate placed with some gap above the delay line with propagating piezoactive shear – horizontal acoustic wave of zero order. The excitation of slot wave in such structure leaded to the appearance of the clearly expressed resonant peaks on the frequency dependencies of insertion loss and phase of output signal of delay line. It has been shown that such structure may be used for estimation of acoustic properties of various materials. In this paper the influence of liquids with various values of electrical conductivity, viscosity, and permittivity contacting with upper plate on characteristics of slot wave in such structure was investigated.

Statement of Contribution/Methods

As the main element of the device for study of influence of liquid on slot wave the delay line based on piezoelectric plate of Y–X lithium niobate was used. Two interdigital transducers (IDTs) for excitation and reception of acoustic wave with shear – horizontal polarization of zero order (SH0) were deposited on the plate surface. The liquid container was placed above the waveguide of delay line between IDTs. The bottom of the container was made of Z–X lithium niobate plate in such a way that axis X was parallel to wave vector of the SH0 wave in delay line. The given width of the gap between waveguide of delay line and bottom of liquid container was provided by peaces of the aluminum foil. The measurement of the frequency dependence of the insertion loss of output signal was carried out by using meter of S – parameters. At first the frequency dependency of the insertion loss of the device with empty container was measured. The clearly expressed resonant peaks caused by excitation of slot wave were observed on the frequency dependence of insertion loss. Then liquid container was filled by liquid with given properties and the measurement was repeated. For investigation we used water solution of sodium chloride with conductivity from 2 up to 25000 μS/cm, water solution of ethyl alcohol with permittivity from 24 up to 80, and water solution of glycerol with viscosity from 1 up to 1490 mPa c.

Results/Discussion

It was found that change in parameters of liquid under study leads in changes of resonant frequency and depth of peaks on frequency dependencies of insertion loss. The dependencies of these peak parameters on liquid conductivity, permittivity, and viscosity were obtained and discussed. These results showed the possibility to use the slot wave in device based on delay line with shear – horizontal wave for identification of liquids with various values of conductivity, viscosity, and permittivity.

The work is supported by grant of RFBR 16-07-00818.

P2-A2-3

Measurements of Oil Quality Using Shear Horizontal Surface Acoustic Wave Sensor

Saya Kobayashi[1], **Jun Kondoh[2]**; [1]*Graduate School of Integrated Science and Technology, Shizuoka University, Hamamatsu-shi, Japan,* [2]*Graduate School of Science and Technology, Shizuoka University, Hamamatsu-shi, Japan*

Background, Motivation and Objective

Oil has been used in many fields, such as transportation systems and machine tools. Performances of those depend on oil quality. However, quality is normally checked by visual inspection. Therefore, it is required to develop a sensor for monitoring oil quality to measure online and real time. A shear horizontal surface acoustic wave (SH-SAW) sensor can detect liquid properties. In this paper, particles in oil were measured using the SH-SAW sensor.

Statement of Contribution/Methods

The SH-SAW sensors for detecting mechanical and electrical perturbations were fabricated on 36YX-LiTaO3. Operating frequency was 51.5 MHz. Sensor responses were the velocity shift (ΔV/V) and the attenuation change normalized by the wavenumber (Δα/k). As olive oil has the same viscosity with an oil for cars, it was used. Iron particles (diameter: 5-9 µm) of 1.5 mg were added into the oil.

Results/Discussion

The results for electrical and mechanical perturbations are shown in Figs. 1 and 2. The arrows are the time when the particles of 0.5 mg were injected. For Fig. 1, ΔV/V and Δα/k decrease. Using the electrical perturbation theory, electrical property changes were estimated. The relative permittivity increases with increasing particles. For Fig. 2, ΔV/V and Δα/k increase. If the detection mechanism is mass loading, Δα/k is zero. As Δα/k only increases at the first particle injection, we assumed the change was a cause of the viscosity change. Then, due to mass loading, Δα/k is almost constant. ΔV/V normally decreases during the mass loaded. The theory for the mass loading is derived when uniform layer is formed on a surface. In this paper, sphere particles were used. Considering the shape of particles, increase of ΔV/V was explained. The experimental results strongly suggest that the SH-SAW sensor can be measured particles in oil.

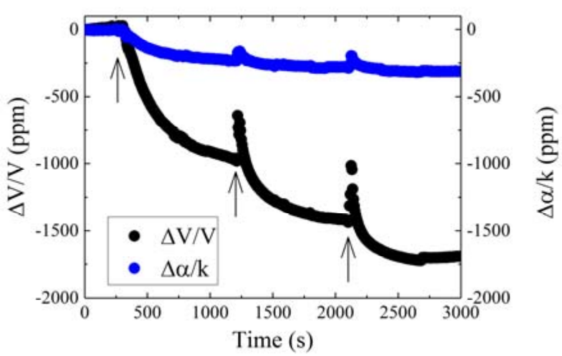

Fig. 1 ΔV/V and Δα/k obtained SH-SAW sensor for electrical perturbation.

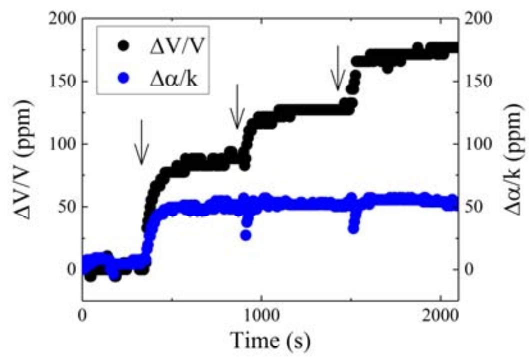

Fig. 2 ΔV/V and Δα/k obtained SH-SAW sensor for mechanical perturbation.

P2-A2-4

Design and Enhancement of a Magnetostrictive Generating EMAT without Magnet

Jianpeng He[1], Ke Xu[2]; [1]*National Engineering Research Center of Advanced Rolling Technology, University of Science and Technology Beijing, Beijing, China, People's Republic of,* [2]*Collaborative Innovation Center of Steel Technology, University of Science and Technology Beijing, Beijing, China, People's Republic of*

Background, Motivation and Objective

Electromagnetic acoustic transducers (EMATs) are non-contact ultrasonic transducers capable of generating and receiving ultrasonic wave on metallic samples. The lack of physical contact makes EMATs suitable for detecting material properties or cracks where samples be moving or hot. However, one important problem associated with operation on ferromagnetic material is that the strong attraction force between the magnet and ferromagnetic plate makes canning difficult. In this work, EMATs which do not contain magnets, are designed and investigated to solve the aforementioned problem.

Statement of Contribution/Methods

A coil only EMAT driven by a large current pulse is used to produce a large dynamic magnetic field in the steel plate. The experimental results shows that broadband, low frequency, S0 Lamb wave can be generated in the steel plate by the dynamic magnetic field via magnetostrictive mechanism. Moreover, a ferrite core with high permeability and low conductivity is employed to enhance the generation efficiency of the coil only EMAT. The influence of the ferrite on coil inductance and lift-off performance is also investigated.

Results/Discussion

The coil only EMAT is able to work at a lift-off higher than 5mm, which is the utmost limit for most typical EMATs. By using a ferrite core, the peak-to-peak amplitude of S0 Lamb wave is increased by a factor of ~1.96 without much changing the inductance of the coil. Although the signal generated by the EMAT with ferrite core attenuates more rapidly than that from the bare coil, enhancement can be achieved at all lift-offs.

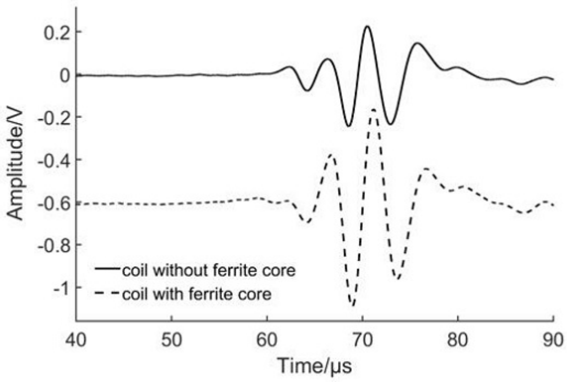

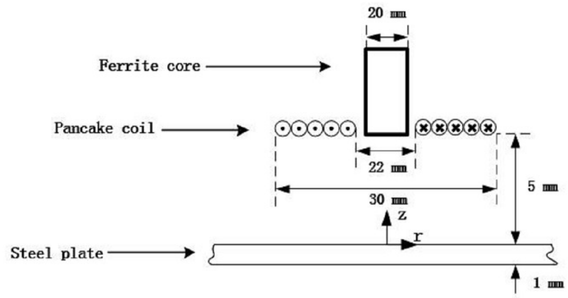

P2-A2-5

Fabrication and Characterization of a Photoacoustic Lens Using a CNT Gel-PDMS Composite Film

Jeongmin Heo[1], Erwin J.Alles[2], Sacha Noimark[2,3], Radhika Poduval[2,3], Richard J.Colchester[2], Ivan P. Parkin[3], Ioannis Papakonstantinou[4], Adrien E. Desjardins[2], Hyoung Won Baac[1]; [1]*School of Electronic and Electrical Engineering, Sungkyunkwan University, Suwon 440-746, Korea, Republic of,* [2]*Department of Medical Physics and Biomedical Engineering, University College London, London, United Kingdom,* [3]*Materials Chemistry Research Centre, Department of Chemistry, University College London, London, United Kingdom,* [4]*Department of Electronic and Electrical Engineering, University College London, London, United Kingdom*

Background, Motivation and Objective

Carbon nanotube (CNT)-polydimethylsiloxane (PDMS) composite films have been used to generate high-amplitude ultrasound pressures (>MPa) under pulsed laser irradiation. A film deposited on concave substrate, which forms a photoacoustic lens, can generate strong, focused ultrasound in a tight spot of <100 µm to enable shock and cavitation effects. Although this technology has been demonstrated for micro-histotripsy and thrombolysis, the fabrication of a high-efficiency photoacoustic lens is still challenging when a large aperture lens with a long radius of curvature (>10 mm) is needed. Previous CNT films were fabricated by a chemical vapour deposition (CVD) process, but the diameter of lenses were limited to 10 to 15 mm to maintain spatial a uniformity of the films. In this study, we utilize spin-coating methods in combination with a CNT-gel and PDMS to make uniform composite films on concave lenses. The films could be fabricated with a higher yield than the case obtained by the CVD process. We characterize photoacoustic lenses in terms of pressure waveforms and amplitudes, frequency spectra, cavitation threshold, and focal spot widths.

Statement of Contribution/Methods

CNT gel-PDMS composite films were fabricated on concave lenses (20 mm and 25 mm in diameter) with a spin-coating process. A functionalized CNT gel solution was first spin-coated on concave substrates; subsequently, PDMS was spin-coated over the CNT film. Focused ultrasound was generated by irradiating the lenses with a pulsed laser beam (Nd:YAG 532-nm wavelength, 6-ns width). Focal waveforms and frequency spectra were characterized below the cavitation threshold. A laser pulse energy for cavitation threshold was measured to evaluate the capability for mechanical destruction.

Results/Discussion

Cavitation was observed at a low pulse energy fluence of 0.24 mJ/cm^2 (0.76 mJ/pulse). Figure 1 shows focal waveforms below and above the cavitation threshold. This result means that our photoacoustic lens can produce cavitation-induced destruction effects using a relatively low input laser energy as compared to previous ones. A centre frequency of 24.5 MHz was measured, resulting in a tight focal width of 50 µm and 210 µm in lateral and axial directions, respectively. We expect that the current lenses will be useful to perform precise ablation on soft tissue using the excitation with low pulse laser energies.

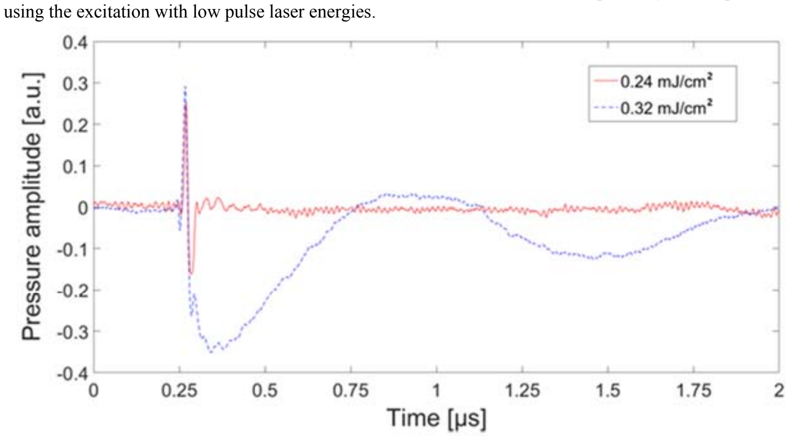

Figure 1. Focused ultrasound waveforms obtained by using a CNT gel-PDMS lens. The red line was measured near cavitation threshold (laser energy = 0.24 mJ/cm^2). Cavitation-induced distortion is clearly shown for the case above the threshold (0.32mJ/cm^2).

P2-A3 - NDE

Exhibit Hall

Thursday, September 7, 2017, 9:30 am - 4:00 pm

Chair: **Jafar Saniie**
Illinois Institute of Technology

P2-A3-1

Ultrasonic Flaw Detection based on Temporal and Subband Signals Applied to Neural Network

Boyang Wang[1], Jafar Saniie[1]; [1]*Illinois Institute of Technology, USA*

Background, Motivation and Objective

Ultrasonic NDE uses high frequency acoustic waves to evaluate materials, and often signal processing is required to detect echoes from defects in the presence of microstructure scattering noise. Scattering noise, also known as clutter, interferes with the flaw signal and cannot be completely eliminated by using classical signal processing methods such as band-pass filtering. In this paper, neural network (NN) is used for ultrasonic flaw echo detection using temporal data and subband signals to design and train the network. This paper also discusses the implementation of the NN algorithm on an FPGA platform using ZYNQ System-on-Chip (SoC).

Statement of Contribution/Methods

To collect sufficient inputs for training the NN, a specimen with a crack is being tested by the system. The position of the transducer, and the location of defects within the material is already known in the test setup. With this arrangement, the position of the crack in the captured signal can be effortlessly identified. Two different training methods are applied for flaw detection. The first algorithm applied to the captured signal was Split Spectrum Processing (SSP) to split the signal into 8 frequency bands. These frequency bands form an 8-dimensional input signal for training the NN. The second algorithm uses a moving window to segment the input data for training the NN. To explore the effectiveness of the data for training the NN, the Embedding Projector Data Visualization (EPDV) is used to project high dimension data into a 3-dimentional (3D) space. This 3D projection space shows that both temporal and subband data cluster in a different way for the flaw signal compared to the clutter. In the hardware realization of these NN, Xilinx Vivado HLS is used to generate the HDL codes for algorithms. The codes for these algorithms were downloaded into the FPGA fabric to customize an acceleration unit for ultrasonic flaw detection. This hardware acceleration unit will be used as a custom peripheral for the embedded ARM processors within the FPGA. With the help of Direct Memory Access (DMA), the input and processed data are transferred very efficiently between DDR RAM (Double Data Rate Random Access Memory) and the custom designed acceleration unit.

Results/Discussion

In this paper, the feasibility of using NN for ultrasonic NDE applications and flaw detection is discussed. The performance and efficiency of training methods are compared. The algorithm is designed to be executed on an ultrasonic testing platform based on ZYNQ SoC. The algorithm acceleration unit is generated by HLS and tested within the ZYNQ platform. The overall system performance is also compared with software-only implementation.

P2-A3-2

Block Sparse Compressed Sensing in Ultrasonic NDE Echo Analysis and Parameter Estimation

Yufeng Lu[1], Jafar Saniie[2]; [1]*Bradley University, USA,* [2]*Illinois Institute of Technology, USA*

Background, Motivation and Objective

In ultrasonic NDE applications, the received signal carries valuable physical information along the wave propagation path such as locations, orientation and sizes of discontinuities. Various signal processing algorithms have been utilized to interrogate ultrasonic echoes, highly overlapped and sometimes noise-contaminated. As of assessing and monitoring the in-situ outsized structures, it becomes challenging to collect and analyze a large volume of data due to the workload time and computational expense. Recently, compressed sensing (CS) has been introduced to exploit signal sparsity, where most coefficients are null or close to zero in the sparse domain. It significantly reduces the system sampling rate. This study aims to explore the CS application in ultrasound echo estimation and analysis.

Statement of Contribution/Methods

The CS sampling scheme together with ultrasonic model-based analysis has been studied for echo acquisition and parameter estimation, where a commonly used model, i.e., Gaussian chirplet (GC), is adopted. Annihilating filter is applied to estimate the time-of-arrivals (TOAs) and amplitude of GCs from the sparse samples through matrix operations. Nevertheless, the size of matrix is proportional to the number of GC echoes. It becomes problematic when outnumbered highly overlapped echoes present in the application. In this investigation, block sparse representation is introduced to limit the number of echoes, subsequently reduces the computation. Additionally, the echo estimation results from previous assessment are used as priori information to assist the sampling scheme and the parameter estimation.

Results/Discussion

An experimental ultrasonic signal with highly backscattered echoes has been evaluated. It has been shown that the block sparse CS can accurately estimate the TOAs and amplitudes of ultrasound echoes in the presence of noise with SNR as low as -5 dB. It also assures the sampling efficiency, while providing computational reduction in one order of magnitude. Furthermore, priori information has successfully applied to improve signal decomposition and parameter estimation. In this study, an efficient block sparse CS approach is introduced to improve the sampling and computation efficacy of ultrasonic echo estimation for NDE applications. The study may have a great potential in material evaluation and structural health monitoring, especially real-time defect detection and pattern recognition.

P2-A3-3

Using SAM Technology and Fuzzy C-Means Algorithm for Defect Inspection of Solder Bumps

Xiangning Lu[1], Zhenzhi He[1], Minghui Shao[1], Lei Su[2]; [1]*Jiangsu Normal University, China, People's Republic of,* [2]*Jiangnan University, China, People's Republic of*

Background, Motivation and Objective

Solder bumps are widely used in surface mount components, which provide electrical and mechanical connection between the chip/package and the substrate. With the decrease of solder bump in dimension and pitch, it becomes more difficult to inspect the solder defects as they are hidden in the IC package.Non-destructive methods have been used for defect inspection of the solder bumps. Scanning acoustic microscopy (SAM) has also been applied to IC devices for screening the internal defects. However identifying defect by human visual in SAM test is prone to fatigue and errors. An intelligent diagnosis system for defect identification is necessary.

Statement of Contribution/Methods

In this paper, an intelligent inspection method using the scanning acoustic microscopy (SAM) and the fuzzy c-means (FCM) algorithm is investigated.FCM is one of the most well-known and powerful intelligent algorithms in clustering analysis. The statistical features in SAM image are calculated and selected to characterize the solder bumps in FCM clustering.

Results/Discussion

The flip chip FA10 with many missing solder bump was chosen as the test vehicle. An ultrasonic transducer of 230MHz was used to capture the image of the flip chip. Sub-images of every solder bump was then segmented and the statistical parameters were calculated, the area of solder bump, the variance of gray-value and the kurtosis were selected to characterize the corresponding solder bump, and were used in fuzzy clustering. The results show that the FCM algorithm reaches a high recognition accuracy of 91.2%, and the intelligent diagnosis method is effective for defect inspection of solder bumps in high density packaging.

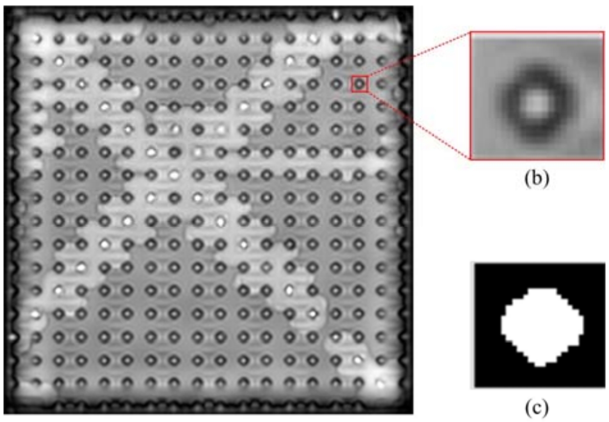

(a) (b) (c)

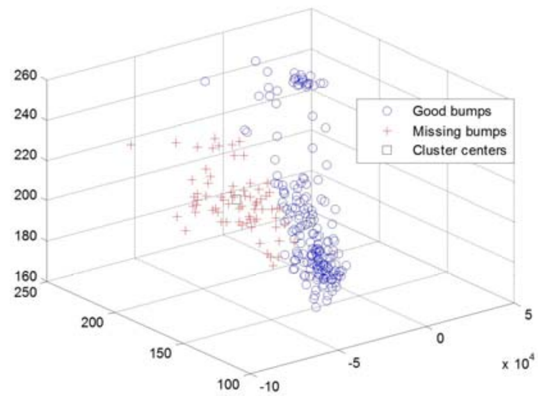

P2-A3-4

Dynamic Shear Strain Analysis for Silhouette Reconstruction of Defects in Anisotropic Laminated Composites

Kenbu Teramoto[1], Haruka Ishibashi[1]; [1]*Saga University, Saga-shi, Japan*

Background, Motivation and Objective

In last decade, composite materials have been used widely in industrial area. Structural elements produced from the composites possess more complicate mechanical properties than components manufactured from isotropic materials. Therefore, imaging algorithms of defects in anisotropic materials have not yet been developed well, because of anisotropic properties of elastic media affect much on the shape reconstruction. This paper proposes a novel method which has an ability to reconstruct images of subsurface defects through evaluating the linearity between the orthogonal pair of out-of-surface shear strains. Numerical simulation and several acoustical experiments are performed to show accuracy and applicability of our proposed approach for imaging of defects in an anisotropic laminated composites.

Statement of Contribution/Methods

In this study, focusing on the normal displacement of the A0 mode Lamb wave field on the surface, we show the reconstruction of the image of subsurface defects. However these media are often featured by multimodal and frequency dispersiveness. This implies that the received signals can be expressed as a sum of wave modes that travel at different frequency dependent velocities. Thus the algorithm of the proposed image reconstruction is shown as follows:[1] obtaining a time series signals of the orthogonal pair of out-of-surface shear strains, [2] calculating the determinant of covariance matrix composed of above vector. [3] reconstructing the wave frontal image of the scattered wave field from the boundary of the corroded region.

Results/Discussion

The experimental results through the proof-of-concept model are summarized with following conclusions and remarks: 1. A near-field imaging method based on the analysis of the covariance matrix of dynamic shear strains is proposed as a novel NDE method. 2. The figure shows the example of reconstructed image of subsurface cylindrical cavities in the CFRP plate. Therefore the proposed imaging method has a super-resolution 2mm which is 1/12 of the wavelength 24mm.

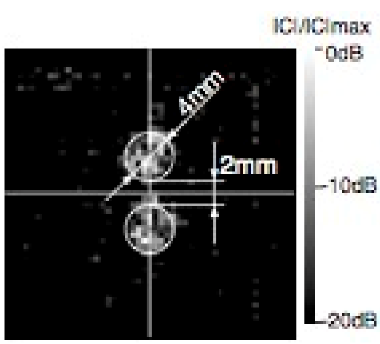

P2-A3-5

Extraction of Healthy Part Using Two Acoustic Characteristics for Defect Detection by Non-Contact Acoustic Inspection Method

Kazuko Sugimoto[1], Tsuneyoshi Sugimoto[1], Takeyuki Oodaira[1], Itsuki Uechi[1], Noriyuki Utagawa[2]; [1]*Graduate School of Engineering, Toin University of Yokohama, Yokohama, Japan,* [2]*Sato Kogyo Co.,Ltd., Japan7*

Background, Motivation and Objective

We have studied a non-contact nondestructive acoustic inspection method using a long range acoustic device (LRAD) and a laser Doppler vibrometer (SLDV) to detect internal defects of concrete. Specimens or actual concrete structures have been measured from 5 m or more. Internal defects were detected and can be visualized. In order to detect internal defects of real concrete structures, quantitative evaluation of healthy part of concrete is important. The purpose is to detect defective parts by identifying and extracting healthy part of concrete.

Statement of Contribution/Methods

Two quantities of acoustic characteristics called 'Vibrational Energy Ratio (VER)' and 'Spectrum Entropy (SE)' are introduced. VER is calculated by integrating measured vibration velocity spectrum in measured frequency range, and the ratio with the minimum value is expressed in decibels. SE is a feature quantity representing 'whiteness' of a signal. Using SE, it is possible to identify optical noise, which is generated depending on the surface condition of concrete, shows frequency characteristics similar to white noise. By two acoustic characteristics, it is possible to distinguish between defective part, healthy part and an abnormal measurement point.

Results/Discussion

For concrete specimens, our defect detection algorithm is effective. However, for actual concrete structures, it is occasionally difficult to distinguish using it. Because an ambiguous region exists between healthy part and defective part. Therefore, we propose a new method for evaluating and extracting healthy part using a statistical method. Fig.1 shows correlation diagram between VER and SE as a result of real concrete structure. A healthy part can be identified, then a defective part can be separated and visualized clearly (Fig.2).

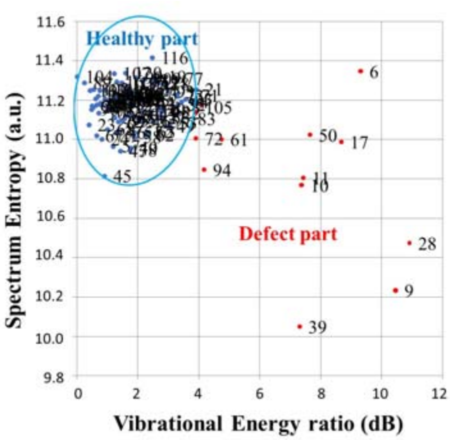

Fig.1. Spectrum entropy (a.u.) vs. vibrational energy ratio (dB).

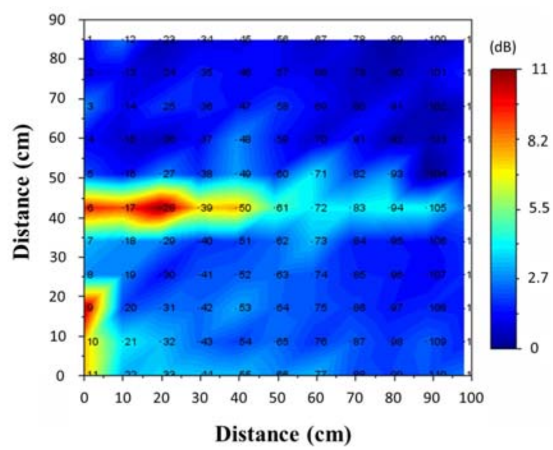

Fig.2. An example of the distribution of vibrational energy ratio.

P2-A3-6

Generation and Propagation of Rayleigh Surface Wave in Anisotropic Materials by Line-focus Ultrasonic Transducer

Qiuyan Li[1], Yuxiang Wang[1], Chenglong Ji[1], Qing-Ming Wang[1]; [1]*Mechnaical Engineering and Materials Science, University of Pittsburgh, Pittsburgh, PA, USA*

Background, Motivation and Objective

Single crystal materials are anisotropic due to their direction-dependent structures and properties, while most metal alloys are often taken as isotropic when their elastic and mechanical properties are evaluated. However, as the additive manufacturing (AM) technologies become widely used in materials and components fabrication, it has been noticed that due to the directional manufacturing processing, the mechanical properties of some alloys show some anisotropic behavior. In this study, we propose a non-destructive testing system using a line-focus ultrasonic transducer to characterize the elastic property anisotropy by evaluating the Rayleigh Surface Wave velocity on the solid surface. The elastic property anisotropy of metal alloys caused by fabrication process is investigated by measuring metal alloys fabricated by different additive manufacturing approaches, while the elastic anisotropy of single crystal silicon wafer is studied along different surface wave propagation directions.

Statement of Contribution/Methods

A line focus ultrasonic system is built for Rayleigh wave velocity measurement. In the system, ultrasonic wave is generated, received and processed by a PVDF piezoelectric transducer, a pulser/receiver and an oscilloscope. Motorized stages are used to control the defocus position and relative angle between the transducer and samples. By measuring the time delay between the surface wave and the direct reflected wave at different defocus position, the Rayleigh Wave velocity of the material at the specific measurement direction is obtained. This velocity can indicate the anisotropy of the material. Metal alloys to be tested are made from Binder jetting (SS316 provided by ExOne) and Laser sintering method [Al alloy (AlSi), nickel alloy (IN718) and Titanium alloy (Ti) by EOS]. The Rayleigh wave velocities are measured at parallel and orthodox direction to the fabrication direction. The Rayleigh velocities of a silicon wafer on four directions are also measured.

Results/Discussion

Figure 1 shows the Rayleigh wave velocity variation on 0° and 90° directions of metal alloys fabricated by additive manufacture methods. The commercial SS420 is tested as reference, which is clearly isotropic. The other alloys show some degree of Rayleigh wave velocity anisotropy, indicating their elastic properties differ at the two different directions.

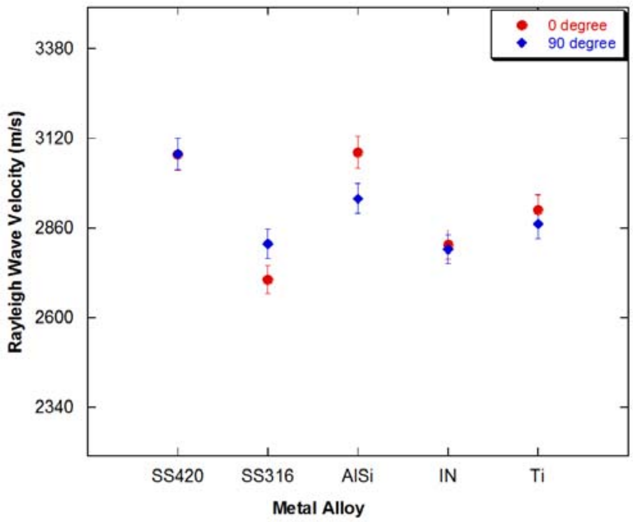

P2-A3-7

Estimation of the Thickness of Refractory Ceramics by the Impact-Echo Method

Seongmin Lee[1], Namho Shin[2], Yongrae Roh[1]; [1]*School of Mechanical Engineering, Kyungpook National University, Daegu, Korea, Republic of,* [2]*Technical Research Laboratory, POSCO, Pohang, Korea, Republic of*

Background, Motivation and Objective

A blast furnace surrounded by steel plates from its outer side and by a refractory lining from its inner side is used to acquire pig iron from iron ores. The refractory lining is a wall of refractory bricks which can withstand elevated temperature as high as 1600 degrees. Although the refractory lining has high thermal resistance, it is inevitable for the lining to suffer from degradation of its thickness and properties when the furnace is operated over a long period of time. Therefore, researches using non-destructive testing technique have been carried out to do accurate measurement of the remaining thickness of the refractory lining in a blast furnace. In this work, the state of the refractory ceramics was characterized by the impact-echo technique. To measure the thickness of a refractory lining by the impact-echo technique, the vibration characteristics of the refractory ceramic should be identified first. The vibration characteristic of refractory ceramics has been identified by assuming the ceramics as an isotropic material. However, in practice, refractory ceramics exhibit anisotropic properties since they are manufactured by pressing ceramic powder along one particular direction. Hence, the impact-echo technique should be well refined to reflect the detailed properties of the refractories for accurate characterization of present state.

Statement of Contribution/Methods

Therefore, in this research, the dimension of refractory ceramic bricks along their width, length, and height directions were estimated by assuming the ceramics to have tetragonal symmetry in their material properties. For the purpose, material properties of the refractory were measured first. Measured properties were longitudinal and shear wave velocities along three orthogonal symmetry directions of the ceramics and overall density. Then, the vibration characteristics of the refractory specimens were investigated through modal analysis using the finite element method. The validity of the numerical analysis was verified by comparing the results with those of experimental modal analysis. Based on the results, the thicknesses of the bricks along the three different directions were evaluated using the impact-echo technique.

Results/Discussion

Accurate characterization of the anisotropic properties of the refractory bricks led to the close agreement of numerical modal analysis results with those of experimental measurement. The discrepancy was less than 2%, which was not possible in precedent works reported so far. The estimated thicknesses of the experimental refractory bricks turned out to differ from actual thicknesses by less than 3.3%. This result confirmed the effectiveness of the impact-echo technique along with anisotropic property characterization to evaluate the thickness of the refractory ceramics. The procedure adopted in this research can be conveniently applied to the thickness estimation of other ceramics as well as isotropic materials.

P2-A3-8

Damage Identification in Plate-Like Structures Based on Lamb Waves Mode-Conversion Sensing Using 3D Laser Vibrometer

Lukasz Ambrozinski[1], Jakub Spytek[1], Kajetan Dziedziech[1], Lukasz Pieczonka[1]; [1]*Robotics and Mechatronics, AGH University of Science and Technology, Krakow, malopolskie, Poland*

Background, Motivation and Objective

Interpretation of Lamb waves signals raises serious difficulties due to their multi-modal and dispersive nature. Different modes propagating with different velocities can be confused and erroneously interpreted as damage-originating components. The S0 and A0 Lamb wave modes, most commonly used for damage identification, exhibit elliptical polarization. Therefore, their in-plane and out-of plane motion components are shifted by ± 90°. In addition, the ratios of in-plane and out-of-plane displacements between these components vary and the direction of particle motion is opposite for both modes. Using a 3D scanning laser vibrometer it is possible to capture the full-field in-plane and out-of-plane wave motion.

Statement of Contribution/Methods

The fundamental A0 and S0 Lamb wave modes differ not only in their polarization but also in group velocities, therefore, they are normally well separated in time. The two modes can occur simultaneously only close to the wave source or to a defect that leads to mode conversion. Since the in-plane and out-of plane motion components are generally out-of-phase, a comparison of these components permits the detection of mode conversion, which leads to a superior and reliable damage detection. Here, we present a damage imaging method based on mode-conversion indicator (MDI) and illustrate the performance of this technique for both metallic and composite panels.

Results/Discussion

Fig. 1 presents exemplary experimental responses of in-plane and out-of-plane Lamb waves components acquired from a composite plate using a 3D scanning laser vibrometer. Both waveforms sets were obtained at points equidistant form the wave source. Fig. 1a presents a set of signals from an undamaged area. The initial part of the responses is dominated by in-plane motion (mainly y axis) which suggests presence of S0 mode. The signals presented in Fig. 1b, on the other hand, were taken from a damaged section of the plate. A significant contribution of the out-of plane (z axis) motion can be observed. Since the in-plane and out-of-plane motion signals are in phase it suggests simultaneous S0 and A0 mode occurrence resulting from proximate mode conversion. We demonstrate that the analysis of such vibration signals measured over a grid of points on a plate-like component can be used for a robust damage identification.

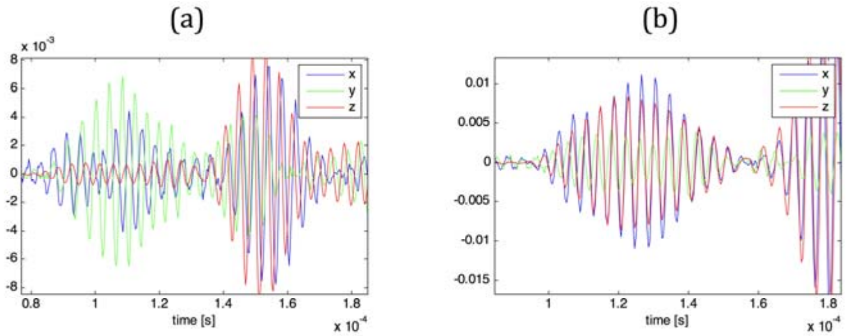

Figure 1. Exemplary experimental time signals acquired at an undamaged area (a) and on a damaged area (b) of a laminated composite plate

P2-A4 - Flow Measurement

Exhibit Hall

Thursday, September 7, 2017, 9:30 am - 4:00 pm

Chair: **Mario Kupnik**
Technische Universität Darmstadt

P2-A4-1

Splitting of the Ultrasounic Beam Path in Clamp-On Ultrasonic Flowmeters due to Propagation through Dispersive Materials

Oliver Millán-Blasco[1], Jordi Salazar[1], Juan A. Chávez [1], Antoni Turó[1], Miguel J. García-Hernández[1]; [1]*Electronic Engineering, Universitat Politècnica de Catalunya, Barcelona, Barcelona, Spain*

Background, Motivation and Objective

Dispersive materials are commonly used in the manufacture of transducer wedges and pipes. Focusing on Clamp-on ultrasonic flowmeters, the incident angle is not normal to the pipe surface and a coupling wedge is necessary. In dispersive materials, the propagation velocity depends on the frequency. Therefore, when the excitation signal contain several frequential components, according to Snell's law, different diffraction angles are produced for each frequency at the boundaries between materials, producing the splitting of the ultrasound beam path. The objective of this work is to describe this phenomenon and analyses the implications it has in flow measurement in Clamp-on ultrasonic flowmeters.

Statement of Contribution/Methods

In our analysis, commercial elements were used. The splitting of the ultrasonic beam will be demonstrate by a two-dimensional numerical ray model based on the Clamp-on flowmeter geometry and by experimental measurement. Figure 1 is an example of how the ultrasonic beam widens due to the propagation through dispersive material, in this case, both pipe and transducer wedge materials were dispersive.

Results/Discussion

As a result of split path, the ultrasonic beam widens and the transducer aperture become too small to receive all the frequential components contained in the ultrasonic beam. Thus, when the ultrasonic beam is carried by the liquid that flows inside the pipe, the reception transducer receives different frequency contributions, producing a change in its spectral composition. The mixing of these frequencies (phasors), generates a reception signal altered in phase and amplitude by the flow. Moreover, modulation will change as a function of which frequencies are combined at the reception aperture. This produces nonlinear changes in the signal phase affecting the flow measurement in Clamp-on ultrasonic flowmeters. By experimental measurement, the flow linearity error could reach values up to 6.4%.

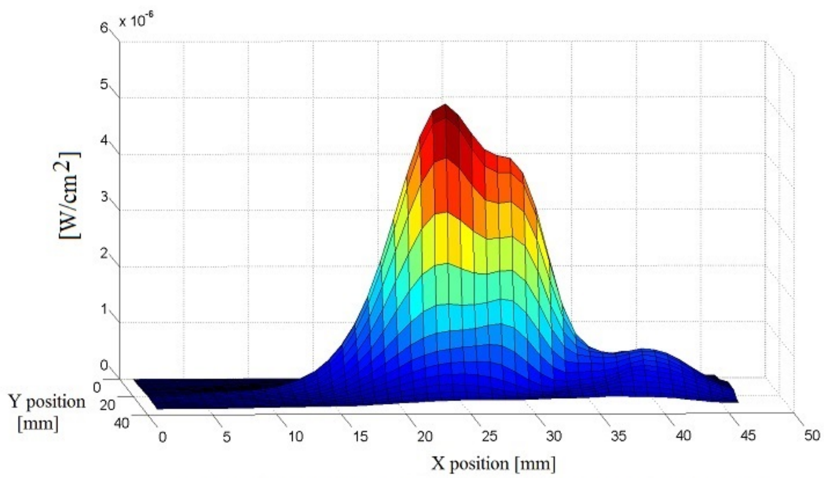

Fig.1. Beam widening due to the splitting of the ultrasonic beam path

P2-A4-2

Influence on the Accuracy of Clamp-On Ultrasonic Flowmeters due to the Recombination of Multiple Propagation Paths

Oliver Millán-Blasco[1], Jordi Salazar[1], Juan A. Chávez [1], Antoni Turó[1], Miguel J. García-Hernández[1]; [1]*Electronic Engineering, Universitat Politècnica de Catalunya, Barcelona, Barcelona, Spain*

Background, Motivation and Objective

Clamp-on ultrasonic flowmeters geometry includes four different materials in the ultrasound propagation path: wedge, coupling material, pipe and liquid. In this case, oblique incidence ray generated by the emitter transducer is splitted into several rays caused by multiple reflections in pipe wall or because of propagation mode conversion at interfaces. These multiple paths are recombined at the reception transducer aperture, producing a single signal whose amplitude and phase depend on which proportion each paths contributes. The objective of this work is to quantify this phenomenon and analyses the implications it has on the accuracy of Clamp-on ultrasonic flowmeters

Statement of Contribution/Methods

The influence on the accuracy caused by the recombination of multiple paths will be demonstrated by a two-dimensional numerical model based on the Clamp-on flowmeter geometry and validated experimentally. Figure 1 shows a possible propagation paths distribution in Z-mode measurement configuration, taken into account just one reflection inside the pipe wall.

Results/Discussion

In this work has been proven that the difference in the recombination of ultrasonic signal in upstream and downstream produce a linearity error in the flow measurement. This error will depend on the geometry where the Clamp-on ultrasonic flowmeters is installed. The factors involved on the geometry are pipe material, wall thickness, pipe diameter, the velocity and the type of the liquid that flow inside the pipe. The mixing of multiple paths, generates a reception signal altered in phase and amplitude by the flow. Moreover, modulation will change as a function of the proportion each path contributes at the reception aperture.

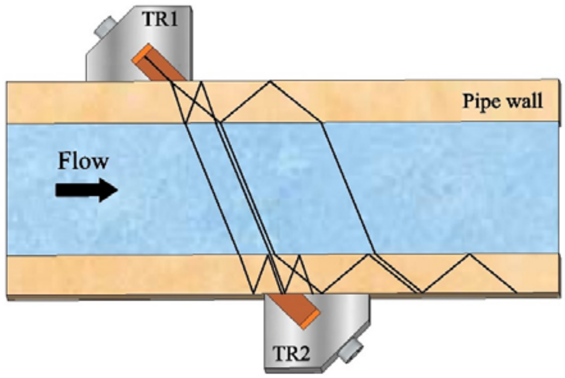

Fig. 1. Propagation paths in Z-mode configuration

P2-A4-3

Characterization of Nonhomogeneity in the Dispersive Properties of the Materials Used in Pipes

Oliver Millán-Blasco[1], Jordi Salazar[1], Juan A. Chávez [1], Antoni Turó[1], Miguel J. García-Hernández[1]; [1]*Electronic Engineering, Universitat Politècnica de Catalunya, Barcelona, Barcelona, Spain*

Background, Motivation and Objective

Accurate measurement of acoustic dispersion has important applications in theoretical acoustics, ultrasound tissue characterization, ultrasound measurement systems, etc. Usually, the parameter of interest associated to dispersion is the variation in the propagation velocity as a function of the frequency or the temperature. Nevertheless, this work is focused on the study of the variation in the propagation velocity caused by the intensity of the acoustic signal. As a consequence, the lack of homogeneity in dispersive properties of polymeric materials, as a function of the signal power, produces a measurement error in Clamp-on ultrasonic flowmeters.

Statement of Contribution/Methods

Three pipes made of polymeric materials (PVC, PP and PVDF), which are commonly used in industrial installations, have been characterized. For each pipe, two acoustic maps with two different acoustic intensity signals, 1.18W/cm2 and 16.2mW/cm2, were obtained (these acoustic field levels are similar to those that appear, during operation, below the transducers in commercial Clamp-on ultrasonic flowmeters). These maps show the propagation velocity along the pipe surface as a function of the power of the signal. The method used to calculate the propagation velocity is based on the utilization of both transmitted and reflected pulse. The advantage of this method is that it is not necessary to measure the pipe wall thickness. Therefore, the accuracy of the propagation velocity is not affected by the uncertainly of the thickness measurement or by the irregularity that the pipe wall may have.

Results/Discussion

Figure 1 is an example of the acoustic maps obtained for a pipe made of PP material. These maps reveal two effects that are not usually taken into account. The first one is the variation of the propagation velocity with the power of the signal and the second one is the nonhomogeneous behavior along the whole pipe surface. The combination of both effects, produces a variation of the zero-flow measurement in ultrasonic Clamp-on flowmeter caused by not fulfilling the reciprocity criterion.

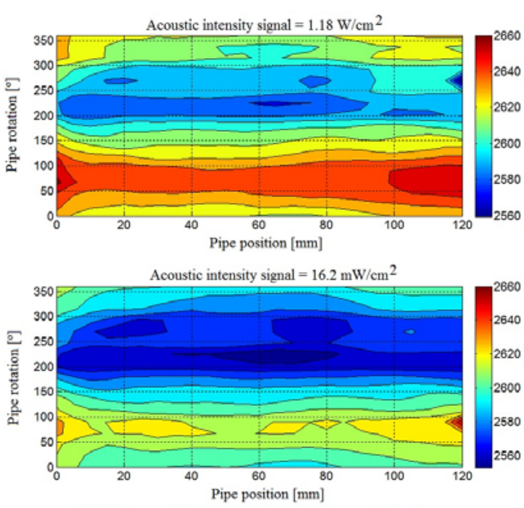

Fig.1. Maps with the acoustic behaviour of PP pipe.

P3-A1 - POA - Opto-Acoustics

Exhibit Hall

Thursday, September 7, 2017, 9:30 am - 4:00 pm

Chair: **Sarah Benchabane**
CNRS, Université de Bourgogne Franche-Comté

P3-A1-1

Spatio-Temporal Superposition of LGFU and HIFU to Facilitate Acoustic Cavitation

Lee Seung Jin[1], Baac Hyoung Won[1]; [1]*Sungkyunkwan University, Korea, Republic of*

Background, Motivation and Objective

Laser-generated focused ultrasound (LGFU) is a promising modality for micro-precision therapy, relying on cavitation-induced mechanical disturbance. However, conventional LGFU systems still require a high laser energy (several to tens of mJ/pulse), irradiated onto an optoacoustic lens, to generate a focal pressure sufficient for acoustic cavitation at focus. Acoustic attenuation over the tissue depth requires even higher pressure and laser energy to perform cavitational therapy. In an effort to lower the input laser energy to meet cavitation threshold, we propose a dual focused system of LGFU and high-intensity focused ultrasound (HIFU) generated by a secondary transducer. As the HIFU plays a role of increasing the temperature at the superposed focus, the cavitational requirement for LGFU is significantly mitigated, thus enabling more efficient therapeutic treatment.

Statement of Contribution/Methods

An optoacoustic transmitter for laser-generated ultrasound was fabricated by using a CNT-PDMS composite film on a plano-concave lens. An Nd:YAG pulsed laser beam (7-ns width and 532-nm wavelength) was irradiated on the focal transmitter to produce LGFU. LGFU amplitudes and spatial profiles were characterized by a fiber-optic hydrophone. A thermal effect induced by a piezoelectric transducer was measured by a k-type thermocouple attached 1 mm apart from the hydrophone. Both LGFU and HIFU waveforms were overlapped at the focus. Finally, the cavitation threshold for LGFU was measured as the temperature at the focal region is raised.

Results/Discussion

We demonstrated the superposition of two transmitters: LGFU (13 MHz) and HIFU (4.1 MHz) to lower the cavitation threshold by controlling the temperature at the focal zone. For fixed LGFU amplitudes in a subthreshold regime for cavitation, we could significantly increase the temperature at focus by the HIFU and observe the cavitation. Figure 1 shows example waveforms of LGFU (produced by a laser energy of 4.35 mJ/pulse), HIFU for 10°C enhancement, and superposition. It is clear that the LGFU alone operated in the subthreshold does not produce cavitation, but the dual focusing enables the cavitational disturbance at the focus. This means that the dual focusing can produce cavitation over a deeper region (e.g. in the tissue) under the same input laser energy, which enables micro-precision therapy over a deep range as well.

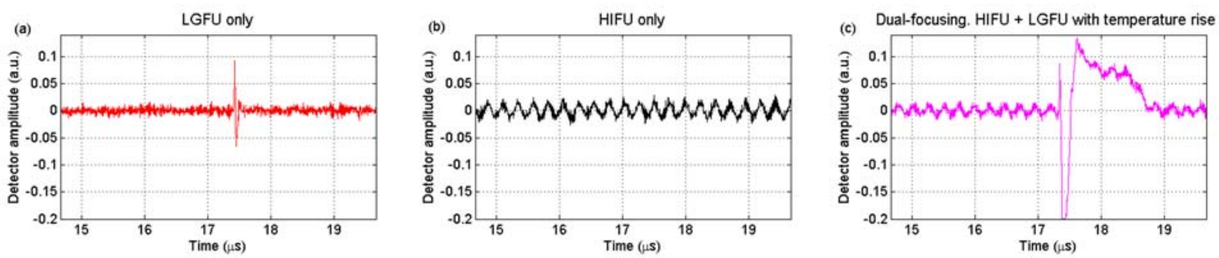

P3-A1-2

Photoacoustic-Based SO_2 Assessment Oo Femoral Bone Marrow in a Murine Model of Leukemia

Cayla Wood[1,2], Karine Harutyunyan[3], Jorge Delacerda[1], Niki Zacharias Millward[2,4], Sriram Shanmugavelandy[4], Caterina Kaffes[1], Marina Konopleva[2,3], **Richard Bouchard**[1,2]; [1]*Department of Imaging Physics, The University of Texas MD Anderson Cancer Center, Houston, Texas, USA,* [2]*Graduate School of Biomedical Sciences, The University of Texas MD Anderson Cancer Center UTHealth, Houston, Texas, USA,* [3]*Department of Leukemia, The University of Texas MD Anderson Cancer Center, Houston, Texas, USA,* [4]*Department of Cancer Systems Imaging, The University of Texas MD Anderson Cancer Center, Houston, Texas, USA*

Background, Motivation and Objective

Leukemia commonly leads to hypoxia in the bone marrow, which can then result in increased resistance to chemotherapy. However, the relationship between local hypoxia and disease progression is not well understood, and it is unclear whether hypoxia in the bone marrow is diffuse or focal in presentation. Spectroscopic photoacoustic (PA) imaging-based estimation of blood oxygen saturation (SO_2) can be used as a biomarker for tissue hypoxia. In this study, we investigate the longitudinal repeatability of PA-based SO_2 estimates in the femoral bone marrow of a murine model of leukemia.

Statement of Contribution/Methods

C57ALB mice were injected with p190-BCR-ABL acute lymphoblastic leukemia cells, while control mice were not injected. Engraftment of cells expressing luciferase was confirmed with IVIS imaging (Fig. 1E, upper right). Axial PA images (Fig. 1B) were obtained in two-day intervals at six wavelengths through the full femoral extent to allow for linear unmixing of the oxy- and deoxyhemoglobin (HbO_2, HHb) signals using the inVision 256-TF (iThera Medical) PA small-animal imaging system (Fig. 1A). Regions of interest (ROIs) were then manually applied to images over the blood-laden area of bone marrow, as identified by PA-based hemoglobin signatures. Mean and standard deviation of SO_2 in each axial slice were then compared to different femoral locations and time-points to assess the spatial and temporal stability of the imaging technique (Fig. 1E). A matched CT scan of murine hind limbs was co-registered with 800-nm PA volumetric data to confirm that the PA signature co-located with the bone marrow cavity (Fig. 1C,D).

Results/Discussion

In control mice, the mean PA-based SO_2 estimate was 43.0% with a standard deviation of 2.0% over the four time-points. In the diseased mice, mean SO_2 signal was 38.6%, so the overall SO_2 was not significantly lower than the control mouse. However, the standard deviation of the SO_2 as a function of position along the femur increased from 1.2% on day 0 to 5.8% on day 6 in one of the diseased mice, whereas the standard deviation in the control mouse did not exceed 2.6%. This indicates that the SO_2 over the length of the femur may become less uniform as the disease progresses, implying that there are local cell clusters where hypoxia develops more rapidly than in others.

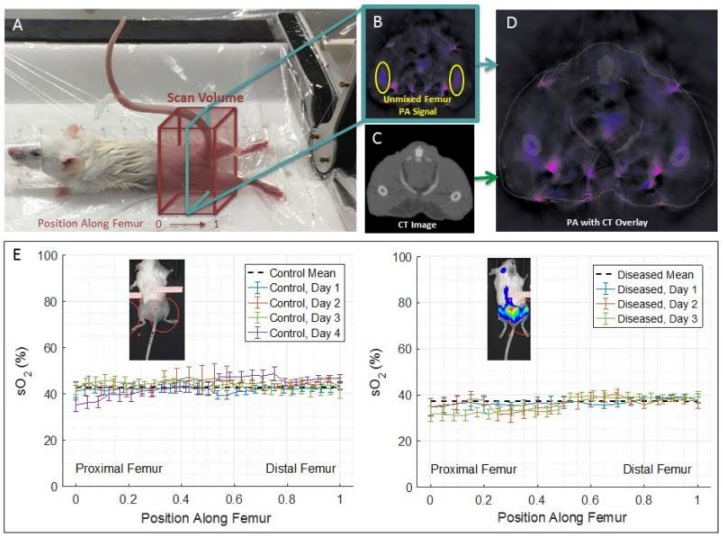

P3-A1-3

Evaluation of Wave Velocity in C-Axis Oriented Hydroxyapatite Film by Brillouin Scattering Technique

Hiromichi Hayashi[1], Mami Matsukawa[1], Takafumi Kubota[1], Shohei Tokuda[1], Yoshiaki Shibagaki[1], Mami Kawase[1]; [1]*Doshisha Univ, Kyotanabe, Kyoto, Japan*

Background, Motivation and Objective

Hydroxyapatite (HAp) is a useful biocompatible material and is used for the surface coating of artificial bone. It has been reported that the oriented HAp promotes rapid recovery of the bone fracture[1], although most of coating HAp layers on the commercial artificial Titanium (Ti) bones are not oriented. As a new coating layer, our group has reported the highly oriented HAp film on Ti substrate fabricated by RF magnetron sputtering[2]. This study reports the evaluation of longitudinal wave velocities in the oriented HAp film, which are related to the elastic properties and the adhesion performance. The velocity in the oriented HAp film was experimentally observed by a Brillouin scattering technique.

Statement of Contribution/Methods

A HAp film was fabricated on a Pyrex glass substrate (25×100×0.5 mm) coated with Ti by RF magnetron sputtering. The film thickness was about 4.6 μm. The preferred crystalline orientation of HAp was evaluated by an X-ray diffractometer (PANalytical). The in-plane longitudinal wave velocities were measured by a Brillouin scattering system, which composed of a tandem Fabry-Pérot interferometer (JRS Instruments) and a solid-state laser (Laser Quantum). This system enables non-destructive and non-contact measurement in a small area (diameter: 50 μm). Velocity of the wave propagating along the longitudinal direction of the substrate could be observed.

Results/Discussion

The HAp orientation gradually changed due to the position on the substrate. Fig. 1 shows relation between in-plane averaged longitudinal wave velocities and (002) plane peak intensities of the HAp film. (002) peak intensity shows the degree of HAp c-axis alignment normal to the film surface. Longitudinal wave velocity decreased as the (002) peak intensity increased. This means that the in-plane elastic properties decreased as the HAp crystallites align normal to the surface. The velocity values were reasonable to the reported moduli of HAp, telling that the film seemed appropriate as the coating material. Using this Brillouin scattering technique, the measurement of velocity in the thickness direction also seems possible in the future work.

[1] K.Grandfield, et al. *J. R. Soc. Interface.* 7, 1497 (2010)

[2] K.Hirata, et al. *Proc. Joint ISAF. ECAPD. PFM Conference.* 5453(2016)

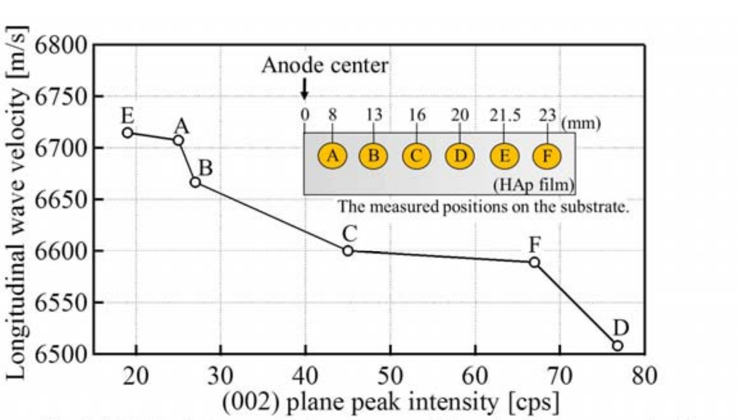

Fig. 1 Relation between in-plane averaged longitudinal wave velocities and (002) plane peak intensities of the HAp film.

P3-A2 - PPN - Phononics

Exhibit Hall

Thursday, September 7, 2017, 9:30 am - 4:00 pm

Chair: **Sarah Benchabane**
CNRS, Université de Franche-Comté

P3-A2-1

Phononic Lens for Suppressing Diffraction of Surface Wave in Lithium Niobate Substrate

Jia-Hong Sun[1], Yuan-Hai Yu[1]; [1]*Department of Mechanical Engineering, Chang Gung University, Tao-Yuan, Taiwan*

Background, Motivation and Objective

Surface acoustic wave (SAW) devices are widely used as acoustic-electronic components today. The lithium niobate was often used as the substrate of SAW devices for its higher electromechanical coupling coefficient. In some applications like RFID tags and sensors, SAW devices have a long delay line and the energy loss of diffraction is considerable. Phononic crystals (PnC) have properties of band gaps and anisotropic propagation. Band gaps were proposed as filters, reflective gratings, and waveguide [1-2]. In our previous study, self-collimation of SAW propagating in a tungsten/lithium niobate PnC was studied, and a PnC delay line was used to lower beam spreading [3]. In this paper, we further analyze the anisotropic SAWs in PnCs systematically and then phononic lenses were designed to suppress diffraction in SAW devices.

Statement of Contribution/Methods

Finite element method was used to analyze the surface acoustic waves in the PnCs. The lithium niobate-substrate PnC in Ref. [3] was adopted in this study. Periodic cylindrical tungsten films formed a square lattice and the ΓM direction aligned with X direction of the 128° rotated Y-cut lithium niobate substrate. A unit cell was defined to compute acoustic dispersion curves firstly. Eigenmodes of Rayleigh wave, Love wave and other high order modes inside the unit cell were identified. Then equal frequency contours (EFC) were calculated at selected frequencies to observe the anisotropic propagation. For a PnC with 4 µm lattice constant, 1.6 µm cylinder radius, and 400 nm cylinder height, the 445 MHz Rayleigh performed a concave EFC. A flat phononic lens was then defined accordingly and negative refraction of energy velocity of SAW at the interfaces of lens was promised.

Results/Discussion

SAW propagating through PnC was simulated to design the flat phononic lens. The negative refraction of energy velocities let lens converged SAW. Then phononic lens was optimized according to the transmission of SAW passing through it. Tapered PnC was defined at boundaries of the lens to reduce the discontinuity. The layer numbers of the PnC in the lens affected both the transmission and focal length of SAW. Some proper designed phononic lenses were set in front of inter-digital transducers. The simulation showed these lenses can suppress diffraction of SAW.

[1] T.-T. Wu, W.-S. Wang, J.-H. Sun, J.-C. Hsu, and Y.-Y. Chen, Appl. Phys. Lett., vol. 94, no. 101913, 2009.
[2] V. Yantchev, Appl. Phys. Lett., vol. 104, no. 103503, 2014.
[3] J.-H. Sun and Y.-H. Yu, 2015 IEEE Ultrason. Symp., Taipei, Taiwan.

P3-A2-2

Proposal for Topological Insulator Realized with Piezoelectric Resonators

Sean McHugh[1]; [1]Resonant Inc., Santa Barbara, CA, USA

Background, Motivation and Objective

Topological Insulators (TI) have been the subject of intense research by condensed matter physicists over the last decade for many reasons. One of which is the existence of helical edge modes, which can occur even when wave propagation through the bulk of the material is impossible. Eager to engineer devices that support these helical modes, researchers have invented classical systems analogous to the quantum mechanical TI. However, the path to miniaturization for most of these systems for practical devices is not always clear. Here, I propose a classical TI which can be realized with piezoelectric resonators. By using piezoelectric resonators, one may take advantage of the high linearity, compact design, and established micro-fabrication techniques.

Statement of Contribution/Methods

This paper describes an analytical method for designing a piezoelectric TI. Numerical simulations are performed to confirm and visualize the expected helical edge modes.

Results/Discussion

The object in consideration is an array of metal resonators coupled by a piezoelectric material. The resonators of this system are assumed to be mechanically and electrically coupled to one another similar to the metal fingers of an interdigital transducer. The conditions necessary for the array to form a TI are found explicitly. In particular, the admittance matrix describing the electrical interactions between resonators is found. Although complicated, the electrical interactions for resonator arrays of modest size should be realizable. Prospective realizations are discussed.

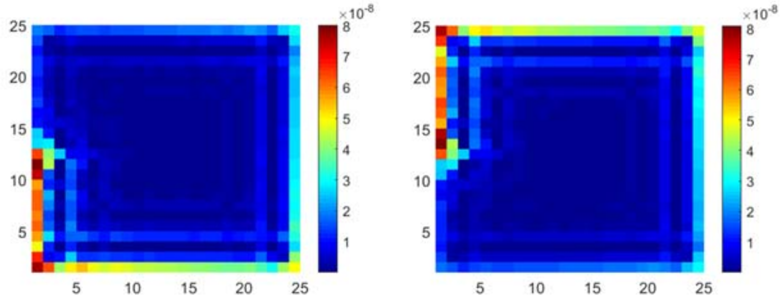

Figure. Mechanical amplitudes of two helical edge modes on a two-dimensional array of piezoelectric resonators.

P3-A2-3

Observation of Band Gaps in Chirped Interdigital Transducers

Anurupa Shaw[1], Damien Teyssieux[2], Vincent Laude[1]; [1]*FEMTO-ST, Besançon, France,* [2]*FEMTO-ST, France*

Background, Motivation and Objective

A grating structure serves as the most fundamental element of inter-digital transducers (IDTs). IDTs are used for excitation and detection of surface acoustic waves (SAW) in Ultra wide band (UWB) SAW devices. Reflections on the metal fingers greatly affect the functionality of IDTs, and thus that of the SAW devices they are used in. Hence, this effect has been studied extensively and several models and theories have been proposed for this purpose. The signal properties of IDT devices can be controlled by varying several parameters like the number of fingers (electrodes) of the IDT or the spatial distribution of the pitch of the array of fingers. Here, we wish to study the generation and propagation of SAW inside a chirped IDT.

Statement of Contribution/Methods

In the case of bidirectional IDts, SAWs are excited toward both right and left directions. When an input chirp signal is sent through the IDT with a continuously varying pitch, there is a superposition of forward and backward propagating SAW with different amplitudes. The final response at each position within the IDT is due to the interference of these waves. At certain positions, due to destructive interference, a band gap is observed. Such a phenomenon has been reported previously, e.g. in grating based Surface Plasmon generation studies.

Results/Discussion

In this work, the occurrence of band gaps is investigated in UWB SAW devices working within a frequency range of 200 MHz – 400 MHz. A p-matrix approach is used to model the response of a chirped IDT. Three cases are studied in which the pitch of the chirped IDT is varied linearly, hyperbolically, and as a mean of the two, respectively. As we move from the entrance to the exit of the chirped IDT, the band gap is observed to shift in frequency. The superposition of the forward and backward propagating SAW is observed within the chirped IDT with a differential interferometer setup specially designed to measure short pulses. A comparison between the modelled response and experimental results for the different cases is presented. Pulse compression or dilatation as a function of position is observed depending on the input signal.

P3-A2-4

Tuning Waves in Soft Phononic Rods via Large Deformation and Electromechanical Coupling

Bin Wu[1], **Weiqiu Chen**[2]; [1]*Department of Engineering Mechanics, Zhejiang University, Hangzhou, China, People's Republic of,* [2]*Department of Engineering Mechanics, Zhejiang University, Hangzhou, Zhejiang, China, People's Republic of*

Background, Motivation and Objective

Phononic crystals have attracted intensive research interest for decades since the early 1990s. They exhibit a spatially periodic feature regarding the distribution of physical properties, geometry, boundary conditions, or/and external stimuli, making their wave spectrum quite different from the conventional continuous one, usually with frequency band gaps where waves cannot propagate through them. These band gaps are formed due to the Bragg scattering and can be used to manipulate waves that are the basis of many wave devices.

In 2008, Bertoldi and Boyce found that buckling and large deformation can be used efficiently to tune the band gaps in soft phononic crystals. Inspired by the work of Bertoldi and Boyce, recently we have conducted a series of study on wave propagation in soft phononic crystals of various configurations. In this report, we show that the combination of large deformation and electromechanical coupling can lead to a more flexible and efficient way to tune the band gaps by considering a simple phononic rod of soft electroactive elastomer with periodically spaced electrodes.

Statement of Contribution/Methods

We consider a circular solid phononic rod made of dielectric elastomer, whose constitutive behavior is governed by the generalized new-Hookean model. A series of mechanically negligible electrodes are placed periodically along the rod. A large deformation is induced by an axial force to form a uniformly pre-deformed configuration. Then we consider two paths to form the periodicity of the pre-deformed rod, and to arrive at the desired initial configuration. For Path A, we keep the longitudinal stretch unchanged, and apply an electric voltage over any two neighbouring electrodes. For Path B, we keep the axial force unchanged, and then apply the voltage. These two paths give birth to two macroscopically different phononic rods. Based on the nonlinear theory of electroelasticity proposed by Dorfmann and Ogden, we are able to derive exactly all nonlinear field variables without any approximation.

Then we use an analytical method to derive the explicit dispersion equation for the infinitesimal incremental wave motion that is further superimposed on the initial configuration. The only approximation made in the derivation is the stress relaxation which is well-accepted in the classical rod theory. Based on the derived dispersion equation, we numerically calculate the band structures of the two different phononic rods that are formed through Paths A and B respectively.

Results/Discussion

Comprehensive numerical simulations have been conducted. From the results including those not shown here, we find that the both the large deformation and electromechanical coupling play an important role in wave propagation in the phononic rod under consideration. Thus, they can be efficient means to engineer the band structure, and in particular to tune the band gaps in soft electroactive phononic crystals.

P3-A3 - PNL - Nonlinear Ultrasound

Exhibit Hall

Thursday, September 7, 2017, 9:30 am - 4:00 pm

Chair: **Andreas Mayer**
HS Offenburg - Univ. of Applied Sciences, Gengenbach

P3-A3-1

Investigation of the Nonlinear Propagation of Ultrasound through a Bubbly Medium Including Multiple Scattering and Bubbl-Bubble Interaction: Theory and Experiment

Amin JafariSojahrood[1,2], Qian Li[3], Hossein Haghi[1], Tyrone M. Porter[3], Michael C. Kolios[1]; [1]*Physics, Ryerson University, Toronto, Ontario, Canada,* [2]*Institute for Biomedical Engineering, Science and Technology (iBEST), a partnership between Ryerson University and St. Michael's Hospital, Toronto, Canada,* [3]*Biomedical Engineering, Boston University, Boston, MA, USA*

Background, Motivation and Objective

Understanding of the propagation of ultrasound through a bubbly medium is a challenging task because of the nonlinear dynamics of the bubbles and their effect on the attenuation and sound speed of the medium. The majority of the studies on this subject apply linear models, which will generate inaccurate results, especially at higher-pressure excitations. These studies have also ignored the effect of bubble-bubble interaction and nonlinear multiple scattering.

Statement of Contribution/Methods

In this work, we have numerically simulated the attenuation and sound speed of a bubbly medium by solving our recently developed nonlinear model. An efficient method to investigate the nonlinear bubble-bubble interaction and multiple scattering is developed, and this phenomenon is included the numerical investigations through considering a cluster of 130 randomly distributed interacting bubbles with sizes derived from experimental measurements. Broadband experimental attenuation measurements of monodisperse lipid-coated microbubble solutions were performed with peak acoustic pressures ranging within 10-100kPa. The bubble solutions had mean diameters of 4-6 micron and peak concentrations of 1000 to 15000 bubbles/ml.

Results/Discussion

At lower concentrations (with minimal bubble-bubble interactions), predictions of the model (attenuation and sound speed vs frequency) in the absence of interaction are in good agreement with experimental measurements (Fig 1&2). At higher concentrations, secondary peaks in the attenuation and sound speed diagrams as a function of frequency appear. Through considering the bubble-bubble interactions, the numerical results can predict the quantitative changes in the attenuation and frequency as well as the generation of secondary peaks.

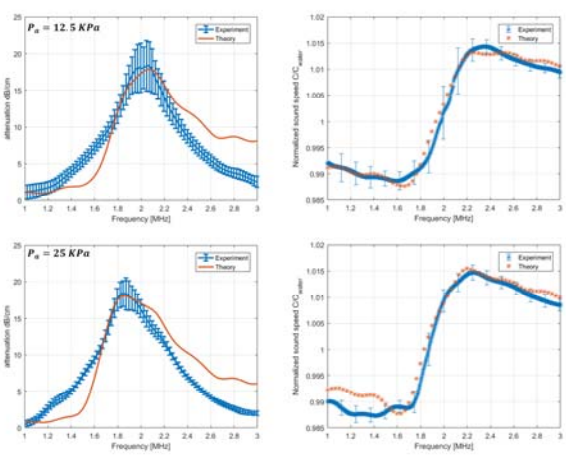

figure 1

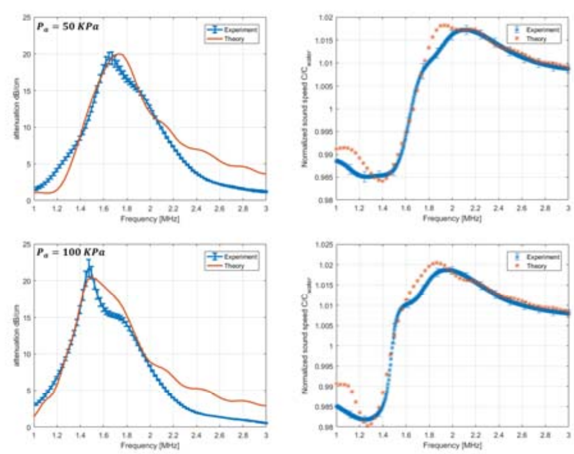

figure 2

P3-A3-2

Selecting the Number and Location of Sources and Receivers for Non-Linear Time-Domain Inversion

Ana B. Ramirez[1], Sergio A. Abreo[1], Koen van Dongen[2]; [1]*Universidad Industrial de Santander, Colombia,* [2]*Delft University of Technology, Netherlands*

Background, Motivation and Objective

The design of ultrasound scanning systems for breast cancer detection is a challenging task. To decide on the number of transducers and where to place them, several approaches could be followed. A simple and straightforward approach is to compute for several configurations the energy distribution in the region of interest, and treat each receiver as if it is a transmitter. In that case, the assumption is made that the effect a source or a receiver has on the resulting image is on an equal level. This assumption is mainly based on reciprocity; the observation that the response RAB measured by a receiver at the location B and for a transmitter at location A is identical to the response RBA obtained after interchanging the source and receiver. This is true for linear imaging methods, where a source can be interchanged with a receiver without affecting the resulting image. However, for the non-linear imaging method named Contrast Source Inversion, it does matter. In the past we showed that interchanging sources with receivers does affect the image. To test the hypothesis that this is the case for any non-linear inversion method, we also investigated this effect for a completely different imaging method: non-linear time-domain inversion.

Statement of Contribution/Methods

We tested the time-domain imaging method for two different setups. We have a circular aperture with a radius of 63 mm. In all cases, all sources and receivers are equally distributed over the aperture. For the first configuration, the number of sources is NS=10 and the number of receivers NR=100 and for the second configuration NS=100 and NR=10. The embedding has a speed of sound of 1540 m/s, with three different contrast objects, two of them having speed of sound of 1437 m/s, and one having a speed of sound of 1572 m/s. For each source, the forward problem is solved using a time-domain full-wave method. For imaging, the non-linear time domain inversion (TDI) method is applied.

Results/Discussion

For the non-linear TDI inversion method, the configuration of the transducers is of importance for obtaining a correct image of the speed of sound profile. Moreover, we also conclude that increasing the number receivers has a more positive effect on the resulting images (i.e. obtaining a higher quality images in less iterations) than increasing the number of sources. Consequently, it is likely, that for any non-linear inversion method it is more advantageous to increase the number of receivers than the number of sources.

P3-A3-3

Ultrasound Nonlinearity Parameter Assessment with the Plane Wave Imaging

Michał Byra[1], Janusz Wójcik[1], Andrzej Nowicki[1]; [1]*Institute of Fundamental Technological Research PAS, Warsaw, Poland*

Background, Motivation and Objective

Assessment of medium nonlinearity parameter in pulse-echo mode usually demands information on the second harmonic. However, the acquisition of quantitative data on backscattered amplitude at the fundamental and second harmonic components is difficult using the same probe due to its limited bandwidth. In this paper we propose how to assess medium nonlinearity using only the fundamental harmonic and the plane wave imaging. We utilize the fact that the backscattered echo amplitude at the fundamental is not linearly proportional to the initial plane wave amplitude. This relation is modified due to the wave nonlinear propagation.

Statement of Contribution/Methods

The proposed method is based on the modified Fubini equation which describes the nonlinear propagation of ultrasound plane waves. We derive a relation between the backscattered echo amplitude at the fundamental harmonic and the initial plane wave amplitude, which depends i. a. on the nonlinearity parameter, propagation distance and tissue attenuation.

Experiments were performed to validate the model. First, a wire phantom was immersed in water and the Verasonics scanner equipped with the linear probe L12-5 was used to perform plane wave imaging. For the wire positioned at a fixed depth several scans were acquired varying the initial plane wave amplitude value from around 0.25 MPa to 0.9 MPa. The initial amplitude was measured with a needle hydrophone positioned 1 mm below probe surface. Acquisition was repeated for the wire positioned at various depths. Radiofrequency signals were reconstructed. The maximum amplitude of the signal backscattered on wire was analyzed as a function of the initial plane wave amplitude. Next, we performed a similar experiment investigating nonlinear response of the porcine meet sample in vitro.

Results/Discussion

Fig. 1 shows the relation between the backscattered echo amplitude and the initial plane wave amplitude for the wire positioned at various depths. The relation is clearly nonlinear, especially for the wire positioned at greater depths. This deviation can be used to assess the nonlinearity parameter. The greater the deviation at the distance between the probe and the wire, the greater is the mean nonlinearity parameter in medium. We show that the nonlinearity parameter can be similarly assessed in the case of the tissue sample and provide its quantitative characterization.

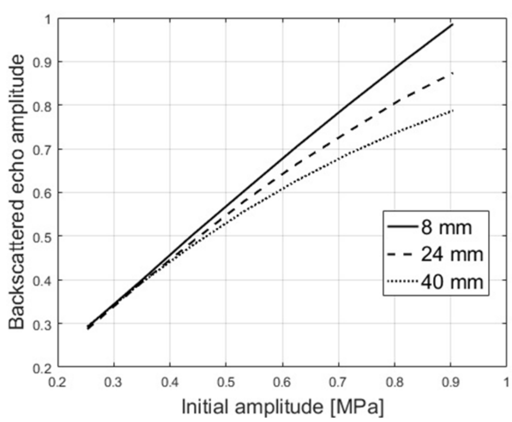

Fig. 1. The relation between the backscattered echo amplitude and the plane wave initial amplitude at various depths for the wire phantom immersed in water.

P3-A3-4

Dynamic Nonlinear Focal Shift and Acoustic Radiation Forces in Amplitude-Modulated Focused Beams

Noé Jiménez[1], **Francisco Camarena**[2], Nuria González-Salido[3], Sergio Giménez-Gambín[2]; [1]*CNRS, LUNAM Université, Université du Maine, Le Mans, France,* [2]*Instituto de Instrumentación para Imagen Molecular, Universitat Politècnica de València, Valencia, Valencia, Spain,* [3]*CSIC, Madrid, Spain*

Background, Motivation and Objective

Finite amplitude focused beams change its spatial distribution accordingly to the wave amplitude. In this work, we numerically and experimentally report the dynamic nonlinear focusing and the nonlinear acoustic radiation forces (ARF) of a moderately focused ultrasonic beam under amplitude modulated (AM) excitations for both, thermo-viscous media (water) and media showing a frequency power-law dependent attenuation (human soft-tissue).

Statement of Contribution/Methods

The pressure fields were measured in water and compared to those obtained by time-domain simulations of the KZK equation for a moderately focused beam excited with 1.1 MHz sinusoidal continuous and 25 kHz amplitude modulated signals. We study the displacement of the position of the focus along the axis of a focused acoustic beam as a function of the driving amplitude. The different behaviour of the pressure maxima, intensity and specially the ARF is discussed.

Results/Discussion

We observe that the location of the maximum value of the ARF do not follow the location of the intensity maxima. Instead, in the moderate nonlinear regime the ARF focus is located between the intensity maximum and the peak positive pressure, even surpassing the peak pressure location in the strong nonlinear regime. Once shock waves begin to appear, the nonlinear shifts for all the singular points of the beam begin to decrease. These phenomena are link to the balance between harmonic generation and absorption during propagation in a lossy nonlinear medium. Thus, different behaviour is obtained between thermos-viscous fluids and frequency power-law attenuation media (human liver). The fact that in AM beams the linear and nonlinear propagation regimes coexists allows to control the dynamical axial focusing using a single element ultrasonic source. The obtained results demonstrate the ability of nonlinear AM beams generated with a mono-element transducer to produce dynamical axial focal displacements.

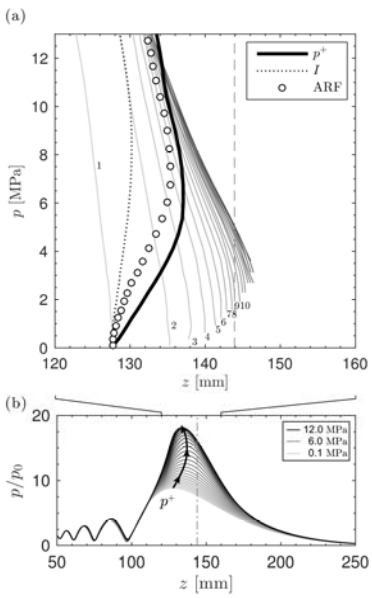

P3-A3-5

Nonlinear Ultrasound Propagation in Homogeneous and Heterogeneous Media: Factors Affecting the in Situ Mechanical Index (MI)

Bofeng Zhang[1], Gianmarco Pinton[2,3], Bharat Tripathi[2,3], Yufeng Deng[1], Kathryn Nightingale[1]; [1]*Duke University, USA,* [2]*University of North Carolina at Chapel Hill, USA,* [3]*North Carolina State University, USA*

Background, Motivation and Objective

We have previously reported increases in diagnostic shearwave and harmonic SNR using pressures that exceed the US FDA guideline for the Mechanical Index (MI). The MI is calculated using peak rarefaction pressure (PRP) measured in water with linear derating to account for tissue attenuation. However, acoustic propagation through water is a highly nonlinear process that inherently differs in attenuation, nonlinearity, and path heterogeneity from propagation in tissue. We hypothesize that MI overestimates the in situ acoustic output for many clinical scenarios and that PRP can occur in spatially offset locations when imaging through heterogeneous media such as the abdominal wall. Herein we demonstrate how these parameters affect in situ PRP as compared to that predicted by linear derating.

Statement of Contribution/Methods

A full-wave ultrasound package simulated acoustic propagation. Source pressures were obtained for a 2cycle, 2.2 MHz pulse from a 4C1 curvilinear (clinical abdominal) probe focused at 5cm, using a transmit voltage that produced focal MI=1.9. Simulations were performed varying parameters over the following ranges: attenuation (α): 0.3-1.1 dB/cm/MHz; nonlinearity (B/A): 7-10; and focal configuration: F/1-F/5 (by changing aperture size). Propagation through a range of heterogeneous bodywalls derived from histological images was also performed. For each simulation, the PRP amplitude and location were evaluated and compared to the corresponding linearly derated reference value.

Results/Discussion

As expected, increasing α in homogeneous media was associated with decreasing PRP, and the location of the PRP did not move appreciably (< 1mm). In addition, changing B/A varied PRP <5% and shifted PRP location <1mm. In contrast, changing F/ caused large shifts in PRP location, from the focus (F/1.5) to 2 cm proximal of the focus (F/5). For tightly focused beams (F/ < 3) though a bodywall, the PRP remained near the focus (Fig 1a, red dot). However, for weakly focused configurations (F/ >= 3), the location of PRP was often inside the bodywall (Fig 1b, red dot). Fig 1c demonstrates the % change in PRP vs. the linearly derated reference value across 6 different bodywalls at each F/, propagation through the bodywall leads to considerable variation in PRP, suggesting that elevating source pressures on a patient specific basis could increase SNR without increasing risk.

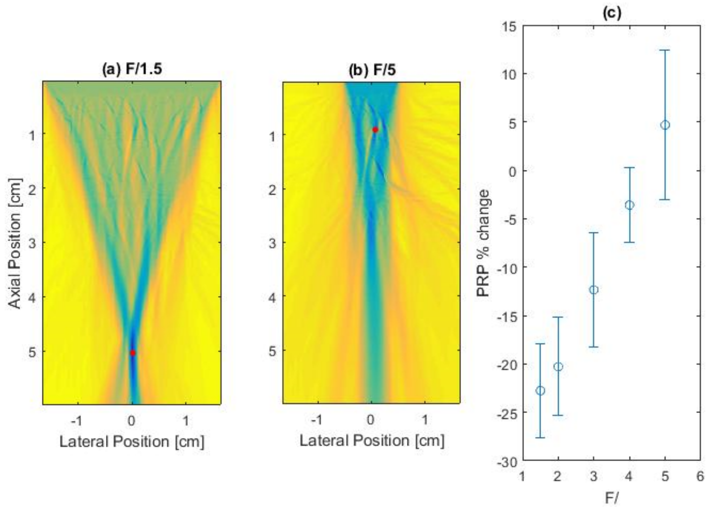

(a) F/1.5
(b) F/5
(c)
Axial Position [cm]
Lateral Position [cm]
Lateral Position [cm]
PRP % change
F/

P3-A4 - PUM - Ultrasonic Motors and High Intensity Applications

Exhibit Hall

Thursday, September 7, 2017, 9:30 am - 4:00 pm

Chair: **Vincent Laude**
Université'de Bourgogne Franche-Comté, CNRS

P3-A4-1

Design and Experimental Evaluation of a Linear Piezoelectric Ultrasonic Motor Using Longitudinal Transducers

Hongpeng Yu[1], **Yingxiang Liu[1]**, Shengjun Shi[2], Xinqi Tian[2]; [1]*State Key Laboratory of Robotics and System, Harbin Institute of Technology, Harbin, Heilongjiang, China, People's Republic of,* [2]*Harbin Institute of Technology, China, People's Republic of*

Background, Motivation and Objective

Piezoelectric ultrasonic motors (PUMs) are based on the concept of driving the runner by a mechanical vibration excited on the stator via the converse piezoelectric effect. They exhibit merits of small size, simple structure, quick response, high accuracy and resolution, self-locking when power off and a lack of electromagnetic radiation. The linear PUMs become the research focus in recent years as the increase demand of the engineering application. Linear PUMs using longitudinal transducers have been shown the potential on large force and high speed by the previous studies.

Statement of Contribution/Methods

A linear piezoelectric ultrasonic motor was proposed, designed and tested in this work, in which three longitudinal transducers were used together to achieve the linear driving by two feet synchronously. Longitudinal vibrations of the transducers were generated with certain temporal shift to from the desired elliptical movements on the two driving feet. The two feet are machined into trapezoid-shape to ensure the particles on the contact surfaces have close vibration amplitudes. Finite element method was used to accomplish the design process, in which the resonance frequencies of the transducers were tuned to be very close, and the movement trajectories of the driving feet were gained. The calculated results shown the feasibility of the PUM initially; then, a prototype was fabricated and tested to verify the proposed design further.

Results/Discussion

The resonance frequencies of the two vibration modes of the prototype were tested to be about 30.024 kHz and 29.714 kHz by using the Scanning Laser Doppler Vibrometer (PSV-400-M2, Polytec, Germany). The optimal working frequency of the prototype was tested to be about 29.35 kHz under voltage of 175 V. The maximum output speed and maximum thrust force were tested to be about 306 mm/s and 12 N, respectively. Theoretically speaking, the proposed PUM can achieve higher output speed and force by using a high power supply. This piezoelectric ultrasonic motor is very suitable for the linear driving of a platform, which has good potential in engineering application.

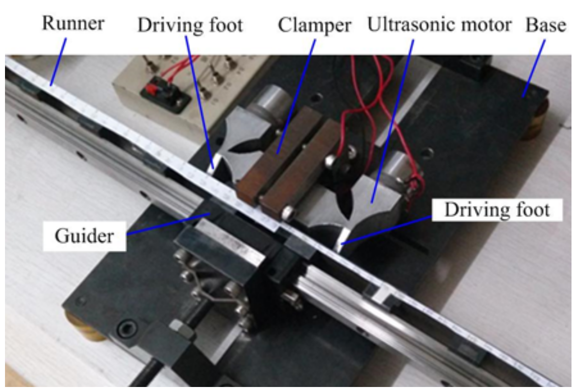

P3-A5 - PTF - Thin Films

Exhibit Hall

Thursday, September 7, 2017, 9:30 am - 4:00 pm

Chair: **Vincent Laude**
Université'de Bourgogne Franche-Comté, CNRS

P3-A5-1

Mechanisms of Appearance of Backward Shear-Horizontal Waves in Potassium Niobate Plates

Ilya Nedospasov[1], Vladimir Mozhaev[2], Iren Kuznetsova[1]; [1]*Kotel'nikov Institute of Radio Engineering and Electronics, Russian Academy of Sciences, Moscow, Russian Federation,* [2]*Physics Faculty, Lomonosov Moscow State University, Moscow, Russian Federation*

Background, Motivation and Objective

The backward waves with opposite directions of energy transport and phase velocity are in the focus of current studies in physics. Besides they are of interest for possible technical applications. This type of wave motion was previously studied in acoustics mainly in the case of Lamb modes. Nevertheless, shear-horizontal (SH) plate modes, as known, can also be backward waves if the plates are piezoelectric. However, SH backward waves were never observed experimentally. The reason for that is a very narrow frequency range where these waves are found numerically in common piezoelectric materials like ZnO with a relative frequency range of only $2 \cdot 10^{-5}$. As we have recently shown [J. Commun. Technol. Electron., November, 2016], the situation is opposite in the case of superstrong piezoelectric crystals of potassium niobate, for which the wide frequency ranges of the existence of backward waves occur in the *X*-cut plates, while they are absent in the Y-cut plates. The aim of the present work is to study quantitatively the possible mechanisms that affect the appearance of waves under consideration.

Statement of Contribution/Methods

The stated aim is achieved by using the asymptotic expansion of the secular equations for symmetric and antisymmetric modes at points of thickness resonances where the backward waves appear. In addition, the perturbation method based on the divergence relation is applied to this problem. The modification of the existing method is performed to take into account both linear and quadratic terms in the small parameter in this expansion. Iterative computations are also used to construct the dispersion curves for waves studied.

Results/Discussion

There is no difference between formulas obtained by two mentioned methods that confirms their validity. Their analysis allows us to identify and quantify three different mechanisms responsible for the occurrence of backward waves. Among them are (i) the curvature of the slowness surface for bulk acoustic waves, that constitute the guided modes, along the normal to the plate surface, (ii) the negative displacement of wave rays at oblique reflection from the surfaces in piezoelectric plates, (iii) the specific contribution for antisymmetric modes caused by spatially uniform electrical fields of capacitor type in the plates. The co-action or counteraction of these factors with a dominant role of one of them determine the final result of the existence of backward shear waves in the *X*-cut case or their absence in the Y-cut case in potassium niobate plates. The overlapping of the existence domains of backward waves on the higher-mode branches is observed for modes of fifth and higher order. It is found that, for the backward waves in contrast to the forward ones, an additional possibility of pulse compression instead of spreading appears due to the special form of their dispersion curves. The study is supported in part by the RFBR grants 16-07-00629_a, 17-07-00608_a, 17-57-53101_a.

P3-A5-2

Film Growth of C-Axis Tilted ScAlN on the Sapphire Substrate for SAW Devices

Shohei Tokuda[1], Shinji Takayanagi[2], Mami Matsukawa[1], Takahiko Yanagitani[3]; [1]*Doshisha Univ, Kyoutanabe, Japan,* [2]*Nagoya Institute of technology, Japan,* [3]*Waseda Univ, Japan*

Background, Motivation and Objective

Recently, it was shown that heavily doped AlN film possess the high piezoelectricity by Akiyama et al [1]. On the other hand, SAW devices were widely used as filters and sensors. Among them, SAW in ScAlN film is attracting a lot of attention because this SAW devices have high electromechanical coupling coefficient K2. We analyzed the K2 value in Sc0.4Al0.6N was increased by c-axis tilted angle θ becoming bigger [2]. In this study, changing the angle of c-axis tilted ScAlN films, we have tried to improve the K2 value of SAWs in c-axis tilted ScAlN/R-sapphire.

Statement of Contribution/Methods

At first, ScAlN film was deposited on the R-sapphire substrate by using RF magnetron sputtering. Scandium ingot grains were positioned on an Al target. While sputtering deposition, the substrate angle  to the target surface plane was adjusted to be 0º and 45º. The crystalline orientation of the films were measured by XRD pole figure analyses and it was estimated that the K2 values of SAW in the c-axis tilted ScAlN/R-sapphire structure theoretically.

Results/Discussion

Fig. 1(a), (b) shows AlN (0002) X-ray pole figure of the ScAlN film ( = 0, 45). In Fig.1 (a), c-Axis of this film sample was normally oriented to the substrate and FWHM value of the ω-rocking curve was 2.03º. In Fig. 1(b), the pole was observed at  = 50º and the -scan FWHM, indicating the dispersion of the c-axis tilted, was 8.9º.

P4-A1 - Simulation of Microacoustic Devices and Effects

Exhibit Hall

Thursday, September 7, 2017, 9:30 am - 4:00 pm

Chair: **Maximilian Pitschi**
RF360 Europe GmbH

P4-A1-1

Selection of Materials for Multilayered Structures to Be Used in Packageless Sensors

Natalya Naumenko[1]; [1]*National University of Science and Technology "MISIS", Moscow, Russian Federation*

Background, Motivation and Objective

Recently a multilayered structure with a low-velocity layer sandwiched between two high-velocity materials, one of which also works as a supporting substrate and another one as a coat isolating the wave from the influence of undesired external factors, was suggested for application in packageless sensors [1,2]. The thickness of a middle piezoelectric layer must be sufficient to confine the wave within this layer. The suggested combinations of materials included ZnO or GaN as a waveguiding layer, sapphire or diamond as a supporting substrate and Al_2O_3 (alumina) or AlN as a coating. In the present work, two previously reported structures were analyzed and compared to find the selection criterion for optimal combination of materials enabling high coupling of the useful mode and suppression of parasitic modes.

Statement of Contribution/Methods

Velocities and coupling coefficients k^2 were calculated using SDA-FEM-SDA software for acoustic waves propagating in AlN/Pt/ZnO/diamond and in Al_2O_3/Pt/GaN/sapphire with ZnO or GaN thickness h=1λ. Two high-velocity materials were assumed thick (half-infinite). Due to the high-velocity upper material, the analyzed wave propagates with $V_{BAW1}<V<V_{BAW2}$, where V_{BAW1} and V_{BAW2} refer to shear BAWs in the piezoelectric layer and in the coat, respectively, but shows different k^2. In the first structure (Fig.1a), due to the large difference between the useful wave and BAW velocities, it does not couple with other modes and shows high k^2=1.59%. In the second structure (b) the main mode with mostly vertical polarization interacts strongly with slightly slower propagating SH-polarized BAW and decouples into two modes, both having low k^2. If Al_2O_3 is replaced by lower-velocity Si_3N_4 (c), which is often used as a coating in devices for high-temperature applications, the useful mode has $V<V_{BAW1}$ and propagates as a boundary wave with energy confined around IDT, does not couple with parasitic modes and shows k^2 only twice lower than in GaN substrate.

Results/Discussion

The anisotropy of materials and the ratio between BAW velocities in piezoelectric and coating films plays an important role in selection of a proper combination of materials for a multilayered structure promising for application in packageless sensors or resonators.

[1] O.Elmazria et al., Appl. Phys. Lett. 95, 233503 (2009).
[2] F.Bartoli et al., IUS-2016, Abstract book, p.452.

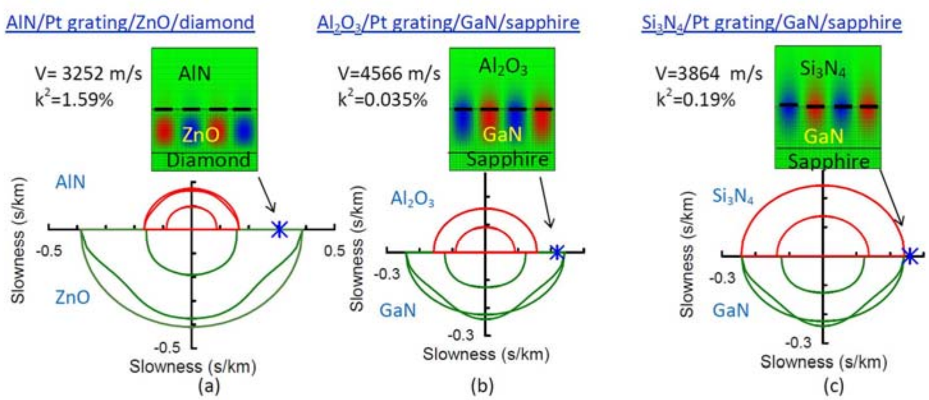

Fig.1. Displacement u_3 as function of depth in AlN/ZnO/diamond (a), Al_2O_3/GaN/sapphire (b) and Si_3N_4/GaN/sapphire (c) and the ratio between slowness surfaces of piezoelectric and upper layers.

P4-A1-2

Traveling Wave Excitation for FEM Simulation of RF SAW/BAW Devices

Xinyi Li[1,2], Jingfu Bao[1], Yulin Huang[1,2], Benfeng Zhang[2,3], Gongbin Tang[2,3], Tatsuya Omori[2], Ken-ya Hashimoto[2,3]; [1]*University of Electronic Science and Technology of China, Chengdu, Sichuan, China, People's Republic of,* [2]*Chiba University, Chiba, Japan,* [3]*Shanghai Jiao Tong University, Shanghai, China, People's Republic of*

Background, Motivation and Objective

Design of side edges is one of the most important tasks for realization of high performance RF SAW/BAW devices. For the purpose, the authors proposed an FEM based technique where the specified mode is injected to the border under concern through a damping mechanism, and scattering coefficients are estimated from calculated BAW field [1]. Even though this technique is effective, its setup is too complicated to apply it to complex structures such as SAW devices.

[1] F.Thalmayr, et al, IEEE Trans. UFFC, 57 (2010) p. 1641

Statement of Contribution/Methods

This paper proposes use of traveling wave type excitation sources for the scattering analysis of RF SAW/BAW devices. They are artificial but can be easily implemented into FEM.

For example, we analyzed SAW scattering at side edges of an infinitely long IDT, which is fully covered by SiO_2. Fig. 1 shows its 3D FEM model. Symmetrical boundary condition is applied to the longitudinal sides. Our idea is to set the applied voltage in the active region to vary in form of $\exp\{j(\omega t - \beta_y y)\}$, where ω is the driving angular frequency. Then a particular mode having the lateral wavenumber of β_y is predominantly excited provided that the β_y-ω relation is known a priori. Passive regions are placed next to the active region. After the FEM calculation, surface displacements in the passive regions are extracted, and their FFT is used to estimate amplitudes of incident and reflected modes selectively.

Results/Discussion

Fig. 2 shows calculated field distribution at 941.5 MHz and β_y=0.15 rad/μm. In the calculation, the SiO_2 thickness on the IDT is $0.35p_I$ while that in the border region is $0.15p_I$. It is seen that almost 100% reflection is achieved at the boundary. The reflection angle can also be estimated.

Other examples including FBAR analysis will be also demonstrated at the presentation.

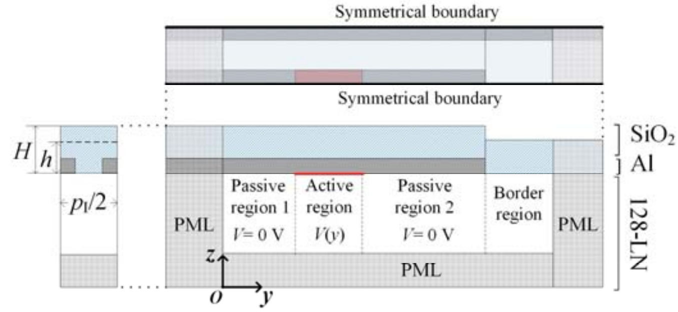

Fig.1 Schematic diagram of FEM model

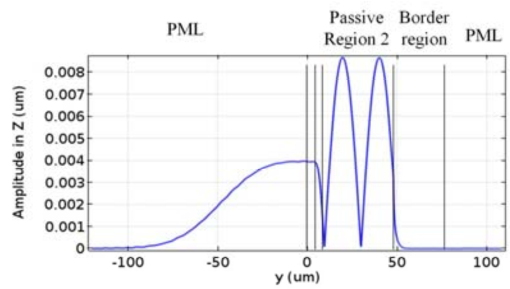

Fig.2 Vibrating Amplitude in Z of top sideline

P4-A1-3

Parametric Study of the Resonant TC-SAW Piston-mode Configurations

Ventsislav Yantchev[1,2], **Sean McHugh[3]**, Patrick Turner[3]; [1]*Q-Arts Consulting Ltd., Sofia, Bulgaria,* [2]*Chalmers University of Technology, Goteborg, Sweden,* [3]*Resonant Inc., Santa Barbara, CA, USA*

Background, Motivation and Objective

Recent trends in RF filter design has brought the necessity to design SAW resonators with boosted performance. Most importantly, improvements in both the resonators' quality factors (Q) and temperature coefficient of frequency (TCF) are needed. TC-SAW concept employing 128 Y-cut $LiNbO_3$ has attracted considerable practical interest in this view. Some excellent works from Qorvo have demonstrated the viability of this technology. Here we present some more detailed theoretical and experimental studies on the scaling rules regarding the design of TC-SAW resonators with suppressed spurious transverse mode responses.

Statement of Contribution/Methods

3D finite element analysis (FEA) has been used to perform parametric analysis of the piston mode waveguide as integrated into a TC-SAW resonator (see Fig. 1). The analysis was performed for the frequency band 1.7GHz – 2.0 GHz with the aim to design RF filter meeting the requirements for B3 and B66. TC-SAW resonators with varying parameters of the piston region are fabricated, characterized and discussed in light of the theoretical predictions. Scaling rules for the design of piston mode resonators are deduced in view of the design of high performance TC-SAW B3 and B66 filters.

Results/Discussion

For the suggested TC-SAW geometry (Fig 1) the FEA simulations predicted that the length of the border region scales proportionally with the wavelength and inverse proportionally with border layer thickness. The length of the border region was found insensitive to the metallization ratio and aperture. The experimental results from 1.8GHz TC-SAW resonators confirm to a large extent the FEA predictions. Spurious free responses were measured (see Fig. 2). We will present a complete set of experimental data and summarize some practical rules for piston mode design.

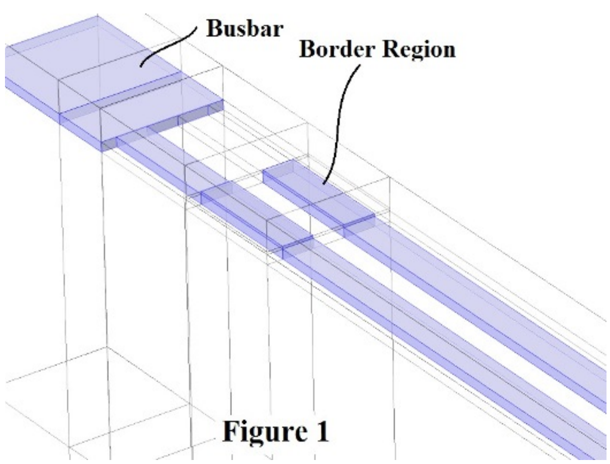

Figure 1

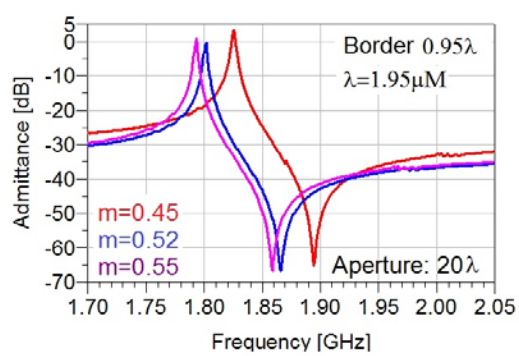

Figure 2

P4-A1-4

Effective SAW Excitation on the Non-Piezoelectric Substrate Using the AlScN Piezoelectric Film BAW/SAW Hybrid Transducer

Vladimir Pashchenko[1], Mohammad Fazel Parsapour kolour[1], Sylvain Ballandras[2], Paul Muralt[1]; [1]*Electroceramic Thin Films Group, Swiss Federal Institute of Technology in Lausanne, Lausanne, Switzerland,* [2]*Frec|n|sys, Besançon, France*

Background, Motivation and Objective

Recently we reported on fabrication and characterization of a novel type of hybrid resonator in which BAW transforms into SAW due to a periodic pillar pattern of piezoelectric material. This device looks promising thanks to high achievable electromechanical coupling (over 4%) and possibility for application as sensor in harsh environment when using AlScN as piezoelectric. The main feature of the device is the concentration of BAW energy inside the AlScN pillars (figure). Because of the opposite phase connection of the neighbor pillars and the spatial period≈λ_{SAW} (SAW wavelength on the substrate), SAW waves are excited, which in principle contain evanescent solutions onto the non-piezoelectric substrate. However, it turns out that the main solutions are 180° phase shifted and compensate each other outside the pillar structure on the free substrate, resulting in a weak SAW emission. Some additional features must be added to avoid this compensation. Otherwise the SAW/BAW hybrid is inferior to an ordinary thin film SAW structure on a high SAW velocity substrate like Si, SiC, sapphire, etc.

Statement of Contribution/Methods

Several designs of SAW-BAW structures were studied by finite element simulation (COMSOL). In addition, some devices were fabricated and characterized.

Results/Discussion

The main SAW propagation condition is an acoustical impedance matching of the longitudinal wave of the piezoelectric pillars and substrate, i.e. acoustical impedance ratio of the AlScN transducer and substrate: Zp/Zs. There are two possible operation regime of the described device: 1) Zp/Zs ≥1: The AlScN transducer is "free" with respect to the substrate surface, leading to BAW excitation in the pillars; 2) Zp/Zs<1: The AlScN pillars are acoustically "loaded" with respect to the substrate, and work like micro-hammers which excite a SAW on the substrate surface. The acoustical impedance matching at the operational frequency was achieved by the selection of suitable substrates. Simulation results confirm the SAW propagation on the substrate. In the device, K^2 of 4.8 % was achieved at an operational frequency of 1 GHz. Sweeping the pillars depth and AlScN film thickness leads to K^2 tuning, however, spurious modes are excited as well. We identified optimal values of the AlScN thickness and the pillar depth. Experimental results will be presented as well.

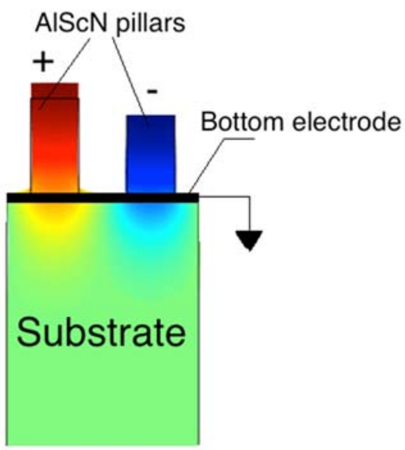

P4-A1-5

Investigation of Interaction of Surface Acoustic Wave with Controlled Electroinduced Domain Structures in the Crystal

Siarhei Barsukou[1], Jun Kondoh[2], Sergei Khakhomov[3]; [1]*Shizuoka University, Hamamatsu, Japan,* [2]*Graduate School of Science and Technology, Shizuoka University, Hamamatsu, Japan,* [3]*Optic, Gomel State University, Gomel, Belarus*

Background, Motivation and Objective

The creating different kinds of the phononic crystals and acoustic metamaterials, which has advanced ultrasound properties, have generated considerable recent research interest. The new kind acoustic materials, allows to studying the new effects of the ultrasound interaction and developing different types of the surface acoustic wave (SAW) devices for electronic industry. We represented the possibilities to creating of the controlled SAW devices on the base 36˚ rotated Y-cut, X-propagating $LiTaO_3$ single crystal with the volume electroinduced periodical domain structure. We are focusing on the theoretical and experimental investigations of volume induced and controlled domain structures.

Statement of Contribution/Methods

The principle of the proposed SAW device is illustrated in Fig. 1. The controlled SAW device includes a single crystalline waveguide, two inter digital transducers (IDT1, IDT2) and electrode structures (E1, E2, E3 and E4). Two pairs of electrodes were crossed on the surface of the crystal. The applying electric potential to the electrodes and due to linear electrostatic effect, in the volume of the crystal was induced periodical acoustic impedance structure. The value and configuration of the electroinduced structure can be controlled by changing electrodes electric potential.

Results/Discussion

The finite element method (FEM) was used for studying of the domain formation process. Figure 2 shows the theoretical results of the static total displacement distribution in the volume of the studied domain unit cell with periodical boundary conditions. From the figure, the domain area, obtained for different domain configurations (Fig. 2(a) – four individual domains with the same direction of polarization and Fig. 2(b) – two domains with opposite polarization) it can be observed.

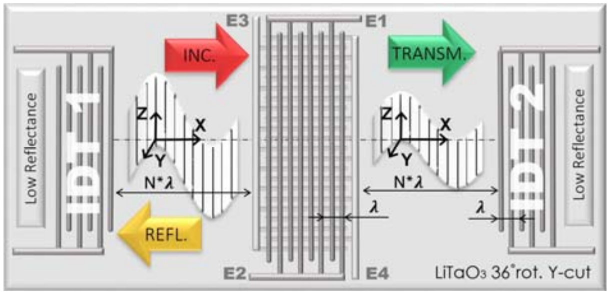

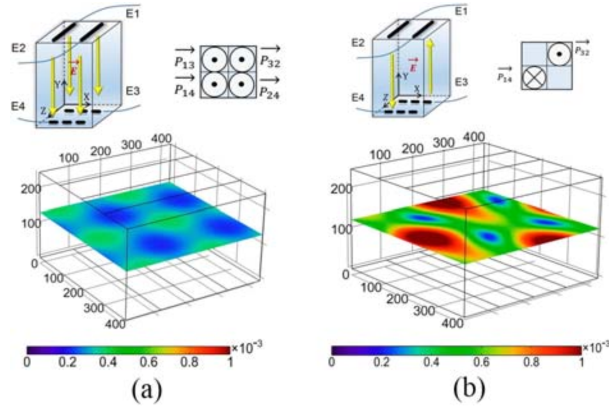

P4-A1-6

SAW Based Rotation Force of a Cylindrical Solid

Sergey Biryukov[1], **Manfred Weihnacht[2]**, Andrei Sotnikov[1,3], Hagen Schmidt[1]; [1]*IFW Dresden, SAWLab Saxony, Dresden, Germany,* [2]*innoXacs, Dippoldiswalde, Germany,* [3]*Ioffe Institute, St. Petersburg, Russian Federation*

Background, Motivation and Objective

It was shown experimentally in [1], [2] that a macroscopic cylindrical solid can be rotated due to the excitation of two counter-propagating surface acoustic waves (SAWs) with different amplitudes on its surface. Arising internal distributed rotation force has been calculated phenomenologically in the partial case of a piezoelectric tube with a ring unidirectional electrode transducer (RUDT) using the torsion pendulum equation of motion. The rotation force is proportional to applied voltage squared. The cylindrical rotating structure can be considered as a prototype of new kind of motor without any stator and needs to be investigated and optimized for possible applications. The objective of the present work is to give the first estimation of the rotation force on the basis of physical principles and equations of motions in periodic structures. Hereby, this approach makes it possible to relate the rotation force with both material parameters and geometry of the structure.

Statement of Contribution/Methods

The idea of rotation force estimation for the cylindrical solid is based on a natural effect. This effect is a recoil of UDT on a SAW train excitation with its inherent momentum [2]. In the case of RUDT there is no obstacle for SAW propagation around the cylinder surface and the rotation effect has been detected as a permanent rotating force due to a permanent SAW excitation. As was mentioned in [2] this force can be estimated as the integral density of energy across the structure, E=W/V, where W is the integral energy flux and V is the group velocity of SAW. As known, the integral energy flux W is related by a simple formula to the amplitude square of the surface electric potential of SAW. The amplitudes of this potential for two counter-propagating waves can be found from the well-known COM equations as a function of so-called COM parameters. In turn, these parameters are calculated here as a function of material parameters and structure geometry. Thus the rotation force can be estimated.

Results/Discussion

First theoretical investigations of the rotation force show up its strong dependency on propagation losses. There is the optimum value of losses to get the maximum effect in the case of the perfect RUDT directivity (phase shift between reflection and transduction center is equal to 45°). Interestingly, that rotation effect completely disappears if losses are zero in spite of the transducer unidirectivity. In this case the COM equations on the closed surface give equal amplitudes for both counter-propagating waves. Calculations of the electrical admittance and the rotation force have been performed for RUDT with two electrodes per period and different electrode widths like in [1]. An analytical expression for the rotation force arising in the passband frequencies will be presented.

[1] S. V. Biryukov, A. Sotnikov, and H. Schmidt, APL, 108, 134103, 2016.

[2] S. V. Biryukov, A. Sotnikov, and H. Schmidt, In Proc. 2016 IEEE IUS, ID 318.

P4-A2 - Experimental Characerization Methods for Microacoustics

Exhibit Hall

Thursday, September 7, 2017, 9:30 am - 4:00 pm

Chair: **Amelie Hagelauer**
University Erlangen-Nuernberg

P4-A2-1

Temperature Behavior of Sound Velocity of SiON Thin Films Studied by Picosecond Ultrasound

Seiya Tsuboi[1], Hirotsugu Ogi[1], Akira Nagakubo[1], Nobutomo Nakamura[1], Satoru Matsuda[2], Yoshiro Kabe[2]; *[1]Osaka University, Japan, [2]Skyworks Filter Solutions Japan Co., Ltd., Japan*

Background, Motivation and Objective

Amorphous thin films are used as components of acoustic resonators because they could control temperature coefficient of resonator. Because elastic constants of thin films are often different from those of bulk materials, the direct measurement of sound velocity and temperature coefficient of velocity (TCV) for individual thin films becomes important in designing resonators. Because The TCV of amorphous silicon oxide is opposite in sign to that of silicon nitride, we expect that a specific-composition SiON thin film show the zero TCV. We here measure the longitudinal-wave velocity of SiON thin films with various nitride concentrations using picosecond ultrasound method.

Statement of Contribution/Methods

The SiON thin films were deposited on silicon substrates with a sputtering method for a silicon target under nitrogen and oxygen gasses. We fabricated various nitrogen-concentration SiON thin films. The 800-nm pump light pulse with 200-fs duration was focused on the thin-film surface to generate the high-frequency longitudinal wave, which propagates in the film-thickness direction and repeat reflection between the surface and interface with the substrate. The time-delayed pump light pulse with 400 nm wavelength was then applied to the surface to detect the diffracted light from the acoustic pulse. The reflectivity change of the probe light pulse deduces the sound velocity.

Results/Discussion

Figure 1 shows typical reflectivity changes (waveforms) obtained at various temperatures for the SiON thin film with 33% nitrogen content. The low-frequency (~85 GHz) oscillation in the reflectivity first appears, and the high-frequency (~ 230 GHz) oscillation follows. The former indicates Brillouin oscillation from the SiON thin film, whose frequency provides us with the sound velocity, and the latter indicates Brillouin oscillation from the silicon substrate. The inset shows the enlarged second Brillouin oscillation from the substrate; the sound velocity is also obtained from the round trip time at the film-substrate interface and the film thickness measured by the ellipsometry. We obtain very good correlation between the sound velocity and the chemical composition, and we find a very small TCV with a specific content, which will be reported in detail at the presentation.

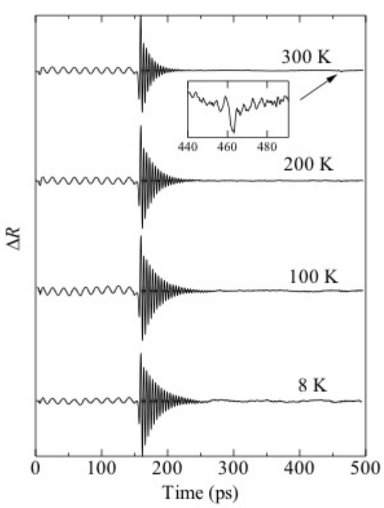

P4-A2-2

Accuracy Analysis and Deduced Strategy of Measurements Applied to $Ca_3TaGa_3Si_2O_{14}$ (CTGS) Material Characterization

Manfred Weihnacht[1], Andrei Sotnikov[2], Yurij Suhak[3], Holger Fritze[3], Hagen Schmidt[2]; *[1]innoXacs, Germany, [2]IFW Dresden, Germany, [3]TU Clausthal-Zellerfeld, Germany*

Background, Motivation and Objective

Since the beginning of using piezoelectric single crystals for highly-precise microacoustic components rigorous knowledge of material constant (MC) sets was an indispensable requirement for mastering the subject. The sets have to be both accurate and complete. Accuracy is important for acceptable agreement between device simulation and experimental reality, completeness preferentially plays a role for finding out optimum figure-of-merit issues, because in cases of complex acoustoelectric situations single MC can cause unexpected behavior. There exist many publications presenting new sets of “accurate” named MC’s for piezoelectric crystals, most of them with full sets but without any specification of accuracies. The aim of this paper is to demonstrate for the case of CTGS (member of langasite family) the calculation way of accuracies and to use this knowledge for finding out optimum combinations of experimental measurements.

Statement of Contribution/Methods

On the base of least squares method which is arranged to our problem of fitting theoretical to experimental values (EV) (i.e. phase velocities of acoustic waves and/or resonant frequencies) the surroundings of the minimum sum of squares (MSS) has been analyzed, similarly to [1]. This was done by forming a "sensitivity matrix" (or Jacobian matrix: derivatives of EV's w.r.t. each searched MC) based on a MC set found in first approximation. Subsequently, the quadratic dependence of MSS on all MC's was evaluated. As a result, the full set of MC accuracies is available. In such a way the overall evidence of used experimental method can be seen. A special treatment is necessary in the case of incorporating inaccurate "given" MC's in the procedure.

Results/Discussion

The described method has been applied to different series of own measurements of surface acoustic wave (SAW) and bulk acoustic wave (BAW) velocities, and of resonant frequencies on CTGS samples. The method was utilized to exhibit accuracy differences depending on the combination of experiments. In principle, SAW measurements are known to deliver well reproducible MC's [2, 3], but there exist substrate orientations with quite different suitability, and also substrate combinations providing considerable improvements of MC accuracy. From that, the possibility to optimize the experimental strategy is evident. Besides, the Jacobian can also be used for fast solving the inverse problem, i.e. the variation of MC's at given variation of EV. For example, the imaginary parts of MC's can be directly determined from imaginary parts of EV's which represent the losses being small as a rule. Similarly, the temperature behavior of EV's can be converted to the temperature dependence of MC's (see also [4]). Examples are given for CTGS.

[1] G. Kovacs et al., Proc 1988 IEEE Ultrason. Symp., pp.269.

[2] S. V. Biryukov et al., Proc. 2014 IEEE Ultrason. Symp., ID 318

[3] Y. Ohashi et al., IEEE TUFFC, 51, 2004, pp. 687.

[4] P. Nicolay, Proc. 2016 IEEE Ultrason. Symp.

P4-A2-3

Implementation of Frequency Scanning Function in Phase Sensitive Laser Probe System for RF SAW/BAW Devices

Tatsuya Omori[1], Tasuku Suzuki[1], Ken-ya Hashimoto[1]; [1]*Chiba University, Japan*

Background, Motivation and Objective

The authors developed phase-sensitive and fast mechanical scanning laser probe system as a diagnosis tool for RF SAW/BAW devices[1]. Captured 2D image of wave field brings valuable information such as energy leakage and standing wave pattern with a help of a wavenumber domain analysis[2] for a specified driving frequency.

Although the system is frequently used by external researchers and engineers from all over the world and its effectiveness is well recognized, inclusion of the frequency scanning function is highly demanded to investigate how the field pattern changes with the frequency.

Statement of Contribution/Methods

This paper describes implementation of the frequency scanning function to the current laser probe system. The operation is as follows: (a) importing parameters such as frequency span and interval through GUI, (b) setting the oscillator frequency, (c) data acquisition with 2D stage scanning, and (d) data storage, (e) stage control to return back to the original position, and repeating steps (b) to (g) for specified times. This operation is mainly performed by executing preexisted hardware-dependent control programs from newly developed one.

Since one 2D scan takes about ten minutes, about 400 images can be captured autonomously in a week end.

After all scans are completed, captured 2D images are converted to easy-to-see animations by another software.

Results/Discussion

As a demonstration, field images of a one-port SAW resonator on 42-LT were captured for the frequency span from 820 to 880 MHz with an interval of 0.25 MHz. The scanning area is 390x130 μm^2, and the spatial resolution is 0.4 µm. It took 31.5 hours for the whole scan. Fig. 1 shows a snapshot of created GIF animations. They consist 241 frames of amplitude (top) and phase (middle) of 2D field distribution and intensity (bottom left) in the wavenumber domain. Their motion is synchronized with a marker displayed on the impedance plot (bottom right).

At the presentation, we will show variation of SAW propagation in the device structure with the frequency, and demonstrate how animation is effective to understand wave phenomena such as energy trapping and leakage intuitively.

[1] K.Hashimoto, et al., IEEE Trans. UFFC, 58 (2011) p. 187.

[2] K.Hashimoto, et al., IEEE Trans. UFFC, 54 (2007) p. 1072.

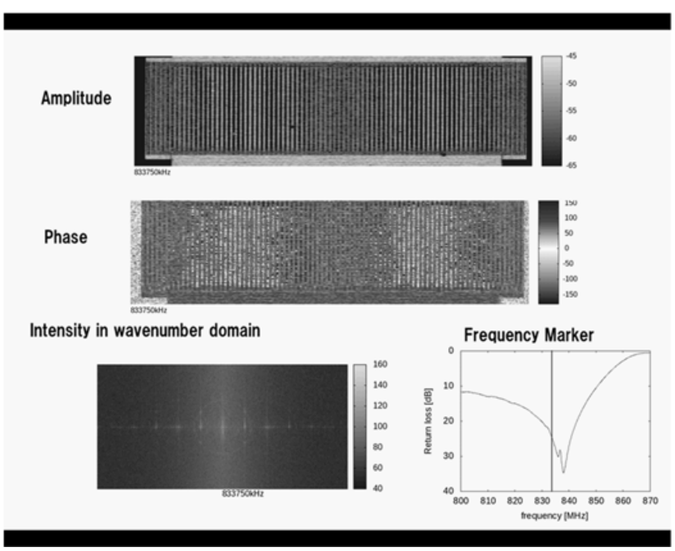

P4-A2-4

Design and Characterization of SAW filters for High Power Performance

Jim Costa[1], **Sean McHugh[1]**, Patrick Turner[1], Balam Willemsen[1], Neal Fenzi[1], Bob Hammond[1], J.D. Ha[2], C.H. Lee[2], Takahiro Sato[3]; *[1]Resonant Inc., USA, [2]Wisol Co, Ltd., Korea, Republic of, [3]Wisol Japan Co, Ltd., Japan*

Background, Motivation and Objective

Mobile filters are required to process increasing RF power levels, driven by the need for higher data-rates and improved cell-edge coverage. This results in more demanding filter specifications for loss, rejection, isolation, linearity and reliability, while, at the same time, handset OEMs require smaller filter footprints.

Statement of Contribution/Methods

This paper describes how a combination of modeling of the RF power dissipated in an acoustic wave filter and thermal characterization using IR microscopy can provide filter designs with improved power performance.

Results/Discussion

At high RF input power levels in the range of 1 Watt, the output power becomes sublinear with increasing input power. The cause for this lies in the highly non-uniform heating of individual resonators within a complex SAW filter leading to filter detuning and ultimately thermal runaway and destructive failure. Real-time IR microscope images confirm that the steady-state localized heating at individual resonators depends on the input power level and the details of the filter design. By modeling the thermal environment and RF power dissipation within individual resonators, filters with improved power handling can be designed. In the best case, filters made on inexpensive substrates such as LiTaO3 can compete with those requiring exotic temperature-compensated substrates with improved TCF performance.

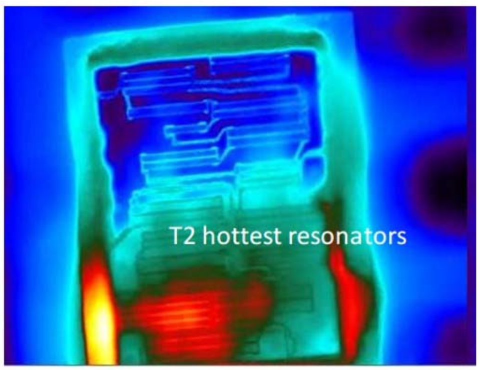

Fig. 1 – Infrared microscope image showing local heating of a resonator within a SAW duplexer.

P4-A2-5

Validation of a Thermal Model for TC SAW Resonators

Wolfgang Akstaller[1], Kimmo Kokkonen[2], Jan Kuypers[3], Robert Weigel[1], Amelie Hagelauer[1]; *[1]Institute for electronics engineering, Erlangen, Bavaria, Germany, [2] Qorvo Munich GmbH, Germany, [3]Qorvo, Inc., Apopka, FL, USA*

Background, Motivation and Objective

Ongoing miniaturization of RF frontend modules for mobile hand-sets is causing power densities in the electrical components to increase. Filters based on temperature compensated surface acoustic wave (TC SAW) technology are widely used, as for example in a B26 duplexer. However, even with a reduced TCF of typically -20 to -30 ppm/K for standard TC SAW, the observed frequency shifts of a Tx filter operating at high transmit power levels can be substantial due to the dissipated power and miniature die size. Furthermore, increasing temperatures accelerate the failure of the filter, possibly affecting the reliability. This effect is exacerbated with an effect referred to as thermal runaway [1], i.e. a high-power transmit tone at the upper band edge causing the frequency skirt to shift down, leading to even more power being dissipated, and in turn the temperature rising further, the filters shifting further, and so on. In order to avoid such phenomena and to include the thermal aspect early on in the filter design phase we have developed an efficient FEM based electro-thermal model.

Statement of Contribution/Methods

Close agreement of the predicted and measured temperature dependent on the electrical input signal is observed for a TC SAW resonator, illustrated in Fig. 1a. The thermal behavior of the resonator is included in the RF simulator, by combining a temperature dependent resonator model with a thermal behavioral model. A thermal impedance matrix is computed based on FEM-simulations in COMSOL®. To efficiently compute the thermal model an optimization of the geometry was developed. The validity of the electro-thermal model was confirmed with measurements.

Results/Discussion

Here we present the results of the temperature rise of the resonator dependent on the power and frequency of an electrical CW load tone. The comparison of the simulated and measured temperature increase versus a 30 dBm CW load tone for different frequencies is shown in Fig. 1b. Excellent agreement is observed. The discrepancy around 859 MHz is due to the effect of a parasitic mode. This implementation of the electro-thermal model can be applied to arbitrary filter geometries and the design optimization thereof.

[1] K. Gamble and W. Buettner, “Steady-state and transient thermal modeling for a SAW duplexer,” 2016 IEEE International Ultrasonics Symposium (IUS), Tours, pp. 1-6, 2016.

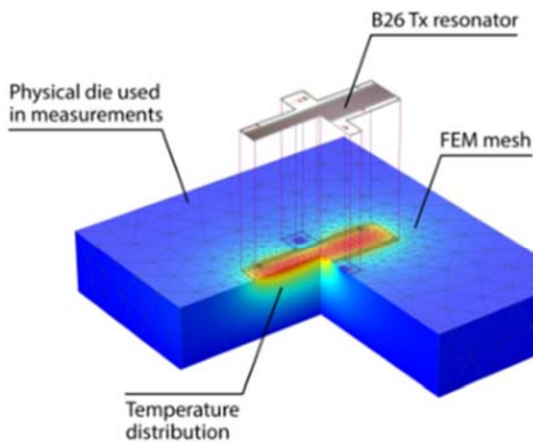

Fig. 1(a) 3D FEM model including photograph of resonator.

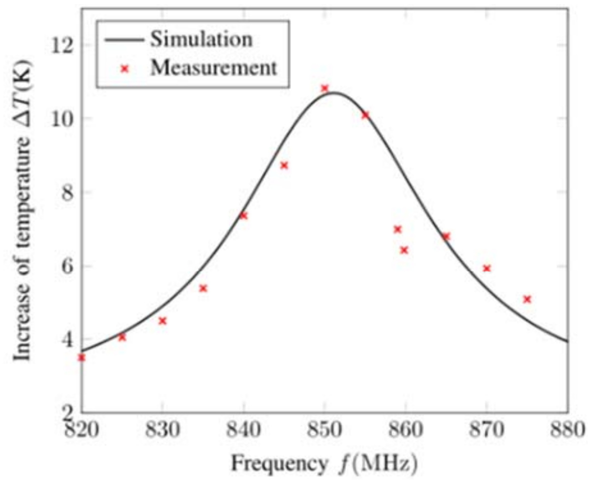

Fig. 1 (b) Simulated and measured temperature increase for different CW load tone frequencies at a power of 30 dBm.

P5-A1 - Imaging Transducers

Exhibit Hall

Thursday, September 7, 2017, 9:30 am - 4:00 pm

Chair: **Lynn Ewart**
NUWC

P5-A1-1

Translational Trial Outcomes for Capsule Endoscopy Test Devices

Holly Lay[1], Gerard Cummins[2], Benjamin Cox[3], Yongqiang Qiu[1], Ciarán Connor[1], Vipin Seetohul[4], Michnea Turcanu[1], Rachael McPhillips[1], Marc Desmulliez[2], Eddie Clutton[5], Sandy Cochran[1]; [1]*University of Glasgow, United Kingdom,* [2]*Heriot-Watt University, United Kingdom,* [3]*University of Dundee, United Kingdom,* [4]*Micrima Limited, United Kingdom,* [5]*University of Edinburgh, United Kingdom*

Background, Motivation and Objective

Endoscopy and colonoscopy are the clinically recognised standards for imaging and diagnosis of diseases of the gastrointestinal (GI) tract. While 'scope-based approaches combine optical and ultrasound imaging to allow both imaging of the surface and full thickness of the bowel wall, they are limited in their ability to access the full length of the GI tract particularly the small bowel. Wireless video capsule endoscopy (VCE) devices designed to transit the entire GI tract are currently limited to optical imaging of the superficial surface. Work is thus under way to implement additional capsule endoscopy (CE) functionality through the development of devices incorporating both optical and microultrasound imaging.

Research to date has identified several gaps in the literature, which have been addressed through early translational trials in vivo. The areas of concern can be classified by sensing modality and necessary support circuitry, and resulting research questions addressed through bespoke, single system capsules.

Statement of Contribution/Methods

Two types of test CE device were designed to address questions about capsule integrity and temperature tolerance (device termed Thermocap) and ultrasound coupling and sensitivity (device termed Sonocap). Two versions of Thermocap were used in sequential tests, one containing 14 thermistors and a power resistor and the other containing 6 thermistors, a power resistor and a combined humidity / temperature measurement integrated circuit. All Sonocaps contained four focused, single element PVDF transducers operating at approximately 30 MHz, with transmit/receive protection circuits and 12 dB of receive amplification on all four channels. With diameter 10 mm and length 30 mm, all CE devices matched the dimensions of existing clinical VCE devices. Control and data transfer were managed via tethers 3 m in length. In vivo tests were performed in porcine models in collaboration with the Wellcome Trust Critical Care Laboratory for Large Animals (Roslin Institute) under license from the UK Home Office (PPL 70/8812). Tests were performed in the oesophagus and small intestine.

Results/Discussion

Initial Sonocap testing in the oesophagus showed poor coupling with the use of traditional ultrasound gel due to air bubble build-up. The protocol was adjusted to use a continuous flow saline solution and images resolving the layers of the gut were obtained successfully from multiple Sonocap pull-backs in the small bowel. Thermocap measurements in both the oesophagus and the small bowel showed a linear relationship between input (dissipated) power and Thermocap surface temperature increase and 100 mW continuous power dissipation was achieved in all test runs without exceeding safety tolerances.

P5-A1-2

An Optimized High Resolution Radial Ultrasound Endoscope for Digestive Tract Imaging

Jue PENG[1,2], Xiaozhen Li[1,2], Hu Tang[1,2], Xiaojian Peng[1,2], Siping CHEN[1,2]; [1]*National-Regional Key Technology Engineering Laboratory for Medical Ultrasound, Department of Biomedical Engineering, School of Medicine, Shenzhen University, Shenzhen, China, People's Republic of,* [2]*Guangdong Key Laboratory for Biomedical Measurements and Ultrasound Imaging, Department of Biomedical Engineering, School of Medicine, Shenzhen University, Shenzhen, China, People's Republic of*

Background, Motivation and Objective

EUS is performed with radial imaging perpendicular to the endoscope shaft, and lateral imaging parallel to the shaft and biopsy channel. Radial imaging is preferred for some diagnostic and staging purpose because of ease of use as well as the production of a full 360-degree field of view. For operation smoothly and safety, the smaller external diameter (less than 11mm), the higher optical and ultrasonic resolution are required. In this paper, an EUS probe integrating an 8 MHz, 128 elements radial electrical scanning transducer and a wide-angle 8-million-pixel CMOS camera module is presented.

Statement of Contribution/Methods

We designed an optimized process to fabricate of the 8 MHz, 128 elements radial ultrasound transducer, which can provide the reliable electrical connection, and avoid the image incoherence between elements. A 128.3-degree wide-angle lens driving with an 8-million-pixel CMOS camera module can improve optical imaging resolution. After the optical and ultrasound parts integrated and packaged, a 9.58 mm external diameter EUS produced. This integrated radial EUS can simultaneously provide a forward 128.3-degree optical view and a sideward 360-degree ultrasound view. We use PZT ceramics as the functional active materials at present state. High performance piezoelectric single crystals and other composite materials will be considered in the future.

Results/Discussion

The schematic of the radial EUS probe is shown in Fig.1 (a). The 128.3-degree optical vision of 8 million pixels can be achieved by the miniatured camera module. The anthropomorphic digestive tract phantom can be distinctly imaged with camera module. Photograph of the EUS radial array is shown in Fig.1 (b). The measured center frequency and -6 dB fractional bandwidth of the radial array were 7.94 MHz and 83.4%, respectively as shown in Fig.1 (c). A two-way insertion loss of -41 dB was obtained at the average center frequency. The wire phantom image with the radial array was tested, and the measured full-width at half-maximum spatial resolutions was respectively 695 µm and 133 µm in lateral and axial directions at the depth of 10 mm respectively. According to the measured results, the radial EUS ensure a desirable imaging resolution in digestive tract imaging.

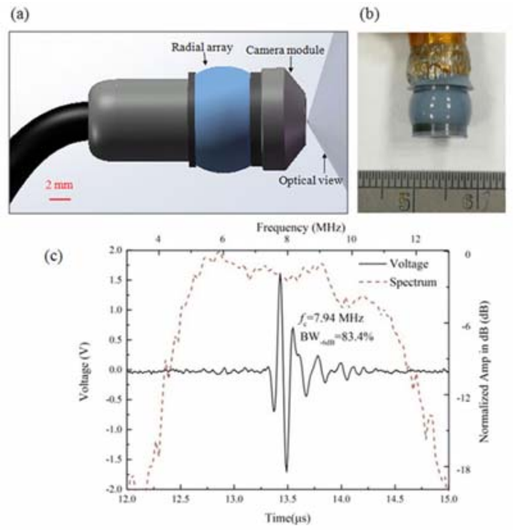

Fig. 1 (a) Schematic of an integrated radial EUS. (b) Photograph of the EUS radial array. (c) The measured echo waveform (black line) and spectrum (red line).

P5-A1-3

Improved CMUT Structure and Method of Operation for Dual-Frequency Acoustic Angiography

Marzana M. Mahmud[1], Oluwafemi J. Adelegan[1], Jean L. Sanders[1], Xiao Zhang[1], Feysel Y. Yamaner[1], Paul A. Dayton[2], Ömer Oralkan[1]; [1]*Department of Electrical and Computer Engineering, North Carolina State University, Raleigh, NC, USA,* [2]*UNC and NCSU Joint Department of Biomedical Engineering, USA*

Background, Motivation and Objective

"Acoustic angiography" is a super-harmonic contrast imaging technique. When the ultrasound contrast agents (microbubbles) are excited with a moderate acoustic pressure (MI of ~0.5-0.7) near their resonance (2-4 MHz), they produce broadband content which extends well past 15 MHz. By detecting the higher order harmonic energy while transmitting at a low frequency fundamental, exquisite resolution and tissue-contrast (microvascular) sensitivity can be achieved. The primary challenge with this technique is it requires transducers that can transmit a low-frequency (LF) pulse and receive high-frequency (HF) harmonics. We propose a novel scheme to transmit a LF high-pressure pulse from a capacitive micromachined ultrasonic transducer (CMUT) operating in conventional model and then switching to collapse mode to receive the HF microbubble harmonics in the same transmit-receive cycle.

Statement of Contribution/Methods

Previously we demonstrated vacuum-backed CMUT arrays realized on an insulating glass substrate. Now we pattern and etch the substrate to create glass spacers inside the device cavity (Fig.1a, b). These spacers eliminate the need for an insulation layer and consequently the dielectric charging. In case of pull-in, the top electrode rests on these spacers that prevent electrical shorting. The improved design allows operation in LF transmit and HF receive modes in the same pulse-echo cycle.

Results/Discussion

We designed CMUT cells with 7 and 19 spacers in the device cavity. Two etch steps are performed to realize the spacers and the device cavity. The first etch sets the gap between the top electrode and the spacer. The second etch step defines the bottom metal electrode regions and spacers. Metal deposition into the cavities consequently defines the spacers and the gap height.

We developed a 3D finite element model (FEM) of the structure. The simulations for 7-spacer design verify LF (3-MHz) transmit and HF (10-40 MHz) receive capability in the same pulse-echo cycle (Fig.1c-f). A custom high-frequency (<40 MHz) FPGA-based imaging system will be used to test the fabricated devices for the presented application in phantoms.

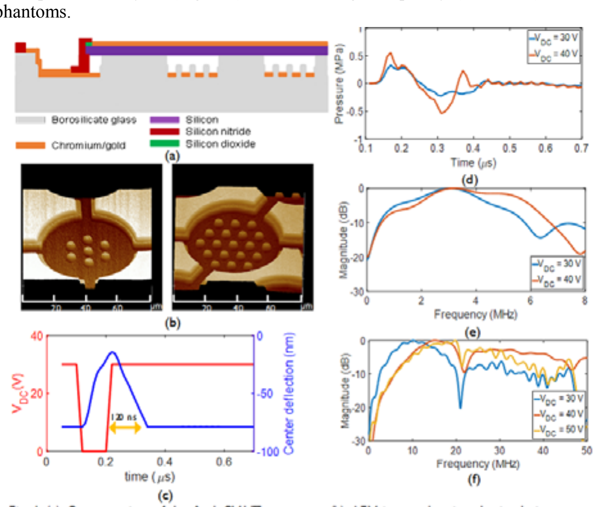

Fig 1 (a) Cross-section of the final CMUT structure. (b) AFM image showing the insulating spacers and the bottom metal in the cavity. (c)FEM analysis showing quick switching between conventional and collapse mode. (d) High-pressure during transmit cycle. (e) Low-frequency (3 MHz) transmit capability. (f) High-frequency (10-40) MHz receive capability.

P5-A1-4

A Shear Wave Endoscopic Elasticity Imaging Approach with Micro Focused Piezoelectric Transducer

Yang Jiao[1], Yaoyao Cui[1], Jibing Wu[1], Zhangjian Li[1], Pengbo Liu[1], Zhile Han[1]; [1]*Suzhou Institute of Biomedical Engineering and Technology, Chinese Academy of Sciences, Suzhou, JiangSu, China, People's Republic of*

Background, Motivation and Objective

Esophageal cancer is an aggressive disease with poor survival rate in surgery or chemoradiation therapy. Early diagnosis of the space occupying lesion in esophagus are crucial for the prevention of the esophageal carcinoma. Comparing with the present clinical methods, such as Chest X-ray (with Barium swallow) and Esophagoscopy, Shear Wave Elasticity Imaging (SWEI) which take advantage of quantitative measurement of elasticity in deeper biological soft tissues is capable of analyzing the components of the lesion. In this paper, we propose an endoscopic elastography approach which combine the endoscopic techniques and SWEI to achieve both morphological and mechanical parameters of esophagus in clinical diagnosis, Fig.1(a). It will overcome the shortcomings of current methods for poor penetration depth and lack of elastic information.

Statement of Contribution/Methods

The major problem of the invasive shear wave elasticity imaging is that the output acoustical power of the micromachined ultrasonic transducer is not enough for the excitation of shear wave in biological tissue. In this work, a micro focused piezoelectric transducer was developed as excitation source of the acoustic radiation force. Then a linear array transducer with 8 micro high-frequency piezoelectric elements was used to detect the propagation of the shear wave, Fig.1(b). With an 8 channels high-frequency Pulser/Receiver system, Fig.1(c) multi-angle plane waves were emitted to examine the tissue deformation caused by shear wave in ROI. Finally, the shear wave velocity was calculated by applying the Modal Assurance Criterion (MAC) to shear wave tracking algorithm which we had proposed in IUS 2015.

Results/Discussion

Fig. 1(d) shows the results of shear wave tracking by MAC matrix. It is bounded between 0 and 1, with 1 (red) indicating no displacements in the tissue and value near 0 (blue) indicates to the contrary.The MAC matrix shows the propagation process of shear wave. These results demonstrate that this endoscopic elastography method based on the invasive shear wave imaging was capable of detecting the shear wave velocities in esophagus. And with the effectiveness and stability of the MAC tracking algorithm, we are looking forward to achieve a thin, flexible esophagoscopy probe with an effective and stable real-time invasive shear wave imaging method in clinical diagnosis of esophageal cancer.

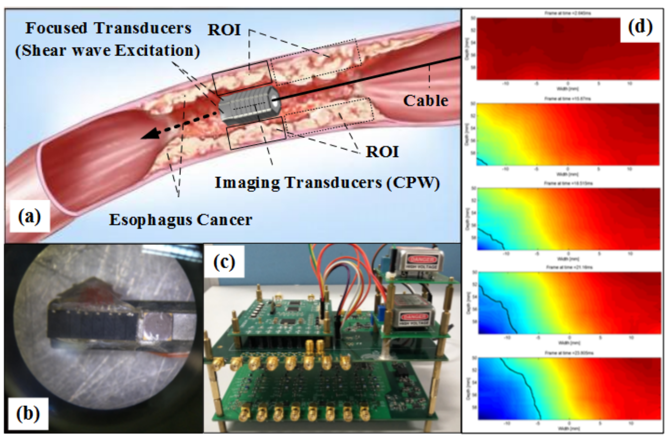

Fig. 1. (a) *The working scheme of Shear Wave Endoscopic Elasticity Imaging Approach*; (b) *The invasive shear wave elasticity esophagoscopy probe under microscope (×100 times)* ; (c) *8 channels high-frequency Pulser/Receiver system*; (d) *The experimental results of shear wave tracking with MAC where color blue indicating the shear wave propagation has been tracked in this line and red representing the opposite*

invasive shear wave imaging

P5-A1-5

Hybrid Dual Frequency Transducer / Array Probe For Super-Harmonic Imaging

Jianhua Yin[1], Emmanuel Cherin[1], Christine Demore[1], Paul Dayton[2], F. Stuart Foster[1]; [1]*Imaging Research, Sunnybrook Research Institute, Toronto, Ontario, Canada,* [2]*Department of Biomedical Engineering, University of North Carolina, USA*

Background, Motivation and Objective

In previous work, the advantage of using super-harmonic contrast imaging to visualize the microvasculature in tumors and organs has been demonstrated [1]. This was performed using dual frequency (DF) probes consisting of a high frequency single element transducer from a motorized probe concentric with a low frequency ring [2]. However, mechanically scanned systems have limitations, including single focal zone and slow frame rate, which can be alleviated using array technology. In this work, the design and performance of new hybrid dual frequency transducer/array probes are presented.

Statement of Contribution/Methods

The hybrid probe combines a pair of two identical rectangular low frequency (LF, 1.7 MHz) piezocomposite transducers aligned symmetrically and parallel to a high frequency (HF, 21 MHz) array (MS250, VisualSonics, Toronto). The two matched and backed LF stacks are angled such that their beams interfere constructively in the HF imaging plane, creating an LF elevation focal zone overlapping that of the array. LF transducers have been designed with an electric impedance of 50Ω to maximize transmission efficiency. Probe design, LF stack and dimensions, and expected performance, have been investigated and optimized using finite element analysis (PZFlex, Cupertino).

Results/Discussion

A hybrid dual frequency (1.7 MHz/21 MHz) probe was assembled as shown in Fig 1A and B. The 3D printed casing housing the LF stacks was designed to accurately center the HF array and tightly hold the two devices. Two inclined slots in the casing allow for simple, precise and repeatable integration (or replacement) of the LF transducers. The electrical impedance measured at central frequency of 1.7 MHz is around 50Ω, agreeing with the simulation. The acoustic fields generated by the LF elements and HF array were measured.

A good agreement between simulated (Fig 1C) and measured (Fig 1D) LF beams was found. The LF focus was located as designed in the elevation focal zone of the array (Fig 1E), and both LF and HF beam are accurately aligned in the elevation direction (Fig 1F). The focal zone of the LF transducer overlays the focal zone of the HF array.

[1] Gessner et al. IEEE UFFC 57(8):1772-1781, 2010.
[2] Lukacs et al. IEEE 2009 IUS:1000-1003, 2009.

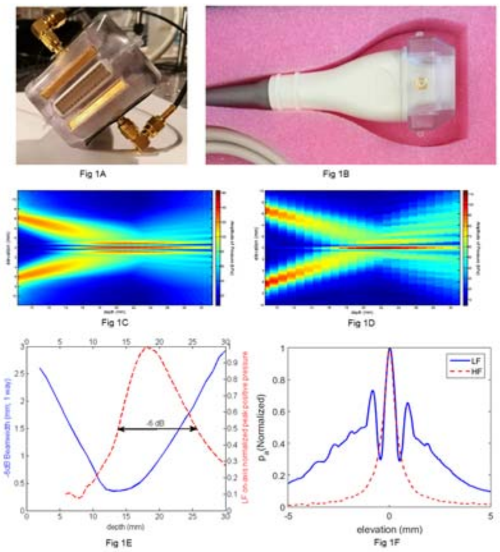

P5-A1-6

An Intracranial Implantable Ultrasound Device for Seizure Mapping

Weiwei Shao[1], Zhangjian Li[1], Zhile Han[1], Jibing Wu[1], Dan Li[2], Hongtao Ma[3], Yaoyao Cui[1]; [1]*Suzhou Institute of Biomedical Engineering and Technology (SIBET), Chinese Academy of Sciences, China, People's Republic of,* [2]*Jilin University, China, People's Republic of,* [3]*Cornell University, USA*

Background, Motivation and Objective

Epilepsy is the third most commonly diagnosed neurological disorder. For drug-resistant patients, epilepsy surgery is the only option. The outcome of epilepsy surgery largely depends on an accurate mapping of epileptogenic zone. In clinic, this is done with subdural electrode array to monitor the Electrocorticography (ECoG) with a disappointing low spatial resolution of ~ 1cm. As a result, the cure rate of neocortical epilepsy can barely reach ~ 30%. Recent study showed that the neurovascular based CBV (Cerebral Blood Volume) increases spatially overlapped with seizure focus and functional ultrasound imaging can provide high resolution 3D maps of seizure focus in animal models. To apply ultrasound imaging techniques in clinic, we propose to develop implanted ultrasound transducers 3mm*1.5mm*0.8mm which can be incorporated with the electrode array to record the CBV changes during seizure onset. This device can provide high resolution 3D seizure maps to guide the epilepsy surgery.

Statement of Contribution/Methods

In order to verify our proposals, phantom was employed to investigate the penetration of ultrasound in the brain. The 12MHz, 20MHz transducers and the corresponding ultrasound system were designed and fabricated. Acute rabbit epilepsy model was employed to verify the efficiency of our device in detecting seizure related CBV changes.

Results/Discussion

The 12MHz and 20MHz ultrasound transducer can penetrate ~ 35 mm and ~ 17.5 mm in phantoms, respectively. In animal studies, the pulse-echo voltage of 20MHz (with 40% bandwidth) from the brain tissue showed obvious periodical variation following respiration. We will further conduct experiment on the seizure induced ultrasound change animal model and develop data analysis method.

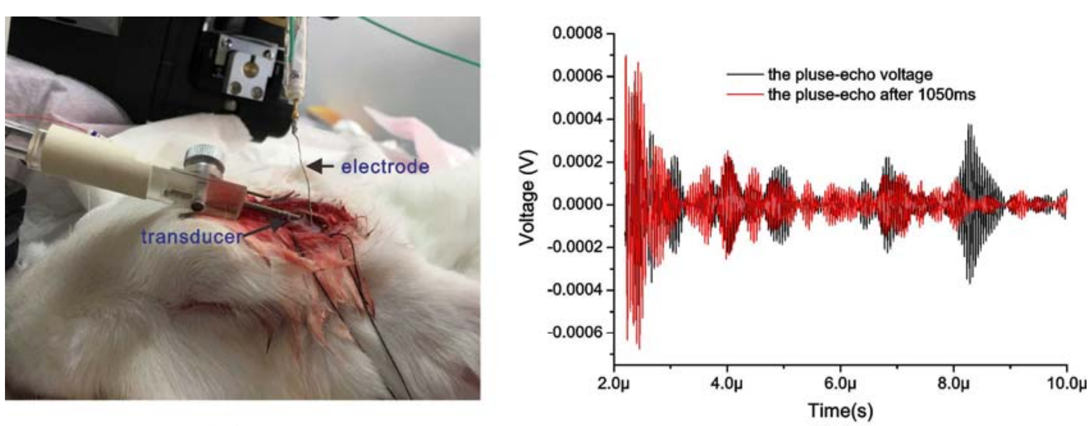

(a) (b)

Fig. 1 the rabbit epilepsy experiments and pulse-echo voltage of brain

A Feasibility Study for MRI Guided CMUT-based Intracardiac Echocardiography Catheters

Seyedabdollah Mirbozorgi[1], Coskun Tekes[2], Amirabbas Pirouz[2], Ozgur Kocaturk[3], Robert J. Lederman[3], Maysam Ghovanloo[1], **F. Levent Degertekin[2]**; *[1]School of Electrical and Computer Engineering, Georgia Institute of Technology, Atlanta, GA, USA, [2]George W. Woodruff School of Mechanical Engineering, Georgia Institute of Technology, Atlanta, GA, USA, [3]Division of Intramural Research, National Institute of Health, Bethesda, MD, USA*

Background, Motivation and Objective

Intracardiac echocardiography (ICE) is routinely used in many interventional procedures in cardiology. In these procedures ICE catheter is positioned with fluoroscopy guidance, which can be harmful due to ionizing X-ray radiation exposure. Positioning the ICE catheter using an interventional magnetic resonance imaging (MRI) system would enable procedures that are free of ionizing radiation, and complement MRI with its speed and image resolution. This paper presents a feasibility study of potential combination of these modalities demonstrating the visibility of a CMUT-based ICE catheter tip for positional guidance, minimum distortion of the MRI image, and the functionality of catheter components under high static and RF magnetic fields in MRI room.

Statement of Contribution/Methods

A custom ICE catheter prototype was built to test the feasibility of using the catheter under MRI system (Fig 1-a). The catheter includes an 8-element 1-D CMUT array placed on the distal end, a tracking coil mounted at the tip and a 1-m long catheter body enclosing 48 AWG µ-coax cables which provides the electrical connections between CMUT array and the handle (Fig. 1-a). The handle device contains Tx/Rx circuitry to generate up to 100V, 50ns duration pulses and receiver front-ends to amplify the received ultrasound echo signals with 23 dB gain and 15 MHz bandwidth. For a separate experiment to test CMOS IC functionality for possible CMUT-on-CMOS implementation under MRI, a catheter prototype with a custom designed buffer circuit (implemented in 0.18um HV TowerJazz CMOS process) at the tip was used.

Results/Discussion

The functionality of the catheter prototype system was characterized both electrically and acoustically before MRI imaging test. Immersion pulse-echo measurements from water-air interface were performed and recorded with a CMUT bias of 21V and excitation pulse of 60-ns unipolar pulse with a 46-V amplitude. The catheter prototype was then imaged in a water tank under 1.5T open magnet MRI system. The tracking coil can be clearly seen under MRI without any distortion (Fig.1-b). The system was fully functional after the MRI imaging test as indicated by pulse-echo measurements (Fig.1-b). Similarly, the IC at the tip of the other catheter was functional before and after MRI imaging. The results indicate that time multiplexed ICE/MRI imaging would be possible for MRI guided ICE.

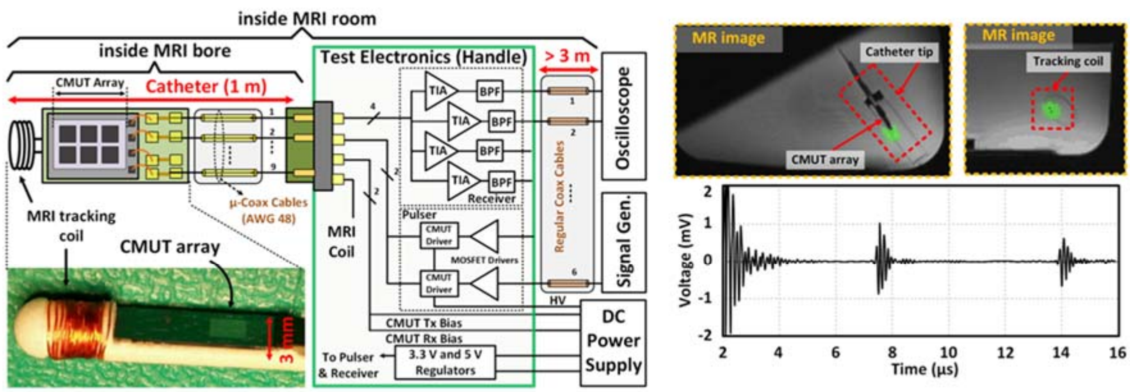

(a) (b)

Fig. 1. (a) The block diagram of the ICE catheter test system to evaluate the MRI magnetic fields effect on the performance of catheter and handle including the catheter tip with the CMUT array and MRI tracking coil (b) MR image showing the ICE catheter tip clearly visible without any distortion and the pulse-echo signals after MRI.

P5-A2 - Front End and Integrated Devices

Exhibit Hall

Thursday, September 7, 2017, 9:30 am - 4:00 pm

Chair: **Doug Wildes**
GE Global Research

P5-A2-1

Development of Wide Dynamic Range Receiver for Intravascular Ultrasound Imaging

Ju-Young Moon[1,2], Junsu Lee[3], Jin Ho Chang[3,4]; [1]*Institute of Integrated Biotechnology, Sogang University, Seoul, Korea, Republic of,* [2]*Department of Biomedical Engineering, Sogang University, Seoul, Korea, Republic of,* [3]*Department of Electronic Engineering, Sogang University, Seoul, Korea, Republic of,* [4]*Sogang Institutes of Advanced Technology, Sogang University, Seoul, Korea, Republic of*

Background, Motivation and Objective

Intravascular ultrasound (IVUS) imaging systems use high frequency ultrasound (HFU) ranging from 20 MHz to 100 MHz, or even higher to acquire high spatial resolution images of vessel diseases such as atherosclerosis. To take full advantage of HFU, imaging systems should have the capability to accommodate HFU with a relatively small amplitude and a wide dynamic range due to the small aperture of IVUS transducers and the frequency dependent attenuation of ultrasound, respectively. However, it is difficult to implement a signal receiver with off-the-shelf components that can provide high amplification gain and wide dynamic range simultaneously. Here, we present the analog frontend signal receiver recently developed for high quality IVUS imaging.

Statement of Contribution/Methods

The receiver was implemented using two 20-dB LNAs (AD8000, Analog Devices Inc.) and two 24-dB ranged VGAs (AD8337, Analog Devices Inc.) to secure both wide dynamic range and high amplification gain. For stable operation, the LNAs and VGAs were arranged alternately and the amplification gain range of each VGA was set at -6 dB to 18 dB (Fig. 1(a)). The electrical performance of the developed receiver was evaluated after measuring the amplification gain as a function of frequency and variable gain of the VGAs. The imaging performances were evaluated by comparing SNR and CNR of the developed receiver with those of the receive module in a commercial pulser/receiver system (UT340, UTEX Scientific Instruments Inc.). For the experiment, the images of a tissue mimicking phantom were acquired using a custom-made 52 MHz IVUS transducer.

Results/Discussion

Fig. 1(a) shows the amplification gain range of the developed receiver when changing the TGC gain from -12 dB to 36 dB, its operating frequency range of higher than 100 MHz and maximum gain of 73 dB. The SNR of the IVUS image acquired by the developed receiver was almost 45 dB, whereas that by the UT340 was 34 dB (Fig. 1(b)). Also, the developed receiver provided CNR higher than the commercial receiver: 15.4 dB vs. 10.5 dB for the hole at 2 mm and 11.2 dB vs. 7.5 dB at 3 mm (Fig. 1(c), (e)). From the results, it was confirmed that the developed receiver has the capability to improve SNR and CNR of IVUS images compared to the commercial receiver, which is a desired feature for high quality IVUS imaging.

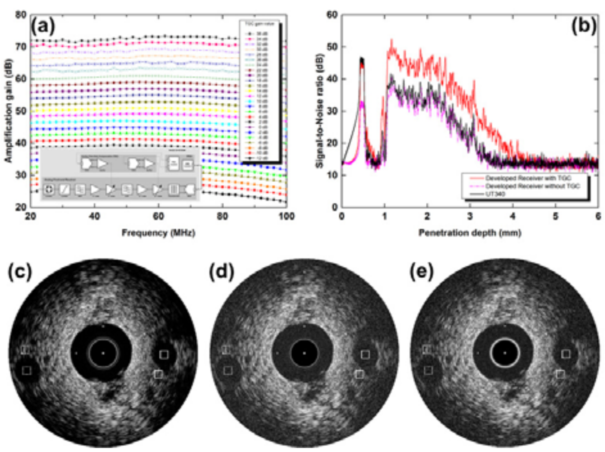

P5-A2-2

New Generation of High Voltage Pulser for Ultrasound: 16 Channels 5 Levels with Integrated Transmit Beamformer

Federico Guanziroli[1], Davide Ghisu[1], Stefano Passi[1], Sandro Rossi[1]; [1]*STMicroelectronics, Italy*

Background, Motivation and Objective

During the last decade the devices used in the transmission chain of an ultrasound machine had a huge boost towards the integration. Starting from a discrete solution the trend is to integrate multichannel solution into a single chip. One or two half bridges, a clamp to GND and the TRSW are a standard integrated channel. Actually solutions with 8 channels are the state of the art. However the transmission beamformer and the waveform generator are still managed by the FPGA.

Next step towards the integration in these devices is a challenge and the block diagram partitioning must change mainly for three reasons:

- high current values, high number of high voltage nets must be managed on single chip
- the number of inputs become a limit (at least 3 independent high frequency signals for each channel)
- single technology to manage voltage up to 200V and high density logic.

The objective of this work is to study a new approach in the transmission chain and to integrate 16 channels in a single chip with a digital machine embedded.

Statement of Contribution/Methods

The goal of this work is 16 channels 5 levels at +/-100V that means up to 64 ampere flowing in the device in the same time. The ST technology BCD8soi was used allowing to coexist HV and digital part on the same silicon.

A new and complex package solution was adopted using copper pillar on BGA substrate.

To reduce the number of the driving input signals a complex digital portion was introduced with a RAM embedded. It allows to manage the TX beamforming, to store the used waveforms, to manage all phases using only a single trigger and to introduce flexibility. The new driving technique allows to improve the performances of the device according with different applications.

Results/Discussion

The first prototypes were realized and they confirm the expected results in term of integration, compactness and performances.

The last silicon assures the optimization of some parameters like harmonic distortion and power consumption according with different final applications.

Below a short list of the main parameters:

- Rising and falling edge up to 30V/ns
- Ron TRSW of 9 ohm
- Up to 200MHz of system clock so 5ns of time resolution
- 65kbit of RAM embedded

The last version is under industrialization and it will become a new product. It enables the possibility to simplify the actual cart solution or to start moving part of the electronics directly into the probe.

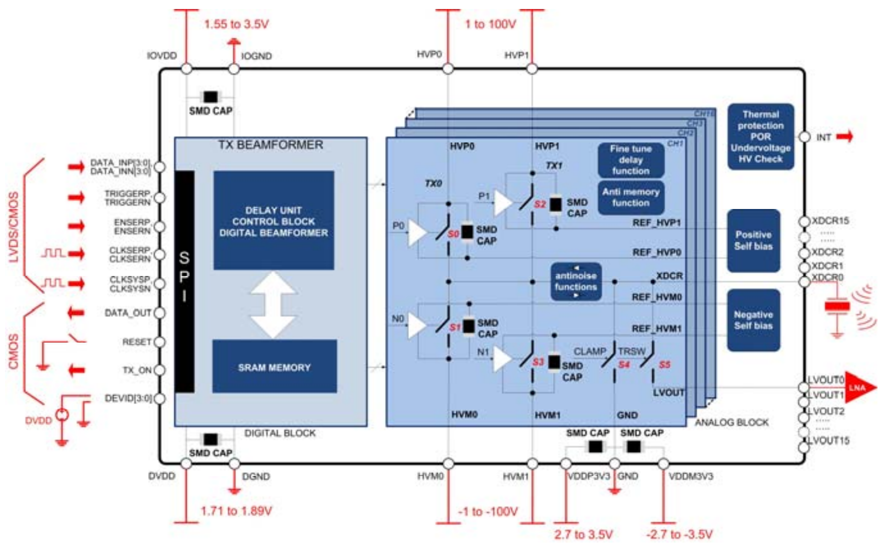

P5-A2-3

Thermal Resistance of Ultrasound Probe Cable

Richard Roth[1], Tomonori Watanabe[2], Takumi Kobayashi[2], **Koki Hirano[2]**; *[1]Research & Development, Hitachi Cable America, Manchester, NH, USA, [2]Hitachi Metals, Japan*

Background, Motivation and Objective

Ultrasound probe cable for 3D and 4D designs must efficiently dissipate the higher heat of probe head piezoelectric elements. A typical ultrasound probe cable consists of many micro-coaxial cables with an overall shield and jacket. By simply changing materials and termination methods, a significant reduction of heat can be transferred and dissipated through the cable. We will show our analysis of the ability of removing this heat through a redesigned thermal connection of the probe head to the shielding material.

Statement of Contribution/Methods

To evaluate the heat transfer, we measured the thermal resistance R of the cable. The R value depends on cable length and the surrounding environment, so we also evaluated the heat transfer coefficient h and heat conduction coefficient λthat are not dependent on cable length.

We assumed the probe cable is a thermal resistant structure and used a fin model for the cable. We connected copper rods to both sides of the shield inside the probe cable with solder (for the thermal connection) and with epoxy resin (for the non-thermal connection comparison), and applied heat to one-side of the copper rod and kept the other side at a constant temperature. We then thermally insulated the prepared samples to precisely measure the parameters. We estimated the heat transfer coefficient of h by the applied heat and the surface temperature of the cable, and the heat conduction coefficient λ by the applied heat and temperature gradient inside the cable.

We used and compared the two types of braid shielding material, (1) nylon fibers wound by thin copper tape (called SX) and (2) tinned copper alloys (called SB).

Results/Discussion

Fig.1 shows the measurement results when comparing the thermal resistance. The SB braid shielding when compared to the conventional probe cable with the SX braid shielding, shows a 10% reduction in the thermal resistance of the cable. By providing a soldered thermal connection between the cable and heat source, there is a greater than 30% reduction in thermal resistance as compared to the non-thermal connection.

In total, at least 40% of the heat could be efficiently transferred to the cable simply by changing the braid shielding material and by implementing a thermal connection method to the heat source. Further, we expect even higher thermal transfer effects by altering the thermal connection structure and method.

Figure 1

	Without thermal connection of shield material		With thermal connection of shield material	
	Setup of λ measurement 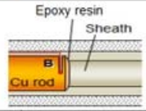		Setup of λ measurement 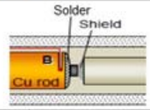	
	SX	SB	SX	SB
Heat conduction coef λ [W/mK]	6.1	7.0	18.5	34.1
Heat transfer coef h [W/m^{2}K]	17.6	18.9	17.5	17.5
Thermal resistance[K/W] @cable length 1m	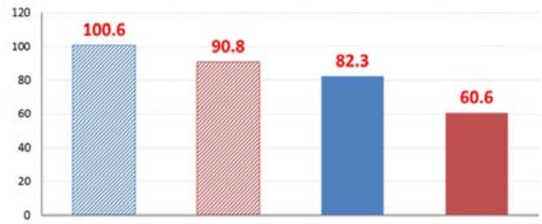			

P5-A2-4

Design of a Smartphone based Wearable Doppler Device for Continuous Blood Flow Monitoring and Prediction of Abnormalities of Vascular Function in the Common Carotid Artery

Junil Park[1], Jinbum Kang[1], Ilseob Song[1], Yangmo Yoo[1]; [1]*Electronic Engineering, Sogang University, Seoul, Korea, Republic of*

Background, Motivation and Objective

Continuous monitoring of cardiovascular system is crucial for today's healthcare system. Doppler ultrasound has been found to be of great value for assessing blood flow and diagnosing vascular diseases. However, conventional rack-based Doppler ultrasound systems is not suitable for monitoring continuous vascular function due to the low accessibility. In this paper, a new vascular function prediction protocol in the home health care environment using a smartphone based wearable Doppler device based on deep learning is presented and a sub-miniaturized CW Doppler system for the wearable Doppler device is introduced.

Statement of Contribution/Methods

The overall scheme of the proposed protocol is illustrated in Fig. 1(a). The wearable Doppler device transfers the Doppler audio signal into the smartphone for continuous blood flow monitoring in a carotid artery. The blood flow data in the smartphone are concurrently transferred into the external PC, and then deep learning with CNN and RNN algorithm is performed. The CNN for assessing the presence of the cardiovascular disease (CVD) employs the acquired Doppler audio signal with the pre-built database and the RNN predicts the risk of the outbreaks of the CVD with the accumulated database. For the wearable Doppler device to obtain the audio signal, the sub-miniaturized 2-channel CW Doppler system (50×90 mm) was developed with the two 5.0-MHz single-element transducer (Fig. 1(b)). As shown in Fig. 1(c), the received data from an ADC are fed directly to the FPGA and Doppler processing is digitally conducted in FPGA. The acquired Doppler audio signal is then transferred into the smartphone through a USB module in real time.

Results/Discussion

Fig. 1(d) represents the obtained Doppler audio signal from the flow phantom and its externally processed spectrogram. The carotid flow was successfully measured by the developed system with moderate sensitivity. In the next step, we are customizing the necklace-type wearable Doppler device using the sub-miniaturized Doppler system and the software implementation on the Android developer is performing on the smartphone for the data transmission and continuous blood flow monitoring. After that, the deep learning using the accumulated audio data is conducted for predicting of abnormalities of vascular function and the further results with *in vivo* data will be presented.

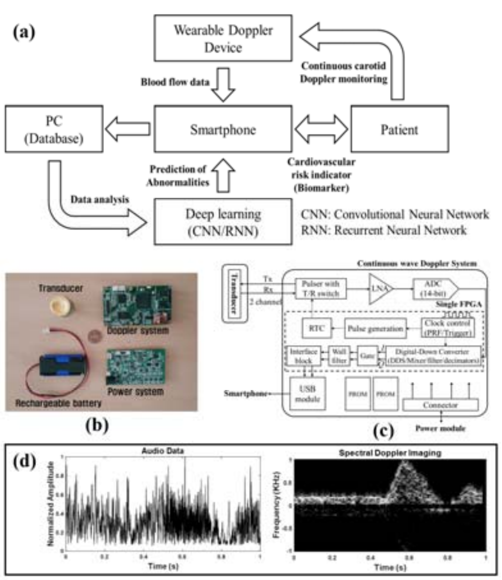

Fig. 1. (a) Overall block scheme of the proposed vascular function prediction protocol using smartphone based wearable Doppler device with deep learning. (b) Sub-miniaturized CW Doppler system for the wearable Doppler device. (c) Block diagram of the CW Doppler system. (d) The results of the Doppler audio signal (left) and its spectrogram (right) acquired using the CW Doppler system in the phantom study.

P5-A2-5

A FPGA-based Home-Care Ultrasound Device for Measuring the Flow Volume of Arteriovenous Fistula in Dialysis Patients

Po-Yang Lee[1], Chih-Chung Huang[1]; [1]*Department of Biomedical Engineering, National Cheng Kung University, Taiwan*

Background, Motivation and Objective

In general, kidney patients often have hemodialysis three to four times a week, and need to take few hours once. Before hemodialysis, the medical staff must often measure the flow volume within the vessel for the patient. If blood flow is found to be insufficient, it denotes that the blood vessels are blocked for some reasons. However, it is a very serious event for the patient, which means that patients cannot be hemodialysis and must be done the repair surgery of arteriovenous fistula immediately, otherwise it will cause the patient's life risk. In order to reduce this occurrence, the surgeon suggested that could develop a device for the patients who can measure the blood flow volume by himself or families at home. In this study, we developed a FPGA-based home-care ultrasound device for measuring the flow volume of arteriovenous fistula in dialysis patients.

Statement of Contribution/Methods

This study used the pulsed-wave Doppler ultrasound approach and M-mode to estimates the volume of blood flow. Through this way, we can get the size of the diameter and blood flow velocity in the blood vessels. Figure 1(a) shows the block diagram of FPGA-based home-care ultrasound device. It is a portable system which is includes 3 parts, button type ultrasound transducer, analog front-end board, and personal computer (PC). The special transducer (3 MHz) of button type is made for this study which package has a built-in Doppler angle transducer. This makes it easy for us to estimate the current Doppler angle on vessel and to correct the flow velocity. Then the AFE board includes pulser, pre-amplifier, variable-gain amplifier, and 14-bit analog-to-digital converter (ADC) running at a sampling frequency of 25 MSPS.

Results/Discussion

Figure 1(b) shows the graphs of whole system which size is 8×15 cm. The Fig. 1(c) shows the diameter of blood vessel, and the position of top and bottom vessel walls. And Fig. 1(d) shows a typical Doppler spectrogram of patient and its mean power spectral density. For this patient, the cross-sectional area is 1.13 cm^2 and velocity is about 25 cm/s, and its flow volume is 1695 cc/min. The challenge here is due to the vortex of blood flow caused by arteriovenous fistula, this make it very difficult to estimate the true average flow rate simply and accurately. In the estimation of blood flow velocity, some autoregressive algorithms should be applying into the spectrogram calculation.

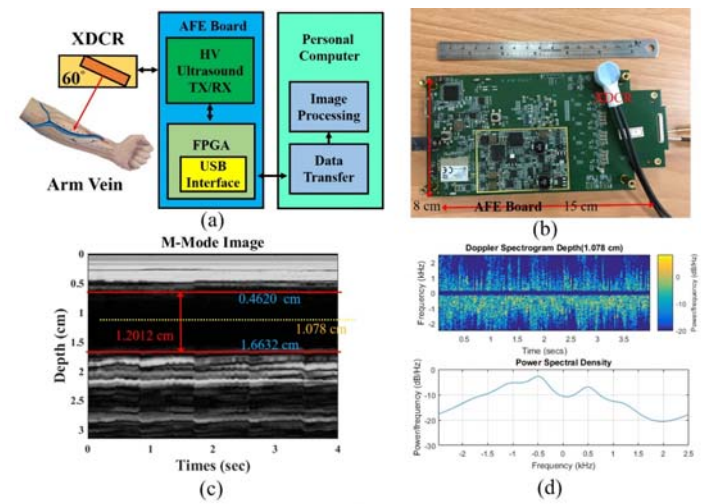

Figure 1

P5-A2-6

Doppler-based Blood Pressure Measurement System for Patients Supported by a Continuous-Flow Rotary Left Ventricular Assist Device

Jakub Rozbicki[1], Beata Witek[1], Tomasz Steifer[1], **Marcin Lewandowski**[1]; [1]*Laboratory of Professional Electronics, Institute of Fundamental Technological Research, Warsaw, Poland*

Background, Motivation and Objective

The medical management of patients with continuous-flow left ventricular assist devices (LVADs) requires frequent measurement and analysis of various physiological parameters. Among the most important is blood pressure (BP), which cannot be reliably measured by the standard oscillometric method because of an impaired pulsation due to continuous flow.

The objective of this work is to show the feasibility of ultrasound-based BP measurement in a portable, easy to use device for patients with LVAD in home-based rehabilitation environments, enabling long-term remote monitoring.

Statement of Contribution/Methods

We have implemented a BP measurement system which uses continuous wave (CW) Doppler ultrasound for blood flow detection. The system is based on a standard cuff design with custom analog CW circuitry connected to a high-performance, low-power 32-bit microcontroller (ARM Cortex-M7). The uC is responsible for system control, as well as Doppler signal acquisition and processing. A dedicated ultrasound probe equipped with an elastic strap is placed over a radial artery.

In the target solution, the cuff pressure and CW signal will be analyzed in real-time to provide systolic and/or mean blood pressure. At present, we have acquired raw signals for off-line analysis. The system was tested in a clinical experiment both on healthy patients and patients with three types of commercially available LVADs (HeartWare, HeartMate II and HeartMate III).

Results/Discussion

In healthy patients, we found a good correlation between our automatic algorithm and the standard BP measurement based on the Korotkov method. The morphology of Doppler signals in patients with LVADs were much more variable between patients and pumps. In most cases, we were able to estimate the systolic pressure, but the measurement of diastolic pressure was not conclusive. We observed variable blood flow patterns generated by the Lavare cycle (a periodic speed modulation feature of some LVADs), which further complicates the estimation.

A prototype of automatic BP measuring devices for patients with rotary LVADs has been demonstrated. In the next step, we are planning an animal validation study with invasive blood pressure monitoring.

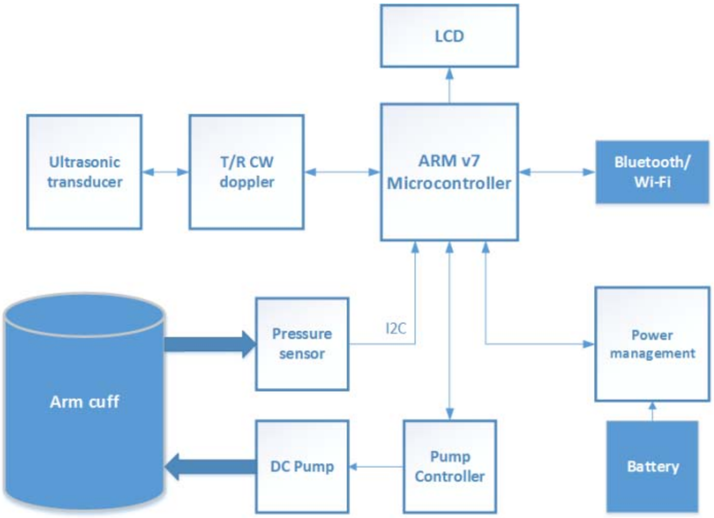
LCD
Ultrasonic transducer
T/R CW doppler
ARM v7 Microcontroller
Bluetooth/ Wi-Fi
Arm cuff
Pressure sensor
I2C
Power management
DC Pump
Pump Controller
Battery

P5-A3 - Transducer Optimization

Exhibit Hall

Thursday, September 7, 2017, 9:30 am - 4:00 pm

Chair: **Anne-Christine Hladky**
IEMN

P5-A3-1

Development of a Rotary-Percussive Ultrasonic Drill for Extraterrestrial Rock Sampling

Qiquan Quan[1], **Deen Bai[1]**, Zongquan Deng[1], He Li[1], Yinchao Wang[1]; [1]*School of Mechatronics Engineering, Harbin Institute of Technology, Harbin, China, People's Republic of*

Background, Motivation and Objective

Compared with traditional rotary-percussive drill driven by magnetic motors, ultrasonic drill which usually employs the high frequency longitudinal vibration of Langevin transducer to break down rocks, shows advantages of small size, low power, low axial load, and lubrication free, making it available for the extraterrestrial rock sampling, especially for the minor planet with a weak gravitational field. To solve the problem that the conventional percussive ultrasonic drill cannot remove cuttings effectively, we proposed a scheme of rotary-percussive ultrasonic drill which realizes both rotary and percussive motions simultaneously to remove the cuttings by the spiral groove of the drill bit.

Statement of Contribution/Methods

The conventional percussive ultrasonic drill employs the vibration energy of the front mass of the Langevin transducer to generate mechanical vibration at the bottom surface of the horn, however, the vibration energy of the back mass is not utilized. Thus, we proposed to use the vibration energy of the back mass to generate a rotary motion via a LT (longitudinal-torsional) coupler. The rotary shaft drives the drill bit to rotate continuously to deliver the cuttings out so as to increase drilling efficiency.

Results/Discussion

The experiments show that the RPUD prototype, of which preload force is 18 N, achieved no load speed of 94 rpm and maximum continuous torque of 39 mNm when excited by a voltage with amplitude of 300 Vp-p and frequency of 16.17 kHz. Under the same conditions that the diameter of the drill bit is 5 mm and the axial load is 3 N, RPUD can drill the sandstone in rotary-percussive mode with a speed of 11 mm/min while RPUD can only drill the sandstone at a speed of 9 mm/min in percussive mode where the rotor and preload spring are disassembled. Contrastive experiments show that the rotary-percussive drilling can actually raise the drilling efficiency compared with percussive drilling. This indicates that the RPUD is superior to conventional percussive ultrasonic drill.

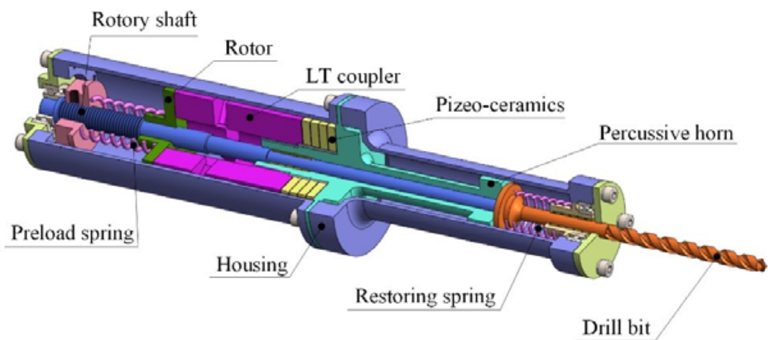

P5-A3-2

Linear Ultrasonic Array incorporating a Cantor Set Fractal Element Configuration

Haoyu Fang[1], Zhen Qiu[1], Anthony Mulholland[2], Richard O'Leary[1], **Anthony Gachagan[1]**; [1]*Electronic & Electrical Engineering, University of Strathclyde, Glasgow, United Kingdom,* [2]*Department of Mathematics, University of Strathclyde, Glasgow, United Kingdom*

Background, Motivation and Objective

The resonance frequency of an active element in a piezoelectric ultrasonic transducer is dependent on its length scale. Inspired by natural occurring auditory systems, incorporation of elements with varying length scales in the piezoelectric transducer design can result in a wider operational bandwidth. A mathematical algorithm has been developed to define the feature of a fractal geometry called the Cantor Set (CS), which will be used to design a phased array transducer. The performance of this fractal array is explored using a Finite Element (FE) model (PZFlex, Thornton Tomasetti), and compared with a conventional linear array incorporating a 2-2 piezocomposite microstructure.

Statement of Contribution/Methods

In this paper, a developed mathematical algorithm controls the scaling ratio of the CS fractal geometry, which determines the array element basic structure. A series of FE parameter simulation sweeps are used to find the optimal design of a single array element for both fractal and conventional configurations. Subsequently, linear array performance for both configurations has been simulated using an extended FE model comprising 24 elements. Consistency is maintained between the two array designs, where the thickness of both arrays is 1.5 mm and pillar width of the fractal array at Level II and conventional array is 0.15 mm. Finally, the bandwidth and beam shape of these two arrays were investigated and compared.

Results/Discussion

According to the FE parameter simulation sweep results, optimal designs have been selected for a single element of the CS and conventional array, with a single CS fractal array element illustrated in Figure 1. The FE simulation results indicate that for one single CS element, a -3 dB transmission bandwidth of 38.6 % can be achieved compared to 26.6 % for the conventional design. Moreover, the 24-element array transducer simulation produces a -3 dB transmission bandwidth of 50.1 % for the CS fractal array, against 45.2 % for the conventional linear array. When both arrays were focused 15 mm away from the transducer front face, a predicted 5 dB side lobe reduction can be achieved by using the CS fractal array design compared to the conventional linear array design. The initial prototype of this fractal array is under construction using the dice and fill approach and experimental results will be compared to an equivalent 2-2 composite substrate.

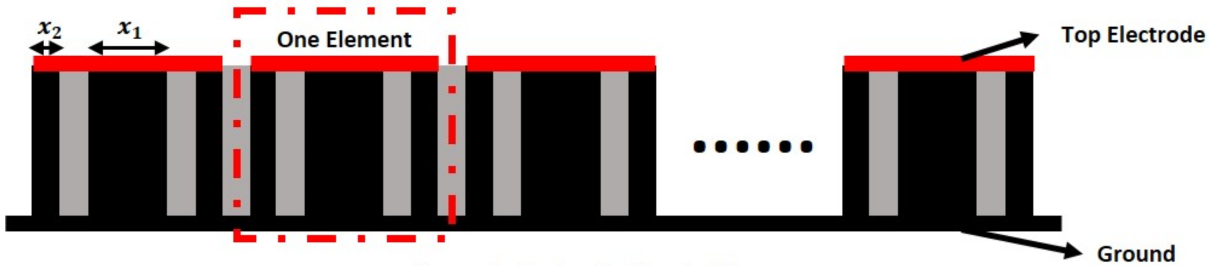

Figure 1: Cantor Set Fractal Array
Black: Ceramic Phase; Grey: Polymer Filler
x_1 = 0.47 mm; x_2 = 0.15 mm

P5-A3-3

Coupled Model for the Determination of full Electroelastic sets of 1-3 Piezocomposites with Various Pillar Shapes

Antoine Balé[1,2], Franck Levassort[1], Anne-Christine Hladky-Hennion[2]; [1]*GREMAN UMR7347 CNRS, Université de Tours, INSA Centre Val de Loire, Tours, France,* [2]*IEMN-ISEN UMR8520, Université de Lille, CNRS, Centrale Lille, Université de Valenciennes, Lille, France*

Background, Motivation and Objective

Due to their enhanced properties with respect to conventional piezoelectric ceramics, 1-3 piezocomposite materials are predominant in high performance transducer applications. The determination of their effective electroelastic modulus has been the subject of numerous investigations. Simple modeling of the thickness mode is well documented in literature, however precise simple modeling of the full effective modulus is less abundant. A coupled model is proposed to predict the complete electroelastic moduli of 1-3 piezocomposites. The main aim of this model is to deliver accurate effective elastic, dielectric and piezoelectric parameters while taking into account the internal geometry of the composite. Various piezoelectric pillar shapes and spatial distribution were tested to assess the effect on the effective parameters.

Statement of Contribution/Methods

In order to homogenize the composite, slowness surfaces of bulk waves were computed in the large wavelength approximation using the Finite Element method. Slowness surfaces are obtained by examining the response in terms of phase velocity of a bulk wave propagating within the composite with varying incidence (every 1 degree). These numerical results were fitted using relations deduced from Christoffel's equation for wave propagation in piezoelectric media which takes into account the symmetry class of the composite. Three symmetry classes were considered: 6mm, 4mm and mm2 according to the spatial arrangement and shapes of the pillars. In an effort to reduce computational time, an investigation was performed with the objective of reducing the number of computed velocities needed in order to extract the full effective modulus while keeping accurate parameters.

Computations were carried out on 1-3 PZT4 Epoxy resin piezocomposites with volume fraction ranging from 10% to 70% for square, circular and triangular shaped pillar geometry. A staggered row configuration with square pillar shape was also considered.

Results/Discussion

Complete effective electroelastic moduli were obtained for all configurations. For varying pillar geometry, related thickness mode coefficients are seen to be in agreement but notable differences appear for other coefficients such as e_{31} at high ceramic volume fraction. This is attributed to the different packing factor of the pillars. When considering the hydrostatic figure of merit F=dh×gh, results show a maxima at low volume fraction (≈ 10%) with a strong dependence of the internal structure with typically a difference of 18% between two configurations. This allows to tend toward an optimization process to maximize F for underwater applications.

Finally, the investigation into the reduction of the number of computed velocities showed that data obtained from 4 well chosen incidence angles are sufficient to obtain the electroelastic moduli with the same accuracy. This data reduction opens up the possibility of an experimental characterization.

P5-A3-4

The Directivity of Piezoelectric Matrix Transducer Elements Mounted on an ASIC

Maysam Shabanimotlagh[1], Shreyas Raghunathan[1], Verya Daeichin[1], Pieter Kruizinga[1,2], Hendrik J. Vos[1,2], Michiel A.P. Pertijs[1], Johannes G. Bosch[2], Nico de Jong[1,2], Martin D. Verweij[1,2]; [1]*Technical University of Delft, Netherlands,* [2]Erasmus MC, Netherlands

Background, Motivation and Objective

Over the last decade, clinical studies show a strong interest for real-time 3D imaging. This calls for ultrasound probes with high-element-count 2D matrix transducer array, interfaced to an imaging system using an in-probe Application Specific Integrated Circuit (ASIC) that takes care of element selection, signal amplification, sub-array beamforming, etc. Since the ASIC is based on silicon and is mounted directly behind the transducer elements, it can be regarded as a rigid plate that can sustain travelling waves, which effectively lead to acoustical cross-talk between the elements. We hypothesize that the cross-talk can be diminished by reducing the thickness of the ASIC and using a proper backing, and we investigate this by simulation.

Statement of Contribution/Methods

A finite element simulation is conducted in PZFlex, which considers a matrix of 20×20 elements with 100 µm pitch and central frequency of 7.5 MHz, which are mounted on a silicon layer and then a backing. The directivity pattern of a single element in the matrix transducer is calculated in the far field by extrapolating the pressure field generated at the surface of the transducer for the overall band. Silicon layers with four different thicknesses (30, 100, 300 and 500 µm), and two different backing materials (highly damped backing material, and an epoxy mimicking a Printed Circuit Board or PCB) are investigated.

Results/Discussion

Fig. 1 shows the simulated directivity pattern. For both backing materials, positive peaks are observed when having a thick silicon. We hypothesize that these peaks are due to a wave travelling in the ASIC and bouncing back into the medium by the neighboring elements. The peaks occur at angles that are related to the velocity of the first anti-symmetric Lamb wave travelling in the ASIC. Decreasing the thickness of the silicon results in a lower Lamb wave speed, causing the peaks to appear at higher angles. Conversely, by increasing the silicon thickness, the Lamb wave speed converges to the Rayleigh wave speed (3989 m/s for silicon), causing a peak at an angle of 22° for the highest silicon thickness. Moreover, a highly damped backing clearly decreases such acoustic cross-talk between the neighboring elements. We conclude that the acoustic cross-talk caused by the silicon layer can be suppressed when a silicon layer with thickness less than 100 µm and a highly damped backing material is used.

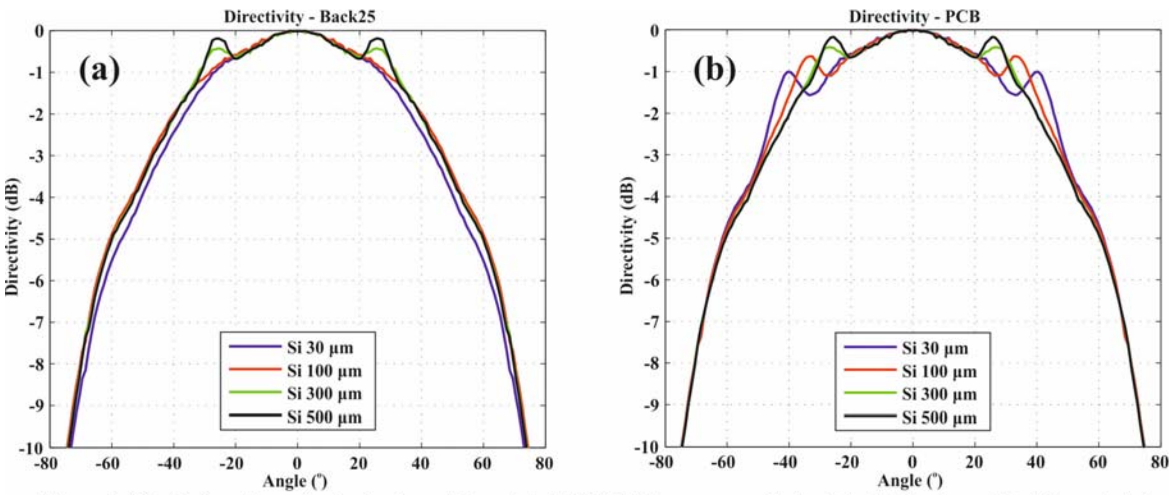

Figure 1. Directivity pattern of a single element for selected ASIC thicknesses, considering **(a)** a highly damped backing material, **(b)** a PCB epoxy backing.

P5-A3-5

Numerical Optimization of Ultrasound Transducers by the Linearity of the Phase Spectrum

Kenneth K. Andersen[1], Martijn Frijlink[1], Lars Hoff[1][3] H. Chen, [1]*Department of Microsystems, University College of Southeast Norway, Horten, Norway*

Background, Motivation and Objective

New ultrasound imaging and therapeutic modalities may require complex transducer designs that are not easily facilitated by conventional design guidelines. This motivates the investigation of numerical optimization methods that can include the effect of structural layers (e.g. bonding and electrodes), electrical loading, and more than one piezoceramic layer in the design and optimization procedure. The aim of his paper is to investigate such numerical design methods and apply this to optimize a transducer by linearizing the phase spectrum.

Statement of Contribution/Methods

We have developed a numerical design method that utilizes the linearity of the phase spectrum as the design criterion. The motivation for this choice is to obtain short pulse lengths: A system with a linear phase has a constant group delay, which for a given transducer corresponds to the shortest possible impulse response [1]. The optimization is done by the Simulated Annealing algorithm where the characteristic impedance and thickness of each matching layer are changed stochastically. The deviation between the transducer's spectral phase and an ideal linear phase, obtained by linear regression within a specified bandwidth, is used as the measure of the performance.

Results/Discussion

The linear phase (LP) method is used to optimize the matching section of an air-backed transducer (bonding layers are included) and the results are compared to the established analytical equations derived by Desilets [2]. The magnitude of the transmit transfer function and corresponding impulse response are shown in Fig. 1 (a) and (b), respectively. The -6 dB relative bandwidth and -20 dB impulse length obtained by the LP method are 63% and 0.62 µs, respectively. For comparison, the same quantities obtained by Desilets' equations are 71% and 0.91 µs, respectively. Compared to Desilets' equations, the LP method shows a reduction in the bandwidth; however, the impulse response also shows a reduction in the ringing, which yields a 30% shorter impulse length. We therefore conclude that the LP method may lead to transducers with potential for shorter pulses and subsequently improved axial resolution in ultrasound imaging applications.

References:

[1] S. C. Pohlig, Proc. IEEE, 68(5), 1980.

[2] C. S. Desilets et al., IEEE Trans. Son. Ultrason., 25(3), 1978.

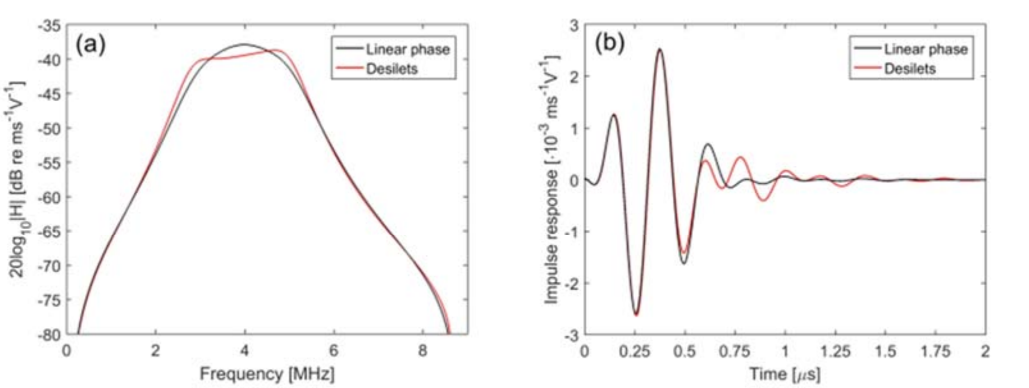

Figure 1: (a) Magnitude of the transmit transfer function $H = U/V$, where U is the normal particle velocity at the face of the transducer and V is the voltage across the transducer terminals. (b) Corresponding impulse response.

PA - Student Poster Competition

Exhibit Hall

Thursday, September 7, 2017, 9:30 am - 4:00 pm

Chair: **0**
0

PA-1

3D Rendering of Electromechanical Wave Imaging for the Characterization and Optimization of Biventricular Pacing Conditions in Heart Failure Patients Undergoing Cardiac Resynchronization Therapy

Lea Melki[1], Ethan Bunting[1], Daniel Wang[2], Pierre Nauleau[1], Elisa Konofagou[1,3][3] H. Chen, [1]*Biomedical Engineering, Columbia University, New York, NY, USA,* [2]*Medicine - Division of Cardiology, Columbia University, New York, NY, USA,* [3]*Radiology, Columbia University, New York, NY, USA*

Background, Motivation and Objective

Assessing the response of heart failure (HF) patients to Cardiac Resynchronization Therapy (CRT) currently relies on the ECG and left ventricular (LV) ejection fraction. Electromechanical Wave Imaging (EWI) is a high frame-rate (2000 Hz) ultrasound-based technique capable of non-invasively mapping the electromechanical activation in all four cardiac chambers in vivo. In this study, we aim to show the capability of EWI in identifying different pacing conditions in patients with CRT and to characterize the resulting activation pattern directly following biventricular (BiV) device placement.

Statement of Contribution/Methods

A total of nine HF patients, each in three different pacing conditions (RV only, LV only and BiV), were imaged following their ICD implantation in four transthoracic standard echocardiographic apical views (4-, 2-, 3- and 3.5-chamber). Electromechanical strains and activation maps were computed in each view with EWI processing. Axial displacements were estimated using 1D RF cross-correlation, and strains were derived with a 5 mm least squares kernel. Activation times were defined by the sharp transition from positive to negative values on the incremental strain curves. LV lateral wall activation times (LWAT) and RV free wall activation times (FWAT) were quantified on the apical 4-chamber view for each patient and each pacing protocol. 3D rendering of the ventricular activation maps were then generated by registering the four multi-2D views around the LV base to apex axis of symmetry and performing a linear interpolation circumferentially between them.

Results/Discussion

EWI was shown capable of mapping and distinguishing the electromechanical activation in the three standard pacing protocols arising from CRT (Figure). LWAT in BiV pacing (71 ± 16 ms) were found to be lower compared to LV (94 ± 21 ms) and RV pacing only (123 ± 21 ms). FWAT were the highest in LV pacing (104 ± 17 ms), while RV (74 ± 18 ms) and BiV (72 ± 20 ms) pacing conditions resulted in similar FWAT values. LWAT was significantly different in each of the three pacing conditions (p=0.05), while FWAT was able to distinguish between LV pacing and the other two conditions (p=0.02). These findings indicate that EWI could be a valuable monitoring tool for clinicians to optimize the pacing vectors after ICD placement and potentially identify super-responders.

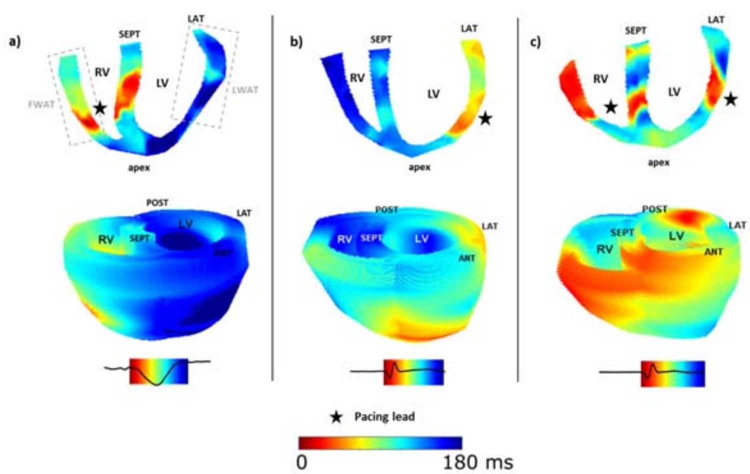

Fig. EWI ventricular activation maps in HF patient undergoing CRT. a) RV pacing only (LWAT = 154 ms, FWAT = 84 ms), b) LV pacing only (LWAT = 84 ms, FWAT = 129 ms), c) BiV pacing (LWAT = 96 ms, FWAT = 57 ms). Top row: four-chamber apical view isochrones, bottom row: 3D rendering of the ventricular activation maps.

PA-2

Multispectral Ultrafast Ultrasound Imaging: A Versatile Tool Probing Dynamic Phase-Change Contrast Agents

Heechul Yoon[1], Stanislav Emelianov[1,2]; [1]*School of Electrical and Computer Engineering, Georgia Institute of Technology, Atlanta, GA, USA,* [2]*Wallace H. Coulter Department of Biomedical Engineering, Georgia Institute of Technology and Emory University School of Medicine, Atlanta, GA, USA*

Background, Motivation and Objective

Optically triggered perfluorohexane nanodroplets (PFHnDs) can repeatedly vaporize and recondense, providing photoacoustic (PA) and blinking ultrasound (US) signals in response to pulsed laser irradiation. This property of PFHnDs has led to the development of various US imaging modes, including super-resolution and background-free contrast-enhanced imaging. However, to utilize the full potential of PFHnDs, multi-wavelength PA imaging, followed by ultrafast US imaging, referred to as multispectral ultrafast US/PA imaging, is required. Thus, we built a combined system that can trigger and image the dynamic behavior of PFHnDs with various optical wavelengths.

Statement of Contribution/Methods

A programmable US system (Vantage-256, Verasonics Inc., Kirkland, WA) and a multi-wavelength pulsed laser (Phocus, Opotek Inc., Carlsbad, CA) were interfaced and synchronized with a host controller (HC) and a function generator (FG) as shown in Fig. 1a. Using a MATLAB programming environment of the HC, we developed customized routines to irradiate tissue using laser pulses of desired optical wavelengths and to acquire post-laser-pulse PA and US images. To tune the laser wavelength, the HC communicated with the laser system using dynamic linked library functions. An image acquisition sequence that can be repeated with various optical wavelengths is illustrated in Fig. 1b. To test the performance of the system, we spectroscopically (from 700 nm to 940 nm with a 30-nm step) imaged a tube containing PFHnDs with a peak absorption at 760 nm.

Results/Discussion

As expected, both PA and differential US (ΔUS) images exhibit higher contrast at 760 nm compared to the image obtained with longer wavelengths (Fig. 1c). In addition, temporal behavior of differential US signal changes with laser wavelength (Fig. 1d) allowing for the US-based spectroscopic characterization of PFHnD dynamics. Furthermore, multi-wavelength PA imaging can visualize PFHnDs in the presence of endogenous chromophores (not shown). The developed multispectral ultrafast US/PA system could be used in various applications, including simultaneous detection and assessment of micro-metastasis in sentinel lymph node (SLN), where the location of SLN is determined by multispectral US imaging of PFHnDs and micro-metastases are detected by spectroscopic PA imaging of blood oxygen saturation.

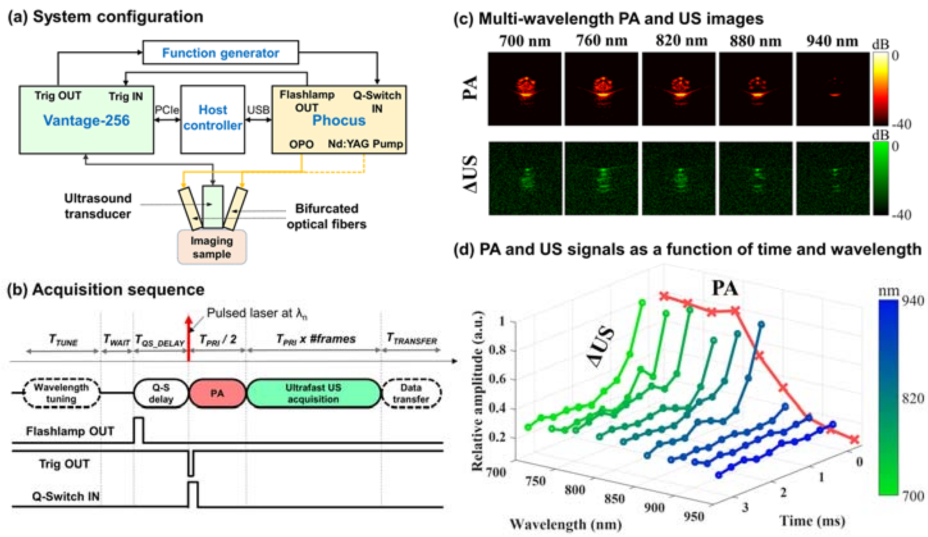

PA-3

In Vivo Photoacoustic Detection of Lymph Node Metastasis using Glycol-Chitosan-Coated Gold Nanoparticles

Diego Dumani[1,2], In-Cheol Sun[1,2], Stanislav Emelianov[1,2]; *[1]Wallace H. Coulter Department of Biomedical Engineering, Georgia Institute of Technology and Emory University School of Medicine, Atlanta, GA, USA, [2]School of Electrical and Computer Engineering, Georgia Institute of Technology, Atlanta, GA, USA*

Background, Motivation and Objective

Metastasis rather than primary tumors determines prognosis and mortality in the majority of cancer patients. Detection of metastatic lesions is critical to determine prognosis and suitable treatments. We developed a method for identifying sentinel lymph node (SLN) metastasis, using combined ultrasound and photoacoustic (US/PA) imaging augmented with glycol-chitosan-coated gold nanoparticles (GC-AuNP). Presence of metastasis affects accumulation of GC-AuNP in the SLN, which can be monitored via US/PA imaging (A).

Statement of Contribution/Methods

GC-AuNP colloid (100 µl, 0.1 mg Au/ml) was injected peritumorally for drainage into the SLN of breast tumor-bearing mice (A). US/PA imaging of the SLN was performed before and immediately after the injection, and then 1 h, 24 h, and 48 h after the injection. Accumulation of GC-AuNP in the LN after cellular uptake by immune cells (macrophages) was visualized using PA imaging in the near-infrared wavelength range. To quantify accumulation, we used spectroscopic PA (sPA) in the 680-970 nm wavelength range, which allows for isolation of signal corresponding to GC-AuNP. At the conclusion of the imaging studies, we harvested the tissue and performed histological analysis. Immune cells, metastatic cells, and GC-AuNP were identified by H&E stain, GFP fluorescence, and dark-field microscopy, correspondingly.

Results/Discussion

US/PA imaging showed that accumulation of GC-AuNP in the SLN was reduced due to metastasis (B). While single-wavelength PA images demonstrated the effect qualitatively, the accumulation of GC-AuNP was quantified using sPA analysis. The overall sPA signal (area of sPA image relative to area of LN) within the lymph node was reduced by more than 20% (statistically significant) when compared to healthy controls (C). No changes were observed between 24 h and 48 h drainage. Histology (D) confirmed that metastatic cells inside the SLN disturb the distribution of particles inside immune cells, stopping them from spreading across the SLN, as identified by US/PA. In healthy controls, GC-AuNP were found in macrophages across the lymph node. In conclusion, the developed US/PA imaging method can aid physicians in detection of micrometastasis thus guiding and avoiding unnecessary SLN biopsy. Future studies will focus on studying cell uptake mechanisms to optimize GC-AuNP, improve delivery, and minimize the dosage.

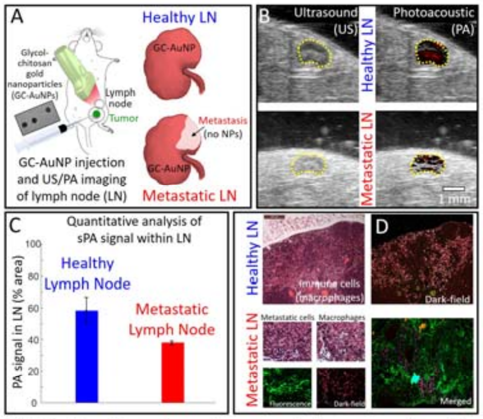

A) GC-AuNP are injected near primary tumor in the mammary fat pad for drainage into the inguinal lymph node. Distribution of GC-AuNP in LN is affected by metastasis. B) The SLN is identified using ultrasound. Spectroscopic PA imaging shows the difference in nanoparticle accumulation/distribution. C) Healthy LN showed enhanced accumulation of GC-AuNP in the dark-field microscopic images. In contrast, accumulation of GC-AuNP (dark-field) is reduced in LN with metastatic cancer cells (fluorescence). D) Quantitative analysis shows significant reduction in sPA signal in the metastatic SLN.

PA-4

Full 4D Functional Ultrasound Imaging in Rodents Using a Matrix Array

Claire Rabut[1], Victor Finel[1], Mafalda Correia[1], Mathieu Pernot[1], Thomas Deffieux[1], Mickaël Tanter[1]; [1]*INSERM U979, PARIS, France*

Background, Motivation and Objective

In vivo brain activity imaging is a key to understanding the mechanisms of complex neural behavior. Functional MRI records brain-wide mechanisms, but at the cost of subject sedation which excludes behavioral experiments. Functional Ultrasound (fUS) Imaging, based on Doppler Imaging, is a powerful new tool for imaging brain activation with high spatiotemporal sampling (80µm, 1ms). It has been successively applied in anesthesized and awake rodents and in humans in preoperative settings.

However, the brain mechanisms and functional connectivity are inherently three-dimensional, it is thus crucial to work toward imaging of the full brain in 3D.

In this study, we present the first full 3D fUS Imaging of a mouse using a matrix array.

Statement of Contribution/Methods

To address the issue of 3D, the concept of 2D Ultrafast Ultrasound Imaging is extended to 3D Ultrafast Volumetric Imaging. A 1024 channel ultrasound platform is used to drive a 32x32 matrix phased array (0.3mm pitch, 9MHz). Ultrasound plane wave compounding (12 angles, PRF=500) is used to insonify the region of interest and volumetric images are reconstructed using a 3D GPU-based beamformer.

During functional acquisition experiments, the matrix array was setup on top of craniotomized and anesthetized mice (n=3). Mice whiskers were mechanically stimulated (12sc ON period- 12sc OFF period stimulations).

Results/Discussion

High-quality 3D vascular volumes were obtained in mice with the craniotomy procedure and showed the feasibility of task-activated 3D functional ultrasound imaging. The 3D activation map shows the spatial distribution of the hemodynamic response to manual stimulation of whiskers with the activation of both the S1BF and VPM structures. A strong correlation is observed (r=0.5, figure 1b) between the stimulus and the vascular response.

This proof of concept demonstrates 3D fUS and the reconstruction of activated. Those results pave the way to the study of brain connectivity between all structures in the mouse brain. Nevertheless, the setup sensitivity still need to be improved to allow transcranial imaging and the sequence processing must be improved to allow much longer acquisition.

Those results demonstrate how 3D fUS could be useful for preclinical research or clinical applications.

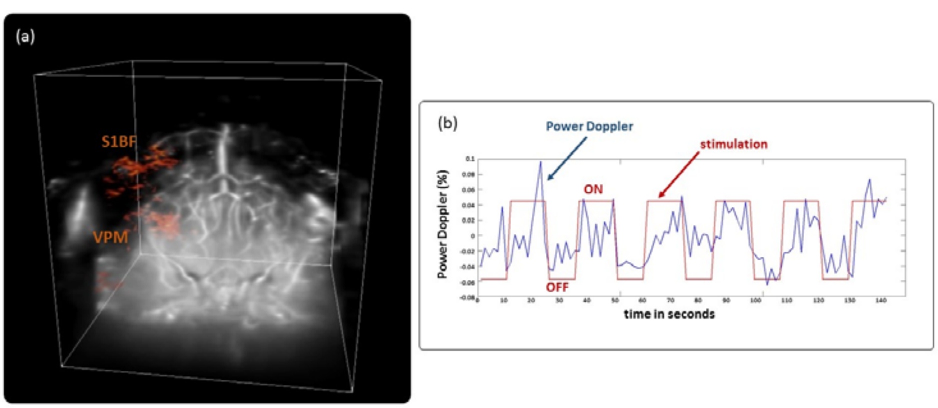

Figure: (a): Representative example of an 3D activation map obtained when stimulating the right whiskers. Map was obtained as the correlation coefficient between the power Doppler signal and the stimulus pattern. S1, primary somatosensory barrel cortex; VPM, ventral posterior medial nucleus. S1BF and VPM regions were delineated from a mouse brain atlas. (b) Doppler signal of task-evoked brain activation in the mouse brain. Power Doppler (PD) fUS images are acquired every 1.5 s. The whisker stimulation pattern (red line) consisted of 12 s ON and 12 s off repeated 6 times. The PD is plotted in percentage relative to the whole brain volume.

PA-5

3D Functional Ultrasound Imaging of the Visual System in the Pigeon Brain

Richard Rau[1], Wolfgang Scheffer[1], Markus Belau[1], Pieter Kruizinga[2], Nico de Jong[2,3], Johan G. Bosch[2], Georg Maret[1]; [1]*University of Konstanz, Germany,* [2]*Thorax Center, Erasmus MC, Rotterdam, Netherlands,* [3]*Faculty of Applied Sciences, Delft University of Technology, Delft, Netherlands*

Background, Motivation and Objective

Recently, a new functional neuroimaging method called fUS was proposed, which is based on high-frame-rate Power Doppler imaging. So far, fUS has only been performed on rodents, but major issues in neuroscience such as cerebral asymmetries and language learning are mainly studied in birds. Here, we show the first successful fUS measurements on a non-mammalian species without cortical brain architecture, such as pigeons. These measurements are based on a framerate enhanced fUS acquisition algorithm, which was necessary to suppress the signal variations originating from the slower heartrate of pigeons.

Statement of Contribution/Methods

The study was carried out on anesthetized healthy pigeons (Columba livia domestica) with a thinned skull (isoflurane narcosis). The stimulation pattern consisted of unilateral flickering (5Hz) LEDs, ~5.5cm away from the eye (15s on / 30s off). A 128-element linear array probe (L22-14v, Verasonics) operating at 16MHz was used. The probe was connected to a fully programmable ultrasound system (128 chan. Vantage, Verasonics). The fUS signal was recorded continuously at a transmission rate of ~11kHz (36 angled plane waves and ensemble length of 160 per Power Doppler image), making use of a dedicated beamforming and SVD filtering algorithm on the graphics processing unit (GPU) using Matlab 2015a. For the 3D datasets, we acquired 21 slices using a manual translation stage, 500µm apart, and evoked a response in each visual wulst by stimulating the contralateral eye.

Results/Discussion

Fig.1a shows an evoked response of ~6% cerebral blood volume change by contralateral stimulation, whereas the ipsilateral control signal remains at the baseline level. The signals correspond to the mean Power Doppler intensity in the regions of interest (ROI) marked in Fig.1b. The activity map overlay (correlation coefficient with stimulus pattern) in Fig.1b shows that the spread of activation within the fUS measured brain slice can be robustly evaluated with values up to r≅0.4. In Fig.1c, the whole activated visual wulsts (red/green regions) in the pigeon brain are revealed in 3D, where only r>0.2 is shown. The activity resulted as a response to contralateral visual stimulation and has volumina of (6.4±0.3) mm³ (right hemisphere) and (8.7±0.4) mm³ (left), respectively. Future work will concentrate on characterizing the cerebral asymmetries in more detail.

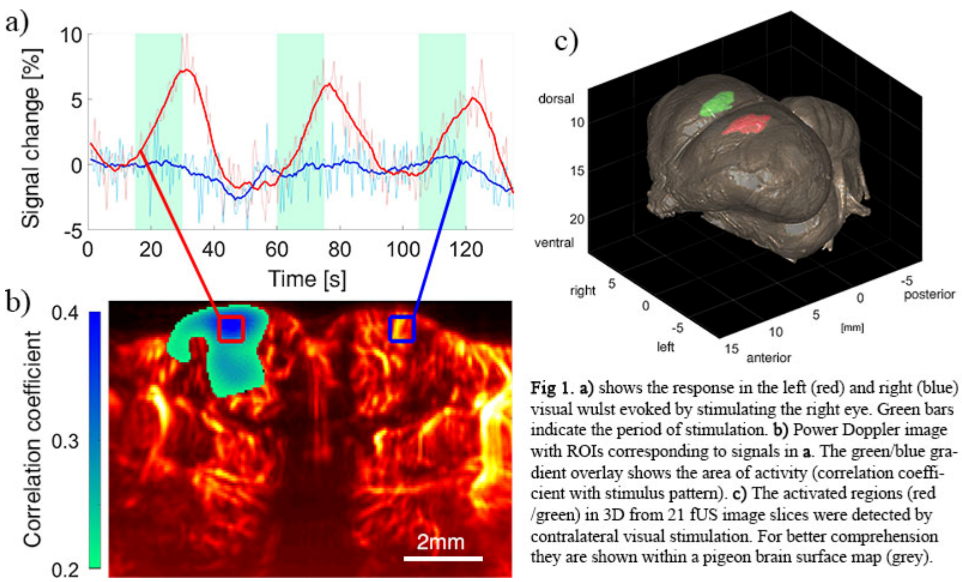

Fig 1. a) shows the response in the left (red) and right (blue) visual wulst evoked by stimulating the right eye. Green bars indicate the period of stimulation. **b)** Power Doppler image with ROIs corresponding to signals in **a**. The green/blue gradient overlay shows the area of activity (correlation coefficient with stimulus pattern). **c)** The activated regions (red /green) in 3D from 21 fUS image slices were detected by contralateral visual stimulation. For better comprehension they are shown within a pigeon brain surface map (grey).

PA-6

Volumetric Imaging of Fast Mechanical Waves in the Heart Using a Clinical Ultrasound System: A Feasibility Study

Pedro Santos[1,2], Lasse Løvstakken[2,3], Eigil Samset[2,4], Jan D'hooge[1]; [1]*Department of Cardiovascular Sciences, KU Leuven, Belgium,* [2]*GE Vingmed Ultrasound, GE Healthcare, Norway,* [3]*Department of Circulation and Medical Imaging, NTNU, Norway,* [4]*Center for Cardiological Innovation, Norway*

Background, Motivation and Objective

Fast mechanical waves following e.g. electromechanical activation and aortic valve closure (AVC) have been imaged using 2D diverging waves (DW). However, their full characterization requires multiple 2D recordings in subsequent heartbeats. Given the heart cycle variability and short-lived nature of these waves, temporal alignment is challenging. Moreover, clinical matrix arrays hinder the straightforward implementation of DW, due to sub-aperture (SAP) beam forming.

We have recently proposed a sparse DW sequence capable of imaging a 70°x70° volume in a clinical system and reported its preliminary validation *in vivo* against 2D Tissue Doppler Imaging (TDI).

Herein, the feasibility of measuring fast mechanical events in 3D *in vivo* was investigated.

Statement of Contribution/Methods

A GE Vivid E95 clinical scanner with a GE 6VT-D transesophageal (TEE) matrix array was used to transmit a sparse sequence consisting of 9 DW (3 in azimuth, 3 in elevation). Ultrafast 3D TDI was recorded on a healthy volunteer in both apical and parasternal views. A TDI frame rate of 610 vol/s was achieved with frame-to-frame autocorrelation method on IQ data.

The datasets were subsequently contoured in 3D at the isovolumetric contraction (IVC) and relaxation (IVR) periods. TDI, strain rate and tissue acceleration (i.e. forward difference of TDI) were computed at the mesh nodes. Moreover, anatomical colour M-modes were extracted at the anteroseptal wall. These were used to detect the mechanical waves following mechanical activation and AVC.

Results/Discussion

Given the 610 vol/s, the 3D DW sequence detected fast mechanical events occurring in all directions. The figure shows a mechanical wave captured by 10 subsequent frames during a 15 ms interval starting at AVC. The wave starts at the basal anteroseptal segment and propagates towards the apex, as well as laterally and therefore matches the shear wave associated with AVC as described previously using 2D techniques.

This study demonstrated the feasibility of the proposed sequence for the detection of clinically-relevant fast mechanical waves in 3D *in vivo* using a clinical scanner. This allows the assessment of the whole ventricle in a single heartbeat, unlike the conventional 2D imaging sequences used nowadays.

A clinical study using this acquisition sequence is currently being planned, in order to confirm these observations in a larger cohort.

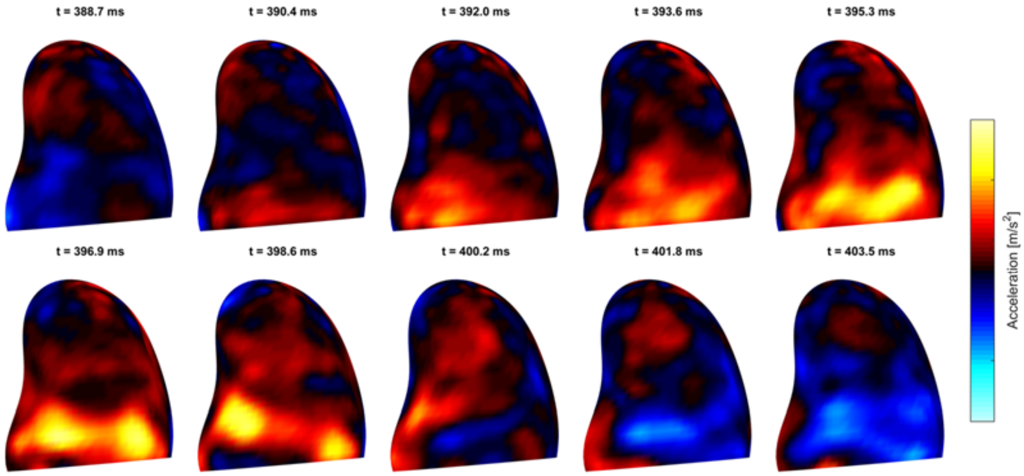

Fig – Propagation of the mechanical wave created by the aortic valve closure, as seen from the anteroseptal wall. The image shows tissue acceleration over 10 subsequent volumes acquired at 610 Hz (1.6 ms temporal resolution) around the aortic valve closure time.

PA-7

Prevent Lithium Dendrite Formation in Rechargeable Batteries through Surface Acoustic Waves

Ann Huang[1], James Friend[1]; [1]*Center for Medical Devices and Instrumentation, University of California, San Diego, La Jolla, CA, USA*

Background, Motivation and Objective

Lithium (Li) has long been known to be the best anode material for rechargeable batteries, however, lithium **metal** batteries (LMB) have never been commercialized due to dendrite formation, resulting in thermal runaway and fire or explosion. During charging, Li ions deposit onto Li anode from the cathode via electrolyte. However, the deposition is not uniform due to the inhomogeneous ion distribution in the electrolyte from a thick Li ion depletion layer, typically >400 µm. Our objective is to reduce the diffusion layer from 400 µm to only 1 µm by using surface acoustic wave (SAW)-driven mixing flow of the electrolyte during charging and to prevent dendrite formation.

Statement of Contribution/Methods

We solve the dendrite problem in LMBs via an efficient, SAW-driven internal recirculation of the electrolyte during charging. In suppressing dendrite growth, we preserve the charge capacity of the battery. The small, 100 MHz single-crystal lithium niobate SAW device is compatible with lithium electrochemistry. By externally inducing the flow along the anode, we avoid interfering with the anode's solid electrolyte interphase (SEI) layer that forms during use. Outside this 1 µm viscous boundary layer, the Li ion concentration is homogeneous: dendrites are precluded.

Results/Discussion

Rapid recharging of a SAW LMB at up to 0.8C (1.25 hr at 1.5 mA/cm^2) is now possible without dendrites. Thus, after 5 cycles, the SAW LMB retains 90% of the battery's *theoretical* 170 mAh/g capacity; after 50 cycles it retains 70%. A traditional LMB's capacity fades to only 40% after 5 cycles, as shown in Figure 1(a). Dendrites are a problem in the standard LMB as shown via a scanning electron microscope image in Figure 1(b); the dendrites are absent with SAW in Figure 1(c). Lastly, as shown in Figure 1(d), Li dendrites grow in a SAW-absent LMB regardless of charge rate, but upon application of SAW to reduce the Li ion concentration gradient, charge rates up to 85% of the maximum rate are possible without dendrites according to calculations based on convection-diffusion equations incorporating acoustic streaming.

This result indicates that, with application in an electric vehicle for example, the 280-mile range of a car using today's latest lithium-ion battery technology would be almost *doubled* to over 500 miles, with a reduction in battery cost of 20% per mile. Further, such a battery will charge in only 10 min.

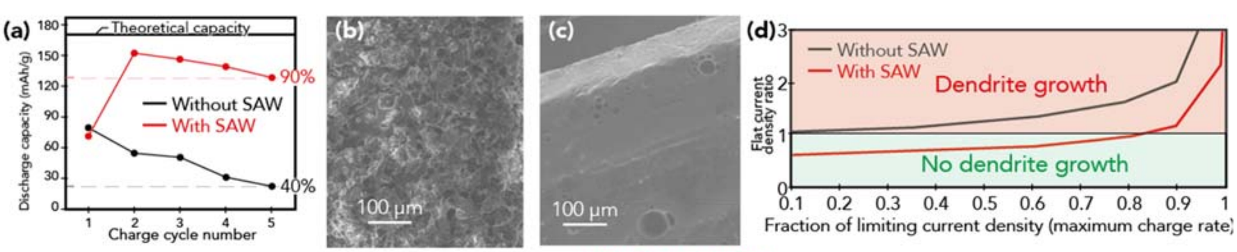

Figure 1. (a) The charging performance of an LMB cycled with SAW (red line): 90% capacity after 5 cycles. Without SAW (black line) it is only 40% after 5 cycles. SEM images of the Li anode charged (b) without SAW, Li dendrite is shown, while (c) with SAW, the Li anode remains pristine after 5 cycles. (d) Computed dendrite growth rate in a LMB without SAW, compared to with SAW to reduce the Li concentration gradient. Flat current density ratios of less than one imply no dendrite growth. Charge rates up to 85% of theoretical are possible without dendrite growth using SAW irradiation.

PA-8

Directivity of a Planar Fabry-Perot Optical Ultrasound Sensor

Danny Ramasawmy[1], James Guggenheim[1], Paul Beard[1], Benjamin Cox[1], Bradley Treeby[1]; *[1]Medical Physics and Biomedical Engineering, University College london, United Kingdom*

Background, Motivation and Objective

The Fabry-Perot (FP) polymer film sensor can detect ultrasound over a broadband frequency range (tens of MHz), with small element sizes (tens of microns), and high sensitivity. It has been used extensively in photoacoustic imaging as well as general ultrasound field characterisation. Although it will clearly affect the ultrasound field measurements, the directional response of the sensor has not been widely studied. The objective of this work was to develop an analytical model to study how the various wave types propagating in the multilayer FP sensor affect the directionality. This is critical to optimise the design of the FP sensor, and to reduce sensor-related image artefacts.

Statement of Contribution/Methods

The global matrix (GM) method was used as the basis for a model of the FP sensor directivity. This can incorporate an arbitrary number of layers with different elastic properties, as well as acoustic absorption. The sensors were modelled as 6 layer structures, including the propagation medium, barrier coating, mirrors, spacer, and backing.

The elastic properties of the sensor layers were estimated using a multi-parameter optimisation to fit the model (Fig. 1b) to measurements of the directivity made using a broadband laser-generated ultrasound pulse (Fig 1a). To understand the effect of the various wave modes on the directivity, dispersion curves (Fig. 1c) were calculated by finding pairs of values for frequency and phase speed for which the determinant of the GM became singular.

Results/Discussion

The multi-layered model of the FP ultrasound sensor directivity gives very good agreement with experimental measurements. Using the model, this allows the features in the angle-dependent frequency response to be associated with different wave phenomena, giving greater insight into the sensor's response. In particular, the vertical banding was associated with critical angles for different wave types, and the curved peaks were associated with different combinations of Scholte and Stoneley waves. The developed model will underpin future attempts to design sensors with improved directional responses, and - when the sensor is used as an imaging array - will be a key component in the amelioration of image artefacts.

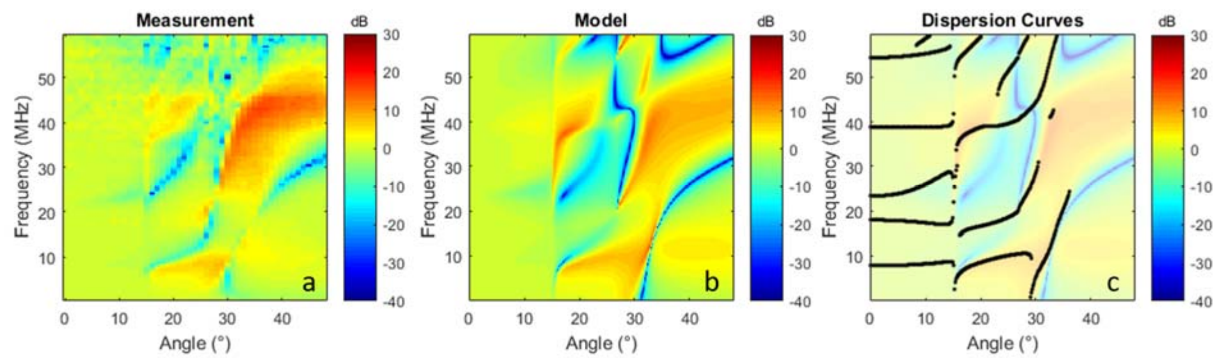

PA-9

Ultrasound Flow Mapping of 3D Turbulent Liquid Metal Flows

Norman Thieme[1], Karl Büchner[2], Richard Nauber[1], Lars Büttner[1], Olf Pätzold[2], Jürgen Czarske[1]; *[1]Laboratory for Measurement and Sensor System Techniques, TU Dresden, Germany, [2]*TU Freiberg, Germany

Background, Motivation and Objective

Conductive fluids, e.g. metallic melts, can be driven by magnetic fields, which is a branch of magnetohydrodynamics (MHD). MHD can be used for driving a melt flow during the crystal growth of photovoltaic silicon in order to improve the mass and heat transfer in the melt for better structural and electrical properties of the silicon crystals. However, the optimal application of MHD requires a good understanding of the flow, which is generally complex and unsteady during crystal growth. Substantial knowledge about the flow is usually gained through numerical simulations and MHD model experiments at room temperature. For model experiments, a comprehensive flow mapping of complex and unsteady flow phenomena is required.

Statement of Contribution/Methods

We present an ultrasound array Doppler velocimeter (UADV) suited for model experiments with low-melting metals, e.g. the alloy gallium-indium-tin (GaInSn, melting point 10.5°C). The UADV measures flow maps by a line-scanning approach with arrays of large US elements (pitch > λ). With the line-scanning approach 2-d vector flow maps can be measured and processed effectively, since beamforming calculations are not necessary. In a typical configuration, the UADV is equipped with four ultrasound arrays with 25 elements each. The arrays span two planes measuring two 2-d vector flow fields. The investigation of unsteady flows may take several hours. Therefore, the I-Q demodulation and the velocity estimation are executed on an FPGA, which can reduce the measurement data by a factor of 100. A combined spatial and time multiplexing scheme enables high frame rates of several 10 Hz, which qualifies the UADV for the measurement of turbulent melt flows.

Results/Discussion

The UADV was applied to a model experiment consisting of a cylindrical container filled with the alloy GaInSn and ring coils with a current source generating a magnetic field. The melt flow was driven by a travelling magnetic field. The figure shows a sketch of the experiment and measured instantaneous flow patterns that show the transition from an almost symmetric, stationary to a complex, time-dependent flow.

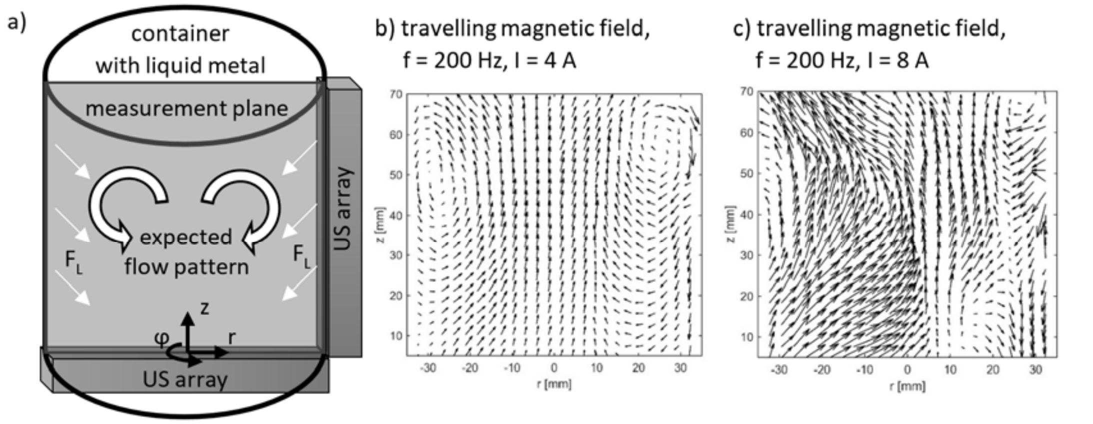

Figure: a) Sketch of the container with the Lorentz force F_L and the expected toroidal flow pattern. b) and c) Vector flow maps measured at the sketched model experiment.

PA-10

Design of Multi-Frequency Acoustic Kinoforms

Michael Brown[1], Ben Cox[1], Bradley Treeby[1]; [1]*University College London, London, United Kingdom*

Background, Motivation and Objective

The control of acoustic fields in 3-D is vital in many areas of physical acoustics. Recently, a new approach for the generation of complex diffraction limited acoustic fields in 3-D was introduced. This works by calculating a phase hologram designed to generate a desired acoustic field. The output of a simple planar transducer is then mapped onto this phase distribution using a 3-D printed kinoform attached to the transducer.

One limitation of this approach is that the acoustic field generated by each kinoform is fixed. A way to overcome this is to adapt a technique from optical holography and encode several target distributions onto different frequencies. The field can then be changed by varying the driving frequency of the transducer. The goal of this work was to demonstrate this approach and to investigate the design of these kinoforms.

Statement of Contribution/Methods

An optimisation approach based on direct-binary-search was implemented to calculate multi-frequency kinoforms. This searched, sequentially, for the thickness at each position that minimised a cost function penalising variations between the actual field and the target field for each frequency. Two other algorithms were also implemented. One based on combining several phase holograms using a >2π modulation depth to minimise the combined error, and another based on dividing the aperture for each frequency.

The fields generated by the output kinoforms were simulated using the k-Wave toolbox and measured experimentally. For the experiments, kinoforms were fabricated using 3-D printing and attached to the front face of a planar transducer. The acoustic field was then measured driving the transducer at each encoded frequency.

Results/Discussion

Both the simulated and experimental results demonstrated that acoustic kinoforms encoding multiple field patterns onto different frequencies can be generated with a direct-search approach. This is illustrated by the figure which shows a calculated kinoform and its simulated field in one plane when driven at two different frequencies. The efficiency of this approach is sensitive to the choice of design method and the separation and number of encoded frequencies.

This work enables some of the functionality of a large phased array to be encoded onto a single element transducer using a cheap 3-D printable structure.

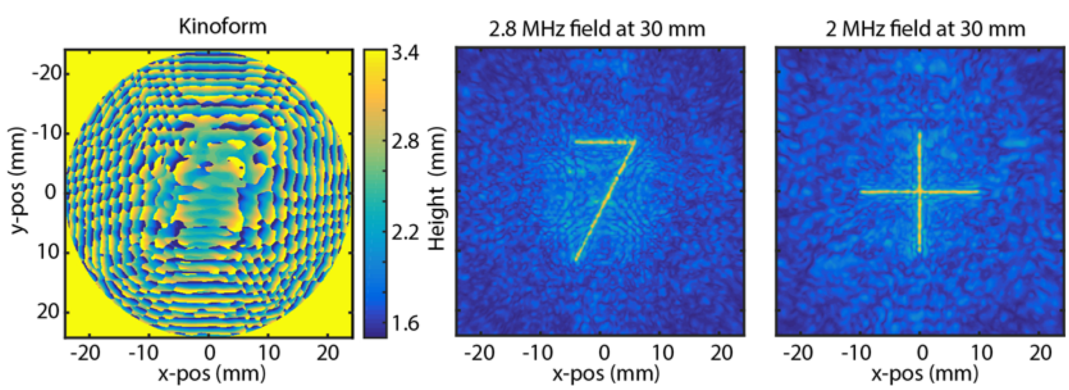

PA-11

High Electromechanical Coefficient k_t^2=19% thick ScAlN Piezoelectric Films for Ultrasonic Transducer in Low Frequency of 80 MHz

Ko-hei Sano[1], Rei Karasawa[1], Takahiko Yanagitani[1,2]; [1]*Waseda university, Japan,* [2]*JST-PRESTO, Japan*

Background, Motivation and Objective

Ultrasonic in the frequency ranges of 20-100 MHz is not well-developed because of less applications or less suitable piezoelectric materials as shown in Table I. In a photoacoustic imaging, PVDF are usually used for ultrasonic transducers in the 10–50 MHz band. However, their electromechanical coupling coefficient k_t^2 of 4% is not enough for the practical uses. To excite ultrasonic in the 20-100 MHz, 125 μm-25 μm thick piezoelectric film is required. It is difficult to fabricate such a thick piezoelectric film without a crack caused by the internal stress during the deposition. A film deposition technique can realize the piezoelectric layer on a complicated surface such as curved or concave surface, which is difficult in the case of the single crystal plate. In this study, we demonstrated high efficient 81 MHz ultrasonic generation by using 43 μm extremely thick ScAlN films.

Statement of Contribution/Methods

ScAlN thick films were grown on (0001) oriented Ti electrode films/silica glass substrate. We achieved stress free film growth by employing the unique hot cathode sputtering technique without heating substrate. Next, the k_t of the ScAlN thick film were determined by comparing the experimental and theoretical longitudinal wave conversion losses. The experimental conversion losses were measured using a network analyzer. The theoretical conversion loss curves were simulated using multilayered Mason's equivalent circuit model.

Results/Discussion

The k_t^2 of the ScAlN thick film is determined to be 18.5% at 81 MHz, which is much larger than k_t^2=4% of PVDF. ScAlN and PVDF transducer performance used in water medium were simulated by using Mason's model, as shown Fig.1. We can see narrow frequency characteristics due to the difference of acoustic impedance between the piezoelectric layer and the water medium. Although these bandwidths around 80 MHz are almost same, the ultrasonic conversion efficiency of ScAlN is much better than PVDF. Furthermore, we simulated the effect of λ/4 acoustic matching layer of SiO_2 inserted between the ScAlN piezoelectric layer and the water medium. The results indicate the broadband frequency characteristics with high efficiency. Therefore, this ScAlN thick film transducer is promising for photoacoustic imaging applications.

Table I Frequency ranges in the ultrasound imaging and the typical properties of the piezoelectric film materials

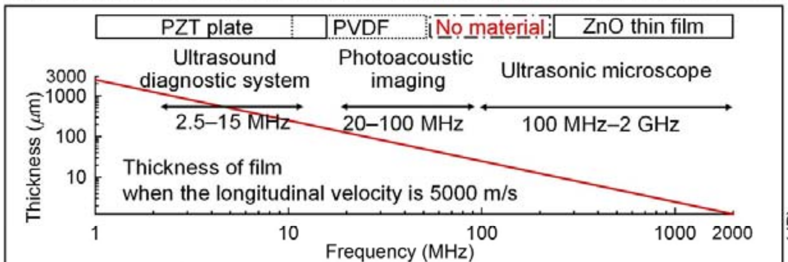

	k_t	k_t^2	Ref.
PMN-PT (PT 33%)	0.55	30%	[1]
PZT (sol-gel)	0.40	16%	[2]
PZT (hydrothermal synthesis)	0.51	26%	[3]
PVDF	0.20	4%	[4]
ZnO thin film	0.29	8.4%	[5]
ScAlN thin film	0.39	15%	[6]
ScAlN thick film (43 μm)	0.43	18.5%	This study

[1] Xiang Li, et al. IEEE TUFFC 58, 2281 (2011).
[2] R. Nanjo, et al. IEICE Tech Rep 97, 39, (1997).
[3] Q. Su, B Zhu, et al. J. Mater. Res. 26, 1431 (2011).
[4] G. Teyssedre, et al. J POL SC PP. 33, 879, (1995).
[5] R.T. Smith and V.E. Stubblefield, JASA. 46, 105 (1969).
[6] T. Yanagitani, et al., Proc. IUS., pp. 2095–2098, (2010).

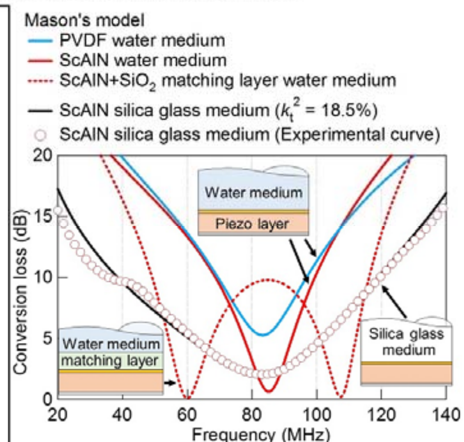

Fig.1 Experimental and theoretical conversion loss curves in the silica glass and water medium.

PA-12

Variable-Focus Liquid Crystal Lens Using Ultrasound Vibration

Yuki Shimizu[1], Daisuke Koyama[1], Akira Emoto[1], Kentaro Nakamura[2], Mami Matsukawa[1]; [1]*Faculty of Science and Engineering, Doshisha University, Kyotanabe, Kyoto, Japan,* [2]*Laboratory for Future Interdisciplinary Research of Science and Technology, Tokyo Institute of Technology, Yokohama, Kanagawa, Japan*

Background, Motivation and Objective

Nematic liquid crystal is widely used in optical devices such as liquid crystal displays. The optical characteristics of liquid crystal devices (ex, birefringence) can be controlled by applying an electric field because the liquid crystal molecules have electric dipoles. Although indium tin oxide (ITO) is generally employed as the transparent electrode material, ITO needs the rare metal indium and has problems of low electric conductivity and transparency. Our group has proposed a novel control technique of liquid crystal molecular orientation using ultrasound vibration without using ITO [1]. In this report, an optical variable-focus liquid crystal lens using ultrasound was discussed.

Statement of Contribution/Methods

An ultrasonic liquid crystal lens was fabricated (see Fig. 1(a)). The lens has no moving mechanical parts and no transparent electrodes and consists of a simple structure; a nematic liquid crystal layer with a thickness of 50 μm is formed between two circular grass plates (Φ_a = 30 mm; Φ_b = 15 mm) with a thickness of 0.7 mm. An annular PZT ultrasonic transducer (outer diameter: 30 mm; inner diameter: 20 mm; thickness: 1.0 mm) was bonded on the glass plate (a). By exciting the transducer at the resonance frequencies, the flexural vibration modes were generated on the liquid crystal lens. The acoustic radiation force changed the molecular orientation of the liquid crystal so that the incident light to the lens was refracted and the transmitted light could be focused.

Results/Discussion

In the default condition with no input voltage, the transmitted light was not refracted and focused because the liquid crystal molecules oriented perpendicularly to the glass plates (Fig. 1(b)). With the ultrasound excitation at the fundamental resonance frequency of 36.1 kHz, the concentric flexural vibration mode with the half wavelength of approximately 11 mm was generated on the glass plates. The liquid crystal molecular orientation then was changed by acoustic radiation force, and the transmitted light was refracted and focused on the target (Fig. 1(c)). The focal point could be controlled rapidly and simply by the input voltage.

[1] S. Taniguchi, D. Koyama, Y. Shimizu, A. Emoto, K. Nakamura, and M. Matsukawa. Appl. Phys. Lett. 108 (2016) 101103.

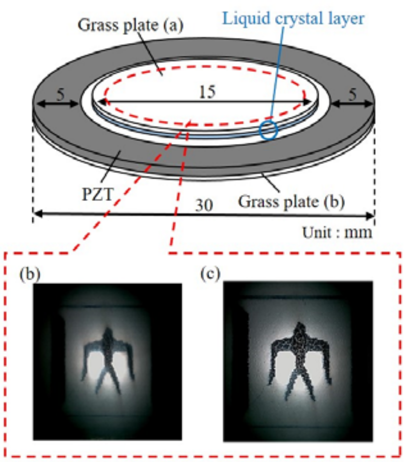

Figure 1. Ultrasonic liquid crystal cell; (a) configuration, (b) the vibrational distribution, and (c) the transmitted light distribution at 36.1 kHz.

PA-13

Role of Metal Electrodes in the Generation of Third Order Non-Linearities in Surface Acoustic Wave Components

Vikrant Chauhan[1], Markus Mayer[2], Andreas Mayer[3], Elena Mayer[3], Werner Ruile[2], Thomas Ebner[2], Karl Wagner[2], Robert Weigel[1], Amelie Hagelauer[1]; [1]*Institute of Electronics Engineering, Erlangen Nuremberg University, Erlangen, Bayern, Germany,* [2]*Advanced development discreet, RF360jv, Munich, Bayern, Germany,* [3]*Hochschule Offenburg, Germany, Offenburg, Germany*

Background, Motivation and Objective

The growing complexity in RF front-ends, which support carrier aggregation and a growing number of frequency bands, leads to tightened nonlinearity requirements in all sub-components. The generation of third order intermodulation products (IMD3) are typical problems caused by the non-linearity of SAW devices. In the present work, we investigate temperature compensating (TC) SAW devices on Lithium Niobate-rot128YX. An accurate FEM simulation model [1] is employed, which allows to better understand the origin of nonlinearities in such acoustic devices.

Statement of Contribution/Methods

The nonlinear tensor data of the different materials involved in a TC-SAW device have been determined. Thereto we compared IMD3 measurements of test filters with FEM simulations and obtained nonlinear tensor data of the various materials. We employed the periodic FEM tool presented recently [1]. Since the FEM model is periodic we did not compare results directly to measurement, but at first determined an effective nonlinearity constant by comparison of nonlinear P-matrix simulations [2] to measurement. The effective nonlinearity constant obtained in this way was then applied in nonlinear periodic P-matrix simulations for comparison to the FEM-simulations.

Results/Discussion

In this investigation we focused on the role of the metal electrodes. We investigated test TC-SAW filters with varying metalization ratios. In order to reduce the number of unknowns we assumed the nonlinear tensors of each material to depend on a single parameter only. The substrate nonlinear tensor data are known from literature and were not optimized. Based on FEM simulations the contribution of the different materials to the nonlinear behavior of SAW devices is discussed.

[1]. A. Mayer, E. Mayer, M. Mayer, P. Jager, W. Ruile, I. Bleyl and K. Wagner, “Full 2DFEM calculations of third-order intermodulation in SAW devices”, IEEE International Ultrasonics Symposium 2016.

[2] M. Mayer, W. Ruile, J. Johnson, I. Bleyl, K.Wagner, A. Mayer, E. Mayer, “Rigorous COM and P-matrix approaches to the simulation of third-order intermodulation distortion and triple beat in SAW filters”, IEEE International Ultrasonics Symposium 2013

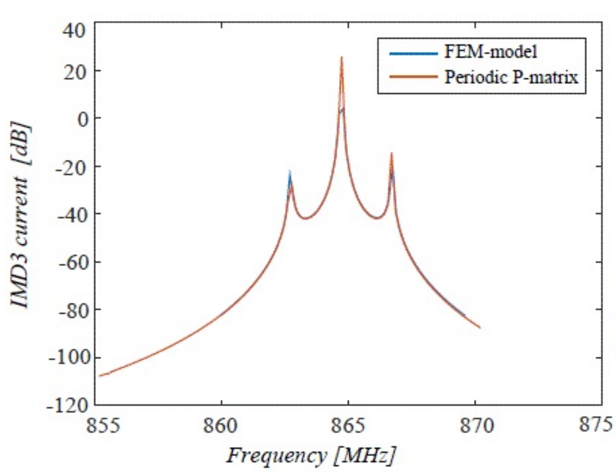

Figure. 1: Comparison of IMD3 current from nonlinear 2D-FEM and periodic P-matrix simulation model.

PA-14

Piston Mode Operation of SAW Resonators Using Coupling Between Multiple SAW Modes

Benfeng Zhang[1,2], Tao Han[1], Gongbin Tang[1,2], Xinyi Li[2,3], Yulin Huang[2,3], Tatsuya Omori[2], Ken-ya Hashimoto[2]; *[1]School of Electronic Information and Electrical Engineering, Shanghai Jiao Tong University, China, People's Republic of, [2]Graduate School of Engineering, Chiba University, Japan, [3]School of Electronic Engineering, University of Electronic Science and Technology of China, China, People's Republic of*

Background, Motivation and Objective

The piston mode operation (PMO) is quite effective for realization of spurious-free and low-loss SAW resonators. The scalar potential (SP) analysis indicates that "phase shifters" are necessary for PMO at edges of the acoustic aperture. Nakamura, et al., pointed out that for SAW resonators using $SiO_2/LiNbO_3$ structure, PMO is possible by simply removing SiO_2 in the dummy electrode region [1]. This phenomenon cannot be explained by the SP theory, and was expected to be due to existence of the spurious SH SAW in addition to the main Rayleigh SAW or vice versa.

Statement of Contribution/Methods

This paper investigates SAW reflection at aperture edges of SAW resonator structures when multiple SAWs exist and couple with each other. The extended thin plate model [2] which can take the coupling into account is used for the analysis. It is shown that the coupling causes additional phase shift at the reflection, and PMO is possible without any tricks at aperture edges when the device structure is designed properly.

Results/Discussion

The simulation model gives the PMO condition in a closed form. It is governed by velocities of the main and spurious SAW modes in the aperture and dummy electrode regions and their anisotropy factors in the dummy electrode regions.

Fig. 1 shows calculated input admittance of infinitely long IDT with finite aperture when the parameters are set to satisfy the condition. Transverse resonances are completely suppressed. Fig. 2 shows the field distribution of the main resonance. It is seen that the main mode is well trapped in the aperture region, and the boundary condition is satisfied with a help of evanescent fields near the aperture edges.

[1] H. Nakamura, et al., IEEE Trans. UFFC., 58, (2011), p.2188.

[2] B. Zhang, et al., Proc. IEEE Ultrason. Symp. (2016) 10.1109/ULTSYM.2016.7728496.

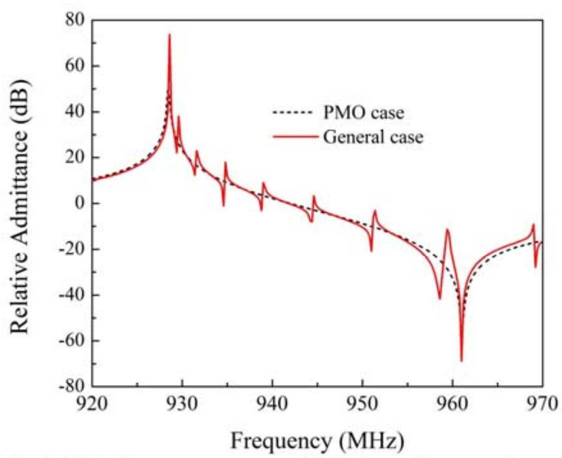

Fig.1 Admittance curves of PMO and general cases

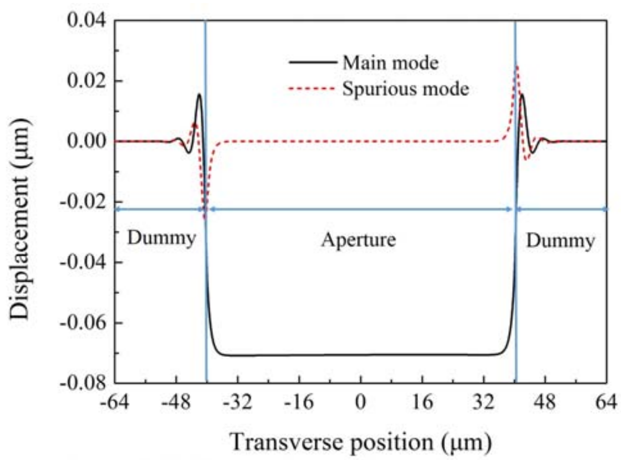

Fig.2 Field distribution of the main resonance

PA-15

AlN/ZnO/LiNbO₃ Packageless Structure as a Low-Profile Sensor for On-Body Applications

Cécile Floer[1], Mohammed Moutaouekkil[1], Florian Bartoli[1,2], Harshad Mishra[1], Sami Hage-Ali[1], Stefan Mc Murtry[1], Philippe Pigeat[1], Thierry Aubert[2], Olivier Bou Matar[3], Abdelkrim Talbi[3], Omar Elmazria[1]*; [1]Institut Jean Lamour UMR 7198, Université de Lorraine - CNRS, Nancy, France, [2]LMOPS EA 4423, CentraleSupélec - Université de Lorraine, Metz, France, [3]LIA LEMAC/LICS - IEMN UMR CNRS 8520, ECLille - USTL, PRES Université Lille Nord de France, Villeneuve d'Ascq, France*

Background, Motivation and Objective

Surface acoustic wave (SAW) devices are widely used as filters or resonators for mobile communications or radars applications. However, the velocity of the wave can be very sensitive to physical parameters of the environment (temperature, strain…), which allows the device to be used as a sensor. SAW devices are passive (batteryless) and wireless, but are often bulky due to the package. To dramatically reduces their profile, it is possible to use a Wave-guiding Layer Acoustic Wave (WLAW) structure, which consists of a low velocity layer between two higher velocity layers. These structures have the potential to be ultra-thin and conformable and thus could be used for flexible on-body biomedical applications. This work investigates the $AlN/ZnO/LiNbO_3$ structure as a candidate for a WLAW temperature sensor.

Statement of Contribution/Methods

First, the structure was studied by a 2D-FEM modelling to maximize the electromechanical coupling coefficient K^2 (ZnO thickness) and to determine the minimum required AlN thickness for the wave confinement (see Fig.1a and 1b). Then, for the experimental part, a single port synchronous resonator with a wavelength of 4.4 µm, was designed and then fabricated with e-beam lithography and chemical etching on the piezoelectric substrate ($LiNbO_3$). Then, 2 µm of ZnO followed by 8 µm of AlN (in two steps: 2 µm AlN, then 6 µm AlN) were deposited on the top of the electrodes using reactive magnetron sputtering (see Fig.1c).

In order to check experimentally the confinement of the wave in a WLAW device, a soft matter can be placed on the top of it at different stages of the process. Here the silicone elastomer Solaris has been chosen (see Fig.1d) for its simplicity of use and its properties which are comparable to those of the skin (E_{Young}=50 kPa). If no change occurs to S parameters, then it proves that the wave is confined.

Results/Discussion

Considering large thickness of top and bottom layers, calculations show that the maximum K^2 is obtained for 2 µm of ZnO. With this thickness, at least 7 µm of AlN are required to fully confine the wave. Experimentally, with 2 µm of AlN, an impedance change is clearly notable and confirms that the wave requires a thicker layer of AlN to be confined. With 8 µm of AlN, the Solaris perturber has no impact on the signal and thus prove that the studied structure can be used for packageless SAW sensors.

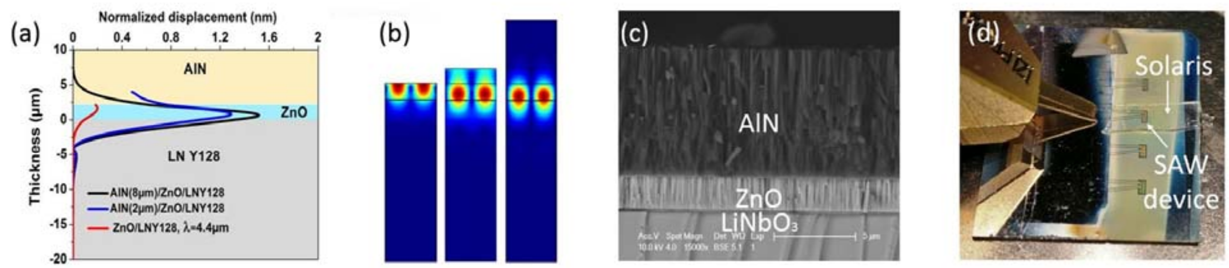

Fig. 1. (a) (b) 1D/2D Comsol modellings of particle displacements in a $LiNbO_3$/ZnO structure with 0 µm, 2 µm and 8 µm of AlN, respectively, on top of it: the wave is confined in the latter case, (c) SEM visualization of the device cross-section ($LiNbO_3$/ZnO/AlN), (d) Probe station measurement of the electrical impedance of a SAW resonator with an elastomeric Solaris perturber

PA-16

An Optically Transparent Air-Coupled Capacitive Micromachined Ultrasonic Transducer (CMUT) Fabricated Using Adhesive Bonding

Xiao Zhang[1], Feysel Y. Yamaner[1], Oluwafemi Adelegan[1], Ömer Oralkan[1]; [1]*Electrical and Computer Engineering, North Carolina State University, Raleigh, North Carolina, USA*

Background, Motivation and Objective

Transparent transducers are desired in the applications where optics and acoustics are combined, such as integrating ultrasound sensing or parametric arrays for directional sound in display, combined optical and acoustical microparticle manipulation, and backward-mode photoacoustic imaging. Some piezoelectric materials, e.g., PVDF, LNO, and PLZT, have been investigated for such applications. Besides, a Fabry-Perot (Etalon) optical ultrasound sensor can be used as a transparent ultrasound receiver. Implementing a transparent transducer in CMUT technology is desired to take advantage of wide bandwidth, ease of fabrication, and broad selection of processing materials. We have demonstrated a CMUT with ITO bottom electrode for improved transparency fabricated using anodic bonding. The main hurdle for the transparency in the visible wavelength range was a 2-µm silicon plate. In this work, we have designed and fabricated a CMUT with a glass plate using adhesive bonding and achieved improved transparency in the full visible wavelength range.

Statement of Contribution/Methods

The presented transparent CMUT was fabricated by a two-mask process using adhesive bonding (Fig. 1a), specifically for display-based air-coupled applications. A 1-mm-thick, 100-mm-diameter glass wafer with 200-nm ITO coating was used as the starting substrate. The ITO was etched to form the bottom electrodes and then a 4.5-µm thick SU-8 was spun and patterned to serve as the post and also the base for adhesive bonding. A 175-µm-thick glass wafer with 200-nm ITO coating was used as the top plate wafer. A 1-µm thick SU-8 layer was coated on the ITO to serve as the insulation layer. The plate wafer was flipped and bonded on the thick wafer at 120°C under 0.3-MPa pressure in vacuum.

Results/Discussion

The completed wafer is a single CMUT element. The wafer was placed on a "NC State University" logo to show the transparency (Fig. 1b top). The average transmission of the device is measured as ~70% in the 400-1000-nm wavelength range (Fig. 1b bottom). The electrical input impedance was measured in air (Fig. 1c). The resonant frequency of the fabricated device is ~ 62 kHz and the series resistance is ~30 Ω.

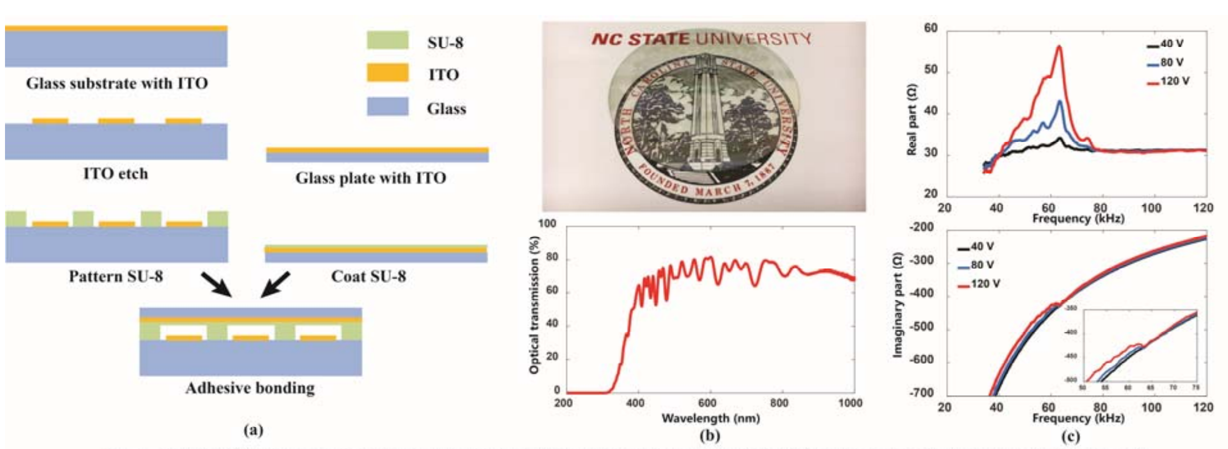

Fig. 1. (a) Simplified fabrication process flow; (b) Photo of the finished wafer on NCSU logo (top); Optical transmission measurement (bottom); (c) Electrical input impedance: Real part (top); Imaginary part (bottom).

PA-17

A Front-End ASIC for Miniature 3-D Ultrasound Probes with In-Probe Receive Digitization

Chao Chen[1], Zhao Chen[1], Deep Bera[2], Emile Noothout[3], Zu-yao Chang[1], Hendrik Vos[2,3], Johan Bosch[2], Martin Verweij[2,3], Nico de Jong[2,3], Michiel Pertijs[1]; *[1]Electronic Instrumentation Lab., Delft University of Technology, Delft, Netherlands, [2]Biomedical Engineering, Erasmus MC, Rotterdam, Netherlands, [3]AcousticalWavefield Imaging, Delft University of Technology, Delft, Netherlands*

Background, Motivation and Objective

Data acquisition from 2-D transducer arrays has become one of the main challenges for the development of endoscopic and catheter-based 3-D ultrasound imaging devices. Front-end ASICs with sub-array pre-beamforming have been reported that reduce the cable number by an order of magnitude. Further channel reduction requires digitization in the front-end ASIC to facilitate more in-probe data processing functions. Prior solutions, however, are too large and power-hungry to be integrated in a miniature ultrasound probe. In this work, we present a front-end ASIC with an element-pitch-matched layout that combines sub-array beamforming, digitization and high-speed data transmission. It achieves a 36-fold channel-count reduction and a record power-efficiency with less than 1 mW/element power dissipation in receive.

Statement of Contribution/Methods

Realized in a 0.18 μm CMOS process, the ASIC was designed for direct integration with a 5-MHz 150-μm-pitch PZT matrix, consisting of 3×24 transmit (TX) elements and 6×24 receive (RX) elements (Figs. A, B). For initial tests, the ASIC was wire-bonded to a similar PZT matrix built on a separate test chip. In RX, pre-beamforming is applied on 3×3 elements, realizing a 9-fold channel reduction. Each sub-array receiver consists of 9 LNAs, 9 TGCs, 9 S/H delay lines and a 10-bit 33 MS/s SAR ADC. The ADC directly digitizes the beamformer output in the charge domain to eliminate the need for intermediate buffers, resulting in significant reduction in power consumption and silicon area. The 10-bit parallel outputs of 16 sub-array ADCs are serially exported to datalinks at the ASIC periphery, where the outputs from every 4 sub-arrays are combined and transmitted to the FPGA via a LVDS port.

Results/Discussion

The ASIC consumes 135 mW in receive, equivalent to only 0.94 mW/element, which is acceptable even when scaled up to a 1000-element probe. The peak SNDR was measured as 51.3 dB within 100% RX bandwidth for a 5.5 MHz sinewave input (Fig. C-a). Fig. C-b shows the digitized acoustic signal received by one sub-array for 2 different steering angles. The aggregate output data rate is 6.6 Gb/s (1.65 Gb/s per output channel). In conclusion, our prototype ASIC with low-power ADCs realizes an additional 4-fold channel-count reduction compared to prior analog pre-beamformer designs, which is essential for endoscopic and catheter-based 3-D imaging systems.

PA-18

A Front-end Integrated Circuit for a 2D Capacitive Micromachined Ultrasound Transducer (CMUT) Array for a Noninvasive Neural Interface to the Retina

Chunkyun Seok[1], Xun Wu[1], F. Yalcin Yamaner[1], Omer Oralkan[1]; *[1]Electrical and Computer Engineering, North Carolina State University, Raleigh, NC, USA*

Background, Motivation and Objective

A recent study showed that focused ultrasound can noninvasively create neural response in the retina in a similar way to light stimulus. To implement such functionality, we developed an algorithm for a 2D transducer array to project an image to the retina as an ultrasound field pattern (USFP) in a previous study. In this work, we report a front-end integrated circuit (IC) for a 2D CMUT array that realizes a USFP with quantized phases and amplitudes. In addition, we evaluated the projected image quality with Field II simulations considering non-linearity in phases extracted from a fabricated prototype chip.

Statement of Contribution/Methods

The IC consists of a pitch-matched (250 μm in x and y) 16x16 transmitter (TX). The TX circuitry is capable of generating a 3-level pulse-shaped excitation signal, and driving capacitive loads of up to 20 pF. A single TX circuit [Fig. 1 (a)] consists of a voltage-controlled delay line (VCDL), a pulse-shaping block, level shifters, and a 3-level 13.5-V pulser.

The TX circuit works in either pulse-width modulation (PWM) mode for low frequency pulses (< 10 MHz) or pulse-level modulation (PLM) mode for high frequency (10-40 MHz) pulses. In PWM mode, four different levels of symmetric PWM signals are generated by selecting appropriate clocks from a VCDL. In PLM mode, the level of the excitation signal is quantized into two levels, 13.5 V or 6.75 V. For both modes, a phase delay is implemented by selecting a clock from the 16 multiphase clocks generated by the VCDL.

Results/Discussion

The front-end IC was fabricated in a 0.35-μm 13.5-V DDD process [Fig. 1 (b)]. Fig. 1 (c) shows the pulse shapes with different levels in both PWM and PLM modes. Although all the VCDLs are controlled by the same global delay-locked loop (DLL), there exist non-uniform delays due to local mismatch and clock skew. Statistical data [Fig. 1 (d)] for the static non-linearity in phases were extracted from the 16-channel outputs operating at 6.25 MHz. To evaluate the effects of the non-linearity, we simulated a 128x128 array by applying the measured statistical variation to TX signals in Field II. The resulting projection of character "A" did not degrade significantly compared to the case with ideal delays (Fig. 1 [e]). This work proves the basic functionality of our US neural stimulator IC, which will be interfaced with a 16x16 CMUT array for full acoustic characterization.

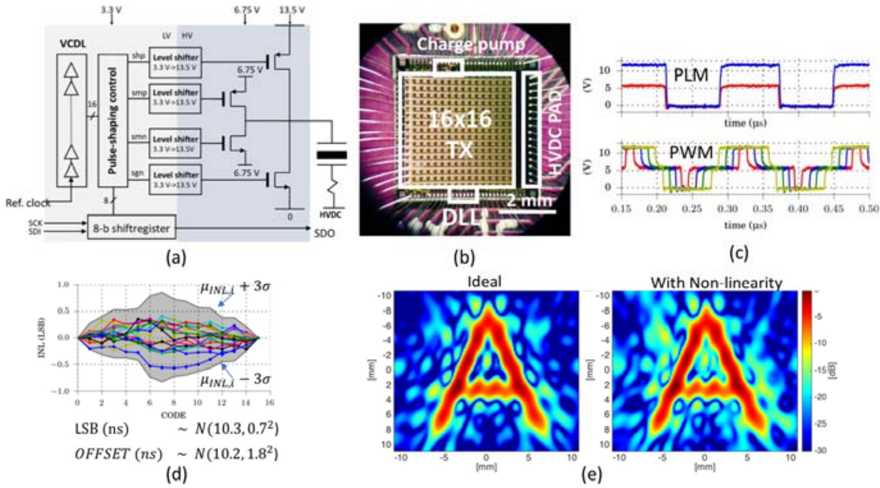

Fig. 1. (a) Block diagram of a single element TX. (b) Die photo of the IC after wire bonding. (c) Measured pulse shapes in PLM (upper) and PWM (lower) modes. (d) Measured statistical variation in phases. (e) Projected images of character "A" with ideal delays (left) and non-linear delays (right) in Field II.

1D - MIM: Brain and Acoustoelectric Imaging

Regency Ballroom

Friday, September 8, 2017, 8:00 am - 9:30 am

Chair: **Mickael Tanter**
INSERM

1D-1

8:00 am Full 4D Functional Ultrasound Imaging in Rodents Using a Matrix Array

Claire Rabut[1], Victor Finel[1], Mafalda Correia[1], Mathieu Pernot[1], Thomas Deffieux[1], Mickaël Tanter[1]; [1]*INSERM U979, PARIS, France*

Background, Motivation and Objective

In vivo brain activity imaging is a key to understanding the mechanisms of complex neural behavior. Functional MRI records brain-wide mechanisms, but at the cost of subject sedation which excludes behavioral experiments. Functional Ultrasound (fUS) Imaging, based on Doppler Imaging, is a powerful new tool for imaging brain activation with high spatiotemporal sampling (80µm, 1ms). It has been successively applied in anesthezied and awake rodents and in humans in preoperative settings.

However, the brain mechanisms and functional connectivity are inherently three-dimensional, it is thus crucial to work toward imaging of the full brain in 3D.

In this study, we present the first full 3D fUS Imaging of a mouse using a matrix array.

Statement of Contribution/Methods

To address the issue of 3D, the concept of 2D Ultrafast Ultrasound Imaging is extended to 3D Ultrafast Volumetric Imaging. A 1024 channel ultrasound platform is used to drive a 32x32 matrix phased array (0.3mm pitch, 9MHz). Ultrasound plane wave compounding (12 angles, PRF=500) is used to insonify the region of interest and volumetric images are reconstructed using a 3D GPU-based beamformer.

During functional acquisition experiments, the matrix array was setup on top of craniotomized and anesthetized mice (n=3). Mice whiskers were mechanically stimulated (12sc ON period- 12sc OFF period stimulations).

Results/Discussion

High-quality 3D vascular volumes were obtained in mice with the craniotomy procedure and showed the feasibility of task-activated 3D functional ultrasound imaging. The 3D activation map shows the spatial distribution of the hemodynamic response to manual stimulation of whiskers with the activation of both the S1BF and VPM structures. A strong correlation is observed (r=0.5, figure 1b) between the stimulus and the vascular response.

This proof of concept demonstrates 3D fUS and the reconstruction of activated. Those results pave the way to the study of brain connectivity between all structures in the mouse brain. Nevertheless, the setup sensitivity still need to be improved to allow transcranial imaging and the sequence processing must be improved to allow much longer acquisition.

Those results demonstrate how 3D fUS could be useful for preclinical research or clinical applications.

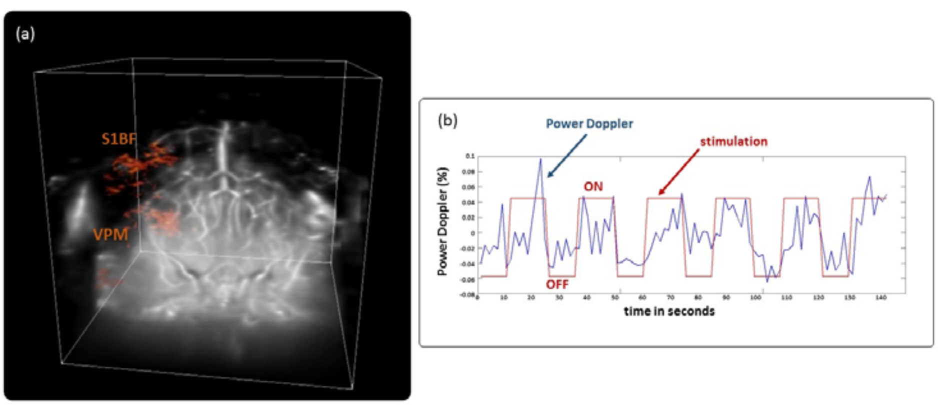

Figure: (a): Representative example of an 3D activation map obtained when stimulating the right whiskers. Map was obtained as the correlation coefficient between the power Doppler signal and the stimulus pattern. S1, primary somatosensory barrel cortex; VPM, ventral posterior medial nucleus. S1BF and VPM regions were delineated from a mouse brain atlas. (b) Doppler signal of task-evoked brain activation in the mouse brain. Power Doppler (PD) fUS images are acquired every 1.5 s. The whisker stimulation pattern (red line) consisted of 12 s ON and 12 s off repeated 6 times. The PD is plotted in percentage relative to the whole brain volume.

1D-2

8:15 am Imaging of Tissue Displacement during Focused Ultrasound Neuromodulation *In Vivo*

Stephen Lee[1], Matthew Downs[2], Niloufar Saharkhiz[2], Yang Han[2], Elisa Konofagou[3]; [1]*Biomedical Engineering, Columbia University, New York City, New York, USA,* [2]*Biomedical Engineering, Columbia University, USA,* [3]*Columbia University, USA*

Background, Motivation and Objective

Focused Ultrasound (FUS) has been shown to modulate neural activity in the brain. Our group has recently shown feasibility of FUS modulation of peripheral nerves *in vivo*. However, the mechanism of FUS on the peripheral nervous system (PNS) is not known and has never been imaged in vivo. In order to unveil both the mechanism as well as provide an image-guided approach to modulation monitoring, we designed a new transducer set-up incorporating both a FUS transducer and an imaging array. Thus, we can simultaneously image the mechanical perturbation of the tissue during modulation in vivo.

Statement of Contribution/Methods

The FUS stimulation system consists of a 96-element, 4.5 MHz HIFU therapeutic ultrasound transducer confocally aligned with a 104-element, 7.8-MHz, pulse-echo imaging transducer. The pulse length was equal to 6 ms and *in vivo* mice were used to determine feasibility. Activation of the sciatic nerve in the upper thigh of the mouse at 5 different locations were induced with the same parameters previously reported. A Verasonics Vantage system was used to acquire 200 RF frames, at a 10 kHz pulse repetition frequency, and 1D cross-correlation, with a 20 λ kernel and 90% overlap, was applied to image the inter-frame axial displacement before, during, and after modulation.

Results/Discussion

Displacement maps overlaid on the B-mode images are shown for one location in a mouse leg illustrated in figure 1. Before FUS, no displacement was registered. Once FUS was applied (at 2ms), downward displacement is detected with the highest displacement at the focus of the FUS beam. During modulation, the average peak displacement at the focus was 9.8 microns with the parameters used to induce sciatic nerve stimulation. After FUS is stopped (at 7ms), displacement steadily decreases during 0.5 - 0.8 ms before complete recovery of the tissue. Our findings indicate that FUS neuromodulation is associated with the radiation force effect and therefore its successful application is dependent upon sufficient displacement generation. Ongoing studies are investigating the link between the nerve displacement amplitude and induced muscle activity *in vivo*.

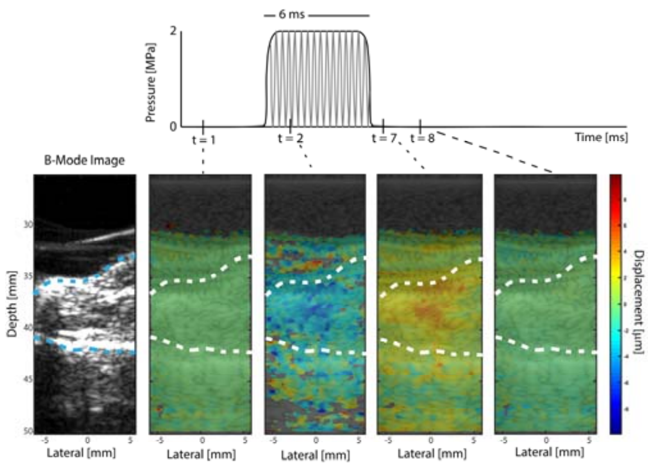

Figure 1: B-mode image of the mouse leg (outlined) with displacements overlaid at various timepoints in the FUS stimulation sequence. The ultrasound source is located above each displacement map and the imaging. probe plane is aligned cross-sectionally with the mouse thigh. Red displacements indicate tissue movement away from the transducer and blue indicates tissue movement towards the transducer.

1D-3

8:30 am Laser-Activated Perfluorocarbon Nanodroplets as a New Tool For Image-Guided Blood Brain Barrier Opening and Delivery of Imaging/Therapeutic Agents to the Brain

Kristina Hallam[1], Eleanor Donnelly[2], Andrei Karpiouk[2], Robin Hartman[2], Stanislav Emelianov[1,2]; [1]Wallace H. Coulter Department of Biomedical Engineering, Georgia Institute of Technology and Emory University School of Medicine, Atlanta, Georgia, USA, [2]School of Electrical and Computer Engineering, Georgia Institute of Technology, Atlanta, Georgia, USA

Background, Motivation and Objective

Perfluorocarbon nanodroplets (PFCnDs) are a tool used in ultrasound (US) as a contrast agent and therapeutic delivery vehicle. When loaded with a photoabsorber, PFCnDs can also provide photoacoustic (PA) contrast, as they undergo a laser-triggered phase change from droplet to bubble. Utilizing this phase-changing behavior, we have investigated the ability of laser-activated PFCnDs to open the blood brain barrier (BBB) and deliver an encapsulated photoabsorber across the BBB. This method of BBB opening could enable non-invasive delivery of contrast or therapeutics to the brain tissue under US/PA image guidance, resulting in a safe, efficient, and cost-effective approach to studying neurological diseases.

Statement of Contribution/Methods

A solution of Evans Blue (EB) dye and PFCnDs, composed of liquid perfluorohexane, a zonyl FSO shell, and a 1064 nm NIR dye for laser triggering, was introduced via systemic delivery. Injected PFCnDs had a distribution of 252 ± 51 nm in size. To enable sufficient light delivery, mice (n=5) were prepared by depilation of the scalp. To activate PFCnDs, a pulsed laser (1064 nm, 10 Hz PRF, 60 seconds exposure) was used to deliver light with an energy output of 38 mJ through a 1.5 mm diameter optical fiber positioned over the right side of the mouse brain (Fig. 1A-B). After 4 hours, mice were sacrificed by cardiac perfusion, and brains were excised. To assess delivery of the NIR dye to the tissue, brains were imaged using a 40 MHz Vevo LAZR system (Fig.1C). In addition, BBB opening was confirmed ex vivo via EB staining of tissue slices (Fig.1D).

Results/Discussion

Results of our studies demonstrate the ability of laser-activated PFCnDs to open the BBB and deliver agents to the brain. Furthermore, these results indicate that PFCnDs can enable localized delivery of a sufficient quantity of contrast agents for US/PA imaging (Fig. 1C). These initial studies provide insight into how laser activated PFCnDs can be harnessed for BBB disruption and delivery of contrast agents and therapeutics. Additionally, delivery could be monitored via US/PA imaging given the ultrasonic and photoacoustic contrast produced by both PFCnDs and the photoabsorber used to activate the droplets (Fig 1B-C). In conclusion, laser-activated PFCnDs can be used for BBB opening, delivery, and US/PA imaging, making them a versatile tool for neurological studies.

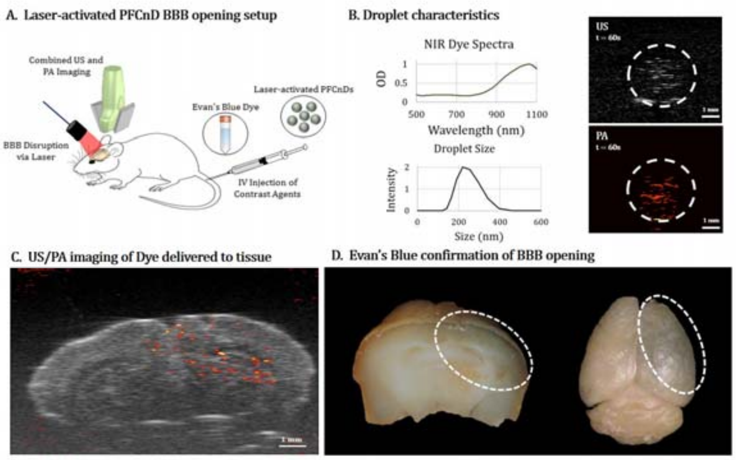

Figure 1 **A** Summary of the setup used to activate PFCnDs, open BBB, and image. **B** PFCnDs characterized by UV-VIS spectroscopy, size, and US/PA contrast produced via laser vaporization of droplets in a pipette under parameters similar to those used *in vivo*. **C** *Ex vivo* US/PA image of NIR dye delivered to the brain tissue via laser-activated PFCnDs and 1064 nm laser irradiation of the brain on the right side. **D** Images depicting delivery of Evan's Blue dye to the right side of the brain.

1D-4

8:45 am **Acoustoelectric Imaging of Time-Varying Current Produced by a Clinical Deep Brain Stimulator**

Chet Preston[1], Yexian Qin[2], Alex Burton[1], Pier Ingram[2], Willard Kasoff[3], Russell Witte[1,2]; [1]*Biomedical Engineering, University of Arizona, Tucson, AZ, USA,* [2]*Medical Imaging, University of Arizona, Tucson, AZ, USA,* [3]*Surgery, University of Arizona, Tucson, AZ, USA*

Background, Motivation and Objective

Deep brain stimulation (DBS) is an effective therapy for dyskinesia associated with treatments for Parkinson's disease (PD). While current surgical placement of a DBS implant depends on stereotactic coordinates with computed tomography and magnetic resonance imaging for precise localization of the electrode sites, the actual current densities produced by the DBS are not directly observed. This study proposes a novel ultrasound (US) method to visualize these current distributions produced by a DBS via acoustoelectric (AE) imaging. AE imaging uses a focused US beam to locally modulate tissue resistivity due to the AE effect, producing a detectable oscillating voltage from a current flow. The primary goal for this study is to assess baseline performance of AE technology for detecting and resolving current densities near a DBS implant using clinically-relevant stimulation parameters.

Statement of Contribution/Methods

A commercial DBS implant (Medtronic #3389) with four platinum-iridium electrodes (Fig. 1a) was placed in a bath of 0.9% NaCl. Time-varying current was generated by applying pulses up to 4V between two electrodes (4 square pulses, 1 ms duration, 5 ms inter pulse interval). A single element transducer (1 MHz, Olympus NDT A392S) produced a focused US beam at 4 kHz repetition rate near the DBS, generating an AE signal proportional to local current density. The AE signal was recorded on a contact between the stimulating sites. The US transducer was mechanically scanned in the lateral plane to form 4D AE images. Raw signals were band-pass filtered between 100 and 1200 Hz in physiologic time and 0.5 and 1.5 MHz in US time. The signal-to-noise ratio (SNR), sensitivity, and spatial extent of the dipole were calculated based on the AE images.

Results/Discussion

Fig. 1b displays an M Mode AE image of time-varying current densities between the stimulating sites. Fig. 1c describes a cross-sectional AE image (hot) near the same site along with a co-registered pulse echo image (gray) corresponding to the tip of the DBS. The sensitivity for detecting the AE signal was 0.038 μV/(MPa*mA/cm^2) with SNR measurements presented in Fig. 1d. The axial and lateral dimensions of the dipole were 3.3x3.0 mm (full width half maximum). Future tests will evaluate AE imaging as a noninvasive tool for guiding placement of the DBS and non-invasive long-term monitoring of stimulation patterns in the brain.

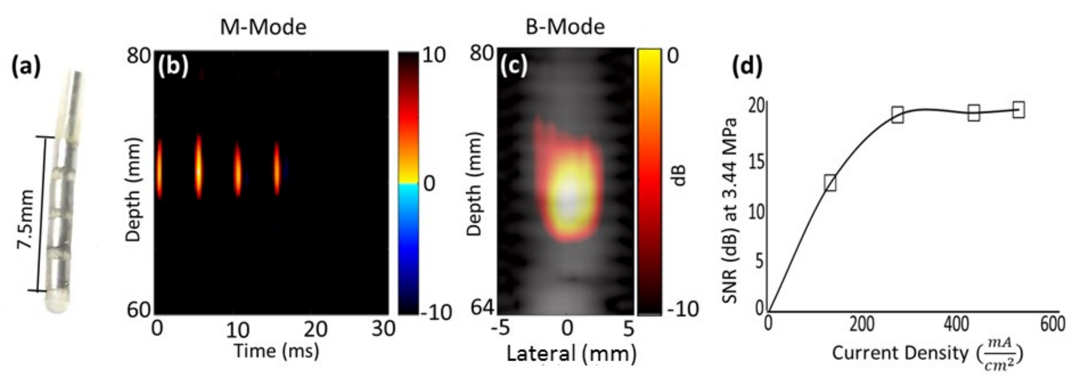

1D-5

9:00 am **Coded Excitation with Optimized Inverse Filter for Improving Sensitivity in Acoustoelectric Imaging**

Hsin-Wu Tseng[1], Yexian Qin[1], Matthew O'Donnell[2], Russell Witte[1]; [1]*Medical Imaging, University of Arizona, Tucson, Arizona, USA,* [2]*Bioengineering, University of Washington, Seattle, Washington, USA*

Background, Motivation and Objective

Noninvasive imaging of physiologic currents in the body is limited by poor spatial resolution due to the ambiguous conductivity distribution between the current sources and recording electrodes. Acoustoelectric imaging (AEI), based on the interaction between pressure and resistivity, provides higher spatial resolution. Although we have demonstrated AEI of the cardiac activation wave in the live rabbit heart, weak physiologic currents (e.g., in the heart or brain < 1 μV) and ultrasound (US) pulses of balanced shape (zero mean) make detection especially challenging. This study investigates the use of standard US transducers with coded excitation with optimized inverse filter to produce quasi-unipolar pulses that amplify the AE signal.

Statement of Contribution/Methods

We performed AE modeling with COMSOL™, varying the diameter of the cylindrical current source along the z-axis (depth), to study effects of different pulse shapes towards improving signal-to-noise ratio. The beam of a focused single element US transducer was modeled in FOCUS™. Different types of excitation waveforms and corresponding filters were evaluated. First, the standard linear chirp with matched filter was used to compress the signal and improve spatial resolution. Then, nonlinear chirps with low frequency weighting were combined with an inverse filter for both compression and pulse shaping. The coefficients of the inverse filter were calculated by convolving a matched filter and parameterized finite impulse response filter, guided by a target quasi-unipolar signal and optimized through error minimization.

Results/Discussion

Fig. 1a displays the orientation of the US beam and current geometry for simulation, as well as the linear and nonlinear chirp excitations. Fig. 1b presents the AE signal after compression (linear chirp; black) or inverse filter (nonlinear chirp; red) producing a quasi-unipolar AE signal. Fig. 1c indicates when the thickness of the current source is larger than twice the US wavelength (λ), the AE magnitude increases by 5.2 dB (80.28%), which is a significant improvement for detecting weak currents. The simulation demonstrates that waveform engineering of quasi-unipolar pulses may play an important role for optimizing detection of AEI in peripheral nerve, brain, and heart.

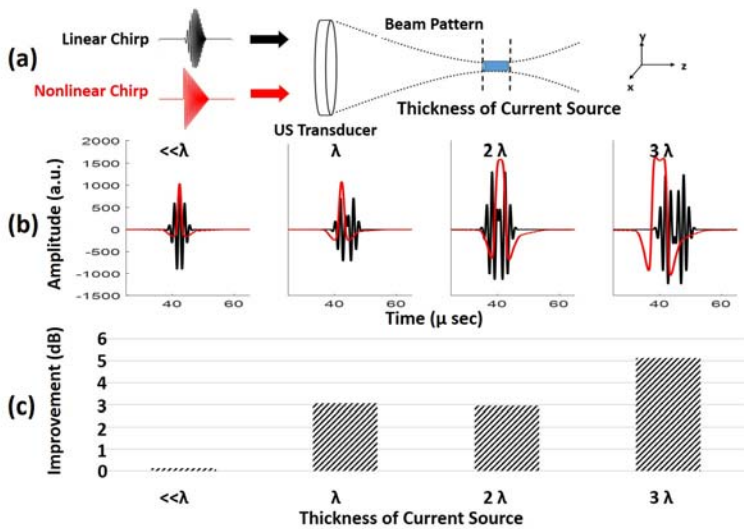

1D-6

9:15 am Ultrafast Acoustoelectric Imaging for Direct Mapping of Cardiac Electrical Activation In Vivo.

Beatrice Berthon[1], Philippe Mateo[1], Nathalie Ialy-Radio[1], Mickaël Tanter[1], Mathieu Pernot[1], Jean Provost[1]; [1]*Institut Langevin, ESPCI Paris, PSL Research University, CNRS UMR 7587, INSERM U979, France*

Background, Motivation and Objective

Direct access to the electrical activation in the heart is crucial for understanding and diagnosing cardiac activation diseases such as arrhythmias. We have recently presented a fully integrated Ultrafast Acoustoelectric Imaging (UAI) system based on the acoustoelectric effect[1], i.e., the modulation of the electrical impedance of a tissue by an ultrasound wave, which uses plane wave emissions to provide 2D maps of electrical current densities with 1-mm and 5-ms spatial and temporal resolutions, respectively[2]. In this work, we present its application to direct measurements of cardiac activation in isolated live rat hearts and in pig hearts in vivo.

Statement of Contribution/Methods

UAI was performed in isolated rat hearts (n = 4) and in open-chest pigs (n = 1) using a 5-MHz ultrasound linear array probe fitted to a Vantage ultrasound system (Verasonics Inc., WA, USA), using up to 33 tilted plane waves emitted at up to 10000 Hz during up to 6 s with a 3 MPa peak negative pressure (MI=1.4). The signal from two electrodes positioned on the heart was used to measure the electrocardiogram, and was also fed to the Vantage system after differential amplification and high pass filtering, for the acoustoelectric measurement. Both B-mode and UAI images of the electrical activation were produced, from the backscattered echoes and from the detected acoustoelectric signals, respectively, using a holographic image formation approach described previously[3].

Results/Discussion

Current density images were obtained from the received UAI signals, and overlaid onto B-mode images obtained simultaneously for rat and pig hearts. For the rat hearts, electrical activation was observed in the atrial node, ventricular wall and apex with an average SNR over 100 frames of 6.4 ± 2.6, 6.6 ± 2.9 and 6.3 ± 2.9, respectively. The frequency of the signals measured matched the simultaneously acquired ECG and propagation of the electrical activation propagation was visible from the atrial node to the apex via the ventricular walls. Data obtained in vivo in pig's hearts showed electric activation signals with an SNR of up to 13.3 ± 0.12 without averaging.

We show, for the first time, that Ultrafast Acoustoelectric Imaging provides direct access to electrical current density in-vivo, allowing for mapping of the electric activation spatially and temporally. These results suggests that UAI may become a new biomarker for the diagnosis and study of cardiac activation diseases such as arrhythmias.

References

1. Olafsson et al. 2008 IEEE Trans. Biomed. Eng. 55 1840–8

2. Berthon et al. 2016 IEEE Physics in Med. Biol. (in review)

3. Berthon et al. 2016 IEEE IUS

2D - MSD: Novel Real-Time Implementations

Ambassador Ballroom

Friday, September 8, 2017, 8:00 am - 9:30 am

Chair: **Kai Thomenius**
Massachusetts Institute of Technology

2D-1

8:00 am **Towards Real-Time Adaptive Color Flow Imaging: A GPU-Optimized Eigen-Based Clutter Filter Core**

Adrian J. Y. Chee[1], Billy Y. S. Yiu[1], Alfred C. H. Yu[1]; [1]*Schlegel Research Institute for Aging, University of Waterloo, Waterloo, Canada*

Background, Motivation and Objective

Eigen-filters with attenuation response adapted to clutter statistics in color flow imaging (CFI) have shown improved flow detection sensitivity in the presence of tissue motion. However, its practical adoption for routine use in clinical scanners is hindered by the long processing time required to derive the eigen-components. In this work, we seek to overcome this issue by formulating a parallel-computing framework that enables fast execution of eigen-filtering so as to foster their practical adoption in CFI. Our framework readily differs from commercial eigen-solvers available on numerical software packages. In particular, our algorithm is the first that is optimized for parallel execution of multiple eigen-computation tasks on small matrices (a typical scenario in CFI processing).

Statement of Contribution/Methods

Our framework is devised upon: 1) eigen-computation using first principles in algebra; 2) use of single-instruction, multiple-data (SIMD) computing for parallelized eigen-computation; 3) use of single-ensemble-based (Hankel-SVD) eigen-filtering that fits well with SIMD computing. A two-level parallelization strategy is adopted to process multiple CFI pixels concurrently while further exploiting parallelism during slow-time processing. For each CFI pixel, its slow time ensemble is arranged into Hankel matrix. SVD is then applied to obtain the eigen-components through a two-stage algorithm: 1) reduction of Hankel matrix into its bi-diagonal form through Householder transform, 2) further reduction to a diagonal matrix using Givens rotation. Then, Doppler frequencies of each component were estimated before performing clutter rejection to derive its Doppler power. Our SIMD eigen-filter was implemented using CUDA and was executed on a single GPU device (GTX Titan X).

Results/Discussion

Our framework's computing throughput was tested for various scan depth and slow-time ensemble lengths (fig 1a). Real-time throughput (24 fps) can be attained for CFI frames with 128 scanlines, up to a scan depth of 5cm for ensemble size of 16 samples. As demonstrated in a carotid imaging case example (fig 1b), our framework delivered enhanced flow detection sensitivity over a non-adaptive polynomial regression clutter filter. These findings indicate that the GPU-enabled eigen-based clutter filtering can improve CFI flow detection performance in real time.

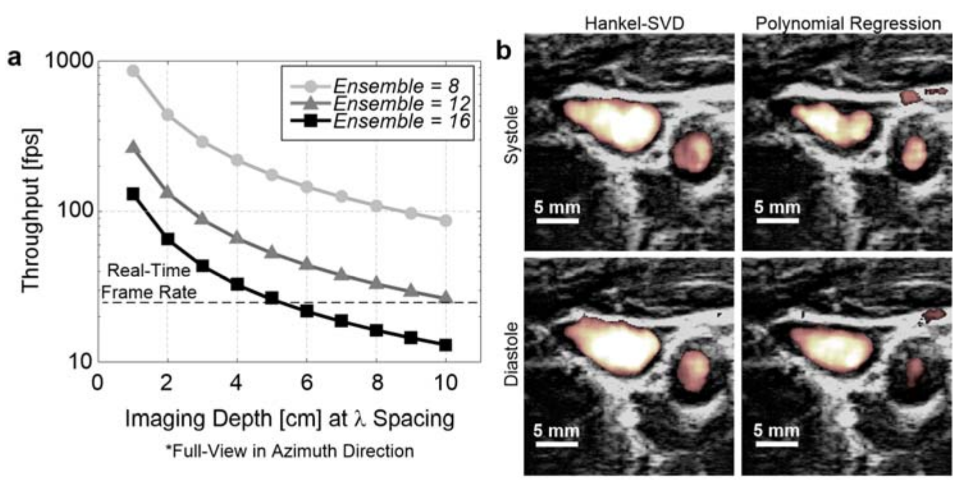

(a) Throughput of eigen-processing framework: Real-time video frame rate attainable.
(b) Case example of carotid imaging: Hankel-SVD filter demonstrates better flow detection.

2D-2

8:15 am **High Dynamic Range Ultrasound Imaging with Real-Time Filtered-Delay Multiply and Sum Beamforming**

Alessandro Ramalli[1], Alessandro Dallai[1], Luca Bassi[1], Monica Scaringella[1], Enrico Boni[1], Gabriel Emile Hine[2], Giulia Matrone[3], Alessandro Stuart Savoia[2], Piero Tortoli[1]; [1]*Department of Information Engineering, University of Florence, Florence, Italy,* [2]*Department of Engineering, Roma Tre University, Rome, Italy,* [3]*Department of Electrical, Computer and Biomedical Engineering, University of Pavia, Pavia, Italy*

Background, Motivation and Objective

Most commercially available ultrasound imaging systems currently implement the delay and sum (DAS) beamforming. Alternative beamformers have been presented, offering higher performance at the expense of computational complexity, which has so far limited their actual implementation. In particular, the Filtered-Delay Multiply and Sum (F-DMAS) beamformer, which adds the computation of signed square roots, absolute values and multiplications to DAS, was recently shown to be effective in improving resolution, dynamic range and overall image quality (DOI: 10.1109/TMI.2014.2371235). In this work, we present the real-time implementation of the F-DMAS beamformer on the ULA-OP256 research system.

.

Statement of Contribution/Methods

ULA-OP256 hosts up to 8 front-end boards (FEB) and a master control board (MCB) arranged in a closed loop architecture by means of a high throughput serial link. Each FEB embeds the electronics (one FPGA and two DSPs) to manage transmission, beamforming and primary processing for 32 channels.

For its real-time implementation, the F-DMAS beamforming procedure is re-formulated as a compact algebraic expression and split in two stages: each FPGA dynamically delays the 32 acquired RF signals, extracts the absolute value, computes the signed squared root by employing look-up-tables, and performs first-stage sums; the DSPs perform second-stage sums by collecting the partially summed signals from the other FEBs in the loop. The beamformed signal is coherently demodulated at twice the frequency of the transmitted burst, and transferred to the MCB where it is converted to a grayscale frame for B-mode imaging.

The system was set to perform a linear scan of a tissue mimicking phantom, transmitting Hanning-tapered sine bursts at 8 MHz with different number of cycles (6, 8, 10). Baseband data for both DAS and F-DMAS beamformed images were acquired and post-processed in Matlab to compare the achievable resolution, CR and CNR.

.

Results/Discussion

The proposed architecture allows reconstructing B-mode images with the F-DMAS beamformer in continuous real-time. Compared to DAS, F-DMAS real-time phantom images (see figure) show a higher dynamic range, darker cysts with sharper borders and an increased speckle variance that corresponds to higher CR (up to +7 dB), better spatial resolution (up to 20%), but lower CNR (-40%).

.

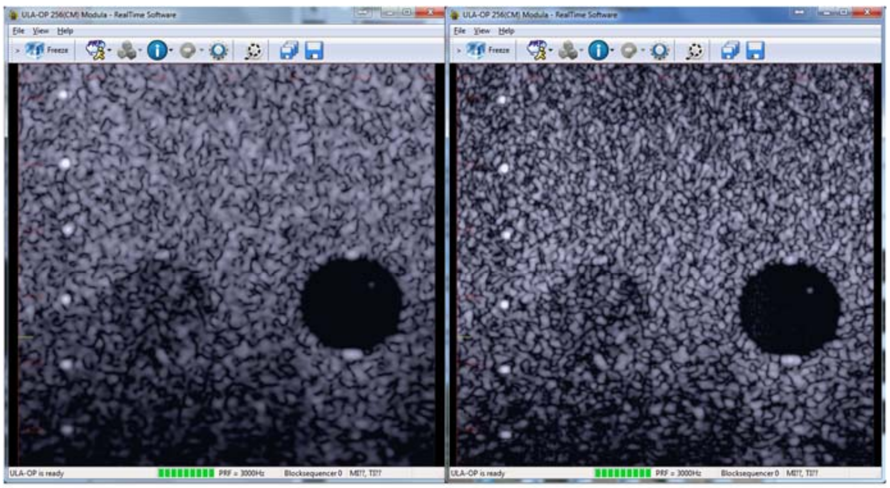

Fig. 1: The ULA-OP 256 real-time interface during phantom acquisitions: DAS (left) and F-DMAS beamforming (right) images; the dynamic range is 33 dB and 45 dB, respectively.

2D-3

8:30 am Real-Time Implementation of Synthetic Aperture Vector Flow Imaging in a Consumer-Level Tablet

Tommaso Di Ianni[1], Thomas K. Kjeldsen[2], Carlos A. Villagòmez Hoyos[1], Jesper Mosegaard[2], Jørgen A. Jensen[1]; [1]*Technical University of Denmark, Lyngby, Denmark,* [2]*Alexandra Institute, Aarhus, Denmark*

Background, Motivation and Objective

In this work, a vector flow imaging (VFI) method based on synthetic aperture sequential beamforming and directional transverse oscillation (TO) is implemented in a commercial tablet. In comparison with previous tablet-based flow imaging implementations, the velocity estimation is extended to a 2-D angle-independent setup. The received data are pre-beamformed in the probe, which leads to a 64x data reduction that enables real-time wireless transfer. The second stage beamforming and velocity estimation are performed in the tablet. The objective of the work is to investigate the feasibility and performance of synthetic aperture VFI implemented in a commercial hand-held device.

Statement of Contribution/Methods

A laminar, parabolic flow was created in a flow rig system with a peak velocity of 0.2 m/s. A 6-mm-radius vessel was positioned at a depth of 20 mm. The first-stage data were acquired using a BK Ultrasound 8L2 linear array (4.1 MHz; 4 cycles; 9 kHz PRF) connected to a BK5000 scanner, and transferred to a HTC Nexus 9 (2 years old) through a Wi-Fi link to simulate a wireless probe. Six focused emissions were used to create a flow high-resolution image (HRI), where a TO was obtained due to the lateral separation of the first-stage focal positions. The lateral and axial velocities were estimated from 16 HRIs in a region of 0.8x1.9 cm using a phase-shift estimator. Sixty-four emissions were used for each B-mode image. B-mode and VFI processing, including beamforming, velocity estimation, clutter filtering, and displaying, were implemented on the GPU (Nvidia Tegra K1) through the OpenGL ES 3.1 API.

Results/Discussion

The figures below show a VFI frame processed and displayed on the tablet (left) and in Matlab (right) for comparison. The peak frame rate was 27 fps (37 ms/frame), which corresponds to a data rate of 14 MB/s. This is lower than the maximum Wi-Fi throughput between the tablet and the ASUS RT-AC68U wireless router, which was tested to exceed 30MB/s. The frame rate was gradually lowered due to heating of the chipset, and was 15 fps after 12 min of continuous scanning.

In conclusion, synthetic aperture VFI is feasible in a commercial tablet with real-time performance. The computational tasks were efficiently implemented on the GPU, and the data reduction of the sequential beamforming enables real-time wireless transmission.

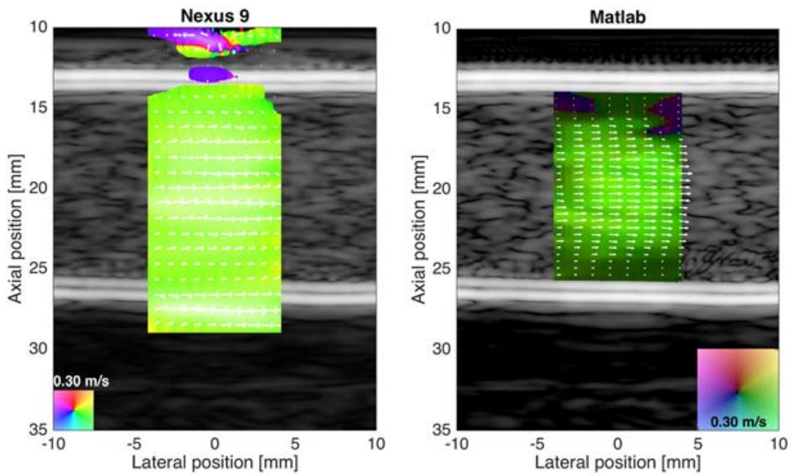

2D-4

8:45 am **A New Preclinical Ultrasound Imaging Platform for Whole-Body Multiplexed Imaging**

Tomek Czernuszewicz[1], James Butler[1], Max Harlacher[1], Graeme O'Connell[1], Jonathan Perdomo[1], Virginie Papadopoulou[2], Juan Rojas[2], Paul Dayton[2], **Ryan Gessner[1]**;
[1]SonoVol, Inc., Research Triangle Park, NC, USA, [2]Biomedical Engineering, UNC Chapel Hill, NC, USA

Background, Motivation and Objective

Rodents are used extensively in research to study disease and evaluate drugs. Preclinical imaging systems allow for non-invasive assessments of animals. High frequency ultrasound systems have emerged over the last 15 years as valuable tools for evaluating numerous diseases and organs. When compared against other anatomical imaging systems, such as MRI and CT, ultrasound is the most cost effective, but is often criticized for a limited field of view and large operator dependence. We have built a novel system which addresses these two weaknesses. The robotic system allows the entire body of a rodent to be scanned in <2 min in multiple imaging modes (tissue, vasculature, elastography, etc.), and up to 5 animals at once.

Statement of Contribution/Methods

The benchtop device uses a 2D motion stage to manipulate one or more transducers beneath an acoustically transparent membrane on which the animal is positioned. Fluid and gel couple the transducer to the animal below and above the membrane, respectively. The robotic system's encoders are used to reconstruct the timestamped CINE image data in near real-time. The system has two transducers included in it: a dual-frequency annular array (2 and 35 MHz), and a linear array (15 or 18 MHz). This enables Acoustic Angiography, high frequency b-mode, m-mode, and elastography modes.

Results/Discussion

Preliminary in vivo data is presented for images of 3 mice acquired side by side in high frequency b-mode, followed by a targeted Acoustic Angiography microvasculature images of a tumor located in the thoracic mammary pad. Acquisition time for the data of each mouse approximately 1.3 and 3 min for b-mode and Acoustic Angiography respectively. The tumor's microvascular network can be seen branching from both the axillary and mammary arteries. To our knowledge this is the first demonstration of a multi-mouse, multi-transducer robotic ultrasound imaging system for high frequency preclinical imaging. Mice can be automatically scanned in minutes, and vasculature throughout the body can be visualized with the use of a microbubble contrast agent. The system still requires mice to be shaved prior to scanning, and cannot visualize the brain or lungs (unlike MR and CT), though images can be acquired with nearly the same field of view and in a fraction of the time.

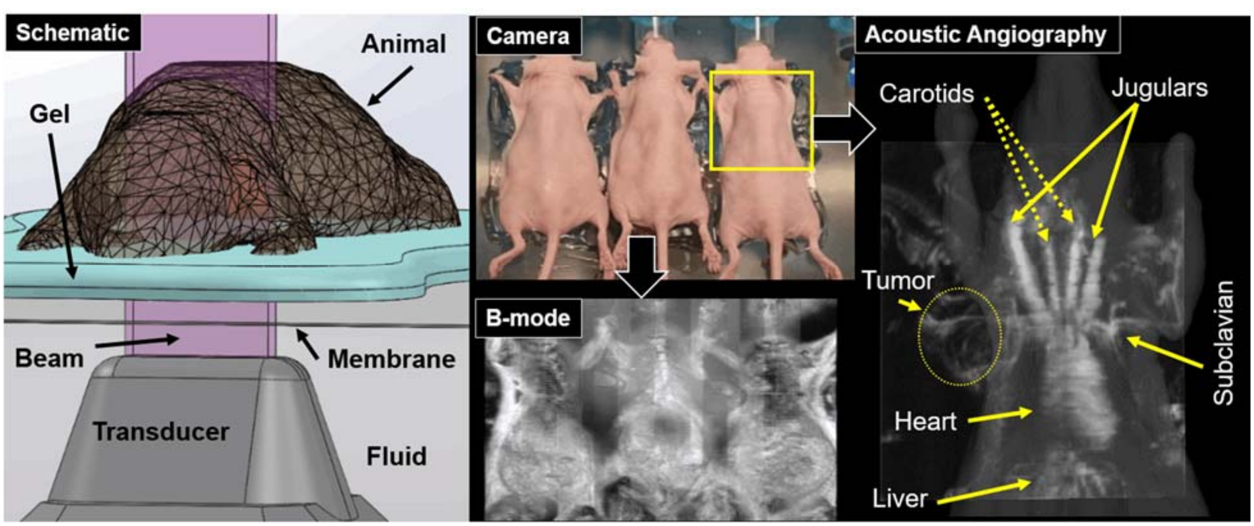

2D-5

9:00 am Ultrasound Neuro-Modulation Chip for Activating the Pyramidal Neurons in Hippocampal CA1 Slices

Zhengrong Lin[1], Lili Niu[1], Long Meng[1], Wei Zhou[1], Xiaowei Huang[1], Hairong Zheng[1]; [1]*Paul C. Lauterbur Research Center for Biomedical Imaging, Shenzhen Institutes of Advanced Technology, Chinese Academy of Sciences, Shenzhen, China, People's Republic of*

Background, Motivation and Objective

Recent studies have proven that ultrasound as a non-invasive method enable to delivery energy to deep brain for both excitation and reversible suppression of neuronal activity in cell, animal, human experiments (Scientific Reports 6:24170, 2016; Neuron 66(5):681-694; Nature Neuroscience 17(2):322-9, 2014). Due to bulk ultrasound transducer, it is difficult to compatible the ultrasound stimulation system with the classical electrophysiological technique, such as path clamp and the mechanism underlying ultrasound neuro-modulation remains unclear. In this study, we developed an ultrasound neuro-modulation chip and recorded the effects of the hippocampal CA1 slices responded to the ultrasound stimulation by the whole-cell patch-clamp.

Statement of Contribution/Methods

Fig. 1a shows the schematic of the on-chip ultrasound stimulation of the neurons. During the ultrasound stimulation, the activity of single CA1 pyramidal neuron could be recorded in a real time manner. The ultrasound was generated by ultrasound neuro-modulation chip (Frequency: 27.38 MHz; stimulation duration: 30 s; stimulus intensity: 0.3 W/cm^2). To characterize the firing pattern of CA1 neurons, current-clamp and voltage-clamp were utilized to investigate the neuronal properties and the isolated NaV current, respectively.

Results/Discussion

Fig. 1b shows ultrasound stimulation was capable of triggering membrane potential depolarization and evoking the action potential in CA1 pyramidal neurons. With the increment of the acoustic intensity, the action potentials of neurons increased correspondingly. Simultaneously, ultrasound stimulation increased neurons excitability by decreasing action potential threshold (Fig 1c) and increasing the total TTX-sensitive sodium currents. In addition, ultrasound stimulation lead to the increased availability of sodium channels by accelerating the activation and the recovery of sodium channels, and thus contributing to increased neuronal excitability. The results suggested that the ultrasound neuro-modulation chip enable to activate the neurons and provide a convenient, powerful tool for understanding the mechanism of ultrasound neuro-stimulation.

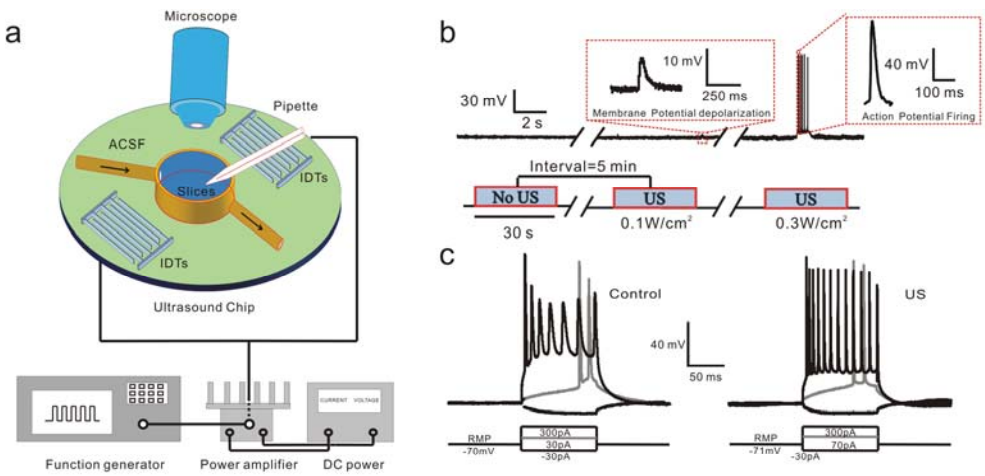

Fig 1. a. The schematic of ultrasound stimulation system; b. Ultrasound are capable of triggering membrane potential depolarization in low stimulus intensity and evoking action potentials in high stimulus intensity; c. Voltage traces recorded in the same pyramidal neuron before and after sonication.

2D-6

9:15 am Ultrasound Imaging Using Transmit Wavefront Synthesis: Spatial and Frequency Diversity Approach to Compounding

Parker O'Brien[1], Dalong Liu[1], Emad Ebbini[1]; [1]*Electrical Engineering, University of Minnesota, Minneapolis, Minnesota, USA*

Background, Motivation and Objective

We have developed a modern array driver employing multi-channel arbitrary waveform generator and linear amplifiers for transmit wavefront synthesis. The system utilizes deep waveform memory that can be configured for switching between transmit patterns seamlessly thus allowing for the use of spatial and frequency diversity in image acquisition. In this paper, we present the first experimental results demonstrating dramatic reduction in sidelobe artifacts as well speckle reduction.

Statement of Contribution/Methods

A 3.5 MHz, 32-element concave array with 40-mm radius of curvature was used. The array was designed as a dual mode transducer for imaging and therapy. It was shown to have 60% FBW and was fully characterized for imaging and therapy, including image-guided *in vivo* transcranial application of focused ultrasound (FUS). Synthetic aperture (SA) imaging with this array provided 60 dB dynamic range and was used for guidance. We have also demonstrated the use of the array in single-transmit focus (STF) mode for continuous monitoring of therapeutic FUS application. STF imaging provides unique form of feedback about the FUS-tissue interactions, but is prone to sidelobe artifacts. The use of multiple transmit beams with different spatial and frequency characteristics allows for reduction of these artifacts. To demonstrate this, we used the array to image two fine wires that were embedded very closely to each other in a tissue-mimicking phantom. The distance between the wires was determined using SA imaging to be approximately 0.5 mm. Three transmit beams were used to acquire STF multiframe images (up to 1000 fps). A standard wideband STF, a narrowband 3-focus STF and a wideband 3-focus STF. Beamformed echo data from the 3 transmit wavefronts were incoherently compounded.

Results/Discussion

The figure shows grayscale images (80 dB) from standard STF (WB), MTF wavefronts (NB and WB) as well as the compounded image. The STF and MTF images exhibited the classical butterfly sidelobe pattern, which is completely absent from the compounded image. The sidelobe structure and the speckle patterns are distinctly different different in the in the STF and MTF images, which explains the effectiveness of the compounding. A lateral echogenicity profile through the wire on the left is also shown to provide a quantitative measure of dynamic range. In addition to the reported increase in dynamic range, the use of coded wavefront and image reconstruction allows for significant improvement in resolution.

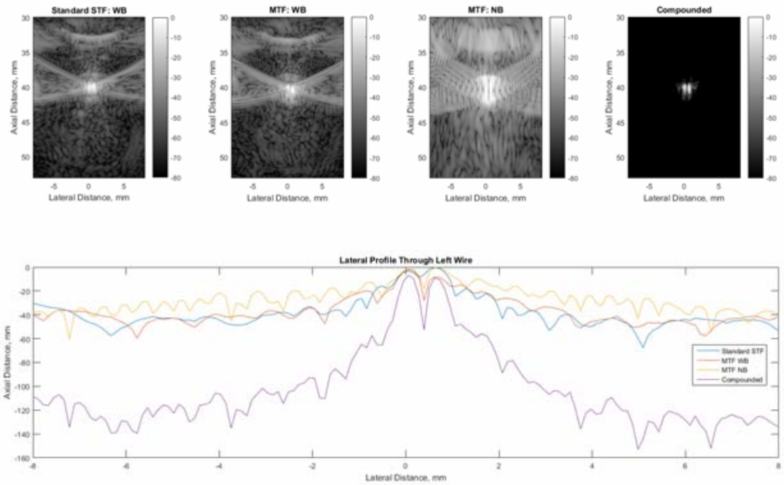
Standard STF: WB
MTF: WB
MTF: NB
Compounded
Axial Distance, mm
Lateral Distance, mm
Lateral Profile Through Left Wire
Standard STF
MTF WB
MTF NB
Compounded

3D - MEL: New Elasticity Methods

Palladian Room

Friday, September 8, 2017, 8:00 am - 9:30 am

Chair: **Damien Garcia**
CREATIS

3D-1

8:00 am Single Track Location Comb-Push Ultrasound Shear Elastography (STL-CUSE)

Peter Hollender[1], Nicholas Bottenus[2], David Bradway[2], Gregg Trahey[1,3]; [1]*Biomedical Engineering, Duke University, Durham, NC, USA,* [2]*Biomedical Engineering, Duke University, Durham, North Carolina, USA,* [3]*Radiology, Duke University Medical Center, Durham, North Carolina, USA*

Background, Motivation and Objective

Single Track Location Shear Wave Elasticity Imaging (STL-SWEI) creates high resolution shear wave speed maps by comparing the tissue motion at each tracking location between spatially-offset radiation force excitations. While STL-SWEI circumvents the resolution-limiting effects of speckle noise, it requires a series of excitation-tracking ensembles to build up a lateral field of view, increasing the acquisition time. Comb-push ultrasound shear elastography (CUSE) is another novel shear wave method that uses adjacent subapertures to simultaneously excite multiple shear waves. We propose here a combination of the two methods, called single track location comb-push ultrasound shear elastography.

Statement of Contribution/Methods

A 128-element L7-4 linear array was used with a Verasonics Vantage 128 ultrasound system, scanning a CIRS stepped-cylinder elasticity phantom. Three adjacent 32-element subapertures were used to excite a three-focal zone comb push excitation with 1 cm lateral spacing. Channel data were recorded every 75 microseconds after the excitation, using three sequentially- steered plane waves for each tracking frame. 33 push-track ensembles were recorded, each offset from each other by 1 element (0.3125 mm), so that every possible subaperture was excited once. Directional filters were used to separate the right-going from the left-going waves. Shear wave velocities were estimated across push beams using normalized cross correlation. For comparison, conventional CUSE images and STL-SWEI images were created of the same targets.

Results/Discussion

The figure shows the results of one of the elasticity phantom targets for STL-CUSE. The target is well visualized with good contrast to noise ratio (CNR) and lateral resolution. Across all targets, STL-CUSE shows the benefits of STL-SWEI with improved lateral resolution and CNR and a threefold reduction in acquisition time over conventional STL-SWEI. The wide tracking field of view allows for a robust estimation of shear velocity by using many tracking lines simultaneously in the velocity estimation. There is a trade-off between the number of pushes used to improve acquisition time and the robustness of isolating the pushes from each other to track the correct STL shear wave. This method may provide a means for realizing the benefits of STL-SWEI imaging with shorter acquisition times.

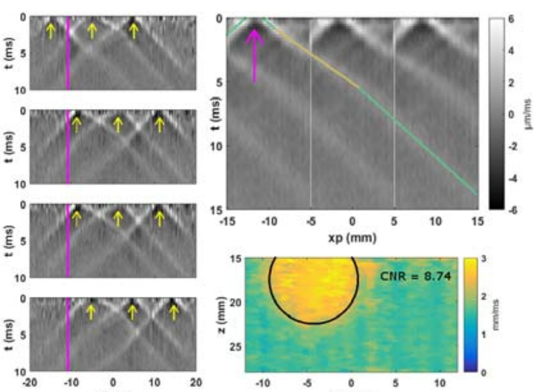

Left: Recorded CUSE particle velocity maps. Yellow arrows indicate the comb push foci in each image.
Top Right: Synthesized STL-CUSE particle velocity map from the magenta line. Each track line appears three times in the STL-CUSE map. The STL-CUSE shear wave of interest is the one originating from the track location (magenta arrow). It's propagation is marked with lines colored by approximate shear wave speed.
Bottom Right: The STL-CUSE shear wave speed map shows clear delineation of the circular inclusion with CNR = 8.74.

3D-2

8:15 am Combination of Air-Coupled Acoustic Micro-Tapping and Phase Sensitive OCT for 4-D Real-Time, Non-Contact Imaging of Soft Tissue Elastic Moduli

Shaozhen Song[1], Łukasz Ambroziński[2], Soon Joon Yoon[1], Mitchell Kirby[1], Liang Gao[1], **Ivan Pelivanov**[1], David Li[3], Tueng T. Shen[4], Ruikang Wang[1], Matthew O'Donnell[1]; [1]*Bioengineering, University of Washington, Seattle, Washington, USA,* [2]*AGH University of Science and Technology, Kracow, Poland,* [3]*Chemical Engineering, University of Washington, Seattle, Washington, USA,* [4]*Ophtalmology, University of Washington, Seattle, Washington, USA*

Background, Motivation and Objective

Elastography plays a key role in characterizing soft tissue. Although it has found widespread use in clinical diagnostics, nearly all methods require direct physical contact with tissue and can even be invasive. However, for a number of applications (ophthalmic, for instance) physical contact is not desired and may not even be allowed. Recently, we proposed a fundamentally new approach to 4-D dynamic elastography using non-contact mechanical stimulation (e.g. from air) of soft media with an air-coupled focused US transducer (we call it acoustic micro-tapping, AμT) combined with ultrafast phase sensitive (PhS) OCT [1]. Here, we report on new AμT-OCT system developments and new results obtained in ex-vivo and in-vivo studies on eye and skin.

Statement of Contribution/Methods

The AμT-OCT method uses transient mechanical waves excited in the object under study from air (i.e., non-contact) with air-coupled focused ultrasound and resultant displacements detected with a 16 kHz frame rate, phase-sensitive (PhS)-OCT system. The air-coupled focused US beam reflected from the air/medium interface provides acoustic radiation force (ARF) to the medium surface, launching a transient mechanical wave. Real-time tracking/imaging of resultant mechanical wave propagation can be used to reconstruct tissue elastic properties.

Results/Discussion

Figure 1 shows the AμT-OCT imaging principle (left panel) with wavefield snapshots at different times after AμT excitation in ex-vivo porcine cornea kept under a 20 mmHg intraocular pressure in the right panel.

Detailed analysis of the guided wavemode content as well as the measured phase velocity dispersion and US attenuation allows us to reconstruct real and imaginary components of tissue elasticity. In addition, it has been shown that the frequency content of generated mechanical waves near the source provides a local estimate of elastic modulus.

Results of experiments strongly suggest that the AμT-OCT technique holds great promise for non-invasive characterization of soft media, in general, and for translation to in-vivo elasticity measurements in delicate soft tissues and organs in particular.

[1] Ł. Ambroziński et al., "Acoustic micro-tapping for non-contact 4D imaging of tissue elasticity," Scientific Reports, Article number: 38967 (2016).

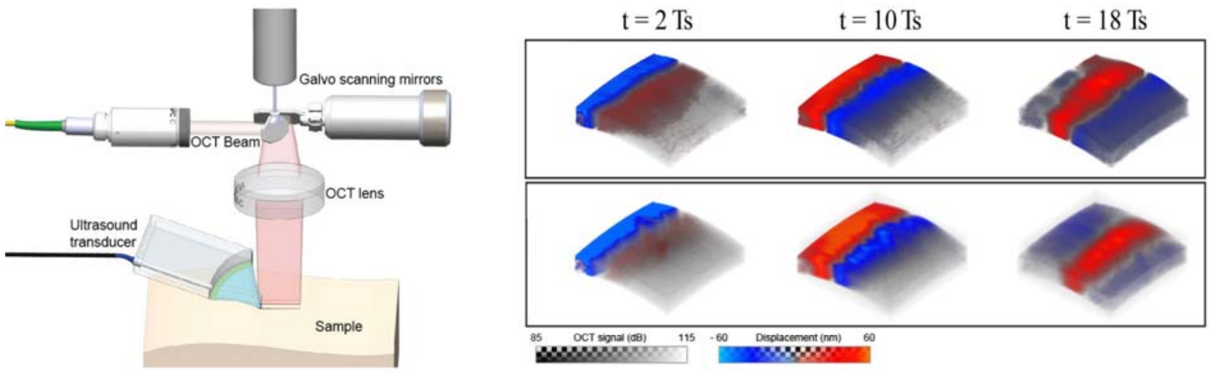

Figure 1. Schematics of the AμT-OCT technique (left panel) and wavefield snapshots of the mechanical wave propagation in an ex-vivo porcine cornea at a 10 mmHg (upper right panel) and 20 mmHg (lower right panel) intraocular pressure.

3D-3

8:30 am A Model-Free Approach to Probe Motion Artifacts Suppression for *in vivo* Imaging with Probe Oscillation Shear Wave Elastography (PROSE)

Daniel Mellema[1], Pengfei Song[1], Armando Manduca[2], Matthew Urban[1], Randall Kinnick[2], James Greenleaf[2], Shigao Chen[1]; [1]*Radiology, Mayo Clinic, Rochester, MN, USA*, [2]*Physiology and Biomedical Engineering, Mayo Clinic, Rochester, MN, USA*

Background, Motivation and Objective

Probe oscillation shear wave elastography (PROSE) can achieve high frame-rate two-dimensional (2D) shear wave elastography by utilizing a continuously vibrating ultrasound probe to simultaneously generate and detect shear waves (Mellema, IEEE TMI 0278-0062). Strategically detecting when the probe returns to the same physical location allowed the shear waves to be decoupled from probe motion artifacts; however, complicated wave patterns observed when imaging *in vivo* liver prevented full suppression of these artifacts. This work proposes Empirical Mode Decomposition (EMD) as a model-free approach to decouple probe motion artifacts from the shear wave signal.

Statement of Contribution/Methods

A Verasonics Vantage system with a C5-2v probe (3.7 MHz) was mounted co-axially with an in-house voice coil vibration system. Under an IRB approved protocol, the livers of five healthy volunteers were imaged through the intercostal space. A 30 Hz sinusoidal signal was used to drive the vibration system and motion was captured over a single vibration cycle using a plane wave imaging sequence with a 1 kHz effective pulse repetition frequency. For each frame, EMD was used to estimate probe motion artifacts and these were subtracted from the data to isolate the shear wave signal. A temporal band pass filter (BPF) was applied to remove any motion outside the vibration frequency and a spatial BPF was used to suppress residual artifacts. A local frequency estimation technique was used to reconstruct 2D shear wave speed (SWS) maps. For comparison, the SWS of each liver were also obtained using a General Electric Logiq E9.

Results/Discussion

Fig. 1a shows a representative motion profile from a healthy volunteer (blue), with an estimation of the artifact (red), and the isolated shear waves (black) allowing detection at depths greater than 80 mm. The corresponding 2D shear wave image is shown in Fig. 1b. The shear waves have good penetration allowing for SWS to be estimated for a majority of the 2D cross section, and a region-of-interest (ROI) was manually drawn to isolate areas with high shear wave signal. Fig. 1c shows the resulting SWS map with a SWS of 1.22 ± 0.15 m/s within the ROI. This agrees well with the Logiq E9 value of 1.15 m/s. Fig. 1d shows a comparison of PROSE to the Logiq E9 for all of the volunteers resulting in an R^2 value of 0.94, demonstrating that PROSE is an effective elastography method.

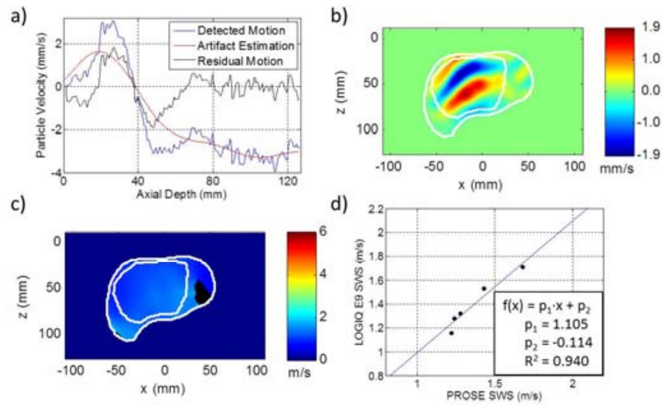

Figure 1. (a) Motion profiles representing the detection with probe motion artifact removal (blue), the estimated artifact (red) and the shear wave signal (black). (b) The shear waves after the probe motion artifact removal; the larger ROI denotes the boundary of the liver while the smaller ROI denotes region with good shear wave signal. (c) The resulting shear wave speed reconstruction. The shear wave speed within the smaller ROI was 1.22 ± 0.15 m/s compared to 1.15 m/s reported by the LogiqE9. (d) A comparison of the 5 healthy volunteers imaged with PROSE and the LogiqE9.

3D-4

8:45 am Multi-row Array Transducer for Elevational Motion Consideration in Strain Imaging

Elisabeth Brusseau[1], Adeline Bernard[1], Cyril Meynier[2], Guillaume Férin[2], An Nguyen-Dinh[2], Olivier Basset[1]; [1]*CREATIS, Villeurbanne, France,* [2]VERMON, France

Background, Motivation and Objective

Ultrasound is a widely used imaging modality, both for diagnosis and guidance of interventional procedures such as biopsies. Ultrasound imaging commonly provides 2D data, which can be a limitation for further data processing, since information like out-of-plane motion is inaccessible. In this study, a specific multi-row array transducer – developed for the elastography application – is presented. This prototype acquires series of three adjacent imaging planes over time and makes therefore possible to compute 2D strain images of the central plane, with consideration of out-of-plane motion.

Statement of Contribution/Methods

The developed transducer is a 7-MHz central frequency probe, composed of 640 elements organized in five rows of 128 elements. Their dimensions vary with the row. The elements from the rows #1, 2, 4 and 5 all measure 0.725 mm x 0.275 mm (height x width), while those from the central row are larger, measuring 3.125 mm x 0.275 mm. The horizontal and vertical spacing between elements (kerf) is 25 µm. This probe allows the acquisition of three adjacent imaging planes by electronically switching between element rows. The first plane is obtained by the simultaneous activation of rows #1, 2 and 3, the second one (or central plane) of the rows #2, 3 and 4 and the third imaging plane by activation of the rows #3, 4 and 5. This strategy permits to vary the position of the emitting surface in 0.75-mm step in elevation, without mechanical translation of the array.

This probe was connected to an Ultrasonix ultrasound scanner and initial tests were conducted with phantoms and bovine tissue samples. Data were acquired at 40 MHz and 2D axial strain images of the central plane were computed using a 3D motion estimation method, based on correlation coefficient maximization.

Results/Discussion

Fig. 1 provides an example of results, obtained with a CIRS phantom (model 049), along with the axial strain images from the same technique but restricted to in-plane motion analysis. Elastograms are given for increasing steps of probe displacement in elevation (a,b,c). Results show the interest of the proposed approach – compared to a 2D technique – for larger elevational motion, with an increase in the mean correlation coefficient values achieved during elastogram computation: 0.95, 0.91, and 0.82 versus 0.96, 0.94, and 0.89 for the 2D vs 3D estimation technique and increasing probe displacements.

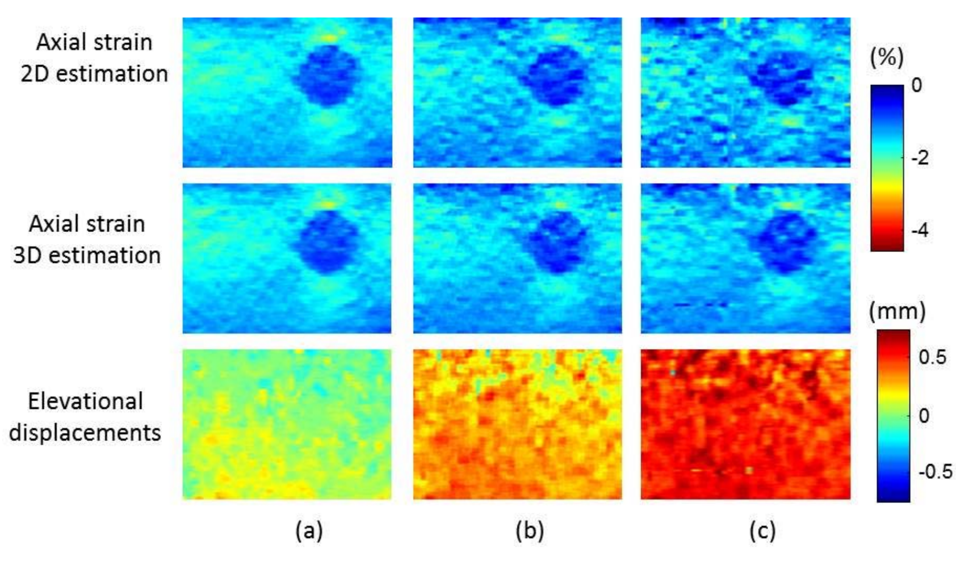

3D-5

9:00 am **Shear-Wave Imaging Of Viscoelasticity Using Local Impulse Response Identification**

Ruud J.G. van Sloun[1], Rogier R. Wildeboer[1], Hessel Wijkstra[1,2], Massimo Mischi[1]; [1]*Eindhoven University of Technology, Eindhoven, Netherlands,* [2]*Academic Medical Center University of Amsterdam, Netherlands*

Background, Motivation and Objective

Imaging technologies that allow assessment of the elastic properties of soft tissue provide clinicians with an important asset for several diagnostic applications. A quantitative measure of stiffness can be obtained by shear-wave (SW) elasticity imaging, a method that uses acoustic radiation force to produce laterally-propagating shear waves that can be tracked to obtain the velocity, which in turn is related to the shear modulus. If one considers the medium to be purely elastic, its local shear modulus can be estimated by determining the local SW velocity. However, this assumption does not hold for many tissue types, whenever the shear viscosity plays an important role. In fact, there is increasing evidence that viscosity itself could be an important marker for malignancy [1]. In this work, we therefore aim at providing a joint local estimate of tissue elasticity and viscosity based on SW elastography.

Statement of Contribution/Methods

We consider the viscoelastic material as a dynamic linear system, whose impulse response can be locally identified by point-to-point analysis of SW time-displacement curves. Starting from the Navier-Stokes equation, a model-based impulse response was derived and locally fitted to the data in a least-squares fashion. The method extends beyond time-of-flight based methods [2] by estimating the kinetics between laterally sampled time-displacement curves instead of just their time-delay, permitting the extraction of the viscoelastic material parameters at a high spatial resolution.

In our experiments, tofu served as a typical high-viscosity material. To mimic low-viscosity tissues, water-based gelatin with graphite scatterers was prepared. Mechanical characterization confirmed that the gelatin material showed little to no viscous creep, whereas the tofu phantom clearly displayed viscous behavior. The proposed method was tested on a tofu phantom containing a cylindrical inclusion of gelatin.

Results/Discussion

From Figure 1, we can observe that the less-viscous gelatin inclusion is indeed revealed by the viscosity maps, whereas the velocity images (showing elastic behavior) fail to expose it.

[1] Hoyt et al., "Tissue elasticity properties as biomarkers for prostate cancer", Cancer Biomarkers, 2008

[2] Palmeri et al. "Quantifying hepatic shear modulus in vivo using acoustic radiation force", UMB, 2008

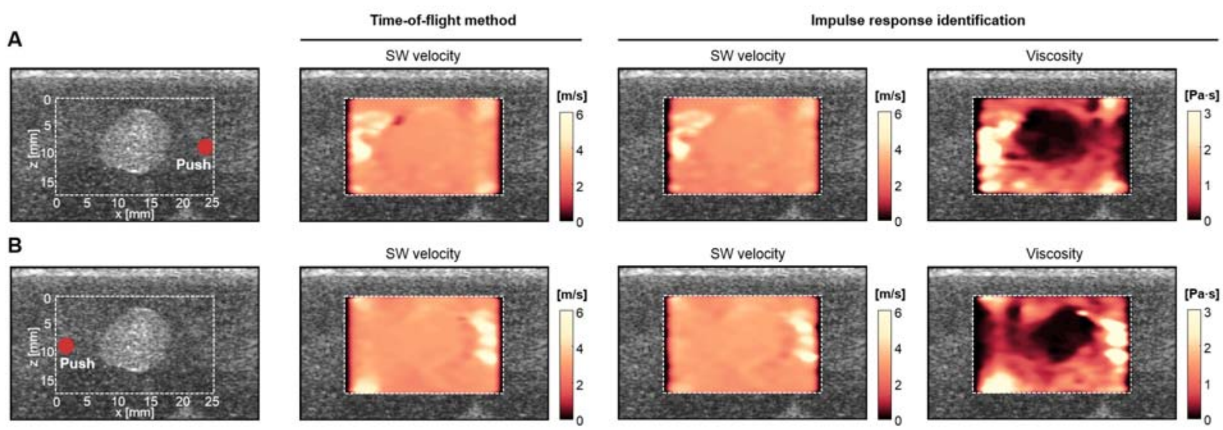

Figure 1. Proposed shear wave viscoelasticity imaging on a tofu phantom containing a cylindrical inclusion of gelatin, as compared to a typical correlation-based time-of-flight approach. The results obtained with the acoustic push focus positioned on the right lateral side (A) are compared to those obtained with a push on the other side (B).

3D-6

9:15 am **Comparison of Shear Velocity Dispersion in Viscoelastic Phantoms Measured by Ultrasound-Based Shear Wave Elastography and Magnetic Resonance Elastography**

Matthew Urban[1,2], Jun Chen[1], Richard Ehman[1]; [1]*Department of Radiology, Mayo Clinic College of Medicine and Science, Rochester, MN, USA,* [2]*Department of Physiology and Biomedical Engineering, Mayo Clinic College of Medicine and Science, Rochester, MN, USA*

Background, Motivation and Objective

Pathological processes in soft tissues cause changes in mechanical properties. Elastography methods have emerged to make quantitative measurements of the shear modulus or shear wave speed (SWS) as a noninvasive way to provide diagnostic information. In an effort to standardize ultrasound-based measurements of SWS, the Radiological Society of North America Quantitative Imaging Biomarkers Alliance (RSNA QIBA) has established working groups to develop profiles for different biomarkers including the use of SWS for staging of patients with liver fibrosis. To understand how ultrasound-based measurements vary with tissue viscoelasticity, measurements were made in viscoelastic phantoms with ultrasound-based shear wave elastography (US-SWE) and magnetic resonance elastography (MRE) over a wide frequency range.

Statement of Contribution/Methods

Three different viscoelastic phantoms (CIRS, Inc., Norfolk, VA) were tested with US-SWE and MRE and analysis was considered over a range of frequencies (60-600 Hz). MRE was performed with an electro-mechanic driver driven with continuous vibration at various frequencies (60, 80, 100, 120, 140, 160, 180, 200, 300, 400, 500, 600 Hz). Shear wave motion was measured with a phase-sensitive pulse sequence and the complex modulus and SWS at each frequency was estimated. The SWS in each phantom were fit with a power-law. US-SWE was performed with a Verasonics system and curved array transducer. An acoustic radiation force push of 800 µs was focused at 30, 45, and 70 mm and shear wave motion was measured and two-dimensional Fourier analysis was used to measure SWS dispersion.

Results/Discussion

The figure shows the SWS dispersion from the MRE power law fits ($R^2 > 0.98$) and the mean of 20 measurements made with US-SWE with a focal depth of 45 mm. The agreement was generally good and the percent differences for a focal depth of 45 mm ranged from -6.35-11.99% over the range of 60-300 Hz. The results for a focal depth of 30 mm had percent differences ranging from -4.37-12.17% from 60-300 Hz, and for a focal depth of 70 mm -1.05-16.46% from 80-200 Hz. The percent differences were typically above 15% at frequencies of 400-600 Hz. These measurements showed very good agreement between US-SWE and MRE methods in viscoelastic phantoms as MRE is being considered as a QIBA reference standard for US-SWE methods for liver SWE measurements.

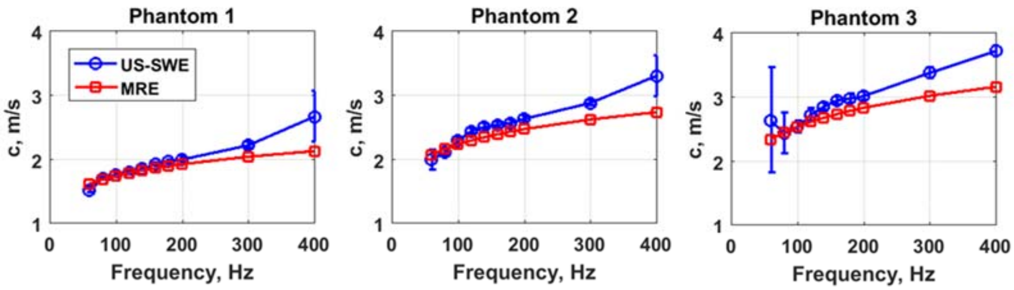

Figure 1. Comparison of SWS dispersion in three viscoelastic phantoms between MRE and US-SWE. US-SWE measurements were made with a focal depth of 45 mm and are shown as the mean and standard deviation of 20 measurements. The agreement between the two methods is high from 60-200 Hz, and the deviation between the two methods increases at frequencies 300 Hz and above.

4D - MPA: Photoacoustic Reconstruction Approaches and Technical Developments

Diplomat Room

Friday, September 8, 2017, 8:00 am – 9:30 pm

Chair: **Pai Chi Li**
National Taiwan University

4D-1

8:00 am **Aberration Correction in Photoacoustic Imaging using Paraxial Backpropagation**

Hans-Martin Schwab[1], Andreas Ihrig[1], Dominic Depke[2], Sven Hermann[2], Michael Schäfers[2], Georg Schmitz[3]; [1]*Ruhr-University Bochum, NRW, Germany,* [2]*European Institute for Molecular Imaging, Westfälische Wilhelms-Universität Münster, Germany,* [3]*Medical Engineering, Ruhr-University Bochum, Germany*

Background, Motivation and Objective

Photoacoustic (PA) imaging aims for the reconstruction of acoustic sources that originate in pulsed light absorption. While the speed of sound (SOS) in biological tissue is heterogeneous, standard reconstruction algorithms usually assume a constant SOS. This results in deformations of the reconstructed sources, which are referred to as aberration and can have a severe impact on the spatial resolution.

If the SOS is known, aberrations can be compensated during the reconstruction at the expense of an increasing computational effort. Algorithms that account for heterogeneous SOS usually compute individual delays for each reconstructed pixel or perform an entire wave field simulation. In this contribution, we present an alternative approach by introducing a PA backpropagation based on a paraxial approximation of the wave equation that can be computed with almost the computational efficiency of a standard frequency domain reconstruction (FSAFT). The method accounts for refraction and neglects unwanted back-reflections during the backpropagation process.

Statement of Contribution/Methods

The reconstruction method is derived as a frequency domain backpropagation based on a paraxial approximation of the wave equation using a Fourier split step method.

In order to successfully apply an aberration correction, the SOS distribution needs to be known. Therefore, we demonstrate two approaches to approximate an SOS map for the paraxial reconstruction. In the simulation experiment, plane wave ultrasound measurements are simulated in addition to the PA measurement. The ultrasound measurements are processed in a CUTE [1] reconstruction yielding the required SOS distribution. In a second experiment, which is acquired in vivo with a Vevo 2100 LAZR (Visualsonics), the SOS distribution is derived from a simple segmentation of the B-Mode ultrasound image assuming two areas, ultrasound gel and tissue, using reference SOS values from literature.

Results/Discussion

In the simulation experiment, the position and shape of PA sources behind an inclusion with 2% SOS deviation are correctly restored. In the in vivo experiment, which is depicted in the figure below, the lateral resolution of a structure at 9.6 mm depth could be improved by 32% and 152% compared to homogeneous reconstructions with the SOS of only ultrasound gel or only tissue.

[1] Jaeger et. al, Ultrasound Med. Biol., (2015)

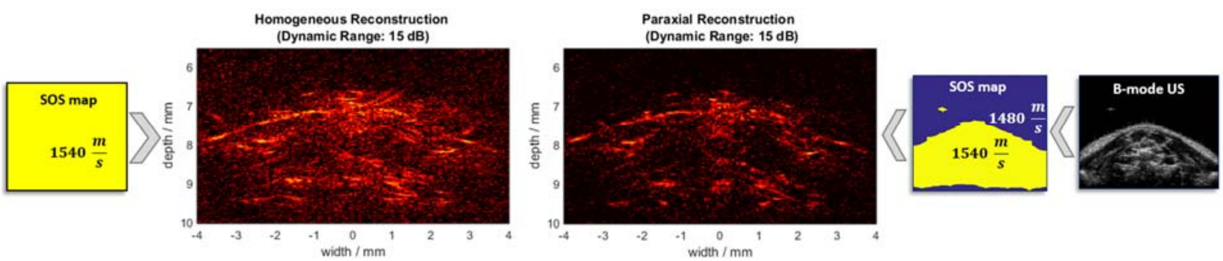

4D-2

8:15 am **Elevation Resolution Enhancement in 3D Photoacoustic Imaging Using FDMAS Beamforming**

Abdulrhman Alshaya[1], Sevan Harput[1], David M. J. Cowell[1], James McLaughlan[1], Steven Freear[1]; [1]*University of Leeds, United Kingdom*

Background, Motivation and Objective

Photoacoustic imaging is a non-invasive and non-ionizing imaging technique that combines the spectral selectivity of laser excitation with the high resolution of ultrasound imaging. It is possible to identity the vascular structure of the cancerous tissue using this imaging modality. However, elevational and lateral resolution of photoacoustic imaging is usually poor for imaging target. In this study, a 3D imaging protocol was created using a linear array transducer and two dimensional synthetic aperture filter delay multiply and sum beamforming (2D-FDMAS). Implementation of 2D-FDMAS improves the elevation and lateral resolutions and enhances SNR of the photoacoustic image.

Statement of Contribution/Methods

A turbid polyacrylamide hydrogel phantom was created with carbon fibre rods which its size was 2.5λ (fig.1 (A)). The optical scattering coefficient of the phantom was 0.3 mm^{-1}. Photoacoustic emissions were generated from the phantom by a tuneable Nd:YAG pulse laser. The output optical energy and wavelength were 3.7 mJ and 850 nm respectively. In this experiment, photoacoustic emissions were acquired by using an Ultrasound Array Research Platform II (UARP II), with a 128-element linear transducer (4-11 MHz). The scan step, in the probes elevation plane was 0.1 mm. The received photoacoustic emissions from each element were averaged 100 times before beamforming. Results were analysed comparing the SNR and spatial resolution of maximum amplitude projection (MAP) photoacoustic images after beamforming by 2D delay and sum (2D-DAS), 3D-DAS and 2D-FDMAS.

Results/Discussion

Fig.1 (B), (C) and (D) show the photoacoustic images of two carbon fibre rods processed by the three different beamforming techniques described. It showed that 2D-FDMAS beamforming improved the SNR by 5 dB and 3.7 dB compared with 2D-DAS and 3D-DAS respectively. The -6 dB lateral resolution was measured along the dashed line (1) in Fig.1 (B), where 2D-FDMAS performed 17% and 22% better than 2D-DAS and 3D-DAS respectively, see Fig.1 (E). The -6 dB elevation resolution was calculated for the dashed line (2) is Fig.1 (B), which was improved by 52% and 20% for 2D-FDMAS compare with 2D-DAS and 3D-DAS respectively as shown in Fig. (F). From these results, the 2D-FDMAS achieved noticeable improvement in elevation revolution and SNR.

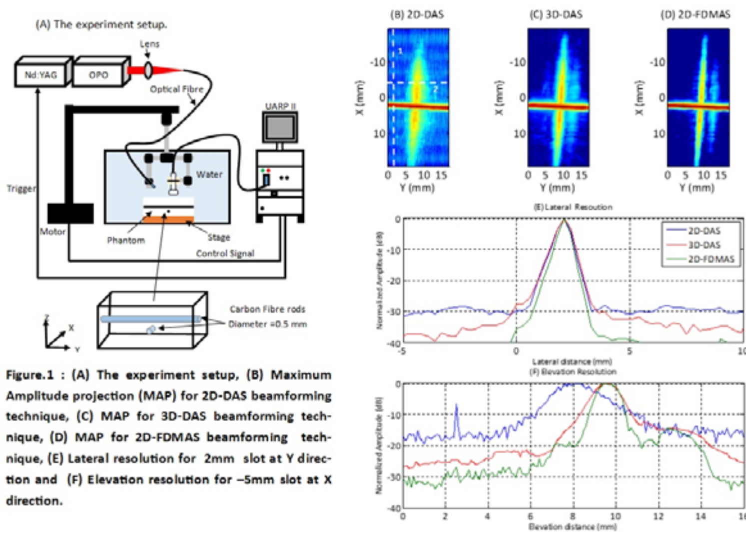

Figure.1 : (A) The experiment setup, (B) Maximum Amplitude projection (MAP) for 2D-DAS beamforming technique, (C) MAP for 3D-DAS beamforming technique, (D) MAP for 2D-FDMAS beamforming technique, (E) Lateral resolution for 2mm slot at Y direction and (F) Elevation resolution for –5mm slot at X direction.

4D-3

8:30 am **Visualization of the Microcirculation in Micro Vasculatures by Photoacoustic Tomography with High Frequency Spherical Array Transducer**

Ryo Nagaoka[1], Takuya Tabata[1], Ryo Takagi[2], Shin Yoshizawa[2], Shin-ichiro Umemura[2], Yoshifumi Saijo[1]; [1]*Biomedical Imaging Laboratory, Graduate School of Biomedical Engineering, Tohoku University, Sendai, Japan,* [2]*Ultrasound Enhanced Nanomedicine Laboratory, Graduate School of Biomedical Engineering, Tohoku University, Sendai, Japan*

Background, Motivation and Objective

A spatial resolution of photoacoustic tomography (PAT) has been limited by the receive frequency significantly lower than that of photoacoustic microscopy. In the present study, an in vivo microcirculation is visualized by a PAT system by using a newly developed spherical array transducer with a center frequency of 10 MHz. Additionally, we propose a novel reconstruction method suppressing the side lobe level with Wiener filtering.

Statement of Contribution/Methods

Assuming the photoacoustic signal (PAS) is one sinusoidal wave with an initial phase of 0 rad, the first side lobe is attributable to a negative peak with a relative phase of π. Hence, the first side lobe can be suppressed by not using the negative values from the Delay-And-Sum (DAS) reconstruction. The spherical array transducer consisting of 256 elements had a center frequency of 10 MHz, a diameter of 42.4 mm, and an opening angle of 90 degrees. PAS was acquired by a programmable acquisition system with 256 Tx/Rx channels (Verasonics, Redmond) at a sampling frequency was 62.5 MHz. A short-pulsed (< 10 ns) laser (opolette, Opotek Inc.) at a wavelength of 532 nm wavelength with a repetition frequency of 20 Hz was used for generating PAS in vivo experiment to visualize microcirculation of a human hand. Three dimensional image was reconstructed by DAS beamforming from Wiener-filtered PAS. The first side lobe can be suppressed by thresholding the minus values of the signals after beamforming.

Results/Discussion

By the proposed method, the side lobe level was suppressed by almost -7 dB, and the spatial resolution was improved from 95 µm to 85 µm. A following figure shows the in vivo PA C-mode image of the microvasculatures in the hand. Arrows indicated the microcirculation through the vasculatures. According to the figure, a flow speed was approximately estimated to be 1 mm/s, which agreed well with the values (1-5 mm/s) in references. The PAT system by using the newly transducer with the proposed method clearly could visualize the vasculatures and its circulation in real time at 20 fps.

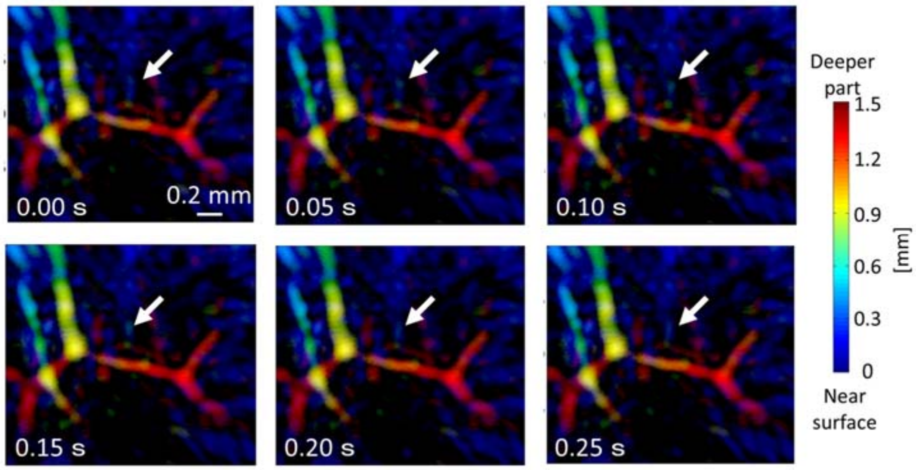

4D-4

8:45 am Simultaneous Dual-Modality Imaging of the Vasculature and Gross Anatomy of the Zebrafish Embryo Trunk

Michael Moore[1,2], Youdong Wang[3,4], Xiao-Yan Wen[3,4], Michael Kolios[1,2]; *[1]Department of Physics, Ryerson University, Toronto, Ontario, Canada, [2]Institute for Biomedical Engineering Science and Technology, St. Michael's Hospital, Toronto, Ontario, Canada, [3]Keenan Research Centre, Li Ka Shing Knowledge Institute, St. Michael's Hospital, Toronto, Ontario, Canada, [4]Departments of Medicine and Physiology, University of Toronto, Toronto, Ontario, Canada*

Background, Motivation and Objective

One of the main advantages of photoacoustic (PA) microscopy is its ability to generate high-resolution maps of vasculature due to strong endogenous absorption. In contrast the optical absorption of the gross anatomy surrounding the vasculature is negligible, and it is thus not readily imaged using PA. We have previously reported on a new imaging technique, termed Photoacoustic Radiometry (PAR), which derives contrast from the sample's optical attenuation properties (doi:10.1117/12.2212961). In this work, we use a dual PA and PAR technique to simultaneously acquire co-registered images of the vasculature and gross anatomy of the trunk of a zebrafish embryo from a single PA scan.

Statement of Contribution/Methods

A 3 day post fertilization zebrafish embryo was anesthetized using clove oil and fixed overnight in a 4% PFA in PBS (v/v) solution. The embryo was mounted on a glass bottom petri dish and covered with 200 µL of 0.5% agarose to prevent sample movement during image acquisition. A photoacoustic microscope equipped with a 200 MHz transducer and a 532 nm laser focused through a 10X optical objective was used to raster scan the embryo. The resultant RF data was time gated to separate the PAR and PA signals (top row, Fig. 1). Two maximum amplitude projection (MAP) images were formed, one for the PAR data and the other for the PA.

Results/Discussion

An optical image of the zebrafish embryo trunk is shown in Fig. 1a. The corresponding PAR image in Fig. 1b depicts several features of the gross anatomy, most notably the vertical myosepta (arrowhead), notocord (N), and mytotomes (M). Melanin spots on the epidermis are indicated with arrows. When compared with the optical image, the PAR image demonstrates enhanced contrast between the notocord and myotmes, as well as additional fine structure within the myotomes. Figure 1c shows the PA image formed from the same RF data as Fig. 1b. The dorsal aorta (arrow) and intersegmental vessels (arrowhead) are clearly visible, along with the posterior cardinal vein (PCV). Superimposing the vasculature from the PA image onto the gross anatomy from the PAR image reveals that the intersegmentental vessels follow the contour of the myosepta, with the dorsal aorta directly ventral to the notochord. In the future, the dual imaging technique presented herein will be used to monitor blood vessel development, and quantify the oxygen saturation of trunk vessels *in vivo*.

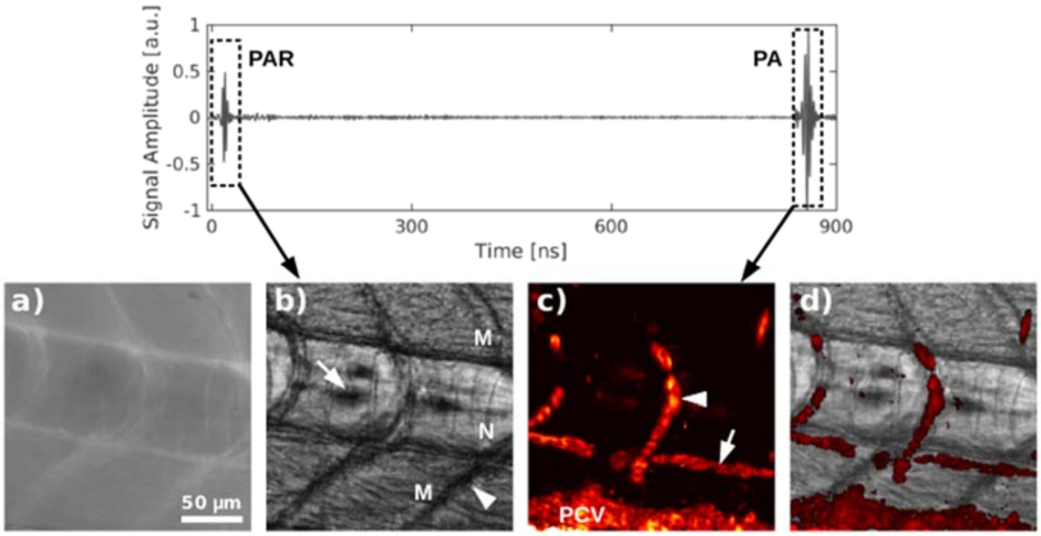

4D-5

9:00 am Fast Scanning Wide-Field Clutter Elimination in Epi-Optoacoustic Imaging using Comb-LOVIT

Tigran Petrosyan[1], Maria Theodorou[2], Jeffrey Bamber[2], Martin Frenz[1], Michael Jaeger[1]; [1]*Institute of applied Physics, University of Bern, Switzerland,* [2]*Joint Department of Physics and CRUK Cancer Imaging Centre, Institute of Cancer Research, United Kingdom*

Background, Motivation and Objective

Epi-optoacoustic (OA) imaging allows flexible clinical use, but out-of-plane and echo clutter from strong OA sources limits contrast. In localized vibration tagging (LOVIT), a focused ultrasonic pushing beam creates transient localized displacement and thus a signal phase shift. Subtraction of OA acquisitions before and at the peak displacement highlights signal from the focus and eliminates out-of-plane clutter. However, residual echo clutter remains, from structures inside the pushing beam above the focus where non-zero displacement also occurs. It also requires time to scan a single focus through the region of interest (ROI). We present a novel approach, by which acquisition speed is increased and residual clutter is reduced almost to the noise level.

Statement of Contribution/Methods

Multiple horizontally aligned foci are created in parallel, forming a comb displacement pattern. Two OA images are acquired, each preceded by a comb where the two combs have interleaved foci. Both combs have a similar displacement above the focal depth, leading to near-zero relative displacement in the region from where residual clutter would originate. Subtraction of the two images therefore results in simultaneous clutter reduction with minimized residual echo clutter inside multiple foci in parallel. A comparative study between comb- and single-focus LOVIT is presented, with phantoms that mimic optical and elastic properties of breast tissue and contain optically absorbing inclusions.

Results/Discussion

Referring to the figure. a) Significant clutter is noticed in the conventional OA image. b) Comb substantially reduces clutter and improves visibility of the inclusions (arrows). c) Displacement between interleaved combs with 6 parallel foci at one focal depth, determined by pulse-echo phase tracking. Multiple depths were scanned to achieve the ROI indicated in (b). d) The displacement in single-focus and comb LOVIT along the line in (c), indicating a smaller displacement with comb above the focal depth. e) Mean square background when averaging multiple acquisitions – evaluated inside the dashed rectangle in (b) – in comparison to the noise level. Single-focus LOVIT results in residual background far above the noise. Comb-LOVIT – in addition to a 6x faster scanning speed – demonstrates a substantial residual clutter reduction towards the noise level.

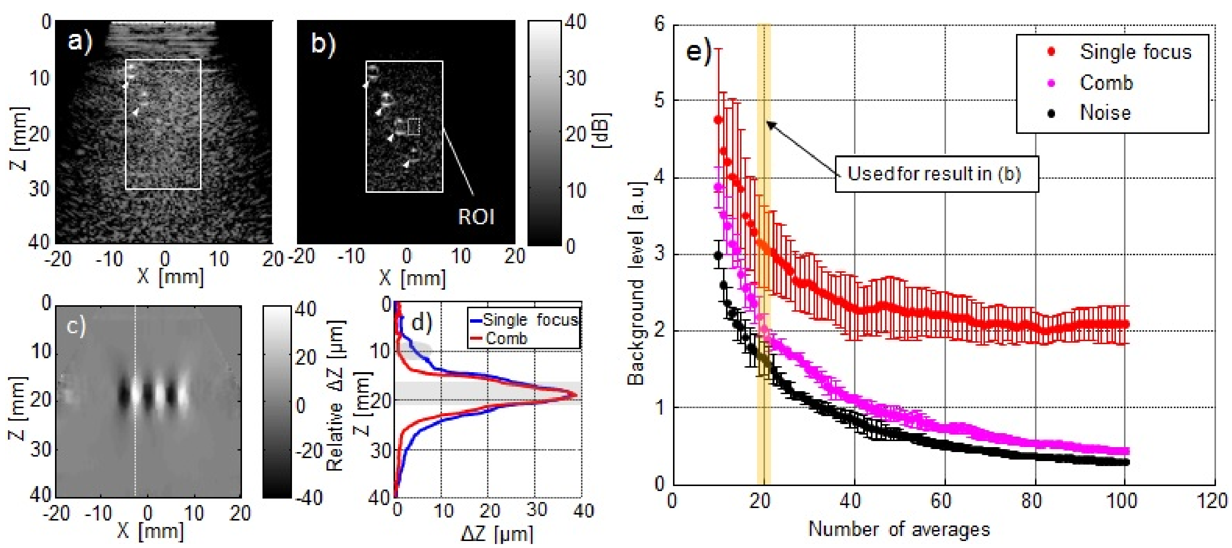

4D-6

9:15 am Photoacoustic Microscopy of Lipids at 1.2 and 1.7 µm Using a Pulsed Supercontinuum Laser

Nicole Conley[1], Sang Won Choi[1], **Takashi Buma**[2]; [1]*Union College, USA,* [2]*Union College, Schenectady, NY, USA*

Background, Motivation and Objective

Photoacoustic microscopy (PAM) is promising for label-free histology of lipid-rich tissue. Lipids have optical absorption peaks at 1.2 and 1.7 µm, but these wavelengths are typically produced with expensive optical parametric oscillator (OPO) lasers. We have been exploring nonlinear fiber optics to convert inexpensive pulsed lasers into multi-wavelength sources for PAM. Photonic crystal fibers (PCFs) have nonlinear optical properties that enable a single-wavelength laser to produce an ultra-broadband supercontinuum spanning the visible and near-infrared.

Statement of Contribution/Methods

In this paper, we demonstrate near-infrared PAM of lipids using a supercontinuum PCF laser. Our system starts with a 1047 nm Q-switched Nd:YLF laser producing 14 ns pulses with 120 uJ of energy at a 2.5 kHz repetition rate. These pulses are sent through 30 meters of polarization-maintaining large-mode area photonic crystal fiber (LMA-PCF) with a 10 µm core diameter. The desired PAM wavelength is selected with a dielectric band-pass filter (50 nm bandwidth) and focused onto the sample with a 4X microscope objective. Photoacoustic signals are detected with a 25 MHz f/2 transducer. Imaging experiments are performed on a lipid phantom consisting of small butter droplets placed between approximately 1 mm thick gelatin layers.

Results/Discussion

The fiber output spectrum from 1000 to 1800 nm is shown in Fig. 1a. The discrete peaks at 1098 and 1153 nm are due to stimulated Raman scattering. Wavelengths greater than 1200 nm experience negative dispersion, where a variety of nonlinear phenomena produce a supercontinuum. The laser pulse energies at 1100, 1225, 1325, 1600, and 1710 nm are 3.12, 0.47, 0.52, 0.32, and 0.13 µJ, respectively. Multispectral PAM images of the lipid phantom are shown in Fig. 1b. All C-mode images span a 3.75 x 1.25 mm region and are shown over the same 15 dB scale. All signals are averaged 64 times. As expected, the lipid regions are most apparent at 1225 and 1710 nm and lipid contrast is higher at 1710 nm. Image contrast at 1600 nm is actually due to optical absorption from gelatin, rather than lipid, at the gelatin-lipid interface. To our knowledge, this is the first demonstration of a supercontinuum laser for near-infrared PAM of lipids. We believe our system's wavelength flexibility make it promising for label-free histology of lipid-rich tissue.

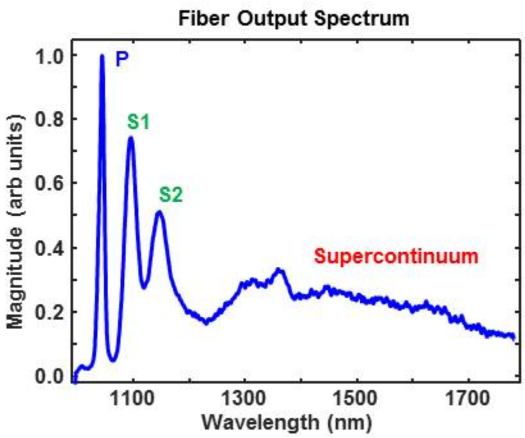

Fiber Output Spectrum
Magnitude (arb units)
Wavelength (nm)
1.0
0.8
0.6
0.4
0.2
0.0
1100
1300
1500
1700
P
S1
S2
Supercontinuum

(a)

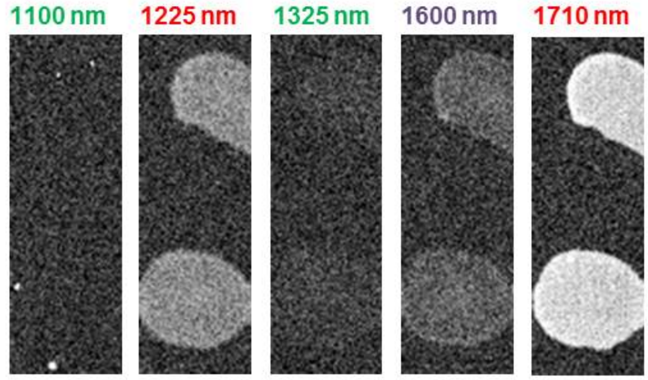

1100 nm
1225 nm
1325 nm
1600 nm
1710 nm

(b)

5D - Acoustic Nonlinearity

Blue Room

Friday, September 8, 2017, 8:00 am - 9:30 am

Chair: **Ken-ya Hashimoto**
Chiba University

5D-1

8:00 am **An Alternative Method for Determining the 2nd Order Nonlinear Coefficients of BAW Resonators**

Jing Wu[1], Dave Feld[1], Dong Shim[1], Zongliang Cao[1]; [1]*Wireless Semiconductor Division, Broadcom, San Jose, CALIFORNIA, USA*

Background, Motivation and Objective

Filters operated at high power levels and comprising BAW resonators produce 2nd harmonic emissions. To model the emissions of a BAW resonator, Feld and Shim constructed a nonlinear Mason model, which implements an "extended" pair of piezoelectric constitutive equations containing arbitrary 2nd order terms:

$T = c^E S - eE + [1/2\delta_3 c^E S^2 - \delta_1 eSE + 1/2\delta_2 \varepsilon^S E^2]$

$D = eS + \varepsilon^S E + [1/2\delta_1 eS^2 - \delta_2 \varepsilon^S SE + 1/2\delta_4 \varepsilon^S eE^2/c^E]$ (1)

c^E, e, ε^S, δ_1-δ_4 are the 1-D stiffness, piezoelectric, and dielectric, and 2nd order constants respectively. The values of the 2nd order coefficients, δ_1 & δ_4, which are found to be the dominant terms – can be found by measuring the on- and off-resonance levels of H2 respectively. We present an alternate measurement technique to determine these coefficients by measuring linear parameters of a resonator under large DC bias voltage conditions.

Statement of Contribution/Methods

Using a network analyzer and a dc bias tee, we measured the linear relationship f_p vs. V_{dc} of a resonator. This can be expressed by the parameter: $\alpha_{fp} = (df_p/dV_{dc})/f_p$. A simple theory, expresses δ_1 in terms of α_{fp}:

$\delta_1 = 2\alpha_{fp} c^E t/(e(1-3k_t^2))\cdot F$, $F = (Y / \mathrm{Sin}Y + X / \mathrm{Sin}X) / (1 + X / \mathrm{Sin}X)$, $X = 2\pi f_p t/v_{AlN}$, $Y = 2\pi f_p d/v_{Mo}$ (2)

where t, v_{AlN}, d, v_{Mo}, k_t^2, F are are piezo thickness and velocity, electrode thickness and velocity, coupling coefficient, and geometric factor of the layer stack respectively.

Similarly, by measuring the capacitance at 100 MHz (below resonance) vs. V_{dc} using an impedance analyzer, δ_4 can be computed from the linear relationship between C_0 and V_{dc} (fig. 1a). $\alpha_{C0} = (dC_0/dV_{dc})/C_0$:

$\delta 4 = (\alpha_{C0} c^E t)/e - 3\delta_1 e^2/(\varepsilon c^E)$ (3)

Results/Discussion

We selected a piezoelectric AlN resonator for study fabricated using an arbitrarily chosen layer stack. For this resonator, we measured the DC sensitivity parameters to be: α_{fp} = -3.6e-5 & α_{C0} = -1.5e-4, and from these parameters, using the equations stated above, we computed the nonlinear constants of the AlN to be: $\delta_1 \approx -20$, $\delta_4 \approx -21.1$. To verify these parameters, we plugged these constants, along with the linear materials properties and thicknesses of the piezo and metal films, into our non-linear Mason model. We simulated the response of our resonator by applying a 27dBm, frequency-swept fundamental tone incident on our resonator. The measured and simulated responses of the 2nd harmonic were in strong agreement -fig. 1(b).The work in this paper is an important confirmation of our model.

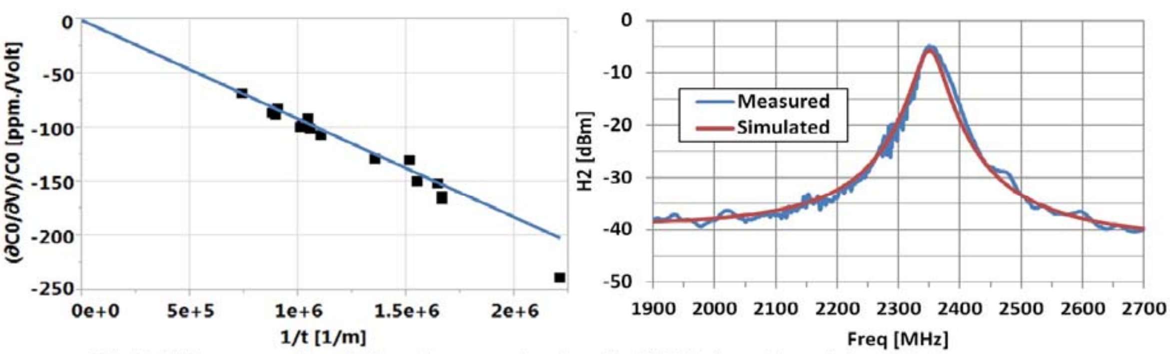

Fig.1(a) The measured α_{C0} is linearly proportional to 1/t. δ4 is independent of piezo thickness;
(b) Measured response (blue) at second harmonic frequencies strongly agrees with the simulation (red).

5D-2

8:15 am **Second Harmonic Generation and Detection in a Rayleigh-type SAW Structure**

Werner Ruile[1], Markus Mayer[1], **Andreas Mayer**[2], Elena Mayer[2], Vikrant Chauhan[3], Ingo Bleyl[1], Karl Wagner[1]; [1]*RF360 Europe GmbH, Germany,* [2]*Hochschule Offenburg, Germany,* [3]*Friedrich Alexander Universität Erlangen-Nürnberg, Germany*

Background, Motivation and Objective

With ever increasing requirements on the linearity of SAW signal processing devices in mobile communication, nonlinear effects like harmonic generation and intermodulations have gained renewed interest and have become an active field of research with the aim of identifying their origin, analyzing and counteracting them.

In this contribution we focus on second-harmonic generation in SAW resonators. Like counter-propagating surface waves in SAW-type convolvers [1,2], part of the second-harmonic is a bulk wave propagating from the surface into the substrate [3,4]. In SAW resonators, this bulk wave has recently been investigated experimentally in detail [4]. Its reflections from the bottom of the substrate were found to give rise to Fabry-Perot-type resonances which were measured electrically at the output port. An open question remained: Why is the second harmonic visible in electrical measurements in a device with symmetrically arranged electrodes on the surface, since the nonlinear driving terms resulting from the fundamental via second-order nonlinearity of the materials contain equal charges on adjacent electrodes. This suggests that an electrical output signal at the second harmonic is not visible unless symmetry-breaking deviations from a perfect system are present.

Statement of Contribution/Methods

An L-section of a ladder-type filter is considered with a series and a parallel resonator. It is shown that in this configuration, the second harmonic generated in the two SAW resonators does in fact lead to an electrical signal at the output port of the L-section, even in the case of perfectly symmetric resonators. With the help of FEM calculations the wave field of the second harmonic as well as the electrical output signal have been determined. In a first step, the resonators are modeled as a periodic arrangement of Cu-electrodes on $LiNbO_3$ as the piezo-electric substrate, covered with an SiO_2 layer. For all materials involved, second-order and third-order material constants are available in the literature and have been used in the FEM calculations.

Results/Discussion

Results are presented for the displacement field and electric field in the resonators, associated with the second harmonic, as well as for the output voltage of the L-section at the second-harmonic frequency. The dependence of these quantities on the input frequency and on variations of the geometry of the resonators is analyzed in detail.

Consequences of the second-harmonic acoustic bulk wave for third-order intermodulations via cascaded second-order nonlinearity are also discussed.

[1] Y. Nakagawa, T. Dobashi, Y. Saigusa, J. Appl. Phys. 49, 5924 (1978).

[2] H.P. Grassl, L.Reindl, H.-W. Wörz, W.Ruile, Electron. Lett. 22, 1288 (1986).

[3] A. Mayer, E. Mayer, M. Mayer, P. Jäger, W. Ruile, I. Bleyl, K. Wagner, Int. Ultrason. Symp. Proc. 2016.

[4] M. Solal, K. Kokkonen, S. Inoue, J.B. Briot, B. Abbott, K. Gamble, Int. Ultrason. Symp. Proc. 2016.

5D-3

8:30 am **Lateral Mode Modeling and H2 Prediction of an FBAR Resonator Using an E-BVD Model**

Tao Yang[1], Zongliang Cao[1], David Feld[1]; [1]*Broadcom, USA*

Background, Motivation and Objective

Transmit filters comprising piezoelectric resonators are fabricated in a Thin Film Bulk Acoustic Resonator (FBAR) technology. A filter's 2nd harmonic emissions (H2), generated by the resonators in the filter's output stage must be sufficiently small to prevent the filter from desensitizing a nearby receiver. Anti-parallel and anti-series connected resonator configurations, in which the H2 emissions of a pair of resonators annihilate one another are often used to suppress such emissions. Such topologies are effective in suppressing H2 when the constituent resonators can be modeled as 1-D pistons. But certain resonators exhibit poorly suppressed lateral mode "rattle" behavior over a range of frequencies indicating that they can't be modeled as 1-D pistons. Such resonators produce 2nd harmonic emission "spikes" when they are excited over this same range of frequencies. When pairs of such resonators comprise H2-suppressing circuit configurations, tiny imbalances in the H2 spike emissions of each resonator prevent H2 annihilation. An effort to characterize and to model lateral modes and their corresponding H2 spike emissions in such resonators is warranted in understanding H2 emissions in filters.

Statement of Contribution/Methods

The S11 parameters of a poorly apodized square resonator were measured and fitted to an Extended Butterworth-Van Dyke (EBVD) model. The rattles of each branch were modeled using an L-C resonant tank circuit whose frequency, impedance, and Q were extracted using a fitting algorithm. The capacitor in each branch of the model was modified to include one global 2nd order non-linear parameter common to all branches.

Results/Discussion

As shown in Fig. 1a, the S11 parameters of the resulting 22 branch EBVD fit was in good agreement with measurement. A harmonic balance circuit simulator was used to simulate the H2 response of the EBVD model. By adjusting the global second order coefficient it was found that the simulated emissions could be brought into near perfectly agreement with the measured H2 as is shown in Fig. 1b.

This simple relationship between lateral mode rattles and H2 emissions in the square resonator has implications in modeling H2 in more complex resonator geometries found in the real world. We'll discuss how our methodology can be applied to understanding H2 emissions in the aforementioned H2 suppressing resonator configurations.

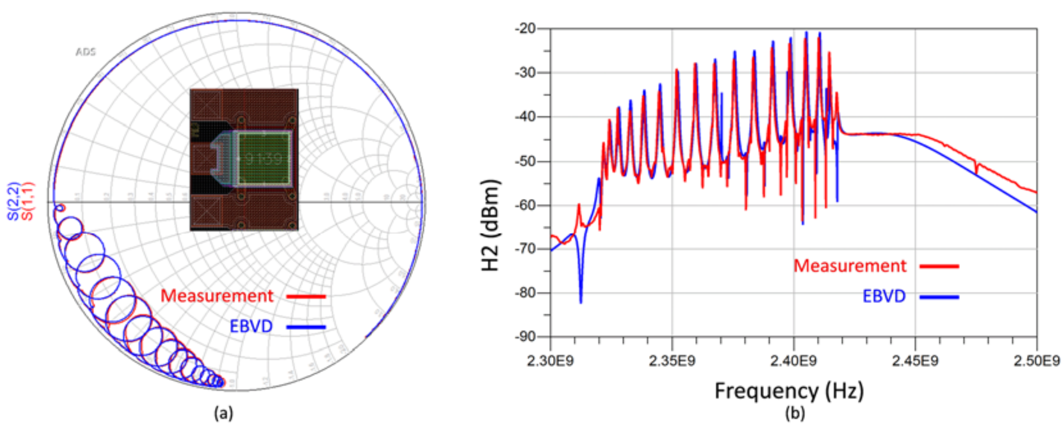

Fig. 1. (a) Fitted and measured S_{11} of a square FBAR. (b) Fitted and measured H2 emission of the square FBAR

5D-4

8:45 am **Improvement of Non-linear Performance in BAW Filters using Balancing Capacitors**

Susanne Kreuzer[1], Robert Aigner[1], Alexandre Volatier[1]; [1]*BAW R&D, Qorvo, Apopka, FL, USA*

Background, Motivation and Objective

The constantly rising demand for higher data rates is addressed by advanced communication standards like carrier aggregation (CA) in combination with LTE. The increased complexity of the RF frontend has put tremendous pressure on improving linear performance of BAW filters over the last years. On top of that a large number of intermodulation (IMD) specification have been added to safeguard all CA modes. It is obvious that improving intrinsic linearity on a filter level is of great advantage. Doubling up resonators in perturbing stages is a common approach to decrease non-linear contribution in a filter as power density in resonators decreases and – in theory – a perfect cancellation of non-linear

2nd order response occurs when the resonators are connected such that they operate in anti-phase. Focusing on cascaded resonator stages, the authors present a novel way to achieve improved cancellation so resonator stages exhibit an even more linear behavior than for the regular cascaded pair.

Statement of Contribution/Methods

Cascaded resonator configuration in BAW filters leads to an imperfect cancellation due to unavoidable asymmetry of parasitic effects. The lead connection and electrodes at the inner node of the cascade have an inherent parasitic capacitance to RF ground. The current flowing into this parasitic capacitance destroys the perfect amplitude and phase anti-symmetry required to achieve full cancellation of the 2nd order non-linear response. As a consequence linear and non-linear performance of the filter die deteriorate and spikes show up in the response. Using an accurate EM model of the filter die those parasitics can be predicted and a capacitor can be placed in the circuit to counter act the perturbing parasitic, thus re-balancing the situation. On-wafer H2 and IMD measurement were used to characterize the performance of the die with different balancing capacitors.

Results/Discussion

In this article we present the basic concept of a novel approach to linearize cascaded resonator stages in BAW filters using balancing capacitors. Part-to-part variation in the on-wafer measurements can be significant, nevertheless a statistical analysis clearly shows spike reduction using the balancing capacitors. Analysis of the impact of balancing capacitors on BAW filter dies using on-wafer H2 and IMD2 probing will be presented. Response variation due to the effect of non-identical resonator pairs in cascaded resonator stages will be discussed. The results are compared to EM simulation and are in good agreement with measurements.

5D-5

9:00 am Influence of Electrode Width of Interdigital Transducer on Third-order Nonlinear Signals of SAW Devices on 42°YX-$LiTaO_3$ Substrate

Ryo Nakagawa[1], Ken-ya Hashimoto[2]; [1]*Murata Manufacturing Co., Ltd., Japan,* [2]*Chiba Univ., Japan*

Background, Motivation and Objective

Recently, a generation mechanism of nonlinear signals of SAW devices is one of the most important topics in the RF front-end field, because essential improvement of linearity is strongly demanded to SAW multiplexers to realize the uplink inter-band carrier aggregation.

Statement of Contribution/Methods

In this study, we investigate the influence of the metallization ratio (w/p) of an interdigital transducer on the third-order nonlinearity of the SAW devices fabricated on 42°YX-$LiTaO_3$ substrates.

First, variation of acoustic strain in the Al electrode with w/p is estimated by 2D-FEM, and the third harmonic (H3) is estimated from integration of its cube. This is because the acoustic strain is considered as one of the predominant causes of the third-order nonlinearity. Then some test resonators with different w/p are fabricated and their linearity are compared with the simulation results.

Results/Discussion

Figure 1 shows variation of the calculated H3 with w/p relative to the value when w/p=0.5. This result shows that the H3 level decreases when electrode width is narrow.

Figure 2 shows variation of experimental H3 with w/p. In Fig. 2(b), the H3 level increases with increment of w/p in the case where w/p≥0.4. This behavior agrees with the estimation result by FEM well. When w/p=0.65, a steep peak appears at approximately 2.6 GHz. This peak is caused by coincidence of the third over-tone resonance to the output frequency of H3.

On the other hand, Fig. 2(a) shows that the H3 level increases with decrement of w/p when w/p≤0.4, and this phenomena can ft be explained by the simulation result in Fig. 1. This result indicates existence of another factor of third-order nonlinearity other than acoustic strain in Al electrodes.

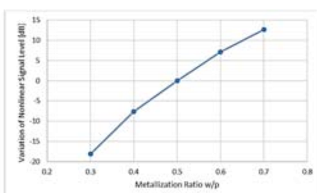

Fig. 1 Variation of nonlinear signal level with w/p on the basis of the value when w/p=0.5.

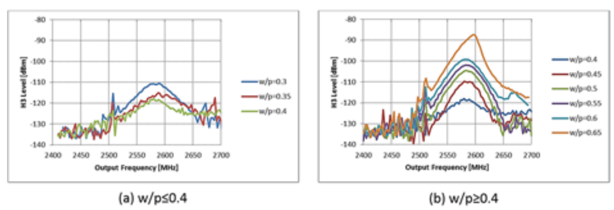

Fig. 2 Variation of H3 level with w/p (measured value).

5D-6

9:15 am FEM Modeling of an Entire 5-IDT CRF/DMS Filter

Victor Plessky[1], Julius Koskela[1], Balam Willemsen[2], Panagiotis Maniadis[2], Patrick Turner[2], Filip Iliev[2], Bob Hammond[2], Neal Fenzi[2]; [1]*GVR Trade SA, GORGIER, Switzerland,* [2]*Resonant Inc., Goleta, California, USA*

Background, Motivation and Objective

SAW filter technology includes different substrates, multilayered electrodes from Al, Cu, Pt, …, dielectric sublayers and over-layers, etc. Temperature compensated SAW filters have been developed that have performance competitive with FBARs. Traditional design tools, such those as based on COM models, demand experimental characterization of wave propagation parameters. FEM/BEM models cannot be easily adopted to new substrates and calculations are slow. The advantage of FEM methods is their remarkable generality. FEM can handle arbitrary materials and crystal cuts, different electrode shapes, and structures including multiple metal and dielectric layers. The main challenge in applying FEM to SAW devices has been unacceptably long computation times. Recently, we proposed "hierarchical cascading" FEM software called "Layers" [1], suitable for simulating any 2D SAW device with hundreds of electrodes with a speed of 1sec.- 4 sec. per frequency point on a 32 processor PC. Note that exact acoustic and electric field distributions can be calculated for all points of the device. A 5-IDT CRF/DMS TC SAW filter has been simulated using "Layers" [1]. In addition to the 10-port electrical network parameters for the filter, a visualization of acoustic field and power flow is presented (Fig. 1). Simulation reveals the resonances in the structure, radiation of energy at the interfaces between IDTs, and the origin of notches in passband including parasitic acoustic modes.

Statement of Contribution/Methods

We analyze the 10-port CRF device with passband frequency close to 1842.5 MHz including 5 IDTs, 8 "gap IDTs" and 2 reflectors. This TC SAW structure has a thick SiO2 over layer with 274 Cu electrodes on a 128° LiTaO3 substrate. We simulate 1601 frequency points and present acoustic fields, power flows inside the whole device for selected frequencies of interest and generated bulk waves.

Results/Discussion

Matlab software “Layers” was used for simulation of a 5-IDT CRF TC SAW filter and visualization of acoustic fields and power flows (Fig. 1). On a PC with 32 processors and 128 GB RAM, a device with 274 electrodes was simulated, with about 3 second simulation time per frequency point (1601 points in total). Losses due to bulk wave generation are estimated. Experimental results will be presented too.

[1] Koskela, J., et al. "Hierarchical cascading in 2D FEM ..." Ultrasonics Symposium, 2016.

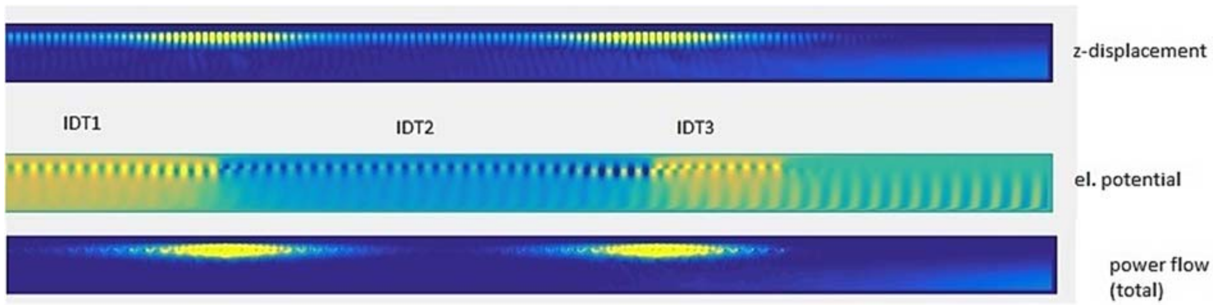

Fig.1 Vertical displacements, potential and power flow; left end corresponds to the center of symmetric 5-IDT CRF structure.

6D - Microfluidics

Hampton Room

Friday, September 8, 2017, 8:00 am - 9:30 am

Chair: **James Friend**
University of California, San Diego

6D-1

8:00 am **Shaping Acoustofluidic Landscapes to Profile and Separate Cells and Sub-micron Particles**

Per Augustsson[1]; [1]*Biomedical Engineering, Lund University, Lund, Sweden*

Background, Motivation and Objective

Acoustophoresis, where flow and acoustic fields are used to separate suspended objects, is getting increasingly more attention for cell and bacteria-handling applications relating to medicine and biology. Major benefits are flexibility in design, gentleness to cells and that relatively large forces can be exerted on suspended objects compared to competing technologies.

Two important features limit acoustophoresis. First, the strong size dependency hampers separation of cells based on the underlying properties density and compressibility. Second, the presence of acoustic streaming introduces a lower size limit of objects that can be manipulated by primary radiation forces.

To address these problems, we explore the action of acoustic fields on liquids of inhomogeneous acoustic properties which introduce stabilizing forces in the bulk.

Statement of Contribution/Methods

The work that I will present is primarily experimental but a theoretical framework is evolving which I will briefly touch upon.

Liquids of different acoustic properties are laminated side by side inside a microchannel and exposed to a standing wave field directed transversely to the flow. We then observe the acoustic migration of suspended cells or sub-micron particles that are seeded in the flow.

Results/Discussion

We show that cells and liquids re-organize themselves in a systematic way when exposed to an acoustic standing wave. This enables size-insensitive phenotype-specific separation of cells based on their acoustic properties. In this iso-acoustic focusing process liquids and suspended cells arrange themselves in a way that can be predicted from their effective acoustic impedances, Fig. 1.

We found that acoustic streaming in the bulk can be reduced by the stabilizing forces that arise in liquids of inhomogeneous acoustic properties. This enabled us to actively transport and concentrate 500-nm-particles and we also demonstrated fractionation of 1-µm-dimeter particles from 500-nm-particles in this streaming free acoustofluidic landscape.

The precise spatiotemporal control offered by microfluidics leads us to envision that the IAF method can be developed into tunable bio-particle profiling and separation platforms for particles ranging from a few hundred nanometers and higher.

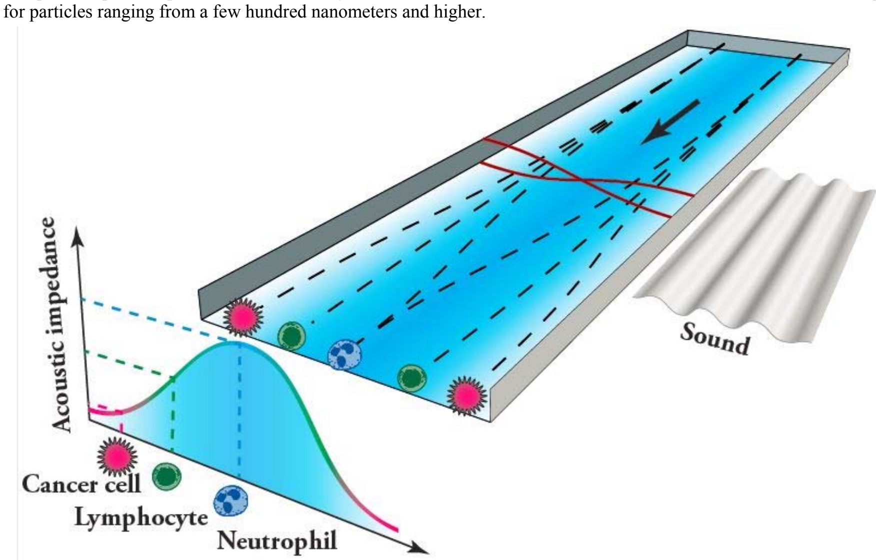

6D-2

8:30 am **Human Blood Cell Separation Using Bulk Acoustic Waves in a Machined PMMA Microchannel**

Erin Dauson[1], Kelvin Gregory[1], Irving Oppenheim[1], Kris Dahl[2]; [1]*Civil and Environmental Engineering, Carnegie Mellon University, USA,* [2]*Chemical Engineering and BioMedical Engineering, Carnegie Mellon University, USA*

Background, Motivation and Objective

In prior research we demonstrated the separation of particles using bulk acoustic waves coupled from PZT (lead zirconate titanate) transducers into a PMMA (poly (methyl methacrylate)) prism containing a microfluidic channel. By directing fluid flow at an angle to a standing acoustic node field this device creates a field of drag and acoustic forces that separates particle based on size and compressibility. In contrast to other microfabricated devices the strength of the PMMA core allows it to be interchangable and inexpensive.

Applying this technology to human blood cell separations in a high-throughput, low-cost, low-volume device has potential for a point-of-care diagnostic tool. Specifically, the separation of red blood cells (RBCs) from white blood cells (WBCs) enables diagnostic of systemic infections; the separation of RBCs by differential compressibility enables diagnosis of RBC infection including malaria.

Statement of Contribution/Methods

A 1.27 mm wide by 500 µm deep microchannel is machined on a rectangular prism of PMMA and bonded to a matched, flat prism to form a closed channel. The microfluidic channel, parallel to the prism edges prism at the inlets and outlets, lies at a 30 degree tilt angle. A pair of 1 mm thick PZT wafers excited at 6.74MHz create a standing acoustic wave field in the channel. Cells flowed via syringe pump are focused prior to separation both hydrodynamically and acoustically. P-waves travel through the PMMA and into the channel, refract at the tilted sides of the channel, and create standing acoustic node lines at an angle with respect to fluid flow. Simulations in COMSOL 5.2a inform device design and operation parameters.

Human blood is washed in phosphate buffered saline (PBS) to remove coagulant proteins. Less than 5 µL of blood is required per test. RBCs fixed with 3.7% formaldehyde and stabilized in 2% bovine serum albumin in PBS are used to test the effect of compressibility changes on cell trajectory through the device.

Results/Discussion

Our rapidly prototyped PMMA device, guided by simulation, has been shown experimentally to deflect or separate RBCs, stiffened RBCs, and WBCs through a tilted angle acoustic field, based on differences in cell sizes and compressibilities. This device, which is mechanically robust, inexpensive and modular has numerous potential biomedical applications.

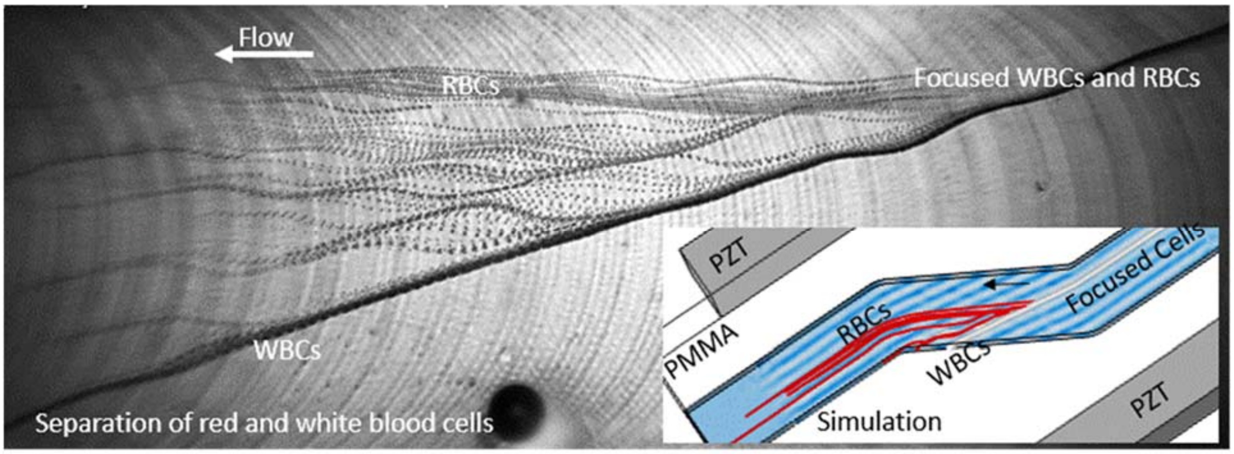

6D-3

8:45 am Prevent Lithium Dendrite Formation in Rechargeable Batteries ihrough Surface Acoustic Waves

Ann Huang[1], James Friend[1]; [1]*Center for Medical Devices and Instrumentation, University of California, San Diego, La Jolla, CA, USA*

Background, Motivation and Objective

Lithium (Li) has long been known to be the best anode material for rechargeable batteries, however, lithium **metal** batteries (LMB) have never been commercialized due to dendrite formation, resulting in thermal runaway and fire or explosion. During charging, Li ions deposit onto Li anode from the cathode via electrolyte. However, the deposition is not uniform due to the inhomogeneous ion distribution in the electrolyte from a thick Li ion depletion layer, typically >400 µm. Our objective is to reduce the diffusion layer from 400 µm to only 1 µm by using surface acoustic wave (SAW)-driven mixing flow of the electrolyte during charging and to prevent dendrite formation.

Statement of Contribution/Methods

We solve the dendrite problem in LMBs via an efficient, SAW-driven internal recirculation of the electrolyte during charging. In suppressing dendrite growth, we preserve the charge capacity of the battery. The small, 100 MHz single-crystal lithium niobate SAW device is compatible with lithium electrochemistry. By externally inducing the flow along the anode, we avoid interfering with the anode’s solid electrolyte interphase (SEI) layer that forms during use. Outside this 1 µm viscous boundary layer, the Li ion concentration is homogeneous: **dendrites are precluded**.

Results/Discussion

Rapid recharging of a SAW LMB at up to 0.8C (1.25 hr at 1.5 mA/cm^2) is now possible without dendrites. Thus, after 5 cycles, the SAW LMB retains 90% of the battery's *theoretical* 170 mAh/g capacity; after 50 cycles it retains 70%. A traditional LMB's capacity fades to only 40% after 5 cycles, as shown in Figure 1(a). Dendrites are a problem in the standard LMB as shown via a scanning electron microscope image in Figure 1(b); the dendrites are absent with SAW in Figure 1(c). Lastly, as shown in Figure 1(d), Li dendrites grow in a SAW-absent LMB regardless of charge rate, but upon application of SAW to reduce the Li ion concentration gradient, charge rates up to 85% of the maximum rate are possible without dendrites according to calculations based on convection-diffusion equations incorporating acoustic streaming.

This result indicates that, with application in an electric vehicle for example, the 280-mile range of a car using today's latest lithium-ion battery technology would be almost *doubled* to over 500 miles, with a reduction in battery cost of 20% per mile. Further, such a battery will charge in only 10 min.

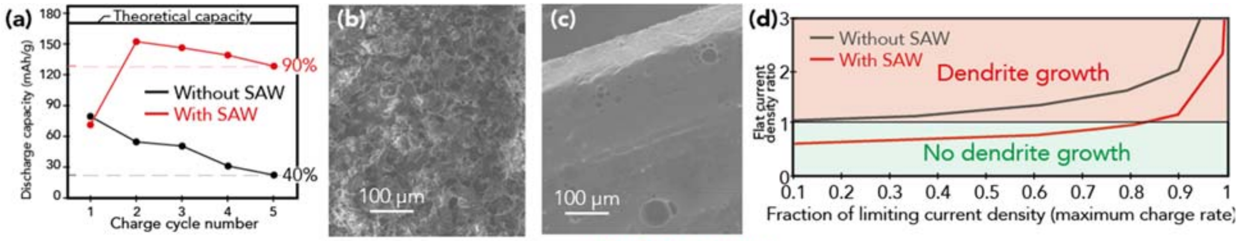

Figure 1. (a) The charging performance of an LMB cycled with SAW (red line): 90% capacity after 5 cycles. Without SAW (black line) it is only 40% after 5 cycles. SEM images of the Li anode charged (b) without SAW, Li dendrite is shown, while (c) with SAW, the Li anode remains pristine after 5 cycles. (d) Computed dendrite growth rate in a LMB without SAW, compared to with SAW to reduce the Li concentration gradient. Flat current density ratios of less than one imply no dendrite growth. Charge rates up to 85% of theoretical are possible without dendrite growth using SAW irradiation.

6D-4

9:00 am **A New Type Wide-Frequency-Range Shear Viscosity Sensor Using C-Axis Tilted ScAlN Thin Film on Temperature Stable AT-cut Quartz Thick Plate**

Yui Yamakawa[1], Kohei Sano[1], Rei Karasawa[1], Takahiko Yanagitani[1,2]; [1]*Waseda University, Japan,* [2]*JST PRESTO, Japan*

Background, Motivation and Objective

In order to study relaxation characteristics of viscoelasticity of the liquid, a wide frequency sweep in the range of MHz to GHz is desired. We, therefore, report a new type HBAR (High-overtone Bulk Acoustic Resonator: shear mode ScAlN film on AT-cut quartz plate) sensor which makes it possible to operate in a wide frequency range as shown in Fig. 1. When a thickness shear acoustic mode (TSM) resonator is in contact with a liquid sample, the shear wave penetrates into the liquid by the depth of δ (called penetration depth [1]). Thus, the liquid viscosity can be determined from the amount of the resonant frequency shift due to a δ thick mass loading layer mounted on the resonator. We choose AT-cut quartz as the substrate whose TCF is zero at room temperature to suppress frequency shifts due to the temperature change. TCF of the whole resonator stack greatly decreases considering the mass ratio between the thin piezoelectric film and the much thicker substrate. In this study, frequency shifts were measured for various concentration of glycerine solutions in order to demonstrate usefulness of the HBAR.

[1] T. Nakamoto and T. Moriizumi, Jpn. J. Appl. Phys., **29** 963 (1990).

Statement of Contribution/Methods

Viscosity standard liquids at 25°C were in contact with the HBAR in a thermostatic chamber. The real part of impedance *Z* of HBAR was measured by a network analyzer (Agilent Technologies, E5071C). Anti-resonance frequencies are determined from peaks of the Z.

Results/Discussion

Experimental TCF of the HBAR in air is -3.2 ppm/°C, which demonstrates the great decrease of TCF compared with single ScAlN films (-62 ppm/°C [2]) due to the zero TCF AT-cut quartz substrate. Fig. 2 shows the experimental frequency shifts. The tendency of resonant frequency decreasing caused by liquid viscosity increasing is observed. Overall, 97 wt.% data is estimated smaller than the theoretical curve, while 40 wt.% and 80 wt.% data show good agreement with the theoretical one, as shown in Fig. 3. This is probably because the viscomodel cannot represent the viscoelasticity of 97 wt.% glycerine. This HBAR sensor achieves the wide frequency measurement unlike other types of viscosensors such as QCM, FBAR, and SH-SAW.

[2] T. Yanagitani, K. Arakawa, K. Kano, A. Teshigahara, and M. Akiyama, in Proc. IEEE Ultrason. Symp., 2095, (2010).

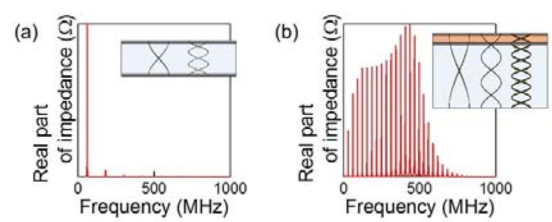

Fig. 1 Simulated results of resonant frequency peaks in (a)QCM and (b)HBAR

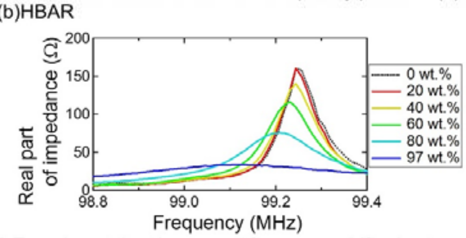

Fig. 2 Experimental anti-resonant frequency shifts due to the change in liquid viscosity

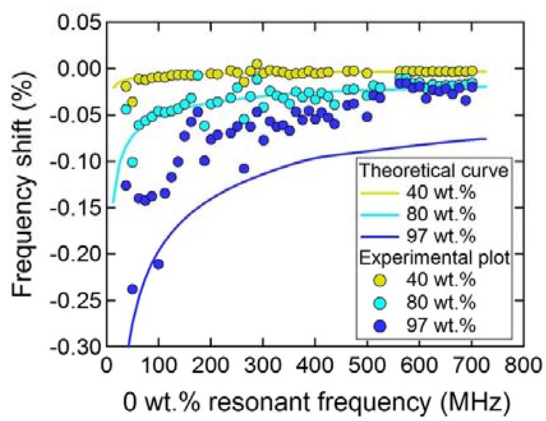

Fig. 3 Experimental and theoretical anti-resonant frequency shifts of HBAR in the case of 40 wt.%, 80 wt.%, and 97 wt.% glycerine solutions

6D-5

9:15 am **The Influence of a Background Flow on Acoustic Streaming**

Marcus A. Hintermüller[1], Erwin K. Reichel[1], Bernhard Jakoby[1]; [1]*Institute for Microelectronics and Microsensors, Johannes Kepler University, Linz, Austria*

Background, Motivation and Objective

The modeling of acoustic streaming problems is usually treated by using simulation schemes based on perturbation theory to reduce the computational effort, where a quiescent fluid is assumed in the unperturbed state. However, when considering situations and applications where a steady background flow is present, this zero-order field would directly influence the first- and second-order velocity fields of the perturbation expansion. The investigation of the associated impact on the acoustic streaming effect is the main objective of this contribution.

Statement of Contribution/Methods

Following the approach proposed in [1], we implement the zero- to second-order equation systems issuing from the perturbation approach using the ‘Weak Form PDE’ module of the commercial finite element software COMSOL Multiphysics 5.1. The whole simulation is split into three separate steps, (i) the stationary solution of the zero-order fields, (ii) the solution of the first-order fields in the frequency domain and (iii) the stationary solution of the second-order fields.

As our benchmark problem we investigate our previously reported design of a microfluidic pump based on boundary-driven acoustic streaming (Fig. 1 (a)) [2], and the streaming arising from a half-wavelength resonance in a fluid cavity (Fig. 1 (c)). A parabolic flow profile ranging from 10^{-1} - 10^{3} mm/s was introduced at the inlets, which represents the assumed background flow in the channel.

Results/Discussion

The results from the simulations (Fig. 1 (b) and (d)) show, that the background flow affects the acoustic streaming fields only at speeds that are unreasonably high compared to the dimensions of the investigated devices.

These results imply that the acoustic streaming effect can be computed independently from a background velocity. The total net flow can then be calculated from the superposition of the zero-order and second-order velocities (the first-order fields have a zero time average and do not contribute to the net flow).

[1] N. Nama, P.-H. Huang, T. J. Huang, and F. Costanzo, “Investigation of micromixing by acoustically oscillated sharp-edges,” Biomicrofluidics, vol. 10, no. 2, p. 24124, Mar. 2016.

[2] M. A. Hintermüller, B. Jakoby, and E. K. Reichel, “Acoustic Streaming via a Flexible PCB for Micropumping Applications,” Procedia Eng., vol. 168, pp. 856–859, 2016.

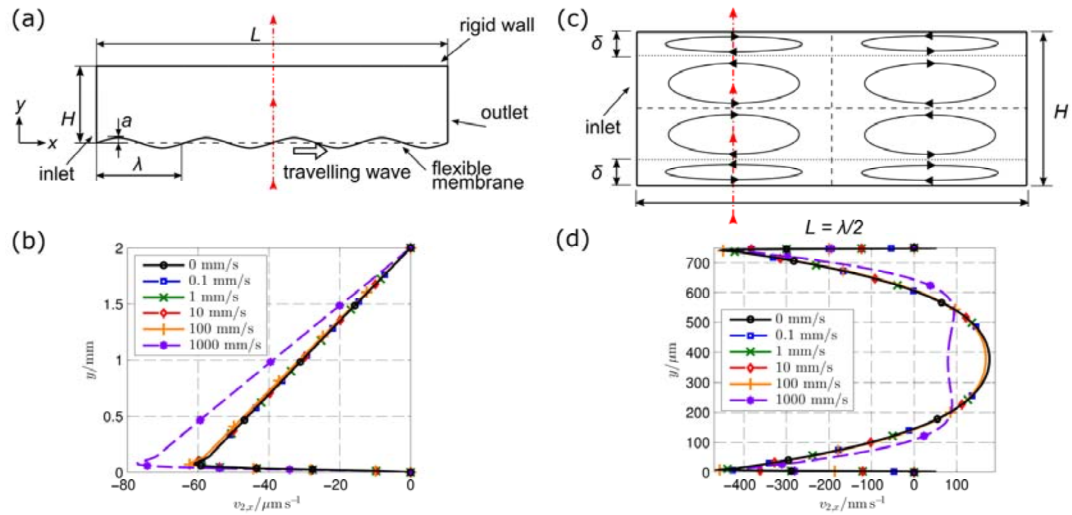

Fig. 1. (a) and (c) show schematic drawings of the considered geometries. (b) and (c) show the second-order velocity in *x*-direction along the red dashed-dotted lines in the schematics for different background velocities.

7D - Medical Ultrasound Devices and their Applications

Empire Room

Friday, September 8, 2017, 8:00 am - 9:30 am

Chair: **Christine Demore**
Sunnybrook Research Institute

7D-1

8:00 am Capsule Ultrasound Device: Characterization and Testing Results

Junyi Wang[1], Farah Memon[1], Gerard Touma[1], Spyridon Baltsavias[1], Ji Hoon Jang[1], Chienliu Chang[1], Morten Fischer Rasmussen[1], Eric Olcott[2,3], R. Brooke Jeffrey[2], Amin Arbabian[1], Butrus (Pierre) T. Khuri-Yakub[1]; *[1]Stanford University, Stanford, CA, USA, [2]School of Medicine, Stanford University, Stanford, CA, USA, [3]Veterans Affairs Palo Alto Health Care System, Palo Alto, CA, USA*

Background, Motivation and Objective

In order to overcome the limitations of conventional ultrasound endoscope, we propose to develop a capsule ultrasound (CUS) device: an ingestible and disposable pill to inspect the multiple layers of the entire gastrointestinal (GI) tract as well as its surrounding organs, and to provide a convenient method for diagnosing GI diseases, such as abdominal cancers and lesions. The CUS device is composed of three building blocks: the cylindrical capacitive micromachined ultrasonic transducer (CMUT) array, front-end electronics, and wireless transmitter. All of the components are functioning successfully and in this paper, we describe our characterization and testing results.

Statement of Contribution/Methods

To characterize the CMUT array, we measured its output pressure, center frequency, and frequency response using a hydrophone. In addition, we assessed the performance of the transmit (TX) and receive (RX) circuitries of the front-end electronics. For the TX channel, we tested the one-shot circuit and the unipolar pulser, and for the RX channel, we tested the transimpedance amplifier (TIA), time-gain-compensation (TGC) amplifier, and the analog-to-digital converter (ADC). The wireless transmitter has also been characterized. Currently, we are working on integrating the CMUT array with the front-end electronics and the wireless transmitter for imaging experiments.

Results/Discussion

We characterized the CMUT array by measuring its output pressure using the hydrophone. When biased at 20 V DC and provided with a 28 V unipolar pulse, the 3 dB bandwidth of the transmit signal was greater than 80%. Furthermore, all the major individual components of the TX and RX circuitries were tested. In the TX channel, the one-shot provided a tunable pulse-width with a frequency range of 4-6 MHz, which would drive the high voltage pulser to provide a unipolar pulse of up to 20 V. The RX channel included the TIA with a gain of 89 dB, the TGC amplifier with 25 ns recovery time when switching between five gain levels, and the 20 MSample/s ADC with SNDR of 46.5 dB. The wireless transmitter finally provided a data rate of 10 Mbps, and a measured BER < 10-5 for an expected link attenuation through more than 10 cm of body tissue.

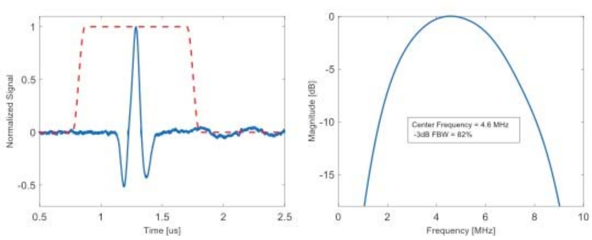

Figure 1: CMUT Transmit Pulse and Frequency Spectrum.

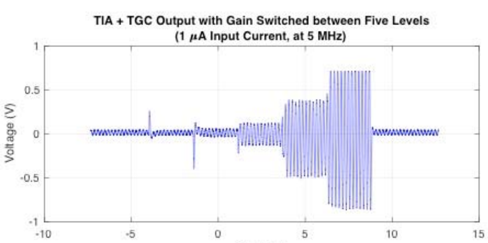

Figure 2: TIA and TGC Output

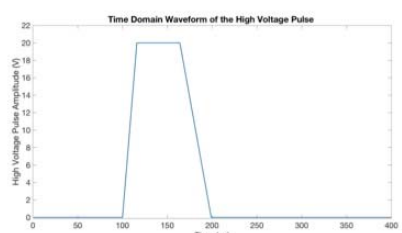

Figure 3: Pulser Output Piecewise Linear Fit Waveform

7D-2

8:15 am The Fabrication and Integration of a 15 MHz Array within a Biopsy Needle

Rachael McPhillips[1,2], David Watson[3], Jun Gao[3], Marc P.Y. Desmulliez[3], Sarah Vinnicombe[2], Sandy Cochran[1], Christine Demore[4,5]; *[1]Medical and Industrial Ultrasound Group, University of Glasgow, Glasgow, United Kingdom, [2]Division of Cancer Research, University of Dundee, Dundee, United Kingdom, [3]Multimodal Sensing and Micromanipulation Group, Heriot Watt University, Edinburgh, United Kingdom, [4]Physical Sciences, Sunnybrook Research Institute, Toronto, ON, Canada, [5]Medical Biophysics, University of Toronto, Toronto, ON, Canada*

Background, Motivation and Objective

Microultrasound is a real-time imaging modality that can resolve features <200 µm using frequencies of 15 MHz and above. While attenuation limits the penetration depth, incorporating a miniature transducer within a biopsy needle enables in vivo imaging of structures deep within the body. Imaging from the tip of minimally invasive needles has potential in applications in guiding intervention and tissue characterisation for diagnosis, for example, accurate navigation of interventional neurosurgical tools, and high resolution diagnostic imaging of breast lesions and axillary lymph nodes.

Statement of Contribution/Methods

In this paper, a 16-element, 15 MHz transducer array housed within a biopsy needle is presented. The approaches taken to overcome challenges in fabrication, interconnection and packaging are described along with relevant characterisation results. A fabrication process was developed to produce multiple 15 MHz array stacks from the micromachining of a single PIN-PMN-PT piezocrystal-polymer dice-and-fill composite plate. The array stack comprised a 118 µm thick composite and a cast alumina-epoxy quarter wavelength matching layer. For electrical connection to the array elements, a flexible printed circuit was bonded to the piezocomposite. Bonding with both isotropic and anisotropic conductive adhesives (ACAs) was tested. Array elements were defined with precision dicing and a alumina-epoxy backing cast in place after integrating the array in a 7G (ID 3.8 mm) biopsy needle. Electrical impedance and pulse echo measurements confirmed operation of each of the 16 array elements. Using an FI Toolbox array controller (Diagnostic Sonar Ltd, Livingston, UK) preliminary images of 20 µm wire targets were acquired.

Results/Discussion

Fabrication and characterisation results, Fig. 1, demonstrated the feasibility of producing transducers via small wafer-scale production for incorporation within needle packages. The suitability of such devices for minimally invasive microultrasound imaging and, potentially, *in vivo* characterisation of tissues has been examined. Work is underway to miniaturise the dimensions of such devices further and to create an automatic process for reliable bonding of the arrays to flexible circuits using ACAs.

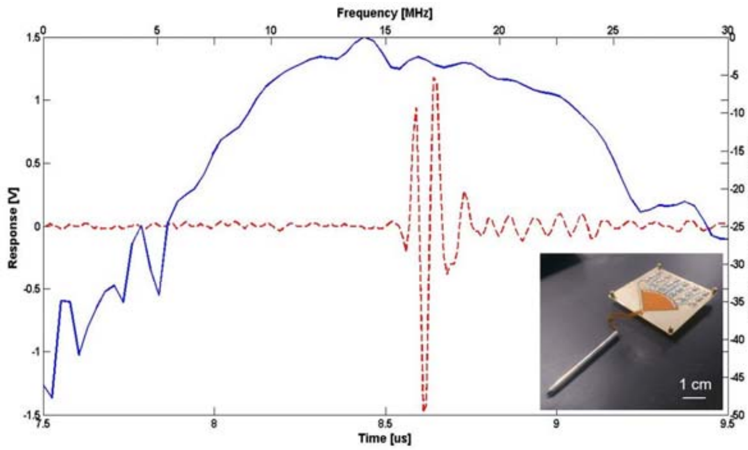

Figure 1. A pulse-echo response measured using element 6 as an example from the fabricated array. From this figure, a -6 dB fractional bandwidth of 78% is shown. The -20 dB pulse length for this element is approximately 0.1 µs. The inset image shows the completed needle device in a 7G breast biopsy needle (ID 3.8 mm).

7D-3

8:30 am Design of an Ultrasound Transducer for Continuous Fetal Heartbeat Monitoring¬

Assel Ryspayeva[1], Kenneth K. Andersen[1], Lars Hoff[1], Kristin Imenes[1]; [1]*Department of Microsystems, University College of Southeast Norway, Borre, Norway*

Background, Motivation and Objective

Stillbirth is when a baby is born without signs of life after 28 weeks of gestation. It is estimated that 2.6 million stillbirths occurred in 2015 [Lawn et al. 2016]. Today, the fetus is examined at regular hospital checks during pregnancy, but no checks are done between these hospital visits. These antenatal tests are not always effective to prevent stillbirth [O'Neill et al. 2012]. More frequent investigation of the fetal heart rate (FHR), preferably by the mother at home, may contribute to prevent stillbirth. FHR monitors using ultrasound Doppler are widespread, but can be difficult to use as they require frequent position adjustment [Wolfberg 2012]. The aim of this study is to investigate transducer solutions to make Doppler FHR monitors more robust against movements, making them suitable for home monitoring. The aim is to find a design that is portable, reliable, easy to use, and affordable for low-income countries.

Statement of Contribution/Methods

A model for the FHR monitor was set up in MATLAB using Field II, and analytical calculations were done to support the simulations. The FHR was estimated from simulated Doppler signals. The model was set to describe an average maternal size with a fetus in 28 weeks of gestation. In the 3rd trimester, the fetus normally lies with the head down as in Fig.1 (a). The transducer is placed at position 2, and only maternal movements are assumed to perturb the signal. If fetus switches to a head up position, the transducer is to be attached at position 1. Possible angle uncertainties due to transducer and fetus shifts are shown in Fig. 1 (b). Transducers with different values of focal length, aperture diameter and concave vs. convex shape were studied to find the optimum shape and beam pattern.

Results/Discussion

Concave, flat and convex transducer shapes with 2 MHz center frequency were studied, with diameters from 5 mm to 30 mm.Focal lengths for concave transducers were varied from 50 mm to 150 mm, while convex transducers with radii of curvature between 60 mm and 120 mm were studied. We found that the concave transducers lost the signal for an angle misalignment of 25°, while the convex transducer with a radius of curvature of 100 mm was robust for an angle deviation up to 40°. We found the best balance between signal strength and robustness to maternal and fetus movements was a convex transducer with a height & width of 10 mm & 30 mm and radius of curvature 100 mm.

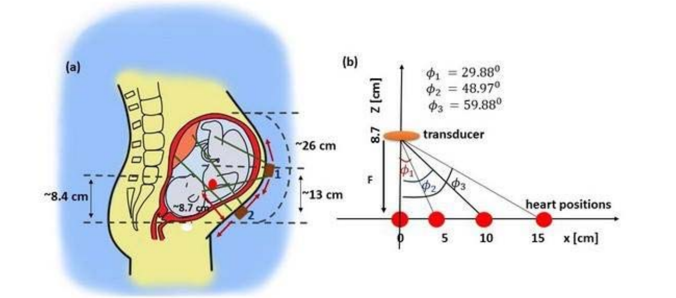

Figure 1: Schematic of a woman in the 28th week of gestation showing transducer at position 1 and 2 (a), misalignment between the transducer surface and fetal heart (b).

7D-4

8:45 am **Closed-Loop Ultrasonic Power and Communication with Multiple Miniaturized Active Implantable Medical Devices**

Max Wang[1], Ting Chia Chang[1], Marcus Weber[1], Jayant Charthad[1], Sawson Taheri[1], Amin Arbabian[1]; [1]*Electrical Engineering, Stanford University, Stanford, CA, USA*

Background, Motivation and Objective

Networks of miniaturized implantable medical devices (IMDs) capable of operating deep in the body are crucial for many novel diagnostic and therapeutic applications. An external portable base station to power, coordinate, and communicate with IMDs can enable these networks. Ultrasonic (US) wireless power transfer is utilized to shrink device dimensions, raise available power, and increase operation depth due to its small wavelength and low attenuation in the body. Building on previous demonstrations of US-powered IMDs for neuromodulation and active communication, we investigate and design an US linear array base station to interface with multiple implants. This allows for programmable focusing for multi-access control and higher power transfer efficiency (PTE), as well as bidirectional communication for closed-loop operation.

Statement of Contribution/Methods

A linear array, operating around 1 MHz, is designed with piezoelectric transducers on a printed circuit board with optional air backing for increased transduction efficiency. The array is driven by front-end electronics with both transmit and receive capabilities including variable-gain amplifiers and analog-to-digital converters. The system controller and beamforming are designed and implemented on a field-programmable gate array (FPGA). To determine the PTE and robustness of the system, we test its operation in an acoustic tissue phantom. The beam steering and bidirectional communication are also demonstrated using previously developed US-powered active IMDs.

Results/Discussion

Simulations of the design revealed the optimal size and spacing for 8-64 element linear arrays capable of focusing at least 5 cm away, beam steering at least 40°, and delivering up to the diagnostic US intensity limit. The measured intensity from the US base station shows a steerable focus and programmable intensity for simultaneous power and communication. High conversion efficiency is achieved using IMDs with US receivers, resulting in efficient wireless power transfer. Interfacing with multiple implants is shown by beamforming to one implant at a time, activating its sensor or stimulator, and extracting data. Thus, a closed-loop multi-access system is demonstrated, enabling the development of coordinated sensing and treatment deep in the body.

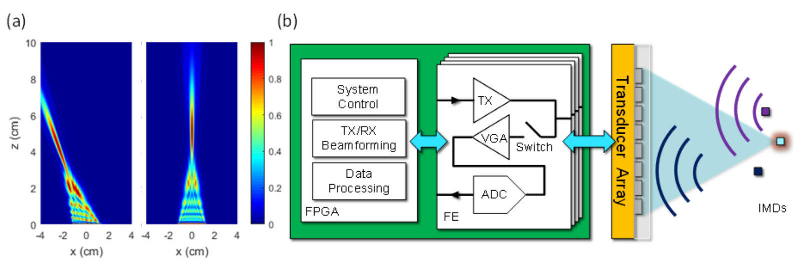

Fig. 1 (a) Simulated normalized intensity from ultrasonic beam steering 30° (left) and 0° (right) with 1 dB/MHz/cm attenuation using a 32-element array (0.5 mm width and 0.8 mm pitch) at 1 MHz. (b) Diagram of the system architecture showing beamforming, multi-access, and active communication.

7D-5

9:00 am **Regulation of Medical Ultrasound Devices in the United States of America**

Keith Wear[1]; [1]*Food and Drug Administration, USA*

Background, Motivation and Objective

In the United States of America, the Food and Drug Administration is the government agency responsible for regulating medical ultrasound devices. The objective of this presentation is to give an overview of current FDA regulatory activities regarding ultrasound devices for diagnostic and therapeutic applications.

Statement of Contribution/Methods

Medical devices are classified into three classes: I, II, and III. Classification depends on risk, intended use, indications for use, and other factors. Most diagnostic ultrasound imaging systems are class II and therefore require a 510(k) for marketing. The objective of a 510(k) submission is to demonstrate that a device is substantially equivalent, in terms of safety and effectiveness, to a predicate device that is already legally marketed in the United States. Therapeutic ultrasound devices may be class II or class III. Class III devices require premarket approval (PMA). The objective of a PMA submission is to demonstrate the safety and effectiveness of the class III device. For most medical ultrasound devices, an important component of the FDA submission involves measurement of acoustic output, which is often accomplished with hydrophones.

Results/Discussion

The FDA regulatory framework is applied to a variety of medical ultrasound devices of current interest including conventional imaging systems, tomographic imaging systems, point-of-care ultrasound systems, high-intensity therapeutic systems, low-intensity therapeutic systems, devices that utilize ultrasound-based data and power transfer to implants, neuromodulation devices, and microbubbles.

1E - MBF: Cerebrovascular and Microvascular Imaging

Regency Ballroom

Friday, September 8, 2017, 10:30 am - 12:00 pm

Chair: **Matthew Bruce**
University of Washington

1E-1

10:30 am Functional Ultrasound Imaging in Awake Non-Human Primates Performing Voluntary Saccade

Alexandre Dizeux[1], **Marc Gesnik[1]**, Nicolas Wattiez[2], Thomas Deffieux[1], Pierre Pouget[2], Mickaël Tanter[1]; [1]*Institut Langevin, ESPCI, CNRS, INSERM, Paris, France,* [2]*Institut du Cerveau et de la Moelle épinière, INSERM, CNRS, UPMC, Paris, France*

Background, Motivation and Objective

Functional ultrasound (fUS) is a novel technique for in vivo neuroimaging which allows to map subtle changes of the Cerebral Blood Volume (CBV) due to neurovascular coupling with a very high sensitivity, and thus map dynamics of brain activity [1].In this study, we apply fUS to awake and behaving non-human primate to investigate the monitoring of saccadic eye movement by the supplementary eye field (SEF) brain region [2]. This represents the first fUS images in non-human primate, doing complex tasks, which generally remains very challenging to perform in an MRI environment in awake and behaving conditions.

Statement of Contribution/Methods

2 trained captive-born macaques (Maccaca Mulatta) performed in a row, baseline (rest phase), fixation, pro-saccade and anti-saccade trials in a blocked design of 60s each (~ 20 trials/task) and this block of 300s was repeated 5 times. A 1 kHz infrared video eyetracker (Eyelink 1k, SR-Research) enables live control and delivery of reward based on success of visual task. CBV is measured with a linear ultrasonic probe (128 elements, 15 MHz, 0.11 mm pitch, Vermon, France) driven by an ultrafast research scanner and taking advantage of an existing cranial window used for electrophysiology measurements.

During the 300s of task, the brain is continuously insonified with a frame rate of 500 frames/s. Each frame is a coherent compounding of 8 plane waves with a 20 kHz pulse repetition frequency. After high-pass filtering and incoherent summation, the 600 CBV images are correlated with the task pattern to extract the activated areas. The CBV time course for a given region is obtained by averaging the signal over the responding pixels.

Results/Discussion

As presented in figure, for both primates, bilateral SEF regions show a strong increase of CBV between 30 to 70% compared to rest with pro-saccade movement phase. Similar responses were observed when comparing anti-saccade task with baseline condition. However, no significant variation of CBV were observed in SEF when comparing anti or pro-saccade to fixation tasks.

This confirm the crucial role of SEF in processing information about oculomotor goals and relationship between actions and their outcomes. In that perspective, fUS represents an imaging modality able to monitor complex cognitive tasks in awake behaving primate with high spatial resolution.

[1] Macé E, *Nat. Methods* (2011)
[2] Pouget P, *Eye* (2015)

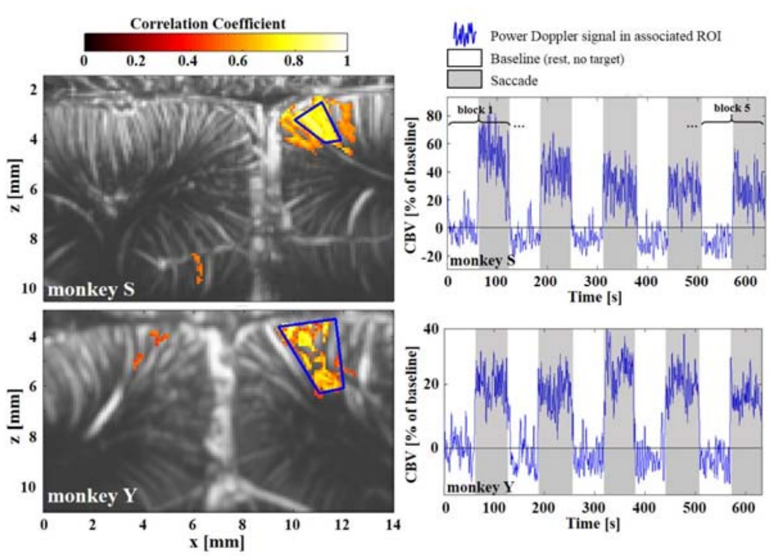

Figure: fUS imaging of SEF activity for both monkeys while performing complex visual task (Left). Activated pixels are related to regions where variation of cerebral blood volume correlates temporally with visual stimulus pattern. These correlations are superimposed (hot scale) to brain vasculature (gray scale). Activation was considered significant for a correlation r > 4σ, where σ is the spatial standard deviation of correlation values from non-active areas of the correlation map. Power Doppler signal was averaged in ROI, delineated by the blue quadrilateral, and plot against time and superimposed to visual stimulus pattern (Right). Similar patterns of activation were observed comparing rest phase with other visual tasks (fixation and anti-saccade).

1E-2

10:45 am Background-Free Visualization of Microvasculature Networks

Mahdi Bayat[1], Mostafa Fatemi[1], Azra Alizad[2]; [1]*Physiology and Biomedical Engineering, Mayo Clinic, USA,* [2]*Radiology, Mayo Clinic, USA*

Background, Motivation and Objective

Recent studies have shown the ability of concurrent spatial-temporal processing methods such as singular value decomposition (SVD) filtering in visualization of the small vessels without using any type of contrast agents. The vessel images resulting from SVD filtering suffer from local and global residual background that limit the visibility of the entire vessel networks within a fixed dynamic range. This mainly stems from ultrasonic intensity variations which are not accounted for in obtaining dominant singular values representing clutter signals. In this study, we present a novel approach for removal of local and global background signals and enhancement of the vascular objects. The final images present superb vessel background separation and make them suitable for further processing such as quantitative morphology analysis.

Statement of Contribution/Methods

With informed IRB consent, plane wave imaging using 5-angle compounding was performed on a patient with a malignant thyroid nodule using Alpinion Ecube-12R (Alpinion, Soul, South Korea) at 608fps for 3 seconds. A L3-12H transducer (ALPINION Medical Systems, Seoul, Korea) was used at 11.5MHz. SVD filtering was used for tissue clutter removal, creating gross microvasculature image after excluding first 1200 largest eigenvalues (out of 1824). A global top-hat morphology filtering with a disk structuring element (size: 347μm) was used to remove local and global background signals. A multi-scale Hessian-based vessel filtering was used to promote tubular structures with sizes less than 347μm and penalize random unstructured residual background.

Results/Discussion

Fig.1(a) shows the B-mode image of a malignant thyroid papillary carcinoma nodule. The SVD-filtered, top-hat filtered and, multi-scale Hessian based filtered images are shown in Fig.1(b), (c) and (d) respectively. The local and global background removal achieved by the top-hat filtering is evident in Fig.1(c). The Hessian-based filtering has considerably enhanced the vessel visibility, smoothness and continuity of the microvasculature network without scarifying spatial resolution as seen in Fig.1(d). The final image is mostly background-free and ready for additional processing such as morphology analysis which might reveal information about disease induced morphology changes in the underlying microvasculature network.

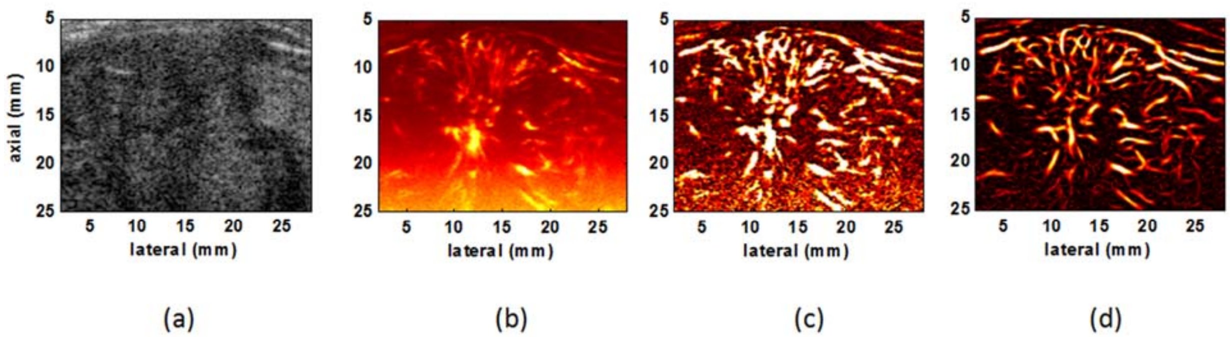

Figure 1: (a) B-mode image of a malignant thyroid papillary carcinoma nodule (a) SVD-filtered image (b) top-hat filtered image and (c) multi-scale Hessian-based filtered image

1E-3

11:00 am 3D Functional Ultrasound Imaging of the Visual System in the Pigeon Brain

Richard Rau[1], Wolfgang Scheffer[1], Markus Belau[1], Pieter Kruizinga[2], Nico de Jong[2,3], Johan G. Bosch[2], Georg Maret[1]; *[1]University of Konstanz, Germany, [2]Thorax Center, Erasmus MC, Rotterdam, Netherlands, [3]Faculty of Applied Sciences, Delft University of Technology, Delft, Netherlands*

Background, Motivation and Objective

Recently, a new functional neuroimaging method called fUS was proposed, which is based on high-frame-rate Power Doppler imaging. So far, fUS has only been performed on rodents, but major issues in neuroscience such as cerebral asymmetries and language learning are mainly studied in birds. Here, we show the first successful fUS measurements on a non-mammalian species without cortical brain architecture, such as pigeons. These measurements are based on a framerate enhanced fUS acquisition algorithm, which was necessary to suppress the signal variations originating from the slower heartrate of pigeons.

Statement of Contribution/Methods

The study was carried out on anesthetized healthy pigeons (columba livia domestica) with a thinned skull (isoflurane narcosis). The stimulation pattern consisted of unilateral flickering (5Hz) LEDs, ~5.5cm away from the eye (15s on / 30s off). A 128-element linear array probe (L22-14v, Verasonics) operating at 16MHz was used. The probe was connected to a fully programmable ultrasound system (128 chan. Vantage, Verasonics). The fUS signal was recorded continuously at a transmission rate of ~11kHz (36 angled plane waves and ensemble length of 160 per Power Doppler image), making use of a dedicated beamforming and SVD filtering algorithm on the graphics processing unit (GPU) using Matlab 2015a. For the 3D datasets, we acquired 21 slices using a manual translation stage, 500μm apart, and evoked a response in each visual wulst by stimulating the contralateral eye.

Results/Discussion

Fig.1a shows an evoked response of ~6% cerebral blood volume change by contralateral stimulation, whereas the ipsilateral control signal remains at the baseline level. The signals correspond to the mean Power Doppler intensity in the regions of interest (ROI) marked in Fig.1b. The activity map overlay (correlation coefficient with stimulus pattern) in Fig.1b shows that the spread of activation within the fUS measured brain slice can be robustly evaluated with values up to $r \cong 0.4$. In Fig.1c, the whole activated visual wulsts (red/green regions) in the pigeon brain are revealed in 3D, where only $r > 0.2$ is shown. The activity resulted as a response to contralateral visual stimulation and has volumina of (6.4 ± 0.3) mm³ (right hemisphere) and (8.7 ± 0.4) mm³ (left), respectively. Future work will concentrate on characterizing the cerebral asymmetries in more detail.

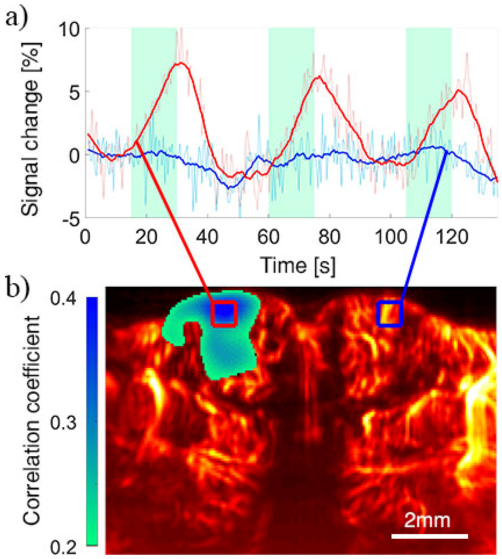

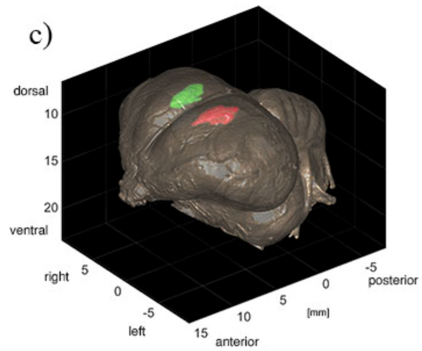

Fig 1. a) shows the response in the left (red) and right (blue) visual wulst evoked by stimulating the right eye. Green bars indicate the period of stimulation. **b)** Power Doppler image with ROIs corresponding to signals in **a**. The green/blue gradient overlay shows the area of activity (correlation coefficient with stimulus pattern). **c)** The activated regions (red /green) in 3D from 21 fUS image slices were detected by contralateral visual stimulation. For better comprehension they are shown within a pigeon brain surface map (grey).

1E-4

11:15 am ***In vivo*** **Imaging of Blood Flow in Murine Brain using Angular Coherence Methods**

Marko Jakovljevic[1], Lotfi Abou-Elkacem[1], Dongwoon Hyun[1], Jason Yoon[1], You Li[1], Jeremy Dahl[1]; [1]*Radiology, Stanford University, Palo Alto, CA, USA*

Background, Motivation and Objective

Recently, ultrafast Doppler techniques have been proposed for imaging brain and other slow flow targets. These techniques rely on synthetic focusing and the use of large ensemble lengths to separate slow-flow signal from the stationary clutter, but are susceptible to high acoustic and thermal noise. We have recently developed the short-lag angular coherence (SLAC) method, which suppresses the incoherent portion of the beam-summed signals and utilizes fast beamforming techniques for processing large Doppler ensembles. Here, we demonstrate SLAC-based PD by imaging blood flow in the brain of a mouse through the intact skull and show improved sensitivity compared to conventional PD.

Statement of Contribution/Methods

Plane-wave Doppler data was collected on a mouse brain using a Verasonics L12-3v linear array attached to a Verasonics Vantage 256 research scanner. Plane waves were transmitted with a 9 MHz center frequency and at a rate of 2100 Hz over 7 angles, resulting in a Doppler PRF of 300 Hz. Spatiotemporal filtering was used to remove stationary tissue signal from the individual Doppler frames. The angular coherence function between the 7 angles was computed from the filtered beam-summed data. Matched conventional PD and SLAC images were created from the filtered data and the angular coherence function, respectively, as a function of ensemble length. Doppler signal-to-noise ratio (SNR) was calculated from the vasculature in the mouse brain. Control data was also collected from a phantom with a 200 um-vessel under ideal imaging conditions.

Results/Discussion

Sample *in vivo* images acquired from the mouse brain are shown below. The Doppler images are reconstructed from 300 and 200 frames using conventional PD and SLAC-based PD methods, respectively. The B-mode image is created from a single frame of data and indicates the region of brain used for Doppler reconstruction (red rectangle). The transverse sinus vein is visible in both Doppler images, but the SLAC image shows improved delineation of the vessel and reduced noise in the lower part of field of view. Doppler SNR is computed for the lower part of the vessel and is plotted as a function of Doppler ensemble length. SNR in the SLAC-based PD images is up to 4 dB higher than in the matching conventional PD images. The results suggest that angular coherence processing can be used to reduce ensemble length and improve Doppler frame-rate.

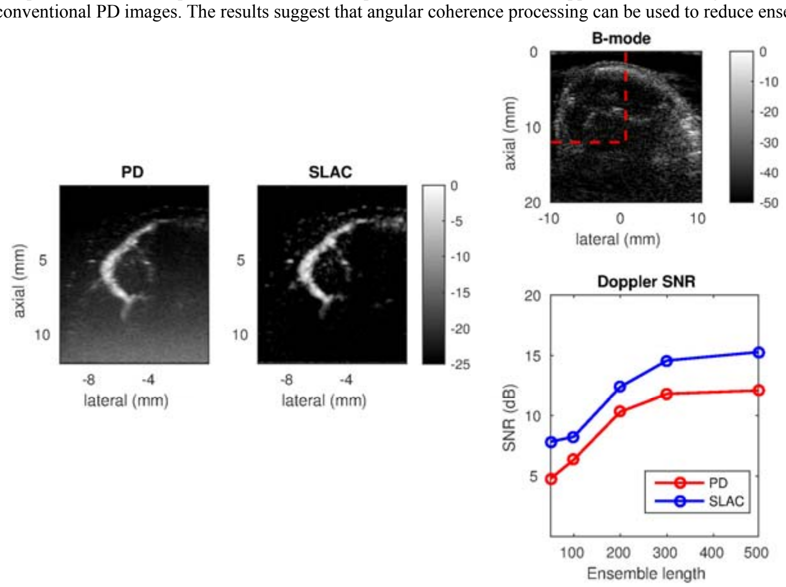

1E-5

11:30 am Functional Ultrasound (fUS) Allows Measurements of Cerebral Blood Volume Response Delays

Marc Gesnik[1], Kevin Blaize[2], José-Alain Sahel[2], Mathias Fink[1], Thomas Deffieux[1], Jean-Luc Gennisson[1], Serge Picaud[2], Mickaël Tanter[1]; [1]*Institut Langevin, ESPCI, France,* [2]*Institut de la Vision, Paris, France*

Background, Motivation and Objective

Functional ultrasound (fUS) imaging of the brain is a novel technique for *in vivo* neuroimaging which can acquire and map the cerebral blood volume (CBV) with a very high sensitivity. While fUS has demonstrated its ability to map cerebral activity through CBV subtle changes due to neurovascular coupling, [1], its temporal resolution has yet to be fully exploited. On the other hand, recent neuroscience studies point cerebral hemodynamic delays as a promising cerebral biomarker [2].

In this study, we leverage the high temporal resolution of fUS, within the framework of visual stimuli, to detect CBV response delays between vision involved structures.

Statement of Contribution/Methods

In vivo experiments were performed on anesthetized (Ketamine 60mg/kg, Domitor 0,4mg/kg) and trepanned rats. A 15MHz ultrasonic probe (128 elements, 0.11mm pitch, Vermon, France) driven by an ultrafast research scanner is placed on top of the brain over a coronal cross-section containing visual areas thanks to a motorized system (PI micos, VT80). The ultrasonic sequence consists in 5 min and 30s acquired at 500 frames/s. Each frame is a coherent compounding of 11 plane waves with a 20 kHz pulse repetition frequency. Acquired data are high-passed filtered to get the spatiotemporal CBV, and correlated with the episodic stimulus pattern to recover the vision-activated areas. The CBV signal is averaged over cortical and sub-cortical visual areas. The CBV response delays are obtained with parabolic interpolation of the maximum of correlation between these two signals [3].

Results/Discussion

The cross-correlation curves between Superior Colliculus (SC) and visual cortex (V1/V2) show that the response in SC arises earlier than in V1/V2. We repeated the measurement on 8 rats and found significant delays of 0.35s ($p<0.001$).

On one rat, we performed a fUS measurement in 6 coronal slices from Bregma -6mm to Bregma -3.5mm, and measured the response delays between the sub-cortical structures and V1/V2 and found a mean delay of 0.37s ($p<0.001$) consistent with the single slice measurements.

This work demonstrates the ability of fUS to measure consistent cerebral hemodynamic response delays between coactivated brain structures.

[1] Macé E, *Nat. Methods* 2011

[2] Siegel JS, *JCBFM* 2015

[3] Carter G.C., *Proc. IEEE*, 1987

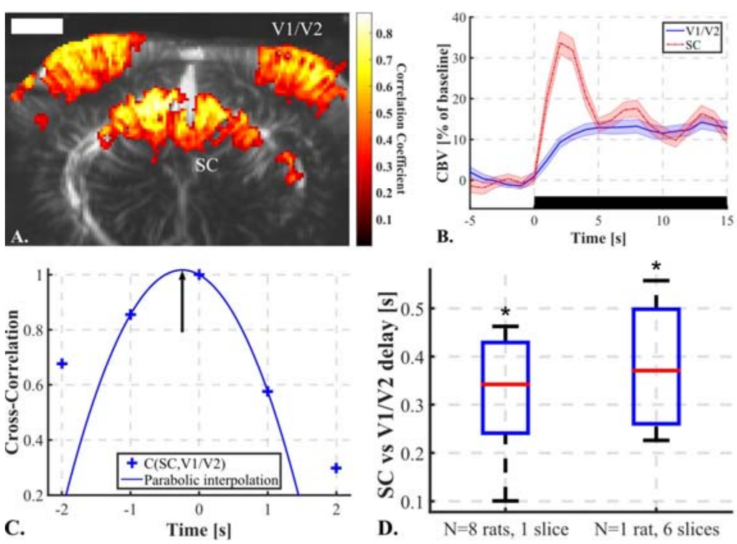

Figure: CBV response delay measurement using fUS. A. Visual areas responding to an episodic visual flickering stimulus in coronal cross-section at Bregma -5.5mm. Visual cortex (V1/V2), and Superior Colliculus (SC). Scale bar = 2mm. B. Average CBV response curves to the stimulus in V1/V2 (solid blue line) and SC (dashed red line) to N=30 stimuli. V1/V2 seems to respond earlier. Error: SEM. Black rectangle = Stimulus. C. Example of cross-correlation curve between the CBV responses to 5 successive stimuli in SC and in V1/V2. Experimental data points (blue crosses) interpolated by a parabol (solid blue line) show a maximum happening shortly before t=0s (black arrows). This allows the measurement of the delay of activation between SC and V1/V2. D. CBV response delays measured between SC and V1/V2 (N=8 rats) in the Bregma -5.5mm coronal slice (left), and between SC and V1/V2 in 6 different coronal slices for the same animal (right). Both series show a significant non-zero delay *$p<0.001$.

1E-6

11:45 am Visualization of Blood Flow in Brain Tumor in Small Animal with Ultrafast Ultrasound

Yi Yang[1], Jingjing Xia[1], Chenwenbao Hu[1], Rui Meng[1], Qiuju Jiang[1], Rong Liu[1], Hairong Zheng[1], Weibao Qiu[1]; [1]*Shenzhen Institutes of Advanced Technology, Chinese Academy of Sciences, Shenzhen, China, People's Republic of*

Background, Motivation and Objective

How to precisely evaluate the characteristics of glioma tumor *in vivo* is a challenging question for surgical resection clinically. Due to the infiltration feature of the tumor, precise resection remains challenging because of the uncertainties of surrounding vasculature. The sensitivity of flow measurement is improved by ultrafast plane-wave imaging which is capable of delineating the flow information in the brain. In this study, we first time visualize the blood flow distribution of glioma tumor in a small animal with plane-wave Doppler ultrasound imaging method, yielding highly resolved neurovascular map of the glioma.

Statement of Contribution/Methods

Fig. 1 shows the general illustration of our experimental setup and data acquisition scheme. The experiment object was the C6 glioma rat model. All imaging data were acquired by a Verasonics Vantage system (Verasonics Inc., Redmond, WA, USA) with a linear array transducer (L15-128, Center frequency of 15 MHz, 128 elements, 0.1 mm pitch, Vermon, France). We developed a plane-wave imaging sequence of 11 tilted angles for coherence compounding with a total degree of 21^{o} to scan the entire brain at a pulse repetition frequency of 3000 Hz. We transmitted three pulses at each transmission and received the echoes three times for averaging to reduce background noise. Then the averaged signal was considered as the final echo for delay-and-sum beamformer process to form an image at one tilted angle.

Results/Discussion

The glioma rats were performed with the T2-weighted MRI scan one day before conducting the ultrasound imaging. Because of the low resolution of MRI, there is no flow information can be acquired (Fig. 2(a, b)). However, after a series of post-processing of the ultrasound images, the high-resolved vasculature images shown in Fig. 2(e, f) have been acquired. In Fig. 2(e), comparing to the normal regions in the images, the flow format of the tumor region presents more flow and curved segments. In addition, the different tumor growth period may lead to quite different blood flow distributions in the tumor region. The tumor which has grown a longer time (Fig. 2(f)) may possess poor blood flow in the center according to the results. As a conclusion, the proposed pane-wave imaging method is able to visualized detailed flow information of the glioma tumor, which would be a valuable tool for characterization of the tumor.

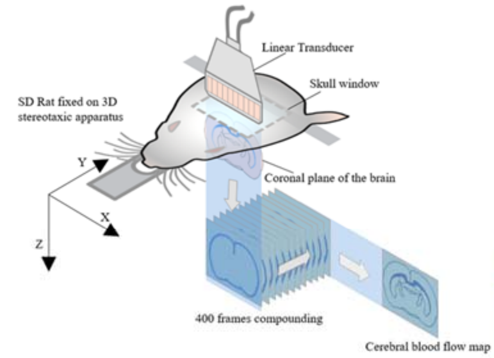

1

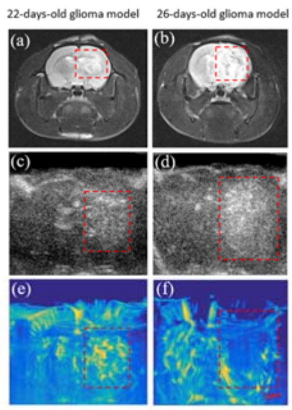

2

1. The framework diagram of this study shows the principle of the plane wave Doppler imaging.
2. Comparison between MRI, plane-wave B-mode images and plane-wave ultrasound Doppler images for the brain tissue with glioma tumor. Fig. 2(a, c, e) present the images of the 22-days-old glioma rat model and Fig. 2(b, d, f) present the 26-days-old one.

2E - MSD: Towards Real-Time 3D Imaging

Ambassador Ballroom

Friday, September 8, 2017, 10:30 am - 12:00 pm

Chair: **Steven Freear**
Univ. of Leeds

2E-1

10:30 am **Next-Generation Ultrasound Research Scanners Design**

Piero Tortoli[1], Enrico Boni[1], Luca Bassi[1], Alessandro Dallai[1], Francesco Guidi[1], Alessandro Ramalli[1], Stefano Ricci[1]; [1]*Information Engineering, Università di Firenze, Firenze, Italy*

Background, Motivation and Objective

In a few years, ultrasound research platforms, also known as open scanners, have become a great tool for facilitating the experimental activities of ultrasound labs. An ideal platform should be easily programmed to permit the transmission of arbitrary sequences of arbitrary waveforms, the acquisition of huge amounts of raw echo-data, the visualization of the region of interest and, possibly, the real-time implementation of novel processing methods. In this talk, the design criteria followed in the recent development of our 256-channel research scanner, ULA-OP 256, to meet such requirements, are reported, and some illustrative applications are presented.

Statement of Contribution/Methods

Differently from open scanners that adopt a software approach, based on the acquisition of raw data through high-speed parallel links followed by elaboration performed by Graphical processing units (GPUs), ULA-OP 256 was designed to permit continuous real-time processing of data before their transmission to a host CPU. The system core is the front-end board (FE), which embeds the electronics needed to manage transmission, beamforming and processing for 32 channels. 8 FEs are connected through a high throughput serial link in a closed ring architecture, to permit the real-time full control of 256 active probe elements. A high speed multi-line parallel beamformer is implemented in one FPGA, while two DSPs are usually in charge of operations like beamformed data demodulation and compounding. A further board, the Master Control board, hosts another DSP, which collects the data from all the FEs and performs custom elaboration functions like B-Mode or Multigate Spectral Doppler. The board is connected to a PC through an USB3.0 super-speed link. A control software shows in real-time the elaboration results.

Results/Discussion

The ULA-OP 256 scanner can be programmed to satisfy the requirements of different applications. The capability of transmitting arbitrary sequences and waveforms is fundamental in the multi-line transmit modes used in cardiac imaging. Here, up to 16 beams are transmitted into different directions and real-time high frame rate (HFR) imaging is obtained thanks to the FPGA-based parallel beamformer. The same beamformer can be exploited in association with the transmission of plane waves to achieve continuous real-time frame rates higher than 5 kHz for 64-line images. The acquisition of up to 64 GB of raw radiofrequency data allows the development and test of novel methods such as the filtered delay multiply and sum beamformer, before their real-time implementation. The processing power of DSPs is finally exploited exploited in multi-line vector Doppler applications in which the velocity profiles along multiple (up to 8) lines are detected at PRF higher than 10 kHz. Future directions for possible further improvement of research scanners performance will be discussed.

2E-2

11:00 am **A New High Channels Density Ultrasound Platform for Advanced 4D Cardiac Imaging**

Lorena Petrusca[1], François Varray[2], Rémi Souchon[3], Adeline Bernard[2], Jean-Yves Chapelon[3], Hervé Liebgott[2], W.Apoutou N'Djin[3], Magalie Viallon[1,2]; [1]*Univ Lyon, UJM-Saint-Etienne, INSA, CNRS UMR 5520, INSERM U1206, CREATIS, F-69100, LYON, France, France,* [2]*Univ Lyon, UCBL, INSA, CNRS UMR 5520, INSERM U1206, CREATIS, F-42023, SAINT-ETIENNE, France, France,* [3]*Inserm, U1032, LabTAU, Lyon, F-69003, France ; Univ Lyon, Université Lyon 1, Lyon, F-69003, France, France*

Background, Motivation and Objective

A novel ultrasound (US) platform with high channels density that offers flexibility, precision and open access is a pre-requisite to open new frontiers in diagnostic and/or therapy by experimental implementation of new enabled advanced techniques: dual-mode US imaging/therapies in the heart, new approaches to study the myocardial tissue (structure/characterization), fast sparse array strategies, multi-line transmit (MLT), powerful motion correction strategies. To date few systems in the world permit to have a full control both in transmit and receive of all single elements simultaneously of arrays with more than 1000 transducers. This paper presents a powerful US platform for implementing 4D (real-time 3D) advanced US strategies.

Statement of Contribution/Methods

An US platform was developed including a 1024-element US prototype designed for 4D cardiac dual-mode US imaging/therapy (Vermon, 2D 32x32 planar phased-array transducer, fc = 3.4 MHz) and a high channels density (1024-channels) US scanner, made of 4 256-Vantage systems (Verasonics) synchronized together (Fig1e). These systems have per-channel arbitrary waveform transmit/receive generation capability with easy access to RF data. The physical addressing of each US element was properly chosen for allowing various array sparsity combinations while minimizing the number of Vantage driving systems needed. Numerical simulations of US imaging were performed and experimental data of identical configuration were acquired to compare full and sparse array strategies, testing 4D imaging sequences and reconstruction processes.

Results/Discussion

Real-time 4D US imaging was successfully performed in full array mode by synchronizing in emission/reception up to 1024 elements independently. The modular US platform could be reconfigured depending on the number of available Vantage (1 to 4 systems) allowing to use dense halves/quarters of the array, or downsampled full array (Fig1b-d). The validation of image sequences involved plane, diverging and focused waves (SPW, SDW, MLT) and the technical feasibility of real-time 4D US for low therapy focused US and imaging was confirmed with this 1024-channels density US system, offering full research access for developing advanced US strategies.

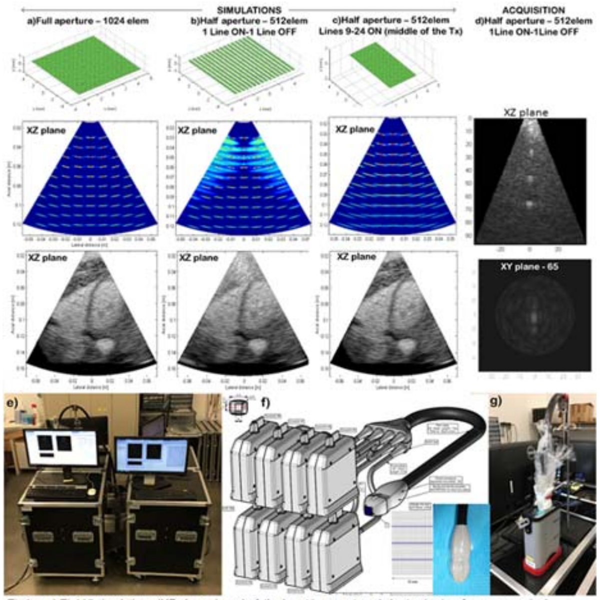

Fig1. a-c) Field II simulations (XZ plane shown) of the heart in parasternal short axis view from a numerical phantom obtained using a slice of a high resolution 3D MRI acquisition of the heart: from left to right: a) full array, b) ½ sparse full array, c) dense half array. d) Example of results obtained using half aperture 512 elements SPW mode e) Setup of the 4 synchronized Verasonics systems f-g) The 3D US probe (Vermon) with 1024 elements, 128 per connectors and validation setup on cyst phantom.

2E-3

11:15 am Low-cost 3D Ultrasound with Any Probe: A Sensor-based Approach

Carl Herickhoff[1], Matthew Morgan[2], Joshua Broder[3], Jeremy Dahl[1]; [1]*Radiology, Stanford University, Palo Alto, CA, USA,* [2]*Biomedical Engineering, Duke University, Durham, NC, USA,* [3]*Surgery - Emergency Medicine, Duke University Medical Center, Durham, NC, USA*

Background, Motivation and Objective

Volumetric 3D ultrasound captures a region of interest more completely than cross-sectional 2D imaging, but 3D implementation has been limited. Mechanical wobbler and matrix-array probes can do 3D imaging, but these probes tend to be bulky and/or expensive, and precise orientation of the image with respect to the patient is not measured.

In this work, we present a method of acquiring volumetric 3D ultrasound images with known patient orientation by utilizing a low-cost sensor. This method enables 3D imaging with any 2D imaging probe; this versatile and practical approach may increase the clinical utilization of 3D ultrasound.

Statement of Contribution/Methods

A $10 inertial measurement unit (IMU) sensor incorporating 3-axis gyroscope, accelerometer, and magnetometer MEMS provides a unit quaternion reading to precisely indicate orientation in space relative to Earth's gravitational and magnetic fields. An IMU sensor was attached to an ultrasound probe to measure its orientation at a rate up to 400 Hz, and a calibration reading was recorded with the probe in a known position on the patient. A simple plastic fixture was designed to mate with the probe and limit its motion to pivoting about a fixed axis, and a video capture box was used to stream 2D image data from an ultrasound scanner.

While pivoting the probe about the fixture axis to 'fan' sweep the image plane through a volume of interest, the sensor's orientation reading was synchronized with each 2D image acquired and displayed on the scanner. The orientation readings were then used as part of a voxel-based reconstruction method to stitch each 2D image into a 3D voxel grid in position relative to the pivot axis. This acquisition and reconstruction routine was used to acquire volumetric 3D images of a fetal phantom and in vivo abdominal targets, including the gallbladder and kidney.

Results/Discussion

Volumetric 3D images were acquired with various 2D imaging probes using a low-cost sensor and motion-limiting fixture, with quality acquisition sweeps performed in under 5 seconds and reconstruction taking less than 30 seconds. In vivo 3D images gave better visualization of gallstones in multi-planar and volume-rendered views (see figure: b and e). The method is susceptible to cardiac or respiratory motion artifacts, but the method can be applied to any existing 2D imaging probe and scanner to acquire 3D images of stationary targets.

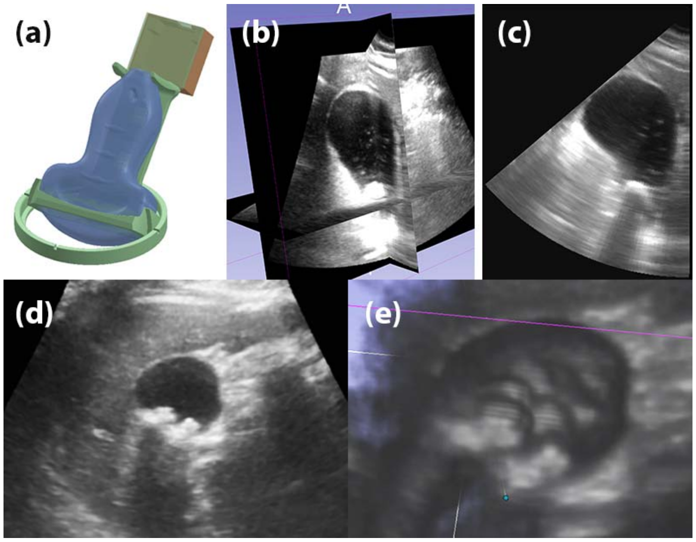

2E-4

11:30 am **Performance of a Transcranial Ultrasound Array Designed for 4D Acoustoelectric Brain Imaging in Humans**

Yexian Qin[1], Pier Ingram[1], Zhen Xu[2], Matt O'Donnell[3], Russell Witte[1,4]; [1]*Department of Medical Imaging, University of Arizona, Tucson, Arizona, USA,* [2]*Department of Biomedical Engineering, University of Michigan, Ann Arbor, Michigan, USA,* [3]*Department of Bioengineering, University of Washington, Seattle, Washington, USA,* [4]*Department of Biomedical Engineering, University of Arizona, Tucson, Arizona, USA*

Background, Motivation and Objective

Noninvasive electrical brain imaging in humans often suffers from poor spatial resolution due to the uncertain spread of electric fields through the head. To overcome this limitation, we propose 4D transcranial acoustoelectric brain imaging (tABI) for mapping current densities at a spatial resolution confined to the ultrasound (US) focus. Acoustoelectric (AE) imaging exploits an interaction between a pressure wave and tissue resistivity, which was demonstrated for mapping the cardiac activation wave in the rabbit heart. Our goal is to extend this modality for mapping the human brain noninvasively. This study describes the performance of a 2D US array designed for tABI in humans.

Statement of Contribution/Methods

A 0.6 MHz handheld 2D US array was designed and fabricated for tABI. The acoustic pressure was measured using a hydrophone with and without a 5mm thick skull cap of an adult human. Two electrodes separated by 10mm were placed in a 0.9% saline bath (Fig. 1a) to produce time-varying currents, which were controlled by a waveform generator. A recording electrode was placed in the bath to detect AE signals. The array was placed in contact with the acoustic window using coupling gel. To form 4D AE images of current densities, the US beam was electronically steered near the dipole. At each position, a burst of US pulses was delivered to reconstruct the time-varying current. Pulse echo images were simultaneously captured to reveal the location of structures co-registered with ABI.

Results/Discussion

With a 20V excitation, the pressure at the geometrical focus was 2.33 MPa (no skull) and 0.68 MPa (with skull) (Fig. 1b). Fig. 1c depicts a cross-sectional tABI of current densities near the dipole. AE amplitudes vs. current densities were measured with and without the skull (Fig. 1d). Sensitivity for detecting the AE signal was 1.47µV/(MPa*mA/cm2) for both scenarios based on a linear fit. The noise equivalent current densities (normalized to 1 MPa) with and without skull were 1.3 and 1.8 mA/cm2, respectively (Fig. 1e). Further optimization of tABI may push the detection limit toward neural currents through the human skull. It may thereby be feasible to build a portable, noninvasive, real-time platform based on tABI for 4D electrical human brain imaging, advancing our understanding of brain function and help diagnose and treat a variety of neurologic, psychiatric and behavioral disorders.

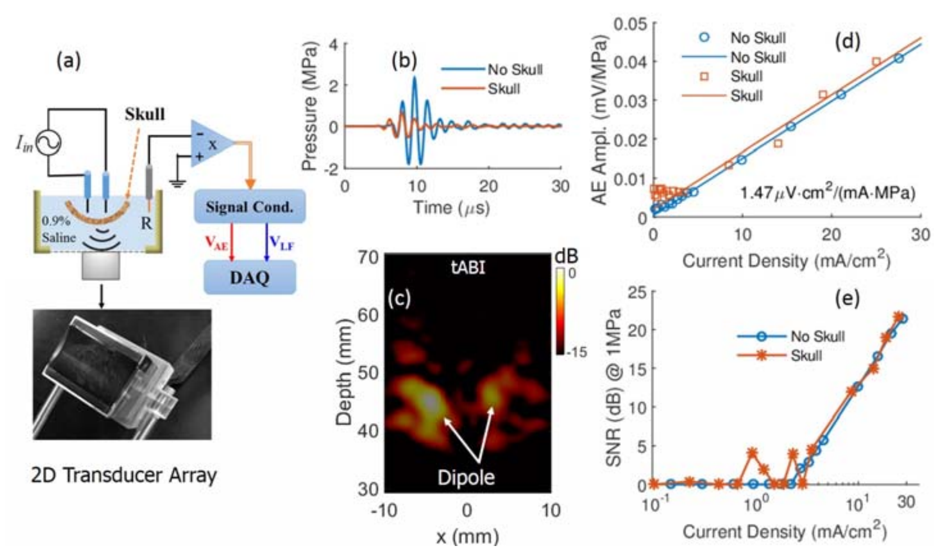

11:45 am **Acoustical Compressive 3D Imaging with a Single Sensor**

Pieter Kruizinga[1], Pim van der Meulen[2], Frits Mastik[1], Andrejs Fedjajevs[2], Geert Springeling[1], Nico de Jong[1,3], Geert Leus[2], Johannes G. Bosch[1]; [1]*Thorax Center - Biomedical Engineering, Erasmus MC, Rotterdam, Netherlands,* [2]*Circuits and Systems – EEMCS, Delft University of Technology, Netherlands,* [3]*Faculty of Applied Sciences, Delft University of Technology, Netherlands*

Background, Motivation and Objective

3D ultrasound (US) requires expensive transducers comprising thousands of elements and complicated hardware. This complexity originates from the classical idea on spatial sampling requirements for US imaging. The discovery of compressive sensing allows to ease this sampling constraint, enabling smarter ways of recording the required information. Inspired by this work we introduce a US imager that can perform 3D imaging using one acoustic sensor. Our device sends and detects US waves through a random coding mask that enables unique signals at every voxel. Rotation of the mask allows for several compressed measurements. By knowing the voxel signals, a full 3D reconstruction of the object can be obtained, as we demonstrate in this work.

Statement of Contribution/Methods

The coding mask was made from plastic with 1mm holes drilled with varying depths. This variation in depth causes the transmit and receive acoustic field to produce a unique interference pattern. We used a commercial single element transducer (5 MHz, 17mm, C309-SU Olympus) coupled to a pulser/receiver box (5077PR – Olympus). For calibration purposes we recorded the transmit field in a plane perpendicular to the acoustic propagation axis using a hydrophone (0.5 – 20 MHz Precision Acoustics). To estimate the signal originating from every voxel we used the angular spectrum approach to calculate resulting voxel signals at greater depth; auto-convolution to account for the pulse-echo acquisition; and linear interpolation to account for additional rotation measurements. We formalized our image reconstruction problem in a set of linear equations **Ax** = y, where A is the system matrix (obtained from calibration), y contains our pulse-echo measurements and x is the recovered image. The image was found by iteratively minimizing the least-squares error between Ax and y using the MATLAB LSQR algorithm. For the imaging experiment we placed two 3D printed plastic letters 'E' and 'D' inside water.

Results/Discussion

Figure 1(a) shows a schematic overview of our imaging device and setup, Fig1(b) the mean projections of the two reconstructed letters. We used 72 rotations and 15 LSQR iterations. Future work includes optimal mask design to mitigate the need for mask rotation. In this paper we presented the first hardware implementation of compressive 3D US imaging consisting of one acoustic active element and a random coding mask.

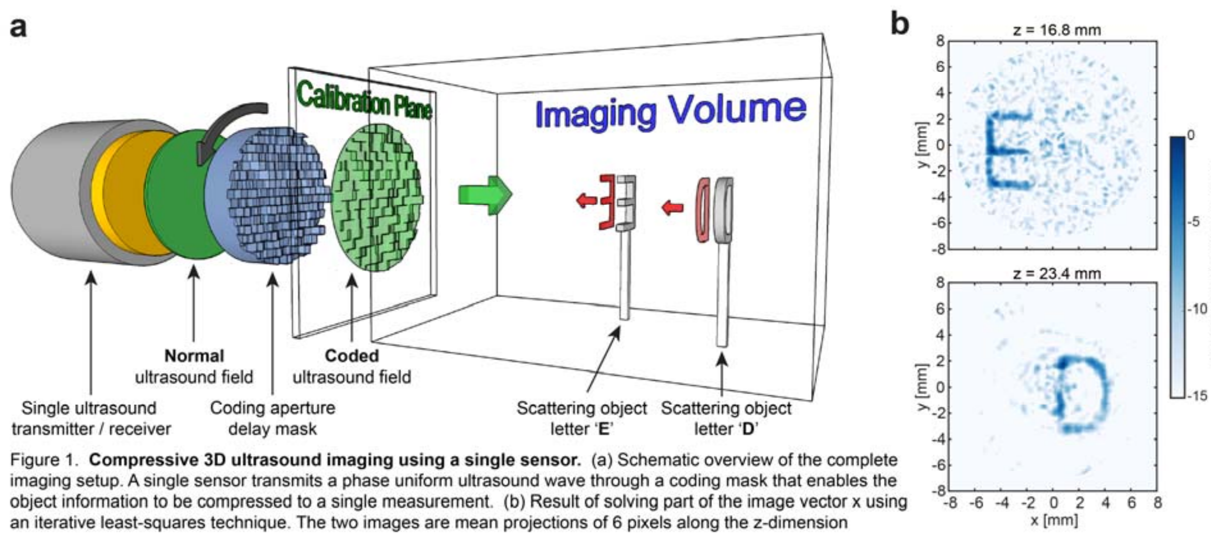

Figure 1. **Compressive 3D ultrasound imaging using a single sensor.** (a) Schematic overview of the complete imaging setup. A single sensor transmits a phase uniform ultrasound wave through a coding mask that enables the object information to be compressed to a single measurement. (b) Result of solving part of the image vector x using an iterative least-squares technique. The two images are mean projections of 6 pixels along the z-dimension

3E - MEL: Elasticity Based Tumor Detection

Palladian Room

Friday, September 8, 2017, 10:30 am - 12:00 pm

Chair: **Kathy Nightingale**
Duke University

3E-1

10:30 am Viscoelastic Properties of Breast Masses: A Frequency Dispersion Analysis Using Acoustic Radiation Force

Viksit kumar[1], Mahdi Bayat[1], Max Denis[1], Adriana Gregory[1], Jeremy Webb[1], Dana Whaley[1], Mostafa Fatemi[1], Azra Alizad[1]; [1]*Mayo Clinic, Rochester, MN, USA*

Background, Motivation and Objective

Elasticity values reported by shear wave elastography techniques for Breast tissue/mass are a combination of elasticity and viscosity at the frequency with peak shear wave energy; thus, resulting in overestimation of tissue elasticity. To better estimate shear elasticity and to understand the role of shear viscosity in suspicious breast masses at different frequencies, the frequency dispersion of shear wave propagating inside suspicious breast masses is investigated.

Statement of Contribution/Methods

10 female patients with suspicious breast masses undergoing biopsy are recruited prior to their biopsy. An acoustic radiation force push of 600µs is used to create a shear wave just outside the suspicious mass boundary. The shear wave propogating inside the suspicious mass is imaged at 3.3 kHz. 2D auto correlation techniques are used to calculate the particle velocity followed with a K-space analysis to estimate the phase velocity. The phase velocity is used to inversely estimate elasticity and viscosity using a simple Voigt model.

Results/Discussion

The mean values of elasticity, viscosity and retardation time (η_{Voigt}/μ_{Voigt}) is reported for 5 benign and 5 malignant breast masses in Table 1 along with values of normal breast tissue observed from the same patient. Figure 1(a), (b) and (c) show the box plot for shear elasticity, shear viscosity and retardation time respectively. Statistically significant difference is observed between benign and malignant cases for all the parameters with retardation time having the lowest p-value.

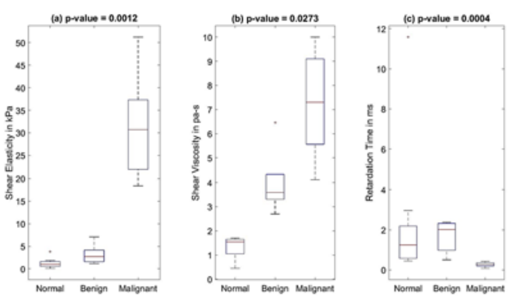

Histopathology	Shear Elasticity (kPa)	Shear Viscosity (Pa-s)	Retardation Time (ms)
Malignant (n=5)	31.26±12.55	7.25±2.30	0.27±0.13
Benign (n=5)	3.19±2.32	3.98±1.44	1.67±0.82
Normal (n=10)	1.25±1.05	1.34±0.43	2.38±3.34

3E-2

10:45 am Quasi-Static Elastography and Ultrasound Plane-Wave Imaging: The Effect of Beam-Forming Strategies on the Accuracy of Displacement Estimations

Gijs A.G.M. Hendriks[1], Chuan Chen[1], Hendrik H.G. Hansen[1], Chris L. de Korte[1,2]; [1]*Medical UltraSound Imaging Center (MUSIC), Department of Radiology and Nuclear Medicine, Radboud university medical center, Nijmegen, Netherlands*, [2]*Physics of Fluids Group, University of Twente, Enschede, Netherlands*

Background, Motivation and Objective

Quasi-static elastography is a widely applied ultrasound method in which RF data acquired in tissue at different states of deformation are correlated to estimate displacements and strain (displacement gradient). A recent development is the introduction of ultrafast plane-wave imaging where element data are beam-formed after collection to reconstruct the image lines. Several beam-forming strategies are available: time-domain based delay-and-sum (DAS) based on time-of-flight, and frequency domain based techniques like Stolt's f-k (Stolt) and Lu's method (Lu) based on an exploding reflector model and ideal transmit-receive model, respectively. Plane-wave beam-forming allows arbitrary grid designs not limited by probe pitch etc. In this study, we investigated the influence of beam-forming strategies and grid designs on the performance of displacement estimation.

Statement of Contribution/Methods

Element data were collected by a 0° plane-wave transmit-receive acquisition in a phantom pre- and post-rotation (1°) using four different probes connected to a Verasonics V1 (fig 1d). RF data were reconstructed by DAS (F# 0.9) with rectangular (DAS_{Rect}) and hanning apodization (DAS_{Apod}), Stolt and Lu, and Stolt and Lu with angular weighting to incorporate element sensitivity ($Stolt_{Ang}$ and Lu_{Ang}). Grid resolution was 8 samples per wavelength axially (ax) and 1-4 lines per pitch (l_{pitch}) laterally (lat). Displacements (d) were estimated by two step cross-correlation (envelope and RF). Root-mean-squared errors (RMSE) were calculated by comparing estimated and expected radial displacements ($d_{rad} = \sqrt{(d_{ax}^2 + d_{lat}^2)}$).

Results/Discussion

As expected, due to the applied rotation, d_{ax} (fig 1a) and d_{lat} (fig 1b) showed a clear gradient in lat and ax direction respectively and increasing d_{rad} (fig 1c) diverging from the rotational point for all probes and strategies. The optimal method for all probes was Lu's method for 3 lines per pitch (table 1). However, for MS250 (13-24 MHz), DAS_{Rect} seemed to have slightly improved RMSE and l_{pitch} seemed to hardly affect results for Lu and Stolt. Furthermore, applying weighting or apodization to improve contrast in RF data deteriorates displacement estimation probably caused by compromised resolution. In conclusion, beam-forming 3 lines per pitch by Lu seemed to provide the most accurate cross-correlation-based displacement estimates.

Fig 1a-c: example of d_{Ax}, d_{Lat} and d_{Rad} (L7-4, Lu, l_{pitch} 3) by phantom rotation (**1d**). **Table 1:** RMSE (µm) for all probes, beam-forming strategies and l_{pitch}. Grey areas indicate lowest RMSE for each probe and strategy.

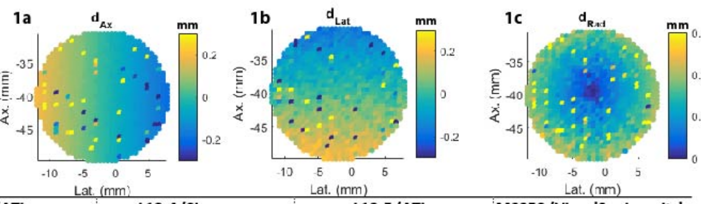

Table 1	L7-4 (ATL; pitch 298 µm)				L12-4 (Siemens; pitch 266 µm)				L12-5 (ATL; pitch 195 µm)				MS250 (VisualSonics; pitch 88 µm)			
l_{pitch}	1	2	3	4	1	2	3	4	1	2	3	4	1	2	3	4
Lu	183	161	158	158	270	185	149	159	170	129	129	137	112	105	106	108
Lu_{Ang}	202	216	225	224	277	183	152	160	175	161	169	165	110	112	111	114
Stolt	160	191	202	182	321	168	183	176	182	148	142	152	114	113	114	118
$Stolt_{Ang}$	205	211	229	210	246	174	179	168	205	180	179	173	115	117	115	116
DAS_{rect}	180	161	157	183	336	188	201	204	197	141	146	154	105	106	98.1	99.5
DAS_{Apod}	211	228	242	236	259	231	186	212	210	200	186	196	109	108	107	111

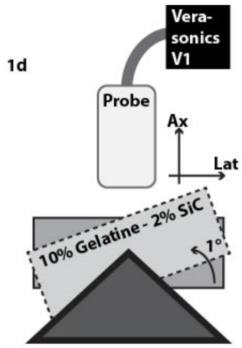

3E-3

11:00 am Evaluation of the Feasibility of Measuring the Fourth-order Nonlinear Parameter *D* in *Ex vivo* Kidneys

Tomas Echavarria Bayter[1], **Sara Aristizabal[2]**, Matthew Urban[2,3]; [1]*Universidad EIA, Envigado, Antioquia, Colombia,* [2]*Physiology and Biomedical Engineering, Mayo Clinic, Rochester, Minnesota, USA,* [3]*Radiology, Mayo Clinic, Rochester, Minnesota, USA*

Background, Motivation and Objective

Current elastography techniques can measure mechanical properties of soft tissues by estimating the elastic shear modulus, μ_0. Recently, the assessment of tissue nonlinearity using acoustoelasticity (AE) has shown some promising results in differentiating healthy from malignant tissue by estimating a third-order nonlinear coefficient *A*. To fully characterize the nonlinear properties of the tissue, it may be necessary to develop techniques to also reliably estimate the fourth-order elastic constant D as the combination with the other parameters µ and A could provide diagnostic discriminatory power. This study evaluates the implementation of a three-parameter fit (μ_0, A, D) to estimate the nonlinear properties of ex vivo kidneys using the shear modulus, µ vs. strain, ε estimates obtained when the phantoms are subjected to compression.

Statement of Contribution/Methods

The study was performed using µ vs. ε data we previously acquired in 10 porcine kidneys embedded in 10% porcine gelatin by inducing stress on the phantoms using a linear array transducer attached on a stepper motor programmed to compress in 7 steps until reaching 25% strain given the phantom's initial thickness. The phantoms were evaluated under 3 different configurations: 1) In the presence and absence of a plate attached to the transducer, 2) in the longitudinal and transverse view of the kidney, 3) with progressive and regressive directions of compression. For the AE measurements, we previously estimated *A* by applying the AE theory using a two parameter fit. For this study the parameters A and D were estimated using the same data but evaluated using a three-parameter fit (μ_0, A, D). The variability of D was evaluated for each phantom and experimental configuration to evaluate the consistency of the results. The variability and results of each case were compared among each other, and the precision of the fits was assessed using the root mean square error (RMSE).

Results/Discussion

The fit of the shear modulus vs. strain using two-parameter and three-parameter equation is shown on Fig. 1(a) The standard deviation of the *A*, μ_0, and D values for all the different configurations is shown in Fig. 1 (b). The values of A and D were evaluated in ex vivo porcine kidneys with larger variability in the values, but the value of D is a novel characterization in soft tissues.

(a)

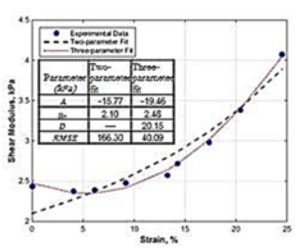

(b)

		Progressive (kPa)		Regressive (kPa)	
		Plate	No Plate	Plate	No Plate
Two-parameter fit	*A*	-9.46 ± 3.02	-5.51 ± 2.23	-7.51 ± 2.04	-5.24 ± 1.18
	μ_0	2.03 ± 0.21	1.8 ± 0.10	1.89 ± 0.10	1.82 ± 0.09
Three-parameter fit	*A*	-6.95 ± 4.89	-17.98 ± 6.49	-11.48 ± 10.82	-11.59 ± 6.50
	μ_0	2.19 ± 0.20	2.08 ± 0.09	2.09 ± 0.20	1.98 ± 0.10
	D	11.74 ± 4.86	14.08 ± 4.08	12.69 ± 6.10	9.51 ± 3.35

(c)

$$\mu_i = \mu_0 + \frac{A * \xi_i}{4} + (2\mu_0 + A + 3D)\xi_i^{\,2}$$

μ_0 = shear modulus at baseline (0% Strain)

Figure 1. a) Strain (%) vs Shear Modulus (kPa) is shown for a progressive compression with plate attached to the transducer for one phantom. The values for each parameter is shown. **b)** Variability of each parameter was calculated with the standard deviation of the values across acquisitions and then averaged between phantoms. (Mean ± standard deviation is shown). **c)** The three-parameter equation is shown were the fourth order coefficient *D* is introduced.

3E-4

11:15 am Shear Wave Elasticity Imaging of Pancreatic Cancer Tumors Treated with Immunotherapy and Radiotherapy

Hexuan Wang[1], Rifat Ahmed[1], Kelli Connolly[2], Scott Gerber[2], Brian Pogue[3], Marvin Doyley[1]; [1]*Electrical and Computer Engineering, University of Rochester, USA,* [2]*School of Medicine and Dentistry, University of Rochester, USA,* [3]*Thayer School of Engineering, Dartmouth College, USA*

Background, Motivation and Objective

Pancreatic cancer is an aggressive disease a 5-year-survival rate less than 7%. To improve the patient overall survival, recent developments in pancreatic cancer research have been targeting various components of the tumor microenvironment such as the extracellular matrix, blood vessels and immune cells. We hypothesize that targeted therapies will affect the biomechanics of the tumor microenvironment. To corroborate this hypothesis, we used shear wave elasticity imaging (SWEI) to investigate how different therapies (immunotherapy and radiotherapy) impact tumor stiffness.

Statement of Contribution/Methods

We implanted orthotopic KCKO pancreas tumors in 15 C57B/6 mice. The mice were treated with 10% Hydroxypropyl-beta-Cyclodextrin and 5% Solutol HS15 in sterile water (control group, n = 5), CCR2/CCR5 antagonist immunotherapy (CVC group, n = 5) or 5Gy radiotherapy over five days using a 3200 Curie-sealed 137 Cesium source (RT group, n = 5). Excised tumors were implanted in a gelatinous solution consisting of 15% gelatin, 2% corn starch, and water. Shear wave elasticity imaging was implemented on a Verasonics Vantage 64 scanner with a 5 MHz L7-4 transducer. Shear wave speed maps were generated using a time-of-flight algorithm and were converted to Young’s modulus using the infinite medium assumption.

Results/Discussion

SWEI measurements showed a variance in stiffness among the three treatment groups. The average Young’s moduli (E) measured in the tumors were 76.625 kPa, 58.415 kPa, 42.245 kPa for the control, immunotherapy-threated, and RT-treated groups, respectively (figure 1a). To validate the SWEI results, we also performed model-based quasi-static ultrasound elastography on the same tumors. We observed a strong correlation (R^2 = 0.934) between E recovered using shear wave and model-based ultrasound elastography, as indicated in figure 1b. Those results demonstrated that SWEI can characterize the mechanical properties of murine pancreatic cancer tumors and detect changes in tumor microenvironment in response to treatment plans, thus potentially facilitating the in vivo evaluation of novel therapeutic approaches.

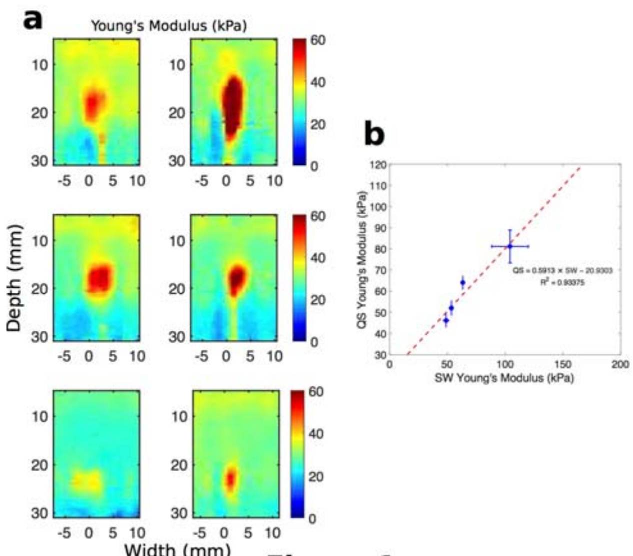

Figure 1

3E-5

11:30 am Pancreatic Ductal Adenocarcinoma Detection and Treatment Monitoring In Vivo and in Post-surgical Human Specimens Using Harmonic Motion Imaging (HMI)

Thomas Payen[1], Yang Han[1], Alireza Nabavizadehrafsanjani[1], Kenneth P Olive[1], Elisa E Konofagou[1]; [1]*Columbia University Medical Center, USA*

Background, Motivation and Objective

Pancreatic ductal adenocarcinoma (PDA) has one of the lowest prognosis due to non-specific symptoms leading to late diagnosis. The tumor is characterized by an unusually dense stroma limiting chemotherapeutic perfusion. Harmonic Motion Imaging (HMI) assesses tissue mechanical properties by inducing localized oscillation resulting from a periodic acoustic radiation force. The amplitude of the displacement is inversely related to the underlying tissue stiffness. The objective of this study was to evaluate the utility of HMI in post-surgical human pancreatic cancer specimens to detect the tumor, and assess the tumor response to neoadjuvant treatments.

Statement of Contribution/Methods

A 4.5-MHz focused ultrasound transducer generates an amplitude-modulated beam resulting in harmonic tissue oscillations at its focus. Axial tissue displacement is estimated using 1D cross-correlation of RF signals acquired at 2.5-MHz using plane waves with a framerate of 1 kHz. Thirteen human pancreatic specimens (average dimensions = 24 x 12 x 80 mm3) were assessed immediately after surgery. Six of these patients had received neoadjuvant treatment (gemcitabine-based chemotherapy alone or in combination with radiations). The full volume of the specimen was scanned with HMI in less than 90 minutes before histology was performed.

Results/Discussion

The full volume of the specimens was successfully scanned with measurements as deep as 3 cm in the tissue without damage to the tissue. A sharp mechanical contrast was evident on the HMI maps between the stiff tumor and the softer adjacent tissue (Figure). Mean HMI displacements were significantly different in the normal pancreas, fibrotic perilesional tissue, and PDA (16.9 ± 3.5 µm, 12.7 ± 2.5 µm, and 2.6 ± 1.5 µm, respectively). Further analysis showed that HMI is also capable of detecting the effects of neoadjuvant treatment (Figure). Response to therapy resulted in significantly softer PDA reflecting tumor cell death. In addition, HMI detected that neoadjuvant treatment lead to significantly stiffer normal parenchyma due to higher fibrosis.

HMI can assess the mechanical properties of the entire pancreas and distinguish between PDA, fibrotic tissue and normal parenchyma. Neoadjuvant treatment response could also be detected both in the tumor and in the normal tissue. HMI could thus constitute a crucial tool to improve PDA poor prognosis.

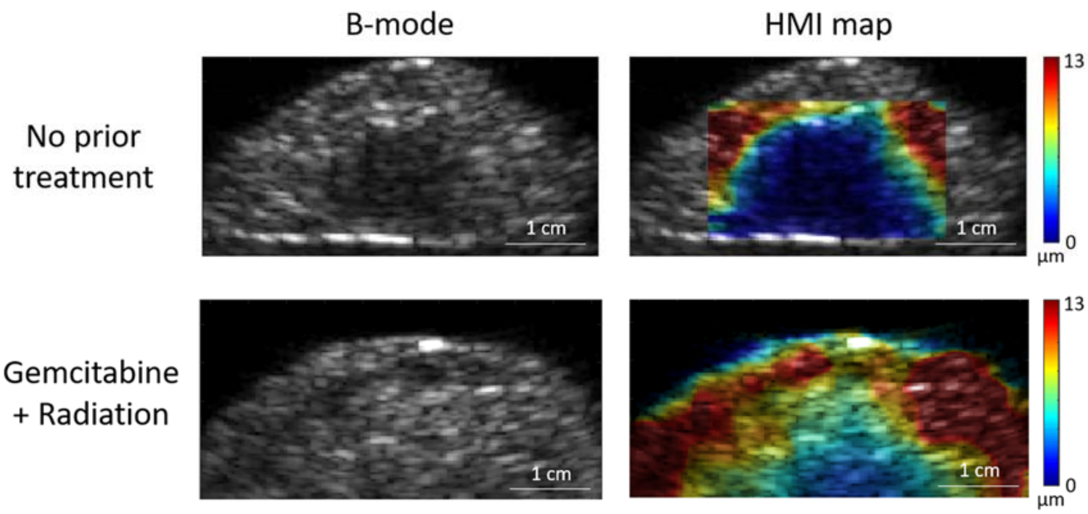

3E-6

11:45 am Viscoelastic Response (VisR)-Derived Relative Elasticity and Relative Viscosity Reflect Tissue Elasticity and Viscosity: *In Silico* and Experimental Demonstration in Liver

Md Murad Hossain[1], Timothy Nichols[2,3], Elizabeth Merricks[3], Caterina Gallippi[1]; [1]*Department of Biomedical Engineering, University of North Carolina, Chapel Hill, Chapel hill, North Carolina, USA,* [2]*Department of Medicine, University of North Carolina, Chapel Hill, USA,* [3]*Department of Pathology and Laboratory Medicine, University of North Carolina, Chapel Hill, USA*

Background, Motivation and Objective

VisR ultrasound characterizes the viscoelastic properties of tissue by fitting acoustic radiation force (ARF)-induced displacements in the region of ARF excitation to a 1D mass-spring-damper (MSD) model. Viscosity and elasticity are found separately from each other but relative to the applied ARF amplitude. We refer to these parameters as 'relative elasticity (RE)' and 'relative viscosity (RV)'. *We hypothesize that RE and RV linearly correlate to true elasticity and viscosity in tissue.*

Statement of Contribution/Methods

In silico, VisR imaging was simulated using finite element (FE) models of displacements induced in 200 Voigt viscoelastic materials with varying shear modulus (1.7 to 34 kPa in steps of 1.66 kPa) and viscosity (0.17 to 3.2 Pa.S in steps of 0.33 Pa.S). The modeled displacements were ultrasonically tracked using Field II. Experimentally, VisR imaging was performed using a Siemens S3000 Helix and 9L4 on 4 homogeneous oil-gelatin phantoms with oil (5%, 10%, or 20%) and gelatin (6% or 12%) concentrations; on excised livers from 2 pigs and 1 dog; and on an excised dog liver with an oil-gelatin inclusion. Peak displacement (PD), RE, and RV were calculated after correction of the relaxation time constant for constant stress, τ. VisR RE and RV were compared to Shearwave Dispersion Ultrasound Vibrometry (SDUV) elasticity and viscosity.

Results/Discussion

See Fig. 1. *In silico*, VisR RE increases with increasing material elasticity. For a given elasticity, RE values vary by 1.74% on average when viscosity varies from 0.5 to 2.2 Pa.S (panel a). Similarly, RV increases with increasing material viscosity, and for a given viscosity, RV values vary by 6% on average when elasticity ranges from 3.3 to 25 KPa (panel b). PD decreases with both increasing elasticity and increasing viscosity. For a given elasticity, PD varies by 39.95% on average when viscosity ranges from 0.5 to 2.2 Pa.S (panels c). Experimentally, RE and RV linearly correlate to SDUV elasticity and viscosity in phantoms with R^2 values of 0.98 and 0.90, respectively, and in excised livers with R^2 values of 1.0 and 0.85, respectively (panels d-e). Finally, RE and RV contrast a stiffer, more viscous inclusion in the liver background with contrast comparable to SDUV (panels f-g). These results suggest that VisR RE describes the elastic, and RV the viscous, properties of tissue without observing shear wave propagation.

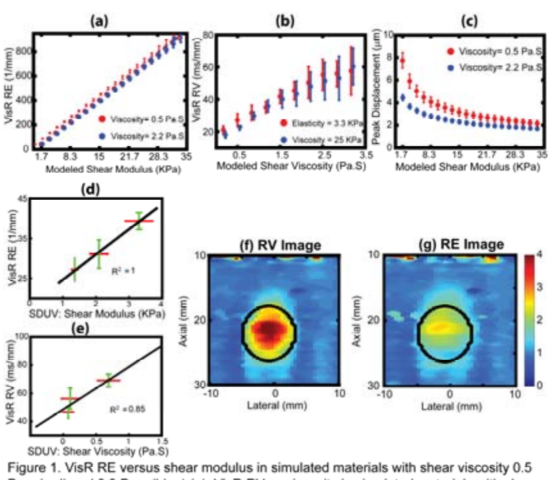

Figure 1. VisR RE versus shear modulus in simulated materials with shear viscosity 0.5 Pa.s (red) and 2.2 Pa.s (blue) (a). VisR RV vs viscosity in simulated materials with shear modulus 3.3 KPa (red) and 25 KPa (blue) (b). PD vs shear modulus (c) in the simulated materials. RE, RV, and PD are shown as mean ± 1 standard deviation over 10 independent speckle realizations. VisR RE (d) and RV (e) versus SDUV shear elasticity and viscosity, respectively, in excised pig and dog livers. VisR RE and RV and SDUV measures are shown as mean ± standard deviation over 10 different measurements in 5 different locations. Parametric images, showing VisR RV (f) and RE (g), of a stiff and viscous inclusion in a liver background. The black contour, derived from the B-mode image, represents the inclusion boundary.

4E - MPA: Clinical and Pre-Clinical Models

Diplomat Room

Friday, September 8, 2017, 10:30 am - 12:00 pm

Chair: **Michael Kolios**
Ryerson University

4E-1

10:30 am Preliminary Photoacoustic Imaging of the Human Radial Artery for Simultaneous Assessment of Red Blood Cell Aggregation and Oxygen Saturation *In Vivo*

Tae-Hoon Bok[1,2], Eno Hysi[1,2], Michael Kolios[1,2]; [1]*Physics, Ryerson University, Toronto, Ontario, Canada,* [2]*Institute for Biomedical Engineering, Science and Technology, Toronto, Ontario, Canada*

Background, Motivation and Objective

The main role of red blood cell (RBC) is oxygen delivery to body tissues via blood flow. When flowing blood is exposed to stasis or low shear rate (the radial gradient of velocity profile) in blood vessels, RBCs become aggregated resulting in alterations of blood viscosity affecting blood flow dynamics. Our group demonstrated that lower shear rate yielded greater aggregation and a higher PA signal while higher shear rates led to disaggregation thereby decreasing the PA signal amplitude (Bok *et al.*, Biomed. Opt. Express, 2016). In this way, the relation between oxygen saturation (sO_2) and RBC aggregation may provide a new biomarker in diagnosis of blood flow. In this paper, we present a pilot study where high-frequency photoacoustic imaging (PAI) is used to for the simultaneous assessment of RBC aggregation and sO_2 in vivo from the human radial artery (RA).

Statement of Contribution/Methods

A human participant experiment was approved by the Research Ethic Board of Ryerson University (REB 2017-040). The US and PA images in the RA were acquired using a US/PA imaging system equipped with a 21 MHz linear-array probe (Vevo LAZR; LZ250, FUJIFILM VisualSonics, Canada), varying the wavelength of optical illumination (700, 750, 800, 850 and 900 nm). The blood flow velocity at the RA was assessed by pulsed wave Doppler in the same device.

Results/Discussion

The PA signals in the RA were observed at all wavelengths (Fig. 1a). The intensity of PA images was reduced with increasing wavelengths since the optical energy in the PA device decreased (0.96 to 0.31 mJ from 700-900 nm). The energy compensated PA signals cyclically varied as function of time, and increased with wavelength (Fig. 1b), i.e., 3.69 ± 0.2 to 7.21 ± 0.17 dB. Optical absorption of hemoglobin inside RBCs dominated the PA signals in the vessel lumen. The phase of variation in PA signals was inversely proportional to that in systolic blood flow velocity (Fig. 1c). The sO_2 is proportional to the cell surface area exposed to the surrounding media, and RBC aggregation decreases the exposed area. As such, in Fig. 1d, the sO_2 was higher for aggregated cells (diastolic state) than single cells (systolic state). This preliminary PAI study of RBC aggregation and sO_2 *in vivo* in the RA is the first attempt to study the hemodynamics and physiological function of RBC, which can be used as a potential tool for the diagnosis of blood flow conditions in the RA.

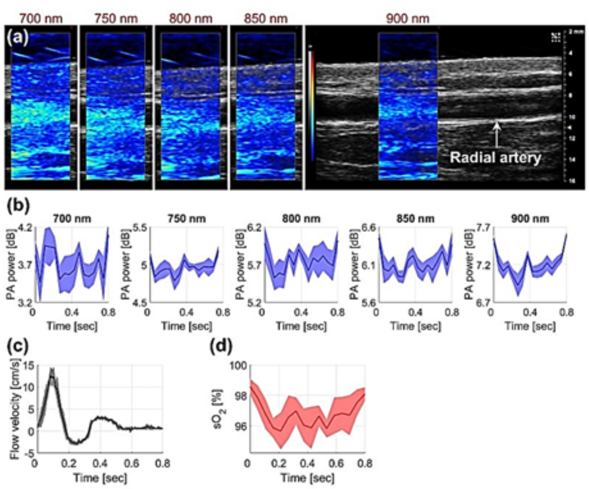

Figure 1. (a) The overlapped ultrasound/photoacoustic images at 700 ~ 900 nm of optical illumination in the human radial artery. The average of photoac oustic signal amplitude (b), blood flow velocity (c) and oxygen saturation (d) per one cycle in the vessel lumen.

4E-2

10:45 am Chemical Imaging of Tumor Microenvironment by Using Multi-Spectral Photoacoustic Imaging Powered by Functional Nanosensors

Janggun Jo[1], Chang Lee[2], Raoul Kopelman[2], **Xueding Wang**[1]; [1]*Department of Biomedical Engineering, University of Michigan, USA,* [2]*Department of Chemistry, University of Michigan, USA*

Background, Motivation and Objective

Tumor acidosis, as a consequence of increased fermentative metabolism and poor perfusion, plays an important role in almost all steps of invasive growth and metastasis. Successful measurements of the extracellular pH of the tumor microenvironment can contribute to clinical management of cancer and basic science research. We herein report on an in vivo tumor pH mapping nanotechnology that includes the development of a pH sensing nanoprobe and multi-wavelength photoacoustic imaging (PAI) integrated with ultrasound imaging.

Statement of Contribution/Methods

The optical pH indicator, SNARF-5F, i.e., 5-(and-6)-Carboxylic Acid, was encapsulated into polyacrylamide nanoparticles with surface modification for tumor targeting. Protected by the polyacrylamide nanoparticles, the pH indicator's optical performance is not affected anymore by proteins or enzymes, making possible for quantitative assessment of tumor pH in vivo. Facilitated by the multi-wavelength PAI plus spectral unmixing technique, both the pH levels and the hemodynamic properties in the entire tumor can be quantitatively evaluated with high sensitivity and in high spatial resolution.

Results/Discussion

The experiments on phantoms validated the accuracy and robustness of this pH imaging technology; while the later experiments on a mouse cancer model demonstrated its good performance in vivo. The statistical analysis shows that the average pH levels quantified in tumors were lower than those in normal tissue, which was also confirmed by the measurements from an invasive pH electrode used as a gold standard. Using the same nanosensors carrying oxygen sensing dye or potassium sensing dye, the oxygen saturation or the potassium concentration in a solid tumor can also be quantitatively mapped, which will also be presented in this paper. The imaging technology reported here holds potential to be developed into a new and powerful tool for real-time evaluation and repeated monitoring of cancer microenvironment.

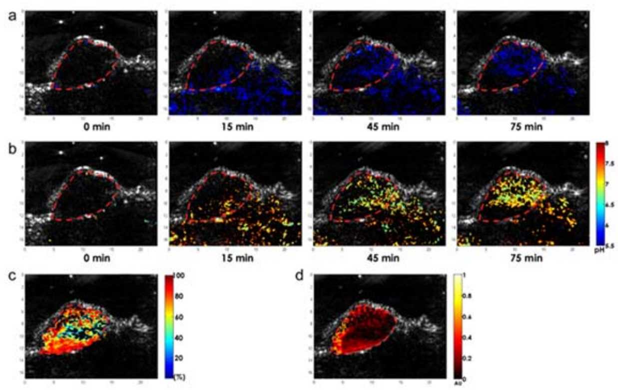

Figure 1: ***In vivo*** **photoacoustic imaging (PAI) of cancer microenvironment.** (a) PA images showing the distributions of SNARF-PAA NP (shown in blue) at different time points after injection. The PA images in pseudo-color are superimposed on the gray-scale US images. The tumor area is marked by a dashed circle in each image. (b) Quantitative PA pH image at different time points after SNARF-PAA NP injection. The pH images in pseudo-color are superimposed on the gray scale US images. (c) PA images showing the spatially distributed blood oxygen saturation (sO_2) in the tumor area. (d) PA images showing the spatially distributed total hemoglobin concentration (THb) in the tumor area.

4E-3

11:00 am Evaluating the Physiology of Inflammatory Arthritis with Functional Photoacoustic Imaging

Janggun Jo[1], Guan Xu[2], Sheeja Francis[3], April Marquardt[3], Gandikota Girish[2], **Xueding Wang[1]**; *[1]Biomedical Engineering, University of Michigan, USA, [2]Radiology, University of Michigan, USA, [3]Internal Medicine, University of Michigan, USA*

Background, Motivation and Objective

Presenting highly sensitive and clinically relevant functional information from soft tissues in and around the joint with spatial resolution comparable to ultrasound (US) imaging, photoacoustic (PA) imaging may shed new light on early diagnosis and treatment evaluation of human inflammatory arthritis. In this study on severe arthritis patients and healthy control subjects, we explored the potential contribution of PA imaging to rheumatology clinic. The feasibility of a point-of-care device built on a LED based PA imaging system for evaluating human finger joints was also studied.

Statement of Contribution/Methods

By performing imaging at a single laser wavelength, the spatially distributed hemoglobin content reflecting the hyperemia in synovial tissue in the finger joints of arthritis patients were imaged. By performing imaging at two laser wavelengths, the spatially distributed hemoglobin oxygenation reflecting the hypoxia in the finger joints of arthritis patients were also imaged. The measurements from the arthritis patients and the healthy controls were statistically analyzed by using two-tailed student t-tests.

Results/Discussion

The statistical analyses of the imaging results demonstrated significant differences in quantified hemoglobin content and in quantified hemoglobin oxygenation between the arthritis joints and the normal joints. PA imaging is capable of identifying inflammation in human peripheral joints based on the detection of increased hyperemia and increased hypoxia in affected synovium. These two physiological biomarkers of synovitis reflecting the increased metabolic demand and the relatively inadequate oxygen delivery can both be non-invasively evaluated. The results from the LED-based PA imaging system demonstrated satisfactory sensitivity and depth for evaluating the physiological biomarkers in human joints affected by arthritis.

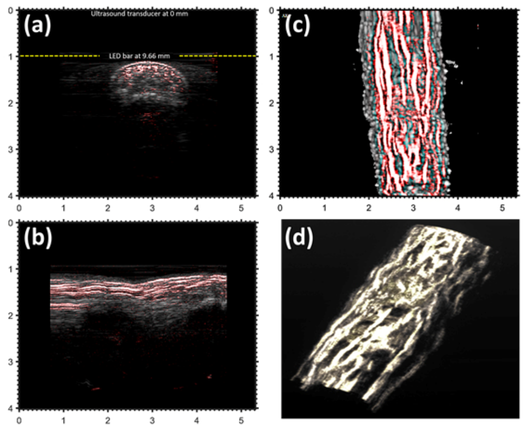

Fig. 1. 3D photoacoustic (PA) and ultrasound (US) dual imaging of a human finger joint. The PA image (in pseudo-color) acquired using a LED-based imaging system is super-imposed on the B-scan US image (in gray-scale) acquired from the same joint. (a)-(c) Display of the imaging result along the axial, the coronal, and the sagittal planes, respectively. (d) 3D rendering of the PA image demonstrating the spatially distributed vasculature in the finger digit.

4E-4

11:15 am Photoacoustic-Ultrasonic Imaging Biomarkers for Treatment-Response Assessment of Sorafenib in a Rat Model of Hepatocellular Carcinoma

Houra Taghavi[1], Nina Munoz[2], Mohamed Naser[1], Kiersten Maldonado[1], Charles Kingsley[1], Yugi Tang[1], Katherine Dextraze[1], Rony Avritscher[2], Richard Bouchard[1];
[1]Imaging Physics, The University of Texas MD Anderson Cancer Center, USA, [2]Interventional Radiology, The University of Texas MD Anderson Cancer Center, USA

Background, Motivation and Objective

Sorafenib is the only clinically approved drug for hepatocellular carcinoma (HCC), but its response rate is relatively poor. Recently, it has been shown that tissue hypoxia and perfusion have predictive correlation with HCC response to sorafenib treatment. In this study, we investigate the correlation of photoacoustic-ultrasonic (PAUS) imaging biomarkers for oxygen saturation (SO_2) and perfusion to the treatment response from sorafenib in an orthotopic rat model of HCC.

Statement of Contribution/Methods

McA-RH7777 HCC cells were implanted into the left liver lobe of twenty-two Buffalo male rats. Two weeks post inoculation, rats were randomly assigned to untreated (n=10) and treated (n=12; daily dose of 7.5 mg/kg sorafenib) cohorts. PAUS imaging (Vevo LAZR; FUJIFILM VisualSonics) was performed on all the rats at 2-week and 4-week time points. Volumetric multi-wavelength (710, 734, 760, 800, & 850 nm) PA imaging data were acquired during an oxygen challenge (i.e., pure O_2 vs. medical air), and linear unmixing was implemented for SO_2 assessment. Following PA imaging, 300-µl of MicroMarker microbubble contrast was introduced via tail-vain injection, and harmonic imaging data were acquired during the wash-in/wash-out phases through midsection of each tumor. The average value of each metric within a tumor was used for comparisons.

Results/Discussion

Microbubble peak enhancement (Fig. 1A-B), which provides a relative indication of blood volume, and the wash-in perfusion index, which provides a relative indication of perfusion, was found to significantly decrease ($p \leq 0.05$) compared to their baseline pre-treatment measurements and to the untreated control cohort. PA-based SO_2 estimates of the difference observed during the oxygen challenge was also found to be significant, with the treatment cohort presenting a larger average difference (15.1%) than the control cohort (9.3%). This result could indicate that reduced treatment-mediated perfusion leads to decreased overall oxygen availability, and thus a higher percentage of oxygen diffuses out of capillaries to meet the demands of local cell metabolism. Alternatively, it could also occur from increased cellular metabolism resulting from therapy, which would increase local oxygen consumption. This study demonstrates the potential of PAUS imaging in monitoring HCC tumor response to sorafenib therapy.

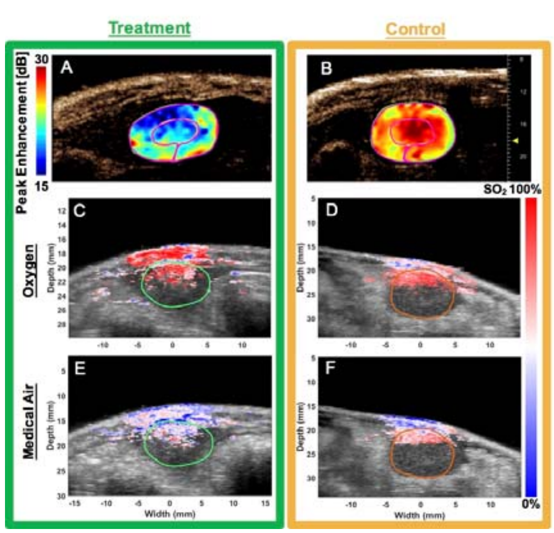

4E-5

11:30 am **_In Vivo_ Photoacoustic Quantification of Brain Tissue Oxygenation for Neonatal Piglet Graded Ischemia Model using Microsphere Administration**

Jeeun Kang[1], Haichong Zhang[1], Ewa Kulikowicz[2], Ernest Graham[2], Raymond Koehler[2], Emad Boctor[1,2,]; [1]*Johns Hopkins University, Baltimore, USA,* [2]*Johns Hopkins University School of Medicine, USA*

Background, Motivation and Objective

Perinatal arterial ischemic stroke can result in long-term deficits in motor, cognitive, attention, and executive functions as well as persistent seizures. Rapid diagnosis is critical for newborns who suffer a focal ischemic stroke in order to distinguish prenatal vs. postnatal stroke, and to differentiate perinatal stroke from global hypoxic ischemia (HI). In this study, we present photoacoustic (PA) quantification for brain tissue oxygenation on an in vivo focal stroke model based on a newborn piglet.

Statement of Contribution/Methods

We injected incremental doses of 15-µm microspheres into a single hemisphere to produce graded ischemia and track the changes in HbO2, deoxyHb, and tHb as a function of the percent change of laser Doppler flowmetry (LDF) bilaterally placed. Near-infrared PA spectrum at 21 wavelengths (700 to 900 nm in 10 nm increments) was acquired from the sagittal sinus using an optical parametric oscillator fed by an Nd:YAG pulsed laser (Phocus, Opotek Inc., USA) and ultrasound research package (SonixDAQ, Ultrasonix Corp, Canada). To calculate deoxy Hb, HbO2, and tHb, we derive a least square error fit between PA spectrum and the reference absorbance of Hb at varying O2 saturation. The in vivo experimental protocol is as follows; after obtaining baseline measurements of arterial blood gases, arterial blood pressure, LDF, and PA spectrum, we injected 3 million spheres over a 5-min period through a catheter placed in an ascending pharyngeal artery. Additional doses of 3 million spheres were made, and measurements were repeated until LDF in the affected hemisphere is < 20% of baseline.

Results/Discussion

We found that subsequent injections of 3 million microspheres into the right ascending pharyngeal artery produced graded reductions in tHb and tissue HbO2 saturation (Fig. 1). The contralateral tHb and HbO2 saturation showed only minor changes, indicating that most of the microsphere emboli remained unilateral. LDF fell to <20% of baseline on the right side with little change on the left side. The results indicate that the PA imaging can quantify the graded reductions in tHb and tissue HbO2 saturation using the microsphere-induced graded ischemia, which occurs unilaterally, while the contralateral tHb and HbO2 saturation showed only minor changes, which are well correlated with LDF measurement.

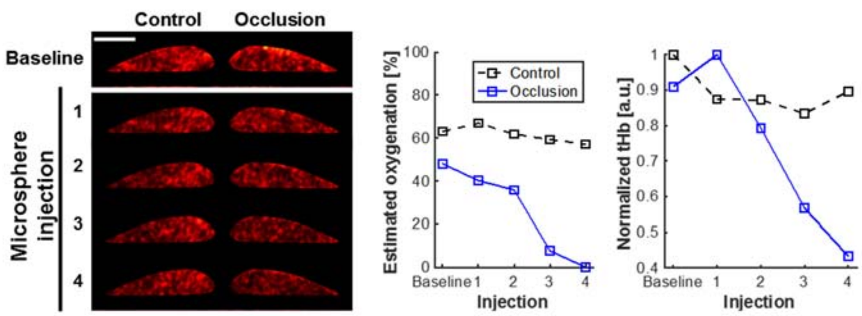

Figure 1. Left, tHb PA images of piglet cortex after serial injections of 15-µm plastic microspheres into the right ascending pharyngeal artery (Occlusion side). Scalp and skull image portion removed for clarity. Middle, multi-spectral-derived tissue HbO2, and Right, tHb intensity at 790 nm (near isobestic point) display progressive decreases over the 1st – 4th injection. 1st & 2nd dose =1.5 million spheres each; 3rd & 4th dose = 3 million spheres each.

4E-6

11:45 am **Endocavity Ultrasound and Photoacoustic Imaging System to Evaluate Fetal Brain Perfusion and Oxygenation: Preliminary ex vivo studies**

Yan Yan[1], Maryam Basij[1], Edgar Hemandez-Andrade[2,3], Sonia Hassan[2,3], Mohammad Mehrmohammadi[1]; [1]*Department of Biomedical Engineering, Wayne State University, Detroit, Michigan, USA,* [2]*Department of Obstetrics and Gynecology, Wayne State University, Detroit, Michigan, USA,* [3]*Perinatology Research Branch, Wayne State University, Detroit, Michigan, USA*

Background, Motivation and Objective

Perinatal asphyxia, or oxygen deprivation during the birth, is believed to cause approximately 23% of newborn deaths worldwide and to lead to neurological disorders that can persist throughout the child's lifetime [1-4]. Unfortunately, FHRM is associated with false-negative and false-positive diagnoses, limiting the ability of clinicians to identify fetuses at risk of metabolic acidosis [5-9]. Ultrasound (US) and Photoacoustic (PA) imaging have shown to be capable of imaging blood flow and hemoglobin oxygen saturation (SO_2) in tissues and blood vessels. Photoacoustic (PA) imaging has been steadily growing in recognition as a complement to US, by providing functional information, such as blood oxygen saturation. In this study, we implemented and characterized a transvaginal USPA imaging system and demonstrated its utility for imaging ex vivo animal brain (in a sheep model) and its reliability in measuring blood SO_2.

Statement of Contribution/Methods

Endocavity US and PA (ECUSPA) imaging probe consists of a transvaginal US transducer (ATL C9-5) and an optimized integrated light delivery using large-core multimode optical fibers. The developed ECUSPA imaging system could be utilized to acquire the co-registered US, Doppler US and spectroscopic PA (sPA) images. The system was characterized by a course of tissue- mimicking and ex vivo experiments. Specifically, a set of experiments were performed in which excised sheep brain was imaged to demonstrate the accessible imaging depth. In addition, the accuracy of sPA (λ varies between 750 and 840 nm) in measuring blood SO_2 was evaluated in an ex vivo blood chamber experiment in which the blood oxygenation was varied using O_2 and N_2 gas purge. The SO_2 obtained from sPA measurements were compared to a standard blood gas analyzer (BGA).

Results/Discussion

Our results indicate the possibility of detecting PA signal arises from injected blood inclusions (within an excised sheep brain through a cut cranial window) up to a depth of 25 mm which could be sufficient to monitor cortical blood flow in vivo. We also previously demonstrated the penetration depth of 38 mm in imaging blood samples embedded in porcine tissue. Regarding blood SO_2 measurements, our results indicate a high correlation between sPA and BGA measurements (R^2=0.87) when the blood SO_2 was varied between 47 and 100 percent (heparinized sheep blood). In addition, we demonstrated the ability of the system to measure blood perfusion through calculating fractional moving blood volume (based on Doppler US) and the vessel sizes.

The results of this study can pave the way for further development and validation of the system in vivo. While USPA imaging of the adults' brain is associated with certain limitations due to the presence of skull, thin and relatively soft skull bone in fetus and neonates, and especially the presence of fontanelles allows for accessing the cortical regions of brain for imaging [10].

5E - PAT - Acoustic Tweezers and Particle Manipulation

Blue Room

Friday, September 8, 2017, 10:30 am - 12:00 pm

Chair: **Koen van Dongen**
Delft University of Technology

5E-1

10:30 am **Variable-Focus Liquid Crystal Lens Using Ultrasound Vibration**

Yuki Shimizu[1], Daisuke Koyama[1], Akira Emoto[1], Kentaro Nakamura[2], Mami Matsulawa[1]; [1]*Faculty of Science and Engineering, Doshisha University, Kyotanabe, Kyoto, Japan,* [2]*Laboratory for Future Interdisciplinary Research of Science and Technology, Tokyo Institute of Technology, Yokohama, Kanagawa, Japan*

Background, Motivation and Objective

Nematic liquid crystal is widely used in optical devices such as liquid crystal displays. The optical characteristics of liquid crystal devices (ex, birefringence) can be controlled by applying an electric field because the liquid crystal molecules have electric dipoles. Although indium tin oxide (ITO) is generally employed as the transparent electrode material, ITO needs the rare metal indium and has problems of low electric conductivity and transparency. Our group has proposed a novel control technique of liquid crystal molecular orientation using ultrasound vibration without using ITO [1]. In this report, an optical variable-focus liquid crystal lens using ultrasound was discussed.

Statement of Contribution/Methods

An ultrasonic liquid crystal lens was fabricated (see Fig. 1(a)). The lens has no moving mechanical parts and no transparent electrodes and consists of a simple structure; a nematic liquid crystal layer with a thickness of 50 μm is formed between two circular grass plates (Φ_a = 30 mm; Φ_b = 15 mm) with a thickness of 0.7 mm. An annular PZT ultrasonic transducer (outer diameter: 30 mm; inner diameter: 20 mm; thickness: 1.0 mm) was bonded on the glass plate (a). By exciting the transducer at the resonance frequencies, the flexural vibration modes were generated on the liquid crystal lens. The acoustic radiation force changed the molecular orientation of the liquid crystal so that the incident light to the lens was refracted and the transmitted light could be focused.

Results/Discussion

In the default condition with no input voltage, the transmitted light was not refracted and focused because the liquid crystal molecules oriented perpendicularly to the glass plates (Fig. 1(b)). With the ultrasound excitation at the fundamental resonance frequency of 36.1 kHz, the concentric flexural vibration mode with the half wavelength of approximately 11 mm was generated on the glass plates. The liquid crystal molecular orientation then was changed by acoustic radiation force, and the transmitted light was refracted and focused on the target (Fig. 1(c)). The focal point could be controlled rapidly and simply by the input voltage.

[1] S. Taniguchi, D. Koyama, Y. Shimizu, A. Emoto, K. Nakamura, and M. Matsukawa. Appl. Phys. Lett. 108 (2016) 101103.

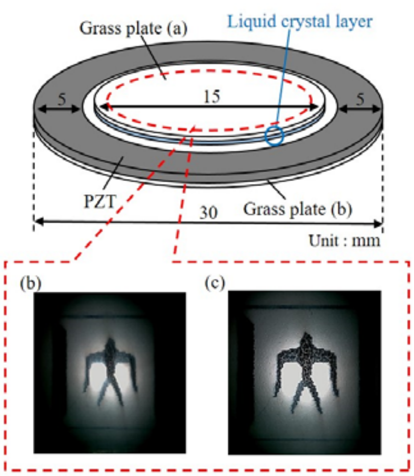

Figure 1. Ultrasonic liquid crystal cell; (a) configuration, (b) the vibrational distribution, and (c) the transmitted light distribution at 36.1 kHz.

5E-2

10:45 am **Acoustic Wave Directed Assembly of Conjugated Polymers**

Yuyin Xi[1], David Li[1], Greg Newbloom[1], Matthew O'Donnell[2], Lilo Pozzo[1]; [1]*Chemical Engineering, University of Washington, seattle, Washington, USA,* [2]*Department of Bioengineering, University of Washington, Seattle, USA*

Background, Motivation and Objective

Conjugated polymers (CP) have attracted a great deal of attention because they are flexible, light weight, economical, and highly scalable. They are widely used in organic electronics, such as organic field effect transistors, photovoltaics, thermoelectrics, spintronics and electronic skins. However, the electrical performance of CP is still limited due to the inefficient charge hopping between polymer chains.

Statement of Contribution/Methods

To facilitate long range charge transport, thus enhancing the conductivity, π-π stacking is usually desired. In this study, acoustic waves have been demonstrated to effectively assemble poly(3-hexylthiophene) (P3HT) into nanofibers that are micrometers long and have ordered molecular structures. The mechanism was revealed by systematically exposing the sample solutions to peak negative acoustic pressure varying from 0.05 to 7.2 MPa generated from a 1.24 MHz spherically focused transducer outputting 40 cycle bursts at a pulse repetition rate of 6.2 KHz. A custom-made polyvinylidene fluoride unfocused transducer was positioned off-axis from the transmitting transducer to passively detect cavitation. In addition to varying pressure, the effect of varying sonication time was investigated. The percentage of aligned polymer fibers was estimated using ultraviolet-visible spectroscopy as well as small-angle neutron scattering (SANS). The fiber dimensions were quantified by transmission electron microscopy and SANS.

Results/Discussion

The study demonstrated that acoustic energy can be used to assemble and enhance the crystallinity of conjugated polymers in solutions. Although the percentage of polymer fibers increases with increasing acoustic pressure and sonication period, the results indicate that cavitation must be present for directed assembly. The use of acoustic energy is a simple, highly tunable, and versatile method to effectively promote nanofiber formation. It opens doors to engineering the structure of conjugated polymers for better charge transport, which can enhance the performance of various organic electronics.

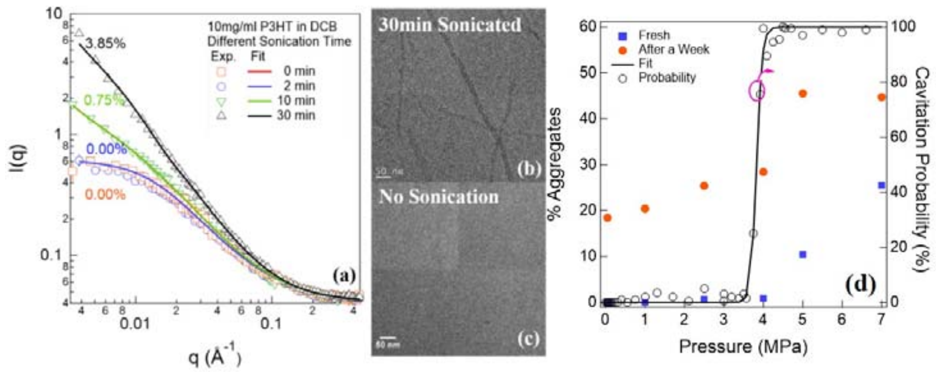

Figure (a) 1-D SANS scattering profile of P3HT in dichlorobenzene sonicated for different durations. TEM images of P3HT samples sonicated for (b) 30 and (c) 0 min. (d) Cavitation probability plotted along with percent aggregates of P3HT in chloroform immediately after and one week after the sonication as a function of peak negative pressure. The right axis is associated with the filled markers and while the left axis is the open markers and black line.

5E-3

11:00 am A Few Twists Regarding the Momentum of Shaped Beams

Gabriel Spalding[1], Patrick Dahl[2], Zhengyi Yang[3], Peter Glynne-Jones[4], Michael P. MacDonald[5], Christine Demore[6], Sandy Cochran[7]; [1]*Physics, Illinois Wesleyan University, Bloomington, IL, USA,* [2]*ECE, University of Illinois at Chicago, Chicago, IL, USA,* [3]*School of Physics & Astronomy, University of St Andrews, St Andrews, United Kingdom,* [4]*Engineering Sciences, University of Southampton, Southampton, United Kingdom,* [5]*Physics & Medicine, University of Dundee, Dundee, United Kingdom,* [6]*Sunnybrook Research Institute, University of Toronto, Toronto, Ontario, Canada,* [7]*School of Engineering, University of Glasgow, Glasgow, United Kingdom*

Background, Motivation and Objective

In the acoustic tweezers literature, it is sometimes stated that there would be no radiation pressure in the absence of nonlinearity. In fact, such a circumstance would allow violation of the Second Law of Thermodynamics, an issue we discuss in this talk. In the limit where the Second Law applies, all radiant forms of energy must carry an associated momentum. Shaped beams offer (along with shaped targets) opportunity for discussion of the respective advantages of conservative and non-conservative forces. Commonly in acoustic trapping, conservative, gradient-induced mechanisms (e.g., standing waves) are used to manipulate matter. Such situations are reasonably described in terms of potential energy landscapes, an approach also applied to optics, for applications such as cell sorting [MacDonald et al, Nature 426 (2003)]. No such description is possible for radiation pressure, which is non-conservative, a distinction that is sometimes muddled in the literature, although it was made clear even in early landmark papers.

Statement of Contribution/Methods

Our ``sonic screwdriver'' makes use of two non-conservative mechanisms: levitation by radiation pressure and rotation by transfer of azimuthal momentum components [Demore et al, PRL 108 (2012)], and extends what has been learned from analogous experiments in optics. We also note that the term ``tractor beam'' has often been reserved to describe an effect involving non-conservative forces, and demonstrate an attractive force produced in such an arrangement, even against a net momentum flux [Demore et al, PRL 112 (2014)]. 

Results/Discussion

We place the discussion of shaped beams in the larger context of ongoing work within acoustics, analogous work in optics, and within the broader field of physics and its history. It is hoped that providing such context may help to broaden awareness of the options within the experimentalist's toolkit.

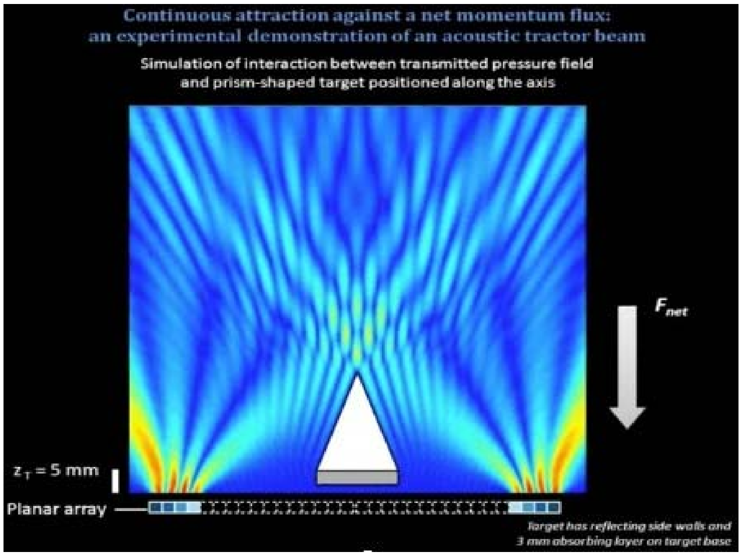

5E-4

11:30 am Massive Manipulation of Cells for Drug Delivery Using Phononic Crystals

Fei Li[1], Jinsui Yu[1], Chen Wang[1], Long Meng[1], Mian Chen[1], Fei Yan[1], Feiyan Cai[1], Hairong Zheng[1]; [1]*Shenzhen Institutes of Advanced Technology, Chinese Academy of Sciences, China, People's Republic of*

Background, Motivation and Objective

The acoustic microstreaming originating from microbubbles′ linear oscillations can be used as a potential cell sonoporation tool for drug delivery and gene transfection. However, this bubble-based method suffers from bubble instability, non-uniform size, unreliable performance, and inconvenient trapping. In order to overcome the above drawbacks, in this study, we proposed a massive drug delivery method based on the modulated acoustic field through phononic crystal plate (PCP), which combined with the localized acoustic radiation force (ARF) for trapping and aligning cells and tunable acoustic-induced vortex array around the trapping positions for the enhancement of cell permeability.

Statement of Contribution/Methods

The PCP was made of a thin steel plate patterned with a periodical array of rectangular gratings on the bottom sides.The corresponding A_0 mode of the plate can be excited at the frequency of 3.77 MHz at normal incidence. The water chamber was constructed by PDMS walls, a quartz substrate and a piece of glass cover. Continue sine signals were generated to excite a PZT adhering to the substrate. Polystyrene (PS) spheres with a diameter of 1µm were used as tracers for the streaming visualization. Cancer cells with a diameter of 15µm were injected into the water chamber. Propidium iodide (PI) and calcein-AM were used to determine the cell membrane permeability and verify the cell viability, respectively. The vortex can be modelled as the second order forced creeping flow driven by the volume force from the first order acoustic field.

Results/Discussion

Both the simulation and experiment showed the existence of acoustic-induced vortex array. The rotation speed of tracers was dependent on the acoustic power. We experimentally observed that cancer cells were aligned and trapped by the acoustic trapping force generated from the periodic gradient field of the A_0 mode Lamb wave under a low voltage, and can only be observed by the optical imaging. As the voltage increased, the increase of vortex rotation speed led to the enhancement of cell permeability. And due to the permeation of PI, the cancer cells can be observed by the fluorescent imaging. The viability of cells was verified by the calcein-AM staining assay (green fluorescence). This system might provide massive drug delivery with a simple, disposable, scalable and reliable microfluidic device.

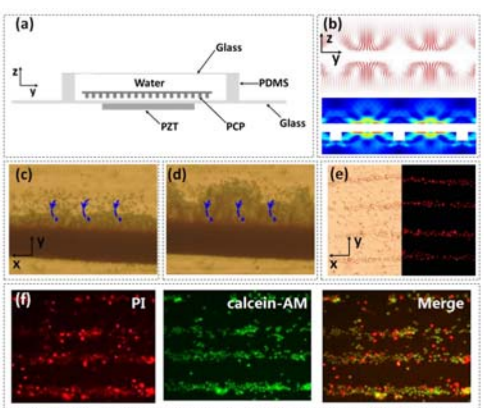

Figure 1 (a) Scheme of experimental setup in yz plane; (b) Simulated acoustic-induced vortex array of the resonant PCP and its shear stress distribution; (c) Vortices under a low acoustic power; (d) Vortices under a high acoustic power; (e)Observations of trapping and aligning cancer cells by the optical (left) and fluorescent imaging (right); (f) PI/calcein-AM double staining assay to verify the cell permeability and viability.

11:45 am **Noncontact Manipulation and Evaluation of Hela Cells Using Ultrasound Vibration**

Tomohiro Otuska[1], Ryota Yamamoto[1], Daisuke Koyama[2], Mami Matsukawa[2]; [1]*Faculty of Life and Medical Sciences, Doshisha University, Japan,* [2]*Faculty of Science and Engineering, Doshisha University, Japan*

Background, Motivation and Objective

Contact manipulation using a micropipette is widely used for cell culture and evaluation. However, the operation efficiency and the damage on the cells depend on the individual skills. A technique for manipulating a micro biological material with high accuracy and selectivity is required. Our group has been investigating noncontact ultrasonic manipulation techniques using acoustic standing wave. In this report, ultrasonic manipulation, separation, and evaluation of HeLa cells in a microchannel are discussed.

Statement of Contribution/Methods

Two ultrasound PZT transducers (10.0×10.0×1.0 mm3) were attached to both ends of a glass substrate (60.0×10.0×2.0 mm3) with a microchannel (40.0×1.0×1.0 mm3) filled with the suspension of HeLa cells (average diameter of 15 µm) and a culture medium (E-MEM) (Fig. 1). By applying an input voltage to the two transducers at the resonance frequency of 1.4 MHz, an acoustic standing wave was generated in the channel by flexural vibration of the substrate, and the HeLa cells can be trapped along the nodal lines. The position of the standing wave can be controlled by the driving phase difference between the two transducers so that the HeLa cells can be manipulated.

Results/Discussion

By changing the driving phase difference, the HeLa cells could be trapped and moved in the same direction of the movement of flexural vibration along the channel (286~350°, 0.478 µm/deg.) (Fig. 1(a)). Also the HeLa cells trapped by the standing wave were deformed due to the acoustic radiation force, the change in shape of cells increased by increasing the input voltage (Fig. 1(b)). Non-contact evaluation of cell stiffness seems possible by comparison between cell shapes before and after the acoustic compression. In addition, the intensity of the acoustic radiation force to the HeLa cells depended on the condition of the cell; the voltage threshold for trapping of the live cells (4.0 Vpp) was lower than that of the dead cells (5.0 Vpp). This is attributed to the difference in the acoustic impedance of cells, enabling the noncontact separation techniques of cells.

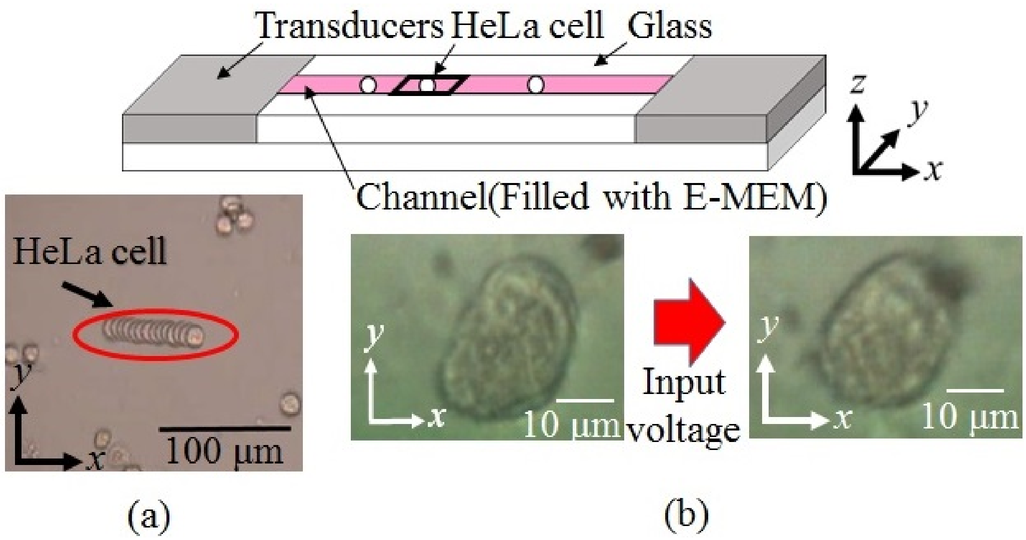

6E - Sensors

Hampton Room

Friday, September 8, 2017, 10:30 am - 12:00 pm

Chair: **David Greve**
Carnegie Mellon University

6E-1

10:30 am Thermal Wavefront Imaging Using GHz Ultrasonics

Mamdouh Abdelmejeed[1], Justin Kuo[1], Amit Lal[1]; [1]*Electrical and computer engineering, Cornell University, Ithaca, NY, USA*

Background, Motivation and Objective

In many cases it is important to measure the temperature and the thermal conductivity of an object by contact. Examples include sensors in robot hands, and sensors to measure material properties during manufacturing. In this paper, we demonstrate the ability to measure the time-of-flight (TOF) as a function of time after mechanical contact to the transducer, and show that the rate of TOF change can indicate the thermal conduction properties of the object being contacted. Using this data we can distinguish different materials with small differences in structure. We have previously reported the use of thin film GHz Aluminum Nitride (AlN) piezoelectric transducers on top of a silicon wafers in configurable ultrasound communications, through-silicon-vias (TSVs), fingerprint sensing, and delay references. Our device is expected to have high yield and reliability owing to elimination of a release step, integration with CMOS and compatibility with CMOS drive voltage (< 3 Vpp).

Statement of Contribution/Methods

The outer ring of the AlN Transducer (Fig 1A.) is used to transmit the RF wave packet through silicon wafer. The inner and outer radiuses of the transmitting ring are 73 µm and 93 µm , respectively. As shown in Fig. 1B, the acoustic wave packet propagates through silicon, reflects from the back side of silicon and is received by the circular transducer in the middle of the transmitting ring transducer. The acoustic wave speed has a negative temperature coefficient. As a result, as a material touches the back side of silicon, the temperature of silicon is changed by heat conduction, that causes the TOF of the wave packet to increase. The rate of TOF change is affected by the thermal conductivity of the contacted material – therefore both temperature and thermal conductivity can be measured by measuring TOF.

Results/Discussion

The transmit ring was driven with an RF pulse of 100ns at 3.1 GHz, and a 4 GHz Agilent Oscilloscope is used to measure the TOF of received pulse. The received signal is shown in Fig. 1C. A human finger (~37°C) touches the silicon chip and the TOF of the wave packet is measured after touching and removing the finger (Fig. 1D). The final TOF is 159.57 ns, corresponding to body temperature (37° C), and dToF/dt can be used to model the heat permeation resistance at the skin-silicon interface due to air in the fingerprint ridges.

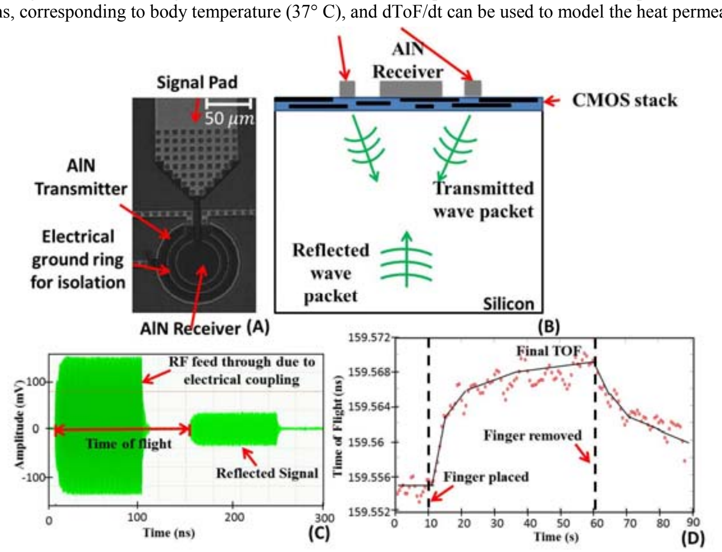

6E-2

10:45 am Directivity of a Planar Fabry-Perot Optical Ultrasound Sensor

Danny Ramasawmy[1], James Guggenheim[1], Paul Beard[1], Benjamin Cox[1], Bradley Treeby[1]; [1]*Medical Physics and Biomedical Engineering, University College london, United Kingdom*

Background, Motivation and Objective

The Fabry-Perot (FP) polymer film sensor can detect ultrasound over a broadband frequency range (tens of MHz), with small element sizes (tens of microns), and high sensitivity. It has been used extensively in photoacoustic imaging as well as general ultrasound field characterisation. Although it will clearly affect the ultrasound field measurements, the directional response of the sensor has not been widely studied. The objective of this work was to develop an analytical model to study how the various wave types propagating in the multilayer FP sensor affect the directionality. This is critical to optimise the design of the FP sensor, and to reduce sensor-related image artefacts.

Statement of Contribution/Methods

The global matrix (GM) method was used as the basis for a model of the FP sensor directivity. This can incorporate an arbitrary number of layers with different elastic properties, as well as acoustic absorption. The sensors were modelled as 6 layer structures, including the propagation medium, barrier coating, mirrors, spacer, and backing.

The elastic properties of the sensor layers were estimated using a multi-parameter optimisation to fit the model (Fig. 1b) to measurements of the directivity made using a broadband laser-generated ultrasound pulse (Fig 1a). To understand the effect of the various wave modes on the directivity, dispersion curves (Fig. 1c) were calculated by finding pairs of values for frequency and phase speed for which the determinant of the GM became singular.

Results/Discussion

The multi-layered model of the FP ultrasound sensor directivity gives very good agreement with experimental measurements. Using the model, this allows the features in the angle-dependent frequency response to be associated with different wave phenomena, giving greater insight into the sensor's response. In particular, the vertical banding was associated with critical angles for different wave types, and the curved peaks were associated with different combinations of Scholte and Stoneley waves. The developed model will underpin future attempts to design sensors with improved directional responses, and - when the sensor is used as an imaging array - will be a key component in the amelioration of image artefacts.

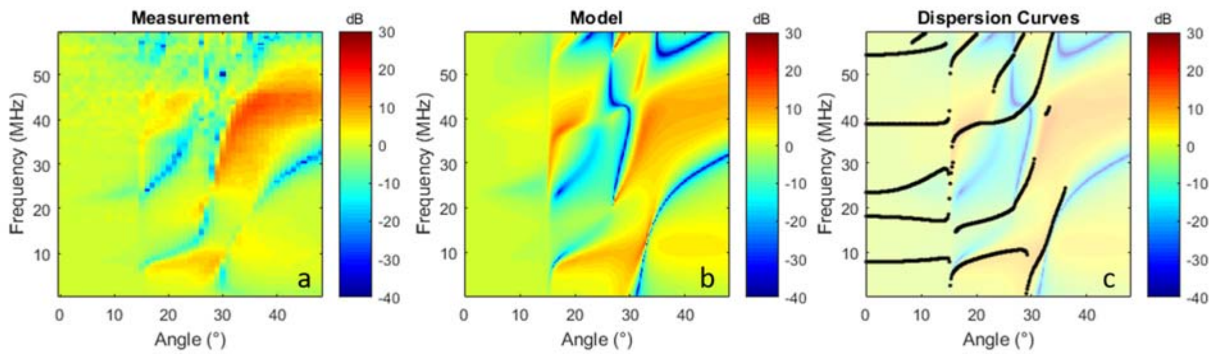

6E-3

11:00 am Stability of $PtAl_2O_3$-Based Electrode Langasite SAW Sensors with Al_2O_3 Capping Layer and Yttria-Stablized Zirconia Sensing Layer

Anin Maskay[1,2], Armando Ayes[1,2], Mauricio Pereira da Cunha[1,2]; [1]*Department of Electrical and Computer Engineering, University of Maine, Orono, Maine, USA,* [2]*Laboratory for Surface Science and Technology, University of Maine, Orono, Maine, USA*

Background, Motivation and Objective

Surface acoustic wave (SAW) sensors have been finding increased usage in a variety of manufacturing and automotive industries as torque, temperature, and pressure sensors. Gas, liquid, biochemical, strain, and mass sensors are other promising applications for aerospace, power plants, process dynamic monitoring, structural health monitoring, and condition-based maintenance. For high-temperature harsh-environment applications, battery-free wireless operation associated with sensor robustness, small profile, and mass fabrication capability make SAW sensors a very attractive solution. For high-temperature (<800°C) gas sensor applications, the stability of SAW sensor platform including protective and sensing film layers must be guaranteed over time and under temperature cycling conditions.

Statement of Contribution/Methods

This paper reports on the performance and stability of langasite SAW sensor resonator platform using $PtAl_2O_3$-based electrode (LGS $PtAl_2O_3$ SAWR), using atomic layer deposited (ALD) Al_2O_3 protective layer and yttria-stabilized zirconia (YSZ) gas sensing layer. The effect of 50nm thick Al_2O_3 or YSZ layers on resonator-based SAW sensor amplitude, resonant frequency, and temperature sensitivity responses were investigated. In addition, the stability of the frequency responses of SAW sensors have been monitored during multiple 110-hour temperature cycling (over 620 hours in total) from 300°C to 750°C.

Results/Discussion

The figure shows a 110-hour cycling test of a LGS $PtAl_2O_3$ SAWR sensor with an ALD Al_2O_3 protective layer (4-hour holds at 750°C and 300°C; 10-hour soaking at 750°C). The measured frequency deviation at 750°C over six of these 110-hour cycling tests was 0.04%. Similar stable responses were measured for YSZ covered SAW sensors. The inset shows fractional frequency variation as a function of temperature for two SAW sensors, with and without ALD Al_2O_3, with respective slopes of -4.48 x 10^{-5}ppm/ºC and -4.63 x 10^{-5}ppm/ºC. This 3.2% discrepancy is within experimental error, suggesting that the film does not significantly affect the SAW sensor temperature coefficient of delay. The results obtained confirm that the presence of the ALD Al_2O_3 protective layer or the YSZ sensing layer do not compromise the stability of high-temperature harsh-environment SAW sensors, validating their use for the aforementioned applications.

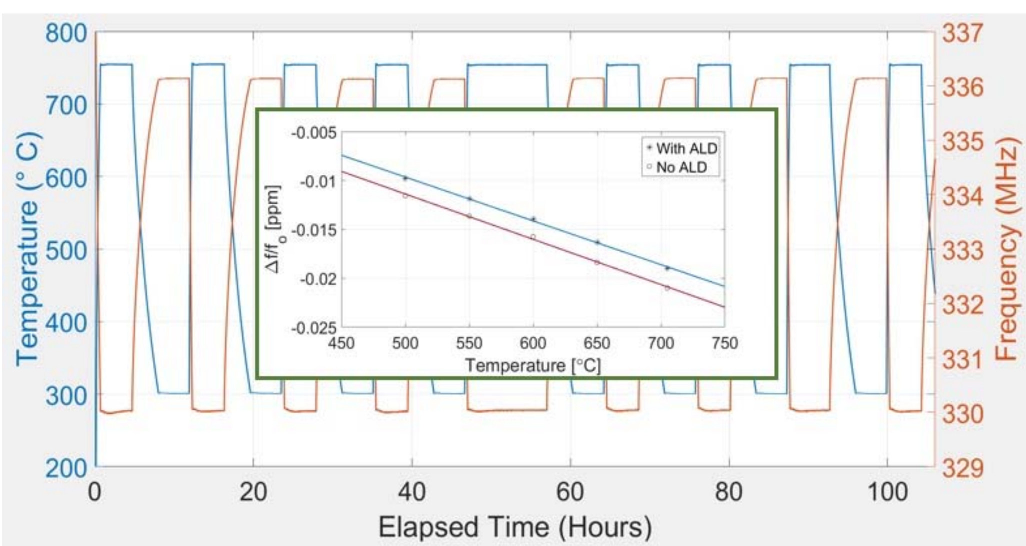

6E-4

11:15 am Multitouch Touchscreen using Reverberant Lamb Waves

Kamyar Firouzi[1], Amin Nikoozadeh[1], Thomas E. Carver[1], Butrus T. Khuri-Yakub[2]; [1]*EE, Ginzton Lab, Stanford university, STANFORD, CA, USA,* [2]*EE, Stanford University, STANFORD, California, USA*

Background, Motivation and Objective

Touchscreen sensors are widely used in many devices such as smart phones, tablets, laptops, etc. There are many different types of modalities that enable sensing the touch. The dominant technologies on the market are the capacitive, resistive, acoustic or ultrasound, and optical touch systems. None of these technologies are perfect and each has some advantages and disadvantages. Capacitive touch technologies are the most common in the industry. However, hardware complexity, high manufacturing cost, and high power consumption have impeded their feasibility for certain applications such as larger screens. Acoustic/ultrasound technologies due to their simplicity, ease of manufacturing, and low cost have been identified as suitable alternatives for a wide spectrum of applications. However, lack of robustness and multi-touch capability have made them fall short as competitive technologies.

We present design, analysis, and implementation of an ultrasonic touchscreen system that utilizes interaction of transient Lamb waves with objects in contact with the screen. It attempts to improve on the existing ultrasound technologies, with the potential of addressing some of the weaknesses of the dominant technologies, such as the capacitive or resistive ones. Compared with the existing ultrasonic and acoustic modalities, among other advantages, it provides the capability of detecting several simultaneous touch points and also a more robust performance.

Statement of Contribution/Methods

The Lamb wave touchscreen attempts to reconcile the key features of the reverberant field with the benefits of the lowest order Lamb modes. Spreading of the wave energy in a reverberant field leads to multiple interrogations of each point in the enclosure, suggesting that upon registering a longtime response of the system at only a few locations in the domain, any substructural changes in the enclosure can be sensed with sufficient information carried by the wave energy flow.

This motivates a system consisting of small transducers integrated with a plate. The transducers are pulsed selectively and repeatedly to create propagating Lamb waves inside the plate. The field is then measured at a selection of the transducers (which can include the transmitters as well). Upon having a touch, a local perturbation is created at the touched region, and hence, a portion of the wave field is absorbed through the touch(es). This absorption alters the base signals in many ways such as by reducing the energy, introducing phase-shifts, etc. We also present a localization algorithm that can detect several touch points with a very limited number of measurements (one or two).

Results/Discussion

We will present an in-lab prototype, implementation, and several test results demonstrating the capability of detecting many simultaneous touch points. We will discuss robustness and sensitivity to temperature and environmental noise and present a noise compensation strategy.

6E-5

11:30 am Chemical and Biological Sensing using Acoustic Wave Propagation and Nano-scale Phenomena

Venkat Bhethanabotla[1]; [1]*Chemical & Biomedical Engineering, University of South Florida, Tampa, Florida, USA*

Background, Motivation and Objective

Surface acoustic wave propagation in piezoelectric substrates is combined with nano-scale phenomena in sensing layer materials to realize practically viable chemical and biological sensors in our group. Ab initio electronic structure, molecular dynamics and finite element models are constructed to design these sensors and sensing materials, and understand sensing mechanisms at multiple length and time scales. Several design advances to the surface acoustic wave (SAW) device to improve sensitivity, enable non-specific binding removal and increase incubation times will be presented. One result of these studies is a SAW biosensor in which Rayleigh and Love waves are propagated in orthogonal directions to achieve mixing, non-specific binding removal and sensing in the same device for biosensing applications. Improved incubation times, removal of non-specifically bound proteins to improve sensitivity, reduce false determinations and improve selectivity, and sensing are simultaneously realized in devices constructed in Langasite and ST quartz, and results will be presented.

Several applications of SAW devices in chemical and biological sensing wherein nano-scale phenomena in sensing materials is utilized to improve sensor properties will be presented. In one application, interaction of hydrogen with a palladium film is replaced with interaction with palladium nanoparticles loaded on flexible single-walled carbon nanotube (SWCNT) surfaces. This allows for a robust hydrogen sensor using acoustic wave devices. In the second application, enhancement of luminescence by silver nanocubes is leveraged to construct an immunofluorosensor which is orders of magnitude more sensitive than without this plasmonic enhancement. Combined with a Rayleigh wave SAW device, a sensitive, selective and fast-responding immunofluorosensor is realized. In a third application, carcionoembryonic antigen (a cancer biomarker) is detected at clinically-relevant pg/ml levels with a Love wave device using gold nanoparticle-based nanoprobes. Details will be presented in this talk.

Statement of Contribution/Methods

Results/Discussion

7E - CMUT Technology

Empire Room

Friday, September 8, 2017, 10:30 am - 12:00 pm

Chair: **Tomas Gomez**
CSIC, Madrid

7E-1

10:30 am Wireless Power Recovery for Internet of Things Devices Using Pre-Charged CMUTs

Angad Rekhi[1], Butrus Khuri-Yakub[1], Amin Arbabian[1]; [1]*Electrical Engineering, Stanford University, Stanford, California, USA*

Background, Motivation and Objective

Capacitive micromachined ultrasonic transducers (CMUTs) are currently used in diagnostic ultrasound imaging systems, and are also attractive solutions for therapeutic and tracking applications in the body. Most CMUTs require a voltage bias for operation with high sensitivity and efficiency; this requirement can be inconvenient for some applications, such as catheter- and capsule-based endoscopy, while being prohibitive for others, such as wirelessly-powered millimeter-sized nodes for the Internet of Things.

The use of *pre-charged* CMUTs, which can operate without a voltage bias, holds the potential to open up an entire class of previously inaccessible applications for CMUTs that are incompatible, due to issues of size, complexity, or safety, with a voltage bias. Pre-charging can also greatly increase the safety and simplicity of system-level design for applications that are compatible with a voltage bias, but that do not require tuning of the bias in the course of operation.

Statement of Contribution/Methods

In this work, we present a methodology to experimentally demonstrate wireless power recovery using pre-charged CMUTs, accompanied by measurements of a long-term pre-charged CMUT operating in air. We also discuss ways of benchmarking acoustic transducers for the purpose of comparing their suitability for wireless power recovery.

Results/Discussion

Based on the methodology presented in this work, we are able to use a pre-charged CMUT to recover 5 µW at a simulated distance of 1.05 m from a ~60 kHz, 25 cm^2 transmitter array operating in air.

Our methodology and measurements demonstrate the potential of using pre-charged CMUTs for wireless power recovery in Internet of Things applications. More broadly, these results support the case for using pre-charged CMUTs in any application that is incompatible with the requirement of a voltage bias.

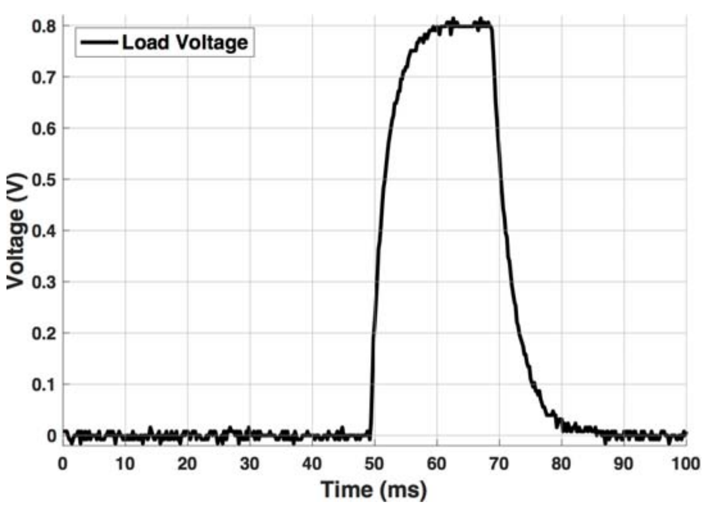

7E-2

10:45 am A Novel Amplitude Modulated Pulse Inversion Technique for High SNR of Tissue Harmonic Imaging using CMUT

Hiroaki Hasegawa[1], Shuntaro Machida[1]; [1]*Research and Development Group, Hitachi, Ltd., TOKYO, Japan*

Background, Motivation and Objective

Capacitive micro-machined ultrasonic transducer (CMUT) has various advantages in superior imaging quality and circuit integration capability compared with piezoelectric transducer. One of major challenges for CMUT is to perform tissue harmonic imaging (THI) that is widely used in clinical practice because it is difficult to obtain enough because of low signal-to-noise ratio (SNR) due to CMUT fs intrinsic nonlinear behavior. Conventional pulse inversion (PI) uses inverted transmit pulse pair with equal amplitude between the first (TX1) and the second pulse (TX2). Such inverted pulse is not practical for CMUTs due to the asymmetric transmission performance caused by the offset of initial membrane position of membrane. Although amplitude modulation (AM) technique has been proposed (Tanaka et al. IUS 2015) for THI using CMUT, the extracted harmonic signal lacks SNR for practical use. Here, we propose a novel technique that realizes high SNR under the restriction of nonlinear asymmetric behavior of CMUT.

Statement of Contribution/Methods

A novel Amplitude Modulated Pulse Inversion (AMPI) is proposed to suit asymmetric characteristics of CMUT. AMPI reduces the amplitude of TX2 to affordable value for CMUTs. Major drawback of reduced amplitude is noise increase due to from amplification of received echo. To suppress this side-effect, we added low frequency (LF) drive voltage which preserves movable room of membrane to maximize TX2 amplitude. Based on these concepts, TX1 and TX2 waveforms were arranged for ALOKA Arietta 850 ultrasound scanner and SML44 CMUT probe. The harmonic signals were calculated by pseudo-spectral nonlinear ultrasound propagation simulator.

Results/Discussion

Figure 1 shows simulated waveforms and power spectra comparing AM and AMPI techniques. The transmitted pressure amplitude for TX1 and TX2 is 1.3 and 0.65 MPa, respectively. Extracted harmonic signal of AMPI+LF improved by 10 dB compared to AM technique. Although LF component appeared around 0.5 MHz of harmonic signal in AMPI+LF result, this is easily removed by using a band-pass filter because this component is sufficiently low power and frequency.

These results indicates that Tthe proposed technique, AMPI+LF can was verified to improve extracted harmonic signal by 10 dB, and achieved enough SNR for practical tissue harmonic imaging for CMUT probes.

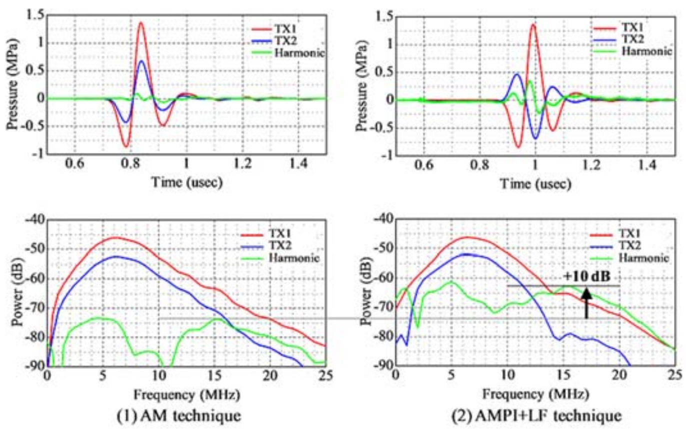

Fig. 1: Waveforms and power spectra of simulated harmonic signals extracted by (1) AM and (2) AMPI+LF techniques; Amplitude of both transmit pulses are equal. Polarity of 2nd pulse is inverted.

7E-3

11:00 am A Nonlinear Large Signal Equivalent Circuit Model for a Square CMUT Cell

Mohammad Maadi[1], Roger Zemp[1]; [1]*Electrical and Computer Engineering, University of Alberta, Edmonton, Alberta, Canada*

Background, Motivation and Objective

An accurate nonlinear lumped equivalent circuit model is used for modeling of capacitive micromachined Ultrasonic Transducers (CMUTs). Finite element analysis (FEA) is a powerful tool for the analysis of CMUT arrays with a few number of cells while with the equivalent circuit model, the entire behavior of a large-scale arbitrary CMUT array can be modelled in a very short time. Recently, an accurate nonlinear equivalent circuit model for un-collapsed single circular CMUT cells has been developed. However, the need for an accurate circuit model for CMUT cells with square membranes motivated us to produce a new nonlinear equivalent circuit model for un-collapsed CMUT cells on an infinite rigid baffle.

Statement of Contribution/Methods

Using analytical calculations, a precise large signal equivalent circuit model of square CMUT dynamics was developed. The model predicts many intrinsic properties of a square CMUT cell including resonance frequency, phase and magnitude of the membrane displacement, membrane velocity, electrical conductance, collapse voltage and etc. ANSYS 3D FEA was used to validate the equivalent circuit model predictions by performing static, pre-stressed harmonic and nonlinear transient analysis. The model was designed and implemented in a circuit simulator and then compared with FEM and experimental results. The results were compared with circular CMUT cells when the half side length of the square CMUT is assumed to be equal to the radii of the circular CMUT cell.

Results/Discussion

A single CMUT cell with square shaped silicon nitride membrane is considered in water immersion. The analytical relations of the square CMUT with arbitrary parameters were obtained and implemented in the nonlinear large signal equivalent circuit (Figure 1-a). The periodic portions of two CMUTs with 93 µm and 110 µm half-side-length and 14 µm thickness were modelled separately using FEM by applying the rigid boundary conditions (Figure 1-b). As shown in Figures 1-c and 1-d, the results show an excellent agreement with FEM results and there is a considerable error if we only use the equivalent circuit model of a circular CMUT cell. Model predictions of resonance frequencies and displacements (Figure 1-e) closely matched experimental vibrometer measurements of fabricated square CMUT cells.

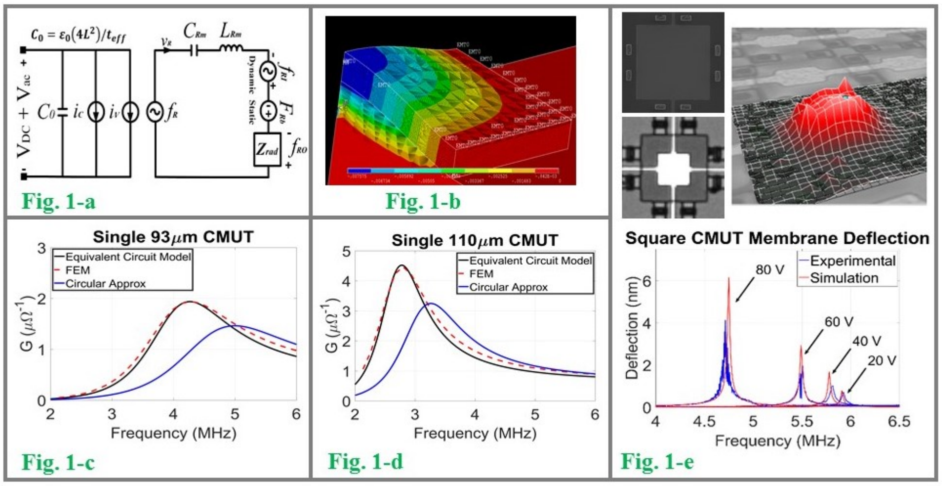

7E-4

11:15 am Ultra-Narrow Gap CMUT Cell Structure for Highly Sensitive Photoacoustic Imaging

Taiichi Takezaki[1], Masakazu Kawano[1], Hiroaki Hasegawa[1], Shuntaro Machida[1], Daisuke Ryuzaki[1]; [1]*Hitachi, Ltd., Japan*

Background, Motivation and Objective

Capacitive micro-machined ultrasonic transducers (CMUTs) offer several advantages over conventional piezoelectric transducers in terms of acoustic performance and circuit integration capability. In this study, we focus on the potential of CMUTs for the high receiving sensitivity which is strongly required for photoacoustic imaging applications. We propose an advanced CMUT cell design with an ultra-narrow gap to increase the receiving sensitivity.

Statement of Contribution/Methods

To realize a CMUT with a narrow gap of several tens of nanometers, sticking between the membrane and the bottom of the gap during fabrication must be avoided. To solve this issue, we precisely controlled the residual stress of materials of the membrane. The electromechanical coupling coefficient (k_t) of the fabricated CMUTs was estimated by measuring capacitance characteristics and compared with that of piezoelectric transducers.

Results/Discussion

Figure 1 (a) shows a cross-sectional SEM image of the fabricated 30 MHz CMUT with a 30 nm gap. Total thickness of the dielectrics between the top and bottom electrodes is 100 nm. The ultra-narrow gap CMUT was successfully fabricated without sticking between the membrane and the bottom of the gap. The effective distance between the top and bottom electrodes (g_{eff}) is 55 nm, which is the sum of the gap height of 30 nm and the effective thickness of 25 nm in 100 nm thick dielectrics with the dielectric constant of 4. Figure 1 (b) shows the dependence of k_t of the fabricated CMUTs on g_{eff}. At g_{eff} of 55 nm, k_t reaches 0.67. This value exceeds that of single crystal PZNT which is the most sensitive transducer at present. This result indicates that the proposed ultra-narrow gap CMUT can be a promising transducer for photoacoustic imaging application.

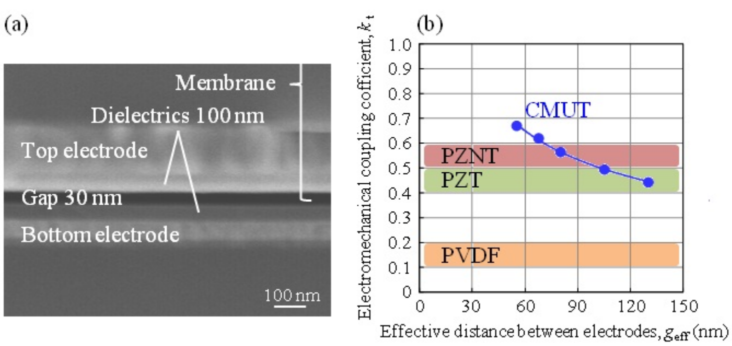

Figure 1: (a) Cross-sectional SEM image of a fabricated narrow gap CMUT with the effective distance between electrodes of 55 nm. (b) Dependence of electromechanical coupling coefficient (k_t) on effective distance between electrodes in the proposed CMUT.

7E-5

11:30 am Cavity Edge Insulator Extension in CMUT Cell for High Ultrasound Power Transmission

Shuntaro Machida[1], Taiichi Takezaki[1], Hiroaki Hasegawa[1], Hiroki Tanaka[1], Daisuke Ryuzaki[1]; [1]*Hitachi, Ltd., Tokyo, Japan*

Background, Motivation and Objective

As an ultrasonic transducer in medical imaging diagnostics, capacitive micro-machined ultrasonic transducers (CMUTs) have various advantages over conventionally used piezoelectric transducers, such as superior image quality and feasibility of circuit integration. CMUTs must be operated by applying not only high AC driving voltage (V_{AC}) but also high DC bias voltage (V_{DC}) to generate enough ultrasound power especially in the case of tissue harmonic imaging (THI). Applying high V_{DC} results in high electromechanical coupling constant required for THI, however, that causes electric breakdown between the top and bottom electrodes at the edge of the cavity where electric field concentrates. In this research, we propose a novel CMUT cell structure which has long breakdown lifetime against high V_{DC} at the edge of the cavity.

Statement of Contribution/Methods

The proposed CMUT cell structure extends the distance of the top and bottom electrodes only at the edge of the cavity by inserting an additional insulator between top and bottom electrodes. To maintain electromechanical coupling coefficient, the insulator thickness of the center part of the cavity is kept the same thickness of the conventional one. The total thickness of the insulator at the edge of cavity in the proposed structure is 1.75 times thicker than that in conventional structure. CMUT cells with and without the additional insulator at the edge of the cavity was fabricated. Electric breakdown voltage was measured by applying V_{DC}. Electric breakdown lifetime at a failure rate of 0.1% for standard linear probe used in medical imaging was estimated.

Results/Discussion

The electric breakdown voltage of the proposed structure became about 1.1 times higher than that of the conventional one. This is attributed to the decrease of electric field at the cavity edge by inserting the insulator between electrodes. The estimated breakdown lifetime of the proposed structure was estimated 25 orders of magnitude longer than that of the conventional one. As a result, the applicable V_{DC} which ensures the lifetime of ten years was increased from 0.68 of the ratio of V_{DC} to the collapse voltage (V_C) to 0.95 of V_{DC}/V_C for the proposed structure. This results shows that the proposed CMUT structure has enough endurance for high V_{DC} and enables high ultrasound transmission power for THI.

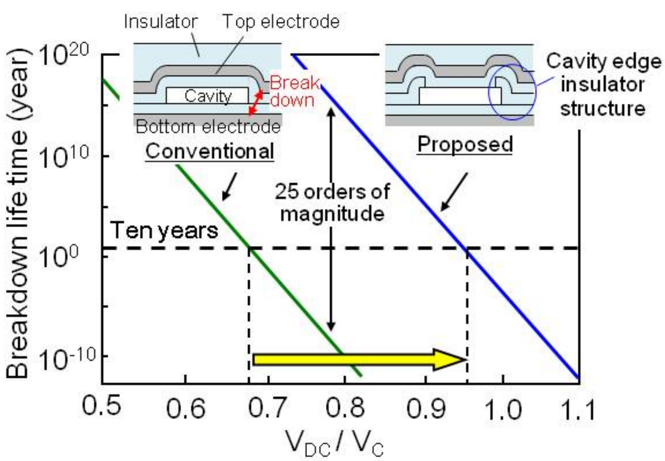

Figure: Estimated breakdown lifetime at 0.1% failure rate for 192 channel probe.

7E-6

11:45 am An Optically Transparent Air-Coupled Capacitive Micromachined Ultrasonic Transducer (CMUT) Fabricated Using Adhesive Bonding

Xiao Zhang[1], Feysel Y. Yamaner[1], Oluwafemi Adelegan[1], Ömer Oralkan[1]; [1]*Electrical and Computer Engineering, North Carolina State University, Raleigh, North Carolina, USA*

Background, Motivation and Objective

Transparent transducers are desired in the applications where optics and acoustics are combined, such as integrating ultrasound sensing or parametric arrays for directional sound in display, combined optical and acoustical microparticle manipulation, and backward-mode photoacoustic imaging. Some piezoelectric materials, e.g., PVDF, LNO, and PLZT, have been investigated for such applications. Besides, a Fabry-Perot (Etalon) optical ultrasound sensor can be used as a transparent ultrasound receiver. Implementing a transparent transducer in CMUT technology is desired to take advantage of wide bandwidth, ease of fabrication, and broad selection of processing materials. We have demonstrated a CMUT with ITO bottom electrode for improved transparency fabricated using anodic bonding. The main hurdle for the transparency in the visible wavelength range was a 2-µm silicon plate. In this work, we have designed and fabricated a CMUT with a glass plate using adhesive bonding and achieved improved transparency in the full visible wavelength range.

Statement of Contribution/Methods

The presented transparent CMUT was fabricated by a two-mask process using adhesive bonding (Fig. 1a), specifically for display-based air-coupled applications. A 1-mm-thick, 100-mm-diameter glass wafer with 200-nm ITO coating was used as the starting substrate. The ITO was etched to form the bottom electrodes and then a 4.5-µm thick SU-8 was spun and patterned to serve as the post and also the base for adhesive bonding. A 175-µm-thick glass wafer with 200-nm ITO coating was used as the top plate wafer. A 1-µm thick SU-8 layer was coated on the ITO to serve as the insulation layer. The plate wafer was flipped and bonded on the thick wafer at 120°C under 0.3-MPa pressure in vacuum.

Results/Discussion

The completed wafer is a single CMUT element. The wafer was placed on a "NC State University" logo to show the transparency (Fig. 1b top). The average transmission of the device is measured as ~70% in the 400-1000-nm wavelength range (Fig. 1b bottom). The electrical input impedance was measured in air (Fig. 1c). The resonant frequency of the fabricated device is ~ 62 kHz and the series resistance is ~30 Ω.

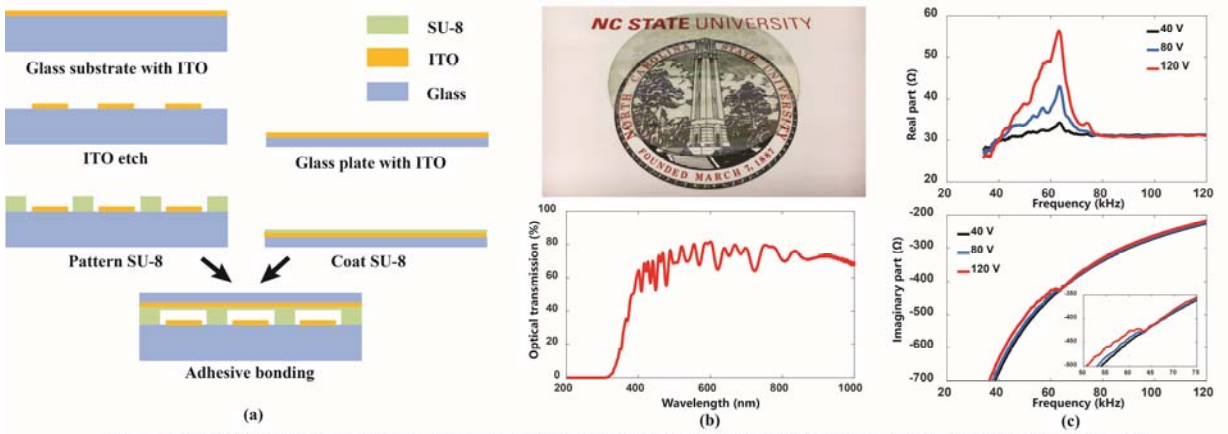

Fig. 1. (a) Simplified fabrication process flow; (b) Photo of the finished wafer on NCSU logo (top); Optical transmission measurement (bottom); (c) Electrical input impedance: Real part (top); Imaginary part (bottom).

1F - MTH: Brain

Regency Ballroom

Friday, September 8, 2017, 1:30 pm - 3:00 pm

Chair: **Jean-Yves Chapelon**
INSERM

1F-1

1:30 pm Targeted Brain BRICHOS Domain Delivery Induced by Focused Ultrasound for the Treatment of Alzheimer's Disease

Carlos Sierra[1], Lorena Galan-Acosta[2], Jenny Presto[2], Per Nilsson[2], Janne Johansson[2], Elisa Konofagou[1,3]; [1]*Biomedical Engineering, Columbia University, New York, NY, USA,* [2]*Neurobiology, Karolinska Institutet, Huddinge, Sweden,* [3]*Radiology, Columbia University, New York, NY, USA*

Background, Motivation and Objective

The BRICHOS domain is encoded in more than 30 genes associated with cancer, dementia (BRI2/ITM2b) and amyloid lung disease (proSP-C). Studies have demonstrated that it delays fibril formation and toxicity of amyloid-β peptide (Aβ) *in vitro* and in vivo, which plays a central role in the development of Aβ amyloid plaques, one hallmark of Alzheimer´s disease (AD). It has been shown that overexpression of proSP-C or Bri2-BRICHOS proteins delayed Aβ42 fibril formation in the brain and improved lifespan and locomotor function in Drosophila flies. Also, after peripheral administration, a low amount of Bri2-BRICHOS was detected in the brain parenchyma of wild-type mice, suggesting a poor passage through the blood-brain barrier (BBB). Hence our main objective is to increase the delivery rate in a safe and non-invasive way. Focused ultrasound (FUS) in presence of microbubbles has been proven to open the BBB locally, transiently and non-invasively.

Statement of Contribution/Methods

A spherical, single-element FUS transducer (center frequency 1.5 MHz) and a pulse-echo transducer (center frequency 10 MHz), used for passive cavitation detection, confocally mounted at the center of the FUS transducer, were used. FUS (pulse length 6.56 ms; pulse repetition frequency 5 Hz; duration 2 min; acoustic pressure 450 kPa) targeted mouse brains *in vivo* in the presence of lipid microbubbles for trans-BBB delivery of BRICHOS domain. The delivery was assessed by ex vivo immunohistochemistry (IHC) using a primary rabbit anti-surfactant protein-C antibody and permanent Alkaline Phosphatase red for developing the stains. BBB opening was confirmed in vivo by T_1-w magnetic resonance imaging. The overall brain histology was evaluated by hematoxylin & eosin staining for microscopic damage.

Results/Discussion

Successfully targeted brain BRICHOS domain delivery was achieved in 6 out of 10 cases. The delivery was assayed using IHC for proSP-C. In Figure 1, IHC visualized a significant uptake of the BRICHOS protein to neuronal cells according to their morphology in the FUS-targeted hippocampus section, confirming successful delivery. Mice were survived for 2 hours after sonication to allow the BRICHOS domain to diffuse to the parenchyma. Microhemorrhages were not detected in any mice. This study indicates a safe methodology for targeted brain BRICHOS domain delivery, with application to AD treatment.

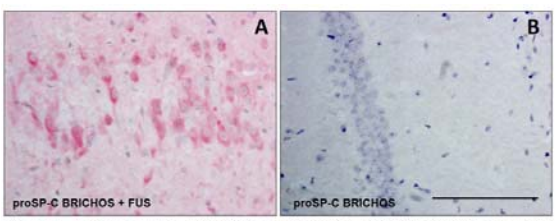

Figure 1. Representative IHC of delivered proSP-C BRICHOS (10 mg/kg) in FUS-targeted left hippocampal section (A) compared to the contralateral side (B) of wild-type mouse. Magnifications are 40X and scale bar in B, applied to both images, is 500 μm.

1F-2

1:45 pm Ultrasound-Induced Delivery of Erlotinib to the Brain is Not Enough to Counter Efflux Pumps

Matthieu Gerstenmayer[1], Sebastien Goutal[2,3], Sylvain Auvity[2], Fabien Caille[2], Irène Buvat[2], Dominique Vodovar[2], Geraldine Pottier[2], Michel Bottlaender[1,2], Nicolas Tournier[2], Benoit Larrat[1]; [1]*NeuroSpin, CEA, France,* [2]*SHFJ, CEA, France,* [3]*MIRcen, CEA, France*

Background, Motivation and Objective

The tyrosine kinase inhibitor (TKI) erlotinib (Tarceva©) is an efficient therapy for patients with mutated epidermal growth factor receptor non-small-cell lung cancer. Unfortunately, the brain is a common site of progression and 40% of patients develop brain metastases. This may be explained by the low brain disposition of erlotinib, due to poor permeability across the blood-brain barrier (BBB). ATP-binding cassette efflux transporters at the BBB, the P-glycoprotein (ABCB1) and the Breast Cancer Resistance Protein (ABCG2), were shown to work in concert to restrict brain distribution of most TKIs, including erlotinib. Focused ultrasound (FUS) and microbubbles is a reliable technical approach to safely and temporarily overcome the "physical" properties of the BBB by loosening the tight junctions. Here, we hypothesized that opening the paracellular route using FUS may overcome the ABCB1/ABCG2-mediated efflux of erlotinib at the BBB.

Statement of Contribution/Methods

^{11}C-erlotinib Positron Emission Tomography (PET) imaging was performed in rats after ultrasound-induced BBB disruption or ABCB1/ABCG2 inhibition. Five rats underwent a hemispheric BBB opening using continuous waves (PNP 0.6 MPa, f 1.5 MHz) and a head-foot displacement of the transducer over the left hemisphere. Then rats were intravenously injected with Evans Blues (EB), placed in an Inveon MicroPET scanner, injected with ^{11}C-erlotinib and PET image series were acquired for 40 min. Five rats received an ABCB1/ABCG2 inhibition protocol with elacridar followed by EB + ^{11}C-erlotinib injection and PET imaging. A baseline group of 4 rats underwent EB + ^{11}C-erlotinib and PET imaging.

Results/Discussion

EB extravasation was obvious in all rats of the FUS group and absent in the two other groups. However, BBB disruption did not significantly impact the brain kinetics of ^{11}C-erlotinib (FUS AUC = 6.9 ± 1.4 SUV.min, Baseline AUC = 6.6 ± 1.1 SUV.min). Comparatively, ABCB1/ABCG2 inhibition significantly increased erlotinib uptake (Elacridar AUC = 9.1 ± 1.1 SUV.min, p<0.05), suggesting that ABCB1/ABCG2-mediated efflux is the major component of the low brain disposition of erlotinib. Interestingly, transporter function efflux seems to persist in the presence of a disrupted BBB. We conclude that opening the "physical barrier" using FUS may not be sufficient to overcome the carrier-mediated efflux at the BBB.

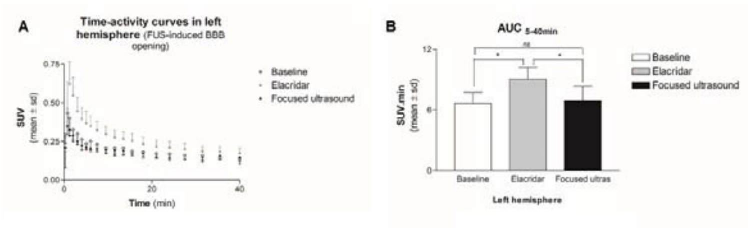

Figure: ^{11}C-erlotinib left hemisphere TACs (A) and ^{11}C-erlotinib left hemisphere AUCs (B) for each experimental group : baseline (n=4), elacridar pretreated (n=5) and ultrasound focused rats (n=5). (*, P<0.05, one-way ANOVA followed by Tukey's post hoc). The brain exposure to ^{11}C-erlotinib was estimated as the area under the time-activity (AUC) of the brain kinetics of ^{11}C-erlotinib in the left hemisphere.

1F-3

2:00 pm Pulsed Focused Ultrasound Effects on the Brain Interstitium

Victor Frenkel[1], David Hersh[2], Pavlos Anastasiadis[1], Ali Mohammadabadi[1], Jimena Dancy[2], Jeffrey Winkles[3], Asaf Keller[4], Graeme Woodworth[2], Anthony Kim[2]; *[1]Diagnostic Radiology and Nuclear Medicine, University of Maryland School of Medicine, Baltimore, Maryland, USA, [2]Neurosurgery, University of Maryland School of Medicine, Baltimore, Maryland, USA, [3]Surgery, University of Maryland School of Medicine, Baltimore, Maryland, USA, [4]Anatomy and Neurobiology, University of Maryland School of Medicine, Baltimore, Maryland, USA*

Background, Motivation and Objective

The ability to generate changes in the interstitial components of various tissues has a host of potential clinical applications. These include enhancing the delivery of drugs and genes, increasing oxygenation and blood flow for radiosensitization, altering fluid and pressure dynamics in the setting of inflammation, and increasing the clearance of detrimental factors such as amyloid plaques in the brain of patients with Alzheimer's disease. Our previous studies have shown how pulsed focused ultrasound (pFUS) can enhance the delivery of various chemotherapeutic agents in solid tumor models for reduced growth rates and improved survival. More recently we showed how pulsed ultrasound exposures can safely enlarge both the extracellular and perivascular spaces in an ex vivo brain model. The goal of the current study was to determine whether these effects could be reproduced noninvasively in the living brain.

Statement of Contribution/Methods

Female Sprague Dawley rats were treated with transcranial pFUS using an MRI-guided focused ultrasound system. Sham or pFUS exposures were given in the left striatum, followed by injections of Evans blue dye (EBD) or polyethylene glycol-coated nanoparticles of various diameters (2.5 microliter; 0.2 microliter per minute). Two hours post-treatment, animals were euthanized and brains removed and sectioned. Digital images of the sections were captured and processed in MATLAB to determine overall volume of distribution. Additional treatments evaluated the safety of the exposures by histological analysis and electrophysiology.

Results/Discussion

In pFUS-treated animals, EBD distribution was unaffected, but enhanced distribution was observed for the 60 nm (0.21-fold, p=0.01), 200 nm (0.46-fold, p=0.01) and 500 nm (0.39-fold, p=0.02) nanoparticles compared to untreated controls (Figure). Histological analysis did not reveal damage in response to pFUS. Electrophysiology, using whole cell patch clamp recordings, showed only one of several neuronal health indicators evaluated (mean amplitude of post-synaptic currents) to be significantly different for pFUS compared to sham controls. Future experiments are underway to evaluate the reversibility of these effects, as well as their therapeutic potential in an invasive brain tumor model.

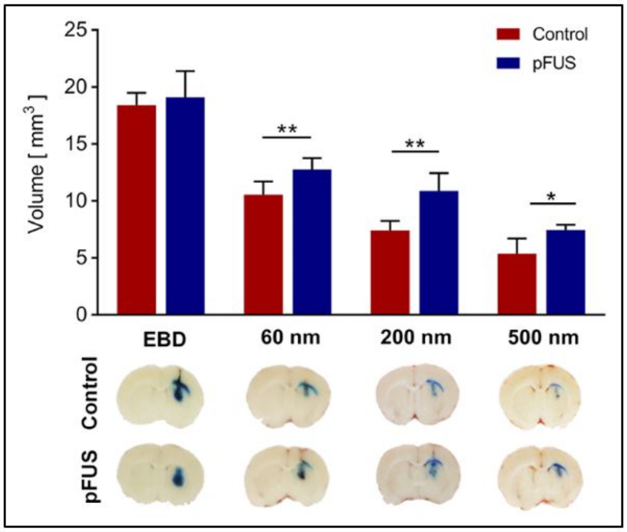

1F-4

2:15 pm Local Field Potentials Responses to Ultrasonic Neuromodulation on Freely Moving Mouse

Guofeng Li[1,2], Min Su[1], Qiuju Jiang[1], Huixia Zhao[1], Wenbin Yan[1], Weibao Qiu[1], Hairong Zheng[1]; [1]*Shenzhen Institutes of Advanced Technology, Chinese Academy of Sciences, China, People's Republic of,* [2]*Guangdong Medical University, China, People's Republic of*

Background, Motivation and Objective

Ultrasound (US) brain stimulation has been demonstrated to be a promising approach for noninvasive neuromodulation. However, traditional methods always demand animals to be under anesthesia and body constraint to achieve stable operation with bulky US transducer, while those demands would result in interference to the neural activity related to perception, cognition, and behavior. Appling a miniature US stimulator on freely moving mouse will greatly benefit for obtaining credible neural response from ultrasonic neuromodulation. This study investigates the local field potentials (LFPs) responses to ultrasonic neuromodulation on freely moving mouse by using a customized head-mounted US transducer.

Statement of Contribution/Methods

Miniature head-mounted focused US transducers (PZT-4, 2MHz, 5mm, 0.49g), were installed on the intact skulls (above the prefrontal cortex) of five C57BL/6 mice before stimulating experiment. Stimuli signals are generated by a functional generator and amplified by a power amplifier, and finally drive the transducer to achieve non-invasive neuromodulation. LFPs were acquired from the hippocampus region with microelectrodes. Power spectral densities (PSD) of the LFPs were used to quantitatively evaluate the ultrasonic neuromodulation effects on five mice in anesthetized and freely moving states, respectively.

Results/Discussion

Figure (a) shows a mouse under ultrasonic neuromodulation by a head-mounted US stimulator. (b) shows four typical LFPs waveforms at different states. (c) illustrates that US stimuli can not only increase PSD in delta band (1-4 Hz), but also significantly evoke LFPs responses at the frequency higher than 6.5 Hz for the awake mice. (d) illustrates that US stimuli can increase PSD in delta band, but not at frequencies higher than 6.5 Hz for anesthetized mice. Consistently, LFPs in the 4-6.5 Hz band can be suppressed by US stimuli, no matter for anesthetized or awake mice. This study first time illustrates the different LFPs responses evoked by ultrasonic neuromodulation on mice in freely moving and anesthesia states, and emphasizes the significance of ultrasonic neuromodulation on conscious rodents. The proposed head-mounted US device could potentially promote the development of ultrasonic neuromodulation to more extensive neuroscience studies.

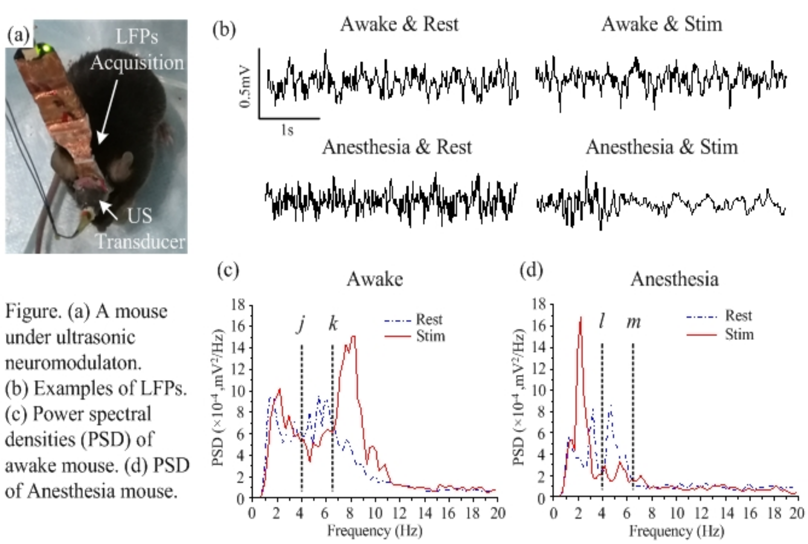

Figure. (a) A mouse under ultrasonic neuromodulaton. (b) Examples of LFPs. (c) Power spectral densities (PSD) of awake mouse. (d) PSD of Anesthesia mouse.

1F-5

2:30 pm **Rapid Short-Pulse (RaSP) Sequences Improve the Distribution of Drug Delivery to the Brain In Vivo**

Sophie V Morse[1], Antonios N Pouliopoulos[2], Tiffany Chan[1], Julien Lin[1], Matthew Copping[1], Nicholas J Long[1], James J Choi[1]; [1]*Imperial College London, United Kingdom,* [2]*Columbia University Medical Campus, USA*

Background, Motivation and Objective

Focused ultrasound and microbubbles have been shown to locally and noninvasively open the blood-brain barrier. Despite encouraging results in human patients, several performance and safety features, such as poor drug distribution, high drug accumulation along vessels and small sites of red blood cell extravasation, have been unavoidable. We have recently developed a new ultrasound sequence – rapid short-pulse (RaSP) sequence – designed to suppress these adverse features by promoting safer modes of cavitation activity throughout capillaries. In our RaSP sequences, low-pressure short ultrasonic pulses are emitted at kHz pulse repetition frequencies (PRF) and grouped into bursts. We have shown in vitro that RaSP sequences prolong microbubble lifetime and increase their mobility, enhancing the distribution of acoustic cavitation activity. Here we evaluate the ability of RaSP sequences to improve the in vivo performance and safety of ultrasound-mediated drug delivery to the brain.

Statement of Contribution/Methods

The left hippocampus of mice was exposed to 1 MHz focused ultrasound after systemically administering SonoVue® microbubbles and fluorescent 3 kDa dextran. The mice were exposed to RaSP sequences (pulse length (PL): 5 cycles; PRF: 1.25 kHz; burst length: 30 ms) or conventionally used ms-long sequences (PL: 10,000 cycles; PRF: 0.5 Hz; burst length: 10 ms) at nonderated 400 $kPa_{pk\text{-}neg}$. Microbubble acoustic emissions were captured with a 7.5 MHz passive cavitation detector. Brains were sectioned into 30 µm slices and imaged by fluorescence microscopy.

Results/Discussion

Despite emitting 150 times less acoustic energy, RaSP sequences delivered a similar drug dose and produced a more uniform drug distribution compared to long-pulse sequences (Figure (1-2)). RaSP sequences resulted in less dextran accumulation along arteries, suggesting that these sequences reduce the likelihood of unnecessary arterial treatment. For both sequences, neuronal uptake of dextran was observed in areas where high doses of dextran were present in the parenchyma (Figure (3)). Acoustic emissions, which are related to the magnitude and duration of cavitation activity, were more stable for RaSP sequences than for the long-pulses. These results indicate that low-pressure RaSP sequences could deliver a more efficient and safe drug dose to treat brain diseases such as Alzheimer's.

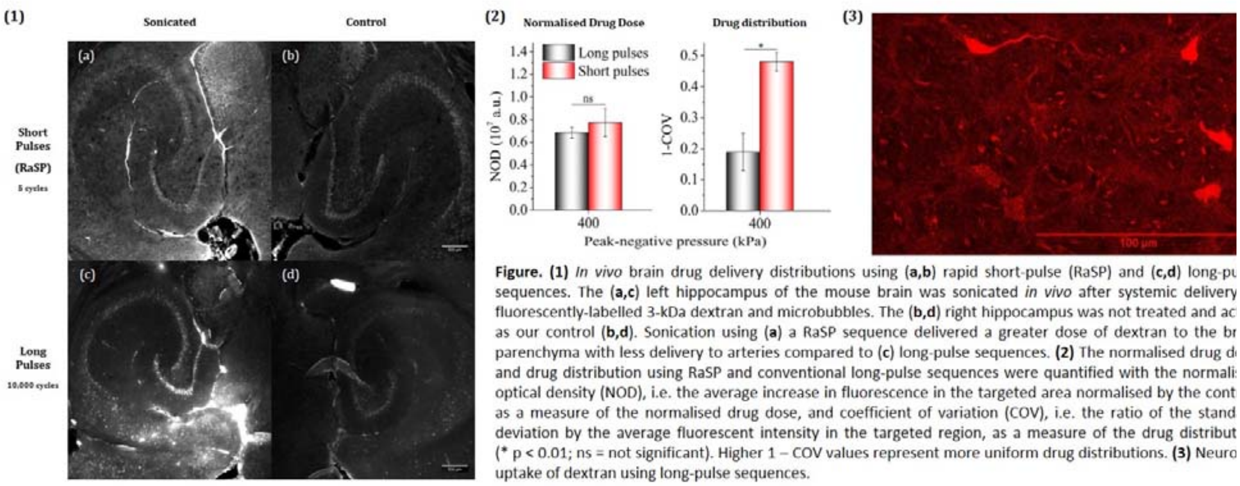

Figure. **(1)** *In vivo* brain drug delivery distributions using **(a,b)** rapid short-pulse (RaSP) and **(c,d)** long-pu sequences. The **(a,c)** left hippocampus of the mouse brain was sonicated *in vivo* after systemic delivery fluorescently-labelled 3-kDa dextran and microbubbles. The **(b,d)** right hippocampus was not treated and ac as our control **(b,d)**. Sonication using **(a)** a RaSP sequence delivered a greater dose of dextran to the br parenchyma with less delivery to arteries compared to **(c)** long-pulse sequences. **(2)** The normalised drug d and drug distribution using RaSP and conventional long-pulse sequences were quantified with the normali optical density (NOD), i.e. the average increase in fluorescence in the targeted area normalised by the cont as a measure of the normalised drug dose, and coefficient of variation (COV), i.e. the ratio of the stand deviation by the average fluorescent intensity in the targeted region, as a measure of the drug distribut (* $p < 0.01$; ns = not significant). Higher 1 – COV values represent more uniform drug distributions. **(3)** Neuro uptake of dextran using long-pulse sequences.

1F-6

2:45 pm **Weekly Ultrasound Induced Blood-Brain Barrier Openings Seem to Restore Memory in APP/PS1dE9 Amyloid Mice Model**

Matthieu Gerstenmayer[1], Erwan Selingue[1], Francoise Geffroy[1], Sebastien Meriaux[1], Benoit Larrat[1]; [1]*MIDAS, NeuroSpin, CEA, France*

Background, Motivation and Objective

Blood-Brain Barrier opening (BBBO) with Focus Ultrasound (FUS) seems to give significant results in clearing amyloid plaques and restoring memory in Alzheimer's disease (AD-Tg) transgenic mice models. So far, only few teams have produced results [Burgess, 2014 - Leinenga, 2015] which motivates more investigations. To do so we set up two protocols: one on wild type (WT) mice and one AD-Tg mice.

Statement of Contribution/Methods

In a first experiment, a group of WT mice (n=8, male, 3 months old) underwent whole brain weekly BBBO for 8 weeks. The global BBBO was perform by moving the transducer (F/D = 20/25 mm,) on the horizontal plane over the head of the animal. The acoustic parameters are as follow: Peak Negative Pressure 0.6 MPa, frequency 1.5 MHz, duty cycle 3% for 5 minutes. Success of the BBBO was confirmed by T_1 weighted MRI acquisitions after injection of a MR-contrast agent. Absence of hemorrhages was assessed by acquiring anatomical images. After the last FUS session, locomotion, stress (Open Field) and memory (Y-maze) of the mice was evaluated by behavior tests and compared to a control group of 8 littermates. In a second experiment, 3 groups were made: 5 APP/PS1dE9 AD-Tg mice which received FUS weekly (AD+FUS), 6 AD-Tg mice without FUS (AD) and 8 WT mice. All animals were 10 months old male littermates. The AD+FUS group underwent a 6 weeks BBBO protocol with the same conditions as the first experiment. Same behavior testing protocol for all groups was performed as for the first experiment.

Results/Discussion

In the first experiment, MR images confirmed a success rate of BBBO greater than 85%, mice did not lose weight and anatomical images showed no major damages to the brain. Behavior tests showed no significant differences in term of locomotion, stress and memory between the BBBO group and the control group. It leads us to think that our BBBO protocol is efficient, safe and does not alter behavior. In the second experiment, AD+FUS mice showed memory improvement in the Y-maze (see figure) with on average 37% more distance walked in the new arm, 40% more entries in the new arm and 41% more alternation triplets than untreated AD mice. However, these differences were not significant, maybe due to small number of mice per group. High resolution *ex vivo* MR imaging and brain histology for quantification of amyloid load is ongoing and will give more understanding of the observed effects.

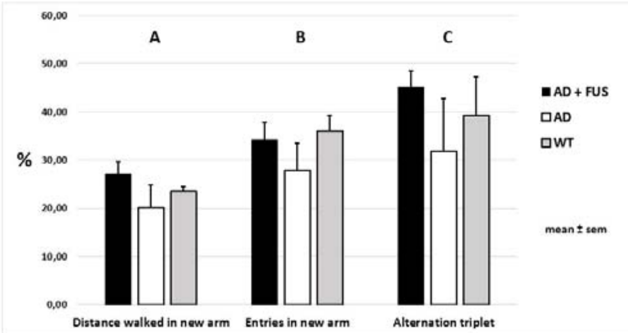

Figure, Results of the Y-maze: During 10 minutes the new arm is closed and mice walk freely in two arms. They rest for 1 hour. During the probe trial, mice walk freely in the three arms for 5 minutes and their trajectories are tracked with a camera. They natural curiosity lead them to explore new areas (the new arm), to do so they have to remember what is new. (A) Distance (%) walked in the new arm. (B) Number of entries (%) in the new arm. (C) Percentage of alternation triplet.

2F - MIM: Fast Cardiac Imaging: Methods and Applications

Ambassador Ballroom

Friday, September 8, 2017, 1:30 pm - 3:00 pm

Chair: **Jan Dhooge**
University of Leuven

2F-1

1:30 pm **Ultrafast Ultrasound Imaging of the Heart: from 2D to 3D Quantitative Imaging of the Myocardium and Blood Flows**

Mathieu Pernot[1]; [1]*Institut Langevin, INSERM, ESPCI, Paris, France*

Background, Motivation and Objective

Cardiac pathologies are often characterized by important changes of myocardial properties such as the myocardial stiffness, re-organization of muscle fiber structure, modification of the microcirculation flow, all of which remain challenging to assess quantitatively and non-invasively in vivo. Over the last decade, the advent of software-based systems has enabled the implementation of ultrafast ultrasound imaging of the heart at 5000 images/s. Such a high frame rate has offered new possibilities for imaging quantitatively the myocardial function in 2D and 3D.

Statement of Contribution/Methods

Ultrafast imaging of the heart was implemented on 2D and 3D research scanners and enabled (1) quantifying non-invasively the myocardial stiffness and its dynamics by using myocardial shear wave elastography (2) mapping the myocardial fibers orientation using Backscattering Tensor Imaging and (3) mapping the coronary vasculature with high sensitivity thanks to ultrafast Doppler imaging. These techniques were first validated on animal models and recently translated to human applications.

Results/Discussion

Ultrafast imaging of the heart offers new opportunities for the diagnosis of various cardiovascular diseases. Unavailable information such as the myocardial stiffness, the fibers orientations or the intramyocardial coronary vasculature can be imaged with 2D and 3D ultrafast imaging and will help to better characterize the myocardial function.

2F-2

2:00 pm **Comparison of Motion Corrected Multi-Plane-Transmit Beamforming and 3D Diverging Wave Compounding: A Simulation Study**

Yinran Chen[1], Jianwen Luo[1], Jan D'hooge[2]; [1]*Department of Biomedical Engineering, Tsinghua University, Beijing, Beijing, China, People's Republic of,* [2]*Laboratory of Cardiovascular Imaging and Dynamics, Department of Cardiovascular Sciences, KU Leuven, Leuven, Belgium*

Background, Motivation and Objective

3D diverging wave compounding (DWC) was recently demonstrated to be capable of providing high-frame-rate imaging, but at the risk of introducing motion artifacts. As an alternative, a hybrid beamforming approach combining the features of DWC and multi-line-transmit (MLT) beamforming was proposed (i.e., multi-plane-transmit, MPT), showing some superiority when compared with 3D DWC [1]. However, in our prior study, motion correction (MoCo) was not used for either beamforming approach. The aim of this study was therefore to extend the comparison of both approaches by incorporating MoCo for both of them.

Statement of Contribution/Methods

A 32×32 element matrix array was simulated in Field II. For MPT imaging, a 3MPT-2MLA system was set up (see Fig. b), with compounding of 5 *planar* diverging waves (DWs) in their respective planes [1]. Such setup led to a frame rate of ~66 Hz (PRF = 5 kHz). A 2-step MoCo was applied in this system. The 1st step was performed within the individual plane to correct the motion in the successive transmitted DWs before compounding; the 2nd step was performed in between the MPT planes in order to correct for time lag between subsequent MPT planes.

For fair comparison, a 9×9 DWC system with 16×16 element transmit sub-aperture and 60° opening angle in a ″round-trip″ Diagonal-shape scan sequence was simulated (see Fig. d). The frame rate was ~61 Hz. MoCo was applied in the volume before compounding by extending the method in [2] to 3D. The imaging object was a cystic phantom in a static state and in motion in the axial direction at a speed of 10 cm/s. The contrast-to-noise ratio (CNR) of the cyst was quantified for the tested systems before and after MoCo.

Results/Discussion

In static state, the CNRs were [5.91, 5.95] for 3MPT-2MLA and 9×9 DWC, respectively. Although the CNRs decreased to [4.59, 3.57] during motion, they were restored with MoCo to [6.39, 4.87] for the two systems respectively. The inferior outcome of MoCo in 9×9 DWC is likely due to the massive compounding operation in combination with the bias in the Doppler-based motion estimator.

To conclude, MoCo showed to be beneficial for both the MPT and the DWC systems but – when running at similar frame rate – the MoCo 3MPT-2MLA system outperformed the 9×9 DWC one. Experimental verification of these results is the topic of ongoing work.

[1] Chen *et al*. 10.1109/TUFFC.2017.2651498.

[2] Porée *et al*. 10.1109/TMI.2016.2523346.

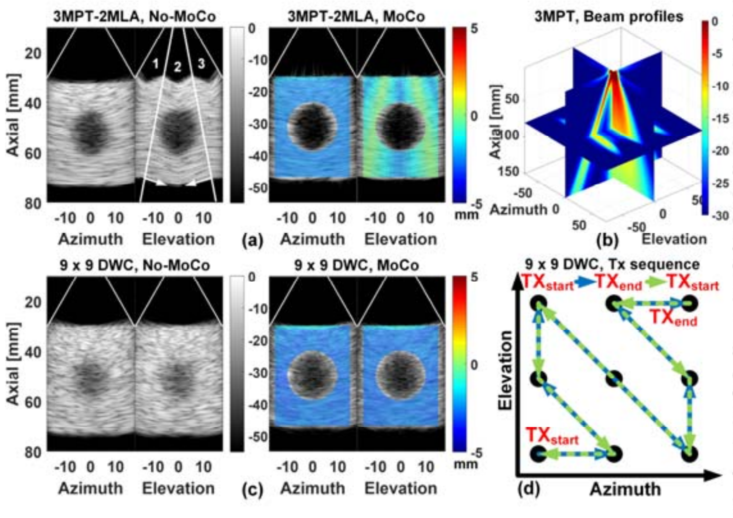

Figure (a) Images of 3MPT before and after MoCo, please note that it followed an "edge-to-center" interleaved scan sequence in the elevation dimension. (b) Beam profiles of 3MPT. (c) Images of 9×9 DWC before and after MoCo. (d) "Diagonal" scan sequence of 9×9 DWC (simplified to 3×3). The phase shifts of the forward and backward sequences were combined to get the Doppler velocity.

2F-3

2:15 pm 3D Ultrafast Imaging of the Heart: Application to the Mapping of Electromechanical Activation

Victor Finel[1], Philippe Mateo[1], Clement Papadacci[1], Jean Provost[1], Mickael Tanter[1], Mathieu Pernot[1]; [1]*Institut Langevin, ESPCI ParisTech, CNRS UMR 7587, INSERM U979, Université Paris 7, Paris, France*

Background, Motivation and Objective

Cardiac conduction abnormalities and arrhythmias are linked to stroke, heart failure, and sudden cardiac death and continue to be a major cause of death and disability worldwide. However, the evaluation of cardiac conduction remains challenging in the clinical setting. Electromechanical Wave Imaging (EWI) [1] was recently developed to map the transient displacements [1] and deformations [2] of the myocardium following electrical activation in multiple 2D imaging planes and was shown to be highly correlated with electrical activation times. In this study, we demonstrate the feasibility of performing EWI in isolated rat hearts using a 3D ultrafast ultrasound scanner.

Statement of Contribution/Methods

A 2D matrix array (8MHz, 32x32 elements, 0.3mm pitch) driven by a customized, programmable, 1024-channel ultrasound scanner was used to perform 600-ms-long 2D plane-wave acquisitions during sinus rhythm and during pacing at 3000 volumes/s in two isolated rat hearts in the apical view. Inter-frame axial displacements and strains were mapped in the myocardium using the Kasai algorithm and a least-squares estimator with a kernel size of 0.94mm, respectively. Displacements and strains were overlaid onto B-mode ciné-loops. Two-lead electrocardiogram was recorded simultaneously during ultrasound acquisitions.

Results/Discussion

The electromechanical activation was successfully imaged in 3D in two rat hearts with the probe placed on the apical view. In sinusal rhythm, activation times were quantified and ranged between 100 ms and 120 ms after P-wave. The conduction pattern was completely modified during pacing and the pacing location was correctly identified on the activation map.

These results suggested that 3DEWI could be used to detect and follow abnormalities of electrical conduction in the heart in entire volumes.

[1] Konofagou et al., Ultrasonics, 50(2):208-15, 2010

[2] Provost et al., Proc. Nat. Acad. Sci., 108(21):8565-70, 2011

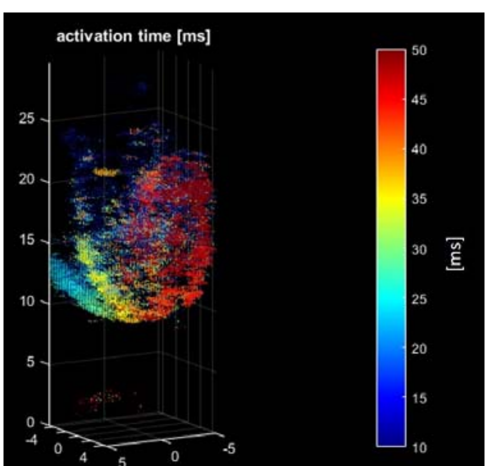

Figure 1 : Activation map of an isolated rat heart. Right ventricule on the left side of the image, apex on the bottom. Axes in mm. Color represent activation times in ms

2F-4

2:30 pm **Volumetric Imaging of Fast Mechanical Waves in the Heart Using a Clinical Ultrasound System: A Feasibility Study**

Pedro Santos[1,2], Lasse Løvstakken[2,3], Eigil Samset[2,4], Jan D'hooge[1]; [1]*Department of Cardiovascular Sciences, KU Leuven, Belgium,* [2]*GE Vingmed Ultrasound, GE Healthcare, Norway,* [3]*Department of Circulation and Medical Imaging, NTNU, Norway,* [4]*Center for Cardiological Innovation, Norway*

Background, Motivation and Objective

Fast mechanical waves following e.g. electromechanical activation and aortic valve closure (AVC) have been imaged using 2D diverging waves (DW). However, their full characterization requires multiple 2D recordings in subsequent heartbeats. Given the heart cycle variability and short-lived nature of these waves, temporal alignment is challenging. Moreover, clinical matrix arrays hinder the straightforward implementation of DW, due to sub-aperture (SAP) beam forming.

We have recently proposed a sparse DW sequence capable of imaging a 70°x70° volume in a clinical system and reported its preliminary validation *in vivo* against 2D Tissue Doppler Imaging (TDI).

Herein, the feasibility of measuring fast mechanical events in 3D *in vivo* was investigated.

Statement of Contribution/Methods

A GE Vivid E95 clinical scanner with a GE 6VT-D transesophageal (TEE) matrix array was used to transmit a sparse sequence consisting of 9 DW (3 in azimuth, 3 in elevation). Ultrafast 3D TDI was recorded on a healthy volunteer in both apical and parasternal views. A TDI frame rate of 610 vol/s was achieved with frame-to-frame autocorrelation method on IQ data.

The datasets were subsequently contoured in 3D at the isovolumetric contraction (IVC) and relaxation (IVR) periods. TDI, strain rate and tissue acceleration (i.e. forward difference of TDI) were computed at the mesh nodes. Moreover, anatomical colour M-modes were extracted at the anteroseptal wall. These were used to detect the mechanical waves following mechanical activation and AVC.

Results/Discussion

Given the 610 vol/s, the 3D DW sequence detected fast mechanical events occurring in all directions. The figure shows a mechanical wave captured by 10 subsequent frames during a 15 ms interval starting at AVC. The wave starts at the basal anteroseptal segment and propagates towards the apex, as well as laterally and therefore matches the shear wave associated with AVC as described previously using 2D techniques.

This study demonstrated the feasibility of the proposed sequence for the detection of clinically-relevant fast mechanical waves in 3D *in vivo* using a clinical scanner. This allows the assessment of the whole ventricle in a single heartbeat, unlike the conventional 2D imaging sequences used nowadays.

A clinical study using this acquisition sequence is currently being planned, in order to confirm these observations in a larger cohort.

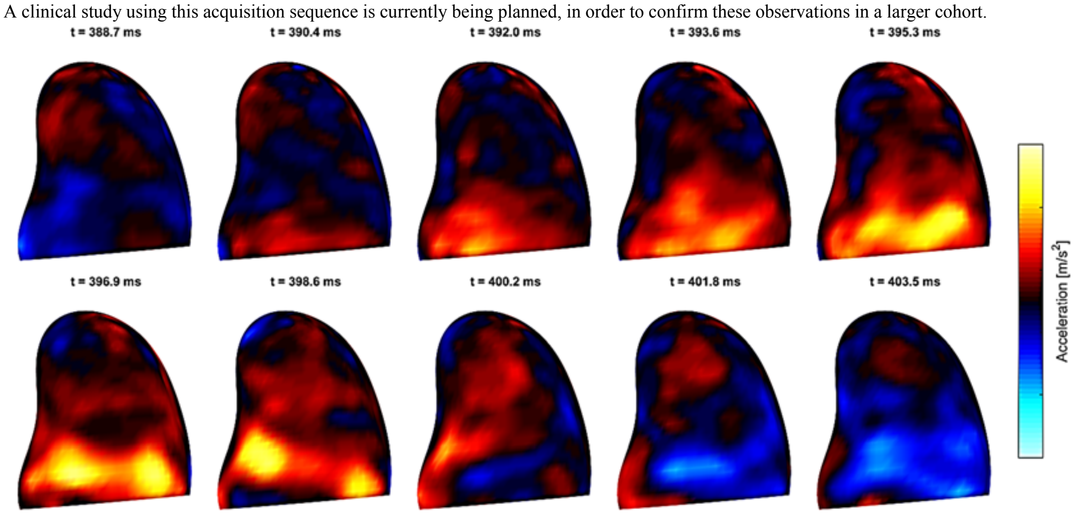

Fig – Propagation of the mechanical wave created by the aortic valve closure, as seen from the anteroseptal wall. The image shows tissue acceleration over 10 subsequent volumes acquired at 610 Hz (1.6 ms temporal resolution) around the aortic valve closure time.

2F-5

2:45 pm **3D Rendering of Electromechanical Wave Imaging for the Characterization and Optimization of Biventricular Pacing Conditions in Heart Failure Patients Undergoing Cardiac Resynchronization Therapy**

Lea Melki[1], Ethan Bunting[1], Daniel Wang[2], Pierre Nauleau[1], Elisa Konofagou[1,3]; [1]*Biomedical Engineering, Columbia University, New York, NY, USA,* [2]*Medicine - Division of Cardiology, Columbia University, New York, NY, USA,* [3]*Radiology, Columbia University, New York, NY, USA*

Background, Motivation and Objective

Assessing the response of heart failure (HF) patients to Cardiac Resynchronization Therapy (CRT) currently relies on the ECG and left ventricular (LV) ejection fraction. Electromechanical Wave Imaging (EWI) is a high frame-rate (2000 Hz) ultrasound-based technique capable of non-invasively mapping the electromechanical activation in all four cardiac chambers in vivo. In this study, we aim to show the capability of EWI in identifying different pacing conditions in patients with CRT and to characterize the resulting activation pattern directly following biventricular (BiV) device placement.

Statement of Contribution/Methods

A total of nine HF patients, each in three different pacing conditions (RV only, LV only and BiV), were imaged following their ICD implantation in four transthoracic standard echocardiographic apical views (4-, 2-, 3- and 3.5-chamber). Electromechanical strains and activation maps were computed in each view with EWI processing. Axial displacements were estimated using 1D RF cross-correlation, and strains were derived with a 5 mm least squares kernel. Activation times were defined by the sharp transition from positive to negative values on the incremental strain curves. LV lateral wall activation times (LWAT) and RV free wall activation times (FWAT) were quantified on the apical 4-chamber view for each patient and each pacing protocol. 3D rendering of the ventricular activation maps were then generated by registering the four multi-2D views around the LV base to apex axis of symmetry and performing a linear interpolation circumferentially between them.

Results/Discussion

EWI was shown capable of mapping and distinguishing the electromechanical activation in the three standard pacing protocols arising from CRT (Figure). LWAT in BiV pacing (71 ± 16 ms) were found to be lower compared to LV (94 ± 21 ms) and RV pacing only (123 ± 21 ms). FWAT were the highest in LV pacing (104 ± 17 ms), while RV (74 ± 18 ms) and BiV (72 ± 20 ms) pacing conditions resulted in similar FWAT values. LWAT was significantly different in each of the three pacing conditions (p=0.05), while FWAT was able to distinguish between LV pacing and the other two conditions (p=0.02). These findings indicate that EWI could be a valuable monitoring tool for clinicians to optimize the pacing vectors after ICD placement and potentially identify super-responders.

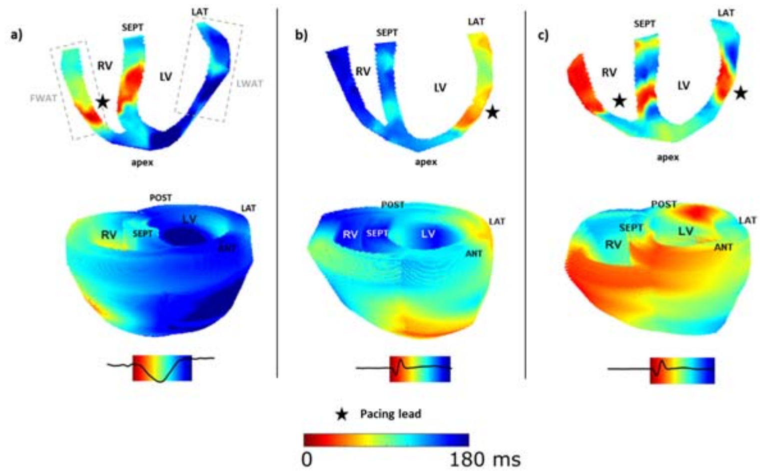

Fig. EWI ventricular activation maps in HF patient undergoing CRT. a) RV pacing only (LWAT = 154 ms, FWAT = 84 ms), b) LV pacing only (LWAT = 84 ms, FWAT = 129 ms), c) BiV pacing (LWAT = 96 ms, FWAT = 57 ms). Top row: four-chamber apical view isochrones, bottom row: 3D rendering of the ventricular activation maps.

3F - MEL: Elastography in Anisotropic Tissue

Palladian Room

Friday, September 8, 2017, 1:30 pm - 3:00 pm

Chair: **Matthew Urban**
Mayo Clinic

3F-1

1:30 pm **Estimating Degree of Mechanical Anisotropy in Healthy and Dystrophic Rectus Femoris of Boys using VisR Ultrasound, *In Vivo***

Christopher Moore[1,2], Melissa Caughey[3], Diane Meyer[4], Regina Emmett[4], Manisha Chopra[5], James Howard Jr. [3,5], Caterina Gallippi[1,2]; [1]*Department of Electrical and Computer Engineering, North Carolina State University, Raleigh, NC, USA,* [2]*Joint Department of Biomedical Engineering, University of North Carolina at Chapel Hill, Chapel Hill, NC, USA,* [3]*Department of Medicine, University of North Carolina at Chapel Hill, Chapel Hill, NC, USA,* [4]*Rehabilitation Services, University of North Carolina Hospital, Chapel Hill, NC, USA,* [5]*Department of Neurology, University of North Carolina at Chapel Hill, Chapel Hill, NC, USA*

Background, Motivation and Objective

In Duchenne muscular dystrophy (DMD), muscle fiber necrosis and subsequent progressive replacement of muscle by fibrous tissue and fat impacts the degree of anisotropy (DoA) in mechanical properties. Mechanical DoA can be assessed in skeletal muscle using Viscoelastic Response (VisR) ultrasound. We hypothesize that in vivo VisR DoA measures in the rectus femoris (RF) muscles of boys with DMD statistically differ from those in control boys. Further, we hypothesize that VisR DoA is correlated to RF functional output.

Statement of Contribution/Methods

In vivo VisR imaging was performed on the RF muscles of 4 boys with DMD and 3 control boys with no known neuromuscular disorders ranging in age from 7.9-10.8 years. In some subjects, repeated imaging occurred at an interval of no less than 4 months for a total of 11 data acquisitions in DMD and 7 in control subjects. Data were collected using a custom VisR beam sequence (two 70-μs, F/3.0 ARF excitations spaced 0.3 ms in time and followed by 37 tracking lines) and a linear array transducer oriented such that the long axis of the ARF PSF was aligned parallel (90°) and perpendicular (0°) to the muscle fibers. Induced displacements were fit to the 1D mass-spring-damper model to estimate tissue elasticity relative to the applied ARF amplitude ('relative elasticity', RE), and median RE in a 2-mm lateral by 1-mm axial ROI at the focal depth was calculated. The ratios of median RE in the 90° to the 0° orientations were computed to reflect DoA and compared between DMD and control RF. Finally, linear regression was used to correlate VisR DoA to functional muscle output, which was measured using a handheld dynamometer.

Results/Discussion

Results are presented as: median [IQR]. DoA in the DMD RF is significantly (Wilcoxon, $p<0.05$) higher than in control (DMD: 1.41 [1.06, 1.97], control: 0.86 [0.71, 1.17]) (Fig 1(a)). Note that DMD DoA > 1 suggests that the transverse shear modulus was greater than the longitudinal shear modulus, which is consistent with expected fibrosis between muscle fibers transversely and myofiber fragmentation longitudinally. DoA is negatively correlated to force output in both DMD and control RF but with a larger slope in DMD (DMD: slope = - 0.027 lb^{-1}; control: slope = -0.008 lb^{-1}) (Fig 1(b)). These results suggest that VisR DoA is relevant to differentiating dystrophic muscle degeneration in the RF muscles of boys with DMD, *in vivo*.

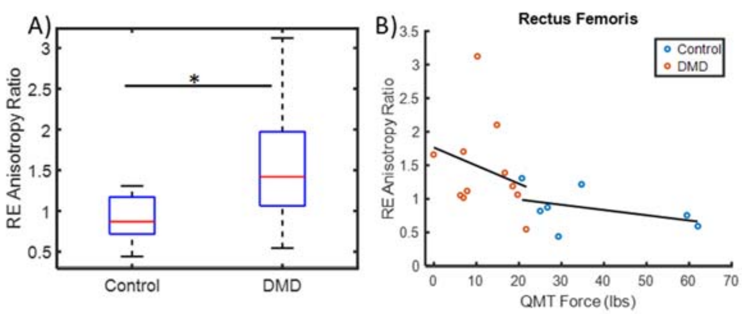

Figure 1A) Distributions of VisR Derived DoA in control and DMD boys. DMD group has DoA which is significantly higher and more varying than control. The control group has a median value less than 1 (0.86), which is expected for muscle, while DMD has a ratio greater than 1 (1.41), suggesting modulus across the muscle fibers is greater than along the fibers. B) VisR Derived DoA for control (blue) and DMD (orange), plotted against peak muscle output. The black lines shows the linear regression for each of the groups. The slope of the regression line is greater for DMD (-0.027 lb^{-1}) compared to control (-0.008 lb^{-1}). DMD = Duchenne Muscular Dystrophy, DoA = Degree of Anisotropy, VisR = Viscoelastic Response Ultrasound

3F-2

1:45 pm **Shear Wave Attenuation Quantification in Viscoelastic Transverse Isotropic Soft Tissue Using Shear Wave Elastography**

Eliana Budelli[1,2], Javier Brum[3], Patricia Lema[1], Mickaël Tanter[2], Carlos Negreira[3], **Jean-Luc Gennisson**[2]; [1]*Instituto de Ingeniería Química, Facultad de Ingeniería - Universidad de la República, Uruguay,* [2]*Institut Langevin, Ondes et Images, ESPCI ParisTech, CNRS UMR 7587, INSERM U979, France,* [3]*Laboratorio de Acústica Ultrasonora, Facultad de Ciencias - Universidad de la República, Uruguay*

Background, Motivation and Objective

Evaluation of rheological behavior of soft tissues provides an important diagnosis tool. Nowadays, most of the available commercial ultrasound systems assume tissues as isotropic and purely elastic. Recently in order to fully characterize the rheological behavior of tissues, methods to estimate both shear wave speed (V) and attenuation (α) were developed for isotropic media [1, 2]. In acoustic radiation force elastography, generated shear waves are not plane and a diffraction correction is needed to estimate α [1]. Here a diffraction correction is studied through numerical simulation and experimentally to measure α for a homogeneous transverse isotropic, viscoelastic (TIV) medium.

Statement of Contribution/Methods

Field II [3] ultrasound simulation program was used to simulate the acoustic radiation force generated by an 8MHz, 256 elements probe. The resulting numerical focusing was used as the shear wave source in a Green's function algorithm (TIV medium defined by two V and two α, parallel (1) and perpendicular (2) to the fibers) [4]. Then shear wave propagation was calculated in a numerical representation of a fusiform muscle. By using these numerical tools the validity of a cylindrical approximation was carried out. Experiments were conducted in anisotropic PVA phantoms, in ex vivo beef muscle and in vivo on volunteers. Shear waves were generated by using the Supersonic Shear Imaging technique on an ultrafast ultrasound scanner (Aixplorer with SL15-4 probe, same probe used in simulation). V and α at each frequency were recovered from the phase and amplitude (corrected from diffraction) decay versus distance respectively.

Results/Discussion

Simulation results show that for low anisotropy ratio (V1 / V2 < 1.5), the cylindrical correction available for isotropic medium [1], should be sufficient with an error < 15%. For higher ratios, numerical simulation is needed. Experimentally, shear waves were generated in a large bandwidth (100-500 Hz) and V and α were calculated at each frequency. As an example, at 150 Hz, two values of V and α, parallel (1) and perpendicular (2) to the fibers, were recovered in PVA phantoms: V1 = 4.7±0.2 m/s, V2 = 3.6±0.2m/s, α1 = 24 Np/m, α2= 62 Np/m. In ex vivo beef muscle, the values recovered at 150 Hz were: V1 = 4.8±0.2 m/s, V2 = 3.4±0.2m/s, α1 = 76 Np/m, α2= 130 Np/m, which are in good agreement with literature [5]. Frequency analysis of V and α will be presented. From such measurement, conservation and loss moduli can be retrieved and any rheological model can be used in order to determine elasticity and viscosity [1]. Future works will focus on using this technique to choose the right rehological model of biceps during contraction.

[1]Budelli PMB 2017 [2] Bernard IEEE-UFFC 2017 [3] Jensen JASA 1991 [4] Chatelin PMB 2015 [5] Catheline JASA 2004.

3F-3

2:00 pm ***Ex Vivo* and *In Vivo* Demonstration of 2D Viscoelastic Response (VisR) Anisotropy Imaging in Skeletal Muscle**

Christopher Moore[1,2], MD Murad Hossain[2], Caterina Gallippi[1,2]; [1]*Department of Electrical and Computer Engineering, North Carolina State University, Raleigh, NC, USA,* [2]*Joint Department of Biomedical Engineering, University of North Carolina at Chapel Hill, Chapel Hill, NC, USA*

Background, Motivation and Objective

Degree of anisotropy (DoA) has been evaluated for clinical significance in several organs. In skeletal muscle, mechanical DoA has been shown to increase with passive extension, i.e. the shear modulus parallel to muscle fibers (μ_l) increases relative to that perpendicular (μ_t). Imaging such variations in DoA could facilitate diagnosing and monitoring muscle pathologies. We have previously demonstrated the feasibility of imaging DoA with VisR ultrasound, *in silico*. The purpose of this work is to experimentally demonstrate VisR DoA imaging ex vivo in pig and in vivo in human muscles. We hypothesize that 2D VisR anisotropy images represent mechanical anisotropy in muscle.

Statement of Contribution/Methods

Ex vivo, swine psoas major muscle was surgically sectioned into a 0.8-cm diameter cylinder (with muscle fibers aligned along the cylinder's long axis) and embedded in an isotropic gelatin phantom for imaging. In vivo, the right biceps brachii of a 41 year-old woman with no known neuromuscular disorders was held in neutral flexion or passive extension (115° or 140° elbow angles, respectively) during imaging. The imaging linear array transducer was mounted to a motion stage such that, for each of the 72 lateral positions across the 2.5-cm field of view, raw RF data were acquired with the transducer oriented both parallel (0°) and perpendicular (90°) to the muscle fibers. The VisR beam sequence consisted of two, 70-µs acoustic radiation force (ARF) excitations and 40 tracking pulses. VisR relative elasticity (RE), relative viscosity (RV), and peak displacement (PD) were computed for each location and transducer orientation. Then, the ratio of each measure in the 90° to the 0° transducer orientation was calculated to reflect the DoA, and parametric images of the ratios were rendered.

Results/Discussion

Ex vivo, CNR of the muscle inclusion in the isotropic phantom was 2.09, 2.41, and 3.26 for RE, RV, and PD DoA images, respectively. In the biceps brachii, VisR suggested higher DoA (values further from 1) during passive extension (RE = 0.50 ± 0.11, RV = 0.57 ± 0.13, PD = 1.59 ± 0.29) relative to neutral flexion (RE = 0.58 ± 0.18, RV = 0.69 ± 0.18, PD = 1.30 ± 0.28), which is consistent with the expected increase in μ_l during passive extension (Fig. 1). These results suggest that 2D VisR anisotropy imaging delineates anisotropic features and supports evaluation of DoA changes in muscle, in vivo.

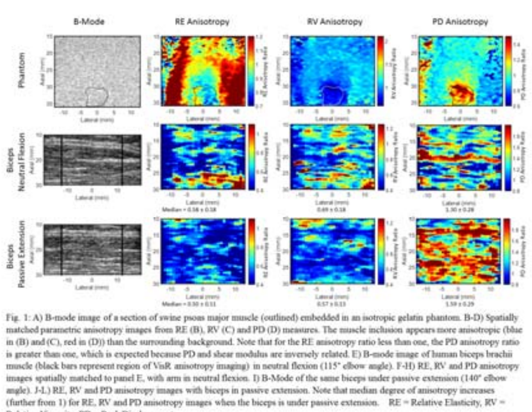

Fig. 1: A) B-mode image of a section of swine psoas major muscle (outlined) embedded in an isotropic gelatin phantom. B-D) Spatially matched parametric anisotropy images from RE (B), RV (C) and PD (D) measures. The muscle inclusion appears more anisotropic (blue in (B) and (C), red in (D)) than the surrounding background. Note that for the RE anisotropy ratio less than one, the PD anisotropy ratio is greater than one, which is expected because PD and shear modulus are inversely related. E) B-mode image of human biceps brachii muscle (black bars represent region of VisR anisotropy imaging) in neutral flexion (115° elbow angle). F-H) RE, RV and PD anisotropy images spatially matched to panel E, with arm in neutral flexion. I) B-Mode of the same biceps under passive extension (140° elbow angle). J-L) RE, RV and PD anisotropy images with biceps in passive extension. Note that median degree of anisotropy increases (further from 1) for RE, RV and PD anisotropy images when the biceps is under passive extension. RE = Relative Elasticity, RV = Relative Viscosity, PD = Peak Displacement.

3F-4

2:15 pm ***In Vivo* Contractile Properties Measurement of the Biceps *Brachii* Muscle Using High Frame Rate Plane Waves And k-Space Transverse Oscillation**

Rémi Rouffaud[1], Steve Beuve[1], Léopold Kritly[1], **Jean-Pierre Remenieras**[1]; [1]*INSERM U930, Tours, France*

Background, Motivation and Objective

Amyotrophic Lateral Sclerosis (ALS) is a fatal motor neuron progressive disorder that leads to muscle deterioration and paralysis. There is a crucial need to identify new therapeutic approaches and validate methods to assess their efficacy. The objective was to develop a high frame rate vectorised approach to visualize and analyze the 2D transient contractile wave propagation of muscle tissue with the perspective to understand the link between its electrical and mechanical activities.

Statement of Contribution/Methods

An electrostimulation device (COMPEX, France) generated a transient contraction in the biceps *brachii* muscle. We have placed the cathode on the proximal portion of the biceps, the anode on the distal one. US scanning was performed with an L11-4v probe positioned between the electrodes parallel to the fiber's principal orientation. Verasonics Platform for fast imaging with 3 plane waves emitted at -10°, 0° and +10° at 50µs intervals was used. The acquired RF data were individually beam formed and summed to obtain high-resolution RF data sets. Post processing of the resultant data executed in the f-k space domain by filtering and 2D Hilbert transform (2 Gaussian pics width σ_x centered at $\pm 1/\Lambda_x$) allowed us to obtain a Doppler complex signal $h_x=\exp(2i\pi x/(\Lambda_x/2))$ with $x=V_x t$ only sensitive to lateral V_x velocity. We obtained the axial velocity V_z in parallel from the original RF data sets.

Results/Discussion

Fig.1.A) shows the temporal displacement, computed from the integration of the tissue velocity. During the 150ms acquisition time, the axial displacement u_z of this ROI varied from -60µm to 175µm while the transverse displacement along the fibers varied from 0µm to 75µm. We showed for the first time that these measured displacements have the same order of magnitude. Fig.1.B) shows a muscle vector velocity imaging 70ms after the beginning of the electrical excitation superposed to the B mode image. We computed movies of vector evolutions as a function of time that showed the 2D transient motions of the muscle due to the propagation contraction wave. Finally, the determination of maximum cross-correlation between particle velocity curves obtained at constant depth for different lateral distances of propagation allowed us to measure a wave contraction speed of 100m/s which corresponds to the mean conduction velocity of α-axons connected to the muscle fibers.

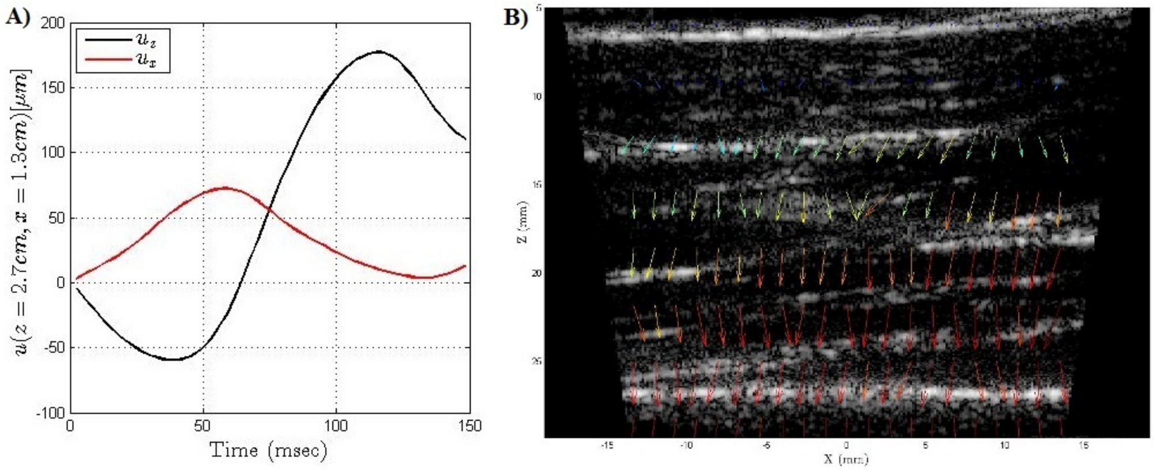

Figure 1: A) Temporal variations (with resolution of 1.8ms) of particle displacements in the axial (u_z) and lateral (u_x) directions of the probe for a 0.86x0.6mm² axial/lateral ROI at z=27mm and x=13mm. B) velocity vectors superposed to B-mode image with spatial discretizations Δz=630µm and Δx=450µm.

3F-5

2:30 pm ***In Vivo* Mechanical Anisotropy Assessment in Renal Parenchyma Using ARFI Peak Displacement**

Md Murad Hossain[1], Randal Detwiler[2], Emily Chang[2], Melissa Caughey[2], Melrose Fisher[2], Timothy Nichols[2,3], Elizabeth Merricks[3], Robin Raymer[3], Margaret Whitford[3], Bellinger Dwight[4], Lauren whimsey[4], Caterina Gallippi[1]; [1]*Department of Biomedical Engineering, University of North Carolina, Chapel Hill, Chapel hill, North Carolina, USA,* [2]*Department of Medicine, University of North Carolina, Chapel Hill, USA,* [3]*Department of Pathology and Laboratory Medicine, University of North Carolina, Chapel Hill, USA,* [4]*Department of Laboratory Animal Medicine, University of North Carolina, Chapel Hill, USA*

Background, Motivation and Objective

Renal parenchyma is strongly anisotropic; mechanical properties differ along versus across nephron alignment. In this work, the feasibility of interrogating such directional differences in mechanical property using ARFI is investigated. *We hypothesize that: 1) the ratio of ARFI peak displacements (PDs) achieved with the long axis of an asymmetrical ARF PSF oriented along versus across nephron alignment reflects the mechanical degree of anisotropy (DoA); and 2) directional differences in parenchymal mechanical property are detected when using an asymmetrical ARF PSF but obviated when using a symmetrical ARF PSF.*

Statement of Contribution/Methods

In vivo ARFI imaging was performed in 3 pigs with surgically exposed right kidneys and in 11 renal transplant patients 1 month (N=11) and 3 months (N=8) after transplantation. ARF excitations were 70 µs and centered at 4.21 MHz with F/1.5 or F/5.0 for asymmetrical or symmetrical ARF PSFs, respectively, at a focal depth of 36 mm. The elevational dimension of the PSF was oriented along and then across the nephron alignment during data acquisitions. ARFI induced displacements were monitored using ensembles of 43 tracking pulses, centered at 6.15 MHz, with a 10-kHz PRF. Normalized 1D axial cross-correlation was used to measure the induced displacements, and PD was evaluated. Then, the ratio of PDs achieved with the elevational dimension of the ARF PSF oriented along versus across nephrons was measured to reflect DoA. In pigs, this PD ratio was compared to the ratio of shear wave velocities (SWV) along versus across nephrons.

Results/Discussion

See Fig. 1. In pig kidneys, the ratio of PDs achieved using the asymmetrical (F/1.5) ARF is linearly correlated to the ratio of SWVs with $R^2=1$ (panel a). The ratio of PDs is greater than 1 (indicating directionally dependent PDs) for the asymmetrical ARF but approximately 1 (indicating directionally independent PDs) for the symmetrical (F/5.0) ARF (panel b). Similarly, in renal transplant patients, ratio of PDs is greater than 1 for the asymmetrical ARF but approximately 1 for the symmetrical ARF (panel c). Finally, the ratio of PDs achieved using the asymmetrical ARF is not statistically different at 1 versus 3 months post transplantation (panel d). These results demonstrate that mechanical DoA in renal parenchyma may be selectively interrogated or obviated, *in vivo*, using ARFI imaging.

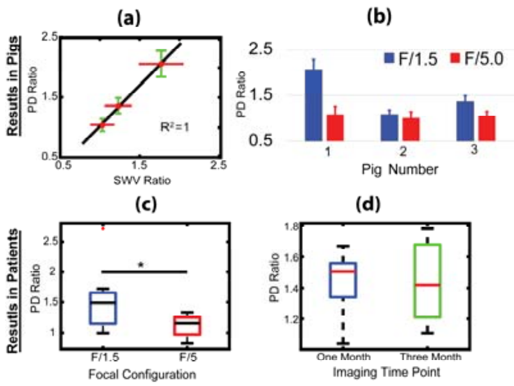

Figure 1. The ratios of PDs achieved using an asymmetrical F/1.5 ARF focal configuration is linearly correlated (R^2=1) to the ratios of SWVs in surgically exposed pig kidneys, *in vivo* (a). PD ratios measured *in vivo* in 3 pig kidneys (b) and in 11 renal transplant patients (c) using an asymmetrical F/1.5 ARF focal configuration (blue) is greater than 1, while the ratios achieved using a symmetrical F/5.0 ARF focal configuration (red) are approximately 1. In patients, the F/1.5 and F/5.0 PD ratios are statistically different (Wilcoxon, $p<0.05$). PD ratios measured in vivo in 8 renal transplant patients using an asymmetrical F/1.5 ARF focal configuration at 1 month (blue) and three months (green) after transplantation do not statistically differ (d). Note that, the transplant patients had stable creatinine levels and renal function at the one and three month post transplant or were excluded if rejection was detected clinically.

3F-6

2:45 pm **Characterization of Local Muscle Fiber Anisotropy Using Shear Wave Elastography in Patients with Chronic Myofascial Pain**

David Le[1], **Matthew Bird[1]**, Jay Shah[2], Naomi Gerber[1], Hannah Tandon[2], Secili DeStefano[1], Siddhartha Sikdar[1]; *[1]George Mason University, USA, [2]National Institute of Health, USA*

Background, Motivation and Objective

Previous studies have reported that shear wave speed along muscle fibers is distinct from the speed across the fibers. Therefore, the shear speed may be a sensitive method to determine muscle fiber orientation in vivo. The purpose of this study is to develop a reproducible method to determine anisotropy in muscle fibers using Shear Wave Elastography (SWE). This technique was used to study myofascial trigger points (MTrPs) which are palpable tender nodules found in skeletal muscle. MTrPs are a characteristic finding in myofascial pain syndrome (MPS), a widely prevalent chronic pain condition. The relationship between MTrPs and the pathophysiology of MPS is still largely unknown. We hypothesized that muscle containing MTrPs have heterogeneous fiber orientation within the affected zone and surrounding areas compared to normal muscle.

Statement of Contribution/Methods

Subjects (N=7) with chronic neck pain and active MTrPs were recruited. The MTrPs for each subject were identified through physical examination by trained clinicians, and the MTrPs as well as normal muscle were both imaged. A Supersonic Aixplorer system with an L10-4 ultrasound transducer was used. A custom holder was created that enabled the transducer to be rotated to precise angles, while imaging through a window of diameter (20 mm). The holder was placed on the skin with the window located over the manually palpated MTrP allowing the US images to be registered with the MTrP as identified on examination. The holder was fastened to the skin surface with adhesive. SWE images were acquired by rotating the transducer from -90° to +90° (0° denotes the expected orientation along the fibers) and shear wave speed was noted as a function of fiber angle. The asymmetry in the profile of the shear modulus was quantified at half peak value.

Results/Discussion

Shear wave speed in muscle showed changes with the fiber orientation as expected. Preliminary results suggest that in muscles with active (symptomatic) MTrPs (N=5), shear wave speed as a function of angle exhibits an asymmetric distribution around the peak (13.6 ± 7°), unlike normal, asymptomatic muscle tissue (N=5), which is more symmetric (5 ± 4.3°) (Fig. 1). This preliminary analysis indicates that muscle containing active MTrPs may have more heterogeneous fiber architecture than asymptomatic muscle ($p<0.05$). Studies are ongoing to confirm this in a larger population.

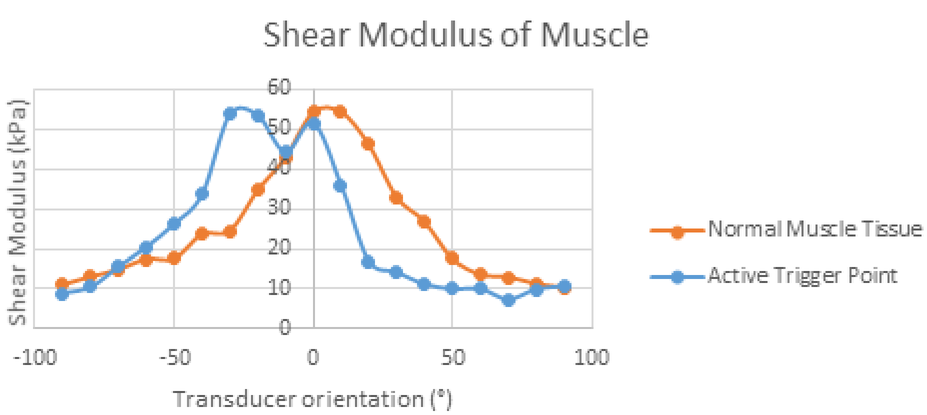

Figure 1: Example variation of shear modulus with orientation between normal muscle tissue and an active trigger point

4F - MPA: Molecular Imaging and Photoacoustic Contrast Agents

Diplomat Room

Friday, September 8, 2017, 1:30 pm - 3:00 pm

Chair: **Stuart Foster**
Univ of Toronto

4F-1

1:30 pm **Photoacoustic Assessment of Nanoparticles Distribution Pattern in the Mouse Brain following Blood-Brain Barrier (BBB) Disruption**

Johann Le Floc'h[1], Hoang D. Lu[2], Christine Démoré[1], Robert K. Prud'homme[2], Kullervo Hynynen[1], F. Stuart Foster[1]; [1]*Physical Sciences, Sunnybrook Research Institute, TORONTO, Ontario, Canada,* [2]*Princeton University, USA*

Background, Motivation and Objective

Focused ultrasound (FUS) with circulating microbubbles creates transient and reversible permeabilization of vasculatures which provides an essential means to deliver therapeutics and imaging agents, for instance across the BBB. We have previously shown that 3D color Doppler and photoacoustic imaging can monitor BBB disruption (BBBD) in mice. Here we study how changes in NPs size, concentration and dye properties play an important role in their spatial deposition.

Statement of Contribution/Methods

MRI guided FUS (MRIgFUS) was performed to create 4 openings on the left hemisphere in healthy mice (n=3). Immediately following the injection of microbubbles, three sizes of NPs loaded with dyes at different concentration and absorbance (NPs [40 nm, 784 (dye), 5 mg/mL (dye concentration), 17.1 (absorbance)]; [100 nm, 867, 10 mg/mL, 85.4]; [240 nm, 774, 15 mg/mL, 110]) were simultaneously injected *i.v.* in the mouse tail vein. NPs have well separated spectra and were labeled with fluorophores (Alexa 405, 488 and 647, respectively) for microscopic analysis. Mice were scanned, 2 h following BBBD, with a photoacoustic (PA) system equipped with a 15 MHz PA probe to monitor in vivo the spatial distribution of NPs infiltration in brain tissues at specific wavelengths. Mouse brains were then collected following formalin fixation, scanned with a 40 MHz PA probe and later sectioned for fluorescence imaging.

Results/Discussion

MRIgFUS confirmed openings (Fig. 1A). At the same NP and dye concentrations, spectral unmixing of perfused & excised PAI showed a similar in-plane NPs spatial distribution independent of their sizes (Fig. 1B). *In vivo* PAI confirms these results and revealed that absorbance larger than 85 is not suitable for in vivo monitoring. The slightly smaller depth of penetration of 40 nm NPs observed is likely attributed to their lower absorbance as no large differences were observed in fluorescent microscopy at this location (Fig. 1C). In contrast, spectral unmixing of perfused & excised in vivo PAI with normalized absorbance, same NP and dye concentrations showed a consistent and marked difference in NPs spatial in-plane distribution (Fig. 1D). This suggests that size might influence NPs distribution in brain under specific conditions. In conclusion, NPs as large as 240 nm in diameter could potentially be used to maximize drug delivery in brain tissues following BBB opening.

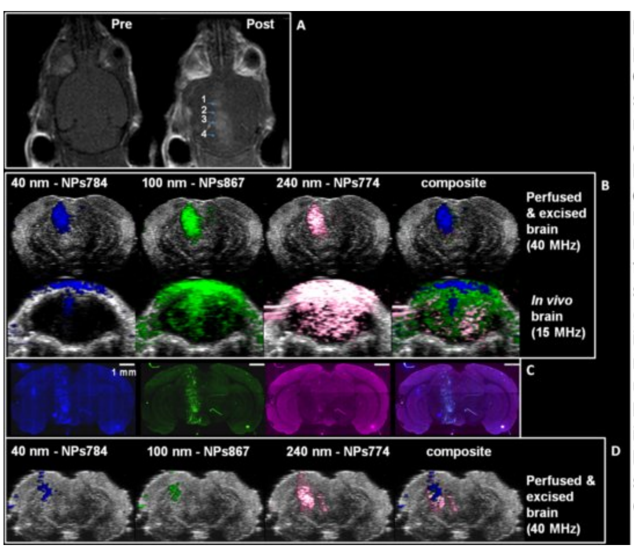

Figure 1. A. MRI of mouse brain pre and post blood-brain barrier disruption by focused ultrasound showing 4 openings (region, mouse#1). **B.** Spectral unmixing of perfused & excised and *in vivo* PAI showed similar spatial distribution of NPs (40 nm in blue, 100 nm in green and 240 nm in pink, color coded to match fluorescence microscopy) at same dye concentration (mouse#1). **C.** Fluorescent images of brain slices within region 3 (mouse#1). **D.** Spectral unmixing of perfused & excised PAI showed dramatic differences in spatial distribution of 3 sizes of NPs at normalized absorbance, same NP concentration and dye concentration (mouse#2).

4F-2

1:45 pm **Sono-Photoacoustic Imaging using Polypyrrole Coated Phase-Change Contrast Agents**

Soon Joon Yoon[1], David Li[2], Ivan Pelivanov[1], Martin Frenz[3], Thomas Matula[4], Lilo Pozzo[2], Matthew O'Donnell[1]; [1]*Department of Bioengineering, University of Washington, Seattle, Washington, USA,* [2]*Department of Chemical Engineering, University of Washington, Seattle, Washington, USA,* [3]*Institute of Applied Physics, University of Bern, Switzerland,* [4]*Center for Industrial and Medical Ultrasound, University of Washington, Seattle, Washington, USA*

Background, Motivation and Objective

Photoacoustic (PA) imaging is an emerging molecular imaging modality. Image contrast, however, strongly decreases with depth due to light attenuation in tissue. Recently, PA phase-change contrast agents (PCCAs) have been proposed as alternative PA agents because the rapid expansion from droplet vaporization provides contrast orders of magnitude higher than that of conventional PA agents. Current PA PCCAs still require a minimum of 10 mJ/cm2 to activate, making them unsuitable for deep tissue imaging.

Statement of Contribution/Methods

Sono-photoacoustic (SPA) imaging is a non-linear imaging modality using simultaneous optical and acoustic activation of the PCCAs. The SPA pulse sequence, given by SPA = (PAUS+ - US +) - (PAUS- - US -), requires four pulses to isolate non-linear signals generated by vaporizing droplets from PA signals, producing integrated PAUS images at frame rates equal to ½ the laser repetition rate. US refers to a conventional ultrasound (US) image, PAUS is a US image with a time delayed laser pulse, and the superscript +/- refers to positive or negative phase acoustic pulses. SPA imaging was performed using a Verasonics Vantage equipped with an ATL L7-4 with a 1064 nm wavelength pulsed laser source. The PCCA used was 190 nm in diameter featuring a broad optically absorbing polypyrrole (PPy) shell and a liquid perfluoropentane core (TBoiling = 29°C). The agent was imaged in chicken breast.

Results/Discussion

The study revealed that SPA imaging using PPy-coated emulsions provides greater contrast enhancement than conventional PA imaging while suppressing PA image artifacts. Optical and acoustic intensities required to activate the droplets were well within FDA and ANSI safety limits. By modulating acoustic pressure and optical fluence, the optical fluence needed to vaporize the droplets can be reduced by more than a factor of 10. SPA activation not only provides improved contrast enhancement and selectivity over conventional PA imaging, but can also be used for theranostics.

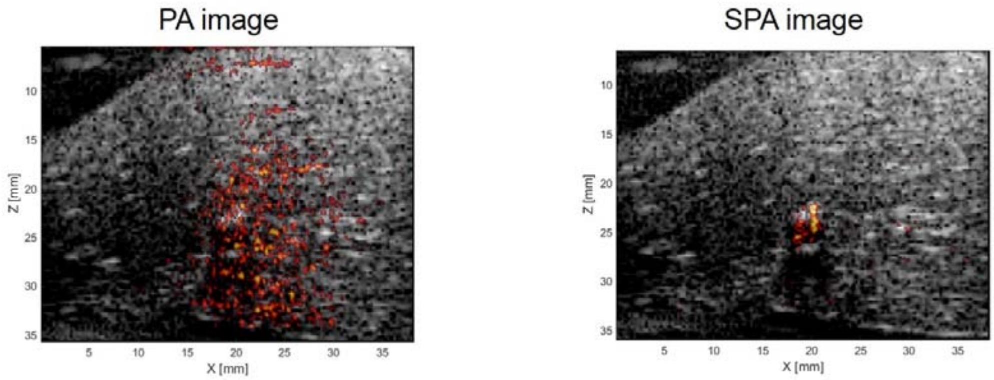

Figure 1: (A) Photoacoustic (PA) versus (B) sono-photoacoustic (SPA) image of SPA contrast agents in chicken breast at an 0.65 pM concentration. This agent is easily identified in the SPA image. Furthermore, imaging artifacts from endogenous absorbers are suppressed in the SPA image. These images represent a single frame in a real-time imaging loop operating at a display rate equal to ½ the laser repetition rate.

4F-3

2:00 pm Gold Pickering Emulsions as a Phase-change Contrast Agent for Photoacoustic Imaging

Yi-Ting Lee[1], David Li[1], Matthew O'Donnell[2], Thomas Matula[3], Lilo Pozzo[1]; [1]*Chemical Engineering, University of Washington, Seattle, Washington, USA,* [2]*Bioengineering, University of Washington, Washington, USA,* [3]*Center for Industrial and Medical Ultrasound, University of Washington, USA*

Background, Motivation and Objective

Photoacoustic (PA) imaging is an emerging technique used with ultrasound imaging to provide molecular specificity. Even with contrast agents, PA imaging suffers from poor penetration depth due to strong light attenuation in tissue. Recently, Phase-change contrast agents (PCCAs) have been proposed as an alternative agent since volume expansion during the vaporization process results in significantly larger signals than those from traditional photo-thermal expansion based contrast agents.

Our PCCA is a Pickering emulsion featuring a low boiling point liquid perfluorocarbon (PFC) core decorated by 12 nm diameter gold nanoparticles (GNP). The agents can undergo a reversible phase change with the application of either optical or acoustic energy. Photo-thermal heating of the GNP shell or acoustic cavitation causes vaporization of the PFC core. The non-bonded shell can easily recover after vaporization and condensation for multiple activation events. In this study, the synthesis and imaging contrast performance of gold stabilized Pickering is presented.

Statement of Contribution/Methods

The necessity of sonication for Pickering emulsion formation was investigated as a function of pressure and time. PFC emulsions were insonated in the presence of GNPs using a spherically focused 1.24 MHz transducer. Threshold measurements for contrast agent activation was evaluated as a function of acoustic pressure (1.24 MHz) and laser fluence at 750 nm in wavelength. The activation (i.e. vaporization) of the agents was detected using a custom-made, broadband, high-sensitivity transducer positioned off-axis from the optical beam path.

Results/Discussion

The study reveals that cavitation events are crucial in synthesizing Pickering emulsions. Cavitation from either the PFC emulsion or water results in inducing a strong mechanical force into the system, driving the GNPs onto the PFC-water interface. Once the agent is synthesized, the extinction spectrum of the Pickering emulsion red-shifts into the NIR region due to plasmonic interactions between GNP decorating the PFC interface. This highly efficient agent reduces optical and acoustic energies required for phase transition to levels significantly lower than FDA and ANSI safety regulations, indicating these emulsions are potential contrast agents for PA imaging.

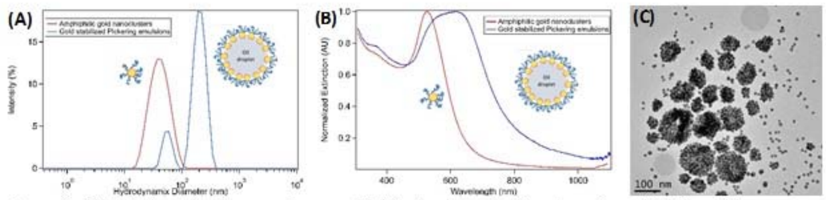

Figure 1. (A) UV-vis extinction spectrum and (B) hydrodynamic diameter of amphiphilic gold nanoparticles versus gold stabilized Pickering emulsions. (C) TEM images of the synthesized Pickering emulsion demonstrating the PFC core is densily decorated with gold nanoparticles.

4F-4

2:15 pm In Vivo Photoacoustic Detection of Lymph Node Metastasis using Glycol-Chitosan-Coated Gold Nanoparticles

Diego Dumani[1,2], In-Cheol Sun[1,2], Stanislav Emelianov[1,2]; [1]*Wallace H. Coulter Department of Biomedical Engineering, Georgia Institute of Technology and Emory University School of Medicine, Atlanta, GA, USA,* [2]*School of Electrical and Computer Engineering, Georgia Institute of Technology, Atlanta, GA, USA*

Background, Motivation and Objective

Metastasis rather than primary tumors determines prognosis and mortality in the majority of cancer patients. Detection of metastatic lesions is critical to determine prognosis and suitable treatments. We developed a method for identifying sentinel lymph node (SLN) metastasis, using combined ultrasound and photoacoustic (US/PA) imaging augmented with glycol-chitosan-coated gold nanoparticles (GC-AuNP). Presence of metastasis affects accumulation of GC-AuNP in the SLN, which can be monitored via US/PA imaging (A).

Statement of Contribution/Methods

GC-AuNP colloid (100 µl, 0.1 mg Au/ml) was injected peritumorally for drainage into the SLN of breast tumor-bearing mice (A). US/PA imaging of the SLN was performed before and immediately after the injection, and then 1 h, 24 h, and 48 h after the injection. Accumulation of GC-AuNP in the LN after cellular uptake by immune cells (macrophages) was visualized using PA imaging in the near-infrared wavelength range. To quantify accumulation, we used spectroscopic PA (sPA) in the 680-970 nm wavelength range, which allows for isolation of signal corresponding to GC-AuNP. At the conclusion of the imaging studies, we harvested the tissue and performed histological analysis. Immune cells, metastatic cells, and GC-AuNP were identified by H&E stain, GFP fluorescence, and dark-field microscopy, correspondingly.

Results/Discussion

US/PA imaging showed that accumulation of GC-AuNP in the SLN was reduced due to metastasis (B). While single-wavelength PA images demonstrated the effect qualitatively, the accumulation of GC-AuNP was quantified using sPA analysis. The overall sPA signal (area of sPA image relative to area of LN) within the lymph node was reduced by more than 20% (statistically significant) when compared to healthy controls (C). No changes were observed between 24 h and 48 h drainage. Histology (D) confirmed that metastatic cells inside the SLN disturb the distribution of particles inside immune cells, stopping them from spreading across the SLN, as identified by US/PA. In healthy controls, GC-AuNP were found in macrophages across the lymph node. In conclusion, the developed US/PA imaging method can aid physicians in detection of micrometastasis thus guiding and avoiding unnecessary SLN biopsy. Future studies will focus on studying cell uptake mechanisms to optimize GC-AuNP, improve delivery, and minimize the dosage.

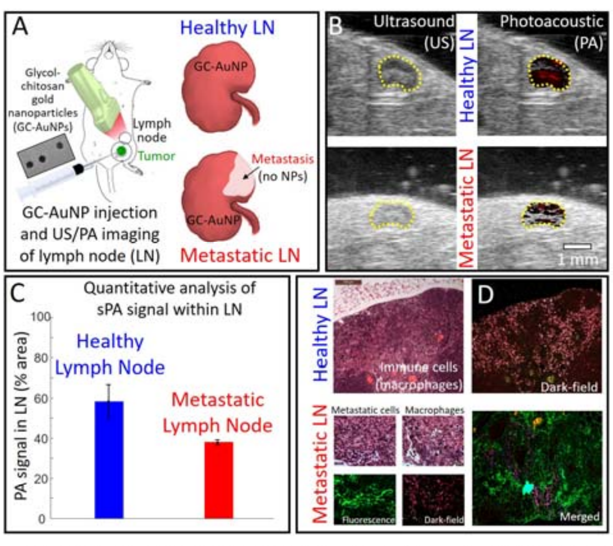

A) GC-AuNP are injected near primary tumor in the mammary fat pad for drainage into the inguinal lymph node. Distribution of GC-AuNP in LN is affected by metastasis. B) The SLN is identified using ultrasound. Spectroscopic PA imaging shows the difference in nanoparticle accumulation/distribution. C) Healthy LN showed enhanced accumulation of GC-AuNP in the dark-field microscopic images. In contrast, accumulation of GC-AuNP (dark-field) is reduced in LN with metastatic cancer cells (fluorescence). D) Quantitative analysis shows significant reduction in sPA signal in the metastatic SLN.

4F-5

2:30 pm **Optically and Acoustically Triggerable Sub-micron Phase-change Contrast Agents for Enhanced Photoacoustic and Ultrasound imaging**

Shengtao Lin[1], Anant Shah[2], Javier Hernández-Gil[3], Antonio Stanziola[1], Bethany Harriss[3], Terry Matsunaga[4], Nicholas Long[3], Jeffrey Bamber[2], Meng-Xing Tang[1]; [1]*Department of Bioengineering, Imperial College London, London, United Kingdom,* [2]*Joint Department of Physics and Cancer Imaging Centre, The Institute of Cancer Research and The Royal Marsden NHS Foundation Trust, London, United Kingdom,* [3]*Department of Chemistry, Imperial College London, London, United Kingdom,* [4]*Department of Medical Imaging, University of Arizona, Tucson, Arizona, USA*

Background, Motivation and Objective

To explore the extravascular space, sub-micron phase-change droplets show widespread interest in medical imaging and therapy with various modalities, such as ultrasound and photoacoustic. Existing studies (Wilson 2012, Wei 2014) on such dual-modality contrast agents have demonstrated the generation of both optical and ultrasound contrast after optical activation. However these studies did not explore the option of acoustic activation. Furthermore, high boiling point perfluorocarbons were used in these studies. A low boiling point may be preferred, to minimise un-wanted bioeffects, especially when activating in deeper tissues. In this study, we demonstrate a versatile phase-change sub-micron contrast agent that can provide three modes of contrast enhancement: 1) photoacoustic imaging contrast, 2) ultrasound contrast with optical activation, and 3) ultrasound contrast with acoustic activation. This would add versatility of vaporisation triggering, offering new possibilities in dual mode imaging, molecular imaging and drug delivery.

Statement of Contribution/Methods

The contrast agent, ‘Cy-droplet’ (Fig 1a), comprises of a volatile perfluorocarbon core and a near infrared dye (Cyanine7.5, peak absorption: 788 nm), and was prepared via ‘microbubble condensation’ (Sheeran, 2011). The size-selected Cy-droplet revealed an average diameter ~220 nm, and ~400 nm for stock Cy-droplet. For optical activation, the pre-clinical MSOT system (iThera) was employed to deliver laser pulses (788 nm, 22.6 mJ/cm^2) to optically activate Cy-droplets, and to acquire photoacoustic signal. For acoustic activation, ‘imaging-activation-imaging’ sequence on a Verasonics ultrasound research platform (with L12-5) was delivered to activate (mechanical index =1.2) and image Cy-droplets.

Results/Discussion

The phase-shift of Cy-droplets by optical activation was achieved and offer both photoacoustic (8 dB, Fig 1c) and ultrasound (11 dB, Fig 1d) signal enhancement, or by diagnostic ultrasound pulses to provide ultrasound echo enhancement (12-fold, Fig 1f). Both *in vitro* experiments and initial in vivo experiments have been conducted and results show that activation of the Cy-droplets using either approach forms acoustically detectable gas bubbles, which could potentially offer extravascular ultrasound contrast enhancement due to their sub-micron initial size.

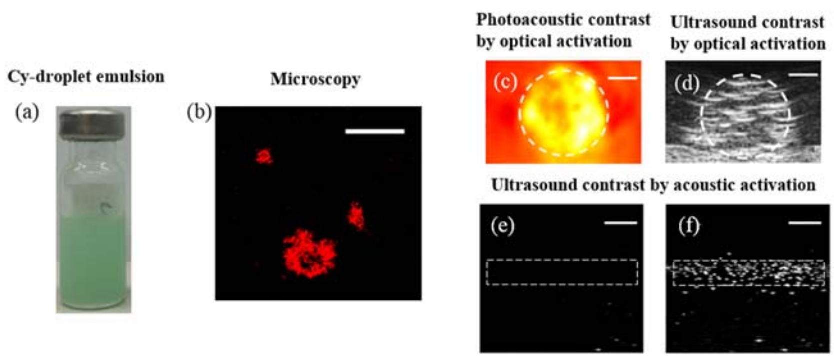

Figure 1. (a) Cy-droplet emulsion in a 2-mL glass vial. (b) Confocal fluorescence of Cy-droplets. ‘Large ones’ (size outliers) were demonstrated for the purpose of visualisation of the location of fluorescent lipid. Scale bar 10 μm. (c) Photoacoustic contrast induced by optical activation of Cy-droplets embedded in a phantom using a MSOT system. Scale bar 5 mm. (d) Ultrasound contrast generated after optical activation of Cy-droplets embedded in a phantom. Scale bar 5 mm. (e, f) Ultrasound images before and after acoustic activation of Cy-droplets dispersed in a 37° C water tank. It was conducted using a programmable ultrasound research platform (Verasonics). Scale bar 5 mm.

4F-6

2:45 pm **Photoacoustic Detection of Targeted Cancer Cells Using Gold Nanorod Loaded PLGA Nanoparticles**

Yanjie Wang[1,2], Maurice Pasternak[3], Michael Kolios[1,2]; [1]*Physics Department, Ryerson University, Toronto, Canada,* [2]*Institute for Biomedical Engineering, Science and Technology (iBEST), Toronto, Canada,* [3]*Biological Sciences Department, Sunnybrook Research Institute, Toronto, Canada*

Background, Motivation and Objective

Medical imaging through a targeting agent promises to improve the specificity and sensitivity of cancer detection. Nanoparticles (NPs) may provide advantages for targeted photoacoustic (PA) imaging due to their unique physical and optical properties. In our previous study, we developed a phase-change contrast agent made from a biodegradable polymer, poly(lactic-co-glycolic acid) (PLGA) and loaded with perfluorohexane (PFH) liquid, gold NPs and fluorescent dyes for PA imaging and cancer therapy [1]. In this study, The PLGA NPs were conjugated to an anti-HER2 antibody (Herceptin) for specific binding to breast cancer cells that overexpress HER2 receptors. The targeting specificity of PLGA-GNR-Herceptin NPs and the resultant PA enhancement in cells were examined using fluorescent imaging, flow cytometry, and PA imaging.

Statement of Contribution/Methods

PLGA NPs (d ≈ 560 nm) loaded with PFH liquid, gold nanorods (GNRs), and DiD fluorescent dye were synthesized using a double emulsion technique. Two breast cancer cell lines, BT474 as HER2-positive and MDA-MB-231 as HER2-negative were incubated with NPs for 1h. For flow cytometry, following incubation with PLGA-DiD-Herceptin NPs, percent DiD-positive fluorescence was assessed. For PA measurements, after incubation with PLGA-GNRs-Herceptin, methanol-fixed cells were injected into a cylindrical cavity in a tissue-mimicking phantom and the phantom was scanned using a 21 MHz transducer at 700 nm laser wavelength with a fluence of 10 mJ/cm^2 using a Vevo LAZR 2100 device. PA signals were recorded and images were reconstructed using MATLAB.

Results/Discussion

Flow cytometry results demonstrated that 53.17% DiD-positive staining was found in HER2-positive BT474 cells, while only 3.80% DiD-positive staining was found in HER2-negative MDA-MB-231 cells, indicating receptor-specific binding of the conjugated PLGA NPs. These results were confirmed by fluorescent imaging. In the PA study, the average PA signal of PLGA-GNRs conjugated BT474 cells was 15 ± 2 mV, while signal of PLGA-GNRs conjugated MDA-MB-231 cells was 0.75 ± 0.1 mV. In conclusion, the PA image enhancement was demonstrated *in vitro* using targeted NPs. This particle can be loaded with chemo drugs and may be a potential cancer biomarker and therapeutic agent using PA technique.

[1] Y. Wang, et al., Biomed. Opt. Express, vol. 7, no. 10, p4125, 2016.

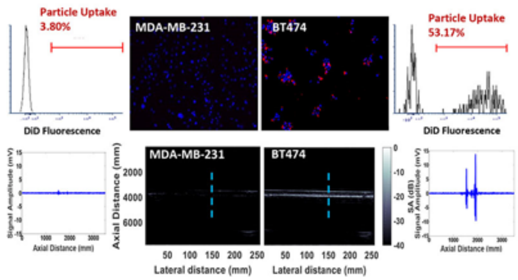

Fig 1 (Top) Fluorescent intensity and fluorescent images of PLGA-DiD-Herceptin NP conjugated cancer cells MDA-MB-231 and BT474 were obtained using flow cytometry and fluorescent microscopy. The nuclei stained with Hoechst are shown in blue, and the PLGA-DiD-Herceptin NPs are shown in red. (Bottom) PA signals and images of cancer cells conjugated with PLGA-GNRs-Herceptin. The dashed blue lines are the locations of the RF lines.

5F - Optimization of Quality Factor of Acoustic Resonators

Blue Room

Friday, September 8, 2017, 1:30 pm - 3:00 pm

Chair: **Marc Solal**
Qorvo

5F-1

1:30 pm **Solidly Mounted Plate Mode Resonators Based on 42°-48°YX LT Cuts: Loss Mechanisms**

Natalya Naumenko[1]; [1]*National University of Science and Technology "MISIS", Moscow, Russian Federation*

Background, Motivation and Objective

SH-polarized plate modes propagating in thin membranes of 42°-48°LT cuts can combine high Q-factors with electromechanical coupling up to 20% and zero TCF. For high frequency applications the main challenge is fabrication of thin membranes, less than 1 micron at GHz frequencies. Thin LT plates solidly mounted on supporting substrates can help avoid fabrication of fragile membranes. The nature of plate modes modifies in such structures and their main characteristics may change strongly. In addition, SH-wave leaks into the low-velocity substrate. In the paper, loss mechanisms are investigated for Solidly Mounted Plate Mode Resonators (SMPMR) with thin LT plates mounted on silicon or glass substrates directly or via one or few isolating layers.

Statement of Contribution/Methods

The characteristics of SH-waves propagating in LT/Si and LT/glass were analyzed using SDA-FEM-SDA software. For LT/glass propagation losses were extracted from admittance functions at resonant and anti-resonant frequencies. To improve Q-factors of SMPMRs AlN film was introduced between LT and the substrate. If LT thickness is optimized to avoid generation of spurious modes, propagation losses reduce continuously to zero when h_{AlN}/λ=0.3-0.4. To understand the mechanisms of wave transformations in multilayered structures the improved version of the software was developed. It extracts acoustic fields from Spectral Domain Analysis (SDA) of each layer in a multilayered structure. Acoustic fields were visualized for LT/Si, LT/glass, LT/AlN/glass and the structures with alternating AlN/SiO_2 layers between the plate and the substrate.

Results/Discussion

Fig. 1 shows examples of acoustic fields obtained for LT/glass (a), LT/AlN/glass (b) and the structures with two (c) and three (d) AlN/SiO_2 pairs between LT and glass. With AlN of sufficient thickness the leakage tends to zero, the wave is localized near the surface but also builds a pattern in the glass substrate. The spurious mode can be suppressed by proper selection of cut angle, electrode and LT thicknesses or optimization of AlN and SiO_2 thicknesses, with further multiplication of these layers for higher Q-factor. The alternating AlN/SiO_2 layers transform the wave into the mode totally confined in LT. The waves propagating in the structures (b) and (d) have different nature but both are able to provide zero losses and high Q-factors of SMPMRs.

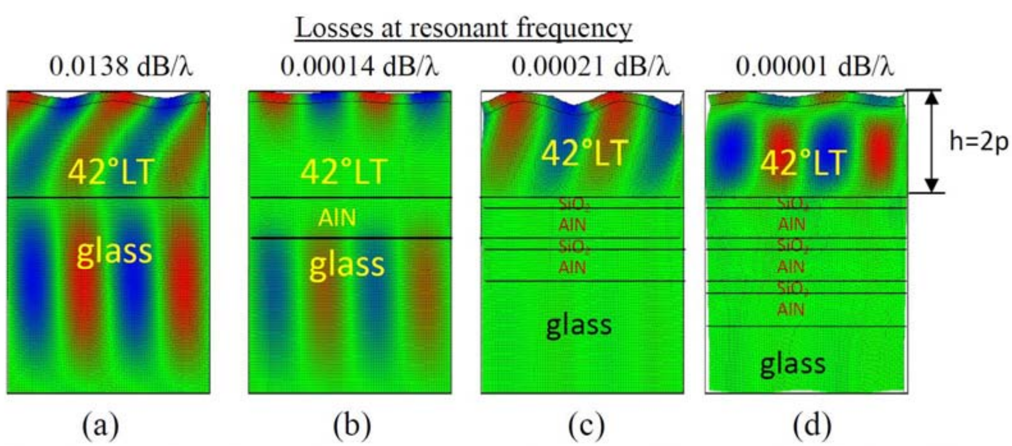

Fig. 1. Examples of acoustic waves propagating under Al grating (10%λ) in multi-layered structures including 42°LT (color refers to $\mathbf{u}_2$).

5F-2

1:45 pm **I.H.P.SAW Technology and its Application to Micro Acoustic Components**

Tsutomu Takai[1], Hideki Iwamoto[1], Yuichi Takamine[1], Takeshi Nakao[1], Masahiro Hiramoto[1], Masayuki Koshino[2]; [1]*Thin Film Engineering Dept, Murata Manufacturing Co., Ltd., Kyoto, Japan,* [2]*Murata Manufacturing Co., Ltd., Kyoto, Japan*

Background, Motivation and Objective

I.H.P.SAW (Incredible High-Performance SAW) has a novel multi-layered structure to confine SAW energy in substrate surface area, and it shows extremely high quality (Q) factor, low temperature coefficient of frequency (TCF) and improved electromechanical coupling coefficient (K2). This paper introduces its mechanism of the high acoustic Q factor, both theoretically and experimentally, and its applications to new LTE band filters and multiplexers for Carrier Aggregation service.

Statement of Contribution/Methods

Basic construction of I.H.P.SAW is following multilayered structure: piezoelectric-layer/low-impedance-layer/high-impedance- layer/support-substrate, as reported in IUS2016 [1]

In this paper, it is shown that by using high impedance material as a support substrate, simple construction with only two thin film layers (a piezoelectric-layer and a low-impedance-layer), can realize high Q characteristics.

Acoustic wave propagation characteristics, and thickness dependency and propagation direction dependency of the acoustic energy confinement have been simulated using a finite element method (FEM). As the piezoelectric material and low impedance material, a rotated YX-LiTaO3 (LT) and a SiO2 are employed. The support substrate is silicon wafer. Furthermore, the thickness of each layer is optimized to realize low TCF and improved K2. Experimental results using fabricated one-port resonators indicate high Q and low TCF.

Results/Discussion

Propagation profiles derived from the FEM simulation show that the confined acoustic wave mode is a shear-horizontal (SH) mode and the SH wave propagates along the LT and the SiO2 layers as if it were traveling wave in a waveguide. This phenomenon can be observed not only in depth direction but in the surface of piezoelectric layer. The SiO2 thickness acts important role in the confinement of the SH-SAW according to the analysis. Frequency responses and temperature characteristics of fabricated one-port resonators using the two-layered substrate with optimized structure were measured. High Q values of over 5000 and 2500 have been obtained at 1GHz and 2.7GHz, respectively. The measured TCFs have been less than 10 ppm/deg C. Using the novel substrate, a Band 41 filter and a WiFi filter with the center frequency of 2.5GHz band have been developed, which show very low loss and steep skirt characteristics. Applications to multiplexers for Band 25, Band 66 and Band 30 are also studied.

[1] T. Takai, H. Iwamoto, Y. Takamine, H. Yamazaki, T. Fuyutsume, H. Kyoya, T. Nakao, H. Kando, M. Hiramoto, T. Toi, M. Koshino and N. Nakajima, gIncredible high-performance SAW resonator on novel multi-layered substrate, hIEEE Intl. Ultrason. Symp. (2016) pp. 1-4

5F-3

2:15 pm **Piston Mode Operation of SAW Resonators Using Coupling between Multiple SAW Modes**

Benfeng Zhang[1,2], Tao Han[1], Gongbin Tang[1,2], Xinyi Li[2,3], Yulin Huang[2,3], Tatsuya Omori[2], Ken-ya Hashimoto[2]; *[1]School of Electronic Information and Electrical Engineering, Shanghai Jiao Tong University, China, People's Republic of, [2]Graduate School of Engineering, Chiba University, Japan, [3]School of Electronic Engineering, University of Electronic Science and Technology of China, China, People's Republic of*

Background, Motivation and Objective

The piston mode operation (PMO) is quite effective for realization of spurious-free and low-loss SAW resonators. The scalar potential (SP) analysis indicates that "phase shifters" are necessary for PMO at edges of the acoustic aperture. Nakamura, et al., pointed out that for SAW resonators using $SiO_2/LiNbO_3$ structure, PMO is possible by simply removing SiO_2 in the dummy electrode region [1]. This phenomenon cannot be explained by the SP theory, and was expected to be due to existence of the spurious SH SAW in addition to the main Rayleigh SAW or vice versa.

Statement of Contribution/Methods

This paper investigates SAW reflection at aperture edges of SAW resonator structures when multiple SAWs exist and couple with each other. The extended thin plate model [2] which can take the coupling into account is used for the analysis. It is shown that the coupling causes additional phase shift at the reflection, and PMO is possible without any tricks at aperture edges when the device structure is designed properly.

Results/Discussion

The simulation model gives the PMO condition in a closed form. It is governed by velocities of the main and spurious SAW modes in the aperture and dummy electrode regions and their anisotropy factors in the dummy electrode regions.

Fig. 1 shows calculated input admittance of infinitely long IDT with finite aperture when the parameters are set to satisfy the condition. Transverse resonances are completely suppressed. Fig. 2 shows the field distribution of the main resonance. It is seen that the main mode is well trapped in the aperture region, and the boundary condition is satisfied with a help of evanescent fields near the aperture edges.

[1] H. Nakamura, et al., IEEE Trans. UFFC., 58, (2011), p.2188.

[2] B. Zhang, et al., Proc. IEEE Ultrason. Symp. (2016) 10.1109/ULTSYM.2016.7728496.

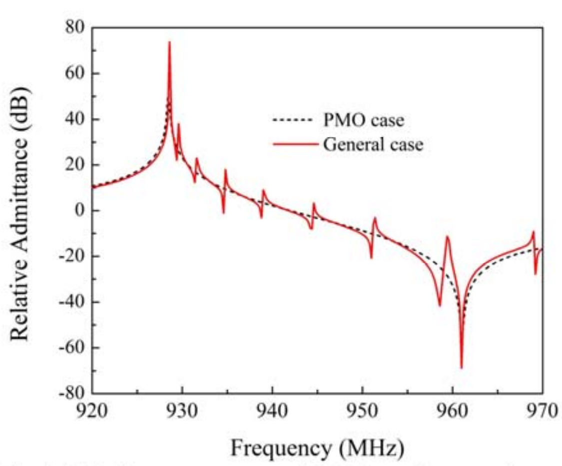

Fig.1 Admittance curves of PMO and general cases

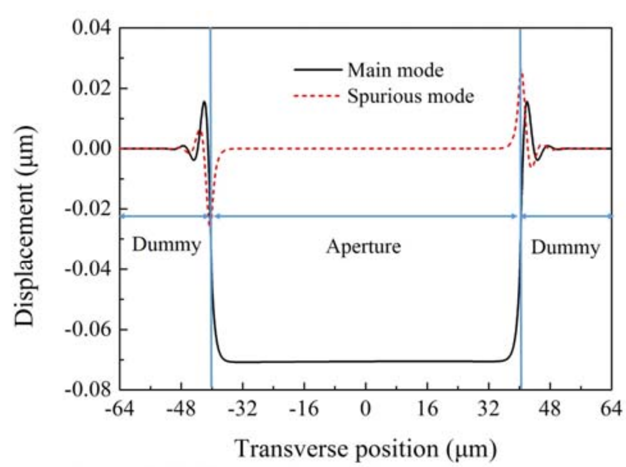

Fig.2 Field distribution of the main resonance

5F-4

2:30 pm **Acoustic Radiation from Ends of IDT in Synchronous Resonators**

Victor Plessky[1], Julius Koskela[1], Panagiotis Maniadis[2], Balam Willemsen[2], Patrick Turner[2], Filip Iliev[2], Bob Hammond[2], Neal Fenzi[2]; *[1]GVR Trade SA, GORGIER, Switzerland, [2]Resonant Inc., Goleta, California, USA*

Background, Motivation and Objective

The SAW on rotated "leaky" Y-cuts LiTaO3 and LiNbO3 is a dominantly localized near surface slow shear-horizontal wave, which is weakly coupled to the fast shear bulk wave. Any surface perturbation can lead to radiation of bulk-acoustic waves from the device, increasing losses. To minimize this radiation, LSAW resonators are typically synchronous, with all electrodes in the IDT and in the reflectors having the same periodicity and shape. Moreover, the crystal cut and the thickness of the metallization are typically optimized to minimize the acoustic radiation [1]. We show here that the ends of the IDTs can be a source of bulk wave radiation and, hence, cause additional losses, similar to known effect of the leaky SAW scattering on gaps between IDTs.

Statement of Contribution/Methods

In this work, we employ a recently introduced 2D hierarchical cascade-FEM method [2] to simulate acoustic radiation from synchronous resonators. Cascade-FEM program "Layers" allows rapid evaluation and visualization of full acoustic and electric field distributions in 2D finite SAW devices on typical workstations. Integral radiated power can then be calculated.

Results/Discussion

The contribution of acoustic radiation to losses are characterized in different frequency ranges for synchronous resonators used in "ladder" -type filters. In particular, we find that the transition between the IDT and the reflectors serves as a localized source of BAW radiation on 42°LiTaO3. As the structure is mechanically periodic at the transition, this radiation is probably solely due to the electric discontinuity at that transition. In comparison, such radiation looks less significant in a TC SAW resonator on SiO2-covered 128°-LiNbO3 with Cu electrodes. Numerical estimation of this effect on the Q-factor of resonator will be presented.

[1] O. Kawachi, G. Endoh, M. Ueda, O. Ikata, K. Hashimoto, and M. Yamaguchi, "Optimum cut of LiTaO3 for high performance leaky surface acoustic wave filters", Proc. IEEE Ultrasonics Symp., 1996, pp. 71-76.

[2] J. Koskela, P. Maniadis, B.A.Willemsen, P.J.Turner, R.B.Hammond, N.O.Fenzi, and V. Plessky, "Hierarchical cascading in 2D FEM simulation of finite SAW devices with periodic block structure", in 2016 IEEE International Ultrasonics Symposium, 2016.

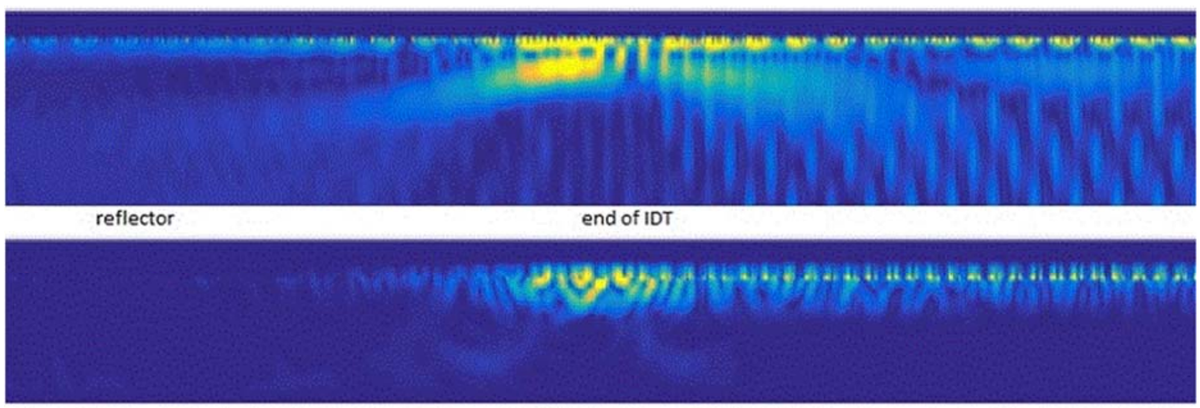

Figure 1. Top: magnitude of power flow in a synchronous LSAW resonator on 42°YX-cut $LiTaO_3$, at a frequency within the stopband. The local radiation of BAWs, which can be seen at the center of the image, originates from the electric discontinuity between a reflector (left) and an IDT (right). Bottom: magnitude of power flow in a synchronous TCSAW resonator on 128°YX-cut $LiNbO_3$, at corresponding location and within the stopband frequencies. No traces of BAW radiation can be seen.

5F-5

2:45 pm Improvement of Quality Factro by Hetero Acoustic Layer (HAL) Structure SAW combining LiTaO3 Thin Plate and Quartz Substrate

Michio Kadota[1], Shuji Tanaka[2]; [1]*Graduate School of Engineering, Tohoku university, Sendai, Miyagi prefecture, Japan,* [2]*Graduate School of Engineering, Tohoku University, sendai, Miyagi prefecture, Japan*

Background, Motivation and Objective

For mobile communication, acoustic wave filters are being continuously required better steepness of a passband and a smaller temperature coefficient of frequency (TCF). Recently, various Hetero Acoustic Layer (HAL) types of surface acoustic wave (SAW) devices were reported by different groups including us[1-5]. HAL SAW devices inherently have many variations of structure and a lot of potentials. In this study, we report the bandwidth (BW) and impedance ratio (Z ratio) of different designs of HAL SAW resonators using a $LiTaO_3$ thin plate on a quartz substrates.

Statement of Contribution/Methods

Fig. 1 shows the simulated resonance characteristics of (a) 42°YX-LT (42LT), (b) 42LT/42°45′YX quartz and (c) 42LT/42°45′Y90°X quartz with Al electrodes. Compared with the standard 42LT SAW resonator (a), the HAL SAW resonators (b) and (c) show higher Z ratios. Also, the TCF is smaller, because a positive TCF of leaky SAW on quartz compensates a negative TCF of 42LT. The 42LT/42°45′YX quartz HAL SAW resonator and the standard 42LT SAW resonator as a reference were fabricated, for both of which the Euler angle is not suitable but commercially available. An LT thickness after bonding and polishing is 0.5 µm ± 25%. The electrodes are made of 0.12 µm thick Au.

Results/Discussion

Fig. 2 compares the frequency characteristics of the 42LT and 42LT/42°45′YX quart resonators with Au electrodes. Both resonators share the same electrode design; a wavelength λ of 3.26 µm, an aperture of 16λ, and 68 pairs of IDT. The HAL SAW resonator shows better performance in BW and Z ratio compared with the reference (4.5% vs. 3.3% in BW and 66 dB vs. 50 dB in Z ratio). In terms of Q factor, this is 4.6 times improvement. The same comparison was done for Cu-metalized resonators, and a smaller Q improvement of 2.9 times was confirmed (IFCS 2017). The TCF was also evaluated. The TCF of the HAL SAW resonator is about 3/5 of that of the standard SAW resonator. In conclusion, the Q factor of SAW resonators can be drastically improved by HAL structure combing thin LT and quartz.

References

[1] Jpn. J. Appl. Phys., 54, 2015, 07HD09-1-4.

[2] Proc. IEEE Freq. Cont. Symp. (2016) p361.

[3] Proc. IEEE Ultrason Symp. (2016) 6A2.

[4] Proc. Symp. On Ultrasonic Electronics, (2016) 1P3-2.

02:

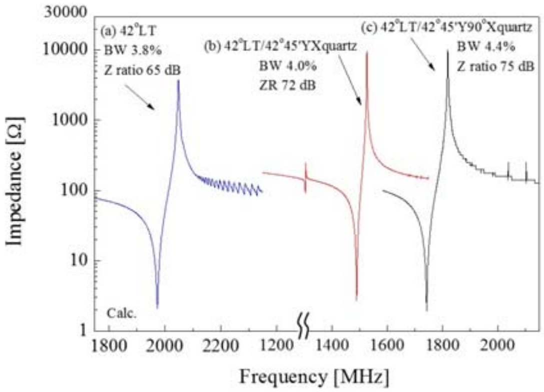

Fig. 1 Simulated frequency characteristics of resonators using (a) 42LT, (b) 42LT/42º45`YXquartz, and (c) 42LT/42º45'Y90ºX quartz.

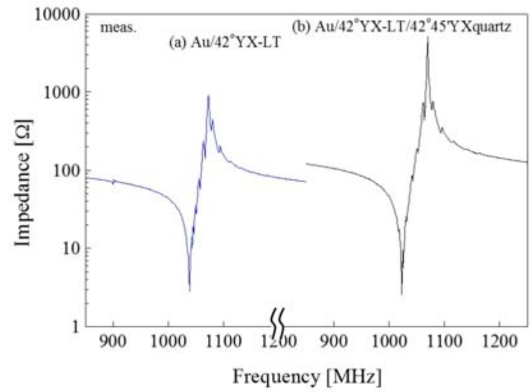

Fig. 2 Measured frequency characteristics of resonators using (a) Au IDT/42LT and (b) Au IDT/42LT/42º45`YX quartz.

6F - NDE and Industrial Applications

Hampton Room

Friday, September 8, 2017, 1:30 pm - 3:00 pm

Chair: **Lawrence Kessler**
Sonoscan Inc.

6F-1

1:30 pm **Long Distance Measurement over 30m by High-Speed Non-Contact Acoustic Inspection Method using Acoustic Irradiation Induced Vibration**

Tsuneyoshi Sugimoto[1], Kazuko Sugimoto[1], Itsuki Uechi[1], Takeyuki Oodaira[1], Akihiko Kawakami[2], Noriyuki Utagawa[3]; [1]*Graduate School of Engineering, Toin University of Yokohama, Yokohama, Japan,* [2]*Honsyu-Shikoku Bridge Expressway Co., Ltd., Japan,* [3]*SatoKogyo Co., Ltd., Japan*

Background, Motivation and Objective

The non-contact acoustic inspection method has been studied using a laser Doppler vibrometer of high sensitivity and a sound source which can generate big sound pressure at a long distance. However, the inspection at the long distance over 10 m was carried out only with the concrete test object. Therefore, for an actual concrete bridge in Japan, the long distance measurement experiment over 30 m was conducted this time.

Statement of Contribution/Methods

Long range acoustic device (LRAD) was used as the excitation sound source and a scanning laser Doppler vibrometer (SLDV) was used as a measurement LDV, both of which were located at a distance of about 34 m from the surface of target under the bridge as shown in Fig.1. Multi tone burst wave (pulse length: 3 ms, interval time: 200 ms, total signal length: 400 ms) with a frequency range of 300-4000 Hz were used as the emitted sound wave. The sound pressure on the surface of concrete is set to about 100 dB, and the number of average is three. The size of the measurement area was about 57 cm in length and about 72 cm in width (7x11points). The measurement time is about 284 seconds.

Results/Discussion

Figure 2 shows an example of the distribution of the vibration energy ratio. The ratio is based on the minimum vibration energy. The measured 300-4000 Hz band is used excluding the resonance frequency band of the laser head. Near white crack line of this figure, high vibration energy area can be seen. As a comparison, vibration measurement experiment by hammer method was carried out. Since based on the difficulty of hammer method at high places, the measurement was made with only one horizontal line (17 points). Since the same experimental result using hammer method was obtained, it was confirmed that this method can detect defects even at a distance exceeding 30 m.

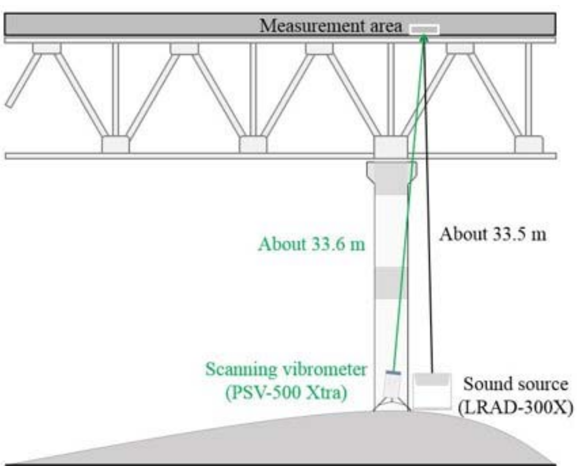

Fig.1. Experimental setup. LRAD-300X was used as a sound source, PSV-500 Xtra was used as a scanning vibrometer.

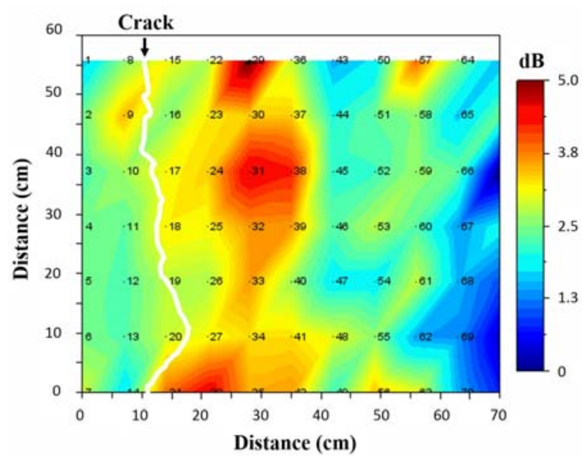

Fig.2. An example of the distribution of the vibrational energy ratio (300-4000Hz).

6F-2

1:45 pm **A Hardware/Software Co-Design Architecture for Ultrasonic Flaw Detection with Hidden Markov Model and Wavelet Transform**

Kushal Virupakshappa[1], Erdal Oruklu[1]; [1]*ECE Department, Illinois Institute of Technology, Chicago, IL, USA*

Background, Motivation and Objective

This work presents an embedded hardware architecture for real-time ultrasonic NDE applications that incorporate Hidden Markov Model (HMM) based statistical signal methods. HMM has been successfully used in applications like audio segment retrieval, speech/language recognition and image processing applications. Recently, we proposed a new Hidden Markov Model (HMM) based ultrasonic flaw detection algorithm which can not only detect the presence of flaw echoes but also determine the exact location of the flaw within the A-scans. The proposed method is computationally complex and it also involves a supervised training phase for determining the algorithm parameters.

Statement of Contribution/Methods

HMM provides signal analysis based on state machine based approach with the assumption that each emission corresponds to a sample in the ultrasonic A-scan emitted in a sequential manner. The A-Scan is subjected to three levels of discrete wavelet transform (DWT) and the wavelet filter output is considered as the feature input to HMM. The feature set is subjected to quantization to accommodate HMM training. The training algorithm calculates the transition and emission probability matrices. The maximum likelihood estimates of the transmission and emission probability parameters are calculated with Baum-Welch forward-backward algorithm. Finally, Viterbi algorithm predicts the probability of a given observation belonging to a particular hidden state. This probability determines the location of the flaw echoes.

For this work, a ZedBoard with Xilinx Zynq-7020 System-on-Chip (SoC) is chosen for the hardware implementation. Zynq-7020 has a dual-core ARM Cortex A9 processor within the FPGA fabric. Therefore, a hardware/software approach is used for maximizing the resource usage. Three-layer wavelet decomposition is implemented via hardware description language (HDL) within the FPGA programmable fabric. HMM implementation utilizes both software and hardware pipelines. In particular, Baum-Welch algorithm runs on the ARM processor core while the Viterbi decoder is realized inside the programmable logic.

Results/Discussion

Overall, a total of 395 A-scans (each one has 1024 data samples) were used in this study. Out of 395 A-scans, 40 were used for training and the remaining 355 A-scans were used for testing purpose. Flaw echo location was detected correctly for 317 A-Scans, indicating 90% detection accuracy. Results demonstrate that HMM algorithm with wavelet features provide significant SNR improvement. Furthermore, training for transition and emission matrices is accomplished with a relatively small data set compared to other learning algorithms such as neural networks or support vector machines. Although Zynq-7020 is a low-cost embedded system, it is shown to be capable of executing the proposed algorithm successfully.

6F-3

2:00 pm **Contactless Ultrasonic Wavefield Imaging of Concrete Elements Using an Automated Scanning MEMS Ultrasonic Sensor Array**

Homin Song[1], John Popovics[1], Jongwoong Park[2]; [1]*Department of Civil and Environmental Engineering, University of Illinois at Urbana-Champaign, Urbana, IL, USA,* [2]*School of Civil and Environmental Engineering, Chung-Ang University, Seoul, Korea, Republic of*

Background, Motivation and Objective

Concrete is the most widely used material to construct critical large infrastructure systems such as dams, bridges and nuclear power plants. These concrete structures are generally subjected to various degradation mechanisms including alkali-silica reaction (ASR), freezing-thawing cycles and steel bar corrosion during their service life. Prolonged and repeated exposure to these mechanisms can result in distributed cracking in the structures. This paper presents a contactless ultrasonic wavefield imaging approach for visualizing distributed cracks in concrete.

Statement of Contribution/Methods

The approach uses an air-coupled ultrasonic transducer for sending and a MEMS ultrasonic air-coupled sensor array for sensing and thus enables rapid acquisition of ultrasonic wavefield data with high signal-to-noise ratio (SNR) and spatial resolution. The approach does not require physical contact between the sensors and test specimens nor special surface treatment.

Results/Discussion

In the paper, the experimental testing set-up is described. A series of ultrasonic scanning tests are performed on a sound and damaged (containing simulated distributed cracks) concrete samples. The ultrasonic wavefield data obtained from the experiments are analyzed in frequency-wavenumber domain to extract the multiply scattered wavefields set up by heterogeneity of concrete (aggregates and distributed cracks). The experimental results show that the high sensitivity of the MEMS sensors enables acquisition of leaky ultrasonic wavefields from concrete with suitable SNR and their small size provides high spatial resolution in the obtained images. Analysis of the obtained scattered field data reveals that incident ultrasonic surface waves undergo complicated random scattering within the cracked region and further that the randomly scattered wavefield energy is closely related to the density of distributed cracks.

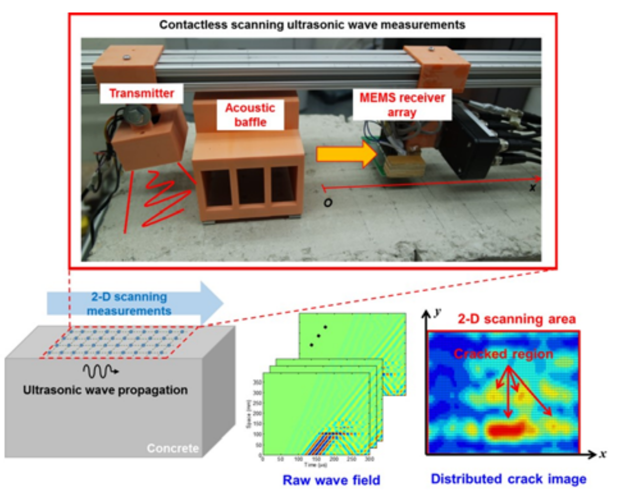

Figure 1. Conceptual illustration of the proposed approach. A fully contactless air-coupled scanning measurement setup obtains ultrasonic surface wave data in concrete; the resulting wave field data can be used to visualize distributed cracks within the scanned region.

6F-4

2:15 pm **One-Dimensional Model for the Ultrasonic Response of Resin-Filled Gaps in Automated Tape Layup Composites**

Patrick Johnston[1], Peter Juarez[2]; [1]*Nondestructive Evaluation Sciences Branch, NASA Langley Research Center, Hampton, VA, USA,* [2]*Nondestructive Evaluation Sciences Branch, NASA Langley Research Center, USA*

Background, Motivation and Objective

Automated tow placement has become a widely-used fabrication technique, especially for large aerospace structures. Robotic heads lay down strips of pre-impregnated fiber (called tows) along programmed paths. While the intention is to lay adjacent tows abutted to one another, occasionally a tow is placed leaving a non-zero gap between it and the previously-placed tow. In order to preserve the intended stiffness properties in the finished composite, it is important to control gap formation, to keep gaps below a certain width.

If a gap between tows exists, it tends to fill with resin during the cure, forming a fiber free (resin-rich) volume. In immersion ultrasonic pulse-echo measurements of a cured laminate, the gap can be observed to produce a noticeable echo, lacking the image "texture" of the surrounding fiber-filled resin. Furthermore, the gap does not appear to significantly attenuate the sound, as indicated by the reflection from the far surface of the laminate.

Statement of Contribution/Methods

As an aid to understand this behavior, we considered a one-dimensional model of the composite laminate, with a thin layer having the ultrasonic sound speed and density of neat resin, sandwiched between two layers of material having the sound speed and density of fiber-reinforced composite and surrounded on both sides by water. Neglecting attenuation, we considered the transmission and reflection coefficients of each interface, as well as that of the thin resin layer, using the impedance for a thin layer from Brekhovskikh [1].

[1] L.M. Brekhovskikh, Waves in Layered Media, 2nd ed., trans. by R.T. Beyer, Academic Press, New York, (1980), p. 17.

Results/Discussion

Using the initial water/composite reflection as a reference, we computed the relative magnitude of the back surface/water reflection in the presence and in the absence of a resin-only layer, as well as the relative magnitude of the reflection arising from a thin resin layer in composite. These magnitudes compared favorably with those experimentally measured in several composite specimens.

6F-5

2:30 pm The Structure Design of Two-dimensional Graphene-based Acoustic Arrays

Kaihua Cao[1], Xiaodong Ye[1], Xinhua Guo[1]; [1]*School of Mechanical and Electronic Engineering, Wuhan University of Technology, Wuhan, China, People's Republic of*

Background, Motivation and Objective

Acoustic sensors are used for tracking, amplifying, and transferring sound signal widely. There are some limitations on the traditional acoustic sensors. However, such as narrow bandwidth and low sensitivity. It is extremely difficult to capture pure sound signal with a single acoustic sensor since the noise signal and speech signal are often overlapped in the spectrum.We present a two-dimensional graphene-based acoustic sensors array since graphene film is proved to be suitable for broadband sound signal processing.

Statement of Contribution/Methods

The two-dimensional graphene-based acoustic array consists of two parts: upper plate and lower plate. Fig.1 shows that there is a 16×16 perforated array (each opening is 5 mm in diameter) on the upper plate. The multi-layer graphene film (~100 nm thick, 120×120 mm in size) attached on the upper plate can vibrate with external sound source. As a result, the distance between the graphene film and lower plate will change with the vibration of sound wave. The lower plate consists of a metal lattice (a 16×16 array, each metal dot is 5 mm in diameter) and amplifying circuit designed on the other side of the plate. The combination of graphene film and metal lattice constitutes a capacitor array. There is an external power to keep the voltage between the upper and lower plates constant, which means the voltage of each capacitor is constant. In this condition, the charge of each independent capacitor will change with the vibration of graphene film, creating a current. Then a large resistor (5.5 M Ohm) is used to covert the current into voltage. The displacement of different locations on the film is different, which means that the changes in capacitance value are different. We can have more detail information about the sound source by reverting these changes.

Results/Discussion

It is shown that the graphene-based acoustic array provides an excellent sensitivity and a flat frequency response with a wide bandwidth, which can be used to transmit/receive ultrasonic wave due to the excellent mechanical properties of the graphene film.The acoustic arrays can be used in industrial nondestructive evaluation, sound source localization and sound imaging through related algorithm.

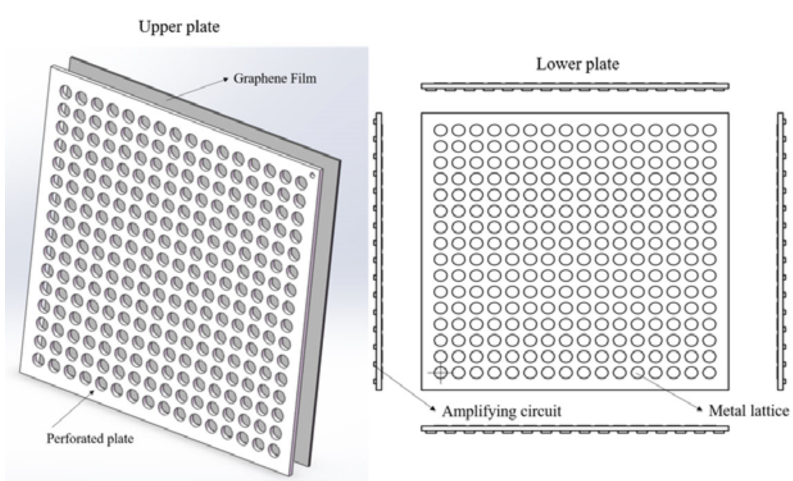

6F-6

2:45 pm Acoustic Hybrid Sensor for BDV Monitoring in Insulating Oil

Matthias Wrobel[1]; [1]*Ludwigs-Maximilians-University, Munich, Germany*

Background, Motivation and Objective

The flawless operation of a power transformer is essential to a functioning "smart" grid. Measurement of the dielectric breakdown voltage (BDV) of insulating oil in real-time and online, is the most crucial and desired feature to manage the high-energy power network. Established good laboratory practices have shown that the BDV is mainly dependent on two major factors: absolute moisture (Wc) and total acid number (TAN) of the oil1. Absolute moisture can easily be measured on-line by already established methods, while a metering of the TAN could not be realized until now. This confinement inspired us to create a piezo-acoustic-resonator sensor to estimate these two critical factors Wc and TAN.

Statement of Contribution/Methods

The hybrid measurement configuration includes a piezo acoustic resonator and a semiconducting humidity sensor. The beneficial spectrum of the piezo-plate resonator is ranging from 75-750 kHz and allowed very good estimations on the misbalance between Wc and TAN in different insulting oils. The humidity-sensing part contains an ultra-thin polyimide film with little hysteresis, fast response time and excellent stability. Initially executed measurements have tested 47 different oil samples from real power transformers under the oil testing standards for water, acidity and breakdown voltage (IEC 60156/62021-1/60814). Parallel data from our hybrid measurement configuration was extracted and additional fast Fourier transformation (FFT) was performed allowing to build a mathematical model that is also able to predict possible variations and establishing a database, creating a matrix and founding a lookup table. (Fig.1)

Results/Discussion

30 known and 30 unknown oil samples where measured with standard methods and the acoustic hybrid sensor. Fisher's Exact Test shows that this correlation is highly significant ($p<0.001$). In the next step 32 sensors will be placed on selected transformers on the "grid" of one of Germanys biggest energy providers.

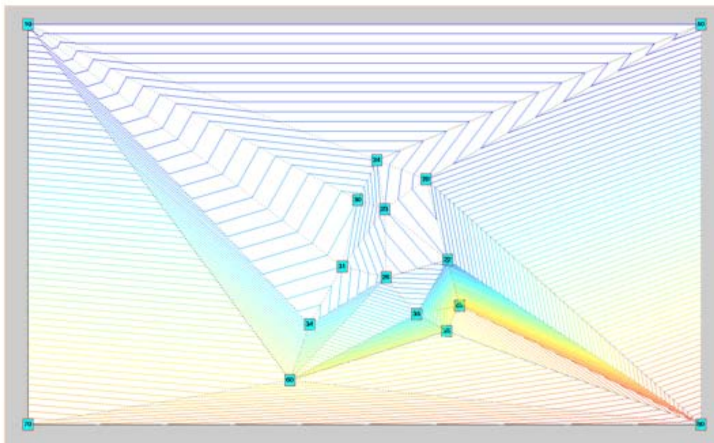

Fig.1: Lookup Table for BDV based on relative moisture (y-axis) and acoustic-resonator dissonance (x-axis)

7F - Ultrasound Electronics and Systems

Empire Room

Friday, September 8, 2017, 1:30 pm - 3:00 pm

Chair: **David Cowell**
University of Leeds

7F-1

1:30 pm A Front-End ASIC for Miniature 3-D Ultrasound Probes with In-Probe Receive Digitization

Chao Chen[1], Zhao Chen[1], Deep Bera[2], Emile Noothout[3], Zu-yao Chang[1], Hendrik Vos[2,3], Johan Bosch[2], Martin Verweij[2,3], Nico de Jong[2,3], Michiel Pertijs[1]; [1]*Electronic Instrumentation Lab., Delft University of Technology, Delft, Netherlands,* [2]*Biomedical Engineering, Erasmus MC, Rotterdam, Netherlands,* [3]*AcousticalWavefield Imaging, Delft University of Technology, Delft, Netherlands*

Background, Motivation and Objective

Data acquisition from 2-D transducer arrays has become one of the main challenges for the development of endoscopic and catheter-based 3-D ultrasound imaging devices. Front-end ASICs with sub-array pre-beamforming have been reported that reduce the cable number by an order of magnitude. Further channel reduction requires digitization in the front-end ASIC to facilitate more in-probe data processing functions. Prior solutions, however, are too large and power-hungry to be integrated in a miniature ultrasound probe. In this work, we present a front-end ASIC with an element-pitch-matched layout that combines sub-array beamforming, digitization and high-speed data transmission. It achieves a 36-fold channel-count reduction and a record power-efficiency with less than 1 mW/element power dissipation in receive.

Statement of Contribution/Methods

Realized in a 0.18 µm CMOS process, the ASIC was designed for direct integration with a 5-MHz 150-µm-pitch PZT matrix, consisting of 3×24 transmit (TX) elements and 6×24 receive (RX) elements (Figs. A, B). For initial tests, the ASIC was wire-bonded to a similar PZT matrix built on a separate test chip. In RX, pre-beamforming is applied on 3×3 elements, realizing a 9-fold channel reduction. Each sub-array receiver consists of 9 LNAs, 9 TGCs, 9 S/H delay lines and a 10-bit 33 MS/s SAR ADC. The ADC directly digitizes the beamformer output in the charge domain to eliminate the need for intermediate buffers, resulting in significant reduction in power consumption and silicon area. The 10-bit parallel outputs of 16 sub-array ADCs are serially exported to datalinks at the ASIC periphery, where the outputs from every 4 sub-arrays are combined and transmitted to the FPGA via a LVDS port.

Results/Discussion

The ASIC consumes 135 mW in receive, equivalent to only 0.94 mW/element, which is acceptable even when scaled up to a 1000-element probe. The peak SNDR was measured as 51.3 dB within 100% RX bandwidth for a 5.5 MHz sinewave input (Fig. C-a). Fig. C-b shows the digitized acoustic signal received by one sub-array for 2 different steering angles. The aggregate output data rate is 6.6 Gb/s (1.65 Gb/s per output channel). In conclusion, our prototype ASIC with low-power ADCs realizes an additional 4-fold channel-count reduction compared to prior analog pre-beamformer designs, which is essential for endoscopic and catheter-based 3-D imaging systems.

7F-2

1:45 pm A Front-end Integrated Circuit for a 2D Capacitive Micromachined Ultrasound Transducer (CMUT) Array for a Noninvasive Neural Interface to the Retina

Chunkyun Seok[1], Xun Wu[1], F. Yalcin Yamaner[1], Omer Oralkan[1]; [1]*Electrical and Computer Engineering, North Carolina State University, Raleigh, NC, USA*

Background, Motivation and Objective

A recent study showed that focused ultrasound can noninvasively create neural response in the retina in a similar way to light stimulus. To implement such functionality, we developed an algorithm for a 2D transducer array to project an image to the retina as an ultrasound field pattern (USFP) in a previous study. In this work, we report a front-end integrated circuit (IC) for a 2D CMUT array that realizes a USFP with quantized phases and amplitudes. In addition, we evaluated the projected image quality with Field II simulations considering non-linearity in phases extracted from a fabricated prototype chip.

Statement of Contribution/Methods

The IC consists of a pitch-matched (250 µm in x and y) 16x16 transmitter (TX). The TX circuitry is capable of generating a 3-level pulse-shaped excitation signal, and driving capacitive loads of up to 20 pF. A single TX circuit [Fig. 1 (a)] consists of a voltage-controlled delay line (VCDL), a pulse-shaping block, level shifters, and a 3-level 13.5-V pulser.

The TX circuit works in either pulse-width modulation (PWM) mode for low frequency pulses (< 10 MHz) or pulse-level modulation (PLM) mode for high frequency (10-40 MHz) pulses. In PWM mode, four different levels of symmetric PWM signals are generated by selecting appropriate clocks from a VCDL. In PLM mode, the level of the excitation signal is quantized into two levels, 13.5 V or 6.75 V. For both modes, a phase delay is implemented by selecting a clock from the 16 multiphase clocks generated by the VCDL.

Results/Discussion

The front-end IC was fabricated in a 0.35-µm 13.5-V DDD process [Fig. 1 (b)]. Fig. 1 (c) shows the pulse shapes with different levels in both PWM and PLM modes. Although all the VCDLs are controlled by the same global delay-locked loop (DLL), there exist non-uniform delays due to local mismatch and clock skew. Statistical data [Fig. 1 (d)] for the static non-linearity in phases were extracted from the 16-channel outputs operating at 6.25 MHz. To evaluate the effects of the non-linearity, we simulated a 128x128 array by applying the measured statistical variation to TX signals in Field II. The resulting projection of character "A" did not degrade significantly compared to the case with ideal delays (Fig. 1 [e]). This work proves the basic functionality of our US neural stimulator IC, which will be interfaced with a 16x16 CMUT array for full acoustic characterization.

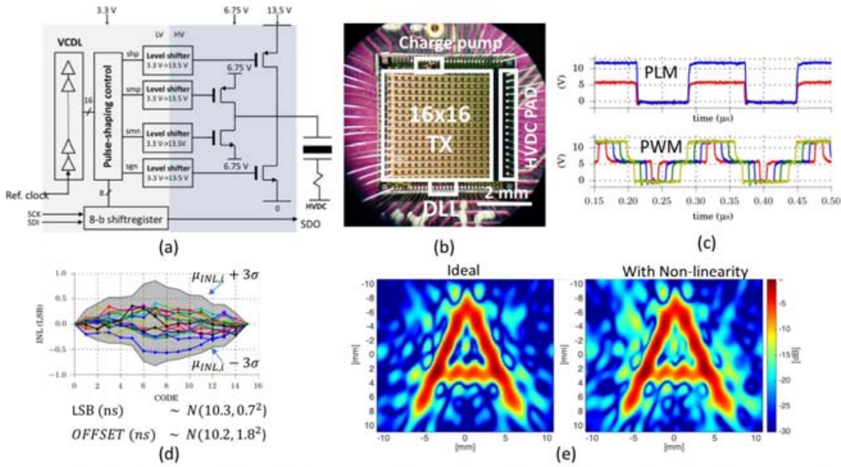

Fig. 1. (a) Block diagram of a single element TX. (b) Die photo of the IC after wire bonding. (c) Measured pulse shapes in PLM (upper) and PWM (lower) modes. (d) Measured statistical variation in phases. (e) Projected images of character "A" with ideal delays (left) and non-linear delays (right) in Field II.

7F-3

2:00 pm A High-Frequency and High-Frame-Rate Ultrasound Imaging System Design for Capacitive Micromachined Ultrasonic Transducer Arrays on an FPGA Evaluation Board

Xun Wu[1], Jean Sanders[1], Xiao Zhang[1], F. Yalcin Yamaner[1], Ömer Oralkan[1]; [1]*Department of Electrical and Computer Engineering, North Carolina State University, Raleigh, North Carolina, USA*

Background, Motivation and Objective

Dynamic receive beamforming (DRBF) is challenging for FPGA-based ultrasound (US) imaging because it is computationally intense. Work has been done to either simplify the delay calculation or precalculate the delays and store them on the FPGA. The former sacrifices image quality and the latter is challenged by limited memory resource. In this work, we report on the design of an US imaging system for capacitive micromachined ultrasonic transducer (CMUT) arrays implemented on an FPGA evaluation board. The system features high frequency, high framerate, and full DRBF for every pixel.

Statement of Contribution/Methods

The system is composed of four parts: a custom frontend analog circuit board for US transmission and reception, an analog-to-digital converter board (FMC116, 4DSP LLC, Austin, TX) to digitize echo signals, an FPGA evaluation board (VC707, Virtex-7, Xilinx Inc., San Jose, CA), and a PC (OptiPlex 9010, Dell Inc., Round Rock, TX) for post processing (PP) and image display (Fig. 1a).

The system works in either imaging mode or data acquisition (DAQ) mode.

In imaging mode, the delays are precalculated on the PC, sent to the FPGA through a 1-Gb Ethernet link, and written to the 1-GB DDR3 memory on the FPGA board. For each scanline, its delay information is read from the DDR3 and pushed into a control FIFO (Fig. 1b) before transmit beamforming. DAQ and DRBF (Fig. 1c) are pipelined to save time and space. The beamformed scanline is sent back to the PC for PP and image display.

In DAQ mode, the system waits for the PC to send a transmit delay pattern. Once it is received, the system excites the CMUT array with the pattern and sends the A-scans to the PC. Imaging software is developed to cooperate with the system in this mode. DRBF and PP are done on the PC.

Results/Discussion

Fig. 1d shows the parameters of the system and the CMUT array. In imaging mode, the highest achieved framerate is 220 fps. The 125 MS/s sampling rate, wideband preamplifiers, and 8-ns FPGA time resolution allow for high-frequency US imaging. In DAQ mode, the highest framerate is 8 fps, which is lower due to the large A-scans data set, but this mode provides access to A-scans and more flexibility in implementing new imaging algorithms. Both modes provide good image quality for a fishing wire imaging phantom (Fig. 1e, f). The demonstrated backend system is especially useful for imaging catheters with high frequency and low channel count.

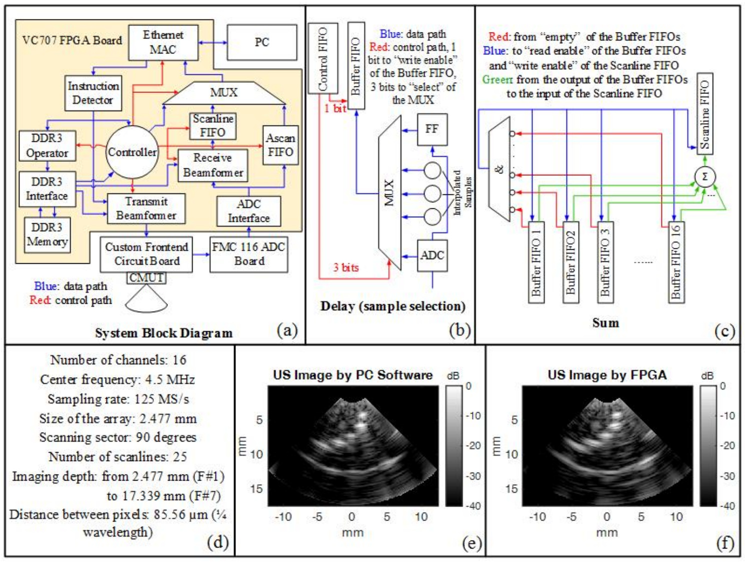

7F-4

2:15 pm Towards 3D Ultrasound Imaging of the Carotid Artery Using a Programmable and Tileable Matrix Array

Pieter Kruizinga[1,2], Eunchul Kang[3], Maysam Shabanimotlagh[2], Qing Ding[3], Emile Noothout[2], Zu Yao Chang[3], Hendrik J. Vos[1,2], Johannes G. Bosch[1], Martin D. Verweij[1,2], Michiel A.P. Pertijs[3], Nico de Jong[1,2]; [1]*Thorax Center - Biomedical Engineering, Erasmus MC, Rotterdam, Netherlands,* [2]*Lab. of Acoustical Wavefield Imaging, Delft University of Technology, Netherlands,* [3]*Electronic Instrumentation Lab, Delft University of Technology, Netherlands*

Background, Motivation and Objective

Accurate assessment of carotid artery disease by measuring blood flow, plaque deformation and pulse wave velocity using ultrasound (US) imaging requires 3D information. Additionally, the volume rates should be high enough (> 1 kHz) to capture the full range of these fast transient phenomena. For this purpose, we have built a programmable, tileable matrix array that is capable of providing 3D US imaging at such volume rates. This array contains an application-specific integrated circuit (ASIC) right beneath the acoustic piezo-stack (see Fig. 1a). The ASIC enables fast programmable switching between various configurations of elements connected to the acquisition system. This design also allows for expanding the footprint by tiling several of these arrays together into one large array. We explain the working principles and show the first basic imaging results of a single matrix array.

Statement of Contribution/Methods

One matrix array contains 24 x 40 (rows x columns) elements with a 150µm pitch and 7.5 MHz centre frequency. Finally, 10 of these arrays will be tiled to an overall aperture of 18 x 12 mm, sufficient for imaging the carotid artery. Each element in the array can be addressed via a row-level transmit (tx) and receive (rx) bus within the ASIC. These row busses are interfaced via an external circuit board to an open US system (Verasonics V1). A reconfigurable switch matrix in the ASIC allows any subset of elements per row to be selected. Row-level amplifiers and matching circuits boost the rx signal transmission to the US system. The design of the switch matrix with integrated configuration memory allows for dynamic reconfiguration of the elements connected to each tx/rx bus. Fig. 1b shows two possible acquisition schemes useful for carotid artery imaging. For the first experiment we imaged two metal wires in water. The volume reconstruction (121x73x241 50µm voxels) was done using a delay-and-sum algorithm implemented on a GPU using CUDA and MATLAB software.

Results/Discussion

Figure 1c shows a 3D rendering and 3 orthogonal mean intensity projections of the reconstructed volume of the two wires in water. Although the point-spread-function (psf) of this single array is still quite wide, it shows that this array can be used for 3D US imaging. In the upcoming months we will build tiled arrays and we will focus on acquiring 3D Doppler images from a phantom with complicated flow patterns.

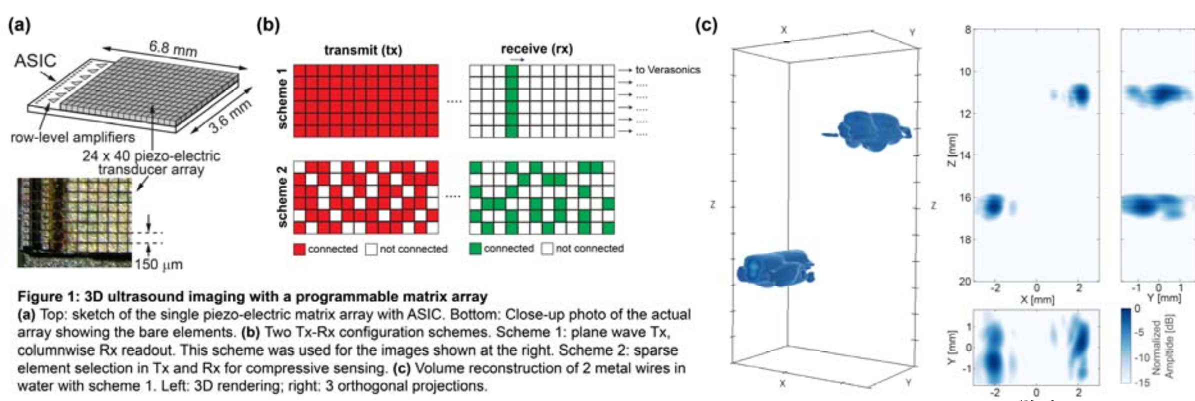

Figure 1: 3D ultrasound imaging with a programmable matrix array
(a) Top: sketch of the single piezo-electric matrix array with ASIC. Bottom: Close-up photo of the actual array showing the bare elements. **(b)** Two Tx-Rx configuration schemes. Scheme 1: plane wave Tx, columnwise Rx readout. This scheme was used for the images shown at the right. Scheme 2: sparse element selection in Tx and Rx for compressive sensing. **(c)** Volume reconstruction of 2 metal wires in water with scheme 1. Left: 3D rendering; right: 3 orthogonal projections.

7F-5

2:30 pm Performance Evaluation of ASICs for CMUT-Based Portable Ultrasound Scanners

Pere Llimós Muntal[1], Søren Elmin Diederichsen[2], Jørgen Arendt Jensen[3], Ivan Harald Holger Jørgensen[1], Erik Vilain Thomsen[2]; *[1]Department of Electrical Engineering, Electronics Group, Technical University of Denmark, Kongens Lyngby, Denmark, [2]Department of Micro- and Nanotechnology, Technical University of Denmark, Kongens Lyngby, Denmark, [3]Department of Electrical Engineering, Center for Fast Ultrasound Imaging, Technical University of Denmark, Kongens Lyngby, Denmark*

Background, Motivation and Objective

Portable ultrasound scanners (PUS) have shown to have advantages over stationary scanners such as ease of use, accessibility, transportability and cost. However, PUS are severely restricted on size and power which directly limits the area and power consumption of the electronics. In order to fully utilize the available area and power budget to achieve the best picture quality, application specific integrated circuits (ASICs) are required for the electronics. The ASICs are optimized to drive a specific transducer while minimizing the area and power consumption, which is a key target for PUS. For the purpose of implementing compact probes, CMUTs are used due to their highly compatible integration with ASIC fabrication processes. The goal of this work is to assess the impact of the area and power consumption reduction on the acoustic performance of the scanner. For this purpose, a comparison between a commercial ultrasound pulser and an ASIC optimized for CMUT-based PUS is presented.

Statement of Contribution/Methods

Typically, the performance of electronics is evaluated using voltage or current measurements. However, in systems with complex loads, such as CMUTs, the electronics performance is best assessed in the acoustic domain. An ASIC for PUS designed to minimize area and power is compared to a generic commercial ultrasound pulser from Hitachi (HDL6V5582). The ASIC occupies a die area of 0.94 mm^2. For the purpose of achieving a fair comparison, the same CMUT, pulsing frequency (5 MHz), duty cycle (1 %), DC bias voltage (80 V), and pulsing voltage amplitude (20 V) are used. The CMUT was fabricated using two consecutive local oxidation of silicon processes and has an element capacitance of 18 pF. The transducer is mounted on a PCB and placed in a water tank in 1 cm distance from a 5 MHz Optel hydrophone.

Results/Discussion

One CMUT element is pulsed with a two-period square pulse using the ASIC and the HDL6V5582, and the hydrophone signal received is shown in the left figure. The right figure shows the corresponding frequency spectra (FFTs) normalized to the maximum hydrophone voltage. The acoustic performance achieved is comparable, with a minor amplitude difference of -1.9 dB at the center frequency of the CMUT. The one-channel ASIC power consumption is 5.78 mW, whereas the HDL6V5582 consumes approximately 250 mW, i.e. the ASIC consumes 2.3 % of the total power consumption of the HDL6V5582.

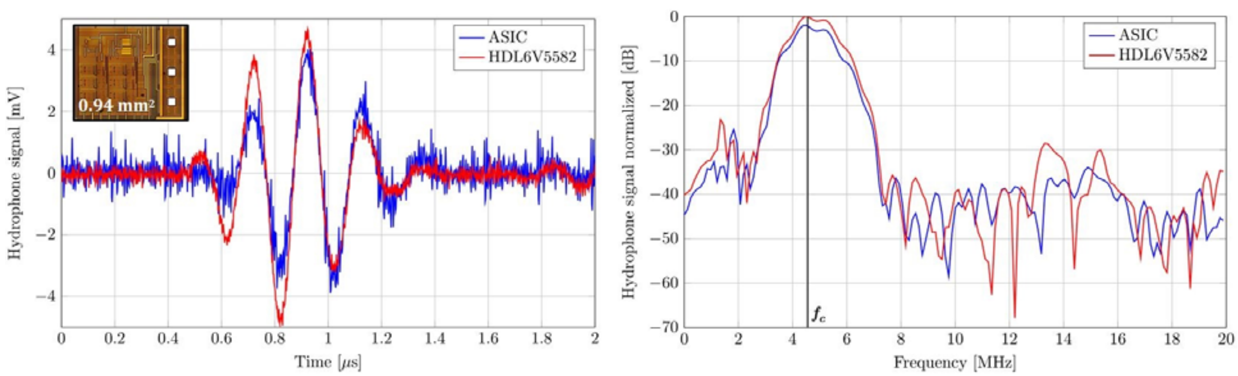

7F-6

2:45 pm Supply-Inverted Bipolar Pulser and Tx/Rx Switch for CMUTs Capable of Tolerating Voltage Levels above Process Limit

Gwangrok Jung[1], Amirabbas Pirouz[1], Coskun Tekes[2], F. Levent Degertekin[2], Maysam Ghovanloo[1]; *[1]School of Electrical and Computer Engineering, Georgia Institute of Technology, Atlanta, Georgia, USA, [2]School of Mechanical Engineering, Georgia Institute of Technology, Atlanta, Georgia, USA*

Background, Motivation and Objective

Capacitive micromachined ultrasonic transducers (CMUTs) are prone to having low transmit sensitivity. According to large signal CMUT models, this shortcoming can be overcome with higher pulse voltages and optimized bipolar pulse drives [1]. Therefore, a supply-inverted bipolar pulser and a Tx/Rx switch are proposed to drive CMUTs in medical ultrasound imaging applications. These circuits are particularly suitable for intracardiac echocardiography (ICE) catheters where interface electronics and transducer arrays are integrated at the tip and low supply voltages are desired for safety. The proposed pulser generates a bipolar signal with a peak-to-peak voltage that is almost twice the supply level, which improves the driving capability compared to conventional supply-limited pulser, enabling operation at lower supply voltage, and the switch is able to protect Rx electronics during the transmit phase.

Statement of Contribution/Methods

A prototype driver has been implemented in 0.18-μm HV CMOS/DMOS technology with 60 V devices. H-bridge circuit enables charging of an extra capacitance, C, to drive the bipolar HV pulse at output (Fig. 1, Left). The capacitance C, can be implemented on chip as part of the CMUT fabrication process. The negative HV pulse level is defined by the capacitive division between C and CMUT capacitance. Thus, it is key to select proper C based on the output level, slew rate, and power consumption. The supply-inverted bipolar pulser adopts a bootstrap circuit combined with stacked transistors and protection diode, which guarantee HV operation above process limit without lowering device reliability. It generates a bipolar pulse, controlled by three low voltage signals and a single HV positive supply. The Tx/Rx switch has a diode-bridge structure with HV protection scheme, enabling integration of the receiver with the proposed pulser by protecting against the HV signal without adding extra loading.

Results/Discussion

Measurement results, which are in good agreement with simulations, show that proposed pulser can safely generate a bipolar pulse of -34.6 to +45 V from +45 V supply voltage with C = 30 pF for 8 pF CMUT (Fig. 1, Right). Using the same supply, simulations show that the pulser is able to drive 2 pF CMUTs up to 85 Vpp. The Tx/Rx switch blocks the HV bipolar pulse, resulting in less than 1.6 V at the receiver output, allowing safe Rx operation.

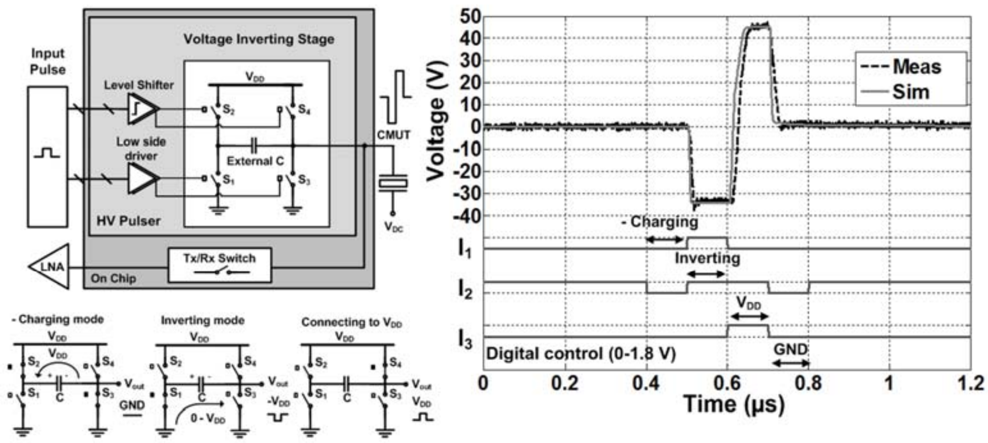

Fig. 1. Left: Simplified schematic diagram of the proposed pulser and Tx/Rx switch. Lower left: Operation of the bipolar voltage stage. Right: Measured and simulated supply-inverted output pulse along with three input control signals. C = 30 pF, CMUT capacitance (C_{CMUT}) = 8 pF.

[1] S. Satir, J. Zahorian and F. L. Degertekin, "Transmit optimization of CMUTs in non-collapse mode using a transient array model," *IEEE Ultrasonics Symp.*, pp. 85-88, 2012.

1G - MTH: Blood-Brain-Barrier

Regency Ballroom

Friday, September 8, 2017, 4:00 pm - 5:30 pm

Chair: **Charles Cain**
Univ of Michigan

1G-1

4:00 pm **Breaching the Blood-Brain Barrier Noninvasively**

Kullervo Hynynen[1]; [1]*University of Toronto, Toronto, Ontario, Canada*

Background, Motivation and Objective

Magnetic Resonance imaging (MRI) guided focused ultrasound (FUS) has been shown to be able to safely ablate deep tissues in the brain in clinical settings resulting in reduction in recovery time and complications. Pre-clinical work has demonstrated that FUS energy deposition with intravascular micro-bubbles could be used also for non-invasive MRI-guided drug delivery into tumours and brain. The preclinical studies have shown significant survival benefits when FUS has been used to open the blood-brain-barrier (BBB) for large molecular chemotherapy agents, antibodies and natural killer cells. Effective and local delivery of nanoparticles and viral vectors has also been shown.

Statement of Contribution/Methods

This talk will briefly review the physical and engineering aspects related to the FUS exposures needed to enhance the permeability of the BBB. The potential therapeutic value of the FUS exposure with micro-bubbles alone will also be shown.

Results/Discussion

The first clinical experiences with noninvasive drug delivery will be reviewed. Finally, the next generation phased array technology, the feasibility for closed-loop control using acoustic feedback and the ultimate clinical potential of the FUS brain treatments will be discussed.

1G-2

4:30 pm **Blood-Brain Barrier Disruption for the Delivery of Non-Infectious Viral Vectors and Proteins, Preliminary Study**

Josquin Foiret[1], Hua Zhang[1], Brett Z. Fite[1], Lisa Mahakian[1], Sarah Tam[1], David J. Segal[2], Katherine W. Ferrara[1]; [1]*Department of Biomedical Engineering, UC Davis, Davis, CA, USA,* [2]*MIND Institute, Department of Biochemistry and Molecular Medicine, UC Davis, Davis, CA, USA*

Background, Motivation and Objective

Human studies aimed at opening the blood brain barrier (BBB) to deliver therapeutic agents through a combination of focused ultrasound (US) and microbubbles (MB) are currently underway [1]. Our goal was to develop an US-guided BBB opening system capable of steering the US beam throughout the rodent brain and registering the coordinates with high field MRI. Our ultimate goal is to deliver therapy for Angelman Syndrome which requires the ability to deliver protein or adeno-associated virus (AAV) across the BBB over a large field of view. We sought to interface a modular imaging and therapeutic array capable of 3D electronic steering of the therapeutic beam to the Verasonics and MRI.

Statement of Contribution/Methods

BBB opening was performed on FVB mice (Charles River) and the study was approved by the UC Davis Institutional Animal Committee on Use and Care. A 1.5 MHz 128-element therapeutic array (Imasonic; focus size $2.7\times0.7\times0.4$ mm^3) with a center void that contains a user-selectable US array (Fig. 1) was interfaced to the Vantage platform (Verasonics) [2]. A 50 µL bolus of 1.5×10^7 non-targeted MBs was injected into the tail vein of the animal prior to US. The treatment consisted of 1.3 ms bursts rapidly swept over a grid pattern (3×3 locations, 0.5 mm step) with a PNP of 0.51 MPa at focus. The pattern was repeated at a PRF of 5 Hz for a total duration of 11 min [3]. Following US treatment, BBB opening was imaged with contrast MR on a 7T MRI (Bruker): 275ms/10ms/90°, FOV: 19.2×19.2 mm^2, ST/SI: 0.7mm/0.7mm, MTX = 256×256. The first animal received ip Prohance 0.5 mmol/kg Gd; the second animal received iv Gadomer-17 0.25 mmol/kg Gd equiv.

Results/Discussion

The BBB was successfully opened with both Prohance and Gadomer at the targeted site (Fig. 1). The square outline of the treated region was evident using Gadomer ($2.6\times2.1\times2.0$ mm^3). The combination of small focus size and electronic steering of the FUS array, designed for small animal therapy, allows precise delimitation of the disrupted area, and extending the treated volume can be set by choosing a larger grid size. Current work focuses on optimizing delivery of AAVs as well as real-time monitoring of MB cavitation.

Acknowledgment: NIH R01CA112356 and the Foundation for Angelman Syndrome Therapeutics

[1] https://clinicaltrials.gov/ct2/show/NCT02343991

[2] Liu *et al.*, Phys. In Med. Biol., 2016.

[3] H. Chen, J. of Cereb. Blood Flow & Met., 34, 2014

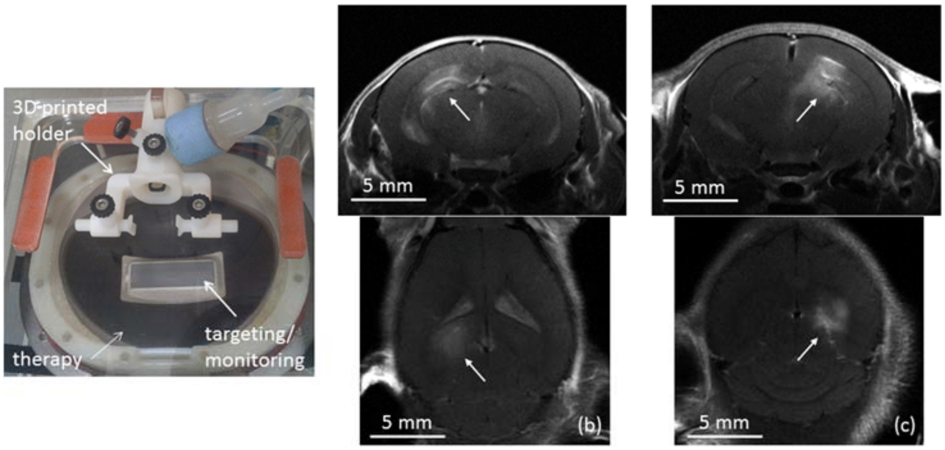

Figure 1. (a) Experimental setup. (b)-(c) MR images (top: transverve, bottom: coronal) showing contrast uptake at different targeted sites (arrow) indicate successful BBB opening. (b) Animal 1 injected with Prohance. (c) Animal 2 injected with Gadomer.

1G-3

4:45 pm MRI Guided Ultrasound-Mediated Blood-Brain Barrier Opening in Non-Human Primates Using Passive Cavitation Detection-Based Feedback Control

Hermes Kamimura[1,2], Julien Flament[1,3], Julien Valette[1], Andrea Cafarelli[4], Romina Badin[1], Philippe Hantraye[1], Benoit Larrat[2]; [1]*Molecular Imaging Research Center, CEA, France,* [2]*Neurospin, CEA, France,* [3]*INSERM, France,* [4]*The BioRobotics Institute, Scuola Superiore Sant'Anna, Italy*

Background, Motivation and Objective

Noninvasive focused ultrasound (FUS) combined with microbubbles has been proven capable of locally and reversibly increasing the blood-brain barrier (BBB) permeability allowing the extravasation of several clinical relevant substances (Hynynen et al. 2001). Despite its progress, neuro-inflammatory responses (Kovacs et al. 2016) and the high variability of the FUS transmission in the brain due to skull heterogeneity make the control of the acoustic parameters challenging. Based on that, real time microbubble activity monitoring has been employed to ensure efficacy and safety. However, further pre-clinical investigations using large animals are necessary for obtaining reliable acoustic parameters control to avoid harmful bio-effects. In this study, we developed a high-field magnetic resonance (MR) guided FUS system with passive cavitation detection (PCD) feedback control for exploring BBB opening in non-human primates (NHP).

Statement of Contribution/Methods

The animals (n= 4; 7 sessions) had the head shaved and were positioned in a 2D stereotaxic frame in sphinx position inside a 7-T Agilent MR imaging system. The FUS transducer was fixed in the stereotaxic frame and coupled to the animal's head with an expandable balloon filled with degassed water. A 14-element annular array transducer was driven at 500 kHz during 2 min with pulse length of 10 ms and pulse repetition frequency of 5 Hz. The PCD was performed by a planar mono-element 1.5 MHz transducer positioned at the center of the FUS transducer. A bolus of gadolinium (Gd) (MRI contrast agent) and microbubbles was injected intravenously before sonications. PCD baseline acquisitions were performed before injections.

Results/Discussion

The targeting and acoustic coupling quality (optimal with no bubbles trapped in the gel/balloon) were confirmed using T_2-w (weighted) MR images. Contrast enhanced T_1-w dynamic MR images after contrast agent injection confirmed the BBB opening and measured its uptake kinetics. T_2- and T_2*-w MR images acquired after sonication revealed potential hemorrhages. Safe pressure range from 228±27 to 328±4 kPa was found during sessions with no feedback-controlled sonications. The amount of Gd in the sonicated area was maximum around 15-20 min post injection. PCD harmonic emissions correlated with safe BBB opening, whereas broadband and sub-harmonic emissions were present in 1 sonication that resulted in permanent lesion (400 kPa estimated in the brain). Safe sonications were achieved in 3 sessions using real-time PCD-based feedback control of the acoustic pressure. The high resolution anatomical images and the high temporal/spatial resolution of contrast agent diffusion provide a unique tool for studying the mechanisms of BBB disruption and drug delivery in NHP. Furthermore, the PCD-based feedback control allows repeatable safe sonication regardless variation of skull attenuation.

Hynynen et al. Radiology 220, 640–646, 2001

Kovacs et al. PNAS 201614777, 2016

1G-4

5:00 pm Analysis of Focused Ultrasound with Microbubbles Induced BBB Disruption on Tight Junction Morphology

Tara Kugelman[1], Camilo Acosta[1], Shutao Wang[1], Marilena Karakatsani[1], Dritan Agalliu[2], Elisa Konofagou[1,3]; [1]*Biomedical Engineering, Columbia University, New York, New York, USA,* [2]*Pathology and Cell Biology, Columbia University, New York, New York, USA,* [3]*Radiology, Columbia University, New York, New York, USA*

Background, Motivation and Objective

Focused ultrasound (FUS) with systemically delivered microbubbles has been established to locally, reversibly and non-invasively increase the permeability of the blood brain barrier to facilitate targeted drug delivery to the brain. Despite FUS constituting a promising therapeutic technique, the cellular mechanism of FUS-mediated BBB opening has yet to be fully described. Immunoelectron microscopy of vessels has reported the removal of tight junction (TJ) proteins from the junctional cleft, yet no study has examined the structural integrity of the entire length of the TJ strand following FUS with microbubbles. Furthermore, permeability studies have identified differences in the rate of leakage between large and small vessels, but it remains to be studied if TJ strand morphology differs among vessel types. The aim of the current study is to investigate TJ strand morphology for structural abnormalities in different vessel types following FUS-induced BBB opening.

Statement of Contribution/Methods

Tg eGFP-Claudin-5 mice were intravenously co- injected with polydisperse microbubbles with the small molecular weight fluorescent tracer, 5-(and-6-) tetramethylrhodamine biocytin (biocytin-TMR, MW = 869 Da) prior to sonication. The FUS parameters used were as follows: frequency 1.5 MHz, peak-rarefactional pressure 0.45 MPa or 0.75MPa, pulse length 10 ms, pulse repetition frequency 5 Hz, and a duration of 120 s. Mice were survived for one hour and biocytin-TMR leakage and TJ integrity was examined with confocal imaging of the brain (25μm).

Results/Discussion

TJ strand abnormalities including complete removal of the TJ strand, strand discontinuities, and bulbous protrusions from the TJ strand were observed in arterioles, venules, and capillaries after FUS-induced BBB opening, at both 450kPa and 750kPa. In the treated hemisphere at 750kPa there was a significantly ($p<0.001$) greater percent of TJ strands with gaps only in capillaries at 750kPa, but not at 450kPa. No other TJ structural abnormalities in either arterioles or venules, at 450kPa or 750kPa, were found to be significantly different between treated and untreated hemispheres. These findings suggest a primarily transcellular mode of transport in all vessels at 450kPa and in large vessels at 750kPa, compared to primarily paracellular transport in capillaries at 750kPa.

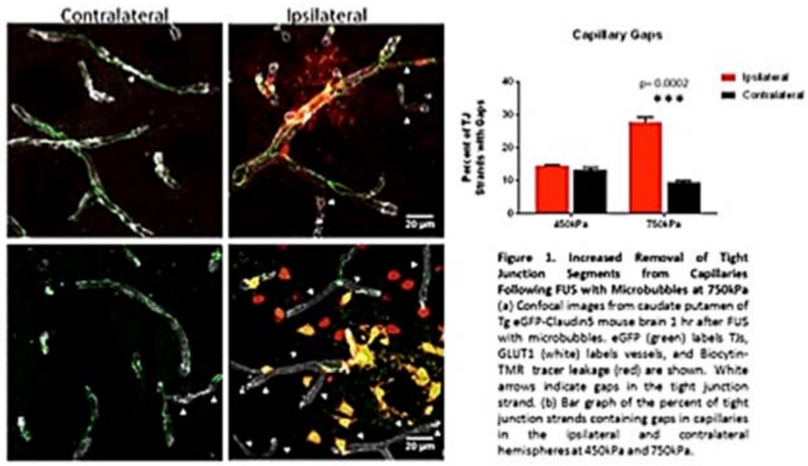

Figure 1. Increased Removal of Tight Junction Segments from Capillaries Following FUS with Microbubbles at 750kPa (a) Confocal images from caudate putamen of Tg eGFP-Claudin5 mouse brain 1 hr after FUS with microbubbles. eGFP (green) labels TJs, GLUT1 (white) labels vessels, and Biocytin-TMR tracer leakage (red) are shown. White arrows indicate gaps in the tight junction strand. (b) Bar graph of the percent of tight junction strands containing gaps in capillaries in the ipsilateral and contralateral hemispheres at 450kPa and 750kPa.

1G-5

5:15 pm Repeated Hippocampal Blood-Brain Barrier Opening Controlled via Three-Dimensional Transcranial Acoustic Imaging: Safety Study in a Porcine Model

Ryan Jones[1,2], Lulu Deng[2], Kogee Leung[2], Dallan McMahon[1,2], Meaghan O'Reilly[1,2], Kullervo Hynynen[2,3]; [1]*Department of Medical Biophysics, University of Toronto, Canada*, [2]*Physical Sciences Platform, Sunnybrook Research Institute, Canada*, [3]*Department of Medical Biophysics and Institute of Biomaterials and Biomedical Engineering, University of Toronto, Canada*

Background, Motivation and Objective

Transient blood-brain barrier (BBB) opening via focused ultrasound (FUS) combined with intravenously circulating microbubbles (MBs) may have a role in the treatment of Alzheimer's disease (AD). Spectral characteristics of MB emissions recorded during the procedures using single-element detectors have correlated with biological outcomes [McDannold *et al. PMB* 2006], leading to the development of acoustic emissions-based controllers that aim to achieve safe and consistent BBB opening [O'Reilly et al. Radiology 2012]. We recently demonstrated that 3D mapping of subharmonic MB activity can be used to calibrate FUS exposure levels for BBB opening [Jones et al. IEEE IUS 2016]. Here we evaluate the safety of this imaging-based calibration approach during repeated volumetric sonications targeted to the hippocampus in a large animal model.

Statement of Contribution/Methods

FUS and Definity[TM] MBs were used to open the BBB unilaterally in the hippocampus of Yorkshire pigs (Male, 10-20 kg) using a multi-frequency, dual-mode sparse hemispherical array (30 cm diam., 256 modules, 3 concentric PZT4 tube elements per module: 306/612/1224 kHz). The array was focused through the intact pig skull without aberration correction and 10 ms bursts of 612 kHz ultrasound were applied at a 1 Hz PRF, starting concurrently with MB infusion (20 µL/kg, 1 min). Receiver signals were captured using elements tuned to the subharmonic (306 kHz) and beamforming was performed over a 3D volume near the target. The pressure was increased after each burst (10-20 kPa steps *in situ*) until spatially coherent MB activity was detected, at which point the sonication was terminated. Proximal tissue volumes were exposed at 50-100% of the value required to induce this MB behavior via electronic focusing (6 x 6 grid, 1 mm spacing, 10 ms bursts & 1 Hz PRF per point, 2 min). MRI was performed at 3T to detect BBB opening and monitor for tissue damage post-treatment. Animals received 1-4 weekly treatments, underwent daily neurological testing starting 24 h before the first session, and were sacrificed 1 h - 7 days following their final session for histological examination.

Results/Discussion

Subharmonic activity was detected at a peak pressure of 0.24 ± 0.05 MPa *in situ* 1.1 ± 0.9 mm from the target during calibration. Following subharmonic detection, multi-point sonications induced volumetric BBB opening (0.10 ± 0.03 cm^3 on T_1w MRI). Neurological testing did not show any effects from the treatments. Follow-up T_1w MRI confirmed BBB integrity was restored 1 week following each session. Hypointense regions on T_2^*w MRI were occasionally seen at target levels of 75% and above. H&E staining revealed small regions of petechiae within the treated volumes (10.7 ± 2.3 vs. 1.3 ± 2.3 on control side). Our results suggest that subharmonic MB imaging can be used to calibrate FUS exposures for safe BBB opening over large volumes, and that repeated exposures in a structure relevant to the treatment of AD is tolerated in healthy swine.

2G - MEL: Carotid Elastography

Ambassador Ballroom

Friday, September 8, 2017, 4:00 pm - 5:30 pm

Chair: **Chris de Korte**
Radboun University Medical Center Nijmegen

2G-1

4:00 pm **Estimation of the 2D Motion Induced by an Acoustic Radiation Force Push Pulse in Transverse Cross-Sections of Vessel-Mimicking Phantoms Using High Frequency Ultrasound Displacement Compounding**

Hendrik Hansen[1], Gijs Hendriks[1], Stein Fekkes[1], Chris de Korte[1,2]; *[1]Medical ultrasound imaging center (MUSIC), Department of Radiology and Nuclear Medicine, Radboud university medical center, Nijmegen, Netherlands, [2]Physics of Fluids Group, University of Twente, Enschede, Netherlands*

Background, Motivation and Objective

Quantification of local arterial wall elasticity may assist in differentiating lipid rich rupture prone atherosclerotic plaques from stable fibrous plaques. Because lipid cores can be present anywhere along the circumference, we focus on developing a noninvasive shear wave elastography technique for transverse carotid cross-sections. Tracking the induced wave is not trivial because the circular geometry will result in particle motion in both the axial as well as the lateral direction. This study investigates the possibility to measure the minute 2D motion field using a single high frequency ultrasound transducer by combining axial displacements estimated at multiple beam-steering angles.

Statement of Contribution/Methods

A Verasonics V1 equipped with an L7-4 probe (fc = 5 MHz) was used to induce waves in the top wall of vessel-mimicking polyvinyl alcohol phantoms by a single focused ultrasonic push (200 µs, F# = 1). The push was followed, after a delay of 240 µs, either by plane wave acquisitions (n = 100, PRF = 10 kHz) on the L7-4 probe (only 0°) or using a perpendicularly placed high frequency L22-8v CMUT transducer (beam-steered) connected to a Verasonics Vantage 256 system. Beam-steering angles were varied from -25° to +25° with an angular increment of 5°. For each angle, axial displacements were estimated based on the phase shift in the IQ data. Triangulation of axial displacements of two opposite angles yielded horizontal displacement estimates (displacement compounding). The 0° axial L22-8v acquisition yielded the vertical displacements. The axial displacements measured by the L7-4 probe were used as a reference to assess the quality of the compounded horizontal displacements for the L22-8v probe as a function of steering angle.

Results/Discussion

Figure 1 shows the estimated horizontal displacements (both probes) for beam-steering angles of 5° and 25° and the vertical estimates for the L22-8v at t = 1.7 ms and t = 3.4 ms. As can be observed, it was possible to estimate the horizontal displacement component independently of the vertical component. The compound horizontal estimates improved monotonically with increasing steering angle. The ability to estimate both 2D motion components is an important achievement. 2D motion information will aid in understanding the wave propagation in vessels and might be essential to quantify elasticity in complex in vivo arteries.

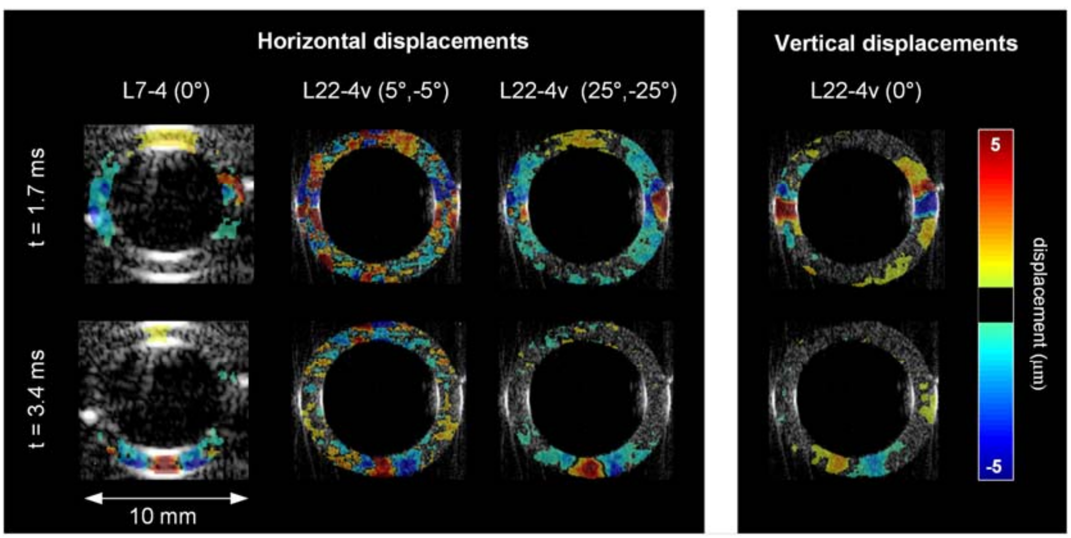

2G-2

4:15 pm **Guided Wave Elastography of Pressurized Artery in both Longitudinal and Transverse Sections: Validation in Phantom Experiments**

Qiong He[1], Guoyang Li[2], Yanping Cao[2], Jianwen Luo[1]; *[1]Department of Biomedical Engineering, Tsinghua University, China, People's Republic of, [2]Department of Engineering Mechanics, Tsinghua University, China, People's Republic of*

Background, Motivation and Objective

Guided wave elastography (GWE) is promising to measure the local arterial stiffness. However, most studies focus on the longitudinal section, with a guided axial wave (GAW). In addition, the dispersion curve of GAW can be well approximated by immersed Lame wave model only at high frequencies (Li et al, UMB 2017). In the transverse section, guided circumferential wave (GCW) can be utilized to obtain the arterial Young′s modulus (Li et al, JBM 2017). In this study, the effect of the lumen pressure on the dispersion curves of GAW and GCW was investigated, and a pressure quantification method from GCW at different pressures was developed.

Statement of Contribution/Methods

A Verasonics V1 system with an L10-5 probe was used to induce shear wave in a homogeneous vessel-mimicking PVA phantom. Coherent plane-wave compounding images were acquired at ~5k fps at different inner pressures from 0, 10, 20 and 30 mmHg. In the longitudinal section, axial displacements were calculated from RF based 2D cross-correlation; directional filtering was applied to remove the reflected waves. In the transverse section, the RF data were transformed from Cartesian to polar coordinates so as to perform radial displacement estimation; directional filtering was applied in polar coordinates to obtain the forward shear wave in the circumferential direction (He et al, UMB 2017). Finally, the dispersion curve was obtained from the spatio-temporal distribution of the axial or radial displacements. The Young′s modulus was obtained from GAW and GCW respectively at 0 mmHg according to the theoretical model. The relationship of the dispersion curves of GAW and GCW and the pressure was also derived in theory. The pressure was then estimated from the Young′s modulus and the experimental dispersion curve of GCW.

Results/Discussion

The shear waves are guided along the vessel wall (a, b). When the pressure increases, the dispersion curves changed only slightly in the longitudinal section (c) but raised in the transverse section (d) due to the circumferential stress. The Young′s modulus obtained from GAW (190 kPa) was larger than that from GCW (110 kPa). These results are in good agreement with our theoretical analysis. The pressures estimated from GCW are 10.3, 20.7 and 35.2 mmHg respectively, close to the pressures applied (r = 0.99). In conclusion, both the Young′s modulus and pressure of the vessel can be estimated from GWE.

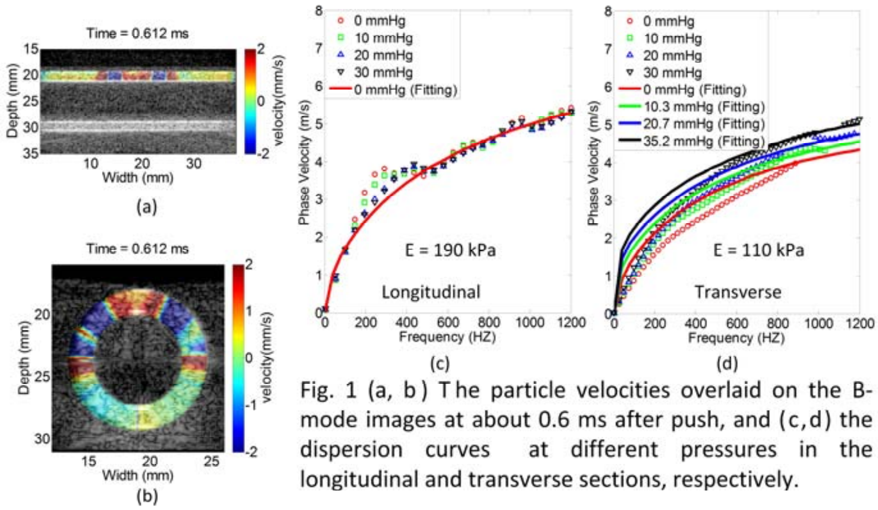

Fig. 1 (a, b) The particle velocities overlaid on the B-mode images at about 0.6 ms after push, and (c,d) the dispersion curves at different pressures in the longitudinal and transverse sections, respectively.

2G-3

4:30 pm Visualizing Angle-Independent Principal Strains in the Longitudinal View of the Carotid Artery: Phantom and In Vivo Evaluation

Rohit Nayak[1], Giovanni Schifitto[2], Marvin Doyley[1]; [1]*Department of Electrical and Computer Engineering, University of Rochester, Rochester, NY, USA,* [2]*Department of Neurology, University of Rochester, Rochester, NY, USA*

Background, Motivation and Objective

Arterial stiffness is a strong indicator of atherosclerosis, and can be evaluated by computing the arterial strain in the carotid artery using ultrasound elastography. Researchers have used axial strain to visualize the radial motion in the longitudinal plane of the carotid artery. However, axial strains can be influenced by the geometry of the vessel (Fig. 1 a,b), and thus could limit the scope of vascular elastography in the clinic. In this study we hypothesize that principal strain elastograms computed using compounded plane wave (CPW) imaging could reliably estimate angle-independent vascular strains in the carotid artery.

Statement of Contribution/Methods

To test our hypothesis, we conducted phantom and in vivo studies. The phantom studies were conducted using a homogenous cryogel vessel phantom, at different transducer angles (±30°, ±20°, ±10°, 0°). The in vivo studies were conducted on 20 healthy volunteers in the age group 50-60 years. The volunteers were screened to ensure there were 10 participants for each category, i.e. (i) artery parallel and (ii) non-parallel to the elements of the transducer. All echo imaging were performed at a transmit frequency of 5 MHz, using a commercially available ultrasound scanner (Sonix RP, Analogic, Canada).

Results/Discussion

The results of the phantom study demonstrated that for parallel vessel-transducer configurations, principal strains were similar to axial strain (Fig. 1 c). However, at non-parallel configurations, the magnitude of the axial strain decreased with increase in angle. In comparison, the co-ordinate independent principal strains were relatively unaffected, and measured at approximately 1%. The in vivo study demonstrated that for subjects with vessel lumen parallel to the transducer, principal and polar strain elastograms were similar ($p>0.01$). However, when the vessels were arched, principal strains were significantly higher than axial strains ($p>0.01$), which corroborated the phantom study results. In conclusion, the results demonstrate that the principal strain elastograms computed using CPW imaging could reliably estimate the vascular strain in the longitudinal plane of the vessel wall, regardless of the transducer angle.

2G-4

4:45 pm Measurement of Carotid Artery Viscoelasticity in Young and Older Individuals Using Acoustic Radiation Force-Induced Waves and Fourier Analysis

Matthew Urban[1,2], Murthy Guddati[3], Wilkins Aquino[4], James Greenleaf[2]; [1]*Department of Radiology, Mayo Clinic College of Medicine and Science, Rochester, MN, USA,* [2]*Department of Physiology and Biomedical Engineering, Mayo Clinic College of Medicine and Science, Rochester, MN, USA,* [3]*Department of Civil Engineering, North Carolina State University, USA,* [4]*Department of Civil and Environmental Engineering, Duke University, USA*

Background, Motivation and Objective

Techniques that can quantitatively measure viscoelastic mechanical properties in arteries may be very useful to detect early disease processes. We propose the use of inducing waves in the arterial walls with acoustic radiation force (ARF) and measuring their propagation characteristics to solve for the viscoelastic material properties.

Statement of Contribution/Methods

A pilot study was performed with 20 subjects. The cohort consisted four categories: young males (YM, 30.2±7.1 yo), young females (YF, 27.4±4.5 yo), older males (OM, 68.2±8.2 yo) and older females (OF, 62.0±2.9 yo) with 5 subjects in each group. Subjects lay on a bed and ARF-based measurements were performed in the right and left common carotid arteries. A Verasonics system was used with a linear array transducer, and ECG was used for triggering. A wave measurement was made on 10 consecutive heartbeats with different levels of delay with respect to the R-wave depending on the heart rate of the subject to obtain several measurements throughout the cardiac cycle. Wave motion from the arterial walls were extracted, and we used two-dimensional Fourier transform analysis for each subject and extracted the wave (phase) velocity and attenuation at 400 Hz for further analyses.

Results/Discussion

We summarized the variation of the wave velocity and attenuation for all subjects in the different groups through the cardiac cycle at 400 Hz in Figs. 1(a) and 1(b), respectively. We calculated the model-free storage and loss moduli from the mean values for each group through the cardiac cycle (Figs. 1(c)-(d)). It was found that the older groups had higher wave velocities and storage and loss moduli while attenuation did not differentiate the groups. We isolated two time points that we termed as diastole (t = 0) and systole (when maximum wave velocity was reached) for further comparisons among the different groups and found that systolic measurements were larger in each group (Fig. 1(e)). We also evaluated the differences in systolic and diastolic speeds, $\Delta c = c_{Sys} - c_{Dia}$, and observed that the older subjects had larger differences than younger subjects (Fig. 1(f)). The ability to examine arterial model-free viscoelastic parameters dynamically through the heart cycle has not been previously demonstrated and will provide new insight into the dynamic response of the artery so that comparisons between diastole and systole can be made.

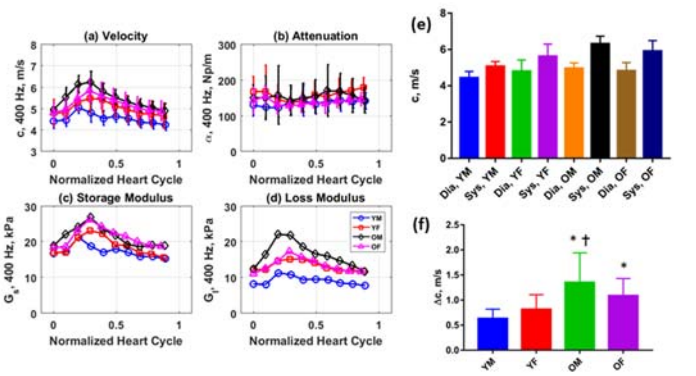

Figure 1. Variation of mean wave velocity (a) and attenuation (b) with normalized heart cycle. Error bars are standard deviations. Mean storage (c) and loss (d) moduli through the heart cycle. The legend in (d) applies to (a)-(d). (e) Comparison of wave velocities at 400 Hz between diastole (Dia) and systole (Sys), (f) Comparison of wave velocity differences between diastole and systole (* p<0.05 compared to YM, † p<0.05 compared to YF).

2G-5

5:00 pm **Elastographic Imaging of the Carotid Arteries of HIV Infected Patients with and without Cardiovascular Disease: A Pilot Study**

Marvin Doyley[1], Rohit Nayak[2], Nancy Carson[3], Giovanni Schifitto[4]; [1]*Electrical and Computer Engineering, Univeristy of Rochester, Rochester, NY, USA,* [2]*Electrical and Computer Engineering, University of Rochester, Rochester, NY, USA,* [3]*Medical Center, Univeristy of Rochester, Rochester, USA,* [4]*Neurology, Univeristy of Rochester, Rochester, USA*

Background, Motivation and Objective

Individuals infected with the human immunodeficiency virus (HIV) are prone to develop cardiovascular disease (CVD) because the HIV infection and combination antiretroviral therapy (cART) produces atherosclerosis. Clinicians need sensitive tests to monitor interventions designed to prevent CVD in patients with HIV on long term cART. We hypothesize that vascular elastography can fulfill this role. To corroborate this hypothesis, we performed vascular elastography on 60 volunteers (mean age of 55.5 y), which we divided into four groups: (a) HIV positive with CVD (HIV++), (b) HIV positive without CVD (HIV+-), (c) HIV negative with CVD (HIV-+), and (c) HIV negative without CVD (HIV--).

Statement of Contribution/Methods

Echo imaging was performed with a commercially available ultrasound scanner (Sonix RP, Analogic, MA, USA) equipped with a 128 element linear transducer array (L14-5/38) operating at 5 MHz. We configured this system to acquire plane wave images from transmission angles of -14 to 14 degrees in angular increments of 2 degrees. Principal strain elastograms were computed by solving the 2D eigenvalue equation as described in [1].

Results/Discussion

Figure 1A shows a box-plot of IMT for the four groups of patients. This result demonstrates that the IMT of HIV++ patients was higher than their HIV+- peers. The controlled group displayed a similar trend. Figure 1B shows a box-plot of the normalized strain. The peak strain of HIV++ patients was significantly lower than those of HIV+- patient ($p<0.05$). The peak strains of HIV-+ patients were lower than their HIV-- counterpart. It was also apparent that the peak strain in HIV infected individuals were consistently lower than their aged matched HIV negative peers, which suggest that the disease and cART stiffens the carotid artery. Figure 1C shows a plot of IMT as function of peak strain (normalized), which demonstrates that IMT is inversely proportional to peak strain. This pilot study demonstrates that vascular elastography could prove to be useful tool for detecting CVD in HIV infected patients undergoing long-term cART.

[1] Rohit Nayak, Steven Huntzicker, Jacques Ohayon, Nancy Carson, Vikram Dogra, Giovanni Schifitto, Marvin M. Doyley "Principal Strain Vascular Elastography: Simulation and Preliminary Clinical Evaluation" Ultrasound in Med. Biol. 43 (3), 2017

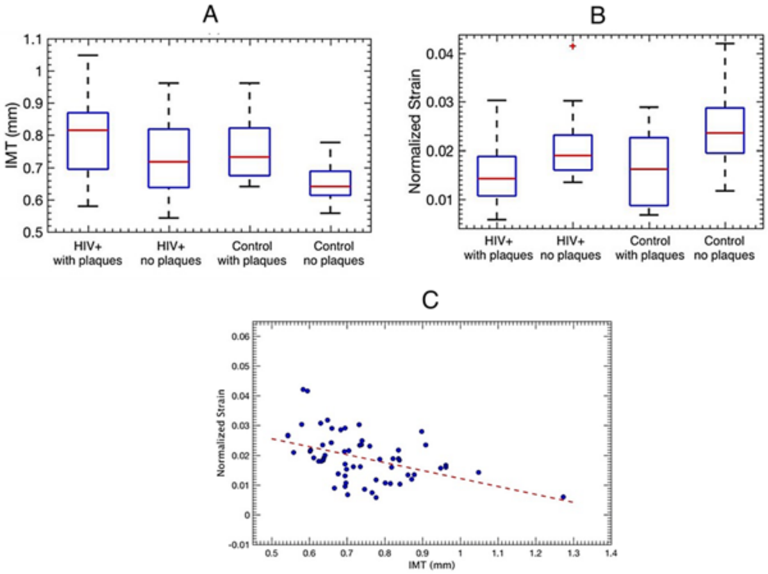

2G-6

5:15 pm **In Vivo Delineation of Human Carotid Plaque Features with ARFI Variance of Acceleration (VoA)**

Gabriela Torres[1], Tomasz J. Czernuszewicz[1], Jonathon W. Homeister[2], Mark A. Farber[3], Caterina M. Gallippi[1]; [1]*Joint Department of Biomedical Engineering, University of North Carolina at Chapel Hill, USA,* [2]*Department of Pathology and Laboratory Medicine, University of North Carolina at Chapel Hill, USA,* [3]*Department of Surgery, University of North Carolina at Chapel Hill, USA*

Background, Motivation and Objective

Stroke is commonly caused by thromboembolic events originating from ruptured carotid plaque, with rupture potential related to plaque composition. We have previously shown that soft (intraplaque hemorrhage/necrotic core) and stiff (collagen/calcium) plaque components are differentiated with high sensitivity and specificity by peak displacement (PD) in Acoustic Radiation Force Impulse (ARFI) imaging. However, PD showed low performance for distinguishing between soft and between stiff features. *We hypothesize that soft and stiff feature delineation will be improved using a new ARFI outcome metric - the variance of acceleration (VoA).* We test our hypothesis using histological validation.

Statement of Contribution/Methods

This study analyzed 20 carotid plaques imaged in vivo in patients undergoing carotid endarterectomy (CEA). Prior to CEA, raw RF data were acquired using a Siemens Acuson Antares and a VF7-3 linear array. For ARFI imaging, excitation pulses were 300 cycles at 4.21 MHz, and tracking pulses were 2 cycles at 6.15 MHz. After imaging, CEA specimens were harvested for histological validation. VoA was calculated as the variance of the second time derivative of displacement over 3-5 ms in tracking ensemble time. For both VoA and PD images, values were normalized to median ± 2 mean absolute deviations within the plaque.

Results/Discussion

Normalized VoA was statistically significantly different (Wilcoxon, $p < 0.01$) between all examined plaque features (Fig. 1). Notably, VoA was statistically higher in intraplaque hemorrhage than in necrotic core and lower in calcium than in collagen. This suggests that, unlike PD, VoA is relevant to separately discriminating these regions. Overall, contrast between soft plaque features was 46% higher for VoA (0.79 ± 0.19) versus PD (0.54 ± 0.35); contrast between stiff components was 124% higher for VoA (0.74 ± 0.16) versus PD (0.33 ± 0.21). CNR between soft features was 126% higher for VoA (1.47 ± 0.56) versus PD (0.65 ± 0.58), and CNR between stiff components was 179% higher for VoA (1.59 ± 0.31) versus PD (0.57 ± 0.58). These results suggest that VoA analysis improves ARFI discrimination between soft and between stiff carotid plaque components that are correlated to vulnerability for rupture.

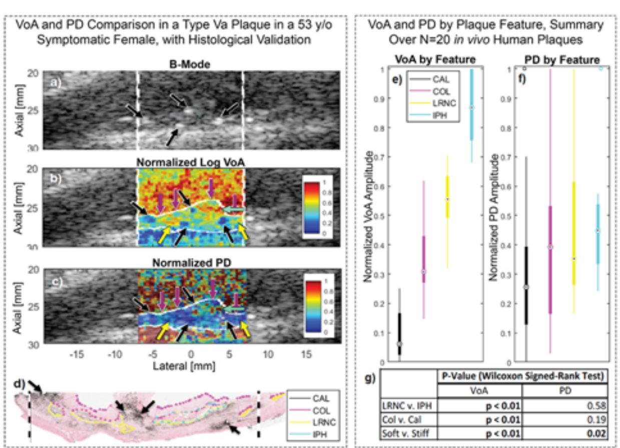

	VoA	PD
LRNC v. IPH	**p < 0.01**	0.58
Col v. Cal	**p < 0.01**	0.19
Soft v. Stiff	**p < 0.01**	**0.02**

Figure 1: Matched B-Mode (a), ARFI normalized log VoA (b), ARFI normalized PD (c), and hematoxylin and eosin stain histology (d) images for a plaque in the carotid artery of a 53 y/o symptomatic female. Arrows show calcium deposits (Cal - black), fibrous cap (Col - magenta), necrotic core (LRNC - yellow) and intraplaque hemorrhage (IPH - teal) marked by a pathologist. Panels (e) and (f) show the distributions of in vivo VoA and PD values, respectively, measured in histologically confirmed regions across 20 human carotid plaques. Panel (g) reports the statistical significance of the differences between LRNC and IPH, between COL and CAL, and between grouped soft (LRNC/IPH) and stiff (COL/CAL) features for VoA and PD.

3G - MTC: In Vivo Soft Tissue Characterization

Palladian Room

Friday, September 8, 2017, 4:00 pm - 5:30 pm

Chair: **Roberto Lavarello**
Pontificia Universidad Católica del Perú

3G-1

4:00 pm **In-vivo Quantitative Ultrasound Evaluation of Carotid Plaque**

Catherine Steffel[1,2], Kayvan Samimi[2], Tomy Varghese[2], Shahriar Salamat[3,4], Stephanie Wilbrand[3], Robert Dempsey[3], Carol Mitchell[5]; *[1]Cardiovascular Research Center, University of Wisconsin-Madison School of Medicine & Public Health, Madison, Wisconsin, USA, [2]Medical Physics, University of Wisconsin-Madison School of Medicine & Public Health, Madison, WI, USA, [3]Neurological Surgery, University of Wisconsin-Madison School of Medicine & Public Health, Madison, WI, USA, [4]Pathology and Laboratory Medicine, University of Wisconsin-Madison School of Medicine & Public Health, Madison, WI, USA, [5]Medicine, Cardiovascular Division, University of Wisconsin-Madison School of Medicine & Public Health, Madison, WI, USA*

Background, Motivation and Objective

Carotid atherosclerotic plaque is a contributor to cerebrovascular disease. Noninvasive quantitative ultrasound (QUS) evaluations of plaque morphology are requisite for comprehensive risk assessments, as system and setting dependencies limit current grayscale analyses. Here, integrated backscatter (IB) and attenuation coefficient (AC) were calculated in-vivo and compared with pathology scores of excised plaque.

Statement of Contribution/Methods

Radiofrequency data were acquired prior to carotid endarterectomy and were processed on 6 subjects. Average % stenosis(SD) was 71.67(11.69). QUS parameters were calculated in-vivo with 70% axial overlap at end-diastole using the reference phantom method (IB) and optimum power-spectral shift estimator (AC). QUS parameter images were created to visualize parameter variation through plaque. Histopathology examination on fixed plaque was reported for a representative section of plaque. Plaque was scored for hemorrhage, hemosiderin, and inflammation on an ordinal scale and was assessed for percent cholesterol and calcium. Relationships between IB and AC in-vivo and histopathological tissue composition of plaque were examined. Figure 1: QUS parameter images of carotid plaque (80% stenosis, 25% calcified, 70% cholesterol). Left-IB image, min IB = -26.04 dB. Right-AC image, max AC = 1.09 dB/cm-MHz.

Results/Discussion

Plaques with more calcium on histopathology (n=2, >20% calcium) have high IB (approaching 0 dB) and elevated AC (approaching 1.5 dB/cm-MHz). Plaques with high percent cholesterol on histopathology (n=4, >60% cholesterol) have low IB (approaching -30 dB) and moderate AC (approaching 1 dB/cm-MHz). We are also able to distinguish calcified and soft plaque regions on QUS parameter images (see Figure 1). These findings suggest that IB and AC can be used to noninvasively distinguish plaques by tissue composition. Thus, these QUS parameters provide important information for a risk-assessment model of carotid plaque. Future work will compare QUS parameters in-vivo with high frequency characterizations of plaque ex-vivo and 3D reconstructions of histopathology sections.

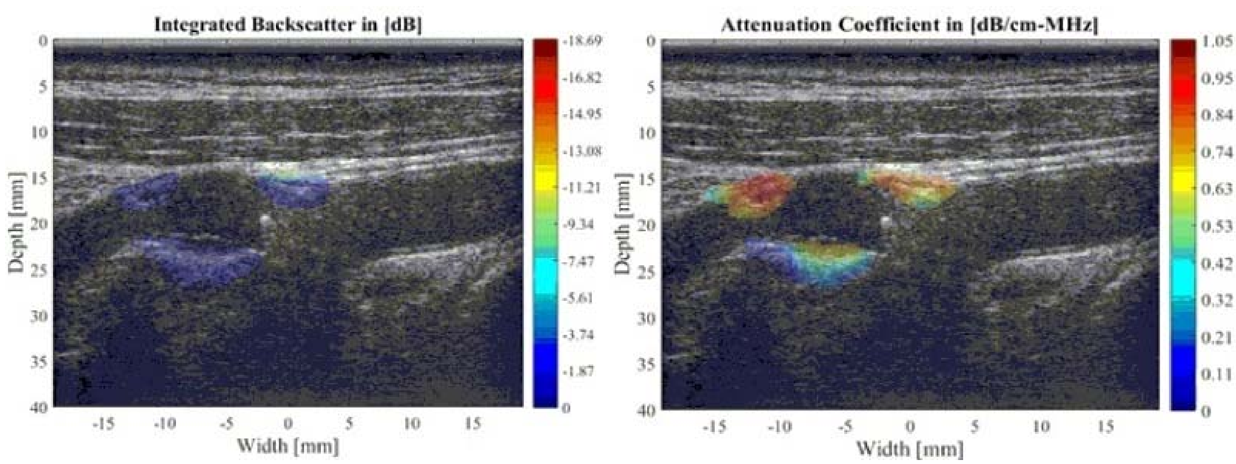

3G-2

4:15 pm **In-vivo Quantitative Assessment of Pulmonary Edema and Fibrosis Using Ultrasound Multiple Scattering.**

Kaustav Mohanty[1], Marie Muller[1], Thomas Egan[2], John Blackwell[2]; *[1]Mechanical and Aerospace Engineering, North Carolina State University, Raleigh, North Carolina, USA, [2]Division of Cardiothoracic Surgery, Dept. of Surgery, University of North Carolina, Chapel Hill, North Carolina, USA*

Background, Motivation and Objective

The lung parenchyma is a highly complex and diffusive medium for which ultrasound (US) techniques have remained qualitative. US quantitative characterization of the lung has remained elusive due to the presence of air- filled alveoli which is responsible for Multiple Scattering (MS). There is a need from pulmonologists for a method which would enable them to stage and monitor pulmonary edema and fibrosis using US.

Statement of Contribution/Methods

We present an approach based on ultrasound MS, which exploits the complexity of US propagation in the lungs. Diffusion constant (D), mean free path (L*) and backscattered frequency shift (BFS) are proposed as prediction parameters for the quantitative assessment of pulmonary edema and fibrosis. Two sets of experiments were conducted. First, edema was simulated in ex vivo rat lungs, by inflating them to their tidal volume and injecting PBS (Phosphate Buffered saline) in increments of 1ml. Second, in vivo experiments were conducted in Sprague-Dawley rats, in which the lungs were exposed by sternotomy and connected to a rodent respirator. Edema was induced in the left lung using ischemia-reperfusion injury, while the right lung was used as control. Bleomycin was used to induce fibrosis in other rats. The experimental setup consisted of a linear transducer array (Verasonics L11-4v) with a 7.8 MHz central frequency in contact with the lung surface. D and L* were estimated by separating the incoherent and coherent backscattered intensities in the near field and measuring the growth of the incoherent diffusive halo over time. BFS was evaluated using plane wave transmission and calculating the frequency shift of the peak backscattered amplitudes over time.

Results/Discussion

In engineered edema experiments, L* values were 404, 748, 1002 and 1446 µm for injected PBS amounts of 0, 1, 2 and 3 ml respectively. In-vivo values of L* for control, edema and fibrosis were 330 (±79, N=6), 876 (±179, N=5) and 1103 µm (±356, N=5) respectively. By measuring L*, we were able to discriminate control from pathological subjects, but not fibrosis from edema. The BFS values enabled to distinguish between fibrosis and edema. Combining BFS and L* enabled the diagnosis of fibrosis and edema, as shown in Fig.1B. These results suggest the potential of these approaches for the diagnosis and monitoring of pulmonary fibrosis and edema.

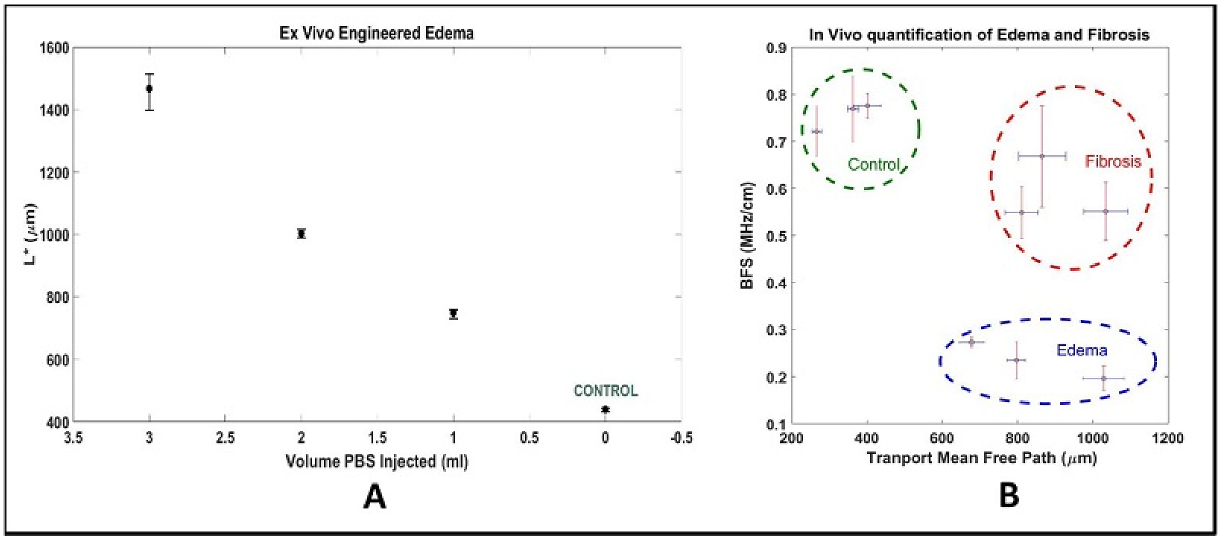

3G-3

4:30 pm In-vivo Characterization of Angiogenesis in Tumor-Bearing Rats Using Multiple Scattering of Ultrasound

Aditya Joshi[1], Sarah Shelton[2], Virginie Papadopoulou[2], Brooks Lindsey[2], Gianmarco Pinton[2], Paul Dayton[2], Marie Muller[1]; *[1]Mechanical and Aerospace Engineering, North Carolina State University, Raleigh, North Carolina, USA, [2]UNC - NCSU Joint Department of Biomedical Engineering, University of North Carolina at Chapel Hill, Chapel Hill, NC, USA*

Background, Motivation and Objective

There are significant differences in microvasculature density, tortuosity, and anisotropy of cancerous and benign tissue, which makes non-invasive methods to quantify these microvascular architectural properties highly relevant for applications like monitoring the response to anti-angiogenic treatments. We present a method to quantify these properties using ultrasound multiple scattering from contrast agent microbubbles injected into the vasculature.

Statement of Contribution/Methods

Subcutaneous fibrosarcoma tumors were grown in the right flank of 16 rats by implanting 1 mm^3 tissue fragment. Lipid shelled ultrasound contrast agent at a concentration of 10^9 microbubbles/ml was infused through a catheter inserted into the tail vein. Verasonics L11-4 linear transducer array operating at 8 MHz recorded ultrasound signals backscattered from the vasculature in the form of inter-elemental response matrix (IRM). This was done by using all elements of the array as transmitters one by one and recording the backscattered signals on the whole array for each transmit. In highly diffusive media the spatial spread of the incoherent intensity grows exponentially over time. Thus by computing the incoherent backscattered intensity, we were able to quantify the scattering mean free path (L). Values of L obtained using the whole array quantify the mean density of the vasculature. We also obtained 1D maps of semi-local L values along the array length by acquiring sub-IRMs using sub-apertures translated along the length of the array. This enabled the computing of a semi-local L from each sub-IRM. The tortuosity was computed from multiple 1D maps using a modified sum of angles metric (modified SOAM), an approach that estimates integral of curvature along vessels. To quantify the anisotropy of the vasculature, we measured the ratio of L along perpendicular orientations (Anisotropy ratio).

Results/Discussion

The values of anisotropy ratio, L, and SOAM were significantly different for control (benign) and tumor tissues, as shown in the figure. Anisotropy ratio,SOAM, L were 1.19 +- 0.03, 21.7 +- 4.4 and 138.2 +- 37.35 micron for control and 1.46 +- 0.13, 34 +- 5 and 52.6 +- 9.3 micron for control respectively. By using these parameters we can distinguish tumor from benign tissue. These results show the potential of proposed quantitative method for characterization of vascular networks.

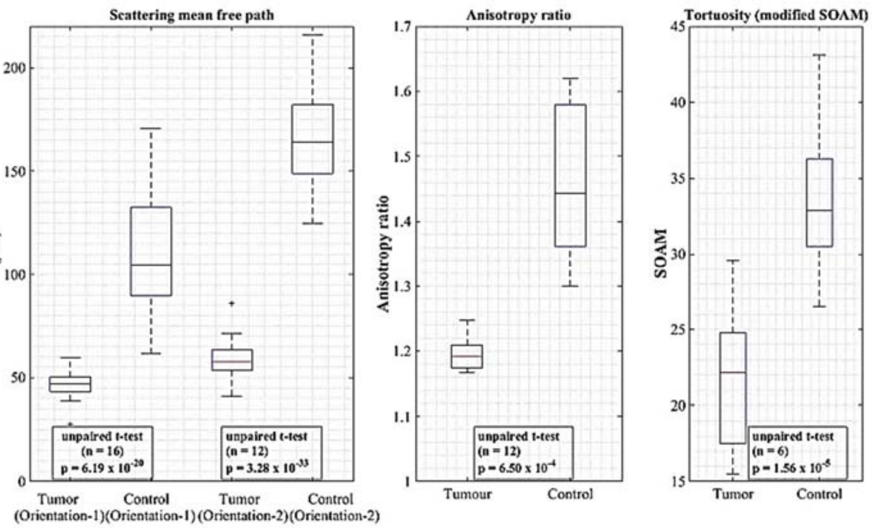

3G-4

4:45 pm **Contrast and Quantitative Ultrasound Mapping of Heterogeneous Tumor Function and Structure**

Jerome Griffon[1], Delphine Le Guillou-Buffello[1], Oumeima Laifa[1], Maxime Doury[1], Alexandre Dizeux[1], Michele Lamuraglia[2], Michael Oelze[3], S. Lori Bridal[1]; [1]*Laboratoire d'Imagerie Biomedicale, UPMC, CNRS, INSERM, Paris, France,* [2]*Beaujon Hospital, AP-HP, Paris, France,* [3]*Bioacoustics Research Laboratory, University of Illinois at Urbana-Champaign, Urbana-Champaign, USA*

Background, Motivation and Objective

Tumor heterogeneity is associated with increased risk of therapeutic resistance and challenges evaluation of therapeutic response based on whole-tumor microvascular function or volume. To better interpret and relate ultrasonic maps of functional and structural properties in heterogeneous tumor, we compared matched regions of CEUS (Contrast-enhanced ultrasound) and QUS (Quantitative Ultrasound) maps with whole-slice, virtual histology sections stained for vascular and microstructural features.

Statement of Contribution/Methods

An ectopic model of murine colorectal carcinoma (CT26) was implanted in 9 mice (BALB/c). On 14 days after start of daily, *per os* therapy with an anti-angiogenic (AA: n = 4, Pazopanib) or placebo (P: n = 5), US radiofrequency data were acquired for the longitudinal plane of tumors *in vivo* (SSI, Aixplorer, SL15-4 probe, research mode) and contrast data were acquired after realignment in the same plane (Sequoia 512, 7-14 MHz probe, cadence contrast pulse sequencing).

Regions with no contrast-enhancement were identified to construct masks of the perfused and non-perfused tumor regions. A lognormal bolus model was fit to the resulting echo-power curve to assess flow within the perfused region of the tumor. Average backscattered power spectra were calculated (FFT, 512 pts, Rectangular gated RF), normalized with respect to a reference phantom and corrected for attenuation (0.4 dB/cm/MHz) to map (2 x 2 mm blocks, with 75% axial and lateral overlap) effective scatterer diameter (ESD, µm) and effective acoustic concentration (EAC, dB/cm).

Tumors were excised and marked to conserve orientation and approximate position relative to US imaging plane. Whole-slice, histological sections were prepared with fluorescent immunohistochemical markers for reference assessment of cell nuclei, apoptosis and vascular endothelium. The Number of Nuclei per mm^2 (NU), the % area of Apoptosis (AP) and % area of Vascular (VA) marker were calculated with image analysis processing for each 670 by 670 mm^2 region of histological sections. CEUS, QUS and histological parameter correlations were tested in the vascularized and nonvascularized zones. The median values of parameters between vascularized and nonvascularized zones were also compared.

Results/Discussion

Most different immunohistochemical markers between vascularized and nonvascularized regions were AP in AA (0.0120% vs 0.0308% respectively), AP in P samples (0.0092% vs 0.0769%) and the NU in P (5700/mm^2 vs 4510/mm^2). The EAC was slightly elevated in the nonvascularized (more apoptotic) zones in AA (19dB/cm) as well as for the nonvascularized zones (more apoptotic, lower density of nuclei) in P (14dB/cm). By selecting more homogeneous region of heterogeneous tumor based on vascular function, localized changes in QUS parameters and the underlying structural changes may be better visualized and interpreted.

Work funded by FRM (grant DBS20131128436).

3G-5

5:00 pm **Volumetric Contrast-Enhanced Ultrasound Parametric Maps and Texture Feature Extraction for Tissue Treatment Response Characterization**

Ahmed El Kaffas[1], Assaf Hoogi[1], Albert Tseng[1], Jianhua Zhou[1], Huaijun Wang[1], Hersh Sagreiya[1], Dimitre Hristov[2], Daniel Rubin[1], Juergen Willmann[1]; [1]*Radiology, Stanford University, USA,* [2]*Radiation Oncology, Stanford University, USA*

Background, Motivation and Objective

Volumetric dynamic contrast-enhanced ultrasound (DCE-US) can be used to yield 3D parametric maps to assess spatial changes in tumor perfusion heterogeneity during cancer treatment. Here, quantitative image features (texture and histogram-based features) extracted from 3D parametric maps were evaluated as surrogates of treatment response, and compared to conventional perfusion parameters.

Statement of Contribution/Methods

Mice bearing LS174T (n = 10; responders to therapy) or CT26 (n=10; non-responders to therapy) colon tumors on the hind leg were imaged during anti-angiogenic therapy (Bevacizumab; 3x10 mg weekly) at 0, 1, 3, 7, and 10 days. A control subset of animals was left untreated (n=10 for each cell line). A separate cohort of animals with LS174T tumors (n=20) was used to assess repeatability of measurements through repeated acquisitions. Imaging was performed using Philips EPIQ7/iU22 with an X6-1 transducer. Animals were imaged following a bolus of 5x107 Definity microbubbles. Parametric map generation was carried out on high-performance computing cluster by: (1) motion correction; (2) linearization of signal and isotropic resampling; (3) automatic identification of contrast arrival and volume of interest (VOI) selection around lesion; (4) time intensity curve (TIC) fitting to each voxel based on perfusion model (lognormal using least-square); (5) generation of parametric maps for each perfusion parameter (peak enhancement, time to peak, mean transit time, area under the curve). Quantitative image features were extracted from parametric maps (46 features per map). These were classified as low-level (i.e. mean) and high-level (i.e. co-occurrence). Repeatability and sensitivity to treatment for each feature was compared to conventional perfusion parameters. Response confirmation was based on tumor growth and histology.

Results/Discussion

Results confirmed heterogeneity of conventional DCE-US parameters in tumor volume. Texture features were more repeatable and sensitive to therapy than conventional parameters; preliminary results indicate that > 30 features were more repeatable (intra class correlation coefficient > 0.9) and highly sensitive ($p < 0.01$) to treatment (Figure). Results demonstrate that 3D parametric map-based texture features are promising to characterize treatment response in a radiomics approach.

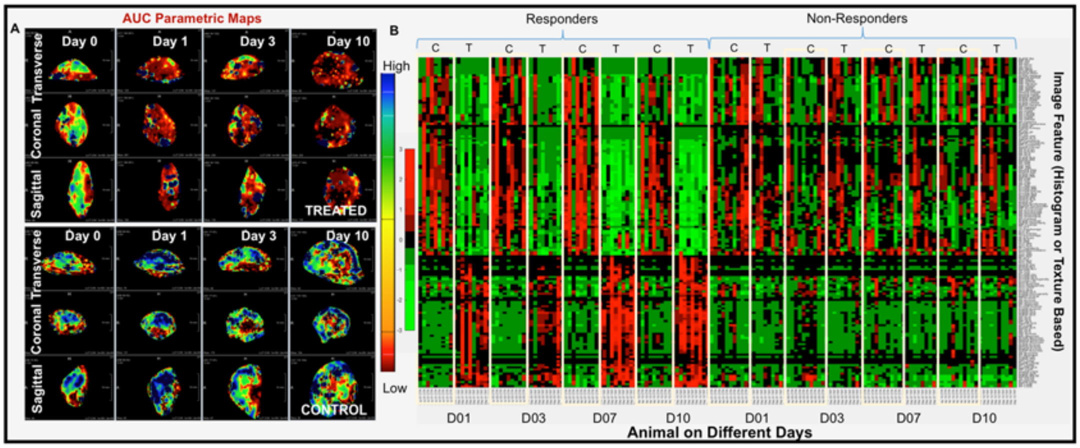

Figure: (A) 3D area under the curve (AUC) parametric maps for one treated and one control animal at four different days – maps show heterogeneous perfusion response to treatment. **(B)** Clustergram showing several change in features extracted from different parametric maps (y-axis) for each animal on each day following start of treatment (D01, D03, D07, D10), for both responder (LS174T) and non-responder animals (CT26). T indicates treated animals; C indicates control animals.

3G-6

5:15 pm Motion Correction for 3D Ultrafast Ultrasound: Application to 3D Backscattered Tensor Imaging of Soft Tissues Anisotropy

Victor Finel[1], Clement Papadacci[1], Jean Provost[1], Mickael Tanter[1], Mathieu Pernot[1]; [1]*Institut Langevin, ESPCI ParisTech, CNRS UMR 7587, INSERM U979, Université Paris 7, Paris, Paris, France*

Background, Motivation and Objective

3D Ultrasound Backscatter Tensor Imaging (3D-BTI) is a novel approach based on 3D Ultrafast Ultrasound Imaging to map fiber orientation in tissues such as the human heart in vivo [1]. Fiber orientations are obtained in entire volumes at high frame rate by computing and analyzing a voxel-wise coherence function relying on the synthetic focusing of multiple tilted plane waves. However, in rapidly moving organs such as the heart, the quality of the synthetic focusing and thus of the computed fiber orientation will be altered by motion. In this study, we quantify the effect of axial tissue motion on the quality of 2D spatial coherence functions, propose a novel motion-correction scheme, and demonstrate its application.

Statement of Contribution/Methods

Acquisitions were performed using a programmable 1024-channel ultrasound system and 2D matrix arrays (10 MHz, 16*16 elements, 0.3-mm pitch, and 8 MHz, 32*32 elements, 0.3-mm pitch). In vitro acquisitions were performed in tissue mimicking gels mounted on a linear stage motor. Ultrafast volumes were acquired using 81 tilted 2D plane waves. IQ beamforming of volumes corresponding to each tilted plane wave was performed and motion was estimated by measuring their phase shift. The 2D coherence function was computed for each voxel with and without motion, and with motion correction by applying phase shifts. Finally, the correction was applied in vivo in the left ventricular wall of a healthy volunteer at a volume rate of 91 Hz over a cardiac cycle.

Results/Discussion

The 2D coherence functions were strongly altered by axial motion. In absence of motion, the 2D coherence function was found to be isotropic (FA=0.04) (figure 1a), as expected. In the presence of motion, the 2D coherence function changed shape and became anisotropic (FA=0.61): this distortion was directly linked to the succession of plane wave's angles (figure 1b). Motion estimation and correction allowed for the rectification of 2D coherence function toward the expected isotropic shape (FA=0.14) (figure 1c). Finally, we showed the feasibility of the motion correction for 3D BTI in the heart of a healthy volunteer. These results showed that motion can distort the coherence functions. We also demonstrated that the motion correction method enabled to retrieve the coherence function obtained without motion and were able to apply it to a human heart to retrieve the fiber dynamic.

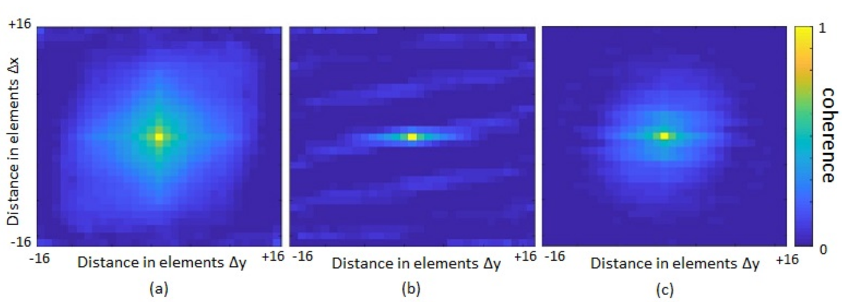

Figure 1: 2D coherence functions calculated in the following cases:
(a) without motion on an isotropic phantom.
(b) with a motion of 12mm/s
(c) calculated with a motion of 12mm/s with motion estimation and correction

4G - MCA: New US Contrast Agents for Imaging and Therapy

Diplomat Room

Friday, September 8, 2017, 4:00 pm - 5:30 pm

Chair: **Paul Dayton**
Univ. North Carolina/NCSU

4G-1

4:00 pm **Sensitization of Hypoxic Tumors to Radiation Therapy Using Ultrasound Sensitive Oxygen Microbubbles**

John Eisenbrey[1], Rawan Shraim[2], Ji-Bin Liu[1], Jingzhi Li[3], Maria Stanczak[1], Brian Oeffinger[2], Flemming Forsberg[1], Patrick O'Kane[1], Margaret Wheatley[2]; [1]*Radiology, Thomas Jefferson University, USA,* [2]*Biomedical Engineering and Health Sciences, Drexel University, USA,* [3]*Vascular Ultrasonography, Xuanwu Hospital, Capital Medical University, China, People's Republic of*

Background, Motivation and Objective

Tumor hypoxia has been shown to decrease the sensitivity of solid tumors to radiation. Systemic efforts to increase tumor oxygenation levels immediately prior to therapy, however, have largely proven unsuccessful. The objective of this work was to determine the utility of oxygen-filled, ultrasound sensitive microbubbles for locally delivering oxygen and sensitizing tissue to radiation in a breast cancer model.

Statement of Contribution/Methods

Surfactant-shelled oxygen microbubbles (SE61O2) or nitrogen microbubbles (SE61N2) were prepared using previously described techniques. Human breast cancer cells (MDA-MB-231) were subcutaneously implanted into the hind limb of 28 female athymic mice and grown to maximum diameters of 5-7 mm. Animals received 0.1 ml injections of each SE61 agent or saline with and without ultrasound (S3000 Helx with a 9L4 probe generating 1.5 second flash pulses (MI=1.35) with 3 second microbubble replenishment periods; Siemens Healthineers, Mountain View, CA). In the first 8 animals, the ability of microbubbles to elevate tumoral partial oxygen pressure (pO2) was monitored using an OxyLite 2000 with a bare fiber probe (Oxford Optronix, Oxford, UK). The remaining 20 animals were assigned to treatment groups receiving A) SE61O2 + ultrasound + radiation (5 Gy), B) SE61O2 + ultrasound (no radiation), C) ultrasound + radiation (no SE61O2), D) SE61N2 + ultrasound + radiation, or E) SE61O2 + radiation (no ultrasound). Tumor growth was monitored over 5 weeks and compared to determine if SE61O2 sensitized tumors to radiation.

Results/Discussion

In the oxygenation monitoring experiments, tumors treated with SE61O2 and ultrasound showed a pO2 increase in all animals with a peak increase of 22.9±6.4 mmHg. No changes in pO2 levels were detected after injection of SE61O2 without ultrasound or saline or SE61N2 with ultrasound (largest change < 0.5 mmHg). Peak oxygenation was achieved 75±28.9 seconds post injection. For therapy experiments, normalized tumor volume 1 month post treatment was found to be A) 1.5±1.2 fold for SE61O2 + ultrasound + radiation, B) 41.7±62.7 fold for SE61O2 + ultrasound, C) 4.3±1.2 fold for ultrasound + radiation, D) 9.3±4.7 fold for SE61N2 + ultrasound + radiation, and E) 14.7±14.4 fold for SE61O2 + radiation. These preliminary results indicate that the combination of SE61O2 with ultrasound elevates breast tumor oxygenation levels, and that this elevation leads to improved tumoral radio-sensitivity and treatment response.

4G-2

4:15 pm **A Flow Focusing Microfluidic Device with an Integrated Micro Coulter Particle Counter for Sequential Production and Characterization of Size Tunable Microbubbles**

J.M. Robert Rickel[1], Adam J. Dixon[1], Alexander L. Klibanov[1], John A. Hossack[1]; [1]*Biomedical Engineering, University of Virginia, Charlottesville, Virginia, USA*

Background, Motivation and Objective

Flow-focusing microfluidic devices (FFMDs) provide a means to customize microbubble (MB) populations for imaging or therapy. FFMDs produce monodisperse MBs characterized by relatively low production rates, large diameters and short lifetimes compared to batch methods of MB production. Previously, we proposed exploiting these qualities in the context of tPA delivery for more rapid blood clot erosion where the device is integrated into a catheter to mitigate the impact of low MB count and lifetime (Dixon *et al*. IEEE IUS 2015). Conventionally, MBs produced by FFMDs are characterized optically; however, this is incompatible with a catheter application. In this work, we demonstrate integrated Coulter-based counting and sizing of MBs produced *in situ*.

Statement of Contribution/Methods

The measurement circuit design was informed by finite element analysis. Coplanar electrodes were integrated into a FFMD (Fig 1A, B) and excited by a 3V, 1MHz sinusoid. The accuracy of the integrated measurement circuit was validated by simultaneous optical measurement with a high speed camera setup (Specialised Imaging, Inc.). The time-varying electrical impedance from MB production modulates the amplitude of the excitation waveform in accordance with the Coulter Principle. However, this modulation is also a function of the distance between successively produced MBs (Fig.1C). MBs were produced using a 99.999% purified nitrogen gas core stabilized by a shell comprised of 3% bovine serum albumin and 10% dextrose in 0.9% physiologic saline. Liquid flow rate and gas pressure were varied to produce MBs with a range of diameters and production rates.

Results/Discussion

MBs between 8-20 μm were electrically assessed at production rates up to 325,000 MBs/s. Electrical, as opposed to optical, detection enables continuous versus discrete measurement of production rate. Electrical measurements validated the predicted changes in impedance for 17.5, 15, 12.5 and 10 μm diameter MBs (R^2 = 0.954, 0.911, 0.907 and 0.773, respectively (Fig. 1C)) using experimental data of optically determined MB diameter and distance between successively produced MBs. The smallest MBs that can be detected are 5 μm in diameter, as determined by the electronic noise floor. In conclusion, the system is able to count and size MBs at production rates and diameters that meet, or exceed, projected needs relevant to our application.

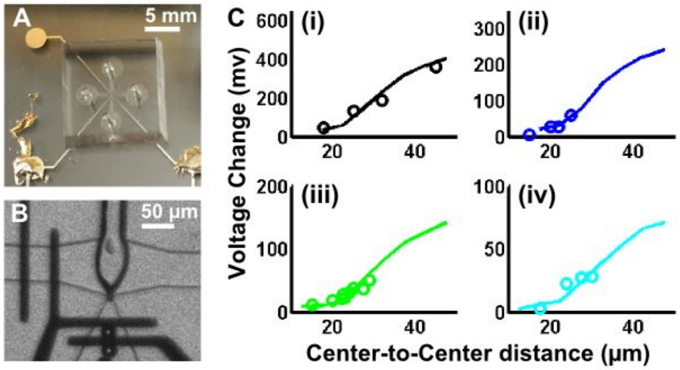

Figure 1 (A) Image of microfluidic device. (B) Microfluidic device producing 15 μm microbubbles under 20x magnification. (C) Voltage modulation as a function of center-to-center distance between successively produced microbubbles for (i) 17.5, (ii) 15, (iii) 12.5 and (iv) 10 μm microbubbles. Each curve depicts simulated data and open circles are experimental data.

4G-3

4:30 pm Accelerated Clearance of Ultrasound Contrast Agents Containing Polyethylene Glycol (PEG) is Associated with a PEG-Specific Immune Response

Samantha M. Fix[1], A. Gloria Nyankima[2], Morgan D. McSweeney[1], James K. Tsuruta[3], Samuel K. Lai[1], Paul A. Dayton[2]; *[1]Eshelman School of Pharmacy, University of North Carolina at Chapel Hill, Chapel Hill, North Carolina, USA, [2]Joint Department of Biomedical Engineering, University of North Carolina at Chapel Hill and North Carolina State University, Chapel Hill, North Carolina, USA, [3]Department of Pediatrics, University of North Carolina at Chapel Hill, Chapel Hill, North Carolina, USA*

Background, Motivation and Objective

Lipid-shelled microbubbles (MBs) are routinely used as contrast agents for ultrasound imaging. Such MBs are often formulated with polyethylene glycol (PEG), with the intention of shielding them from recognition and clearance by the innate immune system, prolonging their intravenous circulation time. Paradoxically, the immune system is able to generate specific antibodies that bind PEG. This has been associated with accelerated blood clearance of PEGylated particles when dosed repeatedly over multiple days. Here we aim to (1) study how PEGylated MB pharmacokinetics changes during repeat contrast-enhanced ultrasound imaging schedules and (2) investigate whether administration of these MBs generates an anti-PEG antibody response in rats.

Statement of Contribution/Methods

One group of rats received multiple doses of PEGylated MBs over a 28-day period. At each time point, MB circulation kinetics was quantified by contrast time intensity curve (TIC) analysis. A second group of animals received a single dose of PEGylated microbubbles on Day 0 and resultant changes in clearance due to this single dose were assessed by TIC analysis at the study end point (Day 28). Finally, serum samples collected from all animals at each time point were tested for anti-PEG antibodies via ELISA.

Results/Discussion

We observed accelerated clearance starting 2-days after the initial MB dose in animals receiving multiple doses, which persisted throughout the remainder of the study (Fig 1). MB clearance was found to be most rapid on Day 14 with a 4.2× reduction in MB half-life. This maximally accelerated clearance was maintained out to the 28-day time point. Additionally, we found that a single dose of MBs on Day 0 was sufficient to cause accelerated clearance of a second dose administered 28-days later. Analysis of the animals' serum indicated a robust anti-PEG IgM and anti-PEG IgG response that peaked 7 and 14 days after the initial MB dose, respectively. We conclude that repeat dosing of PEGylated MBs results in dramatically accelerated MB clearance, which is associated with a PEG-specific immune response. We believe that these data will have important implications for many contrast-enhanced ultrasound-imaging techniques that (1) involve repeat administration PEGylated MBs over multiple days or weeks and (2) require precise knowledge of circulating MB concentration for proper interpretation.

Figure 1. Change in microbubble circulation over 28 days of repeat administration.

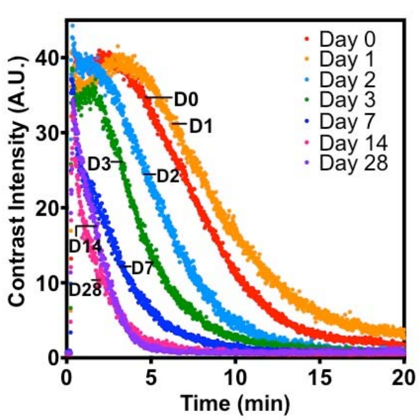

4G-4

4:45 pm **Altering Lipid Shell Composition Enables the Tunability of Perfluorocarbon Nanodroplets**

Steven Yarmoska[1], Heechul Yoon[2], Stanislav Emelianov[1,2]; [1]*Wallace H. Coulter Department of Biomedical Engineering, Georgia Institute of Technology and Emory University School of Medicine, Atlanta, Georgia, USA,* [2]*School of Electrical and Computer Engineering, Georgia Institute of Technology, Atlanta, Georgia, USA*

Background, Motivation and Objective

Perfluorocarbon nanodroplets (PFCnDs) are emerging ultrasound (US) contrast agents that seek to enable contrast-enhanced imaging of extravascular spaces and offer increased biological stability and circulation times compared to traditional microbubbles (MBs). However, rigorous studies have not analyzed the impact of shell composition on PFCnDs. In particular, lipid-shell PFCnD formulations borrow their shells from liposomes or MBs, and these formulations may not be ideal for phase-changing PFCnDs. The objective of this work was to assess the impact of variable lipid shell composition on phase-changing PFCnD size and their US and photoacoustic (PA) imaging parameters.

Statement of Contribution/Methods

PFCnDs were synthesized via a sonication-based method using perfluorohexane, variable molar ratios of lipids DSPC and DSPE-mPEG2000, near-infrared dye, and PBS as solvent (**Fig. 1A**). Four batches of each PFCnD formulation were sized using a Zetasizer Nano ZS (Malvern Instruments, Malvern, UK). Imaging experiments were conducted with a 16 MHz linear array transducer (LZ201, FUJIFILM Visualsonics Inc., Toronto, ON) interfaced with a Vantage 256 US system (Verasonics Inc., Kirkland, WA) and a 10 Hz Nd:YAG laser (Phocus, Opotek Inc., Carlsbad, CA) outputting near-infrared light at 1064 nm. The integrated system was able to capture both PA images as well as post-laser ultrafast US images acquired at 1 kHz frame rate. Imaging phantom experiments were performed with a PFCnD-filled tube submerged within a water bath.

Results/Discussion

PFCnDs with an inverted molar ratio of DSPC to PEGylated DPSE (1:9) compared to the typical formulation (9:1) produced consistently smaller (initially <200 nm) PFCnDs with significantly lower inter-batch variance (**Fig. 1B**). The 1:9 PFCnDs gradually increased in size over time (+100 nm over 6 hr). PA signal from the 1:9 PFCnDs increased as a function of their volumetric expansion (**Fig. 1C**). Changes in US signal from these PFCnDs were observed only within the first 6 ms post-laser pulse, supporting repeatable vaporization-recondensation or "blinking" (**Fig. 1C**). Our studies indicate the ability to tune the size of, and by extension the signal produced by, PFCnDs by varying the lipid shell composition. Future studies will explore intermediate lipid ratios and characterize recondensation dynamics as a function of droplet size and composition.

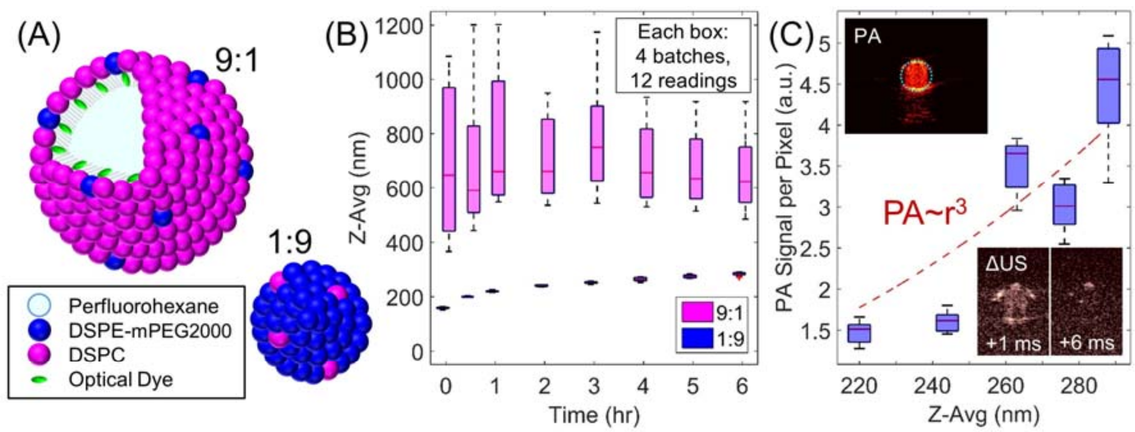

Figure 1. (A) Cartoon of optically-triggered perfluorocarbon nanodroplets (PFCnDs) with 9:1 (left, pink) and 1:9 (right, blue) molar ratios of DSPC:DSPE-mPEG2000. **(B)** Boxplot showing DLS size data from the two PFCnD populations over six hours. **(C)** Boxplot displaying photoacoustic (PA) signal as a function of PFCnD size overlaid with a cubic fit (red dashed line). Insets show representative PA and differential ultrafast ultrasound images.

4G-5

5:00 pm **High Frame Rate Ultrasound Imaging of Vaporised Sub-micron Phase-Change Contrast Agents**

Shengtao Lin[1], Ge Zhang[1], Chee Hau Leow[1], Meng-Xing Tang[1]; [1]*Department of Bioengineering, Imperial College London, London, United Kingdom*

Background, Motivation and Objective

Contrast-enhanced high-frame-rate (HFR) ultrasound imaging offers enriched temporal information. As one of the most actively researched alternative contrast agent, the sub-micron phase-change contrast agent (PCCA) has shown attractive advantages in ultrasound imaging and therapy. Post-vaporisation of PCCAs has been optically evaluated (Reznik, 2013) and acoustically characterised (Reznik, 2011) with fluorinate-shelled PCCAs. In this study, for the first time, we employed HFR ultrasound to image the vaporised lipid-shelled PCCAs immediately after acoustic activation on a microvascular phantom with microscopic validation. This will provide an understanding of the stability and lifetime of vaporised PCCAs after activation in the context of HFR ultrasound imaging.

Statement of Contribution/Methods

The PCCA (averaged 243±54 nm) solution was administrated into a 200-µm-cellulose tube submerging in a 37°C water tank. An ultrasound research platform (Verasonics) equipped with a L11-4 array was used to deliver the imaging sequence, 'imaging-activation-imaging'. The PCCAs were acoustically activated by focus-pulses (8 MHz, MI=1.7, 5-cycle). The 3 kHz HFR plane-wave (3 angles, 4 MHz, MI=0.065) pulse-inversion imaging was applied. The data was analysed using differential imaging, where image subtraction was performed from the baseline image (acquired prior to vaporisation). The high-speed camera (1 kHz) was used to observe the microbubble (MB) generation and MB dynamics afterwards.

Results/Discussion

The selected HFR differential images are shown in Fig 1a-d, and the quantification result is revealed in Fig 1e. The significant contrast enhancement was generated immediately after PCCA activation (Fig 1b), and then the intensity decreased significantly (>50%) in the first ~50 ms at a rate of ~0.2 dB/ms; y=-0.208x+17.88, R^2=0.997 (Fig 1c), followed by a gradual and small decay (~2 dB) in the next 950 ms (Fig 1d). The optical observation shows the vaporised PCCAs presented (Fig 1g) immediately after activation (Fig 1f is before activation), followed by an obvious disappearance of some MBs in the next frame (Fig 1h). The control experiment performed using the same imaging settings with water (Tissue) and precursor MBs shows signals of different characterises, suggesting the vaporised contrast agents being acoustically less stable than their precursor MBs.

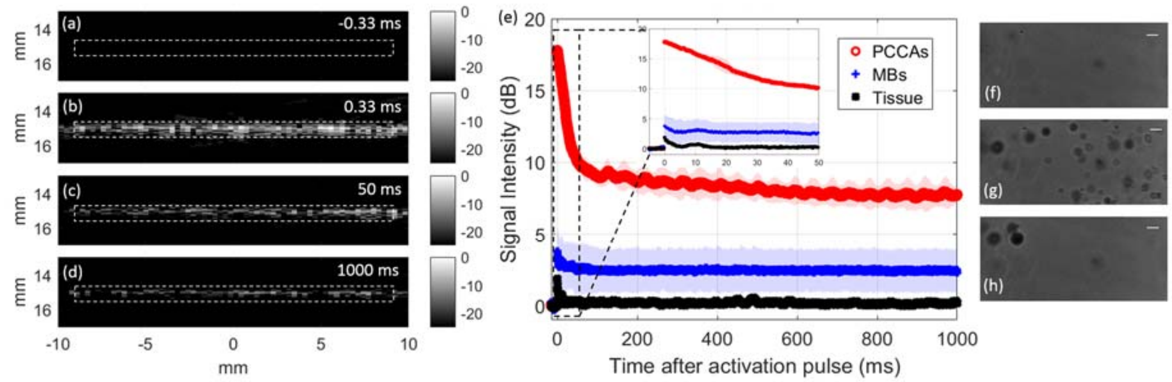

Figure 1. (a-d) High frame rate ultrasound differential imaging of PCCAs in a 200-µm-cellulose tube imaged at 3 kHz with an MI of 0.065. The time after acoustic vaporisation for these selected images is (a) -0.33 ms (b) 0.33 ms (c) 50 ms (d) 1000 ms. The images are presented in a 25 dB scale. The white dash lines present the region-of-interest for data analysis. (e) Quantitative image intensity over the time after PCCA activation. Tissue and MBs were the control experiment by imaging water and MBs in the tube respectively. (f) Optical image acquired before PCCA activation. (g) The image shown the vaporised PCCAs immediately after acoustic vaporisation. (h) Some small vaporised PCCAs disappeared in the next frame. Scale bar is 10 µm.

4G-6

5:15 pm Improved Selection of Optimal Acoustic Output Power for Subharmonic Aided Pressure Estimation of Portal Hypertension

Ipshita Gupta[1,2], John Eisenbrey[1], Maria Stanczak[1], Colette Shaw[1], Susan Schultz[3], Susan Shamimi-Noori[1], Stephen Hunt[3], Michael Soulen[3], Jonathan Fenkel[4], Chandra Sehgal[3], Kirk Wallace[5], Flemming Forsberg[1]; *[1]Radiology, Thomas Jefferson University, Philadelphia, PA, USA, [2]School of Biomedical Engineering, Sciences and Health Systems, Drexel University, Philadelphia, PA, USA, [3]Radiology, Hospital of the University of Pennsylvania, Philadelphia, PA, USA, [4]Gastroenterology & Hepatology, Thomas Jefferson University, Philadelphia, PA, USA, [5]GE Global Research, Niskayuna, NY, USA*

Background, Motivation and Objective

Subharmonic aided pressure estimation (SHAPE) is based on the inverse relationship between the subharmonic amplitude of contrast microbubbles and the ambient pressure. A noninvasive ultrasound based pressure estimation procedure would be a major development in the diagnosis of portal hypertension and less invasive than the current hepatic venous pressure gradient (HVPG) measurement. The hypothesis of this study was that portal vein pressures could be monitored and quantified noninvasively in humans using SHAPE. For maximum SHAPE sensitivity, the optimum acoustic power is currently selected using an algorithm, which collects subharmonic data at power levels increasing from 0 % to 100 % in 8 cine clips. The ROI is selected on a common Maximum Intensity Projection (MIP) for all these 8 clips, data is plotted against the power levels and the point of maximum inflection gives the optimum power. However, this algorithm is prone to motion due to breathing and can greatly affect the results, hence was improved to minimize the error.

Statement of Contribution/Methods

A modified Logiq 9 ultrasound scanner with a 4C curvi-linear probe (GE, Milwaukee, WI, USA) was used to acquire SHAPE data transmitting at 2.5 MHz and receive subharmonic signals at 1.25 MHz. The improved algorithm was developed *in vitro*. A sonographer mimicked breathing motion by moving the probe across a flow phantom with Sonazoid microbubbles (GE, Oslo, Norway) circulating. The optimization algorithm was improved by creating a separate MIP for each of the 8 cine clips so the ROI could be repositioned each time to reduce noise. SHAPE results were compared between the existing and the improved algorithm for pressures increasing from 10 to 40 mmHg. Next, this IRB approved study enrolled 98 transjugular liver biopsy subjects (median age 60 yrs, 58 % males). Post biopsy, the contrast agent Sonazoid was infused at a rate of 0.024 µL/kg/min. SHAPE data was collected from the portal and hepatic vein in triplicate at the optimal acoustic power and compared to invasive HVPG measurements.

Results/Discussion

An improved algorithm to identify optimum acoustic power levels has been developed and validated *in vitro*. The new algorithm gives better or similar correlation for all the setups (r ranging from -0.85 to -0.95 vs. -0.39 to -0.98). Also, the linear relationship between the SHAPE gradient and HVPG over the patient dataset showed good correlation ($r = 0.76$). Patients at increased risk for variceal bleeding (HVPG > 12 mmHg) had a significantly higher mean subharmonic gradient than patients with lower HVPGs (-0.14 ± 2.11 vs. -4.43 ± 2.88 dB; $p < 0.0001$). Current results indicate that SHAPE may be useful for non-invasive estimation of portal pressures.

5G - PGP - General Physical Acoustics

Blue Room

Friday, September 8, 2017, 4:00 pm - 5:30 pm

Chair: **Robert Thalhammer**
Broadcom Ltd

5G-1

4:00 pm **Design of Multi-Frequency Acoustic Kinoforms**

Michael Brown[1], Ben Cox[1], Bradley Treeby[1]; [1]*University College London, London, United Kingdom*

Background, Motivation and Objective

The control of acoustic fields in 3-D is vital in many areas of physical acoustics. Recently, a new approach for the generation of complex diffraction limited acoustic fields in 3-D was introduced. This works by calculating a phase hologram designed to generate a desired acoustic field. The output of a simple planar transducer is then mapped onto this phase distribution using a 3-D printed kinoform attached to the transducer.

One limitation of this approach is that the acoustic field generated by each kinoform is fixed. A way to overcome this is to adapt a technique from optical holography and encode several target distributions onto different frequencies. The field can then be changed by varying the driving frequency of the transducer. The goal of this work was to demonstrate this approach and to investigate the design of these kinoforms.

Statement of Contribution/Methods

An optimisation approach based on direct-binary-search was implemented to calculate multi-frequency kinoforms. This searched, sequentially, for the thickness at each position that minimised a cost function penalising variations between the actual field and the target field for each frequency. Two other algorithms were also implemented. One based on combining several phase holograms using a $>2\pi$ modulation depth to minimise the combined error, and another based on dividing the aperture for each frequency.

The fields generated by the output kinoforms were simulated using the k-Wave toolbox and measured experimentally. For the experiments, kinoforms were fabricated using 3-D printing and attached to the front face of a planar transducer. The acoustic field was then measured driving the transducer at each encoded frequency.

Results/Discussion

Both the simulated and experimental results demonstrated that acoustic kinoforms encoding multiple field patterns onto different frequencies can be generated with a direct-search approach. This is illustrated by the figure which shows a calculated kinoform and its simulated field in one plane when driven at two different frequencies. The efficiency of this approach is sensitive to the choice of design method and the separation and number of encoded frequencies.

This work enables some of the functionality of a large phased array to be encoded onto a single element transducer using a cheap 3-D printable structure.

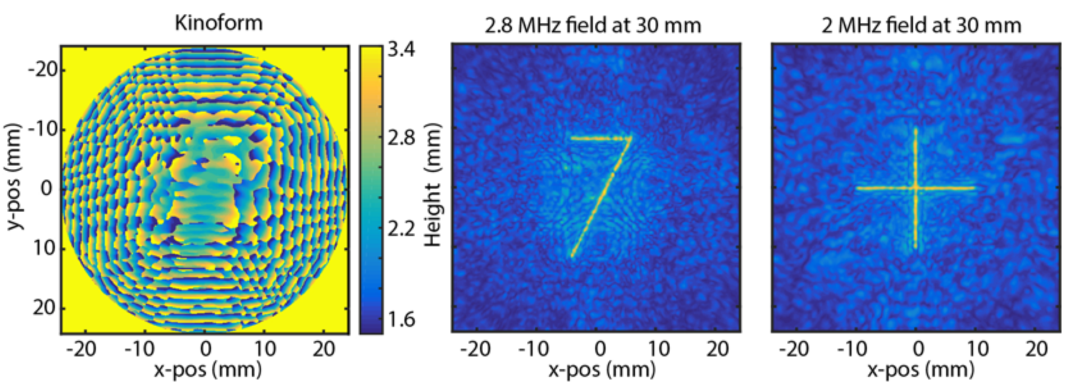

5G-2

4:15 pm **Dirac Cone Dispersion of Lamb Waves in Plates**

David Stobbe[1], Todd Murray[1]; [1]*University of Colorado Boulder, Boulder, Colorado, USA*

Background, Motivation and Objective

Electromagnetic [1] and acoustic [2] metamaterials that exhibit linear dispersion at a nonzero frequency and a wave vector (k) of zero, leading to a conical dispersion surface or so-called Dirac cone dispersion, have been demonstrated recently. These materials display unusual behavior associated with the occurrence of a finite group velocity at $k = 0$, leading to a wave which propagates with a uniform phase distribution over space or infinite wavelength. The existence of similar conical dispersion in homogeneous plates due to accidental degeneracy of longitudinal and transverse resonances has also been discussed [3]. In this work, we provide an experimental and numerical study of Lamb waves generated in plates with conical dispersion and the interaction of these waves with boundaries.

Statement of Contribution/Methods

A degeneracy of longitudinal and transverse resonances associated with the S_2 and S_{2B} symmetric Lamb modes at $k = 0$ occurs in materials in which the longitudinal wave velocity is twice the shear wave velocity, corresponding to a Poisson's ratio of $\nu = 1/3$. Aluminum alloy 6061-O plates having a room temperature Poisson's ratio near the required value were cooled to tune the elastic properties to $\nu = 1/3$. Lamb waves were excited in the plate using a contact transducer and detected using a photorefractive crystal based interferometer. The plate response measured as a function of source to receiver distance was collected and processed to obtain the dispersion curves. In addition, two dimensional scans of the wave field were collected to investigate the interaction of $k \sim 0$ Lamb waves with plate boundaries. The results were compared to numerical simulations.

Results/Discussion

The experimentally measured dispersion curve for the degenerate case demonstrates that linear dispersion near k = 0 can be achieved in homogeneous plates as the wave field transitions between forward and backward propagating waves. In addition, we demonstrates that when k ~ 0 the wave field exhibits a degree of spatial invariance. Mode converted Lamb waves at a plate edge, for example, have an angle of reflection of 900 regardless of the angle of incidence. We demonstrate that a lens for mode converted k ~ 0 Lamb waves can be created by a machining a semicircular plate boundary and that such a lens is independent of the position of the excitation source. Finally, interesting features of k ~ 0 Lamb wave interactions with defects in the plate are discussed. Numerical results show excellent agreement with experiments. Dirac cone dispersion in homogeneous elastic plates provides a new means to manipulate and control wave propagation.

References

[1] *X. Huang, Y. Lai, Z. H. Hang, H. Zheng, and C. T. Chan, Nature Mater. 10, 582 (2011).*

[2] *F. Liu, X. Huang, and C. T. Chen, Appl. Phys. Lett. 100, 071911 (2012).*

[3] *A. A. Maznev, J. Acoust. Soc. Am. 135 (2014).*

5G-3

4:00 pm Staircase-Free Acoustic Sources for Grid-Based Models of Wave Propagation

Elliott Wise[1], Ben Cox[1], Bradley Treeby[1]; [1]*Medical Physics and Biomedical Engineering, University College London, United Kingdom*

Background, Motivation and Objective

The k-Wave MATLAB toolbox is widely used to conduct medical ultrasound simulations. These require accurate models of acoustic sources. In k-Wave, a k-space pseudospectral time domain model of acoustic propagation, sources are introduced by adding acoustic pressure at points on a uniform, orthogonal grid. For curved sources two issues arise: First, points on the source's surface do not necessarily align with the grid, and so are typically moved to nearby grid nodes. This produces local phase errors in the discretised source. Second, the resolution of the grid is lower in directions which are unaligned with the grid axes. This results in fewer source points in these directions, and hence in local amplitude errors. These errors are collectively referred to as 'staircasing'. The present work outlines a method for introducing acoustic sources that is free from staircasing errors.

Statement of Contribution/Methods

When an acoustic pressure source is added at a single grid node in k-Wave, some pressure is added globally through the band-limited interpolant (BLI), which is zero at all other grid nodes but non-zero between them. This is due to k-Wave's use of the Fourier collocation method. To introduce acoustic pressure at a point which is off-grid, one can evaluate a BLI centred at this point over the grid. General acoustic source terms can thus be discretised in a manner that is free from staircasing by convolving the BLI with the source. This approach minimises the least-squares error between the discretised and continuous sources.

Results/Discussion

In this work, two algorithms are presented to introduce acoustic sources without staircasing errors. The first numerically convolves the BLI with the source, demonstrating optimal introduction of a continuously defined source into a discrete k-Wave simulation. The second evaluates BLIs which are uniformly distributed over the source geometry at twice the resolution of the simulation grid. This is faster and more easily implemented for general source geometries. A comparison is made with current k-Wave source algorithms and with the FOCUS ultrasound simulation code. The simulation depicted below shows an acoustic field which was generated for a bowl-shaped source. The staircasing-free (i.e. off-grid) approach produced a maximum error in the axial pressure 17 times lower than that produced by the usual on-grid approach.

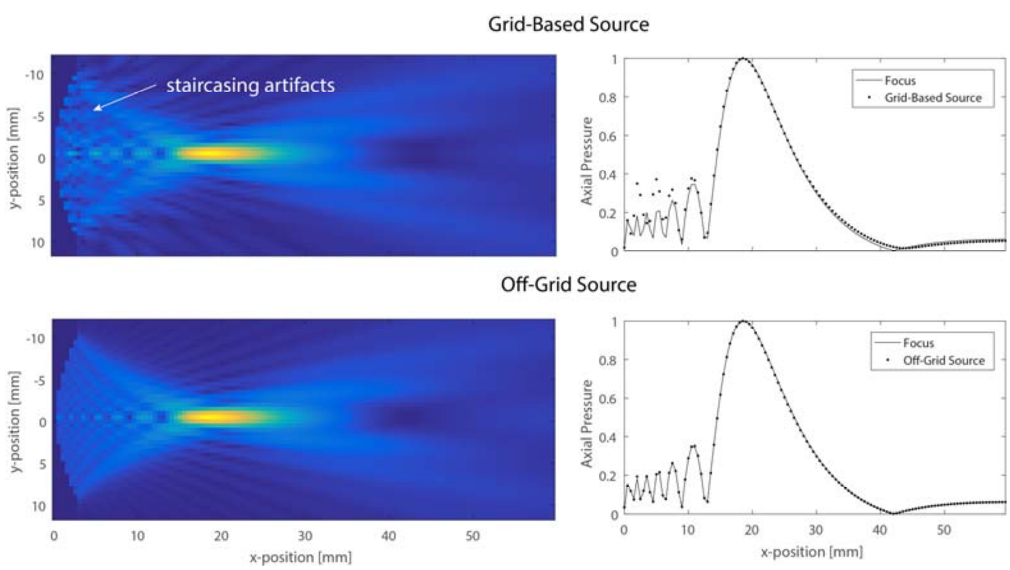

5G-4

4:45 pm Blind Deconvolution of a Hydrophone with a Bubble-Collapse Shock Wave

Kristoffer Johansen[1], Jae Hee Song[1], Paul Prentice[1]; [1]*CavLab, School of Engineering, University of Glasgow, Glasgow, United Kingdom*

Background, Motivation and Objective

Measuring broadband signals demands complex calibration of a detector over a sufficient bandwidth. For inertial cavitation emissions, the shock waves will be convolved with the transfer function of the hydrophone, and introduce artefacts to the measurement. Use of appropriately calibrated detectors would thus facilitate meaningful comparison of the cavitation emission data reported from groups using different detectors. However, complex calibration (magnitude and phase) is costly and time consuming, typically requiring hydrophone relocation to an institute with accredited and standardized instrumentation. This paper describes an economical, one-shot concept for 'blind characterization' of the magnitude of the transfer function of a hydrophone, utilizing the broadband nature of an experimental bubble collapse shock wave, an established bubble collapse model and shock wave propagation simulation.

Statement of Contribution/Methods

A commonly reported technique for studying single bubbles involves focusing a short laser pulse, of energy above the plasma forming threshold, into water to generate a laser-induced bubble (LIB). LIBs are acoustically characterized by the emission of two shock waves, the first on formation of the plasma and the second during the bubble collapse. We detect both shock waves with a PVdF needle hydrophone (NH) Fig. 1(b), with complex calibration over a bandwidth of 125 kHz to 20 MHz (National Physical Laboratory (NPL), 2016), Fig. 1 (e). The Rayleigh-collapse time for the LIB is deduced as half the time between the shock waves, proportional to the maximum radius, confirmed by shadowgraphic high-speed imaging, Fig. 1(a). The Keller-Miksis equation for inertial bubble dynamics is solved, and a bubble-collapse shock wave (BCSW) computed.

Results/Discussion

The spectral content of the computed BCSW, Fig. 1(d), is used to characterize the magnitude of the transfer function of the NH, for comparison to the NPL calibration. Fig. 1(e) indicates that the main features of the calibration are reasonably reproduced, within 6 dB. The accuracy of this technique relies critically on the physical BCSW being well represented by the computed BCSW, which includes the bubble collapse model and simulation of the BCSW propagation to the detector. A computed BCSW of sufficient accuracy should also allow the phase response to be blindly characterized.

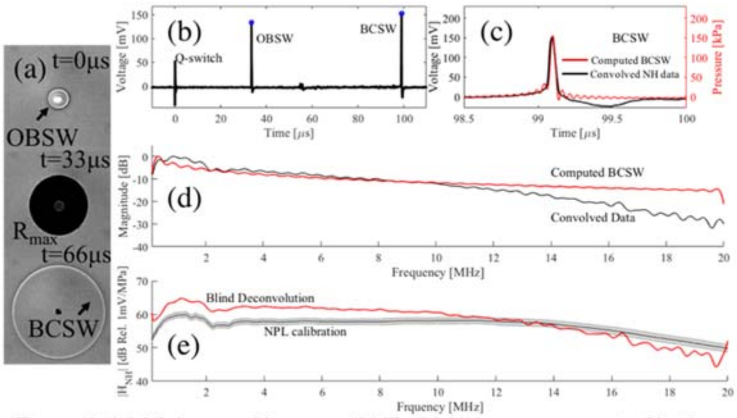

Figure 1: (a) High-speed images of LIB. (b) NH measurement of both shock waves. (c) NH measurement (black) and computed BCSW (red). (d) Convolved NH measurement (black) and computed BCSW (red). (e) NPL calibration of sensitivity (black) with grey shadow representing the uncertainty, and blindly deconvolved sensitivity (red).

5G-5

5:00 pm Investigations on the Correlation between Particle Velocity Distribution and PMMA Heating Effect Induced by High-Intensity Focused Ultrasound

Coralie Koo Sin Lin[1], Lukas Oehm[2], Marko Liebler[1], Holger Brehm[1], Klaus-Vitold Jenderka[3], Jens-Peter Majschak[2], Bernd Wilke[1]; [1]*Robert Bosch GmbH, Germany,* [2]*Chair of Processing Machines and Processing Technology, Dresden University of Technology, Germany,* [3]*Departement of Engineering and Natural Sciences, Merseburg University of Applied Sciences, Merseburg, Saxony-Anhalt, Germany*

Background, Motivation and Objective

High-intensity focused ultrasound (HIFU) is increasingly getting in focus of interest for polymer layer joining (Liebler 2008). Previous studies investigated the heating effect in polymer materials induced by HIFU with liquid sound conductor (Bo Liu et al. 2013) and with solid sound conductor (Oehm et al. 2016). An improved understanding of the physical mechanisms of HIFU to heat thin polymer layers, particularly the correlation between sample heating and particle velocities at the top of the solid sound conductor, is essential to advance polymer processing, where liquids are prohibited.

Statement of Contribution/Methods

A focusing ultrasound transducer (R=48.5 mm, f=1.1 MHz) coupled to a solid sound conductor is used to heat PMMA samples (electrical power 175 W). The effect of the particle velocity distribution at the top of the sound conductor on the heating effect is studied. The particle velocities were measured with scanning Laser-Doppler-Vibrometry (Polytec, PSV-500). The heating of the samples was measured by infrared thermography (Infratec, ImageIR 8300). The results of a finite element simulation model are compared to the vibrometry measurements.

Results/Discussion

A maximal particle velocity of 0.38 m/s for 2.3 W electrical power was measured and the maximal temperatures recorded inside the samples of 0.37 mm, 0.5 mm and 1 mm thickness were 163 °C, 196 °C and 226 °C respectively for 175 W electrical power (Figure 1(a)). The simulation is in good qualitative (Figures 2(a) and (b)) and quantitative (Figure 1(a)) agreement with the experiments (8 % deviation between the maximal measured and simulated particle velocity amplitudes). A qualitative correlation between particle velocities, heat distribution and position of generated gas bubbles in the PMMA sample is found (Figure 2).

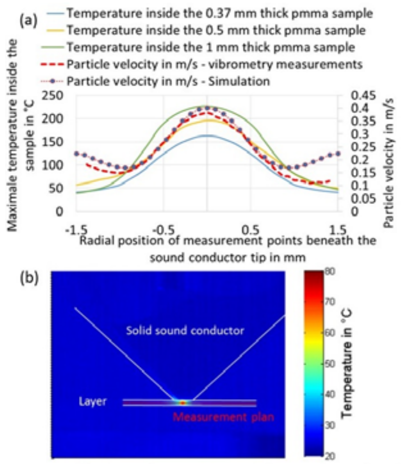

Figure 1: (a) maximal temperature of the sample irradiated with a solid sound conductor transducer compared to the particles velocity distribution for different sample thicknesses, (b) infrared image, lateral view (sample thickness 0.375 mm)

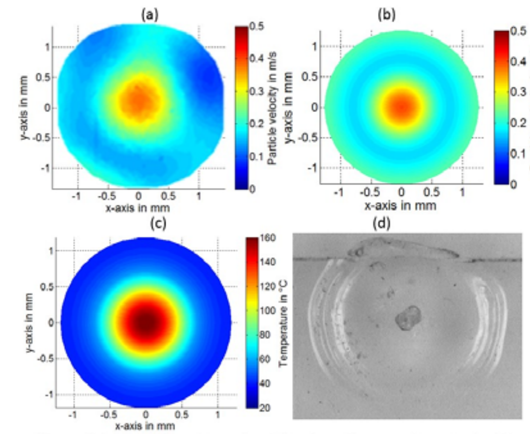

Figure 2: (a) scanning vibrometry of the top of the sound conductor (b) FE-simulation (Software: Abaqus) (c) infrared temperature recording inside the PMMA sample (sample thickness 0,37 mm – temperature measured 0.150 mm under the sound conductor surface) (d) microscope image of the cooled down irradiated PMMA 0.37 mm thickness sample

5G-6

5:15 pm Validity of the Keller-Miksis Equation for "Non-stable" Cavitation and the Acoustic Emissions Generated

Kristoffer Johansen[1], Jae Hee Song[1], Paul Prentice[1]; [1]*CavLab, School of Engineering, University of Glasgow, Glasgow, United Kingdom*

Background, Motivation and Objective

The Keller-Miksis equation (KME) is commonly used for numerical studies of inertial and stable-inertial cavitation. However, experimental validation of KME under clinically relevant exposure settings is scarce, particularly in terms of the acoustic emission signal generated by the cavitation. Validation of KME for strongly driven bubbles could significantly aid the design of arrays for passive acoustic mapping (PAM), quantification of cavitation dose, and the study of novel cavitation configurations such as dual-frequency exposures and control systems.

Statement of Contribution/Methods

Laser-nucleation of acoustic cavitation is used to initiate single events for imaging at unprecedented spatiotemporal resolution, in a characterized focused ultrasound field of $f_0 = 692$ kHz. A Shimadzu HPV-X2 high-speed camera, capable of recording 256 frames at up to 10 MHz, is configured with synchronous 10 ns laser pulses for illumination, such that an effective temporal resolution of 10 GHz is achieved. In parallel, the acoustic emissions are collected through a PVdF needle hydrophone (NH), the tip of which is located within a few millimeters of the driven bubble(s). The resolved oscillations are modeled using the KME, and the acoustic emissions computed for both $f_0/2$ and $f_0/3$ stable-inertial cavitation, via an oscillating sphere assumption.

Results/Discussion

The high-speed images of Fig. 1(a) captured at 5 MHz (sampled at 10 GHz), depict successive strong collapses with coincident shock wave emission, and therefore represent a full subharmonic oscillation cycle. The KME simulation of an equivalent driven bubble is shown, Fig. 1(b), and the inferred acoustic emissions, Fig. 1(c) red, bandpass filtered according to the complex calibration of the NH (125 kHz – 20 MHz). The control-subtracted experimental NH data, the tip of which is visible at the full field-of view (Fig 1(a), 5.2 µs) is also presented, Fig. 1(c) grey.

Practicable agreement between experimental and simulation acoustic emission data is demonstrated for the single $f_0/2$ event. For higher driving amplitudes, and higher-order subharmonic cavitation regimes, the agreeance deteriorates principally due to bubble fragmentation. Progress toward validation for multiple simultaneous cavitation events, and the emissions generated, will also be discussed.

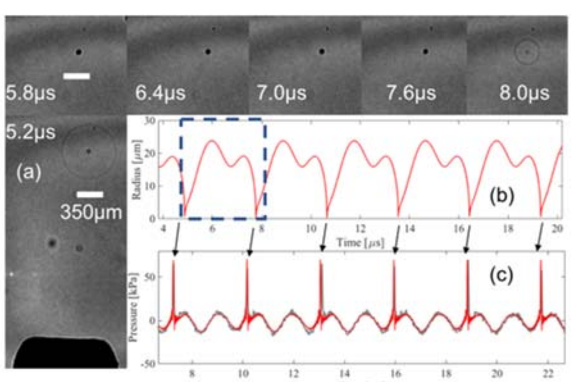

Fig. 1: (a) high-speed images of a single $f_0/2$ cavitation event, 2.7mm from NH tip. (b) Simulated radius-time curve from KME, with dashed rectangle representing the subharmonic oscillation imaged. (c) acoustic emissions from the driven bubble, measured by the NH (grey) and simulated (red), with periodic shock wave features arrowed from collapses in (b).

6G - Signal Processing

Hampton Room

Friday, September 8, 2017, 4:00 pm - 5:30 pm

Chair: **Erdal Oruklu**
Illinois Institute of Technology

6G-1

4:00 pm **Implementation Issues of 3D SAFT in Time and Frequency Domain for the Fast Inspection of Heavy Plates**

Fabian Krieg[1,2], Jan Kirchhof[2], Florian Römer[2], Alexander Ihlow[2], Christian Grandinetti[1], Giovanni Del Galdo[2,3], Ahmad Osman[1,4]; [1]*NDT of Components and Assemblies, Fraunhofer Institute for Non Destructive Testing IZFP, Saarbrücken, Germany,* [2]*Institute for Information Technology, Technische Universität Ilmenau, Ilmenau, Germany,* [3]*Fraunhofer Institute for Integrated Circuits IIS, Germany,* [4]*Hochschule für Technik und Wirtschaft des Saarlandes, Germany*

Background, Motivation and Objective

The Synthetic Aperture Focusing Technique (SAFT) is a reconstruction strategy for ultrasonic non-destructive inspection, which allows the focusing of multiple measurements by superposition. Here, it is applied for the inspection of heavy plates, where a plate is scanned with a fast feed rate by an ultrasonic sensor and a decision about material quality (inclusions, holes, cracks, etc.) has to be made virtually in real-time. This raises high demands on the SAFT-reconstruction, which is due to its computational expense usually applied in post-processing. Consequently, specific tuning of the algorithm and a compromise in reconstruction quality vs. speed is required.

Statement of Contribution/Methods

We investigate and tune SAFT algorithms in time- and frequency domain for planar objects regarding computational cost under the constraint of obtaining a sufficient reconstruction quality. As frequency-domain approaches, we compare Phase-shift migration and tuned versions of Stolt's migration with different interpolation strategies (linear, spline, non-uniform FFT). In time domain, we propose and compare several heuristics for delay-and-sum SAFT.

Results/Discussion

We compare and discuss reconstruction results from the aforementioned SAFT algorithms based on measurement data of a steel specimen in connection with computation times and memory requirements. It is shown that algorithm tuning can dramatically reduce computation times while maintaining virtually perfect reconstruction results. Theoretic bounds for computation times and memory requirements related to the parameters of the algorithms and reconstruction scenario are given and backed by measurements.

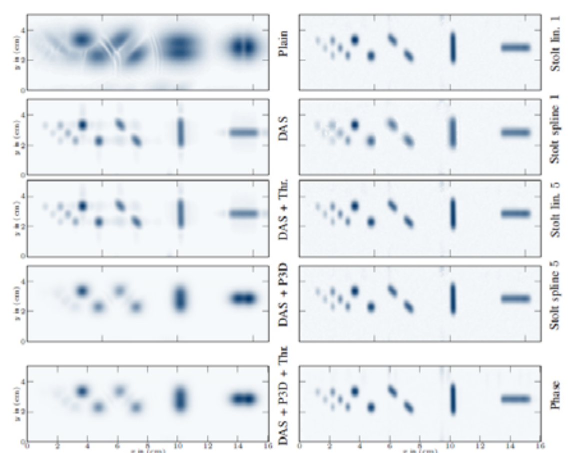

Fig. 1: C-images for the reconstruction of measurement data: DAS denotes delay-and-sum time domain SAFT, Thr. the thresholding heuristic, P3D the pseudo 3D heuristic, Stolt lin. n the Stolt migration with linear interpolation and oversampling n, Stolt spline n Stolt migration with spline interpolation and Phase the phase migration algorithm.

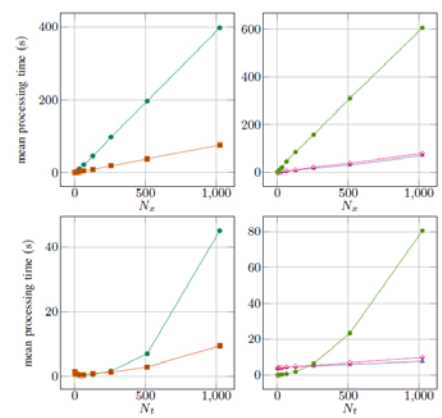

Fig. 2: Measured scaling of the computation time for varying problem size for the base algorithms - first row: N_x is the number of spatial samples, second and third dimension are held fixed; second row: N_t is the length of each A-scan, spatial dimensions are held fixed; left side: DAS + Thr. heuristic, DAS + P3D heuristic; right side: Phase migration, Stolt migration lin. 5 interpolation, Stolt migration spline 5 interpolation.

6G-2

4:15 pm **Impulse Response Estimation Method for Ultrasound Arrays**

Pim van der Meulen[1], Pieter Kruizinga[2], Johannes G Bosch[2], Geert Leus[1]; [1]*Circuits and Systems, Delft University of Technology, Netherlands,* [2]*Biomedical Engineering, Erasmus Medical Center, Netherlands*

Background, Motivation and Objective

Accurate knowledge of the electro-mechanical impulse response for each element in an ultrasound array is important for e.g. model-driven beamforming techniques, coded excitation, etc. Typically, one would use a hydrophone to measure the transmitted pulse of an element excited by a delta-pulse. However, hydrophone setups are expensive, the procedure time is costly, and the measurement is sensitive to the hydrophone position relative to the element. Here we present a procedure to estimate the impulse response for each array element using simple pulse-echo measurements of the elements themselves by means of a new de-autoconvolution algorithm, not involving hydrophones.

Statement of Contribution/Methods

We developed an algorithm that, given an auto-convolved signal $x[n]=h[n]*h[n]$, estimates the original signal $h[n]$. A flat surface parallel to the transducer surface is placed in front of the array. Each element is excited one by one. The flat surface will act as a mirror to the ultrasound waves, so that on element i one measures $x_{i,i}[n]=h_i[n]*h_i[n]$, where $h_i[n]$ is the electro-mechanical impulse response of element *i*. The square root of the DFT of $x_{i,i}[n]$ is a potential solution for $h_i[n]$, but every frequency bin has a sign ambiguity. Note that using the DFT implies $x_{i,i}[n]$ is the result of a circular auto-convolution instead of a linear auto-convolution. Therefore, we only look for solutions $h_i[n]$ of which the circular and linear auto-convolutions are equal, which can be cast as a semidefinite program. Using our de-autoconvolution algorithm, we estimate $h_i[n]$ for each element, and subsequently compute any pulse-echo cross-channel impulse response $h_i[n]*h_j[n]$ as well, which is essential for synthetic aperture techniques.

Results/Discussion

We performed the proposed procedure, using a 5 MHz, 128-element ultrasound array (L7-4 coupled to a Verasonics Vantage system) using a flat perspex surface in water placed 25 mm from the transducer. First two figures: the measured echo signals, as well as the estimated impulse responses are distinctly different. Rightmost figure: the measured cross-channel convolution of two channels *i* and *j* is nearly equal to the signal obtained by convolving the *estimated* impulse responses h_i and h_i. Comparing other cross-channel measurements, we report an average correlation coefficient between the measurement and the estimate of more than 0.97.

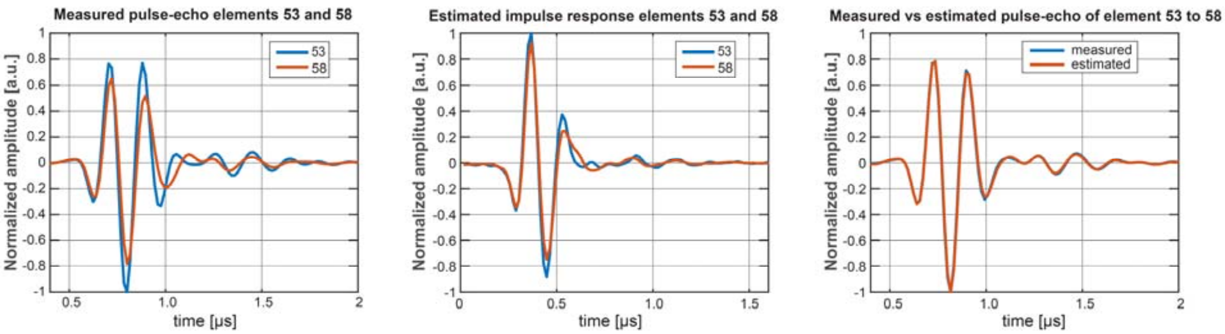

Left: pulse-echo signal for element 53 and 58. Centre: estimated impulse responses computed from the pulse-echo signals. Right: estimated pulse-echo signal (obtained by convolving estimated impulse responses) from channel 53 to 58 compared to an actual pulse-echo measurement.

6G-3

4:30 pm Improvement of the Total Focusing Method Using an Inverse Problem Approach

Ewen Carcreff[1], Nans Laroche[1], Sébastien Bourguignon[2], Dominique Braconnier[1]; *[1]The Phased Array Company, USA, [2]LS2N, France*

Background, Motivation and Objective

Imaging using the total focusing method (TFM) is a popular tool in nondestructive evaluation and it becomes a standard. From full matrix capture, this method consists in focusing at each point of a defined reconstruction zone. It is generally more efficient than conventional phased array focusing that can focus at only a few points. Despite the good quality of TFM images, TFM suffers from a lack of resolution and contrast, in particular when the defects are close or in scattering materials.

Statement of Contribution/Methods

We propose to formalize the TFM algorithm as a linear operation. The contribution of this paper is then to include a sparse penalization to the TFM procedure. The image is therefore considered null with few non zero values, corresponding to flaws or geometry. The final image is obtained by minimizing a penalized least-squares criterion within an iterative procedure.

Results/Discussion

The first example uses data acquired from two close side drilled holes (SDH) in an aluminum block. The proposed algorithm shows good echo separation whereas the reference method has overlapping, also demonstrating resolution improvement. The second example comes from an austenitic stainless steel specimen where scattering noise in high. The proposed method reduces the scattering noise producing contrast improvement.

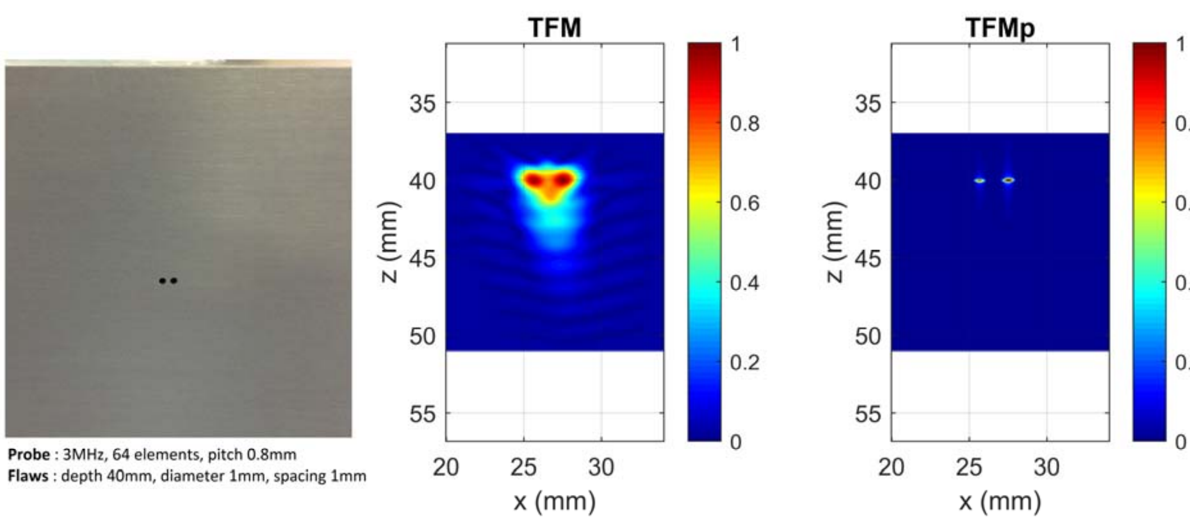

6G-4

4:45 pm Guided Wave Retrieval from Temporally Undersampled Data

Soroosh Sabeti[1], **Joel B. Harley[1]**; [1]*Electrical and Computer Engineering, University of Utah, Salt Lake City, Utah, USA*

Background, Motivation and Objective

Within the realm of structural health monitoring (SHM), employing guided waves as an efficacious means of inspecting structures for potential defects has been steadily gaining ground, owing to the numerous advantages it provides, including accessibility and low cost of transducers as well as suitability for scanning large areas due to minimal attenuation of guided waves. While effective, practical SHM systems will collect and process excessively large data sets from many sensors across structure, over prolonged periods of time (i.e., years to decades). To improve storage efficiency, it is desirable to retrieve information from partial data. Recently, methodologies based on compressive sensing have been proposed to recover guided wave dispersion curves from spatially undersampled experimental data. In this paper, we present a similar technique to estimate dispersion curves and reconstruct wavefields from temporally undersampled data.

Statement of Contribution/Methods

By utilizing a general model derived for Lamb waves propagating in an isotropic medium, we assume a sparse model for a wavefield in the time-wavenumber domain. Given the knowledge that Lamb waves are generally sparse in the frequency-wavenumber (f-k) domain, we use compressive sensing methods, such as orthogonal matching pursuit (OMP), to estimate the desired sparse representation with a limited number of randomly generated time samples from the wavefield.

Results/Discussion

Figure 1(a) shows one simulated temporally undersampled signal from the wavefield, which preserves five percent of the temporal information. Figure 2 depicts the recovered sparse representation of the wavefield in the (f-k) domain (i.e., the dispersion curves). The two dominant propagating modes of the wave and the corresponding curves are visible. Figure 1(b) shows the reconstructed signal from the dispersion curves. We observe a correlation coefficient of approximately 0.95 between the reconstructed signal and the true signal. In this paper, we discuss the benefits and limitations of our method with experimental data.

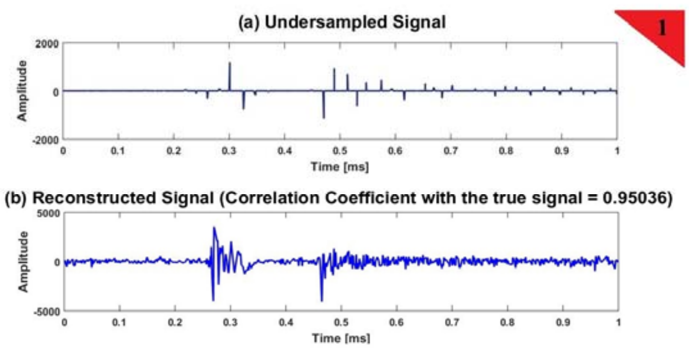

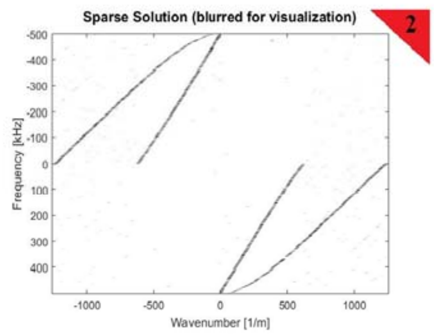

6G-5

5:00 pm Accelarated Guided Waves Inspection Using Compressive Sensing and Local Wavenumber Domain Analysis

Yasamin Keshmiri Esfandabadi[1], Alessandro Marzani[2], Nicola Testoni[1], Luca De Marchi[1]; [1]*Department of Electrical, Electronic and Information Engineering, University of Bologna, Italy,* [2]*Department of Civil, Chemical, Environmental, and Materials Engineering, University of Bologna, Italy*

Background, Motivation and Objective

Many structural health monitoring techniques rely on the full field analysis related to stress guided waves propagation. Such techniques can be quite slow as in general the acquisition of the full wave field and its processing, aimed at extracting damage related information, are time consuming processes. Therefore, strategies to reduce the acquisition time and improve the damage detection and quantification are sought. This research describes a method based on Compressive Sensing (CS) and a local wavenumber estimation technique that can lead to fast scanning and improved damage detection. CS theory [Donoho, IEEE TIT, 2006] states the possibility of reconstructing a signal by feeding a limited number of measurements into an L1 norm minimization procedure. As a prerequisite, the signal must be sparse, i.e. it should be well approximated by a linear superposition of a few atoms of an appropriate basis.

Statement of Contribution/Methods

In the experiments detailed in this work, guided waves are excited with a piezoelectric transducer bonded to the inspected structure and sensed by an air-coupled probe mounted on a CNC machine for horizontal and vertical scanning with the sub-sampling procedure described in [Di Ianni et al, IEEE TUFFC 2015]. First, full wavefields are rapidly reconstructed by applying the CS technique. Then, frequency wavenumber processing is performed to isolate each wave mode and identify the center wavelength. Finally a dedicated masking procedure is implemented to enhance the defect-induced scattering. To image the defect itself, we employed two techniques: the first is based on the Cumulative Kinetic Energy (CKED) [Sohn et al, EWSHM, 2010], and the second one is based on the computation of the wavefield 3D envelope [Flynn et al, NDT&E International, 2013]. Both techniques were combined with Discrete Laplacian operators for improving damage area visualization.

Results/Discussion

The proposed method was applied to two different setups related to: a) an aluminum, and b) a composite plate, emulating defects with a mass. The results demonstrate that the proposed technique allows to reduce the amount of measurements needed and therefore the needed scanning time, as just the 20% of the Nyquist scanpoints were measured, and improves the performance of damage imaging tasks by removing automatically noise artifacts.

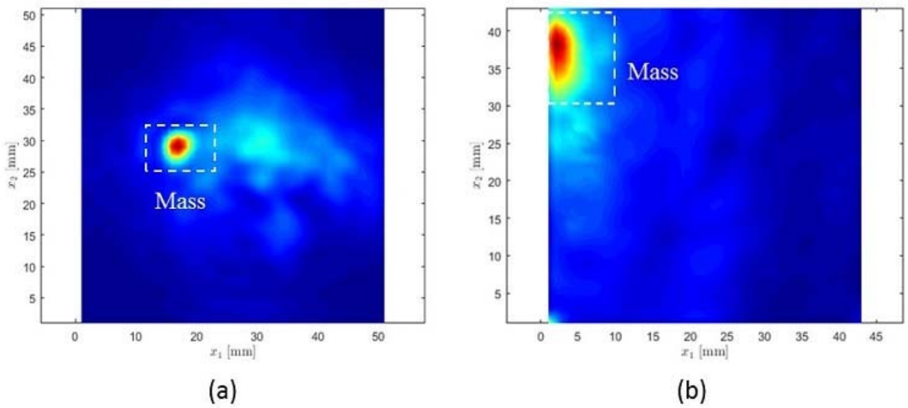

Figure1: Damage detection results: Mass detection in an aluminum plate (a); Mass detection in a composite plate (b);

6G-6

5:15 pm Mbit/Second Communication through a Rock Bolt Using Ultrasound

Johan E. Carlson[1], Jaap van de Beek[1], Medhat Mohamad[1]; [1]*Signals and Systems, Lulea University of Technology, Lulea, Sweden*

Background, Motivation and Objective

In most industrial processes transfer of data and software from or to sensors is an essential part of the monitoring and control systems. Many of the older, wired communication systems have been or are being replaced with wireless alternatives. A number of challenges are associated with this replacement: Radio receivers are subject to interference from other radio sources. Similarly, radio transmitters may cause undesired interference into other equipment and environments. Compared to wired solutions, security becomes an issue as radio communication links are more vulnerable to eavesdropping than wired schemes.

Radio communication with sensors and sensor platforms embedded deep inside large metal structures or fluid tanks may be difficult or even impossible.

The objective of this work is to develop and evaluate a high data-rate communications scheme based on ultrasound, which can be used to transmit wirelessly through solid structures. An example will be given using a one-meter segment of a rock bolt.

Statement of Contribution/Methods

In all digital communications, the propagation path, i.e. the channel has to be known in order to reliably transfer data. From an ultrasound measurement point of view, this is analogous to knowing the combined transfer function of the transducer(s) and the medium. We will show that, adopting a communications scheme known as Orthogonal Frequency Division Multiplexing (ODFM), the channels estimation becomes trivial. We then show using a real-world experiment on a one-meter segment of a rock bolt that using this scheme, we can achieve data rates in excess of one Mbit/s. This example serves to show that ODFM over ultrasound can be used for high data rate transfer in environments where traditional radio communications is not possible, and where retro-fitting wired equipment is impractical or infeasible.

Results/Discussion

The system was evaluated using two off-the-shelf Olympus transducers and a universal software radio platform (USRP) from Ettus Research. Adapting the transmit symbol spectrum to the bandwidth of the transducer, a data rate of approximately 1.3 Mbit/s was achieved, excluding overhead for synchronization and channel estimation (which can be kept low in a fairly static environment). The figure shows a schematic view of the system, with some key system parameters.

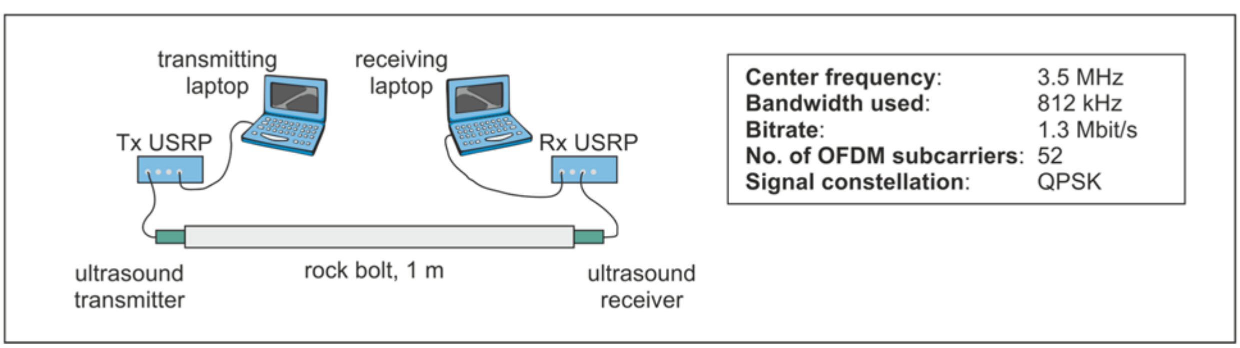

7G - Devices for Therapeutic Ultrasound

Empire Room

Friday, September 8, 2017, 4:00 pm - 5:30 pm

Chair: **Paul Reynolds**
Siemens Healthcare

7G-1

4:00 pm **Integration of Percutaneous Cardiac Catheter for HIFU Ablation and Image Guidance**

Ji Hoon Jang[1], Chienliu Chang[1], Morten Fischer Rasmussen[1], Azadeh Moini[1], Hyo-Seon Yoon[1], Ronald D Watkins[2], Jung Woo Choe[1], Amin Nikoozadeh[1], Douglas Stephens[3], Omer Oralkan[4], Kim Butts Pauly[2], Butrus Khuri-Yakub[1]; [1]*Electrical Enginnering, Stanford University, Stanford, California, USA,* [2]*Radiology, Stanford University, Stanford, California, USA,* [3]*Biomedical Engineering, University of California, Davis, Stanford, California, USA,* [4]*Electrical and Computer Engineering, North Carolina State University, Stanford, California, USA*

Background, Motivation and Objective

Image-guided high intensity focused ultrasound (HIFU) is widely used not only for non-invasive therapy but also as a precise approach for cardiac tissue ablation. However, most HIFU systems use piezoelectric transducers, which are typically bulky due to active cooling, and separate imaging and HIFU transducers, and therefore impractical for catheter-based applications. Taking advantage of a single 2-D capacitive micromachined ultrasonic transducer (CMUT) array, we developed a percutaneous cardiac catheter that can switch between ultrasound imaging mode and HIFU ablation mode.

Statement of Contribution/Methods

The catheters are equipped with an application-specific integrated circuit (ASIC) and a 32 × 32-element CMUT array. Both of ASIC and CMUT are flip-chip bonded to a custom-designed flexible printed circuit board (flex) via 100-um and 80-um solder balls. Then, the flex legs are folded and terminated with pads for a micro zero insertion force (ZIF) connector as shown in the figure, allowing easy assembly replacement without the extra cost of coaxial cable termination. Next, the micro coaxial cables are assembled at the end of the micro ZIF connectors. After assembling with a 3-D printed tip and encapsulating with polydimethylsiloxane (PDMS), the catheter is finalized in a 22-mm shaft.

Results/Discussion

We have successfully integrated the dual-mode flex assembly into a catheter shaft and validated the functionality of both modes in bench-top tests with the back-end system. The back-end system includes an 8-channel phase generating system for HIFU, an image reconstruction system, and a field-programmable gate array (FPGA). The FPGA sends the imaging beam patterns and switches the operating mode. The imaging system processes the data to reconstruct real-time ultrasound images. The phase generating system drives eight HIFU channels for F#1 focal depth. We are currently working on preparing the setup for an animal study. This work was supported by the National Institutes of Health (NIH) under grant R01HL117740.

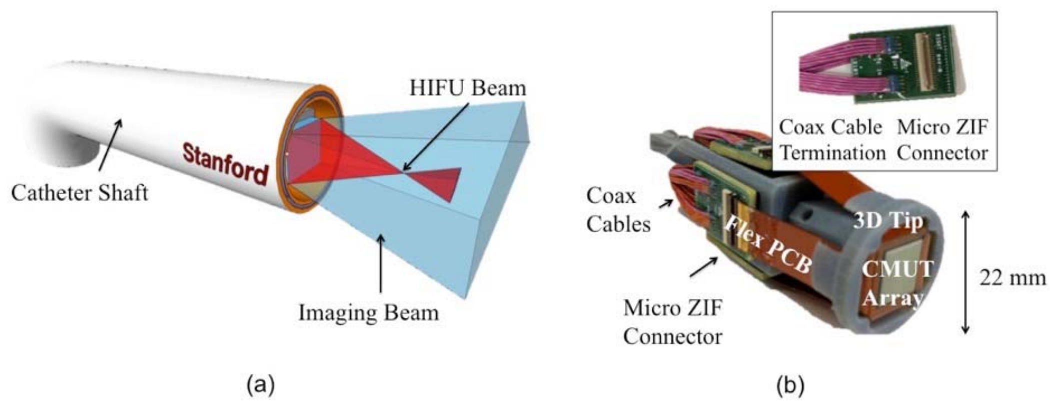

Fig 1. (a) Conceptual drawing of the dual-mode catheter. (b) Optical picture of the assembled dual-mode catheter.

7G-2

4:15 pm **Mechanical Wobbling High Intensity Focused Ultrasound (HIFU) Transducer for Volumetric Ultrasound Guided Treatment of Uterine Fibroids**

Euna Choi[1], Wonseok Lee[2], Jeongdong Woo[2], Yongrae Roh[1]; [1]*School of Mechanical Engineering, Kyungpook National University, Daegu, Korea, Republic of,* [2]*Probe Development Team, Alpinion Medical Systems Co., Ltd., Seoul, Korea, Republic of*

Background, Motivation and Objective

Uterine fibroids are noncancerous growths that develop in or just outside a woman¡¯s uterus. For treatment of these, high intensity focused ultrasound (HIFU) surgery is gaining more and more popularity. Presently, two representative types of HIFU treatment are used: magnetic resonance guided and ultrasound (US) guided HIFU treatment depending on the method to monitor the treatment. This work is about the development of a new transducer for a more versatile US guided HIFU system to treat uterine fibroids. Normally, HIFU treatment of the uterine fibroids has been carried out with an extracorporeal transducer mounted on abdomen. Use of the extracorporeal transducer requires the US to be delivered through an external surface of a human body, which causes unnecessary exposure of interstitial cells to the high intensity US. In order to resolve the problem, the HIFU needs to be insonated into only the tumors. For that purpose, the HIFU transducer incorporating both a treatment module and a US imaging module should be small enough to be inserted into vagina while providing enough acoustic power to heat the uterine fibroid tumors.

Statement of Contribution/Methods

In this work, a new HIFU transducer has been developed for volumetric ultrasound guided treatment of uterine fibroids. The transducer is composed of an imaging module (6.8 MHz, 84 elements, micro-convex array) and a HIFU module (3 MHz, ten channels, annular array of concave geometry, 30 mm in diameter). The imaging module is installed at the center of the HIFU module. The transducer also incorporates a mechanical wobbling mechanism that can rotate the assembly of the imaging and HIFU modules along azimuthal directions. The whole transducer is rotated again by another external mechanical system to control the orientation of the transducer along elevation directions. The transducer can do both HIFU treatment and US imaging of the uterine fibroids in three dimensions, which is the first in its kind. The HIFU treatment module and micro-convex imaging mode have been designed through finite element analysis with PZFlex.

Results/Discussion

Based on the design, a prototype of the transducer was fabricated and its performance was measured, which showed excellent agreement with the design. The annular HIFU treatment module was made of a 1-3 piezocomposite material. The focus of the HIFU treatment module was steerable from 30 to 50 mm from the zenith of the concave treatment module. The total acoustic power from the treatment module was 55 Watts and the acoustic pressure at the focus was 18 MPa. The imaging module had the field of view of 90 degrees to do clear monitoring of the lesion. The rotating mechanism wobbled the module assembly at the speed of 1 Hz and showed negligible mechanical backlash even after wobbling two million times. These results confirmed the efficacy and effectiveness of the new HIFU transducer for volumetric treatment of uterine fibroids. The HIFU transducer is presently under preclinical tests with pigs.

7G-3

4:30 pm Preliminary Investigation of Dual Mode CMUT Probe for Ultrasound Image Guided HIFU Therapy

Christopher Bawiec[1,2], W. Apoutou N'Djin[1,2], Guillaume Bouchoux[1,2], Nicolas Sénégond[3], Nicolas Guillen[4], Jean-Yves Chapelon[1,2]; [1]*Inserm, U1032, LabTau, Lyon, Rhone-Alpes, France,* [2]*Univ Lyon, Université Lyon 1, Lyon, France,* [3]*Vermon, Tours, France,* [4]*Edap TMS, Vaulx-en-Velin, France*

Background, Motivation and Objective

The primary aim of this work was to develop and study the potential of Capacitive Micro-machined Ultrasound Transducers (CMUTs) for dual-mode ultrasound therapy and imaging. This was investigated in the context of Ultrasound-guided High Intensity Focused Ultrasound (USgHIFU) designed for endocavitary HIFU tissue ablation of the prostate gland. The hypothesis is that this CMUT design could offer potential advantages over currently used piezoelectric probes such as ease of miniaturization, increased elements for improved imaging and more control over electronic focusing allowing focal therapy.

Statement of Contribution/Methods

A planar dual mode CMUT probe consisting of a 3 MHz, 64 element annular array for therapy and 7 MHz, 256 element linear array for imaging (Fig. 1A) were investigated in simulation and experimentally for validating the probes ability to create mm sized lesions from 3-7cm using electronic focusing. Numerical models of the pressure field and tissue heating simulations were performed and compared with an existing piezo-based geometrically focused annular array HIFU probe (16 rings) with a hole in the center that possesses a curvilinear imaging array (128 elements). To validate the modelling and the focusing capabilities, pressure field hydrophone measurements were performed. To validate the HIFU capabilities, radiation force measurements were performed, followed by the creation of lesions in thermally-sensitive, optically-transparent tissue mimicking phantoms.

Results/Discussion

Simulations showed that the planar annular CMUT design could dynamically focus from 3-7cm which matched well with the experimentally obtained pressure field data (Fig. 1B). Radiation force balance measurements confirmed the desired 5 W/cm^2 surface acoustic intensity. The generation of lesions in the phantoms confirmed the ability to deposit energy focally and to create lesions in non-perfused tissues. This CMUT prototype will require further investigation for determination of the robustness of this technology and the ability to create lesions perfused tissues in vivo, yet according to the modelling and experimental validation thus far, this CMUT design shows promise for improved USgHIFU treatment strategies.

This project was supported by the French Single Interministerial Fund (FUI, 2013).

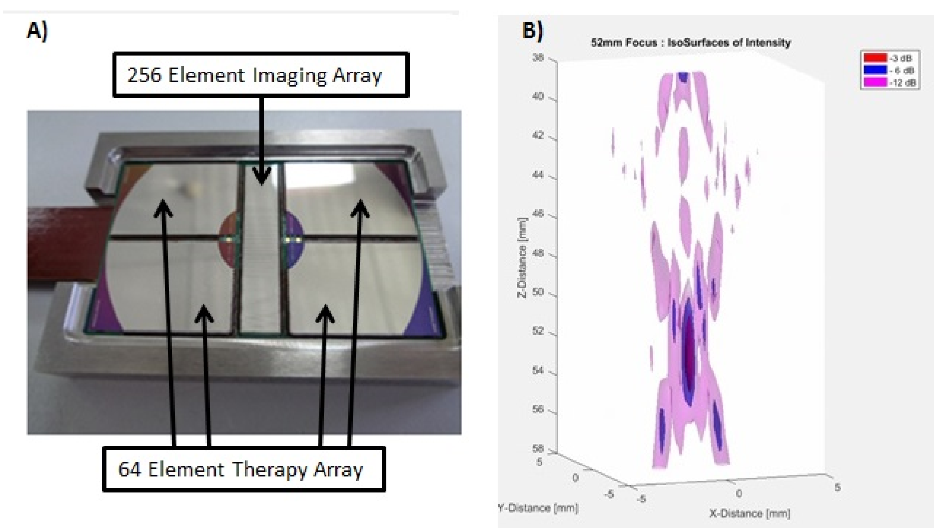

7G-4

4:45 pm A Fully-Automated Insonation System for *In Vitro* Investigations of Ultrasound-Mediated Targeted Drug Delivery

Fraser Stewart[1], Yangminghao Liu[2], Pierre Roncin[3], Ian P Newton[1], Zhihong Huang[2], Inke Näthke[1], Sandy Cochran[4]; [1]*School of Life Sciences, University of Dundee, Dundee, United Kingdom,* [2]*School of Science and Engineering, University of Dundee, Dundee, United Kingdom,* [3]*School of Engineering, ESEO, Angers, France,* [4]*School of Engineering, University of Glasgow, Glasgow, United Kingdom*

Background, Motivation and Objective

Focused ultrasound (US) produces clinically useful bioeffects such as hyperthermia, cavitation and radiation force. A focused US mediated targeted drug delivery (UmTDD) capsule endoscope was developed previously to explore treatment of gastrointestinal conditions such as Crohn's disease (SonoCAIT [1]). This included focused US transducers to enhance drug uptake into the bowel wall. In further development, a benchtop system was developed [2] using the same ultrasound sources. However, this system was limited and could only insonate single samples, required significant human intervention, and could only work on therapeutic agents in suspension rather than introduce them selectively. This paper describes the development of a fully automated system to overcome these issues and describes the development of application-specific focused US transducers.

Statement of Contribution/Methods

The automated system, Fig. 1a, comprises three translation stages (Velmex Inc., NY, USA) mounted on an optical breadboard (Thorlabs Inc., NJ, USA). Transducers were held in an additively-manufactured bracket (MakerBot, NY, USA) and attached to the stage carriage. Transducers were driven by a waveform generator (DG4102, RIGOL Technologies, Beijing, China) and therapeutic agents were delivered by syringe pump (NE-1000, New Era Pump Systems Inc., NY, USA). The cell plate holder was mounted on an optical base and raised 50 mm by mounting posts (Thorlabs Inc., NJ, USA). A LabView (National Instrument, TX, USA) interface controlled the system allowing different parameters to be applied in each well.

Focused US transducers, Fig. 1b, were constructed with perforated PZ26 spherical-section bowls (Meggitt Sensing Systems, Kvistgaard, Denmark) with outer dia., OD = 5 mm, 1 mm dia. centre hole, radius of curvature, R_c = 15 mm, and operating frequency, f = 4 MHz. The transducers had additively-manufactured cases (Stratasys Ltd, MN, USA) with SMA connectors.

Results/Discussion

The transducers provided acoustic pressure, $10 < p_{ac} < 170$ kPa, with focal zone beam dia., BD = 2 mm, and acoustic power, $10 < P_{ac} < 140$ mW. Caco-2 cells, an FDA approved model of the small bowel, were insonated and fluorescent particles (FP) were introduced. The cells were visualised by immunofluorescence and FPs were found to be inside the cells.

[1] Stewart et al. IEEE IUS, Oct. 2015.

[2] Stewart et al. IEEE IUS, Sept. 2016.

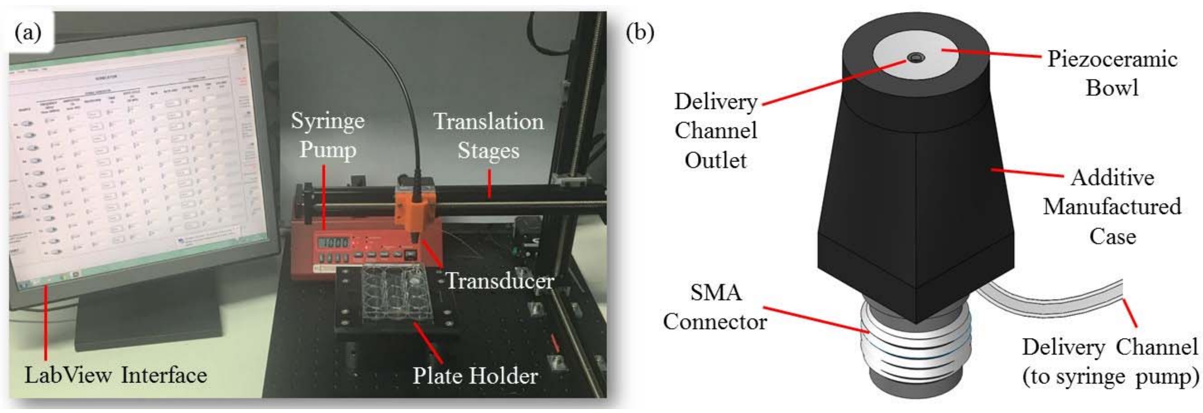

7G-5

5:00 pm Optical Fiber Laser-Generated-Focused-Ultrasound Transducers for Intravascular Therapies

Jinwook Kim[1], Wei-Yi Chang[1], Huaiyu Wu[1], Xiaoning Jiang[1]; [1]*Mechanical Engineering, North Carolina State University, Raleigh, North Carolina, USA*

Background, Motivation and Objective

Catheter-delivered ultrasound has been widely utilized for intravascular therapies such as thrombolysis, drug delivery, and plaque removal. High amplitude pressure is required for cavitation induced-microstreaming, which is considered main factor for therapeutic efficiency. Precise spatiotemporal control of insonation is important to relieve concerns on ultrasound-induced damaging of surrounding healthy tissue and vessel wall. Recent advances in laser-generated focused ultrasound (LGFU) have demonstrated precisely controlled ultrasound therapies owing to its capability of generating high-pressure (up to 20 MPa), high-frequency (>10 MHz) shock waves at a tight focal spot. Despite of the promising intravascular ultrasound therapies, to date, relatively large (diameter > 12 mm) LGFU transducers composed of carbon-based composite lens have demonstrated their capability only for extracorporeal ultrasound therapies. We hypothesize that the optical fiber LGFU transducer can be used for precise and efficient intravascular therapies taking advantage of high-frequency, high-amplitude shock waves as well as the optically efficient, small aperture optical fibers (Fig. A).

Statement of Contribution/Methods

We developed optical fiber LGFU transducers for intravascular therapies. Miniaturized transducers with a diameter of 1 mm PDMS lens was designed and fabricated by using carbon nanoparticles (CNP)/PDMS composite film (Fig. B). The PDMS lens (approximated radius-of-curvature of 1 mm) was fabricated by the dip-coating method, and the CNP composite film was coated on the concave surface by using a candle soot process. The fabricated transducer was integrated with an optical fiber (diameter of 0.6 mm), followed by acoustic characterizations to evaluate the wave form, center frequency, and pressure output.

Results/Discussion

We confirmed that the optical fiber CNP/PDMS LGFU transducer with a custom PDMS lens is able to generate 11 MHz, high pressure shock wave (peak pressure of 16 MPa) at 0.5 mm away from the transducer surface (Fig. C). The corresponding mechanical index of the achieved pressure output is 1.9, which is sufficient to induce inertial cavitation in microbubble-mediated therapies. The used laser input was only 1.5 mJ of a 532 nm pulsed laser (6 ns pulse duration), thus higher pressure output can be possible with higher laser input.

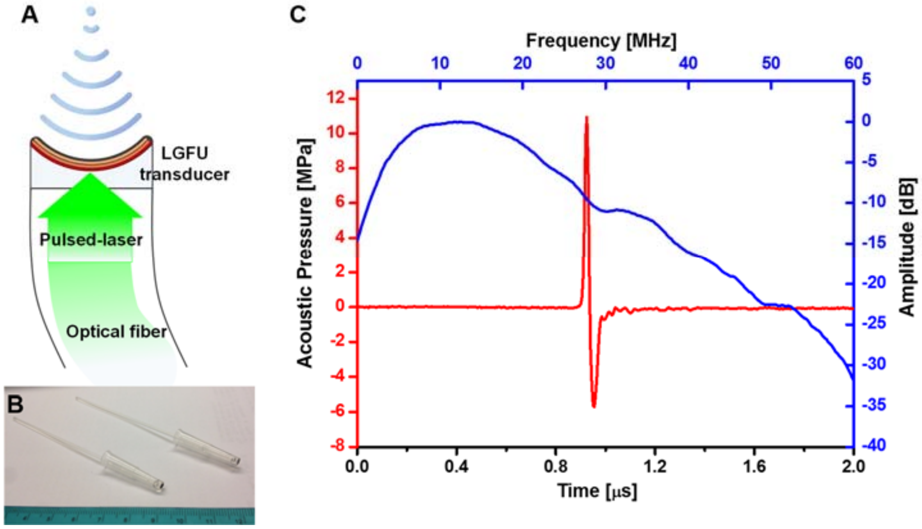

7G-6

5:15 pm Development of Forward-Looking Ultrasound Transducers for Microbubble-Aided Intravascular Ultrasound-Enhanced Thrombolysis

Jinwook Kim[1], Brooks D. Lindsey[2], Wei-Yi Chang[1], Paul A. Dayton[2], Xiaoning Jiang[1]; [1]*Mechanical Engineering, North Carolina State University, Raleigh, North Carolina, USA,* [2]*Biomedical Engineering, University of North Carolina, Chapel Hill, North Carolina, USA*

Background, Motivation and Objective

Pulmonary embolism (PE) is the third-leading cause of death from cardiovascular disease. Currently, PE is treated via catheter-delivered, ultrasound-enhanced thrombolysis using side-fired, low-intensity ultrasound energy (0.5 W/cm^2) at ~2 MHz to reduce the required dose of thrombolytic drugs because of the enhanced drug penetration into the clot. However, several clinical studies have shown that the relatively high-frequency (2 MHz), low-power ultrasound is insufficient for improving thrombolytic efficacy. Low-frequency (< 1 MHz), higher intensity ultrasound yields a higher thrombolytic rate, however, the propagation of ultrasound toward the vessel wall (side looking) results in increased likelihood of healthy tissue damage from overexposure of acoustic energy. We hypothesize that a forward-looking intravascular ultrasound transducer design will enable generation of higher pressures at a lower operating frequency, which can enhance the lytic rate and reduce the required dose of the drug.

Statement of Contribution/Methods

We designed forward-looking transducers for intravascular microbubble-mediated ultrasound-enhanced thrombolysis. Transducers were fabricated with planar and concave apertures for integration with an 8F-catheter that has a bubble-injection tube (Figure A). These transducers operate at 620 kHz and are composed of 6 layers of PZT-5A ceramic with an aperture diameter of 1.5 mm. *In vitro* tests with bovine blood clots were conducted using the prototype transducers. 200 mg ± 10% clot samples were positioned in a vessel-mimicking tube, and exposed to ultrasound with an input condition of 80 V, 10%-duty cycle at 620 kHz. Microbubbles were injected at a concentration of 1x10^7/mL at a flow rate of 0.1 ml/min. The clot mass was measured before and after the 30 min-treatment.

Results/Discussion

We observed significant reductions in clot mass for both planar and concave apertures after 30 min treatments relative to the control case (no ultrasound, Figure B and C). Despite the different focal spot sizes, both apertures yielded an average thrombolytic rate of ~0.7 %/min, as the planar aperture has a larger cavitation zone but lower peak negative pressure compared to the concave aperture (i.e. 320 vs. 790 kPa). Further in vitro tests will evaluate the efficacy of these transducers with a low dose of thrombolytic agent (<25% of typical clinical dose).

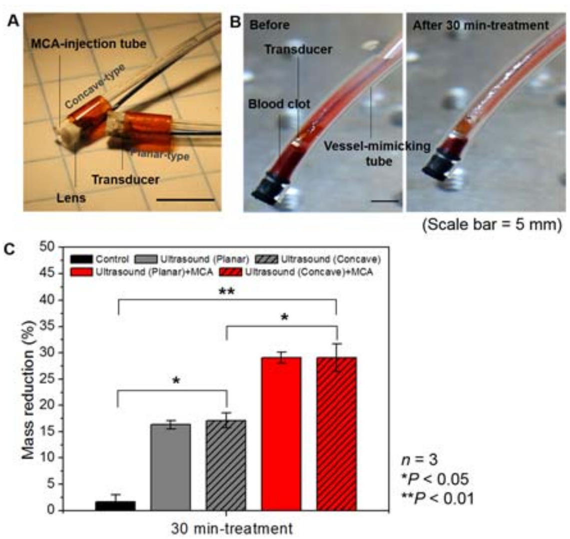

P1-B1 - MBB: 3D

Exhibit Hall

Friday, September 8, 2017, 9:30 am - 4:00 pm

Chair: **Matthias Bo Stuart**
Technical University of Denmark

P1-B1-1

Improved Focusing Method for 3-D Imaging Using Row–Column Addressed 2-D Arrays

Hamed Bouzari[1], Mathias Engholm[2], Matthias Stuart[1], Erik Thomsen[2], Jørgen Arendt Jensen[1]; [1]*Electrical Engineering, Technichal University of Denmark, Lyngby, Denmark,* [2]*Micro- and Nanotechnology, Technichal University of Denmark, Lyngby, Denmark*

Background, Motivation and Objective

A row–column-addressed (RCA) 2-D array can be interpreted as two orthogonal 1-D arrays. Since the transmit and receive 1-D arrays are orthogonal to each other, only one-way focusing is possible in each transmit or receive plane. By transmitting with row elements and receiving the echoes through column elements, a rectilinear volume in front of the array can be beamformed. This study suggests to use the RF-data received by the row elements as well as the column elements to improve the focusing. This study investigates the performance of the new focusing scheme based on simulations in Field II in terms of full-width-at-half-maximum (FWHM) and cystic resolution (CR).

Statement of Contribution/Methods

In the proposed method, at each point an improved focusing profile in transmit direction and a one-way focusing profile in receive direction can be achieved. An improved focusing in the transmit direction is possible since the transmit and receive focus lines are both in the same plane and therefore the effective aperture is squared. This is achieved by taking the minimum value of the two beamformed data sets. In a similar way, by switching the transmit and receive elements, an improved profile in the other direction is produced. Ultimately, by summing the two beamformed volumes in phase, a full volume with an improved focusing profile in each lateral direction is produced compared to traditional row-column focusing. The performance of the proposed focusing method is investigated using a λ/2-pitch 3 MHz 62+62 RCA 2-D array. A synthetic aperture imaging sequence with single element transmissions is designed for imaging down to 14 cm at a volume rate of 44 Hz. On each emission a three-cycled sinusoidal impulse with a center frequency of 3 MHz is transmitted.

Results/Discussion

Using the proposed focusing method has improved the FWHM and CR at all depths compared to the normal RCA beamforming method, specifically at 20 mm depth by 17% and 12%, respectively. The top row in the figure shows a point target beamformed with normal RCA method, and the bottom row shows the proposed focusing method. In this method, the acquisition volume rate is halved compared to the normal RCA beamforming and also it is susceptible to motion artifacts. However, due to the provided increase in the spatial resolution, the number of emissions can get lowered, therefore the volume rate can be recovered.

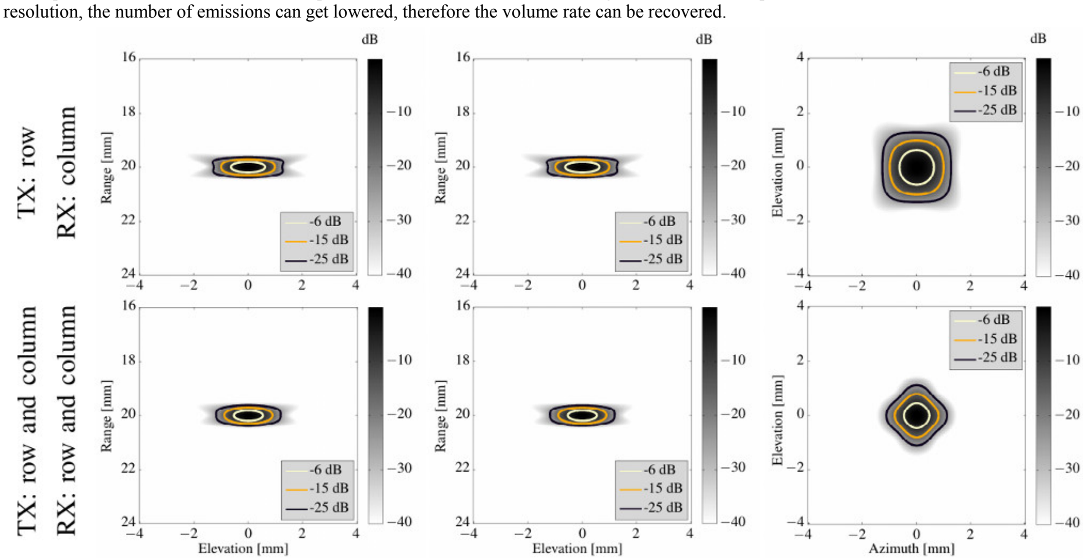

P1-B1-2

3D Diverging Waves with 2D Sparse Arrays: A Feasibility Study

Emmanuel Roux[1], François Varray[2], Lorena Petrusca[2], Christian Cachard[2], Piero Tortoli[1], Hervé Liebgott[2]; [1]*Department of Information Engineering, Università Degli Studi di Firenze, Firenze, France,* [2]*Univ.Lyon,-INSA-Lyon, UCBL1, UJM-Saint Etienne, CNRS, Inserm, CREATIS UMR 5220, U1206, F-69100, Villeurbanne, France*

Background, Motivation and Objective

Very high frame rates can be reached both in 2D and 3D ultrasound imaging thanks to diverging waves (DWs) transmission. Up to now 3D ultrafast imaging has been performed controlling full 2D arrays with thousands of active elements which cannot be directly controlled by scanners with limited number of channels. The motivation here is to perform 3D ultrafast imaging with 128, 192 or 256 active elements. We recently addressed a similar issue in focused mode [Roux et al. IEEE UFFC17]: three optimal arrays (opti128, opti192 and opti256) were obtained by reducing the amount of energy out of the main lobe at multiple depths. In this work we experimentally investigate the feasibility of acquiring 3D volumes at high frame rate by transmitting DWs with the opti128, opti192 and opti256 sparse arrays under the hypothesis that these optimal arrays for focused imaging are also the most adequate sparse configurations to produce well resolved and artifactless virtual sources based on time reversal principle.

Statement of Contribution/Methods

The 1024 (32x32) elements of a 3 MHz array made by Vermon were individually driven by four synchronized Verasonics Vantage 256 systems. The systems were programmed to transmit 2.5-cycle sine bursts at 3 MHz. The evaluated image was made by compounding 25 images produced by 5x5 virtual sources located at 25 mm behind the array with span ±15° in both azimuth and elevation. Six arrays were compared: opti128, opti192, opti256, an array whose active elements where randomly selected (rand256) and two references (REF716 and REF1024). The circular dense array REF716 corresponds to the full 32x32 REF1024 array without the corner elements. The comparison criteria were the full width at half maximum (FWHM) and the contrast to noise ratio (CNR).

Results/Discussion

The results are reported in Table 1. The performance of rand256 in resolution is very close to REF1024 and even better than REF716 whereas the optimized arrays (opti128, opti192 and opti256) yield a resolution about 30 % coarser. However opti256 yields +1dB CNR improvement compared to rand256. The REF716 array is very competitive with REF1024 (+0.3 mm, -0.9 dB) using only 70% of the active elements. As a conclusion, is has been shown that 3D ultrafast imaging can be performed using 2D sparse arrays but potential improvements may be achieved with dedicated optimization e.g. cost function to homogenize DW wavefront.

TABLE I: FULL WIDTH AT HALF MAXIMUM - FWHM (AVERAGED OVER THREE SCATTERERS LOCATED AT DEPTHS 20, 40, 60 MM) AND CONTRAST-TO-NOISE RATIO (CNR) EVALUATED ON IMAGES OF FIGURE 1.

	opti128	opti192	opti256	rand256	REF716	REF1024
Lat. resolution (mm)	2.8	2.8	3.0	1.9	2.1	1.8
CNR (dB)	2.8	1.4	6.6	5.6	9.8	10.7

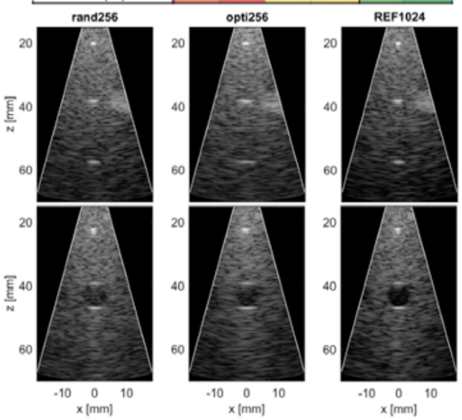

Figure 1 *In vitro* 3D diverging wave image slices for resolution (top line) and contrast (bottom line) evaluation comparison between two sparse arrays (opti256 and rand256) and the reference array (REF1024). The dynamic range is 60 dB.

P1-B1-3

Fourier-based 3D Ultrafast Ultrasound Imaging with Diverging Waves: In Vitro Experiment Validation

Miaomiao Zhang[1], François Varray[1], Lorena Petrusca[1], Denis Friboulet[1], Hervé Liebgott[1], Olivier Bernard[1]; [1]*Univ Lyon, INSA-Lyon, Université Claude Bernard Lyon 1, UJM-Saint Etienne, CNRS, Inserm, CREATIS, Villeurbanne, France*

Background, Motivation and Objective

Ultrafast imaging based on diverging wave (DW) is an active area of research in ultrasound sectorial acquisition because of its capacity of reaching high frame rate. Recently, we have introduced a 3D Fourier-based formalism for the reconstruction of 3D sectorial images with DW insonifications and validated with numerical simulations [Zhang et al. IUS 2016]. The proposed method can provide comparable image quality as DAS but with a much lower computational complexity. This study aims to experimentally verify these theoretical conclusions in vitro.

Statement of Contribution/Methods

A 32-by-32 matrix array centered at 3 MHz with a 0.3 mm pitch (Vermon, Tours, France) interfaced with 4 Verasonics systems was used to transmit 3D DW sequences and acquire the reflected echoes. The experiment was performed on an ultrasound phantom (CIRS model: 054GS). Each DW was emitted from a virtual source point with an angular aperture of 90º and a sub-aperture of 16×16 elements as in [Provost et al. 2014]. The received rawdata was post-processed in Matlab using the proposed Fourier-based algorithm in [Zhang et al., IUS 2016].

Results/Discussion

Figure1 displays the orthogonal slices along x-z direction of the volumetric images reconstructed from the proposed Fourier-based method using 1 and 81 DWs, respectively. This result shows, visually, the image quality (i.e. both lateral resolution and image contrast) can be improved with 81 DW for compounding, which is consistent with what have been observed from simulations [Zhang et al., IUS 2016].

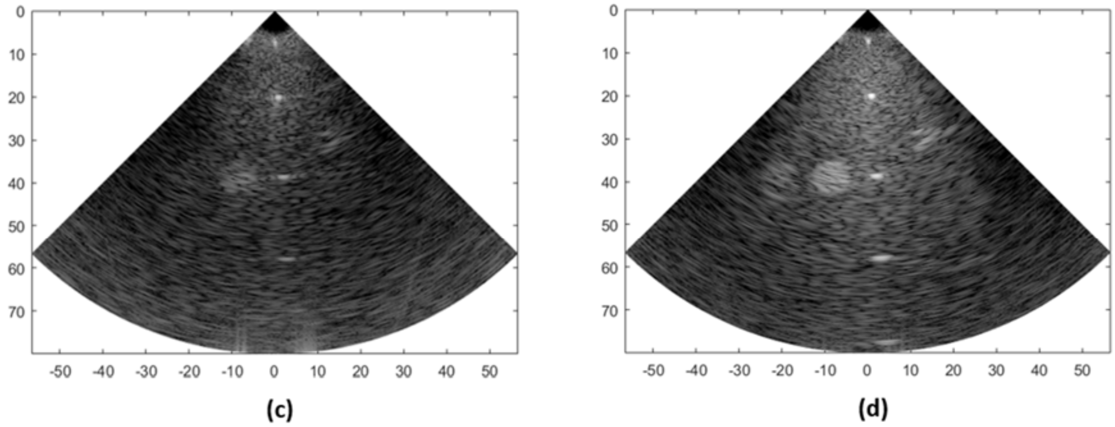

Figure1. Orthogonal slices along x – z direction of the reconstructed volumes from the proposed Fourier-based method using (a) 1DW and (b) 81 DW, respectively.

P1-B1-4

High Volume Rate 3D Ultrasound Imaging Based on Synthetic Aperture Sequential Beamforming

Jian Zhou[1], Siyuan Wei[1], Richard Sampson[2], Rungroj Jintamethasawat[3], Oliver D. Kripfgans[3], J. Brian Fowlkes[3], Thomas F. Wenisch[2], Chaitali Chakrabarti[1]; [1]*School of Electrical, Computer and Energy Engineering, Arizona State University, Tempe, Arizona, USA,* [2]*Department of Electrical Engineering and Computer Science, University of Michigan, Ann Arbor, Michigan, USA,* [3]*Department of Biomedical Engineering and Radiology, University of Michigan, Ann Arbor, Michigan, USA*

Background, Motivation and Objective

Synthetic Aperture Sequential Beamforming (SASB) [1] divides the beamforming process into two stages so that only the first stage needs to be done in the front-end and the compressed data for processing the second stage is computed off-chip. However, 3D SASB suffers from low volume rate. Our objective is to increase the volume rate of 3D SASB without increasing the front-end computational rate.

Statement of Contribution/Methods

In 3D SASB, volume rate is a function of the number of transmit events and the ultrasound signal's round-trip propagation time. To increase the volume rate, we propose to fire several subapertures simultaneously, resulting in a proportional increase in the front-end's computational rate. Since the number of computations in the first stage is proportional to the number of transducers in the receive subaperture, we propose to use sparse arrays to reduce the number of such elements. Our method is based on the bin-based random array [2], which reduces grating lobes at the expense of increased sidelobes. We use simulated annealing to optimize the locations of transducer elements within each bin, to mitigate the sidelobes in the directions of other simultaneous firings. As a result, the image quality due to sparse arrays is comparable with that due to uniformly distributed arrays which have higher computational complexity.

Results/Discussion

We present results of point targets computed using Field II with a center frequency of 4 MHz and subaperture size of 32x32. The full width at half magnitude (FWHM) shows that the proposed method using 256 elements and 4 simultaneous firings has comparable resolution with the original 3D SASB system. And the lateral sidelobe level (LSLL) of the proposed method are still below -40 dB which is the dynamic range. Compared to the baseline scheme which has a volume rate of 11.4 Hz, the proposed scheme operates with 1/4 the receive elements and has a volume rate of 45.6 Hz with no increase in the computational rate in the front-end.

[1] J. Kortbek, J. Jensen and K. Gammelmark, "Sequential beamforming for synthetic aperture imaging", Ultrasonics, vol. 53, no. 1, pp. 1-16, 2013.

[2] W. Hendricks, "The totally random versus the bin approach for random arrays", IEEE Trans. on Antennas and Propagation, vol. 39, no. 12, pp. 1757-1762, 1991.

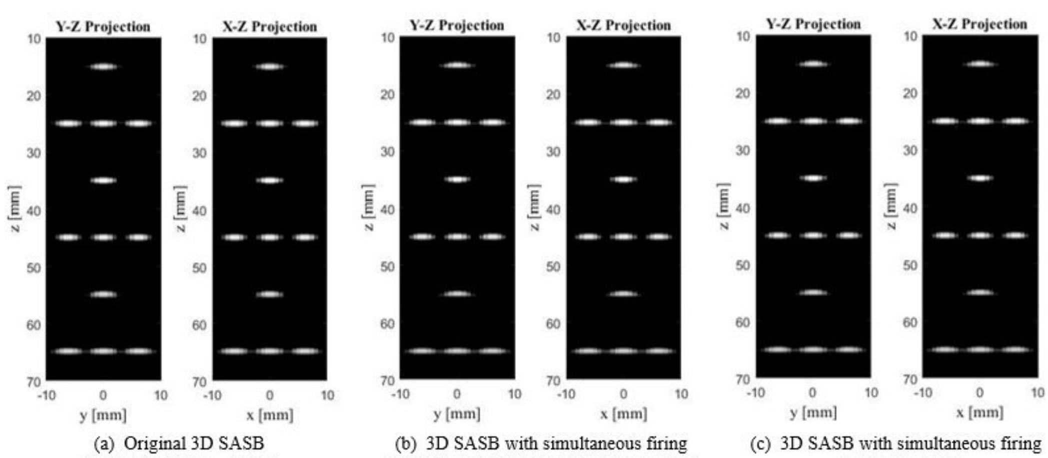

(a) Original 3D SASB
Average FWHM = 2.3mm
LSLL at 15mm, 35mm, 55mm:
-43 dB, -80 dB, -78 dB

(b) 3D SASB with simultaneous firing and uniformly distributed transducer array
Average FWHM = 2.3mm
LSLL at 15mm, 35mm, 55mm:
-41 dB, -75 dB, -52 dB

(c) 3D SASB with simultaneous firing and sparse array
Average FWHM = 2.3mm
LSLL at 15mm, 35mm, 55mm:
-41 dB, -52 dB, -45 dB

P1-B1-5

Real-time Anatomical Imaging of the Heart on an Experimental Ultrasound System

João Pedrosa[1], Vangjush Komini[1], Jan D'hooge[1]; [1]*KU Leuven, Belgium*

Background, Motivation and Objective

Fast cardiac imaging requires a reduction of the number of transmit events. This is typically achieved through multi-line-transmission (MLT) and/or multi-line-acquisition (MLA) techniques. However, restricting the field-of-view (FOV) to the anatomically relevant domain, e.g. the myocardium, can increase frame rate (FR) further. Using computer simulations, we previously proposed an anatomical scan sequence by performing automatic myocardial segmentation on conventional B-mode images and feeding this information back to the scanner in order to define a fast myocardial scan sequence. The aim of this study was to implement and test this approach experimentally.

Statement of Contribution/Methods

Ultrasound imaging was performed using HD-PULSE, an experimental fully programmable 256 channel ultrasound system equipped with a 3.5MHz phased array. A univentricular PVA phantom was connected to a pump to simulate the cardiac cycle and imaged from an apical view using a 2MLT 2MLA approach (FR 150Hz). The B-mode images were segmented real-time using an in-house developed algorithm (BEAS) in order to quantify the percentage of each scan line covering the myocardium. Based on this coverage function, the anatomical FOV was automatically defined by excluding scan lines with smaller myocardial coverage while retaining a predefined overall myocardial coverage T. An identical experiment was subsequently conducted on a volunteer.

Results/Discussion

Fig. 1a and b show an example of a real-time segmented B-mode and the associated myocardial coverage function at two time points in the cardiac cycle. Based on this function, the anatomical FOV was automatically defined resulting in Fig. 1d (T=85%) thereby increasing FR 2.3 times to 350Hz. Fig. 1c and f show the in vivo results with the anatomical scan running at a FR of 220Hz. Obviously, T will compromise FOV against FR according to the relation in Fig. 1e. Although the anatomical image preferably excludes the apical cap of the ventricle, this region is often unanalyzable due to near field clutter anyway. In comparison to other techniques such as diverging waves this method has the advantage that it is able to maintain the spatial resolution and SNR/CNR of conventional ultrasound imaging while operating at competitive FR.

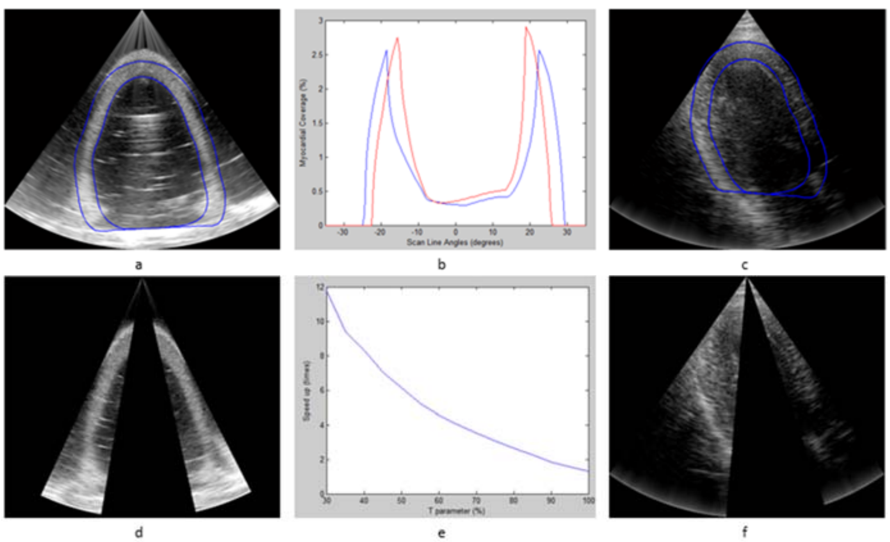

P1-B1-6

Multi-line Transmission for 3d Ultrasound Imaging: An Experimental Study

Emilia Badescu[1], Denis Bujoreanu[1], Lorena Petrusca[1], Denis Friboulet[1], Hervé Liebgott[1]; [1]*Univ.Lyon, INSA-Lyon, UCBL1, UJM-Saint Etienne, CNRS, Inserm, CREATIS UMR 5220, U1206, Lyon, France*

Background, Motivation and Objective

Achieving a high frame rate in echocardiography is highly important for quantifying the short phases of the cardiac cycle that contain valuable information for medical diagnosis. Additionally, the 3D quantitative assessment of the heart would significantly improve the current measurements used in daily clinical routine. Nevertheless, obtaining ultrafast images remains a challenge due to the trade-off between the image quality and a high frame rate, especially when volumetric data is acquired. Among the current ultrafast imaging methods, multi-line-transmit imaging (MLT) provides an increased frame rate but in the same time mostly preserves the image quality. However, the current implementation of this method in 3D proposed by Ortega et al. [IEEE TUFC 2016] is based on generating the MLT data synthetically by summing up the raw data before beamforming. In this paper we present the first real-time implementation of the MLT in 3D ultrasound.

Statement of Contribution/Methods

Multi-line-transmission was performed by dividing the angular aperture into three regions. Then, due to practical limitations, three equally spaced focused beams were transmitted simultaneously in the first YZ plane of the first region. Once the transmission for a full YZ plane was completed, the process was repeated for the first YZ plane of the second region. The same steps were followed till the full volume was insonified. Data acquisition was performed using four Verasonics systems synchronized to drive a 32x32 matrix probe. A transmit frequency of 2.97 MHz was used and the images were acquired using a sampling frequency of 11.9 MHz. The focal point was set to 6.7 cm depth along 27 different angles in elevational direction (YZ) and 30 angles in azimuthal direction (XZ) between -20º and 20º.

Results/Discussion

The contrast and the resolution assessment, performed on a CIRS ultrasound phantom (Figure 1) showed a contrast of 6.36 dB and a mean axial (lateral) resolution of 0.9 mm (1.77 mm) measured for different depths. These values are comparable with those obtained for a 3D focused sequence obtained by using the same emission parameters. The results indicate the potential of MLT 3D for achieving high contrast and resolution while increasing the frame rate. This study thus demonstrates the feasibility of 3D MLT in real-time and extends its possible applications to dynamic cardiac imaging.

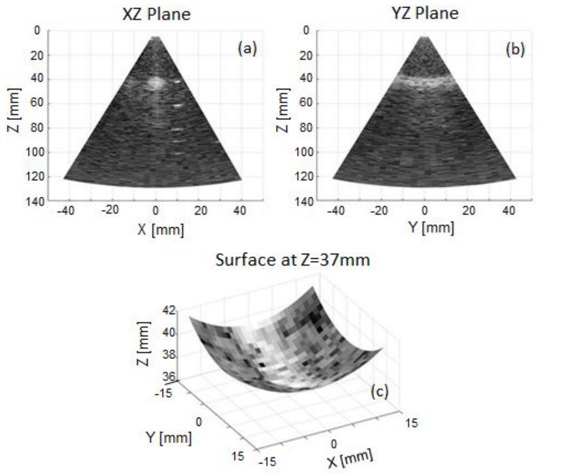

Figure1: 3D MLT results.
(a) XZ and (b) YZ reconstructed planes and (c) a surface at a constant depth

P1-B1-7

The Influence of Speckle Statistics on Contrast Metrics in Ultrasound Imaging

Stine M. Hverven[1], Ole Marius Hoel Rindal[1], Alfonso Rodriguez-Molares[2], Andreas Austeng[1]; [1]*Department of Informatics, University of Oslo, Oslo, Norway,* [2]*Department of Circulation and Medical Imaging, Norwegian University of Science and Technology, Trondheim, Norway*

Background, Motivation and Objective

Quality assessment of ultrasound images is difficult since image quality is subjective to the human observer. Nevertheless, image quality metrics are imperative when benchmarking different beamforming techniques. However, if we do not know how a beamformer alters an image, a quality metric might give an incorrect measurement of the image quality. Using the standard Delay-And-Sum (DAS) beamformer as a reference, we examine many of the most popular adaptive beamformers presented in literature; Capon's Minimum Variance (MV), Eigenspace Based Minimum Variance (EBMV), Coherence Factor (CF), Delay-Multiply-And-Sum (DMAS), Generalized Coherence Factor (GCF), and Phase Coherence Factor (PCF). We show that the speckle statistics for some of these adaptive beamformers are dependent on reflection amplitude, resulting in contradicting measurements of contrast metrics.

Statement of Contribution/Methods

The two most common contrast metrics are contrast ratio (CR) and contrast-to-noise ratio (CNR). CR measures the difference between the mean intensity of a region of interest and the background, while CNR adjusts the CR by the square root of the mean of the variances.

To investigate the speckle statistics of the beamformers we have simulated three speckle regions with three different amplitudes using Field II. A synthetic transmit aperture sequence was simulated using a L7-4 probe transmitting at 5 MHz. The speckle intensity distribution and statistical properties were estimated for each region.

Results/Discussion

The figure shows the ultrasound image for the DAS and CF beamforming techniques, as well as the estimated probability density functions for the speckle regions with the lowest and highest intensity. As expected, the DAS beamformer has a Rayleigh distribution for all regions (SNR=$\mu/\sigma \approx$ 1.91). However, the CF beamformer obtains different statistical speckle distributions depending on the amplitude. This gives us a strange result when measuring the contrast between the regions in the figure. The CR metric favors the CF beamformer while the CNR favors the DAS beamformer. Similar alterations of speckle statistics were also found for some of the other adaptive beamforming techniques. This opens up for cherry-picking image quality metrics when benchmarking beamforming performance, resulting in an arbitrary ranking.

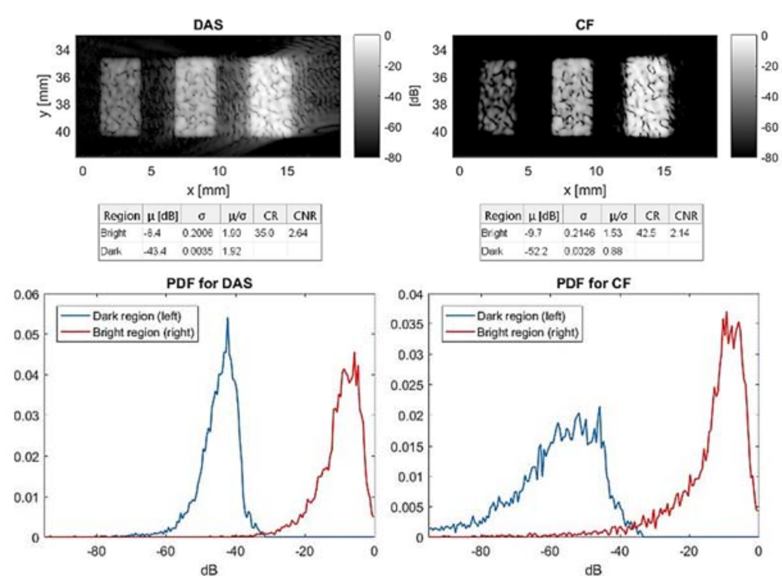

DAS:

Region	μ [dB]	σ	μ/σ	CR	CNR
Bright	-8.4	0.2006	1.90	35.0	2.64
Dark	-43.4	0.0035	1.92		

CF:

Region	μ [dB]	σ	μ/σ	CR	CNR
Bright	-9.7	0.2146	1.53	42.5	2.14
Dark	-52.2	0.0028	0.88		

P1-B2-1

Non-contact High Frequency Ultrasound Microbeam Stimulation for Determination of Invasion Potential of Breast Cancer Cells

Luchao Qi[1], Ming Qian[1], Runkang Chen[1], Yan Tan[1], Hairong Zheng[1]; *Paul C. Lauterbur Research Center for Biomedical Imaging, Shenzhen Institutes of Advanced Technology, Chinese Academy of Sciences, China, People's Republic of*

Background, Motivation and Objective

Invasiveness research is an essential step in breast cancer metastasis. The application of non-contact high frequency ultrasound microbeam stimulation (HFUMS) offers a manner of determining the invasion potential of breast cancer cells. In this article, we compare the calcium elevations elicited in breast cancer cells.

Statement of Contribution/Methods

We fixed the 50MHz single element LiNbO3 transducer to a three-dimensional stereotaxic apparatus. In order to generate the ultrasound microbeam, 50-MHz sinusoidal bursts from a function generator together with a tunable (0dB~100dB) power amplifier were used to drive transducer. Cancer cells were added with Fluo4-AM solution, a fluorescent calcium indicator diluted with the external buffer solution, for 30 minutes at room temperature before calcium fluorescence imaging. Then we put the stimulation system onto an inverted epi-fluorescence microscope to perform live-cell fluorescence imaging(figure A). By adjusting the parameter of power amplifier, we localized an ultrasound microbeam focus(figure B). Finally, a 50-MHz highly focused ultrasound microbeam is applied to breast cancer cells.

Results/Discussion

As figure C shows, the fluorescent intensity of MDA-MB-231 rise when HFUMS on and decline when HFUMS off. Then we used different power gain to stimulate cancer cells and get figure D. From figure D, as we increase power gain, the percentage changes of fluorescent intensity (Delta intensity/Initial intensity) from MDA-MB-231 increase which is in stark contrast with MCF-7. We prepared to use different channel blocker such as GsMTx4T, blocker of piezo channel, SKF-96365, blocker of TRP channel to investigate the role channels play in HFUMS. The results of HFUMS suggested that HFUMS is capable of eliciting cytoplasmic calcium elevations in breast cancer cells. This non-contact manner provides an unconventional way to study cellular mechanotransduction especially when atomic force microscope shows that pure force stimulation could elicit cytoplasmic calcium changes.

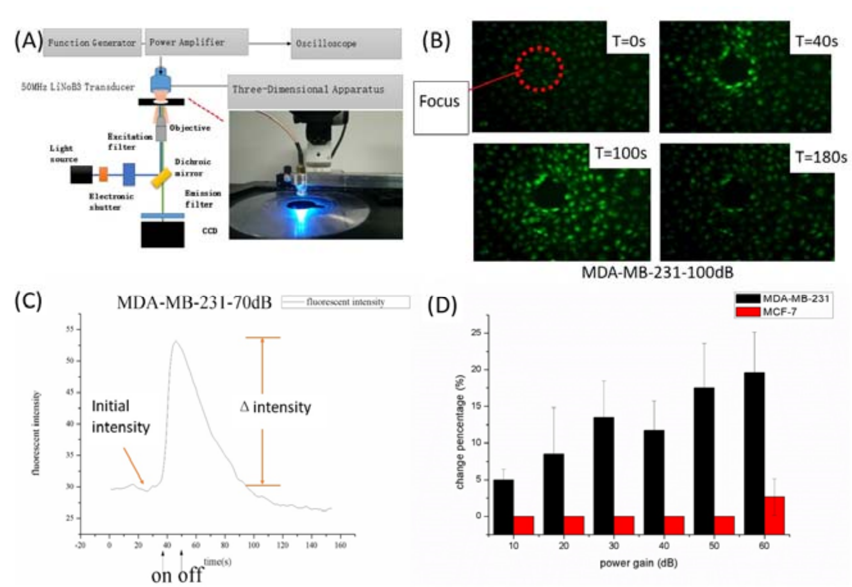

P1-B2-2

Precise Control of Neuronal Activity by Ultrasound: Fundamentals and Toolkits

Zhihai Qiu[1], Jinghui Guo[2], Yaoheng Yang[1], Jingyao Wang[1], Rui Zhang[1], Jiejun Zhu[1], Shashwati Kala[1], Hsiao Chang Chan[2], Lei Sun[1]; [1]*Interdisciplinary Division of Biomedical Engineering, The Hong Kong Polytechnic University, Hong Kong,* [2]*School of Biomedical Sciences, The Chinese University of Hong Kong, Hong Kong*

Background, Motivation and Objective

Ultrasonic (US) brain stimulation, has been demonstrated to noninvasively alter neuron activity in animals and humans. Capable of non-invasive transmission trough skull with fine focal size (~mm), it is an encouraging means and a good alternative to existing stimulating strategies. However, the bio-effects of US are diverse and thus it is crucial to develop precise neuron control strategies for later translation. Here we focus on the mechanisms of gating mechanosensitive ion channels (MCs) by US and explored as fundamentals for the developing selective US neuron stimulation.

Statement of Contribution/Methods

The cell membrane tension was approximated by various models and then calculate the interaction with MCs. On gating MCs by US was verified on Piezo1 expressed HEK293t cells and primary cultured neurons. In addition, neurons with Piezo1 targeted nano-bubbles were utilized to verify the tether model for MCs activation. Calcium imaging and whole cell patch clamp techniques were utilized to characterize the responses. Based on these proof of concept results, sono- and acoustic mechano-genetic toolkits for neuron activity controlling and visualization simultaneously were developed.

Results/Discussion

It is shown that US can mediate membrane tension which can be tuned up to one order magnitude higher than which required for gating MCs, here Piezo 1. The open probability of MCs as a function of acoustic pressure highly depends on frequency, as indicated in Fig. 1. The MCs is more sensitive to lower frequency US. Experimental results clearly demonstrated that US can activate Piezo1-HEK293t cells while no response can be detected for the control cells (Fig. 2). The induced inward current and calcium influx are US pressure dependent for Piezo1 overexpressed HEK293T and neurons. On the other hand, the nano-bubble targeted neurons can be activated by low acoustic pressure as well (Fig. 3). These results show that ultrasound is able to modulate neuronal activity by gating mechanosensitive ion channels by membrane tension or localized tether force. It demonstrates reliable precise control of neuron activity by ultrasound (Fig. 4 A) and B)). The toolkit for sonogenetics and acoustic mechanogenetics are being developed (Fig. 4 C) and D)). We envision that these toolkits could be powerful tools for understanding our brain function.

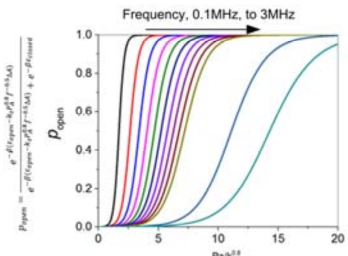

Fig. 1 MCs open probability in response to ultrasound pressure

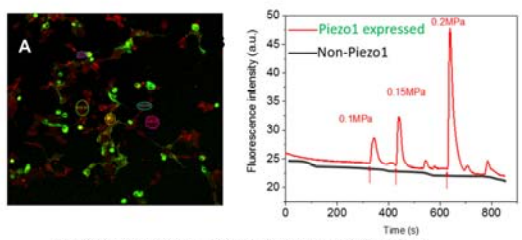

Fig. 2 A) Piezo1 expressed HEK293T; and its B) calcium response to ultrasound

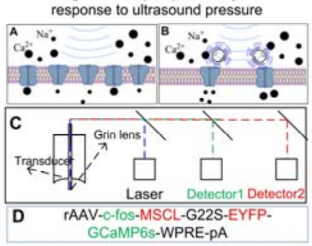

Fig. 4 Concept for A) sonogenetics; B) acoustic mechanogenetics; C) In vivo ultrasound stimulation and response monitoring system and D) viral partical design for targeting neuron circuts

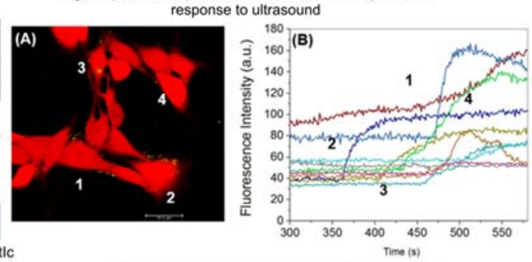

Fig. 3 A) Nano-bubble targeted neurons; and its B) calcium response to ultrasound

P1-B2-3

FUS Cavitation Induced Injury and Localized Atherosclerosis Plaques of Rabbit Abdominal Arterial Endothelium

Yujin Zong[1], Gang Liu[1], Jiangying Long[1], Lei Zhang[1], Di Zhou[1], Yi Feng[1], Mingxi Wan[1]; [1]*Department of Biomedical Engineering, Xi'an Jiaotong University, Xi'an, Shaanxi, China, People's Republic of*

Background, Motivation and Objective

Early detection and diagnosis of high-risk vulnerable plaques can reduce the death rate attributable to atherosclerosis. Many attempts to identify plaques have focused on *in vivo* imaging techniques. Animal models with foregone plaque sites will be valuable to evaluate the validity of the imaging methods. However, in traditional balloon injury models, the sites and size of generated plaques are uncertain and uncontrolled. Based on the "response-to-injury" hypothesis, lesions in the artery's endothelium might be the main mechanism. Therefore, we utilized focused ultrasound(FUS) cavitation to generate localized endothelial lesions instead of balloon, and thereby induced localized, size-controlled plaques combined with high cholesterol diet.

Statement of Contribution/Methods

Rabbit abdominal aortas were processed by phase-shifted nanodroplets(PSND) enhanced FUS cavitation and balloon separately. Briefly, a catheter was introduced into the aorta via femoral artery and withdrawn with inflated balloon five times to damage the endothelium. In cavitation case, the aortas were exposed to short FUS pulses under US image guidance after PSND injection. Evans blue staining was used to visualize the endothelial injury. Furthermore, rabbits were divided into three groups besides control group and developed plaques using high fat feeding, balloon injury plus fat feeding, and cavitation injury plus fat feeding separately. The abdominal aortas were isolated for macroscopic visualization of plaques and HE stained for routine microscopic evaluation after 6 weeks.

Results/Discussion

Evans blue stained endothelial lesions were observed in both situations. The bolloon injury regions were distributed on the whole vessel wall(Fig.1b), while cavitation injuries were just located at US exposure sites(Fig.1a). And the lesions with different sizes (white arrows in a1,a2) can be generated by adjusting US intensity, exposure time, etc.,. As a result of cavitation injury, the induced plaques were size-controlled and localized at the predictable sites(Fig.2a,b), while the plaques induced by balloon injury occurs randomly within the injury region (Fig.2c). There were no obviously visible plaques in only fat-fed group (Fig.2d). Therefore, cavitation injury might become an alternative and potential strategy to develop a localized and controllable atherosclerosis model.

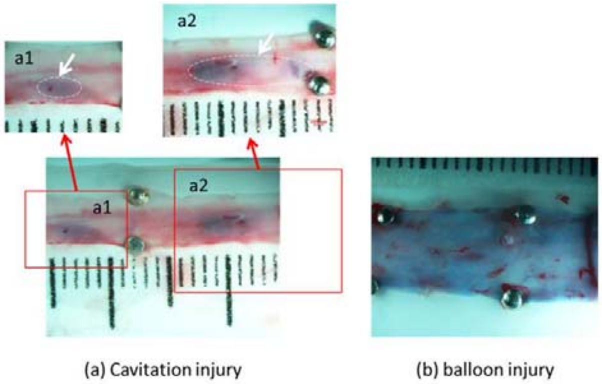

Fig. 1 Evans blue stained endothelial injuries

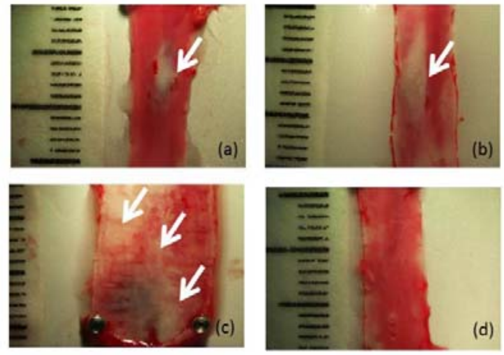

Fig. 2 Plaques induced by cavitation injury (a and b), balloon injury (c) and high fat feeding

P1-B2-4

HIFU Waveform Measurement at Clinical Amplitude Levels: Primary Hydrophone Calibration, Waveform Deconvolution and Uncertainty Estimation

Martin Weber[1], Volker Wilkens[1]; [1]*1.62 Ultrasonics, Physikalisch-Technische Bundesanstalt, Braunschweig, Lower Saxony, Germany*

Background, Motivation and Objective

High intensity focused ultrasound (HIFU) is being increasingly used in medical therapeutics. The properties of the ultrasonic fields applied entail challenging acoustic output measurement tasks: the generation of high-pressure amplitudes sufficient for cavitation; the use of high-frequency components due to the non-linear sound propagation in water; and narrow beam widths at the focus. Conventional piezoelectric hydrophones can easily be destroyed in HIFU fields, but specially designed and recently developed robust hydrophones may be applied instead. Due to the use of protection layers, the frequency response of such hydrophones is less uniform than that of conventional unprotected membrane hydrophones, and waveform deconvolution is indispensable for correct determination of the high-amplitude broadband waveforms.

Statement of Contribution/Methods

A robust HIFU membrane hydrophone with a stainless-steel front protective layer and a silicon oil backing component was calibrated using a new, recently developed primary calibration setup. The method uses an optical vibrometer as a reference receiver, in conjunction with broadband ultrasonic pulse excitation, and provides frequency response data of up to 100 MHz in amplitude and phase, including a full description of uncertainties. After calibration, the hydrophone was applied to HIFU measurements at working frequencies of about 1 MHz and 3 MHz, and the complex-valued frequency response data was used to deconvolve the broadband waveforms. Uncertainty-optimized regularization filtering was applied in order to suppress high-frequency noise from the deconvolved signals, and the overall uncertainty of the pressure waveforms in the time domain was determined considering the frequency-dependent calibration uncertainties, as well as a recently proposed method for estimating the maximum regularization error.

Results/Discussion

New primary calibration facilities were incorporated into the characterization of a robust hydrophone for HIFU measurements. The frequency response was obtained in the range from 1 MHz to 100 MHz, with uncertainties on the order of 5 % at frequencies around 7 MHz, increasing to about 20 % at 50 MHz (95 % confidence level). The hydrophone has a low-pass characteristic, with a decrease in sensitivity of about 9 dB between 5 MHz and 50 MHz. To compensate for the resulting low-pass characteristic of the sensor, the calibration data obtained is used to deconvolve HIFU measurement data. Waveforms with peak-compressional pressures of up to 90 MPa were determined in this way at the focus of a single-element transducer. A comprehensive uncertainty estimation for the deconvolved pressure waveform results was provided. It may serve as an example of how to treat frequency-dependent calibration data uncertainties in combination with deconvolution and regularization in hydrophone-based exposimetry.

P1-B2-5

Bioeffects of Acoustic Droplet Vaporization-Generated Bubbles in Tissue

Yi-Ju Ho[1], Yi-Tim Lin[1], Chih-Kuang Yeh[1]; [1]*Biomedical Engineering and Environmental Sciences, National Tsing Hua University, Taiwan*

Background, Motivation and Objective

Acoustic droplet vaporization (ADV) is a process when a droplet is converted into a gaseous bubble under ultrasound (US) stimulation. Our previous study has shown that the mechanical force generated by ADV can release drugs and disrupt vessels. It would result in the streaming intact droplets leaking into tissue. In addition, the intact droplets may occur ADV process by subsequent US stimulation. Therefore, this study explored the bioeffects between ADV-Bs and cells within tissue.

Statement of Contribution/Methods

In vivo window chamber model was used to provide the optical visualization of ADV-Bs with an intravenous injection of 1×10^8 lipid-based droplets (1.1±0.1 μm). The behaviors of ADV-B formation, cavitation, and movement in tissue were observed during subsequent US stimulation. To further discuss the possible reasons of cell death by ADV, cell culture experiments were conducted by using a C6 glioma-astrocytoma cell line incubated with the droplets. The calcein-blue AM, propidium iodide (PI), and Hoechst were conducted to verify the cell viability, cell membrane disruption, and DNA distribution, respectively. Besides, cells were transfected with lyn-CFP to visualize the membrane dynamics when ADV-Bs attached to cells.

Results/Discussion

Intravital images showed ADV-B formation, cavitation, and movement in tissue during US stimulation. The intertissue ADV-Bs were coalesced and pushed away by US pulse from the original location, and the movement distance of ADV-Bs was 32.7±13.3 and 21.7±14.8 μm per pulse (5-MPa and 100-cycle) for smaller (≤20 μm) and larger (>20 μm) ADV-Bs, respectively (Fig. A). Since the adjacent cell damage was observed after intertissue ADV-B stimulation, our study further evaluated the interaction between cellular bioeffect and ADV-Bs *in vitro*. The phenomena of cell viability decreasing (calcein-blue AM decreasing) and cell membrane disruption (PI increasing) were visualized after ADV (Fig. B). The PI distribution in whole cells and Hoechst decreasing in cell nuclei indicated the permeability of nuclear envelope increasing. Moreover, the fraction of cell membrane was observed on ADV-B surface because of occurrence of lipid exchange process. Therefore, these above bioeffects induced by ADV-Bs would cause cell apoptosis to provide an ability to directly kill tumor cells by intertissue ADV-Bs for physical therapy.

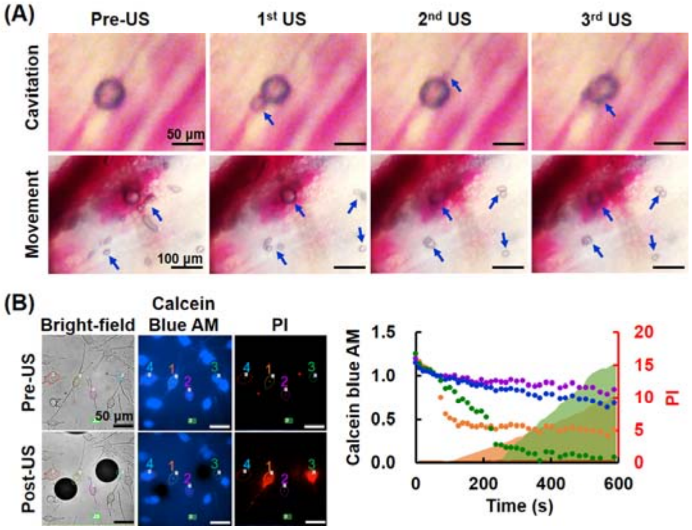

P1-B2-6

Controlled Permeation of Cell Membrane by a Single-Bubble Stable Cavitation in a Microfluidic Device

Yuchen Wang[1,2], Ruoyan Meng[1], Wei Zhou[1], Kaiyue Wang[1], Lili Niu[1], Long Meng[1], Hairong Zheng[1]; [1]*Shenzhen Institutes of Advanced Technology, Chinese Academy of Sciences, shenzhen, Guangdong, China, People's Republic of,* [2]*Northeastern University, shenyang, liaoning, China, People's Republic of*

Background, Motivation and Objective

Enhancing the cell's membrane permeability enables to promote foreign substance into the cell and has various applications in biomedical engineering.Sonoporation employs the microbubble inertial cavitation to induce reversible cell-pores in the membranes allowing some impermeable molecules to be transferred into cells. However, the inertial cavitation is the violent collapse of bubbles and thus sonoporation process is difficult to control. In this paper, we developed a reversible sonoporation method based on stable cavitation with highly controllable membrane permeability.

Statement of Contribution/Methods

A PDMS microchannel was fabricated by the standard soft lithography method and a rectangular hole with the length of 40 μm was located at the side wall. A piezoelectric transducer (PZT) whose resonance frequency equals to the resonant frequency of air bubble was glued to the glass slide to excite the bubble stable cavitation. Human breast cancer cell of MDA-MB-231 with Propidium Iodide (PI) was infused in the microchannel through a pressure driven flow. PI is a molecule that can bind to DNA and RNA and become fluorescent.

Results/Discussion

When the cell solution flowed through the microchannel, a semicircular air bubble at the opening hole was generated due to the discontinuity at the fluid/PDMS interface, as shown in Fig. 1(a). Before ultrasound irradiation, no fluorescence was observed, illustrating the membrane of the cell was intact. When the PZT was applied to the input power, the air bubble membrane started to oscillate and the cell was attracted to the air bubble and trapped at the bubble surface. The fluorescence intensity of the cell increased significantly with time which indicated the membrane permeability was improved by the stable cavitation. Fig. 1(b) shows the quantitative analysis of the fluorescence intensity. It obvious that there was a sharp rise in the fluorescence at 40 s and the fluorescence remained stable after 41 s.

We have demonstrated that this approach is a promising technique to realize the sonoporation in a controllable manner. As the cells are trapped by the bubble, the vibration of the bubble could open the repairable pores efficiently. Using this principle, it is possible to improve the membrane permeability with a high-throughput by fabrication the microchannel in a parallel fashion.

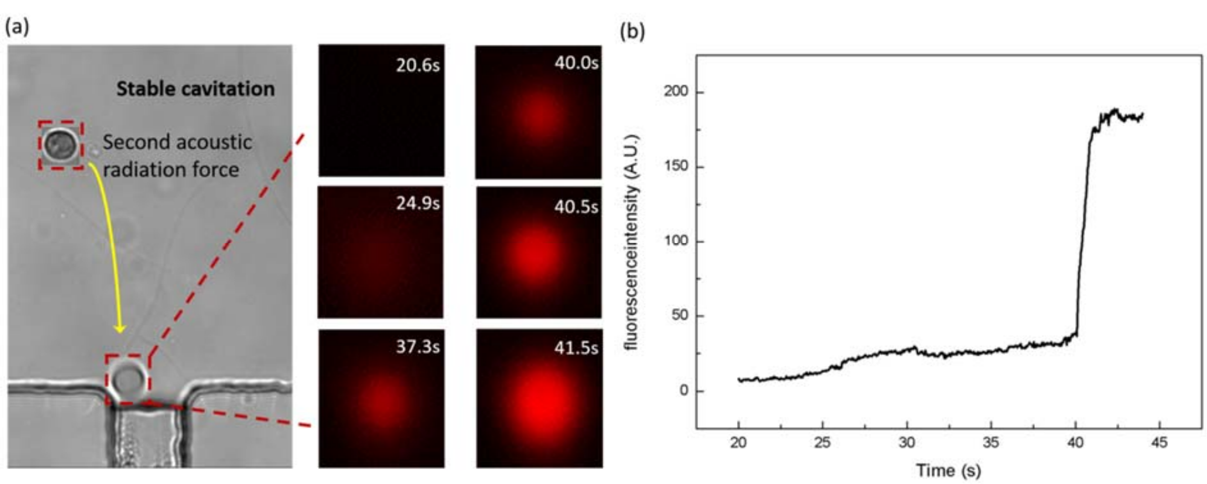

P1-B2-7

Three Dimensional Pressure Field Measurement of Focused Ultrasound by Optical Phase Contrast Method

Shin Yoshizawa[1], Takuya Nakamura[2], Yohei Sasaki[1], Maxime Lafond[2], Shin-ichiro Umemura[2]; [1]*Communications Engineering, Tohoku University, Sendai, Japan,* [2]*Biomedical Engineering, Tohoku University, Japan*

Background, Motivation and Objective

A hydrophone scanning method is gold standard for the ultrasound filed measurement. However, the hydrophone scanning is time consuming especially for the three-dimensional measurement. On the other hand, two-dimensional data can be acquired simultaneously by an optical measurement method using a camera. In this study, the optical phase contrast method was used to measure a three-dimensional pressure filed generated by a focused transducer.

Statement of Contribution/Methods

The experimental setup for the optical phase contrast method is similar to that for the schlieren method. The difference is the use of a phase plate in the phase contrast mesurement, instead of an optical stop in the schlieren optics. The phase plate has an advanced column, with a diameter of 100 µm, etched into its surface to give an optical phase shift to the undisturbed optical component. A spherical PZT transducer with both diameter and focal length of 72 mm was placed in a water tank. It was continuously driven at a frequency of 1.14 MHz. The light source is a pulsed green lase with a wavelength of 532 nm, pulse width of 1.8 ns, and pulse energy of 20 µJ. 60 images with & without ultrasound exposure, respectively, were taken to obtain the two-dimensional optical phase modulated by the acoustic filed. Then they were averaged to increase SNR. The transducer was rotated to obtain the optical phase distribution from angles of 0 to 180 degrees at every 2 degrees. The rotation axis was approximately 6-mm away from the beam axis of the focused ultrasound. Therefore, the acquired optical phase distribution was not axisymmetric along the rotation axis, although the acoustic field itself is ideally axisymmetric. The pressure distribution was reconstructed using the inverse radon transformation.

Results/Discussion

Figure 1 shows the measured pressure field by the optical and hydrophone methods. The peak-to-peak pressures measured by the hydrophone scanning and phase contrast method were 0.52 and 0.51 MPa, respectively. The good agreement was seen in both of the axial and radial pressure distributions. However, there is an optical phase-wrapping problem in the measurement at a higher acoustic intensity. In the presentation, the reconstructed three-dimensional acoustic field with a much higher focal pressure will be also shown by acoustic holography using the optical measurement data.

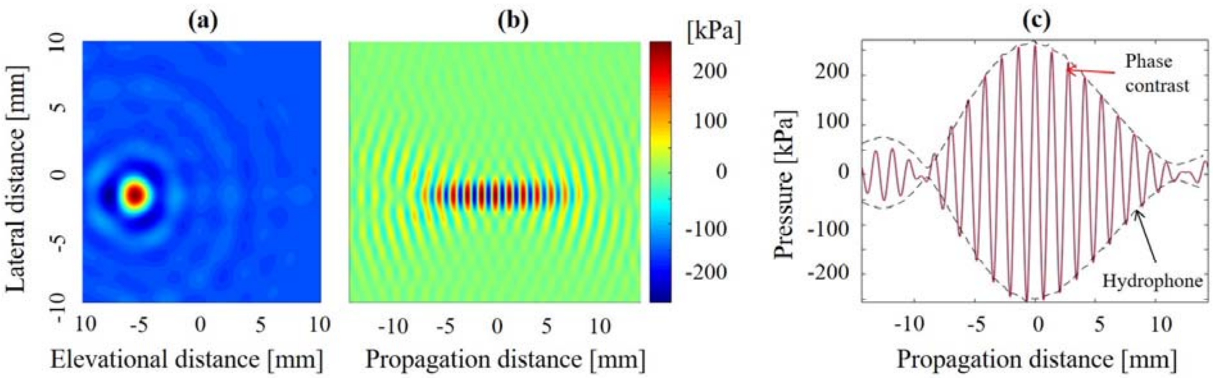

Figure 1 Pressure field measured by the optical phase contrast and hydrophone methods. Pressure distributions in perpendicular (a) and parallel (b) to the ultrasound propagation axis obtained by the optical method. Pressure distributions along the ultrasound propagation axis (c).

P1-B2-8

Design and Characterization of a Research Phantom for Shock-Wave Enhanced Irradiations in High Intensity Focused Ultrasound Therapy

Wayne Kreider[1], Barbrina Dunmire[1], John Kucewicz[1], Christopher Hunter[1], Tatiana Khokhlova[2], George Schade[3], Adam Maxwell[3], Oleg Sapozhnikov[1,4], Lawrence Crum[1], Vera Khokhlova[1,4]; [1]*CIMU, Applied Physics Laboratory, University of Washington, USA,* [2]*Gastroenterology, University of Washington School of Medicine, USA,* [3]*Urology, University of Washington School of Medicine, USA,* [4]*Physics Faculty, Moscow State University, Russian Federation*

Background, Motivation and Objective

The use of shock waves for enhancing thermal effects and mechanically ablating tissue is gaining increased attention in high intensity focused ultrasound (HIFU) therapies for applications such as tumor treatment, drug delivery, and immunotherapy. For abdominal targets, the presence of ribs and inhomogeneous adipose tissue can affect shock formation through aberration, absorption, and diffraction. The goal of this study was to design and characterize a phantom that simulates an abdominal body wall, ribs, and target tissues for investigating the impact of different structures on shock formation in situ.

Statement of Contribution/Methods

A transducer with driving electronics was developed to operate at 1.2 MHz with the ability to deliver either short pulses at high powers (10 ms pulses at 1% duty cycle at up to 5 kW electrical power) or continuous output at moderate powers up to 700 W (Sonic Concepts, Bothell, WA). To represent fat and muscle in body wall, phantom layers were made from polyvinyl alcohol. Ribs were fabricated by 3D-printing based on a human anatomical model relevant to liver or kidney treatments. Phantom targets comprised optically transparent alginate or polyacrylamide gels. These components were assembled in a water tank to provide coupling between layers and allow shifting of relative positions. Free-field hydrophone measurements were performed for transducer characterization; in situ fields behind ribs and body wall were then characterized both by hydrophone measurements and observations of lesion formation.

Results/Discussion

Shocked waveforms with peak positive/negative pressures of +100 / -20 MPa were measured in free-field in water at 1 kW. When ribs were present, shocks formed at about 50% amplitude at the same power, and higher pressures were measured with ribs positioned closer to the transducer (see Figure). A uniform body wall structure attenuated shock amplitudes by a smaller amount and was insensitive to axial position. In addition, boiling histotripsy lesions were visualized in target gels. A phantom was developed and tested, demonstrating that that the presence of ribs and absorptive tissue-mimicking layers do not prevent shock formation at the focus. With real-time lesion visualization, the phantom is suitable for adaptation as a training tool. Work supported by NSBRI through NASA NCC 9-58, NIH R01EB007643, K01 EB015745 and DK104854.

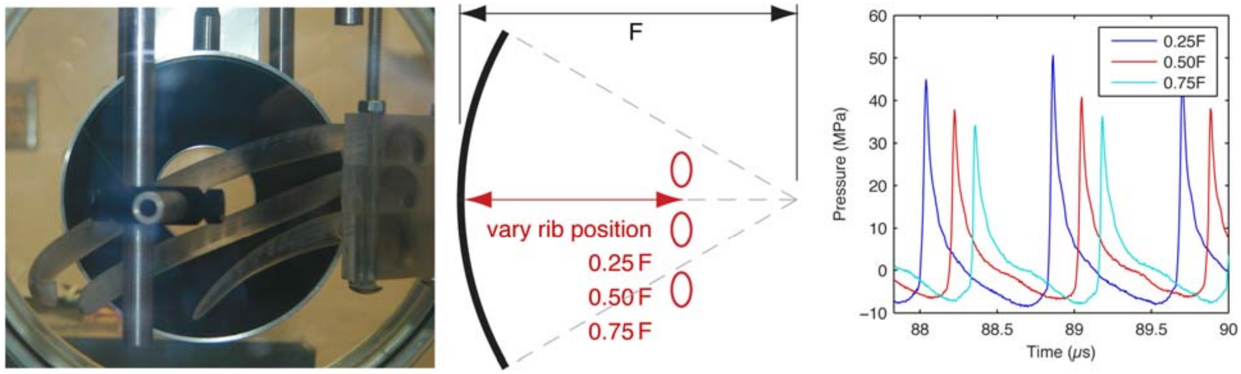

Figure. Photograph of the test configuration for irradiation through ribs (left). Schematic representation of rib positions (middle). Pressure waveforms measured at the focus using a fiber optic hydrophone behind ribs positioned in three different axial locations (right).

P1-B2-9

A Reliable and Convenient Acoustic Field Characterization Method of a Clinical MR-HIFU System Using Electronic Beam-steering

Satya VVN Kothapalli[1], Ari Partanen[2], Lifei Zhu[3], H. Michael Gach[4], Michael Altman[5], Hong Chen[6]; [1]*Biomedical Engineering, Washington University in Saint Louis, Saint Louis, Missouri, USA,* [2]*Clinical Science MR Therapy, Philips, Andover, Massachusetts, USA,* [3]*Biomedical Engineering, Washington University in Saint Louis, Saint Louis, USA,* [4]*Radiation Oncology, Washington University in St. Louis, St. Louis, USA,* [5]*Radiation Oncology, Washington University in St. Louis, St. Louis, USA,* [6]*Biomedical Engineering and Radiation Oncology, Washington University in St. Louis, Saint Louis, Saint Louis, USA*

Background, Motivation and Objective

With a growing number of magnetic resonance-guided high-intensity focused ultrasound (MR-HIFU) clinical applications, acoustic field characterization tools and methods for quality assurance are needed to ensure safe treatment outcomes. However, the established methods typically use equipment that cannot be used in a magnetic resonance imaging (MRI) suite. Herein, we propose a technique for convenient and reliable acoustic field characterization of clinical MR-HIFU systems with the aid of MRI-based HIFU focus localization and electronic HIFU beam-steering.

Statement of Contribution/Methods

A clinical MR-HIFU system (Sonalleve V2, Philips) was used to assess the proposed technique. A fiber-optic hydrophone with a 20-m long fiber was fixed inside a water tank located on the HIFU table above its acoustic window, allowing the hydrophone control unit to be located outside the MRI suite. MR images of the setup allowed the HIFU focal point to be roughly positioned at the fiber tip using the MR-HIFU therapy planning software. The HIFU focus was electronically steered against the fiber tip within a 3D volume (5×5×20mm3) with step sizes of 0.5mm and 2mm in-plane and along the beam path, respectively, followed by 2D pressure field mapping in a 3×3mm2 plane (step size 0.1mm). Then, peak positive (p+) and negative pressures (p-) were measured for acoustic powers of 10-500W. For validation, the HIFU table was moved out of the MRI suite, and a standard laboratory hydrophone measurement setup equipped with a high precision 3D stage was used to perform acoustic field characterization using the same acoustic powers.

Results/Discussion

The MRI-based focus localization indicated a maximum offset of 2mm from the actual focus location identified using electronic beam steering. MRI guidance with electric beam steering allowed 3D focus localization in 50 minutes, i.e., faster than with the standard setup. Acoustic field calibration with electrical beam-steering eliminated the need of using a 3D stage. The pressures acquired using electronic steering were not significantly different from the pressures acquired with standard laboratory equipment (Fig. 1). In conclusion, this method offers convenient and reliable acoustic field characterization of clinical MR-HIFU systems.

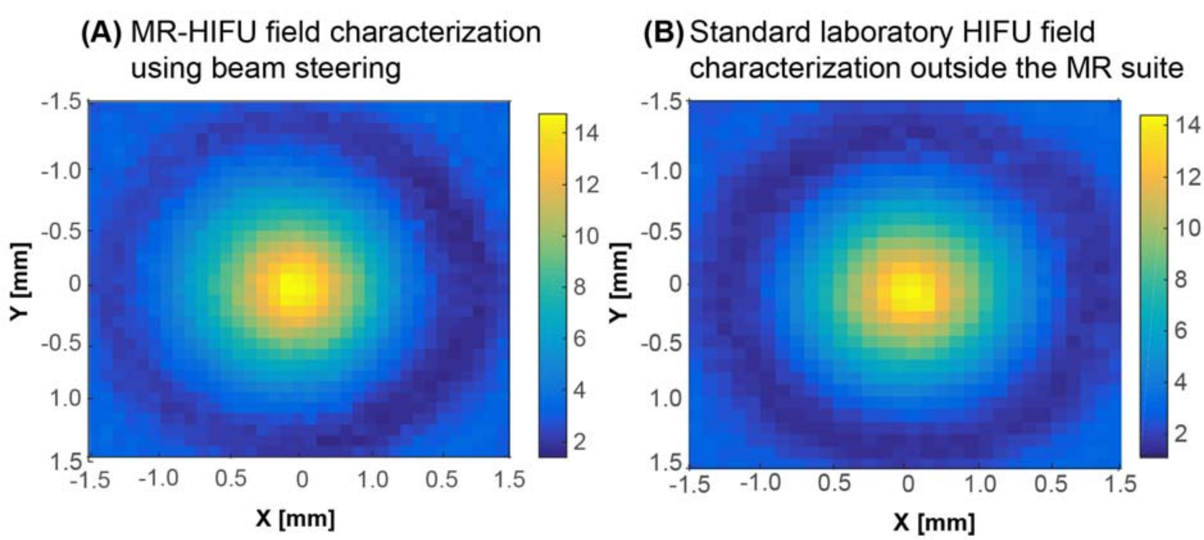

P1-B2-10

Real-time Investigation of Irreversible Cell Membrane Damage Induced by Acoustic Droplet Vaporization

Dui Qin[1], Lei Zhang[1], Nan Chang[1], Yujin Zong[1], Mingxi Wan[1], Yi Feng[1]; [1]*Department of Biomedical Engineering, School of Life Science and Technology, Xi'an Jiaotong University, China, People's Republic of*

Background, Motivation and Objective

Acoustic droplet vaporization (ADV) has shown a great potential in extravascular tumor-targeting theranostics. During ADV, its mechanical effects on the nearby cells could cause cell dysfunction with irreversible cell membrane damage or facilitate drug delivery by sonoporation. Understanding the real-time characteristics and bio-effects of ADV on cells is significant to develop the approach *in vivo* and then *in clinic*.

Statement of Contribution/Methods

A confocal acousto-optical microscopic system was used to investigate the bioeffects of ADV on nearby cells in real time with high speed microscopic imaging and fluorescence imaging. HeLa cervical cancer cells were cultured in the Opticell chamber. A 5 MHz single-element transducer driven by a high power pulser was focused to induce ADV on the cells. Propidium iodide (PI) and Calcein-AM were added for real-time tracking cell membrane integrity and evaluating cells viability after ADV, respectively.

Results/Discussion

Upon ultrasound exposure, the rapid vaporization of perfluoropentane (PFP) nanodroplets into gaseous bubbles and subsequent ADV bubble-cell interactions were observed (Fig.1 b), including the bubble growth, coalescence and translational motion above the apical cell membrane layer or near the cells. A rapid and continuous increase in the intracellular PI fluorescence intensity in the cells near ADV was observed post-ADV (Fig. 1 c and d). It indicated the loss of cell membrane integrity, which was also confirmed by a complete leakage of Calcein-AM (Fig. 1 d). It revealed that the rapid ADV event and formed ADV bubbles forced by ultrasound pulses can cause the irreversible pores on the cancer cell membrane, and then cell damage or death. Its real-time characteristics would help to develop the new ADV-mediated theranostic approach.

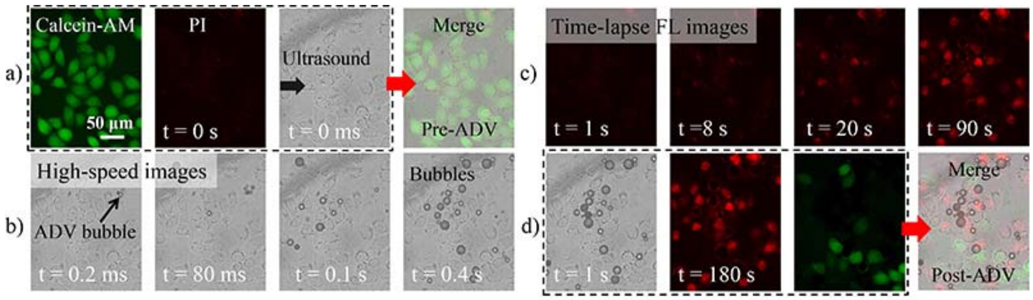

Figure 1. (a) Bright-field, Calcein-AM and PI fluorescence images of HeLa cells pre-ADV; (b) High speed imaging of the ADV process; (c) Time-lapse PI fluorescence images post-ADV; (d) Bright-field, Calcein-AM and PI fluorescence images post-ADV. Ultrasound amplitude: 1.2 MPa, pulse duration: 2 μs, pulse repetition frequency: 50 Hz, time: 1 s.

P1-B2-11

On-chip Spatial Controlled Single Cell Sonoporation by Vibrating Targeted Microbubbles

Ruoyan Meng[1,2], Yuchen Wang[1,2], Xuelian Shen[1], Wei Zhou[1], Kaiyue Wang[1,2], Lili Niu[1], Long Meng[1], Hairong Zheng[1]; [1]*Paul C. Lauterbur Research Center for Biomedical Imaging, Shenzhen Institute of Advance Technology Chinese Academy of Sciences, China, People's Republic of,* [2]*School of Sino-Dutch Biomedical and Information Engineering, Northeastern University, China, People's Republic of*

Background, Motivation and Objective

It is crucial to transport foreign substance into living cells efficiently and minimize adverse side-effects. Using ultrasound microbubble, it is possible to enhance the cellular uptake and transfer the extracellular molecules into cells, this process is called sonoporation. However, the spatial location of microbubbles appears to be a stochastic process, which makes the targeted sonoporation at specific location difficult to realize. In this paper, we developed a microfluidic device which enables to realize the spatially controlled sonoporation at single cell level by the manipulation of the targeted microbubble precisely.

Statement of Contribution/Methods

By the Biotin-Avidin method, the ligand was attached to the microbubbles so they could bind to a certain cell membrane specifically. The diameter of the microbubbles ranged from 0.5μm to 10μm. A pair of straight interdigital transducers (IDTs) which having a 200μm pitch was fabricated on a 128° Y-rotated, X-propagating LiNbO3 substrate to generate a plane standing surface acoustic wave (SSAWs) to control the spatial distribution of the targeted microbubbles. Simultaneously, the microbubble vibration was induced by SAWs irradiation.

Results/Discussion

When targeted microbubbles were delivered to microchannel, the membrane surface of breast cancer cells MDA-MB-231 were adhered to the targeted microbubbles (Fig.1). Then, a pulsed radio frequency signal was applied to IDTs, the adhered microbubbles began to vibrate and induced localized membrane disruption. Fig. 2a shows the single cells generated red fluorescence as the increased permeability of the membrane. Simultaneously, strong green fluorescence emitted by the single cells was also observed which confirmed the viability (Fig.2b). In addition, when the SSAWs was established, targeted microbubbles were aggregated at the pressure nodes and the corresponding cells adhered to the targeted microbubble could be sonoporated efficiently, forming a multi-line pattern. In conclusion, we have demonstrated the permeability of the cell membrane could be altered by vibrating targeted microbubbles. By manipulation of the location of the targeted microbubble, spatially controlled sonoporation was achieved.

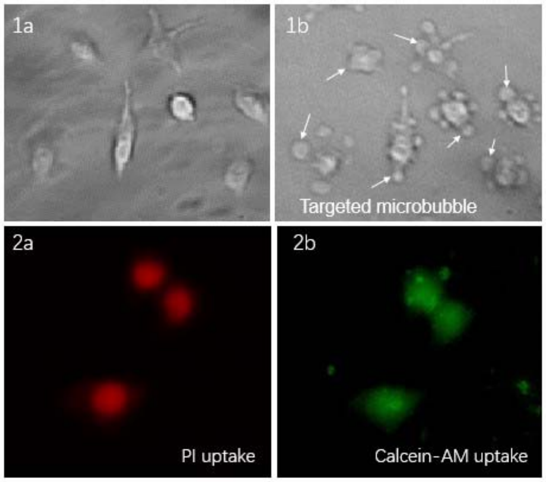

Fig 1. The adhension of the targeted microbubble to the specific cells
Fig 2. The single cells generated red fluorescence as the increased permeability of the membrane (a) while maintaining cell viability (b)

P1-B2-12

Heterogeneous Responses of Reactive Oxygen Species in the Sonoporated Cells at the Single-cell Level

Caixia Jia[1], Tao Han[1], Lin Xu[2], Alfred.C.H. Yu[3], Peng Qin[1]; [1]*Department of Instrument Science and Engineering, Shanghai Jiao Tong University, China, People's Republic of,* [2]*Institute of Plant Physiology and Ecology, Shanghai Institutes for Biological Sciences, Chinese Acad, China, People's Republic of,* [3]*Department of Electrical and Computer Engineering, University of Waterloo, Canada*

Background, Motivation and Objective

To develop and realize the sonoporation-based therapeutic applications, it is important to understand underlying cellular bioeffects involved in the sonoporation. It is known that appropriate reactive oxygen species (ROS) is necessary to maintain normal physiological functionality, but excessive ROS would trigger downstream adverse bioeffects. However, it is still unclear about ROS response in the sonoporated cells. This study aims to investigate how the intracellular ROS responds to the perforated membrane triggered by acoustic cavitation.

Statement of Contribution/Methods

Hela cervical cancer cells, as a model, were employed to perform the following investigations at the single-cell level. The microbubbles (DSPC, DSPE-PEG2000, C3F8) were fabricated by film dispersion method. The fluorescence intensities of the internalized Propidium iodide (PI) and pre-stained intracellular H2DCFH were evaluated to determine the degree of sonoporation and the level of intracellular ROS response, respectively. 1.5 MHz ultrasound with 30 ¦Ìs duration and 0.85 MPa peak negative pressure was applied to trigger the collapse of bubbles. The time-lapse fluorescence images of PI and DCF were acquired by confocal microscope at 30 sec interval over 6-min period after exposure, and then were quantified by software. Cell viability was evaluated by Calcein blue images at 15 min.

Results/Discussion

Our results revealed heterogeneous change of intracellular ROS level was correlated with the degree of the sonoporation. 1) Within about 100 s after the onset of ultrasound, which covered intervals from membrane perforation to the completion of membrane resealing, intracellular ROS level rapidly decreased because of extracellular diffusion of DCF through perforated membrane, similar to the extracellular PI influx. In the following 260 s, ROS level in the reversibly sonoporated cells exhibited gradual increase. The increasing amplitude was positively correlated with the degree of the sonoporation. 2) For the irreversibly sonoporated cells, although intracellular ROS level also decreased in the first 100 s and increased in the following 260 s, they subsequently exhibited severe decrease and approximate disappearance. We think heterogeneous ROS responses may be related with the long-term fate of the sonoporated cells.

Figure 1

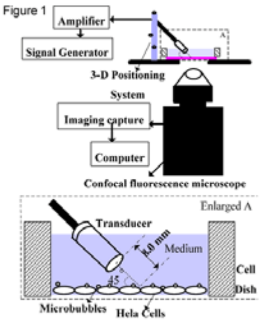

Figure 2

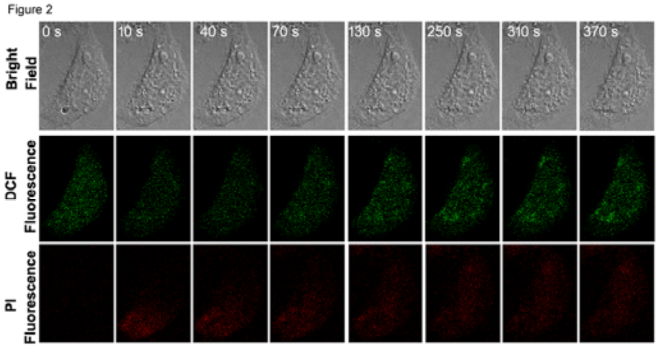

Figure 3

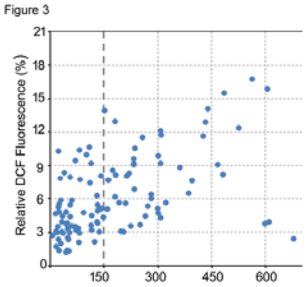

Figure 1: the ultrasound exposure and real-time observation plateform at the single-cell level
Figure 2:Images of bright-field, DCF and PI fluorescence at different time points before and after ultrasound exposure
Figure 3: Scatterplot of relative DCF and PI fluorescence intensity change of 128 sonoporated cells

P1-B3 - MBF: Flow Estimation: Simulators, Phantoms, and Filtering Methods

Exhibit Hall

Friday, September 8, 2017, 9:30 am - 4:00 pm

Chair: **Shigao Chen**
Mayo Clinic

P1-B3-1

Fast Ultrasound Simulation Method for Evaluation of Velocity Estimators

Jørgen Avdal[1], Hans Torp[1]; [1]*Centre for Innovative Ultrasound Solutions (CIUS), Norwegian University of Science and Technology, Norway*

Background, Motivation and Objective

Both mean velocity and spectral Doppler techniques are prone to estimation errors and variance, and new velocity estimation techniques need to be validated extensively before they can be considered for clinical use. Quantitative validation is commonly performed using simulations, with the advantage that the underlying velocity field is known. However, simulations typically produce only realizations of the signal, so that multiple simulations or long temporal windows are necessary to estimate the statistical properties of the estimators.

Statement of Contribution/Methods

We propose a method for calculating the statistical expectation value and variance of a velocity estimator when applied to *in silico* stationary flow fields. The flow field is first decomposed into flow lines. The software Field II is then used to calculate the spatial and temporal correlation functions of the received signal for a point scatterer moving along each flow line, before summing the correlation functions. The result is filtered through white noise to generate many realizations of the signal. Finally, the expected value and variance of the estimator is obtained by applying it to all realizations. The method is general and can be used to evaluate 1D, 2D and 3D mean velocity and spectral estimators. Because producing realizations from the correlation function is computationally cheap, and because only one scatterer is needed for each flow line, this approach is faster than estimating the same properties from simulations with randomly positioned point scatterers.

Results/Discussion

The left panel of the figure shows a 2D *in silico* cylindrical tube phantom with a narrowing, producing a flow jet with maximum velocity of 3 m/s. The phantom was insonated using unsteered plane waves from a phased array probe using center frequency 2.5 MHz, PRF 10 kHz, and beam-to-flow angle 60 degrees. The two rightmost panels show expectation values of PW Doppler and 2D Tracking Doppler (Fredriksen *et al*, 2013) estimators when using temporal observation window 6.5 ms and spatial tracking length 2 cm, with noise floor scaled to 0 dB. Also shown are spectral estimates produced from realizations of the signal, averaged over 40 independent temporal windows, showing that many realizations would be necessary to accurately estimate the expected value using randomly positioned point scatterers.

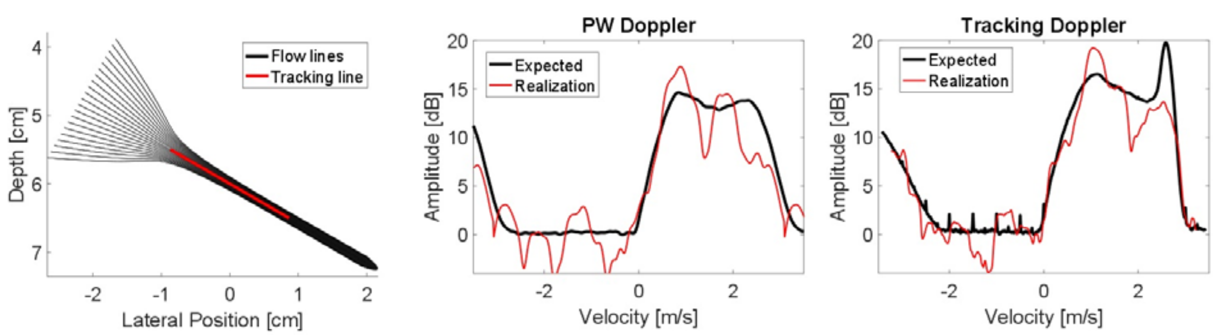

P1-B3-2

Perfusion Flow Phantoms with Many Variably Oriented Micro Channels

Mark George[1], Jaime Tierney[1], Shannon Faley[1], Kathryn Ozgun[1], Leon Bellan[1], Brett Byram[1]; [1]*Vanderbilt University, USA*

Background, Motivation and Objective

Ultrasound perfusion imaging with and without contrast agents continues to be an exciting pre-clinical and clinical problem as ultrasound systems and algorithms get more sensitive to slow blood flow. Unfortunately, there have been few phantoms to help develop these techniques. Some have used very small straight tubes, while others have adapted dialysis cartridges. Here, we form a gelatin phantom around a polymer resin template. Then, the resin structure is dissolved leaving behind a network of small randomly oriented channels. These small microchannels are connected to a large channel and then connected to a pump to perfuse blood-mimicking fluid through the phantom

Statement of Contribution/Methods

The base phantom was gelatin doped with graphite to add diffuse scattering. Before mixing the gelatin, a polymer resin was spun into interconnected microfibers using a cotton candy machine. Microfibers were treated to make them less hydrophobic, and then the gelatin (with a crosslinking agent) was poured over the fibers into a mold. The phantom was rotated for an hour while it gelled. The phantom was then immersed in an ammonia bath for 2 days to dissolve the polymer resin and leave behind the empty microchannel network. The microchannels were then perfused with CIRS' blood mimicking fluid at a constant flow rate of 90 (70 – 100) µL/min. To determine whether flow was present, we acquired data with a Verasonics system and an L12-5 transducer operating at 7.8 MHz. To visualize perfusion we used a previously reported adaptive tissue demodulation technique for imaging perfusion without contrast.

Results/Discussion

In the figure below, we show a confocal microscopy image of the phantom microchannels in a gel without graphite (left). The fiber sizes are 1-198 µm in diameter with an expected average of 33 µm. We also show a phantom hooked up to a syringe pump (middle), and a power Doppler image made with our adaptive demodulation technique (right). For this we cut the phantom in half so that only the left side was perfused. The location of the cut is noted on the image. Here we can see that on the left side we still see perfusion as evidenced by the power Doppler image, but on the right side we no longer see any perfusion. We expect these phantoms to be extremely useful for evaluating slow flow algorithms and in establishing new minimum bounds for flow detection given the newest techniques for detecting slow flow.

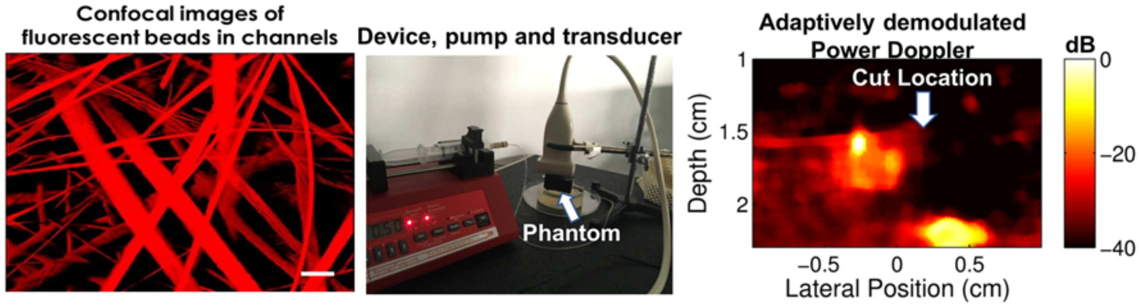

P1-B3-3

Quantitative 3D Assessment of Flow in a Printed Hydrogel Vascular Phantom

Samantha Paulsen[1], James Long[1,2], Bagrat Grigoryan[1], Wolfgang Stefan[2], Jordan Miller[1], **Richard Bouchard[2]**; *[1]Rice University, USA, [2]University of Texas MD Anderson Cancer Center, USA*

Background, Motivation and Objective

While tissue-mimicking phantoms have been useful in the validation of ultrasonic equipment and image processing techniques, they are often restricted to simple vascular geometries due to limitations in fabrication techniques. To address this need, a novel technique has been employed to fabricate 3D-printed photo-curable poly(ethylene glycol) (PEG) hydrogel constructs containing complex, small-scale (e.g., 100s of µm in diameter) vascular channels that can be imaged with ultrasound. In this study, we use color Doppler ultrasound to obtain 3D velocity vector fields through vascular geometries within hydrogel phantoms and compare these results to optical flow assessment and numerical modeling results.

Statement of Contribution/Methods

The geometry of each phantom was first encoded in a CAD program (Fig. 1A) and printed using photomask projections in an iterative process of photo-curing and hydrogel extrusion. A water-based blood substitute containing 25% glycerol and 3µm polystyrene beads was then infused into the channel at constant velocity, during which ultrasonic B-mode and color Doppler images were acquired with the Vevo 2100-LAZR photoacoustic-ultrasonic imaging platform at 24 MHz. Six partially correlated color Doppler acquisitions were obtained at transducer orientations of 0°, 45°, and 90° and transmit steering angles of +/-15°. Acquisitions were then retrospectively co-registered based on B-mode data of the lumen. Matched COMSOL-based numerical modeling and optical flow tracking were implemented for comparison and validation, respectively.

Results/Discussion

Throughout each channel, a radially symmetric, parabolic flow profile was observed (Fig. 1C,D), with maximum velocities of 12 mm/s, considerably greater than estimates from numerical modeling (Fig. 1B,E), at the radial center of the channel. Profile inconsistencies were found near regions containing irregularities – confirmed from B-mode – from the intended print geometry (Fig. 1E). Doppler flow velocity profiles were found to correlate well with optical measurements for planar geometries. As phantom technologies progress and become more physiologically relevant, 3D Doppler-based flow assessment will play a critical role in characterizing complex flow to ensure numerical modeling assumptions match phantom-based experimental analogs.

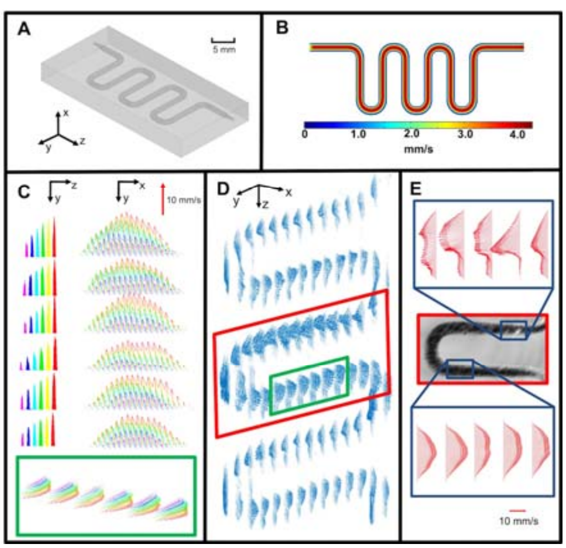

P1-B3-4

Real-time Assimilation and Regularization of Ultrasound Blood Velocity Measurements Using Smoothed Particle Hydrodynamics

Thomas Grønli[1], Abigail Swillens[2], Patrick Segers[3], Lasse Lovstakken[1]; *[1]Department of Circulation and Medical Imaging, Norwegian University of Science and Technology, Trondheim, Sør-Trøndelag, Norway, [2]Barco Healthcare, Ghent, Belgium, [3]Biommeda, Ghent University, Ghent, Belgium*

Background, Motivation and Objective

Ultrafast vector flow imaging can provide detailed measurements of 2D/3D blood velocity patterns, but suffers from an increased variance due to reduced SNR and inherent estimator properties. Further, clutter filtering causes measurement dropouts during parts of the cardiac cycle and imposes an angle-dependent measurement accuracy. This work aims to demonstrate how simulation of the incompressible Navier-Stokes (NS) equations using Smoothed particle hydrodynamics (SPH) can improve the quality of blood flow estimates, and provide reconstruction in regions suffering from filter dropouts.

Statement of Contribution/Methods

A real-time 2D/3D SPH simulator was developed and setup to model intracardiac blood fields using an ensemble of particles suspended in a field potential. The data driven model is continuously updated with motion estimates from blood speckle tracking (BST) and domain boundaries obtained by a real-time segmentation framework. The flow estimates are imposed using the interpolating rules of the SPH framework and a tracking variance measure. The particles are subsequently evolved according to the established system dynamics before a flow grid extraction is performed. A computational fluid dynamic (CFD) model of simplified intracardiac flow (Ansys Fluent) was used as reference, as well as a basis for ultrasound blood speckle simulations (FUSK simulation model) for generating *in silico* BST measurements. The dynamic SPH approach was compared to a static B-spline smoothing with incompressible flow regularization.

Results/Discussion

The GPU-based simulator achieved real-time particle evolution for 2D systems and approximately so for coarse 3D systems, providing bedside applicability. Results showed that the dynamic regularization of SPH was able to reduce the measurement error in the domain on average better than the static B-spline grid (see Figure). The SPH approach was, however, more dependent on boundary conditions, and suffered from spurious and large errors due to improper handling of inlet and outlet paths. Simple gauge pressure models at the valves showed promise in correcting this despite the strong ad hoc nature of the method. Moving forward, more sophisticated models should be devised. This work demonstrates that real-time computational fluid simulation is feasible and can aid in regularizing and reconstructing blood flow estimates.

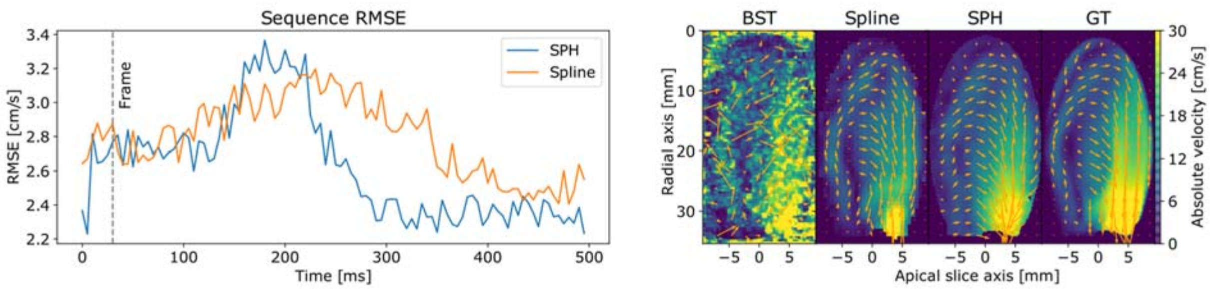

P1-B3-5

Adaptive Clutter Filtering based on Tissue Vector Velocities

Ingvild Kinn Ekroll[1,2], **Jørgen Avdal[1]**; [1]*Centre for Innovative Ultrasound Solutions (CIUS), Norwegian University of Science and Technology (NTNU), Trondheim, Norway,* [2]*Kirurgisk klinikk, St Olav's Hospital, Trondheim, Norway*

Background, Motivation and Objective

Signal from tissue will always be present within the lumen of vessels or in the heart. To image blood flow, this clutter needs to be suppressed sufficiently for the weaker blood signal to appear. As the magnitude and direction both of surrounding tissue and blood flow varies throughout the cardiac cycle, non-adaptive clutter filters will inevitably either yield dropouts or a significant tissue velocity bias in some color flow frames. The individual Doppler measurement biases will further contribute to missing or erroneous vector Doppler estimates. In this work, we propose to use tissue vector velocities to generate clutter filters adapted to the tissue motion in each Doppler frame.

Statement of Contribution/Methods

The carotid artery bifurcation of a healthy volunteer was imaged using a coherent compounding setup (L9, Verasonics Vantage 256) with three transmit angles (-15, 0, 15) degrees and a Doppler PRF of 3 kHz. Using modified autocorrelation estimates of tissue motion in conjunction with the least squares vector Doppler technique described previously (Ekroll et al. 2016), tissue vector velocity fields were generated in a region surrounding the vessel. For each frame, the mean tissue vector velocity was projected onto the different Doppler measurement directions, and used for automatic selection of filter cutoff frequency.

Results/Discussion

Figure 1 shows three vector velocity images from different parts of the cardiac cycle. The first frame is at peak tissue velocity, the second at peak flow velocity and the third is a frame with more complex flow patterns. The lower right panel shows the frequency response of the applied adaptive FIR filter as a function of time, corresponding well with the tissue velocity magnitude (orange color). A FIR filter design was utilized in this work to allow (distortion free) spectral estimation after clutter filtering, but further work will include comparing this approach to other adaptive filtering techniques.

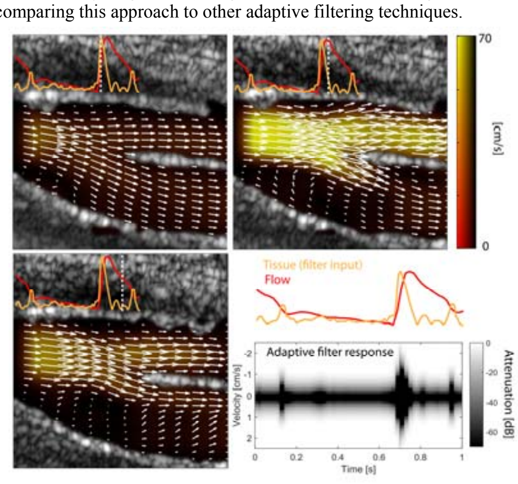

P1-B3-6

Fast and Robust Spatiotemporal Microvessel Clutter Filtering with Randomized Singular Value Decomposition (rSVD) and Randomized Spatial Downsampling

Pengfei Song[1], Joshua D. Trzasko[1], Armando Manduca[2], Bo Qiang[2], Ramanathan Kadirvel[1], David F. Kallmes[1], Shigao Chen[1]; [1]*Department of Radiology, Mayo Clinic College of Medicine, Rochester, Minnesota, USA,* [2]*Department of Physiology and Biomedical Engineering, Mayo Clinic College of Medicine, Rochester, Minnesota, USA*

Background, Motivation and Objective

Singular value decomposition (SVD)-based clutter filtering has demonstrated superior clutter rejection performance in the emerging field of ultrasound microvessel imaging. To alleviate the computational burden of SVD, here we present a fast and robust clutter filter using randomized SVD (rSVD) and randomized spatial downsampling (rSD). rSVD accelerates SVD by approximating and removing the first *k*-order singular values that represent tissue, and rSD achieves further speed-up by allowing parallel processing without introducing artifacts associated with regularized downsampling.

Statement of Contribution/Methods

rSVD first multiplies the spatiotemporal ultrasound data S ($xz \times t$) by a random matrix Ω ($t \times k$, k = assumed tissue rank) to generate a new matrix S' ($xz \times k$), and then performs a QR factorization of S' to obtain a matrix Q whose columns form an approximate orthonormal basis for the column space of S. Tissue signal is equal to QQ^*S, and blood signal is obtained by subtracting QQ^*S from S. rSVD reduces the computational cost from $O(xzt)$ of a full SVD to $O(xzlog(k))$. rSD uses randomized spatial downsampling patterns to create naturally appearing dithering and rendering patterns. This effectively disperses discrepancies among filtered downsampled blocks in an incoherent manner throughout the image. The downsampled blocks can then be parallel processed for enhanced computational performance.

Results/Discussion

An *in vitro* blood flow phantom (Mini-Doppler 404, Gammex) study with external vibration simulating tissue clutter and an *in vivo* rabbit kidney study were conducted with a Verasonics Vantage system (Verasonics Inc.). The phantom study (Fig. 1(a-b)) showed a maximum 9-fold increase in processing speed as compared to a conventional full SVD filtering with minimal deterioration to the clutter filter performance: <3dB reduction in blood to clutter ratio; <0.2 cm^2/s^2 increase in speed mean squared error; <0.1 cm/s increase in flow signal standard deviation; and <0.3 cm/s increase in tissue clutter velocity. The *in vivo* study (Fig. 1(c-e)) showed comparable performance of the proposed filter to a conventional SVD filter in the presence of heavy tissue clutter and showed no artifacts throughout the downsampling range (4× ~ 40×). We also demonstrated real-time imaging capability with ~40 ms processing time per frame (31200 spatial samples and 50 ensembles).

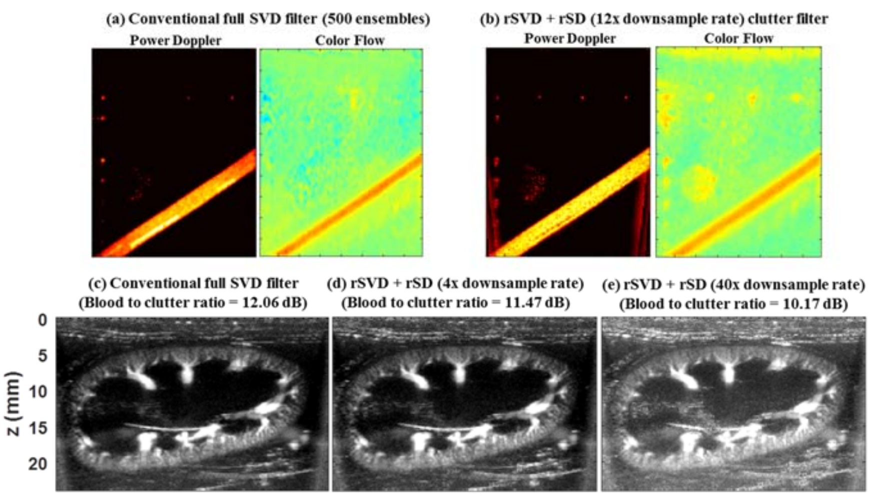

Figure 1. (a)-(b): Selected flow phantom results filtered by conventional full SVD clutter filter and the proposed rSVD and rSD filter. (c)-(e): Selected power Doppler images of the rabbit kidney processed by full SVD and the proposed filter with different downsample rates.

P1-B3-7

Adaptive Clutter Filtering in High Frame Rate 3D Coronary Imaging

Cristiana Golfetto[1], Hans Torp[1], Ingvild Kinn Ekroll[1,2] ; [1]*Centre for Innovative Ultrasound Solutions (CIUS), Dept. Circulation and Medical Imaging, Norwegian University of Science and Technology (NTNU), Norway,* [2]*St. Olavs Hospital, Norway*

Background, Motivation and Objective

Doppler measurements in coronary arteries are difficult due to rapid motion of the myocardium and small vessel dimensions. High frame rate 3D Doppler imaging with retrospective spectral Doppler processing could potentially solve this.

However, the combination of low blood flow velocities and excessive tissue motion in parts of the cardiac cycle makes clutter suppression challenging. In the present work, we propose to use adaptive clutter filtering to reduce power Doppler artefacts such as flashing and dropouts.

Statement of Contribution/Methods

A high frame rate (4545 fps) 3D dataset from the left anterior descending coronary artery of a healthy volunteer was acquired with a locally modified commercial scanner (GE-Vingmed Vivid E95, GE 4V-D matrix array probe). A total of 6000 frames was acquired with plane wave transmissions covering a 3D volume of 19.2 x 15 x 29.8 mm, over one cardiac cycle. Through eigenvector decomposition of the signal correlation matrix, the clutter signal was represented as a linear combination of 8 basis vectors, using an ensemble of 64 frames. After analysing the frequency response of the eigenvector filter, two butterworth filters were used for comparison, showing similar cut off at positive and negative frequencies; see figure.

Results/Discussion

Figure 1 shows 3D power Doppler images of the left anterior descending coronary artery after applying the filters depicted in panel d). The power Doppler isosurfaces represent the same dB level for all filters. When using the low-cutoff butterworth filter, the coronary is partly obscured by clutter noise. The high-cutoff butterworth filter is able to suppress the clutter, but results in (coronary artery) dropouts. The eigenvector filter reduces clutter noise in a pronounced way without removing significant blood components.

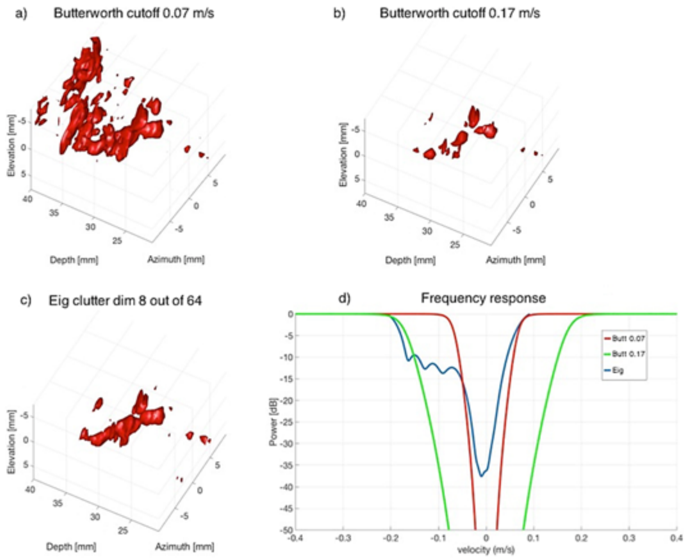

P1-B3-8

Energy Based Clutter Filtering for Vector Flow Imaging

Carlos Armando Villagómez Hoyos[1], Jonas Jensen[1], Caroline Ewertsen[2], Kristoffer Lindskov Hansen[2], Michael Bachmann Nielsen[2], Jørgen Arendt Jensen[1]; [1]*Electrical Engineering, Technical University of Denmark, Kgs. Lyngby, Denmark,* [2]*Department of Radiology, Copenhagen University Hospital, Copenhagen, Denmark*

Background, Motivation and Objective

Over the past years, the design principle for clutter removal has remained basically the same. The clutter signal has been separated from the blood signal based on the difference in their spectral frequencies. This design presents a major challenge for angle independent estimators, because at high beam-to-flow angles tissue and blood frequency spectra tend to overlap. This work presents a novel filtering scheme to better suppress the clutter signal originating from a moving vessel wall. The filter operates on the energy content instead of frequency discrimination, allowing it to maintain a larger portion of the blood velocity spectrum. The use of energy based clutter filtering is explored using simulated and a measured data.

Statement of Contribution/Methods

The energy based filter uses the energy or amplitude characteristic of the velocity (Doppler) spectrum to discriminate between blood and tissue signals. The frequency components are classified as tissue, when they are above a selected threshold. The tissue signal is attenuated by limiting the amplitude of the spectrum to the threshold.

A synthetic aperture flow sequence (using 8.0 MHz; 3-cycle pulse; 12.5 kHz PRF; 5 emissions) on a 128 elements linear array was used for both the simulated and measured investigations. Field II simulation of a 90° beam-to-flow angle straight vessel with parabolic profile and vessel wall movement was investigated. The vessel wall was either expanded radially at a constant velocity or remained static. The vessel wall scatterers mean amplitudes were set 10 dB above the tissue signal mean amplitude, while the blood scatterers amplitude were set 40 dB below. The measurements data is obtained from the carotid bifurcation of a healthy 27 yo male during peak systole, when the wall movement is the largest.

Results/Discussion

The results from the simulations (left) and measurements (right) are shown on the Fig. 1, where the left column presents the results from a moving average and the right column from the proposed energy based filter. Simulations showed an improvement of bias, specially for estimates closer to the vessel wall. In vivo measurements showed an improvement, providing a better filtering of the tissue clutter compared to the moving average during this cardiac stage. In conclusion, the energy based filter performs better when a higher clutter signal originated from tissue movement is present.

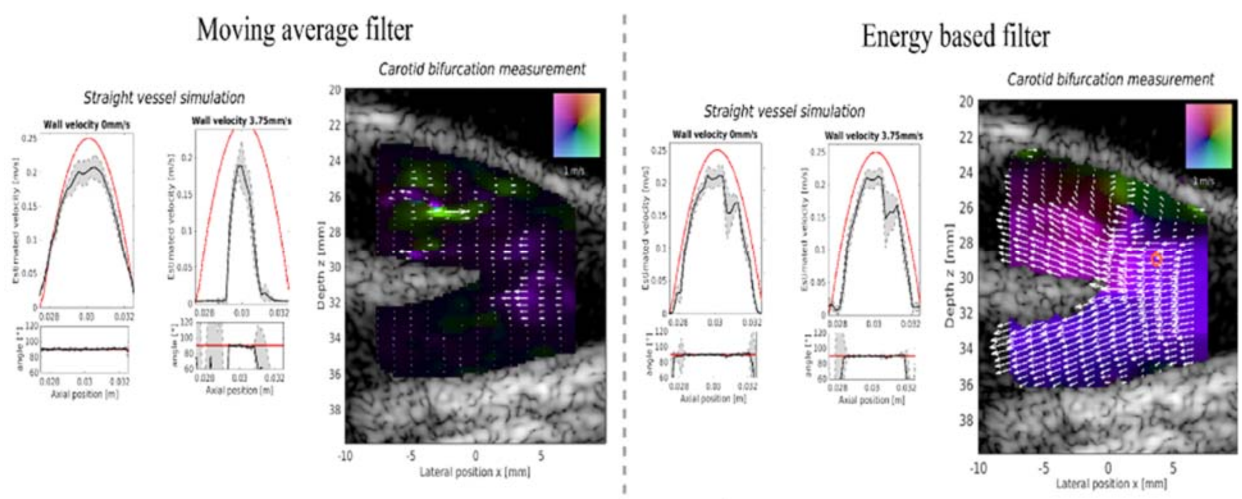

An Improved Spread-Spectrum Method for High-Frame-Rate Color Doppler Ultrasound Imaging

Omar Mansour[1,2], Tamie L. Poepping[3,4], **James C. Lacefield[1,4]**; *[1]Electrical & Computer Engineering, Western University, London, Ontario, Canada, [2]Robarts Research Institute, Western University, London, Ontario, Canada, [3]Physics & Astronomy, Western University, London, Ontario, Canada, [4]Medical Biophysics, Western University, London, Ontario, Canada*

Background, Motivation and Objective

Ultrasound plane-wave imaging is desirable for its ability to achieve high frame rates, allowing the capture of fast dynamic events and continuous Doppler data. In most implementations, multiple low-resolution images from different plane-wave azimuthal steering angles are compounded to form a single high-resolution image, thereby reducing the effective frame rate and attenuating signals with high Doppler shifts. We recently introduced a spread-spectrum color Doppler imaging method [1] that produces high-resolution images without the use of compounding, thereby eliminating the trade-off between beam quality, frame rate, and the unaliased Doppler frequency limit. The method uses a Doppler ensemble formed from a long random sequence of transmit angles that randomizes the phase difference between echoes from the focal point and the out-of-cell (clutter) echoes, thereby spreading the clutter power in the Doppler frequency domain. The original spread-spectrum method suppressed vessel wall echoes, but did not address tissue clutter.

Statement of Contribution/Methods

To reduce both tissue and wall clutter, we redesigned the spread-spectrum method to partition the random transmit angle sequence into multiple segments. Each segment includes the same set of angles, so each angle repeats once per segment, but in a unique random sequence within each segment. After re-arranging the Doppler ensemble into an angle-ordered sequence with periodically repeated angles, the stationary clutter forms a periodic signal represented by discrete spectral lines whose frequency bin spacing is equal to the number of angle segments. The clutter signal is then removed by clearing the corresponding bins in the FFT domain by applying a multi-tap comb filter. The improved method was demonstrated by imaging a carotid artery phantom, perfused with continuous flow, using an Ultrasonix Sonix RP system equipped with an L14-5W/60 linear array and a SonixDAQ module. Spread-spectrum processing was performed offline in MATLAB.

Results/Discussion

The flow-phantom experiments demonstrate that the improved method outperformed the original spread-spectrum technique as measured by a higher probability of detecting flow within the vessel lumen (69% vs. 23%) and an increased blood-to-clutter signal power ratio (18 dB vs. 14 dB). The spread-spectrum method enables acquisition of color Doppler images at high frame rates with high spatial resolution, low side lobes, and high unaliased Doppler velocity limits. The method is promising for improved imaging of rapidly changing fast flows such as those in a stenosed carotid artery, aortic arch, or within the heart chambers.

[1] O. Mansour, T.L. Poepping, and J.C. Lacefield, "Spread-spectrum beamforming and clutter filtering for plane-wave color Doppler imaging," *IEEE Trans. UFFC*, vol. 63, pp. 1865-1877, 2016.

P1-B4 - MCA: Novel Contrast Agents

Exhibit Hall

Friday, September 8, 2017, 9:30 am - 4:00 pm

Chair: **Mark Bordon**
University of Colorado

P1-B4-1

Engineering Acoustic Biomolecules as Dynamic Molecular Sensors for Ultrasound

Anupama Lakshmanan[1], Suchita P. Nety[2], David Maresca[2], Mikhail G. Shapiro[2]; [1]*Biology and Biological Engineering, California Institute of Technology, Pasadena, CA, USA,* [2]*Chemistry and Chemical Engineering, California Institute of Technology, Pasadena, CA, USA*

Background, Motivation and Objective

Ultrasound is currently limited in its ability to image dynamic molecular and cellular processes due to the lack of appropriate contrast agents. Gas Vesicles (GVs) - hollow protein nanostructures isolated from buoyant microbes, have emerged as a new class of nanoscale imaging agents for ultrasound (Shapiro et al., Nat. Nano. 2014). The genetic encodability of these acoustic biomolecules provides a unique platform for engineering mechanical and functional properties at the protein level. Recently, we demonstrated that removal or sequence modification of a key GV shell protein results in nanostructures with enhanced non-linear contrast as well as tunable collapse pressures for multiplexed imaging (Lakshmanan et al., ACS Nano 2016; Maresca et al., Appl. Phys. Lett. 2017). Now, we extend this platform to engineer GVs whose ultrasound signals change dynamically in response to the activity of specific molecules in their environment. In particular, we set out to produce GVs that change their non-linear ultrasound contrast in response to specific proteases, an important class of enzymes underlying homeostatic and disease processes and a target of drug discovery.

Statement of Contribution/Methods

Here, we present initial evidence that genetic engineering of the GV shell protein GvpC (gas vesicle protein C) can be used to generate GVs whose non-linear ultrasound signals depend on activity of two proteases. Incorporation of protease recognition motifs at specific sites within the GvpC sequence enables its cleavage by the active enzyme, producing a change in GV acoustic properties (Fig 1A). The target enzyme may be an always-on protease or one whose function depends on the concentration of another analyte of interest, such as calcium.

Results/Discussion

Incubation of engineered GVs with the always-on Tobacco Etch Virus (TEV) protease or the calcium-activated protease calpain causes a change in mechanical properties of GVs, as seen by a reduction in their critical hydrostatic collapse pressure (Fig 1B). Furthermore, we show that protease activity results in increased harmonic backscattering, as observed by in vitro imaging in agarose phantoms (representative data for calcium-dependent calpain activity shown in Fig 1C). These results demonstrate that GVs can be engineered as dynamic molecular sensors for ultrasound, adding a new capability to this imaging modality.

Figure 1: Engineering Acoustic Biomolecules as Dynamic Molecular Sensors

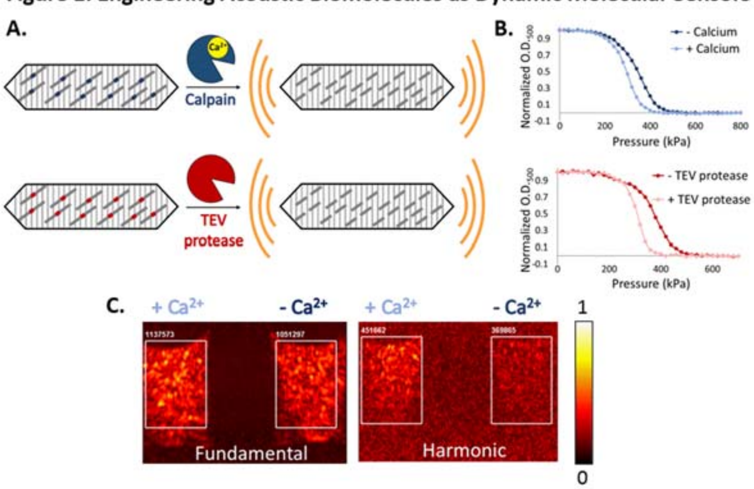

P1-B4-2

Effect of the Surfactant Pluronic on the Stability of Lipid-Stabilized Perfluorocarbon Nanobubbles

Lenitza Nieves[1], Christopher Hernandez[2], Jacob Lilly[1], Joey Mangadlao[1], Rigoberto Advincula[3], Agata Exner[1,2]; [1]*Radiology, Case Western Reserve University, Cleveland, Ohio, USA,* [2]*Biomedical Engineering, Case Western Reserve University, Cleveland, Ohio, USA,* [3]*Macromolecular Science and Engineering, Case Western Reserve University, Cleveland, Ohio, USA*

Background, Motivation and Objective

Microbubble (MB) contrast agents are widely used in diagnostic and therapeutic ultrasound (US) applications. However, due to their 1-10 µm size range, MBs have limited use in cancer detection and treatment. To expand contrast enhanced US capabilities, we have developed sub-micron contrast agents, nanobubbles (NB), via the addition of Pluronic, a nonionic triblock copolymer surfactant, to the phospholipid shell stabilizing perfluoropropane (C_3F_8) gas (Fig 1A). NBs, with diameter of ~200nm, can take advantage of the EPR effect, extravasate the leaky tumor vasculature and accumulate in tumors. Prior work has shown that bubble echogenicity and stability are, in part, dependent on the surface tension of the stabilizing shell. In this study, we evaluate the effect of Pluronic on surface tension of the lipid films and how its presence in the NB shell affects echogenicity and signal decay at clinically-relevant imaging frequencies.

Statement of Contribution/Methods

Pluronic L10 (MW 3200, PPO/PEO units of 49.7/7.3), at three Pluronic:lipid molar ratios (0.02, 0.2, and 0.4), was incorporated into the lipid film composed of a mixture of DPPC, DPPE, DPPA and DSPE-PEG. Bubble diameter was measured with dynamic light scattering (DLS). The surface tension of each composition was measured using pendant drop tensiometry. To test the effect of Pluronic concentration on bubble stability, NBs with the same Pluronic:lipid ratios were formulated by hydrating the lipid mixture described above with the appropriate Pluronic concentration and exchanging air with C3F8. Bubbles were then activated using mechanical agitation and imaged in PBS inside an agarose phantom using a standard diagnostic US scanner (Toshiba Aplio) in contrast harmonic mode at 12 MHz, MI 0.1, and 0.2 frames per second.

Results/Discussion

The incorporation of Pluronic L10 significantly decreased the surface tension, especially at a ratio of 0.2, where this value decreased by 27% ($p < 0.0001$) (Fig 1 B). This led to a significant decrease in the signal decay over time resulting in a stability increase of 39% ($p < 0.0001$) (Fig 1C-D). The Pluronic had little impact on size; NBs had an average diameter of 208 ± 21.3 nm. Future work will evaluate surface tension effects Pluronics of different PEO-PPO ratios to further optimize the NB formulation.

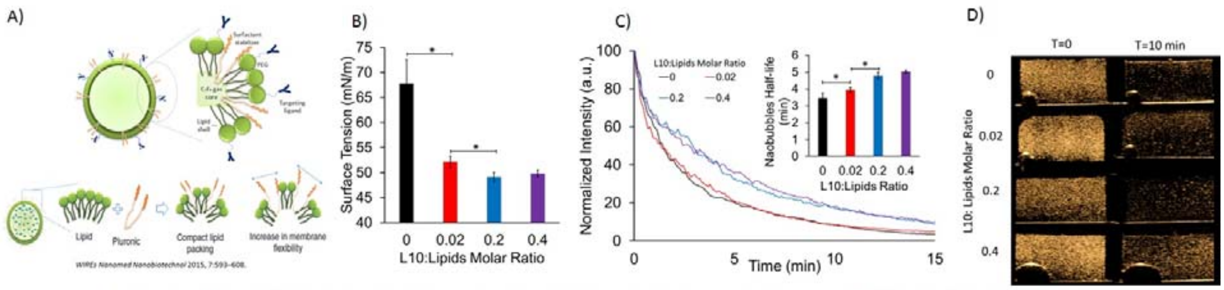

Figure 1: A) Nanobubble Schematic. B) Average surface tension measurements of solutions with different Pluronic L10: Lipids molar ratio. C) Nanobubble stability in US representative curves and half-life calculations for different Pluronic L10: Lipids molar ratio bubbles. D) US images of bubbles in vitro using custom-made agarose mold .

P1-B4-3

Effect of Boundary Constraints on the Vaporization Threshold of Low Boiling-Point Phase-Change Contrast Agents

Juan Rojas[1], Paul Dayton[1,2]; [1]*Biomedical Engineering, The University of North Carolina and North Carolina State University, USA,* [2]*The University of North Carolina Lineberger Comprehensive Cancer Center, USA*

Background, Motivation and Objective

Phase-change contrast agents (PCCAs) provide advantages over conventional microbubble contrast agents, including increased circulation time and the ability to extravasate from leaky tumor vasculature. Additionally, PCCAs can be vaporized into echogenic microbubbles for diagnostic ultrasound imaging. Previous studies have demonstrated that the vaporization threshold of PCCAs is higher in vivo than in vitro. In this work, the role of boundary constraints imposed by blood vessels on the vaporization threshold of PCCAs is explored. We hypothesize that boundaries raise the vaporization threshold of PCCAs.

Statement of Contribution/Methods

PCCAs were perfused through microtubes with diameters of 12.5, 50, 108, and 160 µm and vaporized using an L11-5 linear array driven by a Verasonics ultrasound system. The signal produced by the vaporization event was captured using a 1 MHz piston transducer. Vaporization pulses consisted of 5 cycle, 5 MHz sinusoids with peak negative pressures (PNP) ranging between 1 and 4 MPa, and the pressure was increased in increments of 500 kPa for the entire range. A 10 % dilution of droplet solution was used, and the amount of vaporization was calculated by finding the area under the curve of the frequency spectrum of the signals resulting from each of the pulses. The vaporization threshold was calculated as the first pressure to produce 10 % of the maximum AUC value.

Results/Discussion

The results show that smaller tube diameters increase the vaporization threshold (Figure 1). The threshold in 160, 108, and 50 µm tubes were 1.5 ± 0.0 MPa, 1.67 ± 0.24 MPa, and 2.33 ± 0.24 MPa, respectively, and vaporization was not detected in the 12.5 µm tube at any of the tested pressures. The number of PCCAs inside the 12.5 µm tube (based on inner volume) was approximately matched in a 105 µm tube using a very dilute solution (0.13 %), and vaporization in the larger tube was detected at various pressures. Therefore, our system was sensitive enough to detect vaporization of few PCCAs, implying that if vaporization in the 12.5 µm tube had occurred, we would have been able to detect it. Thus, we conclude that boundary constraints imposed by microtubes of decreasing diameter raise the vaporization threshold of PCCAs. However, more work is required to understand what other factors such as hydrostatic pressure may be involved.

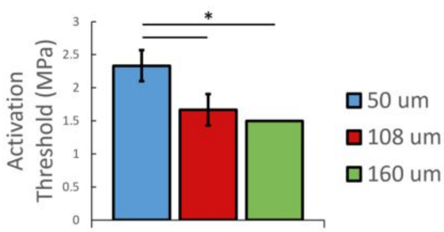

Figure 1. Vaporization thresholds for PCCAs in tubes with different diameters. Vaporization was not achieved in the 12.5 µm tube, so no threshold value is displayed. The asterisk represents significance ($p < 0.05$).

P1-B4-4

Microfluidic Shrinking of Microbubble Contrast Agents

Vaskar Gnyawali[1,2], Byeong-Ui Moon[1,2], Jennifer Kieda[2,3], Raffi Karshafian[2,4], Michael C. Kolios[2,4], Scott S. H. Tsai[1,2]; [1]*Department of Mechanical and Industrial Engineering, Ryerson University, Toronto, Canada,* [2]*Institute for Biomedical Engineering, Science and Technology (iBEST), Toronto, Canada,* [3]*Department of Electrical and Computer Engineering, Ryerson University, Toronto, Canada,* [4]*Department of Physics, Ryerson University, Toronto, Canada*

Background, Motivation and Objective

Lipid-stabilized microbubbles are used in various clinical ultrasound (US) applications such as diagnostics imaging and therapeutics. The characteristics of the microbubbles such as size, shell material, and US frequency dictate the acoustic response of these microbubbles. Therefore, monodispersed microbubbles with the length-scale (1-7 µm in diameter) relevant to the biomedical ultrasound applications are highly desirable. However, generating monodispersed microbubbles with sub-micron size control has been challenging.

Statement of Contribution/Methods

We developed a new microfluidic technique to generate lipid-stabilized microbubbles of 1-7 µm in diameter by shrinking the microbubbles from O(100) µm in diameter by applying a suitable vacuum pressure. We use polydimethylsiloxane (PDMS) microfluidic devices with a conventional flow focusing orifice for generating the lipid stabilized microbubble before shrinking them to O(1) µm in diameter as they passage through a serpentine channel. In the microfluidic system, we adjust a single parameter, the vacuum pressure, to control the resulting size of the microbubbles.

Results/Discussion

Negative pressure environment in the interdigitated vacuum microchannels adjacent to the serpentine channel (Fig. 1a) removes air components dissolved in the continuous phase liquid through the PDMS wall. As a result, air molecules inside the microbubbles diffuse into the surrounding liquid causing the microbubbles to shrink (Fig.1c-f). During the diffusion process, the liquid-lipid interface continually maintains the thermodynamic equilibrium. Hence, the shrunk microbubbles remain stable. We demonstrate that the final shrunk microbubbles of O(1) µm in diameter are stable in the atmospheric condition for at least 25 minutes.

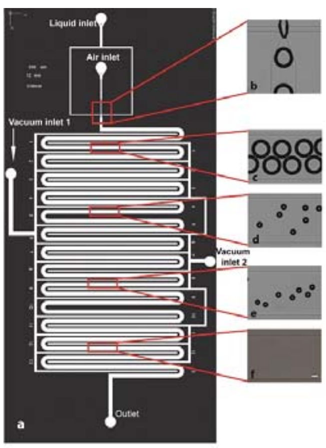

Fig. 1: a) Schematic illustration of design of our microfluidic device. b) Experimental images of microbubbles generated at the orifice (c-f) continuously shrink while flowing downstream the serpentine channel. Vacuum inlets connect vacuum source to the vacuum channels adjacent the serpentine channel. The scale bar represents 50 µm.

P1-B4-5

On-demand Gas-generating Nanoparticles as an Ultrasound Imaging Contrast Agent

In-Cheol Sun[1], Heechul Yoon[2], Stanislav Emelianov[1,2]; [1]*Wallace H. Coulter Department of Biomedical Engineering, Georgia Institute of Technology and Emory University School of Medicine, Atlanta, Georgia, USA,* [2]*School of Electrical and Computer Engineering, Georgia Institute of Technology, Atlanta, GA, USA*

Background, Motivation and Objective

Microbubbles (MBs) are often used as ultrasound imaging contrast agents. Given their micrometer size, MBs are confined in vascular compartments because they cannot escape through endothelial barriers and, as such, MBs are primarily useful in microcirculation or vascular-targeting molecule imaging. To penetrate outside of vasculature, the size of the ultrasound contrast agent should be in the nanometer scale range. When gas bubbles are reduced to nanometer size, they have low echogenicity and limited response to acoustic field. A desired ultrasound contrast agent should consist of nanoparticles that are capable of escaping from vasculature, penetrating into tissue, and generating sufficient contrast once they reach the target site. Here we report the development of a novel contrast agent (panel A) consisting of gold nanoparticles that are covered by azide compounds and capable of on-demand laser-induced gas generation via photolysis.

Statement of Contribution/Methods

Gold nanoparticles were synthesized by reducing chloroauric acid with glycol chitosan at 70°C for 24 h. Then, azidobenzoic acid was conjugated with EDC/NHS. The absorption spectrum, particle size distribution/zeta potential, and morphology were characterized using UV-vis spectroscopy, DLS, and TEM, respectively. Contrast enhancement by gas generation upon laser irradiation was visualized using the Vevo LAZR imaging system (40 MHz ultrasound array transducer and 5-7 ns, 532 nm laser pulses).

Results/Discussion

The size of gas-generating nanoparticles (ggNPs) was 35.72 ± 8.83 nm (TEM image in Panel B). UV-vis spectrophotometer measurements confirmed the stability of ggNPs since the surface plasmon resonance peaks were preserved at around 532 nm after surface modification. Upon laser irradiation, ggNPs generated gas bubbles (panel C) resulted in significant enhancement of contrast in US images (panel D). The significance of this proof-of-principle study is in the discovery of the photocatalytic function of gold nanoparticles in the photolysis of azide and the gas generation for contrast-enhanced ultrasound imaging. These ggNPs may enable the ultrasound diagnosis of various diseases that conventional microbubbles cannot detect. Furthermore, these particles can also be used for ultrasound-guided photoacoustic imaging, focused ultrasound, and photothermal therapy.

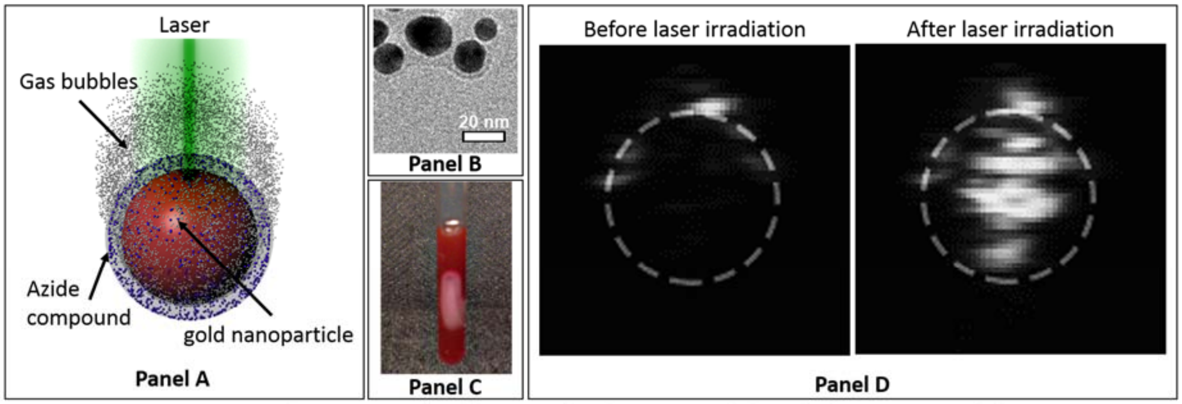

Gas-generating nanoparticle consisting of gold core and azide compounds (Panel A). TEM image of the gas-generating nanoparticles (Panel B). Photograph of a glass tube with gas-generating nanoparticle colloid showing the formation of gas bubbles upon irradiation with a single laser pulse (Panel C). Ultrasound images of microtube (0.28 mm diameter) containing gas-generating nanoparticles: before (left) and after (right) laser irradiation (Panel D).

P1-B4-6

Ultrasound Signal from Sub-Micron Lipid-coated Bubbles

Christopher Hernandez[1], Jacob Lilly[2], Gabriellla Fioravanti[1], Judy Hadley[3], Agata A. Exner[2]; *[1]Department of Biomedical Engineering, Case Western Reserve University, USA, [2]Department of Radiology, Case Western Reserve University, USA, [3]Malvern Instruments, USA*

Background, Motivation and Objective

Sub-micron bubbles have recently gained interest in cancer imaging and therapy for their ability to enter the tumor parenchyma through the enhanced permeability and retention (EPR) effect. It remains unclear whether nanoscale lipid-stabilized bubbles can produce the observed enhanced acoustic backscatter at clinically relevant frequencies. Because NB polydispersity is high, micron sized bubbles are thought to contribute to experimental observations. Accordingly, this study examined echogenicity of lipid- and surfactant-stabilized perfluoropropane (C_3F_8) nanobubbles (NBs), rigorously controlling for the presence of microbubbles in the solution.

Statement of Contribution/Methods

NBs were formulated by mechanical agitation of a PBS solution of lipids (DBPC:DPPE:DPPA), Pluronic L10, and glycerol in the presence of C_3F_8 gas. Microbubbles were separated from NBs based on their buoyancy by centrifugation. According to the Stokes equation (Fig 1A), when centrifuged at 50g for 5 min a bubble larger than 0.7 µm should rise a distance of 0.5 cm. Care was taken to only collect samples below this distance. Particle size and buoyant mass were measured using Resonant Mass Measurement (RMM), Archimedes, Malvern Instruments). Isolated NBs were filtered using track-etched polycarbonate filters of 1000 nm and 400 nm using a syringe pump at 0.125 mL/min and 0.5 mL/min and were imaged in an agarose mold in PBS using contrast harmonic imaging (Toshiba, 12 MHz, MI 0.1).

Results/Discussion

RMM results (Fig. 1B) show that mean NB size was 469 nm and all buoyant particles (positive mass) were below 1 µm. These large positive mass particles are likely large lipid aggregates and should not produce ultrasound (US) signal. US images of isolated NBs (Fig. 1C) demonstrate considerable echogenicity. A reduction in signal after filtration was noted (Fig 1C), but NB activity was observed under all conditions. It is not clear whether the signal decrease is due to lower NB concentration or smaller bubble size. It is likely that filter pore blockage by lipid aggregates is responsible for some of the signal loss. While the mechanism of the strong NB activity at 12 MHz is not fully understood, a reduction of surface tension by the surfactant Pluronic, or buckling of the shell in response the US field, are likely contributors.

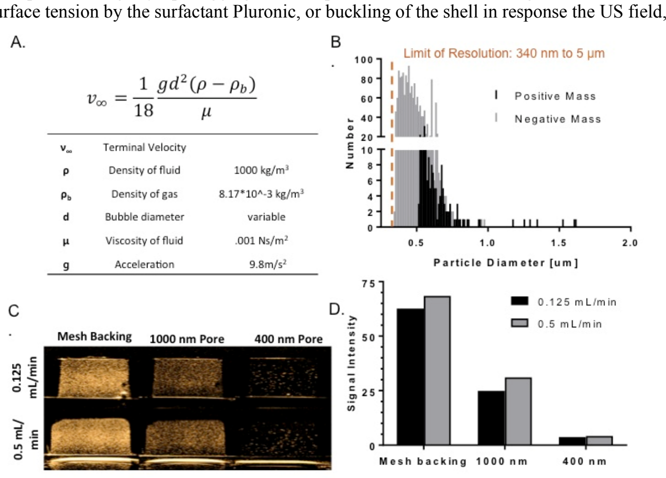

Figure 1. (A) Stokes law for the terminal velocity of a bubble. (B) Particle size distribution based on buoyancy determined by RMM with a lower limit of detection at 340 nm; prior dynamic light scattering results which analyze particles to <10 nm show mean NB diameter to be 0.19 µm. US images (C) and corresponding grayscale intensity (D) of isolated NBs before and after being filtered through 1000 nm and 400 nm pores.

P1-B4-7

Experimental Investigation on Chemical Kinetics between Biotinylated Microbubbles and Streptavidin

Yuta Otsuki[1], Kenji Yoshida[2], Yoshiaki Watanabe[1]; [1]*Doshisya univ, Japan,* [2]*Chiba univ., Japan*

Background, Motivation and Objective

For ultrasonic molecular imaging, evaluation for molecular expression has been discussed for decades. However, there is no method to quantify the precious expression level of molecules using ultrasonography. To solve this problem, it is important to understand the chemical kinetics between targeted microbubbles (TMBs) and target molecules as a fundamental study. Therefore, we construct the system composed of a quartz crystal microbalance (QCM) sensor and flow system. By using the proposed system, we evaluated the adsorption rate and amount of TMBs to target molecules and investigated how these parameters relate to the number density of TMBs.

Statement of Contribution/Methods

MBs with biotinylated phospholipid shell was fabricated as TMBs where the number density was$7.2*10^6$ bubbles/mm^3 and the average diameter was 1.2 µm in original suspension. Suspensions with different number density of TMBs were prepared by diluting the original suspension. Streptavidin as target molecule was fixed on the whole surface of QCM. TMBs specifically absorbed to the streptavidin in sending the TMBs suspension to the surface of QCM. To wash the non-specifically absorbed TMBs, ultrapure water was finally sent to the QCM surface. We monitored the frequency shift (Δf) of QCM during the interaction between TMBs and streptavidin. An adsorption rate (time constant τ) was measured by fitting an exponential curve ($\Delta f = A*\exp(-t/\tau)+\Delta f_c$) to the experimentally-obtained Δf -time curve. The frequency shift Δf_B as defined in Fig.1 (a), corresponded to the amount of specifically-adsorbed TMBs, also was measured.

Results/Discussion

Figure 1(a) shows Δf –time curves in sending TMBs suspensions with different number density (20 and 890 bubbles/mm^3). It was found that Δf decreased exponentially in both cases. In addition, τ in case of 890 bubbles/ mm^3 was clearly smaller than that in case of 20 bubbles/ mm^3. Fig. 1 (b) shows τ -C characteristic and Δf_B –C characteristic, where C means the number density of TMBs. It could be found that there was a power law dependence in τ -C characteristic and a logarithmic dependence in Δf_B –C characteristic. Based on this result, fitting was performed with $\tau = 10^B *C^A$, and $|\Delta f_B| = A' * \log C + B'$ (A=-0.73,B=3.85, R^2=0.975 and A'=59.7, B'=17.8, R^2=0.939). This result provides effective insights to chemical kinetics between TMBs and target molecule.

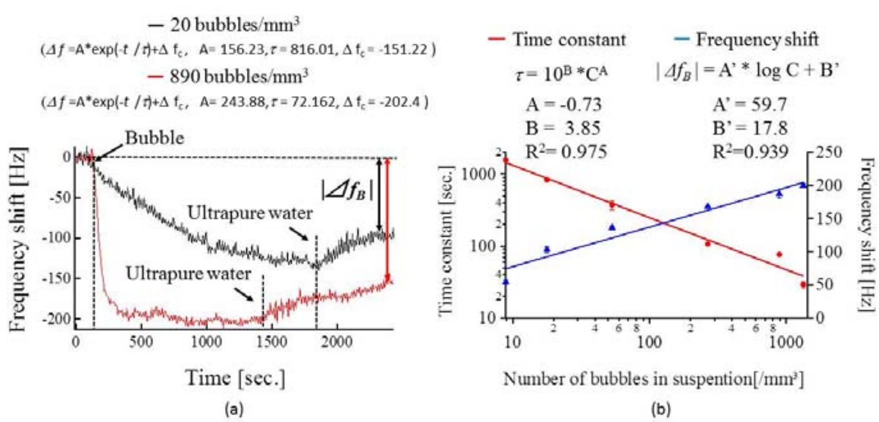

Figure.1 (a) Δf -time curve in case of 20 and 800 bubbles/mm^3
(b) Time constant and frequency shift VS Number of bubbles in suspension

P1-B4-8

A Preliminary Study of Amorphous Calcium Carbonate-Doxorubicin Nanoparticles (ACC-DOX NPs) for Ultrasound Theraonstics

Pei-Hua Chiang[1], Qiaofeng Jin[1], Chih-Kuang Yeh[1]; [1]*Department of Biomedical Engineering and Environmental Sciences, National Tsing Hua University, Taiwan*

Background, Motivation and Objective

Microbubbles in ultrasound-triggered drug and gene delivery have been widely used for biomedical applications. However, the properties of micron-sized, short lifespan and low drug payload limit their applications. The pH sensitive nanoparticles (NPs) that can generate bubbles and release drugs quickly within acidic tumor microenvironment would be a promising theranostic agent. Among them, Amorphous calcium carbonate-Doxorubicin (ACC-DOX) NPs are the typical one with high DOX payload. However, they are unstable in aqueous environment. Herein, we propose that superhydrophobic modification would greatly improve their stability. Our previous studies showed that air bubbles adsorbed on superhydrophobic surface can be served as cavitation nuclei to enhance blood vessel permeability and drug accumulation in tumor. Moreover, the CO_2 bubbles generated in tumor can enhance ultrasound imaging and trigger dox release simultaneously (Figure A).

Statement of Contribution/Methods

ACC-DOX NPs were synthesized by using a vapor-diffusion method. Then, ACC-DOX NPs were coated with silica layers by Stober method and fluorinated with Perfluorodecyltriethoxysilane to obtain the superhydrophobic NPs (ACC-DOX@silica-F). Inertial cavitation doses of the fabricated NPs were detected by a 15-MHz focused transducer under 2-MHz ultrasound excitations at 2-6 MPa. The amounts of Dox release from ACC-DOX@silica-F in various pH-value phosphate buffers were measured by plate reader. The TRAMP cell experiments were conducted to assess the cytotoxicity under 2-MHz ultrasound excitation (50-cycle and 5 MPa at a PRF of 100).

Results/Discussion

TEM images show the sizes of both ACC-DOX and ACC-DOX@silica NPs about 100-200 nm in an amorphous morphology and their silica shells are 20-30 nm (Figure B). The ξ-potentials were varied from +37.2 mV (ACC-DOX) to -35.8 mV (ACC-DOX@silica), and ACC-DOX@silica-F became superhydrophobic after fluorination. The inertial cavitation dose of ACC-DOX@silica-F shows a 4.5-fold increasing with respect to that of ACC-DOX@silica and DI water (Figure C). Furthermore, Dox release was augmented under pH 6.5 than pH 7.4 to demonstrate the pH-sensitive character. The TRAMP cells incubated with ACC-DOX@silica-F NPs presented a 34% cytotoxicity under ultrasound exposure. Future work includes assessment of their capability as theranostic agent in vivo.

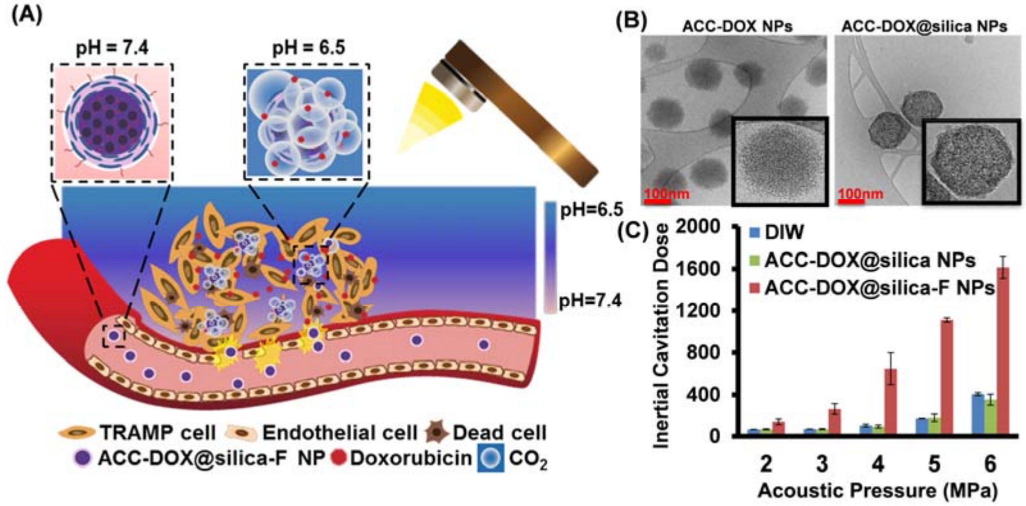

P1-B4-9

Magneto-motive Ultrasound Imaging Using Superparamagnetic Ferrite Nanoparticles with Enhanced Saturation Magnetization Synthesized by a Simple Copreciptation Method

Yaser Hadadian[1], Ana Paula Ramos[2], Diego Sampaio[1], Antonio Carneiro[1], **Theo Pavan[1]**; [1]*Department of Physics, University of Sao Paulo, Ribeirão Preto, SP, Brazil,* [2]*Department of Chemistry, University of Sao Paulo, Ribeirão Preto, SP, Brazil*

Background, Motivation and Objective

Detecting cancer at earlier stages is critical for effective therapeutic procedures and reduction of mortality. Molecular imaging plays a crucial role to improve the early diagnosis of cancer. Magneto-motive ultrasound (MMUS) imaging is a technique developed to improve the detection of magnetic nanoparticles (MNPs) by ultrasound. The advantage of using contrast agents with nanoscale dimensions is their ability to target biologic events at the molecular and cellular levels. In MMUS, MNPs are used to label a specific tissue and an induced displacement, due to the interaction of MNPs with an alternating magnetic field, is detected by ultrasound imaging. Therefore, it is desirable to use MNPs with high saturation magnetization to enhance the induced displacements, consequently, improving the visualization of the contrast agent at lower concentrations.

Statement of Contribution/Methods

In this study, five different Zn-substituted magnetite nanoparticles, $Zn_xFe_{1-x}Fe_2O_4$ (x=0.0, 0.1, 0.2, 0.3, 0.4) prepared by a one-pot simple coprecipitation reaction were used as contrast agents in MMUS imaging. All samples were in superparamagnetic state with the size distribution between 30-40 nm. Prepared MNPs had different magnetization values at the field strength of 900 Oe, the maximum strength for our MMUS setup. MMUS images were obtained from five different gelatin phantoms with semi-spheres inclusions of 1 cm in diameter and 0.7 wt% concentration of MNPs. The setup for MMUS consisted of a custom build coil for generating the magnetic field and an ultrasound system used for echo signal acquisition, which used a linear ultrasound transducer operating at 9.5 MHz and was positioned opposite the coil. An interface software system developed in MatLab was used for data acquisition and processing.

Results/Discussion

The results showed that the magnetization of magnetite was enhanced by substituting Zn for Fe in its structure. All nanoparticles showed good potential to be used in MMUS imaging as a contrast agent and the induced displacement, in the inclusion area, changed according to their magnetization values (see Fig). The highest displacement was 60 µm related to the composition with x=0.1, which had the highest magnetization. This relative high magnetization can lead to use less concentration of nanoparticles in MMUS imaging.

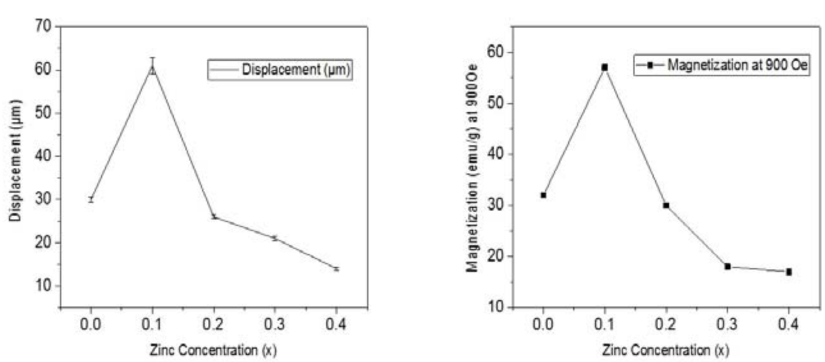

P1-B5 - MEL: Emerging Methods for Elasticity Imaging

Exhibit Hall

Friday, September 8, 2017, 9:30 am - 4:00 pm

Chair: **Muyinatu Lediju Bel**
Johns Hopkins University

P1-B5-1

Air-coupled ARF-based Excitation of Broadband Mechanical Waves for Dynamic Elastography

Liang Gao[1], Piotr Kijanka[2], Mitchell Kirby[1], Ivan Pelivanov[1], Łukasz Ambroziński[2], Shaozhen Song[1], David Li[3], Soon Joon Yoon[1], Ruikang Wang[1,4], Matthew O'Donnell[1]; [1]*Department of Bioengineering, University of Washington, Seattle, WA, USA,* [2]*AGH University of Science and Technology, Krakow, Poland,* [3]*Department of Chemical Engineering, University of Washington, Seattle, WA, USA,* [4]*Department of Ophthalmology, University of Washington, Seattle, WA, USA*

Background, Motivation and Objective

Recently we demonstrated non-contact excitation of broadband mechanical waves in soft media for transient elastography. Using US from an air-coupled transducer focused on an air/medium interface, this method (called "acoustic micro-tapping", or AμT) provides sufficient radiation force to launch a transient displacement. Combined with ultrafast phase sensitive OCT, AμT-OCT can track propagating mechanical waves with a fully non-contact system appropriate for many applications. Complementary methods are now needed to properly reconstruct the elastic modulus from imaged wavefields.

Here we explore the different modes launched by an AμT source that can be tracked efficiently with OCT. The motivation is an optimal method to reconstruct the elastic modulus from complex displacement fields given the highly dispersive nature of waves in bounded media such as the cornea.

Statement of Contribution/Methods

Both theoretical and computational approaches were used to analyze wave propagation. Far from the AμT source, simple mode types can be identified theoretically. Close to the source, however, computational methods are needed to describe complex displacements. Both finite difference and finite element methods have been used and compared to minimize inaccuracies due to the specific method.

Experiments were also performed on bulk and bounded gelatin phantoms to compare with theoretical and computational predictions.

Results/Discussion

Under AμT excitation, both shear and surface waves are efficiently generated [Fig. 1]. Note that the shear wave propagation direction is independent of soft medium properties and source characteristics. Separating these waves with generalized directional filters over a wide bandwidth is needed to accurately reconstruct real and imaginary components of the elastic modulus.

For bounded media, 2D Fourier and time-frequency transforms help select modes and evaluate dispersion relations for accurate elasticity reconstruction. These methods are applied to AμT-OCT measurements in pilot ex-vivo and in-vivo studies as part of initial translational work.

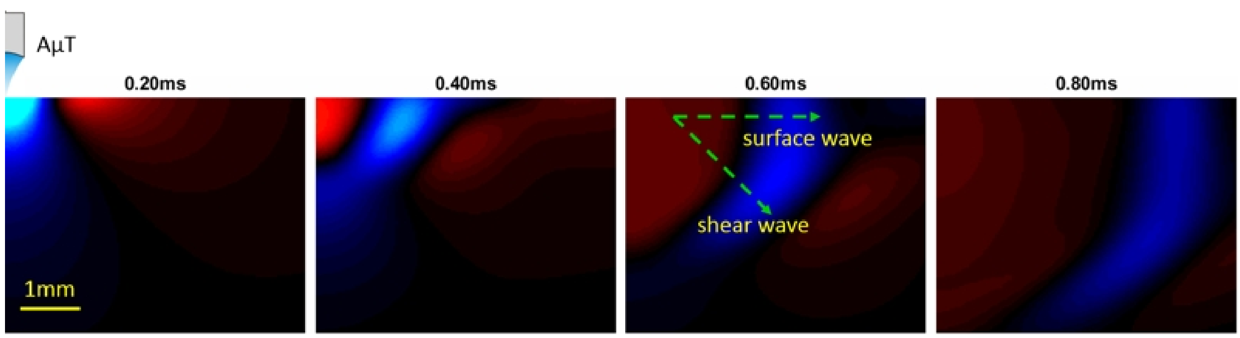

Figure 1. Numerically simulated wavefield snapshots in a soft medium model at different times after AμT excitation. The air-coupled ultrasound transducer is aimed at the center of the phantom and generates mechanical waves within. Due to symmetry, only the right half is shown. Note that the shear wave direction is at an angle to the surface normal.

P1-B5-2

Experimental Validation of Simultaneous Excitation of Orthogonal Coded Push Pulses for Fast Shear Wave Elastography

Takuya Matsumoto[1], Kengo Kondo[1], Takeshi Namita[1], Makoto Yamakawa[1], Tsuyoshi Shiina[1]; [1]*Graduate School of Medicine, Kyoto University, Kyoto, Japan*

Background, Motivation and Objective

Shear wave elastography is useful for quantitatively evaluating tissue elasticity by measuring the speed of a shear wave induced within the body by acoustic radiation force. We proposed a pushing-and-tracking sequence, coded push-pulse excitation to increase the signal-to-noise ratio (SNR) of the observed shear wave propagation without increasing measurement time and push-pulse amplitude[1)]. In this study, we irradiate multiple coded-pulse sequences from different locations at the same time and separate overlapped shear waves by decoding to quickly image a wider area with high SNR. The feasibility of the proposed method was validated in phantom experiments.

Statement of Contribution/Methods

Assuming linear tissue deformation with excitation enables us to code tissue displacement by push pulses. Coded displacement can be decoded by post-processing, and the decoded displacement is equivalent to the result of short, high-amplitude excitation. Such sequences can be achieved by interleaving push and track pulses. We divided the aperture into two sub-apertures and irradiated coded pulse sequences from each sub-aperture at the same time using Orthogonal Golay Code (OGC)[2]. The received shear waves induced by two push-pulse sequences are overlapped but are separated by orthogonality after post-processing. As a result, measurement time decreases and SNR increases due to push-pulse compression.

Results/Discussion

The proposed method was validated with elasticity QA phantom using linear probe (VeraSonics, L7-4). The PRF was 2500 Hz. Figs. 1 (a), (b) depicts the conventional one-time measurement. We irradiated pulse sequences from the right and left sides of the probe (Figs. 1 (c), (d)). Two shear waves were separated by post-processing (Figs. 1 (e), (f)). Compared with conventional method, the SNR increases by 14.5dB (32-bit OGC), 14.9dB (32-bit Golay Code (GC)), 15.0dB (32 average procedure), and 15.1dB (theoretical value of all methods). The measurement times were 0.129sec (32-bit OGC), 0.258sec (32-bit GC), and 1.28sec (32 average procedure).

As a result, the measurement time for one irradiation by 32-bit OGC was half of that for two irradiations from the left and right sub-apertures by 32-bit GC and reduced to 10 percent of the time of the 32 average procedure.

Reference

1) K. Kondo et al., Proc. IEEE IUS, 341, 2013.

2) R. Y. Chiao et al., Proc. IEEE IUS, 1677, 2000.

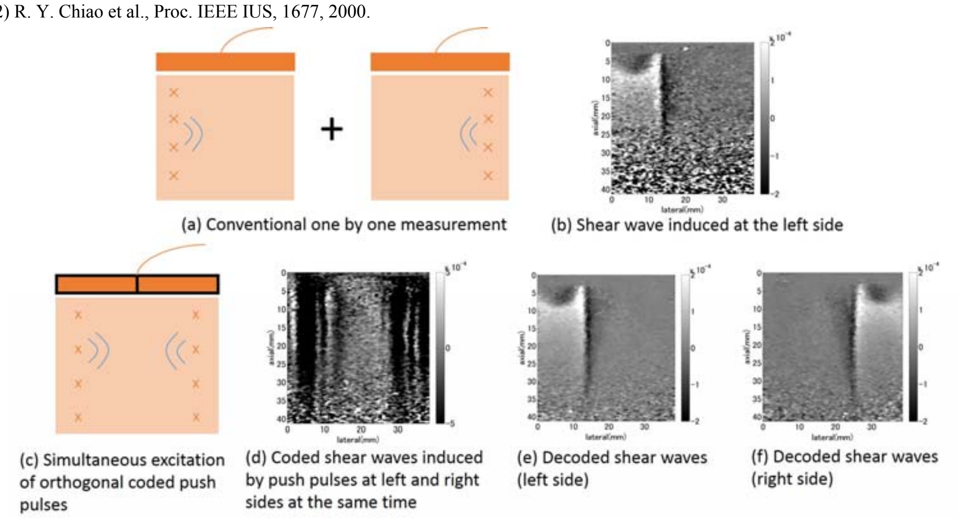

Fig. 1. Shear waves 4msec after the irradiation of pulse sequences.

P1-B5-3

Clutter Filter Wave Imaging (CFWI): A New Way to Visualize and Detect Mechanical Waves Propagation.

Sebastien salles[1], Svein Arne Aase[2], Tore Bjastad[2], Lasse Løvstakken[1], Hans Torp[1]; [1]*Norwegian University of Science and Technology, Department of Circulation and Medical Imaging, Norwegian University of Science and Technology, Norway,* [2]*GE Vingmed Ultrasound, Norway*

Background, Motivation and Objective

In the last 10 years the advent of high frame rate ultrasound imaging has allowed the visualization and study of mechanical wave propagation in order to estimate the elastic properties of tissue. Theses waves are detected through the estimation of motion induced by the wave propagation. Despite efficient motion estimator such as speckle tracking or Tissue Doppler Imaging (TDI), the detection of mechanical waves still remains challenging. Moreover, such techniques can be time consuming and dependent on several tunable parameters. In this work, we present a new, simple and fast method allowing the detection of mechanical waves without using any motion estimator.

Statement of Contribution/Methods

This method only consists in applying a temporal clutter filter, for instance a third-order high-pass Butterworth filter, on the radio-frequency data. Instead of using a clutter filter to remove all the tissue, as it used in blood flow imaging, we set the clutter filter to remove or attenuate only a range of velocities along the beam direction. The propagation of this attenuated tissue motion will be visible as a darker band in the B-mode sequences. By taking the time gradient and extracting the spatiotemporal map of a specific region, the wave propagation velocity can be estimated. The feasibility of this technique was studied, first using acoustic radiation force imaging on a tissue-mimicking phantom in order to visualize and extract the acceleration map of shear wave (Verasonics Inc., 1000 fps). And secondly by studying the “natural” mechanical wave which propagate along the left ventricle wall in 2D (GE Vivid, 820 fps).

Results/Discussion

In panel a, the results show that CFWI is able to better distinguish the propagation slope than using TDI. Moreover, we can see that the propagation slope is clearly visible, with a better spatial resolution, without any smoothing needed. In panel b, the use of CFWI allows a better description of the wave propagation in term of resolution and signal-to-noise ratio, all along the wall. The estimated wave velocities of two different mechanical waves, of one healthy voluntary, were more homogeneous with a better standard deviation, over 5 cardiac cycles (Tab b).

In this work, a new method able to detect the propagation of mechanical waves was presented and compared to TDI. This technique is able to better detect the propagation of waves in term of resolution and SNR

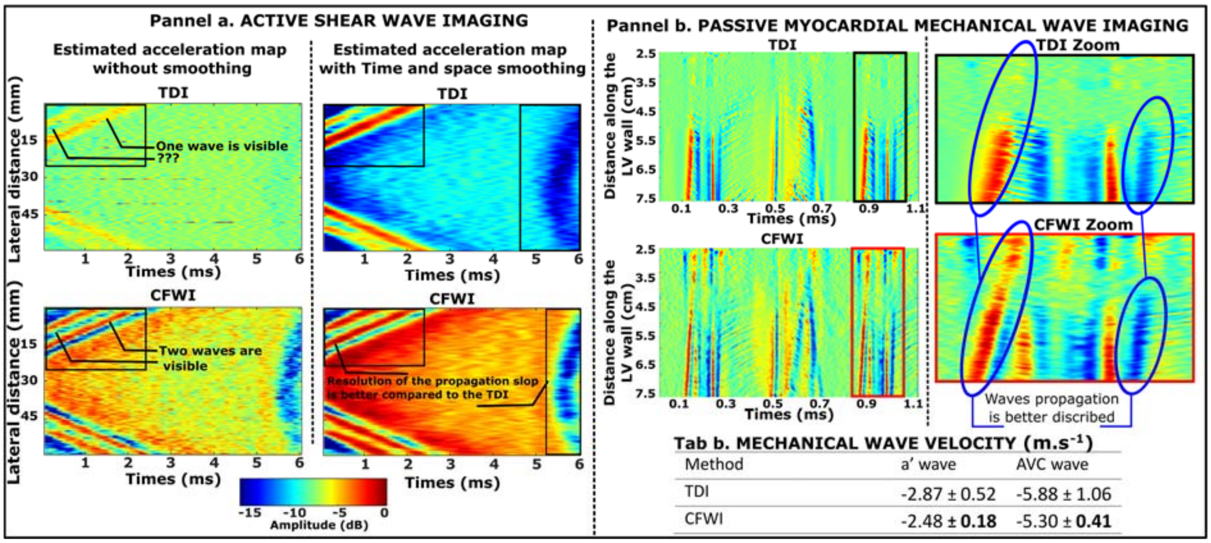

P1-B5-4

A New Method for Shear Wave Speed Estimation in Anisotropic Tissues Using Wavelet Transform and Dynamic Programming

Pak-Hei Yeung[1], Wei-Ning Lee[1,2]; [1]*Medical Engineering Programme, The University of Hong Kong, Hong Kong,* [2]*Department of Electrical and Electronic Engineering, The University of Hong Kong, Hong Kong*

Background, Motivation and Objective

Ultrasound shear wave imaging is a rapidly emerging technique that noninvasively quantifies shear wave speed (SWS), which is directly linked to the stiffness of soft tissues. Targeting sources of estimation errors entailed in *in vivo* data, previous studies have proposed different methods, e.g. radon sum (RS) (Rouze *et al*. 2010), under the assumption of tissue homogeneity, which significantly limits its application in tissues with complex structure. In this study, we propose dynamic programming regularized wavelet transform (DPRWT) towards robust estimation of local SWS in inhomogeneous and anisotropic soft tissues.

Statement of Contribution/Methods

In each shear wave event, a spatial-temporal map (STM) was obtained from each depth of interest (Fig. a). Wavelet transform was first performed at every time point of STM to generate a series of spatial frequency-translation maps (SFTMs) for tracking the shear wavefronts. Cross correlation among SFTMs therefore yielded likelihood maps for identifying potential shear wave propagation (SWP) pathways. Dynamic programming was then employed to search for the optimal SWP pathway by incorporating physical constraints, i.e., bounded propagation speed and direction, into the optimization process. This effectively eliminated noise interference. Local SWS was finally estimated by taking piecewise gradient of the optimal SWP curve.

Results/Discussion

In vivo porcine myocardium (P_H) and patients′ back muscle (H_{BM}) were examined. Fig. a shows that wavelet-transform-based methods were less susceptible to noise than the conventional time-of-flight (TOF) method as quantitatively verified by the largely distinct goodness-of-fit (Fig. b) and Frechet distance in DPRWT-RS (P_H: 23.1, H_{BM}: 38.2) and TOF-RS (P_H: 88.1, H_{BM}: 189.1). Fig. c shows that shear wavefronts traced by DPRWT exhibited less amplitude variation, indicating that shear wave energy during propagation could be more accurately followed by DPRWT than RS method. Our findings demonstrated that DPRWT outperformed RS in inhomogeneous and low SNR regions (Fig. a). Local muscle fiber orientations of P_H (Fig. d) and H_{BM} (Fig. e) were further derived from the DPRWT-estimated SWS. Our results demonstrated the good performance of SWS estimation by DPRWT and its potential application in retrieving local anatomical information and stiffness of anisotropic tissues.

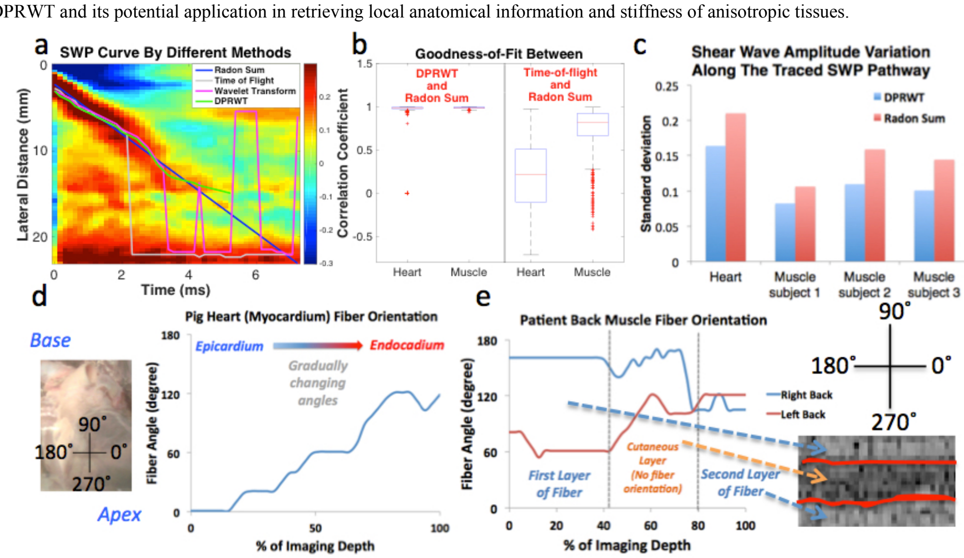

P1-B5-5

A Novel Tracking Strategy for Single Tracking Location Shear Wave Elasticity Imaging

Rifat Ahmed[1], Stephen A. McAleavey[1,2], Marvin M. Doyley[1,2]; [1]*Department of Electrical and Computer Engineering, University of Rochester, New York, USA,* [2]*Department of Biomedical Engineering, University of Rochester, New York, USA*

Background, Motivation and Objective

Single tracking location shear wave elasticity imaging (STL-SWEI) follows shear waves either at a fixed point in space or at equidistant points from push beam pairs. The former method uses directional filtering to reduce reflection artifacts, the latter approach provides more accurate shear wave speed (SWS) estimates. To exploit the advantages of both tracking strategies, we propose to use compounded plane wave (CPW) imaging to perform STL-SWEI. This will reduce both reflection artifacts and the variance incurred when estimating SWS in suboptimal imaging conditions.

Statement of Contribution/Methods

To investigate this hypothesis, we developed a novel approach known as plane-wave based single tracking location shear wave elasticity imaging (pSTL-SWEI). The method consists of a set of push beams at multiple lateral sites, each followed by CPW imaging. During the post-processing stage, we use the temporal wave profiles corresponding to a push beam pair at a common tracking location to estimate SWS. We change the tracking distance relative to the push beam pair to obtain multiple estimates of SWS and reduce the estimation variance by averaging. This is different from standard STL-SWEI, which uses a pair of push beams with a common focused tracking beam to estimate SWS. Specifically, 2D SWS images are produced by keeping the tracking beam static while pushing at different spatial locations (sSTL) or translating a pair of push beams and a common track beam laterally (mSTL). To assess the performance of pSTL-SWEI relative to sSTL-SWEI and mSTL-SWEI, we implemented all three approaches on a Vantage 64 research scanner (Verasonics, Inc., Kirkland, WA). We performed studies on custom-made homogeneous phantoms (10%, 13% and 16% gelatin concentrations) and a commercially available (CIRS Model 049A, Norfolk, VA) phantom.

Results/Discussion

Figure 1(a) shows SWS estimates of homogeneous phantoms measured with all three approaches. The mean and standard deviations are similar, which is expected due to optimal imaging conditions. Figure 1(b) shows the standard deviation of SWS plotted as a function of sonographic SNR. Figure 1(c) shows representative shear wave images produced with the three methods. The pSTL-SWEI depicts the lesion shape more accurately than the other two approaches, which demonstrates that it is more noise resistant than other STL-SWEI techniques.

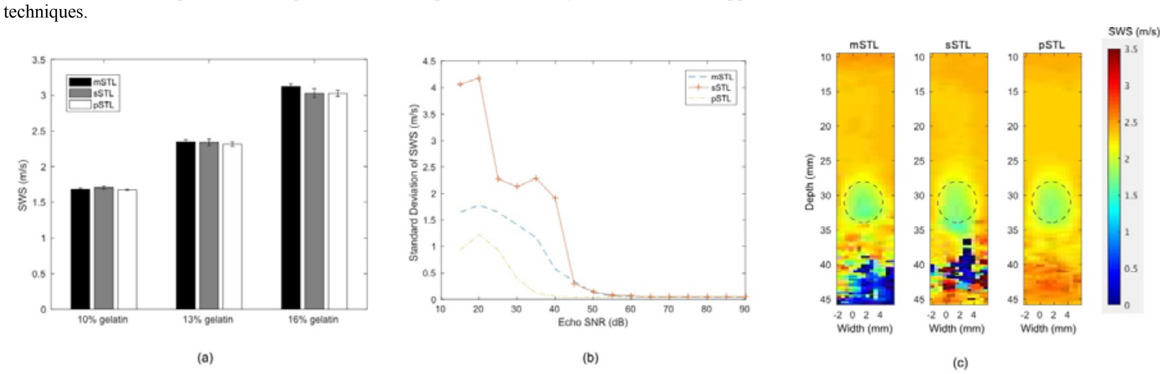

Figure 1

P1-B5-6

Reduced Jitter in Displacement Estimation Using the Spatial Coherence of Backscatter

Dongwoon Hyun[1,2], Yufeng Deng[1], Arsenii Telichko[3], Jeremy Dahl[3]; [1]*Biomedical Engineering, Duke University, Durham, NC, USA,* [2]*Bioengineering, Stanford University, Stanford, CA, USA,* [3]*Radiology, Stanford University, Stanford, CA, USA*

Background, Motivation and Objective

Displacement estimation is a critical component of elastography. The measurement of sub-resolution displacements relies on high cross-correlation (CC) between repeated collinear RF acquisitions. CCs are degraded by common sources of acoustic noise, such as reverberation clutter, in addition to the displacement of scatterers within the radiation force field. CCs are also degraded spatially across the aperture when imaging diffuse scatterers. Previously, we proposed a method that defines an equivalent CC calculation utilizing the CCs of the individual channel signals. In this method, poor CCs are rejected from the channel-signal pairs, resulting in reduced jitter in simulation experiments. Here, we characterize the performance of the channel-based method in radiation force displacement estimation in a phantom study under ideal and noisy imaging conditions.

Statement of Contribution/Methods

Acoustic radiation force impulse (ARFI) imaging was performed in a calibrated phantom using a Verasonics research scanner with the VF7-3 transducer. Imaging was performed with and without a layer of porcine tissue for low and high SNR imaging, respectively. The standard 1D (Kasai) and 2D (Loupas) autocorrelation phase-shift estimators were compared to their channel-based formulations C-Kasai and C-Loupas, respectively. In these methods, CCs with a magnitude below 95% of the channel autocorrelation were rejected. Displacements were estimated using axial kernels of 0, 1, and 2 wavelengths (WL). Jitter was measured as the sample standard deviation of the displacements in a uniform region.

Results/Discussion

The C-Kasai estimator improved ARFI image quality by suppressing the texture variance as compared to the conventional Kasai estimator. In a speckle region with a mean displacement of 1.2 um, the jitter measured by C-Kasai (0.20 um) and C-Loupas (0.17 um) were both smaller than the jitter measured by Kasai (0.39 um) and Loupas (0.32 um). The channel-based estimators reduced jitter approximately two-fold under both the low and high SNR imaging conditions for multiple axial kernel lengths. Furthermore, the C-Kasai and C-Loupas estimates with a single-sample (0 WL) kernel had lower jitter than Kasai and Loupas with a 2 WL kernel. By selectively utilizing only the highly coherent CCs, the channel-based estimators significantly reduced jitter in the displacement estimates.

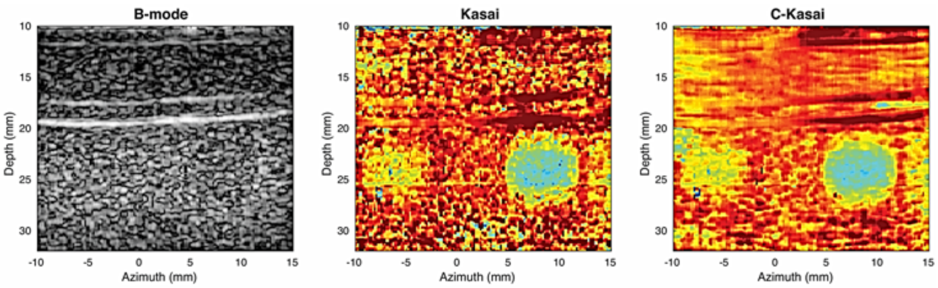

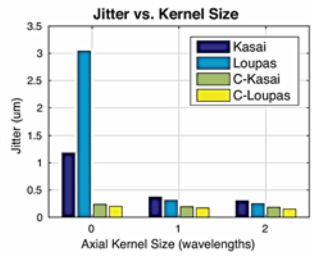

Figure 1 - B-mode and ARFI images of elasticity targets in a CIRS 040GSE phantom were formed using a VF7-3 transducer. (*top left*) The targets were not visible in the B-mode image. (*top middle*) An ARFI image was formed using the conventional Kasai estimator on summed channel data. (*top right*) An ARFI image was formed using the proposed C-Kasai estimator on the full channel data. The C-Kasai ARFI image exhibits reduced jitter in the speckle-like texture throughout the image. (*bottom right*) The measured jitter is plotted for the estimators for a mean displacement of 1.2 um. For all kernel sizes, C-Kasai and C-Loupas each outperformed both Kasai and Loupas.

P1-B5-7

Comparison Study of Displacement Estimation Methods for Microwave Ablation Procedures using Electrode Displacement Elastography

Robert Pohlman[1,2], Jingfeng Jiang[3], Wenjun Yang[1], Timothy J Ziemlewicz[4], Marci Alexander[4], Kelly Wergin[4], Meghan Lubner[4], James Louis Hinshaw[4], Fred T Lee Jr. [4], Tomy Varghese[1,2]; [1]*Department of Medical Physics, University of Wisconsin School of Medicine and Public Health, Madison, Wisconsin, USA,* [2]*Department of Electrical and Computer Engineering, University of Wisconsin-Madison, Madison, Wisconsin, USA,* [3]*Department of Biomedical Engineering, Michigan Technological University, Houghton, Michigan, USA,* [4]*Department of Radiology, University of Wisconsin School of Medicine and Public Health, Madison, Wisconsin, USA*

Background, Motivation and Objective

Minimally invasive procedures such as microwave ablation (MWA) are growing in popularity as a substitute for surgical resection of hepatocellular carcinomas. Ultrasound electrode displacement elastography (EDE) has demonstrated the potential to provide a feasible non-invasive and non-ionizing approach for monitoring the region of thermal necrosis.

Statement of Contribution/Methods

We present results on a comparison of the signal-to-noise (SNR) and contrast-to-noise (CNR) ratios for two displacement estimation algorithms, the Quality-Guided Displacement Tracking (QGDT) [1] and the Coupled Subsample Displacement Estimation (CSDE) [2] method. Twenty patients with strain images processed with both algorithms were recruited in this study. QGDT, using a kernel size of 3.5 wavelengths x 7 A-lines, selects certain pixels as seeds whose quality, correlation coefficient >0.75, are tested among its 4 neighbors. The neighbor with the highest quality is then selected next for processing and this is continued until all estimates of the displacement map are computed [1]. CSDE uses a modified block matching (MBM) algorithm with a kernel size of 7.5 wavelengths x 29 A-lines to estimate initial integer displacement from high quality seeds followed by "motion-compensation". Finally, an iso-contour of the correlation function is fitted to an ellipse to produce the subsample displacement vectors. The final displacement is the sum of the initial integer and subsample displacements [2].

Results/Discussion

Figure 1 shows images from both modalities. The CSDE shows a well delineated ablated region, while the QGDT shows an unclear, noisy boundary. Quantitatively, the strain contrast obtained using both methods are similar. On the contrary, the SNR and CNR of the QGDT was found to be 9.93±6.83 dB and 2.42±6.62 dB, while the CSDE showed an SNR and CNR of 16.8±6.64 dB and 3.68±3.57 dB, respectively. This study indicates that EDE using the CSDE provides higher SNR and CNR however, both approaches produced reproducible results.

Acknowledgement: Funded in part by National Institutes of Health grant 2R01 CA112192 and an academic hardware grant from NVIDIA.

Figure 1: B-mode and EDE strain images obtained using the two algorithms.

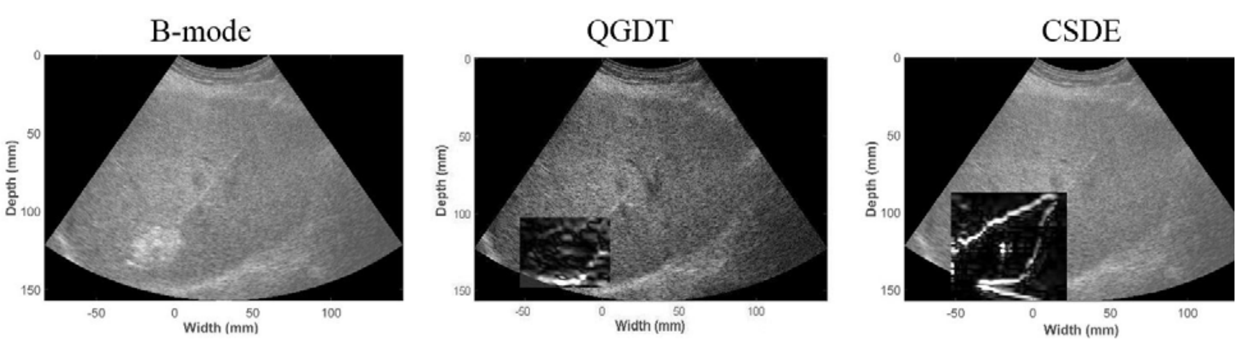

P1-B5-8 ____

Performance Comparison of Optical Flow and Block Matching Methods for Strain Estimation in Spatial Angular Compounding with Plane Wave

Zhi Liu[1], Qiong He[1], Jianwen Luo[1]; [1]*Biomedical Engineering, Tsinghua University, Beijing, China, People's Republic of*

Background, Motivation and Objective

Spatial angular compounding (SAC) with plane wave has been proposed to improve the performance of motion and strain estimation at high frame rate. A previous study shows that the accuracy of 2D estimation depends on the number of steering angles, maximum steering angle, and accuracy of axial estimation at different angles (He et al, Ultrasonics 2017). We have demonstrated (Pan et al, TUFFC 2015) that optical flow (OF) with affine model obtains better axial estimation than normalized cross-correlation based block matching (BM) with rigid model. The objective of this study was to investigate whether OF combined with SAC performs better in plane wave imaging (PWI).

Statement of Contribution/Methods

A homogeneous model was axially compressed by 2% in simulations. The pre- and post-compression channel data of PWI were simulated in Field II (f_0 = 6.25 MHz, f_s = 100 MHz) without (0°) and with steering the transmit beams (±20°), and then were beamformed using delay-and-sum. In phantom experiments, a homogeneous polyvinyl alcohol phantom was laterally compressed by ~1.8% with a customized holder. The channel data were acquired with a Verasonics Vantage System equipped with an L12-5 probe (f_0 = 6.25 MHz, f_s = 50 MHz), and then were beamformed for post-processing. The axial displacements along the steering angles were estimated by OF and BM respectively, and then were compounded to obtain 2D displacements using the least-squares method. The strain was calculated from the spatial derivative of the displacement.

The root-mean-square error (RMSE) and signal-to-noise ratio (SNR) were used to evaluate the strain estimation performance in simulations and phantom experiments, respectively.

Results/Discussion

For both OF and BM, SAC improves the lateral strain estimation, compared with no compounding [Figs. 1(b), 1(d), 2(b), and 2(d)]. OF with compounding obtains smoother lateral strains [Figs. 1(b) and 2(b)], lower RMSEs [Fig. 1(d)] and higher SNRs [Fig. 2(d)]. Specifically, it reduces the RMSE by up to 27.78% and increases the SNR by up to 6.2 dB, respectively. Regardless of whether compounding or not, OF obtains smoother axial strains [Figs. 1(a) and 2(a)], lower RMSEs [Fig. 1(c)] and higher SNRs [Fig. 2(c)] than BM. It reduces the RMSE by up to 59.45% and increases the SNR by up to 5.9 dB, respectively. OF is proved to be superior to BM and thus is suggested for strain estimation in SAC with plane wave.

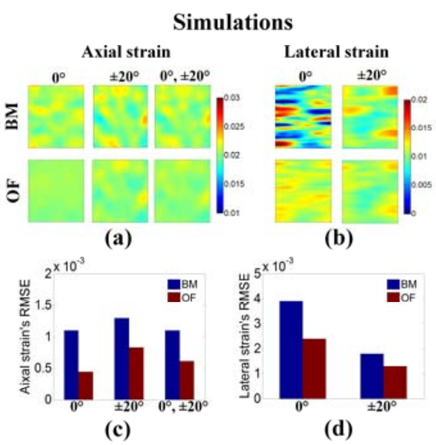

Fig. 1. The estimated (a) axial and (b) lateral strains by BM and OF without and with SAC respectively, and the RMSEs of (c) axial and (d) lateral strains in simulations.

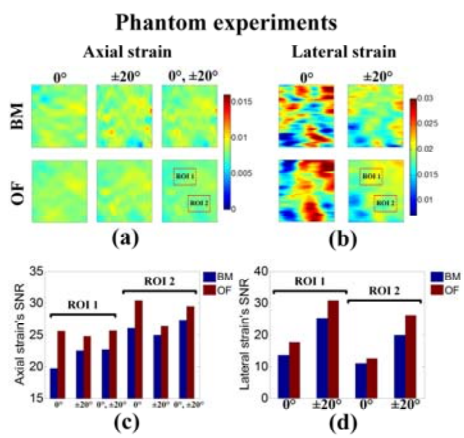

Fig. 2. The estimated (a) axial and (b) lateral strains by BM and OF without and with SAC respectively, and the SNRs of (c) axial and (d) lateral strains in phantom experiments.

P1-B5-9 ____

Constructive Shearwave Imaging: Feasibility and Improvements In SNR

Anna Knight[1], Peter Hollender[1], Kathryn Nightingale[1], Mark Palmeri[1]; [1]*Biomedical Engineering, Duke University, Durham, North Carolina, USA*

Background, Motivation and Objective

Shear wave elasticity imaging (SWEI) measures mechanical properties of tissues and has been used to characterize tissue stiffness, but SWEI is limited by low displacement SNR in stiff media such as skin. A method for repeatable measurement of skin elasticity is critical for longitudinal monitoring of sclerotic diseases such as morphea. Constructive Shearwave Interference (CSI) overcomes the SNR limitations of conventional SWEI in skin by generating greater shear wave displacements at the constructive center of an acoustic radiation force ring of excitation. The objective of this study is to characterize the increase in displacement SNR from constructively-interfering shear waves.

Statement of Contribution/Methods

We are developing a CSI skin elasticity measurement device that uses an annular ring transducer to provide an acoustic radiation force excitation, and a concentric single tracking element in the center of that ring. High SNR shear waves are generated by exciting tissue with the ring and measuring displacements at the point of constructive shear wave interference at the ring center. These higher displacement signals are generated without increasing the peak acoustic exposure in the tissue. Using FEM models, the increases in resultant displacement using CSI are evaluated by comparing the maximum displacement at the constructive center with the maximum displacement at equidistant radial positions outside of the ring. A 7.5 mm outer radius, 2.5 mm inner radius annular ring transducer (Fig A) was modeled using Field II and LS-DYNA in elastic media ranging from E=10-50 kPa and ν=0.45, 0.499. Varying outer radii from 7.5 mm to 17.5 mm transducers were also modeled for E = 10 kPa to test geometric limits.

Results/Discussion

The average ratio of displacement at the constructive center relative to displacement at equidistant positions outside the ring was 12.85 ± 1.11 (Fig B). The maximum displacements and ratios did not appreciably differ for varying ν (Fig C). Using an arrival-time based reconstruction algorithm, the RMSE of reconstructed shear wave speed relative to analytic speed was 0.0576 m/s. CSI accurately predicts shear wave speed across a wide range of tissue stiffnesses and achieves appreciably greater displacement SNR than traditional SWEI methods, making it a promising methodology for measuring skin in longitudinal sclerotic disease studies.

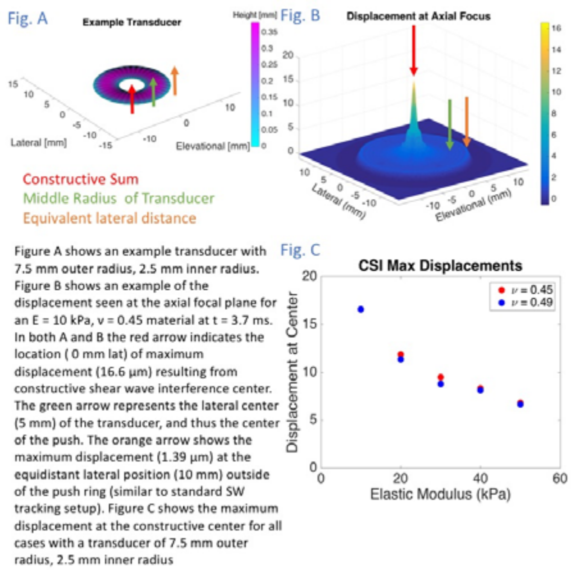

P1-B5-10

Tomographic Shear Wave Imaging: Feasibility Study

Yung-Shao Yang[1], Pei-Yu Chao[2], Pai-Chi Li[1]; [1]*National Taiwan University, Taipei, Taiwan,* [2]*National Taiwan University, Taiwan*

Background, Motivation and Objective

Ultrasound shear wave imaging has been successfully developed with wide clinical applications. Typically, the shear wave image format is the same as the corresponding B-mode so that the shear modulus distribution can be overlaid with the anatomy. However, in certain applications the B-mode cross-sectional view may not be ideal. In this study, we propose a system for shear modulus computed tomography. Such a system inherently can achieve higher spatial resolution and the imaging setup is more suitable for cell studies using 3D culture systems.

Statement of Contribution/Methods

As shown in Figures 1, data acquisition is similar to that of X-ray computed tomography. A 20MHz transducer is used to generate shear waves. A 40MHz transducer is used to detect the shear wave arrival time. The distance between focal points of the two transducers is 5mm and the shear wave speed is calculated based on the time-of-flight. The reconstruction is performed at the focal depth at 12mm. A step motor stage is used to move and rotate the sample. At each angle, linear projection of the shear wave propagation time is done by linearly translating the two transducers at 51 steps with a step size of 0.1mm. The rotation is from 0 to 180 degrees with a 1 degree step size. The filtered back projection method is used for reconstruction of shear wave speed.

Results/Discussion

As shown in Figure 2, three types of agar based elasticity phantoms were constructed and tested (half circle, layer and circle). The diameter of the reconstruction area is 5mm and shear wave speed ranges from 2.4m/s to 3m/s. The reconstruction results generally agree with the original phantom designs with a spatial resolution at the order of 100 microns. The proposed system is being applied to elasticity measurements of 3D cell culture systems as part of the ongoing work.

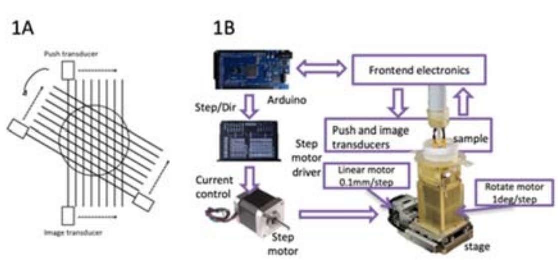

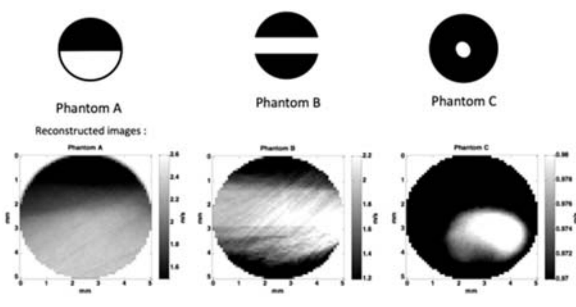

P1-B5-11

Beyond Diffraction Limit in Shear Wave Imaging

Stefan Catheline[1], Ali Zorgani[1], Chadi Zemzemi[1], Loic Daunizeau[1], Remi Souchon[1]; [1]*INSERM, University of Lyon, France*

Background, Motivation and Objective

When a wave field is measured within a propagative medium, it is widely accepted that the resulting image resolution depends on the measuring point density, and no longer on the wavelength. Indeed, in-situ measurements allow the near-field details needed for super-resolution to be retrieved. This is supported here by two experiments conducted in elastography. In the first, the virtual source and sink fields known to overcome the diffraction limit are extracted from a time-reversal experiment in the bulk of an elastic soft solid. In the second, imaging is shown with a resolution down to 1/27th of a shear wavelength.

Statement of Contribution/Methods

In the first part of this report, a time-reversal elastic field is reconstructed from the local measurement of a diffuse field. From a time-reversal point of view, even if the source is point-like, because of diffraction the wave refocuses on a spot size that cannot be smaller than half a wavelength, except in the presence of an acoustic sink. Thus, overcoming the diffraction limit implies that a sink or its equivalent counterpart, a source field, can be recreated. This is achieved by using a simple directional filter applied to the experimental time-reversal field. This demonstrates the close link that relates the nature of super-resolution in elastography to the present methods listed here. The second part of this report is devoted to a quantitative experimental estimation of the resolution in elastography.

Results/Discussion

As can be extended to other fields of wave physics, the conclusion here is that in the absence of noise in the data, the tomography resolution in magnetic resonance elastography ultimately depends on the magnetic resonance imaging, in optical coherent elastography on the optical coherent tomography, and in seismology on the distance between the geophones.

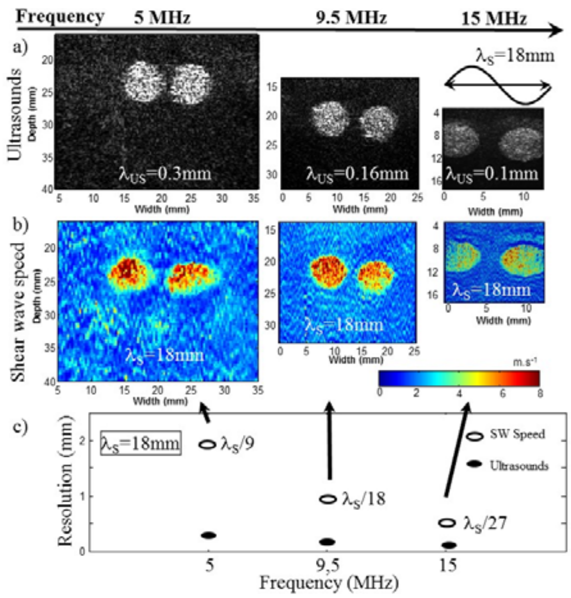

P1-B6 - MIM: Contrast

Exhibit Hall

Friday, September 8, 2017, 9:30 am - 4:00 pm

Chair: **Kenneth Hoyt**
University of Texas at Dallas

P1-B6-1

Transcranial Dual Frequency Ultrasound for Contrast Enhanced Ultrafast Brain Functional Imaging – An in vitro Feasibility Study

Thomas Robins[1], Mengxing Tang[1]; [1]*Bioengineering, Imperial College London, London, United Kingdom*

Background, Motivation and Objective

Functional Ultrasound (fUS) has shown to be a promising new neuroimaging modality that uses ultrafast plane waves to detect changes in cerebral blood flow for imaging brain activity at high spatiotemporal resolution. An existing challenge is the ultrasound penetration of skull which decreases with frequency. In the initial study (Macé et al., 2011)[1] a craniotomy was required to perform fUS. Since then non-invasive fUS has been demonstrated through the introduction of microbubble (MB) contrast agent to produce a 9 dB gain in contrast to noise ratio (CTR) (Errico et al., 2016)[2]. Even with MB, attenuation of skull still places constraints on imaging depth. Decreasing the frequency reduces this attenuation and allows for greater depth of penetration while also producing more MB resonance, but this is at the cost of decreasing resolution. We propose a dual transducer, dual frequency system for transmitting at low frequency to stimulate microbubbles at greater depths and producing superharmonic echoes that can be detected by a high frequency transducer. The aim of this dual frequency system will therefore be to achieve high resolution transcranial functional imaging at greater depths while improving the CTR.

Statement of Contribution/Methods

Two transducers (P4-1, L22-14v) were secured at 90^o to each other while coplanar through the centre of the two apertures, resulting in a shared imaging plane. An ultrafast ultrasound scanner (Verasonics Vantage 256 system, Washington, USA) was used to define a virtual transducer of 256 elements for the dual frequency system. The P4-1 was set to transmit plane wave pulses (PRF = 3500 Hz, without compounding, single angle = 0^o) while both transducers receive echoes. An ex-vivo flow phantom was constructed using a macerated mouse skull containing a 200 µm cellulose vessel with contrast enhanced flow (10^6 MB ml^{-1}). Acquisitions were taken at transmit frequencies 1.5, 2.0 and 2.5 MHz for 4 increasing MI values. This was repeated with the L22_14v for comparison. The data then underwent high pass filtering to remove clutter signal and power Doppler signals were calculated.

Results/Discussion

The signal to noise ratio (SNR) was found to be higher when imaging using the dual frequency system. However, there is also a reduction in spatial resolution, especially when no compounding was used in this study. Further optimisation of the approach is required.

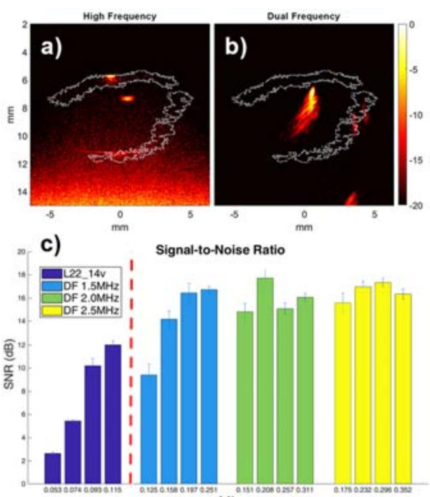

Figure 1: a) L22_14v and b) Dual Frequency acquisitions (skull cross section can be seen superimposed in white). The cross section of the tubing can be seen at a depth of ~8mm. The P4_1 is aligned along the left of the frame, the L22_14v is positioned along the top edge, c) SNR plot for L22_14v (left of dotted line) and the 4 Dual Frequency transmit frequencies.

P1-B6-2

Real-Time Optical Tracking to Provide Feedback during Blinded Contrast-Enhanced Ultrasound Imaging: Clinical Evaluation of System and Protocol

Ahmed El Kaffas[1], Renhui Gong[2], Rosa Sigrist[1], Juergen Willmann[1], Dimitre Hristov[2]; [1]*Radiology, Stanford University, USA,* [2]*Radiation Oncology, Stanford University, USA*

Background, Motivation and Objective

Current commercial matrix transducers for 3D Dynamic Contrast-Enhanced Ultrasound (3D DCE-US) do not display side-by-side B-mode and contrast-mode images, thus leaving the operator with no position feedback during lengthy acquisitions. The purpose of this study was to demonstrate the feasibility of using tracking to provide positioning feedback and to assess resulting improvements in maintaining imaging position.

Statement of Contribution/Methods

A tracking system was developed in house using infrared camera (Polaris, NDI, Canada) and a 3D-printed tracking target attached to a X6-1 matrix transducer. Cameras were connected to a PC, enabling real-time streaming of transducer coordinates and display of virtual probe on a separate screen. The tracking system captures a reference position to provide operators positioning feedback when no B-mode image is available. To test this set-up, five experienced operators were asked to locate an image landmark within a healthy volunteer liver in B-mode images using the X6-1 connected to an EPIQ7 system (Philips, Bothell, WA). Operators were then asked to maintain the transducer position for 4 min under three feedback methods: i) B-mode, ii) display of real-time virtual transducer, iii) blind. The magnitude of displacement of a voxel over the cine was computed relative to the reference position as an estimate of the imaging position error.

Results/Discussion

Results suggest that tracking can assist operators maintain a position during a lengthy acquisition. An average displacement of 3.75 mm with standard deviation (S.D.) of 3.31 mm and displacement histogram skewness of -0.18 was noted when using B-mode feedback. When blinded, an average displacement of 4.58 mm (S.D. 2.65 mm; skewness 6.19) was noted. In contrast, the average displacement for tracking-feedback was comparable to that from B-mode at 3.48 mm (S.D. 0.8 mm; skewness 0.09). One operator performed better with tracking than B-mode; one operator performed better blinded than with tracking and B-Mode. To the best of our knowledge, this study is the first to demonstrate the feasibility of tracking for 3D DCE-US to provide feedback during lengthy scan sessions.

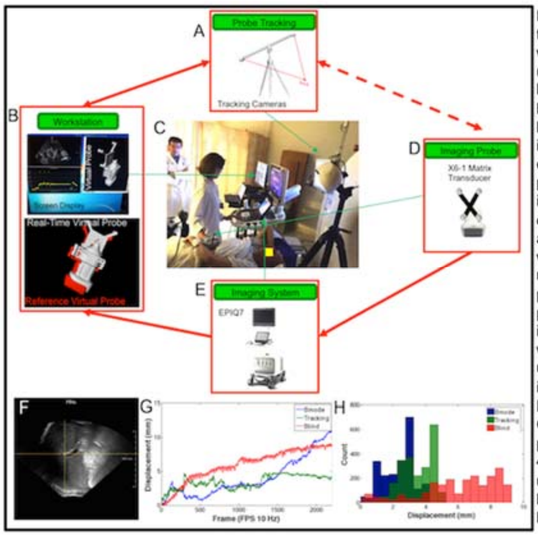

Figure 1: A, Stereo cameras used to track transducer. **B**, Interventional workstation for acquisition of data (Ethernet transfer) and visualization of live virtual probe. For live virtual probe based on tracking, an anatomical location is identified; a reference image is captured linked to a set of coordinates. A red still virtual reference probe (see lower picture; remains still) is then placed on the display to provide operator feedback. The user can then align the live virtual transducer (grey) with the red virtual transducer to reposition or maintain the same position. **C**, Image of set-up around a patient showing location of each instrument. **D**, X6-1 matrix transducer with tracking markers. **E**, EPIQ7 system used to acquire data – the system is interfaced with workstation. **F**, Representative B-mode for feedback. **G**, Representative displacement of probe from reference position over the 4 min cine for one operator shown under B-mode/tracking feedback, and blind. **H**, Representative displacement histograms.

P1-B6-3

Adaptation of the Acoustic Angiography Technique for Use with a Capacitive Micromachined Ultrasound Transducer (CMUT)

Isabel G. Newsome[1], Juan D. Rojas[1], Virginie Papadopoulou[1], Fanglue Lin[1], Anthony Novell[1,2], Omer Oralkan[3], Paul A. Dayton[1]; *[1]Joint Department of Biomedical Engineering, University of North Carolina at Chapel Hill and North Carolina State University, North Carolina, USA, [2]Imagerie et Cerveau, UMR Inserm 930-Université François Rabelais de Tours, France, [3]Department of Electrical and Computer Engineering, North Carolina State University, North Carolina, USA*

Background, Motivation and Objective

Though a fairly new technology, CMUTs present many advantages over traditional piezoelectric transducers, including wider frequency bandwidths, easier integration with circuitry, and cheaper and easier production. The wide frequency bandwidth of CMUTs makes them ideal for multi-frequency ultrasound (US) applications in particular. In this work, we present a CMUT-specific version of the dual-frequency superharmonic imaging technique known as “acoustic angiography” (AA). This contrast US method combines a low frequency transmit with a high frequency receive to create microvascular images, but two-element prototypes are required to do so. These probes are confocally aligned and must be mechanically scanned to create an image. Here, this technique has been optimized for use with a single CMUT array.

Statement of Contribution/Methods

The transducer used in this work was a CMUT from Vermon (Tours, France) that operates with the Verasonics research US platform. For the purposes of this work, this CMUT was operated in the conventional regime. A focused imaging script was developed that incorporates an aperture of 100 elements and 86 scan lines. The CMUT was used to transmit at 4 MHz and receive above 12 MHz. Various highpass filters were tested. A type of amplitude modulation is employed to remove the device’s inherent nonlinearity. The pressure profile of the CMUT was characterized with hydrophone measurements, and in vitro testing was performed to evaluate the imaging method. A lipid shelled, perfluorocarbon core microbubble contrast agent and transmit pressure of 440 kPa were used.

Results/Discussion

The -6 dB frequency bandwidth of this probe indicates optimal performance between 3 and 13 MHz. The CMUT provided SNR of 32.4 dB when imaging contrast in a 200 µm cellulose tube at a concentration of 1e8 bubbles/mL (Fig. 1). Like in dual-frequency AA, CMUT AA removes nearly all signal from linear reflectors, like the tube wall, while signals from nonlinear reflectors, such as microbubbles, are preserved. This data has been processed with a high-pass filter of 12 MHz cutoff frequency, showing that this probe can receive at frequencies greater than the bandwidth implies. Future work will focus on transitioning this sequence from in vitro to in vivo imaging.

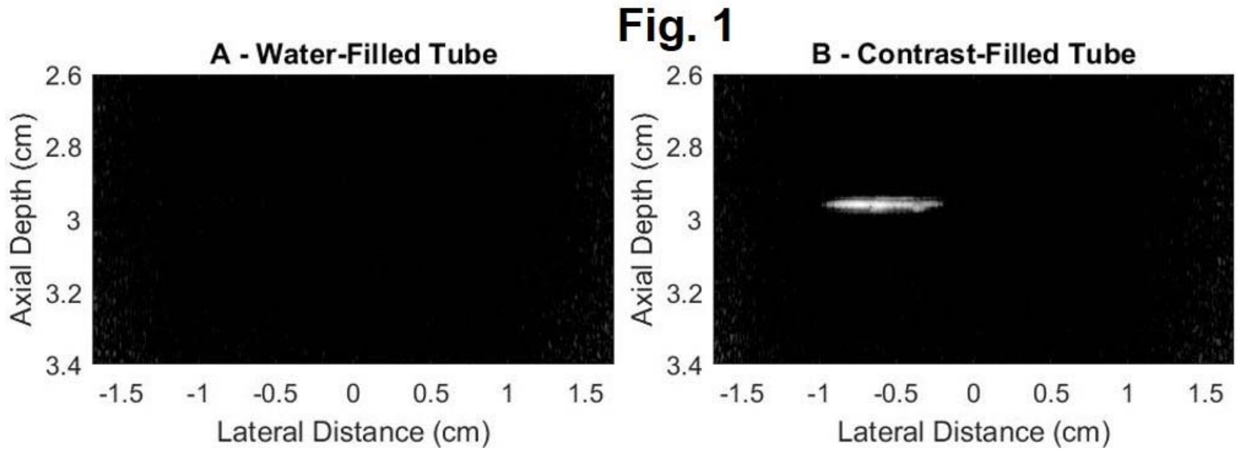

P1-B6-4

Super-resolution Ultrasound Imaging of the Microvasculature In Skeletal Muscle: A New Tool In Diabetes Research

Debabrata Ghosh[1,2], Jun Peng[2], Shashank Sirsi[1,2], Robert Mattrey[2], Philip Shaul[2], Kenneth Hoyt[1,2]; [1]*University of Texas at Dallas, USA,* [2]*University of Texas Southwestern Medical Center, USA*

Background, Motivation and Objective

Diabetes is a major cause of morbidity, mortality, and health care costs worldwide. Studies indicate that an attenuation in the skeletal muscle microvascular response to insulin plays a critical role in type 2 diabetes and obesity-induced insulin resistance. However, the basis of impaired skeletal muscle microvascular function and its correlation to type 2 diabetes remains unclear. An improved knowledge of these processes will lead to new therapeutic strategies to help combat this devastating disease. To that end, the goal of this project was to evaluate the use of super-resolution ultrasound (SR-US) imaging for performing a quantitative analysis of insulin-mediated microvascular changes in skeletal muscle.

Statement of Contribution/Methods

A clinical US scanner (Acuson Sequoia 512, Siemens Healthcare) equipped with a 15L8-S linear array transducer was used for our study. Operation of this system was done using a nonlinear harmonic imaging (transmit/receive at 7/14 MHz). A low transmit power (mechanical index = 0.2) was used to minimize any MB destruction during imaging. C57BL/6J mice (Jackson Laboratory) fed a normal diet (lean model, N = 3) or high-fat diet (obese model, N = 2) were used in this study. After a slow, intravascular injection of 2.5 x 107 MBs, the proximal hindlimb adductor muscle group of each animal was imaged (dynamic contrast-enhanced US, DCE-US) for 10 min (at 10 frames per sec) at baseline and again at 1 h and towards the end of a 2 h hyperinsulinemic-euglycemic clamp. The US transducer was fixed throughout the 2-h imaging period to help capture any microvascular changes along the same image plane. The SR-US imaging technique was developed using custom Matlab software (Mathworks Inc). After collecting a stack of DCE-US images and applying a singular-value-decomposition (SVD) based spatiotemporal filtering, individual MBs were localized and subsequently a SR-US image was generated by mapping the cumulative MB localizations in a single image. The insulin-induced skeletal muscle microvascular recruitment resulting from the clamp procedure was evaluated for the lean and obese animals.

Results/Discussion

Lean animals exhibited a considerably higher increase in microvascular recruitment in skeletal muscle during the hyperinsulinemic-euglycemic clamp procedure compared to the obese animals. More specifically, our SR-US image-derived data from lean animals revealed that relative to baseline, there were 64.4% and 141.2% increases in microvascularity at 1 and 2 h, respectively, of insulin plus glucose administration. In contrast, microvascularity levels (recruitment) in obese animals increased only 20.3% and 33.3%, respectively. These results clearly indicate insulin-induced microvascular recruitment in normal skeletal muscle and an impaired microvascular response to insulin in obese animals. In addition, a new SR-US imaging strategy for studying skeletal muscle microvascularure has been successfully established.

P1-B7 - MIM: Experimental Ultrasound Systems and Applications

Exhibit Hall

Friday, September 8, 2017, 9:30 am - 4:00 pm

Chair: **Marcin Lewandowski**
Institute of Fundamental Technological Research

P1-B7-1

Sentinel Lymph Node Imaging Using Ultrafast Cyclic Pulsed Magnetomotive Ultrasound: Small Animal Study

Yu-Chun Chang[1], Ming-Chen Lu[1], Zhung-Hang Wei[1], Meng-Lin Li[1]; [1]*National Tsing Hua University, Taiwan*

Background, Motivation and Objective

Sentinel lymph nodes (SLNs) are the first draining lymph nodes when metastatic cancer cells are spreading. Sentinel lymph node biopsy (SLNB), which is performed invasively, is the current standard treatment to determine whether the cancer cells are spreading or not. A non-invasive SLN imaging modality along with fine needle aspiration biopsy (FNAB) would be beneficial for staging the axillary lymph nodes without the need of surgical intervention. Photoacoustic imaging has shown its feasibility of SLN mapping. However, it involves laser safety issues and is not available for clinical use yet. MRI has been used with superparamagnetic iron oxide nanoparticles (SPIOs) for the same purpose. MRI is not a good solution owing to its low imaging rate and high cost.

Statement of Contribution/Methods

In this study, we propose an alternative solution – ultrafast cyclic pulsed magnetomotive ultrasound (cMMUS) for noninvasive SLN indentification, which features cyclic pulsed magnetic excitation, MRI SPIOs as contrast agents, and 2.5-kHz ultrafast plane wave imaging for magneto-motion tracking. cMMUS tracks the unique cyclic magneto-motion resulting from the SPIOs drained to the SLNs and excited by the cyclic magnetic pulse to localize the SPIOs; thus identifying the SLNs. Cyclic pulsed magnetic excitation and high frame-rate speckle tracking enable matched filtering for physiological motion artifact suppression.

Results/Discussion

In vivo rat experimental results confirmed that the SLN identification could be done by the proposed method while it was challenging to conventional B-mode ultrasound. Red circle in the B-mode image (figure (a)) labeled the SLN. Figure (b) showed cMMUS displacement map which was overwhelmed by tissue motion artifacts and cannot provide clear identification of the SLN. Matched filtering with the cyclic magnetic pulse helped to suppress the artifacts and localize the excited SPIOs drained to the SLN; thus identifying the SLN (see figure (c)). Overall, we demonstrated the capability of the proposed cMMUS for noninvasive SLN identification in vivo, which owns great potential in image guidance of SLN FNAB. Future work will focus on development of backward mode cMMUS to facilitate clinical translation.

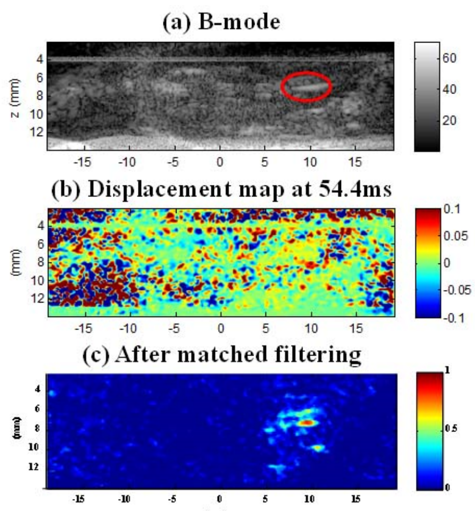

P1-B7-2

Influence of Naturally Occurring Tissue Movements on Magnetomotive Ultrasound Detection of Iron Oxide Nanoparticles for Magnetic Drug Targeting

Michael Fink[1], Helmut Ermert[1], Stefan Lyer[2], Christoph Alexiou[2]; [1]*Sensor Technology, Friedrich-Alexander-University Erlangen-Nuremberg, Erlangen, Germany,* [2]*Section of Experimental Oncology and Nanomedicine, University Hospital Erlangen, Germany*

Background, Motivation and Objective

Magnetic Drug Targeting (MDT) is a cancer treatment technique that enables a local chemotherapy. For this purpose, chemotherapeutic drugs are bound to magnetic nanoparticles and are accumulated in the tumor area by means of an external magnetic field. In order to adapt the position of the magnet the visualization of nanoparticles is of vital importance for MDT. Magnetomotive Ultrasound (MMUS) enables the sonographic detection of magnetic nanoparticles which are not visible directly using ultrasound imaging techniques due to their weak backscattering. In this connection, image artefacts in MMUS applications can be reduced by means of coded magnetic fields.

Statement of Contribution/Methods

In MMUS modes the sonographic detection of magnetic nanoparticles is attributed to the sonographic detection of tissue shifts due to magnetically moved particles. Thereby, harmonic magnetic fields are advantageous in terms of distinctiveness of magnetically induced oscillations, while pulsed magnetic fields are favorable in terms of spatial confinement of the particle loaded tissue. However, the use of coded magnetic fields, such as frequency-modulated signals, combines the advantages of both modes. On the one hand, the signal contains distinctive frequency components. On the other hand, the missing phase-ambiguity enables the detection of time shifts. In our approach a 4 Bit Barker Code employing frequency-modulation was used as excitation signal. For evaluation, the phase φ(x,z) of the rf-data in each image point P(x,z) is observed over time t. If the observed tissue contains nanoparticles the excitation signal can be detected in the variation of the phase φ(x,z,t). Thus, the evaluation can be performed via Fourier transform as in the conventional MMUS case. In addition, due to outstanding cross-correlation properties of Barker codes particle induced movements can be distinguished from noise signals. In this contribution the influence of random noise signals on the presented algorithm is investigated.

Results/Discussion

The algorithm has been tested on a tissue mimicking phantom. The left images of the figure show the tissue mimicking phantom and its B-mode image. The images on the right show the result employing the conventional MMUS algorithm and the result using coded magnetic fields, each with a signal-to-noise ratio of 0 dB.

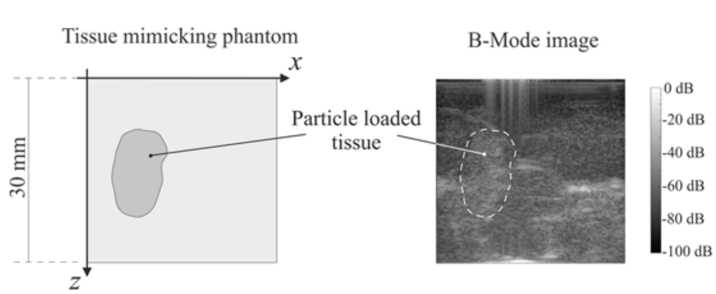

P1-B7-3

Towards Real-time Magnetomotive Ultrasound Imaging

Maria Evertsson[1], Alessandro Ramalli[2], Theo Z. Pavan[3], Luciana C. Cabrelli[3], Roger Andersson[4], Magnus Cinthio[5], Piero Tortoli[2], Tomas Jansson[1,4]; [1]*Department of Clinical Sciences Lund, Biomedical Engineering, Lund University, Sweden,* [2]*Department of Information Engineering, University of Florence, Florence, Italy,* [3]*Department of Physics, University of Sao Paulo, Ribeirao Preto, SP, Brazil,* [4]*Medical Services, Skåne University Hospital, Lund, Sweden,* [5]*Department of Biomedical Engineering, Faculty of Engineering LTH at Lund University, Lund, Sweden*

Background, Motivation and Objective

Magnetomotive ultrasound (MMUS) imaging indirectly enables visualization of magnetic nanoparticles (MNPs) with ultrasound. An external time varying magnetic field displaces MNPs and thus their closest surrounding, the induced displacement is tracked in the US data and color-coded on B-mode images. However, images are currently processed offline, which is time consuming and precludes clinical use of MMUS. In this work, the previously proposed MMUS algorithm (DOI: TUFFC.2013.2591) is automated and implemented online on the ULA-OP scanner.

Statement of Contribution/Methods

The processing exploits the fast Matlab-to-ULA-OP interface. An infinite loop is programmed in Matlab during which ULA-OP acquires a group of 23 frames (192*230 pixels/frame) at a frame rate of 67.5 Hz and automatically streams them to the PC; here, they are processed according to the MMUS algorithm based on quadrature detection and phase gating at the precise frequency of magnetic particle movement (f0); then the loop is repeated. To synthesise the phase of the magnetic field reference signal, the phases from all pixels at f0 were grouped into a 360 bin histogram. The peak bin was considered as in-phase with the MMUS displacement and the zero passes of the second derivative of the histogram envelope closest to the peak bin was set as cut off for the phase gated interval.

The ULA-OP, connected to a 192-element linear array, was used to scan a phantom (Styrene-ethylene/butylene-styrene (10 %)/mineral oil (90 %)) with a 2 % magnetic ferrite particle inclusion. MMUS displacement was calculated in the entire image area and in a sub region of 130*90 pixels, covering the insert. Magnetic fields with different magnitudes were applied (0.075, 0.10 and 0.15 Tesla) as measured closest to the coil.

Results/Discussion

The automated online implementation computes one full MMUS image in 2.8 ± 0.06 seconds and the sub region in 1.17± 0.05 seconds, compared to 1-2 minutes in post processing mode. Most processing time is needed for unwrapping the temporal IQ-phase data (23 %) and for calculating the displacement and phase in each pixel (67%), pointing at parts of the algorithm that need to be streamlined. When the magnetic field was increased with 30 or 100 % the mean displacement in the particle laden area was seen to increase correspondingly. This could be noted immediately on-screen as the magnetic flux setting was altered (see Fig).

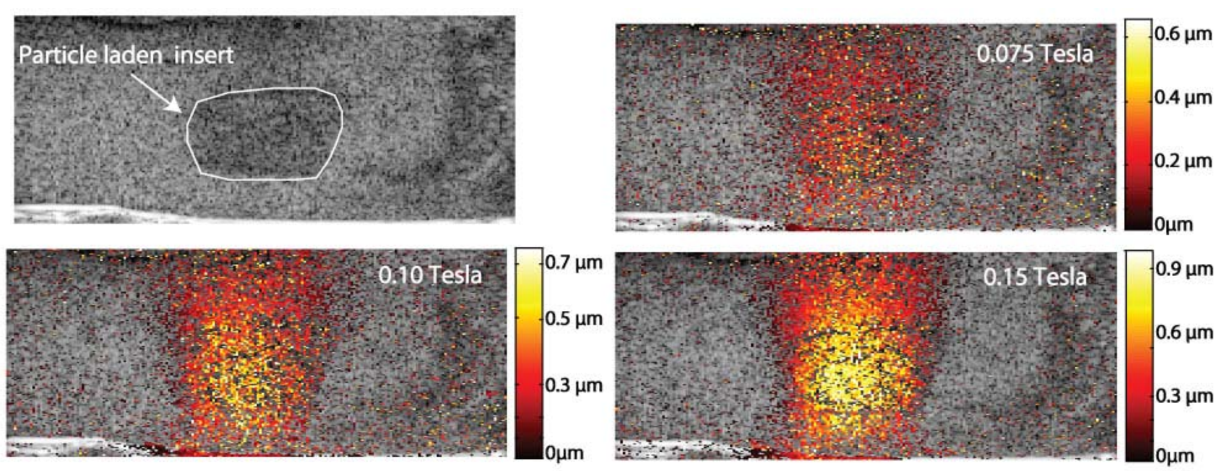

P1-B7-4

Ultrasound Imaging of Muscle Contraction of the Tibialis Anterior in Patients with Facioscapulohumeral Dystrophy

Kaj Gijsbertse[1], Rianne Goselink[2], Saskia Lassche[2], Maartje Nillesen[3], André Sprengers[1,4], Nico Verdonschot[1,4], Nens van Alfen[2], Chris de Korte[3,5]; [1]*Orthopaedics, Radboud university medical center, Nijmegen, Netherlands,* [2]*Department of Neurology, Radboud university medical center, Netherlands,* [3]*Radiology & Nuclear Medicine, Radboud university medical center, Netherlands,* [4]*Laboratory of Biomechanical Engineering, University of Twente, Netherlands,* [5]*Physics of Fluids Group, University of Twente, Netherlands*

Background, Motivation and Objective

In fascioscapulohumeral muscular dystrophy (FSHD) and many other neuromuscular disorders there is a need for biomarkers to diagnose, quantify and longitudinally follow muscle disease. Furthermore, the pathophysiological mechanisms leading to muscle weakness in most neuromuscular disorders are not completely understood. Speckle tracking allows to quantify muscle deformation. This dynamic information provides insight in the pathophysiological mechanisms and may help to distinguish the different stages of diseased muscle in FSHD.

Statement of Contribution/Methods

In this study we applied a speckle tracking technique to dynamic ultrasound image sequences to quantify the deformation of both tibialis anterior muscles in 4 patients with FSHD and 4 healthy controls. The resulting deformation patterns were compared to muscle ultrasound echo intensity analysis as a measure of fat infiltration and dystrophy (expressed as z-scores, *i.e.* the number of standard deviations from the mean), and clinical outcome measures.

Results/Discussion

The results from the displacement estimation revealed a distinctively different tissue motion pattern between patients with peroneal weakness and healthy controls (Figure 1). Patients with severe peroneal weakness showed a displacement pattern of the tibialis anterior with overall less motion of the central tendon region (-2.1 ± 1.0 mm), while healthy subjects showed a non-uniform displacement pattern, with the central aponeurosis showing the largest displacement (-9.7 ± 1.8 mm). Furthermore, this change in muscle motion pattern of patients shows good agreement with clinical measures (*e.g.* decrease in force generation) and quantitative muscle ultrasound measurements. Ultrasound echo intensity values were highest for patients with severe peroneal weakness with z-scores between 2.7 and 4.78 corroborating that these muscles were (severely) affected. In conclusion, dynamic ultrasound in combination with speckle tracking allows to study the effects of muscle pathology in relation to strength, force transmission and movement generation. Although further research is required, this technique can develop into a biomarker to quantify muscle disease severity.

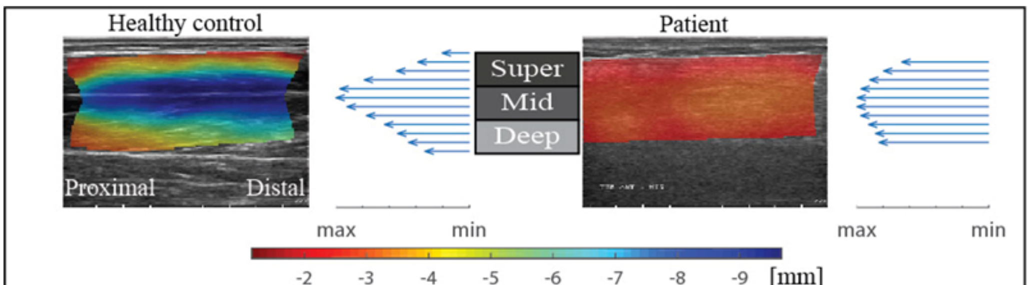

Figure 1. Tibialis anterior muscle motion patterns of a healthy control and a FSHD patient with severe peroneal weakness. The displacement maps depict the longitudinal displacement [mm] of the muscle in the sagittal ultrasound plane. The arrows represent the averaged normalised muscle displacement across the thickness of the muscle.

P1-B7-5

Non-invasive Spinal Vibration Testing Using Ultrafast Ultrasound Imaging: A New Way to Measure Spine Function.

Tarek Kaddoura[1], Anthony Au[2], Richard Uwiera[2], Richard Fox[2], Greg Kawchuk[2], Roger J. Zemp[1]; [1]*Electrical and Computer Engineering, University of Alberta, Edmonton, Alberta, Canada,* [2]*University of Alberta, Canada*

Background, Motivation and Objective

The extremely high frame-rate of ultrafast ultrasound imaging has enabled the possibility to image extremely fast events on the order of thousands of frames/sec. With the success of ultrafast imaging across a wide variety of disciplines, we now explore the ability of ultrafast imaging to capture spinal vibrations for non-invasive spinal testing in living subjects. Previously, we have shown that accelerometer-based vibration testing in cadaveric models can reveal the presence, location and magnitude of spinal pathology. However, this process remains an invasive procedure as current non-invasive sensors are inadequate. In this experiment, we investigate the ability of non-invasive ultrafast ultrasound to quantify in-vivo vertebral vibration response across a broad range of frequencies (10–100 Hz) in an anesthetized pig model.

Statement of Contribution/Methods

Seven pigs (58-68kg) were used in this experiment. Vibration was provided to the L4 vertebra in each anesthetized animal via a computer-controlled stylus lowered on to the skin posterior to the L4 spinous process. The reference system consisted of a 3mm diameter bone pin drilled through the surface of the skin and into the left L4 vertebral body. A tri-axial accelerometer was then connected to the exposed pin. The experimental system consisted of an ultrasound transducer placed posterior to the right L4 transverse process to collect images of vertebral position at 500 images/sec using plane wave imaging. Vibration was then applied with single-frequency sine waves ranging from 10-100Hz in 10Hz increments for 10 seconds each. Displacement of the spine as measured by ultrasound was calculated in between image frames using cross-correlation. A differentiation filter was then applied twice to convert the displacement vectors to acceleration. Pearson correlation coefficients were calculated to compare the power-spectral-density estimates of acceleration between the ultrasound and the accelerometer.

Results/Discussion

Here we present power-spectral-density correlation data from 4 pigs as a function of frequency (Fig. 1). The correlation is consistent across all frequencies with an average correlation coefficient of 0.97. Hence, ultrafast ultrasound imaging enables the ability to non-invasively capture vibrational responses in the spine, and possibly to non-invasively diagnose spine pathologies.

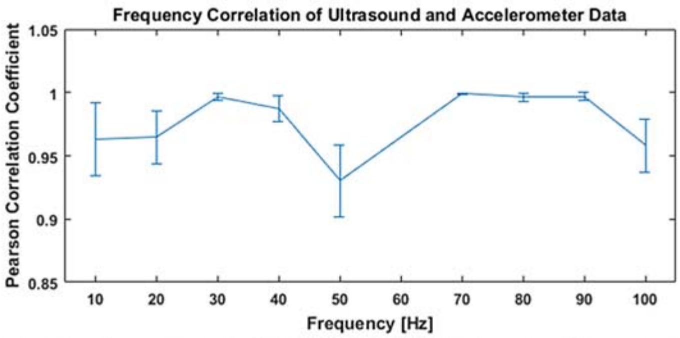

Fig. 1. Correlation of the power-spectral-density of the acceleration obtained by ultrasound and by the accelerometer. For each frequency, the mean of the correlation was calculated from 4 pigs. Error bars represent standard error. The correlation is consistently good across all frequencies. 60 Hz was omitted due to electrical interference.

P1-B7-6

Low-power Ultrasound Imaging Systems Using Time Delay Spectrometry

Elizabeth Tarbox[1], **Nima Akhlaghi[2]**, Ananya Dhawan[3], Paul Gammell[4], Parag Chitnis[1], Siddhartha Sikdar[1]; *[1]Bioengineering, George Mason University, USA, [2]Electrical Engineering, George Mason University, USA, [3]Computer Science, George Mason University, USA, [4]Gammell Applied Technologies LLC, USA*

Background, Motivation and Objective

Ultrasound (US) imaging systems have undergone substantial miniaturization leading to many clinical applications that rely on batteries. However, current clinical US systems utilizing pulse-echo imaging require a high voltage and short duration transmit pulse along with electronics that operate in the MHz frequency range. We are investigating a novel imaging method that employs time-delay spectrometry (TDS) as an alternative to pulse-echo and uses low-voltage (~5V peak-to-peak) transmit pulses along with low-power electronics operating in the kHz frequency range.

Statement of Contribution/Methods

We have developed a battery-powered benchtop 4-channel TDS system comprised of a frequency sweeper, a custom-designed mixer, a 7.5 MHz dual-element transducer, a low-pass filter (20-kHz) to remove the high frequency sidebands, and an audio-frequency digitizer. The digitized data are processed in MATLAB to reconstruct A-lines.

TDS is a frequency-domain signaling modality, in which the transmit signal is swept across a range of frequencies (~5-15 MHz) over a long duration (~20 ms). As this signal propagates through the media, it is modulated by its frequency response; the received signal is mixed with the transmitted signal and low-pass filtered to recover these audio frequency modulations. Within the received signal, time delays corresponding to reflections at different interfaces are encoded as frequency shifts in the kHz range. The signal is processed with the Fourier transform to recover the corresponding time delays and generate an A-line.

Results/Discussion

We have successfully generated M-mode images in real time to 5 cm of depth with a pulse repetition frequency of 50 Hz. M-mode images mimicking tissue motion were generated by moving the transducer sinusoidally over a 2 cm gel pad, with a peak displacement of 0.5 cm. Fig1 shows an M-mode image generated using the TDS approach. These results are comparable to those generated using conventional pulse-echo US systems and have a comparable signal to noise ratio. The image accurately reflects the dimensions of the gel pad as well as the displacement. These results demonstrate the feasibility of US imaging using the TDS approach. TDS could lead to a new generation of low-power US imaging systems.

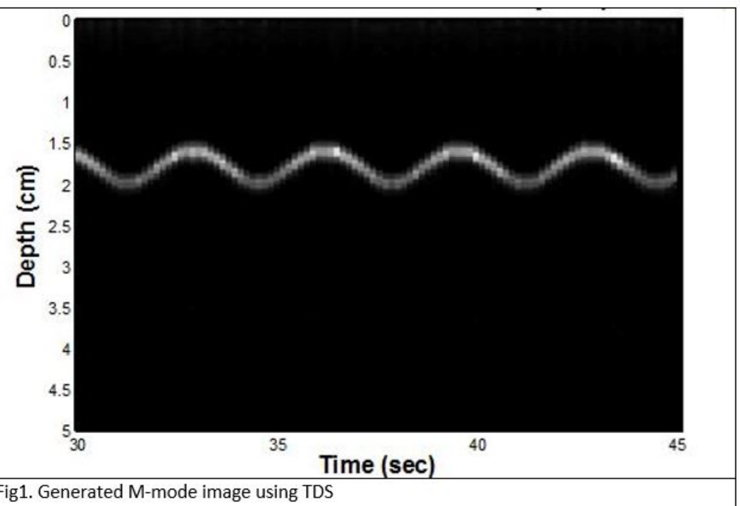

Fig1. Generated M-mode image using TDS

P1-B7-7

Monitoring Treatment Response in Patient-derived Orthotopic Glioblastoma Xenograft Models with Multi-parametric Ultrasound and Photoacoustic Imaging

Srivalleesha Mallidi[1], Meguimi Ichikawa[1], Tayyaba Hasan[1]; [1]*Harvard Medical School, USA*

Background, Motivation and Objective

Glioblastoma (GBM) is a disease with less than a year overall patient survival. Poor prognosis is due to local recurrence post treatment or growth of "left-over" residual disease post surgical resection. To personalize treatment strategies and reduce rate of recurrence, it is important to monitor treatment response and develop imaging based prediction markers to identify GBM recurrence. Given the role of vasculature in tumor growth and survival, here we utilize multi-parametric ultrasound and photoacoustic imaging to validate if changes in vascular structure and function could be predictive of treatment response in patient-derived orthotopic Glioblastoma xenograft models.

Statement of Contribution/Methods

Patient-derived GBM cell lines were implanted in the brain of Swiss nu/nu mice. 10 days post implantation, the mice were divided into 4 groups namely – no treatment, surgical resection, therapy and surgical resection with therapy. Surgery was performed in the mice to establish cranial window for longitudinal in-vivo imaging. Photodynamic therapy (PDT), a light based cytotoxic therapy, with photosensitizer Benzoporphyrin derivative (BPD) or FDA approved chemotherapy temozolomide (TMZ) were administered in the mice. Fujifilm VisualSonics LAZR system with a 20 MHz transducer was used to obtain power Doppler (vascular density in tumors) and oxygen saturation (StO2) maps of the brain tumors at different time points pre and post treatment (immediately, 6, 24 and 72 hours). The mice were either euthanized for immunofluorescence to validate the imaging markers or longitudinally monitored for tumor volume until moribund

Results/Discussion

The no-treatment group or the surgery only group did not have significant changes in vascular density or StO2. We observed statistically significant decrease in vascular density and StO2 post BPD-PDT (primarily a vascular therapy) but not with TMZ (a cellular therapy) in both therapy and surgery plus therapy groups. Furthermore we also observed that the sustenance of hypoxia or low StO2 in tumors for 24-72 hours can be a predictive biomarker for tumor recurrence. Overall, these results suggest the utility of ultrasound and photoacoustic imaging in monitoring treatment response and developing treatment prediction strategies for glioblastoma.

P1-B7-8

Design Considerations and Performance of a Variable Gain, Variable Bandwidth Signal Processing Circuit for Acoustoelectric Imaging

Tushar Kanti Bera[1], Pier Ingram[1], Yexian Qin[1], Russell S. Witte[1]; [1]*Department of Medical Imaging, University of Arizona, Tucson, Arizona, USA*

Background, Motivation and Objective

Acoustoelectric (AE) imaging is a new technique for mapping current densities in the heart and brain at a high resolution determined by the size of the ultrasound (US) focus. Because the amplitude of the AE interaction signal in biological tissue is weak (on order of 1 μV), detection of small currents is challenging with poor signal-to-noise ratio (SNR). Because optimal detection depends on minimizing background noise, the design and performance of the recording system, especially amplifiers and filters, is crucial for efficient and sensitive AE imaging. The amplitude and bandwidth of the AE signal depends on a variety of factors, including the US bandwidth and beam pattern, distribution of current densities, properties of the recording electrodes, and amount of averaging/sampling. The primary goal of this work was to optimize the design and performance of the acoustoelectric differential amplifier, including signal processing circuits, to minimize noise and maximize sensitivity for detection of the AE signal. Variable gain, band-pass filter (BPF) cutoffs, and bandwidth are critical design parameters for optimizing the AE imaging platform for mapping weak electric currents in tissue.

Statement of Contribution/Methods

Signal processing instrumentation (Fig. 1a) is developed with a pre-filter, an analog amplifier block (AAB) with variable gain for low amplitude AE signals, and an active filter block (AFB) with variable bandwidth BPF (VBW-BPF) followed by a 60 Hz-notch filter and filter gain controller. The pre-filter is studied with a quasi-AE produced with a low voltage high frequency signals mixed with a high voltage low frequency pulses. Band pass filters are developed with three low pass filters and three high pass filters which can be connected in different combinations to obtain different frequency bands (Fig. 1b) for AE signal filtering and processing.

Results/Discussion

The AAB provides a variable gain ranging from 0.1 to 350. The VBW-BPF provides 10 kHz-10 MHz, 100 kHz-5 MHz, 500 kHz-2.5MHz bandwidths or else. The 60-Hz Notch filter successfully filters out the 60-Hz signal. The circuit removes 2V pulses from the quasi-AE signals (Fig. 1c) of different frequencies (50 kHz, 100 kHz, 500 kHz and 1 MHz). Future studies will compare different parameters of the signal processing circuit and its effect towards minimizing in-band noise and maximizing SNR of the AE signal.

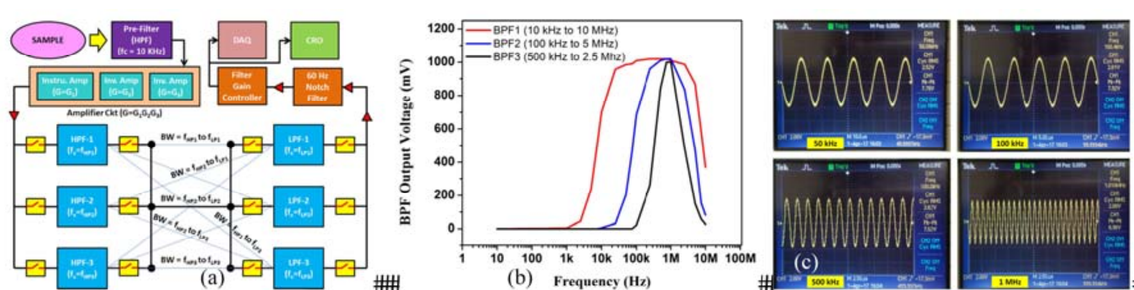

Figure 1: (a) Circuit block diagram, (b) frequency response of the variable BW BPF, (c) quasi-AE signal removed from high voltage pulses.

P1-B7-9

Imaging *In Situ* Human Kidney Stones with the Color Doppler Ultrasound Twinkling Artifact

Julianna Simon[1], Barbrina Dunmire[2], Bryan Cunitz[2], Oleg Sapozhnikov[2,3], Jeffrey Thiel[2], James Holm[4], Michael Bailey[2]; [1]*Graduate Program in Acoustics, The Pennsylvania State University, University Park, PA, USA,* [2]*Center for Industrial and Medical Ultrasound, Applied Physics Laboratory, University of Washington, Seattle, WA, USA,* [3]*Department of Acoustics, Physics Faculty, Moscow State University, Moscow, Russian Federation,* [4]*Center for Hyperbaric Medicine, Virginia Mason Medical Center, Seattle, WA, USA*

Background, Motivation and Objective

Hyperbaric pressures of 3-100 atmospheres absolute (ATA) have been shown to reduce the color Doppler ultrasound twinkling artifact on *ex vivo* human kidney stones, leading to the hypothesis that surface crevice microbubbles cause twinkling. Similarly supportive for the crevice bubble hypothesis is the suppression of kidney stone twinkling in animals breathing elevated levels of carbon dioxide. However, it is unclear whether stable microbubbles can exist on the surface of kidney stones in the human body. For the first time, we investigate the effect of hyperbaric pressure on *in situ* human kidney stones to determine whether stable microbubbles exist as measured by the color Doppler ultrasound twinkling artifact.

Statement of Contribution/Methods

Seven human subjects with kidney stones known to twinkle were imaged with a Philips/ATL P4-2 transducer and Verasonics® ultrasound system while inside a multiplace hyperbaric chamber. Subjects breathed ambient air while exposed to a maximum pressure of 4 ATA except for a scheduled decompression stop of 10 minutes at 1.6 ATA where subjects breathed pure oxygen. Twinkling was quantified in terms of Doppler power for 2-minute intervals before pressurization (baseline), at 4 ATA, at 1.6 ATA, and after pressurization. A paired t-test was used to determine statistical significance ($p<0.05$).

Results/Discussion

As shown in fig. 1, preliminary results of the first 4 subjects show no change in twinkling at 4 ATA compared to baseline levels ($p=0.30$). However, a statistically significant increase in twinkling was observed when subjects breathed pure oxygen during the decompression stop at 1.6 ATA compared to baseline levels ($p=0.046$). At the end of the study with subjects once again breathing ambient air, twinkling was similar to what was initially observed ($p=0.44$). The increase in twinkling associated with breathing pure oxygen supports the crevice microbubble hypothesis. As with *ex vivo* kidney stones, higher pressures than explored in this study may be needed to reduce twinkling on kidney stones. The results from this study can be used to improve stone detection with Doppler ultrasound. [Work supported by the National Space Biomedical Research Institute through NASA NCC 9-58 and National Institutes of Health NIDDK grant DK043881].

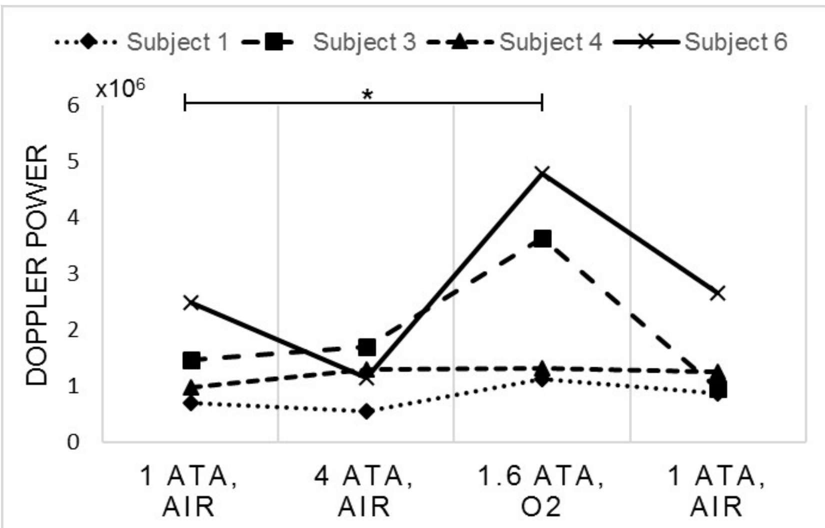

P1-B8 - MPA: Technincal Developments in Photoacoustic Imaging

Exhibit Hall

Friday, September 8, 2017, 9:30 am - 4:00 pm

Chair: **Kang Kim**
University of Pittsburgh

P1-B8-1

Handheld Optical-Resolution Photoacoustic Microscopy Probe for Preclinical Application

Kyungjin Park[1], Jin Young Kim[2], Seungwan Jeon[2], Sungjo Park[2], Ki Jong Lee[2], **Hyung Ham Kim[2]**, Chulhong Kim[2]; [1]*School of Interdisciplinary Bioscience and Bioengineering, Pohang University of Science and Technology, Pohang, Korea, Republic of,* [2]*Department of Creative IT Engineering, Pohang University of Science and Technology, Pohang, Korea, Republic of*

Background, Motivation and Objective

In this study, we developed an imaging device for preclinical and clinical application using photoacoustic effect. The photoacoustic effect is to make ultrasound images using light as its name illustrates. Light irradiated in a short time (nano seconds) is absorbed by the tissue, and the local pressure is generated by the thermo-elastic expansion. The photoacoustic effect is a safe method of imaging because it uses an endogenous chromophore in the human body without the use of an external contrast agent. In this study, the image uses an optical-resolution photoacoustic microscope (OR-PAM) which has a resolution of 12 ¥ìm. The conventional or-pam has the disadvantage of being slow and bulky using mechanical motors. To overcome this problem, our research team developed a photoacoustic imaging system that uses a MEMS scanner to equip a fast image capability into a compact handheld probe.

Statement of Contribution/Methods

To make the handheld OR-PAM probe, a two-axis waterproof MEMS scanner (2A-WP-MEMS scanner) was first created. The 2-axis MEMS scanner consists of a front part with an aluminum mirror and a rear part that drives the mirror. The main feature of this structure is that the movable part of the front structure is made of waterproof PDMS. This scanner uses the magnetic force between the magnet and the magnet for driving. Applying AC voltage here enables fast scanning at the resonant frequency with low voltage. To increase the SNR, an optical ultrasound coupler (OUC) was used to reflect the ultrasound and pass the light. We also used a 3D printing housing to connect scanners, transducers, light guides, and scanning windows. The probe thus developed is mounted on the 3-axis artificial joint for ease of use.

Results/Discussion

The axis resolution was measured after the system was built. We took a B scan image of carbon fiber 6 µm in diameter to measure the axial resolution. The measured axis resolution is 30 µm. From the in vivo demonstration, we visualized microvasculature of a mouse ear. Mouse was anesthetized and injected with isoflurane gas. In the photoacoustic image, we were able to identify capillaries and single capillaries as well as arterial and venous pairs of blood vessels. The time for the image of 700 x 700 pixels took for 20 seconds.

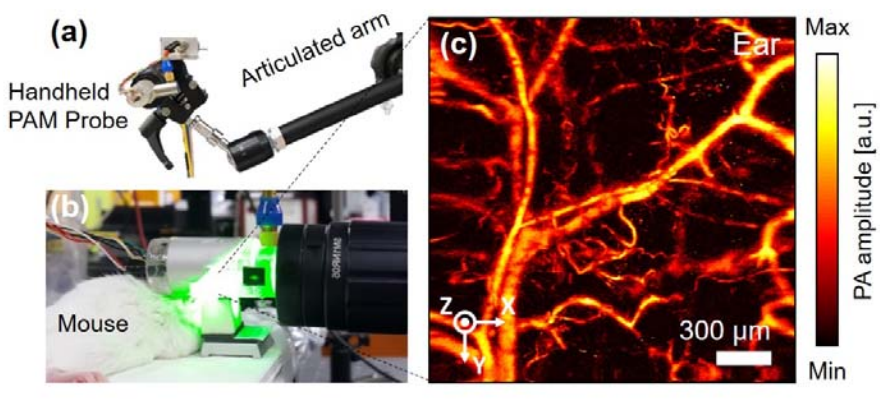

Figure 1. Handheld photoacoustic microscopy (PAM) probe. (a) Photograph of the handheld PAM probe with a articulated arm. (b) in vivo experiment of mouse ear. (c) *In vivo* PA images of microvasculature in a mouse ear

P1-B8-2

Source Density Apodisation in 2D All-Optical Ultrasound Imaging

Erwin J. Alles[1], Sacha Noimark[1,2], Edward Zhang[1], Paul C. Beard[1], Ivan P. Parkin[2], Adrien E. Desjardins[1]

Background, Motivation and Objective

All-optical ultrasound imaging, where ultrasound is generated photoacoustically and back-scattered fields are detected with optically resonant structures, has distinct advantages over conventional piezoelectric or capacitive transducers. An absence of electrical connections facilitates probe miniaturisation and confers MRI compatibility, while similar or better sensitivities and bandwidths can be achieved. Previously reported all-optical systems used mechanical translation of a single source and receiver to scan a synthetic aperture, resulting in image acquisition times ranging from seconds to minutes. This frame-rate can be improved by reducing the number of A-scans per image; however, this increases the noise and artefact levels of the image. For conventional probes, typically employing unalterable periodic arrays, side- and grating lobes can give rise to substantial artefacts that are commonly suppressed using amplitude-weighted apodisation. In this work, however, the spatial density of the acoustic sources rather than their amplitudes is weighted to avoid array periodicity, in order to achieve a better image quality using the same aperture and number of A-scans.

Statement of Contribution/Methods

An ultrasound source (width: 50 µm, bandwidth: 2-15 MHz) was generated by focussing pulsed light onto an optically absorbing film. Using a galvo mirror, this source could be positioned arbitrarily within a 1D aperture (width: 15 mm), resulting in a reconfigurable source array geometry. A single stationary fibre-optic acoustic detector was used to detect back-scattered signals. To demonstrate the efficacy of source density apodisation, images were acquired of a tungsten wire phantom using both a periodic array comprising 128 equidistantly spaced sources and an array where the source density was given by the Hamming apodisation function. Images were reconstructed both with and without amplitude apodisation.

Results/Discussion

Numerical and experimental results (Fig 1) confirm that applying source density apodisation yielded lower artefact levels by 5 dB and similar resolutions. The lowest artefact levels were observed when both source density and amplitude apodisation were applied. Thus, using source density apodisation, fewer source locations and correspondingly lower acquisition times were required to achieve the same image quality.

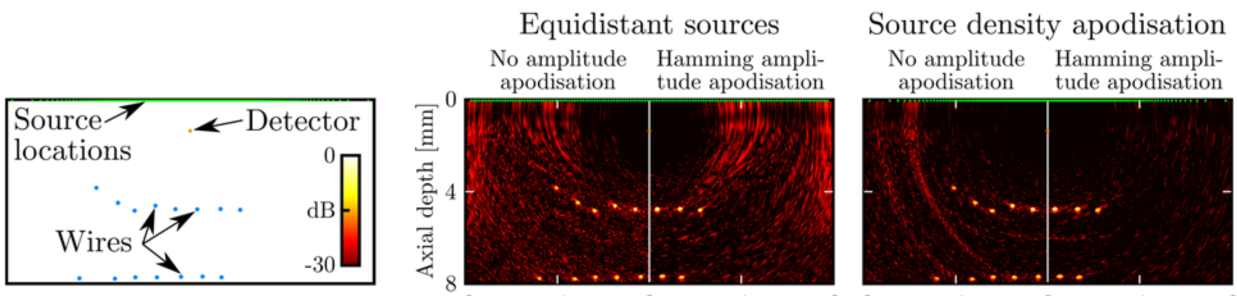

Fig. 1

P1-B8-3

Non-Contact Laser Ultrasound for Medical Imaging

Rob Haupt[1]; [1]*Active Optical Systems, MIT Lincoln Laboratory, Lexington, MA, USA*

Background, Motivation and Objective

Ultrasound (US) is an ideal imaging modality used in medical practice: it is portable, has no known bio-effects and produces images with excellent resolution. Despite these advantages, MRI and CT are dominant modalities used for most medical imaging, while accepting much higher cost and health risks. US is acquired with hand held transducers dependent on operator applied pressure and angle plane selection with no fixed acquisition frame. This leads to inter-operator variability – significant image distortion with limited feature accuracy/confidence, especially upon repeat measurement and is the primary reason US is unable to compete with MRI and CT. For example, the standard criteria for determining tumor progression in cancer trials do not permit tumor measurements made with US.

Statement of Contribution/Methods

The N-CLUS system employs a pulsed near IR source (1550nm wavelength) that converts optical energy to ultrasonic waves within the skin surface via photoacoustic (PA) mechanisms. Laser Doppler vibrometry is then used to measure probing US signals that return to the skin surface. Fast steering mirrors can move both transmit and receive laser beams to provide operational coverage rates. We employ 3D lidar to accurately map out patient skin topography while locating each on the surface using a fast frame rate SWIR camera providing a fixed reference frame.

We have demonstrated the N-CLUS system can produce useful US images in tissue and bone while operating within laser eye and skin safety limits. Our studies show PA mechanisms can produce the full compilation of ultrasonic waves including longitudinal and shear waves that can yield not only anatomical images, but also provide elastic property distributions, in-vivo useful for several emerging fields in medicine.

Results/Discussion

The N-CLUS system, if successfully transitioned, will mitigate US inter-operator variability using a standoff optical concept that generates and measures ultrasonic waves without patient contact, thus dramatically expanding the use of US. An optical approach enables a fixed reference frame system that provides repeatable accurate images for 'change detection' of critical internal features. We have demonstrated that an optical non-contact approach can yield the mechanical property distributions which are critical for tissue, bone, and disease feature identification.

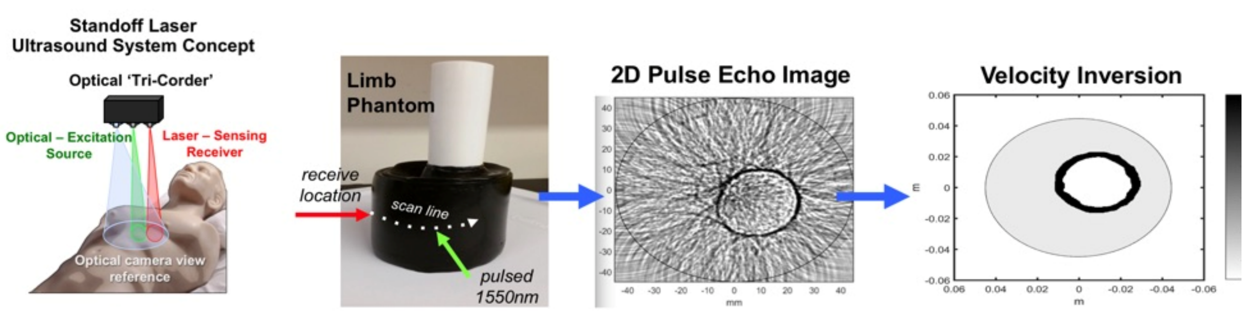

P1-B8-4

Photoacoustic Visual Servoing of Needle Tips to Improve Biopsy Targeting in Obese Patients

Joshua Shubert[1], Muyinatu Bell[1]; [1]*Electrical and Computer Engineering, Johns Hopkins University, Baltimore, Maryland, USA*

Background, Motivation and Objective

Ultrasound guided biopsies are useful for real-time, simultaneous visualization of both the target region and the needle tip. However, localizing the needle tip in traditional ultrasound images often requires complicated image processing with segmentation algorithms that tend to fail in the presence of acoustic clutter, scattering, and attenuation, which is particularly true in obese patients. Photoacoustic imaging is a promising alternative with the potential to provide needle tip localization and segmentation algorithms that are robust in the presence of highly scattering tissues. In addition, segmentation results can be used to visually servo an ultrasound probe to track the needle tip, thus expanding the possibilities for procedures implemented with the biopsy needle separated from the probe. This work presents the development and evaluation of the first robotic photoacoustic system that maintains the needle tip at the center of co-registered photoacoustic and ultrasound images.

Statement of Contribution/Methods

The photoacoustic signal was generated by a Nd:YAG laser with 10 Hz pulse frequency, coupled to an 1 mm core diameter optical fiber. The fiber was inserted into a hollow biopsy needle that punctured ex vivo lamb tissue. The photoacoustic data was acquired with an Alpinion L3-8 linear array ultrasound probe connected to an Alpinion E-Cube 12R ultrasound scanner. The probe was rigidly attached to a 7 DOF Sawyer robotic arm from Rethink Robotics. Photoacoustic images were segmented using local intensity-based thresholding. Needle tip coordinates were calculated to be the centroid of the segmented area. Consecutive frames of segmentation results were compared for consistency before sending a command to the robotic arm. Needle tip pixel coordinates were transmitted via ethernet connection to the robot controller and transformed to the robot coordinate system. A kinematics solution for centering the ultrasound probe over the needle tip was then computed and sent to the robot joint controllers for execution. For each trial, the steady state error was calculated as the horizontal pixel difference between the segmented needle tip centroid and the center of the photoacoustic image.

Results/Discussion

Our system centered the ultrasound probe over the needle tip with a mean error +/- one standard deviation of 0.567 +/- 0.554 mm, as measured from 11 starting positions. The system segmented the location of the needle tip at a rate of 20 Hz. This system has potential to improve the placement and localization of biopsy needles in obese patients.

P1-B8-5

Design and Development of a Full-ring Ultrasound and Photoacoustic Tomography System for Breast Cancer Imaging

Suhail Alshahrani[1], Yan Yan[1], Ivan Avrutsky[2], Mark Anastasio[3], Eugene Malyarenko[4], Neb Duric[4], Mohammad Mehrmohammadi[1]; [1]*Biomedical Engineering, Wayne State University, Detroit, MI, USA,* [2]*Electrical & Computer Engineering, Wayne State University, Detroit, MI, United States Minor Outlying Islands,* [3]*Department of Bioengineering, Washington University in St. Louis, St. Louis, MO, USA,* [4]*Karmanos Cancer Institute, Detroit, MI, USA*

Background, Motivation and Objective

Clinical diagnostic imaging modalities of breast cancer are still having certain limitations such as low sensitivity in dense breast in mammography and low specificity of the B-mode ultrasound [1, 2]. Photoacoustic (PA) imaging has been introduced as an enabling tool to acquire important functional information of the pathologic tissues as well as molecular imaging of cancer when it is augmented with nano-sized contrast agents [3]. US tomography (UST) has shown superior utility imaging of the breast and is growing as reliable tool for characterizing breast lesions [4, 5]. In this study, we demonstrate the development of an US and PA tomography (USPAT) system, consists of a full-ring US acquisition and an all-reflective, aberration-independent, and easy to implement light delivery to achieve an omni-directional co-planar ring illumination.

Statement of Contribution/Methods

The optical system converts a collimated laser beam into a ring-shaped illumination consists of a cone-shaped and two conical ring mirrors. The cone-shaped and the first conical mirrors converts the collimated laser beam into parallel cylindrical beam which will be redirected by the second reflector mirror to the scanned object. A prototype optical system was developed, tested, and characterized through a set of experiments on excised tissue and tissue mimicking phantoms. As an important parameter in PA imaging, we investigated the effect of omni-directional ring illumination on uniformity of light fluence and thus on generated PA signals within tissue-like medium. We also evaluated the utility of using a full-ring US transducer to perform co-registered US and PA imaging. The ring-based UST that been used in this study employs a solid-state ring-array transducer comprising 256 elements.

Results/Discussion

Preliminary evaluation of ring-illumination effect on PA signal amplitude within a breast-mimicking phantom (**Fig 1.**) indicated uniformity of PA signal at distances ranging from 10 to 25 mm from the surface with a low fluence 0.0131 /cm^2. The omni-directional illumination can potentially reduce the effect of light fluence variations in PA imaging, thus achieve larger imaging depth. Other key advantages of developed USPAT system include more efficient PA signal acquisition with an enclosed ring transducer and possibility of using higher laser energies yet remaining below fleucne safety limits.

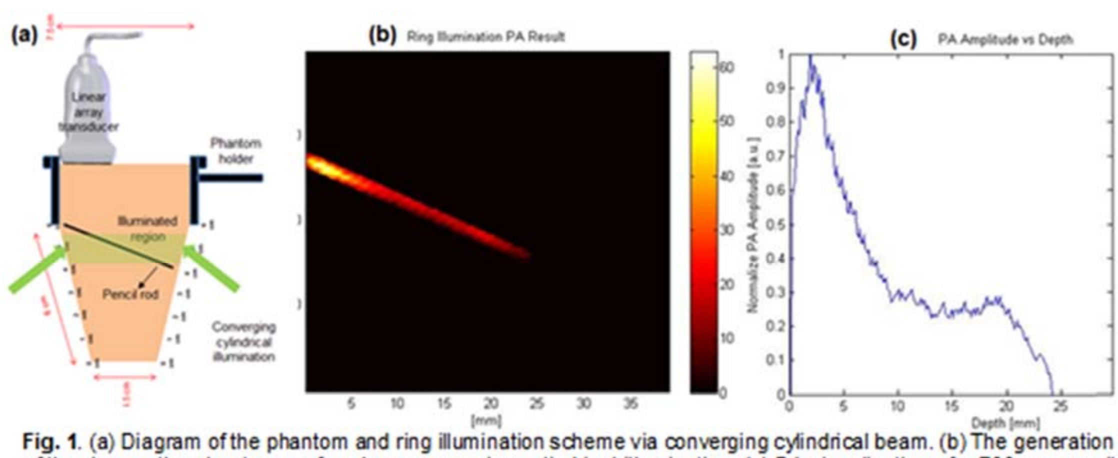

Fig. 1. (a) Diagram of the phantom and ring illumination scheme via converging cylindrical beam. (b) The generation of the ring on the phantom surface by a converging cylindrical illumination. (c) PA visualization of a 700 µm pencil lead embedded inside gelatin background. (e) Normalized PA signal amplitude vs. depth.

P1-B8-6

Structurally Enhanced Contrast in Photoacoustic Microscopy with F-Mode Imaging

Michael Moore[1,2], Michael Kolios[1,2]; [1]*Department of Physics, Ryerson University, Toronto, Ontario, Canada,* [2]*Institute for Biomedical Engineering Science and Technology, St. Michael's Hospital, Toronto, Ontario, Canada*

Background, Motivation and Objective

The maximum amplitude projection (MAP) technique is the gold standard for image formation in photoacoustic (PA) microscopy. While the technique provides high-resolution spatial maps of optical absorption, it neglects the abundance of information encoded in the frequency domain of the broadband PA signals. In this work, we present a new technique for PA image formation, termed 'F-Mode', which capitalizes on variations in the power spectrum of PA signals to produce images with object specific contrast not achievable using conventional MAP techniques.

Statement of Contribution/Methods

A PA microscope equipped with a 532 nm laser and 400 MHz transducer was used to raster scan an agarose phantom containing black polystyrene beads with diameters of 6 µm and 10 µm. Acquired PA signals were sampled at a rate of 8 GHz using a 10-bit digitizer, and were averaged 100 times to increase SNR. The power spectrum of the averaged RF-line at each scan position was computed, and then partitioned into intervals of 1 MHz. For each interval, an independent F-Mode image was formed by summing the power spectrum within the interval. An animation of the resultant image stack was created and used to identify the intervals demonstrating the greatest difference in contrast between the two beads.

Results/Discussion

An optical micrograph of the phantom is shown in Fig 1A, with the corresponding PA MAP image in Fig 1B. Due to the similarity in the optical absorption properties of the beads, the intensity of the 6 and 10 µm bead are comparable in the MAP image. Figure 1C shows the F-Mode image acquired by summing the power spectrum from 244-245 MHz. In this interval, the summed power spectrum for the 10 µm bead is 10 times less than the power in the 6 µm bead power spectrum. As a result, only one of the beads is clearly seen. In the F-Mode image from 394-395 MHz shown in Figure 1D the trend is reversed, and only the 10 µm bead can visualized clearly. These preliminary results demonstrate the efficacy of the F-Mode technique for selectively accentuating the contrast of structures of different size. Future work will involve applying the technique in both *in vivo* and *ex vivo* biological models to selectively analyze blood vessels of different diameters, and investigating the applicability of the technique to PA datasets acquired with transducers with central frequencies ranging from pre-clinical (<40 MHz) to ultra-high (>1 GHz).

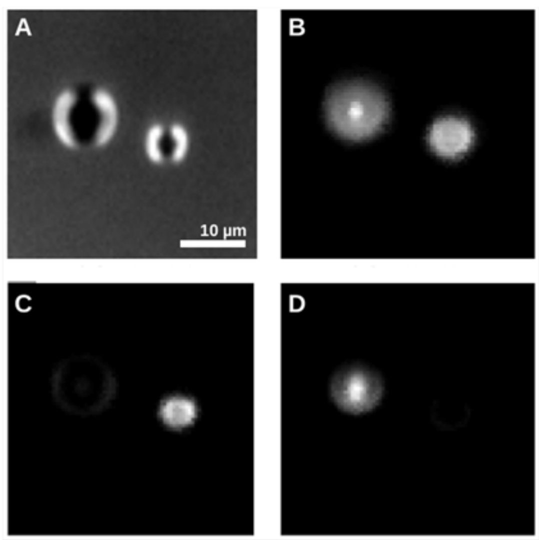

P1-B8-7

Glycerol in Oil-based Phantom with Improved Performance for Photoacoustic Imaging

Felipe Grillo[1], Luciana Cabrelli[1], Diego Sampaio[1], Antonio Carneiro[1], Theo Pavan[1]; [1]*Department of Physics, University of Sao Paulo, Ribeirão Preto, SP, Brazil*

Background, Motivation and Objective

Photoacoustic (PA) is an imaging modality where ultrasound signal is generated when laser pulses are absorbed by tissue. Tissue-mimicking phantom is a useful tool to characterizing PA imaging methods. Our group has previously proposed gels composed by the copolymer styrene-ethylene/butylene-styrene (SEBS) in mineral oil as a stable phantom material for PA imaging. SEBS gel is a translucent material and present acoustic and elastic properties similar to tissue. Recently, we proposed using glycerol dispersion to further tune the acoustics properties of the phantom. Chromophores can be added to tune optical absorption, while additives, such as intralipid and TiO_2 can be incorporated to tune optical scattering. Most additives used to tune optical properties of phantoms are hydrophilic; therefore, not soluble in mineral oil and SEBS molten gel. To overcome this limitation, in this study we propose using the glycerol dispersion technique to incorporate hydrophilic additives to the phantom. We also verified if this approach prevented the diffusion of the chromophores through different parts of heterogeneous phantoms.

Statement of Contribution/Methods

Cubic phantoms with 3.9 x 3 x 1.95 cm^3 containing cylindrical inclusions with 0.8 cm in diameter and 1 cm thick were manufactured. The base material, for both inclusion and background, was made using SEBS in mineral oil in the proportion of 10% w/w. Glycerol was added in a fraction of 15% of the oil mass. To manufacture the background, we mixed glycerol with TiO_2 nanoparticles (285 ± 86 nm) to enhance optical scattering. Mineral oil and SEBS were added to the glycerol/TiO_2 mixture and heated to 110°C until gel formation. For the inclusions, glycerol was mixed with methylene blue or India ink, to increase optical absorption. Acoustic, optical and elastic properties were assessed. PA spectroscopic images were acquired using a Nd:YAG laser (pulses of 10 ns) operating between 680 and 950 nm and the ultrasonic signals were acquired with a linear ultrasound transducer.

Results/Discussion

The speed of sound and attenuation coefficient of the material were 1478 m/s and 0.4 dB/cm at 1MHz, respectively. The presence of glycerol increased the apparent integrated backscattering by 20 dB when compared to SEBS gel in the absence of glycerol. The Young's modulus was 34 kPa. The phantoms presented homogeneous echogenicity in the B-mode images. Microscopic images revealed homogenous TiO_2 distribution in the glycerol droplets which had a diameter between 5 and 30 µm. The presence of TiO_2 increased the optical scattering to values similar to tissue. PA spectroscopy had a peak between 680-690 nm for the methylene blue inclusion; for the India ink case a flat PA signal magnitude in the range of 680-950 nm was obtained. In both cases, the PA spectroscopy is consistent with the absorption spectra. Finally, we observed that the strategy of mixing the chromofores with glycerol prevented them to diffuse to the background material.

P1-B8-8

Photoacoustic Speckle: Theoretical Basis and Experimental Evidence

Eno Hysi[1,2], Michael J. Moore[1,2], Subhajit Karmakar[3], Ratan K. Saha[4], Eric M. Strohm[5], Michael C. Kolios[1,2]; [1]*Physics, Ryerson University, Toronto, ON, Canada,* [2]*Institute for Biomedical Engineering, Science and Technology, Toronto, Ontario, Canada,* [3]*University Science Instrumentation Centre, The University of Burdwan, Bardhaman, India,* [4]*Department of Applied Sciences, Indian Institute of Information Technology Allahabad, Jhalwa, Allahabad, India,* [5]*Institute of Biomaterials & Biomedical Engineering, Mechanical and Industrial Engineering, University of Toronto, Toronto, Ontario, Canada*

Background, Motivation and Objective

Imaging speckle arises from the interference of waves from randomly distributed sources. Here, we provide a theoretical basis and experimental evidence for the presence of speckle in photoacoustic (PA) imaging across multiple ultrasonic (US) detection frequencies.

Statement of Contribution/Methods

PA systems used to image black polystyrene beads suspended in gelatin or agarose phantoms had the following properties:

S1. Ultrasonix RP (Ultrasonix Medical Corp.) 7 MHz linear array, 720 nm illumination

S2. VevoLAZR (FujiFilm VisualSonics) 40 MHz linear array, 680 nm illumination

S3. SASAM PA microscope (Kibero GmbH) 200/400 MHz single element transducers, 532 nm illumination.

In S1, the effect of absorber concentration on the speckle patterns was investigated using 400 µm beads. Influence of absorber size on PA speckle was tested in S2 for beads in what can be thought of as the Rayleigh (ka = 0.3) and Faran (ka = 1.2) regimes. S3 transducers were used to examine the effect of resolution volume on speckle patterns for a phantom containing 0.9 µm beads.

For S3, simulated PA images were obtained by solving the frequency domain solution of the wave equation and calculating the transducers' spatial impulse response using a Green's function approach. The presence of fully developed speckle was confirmed using a Generalized Gamma (GG) statistical model and the full width at half maximum (FWHM) of the autocovarience function (ACF) was used to estimate the speckle size.

Results/Discussion

Fully developed speckle was observed for all frequency regimes (Fig. 1). Figs. 1a and 1b show the changing texture of the speckle pattern with increasing US frequency. For both S1+S2, the GG distribution provides a good fit to the envelope of the PA signals. Specifically, the c/v GG shape parameter increased by 6x as the absorber size increased by 6 µm and by 10x as the number of beads per resolution volume increased from 50 to 500.

Experimental images of S3 revealed that the speckle pattern of the same phantom changes as the resolution of the imaging transducer increases (Figs. 1c and 1d). The ACF estimated speckle size for both experiment (Fig. 1e) and simulations (Fig. 1f) was within 5% of the transducer's axial and lateral resolutions. The findings of this study provide insights into the nature of PA speckle and how it is strongly influenced by the properties of the imaging transducer.

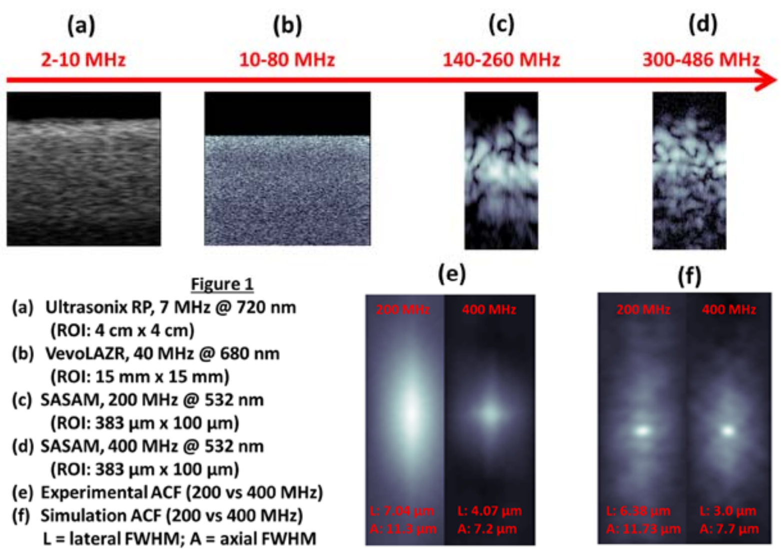

Figure 1
(a) Ultrasonix RP, 7 MHz @ 720 nm (ROI: 4 cm x 4 cm)
(b) VevoLAZR, 40 MHz @ 680 nm (ROI: 15 mm x 15 mm)
(c) SASAM, 200 MHz @ 532 nm (ROI: 383 µm x 100 µm)
(d) SASAM, 400 MHz @ 532 nm (ROI: 383 µm x 100 µm)
(e) Experimental ACF (200 vs 400 MHz)
(f) Simulation ACF (200 vs 400 MHz)
L = lateral FWHM; A = axial FWHM

P1-B9 - MSD: Novel Medical Systems

Exhibit Hall

Friday, September 8, 2017, 9:30 am - 4:00 pm

Chair: **Sevan Harput**
Imperial College London

P1-B9-1

Flexible Sensor Matrix with Dynamic Channel Weighting for improved Estimation of the Fetal Heart Rate by Doppler Ultrasound

Paul Hamelmann[1], Massimo Mischi[1], Rik Vullings[1], Alexander F. Kolen[2], Lars Schmitt[2], Shivani Joshi[3], Jan W.M. Bergmans[1]; [1]*Signal Processing Systems, Eindhoven University of Technology, Eindhoven, Netherlands,* [2]*Philips Research, Eindhoven, Netherlands,* [3]*Electronic Components, Technology and Materials, Delft University of Technology, Delft, Netherlands*

Background, Motivation and Objective

Electronic fetal heart rate (fHR) monitoring is standard in clinical practice to detect deviations from the normal fHR pattern. Typically, an ultrasound (US) transducer, operating in a pulsed-wave Doppler mode, measures the periodic motion of the fetal heart, from which the fHR can be derived. However, as the fetus moves through the birth canal, the fetal-heart location (fHL) changes continuously. Consequently, the clinical staff needs to manually track the fHL and reposition the US transducer accordingly. In this research, a new flexible US patch with multiple elements is designed; it allows measuring the fHR over a large range of possible fHLs. Further, a method for dynamic combination of the receiving channels is presented, with the aim of improving the Doppler signal and, therefore, the accuracy of the fHR estimation.

Statement of Contribution/Methods

A first prototype of a flexible ultrasound patch was realized by casting and curing a 1 mm thick layer of silicone (PDMS) into a mould. After curing at ~65 C°, 25 circular ceramic elements (PZT) were pressed into the layer at predefined positions. Each element was wired via 0.2 mm thick coaxial cables to an open US research platform (Vantage 256, Verasonics), which provides individual control over all elements. Eventually, a second layer of casted PDMS embeds the elements.

Fig. 1a shows the dynamic combination of individual receive channels. In transmission, all elements are active. After extraction of the Doppler signal, the power of each individual Doppler signal is computed. The relative power in each element is then used to dynamically adapt the weighting factors wi. This way, elements not directed towards the fHL will be deemphasized in the summation signal. The obtained signal is finally passed to an fHR estimator, making use of an autocorrelation function (ACF).

A dedicated *in-vitro* fHR setup was realized (Fig. 1b), for validation of the fHR at varying fHL.

Results/Discussion

A new design of a flexible sensor matrix is realized. The dynamic weighting of the channel summation produces improved signal quality. This improvement, along with the possibility to measure the fHR at varying fHLs without user interaction, represents an asset for the clinical assessment of fetal well-being.

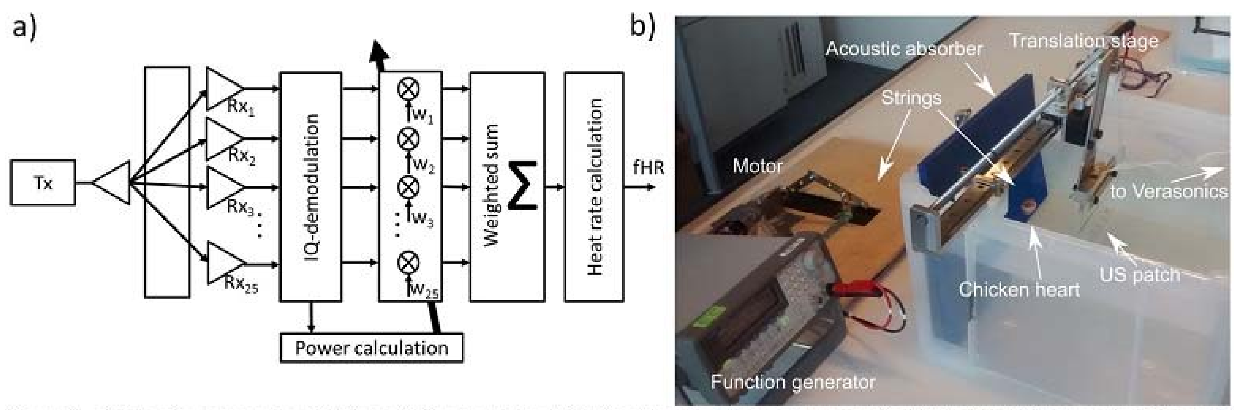

Figure 1: a) Adaptive channel weighting of Doppler signals for fetal heart rate measurements. b) Flexible Ultrasound patch used in dedicated in-vitro beating fetal heart rate setup. The function generator drives the motor with a predefined waveform. The strings attached to the motor pull on the chicken heart, causing a beat-like motion pattern at 120 beats per minute.

P1-B9-2

Imaging from the Implantable Side: Ultrasonic-Powered EIT System for Surgical Site Infection Detection

Bruno M. G. Rosa[1], Guang Z. Yang[1]; [1]*Hamlyn Centre, Imperial College London, London, London, United Kingdom*

Background, Motivation and Objective

Ultrasounds (US) are a proven medical tool to assess a myriad of biological processes, including breast cancer screening, fetal development and blood flow. However, US also have the potential to deliver power and telemetry capability to deeply implanted devices, surpassing some challenges faced by coils or antennas operating inside the human body. In this study we present an implantable device powered by US that can perform in situ tissue impedance imaging. The objective is to provide a tool to evaluate soft tissue healing after surgery, by searching for areas of bacterial infection as the normal conductivity of tissue will be impaired, undetectable by standard imaging methods. The motivation is to reduce not only the morbidity rate associated with wound infections (1/3 of the postoperative deaths) but also to shorten patient's recovery time in hospital, with 5% risk of developing a new infection.

Statement of Contribution/Methods

Electrical Impedance Tomography (EIT) has never been used as an un-tethered application where electrodes are in direct contact with tissues inside the body. The proposed device resorts to ultra-low power electronics to switch the current through each pair of electrodes while recording the voltage developed across the remaining pairs in DC regime. The device can operate with voltage levels as low as 0.8 V, with the energy being delivered via US by harmonic excitation of an external PZT at 400 kHz. In the other direction, the binary pattern from each voltage sample is coded using ON-OFF modulation over the implantable piezo, thereby modifying the acoustic transmission line as seen by the external PZT.

Results/Discussion

Figure 1 shows the results for a calibrated solution tank (1413 uS/cm) surrounded by device electrodes (8 in total), to which perturbations in conductivity (2600 uS/cm) are imposed. A back-projection scheme is implemented to transform the voltage samples into image domain pixels, given the current patterns. The results show a good performance in tracking the correct location of the perturbation within the tank, even in the presence of multiple disturbances. This fact is of paramount importance since bacteria tend to form colonies disseminating all over the surgical site. Moreover, the magnitude for conductivity can provide an indication of the stage of development of such colonies as it changes with the spreading of the perturbation.

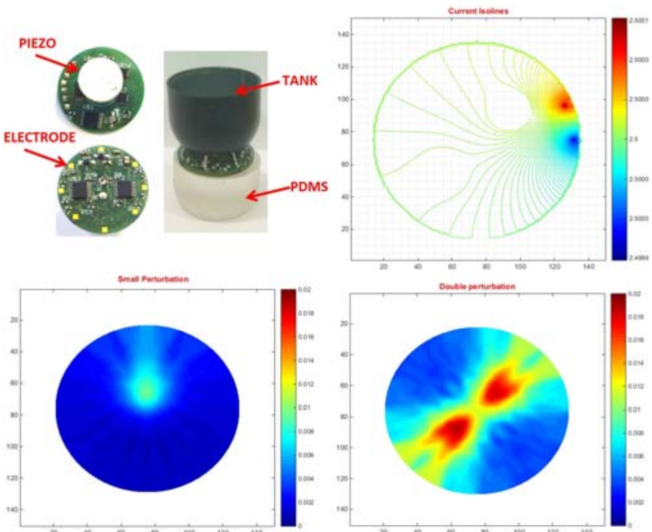

P1-B9-3 ____

Backward-Mode Ultrafast Pulsed Magnetomotive Ultrasound

Ming-Chen Lu[1], Jieh-Yuan Houng[1], Meng-Lin Li[1], [1]*National Tsing Hua University, Taiwan*

Background, Motivation and Objective

Recently, magnetomotive ultrasound (MMUS), which is capable of ultrasonic visualization of in vivo magnetic nanoparticle distribution challenging to conventional B-mode ultrasound, has shown its potential in extravascular ultrasound molecular imaging, magnetic nano-drug delivery monitoring, and sentinel lymph node identification. However, to date, only forward-mode MMUS where the imaging object is placed in between an ultrasound probe and an electromagnet is implemented in the literature. Such a MMUS mode is not suitable for clinical use.

Statement of Contribution/Methods

To facilitate clinical translation of MMUS, we proposes a backward-mode ultrafast pulsed MMUS system, featuring an MMUS probe integrating a 7.5-MHz ultrasound array transducer and an electromagnet, cyclic pulsed magnetic excitation, magnetic nanoparticles as contrast agents, and ultrafast plane wave imaging for magneto-motion tracking. The MMUS probe facilitates the backward-mode MMUS, improving the portability of MMUS. A programmable magnetic pulser is developed to enable cyclic pulsed magnetic excitation and 0.4-Tesla maximum magnetic field intensity. Cyclic pulsed magnetic excitation and ultrahigh frame-rate speckle tracking enable matched filtering for the identification of the unique cyclic magneto-motion from the excited magnetic nanoparticles. With the matched filtering, physiological motion artifacts can potentially be suppressed. In addition, a thresholding technique is also developed to reject the artifact caused by the intrinsic vibration of the working electromagnet in the MMUS probe.

Results/Discussion

Phantom experiments were performed to valid the proposed technique. Figure (a) showed the MMUS displacement image with matched filtering only. It was overwhelmed by the artifact resulting from the intrinsic vibration of the electromagnet in our MMUS probe and it was difficult to localize the embedded magnetic nanoparticles. Figure (b) presented the displacement image of the proposed technique with matched filtering and the developed thresholding method. The intrinsic vibration artifact was suppressed. With the improved contrast, the distribution of the embedded magnetic nanoparticles was clearly imaged. Overall, we demonstrate the capability of the proposed backward-mode ultrafast pulsed MMUS system, which is more clinically translatable.

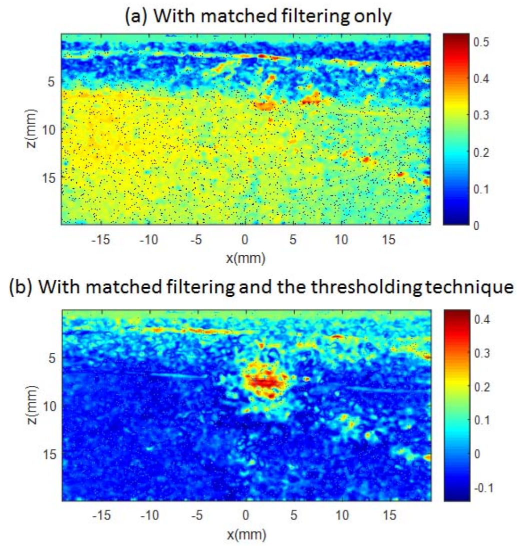

P1-B9-4

Fast Multilevel Lagrangian Carotid Strain Imaging with GPU Computing

Nirvedh Meshram[1,2], Tomy Varghese[1,2]; [1]*Department of Medical Physics, University of Wisconsin School of Medicine and Public Health, University of Wisconsin Madison, Madison, Wisconsin, USA,* [2]*Department of Electrical and Computer Engineering, University of Wisconsin Madison, Madison, Wisconsin, USA*

Background, Motivation and Objective

Lagrangian carotid strain Imaging (LCSI) involves estimation of deformation in the arteries undergoing cardiac pulsation and tracking the local strain over a cardiac cycle which is computationally intensive. We incur long offline processing times for LCSI which is a limiting factor for clinical adoption. We report on computations gains for a parallelized implementation of LCSI our algorithm using CUDA programming for fast computation.

Statement of Contribution/Methods

LCSI is currently performed using a multi-level block matching algorithm written in C++ using the Insight Toolkit (ITK) system. We are implanting this code with a NVIDIA k40 GPU for running CUDA kernels called from the ITK C++ code. This multi-level algorithm consists of three levels, level 1 performing block matching at the coarsest level and level 3 at the finest all on radiofrequency signals. Computational time for a single frame to frame displacement estimation is shown in figure 1A. The regularization step which takes the most time was implemented on the GPU. Analysis in Figure 1B, shows that the new bottleneck appears to be data updating and cross-correlation. Data updating was removed since it is pre-fetched with an existing streaming pattern. Finally, cross-correlation was implemented on GPU with the regularization step avoiding a CPU to GPU data transfer. Shared memory was also used in the regularization step to further reduce the time. Analysis of this optimized implementation is shown in figure 1C.

Results/Discussion

The computation time per frame for LCSI with our initial implementation was about 316.41 secs for an in vivo human carotid, thereby taking 131 minutes for an entire loop over a cardiac cycle of 25 frames. GPU implementation as shown in figure 1B takes 99.92 secs per frame, a speedup of 3.16X. Figure 1C demonstrates further optimization to complete a frame in about 23 secs giving a net speedup of 13.75X, and 9.5 minutes for a cardiac cycle.

Acknowledgement: Funded in part by National Institutes of Health grants R21 EB010098, R01 NS064034, and 2R01 CA112192. Academic hardware grant by NVIDIA)

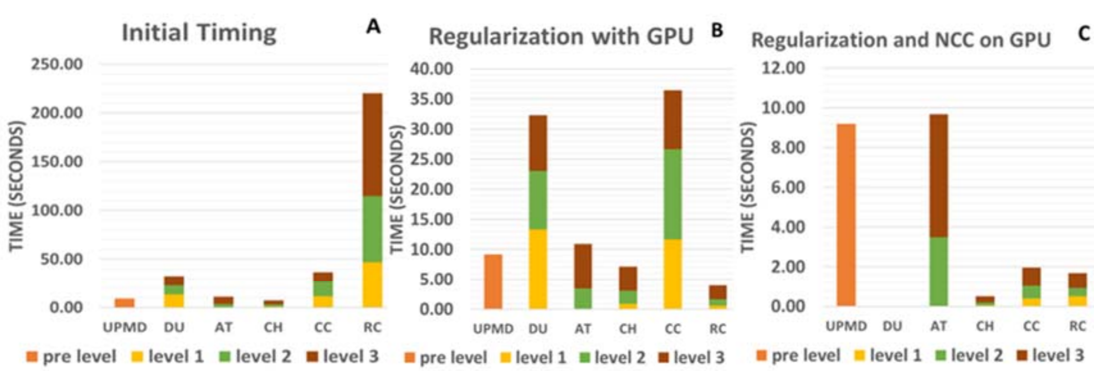

Figure 1 UPMD – Upsample and prepare multilevel Data, **DU** – Data updated and brought into memory to avoid future streaming. **AT**- Affine transform to prepare for block matching, strain in the previous level is used to scale data blocks for accurate inter-frame block matching. **CH** – Normalized cross corelation Helper, calculates mean and standard deviation for block matching. **CC**- Normalized cross corelation Calculator. **RC**- Regularization calculation

P1-B9-5

The Feasibility of Deep-Learning Algorithms Integration on a GPU-based Ultrasound Research Scanner

Piotr Jarosik[1], **Marcin Lewandowski[2]**; [1]*Department of Computational Science, Institute of Fundamental Technological Research, Warsaw, Poland,* [2]*Laboratory of Professional Electronics, Institute of Fundamental Technological Research, Warsaw, Poland*

Background, Motivation and Objective

Ultrasound medical diagnostics is a real-time modality based on a doctor's interpretation of images. So far, automated Computer-Aided Diagnostic tools were not widely applied to ultrasound imaging. The emerging methods in Artificial Intelligence, namely deep-learning, gave rise to new applications in medical imaging modalities.

The work's objective was to show the feasibility of implementing deep-learning algorithms directly on a research scanner with GPU software beamforming.

Statement of Contribution/Methods

We have implemented and evaluated two deep neural network architectures as part of the signal processing pipeline on an ultrasound research platform USPlatform (us4us Ltd., Poland). The USPlatform is equipped with a GPU cluster, enabling full software-based channel data processing as well as the integration of open source Deep-Learning frameworks.

The first neural model ('S-4-2') is a classical convolutional network for one-class classification of baby body parts. We propose a simple 6 layer network for this task. The model was trained and evaluated on a dataset consisting of 786 ultrasound images of a fetal training phantom. The second model ('GU-Net') is a fully convolutional neural network for brachial plexus localisation. The model uses U-Net like architecture to compute the overall probability of target detection and the probability mask of possible target locations. The model was trained and evaluated on 5640 ultrasound B-mode frames.

Both training and inference were performed on a multi-GPU (Nvidia Titan X) cluster integrated with the platform.

Results/Discussion

As performance metrics we used: accuracy as a percentage of correct answers in classification, Dice coefficient for object detection, and mean and std. dev. of a model's response time.

The 'S-4-2' model achieved 92% classification accuracy and a response time of 3.5ms (288 predictions/s). This simple model makes accurate predictions in short time. The 'GU-Net' model achieved 0.63 dice coefficient for object detection and 73% target's presence classification accuracy with a response time of 34ms (29 predictions/s). The brachial plexus detection task is more challenging and requires more effort to find the right solution.

The results show that deep-learning methods can be successfully applied to ultrasound image analysis and integrated on a single advanced research platform.

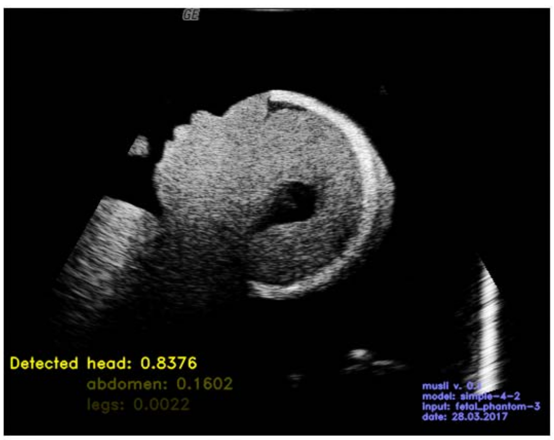

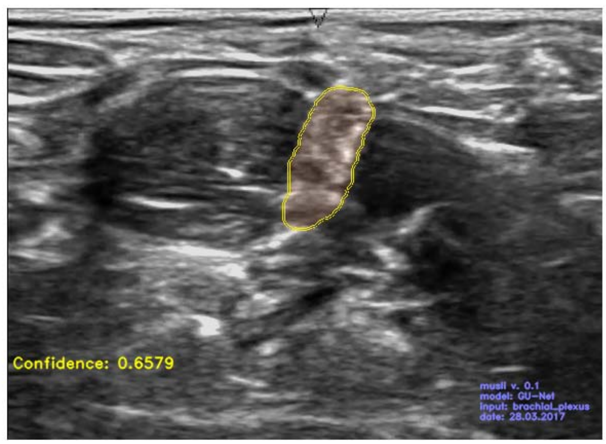

P1-B9-6

Automated System for Point Shearwave Elastography (pSWE) in Rodent Livers

Jonathon Perdomo[1], James Butler[1], Max Harlacher[1], Graeme O'Connell[1], Gabriela Torres[2], Caterina Gallippi[2], Anush Sridharan[2], Kennita Johnson[2], Paul Dayton[2], Ryan Gessner[1], **Tomasz Czernuszewicz[1]**; [1]*SonoVol, Inc., Research Triangle Park, NC, USA,* [2]*Biomedical Engineering, UNC Chapel Hill, NC, USA*

Background, Motivation and Objective

Point shear wave elastography (pSWE) provides noninvasive measures of mechanical stiffness of biological tissue. Over the past decade, research has demonstrated that pSWE is effective at diagnosing a multitude of pathologies such as liver fibrosis and cancer. Life science researchers stand to benefit tremendously from access to pSWE but a number of challenges have limited its use in small animals. First, high frequency pSWE imaging suffers from transducer heating challenges and bandwidth requirements. Second, pSWE measurements are highly susceptible to variations in the environment and operator (e.g. precompression of tissue, transducer placement, etc.) which bias measurements and introduce error. Therefore, the objective of this work is to develop a robotically controlled, non-contact pSWE system capable of measuring liver stiffness in rodents.

Statement of Contribution/Methods

A workflow was developed that uses a robotic system to raster scan through predefined locations (N=14) and automatically collects several pSWE measurements (N=10) at each location. These locations are defined using an initial widefield B-mode "scout scan" (FOV: 2x4 cm, 35 MHz). The system was tested on a set of 10 gel phantoms spanning a shear modulus range of 0.5-4 kPa (0.7-2 m/s). Additionally, the system was evaluated in 10 healthy control mice (C57BL/6). Shearwave parameters were as follows: 12 MHz pushing pulse, 15 MHz tracking pulses, 5 kHz PRF, 8 multiplexed lateral locations spaced 0.2 mm, 6 ms ensembles.

Results/Discussion

Figs. A and B show an example of a coronal B-mode image of a mouse abdomen with 14 targeted pSWE lines in the liver. Fig. C shows shear wave velocity (SWV) measured from phantoms with increasing gelatin concentration. As expected, SWV increased with increasing gel concentration, and measurement reproducibility was high with an average coefficient of variation (CV) of 6±3%. Ten healthy rodents were also scanned (Fig. D) resulting in a median SWV across all animals of 1.04 m/s (IQR: 0.83-1.28) and an average intra-animal CV of 37±8%. This study shows feasibility of a system that robotically manipulates ultrasound transducers beneath rodents in a non-contact manner to allow multiple pSWE acquisitions across a liver. Future work will include improving measurement reproducibility and automating the targeting line placements based on liver boundary segmentation.

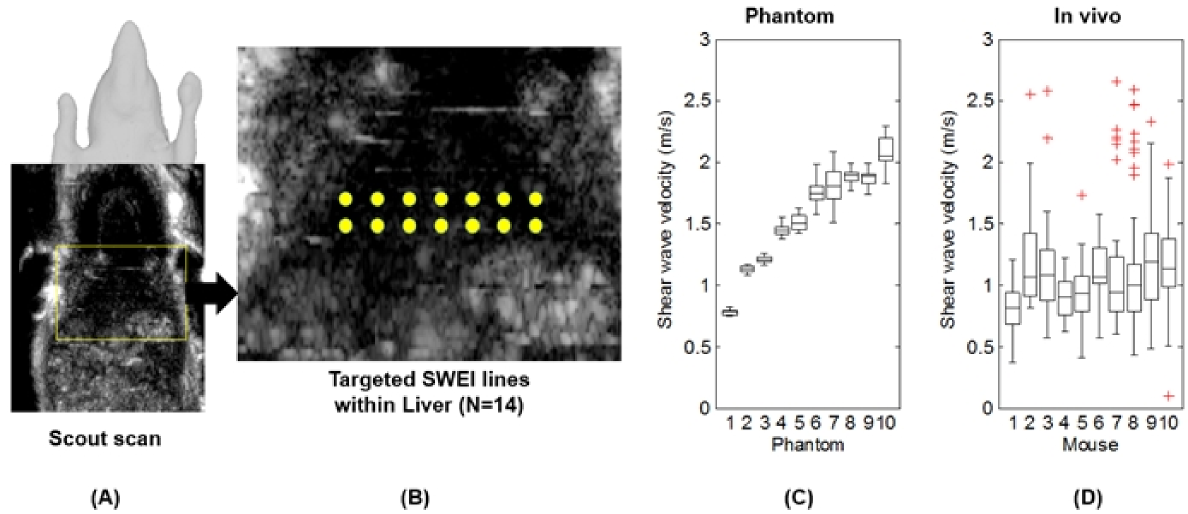

P1-B9-7

A New Method to Increase the Penetration Depth of Intravascular Ultrasound with Coded Excitation Imaging

Jiehan Hong[1], Peitian Mu[1], Xingyin Wang[1], Hairong Zheng[1], Weibao Qiu[1]; [1]*Paul C. Lauterbur Research Center for Biomedical Imaging, Shenzhen Institutes of Advanced Technology, Chinese Academy of Sciences, China, People's Republic of*

Background, Motivation and Objective

Intravascular ultrasound (IVUS) is a well-established diagnostic method that provides high-resolution images of vessel walls and atherosclerotic plaques. High-frequency (>50 MHz) ultrasound enables the spatial resolution of IVUS to approach that of optical imaging methods. However, the penetration depth decreases when using higher imaging frequencies due to the greater acoustic attenuation. In this paper we propose an ultrasound system specifically designed for coded excitation based IVUS (CE-IVUS) applications.

Statement of Contribution/Methods

Fig. 1 shows a block diagram of the proposed imaging system design especially for CE-IVUS applications. A field-programmable gate array device was incorporated for waveform generation and image processing. A high-speed DAC and a linear power amplifier were designed for the generation of an arbitrary waveform with a high voltage and adjustable amplitude and phase. A transmit/receive switch allowed the transducer to be triggered, and echo signals from the transducer were acquired with high-speed data acquisition circuitry. A universal serial bus (USB) was employed for transferring data to a computer. The system is able to generate a linear high-voltage waveform from 20 MHz to 100 MHz into a 50-ohm load. The power amplifier could produce a waveform with an amplitude exceeding 60 Vpp, with the frequency range covering most applications of the CE-IVUS.

Results/Discussion

The speed of data transfer is higher than 200 MB/second for a USB 3.0 interface, which facilitated high speed imaging performance: higher than 50 frames/second at an image size of 512*512 pixels.The anechoic holes could be clearly visualized using the proposed system. The mean contrast-to-noise ratio were 3.0, 3.6, and 4.4 for anechoic holes with diameters of 0.9 mm, 1.4 mm, and 3.0 mm, respectively. The penetration depth (i.e., where the signal magnitude reduced by more than 6 dB) was improved significantly when using the modulated excitation imaging technique compared with the short-pulse imaging technique for both 30-MHz ultrasound (10.3 mm and 7 mm, respectively) and 60-MHz ultrasound (about 5.6 mm and 3 mm).

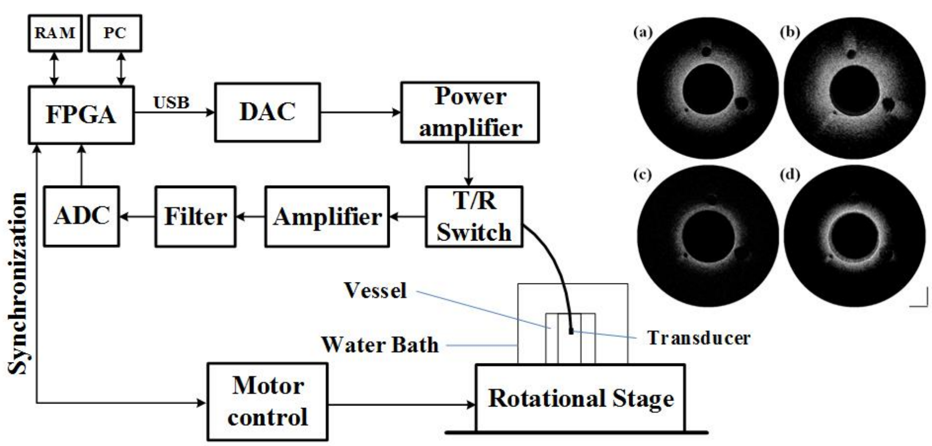

Fig. 1. Block diagram of the proposed system specifically designed for IVUS imaging; and sectional images of the tissue phantom acquired using the proposed system: (a) 30-MHz short pulse, (b) 30-MHz chirp, (c) 60-MHz short pulse, and (d) 60-MHz chirp. Scale bars: 5 mm.

P1-B9-8

Low Cost 3D Doppler Ultrasound: Preliminary *In Vivo* Results

Matthew R. Morgan[1], Carl D. Herickhoff[2], Joshua S. Broder[3], R. Brooke Jeffrey[2], Jeremy J. Dahl[2]; [1]*Biomedical Engineering, Duke University, Durham, NC, USA,* [2]*Radiology, Stanford University, Stanford, CA, USA,* [3]*Emergency Medicine, Duke University, Durham, NC, USA*

Background, Motivation and Objective

Conventional 2D Doppler ultrasound is a valuable screening tool for early detection of cardiovascular disease, including aneurysm of the abdominal aorta (AA) and stenosis of the carotid artery (CA). However, vascular ultrasound screening rates remain low and vary widely among physicians, due to the need for a skilled sonographer, equipment costs and scan time. We have recently developed a low-cost method to acquire 3D B-mode images using existing 2D clinical ultrasound systems, and 3D Doppler is a necessary feature for the application of this technology in vascular screening. Volumetric 3D Doppler ultrasound could enable faster scans by untrained users, and while 3D Doppler is available on some high-end systems, these are prohibitively expensive for deployment at the point-of-care. We demonstrate a fast and reliable method to enable comprehensive 3D Doppler acquisition using low-cost, peripheral hardware.

Statement of Contribution/Methods

A low-cost orientation sensor is mounted on a conventional 2D imaging probe, which is coupled to a plastic fixture designed to limit probe motion to pivoting about a fixed axis. Planar 2D Doppler images are acquired from the ultrasound scanner using a video capture device and tagged with an orientation reading while the user pivots the probe to sweep the image plane through a volume. Custom software on an external laptop uses the orientation-tagged 2D Doppler images to rapidly reconstruct an anatomically-oriented volumetric 3D Doppler dataset, which can be immediately visualized at the point of care in multi-planar or segmented and 3D-rendered views. *In vivo* 3D Doppler scans of the AA and CA were acquired on several patients according to an IRB-approved protocol at the Stanford University Medical Center.

Results/Discussion

We have developed a fast and intuitive augmentation to existing 2D ultrasound systems, allowing reliable volumetric 3D Doppler image acquisition. Preliminary *in vivo* results from the CA and AA demonstrated improved ability to identify and visualize the AA, CA, and an optimal short-axis plane to measure the maximum vessel diameter. Volumetric images were compared to the native 2D images, showing quantitatively accurate measurements and a more comprehensive field of view. This low-cost system has the potential to increase diagnostic information and improve the detection and treatment of cardiovascular disease.

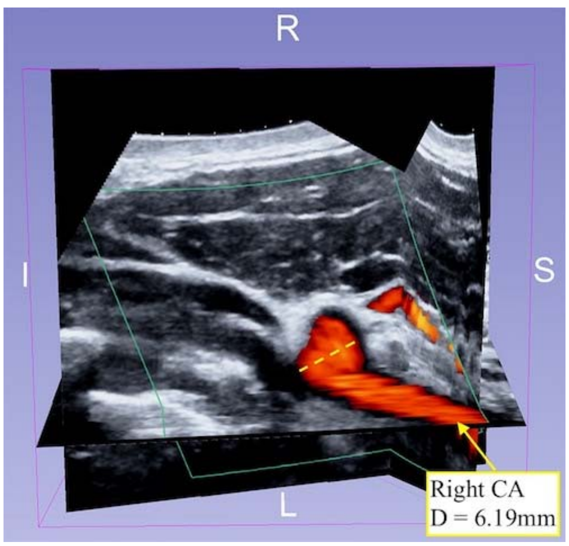

P1-B9-9

Therapeutic Ultrasound System Transducer Coupling Fluid Management System

Ralf Seip[1], Rodrigo Chaluisan[1], Drew Degentesh[2], Craig Campbell[2], Rob Parks[2], Mark Carol[1]; [1]*Sonacare Medical, USA,* [2]*Daedalus, USA*

Background, Motivation and Objective

Water continues to be the most commonly used fluid when coupling the energy emanating from a therapeutic ultrasound transducer to its target tissue. In many therapeutic ultrasound systems, this coupling fluid performs additional functions, such as transducer cooling, target tissue temperature management, and transducer/target tissue separation management, and is typically degassed to prevent the formation and accumulation of cavitation bubbles in the transducer's propagation path. Readying a therapeutic ultrasound system for use normally involves preparing this coupling mechanism, and being able to do this quickly and easily by the clinician or clinical support staff has tremendous implications on procedure workflow and time, as well as on overall system ease of use.

Statement of Contribution/Methods

Incorporating existing user feedback, a smart therapeutic ultrasound system coupling fluid management system was designed, implemented, and tested. It is capable of circulating and degassing coupling water, temperature-controlling this fluid for transducer and tissue temperature management, automatically priming the fluid path without user intervention, and adjusting the transducer/target tissue separation as required by a treatment plan or under user control. To achieve desired temperature control performance (cooling 500ml of water from room temperature to 14°C in less than 10minutes and maintaining it at this temperature during an ultrasound therapy), a novel single-loop disposable waterpath and heat exchanger system was developed. To achieve transducer/target tissue separation, a dual-pump peristaltic pump system was incorporated, capable of adjusting separation dynamically at flow rates in excess of 200ml/min. To achieve fluid degassing, a membrane-based filter cartridge was incorporated into the fluid path, capable of degassing 500ml of water to ≤1ppm of dissolved O_2 in less than 5 minutes, sufficient to avoid the creation of cavitation bubbles during typical sonications. The addition of temperature, vacuum, and water detection sensors and a microcontroller enabled implementation of a variety of use cases and applications, as well as identification and in many cases correction of user errors, and automatic detection of system faults.

Results/Discussion

Initial user feedback of this important but often overlooked therapeutic ultrasound system component has been overwhelmingly positive due to its ease of use and almost intuitive and transparent functionality. Its ability to operate in a stand-alone mode, or interface to an existing HIFU system further enhances the applications of this device.

Real-Time Intra-Operative Guidance Using Combined Photoacoustic and Pulsed Fluorescence Imaging for Robot-Assisted Surgical Operation

Jeeun Kang[1], Hanh Le[1], Jin U. Kang[1], Emad Boctor[1]; [1]*Johns Hopkins University, USA*

Background, Motivation and Objective

Multi-modal interface in medicine has been of interest as it extends clinical vision and diagnostic to a higher dimension. In this paper, we develop a real-time intra-operative guidance for robot-assisted surgical operation using a dual photoacoustic (PA) and fluorescence (FL) imaging based on a common pulsed laser and commercial ultrasound array transducer.

Statement of Contribution/Methods

As indicated in Fig. 1a, the system consists of a pulsed laser light generated from a second-harmonic Nd:YAG laser-pumped optical parametric oscillator system (Phocus Inline, Opotek Inc., USA). The laser pulse focused at 200 mm is delivered to a target through the dual-axis scanning galvo system (GVS 012, Thorlabs, Inc., USA). For each light delivery at 780 nm, the PA pixel data were collected by the transrectal ultrasound array transducer (BPL9-5/55, Ultrasonix Corp., Canada) connected to ultrasound research package (SonixDAQ), while the emitted fluorescence selectively captured by scientific CMOS camera (ORCA-Flash 4.0 V2, Hamamatsu K. K., Japan) through the dichroic mirror (805 nm) and emission filter (>830 nm). The system was validated using an acoustic tissue-mimicking phantoms mixed with indocyanine green for spectral absorption at 780 nm and emission at around 830 nm.

Results/Discussion

We have successfully reconstructed a maximum intensity projection (MAP) of both PA and the corresponding FL images on *ex-vivo* experiments using the designed phantoms. Further *in-vivo* experiments on bovine model will be conducted to support the clinical significance of the system specifically in the navigation for prostatectomy and ovarian cancer surgeries. We believe that the proposed method would provide the novel vision to surgeons for challenging laparoscopic operation such as nerve-sparing procedures in prostatectomy.

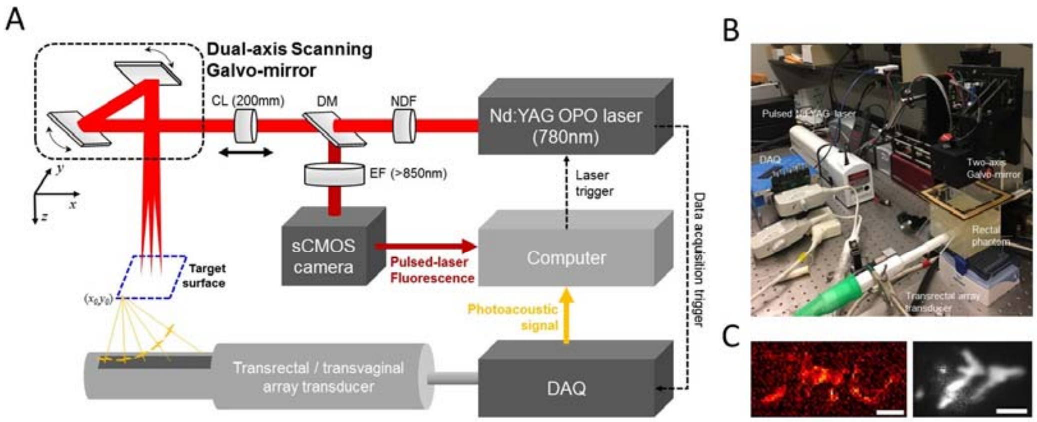

Figure 1. (a) Schematic diagram of dual-modal surgical guidance system; CL: coated piano convex lens (LA1708-C, Thorlabs), DM: dichroic mirror; NDF: neutral density filter; EF: emission filter, (b) system implementation, and (c) preliminary photoacoustic and fluorescence images; White bar indicates 5 mm.

P1-B10 - MTC: Tumor Characterization

Exhibit Hall

Friday, September 8, 2017, 9:30 am - 4:00 pm

Chair: **Aiguo Han**
University of Illinois at Urbana-Champaign

P1-B10-1

Relating Quantitative Ultrasound Parameters to Histologic Texture Parameters in Cancerous Human Lymph Nodes

Rui Venâncio[1], Bassem Ben Cheikh[1], **Alain CORON[1]**, Emi Saegusa-Beecroft[2], Junji Machi[2], Daniel Racoceanu[1], Lori Bridal[1], Jonathan Mamou[3]; *[1]Laboratoire d'Imagerie Biomédicale (LIB), Sorbonne Universités, UPMC Univ Paris 06, CNRS, INSERM, Paris, France, [2]University of Hawaii and Kuakini Medical Center, Honolulu, Hawaii, USA, [3]Lizzi Center for Biomedical Engineering, Riverside Research, New York, New York, USA*

Background, Motivation and Objective

Previous studies have shown that quantitative ultrasound (QUS) methods can provide tissue-microstructure information and are able to successfully detect metastases in human lymph nodes (LNs) harvested from cancer patients. Nevertheless, the gold standard for diagnosis remains pathological evaluation of histology photomicrographs. The goal of the present study is to compare QUS-based and histology-based features which proved to be most valuable for metastatic classification in LNs.

Statement of Contribution/Methods

14 metastatic and 19 non-metastatic LN of colorectal cancer patients were scanned in 3D with a 25.6-MHz center-frequency transducer. After histologic preparation and hematoxylin & eosin (H&E) staining, at least two whole slide histology images were acquired at 20X magnification using a whole slide scanner. For each ultrasound acquisition, QUS parameters (i.e., acoustic concentration (AC) and effective scatterer size (ESS)) were estimated from 3D cylindrical regions of interest in each LN. On each whole slide image, subimages of 1000x1000 pixels (460x460 µm) of LN tissue were extracted. From these subimages, 1755 texture features based on gray-level co-occurrence matrices and Law's filters were extracted from each of the color channels, after stain normalization, or after H&E separation. Best features for metastases detections were obtained by sequential forward selection (SFS). For each selected feature, an average value was estimated for each LN and scatter plots of US and histologic features were drawn (Fig 1).

Results/Discussion

AC and ESS were two of the most important QUS features to classify cancerous/non-cancerous lymph nodes (AUC>0.95 on >100 LNs of similar patients). The SFS selected five features and two first were Laws features computed from the hematoxylin channel after H&E separation (mean of L7E7 and skewness of L5E5). The histologic features successfully classified the LN. L5E5_Skewness and ESS exhibited the strongest linear relation relationship ($R^2 = 0.56$) between any pair of QUS and histologic features (Fig 1). Thus, either QUS or histology features alone successfully classified cancerous LN. Interestingly, only moderate information was shared between most performant QUS and histology features. Results offers an original look at how QUS features relate to features that are discriminant on histology photomicrographs.

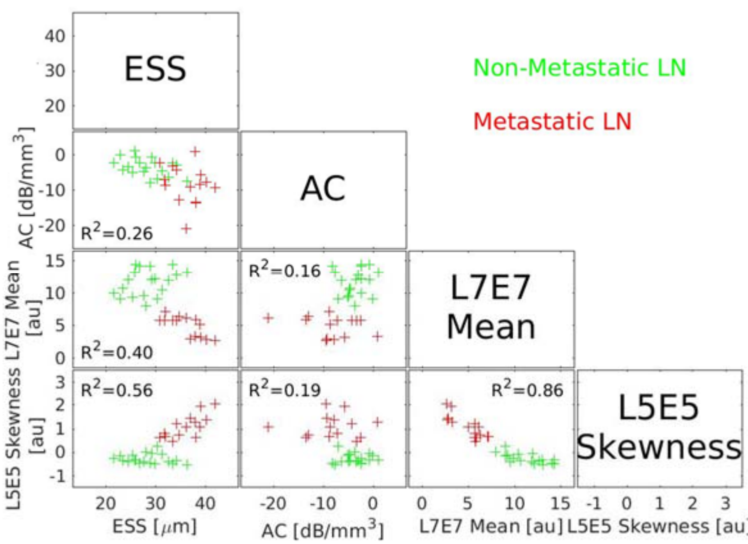

Figure 1: Paired scatter plots between two QUS features and two histology features. (The four features were selected for their demonstrated ability at classifying lymphnodes as metastatic or non-metastatic.)

P1-B10-2

Quantitative Ultrasound Spectroscopy to Differentiate Between Hepatocellular Carcinoma and At-Risk Liver Parenchyma

Ahmed El Kaffas[1], Isabelle Durot[2], Rosa Sigrist[2], Jarrett Rosenberg[1], Nishita Kothary[1], Juergen Willmann[1]; *[1]Radiology, Stanford University, USA, [2]Stanford University, USA*

Background, Motivation and Objective

Early detection of hepatocellular carcinoma (HCC) is critically needed to improve patient survival. Ultrasound is the first-line technology to screen patients at increased risk but has low sensitivity and specify in particular in hepatic cirrhosis. Quantitative ultrasound spectroscopy (QUS) is a promising tool that may increase diagnostic accuracy of ultrasound by enabling quantitative assessment and computerized screening. This study aimed to perform a clinical assessment of QUS parameters for differentiating HCC lesion tissue from liver parenchyma.

Statement of Contribution/Methods

This HIPAA-complied study was approved by the IRB. A total of 30 patients (21 male, 9 female) at increased risk for HCC (25 hepatitis B or C, 2 cirrhosis, 1 polycytemia vera, 1 hemochromatosis, 1 non-alcoholic steatohepatitis) were recruited for QUS assessment. 15/30 patients had at least one HCC lesion confirmed with CT or MRI. Ultrasound RF data was acquired for each patient using an Ultrasonix Tablet (Analogic) coupled to an C7-3/50 transducer. Data was acquired for each of the eight liver segments to survey the whole organ. Each liver location was imaged with 2 center frequencies (3.3 and 5 MHz) and 4 focal depths (3, 6, 9 and 12 cm), for a total of 8 sets of images per liver segment, per patient. ROIs were drawn by one observer on HCC lesions and the liver parenchyma. The average normalized (using glass-bead phantom) power spectrum for each ROI was extracted and a linear regression was fit within the -6 dB bandwidth window of the power spectrum, from which the mid-band fit (MBF), spectral intercept (SI) and spectral slope (SS) were extracted (Oncoustics). Differences in QUS parameters between the ROIs were tested by a mixed-effects regression on ROI location.

Results/Discussion

Results suggest that the MBF and SI parameters can differentiate between HCC positive and at-risk patients. After adjusting for age, sex, focus depth, and cirrhosis, there was a significant difference in MBF and SI values between HCC lesion and surrounding liver parenchyma ($p<0.001$) in the HCC group, as well as between HCC lesion (in HCC group) and the liver parenchyma of at-risk patients ($p<0.001$) (Figure). No statistical significance was noted between the liver parenchyma in HCC group and that in the at-risk group. No statistical significance was noted for the SS parameter between any of groups.

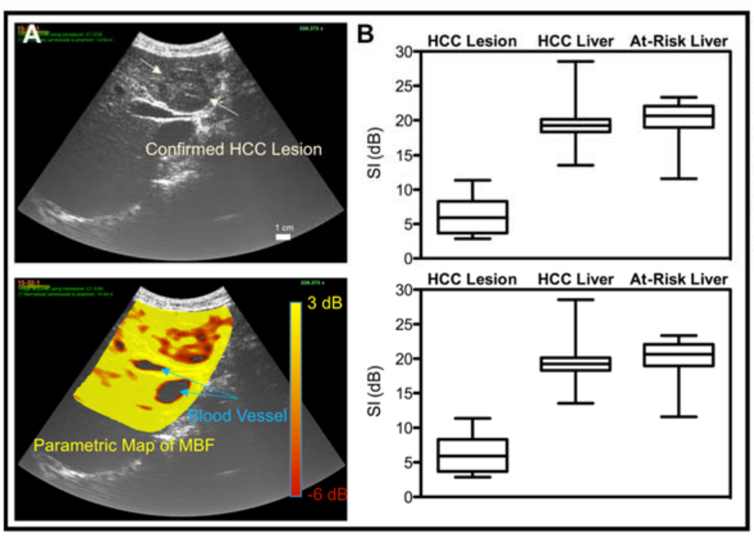

Figure - (A) Top is a Bmode image of patient liver where a confirmed lesion is located at the location of arrows (location of lesion was confirmed by radiologist and through CT). Bottom image shows an overlay parametric map of the mid-band fit (MBF) parameter, where the lesion appears red in the image while the liver parenchyma is a more homogenous yellow. Patient is female, 66 y.o. confirmed 3.2 cm HCC lesion in the left lobe of liver. **(B)** Average MBF and SI value in dB for all patients (15 per group) according to their classification. The first colon is the lesion in patients with confirmed HCC. The middle colon is the liver parenchyma in HCC confirmed patients, and the third colon is the liver parenchyma in at-risk patients.

P1-B10-3

Predicting Treatment Response in Invasive Ductal Breast Carcinoma Using Three-Dimensional Quantitative Ultrasound Analysis

Aisha Meel-van den Abeelen[1], Gert Weijers[2], Jan van Zelst[3], Johan Thijssen[1], Ritse Mann[3], Chris de Korte[4,5]; *[1]Medical Ultrasound Imaging Center, Department of Radiology and Nuclear Medicine, Radboudumc, Nijmegen, Netherlands, [2]Medical Ultrasound Imaging Center, Department of Radiology and Nuclear Medicine, Nijmegen, Nijmegen, Netherlands, [3]Department of Radiology and Nuclear Medicine, Radboudumc, Nijmegen, Netherlands, [4]1Medical Ultrasound Imaging Center, Department of Radiology and Nuclear Medicine, Radboudumc, Nijmegen, Netherlands, [5]Physics of Fluids Group, University of Twente, Enschede, Netherlands*

Background, Motivation and Objective

About 1 in 8 women will develop breast cancer. Histological tumor grade and biological markers such as oestrogen receptors (ER), progesterone receptors (PR), and human epidermal growth factor receptor 2 (HER2) are prognostic indicators for the clinical response to medical treatment and patient prognosis. Breast ultrasound (US) is mainly used to diagnose breast cancer or guide breast biopsies. However, quantitative analysis of US could also be of clinical value by giving additional information on tissue type. The automated breast volume scanner (ABUS) allows an automated assessment of a complete 3D US breast volume. By analyzing the texture of the B-mode images of the ABUS we have already shown that 3D quantitative breast ultrasound (3DQBUS) provides good discrimination between fibroadenomas (benign lesions) and invasive ductal carcinomas (IDC)(AUC=0.89). In this study we investigated whether 3DQBUS can be used to predict grade and receptor status.

Statement of Contribution/Methods

We included 70 3D ABUS datasets with biopsy proven IDC and 20 reference datasets without abnormalities. Of the 70 IDCs, 54 were ER/PR-positive and 16 were ER- and PR-negative, of which 10 were also HER2 negative. Further, 39 were low- and 25 were high-grade tumors (of remaining 6 no grade could be appointed).

As the grey level of US is depth dependent, due to beam diffraction and focusing, calibration of the images is necessary. For this, the grey levels of the reference ABUS images were plotted vs. pixel position and a polynomial was fitted to this curve and averaged over all reference measurements. The scan lines of the US images used in this study were normalised using this reference curve. Hereafter, the lesions were manually delineated and, based on sonographic criteria normally used by radiologists, 3 regions were defined for analysis: ROI (ellipsoid covering the inside of the lesion), PER (peritumoral surrounding: 0.5mm around the lesion), and POS (posterior-tumoral acoustic phenomena: region below the lesion with the same size as the lesion). For ROI, PER, and POS the mean and variance of the echo was calculated and, for the ROI and POS, also the residual attenuation coefficient was calculated. Logistic regression analysis was used to test the association with tumor grade, and receptor status. Classification accuracy was evaluated by leave-one-out cross-validation and receiver operating characteristic curves were constructed.

Results/Discussion

3DQBUS provides good discrimination for ER/PR-positive status vs. double negative (AUC=0.81) and vs. triple negative status (AUC=0.79). 3DQBUS was less able to discriminate between low- and high grade tumors (AUC=0.62).

In conclusion, 3DQBUS is a promising technique to non-invasively predict prognostic breast cancer information. For daily clinical practice, 3DQBUS may be a cheap and quick way to gather predictive information on treatment response for breast cancer.

Combining Nakagami Imaging and Convolutional Neural Networks for Breast Lesion Classification

Michał Byra[1], Hanna Piotrzkowska-Wróblewska[1], Katarzyna Dobruch-Sobczak[1], Andrzej Nowicki[1]; [1]*Institute of Fundamental Technological Research PAS, Warsaw, Poland*

Background, Motivation and Objective

The quantitative ultrasound (QUS) imaging provides additional information on tissue properties in comparison to standard ultrasonography. In this paper we use the Nakagami imaging to address the problem of breast lesion classification. Images of breast lesions may contain areas with calcifications or/and necrosis. These areas are visible on Nakagami maps and their presence make the classification more difficult; efficient texture features for classification are harder to estimate. As a remedy, we propose to use a convolutional neural network which automatically learn task dependent patterns from images. We train the network based on Nakagami maps of breast lesions.

Statement of Contribution/Methods

The analyzed data set contains radiofrequency ultrasound signals from 100 malignant and 100 benign breast lesions collected using the Ultrasonix SonixTouch Research Scanner and a 7.5 MHz linear transducer. Nakagami maps were created using the sliding window technique. The Maximum likelihood method was used to estimate Nakagami parameters based on signal amplitude samples. A convolutional neural network was trained in Tensorflow with the dropout and evaluated by means of the 5-fold cross-validation. Several network architectures were tested. The classification performance was assessed with the area under the receiver operating characteristic (ROC) curve.

Results/Discussion

Fig. 1 shows a B-mode image of a breast lesion and the corresponding Nakagami parameter map. Additionally, The ROC curve for the convolutional neural network trained on the breast lesion Nakagami maps. The AUC was equal to 0.98 which is very encouraging proving that the neural network ensured almost perfect classification. We illustrate network properties and list factors that may have an impact on classification. We state that the Nakagami parameter maps may be more suitable for network training than the standard B-mode images. The proposed method serves as a general approach for tissue characterization and differentiation. The Nakagami parameter used in this study can be replaced with another QUS parameter and the neural network can be trained in a similar fashion.

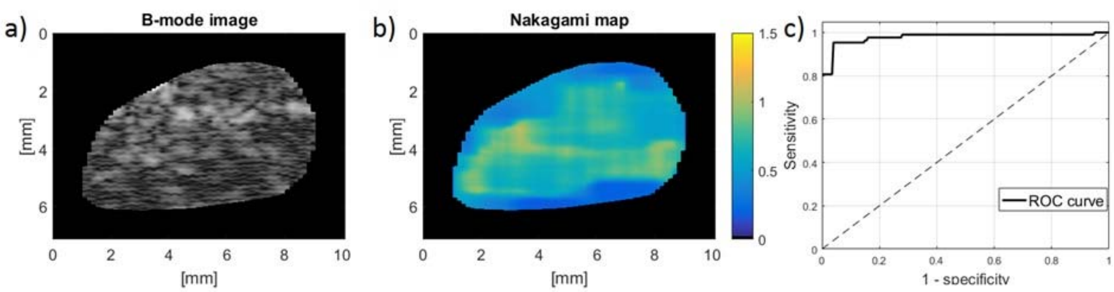

Fig. 1 a) B-mode image of a benign lesion and b) the corresponding Nakagami map, c) the ROC curve for the convolutional neural network trained on breast lesion Nakagami maps.

Three-Dimensional Estimation of Ultrasound-Contrast-Agent Dispersion and Convection in the Prostate

Rogier R. Wildeboer[1], Ruud J.G. van Sloun[1], Stefan G. Schalk[1,2], Christophe K. Mannaerts[2], J.C. van der Linden[3], Pintong Huang[4], Hessel Wijkstra[1,2], Massimo Mischi[1]; [1]*Dept. of Electrical Engineering, Labs of Biomedical Diagnostics, Eindhoven University of Technology, Eindhoven, Netherlands,* [2]*Dept. of Urology, Academic Medical Center, University of Amsterdam, Amsterdam, Netherlands,* [3]*Dept. of Pathology, DNA Laboratories, Jeroen Bosch Hospital, 's-Hertogenbosch, Netherlands,* [4]*Second Affiliated Hospital of Zhejiang University, Hangzhou, China, People's Republic of*

Background, Motivation and Objective

The estimation of Ultrasound-Contrast-Agent (UCA) kinetics from Dynamic Contrast-Enhanced Ultrasound (DCE-US) recordings has shown promise to localize prostatic malignancy. In a two-dimensional (2D) approach, UCA dispersion and velocity provide a characterization of the prostate (micro) vasculature with diagnostic value [1]. To this end, the UCA transport kinetics are modelled with strong assumptions on its directionality. Analysis of three-dimensional (3D) recordings allows clinicians to examine the entire gland with a single UCA bolus injection. In this work, we estimate convective dispersion (D) and velocity (v) of UCAs through the vascular network by directly solving the convective-dispersion equation in 3D, without need for further assumptions. This approach enables us to provide independent 3D maps of D and v for the whole prostate.

Statement of Contribution/Methods

We exploit the representation of UCA dispersion and convection as given by the convective-dispersion equation [2]. By establishing the concentration gradients of the data using Gaussian derivatives in space and time, the impact of noise is mitigated. Assuming D and v to be locally constant, the convective-dispersion equation can then be solved by minimizing a least-squares problem in a moving 3D kernel.

3D DCE-US loops of two minutes were recorded at the Second Affiliated Hospital of Zhejiang University (Hangzhou, Zhejiang, China). Data from four patients referred for radical prostatectomy were selected for this feasibility study.

Results/Discussion

D and v were estimated across the entire volume and compared to 3D reconstructed and registered histopathological models. Our preliminary results (Figure 1) show a good correlation between histopathologically-assessed malignancy and higher UCA velocity and convective dispersion. Although further validation and optimization is required, these results indicate the diagnostic potential of the obtained 3D maps of velocity and convective dispersion for localization of prostatic malignancy.

[1] R. J. G. van Sloun et al., “Ultrasound-contrast-agent dispersion and velocity imaging for prostate cancer localization,” Med. Image Anal., 2017

[2] W. Perl and F. P. Chinard, “A Convection-Diffusion Model of Indicator Transport through an Organ,” Circ. Res., 1968

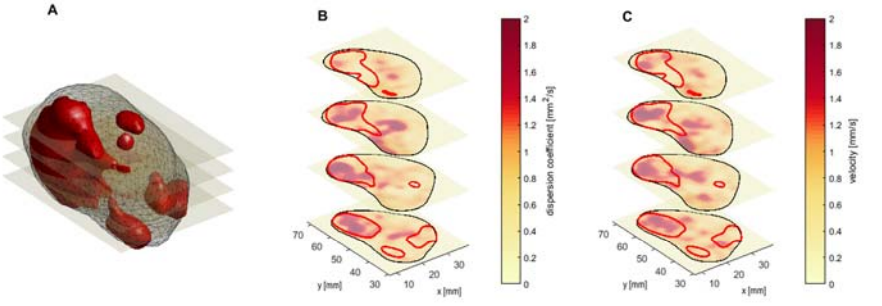

Figure 1 | (**A**) Example of three-dimensional prostate cancer (in red) histopathology and the corresponding (**B**) convective dispersion, *D*, and (**C**) velocity, *v*, maps shown in four slices from the acquired 3D DCE-US dataset. Estimates based on convolution with Gaussian functions of $\sigma = 1$ mm and $\sigma_t = 3.3$ s and least-squares solved in a spherical kernel of diameter 1.25 mm.

P1-B10-6

In Vivo Microcirculation Mapping of Human Skin Keloid by 40-Mhz Ultrafast Ultrasound Imaging

Pei-Yu Chen[1], Yuan-Yu Hsueh[2], Chih-Chung Huang[1]; [1]*Department of Biomedical Engineering, National Cheng Kung University, Taiwan,* [2]*Division of Plastic surgery, National Cheng Kung University Hospital, Taiwan*

Background, Motivation and Objective

Keloids are benign dermal disease that are characterized by the collagen deposition and growth beyond the boundaries of the original wound position. Many studies on keloids have showed that the density of blood vessel within keloids is higher than normal skin, which is a determinant of the physiological conditions of the tissue and also important for understanding the pathogenesis and radiotherapy response to keloids. However, the techniques for extracting the microcirculation of keloids are still lacking, which prompts us to develop a 40 MHz ultrafast ultra-high frequency ultrasound imaging to visualize the microcirculation within keloids.

Statement of Contribution/Methods

Experiments were carried out from a volunteer who is suffering a skin keloid on the abdomen. An ultrafast ultrasound imaging system (Vantage 256) with a 256-element high frequency array transducer (MS550D) were used to acquire the IQ signals from keloids. The operational frequency of transducer is 40 MHz. Seven plane wave angles were transmitted to keloids for acquiring the compounding image of blood vessel at a high frame rate of 1 kHz for 0.1 s. A singular value decomposition (SVD)-based algorithm was used to extract the blood signals in keloids for microvascular imaging.

Results/Discussion

Figure 1(a) shows the typical B-mode images of keloid which the size is about 4×1.5 mm. It is difficult to observe the blood vessel or Doppler mapping in the traditional ultrasound images. However, the microcirculation mapping was obtained clearly by using 40-MHz ultrafast ultrasound imaging based on a SVD algorithm, as shown in Figure 1(b). The angiogenesis in keloid is obvious than it in the normal skin. This result is consistent with previous studies using laser approaches, however, ultrasound image provides deeper information of blood flow. Due to the blood signal in keloids is similar to its surrounding tissues, it is difficult to choose an optimal cutoff frequency for high-pass filter to separate the signal from blood and tissues. Therefore, the SVD-based algorithm was used to overcome this problem in this study. All the results demonstrated the ability of high frequency ultrafast blood flow imaging for keloids, which can provide useful information to assist medical doctor for formulating the heal strategies of keloids.

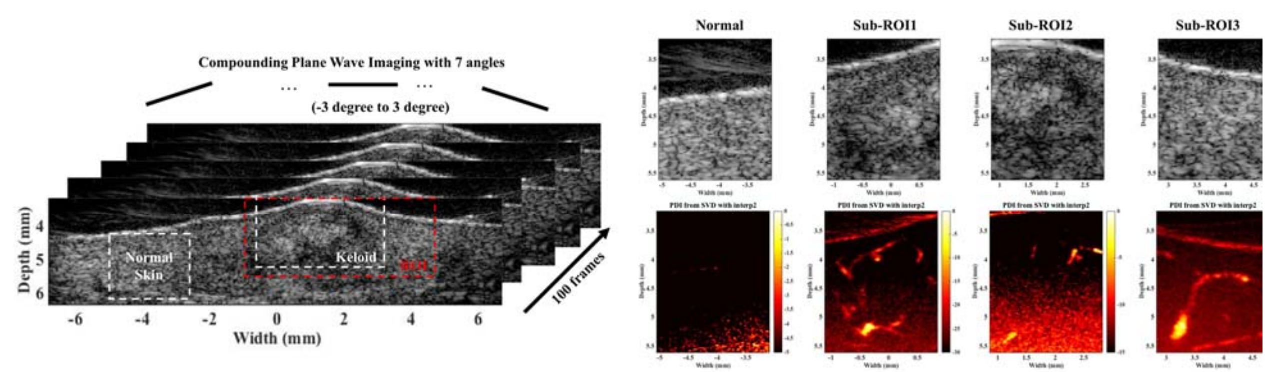

In Vivo Attenuation Estimation in Human Thyroid Nodules Using the Regularized Spectral Log Difference Technique: Initial Pilot Study

Andres Coila[1], Rosa Laimes[2], Claudia Salazar[2], Julien Rouyer[1], Gabriel Jimenez[1], Joseph Pinto[2], Jorge Guerrero[2], **Roberto Lavarello[1]**; *[1]Departamento de Ingenieria, Pontificia Universidad Católica del Perú, San Miguel, Lima, Peru, [2]Oncosalud, San Borja, Lima, Peru*

Background, Motivation and Objective

In vivo estimation of attenuation coefficients is useful because of its potential for tissue characterization and relevance in accurate backscatter coefficient estimation. However, current methods based on spectral analysis for ultrasonic attenuation estimation suffer from a severe trade-off between estimation precision and spatial resolution. Recently, the regularized spectral log difference (RSLD) technique was proposed to extend such trade-off in attenuation coefficient slope (ACS) estimation. The RSLD technique has been tested with simulated data and physical phantoms. Therefore, the aim of this pilot study is to validate the feasibility of in vivo estimation of ACSs from thyroid nodules using the RSLD technique.

Statement of Contribution/Methods

In the traditional spectral log difference technique, ACS values are estimated through a linear regression versus frequency of the logarithm of the spectral ratio from proximal and distal windows within a data block after proper diffraction compensation. In RSLD, the ACSs from all data blocks are jointly estimated regularizing the inverse problem with a total variation cost function. In vivo data from thyroid nodules was acquired in an oncology clinic right before fine needle aspiration (FNA) biopsy procedure. Data acquisition was performed using a SonixTouch (Analogic Ultrasound, Peabody, MA) ultrasound scanner equipped with an L14-5 linear array transducer (nominal center frequency of 10 MHz). The total region of analysis used for ACS estimation was manually selected within the nodule. Six nodules were analyzed in this study, meeting the criteria of being larger than 1 cm in diameter, not exhibiting partially cystic or honeycomb patterns or calcifications, and with FNA results reported as either Bethesda II (benign) or VI (cancer). The nodules had an average diameter of 1.56 cm and their biopsy results were adenomatoid nodules (3), Hashimoto's thyroiditis (2), and papillary carcinoma (1). In addition, healthy thyroid regions in three additional patients were also evaluated. The diffractive effects of the transducer were compensated using a calibrated reference phantom. The ACS estimation was performed with $16\lambda \times 16\lambda$ data blocks.

Results/Discussion

The average ACS values in healthy thyroid tissues and Hashimoto's thyroiditis nodules were found to be 1.63 ± 0.29 and 0.97 ± 0.08 dB.cm^{-1}.MHz^{-1}, which are consistent with the only two previous reports in this subject in the literature [Rouyer et al. (2016) IEEE TUFFC, 63(9), 1253-1261; Fuji et al. (2003) J Ultrasound Med, 22(10), 1067-1073]. The ACS values for the adenomatoid nodules and the papillary carcinoma were 0.94 ± 0.07 and 0.85 dB.cm^{-1}.MHz^{-1}, respectively. All nodules had lower ACS values than the ones in healthy thyroid tissues, which was consistent with the presence of posterior acoustic enhancement in the corresponding B-mode images. These results suggest that the RSLD method is capable of estimating ACS values in vivo.

P1-B11 - MTH: Therapy Guidance and Monitoring

Exhibit Hall

Friday, September 8, 2017, 9:30 am - 4:00 pm

Chair: **Chih-Kuang Yeh**
University of Waterloo

P1-B11-1

Synchronized Passive Microbubble Imaging for Guidance and Monitoring of Focused Ultrasound Therapies

Mark Burgess[1], Iason Apostolakis[1], Elisa Konofagou[1,2]; [1]*Biomedical Engineering, Columbia University, New York, USA,* [2]*Radiology, Columbia University, New York, USA*

Background, Motivation and Objective

Detection of focused ultrasound (FUS)-stimulated microbubble activity (i.e. acoustic cavitation) is a key methodology for monitoring and guidance of FUS therapies that harness the bioeffects of acoustic cavitation. The intensity and location of secondary acoustic emissions emitted by microbubbles can be passively detected and imaged using diagnostic imaging arrays. In turn, ultrasound-guided FUS (USgFUS) systems can be used for planning and evaluating the outcome of microbubble-based FUS therapies. State-of-the-art passive imaging methodologies were developed for monitoring high-intensity focused ultrasound (HIFU) ablation but suffer from poor axial image resolution due to the use of long pulses and asynchronous transmit and receive sequences. The objective of this study was thus to implement passive microbubble imaging (PMI) with short pulses of FUS and synchronous acquisition for improved image resolution by implementing reconstruction techniques similar to B-mode ultrasound imaging. The efficacy of PMI was assessed during blood-brain barrier (BBB) opening with FUS and microbubbles in mice in vivo.

Statement of Contribution/Methods

A 1-MHz FUS transducer was aligned off-axis relative to an 18-MHz imaging array (L22-14v LF, Verasonics, Inc.) and placed above an anesthetized mouse for transcranial application of FUS. A Vantage ultrasound research system (Verasonics, Inc.) was used to synchronize the FUS transmit and receive acquisition of the passive imaging array. Very short FUS pulses (2-3 cycles, 100-500 kPa peak negative pressure) were used at high pulse rates (500-5000 Hz) for simultaneous BBB opening and passive imaging of intravenously-injected microbubbles. Receive acquisition frames were recorded for each FUS transmit and reconstructed off-line using GPU-based delay-and-sum beamforming. PMI was compared with post-FUS dynamic contrast enhanced-magnetic resonance imaging (DCE-MRI) for correlation of BBB permeability with the location and intensity of acoustic cavitation activity.

Results/Discussion

PMI image intensity was found to be proportional to microbubble emission strength and concentration within the microvasculature. The image resolution of PMI was significantly improved compared to existent methods in the literature and is mainly dependent on the duration of cavitation activity and imaging frequency. With the improved resolution, detailed microvasculature PMI images were created using methods similar to power Doppler imaging. These cumulative PMI images revealed a heterogeneous distribution of microbubble activity throughout the focal area and correlated with BBB opening regions imaged with DCE-MRI. PMI also provided high frame rate sampling of the microbubble infusion kinetics and persistence within the focal area of the FUS. The PMI methodology may not only constitute a promising technique for monitoring of BBB opening, but also for other FUS therapies that utilize microbubbles.

P1-B11-2

Feasibility of Thermal Strain Imaging in Noninvasive Monitoring of HIFU-mediated Local Drug Delivery

Xiaolong Liang[1], **Qiong He**[2], Jing Gao[2], Jianwen Luo[2]; [1]*Department of Ultrasonography, Peking University Third Hospital, China, People's Republic of,* [2]*Department of Biomedical Engineering, Tsinghua University, China, People's Republic of*

Background, Motivation and Objective

Thermal strain imaging (TSI) is promising for lesion targeting and dose control in thermal-based treatment. We previously developed HIFU and temperature sensitive cerasomes (HTSCs) for local chemotherapy of cancer (Liang et al, Acs Nano 2015). However, the temperature within tissues cannot be noninvasively measured *in vivo*. The aim of this study was to investigate the feasibility of TSI in noninvasive monitoring of HIFU-medicated doxorubicin (DOX) loaded HTSCs delivery.

Statement of Contribution/Methods

A function generator was used to produce a sinusoid wave (f_0 = 1.64 MHz) modulated by a square wave (PRF = 200 Hz, duty cycle = 50%). The output signal was amplified by an ENI 2100L power amplifier (50 dB gain). The resulting waveform was used to drive a 0.5 MHz single element HIFU transducer (H107, Sonic Concepts). A homogenous PVA phantom was placed in water tank (25 °C) with the region of interest (ROI) located at the focal spot of the HIFU transducer. During HIFU sonication, the plane wave imaging channel data of the phantom were acquired for 5 ms every 100 ms (5 steering angles, 15 kHz PRF) by SonixMDP system equipped with an L14-5 probe and SonixDAQ (Fig. a); the temperature in the ROI was measured by a thermocouple. The axial displacements were estimated from the coherent compounded RF data (3 kHz fps) using cross-correlation, and the thermal strains were calculated from their derivative. The maximum thermal strain (MTS) and the full width at half maximum (FWHM) of the thermal strain lateral profiles at the focal spot were obtained at different time points during heating. Percentage of the released DOX at the focal spot after the temperature reaching the critical value (41 °C) was measured using a fluorescence dequenching assay.

Results/Discussion

The local temperature in the phantom increases and decreases during and after HIFU sonication, respectively (Fig. b). A 500 mV voltage in the function generator was chosen because it can reach 41 °C for drug release and avoid overheating. The MTS and FWHMs increase during heating (Fig. c) and are both linearly correlated with the temperature measured (r = 0.96 and 0.94). After the temperature reaches 41 °C, the percentage of the released DOX increases with the heating time (Fig. d). As a conclusion, TSI may be used to estimate the temperature change for noninvasive monitoring of HIFU-mediated local drug delivery.

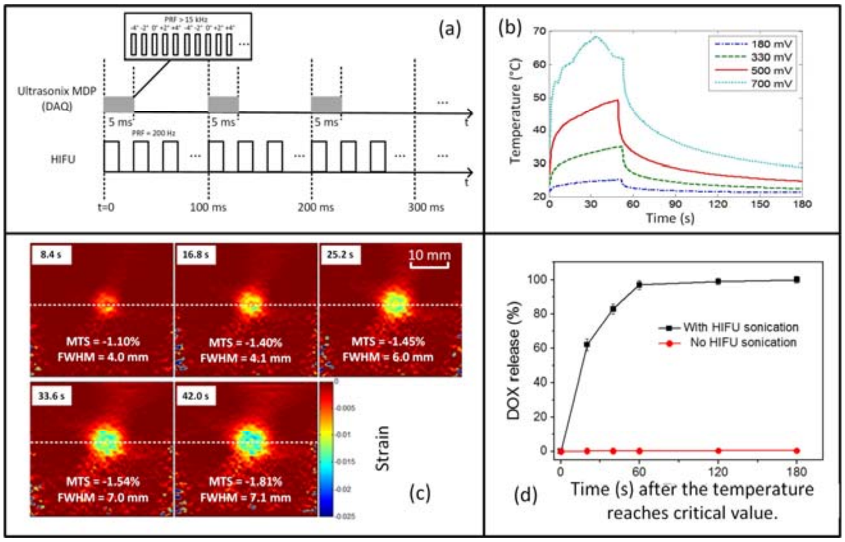

P1-B11-3

Focused Ultrasound Ablation Using Electronically Scanned Grating Lobes with Real-time Echo Decorrelation Imaging Feedback

Michael Cox[1], Mohamed Abbass[1], Allison-Joy Garbo[1], T. Douglas Mast[1]; [1]*Biomedical Engineering, University of Cincinnati, Cincinnati, Ohio, USA*

Background, Motivation and Objective

Focused ultrasound can effectively treat tumors by thermal ablation, but treatment times associated with mechanical or electronic scanning of single foci can be prohibitively long. Maximizing the energy efficiency of focused ultrasound ablation may decrease treatment time while also decreasing sensitivity to perfusion. One proposed approach [Mast et al., US Patent 9132287, 2015] creates multiple foci as grating lobes of a coarse ultrasound aperture, then electronically scans these grating lobes by applying phase rotations to shift the grating lobe positions.

Statement of Contribution/Methods

This study assessed the feasibility of electronic grating lobe scanning to ablate tissue more efficiently than unfocused or single-focus ultrasound ablation. To do this, a 64-element, 5 MHz linear image-ablate array was employed for weakly focused ablation (100-125 W/cm^2 spatial-peak, temporal peak intensity) using a virtual 16-element aperture (5λ pitch) as well as real-time ablation monitoring and control by echo decorrelation imaging. Phase shifts were applied to treat a planar tissue region by alternating between 2 or 3 symmetrical grating lobe patterns. Treatments were assessed in *ex vivo* bovine liver and compared with ablation predicted by numerical simulations and real-time echo decorrelation maps. Lesion dimensions and treatment durations were compared with unfocused and focused ablation treatments performed by the same array using echo decorrelation imaging monitoring and control.

Results/Discussion

Results demonstrate feasibility for this approach, with reasonable agreement between observed thermal lesions, simulations, and echo decorrelation maps. Regions of severe tissue ablation correlated with regions of large simulated thermal dose (EM_{43}>10^7 min) and large observed echo decorrelation (>10^{-2} per ms). Trials employing electronic grating lobe scanning ablated tissue regions faster and more efficiently than either unfocused or single-focused trials.

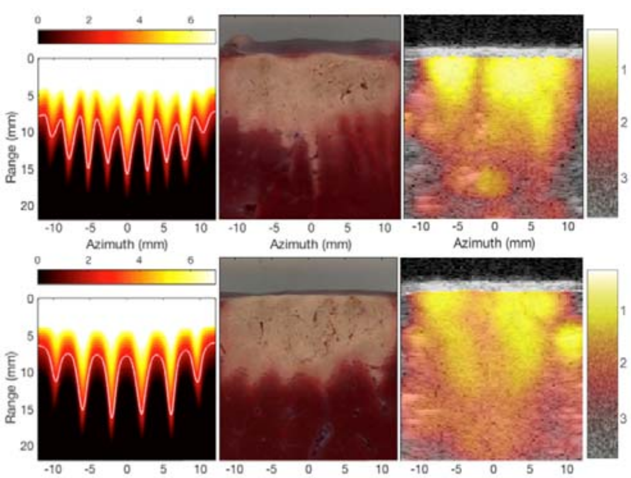

Figure 1. Representative results for grating lobe scanning using 3 (top row) and 2 (bottom row) alternating phase rotations. Left: simulated thermal dose $\log_{10}(EM_{43})$. Middle: TTC-stained cross-sections of treated tissue in the imaging-ablation plane. Right: cumulative echo decorrelation images ($\log_{10}$-scaled decorrelation per ms).

P1-B11-4

Ultrasound Imaging with Enhanced Lesion-to-Bubble Ratio based on Wavelet Transform for Monitoring of High-Intensity Focused Ultrasound

Ting Ding[1], Zhiguo Gui[1], Siyuan Zhang[2], Luyang Ma[1], Mingxi Wan[2]; *[1]Department of Biomedical Engineering, School of Information and Communication Engineering, North University of China, China, People's Republic of, [2]Department of Biomedical Engineering, School of Life Science and Technology, Xi'an Jiaotong University, China, People's Republic of*

Background, Motivation and Objective

B-mode imaging for the guidance and monitoring of high-intensity focused ultrasound (HIFU) treatment mostly relies on the appearance of a hyperechoic region. The hyperechoic region integrates the information from both thermal lesions and cavitation bubbles, making it difficult to visualize thermal lesion formation. In this paper, an approach of ultrasound imaging based on wavelet transform (UIWT) is proposed to enhance the contrast between thermal lesions and cavitation bubbles induced by HIFU, and the efficiency of this approach is evaluated on a transparent tissue-mimicking phantom at various acoustic parameters.

Statement of Contribution/Methods

Radio-frequency data were sequentially collected by a diagnostic ultrasound scanner to obtain the B-mode images over HIFU treatment. The B-mode images were firstly decomposed with multi-scale wavelet transform. The cavitation signals and lesion signals have high and low frequency respectively. Correspondingly their wavelet coefficients have smaller and larger absolute values respectively. The obtained sub-bands images were enhanced by a threshold-based nonlinear method. The coefficient was enhanced or suppressed dependent on if the wavelet coefficient was above or below the threshold value. Subsequently, the UIWT image was obtained by wavelet reconstruction. The lesion-to-bubble ratio (LBR), which was defined as the ratio of the scattered power from the lesion to the bubbles, was calculated at various HIFU exposures. The dynamic changes of LBR over the HIFU treatment were compared with those of the original B-mode images. The lesion areas and shapes were also investigated.

Results/Discussion

The results showed that when a small lesion was induced in the early stage of the HIFU treatment, LBR of the UIWT image was improved by 11.64±2.62 dB compared with that of the B-mode image. When a large lesion was formed, the LBR values increased to 23.87±4.18 dB. When varying acoustic parameters, the difference in LBR dynamic changes over the HIFU exposure were found to rely on the spatial-temporal dynamics of lesion and bubbles, as well as the selections of regions-of-interest (ROIs). The lesions grew towards the HIFU transducer, and the shapes were changed from ellipse to tadpole. This study suggests that UIWT may have potential in enhancing the LBR for better monitoring of thermal lesion formation during HIFU treatment.

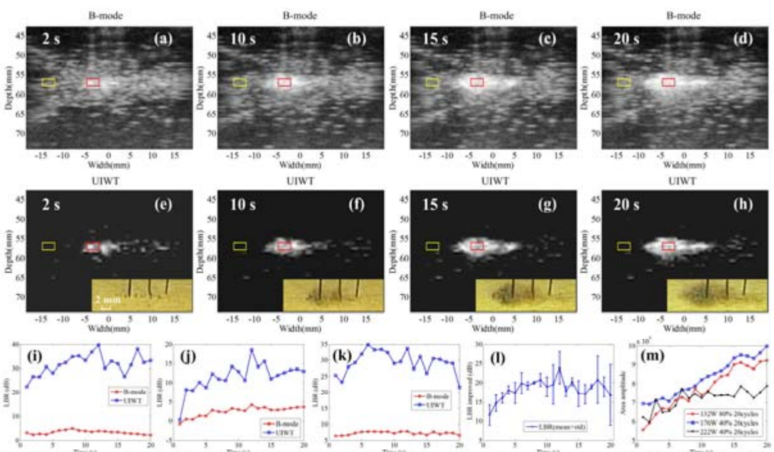

FIG. 1. UIWT images to monitor lesion formation during HIFU treatment. (a)-(d) showed B-mode images at the exposure time of 2 s, 10 s, 15 s and 20 s. (e)-(h) showed UIWT images at the exposure time of 2 s, 10 s, 15 s and 20 s, and in the each image, there is the video photo in the bottom right corner. The yellow and red square ROIs were used for calculating the LBR values. The HIFU transducer was on the left, and the acoustic power was 132 W with a duty cycle of 80% and a total treatment time of 20 s. (i)-(k) showed the dynamic changes of LBR over the HIFU exposure. The various acoustic parameters in (i)-(k) were set as follows: (i) acoustic power=132 W, PD=800 ms, DC=80%, 20 cycles; (j) acoustic power=176 W, PD=400 ms, DC=40%, 20 cycles; and (k) acoustic power=222 W, PD=400 ms, DC=40%, 20 cycles. (l) showed the improved LBR compared with that of B-mode image. (m) displayed the dynamic changes of lesion areas during HIFU treatment.

P1-B11-5

3D Passive Imaging of Ultrasound Cavitation using a 2D Array

Paul Boulos[1,2], Francois Varray[1], Bruno Gilles[2], Jean-Christophe Bera[2], Christian Cachard[1]; *[1]Univ.Lyon, INSA-Lyon, UCBL1, UJM-Saint Etienne, CNRS, Inserm, CREATIS UMR 5220, U1206, lyon, France, [2]LabTau-Inserm U1032, lyon, France*

Background, Motivation and Objective

Ultrasound (US) therapy is, for a large panel of application, a promising technique which still requires an accurate monitoring system. Therefore, the passive acoustic mapping (PAM) beamforming technique is outlined. It reconstructs cavitation activity maps by beamforming acoustic signals passively recorded by an array. This method has already been explored in 2D with optimizations as phase coherence factor (PCF) (Boulos et al, IUS, 2016) or robust capon beamforming (Coviello et al, JASA, 2015). The 3D implementation is a crucial step for real-time monitoring of US therapy. As the cavitation spot is located and spreads in the three directions, the acoustic source information should be retrieved from the recorded radio-frequency (RF) signals in both lateral and elevation directions of the array.

Statement of Contribution/Methods

In this study, the PAM-PCF in 3D was developed and applied to 2 datasets. First, a simulated pre-beamformed data was considered with an acoustic point source positioned at 4 cm from the array. Second, experimental RF signal acquisitions was performed of acoustic waves emitted by a bubble cavitation cloud induced in an agar gel at 4 cm from the array, thanks to a regulated US cavitation generator (Desjouy et al, JASA, 2013). A 2D array with 24x8 elements and a 400 µm pitch was used. For the cavitation experiments, 100 RF signals were acquired with a 1000 Hz pulse repetition frequency. For each acquisition, the cavitation map is computed and then the focal cavitation point (FCP), defined as the maximum acoustic power point, is recovered for the three dimensions: (depth, lateral, elevation).

Results/Discussion

The isosurface at -3dB and two perpendicular cross-section plane (elevation=0 and lateral=0) are displayed for both datasets in Fig. 1. The 3D reconstructed map for cavitation experiment (d,e,f) is very similar to the simulation one (a,b,c). The FCP for the simulation is recovered at (39.9, 0.2, 0.2) mm which is closely equal to the theoretical FCP position at (40, 0, 0) mm. Along the 100 maps of the cavitation experiments, the FCP is equal to (36.2±2.2, -0.4±0.4, -2.2±1.2) mm. A wider cavitation spot is noticed for the elevation direction (Fig. 1. c, f). Indeed, it is related to the probe aperture size which in this direction is three times less than in the lateral direction. Hence with the future use of higher aperture probes, the resolution should be improved.

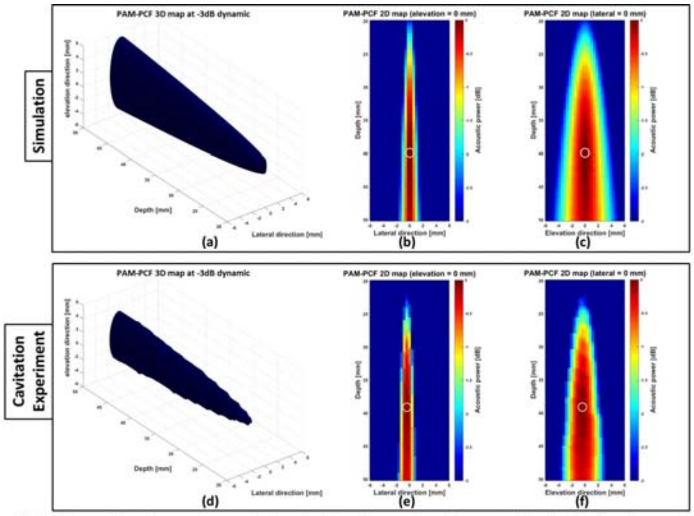

Fig.1: 3D computed passive acoustic maps. On top: simulation of an acoustic point source positioned at 4cm from the array (a,b,c). On bottom: water tank cavitation experiment with a bubble cloud induced in agar gel at 4 cm from the array (d,e,f) for one frame. From left to right: the isosurface at -3 dB dynamic(a,d), the cross-section plane for elevation=0 (b,e), and the cross-section plane for lateral=0 (c,f). The white circle corresponds to the focal cavitation point (FCP) localization.

P1-B11-6

Basic Study on Ultrasonic Tissue Monitoring Using 1.5-Dimensional Ultrasound Phased Array for Ultrasound-guided High Intensity Focused Ultrasound Treatment

Ryo Takagi[1], Shin Yoshizawa[2], Shin-ichiro Umemura[2]; [1]*National Institute of Advanced Industrial Science and Technology, Tsukuba, Japan,* [2]*Tohoku University, Sendai, Japan*

Background, Motivation and Objective

In conventional ultrasonic monitoring of high intensity focused ultrasound (HIFU) treatment, it has been difficult to track the target region when the tissue to be treated deviates from the imaging plane along the elevation axis of the 1-D probe. A 2-D phased array probe providing 3-D imaging capability requires a large number of elements and it is very expensive to build a system to drive all channels simultaneously. A 1.5-D phased array probe can provide a good compromise between conventional 1-D and 2-D phased array probes and has significant cost and implementation advantages. In this study, a new 1.5-D phased array probe consisting of 64×4 elements was designed and developed to track tissue motion within mm order along the elevation direction and the elevational displacement range where the tissue tracking is effective was investigated.

Statement of Contribution/Methods

The new prototype probe with a center frequency of 3 MHz consists of 256 flat elements made of a piezocomposite, where 64 and four flat elements are along the lateral and elevation axes, respectively as shown in Fig.1 (a). The consideration behind the design is that tissue motion of mm order in the elevation direction is to be tracked while keeping the same lateral resolution as a practical 1-D phased array probe. The probe was mounted above the tissue specimen and ultrasound 2.5-D RF volumetric images were produced by applying plane-wave transmission while the probe was moved along the elevation axis at a pitch of 1.0 mm. The displacement vector was calculated from RF image blocks between before and after shifting the probe along the elevation axis to track the 3-D tissue motion.

Results/Discussion

Figure.1 (b) shows the relationship between the actual and estimated elevational displacements using the 1.5-D phased array probe. The dashed line indicates the expected value. As shown in Fig.1 (b), the effective tracking range using this prototype probe was up to 3.0 mm along the elevation axis about three times that for conventional 1-D imaging. We also applied plane-wave transmission followed by parallel beamforming, which led to a 2-D frame rate higher than 5000 fps. Therefore, it is the possible to track tissue motion along the elevation axis at a speed of m/s order during HIFU exposure. We need to investigate the feasibility of this prototype probe for more practical and complicated tissue motion as a future work.

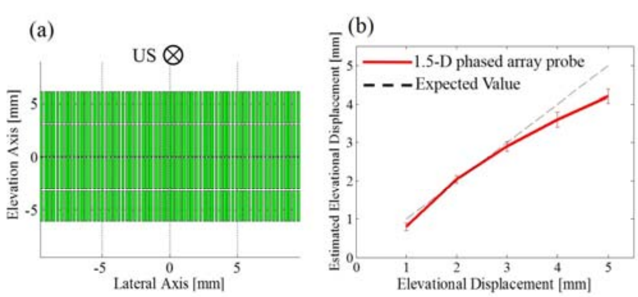

Figure.1 (a) Schematic of 1.5-D phased array probe. (b) Relationship between actual and estimated elevational displacements using 1.5-D phased array probe. The dashed line indicates the expected value.

P1-B11-7

A Novel 3D Ultrasound Thermometry Method for HIFU Ablation Using an Ultrasound Element

Younsu Kim[1], Chloe Audigier[1], Nicholas Ellens[2], Emad Boctor[2]; *[1]Computer Science, Johns Hopkins University, Baltimore, Maryland, USA, [2]Radiology, Johns Hopkins University, Baltimore, Maryland, USA*

Background, Motivation and Objective

High intensity focused ultrasound (HIFU) is a non-invasive thermal ablation technique. Ablating malignant tissue entirely while preserving as much healthy tissue as possible is challenging, requiring real-time monitoring for optimal results. Magnetic Resonance Imaging (MRI) is the current gold standard for HIFU monitoring, providing reliable temperature information in real-time. However, MRI has several disadvantages including its high cost and its lack of portability. Accordingly, there is motivation to guide thermal ablation procedures with real-time ultrasound (US) monitoring techniques exploiting changes in acoustic properties with rising temperature and ablation progression. As the speed of sound (SOS) changes with the increase in temperature, we propose a new method using an active external US element detecting SOS changes to generate temperature images during HIFU ablation.

Statement of Contribution/Methods

We fabricated small active US elements (diameter < 3 mm) which can receive US signals from the HIFU array and produce negligible artifacts on MR temperature images. US pressure waves going through the ablation zone and propagating to the opposite end carry direct time-of-flight (TOF) information that we can use to recover SOS in the intervening tissue and convert into 3D temperature maps. Due to the sparsity of the recorded data, 3D SOS images are generated based on the a priori knowledge of the ablated ROI segmented from a physics-based HIFU simulation.

In our experiment, we built a phantom with 2% agar and 2% silicon dioxide. First, we measured the relationship between SOS and temperature for the phantom. Second, HIFU heating experiments were performed in an MRI (Sonalleve V2 in an Achieva 3T, Philips), consisting of three consecutive interleaved periods of heating (10 s) and element-by-element acoustic interrogation (25 s). The heating was performed at 50 W at 1.2 MHz (all elements continuous wave), while the interrogation used 40 cycle pulses from single elements.

Results/Discussion

3D thermal images were recovered from the TOF information and compared to thermal MR images for validation. The temperature difference in the ROI was 1.1 ± 0.7°C on average, with a maximum difference of 3.7°C. The results establish the feasibility of our method for thermal monitoring with an external ultrasound element.

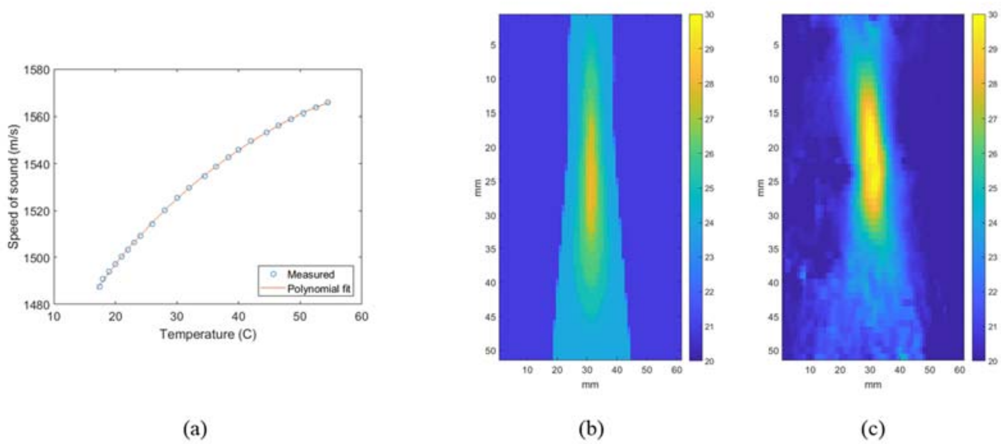

(a) Measured speed of sound of the phantom. (b) US thermometry after HIFU ablation. (c) MR thermometry after HIFU ablation.

P1-B11-8

Estimation and Compensation of In-Situ Ultrasound Intensity Using a 2-D Array Therapy System and High Frame Rate Imaging

Y.M. Peng[1], B.X. He[1], J.Q. Yu[1], M.Y. Chen[1], Z.H. Shuai[1], Y.Y. Hu[1], L.J. Wang[1], S.P. Chen[1,2], **Chien Ting Chin**[1,3]; *[1]Department of Biomedical Engineering, Shenzhen University, P. R. China, Shenzhen, China, People's Republic of, [2]Guangdong Provincial Key Laboratory of Biomedical Information Detection and Ultrasound Imaging, P. R. China, Shenzhen, China, People's Republic of, [3]National-Regional Key Technology Engineering Laboratory of China for Medical Ultrasound, P. R. China, Shenzhen, China, People's Republic of*

Background, Motivation and Objective

Ultrasound had been reported to locate the actual *in situ* focal spot of FUS and to compensate for guidance error due to beam distortion. However it still cannot determine exposure dosage in a clinical setting, therefore monitoring often require MR thermography. The main challenge is that multiple relevant acoustic parameters are not easily isolated from measurable signal characteristics in noninvasive pulse-echo mode.

Microbubbles can be a biocompatible internal "probe" to convert a local parameter to measurable echo characteristics. We sought to exploit highly specific behaviors of microbubble destruction in therapeutic ultrasound. This paper reports the feasibility of a pre-treatment scheme to estimate effective attenuation and other relevant parameters and subsequent compensation during actual treatment.

Statement of Contribution/Methods

A multichannel transmission system and array transducer was designed and built. The system provides 128 physical channels that transmit arbitrary waveform with an analog bandwidth of 12 MHz. The probe consists of a 125-element 2-D array at 2.1 MHz. The system produces a high resolution focal spot of 0.8x0.8x5 mm, steerable to ±8 mm in any direction. Arbitrary exposure fields can be achieved. A phantom containing Sonovue® microbubbles are exposed to the treatment field with an ROI of Ø8 mm. A programmable high frame rate scanner system (Verasonics, Redmond WA) was used to capture echo data. A modified plane wave imaging sequence produced high resolutions B-scan frames at a rate of 1 kHz, which are interleaved between FUS exposure at various burst lengths and amplitudes. The treatment beam is normal to the imaging plane. Reconstructed echo image frames were analyzed to locate the treatment ROI automatically. The dynamics of the averaged echo signal in the ROI as functions of treatment parameters was recorded. The experiment was repeated with various attenuating layers (simulating unknown patient condition) added to the treatment beam path. Four different layers with attenuation between 1.2 to 6.3 dB were used.

Results/Discussion

Extent and rate of destruction of microbubbles by treatment beam increases with amplitude and burst length, as expected. However, any single measurement cannot reliably reveal the *in situ* beam intensity without controlling the microbubble concentration. The data sets of destruction curves obtained with attenuating layers were matched to the un-attenuated reference data set using a multi-parameter fitting algorithm. The resulting fitted beam intensity was found to match closely the actual values, verified by independent measurement of attenuation. The errors of *in situ* beam intensity measured with the proposed method were less than 1.6 dB. Some capabilities of the array therapy system was also demonstrated in this study. An arbitrary ROI is exposed in 30 ms, the fast scanning speed was exploited to ensure that the entire ROI is exposed evenly in between excessive imaging events.

P1-B11-9

Evaluation of the Acoustic Properties of Clots during Sonothrombolysis

Laurent Auboire[1], Damien Fouan[1], Jean-Marc Grégoire[1], Frederic Ossant[1], Jean-Michel Escoffre[1], Ayache Bouakaz[1]; [1]*INSERM U930, France*

Background, Motivation and Objective

Sonothrombolysis with microbubbles (STL) is being explored as a promising therapeutic alternative in ischemic stroke. The objective of this study is to better understand the impact of STL +/- rt-PA on the acoustic properties of blood clot in vitro.

Statement of Contribution/Methods

Clots were made from fresh whole citrated blood. Clots were inserted in a flow circuit with circulating human plasma. Four different conditions were tested: 1) Control 2) rt-PA 3 ng/mL (clinical dose used in stroke) 3) STL: (single element transducer 1MHz, 8% Duty cycle, 600KPa) + BR14, 10^6/min during 30 min exposure time, and 4) rt-PA + STL. When rt-PA was used, the plasma was recalcified to mimick physiological condition.

The acoustic properties of the clots in the 4 different conditions were measured. Vevo 2100 scanner was used at 40 MHz to measure the speed of sound (SS) through the clot every minute over a 30-min time period. Next, Aixplorer scanner was used to assess the clot elasticity (shear wave speed SWS) every 5 min during a 30-min time period. During all these measurements, the STL was turned off.

Results/Discussion

The results showed that the SS through the clot increased for both rt-PA and STL compared to control. However, a clear synergistic effect is obtained when combining rt-PA and STL (A). Elastography measurements showed that SWS does not change for STL alone nor for rt-PA alone. However, the combination of rt-PA and STL induces a significant increase of the SWS. Later on, the SWS seems to decay (B). A delayed action of rt-PA-STL on SWS is observed due to the use of recalcified plasma: Calcium is leading to a fibrino-formation around the clot protecting it in the first 10 minutes, which is lysed by the action of rt-PA afterwards. This is the first study of clot elasticity and SS during STL, showing that the clot is becoming more rigid during the initial treatment with rt-PA-STL. We presume that the hemolysis induced by STL (Ultraschall Med. 2017 Jan;38(1):83-84.) first leads to a compression of the fibrin network accelerating thus the effect of fibrinolysis by rt-PA. These new structural modifications need to be compared to histology to give a new insight on the impact of STL and rt-PA on clots.

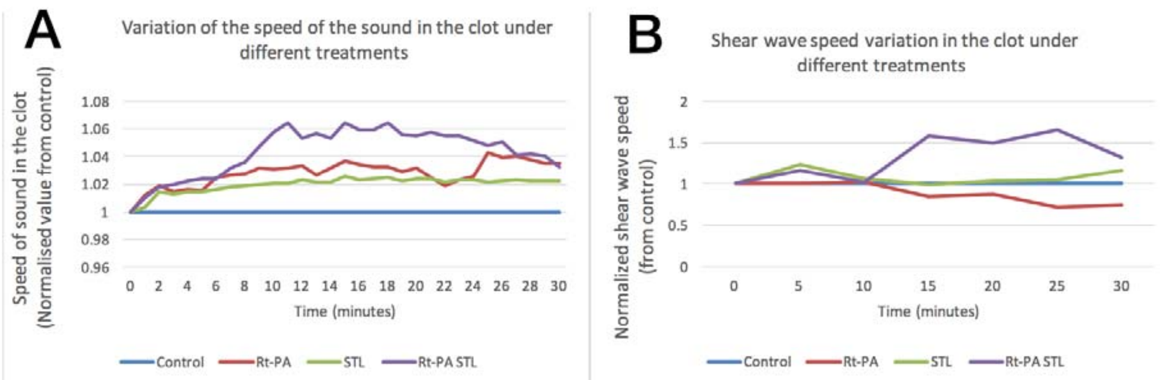

Figure: A) Variation of the speed of sound as measured with the Vevo 2100® using a 40 MHz probe; B) Variation of the shear wave speed measured with the Aixplorer®.

P2-B1 - Signal Processing

Exhibit Hall

Friday, September 8, 2017, 9:30 am - 4:00 pm

Chair: **Erdal Oruklu**
Illinois Institute of Technology

P2-B1-1

Comparison of GPU and FPGA Based Hardware Platforms for Ultrasonic Flaw Detection using Support Vector Machines

Kushal Virupakshappa[1], Erdal Oruklu[1], Yiyue Jiang[1], Yu Yuan[1]; [1]*ECE Department, Illinois Institute of Technology, Chicago, IL, USA*

Background, Motivation and Objective

Our earlier work on support vector machines (SVM) and ultrasonic flaw detection algorithms demonstrated i) highly accurate classifier performance and ii) the feasibility of the algorithm for real-time implementation on low-cost embedded systems with graphical processing units (GPU) and CUDA library (a parallel computing platform and programming model) support. This works extends the implementation to another programmable hardware platform, FPGA, and also evaluates the performance of a different numerical computation library, TensorFlow by Google.

Statement of Contribution/Methods

The proposed ultrasonic flaw detection algorithm is based on subband decomposition of the signal followed by classification with a trained SVM model that uses subband filter outputs as feature inputs. The two different platforms which are being used for implementing the algorithm are FPGA-based Xilinx ZedBoard and GPU-based Tegra TK1 System-on-Chip (SoC). Both platforms utilize ARM processor cores. CUDA is the library provided by NVIDIA for GPU accelerated implementation and TensorFlow is a numerical computation library used primarily for building machine learning algorithms. In TensorFlow, computations are expressed in the form of dataflow graphs and multidimensional arrays are referred to as "tensors". TensorFlow library can work on any platform i.e., CPU, or GPU with CUDA support. In our first approach, the entire flaw detection algorithm is implemented on the ARM CPU core using conventional C code for subband decomposition and CPU based TensorFlow library functions for SVM classification. Next, GPU-based TensorFlow functions for SVM are used to validate the inherent parallelism of the algorithm. Finally, SVM predictor is realized on a Xilinx FPGA. CUDA based implementation on Tegra TK1 board from our earlier work is used as a reference point.

Results/Discussion

The SVM algorithm achieves flaw echo classification accuracy of 95% with 191 experimental A-Scan data (94 data sets were used for training and 97 were for testing). The GPU accelerated CUDA implementation of the algorithm has shown that SVM would execute under 0.174 ms while FPGA implementation takes only 0.02 ms on the Zynq-7000 FPGA. Resource usage for FPGA reaches 70% for DSP slices and 26% for look-up tables (LUTs). Performance discrepancy between GPU and FPGA hardware is partially related to the unoptimized TensorFlow library. The current limitation for using the Tensor Flow SVM function is that only the linear kernel function is available for CUDA acceleration while other kernels (such as the radial basis function kernel used in our algorithm) and their SVM functions are implemented on the ARM CPU core. Currently, we are developing GPU implementations of these functions for enhanced computation with the Tegra boards.

P2-B1-2

Performance Analysis of Deep Learning Architectures for Ultrasonic NDE Applications

Kushal Virupakshappa[1], Erdal Oruklu[1]; [1]*ECE Department, Illinois Institute of Technology, Chicago, IL, USA*

Background, Motivation and Objective

Research on Deep Learning algorithms has progressed rapidly in recent years. Since the inception of deep learning, numerous architectures have been proposed for various applications targeting pattern recognition, image, audio and information analysis. For example, often audio signal classifications use variations of Deep Belief Networks (DBN), while a Deep Neural Network (DNN) called AlexNet is widely used for handwriting and alphabet recognition. Convolutional Neural Network (CNN) and its derivatives are primarily used in machine vision and imaging applications. Convolutional Deep Belief Networks (CDBN) work as a combination of CNN and DBN architectures and can be applied to image, audio and multimodal data. There has been limited studies on the effectiveness of these architectures for ultrasonic NDE applications. Therefore, this work investigates new flaw detection methods based on recent advances on deep learning architectures.

Statement of Contribution/Methods

We use DBN and CNN architectures as the basis of comparison by visualizing outputs of various layers of deep learning architectures. DBN is constructed out of Restricted Boltzmann Machines (RBM) which are stacked to obtain the DBN architecture. Each RBM has a set of hidden and visible nodes/states and the hidden states are connected to visible states obeying the rules of bipartite graph. Based on our earlier preliminary work on signal classification/analysis using deep learning, limited number (1-3) of layers followed by the activation stage is effective for successful classification of flaw echoes (detecting the presence of flaw). A similar approach is employed for CNN and CDBN. CDBN has Convolution RBM as layers, while CNN is comprised of one or more convolutional layers (with a subsampling step) followed by fully connected layers. The key difference between these methods is related to how feature extraction works. DBN and CDBN extract the statistical features from the input while CNN extracts neighboring data differences and spatial structures.

Results/Discussion

For ultrasonic flaw detection, either A-scan, B-scan or their discrete wavelet transform outputs are used as inputs to the deep learning system. Both experimental (data acquired from steel blocks with defects) and simulated data sets are used for training and testing. For implementation of deep learning architectures, we use the TensorFlow platform by Google which is an open source software library for numerical computation with data flow graphs. TensorFlow toolset also enables visualization of extracted features from each deep learning layer. This plays a paramount role in distinguishing the effectiveness of the DBN, CDBN and CNN methods for ultrasonic flaw detection and echo classification. For performance analysis, we present and compare i) training effort (time and number of data sets used), ii) computation time for testing, and iii) classification (flaw detection) accuracy.

P2-B1-3

Architecture of an Ultrasonic Experimental Platform for Information Transmission through Solids

Boyang Wang[1], Jafar Saniie[1], Sasan Bakhtiari[2], Alexander Heifetz[2]; [1]*Illinois Institute of Technology, USA,* [2]*Argonne National Laboratory, USA*

Background, Motivation and Objective

An ultrasonic signal is rarely used for information transmission in solids because it attenuates, scatters, disperses and reverberates in the channel. In some environments, the ultrasonic signal is the only option for communication since radio frequency (RF) electromagnetic waves cannot propagate in the medium. This paper presents the feasibility of using an ultrasonic signal in the frequency range of 100 kHz to 5 MHz as the energy source for communication through elastic solids. A testbed system is assembled for ultrasonic communication experiments. The experiment is conducted with a range of signal frequencies, materials, shapes, and types of transducers. A random message is modulated with different modulation techniques, and the received signal is processed/demodulated to recover the message. The objective is to determine an optimum modulation method for ultrasonic communication in solids having diverse geometrical configurations.

Statement of Contribution/Methods

In our experimental ultrasonic communication platform, a signal function generator is used to excite the transducer. On the receiver side, the signal is picked up by the receiving transducer, and amplified before sampling by a digital oscilloscope. Both devices are interfaced to the computer through an Ethernet cable. For this study, the software is developed to send a modulated message signal from the signal generator and to sample and process the received signal to recover the message. To make the system more compact, efficient, and highly adaptive to communication channel characteristics, and to allow multiple frequency band communications for high computational throughput, we use a ZYNQ SoC, including ARM processors and FPGA fabric. In particular, two types of configuration for ultrasonic communication are examined. The first method utilizes an ultrasonic pulser to excite the transducer. FPGA is used to control the system and to send signals to the ultrasonic pulser with precise message-controlled timings. The second method is to use high speed DAC and a power amplifier to excite the transducer. This architecture allows experimentation with multiple transducers and receivers operating simultaneously at different frequencies.

Results/Discussion

Using an ultrasonic signal for communication is useful in certain environments where other options for information transmission are not practical. For this study, we will present experimental results using different materials such as steel, aluminum, and different geometrical shapes such as rods, tubes, and slabs. We will present the architecture of the platform which includes high speed DAC and ADC interfaces allowing experiments with different modulation techniques, and diverse testing environments with adverse effect of scattering, attenuation, mode conversion, dispersion, and reverberation which are common phenomena in transmitting sound waves in solids.

P2-B1-4

Methods for Correcting Dispersion and Pulse Width Effects During Pulsed Wire Measurements

Matthew Kasa[1,2], Jafar Saniie[1]; [1]*Illinois Institute of Technology, USA,* [2]*Argonne National Laboratory, USA*

Background, Motivation and Objective

Measuring a magnetic field by pulsing electrical current through a wire placed in the magnetic field, followed by measuring the displacement of the wire as a travelling wave passes a displacement sensor, is a technique typically referred to as a pulsed wire measurement. The goal of these measurements is to extract the magnetic field distribution of the magnet from the time dependent wire displacement data. The described technique could be used for measurements of any type of magnet, including undulators.

Statement of Contribution/Methods

The techniques presented will provide a method of correcting for the dispersion in the travelling wave and the averaging effects of pulse duration. The methods used to implement the correction algorithm of dispersion are based on allpass filtering design techniques that allow the filter parameters to be modified on the fly. The correction of errors introduced by the pulse width duration is performed by utilizing deconvolution. Flexibility of the technique and the ability to modify the algorithm parameters during signal processing are two of the main benefits of the technique described. In this study, measurements of a reference magnet and a permanent magnet undulator were performed using the pulsed wire method. Data collected from the pulsed wire measurements were processed using the correction algorithms described, followed by comparing the results to data collected using the Hall probe measurement technique.

Results/Discussion

Measurements of the reference magnet were performed at several distances from the displacement sensor. The plot on the left shows the uncorrected signal of three measurements where the effects of dispersion are evident as the distance between the magnet and sensor is increased. After correcting the three signals with the correction algorithm, the signals were aligned and compared with the Hall probe measurement in the center plot. The right hand plot is the corrected data of a measurement of the permanent magnet undulator and the Hall probe measurement. The two measurements agree to within 1% over most of the magnet.

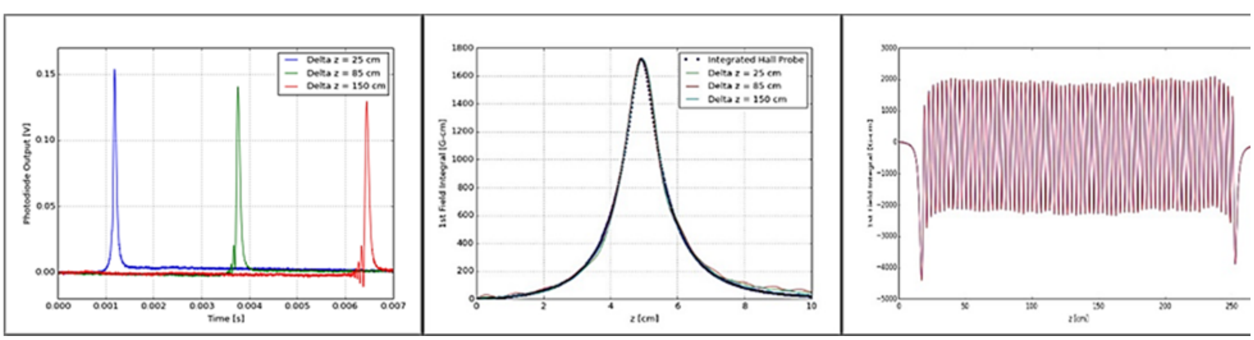

P2-B1-5

Implementation of Sparse Signal Recovery on FPGA for Ultrasonic NDT

Christian Grandinetti[1], Jan Kirchhof[2], Fabian Krieg[1], Florian Roemer[2], Alexander Ihlow[2], Giovanni Delgaldo[3], Hendrik Theado[1], Ahmad Osman[1]; [1]*Fraunhofer IZFP, Saarbrücken, Germany,* [2]*Ilmenau University of Technology, Ilmenau, Germany,* [3]*Fraunhofer IIS, Erlangen, Germany*

Background, Motivation and Objective

For several use cases of complex processing algorithms on ultrasound NDT data, it is mandatory to ensure real-time signal processing speed. This can be achieved by using e.g. a field programmable gate array (FPGA). Sparse signal recovery (SSR) and compressed sensing (CS) methods are used for superior reconstruction of flaws from compressed measurement data. SSR and CS are currently a hot research topic in various fields of application. However, they are not yet implemented for ultrasound NDT in a real-time manner.

Statement of Contribution/Methods

We implement Orthogonal Matching Pursuit both on a µ-processor and a FPGA. The goal of this system is to build a module which can be plugged in the signal chain of an ultrasound NDT system to significantly reduce the amount of raw data while at the same time improving the flaw detection. The system is controlled by software on a pc.

Results/Discussion

In the current state of the development, the SSR processing time of a determined setup on the FPGA is a factor 65 faster than the implementation on the µ-processor.

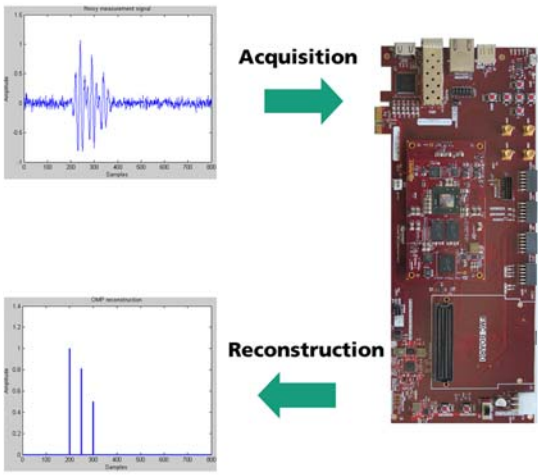

P2-B1-6

Reducing Pulse Compression Sidelobes by Means of a Reactance Transformation

Pietro Burrascano[1], **Stefano Laureti[1]**, Marco Ricci[2], Luca Senni[1], Giuseppe Silipigni[1], Riccardo Tomasello[1]; *[1]Università di Perugia, Terni, Terni, Italy, [2]Università della Calabria, Rende, Cosenza, Italy*

Background, Motivation and Objective

Pulse compression is a well-known technique widely used within the Non-Destructive Testing community [1]. Although pulse compression helps in increasing Signal-to-Noise ratio, the presence of side-lobes in the impulse response retrieved by its use, hampers the range resolution performance. A widely-used approach to face this problem consists in tapering the signal excitation by windowing it in time domain. Several different kinds of windows can be found in literature, and they optimize different aspects related to the sidelobes reduction [2].

Statement of Contribution/Methods

In the present paper, we tackle the problem of the sidelobes reduction by defining a filter operating in the frequency domain. We start by defining the filtering procedure to operate on a signal in the base-band. Since the pulse compression is performed by using bandpass signals as excitation, the useful bandwidth must be tailored to operate on the translated band. As a consequence, we modify the filtering procedure by proposing a reactance transformation of the frequency axis to define the filter for side-lobes reduction in the case of band-pass chirp excitations. The above-mentioned transformation is proposed as an alternative to the Window Translation, which is the standard procedure to obtain the windowing function operating in the translated band.

Results/Discussion

Fig.1 shows the results obtained by applying the proposed method on the impulse response retrieved by using pulse compression on a high-pass filter. It can be seen that the reactance transformation gives the best estimation of the reference impulse response, and this is obtained by optimally reducing the sidelobes level.

References

[1] Hutchins, D., Burrascano, P., Davis, L., Laureti, S., & Ricci, M. (2014). Coded waveforms for optimised air-coupled ultrasonic nondestructive evaluation. Ultrasonics, 54(7), 1745-1759.

[2] Harput, S., Arif, M., McLaughlan, J., Cowell, D. J., & Freear, S. (2013). The effect of amplitude modulation on subharmonic imaging with chirp excitation. IEEE transactions on ultrasonics, ferroelectrics, and frequency control, 60(12), 2532-2544.

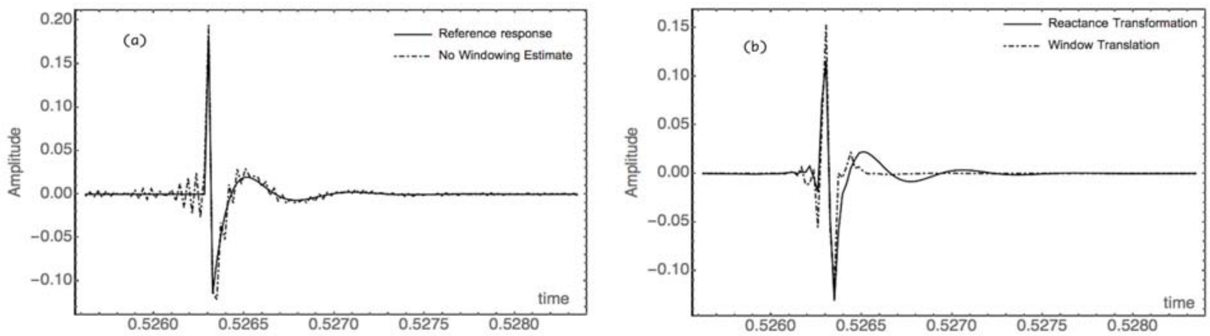

P2-B1-7

Measured Beam Patterns of Biomimetic Receivers Improve Localisation Performance of an Ultrasonic Sonar

Francesco Guarato[1], Charlotte Strang-Moran[1], **James Windmill[1]**; [1]*University of Strathclyde, Glasgow, United Kingdom*

Background, Motivation and Objective

The Beam Based Method (BBM) is inspired by bat echolocation as a novel ultrasonic sonar. The method is designed for a system consisting of an emitter and two receivers with a directional beam pattern and was previously tested in simulation with ideally designed beam patterns of the receivers. This sonar aims to support autonomous robot navigation and provide a bat inspired biosonar to improve target localisation.

In this work, the real measured beam patterns associated with 3D printed bat inspired receivers are imported into the BBM. The biomimetic beam pattern should make it possible for the BBM to efficiently discriminate between orientations, thus being accurate in determining target position. The objective of this work is to investigate how the accuracy of the method depends on the choice of the beam pattern. In particular, the receiver shape with a beam pattern close to that of a bat ear should ensure the most accurate estimations with the BBM. This shape will be included in the final sonar system.

Statement of Contribution/Methods

The BBM estimates the orientation of a target by comparing the amplitude of the received signals to the attenuation provided by the receivers. For all frequencies of the emitted signal, orientations associated with attenuation values in the beam pattern matching those in the received signals are chosen. The one fulfilling geometrical relationships given by the position of the receivers is selected as the estimate of target orientation. This method is strongly affected by the receivers' beam pattern in the sonar system.

The measured beam pattern associated with the ear of a *Phyllostomous discolor* bat and that of 3D printed receiver shapes inspired by it are alternatively imported into the sonar system model. A simulation takes into account the emission of a broadband signal from 20 to 70kHz, the air absorption and the spatial filtering provided by the receivers. Simulations use the filtered received signals in the BBM to estimate target position over a set of locations.

Results/Discussion

Results are the error in degrees between the real target orientation and the one estimated through the Beam Based Method. These angular error values depend on the beam patterns associated with the receivers and on how closely they resemble the shape of that associated with the bat ear: in particular, a beam pattern that is more similar to that of the bat ear ensures the most accurate performance of the BBM in estimating target orientation as angular errors on both cases vary from 0° to 13°. The noise is modelled according to a normal distribution.

This work has imported measured beam patterns of biomimetic 3D printed receivers in the BBM. The measured beam patterns are different from previously simulated beam profiles of geometrically regular receivers and lead to a novel biomimetic sonar system where the performance in determining target orientation depends on the similarities of the acoustical properties of the receivers and their design with real bat ears.

P2-B1-8

Material Impulse Response Estimation from Overlapping Ultrasound Echoes Using a Compressed Sensing Technique

Johan E. Carlson[1], Aziz Kubilay Ovacıklı[1], Patrik Pääjärvi[2]; [1]*Div. of Signals and Systems, Lulea University of Technology, Lulea, Sweden,* [2]*Rubico Vibration Analysis AB, Lulea, Sweden*

Background, Motivation and Objective

In ultrasound examination of thin multi-layered materials, the received signal is, in both through-transmission and pulse-echo configurations, a superposition of multiple reflections from inside the sample. If the layer thicknesses are small compared to the duration of the emitted ultrasound pulse, the received signal will be a sum of overlapping ultrasound pulses. In such scenarios, estimation of the layer thicknesses is challenging. Previous work has adopted model-based decomposition of the overlapping echoes, or various pulse compression or deconvolution schemes, in order to better reveal the arrival times of each individual echo.

Statement of Contribution/Methods

Modeling the multi-layered structure as a linear finite impulse response (FIR) filter enables relating the filter taps to the reflection coefficients at each interface in the material structure. The spacing between the filter taps (i.e. the temporal resolution) is a function of the propagation time of the sound through each layer. If this propagation time can be assumed to be much longer than the sampling time of the system, the resulting filter **h** will be sparse. In other words, the filter will be fairly long (in time) to account for all reflections, but the number of non-zero taps is significantly relatively small. If we assume a signal model for the received signal as $\mathbf{y} = \mathbf{U}\mathbf{h} + \mathbf{e}$, where **U** is the convolution matrix formed from a reference ultrasound pulse **u**, so that **Uh** is equivalent to the convolution of **u** and **h**, and **e** is noise. The task is then to estimate **h** from **u** and **y**. A standard least-squares solution can be made to work on noise-free simulated data, but in practice the problem is ill-posed. In this paper we show that by imposing a sparsity constraint on the solution **h**, the problem can be solved using the method of basis pursuit.

Results/Discussion

In the figure we see the result from a simulation of a 5 MHz ultrasound pulse measured in pulse-echo mode, where the medium is a 2 mm thick glass plate, immersed in water. The true material impulse response is here truncated after 10 reflections. The Signal-to-noise ratio (SNR) in this simulation was set to 20 dB for the output, and to 30 dB on the measured reference echo used in the forming the matrix **U**.

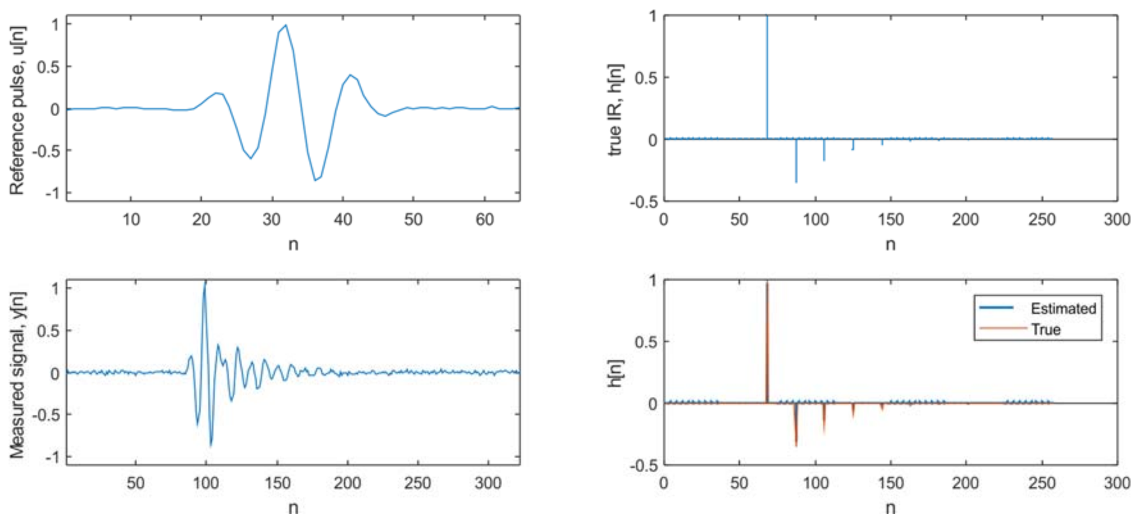

Reference pulse, u[n]
n
true IR, h[n]
n
Measured signal, y[n]
n
h[n]
Estimated
True
n

P2-B2 - Material and Defect Characterization

Exhibit Hall

Friday, September 8, 2017, 9:30 am - 4:00 pm

Chair: **Patrick Johnston**
NASA Langley Research Center

P2-B2-1

Evaluating the Influence of 3D-Printing Parameters on Acoustic Material Properties

Axel Jäger[1], Sarah Johannesmann[2], Leander Claes[2], Manuel Webersen[2], Bernd Henning[2], Mario Kupnik[1]; [1]*Technische Universität Darmstadt, Darmstadt, Germany,* [2]*University of Paderborn, Paderborn, Germany*

Background, Motivation and Objective

We present a non-destructive measurement procedure to obtain acoustic material properties on parts, manufactured using the Fused-Deposition-Modeling (FDM) method. FDM is the most common fabrication method used in desktop 3D printers. During the process, the printer melts the filament of a material and fills the volume of the part, moving in alternating directions. This leads to an anisotropic structure within the part and possible degradation of the material itself due to high temperatures. Because of the open source nature of these printers, they are able to use consumables not only from the printer manufacturer, but also from a variety of suppliers. However, quantitative details about the mechanical properties of the material are usually not provided. Even worse, the properties are changed by the printing process as well. It is of great interest to know the mechanical properties of the final manufactured part, including any anisotropy, to prevent failures and possibly gain information how to optimize the printing process. In this work, we investigate whether ultrasonic non-destructive techniques are suitable to characterize the mechanical properties of such parts after printing.

Statement of Contribution/Methods

We produce plate-shaped specimens with a thickness of 3 mm, made from different regular available thermoplastic materials and vary the process parameters during manufacturing. Using focused laser radiation, broadband ultrasonic Lamb waves are excited in the plates via the photoacoustic effect. A purpose-built ultrasonic transducer detects the resulting waves at different distances to the excitation on the specimen. An optimization process uses the measured signals and matches the four material parameters of Young′s modulus and Poisson′s ratio both parallel and perpendicular to the plate waveguide model.

Results/Discussion

The measurements show an influence of printing temperature and extrusion speed on the Young's modulus and Poisson's ratio: The Young's modulus drops by about 3% both parallel and perpendicular to the plate when the temperature is increased by 20°C. Poisson's ratio parallel to the plate drops by 41% when the extrusion speed is increased from 60 mm/s to 70 mm/s. The Young's modulus perpendicular to the plate is unaffected within the range of temperature and speed conducted in the experiment. The results allow including more design goals, such as maximum strength or maximum isotropy, when preparing a model for manufacturing in addition to already established design goals such as minimum surface roughness or maximum printing speed.

P2-B2-2

Creep Damage Evaluation of P92 Steel Using Nonlinear Lamb Waves

Wujun Zhu[1], Yanxun Xiang[1], Mingxi Deng[2], Fu-Zhen Xuan[1], Chang-Jun Liu[1], Haiyan Zhang[3]; [1]*East China University of Science and Technology, China, People's Republic of,* [2]*Logistics Engineering University, China, People's Republic of,* [3]*School of Communication and Information Engineering, Shanghai University, China, People's Republic of*

Background, Motivation and Objective

P92 martensitic ferritic steels are an attractive material for critical components in power industries due to the excellent creep property. However, these steels are usually susceptible to creep strength degradation during a long service period under the elevated temperature and pressure. Creep damage evaluation is of concern to quantitatively assess the remaining lifespan of the critical components. Nonlinear Lamb waves may offer an efficient method of evaluating these damages for its significant sensitivity to microstructrual evolution. The present research focuses on the evaluation of creep damage in P92 martensitic ferritic steel using nonlinear Lamb waves.

Statement of Contribution/Methods

Continuous creep tests were initially performed on dog-bone specimens in air at an operation temperature of 650 °C. Two sets of P92 specimens were exposed to the creep test at stresses of 100 MPa and 150 MPa with different creep life fractions. Next, nonlinear ultrasonic measurements were conducted on the creep damaged specimens using a S1-s2 Lamb mode pair. The acoustic nonlinearity parameter β was determined from received signals. To further interpret the variation of acoustic nonlinearity with creep life fraction, the microstructural evolutions of the creep damaged specimens were analyzed and identified by OM, SEM, TEM and electron diffraction.

Results/Discussion

An increase-decrease-increase correlation between the β and the creep strain was achieved for both sets of creep damaged specimens. The dominant contribution on the variation of β in the initial increase segment may be the slightly increasing dislocation density with the strain caused by loading stress. The lath martensite conversion to subgrain and consequent reduction of dislocation density would be a main reason for the decrease part because of the lath martensite containing a high dislocation density. The growth of precipitates, which would lead to a local micro-strain due to the precipitate-matrix lattice misfit, induces ultrasonic nonlinearity, which may be the primary effect on the third increase segment. The nonlinear Lamb wave is found to be sensitive to the microstructural evolutions, which may be a promising nondestructive tool to evaluate creep damage evolution in P92 martensitic ferritic steels.

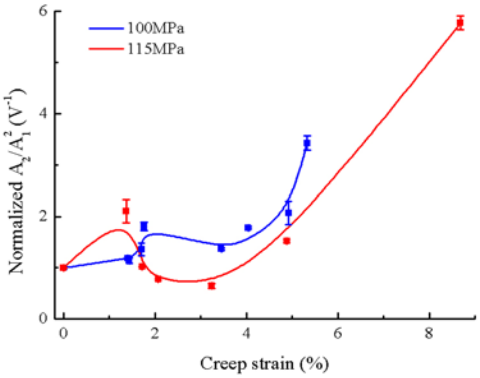

P2-B2-3

Influences on the Ultrasonic Transmission Behavior of Wood based Materials

Torben Marhenke[1], Jens Twiefel[1], Jörg Hasener[2], Jörg Wallaschek[1]; [1]*Institute of Dynamics and Vibration Research, Leibniz Universität Hannover, Hannover, Germany,* [2]*Fagus-GreCon Greten GmbH & Co. KG, Alfeld, Germany*

Background, Motivation and Objective

A standard quality control in the production of wood based materials is the check for delaminations, caused by air inclusions in the material. Plates with delaminations have the risk to burst in the later process or to break, when they are used. A proven measurement method for several decades is the detection by means of air-coupled ultrasound. The defects are identified by the attenuation of the ultrasonic signal at the air inclusions. Some phenomena of this method have not been explored in detail, e.g. the influence of the delamination thickness, the density profile and the flow resistance. The effects will be examined in more detail in this paper.

Statement of Contribution/Methods

The influence of the delamination thickness, in which the minimum detectable thickness is of interest, was calculated analytically according to the model of Brekhovskikh. The results were validated by means of artificial delaminations and transmission measurements by microphones. The density profile, which is built during the pressing process, was analyzed by simulations using the Finite Element Method (FEM). In addition, the propagation of the structure-borne sound waves through wood based materials at cutting edges was measured with a laser vibrometer, whereby the influence of the density on the wave propagation could be visualized.

Current studies on the description of the transmission behavior of wood based materials only take into account the structure-borne sound. Since wood based materials belong to open-pored materials, the transmission behavior of wood based material boards is also determined by the flow behavior, in addition to the structure-borne sound. Therefore the flow resistance of wood based materials was experimentally measured and also simulated by using CT images. The influence on the transmission behavior was analyzed using the Delany-Bazley model.

Results/Discussion

The analysis of the delamination thickness has shown that the minimum thickness is approximately 50 µm when using a frequency of 50 kHz. However, this is only the case, if the surfaces of the delaminations are flat. In the case of rough, uneven surfaces, the delamination could only be detected with a thickness of 1 mm. The result of the investigation of the density influence is that for boards of the same medium density, the plates with a larger boundary layer density exhibit a lower transmission behavior.

Taking into account the flow resistance in addition to the structure-borne sound, the transmission signal doesn't change so much. Although an increase in the receiver signal could be determined, this is in the lower single-digit percentage range. Since the scattering of wood-based materials due to inhomogeneities is in many cases more than 10%, it is legitimate to ignore the influence of the flow resistance on the transmission behavior.

P2-B2-4

Corrosion Evaluation of Additive Manufacture Metal Alloys by Nondestructive Line-focus Transducer

Chenglong Ji[1], Yuxiang Wang[1], Qiuyan Li[1], Qing-Ming Wang[1]; [1]*Mechanical Engineering and Materials Science, University of Pittsburgh, Pittsburgh, PA, USA*

Background, Motivation and Objective

Corrosion of metal alloys is very common in the industrial field, and failure to monitor the seriousness of corrosion can cause serious consequences. Compared with other Non-Destructive Testing methods, the method of ultrasonic surface wave testing has a lot of advantages including portability, efficiency, and un-contamination etc. This makes it a very promising method to evaluate or monitor chemical corrosion. In this study, we are going to evaluate the variation of surface wave velocity when the testing material is subjected to different degree of chemical corrosion, and we will build up a quantitative relationship between the surface wave velocity and the erosion degree.

Statement of Contribution/Methods

A schematic diagram of the Line-Focus Ultrasonic Testing System is shown in figure 1. A PVDF thin film is attached to a cylindrical concave surface as the testing probe at the terminal of the motorized stage. The defocus process of the PVDF probe can be precisely controlled. Connected to the pulser/receiver, the PVDF transducer can emit and receive the ultrasonic signal and convert it into an electric signal. The received signal is sent to an oscilloscope where we can observe and record the variation of the waveform. Distilled water is used as couplant for testing.

Results/Discussion

In figure 2, the testing results of a SS420 sample which was immersed in 34% HNO_3 for 24 hours is shown. As we can see, based on the testing results, the Rayleigh wave velocity can be calculated, and the velocity of the Rayleigh wave becomes larger after the sample is corroded. The change of the elastic properties can be calculated based on the variation of the surface wave velocity. In a similar way, we can quantify the corrosion level by measuring the surface wave propagation using this line-focused transducer system.

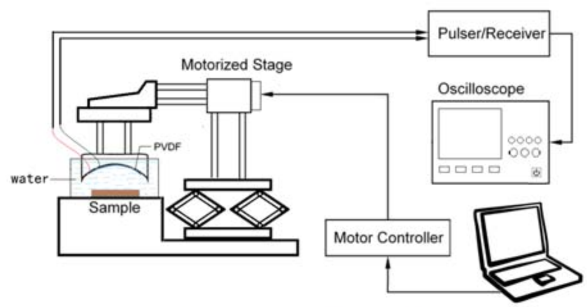

Figure 1. General layout of the testing system*

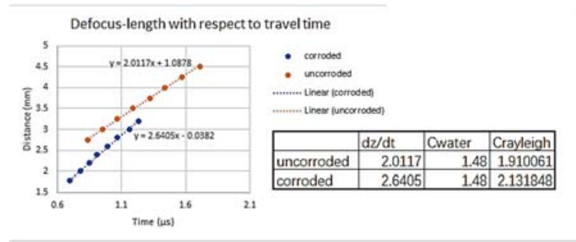

	dz/dt	Cwater	Crayleigh
uncorroded	2.0117	1.48	1.910061
corroded	2.6405	1.48	2.131848

Figure 2 Difference of Rayleigh wave velocity between the references

P2-B2-5

An efficient Non-contact Method for Measuring Physical Parameters of Thin Elastic Multilayers

Ziwen Su[1], Hanmin Peng[1], Dawei Wu[1]; [1]*State Key Lab of Mechanics and Control of Mechanical Structures, Nanjing University of Aeronautics and Astronautics, Nanjing, Jiangsu, China, People's Republic of*

Background, Motivation and Objective

Determining physical parameters of thin elastic multi-layers are essential in the field of scientific research and engineering applications. Routine matrix formulations for multilayered media are very complex and involve intensive computation. At the same time, conventional ultrasonic measurements need coupling agents, which greatly limit practical applications. The objective of this research is to offer an efficient, accurate, non-contact means of measuring important parameters of thin elastic multi-layers with low frequency air-coupled ultrasound.

Statement of Contribution/Methods

Theoretical models of the normal-impinging ultrasound wave propagation in nonporous, homogeneous, sub-wavelength elastic multi-layers were developed with the following assumptions. Frist, diffraction coefficients and attenuation factors in the elastic layers are negligible. Secondly, layers thickness are much smaller than corresponding wavelengths in the layers. Lastly, acoustic impedance of air is much smaller than acoustic impedance of elastic layers. Simplified version of transfer functions for transmission and reflection were derived accordingly. Thereafter, thickness and surface densities of elastic layers were found to be directly determined in terms of transmission coefficients and reflection coefficients.

To validate the theoretical results, a lithium battery film, which is a typical three-layer thin elastic medium, was measured with air-coupled ultrasound asparagus. The lithium battery film used in the study is a 10-¦Ìm copper foil coated with ~100-¦Ìm carbon composite on both sides. Measurements were performed with commercial 200 KHz, 500 KHz and 1 MHz air-coupled ultrasonic transducers, respectively, in both transmission mode and reflection mode. Gold standard X-ray measurements were used in the study to provide reference values.

Results/Discussion

Simplified models to measure thickness and surface densities of thin elastic multi-layers using air-coupled ultrasound were suggested. The efficiency and accuracy of models were confirmed with our experimental study. The errors were found to be about 3% for thickness measurements and 5% for surface densities measurements. The work can be applied to online real-time quality control of industrial processes. In the future, with additional oblique incidence of ultrasound, elastic modulus of the elastic layers can be obtained.

P2-B2-6

Characterization of Microstructure in Ti-6Al-4V through Ultrasonic Scattering Measurements

Andrea P. Arguelles[1], Dan Xiang[1]; [1]*X-wave Innovations, Inc., Gaithersburg, Maryland, USA*

Background, Motivation and Objective

Nondestructive evaluation of material microstructure has become increasingly relevant with the surge of advanced manufacturing methods. Because factors such as grain size and shape dictate material properties, accurate characterization of these features is crucial when implementing novel production methods. Previous ultrasonic approaches to measure grain size in complex media have been hindered by the inability to correlate nominal elastic properties of base metals to those found in post-processed structures. In this presentation, an approach to improve current scattering-based methods for grain size measurements is presented.

Statement of Contribution/Methods

Ultrasonic tests were conducted on a two-phased sample of titanium alloy Ti-6Al-4V. First, a conventional scattering modeling approach was followed to extract representative grain sizes of the specimen. In this method, the spatial variance of A-scan signals from a fixed region in the sample is calculated and fitted with the statistical scattering model by Ghoshal and Turner [J. Acoust. Soc. Am. 128]. Through this approach, the experimental data could not be fitted, likely due to assumptions relating to the elastic properties of the medium. A two frequency approach is employed to eliminate assumptions pertaining to the elastic properties. The peak scattering amplitudes of the scattering model for different grain size/elastic property combinations are compared to the experimental maximum amplitude. The average grain size was then defined by the range where the scattering amplitude difference was less than 10% for both inspection frequencies.

Results/Discussion

The grain sizes obtained through the proposed ultrasonic scattering approach were compared to dimensions obtained through optical micrographs. Reasonable agreement in the grain size values is obtained. However, because the range of grain sizes extracted through ultrasound was larger than that obtained through micrographic techniques, some of the measurements represent overestimation of the actual grain sizes. One possible cause stems from the approach used to compare the experimental spatial variance to the analytical model, namely comparing peak amplitudes only. Considering time dependent features may result in a better grain size estimate and tighter range. Secondly, the proposed approach assumes a single parameter is sufficient to characterize grain size. Considering the case where the two phases present different average grain sizes should be studied. Furthermore, including a grain size distribution characterized by two parameters may also improve the proposed technique.

The Effect of In-Plane and Out-Of-Plane Fiber Waviness on Guided Waves

Peter Juarez[1], Cara Leckey[1]; [1]*Nondestructive Evaluation Sciences Branch, NASA Langley Research Center, Hampton, VA, USA*

Background, Motivation and Objective

In-plane (IP) and out-of-plane (OOP) fiber waviness (sometimes referred to as marcelling and wrinkling, respectively) can occur in composite parts as a result of uneven thermal loading during curing, challenges in manufacturing complex geometry parts or other manufacturing variabilities. The changes in fiber orientations due to waviness can have an impact on the intended strength of the composite part and can create stress concentrations that reduce the overall life of the part. These defects can be difficult to detect in cured parts using traditional ultrasonic approaches.

Statement of Contribution/Methods

Guided waves can be useful in detecting changes in the mechanical properties within a specimen because the waves interact with the full thickness of the material they are traveling through. Guided wave and wavefield-based inspection techniques have been used previously to quantify delaminations in composites. This type of inspection involves exciting guided waves in the part and using a Laser Doppler Vibrometer (LDV) to capture the out of plane velocities created by the guided waves as they travel throughout the part

Results/Discussion

In this study, composite panels with intentional IP and OOP fiber waviness defects were inspected with a LDV while guided waves were excited using a contact transducer. The intentional fiber waviness defects were created at multiple ply levels to test the robustness of the detection methods. Using new and improved data analysis algorithms, the evidence shown in this presentation suggests that guided wave inspection may be useful for detecting and quantifying IP and OOP fiber waviness in composites. This presentation will give an overview of the causes and effects of fiber orientation defects in composites, introduce the methods that were used to make the intentional fiber defects, and present the progress made in measuring the effects of IP and OOP fiber defects using guided waves

P2-B3 - Underwater Acoustics

Exhibit Hall

Friday, September 8, 2017, 9:30 am - 4:00 pm

Chair: **Jafar Saniie**
Illinois Institute of Technology

P2-B3-1

Design of a Sparse Array to Simulate a Fully Dense Underwater Planar Array Transducer for Underwater Vehicles

Yongrae Roh[1], Muhammad Shakeel Afzal[1]; [1]*School of Mechanical Engineering, Kyungpook National University, Daegu, Korea, Republic of*

Background, Motivation and Objective

Planar arrays comprising a two dimensional arrangement of elements have been extensively used in underwater applications for decades. The beam pattern of a planar array depends upon its aperture geometry. Further, the cost and complication of the underwater array system are highly dependent on the total number and geometry of the array elements, which is very important for underwater vehicles. A fully dense planar array transducer provides good imaging but has the limitations such as cross talk, high cost and complexity in fabrication. The drawbacks associated with the fully dense array transducer can be overcome by reducing the number of active elements of the array. Hence, in this work, a sparse planar array was designed to achieve the array performance equivalent to that of a fully dense array for underwater vehicle applications.

Statement of Contribution/Methods

Two square 10 by 10 planar arrays of transmitting and receiving elements were combined using effective aperture approach to compute their beam pattern. The fully dense array was used as a reference so that its effective beam pattern could be achieved with a sparse array that uses only a part of the initial array as transmitters and the other part as receivers. The directional factor of the sparse array was derived as an analytical form. With the derived equation, the structure of the sparse array was designed by optimizing the number and location of transmitting and receiving elements in the array to make its pulse-echo beam pattern comparable to that of the fully dense array in terms of peak sidelobe level (PSLL) and main lobe beam width (MLBW). The optimization was carried out using the OptQuest Nonlinear Programming algorithm. The objective function was to minimize the PSLL difference between the dense and sparse arrays for three azimuthal planes, i.e. 0, 22.5 and 45 degrees with the constraint that the MLBW of the sparse array was to vary within 1 degree from that of the fully dense array. The validity of the optimized beam patterns was verified by comparing them with those from finite element analysis (FEA) of the optimized array structure.

Results/Discussion

The PSLL for the dense and sparse arrays from the analytical calculation were -26.2 dB and -27.9 dB, respectively, while those from the FEA were -26.9 dB and -28.9 dB, respectively, at 100 kHz. Similar closeness was achieved for the MLBW from analytical and FEA results as well. Therefore, the sparse array designed through optimization of the number and location of transmitting and receiving elements in the array was confirmed to have the overall performance equivalent to that of the fully dense array. The small difference between the FEA and analytical results turned out to be due to the crosstalk effect between the array elements, which was not considered in the analytical design. The sparse array transducer designed in this work can provide the beam pattern equivalent to that of a fully dense array while using just a portion of initial array elements.

P2-B3-2

Concentration Profiling Using a Novel Acoustic Backscatter System with Single Transducers Pulsed at Multiple Frequencies

Alastair Tonge[1], Jaiyana Bux[1], David Cowell[2], Jeff Peakall[3], Steven Freear[2], Timothy Hunter[1]; [1]*SCAPE, University of Leeds, Leeds, West Yorkshire, United Kingdom,* [2]*School of Electronic and Electrical Engineering, University of Leeds, Leeds, West Yorkshire, United Kingdom,* [3]*Institute of Applied Geoscience, University of Leeds, Leeds, United Kingdom*

Background, Motivation and Objective

Acoustic backscatter systems offer a flexible technique to measure dispersion concentration and particle size, via inversion of the return echo voltage response of pulse-echo signals in the MHz range. While there have been recent developments in how backscatter models can be broadened in marine applications there is little data available for the Rayleigh regime (ka<1) as direct inversion is not applicable for small particles that attenuate significantly; for engineering applications, however, understanding the limits of current acoustic modelling techniques for these systems would be invaluable.

Statement of Contribution/Methods

The Ultrasonic Array Research Platform II, developed at the University of Leeds, was used to collect acoustic backscatter data for 3 sizes of glass particle species (150-250 µm, 53-106 µm & 4-45 µm) suspended in water. Measurements were taken in an agitated, homogeneous calibration tank over a 0.3 m range using transducers faced perpendicular to the tank base pulsed at frequencies of 2, 2.25 & 2.5 MHz (Olympus & Sonatest) and 0.85, 1 & 1.15 MHz (Sonatest). Suspension samples were taken at multiple depths for gravimetric analysis and compared with *in situ* ultrasonic concentration profiles.

Results/Discussion

A novel calibration, based on a method developed by Rice *et al*., was used to determine attenuation coefficients and hence backscatter cross-sections (χ) for three particle sizes, by measuring homogeneous suspensions at various concentrations up to 133.7 g l^{-1}, and results compared to literature correlations (Fig. (1a)) with deviations from the predicted values caused by the larger size distribution of the glass particles used compared to Betteridge *et al*. Once the backscatter and attenuation parameters were measured, parameterisation of the backscatter voltage was performed to measure solids concentration. Three models for concentration inversion were applied; both iterative-implicit single and dual-frequency inversion (Fig. 1b) and a semi-empirical backscatter correlation developed by Weser *et al*.. Importantly, this work details the flexibility of using single transducers excited at multiple frequencies to enable dual-frequency inversions, while theoretical limitations in terms of particle size, isonification frequencies and solids concentration are discussed for each model as particles approach the Rayleigh regime.

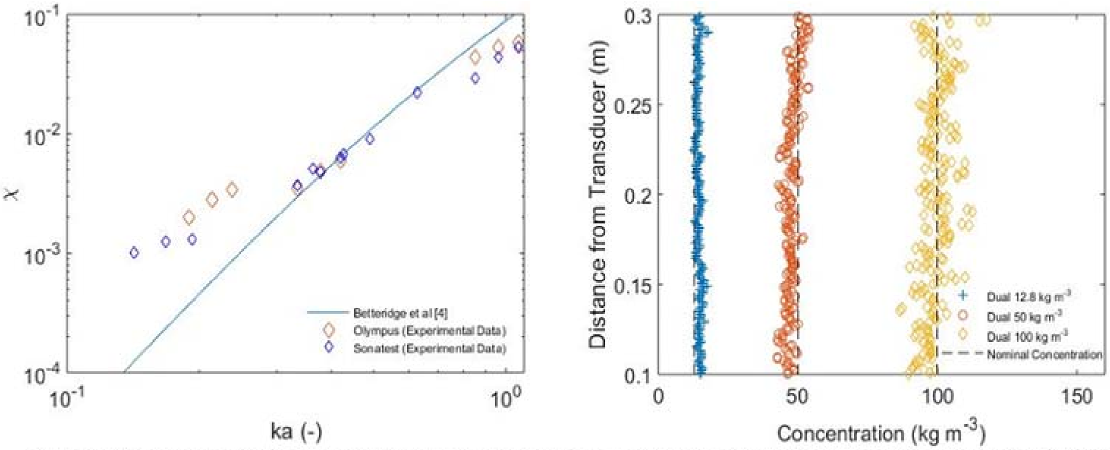

Figure 1a) Showing scattering cross-section as a function of ka for both types of transducer used compared with Betteridge *et al.* model and b) concentration profiles produced for the 53-106 μm glass spheres using the dual frequency method

P2-B3-3

Effect of Underwater Ultrasound Exposure on Growth of Plant Roots and Leaves

Yuta Kurashina[1], Tatsuya Yamashita[1], Shuichi Kurabayashi[2], Keita Ando[1], Kenjiro Takemura[1]; [1]*Keio University, Yokohama, Japan,* [2]*Graduate School of Media and Governance, Keio University, Fujisawa, Japan*

Background, Motivation and Objective

Growth control is an important technique in plant markets, for appropriate shipping time of plants (e.g., flowers and fruits) allows for reducing production costs for post harvesting storage and pesticide. It is favorable to control plant growth without any chemicals; physical stresses are attractive candidates for this purpose. Here, we propose an ultrasound-based technique to control plant growth.

Statement of Contribution/Methods

We fabricated a plant hydroponic cultivation device with ultrasound transducer placed in a plant growth chamber; the details of the device will be presented in the presentation. The underwater pressure at one wavelength of 28-kHz ultrasound from the transducer surface was controlled at either 2kPa or 20 kPa. The concentration of dissolved oxygen was maintained by circulating water. We selected leaf lettuce as a model plant because of its rapid growth rate. Seedlings of leaf lettuce were prepared from 2-week cultivation (without ultrasound exposure) and then cultivated in the developed device to monitor their growth.

Results/Discussion

We evaluate the growth based on length of main root (Lr), length of largest leaf (Ll), total number and weight of leaves (Nl, Wl), and summarize it in Figs. 1 and 2, respectively, for the cases of 2-kPa and 20-kPa ultrasound exposure. It turns out that the lower-intensity ultrasound leads to longer roots and heavier leaves (i.e., growth promoter), while the higher-intensity ultrasound slows the growth in all the respects (i.e., growth inhibitor). This suggests that we may control the growth of plants in hydroponics by tuning the ultrasound intensity.

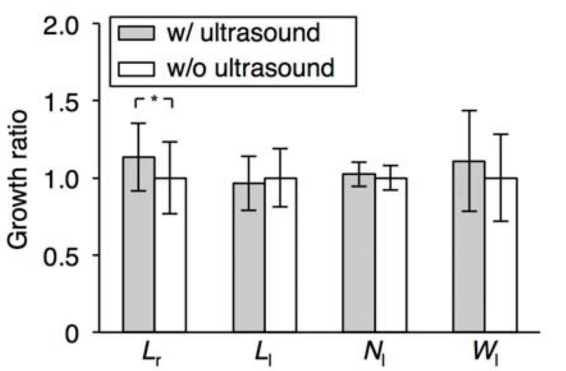

Fig. 1 Growth of leaf lettuce with low ultrasound (2 kPa) normalized by that without ultrasound. (mean ± SD, $n = 25$, *: $p < 0.05$).

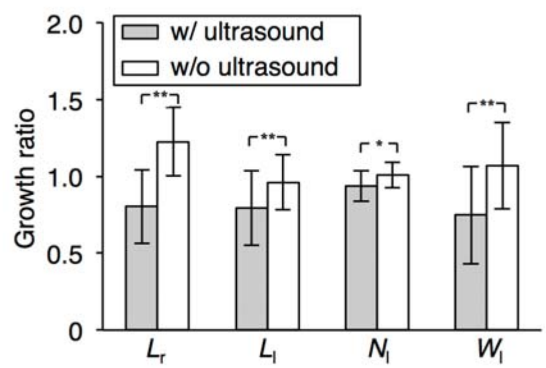

Fig. 2 Growth of leaf lettuce with high ultrasound (20 kPa) normalized by that without ultrasound. (mean ± SD, $n = 25$, *: $p < 0.05$, **: $p < 0.01$).

P3-B1 - PGP - General Physical Acoustics

Exhibit Hall

Friday, September 8, 2017, 9:30 am - 4:00 pm

Chair: **Yook-Kong Yong**
Rutgers University

P3-B1-1

Focusing Beyond the Diffraction Limit with Acoustic Jets

José Henrique Andrade[1], Marco Brizzotti[2], J. P. Leão-Neto[3], Júlio Adamowski[2], Glauber Silva[3]; [1]*Campus Arapiraca, Federal University of Alagoas, Arapiraca, Brazil,* [2]*São Paulo University, Brazil,* [3]*Federal University of Alagoas, Brazil*

Background, Motivation and Objective

In recent years, focusing an ultrasound beam on a subwavelength scale, i.e. beyond the diffraction limit, has attracted much attention. Under this circumstances, the beam is referred to as a superfocused beam. Focusing beyond the diffraction limit may substantially improve the resolution of ultrasound imaging systems, underwater sonar, and acoustic microscopy. Also, it may further enhance particle tweezing with the acoustic radiation force. These new avenues of possibilities have motivated us to seek for a simple scheme to achieve ultrasound superfocusing.To accomplish this goal, we introduce the concept of acoustic jets through a theoretical and computational analysis, with experimental confirmation. An acoustic jet is a superfocused and highly intense ultrasound beam generated in the scattering by a solid or liquid sphere. This phenomenon occurs in the nearfield of the sphere shadow region and propagates over few wavelengths without much diffraction.

Statement of Contribution/Methods

We experimentally demonstrate that superfocusing can be achieved with acoustic jets generated by a Rexolite sphere in a water tank at room temperature. The experimental apparatus used to produce the acoustic jet is described as follows. An ultrasound wave was generated by a 25mm-diameter flat transducer. A 1.01 MHz-pure tone was produced by a function generator and subsequently amplified. A thin string suspended a Rexolite sphere with 12.2 mm-diameter. The sphere was placed along the transducer central axis at 700 mm away from its face. The acoustic pressure field in the sphere shadow zone was measured by raster-scanning a 0.2 mm-diameter hydrophone with transverse and axial steps of 0.2 and 0.4mm, respectively. The detected signals were digitized by an A/D converter at 100 MS/s, and post-processed to obtain the magnitude and phase of pressure for each scanned point. The measured acoustic jet is compared to the results predicted by the scattering theory based on the partial-wave expansion (PWE) method and finite-element simulations.

Results/Discussion

The Rexolite sphere produces an acoustic jet with a 14.4 dB-intensity gain, a subwavelength focal spot with the full width at half maximum (FWHM) and the full length at half maximum (FLHM) of, respectively, half-wavelength and 2.2-wavelengths. The experimental result is in excellent agreement with theory. The normalized RMS error between the theoretical and experimental intensities is smaller than 7%. Our findings demonstrate that a solid sphere can be used as a superlens to focus ultrasound beams in the subwavelength scale. The simplicity of this design may have a great impact on the ultrasound beams applications. A spherical superlens can be readily adapted to ultrasound imaging systems as well as acoustic microscopy technology. Furthermore, acoustic jets may foster novel methods for subwavelength particle manipulation and a new generation of acoustic sensors operating beyond the diffraction limit.

P3-B1-2

Acoustic Radiation Pressure as a Versatile Tool for Cell Compression and Mechanobiology Studies

Valerie Bentivegna[1], Fraser Stewart[1], Sandy Cochran[2], Inke Näthke[1]; [1]*School of Life Sciences, University of Dundee, Dundee, United Kingdom,* [2]*School of Engineering, University of Glasgow, Glasgow, United Kingdom*

Background, Motivation and Objective

Cells not only sense their biochemical and biological environment, they also respond to physical cues. To study the effect of mechanical inputs on cells, techniques commonly rely on growing cells on stretchable substrates or exerting force via directly contacting cells. Our work suggests that acoustic radiation pressure applied with ultrasonic devices can be used to compress cells without requiring direct contact.

Statement of Contribution/Methods

MDCK II (Madine-Darby Canine Kidney, type II) cells were grown to confluence on glass coverslips. Markers for mechanical compression were identified by placing a 2 g weight in the centre of the cell layer for 30 minutes. The same markers were used to confirm compression of cells that were insonated with a single-element focused ultrasound transducer operating at 4.18 MHz with an excitation amplitude of 10 V_{pp} for 30 minutes. The transducer provided a focal zone beam diameter of 2 mm and exerted radiation pressure of 170 kPa. The transducer was controlled by an application–specific automated insonation system[1] that ensured reproducible insonation.

Results/Discussion

Regions of cells that were compressed showed fewer folded nuclei. Smooth nuclei reflect cells under tension[2]. Additionally, compressed cells had more vinculin near membrane regions; when membranes are under tension, vinculin is recruited to the adherence junction[3]. These markers reported compression by weights, and preliminary results show a similar trend in insonated cells (Fig. 1). This suggests that ultrasound could be a versatile new tool for mechanobiology research.

[1] F Stewart et al. A Fully-Automated Insonation System for In Vitro Investigations of Ultrasound-mediated Targeted Drug Delivery. International Ultrasonics Symposium (IUS), 2017.

[2] J Swift and DE Discher. The nuclear lamina is mechano-responsive to ECM elasticity in mature tissue. Journal of cell science, 127(14):3005–15, 2014.

[3] S Dufour et al. α-catenin, vinculin, and F-actin in strengthening E-cadherin cell-cell adhesions and mechanosens- ing. Cell Adhesion and Migration, 7(4):345–350, 2013.

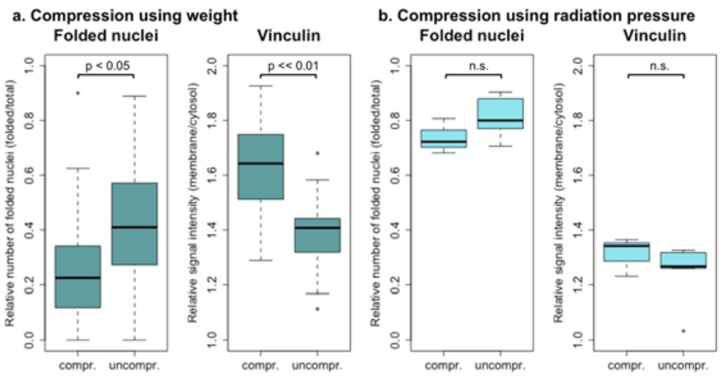

c. sample sizes

	weight		radiation pressure	
	compressed	uncompressed	compressed	uncompressed
number of cells	207	314	225	420
images	24	34	3	5

Fig. 1: Markers for compression in cells after compression with weight (a) and radiation pressure (b). a: compressed cells had fewer nuclei with folds and more membrane-associated vinculin. b: cells compressed by radiation pressure also showed fewer folded nuclei and more vinculin near the membranes.

P3-B1-3

The Ultrasound Needle Pulse

Kevin Parker[1], Shujie Chen[1], Miguel Alonso[2]; [1]*Electrical & Computer Engineering, University of Rochester, Rochester, New York, USA,* [2]*Institute of Optics, University of Rochester, Rochester, NY, USA*

Background, Motivation and Objective

The study of beampatterns and their use in imaging systems has a long history in optics and acoustics. In addition, the topic of limited diffraction fields has received increasing attention since the characterization of Bessel beams in optics. The class of "localized waves" include X-beams, Airy beams, and related monochromatic and broadband solutions.

Statement of Contribution/Methods

Recently, we formulated a new class of propagation invariant fields based on the principle of a wideband source excitation configured through the angular spectrum such that all components propagate with equal phase in the forward propagating direction (Parker and Alonso, Longitudinal iso-phase condition and needle pulses, *Opt Express*, 2016). Analytic solutions are obtained for a one dimensional (1D) source, then for an axial symmetric source, and for a pulsed version of the field. The free space solution has some remarkable properties including vanishing group velocity and a convergence of all energy to a narrow central line as a spatial and temporal crescendo; hence the appellation "needle pulse." Furthermore, there is no focusing in the conventional sense, and the excitation of source array elements can be realized by sampling bounded input waveforms that are expressed in analytical form.

Results/Discussion

A simulated needle pulse is shown in the figure. The needle pulse is formed by arranging all the spatial and temporal frequencies within some practical bandwidth into waves that propagate with constant phase between the source plane and an arbitrary parallel plane. The solutions yield converging stacks of pressure waves that form into a long axis peak and then diverge. At the point of maximum convergence, the lateral beam width is compact with no sidelobes. Figure: the amplitude (left) and pressure waves (right) at three time instants (top to bottom, t = -2, 0, 2 μs from peak) resulting from a 2D array with a center frequency of 6 MHz, 70% bandwidth, 16 mm square.

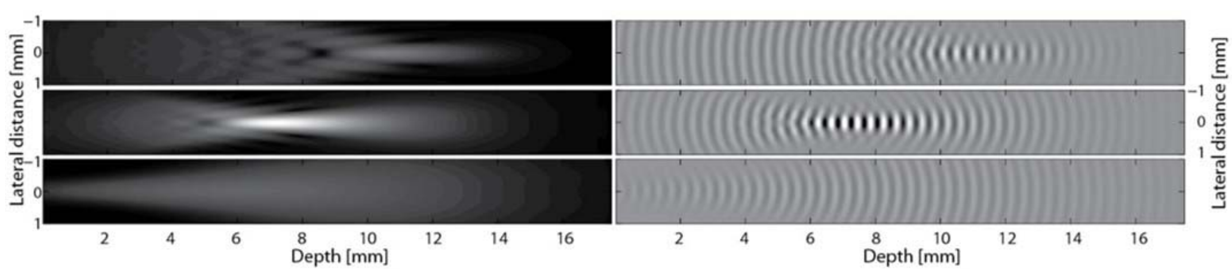

P3-B1-4

Observation of Slow Elastic Waves in Porous Material Using Ultrasound Elastography

Johannes Aichele[1,2], Stefan Catheline[1], Goulven Le Moign[1], Remy Souchon[1], Philippe Roux[2]; [1]*Labtau, INSERM, France,* [2]*ISTerre, CNRS Grenoble, France*

Background, Motivation and Objective

Ultrasound shear wave elastography is a well established tool for characterization of biologic tissues. While it has found applications in various medical disciplines such as oncology and urology its feasibility for pneumology still has to be shown. We provide experimental results of ultrasound shear wave elastography of soft porous materials in phantoms. Shear wave dispersion and evidence of the longitudinal slow ('Biot') wave dispersion allow for better characterization of soft porous materials.

Statement of Contribution/Methods

We use a high frame rate ultrasound scanner and speckle tracking/phase correlation to track shear and longitudinal slow wave propagation in water saturated melamine resin foams from 50 to 600 Hz. Experimental results for phase velocities and attenuation are validated applying a differential form of the Kramers-Kronig relation. Finally, the phantom study is compared to surface waves dispersion curves of porcine lungs obtained with an ultra-fast optical camera and the first results of ex-vivo shear wave elastography in porcine lung.

Results/Discussion

Snapshots of 2D displacement data at consequent timesteps (shear wave - upper row) and displacement gradient data (longitudinal slow wave - lower row) show that two longitudinal waves and one shear wave are propagative in saturated foams. The phantoms show a strong phase velocity dispersion and attenuation increase with increasing frequency. The Kramers-Kronig relation indicates that the main factor are viscous effects. These experimental results are in reasonable agreement with the theory of porous materials. The work shows the feasibility of elastography for porous materials. Its clinical application in the future could offer a noninvasive and non-ionizing alternative for lung characterization.

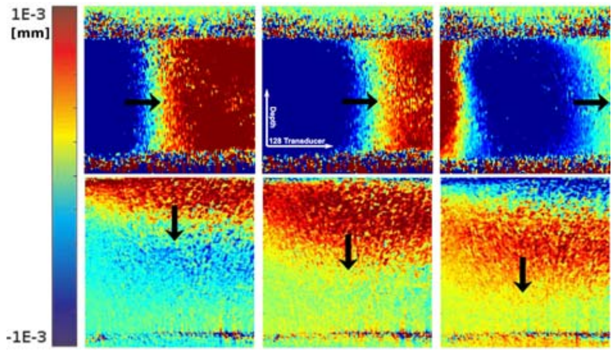

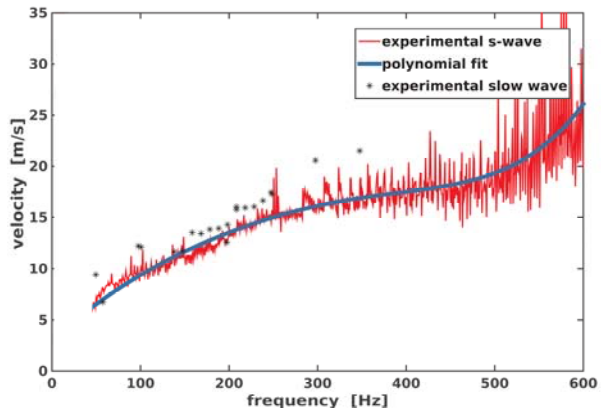

P3-B1-5 ____

Estimation and Measurement of the Streaming Velocity in Presence of Contrast Agents or Blood Mimicking Scatterers

Wojciech Secomski[1], Janusz Wojcik[1], Ziemowit Klimonda[1], Andrzej Nowicki[1]; [1]*Department of Ultrasound, Institute of Fundamental Technological Research, Polish Academy of Sciences, Warsaw, Poland*

Background, Motivation and Objective

Acoustic streaming is a steady flow in a fluid driven by the acoustic wave propagating in a lossy medium. Streaming depends on intensity and absorption of ultrasound in the media. In some cases, such as ultrasound scattered on the blood cells at frequencies ≥ 20 MHz or the presence of ultrasound contrast agents, scattering affects the streaming speed. Parallel to measurements, the streaming theoretical description was modified by introducing the scattering coefficient to equations describing the radiation force and the streaming velocity.

Statement of Contribution/Methods

The velocities of acoustic streaming in blood mimicking starch suspension in water and Bracco BR14 contrast were measured. Suspension of the corn starch in concentration of 1 - 4 g/l ($2•10^6$ - $8•10^6$ particles/mm^3) and BR14 contrast in concentration of $1•10^3$ - $4•10^3$ microbubbles/mm^3 were investigated. The reference was a 0.01 g/l starch suspension in water. The source of the streaming was a plane 2 mm diameter 20 MHz ultrasonic transducer, connected to a pulsed Doppler flowmeter. Velocity was estimated from the averaged Doppler spectrum. The single particle driving force was calculated as the integral of the momentum density tensor components. The scattered acoustic field was determined from the Sturm-Liouville equation.

Results/Discussion

The maximum streaming velocity in reference fluid was 7.9 mm/s, close to the 8 mm/s calculated from the Tjotta equation. For different starch concentrations of 1, 2, 3 and 4 g/l, the streaming velocity was increasing taking values 8.9, 10.1, 11.0 and 12.5 mm/s, respectively. This corresponds to a constant 13% velocity increase for a 1 g/l increase in starch concentration. For BR14, the streaming velocity remained constant at 7.2 mm/s and was independent of the microbubbles concentration. The velocity was less than in reference, within 0.5 mm/s measurement error.

Theoretical calculations showed 15% increase in streaming velocity for 1 g/l starch concentration rise, very similar to the experimental results. The theory has also shown the ability to reduce the streaming velocity by low-density scatterers, as was experimentally proved using BR14 contrast agent.

Figure. Doppler velocity spectrum of the signal scattered on blood mimicking starch in concentrations of 0.01 and 1 - 4 g/l (a), and scattered on BR14 contrast in concentration of 1 - $4•10^3$ microbubbles /mm^3 (b).

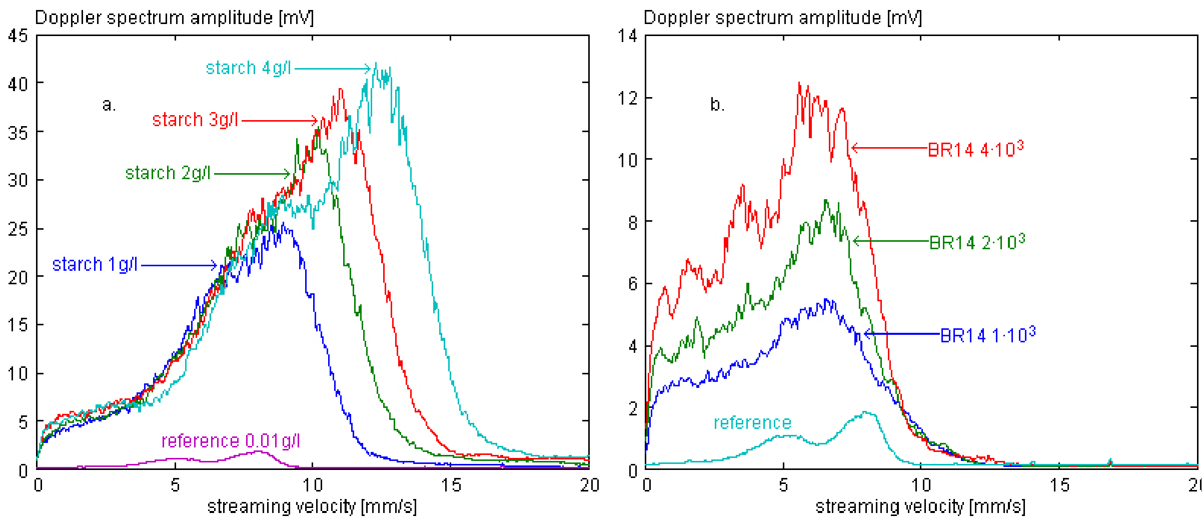

P3-B1-6

The Influence of Rheological Parameters of Viscoelastic Liquids on the Propagation Characteristics of Ultrasonic Love Waves

Piotr Kielczynski[1], Marek Szalewski[1], Andrzej Balcerzak[1], Krzysztof Wieja[1]; [1]*Institute of Fundamental Technological Research, Polish Academy of Sciences, Warsaw, Poland*

Background, Motivation and Objective

Progress in materials engineering has led to development of new materials with improved functional characteristics. One of the new types of materials introduced into industrial practice are plastics and polymers. These materials exhibit rheological (viscoelastic) properties, which combine simultaneously the properties of liquids and solids. Due to their attractive features, such as low specific weight, high resistance to chemical agents, cost effectiveness etc. these materials are widely used in chemical, automotive, aviation and space industry. Thus, it is very important to develop new, robust and accurate methods to measure the rheological parameters (viscosity η, elasticity μ and density ρ) of plastics and polymers. The conventional mechanical methods used so far to this end are outdated, time consuming, and cumbersome. To overcome this problems, the authors propose the use of ultrasonic methods that employ surface Love waves, what is a novelty.

Statement of Contribution/Methods

The aim of this study is to develop a rigorous mathematical model of propagation of shear horizontal (SH) surface Love waves in layered viscoelastic structures, i.e., in layered waveguides with a guiding surface covered with a viscoelastic liquid. This model can constitute the basis of an inverse method to evaluate rheological parameters of polymers. For selected frequencies, energy of Love waves is concentrated mostly in the vicinity of the waveguide surface. Thus, Love waves are ideally suited to investigate the rheological properties of liquid and solid polymers. The Love wave method has many advantages: (1) is non-destructive, (2) is fast and accurate, (3) can be computerized, (4) there are no moving parts and (5) there is a possibility of measuring simultaneously several rheological parameters of material, e.g.,: viscosity, elasticity or density.

Results/Discussion

This work presents formulation and solution of the Direct Sturm-Liouville Problem for Love waves propagating in layered viscoelastic structures. The phase velocity and attenuation of Love waves, propagating in the investigated layered viscoelastic waveguides, were evaluated numerically, as a function of frequency, viscosity and rigidity of the loading viscoelastic liquid. The calculations were performed (in the frequency range from 1 to 10 MHz) for a steel waveguide covered with a copper layer being in contact with a viscoelastic polymer. The Kelvin-Voigt model of the considered polymers was used. The viscosity η of a liquid polymer varies from 0.01 to 100 Pas. The obtained results will form a basis for development of a subsequent inverse method for determining the rheological parameters of viscoelastic media. The obtained results are a novelty and can be useful in design and optimization of ultrasonic sensors, in geophysics and in NDT. So far there is no a complete and rigorous theoretical description of the Love wave propagation in layered structures loaded with a viscoelastic polymer.

P3-B1-7

Transmission of High-Intensity Ultrasonic Waves by Using Sound Wave Transmission Straight Rigid Tube

Norifumi Suzuki[1], Ayumu Osumi[1], Youichi Ito[1]; [1]*Electrical Engineering, Nihon University, Chiyoda-ku, Tokyo, Japan*

Background, Motivation and Objective

Recently, it has been developed a sound source capable of irradiating aerial ultrasonic waves of very high intensity, and researches on applied technologies utilizing the ultrasonic power have been actively conducted. In these applied technologies, it is necessary to irradiate sound waves to the object under optimum conditions. However, this technique has a problem that optimum sound wave irradiation can not be performed when there is an obstacle between the sound source and the object or the distance attenuation of the sound wave due to the propagation to the object.

To solve the above problem, we investigated to propose a method of irradiating the object with sound wave while maintaining the sound pressure by using sound wave transmission.

Statement of Contribution/Methods

Fig.1 shows a schematic view of experimental device. In experiment, we examine to use an ultrasonic sound source that radiates focused sound waves and an acrylic pipe that is a sound wave transmission straight path. The installation position of the pipe is a sound wave focusing point.

Results/Discussion

Fig.2 shows the experimental results. Fig.2 (a) shows the distribution of sound pressure in the pipe (supply electric power is 0.2 W), and (b) shows relationship between the sound pressure at the end of the pipe and supply power to the sound source.

First, as the result of Fig.2 (a), it can be seen that the high sound pressure is obtained at the end of pipe although a sound wave propagation mode is generated in the pipe.

Next, as the result of Fig.2 (b), it can be confirmed that the sound pressure at the end of pipe is only about 20% lower than the sound pressure of the sound wave focusing point in free space.

From the above, it was confirmed that the sound wave can be propagated far away while maintaining high sound pressure by the proposed method.

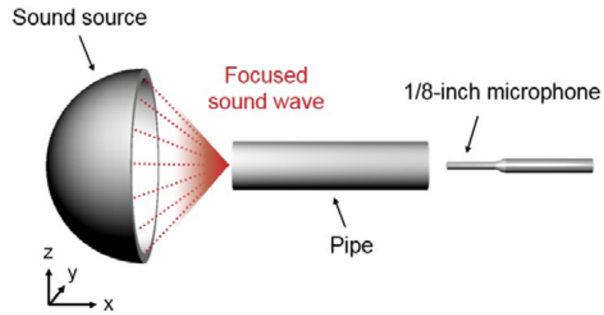

Fig.1 Schematic view of experimental device

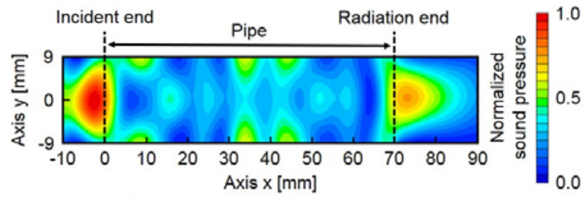

Fig.2(a) Sound pressure distribution

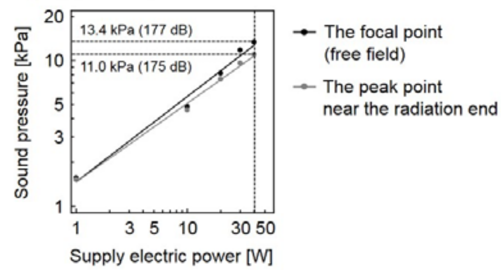

Fig.2(b) Supply power characteristics

P3-B1-8

Experimental Investigations of Ultrasound Speed and Absorption in the Martian Atmosphere

Hanyin Cui[1], Chao Li[1], Weijun Lin[1], Yang Jia[2], Bo Xue[2], Jingchuan Zhang[3], Qian Li[4]; *[1]Institute of Acoustics, Chinese Academy of Sciences, Beijing, China, People's Republic of, [2]Beijing Institute of Spacecraft System Engineering, China, People's Republic of, [3]Beijing Institute of Spacecraft Environment Engineering, China, People's Republic of, [4]Johns Hopkins University School of Medicine, USA*

Background, Motivation and Objective

Future China mission to explore the planet Mars may carry acoustic probes. Because sound interacts with matter intimately, they could be used in Mars to measure the wind speed directly, to record the possible ambient sounds, and to assist the safety of a travelling Lander by inspecting obstacles and by detecting a soft subsurface soil which might cause the Lander being trapped. All these Martian acoustic anemometer, microphone, and ultrasound inspector need to be designed specifically to adapt to the low-pressure, low-temperature, and mainly CO_2 gas Martian atmosphere. The key question is to know the acoustic properties in this extraterrestrial environment of Mars. However, little work has been done to experimentally measure the speed and absorption of ultrasound wave in tenuous Martian atmosphere.

Statement of Contribution/Methods

Experiments to measure the sound speed and absorption in 600-1000 Pa air and CO_2 were carried out in a cylindrical vacuum chamber of 1.6 m length and 0.8 m diameter. The pressure in the chamber, which was respectively filled with air and pure CO_2 gas, drops from 10^5 to 600 Pa. In the chamber, a pair of piezoelectric transducers, which were installed on a remote controlled linear stage, acts as an emitter and a receiver. Four pairs of transducers with central frequencies being 21, 25, 34, and 40 kHz were tested. The pitch-catch technique was applied to measure the speed of sound under different pressures. And the sound absorption was obtained by analyzing the received signals at different transducer separation lengths.

Results/Discussion

From experimental results, the speed of 21-40 kHz ultrasound barely changes when the pressure drops from 10^5 to 600 Pa. And the average speed in the 288 K air and CO_2 are 340.2 and 269.1 m/s. The attenuation rates in air and CO_2 are given in the figure. The sound attenuation in the 600-1000 Pa CO_2 is much stronger than the case of air. And the attenuation in air increases with dropping pressure; however, the variation between the attenuation and pressure is very complicated for 21-40 kHz pulses in the CO_2.

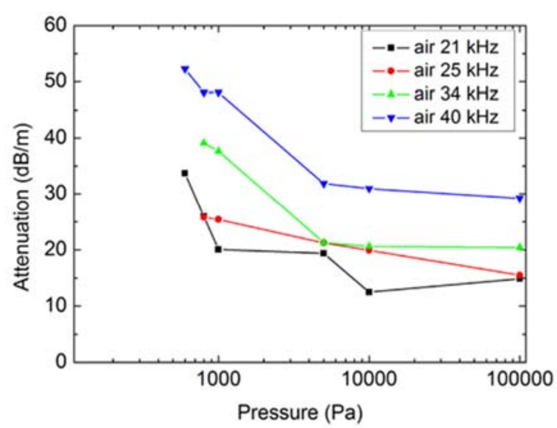

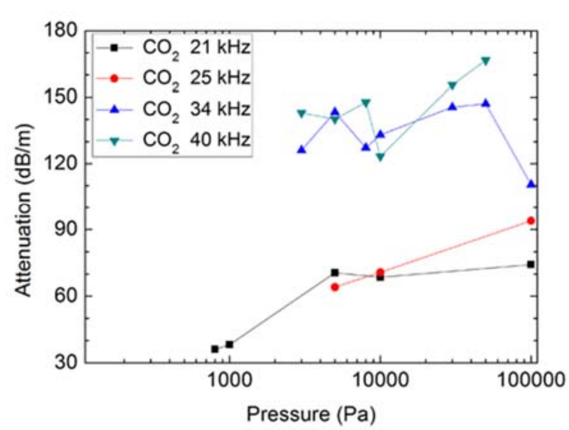

P3-B1-9

Investigation of Regular and Anomalous Behavior of Liquid Media under High Pressure Using Ultrasonic Methods

Piotr Kielczynski[1], Stanislaw Ptasznik[2], Marek Szalewski[1], Andrzej Balcerzak[1], Krzysztof Wieja[1], Aleksander Rostocki[3]; [1]*Institute of Fundamental Technological Research, Polish Academy of Sciences, Warsaw, Poland,* [2]*Meat and Fat Technology Department, Institute of Agricultural and Food Biotechnology, Warsaw, Poland,* [3]*Physics Department, Warsaw University of Technology, Poland*

Background, Motivation and Objective

In many industrial technological processes, liquids are subjected to high pressures, e.g., in the high pressure food preservation. Similarly, in modern fuel injection systems for diesel engines, biofuel is subjected to a pressure up to 300 MPa. In such conditions, in liquids, phase transitions can occur that substantially increase the density and liquid viscosity. This can be very detrimental for the engine or the technological equipment. Thus, it is important to determine at what pressures and temperatures phase transitions occur. Conventional mechanical methods for measuring physicochemical properties of liquids at these extreme conditions do not operate. By contrast, ultrasonic techniques are very suitable for measurements of physicochemical properties of liquids at high pressure, since they are non-destructive and can be fully automated. The aim of this work is to study the high-pressure physicochemical properties of liquids (exemplified by a camelina sativa - false flax oil) using novel ultrasonic methods.

Statement of Contribution/Methods

In this study, phase transitions and physicochemical properties of the investigated liquid (camelina sativa oil) were evaluated in the high-pressure range, using bulk longitudinal ultrasonic waves (f = 5 MHz). The speed of sound in the liquid was determined from the time of flight measured with the cross-correlation method. At the same time, changes in liquid density, as a function of pressure for various temperatures, were specified from the changes in the volume of the investigated oil sample in a high-pressure chamber. The isotherms of the speed of sound and density, as a function of pressure were approximated by analytical expressions. From the measurements performed, a number of crucial physicochemical parameters of the investigated liquid, such as adiabatic and isothermal compressibility, surface tension and thermal pressure coefficient were evaluated.

Results/Discussion

This work presents the following experimental results: 1) high-pressure physicochemical properties of camelina sativa oil and 2) high-pressure phase transitions that occur in the liquid. Sound speed and liquid density isotherms were measured in the range from atmospheric pressure up to 650 MPa, for various temperatures from 3 °C to 30 °C. This oil is increasingly used as a biofuel (green technology) or biofuel component in aviation. The behavior of this oil under high pressure has not hitherto been reported in the literature. The authors stated for the first time the occurrence of high-pressure phase transitions in the camelina sativa oil, which were not discovered up to date. E.g., at 20 °C the phase transition appeared at a pressure of 550 MPa after 72 h, and lasted for 36 h. The results of this study allow for better understanding of the physicochemical properties and the nature of molecular interactions in the liquids. They can also be useful for developing models of physical phenomena occurring in liquids at high pressures.

P3-B1-10

Optimized Acoustic Echoes Simulator in Fourier domain

Norbert Zolek[1], Janusz Wojcik[1]; [1]*Institute of Fundamental Technological Research Polish Academy of Sciences, Warsaw, Poland*

Background, Motivation and Objective

Optimization of ultrasound applications in medical diagnostics as well as in non-destructive testing demands accuracy in prediction of ultrasound propagation. Several attempts were used and few different simulation methods were proposed as a publicly available software toolboxes. Although the *Field II*, *k-Wave*, *Creanuis* belong to most popular ones, we propose new toolbox for the simulation of acoustic wave fields, *USim*, which is designed to make modeling of ultrasound propagation in various scattering media more reliable and fast.

Finite dimensions of scatterers and density inhomogeneities strongly influence the echoes increasing or decreasing impact of speed variations and can generate additional artifacts in the images. It is important to have numerical phantoms of the medium and solver allowing mapping most of its physical and structural properties.

Statement of Contribution/Methods

The simulations of the wave field are based on the solution of Sturm-Liouville equation [J. Wojcik, at ol, J. Acoust. Soc. Am., vol. 130, no. 4, 2011]. The toolbox allows simulating the ultrasound wave excitation, propagation and detection of echoes by arbitrarily shaped (single, multi element) probes in non-homogeneous media with varying speed of sound , density and absorption containing point, cuboidal, cylindrical and ellipsoidal scatterers similar to those building real tissues. The approach of calculations conducted in Fourier space increases the efficiency of stochastic medium properties modeling and allows taking into account the absorption phenomena and density gradients in a simple and correct way.

Results/Discussion

The simulations results from *USim* will be compared with the results of the other ultrasound simulation software - *Field II*, *Creanuis* and *k-wave*. The significant role of inhomogeneities of density δg and scatterer dimension d on the field distributions, the echoes level and shape obtained from plane wave insonification of single scatterer for 5MHz incident frequency and pitch equal to 0.3mm is shown in Fig. 1.

Fig.1. Upper panel: Distribution of the field scattered by a single scatterer with different density characteristics. Lower panel: Influence of the scatterer density characteristics (left panel) and dimensions (right panel) on echo signal amplitude. Speed inhomogeneity is constant δc^2=0.06 in all presented cases.

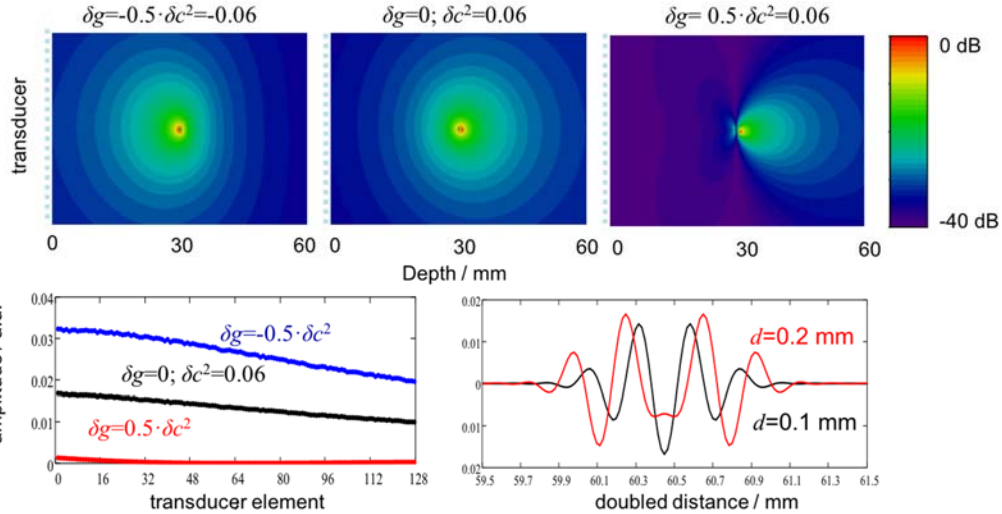

P3-B1-11

Reducing Uncertainties for Spatial Averaging at High Frequencies

David Sinden[1], N. Christopher Chaggares[2], Guofeng Pang[2], Oleg Ivanytskyy[2], **Srinath Rajagopal[1]**; *[1]Ultrasonics, National Physical Laboratory, Teddington, United Kingdom, [2]Fujifilm Visualsonics, Toronto, Ontario, Canada*

Background, Motivation and Objective

Detailed spatial resolution in imaging, requires high frequencies. Indeed, clinical systems with center frequencies up to 50MHz are available. However, at such frequencies, the accuracy in measurements may be compromised if the device may be of comparable size to, or larger than the smallest characteristic length scale of the wave. In such cases, spatial variations in the pressure over the surface of the measurement device will produce a different value from that at the intended location, potentially underestimating the field strength.

Statement of Contribution/Methods

The magnitude and phase uncertainties associated with spatial averaging of a reference hydrophone were investigated. This was performed using a 20µm diameter hydrophone (Chaggares, *2016 IEEE Int. Ultrasound. Symp. Proc*) as a point test device to sample the field. The uncertainty was defined as the ratio between the focal measurement and the average over an area which corresponded to geometric or effective area of the reference hydrophone, (diameter 0.2mm). The field was sampled at 0.025mm. High frequency components were generated by nonlinear propagation, at a fundamental frequency of 5±0.5MHz from a weakly focused 9.525mm diameter transducer with focal depth 71.1mm. Measurements were compared against well-validated nonlinear axisymmetric simulations.

Results/Discussion

Measurements up to 100MHz were made, with all harmonic components with high SNR ratios. Both experiment and computation showed that spatial averaging effects were more produced at higher frequencies. However, there is a discrepancy between the results from two methods beyond the 10th harmonic. Numerical simulations are performed with far higher spatial resolution than the experimental data is acquired. Furthermore, perfect alignment is challenging and the transducer may not produce an exactly axisymmetric field to match the simulations. The main difference was in the tightness of the focus at high frequencies.

That the error for the simulation is not monotonically decreases is due to how the high-frequency field is generated: for nonlinear fields, the location of the axial peaks of the harmonics moves beyond the focus with increased frequency (see Jiménez, *Ultrasonics* 75 p.106, 2017). Thus, for higher harmonics, spatial averages were computed on a prefocal field: the pressure at the focus was not the maximum over the area.

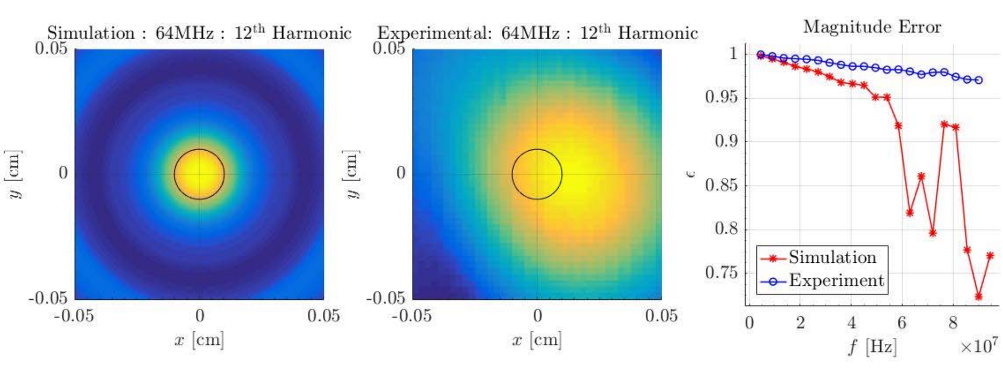

P3-B1-12

Numerical Investigation of Inertial Cavitation Threshold under Multi-Frequency Ultrasound

Dingjie Suo[1], Bala Govind[1], Shengqi Zhang[1], **yun jing[1]**, ; [1]*North Carolina State University, Raleigh, NC, USA*

Background, Motivation and Objective

Through the introduction of multi-frequency sonication in High Intensity Focused Ultrasound (HIFU), efficiency enhancement has been noted in several applications including thrombolysis, tissue ablation, sonochemistry, and sonoluminescence. Researchers reported theoretically and experimentally that the enhanced effect is due to the enhancement of inertial cavitation. One key experimental observation is that multi-frequency ultrasound can help lower the inertial cavitation threshold, thereby improving the power efficiency. However, this has not been theoretically corroborated. Numerical simulation is an important tool for understanding cavitation as well as for optimization purposes. For these reasons, a numerical investigation on the inertial cavitation threshold of microbubbles under multi-frequency ultrasound irradiation was conducted.

Statement of Contribution/Methods

The cavitation threshold was estimated using the Keller-Miksis bubble dynamics model and a common threshold criterion. The relationships between the cavitation threshold and microbubble size at various frequencies and media were plotted as the main outcome of this study. This paper studies different combinations of dual frequencies with different amplitudes and frequency differences. The comparisons of single-, dual- and triple-frequency sonication are conducted and these results are compared with our previous experimental work.

Results/Discussion

The cavitation threshold of microbubbles in blood is found to be higher than that in water. The comparison of single-, dual- and triple-frequency sonication shows a continuous drop of cavitation threshold by adding more frequencies. No significant difference is observed when varying the frequency difference for dual-frequency excitations, which agrees with our previous experiments. In addition, no significant difference between various power allocations on the two frequencies can be observed. We suspect that the reason why multi-frequency excitations could lower the cavitation threshold is mainly because of a higher peak negative pressure. Future work will need to take nonlinearity in the waveform into account.

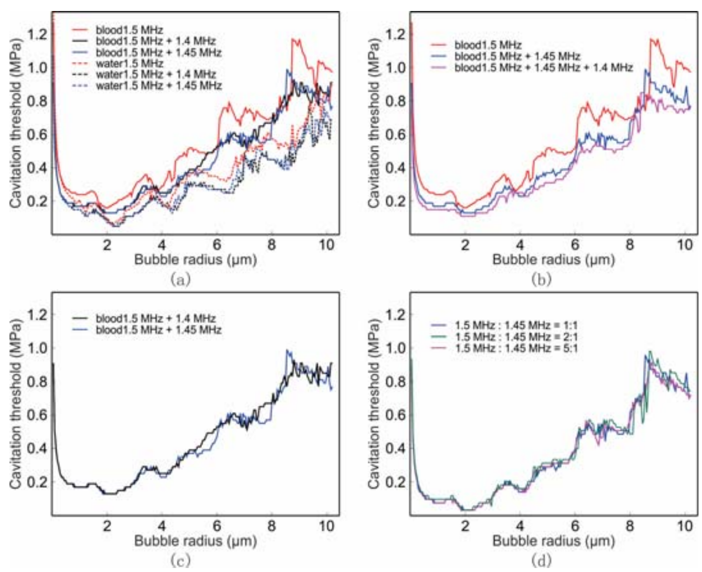

P3-B1-13

Impact-Reduction Effect of Ultrasonic Vibrations on Carbon Fiber-Reinforced Polymer Plate Using a Downsized Transducer

Atsuyuki Suzuki[1], Kai Kimura[1], Futoshi Nishimura[1], Jiromaru Tsujino[2]; [1]*National Institute of Technology, Tokuyama College, Shunan, Japan,* [2]*Kanagawa University, Yokohama, Japan*

Background, Motivation and Objective

There are various technologies available for automobile safety. However, about 1.3 million people die each year as a result of road traffic crashes in the world. We aim to develop an impact-reduction device using ultrasonic vibrations that can change the rigidity of crushable zones instantaneously in the event of traffic crashes. We have previously reported on the deformation and impact-reduction characteristics when applying ultrasonic vibrations to several materials such as high-tensile steel and carbon fiber-reinforced polymer plate (CFRP). An oversized transducer increases the overall weight of the vehicle and reduces fuel economy. Therefore, it is important to downsize the impact-reduction device. The purpose of this study is to confirm the impact-reduction effect of the ultrasonic vibrations using a downsized ultrasonic transducer.

Statement of Contribution/Methods

Practical use of the ultrasonic-impact-reduction device for automobiles will be promoted, if the ultrasonic vibrations by the downsized-ultrasonic transducer show reasonable efficacy. We downsized the ultrasonic transducer and measured the vibration, response, deformation, and impact-reduction characteristics. The length and weight of the downsized transducer were reduced to 45% and 74%, respectively as compared to the ultrasonic transducer that was used in the previous study. Experimental equipment consists mainly of an ultrasonic transducer, an impact weight for impact testing, a jig, and a dynamic force sensor. The crumple plate specimens are 200, 20, and 3 mm in length, width, and thickness, respectively. The material of the crumple plate is the CFRP. Many automakers have committed to the increased use of CFRP components in their vehicles to reduce weight.

Results/Discussion

We developed an experimental device to confirm the ultrasonic-impact-reduction effect using a downsized ultrasonic transducer. The following main results were derived:

(1) The CFRP plate can be bent easily with the application of ultrasonic vibrations.

(2) The impact force was reduced by up to 57.9% with the application of ultrasonic vibrations.

(3) The response time was shorten by downsizing the ultrasonic transducer.

(4) The resonant frequency of the ultrasonic transducer was not match with that of the BLT. The impact- reduction effect will be further enhanced by matching resonant frequency.

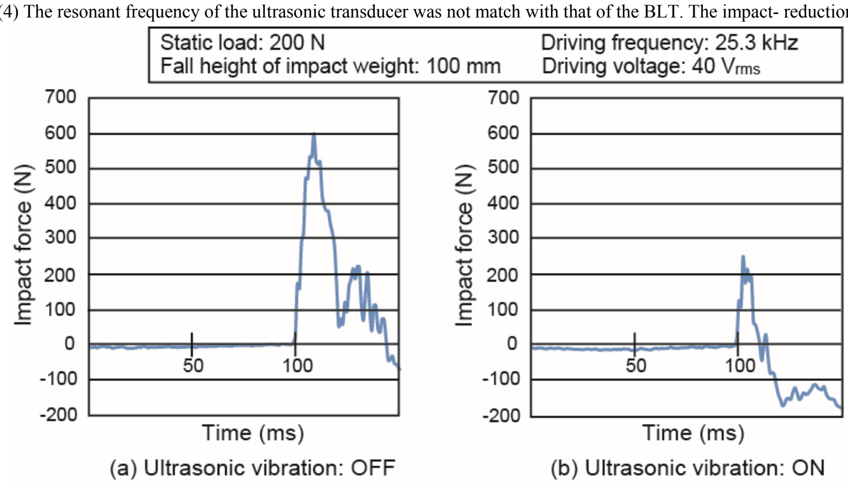

Fig. Impact waveforms (a) without and (b) with the application of ultrasonic vibrations.

P3-B1-14

Temperature Induced Waveguiding in a Resonant 2-port SAW Delay Line on Quartz

Max Madore[1], Pierre Dufilie[1]; [1]*Phonon Corporation, Simsbury, Connecticut, USA*

Background, Motivation and Objective

Over the course of accelerated failure testing of 2-port SAW delay line resonators on quartz, periodic acoustomigration damage patterns with acoustic apertures of less than 6 wavelengths were observed across the fully metalized region between the transducers, while typical electrode stress damage was observed over the acoustic aperture in the transducer gratings. This suggested the power density had become locally concentrated in the fully metalized region by some predictable mechanism. Given the temperature dependence of SAW velocity on quartz and the large acoustic aperture of the transducers (188 wavelengths), it was hypothesized that self-heating in regions of high power density created velocity gradients large enough for acoustic waveguiding to occur. The objective of this work is to verify the presence of temperature induced, self-promoting waveguiding, and determine general design rules for minimizing this effect. The primary motivator is to improve power handling capabilities by maintaining an even power distribution across the die.

Statement of Contribution/Methods

2-port SAW delay line resonators were constructed on various rotated YX quartz cuts to achieve turnover temperatures (Tc) above and below the device's nominal operating temperature (To). The effect of self-heating for Tc << To should result in waveguiding, while Tc > To is expected to eliminate the effect. Packaged resonators were exposed to high RF power in an oscillator circuit for an extended duration and periodically monitored for response shape. The RF power was turned off after changes in the response shape exceeded pre-determined limits. The components were then fully characterized and photographed.

Results/Discussion

Acoustomigration damage distributions due to temperature induced waveguiding will be analyzed and discussed, considering factors such as the quartz cut, power exposure duration and level, ambient and die surface temperatures, and resonator response degradation. Methods to suppress the effect will also be discussed.

P3-B1-15

Magnetoelectric BAW Resonator as a Source of Pure Spin Current

Natalia Polzikova[1], Sergei Alekseev[1], Ivan Pyataikin[1], Iosif Kotelyanskii[1], Valery Luzanov[1], Alexander Raevskiy[1], [1]*Kotel'nikov Institute of Radio Engineering and Electronics of Russian Academy of Sciences, Moscow, Russian Federation*

Background, Motivation and Objective

The generation of spin currents in a ferromagnet/paramagnet junction from acoustically driving magnetization precession, acoustic spin pumping (ASP), in different magnetoelectric structures draws a lot of attention because it offers great opportunities for low-power microwave spintronics. Recently, we have demonstrated for the first time the generation of pure spin current (which does not include charge current) in the high overtone bulk acoustic wave resonator (HBAR) based on YIG-Pt hybrid under resonant excitation of the magnetic dynamics in YIG [N.I. Polzikova, et al., AIP Adv. 6 (2016), 56306.]. For the practical application of this method it is necessary to understand the various factors affecting its efficiency.

Statement of Contribution/Methods

Here, we present systematic studies of the ASP in HBAR with Al-ZnO-Al-GGG-YIG-Pt layered structure (Fig.1). Transversal BAW electrically excited and detected by the transducer (Al-ZnO-Al) drives magnetization oscillations in the epitaxial YIG film in GHz region. We investigate in detail the frequency, the magnetic field, and the angular dependences of the magnitude of the dc voltage induced in the thin Pt stripe. This voltage (U_{ISHE}) arises as a result of a pure spin current (j_s) pumping from insulating YIG film to Pt and its conversion into a charge current (j_c) due to inverse spin-Hall effect (ISHE).

Results/Discussion

The magnetic field dependences of the voltage U_{ISHE} (H) and the shift (Δf_n) of the pumping resonant HBAR frequency f_n have a resonant behavior at the field corresponding to «acoustic FMR» H=H_R. Nevertheless, there is a certain deviation in the values of H_R and the field at which the maximal signal U_{ISHE} (H) is observed.The explanation of this deviation is based on the fact that spin pumping is exclusively an interface effect, while the shift in the resonant frequency is due to magnetoelastic interaction mainly in the volume of the YIG film.

We presented some important features of generation of pure spin current in such a system imposed by crystal and magnetoelastic anisotropy. Namely, the effect of the mutual orientation of the lateral bias magnetic field, the Pt strip and the transverse BAW polarization established by the ZnO film texture axis (**c**) projection on a plane (111) of epitaxial YIG film on the maximal value of HBAR frequency shift, Δf_n, and ISHE voltage, U_{ISHE}, has been studied in detail.

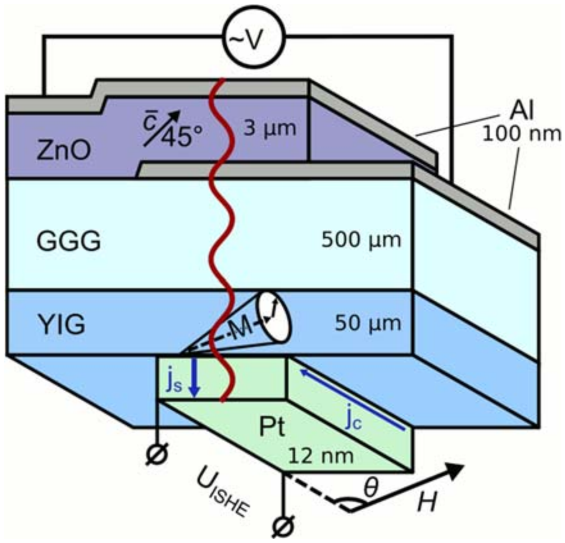

P3-B1-16

SAW Study of Structural Changes in Liquid Crystals Doped with Carbon Nanotubes Induced by Electric and Magnetic Fields

Peter Bury[1], Marek Vevericik[1], Peter Kopcansky[2], Milan Timko[2], Zuzana Mitroova[2]; *[1]Department of Physics, Zilina University, Zilina, Slovakia, [2]Institute of Experimental Physics, Slovak Academy of Science, Kosice, Slovakia*

Background, Motivation and Objective

The doping of liquid crystals (LCs) with carbon nanotubes and magnetic nanoparticles have attracted wide interest in many areas of science, technology and medicine. LCs occur as additional, thermodynamically stable states of matter between the liquid state and the crystal state in some materials. They can be characterized by a long-range orientational order of the molecules and, as a consequence, by an anisotropy in their physical properties. LCs can be oriented under electric or magnetic fields due to the anisotropy of dielectric permittivity or diamagnetic susceptibility. Carbon nanotubes are molecular scaled tubes of graphitic carbon with outstanding properties. The simplest nanotube is composed of a single sheet of a network of carbon atoms, called graphene, which is rolled up into a tubular form. Because of the small value of the anisotropy of the diamagnetic susceptibility of liquid crystals, the idea of doping them with fine magnetic particles was also introduced. Nanotubes can undergo functionalization, including by magnetic particles, to produce novel hybrid materials potentially suitable for applications.

Statement of Contribution/Methods

Acoustic methods are useful tool for the characterization of LCs, particularly their elastic and viscous parameters. Concerning the surface acoustic waves (SAW) they were used to determine the viscosity distribution in LC layer depending on applied electric field, as the SAW-driven LC light shutter or SAW sensor. Recently we have shown [*] that the attenuation of SAW propagating along ferronematic liquid crystals is able to give information about structural changes in LCs, induced by both electric and magnetic fields.

[*] P. Bury, et. all, J. of Magnetism and Magnetic Materials 423 (2017) 57

Results/Discussion

In this contribution we present the utilization of SAW to study structural changes in nematic LC (6CHBT) doped with low concentration (1 ~10-3, 1 ~10-4, 1 ~10-5) of CNs, both single-walled (SWCNT) and multi-walled (MWCNT) and their composites with Fe3O4 induced by electric and weak magnetic fields. The effects of applied electric and magnetic fields on the SAW attenuation for doped LC is illustrated in figure. The obtained results validated that carbon nanotubes causes an effective orientational coupling between both electric and magnetic moments of carbon nanotubes and the director of the LC.

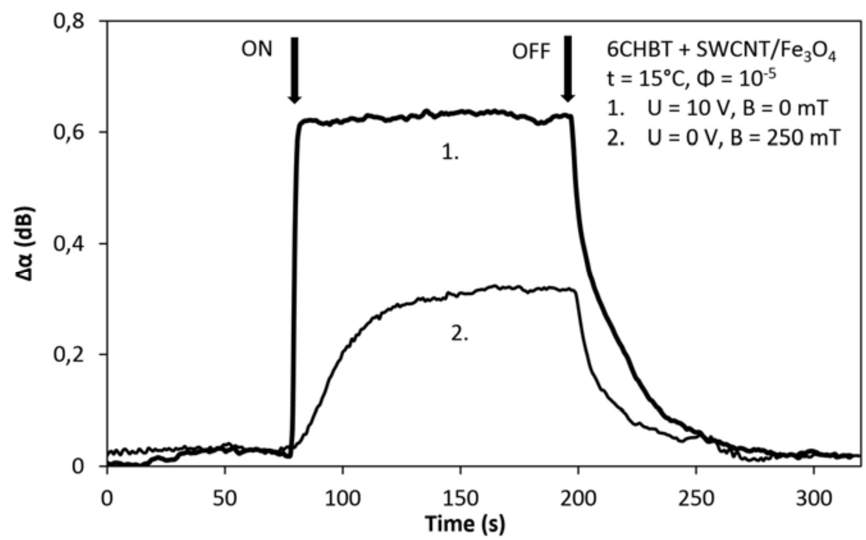

P4-B1 - Nonlinear Signals and Effects in Microacoustics

Exhibit Hall

Friday, September 8, 2017, 9:30 am - 4:00 pm

Chair: **Ventsislav Yantchev**
Chalmers University

P4-B1-1

Role of Metal Electrodes in the Generation of Third Order Non-Linearities in Surface Acoustic Wave Components

Vikrant Chauhan[1], Markus Mayer[2], Andreas Mayer[3], Elena Mayer[3], Werner Ruile[2], Thomas Ebner[2], Karl Wagner[2], Robert Weigel[1], Amelie Hagelauer[1]; [1]*Institute of Electronics Engineering, Erlangen Nuremberg University, Erlangen, Bayern, Germany,* [2]*Advanced development discreet, RF360jv, Munich, Bayern, Germany,* [3]*Hochschule Offenburg, Germany, Offenburg, Germany*

Background, Motivation and Objective

The growing complexity in RF front-ends, which support carrier aggregation and a growing number of frequency bands, leads to tightened nonlinearity requirements in all sub-components. The generation of third order intermodulation products (IMD3) are typical problems caused by the non-linearity of SAW devices. In the present work, we investigate temperature compensating (TC) SAW devices on Lithium Niobate-rot128YX. An accurate FEM simulation model [1] is employed, which allows to better understand the origin of nonlinearities in such acoustic devices.

Statement of Contribution/Methods

The nonlinear tensor data of the different materials involved in a TC-SAW device have been determined. Thereto we compared IMD3 measurements of test filters with FEM simulations and obtained nonlinear tensor data of the various materials. We employed the periodic FEM tool presented recently [1]. Since the FEM model is periodic we did not compare results directly to measurement, but at first determined an effective nonlinearity constant by comparison of nonlinear P-matrix simulations [2] to measurement. The effective nonlinearity constant obtained in this way was then applied in nonlinear periodic P-matrix simulations for comparison to the FEM-simulations.

Results/Discussion

In this investigation we focused on the role of the metal electrodes. We investigated test TC-SAW filters with varying metalization ratios. In order to reduce the number of unknowns we assumed the nonlinear tensors of each material to depend on a single parameter only. The substrate nonlinear tensor data are known from literature and were not optimized. Based on FEM simulations the contribution of the different materials to the nonlinear behavior of SAW devices is discussed.

[1]. A. Mayer, E. Mayer, M. Mayer, P. Jager, W. Ruile, I. Bleyl and K. Wagner, “Full 2DFEM calculations of third-order intermodulation in SAW devices”, IEEE International Ultrasonics Symposium 2016.

[2] M. Mayer, W. Ruile, J. Johnson, I. Bleyl, K.Wagner, A. Mayer, E. Mayer, “Rigorous COM and P-matrix approaches to the simulation of third-order intermodulation distortion and triple beat in SAW filters”, IEEE International Ultrasonics Symposium 2013.

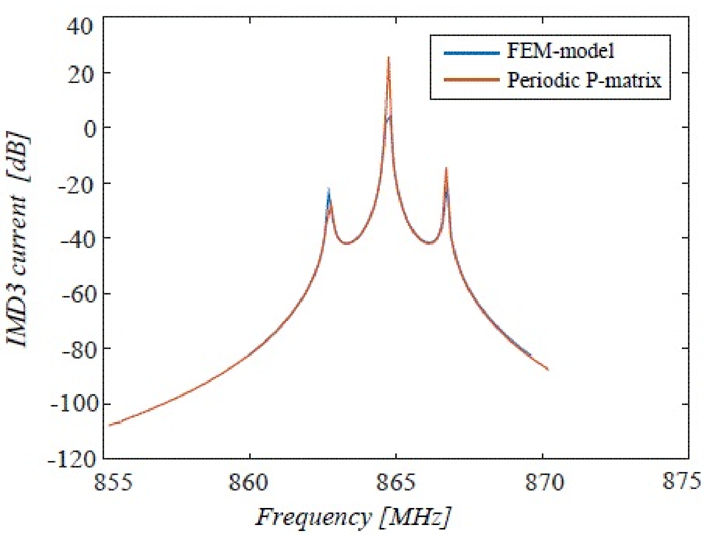

Figure. 1: Comparison of IMD3 current from nonlinear 2D-FEM and periodic P-matrix simulation model.

P4-B1-2

Vector Measurement of Nonlinear Signals Generated in RF SAW/BAW Devices

Masahiro Gawasaw[1], Tatsuya Omori[1], Ryo Nakagawa[2], Haruki Kyoya[2], Ken-ya Hashimoto[1]; [1]*Graduate School of Engineering, Chiba University, Chiba, Japan,* [2]*Murata Manufacturing Co., Ltd., Nagaokakyo, Japan*

Background, Motivation and Objective

Further reduction of nonlinearity is demanded in RF SAW/BAW devices, but even their generation mechanisms have not been fully understood. Although phase possesses comparable information to amplitude, it has not been paid much attention in the nonlinear signal measurement. Nonlinear vector network analyzers (NVNAs) may be used for the purpose. However, NVNAs have limited linearity than spectrum analyzers (SAs), and it seems to be very complex to apply NVNAs for the measurement of intermodulation distortion (IMD).

Statement of Contribution/Methods

This paper proposes a simple technique for vector measurement of nonlinear signals generated in RF SAW/BAW devices. The measurement setup is almost identical with the conventional one using SA, and thus the dynamic range is large. Furthermore, the proposed technique is applicable to the IMD measurement with small efforts.

A key point is use of the cross domain analyzer (XDA) instead of SA. XDA is an SA having two independent receiver channels, and phase difference between the receiver inputs can be measured in addition to their amplitudes for each frequency component. Thus nonlinear signals generated by a target device can be measured provided that a proper reference signal is supplied to the second channel.

Results/Discussion

Figures 1 and 2 show the measured second and third harmonics, respectively, when RF power of +15 dBm is applied to a SAW resonator on 42-LT. Calibration was applied by de-embedding S parameters of all transmission paths from raw data. The figures also show simulated results calculated by the technique described in [1]. Agreement is very well except frequency regions where the signal level is extremely low.

Results for the IMD measurement will be also shown at the presentation.

[1] R.Nakagawa, et al., Proc. IEEE Ultrason. Symp. (2015) 54

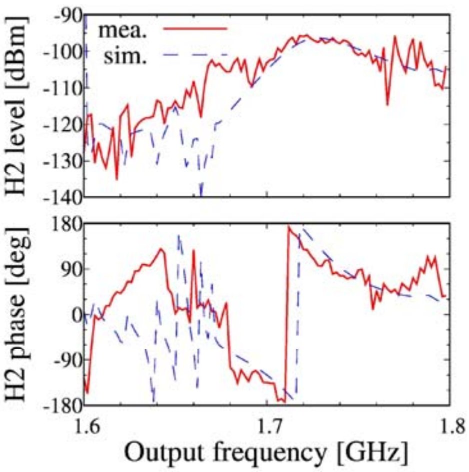

Fig.1 H2 Response

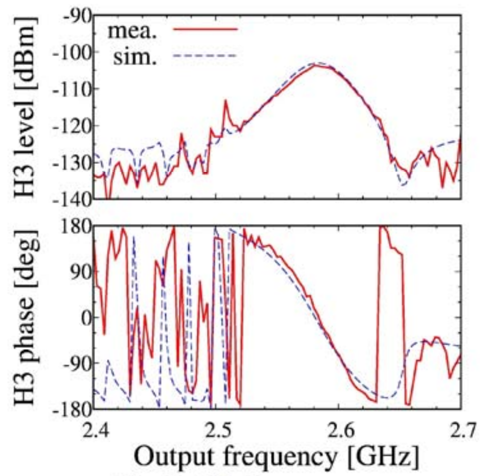

Fig.2 H3 Response

P4-B1-3

Simulating the Frequency Response of Acoustic Resonators with Nonlinear Elastic Constitutive Behavior

Philip Stephanou[1]; [1]*Atlas Sensors, Sunnyvale, CA, USA*

Background, Motivation and Objective

Power handling is a topic of considerable interest in the ultrasonics community as it affects the performance of acoustic devices across multiple fields of study including frequency control, transducers, and NDT / NDE. Harmonic finite element simulations are widely used to model the steady-state linear response of such devices; however, the underlying formulation assumes constant (or frequency-dependent) material properties, and thus cannot be used to model the nonlinearities imparted by phenomena such as strain or temperature dependent constitutive behavior. The aim of this study is to demonstrate a finite element-based approach for modelling the nonlinear frequency response of acoustic resonators.

Statement of Contribution/Methods

The simulation approach for nonlinear resonators is demonstrated within the context of two piezoelectric devices: a 50 kHz piston mode power transducer and a 2 GHz membrane-type BAW resonator. Coupled-field Ansys simulations employing axisymmetric and plane stress assumptions are used to model each device, respectively. Each point in the frequency response is derived from the results of a transient analysis of the model subject to sinusoidal excitation at the corresponding frequency. Each simulation is allowed to reach steady-state, and the magnitude and phase of the response (i.e., admittance or displacement) at the excitation frequency are calculated from the Fourier transform of the solution. Strain softening elastic behavior is modeled by augmenting generalized Hooke's law with a third order term.

Results/Discussion

The nonlinear simulation technique has been validated by demonstrating agreement with corresponding harmonic solutions at low drive levels. At higher drive levels, the effects of the prescribed elastic nonlinearity begin to manifest in the form of Duffing behavior (see figure) in accordance with theory. The analysis tool can be used to solve the direct problem, namely how much signal level a resonator of a given geometry and material properties can handle before exhibiting nonlinear behavior, or to address the inverse problem of inferring unknown material properties by correlating empirically observed nonlinearities to simulation results. Finally, the analysis approach is readily extendable to additional types of nonlinear constitutive behavior such as temperature-dependent elastic moduli.

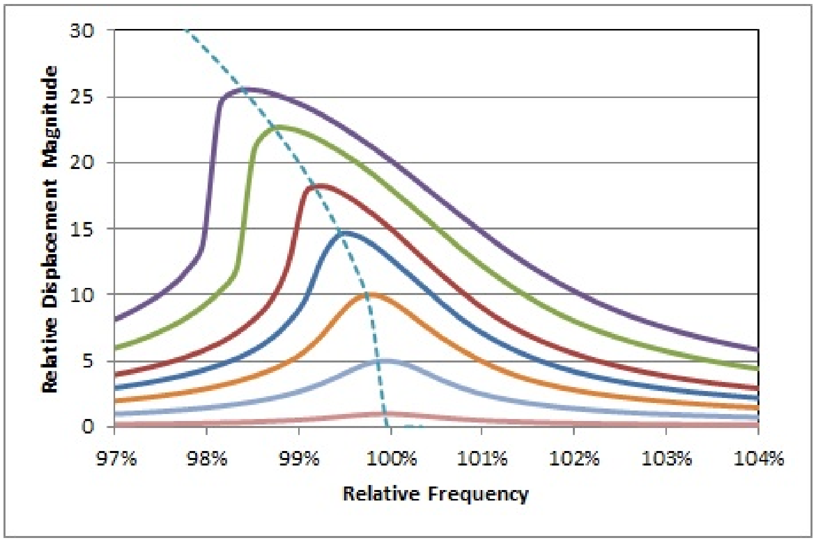

P4-B1-4 ____

Fundamental and 2nd Harmonic Modes, Nonlinear Piezoelectric Equations, Lithium Niobate SAW IDT Resonators

Nonlinear Frequency Response of Second Harmonic Generation in SAW IDT Resonators.

Yook-Kong Yong[1], Xiangnan Pang[1]; [1]*Civil and Environmental Engineering, Rutgers University, Piscataway, New Jersey, USA*

Background, Motivation and Objective

There have been great interests in the nonlinear behavior of SAW resonators but realistic models for their frequency response characteristics have been limited. We present a general purpose finite element model that yields directly the nonlinear frequency response of second harmonic generation in SAW IDT resonators. The nonlinear model enabled us to study the effects of nonlinear material constants, duty factor, and IDT geometry on the f-2f nonlinear interactions.

Statement of Contribution/Methods

A complete set of nonlinear piezoelectric equations along with their material constants for a lithium niobate YX-127^o SAW IDT resonator was implemented in a finite element program. Two sets of finite element matrix equations were derived for the fundamental SAW mode and its 2nd harmonic mode, respectively. We demonstrated how two frequency domain interfaces could be coupled together to simulate the f-2f interactions. The fundamental Rayleigh SAW mode was excited by a drive voltage at the IDT that in turn generated the second harmonic mode at twice the frequency. The model allowed us to study the effects of drive voltage excitation, duty factor and IDT geometry on second harmonic generation and its interaction with the fundamental mode.

Results/Discussion

Effects of drive voltage at the SAW IDT, duty factor and IDT geometry were studied with respect to 2nd harmonic generation. Effects of the 2nd harmonic generation on the fundamental SAW mode and its Q were observed when the voltage drive was greater than 0.6 V. For example, when the drive voltage was 0.1 V the fundamental mode was clean. There was little f-2f interactions (Fig. 1). But when the drive voltage was increase to 0.7 V as shown in Fig. 2 the fundamental mode exhibited Q reduction and modal degeneracy. Strong f-2f interactions were observed

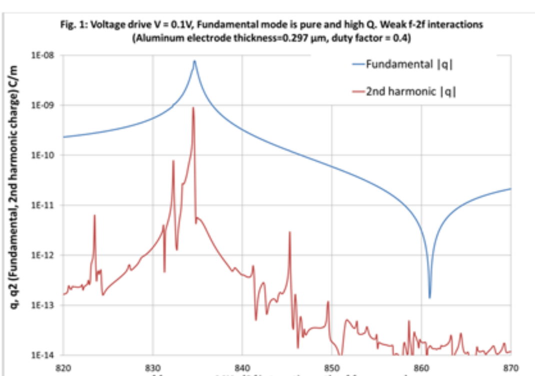

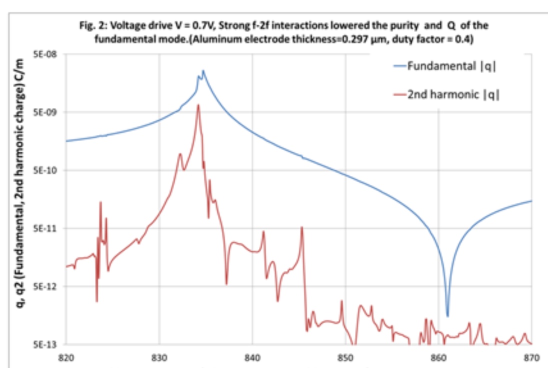

P4-B1-5 ____

Nonlinear Effects of Electrode and Bragg Reflector Materials in BAW Resonators

David García[1], Marta González[1], Alberto Hueltes[1], **Carlos Collado[1]**, Jordi Mateu[1]; Jose M González[1], [1]*UPC, Spain*

Background, Motivation and Objective

Linearity of RF filters is in the focus of system-architects as carrier aggregation (CA) schemes in down- and uplink emerge as a requirement. The nonlinear electro-thermal-acoustic constitutive equations of the piezoelectricity and the number of different materials involved in the manufacturing of BAW resonators make it difficult to discern between different sources of nonlinearity. It is hard to identify the root-cause of undesired effects, such as harmonics, intermodulation products and detuning effects.

A systematic procedure must be defined to unambiguously determine the origin of nonlinearities, and all the nonlinear observations must be consistent with the stated hypothesis. Better understanding of the nonlinear mechanisms is crucial for designing more linear resonators, and consequently improved filters.

Statement of Contribution/Methods

We use a comprehensive distributed Mason model that is able to relate the nonlinear parameters appearing in the constitutive equations governing not only the behavior of the main piezo layer, but also the nonlinear contribution of any other layer in the stack. We show that a given nonlinear observation can be explained by several hypothesis. For example, the 3rd order intermodulation product IMD3 can be explained by the 3rd order term of the elastic constant of the piezo layer, but also by remixing of 2nd order nonlinearities in the SiO2 layers. Additional experiments must be done to unambiguously determine the origin of nonlinearities and a given hypothesis must be consistent with all the experimental results. Specifically, narrowband H2, broadband H2, IMD3 and detuning under a DC bias voltage must be consistent with the established hypothesis. Nonlinear physical parameters have to be independent of the physical dimensions of a device. Results must be consistent not only for a given resonator, but also for other resonators with other dimensions and different stacks.

Results/Discussion

We have measured several resonators with different areas and stacks, and found that the nonlinear contribution of the SiO2 layers can be observed in certain situations. They play a role in the generation of IMD3. The uppermost SiO2 layer is also responsible for a secondary H2 peak that appears below the regular H2 peak. Several experiments (H2, IMD3 and DC detuning) were conducted to reject other hypotheses. As a consequence of the findings the design of the Bragg reflector was modified to prevent undesired nonlinear effects while maintaining small signal resonator performance.

P4-B2 - Contour Mode Resonators and other MEMS

Exhibit Hall

Friday, September 8, 2017, 9:30 am - 4:00 pm

Chair: **Omar Elmazria**
Université de Lorraine

P4-B2-1

High Coupling Two-port Lithium Niobate MEMS Resonators using Capacitive Ground Concept

Abhay Kochhar[1], Gabriel Vidal-Álvarez[1], Luca Colombo[1], Gianluca Piazza[1]; [1]*ECE, Carnegie Mellon University, Pittsburgh, Pennsylvania, USA*

Background, Motivation and Objective

Lithium niobate (LN) based thin film piezoelectrics have being extensively explored [1-3] for the making of high coupling and high performance resonators. The most important bottleneck for the use of LN film is related to fabrication process and it is particularly challenging when a bottom electrode is included in the stack to increase the film capacitance per unit area. We have explored Y-cut LN with both ion-slicing and surface activated bonding types of thin film transfer procedures. However, the patterning of bottom electrode still remains a fundamental issue and prevents designers from implementing two port devices. In this work, we propose the use of capacitive grounding by utilizing high dielectric constant available from Y-cut LN thin film. This demonstration is critical in the development of resonators with high out-of-band rejection and piezoelectric transformers.

Statement of Contribution/Methods

We have fabricated 2-port MEMS resonators in Y-cut LN thin films stacked between a bottom Pt and top Al electrode. The challenge consists in patterning the bottom electrode after bonding of the LN+Pt layers to the Si handle wafer. We have resolved this issue by exploiting the high dielectric constant of Y-cut films and grounding the resonator via large value capacitors, which can be synthesized within a very small footprint. MEMS resonators with a maximum k_t^2 of 8.3% when vibrating in S0 mode were demonstrated.

Results/Discussion

Two-port resonators were modeled via a Butterworth Van Dyke model. Our analysis indicated (Fig.1a) that a minimum capacitance to ground of 1 pF is required in order to preserve large out-of-band rejection and not degrade the device equivalent parameters. We built these capacitors by creating rings made out of Al/LN/Pt around the resonator body (Fig. 1b). The bottom electrode was still patterned and the 1 µm LN film was suspended by AlN . A response of one of these devices is shown in Fig. 1c where Y11 & Y21 responses show that the capacitive ground concept worked successfully. The quality factor recorded in air is much lower than expected. We attribute this to the poor resistance of the interconnect lines as verified by our direct resistance measurement as well as our low temperature measurements, which show that higher Qs approaching 1,000 can be attained.

[1] S. Gong, IEEE TED, 3888, 2013
[2] M. Kadota, IEEE TUFFC, 2564, 2010
[3] A. Kochhar, IEEE MEMS, 962, 2017

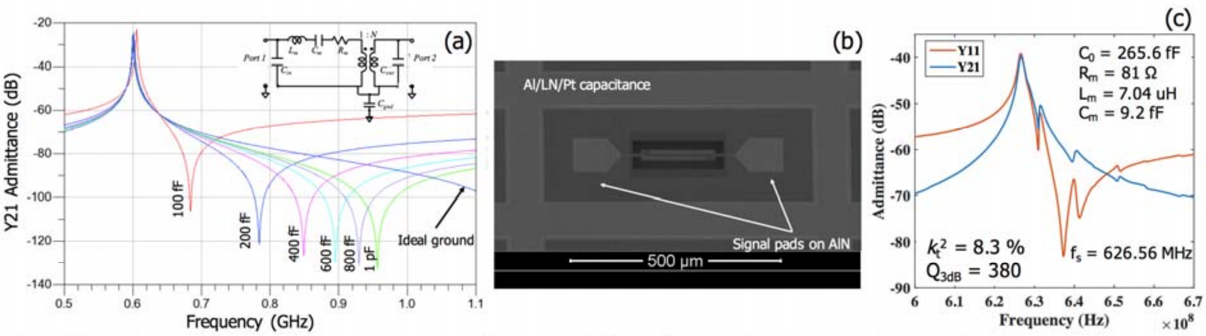

Fig. 1. Capacitive grounding based two-port resonators: (a) 2-port ADS simulation showing the impact of the capacitive ground on the resonator response, (b) SEM image of the device implementation and (c) characterized data of one of two-port resonators fabricated in this process.

P4-B2-2

Fast and Accurate Prediction of Spurious Modes in Aluminum Nitride MEMS Resonators Using Artificial Neural Network (ANN) Algorithm

Changting Xu[1], Mo Li[2], Shuo Zhao[2], Enes Calayir[1], Gianluca Piazza[1]; [1]*Electrical and Computer Engineering, Carnegie Mellon University, Pittsburgh, PA, USA,* [2]*Department of Chemistry, Carnegie Mellon University, Pittsburgh, PA, USA*

Background, Motivation and Objective

Spurious modes (SMs) result in in-band ripples and degrade the out-of-band rejection of filters, thus impeding the synthesis of high performance filters with MEMS resonators. Therefore, the ability to predict the presence of SMs in specific resonator geometries is highly desired and different techniques have been explored such as: 1-D/2-D analytic models, and 2-D/3-D finite element methods (FEM). These methods are either limited or time-consuming. ANN addresses all these challenges simultaneously by capturing the mapping between resonator design parameters and the probability of having spurious modes with connection weight matrix.

Statement of Contribution/Methods

As a proof of concept, we explored how 4 resonator design parameters impact SM: finger length, L, overhang extension, OE, number of fingers, NF, and anchor types, ANC (Fig. 1a-e). Our goal is to build an algorithm that can predict with high confidence the presence of SMs within +/-0.5% of the resonator center frequency, fs (Fig. 1f-g). By varying these 4 design parameters, we collected 106 data samples. These data were used to train an ANN (Fig. 2a). A K-fold cross validation process was used to estimate the prediction accuracy (Fig. 2b).

Results/Discussion

This paper reports for the first time on the effective use of an ANN algorithm for the prediction of SMs for AlN MEMS resonators. The prediction accuracy can be as high as 88.7% when $\Delta p = 0$ (Fig. 2a), which makes the ANN algorithm extremely useful given it only takes micro seconds to do so. Furthermore, we are able to increase the prediction accuracy to 97.7% by assigning $\Delta p = 0.15$, while preserving a confidence level of 81.1%. Most importantly, ANNs can predict the presence of SMs in over 10,000 cases within 0.02 seconds, while it would take years for conventional FEM.

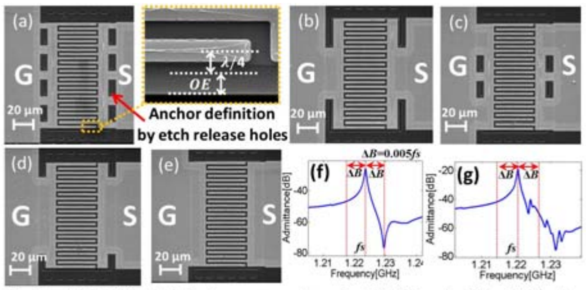

Fig. 1. (a)-(e): Studied design parameters: *L*, OE, *NF* and *ANC*; (f)-(g): the frequency range of interest centered on the resonant frequency, *fs*. Different anchor types are characterized by the ratio of the linearly weighted effective anchor width to the linearly weighted resonator width. The weight is 1 in the center, and 0 at the edge. (a) Anchor type 1, ratio = 0.5, (b) Anchor type 2, ratio = 0.75, (c) Anchor type 3, ratio = 0.64, (d) Anchor type 4, ratio = 0.94, and (e) Anchor type 5, ratio = 1.00, (f) No spurious mode exists within the interested range, which is labelled as 0 in the ANN algorithm. (g) A spurious mode exists within the interested range, which is represented by a 1.

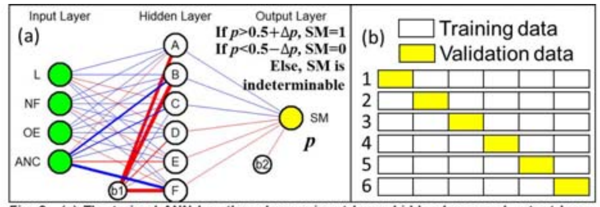

Fig. 2. (a) The trained ANN has three layers: input layer, hidden layer, and output layer. The circles with different filled colors represent neurons, except b1 and b2, which are designated as the biases for the hidden layer neurons and output layer neuron, respectively. The training process consists of determining the optimum weight matrix, which represents the strength of connections between neurons. The line width is proportional to weights (the thicker, the larger), while the color indicates the polarity of connections (blue for positive and red for negative). The ANN establishes the relationship between the probability, *p*, of having SMs and 4 design parameters. The SM value is determined by *p*. (b) K-fold cross-validation (K=6). The original data are randomly partitioned into K disjoint equal-sized subsets. One of subsets (yellow) is used as the validation data for testing the trained ANN (prediction accuracy is estimated), while the rest are used as training data. Such cross-validation process is performed K times (the folds), with a different subset used as validation data each time. From each cross-validation, the training depth (an iteration number, *n*) is determined to produce the best accuracy on the validation set. The final training is performed with all data for the mean *n iterations, with no validation set. This yields the ANN in (a). The average prediction accuracy is the expected prediction accuracy for the ANN.**

P4-B2-3

Sc(0.06)Al(0.94)N Film Evaluation Using Contour Mode Resonators

Benjamin Griffin[1], Michael Henry[1], Bernd Heinz[2]; [1]*MEMS Technologies, Sandia National Laboratories, Albuquerque, NM, USA,* [2]*Evatec, Switzerland*

Background, Motivation and Objective

Recent literature has focused on improving piezoelectric coupling coefficients by alloying aluminum nitride (AlN) with scandium (Sc). Akiyama et al. showed the highest d_33 piezoelectric coefficient increase of >4x at a 41% Sc substitution for Al. Thus far, studies mainly focus on material measurements such as x-ray diffraction or piezoelectric constants to assess the material quality. Although these measurements are useful to assess the improvement in the piezoelectric performance of the material, they do not address improvements in the figure-of-merit (FOM) of resonators (i.e., coupling coefficient times quality factor). Resonator structures are needed to directly extract these key performance parameters for film assessment. Fabrication integration, however, must be minimized to avoid obscuring film performance by extrinsic device effects.

Statement of Contribution/Methods

In this work, we demonstrated a film evaluation tool using contour mode resonators (CMRs) to directly extract resonator FOMs for film comparison. The interdigitated transducer (IDT) electrode CMRs are formed using a two-mask process to minimize integration effects. First, the IDT electrode is deposited and pattern. Next, the piezoelectric film is patterned and etched to form the resonator boundaries. Finally, it is released in XeF2. Arrays of resonator devices are formed to extract coupling coefficients and quality factors as a function of frequencies. An auto-prober is used to measure device arrays across the wafer.

Results/Discussion

In this work, IDT CMRs were formed using 1 µm thick AlN and Sc(0.06)Al(0.94)N. The figure below shows an example result of the coupling coefficients and quality factors extracted from S-parameters for Sc(0.06)Al(0.94)N IDT CMRs with three electrode configurations at 23 wafer locations. The Sc(0.06)Al(0.94)N showed a slight downshift in resonant frequency, likely due to softening of the Young's modulus and increase in density, and an increase in the coupling coefficient. The device level film extraction method clearly shows value as a supplement to direct material measurements by enabling comparison of resonator coupling coefficients and quality factors between films.

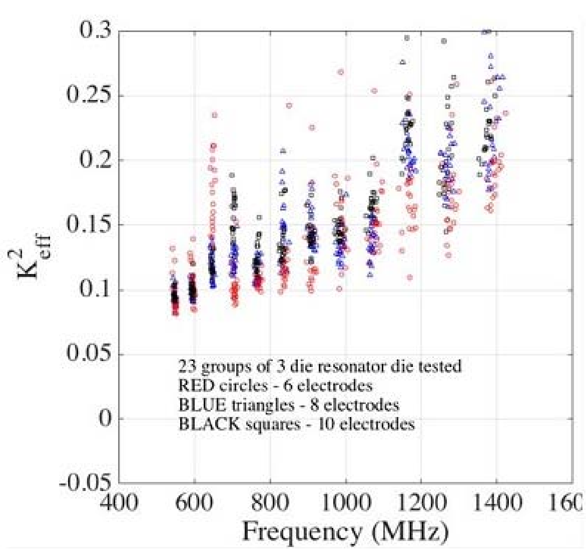

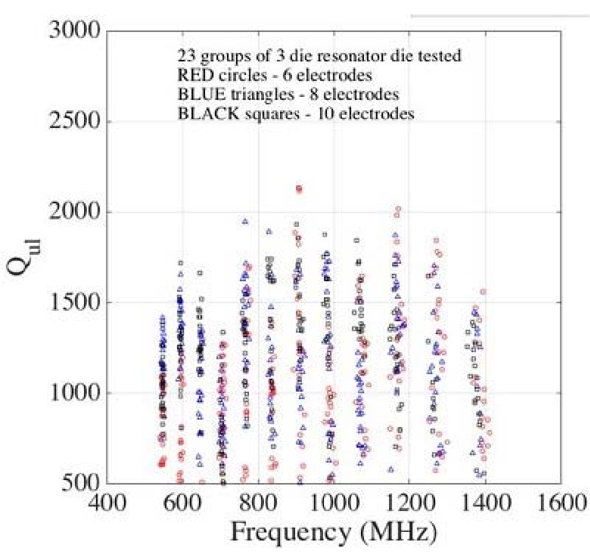

P4-B2-4

Support Loss Evasion in Breathing Mode High-Order Silicon Disc Resonators

Sarah Shahraini[1], Reza Abdolvand[2]; [1]*Electrical Eng & computer science, University of Central Florida, Orlando, Florida, USA,* [2]*University of Central Florida, Orlando, Florida, USA*

Background, Motivation and Objective

Leakage of elastic waves through the anchors is commonly reported as the dominant Q-limiting mechanism in micro-resonators. Bulk mode silicon-based disk resonators are amongst the most attractive designs in literature as they could potentially offer high Q if supported from the center. However, such supporting scheme adds to the fabrication complexity and as such, side supported designs have been explored to achieve high Q for certain resonance modes.

Statement of Contribution/Methods

In this work, silicon anisotropy is exploited to minimize anchor loss for side-supported breathing-mode disc resonators at high frequencies. Contrary to the case of isotropic material, the displacement at the edge of such resonators is not uniform and could be significantly larger in [110] direction relative to the [100] direction and the difference is more prominent in higher order modes (fig 1). With this realization, it is shown through the usage of perfectly matched layers (PML) in finite element modeling that the quality factor could be greatly improved by aligning the anchors to [100]. For such designs, pseudo-nodal points could appear on the side of the disc as shown for the 8th order mode of fig 1.b.

Results/Discussion

Simulated Qs for the resonator with [100]-aligned anchor is significantly higher than the resonator with [110]-aligned supports (table 1). This difference grows for higher order harmonic modes. To experimentally prove the effectiveness of this approach AlN-on-silicon (TPoS) disc resonators on 8µm SOI wafers are fabricated and tested. Piezoelectric transduction facilitates effective excitation of the breathing mode for a large number of harmonics as the top surface of the disc is used for actuation. Measured quality factors are reported in table one agreeing with the predicted trends.

Fig. 1 . a and b shows the displacement plots for 3rd and 8th harmonic. 8th order mode has zero displacement (green color) at the anchor.

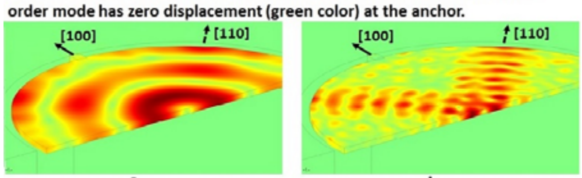

a b

Table 1. Anchor Q is simulated with PML based Comsol model. Measured Q data shows the same trend as the simulation.

Harmonic number	Anchor not rotated (simulated)		Anchor rotated (simulated)		Anchor not rotated (measured)			Anchor rotated (measured)		
	f_0 (MHz)	Q (K)	f_0 (MHz)	Q (K)	f_0 (MHz)	Q (K)	R_m (kΩ)	f_0 (MHz)	Q (K)	R_m (kΩ)
2nd	43.5	0.63	43.4	0.86	43.3	0.46	20.3	42.8	0.45	6.2
3rd	69.4	0.88	69.3	22.6	70.19	0.31	7.7	69.0	2.54	0.33
4th	95.3	0.62	95.5	272	95.91	0.78	33.1	94.7	5.18	1.15
8th	-	-	200.1	4170	-	-	-	195.9	8.74	1.51

Fig. 2 . Measured S21 data for 8th order breathing mode. Anchors in [100] direction.

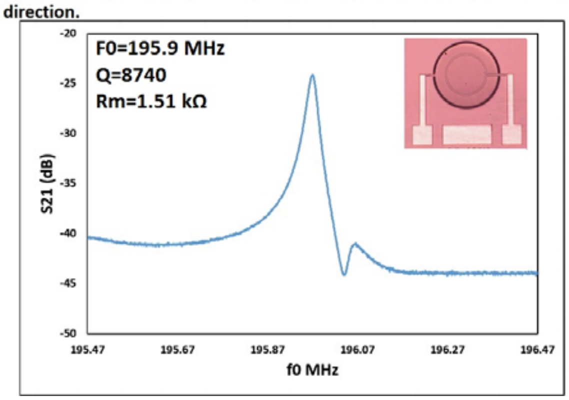

P4-B2-5

Release Area Confinement in Contour Mode Resonators

Andrea Lozzi[1], Annalisa De Pastina[1], Ernest Ting-Ta Yen[2], Luis Guillermo Villanueva[1]; [1]*STI IGM NEMS, École polytechnique fédérale de Lausanne, Lausanne, Switzerland,* [2]*Kilby Labs, Texas Instruments Inc., Santa Clara, CA, USA*

Background, Motivation and Objective

Anchor loss limits quality factor (Q) of contour mode resonators (CMRs) operating below 500 MHz. Studies have shown improvement of Q through geometrical optimization of the resonator's anchors, shape, and inactive region (Lozzi, 2016; Segovia, 2015; Cassella, 2015). A recent study also demonstrated that Q is influenced by the undercut created during the isotropic release (Gibson, 2015).

The objective of this work is to quantify the correlation between Q and the undercut area near the anchors. A novel release boundary design using in-phase reflectors (Harrington, 2011) is also implemented to confine acoustic waves propagating from the anchors, in order to improve Q.

Statement of Contribution/Methods

The fabrication starts with the definition of high aspect ratio trenches (~2×40 um) filled with thermal oxide. As the end of the anchor is a source of circular waves, the trench profile at this region is designed to be an ideal wavefront (Fig.1 b). 220 MHz CMRs with release radius (Rrel) from 25 to 49 um are fabricated for comparison. The release is done in SF_6 (selectivity >200:1 to SiO_2) to preserve the trench walls.

Results/Discussion

Fig. 2 shows a periodic trend of Q in function of Rrel. Distance between peaks corresponds to λ/4 (λ = 40 um) regardless of different anchor designs (Lozzi, 2016). Moreover, comparing identical CMRs with and without confined release, an improvement of Q up to 40% is obtained (Rrel = 25 um). The Q stability was also tested as a function of SF_6 etch time. Two additional etch steps of 90 seconds were performed and Q variation less than 4.5% was recorded after each step.

In conclusion, this work demonstrated a novel method to control the undercut in CMRs and to create in phase reflectors to improve Q. These results agree with FEM simulations which will be presented in the final paper.

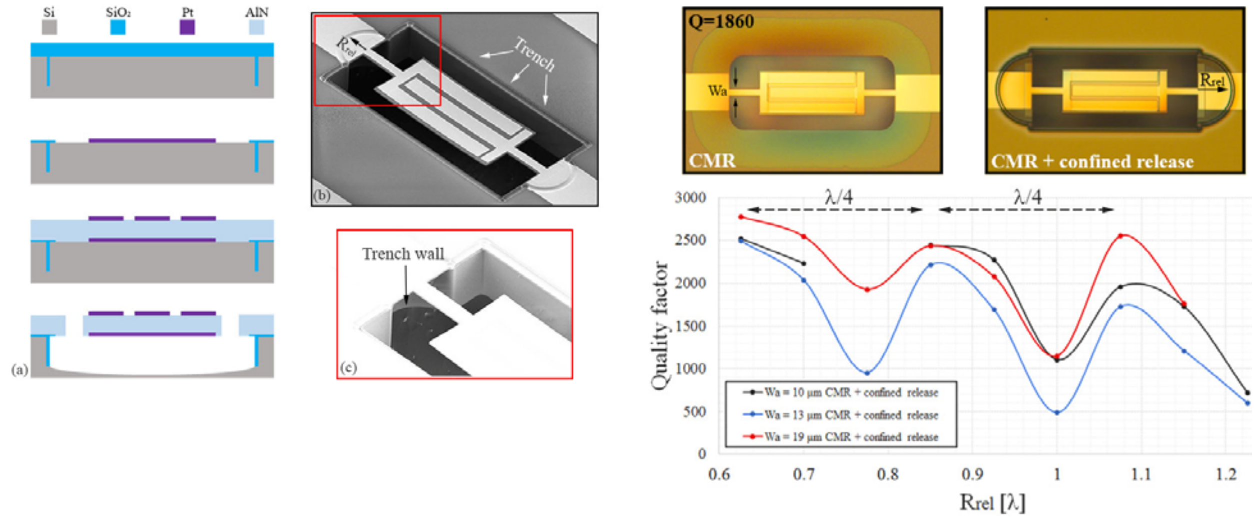

P4-B2-6

Artificial Neural Network (ANN) Based Digital Temperature Compensation Method (DTCM) for Aluminum Nitride MEMS Resonators

Changting Xu[1], Gianluca Piazza[1]; [1]*Electrical and Computer Engineering, Carnegie Mellon University, Pittsburgh, PA, USA*

Background, Motivation and Objective

Temperature stability is critical for commercial oscillators and many methods have been explored such as: a) constant-resistance-based control methods; b) DTCMs with look-up tables; c) phase-lock-loop based control methods. Whereas exemplary results have been attained with these techniques, to be effective they require: a) accurate knowledge of the source of temperature fluctuations; (b) the use of multiple and very accurate calibration curves; c) very high power consumption. ANN-DTCM addresses all these challenges simultaneously by enabling a compensation method that is agnostic about the physical source of temperature-induced frequency fluctuations, performs rapid calibration (>10X faster than b), and results in low power consumption.

Statement of Contribution/Methods

The procedure of the ANN-DTCM to do automatic calibration and testing is shown from Fig. 1(a) to (d).

Results/Discussion

We demonstrate the capabilities of the ANN-DTCM with an ovenized AlN resonator (Fig. 1e). We attain an oven gain, *G*, of 200X, and a power consumption, *P*, of 390 μW over 120 °C (Δ*T*), which result in an overall figure of merit ($G\cdot\Delta T/P$) that is 1 to 2 order of magnitude better than any other compensation methods reported in the literature (Table 1). We achieve a frequency stability of 14 ppm over 120 °C without any additional compensation technique (Fig. 1f) and the uncompensated resonator exhibits a frequency shift of 3000 ppm. Furthermore, this compensation method can be implemented without accurate knowledge of the sources of temperature fluctuation, such as radiation and temperature gradient. Finally, ANN-DTCM can be used to set the initial frequency of the oscillator (within ±500 ppm), thus compensating for fabrication-induced frequency variations.

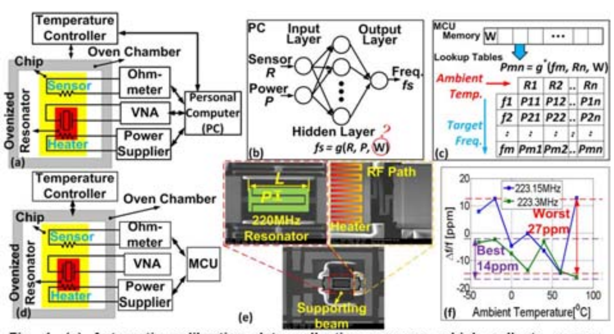

Fig. 1. (a) Automatic calibration data collection process, which collects sensor resistance, *R*, ovenization power, *P*, and corresponding resonator's center frequency, *fs*. The red area stands for the ovenized resonator, and the yellow box represents the tested chip. (b) The calibration data are used to train a 2-Input-n-hidden-1-output ANN, which determines the optimum weight matrix, W. (c) The W matrix is downloaded to a micro-controller-unit (MCU) and then a lookup table for multiple target frequencies is generated. (d) MCU is connected to the ohmmeter to monitor the real-time temperature and adjusts the ovenization power accordingly through the power supply. The real-time frequency is monitored via the VNA . (f) The SEM image of a 220 MHz ovenized resonator. Insets show zoomed-in views of the resonator and RF signal path. *P* is the pitch, which determines the resonator frequency, and *L* is the resonator length. (g) The plot of best and worst frequency change versus temperature after ANN-DTCM for all possible target frequencies between 223.152 and 223.377MHz.

Table 1. Summary and comparison of micro-oven based compensatic methods. CRTC stands for constant-resistance temperature contrc Composite material refers to the insertion of positive TCF material (oxid in the resonator stack. Oven gain is defined as the ratio of the change ambient temperature to the corresponding change in the ovenize resonator's temperature.

	M.-H. Li	K. E. Wojciechowski	Z. Wu	J. Salvia	**This Work**
Year	2015	2015	2014	2009	**2017**
Device Type	Capacitive Oscillator	Piezoelectric Oscillator	Fused Silica Oscillator	Capacitive Oscillator	**Piezoelectri Resonator**
Compensation Technologies	Composite Material, CRTC	Composite Material, CRTC	CRTC, DTCM	Composite Material, PLL, DTCM	**ANN-DTCM**
Frequency Drift Δf/f	< 120ppm /125°C	300ppb /125°C	11ppm /105°C	0.1ppm /100°C	**14ppm /120°C**
Best Oven Gain G	5.1X	~100X	95.5X	704X	**200X**
Ovenization Power P/ΔT	0.47mW /125°C	12.5mW /125°C	15.8mW /105°C	14.9mW /100°C	**0.39mW /120°C**
FoM G·ΔT/P	1356	1000	635	4275	**61538**
Temperature Range	-40 ~ +85 °C	-45 ~ +85 °C	-40 ~ +65 °C	-20 ~ +80 °C	**-40 ~ +80 °C**

P4-B3 - Microacoustic Sensors and Gyroscopes

Exhibit Hall

Friday, September 8, 2017, 9:30 am - 4:00 pm

Chair: **Jidong Dai**
Murata Americas

P4-B3-1

A Love Wave Biosensor with a Phononic Wave Guiding Layer for VEGF Detection in Selective Platelet Activation

Huiyan Wu[1], Guangyi Zhao[2], Hongfei Zu[1], James HC Wang[3], Qing-Ming Wang[1]; [1]*Department of Mechanical Engineering and Materials Science, University of Pittsburgh, Pittsburgh, PA, USA,* [2]*Department of Bioengineering, University of Pittsburgh, Pittsburgh, PA, USA,* [3]*Department of Orthopaedic Surgery, University of Pittsburgh, Pittsburgh, PA, USA*

Background, Motivation and Objective

Platelets are blood cells that play a critical role in a number of pathophysiological processes. After activation, platelets release a variety of growth factors, including PDGF, VEGF, TGF-β and HGF. Using different agonists, platelets can be selectively activated in different ways. For example, PAR-1 agonist activated platelets release VEGF while PAR-4 agonist activated platelets retain VEGF in them. Thus, detection of secreted growth factors under the activation of different agonists is essential for the effective clinical use of platelets for optimal injured tissue repair. Love wave sensor is considered as a promising biosensing platform in biomedical research, and more efforts need be devoted to improve the sensor performance. Phononic crystals are periodic composite materials with periodic scattering centers; and acoustic wave in certain frequencies cannot propagate through this kind of frequency band structure. In this study, a Love wave sensor with an innovative phononic wave guiding layer is proposed to detect the VEGF secreted during the selective platelet activation process.

Statement of Contribution/Methods

Fig.1 shows the structure of a Love wave sensor for VEGF detection in selective platelet activation. Dual delay-line SAW sensors are fabricated on 36º YX-LiTaO3 surface. Parylene-C film is deposited as the wave guiding layer, and the phononic patterns are fabricated by photolithographic process. The cell culture chip is composed of two chambers which are separated by a micro-porous membrane, allowing only macromolecules and small molecules to go through. Firstly, VEGF antibody is added into the bottom chamber so that the Love wave sensor surface would be coated by a thin layer of antibodies. The platelet suspensions are added into the top chamber. By adding PAR-1 agonist, platelets are selectively activated and retained within the top chamber, while released VEGF diffuses through the membrane and bond with the antibodies on the surface of Love wave sensor. In comparison, platelets activated by PAR-4 agonist should have minimal VEGF release.

Results/Discussion

The Love wave sensor with phononic wave guiding layer is investigated theoretically and the optimal device parameters are determined. The experimental results demonstrate that the Love wave sensor is extremely sensitive for detecting VEGF growth factor during selective platelet activation.

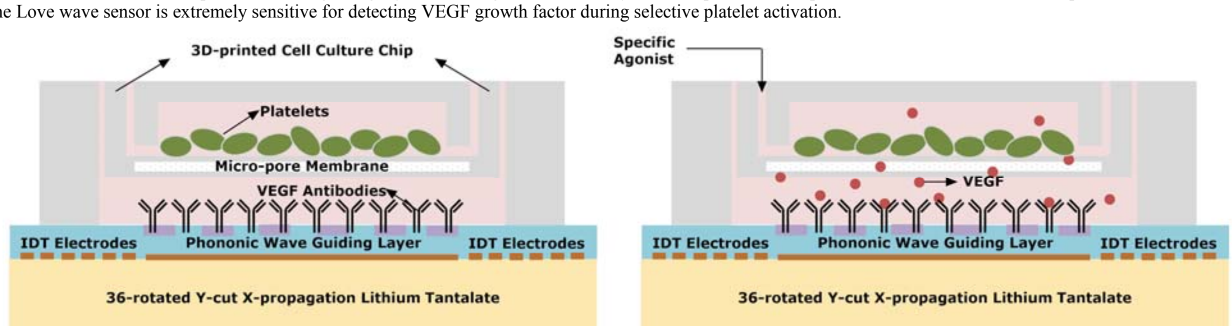

Fig.1 Schematic diagram of a Love wave biosensor with a phononic wave guiding layer for VEGF detection in se-lective platelet activation

P4-B3-2

Combined Colorimetric and Gravimetric CMUT Sensor for Detection Of Phenylacetone

Mathias Mølgaard[1], Milan Laustsen[1], Ida Thygesen[1], Mogens Jakobsen[1], Erik Thomsen[1]; [1]*Nanotech, Technical University of Denmark, Kgs. Lyngby, Denmark*

Background, Motivation and Objective

Detection of phenylacetone is of interest as it is used as a precursor for the synthesis of (meth)amphetamine. The ability to detect illegal drugs at e.g. border crossings is valuable for governments. Capacitive Micromachined Ultrasonic Transducers (CMUTs) have previously been used to detect small amounts of analyte. If the sensitivity of the CMUT is known, the resonance shift can be used to directly calculate the added mass and hereby the amount of an analyte. This typically requires a selective functionalization layer on top of the CMUT in order to differentiate between analytes. However, for some analytes such a layer can be difficult or impossible to obtain.

In this work we use a colorimetric dye which is selective towards phenylacetone in conjunction with a CMUT to detect and quantify the analyte.

Statement of Contribution/Methods

CMUTs were fabricated using a single Local Oxidation of Silicon (LOCOS) process to define the cavities on a highly doped Si substrate wafer. The plate is a tensile stressed Si3N4 layer bonded to the substrate wafer. The CMUTs have a resonance frequency of 36 MHz in air and an experimentally determined sensitivity of 23 zg/Hz/µm2.

To track the resonance frequency, the CMUTs are via a custom-made PCB connected to a lock-in amplifier (Zurich Instruments, HF2LI) with a built-in phase-locked loop. Colorimetric dyes are deposited on the plate of the CMUTs using a spotter. When the analyte is absorbed in the dye a resonance shift is detected due to the increased mass on the plate.

The presence of phenylacetone will for some of the dyes result in a color change. These color changes are subsequently recorded by a digital camera. The analyte can then be identified by the color response.

Results/Discussion

The left figure shows the frequency shift as a function of time for an uncoated CMUT and a CMUT coated with the dye DAB4 when exposed to phenylacetone. The frequency shift of the coated CMUT is seen to be larger than for the uncoated CMUT. The right figure shows part of the dye array where the first and last photograph has been subtracted, hereby showing the color change due to the analyte. The combination of color changes shown in the figure is specific to phenylacetone.

Colorimetric arrays were used to identify phenylacetone while CMUTs were used to quantify the amount.

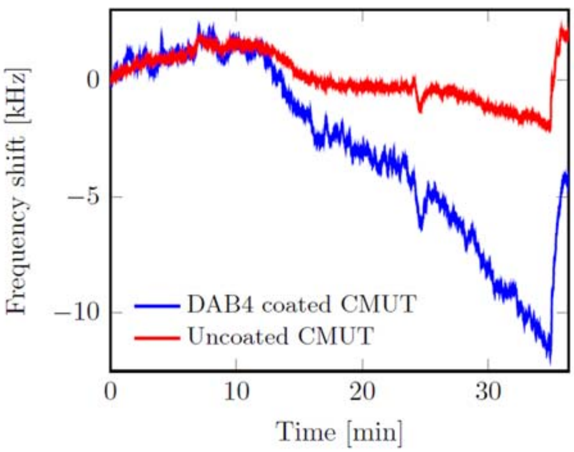

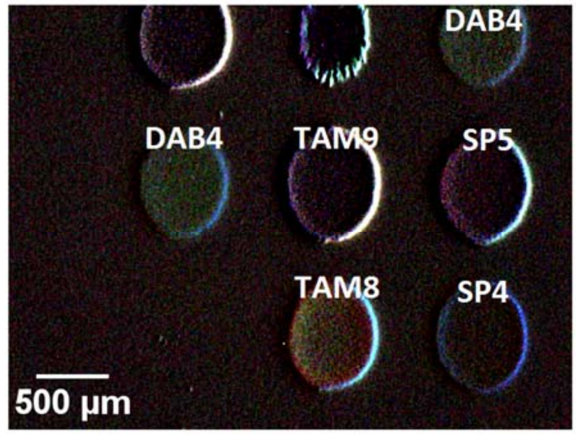

P4-B3-3

Optimal Design for an Innovative Very-High-Temperature Hybrid SAW Sensor

Pascal Nicolay[1], **Natalya Naumenko[2]**; [1]*Carinthian Tech Research CTR AG, VILLACH, Austria,* [2]*National University of Science and Technology "MISIS", Russian Federation*

Background, Motivation and Objective

There is a need for wireless sensors, able to withstand temperatures above 900°C. Promising solutions based on SAW technology have been developed, addressing various technical problems. Material stability, dewetting of the electrodes and damaging of the sensor's housing are some of the main issues that have been tackled over the years. However, there is still no SAW sensor able to withstand very high temperatures for a long time yet. A possible solution would be to stop exposing the SAW sensor to very high temperature, and use it as a transponder only. The sensing could be done by a thermocouple, with a cold junction connected to a thin highly piezoelectric layer, deposited on the SAW track. The voltage generated by the thermocouple would translate into surface strain, which would influence the RF response of the SAW sensor. This concept was tested experimentally at 400MHz, using AlN layers deposited on YZ-LN [1]. In this paper, we present the methodology and results of a theoretical study that was conducted to analyze the acoustic behavior and optimize the design of 2.45GHz version of the sensor, with buried Pt electrodes.

Statement of Contribution/Methods

The acoustic properties of SAW modes propagating in two cuts of LN (YZ and 128ºYX) with platinum grating and AlN overlay were computed using the numerical technique SDA-FEM-SDA. In LN/AlN stacks, the velocities of SAW modes grow with the AlN thickness. In a structure with thin buried Pt electrodes, the Rayleigh SAW (RSAW) velocity becomes eventually bigger than the slowest LN BAW in both LN cuts and transforms into a leaky SAW (LSAW). However, due to negligible coupling between the RSAW and the SH-polarized slow shear BAW in 128ºYX LN, the LSAW can propagate with nearly zero losses. Hence, useful low-attenuated LSAWs propagating with high velocities in the 128ºYX-LN/AlN stack could be advantageously used. When $h_{Pt}/2p=0.1$ and $h_{AlN}/2p \approx 0.6$, the LSAW has the attributes of a boundary mode with its energy focused at the LN/AlN interface and dominant sagittal components of displacements. It propagates at a velocity of 4088 m/s with a coupling factor of 5.65%.

Results/Discussion

For a 1µm-thick AlN layer, the obtained wave characteristics translates into the following optimized devices parameters, to achieve a 2.45GHz operating frequency with buried electrodes: 128°YX LN orientation, pitch=0.834 µm and hPt=0.167µm. Besides, the velocity of the selected LSAW/Boundary mode does not change noticeably with further increasing of the AlN thickness, which could be advantageous from the fabrication point of view.

The measured sensitivity of 0.2 ppm/V at 400MHz was lower than the required value for practical applications. The presented results will help designing the next sensor generation, with improved sensitivity and durability.

[1] P. Nicolay, R. Matloub, J. Bardong, P. Muralt, A new concept of wireless and passive very-high temperature sensor, paper submitted to the Applied Physics Letters in February 2017 (in review)

P4-B3-4

A One-Port SAW In-Liquid Sensor Platform: Design and Fabrication

Kiryl Kustanovich[1], Ventsislav Yantchev[1], Aldo Jesorka[1]; [1]*Chemistry and Chemical Engineering, Chalmers University of Technology, Goteborg, Sweden*

Background, Motivation and Objective

SH-SAW In-liquid sensors have been explored extensively in recent decades. They propose an ability to work at higher frequencies, than the well-known QCM, with the aim to reduce the size and ease the integration in sensor arrays. So far SH-SAW liquid phase sensors are designed in two-port delay line configurations because of the need to protect the IDT from the conductive and dielectric loads from the liquid. A compact one-port resonant SH-SAW liquid sensor is yet to be developed as an alternative of QCM at high frequencies.

Statement of Contribution/Methods

Here we demonstrate the technology and design principles of a new concept for building a SAW in-liquid sensor employing surface acoustic wave resonance (SAR) in a one-port configuration. The reflective gratings of a one-port SAW resonator are employed as sensing elements, while the transducer is a wide-band IDT placed in-between the reflectors and protected from the liquid. Thus the frequency shifts of the SAW resonance will be determined, to a large extent, by the changes in propagation characteristics of SAW under the reflective gratings subjected to mass load.

Results/Discussion

185MHz SAR technological platform integrated with PDMS microfluidic channels is fabricated and characterized (Fig. 1). Specific emphasis in this work is on the fabrication and performance boost of the SAR sensor as well as its integration with impedance spectroscopy through interdigitated reflectors. Few basic designs are identified for their well pronounced resonance and low impedance, while retaining sufficient sensitivity towards liquid loading (about 1000 ppm) (Fig. 2). Inherent for the SAR sensing platform are its low impedance at resonance, retained Q≈200 when immersed in liquid and significantly smaller dimensions.

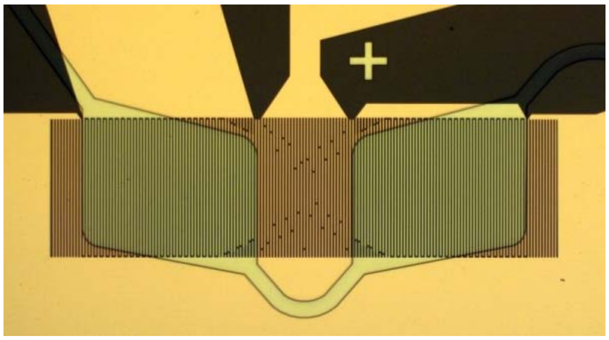

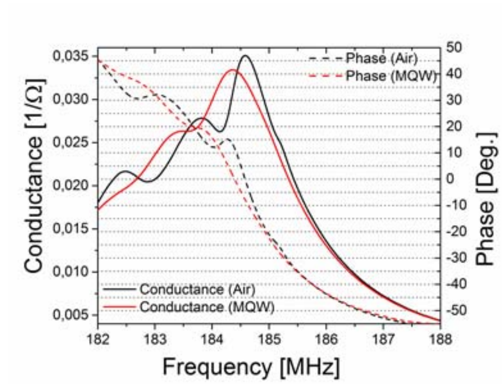

P4-B3-5

A New Threshold Determination Algorithm for SAW Resonant Sensors

Yang Yang[1], Chenrui Zhang[1], Xiaojun Ji[1], Ping Li[1], Yumei Wen[1], Tao Han[1]; [1]*Department of Electronic Information and Electrical Engineering, Shanghai Jiao Tong University, Shanghai, China, People's Republic of*

Background, Motivation and Objective

Wireless SAW resonant sensors have been widely used in many applications, especially in harsh environment. The sensor is detected when the echo signal spectrum processed by Fourier transform exceeds a threshold. Because of complicated noise and electromagnetic interference in wireless channel, the threshold should be adaptive to interference in order to detect the sensor accurately. However, few researches have been reported on the threshold determination of SAW resonant sensors. The only reported minimum identification error probability method for SAW RFID-tags needs prior probability density functions of both the background noise and the signal. In addition, since the resonance frequency of sensor and the reading distance are unknown when the reading system interrogates a SAW resonant sensor, it is difficult to estimate the signal-to-noise ratio (SNR) in real-time before a threshold is determined. A false alarm means the detection of a sensor when it actually does not exist, and it will cause wrong frequency estimation in the reading system; so the false alarm is more unacceptable than the miss-detection. According to the constant false alarm rate (CFAR) method in radar signal processing, a threshold determination algorithm for SAW resonant sensors is proposed, which pursues the detection probability to reach a maximum in complicated noise, and only the probability density distribution of noise is needed to estimate in the algorithm.

Statement of Contribution/Methods

The reading system records the background noise without interrogating SAW resonant sensors. The probability density distribution of noise is estimated and is fitted by double exponential functions. The relationship between threshold and false alarm rate is obtained based on Neyman-Pearson rule, and thus the dynamic and adaptive CFAR threshold is also calculated. A detection index for SAW resonant sensors is proposed, which is a normalized value after the integration of the false-to-correct detection ratio on a range of SNR. The changing trends of threshold and detection probability with signal-to-interference ratio are illustrated. In addition, the proposed algorithm is compared with the minimum error probability method.

Results/Discussion

When the reading system interrogates SAW resonant sensors from a long distance by step frequency sweep, the sensors may not be fully excited. CFAR threshold can change dynamically according to the noise and echo signal, which realizes a longer detection distance than using a constant threshold. Monte Carlo simulation is used to calculate the detection index of CFAR thresholds for SAW resonant sensors, when SNR ranges from 5dB to 15 dB. In experiments, the proposed threshold determination algorithm for SAW resonant sensors is tested in two circumstances: the open space and the multi-reflection environment, respectively.

P4-B3-6

Ultra-High-Frequency Wireless MEMS QCM Biosensor for Direct Detection Of Biomarkers In Serum

Hirotsugu Ogi[1], Arihiro Iwata[1]; [1]*Osaka University, Japan*

Background, Motivation and Objective

It is generally difficult to adopt label-free biosensors, such as quartz-crystal-microbalance (QCM) biosensor and surface-plasmon-resonance biosensor, for diagnosis, because analyte contains many impurity proteins, whose concentrations are much higher than the target protein; they adsorb the sensor surface nonspecifically, obscuring the minute response caused by the target-protein adsorption. Therefore, a sandwich method has been used, which, however, takes a long assay time and deteriorates the label-free advantage.

We then propose a QCM biosensor system, which works at ultra-high frequencies (UHF) (>550 MHz), for minimizing the influence of impurities. QCM principally detects target proteins through the mass-loading effect, and its mass sensitivity significantly improves by thinning the AT-cut quartz resonator. Besides, the resonance frequencies become higher as the resonator becomes thinner, causing a high-speed surface movement. The impurity proteins which are nonspecifically (weakly) bonded on the quartz surface fail to follow the fast movement of the surface and to contribute to the mass loading. On the other hand, the target proteins, which are tightly captured by the receptor proteins immobilized on the surface, can move to the surface movement and they can be detected as the loaded mass. The purpose of this study is thus to directly detect the target proteins in analyte in which many impurity proteins are contained by developing a high-frequency QCM biosensor.

Statement of Contribution/Methods

A bare AT-cut quartz plate with ~25 μm thickness (fundamental resonance frequency: ~65 MHz) was packaged in the microchannel fabricated in silicon wafer with the MEMS technique. The shear vibrations of the AT-cut quartz were excited and detected by line antennas placed outside the microchannel to achieve the wireless measurement. We mainly used the 9th mode at ~585 MHz for detecting target proteins. First, we investigated the effect of impurity proteins on the sensor response using the specific binding between IgG and protein A. We added bovine serum albumin (BSA) as the impurity. Second, we detected the C-reactive protein (CRP) in bovine serum and investigated the applicability of the UHF-QCM assay to the direct detection of targets in serum.

Results/Discussion

The BSA impurity significantly affected the frequency change at a low-frequency (~ 60 MHz) QCM measurement when its concentration is larger than that of IgG by a factor of 1000. However, the 585-MHz QCM assay shows insensitivity to the impurity proteins and identical frequency changes were observed. Furthermore, the UHF-QCM assay reveals that it can detects CRP in the serum directly even in a low-concentration (~ 10 ng/ml) range. Thus, the UHF-QCM is a promising biosensor system for diagnosis.

P4-B3-7

Performance Improvement of the SAW Based Current Sensor Incorporating a Patterned Magnetostrictive Feco Film

Wen Wang[1], Yana Jia[1], Xinlu Liu[1], Yong Liang[1], **Shitang He[1]**; [1]*Chinese Academy of Sciences, Institute of Acoustics, Beijing, China, People's Republic of*

Background, Motivation and Objective

Recently, the idea of Surface acoustic wave (SAW) current sensor utilizing magnetostrictive effect provides a new effective way for sensing current, which exhibits some superior features as fast response, simple structure, and strong anti-jamming. The representative sensor structure is composed of a configuration of dual-delay-line oscillators, and a magnetostrictive film (FeCo) coated onto the sensing device (Fig. 1). Some meaningful results were reported in recent articles. However, due to the strong hysteresis effect of the magnetostrictive material, there occurs obvious asymmetry in sensor response at forward and negative current. To suppress such phenomenon, a patterned design on magnetostrictive coating was performed in this contribution.

Statement of Contribution/Methods

500nm FeCo film was deposited on the SAW propagation path of the 150MHz sensing device by RF magnetron sputtering. The FeCo film produced magnetostrictive strain under the electromagnetic field, and modulates the SAW velocity. The corresponding change in differential oscillation frequency was used to evaluate the current. The striped pattern with strip width of 2λ (λ: wavelength) and strip spacing of 1λ was performed for the FeCo coating. Then, the developed SAW current sensor was characterized by using the Helmholtz coil system.

Results/Discussion

The sputtered patterned FeCo coating was pictured in Fig. 1. The sensor responses of the partnered FeCo-coated sensor towards forward current and negative current were measured in comparison with non-patterned FeCo coated sensor, as shown in Fig. 2. Obviously, due to the patterned design on FeCo coating, the asymmetry induced by the hysteresis effect was reduced significantly. High current sensitivity of 12 KHz/A and excellent linearity were obtained.

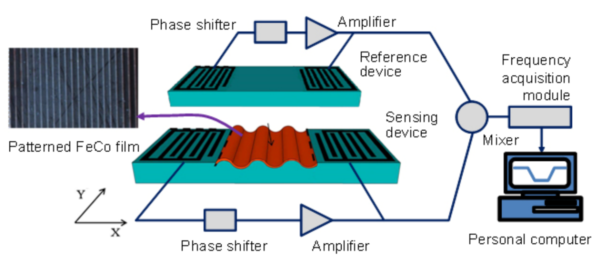

Figure 1 the scheme of the developed SAW current sensor with patterned FeCo film

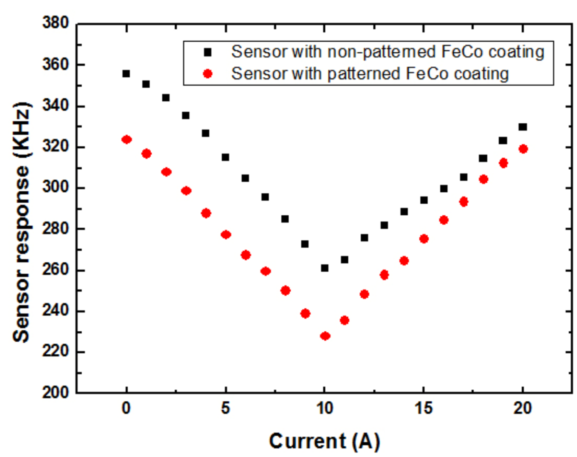

Figure 2 the sensor response from the sensor with non-patterned and patterned 500nm FeCo coating

P4-B3-8

Towards a Surface and Bulk Excited SAW Gyroscope

Benyamin Davaji[1], Amit Lal[1]; [1]*SonicMEMS, Cornell University, Ithaca, NY, USA*

Background, Motivation and Objective

Unreleased gyroscopes are very promising for inertial navigation systems, where the extended dynamic range and structural robustness are not only desirable but expected for many applications. Surface acoustic wave (SAW) gyroscopes, having solid structure, offer high shock survivability and by confining acoustic energy to the surface, may lead to increased sensitivity by avoiding losses to the bulk and edges. The idea of using SAW gyroscopes is not novel, however many untapped areas on performance updates still exist. one of the main challenges is to increase the scale factor, which is a function of the drive amplitude and the Coriolis mass. Though, both the drive and sense resonators have a shared cavity, the direct leakage and scattering results in sacrificing the SNR. In this work, we are investigating the opportunities for driving the distributed Coriolis mass in the SAW cavity from the wafer backside.

Statement of Contribution/Methods

The SAW device was fabricated on 128º Y-cut black lithium niobate substrate with metal (Au/Ti) electrodes patterned (lift off) on both sides. The acoustic gyro (Fig. 1A) was realized with combination of a drive and a sense SAW resonators where the shared acoustic cavity is filled with metal pillars (Coriolis mass) on the top side of the device at a design frequency of 200MHz, with SAW wavelength of 20 microns. The pillars are quarter wavelength in planar dimension and were excited by drive SAW, and any rotation will result in generating a secondary SAW picked up by the sense IDT. The backside IDT electrodes are implemented in the structure to launch acoustic plate mode (APM) waves into the cavity. The backside electrodes are designed to operate at the same frequency as the primary SAW.

Results/Discussion

The top and bottom electrodes are excited at 192.6 MHz and the displacement amplitude for sense and receive electrodes is measured using Doppler vibrometer (Polytec-UHF). Driving the input IDT on the top results in ~2 nm displacement (SAW) at antinodes in the cavity whereas the bottom IDT results in 50 pm displacement (APM) for the same input voltage (Fig. 1C & 1D). In this design, multiple backside IDTs are patterned, which enables the excitation of all or selective parts of the distributed Coriolis mass. In the future, the design of the backside electrodes may extend to a full circular electrode to take advantage of increased wave focusing and better gain.

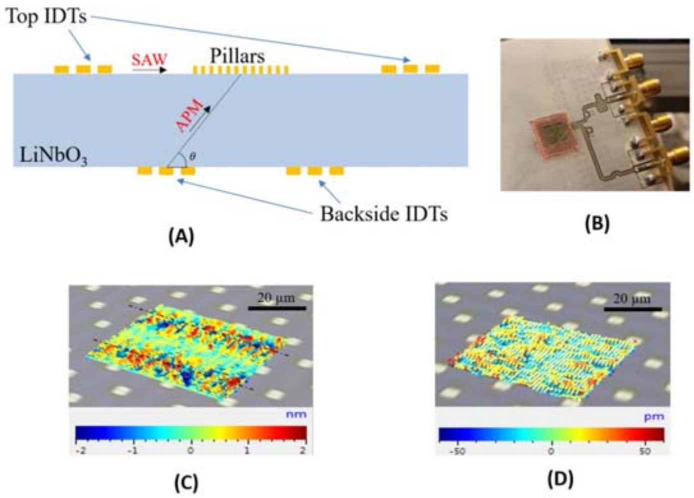

P5-B1 - High-Frequency Transducers

Exhibit Hall

Friday, September 8, 2017, 9:30 am - 4:00 pm

Chair: **Jeremy Brown**
Dalhousie University

P5-B1-1

High Frequency Self-focusing Transducer Fabricated by a Laser Engraving Technique

Xiaohua Jian[1], Zhangjian Li[1], Zhile Han[1], Pengbo Liu[1], Peiyang Li[1], Weiwei Shao[1], **Yaoyao Cui[1]**; *[1]Suzhou Institute of Biomedical Engineering and Technology, China, People's Republic of*

Background, Motivation and Objective

High frequency transducers (>15 MHz) have been widely used in small animal ultrasound, ophthalmic ultrasound, skin ultrasound and intravascular ultrasound et. al. The images obtained by a plane transducer have lower resolution and sensitivity compared with a focusing one. It is usually hard to make the focusing transducer with micro size, short focal length and high frequency. For solving these problems, self-focusing transducers were developed, which pattern a Fresnel half-wave bands on the piezoelectric materials surface as the electrode. Using this method can achieve transducers with micro size (~1-2 mm in diameter), short focal length (~350 µm) and high frequency (>100 MHz). But this method need wire lead to contact each ring separately, so it is hard to keep every annular ring complete. And the instrument accuracy requirements are quite strict. Therefore, based on recent progress on laser cutting, a high frequency self-focusing piezoelectric transducer using laser cutting technique is developed, which engraved the piezoelectric ceramic into annular rings to form Fresnel half-wave-band sources.

Statement of Contribution/Methods

Based on the concept of constructive interference of acoustic waves, the active layer of self-focusing transducer was designed just as Fig. 1(a) showed. It consists of numerous piezoelectric rings, which were Fresnel half-wave pattern on the top view, and their radius were special designed.

The piezoelectric rings will be fabricated by a UV laser cutting system with 50 µm beam width. Firstly, a piezoelectric single crystal PMN-PT was engraved by laser into annular rings with 100 µm thickness, and then filled with epoxy. After curing, the composite will be lapped to the thickness designed, and the Au electrodes will be sputtering on the top and bottom surface.

Results/Discussion

A particular focusing transducer with 50 MHz center frequency and 3 mm focal length has been designed. When the transducer is excited with a burst of RF signal, the acoustic field was distributed as Fig 1.(b) showed. It is clear that the generated acoustic waves converged to the focal point, and then diffused after the focal point. The focal point is extremely small (~50 µm@-6dB in Fig 1.(c)), and its intensity is much stronger than others, which means high lateral resolution and contrast image can be achieved.

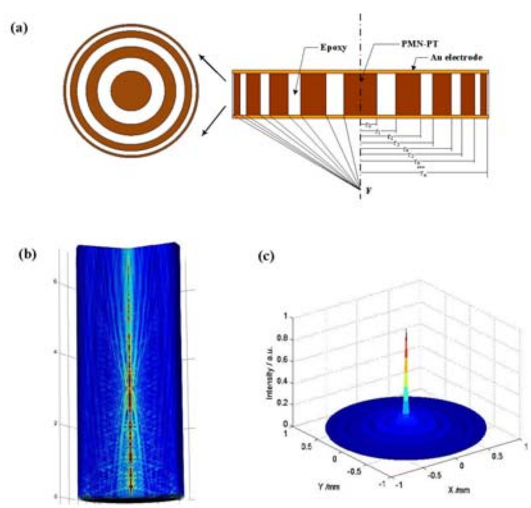

Fig. 1 The designed self-focusing transducer with 50 MHz center frequency and 3 mm focal length: (a)Schematic of laser-cut Fresnel half-wave-band active layer of self-focusing Transducer, (b) Simulation results of the acoustic field distribution,(c) Acoustic intensity distribution on the focal plane

P5-B1-2

High Frequency Array Transducer for Intravascular Ultrasound

Min Su[1], Lining Zhang[1], Zhiqiang Zhang[1], Hairong Zheng[1], **Weibao Qiu[1]**; *[1]Paul C. Lauterbur Research Center for Biomedical Imaging, Shenzhen Institutes of Advanced Technology, Chinese Academy of Sciences, Shenzhen, Guangdong, China, People's Republic of*

Background, Motivation and Objective

Atherosclerotic plaque rupture will cause acute coronary syndrome and sudden cardiac death, so that the diagnosis of this kind disease is crucial in clinical studies. Intravascular ultrasound (IVUS) imaging is an effective means of detecting atherosclerotic plaques. In general, two kinds of transducers were used for IVUS imaging, i.e. single-element transducer and radial array transducer. It should be noted that imaging resolution of single-element transducer was reduced in the deep area. In this study, we propose a high frequency array transducer targeted for IVUS applications.

Statement of Contribution/Methods

In this work, a high frequency array transducer was designed and fabricated for IVUS applications. An Ag-epoxy matching layer was cast onto the front of PZT-5H and a flexible printed circuit was stuck onto the back of the wafer by conductive adhesive. On the other side of the flexible printed circuit was stuck a backing layer which made of a mixture of epoxy and tungsten powder. Then the wafers except backing layer were diced into small elements and epoxy was used to fill into the kerfs between elements (as shown in Figure A). After that, an Au electrode was plated on the surface of matching layer (as shown in Figure B). The schematic of the transducer is shown in Figure (C).

Results/Discussion

The impedance characteristic of the transducer was tested by an impedance analyzer (WK6500B, Wayne Kerr, Inc., UK). The impedance (blue line) and phase (red line) of a typical element of the array were shown in the Figure D, demonstrating a resonant frequency of 24.5 MHz and impedance 136.7 ohm. The pulse echo response was acquired using a glass reflector in a tank of deionized water. A 5073 pulser (Olympus) was used to excite array elements individually, and the receiver on the same unit was used to amplify the echoes before displaying them on a digital oscilloscope (Tektronix DPO 4104). The pulse-echo waveform (blue line) and spectrum (red line) of a typical element of the array were shown in Figure E, presenting a center frequency of 23.9 MHz and a -6dB bandwidth of 55.8%. This type of transducer could be applied for IVUS imaging and therapy applications.

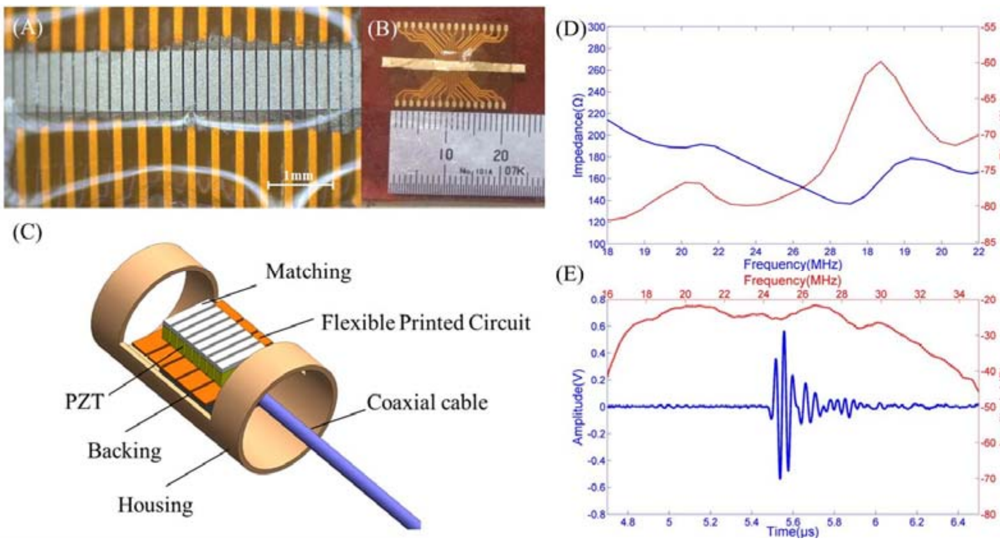

P5-B1-3

Intravascular Ultrasound (IVUS) Imaging Reaching 100 MHz

Xiang Li[1,2], Qifa Zhou[2], K. Kirk Shung[2], Jian Yuan[1]; [1]*Acoustic Life Science Co.,Ltd., Shanghai, China, People's Republic of,* [2]*Biomedical Engineering, University of Southern California, Los Angeles, CA, USA*

Background, Motivation and Objective

Clinically used Intravascular Ultrasound (IVUS) imaging majorly operates in the 20~40MHz range, providing resolution on the order of 100μm. Recent reports showed the potential of higher frequency (60-80MHz) of IVUS improving resolution to the level of 30-60μm, but still inferior to the resolution of OCT (10μm). Whether increasing the working frequency a step further could make IVUS comparable to OCT? What are the challenges we have to face and what are the pros and cons when driving IVUS on extreme high frequency? We have no clear answer yet. In this research, we report a few preliminary results on IVUS imaging closed to 100MHz, including the fabrication of 95MHz IVUS transducer and *ex vivo* imaging test.

Statement of Contribution/Methods

PMN-PT free-standing thick film was fabricated using a modified precursor coating approach and applied as the active material in making ultra-high frequency IVUS transducers. One matching layer was coated to the transducers. Properties of the piezo-film and IVUS transducers were studied and *ex vivo* tests were conducted on human coronary artery specimens.

Results/Discussion

k*t* of PMN-PT film was measured to be 0.46, which was lower than that of bulk PMN-PT single crystal material as expected. Center frequency and bandwidth were 95MHz and 35%. Axial resolutions were determined to be around 20 µm. *Ex vivo* IVUS image acquired on coronary artery is shown in Fig.1(A), which displays superior clarity in differentiating layered structures and plaque cap. RF data was acquired and analyzed in Fig.1(B) showing its spectrum covers 100MHz at -6dB, in agreement with the transducer's impulse response.

PMN-PT free-standing film technology simplified the process of preparation of very thin layers of piezoelectric material compared to lapping from a bulk crystal. The film showed satisfied quality and IVUS transducers made from it was able to generate images with extreme fine speckles. Resolution at 100MHz range was closed to that of OCT. Penetration depth observed in blood free condition could achieve 1~2 mm, which may be further improved by implementing TGC or coded excitation. Blood cells might cause significant scattering and attenuation on such high frequency ultrasound, which needs further investigation. A comparison of 100MHz IVUS and OCT imaging on a controlled condition is necessary to give more detailed information of the benefits of each modality.

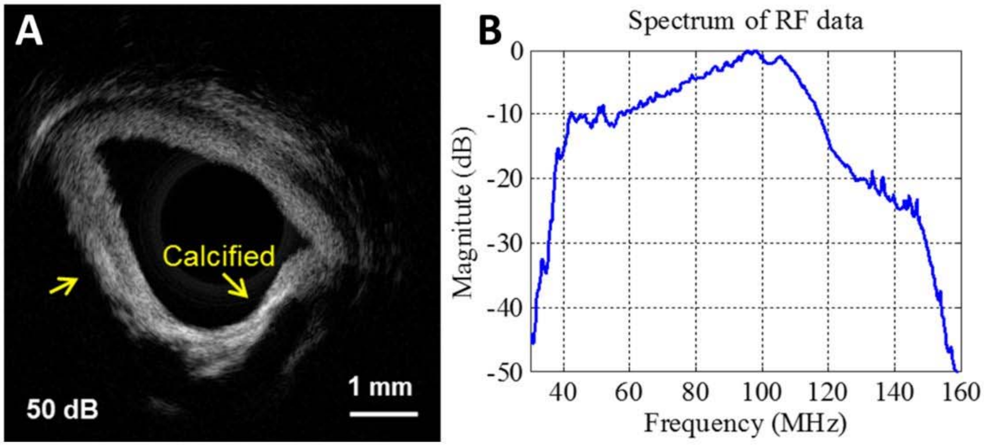

Fig. 1. Ultra-high frequency IVUS imaging of coronary artery (A) and the spectrum of corresponding RF data (B)

P5-B1-4

KNN Single Crystal High Frequency Transducer for Intravascular Photoacoustic Imaging

Benpeng Zhu[1], Wei Wei[2], Xiaofei Yang[3], Yongxiang Li[4], Qifa Zhou[5], K.Kirk Shung[6]; [1]*School of Optical and Electronic Information, Huazhong University of Science and Technology, Wuhan, China, People's Republic of,* [2]*Hubei Cancer Hospital, Wuhan, Hubei, China, People's Republic of,* [3]*School of Optical and Electronic Information, Huazhong University of Science and Technology, Wuhan, Hubei, China, People's Republic of,* [4]*Key Laboratory of Inorganic Functional Materials and Devices, Shanhai, Shanghai, China, People's Republic of,* [5]*University of Southern California, LA, CA, USA,* [6]*Department of Biomedical and Engineering, University of Southern California, LA, CA, USA*

Background, Motivation and Objective

Intravascular photoacoustic (IVPA) imaging, which combines the advantages of high ultrasonic resolution and strong optical absorption contrast, seems to be an alternative method to detect lipid pool and atherosclerotic lesion. A highly sensitive miniaturized ultrasound transducer is required for receiving of intravascular photoacoustic signals. As the core part of the transducer, lead-based piezoelectric materials have been most popular for IVPA applications because of their excellent piezoelectric behavior. However, in view of environmental protection and human safety issues, the use of lead is a problem due to its toxicity. Therefore, it is of urgent need to develop lead-free piezoelectric materials that can be used as intravascular PA signal receivers. The aim of the present study is to demonstrate the feasibility of KNN-based single crystals to be implemented in IVPA applications for the detection of lipid pool and calcification.

Statement of Contribution/Methods

In this study, we present the preparation of KNN-based single crystal with thickness independent high-performance, the fabrication process of a highly sensitive miniaturized high frequency transducer and the ex vivo photoacoustic imaging of the human artery.

Results/Discussion

The KNN-based single crystal exhibits a stable kt value, as high as 0.55, in the frequency/thickness range studied, comparable to the kt values of PMN-PT and PIN-PMN-PT single crystals. The relationship between the frequency constant and sample thickness (t) and suggests that the frequency constant is also a stable parameter. The ultrasound transducer, with a 38 MHz central-frequency and a fractional bandwidth of 56% at -6 dB, which was determined with a pulse echo test, was slightly tilted toward the fiber to achieve a maximized overlap of the optical/acoustic beam. In Fig.1, the PA signal of the calcification area in plaque is around 20 dB higher than the signal of the lipid, revealing that the calcification region in an IVPA image corresponds nicely to that in an IVUS image. These promising results indicate that the KNLN lead free piezoelectric single crystal is competent for the intravascular photoacoustic angiography of atherosclerotic lesion.

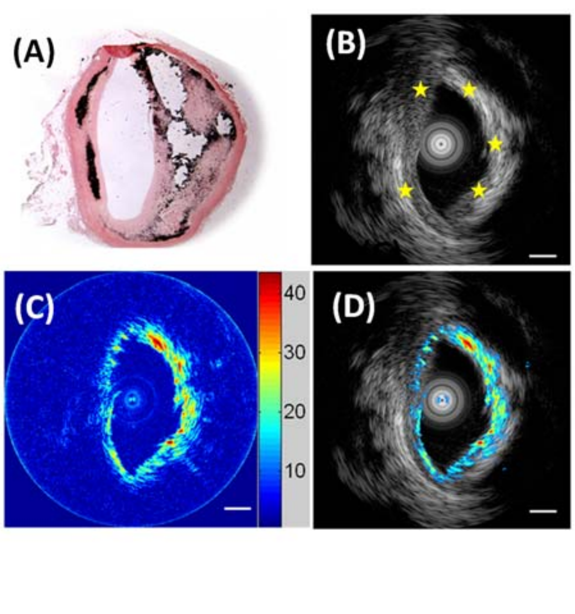

P5-B1-5

A Focused Ultrasound Transducer for Intravascular Ultrasound Application

Min Su[1], Lining Zhang[1], Zhiqiang Zhang[1], Hairong Zheng[1], Weibao Qiu[1]; *[1]Paul C. Lauterbur Research Center for Biomedical Imaging, Shenzhen Institutes of Advanced Technology, Chinese Academy of Sciences, Shenzhen, Guangdong, China, People's Republic of*

Background, Motivation and Objective

Currently, intravascular ultrasound (IVUS) has been frequently used for diagnosing the atherosclerotic plaque due to its good imaging penetration and accurate evaluation. In general, two types of transducers were used for IVUS imaging, i.e. single-element transducer and radial array transducer. It should be noted that imaging resolution of single-element transducer was reduced in the deep area. In this study, we propose a focused ultrasound transducer specifically for intravascular ultrasound applications.

Statement of Contribution/Methods

In this work, a focused single-element ultrasound transducer was designed and fabricated for IVUS applications. Single crystal $Pb(Mg_{1/3}Nb_{2/3})$-$PbTiO_3$ (PMN-PT) was used for the piezoelectric material due to its good performance at electromechanical coupling coefficient (k_t) and piezoelectric coefficient (d_{33}). An Ag-epoxy matching layer was cast on one side of the PMN-PT, and an E-solder baking layer was fabricated on the other side of the material. Then the material was pressed by a 5 mm diameter stainless steel cylinder (as shown in Figure A). After that, the material was diced into small pieces (as shown in Figure B), and this small pieces with coaxial cable were finally placed into a copper housing (as show in Figure C).

Results/Discussion

The impedance characteristic of the transducer was tested by an impedance analyzer (WK6500B, Wayne Kerr, Inc., UK). The impedance (blue line) and phase (red line) of the transducer were shown in the Figure D, demonstrating a resonant frequency of 39.0 MHz and impedance of 40.4 ohm. The pulse echo response was acquired using a glass reflector which was placed at the focal point in a tank of deionized water. A 5073 pulser (Olympus) was used to excite transducer, and the receiver on the same unit was used to amplify the echo before displaying it on a digital oscilloscope (Tektronix DPO 4104). The pulse-echo waveform (blue line) and spectrum (red line) of the transducer were shown in Figure E, presenting a center frequency of 40.3 MHz and a -6dB bandwidth of 70.6%. This type of transducer could be applied for IVUS imaging and therapy applications.

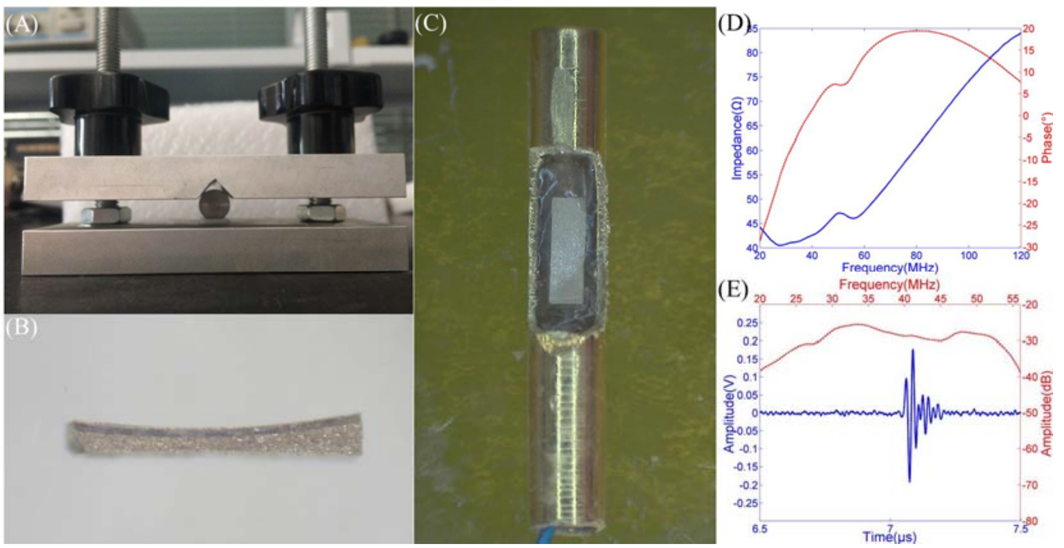

P5-B1-6

Dual-mode Imaging Catheter for Intravascular Ultrasound

Lining Zhang[1,2], Jiehan Hong[1], Min Su[1], Hairong Zheng[1], Weibao Qiu[1]; *[1]Shenzhen Institutes of Advanced Technology, Chinese Academy of Sciences, China, People's Republic of, [2]Northeastern University, China, People's Republic of*

Background, Motivation and Objective

Intravascular ultrasound (IVUS) is a well-established diagnostic method that has been applied frequently for providing high-resolution images of vessel wall and atherosclerotic plaques. Side looking transducer has been employed in a catheter for delineating the structure of vessel wall and lesions. However, it is difficult to get the flow distribution in the vessel by side looking transducer as the ultrasound wave is transmitted perpendicularly to the flow. Doppler ultrasound wire has been proposed and applied to measure the flow information. In this study, we propose a new design of dual mode imaging method by combining side looking transducer together with the forward looking Doppler transducer in one catheter. It could be potentially used for the measurement of both morphology and flow information simultaneously in one catheter.

Statement of Contribution/Methods

Two small size transducers were fabricated using PZT ceramics. The thickness of piezoelectric element is 53 microns and the size is 0.6*0.6 mm. These PZT wafers were coated by sputtering a thin chrome/gold layer. A silver epoxy matching layer made from a mixture of 2-3.5 micron silver particles and Insulcast 502 epoxy is cast onto the negative electrode side. A conductive epoxy (E-SOLDER 3022) then is cast on the wafer as the backing material. Then one element is placed in the front of catheter and the other one is placed in the side of the catheter using insulating epoxy. An electrode sputtered across the silver epoxy matching layer and a needle housing is used to form the ground plane connection. The schematic of the transducer is shown in Figure (a).

Results/Discussion

The resonant frequency and the electrical impedance of the forward looking and side looking transducer are measured by a precise impedance analyzer (WK6500B, Wayne Kerr, Inc., UK). As is shown in the following Figure (b), the resonance frequency of forward looking transducer is 36.7 MHz with the impedance of 40 ohm. The bandwidth is 40.3%. The resonance frequency of side looking transducer is 47.6 MHz with the impedance of 55 ohm, which is shown in Figure (c). The measured bandwidth is 37.2%. This catheter could be applied for measuring the morphology of the vessel wall, as well as the flow speed inside the vessel.

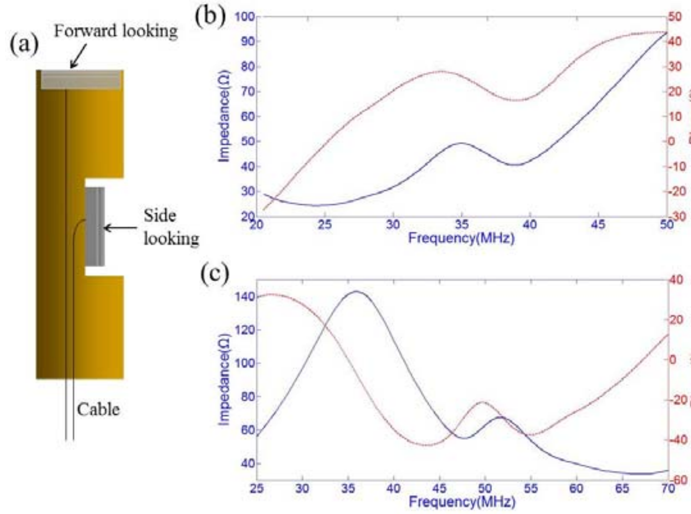

P5-B1-7

High Frequency Single Crystal Ultrasonic Transducers Up to 100 MHz for High Resolution Ophthalmic Imaging Applications

Tianfu Zhang[1,2], Ruimin Chen[1], Zhiqiang Zhang[1], Runze Li[1], Xingui Tang[2], Xueqiao Wang[3], K. Kirk Shung[1], Qifa Zhou[1,4]; [1]*Department of Biomedical Engineering, University of Southern California, Los Angeles, California, USA,* [2]*School of Physics & Optoelectric Engineering, Guangdong University of Technology, Guangzhou, China, People's Republic of,* [3]*Newway Technology, Inc, California, USA,* [4]*Department of Ophthalmology, University of Southern California, Los Angeles, California, USA*

Background, Motivation and Objective

As one of the most important and well established tools, ultrasound imaging provides noninvasive valuable diagnostic information, especially in the form of cross-sectional images of soft tissues. High frequencies are used directly to enable high resolution imaging to be of clinical benefit. As a result, high-frequency ultrasonic transducers with better resolution are needed. The difficulty of a high frequency transducer comes from preparation of a very thin layer of piezoelectric material with piezoelectric properties similar to bulk material.

To date, although there are some reports about high frequency (80 to 100 MHz) ultrasonic transducers for eye imaging applications, but the focal length of those transducers are not enough and the images are not clear enough. In this work, high frequency transducers were prepared and used for eye imaging, high resolution of pig eye imaging were obtained.

Statement of Contribution/Methods

In this work, 36° Y cut Lithium Niobate single crystal was selected due to its good electromechanical coupling (kt ~ 49%), low dielectric permittivity (εs ~ 39), high longitudinal wave velocity (~7340 m/s) and high Curie temperature (~1150 °C). Specific design parameters of the transducers, including the aperture size and proper thickness of acoustic stacks were optimized through a Krimboltz, Leedom, and Mattaei (KLM)14 model-based simulation software PiezoCAD (Sonic Concepts, Woodinville, WA).

Results/Discussion

Figure 1a showed the profile of the transducer structure, prepared transducers with different focal length were shown in Fig.1b, Figs.1c-d showed pig eye imaging obtained by 80 MHz transducer with focal length of 6 mm. Images of pig eye displayed high resolution, good signal-to-noise ratio, clearer structure of cornea, lens surface and iris. In addition, in-vivo imaging for glaucoma disease will be presented.

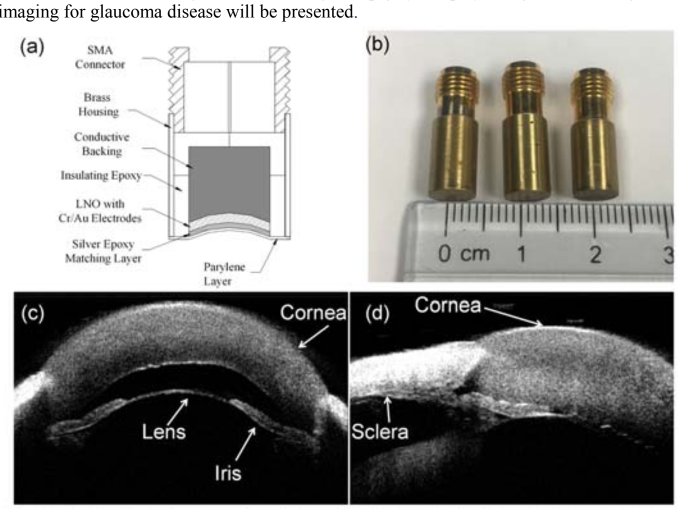

Figure 1. (a) Profile of the transducer structure, (b) Prepared transducers with different focal length, (c) and (d) Pig eye imaging obtained by 80 MHz transducer with focal length of 6 mm.

P5-B1-8

Chirp Coded Ultrasonic Pulses used for Scanning Acoustic Microscopy

Anowarul Habib[1], Frank Melandsø[1]; [1]*Department of Physics and Technology, UiT The Arctic University of Norway, Tromsø, Norway*

Background, Motivation and Objective

Ferroelectric polymers like polyvinylidenefluoride (PVDF) and its copolymer with trifluoroethylene [P(VDF-TrFE)] are widely used in sensor and transducer applications. Good acoustic match to many materials (e.g. water, polymers, and human tissue) and high chemical stability make these materials suitable for ultrasonic applications, especially in the high frequency end (20 MHz-1 GHz). The current work focuses on high frequency P(VDF-TrFE) transducers in combination with chirped pulse coding for scanning acoustic microscopy (SAM). SAM systems typically apply short high voltage square pulses to excite the transducer. The aim of this work has therefore been to investigate experimentally how longer chirped pulses can be used to improve the image quality in SAM systems. Chirped signals are commonly used e.g., in sonar, radar, and optical systems, and also ultrasonic systems involving standard frequencies.

Statement of Contribution/Methods

Several in-house transducer prototypes were built for the investigation. These prototypes illustrated in Fig. 1 (a) were then driven by a chirped and amplitude modulated pulse, and used to image several test objects. Later on, the transducers were also excited with a Ricker wavelet, and a square pulse in order to compare image qualities from different pulse forms. The high-frequency ultrasonic fields generated from the various pulse forms (chirp, Ricker, and square) were also measured in an ultrasonic scanning tank and analyzed in terms of acoustic performance and pressure field distributions.

Results/Discussion

Examples of acoustics imaging performed with different pulse forms are shown in Figs. 1 (b) to (d). The resolutions of these images based on the back scattering amplitude from a coin surface, were found to be consistent with the acoustic lobe widths measured by a 75 µm needle hydrophone. Several lengths for the chirped pulse were also tested out in order to optimize SNR and depth resolution. Complementary to the ultrasonic measurements, the ultrasonic field was also computed from a numeric model including both the transducer and the surrounding water layer. The numerical investigation also showed a close match to the experimental findings.

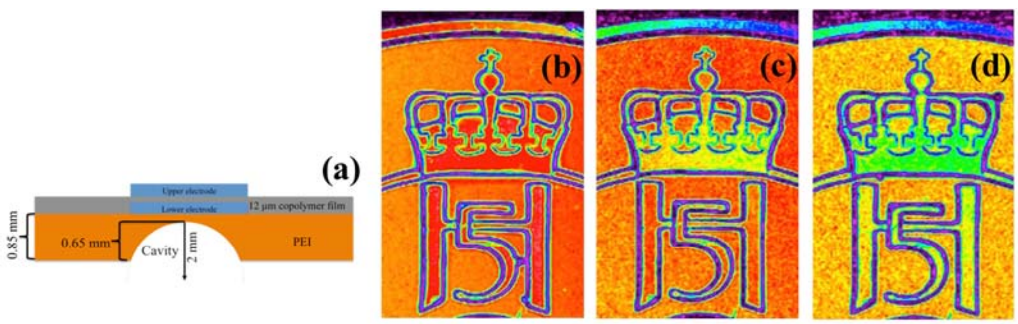

Figure 1: Illustration of the used prototype transducer (a), and acoustic images (b)-(d) of a selected coin area (Norwegian one Krone) used as a test object. The transducer was driven by a chirp signal (b), Ricker wavelet (c), and square pulse (d). The image size was 8.4×4.8 mm² with a 50 µm step size in both directions.

P5-B1-9

Large Aperture, Self-Focused, High-Frequency Ultrasound Transducers for Biomedical Applications

Harold Barquero, Phd. [1], Guillaume Pierre[2]; [1]*R&D Engineer, SONAXIS SA, BESANCON, France,* [2]*CEO, SONAXIS SA, BESANCON, France*

Background, Motivation and Objective

In the recent years, SONAXIS has developed lens-focused ultrasound transducers (LFUTs) with central frequencies greater than 10MHz, and -6dB relative bandwidth larger than 120%. For instance the use of one of these transducers - 78MHz central frequency, 128% relative bandwidth, f/D≈1 - has been reported for biomedical imaging applications [Soliman *et al.*, 2015].

Drawbacks of LFUTs include the attenuation of high-frequency (HF) acoustic waves by the lens material as well as reflexions in the lens. Lensless, self-focused ultrasound transducers (SFUTs) have been proposed as an alternative to LFUTs and have been reported to provide reduced insertion loss compared to the latter [Cannata *et al.*, 2000]. Adequate design of piezocomposite materials (PCMs) make them suitable candidates for biomedical applications, since they can meet requirements in terms of electromechanical coupling coefficient, acoustical impedance, dielectric constant as well as dielectric and mechanical losses [Smith and Auld, 1991]. This study aims at the development and evaluation of SFUTs based on 1-3 PCMs for biomedical applications, as an alternative to LFUTs, with broad bandwidth and high central frequency.

Statement of Contribution/Methods

Prototypes using 1-3 PCMs are currently being designed and manufactured at SONAXIS, with various arrangements and geometries. A variety of designs and manufacturing issues including PCM development, impedance matching, and focusing of the active part, are being addressed to this end.

Characterization of the developed transducers includes the evaluation of their input impedance, central frequency, insertion loss, bandwidth and focusing characteristics, at each step of the manufacturing and with appropriate measurement setups. The comparison with reference, fully-characterized LFUTs (SONAXIS, HFM series) allows to discuss the results and to assess the performance reachable by SFUTs, with respect to their lens-focused counterparts.

Results/Discussion

Preliminary results indicate that broadband, HF SFUTs can be achieved by an appropriate design. Up to now, various prototypes which central frequency lies between 20MHz and 80MHz have been successfully set up and tested. Assessment of their characteristic indicate a relative bandwidth greater than 150% at -20dB. Optimization of the PCM, mechanical setup, as well as the design of the impedance matching and the overall arrangement, is currently carried out to increase this performance.

The first steps of this study confirm the possibility to develop broadband, HF SFUTs as an alternative to LFUTs, and encourage us to push forward with the development of prototypes with optimized design, towards broadband SFUTs operating at high frequencies.

This project has received funding from the European Union's Horizon 2020 research and innovation programme under grant agreement No 687866 (INNODERM).

P5-B2 - MUT Manufacturing

Exhibit Hall

Friday, September 8, 2017, 9:30 am - 4:00 pm

Chair: **Omer Oralkan**
North Carolina State University

P5-B2-1

Optimization of the Efficiency and Reliability of Reverse-Fabricated CMUT Arrays

Alessandro Stuart Savoia[1], Barbara Mauti[1], Alvise Bagolini[2], Luca Maiolo[3], Antonio Minotti[3], Alessandro Pecora[3], Guglielmo Fortunato[3], Pierluigi Bellutti[2], Giosuè Caliano[1]; [1]*Department of Engineering, Roma Tre University, Rome, Italy, Italy,* [2]*Fondazione Bruno Kessler, Trento, Italy,* [3]*Istituto per la Microelettronica e Microsistemi, Consiglio Nazionale delle Ricerche, Rome, Italy*

Background, Motivation and Objective

The electromechanical conversion efficiency and the long-term reliability of Capacitive Micromachined Ultrasonic Transducers (CMUT) are mainly limited by the parasitic capacitance and by charge injection phenomena, which are generated the first, by the portions of the CMUT electrodes used for interconnection, and the second, by the low dielectric strength of the in-cavity passivation materials. Reverse Fabrication Process (RFP) [doi: 10.1088/0960-1317/25/1/015012] is a sacrificial-release low-temperature CMUT technology that employs ultra-low-stress Silicon Nitride (Si_xN_y) dielectrics and Titanium-Aluminum-Titanium metals. In this paper, we investigated the possibility of reducing both the parasitic capacitance, by acting on the electrodes layout, and the charge injection phenomena, by introducing Silicon Oxide (SiO_2) buffer layers between the electrodes and the in-cavity passivation layers.

Statement of Contribution/Methods

The parasitic capacitance reduction was achieved by patterning the metallizations in order to avoid any superposition of the two electrodes outside the CMUT cavity areas [fig.(a)]. The charge injection reduction was obtained by including two high quality SiO_2 thin layers, deposited at very low temperature by electron cyclotron resonance (ECR) PECVD, between the CMUT electrodes and the Si_xN_y passivation layers [fig.(b)]. 256-element, 7.5MHz CMUT arrays were designed and fabricated using both the classical and the modified electrode layouts. Different stacks were investigated by combining various SiO_2 and Si_xN_y film thicknesses, in all cases defined to achieve the same CMUT capacitance and collapse voltage.

Results/Discussion

The electrical impedance of single air-coupled array elements was measured in the 2-20MHz range at different increasing bias voltages up to 160 V. A 32% reduction of the parasitic capacitance, evaluated by fitting the impedance of an accurate CMUT equivalent circuit model with the measured data, was achieved with the modified electrode layout, resulting in a 50% increase of the electromechanical coupling coefficient [fig.(a)]. Finally, the array element capacitance was measured by increasing and successively decreasing the bias voltage in the 0-260V range. The 20nm-thick SiO_2 stack device showed significantly less hysteretic behavior as compared to the conventional device [fig.(b)].

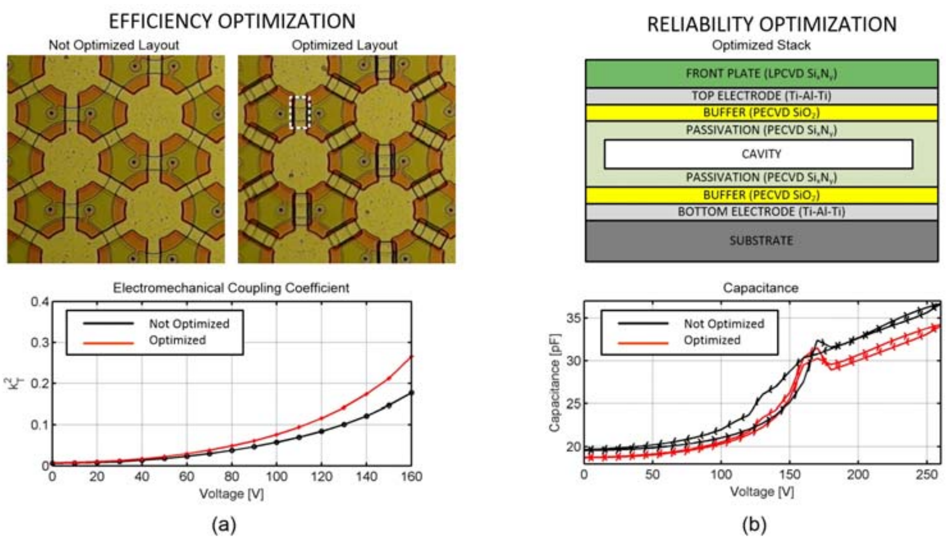

P5-B2-2

Long Term Reliability Test Results of CMUT

Danhua Zhao[1], Costas Simopoulos[1], Steve Zhuang[1]; [1]*Kolo Medical Inc, USA*

Background, Motivation and Objective

The Capacitive Micromachined Ultrasound Transducer (CMUT) technology has been under development for more than 20 years at Universities and industry labs. One of the major limitations for commercial use of CMUT probes has been poor reliability. Kolo Medical Inc. has developed a number of methods to improve reliability of CMUT probes. Kolo performed long term reliability tests to verify the improvements in reliability. This paper presents some of the long term reliability and aging test results.

Statement of Contribution/Methods

The two major reliability problems of CMUT probes are breakdown and charging. High electrical fields are required for the CMUT to meet clinical application requirements. These high fields after long exposures can cause the breakdown of the insulating layers of the CMUT. Charging is a CMUT phenomenon that describes sensitivity degradation caused by the high electric fields present in the CMUT cavity. Typically, an ultrasound probe under normal operating conditions is used between 2 to 5 years. It is impractical to conduct reliability tests for such a long time. Therefore, the test time must be significantly shortened by at least one order of magnitude in order to achieve a reasonable probe development cycle. A CMUT probe requires two voltages to work: the DC voltage and the AC voltage. Since both voltages can cause breakdown and charging, long term tests were performed with DC only and with both voltages. Kolo has developed methods using theoretical models to reduce the test time.

Results/Discussion

A large amount of test data have been collected for both the DC and the DC+AC test cases. For the DC aging test, the reliability of a CMUT is measured by the number of test hours under normal operating conditions for which no significant degradation is observed. The number of test hours can be replaced by the equivalent number of test hours using the accelerated DC aging test methods. For the DC+AC aging test, the reliability of a CMUT can be measured by either the number of test hours for which no significant degradation is observed or by the number of total transmit cycle counts under the accelerated AC aging test. Fig. 1 shows a typical aging test result. The data was generated with a 30 MHz CMUT probe. The figure shows that there was no sensitivity degradation after 100 billion transmit cycles. The 100 billion cycles are equivalent to approximately 2 years of typical clinical use.

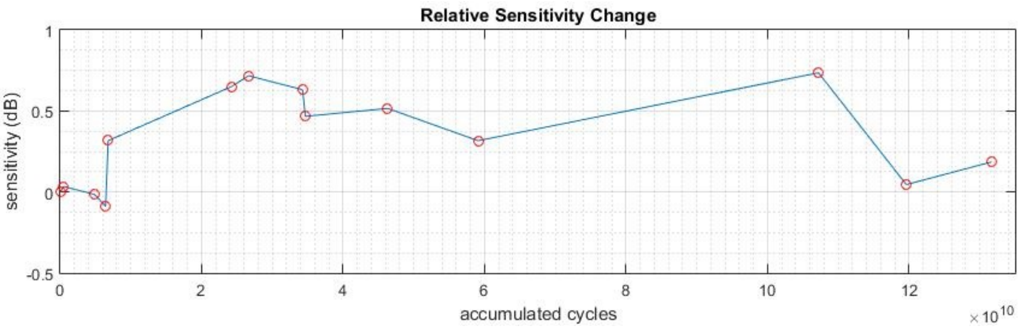

P5-B2-3

Fingerprint Imaging Using Capacitive Micromachined Ultrasonic Transducer Impediography with Glass Waveguide

Yun Sang Kwak[1], Won Young Choi[2], Kwan Kyu Park[1]; [1]*Department of Mechanical Engineering, Hanyang University, Seoul, Korea, Republic of,* [2]*Department of Convergence Mechanical Engineering, Hanyang University, Seoul, Korea, Republic of*

Background, Motivation and Objective

Ultrasonic techniques for fingerprint imaging are emerging as an important alternative technology to the traditional capacitive methods. Recently, a pulse-echo based method using a solid interface layer with a waveguide has been investigated for fingerprint imaging. In addition, an impediography method was previously investigated by measuring the pulse damping of the contact area. Both methods require a complex pulse excitation circuit and short pulse duration. In this work, we present an impediography-based implementation, wherein the fingerprint image was acquired by measuring the device impedance instead of the pulse. By using a pseudo-continuous wave (CW) AC signal, we have performed fingerprint imaging, using a waveguide.

Statement of Contribution/Methods

Our fingerprint sensor is based on a capacitive micromachined ultrasonic transducer (CMUT), with an element size of 168 µm × 168 µm and a 6 MHz center frequency in air. The element is covered by a 500 µm thick glass with a waveguide of a diameter of 200 µm [see schematic in Fig. 1 (a)]. Polydimethylsiloxane (PDMS) was selected as an acoustic medium for the waveguide, with PDMS covering both inside and under the waveguide [refer to Fig. 1 (a)]. To conduct reproducible measurements, a fingerprint phantom was fabricated in the form of a PDMS mold of an actual fingerprint. Another CMUT device without the waveguide was also assembled for comparison. The fingerprint phantom was subsequently scanned by the transducers with a step size of 120 µm. To establish a standing wave inside the waveguide, a pseudo-CW AC signal was applied on the CMUT and the electrical input impedance was subsequently acquired.

Results/Discussion

For the phantom fingerprint in direct contact with the CMUT device, a phase change of 7° was observed for a resonance frequency of 6 MHz. For the CMUT device with a waveguide structure, a lower resonance frequency was accompanied by a smaller phase change of 0.3°. Hence, the direct contact fingerprint image [see Fig. 1 (b)] has a better signal-to-noise ratio than that obtained with the waveguide-based CMUT device. The waveguide-based CMUT device showed confinement of a standing wave and results in an image with an improved resolution [see Fig. 1 (c)]. In summary, in this study, we demonstrate an impediography method with a pseudo-CW AC signal as a viable solution for fingerprint imaging in under-glass applications.

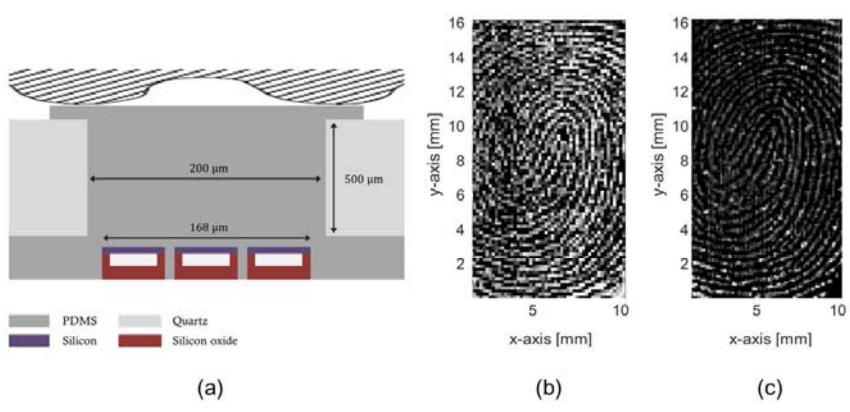

Fig 1. (a) Schematic depicting a cross-sectional view of the waveguide based CMUT finger print imaging system, (b) the direct contact fingerprint image of the phantom obtained with a CMUT device and (c) the fingerprint image of the phantom obtained with the waveguide-based CMUT device.

P5-B2-4

3-D Synthetic Imaging Using 128-Channel 2-D Sparse Capacitive Micromachined Ultrasonic Transducer Array

Won Young Choi[1], Yun Sang Kwak[2], Kwan Kyu Park[2]; [1]*Department of Convergence Mechanical Engineering, Hanyang University, Seoul, Korea, Republic of,* [2]*Department of Mechanical Engineering, Hanyang University, Seoul, Korea, Republic of*

Background, Motivation and Objective

A 2-D array is essential for the construction of a 3-D image. Previous researches have demonstrated how a 3-D ultrasonic image can be constructed by mechanically translating and rotating a 1-D array. For non-mechanical imaging, 2-D dense arrays have been investigated; however, they pose a challenge in practical implementation due to a large number of interconnections. To overcome this problem, we theoretically study a 2-D sparse array with a small number of channels located in a component of the array.

Statement of Contribution/Methods

The 2-D sparse array was implemented by a capacitive micromachined ultrasonic transducer (CMUT). The CMUT was fabricated by a wafer-bonding process with the local oxidation of silicon technique. A CMUT cell is comprised of a silicon plate of radius 24 µm and thickness 1.5 µm with a gap height of 200 nm. Each CMUT element is composed of a 3×3 cell configuration. 128 elements are located on an area of 5.76 mm × 5.76 mm, which is equivalent to the size of a 32 × 32 2-D dense array. The location of each element was optimized by the simulated annealing method.

A 3-D ultrasound image was acquired by the classical synthetic aperture method. A high-voltage transmit AC signal controlled by high voltage analog switches (CPC7601, IXYS Corp., California, USA) was applied. The received signal was controlled by transmit/receive (T/R) switches (TX810, Texas Instruments Inc., Dallas, USA) and pre-amplifiers.

Results/Discussion

The 2-D CMUT array has a center frequency of 3 MHz in oil. The imaging system functions to control the 128 operational elements. From the acquired signal, a volumetric image of 20 mm × 20 mm × 20 mm was constructed. To evaluate the performance of the 3-D imaging system, a point-spread function (PSF) was measured. A thin wire was vertically located on an axis of the array at a distance of 10 mm. Each CMUT element was excited using a 70 V DC and a 7 V AC signal. Preliminary imaging results of a B-mode and C-mode image presents a 3-dB lateral resolution of 1800 µm (3.6 λ) and a 3-dB axial resolution of 200 µm (0.4 λ).

Thus, we have successfully fabricated a 2-D CMUT sparse array for 3-D ultrasound imaging and implemented a 3-D synthetic imaging system. In our presentation, we will discuss the location optimization of the CMUT elements in the sparse array and compare the image quality and the signal-to-noise ratio (SNR) obtained from simulations and measurement.

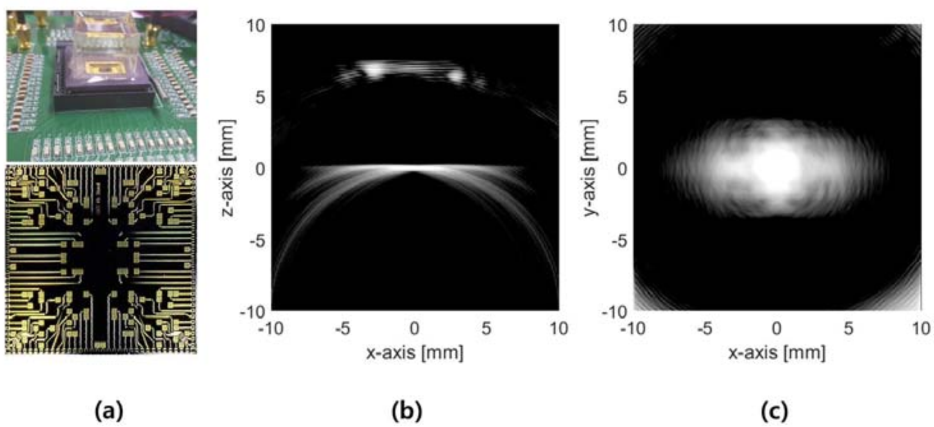

Fig. 1. (a) Photograph of the fabricated sparse CMUT array and synthetic imaging system (b) 20-dB B-mode PSF image (c) 20-dB C-mode PSF image.

P5-B2-5

A Low Temperature Sacrificial Layer Based CMUT Fabrication Process for Improved Reliability

Amirabbas Pirouz[1], F. Levent Degertekin[1,2]; [1]*School of Electrical & Computer Engineering, Georgia Institute of Technology, Atlanta, GA, USA,* [2]*G.W. Woodruff School of Mechanical Engineering, Georgia Institute of Technology, Atlanta, GA, USA*

Background, Motivation and Objective

CMUT efficiency depends on a high electric field over a thin vacuum gap and a dielectric isolation layer. Ideally this high electric field should only exist over the vibrating membrane of the CMUT, but electrical connections between the membranes usually pass over thin dielectric isolation layers (Fig. 1). The resulting high fields on the isolation layer cause charging, dielectric breakdown and reduces CMUT reliability [1, 2]. Although some remedies such as LOCOS regions between the CMUT membranes have been proposed to decouple gap height from isolation layer thickness between membranes, these approaches require high temperatures and thus are not CMOS compatible [3]. In this paper, a simple low temperature solution for reliable sacrificial layer based CMUTs is described.

Statement of Contribution/Methods

The overlap between the top (TE) and bottom electrode (BE) of CMUTs over the thin isolation layer creates charging problems as well as adding parasitic capacitance. The breakdown voltage of the thin isolation layer also limits the maximum voltage applied to CMUTs. In order to mitigate these effects, after etching the sacrificial layer, a lift-off step of a dielectric with a lower relative permittivity (evaporation of SiO_2 with εr of about 3) as compared to the membrane (Si_xN_y with εr of about 6.3) is proposed and implemented (Fig. 1). This simple step does not require an additional mask and the electric field over the TE-BE overlap areas is significantly reduced. This reduces the charging, decouples CMUT sensitivity from the isolation layer thickness, as the lifted off layer is ~2x the gap, and reduces the parasitic capacitance.

Results/Discussion

CMUT arrays suitable for intracardiac imaging in 5-11MHz range are fabricated with the improved process (Fig 2). Parasitic capacitance of the device was reduced by 2pF out of 14pF total capacitance (Fig. 3). Devices fabricated with and without the oxide lift-off step are tested in a water tank to simulate accelerated long-time testing for charging [1]. The hydrophone output as a function of number of 30V pulse cycles applied to the devices indicate that the oxide lift-off device output pressure changes about 5% over 2.5e11 vibration cycles in 72 hours, whereas the comparison device – without oxide - fails after 5e10 cycles, 10 hours, a significant improvement in reliability.

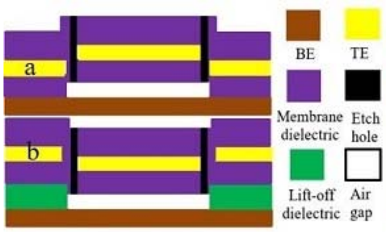

Fig. 1: After depositing BE layer (Cr), and patterning sacrificial layer (Cu), by lifting-off SiO_2 (figure 1.b), the gap height is decoupled from isolation layer (Si_xN_y) thickness in BE-TE(TE is Aluminum) connection region, while in figure 1.a, there is just thin isolation layer in BE-TE connection area.

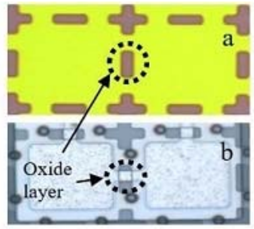

Fig. 2. Optical image of oxide lift-off process, in figure (a), the green parts are the regions where the oxide is lifted-off on top of copper sacrificial layer. Figure (b) is the final CMUT fabricated using the improved method

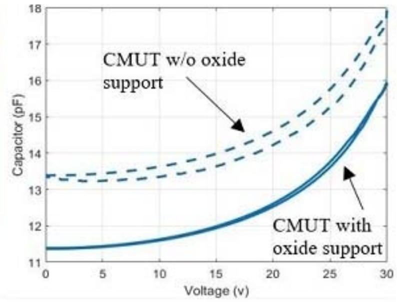

Fig. 3 The C-V curve of the two CMUT array elements which are identical except for the oxide support.

[1] B. Jeong, et al., "Performance and reliability of new CMUT design with improved efficiency" Sens. Actuators, A, Vol 199, pp 325-333, Sep. 2013

[2] S. Machida, et al., "Analysis of the Charging Problem in Capacitive Micro-machined Ultrasonic Transducers", IUS 2008, DOI: 10.1109/ULTSYM.2008.0094

[3] K. K. Park, et al., "Fabricating Capacitive Micromachined Ultrasonic Transducers with Direct Wafer-bonding and LOCOS Technology", MEMS 2008, DOI: 10.1109/MEMSYS.2008.4443662

P5-B2-6

A 3D Packaging Technology for Acoustically Optimized Integration of 2D CMUT Arrays and Front End Circuits

Alessandro Stuart Savoia[1], Barbara Mauti[1], Roberto Bardelli[2], Fabrizio Toia[2], Giulia Matrone[3], Marco Piastra[3], Alessandro Ramalli[4], Fabio Quaglia[2], Giosuè Caliano[1];
[1]*Department of Engineering, Roma Tre University, Rome, Italy, Italy,* [2]*STMicroelectronics, Agrate, Italy,* [3]*Department of Electrical, Computer and Biomedical Engineering, University of Pavia, Pavia, Italy,* [4]*Department of Information Engineering, University of Florence, Florence, Italy*

Background, Motivation and Objective

As compared to piezoelectric technology, MEMS technology employed for Capacitive Micromachined Ultrasonic Transducer (CMUT) fabrication provides increased compatibility with 3D packaging methods, enabling the possible development of advanced transducer-electronics multi-chip modules (MCM) for medical imaging applications. Interconnection of 2D CMUT arrays and analog front end integrated circuits (IC) using die-level packaging methods was demonstrated earlier. However, no effort was devoted to the study and optimization of the acoustic behavior of the resulting MCM. In this paper, we propose an acoustically optimized 3D packaging method for the interconnection of Reverse-Fabricated CMUT [doi: 10.1088/0960-1317/25/1/015012] 2D arrays and front end ICs using a wafer-level compatible process.

Statement of Contribution/Methods

The developed packaging method uses Cu pillars and solder reflow for electrical interconnection, and patterned Benzocyclobutene (BCB) for mechanical bonding [Fig.(a)]. Finite Element Modeling (FEM) was first used to analyze the acoustic behavior of a CMUT supported by a BCB film laying on a silicon substrate. Simulations were carried out with the aim of tuning the BCB film thickness in order to avoid any effect of the film resonant vibration on the acoustic radiation in the CMUT operating frequency band. Dummy CMUTs and ICs, i.e. actual-sized chips provided only with one metal layer and electrical interconnection pads, were then fabricated. The layout of both dummy devices was designed in a way that the pads were positioned following a 256-element spiral 2D array configuration [doi: 10.1109/TUFFC.2015.007035] and interconnected in pairs to form conductive paths accessible from the outside for electrical testing.

Results/Discussion

Dummy CMUT and ASIC wafers were processed targeting a final bonding layer thickness of 10 µm and MCMs were assembled using a chip-to-chip bonding approach [Fig.(d)]. X-ray microscopy and cross section analysis demonstrated successful contact across the entire devices. A dummy probe head was finally assembled by connecting the MCM to a rigid-flex PCB and by etching the dummy CMUT silicon substrate [Fig.(e)]. Electrical continuity measurements were performed successfully before and after silicon etching to monitor the electrical and mechanical stability of the MCM during the entire packaging process.

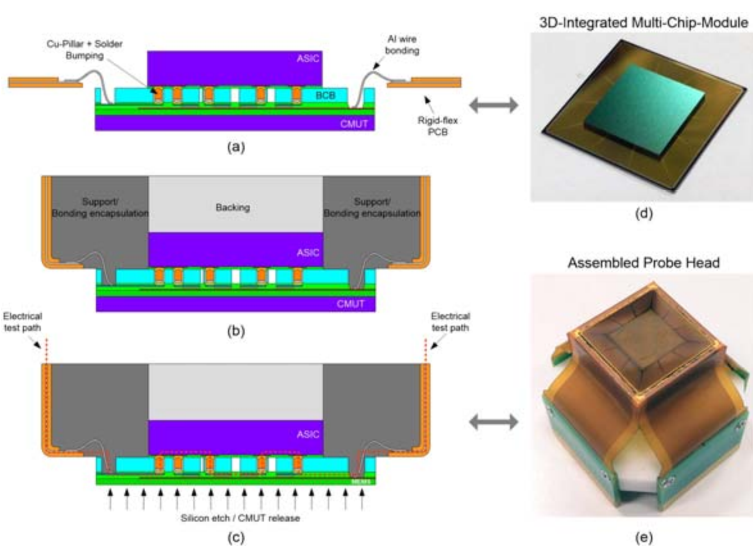

P5-B2-7

Optimization and Characterisation of Bonding of Piezoelectric Transducers using Anisotropic Conductive Adhesive

Gerard Cummins[1], Jun Gao[1], Rachael McPhillips[2], David Watson[1], Sandy Cochran[2], Marc Desmulliez[1]; *[1]Multimodal Sensing and Micromanipulation Group, School of Engineering and Physical Sciences, Heriot Watt University, Edinburgh, United Kingdom, [2]Medical and Industrial Ultrasound Group, School of Engineering, University of Glasgow, Glasgow, United Kingdom*

Background, Motivation and Objective

Microultrasound is of increasing interest in medicine due to the real-time, high-resolution images that can be acquired. The resulting low penetration depth of the image requires the use of multiple transducers laid out as an array and their integration into space-constrained form factors such as needles or capsules to enable minimally invasive access to the site of interest. Miniaturisation of the transducers is possible with modern manufacturing technology but challenges exist in the creation of a reliable interconnection scheme able to produce a series of robust, independent electrical connections between the transducers and external electronics. This paper describes work done to characterise and optimise a low process temperature bonding technology with anisotropic conductive adhesive (ACA) for the production of miniature ultrasound systems with satisfactory yield.

Statement of Contribution/Methods

The development of a reliable integration technology suitable for the production of a 15 MHz ultrasound transducer requires understanding of the underlying physics and the selection of process values that are compatible with dimensional (≤100 µm pitch) and manufacturing (low temperature, low pressure) constraints. The use of a full factorial Design of Experiments (DoE) can identify the sensitivity of the bonding process to alterations in various parameters and the effects of interactions between these parameters on the final result. Three factors were identified to be the most important based on past experience: the ACA stencil mask slit height, the bonding force, and the bonding duration. Each run consisted of eight experiments, and each series was repeated three times to investigate the yield. An initial experiment involved bonding two rigid PCB substrates containing daisy chain electrical test structures with 200 µm track width and 200 µm pitch using magnetically aligned ACA, with the process parameters dictated by the experimental matrix. The daisy chain test structure facilitated measurement of the electrical resistance.

Results/Discussion

Initial analysis of the results shows the contribution of 1st and 2nd order effects on the statistical deviation and average electrical resistance of the bonds, with ACA stencil slit height and bond time being more significant than the bond force. This analysis has identified a set of parameters capable of producing a robust and repeatable bond with the mean electrical resistance along the daisy chain structure measured to be approximately 12Ω. The relevant process parameters are currently being tested to establish PCB connections to piezoelectric arrays with 100 µm element pitch in on-going work.

P5-B2-8

"Pipe Organ" Air-coupled Broad Bandwidth Transducer

Botong Zhu[1], Benjamin Tiller[1], Alan Walker[2], James Windmill[1], Anthony Mulholland[3]; *[1]Centre for Ultrasonic Engineering, University of Strathclyde, Glasgow, United Kingdom, [2]School of Science and Sport, University of the West of Scotland, Glasgow, United Kingdom, [3]Department of Mathematics and Statistics, University of Strathclyde, Glasgow, United Kingdom*

Background, Motivation and Objective

Air-coupled transducers are used to conduct fast non-contact inspections in NDT. Normally, the bandwidth of a conventional transducer can be enhanced, but with a cost to its sensitivity. However, low sensitivity is very disadvantageous in air-coupled NDT. This paper presents a methodology for improving the bandwidth of an air-coupled diaphragm transducer without sensitivity loss by connecting a number of resonating pipes of various length to a cavity in the backplate (see figure 1(a)). The design is inspired by the pipe organ musical instrument, where the resonant frequency (pitch) of each pipe is mainly determined by its length.

Statement of Contribution/Methods

The design, manufacture and experiment are divided into five steps: first, a fast 1D (in space) mathematical model is employed to ascertain the location of resonances and investigate the benefits of an increased number of pipes. Second, a slower but more accurate 3D finite element model provides the optimized parameters of the transducer. Third, a CAD model is built and a commercial stereolithography 3D printer is used to print the "pipe organ" backplate. Fourth, a passive diaphragm is attached onto the cavity/backplate. Finally, a 2D laser vibrometer is used to measure the average velocity of the diaphragm when applying an external sound source in order to estimate the bandwidth.

Results/Discussion

The average velocity of the passive diaphragm in the "pipe-organ" transducer is compared with the standard "cavity-only" transducer. The membrane velocity bandwidth increases with the addition of pipes emanating from the cavity. A common noise floor was defined for both devices as 6dB below the maximum average velocity of the pipe backed device (see figure 1(b)). The bandwidth of this new device was 2.3 times larger than the standard one. Further work is now underway to change the passive diaphragm to an active polyvinylidene fluoride (PVDF) diaphragm. This will allow the bandwidth of the transmission voltage response and the receiving voltage response to be calculated and compared with that of the standard device.

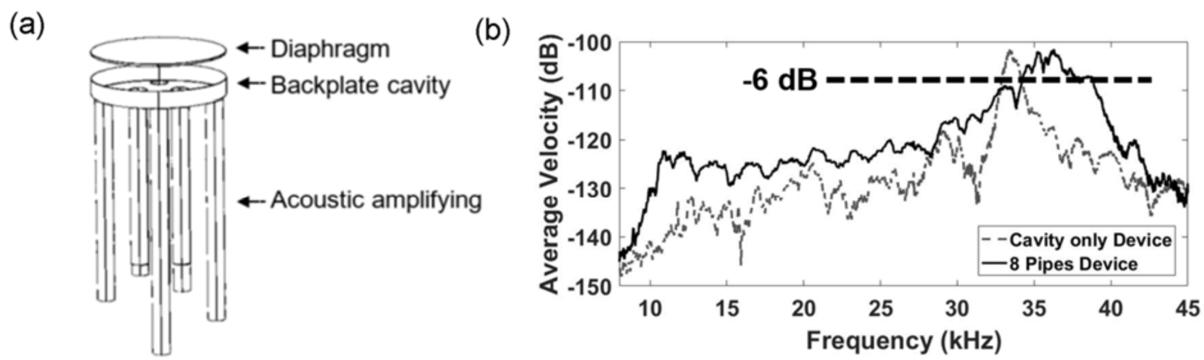

Figure 1. Pipe Organ Transducer. (a) Transducer schematic. (b) Diaphragm passive bandwidth increase.

P5-B2-9

CMUT Isolated Isolation Posts

Benjamin Greenlay[1], Roger Zemp[2]; [1]*University of Alberta, Edmonton, Alberta, Canada,* [2]*University of Alberta, Canada*

Background, Motivation and Objective

A number of novel operating modes could be enabled if CMUTs could effectively operate in collapse or collapse-snapback modes. However, there is little evidence that they can do so without dielectric charging issues modifying the snap-down voltage and ultimately resulting in device failure. Silicon dioxide isolation posts were introduced some time ago and showed promise for mitigating volumetric charging effects, but long-term reliability was not demonstrated and charging effects could not be completely eliminated.

Statement of Contribution/Methods

For this research, wafer bonded CMUTs were fabricated using a modified process utilizing two 5.0 µm device layer SOI wafers, with a resistivity of 0.001-0.005 Ohm-cm. The substrate wafer was thermally oxidized to grow a 340 nm film of silicon dioxide. This film was patterned into isolated isolation post structures using both reactive ion etching and chemical etching processes. This created a CMUT structure with a 300 nm insulation layer and 180 nm silicon dioxide isolated isolation posts, as shown in Fig. 1(a). Each post has a height just below the snap-down distance of the CMUT, so when the membrane collapses there is no longer a large change in displacement as the membrane will just sit on the isolation posts. This larger distance results in a much lower electric field across the isolated isolation posts and combined with the floating silicon segments creates much less charging in these structures.

Results/Discussion

Helium ion microscope images, Fig 1(b), reveal successfully fabricated isolated isolation post structures. The modified wafer bonding approach offered much higher fabrication yields than other previously introduced methods and did not require aligned bonding, thus permitted tighter critical dimensions. Laser doppler vibrometry revealed active device operation. Capacitance-Voltage curves over multiple bias-voltage ramp cycles reveal no charging in the isolated isolation post devices, while charging was apparent in control devices having a contiguous bottom electrode isolation layer. Control devices with only isolation posts exhibited breakdown. Some breakdown was also seen in our isolated isolation post devices and future work should aim to eliminate potential pathways for breakdown.

Fig 1(a)

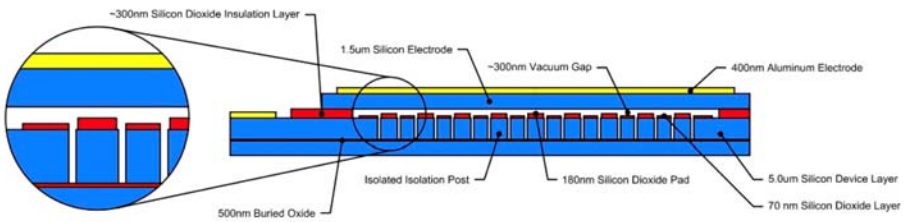

Fig 1(b)

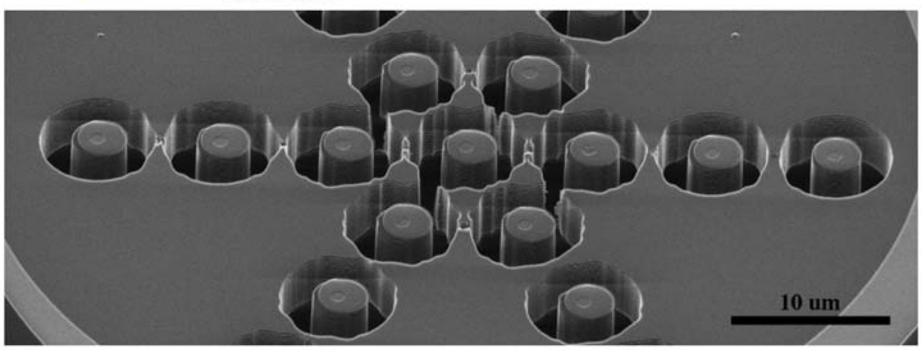

P5-B2-10

BCB Polymer Based Row-Column addressed CMUT

Andreas Havreland[1], Martin Ommen[1], Chantal Silvestre[1], Mathias Engholm[1], Jørgen Jensen[2], Erik Thomsen[1]; [1]*DTU Nanotech, The Technical University of Denmark, Kongens Lyngby, Denmark,* [2]*Center for Fast Ultrasound Imaging, Department of Electrical Engineering, The Technical University of Denmark, Kongens Lyngby, Denmark*

Background, Motivation and Objective

The number of transmit and receive channels needed to perform real-time 3-D ultrasonic imaging can be greatly reduced if row-column (RC) addressed 2-D transducer arrays are used. However, fabricating RC CMUTs have shown to be challenging. The difficulties are typically stress issues related to the high temperature processes and charging effects related to mobile charges in dielectric thin films, overall resulting in low yield and/or a time dependent performance. To overcome these problems a polymer adhesive bonding with Bisbenzocyclobutene (BCB) can be used, and previous work [1] has shown promising results for a single element. This contribution presents a realization of BCB for RC CMUTs with BCB-to-Silicon bonding on a quartz substrate.

Statement of Contribution/Methods

A 62+62 RC 3.0 MHz CMUT is fabricated in a 3 mask process. BCB is patterned in a UV-lithography step and used as bonding material and a spacing layer. A quartz wafer is used as a bottom substrate to lower electrical cross talk between CMUT cells.

The maximum temperature during the fabrication is the curing temperature of BCB (250 °C). Hence, the process contains no high temperature process steps, thus lower thermal stress is expected. The presented design has a patterned bottom electrode surrounded by BCB (see figure A). CMUTs designed this way have minimized parasitic capacitance and electric field inside the spacer region (BCB).

Finally due to the absence of dielectric thin films, charging phenomenons are not expected in this type of CMUT.

Results/Discussion

The presented BCB CMUTs have been electrically characterized by CV measurements, shown in figure B). Hysteresis in a CV curve indicates mobile charges, and the capacitance will depend on the voltage sweep direction. If mobile charges are present the CV curves can potentially be shifted up to several volts depending on the sweep direction. In figure B) the red data corresponds to a sweep going from -100V to 100V where the blue data is the opposite direction. The voltage off-set for the BCB data is identical within the estimation uncertainties. The combination of simple and low temperature fabrication with no charging effects makes BCB a good candidate for solving the issues related to fabrication of RC CMUTs.

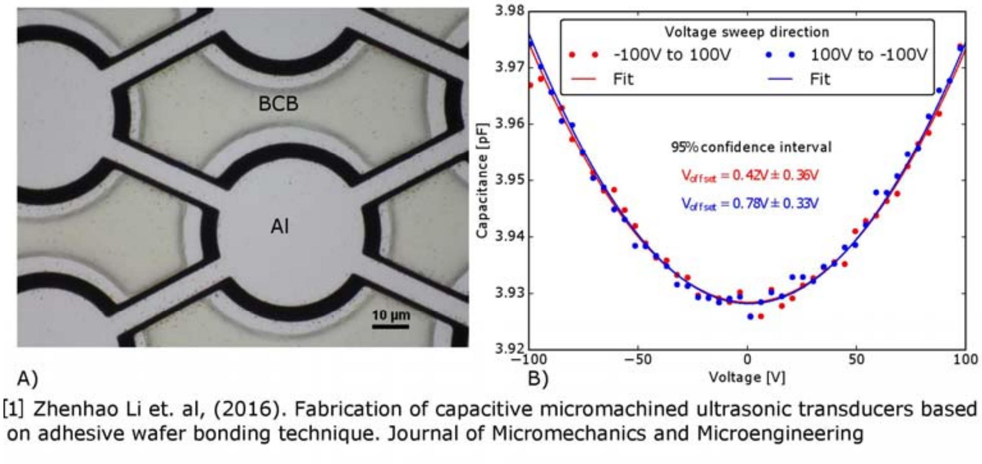

P5-B2-11

A Novel Single-element Dual-frequency Ultrasound Transducer for Image-guided Precise Medicine

Changhe Sun[1,2], Fukang Dai[1,2], Senlin Jiang[2,3], Yufei Liu[1,4]; [1]*Key Laboratory of Optoelectronic Technology & Systems, Ministry of Education, Chongqing University, Chongqing, China, People's Republic of,* [2]*National Key Laboratory of Fundamental Science of Micro/Nano-Device and System Technology, Chongqing University, Chongqing, China, People's Republic of,* [3]*Collaborative Innovation Center for Brain Science, Chongqing University, Chongqing, China, People's Republic of,* [4]*Centre for Intelligent Sensing Technology, Chongqing University, Chongqing, China, People's Republic of*

Background, Motivation and Objective

Single ultrasound device, capable of operating over dual or multiple frequencies, would benefit and expand a series of applications, such as acoustic cavitation enhancement, transdermal drug release, nondestructive testing, ultrasound and photoacoustic imaging. One of the approaches for a dual-frequency operation is to integrate both high- and low-frequency transducer elements in a single chip [1-3]. Meanwhile, another feasible method is for a single element device to be driven by its fundamental and harmonic waves, respectively [4]. However, both of above approaches are hard to well match the acoustic impedance, have poor beam alignment, or rely heavily on nonlinear transient responses of contrast agents.

[1]Kshirsagar, Abhijeet, et al. Multi-frequency CMUT arrays for imaging-therapy applications. (2013):1991-1993.

[2]Martin, K. Heath, et al. Dual-Frequency Piezoelectric Transducers for Contrast Enhanced Ultrasound Imaging. Sensors 14.11 (2014):20825-20842.

[3]Manh, Tung, et al. Dual frequency hybrid ultrasonic transducers - design and simulations. IEEE International Ultrasonics Symposium, 2016:1-4.

[4]Liu, H. L., and C. M. Hsieh. Single-transducer dual-frequency ultrasound generation to enhance acoustic cavitation. Ultrasonics Sonochemistry16.3 (2009):431-438.

Statement of Contribution/Methods

In this paper, a novel single-element dual-frequency ultrasound transducer (DFUT) has been designed and simulated prior to fabrication. The single-element DFUT has been constructed based on the integration of both high-frequency Piezoelectric Micromachined Ultrasonic Transducer (PMUT) and low-frequency Capacitive Micromachined Ultrasonic Transducer (CMUT) in a single transducer element. The schematic structure of the DFUT is shown in Fig. 1(a), consisting of PMUT (centre small piezoelectric membrane) and CMUT (large area membrane) structures. Both numerical modelling and the finite element simulation have been used for optimizing the dimensions of the DFUT.

Results/Discussion

Offering outputs at both low-frequency at 4.1MHz and high-frequency at 20.1MHz (Fig.1(b)), the DFUTs could not only act at treatment and/or imaging modes, but also combined the advantages of high-resolution (<200µm) and a wider working distance (>10cm), which may significantly inspire the imaging-guided precise medical treatment applications.

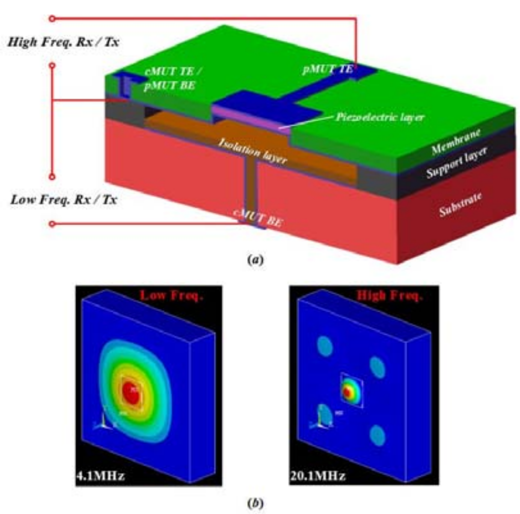

1H - MBE: Cell Dynamics, Microbubbles, and Sonoporation

Regency Ballroom

Saturday, September 9, 2017, 8:00 am - 9:30 am

Chair: **Alfred Yu**
University of Waterloo

1H-1

8:00 am **A High-Speed Microscopic System for Observation of Bubble-Cell Interaction from A Lateral Direction**

Akane Isono[1], Nobuki Kudo[1]; [1]*Graduate School of Information Science and Technology, Hokkaido University, Sapporo, Hokkaido, Japan*

Background, Motivation and Objective

It is widely accepted that cell membrane rupture induced by bubbles oscillating beside the cells is a major mechanism of sonoporation; however, elucidation of bubble dynamics by high-speed observation is still important because the behavior is highly dependent on their surrounding conditions. In this study, a new observation chamber was developed. The observation chamber allows observation of bubble-cell interaction from a lateral direction without obstruction of the view by the oscillating bubbles themselves. Dynamics of bubbles beside cells cultured on a soft scaffold was investigated.

Statement of Contribution/Methods

Figure 1a shows a cross-sectional view of the observation chamber. A pair of small mirrors with a 45-degree light-reflecting surface (Chrovit, Technical, Japan) was added to a conventional observation chamber. Mirror #1 was used to illuminate bubbles and cells from the lateral direction, and mirror #2 was used to incident the lateral image on an objective lens. Cells cultured on an acrylamide gel of 1.4±0.5 kPa in Young's modulus and lipid-shelled bubbles of several microns in resting diameter were used for observation. A single-shot ultrasound pulse of 1 MHz in center frequency and 0.8 MPa in peak-negative pressure was irradiated, and 256 frames were taken at 10 Mfps using a high-speed camera with a CMOS burst image sensor (HPV-X2, Shimadzu, Japan).

Results/Discussion

Figure 1b shows a cell with attached bubbles before insonation, indicating that the camera has sufficient image contrast resolution for visualizing details of almost transparent cells even using bright-field microscopy. Lateral observation showed that bubbles beside a soft scaffold undergo translational movement in a direction separating from the scaffold, whereas bubbles beside a rigid scaffold remain on the scaffold surface (data not shown). **Figures 1c and 1d** show frames taken during and after insonation. Membrane deformation was observed on the left side of the cell (Fig. 1d), suggesting that the bubble oscillating above that location induced damage (Fig. 1c). Removal of a pseudopod was observed on the other side (Fig. 1d), indicating that separation of the bubble adhered to the cell (Fig. 1c) caused the removal. Observation from a lateral direction is important, especially for elucidating the mechanism of *in vivo* sonoporation.

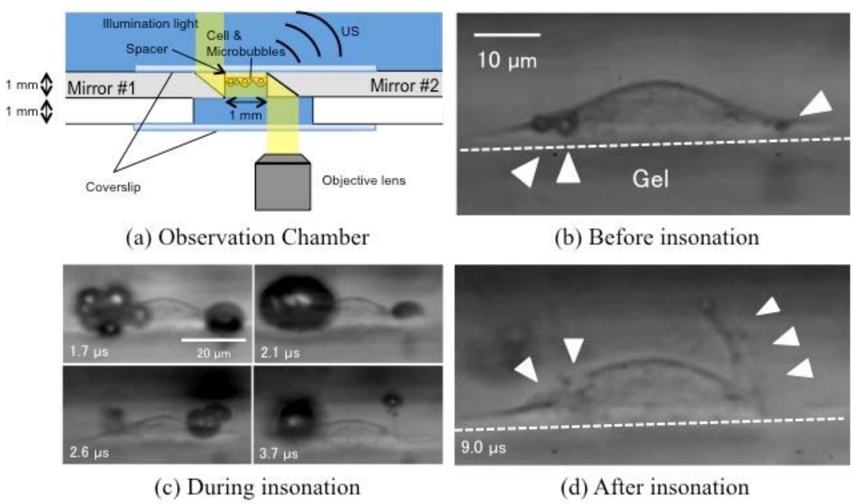

Fig. 1. High-speed Observation from a lateral direction

1H-2

8:15 am **Acoustic-Transfection for Gene Editing Using High Frequency Ultrasound**

Sangpil Yoon[1], Pengzhi Wang[2], Qin Peng[2], Yingxiao Wang[2], K. Kirk Shung[1]; [1]*Department of Biomedical Engineering, University of Southern California, USA,* [2]*Department of Bioengineering, University of California, San Diego, La Jolla, CA, USA*

Background, Motivation and Objective

Controlling cell functions for drug development and therapeutic purposes has been an important method in clinic to treat critical diseases such as cancer and neurodegenerative diseases. Modulation of cancer cells and finding specific mutations in cancer are methods to investigate mechanism of outbreak of cancer. The advancement in molecular biology introduced tools to precisely edit genome of cells. Any molecules spanning from small molecules to extremely large proteins need to be delivered into target cells to express designated gene expression. High frequency ultrasound over 150 MHz can focus its acoustic energy within very confined area less than 10 µm. Here, we introduce a technique to deliver macromolecules into cells using high frequency ultrasound by disrupting cell lipid bilayer without contrast agent such as microbubble. The main contribution of this technique, acoustic-transfection, is that no microbubble is used for the intracellular delivery, which provides much simpler protocol, direct readout from input parameters (Figure 1A), and safe intracellular delivery.

Statement of Contribution/Methods

High frequency ultrasonic transducer was developed using lithium niobate bulk material. The transducer has 1 mm aperture with fnumber of 1. The aperture was placed at the tip of 1.6 mm needle. The center frequency and axial and lateral resolutions were measured to be 150 MHz and 9 µm and 10 µm, respectively. The developed high frequency ultrasonic transducer was attached to a 3D axis stage to precisely control the location of the transducer to target a single-cell. A single-cell was monitored and imaged with a fluorescence microscope. A CRISPR-Cas9 system was cloned to target fibrous actin (F-actin) with TagRFP marker. Three DNA plasmids (Guide RNA, Cas9 nuclease, and donor repair template) were simultaneously delivered by acoustic-transfection. A single-cell was imaged after 36 hours after acoustic-transfection to observe gene expression due to gene editing by CRISPR-Cas9.

Results/Discussion

CRISPR-Cas9 system was successfully delivered by acoustic-transfection. Delivered CRISPR-Cas9 system by acoustic-transfection edited gene of interests at AAVS1 locus by targeting F-actin and expressed TagRFP fluorescence as shown in Figure 1B.

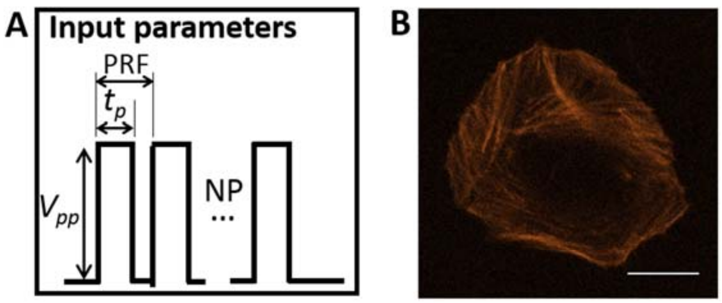

Figure 1. (A) Electrical input signal was generated by commercial electronics to drive developed high frequency ultrasonic transducers. Input parameters were peak-to-peak voltage, *Vpp*, pulse duration, *tp*, pulse repetition frequency, PRF, and number of pulses, NP. (B) CRISPR-Cas9 system was delivered into a HeLa cell by acoustic-transfection. CRISPR-Cas9 targeted F-actin with fluorescence marker TagRFP. Images were taken 36 hours after acoustic-transfection. (Scale bar, 20 µm)

1H-3

8:30 am Insight into the Plasma Membrane Resealing and Calcium Signaling Dynamics Of Sonoporation

Brandon Helfield[1], Xucai Chen[1], Simon Watkins[2], Flordeliza Villanueva[1]; [1]*Center for Ultrasound Molecular Imaging and Therapeutics, University of Pittsburgh, Pittsburgh, Pennsylvania, USA,* [2]*Department of Cell Biology, University of Pittsburgh, Pittsburgh, PA, USA*

Background, Motivation and Objective

Ultrasound (US) and microbubble (MB) treatment has been shown to be a promising approach for localized, non-viral gene delivery. The attributes of MB-target cell interactions that facilitate payload delivery across cell membranes and into extravascular cells, and hence strategies to optimize this platform, remain poorly understood. The objective of this work is to gain insight into the extent of sonoporation by assessing cell membrane dynamics and Ca2+ signaling, both known factors in cell perforation repair, and the role of gap junctional communication (GPC).

Statement of Contribution/Methods

Live-cell confocal microscopy was used to assess the cellular biophysics of sonoporation up to 30 min post-US. Phospholipid MBs adjacent to a cultured endothelial cell (HUVEC) monolayer at 37°C were exposed to a single US pulse (n=39; 1 MHz; 8 µs; 0.1-0.5 MPa) in the presence of propidium iodide (PI), used as a sonoporation marker. Cells were pre-loaded with a Ca2+ indicator dye and their plasma membranes fluorescently labeled. To further examine Ca2+ signaling, a subset of cells were pre-treated with a gap junction blocker (CBX).

Results/Discussion

An individual MB exposed to a single pulse can generate a plasma membrane pore through both sides of the cell that re-seals out-of-plane and initiates Ca2+ influx (Fig. 1). Within sonoporated cells, Ca2+ entry metrics, including the rate of influx and maximum Ca2+, increased linearly with PI uptake ($p<0.0005$). Ca2+ signaling was observed in adjacent, non-sonoporated cells, with time delays (relative to the sonoporated cell) increasing with pore-cell distance ($r=0.71$; $p<0.0001$). The relationship between Ca2+ dynamics PI uptake was amplified with CBX, resulting in ~3-4-fold relative increases in all metrics ($p<0.001$), while Ca2+ entry within adjacent cells was attenuated, both in cell number (86% to 25%, $p<0.0001$) and relative Ca2+ magnitude (0.72 to 0.55, $p=0.007$).

US+MB treatment induces membrane perforations that repair via apical-to-basal membrane resealing, occurring over minutes, and initiates Ca2+ influx in a manner directly related to the extent of sonoporation. While only perforating cells in contact with MBs, the sphere of influence of sonoporation extends to adjacent cells through GPC, suggesting an avenue by which Ca2+, and potentially other messengers, play a role in the remote effects of intravascular sonoporation.

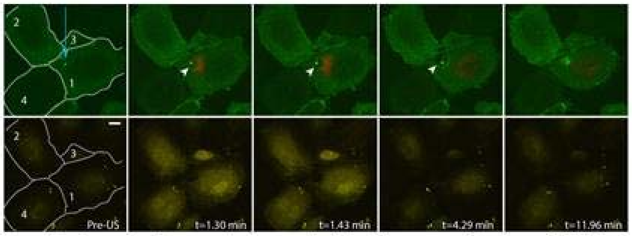

Figure 1: Sonoporation creates a pore in the plasma membrane and initiates Ca^{2+} signaling within perforated and non-perforated, neighboring HUVECs. Maximum intensity projections of live-cell sonoporation, showing (green) plasma membrane, (red) PI and (yellow) intracellular Ca^{2+}. An individual microbubble (blue arrow) adjacent to cell 1 generates a membrane pore (white arrowhead), corresponding with PI entry. Calcium transients are observed in both sonoporated and non-sonoporated cells. US exposure: Peak-pressure of 0.2 MPa, R_0=3.5 µm. Scale bar is 20µm.

1H-4

8:45 am **In Vivo Bioeffects from Phase Change and Microbubble Contrast Agents in the Rodent Kidney: Short Term and Long-Term Effects after Excitation with a Range of Mechanical Indices**

A. Gloria Nyankima[1], Rachel Cianciolo[2], Sandeep K. Kasoji[1], Juan D. Rojas[1], Kennita Johnson[1], Emily H. Chang[3], Paul A. Dayton[1]; [1]*Biomedical Engineering, University of North Carolina at Chapel Hill, Chapel Hill, North Carolina, USA,* [2]*Veterinary Biosciences, The Ohio State University, Columbus, Ohio, USA,* [3]*UNC Kidney Center and Division of Nephrology & Hypertension, University of North Carolina at Chapel Hill, Chapel Hill, North Carolina, USA*

Background, Motivation and Objective

Both microbubble (MB) and phase-change nanodroplet (ND) contrast technology has the potential to enhance ultrasound imaging. However, prior studies have indicated the potential of hemorrhagic bioeffects immediately after sonicating contrast-infused tissue with the low-frequency, high amplitude acoustic energy. To date, little has been reported for NDs or regarding long-term bioeffects of either agent. In this study, we performed short-term experiments to look for bioeffects from MB destruction and ND activation events. We also extended our examination to two weeks post-sonication to explore recovery from cavitation induced bioeffects.

Statement of Contribution/Methods

We explored potential kidney-related bioeffects induced by contrast-enhanced ultrasound imaging in the kidneys of female Fischer rats. For MBs, a clinical system was used with a 4C1 curvilinear array transducer driven at 3MHz. Kidneys were exposed to short pulses with mechanical indices (MIs) of 1.9 or 1.0. For ND contrast studies, activation pulses were transmitted with a research ultrasound system using an L11-5 linear array transducer driven at 5MHz. Activation was performed using MIs ranging from 0.81 to 1.9. For MB and ND studies, the entire kidney volume was imaged by mechanically stepping the transducer with a motion stage. Kidney bioeffects were assessed 24-hours and two-weeks after imaging. Renal injury was analyzed via histopathology and clinically-used serum biomarkers (e.g. creatinine and blood urea nitrogen levels).

Results/Discussion

For moderate-high transmitted pressures and less (MI< 1.4), we observed no statistically significant indications of hemorrhage for MBs or NDs (Table 1). Furthermore, for those parameters that caused hemorrhage in the kidney 24-hours post-imaging (higher MIs of 1.9), we did not observe indications of prior injury two weeks later, suggesting that healing mechanisms resolved any acute effects. To our knowledge this is the first report of long-term observations from NDs and MBs.

Contrast Agent	Filling Gas	Short-term (24 hours)			Long-term (2 weeks)	
		MI<0.9	MI=0.9-1.4	MI=1.4-1.9	MI=0.9-1.4	MI=1.4-1.9
MB	C_3F_8		O	X	O	O
ND	1:1 C_3F_8-C_4F_{10}		O	X		
	C_3F_8	O		X		O
$MI = \frac{PNP_{der}}{\sqrt{f_c}}$ PNP$_{der}$-derated peak negative pressure; f_c-center frequency	X= Indications of hemorrhage in histology; O= No indications of hemorrhage					
	MB= microbubbles; ND= nanodroplets					

1H-5

9:00 am **Focused Ultrasound Setup for the Study of Acoustic Radiation Force Induced Biological Effects in Cells**

Sri Nivas Chandrasekaran[1], Sverre Holm[1], Fabrice Prieur[1]; [1]*Department of Informatics, University of Oslo, Oslo, Norway*

Background, Motivation and Objective

Selective application of shear forces on cells triggers stimulatory biological effects resulting in the manipulation of the cellular mechano-environment and the alteration of cell behavior. The acoustic radiation force (ARF) induced by focused ultrasound (FUS) can generate shear forces as in shear wave elastography imaging. The commonly used setups for *in-vitro* studies of ultrasound-induced mechanotransduction include well plates in which the cells are exposed to unwanted effects like standing waves from the plastic-fluid interface reflections. These well plates lead to additional transmission losses. To effectively study the biological responses in cells due to ARF induced shear stress; an *in-vitro* FUS cell stimulation setup which eliminates the aforementioned effects is described.

Statement of Contribution/Methods

The cell stimulation setup is made of an aluminum box of dimension 194x154x144 mm with a lid providing the footprint for accurate and reproducible positioning of four ATL L7-4 ultrasound probes. The setup can withstand the high temperature in the sterilization autoclave. A 56 mm thick layer of agar-graphite mix is poured at the bottom of the box and the footprints of four cell wells (22x22x6 mm each) are molded at its surface as it sets. In these wells, cells embedded in a collagen matrix can be cultivated. The gap between the agar surface and the probe is filled with cell culture medium which acts as a coolant and minimizes the temperature rise. The large agar substrate attenuates the propagating shear waves and thus avoids reflections from the bottom or the walls of the box. The temperature measurements were made ~2 mm below the surface of the wells using an Omega 0.25 mm T-type thermocouple.

Results/Discussion

The FUS cell stimulation setup provides repeatable exposure conditions. Monitoring of the generated shear waves using ultrafast ultrasound imaging shows that the slab of agar, collagen, and culture medium constitute a large volume through which compressional and shear wave can propagate and be attenuated without reflections or standing waves. The measured temperature rise was 1.2°C for 420 s of pulsed excitation (0.083% duty cycle on 2%-4% agar-graphite mix) which is well within the FDA limit for diagnostic transducers. Further studies on the biological effects of ARF induced shear stress on *in-vitro* tumor spheroids will be carried out with this setup.

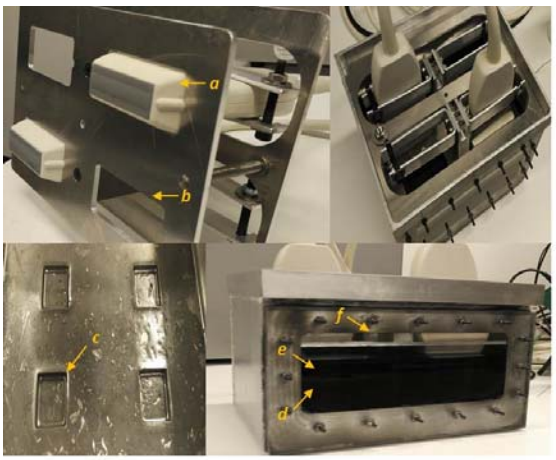

a) *ATL L7-4 US Probe* ***b)*** *Bottom lid with footprints of ATL L7-4 probes* ***c)*** *Footprint of wells on agar* ***d)*** *Slab of Agar* ***e)*** *Water between the agar and the probe* ***f)*** *Sealed plexi-glass window opening*

1H-6

9:15 am New Insights in the Role of Reactive Oxygen Species in Mechanisms of Sonoporation: In-Vitro Validation and Molecular Dynamic Simulations

Jean-Michel Escoffre[1], Pablo Campomanes[2], Mounir Tarek[2], Ayache Bouakaz[1]; [1]*Imagerie et Cerveau, Université François-Rabelais, Inserm, Tours, France,* [2]*CNRS, UMR 7565, Université de Lorraine, Vandœuvre-lès-Nancy, France*

Background, Motivation and Objective

Reactive oxygen species (ROS) are hypothesized to play a role in the sonoporation mechanisms. Sofar, the production of ROS has been mainly reported inside the cytoplasm of cells after sonoporation. However, the acoustical phenomenon triggering the production of ROS is unknown. In this context, we investigated whether the interaction between microbubbles (MBs) and ultrasound (US) induce the production of ROS using biochemical tools and molecular simulation.

Statement of Contribution/Methods

ROS detection assay – A MBs suspension (6.25 or 62.5 µL of BR14 in 1.5 mL) was placed in a plastic cuvette and mixed using magnetic stirrer. In a deionized water tank at 37°C, the MBs suspension was exposed to 1 MHz US waves with a duty cycle of 40% for 30 s, with PNP of 100 kPa and 400 kPa. ROS production was measured, immediately after US application, using fluorescent ROS and OH• detection assays.

Molecular simulations – We used a multi-scale approach in which the reactive fragments are described with a high-level quantum mechanics (QM) method, while the rest of the system (the lipid component of the MBs + surrounding solvent) was treated by molecular mechanics (MM). This hybrid QM/MM strategy offers the best compromise to study the formation and reactivity of ROS while enabling the extensive configuration sampling that was required to compute their behavior and outcome.

Results/Discussion

Our experimental data showed that no ROS was detected at 100 kPa independently of the MB concentrations ($p > 0.05$). At 400 kPa, low concentration of MBs (6.25 µL) did not generate ROS ($p > 0.05$). However, the increase in MB concentration to 62.5 µL induced a significant production of ROS ($p < 0.05$). Using specific OH• detection assay, we confirmed that lipid coated MBs undergo, favored spontaneous formation of a host of free radicals where OH• was the main ROS species after sonoporation. The molecular simulations unveiled how these radicals and under which US condition they form. It also showed that the ROS can easily diffuse though the MB shell toward the surrounding aqueous phase and thus might participate to the permeabilization of plasma membrane. In conclusion, the exposure of MBs to US generates chemical effects, which might play a role in the permeabilization of the cell membrane when generated in its proximity.

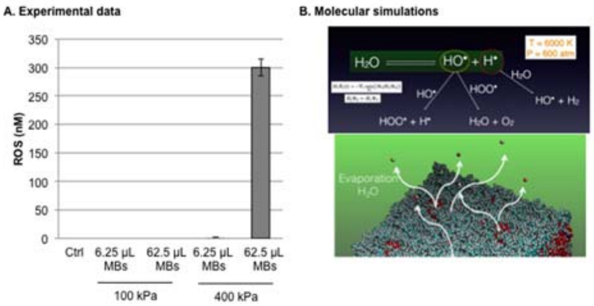
A. Experimental data
ROS (nM)
350
300
250
200
150
100
50
0
Ctrl
6.25 µL MBs
62.5 µL MBs
6.25 µL MBs
62.5 µL MBs
100 kPa
400 kPa
B. Molecular simulations
H2O
HO• + H•
T = 6000 K
P = 600 atm
H2O
HO•
HOO•
HO• + H2
HOO• + H•
H2O + O2
Evaporation
H2O

2H - MTC: Hard and Ex Vivo Human Tissue Characterization

Ambassador Ballroom

Saturday, September 9, 2017, 8:00 am - 9:30 am

Chair: **Pascal Laugier**
Sorbonne Universites

2H-1

8:00 am **In Vivo Radius Bone Evaluation of Teenagers by Modified Two Wave Ultrasound Apparatus**

Mami Matsukawa[1], Isao Mano[2], Kaoru Horii[2], Yutaro Yoneda[2], Shiori Umemura[3], Etsuko Ozaki[3]; *[1]Doshisha University, Japan, [2]OYO Electric, Japan, [3]Kyoto Prefectural University of Medicine, Japan*

Background, Motivation and Objective

The postmenopausal osteoporosis is likely influenced by the events taking place during bone development [1]. To prevent future risk of osteoporosis, the appropriate growth of bone during teenagers is important. The ultrasonic bone densitometry is portable and has no radiation exposure, which is suitable for the evaluation of children′s bone. In this study, an ultrasonic bone measurement system of distal radius was modified for the small bones and applied to teenagers.

Statement of Contribution/Methods

Making use of the fast and slow wave phenomenon in cancellous bone, the two wave apparatus (LD-100, OYO electric and Doshisha university) measures fast, slow and echo waves, and gives us cancellous bone density (mg/cm^3), cancellous bone elasticity (GPa) and the cortical thickness (mm) [2]. In this study, the system was modified and used annular array transducers (diameters: 7-20 mm) to avoid the effects of guided wave along the outer cortical bone on the fast and slow waves. The effects become strong in the smaller bones and the smaller transducers were used for these bones. Under the permission of the ethics committee at Doshisha university, radius bones of 560 teenagers (Ages: 12-18) were measured.

Results/Discussion

We have successfully measured the waves propagated through the teenagers′ radius bone. In the case of late teens women (ages: 15-18), the mean values (MV) of cortical thickness were 93.8 -96.9% of the young adult mean (YAM), whereas those of early teens were 92.4-95.5%. MV of cancellous bone density were 82.0-94.7% (late teens), and 65.3-81.6 % (early teens) of YAM, respectively. In the case of late teens men, MV of cortical thickness were 88.8-104.0 % of YAM and those of early teens were 69.7-78.4 % of YAM. MV of cancellous bone density were 66.3-84.2 % (late teens) and 47.7-55.4 % (early teens) of YAM. The standard deviations of these values were all higher than those of YAM. These data indicate late growth of cancellous bone in both men and women. This tendency was clearer in men. The standard values of each age will be obtained in the future studies with more data and used for the evaluation of young bones.

[1] C.M.Neu, et al., Bone (2001)28;227.

[2] H. Sai, et al., Osteoporos Int (2010) 21:1781.

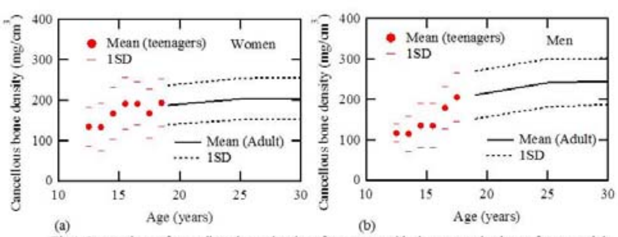

Fig.1 Comparison of cancellous bone density of teenagers with the reported values of young adult.

2H-2

8:15 am **Biological and Spatial Variability of Backscatter Coefficient Parameters in the *Ex Vivo* Human Uterine Cervix**

Andrew Santoso[1], Ivan Rosado-Mendez[1], Quinton Guerrero[1], Lindsey Drehfal[1], Helen Feltovich[1,2], Timothy Hall[1]; *[1]Medical Physics, University of Wisconsin-Madison, Madison, Wisconsin, USA, [2]Maternal Fetal Medicine, Intermountain Healthcare, Provo, Utah, USA*

Background, Motivation and Objective

We are investigating backscatter-based quantitative ultrasound parameters to detect premature cervical remodeling ultimately leading to spontaneous preterm birth. This work systematically assesses the *ex vivo* human cervix microstructure and the effects of cervical ripening based on parameters derived from the acoustic backscatter coefficients (BSCs).

Statement of Contribution/Methods

Hysterectomy specimens (N=14) were collected from non-pregnant women, bisected, pinned to sound absorbing rubber, and immersed in saline. Four samples were normal control while the remaining ten were ripened (endogenously or exogenously). Radiofrequency (RF) echo data were acquired for cervix samples and from a reference phantom under the same settings with a Siemens Acuson S2000. RF power spectra were obtained from 4x4 mm regions of interest (ROIs) and the Reference Phantom Method was used to estimate BSCs for both anterior and posterior cervix sides. BSC frequency dependence and magnitude were parameterized in terms of the effective scatterer diameter (ESD) and average BSC (ABSC), respectively, within 4-9 MHz. Spatial gradients of ESD and ABSC were assessed by computing the slope of a linear fit applied to estimates at various locations along the cervix. Comparison among parameters and their corresponding spatial gradients between ripening states were evaluated using a Kruskal-Wallis H test. A subsample of four ripened cervices was used to quantify anisotropy of frequency dependence assuming a simple cylindrical model for scattering sources. A two parameter secant model was derived dependent on the minimum fiber diameter and fiber orientation angle. Variations of the average ESD spanning ±28° were fit to the model for a stationary 5x5 mm mid-proximal ROI.

Results/Discussion

Parameter variations were observed along the length of the cervix. ESD, ABSC, and their spatial gradients were reduced in ripened samples. Medians and corresponding interquartile ranges (denoted in brackets) of ESD and ABSC among all spatial locations and cervix sides were 80 [65-90] µm and 7.2 [4.1-12.9] $\times 10^{-4}$ cm^{-1} sr^{-1} in ripened samples and 83 [72-94] µm and 10 [6.6-16] $\times 10^{-4}$ cm^{-1} sr^{-1} in unripened samples. ESD gradients on the posterior side differed significantly between ripened and unripened samples ($p<0.05$). The secant model produced minimum fiber diameters of 74.3 and 58.6 µm and fiber angles of 16.8° and 29.0°, for anterior and posterior cervix sides, respectively ($R^2>0.9$ for both sides). Our results suggest BSC parameters can distinguish variability of the uterine cervix tissue microstructure, encouraging further investigation on their use to assess cervical remodeling during pregnancy.

This work was supported by NIH grants T32CA009206, R21HD063031, and R01HD072077. We also thank Siemens HealthCare Ultrasound Division for technical support and equipment loan.

2H-3

8:30 am **Relationships between Cortical Bone Quality Biomarkers: Stiffness, Toughness, Microstructure, Mineralization, Cross-Links and Collagen**

Xiran Cai[1], Rémy Gauthier[2], Laura Peralta[1], Hélène Follet[3], Evelyne Gineyts[3], Max Langer[4], Boliang Yu[4], Cécile Olivier[4], Françoise Peyrin[4], David Mitton[2], Quentin Grimal[1], Pascal Laugier[1]; [1]*Sorbonne Universités, UPMC, INSERM UMR-S 1146, CNRS UMR 7371, Laboratoire d'Imagerie Biomédicale, Paris, France,* [2]*Univ Lyon, Université Claude Bernard Lyon 1, IFSTTAR, LBMC UMR_T9406, Lyon, France,* [3]*Univ Lyon, Université Claude Bernard Lyon 1, INSERM, LYOS UMR 1033, Lyon, France,* [4]*Univ Lyon, INSA Lyon, Université Claude Bernard Lyon 1, CNRS UMR 5220, IINSERM U1206, Creatis, Villeurbanne Cedex, France*

Background, Motivation and Objective

Bone quality encompasses bone properties that contribute to fracture risk, such as bone stiffness, microstructure, matrix constituents or tissue material properties. These aspects cannot be quantified in-vivo except for stiffness, a surrogate biomarker of strength, which can be assessed using quantitative ultrasound techniques. To better predict bone fracture risk, investigating the relationships between stiffness and other bone quality factors is important. Toward this goal, our group adapted resonant ultrasound spectroscopy (RUS) to precisely measure the whole set of stiffness coefficients of cortical bone by improving the signal processing and automatizing the inversion procedure based on a Bayesian framework. In this work, we present the relationships between bone quality biomarkers including stiffness, fracture toughness, microstructure, mineralization, cross-links and collagen.

Statement of Contribution/Methods

From the mid-diaphysis of the femoral cortex of 27 human donors, 54 cuboid specimens (3x4x5 mm^3, axis 1=radial; axis 2=circumferential; axis 3=axial) were prepared. The mesoscale transverse isotropic stiffness tensor C_{ij} of the specimens was measured by RUS. The microstructure (i.e., vascular porosity) and degree of mineralization of bone (DMB) were estimated from synchrotron radiation micro-computed tomography (voxel size 6.5 µm). Another set of 54 samples (3x4x25 mm^3) which were adjacent to the previous ones, was harvested for mechanical testing. Each of them were divided into two samples (1x2x25 mm^3) then notched (1 mm length) in their middle in the transverse direction. Three-point bending tests were conducted at two strain rates 10^{-4} s^{-1} and 10^{-1} s^{-1} to measure the fracture toughness (quasi-static K_{Jc}^{Stat} and dynamic K_{jc}^{Dyn}). Biochemical tests were conducted on small adjacent bone fragments to assess collagen quantity and cross-links.

Results/Discussion

While all the stiffness coefficients significantly correlate with toughness ($-0.35<r<-0.53$, $p<0.05$) except for C_{33}, different biomarkers seem to differently affect toughness and stiffness. Indeed, markers that showed an effect on toughness did not on stiffness (Table 1). This work demonstrates the correlations between cortical bone quality biomarkers and gives insights for a better assessment of bone fracture risk using stiffness measured in-vivo.

Table 1: Spearman's correlation coefficients between stiffness coefficients C_{ij}, fracture toughness (K_{Jc}^{Dyn}, K_{Jc}^{Stat}) and porosity, degree of mineralization of bone (DMB), enzymatic immature cross-links (HLNL, DHLNL), enzymatic mature cross-links (PYD, DPD), non-enzymatic cross-links (PEN) and collagen (coll). Note that DMB values were obtained on 22 specimens. $^*p < 0.05$; $^{**}p < 0.001$; NS: non significant

	porosity	DMB	DHLNL	HLNL	PYD	DPD	PEN	coll
C_{11}	-0.85**	0.41*	-0.42*	-0.39*	NS	NS	NS	NS
C_{33}	-0.79**	0.50*	-0.45*	-0.44*	NS	NS	NS	NS
C_{13}	-0.68**	NS	-0.31*	NS	NS	NS	NS	NS
C_{44}	-0.88**	0.55*	-0.41*	-0.39*	NS	NS	NS	NS
C_{66}	-0.82**	0.44*	-0.34*	NS	NS	NS	NS	NS
K_{Jc}^{Dyn}	NS	NS	NS	NS	NS	NS	-0.31*	0.42*
K_{Jc}^{Stat}	NS	NS	NS	NS	NS	NS	-0.35*	NS

2H-4

8:45 am **Human Breast Tumor Characterization on Post-Surgical Mastectomy Specimens Using Harmonic Motion Imaging (HMI)**

Yang Han[1], Shutao Wang[1], Thomas Payen[1], Elisa Konofagou[1,2]; [1]*BME, Columbia University, New York, NY, USA,* [2]*Radiology, Columbia University, New York, NY, USA*

Background, Motivation and Objective

To overcome the low sensitivity of current breast imaging tools, new tools for breast imaging and evaluation must be developed for reliable identification and differentiation of breast masses based on stiffness. Recently, we have shown that Harmonic Motion Imaging (HMI) can be used to differentiate relative stiffness and monitor HIFU ablations in small lumpectomy human breast specimens. The objective of this study is to apply HMI on post-surgical mastectomy breast specimen to mimic the in vivo environment and characterize tumor at different depth for better tumor localization and identification before and after HIFU treatment.

Statement of Contribution/Methods

Collection and handling of post-surgical breast specimens were approved by the institutional review board (IRB) of Columbia University. Seven mastectomy breast specimens were obtained immediately after surgery for HMI imaging. The HMI setup consists of a 93-element, 4.5-MHz HIFU transducer confocally aligned with a 64-element 2.5-MHz phased array to transmit and receive through a VDAS system. The HIFU transducer was driven by an amplitude-modulated sinusoidal signal to vibrate the tissue at focal area. A point-by-point raster scan acquisition was used with a step size of 3 mm to generate a 2D HMI map. At each spot, 60 RF frames at 1-kHz pulse repetition frequency were acquired for cross-correlation calculation.

Results/Discussion

60mmx20mm HMI displacement maps could be generated to map the induced peak-to-peak displacement that imaged the entire target area within two minutes (Fig. 1) indicating lower displacement in the tumor region and higher displacement in the peripheral tissue. In Fig. 1, the average peak-to-peak displacement in the tumor defined on the B-mode was found to equal 4.93±1.38 µm, and 21.93±2.66 µm in the surrounding tissue. A Student's t-test across all specimens showed significant difference in the HMI displacement ($P < 0.0001$) between the tumor and the perilesional tissue. In addition, the HMI displacement map indicated a larger stiffer region compared to the tumor region identified on the B-mode.

HMI was shown to successfully map the relative stiffness at variable depths in post-surgical human breast mastectomy specimens. This study lays the foundation for upcoming clinical application of HMI on the breast for tumor detection and subsequent thermal ablative treatment.

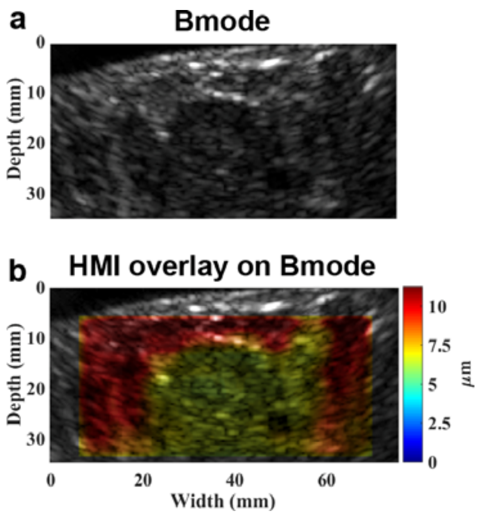

2H-5

9:00 am Assessment of Cortical Bone Pore Dimensions by High-Frequency Backscatter

Vantte Kilappa[1,2], Janos Hackenbeck[1], Gianluca Iori[1], Juan Du[1], **Kay Raum[1]**; *[1]Berlin-Brandenburg School for Regenerative Therapies, Charité-Universitätsmedizin Berlin, Berlin, Germany, [2]Mango Solutions, Jyväskylä, Finland*

Background, Motivation and Objective

Clinical studies using HRpQCT have revealed that cortical bone porosity is a major risk factor for fracture Not only average porosity but also pore size and local accumulation of large basic multicellular units (BMUs) have been associated with a reduction of the hip strength. However, an increase of cortical pore dimensions is poorly captured by X-ray based techniques. A previous in-silico study provided evidence of the dependency of the high-frequency backscatter bandwidth (1-5 MHz) on pore size [1].

Statement of Contribution/Methods

In this study, a conventional 3D medical ultrasound scanner (Ultrasonix Touch Research) was used in combination with a 3D linear transducer array (4DL14-5/38) and a 128-channel data acquisition box. Special beam-steering sequences were developed to send focused beams at multiple inclination angles to the cortical bone surface. The sweep motor of the probe allows to scan a 3D volume (Fig 1b). For each transmitted beam, the full aperture is used to obtain a wide-angle phase-sensitive detection of backscattered signals. The data analysis consists of i) detecting the outer bone surface from the receive-beamformed 3D volume, ii) determining a reference spectrum from surface reflections measured at normal incidence, iii) calculating a depth-dependent normalized backscatter spectrum for each scan position, iv) creating representative parameter maps, e.g. of apparent integrated backscatter amplitude (AIB) and spectral slope (AFB).

The method was applied ex-vivo to 18 human proximal femur shaft bones. Site-matched pore morphology was obtained from 100-MHz acoustic microscopy images (Fig. 1b).

Results/Discussion

An excellent correlation (adj. $R^2 = 0.85$) of the pore diameter was obtained with the slope of the inclination controlled apparent backscatter (AIBslope) (Fig.1c). The method allows a spatially resolved assessment of pore size, which is an early indicator of osteoporosis and treatment related changes in bone remodeling.

References

[1] Potsika VT, Fotiadis DI, Gortsas T, Iori G, Raum K. High-frequency cortical backscatter reveals cortical microstructure - A simulation study. 6th European Symposium on Ultrasonic Characterization of Bone 2015. DOI: 10.1109/ESUCB.2015.7169890

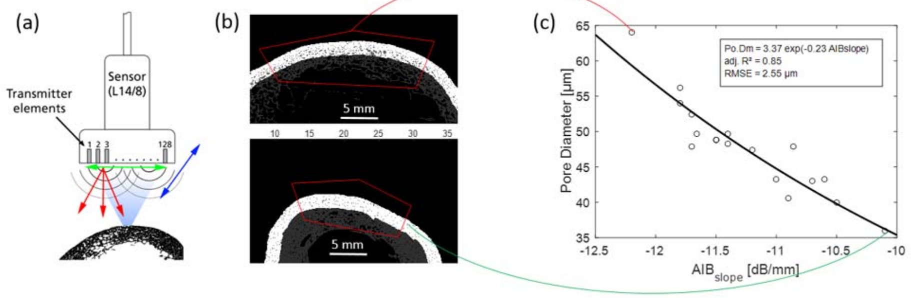

Fig. 1: (a) 3D multi-angle pulse sequence for the cortical backscatter measurement (red: multi-angle beam inclination with respect to the array normal direction; blue: multi-angle sweep of the array along the bone longitudinal direction; green: beam scan along the array direction. (b) Segmented acoustic microscopy images shows two samples with extreme differences in the median pore diameter (only a 2-mm stripe below the outer bone surface was evaluated). (c) Correlation between pore diameter and the depth-dependent slope of AIB.

2H-6

9:15 am Bone Matrix Elastic Properties Determined by FFT-Based Inverse Homogenization

Xiran Cai[1], Laura Peralta[1], Renald Brenner[2], Pascal Laugier[1], Quentin Grimal[1]; [1]*Sorbonne Universités, UPMC, INSERM UMR-S 1146, CNRS UMR 7371, Laboratoire d'Imagerie Biomédicale, Paris, France,* [2]*Sorbonne Universités, UPMC, CNRS UMR 7190, Institut Jean le Rond d'Alembert, Paris, France*

Background, Motivation and Objective

Cortical bone is an anisotropic material with hierarchical structure whose elastic properties are described at different length scales. At millimeter-scale, the whole set of stiffness tensor can be conveniently measured by resonant ultrasound spectroscopy (RUS). At microscopic-scale, micro-indentation and scanning acoustic microscopy are often used to quantify tissue matrix elastic properties. However, the last two methods do not easily provide the entire tissue stiffness tensor, but rather the elasticity or stiffness along a single direction. To overcome this limitation, we introduce a new approach to retrieving the elastic tensor of the tissue based on a numerical optimization procedure using Fast Fourier Transform (FFT)-based homogenization for the forward computation.

Statement of Contribution/Methods

From the mid-diaphysis of 28 human femurs, 55 cuboid cortical bone specimens (nominal dimension 3x4x5mm^3) were harvested and the mesoscopic stiffness coefficients (C_{ij}^{exp}) were measured by RUS. The microstructure was recorded by synchrotron radiation micro-computed tomography (voxel size=6.5µm). A sub volume (around 2.5x3.5x4.5mm^3) from the reconstructed volume of each specimen was used to calculate the effective stiffness coefficients (C_{ij}^{fft}) using FFT-based homogenization (voxel size=15µm) for trial values of the bone matrix stiffness (C_{ij}^{m} assuming transverse isotropy) and assuming the presence of water in pores. The specimen-specific matrix stiffness C_{ij}^{m} (Table 1) were found by inverse homogenization, i.e., by minimizing the root-mean-square-error (RMSE) between C_{ij}^{exp} and C_{ij}^{fft}.

Results/Discussion

The RMSE between C_{ij}^{exp} and C_{ij}^{fft} is 0.36%±0.40% (mean ± standard deviation). The values of bone matrix stiffness are given in Table 1 with their ranges and mean ± standard deviation. This study demonstrates a promising approach to quantifying the average anisotropic elasticity of the tissue matrix of small bone volumes from precisely measured mesocopic bone elasticity by RUS. Determined values of C_{ij}^{m} remain to be validated by independent measurements.

Table 1: The bone matrix elastic coefficients retrieved from the numerical procedure.

	C_{11}^{m}(GPa)	C_{33}^{m}(GPa)	C_{13}^{m}(GPa)	C_{44}^{m}(GPa)	C_{66}^{m}(GPa)
range	21.77∼30.87	31.43∼38.70	12.07∼20.53	6.09∼7.38	4.11∼6.31
mean±std	24.89±1.80	33.78±1.32	15.08±1.62	6.93±0.27	5.39±0.39

3H - MIM: Super-Resolution And Contrast Imaging

Palladian Room

Saturday, September 9, 2017, 8:00 am - 9:30 am

Chair: **Georg Schmitz**
Ruhr-Universität Bochum

3H-1

8:00 am **Two Stage Sub-Wavelength Motion Correction in Human Microvasculature for CEUS Imaging**

Sevan Harput[1], Kirsten Christensen-Jeffries[2], Yuanwei Li[1], Jemma Brown[2], Robert J. Eckersley[2], Christopher Dunsby[3], Meng-Xing Tang[1]; *[1]Department of Bioengineering, Imperial College London, London, United Kingdom, [2]Biomedical Engineering Department, King's College London, London, United Kingdom, [3]Department of Physics and Centre for Pathology, Imperial College London, London, United Kingdom*

Background, Motivation and Objective

The structure of microvasculature cannot be resolved using clinical B-mode or contrast-enhanced ultrasound (CEUS) imaging due to the fundamental diffraction limit. It is possible to overcome this resolution limitation by localizing individual microbubbles (MBs) through multiple frames and forming a super-resolved image. However, super-resolution (SR) imaging bring their own unique problems since the structures to be imaged are on the order of 10s of μm. Therefore, motion correction (MC) is crucial for SR imaging, where tissue movement much smaller than the ultrasound wavelength can significantly reduce the accuracy of SR images created from MB locations gathered through hundreds of frames.

Statement of Contribution/Methods

A two stage MC was applied to compensate for both rigid and non-rigid tissue deformations. The first stage is a rigid MC to minimize the global motion, such as hand-held probe motion or breathing. The second stage is a B-spline based non-rigid registration that can correct for local compression and rarefaction of tissue [1].

To verify the MC accuracy, Field II simulations were performed with a homogeneous tissue phantom. Rigid tissue motion was generated by moving the location of scatterers together. Non-rigid motion was simulated by using a linear stress-strain relation and displacing the scatterers independently to mimic the effect of ultrasound probe compression and muscle contraction. By shifting the scatterers together or independently, a different speckle pattern was created for all tested scenarios.

The proposed method was then applied to clinical data acquired in human lower limb using a 3-9 MHz probe with an MI of 0.06. Several acquisitions with 500 to 700 B-mode and CEUS frames were recorded over a duration of 40 to 55 seconds. B-mode frames were used for motion estimation and the MC was applied on CEUS frames.

Results/Discussion

Results of the non-rigid motion estimation simulations are shown in Fig A for 20 dB SNR. The mean motion estimation error and standard deviation for images with 20 dB SNR or better are less than 25 μm, far smaller than the wavelength (250 μm); however, the error values increase above 50 μm for images with 10 dB SNR, which is not suitable for SR imaging of microvasculature. The benefit of using two stage MC on SR imaging in human microvasculature is illustrated in Fig B and Fig C.

[1] Rueckert et al., IEEE Trans Med Imag, vol 18(8), 1999.

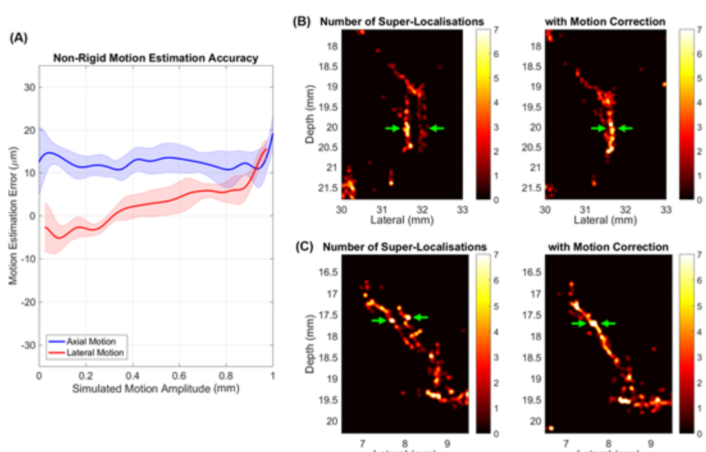

Figure (A) Figure shows the motion estimation error for simulated axial and lateral tissue motion. Axial motion was created by displacing the location of scatterers as a function of depth to mimic ultrasound probe compression. Lateral motion was created by displacing the location of scatterers as a function of lateral distance to mimic muscle contraction in human lower limb. **(B-C)** Two examples of super-resolution images acquired in human lower limb were displayed with and without motion correction. Green arrows show the location of detected microvessels before and after motion correction.

3H-2

8:15 am **Sparsity-Driven Super-Localization in Clinical Contrast-Enhanced Ultrasound**

Ruud J.G. van Sloun[1], Oren Solomon[2], Yonina C. Eldar[2], Hessel Wijkstra[1,3], Massimo Mischi[1]; *[1]Eindhoven University of Technology, Eindhoven, Netherlands, [2]Technion – Israel Institute of Technology, Haifa, Israel, [3]Academic Medical Center University of Amsterdam, Netherlands*

Background, Motivation and Objective

Super-resolution (SR) ultrasound enables detailed assessment of the fine vascular network by pinpointing individual microbubbles (MBs), using ultrasound contrast agents (UCAs). The information in SR images is determined by the density of localized MBs and their localization accuracy. To obtain high densities, one can evaluate extremely sparse subsets of MBs across thousands of frames by using a very low MB dose and imaging for a very long time, which is impractical for clinical routine. While ultrafast imaging somewhat alleviates this problem, long acquisition times are still required to enhance the full vascular bed. As a result, localization accuracy remains hampered by patient motion. Recently, Sparsity-based Ultrasonic Super resolution Hemodynamic Imaging (SUSHI) achieved comparable spatial resolution with a sub-second temporal resolution. However, in the current implementation of SUSHI this temporal resolution was achieved using very high frame-rate, e.g. plane-wave imaging, which is not currently widely available in clinical scanners. The aim of this work is twofold. First, to attain a high MB localization accuracy on dense contrast-enhanced ultrasound (CEUS) data using a clinical dose of UCA and a widespread clinical scanner. Second, to retain a high resolution by motion compensation.

Statement of Contribution/Methods

We performed transrectal imaging of the prostate using a Philips iU22 scanner (frame rate = 10 Hz). To analyze high-density frames in which many MBs are simultaneously present, we formulate the localization task as a sparsity-promoting convex optimization problem. Solving this corresponds to finding the sparse set of locations which, given the point spread function, adequately model the measured data. This process is repeated for a set of frames to accumulate a high number of localized MBs. Elastic registration ensures that the locations are compensated for motion, and is performed using the pure-tissue fundamental mode images. The latter is facilitated by exploiting singular value decomposition to remove the MB signal components.

Results/Discussion

Figure 1 shows the ability of the proposed method to resolve vessels beyond the diffraction limit from clinical prostate CEUS. The method can be applied effectively to achieve SR ultrasound imaging, facilitating a robust implementation in a clinical setting.

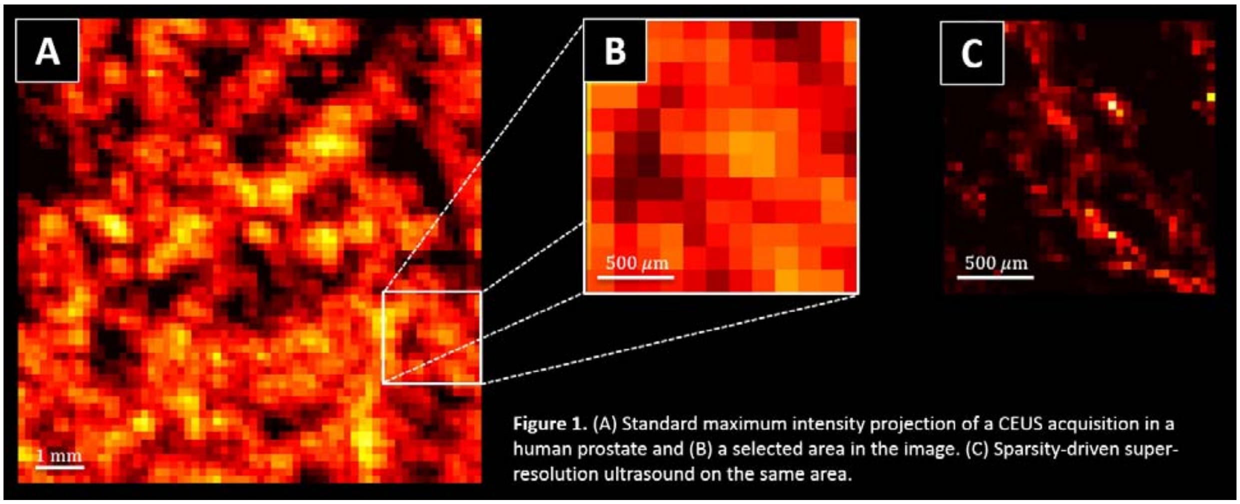

Figure 1. (A) Standard maximum intensity projection of a CEUS acquisition in a human prostate and (B) a selected area in the image. (C) Sparsity-driven super-resolution ultrasound on the same area.

3H-3

8:30 am **Super-Resolution Ultrasound to Aid Testicular Lesion Characterisation**

Kirsten Jeffries[1], Dean Y Huang[2], Jemma Brown[1], Sevan Harput[3], Christopher Dunsby[4,5], Meng-Xing Tang[3], Paul S Sidhu[2], Robert Eckersley[1]; [1]*Biomedical Engineering, Kings College London, London, United Kingdom,* [2]*Radiology, Kings College London, London, United Kingdom,* [3]*Bioengineering, Imperial College London, London, United Kingdom,* [4]*Physics, Imperial College London, London, United Kingdom,* [5]*Centre for Histopathology, Imperial College London, London, United Kingdom*

Background, Motivation and Objective

Changes in microvascular structure and flow is of clinical importance in the study of a number of disease processes such as cancer and diabetes. Ultrasound is often the primary imaging procedure performed to determine appropriate treatment or surgery for testicular lesions. Currently, however, differentiation and diagnosis of both benign and malignant testicular tumours such as seminomas, leydig cell tumours and lymphomas are often challenging. Contrast-enhanced ultrasound (CEUS) has been used to aid their characterisation [1]. There are, however, a variety of benign testicular lesions that can mimic testicular malignancies. Ultrasound super-resolution (US-SR) techniques have been able to visualise vascular structures in vitro and in vivo beyond the diffraction limit by localizing individual microbubble signals. In this work, we aim to apply US-SR processing to clinical data to aid diagnostic confidence.

Statement of Contribution/Methods

US-SR was performed on historical CEUS clinical datasets acquired from a range of benign and malignant intra-testicular lesions using a clinical scanner (Siemens) at 4 MHz. Firstly, sub-pixel rigid cross-correlation motion correction was performed on B-mode frames. A rolling background subtraction was then applied on contrast enhanced frames, before spatially isolated microbubble signals were extracted and localized. Direction and speed maps were generated by tracking individual bubble trajectories. Furthermore, functional measures such as localization rate and flow speed were extracted within regions of interest.

Results/Discussion

Localization maps were able to display the structure and direction of underlying microbubble flow, as demonstrated in Figure 1A. Additionally, functional measures such as localisation rates demonstrated differences between normal and diseased tissue (Figure 1C and D). In the future, structural and functional measures generated using US-SR processing could be used to aid clinical diagnosis of cancerous tissue.

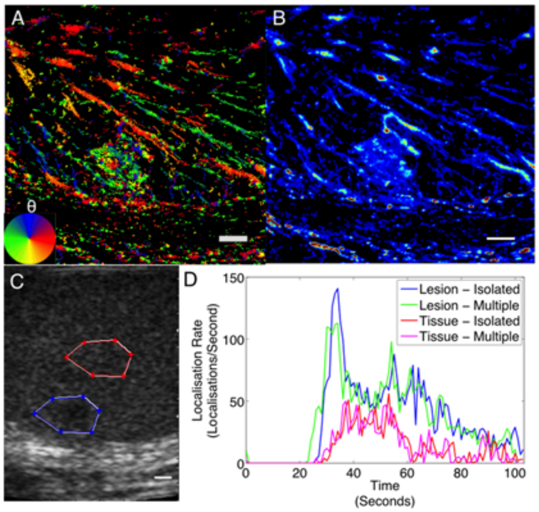

Figure 1. Bubble direction and localization maps are shown in A) and B) for a non-germ cell primary leydig testicular lesion. Regions of interest in the lesion (blue) and tissue (red) shown in C) were analyzed to generate localization rate information shown in D), which demonstrates that the distribution of both multiple and single bubbles exhibit an earlier onset than the surrounding tissue, and a consistently higher localization rate over the time-frame investigated. Scale bar, 2 mm, color wheel, θ = 0-360 degrees.

3H-4

8:45 am **Effects of Motion on High Frame Rate Contrast Enhanced Echocardiography and Its Correction**

Matthieu Toulemonde[1], Antonio Stanziola[1], Yuanwei Li[1], Robert Eckersley[2], Mengxing Tang[1]; [1]*Department of Bioengineering, Imperial College London, London, United Kingdom,* [2]*King's College, United Kingdom*

Background, Motivation and Objective

Contrast enhanced ultrasound (CEUS) has shown great promise in quantifying myocardial perfusion and ventricular flow. More recently high frame-rate contrast enhanced echocardiography (HFR CE), based on pulse inversion (PI) and diverging waves, has shown to significantly improve the image contrast over standard CEUS [M. Toulemonde, IUS 2016]. Both contrast pulse sequences and spatial compounding involve coherent summation of echoes from a target at different time points. Consequently they are susceptible to target motion, and their effects are very different and it is not yet clear of their combined impact on compounded HFR CEUS PI images. Furthermore, there is no study to demonstrate motion corrected compounded HFR CEUS.

The aim of this work is firstly to demonstrate the impact of the motion on compounded HFR CE in simulation and secondly to evaluate the motion correction algorithm in-vivo.

Statement of Contribution/Methods

HFR CE simulation and in-vivo images were obtained by transmitting 11 diverging PI wave pair (3-cycles, 1.5MHz, MI 0.05) and coherently compounding to achieve a compounded frame rate of 250 Hz. In simulation a single moving microbubble (MB) was placed 5 cm below the centre of the transducer. The propagation of the ultrasound wave was simulated via custom software interfaced with Field II, while the MB response was derived by numerically solving the Marmottant model.

Motion compensation is obtained by spatial alignment [D. Rueckert, 1999] of beamformed radio frequency (RF) data with the central angle transmission as reference. Motion corrected data of all beamformed RF angles are then coherently compounded.

Results/Discussion

The simulation results (Figure (a)) show the change of peak image intensity in the beamformed image for different axial velocities of the MB. While larger motion increases image intensity, increasing the number of compounded images modifies the final image intensity, ultimately resulting in a reduced intensity when the number of compounded waves is 11.

Figure (b) and (c) show HFR CE without and with motion correction, respectively. The yellow arrows highlight the areas where the motion correction has the most important impact.

In this work we show the impact of motion on coherent compounding in HFR CEUS acquisition and the importance of motion correction for proper representation of contrast concentration in the chamber.

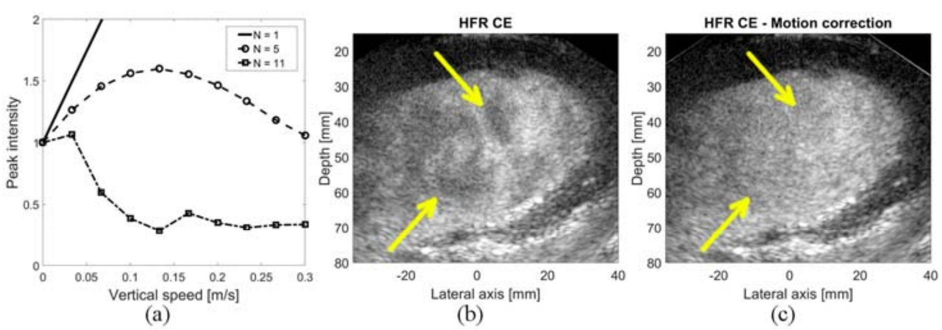

Figure: **(a)** Peak intensity in the beamformed image in ultrasound simulations, for different axial velocities . The peak intensity is normalized with respect to the non-moving case of the microbubble. The value of N highlights the number of compounded waves used. **(b)** and **(c)** are in-vivo HFR CE acquisiton without and with motion correction, respectively. The yellow arrows highlight the areas where the motion correction has the most important impact. Both images are log-compress and displayed with a 50 dB dynamic range.

3H-5

9:00 am High Frame Rate, Three-Dimensional Passive Imaging of Bubble Clouds in Sonothrombolysis Using a Sparse Hemispherical Array

Christopher Acconcia[1,2], Ryan Jones[1,2], Dave Goertz[1,2], Meaghan O'Reilly[1,2], Kullervo Hynynen[1,2]; [1]*Sunnybrook Research Institute, Toronto, Ontario, Canada,* [2]*University of Toronto, Toronto, Ontario, Canada*

Background, Motivation and Objective

Vessel occlusions caused by blood clots can result in severe cardiovascular diseases such as ischemic stroke and deep vein thrombosis (DVT). The current treatment standard for DVT is anticoagulation therapy, which does little to address long term morbidity as opposed to approaches directed at removing clots. High intensity ultrasound can rapidly and non-invasively resolve clots by generating bubble clouds that erode them. However, lack of appropriate methods for treatment monitoring is a limiting factor in its widespread adoption. The objective of this work was to assess the capabilities of passive imaging as a monitoring tool during clot lysis using a near ideal receiver array geometry.

Statement of Contribution/Methods

Blood clots were exposed to 1.5 MHz ultrasound (F#1, spherically focused). Cavitation signals were received with a hemispherical array of 128 sparsely populated, PZT elements (612 kHz center frequency) and beamformed in 3D using a delay, sum, and integrate algorithm. Exposures comprised either long (1 ms, x60) or short (0.1 ms, x100) pulse lengths (0.1% duty cycle) with peak negative pressures of ~8.5 and 15 MPa, respectively. High frequency (30 MHz), 3D B-mode ultrasound imaging identified regions of clot degradation. The frame rate capabilities of the system were explored using integration times of 1, 10 and 100 µs. The number of cavitation events required to induce clot damage was estimated from the mean number along the 3D contour of the degradation volume.

Results/Discussion

The location and volume of clot degradation differed between exposure schemes and was consistent with the spatial distribution of cavitation sources observed on passive imaging. Long pulse exposures produced larger volumes (11.4 vs 4.1 mm3), preferentially at the distal side of vessel. Isolated cavitation events were identified with integration times as short as 1 µs, showing rapid bubble cloud evolution which can be missed with longer integration times (Fig. a,b). The number of accrued events was greatest at the core of degradation, decreasing gradually with distance (Fig. c,d). Using 1 µs integration times the mean number of events along the contour of damage was 2358 ± 547 and 224 ± 149 for the long and short pulse exposures, respectively. This information motivates the development of a device for DVT treatment with receive elements for passive imaging being a key design aspect.

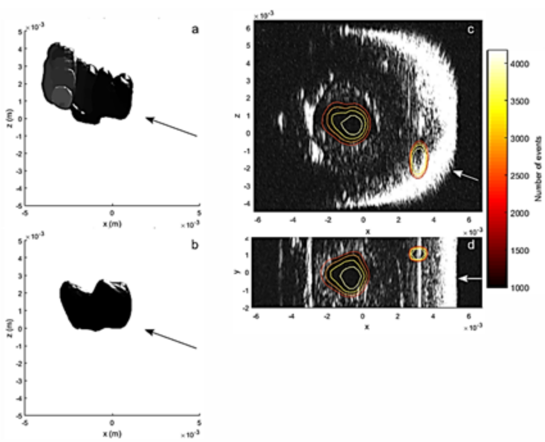

Figure: Cavitation images produced with short (a - 1 µs) and long (b - 100 µs) integration times showing the rapid bubble cloud development over a 100 µs pulse. -3 dB intensity contours are shown color coded in time from light to dark. The spatial distribution of events accrued over exposure was consistent with the size and location of clot damage (c,d). Overlayed on high frequency ultrasound images of clot damage are contours of accrued events presented as maximum intensity projections (data from a long pulse length exposure).

3H-6

9:15 am Multicolor Perfluorocarbon Nanodroplets for Multiplexed Ultrasound And Photoacoustic Imaging

Daniela Santiesteban[1], Kristina Hallam[1], Steven Yarmoska[1], Stanislav Emelianov[1,2]; [1]*Wallace H. Coulter Department of Biomedical Engineering, Georgia Institute of Technology and Emory University School of Medicine, Atlanta, GA, USA,* [2]*School of Electrical and Computer Engineering, Georgia Institute of Technology, Atlanta, GA, USA*

Background, Motivation and Objective

For many diseases, such as cancer, simultaneous imaging of different targets can lead to improved diagnosis, better patient prognosis, and therapy guidance/monitoring. PET-CT multiplexing can be cumbersome, costly, and involve radiation exposure. Other modalities such as fluorescent imaging lack clinical and pre-clinical relevance. Therefore, clinically relevant multiplexed imaging is of interest. Previously, we have shown that laser-activated perfluorocarbon nanodroplets (PFCnDs) can be used as dual PA/US contrast agents. In this work, we present development of a cost-effective, safe and promising platform for multiplexing studies based on PA/US imaging of multicolored PFCnDs.

Statement of Contribution/Methods

We synthesized two sets of lipid shelled PFCnDs (DSPC & DSPE-PEG(2000), Avanti) filled with perfluoropentane (boiling point: 27C). One set of droplets, PFCnD #1, contained a 740 nm peak absorption dye and the other set, PFCnD #2, a dye with a 1000 nm peak absorption. PFCnDs were sized using dynamic light scattering (Zetasizer, Malvern). All imaging studies used a preclinical PA/US system (Vevo LAZR 2100, Visualsonics). We conducted a phantom study with controllable flow rates to test the PA and US signal from PFCnD subsets to determine the activation wavelengths with minimal crosstalk. For the in vivo study, a spleen of a healthy mouse, injected intravenously with a 150 ul cocktail consisting of PFCnD#1 and PFCnD #2, was imaged 30 minutes after the injection.

Results/Discussion

The two sets of color-coded PFCnDs were of comparable hydrodynamic size (~300 nm). Phantom experiments demonstrated that distinct and reliable activation of PFCnD subsets was achieved at 680 nm and 1064 nm wavelengths resulting in a 2-3 fold increase in PA signal (Fig. 1a) and 50% US contrast enhancement (not shown). As expected, PBS control solution showed no PA signal. Preliminary animal studies demonstrated effective multiplexing in vivo (Fig. 1b). Image processing of both US and PA images (Fig. 1b) allowed high contrast, background-free visualization of each particle type (Fig. 1c). In conclusion, we demonstrated a multimodal, multiplexed US/PA imaging platform capable of background-free imaging of multicolored laser-activated PFCnDs. Future studies will exploit multiplexed, targeted PFCnDs in mouse models of primary and metastatic cancer.

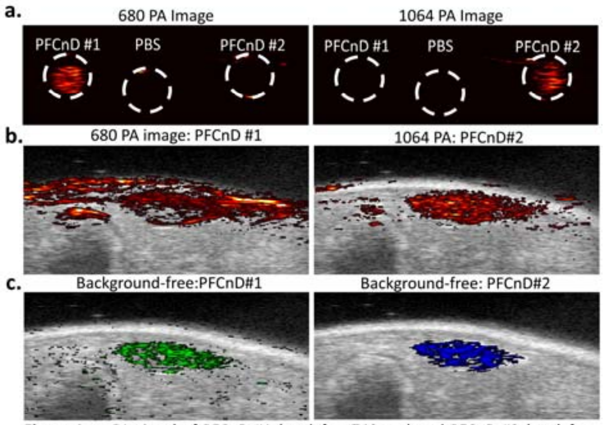

Figure 1. a. PA signal of PFCnD #1 (peak λ = 740 nm) and PFCnD #2 (peak λ = 1000 nm) at 680 nm and 1064 nm pulsed laser irradiation. **b.** Raw PA data at 680, 1064 nm of the spleen *in vivo*. **c.** After processing, each PFCnD group gives high contrast with minimal background. SB = 2 cm.

4H - MBF: Methods in Flow Studies: Phantoms and Algorithms

Diplomat Room

Saturday, September 9, 2017, 8:00 am - 9:30 am

Chair: **Mathieu Pernot**
INSERM

4H-1

8:00 am **Real-Time Staggered PRF for Vector Doppler Blood Velocity Assessment**

Stefano Ricci[1], Luca Bassi[1], Alessandro Dallai[1], Riccardo Matera[1], Piero Tortoli[1]; [1]*Engineering Information Dept., Florence University, Firenze, FI, Italy*

Background, Motivation and Objective

Vector Doppler techniques are ready to substituting the standard methods for blood velocity investigation. However, like in classic Pulse Wave methods, the maximum detectable velocity is related to the Pulse Repetition Frequency (PRF), which is limited by the maximum depth and/or hardware constraints. Unfortunately, the blood velocity, e.g. in stenotic vessels, can easily peak at 2m/s, thus resulting in aliased and unreliable measurements.

Staggered PRF (doi: 10.1109/TMI.2016.2518638) is a technique that recovers the correct velocities by combining aliased data acquired from bursts transmitted at different PRFs. In this work, we extend the capabilities of a 2D real-time vector Doppler method (doi: 10.1109/ULTSYM.2016.7728428) through staggered PRF technique.

Statement of Contribution/Methods

The method was implemented in real-time on the ULA-OP256 research echograph. A linear array probe transmits alternate sequences of 128 plane waves at PRF1 and PRF2=3/4 PRF1. This sequence, according to staggered PRF, allows a 3-folds extension of the velocity limit. In reception, 8 Investigation Lines (ILs) are spaced by 1.25mm in the region of interest, perpendicular to the probe. For each IL, the signal received from a left and a right aperture, is dynamically beamformed along the IL. Thus, for each transmission, the beamformer processes 8 aperture pairs in real-time. The slow-time data go through spectral analysis and mean frequency extraction for 256 depths. The (possibly aliased) frequencies obtained from the 2 PRF-patterns are correlated for generating the de-aliased velocities, which are finally triangulated to calculate the velocity vectors.

Results/Discussion

ULA-OP256 was programmed to transmit 8MHz plane waves in a flow rig with a 0.5 m/s peak velocity flow. The PRF was reduced to 2kHz, and, without staggered PRF, the aliasing was clearly visible in the central region of pipe (Fig. A shows this condition in the live ULA-OP256 display). Then, staggered PRF modality was activated by alternating bursts at PRF1=2kHz and PRF2=1.5kHz. The velocity vectors were correctly recovered as visible in ULA-OP256 display (Fig.B). The velocities on the 8 lines (blue) were compared to the reference (red) in Fig.C. The error outside of the wall region is lower than 10%. Movies showing in-vivo complex flow configurations will be presented.

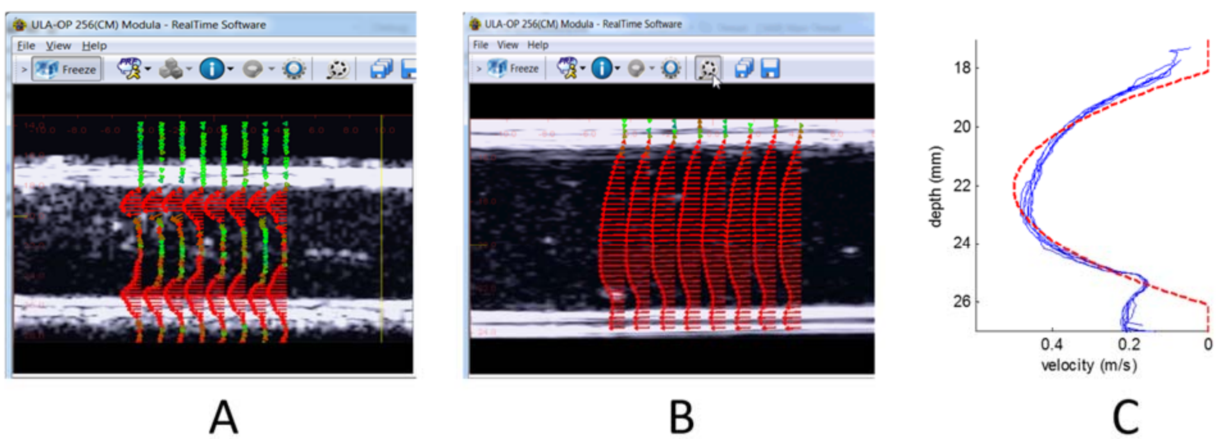

4H-2

8:15 am **Ultrafast Vector Doppler Using RF Sub-Nyquist Sampling**

Craig Madiena[1], Julia Faurie[1], Damien Garcia[1,2]; [1]*University of Montreal, Canada,* [2]*CREATIS, France*

Background, Motivation and Objective

Ultrafast ultrasound has contributed to a renewed interested in vector Doppler. Sampling RF signals at a rate 4 times the carrier frequency is the standard procedure since this rule complies with the Nyquist sampling theorem, regardless of the transducer bandwidth. RF acquisition with a high-performance multi-channel system generates massive datasets, especially in 3-D ultrafast ultrasound. The objective of this *in vitro* and *in vivo* study was to demonstrate that sub-Nyquist sampling can lead to substantial lossless data reduction in vector Doppler.

Statement of Contribution/Methods

Vector Doppler was generated from unsteered plane waves (5-MHz linear array). Two receive sub-apertures were used, with receive angles of ±15°. A staggered dual-PRF sequence ($PRF_2 = \frac{2}{3} PRF_1$) doubled the Nyquist velocity. The effect of RF data undersampling on vector Doppler was investigated in a rotating disc and in a carotid bifurcation. The RF signals were sampled at 20 MHz (center frequency × 4), then downsampled to simulate sub-Nyquist sampling. We used downsampling ratios up to 13; a ratio of 13 means that the RF signals were sampled at 20/13 = 1.54 MHz. The ratios were chosen so that the positive and negative frequency components did not overlap within the -10 dB bandwidth. After I/Q demodulation and beamforming, the Doppler velocities were estimated using an auto-correlator. The Doppler-derived velocity vectors were compared with the actual vector fields.

The *in vitro* phantom rotated at angular velocities up to 15 RPS (maximum outer speed = 1.5 m/s). *In vivo* vector flow images of the carotid bifurcation were produced in one volunteer. We used a high-frame-rate duplex sequence (B-mode + color Doppler) based on plane wave imaging. A spatially-adaptive polynomial regression filter was used to remove the clutter components. Since no *in vivo* reference was available, the velocity vectors produced from the undersampled RF signals were compared with those obtained from the standard Nyquist sampling.

Results/Discussion

The velocity vector errors due to sub-Nyquist sampling were marginal, which illustrates that vector Doppler can be correctly computed with a drastically reduced amount of RF samples. In our study, a 11-fold data reduction was obtained. Sub-Nyquist sampling can be a method of choice in vector Doppler to avoid information overload and reduce data transfer and storage.

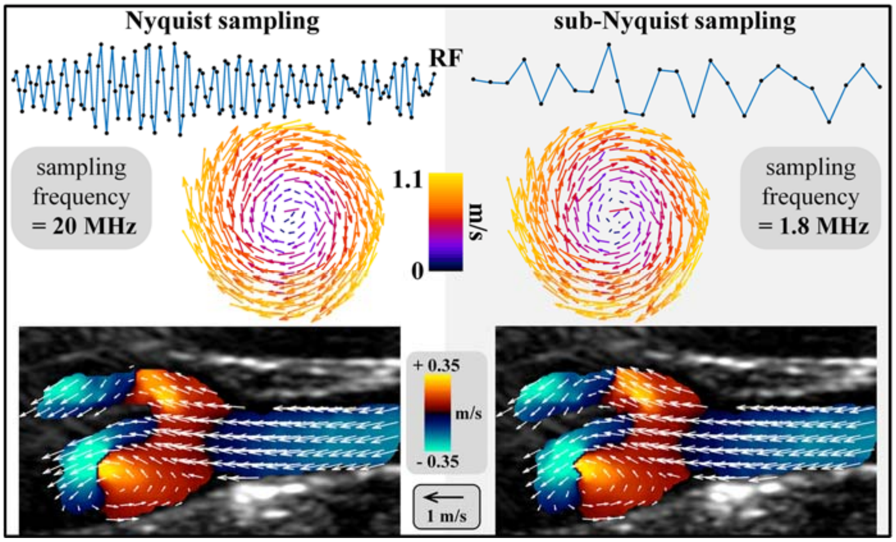

4H-3

8:30 am An MRI-compatible Mock Model for Intra-cardiac Flow Imaging

Qiong He[1], Hang Gao[2], Aiqi Sun[1], Yunduo Li[1], Rui Li[1], Jan D'hooge[2], Jianwen Luo[1]; [1]*Department of Biomedical Engineering, Tsinghua University, China, People's Republic of,* [2]*Department of Cardiovascular Imaging & Dynamics, KU Leuven, Belgium*

Background, Motivation and Objective

Cardiac mock models are helpful to develop new imaging methodologies. Although several mock model setups have been proposed, a good model for the development of intra-cardiac flow imaging is missing. The challenge lies in the fact that mimicking realistic flow patterns requires a realistic left ventricular shape as well as valve systems and a fluid with appropriate rheological properties. Moreover, in order to enable an independent reference method, the model either has to be optically transparent (i.e. for OPIV) or has to be MRI-compatible (i.e. phase-contrast MRI). The goal of this study was therefore to develop such a cardiac mock model.

Statement of Contribution/Methods

A homogeneous phantom was prepared by mixing 10% (by weight) polyvinyl alcohol (PVA), 87% distilled water and 3% Sigmacell cellulose as ultrasound scattering particles at a temperature of 85 °C and pouring it into a 3D-printed mold that was based on an MRI recording of a human left ventricle (LV) in order to ensure a realistic geometry (~100 ml). After that, the mold was put in a freezer and underwent two freeze/thaw cycles. Similarly, based on 3D printing, an in- and outflow track model was produced that allowed implanting prosthetic mechanical valves to ensure unidirectional flow and that could mechanically be attached to the LV model with teflon screws (Fig. 1b). The model was connected to an MRI compatible pump circulating a glycerin-based blood mimicking fluid (CardioFlow 5000, Shelley Medical Imaging Technologies, Canada) to produce realistic LV inflow patterns (Fig. 1a). The model was scanned with color Doppler on a Philips iU22 ultrasound system and with a 4D MRI flow sequence (Philips Achieva 3.0T TX MR scanner equipped with a 32-element cardiac coil).

Results/Discussion

The ultrasound color Doppler image and phase-contrast MRI recording of this model are shown in Figs. 1c and d respectively. Qualitatively, realistic flow fields were observed with appropriate in- and outflow characteristics as well as vortex development. More quantitatively, the measured velocities from both modalities were in good agreement (correlation coefficient of 0.72 at the max velocity of 0.6 m/s). In conclusion, the developed cardiac mock model was demonstrated to function properly and allow for inter-modality comparisons of flow fields. This will be an important tool for further development of ultrasound flow tracking.

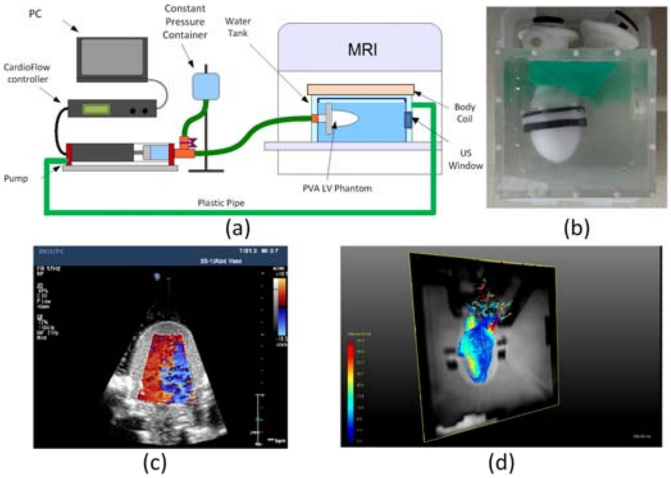

Fig. 1 (a) A schematic overview of the dual-modal mock model. (b) Close-up of the LV model with in- and outflow tracks attached. (c) Ultrasound color Doppler flow imaging. (d) Phase-contrast MRI flow measurements.

4H-4

8:45 am The Spiral Flow Phantom: A New Tool for Vector Flow Estimator Performance Analysis

Billy Y. S. Yiu[1], Alfred C. H. Yu[1]; [1]*Schlegel Research Institute for Aging, University of Waterloo, Waterloo, Canada*

Background, Motivation and Objective

As new flow imaging methods are actively being developed, there is a growing need to devise appropriate phantoms that can holistically assess the accuracy of the derived flow estimates. Straight-tube models simply cannot serve this purpose, nor can spinning discs that simulate tissue motion instead of flow dynamics. Anthropomorphic bifurcation models are also not ideal, because their geometry does not embody all possible curvature angles and thus angle-specific estimation errors are prone to be overlooked. Here, we present a novel spiral phantom design with two unique features: 1) comprehensive multi-directional flow (i.e. from 0 to 360 deg); 2) space-time variability in flow speed. Both features are essential to foster meticulous evaluation of a flow estimator's performance.

Statement of Contribution/Methods

An Archimedes spiral lumen with constant pitch was drafted using Solidworks. It consisted of three loops with constant lumen diameter of 4 mm (Fig a). The outer loop radius was 15 mm, so the entire geometry fitted within the aperture width of an L14-5 array. The spiral radius decreased at a rate of 5 mm per revolution. After appending a horizontal inlet and a vertical outlet connector respectively to the spiral's outermost and innermost positions, a physical phantom of it was fabricated using our established protocol (T-UFFC, 2017; 64: 25-38). The spiral phantom inlet was connected to a gear pump that fed square pulses (10% duty cycle; 5 ml/s peak flow rate; 1 s period). Using a SonixTouch scanner and an L14-5 array (5 MHz freq; 2-cycle duration; 6 kHz PRF), imaging of the spiral phantom's flow dynamics was achieved with multi angle (-10, 0, +10 deg) least squares vector flow imaging (T-UFFC, 2016; 63: 1733-1744). Plane wave color flow imaging was also performed for reference.

Results/Discussion

Color flow imaging yielded unintuitive rendering of spiral flow patterns due to false coloring artifacts [see figure; (b) peak systole, (c) end of systole, (d) diastole; time points marked in (e) spectrogram]. In contrast, vector flow imaging provided a much clearer depiction of spiral flow patterns at those time points [figs (g), (h), (i)]. Differences in flow speeds during (g) systole and (h) diastole can be observed, and spatial variation of flow speeds at (h) end of systole can be seen. These results demonstrate the efficacy of our spiral phantom in the analysis of flow imaging methods.

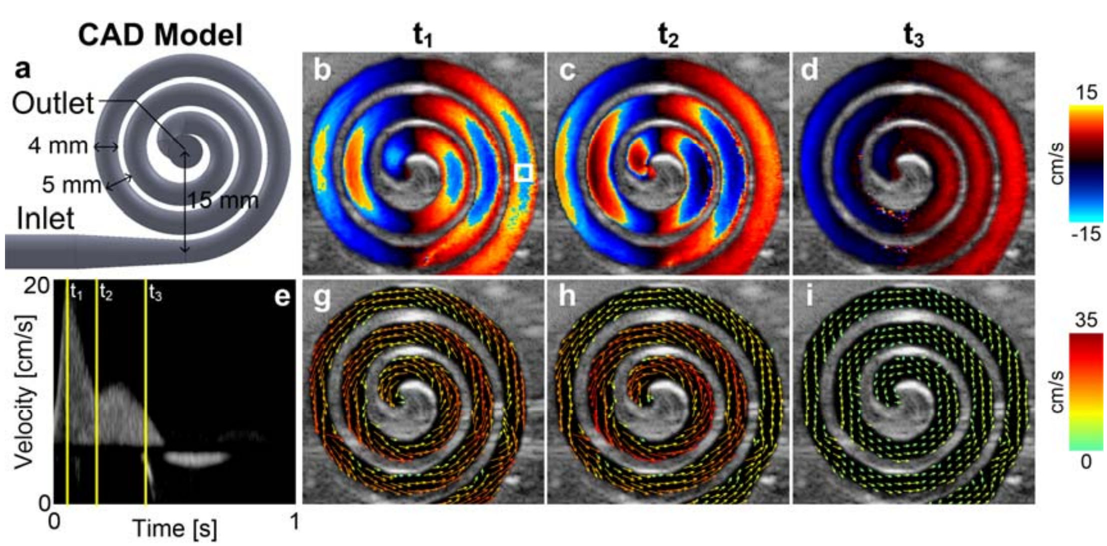

4H-5

9:00 am Singular Value Decomposition-Based Noise Equalization for Ultrafast Plane Wave Microvessel Imaging

Pengfei Song[1], Armando Manduca[2], Joshua D. Trzasko[1], Shigao Chen[1]; [1]*Department of Radiology, Mayo Clinic College of Medicine, Rochester, Minnesota, USA,* [2]*Department of Physiology and Biomedical Engineering, Mayo Clinic College of Medicine, Rochester, Minnesota, USA*

Background, Motivation and Objective

Ultrafast plane wave microvessel imaging significantly improves ultrasound Doppler sensitivity. The rich spatiotemporal plane wave data enables robust clutter filtering based on singular value decomposition (SVD). However, due to the lack of transmit focusing, plane wave microvessel imaging is very susceptible to noise. The mid-to-deep region of the microvessel image is typically saturated by noise, hampering the visibility of microvessels. This study was designed to: 1) study the fundamental relationship between ultrasound system noise and microvessel signal; 2) propose an adaptive and computationally cost-effective noise equalization method derived from the SVD clutter filtering process to improve microvessel image quality.

Statement of Contribution/Methods

An *in vitro* blood flow phantom (Model 1425A, Gammex Inc.) and multiple *in vivo* cases acquired from the Verasonics Vantage system (Verasonics Inc.) and the Alpinion ECUBE-12R system (Alpinion USA) were studied. The relationship among ultrasound system noise, tissue signal, and blood signal was systematically investigated with different gain settings. An adaptive noise equalization method was developed by using the lowest-order singular value and singular vector from the SVD clutter filter process (which primarily represents noise) to reconstruct a 2D noise field. The derived noise field using the proposed method showed good agreement with the experimentally measured noise field.

Results/Discussion

Fig. 1a shows the tissue, blood, and noise measurements along depth and the corresponding power Doppler (PD) image from the flow phantom. Because of the similar signal amplitude between blood and noise, the lower part of the PD image is severely saturated by noise, which increases nonlinearly with increased TGC gain along depth. Reducing the TGC gain (results not shown here) exacerbated the problem. After noise curve equalization (Fig. 1b), the noise saturation is greatly alleviated (although SNR remains the same), which provides a much "quieter" background to visualize the blood flow signal. Figs. 1c-d show *in vivo* examples of noise equalization using the 2D noise field derived from the proposed SVD-based method on pig brain and human liver microvessel imaging. One can see marked improvement of microvessel discernibility (green arrows) after equalization.

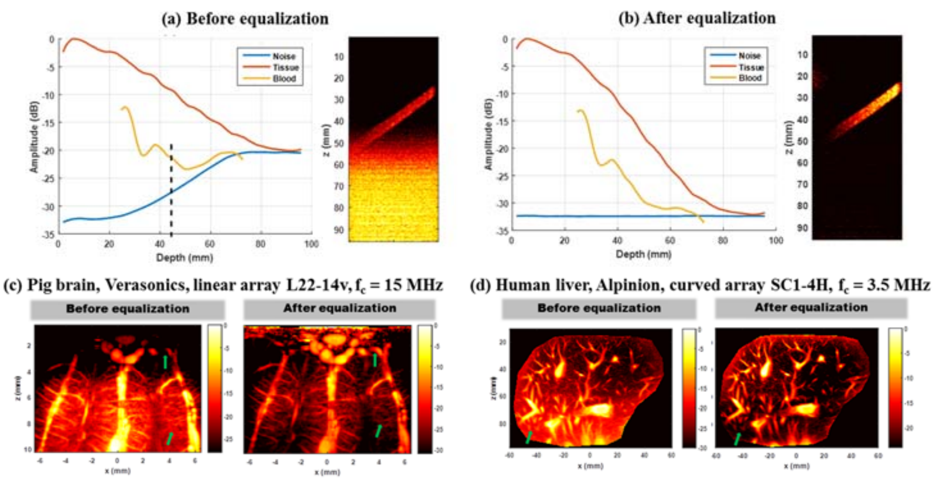

Figure 1. (a)-(b) Measured tissue, blood, and noise and corresponding power Doppler images from the blood flow phantom before and after noise equalization. The black dashed line in (a) indicates the depth where SNR begins to drop below 6 dB. (c)-(d): example power Doppler images from different tissues, transducers, and ultrasound systems before and after noise equalization using the proposed method.

4H-6

9:15 am Beamforming Improvement for Non-Contrast Perfusion Imaging with Adaptive Tissue Clutter Demodulation

Jaime Tierney[1], Brett Byram[1]; [1]*Biomedical Engineering, Vanderbilt University, USA*

Background, Motivation and Objective

Non-contrast blood perfusion imaging with ultrasound is difficult due to tissue clutter caused by patient physiological and sonographer hand motion. This motion causes spectral broadening of the tissue clutter signal, which then overlaps with the perfusion signal. To address this problem, we previously introduced an adaptive frequency and amplitude demodulation scheme to reduce the bandwidth of the tissue clutter signal prior to high-pass filtering. We developed and validated the technique on phantoms and *in vivo* human leg muscles using unfocused single plane wave (SPW) power Doppler imaging to overcome frame rate, ensemble length, and directional limitations associated with conventional scanning.

Statement of Contribution/Methods

To evaluate the benefits of alternative beamforming on adaptive tissue clutter demodulation (ATCD), we used sonographer hand motion phantom data and simulations to compare three different beamforming methods: SPW, plane wave synthetic focusing (PWSF), and short-lag spatial coherence (SLSC)/coherent flow power Doppler (CFPD). For the hand motion study, 6 sonographers acquired data from a quality assurance phantom. For the simulations, a single 0.5mm diameter vessel with 1mm/s parabolic flow of blood scatterers within a 1.5 by 3cm area of tissue scatterers was simulated. Realistic hand motion measurements were used to displace the tissue and blood scatterers. Controlling for tissue clutter, blood, and thermal noise, channel data were simulated using a 7.8MHz center frequency, matching that of the hand motion acquisition. Average blood-to-background SNR was computed on power Doppler data before and after ATCD.

Results/Discussion

Average spectra are shown for each beamforming method before (thick) and after (thin) ATCD in Fig. 1(a). Without ATCD, SLSC suppresses the bandwidth the most, while PWSF performs the best with ATCD. This result is supported by the simulation results. Average blood-to-background SNR (+/- SEM) is plotted for each beamforming method with (orange) and without (teal) ATCD in Fig. 1(b). CFPD produced the best SNR without ATCD (1.67dB). ATCD improved SNR for each beamforming method with PWSF improving the most (6.47dB improvement). These results are supported qualitatively in Fig. 1(c) which shows power Doppler images for one realization and each beamforming method without (top row) and with (bottom row) ATCD.

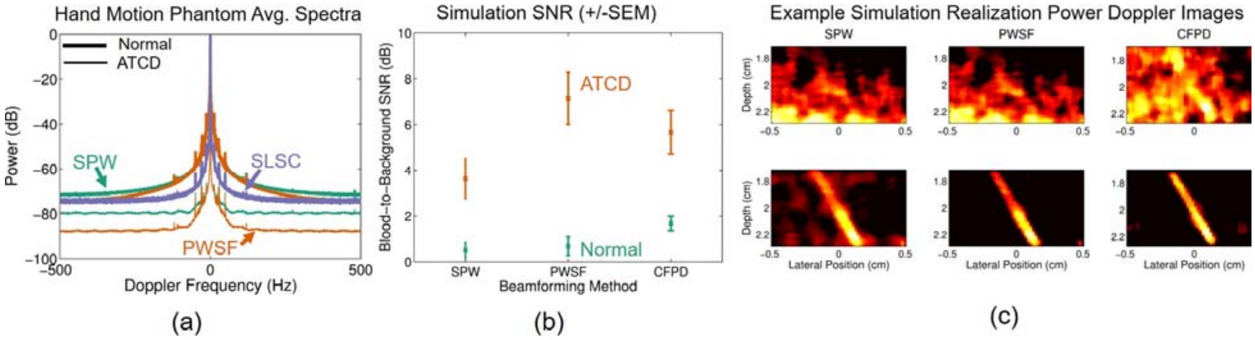

Hand Motion Phantom Avg. Spectra
Normal
ATCD
SPW
SLSC
PWSF
Power (dB)
Doppler Frequency (Hz)
(a)
Simulation SNR (+/-SEM)
ATCD
Normal
Blood-to-Background SNR (dB)
SPW
PWSF
CFPD
Beamforming Method
(b)
Example Simulation Realization Power Doppler Images
SPW
PWSF
CFPD
Depth (cm)
Lateral Position (cm)
(c)

5H - Flow Measurement and Wave Propagation

Blue Room

Saturday, September 9, 2017, 8:00 am - 9:30 am

Chair: **Nishal Ramadas**
Honeywell

5H-1

8:00 am **Ultrasound Flow Mapping of 3D Turbulent Liquid Metal Flows**

Norman Thieme[1], Karl Büchner[2], Richard Nauber[1], Lars Büttner[1], Olf Pätzold[2], Jürgen Czarske[1]; [1]*Laboratory for Measurement and Sensor System Techniques, TU Dresden, Germany,* [2]*TU Freiberg, Germany*

Background, Motivation and Objective

Conductive fluids, e.g. metallic melts, can be driven by magnetic fields, which is a branch of magnetohydrodynamics (MHD). MHD can be used for driving a melt flow during the crystal growth of photovoltaic silicon in order to improve the mass and heat transfer in the melt for better structural and electrical properties of the silicon crystals. However, the optimal application of MHD requires a good understanding of the flow, which is generally complex and unsteady during crystal growth. Substantial knowledge about the flow is usually gained through numerical simulations and MHD model experiments at room temperature. For model experiments, a comprehensive flow mapping of complex and unsteady flow phenomena is required.

Statement of Contribution/Methods

We present an ultrasound array Doppler velocimeter (UADV) suited for model experiments with low-melting metals, e.g. the alloy gallium-indium-tin (GaInSn, melting point 10.5°C). The UADV measures flow maps by a line-scanning approach with arrays of large US elements (pitch > λ). With the line-scanning approach 2-d vector flow maps can be measured and processed effectively, since beamforming calculations are not necessary. In a typical configuration, the UADV is equipped with four ultrasound arrays with 25 elements each. The arrays span two planes measuring two 2-d vector flow fields. The investigation of unsteady flows may take several hours. Therefore, the I-Q demodulation and the velocity estimation are executed on an FPGA, which can reduce the measurement data by a factor of 100. A combined spatial and time multiplexing scheme enables high frame rates of several 10 Hz, which qualifies the UADV for the measurement of turbulent melt flows.

Results/Discussion

The UADV was applied to a model experiment consisting of a cylindrical container filled with the alloy GaInSn and ring coils with a current source generating a magnetic field. The melt flow was driven by a travelling magnetic field. The figure shows a sketch of the experiment and measured instantaneous flow patterns that show the transition from an almost symmetric, stationary to a complex, time-dependent flow.

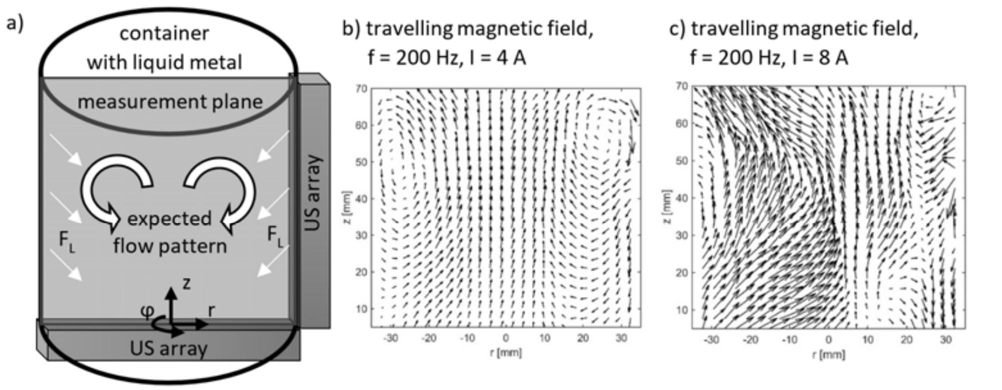

Figure: a) Sketch of the container with the Lorentz force F_L and the expected toroidal flow pattern. b) and c) Vector flow maps measured at the sketched model experiment.

5H-2

8:15 am **Two-Dimensional Flexural Ultrasonic Phased Array for Flow Measurement**

Lei Kang[1], Andrew Feeney[1], Riliang Su[2], David Lines[2], Axel Jaeger[3], Han Wang[3], Yavor Arnaudov[1], Sivaram Ramadas[4], Mario Kupnik[3], Steve Dixon[1]; [1]*University of Warwick, United Kingdom,* [2]*Diagnostic Sonar Limited, United Kingdom,* [3]*Technische Universität Darmstadt, Germany,* [4]*Honeywell, United Kingdom*

Background, Motivation and Objective

Transit-time ultrasonic flow meters, measuring the time difference between upstream and downstream propagation of ultrasonic beams, have been widely utilized to obtain the average velocity of flow in many applications including natural gas flow rate measurement. The signal-to-noise ratio (SNR) of the ultrasonic signals frequently suffers from the sound drift effect, and thus, the arrival time detection probability and the range of the measurement are reduced. Moreover, installation-induced errors of the transducers further degrade the measurement accuracy. To solve these problems, transit-time flow measurements based on 2D flexural ultrasonic phased array technology are investigated. With a phased array, the bend of ultrasonic beams can be compensated by electronic and dynamic beam steering, ensuring optimum SNR and a broader range of measurement. In addition, multiple ultrasonic paths can be realized with an array so that the measurement accuracy can be further improved.

Statement of Contribution/Methods

The flexural ultrasonic phased array used in this research consists of an elastic titanium plate, 16 piezoelectric ceramic discs, a stainless steel baffle with 4×4 holes, and a stainless steel backplate. The baffle is bonded to the titanium plate, with the holes of the baffle defining the boundary conditions of the individual array elements. The piezoelectric discs are bonded onto the 4×4 flexural elements and the backplate is attached to the baffle to improve array's performance. A laser vibrometer (Polytec OFV-5000) is utilized to characterize the array elements, indicating that the centre frequencies of the elements are 48.5 ± 2 kHz. A calibrated microphone (Bruel & Kjaer, 4138-A-015) is chosen to characterize the beam-steering performance, showing that the maximum steering angle can reach to about ± 50°.

Results/Discussion

A flow meter body has been machined to accommodate two flexural ultrasonic phased arrays and a commercial ultrasonic transducer (PROWAVE 500MB120). Preliminary flow tests have been carried out in a calibrated flow rig system, utilizing a commercial turbine gas meter (Elster TRZ G1600, Elster GmbH, Germany), at various gas flow rates ranging from 0 to 2500 m^3/h. The ultrasonic data is acquired using Full Raw Data (FRD) technique by a phased array control system (FIToolbox, Diagnostic Sonar, United Kingdom), which allows various algorithms to be investigated as post-processing operations. Experiments show that, the optimum downstream steering angle decreases from 30° at no flow to about 25° at the highest flow speed, and the upstream steering angle increases from 30° to about 35°. More analysis of the data will be carried out to explore the potentials of the phased arrays in multi-path measurement in the near future. This proof-of-concept design has demonstrated that it is possible to design robust and low-cost flexural ultrasonic phased arrays to improve the accuracy and the range of flow measurement.

5H-3

8:30 am Ultrasound Flow Mapping in a Model of a Secondary Hydraulic Zinc-Air Battery

Christian Kupsch[1], Lukas Feierabend[2], Richard Nauber[1], Lars Büttner[1], Jürgen Czarske[1]; *[1]Laboratory of Measurement and Sensor System Techniques, Technische Universität Dresden, Dresden, Germany, [2]Microsystems & Fluid Mechanics, ZBT GmbH - The Fuel Cell Research Center, Duisburg, Germany*

Background, Motivation and Objective

The investigation of multiphase non-Newtonian flows is of big interest, e.g. for the optimization of the flow field in secondary hydraulic zinc-air batteries (ZAB). These batteries are operated by pumping an opaque suspension of zinc particles and an aqueous potassium hydroxide solution with a binder through an electrochemical cell. Flow investigation is done by means of computational fluid dynamics (CFD), which requires validated numerical models. For multiphase non-Newtonian fluids, new models like the CFD/Discrete Element Method (CFD/DEM) are developed that take particle interaction into account. These models need to be validated, which is done by ultrasound flow mapping. In a model experiment, the planar flow field is measured using a custom research platform, the phased array ultrasound Doppler velocimeter (PAUDV) [1], and compared to the numerical results. For parameterising the PAUDV, the electrolyte suspension has to be acoustically characterized regarding speed of sound and attenuation.

Statement of Contribution/Methods

The particles of the electrolyte suspensions have a non-spherical shape as can be seen in Fig 1a. Hence, a characterization using models like the effective medium model [2] is not applicable and experimental measurements of the speed of sound and attenuation are necessary. We present the acoustical characterization of the electrolyte suspension for volume concentrations in the range of 0 % to 15 % within an ultrasound frequency range from 3 to 13 MHz. For a volume concentration of 4 %, the attenuation calculated using the effective medium model deviates from the measured attenuation by 3 dB/mm, as can be seen in Fig.1b. This underlines the necessity of an experimental characterization, from which we deduce the optimal ultrasound frequency for the flow mapping.

Results/Discussion

Finally, we present the measurement of the flow field inside a model of a ZAB. A scaled up model of the anode channel of a ZAB with an L-shaped flow channel and a gap width of 15 mm and the desired measurement region are shown in figure 1c. A spatial resolution of less than 1.5 mm could be achieved over the whole measurement region.

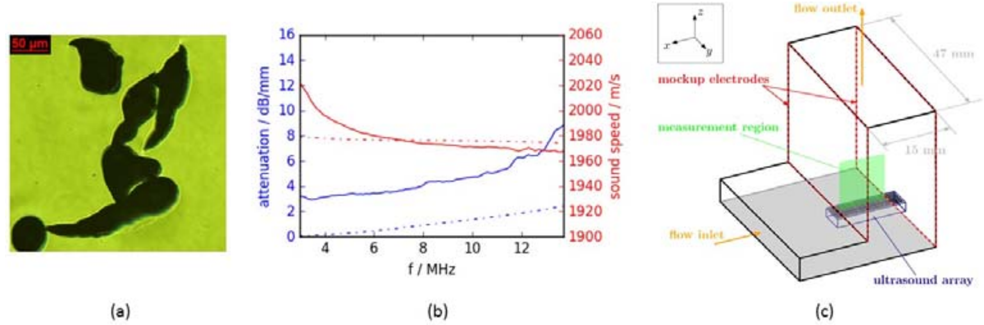

Figure 1: (a) Microscopic recording of zinc particles, (b) continuous line: measured attenuation and speed of sound, dashed line: attenuation and speed of sound from effective medium model [1], (c) flow measurement setup at the ZAB model.

[1] Nauber, R., Beyer, H., Mäder, K., Klaß, A., Thieme, N., Büttner, L., & Czarske, J. (2015, October). Modular research platform for adaptive flow mapping in liquid metals. In *Ultrasonics Symposium (IUS), 2015 IEEE International* (pp. 1-4). IEEE.
[2] Waterman, P. C., & Truell, R. (1961). Multiple scattering of waves. Journal of Mathematical Physics, 2(4), 512-537.

5H-4

8:45 am Ultrasonic Phased Array for Sound Drift Compensation in Gas Flow Metering

Axel Jäger[1], Alexander Unger[1], Han Wang[1], Vavor Arnaudov[2], Lei Kang[2], Riliang Su[3], Dave Lines[3], Sivaram Nishal Ramadas[4], Steve Dixon[2], Mario Kupnik[1]; *[1]Technische Universität Darmstadt, Darmstadt, Germany, [2]University of Warwick, Coventry, United Kingdom, [3]Diagnostic Sonar Limited, Livingston, United Kingdom, [4]Honeywell, United Kingdom*

Background, Motivation and Objective

We present an ultrasonic transit-time gas flow meter (UFM) that features a 40-kHz 2D-phased array for transmitting ultrasonic sound waves up- and downstream to two single element receivers. This allows us to electronically compensate for the well-known parasitic sound drift effect, and, thus, increasing the measurement range by improving the signal-to-noise-ratio (SNR). A regular double-path UFM consists of at least two inclined sound paths to measure the propagation times up- and downstream. However, with increasing flow velocity the sound drift effect reduces the SNR and therefore limits the measurement range. Previous work used rotating [Mylvaganam, TUFFC, 1989] or shifting [Kupnik, IUS, 2006] the ultrasonic transducers to compensate for this parasitic effect. In this work, we consider whether an ultrasonic phased array as a transmitter can be utilized instead. For large diameter flowmeters with ultrasonic transducers, operating at lower frequencies for low attenuation, the array approach not only increases the measurement range but also allows new flowmeter operation modalities, such as adaptive beam steering and off-center measurements for more accurate meter factor determination.

Statement of Contribution/Methods

The UFM fabricated consists of a pipe with an inner diameter of 146 mm with a flush-mounted fully-populated 2D-phased array (8×8 elements, Murata MA40S4S, Murata, Japan, each having a diameter of 10 mm, embedded in a 3D-printed waveguide structure). In order to electronically steer the transmitted beam in both directions, we build custom electronics consisting of an FPGA (Zynq 7010, Xilinx Inc, CA, USA). On the opposite side of the pipe, we use two single element transducers to receive the ultrasonic pulses. The two receiving transducers are positioned towards the phased-array with inclination angles of 30° and -30°, within the maximum beam steering angle ± 55º. Our flowmeter was tested in a calibrated flow rig system, using a commercially available reference meter (turbine gas meter, Elster TRZ G1600, Elster GmbH, Germany), at various gas flow velocities.

Results/Discussion

First, we tested the array without sound drift compensation, i.e. the transmitted waves emitted up- and downstream with beam steering angles of 30° and -30°, respectively. The receiving amplitudes reduced by 39% (downstream) and 26% (upstream) when the flow velocity was ramped up to 40 m/s. Then, when the sound drift compensation was applied by beam steering, the amplitudes only dropped by 13% in both cases at the maximum gas flow velocity. These results prove that the approach of using the phased-array will significantly increase the measurement range. For future work, we plan to repeat the measurements at a stronger flow rig system, capable of generating higher flow velocities. Further, besides using phased arrays as receivers, we also plan to test additional off-centric single element receiver locations for better meter factor determination.

5H-5

9:00 am **Energy Distribution Analysis of Ultrasound Transmission Line Modeled by Cascade-Connection Resonators**

Keita Tachibana[1], **Norio Tagawa[1]**, Takasuke Irie[1,2], Masasumi Yoshizawa[3], Tadashi Moriya[1]; [1]*Department of System Design, Tokyo Metropolitan University, Tokyo, Japan,* [2]*Microsonic Co., Ltd, Tokyo, Japan,* [3]*Tokyo Metropolitan College of Industrial Technology, Tokyo, Japan*

Background, Motivation and Objective

As an application of ultrasonic motors becomes popular, an ultrasound transmission line (UTL) is required to be efficient. Actually, we are developing a puncture type ultrasonic microscope [1] using a miniature ultrasonic motor for scanning. We have to supply a flexural wave through a thin UTL to rotate the motor. In general, when an UTL touches neighboring covers, the propagating wave drastically attenuates. Hence, we are examining the UTL which is fixed to the cover by retainers located every a half wavelength for forming a cascade-connection resonator in it. We reported the resonance property evaluated through simulations as a standing wave for a longitudinal wave [2]. In this study, we confirm the energy distributed in the UTL to clarify the resonance characteristics for a flexural wave that is suitable for driving our motor.

Statement of Contribution/Methods

The left figure shows a 2-D model used in the FEM simulations. The UTL made from stainless steel with a density of 7,930kg/m^3 is placed in the air, and the sinusoidal pressure with 500 kHz generates a flexural wave having a wavelength of 3.1 mm. It is expected that each section between adjacent two retainers behaves as a resonator. We analyze the energy distribution consisting of kinetic and strain energies in the UTL while changing a load density.

Results/Discussion

We confirmed that the both energies in each resonator section in the UTL become larger than the case without fixing, i.e. with no retainers, as the Load density becomes high; in other words, the mechanical impedance matching between the UTL and the load becomes high. The right figure shows the input energy into the UTL, the output energy toward the load and the energy leaking from the retainers. The results indicate that, when the load density is high, the inputted energy increases, which means that the resonance phenomenon occurs. The amplified energy compensates for the leaking energy, and thereby the UTL can provide output energy of the quantity same as a case without retaining. When the retainers are placed at the irregular positions instead of with a half wavelength interval, the output energy decreases obviously. Therefore, our resonator-type UTL can be used for various applications effectively.

[1] T. Irie et al., IEEE Int. Ultrasonics Symp., (2015).

[2] K. Tachibana et al. IEEE Int. Ultrasonics Symp., (2016)

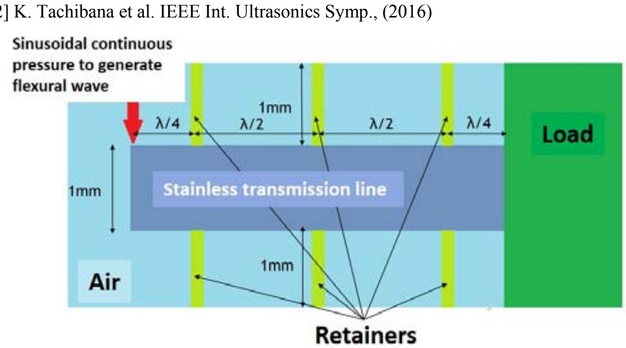

2D simulation model of transmission line

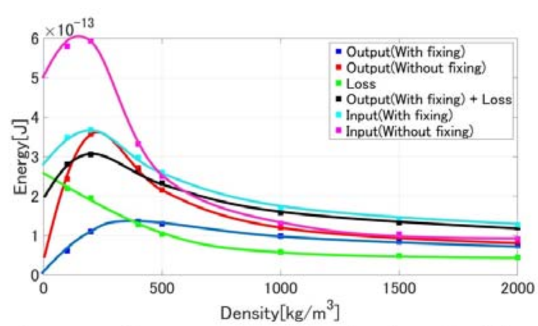

Input and output energies simulated with or without fixing while changing load density

5H-6

9:15 am **Real-Time Staggered PRF for Extended In-Line Industrial Fluids Characterization**

Stefano Ricci[1], Johan Wiklund[2], Valentino Meacci[1]; [1]*Engineering Information Dept., Florence University, Firenze, FI, Italy,* [2]*Bioscience and Materials, Research Institutes of Sweden (RISE), Göteborg, Sweden*

Background, Motivation and Objective

The rheology of a fluid flowing in an industrial pipe can be assessed by combining the pressure drop and the fluid velocity profile, which can be obtained non-invasively through a Pulsed Wave Doppler (PWD) ultrasound investigation. In PWD, the maximum detectable velocity is related to the Pulse Repetition Frequency (PRF), which, in turn, is limited by the maximum investigation depth. Unfortunately, high flow-rates flowing in large industrial pipes produce Doppler frequencies that easily exceed the Nyquist limit, thus resulting in aliased, corrupted measurements.

Staggered PRF is a known technique that allows an extension of the Nyquist limit. The de-aliased velocity is recovered by combining the aliased velocities measured from different PRFs, generated with specific ratios. In this work, we extend the capabilities of an embedded ultrasound system for rheological characterization of industrial fluids (doi: 10.1109/ULTSYM.2015.0273) by implementing, in real-time, the staggered PRF method.

Statement of Contribution/Methods

The Field Programmable Gate Array (FPGA) included in the system is programmed to produce an excitation sequence composed by 2 groups of 128 pulses at PRF1 and PRF2= ¾ PRF1 rate. According to staggered PRF method, the Nyquist limit is extended 3-fold.

The echoes received from each group are sampled in 512 depths, and processed in the FPGA through windowing, 128-point FFT, weighted mean, to obtain the (possibly aliased) Doppler frequencies at each depth. These Doppler frequencies are then combined according to the staggered PRF method for generating the de-aliased velocity profile in each depth. The process is repeated for the next 128+128 pulses.

Results/Discussion

The system with real-time staggered PRF was tested in a flow-rig by investigating a 60 cm/s flow. 5MHz ultrasound bursts were transmitted with PRF1 and PRF2 set at 4kHz and 3kHz, respectively. The echo signal was processed by calculating an FFT every 40 us, and thus a 512-depth frame was produced in about 20 ms. Every 2 frames acquired with different PRF, a de-aliased velocity profile was calculated. The picture below shows an example of FFT frames, coded in grey levels, obtained at PRF1 (left) and PRF2 (center). The reconstructed velocity profile, which exceeds the Nyquist velocity limit (red vertical dashed line, corresponding to PRF 1) is reported on the right.

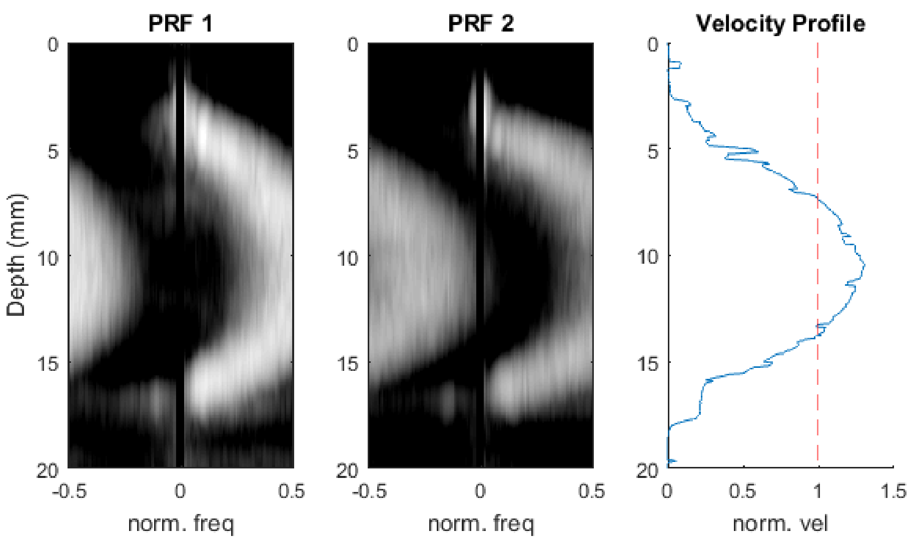

6H - PPN - Phononics

Hampton Room

Saturday, September 9, 2017, 8:00 am - 9:30 am

Chair: **Alex Maznev**
MIT

6H-1

8:00 am Coupling of Mechanical Resonators under Surface Acoustic Wave Excitation

Sarah Benchabane[1], Laetitia Raguin[1], Olivier Gaiffe[1], Roland Salut[1], Valérie Soumann[1], Vincent Laude[1], Abdelkrim Khelif[1]; [1]*FEMTO-ST, CNRS, Université de Franche-Comté, Besançon, France*

Background, Motivation and Objective

Coupling between surface acoustic waves (SAW) and arrays of mechanical resonators has appeared early in SAW history as a potential means to slow down wave propagation through mass-loading, in particular by creating corrugations on the substrate surface. This concept has been revisited over the past few years in the context of locally-resonant phononic crystals where pillars deposited on a homogeneous surface were shown to hybridize with SAW to form band gaps conditioned by the pillar resonance frequencies. Most of the works reported in the literature focus on the interaction between propagating waves and a collection of resonators. We recently considered the interaction of SAW with isolated mechanical resonators and shown that elastic energy can be strongly confined in subwavelength, micron-scale structures. In this work, we experimentally investigate the coupling characteristics of pairs of pillars driven by SAW. The objective here is to set the basics for the realization of waveguides based on compact chains of phononic resonators.

Statement of Contribution/Methods

Pairs of resonators spaced from 0.9 to 6 µm were fabricated on a Y-cut lithium niobate substrate using FIBID (Focused Ion Beam Induced Deposition) of platinum. Although this technique permits the realization of 3D structures with dimensions as low as a few tens of nanometers, we deliberately fabricated cylindrical pillars with a diameter of 4.3 µm in order to be able to distinctly map the displacement field at the pillar surface using optical interferometry. Within each resonator pair, the pillars were fabricated simultaneously to ensure repeatability in shape and size. Annular, chirped interdigitated transducers, exhibiting an electrode shape following the slowness curve of the supporting substrate were used as an excitation source to generate Rayleigh waves in the 50-100 MHz frequency range. The pillar resonance frequencies and the elastic energy distribution were experimentally measured by laser scanning interferometry.

Results/Discussion

The pillars resonate on a first-order flexural mode within the considered excitation frequency range. A shift of the resonator's natural frequency is observed and shown to be dependent on the distance separating two pillars, hence suggesting the occurrence of energy coupling between neighboring resonators and offering the possibility to determine the corresponding coupling strength. Preliminary investigations of the elastic field distribution at the substrate surface reveal that specific geometrical configurations and frequencies tend to favor a strong localization of the elastic energy in between pillars at the substrate surface. These first results suggest that both mechanical and surface mediated coupling can be expected, offering interesting prospects for elastic energy control and waveguiding in compact, SAW-actuated elastic waveguides.

6H-2

8:30 am Numerical and Experimental Demonstration of the Electrical Bragg Band Gaps in Piezoelectric Plates with a Periodic Array of Electrodes

Clement Vasseur[1], Charles Croënne[1], Bertrand Dubus[1], Jérôme Vasseur[1], Claude Prevot[2], Paolo Martins[2], Mai Pham Thi[2], Anne-Christine Hladky[1]; [1]*CNRS, Centrale Lille, ISEN, Univ. Lille, Univ. Valenciennes, UMR 8520 - IEMN, Lille, France,* [2]*Thales Research and Technology, Palaiseau, France*

Background, Motivation and Objective

Recent analytical and numerical studies have shown that Electrical Bragg band gaps (EBBGs) may occur in piezoelectric plates poled along their thicknesses, with a 1D periodic array of electrodes on their two faces (Fig. 1) [C. Vasseur et al, Proceedings of 2016 IEEE IUS 2016, paper P3-C2-7, 4 pages]. These Bragg band gaps can be opened or closed by changing the electrical boundary conditions on the electrodes. In practice, the gap exists when all electrodes are left floating, and disappears when they are all grounded. In this paper, numerical and experimental results are presented for a finite piezoelectric plate and the concept is extended to a 2D periodic array of electrodes on the top and bottom surfaces of the piezoelectric plate, in order to control the propagation path of the wave.

Statement of Contribution/Methods

To evaluate the effect of the EBBG for a finite system, a 10 x 10 x 0.5 mm plate, made of PMN-28PT and poled along its thickness, is used. Ten 0.9 mm-wide electrodes are deposited on its top surface (Fig. 2). Spacing between adjacent electrodes is 0.1 mm, so periodicity is 1 mm. The electrodes at both ends of the plate are used as electrical input and output ports, and the eight intermediate electrodes are all either floating or grounded. Out-of-plane displacements are measured using a scanning laser vibrometer.

Results/Discussion

Fig. 3 shows a comparison between the measured displacements on the output electrode when the intermediate electrodes are floating or grounded. A decrease in amplitude of approximately 10 dB is evidenced in the frequency range of the EBBG. Additional vibratory and electrical measurements on the sample are under progress. The concept is then extended to a 2D periodic array of electrodes on a plate, each one having its own electrical connection, in order to achieve the two-dimensional control of the wave propagation path in the piezoelectric plate.

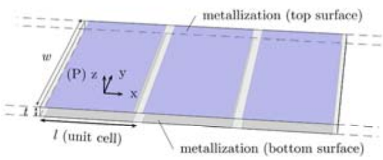

Fig. 1: Schematic view of the device

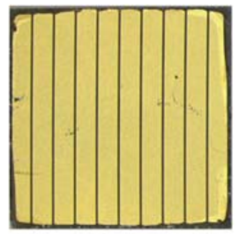

Fig. 2: Fabricated PMN-28%PT plate with an array of electrodes.

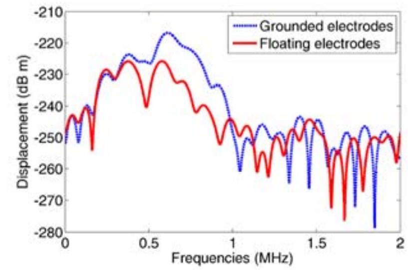

Fig. 3: Measured displacement amplitude of output electrode for grounded and floating electrodes.

6H-3

8:45 am **Focusing of Ultrasonic Waves in Water with a Flat Artificial Composite Plate**

Xiangxiang Xia[1,2], Feiyan Cai[2], Fei Li[2], Di Xu[2], Manzhu Ke[1], Zhengyou Liu[1], Hairong Zheng[2]; [1]*Key Laboratory of Artificial Micro- and Nano-Structures of Ministry of Education, School of Physics and Technology, Wuhan University, China, People's Republic of,* [2]*Paul C. Lauterbur Research Center for Biomedical Imaging, Shenzhen Institutes of Advanced Technology, Chinese Academy of Sciences, China, People's Republic of*

Background, Motivation and Objective

Acoustic lenses, concentrating the acoustic energy into a specific area, have attracted interest due to their broad applications in various domains, such as biomedical imaging, nondestructive testing, etc. For waterborne sound, conventional silicone materials are fabricated with concave shape for focusing wave. However, it is not flexible to design a concave lens than a flat lens to manipulate acoustic focusing. In this research, we investigate a composite structure with flat plate tuning acoustic plane waves focusing in water.

Statement of Contribution/Methods

As shown in Figure 1(a), the schematic of the designed acoustic lens, the center of the slits are all equidistance, and the refractive index (neff) of the composite structure changes with the filling factor of B. The different materials A and B represent PMMA and Silicone, respectively. The acoustic lens is immersed in water, and plane wave at 0.5MHz frequency incident from the bottom of the lens. We simulate the pressure field and the distributions of the field using the COMSOL software.

Results/Discussion

Through analyzing the numerical results of the acoustic properties of composite material, we find that the refractive index changes with the filling factor of the Silicone in the PMMA. The interesting phenomenon originate from the different acoustic properties of the two materials. As shown in Figure 1(d), the range profile of the pressure amplitude distribution, which is along the vertical line shown in Figure 1(b), the predicted focal length is observed. Furthermore, the full width at half maximum (FWHM) ≈0.9λ, less than the wavelength, as shown in Figure 1(c). Thus, this flat artificial composite plate can be used as an acoustic lens to manipulate acoustic plane wave focusing.

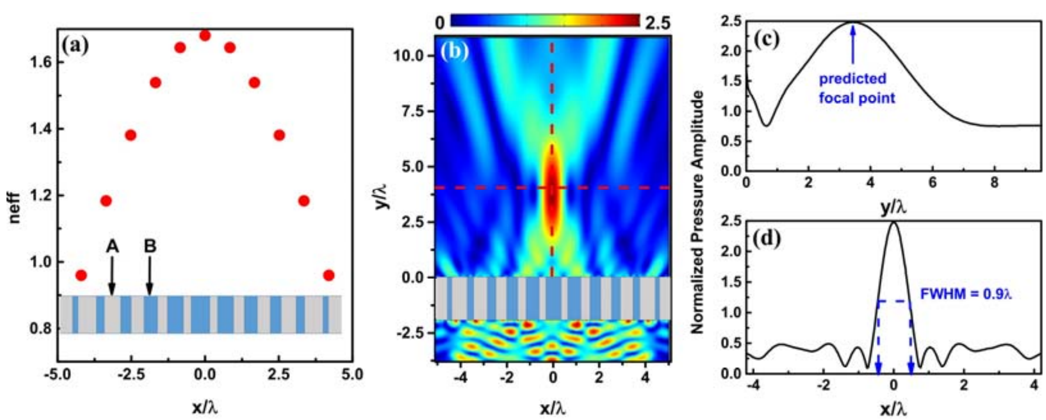

Figure 1(a) The refractive index (neff) as a function of the position of the slit. Schematic of the designed acoustic lens as the inset shows, A and B represent PMMA and Silicone, respectively. (b) The distributions of the pressure field of plane waves at 0.5MHz frequency incident on the bottom of the acoustic lens. (c) Cross-range and (d) range distributions of the pressure field shown in Figure 1(b).

6H-4

9:00 am **Acoustic Topological Insulator Based on Phononic Crystals**

Yuanchen Deng[1], Yun Jing[1]; [1]*NC State University, USA*

Background, Motivation and Objective

Quantum Spin Hall Effects(QSHE) underpins most of the design in topological insulators. The intrinsic spin-0 of the phononics, yet, continue to be the main barrier in designing acoustic topological insulators. Previous research proposed a solution using external fields such as clockwise and counter-clockwise circulating fluids to create artificial acoustic spin-1/2 states. Most recently, several papers provided ideas based on forming two pairs of degenerate Bloch modes in phononic crystals by tuning the filling factor of the honeycomb lattice. In this work, we introduce a new way to form a phononic double Dirac cone based on the idea of “zone folding”. By simple modifications of the geometry, topological protected bulk band gaps can be opened and a helical edge channel can be realized.

Statement of Contribution/Methods

In a traditional triangular lattice phononic crystal, the unit cell could be chosen as a hexagon with a single "atom" at the center. The hexagonal unit cell has a six-fold rotational symmetry C_6 as well as a translational symmetry T_a corresponding to the lattice constant a. A single Dirac cone will exist at the high symmetry point K and K' of the first Brillouin zone (BZ) because of the C_6 symmetry. Here we modify the unit cells so that the physical domain is enlarged. Whereas there is still an "atom" at the center, there are 6 "1/3 atom"s at each corner of the hexagon. The size of the unit cell is enlarged by $\sqrt{3}$ and the size of the Brillouin zone will consequently be reduced by the same factor. Because there is also a 60 degrees rotation from the original orientation, the change of the Brillouin zone will map the Dirac cones from K and K' into the new BZ's Γ point, which will form a double Dirac cone. By either increasing or reducing the radius of the center "atom" of the new unit cell, the translational symmetry will be broken while the C_6 symmetry will be preserved and a topological protected band gap can be created, leading to robust one-way propagation of acoustic waves.

Results/Discussion

A supercell comprising two different types of unit cells (ones with larger center "atom" and ones with smaller center "atom") is built to find the edge states formed at the boundaries, from which the helical channel is designed. The Finite Element Method and experimental results show that the helical edge channel gives rise to robust one- way wave propagation with the presence of a curved edge channel.

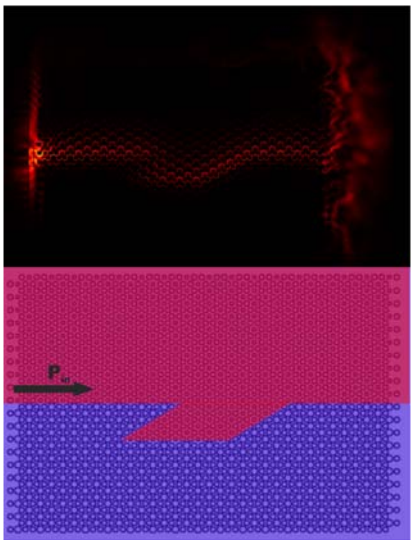

6H-5

9:15 am Stochastic Generation of the Phononic Band Structure of Lossy And Infinite Crystals

Maria Korotyaeva[1], **Vincent Laude[2]**; [1]*Institut FEMTO-ST, Université de Bourgogne Franche-Comté, Besancon, France,* [2]*Institut FEMTO-ST, Université de Bourgogne Franche-Comté, CNRS, Besancon, France*

Background, Motivation and Objective

The concept of the band structure is central to the field of phononic crystals. Indeed, capturing the dispersion of Bloch waves - the eigenmodes of propagation in periodic media - gives invaluable information on allowed propagation modes, their phase and group velocities, local resonances, and band gaps. Band structures are usually obtained by solving an eigenvalue problem defined on a closed and bounded domain, which results in a discrete spectrum. There are at least two cases, however, that cannot be reduced to a simple eigenvalue problem: first, when materials showing dispersive loss are present and second, when the unit-cell extends beyond any bound, as in the case of phononic crystal of holes or pillars on a semi-infinite substrate.

Statement of Contribution/Methods

We introduce a numerical technique to obtain the phononic band structure that does not rely on eigenvalues. In spectral theory, the spectrum (and hence the band structure) is the singular complement of the resolvent set in the complex plane. The idea is then to obtain the resolvent set of the acoustic or elastodynamic operator. In practice, we solve a system of the form $(K(\mathbf{k})-\omega^2 M)\,\mathbf{u}=\mathbf{y}$, where K is a stiffness matrix dependent on wavevector **k**, M is a mass matrix, ω is the angular frequency, **u** is the unknown displacement vector field, and **y** is a stochastic body force. From the solution, we obtain a density of states that has complex poles coinciding with the band structure. For the case of infinite or semi-infinite unit-cells, we employ a perfectly matched layer (PML) to close to computation domain.

Results/Discussion

The method has been applied to several problems in phononic crystal theory. In the case of dispersive loss, the complex poles of the density of states give a direct account of propagation loss of each dispersion branch as a function of frequency. The figure shows a comparison of a classical band structure (left) with the density of states accounting for viscoelastic losses (right), for a square-lattice sonic crystal of rigid rods in air. In the case of phononic crystals of finite-depth holes or of finite-height pillars sitting on a semi-infinite substrate, the dispersion inside the sound cone - or radiative region - is obtained. It is also found that the results can be made almost independent of the particular realization of stochastic body force that is applied.

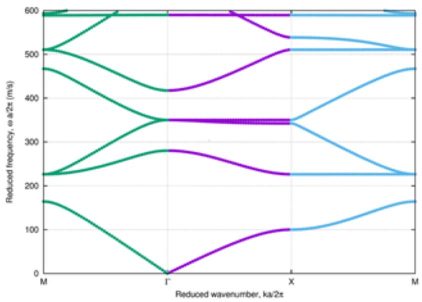
Reduced frequency, ω a/2π (m/s)
Reduced wavenumber, ka/2π
M
Γ
X
M
0
100
200
300
400
500
600

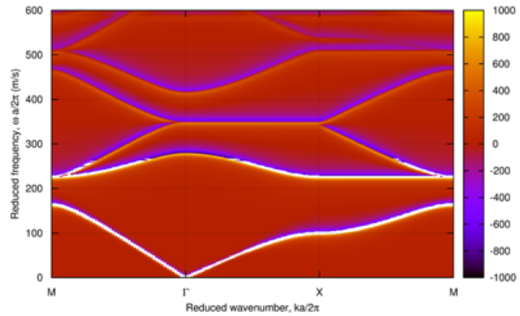
Reduced frequency, ω a/2π (m/s)
Reduced wavenumber, ka/2π
M
Γ
X
M
0
100
200
300
400
500
600
1000
800
600
400
200
0
-200
-400
-600
-800
-1000

7H - Microacoustic Device Design

Empire Room

Saturday, September 9, 2017, 8:00 am - 9:30 am

Chair: **Jan Kuypers**
Qorvo

7H-1

8:00 am **Small Sized Band 20 SAW Duplexer Using Low Acoustic Velocity Rayleigh SAW on $LiNbO_3$ Substrate**

Masakazu Mimura[1], Daisuke Ajima[1], Chihiro Konoma[1], Tomohiko Murase[1]; [1]*Murata Manufacturing Co., Ltd., Japan*

Background, Motivation and Objective

In recent years, numerous SAW filters and duplexers are used in each mobile terminal. In such situations, miniaturization of SAW devices has been required and various efforts have been carried out. As for current SAW devices, most of the surface area of a SAW die is filled with interdigital transducers (IDTs). A size of IDTs highly depends on the wave length of the SAW, which is proportional to the acoustic velocity. Therefore, lowering the acoustic velocity will be essential for further miniaturization. Nowadays, the Rayleigh SAW on $LiNbO_3$ (LN) substrates with a SiO_2 overlay is widely used for temperature compensated SAW devices. Accordingly, lowering the acoustic velocity of this wave mode is significant for current mobile terminals.

Statement of Contribution/Methods

In order to lower the acoustic velocity, we adopted multi layered IDT electrodes of Pt and Al, and increased the thickness of the Pt layer. Several FEM simulations were performed to optimize the Pt thickness and the cut angle of LN substrates, and one port resonators were fabricated to confirm the calculation results. Furthermore, we applied these resonators to a duplexer for Band 20.

Results/Discussion

From FEM simulations, the velocity of 3000 m/s, about 17 % lower than normal SAWs, was obtained at the Pt thickness of 0.08λ. The good cut angle, in which the k^2 of the SH-type SAW is almost zero and that of the Rayleigh SAW is moderate, could be found at 120° Y-X. The acoustic velocity of 3025 m/s at the resonant frequency of the fabricated one port resonator was achieved, and no spurious response could be found around the resonant and anti-resonant frequencies. Its k^2, TCF and Q-value are comparable to those of the conventional Rayleigh SAW on 128° Y-X LN.

Figure 1 shows the measured transmission characteristics of the developed duplexer. Small insertion loss of 1.9 dB in Tx band and 1.8 dB in Rx band and good shape factor have been achieved. The die size of the duplexer is 1.0 mm × 1.3 mm, about 19 % smaller than conventional duplexers.

By lowering the acoustic velocity of the Rayleigh SAW on LN substrates, we successfully achieved remarkable miniaturization of SAW duplexers maintaining high performances.

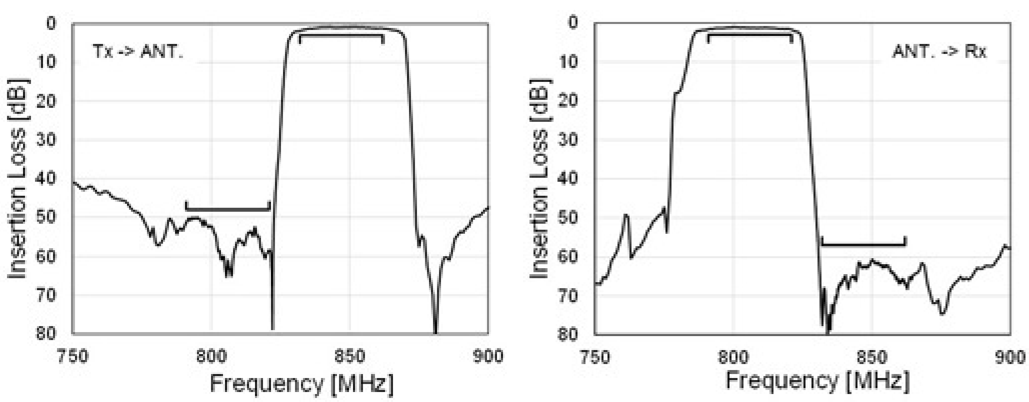

Fig. 1

7H-2

8:15 am **Relation between Electromagnetic Coupling Effects and Network Synthesis for Acoustic Wave Ladder Type Filters**

Angel Triano[1], **Jordi Verdu**[1], Pedro de Paco[1], Thomas Bauer[2], Karl Wagner[2]; [1]*TES, Universitat Autonoma de Barcelona, Cerdanyola del Vallès, Barcelona, Spain,* [2]*RF360 Europe GmbH, Germany*

Background, Motivation and Objective

Factors limiting the isolation of conventional miniaturized filters and duplexers have been considered in the literature. They can be classified into two types of signal leakage: one occurs via the main signal path due to the finite impedance of the RX filter in the TX band in a duplexer; the second one is due to electromagnetic feedthrough (EMF), electromagnetic couplings or imperfect grounding. Because of the existence of these leakages, the isolation of usual duplexers is limited to about 50 to 55 dB.

Statement of Contribution/Methods

A synthesis technique has been developed. Using parameter extraction of the resonators and the desired cross-inverters, a number of topologies are synthesized. Studies on the electric performance due to potential parasitic elements, such as the EMF between ports, have also been developed. The presence of the cross-inverter is not desired, but forced by the physical structure. Then, the resonant frequencies of the resonators are not equal to the transmission zeros as expected.

The numerator of the transmission function polynomial P0(s) is constructed with its' roots, which correspond to the predefined finite transmission zeros (TZ) at the beginning of the process. However, all resonators affected by a cross-coupling (EMF case) have to resonate at different resonant frequencies to keep the position of the original TZs, that is, a frequency shift of the TZs will happen. But also, some of the zeros at kth extraction step may become complex, so that they can not be properly extracted with a Non-Resonant Node / Resonant node pair (NRN-RN). When complex singularities arise, further cross-couplings are required to be extracted. Otherwise, the filter characteristics are degraded because the acoustic resonator is unable to implement complex roots.

Results/Discussion

Two scenarios are shown in the figure. On the left side is the co-simulation of a measured filter with different EMF modelled with a cross inverter, also shown is the floor level. On the right is the simulation of a ladder filter compared for different cases. The transmission response of an isolated filter, the filter response when the EMF is present, the response when one of the roots is complex, and finally, the filter including a cross-coupling to convert the complex root to pure imaginary (black, red, green and blue lines). The blue line well approximates the original filter without EMF.

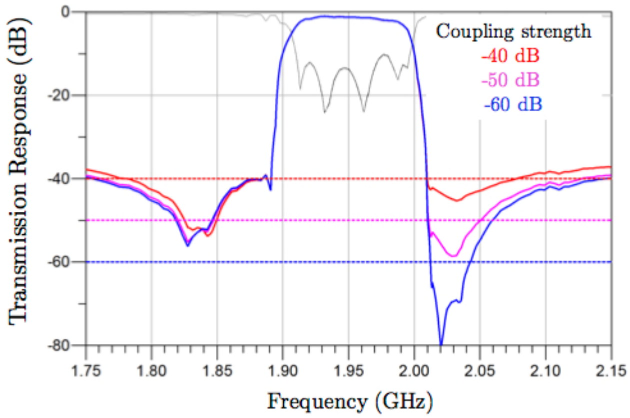

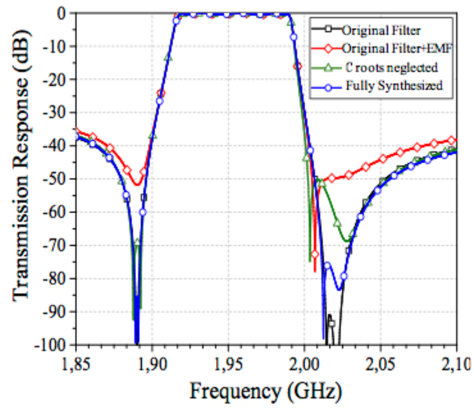

7H-3

8:30 am Temperature Compensated SAW with High Quality Factor

Benjamin Abbott[1], Alan Chen[1], Tim Daniels[1], Kevin Gamble[1], Taeho Kook[1], Marc Solal[1], Kurt Steiner[1], Robert Aigner[1], Svetlana Malocha[1], Curtis Hella[1], Mark Gallagher[1], Jan Kuypers[1]; [1]*Qorvo, USA*

Background, Motivation and Objective

Mark Twain said "There is no such thing as a new idea. It is impossible. We simply take a lot of old ideas and put them into a sort of mental kaleidoscope. We give them a turn and they make new and curious combinations. We keep on turning and making new combinations indefinitely; but they are the same old pieces of colored glass that have been in use through all the ages."

This sentiment rings true for high quality factor temperature compensated SAW devices (TCSAW). The foundations for high Q TCSAW arrived nearly 30 yrs prior to their application in cellular handsets. Two dominant technical foundations are temperature compensation by an SiO_2 overcoat [1], and the suppression of transverse modes by construction of a acoustic waveguide for the so called "piston mode" [2].

[1] K. Yamanouchi, "SAW Properites of SiO2/128o Y-X LiNbO3 Structure Fabricated by Magnetron Sputtering Technique," IEEE Trans. on Sonics and Ultrasonics, Vol. SU-31, No. 1, Jan 1984.

[2] S. Wilkus, C. Hartmann, R. Kansy, "Transverse Mode Compensation of Surface Acoustic Wave Filters," IEEE IUS 1985.

Statement of Contribution/Methods

The kaleidoscope of ideas forming the foundation for TCSAW were in place in 1985. However, the initial prototypes demonstrating feasibility weren't developed until about 30 yrs later. Feasibility was quickly followed by surging volumes high Q TCSAW products. The drivers for demand of these products are new cellular bands with tighter spectrum requirements, and new features such as RX diversity and carrier aggregation.

Using Chebeyshev Type II filter prototypes, the TCF and Q necessary to meet the performance requirements for current wireless handsets may be estimated. Using this approach Q/TCF iso-lines are derived from filter specifications which delineate between feasible and infeasible regions. Figure 1 illustrates examples of iso-lines associated with performance requirements and Q & TCF values of respective TCSAW products.

Results/Discussion

The embodiment of a temperature compensating acoustic thin film stack is presented. The relationship/trade-off between piezoelectric coupling, TCF, and quality factor is examined. Likewise, the construction of the piston mode waveguide is presented.

Using Q and TCF data from TCSAW resonators, the suitability of using high Q TCSAW to meet the performance requirements of several cellular bands is examined.

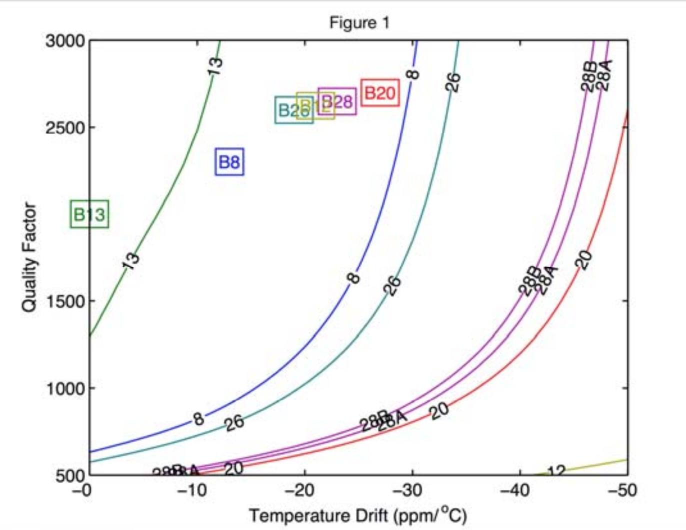

7H-4

9:00 am **Influence of Coupling between Rayleigh and SH SAWs on Rotated Y-cut $LiNbO_3$ to Their Electromechanical Coupling Factor**

Yulin Huang[1,2], Jingfu Bao[1], Xinyi Li[1,2], Benfeng Zhang[2,3], Gongbin Tang[2,3], Tatsuya Omori[2], Ken-ya Hashimoto[2,3]; *[1]University of Electronic Science and Technology of China, Chengdu, Sichuan, China, People's Republic of, [2]Chiba University, Chiba, Chiba, Japan, [3]Shanghai Jiao Tong University, Shanghai, China, People's Republic of*

Background, Motivation and Objective

Suppression of the SH-SAW response is mandatory to design TC SAW devices on θ degree rotated Y-cut $LiNbO_3$. However, it is not easy because K^2 for SH SAW changes rapidly with θ, and its optimal value in terms of the SH-SAW suppression is dependent on electrode and SiO_2 thicknesses. The authors found that the optimal θ always locates close to θ where difference in velocities of two SAWs is minimum. This suggested that their coupling is responsible for variation of their K^2.

Statement of Contribution/Methods

This paper investigates influence of coupling between Rayleigh and SH SAWs to their K^2. For the purpose, a COM model including the coupling between two SAWs is developed, and its validity is confirmed by comparison of its results with the FEM analysis. Then it is discussed how the coupling influences to their excitation in addition to propagation.

Results/Discussion

Fig. 1 compares dispersion curves of SAWs calculated by the FEM with ones obtained by the developed COM model when θ=126.6°, the IDT period is 4.4 µm, and the Cu electrode thickness is 0.162 µm, Agreement is well for both the short-circuited (SC) and open-circuited (OC) grating cases. The dispersion curves of coupled two SAWs change anomalously at 887 MHz due to their interference. In the Figure, the corresponding admittance curve is also given in the bottom. A spurious resonance is seen at 887 MHz.

Fig. 2 shows the results when θ=124.8°. It is seen that two dispersion curves are completely separated, and the spurious response disappears. It should be noted that COM parameters used in the calculation are almost equal to those used in Fig. 1, and K^2 of the uncoupled SH SAW is comparable to that of the uncoupled Rayleigh SAW.

The present COM analysis indicates that K^2 of the coupled SH SAW takes a minimum when that of the coupled Rayleigh SAW takes a local maximum.

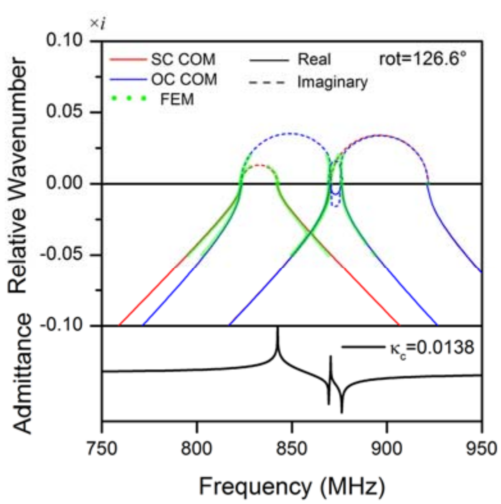

Fig.1 Calculated dispersion curves (θ = 126.6°) and its Admittance

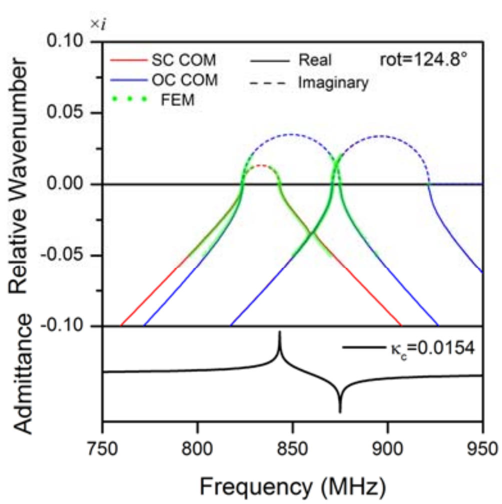

Fig.2 Calculated dispersion curves (θ = 124.8°) and its Admittance

9:15 am Full 3D Simulation of SAW Resonators Using Hierarchical Cascading FEM

MARC SOLAL[1], Alireza Tajic[1]; [1]*Qorvo Inc., Apopka, FL, USA*

Background, Motivation and Objective

The normal way to simulate SAW resonators is to use a phenomenological model like coupling of modes or P matrix. Numerical methods can also be used but are very costly in computing resources. Models based on combination of finite elements and boundary elements models are a possible approach but are mostly limited two dimensional models. Also, they are less versatile than models using only finite elements. A new approach was proposed in 2016 [1]. This approach is based strictly on finite elements and uses a perfectly matched layer to describe the infinite substrate. By taking advantage of the repetitive structure of the resonator, the computation time becomes proportional only to the logarithm of the electrode number. The results shown last year were limited to two dimensions. The goal of this paper is to show that this method can be extended to a full 3D simulation.

Statement of Contribution/Methods

The hierarchical cascading method proposed in [1] is extended to the full 3D simulation of a SAW resonator. The resonator is split into unit cells comprising two electrodes (one wavelength). The unit cell is meshed in 3D including its transverse structure (electrodes, gaps, bussbars). Perfectly matched layers are used for avoiding reflections on the edges of the mesh in the vertical, transverse and propagation directions. The model is used to analyze resonators on lithium tantalate and temperature compensated resonators on lithium niobate.

Results/Discussion

Thanks to the hierarchical FEM approach, it is now possible to fully analyze a SAW device accounting both for its finite length and its finite aperture in a reasonable time. For example, simulation on lithium tantalate show both the effect of busbar radiation and stop band edge. The effect of gap and dummy electrode length is analyzed and compared with measurement.

[1] J. Koskela et al., “Hierarchical cascading in 2D FEM simulation of finite SAW devices with periodic block structure”, 2016 IEEE International Ultrasonics symp. proc.

1I - MTH: Therapeutic Ultrasound Applications

Regency Ballroom

Saturday, September 9, 2017, 10:30 am - 12:00 pm

Chair: **Ralf Seip**
Sonacare Medical

1I-1

10:30 am Combining Ultrasound Ablation with Immunotherapy: Opportunities and Challenges

Brett Z. Fite[1], Matthew T. Silvestrini[1], Michael Chavez[1], Elizabeth S. Ingham[1], Lisa M. Mahakian[1], Azadeh Kheirolomoom[1], Yu Liu[1], Sarah M. Tam[1], Samantha Tucci[1], Andrew W. Wong[1], Katherine W. Ferrara[1]; [1]*Biomedical Engineering, University of California Davis, USA*

Background, Motivation and Objective

Thermal ablation provides local control of cancer; however, pairing ablation with immunotherapy is attractive as there is emerging evidence that focal therapy enhances the efficacy of immunotherapy. The goals of local treatment are to rapidly debulk the tumor and release tumor antigen to stimulate immune recognition. We seek to evaluate combination protocols and their tumor suppressive effects.

Statement of Contribution/Methods

All animal procedures were approved by the local institutional review board. We applied MRI, positron emission tomography (PET), flow cytometry, and tumor histology to characterize the effects of MRgFUS ablation. A total of 210 neu deletion line (NDL) tumor bearing mice and a total of 34 mice bearing B16-OVA and B16-F10 lesions were studied; both are syngeneic mouse models. In the NDL model, αPD-1 was injected i.p. at a dose of 200 µg and CpG was injected intratumorally (i.t.) into a single tumor at a dose of 100 µg. Immunotherapy protocols were initiated either before ablation or coincident with ablation. MRgFUS was performed with a BioSpec 7T (Bruker), 16-element annular transducer (Imasonic SAS, 48 mm diameter, 3 MHz central frequency) and MR-compatible US system (Image Guided Therapy). The treatment plan used 5 acoustic Watts, a PNP of 3.1 MPa, and the focal volume was scanned through the tumor with a diameter selected to ablate within 1-2 mm of the tumor edge; treatment created temperatures >65°C and CEM43 of more than 5,000.

Results/Discussion

Three mechanisms have potential to impact the efficacy of immunotherapy when begun after thermal ablation: antigen release, mechanical changes in the tumor microenvironment and inflammatory-mediated changes in immune phenotype. We confirmed tumor antigen was released and displayed by the innate immune system. Immediately after ablation, protein transport into the lymphatics was enhanced outside of heat-fixed lesions; however, at later time points transport was impaired. Ablation locally enhanced macrophage and myeloid-derived suppressor cells (MDSCs). Preceding ablation with 7 days of immunotherapy (TLR9 agonist and checkpoint blockade) resulted in an anti-inflammatory and anti-tumor effect: macrophages and MDSCs were reduced, IFN-γ producing CD8+ T-cells and the M1 macrophage fraction were enhanced, and PD-L1 expression on CD45+ cells increased. Continued treatment with immunotherapy alone or with immunotherapy combined with ablation produced a complete response in 80% of treated mice at day 90. When the tumor burden was increased by implantation of three orthotopic tumors, successive primed ablation of two discrete lesions resulted in survival of 60% of treated mice as compared to 25% of mice treated with immunotherapy alone. Alternatively, when immunotherapy was begun immediately after thermal ablation, none of the mice within the cohort exhibited a complete response. We conclude that with priming ablation can be synergistic with immunotherapy.

1I-2

10:45 am Development of a Therapeutic Capsule Endoscope for Treatment in the Gastrointestinal Tract: Bench Testing to Translational Trial

Fraser Stewart[1], Ian P Newton[1], Benjamin F Cox[2], Zhihong Huang[3], Inke Näthke[1], Sandy Cochran[4]; [1]*School of Life Sciences, University of Dundee, Dundee, United Kingdom,* [2]*School of Medicine, University of Dundee, Dundee, United Kingdom,* [3]*School of Science and Engineering, University of Dundee, Dundee, United Kingdom,* [4]*School of Engineering, University of Glasgow, Glasgow, United Kingdom*

Background, Motivation and Objective

Video capsule endoscopy (VCE) is a widely accepted clinical alternative to conventional endoscopy for diagnosis in the gut. Its advantages are that it can visualise the entire gastrointestinal tract including the small bowel (SB) and it is less invasive for the patient. However, VCE is suitable only for diagnosis, with little research into therapeutic capsule endoscopy (TCE). Like VCE, TCE has great potential to reach locations that would previously have been difficult, such as the SB. Ultrasound-mediated targeted drug delivery (UmTDD) is a promising modality for TCE: the power required is low compared with ultrasound (US) ablation and focused US can manipulate the position of therapeutic agents using radiation forces, increase uptake into and through cell layers, and thus deliver a higher dose safely to specifically targeted sites of action.

Statement of Contribution/Methods

This paper describes development of a TCE device containing UmTDD components and *in vitro* testing as a precursor to planned translational trials *in vivo*. A particular aim is to investigate if miniature focused US transducers on VCE suitable scale (10 mm dia. x 30 mm length) are useful for UmTDD. The TCE contains a miniature focused-US transducer built and characterised in house, a drug delivery channel and a video camera, all confocal [1]. At its present development stage, the capsule is tethered for power and drug delivery. To investigate the ability of the focused US device for manipulation of therapeutics, microbubbles (MBs) were passed through the delivery channel into the US focus, monitored using the video camera. An FDA approved *in vitro* SB model using Caco-2 cells was established to determine if uptake into and through the SB wall could be enhanced by US. This was carried out using an insonation system [2] with US sources matching those in the TCE device. Intracellular drug delivery was investigated using fluorescent particles that could be visualised by immunofluorescence. Therapeutic delivery through tight junctions was investigated by measuring barrier function via transepithelial electrical resistance (TER) across the cell layer.

Results/Discussion

MB manipulation was demonstrated successfully with the focused-US transducer in the prototype TCE device using +/- 8 V excitation, a level viable in capsule endoscopy. Immunofluorescence demonstrated that fluorescent particles could be delivered into the Caco-2 SB model and the same model also showed a drop in TER of 6.5% during insonation, indicating reduced barrier function. These results may be translated into a procedure for pushing drugs towards the wall of the SB, then delivering it either into or through it using focused US, suggesting TCE merits further study. A translational trial is planned in which the uptake of fluorescent particles delivered by the TCE device *in vivo* will be monitored.

[1] F. Stewart et al. Journal of Medical Robotics Research; CRAS Special Issue. 2017

[2] F. Stewart et al. IEEE IUS, Sept. 2016

1I-3

11:00 am Self-Adaptive Time Reversal Cavity for Ultrasound Therapy Through The Ribcage

Justine Robin[1], Bastien Arnal[1], Mickaël Tanter[1], Mathieu Pernot[1]; [1]*Institut Langevin (ESPCI Paris, Université P7, PSL Research University, CNRS UMR 7587, INSERM U979), paris, France*

Background, Motivation and Objective

Ultrasound therapy requires focusing high pressures in confined focal spots, to ablate tissues. For organs like the heart, the treatment is challenging, as the US beam must cross the ribs. Part of the energy is reflected by the bones, leading to potential injuries at tissue – bone interface and a pressure drop on target. With usual therapy devices – large transducers on spherical shells – an adaptive US beam propagating in the intercostal space is hard to build without losing power. Time reversal cavities (TRC) have shown promising results for shockwave therapy [1], and have been used as compact emitter-receivers [2]. We present here a dual mode TRC that can perform shock wave therapy in large regions and image the ribs. The image is then use to form a therapy beam propagating selectively through the ribs [3].

Statement of Contribution/Methods

A TRC was built by placing a steel rod forest (density 10 rods.cm^{-2}, width 15 mm) in a steel cavity (20 x 5 x 5 cm^{3}, filled with water). A high power linear transducer (128-elements, 1 MHz, Imasonics, France) was placed in the cavity, opposite the aperture, driven by a Verasonic HIFU system. 3 µs US pulses emitted through the cavity were temporally spread to 600 µs, picked up by a HNC 400 hydrophone (Onda, CA) and stored. This calibration step was repeated on a 70 mm control grid (0.75 mm step), that will be used as an imaging plane in front of the TRC. Once temporally reversed, these signals constitute a library for TRF in all grid points. The calibration step was repeated on a point 5 cm behind the grid plane: the therapy target. All calibration was done in free field.

The signals focusing on each grid point were successively emitted in free space. The backscattered signals were recorded and stored, as a reference. Ribs were then placed in the grid plane, and the process was repeated. For each point, the reference was subtracted from the backscattered signals. An image of the ribs was reconstructed using the TR signals for focusing on reception.

From the image of the ribs, we used the grid points as virtual transducers, and built a therapeutic beam propagating in the intercostal space with the DORT method [3].

Results/Discussion

We formed an image of the medium in front of the cavity. The ribs are visible and can be segmented by thresholding the image. In free field, the focal spot on the therapy target is 2 mm thin (-3dB), with -20 dB side lobes. Through the ribs, the side lobes increase to -10 dB, and we observe a focal pressure drop of 60%. In the ribs plane, the energy is homogeneously distributed.

Transcostal therapy is improved by the DORT method. It restores 10 % of the pressure on target, matching TRF calculated through the ribs (our gold standard), and the energy in front of the ribs in the grid plane decreases.

This is a proof of concept of a dual mode TRC, for shockwave therapy and imaging. Having both, we can improve both the efficacy on focus and the safety by decreasing the pressure on the ribs.

1. Robin et al PMB 2017
2. Luong et al Sci Rep 2016
3. Cochard et al Med Phys 2009

1I-4

11:15 am The Application of Antivascular Photo-Mediated Ultrasound Therapy in Removing Microvessels in the Eye

Xinmai Yang[1], Haonan zhang[2], Jia Li[2], Yannis Paulus[2], Xueding Wang[2]; [1]*University of Kansas, USA,* [2]*University of Michigan, USA*

Background, Motivation and Objective

Pathologic microvasculature plays a key role in the leading causes of blindness including diabetic retinopathy, retinal vein occlusions, and macular degeneration. Current treatments, including laser therapy, photodynamic therapy (PDT), and anti-vascular endothelial growth factor (VEGF) therapy, impose significant burdens on patients, their families, and our health system because of frequent administration, and destructive nature. Using a combination of a low intensity laser concurrently with ultrasound, we developed a novel treatment, photo-mediated ultrasound therapy (PUT), which can noninvasively remove microvessels without damaging surrounding tissue in the eye. We present the first evaluation of PUT on rabbit choroidal vessels.

Statement of Contribution/Methods

An integrated therapeutic ultrasound and laser treatment system was devised. Laser pulses, produced by a pulsed (Nd:YAG) laser at 532 nm with 3-ns pulse duration and 10-Hz repetition rate, synchronized with 10-ms ultrasound bursts. New Zealand white rabbits were used. Fundus photography and indocyanine green (ICG) angiography (ICGA) were acquired using the Topcon 50EX Fundus Camera. ICGA was performed before, immediately after, and weekly following PUT treatment for 1 month by injecting 0.2 mL/kg of ICG into the marginal ear vein.

Results/Discussion

Treatment with laser- or ultrasound-only resulted no changes on rabbit choroidal vessels. PUT treatment with concurrent laser and ultrasound was able to stop the blood flow in the choroidal vasculature with optimized parameters. Hemorrhage occurred with 2 MPa ultrasound + 150 mJ/cm2 laser (estimated at the choroidal layer) whereas 2 MPa ultrasound + 30 mJ/cm2 laser caused no effect. The optimal parameters were 2 MPa ultrasound + 75 mJ/cm2 laser, which caused edema immediately after treatment. By 1 week, pallor occurred in the region of treatment with greatly diminished choroidal vessels which persisted to 4 weeks (Fig 1). ICGA demonstrated a decrease in number of choroidal vessels in the region by 1 week that persisted to 4 weeks after treatment. In conclusion, PUT holds significant promise as a novel non-invasive method to precisely remove microvessels in neurovascular eye diseases by more selectively treating vasculature with minimized side-effects and no systemic photosensitizing dye.

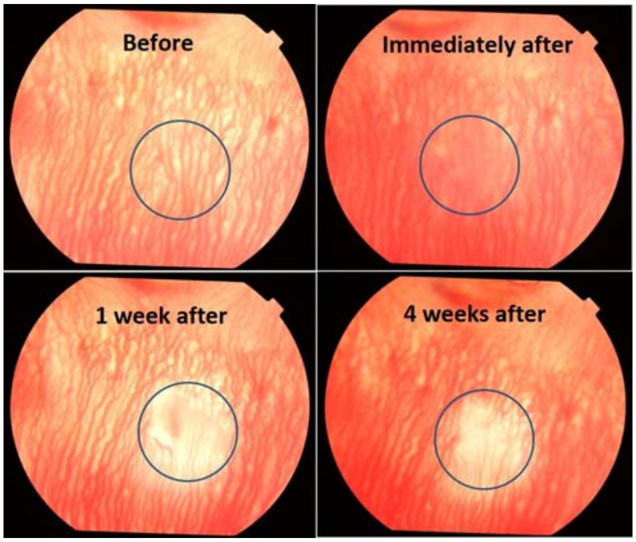

1I-5

11:30 am **Low-Frequency, Low-Intensity Ultrasound as a Potential Novel Treatment for Type 2 Diabetes**

Tania Singh[1], Bogdan Balteanu[1], Ivan Suarez Castellanos[1], Aleksandar Jeremic[2], Vesna Zderic[1]; [1]*Biomedical Engineering, The George Washington University, Washington, District of Columbia, USA,* [2]*Biological Sciences, The George Washington University, Washington, District of Columbia, USA*

Background, Motivation and Objective

The objective of this study was to explore the safety and efficacy of a potential new treatment method that utilizes a non-invasive application of ultrasound energy to induce exocytosis of insulin from pancreatic beta cells. We employed carbon-fiber amperometry and finite-element modeling in our studies.

Statement of Contribution/Methods

Our experiments focused on detecting exocytotic secretions from pancreatic beta cells in response to ultrasound stimulation using carbon fiber amperometry. Neurotransmitters, specifically dopamine and its precursor L-DOPA, were loaded into secretory vesicles in beta cells and co-released with insulin. Cells were stimulated at 800 kHz and an intensity of 0.5 W/cm^2 for 5 s, 10 s, and 15 s. Secretion of insulin was detected through the oxidation of these neurotransmitters using commercially available carbon fiber electrodes. In parallel with these experiments, a finite-element modeling study was used to determine the safety of therapeutic levels of ultrasound to the human pancreas *in vivo* without adverse thermal effects in the surrounding tissues.

Results/Discussion

Secretory amperometric readings were recorded after application of ultrasound at the parameters described above. Ultrasound stimulation produced an immediate response which was sustained until stimulation was terminated. As shown in Figure 1a, cells sonocated in the presence of calcium chelators produced an amperometric response that was approximately six times less than the response solely from ultrasound stimulation (n=6; $p < 0.01$). Ongoing work is focusing on finding the optimal acoustic windows for ultrasound applications in patients through simulations (Figure 1b). These results confirmed that ultrasound stimulation induces secretory events in pancreatic beta cells, and points towards a Ca^{2+} dependent process. We are currently evaluating the safety and effectiveness of this method in clinically relevant models including human pancreatic islets and *in vivo* diabetic rat models. Our proposed technology would directly target beta cell dysfunction, one of the underlying causes of insulin deficiency in type 2 diabetes, potentially resulting in a new therapeutic approach for the treatment of type 2 diabetes.

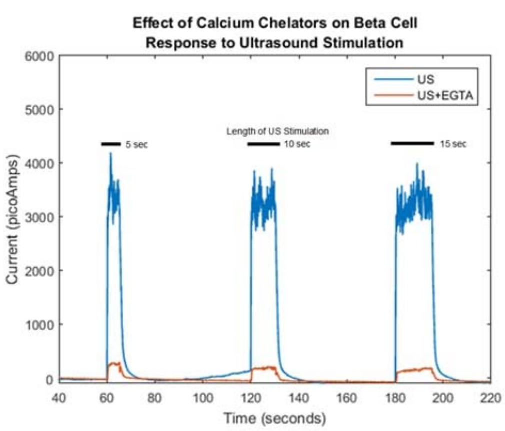

Figure 1a: Amperometric detection of secretory events in ultrasound-stimulated pancreatic beta cells. Cells were sonocated in the presence of calcium chelators (orange) and without chelators (blue).

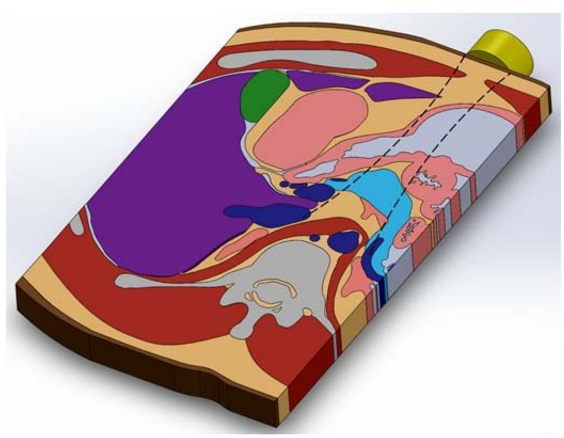

Figure 1b: Simulation of extracorporeal ultrasound application (dashed lines) on a 1.0 cm slice of the abdomen at varying levels of body mass index to determine the thermal effects on the pancreas (light blue).

11:45 am Ultrasound-Mediated Transfection of Endogenous Stem Cells for Regenerative Medicine

Maxim Bez[1], Dmitriy Sheyn[2], Wafa Tawackoli[2], Pablo Avalos[2], Galina Shapiro[1], Joseph Giaconi[2], Xiaoyu Da[2], Shiran BenDavid[2], Jayne Gavrity[3], Hani Awad[3], Hyun Bae[2], Eric Ley[2], Thomas Kremen[2], Zulma Gazit[2], **Katherine Ferrara[4]**, Gadi Pelled[2], Dan Gazit[2]; *[1]The Hebrew University–Hadassah Faculty of Dental Medicine, Israel, [2]Cedars-Sinai Medical Center, USA, [3]Rochester University, USA, [4]University of California, Davis, USA*

Background, Motivation and Objective

The oscillation of microbubbles has long been hypothesized to provide the opportunity to enhance gene delivery as a result of changes in membrane permeability; however, translationally-relevant therapeutic protocols have not yet been realized. We sought to develop and validate a protocol to transfect endogenous mesenchymal stem cells (MSCs) via the local injection of plasmids and microbubbles and the application of ultrasound. We apply this therapy in a pre-clinical model to solve an important clinical problem—that of healing segmental bone defects. More than two million bone-grafting procedures are performed each year using autografts or allografts and these standard of care therapies have substantial disadvantages.

Statement of Contribution/Methods

All animal procedures were approved by the local institutional review board. A critical-size bone fracture was surgically created in the tibiae of Yucatan mini-pigs. A collagen scaffold was implanted in the defect to facilitate recruitment of MSCs into the fracture site. Two weeks later, 107 microbubbles (Definity; Lantheus Medical Imaging) and 1 mg plasmid DNA (reporter gene or BMP-6) were mixed together and injected to the fracture site under the guidance of a fluoroscan mini C-arm (Hologic), followed by application of ultrasound (Sonos 5500; Philips Ultrasound) to the injected location. In particular, the contrast agent imaging mode was applied at a transmission frequency of 1.3 MHz, mechanical index of 0.6, and a depth of 4 cm for approximately 2 minutes until microbubble oscillation could no longer be visualized.

Results/Discussion

Ultrasound-mediated reporter gene delivery successfully transfected 40% of the cells at the fracture site, six times more than control animals ($p < 0.05$), and 80% of the transfected cells expressed MSC markers. In the bone regeneration study, BMP-6 secretion level peaked 5 days post gene delivery. µCT analysis 8 weeks after surgery revealed that 75% of the bone defect was filled with new-formed bone in the ultrasound and BMP-6 gene treated group, which was two times higher than all other control groups ($p < 0.001$) except for autograft treated animals ($p > 0.05$). The newly-formed bone in the BMP-6-ultrasound groups was also significantly more calcified than all other groups ($p < 0.01$). Complete healing was observed only in defects treated with BMP-6 plasmid and ultrasound or autograft. Biomechanical testing showed >2-fold higher mechanical stiffness, strength and toughness of tibiae treated with ultrasound and BMP-6 plasmid compared with negative control groups ($p < 0.05$), and was mechanically equivalent to autograft-treated tibiae ($p > 0.05$). In summary, we find that ultrasound mediated transfection of endogenous MSCs led to transient, localized, transgene expression and resulted in complete healing of bone fractures in minipigs. Further, we conclude that such ultrasound-mediated protocols have potential for translation in regenerative medicine.

2I - MIM: Machine Learning for Image Reconstruction and Interpretation

Ambassador Ballroom

Saturday, September 9, 2017, 10:30 am - 12:00 pm

Chair: **Johan Bosch**
Erasmus Medical Center

2I-1

10:30 am Machine Learning in Medical Ultrasound to Assist Clinical Diagnosis

J. Alison Noble[1]; [1]*University of Oxford, Oxford, United Kingdom*

Background, Motivation and Objective

I describe recent progress in machine learning in medical ultrasound imaging. At a high level, the two technologies appear to be well-matched as the former attempts to make sense of complex patterns, and the latter can generate images of complex acoustic patterns. Thus, the general challenge to the image analysis practitioner is to design machine learning architectures that model the patterns in real world ultrasound images to answer useful clinical questions.

Statement of Contribution/Methods

I will describe a number of machine-learning based 3D ultrasound and ultrasound video object recognition and description methods we have developed to address different ultrasound imaging problems and applications.

Results/Discussion

I will conclude by discussing some current challenges in applying popular machine learning methods (based on deep learning) within the medical image analysis domain more generally, and some of the solutions being developed to overcome them.

2I-2

11:00 am A Deep Learning Approach to Ultrasound Image Recovery

Dimitris Perdios[1], Adrien Besson[1], Marcel Arditi[1], Jean-Philippe Thiran[1,2]; [1]*Signal processing laboratory (LTS5), Ecole Polytechnique Fédérale de Lausanne, Lausanne, VD, Switzerland*, [2]*Department of Radiology, University Hospital Center (CHUV) and University of Lausanne (UNIL), Lausanne, VD, Switzerland*

Background, Motivation and Objective

Compressed sensing (CS) has drawn many interest in the field ultrasound (US) image recovery. It has demonstrated promising results in the recovery of radio-frequency element raw-data [Liebgott *et. al.* ULTRAS13, Besson *et. al.* SPARS17]. The objective of such approaches is to recover the raw-data from undersampled random measurements. It is achieved by means of convex optimization or greedy methods which require a high number of iterations to converge and whose accuracy highly depends on hyper-parameters fine-tuning. Recently, deep-neural networks (DNN) has redefined the paradigm of signal recovery, leading to remarkable results for CS reconstruction of natural images [Mousavi *et. al.* ALBERTON15].

Statement of Contribution/Methods

Inspired by this success, we propose to use a DNN based on stacked denoising autoencoders for US image recovery. The network is composed of 4 layers (*i.e.* encoding - decoding - encoding - decoding). Each layer acts as $\mathbf{y} = F(W\mathbf{x} + \mathbf{b})$, where $\mathbf{x}$ is the input, $\mathbf{y}$ the output, W the weight matrix, $\mathbf{b}$ the bias and F a non-linearity function. For each encoding (decoding) layer, W is a $M \times N$ ($N \times M$) matrix with $M < N$. We use tanh as non-linearity function since US raw-data are zero-centered. During the training, the weights of the 4 layers are learned by minimizing a l_2-loss function on the training set. Once trained, the 1st layer is used to compress the US raw-data, and the remaining layers are used for the recovery. The dataset is simulated using the open source k-Wave toolbox [Treeby *et. al.* JBO10] on a configuration mimicking an acquisition system. The phantoms and medium properties are randomly generated from typical tissue zones (*i.e.* speckle, bright reflectors, inclusions). The simulation accounts for the attenuation and element directivity.

Results/Discussion

We generated the datatest based on a Verasonics system and a L12-5 probe (128 elem., 195µm pitch, 5MHz US freq., 31.2MHz sampl. freq.) with 1 plane wave insonification. We trained the network (100 epochs) over 800000 raw-data traces using Adam optimizer with a learning rate of 0.01. While requiring a fraction of the reconstruction time, Fig. (a) shows that the proposed SDA is competitive and in some cases outperforms state-of-the-art CS algorithm in terms of PSNR on both *in-vitro* and *in-vivo* acquisitions. Fig. (b) shows the reference phantom image (100% of the data) and (c) the image recovered from 15% of the data.

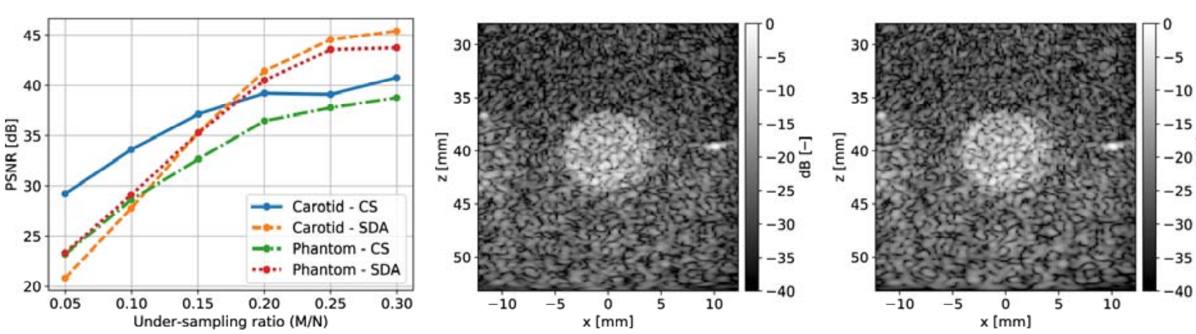

(a) (b) (c)

2I-3

11:15 am Reverberation Suppression Using Dictionary Learning in Optical Resolution Photoacoustic Microscopy

Sushanth Sathyanarayana[1], Bo Ning[2], Song Hu[1], John Hossack[1]; [1]*Biomedical Engineering, University of Virginia, Charlottesville, Virginia, USA,* [2]*Biomedical Engineering, Johns Hopkins University, Baltimore, Maryland, USA*

Background, Motivation and Objective

Optical Resolution Photoacoustic Microscopy (OR-PAM) is uniquely suited to preclinical imaging of the microvasculature due to its high spatial resolution (2.7 µm lateral, 46 µm axial) (Ning et al. Nature Sci. Rep.2015) and high contrast arising from endogenous optical absorption. In preclinical imaging of the mouse brain, large superficial vessels generate strong reverberant artifacts which manifest as repeated copies of the true signal or 'ghosting' that obscures the microvasculature in underlying tissue. In this presentation, we present a method based on dictionary learning to suppress the reverberation and reveal the underlying microvasculature.

Statement of Contribution/Methods

A 3D volume of OR-PAM data was acquired using a 2D raster scan. The A-lines obtained were coded using a learned basis using the K-SVD algorithm (Aharon et al. IEEE Trans. Signal Processing (2006)). Each basis vector is a combination of the signal from multiple photoacoustic emitters and reverberation. Each atom was subsequently reweighted by its correlation with the signal of largest amplitude present in that atom, generating a new basis in which the reverberant echoes are suppressed. Reconstruction using this new basis generates a reverberation suppressed signal. The method was validated in vitro, using an optically transparent PDMS phantom containing embedded red dyed polystyrene beads (Polysciences Inc. (6 µm diameter)). Subsequent in vivo validation on mouse brain images (Fig. 1) acquired using the G3 OR-PAM system developed in Ning et al. (Optics letters. 2015) was also performed.

Results/Discussion

It may be observed from Fig.1 A, B that the reverberant artifacts are suppressed in the scan of the mouse brain (Fig.1 C), while the remaining signal is retained. Coding the A-lines obtained in OR-PAM with a learned dictionary and subsequent reconstruction with reweighted dictionary atoms allow us to suppress reverberant artifacts by 21.04 ± 5.43 dB. This enables visualization of deeper vasculature in the mouse brain. Although the penetration depth is limited by optical scattering loss, we are able to extend effective penetration by eliminating ghosting artifacts. The resulting improved imaging technique could serve as an important tool in perfusion imaging in disease models that involve multiple layers of the murine cortex.

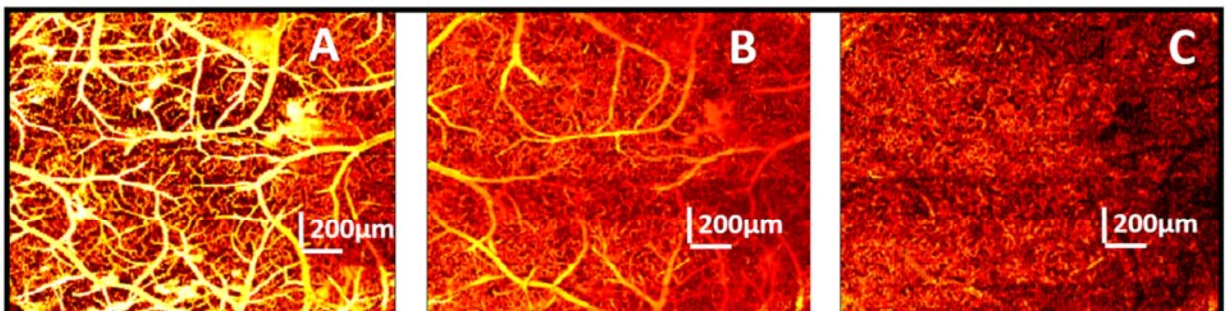

Fig. 1. Maximum Intensity XY Projections of Mouse Brain data calculated over ± 45 µm around the focal plane A. Superficial image (50 µm), B. Deeper image (150 µm) showing 'ghost' artifacts due to reverberation from superficial layer C. Deeper image from (B) after artifact removal

2I-4

11:30 am Tissue Motion Estimation Using Dictionary Learning: Application to Cardiac Amyloidosis

Nora Ouzir[1], Olivier Lairez[2], **Adrian Basarab**[3], Jean-Yves Tourneret[1]; [1]*IRIT, UMR CNRS 5505, University of Toulouse, Toulouse, France,* [2]*INSERM, UMR 1048, Institut des Maladies Métaboliques et Cardiovasculaires, CHU de Toulouse, Université Paul Sabatier, Toulouse, France,* [3]*IRIT, UMR CNRS 5505, University of Toulouse, Toulouse Cedex, France*

Background, Motivation and Objective

Cardiac strain estimation from ultrasound images is an efficient tool for the diagnosis of cardiac diseases. This study focuses on cardiac amyloidosis (CA), a pathology characterized by non-specific early symptoms such as increased wall thickness. Recent clinical studies have demonstrated that patients with CA present an apex-to-base gradient longitudinal strain pattern, i.e., a normal strain in apex and abnormally lower values for base segments. Existing cardiac motion estimation (ME) methods belong to three categories: optical flow, speckle tracking and elastic registration. To overcome the ill-posedness of ME, they use local parametric models (e.g., affine) or global regularizations (e.g., B-splines). The objective of this study is twofold: i) to propose a novel ME method based on dictionary learning, ii) to evaluate this method on patients subjected to CA.

Statement of Contribution/Methods

We formulate the ME problem between two consecutive frames as the minimization of an energy function composed of a data fidelity term and two regularizations. The data fidelity results from the maximum likelihood method exploiting the Rayleigh distribution of envelope images. The first regularization is the conventional total variation ensuring a spatial regularization of the motion fields. The second regularization is the main contribution of this study. It constrains the cardiac motion to be sparse in a dictionary that contains patterns of training motions. Unlike fixed transforms (e.g., wavelet, DCT), the dictionary used in this study is overcomplete (redundant) and is inferred from representative motion fields.

Results/Discussion

Realistic simulated data with ground truth cardiac motion is used to compare the accuracy of the proposed ME algorithm to two existing methods (speckle tracking and elastic B-spline-based registration). The mean values of the squared errors between the estimated and true motion fields and the corresponding standard deviations (std) displayed in Tab. 1 show that the proposed method provides an average accuracy gain of 59.5%. Its efficiency in estimating apex-to-base gradient longitudinal strain patterns was evaluated on three patients suffering from CA. Figs. 1(a,c) show the strain curve evolution over a cardiac cycle for the six cardiac segments and an example of longitudinal strain maps super-imposed to the long-axis view B-mode image.

Tab. 1 Average mean and std values of the squared error (in pixels) between the estimated and true motion fields for a realistic simulated cardiac image sequence.

Method	Mean	+/- Std
Speckle tracking	0.76	0.48
Bspline	0.34	0.13
Proposed	**0.19**	**0.10**

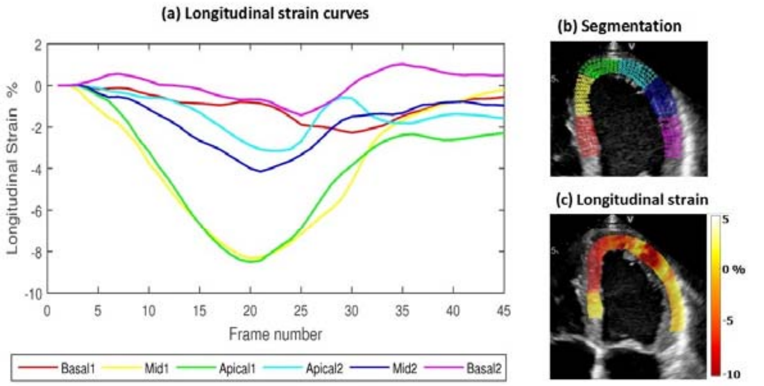

Fig. 1 (a) Segmental longitudinal strain curves of an *in vivo* sequence corresponding to the 6 segments in (b) and (c) longitudinal strains of the 20th frame corresponding to end systole.

2I-5

11:45 am Machine Learning to Understand Anthropomorphic Modulators of Spatiotemporal Myocardial Mechanics

Hanan Khamis[1,2], Peter Claes[3], Nicholas Cauwenberghs[4], Dan Adam[1], Tatiana Kuznetsova[4], Jan D`hooge[2]; *[1]Lab for Ultrasound Signals and Image Processing and Modeling, Department of Biomedical Engineering, Technion, Haifa, Israel, [2]Lab on Cardiovascular Imaging & Dynamics, Department of Cardiovascular Sciences, KU Leuven, Belgium, [3]Lab on ESAT-PSI, Processing Speech and Images, Department of Electrical Engineering, KU Leuven, Belgium, [4]Lab on Hypertension and Cardiovascular Epidemiology, Department of Cardiovascular Sciences, KU Leuven, Belgium*

Background, Motivation and Objective

Speckle tracking echocardiography (STE) is a very promising technique for the assessment of left ventricular (LV) function. Nevertheless, to date, it did not become part of clinical routine due to: i) inter-vendor variability; ii) difficulties in data interpretation. Anthropomorphic patient characteristics (APC) are known to affect the LV strain values as studies have shown the effect of gender, age, body-mass-index (BMI), blood pressure and heart rate on peak global strain. However, to date, it remains unknown how the spatiotemporal strain (STS) patterns across the LV are modulated by these APC. The aim of this study was therefore to statistically determine the effect of APC on the STS measurements.

Statement of Contribution/Methods

144 subjects from a general population were scanned using a Vivid E9 scanner (GE Healthcare, Norway). For each subject, the three apical views were acquired and processed using 2D STE software (GE Healthcare, Norway) to extract segmental strain curves. In addition, APC were collected, including: gender, age, BMI, systolic blood pressure (SBP), diastolic blood pressure (DBP) and heart rate (HR). The proposed method includes 3 parts: (1) temporal interpolation of the strain curves, performed on the systolic and diastolic phases separately; (2) definition of the STS by spatial concatenation of interpolated strain curves following the LV 18-segment model; (3) analysis of the effect of the APC on the STS patterns using partial least square regression (PLSR). PLSR analysis provided spatiotemporal regression coefficient of each APC; coefficient of determination, fitting model and statistical significance.

Results/Discussion

The measured APC were uniformly distributed. PLSR analysis showed that there is a significant effect of some of the APC on the STS patterns: i) aging was associated with changes during diastole for all LV segments but was associated with systolic changes in the Infero-Septal wall only (Figure 1); ii) women were demonstrated to have higher systolic strains; iii) BMI was associated with higher strain values during the filling phase mainly in the Inferior wall. On the other hand, SBP and DBP had negligible effects on the STS patterns while HR had no effect at all. In conclusion, our study showed that LV STS pattern is modulated by APC. These findings are important in order to facilitate interpretation of strain in the clinical setting.

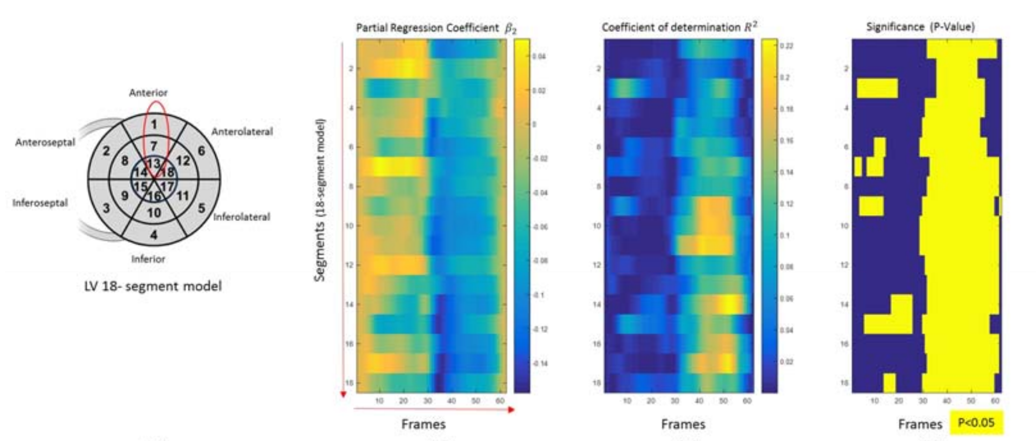

Figure 1: Partial least square regression analysis of the effect age on spatiotemporal strain variation. (a) LV 18-segment model [base: 1-6, mid: 7-12 and apex: 13-18]; (b) partial regression coefficients (rows (up to down): segments 1-18 ordered following the 18-segment model, columns (left to right): time [frames] post interpolation); (c) Coefficient of determination (effect size) expressed as the percentage variance explained of the total amount of variation and (d) significant areas (yellow) p<0.05 of the effect size under permutation with 5000 runs (statistical significance).

3I - MCA: Contrast Imaging: Beamforming and Signal Processing

Palladian Room

Saturday, September 9, 2017, 10:30 am - 12:00 pm

Chair: **Ayache Bouakaz**
INSERM

3I-1

10:30 am Dual Frequency Imaging oicrobubbles Using 1.7-Mhz Transmit Stacks Parallel to A 21-Mhz Receive Array

Emmanuel Cherin[1], Jianhua Yin[1], Alex Forbrich[2], Christine Demore[1,3], Paul Dayton[4], F. Stuart Foster[1,3]; [1]*Physical Sciences, Sunnybrook Research Insitute, Toronto, Ontario, Canada,* [2]*FUJIFILM VisualSonics, Toronto, Ontario, Canada,* [3]*Medical Biophysics, University of Toronto, Toronto, Ontario, Canada,* [4]*Joint Department of Biomedical Engineering, University of North Carolina and North Carolina State University, Chapel Hill, North Carolina, USA*

Background, Motivation and Objective

The concept of contrast imaging using microbubble superharmonic signals was introduced in 2002[1]. A number of implementations with detection above 10 MHz have been reported, in particular by our group using a 25-30 MHz single element receive transducer concentric with a low 2-4 MHz transmit ring[2]. In the present work, the implementation of dual frequency (DF) imaging on a Vevo 2100 (VisualSonics, Toronto) was investigated (Fig.1-A).

Statement of Contribution/Methods

Two single-element rectangular 1.7-MHz transducers flanking a 21-MHz array (MS250, VisualSonics, Toronto) were used to transmit while the array was used to receive. In a scheme based on B-mode, low frequency pulse transmission was triggered for each scan-line acquired by the scanner; therefore exposing the whole field of view (23-mm width) to 256 transmit events per frame. Stationary microbubbles (MB) (MicroMarker, Bracco, Switzerland; ~10^6 MBs/ml) were exposed to 50 and 100% bandwidth (BW) 1.7-MHz pulses of varying amplitudes (20-200 kPa), and their response was analyzed offline.

Results/Discussion

Signal from MBs was detected above the noise floor in the array BW (~10-30 MHz) at peak-negative pressures as low as 52 and 70 kPa with the 50 and 100% BW pulses, respectively. Images of MBs in the phantom obtained in high frequency B-mode (Fig.1-B) and DF-mode (Fig.1-C) show an increase of 30 dB in contrast-to-tissue ratio (CTR) between the two imaging methods. CTR decreases with increasing transmit pulse bandwidth due to the fact that MBs oscillate more strongly with longer pulses, as clearly indicated by the spectra in Fig.1-D. Additionally, these spectra indicate that the MBs signal could originate from both inertial (broadband signals) and non-inertial (harmonic oscillations) cavitations. MB destruction was investigated by estimating MBs backscatter power as a function of frame number. During the experiment, a decrease in backscatter power with number of exposures was observed for both 50% and 100% BW pulses, indicating that MB destruction was occurring (Fig.1-E). The initial rate of decrease is independent from incident pressure above 100 kPa (-0.26 dB/frame for BW=100%, and -0.41 dB/frame for BW=50%). Methods to reduce the number of exposures are under investigation and will be described.

[1] Bouakaz et al. Ultrasound in Med. & Biol. 28(1):59-68, 2002.
[2] Gessner et al. IEEE UFFC 57(8):1772-1781, 2010.

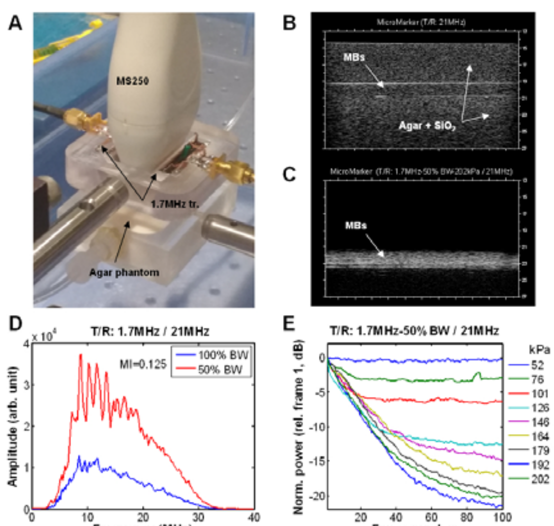

Fig.1 : Setup (A); 21-MHz B-mode image (B); 1.7 / 21 MHz Dual Frequency image (C); MBs backscatter spectra (D); MBs backscattered power as a function of incident pressure and frame number (E)

3I-2

10:45 am Microbubble Signal Classification Using NSSA-Based Filtering Methods

Elizabeth B. Herbst[1], Shiying Wang[1], Alexander L. Klibanov[1,2], F. William Mauldin Jr. [1], John A. Hossack[1]; [1]*Biomedical Engineering, University of Virginia, Charlottesville, Virginia, USA,* [2]*Division of Cardiovascular Medicine, University of Virginia, Charlottesville, Virginia, USA*

Background, Motivation and Objective

Microbubbles (MBs) are capable of binding specifically to molecular markers on the vascular endothelium to enable sensitive detection of early stage disease. Traditional microbubble imaging techniques rely on the nonlinearity of microbubble signal to differentiate it from surrounding tissue. However, the presence of harmonic energy among echogenic tissue interfaces can limit the effectiveness of these methods in enhancing microbubble contrast. In many cases, it is challenging to achieve any quantitative separation between static tissue signal and bound MB signal (Fig. 1B). In this study, we use normalized singular spectrum area (NSSA) to differentiate between static tissue signal, bound MB signal, and free MB signal in a mouse hindlimb tumor.

Statement of Contribution/Methods

Retro-orbital injections of 2*107 VEGFR-2 targeted MBs were administered to mice implanted with subcutaneous adenocarcinoma tumors (MC38 cells). A Verasonics programmable ultrasound scanner and 5-12 MHz linear array transducer was used to collect pulse inversion images at 20 s and 6 min post-injection. Intratumor signals recorded at 20 s post-injection were assumed to derive from free MBs, and those recorded at 6 min post-injection were assumed to derive from bound MBs.

NSSA analysis was performed on sets of 25 sequential frames using blocks of complex data 1mm in depth and 0.5mm in width. A maximum filter was used to record the maximum NSSA value of every 1x0.5 mm block within tissue and MB regions of interest (ROI). Receiver operating characteristic (ROC) analysis was then performed to calculate the sensitivity and specificity of NSSA-based filtering in differentiating between static tissue, free MBs, and bound MBs.

Results/Discussion

For differentiation between static tissue and bound MBs, ROC analysis demonstrated an area under the curve (AUC) greater than 0.99. For differentiation between bound MBs and free MBs, ROC analysis resulted in an AUC greater than 0.93. These results suggest high sensitivity and specificity, particularly in differentiation between nonlinear signals from static tissue artifacts and nonlinear signals from near-static bound MBs (Fig. 1A, red arrow). The improved signal specificity afforded by NSSA-based processing improves the robustness of ultrasound molecular imaging (USMI) techniques and may help to promote the adoption of USMI in a clinical context.

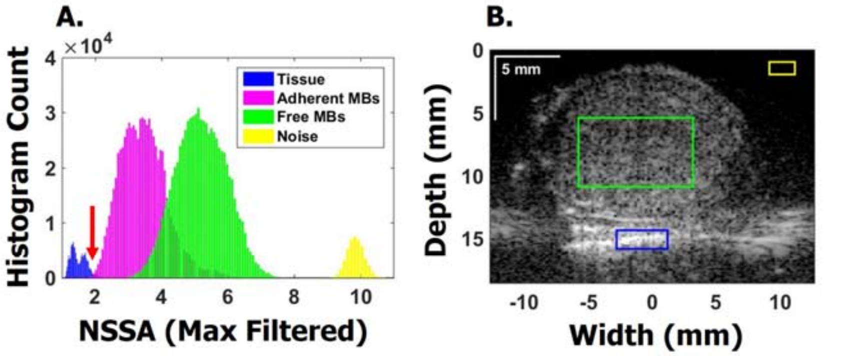

Figure 1. NSSA-based signal mapping is combined with maximum filtering to achieve sensitive and specific signal separation. (A.) Histogram of NSSA signals from static tissue, bound MBs, free MBs, and random electronic noise shows clear delineation between all four types of ultrasound signal, and particularly between the signal of bound MBs and static tissue (red arrow). **(B.)** Representative nonlinear (pulse inversion) image of a mouse hindlimb tumor. Free and bound MB signals were calculated from the green ROI. Static tissue signal was calculated from the blue ROI. Signal from random electronic noise was calculated from the yellow ROI.

3I-3

11:00 am Single Microbubble Measurements of Temperature Dependent Viscoelastic Properties

Jordan Lum[1], David Stobbe[1], Todd Murray[1], Mark Borden[1]; [1]*Department of Mechanical Engineering, University of Colorado, Boulder, Colorado, USA*

Background, Motivation and Objective

Lipid-coated microbubbles are being researched as agents for ultrasound imaging and ultrasound-assisted drug delivery. It is well known that lipid shell composition of a microbubble affects the acoustic response. However, the effect of temperature on lipid shell viscoelasticity has not yet been fully established. The goal of this study was to determine the effect of temperature on the viscoelastic response of individual lipid-coated microbubbles.

Statement of Contribution/Methods

An optical measurement system was used to generate and detect nanometer-scale oscillations of single DPPC microbubbles (Figure 1a). The measurement method did not require gold nanoparticle-coating or direct heating of the microbubbles, as in our previous setup [1]. A modulated continuous wave (CW) infrared laser (1550 nm) was used for microbubble excitation. The light was absorbed in the water adjacent to the microbubble, generating ultrasonic waves through the photoacoustic effect that drove bubble oscillations. Another CW laser (488 nm) was used to track bubble radial displacements. Temperature was set between 20 and 55 oC via resistive heaters and a thermocouple. The modulation frequency of the excitation laser was swept over the frequency range of 1-5 MHz, and bubble resonance curves were generated at each temperature. These curves were processed to determine shell elasticity and viscosity.

Results/Discussion

A plot of the resonance curves for a single microbubble at four different temperatures is shown in Figure 1b. A decrease in resonance frequency and increase in amplitude was observed with increasing temperature. The shell elasticities for n > 20 individual microbubbles were binned and plotted versus temperature (Figure 1c). The colors correspond to the temperatures shown in Figure 1b. In general, shell elasticity decreased monotonically with increasing temperature. For example, a 36% decrease in shell elasticity was observed upon increasing temperature from 21 to 37 °C. These results provide insight into how the viscoelastic response of microbubbles changes with temperature as, for instance, when injected into the body.

References:

[1]J. S. Lum, J. D. Dove, T. W. Murray, and M. A. Borden, Langmuir 32, 9410 (2016).

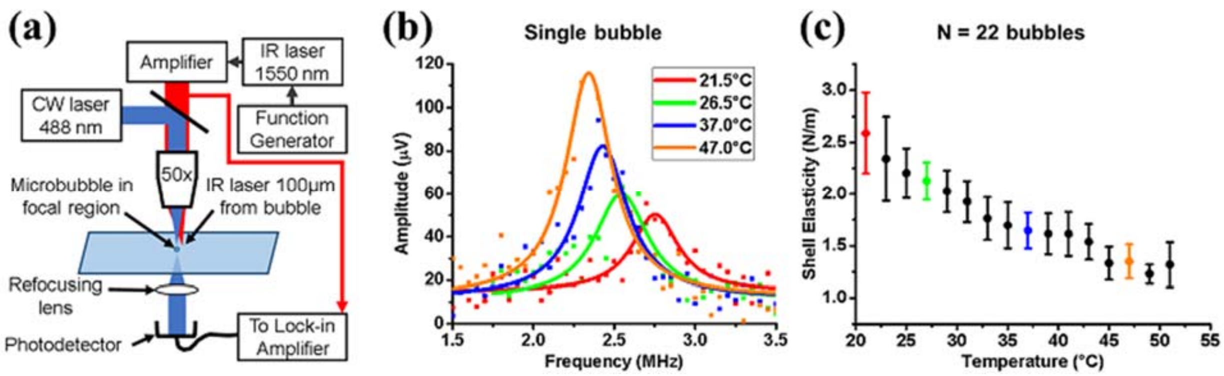

3I-4

11:15 am Differentiation of Vein and Lymphatic Vessel by Photoacoustic Imaging System with Parabolic Array Transducer and Tunable Laser

Takuya Tabata[1], Ryo Nagaoka[1], Shin Yoshizawa[1], Shin-ichiro Umemura[1], **Yoshifumi Saijo[1]**; [1]*Tohoku University, Japan*

Background, Motivation and Objective

Recently, much attention is being paid to lymphatic circulation because intralymphatic immunotherapy and chemotherapy achieved significant clinical benefits. However, conventional ultrasound or photoacoustic (PA) imaging is hard to visualize lymphatic vessels. The objective of the present study is to visualize lymphatic vessels administrated with photoacoustic contrast agents by PA imaging system based on a tunable laser setup.

Statement of Contribution/Methods

Generation of the PA signal is highly dependent on the directions of light and sound to the surface of the target. Multi-angle reception of PA signal has been realized with a real-time PA imaging system with a 256-ch parabolic array transducer (special order, Japan Probe, Yokohama, Japan). The transducer consisted of 1-3-composite elements and the diameter was 42.4 mm, opening angle was 90° and the central frequency of 10 MHz. PA signal was received by a programmable ultrasound data acquisition system (Vantage, Verasonics, Redmond, WA, USA) with a sampling rate of 62.5 MHz. Tunable laser system (special order, MegaOpto, Wako, Japan) emitted the laser with the wavelength between 400 and 2100 nm, the power of 10 mJ and the repetition rate of 20 Hz for generation of PA signal. The ICR mouse was anesthetized and the hair was removed. Indocyanine green (ICG) or gold nanorod (AuNR) was administrated into lymphatic vessels of the mouse. The resonance wavelength of the AuNR was 830 nm. The vein and lymphatic vessel were visualized from the skin surface by the PA imaging system.

Results/Discussion

The three planes such as XY, YZ and XZ plane were processed real-time with a frame rate of 20 Hz by delay and sum beamforming. The resolution of the system was found to be 80 µm by observing a mesh phantom immersed in water. In mouse study, the vein was visualized at the wavelength of 490~600 nm. The lymphatic vessel with ICG was visualized at 670~770 nm and the vessel with AuNR was visualized at 790~890 nm. The figures show macroscopic views from inside and from surface and corresponding PA images at 570 nm and 830 nm. PA imaging system with parabolic array transducer and tunable laser clearly visualized lymphatic vessel with AuNR. The system is clinically applicable for detection of small lymphatic vessels to confirm successful drug delivery during intralymphatic chemotherapy.

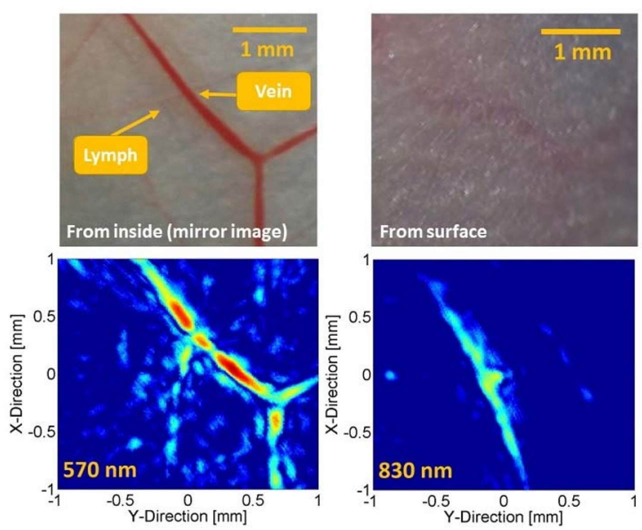

3I-5

11:30 am Acoustic Microbubble Trapping in Blood Mimicking Fluid

Luzhen Nie[1], Sevan Harput[1,2], James McLaughlan[1,3], David M.J. Cowell[1], Thomas Carpenter[1], Steven Freear[1]; [1]*Ultrasonics and Instrumentation Group, School of Electronic and Electrical Engineering, University of Leeds, Leeds, United Kingdom,* [2]*Department of Bioengineering, Imperial College London, United Kingdom,* [3]*Division of Biomedical Imaging, University of Leeds, United Kingdom*

Background, Motivation and Objective

With identical exposures, enhanced cavitation resulting from increased microbubble (MB) concentrations has been demonstrated in the literature. Through the generation of a low-pressure trap, our previous work described a means to locally accumulate MBs within large vessel lumen (fig. a). But the existence of blood in-vivo could impede the MB translation and retention, which calls for preliminary investigations for acoustic MB trap in blood mimicking fluid (BMF). This study validates the feasibility of the MB trapping in the presence of BMF, which could be beneficial for therapeutic regimes involving acoustic cavitation like sonothrombolysis.

Statement of Contribution/Methods

Simultaneous MB trapping and plane wave imaging was achieved through instantaneous switching between two excitation schemes at a rate of 2 kHz. With a 4-11 MHz linear array, the trap was generated by emitting two π phase shifted plane waves. Along the centre of imaging region, destructive wave interference results in a low pressure region that halts MBs. Definity-like MB solutions (1.6x10^6 MBs/ml) were flown into a flow phantom with purified water or BMF at a rate of 28 mL/min. For two sets of experiments, mechanical index were set to 0.09 and 0.42 for trapping and imaging, respectively. A total of 2200 frames were acquired at a rate of 1 kHz. Three ROIs were chosen as given by fig. b and the dashed red line simulates the absolute peak negative pressure profile for bubble trapping. Baseline intensity measurements were performed with 100 frames for all ROIs without MBs. Every 100 frames were averaged and the image intensity containing MBs over time were presented as fig. c and d.

Results/Discussion

In water, compared with its initial intensity, the largest increase was found to be 28 % inside the designed trapping area (fig. c). In BMF, MB accumulation was achieved with an intensity increase of 17% after 800 ms trapping (fig1. d). The higher viscosity of BMF results in delayed MB accumulation after activating the trapping and prolongs intensity increase even after deactivating the trapping (fig. d). This implies that trapping exposure periods need to be specifically determined to achieve optimal MB concentrations in blood for therapeutic use. The flow rate of 28 mL/min is within the upper band of venous flows and results indicate that acoustic MB trapping could benefit deep vein sonothrombolysis.

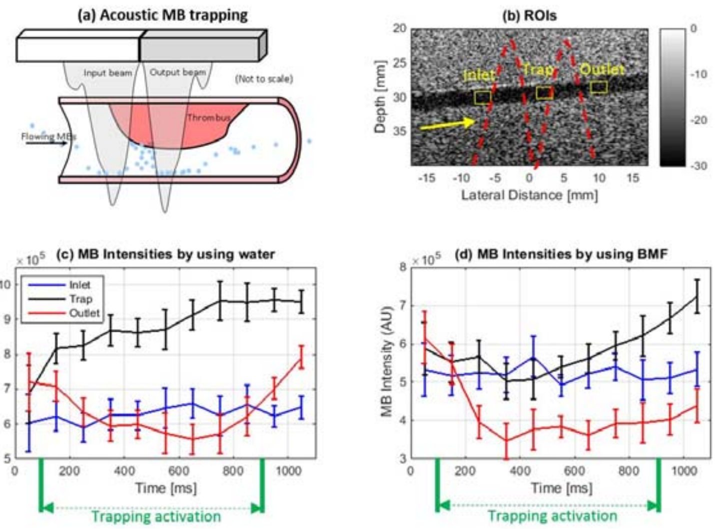

3I-6

11:45 am Adaptive Beamforming Contrast Enhanced Super Resolution Imaging for Improved Sensitivity and Resolution in Deep Tissues

David Espíndola[1], **Fanglue Lin[1]**, Danai Soulioti[1], Paul A Dayton[1], Gianmarco Pinton[1]; [1]*Joint Department of Biomedical Engineering, University of North Carolina at Chapel Hill and North Carolina State University, Chapel Hill, North Carolina, USA*

Background, Motivation and Objective

Ultrasound contrast enhanced super resolution (CESR) imaging, or ultrasound localization microscopy, has recently attracted extensive attention due to its ability to image microvessels at resolutions much smaller than the ultrasound diffraction limit, with the aid of injected microbubble contrast agents. However, to our knowledge, only shallow in vivo images have been presented. This is largely due to the challenge of detecting microbubbles in microvessels in deep tissue, where attenuation substantially degrades the low-amplitude plane wave excitation used for high-frame rate CESR imaging. Therefore, there is a crucial need improve the sensitivity of the imaging system to contrast agents in deep tissues in order to improve the potential clinical translation of this novel imaging approach. We propose a method of adaptive multi-focused-transmit beamforming to overcome this limitation.

Statement of Contribution/Methods

In our approach, a single adaptive multifocal beam is transmitted. Unlike plane waves, which encompass the whole field of view, the focusing simultaneously targets a few specific regions. This technique is achieved via two steps: First, regions requiring improved sensitivity are defined in the imaging field after displaying traditional contrast enhanced images or predefined and loaded into the ultrasound imaging system. Second, a beam with multiple focal regions is generated according to the defined focal regions to deliver higher energy to multiple regions with only one transmit beam. Since these multiple foci are realized with only one transmission, high frame rate achievable with plane wave imaging is not sacrificed to track the microbubbles as they move within the vessels, as would occur with traditional focused imaging. Simulation and ex vivo experiments on beef tissue demonstrate the performance of this technique.

Results/Discussion

Both simulation and ex vivo experiments show the adaptive multifocus imaging provides equivalent or better contrast to tissue ratio than focused imaging (10 dB improvement at 36 mm depth and 8 dB improvement at 53 mm depth, compared with plane wave imaging), while keeping the same high frame rate as plane wave imaging (over 16x fold faster frame rate than focused imaging). These results demonstrate our ability to perform CESR imaging at significant depth in tissue, without a substantial reduction in frame rate.

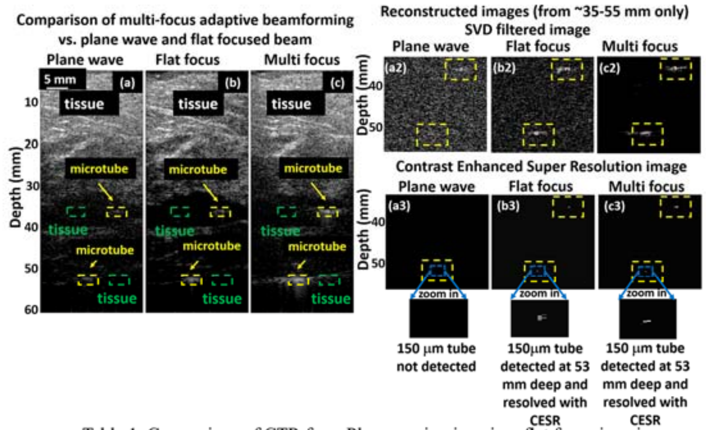

Fig.1. Demonstration of adaptive beamforming multi-focus approach in a deep ex-vivo beef tissue phantom. Left triple panel: (a-c) B-mode image from conventional plane wave imaging, 16 broad focused beams with flat focal depth at 43 mm and one multifocus beam with two targeting foci at the locations of the microtubes (perpendicular to image plane). Yellow squares and arrows show locations of microtubes at 36 and 53 mm deep. Green squares show tissue location for CTR measurements. Right triple panel, top: SVD filtered images of the tubes from the data presented in a-c. Right triple panel bottom, resultant CESR images, and zoom-in (blue) of super-resolution images of deeper tube.

Table 1. Comparison of CTR from Plane waving imaging, flat focus imaging and multifocus imaging before reconstruction. (Fig.1a-c).

	Plane wave	Flat focus	Multi focus
Upper microtube	5.7 dB	15.3 dB	15.7 dB
Lower microtube	7.8 dB	15.1 dB	15.2 dB

4I - MBF: Vector Flow Imaging: Applications and Methods

Diplomat Room

Saturday, September 9, 2017, 10:30 am - 12:00 pm

Chair: **Jørgen Jensen**
Technical University of Denmark

4I-1

10:30 am Vector Flow Imaging of Fetal Circulation using Diverging Waves

Solveig Fadnes[1], Eva Tegnander[2,3], Siri Ann Nyrnes[1,4], Lasse Løvstakken[1]; [1]*Centre for Innovative Ultrasound Solutions (CIUS), NTNU, Norway,* [2]*National Center for Fetal Medicine, St. Olav's University Hospital, Norway,* [3]*Dept. of Laboratory Medicine, Children's and Woman's Health, NTNU, Norway,* [4]*Dept. of Pediatrics, St. Olav's University Hospital, Norway*

Background, Motivation and Objective

Cardiac malformations develop in the first trimester of pregnancy and early detection of abnormalities is important to plan delivery and treatment. Recent reports indicate that blood flow patterns play a significant role in the development of the heart. Our aim is to investigate if vector flow imaging using blood speckle tracking can add useful information to the conventional ultrasound examination of the fetal circulation and cardiac development. We demonstrate the initial feasibility of fetal imaging at gestational weeks 20, 28 and 32 in healthy pregnant volunteers, investigating the quantitative ability of speckle tracking based on an ultrafast diverging wave transmission scheme.

Statement of Contribution/Methods

A Verasonics Vantage system (Verasonics, Inc., USA) with a curvilinear array (C5-2v) was set up with both a duplex (packet) diverging wave acquisition (100fps) and a continuous diverging wave acquisition (3000fps). In the duplex setup, B-mode images were formed using coherent compounding of 11 diverging waves (11 virtual source positions, PRF=4.5kHz, f0=4.46MHz), whereas for the blood flow sequence, 22 diverging waves formed the Doppler packet (fixed source position, PRF=3kHz, f0=2.97MHz). The channel data were stored and beamformed offline. A GPU optimized speckle tracking (ST) method (forward-backward SSD with parabolic subsampling) on the envelope data from the Doppler ensemble provided velocity estimates. The duplex and continuous recordings were programmed to run subsequently without interruption.

Results/Discussion

For the given probe bandwidth and resolution, the small fetal heart (~1.5cm) at week 20 was a challenge. However, when fetal shadowing was avoided, the main flow features like inflow and vortex formations were visualized (see Figure, left panel).

At week 28, the fetus' heart was ~3cm revealing more flow details. To the right in the Figure, a standard view of the RV outflow tract is shown. The main PA branches into the right PA and the DA (a fetal shunt entering the descending aorta). From the corresponding continuous recording, a PW Doppler spectrum was made from the indicated sample volume. The yellow trace is the ST estimates from the same recording showing good agreement between the methods. Overall, angle-independent, quantitative information of the fetal circulation could be obtained from a large field-of-view at high frame rates with speckle tracking and diverging wave imaging.

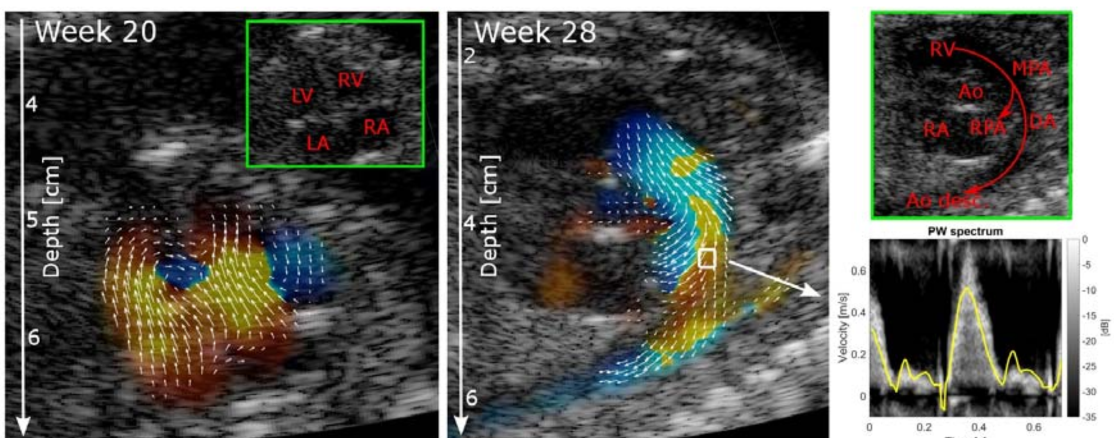

LV/RV,LA/RA=left/right ventricle/atrium, Ao=aorta, MPA/RPA=main/right pulmonary artery, DA=ductus arteriosus

4I-2

10:45 am Time-Resolved Vector Projectile Imaging of Urinary Flow Dynamics

Takuro Ishii[1], Billy Y. S. Yiu[1], Alfred C. H. Yu[1]; [1]*Schlegel Research Institute for Aging, University of Waterloo, Waterloo, Ontario, Canada*

Background, Motivation and Objective

Developing tools to visualize urinary flow dynamics is important, because urinary hydrodynamics is known to have a causal relationship with urethral voiding dysfunction problems. Yet, the design of such an imaging technique is challenging as fine time resolution is essential to track urine passage that can traverse at >2m/s speeds. Previously, we have overcome the time resolvability challenge in flow visualization with a new technique called vector projectile imaging (VPI), which can render flow vector fields with <1 ms time resolution. In this work, we present the first application of VPI to track urinary flow patterns during different voiding phases.

Statement of Contribution/Methods

VPI is based upon the use of: 1) plane wave data acquisition to achieve high frame rate imaging (>1,000 fps); 2) multi-angle Doppler estimation for flow vector estimation; 3) dynamic rendering that depicts individual flow trajectories. This technique was implemented on an ultrasound research scanner (UMB, 2014; 40: 2295-2309) that comprises a programmable transmit front-end (SonixTouch), a pre-beamformed data acquisition tool (SonixDAQ), a GPU beamforming platform, and a L14-5 array transducer (10 kHz PRF, 5

MHz U/S freq). To test the efficacy of VPI in visualizing urinary flow, we designed a new anthropomorphic urinary tract phantom that can reconstruct urine passage under controlled conditions. Both healthy and diseased urinary tract models were devised. The diseased model was in the form of bladder outlet obstruction (BOO): a key characteristic in urinary tracts with voiding dysfunction. The flow system provided urine mimicking liquid at constant water head pressure to assume uniform detrusor function for both models (Fig a).

Results/Discussion

VPI revealed differences in the flow dynamics of normal (Fig b) and diseased urinary tracts (Fig c); space- and time-resolutions were, respectively, 0.1 mm/pixel and 400 µs/frame. In the case with BOO, VPI depicted the presence of BO flow jet and vortices in the prostatic urethra. The corresponding spatial-maximum flow speed was estimated to be 2.43 m/s, which is significantly faster than that for the normal model (1.52 m/s). These results demonstrate the feasibility of VPI in examining flow characteristics related to voiding dysfunction, particularly in locating positions within the urinary tract where disturbed urine passage is evident.

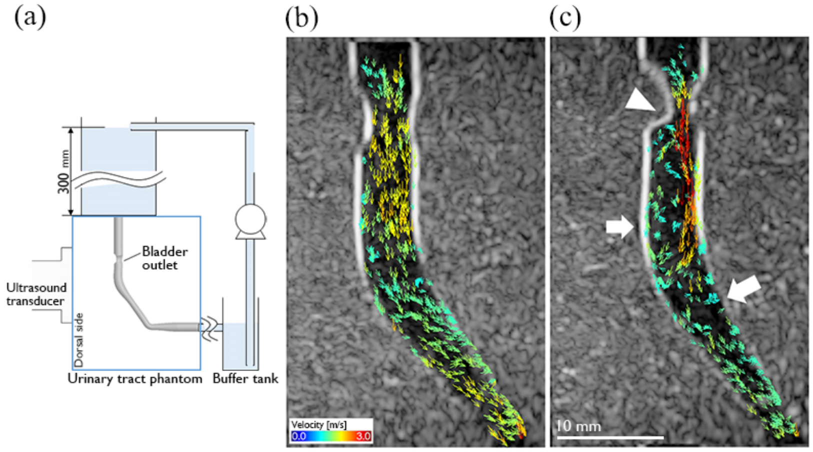

Figure. (a) Experimental setting; (b) VPI of normal urinary tract; (c) VPI of diseased tract with BOO.

4I-3

11:00 am Real-Time Multi-Line Vector Doppler Analysis Based on Layered Array Beams

Alessandro Ramalli[1], Stefano Ricci[1], Piero Tortoli[1]; [1]*Department of Information Engineering, University of Florence, Florence, Italy*

Background, Motivation and Objective

The last decade has seen an extraordinary evolution of vector Doppler techniques, allowing the investigation of full 2D regions of interest (ROI). In particular, we recently proposed a method (DOI: 10.1109/ULTSYM.2016.7728428), which transmits plane waves (PWs), beamforms 8 parallel lines distributed over the ROI, and estimates the flow speed in real-time by using 16 independent sub-apertures in reception. However, the transmission of PWs inefficiently spreads the energy over a wide ROI, thus reducing the contrast of the investigated Doppler lines. In this work, we propose to improve the performance by transmitting the so called "layered array beams" (LBs), which are limited diffraction beams presenting a comb like pattern for a long range of depths.

Statement of Contribution/Methods

First, Field II simulations for an 8 MHz 192-element linear array probe with 245 µm pitch were finalized to find the LB configuration that optimizes the energy distribution along the 8 lines of interest, which are 5-pitch distant from each other. The optimal settings were then used to transmit the same waveforms by the ULA-OP 256 scanner, and the corresponding experimental one-way beams were compared to those obtained in simulation. The side-to-main-lobe energy ratio (SMER), was also evaluated and compared to that obtained with a PW.

Then, steady parabolic flow with different peak velocities (6, 12, 24 cm/s) was pumped in an 8 mm diameter pipe with rigid walls, which was tilted at 0°, 6°, 12°, 18°. The estimated velocity profiles obtained along the 8 lines were compared to the expected ones by evaluating the relative errors. The wall to lumen contrast ratio (CR) was also evaluated and compared to that obtained with a PW.

Results/Discussion

The proposed approach presents -3dB SMER improvement when compared to PW, see the experimental one-way beams for LB (Fig. A, C) and PW (Fig. B, D). The flat lateral pattern of PW (D) spreads the energy over the whole region of interest, while the comb-like pattern (C) mainly focuses the energy along the lines of interest. This result translates to 2.5 dB enhancement of the CRs, which could be significant in difficult Doppler analysis. The velocity vectors are properly reconstructed in the in-vitro test (an example is reported in Fig. E overlaid on the B-mode image); the module of the velocity (Fig. F) for each line of interest is estimated with relative errors lower than 9%.

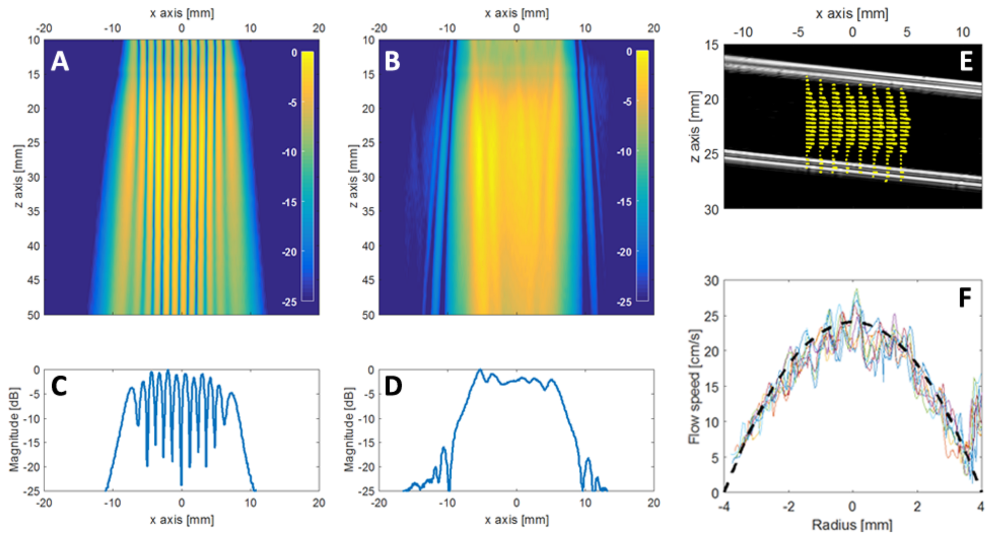

4I-4

11:15 am A Doppler-Based Regularization Problem for Intraventricular Vector Flow Mapping

Kondo Claude Assi[1], Etienne Gay[1], Christophe Chnafa[2], Simon Mendez[2], Franck Nicoud[2], **Damien Garcia[1,3]**; *[1]University of Montreal, Canada, [2]University of Montpellier, France, [3]CREATIS, France*

Background, Motivation and Objective

Recent studies suggest that the analysis of the intracardiac blood flow dynamics *via* vector imaging can provide relevant evaluation of cardiac dysfunction. In particular, the clinical importance of intraventricular vortex formation has been underlined. Cardiac magnetic resonance and contrast-enhanced ultrasound are commonly used. These approaches, however, cannot be integrated into routine clinical practice. For the purpose of offering robust and clinically-compatible intraventricular vector flow mapping (*i*VFM), we generalized the Doppler-based algorithm proposed in [10.1109/TMI.2010.2049656] by using a regularized least-squares method with automatic selection of the regularizing parameters.

Statement of Contribution/Methods

The *i*VFM reconstruction was formulated as an optimization problem based on an *l*2-norm minimization of a functional composed of a Doppler data-fidelity term and a regularizer. The latter contains three physically interpretable expressions related to mass conservation, Dirichlet boundary conditions, and smoothness. A finite difference discretization of the continuous problem was adopted in a polar coordinate system, leading to a sparse symmetric positive-definite system. The three regularization parameters were determined automatically by analyzing the *L*-hypersurface, a generalization of the *L*-curve. The performance of the proposed method was evaluated using 1) simulated flow data from a patient-specific CFD (computational fluid dynamics) model of a human left heart, and 2) *in vivo* echocardiographic data. The main intraventricular vortex was detected by calculating the Okubo-Weiss criterion.

Results/Discussion

In the CFD model, the normalized root-mean-square errors (CFD *vs.* *i*VFM) were less than 5% and 15% for the radial and angular velocities, respectively. They reached maxima during left ventricular filling, when the velocities were the largest. The core vorticities were also in good agreement ($r^2 = 0.91$), although the *i*VFM reconstruction induced some underestimation (maximum = 130 *vs.* 160 s^{-1}). The *in vivo* vector flow maps returned by *i*VFM made the intraventricular flow patterns and vortex formation well discernible. This 2-D *i*VFM method will be clinically relevant for assessing the diastolic function in patients. The proposed algorithm will form the framework for three-component volumetric *i*VFM.

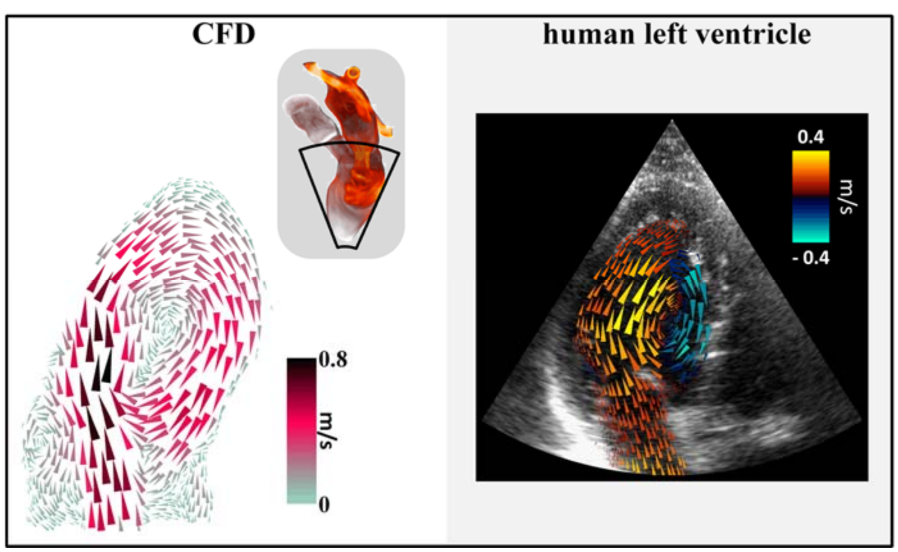

4I-5

11:30 am Accuracy and Precision Study of Plane Wave Vector Flow Imaging for Laminar and Complex Flow *In Vivo*

Jonas Jensen[1], Carlos Armando Villagómez Hoyos[1], Jacob Bjerring Olesen[1], Borislav Tomov[1], Marie Sand Traberg[1], Ramin Moshavegh[1], Matthias Bo Stuart[1], Caroline Ewertsen[2], Kristoffer Lindskov Hansen[2], Michael Bachmann Nielsen[2], Jørgen Arendt Jensen[1]; [1]*Electrical Engineering, Technical University of Denmark, Kgs. Lyngby, Denmark,* [2]*Department of Radiology, Copenhagen University Hospital, Copenhagen, Denmark*

Background, Motivation and Objective

The purpose of this study was to investigate the accuracy and precision of fast plane wave 2-D vector flow imaging (VFI) under laminar and complex flow conditions in a human subject. The method has previously been validated in simulations and straight-vessel phantoms, however, complex flow patterns remain challenging to study, since there are no other imaging techniques accurately enough to compare with. Here, the approach was to study (1) the accuracy by comparing VFI obtained from a patient-specific phantom measurement to computational fluid dynamics (CFD) simulated velocities derived from the same geometry; and (2) the precision *in vivo* by calculating the standard deviation (SD) of VFI estimates at several evaluation points.

Statement of Contribution/Methods

The carotid bifurcation of a healthy subject was scanned using a 4.1 MHz linear probe and a fast plane wave sequence (0° and ± 15°; 10 kHz PRF). Data were acquired for 10 s using the SARUS scanner. The carotid artery of the same subject was scanned with magnetic resonance imaging (MRI). The acquired MRI geometry of the bifurcation was used for fabricating a patient-specific flow phantom, which was ultrasound scanned using the fast plane wave sequence. The same geometry was used in a CFD simulation to calculate the velocity field. Boundary conditions corresponded to those in the phantom. For the processed *in vivo* data, a medical doctor selected evaluation points, where the precision of velocities and angles were calculated as the mean SD of estimates aligned to the heart cycle.

Results/Discussion

The images show a frame during systolic deceleration, where similar flow patterns and a large vortex are estimated in both the CFD simulation and VFI phantom scan. Velocity magnitudes and angles are shown as a function of time at the two estimation points (a) and (b) in the figures to the right. Flow is mainly laminar at (a), and the mean difference between CFD and VFI is 6.6 % for velocities. In the vortex (b), the mean difference is 9.3 % for velocity magnitude, and the angle variation is similar in CFD and VFI except from 0.15 s to 0.3 s. For the *in vivo* scan, the precision was highest in the center of the common carotid artery with a SD of 4.5 % for velocity magnitude and 3.4° for angles, while the SD was 23° for angles in the external branch. In conclusion, plane wave VFI measures flow precisely, and estimates are in good agreement with a CFD simulation.

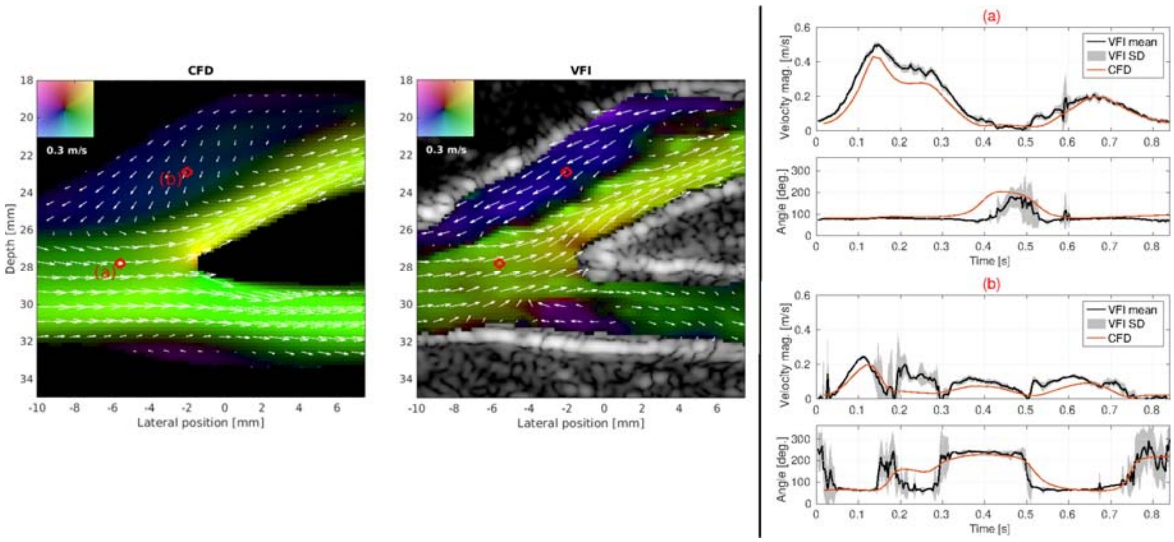

4I-6

11:45 am High-Resolution Vector Doppler for Cerebral Blood Flow Estimation

Jonathan Porée[1], Thomas Deffieux[1], Mathieu Pernot[1], Charlie Demene[1], Jerome Baranger[1], Mickael Tanter[1]; [1]*Institut Langevin (ESPCI ParisTech, PSL Research University, CNRS UMR 7587, INSERM U979), Paris, France*

Background, Motivation and Objective

Functional ultrasound (fUS) imaging is novel neuroimaging modality for brain activity based on the neurovascular coupling. This technique provides non-invasive dynamic mapping of the cerebral blood volume (CBV) variations through high-sensitivity power Doppler measurements. Complementary to CBV measurements, it would be of particular interest to extend fUS to cerebral blood flow (CBF) measurements for the neuroscience community. As power Doppler cannot provide velocity amplitude or the direction of the flow, we developed a high-resolution vector Doppler method dedicated to the evaluation of velocity and CBF in small vessels.

Statement of Contribution/Methods

We present a new computational framework for reconstructing 2D vector flow from beamformed IQ data. High-resolution IQ sequences are first constructed from compounded plane wave transmissions. Tilted IQ images are then computed using k-space Gabor filters for directional power and color Doppler computation. The vector flow is computed as the minimizer of a quadratic cost functional that is the weighted sum of: 1) the vector Doppler residual norm, 2) an anisotropic functional imposing smoothness of the velocity along the blood vessels which are detected using power Doppler and 3) a space-time regularization imposing the overall continuity. The proposed framework was evaluated in-vitro in a pipe flow phantom (3 cm^3s^{-1} Flow/rate) and in-vivo on ultrasonic data acquired on N=3 human neonate brain.

Results/Discussion

High-resolution vector Doppler images were obtained with an Aixplorer V6 scanner and a 6.4 MHz linear array transducer. Three tilted plane waves (-3°,0°,3°) were transmitted with a PRF of 9600 Hz, beamformed with the full aperture and coherently compound. Tilted IQ images were obtained from directional filtering (-10°,0°,10°) with a kernel corresponding to a f# of 5. In vitro, estimated velocities were highly consistent with the expected values with an absolute error of 15±8 % and 6±4° of angular error. In vivo (see Fig.1), we could provide high-resolution 2D vector flow fields in neonate's brain. Flow directions and amplitudes were consistent with the vessel orientation and Pulse wave Doppler respectively. Thanks to this framework, which can easily be extended to 3D, Ultrasensitive Doppler datasets can now be used to give an estimate of the velocity amplitude; direction and blood flow in the brain.

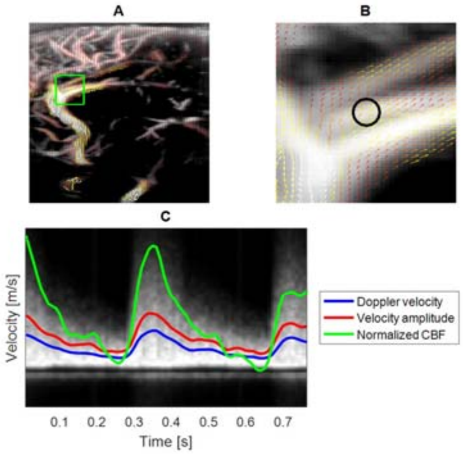

Figure 1: High-resolution vector Doppler in neonate brain. A) High resolution vector flow overlaid on power Doppler in a medial sagital view. B) Zoom of the vector flow corresponding to the green rectangle. C) Doppler velocity; velocity amplitude and Normalized Cerebral Blood Flow overlaid on the Pulse Wave Doppler.

5I - MEL: Cardiac Strain Imaging

Blue Room

Saturday, September 9, 2017, 10:30 am - 12:00 pm

Chair: **Azra Alizad**
Mayo Clinic

5I-1

10:30 am 3-D Electromechanical Wave Imaging in the Heart In Silico and In Vivo

Julien Grondin[1], Dafang Wang[2], Elaine Wan[1], Natalia Trayanova[2], Elisa Konofagou[1]; [1]*Columbia University, USA,* [2]*Johns Hopkins University, USA*

Background, Motivation and Objective

Electromechanical wave imaging (EWI) is an ultrasound-based methodology that can map the electromechanical activation of the heart at high temporal resolution. Previous reports have shown strong correlation between EWI-based and electrical activation times. However, EWI has been performed only with 2D echocardiography, which cannot map the full cardiac volume in a single heartbeat. Our objective in this study was to show the feasibility of 3D EWI in silico and in vivo.

Statement of Contribution/Methods

A 3-MHz 32x32 array was simulated in Field II. The right and left ventricular geometry and displacement fields were obtained from a computational electromechanical model based on a real human heart anatomy. Ultrasound radiofrequency (RF) channel data were simulated at 1000 Hz using diverging wave imaging and inter-volume axial displacements and strains were estimated together with electromechanical activation times. Estimated axial displacements, strains and activation times were compared against their computational equivalents. To investigate in vivo feasibility, RF signals were reconstructed from channel data using a 32x32 array (Vermon) connected to two synchronized Verasonics Vantage systems in an open-chest canine heart and the inter-volume axial displacements and strains were estimated from diverging wave acquisitions at 500 frames per second.

Results/Discussion

Estimated and computational axial displacements in silico were found to be strongly correlated (R2=0.99) in both the right and left ventricles using 3D EWI. Good agreement was found between the estimated electromechanical activation times and the computational electrical activation times (Fig.1). The 3D electromechanical wave propagation was also imaged at different phases of the cardiac cycle in vivo, with earlier contraction in the atria than in the ventricles.

This study shows for the first time that 3-D EWI is feasible and opens new avenues for non-invasive cardiac arrhythmia characterization in 3D.

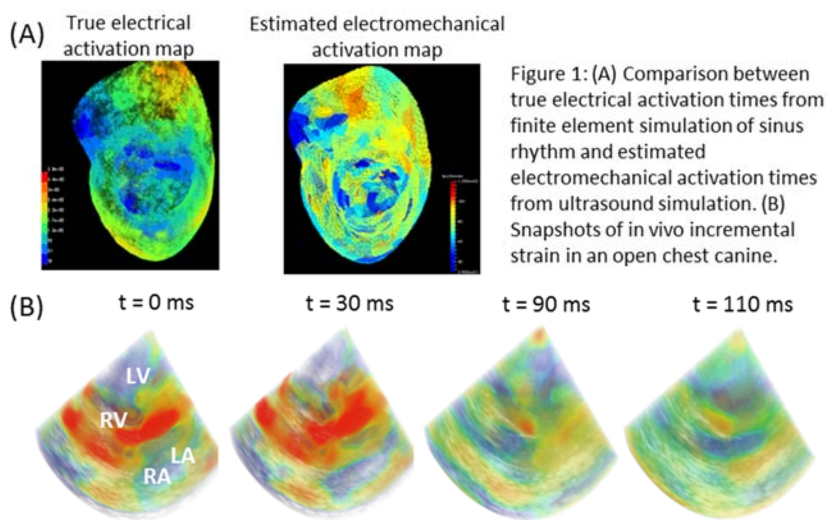

Figure 1: (A) Comparison between true electrical activation times from finite element simulation of sinus rhythm and estimated electromechanical activation times from ultrasound simulation. (B) Snapshots of in vivo incremental strain in an open chest canine.

5I-2

10:45 am In Vivo Mapping of Transverse Shear and Principal Strains in Interventricular Septum Using Coherent Diverging Wave Compounding

He Li[1], Yuexin Guo[1], Wei-Ning Lee[1], Zhe Zhen[2], Songyan Liao[2], Hung Fat Tse[2]; [1]*Department of Electrical and Electronic Engineering, The University of Hong Kong, Hong Kong,* [2]*Department of Medicine, The University of Hong Kong, Hong Kong*

Background, Motivation and Objective

Assessing the interventricular septum (IVS) facilitates the understanding of complex ventricular-ventricular interaction and related cardiac diseases. Previous studies have revealed that the functionally bilayered IVS exhibits distinct radial and circumferential strains in its left (*Ls*) and right (*Rs*) sides. Nonetheless, the transverse shear and principal strains, which reflect the interlayer sliding and the effective contractile function, respectively, in IVS have not been documented yet, and their quantitative mapping by ultrasound strain imaging (USI) is therefore the focus of this study.

Statement of Contribution/Methods

Radio-frequency (RF) data of a normal open-chest beating porcine heart were acquired using a Verasonics® Vantage 256 system with a P4-2 phased array probe (2.5 MHz). Coherent diverging wave compounding (CDWC) was employed to achieve acceptable full-view image quality at 250 fps (subaperture: 21 elements; angular aperture: 90°; compounding set: 9 diverging waves). In-plane displacements were estimated through normalized cross correlation and a recorrelation strategy, and were accumulated to compute in-plane systolic strains, from which cardiac and principal strains were derived through coordinate transformation and eigen decomposition, respectively.

Results/Discussion

Estimated radial (E_{RR}), circumferential (E_{CC}), and longitudinal (E_{LL}) strains were distinct in *Ls* and *Rs* of the IVS (Figs. a and e), in agreement with literature. The radial-circumferential (E_{RC}) and radial-longitudinal (E_{RL}) shear strains showed similar patterns to those reported in a displacement-encoded MRI study, and also revealed distinct values in *Ls* and *Rs* (E_{RC}: -8.3±10.6% vs. 5.6±9.5%; E_{RL}: 16.5±8.5% vs. 10.0±7.9%), indicating different interlayer shearings. The minimum (E_1) and maximum principal strain (E_2) patterns approximated E_{CC}/E_{LL} and E_{RR}, respectively. The relatively small absolute angles between the radial and E_2 directions (θ_{RC} and θ_{RL} in Figs. d and h) were consistent with previous tagged MRI studies, demonstrating systolic wall thickening with E_2 being oriented predominantly in the radial direction. Our findings show that cardiac USI using CDWC could yield myocardial strains with promising quality, and the estimated transverse shear and principal strains may provide additional insights in assessing the IVS function.

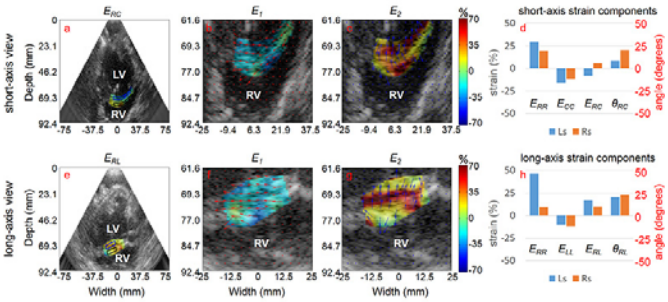

5I-3

11:00 am Ultrafast Myocardial Elastography using Coherent Compounding of Diverging Waves during Simulated Exercise

Diya Wang[1], Jonathan Poree[1], Boris Chayer[1], Amir Hodzic[1,2], Damien Garcia[3,4], François Tournoux[1,2], Guy Cloutier[1,3]; *[1]Laboratory of Biorheology and Medical Ultrasonics, Research Center, University of Montreal Hospital, Montreal, Quebec, Canada, [2]Department of Echocardiography, University of Montreal Hospital, Montreal, Quebec, Canada, [3]Department of Radiology, Radio-Oncology and Nuclear Medicine, Institute of Biomedical Engineering, University of Montreal, Montreal, Quebec, Canada, [4]CREATIS, Lyon, France*

Background, Motivation and Objective

Objective myocardial deformation assessment during exercise could help the clinician to better diagnose myocardial ischemia. However, the use of conventional focus echocardiography is compromised at increased heart rates due to its limited lateral view field and frame rate. Ultrafast echocardiography using coherent compounding of diverging waves improves temporal resolution while maintaining a large view field (*Jonahan, IEEE TMI, 2016*) and could be a valuable alternative during exercise. This study aimed to demonstrate that ultrafast echocardiography combined with a Lagrangian speckle model estimator (LSME) can offer high-quality myocardial strain measurements at increased heart rate.

Statement of Contribution/Methods

Myocardial strain assessment was tested on a dynamic cardiac phantom at heart rates ranging from 60 to 180 beats-per-minute (bpm). Ultrafast echocardiography was obtained by using a Verasonics platform equipped with a 2.5 MHz phased array scanner (PRF: 4500 Hz). Negative effects of side lobes and phase delays during the large tilted compounding were suppressed through a triangle transmit sequence and motion compensation strategy. The robustness and accuracy of affine strain estimation were then enhanced using radiofrequency least-squares-based LSME with a time-ensemble estimation strategy (*Jonathan, IEEE TMI, 2015*). 2D myocardial strain images at systole and early-diastole as well as regional strain curves were finally estimated at low and high heart rates.

Results/Discussion

Myocardial strain assessment was performed with high contrast-to-noise ratio and signal-to-noise ratio at both low and high heart rates. The detailed myocardial deformations were clearly illustrated by the affine strain distributions in one cardiac cycle, even at an *in-vitro* heart rate of 180 bpm. Regional strain curves were accurately estimated and periods matched those of the pump or heart rhythms. These preliminary results suggest that the use of ultrafast echocardiography combined with LSME could be useful clinically to provide an accurate and objective method of myocardial strain assessment at high heart rates.

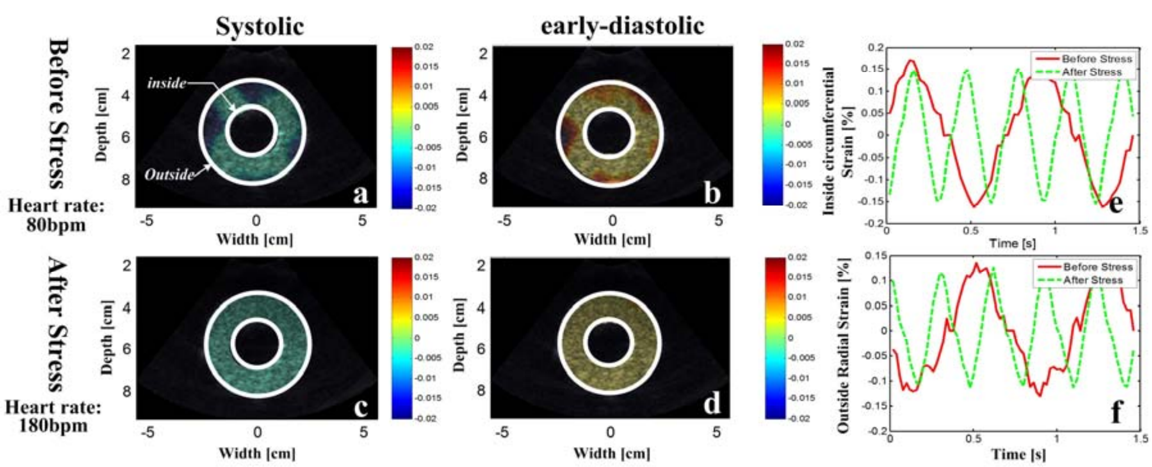

Figure ***In-vitro*** **myocardial elastography during exercise conditions. (a) Systolic and (b) early-diastolic circumferential strain images before stress test at a pump rate of 80 bpm; (c) systolic and (d) early-diastolic circumferential strain images after stress test at a pumb rate of 180 bpm; (e) inside regional circumferential strain curves before and after stress; (f) outside regional radial strain curves before and after stress conditions.**

5I-4

11:15 am Comparison between Fully and Partially Focused Transmit Strategies in Transthoracic Cardiac Strain Estimation

Vincent Sayseng[1], Julien Grondin[1], Elisa Konofagou[2]; [1]*Department of Biomedical Engineering, Columbia University, New York, New York, USA,* [2]*Department of Radiology, Columbia University, New York, New York, USA*

Background, Motivation and Objective

Myocardial elastography identifies ischemia and infarction by estimating strain. Focused beams with ECG-gating offers high spatial resolution and frame rate, but precludes imaging of arrhythmic patients. Wide beam and coherent compounding can estimate strain within a single heart cycle by trading off spatial resolution or frame rate. Compounding and wide beam sequences were optimized in silico and in vivo, and then compared with a focused, ECG-gated sequence in vivo.

Statement of Contribution/Methods

The left ventricle was simulated in Field II as a radially thickening annulus imaged with a 20 mm aperture 2.5 MHz phased array. For compounding, the width of a virtual aperture comprised of 7 equally spaced virtual sources was varied from 0 to 20 mm in silico. The axial position of virtual aperture was varied from 0 to -75 mm. For wide beam, 14 beams were used, varying focal beamwidth from 5 to 34 mm in silico. At 3000 Hz PRF, a human left ventricle was imaged, with compounding sequences at 50, 100, 250, 500, 1000 fps with 60, 30, 12, 6, 3 virtual sources and wide beam sequences at 50, 100, 200, 300, 500 fps with 60, 30, 15, 10, 6 beams. The optimal compounding and wide beam sequences were then tested against a focused, ECG-gated (250 fps and 65 beams) sequence in vivo. Radial and circumferential strains were derived from displacements estimated with 1-D cross-correlation in 2D. In silico, mean difference between estimated and theoretical strains ($\Delta\varepsilon$) was used to evaluate accuracy, while SNR was used in vivo, defined as the mean strain over its standard deviation.

Results/Discussion

In silico, a 20 mm wide virtual aperture positioned at -10 mm estimated strain most accurately ($\Delta\varepsilon_{radial}$ = 6.7%, $\Delta\varepsilon_{circum}$ = 2.3%). In silico, a focal beamwidth of 19 mm estimated strain most accurately ($\Delta\varepsilon_{radial}$ = 11%, $\Delta\varepsilon_{circum}$ = 4.8%). Comparing optimal compounding and wide beam sequences against the focused, ECG-gated sequence in vivo (Fig 1), compounding estimated strain most accurately at 250 fps with 12 virtual sources (SNR_{radial} = 1.2, SNR_{circum} = 0.33), while wide beam estimated strain most accurately at 200 fps with 15 beams (SNR_{radial} = 1.3, SNR_{circum} = 0.32). Compounding and wide beam sequences thus produced similarly accurate strains, while the focused, ECG-gated sequence estimated strain the most accurately in vivo (SNR_{radial} = 1.5, SNR_{circum} = 0.77).

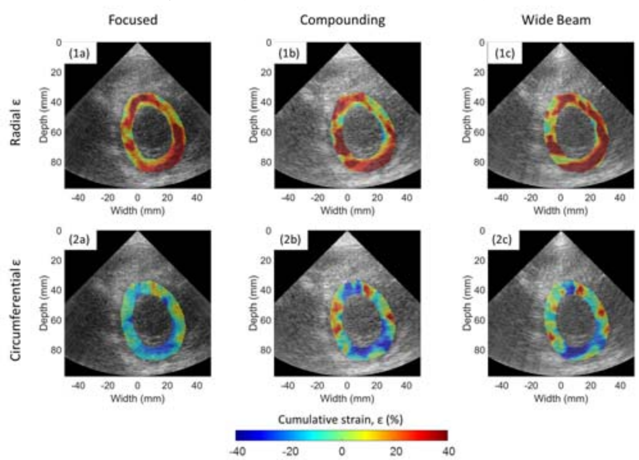

Figure 1. Radial **(1)** and circumferential **(2)** cumulative strains (ε) in a healthy human subject *in vivo*, on cross-sectional views of the left ventricle. ε were overlaid on B-modes generated by each optimized sequence: focused with ECG-gating using 65 beams at 250 fps **(a)**, compounding using 12 virtual sources at 250 fps **(b)**, and wide beam using 15 beams at 200 fps **(c)**. Mean ± standard deviation of the radial and circumferential ε within the masked area was determined to be 23 ± 15% **(1a)** and -8.4 ± 11% **(2a)** for the focused, 23 ± 20% **(1b)** and -6.3 ± 19% **(2b)** for compounding, and 27 ± 21% **(1c)** and -5.4 ± 17% **(2c)** for wide beam, respectively.

5I-5

11:30 am Comparison of 3D Tissue Motion Estimation Methods Using Transverse Oscillations

Solveig Bech[1], Sebastien Salles[2], Hans Torp[2]; [1]*Norwegian University of Science and Technology, Trondheim, Norway,* [2]*Department of Circulation and Medical Imaging, Norwegian University of Science and Technology, Norway*

Background, Motivation and Objective

Cardiovascular diseases are the leading cause of death globally. Such diseases may affect the left ventricular function, which in turn is closely related to the left ventricular stiffness. Estimation of cardiac deformation can give information on the myocardial stiffness, and may therefore be important in assessment of cardiovascular diseases. A 3D motion estimation scheme is necessary to measure the full cardiac motion. To do so, the use of transverse oscillations (TOs), to compute the azimuth and elevation velocity components, has been proposed. The objective of this study was to compare three different ways of introducing 3D TOs, in order to find the method best suited for cardiac motion estimation.

Statement of Contribution/Methods

The three methods use different spatial filters (Figures a-c) to filter the frequency content in order to generate TOs. A phase-based motion estimation scheme is used to estimate the 3D motion by calculating the phase of the autocorrelation after filtering and combining the phase vectors according to the method used to achieve the true velocity components.

Two experiments were performed using a locally modified, university-owned Vivid E95 scanner and a 4V probe. A tissue-mimicking phantom was conventionally scanned using a stepper motor to introduce a known 3D trajectory, and the left ventricle of one healthy volunteer was scanned using 3D high frame rate imaging (820 FPS).

Results/Discussion

Figures a-c show the three filtering techniques used to introduce TOs. Figures d-f show the tracking of a known 3D circle using the three methods. The color of the estimated trajectories gives the mean error of the displacement in relation to the known trajectory. Method b yielded the best result in x-direction with mean error of 0.0204 +/- 0.0174 mm. Methods b and c gave the best results in y-direction with mean errors of 0.0344 +/- 0.0415 mm and 0.0344 +/- 0.0336 mm respectively. Method a yielded the best result in z-direction with mean error of 0.0053 +/- 0.0037 mm. Spatial filtering was used to achieve TOs, hence in all three cases it is possible to apply conventional tissue Doppler, using the entire frequency content, to estimate the motion in z-direction. The TO parameters were chosen independently for each method to yield the best result possible in each case. As method b gave the best result estimating the 3D circle, it was tested on in-vivo data as shown in Figure g.

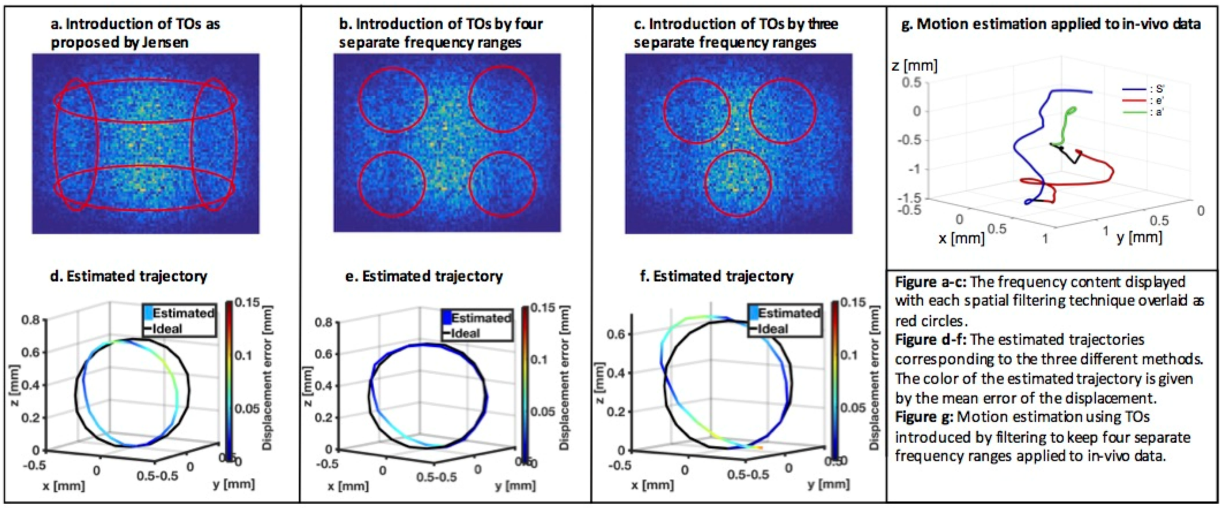

Figure a-c: The frequency content displayed with each spatial filtering technique overlaid as red circles.
Figure d-f: The estimated trajectories corresponding to the three different methods. The color of the estimated trajectory is given by the mean error of the displacement.
Figure g: Motion estimation using TOs introduced by filtering to keep four separate frequency ranges applied to in-vivo data.

5I-6

11:45 am Assessment of Left Bundle Branch Related Strain Dyssynchrony a Comparison with Tagged MRI

Louis Fixsen[1], Anouk de Lepper[2], Marcel van 't Veer[1,2], Marc Strik[3], Lars van Middendorp[3], Frans van de Vosse[1], Frits Prinzen[3], Patrick Houthuizen[2], Richard Lopata[1];
[1]Eindhoven University of Technology, Netherlands, [2]Catharina Ziekenhuis Eindhoven, Netherlands, [3]Maastricht University, Netherlands

Background, Motivation and Objective

Mechanical dyssynchrony caused by left bundle branch block (LBBB) negatively affects cardiac performance and can be treated by cardiac resynchronization therapy. Cardiac strain derived from ultrasound (US) images can be used to quantify and visualise this dyssynchrony at a regional level. Speckle tracking echocardiography is the most commonly used technique, however commercially available methods use extensive post-processing techniques resulting in loss of key local information. In this study, we measure strain using US images of the canine left ventricle (LV) and compare this with tagged cardiac magnetic resonance imaging (CMR), the current gold standard for medical strain imaging.

Statement of Contribution/Methods

In-vivo short axis views of the canine LV were imaged in 16 dogs, before and after LBBB was induced through ablation. US DICOM data was acquired using a General Electric Vivid5, whilst CMR data was acquired using a 1.5T Philips Intera. US short axis views were acquired at papillary muscle level of three cycles, whilst seven cross-sections were acquired using CMR from apex to basal level. All data were manually segmented, and the anterior insertion of the right ventricle free wall was selected. For the US data, displacement fields were calculated for each frame using a coarse-to-fine algorithm and Fourier-based regularisation. The displacements were converted into circumferential strain (e_{cir}) from end-diastole to end-diastole, after estimating the local strain directions by solving a heat diffusion problem for the geometry given. CMR data contained at minimum the entirety of systole and a portion of diastole. e_{cir} was estimated using SinMod (Maastricht University). The local strains were averaged into six standard sectors. US data were down-sampled to match the frame rate of the CMR.

Results/Discussion

CMR data were lag adjusted an average of two frames due to different definitions for systole on-set. Cross-correlating e_{cir} estimations from US and CMR data showed a mean r of 0.85 (±0.14). Presence of LBBB could be observed in both US and CMR data as lateral wall systolic pre-stretch with concurrent early contraction of the septal wall. Preliminary results show Fourier regularisation reduces drift in e_{cir} estimation and increases evidence of LBBB. Future work will include a study in patients using the same method and commercial speckle tracking package.

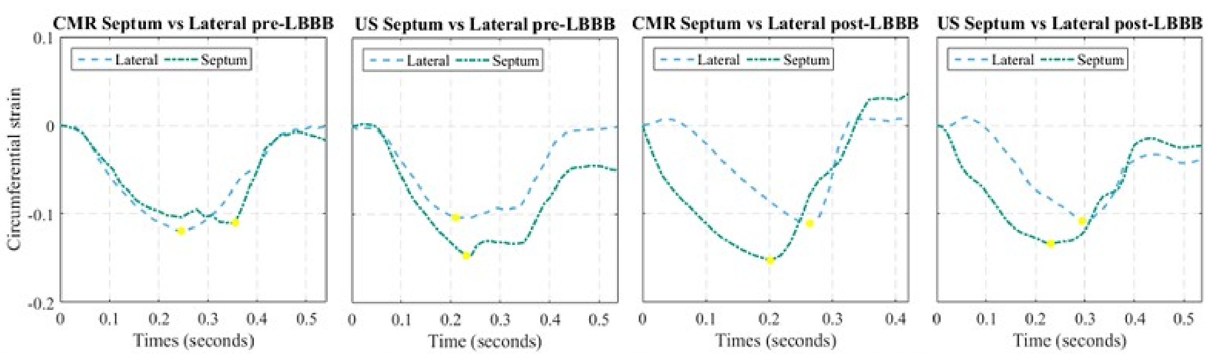

Circumferential strain obtained from CMR and US in the lateral and septal LV wall pre- and post LBBB

6I - Advanced Tranducer Materials and Designs

Hampton Room

Saturday, September 9, 2017, 10:30 am - 12:00 pm

Chair: **Sandy Cochran**
University of Glasgow

6I-1

10:30 am Piezoelectric Materials and Application Oriented Figures Of Merit

Shujun Zhang[1], Fei Li[2], Thomas Shrout[2]; [1]*ISEM/AIIM, University of Wollongong, Wollongong, NSW, Australia,* [2]*Penn State University, USA*

Background, Motivation and Objective

Piezoelectric materials are at the heart of electromechanical devices, such as medical imaging transducer, high intensity focused ultrasound (HIFU), industrial nondestructive evaluation (NDE) and piezoelectric sensors, to name a few. In this presentation, the advantages and disadvantages of piezoelectric materials are discussed based on the requirements (figure of merit) of various applications, with emphasis on recent developments of the high performance relaxor-$PbTiO_3$ (PT) ferroelectric materials and high temperature nonferroelectric piezoelectric single crystals.

Statement of Contribution/Methods

In this presentation, we surveyed relaxor-PT based ferreoelectric materials, including domain engineered relaxor-PT single crystals: Generation I [$Pb(Mg_{1/3}Nb_{2/3})O_3$-PT: PMN-PT], Generation II [$Pb(In_{0.5}Nb_{0.5})O_3$-PMN-PT] and Generation III [acceptor modified relaxor-PT], and modified PNR engineered relaxor-PT ceramics for medical imaging and HIFU applications. In addition, high temperature piezoelectric crystals, such as $ReCa_4O(BO_3)_3$ (ReCOB, Re: rare earth), langasite and fresnoite crystals were surveyed for high temperature industrial NDE applications.

Results/Discussion

Domain engineered PMN-PT single crystals are found to possess high electromechanical coupling factor k_{33} of >0.9, far outperforming commercially available PZT based ceramics (~0.75), greatly enhance the bandwidth and sensitivity of medical imaging transducers, due to the fact that the bandwidth is proportional to $k/[\sqrt{1-k^2}]$, while the power efficiency of transducer $RP=k_t/[\sqrt{c_{33}^D\varepsilon_{33}^S}]$ and $TP=[k_t/(1-k_t^2)][\sqrt{\varepsilon_{33}^S/c_{33}^D}]$. The ternary PIN-PMN-PT crystals are found to possess higher Curie temperature and coercive field, broadening the temperature usage range and drive field stability of the transducer, while acceptor doped relaxor-PT crystals give high mechanical quality factor, greatly decrease the power dissipation, where $P_{disp}=½[\omega Y_r S^2/Q_m]$ and $P=\omega E^2k^2\varepsilon Q_m$, potential for HIFU application[1,2]. Of particular interest is that the modified PNR engineered relaxor-PT ceramics show promising high piezoelectric d_{33} of >1400pC/N and ultrahigh dielectric constant of >10,000, which will benefit the transducer array applications. In addition, the nonferroelectric piezoelectric crystals are found to possess ultrahigh electrical resistivity and mechanical quality factor, warrant the NDE transducers and acoustic emission sensors operational at elevated temperature, up to >1000^{o}C[3,4].

References:

[1] S. Zhang, F. Li, X. Jiang, J. Kim, J. Luo, X. Geng, Prog. Mater. Sci. 68 (2015) 1-66.
[2] S. Zhang, F. Li, J. Luo, R. Sahul, T. Shrout, IEEE Trans. UFFC, 60 (2013) 1572.
[3] S. Zhang and F. Yu, J. Am. Ceram. Soc. 94 (2011) 3153.
[4] X. Jiang, K, Kim, S. Zhang, J. Johnson, G. Salazar, Sensors 14 (2014) 144.

6I-2

11:00 am Piezoelectric Single Crystal Standard

Lynn Ewart[1], Zuo-Guang Ye[2], [1]*U.S. Navy, USA,* [2]*Simon Fraser University, Canada*

Background, Motivation and Objective

Piezoelectric single crystals (piezocrystals) of lead magnesium niobate-lead titante (PMN-PT) and lead zinc niobate-lead titanate (PZN-PT) have extremely large electromechanical coupling coefficients and exhibit strains of over one percent. The technical significance of these properties to devices is enormous and includes a doubling of bandwidth, decreased package size, and increased resolution. The exploitation of electroactive single crystals is currently being pursued for naval sonar and medical ultrasound transducers. To accelerate the maturation and implementation of piezocrystals from the research arena into commercial devices, an international working group completed an IEEE material standard in 2017: The Standard for Relaxor-Based Piezoelectric Single Crystal Materials for Transducer and Actuator Applications. The working group is now working on extensions to this standard including into ternary piezocrystal materials.

Statement of Contribution/Methods

The group has had three major accomplishments to date. First, device designers and materials specialists wrote a standard that serves the two communities. Second, the materials and device communities that use piezocrystals developed mutually agreed upon terminology for discussing piezocrystals and a common understanding of each other's materials needs and concerns. Third, the group has identified near term piezocrystal development areas opportune for future addition to the standard.

Results/Discussion

The standard covers the physical and electromechanical requirements for [001]-poled relaxor-based piezoelectric single crystal materials for use in medical, industrial, and military transducers, actuators, and sensors. The focus is on three compositions from each of the PMNT and PZNT systems. The central content is the eight properties provided for each composition: free relative dielectric permittivity (K3T), dielectric loss tangent (tan del), temperature of the first anomalous event in free relative dielectric permittivity (TRT), rod extensional coupling factor (k33), transversely poled length extensional coupling factor (k31), longitudinal mode piezoelectric coefficient (d33), transversely poled length extensional mode (d31), elastic compliance at constant electric displacement (s33D). This presentation will discuss the standard, the underlying contributions of the working group, and the extensions of the standard, including to ternary piezocrystals, that are underway.

6I-3

11:15 am Design and Characterization of an MR-Compatible FUS Randomized Array for Transcranial Neuromodulation

Vandiver Chaplin[1], Erik Dumont[2], Charles Caskey[1,3]; [1]*Institute of Imaging Science, Vanderbilt University, Nashville, TN, USA,* [2]*Image Guided Therapy, Pessac, France,* [3]*Department of Radiology and Radiological Sciences, Vanderbilt University, Nashville, TN, USA*

Background, Motivation and Objective

Focused ultrasound is a promising method for non-invasive neural stimulation in the brain. Early studies have shown that neurological conditions such as essential tremors can be effectively treated with ultrasound ablation, while sub-thermal stimulation is being explored to probe functional connections in the brain and may have therapeutic benefits in a variety of neurological diseases. Although systems for transcranial ablation exist for human subjects, they are not optimized for cortical stimulation or studies in non-human primates. Here we report on the design and characterization of a new spherically-focused randomized sparse array transducer.

Statement of Contribution/Methods

Our main design goal was to develop a transducer capable of steering over the macaque somatosensory cortex (~2cm) with a focus small enough to selectively stimulate subregions of this circuit (<3mm). At 650kHz sonication frequency we varied radius of curvature, opening diameter, element size, and spacing. 128 elements were randomly placed on spherical caps of varying focal ratio. Beam shape, steering and grating lobes were evaluated with free-field Rayleigh-Sommerfeld simulations. Non-homogenous 3D acoustic simulations were performed to evaluate transcranial targeting, using K-wave and a skull CT to estimate sound speed and density. Imasonic (Besancon, France) fabricated the final design and we measured acoustic output using a needle hydrophone while driving the transducer with a 128-channel amplifier (IGT, Pessac, France).

Results/Discussion

The selected design has radius of curvature of 7.2cm and diameter of 10.3cm at the opening face (focal ratio 0.7). Active elements with diameter of 6.6 mm were randomly placed with a minimum distance of 0.5mm, resulting in an active area of 44cm^2 (~45% area coverage). Pressure FWHM is 9.5mm in the axial direction and 2.3 mm in the transverse direction at the focus and when steered 1 cm off-axis, with no near-field axial grating lobes. Simulations indicate that the focus can be maintained through the skull but is broadened (FWHM roughly doubled in each direction). We are currently measuring skull-induced beam aberrations and implementing methods to improve transcranial focal size, such as time-reversal and radiation force maximization.

The authors acknowledge funding from NIH R24MH109105.

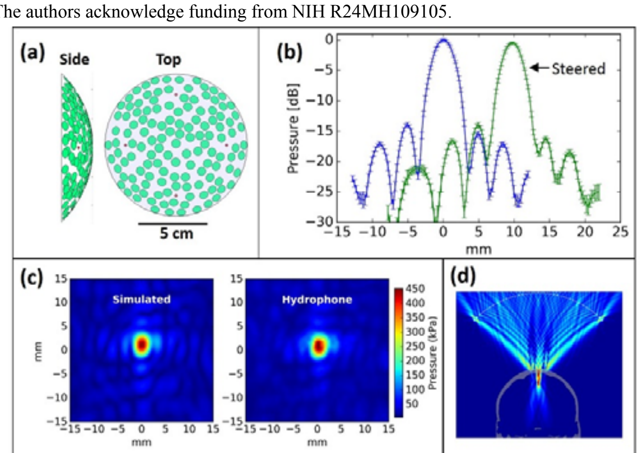

Figure: **(a)** Phased array design. **(b)** Measured pressure profiles (transverse) with and without steering. **(c)** Simulated and measured pressure in the transducer focal plane. **(d)** Transcranial (macaque) simulation with K-wave with no aberration correction.

6I-4

11:30 am Design and Evaluation of Phased Array Transducers for Deep Brain Stimulation in Nucleus Accumbens Region of the Rat Brain

Arif Ergun[1], Mehmet Kilinc[1], Mehmet Aydin[1], Ayhan Bozkurt[2], Erdem Deveci[3]; [1]*Electrical and Electronics Engineering, TOBB, University of Economics, Ankara, Turkey,* [2]*Electrical and Electronics Engineering, Sabanci University, Turkey,* [3]*Department of Psychiatry, Bezmialem University School of Medicine, Turkey*

Background, Motivation and Objective

Neuromodulation with low intensity focused ultrasound has many potential applications. One target of interest is the nucleus accumbens which is the reward center of the brain. It is hypothesized that with proper stimulation of the nucleus accumbens addictive behavior can be suppressed. Carrying out animal studies to understand the effects of LIFU parameters on such behavioral changes is an important step toward achieving addiction control in humans. Our objective is to design and evaluate a transducer array that can deliver enough energy across the rat skull, and target both nucleus accumbens sites simultaneously.

Statement of Contribution/Methods

Skull, being a strong reflector and absorber, is the biggest obstacle in delivering acoustic power into the brain. Achieving high transmission efficiency across the skull is required in order to minimize the surface temperature and damage to the transducer. It has been seen in our previous study that rat skull may act like an acoustic cavity and support standing waves. Consequently, at frequencies at which the skull thickness is half a wavelength, the transmission efficiency is maximized. The first two of these frequencies are 2.5 and 5.0 MHz. The other criterion is exclusive targeting of nucleus accumbens which is located 1.4 mm toward the nose from the bregma. The acoustic window in that region of the skull is 6×6 mm, which limits the transducer area. Since nucleus accumbens is fairly small (approximate dimensions are 1×1.4 mm), a relatively small focal spot is required. So, for evaluation, we designed 10 and 16 element 1D phased arrays at 2.5 MHz and 5.0 MHz, respectively, with ~8 mm elevation focusing. The stacks were designed and manufactured by Imasonics SAS (France). We characterized these arrays with ex-vivo rat skulls, in a water tank, using a HIFU driver, a hydrophone, and a scanning system.

Results/Discussion

With the 2.5 MHz array, we were able to achieve 16 W/cm2 acoustic intensity at focus behind the skull without any matching. We have also shown that we can increase the power 4-fold with a proper matching circuit. We used left and right half of the array independently to achieve two focal spots with beamwidths of 1 mm and 1.35 mm in azimuth (Fig. 1), 0.9 mm in elevation, and 5.5 mm axially. Both the size and location of these focal spots for the 2.5 MHz array are considered to be suitable for proper stimulation of the nucleus accumbens in rats.

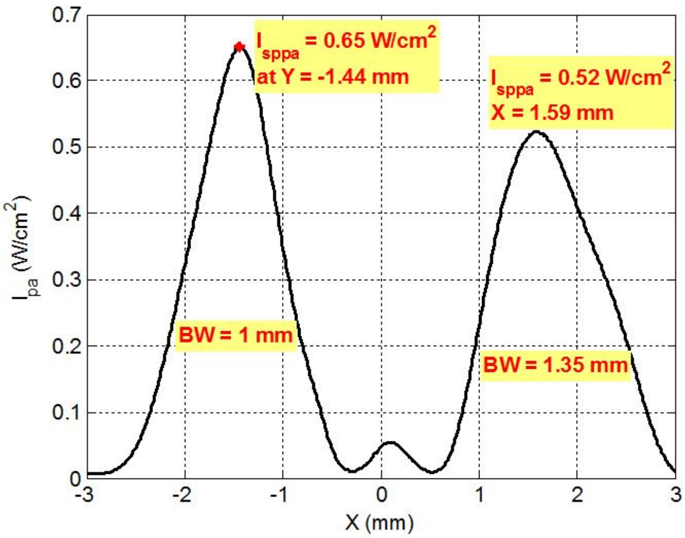

6I-5

11:45 am Design and Characterization of a 2-Dimensional Focused 1.5-Mhz Ultrasound Array with a Compact Spiral Arrangement of 256 Circular Elements

Oleg Sapozhnikov[1,2], Mohamed Ghanem[1], Adam Maxwell[3], Pavel Rosnitskiy[2], Petr Yuldashev[2], Wayne Kreider[1], Bryan Cunitz[1], Michael Bailey[1], Vera Khokhlova[1,2]; *[1]Applied Physics Laboratory, University of Washington, Seattle, Washington, USA, [2]Physics Faculty, Moscow State University, Moscow, Russian Federation, [3]Department of Urology, University of Washington School of Medicine, Seattle, Washington, USA*

Background, Motivation and Objective

Multi-element ultrasound arrays are increasingly used in clinical practice for both imaging and therapy. In therapy, they allow electronic steering, aberration correction, and focusing. To avoid grating lobes, an important requirement for such an array is the absence of periodicity in the arrangement of the elements. A convenient solution is the arrangement of the elements along spirals. The objective of this work was to design, fabricate, and characterize an array for boiling histotripsy applications that is capable of generating shock waves in the focus of up to 100 MPa peak pressure while having a reasonable electronic steering range [Khokhlova et al., Physics Procedia 87 (2016)].

Statement of Contribution/Methods

The array was designed by choosing a special distribution of 256 round elements on the surface of a spherical bowl having a central opening. The chosen array parameters are as follows: frequency 1.5 MHz, focal length 120 mm, outer diameter 144 mm (i.e., F-number = 0.83), diameter of the central opening 40 mm and diameter of the elements 7 mm. Elements are divided into 16 groups, each identifiable as a flexible chain originating at the edge of the central opening. On the bowl surface, each chain bends to minimize the spacing relative to adjacent chains, thereby forming spirals (different from Archimedean ones) that densely cover the surface of the source (see Figure). The designed array was built by Imasonic; array performance was characterized in a water tank using a 0.2 mm active element diameter Onda capsule hydrophone.

Results/Discussion

Electrical circuits were developed for matching each element of the array to an output channel of a Verasonics ultrasound engine to allow for efficient power transfer to the transducer. Measurements of electrical impedances with the matching network and the corresponding voltage signals have shown a fairly uniform distribution of the electric power transmitted to the elements. Reconstruction of the element vibrations using acoustic holography measurements confirmed that elements vibrate in a fairly uniform pattern (Figure). This approach was used to identify individual elements' holograms, calibrate and equalize outputs across all elements, and calculate the steering capabilities of the array. Work supported by NIH P01 DK043881, K01 DK104854, R01 EB007643, NSBRI through NASA NCC 9-58, and RSF 14-12-00974.

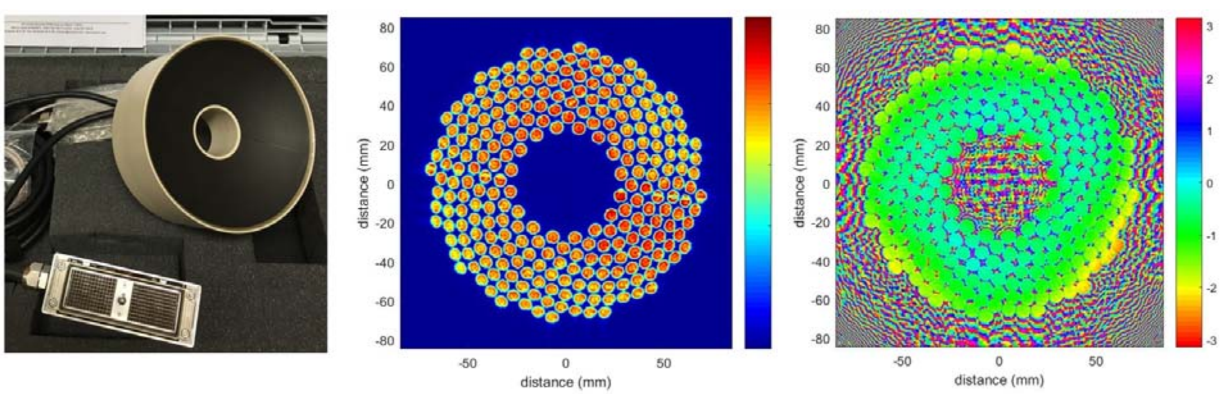

Figure. Photo of the designed array (left) and holographically reconstructed normal velocity distribution along the surface of the array: magnitude (center) and phase (right).

7I - PTF - Thin Films

Empire Room

Saturday, September 9, 2017, 10:30 am - 12:00 pm

Chair: **John Larson III**
Broadcom Ltd

7I-1

10:30 am Enhanced Piezoelectric Properties of C-Axis Textured Aluminium Scandium Nitride Thin Films with High Scandium Content: Influence of Intrinsic Stress and Sputtering Parameters

Stefan Mertin[1], Vladimir Pashchenko[1], M. Fazel Parsapourkolour[1], Cosmin S. Sandu[1], Bernd Heinz[2], Oliver Rattunde[2], Gabriel Christmann[3], Marc-Alexandre Dubois[3], Paul Muralt[1]; [1]*Electroceramic Thin Films Group, EPFL, Lausanne, Switzerland,* [2]*Evatec AG, Trübbach, Switzerland,* [3]*CSEM SA, Neuchâtel, Switzerland*

Background, Motivation and Objective

Aluminium scandium nitride (ASN) exhibits a largely enhanced piezoelectric response as compared to aluminium nitride (AlN), which makes it an upcoming piezoelectric material for next generation RF filters, sensors, actuators and energy harvesting devices. In this work, process-microstructure-property relationships of such ASN films containing up to 40 at% Sc were investigated. Hereby, the influence of the process parameters on the film structure, the intrinsic stress and the piezoelectric response was carefully investigated.

Statement of Contribution/Methods

Like AlN thin films, ASN films were reactively sputter deposited at 300–350 °C with pulsed DC powered magnetrons. The film crystal structure was measured by electron microscopy (SEM/TEM), as well as X-Ray diffraction (XRD), and the chemical composition by energy-dispersive X-ray spectroscopy (EDX). For functional characterisation, Pt/ASN/Pt/SiO_2/Si multilayer stacks were fabricated. The transversal piezoelectric coefficient $e_{31,f}$ of the ASN films was determined with a four-point bending setup using Si(100) cantilevers along [110] direction with a Poisson ratio of 0.064. The longitudinal piezoelectric coefficient $d_{33,f}$ was determined by FEM supported double-beam laser interferometry, which eliminates contributions of substrate bending. The electro-mechanical coupling factor k_t^2 was obtained from high-overtone bulk-acoustic-wave (BAW) resonator structures by fitting the fundamental BAW resonance pattern to a modified Butterworth–van Dyke equivalent circuit.

Results/Discussion

XRD and TEM diffraction (figure b) confirm c-axis textured film growth in the desired piezoelectric wurtzite phase of AlN. For Sc concentrations up to 39 at%, the rocking curve FHWM width of the (002) ASN peak varies in the range of 1.3–2°. The films were further analysed by SEM/EDX. A good compositional homogeneity within 0.5–1 at% was achieved across 200-mm wafers. So far, we obtained ASN films with a response up to $e_{31,f} = -2.37$ C/m^2 and $d_{33,f} = 10.1$ pm/V (for 31.5 at% Sc). The highest value of coupling k_t^2 was determined to 15.2%. The experimental data are close to ab-initio calculations (figure a). The given values for ASN are a factor 2.3, 2.6, and 2.3 times as large as in AlN for the respective parameters.

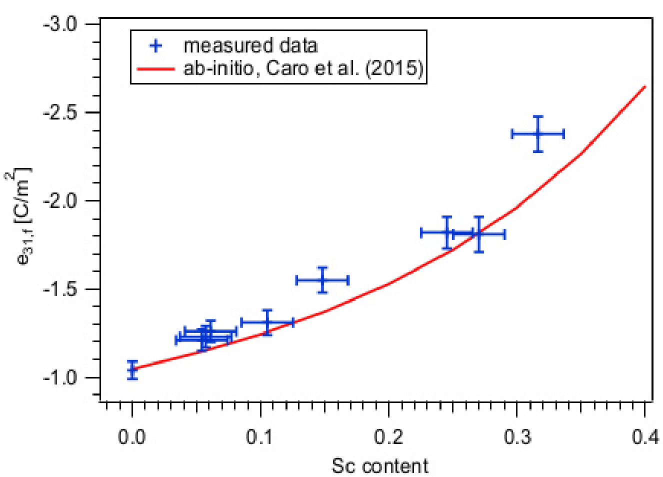

a) Transversal piezoelectric coefficient $e_{31,f}$ versus Sc content

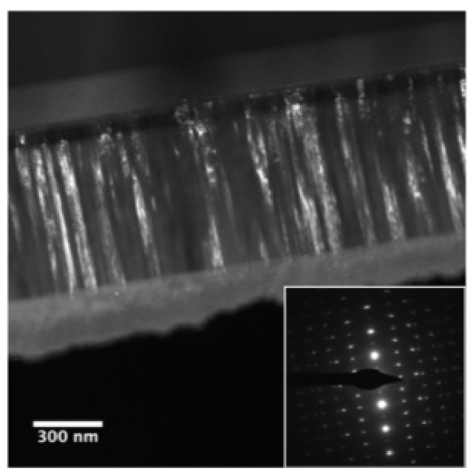

b) TEM dark field and diffraction pattern

7I-2

10:45 am High Electromechanical Coefficient k_t^2=19% Thick ScAlN Piezoelectric Films for Ultrasonic Transducer in Low Frequency of 80 MHz

Ko-hei Sano[1], Rei Karasawa[1], Takahiko Yanagitani[1,2]; [1]*Waseda university, Japan,* [2]*JST-PRESTO, Japan*

Background, Motivation and Objective

Ultrasonic in the frequency ranges of 20-100 MHz is not well-developed because of less applications or less suitable piezoelectric materials as shown in Table I. In a photoacoustic imaging, PVDF are usually used for ultrasonic transducers in the 10–50 MHz band. However, their electromechanical coupling coefficient k_t^2 of 4% is not enough for the practical uses. To excite ultrasonic in the 20-100 MHz, 125 μm-25 μm thick piezoelectric film is required. It is difficult to fabricate such a thick piezoelectric film without a crack caused by the internal stress during the deposition. A film deposition technique can realize the piezoelectric layer on a complicated surface such as curved or concave surface, which is difficult in the case of the single crystal plate. In this study, we demonstrated high efficient 81 MHz ultrasonic generation by using 43 μm extremely thick ScAlN films.

Statement of Contribution/Methods

ScAlN thick films were grown on (0001) oriented Ti electrode films/silica glass substrate. We achieved stress free film growth by employing the unique hot cathode sputtering technique without heating substrate. Next, the k_t of the ScAlN thick film were determined by comparing the experimental and theoretical longitudinal wave conversion losses. The experimental conversion losses were measured using a network analyzer. The theoretical conversion loss curves were simulated using multilayered Mason's equivalent circuit model.

Results/Discussion

The k_t^2 of the ScAlN thick film is determined to be 18.5% at 81 MHz, which is much larger than k_t^2=4% of PVDF. ScAlN and PVDF transducer performance used in water medium were simulated by using Mason's model, as shown Fig.1. We can see narrow frequency characteristics due to the difference of acoustic impedance between the piezoelectric layer and the water medium. Although these bandwidths around 80 MHz are almost same, the ultrasonic conversion efficiency of ScAlN is much better than PVDF. Furthermore, we simulated the effect of $\lambda/4$ acoustic matching layer of SiO_2 inserted between the ScAlN piezoelectric layer and the water medium. The results indicate the broadband frequency characteristics with high efficiency. Therefore, this ScAlN thick film transducer is promising for photoacoustic imaging applications.

Table I Frequency ranges in the ultrasound imaging and the typical properties of the piezoelectric film materials

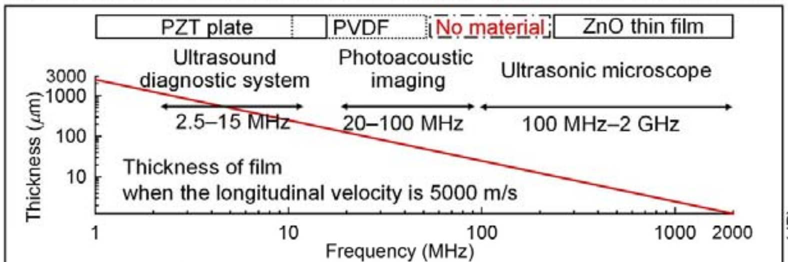

	k_t	k_t^2	Ref.
PMN-PT (PT 33%)	0.55	30%	[1]
PZT (sol-gel)	0.40	16%	[2]
PZT (hydrothermal synthesis)	0.51	26%	[3]
PVDF	0.20	4%	[4]
ZnO thin film	0.29	8.4%	[5]
ScAlN thin film	0.39	15%	[6]
ScAlN thick film (43 μm)	0.43	18.5%	This study

[1] Xiang Li, et al. IEEE TUFFC 58, 2281 (2011).
[2] R. Nanjo, et al. IEICE Tech Rep 97, 39, (1997).
[3] Q. Su, B Zhu, et al. J. Mater. Res. 26, 1431 (2011).
[4] G. Teyssedre, et al. J POL SC PP. 33, 879, (1995).
[5] R.T. Smith and V.E. Stubblefield, JASA. 46, 105 (1969).
[6] T. Yanagitani, et al., Proc. IUS., pp. 2095–2098, (2010).

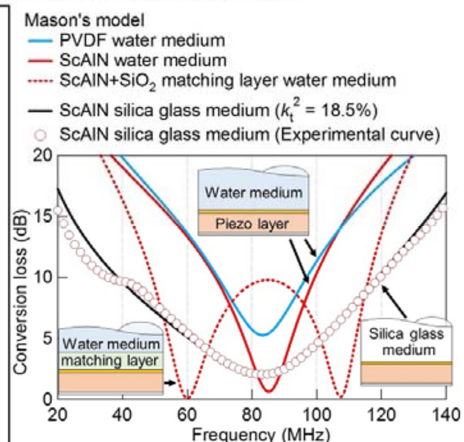

Fig.1 Experimental and theoretical conversion loss curves in the silica glass and water medium.

7I-3

11:00 am Monitoring of Morphological Change of Deposited Metallic Thin Film through Internal Friction of Noncontacting Piezoelectric Oscillator

Nobutomo Nakamura[1], Hirotsugu Ogi[1]; [1]*Graduate School of Engineering Science, Osaka University, Japan*

Background, Motivation and Objective

During deposition of metallic material on substrate, the morphological change from isolated islands to a continuous film occurs. The nano-structures obtained by stopping deposition around the discontinuous-continuous transition show characteristic electrical properties, and film-growth monitoring techniques are required to obtain the structures. Conductivity measurement and surface acoustic wave method have been used for the purpose, but they require electrodes on the substrate. In this study, we develop a method that can detect the morphological change without using the electrodes.

Statement of Contribution/Methods

The proposed method uses the resonant vibration of a piezoelectric oscillator. A substrate is placed in the sputtering chamber, and metallic material is deposited on the top surface. The oscillator is placed blow the substrate, and internal friction of a resonant mode is monitored. When a conductive material is placed close to piezoelectric material, the electric field excited by the vibrating piezoelectric material generates the flow of electric current in the conductive material, which causes energy loss by Joule heating. Then, the internal friction increases, and the change ratio should depend on the conductivity of the conductive material. By using this phenomenon, morphological change of the deposited material on the substrate is detected from the changes in the internal friction of the piezoelectric oscillator.

Results/Discussion

Morphological change of Ag on glass substrate was monitored. $LiNbO_3$ was used as the piezoelectric oscillator. When the film thickness became about 9.5 nm, internal friction increased and showed a peak. Appearance of the internal friction is explained as follows. In the early stage of deposition, the current does not flow between the isolated islands. However, when the intermediate structure that appears between the discontinuous and continuous structures is formed, the electric current starts to flow in the deposited material, which causes energy loss by Joule heating. After a continuous film is formed, the resistivity becomes smaller, and the energy loss also becomes smaller. This interpretation was verified by observing the morphology of the deposited material using the atomic force microscope. Thus, we confirmed that the internal-friction peak can be used as the indication of the morphological transition. In the presentation, further experimental results are shown, and applicability of the proposed method is discussed.

7I-4

11:15 am Ex-situ AlN Seed Layer for (0001)-Textured $Al_{0.85}Sc_{0.15}N$ Thin Films Grown on SiO_2 Substrates for Shear Mode Resonators

Mohammad Fazel Parsapour kolour[1], Cosmin Sandu[1], Vladimir Pashchenko[1], Stefan Mertin[1], Nicolas Kurz[2], Pascal Nicolay[3], Paul Muralt[4]; [1]*Electroceramic Thin Films Group, EPFL, laussane, Switzerland,* [2]*Department of Microsystems Engineering, IMTEK, University of Freiburg, Freiburg, Germany,* [3]*CTR Carinthian Tech Research AG, Villach, Austria,* [4]*Electroceramic Thin films group, EPFL, laussane, Switzerland*

Background, Motivation and Objective

Partial substitution of Al by Sc in AlN wurtzite films leads to a strong enhancement of the piezoelectric properties as long as the wurtzite phase is maintained. This is very promising for improving piezoelectric MEMS devices and enlarging their application range. Nucleation of (0001)-AlScN works particularly well on Pt (111) thin films. However, in some applications, the growth on insulating substrates may be required. Even though AlN can be grown well oriented on smooth amorphous surfaces of SiO_2, it is not the case for AlScN. AlN seed layers are an evident solution when there is no vacuum break between the AlN and AlScN growth. However, when a vacuum break is unavoidable, an oxide layer is formed on AlN, which makes the "regrowth" difficult. In this contribution we show that a mild RF etch can solve the problem.

Statement of Contribution/Methods

For film evaluation, we sputter deposited the following layer stacks: 1 µm $Al_{0.85}Sc_{0.15}N$/100 nm AlN seed layer/100nm Pt (111) / 200 nm amorphous SiO_2/ silicon wafers. The AlScN and AlN films both are grown by pulsed-DC reactive magnetron sputtering at 300°C. TEM investigation is used to study the growth behavior and quality of AlN-AlScN interfaces. FE and analytical modeling are employed to validate the experimental measurements.

Results/Discussion

Growing $Al_{0.85}Sc_{0.15}N$ directly on a well (0001)-textured AlN thin film lead to a poor texture, despite of a close lattice match. The largest XRD peak was still (0002), however, (10-11), (10-12), (10-13) and (10-14) peaks were clearly identified. Double beam laser interferometry yielded a small $d_{33,f}$ (=e33/c33^E) of 1.1 pm/V. High resolution TEM investigations showed the presence of a 8nm thick oxide layer above the AlN seed layer (Fig. 1.a), which prevents a simple epitaxy and leads to badly oriented grains. To remove the oxide layer, a RF etch cleaning step was introduced before depositing the AlScN, reducing the oxide layer to a residual interface layer having about $N_{3/4}O_{1/4}$ on the N-site(Fig. 1.b). X-ray diffraction revealed a completely textured (0002) film with no other orientations. A $d_{33,f}$ of 6.6±0.3 pm/V was measured for this stack allowing to derive a value for AlScN as 6.9 pm/V. Shear mode resonators were fabricated and characterized based on above process.

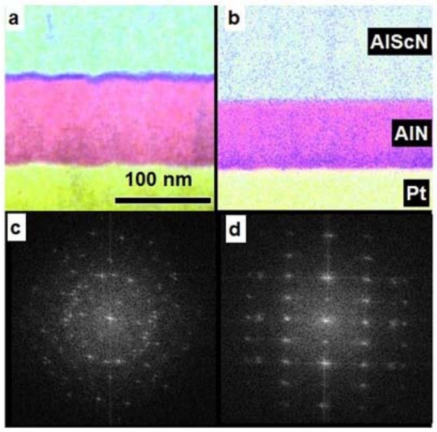

Figure 1. TEM images of AlN/AlScN interface. EDX-Hypermap on samples (a): without etching, (b): with etching. (c) and (d) FFT from HRTEM images of the respective AlScN films.

7I-5

11:30 am Film growth of C-Axis Parallel Oriented ZnO on Entire Surface of Silica Glass Pipe for SH-SAW Pipe Sensor

Yuta Takamura[1], Shinji Takayanagi[2], Mami Matsukawa[3], Chizu Ishida[3], Takahiko Yanagitani[4]; [1]*Doshisha University, Kyotanabe, Kyoto, Japan,* [2]*Nagoya institute of technology, Nagoya, Aichi, Japan,* [3]*Doshisha University, Japan,* [4]*Waseda University, Japan*

Background, Motivation and Objective

SH-SAW is suitable for liquid sensors to measure conductivity and viscosity because it can propagate without the energy leakage into liquid. We have fabricated a SH-SAW sensor consisting of a c-axis parallel (11-20) oriented ZnO film on a silica glass plate [1]. On the other hand, the long-distance propagation is necessary in order to detect the small changes of the velocity and amplitude. One way to increase propagation distance is wave multiple roundtrips around the sensor. In previous study, the c-axis parallel oriented ZnO film was grown on a part of the glass pipe surface and the SH-BAW roundtrips were demonstrated [2]. However, the SH-SAW roundtrips were not observed because the ZnO film was not grown on the entire surface of the pipe. In this study, we demonstrated the entirepipe-surface deposition of c-axis parallel oriented ZnO film to obtain SH-SAW pipe sensor.

Statement of Contribution/Methods

The c-axis parallel oriented ZnO film was grown by an RF magnetron sputtering system, as shown in Fig. 1(a). A glass pipe (20 mm diameter, 50 mm long, 1.5 mm thickness) was used as a substrate. Because the highly-oriented film can be obtained only on the opposite area of the sputtering target, a 6 mm slit was set under the pipe substrate in order to prevent the ZnO film being grown at the side surface of the pipe. Then, the pipe was automatically rotated at 1.2 rpm by connecting a motor to deposit the ZnO film on the entire surface of the pipe. The crystalline orientation of the ZnO film was measured by XRD analyses using an x-ray diffractometer.

Results/Discussion

Fig. 1(b) shows the XRD patterns of ZnO film. Intense ZnO(11-20) peaks, indicating c-axis parallel orientation, were observed at all point on glass pipe. FWHM of the  -scan rocking curve in ZnO(1120) was 5.5-6.8º. In addition, the in-plane direction of the c-axis was determined by an XRD pole figure analysis. We confirmed that the c-axis direction corresponded to the pipe axis direction as expected. Although the further investigation about the rotational speed of the glass pipe during the film deposition, the c-axis parallel oriented ZnO film was grown on the entire surface of the pipe. We will measure the propagation properties of acoustic waves by fabricating IDT on the film.

[1] Y. Nakahigashi, et al., Proc. 2011 IEEE IUS, p.810, 2011.

[2] S. Hiyama, et al., Proc. 2014 IEEE IUS, p.765, 2014.

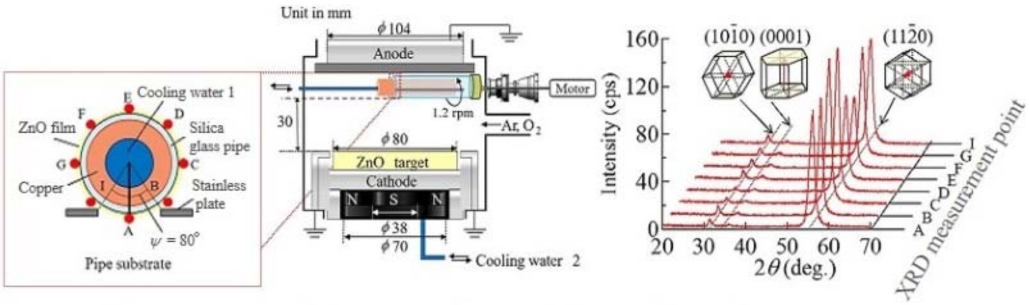

Fig. 1 (a) RF magnetron sputtering apparatus and (b) XRD patterns of the ZnO film sample on a silica glass pipe.

7I-6

11:45 am Effects of Negative Oxygen Ions Generated during Sc Ingot Sputtering on Electromechanical Coupling of ScAlN Film

Shinji Takayanagi[1], Takahiko Yanagitani[2]; [1]*Nagoya Institute of Technology, Nagoya, Japan,* [2]*Waseda University, Japan*

Background, Motivation and Objective

ScAlN films are well-researched for GHz acoustic wave devices. Large-area growth techniques of ScAlN films are necessary for the practical application. A single sputtering source with a ScAl alloy metal target is suitable for the film growth from the point of view of the composition stability. However, it is difficult to alloy Al with Sc in the large-size target. Therefore, a mosaic target of Sc and Al metals is reasonable for the large-area growth. In previous study, we demonstrated Sc ingot sputtering deposition [1] in which Sc ingots were set on an Al metal target as similar conditions with the mosaic target. Oxidization of Sc ingots was seriously problem in this method because the c-axis orientation of ScAlN films was degraded by bombardment with O- negative ions generated from the target. In this study, we investigated the effects of the negative ion bombardment on the crystalline orientations and piezoelectric properties.

Statement of Contribution/Methods

The amount of ion flux and ion energy which enter the substrate during the deposition by using an energy analyzer with a Q-mass spectrometer. We prepared ScAlN film samples by an RF magnetron sputtering with ScAl alloy metal target or Sc ingot on Al metal target. Ar and N2 were used for the process gases. The crystalline orientations were determined by XRD analyses, and the conversion losses were measured by a network analyzer.

Results/Discussion

Fig.1 (a) shows the Energy distributions of O- negative ion during the deposition. The amount of the ion flux decreased with duration, but it remained large in the case of the Sc ingot sputtering. The degrees of crystallization and crystalline orientation in the ScAlN film by the Sc ingot sputtering (sample B) were low compared with those by ScAl alloy metal sputtering (sample A), as shown in Fig. 1 (b). Then, the vacuum chamber was baked for degassing of the chamber wall, resulting in decrease of the negative ion bombardment. Therefore, ScAlN film with higher crystallization was obtained (sample C). Fig.1 (c) shows the longitudinal-mode conversion losses of the samples. Estimated electromechanical coupling coefficient kt of sample C (0.23) was lower than that of sample A (kt = 0.31), but Sc concentration of sample C (27%) was lower. Further investigation in higher-Sc-concentration condition by the Sc ingot sputtering is expected.

[redacted]

1J - MBE: Neuromodulation and Cell Stimulation

Regency Ballroom

Saturday, September 9, 2017, 1:30 pm - 3:00 pm

Chair: **Nobuki Kudo**
Hokkaido University

1J-1

1:30 pm Ultrasonic Neuromodulation

William J Tyler[1]; [1]*School of Biological and Health Systems Engineering, Arizona State University, USA*

Background, Motivation and Objective

To treat brain dysfunction and enhance plasticity in healthy adults, there is a need for new methods of noninvasively modulating neuronal activity. Since the 1950's US has been known capable of modulating electrically-evoked or sensory driven activity in brain circuits. These early observations implemented high-intensity US in a continuous wave mode for long durations and depended on the ability of US to focally heat tissue. The thermal effects of US (for example, HIFU) have been used to therapeutically ablate deep-brain circuits at intensities typically > 200 W/cm2. The peripheral and central nervous systems including the brain are mechanically sensitive. For example, voltage-gated ion channels and neurotransmitter receptors can be activated and inactivated (opened/closed) by mechanical pressures. Because of this we initiated investigations aimed at addressing the possibility of directly stimulating neurons with pulsed US via mechanical actions about a decade ago. This paper describes general information related to the use of US for neuromodulation and it non thermal actions on brain circuits.

Statement of Contribution/Methods

We first described that low-intensity, low-frequency pulsed US is can directly stimulate neuronal activity and synaptic transmission through nonthermal mechanisms in hippocampal slice cultures as assayed using optical imaging and electrophysiology. From a neurophysiological perspective, our observations were fundamentally different from previous ones showing US could modulate evoked activity. Since teaching our methods, US has been shown to nonthermally stimulate neuronal activity in many animals including humans across a range of frequencies ranging from 0.1 MHz to 43 MHz at intensities as low as 0.02 W/cm2. US has also been demonstrated to differentially modulate peripheral somatosensory circuits in humans. In brain, acoustic frequencies greater than 1 MHz are significantly attenuated by the skull, so it has been recommended that acoustic frequencies < 0.65 MHz are used for transcranial applications. Once transmitted across the skull, US < 1 MHz can readily penetrate the deepest extents of the human brain making it an excellent candidate for deep-brain modulation.

Results/Discussion

We originally developed methods and first demonstrated in rodents and humans that pulsed US can transcranially simulate and modulate intact brain circuit activity respectively. Most recently we and others have shown that 0.3 to 0.5 MHz transcranial focused US (tFUS) is capable of noninvasively modulating human brain activity with millimeter spatial resolutions. We have also recently observed that tFUS can achieve deep-brain stimulation of neurons in the reticular formation of non-human primates. A rich history and recent advances should encourage ultrasonic engineers and acoustic physicists to reach out and work closely with neuroscientists to develop new methods for mechanically interfacing with neural circuits.

1J-2

2:00 pm Elucidating the Biophysical Mechanisms of Ultrasonic Neuromodulation

Sangjin Yoo[1], Tomo Sato[2], Doris Tsao[2], Mikhail Shapiro[1]; [1]*Divisions of Chemistry and Chemical Engineering, Caltech, Pasadena, California, USA,* [2]*Divisions of Biology and Biological Engineering, Caltech, Pasadena, California, USA*

Background, Motivation and Objective

Ultrasonic neuromodulation is a promising technology in the field of basic and translational neuroscience because it can control neural activity within the skull without invasive surgery. In particular, low frequency ultrasound has been widely reported to elicit neural excitation and behavior in a number of animal models and humans. However, the cellular and molecular mechanisms of ultrasonic neuromodulation are not yet elucidated, impeding their use in neuroscience and potential clinical translation. To bridge this gap, we investigated the mechanisms of ultrasonic neuromodulation at the levels of single cells and intact organisms.

Statement of Contribution/Methods

For in vitro experiments, primary neurons were cultured on an acoustically permeable substrate and modified to express a fluorescent calcium indicator (GCaMP6f), allowing precise delivery of acoustic energy to target cells and measurement of the cellular events, simultaneously. In parallel with the molecular and cellular approaches, transgenic mice expressing GCaMP6f in cortical neurons were prepared with thinned skulls and used to image the wide field cortical response of neurons to ultrasound stimulation.

Results/Discussion

We tested the neural response to ultrasound stimulation in in vivo using established parameters (500 kHz, PRF 1500 Hz, 120 pulses at 30% duty cycle, ISPPA 4.2 W/cm2). We found that ultrasound stimulation elicited widespread bilateral cortical responses in auditory regions as well as the target area (visual cortex), but that of much activation disappeared after chemical deafening. These results suggest that a major component of the neural response to ultrasound stimulation could be off-target effects caused by activation of somato-auditory organs.

In contrast, clear and reliable neural responses were observed in cultured neurons using a continuous wave (300 kHz, above ISPPA 6 W/cm2 and 200 ms pulse duration). Additional experiments confirmed that the responses do not require transient temperature change or perforation at membrane, and they can respond to ultrasound stimulation without cavitation in the medium. Pharmacological studies demonstrated that the neural responses are amplified by voltage-gated calcium and sodium channels, and not subsequent events resulting from synaptic transmission. Further analysis of response kinetics revealed that latency of the neural responses is on the order of 100 ms, which decrease with higher ultrasound intensity. These results indicate that ultrasound acts directly on neurons through a primarily mechanical mechanism.

In summary, our study provides a combination of direct evidence for neuronal stimulation under carefully controlled conditions, while also showing that in vivo ultrasound causes sensory side-effects. These results suggest that further development of this technology is needed to increase the specificity of direct ultrasound neuromodulation while reducing off-target effects.

1J-3

2:15 pm Feasibility and Main Mechanisms Underlying *In Vivo* Ultrasound Neurostimulation of the Ventral Nerve Cord's Giant Axons of *Lumbricus Terrestris*

Jérémy Vion[1], W. Apoutou N'Djin[1], Jahan Tavakkoli[2], Jean-Louis Mestas[1], Jean-Yves Chapelon[1]; [1]*Therapeutic Applications of Ultrasound, INSERM, Lyon Cedex 03, France,* [2]*Department of Physics, Ryerson University, Toronto, Ontario, Canada*

Background, Motivation and Objective

Several works carried out these last years have demonstrated the ability of ultrasound (US) to activate neurons at a systemic level. However, no complete description of the biophysical mechanisms involved in this phenomenon has been validated so far. In order to identify experimentally these mechanisms, we here present an *in vivo* study of the stimulating effects of US exposures on the ventral nerve cord of the earthworm (*Lumbricus Terrestris*).

Statement of Contribution/Methods

On the basis of preliminary results, we chose to study primarily the effects of cavitation on the nerve response. We used a confocal acoustic transducer driven with an ultrasound sequence specifically designed to generate stable cavitation (f = 1.1 MHz, 44 cycles/pulse, 25-75 pulses/burst, PRF = 125 Hz, P^- = 14.8 MPa), and a hydrophone monitoring the acoustic signature of the cavitation cloud. In each trial, a medial section of the anesthetized worm was placed within the US focal area before being exposed to the ultrasound sequences. The electrophysiological response of the nerve was monitored with two electrodes sunken through the animal in the vicinity of the nerve. Before each trial, the nerve's functionality was tested by applying an electrical stimulation (pulsed, duration = 50 µs, amplitude = 5 V, PRF = 1 Hz, pulses number = 1 to 10). This preliminary test allowed us to identify the characteristic waveform of the action potentials (APs) associated with the medial giant fiber (MGF) and the two lateral giant fibers (LGF).

Results/Discussion

US-induced response of the LGF were observed in 60% of the tested animal (N=10). These responses involved a serial of APs occurring 30 to 80 ms after the first pulse of the burst. The inter-spikes delay and the number of APs following identical ultrasound bursts, sent every 2 s, were highly variable.

The first results of this study allowed to demonstrate the feasibility of the *in vivo* induction of a nervous response in *l. terrestris* by a sequence of pulsed ultrasound. The level of pressure we used, and the associated radiation force, are repeatable effects, while the observed phenomenon of US neurostimulation was not. Cavitation is a complex and random phenomenon, and the acoustic signatures recorded by hydrophone confirmed that identical ultrasound bursts could induce very different bubbles' clouds in the vicinity of the targeted nerve. These observations suggest that, in these experimental conditions, cavitation rather than radiation force is the main biophysical mechanism underlying US neurostimulation. To validate this hypothesis and increase the repeatability and control of US neurostimulation, further investigations are needed to relate with a strong causality the acoustic parameters linked to the cavitation cloud and the biological conditions leading to a nervous response. This project was supported by Mitacs-Campus France (2015), the Labex DEVweCAN (2015) and the French National Research Agency (ANR T-ERC, 2016).

1J-4

2:30 pm Ultrasound Stimulation Enhances the Function Encoding of Bushy Cells in the Rat Anteroventral Cochlear Nucleus

Zhengrong Lin[1], Lili Niu[1], Long Meng[1], Xiaowei Huang[1], Wei Zhou[1], Hairong Zheng[1]; [1]*Paul C. Lauterbur Research Center for Biomedical Imaging, Shenzhen Institutes of Advanced Technology, Chinese Academy of Sciences, Shenzhen, China, People's Republic of*

Background, Motivation and Objective

Transcranial ultrasound is an emerging technology for non-surgical stimulation of the animal and human brain. Previous studies has demonstrated that ultrasound could elicit discharge activity of retinal cells with short latency in animal (Journal of Neuroscience 33(10):4550-4560, 2013) and enhances sensory discrimination abilities of somato-sensory cortex in humans (Nature Neuroscience 17(2):322-9, 2014). In the auditory system, the anterior ventral cochlear nucleus (AVCN) is the origin of major acoustic information and further innervates higher auditory structures. Bushy cells, one of AVCN primary neurons, encode precise temporal information that can be used for sound localization. The aim of this study was to investigate whether ultrasound could enhance the function encoding of bushy cells in the rat anterior ventral cochlear nuclei.

Statement of Contribution/Methods

Prior to recording the bushy cell, the AVCN brain slices were incubated 1h and then transferred to the recording chamber. Fig 1a shows that the experiment system mainly included two parts: an ultrasonic neuro-modulation chip and a whole-cell voltage clamp recording system. The ultrasound was transmitted by an ultrasonic neuro-modulation chip with a set of sonication parameters (Frequency: 27.38 MHz; stimulation duration: 30 s; stimulus intensity: 0.3 W/cm^2). The whole-cell current clamp and voltage clamp were used to record the changes in the function encoding of bushy cells to stimulation with ultrasound waveforms.

Results/Discussion

In the AVCN slices, the biophysical hallmark of bushy cells was the generation of a single onset action potential in response to a sustained depolarizing somatic current injection and a particular morphology with one or two main short, beaded dendrites. Compared to the control group, the onset firing of bushy cells has larger threshold current and a reduction of half width after sonication (Fig 1b). Fig. 1c shows ultrasound stimulation also was capable of enhancing the function encoding of bushy cells through decreasing the latency and jitter. Furthermore, ultrasound stimulation exerted an influence on the membrane properties, such as decreasing the membrane time constant or decreasing the membrane input resistance. The results suggested that ultrasound stimulation could increase ion channels conductance and enhance the function encoding of bushy cells.

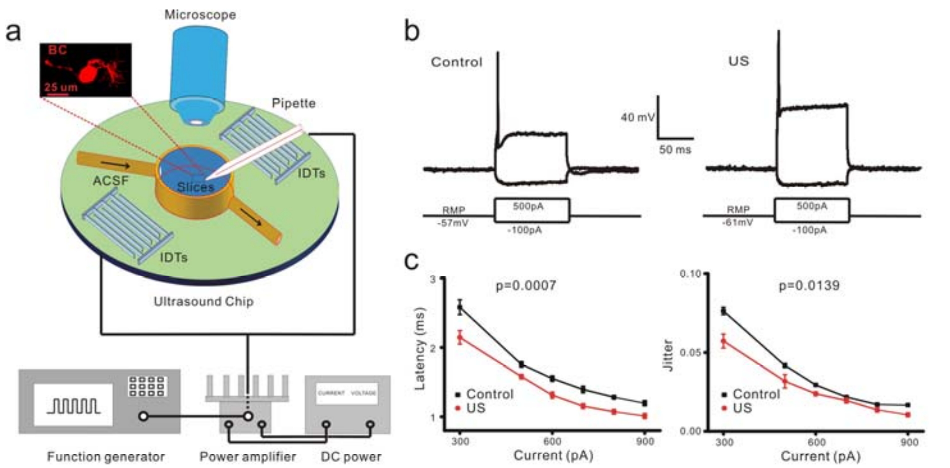

Fig 1. a. Experimental setup; b. Voltage traces recorded in the same bushy cell before and after the sonication ; c. The comparison of functional encoding index. Ultrasound stimulation enhancs the temporal encoding of bushy cells.

1J-5

2:45 pm **Study of Calcium-Dynamics in Ultrasound-Stimulated Secretory Events in Pancreatic Beta Cells**

Ivan Suarez Castellanos[1], Andrew Chen[1], Aleks Klimas[1], Emilia Entcheva[1], Tania Singh[1], Bogdan Balteanu[1], Aleksandar Jeremic[2], Joshua Cohen[3], Vesna Zderic[1]; *[1]Department of Biomedical Engineering, The George Washington University, Washington, DC, USA, [2]Department of Biological Sciences, The George Washington University, Washington, DC, USA, [3]The GW Medical Faculty Associates, Washington, DC, USA*

Background, Motivation and Objective

Type 2 diabetes mellitus is a complex metabolic disease that has reached epidemic proportions. Current pharmacological treatments of this disease include many side effects which can result in complications. We have previously shown that ultrasound is capable of stimulating insulin release from pancreatic beta cells in a safe and effective manner. The aim of this work is to study the role of calcium (Ca2+) dynamics in ultrasound-mediated insulin release from pancreatic beta cells.

Statement of Contribution/Methods

INS cells, an insulinoma beta cell line, were plated on 35 mm glass bottom plates. A planar ultrasound transducer with center frequency of 800 kHz was used to expose cells for durations of 30 s at intensities of 0.5 and 1 W/cm^2. Real-time fluorescence imaging of cells loaded with Ca2+ dye Quest Rhod4AM and voltage-sensitive dye Di-4-ANBDQS was used to measure changes in intracellular Ca2+ and membrane potential in response to ultrasound treatment. Carbon-fiber amperometry was used to characterize the temporal dynamics and Ca2+-dependency of ultrasound-induced secretory events in beta cells loaded with dopamine. To highlight the role of Ca2+ in ultrasound-secretory events, cells were exposed to ultrasound in the presence of EGTA, a known Ca2+ chelator. Cell viability was assessed with MTT cytotoxicity assay.

Results/Discussion

Amperometric recordings showed an immediate and significant secretory response following 5-15 s ultrasound stimulation. The duration of the detected response matched the duration of the ultrasound stimulus. The average amplitude of the amperometric peaks was reduced by ~ 45% (n=5, $p < 0.05$) in samples treated in the presence of 10 mM EGTA compared to samples without the Ca2+ chelator. Our Ca2+ imaging results showed immediate increases in fluorescence intensity after the start of ultrasound exposure at 15 and 75 s (upper-right graph) from the total field of view (FOV), while showing a delayed response (10 s delay) in certain regions of interest (white contour on left hand image) (lower-right graph). Elevations in Ca2+ dye fluorescence intensity were accompanied by increased membrane potential as the fluorescence intensity of the voltage-sensitive dye also increased immediately after the start of ultrasound exposure. No significant difference in cell viability ($p > 0.05$) was obtained in ultrasound-treated cells compared to sham group.

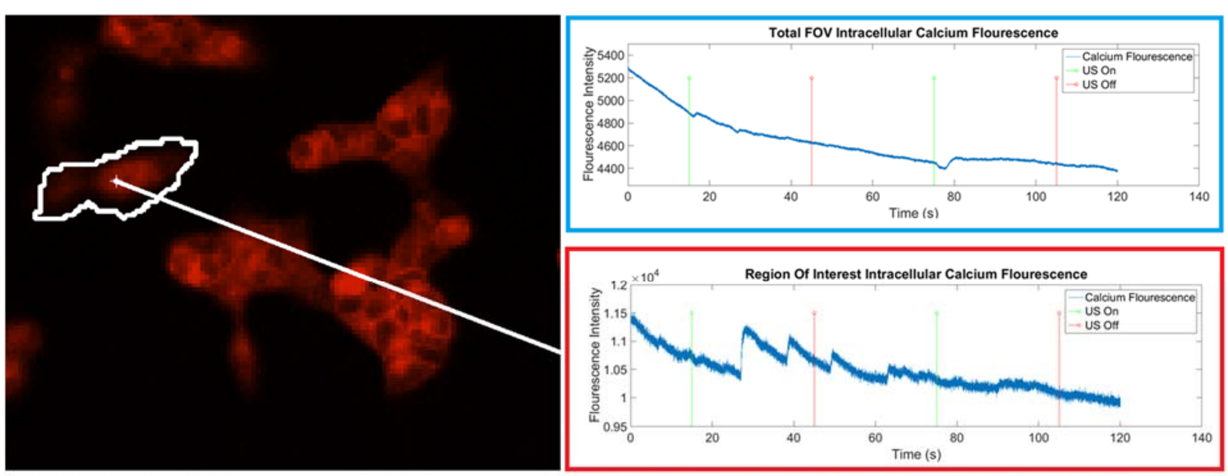

Changes in intracellular Ca^{2+} as measured with fluorescence microscopy in β-cells in response to 800 kHz continuous ultrasound application at intensity of 0.5 W/cm^2. Change in fluorescence intensity with respect to time in the whole field of view (FOV) image on the left (**top-right graph**). Change in fluorescence intensity with respect to time in the region of interest contoured in white on the left-hand image (**bottom-right graph**).

2J - MIM: Improving Image Quality and Analysis

Ambassador Ballroom

Saturday, September 9, 2017, 1:30 pm - 3:00 pm

Chair: **Jeremy Dahl**
Stanford University

2J-1

1:30 pm **Speckle Noise Reduction for High-Frame-Rate Imaging**

Jian-yu Lu[1]; [1]*Bioengineering, The University of Toledo, OH, USA*

Background, Motivation and Objective

Recently, high-frame-rate (HFR) imaging has found many applications such as fast cardiac imaging, elasticity imaging, flow velocity vector imaging, and functional imaging. In late 1990s, a HFR imaging method based on Fourier reconstruction was developed with either plane wave or limited-diffraction beam (LDB).

To increase image resolution and field of view, images obtained with steered plane wave (SPW) or LDB aperture weightings can be coherently superposed. Although image resolution is improved with the coherent superposition, speckle noise of reconstructed images is high, leading to potential misdiagnoses.

Statement of Contribution/Methods

To reduce speckle noise, in this paper, incoherent superposition is used in both SPW and LDB high-frame-rate imaging methods. Images obtained at various steering angles or LDB aperture weightings are first envelope detected and then superposed to form the final image. 91 images corresponding to 91 transmissions (91 TX) are used in the superposition for both SPW and LDB methods. The Fourier method is used in image reconstruction.

To evaluate the efficacy of the speckle reduction method, experiments were performed. During the experiments, a home-made high-frame-rate imaging system was used. The system has 128 transmit and receive channels. The transducer used has 128 elements, a center frequency of 2.5MHz, and a pulse-echo (two-way) bandwidth of about 58% of the center frequency. The dimension of the transducer aperture is 19.2 mm x 14 mm, and the dimension of the reconstructed images is 153.6 mm (w) x 120 mm (h). The ATS539 phantom was used.

Results/Discussion

Images reconstructed with coherent and incoherent superposition are shown in top and bottom rows, respectively, and images reconstructed with SPW and LDB are shown in left and right columns, respectively. The signal-to-noise rations (SNRs) (standard deviation divided by the average) along the horizontal dashed lines (cyan color) are 41.33 and 39.22, respectively, for SPW and LDB images obtained with coherent superposition. The SNRs are increased to 54.27 (31.31% improvement) and 76.72 (95.58% improvement), respectively, for SPW and LDB images obtained with incoherent superposition.

It is clear from the results that the speckle noise is reduced for both SPW and LDB methods with incoherent superposition. However, the LDB method is more effective in speckle noise reduction.

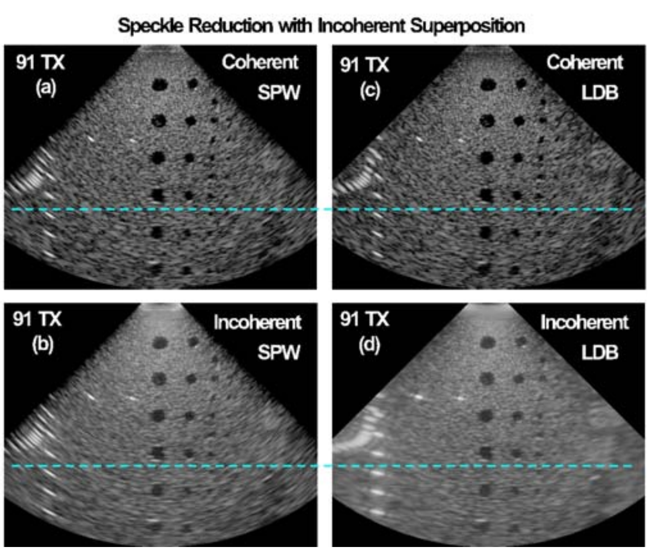

2J-2

1:45 pm **Improved Left Ventricular Wall Visualization in Stress-Echocardiography using Real-Time GPU-Based Harmonic Spatial Coherence Imaging**

Dongwoon Hyun[1,2], Anna Lisa Crowley[3], Jarrett Rosenberg[4], Jeremy Dahl[4]; [1]*Biomedical Engineering, Duke University, Durham, NC, USA,* [2]*Bioengineering, Stanford University, Stanford, CA, USA,* [3]*Cardiology, Duke University Hospital, Durham, NC, USA,* [4]*Radiology, Stanford University, Stanford, CA, USA*

Background, Motivation and Objective

Stress echocardiography is an ultrasound imaging technique to assess the functionality of wall segments of the left ventricle (LV). However, image quality is inadequate in up to 30% of patients, requiring the administration of contrast agents. Coherence-based beamforming methods have shown promise in improving image quality by mitigating clutter, a major source of image degradation. In a previous work, we introduced a coherence imaging system with a GPU-based software beamformer capable of real-time cardiac imaging. Here, the system is used in a clinical study to assess endocardial walls using standard clinical techniques and coherence beamforming.

Statement of Contribution/Methods

LV wall visibility was assessed using both conventional tissue harmonic imaging (THI) and harmonic spatial coherence imaging (HSCI) in a clinical study at Duke University Hospital. Real-time imaging was performed in 15 stress-echocardiography patients who were identified with poor image quality and required contrast agent. For each patient, 100 frames of raw channel data were captured from the live feed at 32 frames per second from 4 standard views of the heart. The raw data was used to form THI and HSCI video clips for review. A cardiologist was presented with 30 sets of video clips (15 THI, 15 HSCI) in randomized order. A standard 17-segment model of the LV was used, and each segment was assigned a score of 0 (not visible), 1 (poorly visualized), or 2 (clinically acceptable). Scores of 0 or 1 in any two contiguous segments indicate a need for contrast agent.

Results/Discussion

In 255 total segments across 15 patients, HSCI improved visibility over THI in 96 segments while THI was better in 11 segments. A total of 45 and 92 segments were well-visualized with THI and HSCI, respectively. There was a clear superiority of HSCI over THI in a comparison of overall segment scores ($p < 0.0001$ by symmetry test unadjusted for clustering). When comparing the number of segments with clinically acceptable image quality per patient, HSCI again showed superiority over THI ($p < 0.0001$ by McNemar test adjusted for clustering). In one patient, HSCI improved visualization sufficiently to eliminate the need for contrast agents altogether. These results indicate that HSCI may provide sufficient improvements in LV wall visualization in certain patients to proceed without contrast agents.

Figure 1 - An apical two-chamber view of the heart was acquired using tissue harmonic imaging (THI, left) and harmonic spatial coherence imaging (HSCI, right). HSCI reduced clutter and improved visualization of the basal, mid-cavity, and apical anterior segments (#1, #7, and #13, respectively). In this patient, image quality was sufficiently improved to eliminate the need for contrast agents.

2J-3

2:00 pm Fast and Fully Automatic 3D Left Ventricular Segmentation Using Shape-Based B-Spline Explicit Active Surfaces

João Pedrosa[1], Sandro Queirós[2], Olivier Bernard[3], Jan Engvall[4], Thor Edvardsen[5], Eike Nagel[6], Jan D'hooge[1]; *[1]KU Leuven, Leuven, Vlaams Brabant, Belgium, [2]University of Minho, Portugal, [3]University of Lyon, France, [4]Linkoping University, Sweden, [5]Olso University Hospital, Norway, [6]University Hospital Frankfurt/Main, Germany*

Background, Motivation and Objective

Cardiac function assessment is a critical step in cardiology and 3D ultrasound plays an increasingly important role. Automatic left ventricular (LV) segmentation remains however challenging particularly in the presence of artifacts and for images with low contrast-to-noise ratio (CNR). It is thus crucial to give segmentation tools prior information on the LV shape in order to fill in the gaps when image content is low. In this work, a fast automatic framework for full cycle LV segmentation is proposed that uses shape information from cardiac magnetic resonance (cMR) for a more accurate segmentation.

Statement of Contribution/Methods

The proposed approach couples B-spline explicit active surfaces (BEAS), an image information approach, with a statistical shape model (SSM) that gives prior information about the LV shape. 289 cMR datasets from a multi-center study, DOPPLER-CIP, were used to build an SSM describing the shape variations of the LV at end-diastole (ED) and end-systole (ES). This SSM is then used within BEAS, restricting the segmentation to the shape variability seen in the SSM.

The framework begins with an automatic initialization of the LV at ED. BEAS is then used with the ED SSM regularization. The segmentation at ED is propagated throughout the heart cycle using a localized anatomical affine optical flow. At ES, the tracking result is refined using BEAS with the ES SSM regularization.

The framework was tested on the CETUS challenge data, a multi-center multi-vendor dataset with manual contouring performed by three experts at ED and ES. The automatic segmentation was evaluated with mean average distance (MAD), Hausdorff (HD) and Dice.

Results/Discussion

The proposed framework took in average 11s for each full cycle segmentation and showed excellent segmentation results, outperforming all state of the art methods presented in the CETUS challenge. Fig. 1 shows the best (left) and worst (right) results at ED (top) and ES (bottom) compared to manual contouring. The proposed framework achieved MAD, HD and Dice of 1.81±0.59mm, 6.31±1.69mm and 0.909±0.034 at ED and 1.98±0.66mm, 6.95±2.14mm and 0.875±0.046 at ES. ED and ES volumes and ejection fraction showed correlations of 0.953, 0.960 and 0.911 with the manual contours. Concluding, a fast and automatic LV segmentation framework based on BEAS and SSM was proposed, outperforming other state of the art LV segmentation tools.

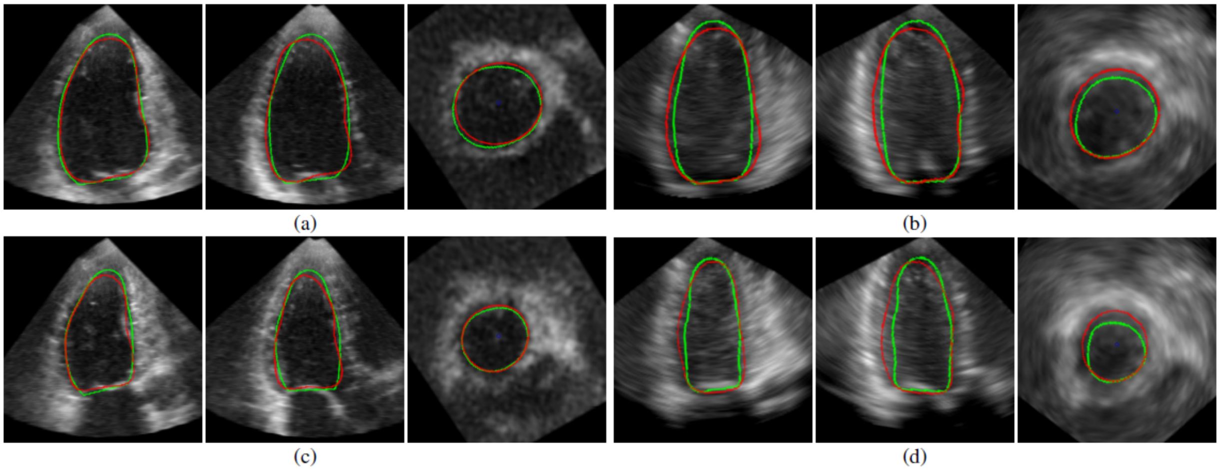

2J-4

2:15 pm **High Frame Rate, Wide-Angle Tissue Doppler Imaging in Real-Time**

Alessandro Ramalli[1], Francesco Guidi[1], Alessandro Dallai[1], Enrico Boni[1], Ling Tong[2], Jan D'hooge[3], Piero Tortoli[1]; [1]*Department of Information Engineering, University of Florence, Florence, Italy,* [2]*Center for Bio-medical Imaging Research, Dept. of Biomedical Engineering, School of Medicine, Tsinghua University, China, People's Republic of,* [3]*Lab. on Cardiovascular Imaging & Dynamics, Dept. of Cardiovascular Sciences, KU Leuven, Belgium*

Background, Motivation and Objective

Tissue Doppler Imaging (TDI) is an excellent tool for early detection of myocardial dysfunction, as well as for prognosis and follow-up of the myocardial function after surgical treatment. However, since it exploits the same principles of color flow imaging, TDI requires to balance frame rate with field of view. A novel TDI technique based on multiline transmission (MLT), i.e. the simultaneous transmission of beams along multiple directions, was shown able to detect tissue motion without making this compromise (DOI: 10.1109/TMI.2015.2480061). However, the technique was only tested by processing acquired data off-line. In this work we present the real-time implementation of this new TDI modality on the ULA-OP256 system and demonstrate its performance in-vivo.

Statement of Contribution/Methods

A 128-element phased array probe was connected to ULA-OP 256 to scan a 90°-wide sector up to the depth of 15 cm. High frame rate was achieved by implementing MLT, which excites each element of the probe with a signal equivalent to the sum of the pulses that would be individually applied to generate distinct single line transmissions. In addition, the frame rate was further increased by exploiting the multiline acquisition (MLA) capability of the ULA-OP 256 to beamform several lines in parallel for each transmission event.

The beamformed signals were demodulated, filtered, TDI processed and transferred to the host PC for continuous real-time display. In particular, the real-time TDI module estimated the phase shift between consecutive samples by standard autocorrelation, averaged it over 4 to 16 estimations, filtered over time and space with a first order IIR and a 3×3 Gaussian filter. The output phase shift values were then mapped to blue-red color coded images which were overlaid to B-mode. Moreover, to assess possible diseases such as ventricular dyssynchrony, the software allowed selecting up to 8 points of interest of which the respective velocities were displayed on distinct graphs. The system was tested by collecting data in healthy volunteers.

Results/Discussion

For 128-line images, the achieved real-time raw data frame rate was 625 Hz for modes 8MLT-2MLA and 4MLT-4MLA, or 1100 Hz for 8MLT-4MLA, which resulted in a real-time 90°-wide TDI frame rate of 39 up to 275 Hz depending on system/processing settings. An example real-time in-vivo TDI recording at 62.5 Hz is shown in Fig. 1.

.

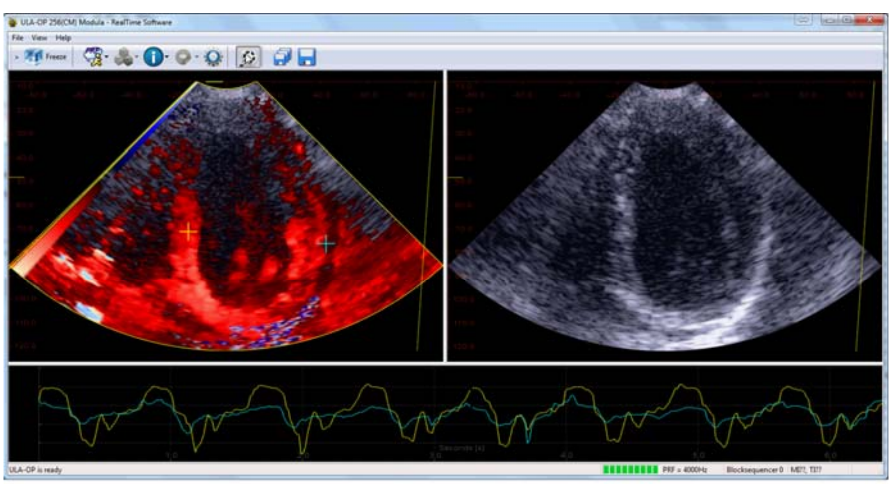

Fig. 1 Screenshot of the ULA-OP 256 real-time interface during an exam of the left ventricle of a healthy volunteer. On the right the B-mode image, at 500 Hz, obtained with 4MLT-4MLA; on the left TDI, at 62.5 Hz, overlaid on B-mode image; on the bottom the velocity time trends on the septal wall (yellow) and on the left ventricular free wall (cyan).

2J-5

2:30 pm Translation of Fetal Short-Lag Spatial Coherence (SLSC) Imaging into Clinical Practice: A Pilot Study

Will Long[1], Dongwoon Hyun[1], Kingshuk Choudhury[2,3], David Bradway[1], Patricia McNally[4], Sarah Ellestad[4], Gregg Trahey[1,2]; [1]*Biomedical Engineering, Duke University, Durham, NC, USA,* [2]*Radiology, Duke University, Durham, NC, USA,* [3]*Biostatistics and Bioinformatics, Duke University, Durham, NC, USA,* [4]*Obstetrics and Gynecology, Duke Univeristy, Durham, NC, USA*

Background, Motivation and Objective

Fetal short-lag spatial coherence (SLSC) imaging has demonstrated 64-85% increases in CNR and 17-29% increases in contrast relative to conventional B-mode imaging. However, despite its proven technical efficacy, the viability of fetal SLSC in the clinical setting remains unknown. The aims of this study were: 1) To demonstrate the feasibility of real-time SLSC imaging on existing hardware and 2) to evaluate expert-user preference between SLSC and B-mode within the clinical workflow.

Statement of Contribution/Methods

Pulse-inversion harmonic SLSC imaging was realized on a Siemens SC2000 clinical scanner. Eighteen healthy subjects were scanned by an expert sonographer using real-time harmonic B-mode and SLSC imaging, during which 2-second channel datasets were acquired for views of the fetal bladder, stomach, and cerebral ventricles. B-mode and SLSC images were formed offline and independently optimized by a blinded sonographer using controls for dynamic range. Optimized settings were applied to the complete channel datasets to generate a series of fully matched B-mode and SLSC video pairs, which were then scored on a 0-5 scale by 3 blinded clinicians based on target conspicuity (TC), border definition (BD), and overall quality (OQ). Dynamic range optimization and scoring were performed on video pairs both without and with manufacturer image post-processing applied.

To ensure clinical relevance, the above protocol was designed to mimic the clinical workflow, in which multi-frame cine loops are acquired and optimized by a sonographer and subsequently reviewed by clinicians. Grading criteria and imaged structures were moreover selected to reflect key clinical tasks associated with 1st and 2nd trimester exams.

Results/Discussion

Real-time coherence imaging was successfully implemented using a standard clinical sequence without modification to scanner hardware. Score distributions revealed consistent SLSC preference across all structures and processing conditions, with SLSC scoring higher than B-mode in 63.9±12.9% and B-mode scoring higher than SLSC in 7.9±5.6% of video pairs. Increases in TC, BD, and OQ with SLSC were statistically significant with $p < 0.01$. Preliminary results indicate that SLSC is readily adaptable to existing clinical technology and shows promise to significantly improve the detectability of clinically relevant fetal structures.

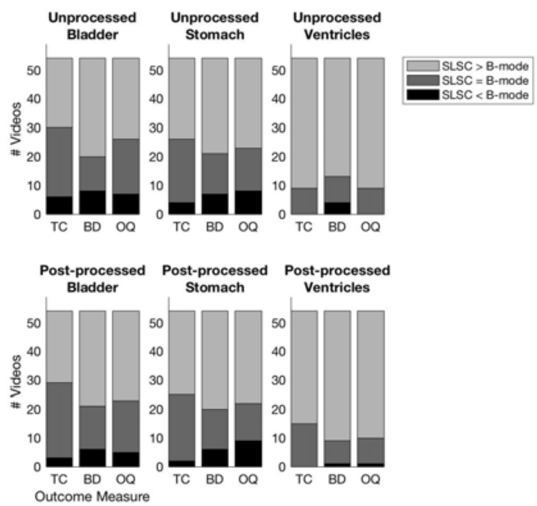

2J-6

2:45 pm Investigating the Impact of Elevated Acoustic Output in B-Mode Harmonic Imaging and Harmonic Motion Tracking

Yufeng Deng[1], Mark Palmeri[1], Ned Rouze[1], Clare Haystead[2], **Kathryn Nightingale**[1]; [1]*Biomedical Engineering, Duke University, Durham, USA,* [2]*Radiology, Duke University, Durham, USA*

Background, Motivation and Objective

Harmonic imaging techniques are widely used in B-mode abdominal imaging and motion tracking in shear wave elasticity imaging (SWEI) to reduce clutter and improve data quality. Harmonic imaging can be both signal-to-noise (SNR) and penetration depth (PD) limited, resulting in decreased diagnostic utility. This work evaluates B-mode harmonic imaging and SWEI harmonic tracking data quality between imaging sequences using a Mechanical Index (MI) within the FDA guideline of 1.9 and an elevated MI ($1.9 < MI < 2.6$), to determine if there is clinical benefit in exceeding the current FDA guideline for MI in the context of hepatic imaging.

Statement of Contribution/Methods

Hepatic B-mode, M-mode and SWEI data have been acquired using a modified Siemens S2000 scanner and a 4C1 curvilinear array in 25 subjects. Three pairs of harmonic images with low MI (1.6) and high MI (2.0-2.6) values were acquired from a range of hepatic hypoechoic vessels. Contrast-to-noise ratio (CNR) was computed on the hypoechoic structures. Repeated firings of beams at the same spatial locations were carried out using a range of MI values. Imaging PD was quantified when the correlation coefficient between the repeated firings dropped below 0.8. SWEI measurements with identical push configurations and low/high MI harmonic tracking were also performed, and shearwave speed (SWS) estimation yield was compared between low (1.6) and high MI (2.8) tracking.

Results/Discussion

A total of 188 hypoechoic structures were identified in harmonic B-mode images. Figure (a) shows that high MI harmonic imaging resulted in modest increases in CNR of hypoechoic structures. The median increase was 4.6%, 7.2%, and 7.6% in easy (1), medium (2) and difficult-to-image (3) subjects. Medium and difficult-to-image subjects had significantly higher CNR increases than easy subjects. Figure (b) shows that imaging PD increased linearly with increasing MI in an example subject. PD increased on average by 4.6 cm per unit MI increase across all subjects for a given focal depth. Figure (c) shows that high MI motion tracking leads to an increase of SWS yield by 27% at 5 cm. In addition, high MI tracking resulted in a 6.5 dB increase of the tracking data SNR and significant decrease in displacement jitter. These results indicate that using elevated acoustic output has the potential to provide clinical benefit for diagnostic ultrasound.

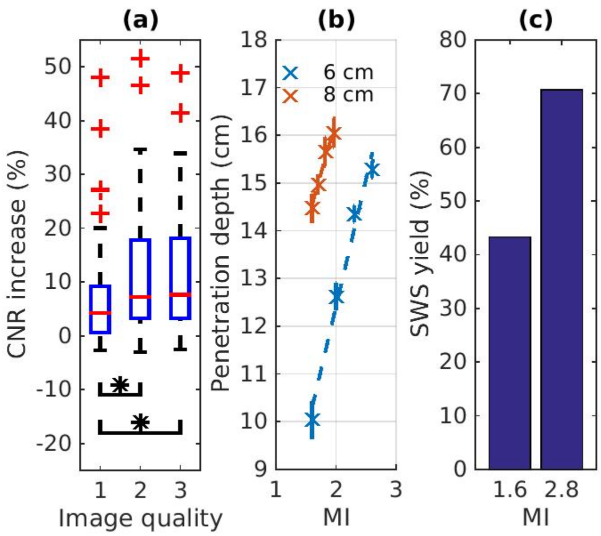
(a)
CNR increase (%)
50
40
30
20
10
0
-10
-20
1
2
3
Image quality
(b)
Penetration depth (cm)
18
17
16
15
14
13
12
11
10
9
6 cm
8 cm
1
2
3
MI
(c)
SWS yield (%)
80
70
60
50
40
30
20
10
0
1.6
2.8
MI

3J - MCA: Contrast Agents and Therapy Assessment

Palladian Room

Saturday, September 9, 2017, 1:30 pm - 3:00 pm

Chair: **Katherine Ferrara**
UC Davis

3J-1

1:30 pm **Assessment of Vascular Remodeling Therapy in Patients with Liver Metastasis with 3D Dynamic Contrast-Enhanced Ultrasound**

Ahmed El Kaffas[1], Isabelle Durot[1], George Fisher[2], Sunitha Bachawal[1], Dimitre Hristov[3], Juergen Willmann[1]; [1]*Radiology, Stanford University, USA,* [2]*Medicine, Stanford University, USA,* [3]*Radiation Oncology, Stanford University, USA*

Background, Motivation and Objective

Vascular remodeling agents that can enhance the effects of chemotherapy have gained significant attention. However, timing and dosing of combinatory treatment regimens requires longitudinal biomarkers to optimize regimens on a patient-by-patient basis. 3D dynamic contrast-enhanced ultrasound (DCE-US) has been proposed as an inexpensive bedside tool to longitudinally guide dosing and scheduling of combined treatments. The purpose of this pilot study was to demonstrate the feasibility of using 3D DCE-US to identify patients with remodeled vasculature before secondary chemotherapy delivery.

Statement of Contribution/Methods

Preliminary 3D DCE-US was acquired in 3 patients through an ongoing HIPAA-compliant IRB-approved Phase II clinical trial of the vascular remodeling agent RRX-001 (EpicentRx, Mountain View, CA). This novel drug acts by increasing reactive oxygen and nitrogen species through a differential stress response in cancer cells, resulting in vascular pruning and normalization/remodeling. Imaging was performed with an EPIC7 (Philips) coupled to an X6-1 matrix transducer over the 2 month course of treatment with RRX-001 (6 scans per patient; Figure), followed by Irinotecan. Image acquisition was performed with Disruption-Replenishment by infusing 0.9 ml of Definity microbubbles in 35.1 ml of saline over 8 min. Volumes-of-interest (VOI) were segmented in each image to extract time-intensity curves (TICs). Parameters were quantified for the whole VOI from both imaging methods. Disruption-Replenishment parameters were: relative blood volume (rBV) and relative blood flow (rBF). Patient response was assessed using the RECIST method in CT images.

Results/Discussion

Initial results suggest that 3D DCE-US is potentially useful to optimize combined treatment regimens. In one patient (Figure – patient 1), we noted a rapid enhancement of perfusion within hours of treatment (relative increase of 450% for rBV); rBV increase remained higher than baseline at the final scan before Irinotecan administration. In a second patient (Figure – patient 2), perfusion enhancement was also present, however, the enhancement was short-lived. These observations confirm differences in patient-by-patient perfusion kinetics, and suggest the feasibility of possibly using 3D DCE-US to identify a window to deliver secondary chemotherapy.

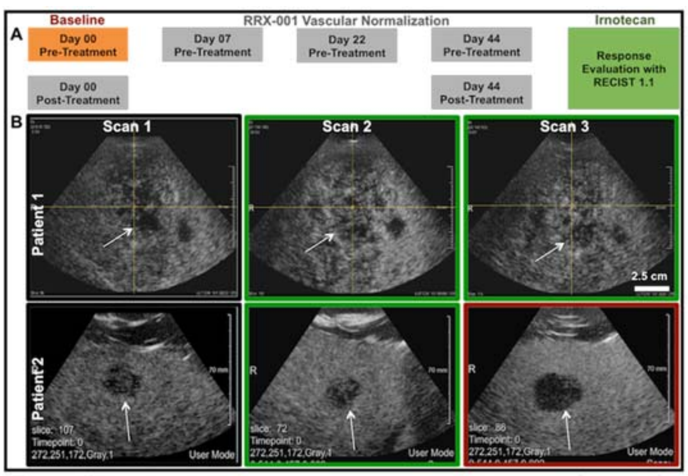

Figure - **(A)** Imaging schedule: each box is an imaging session. Imaging before and after RRX-001 infusion on days 0 and 44 to assess the acute effects. **(B)** Longitudinal scans at contrast infusion steady state from 2 patients receiving RRX-001; green indicates increase in mean perfusion from baseline, red indicates decrease in mean perfusion from baseline.

3J-2

1:45 pm **Contrast Enhanced Ultrasound (CEUS) Imaging of Rat Spinal Cord Injury**

Matthew Bruce[1], Alex Hannah[1], Zin Khaing[1], Charles Tremblay-Darveau[2], Christoph Hofstetter[1], Peter Burns[3]; [1]*University of Washington, Seattle, Washington, USA,* [2]*Philips Medical Systems, USA,* [3]*University of Toronto, Canada*

Background, Motivation and Objective

Traumatic spinal cord injury (tSCI) often leads to debilitating neurological disabilities that in addition to the loss of sensory and motor capabilities, also includes other issues with the bladder, heart and respiration. Overall, tSCI results in a drastic decrease in the quality of life. Traumatic spinal cord injury causes an almost complete loss of blood flow at the site of injury (primary injury) as well as significant ischemia surrounding the injury, resulting in progressive additional cell death over time (secondary injury). Counteracting secondary injury of spinal cord tissue surrounding tSCI is an active area of research to improve outcomes. There are no existing techniques to assess simultaneously both temporal and spatial changes in blood flow of contused spinal cord tissue in experimental settings. The goal of this work was to visualize temporal and spatial changes in blood flow following tSCI in a rat spinal cord injury model.

Statement of Contribution/Methods

We have developed a pre-clinical tool enabling visualization of perfusion changes in a rat injury model utilizing ultrsound contrast agents. This tool provides high resolution and real-time visualization to perfusion changes in and around regions of tSCI. This enables for the first time high-frequency CEUS imaging of rat spinal cord injury. Utilizing an ultrasound research platform (Verasonics Vantage, USA) combined with a 18Mhz linear array transducer (Vermon, France), plane-wave nonlinear Doppler acquisitions enabled visualization of blood flow in the rat spinal cord using PRF's of 10kHz. Four Wistar rats were imaged before and 15 minutes after injury, consisting of a 30 second pinch.

Results/Discussion

Figure 1 shows the results of an amplitude modulated acquisition pre- and post- spinal cord injury. Figure 1a and 1b illustrates the mean perfusion signal over the 300 millisecond acquisition before and after injury respectively. The perfusion deficit of Figure 1b outlines the hypoperfused area of the primary injury. Figure 1c and 1d show the segmentation of the higher velocity flow via a singular value decomposition wall filter. Figure 1d shows a wider disruption of the larger vasculature surrounding the injury site. Figure 1e and 1d show the directional power Doppler signals of the rat spinal cord. This tool can be used to assess the changes in blood flow overtime for different injuries and treatments.

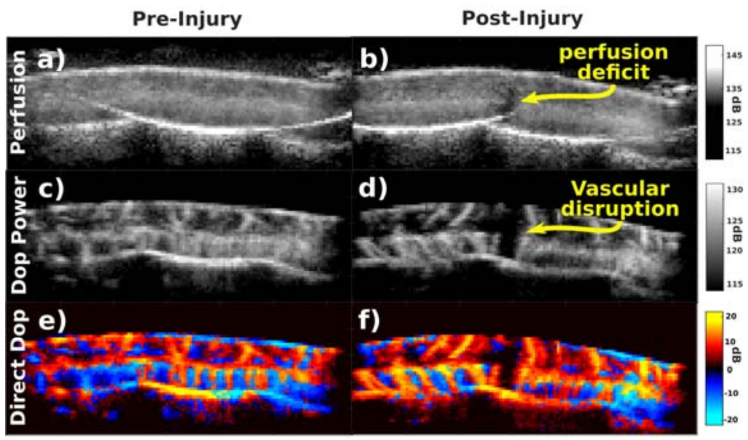

Figure 1. Perfusion and vascular flow changes from spinal cord injury in a rat following a bolus of Definity contrast agent.

3J-3

2:00 pm Nanobubble Contrast Agents Enhance Ultrasound Imaging of Prostate Tumors in Mice

Jacob L. Lilly[1,2], Hansheng Xia[1,2], Afsana Akhter[1,2], Gopalakrishnan Ramamurthy[1,2], James P. Basilion[1,2], Agata A. Exner[1,2]; *[1]Case Center for Imaging Research, Case Western Reserve University, Cleveland, OH, USA, [2]Radiology, Case Western Reserve University, Cleveland, OH, USA*

Background, Motivation and Objective

Prostate cancer biopsies are increasingly guided by ultrasound (US) imaging, yet poor soft tissue contrast makes delineation between normal/abnormal tissue difficult. There is growing interest in US contrast agents (USCA) to improve differentiation of tumors within the prostate gland and facilitate US-guided biopsies. The most widely used formulations are lipid or protein-stabilized perfluorocarbon (PFC) gas microbubbles (MB) typically exceeding 2µm in diameter. These bubbles usually show rapid transient tumor enhancement, as they are confined to vasculature. To achieve longer lasting enhancement and improved delineation of tumors, we have developed sub-micron lipid and surfactant-stabilized PFC nanobubbles (NB). Here we compare tumor kinetics of the NBs compared to commercially available MBs.

Statement of Contribution/Methods

C_3F_8 NBs were formulated by dissolving a cocktail of lipids including DBPC, DSPE-PEG in PBS followed by gas exchange and activation via mechanical agitation. NBs were purified by centrifugation, and size was measured by dynamic light scattering (DLS). Tumors were inoculated in the flank of three male nude mice by injection of PC3 prostate cancer cells in Matrigel®, and grown to 5-8 mm (Fig. 1a). Contrast-enhanced US images were acquired with Vevo 3100 (Visualsonics Fujifilm) at 1fps, 18MHz, and 4% power following tail vein injections of 100 ul of either MicroMarker (Visualsonics) or NBs. Maximum intensity projection (MIP) and time-intensity curves (TIC) were obtained in the same mouse for both contrast agents.

Results/Discussion

NBs have a diameter of 240±95 nm, (compared to 2-3µm for MicroMarker). MIP images (Fig. 1b) show that NB provided more signal throughout the tumor cross section compared to MBs at t=15s. Representative contrast images are shown in Fig. 1c and the mean TIC for all replicates is shown in Fig. 1d. NBs had a half-life of 2.1 min compared to 1min for microbubbles, and at t=2 min showed a signal intensity nearly 3 times higher than MBs. Higher tumor signal during wash out suggests that smaller NBs were able to penetrate out of the leaky tumor vasculature and further into the tumor interstitium. Such NBs may eventually provide a more effective contrast agent compared to MBs and could enhance US guided biopsies.

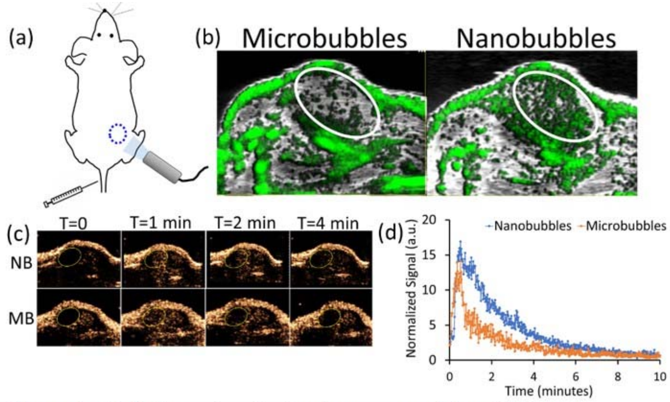

Figure 1: (a) Schematic of animal tumor model and US scan orientation. (b) MIP comparison in PC3 flank tumor 15s after contrast injection. (c) Representative tumor images of NBs and MBs from the same mouse. (d) Mean TIC curves for NBs and MBs

3J-4

2:15 pm **Assessment of 3D Dynamic Contrast-Enhanced Ultrasound of Liver Metastases from Gastrointestinal Tumors to Overcome Sampling Errors: Assessment of Feasibility and Reproducibility**

Ahmed El Kaffas[1], Isabelle Durot[1], Rosa Sigrist[1], George Fisher[2], Sunitha Bachawal[1], Huaijun Wang[1], Jarrett Rosenberg[1], Dimitre Hristov[3], Juergen Willmann[1]; *[1]Radiology, Stanford University, USA, [2]Medicine, Stanford University, USA, [3]Radiation Oncology, Stanford University, USA*

Background, Motivation and Objective

Dynamic contrast enhanced ultrasound (DCE-US) is a low-cost tool proposed for identifying early responders to cancer therapy. To date, sampling errors due to 2D imaging has restricted DCE-US in assessing highly heterogeneous tumors. The purpose of this study was to perform a clinical assessment of 3D DCE-US feasibility and reproducibility.

Statement of Contribution/Methods

Patients with liver metastases from gastrointestinal cancers were imaged with a Philips EPIQ7 coupled to an X6-1 matrix transducer. A total of 16 scan sessions were carried out over 10 patients. Pairs of repeated bolus and disruption-replenishment images were acquired within each scan session to determine reproducibility of parameters. Bolus consisted of intravenous injection of 0.2 ml Definity microbubbles followed by saline. Disruption-replenishment was carried out by infusing 0.9 ml of Definity microbubbles in 35.1 ml of saline over 8 min. Volumes-of-interest (VOI) and regions-or-interest (ROI) were segmented in each image to extract time-intensity curves (TICs). Parameters were quantified for the whole VOI and 4 sub-ROIs. Bolus parameters were: time-to-peak (TP), peak enhancement (PE), area-under-the-curve (AUC), mean-transit-time (MTT). Disruption-replenishment parameters were: relative blood volume (rBV), relative blood flow (rBF) and regional mean flow velocity (rMFV).

Results/Discussion

A large coefficient of variation (CV) was found for ROIs from the same volume confirming potential sampling errors when scanning in 2D. The TP and MTT had the lowest CV while the rBF, rBV and rMFV parameters had the largest plane-to-plane variations with CVs up to 54%. Measurements made in 3D were consistently different than measurements made in 2D with an average percent difference of 60%. Reproducibility, evaluated by the concordance correlation coefficient (CCC) between repeated measurements, was good (0.80) to excellent (0.95). The TP and MTT were the least reproducible with CCCs lesser than 0.80. This first in human study using a matrix transducer for 3D DCE-US confirms 2D DCE-US sampling errors and demonstrates that 3D DCE-US imaging is feasible and reproducible in the clinic.

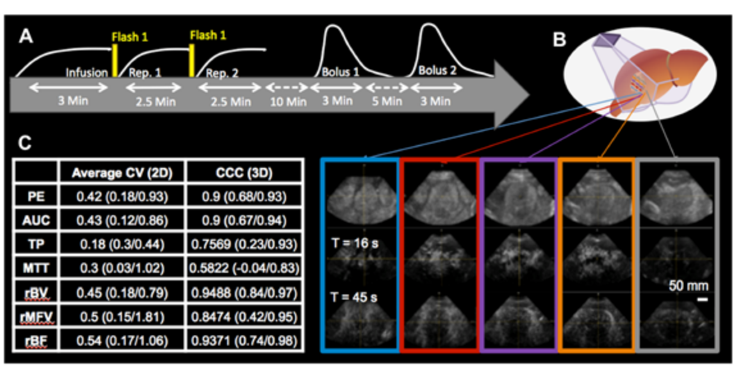

	Average CV (2D)	CCC (3D)
PE	0.42 (0.18/0.93)	0.9 (0.68/0.93)
AUC	0.43 (0.12/0.86)	0.9 (0.67/0.94)
TP	0.18 (0.3/0.44)	0.7569 (0.23/0.93)
MTT	0.3 (0.03/1.02)	0.5822 (-0.04/0.83)
rBV	0.45 (0.18/0.79)	0.9488 (0.84/0.97)
rMFV	0.5 (0.15/1.81)	0.8474 (0.42/0.95)
rBF	0.54 (0.17/1.06)	0.9371 (0.74/0.98)

Figure 1 – A Imaging workflow carried out at each scan session. Contrast infused for up to 3 min to allow steady state, followed by two disruption events ('flash') separated by 2.5 min. Two controlled bolus injections carried out with a syringe pump were administered following a 10 minute pause. **B** Five representative B-mode (top) and contrast mode (middle and bottom) planes out of the hundreds available in each volume at two time points (16 sec and 45 sec). **C** Summary table exhibiting the intra-volume average CV across 4-6 ROIs within a lesion volume, and the CCC between repeated pairs of measurements for each of the parameters.

3J-5

2:30 pm **Evaluation of Transarterial Chemoembolization for Liver Cancer Using 3D Contrast Enhanced Ultrasound Time-intensity Curve Analysis**

Kibo Nam[1], Maria Stanczak[1], Flemming Forsberg[1], Colette Shaw[1], John Eisenbrey[1]; [1]*Radiology, Thomas Jefferson University, USA*

Background, Motivation and Objective

Transarterial chemoembolization (TACE) is a standard care for patients with Barcelona Clinic Liver Cancer stage B hepatocellular carcinoma (HCC) and may also be used as a bridging therapy in patients who are potential transplant candidates. Incomplete treatment is defined as the persistence of enhancing areas inside the treated lesions seen at the first imaging study after locoregional treatment. Current guidelines recommend follow-up MRI or CT imaging 4-6 weeks after treatment. An earlier indicator of residual disease would enable clinicians to re-treat sooner, potentially improving disease control. In this study, a time-intensity curve of 3D contrast-enhanced ultrasound (CEUS) was assessed as a safe, inexpensive, accurate and earlier alternative technique for the identification of TACE patients requiring retreatment.

Statement of Contribution/Methods

To date, sixteen patients undergoing TACE for the treatment of HCC provided informed consent to participate in 3 CEUS exams: prior to TACE treatment, 1-2 weeks post treatment, and approximately one month post treatment. Ultrasound exams were performed using a Logiq E9 scanner with a RAB2-5-D probe (GE Healthcare, Wauwatosa, WI, USA). Following baseline imaging, patients received a bolus IV injection of 0.2-0.3 ml of Definity (Lantheus Medical Imaging, N Billerica, MA, USA), followed by a 10 cc saline flush. 3D volume data was continuously obtained for the entire tumor and surrounding tissue using the scanner's coded harmonics mode at low MI. Data collection was continued until contrast washout was observed (about 3-4 minutes). During post processing, volume data at each time point was extracted as 8 equidistant 2D slices across the mass. The time-intensity curves for tumor and normal tissue volumes were calculated offline by averaging the intensities of corresponding areas over the 8 planes and compared to the patient's treatment response.

Results/Discussion

A total of 11 subjects' data were included for the time-intensity curve analysis. Among the 11 subjects, 5 completed all 3 exams, while the remaining 6 completed 2 out of 3 exams. Based on the post treatment pathology or MRI reports, 6 subjects had complete and 5 subjects had incomplete treatment. The peak enhancement intensity of the tumor prior to TACE was similar between the complete and incomplete treatment group (82.4 ± 43.2 AU vs. 85.1 ± 45.2 AU; p=0.93), while at 1 month post treatment it was significantly lower in the complete treatment group relative to the incomplete treatment group (18.6 ± 3.1 AU vs. 61.2 ± 37.5 AU; p=0.02). The time to peak intensity (wash-in) or time to 70% of the peak value (wash-out) did not differentiate the two groups (p>0.13). The area under the time intensity curve (up to the peak-value) ratio of the tumor to normal tissue showed significant difference at 1 month post treatment (0.23 ± 0.11 vs. 0.78 ± 0.53; p=0.04). In spite of the limited sample size, time-intensity curve analysis from 3D CEUS shows potential to identify the TACE patients requiring retreatment.

3J-6

2:45 pm **Contrast-Enhanced Ultrasound (CEUS) in Patients with Chronic Kidney Disease (CKD)**

Anush Sridharan[1], Sandeep K. Kasoji[1], Emily H. Chang[2], Paul A. Dayton[1]; [1]*Biomedical Engineering, University of North Carolina at Chapel Hill, Chapel Hill, North Carolina, USA,* [2]*UNC Kidney Center, University of North Carolina at Chapel Hill, Chapel Hill, North Carolina, USA*

Background, Motivation and Objective

Chronic kidney disease (CKD) affects over 8 million people in the United States and is a major risk factor for cardiovascular disease, hospitalization and death. Diagnosis is usually made with blood and urine tests, and imaging is used primarily to rule out obstruction or determine size. Blood and urine tests are also used to follow disease progression with imaging used only for specific situations. In this ongoing clinical study, we evaluate the feasibility of using microbubble contrast agents to perform contrast-enhanced ultrasound (CEUS) and develop qualitative and quantitative measures of perfusion in patients with CKD. CEUS imaging may provide information about kidney perfusion that will aid in early diagnosis, disease progression and response to therapy.

Statement of Contribution/Methods

Patients underwent CEUS after providing written informed consent. Imaging was performed on a Siemens Sequoia 512 (Mountain View) by a trained sonographer using a 4C1 transducer (1-4 MHz). Definity (Lantheus Medical Imaging) was administered to the patient as a continuous IV infusion (4–8 mL/min). Contrast infusion was initiated along with cine clip acquisition. Once contrast enhancement reached a steady state (~1.5 min), two repetitions of destruction-reperfusion imaging (40 secs apart) were performed along the lesion and mid-plane of the kidney using a moderate MI pulse (MI; 0.75-0.8, 1 sec duration) followed by low MI imaging (MI; 0.1-0.2, 10 sec duration).

Results/Discussion

CEUS has been performed successfully in 57 patients with CKD and 3 healthy controls. Regions of interest (ROIs) were used to generate time-intensity curves (TICs), maximum intensity projections and reperfusion maps. Preliminary evaluation of the reperfusion maps showed a marked difference between the healthy controls and CKD patients (Figure 1). Wash-in rate based on the slope of the TIC was compared with CKD staging (1-5) and showed a significant correlation (r2:0.30; p=0.0408). TICs will also be used to generate area under the curve and time-to-peak intensity, and compared to blood and urine markers of CKD (serum creatinine and proteinuria). CEUS of CKD patients is shown to be feasible and is able to generate quantitative metrics. The diagnostic accuracy of these metrics is yet to be determined.

Figure 1.Reperfusion map of healthy volunteer (left) and CKD patient (right). ESRD – end stage renal disease.

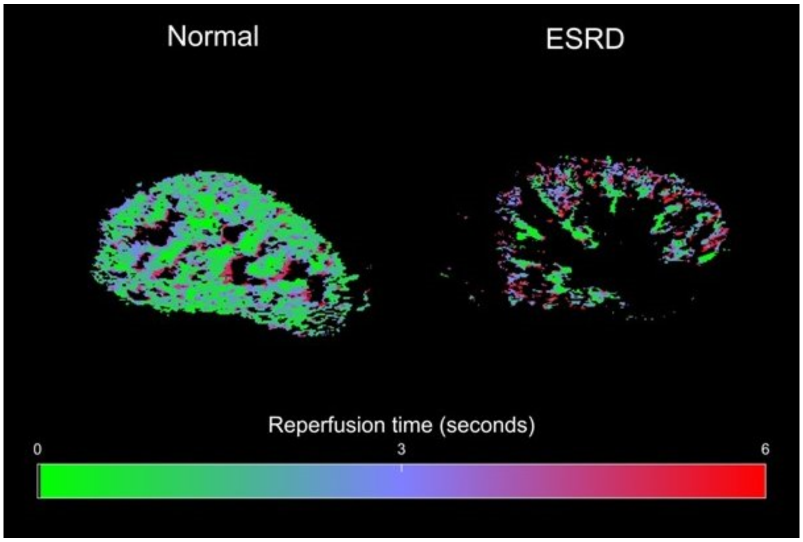
Normal
ESRD
Reperfusion time (seconds)
0
3
6

4J - MBB: Volumetric and Fourier Domain Approaches

Diplomat Room

Saturday, September 9, 2017, 1:30 pm - 3:00 pm

Chair: **Pieter Kruizinga**
Erasmus MC

4J-1

1:30 pm **High-Volume-Rate 3-D Ultrasound Imaging Based on Motion Compensation: A Feasibility Study**

Philippe Joos[1], Hervé Liebgott[1], François Varray[1], Lorena Petrusca[1], Damien Garcia[1], Didier Vray[1,2], Barbara Nicolas[1]; [1]*CREATIS, Université Lyon 1, France,* [2]*INSA Lyon, France*

Background, Motivation and Objective

Echocardiography is the most used modality for the evaluation of cardiac function. To obtain a time-resolved volumetric quantification of cardiac motion, ultrafast 3-D imaging is required. Ultrafast ultrasound imaging with diverging waves has demonstrated its potential for clinical 2-D echocardiography. It has been shown that MoCo (motion compensation) strategies based on a triangle transmit arrangement could produce high-contrast cardiac B-mode images at 500 fps [1]. With the purpose of developing high-volume-rate 3-D echocardiography, we introduced a transmit sequence enabling volumetric MoCo for spherical diverging wave imaging.

Statement of Contribution/Methods

Four Verasonics scanners were combined to get 1024 channels connected to a 2-D 3-MHz phased array of 32x32 elements. A sequence of 49 spherical waves (PRF = 2250 Hz) whose steering angles followed a particular 2-D triangle arrangement was generated using the full aperture of the probe. Motion was compensated by using tissue color Doppler Imaging to avoid destructive interferences issued from frame-to-frame tissue motion. High-frame-rate 3-D ultrasound imaging based on MoCo was evaluated in vitro with a rotating disk. The angle arrangements (cf. Fig.) were defined in the elevation (E) and azimuth (A) directions such that:

- E and A angles increased then decreased linearly to sum the main lobes coherently and mitigate the side lobes
- Small angle increments were used to preserve the frame-to-frame correlation to reduce Doppler variance
- The E and A angles were allocated homogeneously to ensure high spatial resolution

Results/Discussion

A contrast loss due to tissue motion was observed when MoCo was not included in the coherent summation. When MoCo was integrated, the speckles were preserved in the whole field of view (cf. Fig). The estimated in vitro tissue Doppler velocities were consistent with the expected values (mean relative error = 4%). These preliminary results showed that MoCo will be essential in high-volume-rate 3D echocardiography. Further works will help to determine if the temporal and spatial resolutions obtained with this 3-D MoCo method are adapted to 3-D speckle tracking echocardiography.

[1] Porée et al. High-frame-rate echocardiography using coherent compounding with Doppler-based motion-compensation. IEEE TMI, 2016.

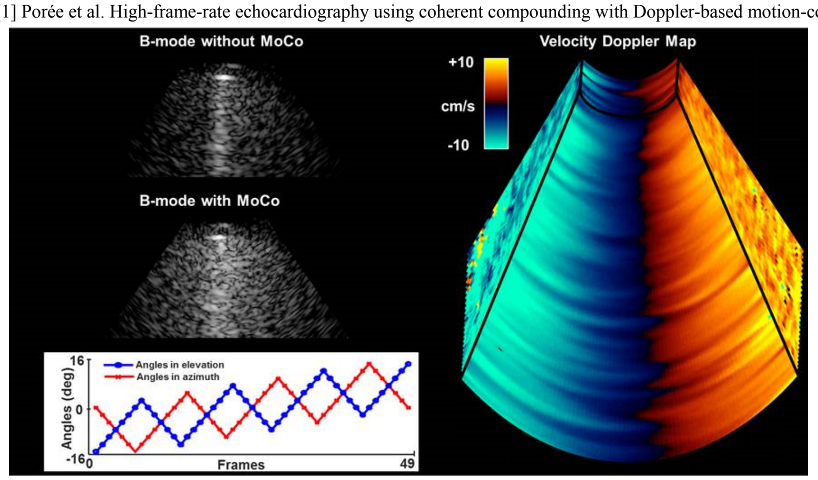

High-frame-rate 3-D ultrasound imaging of a spinning disk. On the left, are represented a plane of the 3-D volume without MoCo (top) and with MoCo integrated in the compounding process (below). The Velocity Doppler Map of the volume is reported on the right. The 49 steered angles used for TDI and compounding are represented on the bottom left.

4J-2

1:45 pm **3-D Imaging Using Row–Column Addressed 2-D Arrays with a Diverging Lens: Phantom Study**

Hamed Bouzari[1], Mathias Engholm[2], Christopher Beers[3], Matthias Bo Stuart[1], Erik Vilain Thomsen[2], Jørgen Arendt Jensen[1]; [1]*Department of Electrical Engineering, Technichal University of Denmark, Lyngby, Denmark,* [2]*Department of Micro- and Nanotechnology, Technichal University of Denmark, Lyngby, Denmark,* [3]*Sound Technology Inc, Analogic Ultrasound Group, USA*

Background, Motivation and Objective

In ultrasound 3-D imaging an N×N element 2-D array can be operated utilizing only 2N connections, when row–column addressing is used. One issue with the row–column-addressed (RCA) arrays is that the imaging can only be performed within a rectilinear region in front of the array. This study proposes and evaluates the possibility of curvilinear 3-D imaging with RCA arrays, using a double-curved diverging lens mounted on the RCA array. A delay-and-sum beamformation scheme specific to double-curved RCA 2-D arrays was proposed by the authors and this study investigates the focusing ability of a mountable acoustic lens based on phantom measurements.

Statement of Contribution/Methods

The imaging performance of a λ/2-pitch 3 MHz 62+62 PZT RCA 2-D array equipped with a diverging lens with f#=1.4 is investigated as a function of depth within its curvilinear field-of-view (FOV). A synthetic aperture imaging sequence with single element transmissions is designed for imaging down to 14 cm at a volume rate of 88Hz. On each emission a three-cycled sinusoidal impulse with a center frequency of 3 MHz and amplitude of ±100 V is transmitted. The manufactured lens is made of RTV silicone casted inside a thermoplastic frame and mounted on the probe with 1 mm gap. The radial curvature of the lens is 12.7 mm. The speed of sound for the RTV silicone rubber is 1 mm/µs. The left two figures illustrate the lens mounted on the RCA PZT probe. The concave cavity of the lens is filled with acoustic gel before measurements. A tissue mimicking phantom with 0.5 dB/cmMHz attenuation (CIRS Model 040GSE) is used for the performance assessment in terms of full-width-at-half maximum (FWHM), and SNR.

Results/Discussion

The figures on the right show two cross-planes (azimuth and elevation) of the tissue mimicking phantom. The dashed lines indicate the FOV using the lens. Measurements on the phantom confirm that the rectilinear imaging FOV is extended to a curvilinear 40°×40° FOV using the lens. The measured lateral FWHM at 55 mm of depth is 2 mm. The penetration depth, where the SNR crosses 0 dB is 11.4 cm. The selection of the lens f# depends on the specific application, which is a trade-off between the penetration depth and the FOV, however the experimental results of this study should be considered as preliminary results. Further investigation on lowering the reflection from the lens needs to be performed.

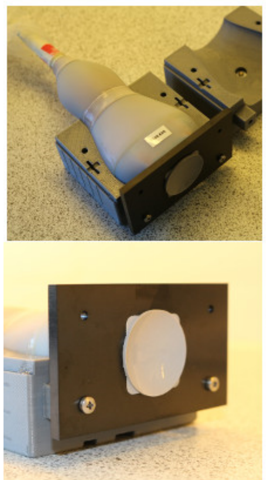

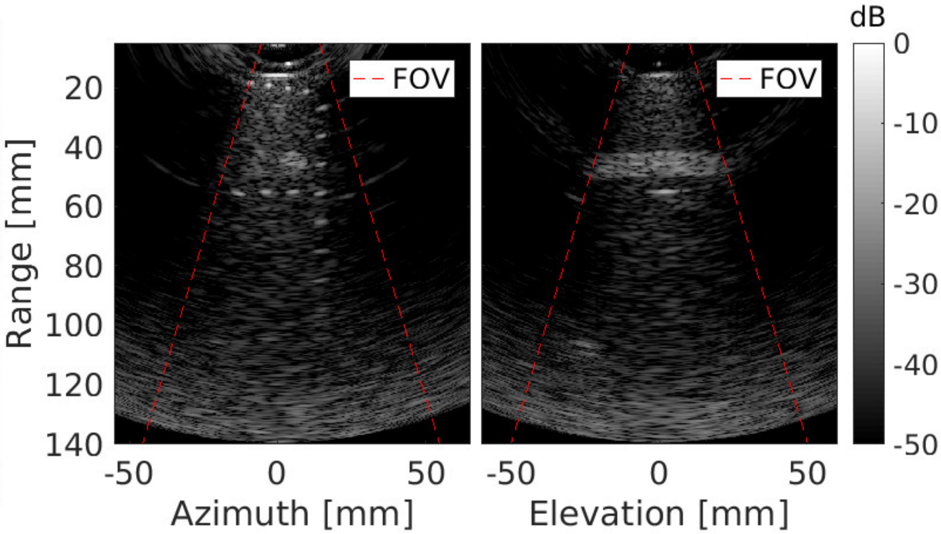

4J-3

2:00 pm Volumetric Imaging Using Adult Matrix TEE with Separated Transmit and Receive Array

Deep Bera[1], Franc van den Adel[2], Nikola Radeljic-Jakic[2], Boris Lippe[2], Mehdi Soozande[1], Michiel Pertijs[3], Martin Verweij[3], Pieter Kruizinga[1], Verya Daeichin[3], Hendrik Vos[1,3], Johan Bosch[1], Nico de Jong[1,3]; [1]*Erasmus Medical Center, Rotterdam, Netherlands,* [2]*Oldelft Ultrasound, Delft, Netherlands,* [3]*Delft University of Technology, Delft, Netherlands*

Background, Motivation and Objective

The design of 3D TEE transducers poses severe technical challenges: channel count, electronics integration with high and low voltages, heat dissipation, etc. We present an adult matrix TEE probe with separate transmit (Tx) and receive (Rx) arrays allowing optimization in both Tx and Rx [1]. Tx elements are directly wired out, Rx employs integrated micro-beamformers in low-voltage (1.8/5.0V) chip technology. The prototype is fully integrated into a gastroscopic tube.

Statement of Contribution/Methods

The 5 MHz matrix array (Fig A) was split into a square Rx array (2048 elements) and a narrow Tx strip (128 elements) at one side. The PZT stack was cut at an angle of 45° (181 µm/0.6λ pitch) with respect to the probe axis. The Rx array is divided in 128 sub-arrays of 4x4 elements. Each sub-array connects to one output channel via an integrated micro-beamformer (µBF) capable of pre-steering in 10 ns delay steps per element. The probe was connected to a Verasonics V1 system. Measurements were compared to FieldII simulations. Volumetric images of a CIRS 040GSE ultrasound phantom were recorded using µBF RF datasets with 3° interval in azimuth (AZ) and 10° in elevation (EL) direction, and sub-volumes were reconstructed with regular delay-and-sum beamforming. Overlapping sub-volumes were linearly combined to make the final volume [2] with an opening angle of 60°x60°. The widths of the PSF were simulated and measured at -6 dB with a point scatterer at 36 mm depth.

Results/Discussion

The AZ width of the PSF was 1.44 mm in simulation and 1.99 mm in measurement (Fig. C and Fig. D). In EL direction simulated PSF was 14% wider compared to AZ and slightly tilted due to the narrow, eccentric Tx array in EL direction. In measurement, EL PSF was 18% wider than AZ PSF. The volume rendered image of the CIRS phantom shows details as expected (Fig. B). From this analysis we conclude that the eccentric, rectangular transmit array has only limited effects on image quality, while avoiding the additional power consumption of high-voltage electronics in the probe tip.

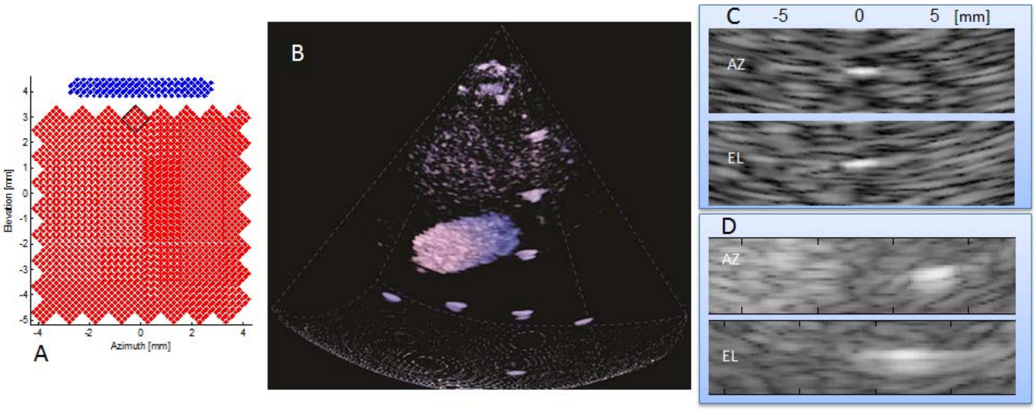

Fig A: Transducer element configuration with Tx sub-array on top, *B:* 3D rendering of CIRS phantom recording, *C:* Simulated point scatterer and *D:* Measured point scatterer (7 mm off-axis).

[1] Blaak et al., IUS 2011, p 2341-2344. [2] Bera et al., IUS 2016.

4J-4

2:15 pm Improved Plane Wave Ultrasound Image Reconstruction Using a Deconvolution-Based Fourier Domain Approach

Chuan Chen[1], Gagm Hendriks[1], Hhg Hansen[1], Cl De Korte[1,2]; [1]*dept. of Radiology, Medical UltraSound Imaging Center (MUSIC), Radboud university medical center, Nijmegen, Netherlands,* [2]*Faculty of Science and Technology, Physics of Fluids Group, University of Twente, Twente, Netherlands*

Background, Motivation and Objective

Different from conventional focused ultrasound, ultrafast ultrasound imaging employs full-field transmission such as a plane wave to achieve frame rates in the order of 10 kHz. Image reconstruction of plane-wave ultrasound is more computational efficient to be processed in Fourier domain than in time domain. A widely-applied seismic wave migration technique, the Stolt's f-k Fourier-domain method, was modified to fit the plane wave transmission-receiving process into the Exploding Reflector Model (ERM). In comparison with the ideal fitting in Lu's f-k method, the fitting in the Stolt's f-k is slightly imprecise for the higher lateral Fourier components that results in residual patterns that degrade the image quality. We propose a template that can be applied in Fourier domain directly to deconvolute the residual point spread function (residual PSF) induced by imprecise fitting.

Statement of Contribution/Methods

After transmitting a non-steered plane wave, received signals were transformed into the Fourier domain by the Stolt's f-k method. The resulting Fourier spectrum (f) can be modelled as f=*f*'h+u, where *f*, h and u represent the Fourier spectrum of the desired image, of the residual PSF and of the noise, respectively. The residual PSF at a certain depth was theoretically derived by locally fitting the plane wave transmission-receiving process with a sequence of ERMs of different depths. The desired spectrum *f* was then approximated by dividing f by the Fourier transform h of the residual PSF. Finally, the desired spectrum was transformed to the spatial domain to form the final image as shown in Fig.1 (a). The proposed method was tested on phantom datasets from two linear-array transducers: a Siemens L12-4 (central frequency 9 MHz) connected to a Verasonics V1 and a Verasonics L11-4 (central frequency 5.2 MHz) provided by the Beamforming Challenge IUS 2016.

Results/Discussion

For the L12-4, the application of deconvolution increased contrast from 4.3 dB to 6.3 dB and improved lateral resolution from 0.56 mm to 0.42 mm. Deconvolution was more effective for the L11-4, where contrast of 5.2 dB and lateral resolution of 1.26 mm were elevated to 8.9 dB and 0.56 mm, respectively (see Fig. 1(b)). To conclude, the proposed deconvolution technique is able to compensate the imprecision in Stolt's f-k and produces improved contrast and resolution.

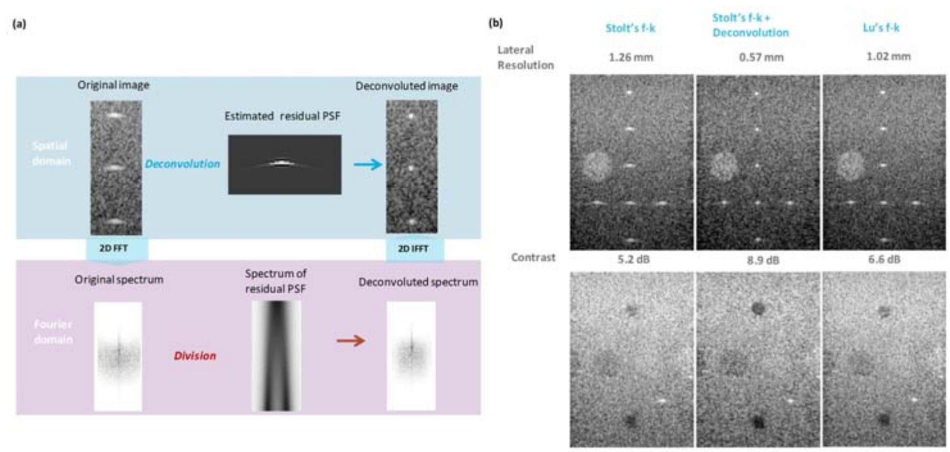

(a) The schematic diagram of deconvoluting estimated residual PSF in Fourier domain and spatial domain. (b) Examples of image quality processed by Stolt's f-k, Stolt's f-k + Deconvolution and Lu's f-k methods (Dataset from Beamforming Challenge IUS 2016).

cityt

4J-5

2:30 pm Orthogonal Golay Pairs-coded Diverging Wave Compounding for High-quality and High-frame-rate Ultrasound Imaging

Feifei Zhao[1], Jianwen Luo[1]; [1]*Department of Biomedical Engineering, Tsinghua University, Beijing, China, People's Republic of*

Background, Motivation and Objective

Coded excitation with complementary Golay codes has been demonstrated to increase the signal-to-noise ratio (SNR) and penetration of diverging wave (DW) coherent compounding for high frame rate cardiac imaging (Zhao et al., PMB 2017). However, the effective gain in frame rate of the Golay coded system is compromised by a factor of 2 because two complementary codes are transmitted. The objectives of this study was to develop the orthogonal Golay pairs-coded sequence for DW compounding scheme while maintaining the high frame rate.

Statement of Contribution/Methods

In a typical sequence (Fig-a), DWs in two steering angles were transmitted simultaneously, coded with orthogonal Golay pairs and their complementary pairs in the 1st and 2nd transmits, respectively. Beamforming was performed on the channel data, followed by pulse compression based on the orthogonality of Golay pairs, and four RF frames corresponding to the two steering angles were obtained. Decoding based on the complementariness of Golay pairs was then applied to obtain two RF frames in the two steering angles. Finally, the two frames were summed for DW coherent compounding. This method was also implemented with more steering angles (even numbers). The point-spread-function (PSF) of the proposed method from a 2 MHz 64 element phased array (pitch = 0.34 mm) was simulated in Field II. Experiments were performed on a CIRS phantom (model 040GSE, 0.5 dB/MHz/cm) using a ULA-OP system equipped with a 2 MHz 64 element phased array (pitch = 0.34 mm). The quality of the orthogonal Golay pairs-coded images was compared with that of the non-coded DW images compounded with different numbers of steering angles and that of the focused image. The SNR of a hypoechoic region and the contrast between a cyst and the background were evaluated.

Results/Discussion

The PSF simulation results demonstrated that the DWs in different steering angles coded with orthogonal Golay pairs in one transmit could be decoded effectively, compared with the separately transmitted DWs. The phantom images showed the contrast improvement at large depths when using orthogonal Golay pairs-coded excitation. The coded images achieved higher SNR and contrast (Fig-b). By using the proposed method for Golay coded excitation, the frame rate of DW compounding system can be maintained. The proposed method can thus obtain DW imaging at both high quality and high frame rate.

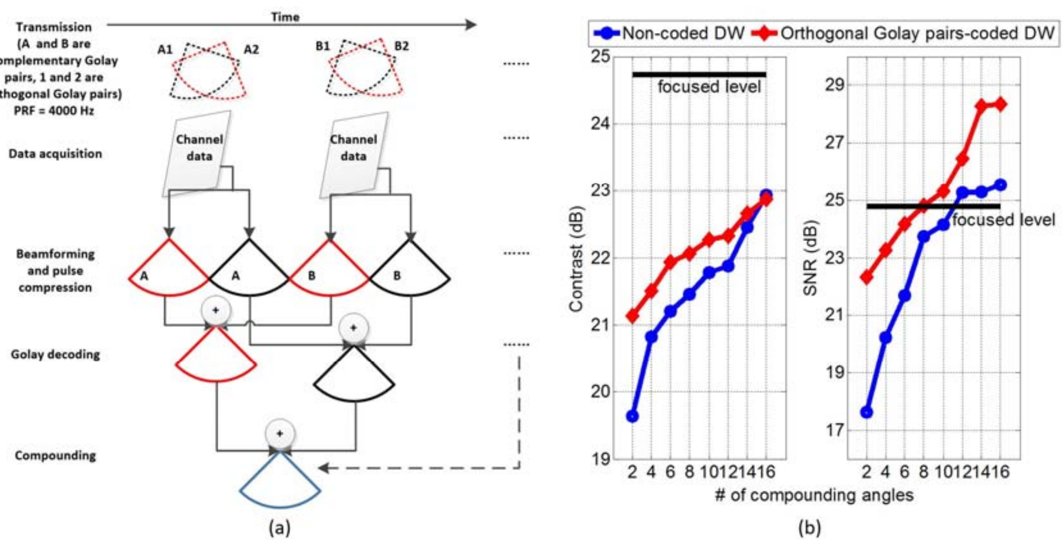

4J-6

2:45 pm Design of an Angular Weighting Template for Coherent Plane Wave Compounding in Fourier Domain

Chuan Chen[1], GAGM Hendriks[1], HHG Hansen[1], CL de Korte[1,2]; [1]*dept. of Radiology, Medical UltraSound Imaging Center (MUSIC), Radboud university medical center, Nijmegen, Netherlands,* [2]*Physics of Fluids Group, University of Twente, Twente, Netherlands*

Background, Motivation and Objective

Coherent plane wave compound imaging has already shown to provide equal image quality as multi-focal conventional imaging at more than ten times higher frame rates. Furthermore, image reconstruction of plane wave ultrasound is more computational efficient in Fourier domain (e.g. Lu's or Stolt's f-k) than in spatial domain (e.g. Delay-and-Sum (DAS)). In this study we fully integrated the Stolt's f-k method and coherent compounding in the Fourier domain to further increase its computational efficiency. Additionally, we introduced a weighting template for Fourier domain methods which is rotated as a function of plane wave transmission angle (angular weighting) and investigated how it affects contrast and resolution of coherently compounded images.

Statement of Contribution/Methods

Experimental plane wave ultrasound data of a contrast and resolution phantom were obtained at 11 beam steering angles linearly spaced between -16° and +16° for a Siemens L12-4, an ATL L7-4 and a Verasonics L11-4 linear array transducer. Data for the first two transducers were obtained with a Verasonics V-1 system, and the last dataset was provided by the IUS 2016 beamforming challenge. Data were transformed to Fourier domain by either Lu's or Stolt's f-k method. To allow coherent compounding in Fourier domain, the original Stolt's f-k process was modified to compensate the coordinate misalignment. The Fourier spectrum Φ_ϑ of a plane wave steered by ϑ was multiplied by a template Ω_ϑ to weight the spectrum ($\Phi_\vartheta = \Phi_\vartheta\Omega_\vartheta$)). As a plane wave was steered by ϑ, its weighting template was designed to be angle-dependent with a Hanning window being symmetric around the orientation of 0.5ϑ. Weighted spectrums were coherently compounded ($\sum\Phi_\vartheta$) followed by inverse 2D Fourier transformation to provide the final reconstructed image.

Results/Discussion

The results for the Fourier methods show enhanced contrast with respect to DAS with and without apodization by using angular weighting for both Lu's and Stolt's f-k method, while slightly degrading the lateral resolution (Table 1). The contrast gain in Stolt's f-k was more significant than in Lu's method. Both methods rendered similar image quality after angular weighting. Our results show that angular weighting improves both Lu's and Stolt's f-k methods and produces images with a quality similar or better than DAS with apodization.

Table 1. Performance of Lu's, Stolt's f-k and DAS, with and without angular weighting or apodization. (cf denotes central frequency.)

		Lu's f-k (no weighting)	Lu's f-k (weighting)	Stolt's f-k (no weighting)	Stolt's f-k (weighting)	DAS (no apodization)	DAS (apodization)
L12-4 (cf: 9.0MHz)	Contrast(dB)	9.0	9.9	7.8	9.9	9.3	9.9
	Resolution(mm)	0.38	0.43	0.36	0.42	0.34	0.43
L12-5 (cf: 9.0MHz, pitch:0.13mm)	Contrast(dB)	8.8	10.3	7.2	10.0	8.9	9.8
	Resolution(mm)	0.34	0.39	0.35	0.39	0.33	0.39
L11-4 (cf: 5.2MHz, pitch: 0.30mm)	Contrast(dB)	8.9	11.4	7.7	11.3	7.9	11.0
	Resolution(mm)	0.49	0.54	0.44	0.52	0.53	0.58

5J - MEL: Vascular Elastography

Blue Room

Saturday, September 9, 2017, 1:30 pm - 3:00 pm

Chair: **Marvin Doyley**
University of Rochester

5J-1

1:30 pm In-Vivo Mechanical Characterization of Abdominal Aortic Aneurysms and Healthy Aortas Using 4D Ultrasound: A Comparison Study

Emiel van Disseldorp[1,2], Niels Petterson[1], Frans van de Vosse[1], Marc van Sambeek[2], Richard Lopata[1]; [1]*Biomedical Engineering, Eindhoven University of Technology, Eindhoven, Netherlands,* [2]*Department of Surgery, Catharina Hospital, Eindhoven, Netherlands*

Background, Motivation and Objective

Abdominal aortic aneurysms are lethal in 80% of all cases when ruptured. Current guidelines for AAA repair are mainly based on the diameter, which has its shortcomings. Hence, a more patient-specific rupture risk assessment is needed. In this study, methods for elastography and wall stress analysis using 4D ultrasound (US) were developed. Patient-specific material properties and peak wall stresses were compared between young and age-matched volunteers, and AAA patients.

Statement of Contribution/Methods

In 40 patients (diameter of 27 – 52 mm), 10 young (age < 30 years), and 8 age-matched (age > 50 years) healthy volunteers 4D-US data were measured using a Philips iU22 (X6-1 transducer) during breath hold for 5 seconds. Brachial blood pressure was measured simultaneously. The US data were manually segmented after which the patient-specific geometry was tracked over time to estimate its displacement field using 3D speckle tracking. The AAA geometry in diastole was converted into a finite element mesh with a wall thickness of 2 mm. Wall stress analysis was performed using a neo-Hookean material model. The model was optimized by iteratively adapting the material properties until the model output matched the 3D displacements. The resulting patient-specific shear moduli (G_{FEA}) were also compared to direct elastometric estimates, G_{ELASTO}.

Results/Discussion

Figure 1 show an increase in arterial stiffness (G_{FEA}) between the young and age-matched volunteers ($p << 0.01$). A significant difference in G_{FEA} between the age-matched healthy volunteers (median 0.16 MPa, IQR: 0.15 – 0.26 MPa) and AAA patients (median 1.05 MPa, IQR: 0.71 – 1.38 MPa) was measured. Moreover, G_{FEA} increases significantly with diameter in the AAA sub-groups. Results for G_{ELASTO}, reveal similar differences between groups, but with a larger spread. The patient-specific 99th percentile wall stress is significantly lower for all healthy volunteers (range: 135 - 258 kPa) compared to AAA patients (range 198 - 390 kPa).

This study shows that 4D US-based wall stress analysis of AAAs is feasible, providing significant differences in material properties and peak wall stresses. Moreover, arterial stiffening observed in AAA patients is significantly higher than age-related changes in healthy volunteers. In future, following these parameters over time could eventually improve AAA rupture risk assessment.

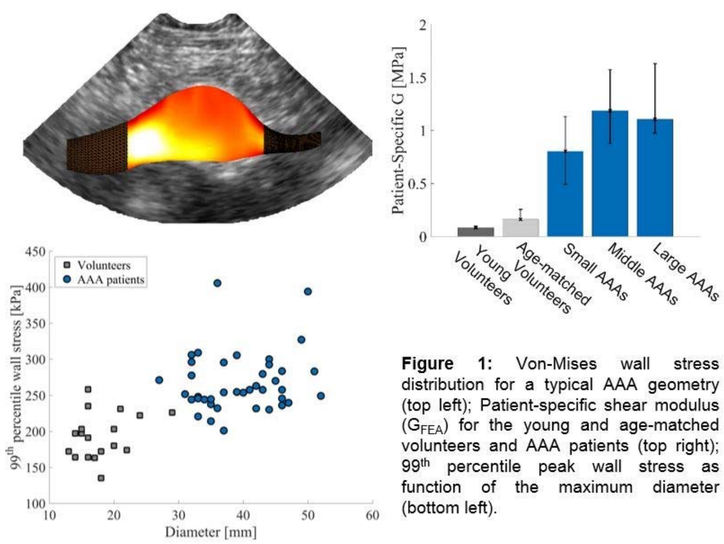

Figure 1: Von-Mises wall stress distribution for a typical AAA geometry (top left); Patient-specific shear modulus (G_{FEA}) for the young and age-matched volunteers and AAA patients (top right); 99th percentile peak wall stress as function of the maximum diameter (bottom left).

5J-2

1:45 pm Insight in Vascular Fragility Induced by Collagen Structural Change Using Ultrafast Ultrasound Imaging in a Mouse Model of Vascular Ehlers-Danlos Syndrome

Guillaume Goudot[1], Tristan Mirault[2], Véronique Baudrie[2], Irmine Ferreira[2], Mickaël Tanter[1], Xavier Jeunemaitre[2], Emmanuel Messas[2], Mathieu Pernot[1]; [1]*Institut Langevin, INSERM U979, Paris, France,* [2]*PARCC, INSERM U970, Paris, France*

Background, Motivation and Objective

Multiple collagen types are critical for proper function of the vascular system, with type III being responsible for imparting strength in the vessel wall. Patients with mutant gene encoding type III collagen experience arterial ruptures, called vascular Ehlers-Danlos syndrome (vEDS). In order to better characterize their arterial mechanical properties, we developed a Knock-In Gly183Arg mice (col3KI-mice) presenting a qualitative default in type III collagen, similar to the human disease. Our goal was to assess the aortic mechanical behaviour by measuring the pulse wave velocity (PWV) at different blood pressure levels.

Statement of Contribution/Methods

We compared Black-6 col3KI-mice to their wild type (WT) littermates. An age of 12-20 weeks was chosen, to anticipate the early high mortality rate in col3KI-mice caused by arterial ruptures. Invasive arterial blood pressure (BP) catheter allowed a follow-up of arterial pressure change to increasing doses of IV phenylephrine (0.01–700 µg/kg), in anesthetized mice with pentobarbital (60mg/kg). PWV was measured by Ultrafast ultrasound imaging, using a 15 MHz probe, with a longitudinal alignment of 1.6cm on the abdominal aorta. The high frame rate (2800 frames/s) was used to measure the PWV at the foot of the waveform (PWV1), generated at the minimal diastolic blood pressure (DBP) and at the dicrotic notch (PWV2), at the systolic blood pressure (SBP). To evaluate the intrinsic properties of the artery, we therefore reported each PWV measured to their corresponding arterial pressure at each level of phenylephrine: PWV1/DBP and PWV2/SBP. The difference of these two PWV (Delta-PWV) is related to the arterial stiffening during the cardiac cycle, and reported to the pulse pressure (PP) as Delta-PWV/PP. Data are expressed as median [25th–75th] and compared by Mann-Whitney tests.

Results/Discussion

Nine col3KI-mice (6 females, 3 males) were compared to 21 WT (10 females, 11 males) of comparable age (123±27 days) and weight (25.8±4.3 g). PWV1/DBP was lower in col3KI-mice (2.76cm.s-1.mmHg-1 [2.66-2.86] vs. 3.07 [2.88-3.26]; p= 0.020). This was also the case at the systolic level, with lower PWV2/SBP (2.91 [2.79-3.02] vs. 3.65 [3.44-3.85]; p<10-8). Delta-PWV/PP (cm.s-1.mmHg-1) was lower in col3KI mice (4.97 [4.12-5.81] vs. 6.79 [6.11-7.47]; p<10-6), showing a lack of stiffening during the cardiac cycle.

In this model of vEDS, arterial rupture may be underlain by the lack of arterial stiffening due to the absence of type III collagen recruitment when pressure rises. This emphasizes the crucial role of type III collagen in the biomechanical properties of the arterial wall. We can expect that using non invasive Ultrafast ultrasound imaging will allow to better characterize the arterial wall property and detect early change of the arterial stiffness.

5J-3

2:00 pm Suppression of Reflected Waves with High-Resolution Radon Transform for Accurate Measurement of Regional Pulse Wave Velocity

Chengwu Huang[1], Jianwen Luo[1]; [1]*Department of Biomedical Engineering, Tsinghua University, Beijing, China, People's Republic of*

Background, Motivation and Objective

Pulse wave velocity (PWV) is a reliable index of arterial stiffness. To date, reflected pulse wave interference is still a major challenge for regional PWV estimation using ultrasound imaging methods. In this study, a high-resolution Radon transform (HRT) method is proposed to eliminate the reflected wave interferences in PWV estimation.

Statement of Contribution/Methods

An inversion-based linear Radon transform was used to transform linear events in pulse wave propagation image (Fig. 1a) to points in Radon domain. The forward and reflected waves were mapped into different regions in Radon domain based on the slope difference (Fig. 1b). To achieve higher resolution, L1-norm regularization was used to obtain the sparse solution of Radon transform (Fig. 1c), in which the reflected waves could be easily removed. Forward wave was then reconstructed with an inverse Radon transform. The method was validated using synthetic data, homogeneous vessel phantom data and *in vivo* common carotid artery (CCA) data of a healthy human subject acquired with a SonixMDP system and an L14-5/38 probe using plane wave imaging, and local PWVs along the vessel were estimated with piecewise linear regression (kernel: 8 mm).

Results/Discussion

For the synthetic data (Fig. 1d), the piecewise PWVs are significantly interfered by the reflected waves [root mean square error (RMSE) = 0.67 m/s)], but can be accurately estimated after reflected wave suppression using the HRT method (RMSE = 0.05 m/s). Directional filtering may not be applicable (RMSE = 1.28 m/s), due to the large wavelength of the pulse wave. For the phantom and *in vivo* healthy CCA, the arterial stiffness is expected to be homogeneously distributed along the imaged segment. The piecewise PWV measurements after wave suppression are much more stable with lower standard deviation and higher correlation coefficient in linear regression (phantom: PWV=2.80 ± 0.02 m/s, R^2 = 1.00 ± 0.00; *in vivo*: PWV = 3.16 ± 0.11 m/s; R^2 = 1.00 ± 0.00), and reveal the homogeneous arterial stiffness distribution better than those without filtering (phantom: PWV = 2.97 ± 0.44 m/s, R^2 = 0.96 ± 0.02 ; *in vivo*: PWV = 3.37 ± 0.78 m/s, R^2 = 0.90 ± 0.08). Therefore, the necessity of reflected wave suppression for regional PWV estimation and the robustness of the HRT method are demonstrated, which may enhance the capability of ultrasound imaging in local arterial stiffness assessment.

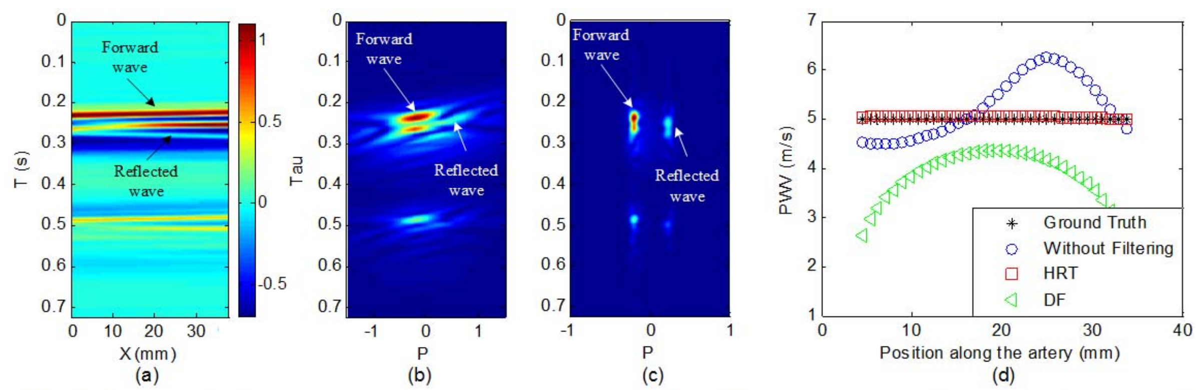

Fig.1. (a) A synthetic pulse wave propagation image, including 128 pulse wave acceleration waveforms, with PWV=5m/s, image width=38mm. (b) Inversion-based Radon transform of (a); the resolution is not enough for wave separation. (c) High-resolution Radon transform of (a). (d) Piecewise PWV estimation along the artery, black dots are ground truth values. HRT, high-resolution Radon transform; DF, directional filtering.

5J-4

2:15 pm Development and Mechanical Evaluation of Nonlinear Anisotropic Aortic Models for In Vitro Experimentation

Miguel Bernal[1], Jorge Saldarriaga[2], John Bustamante[1], Cecilia Cabeza[3], Carlos Negreira[4], Javier Brum[4]; [1]*Grupo de Dinámica Cardiovascular, Universidad Pontificia Bolivariana, Medellin, Colombia,* [2]*Grupo de Investigación sobre Nuevos Materiales, Universidad Pontificia Bolivariana, Medellin, Colombia,* [3]*Grupo de Mecánica Estadística y Física No Lineal, Instituto de Física, Facultad de Ciencias, Universidad de la República, Montevideo, Uruguay,* [4]*Laboratorio de Acústica Ultrasonora, Instituto de Física, Facultad de Ciencias, Universidad de la República, Montevideo, Uruguay*

Background, Motivation and Objective

In the past decades multiple techniques have focused in the characterization of the vasculature elasticity in a clinical setting. In their development in vitro testing and validation is mandatory. Unfortunately, this is done on arterial phantoms that are isotropic, linearly elastic, and that do not match the real mechanical and morphological properties of the vessels. In this work, we developed a series of phantoms made from clinical images and compared them to ex vivo pig aortas.

Statement of Contribution/Methods

MRI images from a healthy volunteer were used to create a mould and contermould of the descending aorta. PVA at 10% bwt was injected between the mould and contermould. Before injection, the contermould was wrapped in a reinforcing fabric (elastic along the circumferential direction and rigid in the longitudinal). The PVA was polymerized by 7 cycles (12 hours) of freezing and thawing. The mechanical properties of the models were assessed using ultrasound elastography and tensile testing. The models were connected to a circulating loop and tested under static and physiological pressure conditions (0 to 200 mmHg). Ten shear wave elastography measurements were performed over one cardiac cycle using a sequence consisting of a 100 µs push and an ultrafast imaging at 6 kHz. To recover the Young's modulus, a thin plate Lamb wave model was fitted to the dispersions curves of the propagating shear waves.

For the tensile testing, the models and pig aortas were open longitudinally and samples (1 X 4 cm2) taken in the longitudinal and circumferential directions. Using an Instron machine a strain rate of 50 mm/s was applied. The strain-stress curves were analyzed and the incremental Young's modulus calculated.

Results/Discussion

The aortic models displayed a nonlinear and anisotropic elastic behavior. The static pressure studies showed significant increases of the Young's modulus from 0.165 MPa at P = 0 mmHg to 1.02 MPa at P = 200 mmHg. The dynamic studies also displayed a significant variation of 56% between systole and diastole (1.33 and 0.58 MPa, respectively) for a mean P = 100 mmHg. The tensile testing for the models and healthy aortas presented a good agreement. Both materials showed a similar increase in Young's modulus as a function of strain in the circumferential direction. Increasing from 200 kPa at low strain (< 10%) to 1 MPa at 40% strain. In the longitudinal direction, the aortic model displayed higher mechanic properties with a Young's modulus of 8MPa at 20% strain. This result is expected due to orientation of the reinforcing fabric. Therefore, it is possible to customize the mechanical properties of these models by changing the orientation and the material of the reinforcement. Finally, this work presents a new type of arterial models that mimic the arterial tissue (anisotropy and nonlinear behavior) which can be used to study the role of arterial elasticity in pathological processes as well as in the development of new imaging methodologies.

5J-5

2:30 pm Guided Wave Elastography of Press-Stressed Thin-Walled Soft Tissues

Guo-Yang Li[1], Qiong He[1], Robert Mangan[2], Guo-Qiang Xu[1], Jianwen Luo[1], Michel Destrade[2], **Yanping Cao[1]**; *[1]Tsinghua University, China, People's Republic of, [2]National University of Ireland Galway, China, People's Republic of*

Background, Motivation and Objective

In vivo measurement of the mechanical properties of thin-walled soft tissues (e.g., mitral valve, artery and bladder) and in situ mechanical characterization of thin-walled artificial soft biomaterials in service are of great challenge. Those thin-walled structures are usually pre-stressed to achieve and/or improve their functional performance, which further complicate the inverse analysis to identify the mechanical properties. In this study, we investigate the properties of guided waves generated by focused acoustic radiation force in immersed pre-stressed plates and tubes, and show that they can address this challenge.

Statement of Contribution/Methods

To obtain the dispersion relation and establish an inverse approach for guided wave elastography (GWE) (Li and Cao, 2017) of the pre-stressed plate and tube, we carried out (i) theoretical analysis, (ii) finite element analysis(FEA), and (iii) phantom experiments. The dispersion equation was firstly derived by incremental theory (Ogden, 2007) and solved to study the effect of the pre-stress. Then frequency-domain finite element model was established to validate the theoretical analysis. Results given by FEA accurately match the theoretical dispersion relation. Experiments were conducted on a polyvinyl alcohol (PVA) cryogel phantom (as shown in the figure). The dispersion relation of the phantom in stress-free and two pre-stressed (stretch ratios were 1.08 and 1.18) states were measured by GWE method, and results shown the theoretical solution can well predict the variation of the dispersion relations.

Results/Discussion

It has been reported the arterial wall stiffness varies with the blood pressure (Couade et al, 2010). However, yet no theoretical solution can address the effect of the blood pressure. By conducting FEA we found in the low frequency range (0-2000 Hz), the curvature of the arterial wall can be ignored and the present theoretical analysis can predict the dispersion relations of both guided axial and circumferential waves. Besides, we also found the variation of the dispersion relation almost only relies on the stretch ratio along the wave propagation direction, instead of the other two stretch ratios along the directions perpendicular the wave propagation direction, which provides convenience in practical used because the accurate deformation state is not necessary.

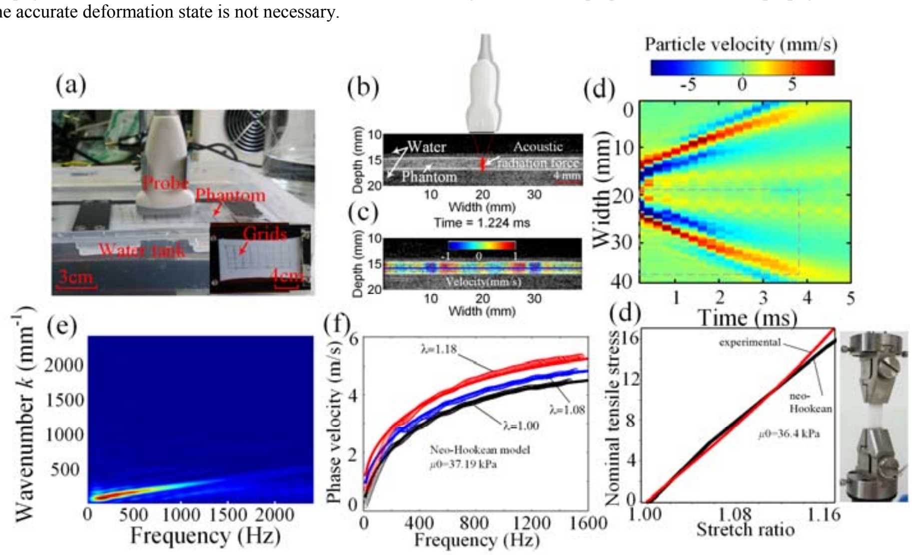

2:45 pm Finite Element Models of Wave Propagation in Embedded Vessels with Simulated Plaques

Matthew Urban[1,2], Kent Carlson[2], Dan Dragomir Daescu[2]; [1]*Department of Radiology, Mayo Clinic College of Medicine and Science, Rochester, MN, USA,* [2]*Department of Physiology and Biomedical Engineering, Mayo Clinic College of Medicine and Science, Rochester, MN, USA*

Background, Motivation and Objective

Carotid plaque vulnerability is difficult to characterize from B-mode ultrasound imaging alone. However, elastographic characterization of plaque mechanical properties may aid in the assessment of vulnerability. As an initial step to understand the complex wave propagation that can occur in plaques, we have developed simulation models that incorporate different shear moduli (μ) of the arterial wall, surrounding medium, and plaque. We explored the wave propagation both in longitudinal and transverse imaging planes.

Statement of Contribution/Methods

We developed three-dimensional finite element models (FEMs) of an artery (1 mm thickness, 8 mm outer diameter, μ = 25 kPa) embedded in a medium with μ = 4 kPa. The plaque had a thickness of 2 mm and extended length of 10 mm with a taper at each end. The plaque covered the full circumference of the artery. The shear modulus of the plaque, μ_p, was varied to 5, 10, 20, 30, 50, 100 kPa. A line source, placed 10 mm away from the plaque, was used for excitation to mimic an acoustic radiation force push that excited both walls of the artery in the longitudinal plane and was offset from the plaque/wall complex in the transverse plane. In the transverse plane a push was located on each side of the plaque. The FEM motion was used to calculate the wave velocity images using a two-dimensional (2D) wave speed algorithm (Song, et al., Ultrasound Med. Biol., vol. 40, pp. 1343-1355, 2014) after directional filters were applied. We also performed 2D Fourier analysis to examine the dispersion of the wave velocities in the wall and plaque in the longitudinal plane.

Results/Discussion

The figure shows wave velocity maps created when the plaque had μ_p = 10 and 100 kPa. There is a distinct difference between the wave velocity in the wall and the plaque for μ_p = 100 kPa. This difference is more subtle when μ_p = 10 kPa. The wave velocities were typically lower than the shear wave velocities of media with the same shear moduli due to the complex wave propagation involving multiple layers as detailed by the data summarized in the table. The percent errors ranged from -47-+18%. These models highlighted the complex wave propagation involved, even in homogeneous plaques, and will provide a foundational tool for understanding the estimation of material properties from measured wave velocities in patient studies.

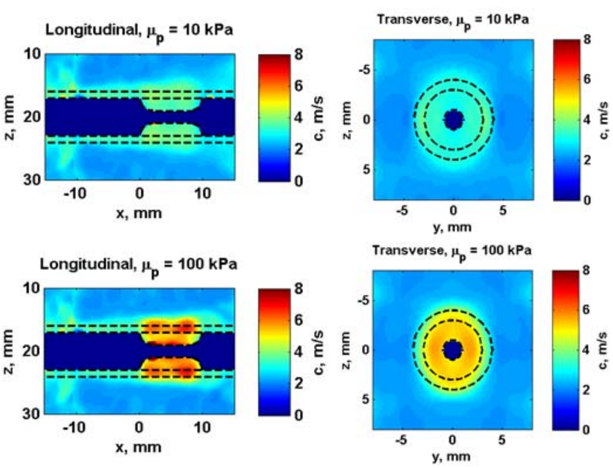

Plaque	Longitudinal			Transverse	
	Distant Wall	Adjacent Wall	Plaque	Wall	Plaque
5 kPa	3.35 ± 0.35	3.55 ± 0.22	3.25 ± 0.42	3.08 ± 0.29	2.65 ± 0.23
10 kPa	3.36 ± 0.36	3.77 ± 0.26	3.65 ± 0.37	3.33 ± 0.20	3.21 ± 0.16
20 kPa	3.38 ± 0.39	4.23 ± 0.28	4.07 ± 0.32	3.74 ± 0.24	3.79 ± 0.14
30 kPa	3.39 ± 0.39	4.44 ± 0.39	4.40 ± 0.47	4.03 ± 0.35	4.23 ± 0.15
50 kPa	3.39 ± 0.38	4.91 ± 0.60	4.95 ± 0.69	4.28 ± 0.51	4.79 ± 0.15
100 kPa	3.38 ± 0.36	5.76 ± 0.70	5.77 ± 1.23	4.28 ± 0.64	5.28 ± 0.23

Figure 1. Longitudinal plane (left column) and transverse plane (right column) wave velocity images for plaque moduli of 10 and 100 kPa. The table summarizes mean and standard deviations of wave velocities in the wall and plaque from the longitudinal and transverse planes for various plaque moduli. The plaque wave velocities increase with plaque modulus but are typically biased low compared to their respective shear wave velocities.

6J - Ultrasound Imaging Devices II

Hampton Room

Saturday, September 9, 2017, 1:30 pm - 3:00 pm

Chair: **Charles Emery**
Ulthera Inc.

6J-1

1:30 pm **Multi-Frequency CMUT Imaging Arrays for Multi-Scale Imaging and Imaging-Therapy Applications**

Mohammad Maadi[1], Benjamin Greenlay[1], Christopher Ceroici[1], Roger Zemp[1]; [1]*Electrical and Computer Engineering, University of Alberta, Edmonton, Alberta, Canada*

Background, Motivation and Objective

Multi-frequency transducers may have a number of emerging applications including multi-scale imaging, superharmonc contrast imaging and imaging-therapy applications. For imaging-therapy applications low-frequencies are typically needed for therapeutic heating or contrast agent destruction, while higher-frequencies are required for high-resolution imaging. However, development of these multi-frequency transducers is challenging owing to disparate focal zones or difficult acoustic impedance matching. Recently we introduced CMUT-based multi-frequency transducers with small- and large- membranes interlaced on a scale smaller than the acoustic wavelengths. We have demonstrated the utility of small feasibility arrays for multi-band photoacoustic imaging but have yet to demonstrate co-aligned low-and-high frequency pulse-echo ultrasound with larger arrays.

Statement of Contribution/Methods

Large- and small CMUT membranes were fabricated in an interlaced fashion such that the pitch of high-frequency sub-arrays were 1λ or 2λ. This design ensures minimization of grating lobes. Arrays were fabricated using a modified sacrificial release process using silicon nitride membranes and metal top electrodes. Arrays of various sizes up to 128 elements were fabricated and wafers were diced to form singulated arrays which were wire-bonded to custom "surf" boards mounted onto a custom interfacing board with voltage-protected pre-amplifiers, connected to a Verasonics programmable ultrasound platform. This system enabled realtime imaging and programmable control over low- and/or high-frequency transmission and reception. To demonstrate co-aligned beams from the low- and high-frequency sub-arrays hydrophone measurements were conducted demonstrating minimal grating lobes and co-aligned beams. To demonstrate multi-band imaging, wire targets were imaged.

Results/Discussion

Fig. 1a illustrates imaging with different of high- and low-frequency transmit and receive combinations. Fig. 1b shows the array, and Fig 1c shows resolution measurements as a function of depth for the high- and low-frequency combinations. Fig 1d shows a photograph of the wirebonded array. Results show promise for novel multi-scale multi-resolution imaging, imaging-therapy modes, superharmonic imaging and other applications.

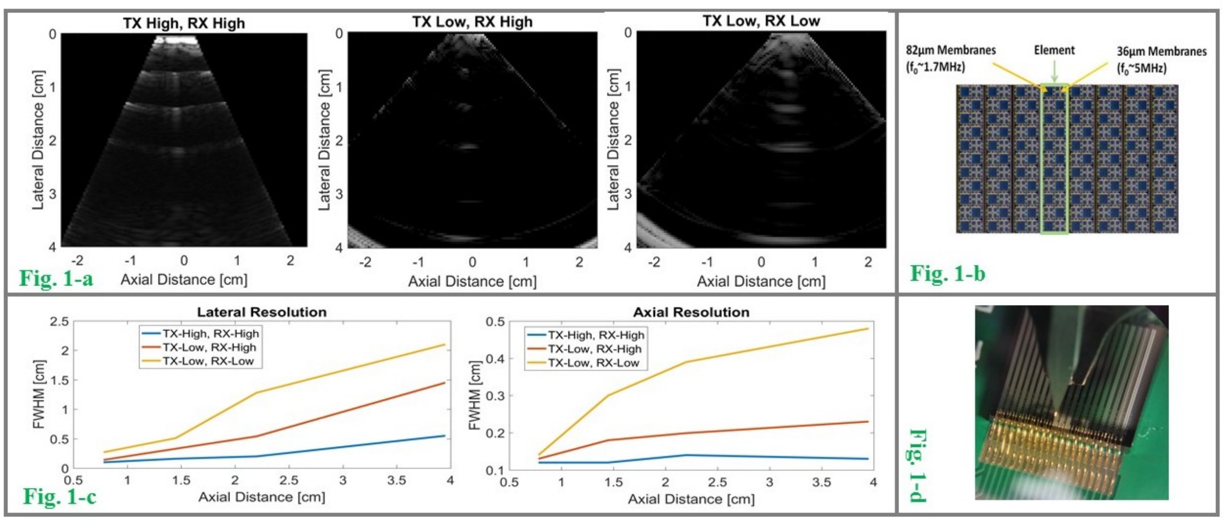

6J-2

1:45 pm **Characterization of a Prototype Transmit 2 MHz Receive 21 MHz Array for Superharmonic Imaging**

Isabel G. Newsome[1], Brooks D. Lindsey[1], Sarah E. Shelton[1], Emmanuel Chérin[2], Jinhua Yin[2], F. Stuart Foster[2,3], Paul A. Dayton[1]; [1]*Joint Department of Biomedical Engineering, University of North Carolina at Chapel Hill and North Carolina State University, North Carolina, USA,* [2]*Sunnybrook Research Institute, Toronto, Canada,* [3]*Department of Medical Biophysics, University of Toronto, Toronto, Canada*

Background, Motivation and Objective

The role of angiogenesis in cancer development has spurred much research in the medical field, including new methods to visualize new vasculature. One such method is "acoustic angiography," a superharmonic contrast-enhanced ultrasound imaging technique. Using prototype dual frequency (DF) transducers to transmit at 4 MHz and receive at 25-30 MHz, this technique is able to resolve vessels of 150 µm and create images for morphological analysis. However, the prototypes used are confocal single element transducers with fixed foci that require mechanical scanning. In this work, we present initial tests of a DF array for superharmonic contrast-enhanced microvascular imaging.

Statement of Contribution/Methods

The DF array used here combines a prototype low frequency (LF) device with the high frequency (HF) MS250 probe and Vevo 2100 scanner from VisualSonics. The LF device is used to transmit at 1.7 MHz, while the HF probe is used to receive at 21 MHz. For this work, an in-house formulation of lipid shelled, perfluorocarbon core microbubble contrast agent was used. The pressure profile of the LF device was characterized by hydrophone measurements. In vitro testing was performed to evaluate the contrast-to-tissue ratio (CTR) of the DF array at various transmit pressures and bubble dilutions. A tissue-mimicking graphite-gelatin phantom with a 1 mm diameter wall-less channel 7.5 mm below the phantom surface was used as a target for CTR measurements.

Results/Discussion

Results of this work illustrate the utility of a DF array transducer for expanding the use of acoustic angiography. Representative images of the in vitro data collected in this work are shown in Fig. 1, parts A and B. Fig. 1A shows a B-mode image of the channel, while Fig. 1B shows an image collected in DF-mode with contrast at the same position. Fig. 1C provides a pressure map (in kPa) of the beam profile of this device, and Fig. 1D presents the CTR data as a function of transmit pressure for contrast concentrations of 1e6, 1e7, and 1e8 bubbles/mL. A maximum CTR of 21.4 dB was obtained. The focal depth for the currently used prototypes is 1.3 cm, while the DF array exhibits a focal depth of 2.2 cm. Similarly, the field of view for the current probes is approximately 2.4 cm in width and 1.5 cm in depth, while the DF array provides a field of view that is 2.3 cm in width and 3 cm in depth.

Fig. 1

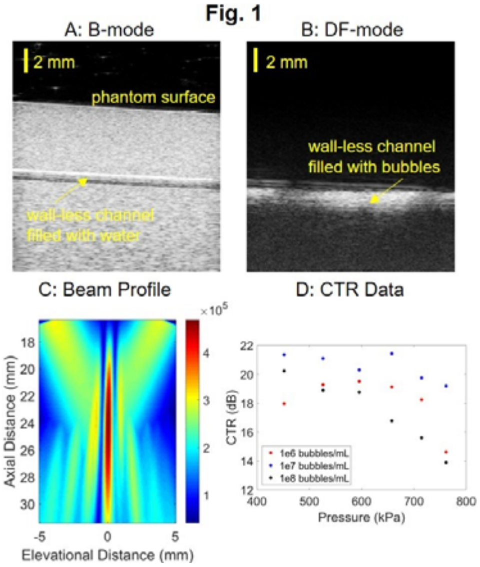

6J-3

2:00 pm Micromachined 1-3 Composite Dual Frequency IVUS Array for Contrast Enhanced Intravascular Ultrasound Imaging

Sibo Li[1], Huaiyu Wu[1], Jinwook Kim[1], Sunny Kasoji[2], Paul A. Dayton[2], Xiaoning Jiang[1]; [1]*Mechanical and Aerospace Engineering, North Carolina State University, Raleigh, NC, USA,* [2]*Joint Department of Biomedical Engineering, University of North Carolina and North Carolina State University, Chapel Hill, North Carolina, USA*

Background, Motivation and Objective

Recent studies suggest that microbubbles based contrast enhanced intravascular ultrasound (CE-IVUS) for vasa vasorum assessment is promising in the identification of vulnerable plaques. However, conventional ultrasound is not suitable for imaging modality which demands up to 5th order harmonics for a receiver. To ensure the imaging performance, high-frequency broadband micromachined 1-3 composites is considered for receivers for their superior electromechanical coupling coefficient and relatively low acoustic impedance. Also, IVUS arrays are desirable for their capability of beam steering, sub-aperture firing, and higher frame rates. In our study, a dual-frequency IVUS array with micromachined 1-3 composites was developed as receiver for superharmonic imaging.

Statement of Contribution/Methods

The dual frequency IVUS array consists of an 8-element 7 MHz PZT-5H 1-3 composite transmitting array (TX) and a 32-element 35 MHz micromachined PMN-PT single crystal 1-3 composite receiving array (RX). A frequency selective isolation layer was designed between RX and TX elements to minimize the acoustic interference from each other. The dimension of TX element is designed 3 mm in elevation and 0.4 mm of pitch spacing, the RX element is designed 1.2 mm in elevation and 0.16 mm of pitch spacing.The TX elements were wrapped onto a Φ1.2 mm needle, and the RX elements were wrapped onto the TX element resulting in ~Φ1.7 mm. The prototyped dual-frequency IVUS array was then acoustically characterized using pulse-echo measurements for the TX and RX elements. Contrast tests are to be performed in a tissue mimicking phantom by exciting microbubbles through a cellulose tube (200 μm) using the 7 MHz transmitting array while detecting the microbubble superharmonics using the 35 MHz receiving array.

Results/Discussion

Characterization results show that the capacitance and dielectric loss of the RX elements are 56 pF and 78 mU, respectively; and those of transmitting elements are 300 pF and 19 mU, respectively. The center frequency of the receiving array is 37 MHz with the -6dB fractional bandwidth of 78 %. The TX elements can be used to produce acoustic pressure > 1 MPa at 100 V excitation, which is sufficient to induce non-linear response from microbubbles. The contrast imaging tests using the prototyped dual frequency array is being performed and the details will be reported in the full paper.

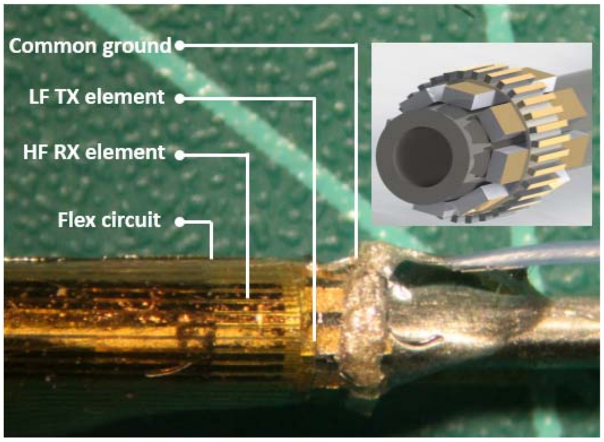

Figure 1 Photograph of dual-frequency IVUS array prototype

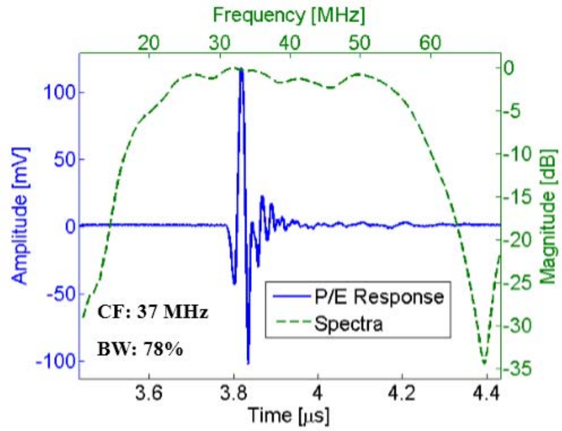

Figure 2 Pulse-echo results of micromachined PMN-PT 1-3 composite receiver

6J-4

2:15 pm Forward-Looking IVUS Transducer with Front-End ASIC for 3D Imaging

Jovana Janjic[1], Mingliang Tan[2], Chao Chen[2], Zhao Chen[2], Emile Noothout[3], Zu-yao Chang[2], Gijs van Soest[1], Martin Verweij[3], Antonius F. W. van der Steen[1], Michiel Pertijs[2], Nico de Jong[1]; [1]*Biomedical Engineering, Erasmus MC, Netherlands,* [2]*Electronic Instrumentation Laboratory, Delft University of Technology, Netherlands,* [3]*Lab. Of Acoustical Wavefield Imaging, Delft University of Technology, Netherlands*

Background, Motivation and Objective

Forward-looking intravascular ultrasound (FL-IVUS) transducers are needed to image complex lesions in the coronary arteries, such as chronic total occlusions (CTOs). To achieve 2D and 3D FL-IVUS imaging, transducer arrays can be integrated at the tip of the catheter. However, connecting the elements is challenging due to the limited space available. In this work, we present a FL-IVUS matrix transducer consisting of 16 transmit and 64 receive elements, which are interfaced with an ASIC that requires only 4 micro-coaxial cables. The transducer performance was characterized by hydrophone measurements and FL imaging of three spherical reflectors.

Statement of Contribution/Methods

The transducer design and a photo of the 2D array on top of the ASIC after dicing are shown in Fig 1 (a) and (b). The circuits on the ASIC are laid out in a donut-shaped area with an outer diameter of 1.5 mm and a central hole of 0.5 mm for guide wire insertion (not visible in Fig. 1(b)). Each transducer element (80x80 μm^2) consists of a stack of backing, PZT and matching material and is connected to the ASIC via a bond pad. High-voltage switches and a multiplexer in receive enable transmission from one or multiple transmit elements and acquisition of the echo signal by one receive element at a time. The ASIC area includes also 5 bond pads connected to 4 micro-coaxial cables and to ground. The ASIC is mounted on a PCB for testing. A water bag made of acoustically transparent material is placed on top of the transducer. Pulse-echo measurements with neighboring transmit and receive elements are performed using a flat steel reflector. For imaging experiments, three needles with steel sphere at the tip are placed in water at different distances from the transducer surface (Fig. 1(d)).

Results/Discussion

Pulse-echo measurements show that the transducer center frequency is 12 MHz and the -6 dB bandwidth is 45 % (Fig. 1(c)). All transmitters were working with an average transmit sensitivity of 0.62 kPa/V at 3 mm, while 46 out of 64 receivers showed acceptable acoustic performance. We were able to successfully image the spheres using synthetic aperture beamforming (Fig. 1 (e)-(g)). These initial imaging results demonstrate the feasibility of 3D FL-IVUS imaging through only 4 cables addressing a total of 80 elements via the front-end ASIC. We will further optimize the acoustic stack fabrication for better imaging performances.

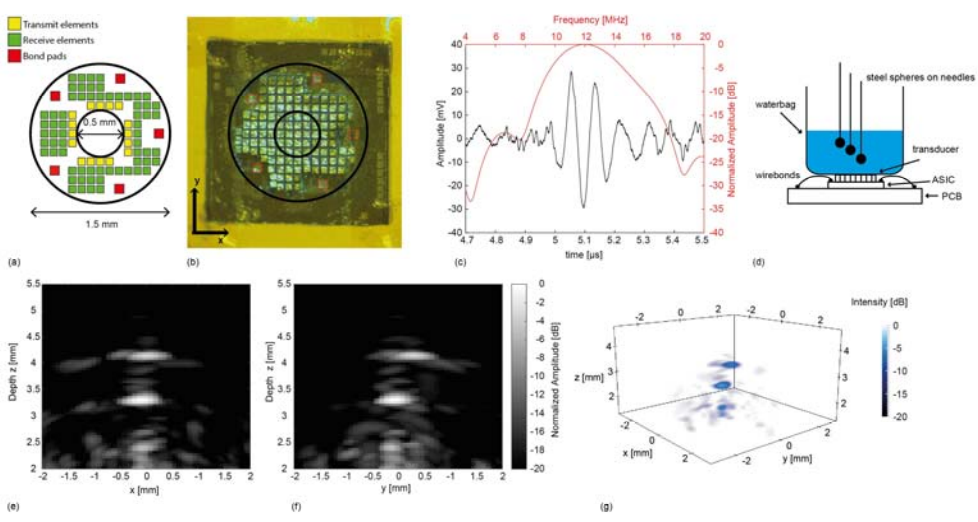

Fig 1. (a) Schematic drawing of the transducer design, (b) picture of the transducer on top of the ASIC after dicing, (c) pulse-echo and frequency response from neighboring transmit and receive elements, (d) experimental set-up for imaging, (e) maximum projections along the y and (f) x direction, (g) 3D rendered ultrasound image.

6J-5

2:30 pm Intravascular Shear Wave Propagation Using Acoustic Radiation Force Generation from a 4.6 Fr Transducer Element

Arsenii Telichko[1], Carl Herickhoff[1], Dongwoon Hyun[2,3], Jeremy Dahl[1]; [1]*Radiology, Stanford University, Stanford, CA, USA,* [2]*Biomedical Engineering, Duke University, Durham, NC, USA,* [3]*Bioengineering, Stanford University, Stanford, CA, USA*

Background, Motivation and Objective

Cardiovascular disease, including atherosclerosis and critical limb ischemia, affects millions of people worldwide. There is a clinical need to base treatment decisions on quantitative analysis of the plaque composition. However, no reliable clinical methods to quantify the mechanical properties of plaque components and detect plaque vulnerability currently exist, particularly for coronary disease.

Here we demonstrate the measurement of shear waves generated by acoustic radiation force (ARF) from an intravascular ultrasound (IVUS) transducer prototype, as a potential means to quantifiably assess vascular plaques.

Statement of Contribution/Methods

A single-element IVUS transducer prototype with shear wave elasticity imaging is a minimally-invasive state-of-the-art technique capable of distinguishing soft lipid cores from stiffer surrounding tissues. The transducer was fabricated using a radially-poled PZT-4 ceramic cylinder, with outer diameter of 4.6 Fr (1.53 mm) and wall thickness of 0.3 mm. The cylinder was cut to a length of 2 mm with a dicing saw and mounted on a stainless steel needle tube.

The cylindrical transducer was connected to a function generator and power amplifier, and placed horizontally at a depth of 20 mm in a gel phantom having a verified shear wave velocity of 0.2 m/s. A high-frequency linear array transducer was placed on top of the phantom to track displacements in planes normal to the prototype's cylindrical axis. A Verasonics ultrasound research scanner was used to (1) trigger an ARF excitation from the prototype transducer to generate radial displacements from a toroidal beam, and (2) subsequently acquire and process RF data from the high-frequency array to track displacement vs. time in the phantom to detect shear waves (see Figure).

Results/Discussion

When measured with a hydrophone in a water tank, the ARF excitation from the single-element IVUS prototype transducer generated a peak-to-peak pressure of 2.6 MPa at a 1-mm radial distance from the transducer face. In the gel phantom, the external linear array measured the maximum displacement from this excitation to be 10.8 microns in a plane 4 mm from the prototype transducer. A shear wave velocity of 0.17 m/s was measured with the external linear array. These results show that it is possible to track the propagation of shear waves generated from an IVUS transducer to assess plaque tissues.

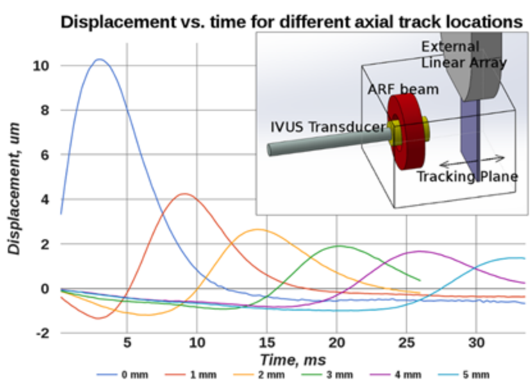

6J-6

2:45 pm Fabrication and Performance of a 128-Element Crossed-Electrode Relaxor Array, for a Novel 3D Imaging Approach

Katherine Latham[1], Christopher Ceroici[2], Christopher Samson[1], Roger Zemp[2], Jeremy Brown[1]; [1]*School of Biomedical Engineering, Dalhousie University, Canada,* [2]*Electrical and Computer Engineering, University of Alberta, Canada*

Background, Motivation and Objective

3D Ultrasound systems present several technical challenges, particularly the large number of elements in a 2D array, high electrical impedance, and image acquisition time. Crossed electrode arrays address some of these issues, especially the huge reduction in number of elements. However, creating a two-way focused 3D image in real-time is difficult with these arrays because azimuth and elevation dimensions cannot be beamformed at the same time. This typically forces one to use a synthetic aperture approach which is inherently slow and requires increased beamforming complexity over a 1D array.

We have developed a new, fast and simple 3D imaging approach referred to as Simultaneous Azimuth and Fresnel Elevation (SAFE) compounding. The principle behind this technique is to perform conventional plane wave compounding with the top set of electrodes, while implementing a reconfigurable Fresnel elevation lens with the bottom electrodes. While a Fresnel lens would usually result in unacceptable secondary lobe levels, these lobes can be suppressed by compounding different Fresnel patterns. Since plane wave imaging already compounds the same slice repeatedly, the elevation Fresnel lens can be simultaneously compounded to increase the beam quality, resulting in no loss in frame rate. In this study, the design, fabrication, and characterization of a crossed electrode array based on an electrostrictive ceramic (eg. Pulse polarity depends on a DC bias) is presented.

Statement of Contribution/Methods

If a Fresnel pattern is changed upon sequential pulsing to focus to n spatially different focal spots that are nearby, but separate enough that the Fresnel pattern changes, the pressure fields can be averaged to reduce side lobe energy. It is equivalent to averaging n pressure fields, each with random beamforming delay errors quantized to $\lambda/2$. The compounded Fresnel lens is also capable of steering, thus enabling collection of multiple elevation slices with no added beamforming complexity.

A 10MHz, 64x64 element crossed electrode relaxor array was fabricated on a electrostrictive 1-3 composite substrate to reduce crosstalk and increase the element directivity. The array was designed with λ pitch and a single quarter wavelength matching layer. 2D images were generated using a Verasonics Vantage system with custom biasing electronics, using plane wave compounding in the azimuth while simultaneously compounding the Fresnel lens in elevation, demonstrating the SAFE compounding technique.

Results/Discussion

The electrostrictive composite array has a measured electromechanical coupling coefficient (kt) of 0.63 with a bias voltage of 90V and a measured two-way pulse bandwidth of 60%. The electrical impedance magnitude on resonance was measured to be 70 ohms with a phase angle of -40 degrees. 2D images were generated of a wire phantom in a water bath using the SAFE compounding technique. Data collection for elevation steering and volumetric 3D imaging is ongoing.

7J - Microacoustic Sensor and Lamb Wave Devices

Empire Room

Saturday, September 9, 2017, 1:30 pm - 3:00 pm

Chair: **Mauricio Pereira da Cunha**
University Maine

7J-1

1:30 pm SAW Resonators for Magnetic Field Sensing with ($TbCo_2$/FeCo) Multilayered IDTs as Sensitive Layer

Harshad Mishra[1], Vincent Polewczyk[1], Mohammed Moutaouekkil[1], Nicolas Tiercelin[2], Cécile Floer[1], Michel Hehn[1], Karine Dumesnil[1], Sami Hage-Ali[1], Abdelkrim Talbi[2], Omar Elmazria[1]; [1]*Institut Jean Lamour UMR 7198, Université de Lorraine - CNRS, Nancy, France,* [2]*LIA LEMAC/LICS - IEMN UMR CNRS 8520, ECLille - USTL, PRES Université Lille Nord de France, Villeneuve d'Ascq, France*

Background, Motivation and Objective

In previous studies [1,2] we have shown the possibility to realize wireless magnetic SAW sensors with a delay line configuration using layered structures. SAW devices in resonator configuration with Ni interdigital transducers (IDT) on the substrate were also investigated by Kadota et al. [3]. The physical phenomena behind sensor behavior is still unclear and the interpretation of the results is not fully in line with the proposed theoretical models. This work aims to understand the physics and the interaction between acoustic waves and magnetostrictive layers under magnetic fields. Here, we investigate multilayer ($LiNbO_3$/($TbCo_2$/FeCo)) SAW structures with different geometries and configurations.

Statement of Contribution/Methods

200nm of 20 × $TbCo_2$ (5nm) /FeCo(5nm) layers were deposited over 128 Y-cut $LiNbO_3$ substrates, one with the easy axis along X and the other along (X+90°). Using photolithography and etching, synchronous single port resonators were fabricated using these stacks as electrodes. Resonators with two wavelengths were fabricated with wave propagation along both X and (X+90°) directions, enabling a comprehensive study. Vibrating sample magnetometer (VSM) tests were conducted from 0° to 90° rotation of the sample (in-plane) to study the effect of the anisotropy on the magnetization. The resonators frequency shifts were measured under magnetic field with a VNA and temperature coefficient of frequency (TCF) measurements provide a base to nullify the effects of the temperature drift.

Results/Discussion

The magnetic properties (Fig 1.a &b) are independent of the substrate crystalline direction. As shown in Fig.1.c, the SAW sensor is sensitive in 3 directions of the magnetic field (parallel and perpendicular to the acoustic wave propagation, and out of plane). The sensitivities range from 0.1 to 1.1 ppm/mT for the 544 MHz Rayleigh wave, considering a measured TCF of -78ppm/°C. Our experimental study includes 3 of the magnetic field, 2 easy axis directions and 2 acoustic wave propagation directions. A bulk acoustic wave was also studied and a sensitivity of 3 ppm/mT was obtained in the 883 MHz range. Theoretical and numerical calculations are in progress to fully comprehend the experimental results.

[1] M. Elhosni et al., Sensors and Actuators A 240 (2016) 41–49.

[2] H. Zhou, PhD Thesis, ECLille, 2014

[3] Kadota et al., Jpn. J. Appl. Phys. 50 (2011) 07HD07

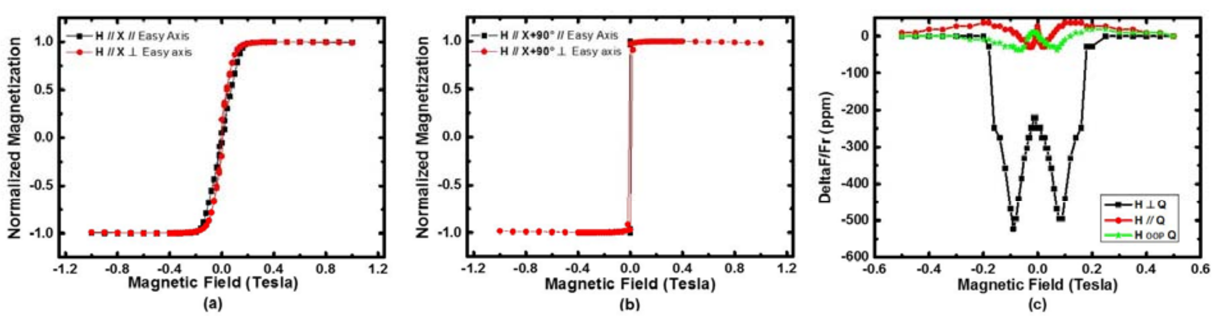

Figure 1. Magnetization curves along in-plane directions X and (X+90°): (a) for parallel and (b) for perpendicular orientation of crystallographic direction (with respect to direction of magnetic field); (b) Comparison of the sensitivity of the sensors for magnetic field (H) applied along the direction of propagation of wave (Q) (parallel), perpendicular to it and out of plane.

7J-2

1:45 pm Wideband Material Detection for Spoof Resistance in GHz Ultrasonic Fingerprint Sensing

Justin Kuo[1], Amit Lal[1]; [1]*Cornell University, USA*

Background, Motivation and Objective

One of the primary motivations for using ultrasound reflectometry for fingerprint imaging is the promise of increased spoof resistance over conventional optical or capacitive sensing approaches due to the ability for ultrasound to determine the elastic impedance of the imaged material. A fake 3D printed plastic finger can therefore be easily distinguished from a real finger. However, ultrasonic sensors are still vulnerable to materials that are similar in impedance to tissue, such as water or rubber.

Previously we demonstrated an ultrasonic fingerprint reader operating with 1.3GHz ultrasound based on pulse echo impedance imaging on the backside silicon interface. In this work, we utilize the large bandwidth of these sensors to differentiate between a finger and materials with similar impedances using the frequency response of elastic impedance obtained by transducer excitation with a wideband RF chirp signal. The reflected signal is a strong function of impedance mismatch and absorption [Hoople 2015].

Statement of Contribution/Methods

An unreleased 100 um wide square AlN transducer fabricated at the Institute of Microelectronics (A*STAR IME, Singapore) is used as the pulse-echo transducer (Fig. 1B). The transducer is driven by a 100 ns wide chirp pulse, with linear frequency variation from 1 GHz to 1.5 GHz, synthesized by an arbitrary waveform generator (Fig. 1A) and amplified to 4 V amplitude. The received echo, after amplification, is acquired by a high frequency oscilloscope. The FFTs of the received echoes for loading with a finger, rubber, water and air are compared to determine frequency response differences.

Results/Discussion

The high resonance frequency and low quality factor of these devices enables measurement of frequency responses over bandwidths of approximately 400MHz and 100 MHz around the 1.3GHz and 2.4 GHz resonances, respectively – a much greater frequency range than what conventional MHz frequency and high Q ultrasonic fingerprint sensors can offer. From the chirp excitation, we see a difference between the spectral responses of the received echoes with different loading conditions (Fig. 1C),. While at several frequencies, the impedances of water, rubber, and finger are indistinguishable, at others, the signal level can vary by as much as 4 to 6%. This contrast can be used to distinguish materials, providing greater spoof tolerance.

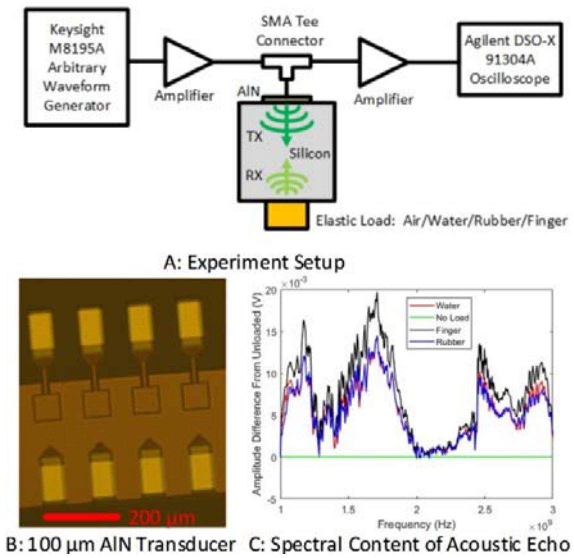

7J-3

2:00 pm An 8-Channel CMUT Chemical Sensor Array on a Single Chip

Quintin Stedman[1], Kwan Kyu Park[2], Butrus T. Khuri-Yakub[1]; [1]*Stanford University, Stanford, CA, USA,* [2]*Hanyang University, Korea, Republic of*

Background, Motivation and Objective

CMUTs make very sensitive gravimetric chemical sensors in air. Selectivity can be improved by using arrays of these sensors with different functionalization coatings. However, operating multiple sensor on the same chip can be challenging because of sensor frequency locking and greater difficulty of functionalization. In prior work, or only two or three sensors have been used at once on the same chip. Here, we present results showing the simultaneous operation of 8 CMUT chemical sensors on a single chip, and demonstrate the ability of the sensor array to recognize chemicals in air.

Statement of Contribution/Methods

Chips with 10 CMUT chemical sensors each were fabricated. The sensors were functionalized using polymers applied in solution to the surface of each sensor using microsyringes. Each sensor was surrounded by isolation trenches etched in the chip to prevent polymer solution from leaking onto neighboring devices. The sensor frequencies were measured simultaneously using op-amp-based oscillator circuits. Different DC bias voltages were applied to different elements using voltage dividers in order to separate the sensor frequencies and prevent the oscillators from locking.

Results/Discussion

The eight sensors exhibit no locking. Part (a) of the figure shows the response of 8 sensors, operated simultaneously, to water vapor in nitrogen. The sensor responses are labeled with the polymer used for functionalization. The sensors operate at 29-31 MHz. Water vapor is introduced at 1 minute and removed at 4 minutes. Part (b) of the figure shows a principal component analysis plot of the sensor responses to mixtures of water vapor and ammonia and demonstrates the ability of the sensor system to distinguish different ammonia levels in a background of water vapor. Additionally, the sensor can distinguish water, methanol, ethanol, acetone, and the ammonia-water mixtures in the plot with 100% accuracy when used with a support vector machine pattern recognition algorithm. This is the first demonstration of more than three CMUT chemical sensors operated simultaneously on a single chip, and represents progress towards a practical CMUT chemical sensor system.

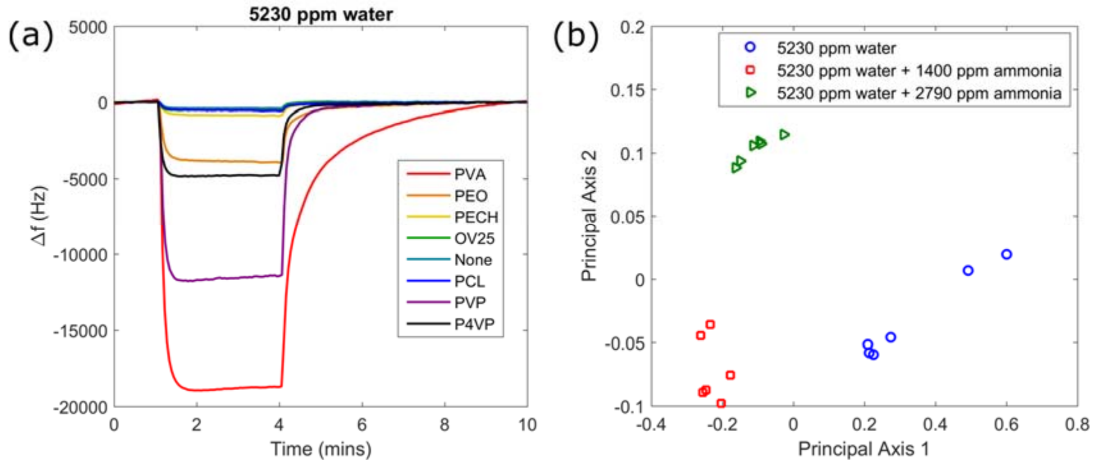

7J-4

2:15 pm **AlN/ZnO/LiNbO$_3$ Packageless Structure as a Low-Profile Sensor for On-Body Applications**

Cécile Floer[1], Mohammed Moutaouekkil[1], Florian Bartoli[1,2], Harshad Mishra[1], Sami Hage-Ali[1], Stefan Mc Murtry[1], Philippe Pigeat[1], Thierry Aubert[2], Olivier Bou Matar[3], Abdelkrim Talbi[3], Omar Elmazria[1]; [1]*Institut Jean Lamour UMR 7198, Université de Lorraine - CNRS, Nancy, France,* [2]*LMOPS EA 4423, CentraleSupélec - Université de Lorraine, Metz, France,* [3]*LIA LEMAC/LICS - IEMN UMR CNRS 8520, ECLille - USTL, PRES Université Lille Nord de France, Villeneuve d'Ascq, France*

Background, Motivation and Objective

Surface acoustic wave (SAW) devices are widely used as filters or resonators for mobile communications or radars applications. However, the velocity of the wave can be very sensitive to physical parameters of the environment (temperature, strain…), which allows the device to be used as a sensor. SAW devices are passive (batteryless) and wireless, but are often bulky due to the package. To dramatically reduce their profile, it is possible to use a Wave-guiding Layer Acoustic Wave (WLAW) structure, which consists of a low velocity layer between two higher velocity layers. These structures have the potential to be ultra-thin and conformable and thus could be used for flexible on-body biomedical applications. This work investigates the AlN/ZnO/LiNbO$_3$ structure as a candidate for a WLAW temperature sensor.

Statement of Contribution/Methods

First, the structure was studied by a 2D-FEM modelling to maximize the electromechanical coupling coefficient K^2 (ZnO thickness) and to determine the minimum required AlN thickness for the wave confinement (see Fig.1a and 1b). Then, for the experimental part, a single port synchronous resonator with a wavelength of 4.4 µm, was designed and then fabricated with e-beam lithography and chemical etching on the piezoelectric substrate (LiNbO$_3$). Then, 2 µm of ZnO followed by 8 µm of AlN (in two steps: 2 µm AlN, then 6 µm AlN) were deposited on the top of the electrodes using reactive magnetron sputtering (see Fig.1c).

In order to check experimentally the confinement of the wave in a WLAW device, a soft matter can be placed on the top of it at different stages of the process. Here the silicone elastomer Solaris has been chosen (see Fig.1d) for its simplicity of use and its properties which are comparable to those of the skin (E_{Young}=50 kPa). If no change occurs to S parameters, then it proves that the wave is confined.

Results/Discussion

Considering large thickness of top and bottom layers, calculations show that the maximum K^2 is obtained for 2 µm of ZnO. With this thickness, at least 7 µm of AlN are required to fully confine the wave. Experimentally, with 2 µm of AlN, an impedance change is clearly notable and confirms that the wave requires a thicker layer of AlN to be confined. With 8 µm of AlN, the Solaris perturber has no impact on the signal and thus prove that the studied structure can be used for packageless SAW sensors.

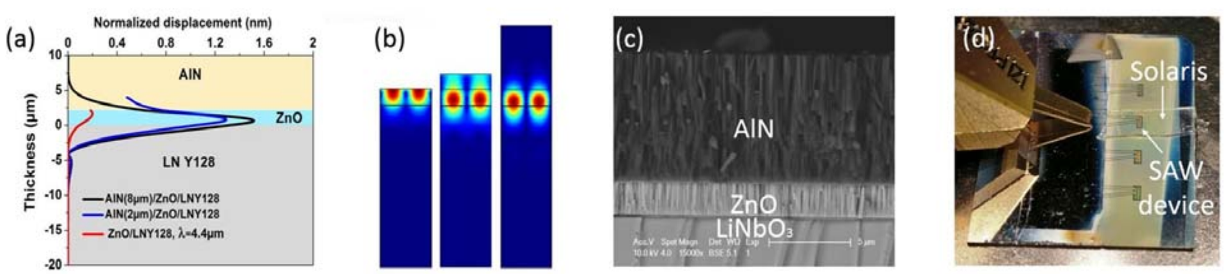

Fig. 1. (a) (b) 1D/2D Comsol modellings of particle displacements in a LiNbO$_3$/ZnO structure with 0 µm, 2 µm and 8 µm of AlN, respectively, on top of it: the wave is confined in the latter case, (c) SEM visualization of the device cross-section (LiNbO$_3$/ZnO/AlN), (d) Probe station measurement of the electrical impedance of a SAW resonator with an elastomeric Solaris perturber

7J-5

2:30 pm A 3.5 GHz Hybrid Wideband RF Filter Using AlN S1 Lamb Mode Resonator

Anming Gao[1], Jie Zou[2], Songbin Gong[1]; [1]*Department of Electrical and Computer Engineering, University of Illinois at Urbana-Champaign, Urbana, IL, USA,* [2]*Department of Mechanical Engineering, University of California, Berkeley, CA, USA*

Background, Motivation and Objective

High frequency bands such as LTE band 42 and band 43 require resonators and filters that can operate at frequencies higher than 3 GHz. However, existing lithium niobate fundamental symmetric (S0) lamb mode resonators and surface acoustic wave (SAW) resonators have operating frequency limitations (<2 GHz) due to their low phase velocities. High frequency AlN film bulk acoustic resonators (FBARs) suffer from the deteriorated crystallization and power handling issues due to the thin AlN film. High frequency AlN S0 lamb mode resonators encounter lithography and power handling challenges because of their narrow pitch. The first-order symmetric (S1) lamb mode in AlN shows a very high phase velocity and is promising in building high frequency resonators and filters. This work thoroughly investigates the S1 lamb mode resonator and extends its application to high frequency RF filters with a hybrid topology.

Statement of Contribution/Methods

Characterizations of the S1 lamb mode in AlN are first carried out to guide the optimization of the resonator design. S1 lamb mode has a much high phase velocity and this qualifies its use for high frequency resonators and filters. The effective electromechanical coupling (k_t^2) of the S1 lamb mode reaches its maximum of 3.6% when $h_{AlN}/\lambda = 0.1$. Duty factor (DF) affects the occurrence of spurious modes. Increasing the DF to 0.8 favors the suppression of spurious modes and the k_t^2. Combining the desire for high frequency, high k_t^2, and smaller spurious modes, h_{AlN} and DF are chosen to be 1 μm and 0.8. The optimized S1 lamb mode resonator consists of top interdigitated transducers (IDTs), a suspended AlN film, and a floating bottom electrode (Fig. 1). Finite element analysis shows an expected S1 lamb mode at 3.44 GHz with a k_t^2 of 3.6% (Fig. 2).

Results/Discussion

With excellent agreement with simulations, the fabricated S1 lamb mode resonator shows a resonating frequency at 3.5 GHz, a k_t^2 of 3.59%, and a Q of 550 (Fig. 3). It has the highest product of $f \cdot Q \cdot k_t^2$ among S1 lamb mode resonators to date. The proposed hybrid filter consists of the fabricated S1 lamb mode resonator, a paralleled inductor L0, and a pair of three lumped-element matching networks. The hybrid filter features a wide FBW of 7.5%, a low IL of 1.4 dB, and a high out-of-band rejection over 28 dB (Fig. 4). Meanwhile, the S0 spurious mode is suppressed to a negligible level in this filter's response.

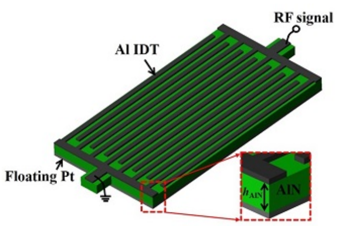

Fig. 1. Mock-up view of the AlN S1 lamb mode resonator.

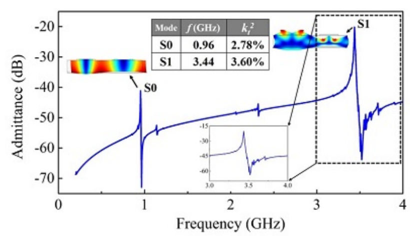

Fig. 2. Simulated response of the AlN S1 lamb mode resonator.

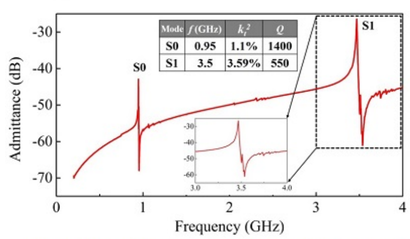

Fig. 3. Measured response of the AlN S1 lamb mode resonator.

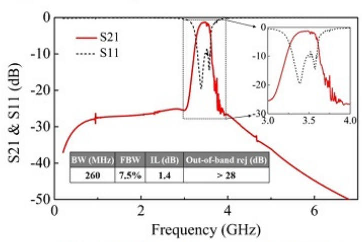

Fig. 4. Simulated response of the hybrid filter.

7J-6

2:45 pm Transverse Mode Suppression in the AlN Lamb Wave Resonators by "Piston Mode"

Jie Zou[1], Chih-Ming Lin[1], CS Lam[1]; [1]*Skyworks Solutions, Irvine, California, USA*

Background, Motivation and Objective

Aluminum nitride (AlN) Lamb wave resonators (LWRs) utilizing the lowest symmetric (S0) mode have attracted much interests since they have high frequencies, low motional impedances, and capability of multiple frequencies on a single chip. However, the transverse spurious modes are often strong in AlN LWR, and largely degrade the performance in application, so suppression the transverse mode is highly desirable to further enable low-loss filters, high-sensitivity sensors and stable oscillators.

Statement of Contribution/Methods

A full analysis on transverse mode of AlN LWR will be done herein. Among various design parameters, the IDT aperture length has the largest impact on transverse modes' position and strengths.

By changing the velocity profile in the direction perpendicular to propagation direction, "piston mode" can be formed which can effectively suppress the transverse modes. Various mass-loading approaches will be compared, including hammer head, extrude on backside, metal strip, and SiO_2 thin layer. The optimized phase velocity profile will be given.

Results/Discussion

As depicted in Fig. 2(a), the transverse modes are very sensitive to the IDT finger aperture length. When the IDT aperture become very small, the transverse modes become fewer but stronger, and the electromechanical coupling coefficient also degrade when the aperture is lower than 10λ; on the contrary, when the IDT aperture become very large, the transverse modes become more in passband but weaker fortunately. Fig. 2(b) shows one example of the strategies to eliminate the transverse modes by lowering the phase velocity near the fast gap region – "piston mode". The optimized DF_{hammer} is found to be 0.7 in this case, in which condition the transverse modes are effectively suppressed. The Lamb wave devices are under fabrication and will be presented in the full paper.

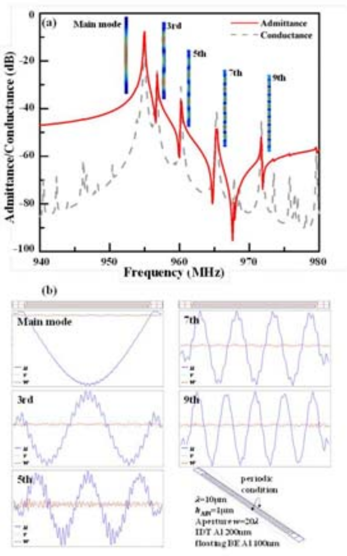

Fig. 1 Transverse modes of AlN LWR (a) in frequency response an (b) their displacement profile.

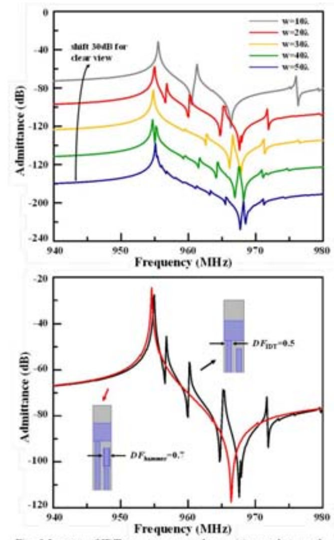

Fig. 2 Impact of IDT aperture w on the position and strengths of the transverse modes (b) suppression of transverse modes by adding loading mass at finger tips to create "piston mode".

1K - MTH: Ultrasound Mediated Delivery

Regency Ballroom

Saturday, September 9, 2017, 4:00 pm - 5:30 pm

Chair: **Elisa Konofagou**
Columbia University

1K-1

4:00 pm **Subwavelength Far-Field Ultrasound Targeted Drug-Delivery**

Vincent Hingot[1], Marine Bezagu[1], Claudia Errico[1], Yann Dessailly[1], Romain Bocheux[1], Mickael Tanter[1], Olivier Couture[1]; [1]*Institut Langevin (CNRS, ESPCI, INSERM), Paris, France*

Background, Motivation and Objective

Recently, the diffraction-limit of resolution for ultrasound imaging has been bypassed in-vivo with the localization of microbubbles [Errico et al, Nature 2015]. However, ultrasound therapy remains bound to the half-wavelength limit, imposing a compromise between the therapeutic precision and its penetration. Exploiting threshold phenomena, such as vaporization or cavitation, could provide a solution to this tradeoff and allow subwavelength energy deposition or drug-delivery.

Statement of Contribution/Methods

In this study, we demonstrate a strategy for subwavelength drug-delivery which relies on the abrupt release threshold of monodisperse (polydispersity<10%) composite droplets along with ultrafast monitoring of their release [Hingot et al, APL 2016]. The inner matrix of the composite droplets, made of perfluorohexane, vaporizes when the pressure reaches a critical level, which releases the aqueous nanodroplets it contains [Couture et al. 2011, Couture et al, 2012]. As the release threshold is very sharp, the release only occurs in the area of the focal spot with a pressure above this threshold. The focal spot can be shaped to make the release spot smaller than the wavelength. We triggered the release of fluorescein droplets at 5 MHz (λ=300 µm) in a cell culture plate with an ultrasound probe connected to a programmable ultrafast ultrasound scanner. A single pulse lasting 4 µs with a peak-negative pressure above 2.5 MPa triggered the release of the droplets. 200 ultrafast images followed the release to highlight the droplets' vaporization.

Results/Discussion

Release spots as small as 70 µm (λ/4.3) could be obtained, and two side-by-side released spots as close as 70 µm could be distinguished with a 8x macroscope (figure 1). We also demonstrated that the release of droplets can be followed acoustically at subwavelength resolution. Such monitoring is essential to the technique, as it highlights the local release threshold. Two side-by-side released spots as close as λ/3 could be distinguished by ultrasound monitoring. Such resolution in drug delivery could improve the accuracy of treatment, especially for very toxic drugs, and limit unwanted delivery in healthy tissues. It could also be useful for therapy in depth or beyond the skull using lower frequencies but maintaining a decent resolution.

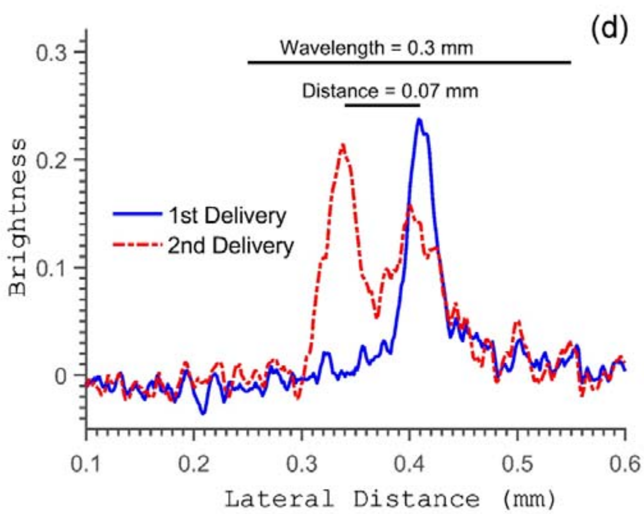

1K-2

4:15 pm **Evaluation of Anticancer Agent Transport in Brain Tumors after Focused Ultrasound-Induced Blood-Brain/Blood-Tumor Barrier Disruption**

Costas Arvanitis[1], Vasileios Askoxylakis[2], Yutong Guo[1], Meenal Datta[2], Jonas Kloepper[2], Miguel Bernabeu[3], Dai Fukumura[2], Nathan McDannold[2], Rakesh Jain[2]; [1]*Georgia Institute of Technology, USA,* [2]*Harvard Medical School, USA,* [3]*University of Edinburgh, United Kingdom*

Background, Motivation and Objective

Blood-brain and blood-tumor barriers (BBB and BTB) constitute a major obstacle to the transport of therapeutics in brain tumors. While several studies have demonstrated the potential of focused ultrasound (FUS) to disrupt transiently the BBB/BTB and improve drug delivery, there is a lack of fundamental understanding of the impact of this method on the pharmacokinetics of anticancer agents in the brain microenvironment. In this study, we examine the impact of FUS-induced BBB/BTB disruption on the transport of two anticancer agent with different properties in a model of breast cancer brain metastases using experimental measurements and drug transport mathematical modeling.

Statement of Contribution/Methods

We implanted human BT474 breast cancer cells in the brain of mice with cranial windows. At a tumor size of ~20-40 mm3, we disrupted the BBB/BTB using FUS exposures in combination with microbubbles. Shortly after sonication, the auto-fluorescent chemotherapeutic agent doxorubicin (Dox) or the antibody-drug conjugate ado-trastuzumab emtansine (T-DM1) was administered i.v.. Using intravital multiphoton microscopy we measured the pharmacokinetics of Dox for 20 minutes. In separate experiments, we also determined the intratumoral penetration of T-DM1 through tissue staining for human IgG. Next, we developed a convection-diffusion-reaction model of drug transport with different reaction terms for the two molecules. We then inferred model parameters (vessel permeability, porosity, etc) from the experimental data under the different conditions tested, using a numerical optimization procedure. Finally, based on the fitted values, we performed a sensitivity analysis in order to determine the most important parameters that affect the drug transport and cellular uptake in the tumor interstitium.

Results/Discussion

Multiphoton microscopy revealed up to one order of magnitude higher Dox extravasation after FUS-BBB/BTB disruption as compared to control. In addition, a five-fold increase of Dox penetration was found after FUS-BBB/BTB disruption compared to control (>100μm vs. <20μm, based on Dox penetration regression). The numerical model indicated that the vessel diffusion coefficient in the FUS-BBB/BTB disruption was tenfold higher from the control (Mean ± SEM (μm2/s) 3.35 ± 1.1 Vs 0.27 ± 0.1). Quantification of the T-DM1 distance from the vessels revealed significant increase penetration after FUS- BBB/BTB disruption as compared to control (Mean ± SEM (μm) 42 ± 7 vs. 11 ± 6). The numerical model indicated that the vessel diffusion coefficient was only 2-fold different between the two cases, which is consistent with the larger molecular weight of this drug. Finally, sensitivity analysis using the optimized values showed that FUS-BBB/BTB disruption eliminates the sensitivity to vessel diffusion coefficient for both agents, suggesting that FUS is able to overcome one of the major obstacles to the transport of therapeutics in brain tumors.

1K-3

4:30 pm Concurrent Anti-Vascular, Sonodynamic and Chemo Therapy in Solid Tumors by Superhydrophobic Dox-Loaded Nanoparticles

QiaoFeng Jin[1], Cheng-Han Wu[1], Chih-Yu Lin[2], Chia-Ming Yang[2], Chih-Kuang Yeh[1]; [1]*Department of Biomedical Engineering and Environmental Sciences, National Tsing Hua University, Hsinchu, Taiwan,* [2]*Department of Chemistry, National Tsing Hua University, Hsinchu, Taiwan*

Background, Motivation and Objective

Microbubbles have been widely studied as ultrasound contrast agents and drug/gene carriers. However, their short lifetime and micron-sized would hamper their applications. Mesoporous silica nanoparticles (MSNPs) with large surface areas and pore volume allow for high drug payload and controllable release feature. Our previous studies showed that superhydrophobic MSNPs can adsorb surface bubbles, which can be served as cavitation nuclei and prevent drug leakage. Moreover, their durable cavitation capability makes it possible to perform repeatable treatments with a single injection. Herein, we apply superhydrophobic Dox-loaded MSNPs to concurrently carry out anti-vascular (vessel disruption to promote nanoparticles accumulation), sonodynamic (cavitation activity to kill tumor cells by free radicals) and chemo (drug release to long-lasting treatment) therapy in solid tumors.

Statement of Contribution/Methods

Mesoporous MCM-48 silica NPs were synthesized with sol-gel method and then fluorinated with perfluorodecyltriethoxysilane (PFDTS) to obtain the superhydrophobic F48-ext. Dox was loaded into F48-ext and denoted as F48-ext-dox. Their inertial cavitation dose (ICD) was assessed by using a 2-MHz HIFU for transmitting pulses (50-cycle and 6 MPa pulse at a PRF of 10) and a 15-MHz transducer for detect cavitation signals. The reactive oxygen species (ROS) were measured using DCFH-DA assay. In vivo window chamber microscopy was applied to directly observe the blood vessels disruption. The experiments of subcutaneous tumor xenograft model were performed to assess the therapeutic efficacy.

Results/Discussion

The F48-ext NPs became superhydrophobic after fluorination and showed a contact angle of about 150 degree and 50 % of Dox leakage was inhibited. Compared with MCM-48 NPs, the ICD and ROS fluorescence of F48-ext NPs was augmented for 3.9 and 10.9 times ($p < 0.05$), respectively. Furthermore, window chamber microscopy showed that at least 57% small blood vessels (diameter < 40 ¦Ìm) were disrupted. The F48-ext and F48-ext-dox with a single dose ultrasound-mediated treatment inhibited 58.2% and 49.2% tumor growth (14 days) with respect to control group ($p < 0.05$) respectively, while F48-ext-dox without ultrasound inhibited 25.7%. Moreover, the cavitation bubbles generated during HIFU therapy could be used to monitor the therapy process by B-mode imaging.

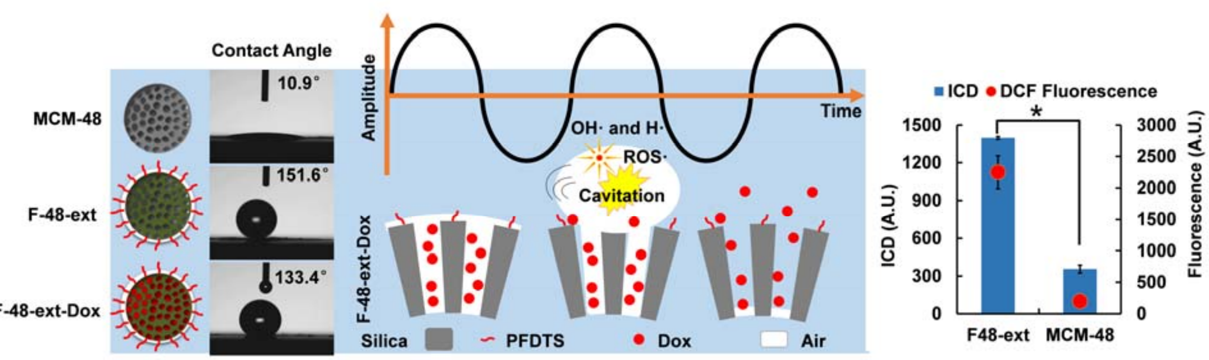

1K-4

4:45 pm Numerical Model Fully Depicting Nanoparticle Uptake within Brain after Ultrasound Induced Blood-Brain Barrier Opening

Allegra Conti[1], Remi Magnin[1], Sébastien Mériaux[1], Benoit Larrat[1]; [1]*NeuroSpin, CEA, Gif-sur-Yvette, France*

Background, Motivation and Objective

Low intensity Focused Ultrasound (FUS) combined with microbubbles open locally and not invasively the Blood-Brain Barrier (BBB) allowing passage of nanoparticles into the brain [Hynynen et al. 2001]. However, since the quantity of particles that can be delivered with this technique depends on tissue properties, on particle properties as well as on acoustic parameters, so far a model fully predicting the result of a FUS induced BBB opening experiment is missing. Here, we introduce a mathematical model depicting both the vascular permeability as a function of time and the diffusion process occurring in brain tissue. This model takes into account acoustic pressure, particle size, blood pharmacokinetics and diffusion rates.

Statement of Contribution/Methods

Our method consists in the numerical solving of the diffusion equation in the presence of a time dependent source term. The source term is derived from the BBB closure model introduced in Marty et al 2012. It relates the amount of Contrast Agent (CA) crossing the BBB at a given time to the concentration in blood CA_{blood} (t), to the distribution of the gap sizes generated in the BBB by ultrasound for various acoustic pressures and to the BBB closure rate. The results from this new model have been corroborated by solving the equation on diffusion data of 3 MR-CA with similar sizes. Thanks to an FUS MR-guided system [Magnin et al 2016], the BBB has been opened in the striatum of 9 rats, inside a 7 T MRI scanner (1.2 MPa at 1.5 MHz, 3% duty cycle for 120s). CA diffusion outside the focal spot has been quantified by acquiring dynamic T_1 maps after BBB opening for at least one hour. Those maps were then converted into CA concentration maps.

Results/Discussion

Figure 1 shows a CA map obtained 1 minute after BBB opening and CA injection. By masking this map for all the time points (A), it is possible to solve the diffusion equation in time and space (B). The model agrees well with the data, as can be seen for example from (C) where the maximum of CA concentrations getting into the brain given by the numerical model are compared to experimental ones. As can be noticed, the match with the experimental data allows us to introduce this approach as a new tool to successfully predict and plan drug distribution after a BBB opening experiment.

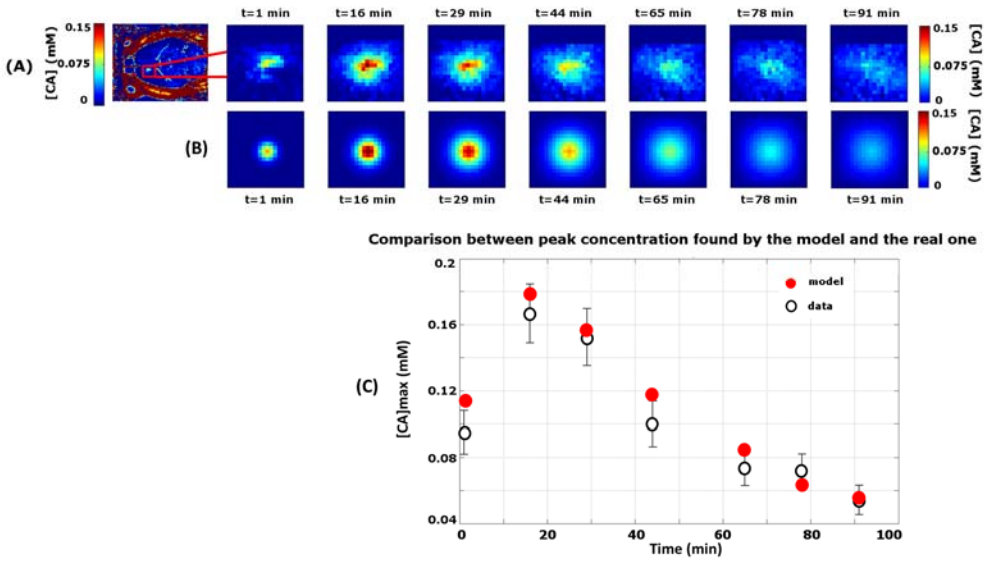

1K-5

5:00 pm MRI-Guided Focused Ultrasound Hyperthermia in Combination with Microbubbles for Improved Drug Delivery at Reduced Power Levels

Marc Santos[1,2], Sheng-Kai Wu[1], Yuexi Huang[1], David Goertz[1,2], Kullervo Hynynen[1,2]; [1]*Physical Sciences Platform, Sunnybrook Research Institute, Toronto, Ontario, Canada*, [2]*Medical Biophysics, University of Toronto, Toronto, Ontario, Canada*

Background, Motivation and Objective

Preclinical studies have shown that MRI-guided focused ultrasound (MRgFUS) can achieve spatially localized thermal exposures in the range of 41-43°C. This presents an advantageous scenario for a plethora of targeted therapeutics. It has been observed that the administration of contrast agent microbubbles (MB) can facilitate increases in temperature with focused ultrasound (FUS), resulting in accelerated ablations. FUS stimulated microbubbles have also been shown to increase vascular permeability which make them useful in a drug delivery context. Here we investigate the combination of MBs and FUS hyperthermia using MRI thermometry for temperature feedback as a means of improving drug delivery at a reduced power level compared to MRgFUS hyperthermia alone and report initial results with this approach.

Statement of Contribution/Methods

Rabbit thigh muscle was targeted using a spherically curved focused ultrasound transducer (frequency 1.17MHz, 60mm focal length, f# 0.8) with an acoustic lens designed to heat large volumes. A single element polyvinylidene fluoride (PVDF, 5mm circular aperture) acoustic receiver was used to monitor the cavitation signals from the muscle tissue during treatment. MR thermometry based PID control of the output power to the transducer was used to maintain the tissue temperature at 42°C for 20 minutes continuously, Fig. 1. Once the tissue was at 42°C for 5 minutes, a slow infusion of Definity® microbubbles (20µL/kg over 5 minutes) was administered to observe the effects on the applied power to the transducer while maintaining the elevated tissue temperature.

Results/Discussion

It was demonstrated that the infusion of MBs during MRgFUS hyperthermia allowed the maintenance of the tissue temperature within the hyperthermia regime at a reduced power level. Further, evidence of drug extravasation was observed when liposomal doxyrubicin was injected prior to the MB infusion. This result will help to expand the utility of MRgFUS as a treatment option designed to improve drug delivery. Both treatments, MRgFUS hyperthermia and FUS stimulated MBs have been shown independently to increase blood vessel permeability and improve local drug delivery, but the combination of the two has not been explored to date and may prove to be an efficacious method of increasing drug delivery at a reduced power level.

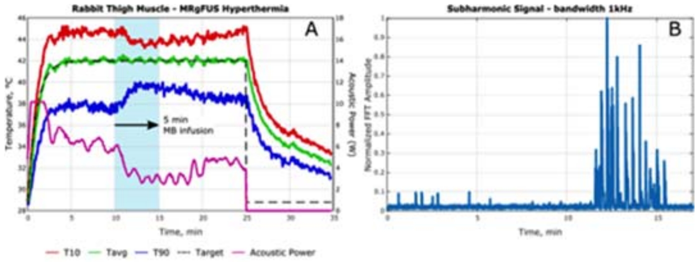

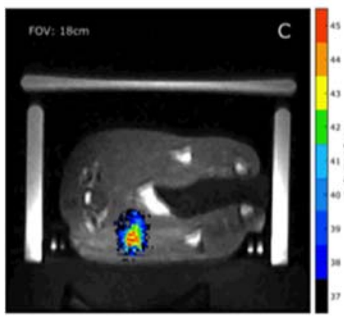

Fig. 1: **A**, MRgFUS hyperthermia exposure at 1.17MHz in healthy rabbit muscle using PID feedback control to achieve a prescribed temperature response, the acoustic power is shown in purple and is seen to drop following the slow infusion of Definity® microbubbles at the clinical dose of 20µL/kg over 5 minutes. **B**, Cavitation detection of the subharmonic signal (585kHz±0.5kHz) using a PVDF receiver during MRgFUS hyperthermia, a noticeable increase in the FFT amplitude of the subharmonic appears to corrsepond with the infusion of microbubbles. **C**, Representative MRI thermometry image with thermometry data overlaid upon a proton density weighted image of the rabbit thigh, 3 B_0 drift correction phantoms filled with heavy mineral oil surround the animal and are used for drift correction in real-time during sonication.

1K-6

5:15 pm **LIFU Triggers Drug Release from Porphyrin-Phospholipid Liposomes and Facilitates Multi-Functional Theranostics**

Xiaobing Wang[1,2], Xiufang Liu[1], Fei Yan[1], Hairong Zheng[1]; [1]*Shenzhen Institutes of Advanced Technology, Chinese Academy of Sciences, China, People's Republic of,* [2]*College of Life Sciences, Shaanxi Normal University, China, People's Republic of*

Background, Motivation and Objective

Externally controlled drug release from nanoscale drug delivery systems hold great potential to increase local deposit. Here, we introduce an ultrasound-activatable porphyrin-phospholipid liposome (PPL) to show its controllable drug release, enhanced imaging signals, and efficient therapeutic actions.

Statement of Contribution/Methods

Dynamic light scattering and transmission electron microscopy were utilized to characterize the features of PPL and PPL loaded with doxorubicin (PPL-DOX). The ultrasound-controllable cargo release was measured at distinct time points with or without free radical inhibitors. In vitro cellular uptake and cytotoxicity were examined in U87 glioma cells by confocal microscopy. In vivo, NIR fluorescent and photoacoustic imaging were applied to indicate the distribution of PPL following intravenous injection, along with the signal changes after ultrasonic irradiation. The tumor inhibition and overall survival time were evaluated by PPL-DOX endowed with the optimal porphyrin-phospholipid ratio, maximum DOX loading and favorable ultrasound-responsible ability.

Results/Discussion

Results: The obtained PPL, PPL-DOX were stable at 4¡æ for at least 4 weeks with appropriate 100 nm diameter. 2 molar % porphyrin-phospholipid in PPL-DOX was compatible with good ultrasound-responsible and drug-loading capacities. DOX release from PPL could be regulated by ultrasound intensity and suppressed with free radical inhibitors. Following intravenous administration, the PPL demonstrates high sensitive photoacoustic and NIR fluorescent imaging by ultrasonic stimulus in xenograft U87-bearing mice. Ultrasound exposure triggered sonodynamic damage of tumors cells and simultaneously initiated local drug release to exert chemotherapy. Exposure to focused ultrasound with PPL suppresses tumor growth several times more than without exposure to ultrasound. What¡¯s more, PPL-DOX displays little damage on normal cells in vitro and even on normal tissues in vivo.Conclusions: The developed ultrasound-activable paradigm achieves simultaneously enhanced bimodal imaging and spatiotemporally regulatable cargo release and initiates sono-chemotherapeutic effects.

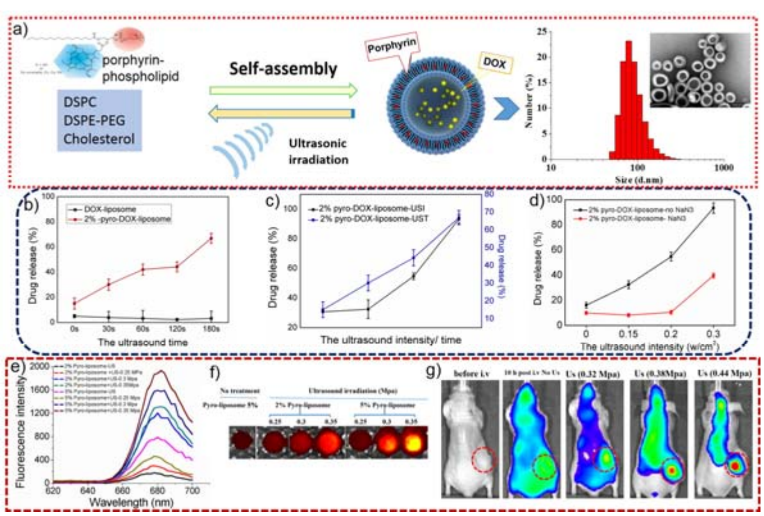

2K - MEL: Elastography in Clinical Application

Ambassador Ballroom

Saturday, September 9, 2017, 4:00 pm - 5:30 pm

Chair: **Caterina Gallippi**
University of North Carolina

2K-1

4:00 pm **Time-Shifted Multi-Tracking of Shear Waves for the Characterization of Scleral Biomechanics**

Heechul Yoon[1], Suhyun Park[2], Salavat Aglyamov[3], Stanislav Emelianov[1,4]; [1]*School of Electrical and Computer Engineering, Georgia Institute of Technology, Atlanta, GA, USA,* [2]*School of Electrical and Electronics Engineering, Chung-Ang University, Korea, Republic of,* [3]*Department of Biomedical Engineering, The University of Texas at Austin, USA,* [4]*Wallace H. Coulter Department of Biomedical Engineering, Georgia Institute of Technology and Emory University School of Medicine, Atlanta, GA, USA*

Background, Motivation and Objective

The biomechanics of the sclera can play a critical role in glaucoma diagnosis and monitoring new treatment methods. Previous studies have used strain elastography and investigated the relationship between scleral stiffness and intraocular pressure. However, applying shear wave elastography (SWE) to scleral tissue is challenging because sclera (100-1000 kPa) is significantly stiffer than normal soft tissue (10-100 kPa). We introduce a time-shifted multi-tracking approach capable of measuring the propagation of fast shear waves in stiff tissues, such as the sclera.

Statement of Contribution/Methods

The time-shifted multi-tracking method is based on the repeated (*M* times) but delayed recording of shear waves created by the same push beam. By combining *M* subsets (Fig. 1a), the overall time-shifted multi-tracking data set captures shear wave propagation with effective pulse repetition frequency (ePRF) increased by a factor of *M*. Because angular compounding (N_θ) is typically required in SWE to improve the signal-to-noise ratio (SNR) and the resolution, the ePRF becomes PRF/$N_\theta \cdot M$. A 16% homogenous gelatin phantom was imaged with four combinations of N_θ and *M*, resulting in ePRFs of 17.5 and 5.8 kHz thus allowing comparison of conventional and proposed methods. For each method, SNR and area (where SNR ≥ 25dB) were measured, and both group and phase shear wave velocities (SWVs) were evaluated. The methods were also compared in *ex vivo* porcine eye experiments where the same N_θ but different *M* (1 and 3) values were used.

Results/Discussion

In phantom experiments (Fig. 1b), our approach outperformed the conventional method in terms of SNR. In addition, even for the same ePRF, the results indicate that our approach has improved SNR. Shear wave velocities were similar, suggesting that the phantom was not stiff enough to show maximum improvement. Compared to the phantom, the porcine sclera was much stiffer (i.e., faster SWVs). Thus, the tracking with *M* of 1 (i.e., ePRF of 5.8 kHz) suffered from insufficient sampling of the shear wave propagation and, as expected, resulted in discrepancies between SWVs (Fig. 1c). Overall, our study indicates that the time-shifted multi-tracking of shear waves can be used to measure the stiffness of extremely hard tissues with improved SNR. Our ongoing studies are focused on monitoring drug-induced changes in scleral stiffness during glaucoma treatment.

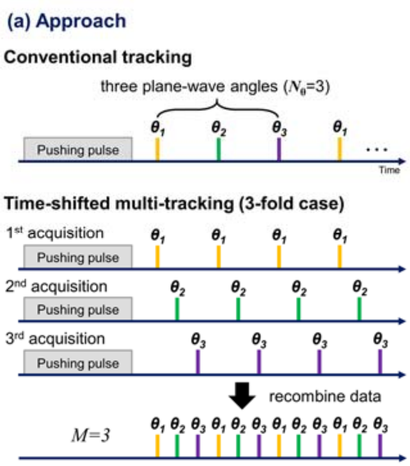

(b) Results from a gelatin phantom

	Conventional tracking		Time-shifted multi-tracking	
N_θ (#angles)	1	3	3	9
M (#acquisitions)	1		3	
PRF (kHz)	17.5			
Effective PRF (kHz)	17.5	5.8	17.5	5.8
SNR (dB)	32.35 ± 0.29	36.16 ± 1.11	36.47 ± 0.23	38.58± 2.36
Area ≥ 25 dB (%)	90.18 ± 1.58	97.76 ± 0.94	98.20 ± 0.26	99.23 ± 0.49
Group SWV (m/s)	6.57 ± 0.07	7.02 ± 0.10	6.50 ± 0.02	6.75 ± 0.03
Phase vel. (m/s)	6.89 ± 0.01	7.14 ± 0.03	6.90 ± 0.01	6.95 ± 0.02
Phase vel. > 1 kHz (m/s)	6.88 ± 0.01	7.31 ± 0.02	6.87 ± 0.01	7.12 ± 0.02

(c) Results from *ex vivo* porcine sclera

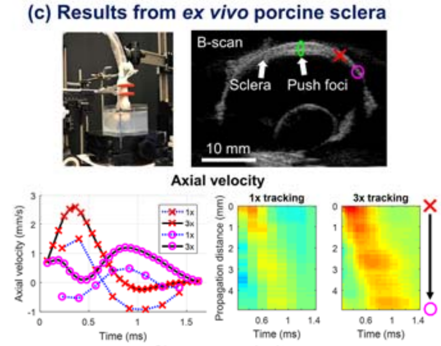

Shear wave velocity

	Effective PRF (kHz)	Group SWV (m/s)	Phase vel. (m/s)	Phase vel. > 1 kHz (m/s)
N_θ=3 & M=1	5.8 kHz	9.49 ± 0.18	5.82 ± 0.11	6.91 ± 0.34
N_θ=3 & M=3	17.5 kHz	8.87 ± 0.21	10.13 ± 0.23	10.98 ± 0.28

2K-2

4:15 pm **Assessment of Corneal Biomechanical Properties Using the Ultrasonic Micro-Elastography**

Xuejun Qian[1,2], Teng Ma[1,2], Martin Heur[1], Jun Zhang[2], K. Kirk Shung[2], Mark Humayun[1,3], Qifa Zhou[1,2]; [1]*USC Roski Eye Institute, University of Southern California, Los Angeles, California, USA,* [2]*Department of Biomedical Engineering, University of Southern California, Los Angeles, California, USA,* [3]*USC Institute for Biomedical Therapeutics, University of Southern California, Los Angeles, California, USA*

Background, Motivation and Objective

Investigating biomechanical properties of the cornea can have many clinical applications, including the diagnosis of keratoconus and post-refractive keratectasia. However, ascertaining the biomechanical properties of cornea remains a challenge because of the low resolution of currently available modalities cannot provide a point-to-point stiffness mapping of cornea. In this study, we reported a high-resolution ultrasonic micro-elastograhy technique for non-invasive mapping of corneal biomechanical properties relative to its morphological structure.

Statement of Contribution/Methods

The ultrasonic micro-elastography imaging system utilized a 4.5 MHz ring transducer and a confocal aligned 40 MHz needle transducer for tissue excitation and detection of micron-level displacement, respectively. The spatial resolution and field of view (FOV) of the system were quantitatively characterized by imaging gelatin tissue-mimicking phantoms. Next, ex vivo imaging of porcine corneas that were either cross-linked using aldehyde or preloaded with various intraocular pressures was performed.

Results/Discussion

The spatial resolution of ultrasonic micro-elastography imaging system within a 2 mm FOV were characterized to be 109.8±6.9 μm axially and 223.7±20.1 μm laterally, which was found to be sufficient for quantifying the biomechanical properties of the cornea. The increase of corneal stiffness (anterior and posterior) and the change in cross-linked volume following aldehyde injection could be both observed in the elastography images. The B-mode structural images remained unchanged (Fig. 1a). The relationship between the stiffness of cornea, sclera, conjunctiva and IOP was shown in Figure 1b. These results demonstrate the ultrasonic micro-elastography has sufficient resolution and FOV to characterize the biomechanical properties of the cornea. Integrating high-resolution elastography imaging with structural imaging of the cornea can provide additional information that can lead to many clinical applications.

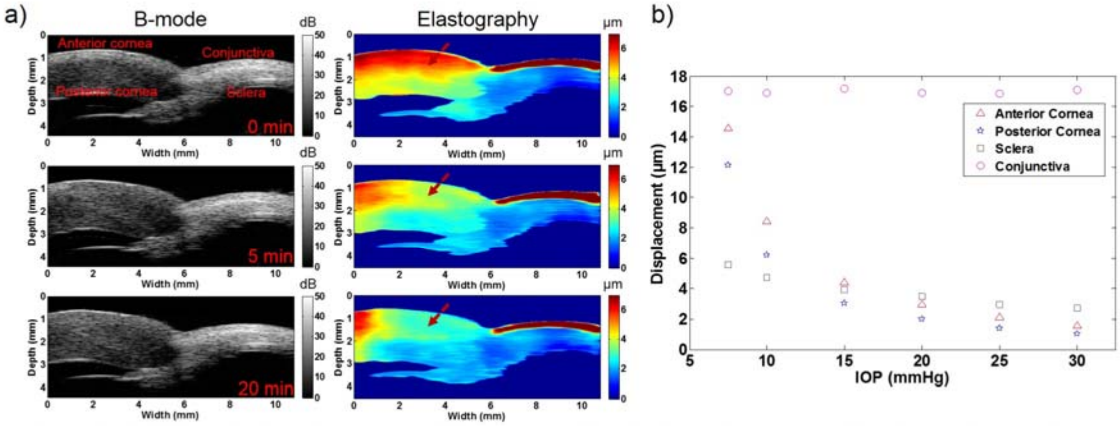

Figure 1. (a) Ultrasonic B-mode images and its corresponding elastography images with an increasing duration of cross-linking; (b) The relationship between stiffness of cornea, sclera, conjunctiva and intraocular pressure (IOP) loading. The red arrows indicate the site of aldehyde injection.

2K-3

4:30 pm In-Vivo Assessing the Age-Related Stiffness of Crystalline Lens in Rabbits by Acoustic Radiation Force Based Ultrasound Elastography

Qingmin Wang[1], Zhen Lv[1], Xuehua Gao[1], Pengpeng Zhang[1], Haoming Lin[1], Yanrong Guo[1], Xin Chen[1], Tianfu Wang[1], Siping Chen[1], Xinyu Zhang[1]; [1]*School of Biomedical Engineering, Shenzhen Univ., Shenzhen, China, People's Republic of*

Background, Motivation and Objective

The pathological or physiological changes of the crystalline lens directly affect the eye accommodation and transmittance, and then increase the risk of the presbyopia and cataract for people in middle and old age groups. This risk has a remarkable rise with age, seriously influencing the living quality of the elderly, and also posing a huge burden on public health. There is no universally accepted quantitative method to measure the lens′ mechanical properties in vivo so far. Acoustic radiation force based ultrasound elastography (ARF-USE) have special advantage for assessing lens′stiffness since it can palpate the tissue remotely and detect the vibration using one ultrasound probe. This study aims to investigate the possibility of assessing the age-related stiffness change of crystalline lens by ARF-USE in a rabbit model in vivo.

Statement of Contribution/Methods

13 New Zealand white rabbits were divided into 4 groups and fed normally till 60, 90, 120, 150 days old, respectively. An USE platform was built up on the basis of Verasonic ™ Vantage 256 ultrasound open system. The rabbits were anaesthetized and a liner ultrasound probe (L11-4) was placed on one eye during the experiment. The ARF were produced by the probe to induce a local deformation in rabbit lens. The plane wave imaging was used to detect the lens′s local deformation and vibration propagating in the lens. After post-processing of the raw RF data, the local displacement, the group velocity and phase velocity was calculated for every eyes of a rabbit. The correlations of group velocity with day-ages and weight of the rabbits were analyzed.

Results/Discussion

The group velocity was used as a biomarker to characterize the lens′stiffness. The results shows that with the increase of day, the maximum displacement of the lens decreased significantly and the group velocity and modulus increased gradually, the group velocities had a strong correlation with day ages ($R=0.84, p<1\times10^{-7}$) and weights ($R=0.83, p<1\times10^{-7}$). In conclusion, this study verified the correlation between lens′stiffness and age and demonstrated the feasibility of in vivo measurement of lens′ mechanical properties based on ARF-USE, which may have great potential in studying the pathogenesis, diagnosis and therapy of presbyopia and cataract in clinical ophthalmology.

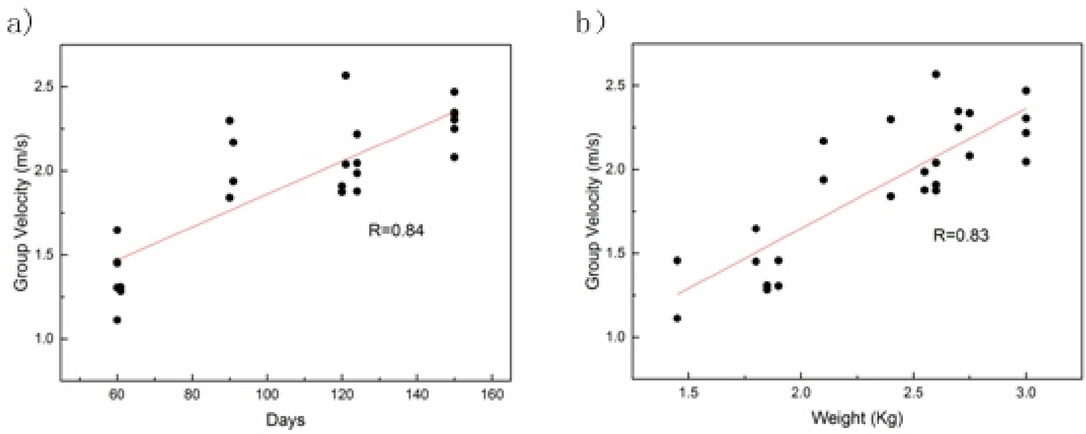

The correlation analysis of group velocity in rabbit crystalline lens with (a) day-ages and (b) weight.

2K-4

4:45 pm Biological and Experimental Factors Affecting the Assessment of Cervical Softening during Pregnancy with Shear Wave Elasticity Imaging

Ivan M. Rosado-Mendez[1], Lindsey C. Drehfal[1], Andrew P. Santoso[1], Quinton W. Guerrero[1], Kaitlin M. Woo[2], Mark L. Palmeri[3], Helen Feltovich[1,4], Timothy J. Hall[1]; [1]*Department of Medical Physics, University of Wisconsin-Madison, Madison, WI, USA,* [2]*Biostatistics and Medical Informatics, University of Wisconsin-Madison, Madison, WI, USA,* [3]*Biomedical Engineering, Duke University, Durham, NC, USA,* [4]*Maternal Fetal Medicine, Intermountain Healthcare, Provo, UT, USA*

Background, Motivation and Objective

Spontaneous preterm birth, the foremost source of neonatal mortality, could potentially be prevented by objectively detecting abnormal changes in the uterine cervix. Shear Wave Elasticity Imaging (SWEI) biomarkers can quantify cervical softening that precedes vaginal delivery. This task can be complicated by biological (i.e., heterogeneity of cervical stiffness and pregnancy history) and experimental confounders (i.e., posture during scanning). Here we investigate how these confounders influence shear wave speed (SWS) as an objective biomarker of cervical softening during pregnancy. We apply SWEI longitudinally in pregnant Rhesus macaques and compare SWS estimates from supine transabdominal (TA) and prone inter-cavitary (IC) approaches.

Statement of Contribution/Methods

Pregnant primates (10 nulliparous, 8 multiparous) from the Wisconsin National Primate Research Center were scanned at weeks 4, 10, 16, 20, and 23 during the 24.5-week gestation. At each scan, each subject's posterior cervix was imaged under the TA (with a linear array transducer) and IC (transrectally, with a catheter transducer) approaches on a Siemens Acuson S2000 scanner (Siemens Healthcare, Mountain View, CA, USA). Five SWS measurements with each approach were performed with an Acoustic Radiation Force Impulse (ARFI) technique, with two wave directions (from uterus to vagina, UTV, or from vagina to uterus, VTU). SWS was estimated with a RANdom SAmple Consensus (RANSAC) method. Linear mixed effects (LME) models were used to model SWS as a function of gestational age, parity (nulliparous vs. multiparous), wave direction (UTV vs VTU), and approach (TA vs. IC) as fixed effects with inter-subject random intercepts and slopes. Interactions between approaches and other fixed effects were also studied.

Results/Discussion

SWS significantly decreased during pregnancy with the IC approach at a rate 0.171 [95% CI: 0.142-0.199] m/s per week ($p<0.001$). The rate of SWS reduction with the TA approach was 0.015 [95% CI -0.012-0.041]m/s per week smaller than with IC, but the difference was not significant ($p=0.27$). Interactions between approach and parity were also significant ($p<0.001$). Results suggest that, although biological and experimental factors contribute to SWS variability, SWEI provides reliable assessment of cervical softening during pregnancy.

Acknowledgements: We thank Michele Schotzko and Sarah Kohn for animal handling and scanning, and Siemens Ultrasound for technical support. Research supported by NIH Grants T32CA009206 from the National Cancer Institute and R21HD061896, R21HD063031, and R01HD072077 from the Eunice Kennedy Shriver National Institute of Child Health and Human Development. The content is solely the responsibility of the authors and does not necessarily represent the social views of the National Institutes of Health.

2K-5

5:00 pm Shear Shock Waves Observed in the Ex-Vivo Brain

David Espindola[1], Gianmarco Pinton[1]; [1]*Joint Department of Biomedical Engineering, University of North Carolina at Chapel Hill and North Carolina State University, Chapell Hill, USA*

Background, Motivation and Objective

Head injury biomechanics has been guided by measurements of accelerometers attached to the skull, which provides a partial and indirect estimate of brain motion because the internal deformation of the brain is far more complex than the rigid motion of the skull. Attempts to measure the *in situ* nonlinear brain mechanics with imaging methods (MRI, CT) have lacked the penetration, frame rate, or motion detection accuracy to capture the rapid brain motion associated with nonlinear transient events during traumatic injury. Here we present a high frame-rate (6200 images/second) ultrasound imaging method that can accurately (<1 µm) measure the internal brain motion during the rapid transient events associated with a mild impact in an *ex vivo* porcine brain. It is shown that shear shock waves are generated in the brain even under low impact conditions.

Statement of Contribution/Methods

Our method relies on two main advancements 1) A flash focus ultrasound sequence which reduces the side lobes by 19dB and increases the SNR deep in the brain compared with a conventional plane wave compounding sequence. 2) An adaptive tracking algorithm which uses a quality weighted median filter to iteratively optimize correlation estimates. To the best of our knowledge no other imaging method (MRI, CT) has been able to achieve this combination of speed, accuracy, and penetration in the brain.

Results/Discussion

By imaging brain motion directly(Fig.1a) we were able to observe the formation of shear shock waves within the brain(Fig.1b). The measured shock waves have a specific odd harmonic signature(Fig.1c) predicted by theory describing a cubically nonlinear elastic soft solid. Measurements of the frequency dependent attenuation and dispersion were used to fit this nonlinear theoretical model to our data. We present the first direct estimate of the cubic nonlinear parameter for brain tissue. This previously unobserved shear shock wave phenomenology dramatically amplifies the acceleration at the shock front, deep in the brain, compared with the acceleration imposed at the brain surface (up to a factor 8.5). Thus a

30 g acceleration at the brain surface develops into a 255 g shock wave deep inside the brain.(Fig.1d) Strain and strain rate are also amplified at the shock front. This highly localized increase in acceleration suggests that the shear shock wave is a primary mechanism for traumatic injuries.

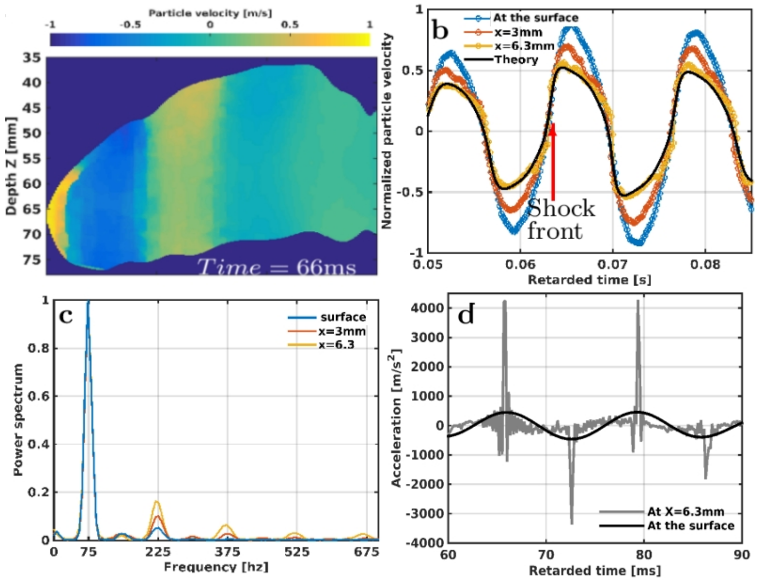

2K-6

5:15 pm **Assessment of Interstitial Lung Disease Using Lung Ultrasound Surface Wave Elastography**

Xiaoming Zhang[1], Boran Zhou[1], Thomas Osborn[2], Brian Bartholmai[1], James Greenleaf[3], Sanjay Kalra[4]; [1]*Radiology, Mayo Clinic, Rochester, Minnesota, USA,* [2]*Rheumatology, Mayo Clinic, Rochester, Minnesota, USA,* [3]*Physiology and Biomedical Engineering, Mayo Clinic, Rochester, Minnesota, USA,* [4]*Pulmonary and Critical Care Medicine, Mayo Clinic, Rochester, Minnesota, USA*

Background, Motivation and Objective

Ultrasonography is not widely used in clinic for lung assessment because ultrasound cannot image deep lung tissue. We have developed a noninvasive technique termed lung ultrasound surface wave elastography (LUSWE) for measuring superficial lung tissue elastic properties. The purpose of this abstract is to demonstrate the clinical use of LUSWE for assessing patients with interstitial lung disease (ILD). ILD consists of multiple chronic lung disorders but, in general, the lung parenchyma of patients with ILD is fibrotic. Reduction in volume and stiffening leads to altered physiology and respiratory symptoms, especially dyspnea, which can eventually progress to respiratory failure. LUSWE may be useful for assessing ILD because patients with ILD have typical fibrotic scars in the peripheral and subpleural regions of the lung.

Statement of Contribution/Methods

In LUSWE, a 0.1 second harmonic vibration is generated on the chest wall of a subject using a handheld vibrator. An ultrasound probe is positioned in the same intercostal space as the indenter of the vibrator to measure the generated surface wave propagation on the lung. The Verasonics ultrasound system with an ultrasound probe of L11-4 with a central frequency of 6.4 MHz is used. A human subject is examined in a sitting position. The lung testing is performed with full inspiration breath hold. Both upper lungs are tested through the second intercostal space in the mid-clavicular line. The bilateral lower lungs are tested one intercostal space above the level of the diaphragm in the mid-axillary line and also one intercostal space above the level of the diaphragm in the mid-scapular line. The surface wave speed of lung is measured at 100 Hz, 150 Hz, and 200 Hz. Three measurements are made at each location and each frequency.

Results/Discussion

In a large prospective clinical study of ILD patients, we measured both lungs through six intercostal spaces for patients and controls. Significant differences in wave speed between healthy subjects and ILD patients were found. For example, the surface wave speed of the lung is 1.98 ± 0.07 m/s at 100 Hz, 2.63 ± 0.46 m/s at 150 Hz, and 3.18 ± 0.58 m/s at 200 Hz for a healthy subject, and the surface wave speed of the lung is 3.30 ± 0.37 m/s at 100 Hz, 4.38 ± 0.33 m/s at 150 Hz, and 5.24 ± 0.44 m/s at 200 Hz for an age matched ILD patient in the same intercostal space.

LUSWE is a safe and noninvasive technique for generating and measuring surface wave propagation on the lung. LUSWE can provide regional lung assessment through an intercostal space and global lung assessment through multiple intercostal spaces. LUSWE may compliment the clinical standard high-resolution computed tomography for assessing ILD, and could be performed in an office setting without use of ionizing radiation.

3K - MCA: Microbubbles Localization Microscopy 2

Palladian Room

Saturday, September 9, 2017, 4:00 pm - 5:30 pm

Chair: **Tomas Jansson**
Lund University

3K-1

4:00 pm **Investigation of Microbubble Detection Methods for Super-Resolution Imaging of Microvasculature**

Jemma Brown[1], Kirsten Christensen-Jeffries[1], Sevan Harput[2], Meng-Xing Tang[2], Chris Dunsby[3,4], Robert Eckersley[1]; [1]*Imaging Sciences & Biomedical Engineering, King's College London, London, United Kingdom,* [2]*Department of Bioengineering, Imperial College London, London, United Kingdom,* [3]*Department of Physics, Imperial College London, London, United Kingdom,* [4]*Centre for Histopathology, Imperial College London, London, United Kingdom*

Background, Motivation and Objective

Super-resolution ultrasound has potential for visualisation of microvasculature[1]. Techniques that localise isolated bubble signals first require detection algorithms to separate the bubble and tissue response. Resolution of the tortuous microvasculature requires localisations with accuracy on the micron scale. Tumour microvasculature blood velocities are ≤1mm/s, and even for vessel diameters approaching 60µm can be an order of magnitude less than normal vasculature[2]. This work compares pulse inversion[1] (PI), differential imaging[3] (DI) and singular value decomposition[4] (SVD) filtering in terms of the localisation accuracy, localisation precision and contrast to tissue ratio (CTR).

Statement of Contribution/Methods

Bubble responses were simulated using the Marmottant model[5] and moving tissue simulated using Field (II). Non-linear tissue propagation was modelled using k-Wave. The implications of SVD filtering on super-resolution in terms of spatial and frequency components of the filtered image was also investigated.

Results/Discussion

Figure 1 shows that at the lowest speeds the bubble displacement between frames is not sufficient to generate a strong differential signal. The separation of bubble and tissue signal with SVD is also more difficult at low speeds. PI is not significantly affected by speed. Lower frame rates could improve slow bubble detection with SVD and DI but an adaptive filtering method would be required to prevent information associated with faster bubbles being lost.

PI signal was largely independent of flow direction. SVD and DI generate higher signal with axial movement compared to lateral.

These results depend on tissue movement and response, acquisition frequency and frame rate. However, for super-resolution of tumour microvasculature, the results suggest that non-linear techniques are necessary. Investigations such as this one will guide the use of detection techniques for specific applications.

References:

[1] Christensen-Jeffries, K., et al., Medical Imaging, IEEE Transactions on, 2015, 34(2): p. 433-440.

[2] Yuan, F., et al., Cancer Research, 1994, 54(17): p.4564 – 4568.

[3] Desailly, Y., et al., Applied Physics Letters, 2013, 103(17), 174107.

[4] Errico, C., et al., Nature, 2015. 527(7579): p. 499-502.

[5] Marmottant, P., et al., The Journal of the Acoustical Society of America, 2005, 118(6): p. 3499-3505.

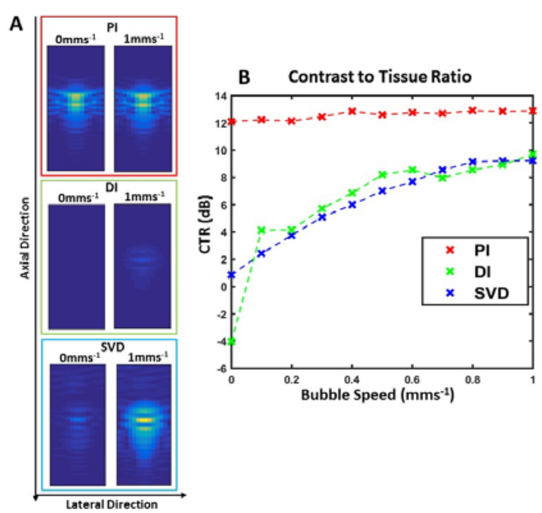

Figure 1: Bubble signals for detection methods at 0mms^{-1} and 1mms^{-1} (A) and dependence of CTR on bubble speed (B). For PRF = 1000Hz, centre frequency = 4.3MHz, SNR = 26.6dB, and linear tissue.

3K-2

4:15 pm **Fast and Background Free Super-Resolution Ultrasound Angiography**

Oren Solomon[1], Avinoam Bar-Zion[2], Dan Adam[2], Yonina C. Eldar[1]; [1]*Electrical Engineering, Technion, Haifa, Israel,* [2]*Biomedical Engineering, Technion, Haifa, Israel*

Background, Motivation and Objective

Spatial resolution in classic contrast-enhanced ultrasound (CEUS) is limited by acoustic diffraction. Ultrafast ultrasound localization microscopy (uULM) has enabled a sub-diffraction spatial resolution of tens of micrometers in-vivo, although at the expense of a scan duration of tens of seconds. In contrast, by exploiting the statistical properties of CEUS, super resolution optical fluctuation imaging (SOFI) recently demonstrated temporal resolution of 90ms in-vivo with a spatial resolution two times better than the diffraction limit. Here, we report on a method which achieves a spatial resolution similar to that of uULM, but with temporal resolution of CEUS SOFI, termed sparsity based ultrasonic super resolution hemodynamic imaging (SUSHI).

Statement of Contribution/Methods

After applying a high-pass clutter filter, each clip was decomposed into sub-scans according to the sign of the Doppler measurements. Statistical analysis was done by calculating the pixelwise temporal-mean, 2nd and 4nd central moment. By exploiting the sparse nature of the bubbles, super-resolved images were produced for each flow direction using an efficient implementation of SUSHI, relying on sparsity in the correlation domain. SUSHI was tested using a New Zealand white rabbit kidney model. Cine-loops of 150 to 1000 frames were acquired using 1 cycle 4.5MHz plane-wave insonations at a PRF of 5kHz using an Aixplorer scanner (Supersonic Imagine, France) and Definity® microbubbles.

Results/Discussion

Upper row panels (red) shows the negative flow images ((a) temporal mean, (b) 4th order SOFI and (c) SUSHI). Lower row depicts the positive flow images ((d) temporal mean, (e) 4th order SOFI and (f) SUSHI). Yellow lines, solid and dashed, in the upper panels correspond to the intensity cross sections below, in the left and right plots, respectively. These profiles show that SUSHI reconstructions have considerable resolution increase (5-6 times reduction in the full-width-half-max compared with the temporal mean), by detecting the vasculature bifurcations compared with the SOFI and temporal mean lines. By dividing the acquired low resolution movie into two sub-movies of different flow directions, sparse recovery is performed more efficiently on each direction than on the movie of combined flows. SUSHI paves the way for super-resolution imaging of living subjects in clinical conditions.

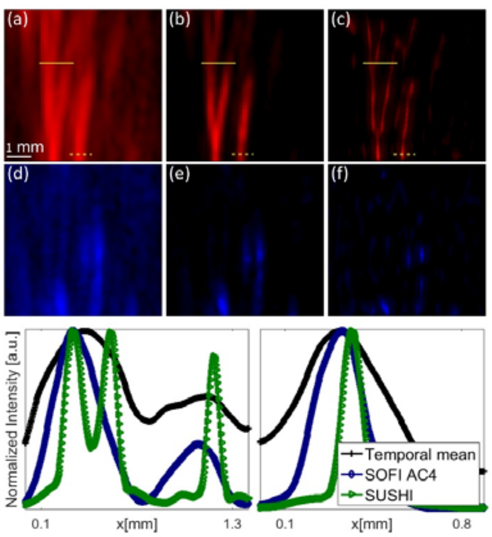

3K-3

4:30 pm **Microbubble Localization Errors in Ultrasonic Super-Resolution Imaging**

Kirsten Christensen Jeffries[1], Sevan Harput[2], Jemma Brown[1], Christopher Dunsby[3,4], Paul Aljabar[5], Meng-Xing Tang[6], Robert Eckersley[1]; [1]*Biomedical Engineering, Kings College London, London, United Kingdom,* [2]*Bioengineering, Imperial College London, London, United Kingdom,* [3]*Physics, Imperial College London, London, United Kingdom,* [4]*Imperial College London, Centre for Pathology, London, United Kingdom,* [5]*Kings College London, London, United Kingdom,* [6]*Imperial College London, London, United Kingdom*

Background, Motivation and Objective

Recently, acoustic super-resolution (SR) imaging has allowed visualization of microvascular structure and flow beyond the diffraction limit through the localization of many isolated microbubble signals. Each bubble position is typically estimated by calculating the centroid, finding a local maximum, or finding the peak of a 2-D Gaussian function fit. However, the backscattered signal from a microbubble depends not only on diffraction characteristics of the waveform, but also on the bubble behavior in the acoustic field, which if not accounted for, may cause localization errors.

Statement of Contribution/Methods

Here, we propose a new localization method to reduce localization errors by identifying the onset of the backscattered signal. We compare the axial accuracy of this method to existing approaches in the literature using *in vitro* experiments performed at 7 cm depth and a low frequency of 2.3 MHz. Simulations of bubble responses to the same measured experimental transmit wave using the Marmottant Model corroborated these experimental findings.

Results/Discussion

Onset detection was demonstrated to provide considerably increased accuracy for SR. Cross-sectional profiles in experimental SR images (Figure 1) demonstrate at least 5.8 times improvement in contrast ratio and more than 1.8 reduction in spatial spread (given by 90% of the bubble localizations) for the onset method over centroiding, peak detection and 2D Gaussian fitting (Figure 2). Simulations estimate that these latter methods could create errors in relative bubble positions as high as 900 µm at these experimental settings, while detecting the onset reduced the interquartile range of these errors by a factor of over 2.2. In the future, localisation using signal onset is expected to considerably improve the accuracy of SR.

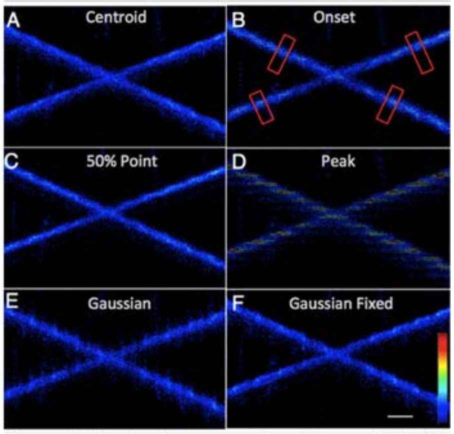

Figure 1. Localization maps using A) centroiding, B) onset, C) 50% point, D) peak detection, E) 2D Gaussian fitting and F) 2D fixed Gaussian fitting. Scale bar 1 mm, color bar 0-12 localizations.

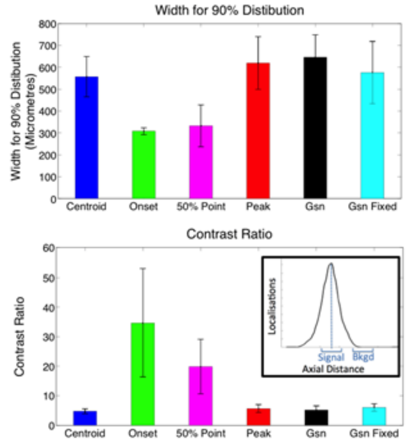

Figure 2. The width for which 90% of localizations exist provide an indication of the proportion of inaccurate localizations. The contrast ratio demonstrates considerable improvement using onset to all other localization methods.

3K-4

4:45 pm **Robust Ultrasound Super-resolution Microvessel Imaging with Spatiotemporal Nonlocal Means Filtering and Bipartite Graph-Based Microbubble Tracking**

Pengfei Song[1], Joshua D. Trzasko[1], Armando Manduca[2], Runqing Huang[3], Ramanathan Kadirvel[1], David F. Kallmes[1], Shigao Chen[1]; *[1]Department of Radiology, Mayo Clinic College of Medicine, Rochester, Minnesota, USA, [2]Department of Physiology and Biomedical Engineering, Mayo Clinic College of Medicine, Rochester, Minnesota, USA, [3]Division of Cardiovascular Diseases, Mayo Clinic College of Medicine, Rochester, Minnesota, USA*

Background, Motivation and Objective

Recently multiple studies have demonstrated microbubble (MB)-based super-resolution imaging (SRI) with ~λ/10 subwavelength resolution on mice and rats. Clinical translation of SRI, however, faces many technical challenges such as low signal-to-noise-ratio (SNR) of the MB signal and physiologic and operator-induced motion in humans. In this study, we take advantage of the rich spatiotemporal information and high frame rate recording of MB signals by ultrafast imaging, and propose a spatiotemporal nonlocal means (NLM) denoising filter and bipartite graph(BG)-based MB pairing and tracking algorithm to achieve robust SRI.

Statement of Contribution/Methods

The SRI signal processing chain consists of signal registration, blinking MB signal extraction, spatiotemporal NLM filtering, MB localization, and BG-based MB pairing and tracking. The NLM filter operates on the spatiotemporal MB data where the moving MB presents unique movement "tracks" while noise manifests in incoherent patterns (Fig. 1a). This distinct contrast provides strong features for NLM to achieve robust denoising without blurring (Fig. 1b). The BG-based MB pairing and tracking is based on the principle that with ultrafast imaging, the most likely position that an MB in frame n will appear in frame n+1 is the location closest to where that MB was in frame n. An MB pairing algorithm was developed to pair MBs between consecutive frames in a BG fashion with the goal of minimizing total pairing distance. A persistence control was also proposed to facilitate more robust MB tracking in multiple consecutive frames.

Results/Discussion

A Verasonics Vantage system and a L11-4v transducer (Verasonics Inc.) were used to image a rabbit kidney with 0.1 ml bolus injection of Optison (GE Healthcare). A 2s data accumulation (PRF = 500 Hz) was obtained from 10s data acquisition, with the rabbit free-breathing and freehand scanning. We found substantially decreased noise and significantly improved SRI imaging quality with NLM filtering and BG-based MB pairing. A comparison study showed that the proposed method had lower overall pairing distance than the classic Hungarian assignment algorithm. Fig. 1c shows the final accumulated SRI microvessel image where ~20 µm microvessels can be visualized in the kidney cortex. Fig. 1d shows the corresponding super-resolution microvessel flow speed image.

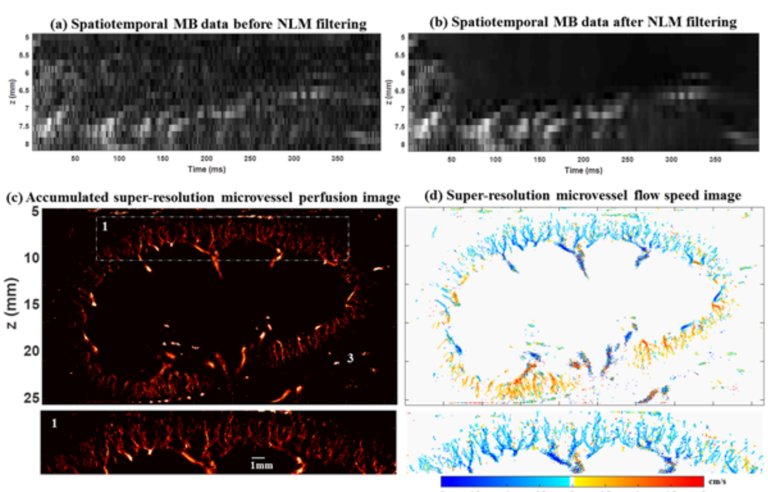

Figure 1. Spatiotemporal MB data before (a) and after (b) spatiotemporal NLM denoising filter. (c) Super-resolution microvessel perfusion images. The region within the white dashed box was magnified to show the detailed microvasculature. (d) Super-resolution microvessel flow speed image. The same region as in (c) was magnified in the lower panel.

3K-5

5:00 pm **Acoustic Response of Phase Change Contrast Agents Targeted with Breast Cancer Cells immediately after Ultrasonic Activation using Ultrafast Imaging**

Ge Zhang[1], Shengtao Lin[1], Chee Hau Leow[1], Kuin Pang[1,2], Javier Hernandez Gil[3], Terry Matsunaga[4], Mengxing Tang[1]; [1]*Department of Bioengineering, Imperial College London, United Kingdom,* [2]*Institute of Molecular and Cell Biology, Agency for Science, Technology and Research (A*STAR), Singapore,* [3]*Department of Chemistry, Imperial College London, United Kingdom,* [4]*Department of Medical Imaging, University of Arizona, USA*

Background, Motivation and Objective

Phase-change contrast agents (PCCAs) have advantageous properties in terms of smaller size, longer half-life and selective activation control compared to conventional microbubble contrast agents (MCAs), which make them ideal for ultrasound cancer imaging. [1] Acoustic signal from tumour site can be further enhanced by receptor targeted PCCAs. However there is still a lack of understanding of the behaviour of these targeted agents. In this work, we report the use of high frame rate (HFR) imaging to investigate the changes in acoustic signal of Folate Receptor (FR)-targeted versus control PCCAs with breast cancer cells immediately after acoustic activation.

Statement of Contribution/Methods

Both FR-targeted and control PCCAs of the same concentration (~4e6/mL) were introduced into two Opticell chambers with MDA-MB-231 breast cancer cells (3.5 million) grown on bottom plane respectively at 37℃. Cells were incubated with PCCAs in the chambers for 15 minutes at 37℃ and 5% CO2. A customised imaging-activation-imaging sequence was designed on a Verasonics platform for imaging and quantification.[2] PCCAs were activated by focused pulses (8MHz, 5-cycles) with MI of 1.9. Acoustic responses before and after activation were imaged by plane wave (4MHz, 1-cycle) with MI of 0.1. The ultrasound high frame rate imaging (500 frames per second with 8-angle compounding) was used to quantify the acoustic signal enhancement after activation and optical microscope imaging were acquired to validate the ultrasound activation (Fig b). All frames were subtracted by the mean pixel intensity measured before activation to remove the background.

Results/Discussion

Experimental results demonstrate that FR-targeted PCCAs can attach to target cells and be vaporised. The acoustic signal of targeted PCCAs is persistent after activation, with 70% acoustic signals remaining 1s after activation, compared to the control where only 40% of the acoustic signals remain (Fig a). This suggests that most of the targeted agents were not detached by the activation pulse (Fig d). The HFR imaging used in this study showed the fast decay of the acoustic signal immediately after the activation, particularly for the control PCCAs. Cytotoxicity test showed the PCCAs used did not appear to affect cell viability during the experiments (Fig c).

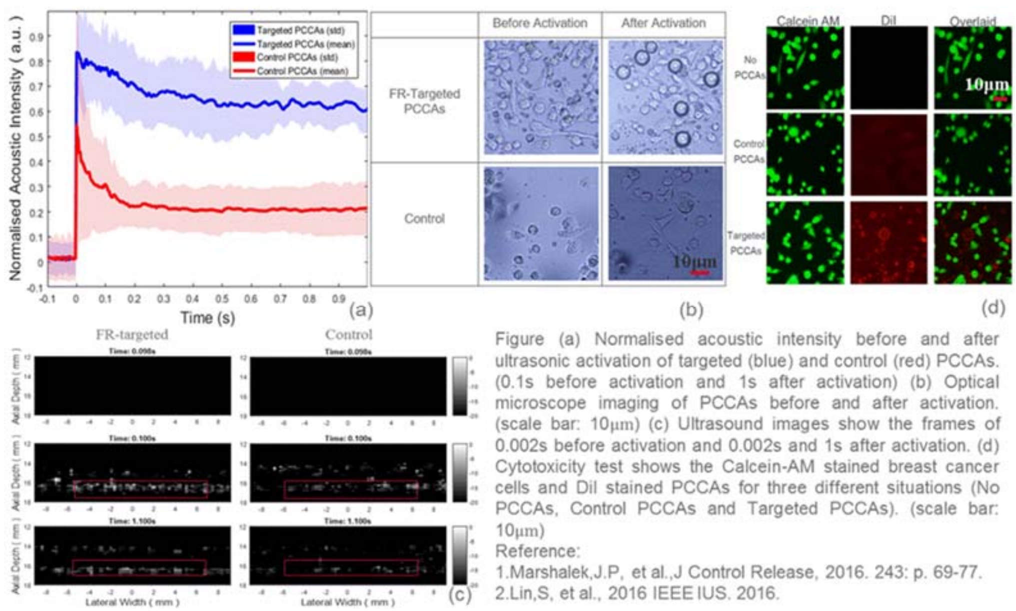

Figure (a) Normalised acoustic intensity before and after ultrasonic activation of targeted (blue) and control (red) PCCAs. (0.1s before activation and 1s after activation) (b) Optical microscope imaging of PCCAs before and after activation. (scale bar: 10μm) (c) Ultrasound images show the frames of 0.002s before activation and 0.002s and 1s after activation. (d) Cytotoxicity test shows the Calcein-AM stained breast cancer cells and DiI stained PCCAs for three different situations (No PCCAs, Control PCCAs and Targeted PCCAs). (scale bar: 10μm)

Reference:

1.Marshalek,J.P, et al.,J Control Release, 2016. 243: p. 69-77.
2.Lin,S, et al., 2016 IEEE IUS. 2016.

3K-6

5:15 pm **Microbubbles Kinetics in Ultrafast Ultrasound Localization Microscopy**

Claudia Errico[1], Olivier Couture[1], Mickael Tanter[1]; [1]*Institut Langevin (CNRS, ESPCI, INSERM), Paris, France*

Background, Motivation and Objective

Ultrafast Ultrasound Localization Microscopy (uULM, Couture et al. IEEE IUS 2011) takes inspiration from the FPALM technique applied in optics as it relies on the detection of single scatters localized at a resolution below the half-wavelength theoretical limit. The tracking of microbubbles injected in the blood stream lead to unprecedented resolution for in-vivo imaging of the rat brain (Errico et al., Nature, 2015). However, due to the microbubble kinetics in small vessels, a trade-off exists between the duration of the ultrasound acquisition, the local concentration of contrast agents (CA), and the detection of fine microvessels, which we explore in this study.

Statement of Contribution/Methods

A programmable ultrafast ultrasound scanner (SuperSonic Imagine, Aix en Provence, France) was used to run a continuous ultrasensitive Doppler sequence (-3°, 0° and 3°, PRF = 1500Hz) at 500 compounded frames per second on the brain of adults Sprague Dawley rats. Microbubbles accumulated for 150s, and uULM image processing was applied to super-resolve the cerebral microvasculature (Errico et al.2015). Microbubble tracking helped us estimate the local concentration of contrast agents C_local (t) in representative vessels of diameter ranging from 8µm to 68 µm. Given the spatiotemporal coordinates of CA within the brain, we calculated the volumetric flow rates in each selected vessel.

Results/Discussion

Larger conduits with lower vascular resistance are perfused faster, hence shorter ultrasound acquisition time were required to achieve super-resolved reconstruction (Figure1A). The effect of the local concentration of contrast agents on the spatial resolution became clearer when we measured the microbubbles accumulation speed (Figure1B). Eventually, we measured the spatiotemporal fluctuation ratio of maximum in-plane velocity distribution in few selected vessels with blood stream oriented in opposite directions (up/down-stream blood flow) to demonstrate that very short ultrasound acquisition (<10s) are suitable for the detection of larger vessels (>40 µm). However, vessels smaller than 20µm require more than ~30s in average to be visible. Ultrasound super-resolution techniques is limited by the incompressible perfusion time of microbubbles in capillaries, which yield a fundamental compromise between the observation scale and the acquisition time.

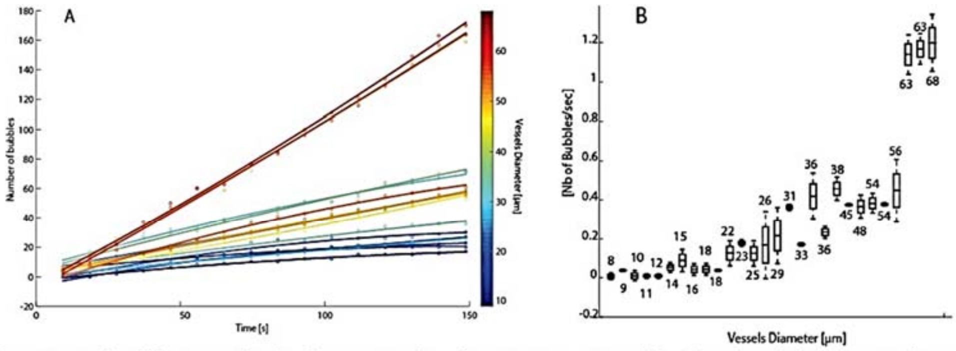

Figure 1: **Trade-off between the local concentration of contrast agents and the duration of the ultrasound acquisition in uULM. (A):** Microbubbles accumulation in vessels of different sizes (8µm to 68 µm). **(B):** Microbubbles accumulation speed within the neurovascular bed

4K - MSP: Optimizing Imaging Performance

Diplomat Room

Saturday, September 9, 2017, 4:00 pm - 5:30 pm

Chair: **Michael Insana**
University of Illinois at Urbana-Champaign

4K-1

4:00 pm **Adaptive Ultrasound Clutter Rejection through Spatial Eigenvector Filtering**

Francois Vignon[1], Jun Seob Shin[2], Sheng-Wen Huang[2], Jean-Luc Robert[2]; [1]*Philips Research North America, Cambridge, Massachusetts, USA,* [2]*Philips Research North America, Cambridge, MA, USA*

Background, Motivation and Objective

Off-axis clutter is a significant cause of image degradation in ultrasound. Adaptive weighting methods based on signal coherence, and adaptive beamforming approaches based on signal direction of arrival, have been proposed to address this problem.

Clutter removal is also an important component of pre-processing prior to flow estimation, and adaptive clutter filters based on singular value decomposition (SVD) to separate clutter from signal have been successfully developed in this context.

In this study, we implement SVD clutter suppression with similar principles as those used in flow imaging, and apply it for beamforming: in flow, the goal is to remove low temporal frequency components (clutter moves slowly), while in beamforming, the goal is to remove high spatial frequency components (clutter comes from off-axis). In both, decomposition of the data matrix into singular vectors is expected to maximize separation between real signal and clutter.

Statement of Contribution/Methods

For each pixel, an M by N per-channel data matrix is estimated from the aligned data received from different observations of that pixel (N = number of channels, M = number of observations, for example all depth samples in 2mm of digitized data). Singular Value Decomposition (SVD) of that matrix yields eigenvectors which correspond to the most important "modes" of the per-channel data. The mean spatial frequency of each eigenvector is estimated, and the eigenvectors with relatively high mean spatial frequencies (corresponding to off-axis signals) are attenuated prior to SVD reconstruction. The filtered per-channel data thus obtained are then summed to yield a pixel value estimate with attenuated contribution of the off-axis signals.

Results/Discussion

The technique is applied on in vivo cardiac data acquired with the S5-1 probe on the Philips iE33 scanner, showing improved contrast through clutter suppression (Figure). Compared to the conventional Delay and Sum (DAS) technique, SVD attenuates left ventricular clutter by a minimum of 5dB without significant tissue signal loss. Larger improvements can be obtained by attenuating off-axis eigenvectors more aggressively.

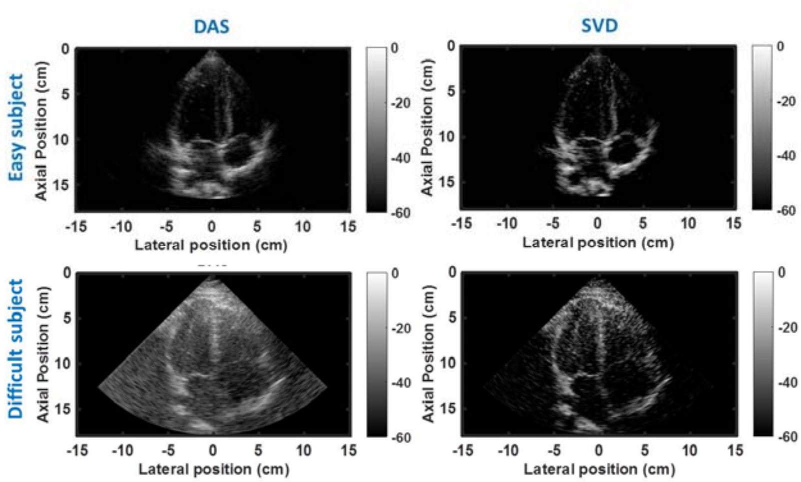

4K-2

4:15 pm **Suppression of Clutter by Rank Adaptive Reweighted Sparse Coding**

Sushanth Sathyanarayana[1], Scott Acton[2], John Hossack[1]; [1]*Biomedical Engineering, University of Virginia, Charlottesville, Virginia, USA,* [2]*Electrical and Computer Engineering, University of Virginia, Charlottesville, Virginia, USA*

Background, Motivation and Objective

Echocardiographic image sequences are frequently corrupted by quasi-static artifacts superimposed on the moving myocardium ("clutter"). Prior work (e.g. Lediju et al., Trans. UFFC 2009) has shown that blind source separation methods can be effective in the removal of clutter. In our prior work (Sathyanarayana et al. IUS 2016), we demonstrated an accelerated method to detect the region of clutter and to remove the clutter signal while retaining the underlying tissue signal. In this approach, clutter was detected and the detection region was held constant while the clutter in the region was removed. However, the spatiotemporal signal characteristics of the clutter are dependent on the underlying physical process from which it is generated, and the same image may be corrupted by clutter from multiple mechanisms or sources.

Statement of Contribution/Methods

In this work, we demonstrate a method to reduce clutter from multiple sources using block sparse coding and alternating between detection and clutter suppression. The clutter is detected using the randomized phase correlation method described in our earlier work. The clutter is effectively an axially sparse, but temporally low rank signal that corrupts the larger rank tissue signal. The estimation of the clutter can be formulated as a sparse coding problem in the principal component domain.

The algorithm initially detects the clutter, and obtains an initial dictionary estimated from principal component analysis (PCA) on the clutter data. The clutter signal is estimated using by performing sparse coding on the detected clutter data and subtracted. This sequence of operations is performed iteratively until clutter is no longer detected, or until a fixed number of steps have been executed as shown in Fig.1. The algorithm was validated using simulated Field-II data and in vivo murine heart data.

Results/Discussion

The performance was quantified in vitro by measuring the RMS error with respect to a ground truth dataset with no clutter. The error with respect to the ground truth was reduced from 153±11.3 a.u. to 2.34±0.22 a.u. The average clutter reduction in the in vivo data was 10.16±0.43 dB. Each iteration of the algorithm is progressively less computationally complex, as there is less clutter to be removed after each iteration.

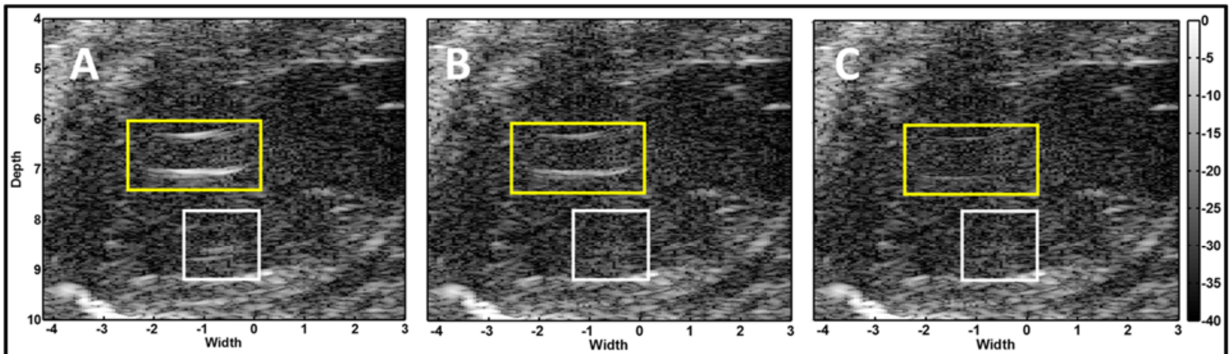

Fig.1. Progressive removal of clutter using the proposed method. The white box encloses the low rank clutter and the yellow box encloses the high rank clutter. A. Original image B. Decluttering (Iteration 1) C. Decluttering (Iteration 2).

4K-3

4:30 pm Optimal Clutter Filtering for Improved Perfusion Sensitivity

MinWoo Kim[1], Jamila Hedhli[1], Lawrence Dobrucki[1], Craig Abbey[2], Michael Insana[1]; *[1]University of Illinois at Urbana-Champaign, USA, [2]Universtiy of California Santa Barbara, USA*

Background, Motivation and Objective

Power Doppler (PD) is the preferred technique for accessing weakly scattering blood cells with low-velocity flow. However, strong clutter decreases sensitivity of the blood signals, which degrades micro-vasculature imaging. Eigen-based filtering methods have been developed to separate the independent scattering sources using both spatial and slow-time statistics of echo data. We recently found that extending data into frame-time sampled on the order of Hz increases the sensitivity of the weak perfusion signal. Higher-order singular value decomposition (HOSVD) effectively decouples these sources. The challenge is to select suitable subspaces to isolate the desired blood components. We propose a subspace selection strategy for optimal HOSVD performance.

Statement of Contribution/Methods

HOSVD decomposes echo data arrays into one core tensor and three eigen-matrices. The core tensor is related to energy distribution of individual eigen-components and the matrices contain spatial, slow-time, and frame-time eigenvectors. The first step of the selection method is using the core tensor to roughly decide subdomains of the clutter and noise, which is attributed by echogenicity disparity between sources. The second step is investigating Doppler frequency contents of the individual temporal eigenvectors. The selection of the slow-time and frame-time domains is based on the flow speed of interest. The final step is through spatial domain selection by comparing texture of post-filtered PD images by using gray level co-occurrence matrix.

Results/Discussion

A murine model of melanoma was used to verify our filtering methods. Mice were injected with tumor cells on the flank, and its vasculature was scanned by using a system (Visualsonics Vevo 2100), 2 weeks after injection. The figure shows non-filtered and post-filtered images in each step. We can see that the first step suppresses considerable clutter and noise from Fig. A to B, the second step enables visualization of fast (Fig. C) and slow-flow patterns (Fig. D) by selecting different temporal subdomains, and the final step clarified the PD images by maximizing contrast (Fig. E and F). Current methods focus on qualitative visualization of blood flow and perfusion. Ongoing experiments involving phantoms aim to quantify these images.

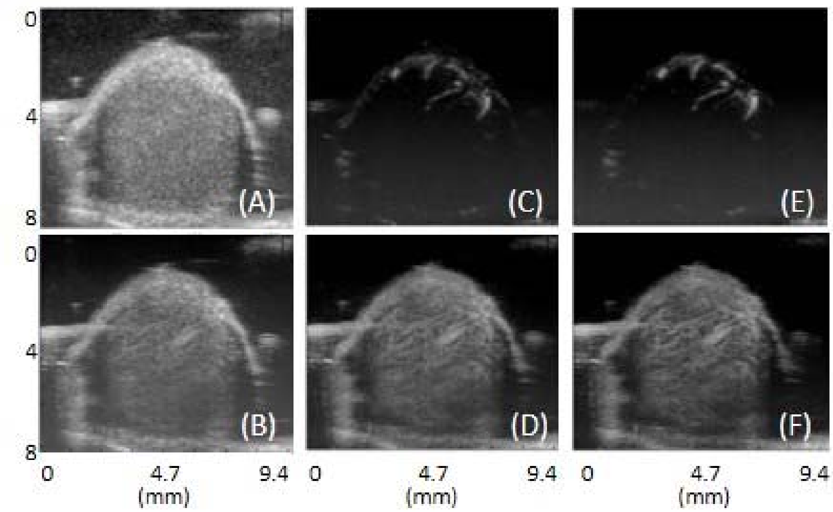

4K-4

4:45 pm Compressed Sensing Based Synthetic Transmit Aperture for Phased Array Imaging

Jing Liu[1], Jianwen Luo[1]; [1]*Tsinghua University, China, People's Republic of*

Background, Motivation and Objective

Based on the linear relationship of channel data between synthetic transmit aperture (STA) and apodized plane wave (PW) firing, we previously proposed compressed sensing (CS) based STA (CS-STA) for linear array (Liu et al, IEEE TMI 2017), which achieves higher frame rate and higher contrast-to-noise ratio (CNR) than STA while maintaining its high resolution. Because diverging wave (DW) instead of PW firing is usually adopted in phased array, CS-STA cannot be directly applied to phased array. In this study, we adapt CS-STA to phased array applications by compensating for the time delays associated with DW firing.

Statement of Contribution/Methods

The procedure of CS-STA for phased array is shown in Fig. 1. First, time delays are applied to transmit multiple DWs and a random partial Hadamard matrix is used to apodize the elements. Then CS reconstruction is adopted to recover the delayed STA channel dataset. At last, the time-aligned STA channel dataset is obtained by compensating for the time delays.

The above method was validated on a 64 element P4-2 phased array (pitch = 0.3 mm) in Field II and a Verasonics Vantage system by comparing CS-STA with 16 and 32 firings (i.e., CS16-STA and CS32-STA, respectively) to STA. A cyst phantom with an attenuation of 0.5 dB/MHz/cm was simulated and the same Gaussian noise was added to the channel data of STA and CS-STA. A CIRS 040 phantom was used in experiments.

Results/Discussion

In simulations, the normalized root-mean-square errors of beamformed data between CS16-STA (6.24%), CS32-STA (4.25%) and STA are tolerable in the noise-free condition. In Gaussian noise condition, CS-STA significantly reduces the visible noise of STA (Fig. 2). The CNRs of the middle cyst of CS16-STA (2.3 dB) and CS32-STA (6.7 dB) are higher than that of STA (-3.3 dB). In experiments, the regions marked as rectangles in Fig. 3 are out of boundary and should be dark. However, there are visible noises in STA image, which is reduced significantly in CS-STA images. The average noise powers of this region are 542, 22.8 and 16 for STA, CS16-STA and CS32-STA, respectively. The CNRs of the cysts marked as arrows are -2.6, 0.1 and 3.2 dB for STA, CS16-STA and CS32-STA, respectively. The difference in the full width at half-maximum of the wires between CS-STA and STA is smaller than 0.05 mm. In conclusion, it is proved that CS-STA in phased array is suitable and has the same advantages in linear array.

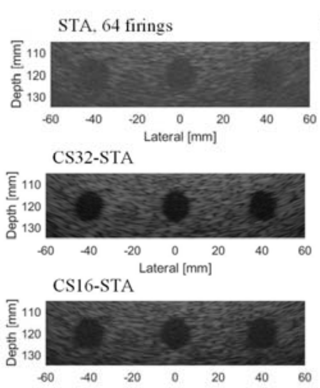

Fig.2. Zoomed-in B-mode images of a simulated cyst phantom with a dynamic range of 75 dB.

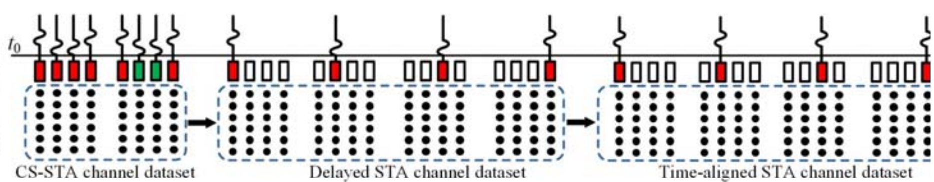

Fig.1. Flow chart of CS-STA for phased array.

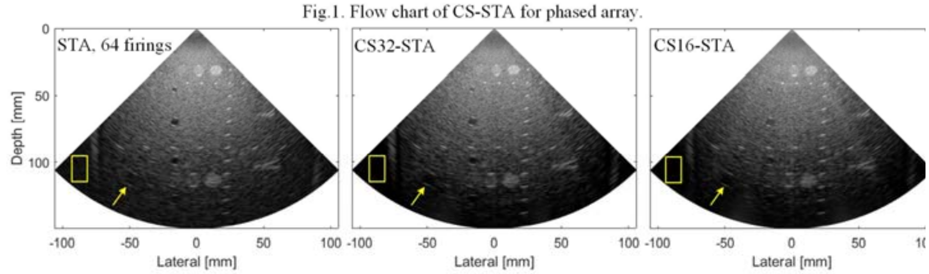

Fig.3. B-mode images of a CIRS 040 phantom with a dynamic range of 75 dB.

4K-5

5:00 pm Random Incident Sound Waves for Fast Compressed Pulse-Echo Ultrasound Imaging

Martin Schiffner[1], Georg Schmitz[1]; [1]*Medical Engineering, Ruhr-Universität Bochum, Bochum, Germany*

Background, Motivation and Objective

Multiple research groups have recently innovated image recovery methods for fast pulse-echo ultrasound imaging (UI) that combine inverse scattering techniques with compressed sensing (CS). These methods alleviate the inherent tradeoff between the image quality and the image acquisition rate. The choice of the incident sound field is a crucial degree of freedom to implement the specific requirements of CS, e.g. incoherent measurements. Previous publications exclusively investigated steered plane waves (PWs).

In this study, we leverage three types of random ultrasonic waves to better conform with the requirements of CS. This increases both the image quality and the speed of convergence.

Statement of Contribution/Methods

We synthesized the random ultrasonic waves by applying pseudorandom time delays, apodization weights, or combinations thereof to the individual elements of a linear transducer array. We recovered spatial fluctuations in compressibility from measurements of the scattered sound by solving a linear inverse scattering problem (ISP). The ISP based upon a realistic physical model, accounting for diffraction, power-law absorption, and dispersion, and was regularized by the CS framework. The postulated nearly-sparse representations of the spatial fluctuations in compressibility were obtained by two linear transforms and recovered by a sparsity-promoting nonlinear method.

We validated the random ultrasonic waves using radio frequency signals acquired from two numerical phantoms, which were sparse in the spatial domain (obj. A) or the Fourier domain (obj. B), for four signal-to-noise ratios and a real phantom consisting of nine wires (obj. C). We emitted only a single wave of each type per phantom.

Results/Discussion

Applying pseudorandom time delays to the transducer elements (cf. a)), for instance, reduces the axial and lateral -6 dB-widths of the point spread function (PSF) (cf. b)) by up to 25 %. The CS-based recovery eliminates the incoherent artifacts in the PSF, whereas the coherent sidelobes remain. For the numerical phantoms, the mean recovery errors are significantly reduced by up to 23.7 % (obj. A) and 43 % (obj. B, cf. c)) while the speed of convergence is up to 29.5 % faster. These findings translate to the other types of random ultrasonic waves and the experimental data (cf. d)).

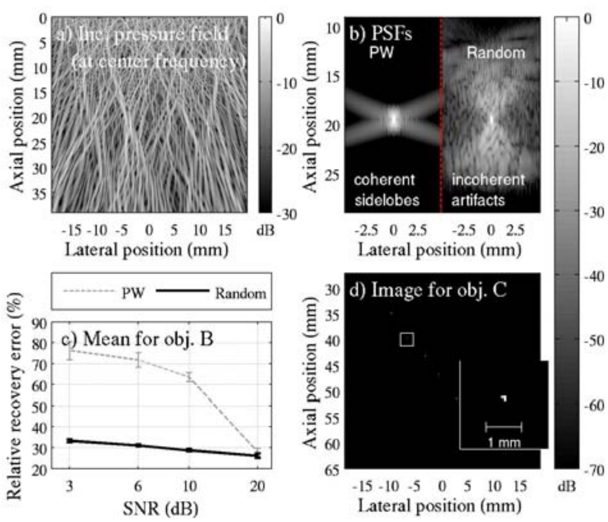

4K-6

5:15 pm Accelerating Plane Wave Imaging through Deep Learning-Based Reconstruction: An Experimental Study

Maxime Gasse[1], Fabien Millioz[1], Emmanuel Roux[2], Hervé Liebgott[1], Denis Friboulet[1]; [1]*Univ.Lyon, INSA-Lyon, UCBL1, UJM-Saint Etienne, CNRS, Inserm, CREATIS UMR 5220, U1206, F-69100, Lyon, France,* [2]*Department of Information Engineering, Università Degli Studi di Firenze, Firenze, Italy*

Background, Motivation and Objective

Obtaining ultrafast images using steered plane wave (PW) imaging remains a challenge due to the trade-off between image quality and frame rate. PW imaging indeed relies on compounding in order to preserve a good image quality, usually using multiple successive emissions, which in turn yields a decrease of the frame rate. As opposed to this classical approach, we propose a new strategy to reduce the number of emitted PWs. This is done using a deep learning technique, i.e. by training a convolutional neural network (CNN) to reconstruct high quality images using a small number of PW emissions (typically two).

Statement of Contribution/Methods

The training data was generated as follows. A standard linear array probe (ATL L7-4 38 mm, 128 elements, bandwidth 4-7 MHz, transmitted frequency 5.208 MHz) was interfaced with a Verasonics system. 31 PWs were emitted (angle spanning ±15° in one degree steps). For each PW emission, the received raw-data was then processed using the f-k migration method [Garcia et al. IEEE UFFC13] to produce the reconstructed RF image. These 31 images were then averaged to get the final compounded image used as a reference in the training process, while only two images corresponding to angles -10° and +10° were given as input to the CNN.

A total of 2000 reference images were acquired, 1000 images from in-vivo tissues (carotid and thyroid), 500 images from a Gammex phantom (410 SCG), and 500 images from a water-based polyamide mixture with air bubbles. 1800 images were used for training, 100 for validation, and 100 for testing. The CNN employed in this study is a fully-convolutional neural network, with 4 hidden layers and maxout activation units. Training is done via stochastic gradient descent and the minimized loss function is the mean absolute error (MAE) between the CNN-reconstructed and the reference RF image, plus a L2 regularization term.

Results/Discussion

Our approach was evaluated by comparing the CNN-based reconstruction of the test images with the conventional compounding method (see Fig. 1). Preliminary results indicate that CNN-based reconstruction is a very promising approach, as the reconstructed images are visually very close to those obtained by standard compounding with 31 PWs, while implying the emission of only 2 PWs.

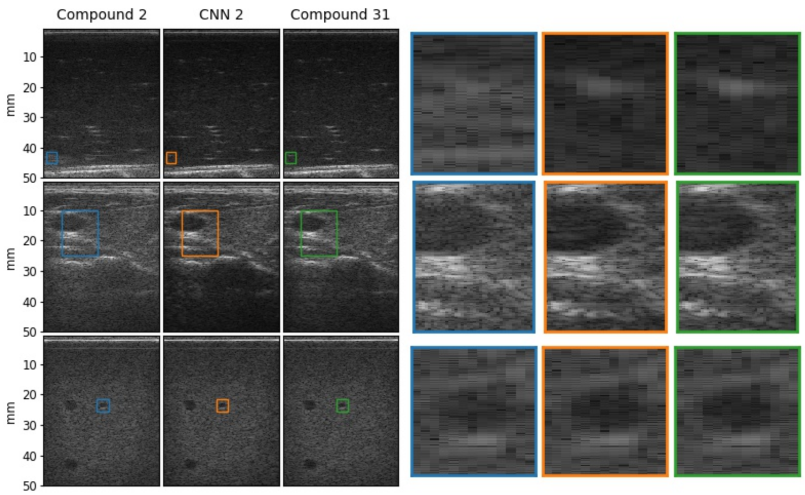

B-mode images obtained from the compounding of 2 PWs (Compound 2), the CNN reconstruction from 2 RF images (CNN 2), and the compounding of 31 PWs (Compound 31). On the left are displayed full images, on the right a zoom on small regions. From top to bottom, data obtained from: a water-based polyamide mixture; in-vivo tissue (thyroid region); a Gammex phantom.

5K - MIM: Medical Imaging

Blue Room

Saturday, September 9, 2017, 4:00 pm - 5:30 pm

Chair: **Roger Zemp**
University of Alberta

5K-1

4:00 pm **Compressed Quantitative Acoustic Microscopy**

Jonghoon Kim[1], Paul Hill[1], Nishan Canagarajah[1], Daniel Rohrbach[2], Denis Kouamé[3], Jonathan Mamou[2], Alin Achim[1], **Adrian Basarab[3]**; *[1]Visual Information Laboratory, University of Bristol, Bristol, United Kingdom, [2]Lizzi Center for Biomedical Engineering, Riverside Research, NYC, New York, USA, [3]IRIT, UMR CNRS 5505, University of Toulouse, Université Paul Sabatier, Toulouse, France*

Background, Motivation and Objective

Scanning acoustic microscopy (SAM) is a well-accepted modality for forming quantitative 2D maps of acoustic properties of soft tissues at microscopic scales. In our SAM studies, the sample is raster-scanned (spatial step size of 2 µm) using a 250 MHz transducer resulting in a 3D RF data cube. Each RF signal is processed to obtain, for each spatial location, acoustic parameters, e.g., speed of sound (SoS). The scanning time is directly dependent on the sample size and can range from few minutes to hours. In order to maintain constant experimental conditions for the sensitive thin sectioned samples, the scanning time is an important practical issue. Hence, the main objective of this work is to reduce the scanning time by reconstructing SAM images from spatially under sampled measurements, based on the theory of compressive sampling (CS).

Statement of Contribution/Methods

The contribution of this study is twofold: i) to propose a spatial sampling scheme that simultaneously meets the CS requirements and the practical constraints of SAM acquisition, ii) to design a dedicated reconstruction algorithm. We investigated a spiral sensing pattern (Fig. 1d) that results in under sampled data compared to 2D raster scan. The classical way of restoring images from CS measurements is to search for the sparsest solution (smallest l1-norm) of an underdetermined linear. In this work, an approximate message passing (AMP) algorithm, previously shown to outperform l1-norm minimization, was implemented. AMP uses an iterative process performing sparse representation-based image denoising. This study demonstrates that a discrete wavelet transform is an appropriate choice for SAM. The Cauchy distribution was used to construct the denoising function embedded in the proposed AMP algorithm.

Results/Discussion

SoS maps of cancerous human lymph nodes were reconstructed using the proposed algorithm (Fig. 1b) and an existing AMP-ST method using soft thresholding denoiser (Fig. 1c) from compressed spiral data (70% less data than classical raster scan). In addition to the sample reduction, the spiral pattern allows fast scanning because it is an indefinitely differentiable continuous curve easily implementable with servo motors. The proposed spiral scanning pattern reduces scan time by ~60%. PSNR and SSIM show improved reconstruction of the proposed algorithm when compared to AMP-ST (Fig. 1e,f).

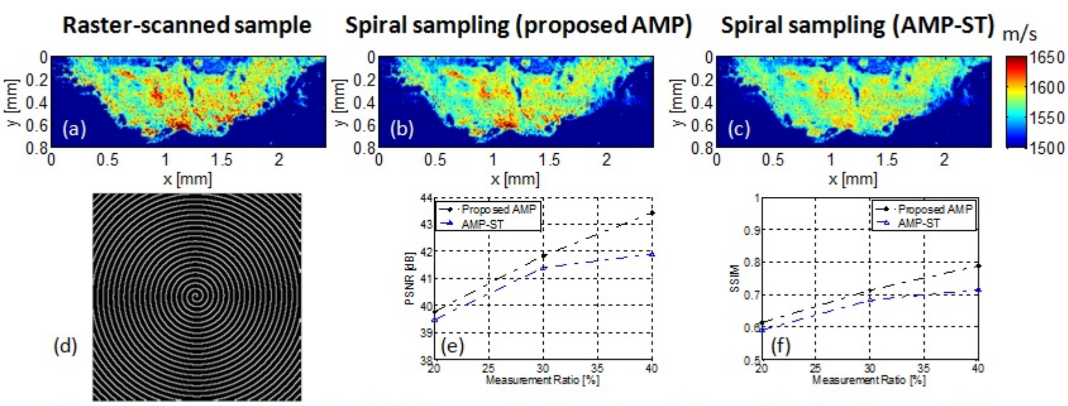

Fig. 1 Illustrative result showing the SoS images of a thin section of a human lymph node acquired from a colorectal cancer patient: (a) conventional raster-scan, (b,c) spiral scan (70% less data points), (d) spiral sensing scheme. (e,f) Evolution of PSNR (peak signal to noise ratio) and SSIM (structural similarity) for different measurement ratios (% of sensed data points compared to stadard raster-scan) for the proposed AMP and existing ST-AMP algorithms.

5K-2

4:15 pm **A Multimodal Microscopic Imaging System based on Multispectral Imaging/Analysis and High-Frequency Ultrasound Elastography for Examination of Resected Human Tumors Ex Vivo**,

Jihun Kim[1], Jun-Young Kim[2], Anna Seo[3], Eunjoo Kim[4], Jae Youn Hwang[1]; *[1]Department of Information and Communication Engineering, Daegu Gyeongbuk Instittue of Science and Technology, Daegu, Korea, Republic of, [2]Department of Orthopedic Surgery, Kyungpook National University Hospital, Daegu, Korea, Republic of, [3]3D Convergence Technology Center, Kyungpook National University Hospital, Daegu, Korea, Republic of, [4]Department of Nano & Energy Research, Daegu Gyeongbuk Instittue of Science and Technology, Daegu, Korea, Republic of*

Background, Motivation and Objective

We report a multimodal microscopic imaging system which offers high-frequency ultrasound B-mode, acoustic radiation force impulse (ARFI), and multispectral image for examination of excised human tumor ex vivo. Examination of excised tumors from the lesions of interest is one of the crucial procedures during surgical operations to treat cancer.

Particularly, if tiny reaming tumors exist at the surgical sites after the resection of tumors, they may result in unwanted outcomes including cancer recurrence or metastasis to the other organs. To avoid them, accurate examination of tumors resected. Thus, we built a multimodal microscopic imaging system to examine the excised tumors quantitatively.

Statement of Contribution/Methods

A multimodal microscopic imaging system based on high-frequency ultrasound and optical imaging techniques was built in an inverted microscope. A 45 MHz high-frequency ultrasound transducer is utilized here for high-resolution ultrasound B-mode and ARFI imaging. The transducer attached to x-, y-, and z- axis motorized stages, which allows both two- and three-dimensional ultrasound imaging. Moreover, a liquid-crystal tunable filter (LCTF) allowing wavelength selections of light with a bandwidth of ~10 nm is integrated with the system for multispectral imaging. Illumination light from a mercury lamp passed through an excitation filter and was directed to a target of interest by a dichroic mirror and an apochromatic objective lens for excitation of the target. Emitted light was recorded using a highly sensitive CCD camera. Each imaging modality of the developed system was evaluated using a tissue-mimicking phantom. After that, the system was applied to examine resected human colorectal tumors ex vivo.

Results/Discussion

This system was evaluated with a tissue-mimicking phantom. In addition, the excised human colorectal tumors were examined accurately as shown in Figure. The proposed system here offers highly resolved anatomical, mechanical, and chemical information on tumors, thus allowing the accurate detection of tumor regions from the surface to deep inside of tissues ex vivo. These results therefore suggest that the multimodal microscopic imaging system has the potential to undertake quantitative examinations of excised tumors for surgical operations ex vivo.

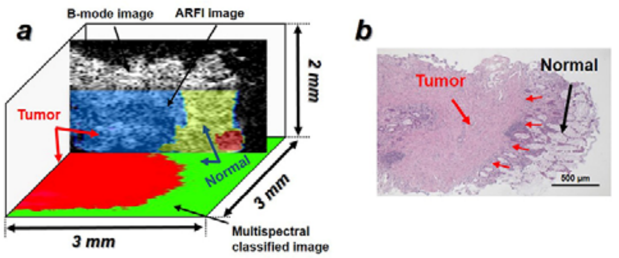

Figure 1. A multimodal image of resected human colorectal tumors obtained using the system
(a) Optical Multispectral classified, high-frequency B-mode, and ARFI image of colorectal tumors (b) H&E stain image of colorectal tumors.

5K-3

4:30 pm Magnetomotive Ultrasound Imaging Using the Nonlinear Magnetization of Nanoparticles

Tim C. Kranemann[1], Thomas Ersepke[1], Georg Schmitz[1]; [1]*Chair for Medical Engineering, Ruhr-Universitaet Bochum, Bochum, NRW, Germany*

Background, Motivation and Objective

In magnetomotive (MM) ultrasound (US) imaging, magnetic nanoparticle (MNP) labeled tissue is moved by a magnetically induced force. Therefore, all MNPs in the field of view are excited simultaneously and a high field strength results in magnetic saturation of MNPs, hence, in a linear response. The linear displacements are spatially resolved by US tracking methods.

Recently [1], it was proposed to detect sound emissions from magnetization changes of MNPs to quantify their concentration and image their distribution. Spatial resolution was achieved with magnetic fields that enable the localized excitation of harmonics by the nonlinear magnetization characteristic of MNPs.

In this contribution, we present a simple magentic field configuration that allows using the nonlinear MNP response to create a localized MM displacement. That could be used to improve the spatial resolution in MMUS.

Statement of Contribution/Methods

For a proof of concept, a field configuration different from the conventional MMUS set-up is used to excite a nonlinear response of MNPs. This is achieved by generating a field-free point (FFP) in a static magnetic gradient field that is moved back and forth along one axis by a homogeneous time-varying field. When the FFP crosses an MNP bolus in a tissue-mimicking phantom, the magnetization changes nonlinearly and thereby generates nonlinear force components leading to harmonics in the bolus displacement. MNPs distant from the FFP are saturated and respond in the conventional, linear way.

An Ø 32 mm x 35 mm cylindrical solenoid is used to generate a spatially homogeneous, sinusoidal field of 18 mT on its center axis. Two opposite permanent magnets are placed outside the solenoid to generate a gradient field of up to 3.4 T/m and thereby an FFP on the solenoid's center axis. On that axis, the gradient is approximately constant and the homogeneous sinusoidal field moves the FFP. Inside the solenoid, a gelatin (15% w/w) phantom is placed with a gelatin-MNP (90% Resovist, Bayer Schering Pharma) cylindrical bolus of Ø 4 mm x 4 mm. The coil set-up is moved so that the FFP crosses the bolus at different positions. To measure the displacement of the bolus quantitatively, a vibrometer is used.

Results/Discussion

The MNP bolus shows a typical MMUS displacement of 0.8 μm at the fundamental frequency. The dependence of additional nonlinear displacement on the bolus position was well detected. The maximum amplitude of the second harmonic was 23 dB lower and the third was 35 dB lower than the displacement at the fundamental.

The space-dependent harmonic response of MNPs agrees well with theoretical expectations. Thereby, the FWHM of the second harmonic is 0.4 mm, which is small compared to the 8.4 mm FWHM of the fundamental. This indicates that the localized excitation can readily be used for an improved localization of an MNP bolus.

[1] B. Gleich, et. al., BMC Med. Imag., 2011.

5K-4

4:45 pm Ultrasound Bandwidth Enhancement through Pulse Compression Using a CMUT Probe

Yanis Benane[1], Roberto Lavarello[2], Denis Bujoreanu[1], Christian Cachard[1], François Varray[1], Alessandro Stuart Savoia[3], Emilie Franceschini[4], Olivier Basset[1]; [1]*Univ.Lyon, INSA-Lyon, Université Claude Bernard Lyon 1, UJM-Saint Etienne, CNRS, Inserm, CREATIS UMR 5220, U1206, F-69100, Lyon, France,* [2]*Laboratorio de Imagenes Medicas, Departamento de Ingenieria, Pontificia Universidad Catolica del Perù, Lima, Peru,* [3]*Dipartimento di Ingegneria, Università degli Studi Roma Tre, Via della Vasca Navale 84, 00146, Rome, Italy,* [4]*Aix-Marseille Université, CNRS, Centrale Marseille, Laboratoire de Mécanique et d'Acoustique, Marseille, France*

Background, Motivation and Objective

In ultrafast imaging using pulse compression, the image quality is limited by the bandwidth of the ultrasonic (US) transducer. Thus extending the effective bandwidth of the US transducers could improve the performance of the current US imaging methods. Resolution Enhancement Compression (REC) allows bandwidth enhancement by exciting the ultrasound transducer with frequency and amplitude modulated signals. By compressing these signals in reception with a Modified Wiener Filter (MWF), REC boosts the energy of the backscattered echoes in the frequency bands where the transducer operates inefficiently. This technique has been successfully applied on piezoelectric US probes. However, no real study was conducted on Capacitive Micromachined Ultrasonic Transducers (CMUT). This work is focussed on the implementation of the REC on a CMUT probe in order to evaluate the resolution improvement.

Statement of Contribution/Methods

The pre-enhanced chirp, V_{pre}, used as the excitation for the US transducer in REC is obtained using Eq1. V_{lin} is a 4µs frequency modulated chirp tapered with a 20% Tukey cosine window. h_1 is the Impulse Response (IR) of the transducer and h_2 is the desired IR, of a bandwidth larger than the one of h_1. The compression of the received signals is performed using the MWF as in Eq2 which represents the emitted signal adjusted with regard to transducer's bandwidth and acquisition noise. REC was implemented in simulation, by considering the experimental IR of the CMUT probe, measured using a hydrophone. Experimental results were obtained using the research platform UlaOP. The performance of the MWF compression was evaluated on a single target and an anechoic cyst centred at 22mm depth. The media was insonified using 13 plane waves with steering angles distributed between ±12°.

Results/Discussion

The objective was achieved by boosting the bandwidth of the CMUT probe by 22 % (at -6 dB and -10 dB) using the REC approach, compared to a Conventional Pulse (CP) emission (E). A better axial resolution is noticed (+ 15 % at -6 dB): respectively 210 µm and 242 µm for REC and CP (A, B). The CNR is also improved using the REC technique 7.45 dB against 6.36 dB for CP (C, D).

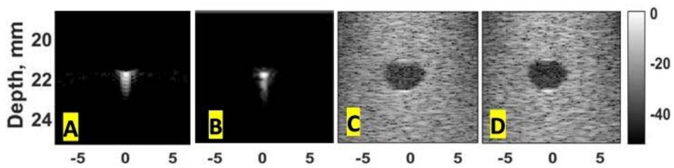

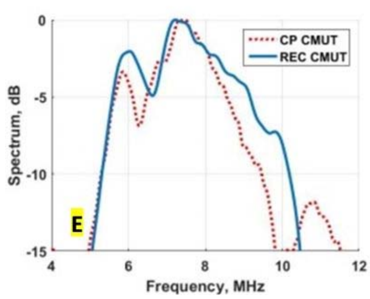

Eq.1: $h_1 * V_{pre} = h_2 * V_{lin}$

Eq.2: $MWF = \frac{V'^{*}_{lin}}{|V'_{lin}|^2 + \gamma \overline{SNR}^{-1}}$

Figure 1.
CMUT probe results: A, C – **CP**; B, D – **REC**.
E – Obtained bandwidths with the CMUT probe using CP and REC

5K-5

5:00 pm **Accelerating Ultrasound Speed of Sound Tomography through Reflection and Transmission Imaging**

Qi You[1], Yingqiao Zheng[1], Yunhao Zhu[1], Rungroj Jintamethasawat[2], Yuxin Wang[1], Jie Yuan[1], Xueding Wang[2], Paul Carson[2]; [1]*School of Electronics Science and Engineering, Nanjing University, Nanjing, Jiangsu, China, People's Republic of,* [2]*Department of Radiology, University of Michigan, Ann Arbor, Michigan, USA*

Background, Motivation and Objective

Imaging of speed of sound holds great promise for medical detection and diagnosis since it is a quantitative, physical property of tissues not imaged by other means. The full Waveform Inversion (FWI) based method can build speed of sound images with high spatial resolution but it is computationally very demanding. The iterative Algebraic Reconstruction Technique (ART) is a favored choice for fast projection reconstruction problems, but its convergence, like that of other algorithms, is strongly limited when used for limited angle tomography, i.e. tomography without full 360º projection data. Limited angle ART is prone to yield inaccurate results and directionally dependent artifacts. Other speed of sound (SOS) imaging methods with fast reconstruction properties can only provide coarse resolution with high variance and bias. Here, we propose a fast SOS imaging method with good quantitative and spatial fidelity.

Statement of Contribution/Methods

In our study, two 128-element linear ultrasound transducer arrays are placed at the opposite side of the imaging target. First, we apply an ultrasound tomography method in classic pulse echo mode, using various steering angles with transmit beamforming. Differences in time-of-flight along different transmission directions are reflected in echo-phase information which gives an approach to a very fast reconstruction of SOS images[1]. Yet, this first step maintains substantial directional blurring lateral to the central beam direction and streak artifacts. Then, we use this poor quality SOS image as an initial result for the iterative optimization implemented in ART. With an approximately correct initial SOS map, blurring from limited angle ART in the axial direction is alleviated and the image is much improved quantitatively. The simulation study was first conducted in a breast tissue-mimicking phantom. The phantom consists of 16 circular and diamond objects with SOS ranging from 1430 m/s to 1590 m/s, mimicking malignant and benign masses. The circular objects are embedded in the homogeneous material that has SOS of 1510 m/s and mimics fatty and glandular tissues. Similar physical experiments are also performed.

[1]Jaeger, Michael, et al. "Computed ultrasound tomography in echo mode for imaging speed of sound using pulse-echo sonography" Ultrasound in medicine & biology, 2015

Results/Discussion

Our reconstructed SOS map shows ART reduces error in every contrast region, where the absolute errors in high contrast regions are greater than those in low contrast regions. The mean relative SOS error with ART applied sequentially is 66% less than that without ART. Meanwhile, the axial artifacts caused by limited angle tomography due to the lack of full information is obviously reduced. Our experimental results in phantoms show improvements in both image quality and computational speed. With optimization, the proposed fast SOS imaging method might help future breast cancer detection and diagnosis.

5:15 pm **Pulse Wave Velocity (PWV) and Compliance Estimation and Mapping Using Pulse Wave Imaging (PWI) in Healthy, Stenotic and Post-Endarterectomy Carotid Arteries *In Vivo***

Iason Zacharias Apostolakis[1], Pierre Nauleau[1], Paul Kemper[1], Edward S. Connolly[2], Elisa Konofagou[1]; [1]*Columbia University, USA,* [2]*Columbia University Medical Center, USA*

Background, Motivation and Objective

Pulse Wave Velocity (PWV), a surrogate marker of arterial stiffness, is associated with cardiovascular mortality and vascular atherosclerotic burden. The Bramwell-Hill equation links PWV with arterial compliance. Pulse wave imaging (PWI) is a noninvasive technique developed by our group for tracking the propagation of pulse waves along the arterial wall at high spatial and temporal resolution. It has been previously enhanced to track piecewise PWVs (pPWVs) and produce PWI compliance maps. This study aims to use PWI to characterize the carotid arteries of healthy, atherosclerotic and post endarterectomy subjects and assess its utility as a monitoring tool.

Statement of Contribution/Methods

The right common carotids of four healthy volunteers, the diseased carotids of four atherosclerotic patients and the operated carotids of four post-endarterectomy patients were scanned using a 5 MHz linear array. Coherent compounding sequences with 3 and 5 plane waves were used. Axial wall velocities (v_{PWI}) were depicted over time to generate spatiotemporal maps of pulse propagation. Regional PWVs and pPWVs with the associated r^2 values were calculated by performing linear regression on Kalman-filtered 50% upstroke markers of the v_{PWI}. The corresponding compliance (C_{PWI}) values were estimated via the Bramwell-Hill equation. Two of the atherosclerotic patients underwent carotid endarterectomy and plaque samples were recovered and histologically examined.

Results/Discussion

Fig. 1 shows C_{PWI} maps of healthy subjects, atherosclerotic and post-endarterectomy patients. For the atherosclerotic patient, the plaque histology is also shown. PWV was higher in atherosclerotic and post-endarterectomy patients (9.52±4.92 m/s,7.92±3.51 m/s) compared to healthy subjects (5.04±1.15 m/s). Significantly higher coefficient of variation of the peak v_{PWI} along the arterial wall and lower r^2 values were found between normal and atherosclerotic carotids ($p \leq 0.05$) followed by decrease and increase, respectively, in the post-operative patients compared to the atherosclerotic ones, indicating that homogeneity along the arterial wall was partially restored after surgery. Thus, these initial findings indicate that PWI could serve as a useful imaging tool of monitoring atherosclerosis progression.

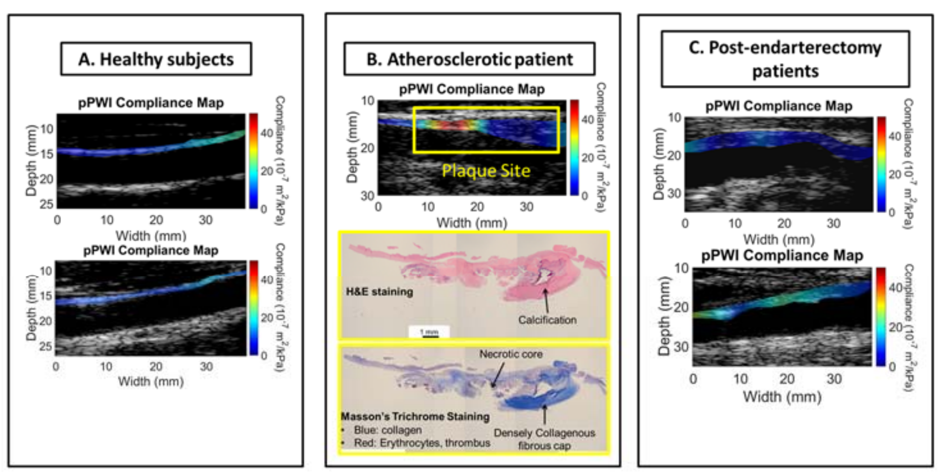

Fig. 1: Compliance maps for A. healthy subjects, B. an atherosclerotic patient and C. post-endarterectomy patients. In the case of the atherosclerotic patient, the histological results corresponding to the plaque region indicated with the yellow rectangle are also shown.

6K - Novel Tranducers and Tranducer Applications

Hampton Room

Saturday, September 9, 2017, 4:00 pm - 5:30 pm

Chair: **Scott Smith**
GE Global Research

6K-1

4:00 pm **Air-Coupled 40-Khz Ultrasonic 2D-Phased Array Based on a 3D-Printed Waveguide Structure**

Axel Jäger[1], Dominik Großkurth[1], Matthias Rutsch[1], Alexander Unger[1], Rene Golinske[2], Han Wang[1], Steve Dixon[3], Klaus Hofmann[1], Mario Kupnik[1]; *[1]Technische Universität Darmstadt, Darmstadt, Germany, [2]Brandenburg University of Technology, Cottbus, Germany, [3]University of Warwick, Coventry, United Kingdom*

Background, Motivation and Objective

We present a fully-populated 2D-phased array, capable of emitting directed air-coupled ultrasound at 40 kHz without any grating lobes. In comparison to our previous work [Konetzke et al, IUS 2015], in which we describe a 1D-phased array, we use 3D printing techniques to realize a wave guide structure that fulfills the half-wavelength criteria of 4.3 mm. The key idea is to use the wave-guide structure to separate the vibrating from the acoustic aperture. This is required, since commercially available air-coupled ultrasound transducers are usually optimized to have a certain directivity, and, thus, require a diameter larger than the wavelength. Therefore, these transducers are unsuitable for being used directly in a phased array.

Statement of Contribution/Methods

In this work, we extend and improve our previous approach by providing a geometric model that describes such a 2D array waveguide structure. It fulfills the reduction of the pitch and diameter from an array of transducers of arbitrary diameter down to an array of channels of the desired smaller pitch size. In addition, a constant channel length ensures a constant wave propagation delay without the necessity of electronic correction. We fabricated such a waveguide structure using a 3D printer from a regular polylactic acid (PLA) blend. It houses an array of 8 by 8 commercial transducers, type Murata MA40S4S, Murata Seisakusho, Japan, each having a diameter of 10 mm. We further developed custom electronics to generate the 64 individual excitation signals allowing 2D-steering and focusing. The electronics consists of an FPGA (Zynq 7010, Xilinx Inc, San Jose, CA, USA) and commercial ultrasound pulsers (HV7355, Microchip Technology, Inc. Chandler, AZ, USA). Focal laws are calculated using a custom PC-based application.

Results/Discussion

The fabricated array shows a symmetric main lobe with 18° width and it can be steered over an opening angle of 110° in both directions without any grating lobes, as expected from theory. In addition, we measure a maximum sound pressure level of 145 dB at a distance of 0.3 m. These measurement results prove that our approach using the 3D printed waveguide structure opens the door to numerous ultrasonic air-coupled applications, such as gas flow metering, range finding, anemometry, gesture sensing and acoustic imaging of entire rooms.

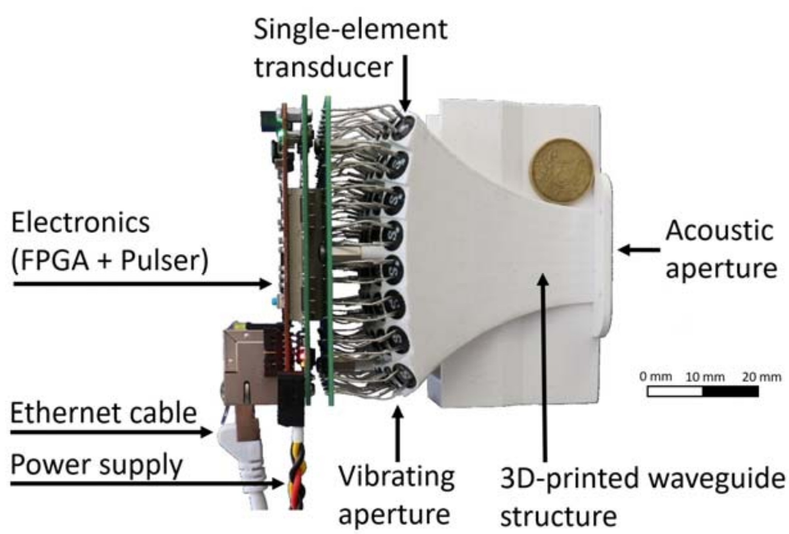

6K-2

4:15 pm **Multi-Focused Acoustic Holograms by 3D printing**

Yang Yang[1,2], Jun Zhang[3], Zeyu Chen[4], Xiangjia Li[5], Jie Jin[5], K.Kirk Shung[4], Yong Chen[5], Qifa Zhou[4,6]; *[1]University Of Southern California, Los Angeles, California, USA, [2]Biomedical Engineering, University Of Southern California, Los Angeles, California, USA, [3]Wuhan University, Wuhan, Hubei, China, People's Republic of, [4]Biomedical Engineering, UNIVERSITY OF southern california, LOS ANGELES, CALIFORNIA, USA, [5]Industrial and Systems Engineering, UNIVERSITY OF southern california, LOS ANGELES, CALIFORNIA, USA, [6]Roski Eye Institute, Department of Ophthalmology, University Of Southern California, Los Angeles, California, USA*

Background, Motivation and Objective

The focused ultrasound (FUS) systems are widely used due to their ability to generate a tight and intense focal region from a distributed source for the non-invasive and safely detection. However, these devices usually require elaborate arrays of a rather complex and cumbersome set of transducers. Holographic techniques are fundamental to applications such as volumetric displays and tweezers. The monolithic acoustic holograms can reconstruct diffraction-limited acoustic pressure fields and arbitrary ultrasound beams.

Statement of Contribution/Methods

The basic of the holography is spatial storage of the phase and/or amplitude profile of the desired wavefront in a manner that allows that to be reconstructed by interference when the hologram is illuminated with a suitable coherent source. Here we introduce a new acoustic hologram that requires only one ultrasonic transducer to generate a complex 3D acoustic field. This hologram placed on top of a transducer is a plastic block that converts a sound wave from a single transducer into a complex sound field.

Results/Discussion

Figure 1 shows a hologram plane will generate 9 focused points by a traditional transducer. The fabrication process starts by defining the desired 2D acoustic field and the plane where it will appear. The image is a square area 20mm in length consisting of 9 focused points (Fig. 1c). The phase map (Fig. 1d) computed by Matlab is rendered into a 3D-printed element whose material has a speed of sound different from the surrounding medium. Then the 3D model needed for printing was generated by Matlab (Fig 1.e) and printed in 2 hours (Fig 1.f). In the reconstruction process (Fig. 1b) a traveling plane wave passes through the hologram, emerges with the required phase distribution and diffracts to form a real image at the desired plane then propagates further. This controllable hologram planes are cost effective and easy to fabricate by a 3D printer. This technique shows a potential application in manipulation of solids in water (particle manipulation), ultrasound therapy, non-destructive testing, medical imaging. More importantly, this could be used in the medical field for 3D imaging as the fields can be adjusted and customized.

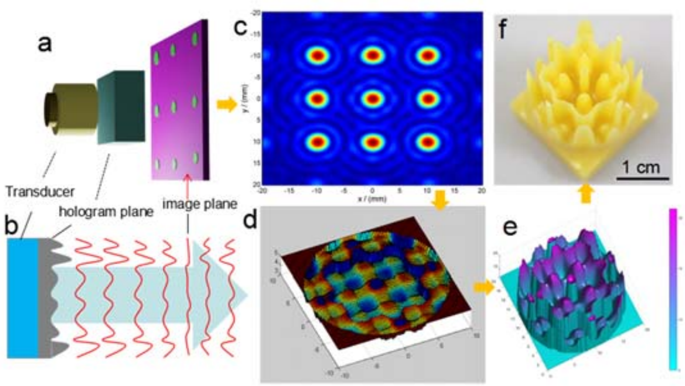

Figure 1. The generation of multi-focused acoustic images. (a) demonstration of the experimental setup with a transducer and 3D printed hologram plane on top; (b) the hologram converts a planar wavefront from the transducer into the required phase distribution; (c) simulated hydrophone pressure by matlab in the image plane showing the reconstructed 9 multi-focused image; (d) computed phase distribution for 2 MHz ultrasound; (e) model generated by Matlab for the 3D printing process; (f) the printed hologram structure, the topology of the hologram surface encodes the desired phase information.

6K-3

4:30 pm In-situ Measurement of Transducer Impedance using AFE Active Termination through Analysis of Ultrasound Echoes

David Cowell[1], Thomas Carpenter[1], Benjamin Fisher[1], Steven Freear[1]; [1]*Ultrasound Group, University of Leeds, United Kingdom*

Background, Motivation and Objective

Periodic calibration of ultrasound imaging and instrumentation systems is critical to identify transducer condition or system failure. Performing impedance measurement allows the monitoring of transducer degradation and cable failure, typically using a dedicated impedance analyzer. This paper proposes a method of concurrent in-situ impedance measurement of all array elements without instrumentation modification through analysis of ultrasound echoes.

Statement of Contribution/Methods

By considering the ultrasound transducer (XDR) and connected analogue front end (AFE) as a voltage source with unknown impedance (Z_S) this paper proposes a method to determine said impedance by performing two voltage measurements using two different known load impedances. Fig A shows a simplified case whereby an XDR is connected to a known load resistor across which a voltage measurement is made. Using measurements across two different resistor values, Z_S of the XDR can be determined. A more realistic system is shown in Fig B whereby the XDR is connected to a switched mode transmit (TX) pulser with integral TX/RX switches and an ADC containing a low noise amplifier (LNA) with active termination (Z_{TERM}). If Z_{TERM} can be adjusted to two distinct known values, then it can be used as the load in the proposed method to determine Z_S without any additional components.

Results/Discussion

Testing was performed using the simplified setup (Fig A) to verify that the proposed methodology can be used to determine the transducer impedance. The resulting impedance measurement was compared with a reference measurement performed using the Omicron Lab Bode 100 analyzer. The two impedance measurements corresponded prompting further investigation. The University of Leeds Ultrasound Array Research Platform (UARP) front end includes a Texas Instruments AFE5807 (Fig B) which contains a software adjustable active termination. This provides the ability to take measurements using multiple distinct load terminations, the impedances of which were measured to ensure accurate known values. Ultrasound echo data was collected using an L11-4V linear transducer and the calculated impedance (Z_s) compared to a reference impedance measurement. Fig C shows that despite the complexity of the AFE, the resulting measurements using the active termination could be used to determine the impedance Z_s of the system.

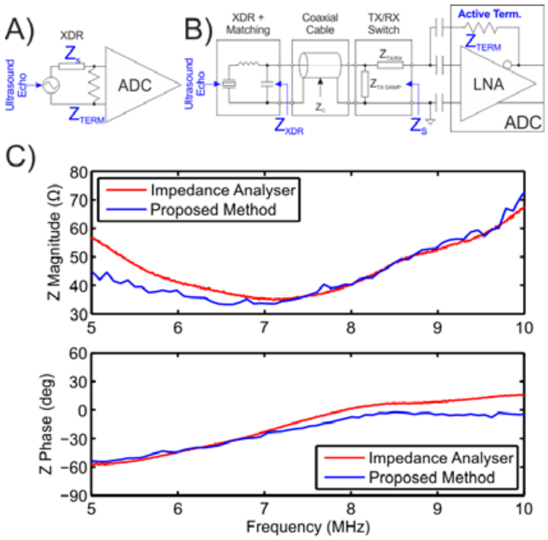

6K-4

4:45 pm AlN on SOI PMUTS for Wireless Communication

Emad Mehdizadeh[1], Gianluca Piazza[1]; [1]*Department of Electrical and Computer Engineering, Carnegie Mellon University, Pittsburgh, PA, USA*

Background, Motivation and Objective

To prevent unauthorized access to ICs, encryption can be enabled via extremely small and practically invisible microscale chips that are embedded inside the packaging of ICs. The authors lately demonstrated an acoustic power link based on AlN HBAR-like structures operating at 500 MHz [1]. Enormous acoustic losses introduced by air at such large frequencies necessitate tight coupling between the transducers and the package. To accommodate for small air gaps in the link, a more versatile route is proposed here based on MHz-range ultrasonic transducers.

Statement of Contribution/Methods

This work reports on vicinity based data transmission using CMOS compatible ultrasonic transducers. Bulk acoustic waves (BAWs) generated by a commercial probe travel through a relatively thick package and are absorbed and converted to an electrical signal using a piezoelectric transducer. The proposed link leverages the enhancement of energy transfer at resonance and is empowered by pMUTs (Fig. 1a). This work is the first step towards the development of next-generation high-efficiency and microscale charging units that could also be used to energize biomedical implants, wearable devices, and microsystems that are embedded in inaccessible areas.

Results/Discussion

The fabricated pMUTs are comprised of a 1 µm thick AlN film sandwiched between a bottom Pt and top Al layer stacked on top of a 2 µm thick silicon substrate (Fig. 1b). A four mask process is used to fabricate the structures on SOI wafers with 5 µm BOX layer. SU-8 is used here as a packaging material that can be photolithographically defined. Due to the specific IC application targeted, the size of the pMUT is constrained to $100\times100 \mu m^2$. To perform the experiments, the amplified RF signal of an arbitrary waveform generator excites the probe into thickness vibrations around 2 MHz. The generated BAWs then travel through the package, are received by the pMUT and detected either via a rectifier or a transimpedance amplifier (Fig. 1c). Comprehensive empirical results from the ongoing experiments will be presented in the final paper submission. However, conducted COMSOL finite element analyses suggest that the package can behave as an acoustic waveguide, hence its thickness is critical in improving link efficiency (Fig. 1d).

[1] E. Mehdizadeh and G. Piazza, "Aluminum Nitride Vicinity-Based Resonant Charging Link," Hilton Head Workshop, 2016.

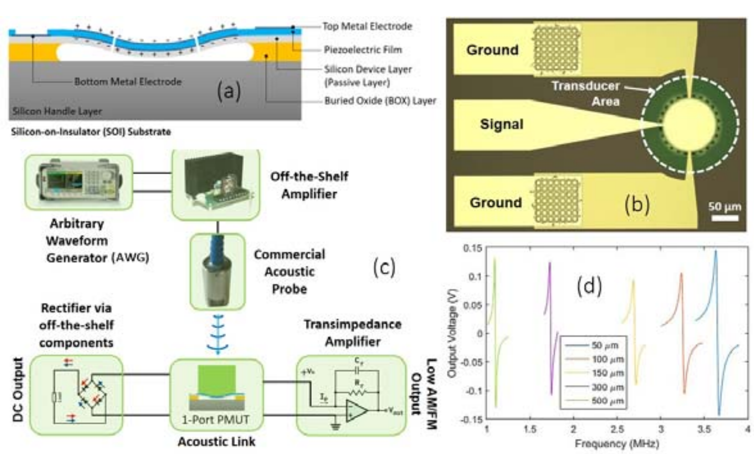

Figure 1. (a) Schematic of the pMUT; (b) Optical microscopic image of a $100\times100 \mu m^2$ pMUT fabricated on SOI wafer with 2µm & 5µm device and BOX layers; (c) Schematic of the proposed system for testing power/data link; (d) Output voltage frequency response of a $100\times100 \mu m^2$ pMUT for different thicknesses of PMMA for an applied pressure of 20kPa on top of the package.

6K-5

5:00 pm Development of a Novel Noncontact Ultrasonic Bearing Actuated by Piezoelectric Transducers

He Li[1], Qiquan Quan[1], Zongquan Deng[1], Deen Bai[1], Yinchao Wang[1]; [1]*School of Mechatronics Engineering, Harbin Institute of Technology, Harbin, China, People's Republic of*

Background, Motivation and Objective

Many high-end power machines demand greater bearing performance in terms of running speed, precision, reliability, longevity, noise reduction, etc. An ultrasonic bearing based on Near-Field Acoustic Levitation (NFAL) effect is a kind of emerging noncontact gas bearing. Due to its self-aligning capability, the ultrasonic bearing can steadily run at a high speed—tens of thousands of revolutions per minute—under high movement precision (micron dimension). Actuated by piezoelectric transducers, the ultrasonic bearings do not produce much noise pollution. As a potential alternative to conventional bearings, study on ultrasonic bearings with different structure forms will expand the bearing's application.

Statement of Contribution/Methods

The existing ultrasonic bearings can only withstand loads in one direction: axial or radial direction. A novel ultrasonic bearing with ability of carrying radical and axial loads simultaneously is first proposed in this study. The "┥ ┝"-shaped slot through the radiator of the bearing is designed using finite element method in order to transform partial longitudinal vibration into flexural vibration to generate axial loads. For purpose of confirming the load-carrying capacity of the designed bearing, the radial and lateral load-carrying models are built based on nonlinear acoustic theory and fluid hydraulic lubrication theory. Ultimately, static mechanics experiments are conducted to validate the correction of the models. Besides, running performance of the bearing at high speeds is tested to study the bearing's running stability and friction torque.

Results/Discussion

The experiments prove that the ultrasonic bearing can carry 15 N radial levitating load and 6 N axial levitating load when excited by a voltage with amplitude150 Vp-p and frequency 16 kHz. The numerical solving results of the levitation force models can interpret the experimental data well. The proposed model will provide a theoretical reference for the design of ultrasonic bearings. The running performance experiments show that the bearing can operate steadily and consistently at a high speed, and the bearing's friction torque at a speed below 20000 rpm is less than 120 μN·m.

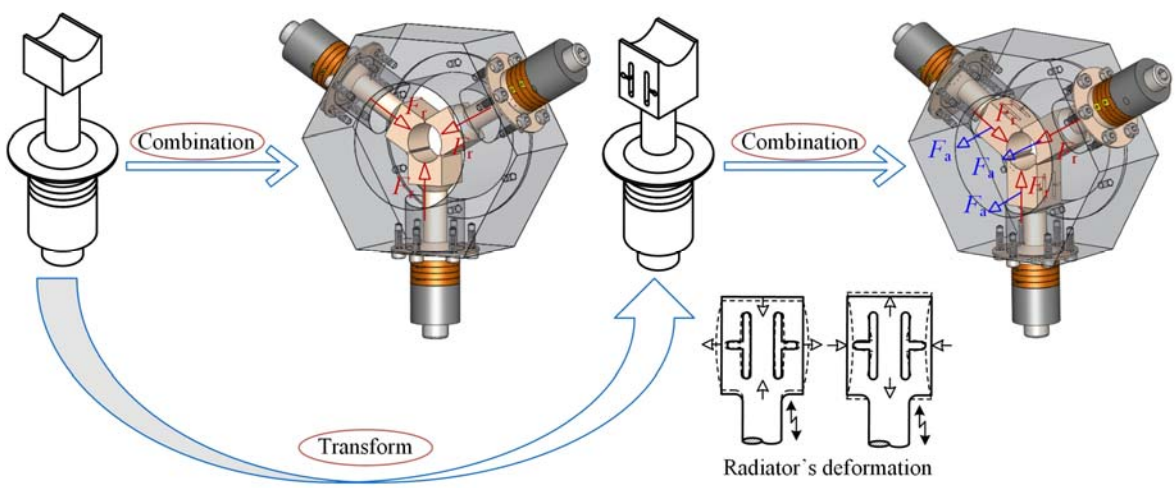

6K-6

5:15 pm LightProbe: A Fully-Digital 64-Channel Ultrasound Probe with High-Bandwidth Optical Interface

Pascal Alexander Hager[1], Daniel Speicher[2], Christian Degel[2], Luca Benini[1]; [1]*Integrated Systems Lab, ETH Zürich, Zürich, Switzerland,* [2]*Fraunhofer Institute for Biomedical Engineering IBMT, Sulzbach, Germany*

Background, Motivation and Objective

A typical medical ultrasound-imaging system consists of a passive probe and a backend system containing the analog frontend and the digital processing unit, to which the probe connects over a coaxial cable harness. Digital processing is increasingly performed in software on powerful GPUs or multicore CPUs. These new system architectures have not only enabled new imaging modalities (Ultrafast Imaging, Vector Flow Estimation), but also reduced system cost, as ultrasound specific hardware is only used for the acquisition of the raw signals. The next step in this evolution are fully-digital ultrasound probes, which integrate the analog frontend and are equipped with a standard digital interface. This allows connecting the probe directly to a standard device, such as a workstation, tablet or mobile phone running an ultrasound software application. So far, this concept has been demonstrated for mobile applications, but is currently limited to a small number of frontend channels (~16) due to the large digital bandwidth (>10 Gb/s) at the interface between the probe and the mobile device.

Statement of Contribution/Methods

We have developed a fully-digital 64-channel ultrasound probe with a high-bandwidth digital optical link. To connect our probe, called LightProbe, with a large range of devices and to support many modalities, we integrated a Xilinx Artix 7 FPGA that provides a high degree of "in-probe" configurability to support different transmit schemes, pre-processing and a scalable link rate (0.5-26.4 Gb/s). The probe consists of a 64-element 4 MHz linear phased array. The TX/RX stage is able to produce programmable 100 Vpp bi-polar pules and provides a sample rate up to 32.5 MS/s @ 12 bit.

Results/Discussion

We successfully put the system in operation and run first tests (The figure shows the current test setup of the LightProbe, with debug attachments) with the probe connected to a workstation. In the current preliminary configuration, the LightProbe captures and transfers emissions at 620 Hz, resulting in a 17.92 Gb/s peak and 1.138 Gb/s average link load. Even without aggressive power optimization, the probe consumes 10.6W and meets handheld size constraints with 220x25x45 mm3 without the housing. Compared to other digital probes, we support 4x more channels and a 5x higher link rate.

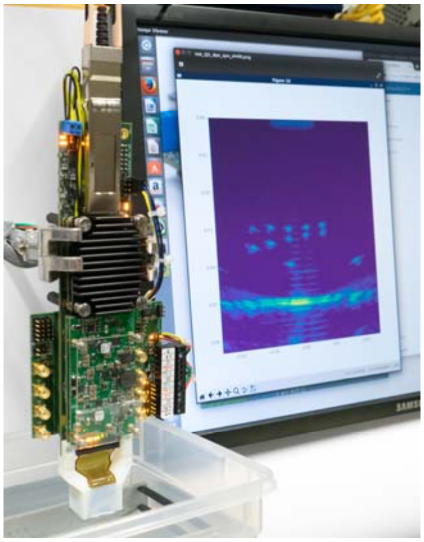

7K - PUM - Ultrasonic Motors and High Intensity Applications

Empire Room

Saturday, September 9, 2017, 4:00 pm - 5:30 pm

Chair: **Margaret lucas**
University of Glasgow

7K-1

4:00 pm **Vibration Response of a High Power Compact Large-Area Ultrasonic Resonator**

Hafiiz Osman[1,2], Fannon Lim[1], Margaret Lucas[1]; [1]*University of Glasgow, United Kingdom,* [2]*Research and Development, Sembcorp Marine Ltd., Singapore*

Background, Motivation and Objective

Ultrasonic water treatment is based on the ability of an ultrasonic device to induce cavitation in the liquid, generating physical and chemical effects that can be exploited to produce effective treatment. This requires that the device be both capable of generating high amplitude pressure waves in the treatment volume and capable of treating a large volume of fluid by having a large radiating surface. Most conventional ultrasonic radiators fulfill only the first of these two objectives, rendering such devices highly unsuitable for use in high-volume, high-flow liquid processes.

Statement of Contribution/Methods

The multiple-orifice radial (MOR) resonators is a new class of power ultrasonic transducer designed to overcome the above limitations by offering both high amplitudes and large radiating area in a relatively compact assembly. In this paper, the vibration characteristics of the Primary-Secondary (PS)-type and Primary-Secondary-Tertiary (PST)-type MOR resonators are presented, where P, S and T refer to the patterns of radial orifices.

Results/Discussion

Modal analysis results show that both resonators operate in the fundamental longitudinal-radial (LR) coupled mode at the operating frequency. Further experimental and modelling results show that the ultrasonic amplitudes achieved at the radiating surfaces are comparable with conventional high-output ultrasonic treatment probes, demonstrating the high acoustic power capability of the MORR devices.

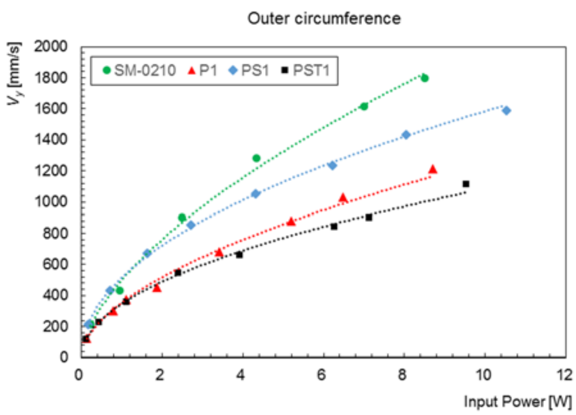

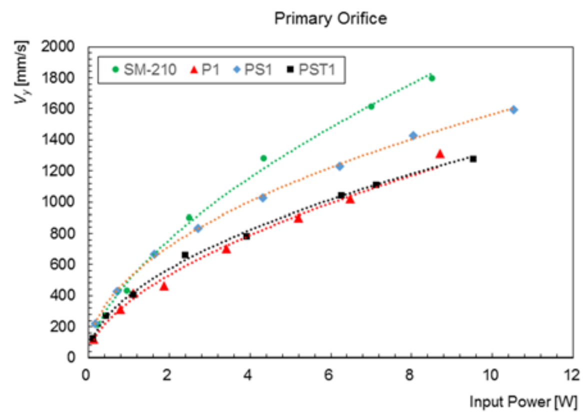

7K-2

4:15 pm **Nanoparticles Generation System Using an Ultrasonic Torsional Transducer**

Nozomu Fujimoto[1], Takefumi Kanda[1]; [1]*Graduate School of National Science and Technology Okayama University, Okayama, Japan*

Background, Motivation and Objective

Nanoparticles have been required in the fields such as medicine, foods and electronic materials. By re-crystallization process, nanoparticles can be formed by quenching a solution. We have generated mono-disperse droplets by using a torsional bolt-clamped Langevin-type transducer and a micropore plate to form fine nanoparticles by quenching the droplets.

Statement of Contribution/Methods

To obtain fine nanoparticles, quenching speed is an important factor. Figure 1 shows internal temperature of droplets estimated by diffusion equations. This results show that smaller micro droplets are much effective for quenching. In addition, uniformity of the formed crystal particles depends on that of micro droplets generated by the transducer.

In previous study, mono-disperse micro droplets were effectively generated by an ultrasonic torsional transducer and a micropore plate[1]. Figure 2 shows system configuration of the nanoparticles generation. When the micropore was oscillated by the ultrasonic torsional vibration, micro droplets were regularly formed. Then the generated droplets of alum solution are quenched with liquid nitrogen. The diameter of micropore is 100μm

Results/Discussion

The average of particle size measured by dynamic light scattering is 380nm when the vibrational velocity of micropore was 96.5mm/s. This results show that the system is effective for the miniaturization and uniformization of the alum crystal particles. As a result, we have successfully obtained fine nanoparticles using mono-disperse droplets generated by the ultrasonic torsional transducer.

[1] T. Murakami et al., 2012 IEEE International Ultrasonic Symposium, pp. 281-284, 2012

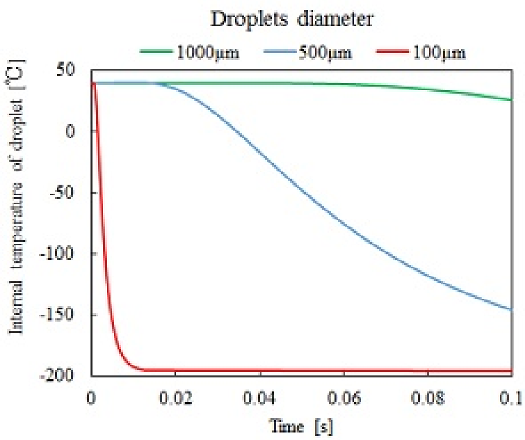

Figure 1 Internal temperature of droplet estimated by diffusion equation

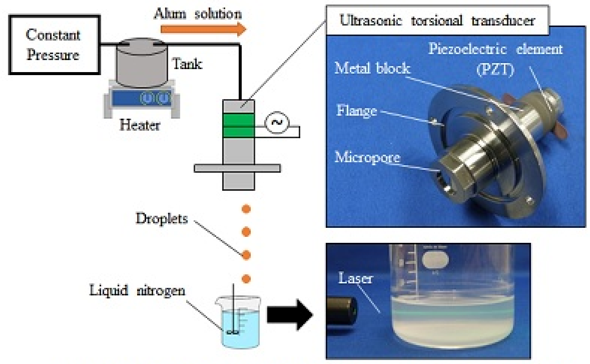

Figure 2 Nanoparticles generation system using an ultrasonic torsional transducer and recovered alum solution

7K-3

4:30 pm **Non-Contact Coating Processing OoSmall Object Levitated in Ultrasonic Standing Wave Field**

Kentaro Nakamura[1], Yoshimasa Sakai[1]; [1]*Institute of Innovative Research, Tokyo Institute of Technology, Yokohama, Japan*

Background, Motivation and Objective

Non-contact processing is an attractive technology for synthesizing new materials and pharmaceutical industry. A technique based on ultrasonic standing waves is a promising method to levitate small object or droplet without contact in air because it is applicable for any materials and easily controllable with electrical signal. The authors have developed various ultrasonic non-contact methods such as transport of droplet [1][2], mixing two liquids [3] and weighing small object under levitation. In this study, we develop a method to coat a small ball with liquid under ultrasonic levitation as one of the necessary technologies for non-contact manipulation.

Statement of Contribution/Methods

A standing wave field was excited between a stepped horn driven by a 27-kHz Langevin transducer and an aluminum plate reflector. A polystyrene ball of 2.75 mm in diameter was levitated at the nodal point of the standing wave field. Red ink was sprayed to the ball through ultrasonic atomizing to achieve non-contact coating. The resonance condition of the air cavity composed of the horn surface and the reflector is varied by inserting the ball. To compensate this change in the resonance condition, a new feedback oscillation system has been proposed in this report. A piezoelectric thin sensor was installed on the reflector to pick up the sound pressure. The sensor output was fed back to the input of the driving power amplifier to excite the ultrasonic field at the resonance frequency of the air cavity. Using this feedback system, the stability of the levitated has been largely improved.

Results/Discussion

Coating test was conducted for a polystyrene ball 2.75 mm in diameter. Red ink was sprayed to the levitated ball using ultrasonic atomizing, and then the coating characteristics were evaluated. The all surface of the ball was successfully painted by the ink. The thickness of the ink was measured from the brightness of the photo of the coated ball. Thickness around the equatorial line of the ball was higher than other parts. It was thought to be caused by the spinning motion of the ball and the acoustic streaming of air around the ball.

* This work was supported by JSPS KAKENHI Grant 26289054.

[1] M. Ding, et al.: Appl. Phys. Express, 5 (2012) 097301.
[2] K. Nakamura: Proc. Int. Cong. Ultrason., (2013) P0495.
[3] R. Nakamura, et al.: Jpn. J. Appl. Phys., 52 (2013) 07HE02.

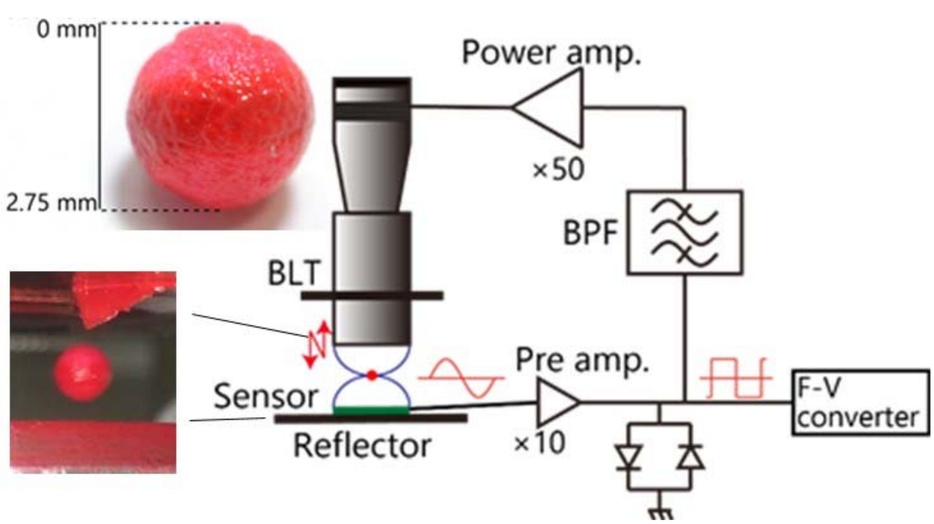

7K-4

4:45 pm **A Small Three-Way Valve for Hydraulic Actuators Using Piezoelectric Transducers**

Hayato Osaki[1], Takefumi Kanda[1], Shoki Ofuji[1], Norihisa Seno[1], Koichi Suzumori[2], Takahiro Ukida[2], Hiroyuki Nabae[2]; [1]*Graduate School of Natural Science and Technology, Okayama University, okayama, Japan,* [2]*Graduate School of Science and Engineering, Tokyo Institute of Technology, Tokyo, Japan*

Background, Motivation and Objective

Hydraulic actuators has been utilized for various types of robots. However, hydraulic control system for multiple degrees of freedom mechanisms has a large volume because such system needs many control components. The purpose of this research is to develop a small hydraulic flow control valve. In the previous research, we have developed a small flow control valve using particle excitation by a piezoelectric transducer [1], and applied this valve to a hydraulic system. In this research, we have fabricated and evaluated a small three-way valve for further miniaturization.

Statement of Contribution/Methods

Figure 1 shows a schema of the proposed three-way valve. The valve consists of two transducers. In each transducers, small particles on an orifice plate are excited by a vibrator. The valve can switch inlet and outlet ports by applying AC voltage of different driving frequencies for each transducer because two transducers have different resonant frequencies. Each port transducer is operated by vibrating the orifice plate, and the flow rate is controlled by applying voltage for piezoelectric vibrator tightened to each orifice plate.

Results/Discussion

Figure 2 shows the relationship between driving frequency and vibration velocity of each orifice plate when the applied voltage was 10 Vp-p for the outlet port transducer. The vibration velocity had peaks at 120 kHz for the inlet, and at 155 kHz for the outlet. Therefore, the proposed valve can switch the open port by changing the driving frequency. Additionally, using this proposed three-way valve, we have succeeded in controlling the speed of hydraulic cylindrical actuator by controlling the flow rate and in switching the moving direction of actuator.

[1] D.Hirooka, et al, 2009 IEEE International Ultrasonics Symposium, pp. 1624-1627, 2009.

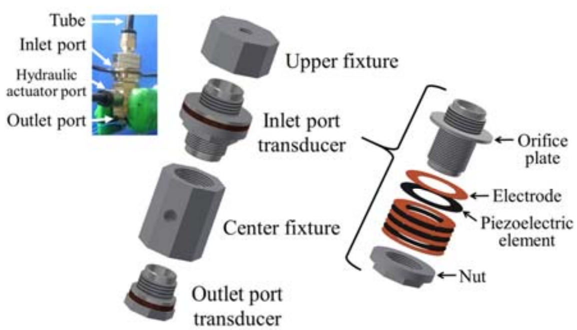

Fig. 1 Structure of the proposed three-way valve

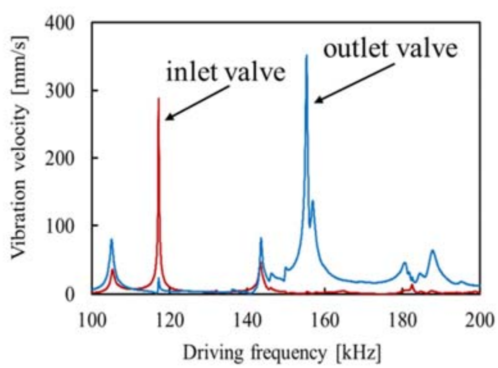

Fig. 2 Vibration velocity of the orifice plate when the applied voltage was 10 Vp-p for the outlet port transducer

7K-5

5:00 pm **A Compact Design for Ultra-Sonic Piezoelectric Motor with Embedded Strain Wave Reducer for High Torque Applications**

Quentin Guilleus[1], Edouard Leroy[1], Laurent Eck[1], Moustapha Hafez[1]; [1]*DIASI / Sensory and Ambiant Interfaces Laboratory, CEA LIST, Gif-sur-Yvette Cedex, France*

Background, Motivation and Objective

Piezo-electric motors are interesting candidates and a good alternative solution to electromagnetic actuation. A limited number of mechanical components is required which leads to simple and compact designs. A high resolution and repeatability can be reached. They do not generate noise nor magnetic fields which make them easy to integrate in different environments. Nevertheless, some limitations remain such as the difficulty to create a piezo-electric motor with high torque capabilities.

Statement of Contribution/Methods

We propose in this paper a new concept for piezo-motor which aims to generate high torque but still have a high compactness and precision. The design consists of merging a mechanical reducer based on the concept of a strain wave gear directly with a piezoelectric motor in a single module.

The motor is composed of three main building blocks: the wave generator, the flexible disk (rotor) and the stator (Figure 1). The wave generator bends the flexible disk by applying pressure through the two rollers. On the other side of the flexible disk a number of teeth mesh with the toothed stator to transmit torque. The wave generator rotates and spreads the deformation of the disk thanks to a US ring shape piezo motor (Figure 2). Due to the difference in the number of teeth (n for the stator and n+2 for the rotor) the rotation of the output shaft is generated.

Results/Discussion

The piezo motor operates at 54.4 kHz, which corresponds to two planar resonant bending modes occurring at the same frequency. A speed of 70rd/s is measured and a torque of 20 mNm is estimated. By adding the reducing stage (1/25 of reduction ration), speed of 2.8 rd/s with an output torque between 200 to 600 mNm is expected.

This proof of concept which has not been optimized at this stage has dimensions of 62mm in diameter and a height of 22mm.

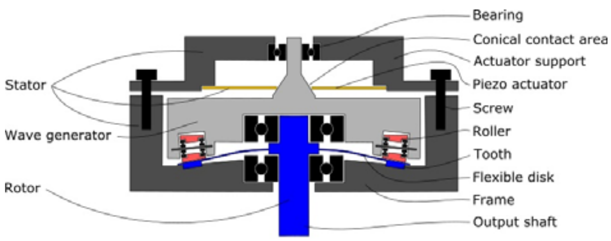

Figure 1 : Cross section of the new piezo motor revealing the Three main building blocks

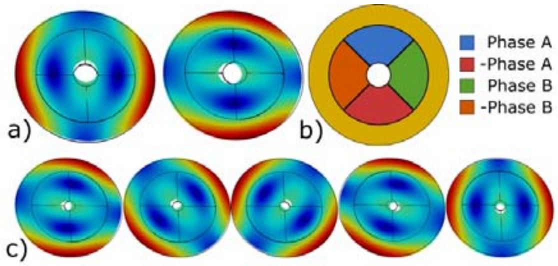

Figure 2 : a) Modal analysis of the 2 resonant frequencies used to generate the rotation (54.5 kHz) b) electrode pattern and signals used to actuate the motor c) Vizualization of the traveling wave thanks to an harmonic response analysis

7K-6

5:15 pm PZT Lateral Bimorph Array Stator Based Ultrasonic Micromotor

Shelly Aggrawal[1], **Sachin Nadig[1]**, Amit Lal[1]; [1]*Cornell University, Ithaca, New York, USA*

Background, Motivation and Objective

Ultrasonic motors generally require high contact force to clamps surfaces. These surfaces are actuated by high forces generated by ultrasonic transducers, typically operating at resonance frequencies. Many actuator types have been explored, the most common being out-of-plane bimorphs. In this paper, we implement a motor utilizing an array of lateral PZT bimorphs. The lateral bimorphs, with vertical slots result in a x-shape motion that can couple into a rotor. The design space of the lateral bimorphs enables lower frequency operation in the 15-40kHz. The lower frequency, as compared to other micromachined motors, allows for higher tip motion coupling to a rotor. The X-shape motion has been used to rotate 3D-printed rotor.

Statement of Contribution/Methods

The ultrasonic motor architecture is an outcome of a novel PZT bimorph fabrication technology developed using a commercial laser machining tool. Through-PZT laser cutting is used to define beams in PZT plates that have a minimum lateral width of 200 microns, providing beams of aspect ratio of 2:5 given the PZT plate thickness is 500 microns. Laser cutting of the electrodes enables definition of electrodes on two sides of the beam that form a bimorph. A valley cut in the middle of the two electrodes shifts the neutral axis of the beam away from the top electrodes leading to a torque for the beam to move in and out of plane producing a X-shape motion. An array of bimorphs can be simultaneously formed to form contact to a rotor mechanically attached to the bimorph array. Unlike previously reported approaches using piezoelectric bimorphs, our process eliminates the need for manual bonding or selective arrangement of PZT of different poling orientations (Figure 1a).

Results/Discussion

The planar integration of the motor elements helps one to envision many co-located motor elements for multi motor systems (Figure 1b). The reported lateral bimorph based motor allows for low-voltage, bidirectional operation with single-phase AC excitation and is shown to operate at 8 Volts Peak-To-Peak drive amplitude, that can produce torques of 5.5 N-mm. Various combinations of rotors and stators were tested to verify the physical model of the motor, with rotation rates of up to 400-600 rpm. One combination of stator and rotor were used to drive a 3D-printed fan load that produced maximum air flow rate of 160 mm/sec at 60 V-Peak motor drive voltage.

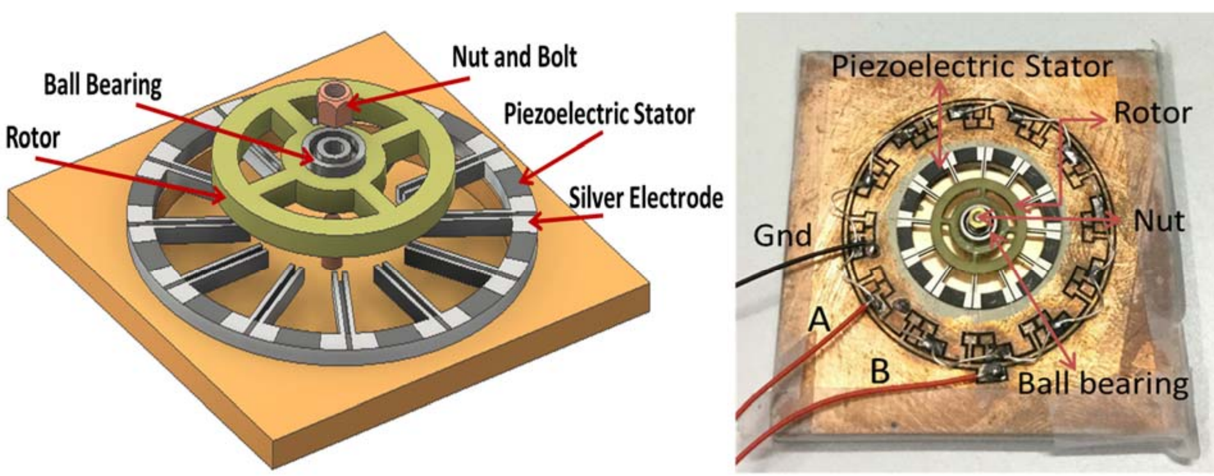

(a) (b)

P1-C1 - MBB: Synthetic Aperture and Multi-zones Imaging

Exhibit Hall

Saturday, September 9, 2017, 9:30 am - 4:00 pm

Chair: **Ling Tong**
Supersonic Imagine

P1-C1-1

Spatial Prediction Filtering for Increased Penetration Depth in Synthetic Aperture Ultrasound

Junseob Shin[1], Yang Lou[2], Jesse Yen[2], Liajie Huang[1]; [1]*Los Alamos National Laboratory, Los Alamos, NM, USA,* [2]*University of Southern California, Los Angeles, CA, USA*

Background, Motivation and Objective

Synthetic aperture (SA) ultrasound imaging is a well-known technique in which RF signals for every transmit and receive element combinations is first obtained and a 2-way-focused image is synthetically formed afterwards. Despite its benefits, one of its main shortcomings is reduced penetration depth caused by low acoustic power from single element firing. To address this challenge, we propose a spatial prediction filtering technique called the frequency-space (F-X) prediction filtering (FXPF), which adaptively constructs a spatial filter that rejects random noise and off-axis clutter components directly from the time-aligned channel data. By utilizing the information in the spatial domain, FXPF enhances the signal-to-noise ratio (SNR) by suppressing random noise within the transducer bandwidth, which typically cannot be filtered by temporal bandpass filters.

Statement of Contribution/Methods

We performed a Field II simulation of point targets located between 4 and 18 cm at an interval of 2 cm. We chose imaging parameters to model a 64-element ATL P4-2 phased array with imaging frequency of 3.3 MHz, 50% bandwidth, and an element pitch of 0.32 mm. We included frequency-dependent attenuation effects in our simulation and added random noise to the simulated data. Then, we applied FXPF on the time-aligned channel data with an axial kernel size of 1 wavelength and a filter order p = 8. We evaluated the increase in penetration depth in terms of the SNR. We validated our simulation results using a synthetic aperture data set from an ATS phantom (Model 549), which was acquired using a Verasonics system and an ATL P4-2 phased array.

Results/Discussion

The improvement in SNR and hence, the penetration depth associated with FXPF is shown with simulated point targets located at varying depths (Fig. 1a). Due to frequency-dependent attenuation effects, the SNR decreases with increasing depth. FXPF improves the SNR by at least 10 dB and makes targets at deep locations more visible. The axial profiles (Fig. 1a) confirm the findings from the corresponding B-mode images. Our simulation results are also confirmed by our ATS phantom images (Fig. 1b), which show improved penetration depth and better target visibility with FXPF, particularly at an axial depth of 12 cm and beyond. Furthermore, FXPF enhances image contrast throughout the entire field-of-view, thereby producing a high-quality image.

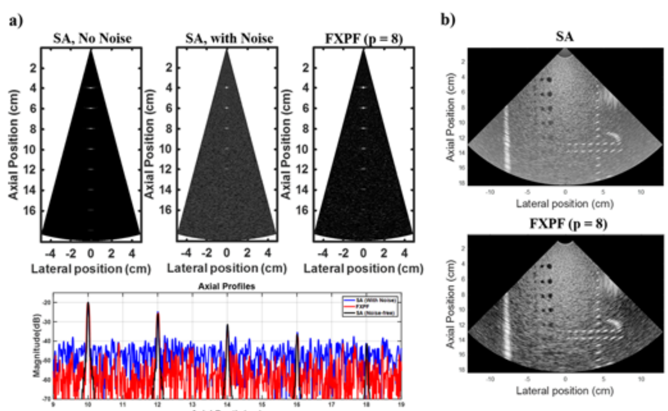

Fig. 1: Comparison of synthetic aperture (SA) imaging and FXPF with a) simulated point targets and b) Experimental ATS phantom. Axial profiles of the simulated point targets at varying depths are also compared for SA with noise, FXPF, and noise-free SA. In both simulation and experiment, SNR improvement of at least 10 dB is achieved and penetration depth is also increased.

P1-C1-2

Swept Synthetic Study of Large Aperture Imaging through Ex Vivo Human Abdominal Wall

Nick Bottenus[1], Will Long[1], Matthew Morgan[1], Gregg Trahey[1,2]; [1]*Biomedical Engineering, Duke University, Durham, North Carolina, USA,* [2]*Radiology, Duke University, Biomedical Engineering, Durham, NC, USA*

Background, Motivation and Objective

Lateral resolution and therefore image quality in ultrasound is tied to aperture size. While this relationship is understood in ideal imaging conditions, the utility of a large aperture in the presence of clutter is unknown. This problem is particularly relevant to abdominal imaging where thick tissue layers and deep targets create a challenging imaging environment. Previous studies have focused on the main lobe width of the beam and were limited by the size of commercially available transducers. Enabled by a synthetic aperture technique to form large coherent apertures, we have performed a more comprehensive study of image quality using excised human abdominal walls in a controlled imaging setting.

Statement of Contribution/Methods

The swept synthetic aperture method was used to experimentally synthesize a large coherent aperture using a commercial 2 cm matrix array (Siemens 4Z1C). The transducer was moved in a prescribed arc of radius 6.4 cm over an arc length of 6.4 cm (F/1 focal configuration) about the target structure – an isolated point target or anechoic lesion phantom. Imaging was performed in a control case (saline path) or through one of three excised cadaveric abdominal wall samples. Array data were focused using knowledge of the transducer position to synthetically create a transmit/receive array with extent equal to the sweep length. A matching conventional full synthetic aperture image was acquired for reference.

Results/Discussion

Lateral resolution was measured for each case using the point target. The percent improvement in resolution for the control and three tissues respectively was 77.9%, 76.0%, 42.1% and 56.9%. One tissue case performed similarly to the control while the other two suffered from aberration due to the abdominal wall. However, resolution improved significantly in all cases and target visibility was improved over the smaller aperture. The lesion contrast-to-noise ratio relative to the speckle background was measured for each image. The large aperture produced CNR improvements of 12.1%, 14.8%, 16.8% and -13.2% for the control and three tissues. This relatively small change was visually outweighed by the large improvement in resolution. Application of spatial compounding over the sweep produced improvements in CNR of 82.2%, 192.5%, 162.7% and 73.0% relative to the smaller aperture with only a modest loss in lateral resolution.

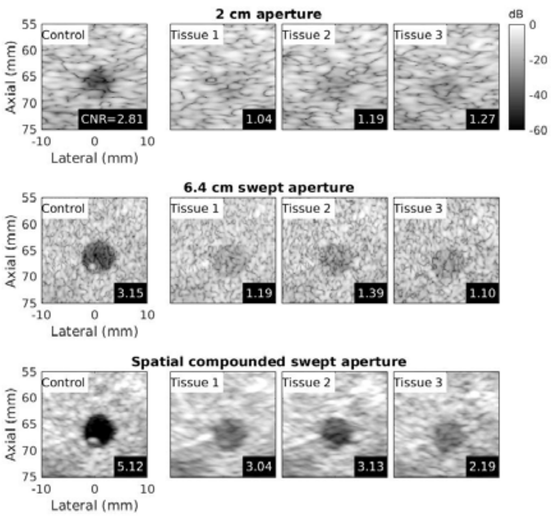

P1-C1-3

Synthetic Aperture Sequential Beamforming Using Spatial Matched Filtering

Mikkel Schou[1], Tommaso di Iannai[1], Jørgen Arendt Jensen[1]; [1]*Department of Electrical Engineering, Technical University of Denmark (DTU), Lyngby, Denmark*

Background, Motivation and Objective

Syntethic Aperture Sequential Beamforming (SASB) has been proven to achieve a better resolution and penetration depth than Dynamic Receive Focusing (DRF). SASB has also shown great potential for use in a handheld device. SASB with a low F# (<= 0.5) has shown even better resolution at the cost of high grating lobes, which cause loss of contrast in the final image. The hypothesis is that Spatial Match Filter (SMF) applied to the second stage can lower these grating lobes thereby obtaining both high contrast and better resolution.

Statement of Contribution/Methods

A 3.3 MHz BK Medical 9040 convex array was simulated in Field-II with a wire phantom and a cyst phantom. The data was simulated with 255 emissions and 64 active channels at each emission and were acquired with two different setups. One setup was optimized to provide a standard DRF image as reference. The setup has a transmit focus at 60 mm with an F# of 4.51 and is dynamically focused in receive with an F# of 0.8. The other setup has a fixed focus at 10 mm in both transmit and receive, which provides an F# of 0.5. The fixed focused data is then used as input to the conventional SASB second stage beamformer and SMF. For each point in the high resolution image, the response of each fixed focus beamformer was matched filtered using a time-reversed version of the expected pulse. Finally SMF-responses from the 255 emissions were coherently summed to obtain the final high resolution image. The resolution is quantified with full-width-half-max(FWHM) and the contrast is measured with the 20dB cystic resolution (CR20dB) together with the contrast-to-noise ratio (CNR) calculated on the cyst phantom.

Results/Discussion

Fig. (a) and (b) shows the two measures as a function of depth calculated on the wire phantom. (c) shows the cyst phantom imaged with SASB and SMF. The effect of SMF is most visible at depths from 10 to 40 mm, seen in (b). The grating lobes caused by the low F# of 0.5 are dominant in SASB, but not in SMF. SMF obtain an almost constant value across all depths in the 20dB cystic resolution, thus, lowering the grating lobes in the range 10-40 mm. The CNR at 20 mm was improved from 1.90 to 22.30 when comparing SASB to SMF, and from 1.05 to 12.03 at 30 mm. The FWHM for SMF is slightly higher than SASB across all depth. In conclusion, it is demonstrated that improved contrast and resolution can be achieved with SASB by using SMFs applied to the second-stage beamformer.

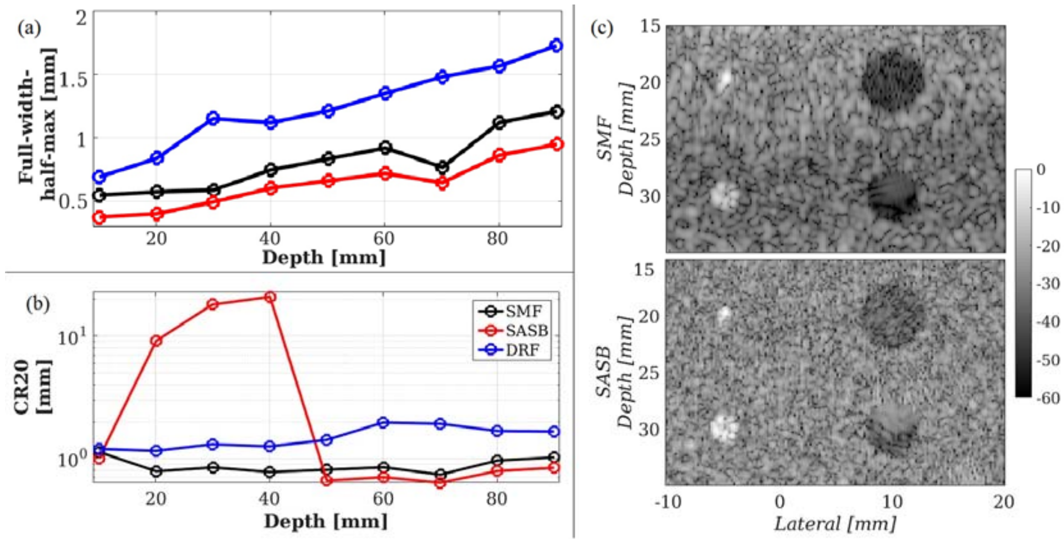

P1-C1-4

Archimedean Spiral Based Compounding for High Quality and High Frame Rate Convex Array Imaging

Jing Liu[1], Jianwen Luo[1]; [1]*Tsinghua University, China, People's Republic of*

Background, Motivation and Objective

Recently plane wave compounding was developed for high resolution convex array (CA) imaging (Bae et al IUS 2015). However, only elements whose directivities cover the plane wave direction were activated in each firing, leading to a narrowed imaging area and reduced frame rate. To solve this issue, we proposed Archimedean spiral (AS) based compounding (ASC) method for high quality and high frame rate CA imaging.

Statement of Contribution/Methods

Fig. 1 shows the ASC setup. As defined in Eq. (1), the transmit delays of the CA elements linearly vary with the element angle with a slope *k* so that the wave front calculated as Eq. (2) is an AS formulated as Eq. (3). The constant t_0 in Eq. (2) indicates the time when an element is first activated. The distance |MP| of an arbitrary point *M* in the imaging area to a point *P* on the AS wave front is calculated as Eq. (4). The minimum |MP| is determined by moving the point *P* along the AS wave front and the time-of-flight is calculated as Eq. (5) for the delay-and-sum beamforming. Different ASes (e.g., the red and green spirals in Fig. 1) are generated by altering the slope *k* in Eq. (1) and compounded to achieve high quality CA imaging. The feasibility of ASC was validated on a CIRS phantom and a C5-2 convex array (radius R = 59 mm, open angle =59°) using a Verasonics Vantage system, with 13 slopes (*k*) uniformly distributed within ±6.6 us.

Results/Discussion

As shown in Figs. 2(a) and (b), ASC does not narrow the imaging area and it performs better than the focused mode out of the focal zone with 9.8-fold higher frame rate. In terms of contrast (Fig. 2(c)) and spatial resolution (Fig. 2(d)), ASC achieves comparable performance to the focused mode in the focal zone and better performance in other zones. ASC is proved to achieve high quality CA imaging with high frame rate while keeping the imaging area of CA.

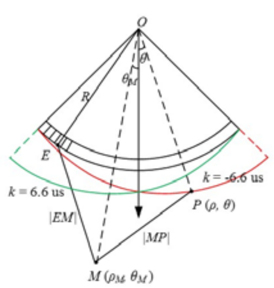

$$Transmit\_delay = k \cdot \theta \quad (1)$$

$$\rho = R + c \cdot t_0 - c \cdot Transmit\_delay = R + c \cdot t_0 - c \cdot k \cdot \theta \quad (2)$$

$$\text{Archimedean spiral: } \rho = a + b \cdot \theta \quad (3)$$

$$|MP|^2 = \rho^2 + \rho_M^2 - 2 \cdot \rho \cdot \rho_M \cdot \cos(\theta - \theta_M) \quad (4)$$

$$\text{time-of-flight} = \frac{|EM| + \min(|MP|)}{c} \quad (5)$$

Fig. 1. An illustration for the setup of Archimedean spiral based compounding for convex array.

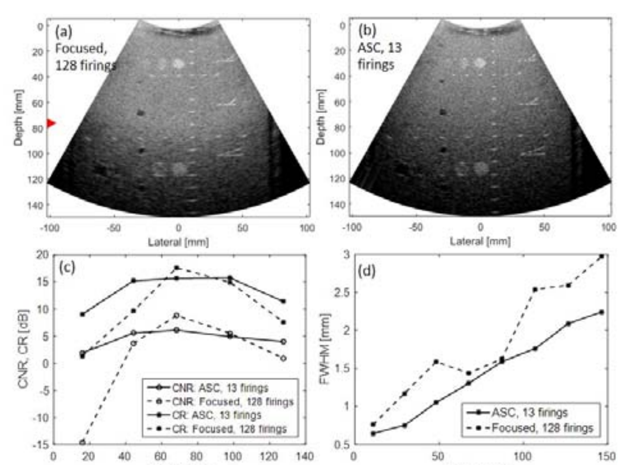

Fig. 2. B-mode images of the CIRS 040 phantom of (a) the focused mode and (b) ASC with a 70 dB dynamic range. (c) Contrast-to-noise ratio (CNR) and contrast ratio (CR) of hypoechoic regions at different depths. (d) Full width at half-maximum (FWHM) of wires at different depths.

P1-C1-5

Diverging Wave Compounding: Direct Comparison of Two Popular Approaches

Vangjush Komini[1], Pedro Santos[1], Jan D'Hooge[1]; [1]*KU Leuven, Leuven, Belgium*

Background, Motivation and Objective

Fast cardiac imaging using diverging waves (DW) is receiving much attention. Coherent compounding is important to keep spatial resolution and CNR acceptable. Two approaches have been presented in literature to do so: i) the full aperture of the probe is used and the virtual focus is moved along an arc centered at the center of the probe (ARC); ii) a sub-aperture is used and the virtual focus is linearly translated across the aperture (TRANS). To date, it remains unclear which approach is most effective. The aim of this study was therefore to directly contrast both approaches.

Statement of Contribution/Methods

Channel data from a point target phantom (10 points 1cm apart in the axial direction) was simulated using FieldII using a phased array (64 elements; 2.7MHz;pitch 0.28[mm]). For both approaches, the number of transmits ranged from 1 (i.e. no compounding) to 11 and was kept odd in order to ensure symmetry in the compounded image. In both the cases the virtual focal point was kept at the same distance relative to the center of aperture. The sub-aperture for TRANS was composed by 21 crystals, whereas the opening angle for ARC was 140 o. All images were reconstructed using delay-and-sum with dynamic receive focusing (90o sector; 140 lines). The resulting point-spread-function was quantified by measuring the -6dB two-way beam profile (FWHM) and the side-to-main-lobe energy ratio (SMER). Similarly, images were reconstructed using both approaches from a cyst phantom (10x10 [cm]) in order to evaluate the contrast-to-noise ratio (CNR). In-vitro data were acquired using our in-house system and a phased array (64 elements; 3.5MHz; pitch 0.22[mm]). A cirs 040 phantom and a thin wire inside a water tank were scanned, using the same setup as in simulation, in order to quantify CNR and FWHM/SMER.

Results/Discussion

Based on simulation and experimental data, compounding using ARC showed little impact on FWHM or SMER while it did significantly improve CNR. TRANS on the other hand benefited more clearly and outperformed ARC for all metrics tested. Our study did not consider the difference in transmit acoustic power for both approaches as this is highly system/transducer specific. Thus, we have focused only on the intrinsic performance of both approaches without taking SNR into consideration. In conclusion, the intrinsic performance of TRANS compounding is better than that of ARC compounding.

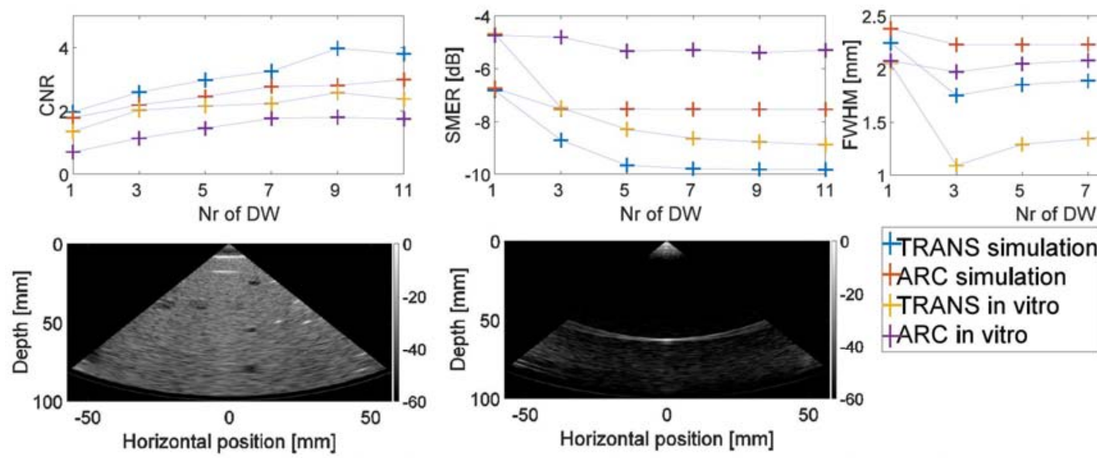

Figure 1. (a) Contrast quantified. (b) Side lobe suppression. (c) Resolution of both the methods. (d) In-vitro image of cirs 040. (e) In vitro image of a wire. (f) Legend for the plots.

P1-C1-6

Inter-Transmission Adaptive Weighting for Suppressing Grating Artifact in High-Frame-Rate Synthetic Transmit Aperture Beamforming

Teiichiro Ikeda[1], Chizue Ishihara[1], Misaki Hiroshima[1], Masanori Hisatsu[1], Kenji Kumasaki[1], Hiroshi Kuribara[1]; [1]*Hitachi Ltd., Japan*

Background, Motivation and Objective

Synthetic Transmit Aperture (STA) is a principal technology of a modern medical ultrasound beamforming. The improved resolution of STA will be a strong feature especially for cardiovascular diagnosis whereas a pitfall exists in increasing the frame rate up to 250 fps without the image degradation. One of the causes is a *grating lobe by the coarse transmission-channel* which manifests in the blurred low brightness region in the accelerated frame-rate images. This is also a general issue for high-frame-rate technologies including plane wave imaging. The purpose of this study is to propose inter-transmission adaptive weighting (ITAW) for the suppressed grating lobe artifacts by the *coarse transmission channel* in the STA imaging.

Statement of Contribution/Methods

ITAW expected to suppress the image blurring caused by the transmission-channel grating lobe because the STA grating lobe has lower coherence compared to the main lobe of the inter-transmit summation. We evaluate several types of adaptive weighting algorithms for the suppressing the grating artifact when the transmission pitch up to 8 times larger than physical channel pitch. First, we examined the characteristics of the ITAW using simplified S/N simulation. Then we evaluate the improved image quality by the computer emulation using RF data obtained by commercialized ultrasound scanner.

Results/Discussion

By the simplified simulation, we confirmed that the effect of grating lobe suppression is much stronger with the smaller noise level, the shorter pulse length (broader frequency band) and the larger number of STA summation. In the in vitro and in vivo experiments, the ITAW suppressed the grating artifact of a pin target and a human heart by 13.2 dB and 8 dB respectively while preserving the spatial resolution of the target structure such as heart wall. The proposed ITAW is a valid method to achieve the high-performance STA images without making a compromise on the trade-off relationships between the frame rate and image resolution.

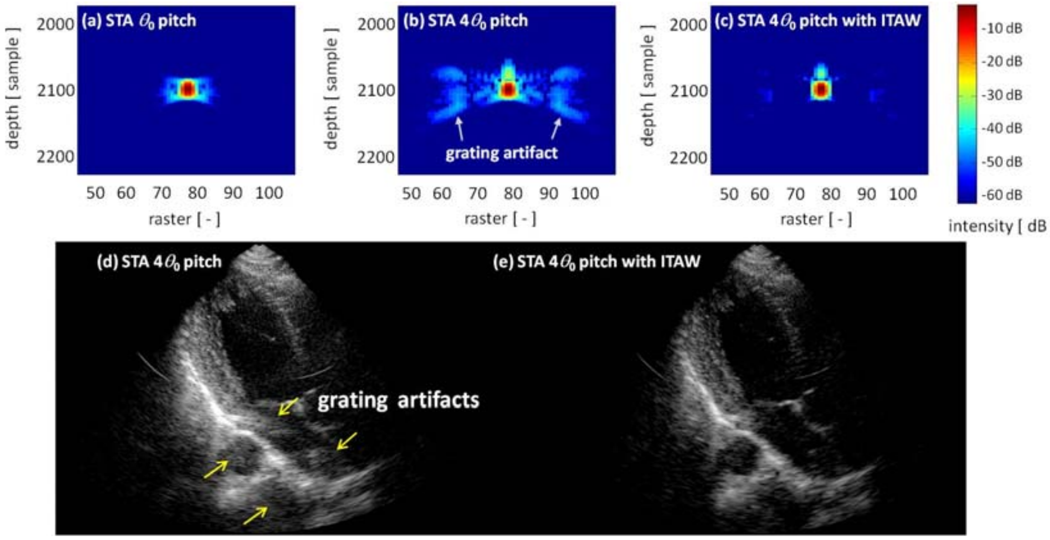

P1-C1-7

High Frame Rate Multi-Plane Echocardiography Using Multi-Line Transmit Beamforming: First Experimental Findings

Pedro Santos[1], João Pedrosa[1], Jan D'hooge[1]; [1]*Department of Cardiovascular Sciences, KU Leuven, Belgium*

Background, Motivation and Objective

Given the limited spatiotemporal resolution of 3D echocardiography, simultaneous assessment of all ventricular myocardial segments can clinically be performed using multi-plane acquisitions (MP) – i.e. biplane (BP) or triplane (TP). However, the wider field of view of MP impairs spatiotemporal resolution, thus hindering the performance of e.g. speckle tracking.

Multi Line Transmit (MLT) beam forming (i.e. simultaneously transmitting multiple focused beams) has been shown an appealing approach to improve temporal resolution without sacrificing image quality.

At IUS 2016, an MLT sequence dedicated for MP imaging was presented and evaluated using computer simulations. The aim of the present study was to implement and validate this sequence on an experimental ultrasound system.

Statement of Contribution/Methods

Two MP imaging sequences, MLT-BP and MLT-TP sequences were implemented and compared against single line transmit (SLT) 2D imaging of the same planes. A sector opening angle of 70° and 72 transmit beams were used for all the sequences. To mitigate MLT cross-talk artifacts, the scan sequences were implemented with asymmetrical beam scanning patterns and with the main direction oriented across the diagonal of the transducer (Fig A).

Experimental validation was done using a 32x32-element 2D array (Vermon, 3.0 MHz, 0.3 mm pitch, 50% bandwidth), driven by a programmable ultrasound system (HD-PULSE).

The point spread function of the system and the cross-talk of the MLT sequences were evaluated by scanning a single wire in a water tank and a CIRS 055A phantom. Subsequently, a simplistic left ventricle mock model was scanned to evaluate the contrast-to-noise ratio and mimic the scanning of multiple cardiac cross-section planes.

Results/Discussion

MP imaging using MLT beamforming has been successfully implemented experimentally. Results have proven that spatial resolution across the multiple planes is preserved (owing to the use of focused beams), whereas frame rate would be increased by a factor of 2 and 3, for BP and TP sequences, respectively. Similarly, comparable contrast was achieved while imaging the heart model with SLT and MP-MLT.

Overall, results seem to corroborate MLT as an attractive approach for characterization of all myocardial segments in a single heartbeat. Further quantitative evaluation is ongoing.

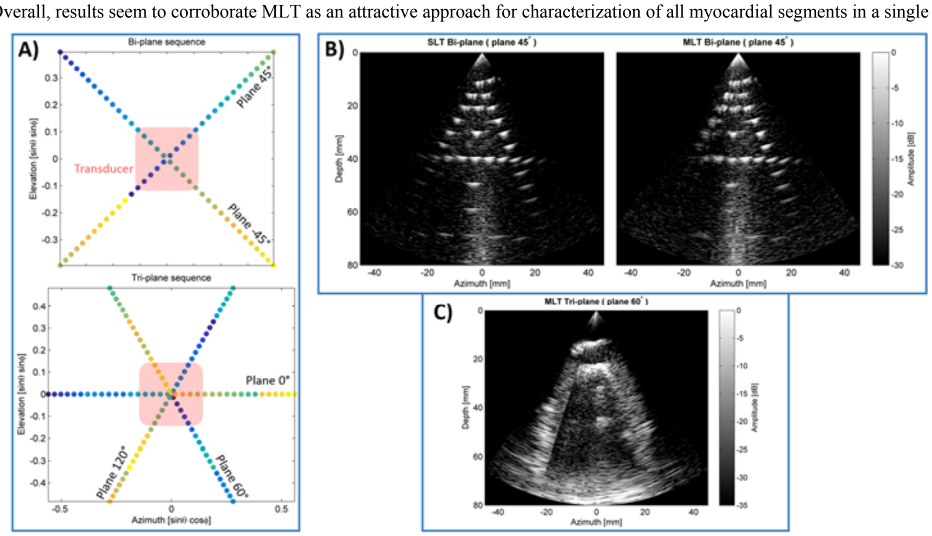

Fig – A) Multi-plane scanning sequences: the colour gradient depicts the order of the MLT transmissions. B) B-mode images of the CIRS 055A acquired with the SLT and MLT bi-plane. C) B-mode image of the cardiac mock model obtained with the MLT tri-plane.

P1-C1-8

Optimization Strategies and Neighbour-Pair Complementary Codes for Massively Parallel Focal-Zone Ultrafast Ultrasound

David Egolf[1], Tarek Kaddoura[1], Roger Zemp[1]; [1]*Electrical and Computer Engineering, University of Alberta, Edmonton, Alberta, Canada*

Background, Motivation and Objective

Plane wave methods for ultrafast ultrasound imaging suffer from a low signal to noise ratio (SNR) and a limited field of view at greater imaging depths. Imaging using multiple focused coded beams in parallel is one strategy for high speed imaging that may improve on these limitations. However, the SNR and resolution of this strategy are degraded by interference between the beams transmitted in parallel. We aim to reduce this interference while retaining acceptable axial resolution by careful design of coded beams.

Statement of Contribution/Methods

To ensure good axial resolution and to increase flexibility of code design, we use two transmit events to form each set of lines in the image. This implies an increase in imaging speed of approximately *K/2*, where *K* is the number of beams fired in parallel. To decode channel data we use a matched filter, summing matched filter output over each pair of transmit events. As a result, the interference between two beams fired in parallel is dictated by the magnitude of the sum of cross-correlations between parallel beam encoding patterns. We have constructed metrics based on this idea, and optimized coded beams for these metrics using the sequential quadratic programming capabilities of MATLAB's nonlinear optimization toolbox.

Results/Discussion

Using our optimization framework, we have generated codes that allow for extremely low interference between two simultaneously transmitted parallel beams. Our optimization framework also enables generation of low-interference codes for many simultaneous parallel focal zones. Codes generated by our optimizer for the case of two simultaneous focal zones have an autocorrelation sum peak magnitude on the order of 10^{15} times larger than the maximum magnitude of their cross-correlation sum. The potential for clutter reduction by using optimized codes is illustrated in the figure below. As shown, clutter is reduced by using optimized codes when imaging point scatterers with two simultaneous beams. To conclude, our optimization framework provides a starting point for applying optimization techniques for the generation of coded beams with minimal interference. Optimized codes may enable ultrafast ultrasound imaging at greater depths and with a greater field of view than flash imaging, with acceptable SNR and resolution.

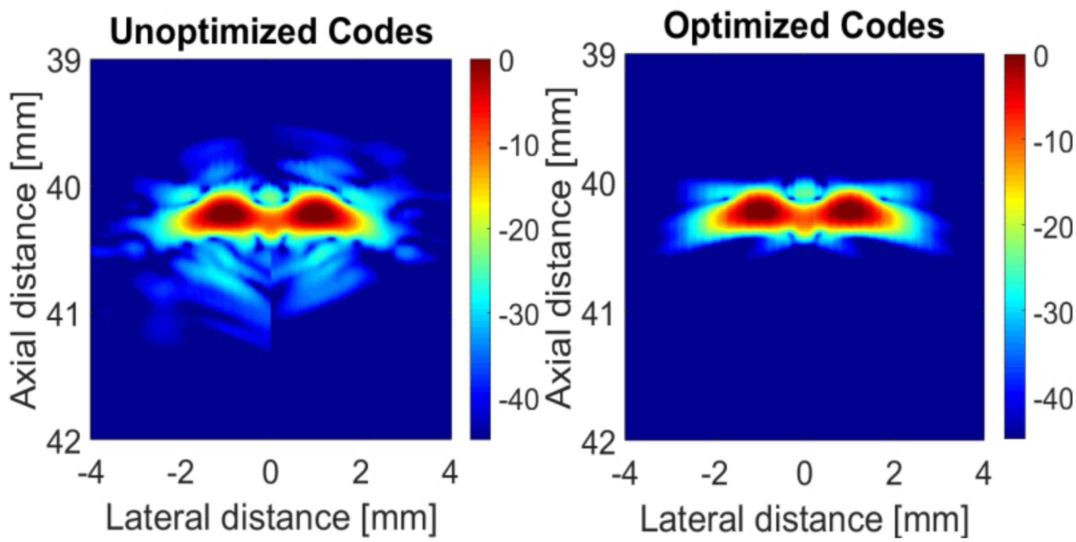

P1-C1-9

Motion Correction for Multi-Plane-Transmit Beamforming: A Simulation Study

Yinran Chen[1], Jianwen Luo[1], Jan D'hooge[2]; [1]*Department of Biomedical Engineering, Tsinghua University, Beijing, Beijing, China, People's Republic of,* [2]*Laboratory of Cardiovascular Imaging and Dynamics, Department of Cardiovascular Sciences, KU Leuven, Leuven, Belgium*

Background, Motivation and Objective

A hybrid beamforming approach combining the strengths of diverging wave compounding (DWC) and multi-line-transmit beamforming (MLT) (i.e., multi-plane-transmit, MPT) was previously proposed by our labs for 3D imaging [1]. Although we demonstrated this approach to be superior to 3D DWC and 3D MLT, we did not account for artifacts induced by motion. The aim of this study was therefore to propose a motion compensation (MoCo) method to further improve the performance of MPT beamforming.

Statement of Contribution/Methods

The proposed 3MPT follows an azimuth-major order. Hereto, 3 *planar* DWs (inter-plane spacing 20°) were simultaneously transmitted repetitively while moving the transmit aperture in the azimuth direction (Figs. c-d) according to a ″round-trip″ compounding scheme as proposed in [2]. This process was repeated while sweeping the 3MPT in the elevation direction in an edge-to-center sequence to avoid motion artifacts at the edges of the respective subsectors (Fig. d). Such setup led to two types of motion: i) the motion within the DW planes due to the compounding process, and ii) the motion in between DW planes due to the scanning process in the elevation dimension.

The proposed MoCo scheme consists of 2 phases: in the 1st step the MoCo was performed within the (3 parallel) DW planes prior to compounding (cf. [2]). In the 2nd step, MoCo was applied to correct for time lag between neighboring DW planes in the elevation direction. Hereto, the cumulative displacement between the measured planes and 3 reference planes (i.e. the 3 planes acquired first) were estimated based on the Doppler velocities within the corresponding DW planes.

A cystic phantom with motion in the axial direction at a speed of 10 cm/s was simulated in Field II. The contrast-to-noise ratio (CNR) of the cystic region before and after MoCo was quantified.

Results/Discussion

The images before MoCo are presented in Fig. a, showing blurring in the azimuth (i.e., DW) dimension and edge-to-center motion artifacts in the elevation dimension. The images were restored qualitatively using the 2-step MoCo (Fig. b) which was confirmed quantitatively by an increase in CNR from 4.59 to 6.39. The proposed method thus allows to reconstruct high quality volumetric images at a frame rate of ~66 Hz (PRF = 5 kHz) that are free of motion artifacts.

[1] Chen *et al*. 10.1109/TUFFC.2017.2651498.

[2] Porée *et al*. 10.1109/TMI.2016.2523346.

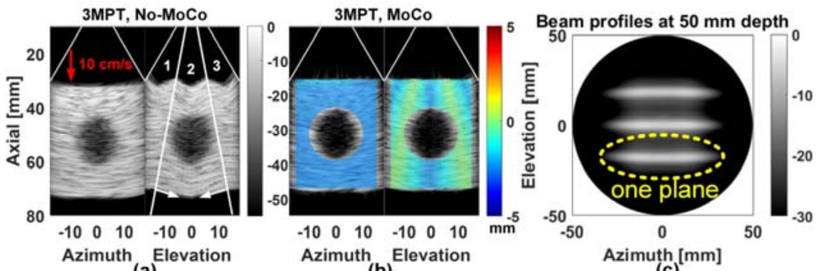

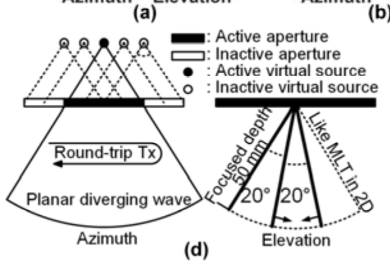

Figure (a)-(b) 3MPT images of a cystic phantom at a speed of 10 cm/s before and after MoCo. (c) the C-plane of the 3MPT beam profiles, where a "plane" was indicated. (d) A detailed illustration of the 3MPT setup with 5 "round-trip" DWC in the azimuth dimension. The beams acted like MLT in 2D in the elevation dimension, with a center-to-edge interleaved scan sequence.

P1-C1-10

Low Complexity Adaptive Beamforming with Multi Line Transmit Cardiac Ultrasound

Grigoriy Zurakhov[1], Ling Tong[2], Alessandro Ramalli[3], Piero Tortoli[3], Jan D'hooge[2], Zvi Friedman[1], Dan Adam[1]; [1]*Biomedical Engineering, Technion - IIT, Israel,* [2]*Department of Cardiovascular Sciences, KU Leuven, Belgium,* [3]*Microelectronics Systems Design lab, University of Florence, Italy*

Background, Motivation and Objective

Multi-line transmission (MLT) is a recently developed method for high frame rate cardiac ultrasound imaging. However, a potential pitfall of this method is the presence of artifacts due to cross-talk between the MLT beams. Low complexity adaptive beamforming (LCA) is a high resolution adaptive beamforming method that chooses a weighting function out of a predefined set of apodization functions assembled from Kaiser windows (regular / with shifted peak response, and also applying the "inverse" window). The objective of the current work was to experimentally examine whether the LCA setup (along with Tukey windowing and additional low-sidelobe apodizations) can attenuate the MLT artifacts better than Tukey windowing alone, at an improved spatial resolution.

Statement of Contribution/Methods

MLT radiofrequency (RF) data was acquired using an ultrasound advanced open platform (ULA-OP). The optimal apodization function was chosen according to the minimization of the cost function applied on the demodulated time delayed data. Spatial resolution was calculated for the -6 dB width of lateral beam profile at four depth values, with different apodizations (Boxcar, Tukey, and modified LCA) each. The results of the improvement are demonstrated using phantom and in-vivo cardiac 4MLT data using the fundamental frequency.

Results/Discussion

In the present study we demonstrate that the modified LCA apodization set outperforms Tukey apodization window by increased spatial resolution and better rejection of receive cross-talk induced artifacts. The mean improvement of the lateral resolution is 70% vs Tukey apodized receive aperture and 62% vs rectangular receive aperture of MLT. Visual inspection suggests a decrease in the lateral extent of transmit cross-talk induced artifacts.

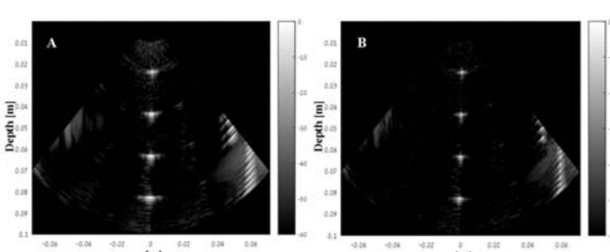

Fig. 1. Wire phantom 4MLT Beamforming: (A) Tukey apodization (B) LCA apodization

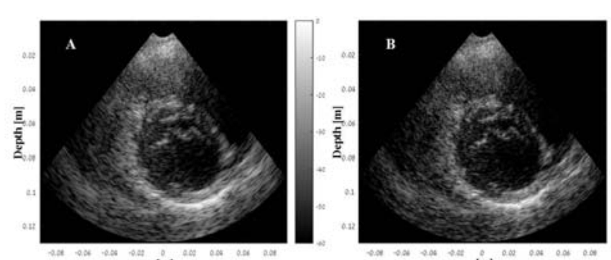

Fig. 2. Cardiac Short Axis 4MLT Beamforming: (A) Tukey apodization (B) LCA apodizatio

P1-C1-11

A Study of Synthetic Aperture Focusing Using Plane Waves to Provide Wider Field of View Ultrasound Imaging without Side-Lobe Artifacts due to the Use of Sampling Angle in Transmitting Inclined Plane Waves

Bae-Hyung Kim[1], Azra Alizad[1,2], Mostafa Fatemi[1]; [1]*Physiology and Biomedical Engineering, Mayo Clinic College of Medicine, Rochester, MN, USA,* [2]*Department of Internal Medicine, Mayo Clinic College of Medicine, Rochester, MN, USA*

Background, Motivation and Objective

Synthetic aperture focusing based on planar waves also known as coherent plane wave compounding (CPWC) was introduced to reduce the diffraction spreading effect of ultrasound at depths (Song et al. US Patent 6736780, 2004). CPWC has been widely used in shear wave elasticity imaging due to its capability of ultrafast frame rate (Montaldo, et al. IEEE TUFFC, vol. 56, 2009). However, CPWC based on unfocused (plane waves) or defocused Tx beams has an inherent limitation in imaging wider field of view (FOV) due to the use of sampling angle in transmitting steered ultrasound wave. The sampling angle causes an unwanted side-lobe artifact if the sampling interval of angle is not small enough to cancel the artifact.

Statement of Contribution/Methods

This paper introduces a theoretical model to control the artifact and presents an approach to provide wider FOV without resorting to increasing the number of firings required (NFR). By using the Rayleigh diffraction formula, the normalized beam pattern of PWC can be described as: $\Psi_{PWC}(x,z) \approx \sin(\pi N \Delta u x/\lambda)/\sin(\pi \Delta u x/\lambda)$ ($u=\sin\alpha$, $\Delta u=\sin\alpha_{n+1}-\sin\alpha_n$) where ($x,z$) is an observation point defined in lateral and axial direction, α_n and N are the n-th inclined angle and the number of Tx waves respectively, and λ is the wavelength. If the angle is not too large, Δu can be regarded as the sampling interval of angle which results in repetitive *sinc* patterns of $m\lambda/\Delta u$ (m=1,2,...) causing the side-lobe artifact in lateral direction. This artifact is separate from the depth while the grating lobe artifact in lateral direction due to the inter-element spacing of source aperture is directly correlated with the depth.

Results/Discussion

To cancel the side-lobe artifact, the sampling interval of angle needs to be small enough as $\Delta u \leq 2\lambda/W$ at given imaging width (W) of FOV. This necessitates increasing NFR. To provide wider FOV without sacrificing the frame rate, traditional approaches to suppress the grating lobe can be adopted. Here we investigate a heuristic approach that uses heterogeneous intervals in sampling angle (e.g. quadratic ($C_1\alpha^2$) or root-square ($C_2\sqrt{\alpha}$) forms) to mitigate the artifact. Field II was used to demonstrate the analysis of CPWC and the side-lobe artifact depending on only the sampling interval of angle as shown in Fig.1. This preliminary study can lead to how to utilize CPWC in using multiple probes to exploit multipath propagation as well as single probe.

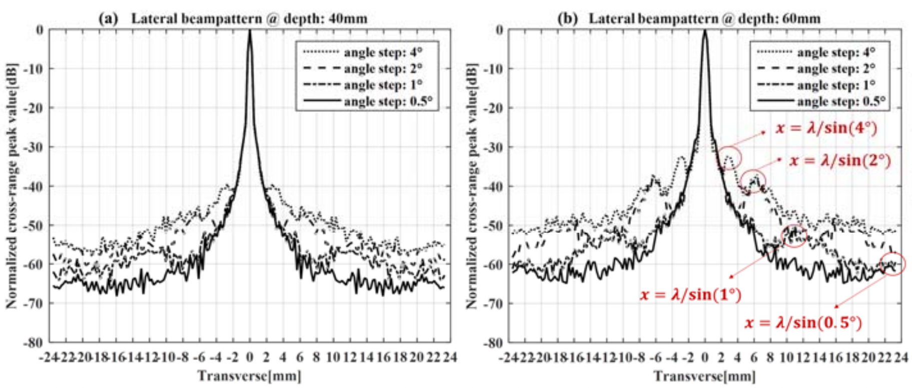

(c) The position of side-lobe artifact according to different sampling intervals of angle (angle step)

$\Delta\alpha$ (angle step)	$x = \lambda/\sin\Delta\alpha$ (mm)
4°	2.94
2°	5.87
1°	11.75
0.5°	23.49
0.2°	58.73

Fig. 1. Pulsed-wave beam-pattern of CPWC at depth of 40mm (a) and 60mm (b), and the position of side-lobe artifact according to the sampling interval of angle (c). In simulation, the maximum angle in transmitting inclined plane wave was 20°, and the element pitch of transducer was 0.245mm, 3 cycles tone-burst with center frequency of 7.5MHz and wavelength of 0.205mm was used, the system of 64 Tx/Rx channels and 80 MHz sampling rate was used.

P1-C2 - MBF: Flow Imaging: From 2D to 4D

Exhibit Hall

Saturday, September 9, 2017, 9:30 am - 4:00 pm

Chair: **Jørgen Avdal**
Norwegian University of Science and Technology

P1-C2-1

Cardiac Flow Mapping Using High Frame-Rate Diverging Wave Contrast Enhanced Ultrasound and Image Tracking

Matthieu Toulemonde[1], Chee Hau Leow[1], Robert J. Eckersley[2], Meng-Xing Tang[1]; [1]*Department of Bioengineering, Imperial College London, London, United Kingdom,* [2]*King's College, United Kingdom*

Background, Motivation and Objective

High frame-rate (HFR) contrast enhanced echocardiography (CE), based on pulse inversion (PI), diverging wave transmission, was recently proposed for improving the image contrast over standard CE with focused transmission [M. Toulemonde, IUS 2016]. Comparing to ~30Hz in standard CE, HFR CE can reach a frame rate of up to 6000Hz, allowing accurate tracking of fast flow structure and dynamics in cardiac chambers.

A recent study shows the benefit of HFR cardiac imaging for flow vortex detection by using a Duplex mode (B-mode + Doppler) but without microbubble contrast agents, the signals from blood cells are weak [J. Faurie, UFFC, 2017]. Another clinical research shows the potential of visualising and tracking vortex with a CE at a frame rate of 204 ± 39 frames / s but the field of view is limited and the frame rate is still low for tracking the very fast cardiac flow [H. Abe, Cardiovascular Imaging, 2013].

The aim of this work is to demonstrate the feasibility of flow mapping using HFR CE in-vivo cardiac imaging.

Statement of Contribution/Methods

In-vivo CE images at a frame rate of 5500Hz are obtained by transmitting diverging PI wave pair (3-cycles, 1.5MHz, MI 0.05) at different steering angles. HFR CE acquisitions were made with using one bolus injection of 1.2 ml Sonovue microbubbles followed by 7 ml of saline solution flush. The data acquisition, started one minute after the bolus injection. The ultrasound imaging velocimetry is performed by using an extension of our particle/speckle image tracking / PIV algorithms [C.H. Leow, UMB 2015].

Results/Discussion

The Figure shows (Top) HFR CE acquisitions at two different time with (Bottom) their corresponding flow velocimetry. The left images show the moment where the valves are opened and where blood is coming inside the left chamber with the highest velocity creating a vortex near the valves. The right images is 0.128 milliseconds after.

In this work we shown the feasibility of microbubbles flow tracking in HFR CE acquisition with a high temporal resolution and low MI as well as the detection of vortex near the valves during filling phases agreeing with previous study [H. Abe, Cardiovascular Imaging, 2013].

Figure: (Top) In-vivo log-compress HFR CE images at two different moment of the left chamber and (Bottom) their corresponding flow velocity mapping based on microbubbles tracking.
The left images show the moment where the valves are opened and where blood is coming inside the chamber.

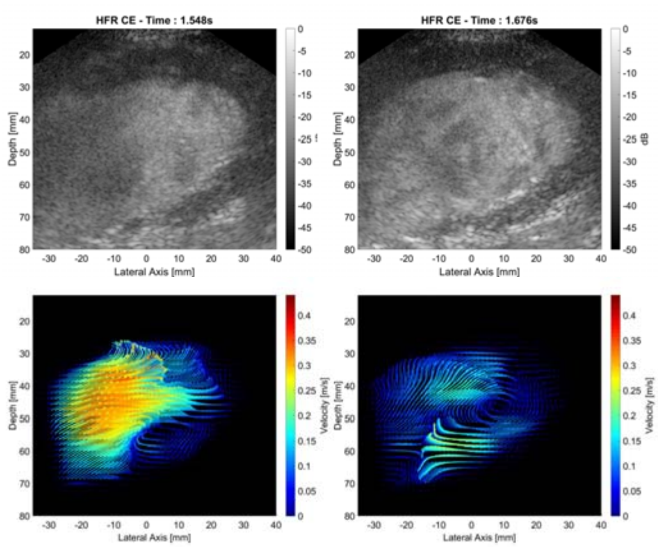

P1-C2-2

In Vivo Blood Flow Mapping of Mice by Ultrafast High Frequency Ultrasound Imaging

Hsin Huang[1], Pei-Yu Chen[1], Chih-Chung Huang[1]; [1]*Department of Biomedical Engineering, National Cheng Kung University, Taiwan*

Background, Motivation and Objective

Recently, ultrafast ultrasound imaging has been proposed for many clinical applications. However, most operational frequencies of ultrafast ultrasound imaging are around 3.5 to 15 MHz. Currently, ultrafast 40 MHz high frequency ultrasound imaging has been developed in our Lab. High frequency ultrasound is a good choice for blood flow mapping because the backscattering signals from blood is increased with the operational ultrasound frequency according to Rayleigh scattering. In order to enhance the blood signals, clutter filter based on singular value decomposition (SVD) is considered as a suitable solution. The purpose of this study is to perform real time blood flow mapping by using a SVD-based algorithm at a frequency of 40 MHz. In vivo experiments were carried out by mice carotid artery imaging.

Statement of Contribution/Methods

Data acquisition was performed by Verasonics Vantage 256 system and 256 high frequency array transducer Visualsonics MS550D. This system can reach a very high frame rate of 10k fps at a 40 MHz center frequency. After data acquisition, slow-time analysis was performed, and the SVD-based algorithm is applied on each slow-time ensemble to separate the clutter signals and blood signals, as shown in Figure 1(a). Subsequently, the blood velocity and Doppler power was estimated, respectively. The blood signals were extracted by thresholding method.

Results/Discussion

Figure 1(b) shows the Doppler power distribution for both blood (red color) and clutter (blue color) after SVD-based algorithm. Under a high frequency range, the blood signals are stronger than clutter in most cases. Therefore, it is quite easy to distinguish blood from clutter in ultrafast ultrasound images. Figure 1(c, top) shows the typical original B-mode image of carotid artery of mice. The lumen exhibits low echogenic as usual. However, the blood signals were enhanced by the proposed method, as shown in Figure 1(c, middle). Figure 1 (c, below) shows the combining image of B-mode and blood signals. This preliminary study indicated that ultrafast high frequency ultrasound imaging can enhance blood signals, which means we may have super-resolution blood mapping without contrast agent in the future.

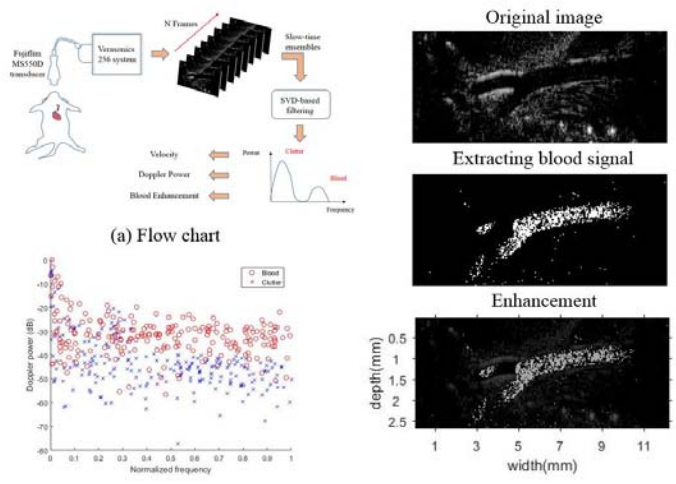

(b) Doppler power distribution (c) Blood enhancement

P1-C2-3

Ultrasound Study of Hemodynamic Changes by Flow Diverting Stents in Idealised and Patient-Specific Anatomies

Ana Paula Narata[1,2], Fernando Silva De Moura[3], Alberto Marzo[4], Cecile Perrault[4], Ignacio Larrabide[5], Ayache Bouakaz[1], **Charles Sennoga[1]**; [1]*Inserm U930, France,* [2]*CHRU Hôpitaux de Tours, France,* [3]*Universidade Federal do ABC, Brazil,* [4]*University of Sheffield, United Kingdom,* [5]*Universidad Nacional del Centro de la Provincia de Buenos Aires, Argentina*

Background, Motivation and Objective

Whereas the use of flow diverter stents (FDs) represents a powerful treatment alternative to surgical clipping of intracranial aneurysms (IAs) presenting at arterial bifurcations, endovascular deployment of FDs often involves the jailing of daughter vessels (DV), and can affect the patency of the jailed DV.

Statement of Contribution/Methods

We studied haemodynamic changes triggered by the deployment of FDs, using computational fluid dynamic (CFD) simulations and sought to validate our CFD findings by using pulse-wave (PW) and colour Doppler ultrasound (cDUS), in idealised and patient-specific flow reconstructions (3D printed phantoms) of bifurcating arteries. Pre- and post-treatment hemodynamic changes were assessed and evaluated for statistical significance. Correlation of PW/cDUS and CFD hemodynamic changes were retrospectively compared against treatment outcomes in patients, at 3-months clinical follow-up that involved n=14 arterial narrowing and n=11 controls.

Results/Discussion

CFD predictions showed that mean wall shear stress (WSS) is significantly affected when FDs are deployed in bifurcations with asymmetric diameter ratios DR<0.65, but were not-significant for bifurcations with symmetric DR≈1. PW and cDUS measurements, correctly reproduced the flow profiles (see Figure) and WSS generated by CFD. As with CFD predictions, hemodynamic PW/cDUS measurements revealed a strong correlation between calibre changes in arterial diameter (narrowing) and bifurcation asymmetry, characterised by a DR<0.7 (p<0.001). This study demonstrated that haemodynamic changes were significant when FDs are deployed within asymmetric bifurcations, and supports our previous suggestion of a higher risk associated with FDs-treatment of IAs presenting at asymmetric bifurcations.

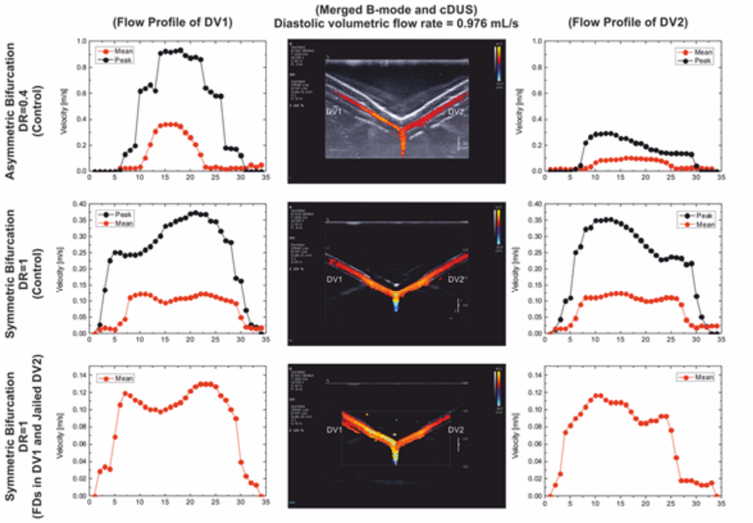

Figure. Merged B-mode/cDUS images (middle row) and corresponding flow profiles for a diastolic volumetric flow rate of 0.976 mL/s in an asymmetric bifurcation (top row); symmetric bifurcation (middle row) and symmetric bifurcation with the FDs deployed along DV1 and subsequent jailing of DV2 (bottom row).

P1-C2-4

3D Flow Velocity Reconstruction in a Human Radial Artery from Measured 2D High-Frame-Rate Plane Wave Contrast Enhanced Ultrasound in Two Scanning Directions – A Feasibility Study

Virginie Papadopoulou[1,2], Richard Corbett[3,4], Xinhuan Zhou[1,4], Matthieu Toulemonde[1], Chee Hau Leow[1], David Cosgrove[3], Neill Duncan[3], Meng-Xing Tang[1];
[1]*Department of Bioengineering, Imperial College London, United Kingdom,* [2]*Recently moved: Department of Biomedical Engineering, UNC Chapel Hill, USA,* [3]*Department of Medicine, Imperial College London, United Kingdom,* [4]*These authors contributed equally to this work, United Kingdom*

Background, Motivation and Objective

Hemodynamics play an important role in the development of cardiovascular disease, with atherosclerosis and intimal hyperplasia arising at sites with low wall shear stress and disturbed endoluminal mixing. Computational fluid dynamics (CFD) can study blood rheology, however performance relies on precise 3D anatomy and accurate blood flow measurements to seed the initial and boundary conditions. Recently, ultrasound (US) 2D high frame-rate (HFR) acquisitions using plane-wave (PW) imaging combined with contrast agent tracking have been used for US image velocimetry (UIV) to measure blood flow profiles (Leow CH, UMB 2015). Here we investigate the experimental feasibility of combining multiple 2D UIV acquired in two non-parallel scanning directions along a human brachial artery for estimating the 3D blood flow velocity profile.

Statement of Contribution/Methods

Sonovue contrast agent was infused into a healthy volunteer with concomitant image acquisition in the volunteer's brachial artery. HFR US images were acquired using an L12-3v linear array probe connected to a Vantage 128 research platform (Verasonics, Redmond, WA, USA). To ensure precise rotation of the transducer through its central axis, this was aligned with a micromanipulator rotator stage. A Velmex controlled translation stage was interfaced with the imaging script so that 11 2D frames are acquired at predetermined positions along the arm direction, before returning to the initial position (Fig.1a). For each position, 1s of HFR US images was acquired with 7 pulse-inversion PW (1 cycle, 4 MHz, MI 0.2, 1000Hz compounded frame rate). The probe was then rotated and the protocol repeated. Data was processed off-line: 2D flow vectors at each frame were tracked (UIV), followed by 3D flow reconstruction using divergence-free interpolation function.

Results/Discussion

This initial feasibility study demonstrated the potential of implementing an acquisition protocol comprised of an initial fast imaging sequence for vessel geometry, followed by 11 separate HFR acquisitions performed for each of the two transducer rotation orientations, all within 25min of total acquisition time. It is thus possible to stay well within the guidelines for human contrast for this method. Data show that it is possible to reconstruct the 3D flow using all 2D positions scanned and aligning for the fastest flow in the cardiac cycle, Fig.1c.

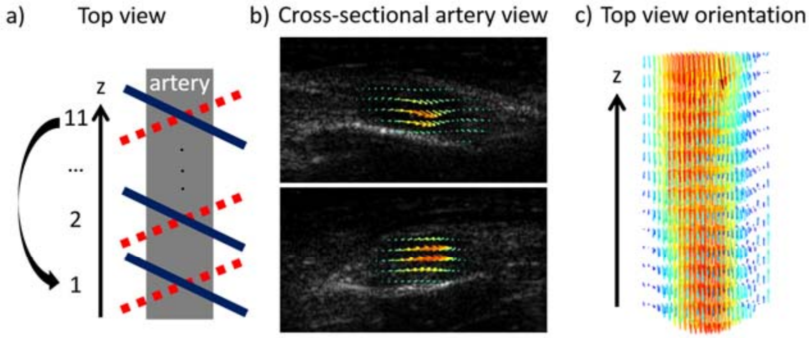

Figure 1: a) Schematic of acquisition strategy along the arm direction (z-axis): angle 1 (blue, solid) frames are acquired, then the probe is rotated and angle 2 (red, dashed) frames are acquired; b) Representative flow-tracked frame from angle 1 (top) and angle 2 (bottom) of the brachial artery at position 1 ; c) 3D reconstruction of the flow for the whole volume scanned for the fastest flow time during the cardiac cycle.

P1-C2-5 ________________________

Three-Dimensional Mapping of Epicardial and Intramyocardial Coronary Circulation In-Vivo Using 3-D Ultrafast Ultrasound Doppler Imaging

Mafalda Correia[1], David Maresca[1], Jean Provost[1], Mickael Tanter[1], Bijan Ghaleh[2], Mathieu Pernot[1]; *[1]Institut Langevin - ESPCI, PSL Research University, CNRS UMR7587, INSERM U979, Université P6 and P7, Paris, France, [2]INSERM U955, Equipe 03, F94000, Créteil et Université Paris Est, Ecole Nationale Vétérinaire, Maisons-Alfort, France*

Background, Motivation and Objective

Dysfunctions on the coronary circulation can lead to adverse and severe clinical outcomes, e.g., ischemic heart failure (IHF) or coronary artery disease (CAD). The evaluation of coronary vasculature is consequently of extreme importance to the diagnosis of these conditions. However, intramyocardial coronary vasculature cannot yet be imaged in-vivo in humans with current angiography techniques or transthoracic conventional ultrasound imaging. Recently, we have shown that in-vivo intramyocardial coronary vasculature can be assessed without any contrast agent injection by 2-D ultrafast ultrasound Doppler Imaging using a dedicated post-processing treatment [1], [2]. Yet, given the complex architecture of these vascular networks, 3-D imaging is of paramount importance for this application. The recent development of high-channel count electronics and 2-D matrix-array probes has enabled the possibility to assess these complex structures [3]. In this study, we propose the use of 3-D Ultrafast Ultrasound Doppler Imaging with coherently compounded plane-wave insonification and a new post-processing treatment to map in-vivo blood flows in three-dimensions of the epicardial and intramyocardial coronary circulation.

Statement of Contribution/Methods

Acquisitions were conducted in-vivo in open-chest swine hearts (N=3) between early and late diastole with a dedicated 3-D Ultrafast Doppler imaging sequence, using a customized, programmable, 1024-channel 3-D ultrafast ultrasound scanner and a 2-D matrix-array probe (9-MHz, 0.3mm pitch, 32x32 elements, Vermon). Acquisitions consisted in 4 successive 2-D tilted plane-wave emissions at a pulse-repetition-frequency of 12 KHz. Backscattered echoes were beamformed using a delay-and-sum algorithm. Tissue clutter was filtered using a new temporal-weighted spatial-temporal clutter filtering approach in order to separate tissue from blood signal throughout the cardiac-cycle. Power Doppler signals of the coronary vessels were finally computed and overlapped on B-mode imaging volumes to explore anatomical and blood flow functional information.

Results/Discussion

We successfully imaged epicardial and intramyocardial coronary vessels in three-dimensions between early and late diastole. The epicardial coronary veins and arteries were assessed exhibiting diameters of a few millimeters. The intramural coronary veins and arteries (i.e. prearterioles) were also assessed exhibiting diameters ranging from 500 µm down to 300 µm. Assessing the full anatomy of the coronary vasculature at high volume rates given by ultrafast imaging could open new insights in cardiovascular imaging. 3-D Ultrafast Doppler imaging could become an important non-invasive imaging tool to evaluate CAD and IHF.

[1] B. Osmanski, et al., IEEE TMI, 2012.
[2] D. Maresca, et al., IEEE IUS, 2015.
[3] Provost et al., PMB, 2014.

P1-C2-6 ________________________

In Vitro & In Vivo 4D Ultrafast Doppler Imaging Using a Large Aperture Row Column Adressed Transducer

Jack Sauvage[1], Martin Flesch[1,2], Thomas Deffieux[1], Mathieu Pernot[1], Bogdan Rosinski[2], Guillaume Ferin[2], Mickael Tanter[1]; *[1]INSERM U979, France, Metropolitan, [2]Vermon, France, Metropolitan*

Background, Motivation and Objective

Ultrafast 3D Doppler imaging can provide volumetric high frame rate and high resolution mapping of the vascular anatomy and function [1]. Current approach relies on the use of matrix arrays connected to high count of electronics channel which remain complex and costly. Row Column Addressed (RCA) approaches have been proposed as a low complexity alternative to matrix probe for imaging of blood flows [2]. Orthogonal Plane Wave (OPW) compounding is a dedicated beamforming strategy introduced recently [3] to perform full 3D ultrafast volumetric imaging using RCA. In this work we apply this technique on a new large aperture RCA probe and validate experimentally 3D blood flow imaging on in vitro flow phantoms and on in vivo human carotid artery.;

Statement of Contribution/Methods

A new prototype of 8MHz ultrasonic RCA probe was designed and built (2×128 orthogonal rows and columns elements, both 0.2 pitch, Vermon ® France). The probe was driven by a VeraSonics® Vantage 256 research ultrasound systems. The acoustic output of the probe was measured using a calibrated acoustic scanning system.

In vitro Power Doppler images were performed with a flow phantom (ATS model 523A Cardiac Doppler flow Phantom) crossed by a 4mm section pipe where blood scatterers mimicking fluid with a max flow velocity of 10cm/s. The frequency of transmitted planes waves was fixed to 10 kHz during 160msfor several set of steered angles. CNR was quantified as a function of the number of angles [Fig1].

Finally, in vivo carotid artery of one volunteer was imaged. The volumetric power Doppler was computed as well as the Doppler spectrum.

Results/Discussion

The pressure amplitude of the transmitted plane waves was +/-600 kPa at 30V. It corresponds to an MI = 0.14 and ISPTA =41 mW/cm² (at PRF= 10kHz).

Image quality assessed on power Doppler images exhibited strong side lobe levels which decreased rapidly with the number of emission angles. For Doppler imaging the contrast was found to increase by 7dB from 5 to 16 plane wave emissions allowing to visualize clearly in 3D the flow phantom (Figure 1). Finally, the in vivo feasibility was shown on the human carotid allowing to reconstruct successively the 3D geometry of the artery.

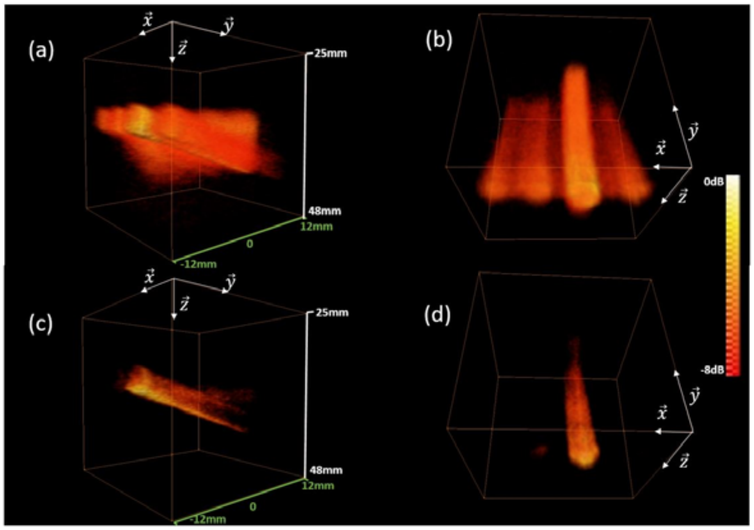

Fig1: 3D power Doppler performed from a 4mm section pipe flow phantom (ATS model 523A Cardiac Doppler flow Phantom). (a) and (b) 3D representation of one acquisition made with 5 steered plane waves. (c) and (d) acquisition from a 16 steered transmits plane waves showing the decrease of the lobes.

P1-C3 - MCA: Microbubbles Physics and Imaging

Exhibit Hall

Saturday, September 9, 2017, 9:30 am - 4:00 pm

Chair: **Emmanuel Cherin**
Sunnybrook Research Insitute

P1-C3-1

Theoretical and Experimental Investigation of the Nonlinear Dynamics of Nanobubbles Excited At Clinically Relevant Ultrasound Frequencies and Pressures: the Role of Lipid Shell Buckling

Amin JafariSojahrood[1,2], Lenitza Nieves[3], Christopher Hernandez[4], Agata Exner[3], Michael C. Kolios[1,5]; [1]*Physics, Ryerson University, Toronto, ON, Canada,* [2]*Institute for Biomedical Engineering, Science and Technology (iBEST), partnership between St. Michael's Hospital and Ryerson University, Toronto, ON, Canada,* [3]*Radiology, Case Western Reserve University, Cleveland, Ohio, USA,* [4]*Biomedical Engineering, Case Western Reserve University, Cleveland, Ohio, USA,* [5]*Institute for Biomedical Engineering, Science and Technology (iBEST), a partnership between St. Michael's Hospital and Ryerson University, Toronto, ON, Canada*

Background, Motivation and Objective

Microbubbles (MBs) excited by ultrasound (Us) are used as contrast agents for the detection of blood vessels. MBs can also be used to enhance drug delivery. However, the usage of MBs is limited to the blood pool due to their large size; where detection of biomarkers on tumor cells and effective drug delivery, requires MBs to reach the tumor tissue outside of the vasculature.

Statement of Contribution/Methods

To tackle these problems, nanobubbles (NBs) are proposed as a potential alternative. NBs can pass through submicron blood vessels and extravasate to tissue and due to their higher number density; higher doses of NBs can be delivered to the target. However, despite their potential, the use of NBs has been limited because of the limited information of their complex dynamics.

In this work, we manufactured lipid and surfactant-stabilized C3F8 NBs (mean diameter 203 nm) with 4 shell compositions of increasing surfactant: lipid ratios, (0, 0.02, 0.2, and 0.4). NB scattering response was investigated by single bubble scattering experiments with narrowband pulses with 16-55 MHz and acoustic pressure of 0.250-1.5 MPa (Vevo-770 Machine,@visualsonics), and in-vivo imaging at 12 MHz using a clinical scanner (Toshiba Aplio). The nonlinear response of the NBs was numerically studied by solving the Marmottant model for US pulses used in the experiments. The results were visualized using the resonance curves and bifurcation diagrams of the oscillations of the NBs versus frequency and pressure.

Results/Discussion

Experimental results demonstrate strong echogenicity of NBs at a frequency range 10-25 MHz. Single NB experiments suggest that NBs generate strong subharmonic and super harmonic responses even at lower acoustic pressures ~250 kPa. This contradicts the linear theoretical predictions, as the resonance frequency (fr) of the NBs is calculated to be ~130 MHz. Results of numerical simulations show that when the initial surface tension of the NBs is ~<0.01 N/m (Fig. 1) the fr of the NBs rapidly decreases as the acoustic pressure increases. Thus, NBs become active at frequencies below 50 MHz due to buckling of the lipid shell. Bifurcation diagrams confirmed the generation of subharmonics and super harmonics only for NBs which are initially close to buckling state. Additionally, we showed that the signal intensity increases for stiffer shell NBs in good agreement with experiments.

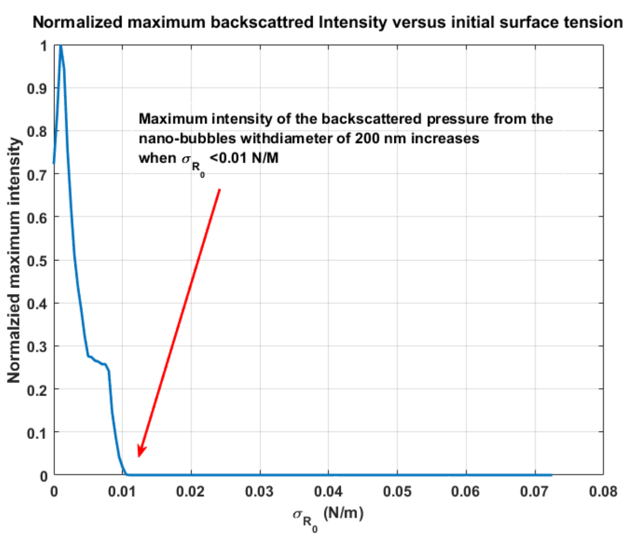

P1-C3-2

Hadamard Encoded Multi-Pulses for Contrast Enhanced Ultrasound Imaging

Ping Gong[1], Pengfei Song[1], Shigao Chen[1]; [1]*Department of Radiology, Mayo clinic, Rochester, MN, USA*

Background, Motivation and Objective

Contrast enhanced ultrasound (CEUS) imaging is widely used in clinic to enhance blood flow signal using microbubbles (MBs). In conventional CEUS methods such as pulse inversion (PI), amplitude modulation (AM), and pulse inversion amplitude modulation (PIAM) (Fig. 1), two pulses are excited individually in each transmission event (i.e. TX #1 and #2). Pulses in TX #2 are modified based on pulses in TX #1 by changing pulse polarity (i.e. PI), amplitude (i.e. AM), or both (i.e. PIAM). Then the echo signals from both transmission events follow the designed recombination to selectively cancel the linear responses from tissue and amplify the nonlinear responses from the MBs. In this paper, we propose a new CEUS pulse sequence using Hadamard-encoded multi-pulses (HEM) with a fundamental bandpass filter (i.e., filter centered on transmit frequency). HEM emits two Hadamard coded pulses consecutively in each of the two CEUS transmission events, as opposed to conventional CEUS methods which emit individual pulses in two separate transmission events. HEM improves the MB responses by: 1) exciting the MBs with a longer transmit pulse; and 2) using the fast polarity change between the HEM coded pulses to excite strong nonlinear MB responses, further enhancing the contrast-to-tissue ratio (CTR) for HEM-CEUS imaging.

Statement of Contribution/Methods

In HEM, the two pulses encoded by a 2nd order Hadamard matrix are emitted consecutively in both transmission events to increase the transmit power. An additional Hadamard decoding step is then applied to recover the signals as obtained from individual pulse excitations, followed by designed recombination to extract microbubble responses.

Results/Discussion

Fig. 1, last row, shows CEUS images obtained with different pulse sequences from a tissue mimicking phantom with a microbubble flow cell in the center. HEM provides the best CTR among these methods. The resolution in HEM is comparable to those in AM and PIAM. These properties of HEM can potentially facilitate more robust CEUS imaging for deep organs such as liver and heart for obese patients.

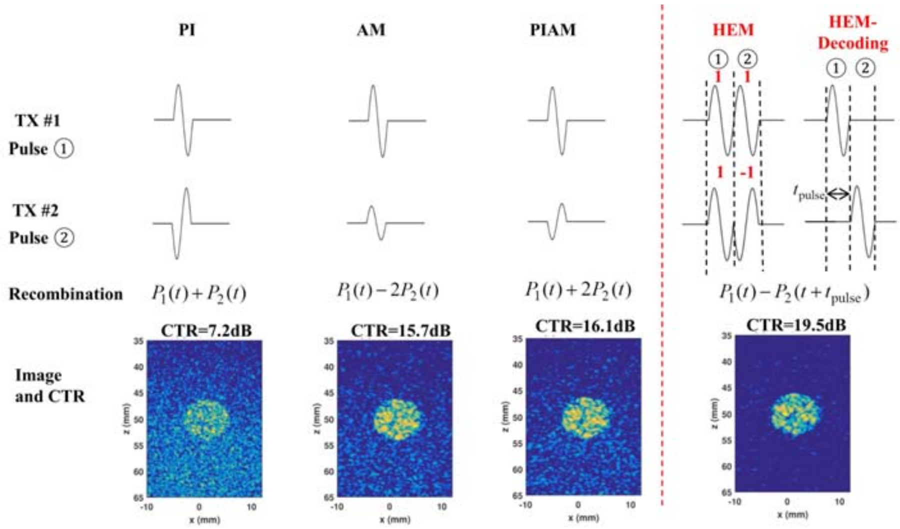

P1-C3-3

Enhanced Subharmonic Emission of Single Microbubbles by Acoustic Deflation

Emma Kanbar[1], Inés Beekers[2], Tom van Rooij[2], Nico de Jong[2], Klazina Kooiman[2], Ayache Bouakaz[1]; [1]*UMR Inserm U930, Université François-Rabelais de Tours, France,* [2]*Biomedical Engineering, Erasmus MC, Rotterdam, Netherlands*

Background, Motivation and Objective

When exposed to ultrasound, microbubbles (MBs) deflate [1]. This occurs due to exchange of the MB filling gas with the gas of its environment, thus implying changes in its gas composition. Moreover, recent studies showed that gas composition affects the subharmonic (SH) response of phospholipid-coated contrast agents [2] [3]. In this work we investigated the SH emission from single MBs and the impact of deflation upon insonification.

Statement of Contribution/Methods

The response of single BR14 MBs was recorded using the Brandaris 128 ultra-high-speed camera. MBs with a diameter ranging from 2.8 to 5.5 µm were insonified at 5 MHz (100 kPa, 10 cycles), since this is the resonance frequency for 3 µm BR14 and twice the resonance frequency for MBs of 5 µm [4], thus ensuring SH emissions. The SH response of deflated MBs was compared with the non treated MBs. The deflation sequence consisted of 10 cycle bursts at 5 MHz and at 200 kPa for medium size bubbles and 350 kPa for larger MBs (above 4 µm). We named deflated the MBs having their size decreased by at least 20%.

Results/Discussion

In total, 32 single MBs were studied. Figure 1 shows that more MBs exhibited SH after deflation (deflated MBs) compared to the non-deflated MBs (Non deflated). Moreover, deflated MBs emit SH with higher amplitudes. Our hypothesis is based on the fact that during deflation the MBs can encounter significant changes such as disruption of the coating and gas exchange. Simulations are currently being performed to predict these changes after deflation.

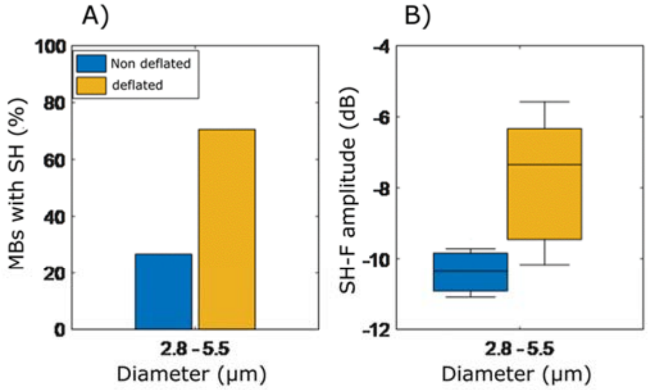

Figure 1. A) Percentage of microbubbles that exhibit subharmonics with a diameter ranging from 2.8 to 5.5 μm, either after deflation or non-deflated. B) The corresponding subharmonic amplitude normalized to the amplitude of the fundamental frequency.

[1] Vos et al, IEEE IUS Proceedings, 2009; [2] Kanbar et al, Ultrasound Med Biol, 2017; [3] Shekhar et al, Ultrasound Med Biol, 2014; [4] van der Meer et al, J Acoust Soc Am, 2007

P1-C3-4

Exploring Mild Bubble Disruption and High Frame Rate Contrast Enhanced Ultrasound for Specific Imaging Of Lymphatic Vessel

Jiaqi Zhu[1], Shengtao Lin[1], Sevan Harput[1], Matthieu Toulemonde[1], Chee Hau Leow[1], Meng-Xing Tang[1]; [1]*Department of Bioengineering, Imperial College London, London, United Kingdom*

Background, Motivation and Objective

Contrast enhanced ultrasound imaging shows great potential for visualising lymphatic vessels and identifying sentinel lymph nodes. However current approaches still have artefacts reducing the lymphatic vessel contrast against background tissue [A. Sever, Clinical Radiology, 2012]. Pulse inversion (PI) detects nonlinear echoes from microbubbles but also from tissue due to nonlinear propagation of ultrasound [M.X. Tang, UMB, 2010]. Doppler acquisition has difficulties due to slow lymph flow rate. In this study, we propose mild bubble disruption imaging (MIDI) that utilises high frame-rate (HFR) plane wave transmission at modest MI to reduce nonlinear tissue artefact for lymphatic imaging with slow flow.

Statement of Contribution/Methods

A lymph vessel mimicking phantom was made consisting of a 200µm cellulose tube was filled with non-flowing microbubbles, and another tube filled with water as control. MIDI is performed by applying HFR PI plane wave (4MHz, 500Hz, 5 compounding angles, MI=0.2) to create mild bubble disruption while imaging data are acquired. The resultant PI images are then processed by differential imaging (DI) or spatiotemporal analysis (STA), both using the high temporal resolution of HFR and filtering to separate fast changing bubble signals from tissue. DI takes the difference between neighbouring frames to suppress static tissue while STA filters off tissue signals based on singular value decomposition. The contrast-to-tissue ratio (CTR) using the two methods at different time points are compared to PI.

Results/Discussion

At 160ms after imaging started, both DI and STA image (Fig 1b and 1c) are able to detect bubbles from the bottom tube while removing nonlinear signals from the control tube present in PI image (Fig 1a). Optical observation under microscope (Fig 1d) further reveals various behaviours of bubble disruption including coalescence, translation and shrinking, which result in bubble signal changes that make MIDI feasible. MIDI improves CTR over PI images by up to 7.5dB, and this improvement decreases over time (Fig 1e). The CTR improvement and its longevity also depends on the MI used. The effects of probe motion is also studied.

In conclusion, preliminary results show that MIDI is a promising contrast imaging technique that can remove nonlinear tissue artefact to improve CTR and is potentially useful for slow flow lymphatic imaging.

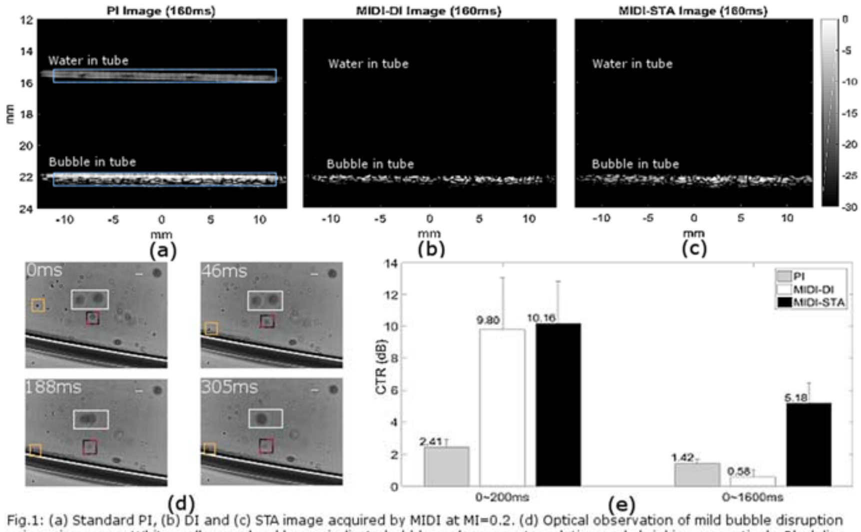

Fig.1: (a) Standard PI, (b) DI and (c) STA image acquired by MIDI at MI=0.2. (d) Optical observation of mild bubble disruption using microscope. White, yellow and red boxes indicate bubble coalescence, translation and shrinking respectively. Black line structure at the bottom of each image is the tube wall. Scale bar:10 µm.(e) Mean CTRs of PI, DI and STA image is computed across time interval of 0-200ms and 1400-1600ms over 5 repeated experiments. CTR is computed as the mean pixel intensity of bubble tube over that of water tube. Mean intensity are computed over regions indicated by the blue boxes in (a).

P1-C3-5

High Frame Rate Contrast Enhanced Echocardiography: Microbubbles Stability and Contrast Evaluation

Matthieu Toulemonde[1], Robert J. Eckersley[2], Meng-Xing Tang[1]; [1]*Department of Bioengineering, Imperial College London, London, United Kingdom,* [2]*King's College, United Kingdom*

Background, Motivation and Objective

High frame-rate contrast enhanced echocardiography (HFR CE), based on pulse inversion (PI) and diverging wave transmission, was recently proposed for improving the image contrast over standard contrast enhanced ultrasound (CEUS) with focused transmission [M. Toulemonde,IUS 2016]. While it has great potential for improved quantification of myocardium perfusion, it is not clear as whether the stability of microbubbles (MBs) is reduced under HFR ultrasound.

Existing studies on MBs stability in HFR CEUS are limited to plane wave imaging at high clinical frequency (3.5 and 7.5 MHz) [O. Couture, 2012 – J. Viti, 2016] where commercial MBs' behaviour is very different from that at lower clinical ultrasound frequency used in cardiac imaging.

The aim of this work is to investigate the MBs stability and the contrast improvement using HFR CE compared to CEUS transmission at an echocardiography relevant frequency for different mechanical indices (MIs).

Statement of Contribution/Methods

An Agar tissue phantom is submerged in a diluted Sonovue suspension (1/40000 dilution). The contrast-to-tissue (CTR) and the destruction of MBs, measured by the disruption ratio, are evaluated at several depth. The HFR CE imaging is obtained by transmitting 7 diverging PI wave pairs (3-cycles, 1.25 MHz) and coherently compounding to achieve a compounded frame rate of 350 Hz. The control experiments using CEUS transmitted PI waves focused at 80 mm with a frame rate of 30 Hz.

Results/Discussion

The Figure shows an example image of the phantom and the quantification of MB disruption and CTR. The disruption of MBs and CTR are the average of two repeated acquisitions close to the probe and at the focus depth 0.5 s after transmission started. For both positions, the disruption of MBs increases with the MI. For MI>0.1 and close to the probe, the disruption is more significant for HFR CE. At the focal depth, both transmission is similar for MI<0.15. In terms of CTR, for both depth and MI<0.1, HFR CE has a better CTR. For MI>0.1 the CTR of HFR CE decreases because of the MBs destruction.

Our initial results shows that the bubble destruction of HFR CE and standard CEUS varies differently as a function of space and MI. At low MIs, HFR CE shows a similar behaviour as focused CEUS with little MB destruction, and generates better CTR (up to 3 folds). As MI increases, the MB destruction is more significant for HFR CE with a reduction of the CTR.

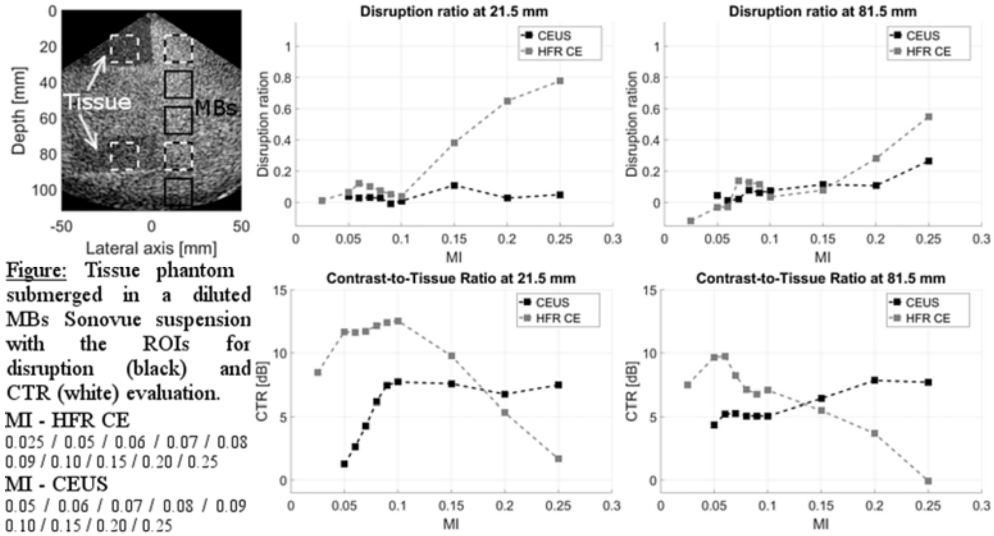

Figure: Tissue phantom submerged in a diluted MBs Sonovue suspension with the ROIs for disruption (black) and CTR (white) evaluation.

MI - HFR CE

0.025 / 0.05 / 0.06 / 0.07 / 0.08 0.09 / 0.10 / 0.15 / 0.20 / 0.25

MI - CEUS

0.05 / 0.06 / 0.07 / 0.08 / 0.09 0.10 / 0.15 / 0.20 / 0.25

P1-C3-6

In-Vitro Contrast Agent Detection Combining Pulse Inversion and SURF Imaging

Stian Solberg[1], Rune Hansen[2,3], Sigrid Berg[2,3], Johannes Kvam[3,4], Bjørn Atle J. Angelsen[3]; [1]*SURF Technology AS, Trondheim, Norway,* [2]*SINTEF Technology and Society, Trondheim, Norway,* [3]*Department of Circulation and Medical Imaging, Norwegian University of Science and Technology, Trondheim, Norway,* [4]*Norsvin SA, Hamar, Norway*

Background, Motivation and Objective

Microbubbles as an ultrasound contrast agent have great diagnostic value, and can be used to visualize the vascularization in a variety of organs, e.g. imaging the neo-angiogenesis in tumors. Pulse inversion (PI) is a common method for detection of these bubbles, implemented in many ultrasound scanners. A dual band imaging technique named SURF has shown the ability to further enhance contrast-to-tissue ratio (CTR) in imaging of microbubbles. A new method is proposed here that combines the two techniques, potentially resulting in even better CTR.

Statement of Contribution/Methods

The method works by transmitting four pulse complexes consisting of an overlapping low frequency (LF) pulse and a high frequency (HF) pulse. For each complex, the polarity of either the HF or the LF is varied. Summing the responses from the complexes with equal LF polarity but opposite HF polarity gives two pulse inversion processed signals, one that is manipulated with a positive LF pressure and one that is manipulated with a negative LF pressure. These sums can be further processed with a SURF imaging method called delay corrected subtraction (DCS) to obtain the final signal that is used to make the image.

The method has been tested both with simulations and in-vitro. Simulations were done using an in-house simulation tool solving the 1D Westervelt equation where the response from the bubble was calculated using a modified Rayleigh-Plesset equation. The in-vitro experiments were conducted with Sonazoid™ in a tissue mimicking phantom using a modified Sonix MDP scanner.

Results/Discussion

Simulations show that the new method has a great potential. At 20 mm depth, the increase in CTR compared to normal B-mode, is 61dB, 34dB and 21dB for the new method, DCS alone and PI alone respectively. The corresponding increase in contrast-to-noise ratio (CNR) is -11dB, -17dB and -8dB.

Initial phantom results also show great promise. A comparison of the new method and a normal B-mode image can be seen in the figure. The strong reflection from the vessel wall is removed with the new method, while still retaining a strong bubble signal. The tissue suppression with DCS alone is about 32dB. With the new method, the remaining tissue signal is buried in the noise floor which means that the tissue signal is suppressed by at least 38dB. The CNR was measured to 13dB for DCS alone, and 15dB for the new method.

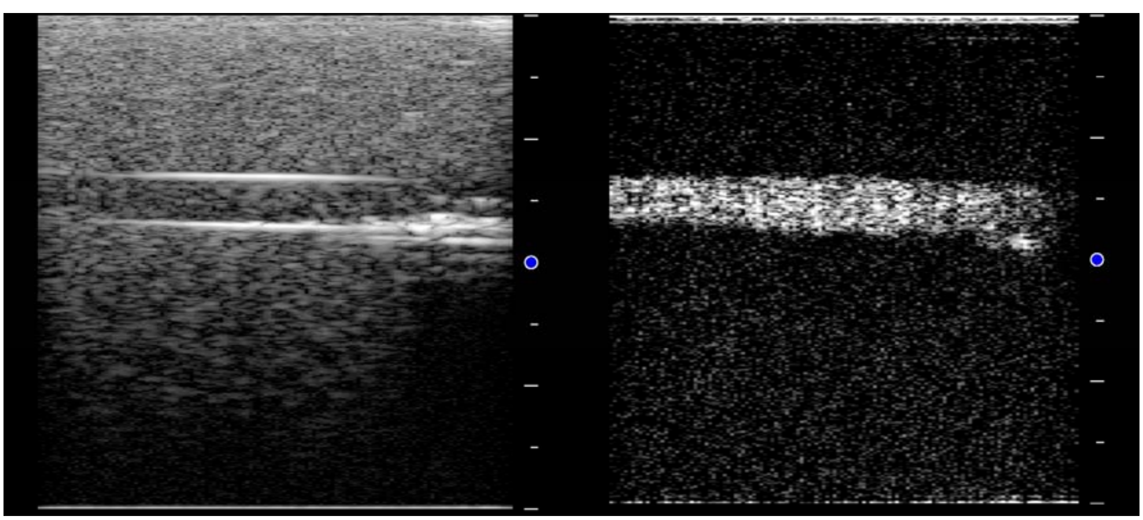

P1-C3-7

The Subharmonic Amplitude of Sonovue Increases with Hydrostatic Pressure at Low Incident Acoustic Pressures

Amanda Nio[1], Alessandro Faraci[1], Kirsten Christensen-Jeffries[1], Robert Eckersley[1], Mark Monaghan[2], Jason Raymond[3], Flemming Forsberg[4], Pablo Lamata[1]; [1]*Biomedical Engineering, King's College London, United Kingdom,* [2]*Cardiology, King's College Hospital, United Kingdom,* [3]*Engineering Science, University of Oxford, United Kingdom,* [4]*Radiology, Thomas Jefferson University, USA*

Background, Motivation and Objective

Physiologically important pressures in the heart and aorta are currently assessed with invasive pressure catheters. The subharmonic signal from ultrasound contrast agents, however, may be exploited to estimate pressures non-invasively. The objective of this work was (i) to develop a static phantom from commercially-available components for easy replication across different laboratories, and (ii) to investigate the subharmonic response of the ultrasound contrast agent SonoVue (Bracco, Milan, Italy) at physiological pressures within the phantom.

Statement of Contribution/Methods

A phantom capable of maintaining 0–200 mmHg static pressures (PRESS-S-000 sensor, PendoTech, USA; INFCS-112B meter, Newport Electronics, Inc., USA) was developed using a cell culture cassette with Luer connections (CLINIcell 25, 175 µm membrane, Mabio International, France). SonoVue was added (0.4 µL/mL degassed water at room temperature) and radiofrequency data were recorded on the ULtrasound Advanced Open Platform (ULA-OP; transmit frequency 5 MHz, 16-cycle pulses, pulse-inversion; LA332E Marzo 2014, bandwidth 3–7 MHz). The mean subharmonic amplitude in a 1 MHz bandwidth (2–3 MHz) was extracted at: (i) 40 scanner acoustic output levels from 1–100% at ambient pressure (0 mmHg), and (ii) 20 levels from 3.5–23.5% at 0–200 mmHg pressures.

Results/Discussion

A single growth phase between 50–250 kPa peak-to-peak acoustic pressures was observed at 0 mmHg (>1 MPa at 100%; measured in a water bath). The subharmonic amplitude of SonoVue increased with hydrostatic pressures of 50 and 100 mmHg (Figure 1)—in line with the buckling effect of microbubbles predicted by the Marmottant model. The strongest direct relationship between subharmonic amplitude and hydrostatic pressure was observed at 10.5% acoustic output (≈130 kPa), with 0.06 dB/mmHg sensitivity. The dampened subharmonic amplitude at 150 and 200 mmHg was accompanied with visual evidence of bubble destruction. Interestingly, the growth phase previously associated with microbubble oscillations at moderate acoustic pressures (300–700 kPa)—within which subharmonic amplitude has been shown to vary inversely with hydrostatic pressure—was not observed in this study. In conclusion, a novel operation window for assessing hydrostatic pressure non-invasively with SonoVue was identified and associated with microbubble buckling.

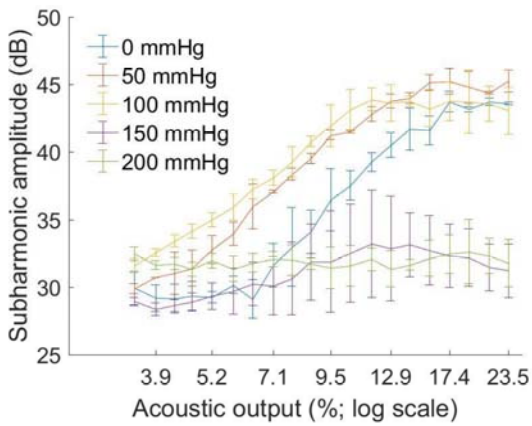

Figure 1: Subharmonic amplitude of SonoVue at 0–200 mmHg hydrostatic pressures (transmit frequency 5 MHz, 16-cycle pulses). Values are mean ± 1SD (n=2).

1-C3-8

Improved Contrast Enhanced Ultrasound Imaging with Multiplane Wave Imaging

Ping Gong[1], Pengfei Song[1], Shigao Chen[1]; [1]*Department of Radiology, Mayo clinic, Rochester, MN, USA*

Background, Motivation and Objective

Contrast enhanced ultrasound (CEUS) imaging offers great opportunities for new ultrasound applications by improving the contrast between blood and tissue using microbubbles. However, the low signal-to-noise ratio (SNR) due to the low mechanical index (*MI*) requirement can be an issue in practice. Multiplane wave (MW) imaging is a technique recently proposed to increase the SNR for compounding plane wave imaging. In this study, we propose to combine CEUS with MW imaging to improve SNR without elevating *MI* in plane-wave-based CEUS imaging.

Statement of Contribution/Methods

The amplitude modulation (AM) CEUS sequence was investigated in this study. Fig. 1 (a) shows a MW-AM pulse design example with two compounding angles (can be extended to more angles). It contains four transmission events (i.e. TX #1- #4), each with four tilted plane wave emissions (i.e. Emission 1-4). These four emissions are further separated into two pairs, each corresponding to one steering angle as Emissions (1, 2) and (3, 4). Two AM pulses (i.e. +1 and +0.5 pulses) are excited consecutively within each pair, with the polarities following a 4th order Hadamard matrix. A short interleaved time delay is added between adjacent pulse emissions as in standard MW compounding. The received radiofrequency (RF) signals can then be Hadamard decoded through addition and subtraction to recover the signals as those obtained with standard AM pulses, for different steering angles. The signal amplitude, however, is enhanced by four times thanks to MW encoding. The recombination in standard AM between +1 and +0.5 pulses at the same angle cancels the tissue linear signals, followed by beamforming and compounding to form the final image.

Results/Discussion

Fig. 1 (b) shows images obtained with standard AM and MW-AM from a tissue mimicking phantom with a microbubble flow cell in the center. MW-AM provides significantly enhanced CTR (shown in sub-titles) with preserved spatial resolution.

Fig. 1 (a)
MW-AM Transmission Design Example

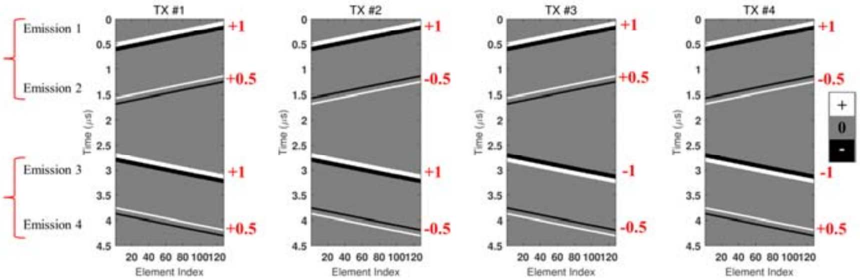

Fig. 1 (b)
AM and MW-AM Images Compa

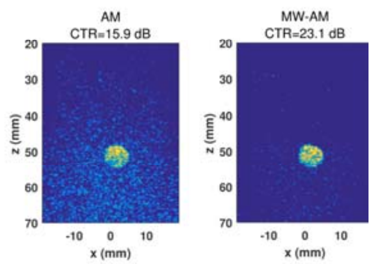

P1-C3-9

Towards Real-Time Implementation of Subharmonic Aided Pressure Estimation (SHAPE) – How to Identify Optimum Acoustic Output for SHAPE?

Cara Esposito[1,2], Kristopher Dickie[3], Flemming Forsberg[1], Jaydev Dave[1]; [1]*Radiology, Thomas Jefferson University, Philadelphia, PA, USA,* [2]*School of Biomedical Engineering, Science and Health Systems, Drexel University, Philadelphia, PA, USA,* [3]*Clarius Mobile Health, Burnaby, BC, Canada*

Background, Motivation and Objective

Pressure measurements within the chambers of the heart yield critical information for diagnosis and management of cardiac patients (~92 million Americans), but cardiac catheterization procedure is invasive and expensive. Subharmonic aided pressure estimation (SHAPE) may be able to estimate intra-cardiac pressures noninvasively, if the optimum incident acoustic output (IAO) for SHAPE can be established. Therefore, the objective of this work was to determine in real-time the optimum IAO for SHAPE.

Statement of Contribution/Methods

We developed a customized interface on a SonixTablet scanner (BK Ultrasound, Richmond, BC, Canada) using C/C++ and Qt libraries (The Qt Company, Oslo, Norway). *In vitro* experiments were conducted using a closed-loop flow system. Activated Definity (Lantheus Medical Imaging, N Billerica, MA, USA; 0.1 ml) was mixed with 750 mL isotonic diluent. A pressure catheter (Millar Inc., Houston, TX, USA) was used to acquire ambient pressure values. A pulsed Doppler gate was placed within the lumen of the vessel in the flow system, then the SHAPE algorithm was initiated ($f_{transmit}$: 5.6 MHz; chirp down transmit pulse in pulse inversion mode). Stepping through all the available IAO levels, the algorithm extracts and processes the subharmonic amplitude and performs a spline fit (subharmonic amplitude vs. IAO) on the scanner in real-time. The IAO level with maximum derivative is then chosen as the optimum IAO level. Simultaneous catheter pressure and subharmonic data were acquired at, below and above the optimum IAO level (10 secs; n=3). Linear correlation between the subharmonic and catheter data was performed using Matlab (MathWorks, Natick, MA, USA).

Results/Discussion

At the optimum IAO level the correlation coefficient between SHAPE and the pressure catheter data ranged between -0.6 and -0.9; for the IAO immediately below and above the optimum IAO, ranges were -0.4 to -0.8, and -0.6 to -0.8, respectively. At the optimum IAO, the sensitivity of the subharmonic signal to the ambient pressure was 13.5±1.0 mmHg/dB. For relatively higher IAO levels (2.9 MPa peak-to-peak), correlation coefficients as high as -0.9 were also noted, presumably due to bubble destruction. In conclusion, optimum IAO level determination (in real-time) for insonating microbubbles to be utilized for SHAPE has been demonstrated; this will assist in real-time clinical applications.

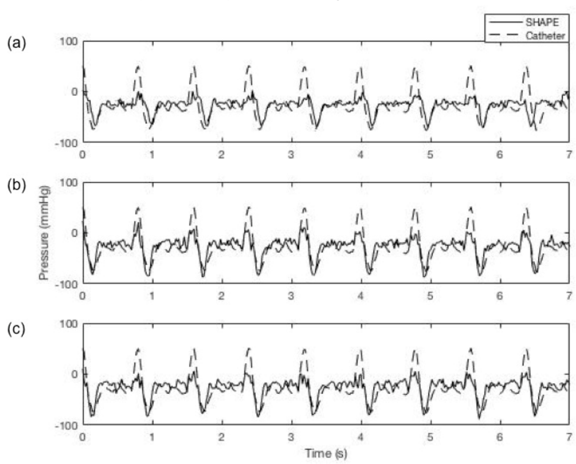

Fig. Relationship between SHAPE (solid line) and catheter pressure (dotted line) data below (a), at (b), and above (c) the optimum IAO, which have a correlation coefficient of -0.49, -0.72 , and -0.68, respectively.

P1-C4 - MCA: Contrast Imaging: Preclinical and Clinical Applications

Exhibit Hall

Saturday, September 9, 2017, 9:30 am - 4:00 pm

Chair: **Jean-Michel Escoffre**
Inserm U930 Imaging & Brain

P1-C4-1

Monitoring Early Tumor Response to Vascular Targeted Therapy using Super-Resolution Ultrasound Imaging

Debabrata Ghosh[1], Fangyuan Xiong[1], Robert Mattrey[2], Shashank Sirsi[1], Kenneth Hoyt[1]; [1]*University of Texas at Dallas, USA,* [2]*University of Texas Southwestern Medical Center, USA*

Background, Motivation and Objective

The standard-of-care for evaluating breast tumor response to chemotherapeutic drug treatment remains the assessment of a tumor size change weeks after therapy begins. However, the tumor microenvironment is known to change drastically before any detectable change in physical size manifests. New clinical tools that can help determine early tumor response are urgently needed so we can both maximize the benefit of an effective therapeutic strategy and minimize the use of drugs that do not improve patient prognosis. To that end, the goal of this research project was to evaluate the utility of super-resolution ultrasound (SR-US) imaging for detecting the early tumor response (or lack thereof) to antiangiogenic-targeted therapy.

Statement of Contribution/Methods

A clinical ultrasound (US) scanner (Acuson Sequoia 512, Siemens Healthcare) equipped with a 15L8-S linear array transducer was used for our study. Operation of this system was done using a nonlinear harmonic imaging (transmit and received at 7 and 14 MHz, respectively). A low transmit power (mechanical index = 0.2) was used to minimize any MB destruction during imaging. Female athymic nude mice (Charles River Laboratories) were implanted orthotopically with 1 million breast cancer cells (MDA-MB-231/Luc, Cell Biolabs) and tumors were allowed to grow for about three weeks. After a slow injection of 2.5 x 107 MBs via a tail vein catheter, each tumor was US imaged for 10 min at baseline and again at 1 and 2 h after dosing with an antiangiogenic (0.2 mg; Avastin, Genentech) or control drug. MBs were produced and characterized using established methods. The US transducer was fixed throughout the 2 h imaging period to help capture any microvascular changes along the same image plane. The SR-US imaging technique was developed using custom Matlab software (Mathworks Inc). After collecting a stack of US images, any images corrupted by respiratory motion were removed using decorrelation filtering. A singular value decomposition-based spatiotemporal filter was then used to localize individual MBs. Subsequently, a SR-US image was generated by mapping the cumulative MB localizations in a single image. SR-US images were reviewed and longitudinal changes in the tumor microvascular network in response to antiangiogenic treatment were evaluated.

Results/Discussion

SR-US images spatially detailed the tumor microvascular network with unprecedented resolution. While there were no notable changes in control tumor studies, SR-US imaging of animals administered an antiangiogenic drug revealed early changes in tumor microvascularity most notably characterized as vascular regression. On average, there was a 53% and 66% decrease (relative to baseline) in microvascularity levels at 1 h and 2 h after dosing, respectively. While mechanisms of action need to be explored further, we hypothesize that these early changes in tumor tissue are due in part to microvascular constriction and impaired function of the vascular bed.

P1-C4-2

Reduced Variability of Contrast-Enhanced Ultrasound Perfusion Estimates in a Patient-Derived Xenograft Model via Analysis of Speckle Statistics

Matthew Lowerison[1,2], Ann Chambers[1,3], Hon Leong[4,5], Nicholas Power[3,4], James Lacefield[1,6]; [1]*Medical Biophysics, University of Western Ontario, London, Ontario, Canada,* [2]*Robarts Research Institute, London, Ontario, Canada,* [3]*Oncology, University of Western Ontario, London, Ontario, Canada,* [4]*Surgery, University of Western Ontario, London, Ontario, Canada,* [5]*Pathology and Laboratory Medicine, University of Western Ontario, London, Ontario, Canada,* [6]*Electrical and Computer Engineering, University of Western Ontario, London, Ontario, Canada*

Background, Motivation and Objective

Contrast-enhanced ultrasound (CEUS) permits quantification and monitoring of tumor vascular changes in response to anti-angiogenic treatment with the goal of informing targeted therapy. Conventional mean-intensity-based CEUS analysis discounts additional information that may be available from the first-order speckle statistics in a CEUS image. In this presentation, we demonstrate that our compound speckle model for analysis of CEUS images [1] reduces the variability in tumor perfusion quantification, particularly for estimates of blood volume, and reduces the sensitive/resistant classification ambiguity caused by heterogeneous tumor samples. This analysis technique has been previously applied to a mouse xenograft model of breast cancer [1], where it significantly improved the classification accuracy between control and bevacizumab-treated tumors over conventional CEUS analysis.

Statement of Contribution/Methods

The model was applied to subharmonic CEUS images acquired at 18 MHz from a high-throughput patient-derived xenograft (PDX) assay of renal cell carcinoma (RCC) in the chicken embryo chorioallantoic membrane (CAM). Control and sunitinib-treated PDX tumors ($N > 30$ of each) from four patients were studied. Uncompressed CEUS images were acquired using a Vevo 2100 ultrasound system (VisualSonics Inc.) and analyzed using MATLAB. Contrast signal intensity was modeled as a compound distribution of exponential probability density functions weighted by a gamma function to approximate the effect of log-normally distributed capillary spacing in tumor vasculature. Destruction-reperfusion curves were constructed by plotting the change in the area of overlap of the weighting function, which was interpreted as an estimate of the enhanced volume fraction. Tumor samples were classified as sunitinib-sensitive or resistant based on significant reductions in tumor relative blood volume as measured by conventional CEUS or enhanced volume fraction measured using the statistical method.

Results/Discussion

We observed intratumoral functional heterogeneity both within untreated core biopsies and in response to antiangiogenic therapy. First-order speckle analysis reduced the coefficient of variation of CEUS estimates of blood volume compared to conventional CEUS methods (CoV of 0.554 vs. 0.828, Brown–Forsythe test, p-value < 0.05) and thereby improved patient classification confidence. Preliminary results indicate that tumor pathology and drug-resistant phenotype are conserved when patient biopsies are grown on the CAM. Therefore, the statistical CEUS method combined with the CAM PDX assay may provide a reliable means of identifying RCC patients who are *de novo* resistant to sunitinib, which is a front-line therapy for metastatic RCC.

[1] M. R. Lowerison, J. J. Tse, et al., *Med. Phys.*, vol. 44, pp. 99–111, 2017.

P1-C4-3

Designing Targeted Ultrasound Contrast for Molecular Imaging of Secreted Frizzled Related Protein-2 (SFRP2) without Biotin-Avidin Linkages.

James Tsuruta[1], Nancy Klauber-DeMore[2], Paul A. Dayton[3]; [1]*Pediatrics, University of North Carolina, Chapel Hill, NC, USA,* [2]*Department of Surgery, Medical College of South Carolina, Charleston, SC, USA,* [3]*Joint Dept of Biomedical Engineering, University of North Carolina & NC State University, Chapel Hill, NC, USA*

Background, Motivation and Objective

Clinical translation of targeted contrast agents for molecular imaging of disease precludes the use of the biotin-avidin cross linking strategy due to the immunogenicity of avidin. Our objective was to cross link targeting ligands to ultrasound contrast using non-immunogenic covalent chemistry, and to validate the resulting targeted contrast agents using a binding assay to cultured cells.

Statement of Contribution/Methods

We compared the efficacy of using maleimide-thiol chemistry to cross link a thiolated antibody fragment (Fab) against SFRP2 (a) directly to maleimide-activated lipid (Fab.lipid) which was then used to formulate size-sorted, targeted contrast, or (b) conventionally to size-sorted ultrasound contrast containing maleimide-activated lipid. We tested the specificity of targeted binding to cell layers by comparing the binding of (a) targeted contrast, and (b) targeted contrast 'inactivated' with Traut's reagent.

Results/Discussion

Size-sorted, targeted contrast formulated with Fab.lipid bound to cell layers at significantly higher levels than size-sorted, maleimide-activated contrast that was subsequently cross linked to thiolated Fab. We suspect that a portion of the maleimide moiety hydrolyzed during the size-sorting protocol, reducing the labeling index of the resulting targeted contrast. Binding of Fab.lipid targeted contrast to cells was antibody-dependent since conversion of active amines with Traut's reagent significantly reduced the number of microbubbles bound to cells producing SFRP2. It was a significant finding to determine that mechanical emulsification of SFRP2 Fab.lipid-containing solutions created an SFRP2-targeted molecular imaging reagent of high activity.

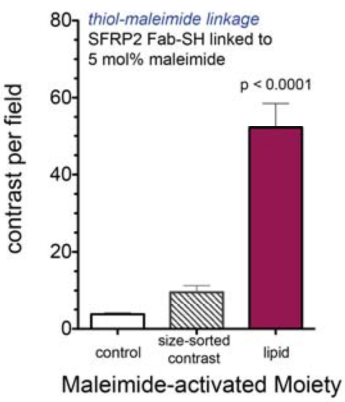

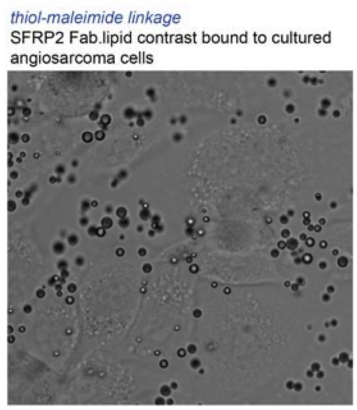

P1-C4-4

Imaging of Cortical Pores Using Ultrasound Contrast Agents: An *Ex-vivo* Study

Juan Du[1], Gianluca Iori[1], Kay Raum[1]; [1]*Berlin-Brandenburg Center for Regenerative Therapies, Charité - Universitätsmedizin Berlin, Berlin, Germany*

Background, Motivation and Objective

Cortical bone porosity (Ct.Po) and pore diameter (Po.Dm) are important factors in determining bone toughness and strength [1-2]. However, the current standard diagnosis, dual-energy X-ray absorptiometry (DXA), doesnot have the sensitivity to those factors. Due to the strong specular reflection from the bone surface and high acoustic attenuation of cortical bone tissue, conventional ultrasound is not feasible for imaging cortical pores. Therefore, we propose an approach in combination of contrast agent (UCA) enhanced nonlinear ultrasound imaging, e.g. pulse inversion (PI) [3], and dynamic processing, i.e., the temporal perfusion index (TPI) [4].

Statement of Contribution/Methods

A cortical bone sample from a human femur was used as *ex-vivo* imaging target. The bone sample was macerated following the procedure in [5]. A 6-mm diameter cylinder was drilled from the femur shaft and connected to plastic tubes. The connections were fastened with heat-shrink tubes (Fig. 1a), in order to ensure a confined flow without leakage. SonoVue (Bracco Imaging S.p.A., Italy) microbubbles with a mean diameter of 2.5 µm were used. The concentration of UCA solution was $(1\sim5)\times10^7$ microbubbles/mL, about one tenth of clinical recommended value. A SonixTOUCH (Ultrasonix, Canada) equipped with a linear transducer array (4DL14-5/38) was used through its research interface. RF data were acquired with PI and beam-steering sequences. The sampling frequency was 40 MHz. After acoustic examination, the sample was microCT scanned (SkyScan, RJL Micro&analytic, Germany) at a resolution of 9.9 µm, in order to measure ground-truth values for Ct.Po and Po.Dm. The CT image was rotated and aligned with ultrasound images. Ct.Po measured from the CT data was 16.83%, using Otsu thresholding.

Results/Discussion

The TPI was computed for each data set after normalization. To compensate for the strong acoustic attenuation, the TPI was computed using a dynamic range (dR) of 30 to 60dB, with a step size of 1dB. The results with each dR were summed together; corresponding maximum projections are plotted in Fig. 1. TPI images showed sensitivity and specificity to large pores, such as the one in the center and the circular pores below that. The TPI may have the potential to estimate Ct.Po and Po.Dm. Further experiments will be performed combining samples with different Ct.Po and Po.Dm and the relation TPI will be analyzed.

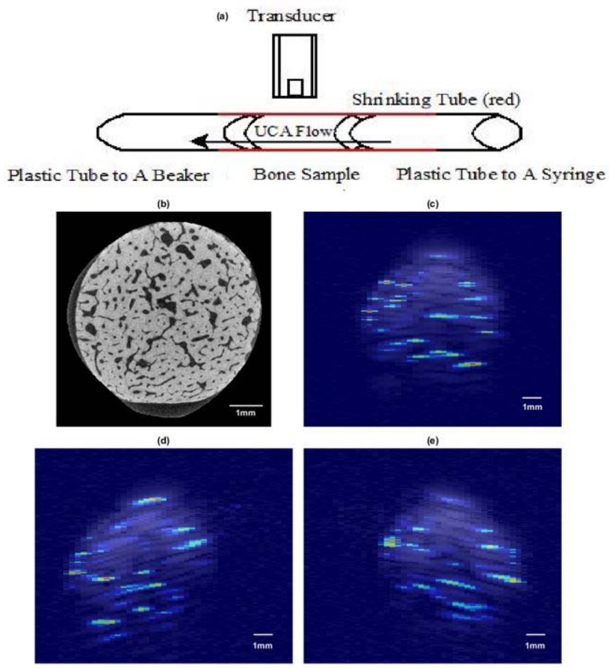

Fig. 1: A schematic of ultrasound experiment setup (a), a microCT minimum projection over 21 slices of the human bone sample in the ultrasonic imaging region (b) and maximum TPI projections mapped on one frame B mode images (c - e) and. The ultrasonic data were acquired using beam-steering sequences with an angle of 0° (c), −10° (d) and 10° (e).

P1-C4-5

High Contrast-to-Tissue Ratio Imaging Technique Using the Unique Vaporization Signature from Phase-Change Contrast Agents

Juan Rojas[1], Paul Dayton[1,2]; [1]*Biomedical Engineering, The University of North Carolina and North Carolina State University, USA,* [2]*The University of North Carolina Lineberger Comprehensive Cancer Center, USA*

Background, Motivation and Objective

Phase-Change Contrast Agents (PCCAs) are liquid core droplets that can be vaporized, or activated, into echogenic microbubbles with the application of ultrasound. The vaporization event produces a unique acoustic signature that is different from that produced by tissue and microbubbles. In this work, the ability to produce high CTR images using the unique low frequency vaporization signature of PCCAs is demonstrated using a clinical array.

Statement of Contribution/Methods

An L11-5 linear array was driven by a Verasonics ultrasound system and used to deliver a series of vaporization pulses to the kidneys of Fischer rats to activate PCCAs. The vaporization pulses consisted of 5 cycle, 5 MHz, sinusoids with a peak negative pressure of 1.5 MPa. Received RF data from PCCA activation was filtered with a low-pass filter with a pass frequency of 1.5 MHz to isolate the activation signal, and Verasonics reconstruction algorithms were used to produce activation-specific images. A pre-activation image was captured using conventional Pulse Inversion (PI), followed by the activation pulses from which a PCCA-specific image was acquired. A post-activation PI frame was also captured to measure the produced contrast. This process was performed before and after the introduction of PCCAs. For PI images, CTR was calculated by dividing the uncompressed mean intensity inside of the kidney of the post-activation image by that of the pre-activation image. For PCCA-specific images, the activation-specific images captured before and after PCCA injection were used to calculate CTR.

Results/Discussion

PI and activation-specific images had CTR values of 11.94 ± 2.89 and 106.55 ± 39.72, respectively. Data show that isolating the activation signal from PCCA vaporization produces images with a CTR that is an order of magnitude greater than when conventional PI was used (Figure 1). Because of the high CTR of this novel technique, it has great potential for molecular or other imaging techniques which require maximum sensitivity to small amounts of contrast agents. However, the resolution is poor since the frequency of activation signals range between 0.2 and 2.5 MHz and consists of several cycles. Therefore, this technique is limited to the overall assessment of a region of interest, rather than delineating small features such as with other high frequency contrast imaging technologies.

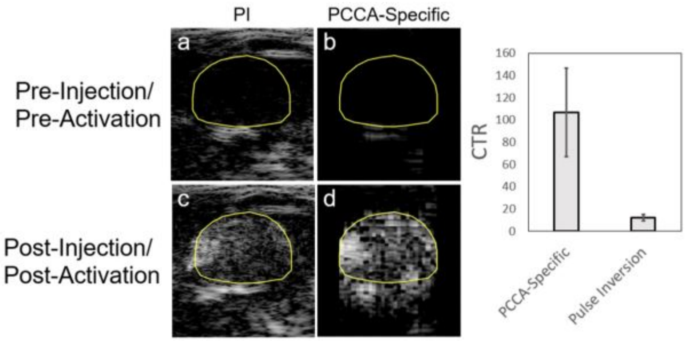

Figure 1. Example of images of PCCA activation in a rat kidney, which is outlined in yellow. The plot on the right shows the CTR values for the PCCA-specific imaging technique and conventional PI.

P1-C4-6

On the Validity of the First-Pass Binding Model for Quantitative Ultrasound Molecular Imaging: Comparison between BR55 and Sonovue

Simona Turco[1], Isabelle Tardy[2], Peter Frinking[2], Hessel Wijkstra[1,3], Massimo Mischi[1]; [1]*Electrical Engineering, Eindhoven Univeristy of Technology, Eindhoven, Netherlands,* [2]*Bracco Suisse SA, Geneva, Switzerland,* [3]*Urology, Academic Medical Center, Amsterdam, Netherlands*

Background, Motivation and Objective

Cancer growth requires angiogenesis; imaging of angiogenesis may thus improve cancer diagnostics and therapy monitoring. Dynamic contrast enhanced ultrasound (DCE-US) permits imaging angiogenesis at the molecular level by using novel targeted ultrasound contrast agents (tUCA). These agents consist of functionalized microbubbles obtained by engineering the shell with targeting ligands able to bind specific biomarkers, over-expressed in tumor angiogenic vasculature. Quantification of binding may thus provide an indirect way of quantifying angiogenesis. Recently, we proposed the first-pass binding (FPB) model to describe the binding kinetics of tUCA. Fitting DCE-US time-intensity curves (TICs) by the FPB model enables quantification of binding by the estimation of the binding rate K_b [1]. After showing the feasibility of the method for angiogenesis imaging in prostate-tumor bearing rats [1], and performing a preliminary validation for anti-angiogenesis therapy monitoring in colon cancer-bearing mice [2], in this work we investigate the validity of the proposed model by comparing K_b estimates in rats injected with non-targeted UCAs (Sonovue) and tUCAs (BR55).

Statement of Contribution/Methods

Conventional and targeted DCE-US was performed in three prostate-tumor bearing rats after injection of Sonovue, followed by BR55 injection about 15 minutes later. In both cases, the proposed quantitative parameter K_b was estimated by fitting each pixel TIC by the FPB model and compared with conventional semi-quantitative US binding parameters (late-enhancement and differential targeted enhancement) in tumor and control regions of interests (ROIs).

Results/Discussion

The estimated Kb showed significantly smaller values for Sonovue, with no significant differences (p-value=0.67) between cancer and control ROIs (Fig. 1). Significant differences (p-value<<0.01) were instead observed for BR55. The non-zero K_b values estimated for Sonovue can be explained by non-selective bubble binding effects [3]. Although further validation is necessary, the results suggest the FPB model to accurately describe the different kinetics of targeted and non-targeted UCAs.

[1] S. Turco *et al*. Phys Med Biol 62 (2017): 2449-2464.
[2] S. Turco *et al*. IUS 2016.
[3] M. Averkiou *et al*. Eur J Ultrasound, 40.9 (2014): 2217-2230.

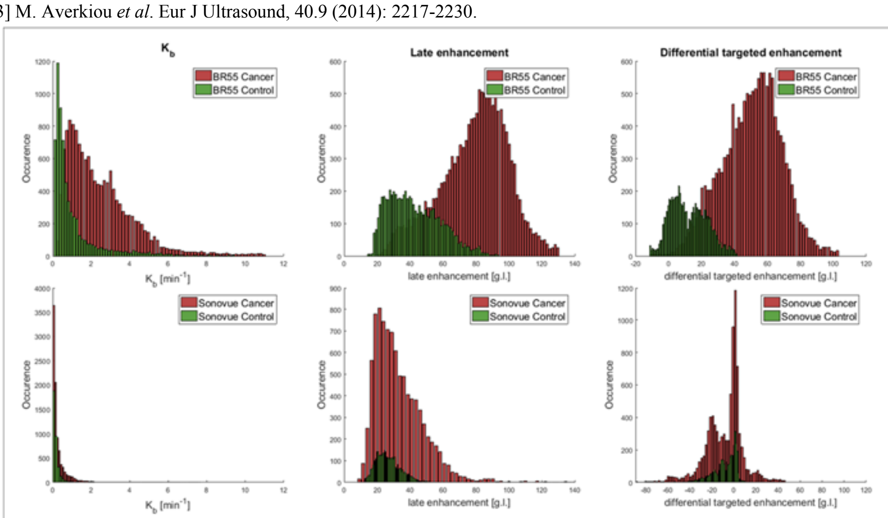

Fig. 1 Histograms comparing the values of K_b, late enhancement, and differential targeted enhancement in control and tumor ROIs for non-targeted (Sonovue) and targeted (BR55) UCAs.

P1-C4-7

Multi-Frame Rate Plane Wave Contrast-Enhanced Ultrasound Imaging for Tumour Vascular Imaging and Perfusion Quantification

Chee Hau Leow[1], Marta Braga[2], Javier Hernández-Gil[2,3], Nicholas J. Long[2,3], Eric O. Aboagye[2], Meng-Xing Tang[1]; [1]*Department of Bioengineering, Imperial College London, United Kingdom,* [2]*Department of Surgery & Cancer, Imperial College London, United Kingdom,* [3]*Department of Chemistry, Imperial College London, United Kingdom*

Background, Motivation and Objective

Angiogenesis and blood flow dynamics play an important role in the development of malignant tumours and their response to treatment. While contrast enhanced ultrasound (CEUS) imaging with microbubble contrast agents as a tool for imaging angiogenesis and flow dynamics has shown great potential [1], recent development of plane wave high frame-rate (HFR) CEUS has offered new opportunities in such applications. In this study, we demonstrate an interleaved multi-frame rate plane wave CEUS imaging to quantify perfusion and to image vascular structure with improved resolution and contrast.

Statement of Contribution/Methods

Customised plane wave imaging pulse sequences are designed which include a long sequence (3 mins, frame rate:2Hz) interleaved with a short but high frame rate sequence (HFR, 2s, frame rate:500Hz). The former is used to quantify tumour perfusion by computing a time-intensity curve whereas the latter is employed to generate high SNR and contrast images for tumour vascular morphology. In both imaging sequences, fifteen 1 cycle plane waves pulses with angles spanning between -100 and 100, were transmitted using a L22-14v probe to form a compounded Bmode images. Power Doppler signals were extracted. Preliminary in-vivo measurements were made on a U2932 mice tumour model. A bolus injection of 50ul home-made bubbles (5x10^9 MB/ml) was injected intravenously through the mice tail. Image acquisition was started immediately after the injection.

Results/Discussion

Figure 1 shows an example of the results obtained from our proposed imaging technique. The mean intensity curve (Fig. 1b) was derived from the tumour region illustrated in the Bmode image (Fig. 1a). Higher contrast vascular persistence image (Fig. 1c) was generated using power Doppler processing to demonstrate the tumour vasculature. The initial results demonstrate the potential of such technique to improve the visualisation and quantification in tumour perfusion and molecular imaging.

[1] J. R. Lindner, “Microbubbles in medical imaging: current applications and future directions,” Nat. Rev. Drug Discov., vol. 3, no. 6, pp. 527–533, Jun. 2004.

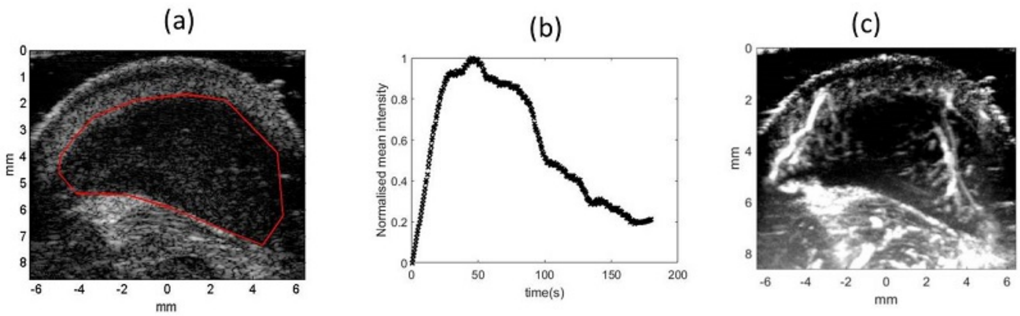

Figure 1: (a) Bmode images of the mouse tumour model with the region of interested selected to compute mean intensity curve (b); (c) Maximum intensity projection of the ultrafast Doppler showing the tumour vasculature.

P1-C4-8

Time Intensity Curve Analysis of Subharmonic Transabdominal and Harmonic Endoscopic Contrast-Enhanced Ultrasound of Pancreatic Masses

Ji-Bin Liu[1], Lauren Jablonowski[1], **John Eisenbrey**[1], Flemming Forsberg[1], Ali Siddiqui[2]; [1]*Radiology, Thomas Jefferson University, USA,* [2]*Gastroenterology and Hepatology, Thomas Jefferson University, USA*

Background, Motivation and Objective

Pancreatic cancer is associated with poor clinical outcomes primarily, due to the advanced stage of disease at diagnosis. Harmonic contrast-enhanced endoscopic ultrasound has been proposed as an imaging approach for characterizing pancreatic masses. As an alternative, transabdominal subharmonic imaging has been proposed to limit invasiveness and better suppress nonlinear tissue echoes. In both of these approaches, time-intensity curve (TIC) analysis can be performed to quantify blood flow dynamics. The purpose of this study was to compare time TICs from both harmonic endoscopic ultrasound and subharmonic transabdominal ultrasound in pancreatic masses.

Statement of Contribution/Methods

Patients scheduled for endoscopic biopsy guidance of a pancreatic mass provided informed consent to undergo both endoscopic and transabdominal contrast-enhanced ultrasound at the time of their procedure. Pulse-inversion subharmonic imaging (transmitting/receiving at 2.5/1.25 MHz) was performed on a modified Logiq 9 system with a 4C probe (GE Healthcare, Milwaukee, WI, USA), while harmonic endoscopic ultrasound (transmitting/receiving at 4.7/9.4 MHz) was performed with a radial endoscope (GF-UTC180; Olympus, Tokyo, Japan) with ProSound SSD -10 scanner (Hitachi-Aloka, Tokyo, Japan). Imaging was acquired during injection of 0.3-0.8 ml of Definity (Lantheus Medical Imaging, N Billerica, MA, USA). TIC analysis was performed on a pixel by pixel basis with moving average filter to generate parametric images of maximum intensity, time to peak enhancement, perfusion, and area under the TIC using a custom program developed in Matlab (Mathworks, Nattick, MA, USA). Quantitative data was then grouped by modality and pathology for comparison.

Results/Discussion

To date, TIC processing has been completed on 10 cases that contained sufficient contrast enhancement without excessive motion. When comparing imaging modes (endoscopic vs. transabdominal), no significant differences were observed in time to peak, perfusion, or area under the time intensity curve ($p > 0.11$), indicating these measures of blood flow are independent of imaging modality. A significant difference between maximum intensity ($p=0.01$) was observed between modalities and attributed to scanner-specific properties such as transmit power, gain, and sensitivity. When grouped by pathology (adenocarcinoma vs. other masses), neither modality showed significant differences in any dynamic parameter, with blood perfusion being the closest to significant separation ($p=0.2$ for transabdominal subharmonic imaging and $p=0.06$ for endoscopic harmonic imaging). While the feasibility of parametric imaging of pancreatic masses has been demonstrated for both endoscopic and transabdominal nonlinear ultrasound, future efforts with increased sample size and motion correction are likely needed to better elucidate differences in blood flow parameters between benign and malignant lesions.

P1-C4-9

Imaging the Rat Liver and Heart with a 3D Motion Corrected Acoustic Angiography System

Tomek Czernuszewicz[1], Virginie Papadopoulou[2], James Butler[1], Max Harlacher[1], Graeme O'Connell[1], Jonathan Perdomo[1], Paul Dayton[2], **Ryan Gessner[1]**; [1]*SonoVol, Inc., Research Triangle Park, NC, USA,* [2]*Biomedical Engineering, UNC Chapel Hill, NC, USA*

Background, Motivation and Objective

Acoustic Angiography enables high resolution and high SNR imaging of microbubble contrast agents. The technique relies on pulsing and receiving at two widely separated acoustic bandwidths to reject signal from the tissue. To date this technique has been used to evaluate microvasculature within tumors and kidneys, but has not been used to visualize in vivo blood flow within heart, or liver. These targets are challenging to image due to their proximal locations to the lungs and thus increased susceptibility to respiration artifacts. We tested a new acquisition approach to allow semi-automated microvascular imaging of these organs without relying on respiratory gating electronics.

Statement of Contribution/Methods

The Acoustic Angiography transducer was constructed as a dual-frequency annular array (outer element 2 MHz, inner element 35 MHz). This transducer is robotically manipulated beneath the animal and can be activated in either high frequency b-mode, or Acoustic Angiography mode using the SonoVol imaging platform. This allows for widefield b-mode tissue scout scans, followed by subsequent Acoustic Angiography vascular images. To eliminate artifacts from respiration, a principal component analysis (PCA)-based algorithm was implemented to identify fluctuations in the data at physiologically relevant frequencies. This can then be used retroactively on the 3D dataset to remove frames corrupted by respiration motion.

Results/Discussion

Preliminary in vivo data is presented of a rat’s thoracic cavity in both b-mode and Acoustic Angiography. A widefield b-mode image was taken to localize the heart and liver. Once localized, two regions of interest were defined on the organs of interest and Acoustic Angiography data acquired at these locations. The data were processed via the PCA gating algorithm to remove corrupted frames. The entire exam took <10 mins. Within the liver, the visible vasculature ranges in diameter from 1.5 mm to 290 um. Future work is necessary to enable the entire cardiac cycle to be visualized, as our approach simply captures it at peak systole. Furthermore, we believe additional branching in the liver can be captured by modulating imaging frame rates to allow smaller vessels to perfuse. This system could be used in the future to study longitudinal disease processes therapeutic effects in rodents.

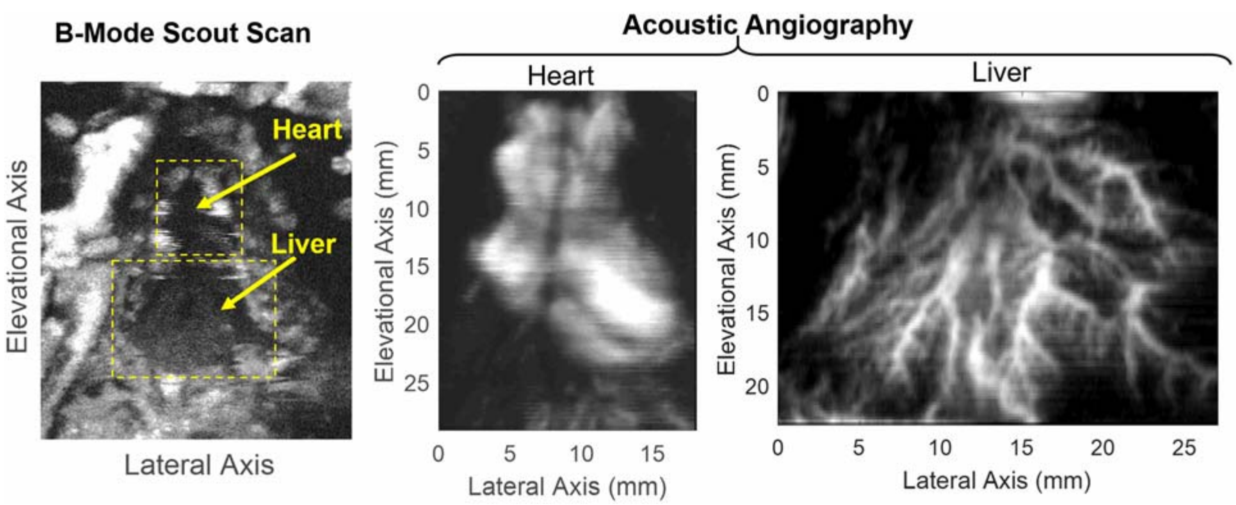

P1-C4-10

Evaluation of Utero-Placental Perfusion in Intrauterine Growth Restriction Rat Model Using CEUS

Anthony Novell[1], Vanda Mendes[1,2], Arthuis Chloé[1,2], Ayache Bouakaz[1], Franck Perrotin[1,2]; [1]*Imagerie et Cerveau, Université François Rabelais, Inserm, Tours, France,* [2]*Department of Obstetrics and Gynecology, CHRU Tours, France*

Background, Motivation and Objective

Intrauterine growth restriction (IUGR) is an anomaly of fetal growth dynamics, which is mainly caused by alterations in the vascular remodeling of utero-placental arteries. With a prevalence of 10% of pregnancies, IUGR remains the leading cause of perinatal mortality. Doppler velocimetry is the common screening tool for IUGR but this imaging modality remains controversial. In this context, we evaluated contrast-enhanced ultrasound (CEUS) as a new modality to monitor the uteroplacental perfusion and to discriminate physiological pregnancy from IUGR in rat model.

Statement of Contribution/Methods

At 17th day of gestation, a ligation of uterine pedicle was performed to induce IUGR in rat. Nine IUGR rats and twelve control rats were examined by CEUS on 19th day of gestation. For each rat, a 200 µL solution of Definity (1 mL/kg) was intravenously injected in the rat tail. CEUS was performed using a MS250 probe (18MHz) connected to a Vevo 2100 scanner and clips of 2.5 minutes were recorded. Data were post-processed using VevoCQTM software and Matlab. Time-intensity curves were analyzed and quantitative perfusion parameters during wash-in were calculated in 3 regions: main maternal vessel, labyrinth, whole placenta and compared to each other.

Results/Discussion

Using CEUS, qualitative and quantitative analyses of uteroplacental perfusion showed low and slow contrast enhancement in IUGR rat model in comparison with control group on the 19th day of pregnancy. In IUGR group, the peak enhancement was lower than control group in whole placenta (p=0.002), in main maternal vessel (p=0.03) and in labyrinth (p=0.006). Wash-in rate was slower in the 3 compartments. For the time to peak, no statistical difference was observed between both groups. Labyrinth congestion might explain the reduced blood perfusion of placenta in IUGR group. Results suggest that CEUS is a suitable imaging modality to discriminate physiological pregnancy from IUGR in rat model.

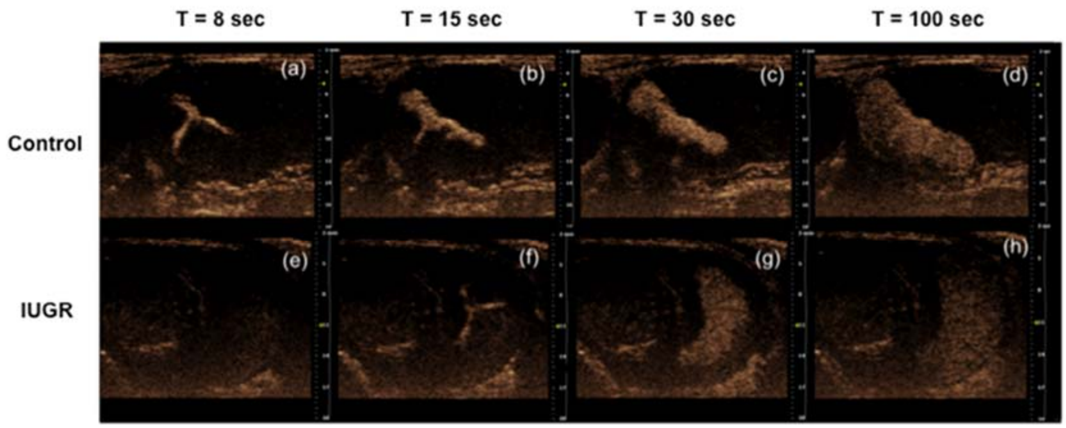

Figure – Contrast-enhanced ultrasound imaging of intrauterin growth retardation

P1-C4-11

Quantitative 3D Subharmonic Imaging for Characterizing Breast Lesions

Anush Sridharan[1,2], John Eisenbrey[1], Maria Stanczak[1], Priscilla Machado[1], Annina Wilkes[1], Alexander Sevrukov[1], Haydee Ojeda-Fournier[3], Robert Mattrey[3], Kirk Wallace[4], **Flemming Forsberg[1]**; *[1]Radiology, Thomas Jefferson University, Philadelphia, PA, USA, [2]Electrical and Computer Engineering, Drexel University, Philadelphia, PA, USA, [3]Radiology, University of California, San Diego, San Diego, CA, USA, [4]GE Global Research, Niskayuna, NY, USA*

Background, Motivation and Objective

Breast cancer is the second most common cancer in the world and the most frequent type of cancer among women (25 % of all cancers). This study used contrast-enhanced 3D subharmonic imaging (SHI) to produce quantitative parametric maps for characterization of breast lesions.

Statement of Contribution/Methods

Women scheduled for biopsy of a suspicious breast lesion (n = 219) were injected with 20 µL/kg of an ultrasound contrast agent (UCA; Definity, Lantheus Medical Imaging, N Billerica, MA, USA) and scanned in 3D SHI mode (transmitting/receiving at 5.8/2.9 MHz) using a modified Logiq 9 scanner (GE Healthcare, Milwaukee, WI, USA) with a 4D10L probe. Time-intensity curves (TIC) of UCA were generated within the center and periphery of the lesions using Matlab (version 2016b; Mathworks, Natick, MA, USA) and mapped onto the raw slice data. Time-points corresponding to baseline, peak intensity and complete washout of contrast were identified to generate vascular heterogeneity plots of the lesion volume (in the center and the periphery as well as the ratio of the two). Likewise, parametric volumes were constructed for perfusion (PER; as the slope of the TIC) and area under the curve (AUC) based on individual voxel values in the lesion volume. ROC analysis and reverse, step-wise logistical regression were used to assess diagnostic accuracy (for individual parameters and in combination) with biopsy results as the reference standard.

Results/Discussion

Biopsies resulted in 164 (75 %) benign and 55 (25 %) malignant lesions, while 3D SHI showed sufficient UCA flow for processing in 83 (58 benign and 25 malignant) lesions. Analysis of vascular heterogeneity using 3D SHI TIC volumes showed a significant difference in vascularity between central and peripheral sections (1.8 ± 0.16 vs 1.2 ± 0.09 dB; p = 0.0003) for the benign cases, whereas malignant lesions showed no significant difference (1.7 ± 0.33 vs 1.3 ± 0.21 dB; p = 0.23), indicative of more vascular coverage. Although both PER and AUC parametric maps were able to visualize vascularity in individual slices in the 3D volume, the AUC maps had noticeably increased image noise due to motion artifacts. Diagnostic accuracy (i.e., area under the ROC curve or A_z) for heterogeneity, PER and AUC (center, periphery and ratio) ranged from 0.52 to 0.75. The best logistical regression model (heterogeneity ratio, PER central and AUC central) achieved an A_z = 0.88. In conclusion, 3D SHI is able to detect UCA flow in vascular breast masses. Evaluation of vascular heterogeneity and parametric maps suggests such quantitative parameters might aid in the characterization of breast lesions.

P1-C4-12

Which Properties of the Vascular Architecture Are Reflected by Dynamic Contrast-Enhanced Ultrasound Imaging Of Dispersion and Wash-In Rate? A Comparison with Acoustic Angiography.

Anastasiia Panfilova[1], Sarah Shelton[2], Ruud JG van Sloun[1], Cristina Caresio[3], Hessel Wijkstra[1,4], Paul Dayton[2], Massimo Mischi[1]; *[1]Electrical Engineering, Technical University of Eindhoven, Netherlands, [2]Joint Department of Biomedical Engineering, University of North Carolina at Chapel Hill and North Carolina State University, USA, [3]Department of Electronics and Telecommunications, Polytechnic University of Turin, Italy, [4]Urology Department, Academic Medical Center, University of Amsterdam, Netherlands*

Background, Motivation and Objective

Tumor growth requires formation of new angiogenic vessels, which differ in their morphology from those of healthy tissue. These vascular abnormalities result in altered blood flow dynamics, which can be assessed by dynamic contrast-enhanced ultrasound (DCE-US). Two distinct approaches are typically employed in DCE-US following an intravenous injection of ultrasound contrast agent: assessment of perfusion or dispersion parameters from the measured time intensity curves [1].

In this paper, we compare maps of dispersion and perfusion with those of acoustic angiography (AA), a 3D high-resolution technique capable of capturing the vascular morphology [2]. We aim at determining those properties of the vascular architecture that are reflected by perfusion and dispersion parameters, as well as their evolution over time as tumor grows. To this end, a longitudinal study has been performed with tumor models in 3 rats.

Statement of Contribution/Methods

Fibrosarcoma tumors were implanted subcutaneously into the flanks of 3 rats. Tumor evolution was imaged with DCE-US and AA starting 8 days after implantation. Subsequent acquisitions were performed every 3 days amounting to 4 time points in total. Dispersion and perfusion were estimated by the correlation coefficient and wash-in rate (WIR), respectively [1]. The obtained parametric maps were overlaid onto the corresponding AA planes. The evolution of both parameters over time and with respect to tumor volume has been assessed.

Results/Discussion

Figure 1a shows a slice of the AA acquisition of a tumor, with bright regions indicating the vasculature. While areas of high WIR (Fig. 1c) correspond to large vessels observed in the AA, preliminary results suggest the correlation coefficient to indicate areas of dense microvasculature (Fig. 1b). The longitudinal analysis does not show consistent trends in the correlation coefficient over time and with respect to volume; however, a decreasing median WIR is observed as tumors increase in size. Further validation is ongoing. Future work will focus on a more reliable registration of the DCE-US plane onto the 3D AA volume, as well as on the characterization of the vasculature in relation to the correlation coefficient.

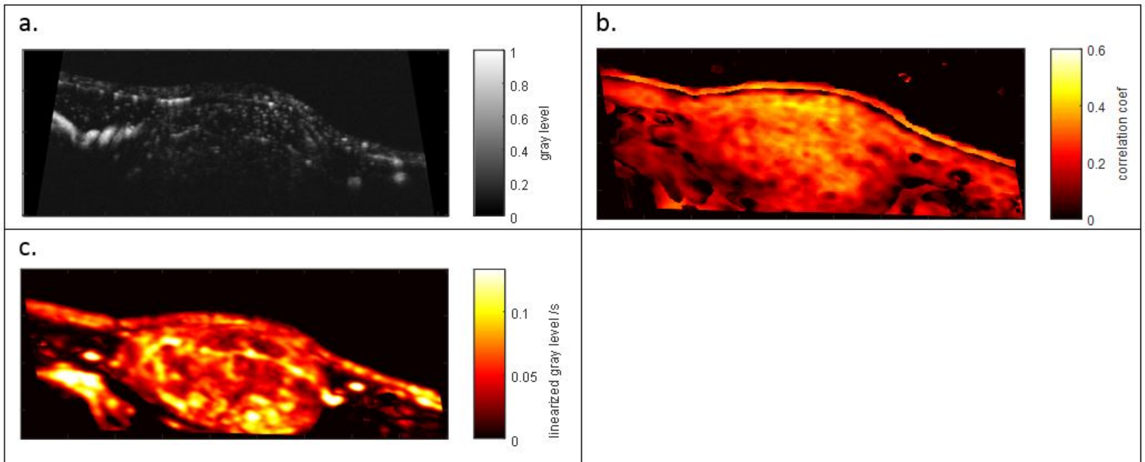

Figure. 1. a. Acoustic Angiography slice. b. Contrast ultrasound dispersion imaging (implemented by correlation coefficient estimation). c. Wash-in rate.

P1-C5 - MEL: Mechanical Parameter Estimation

Exhibit Hall

Saturday, September 9, 2017, 9:30 am - 4:00 pm

Chair: **Mark Palmeri**
Duke University

P1-C5-1

Group-Shearwave Based Viscoelastic Parameter Estimation: Analysis of Sources of Bias

D. Cody Morris[1], Ned Rouze[1], Mark Palmeri[1], Kathryn Nightingale[1]; [1]*Biomedical Engineering, Duke University, Durham, North Carolina, USA*

Background, Motivation and Objective

Shear Wave Elasticity Imaging is used to assess liver fibrosis, as shear wave speed (SWS) correlates with fibrosis stage. We have previously proposed a group SWS-based method to derive the tissue's stiffness (μ) and viscosity (η) using an analytic solution for the shear wave propagation in a Voigt material which accounts for the source excitation geometry [Rouze et al., IEEE IUS 2016]. However, in vivo factors such as phase aberration and nonlinear propagation cause the excitation beam pattern to differ from the modeled geometry. This work assesses the error introduced in material parameter determination by a range of perturbations in source geometry.

Statement of Contribution/Methods

Displacement and velocity shear wave profiles were calculated as a function of space and time for a range of material parameters using the analytic solution derived to model our experimental C5-2 curvilinear array. Sources were created by varying the focal number and using Field-II to simulate the radiation force (Fig b). The resulting shear wave profiles were then used to calculate displacement and velocity group SWSs, the combination of which (sum and difference) relates to specific material properties and excitations. To assess the error introduced by inaccurate source geometries, data from unmatched source geometries were used to determine the material parameters.

Results/Discussion

Figure (a) shows material properties derived from group SWS in relation to fibrosis stage for 43 patients. In simulation, 3 materials with increasing μ and η were analyzed. Figure (c) demonstrates the frequency content at two lateral positions (4 and 15 mm) for the displacement and velocity waveforms in material 2, dashed and dotted lines correspond to F/1.5 and F/3.0 sources. The two geometries have similar frequency distributions, with RMSD < 0.08%. Figure (d) illustrates the calculated SWSs for each material and geometry. The variation in SWS with geometry is <0.5%. Figure (e) shows the bias in material parameter estimates when the listed geometry is used to calculate SWS and the other is used for parameter inversion. These data suggest that the errors in source geometry examined here do not significantly impact this method's accuracy. Ongoing studies include the analysis of errors introduced by aberration and acoustic nonlinearity.

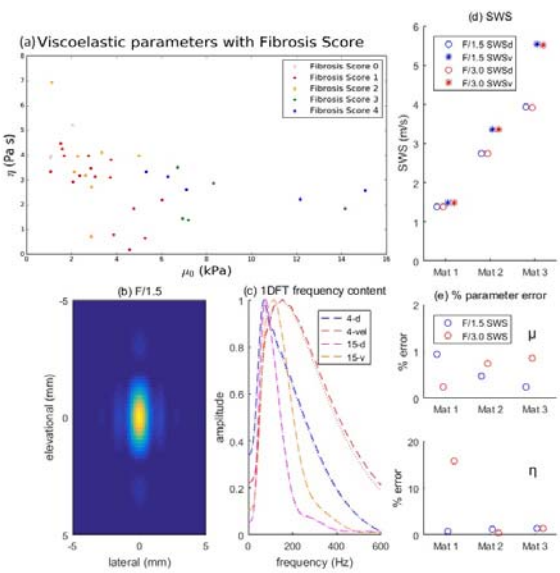

P1-C5-2

Assessing Degree of Mechanical Anisotropy Using the Ratio of ARFI-Induced Peak Displacements at Small Rotation Angles

Md Murad Hossain[1], Leela Goel[1], Caterina Gallippi[1]; [1]*Department of Biomedical Engineering, University of North Carolina, Chapel Hill, Chapel hill, North Carolina, USA*

Background, Motivation and Objective

Many tissues, including muscle, can be described as transversely isotropic (TI) with an axis of symmetry (AoS) perpendicular to a plane of isotropy. Mechanical properties differ along versus across the AoS. We have previously shown that the degree of difference, or the 'degree of anisotropy (DoA)', can be assessed as the ratio of ARFI-induced peak displacements (PDs) achieved when the long axis of an asymmetrical ARF PSF is aligned along versus across the AoS, requiring a 90° PSF rotation. We herein test the hypothesis that *smaller PSF rotation angles, which could facilitate data acquisitions, support DoA assessment.*

Statement of Contribution/Methods

ARFI imaging was simulated for 25 material-ARF PSF orientation angles spanning 0° - 360° using finite element (FE) models of seven linearly elastic and homogeneous TI materials with ranges of elasticity: E_T= 18.06-27.09 KPa;E_L=18.24- 27.36 KPa;μ_T=6- 9.0 KPa; μ_L=10.3-49 KPa; ν_{LT}=0.505;ν_{TT}=0.499, where E = Young's modulus, μ= shear modulus, ν= Poisson's ratio, L= along the AoS, and T= across the AoS. The modeled displacements were ultrasonically tracked using Field II. Experimentally, ARFI imaging was performed in an isotropic phantom and in excised swine psoas major muscle using a rotation stage for 7 material-ARF PSF orientations spanning 0° to 90°. Imaging was performed using a Siemens Acuson Antares™ and a VF7-3 transducer; ARF excitations were 4.21 MHz with F/1.5. Induced displacements were estimated using normalized 1D axial cross-correlation, and PD was evaluated. The ratios of PD at 90° to PDs at 0°, 60°, and 75° material-ARF PSF orientation angles were statistically compared across materials. Finally, DoA assessed using PDs was compared to that using SWV.

Results/Discussion

See Fig. 1. PD varies periodically with increasing material-ARF PSF orientation angle, and the amplitude of variation is larger for more anisotropic materials, particularly near 90° and 270° (panels a, c). *In silico*, DoA derived as the ratio of PDs at 90° and 75° was statistically different ($p<0.05$) in materials with μ_L/μ_T of 1.22 and 1.78, whereas the corresponding ratio of SWVs at 0° and 15° was not statistically different(panel b). Experimental PD and SWV ratios in the isotropic phantom and in muscle are reported in panel (d). These data suggest that ARF PSF rotations as small as 15° could support interrogation of DoA in anisotropic tissue such as muscle.

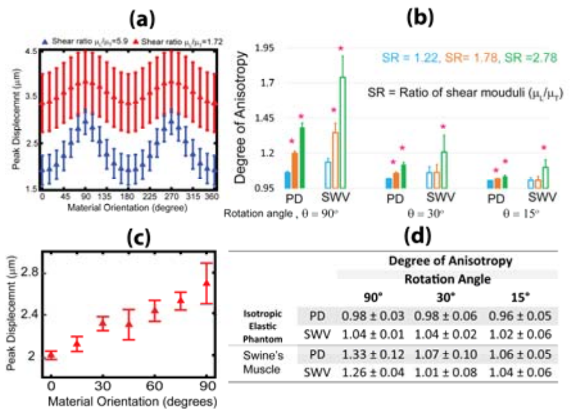

		Degree of Anisotropy		
		Rotation Angle		
		90°	30°	15°
Isotropic Elastic Phantom	PD	0.98 ± 0.03	0.98 ± 0.06	0.96 ± 0.05
	SWV	1.04 ± 0.01	1.04 ± 0.02	1.02 ± 0.06
Swine's Muscle	PD	1.33 ± 0.12	1.07 ± 0.10	1.06 ± 0.05
	SWV	1.26 ± 0.04	1.01 ± 0.08	1.04 ± 0.06

Figure 1. (a) Peak displacement (PD) as a function of material-PSF orientation in two representatives TI materials with ratio of shear moduli (SR) 1.72 (red) and 5.9 (blue). Note that, long axis of ARFI excitation PSF is oriented along and across the AoS at 90° and 0°,respectively. PD is shown as mean ± standard deviation over 10 independent speckle realizations. (b) Degree of Anisotropy (DoA) derived using PD and SWV in three simulated material using rotation angle = 90°, 30°, 15°. Note that, the ratios of SWV at 0° to SWVs at 15°, 30°, and 90° were used to calculate SWV derived DoA because PD and SWV are inversely related. DoA of material with SR =1.22 was always statistically compared against DoA of materials with SR=1.78 and 2.78. (c) PD as a function of material orientation in the swine psoas major muscle. (d) DoA derived using PD and SWV in an isotropic elastic phantom and muscle.

P1-C5-3

Influence of Transmit Beamforming Parameters on Image Quality in Quantitative Elastography

Katelyn Offerdahl[1], Stephen McAleavey[1]; [1]*Biomedical Engineering, University of Rochester, Rochester, NY, USA*

Background, Motivation and Objective

A challenge in the clinical application of shear wave elastography is the level of measurement variance or noise compared to clinically significant changes in shear wave speed. For instance, liver fibrosis staging is challenged by the relatively high variance of shear wave velocity estimates in comparison to the modulus difference between early (F1-F3) fibrosis stages. Recent work has shown that ultrasound speckle can be a significant source of noise in shear wave elasticity imaging (SWEI) when small tracking windows and beam spacings are employed to achieve high spatial resolution. Single tracking location (STL) methods which use multiple or shaped push beams to generate shear waves of known wavelength, and which estimate the speed of these shear waves by timing their arrival at a single tracking location, appear to be nearly immune to speckle noise. Multiple tracking location (MTL) methods are more sensitive to speckle noise, but can allow for more rapid image formation. The objective of this study is to quantify the effects of transmit beamforming parameters on STL and MTL image noise. These data will provide guidance for selection of STL or MTL in a particular imaging situation.

Statement of Contribution/Methods

We report on the effects of beam spacing, track and push aperture size, and SWEI implementation (STL vs MTL) on shear wave speed image noise, spatial resolution, and depth of field. B-mode imaging and shear wave data collection were performed using a Siemens Antares scanner and VF7-3 transducer at a frequency of 4.21 MHz, corresponding to a wavelength of 0.36 mm. Customized beam sequences were implemented for both STL and MTL imaging using control software developed in-house. Beam spacing (tracking and ARFI push) was varied from 0.2 mm to 4.8 mm. Tracking transmit apertures of F/2, F/4, F/6 were evaluated, along with ARFI (push) apertures of F/1.8 and F/3.6. Homogeneous target data was collected in viscoelastic phantoms designed to mimic varying stages of liver fibrosis (CIRS Model 039). SWEI data was also collected from cylindrical inclusions with shear moduli of 0.3, 0.6, 1.8, and 3.2 times the background (G=8 kPA) and diameters 1.6 to 17 mm.

Results/Discussion

At the narrowest beam spacing examined, 0.2 mm, an order-of-magnitude (13x) reduction in the standard deviation of modulus images in homogeneous phantoms is associated with the STL implementation vs MTL, diminishing to a 2.5x reduction at the largest (4.8 mm) spacing. STL exhibited greater sensitivity to track beam aperture size, with increasing image variance with track beam F/#; MTL was comparatively unaffected. The choice of ARFI F/1.8 or F/3.6 did not markedly affect image noise, and the larger F/# exhibited a larger useful depth of field. STL exhibited consistently higher CNR when imaging inclusions for all beam spacings considered. The results support the conclusion that STL is appropriate for high resolution SWEI applications.

P1-C5-4

Comparison of Methods for Measuring the Frequency Dependent Phase Velocity and Attenuation in Viscoelastic Materials

Ned C. Rouze[1], Courtney A. Trutna[1], Yufeng Deng[1], Mark L. Palmeri[1], Kathryn R. Nightingale[1]; [1]*Biomedical Engineering, Duke University, Durham, NC, USA*

Background, Motivation and Objective

Shear wave (SW) propagation in viscoelastic materials is characterized by a complex, frequency-dependent shear modulus μ(f). Measurements of μ(f) typically require Fourier transform techniques to decompose an observed SW signal into discrete frequency components and two independent measurements such as the phase velocity c(f) and attenuation α(f) to determine the real and imaginary parts of μ(f).

Statement of Contribution/Methods

This study considers three methods to determine c(f) and α(f). First, we expanded the two-dimensional Fourier transform (2DFT) method [Nenadic, et al., 2017] to account for a finite spatial window where the SW is observed (fw2DFT). Then, c(f) and α(f) are determined from least squares fitting of the shape of the 2DFT signal. Second, SW spectroscopy determines c(f) and α(f) using the progressive phase and exponential decay of the SW signal [Deffieux, et al., 2009]. Third, we extend our previously described method to determine material model parameters from measurements of group SW speeds to include fractional derivative orders, thereby giving a continuous variation in group speed with derivative order and allowing the use of higher order models such as a three-parameter Standard Linear model.

Results/Discussion

The figure shows measurements of c(f) (left) and α(f) (right) from measurements of SW propagation in a viscoelastic phantom. Shown are the results from fw2DFT measurements (black crosses), SW spectroscopy (red circles), and group SW speed measurements using a Standard Linear model (green line). We observe that the c(f) results are in good agreement for all three methods. For α(f), the fw2DFT and SW spectroscopy measurements are in good agreement, while the group SW speed results differ from these two measurements. Errors in the geometric correction factor employed by the Fourier domain methods modulate the predicted attenuation – which we hypothesize is the source of the disagreement.

The agreement in phase velocity measurements give high confidence in these results and suggests that model-dependent fitting of the dispersion curves can be used to characterize material properties. However, the failure for all measurements of the attenuation to agree lowers the confidence in these measurements and suggest that these measurements cannot be used to obtain model-free measurements of μ(f) from independent measurements of c(f) and α(f).

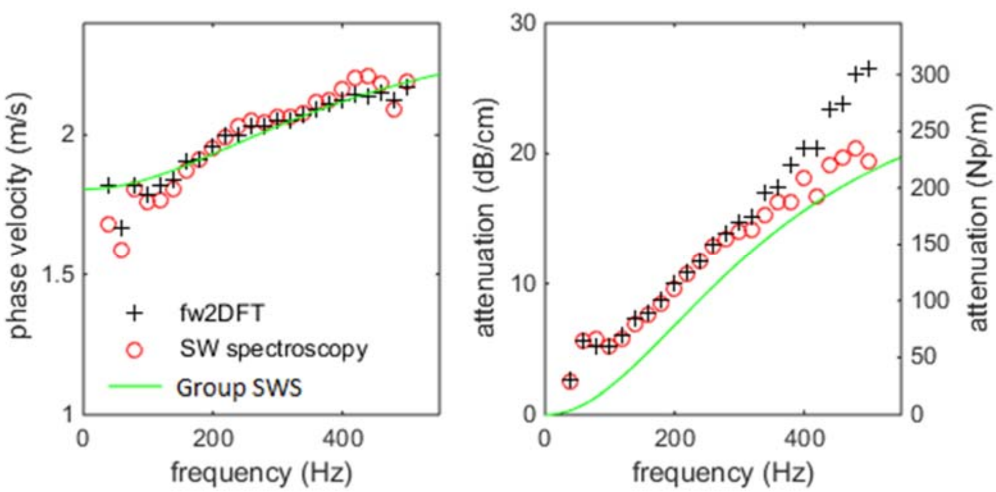

P1-C5-5

Evaluation of the Nonlinear Modulus in Renal Transplant Patients using Progressive and Regressive Compression and Shear Wave Measurements

Sara Aristizabal[1], Carolina Amador Carrascal[1], Tomas Echavarria Bayter[2], James F. Greenleaf[1], Matthew W. Urban[1,3]; [1]*Physiology and Biomedical Engineering, Mayo Clinic, Rochester, Minnesota, USA,* [2]*Universidad Escuela de Ingenieria de Antioquia, Medellin, Antioquia, Colombia,* [3]*Radiology, Mayo Clinic, Rochester, Minnesota, USA*

Background, Motivation and Objective

End-stage renal disease (ESRD) is an irreversible deterioration in the renal function in which the body loses its ability to maintain the fluid and metabolic balance. Transplantation is the treatment of choice for patients with ESRD. After transplantation, biopsies are performed to monitor the function of the kidney transplant over time. Due to the invasive nature of biopsies, we are investigating the potential of noninvasive shear wave based methods such as acoustoelasticity (AE) to estimate the nonlinear mechanical properties of tissues. Using AE by compressing a medium and measuring the shear wave speed at different compression levels, we can estimate the third order nonlinear coefficient, A. The goal of this study was to evaluate the feasibility of performing AE using two directions of compression and to evaluate the potential of A as an indicator of the presence of renal fibrosis in the transplanted kidney.

Statement of Contribution/Methods

The study was conducted on 100 renal transplant patients at the same time of their protocol biopsies. To estimate the parameter A, stress was applied in the transplanted kidney in two manners: progressively, by pressing the ultrasound transducer (C1-6) into the patient in 7 steps until reaching maximum compression and regressively, by applying maximum stress into the tissue and slowly releasing the compression in 7 steps.

In this study, 84 and 76 patients were evaluated using progressive and regressive compression, respectively. Shear waves were generated and measured at each compression step by a GE LOGIQ E9 ultrasound system. For the AE measurements, the shear modulus, μ_i, was quantified at each compression level and the applied strain, ε_i, was assessed in the imaging plane by measuring the change in thickness of the kidney cortex. Finally, A was calculated by applying the AE theory.

Results/Discussion

Fifty-nine (70%) and twenty-eight (37%) patients had adequate data for estimation of *A* when the compression was performed in the progressive and regressive directions, respectively. The estimated values of *A* were compared against the biopsy score for interstitial fibrosis (Banff ci). Boxplots are shown in Figs. 1(a-b). Progressive was more likely to be successful to yield data for measuring *A*, and the values of *A* could be used to distinguish patients with early, mild fibrosis from patients with no fibrosis using a Wilcoxon test, p = 0.005.

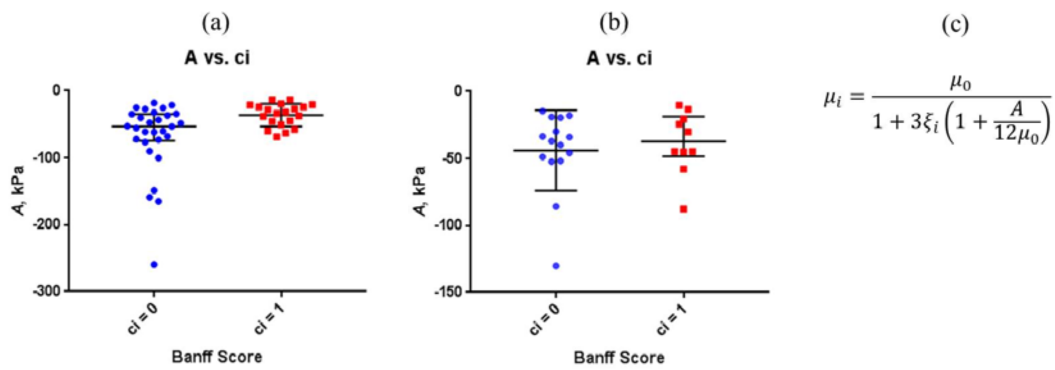

Figure 1: The summary of nonlinear coefficient, *A*, in renal patient data (N = 59) and (N = 28) obtained using progressive and regressive compression are shown in **(a-b)**, respectively. *A* values versus Banff interstitial fibrosis score (ci) of 0 (interstitial fibrosis in up to 5% of cortical area) and 1 (mild interstitial fibrosis in 6-25% of cortical area) obtained with **(a)** progressive and **(b)** regressive compression. The value of *A* was estimated by fitting the shear modulus vs. strain data to equation in **(c)**.

P1-C5-6

Acoustoelasticity Modeling of Bladder Tissue Nonlinearity: Ex Vivo Study

Mahdi Bayat[1], Aparna Singh[1], Jeremy Webb[2], Viksit Kumar[1], Adriana Gregory[1], Azra Alizad[2], Mostafa Fatemi[1]; *[1]Physiology and Biomedical Engineering, Mayo Clinic, USA, [2]Radiology, Mayo Clinic, USA*

Background, Motivation and Objective

Bladder is a complex organ and its proper function is closely tied to the mechanobiology of its multi-layer wall. Characterization of the bladder wall mechanical properties is crucial in diagnosis of diseases that can lead to lower tract infection and incontinence. Ultrasound bladder vibrometry has emerged as a noninvasive method for characterization of the bladder tissue elasticity using Lamb wave model (Nenadic et al. PLOS 2016). Previous studies have shown an increasing trend in bladder elasticity with added fluid which is an indication of a nonlinear behavior. In this study, we use the acoustoelasticity (AE) theory to quantify the bladder tissue nonlinearity parameter A. We show that this parameter can precisely differentiate between the intact and aberrant ex vivo bladder samples treated with formalin.

Statement of Contribution/Methods

Freshly existed ex vivo swine whole bladder samples were positioned in a water tank and were filled at incremental volume steps. At each volume, bladder elasticity was measured based on UBV method using a Verasonics programmable ultrasound machine (Verasonics, Kirkland, WA, USA) using L7-4 linear array transducer (Philips, North America). Ultrasound imaging also provided accurate measurement of the bladder wall thickness. The wall thickness was used to measure the radial strain due to added fluid at each step. Using UBV measurement of the elasticity at each volume, μ_i, and corresponding strain, ε_i, the projected initial unloaded elasticity, $\mu_{0,est}$, strain bias,$\varepsilon_{bias,est}$, and the nonlinearity parameter, A_{est}, can be estimated by solving the following nonlinear least-square problem

$(A_{est},\mu_{0,est},\varepsilon_{bias,est})$=argmin$\sum(\mu_i-\mu_0/(1+3(\varepsilon_i+\varepsilon_{bias,est})(1+A/(12\mu_0))))$^2

Results/Discussion

Fig.1(a) shows elasticity variations with added fluid as a function of strain in one bladder sample. As it can be seen the intact bladder (blue) presents a moderate change in elasticity with increased strain while formalin treated bladder (red) shows a higher rate of elasticity increase with strain. Fig.1(b) shows the box plot for the nonlinearity parameter A for 9 tested ex vivo bladder samples before and after treatment. As it can be seen, A is significantly higher in the treated group, P < 0.002. These outcomes promise an effective tool for measurement of the bladder tissue nonlinearity which might have relevance in assessment of the bladder compliance.

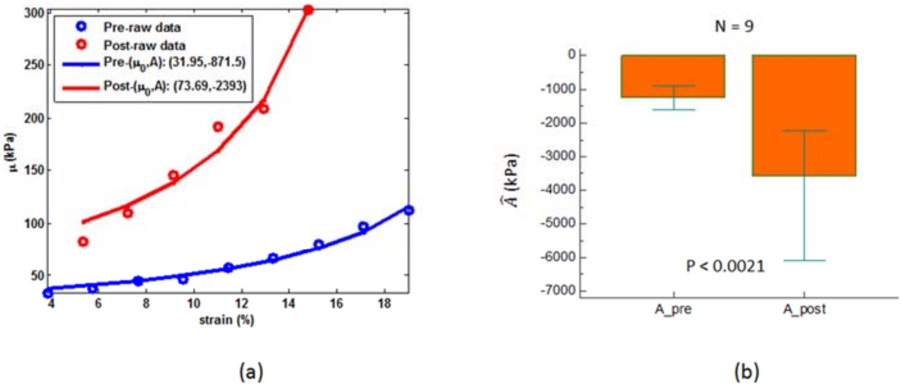

Figure 1: (a) Elasticity measured by UBV at each strain level for pre (blue) and post (red) formalin treated bladder and (b) box plot for nonlinearity parameter *A* in intact (*A_pre*) and formalin treated (*A_post*) from 9 bladder samples.

P1-C5-7

Multi-Plane Estimation of The Third- And Fourth-Order Elastic Constants of Soft Material

Jinping DONG[1], He Li[1], Yang Zhang[1], Yuexin Guo[1], Wei-Ning Lee[1,2]; [1]*Department of Electrical and Electronic Engineering, The University of Hong Kong, Hong Kong,* [2]*Medical Engineering Programme, The University of Hong Kong, Hong Kong*

Background, Motivation and Objective

The nonlinear shear modulus was found to exhibit higher contrast than shear modulus for the detection of breast lesions (Bernal, Chamming's et al. 2016) and may thus serve as a potential diagnostic index of tissue pathology. Such nonlinear elastic constant of soft tissues has been demonstrated to be effectively estimated by combining ultrasound elastography and supersonic shear imaging based on acoustoelastic theory (Latorre-Ossa, Gennisson et al. 2012). Acoustoelastic theory relates shear wave propagation speed to the strain e and the angle θ; between the principal loading direction and the imaging plane (Destrade, Gilchrist et al. 2010), suggesting that 2D distributions of the nonlinear parameters (the third- and fourth-order elastic constants (A, D)) in different planes (θ) could be estimated. We thus aimed to preliminarily validate this concept in vitro.

Statement of Contribution/Methods

A 7wt% polyvinyl alcohol phantom (1% SiO_2; 2 freeze/thaw cycles) was uniaxially stretched at an increment of 2mm to a maximum of 40% strain using a customized stretching device. At each increment, an ultrasound imaging framework that integrated shear wave imaging (SWI) and 2D ultrasound strain imaging (USI) was employed and implemented on a Verasonics Vantage system with an L7-4 probe (fc = 5.2 MHz) mounted on a rotation stage. In SWI, ultrasonic focused beams of 100 us were transmitted to generate shear waves, which were acquired by coherent plane wave compounding (CWPC) with three steering angles (-2°, 0°, 2°) at 5000 Hz for group velocity and thus shear modulus estimation. In USI, radio-frequency (RF) data were acquired using CPWC with 63 angles (-14.3-14.3°) for incremental and cumulative lateral strain estimation (Li et al., 2016). Both the shear modulus and lateral strain in each of the 19 imaging planes (0°: 10°:180°) at each strain increment were estimated and mapped for deriving multi-plane A and D parameters.

Results/Discussion

Reliable USI-estimated lateral strain (i.e., along the stretching direction) (Fig.1(b)) facilitated the estimation of A and D. Fig. 1(c) shows pronounced strain-induced anisotropic behavior, stemming from nonlinearity. The multi-plane A, D estimates (Fig.1(d)-(e)) were in good agreement with literature, demonstrating the feasibility of our integrated imaging framework in mapping muilti-plane nonlinear elastic constants.

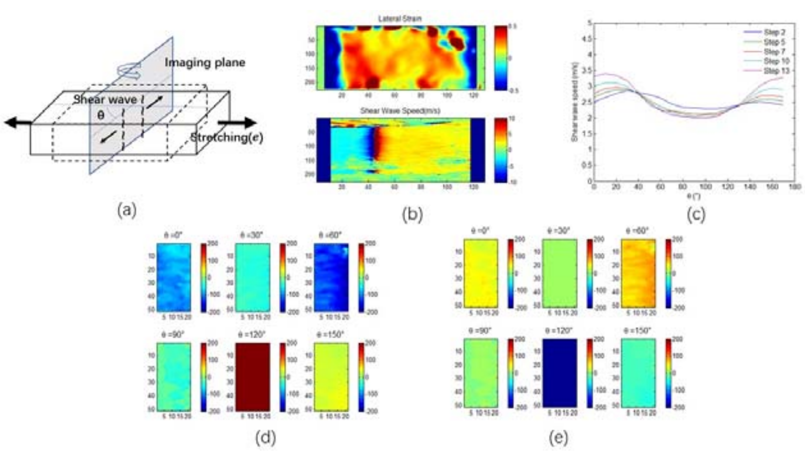

Fig1 (a) Schematic of experimental procedure; (b) 2D lateral strain(stretching strain) and shear wave speed distribution(step5, $\theta = 0°$); (c) Shear wave speed variation with stretching steps; (d) A maps and (e) D maps in different angles

P1-C5-8

Quantification of Nonlinear Elastic Constants Using Polynomials in Quasi-Incompressible Soft Solids

Corin Otesteanu[1], Bhaskara Chintada[1], Orcun Goksel[1]; [1]*Computer-assisted Applications in Medicine, ETH Zurich, Zurich, Switzerland*

Background, Motivation and Objective

Early detection of pathological structures is crucial for the prognosis and treatment of patients. Biomechanical characterization of nonlinear tissue behavior has been shown to significantly improve tumor differentiation compared to linear elastic modulus alone. We aim to characterize the third (A) and fourth (D) order elastic constants.

Statement of Contribution/Methods

In [1], the third order elastic constant was determined from the slope of the shear modulus as a function of applied stress. Both third and fourth order elastic constants were determined in [2], from the quadratic equations relating shear modulus to strain. However, this was found not to be stable for our experimental data. With quasi-incompressibility assumption, we approximate shear modulus with stress ($\sigma=3\mu\varepsilon$), thereby relating stress to strain by a third order polynomial, which leads to more robust parameter fitting

Results/Discussion

Ex-vivo bovine liver was subjected to compression by a motorized stage in 0.5 mm steps, up to 10 mm (20% strain) (Fig. 1a). Ultrasound SWE was used meanwhile to measure the shear modulus of tissue at each compression step, while exerted force (Fig. 1b) was also recorded by a force sensor to estimate uniform uniaxial stress. The strains computed from the RF data via a staggered strain algorithm were found to be within 5% of those known from the motion stage.

Stress-strain plots were computed and a third order polynomial was used to fit the data (Fig. 1c). A = -18.0kPa +/- 1.1kPa and D = 107kPa +/- 23kPa were determined, in line with the literature [3]. A parameter was also recovered using a linear fitting [1], yielding a similar value of -18.1kPa +/-0.2kPa, albeit a narrower confidence interval (Fig. 1d). The results were also compared to the quasi-static (QS) stress-strain measurements computed based on the force/compression measurement system, showing same order of magnitude; with differences potentially originating from uniform uniaxial stress assumption and from tissue mechanical response to the different excitation. We will next corroborate our results with mechanical simulations and indentation tests.

Similarly, nonlinear parameters of a bovine muscle sample was also estimated (Fig. 1e-h).

[1] Bernal, M. et al., IEEE Trans. UFFC, 2016

[2] Destrade, M. et al., Journal of Acoust. Soc. Of America, 2010

[3] Aristizabal, S., et. al., IEEE Ultrason. Symp. Proc. 2016:978-981

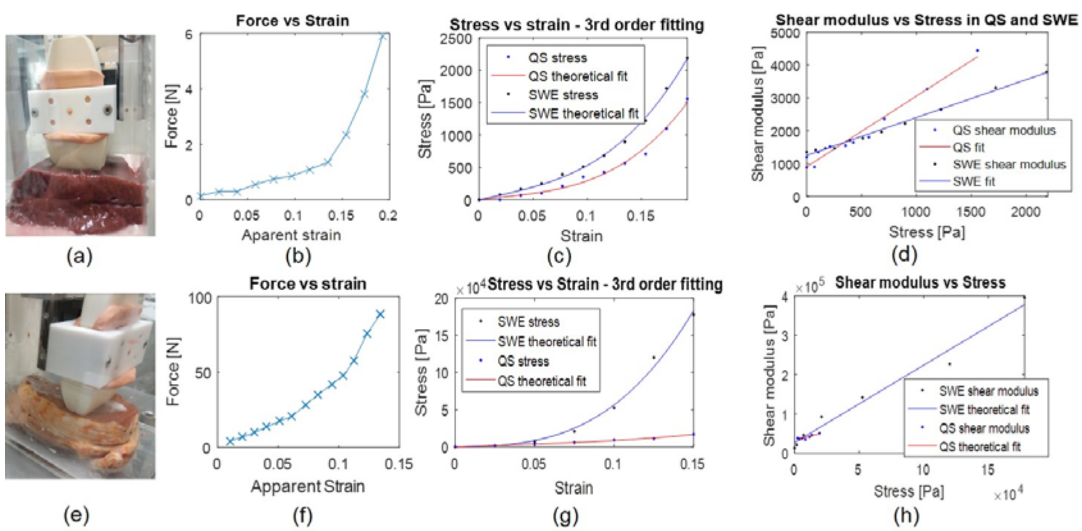

P1-C6 - MEL: Elastography in Pre-Clinical and Clinical Application

Exhibit Hall

Saturday, September 9, 2017, 9:30 am - 4:00 pm

Chair: **Gianmarco Pinton**
University of North Carolina at Chapel Hill and North Carolina State University

P1-C6-1

Improved Delineation Rate of Thermally Ablated Liver Tumors with Electrode Displacement Elastography Compared to Commercial Acoustic Radiation Force Impulse Imaging

Wenjun Yang[1], Tomy Varghese[1], Timothy Ziemlewicz[2], Marci Alexander[2], Kelly Wergin[2], Meghan Lubner[2], J. Louis Hinshaw[2], Shane Wells[2], Fred Lee Jr[2]; [1]*Department of Medical physics, University of Wisconsin-Madison, USA,* [2]*Department of Radiology, University of Wisconsin-Madison, USA*

Background, Motivation and Objective

Ultrasound elastography is an effective imaging modality to delineate thermally ablated regions after ablative liver tumor treatments. The image contrast is based on the difference in the Young's modulus of local tissue. In this work, we compared our previously introduced electrode displacement elastography (EDE) with a commercially available acoustic radiation force impulse imaging (ARFI) technique, for delineating the post ablation regions.

Statement of Contribution/Methods

Forty-nine patients diagnosed with either a hepatic carcinoma or metastases underwent microwave ablation (MWA) procedures with a typical setting of 65 W for 5 minutes. EDE and ARFI images were acquired with a Siemens Acuson S2000 system with a 6C1 HD transducer. EDE images were generated from a continuous loop of ultrasound radiofrequency (RF) data using a 2D cross-correlation based algorithm. ARFI images were obtained using commercial 'Virtual Touch' function available in the Siemens Acuson S2000 system. Delineation of the ablated region was performed by two observers. Imaging depth dependence of EDE and ARFI was evaluated using tissue mimicking (TM) phantoms with the ablation inclusion positioned at different depths.

Results/Discussion

Summary results from the two observers, indicate that the ablated region in ARFI images was recognizable on an average of 20 patients in conjunction with B-mode imaging, while delineable ablation boundaries could be generated on an average of 4 patients. With EDE strain images, delineable ablation boundaries were generated on an average of 40 patients, without obvious imaging depth dependence. The TM phantom studies demonstrate that the difference of dimensions of the inclusion measured with EDE and ARFI images were within 8%, while the image contrast and contrast to noise ratio (CNR) with EDE was 2–3 times higher than that obtained with ARFI. This study showed that the monitoring ability for MWA in terms of the delineation rate and CNR was improved with EDE when compared to the commercially available ARFI function. EDE could therefore become an alternative imaging modality for monitoring the MWA procedure for liver tumors in the ablation suite. EDE is also feasible at deeper tumor locations beyond the rated imaging depth of ARFI.

P1-C6-2

3D Reconstruction of Ablations in Shear Wave Elastography Using the Matérn Kernel

Atul Ingle[1], **Tomy Varghese**[2]; [1]*Department of Biostatistics, University of Wisconsin-Madison, Madison, WI, USA,* [2]*Department of Medical Physics, School of Medicine and Public Health, University of Wisconsin-Madison, Madison, WI, USA*

Background, Motivation and Objective

Radiofrequency and microwave ablation procedures are commonly used for treating hepatocellular carcinoma in patients that are not candidates for surgical resection. Ablation is a minimally invasive procedure which involves insertion of an ablation needle (electrode) into the tumor which produces localized heating to kill the surrounding cancerous cells. Ultrasound can be a valuable tool for real-time monitoring of this procedure, not only to guide the needle into the tumor (using B-mode imaging) but also to monitor the volume of the ablated tissue using tissue elasticity imaging. This work proposes using the ablation needle to produce a pulse displacement with an external actuator and tracking the shear wave velocity (SWV) in the image plane. A 3D reconstruction algorithm is proposed here that uses a kernel based approach to capture the smooth transition zone between the stiff ablated region and the surrounding untreated tissue.

Statement of Contribution/Methods

High frame rate ultrasound echo data is obtained from a tissue-mimicking phantom experiment. A linear array transducer is manually rotated through different imaging planes co-axial with the ablation needle to obtain shear wave arrival time data in a 3D volume. For each scan plane, axial displacements are estimated using a 1D cross-correlation algorithm and the location of peak displacement is tracked laterally to estimate SWV at each pixel. SWV maps are approximated on 2D transverse planes at different depths using a Matérn radial basis kernel. This kernel has two tuning parameters that control smoothness of the resulting reconstruction. These are selected using generalized cross-validation.

Results/Discussion

The Matérn kernel based reconstruction algorithm provides better image quality metrics such as signal-to-noise ratio, contrast and contrast-to-noise ratio compared to a standard nearest neighbor interpolation technique. The choice of kernel parameters through crossvalidation also prevents appearance of "spoke wheel" artifacts. The estimated SWV values provided a contrast of over 5 dB between the stiff and the soft regions and the estimated dimensions of the stiff ellipsoidal region were within 7% along each of the three principal axes.

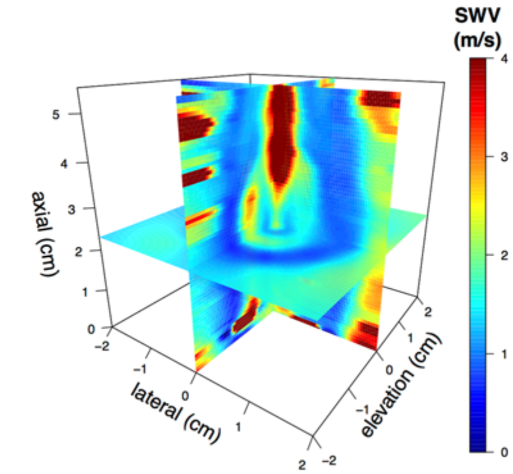

P1-C6-3

Evaluation of the Influence of Severe Steatosis on Fibrosis Measurement in a Rat Model with NAFLD by DMA and ARFI Technology

Yanrong Guo[1], Haoming Lin[1], Changfeng Dong[2], Xinyu Zhang[1], Huiying Wen[1], Yingxia Liu[2], Tianfu Wang[1], Siping Chen[1], **Xin Chen[1]**; [1]*School of Biomedical Engineering, Shenzhen University, China, People's Republic of,* [2]*Shenzhen Third People's Hospital, China, People's Republic of*

Background, Motivation and Objective

Non-alcoholic fatty liver disease (NAFLD) is a major health concern due to the increasing obesity epidemic and it has the risk to progress to liver fibrosis, cirrhosis and hepatocellular carcinoma. In clinical, it is important to assess the severity of hepatic fibrosis for the risk-stratified management of patients with NAFLD. Ultrasound elastography is a new technique for evaluation of liver fibrosis and it has been widely used in routine clinical practice. However, its measurement is usually influenced by the hepatic steatosis in NAFLD patients, and the quantitative estimation of that influence is poorly studied. The aim of this study was to evaluate the influence of severe steatosis on fibrosis measured by elastography technique in a rat model and compare the results with the conventional dynamic mechanical analysis (DMA) technique.

Statement of Contribution/Methods

The experiment was conducted in 110 rats with NAFLD. The right lateral lobe of the liver was harvested for the acoustic radiation force impulse (ARFI) and DMA measurements, and the other lobes were used for a histologic assessment. DMA was performed in a sandwich-type shear oscillation mode, and the results were fitted by a Voigt model to obtain the elasticity and viscosity modulus. ARFI imaging was measured by ACUSON S2000 system (Siemens, German) with an 8-MHz linear ultrasound transducer. Histological scoring was performed according to Brunt.

Results/Discussion

For the DMA measurement, the mean elasticity values were significantly higher in rats with severe steatosis than in those with no or mild steatosis for the F0-F2 fibrosis stages (1.53 versus 1.29 kPa; P = 0.001). However, significant differences were not observed between the rats with severe steatosis and those with no or mild steatosis for the F3-F4 fibrosis stages (3.01 versus 3.21 kPa; P = 0.472). The similar results were observed in the measurements of ARFI. In conclusion, our work indicated that the presence of severe steatosis is a significant factor for assessing lower stages of fibrosis, and should be taken into account to avoid overestimations of liver fibrosis with NAFLD.

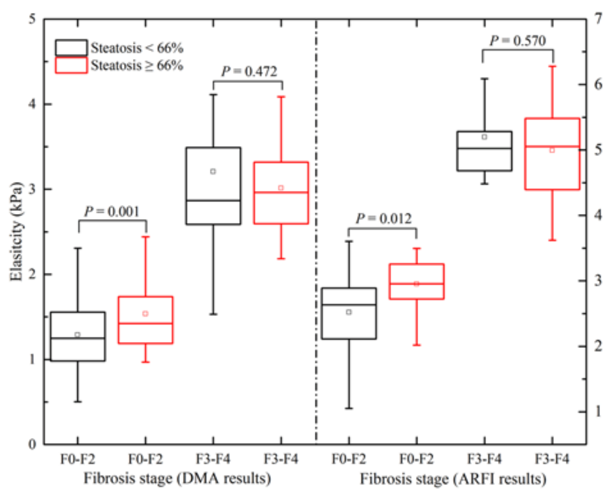

Fig. 1 Elasticity distribution for both DMA and ARFI measurements among rats with F0-F2 vs. F3-F4 stages according to the presence or absence of severe steatosis.

P1-C6-4

Evaluation of Shear Wave Dispersion Caused by Fibrous Structure and Tissue Viscosity Using Hepatic Fibrosis Progression and Histological Models

Shiori Fujii[1], Takeshi Namita[1], Kengo Kondo[1], Makoto Yamakawa[1], Tsuyoshi Shiina[1], Masatoshi Kudo[2]; [1]*Kyoto University, Kyoto, Japan,* [2]*Kindai University Faculty of Medicine, Osaka, Japan*

Background, Motivation and Objective

In chronic hepatitis diagnosis, shear wave elastography is utilized for evaluating fibrosis progression. It is expected that the accuracy will be improved by measuring the viscosity in addition to the elasticity. However, the shear wave dispersion in analyzing liver viscosity is affected by both viscosity and fibrous structure. In order to quantitatively evaluate hepatic fibrosis, we evaluated the effect of liver fibrous structure changes on the shear wave dispersion by using simulation model.

Statement of Contribution/Methods

A liver fibrosis progression model was developed [1]. Normal liver tissue is represented as a set of many hepatic lobules with a mean interval of 1mm. Progression of hepatic fibrosis is simulated by conjugating randomly selected hepatic lobules and generating nodules. The elasticity is given based on the potential at each nodule, with reference to clinical values measured by transient elastography. Shear wave propagation within this model was simulated, and the shear wave dispersion slope in the range of 100-1000 Hz is calculated. In addition to this model, we made other fibrosis model based on hepatitis histological specimen section (histological model) as shown in Fig. 1 and evaluated the shear wave dispersion. Using these models, we investigated how the shear wave dispersion is affected by fibrous structure and tissue viscosity.

Results/Discussion

The shear wave phase velocity at 200 Hz and the dispersion slope were compared at each stage. First, tissue viscosity is set to zero in order to examine the effect of the liver fibrous structure alone. In the fibrosis progression model, the dispersion slopes were 0.02, 0.32, 0.62, 1.25, and 0.73 m/s/kHz for stage F0, F1, F2, F3, and F4, as shown in Fig. 2. In the histological model, the dispersion slopes were 0.09, 0.97, 1.50, 1.80, and 2.90 m/s/kHz for stage F0, F1, F2, F3, and F4. In both models, the dispersion slope tended to increase with progress of the hepatic fibrosis stage. In addition, it was confirmed that both the dispersion slope and the phase velocity at 200 Hz increase as the viscosity increases. These values in Fig. 2 were about 20% of the dispersion slope in in vivo measurement [2]. Therefore, these results suggest that the influence of liver fibrous structure cannot be ignored in evaluating liver viscosity.

[1] T.Shiina et al, JJAP, 51, 07GF11, 2012.
[2] K.R.Nightingale et al, IEEE UFFC, 61, p.165, 2015.

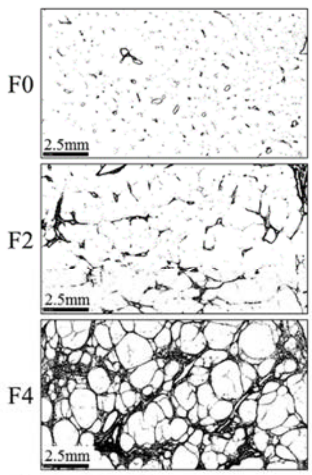

Fig.1 Liver fibrous structure of histological model

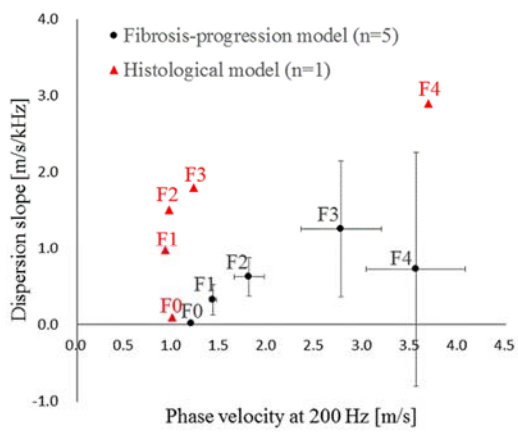

Fig.2 Shear wave dispersion caused by liver fibrous structure

P1-C6-5

Mechanical Effects of Cisplatin on Pancreatic Ductal Adenocarcinoma in a Transgenic Mouse Model Using Harmonic Motion Imaging

Thomas Payen[1], **Niloufar Saharkhiz**[1], Carmine Palermo[2], Steve Sastra[2], Kenneth Olive[2], Elisa Konofagou[1,3]; [1]*Biomedical Engineering, Columbia University, USA,* [2]*Herbert Irving Comprehensive Cancer Center, Columbia University, USA,* [3]*Department of Radiology, Columbia University, USA*

Background, Motivation and Objective

Pancreatic Ductal Adenocarcinoma (PDA) is one of the most lethal cancers with a 5-year survival rate of 8% and 2% for late stage diagnosis. This is due to the dense stroma of PDA at distal stages and increasing drug resistance. Cisplatin, a platinum-based chemotropic drug, is used to treat PDA by damaging DNA of cells through mutation of the Brca gene. In this study, Harmonic Motion Imaging (HMI) which is an all ultrasound based elastography imaging technique, is used to monitor the mechanical effect of Cisplatin on genetically-engineered transgenic mice. HMI generates oscillatory displacements at the focus and is used to measure the viscoelastic properties of wide range of tissues. The high power output of HMI makes it appropriate for characterizing PDA due to the highly stiff nature of PDA and the fact that it is deeply laid in the body.

Statement of Contribution/Methods

Intraperitoneal injection of Cisplatin (3mg/kg) was performed in three KPCB2ff mice and the effect of the drug was monitored for 61 days. The KPC model develops a PDA similar to that of humans. Amplitude modulated acoustic radiation force was generated using a 4.5 MHz focused transducer with the AM frequency of 25 Hz and the RF data was acquired by a confocally aligned 7.8 MHz imaging prob. The axial displacement, which is an indicator to the stiffness of the tissue, was calculated using a 1D-cross correlation technique. 2D images were obtained by moving the transducers in a raster scan regime. The size of the tumor and displacement values at the focal area on the tumor were calculated in each experiment.

Results/Discussion

Tumor decreased in size from day 17 to 29 after every 7-day injection of Cisplatin and increased to its initial size after day 29 due to drug resistance. The correlation between tumor stiffness and size was observed. According to HMI displacements, the softening of the tumor happened three days earlier than its size shrinkage. The tumor stiffened again at day 29 (Figure 1). The softening of the tumor after cisplatin injection has also been shown in literature. This indicates the potential of HMI in the early detection of mechanical effects of chemotherapeutic drugs, before conventional tumor size debulking is manifested. Since PDA patients have a 5-month median survival rate, HMI could be used to indicate the efficacy of the chemotherapy regimens earlier.

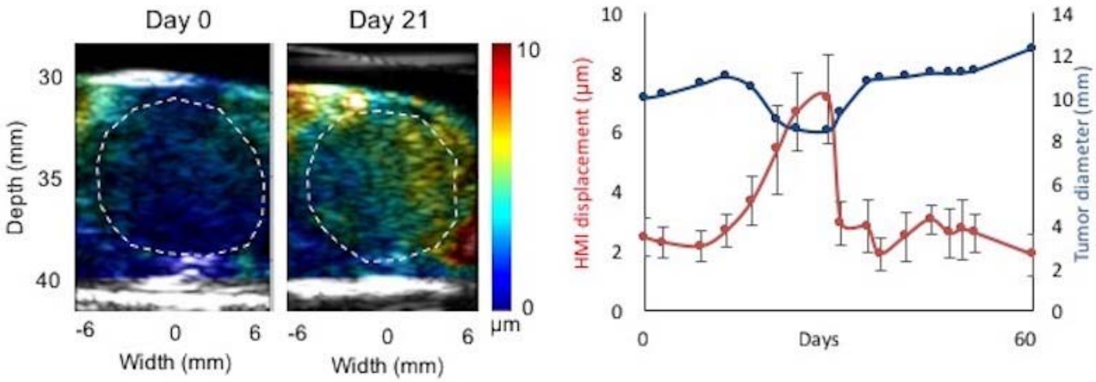

Figure 1: HMI displacement map of tumor before and 21 days after Cisplatin injection (a) and change in HMI displacement (red) and tumor diameter (blue) for 61 days after Cisplatin injection in PDA mouse model (b).

P1-C6-6

Laser Speckle Contrast Shear Wave Imaging of Three-Dimensional Cancer Metastasis Model

Pei-Yu Chao[1], Wei-Wen Liu[1], Shih-Shih Hsu[1], Pai-Chi Li[1]; [1]*National Taiwan University, Taipei, Taiwan*

Background, Motivation and Objective

Biomechanical properties of the extracellular matrix (ECM) are important regulators in cell development, including proliferation, apoptosis and migration. Recent studies have shown that stiffening of the ECM resulting from deposition and crosslinking of collagen may promote invasion and migration of tumor cells. In our previous study, a laser speckle contrast shear wave (SW) imaging system was developed, and a feasibility study on non-invasive, non-superficial and exogenous-tracer-free evaluation of the mechanical property of the 3-D cell matrix was performed. In this report, the system is used to measure the stiffness of 3-D cancer metastasis models. We hypothesize that the developed system can provide temporal and spatial information of the cell matrix during cancer progression related to cancer cell migration and metastasis.

Statement of Contribution/Methods

Both cells and the matrix exhibit optical scattering properties, and when illuminated with a coherent light source, speckle patterns can be observed. The presence of the SW in the cell culture system changes the phase of the transmitted optical waves and thus a decrease in the speckle contrast. The speckle contrast is defined as $K=\sigma_s/\mathbf{I}$, where σ_s and $\mathbf{I}$ are the standard deviation and mean intensity of the image. In this study, colon carcinoma cell lines SW480 and SW620 are used. Since SW480 and SW620 are derived from the primary and secondary tumors of the same patient respectively, they are used as a model for studying the changes in ECM stiffness during metastasis.

Results/Discussion

The imaging system setup and the design of the 3-D cell culture system are shown in Fig. (a) and (b). Fig. (c) shows the stiffness of the cell culture systems measured on 0^{th} hour, which is the time point after the completion of the 2-hours polymerization process, and 24^{th} hour of culture period. Noted that after 2 hours of polymerization process, the measured stiffness of the SW620 model is 9% lower than that of the SW480 model. Furthermore, the stiffness of the SW620 model increased by 16% within 24 hours of the culture period, while no significant changes in the stiffness of the SW480 model was observed. Correlations between the measured stiffness and histology of the cell culture systems will be presented and discussed in the full report.

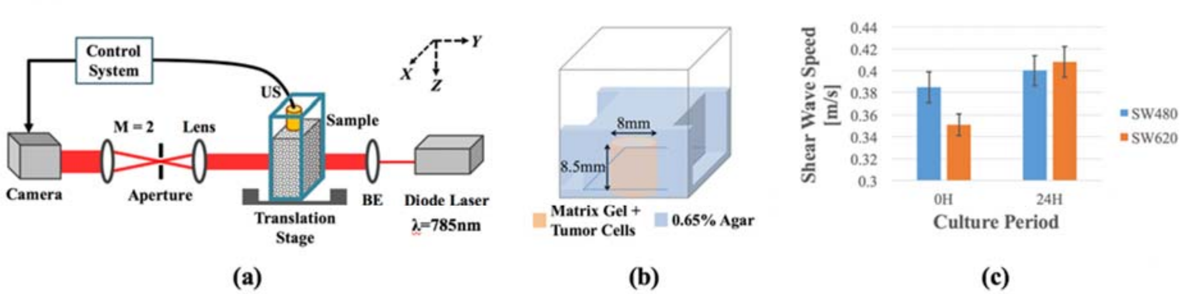

(a) Imaging system, and (b) design of the 3-D cell culture system. (c) Temporal stiffness changes of the cell culture system measured by the imaging system.

P1-C6-7

Delineation of Microwave Ablated Hepatocellular Carcinoma Tumor Regions Using Electrode Displacement Elastography

Wenjun Yang[1], Tomy Varghese[1], Timothy Ziemlewicz[2], Marci Alexander[2], Kelly Wergin[2], Meghan Lubner[2], J. Louis Hinshaw[2], Shane Wells[2], Fred Lee Jr[2]; [1]*Department of Medical physics, University of Wisconsin-Madison, USA,* [2]*Department of Radiology, University of Wisconsin-Madison, USA*

Background, Motivation and Objective

An effective imaging modality to delineate the ablated region after microwave ablation (MWA) therapy is crucial to yield promising treatment outcomes. Ultrasound B mode imaging is widely used to guide the ablation needle. However, the image quality suffers from relatively low imaging contrast due to the similar echogenicity between the ablated and surrounding liver tissue. In this study, we applied a quasi-static ultrasound elastography technique, referred to as electrode displacement elastography (EDE), to delineate the thermally ablated regions for patients diagnosed with hepatocellular carcinoma (HCC) treated with MWA procedures.

Statement of Contribution/Methods

Under our approved institutional review board (IRB) protocol, EDE was used for monitoring MWA on fifty-one patients. The MWA procedures were conducted with a NeuWave Certus 140 (Madison, WI, USA) system, with a typical setting of 65 W and 5 minutes. Ultrasound B mode and radiofrequency (RF) data loops for EDE were acquired with a Siemens Acuson S2000 system and a 6C1 HD transducer. The RF data loops were acquired simultaneously with a manual perturbation of an ablation needle performed by a physician. EDE strain images were generated with a 2D cross-correlation based displacement tracking algorithm with a kernel size of 1.35 mm × 3.29 mm along the axial and lateral direction. Ablation area, contrast and contrast to noise ratio (CNR) of EDE strain and ultrasound B mode images were compared.

Results/Discussion

Delineable ablation regions were observed using EDE for 45 patients, with a success rate of 88.2%. The area of the ablation region in EDE images was 13.3 ± 5.0 cm^2, when compared to 7.7 ± 3.2 cm^2 with B mode images. Contrast and contrast to noise ratios obtained with EDE was on the order of 236% and 102%, respectively, significantly higher than values measured in B mode images ($p < 0.001$). This study showed that the thermally ablated regions were delineated more completely in EDE strain images with enhanced detectability. Potential application of EDE for real-time monitoring of the MWA procedure may improve the treatment outcomes.

P1-C6-8

2D Transient Elastography System Adapted to Shear Wave Speed Dispersion Measurement in Placenta: Ex Vivo Comparison between Normal Pregnancies and Placental Insufficiencies

Emmanuel Simon[1,2], **Jean-Pierre Remenieras**[1], Germain Marcheteau[1], Frédéric Patat[1,3], Franck Perrotin[1,2], Samuel Callé[1,4]; [1]*François Rabelais University, INSERM, Imaging and brain UMR U930, Tours, France,* [2]*Obstetrics, gynecology and fetal medicine, University Hospital Center of Tours, Tours, France,* [3]*CIC-IT, CIC 1415 INSERM, University Hospital Center of Tours, France,* [4]*GREMAN, UMR CNRS 7347, University of Tours, France*

Background, Motivation and Objective

Intrauterine growth retardation (IUGR), and preeclampsia (PE) are major public health challenges. In these situations, significant changes in the villous tree structure probably affect placental elasticity, and their detection could improve diagnostic accuracy and prognosis assessment. To date, no clinical device provides information about placental elasticity or architecture.

Statement of Contribution/Methods

We developed a 2D Transient Elastography (TE) system, dedicated to the placenta and adapted for in vivo measurements, based on the coupling of a shear wave generated by 2 vibrating rods and ultrasound (US) images acquired at an ultrafast rate. Two electrodynamical exciters, decoupled from the US linear probe (128 elements centered at 2.8 MHz), generated the vibration of the rods. For the purpose of measuring shear wave velocity, beamformed demodulated IQ data were acquired with an ultrafast US scanner (Aixplorer): acquisition at 2.8MHz during 128ms with a PRF of 4kHz. The particle velocity was computed using extended autocorrelation method. Calculating the spatial FFTs of Vz(x,ω), the shear wave speed dispersion curve Cs(ω) was obtained between 20 Hz and 80 Hz. The experimental data obtained from TE were fitted with the Voigt model and a fractional rheological model in which the frequency behavior was modeled as a power law (G*(iω)=Ge+K.[iω]n). The exponent parameter n represents a mechanical property inherent to a given material. The method has been applied on delivered placentas, in 20 normal pregnancies, 8 IUGR, and 3 PE (<12h after delivery). Measurements (3 times with repositioning, 2 operators) have been performed on 2 regions, central and peripheral, and compared with Supersonic Shear Imaging measurements.

Results/Discussion

The mean Cs was significantly lower in case of IUGR (1.04m/s +/-SD 0.05) than in control group (1.78m/s +/-0.50, P =2.52x10-6) or in PE cases (1.19m/s +/-0.16). In addition, the mean exponent n value was lower in case of IUGR (0.99+/-0.23) compared to control group (1.27+/-0.11) or PE cases (1.24+/-0.27). We found no difference between central and peripheral regions. Intra and interobserver reproducibility were good for Cs and n values. The frequency analysis could improve the ability of TE to distinguish IUGR cases and normal pregnancies or PE cases. Further work is required to test this hypothesis in vivo.

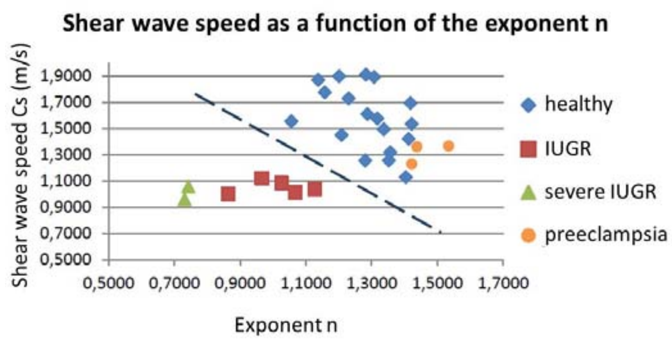

P1-C6-9

Biological Factors Affecting Shear Wave Speed Measurements in the Rhesus Macaque Non-Pregnant Cervix

Ivan M. Rosado-Mendez[1], Lindsey C. Drehfal[1], Andrew P. Santoso[1], Quinton W. Guerrero[1], Mark L. Palmeri[2], Helen Feltovich[1,3], Timothy J. Hall[1]; [1]*Department of Medical Physics, University of Wisconsin-Madison, Madison, WI, USA,* [2]*Biomedical Engineering, Duke University, Durham, NC, USA,* [3]*Maternal Fetal Medicine, Intermountain Healthcare, Provo, UT, USA*

Background, Motivation and Objective

We are studying shear wave speed (SWS) as a biomarker to detect abnormal cervical softening that could lead to spontaneous preterm birth. Elucidating factors affecting the stiffness of the *in vivo* non-pregnant (NP) cervix is the first step to understand the pregnant cervix. Animal models with anatomy and physiology akin to humans, such as the Rhesus macaque, can help achieve this task. Here we investigate biological and experimental factors affecting SWS estimates in the *in vivo* Rhesus macaque NP cervix.

Statement of Contribution/Methods

Ten female primates (5 nulliparous, 5 multiparous) from the Wisconsin National Primate Research Center were scanned transabdominally every week during two sequential ~26-day long menstrual cycles. Shear waves were induced with an Acoustic Radiation Force Impulse technique with a linear array transducer on a Siemens Acuson S2000 scanner (Siemens Healthcare, Mountain View, CA, USA). Two shear waves (one propagating from uterus to vagina (UTV) and one from vagina to uterus (VTU)) were independently tracked within a 6×5mm^2 region of interest placed at the proximal anterior and posterior sides of the cervix. SWS was estimated with a random sample consensus algorithm. Linear mixed effects (LME) models were used to model SWS as a function of menstrual cycle day (day 0 approx. at the beginning of the secretory phase of the uterine cycle), parity (nulliparous/multiparous), cervix side (anterior/posterior) (fixed effects) and subject (random effects) with a $p < 0.05$ (two-sided) criterion for statistical significance.

Results/Discussion

The LME model intercept was 2.98[Standard error=1.09]m/s, corresponding to the average speed of a UTV shear wave in the anterior side of the NP cervix at day 0. This value significantly increased in the posterior side by 1.14[0.51]m/s (p=0.025). SWS increased during the menstrual cycle at a rate of 0.08[0.04]m/s per day (p=0.055). Parity and shear wave direction were not significant. These results point at the importance of accounting for temporal and spatial changes in the NP cervix *in vivo*. We are currently studying the influence of other effects such as the tilt and depth of the cervix with respect to the transducer and the presence of a partially or totally full bladder.

Acknowledgements: We thank Michele Schotzko and Sarah Kohn for animal handling and scanning, and to Siemens Ultrasound for technical support. Research supported by National Institutes of Health Grants T32CA009206 from the National Cancer Institute and R21HD061896, R21HD063031, and R01HD072077 from the Eunice Kennedy Shriver National Institute of Child Health and Human Development. The content is solely the responsibility of the authors and does not necessarily represent the social views of the National Institutes of Health.

P1-C6-10

Ultrasound Elastography in Assessment of Post-Stroke Spasticity of the Biceps Brachii Muscle

Jing Gao[1], Michael O'Dell[2], Johnson Chen[1], Pai-Chi Li[3]; [1]*Radiology, Weilll Cornell Medicine, New York, New York, USA,* [2]*Rehabilitation Medicine, Weilll Cornell Medicine, New York, New York, USA,* [3]*Electrical Engineering, Taiwan National University, Taipei, Taiwan*

Background, Motivation and Objective

Approximately 15 million people experience a stroke each year worldwide and two-thirds of these individuals require rehabilitation. Post-stroke spasticity is one of the common consequences characterized by excessive muscle tone resulting in an increase of muscle stiffness. To date, the assessment of spasticity is still a lack of gold standards. We prospectively evaluated the feasibility of ultrasound strain imaging (USI) to assess biceps brachii muscle (BBM) stiffness and dynamic motion in subjects with post-stroke spasticity.

Statement of Contribution/Methods

USI of BBM was performed in 4 healthy adults and 2 subjects with post-stroke spasticity. The BBM axial deformation was produced by external compression with a sandbag (1.0 kg) tied onto the transducer. The BBM lateral movement was produced by manual passive elbow flexion and extension. Using 2-D speckle tracking, captured 5-second real time ultrasound data of BBM axial deformation and lateral movement were processed to estimate USI parameters including axial strain representing muscle stiffness, and lateral strain and tissue velocity representing muscle dynamic motion. Unpaired t test was used to analyze the difference in USI parameters between healthy and spastic BBM. A paired t test was applied to test the difference in USI parameters before and after Botulinum Toxin (BoNT) injection treatment for spasticity.

Results/Discussion

There was no significant difference in peak axial strain, lateral strain, and tissue velocity between the left and right BBM (all $p > 0.05$). The difference in USI parameters was significant between healthy and spastic BBM, and between affected and non-affected BBM in individuals with stroke (all $p < 0.05$). Significant differences in all USI parameters were also found before and after BoNT injection (all $p < 0.05$). Good inter- and intra-observer reliability in performing USI of the BBM were observed (all ICC > 0.75). Our results suggest that USI is potentially feasible for determining the spasticity and assessing the treatment effect of BoNT injection in post-stroke spasticity rehabilitation. More data continue to be collected as part of our on-going study.

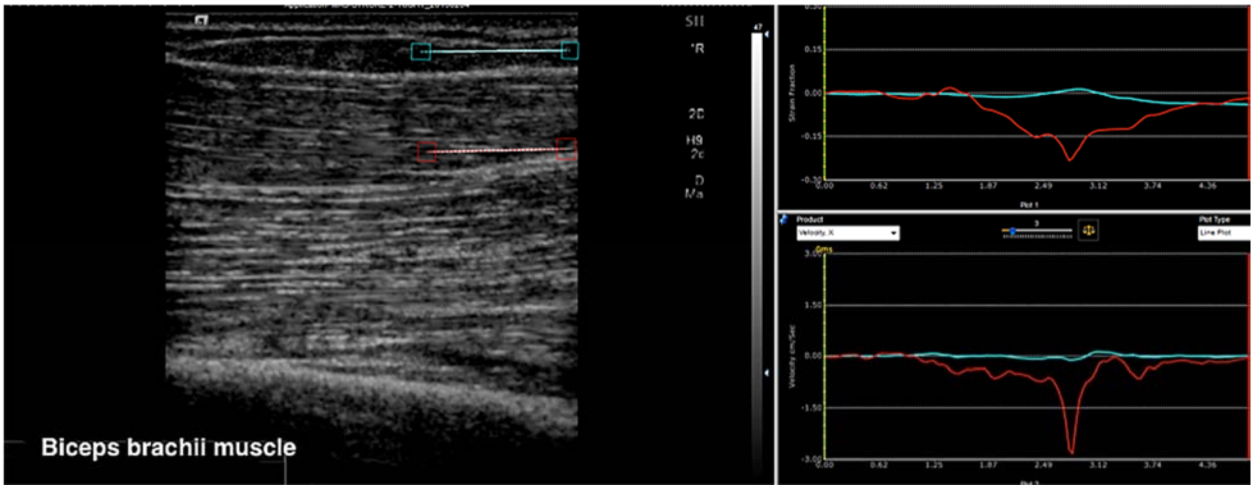

P1-C6-11

Assessment of Anisotropy Using Viscoelastic Response (VisR) Ultrasound in the Biceps Brachii of Healthy Older Adults and Stroke Patients

Leela Goel[1], Christopher Moore[2], Jason Franz[1], Xiaogang Hu[1], Caterina Gallippi[1]; [1]*Joint Department of Biomedical Engineering, UNC at Chapel Hill and NC State, The University of North Carolina at Chapel Hill, Chapel Hill, NC, USA,* [2]*Department of Electrical and Computer Engineering, North Carolina State University, Raleigh, NC, USA*

Background, Motivation and Objective

While skeletal muscle is often assumed to be structurally transversely isotropic, its mechanical anisotropy is not well characterized *in vivo*. Such *in vivo* characterization can be achieved using VisR ultrasound, a technique that provides information about the viscoelastic mechanical response of tissue. Specifically, VisR-derived Relative Elasticity (RE) provides directionally dependent information about the shear modulus of materials. *We hypothesize VisR RE can be used in healthy older adults and in stroke patients to 1) assess the degree of anisotropy (DoA) of the biceps brachii (BB) and 2) characterize the effect of passive loading on the BB.*

Statement of Contribution/Methods

VisR imaging was performed in the BB long head of 2 healthy controls (1M 68y; 1F 75y) and 1 stroke patient (1F ~70y) with neuromuscular impairment in one arm. The subjects' arms were imaged in full extension and approximately 90° flexion at rest. Data were acquired in the transverse and longitudinal imaging planes at the medial location of the BB, and measured displacements were fit to the 1D mass-spring-damper model to estimate RE. The ratio of RE obtained in the longitudinal to the transverse muscle views was found to reflect the DoA in shear modulus, where DoA = 1 indicates perfect isotropy. Changes in RE values and ratios without (flexion) vs with (extension) passive loading were examined.

Results/Discussion

See Table 1. In control subjects, RE values for flexion and extension in the transverse imaging plane (previously shown to reflect the longitudinal shear modulus, μ_L) are higher than the RE values in the longitudinal imaging plane (which primarily reflect the transverse shear modulus, μ_T), and DoA indicates more anisotropy in extension than flexion. In the stroke patient's unaffected BB, RE-assessed μ_L is lower than μ_T with flexion, but the same as μ_T with extension. DoA indicates the unaffected BB becomes less anisotropic in extension than flexion. In the stroke patient's affected BB, RE-derived μ_L is higher than μ_T with flexion, but lower with extension. DoA indicates the affected BB becomes less anisotropic with extension. Panels a-h show representative RE images. The results suggest that VisR can be used to assess DoA in skeletal muscle of older adults and to examine the effects of passive loading on mechanical properties *in vivo*, which may be clinically relevant to studying impairment post stroke.

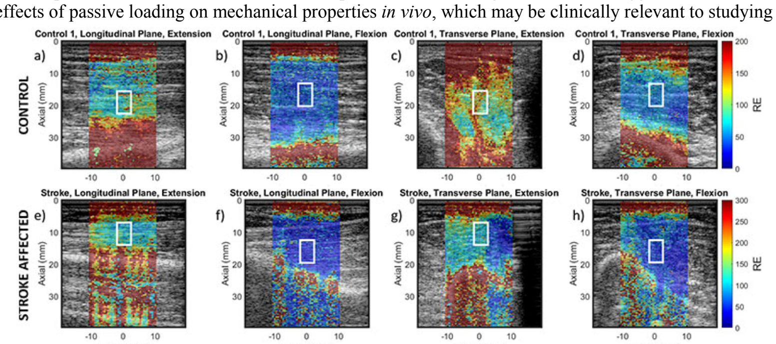

Subject	RE Longitudinal Shear Modulus (μ_L)		RE Transverse Shear Modulus (μ_T)		Degree of Anisotropy (μ_T / μ_L)	
	Flexion	Extension	Flexion	Extension	Flexion	Extension
Control 1	54.15±4.79	118.93 ±14.39	39.62±5.38	80.93±15.19	0.75±0.11	0.68±0.17
Control 2	42.09±4.45	84.78 ±19.69	33.07±4.84	62.63±7.05	0.82±0.17	0.72±0.16
Stroke 1 (Unaffected Side)	52.86±7.61	96.04 ±22.43	63.23±17.03	96.81±40.21	1.15±0.38	1.07±0.24
Stroke 1 (Affected Side)	50.41±3.27	107.16 ±9.38	37.54±3.44	117.73±44.12	0.75±0.13	1.12±0.36

Panels a-h) Parametric relative elasticity (RE) images in the biceps brachii (BB) of a healthy control subject (top row) and in the BB of a stroke patient with neuromuscular impairment (bottom row) with arm flexion and extension in transverse and longitudinal imaging planes. **Table 1)** Summary of relative elasticity (RE) measures reflecting the longitudinal shear modulus, transverse shear modulus, and degree of anisotropy (DoA) in the two control subjects and the affected and unaffected arms of the stroke patient.

P1-C6-12

Combination of Acoustic Radiation Force Impulse Technique and Optical Coherence Tomography to Measure Elastic Properties of the Crystalline Lens as a Function of Intraocular Pressure

Chen Wu[1], Chih-Hao Liu[1], Zhaolong Han[1], Manmohan Singh[1], Kirill Larin[1,2], **Salavat Aglyamov[3]**; [1]*Biomedical Engineering, University of Houston, Houston, Texas, USA,* [2]*Molecular Physiology and Biophysics, Baylor College of Medicine, Houston, Texas, USA,* [3]*Biomedical Engineering, University of Texas at Austin, Austin, Texas, USA*

Background, Motivation and Objective

Elastic properties of the ocular tissues are significantly affected by intraocular pressure (IOP) in the eye. For example, the speed of the elastic wave in the cornea dramatically increases with IOP. In our previous studies using ultrasound shear wave imaging we demonstrated that, for the lens, the increase in IOP does not result significant changes in the wave velocity. Compared with ultrasound imaging, optical coherence tomography (OCT) provides advantage in both spatial resolution and signal-to-noise ratio. Previously, we developed a combined acoustic radiation force impulse (ARFI) and OCT approach where the acoustic radiation force is applied to the anterior surface of the crystalline lens, while displacement of the lens surface is measured using phase-sensitive optical coherence tomography (OCT) system. In this study, we utilized a combine ARFI/OCT system to investigate the influence of IOP on the biomechanical properties of porcine crystalline lenses ex vivo.

Statement of Contribution/Methods

A 3.5 MHz single element transducer was used to remotely disturb the anterior surface of the porcine lenses through the cornea and the aqueous humor. In the phase-sensitive OCT system, a superluminescent laser diode was utilized as the light source with a central wavelength of 840 nm and bandwidth of 49nm. The A-line acquisition rate of this system was 25 kHz. Acoustic radiation force excitation and OCT recording were synchronized by a computer-generated TTL signal. Ultrasound transducer and OCT system were co-focused, and the measurements of the displacement were performed at the focal point. Four porcine eyes were used in the experiments. The measurements were repeated at IOPs increasing from 5 to 30 mmHg at increments of 5 mmHg, and then decreased from 30 to 5 mmHg with the same increments to investigate the elastic hysteresis.

Results/Discussion

The ultrasound-induced displacements were analyzed, and the results show that the amplitude of displacement decreases, while the relaxation rates and natural frequency of vibrations increase when the IOP was elevated (see Fig. 1). Therefore, and stiffness of the lenses grows with IOP. In addition, hysteresis phenomenon was observed in all lenses, such that displacement at 5 mmHg in the beginning of IOP increase higher than at the end of the cycle.

This study was supported by National Institute of Health grants EY022362.

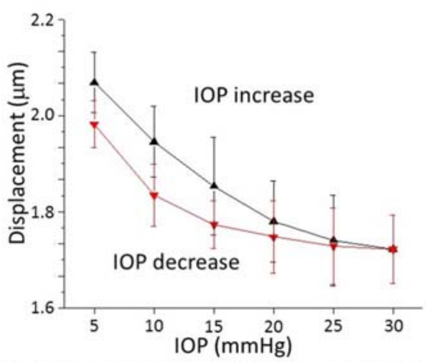

Fig. 1 Hysteresis in the crystalline lens during IOP change.

P1-C6-13

High Frame-Rate Imaging and Adaptive Tracking of Shear Shock Wave Formation in the Brain: A Fullwave and Experimental Study

David Espindola[1], **Gianmarco Pinton[1]**; [1]*Joint Department of Biomedical Engineering, University of North Carolina at Chapel Hill and North Carolina State University, USA*

Background, Motivation and Objective

Nonlinear shear waves have a cubic nonlinearity which generates a unique odd harmonic signature. This behavior was first observed in a homogeneous gelatin phantom with ultrafast plane wave compounding ultrasound imaging and correlation-based tracking algorithm that determines particle motion. However, in heterogeneous tissue, like brain, clutter degrades motion tracking and destroys the weak odd harmonics that are distinctive of shear shock waves. We show that under these imaging conditions, conventional plane wave compounding is not sufficient to detect sharp motion from a shear shock wave. We present a high frame-rate ultrasound imaging sequence consisting of multiple focused emissions that improves the image quality. This imaging sequence reduces the clutter artefacts generated by an *ex-vivo* porcine brain allowing us to track the internal and discontinuous movement.

Statement of Contribution/Methods

The proposed imaging sequence (B) is compared experimentally to conventional plane wave compounding (A). Then the adaptive tracking algorithm was optimized to determine the specific odd harmonic signature generated by the cubic nonlinearity of shear shock waves. This optimization was determined with a numerical description of shear shock waves using a Rusanov-Fourier scheme, that supports nonlinearity and an arbitrary frequency dependent attenuation law with third order accuracy. Fullwave simulations were used to generate ultrasound images of shear shock waves propagating through a medium displaced according to the Rusanov-Fourier predictions.

Results/Discussion

We demonstrate that the point spread function of the proposed imaging sequence reduces the side lobes by 19dB compared to plane wave compounding. Experimentally, we show that our sequence increases our ability to track the harmonics signature significantly (C,D). Optimal values of the tracking parameters (median filter size, kernel length, interpolation factor) are presented. The performance of the adaptive tracking algorithm is compared to the Cramer Rao Lower Bound in terms of bias, jitter, and false peak errors under different imaging scenarios. The overall improvements are even more significant in a high noise imaging environment. Our optimized adaptive tracking algorithm produces displacements that are in agreement with theoretical predictions of the odd harmonic development.

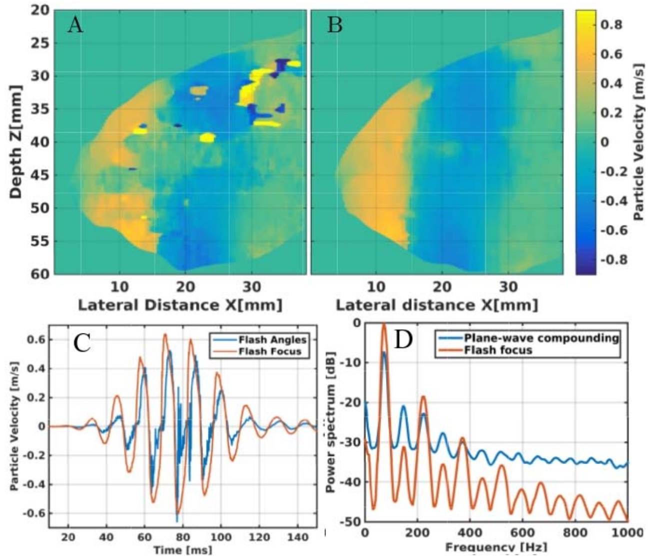

P1-C6-14

Tracing the Shear Modulus Oo Blood Plasma during Clotting and based on Acoustic Radiation Force Induced Vibration of an Embedded Sphere

José Francisco Costa Júnior[1], Guilherme Crossetti Parcero[1], **João Carlos Machado[1,2]**; *[1]Biomedical Engineering Program, Federal University of Rio de Janeiro, Rio de Janeiro, Brazil, [2]Post-Graduation Program in Surgical Sciences, Federal University of Rio de Janeiro, Rio de Janeiro, Brazil*

Background, Motivation and Objective

Blood clotting, a process to avoid bleeding, involves vasoconstriction, platelet plug build-up, coagulation, clot retraction and fibrinolysis. During coagulation, blood changes from liquid to gel, and the clot viscoelastic properties continue modifying until fibrinolysis. Tests to analyze bleeding disorders and anticoagulant therapy include clot-based assays, to detect the end-point of fibrin network in a plasma sample, and viscoelastic methods to trace the kinetics of whole blood coagulation. Ultrasound (US) methods are reported to measure clotting times, similar to clot-based assay findings, and shear modulus, μ, and viscosity, η, of the formed clot. This work objective was to measure μ during plasma clotting, based on the vibration signature induced by impulsive acoustic radiation force (iARF) on an embedded sphere.

Statement of Contribution/Methods

An US method was implemented to trace the time-changing μ of a plasma sample along its clotting process induced based on the aPTT (activated partial thromboplastin time) assay. A push system transmitted bursts of US pulses (2.09 MHz, 500 cycles and 1.25 Hz of PRF-pulse repetition frequency) to generate an iARF on a glass sphere (4.0 mm in diameter and density of 2500 kg•m^{-3}) immersed in a cuvette filled with the components of the aPTT test. The sphere displacement, induced by iARF, was monitored by a 5.0 MHz pulse-echo probing system with a 5.0 kHz PRF. Spherically focused transducers of push and probing systems, immersed with the cuvette in a water tank at 37 °C, were aligned confocal on the sphere inside 250 μL of Actin® FSL in the cuvette. Thereafter, 250 μL of reconstituted lyophilized control plasma was added to the cuvette and one minute later 250 μL of $CaCl_2$ was pipetted to the mixture, initiating the coagulation process synchronized with the operation of push and probe systems. The rf-echo signals from the sphere were sampled, at 50.0 MHz, and their relative delays were determined to yield a sequence of signals representing the sphere damped oscillations along the iARF sequence. Each damped-signal in the sequence was fitted, based on the least square error criterion, with a theoretical-model displacement function whose unknowns are the iARF amplitude and the medium μ and η. The method was repeated five times and the time-changing mean μ was determined along 2100 s of the clotting process.

Results/Discussion

During the first 15 s of plasma clotting, the estimated μ remained stable at 20 Pa and then varied rapidly until 60 s, at a rate of 2.2 Pa•s^{-1}. Between 60 and 800 s, μ varied slowly at a rate of 0.21 Pa•s^{-1}. From 800 to 2100 s the value of μ remained stable at about 300 Pa. The interval of fast changing μ corresponds to the fibrin formation period and comprehends the clotting time of 25 s typically obtained with the aPTT assay for control plasma. The results indicate that μ continued increasing after 60 s and reached a value 2.5 times higher than the value of μ corresponding to the clotting end-point of the aPTT assay.

P1-C6-15

Quantitative Assessment of Scleroderma Using Ultrasound Surface Wave Elastography

Xiaoming Zhang[1], Boran Zhou[1], Sanjay Kalra[2], Brian Bartholmai[1], James Greenleaf[3], Thomas Osborn[4]; *[1]Radiology, Mayo Clinic, Rochester, Minnesota, USA, [2]Pulmonary and Critical Care Medicine, Mayo Clinic, Rochester, Minnesota, USA, [3]Physiology and Biomedical Engineering, Mayo Clinic, Rochester, Minnesota, USA, [4]Rheumatology, Mayo Clinic, Rochester, Minnesota, USA*

Background, Motivation and Objective

Skin stiffening is an early biomarker of many systemic sclerosis or fibrosis diseases. The Modified Rodnan Skin Score (MRSS) is considered the gold standard measurement in the majority of clinical studies of scleroderma or systemic sclerosis (SSc). However, the MRSS is a subjective palpation method. We have developed a noninvasive ultrasound surface wave elastography (USWE) technique for measuring skin elastic properties. The purpose of this abstract is to demonstrate the clinical use of USWE for assessing patients with SSc.

Statement of Contribution/Methods

In USWE, a low intensity 0.1 second harmonic vibration is generated on the skin of a subject using a handheld vibrator. The subject's skin is tested on the forearm and upper arm bilaterally while in a seated position. An ultrasound probe is aligned with the indenter of the vibrator to measure the generated surface wave propagation on the skin. The Verasonics ultrasound system with an ultrasound probe of L11-4 with a central frequency of 6.4 MHz is used. The surface wave speed of skin is measured at 100 Hz, 150 Hz, and 200 Hz. Three measurements are made at each location and each frequency.

Results/Discussion

In a large prospective clinical study to measure skin changes in diseases such as SSc or in subjects with interstitial lung disease, we measured USWE properties of skin on patients with disease and healthy control subjects. Significant differences in wave speed between healthy subjects and SSc patients were found. For example, the surface wave speed of the skin is 1.83 ± 0.04 m/s at 100 Hz, 2.33 ± 0.25 m/s at 150 Hz, and 3.04 ± 0.37 m/s at 200 Hz for a healthy subject, and the surface wave speed of the skin is 2.82 ± 0.31 m/s at 100 Hz, 3.60 ± 0.38 m/s at 150 Hz, and 5.36 ± 0.55 m/s at 200 Hz for an age matched SSc patient in the same location.

USWE is a noninvasive technique for generating and measuring surface wave propagation on the skin. USWE can provide objective measurement of skin elastic properties in various regions of the body which may be useful for assessing the presence, status and potentially the progression of disease.

P1-C6-16

High Speed Clinical Strain Measurements

Martin Andersen[1], Cooper Moore[2], Kristine Ages[3], Melissa Lefevre[3], Samuel Schmidt[1], Joseph Kisslo[3], Olaf T. von Ramm[2]; [1]*Health Science and Technology, Aalborg University, Aalborg Øst, Denmark,* [2]*Duke University, Durham, NC, USA,* [3]*Duke University Hospital, Durham, NC, USA*

Background, Motivation and Objective

High speed ultrasound imaging is a new imaging method particularly applicable to cardiology. At Duke we have developed a real time high speed imaging system capable of producing up to 2500 images per second while maintaining the live imaging feature so essential in clinical scanning. For high speed 2D the Duke system, T5, uses 96 transmitters and 96 receivers at 32:1 parallel processing in conjunction with a 96 element 3.5 MHz linear array measuring 21 by 14 mm. Images are displayed at 60 images per second and up to 20 seconds of high speed data can be stored to permit immediate slow motion playback.

Statement of Contribution/Methods

The first clinical application designed for high speed data has been developed to derive contractile strain curves from patients and compare these to strain curves derived from commercial (GE and Phillips) scanners. Custom software has been developed at Aalborg and Duke University to estimate myocardial motion and strain in high speed ultrasound images. The software uses features derived from speckle. A three-stage process is used to calculate the motion of the myocardial wall, by extracting features, tracking individual features and calculating the weighted average motion of the myocardial wall areas, which in turn can be used to calculate strain.

Results/Discussion

To date upwards of 60 patients have been studied where timing sequences of wall contraction have been identified. Onset of contraction, contraction velocities, peak contraction and relaxation rate can be computed with 1 – 2 ms temporal resolution. Figure 1 illustrate strain rate from a subject with normal cardiac function derived from high speed ultrasound images recorded at 365 images per second. High speed velocity, strain and strain rate show temporal information not easily resolved using conventional ultrasound systems. Results indicate that this technique may become an important new tool in defining cardiac function in the clinic.

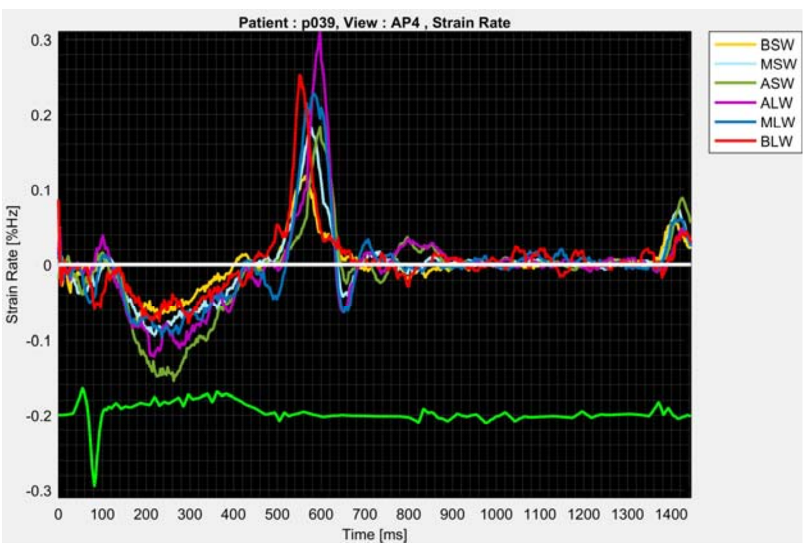

P1-C6-17

Frequency Response of Soft Tissue Displacements Induced by the Force on Magnetic Nanoparticles

Thomas Ersepke[1], Tim C. Kranemann[1], Georg Schmitz[1]; [1]*Chair for Medical Enginnering, Ruhr-University Bochum, Germany*

Background, Motivation and Objective

In Magnetomotive Ultrasound (MMUS), tissue embedded magnetic nanoparticles (MNP) are mechanically excited by a magnetic field. Relatively small forces on the MNP result in small tissue displacements and a low SNR, when US-based displacement tracking is performed. From the application of elastography techniques it is known that the axial displacement of soft tissues shows a resonant behavior depending on the excitation frequency. Therefore, capturing the tissue's frequency response which is related to the corresponding stiffness, might allow to identify and apply appropriate MMUS excitation frequencies in order to increase displacement amplitudes and SNR. However, MMUS studies commonly utilize solenoid/yoke setups with excitation frequencies limited up to a few Hz.

In this work, we present an MMUS setup which allows to measure the entire frequency range, relevant in elastography, by separating the gradient field from the excitation field. We further demonstrate the gain in displacement amplitudes when excitation at the resonance frequency is performed.

Statement of Contribution/Methods

A cylindrical inclusion (Ø 4mm x 4mm) containing 90 % nanoparticle solution (Resovist, Bayer Schering Pharma) and 10 % gelatin by weight is embedded in phantoms of different gelatin concentrations (10 %, 15 % w/w). A static, magnetic field is generated by two permanent magnets arranged opposite each other, producing a constant gradient of 3.4 T/m along the displacement direction. A solenoid produces a superimposed, sinusoidal excitation field of 18 mT at frequencies between 50-1000 Hz. The velocity of the inclusion is tracked at its surface due to reflections at a thin slice of glass powder by a laser vibrometer (OFV 303/3001, Polytec, Germany).

Results/Discussion

The velocity responses (Fig. 1) of the phantom measurements show resonance frequencies of 310 Hz and 500 Hz for the soft (10 %) and the stiff (15 %) phantom. By using these frequencies for excitation, the resulting displacement amplitudes can be increased by 20 dB compared to commonly used MMUS excitation at or below 50 Hz. The proposed setup is capable of tracking the mechanical tissue dynamics precisely within the relevant frequency range. Additionally, a viscoelastic model could be applied for characterization of absolute viscoelastic parameters.

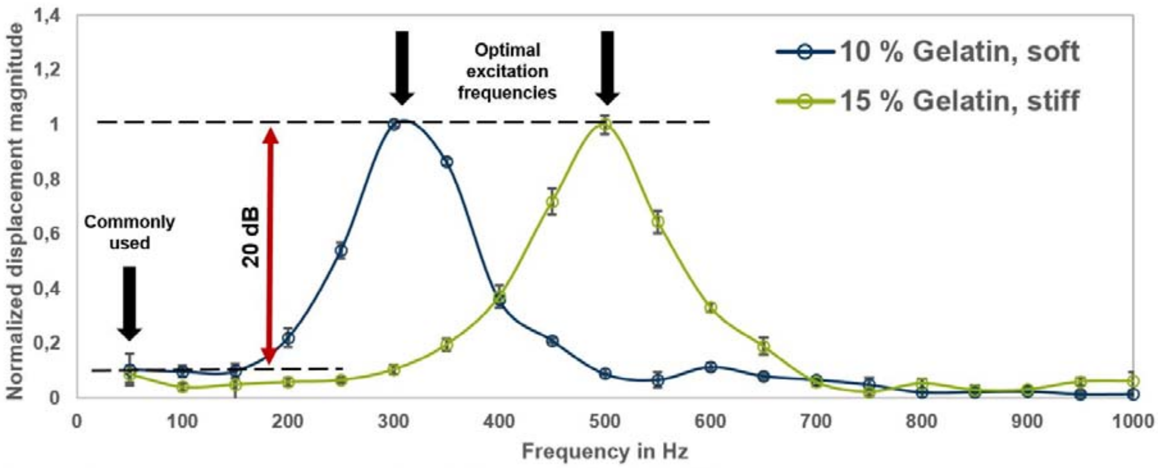

Fig. 1: Measured frequency responses for the soft (10% gelatine) and stiff (15% gelatine) phantom. Excitation at the distinct resonance frequencies yields a 20 dB higher displacement compared to commonly used frequencies.

P1-C7 - MIM: Image Reconstruction

Exhibit Hall

Saturday, September 9, 2017, 9:30 am - 4:00 pm

Chair: **Marko Jakovljevic**
Stanford University

P1-C7-1

Virtual Source Synthetic Aperture Focusing and Coherence Factor Weighting for Intravascular Ultrasound (IVUS)

Mingyue Yu[1,2], Teng Ma[1,2], Yang Li[1], K. Kirk Shung[1], Qifa Zhou[1,2]; [1]*Department of Biomedical Engineering, University of Southern California, Los Angeles, California, USA,* [2]*USC Roski Eye Institute, University of Southern California, Los Angeles, California, USA*

Background, Motivation and Objective

Intravascular ultrasound (IVUS) has frequently been used by the cardiologist to diagnose atherosclerosis and guide the interventional procedures. IVUS has gained widely clinical acceptance over the past twenty years because of its superior capability to assess plaque burden and monitor artery remodeling, which also makes it as the irreplaceable image modality for most innovative multimodality intravascular imaging techniques. However, in current IVUS image, the lateral resolution and contrast-to-noise ratio (CNR) are dramatically downgraded along with the axial direction due to beam divergence of single element transducer, which hinders it from imaging the deeper region of artery wall explicitly. In this study, we report on the application of an ultrasound beamforming method that combines virtual source synthetic aperture (VSSA) focusing and coherence factor weighting (CFW) to improve the IVUS image quality over the entire field of view (FOV).

Statement of Contribution/Methods

Mono-static VSSA focusing technique was implemented to improve the resolution beyond the focal region by summing the RF signals from adjacent emissions with focusing delay relative to the virtual source (natural focal point). However, the aperture synthesis brings in high sidelobes. To suppress the sidelobes and further improve the focusing quality, CFW based on the signal coherence of delayed RF signals was applied to the synthesized beam. Wire phantom and agar-based anechoic cyst phantom were imaged to quantitatively demonstrate the improvement in lateral resolution and CNR. Ex vivo imaging of cadaver human coronary arteries was also performed to evaluate the overall performance of the proposed method.

Results/Discussion

The proposed method improves -6dB lateral resolution by up to 40% (Fig. 1(a)), and enhances CNR by up to 1.5 (Fig. 1(b)). Superior contrast resolution can be observed through the more distinct boundary of the cyst area in Fig. 1(d). As a result of the improvement in both image resolution and contrast, the media layer and the thickened layer of the atherosclerotic artery were better differentiated, as indicated by the red arrowheads in Fig. (f). These preliminary results demonstrate that VSSA-CFW method holds the promising potential to be integrated into the current IVUS imaging system for enhanced clinical diagnosis.

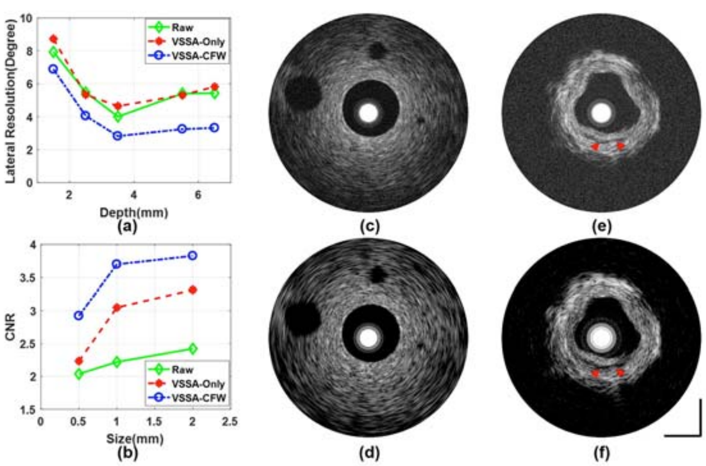

Fig. 1: (a): Lateral resolution of wire target imaging result in degree. (b): CNR results of anechoic cyst phantom of different sizes. (c),(d) are the raw and VSSA-CFW processed image of cyst phantom, respectively. (e), (f) is the raw and VSSA-CFW processed image of human artery, respectively. Dynamic Range: 50dB. Scale bar: 2mm.

P1-C7-2

New Model of Echo-Phase Relating to Speed-of-Sound for Quantitative Reflection-Mode Ultrasound Tomography

Michael Jaeger[1], Martin Frenz[1]; [1]*Institute of Applied Physics, University of Bern, Switzerland*

Background, Motivation and Objective

Computed ultrasound (US) tomography in echo-mode (CUTE) allows sonographic imaging of speed-of-sound (SoS) using handheld probes, based on measuring – in a spatially resolved way – the phase shift of echoes when changing the US transmission (Tx) angle. The phase shift relates to the error of time-of-flight (TOF) of the Tx pulse when propagating through a non-anticipated distribution of SoS. Quantitative imaging was demonstrated in layered phantoms mimicking the abdominal wall, with promise for diagnosis of e.g. fatty liver disease. Recent studies, however, have shown inconsistencies of the so-far assumed relation between TOF error and echo phase when comparing results between layered and laterally confined contrast regions. The goal of the present study was to develop a model that would solve these inconsistencies.

Statement of Contribution/Methods

The TOF error leads to a deviation of the reconstructed echo position from the true position. The new model takes into account that this deviation also depends on the TX angle. Even if the TOF error is constant across Tx angles, this leads to an echo phase shift that depends on the TOF error itself, whereas the old model assumed a dependence on only relative changes of TOF error. The new model was verified in phantoms with varying geometry, and its implications on SoS reconstruction were investigated.

Results/Discussion

Phantom results demonstrate that the new model predicts the echo phase shift for a layered structure (a) and a cylindrical inclusion (b) in a consistent way: Grey lines show the measured shift as function of depth (a) and lateral position (b), whereas black lines are the model predictions. Dotted lines represent the old model. As a result of the direct dependence of phase shift on TOF error, the new model allows a quantitative SoS reconstruction that is robust against ultrasound refraction: In digital phantoms of the abdominal layers, the fat behind the abdominal muscle acts as a lens that leads to distortion of the SoS inside the liver when using the old model (c). The new model allows an accurate reconstruction of liver SoS as well as of the anatomical distribution in general. The proposed model is thus an imperative requirement for further development of CUTE towards successful clinical application.

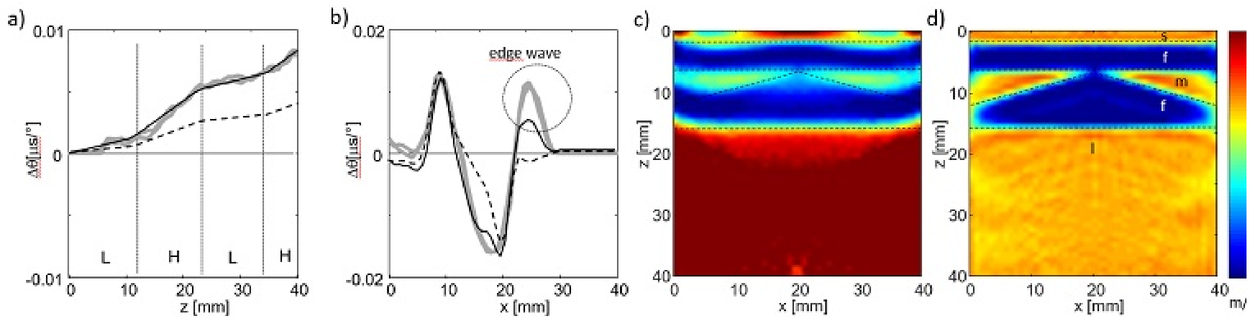

a) Phase shift per angle step at -15° Tx angle for layered phantom, axial profiles. L: 1520 m/s, H: 1560 m/s, *a priori* SoS for pulse-echo reconstruction: 1500 m/s.
b) Phase shift per angle step at -15° Tx angle for cylindrical inclusion, lateral profiles at 30 mm depth. Inclusion: 40 m/s contrast, 10 mm Ø at 15 mm depth. *A priori* = background SoS: 1 The discrepancy between the new model (solid black line) and the measurements (gray lines) is due to the edge wave from the limited probe aperture in the experiment.
c) and d): Reconstructed SoS of digital phantom of the abdomen, using old (c) and new (d) model. The anatomy is delineated by dashed lines. Assumed SoS values: Skin (s) 1590 m/s; fat (f) 1450 m/s; muscle (m) 1590 m/s; liver (l) 1590 m/s. A priori SoS: 1560 m/s.

P1-C7-3

A Wide Field-of-View Microvascular Imaging Using Diverging Transmit Beams in a Curved-Array Transducer

Dooyoung Go[1], Jinbum Kang[1], Yangmo Yoo[1,2]; [1]*Electronic engineering, Sogang university, Seoul, Korea, Republic of,* [2]*Biomedical engineering, Sogang university, Seoul, Korea, Republic of*

Background, Motivation and Objective

Ultrafast compound Doppler imaging enables high-sensitivity microvascular imaging using the large amount of spatial and temporal samples within a short acquisition time. In addition, the longer ensemble length from the ultrafast transmit strategy facilitates efficient clutter rejection filtering. However, the ultrafast microvascular imaging using plane-wave excitation, which is widely used in linear array transducer, may not be suitable for abdominal applications such as hepatic or kidney vessels due to limited field-of-view (FOV) and imaging depth. In this paper, we presents a wide FOV microvascular imaging method using diverging transmit beams in a curved array transducer.

Statement of Contribution/Methods

In the diverging-wave excitation in a curved array transducer, a virtual source for the transmit delay calculation can be located following the arc. In addition, the diverging beams in the curved array transducer allow the full transmit aperture regardless of the steering angles with the same scan angles of the beam. Therefore, unlike the plane-wave compounding in a curved array transducer, the diverging-wave compounding provides a wider fully overlapped region so that the increased SNR and the wide FOV imaging is enabled. To compare the performances of the ultrafast microvascular imaging based on the plane-wave and diverging-wave, a kidney from a healthy volunteer was scanned using an ultrasound research platform (Vantage, Verasonics Inc., Kirkland, WA, USA) with a C5-2 curved array transducer. For ultrafast Doppler imaging, 10 angles ($-18^{\circ}\sim+18^{\circ}$) and 250 ensemble (PRF=250Hz) were used in both methods.

Results/Discussion

In Figs. 1(a)-(b) show B-mode images with the relevant FOV (dotted lines) in accordance with the number of overlapped angles in both methods. As shown in Figs. 1(a)-(b), the diverging-wave image provides wider FOV and increased SNR due to increased fully overlapped region (e.g., yellow arrow). Also, the microvascular imaging using the diverging-waves shows wider FOV (e.g., yellow arrows) and higher signal-to-clutter ratio compared to the plane-wave (i.e., 11.9 vs. 9.9 dB) at the box region as shown in Figs. 1(c)-(d). These results indicate that the diverging-wave excitation is of great advantage of the ultrafast microvascular imaging in a curved-array transducer.

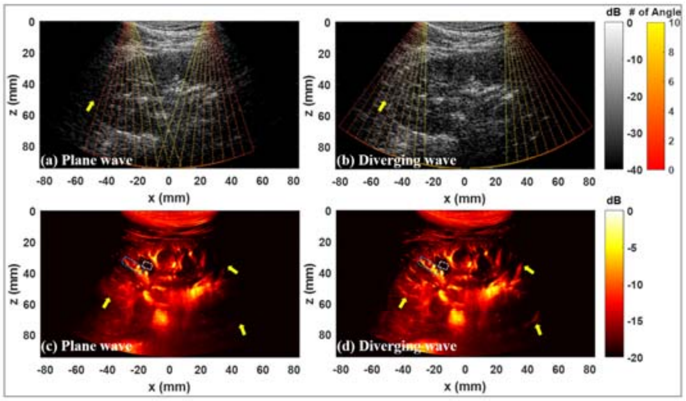

Fig. 1. B-mode images using (a) the plane-wave and (b) diverging-wave with the relevant FOV (dotted lines) in accordance with the number of overlapped angles. Ultrafast microvascular imaging using (a) the plane-wave and (d) diverging-wave in a curved array transducer.

P1-C7-4

Reduction of Transmitted 2nd Harmonics Using an Adaptive Method by Simulated Annealing

Thong Huynh[1], Geir Haugen[2], Lars Hoff[1]; [1]*University College of Southeast Norway, Vestfold, Norway,* [2]*GE Vingmed Ultrasound AS, Norway*

Background, Motivation and Objective

Tissue harmonic imaging is often the preferred ultrasound imaging modality due to its ability to improve image quality by suppressing reverberations [1]. The method relies on the 2nd harmonic of the transmit frequency being generated as the waves propagation in tissue. For such imaging the backscattered harmonics are weak, so for successful imaging the level of undesired transmitted 2nd harmonic must be about 30dB below the fundamental energy. Transmitted 2nd harmonic energy may be caused by both linear, e.g. sidebands in the transmit spectrum, and nonlinear effects in the transducer and transmitting electronics. This paper presents a method where the electrical excitation waveforms are optimized to suppress the 2nd harmonic components of the emitted ultrasound pulses.

Statement of Contribution/Methods

Transmitted pulses from an ultrasound scanner were measured in a water tank close to the transducer surface, using a calibrated Onda HGL0200 hydrophone. The measured pulses were stored on a computer, and their quality was scored by a cost-function designed to minimize 2nd harmonic contents while preserving a short pulse at the desired at center frequency of 1.7MHz. The result of this evaluation was fed into a simulated annealing algorithm, using it to alter the excitation pulse shape, and sending this to the scanner to reprogram the transmit stage. The scanner was connected to the measurement system with ethernet, so that the optimization procedure could run automatically in a loop. This method was applied to two different types of waveforms, where the first was a three-level pulse and the second was a multilevel pulse.

Results/Discussion

We found that the described method could find excitation waveforms that suppressed the transmitted 2nd harmonic level to 30dB below the main lobe for both types of transmit waveforms, by iteratively reducing transmitted 2nd harmonics from the ultrasound transducer. 20000 iterations were used to obtain this result. This is particularly relevant for probes or electronics where the behavior is not fully described by a linear impulse response. The optimization method can be adapted to meet other criteria than reduction 2nd harmonics, by defining a different cost function from the measured pulses. The authors would like to point out that the results presented are experimental and have no relation to the released scanner and its performance.

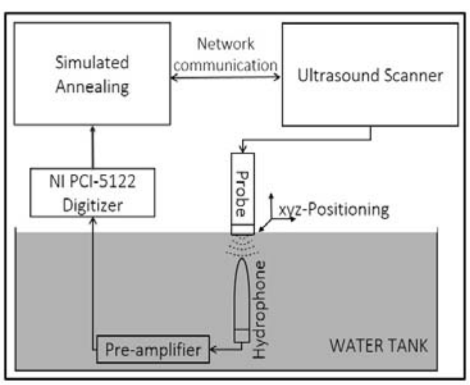

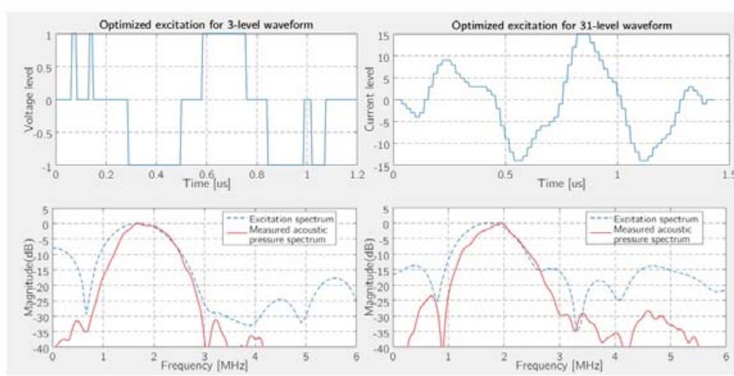

P1-C7-5

Simultaneous Pulse Wave and Flow Estimation at High-Framerate Using Plane Waves and Transverse Oscillations on a Carotid Phantom

Vincent Perrot[1], Lorena Petrusca[2], Adeline Bernard[1], Didier Vray[1], Hervé Liebgott[1]; [1]*CREATIS, Univ. Lyon, INSA‐Lyon, Univ. Lyon 1, UJM-Saint-Étienne, CNRS, Inserm, UMR 5220, U1206, Villeurbanne, France,* [2]*CREATIS, Univ. Lyon, INSA‐Lyon, Univ. Lyon 1, UJM-Saint-Étienne, CNRS, Inserm, UMR 5220, U1206, Saint-Étienne, France*

Background, Motivation and Objective

Pulse wave velocity and blood flow velocity are two different physiological parameters which are generally assessed using two different ultrasound sequences and processing techniques. This can be explained by the difference in term of signal intensity between the tissue and blood (approx. 40 dB). On one side, blood velocity can be estimated using

Doppler, speckle tracking or transverse oscillation techniques… On the other side the arterial wall motion can be obtained using block matching, differential methods or adapted transverse oscillations. In order to better evaluate and understand blood-wall interaction an imaging technique able to provide simultaneously both information from the same sequence would be highly relevant. Accordingly, our objective is to extract pulse wave velocity and flow all at once.

Statement of Contribution/Methods

In this study, we used a Verasonics ultrasound system with a linear array probe. A PVA carotid phantom filled with blood mimicking fluid was constructed to mimic the human carotid artery and blood flow. The variation of pressure was carefully driven with a fluid column and a solenoid valve. In order to produce a pulse wave, the valve was opened during 150 ms and closed during 850 ms. The phantom was imaged with a unique plane wave sequence without compounding (f0: 5 MHz, excitation: 1-cycle sinusoidal pulse, PRF: 5 kHz, 128 elements). The motion was estimated from the same dataset both in the blood and in the wall using transverse oscillations. These latter were obtained with our previously proposed filtering approach.

Results/Discussion

Figure (a) shows the pulse wave arriving from the left part of the image. PWV was estimated at 3.1 m/s based on the acceleration of the wall computed along the upper wall over time. The longitudinal flow and the pulse wave propagate at different speed and are delayed in time as illustrated by panel (b). After processing, visualization is used to extract flow variations and wall positions as a function of time ((c) and (d)). Both spatial and temporal results are coherent with our expectations and confirmed, for flow, with a medical scanner (Doppler mode, Ultrasonix MDP).

As a conclusion our work demonstrated the ability of the transverse oscillations technique to simultaneously extract pulse wave velocity and flow profiles by using a unique plane waves sequence at high-framerate and the same estimation algorithm.

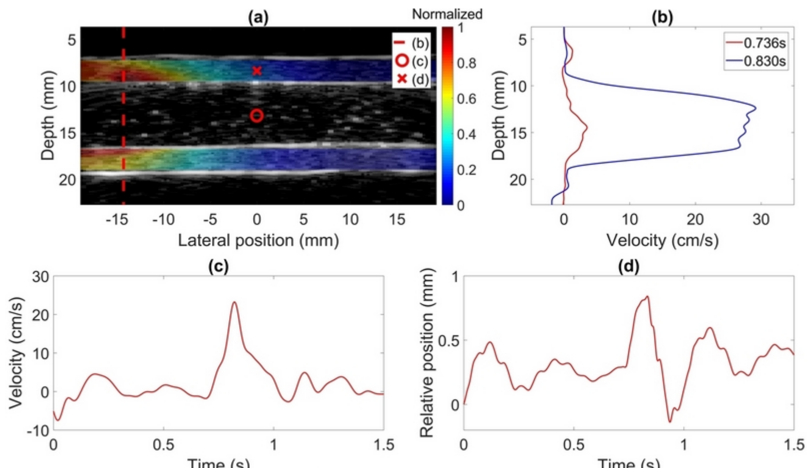

(a) B-mode image (40dB) at 0.736s with axis and points of interest superimposed with axial velocities in the walls.
(b) Two longitudinal flow profiles (0.736s and 0.830s) at the same lateral position.
(c) Flow velocity at the central point of the lumen.
(d) Relative position of the upper wall at the central point.

P1-C7-6

Multispectral Ultrafast Ultrasound Imaging: A Versatile Tool Probing Dynamic Phase-Change Contrast Agents

Heechul Yoon[1], Stanislav Emelianov[1,2]; [1]*School of Electrical and Computer Engineering, Georgia Institute of Technology, Atlanta, GA, USA,* [2]*Wallace H. Coulter Department of Biomedical Engineering, Georgia Institute of Technology and Emory University School of Medicine, Atlanta, GA, USA*

Background, Motivation and Objective

Optically triggered perfluorohexane nanodroplets (PFHnDs) can repeatedly vaporize and recondense, providing photoacoustic (PA) and blinking ultrasound (US) signals in response to pulsed laser irradiation. This property of PFHnDs has led to the development of various US imaging modes, including super-resolution and background-free contrast-enhanced imaging. However, to utilize the full potential of PFHnDs, multi-wavelength PA imaging, followed by ultrafast US imaging, referred to as multispectral ultrafast US/PA imaging, is required. Thus, we built a combined system that can trigger and image the dynamic behavior of PFHnDs with various optical wavelengths.

Statement of Contribution/Methods

A programmable US system (Vantage-256, Verasonics Inc., Kirkland, WA) and a multi-wavelength pulsed laser (Phocus, Opotek Inc., Carlsbad, CA) were interfaced and synchronized with a host controller (HC) and a function generator (FG) as shown in Fig. 1a. Using a MATLAB programming environment of the HC, we developed customized routines to irradiate tissue using laser pulses of desired optical wavelengths and to acquire post-laser-pulse PA and US images. To tune the laser wavelength, the HC communicated with the laser system using dynamic linked library functions. An image acquisition sequence that can be repeated with various optical wavelengths is illustrated in Fig. 1b. To test the performance of the system, we spectroscopically (from 700 nm to 940 nm with a 30-nm step) imaged a tube containing PFHnDs with a peak absorption at 760 nm.

Results/Discussion

As expected, both PA and differential US (ΔUS) images exhibit higher contrast at 760 nm compared to the image obtained with longer wavelengths (Fig. 1c). In addition, temporal behavior of differential US signal changes with laser wavelength (Fig. 1d) allowing for the US-based spectroscopic characterization of PFHnD dynamics. Furthermore, multi-wavelength PA imaging can visualize PFHnDs in the presence of endogenous chromophores (not shown). The developed multispectral ultrafast US/PA system could be used in various applications, including simultaneous detection and assessment of micro-metastasis in sentinel lymph node (SLN), where the location of SLN is determined by multispectral US imaging of PFHnDs and micro-metastases are detected by spectroscopic PA imaging of blood oxygen saturation.

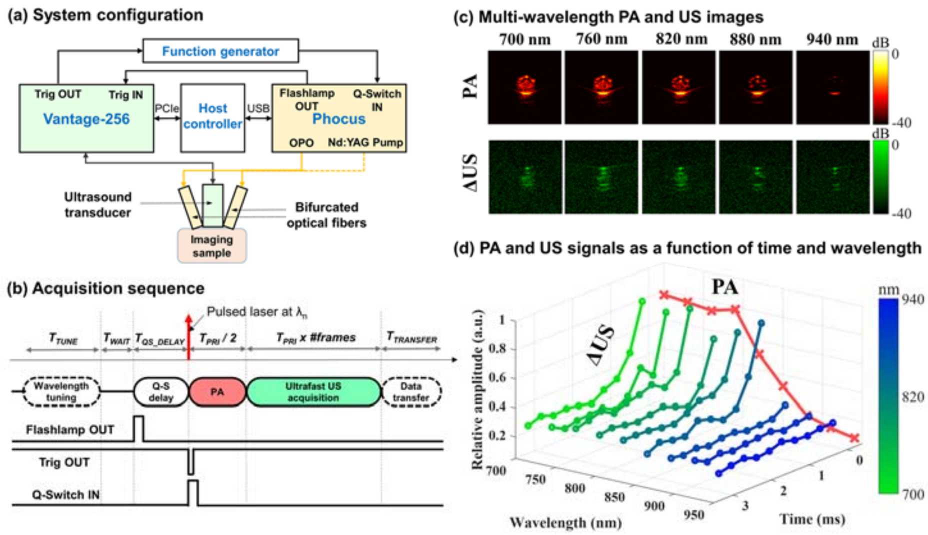

P1-C7-7

Reconstruction of Three-Dimensional Blood Vessel Network Using Multiple Ultrasound Volumes Constructed By Weighted Fusion between B-Mode and Doppler-Mode

Kohji Masuda[1], Tomoki Yamashita[1], Takuya Katai[1], Takashi Mochizuki[1], Shinya Onogi[2]; [1]*Tokyo Univ. of A&T, Japan,* [2]*Kyushu Univ., Japan*

Background, Motivation and Objective

We have previously proposed the use of acoustic microbubble delivery in blood vessels to improve the efficacy of acoustic targeted drug therapy. The technical requirement is the detailed visualization of the blood vessel network (BVN) for navigation around a target such as a tumor. To obtain the accurate shape of BVN for this purpose, we have experienced a problem of expansion and deficiency in 3D Doppler-mode volumes. Therefore, we have proposed a new BVN reconstruction method by fusing B-mode and Doppler-mode volumes, which were acquired simultaneously in the same coordinate space, considering the weight coefficient in each volume. In this presentation, we introduce the accuracy improvement to extract the weight coefficients.

Statement of Contribution/Methods

First, we configured a tube phantom to quantitatively evaluate the degrees of expansion and deficiency in both volumes, where we have examined various flow velocities to reflect the results for the accuracy improvement. Using the the results of the analysis, we have newly established the weight coefficients varied with not only the dot product angle between the tangent vector of the centerline in the volume and the direction of ultrasound propagation to correct the shape of each volume, but also the flow velocity. Then we fused the corrected B- and D-volumes to reconstruct the shape of the tube phantom and human liver vessels.

Results/Discussion

Regarding the reconstruction accuracy, the maximum error of the tube diameter in the proposed method was 20% with the diameter between 1.5 and 3.0 mm. From the results of the phantom experiments, we analyzed the shape of the constructed B- and D-volumes and experimentally obtained the approximation function between the dot product angle and the weight coefficients. Figure shows the 3D fused volume superimposed on the original B-mode image, which was extracted from the human liver of healthy subject, 24 y.o. male. The red and blue volumes indicate B- and D-volumes, respectively. Comparing the results with the original volumes, compensation of deficiency in B- and D-volumes contributes more effective comprehension of BVN. Fusion of the weighted volume has advantages in the points of diameters of blood vessel are more clear and consistent, which makes easier to identify blood vessels.

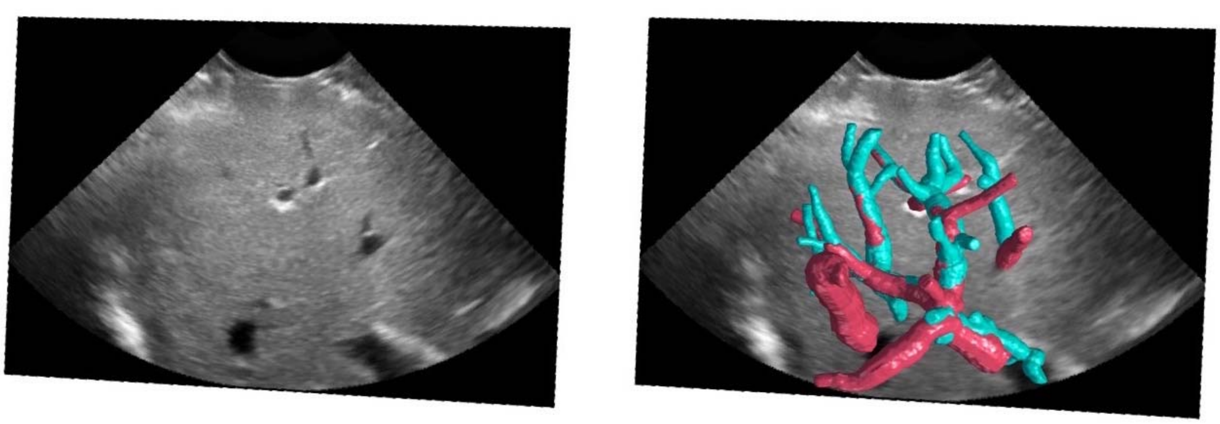

Passive Acoustic Mapping of Cavitation Based on Frequency Sum and Robust Capon Beamformer

Shukuan Lu[1], Xianbo Yu[1], Nan Chang[1], Yujin Zong[1], Hui Zhong[1], Mingxi Wan[1]; [1]*Department of Biomedical Engineering, School of Life Science and Technology, Xi'an Jiaotong University, Xi'an, Shaanxi, China, People's Republic of*

Background, Motivation and Objective

Real-time dynamic monitoring of cavitation is essential for the safety and efficiency of high intensity focused ultrasound (HIFU) therapy. Unlike pulse-echo imaging, which can only be of use while HIFU is turned off, passive acoustic mapping (PAM) can enable monitoring of cavitation during HIFU exposure. But the conventional used PAM has low resolution and interference artifacts. For this, a unique PAM algorithm that combines frequency-sum beamforming with robust Capon beamformer (FS-RCB-PAM) was proposed in this study.

Statement of Contribution/Methods

The performance of the proposed PAM was validated by both simulations and *in vitro* experiments. In simulations, a multi-bubble model, which defined the signal received by single sensor as a rand pulse train, was used to generate the prebeamformed data of cavitation sources. In *in vitro* experiments, a linear array was used to receive cavitation signals in 1.2MHz HIFU-induced histotripsy. The full width at half maximum (FWHM) of the normalized source energy was used to evaluate the resolution improvement. The cavitation artifact ratio (CAR) was used for the evaluation of reduced artifacts.

Results/Discussion

In simulations, DAS-PAM images yield the tail artifact, which is caused by multiple bubbles interfering with each other and become serious with increasing bubbles. From DAS-PAM to FS-PAM, cavitation is more easily to differentiate, therefore making localization of cavitation more accurate. When RCB is added in FS-PAM, a majority of artifacts are reduced, and then cavitation is confined to a small region. The lateral (axial) resolution of FS-PAM is 1.65 ± 0.34 (1.80 ± 0.29) times higher than DAS-PAM. The CAR can be improved by 11.6 dB~12.6 dB. In *in vitro* experiments, pulse-echo image of the residual bubbles around a fluid-tissue interface in histotripsy can reflect the position of tissue damage and is used as a reference to validate the feasibility of FS-RCB-PAM. The results show that FS-RCB-PAM can effectively localize histotripsy damage. The lateral (axial) resolution of the proposed PAM is 1.51 ± 0.18 (1.75 ± 0.11) times higher than DAS-PAM. The CAR is improved by about 11 dB. Both simulations and experiments show that the proposed PAM can realize cavitation imaging with high spatial resolution and greatly reduced artifacts, and therefore allowing precise localization of cavitation activity during HIFU therapy.

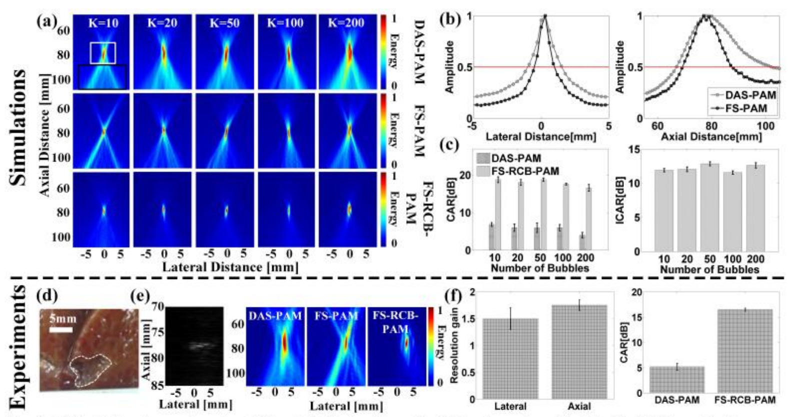

Fig. 1 (a) Cavitation images based on different PAM algorithms for different number of bubbles K. (b) Normalized source energy curve along the lateral and axial direction for DAS-PAM and FS-PAM. (c)Statistical CARs of DAS-PAM and FS-RCB-PAM and ICARs. (d) Cross section of tissue damage. (e)Pulse-echo image of the residual bubbles (differenced by two adjacent frames to remove tissue signal) and cavitation images. (f) The statistical results of resolution gain and CARs. DAS: delay and sum; FS: frequency sum; RCB: robust Capon beamformer.

$CAR=20\lg\left[\max_{(x,z)\in\{\text{cavitation}\}} I(x,z) \,/\, \max_{(x,z)\in\{\text{artifact}\}} I(x,z)\right]$;

$ICAR$(improved cavitation artifact ratio)$=CAR_{FS\text{-}RCB}-CAR_{DAS}$

P1-C8 - MIM: Machine Learning

Exhibit Hall

Saturday, September 9, 2017, 9:30 am - 4:00 pm

Chair: **Olivier Bernard**
CREATIS

P1-C8-1

2D Left Ventricle Segmentation using Deep Learning

Erik Smistad[1,2], Andreas Østvik[1], Bjørn Olav Haugen[1], Lasse Lovstakken[1]; [1]*Centre for Innovative Ultrasound Solutions (CIUS), Norwegian University of Science and Technology (NTNU), Norway,* [2]*Medical Technology, SINTEF, Norway*

Background, Motivation and Objective

Automatic segmentation of the left ventricle (LV) can become a useful tool in echocardiography, for instance to provide automatic ejection fraction measurements or to initialize deformation imaging algorithms. Deep neural networks have recently shown very promising results for improving image classification and segmentation. These methods learn using only a set of input and output data, but require a large and representative amount of annotated data to be successful. This means an expert has to draw the LV border in potentially thousands of images, which is highly tedious and time consuming.

Statement of Contribution/Methods

In this work, we investigate if the need for manual annotation can be reduced by pretraining the NN using an automatic Kalman filter (KF) segmentation approach as the expert. The hypothesis is that the NN is able to reproduce the KF results.

The dataset consisted of apical ultrasound images from 100 patients referenced to the outpatient clinic, containing 1,536 image sequences and a total of about 100,000 image frames with varying image quality. The data was processed with the KF using a LV shape model and edge detection measurements along the shape model. For the evaluation, 13 of the 100 patients were excluded from training and used for validation. An expert cardiologist manually segmented the LV in 52 images.

The B-mode images were resized to 256x256 pixels and used to train a fully convolutional NN. A U-net architecture with 23 convolutional and transpose convolutional layers was used, and the network was trained using stochastic gradient descent for 10 epochs.

Results/Discussion

The dice similarity coefficient (DSC) and the Hausdorff distance was calculated for the KF and NN method. The average DSC was 0.86±0.06 for the KF and 0.87±0.06 for the NN. Thus, the NN achieved comparable performance to the KF by training it on output data from the KF. The average Hausdorff distance, representing the maximum error, was higher for the KF with 7.5±5.6 mm, compared to 5.9±2.9 mm for the NN. Some image sequences where the KF did not work properly were excluded from training, which may be the reason for a lower maximum error. The DSC was observed to increase with the number of patients included in training. The inference runtime of the network was 90±8 ms using a CPU.

In future work, this may enable deep NNs to exceed state-of-the-art with a small set of expert annotations for fine-tuning the NN.

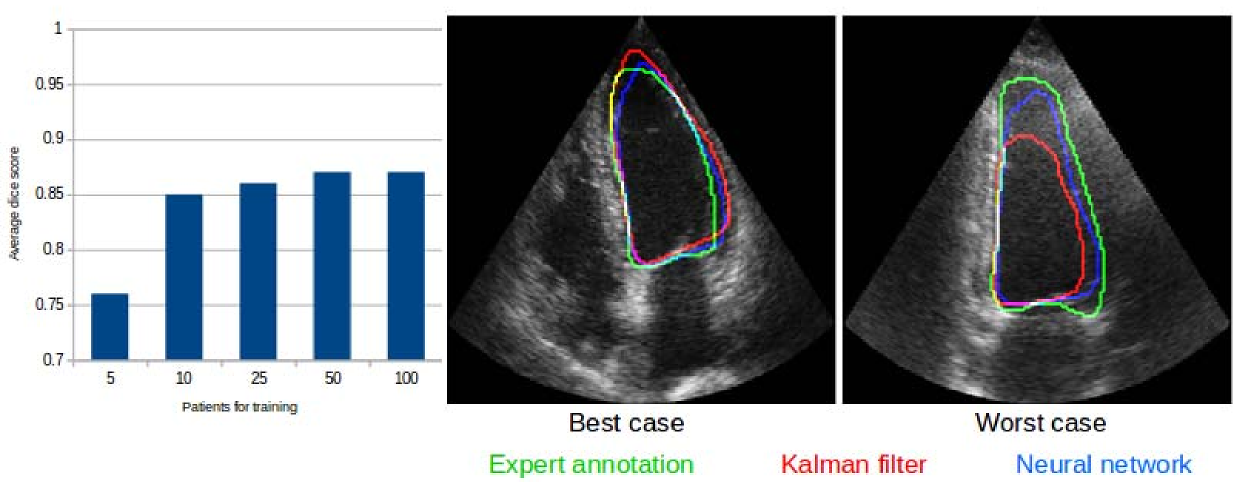

P1-C8-2

A fully Automatic and Multi-Structural Segmentation of the Left Ventricle and the Myocardium on Highly Heterogeneous 2D Echocardiographic Data

Sarah Leclerc[1], Thomas Grenier[1], Florian Espinoza[2], Olivier Bernard[1]; [1]*CREATIS, Lyon, France,* [2]*University Hospital of Saint-Etienne, Saint-Etienne, France*

Background, Motivation and Objective

Although 3D ultrasound plays an increasingly important role, 2D echocardiography remains the main clinical imaging modality for cardiac function assessment in daily practice. This requires precise delineation of the myocardium at end diastole (ED) and systole (ES). Because of intrinsic high variability in image quality, manual interactions are still needed. In this study, we investigate a machine learning solution to fully automate the segmentation of the myocardium on heterogeneous dataset.

Statement of Contribution/Methods

Our approach is based on the Structured Random Forest (SRF) algorithm, introduced in computer vision and applied to cardiac border detection during the MICCAI CETUS challenge. It is designed as a fast learner, able to contextualize the information even on small databases (interesting property for medical applications) where Neural Networks prove to have trouble generalizing. Our contributions are the following: i) integrate the capacity of performing segmentation instead of edge detection; ii) extend the formalism to multiclass segmentation, i.e both the left cavity and the myocardium in our case; iii) enhance the contextual information by mixing global and local gradient-based features.

We compare our results with a semi-automatic state of the art Active Shape Model (ASM) which requires five initialization points: 2 at the basis, 1 at the apex and 2 at the septum.

The database comes from the university Hospital of St-Etienne and contains the full cardiac cycle of daily exams (apical 4-chambers view) from 250 patients. The myocardium was manually delineated by an expert at ED and ES. No restriction on the quality of the image was imposed, making the database highly challenging to process.

Our method was trained using 200 patients and the two algorithms were evaluated on the remaining 50 patients using mean absolute distance (MAD), Hausdorff and Dice metrics.

Results/Discussion

The proposed method showed fairly good results considering the challenging dataset but also competitive results compared to the semi-automatic ASM (see table 1). In particular the proposed framework achieved a MAD of 2.21±0.90mm (endo.) and 2.84±1.45mm (epi.) at ED and 2.22±1.03mm (endo.) and 2.96±1.75mm (epi.) at ES.

The figure below shows the results obtained using our method (continuous line) on two particular patients along with the manual references (dotted lines)

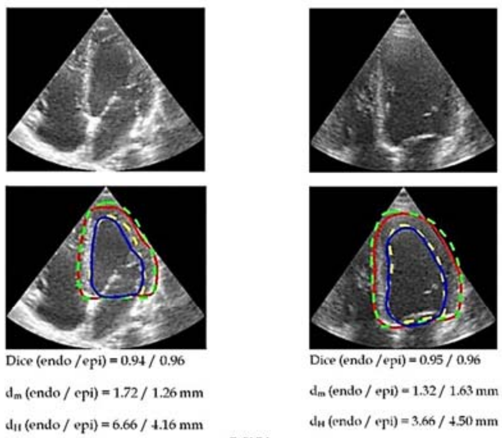

TABLE I

LEFT VENTRICULAR ENDOCARDIUM AND EPICARDIUM SEGMENTATION ACCURACY ON THE TESTING DATASET (50 PATIENTS). ED, ES, d_m, d_H AND MEAN END DIASTOLE, END SYSTOLE, MEAN ABSOLUTE DISTANCE AND HAUSDORFF DISTANCE, RESPECTIVELY.

Experiments			ED						ES					
			Dice		d_m		d_H		*Dice*		d_m		d_H	
			mean	*std*	*mean*	*std*	*mean*	*std*	*mean*	*std*	*mean*	*std*	*mean*	*std*
Method	Category	Structure	mm		mm		val.		mm		mm		val.	
ASM	Semi-auto.	endocardium	0.90	0.04	2.84	1.20	7.24	2.77	0.89	0.06	2.25	1.29	5.69	3.04
Proposed	Fully-auto.	endocardium	0.92	0.03	2.21	0.90	9.18	6.11	0.89	0.06	2.22	1.03	7.89	5.54
ASM	Semi-auto.	epicardium	0.92	0.03	2.91	1.10	7.51	2.37	0.93	0.03	2.43	0.90	6.64	2.16
Proposed	Fully-auto.	epicardium	0.93	0.03	2.84	1.45	10.35	6.29	0.91	0.05	2.96	1.75	10.81	8.42

P1-C8-3

Real-Time Classification of Standard Cardiac Views in Echocardiography Using Neural Networks

Andreas Østvik[1], Erik Smistad[1,2], Svein Arne Aase[3], Bjørn Olav Haugen[1], Lasse Løvstakken[1]; [1]*Centre for Innovative Ultrasound Solutions (CIUS), Dept. Circulation and Medical Imaging, Norwegian University of Science and Technology (NTNU), Trondheim, Norway,* [2]*Dept. Medical Technology, SINTEF, Trondheim, Norway,* [3]*GE Vingmed Ultrasound AS, Horten, Norway*

Background, Motivation and Objective

Echocardiograms are acquired from standard views to ensure correct assessment of cardiac function. There is an increasing use of quantitative tools where specific views are required. Further, non-expert users of echocardiography are increasing, and thus a need for quality assurance during imaging. The aim of this project is to develop automatic and robust real-time classification of cardiac views based on 2D B-mode images.

Statement of Contribution/Methods

A convolutional neural network (CNN) was designed to classify five cardiac views: apical two-, four- and long-axis, and parasternal long- and short-axis. Training data was acquired from 205 patients from the outpatient clinic, containing approx. 4,400 sequences. A tenfold patient-based cross-validation was used for evaluation. One model only considered valid views, intended for applications emphasising high sensitivity, while another was designed to increase specificity by adding an unknown class and by including invalid cardiac images during training. Test data was then generated from 2D slices of a 3D volume, mimicking a scenario with all image views by rotating slices around a fixed depth axis.

The CNN consisted of repeating layers of convolutions, batch normalization, parametric rectified units (PReLU) and max pooling. The classification part employed global average pooling and softmax activation. Training was performed with adaptive moment estimation.

Results/Discussion

An average accuracy of (97.4±0.8) % and (98.3±0.7) % was achieved on unknown frames and sequences respectively, surpassing current state of the art. Accuracy reduced to (96.7±0.9) % for frames when including invalid views for training. The models achieved real-time performance with an average computation time of (20±5) ms per frame on a single CPU core.

In the figure, view confidence applying the extended model on image slices from the 3D volume is shown, where example images correspond to marked peaks. The classes are clearly distinguishable, but also tends to saturate in certain angle intervals complicating assignment of optimal views. A remaining challenge thus involve incorporating the model with ability of assessing view quality.

The results show that CNNs can achieve high performance for cardiac view classification, with potential of becoming a robust tool for quality assurance while imaging in echocardiography.

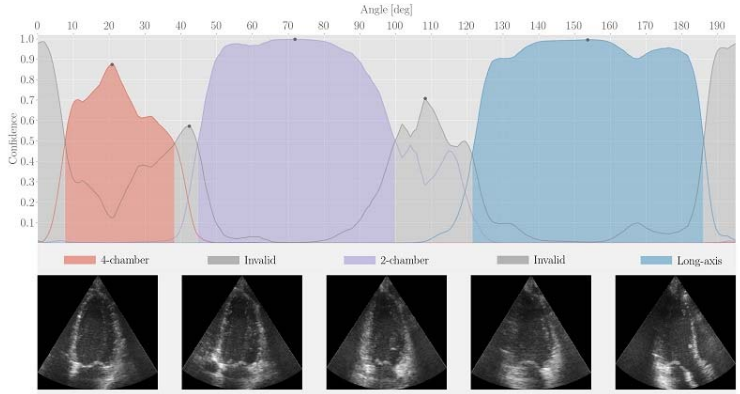

P1-C8-4

Application of Wavelet Scattering Networks in Classification of Ultrasound Image Sequences

Amir Khan[1], Ananya Dhawan[1], Nima Akhlagi[1], Joseph Majdi[1], Siddhartha Sikdar[1]; [1]*Department of Bioengineering, George Mason University, Fairfax, VA, USA*

Background, Motivation and Objective

Recently, ultrasound imaging of muscle contractions has been used by several research groups to infer volitional motor intent of the user, and has shown promise as a novel muscle computer interface. Learning spatiotemporal features from ultrasound image sequences is challenging because of deformations introduced by probe repositioning. The image features are sensitive to probe placement and even small displacements during donning and doffing of the probe compromises the classification accuracy while using a model trained on a previous session. This requires frequent recalibration. Deep learning based feature extractors have been shown to be invariant to translation, rotation and slight deformations. In this study, we investigate the feasibility of wavelet-based deep scattering features to preserve motion classification accuracy across multiple donning and doffing sessions.

Statement of Contribution/Methods

The forearm muscles were visualized using a linear array (L15-4) transducer on a SonixOne ultrasound system while an able-bodied subject performed 10 repetitions of 5 hand motions over 7 different sessions spread across different days. The probe was repositioned at a predefined location. The peak activity location for each motion was extracted for each session, motion and trial. We tested a correlation based k-nn classifier using a leave-one-out approach by averaging the respective peak motion images across 6 sessions while testing on the remaining session. We then compared its results with wavelet scattering transform features in 2 layers. The scattering cascades wavelet transforms and non-linearities at different spatial, angular and scale transformations of a mother wavelet and computes deep layer features with pre-determined weights. We used these scattering features with a k-nn classifier to test different combinations of training sessions and evaluate their performance with training on a limited number of sessions.

Results/Discussion

We found that the k-nn classifier applied directly to the original images requires training on 6 of the 7 sessions (leave one out approach) to achieve an accuracy of 89% on the 5 motions. The accuracy falls if the number of training sessions are reduced. The scattering features achieve a 99.5% accuracy for the leave-one-out approach. The accuracy with 4 sessions used for training and 3 for testing was 98.6% and for 3 training and 4 testing session was 92.5%. Finally, the training on only a single session and testing on all the other sessions revealed a mean accuracy of 82%. Our preliminary results indicate that scattering transform is feasible to extract geometrically invariant features that can alleviate the problem of sensor displacement to maintain motion classification accuracy. Studies are ongoing to validate this method across multiple subjects.

P1-C8-5

Assessment of Myocardial Viability Using Speckle Tracking Echocardiography at High Spatial Resolution

Mahdi Tabassian[1], Serkan Ünlü[1], Oana Mirea[2], Jens-Uwe Voigt[1,3], **Jan D'hooge**[1]; [1]*Department of Cardiovascular Sceinces, KU Leuven, Leuven, Belgium,* [2]*Department of Cardiology, University Hospital Craiova, Craiova, Romania,* [3]*Division of Cardiology, University Hospitals Leuven, Leuven, Belgium*

Background, Motivation and Objective

Speckle tracking echocardiography (STE) is a well-established method to assess regional cardiac function. Traditionally, the left ventricular (LV) walls are divided into 18 segments (6 LV walls each with 3 segments) and the deformation parameters are measured for each of the segments. However, usually, segmental deformation curves are obtained by taking the average of an underlying strain field that is denser than this resolution level. The aim of this study was therefore to investigate whether the dense STE-derived strain data contain meaningful functional information at a sub-LV-segment level.

Statement of Contribution/Methods

Longitudinal strain (rate) traces were extracted using GE EchoPac from 4 LV walls (i.e. 2 views) in a set of 53 patients with myocardial infarction imaged with a GE Vivid E9 at 60 Hz. On average, the dense strain field consisted of 65 strain traces per view that could then be converted to a 24- and 12-segment model by averaging. Based on co-registered correlative MRI delayed enhancement data, each segment (at all resolutions) could be attributed a transmural extend of scar in the range of 0 to 100%. Principal Component Analysis (PCA) was used for statistical modeling of the data. At each resolution, two independent PCA models were built with the strain and strain rate data. Distance-weighted k-nearest neighbor (DWKNN) was used to regress transmurality of scar tissue corresponding to a given test curve based on the PCA-derived features. In order to evaluate the DWKNN performance, the scar was considered transmural if transmurality > 75% and as non-transmural otherwise. This enabled receiver operator characteristic (ROC) and classification analyses. Experiments were performed using leave-one-patient-out cross validation.

Results/Discussion

The best ROC curves and their corresponding classification results, obtained with the optimal number of PCA features and KNNs, of the strain (rate) data at the different resolutions are shown in Figure 1. It can be seen that: 1) for both strain and strain rate, the results at the different spatial resolutions are comparable implying that meaningful data is available at a higher resolution and, 2) strain rate lead to slightly better results than the strain traces. In conclusion, the deformation data can reliably be measured at a higher spatial resolution than what is currently used in clinical practice.

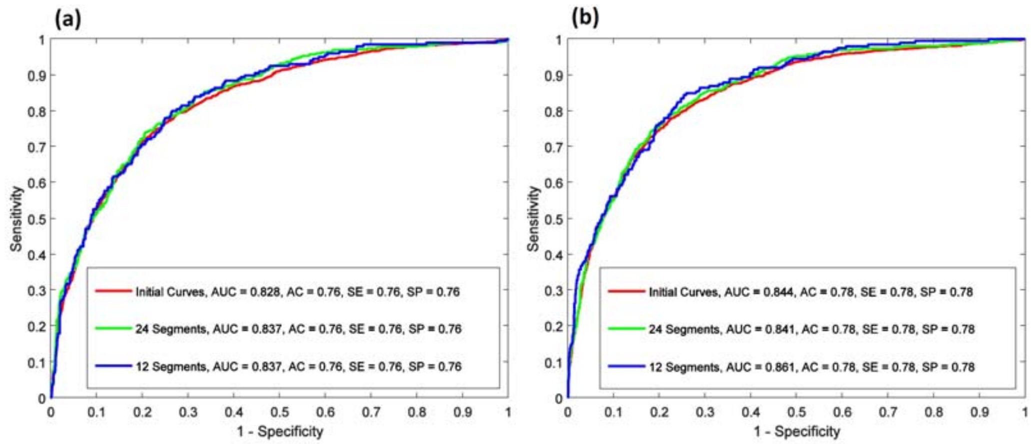

Figure 1. Area under the curve (AUC), accuracy (AC), sensitivity (SE) and specificity (SP) rates obtained with the initial curves (red), 24 segments (green) and 12 segments (blue) per view with the (a) strain and (b) strain rate data.

P1-C8-6

Automated Super-Resolution Image Processing in Ultrasound using Machine Learning

Kirsten Christensen Jeffries[1], Markus Schirmer[2,3], Jemma Brown[1], Sevan Harput[4], Meng-Xing Tang[4], Christopher Dunsby[5,6], Paul Aljabar[1], Robert Eckersley[1]; [1]*Biomedical Engineering, Kings College London, London, United Kingdom,* [2]*Neurology, Harvard Medical School, Boston, MA, USA,* [3]*Computer Science and Artificial Intelligence Lab, Massachusetts Institute of Technology, Boston, MA, USA,* [4]*Bioengineering, Imperial College London, London, United Kingdom,* [5]*Physics, Imperial College London, London, United Kingdom,* [6]*Centre for Pathology, Imperial College London, London, United Kingdom*

Background, Motivation and Objective

Clinical implementation of super-resolution (SR) ultrasound imaging requires accurate single microbubble detection, and would benefit greatly from automation in order to minimize time requirements and user dependence. We present a machine learning based post-processing tool for the application of SR ultrasound imaging, where we utilize superpixelation and support vector machines (SVMs) for foreground detection and signal differentiation.

Statement of Contribution/Methods

Superpixelation is implemented using Simple Linear Iterative Clustering (SLIC) [1] for automated foreground-background differentiation, i.e. two superpixels. Resulting foreground regions are then classified using SVMs as either single bubbles, multiple bubbles, or noise. Manually labelled data were used to train an SVM classifier to categorize candidate signals. The approach was tested on *in vitro* experimental phantoms using a Siemens Acuson Sequoia clinical system (Siemens, Issaquah, WA) at 2.3 MHz on crossed, 200 µm tubes, and its performance was assessed by comparing results to thresholding methods. Each dataset was analysed using two independent training sets generated by two users individually. Microbubble localization was then performed on the classified regions.

Results/Discussion

Results show improved performance compared to existing thresholding techniques, where the resulting single bubble images using SVM displayed a more well defined outline and image measurements of the expected angled cross-sectional tube width (231 µm) corresponded considerably better using the proposed approach, while for thresholding was over 50% wider (see Figure 1). Furthermore, the average classification accuracy was 84 ± 15% for each training and data set. This demonstrates the significant potential of machine learning techniques for SR processing and can provide the basis for clinically viable SR ultrasound imaging.

References:

[1] R. Achanta, A. Shaji, K. Smith, A. Lucchi, P. Fua, and S. Susstrunk, "SLIC Superpixels," EPFL Tech. Rep. 149300, no. June, p. 15, 2010.

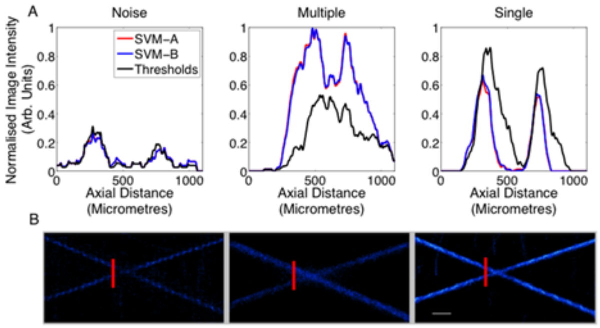

C

Measurement (µm)	SVM-A	SVM-B	Thresholds
S1	305	306	450
S2	212	212	352

Figure 1. (A) Average vertical intensity profiles using two training sets and thresholding across a 200 µm profile (red lines in (B)) (example based on SVM). Table (C) summarises the estimated spatial extents (S1 and S2) of the tube profiles, measured along the dashed line in graph (0.04 AU). We observe that both training sets (SVM-A and B) result in almost identical profiles and spatial extents, thereby removing inter-rater variations.

P1-C8-7

Identification and Removal of Reflection Artifacts in Photoacoustic Images Using Convolutional Neural Networks

Derek Allman[1], Austin Reiter[2], Muyinatu Bell[1]; [1]*Electrical and Computer Engineering, Johns Hopkins University, USA,* [2]*Computer Science, Johns Hopkins University, USA*

Background, Motivation and Objective

Photoacoustic imaging is a useful technique that is often hampered by acoustic reflections from nearby, hyperechoic ultrasound structures. Current beamforming methods are not well suited to remove these reflection artifacts. The objective of this work is to evaluate the potential of a region-based convolutional neural network (RCNN) to identify and remove reflection artifacts.

Statement of Contribution/Methods

A total of 17,340 photoacoustic images were simulated in k-Wave, with 80% used for training and 20% used for testing. Each image contained two acoustic wavefronts, one originating from a true source and the other representing an acoustic reflection artifact. In addition, white Gaussian background noise resulting in -3dB, -9dB, -15dB, and -21dB SNR was added to each image. For each noise level, images were trained using the Faster-RCNN algorithm VGG16 network architecture. Detections were classified as correct if the confidence and the intersect-over-union of the ground truth and detection bounding boxes were both greater than 0.5.

Results/Discussion

The noiseless dataset achieved 100% classification accuracy (i.e. all signals were correctly classified as a source or artifact). The -3dB and -9dB SNR trained networks performed similarly well, both achieving >99% classification accuracy. The -15dB SNR network achieved 91% and 88% accuracy in classifying sources and artifacts, respectively, while the -21dB SNR network achieved 33.8% and 25.1% accuracy in classifying sources and artifacts, respectively. The mean and standard deviation of the distance errors for correct detections for the noiseless, -3dB, -9dB, -15dB, and -21dB were 0.260.15, 0.240.14, 0.200.14, 0.280.17, and 0.300.17 mm respectively. True signal locations were displayed with a size corresponding to 2 standard deviations. We defined a misclassification as a source being classified as an artifact and vice versa. The noiseless and -3dB SNR datasets had no misclassifications. When increasing the noise level to -9dB, -15dB, and -21dB SNR the misclassification rates increased to 0.2%, 2%, and 6.3% respectively. Results demonstrate promise for using machine learning to identify and remove reflection artifacts and to detect low-amplitude signals.

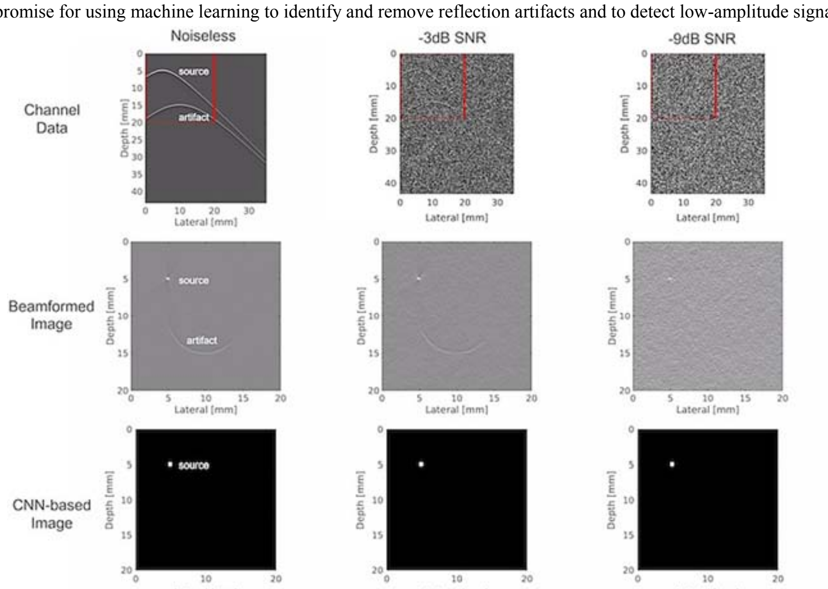

P1-C9 - MTC: Bone and Abdominal Organs

Exhibit Hall

Saturday, September 9, 2017, 9:30 am - 4:00 pm

Chair: **Mami Matsukawa**
Doshisha University

P1-C9-1

The Elastic Properties of Human Cortical Bone Measured by Resonant Ultrasound Spectroscopy at Multiple Skeletal Sites

Xiran Cai[1], Laura Peralta[1], Quentin Vallet[1], Nicolas Bochud[1], Oliver Boughton[2,3], Richard Abel[2], Justin Cobb[2], Kay Raum[4], Jean-Gabriel Minonzio[1], Pascal Laugier[1], Quentin Grimal[1]; [1]*Sorbonne Universités, UPMC, INSERM UMR-S 1146, CNRS UMR 7371, Laboratoire d'Imagerie Biomédicale, Paris, France,* [2]*The MSk Lab, Imperial College London, London, United Kingdom,* [3]*The Biomechanics Group, Imperial College London, London, United Kingdom,* [4]*Berlin Brandenburg School of Regenerative Therapies, Charité-Universitätsmedizin Berlin, Berlin, Germany*

Background, Motivation and Objective

Human cortical bone is an anisotropic material, although isotropic stiffness is generally assumed in most finite element analysis. Detailed information about the anisotropic stiffness at a mesoscopic (mm) scale would improve our understanding of bone's macroscopic mechanical properties. In this work, we report on the anisotropic stiffness of human cortical bone from different sites, and the variation in anisotropy seen.

Statement of Contribution/Methods

Bone specimens were harvested from different locations within the femur, radius and tibia: femoral neck (19 specimens), upper shaft (55) and mid shaft (73), proximal one-third radius (42) and mid shaft tibia (55). All specimens were prepared into cuboid shape, sized ~1-5mm and specimen orientation was defined by the anatomical shape of each type of bone: radial (axis 1), circumferential (axis 2) and axial direction (axis 3). The stiffness coefficients C_{ij} of all the specimens were measured by a custom-made resonant ultrasound spectroscopy setup.

Results/Discussion

Transverse isotropic elastic symmetry was found for the specimens from the radius, tibia and femoral mid shaft, while the femoral neck and upper-shaft were orthotropic. Overall, the radius showed the highest compressional and shear stiffness coefficients(Figure 1). The mean values of C_{11}, C_{22} and C_{66} of the femur were larger compared to the tibia, while there was a good overlap between skeletal sites for C_{33}, C_{44} and C_{55}. The sorted mean values of C_{ij} (from the largest to the smallest) were femoral mid-diaphysis>upper-shaft>neck, which may be due to lower mass density at the proximal location of femur. A negative relationship between the anisotropy ratio C_{33}/C_{11} and mass density was observed for the tibia, while C_{33}/C_{11} of the femur and radius remained constant (Figure 1). The mean C_{33}/C_{11} of the tibia>radius>femur and the mean C_{44}/C_{66} of tibia≈radius>femur. This study shows possible skeletal site and location dependency of anisotropic elastic properties of human cortical bone.

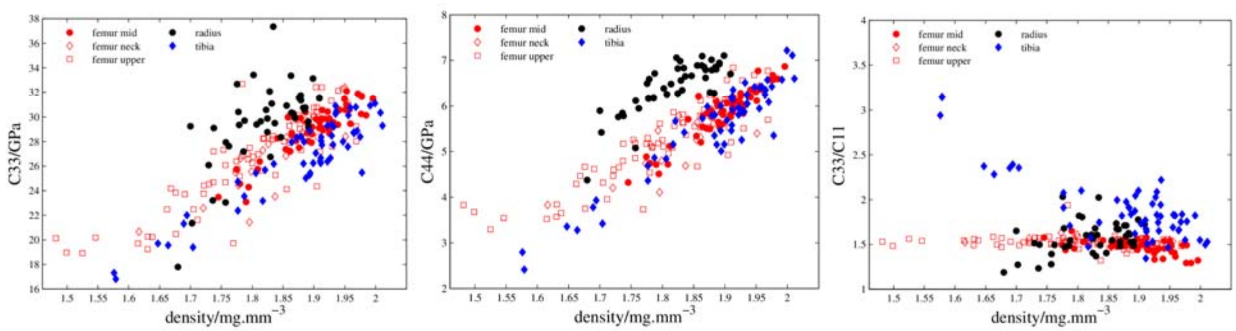

Figure 1: The relationships between stiffness coefficients C_{33} and C_{44}, anisotropy ratio C_{33}/C_{11} and mas density of the bone specimens from femoral mid shaft (femur mid), neck (femur neck), upper-shaft (femu upper), radius and tibia.

P1-C9-2

The Acoustical Properties of Brain, Liver and Kidney Soft Tissue from Small Animals over the Frequency Range 12 – 33 MHz.

Adela Rabell-Montiel[1], Steve Pye[2], Tom Anderson[1], **Carmel Moran**[1]; [1]*Cardiovascular Science, University of Edinburgh, Edinburgh, United Kingdom,* [2]*Medical Physics, NHS Lothian, Edinburgh, United Kingdom*

Background, Motivation and Objective

Commercially available tissue-mimicking-materials (TMMs) and phantoms are designed to exhibit acoustic properties similar to those measured from soft tissue at ultrasound frequencies up to 15MHz. Many of these phantoms are manufacturing using the IEC agar-TMM. However, there are increasing applications of ultrasound at frequencies above 15MHz for both clinical (skin and vascular) and preclinical (small animal) applications and the suitable of these tissues and phantoms to mimic tissue at higher frequencies has not previously been confirmed primarily due to the limited knowledge of the acoustic properties of soft tissue at these higher frequencies.

The aim of this study is to measure the acoustic properties from *ex vivo* brain, liver and kidney from available male mice (6 months old) in the frequency range of 12–32MHz.

Statement of Contribution/Methods

Twenty samples from each organ were analysed from 50 recently euthanized healthy C57/6BL male mice. Within 6 minutes of death, the organs were extracted, sliced and immersed in a bath of phosphate-buffered saline (PBS) at 37.2 ± 0.4°C (reference medium). A broadband reflection substitution technique was employed to calculate the acoustic properties of the soft tissues. Measurements were made with a preclinical ultrasound scanner Vevo 770® (Visualsonics, Inc) over the frequency range of 12–33MHz (RMV 707B). The PBS at 37°C was also acoustically characterised.

Results/Discussion

The mean speed of sound was found to be 1604.4 ± 16.5 ms^{-1} for liver tissue, 1575.3 ± 10.8 ms^{-1} for kidney tissue and 1565.9 ± 9.6 ms^{-1} for brain tissue. Figure 1 shows the polynomial fit for the mean attenuation over the organ samples. A second degree polynomial fit was calculated for each organ. These were found to be $0.3665f+0.003194f^2$ (R^2=0.89) for brain tissue, $0.5168f+0.004411f^2$ (R^2=0.50) for kidney tissue and $0.008778f+0.04482f^2$ (R^2=0.44) for liver tissue, where *f* is the frequency in MHz and the attenuation coefficient is in dB cm^{-1}.

We have measured the acoustical properties of small animal soft tissue at high ultrasound frequencies. This data can be used as the baseline upon which to manufacture a TMM for manufacture of ultrasound phantoms above 15MHz.

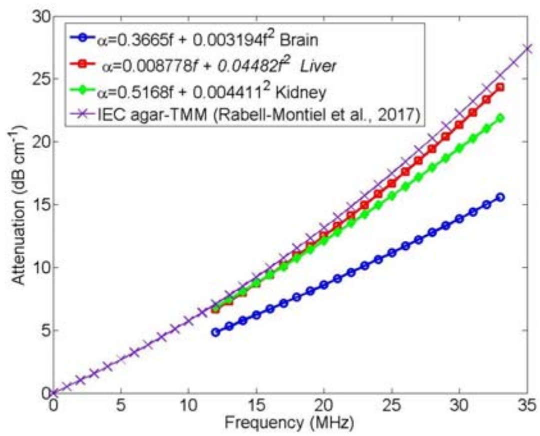

Figure 1. Attenuation versus frequency measured from 20 livers, 20 kidneys and 20 brains. The IEC-agar TMM attenuation was added for comparison purposes. *Rabell-Montiel et al., 2017 Ultrasound in Medicine and Biology in press*

P1-C9-3

Speed of Sound Evaluation of Organelles of NASH Livers in Rats with 250-MHz Ultrasound

Kazuyo Ito[1], Kenji Yoshida[2], Jonathan Mamou[3], Hitoshi Maruyama[4], Tadashi Yamaguchi[2]; [1]*Graduate School of Engineering, Chiba University, Chiba, Japan,* [2]*Center for Frontier Medical Engineering, Chiba University, Chiba, Japan,* [3]*Lizzi Center for Biomedical Engineering, Riverside Research, New York, NY, USA,* [4]*Graduate School of Medicine, Chiba University, Chiba, Japan*

Background, Motivation and Objective

Accurate diagnosis of non-alcoholic steatohepatitis (NASH) is a critical issue in current clinical practice. Non-invasive diagnosis of NASH can be achieved by quantitative ultrasound (QUS), which requires a detailed understanding tissue-specific acoustic microstructure at cellular scale (i,e., 10 µm). Therefore, QUS methods would benefit from the knowledge of the acoustic properties of organelles in NASH livers because they may represent the dominant scattering source at conventional frequencies used for *in vivo* assessments (i.e., < 15 MHz). This study focuses on obtaining speed of sound (*c*) of organelles (i.e., nucleus, cytoplasm, and fibers) using 250-MHz ultrasound in rat livers.

Statement of Contribution/Methods

Three different pathological stages were investigated in rat models: normal (untreated: n = 2), NASH (n = 3), and fibrosis model (n = 6). After animal sacrifice, each liver was fixed in formalin and a 7-µm thin section was affixed to glass slide using a microtome. A scanning acoustic microscopy system equipped with a 250-MHz center-frequency transducer was employed to obtain two-dimensional (2D) maps of *c* with a spatial resolution of 7-µm. Values of *c* were estimated using the phase difference of the RF echo from the interface between the sample slide surfaces compared to that from the exposed microscopy slide. Following SAM scanning, stained photomicrographs were acquired from the same samples. The histological images were used to detect the positions of the nuclei, cytoplasm and fibers, and the corresponding *c* values from obtained from the co-registered 2D *c* map.

Results/Discussion

Figures 1 (a) and (b) show co-registered SAM and histology images showing the positions of nuclei cytoplasm, and fibers. For all organelles, Kruskal-Wallis test reveals a significant difference ($p < 0.01$) between all paired stages (Fig. 1c). These results reveals that *c* is the highest in fibrosis livers for all organelles. Additionally, in NASH livers, *c* of nuclei and cytoplasm were the lowest, which could be due to intracellular fluid or ballooning of the whole cell. As expected, *c* in fiber changes with pathologic state. Results reveal that *c* of the nucleus and cytoplasm also changes with pathologic state and that we were able to carefully assess these differences using 250-MHz ultrasound. These results could prove invaluable to improve *in vivo* QUS investigations of livers.

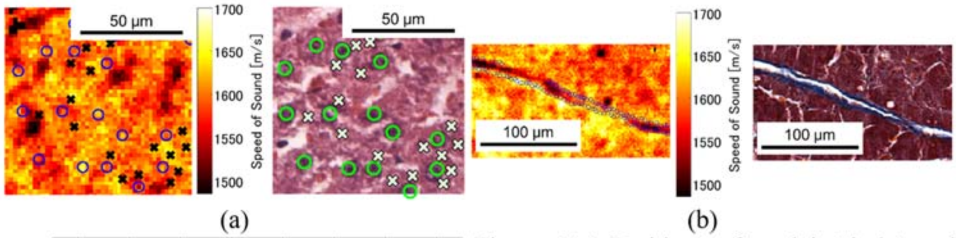

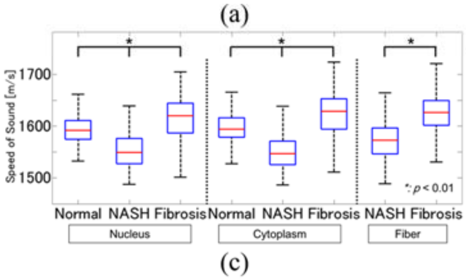

Figure 1(a) Positions of nuclei (circle) and cytoplasm (x-mark) in 2-D c map (left) and co-registered stained histology (right), (b) Position of fiber (blue line) in 2-D c map (left) and co-registered stained histology (right), (c) Distribution of c values in nucleus, cytoplasm and fibrosis for all 3 stages. The "*" symbol signifies statistically-significant difference ($p < 0.01$).

P1-C9-4

Measurement of Ultrasound Attenuation, Phase Velocity and Scattering Mean Free Path in Cortical Bone Using Independent Scattering Approximation

Omid Yousefian[1], Yasamin Karbalaeisadegh[1], Gianluca Iori[2], Kay Raum[2], Marie Muller[1]; [1]*Mechanical and Aerospace Engineering, North Carolina State University, Raleigh, NC, USA,* [2]*Acoustic Microscopy and Ultrasound Spectroscopy, Charité - Universitätsmedizin Berlin, Berlin, Germany*

Background, Motivation and Objective

In cortical bone, osteoporosis impacts both pore size and porosity. A theoretical model predicting ultrasonic parameters based on cortical micro-architectural parameters remains to be developed, and the independent effect of pore size and porosity on ultrasonic parameters remains unclear. Here, we propose a model predicting the attenuation, phase velocity and scattering mean free path (SMFP) in cortical bone. First we validate the proposed model by comparing its predictions to Finite Differences Time Domain (FDTD) simulations. Then, we use the proposed model to measure the SMFP from FDTD simulations, and show that it is possible to differentiate between healthy and osteoporotic bone in human samples.

Statement of Contribution/Methods

The proposed model is based on the Independent Scattering Approximation (ISA) describing the first order multiple scattering interactions of wave propagation in heterogeneous media. 2-D FDTD simulations of the propagation of elastic waves at 5MHz were conducted in numerical models of axial cross-section of cortical bone structures, obtained from Scanning Acoustic Microscopy (SAM) in human cortical bone. The attenuation and phase velocity were measured and compared with the ISA predictions. Next, the pore size was artificially modified in these images, ranging from 60 µm and 1% porosity originally to 120 µm and 4% porosity, to mimic osteoporosis. The SMFP was compared in the healthy and osteoporosis cases.

Results/Discussion

Attenuation and phase velocity measurements in SAM images were in good agreement with the ISA prediction for low porosities, which validates the ISA model for ultrasound propagation in bone for the porosities considered. The SMFP was significantly different in the original bone images and in the images where the porosity was artificially modified, suggesting the potential of this parameter for the assessment of cortical porosity. The SMFP had never been measured before in cortical bone. Through-transmission experiments were also conducted on bovine samples and the attenuation was compared with the ISA prediction for attenuation in order to address the effect of absorption. The experimentally measured attenuation was twice higher than the attenuation predicted from ISA, due to absorption in cortical bone.

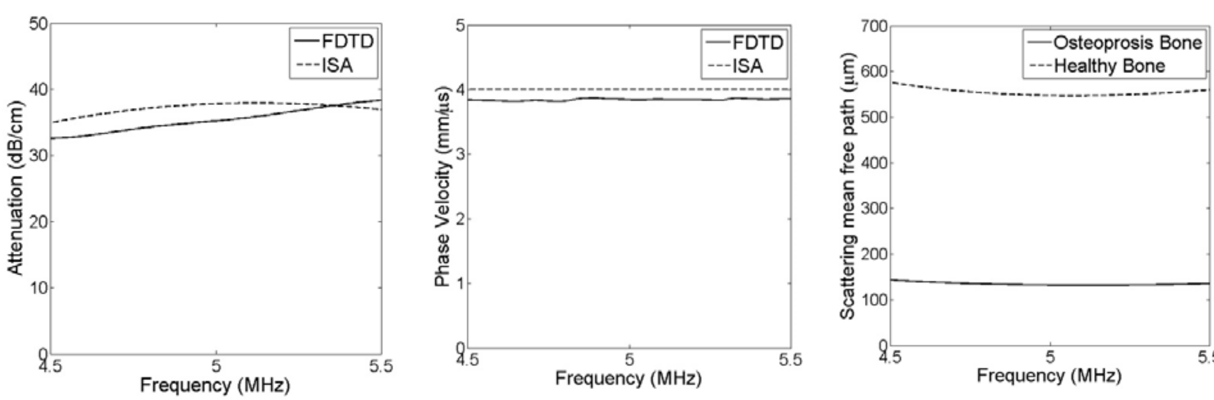

Fig1. Measured attenuation, phase velocity and scattering mean free path in SAM image

P1-C9-5

Comparison of Quantitative Ultrasound Parameters for Fat Content Liver Detection and Monitoring

Pauline Muleki-Seya[1], Aiguo Han[1], Michael P. Andre[2], John W. Erdman, Jr.[3], William D. O'Brien, Jr.[1]; [1]*Electrical and Computer Engineering, University of Illinois at Urbana-Champaign, Urbana, Illinois, USA,* [2]*Department of Radiology, University of California at San Diego, San Diego, California, USA,* [3]*Department of Food Science and Human Nutrition, University of Illinois at Urbana-Champaign, Urbana, Illinois, USA*

Background, Motivation and Objective

There are two generally used ultrasonic approaches to extract sets of quantitative parameters: the Lizzi-Feleppa (LF) and quantitative ultrasound (QUS) approaches. The LF approach estimates LF parameters from the linear fit of the backscatter coefficient (BSC), and yields slope, intercept and midband. The QUS approach relies on the attenuation coefficient (AC) and BSC versus frequency, and yields the mean AC and BSC over a defined bandwidth. By using the spherical Gaussian model, QUS-derived parameters are estimated: the effective scatterer diameter (ESD) and effective acoustic concentration (EAC). LF, QUS and QUS-derived parameters have been used for multiple applications. The goal is to examine which parameter(s) are better for estimating liver fat content, and distinguish between healthy and fatty livers.

Statement of Contribution/Methods

40 C57BL/6J mice were fed a control (n=25) or high-fat diet (n=15) for which the liver fat content, estimated by the Folch biochemical lipid assay, ranged from 4% to 24%. Liver RF data were acquired in vivo [Visualsonic Vevo 2100 the MS-400 (12-33 MHz) array transducer] and ex vivo [40 MHz single-element transducer]. From the acquired RF data, the LF, QUS and QUS-derived parameters were estimated. BSC and AC were averaged in vivo over the 18-28 MHz bandwidth and ex vivo over the 33-47 MHz bandwidth to yield the respective mean BSC and mean AC.

Results/Discussion

The *ex vivo* data generally yielded better parameter correlations with fat content; best correlations were EAC (R^2=0.78), mean BSC (R^2=0.73), and LF midband (R^2=0.70). The *in vivo* data generally yielded worse parameter correlations with fat content: best correlation was mean AC (R^2=0.18). If a threshold fat content of 11.6% in mouse livers were to be defined to represent normal vs. fatty livers, then the parameter yielding the best sensitivities and specificities to differentiate normal vs. fatty liver *ex vivo* would be the mean AC (sensitivity=1, specificity=1), then mean BSC (sensitivity=0.87, specificity=1). *In vivo*, mean BSC and LF midband are (sensitivity=1, specificity=0.41 for both) but mean AC present a better compromise (sensitivity=0.77, specificity=0.68) to differentiate between normal and fatty liver. It is not surprising to obtain better results *ex vivo* than *in vivo* because of the mathematics between the planar reference method (*ex vivo*) and the reference phantom method (*in vivo*), and without (*ex vivo*) and with (*in vivo*) the interposed tissue present between skin and liver. [Support: NIH R37EB002641]

P1-C9-6

Long-term Movement Analysis of Cervical Vertebrae with Normalized Cross-Correlation and Subsample Estimation

Mingxin Zheng[1,2], Amin Mohamadi[2], Thomas Szabo[1], Brian Snyder[1,2]; [1]*Department of Biomedical Engineering, Boston University, Boston, MA, USA,* [2]*Beth Israel Deaconess Medical Center, Boston, MA, USA*

Background, Motivation and Objective

Imaged-based motion analysis of human musculoskeletal systems is a burgeoning area of research. We have previously demonstrated the capability of B-mode ultrasound (US) to statically and dynamically image cervical spine kinematics both *ex-vivo* and *in-vivo*. However high frame rates and long exposure time are required to successfully track the displacement of contiguous spinal units over thousands of US frames. We present a multi-frame tracking algorithm to analyze the motion of vertebrae using US over prolonged time periods and its validation using both idealized phantoms and human cadaver functional spine units.

Statement of Contribution/Methods

Framework: Conventional methods tracking large strain sum displacements pre- and post- deformation, which can accumulate large errors over time. Our proposed multi-frame method obtains displacements between the frame to track with designated previous frames of RF data, and uses the redundant information to optimize results.

Displacement Estimation: After outlining the vertebrae in the first frame of the US image sequence, a box blur filter was applied to segment vertebral surface defining a region of interest (ROI) that corresponded to the vertebral body. The ROI was tracked by Normalized Cross-Correlation (NCC) to estimate the translational displacement. Since US resolution is lower in the lateral direction, parabolic fitting subsample estimation was applied.

Validation: A 3D printed phantom of an isolated cervical vertebra and 6 human cadaver specimens with soft tissue retained were mounted to the piston that provides accurately controlled displacements. Series of sinusoidal displacements (amplitude: 1-4mm, frequency: 1-10Hz) were imaged with a Terason t3200 US probe with a 7.5 MHz linear transducer 8IOL4 oriented over a range of imaging plane trajectories.

Results/Discussion

Comparison of our multi-frame tracking method to traditional frame-by-frame methods demonstrated stable error variances that were 1~2 magnitudes lower than conventional methods for 600 frames (Fig 1.). The root mean square error depended on motion frequency, amplitude, and extent of retained soft tissue surrounding the vertebrae. These results demonstrate the multi-frame approach has significant advantages when tracking complex spine motions over prolonged time periods.

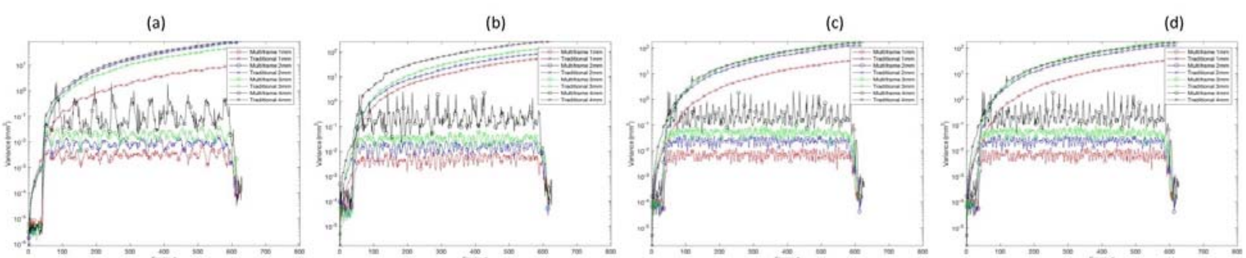

Figure 1. Displacement estimate error variance as a function of number of frames in sinusoidal motion at (a)1Hz; (b)2Hz; (c) 5Hz; (d) 10Hz. Performance between traditional method (marked by ×) and multi-frame method (marked by ○) is compared for long-term movement.

P1-C9-7

Quantitative Ultrasound Parameters in Ex-Vivo Fibrotic Rabbit Livers: Liver Stiffness and Tissue Microstructure Estimation

Jean-Michel Escoffre[1], Anthony Novell[1], Ayache Bouakaz[1], Yanis M. Benane[2], Olivier Basset[2], **Emilie Franceschini[3]**; [1]*Imagerie et Cerveau, Université François-Rabelais, Inserm, Tours, France,* [2]*Creatis, Univ.Lyon, INSA-Lyon, Université Claude Bernard Lyon 1, UJM-Saint Etienne, CNRS, Inserm, Villeurbanne, France,* [3]*Aix-Marseille Université, Centrale Marseille, Laboratoire de Mécanique et d'Acoustique, CNRS, Marseille, France*

Background, Motivation and Objective

Diagnosis and assessment of liver fibrosis grade required for management is mainly based on blood tests and invasive hepatic puncture-biopsy. Quantitative UltraSound (QUS) techniques provide insight into tissue microstructure and are based on the frequency-based analysis of the signals from biological tissues. This study aims to explore the diagnostic performance of QUS technique in high frequency (10-50 MHz) for detection of liver fibrosis. The changes in QUS parameters of healthy and fibrotic livers were investigated and were compared to the changes in liver stiffness using supersonic shear elastography.

Statement of Contribution/Methods

CCL4 was s.c. injected in the rabbit neck for 6, 9 or 12 weeks to induce different liver fibrosis stages (2-3 rabbits/group). Attenuation and backscatter coefficients (BSCs) were estimated (in the 10-30 MHz [MS250 probe] and 20-40 MHz [MS550S probe] frequency bandwidth, with Vevo2100 scanner) using the spectral difference method and the reference phantom method, respectively. Effective scatterer diameter and effective acoustic concentration were estimated by fitting the measured BSC to an estimated BSC calculated with a spherical Gaussian model. Liver stiffness was measured using shear wave elastography (SSI). Finally, histopathological analysis of livers was performed using picrosirius red staining in order to rank the livers according to the Ishak fibrosis staging scale (A,B).

Results/Discussion

In agreement with the literature, our data showed that the elastic modulus values were on the order of several thousand of Pascals and increased with the fibrosis grade (C). In addition, mean attenuation at 40 MHz was higher in fibrotic livers: 0.85 dB/cm/MHz for grades 2 and 3, 0.89 dB/cm/MHz for grades 4 and 5, when compared to 0.52 dB/cm/MHz for healthy livers. Mean acoustic concentration estimated in the 10-40 frequency bandwidth was lower in fibrotic livers: 51 dB.cm-3 for grades 3, 4 and 5, and 54 dB.cm-3 for grade 2, when compared to 57 dB.cm-3 in healthy livers (D). These data demonstrated that the microstructures of liver tissue changed during the fibrosis process. Altogether, these results showed that both US imaging tools are complementary to investigate the pathophysiological process of liver fibrosis.

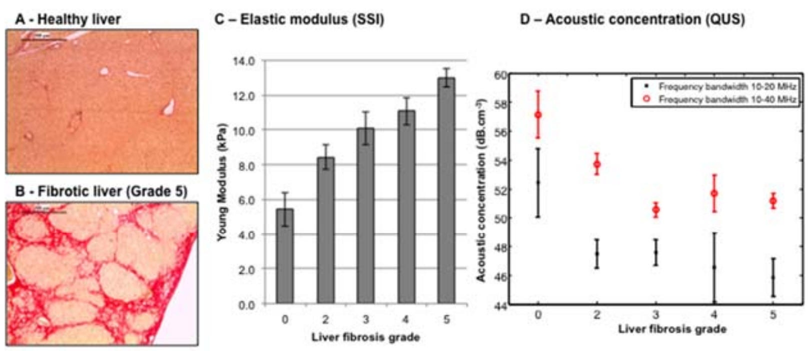

P1-C9-8

Effect of Medullary Cavity on the Two Wave Phenomenon in the Distal Part of Long Bone

Shoko Nakanishi[1], Yumiko Kinoshita[1], Mami Matsukawa[1]; [1]*Doshisha University, Kyoto, Japan*

Background, Motivation and Objective

Osteoporosis is a skeletal disease which increases the risk of bone fracture. We have proposed a ultrasound technique for the early detection of osteoporosis using two wave phenomenon in cancellous bone. In this phenomenon, we can find the fast wave mainly propagating along trabeculae, and the slow wave propagating in the bone marrow [1].

In the early stage of osteoporosis, the medullary cavity (a hole in the cancellous bone) becomes larger in addition to the decrease of bone volume. The effects of such structural changes seem important to understand two wave phenomenon. In this study, we experimentally studied effects of medullary cavity on the two wave phenomenon.

Statement of Contribution/Methods

Human radius bone model were prepared from left and right swine femora. The samples partly include cancellous bone as shown in Fig. 1(a). The structures of cancellous bone and medullary cavity were observed by the X-ray micro CT (Shimadzu, SMX-160CTs). The end of cancellous bone area was confirmed by 3D CT image. Ultrasonic pulse immersion measurements were performed using focus PVDF transducers (Custom-made, Toray, Japan, focal length 40 mm). A single sinusoidal wave at 1 MHz was applied to the transmitter, and the ultrasound was irradiated at the center part of the model (Fig. 1 (a)). By changing the measurement points, the changes of transmitted slow waves were observed. After removing the inside cancellous bone, the transmitted waves were again observed.

Results/Discussion

Fig. 1 (b) shows the wave amplitudes as a function of measurement points. The slow wave amplitudes showed a peak at the end of cancellous bone area. In the area where both cortical and cancellous bones exist, slow wave amplitudes decreased with the decrease of the medullary cavity area. This is due to the increases of cancellous bone part. The slow wave then seems to be a good indicator to evaluate the existence of inside cancellous bone. On the other hand, in the area of cortical bone only, the thickness of cortical bone affected wave amplitudes, which was found as the decrease of wave amplitude.

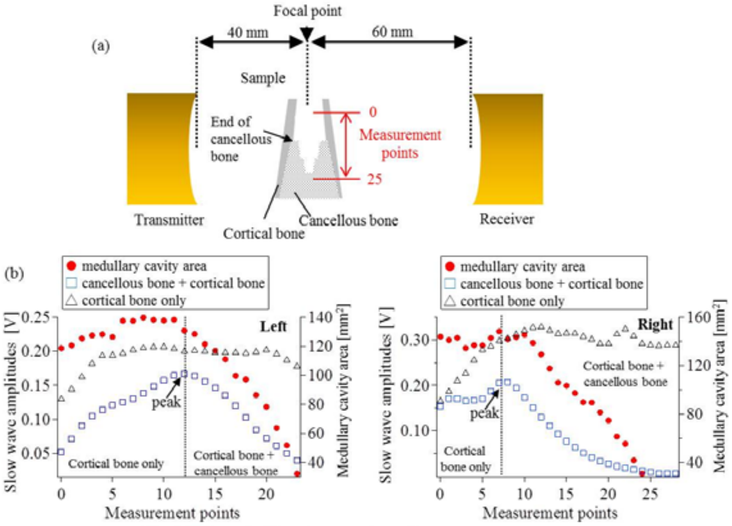

Fig. 1 (a) Layout of transducers and sample
(b) Relationship medullary cavity and amplitude of slow waves

P1-C9-9

Quantitative Ultrasound and the Pancreas: Demonstration of Early Detection Capability

Rita Miller[1], Aiguo Han[1], John Erdman[2], Joanna Shisler[3], Matthew Wallig[4], **William O'Brien[1]**; *[1]Department of Electrical and Computer Engineering, University of Illinois, USA, [2]Department of Food Science and Human Nutrition, University of Illinois, USA, [3]Department of Microbiology, University of Illinois, USA, [4]Department of Pathobiology, University of Illinois, USA*

Background, Motivation and Objective

Identifying real-time changes in tissues via quantitative ultrasound (QUS) approaches are clinically significant, particularly if QUS changes correspond to early detection of disease or provide early assessment of treatment success. Thus, understanding sequential steps in disease progression is key for success. Cerulein-induced inflammation of the pancreas (pancreatitis) in rodent models causes a significant release of pancreatic enzymes into blood, and it induces interstitial edema and inflammatory cell infiltration into the pancreas. This degree of pancreatitis is relatively mild: all animals survive the induction of pancreatitis that resolves itself in ~7 days. This makes this model an excellent one for studying ultrasonic attenuation coefficient (AC: dB/cm-MHz) and backscatter coefficient (BSC: 1/cm-sr) over time. The edematous stroma, cell shrinkage and death, followed by repopulation by dedifferentiated acinar cells, has certain similarities with the morphologies of some forms of pancreatic carcinoma (PCa).

Statement of Contribution/Methods

The study has several unique contributions: 1) The cerulein-induced pancreatitis model can be used as a surrogate for the PCa model, particularly for detecting early responses to PCa onset/treatment. 2) Understanding the progression of acute pancreatitis per se is imperative for successful intervention and treatment, especially in the early phases of the disease, before other clinical changes are manifest.

Pancreatic AC and BSC (25-50 MHz) were estimated in vivo (VEVO2100) and ex vivo (40-MHz transducer) at baseline (no cerulein injections) and at 2, 4, 15, 24, 48, 60, 72 and 168 h after cerulein injections (40 µg/kg injected intraperitoneally, hourly four times) in Sprague-Dawley rats (N = 66). Following euthanasia, the pancreas was removed en mass and evaluated histopathologically on H&E stained sections by a board-certified veterinary pathologist.

Results/Discussion

There are significant measureable early effects on both in vivo AC and BSC (and their respective ex vivo estimates) relative to baseline controls that reflect the temporal biochemical and morphological effects of cerulein. The general trend is decreased AC and BSC at early time points and then rebound increases relative to controls at later time points. The greatest AC and BSC decreases occurred at 2 hr post-cerulein injections [29% AC (in dB/cm-MHz) decrease and 34% BSC (in dB) decrease, at 25 MHz)], suggesting high likelihood for early detection of either disease onset or response to therapy using quantitative ultrasound measures. [Support: NIH R37EB002641]

P1-C9-10

Evaluation of In-Vivo Kinematics of Cervical Spines by Co-Registering Dynamic Ultrasound with MRI

Mingxin Zheng[1,2], Amin Mohamadi[2], Thomas Szabo[1], Brian Snyder[1,2]; *[1]Department of Biomedical Engineering, Boston University, Boston, MA, USA, [2]Beth Israel Deaconess Medical Center, Boston, MA, USA*

Background, Motivation and Objective

Neck pain is a common occupational health complaint associated with exposure to repetitive loads and vibrations. Currently there are no methods to measure the dynamic motion of the cervical spine in at-risk individuals in the work environment. The aim of the current study is to develop a methodology for calculating real-time in-vivo C4-5-6 functional spinal unit (FSU) kinematics by co-registering static MRI images of each individual's cervical spine with dynamic ultrasound (US) image profiles of C4-5-6 during jump tests.

Statement of Contribution/Methods

Experiment Design: With IRB approval, T2-weighted MRI scans were obtained from 12 subjects (21 – 45 yrs, 9 males and 3 females). Each subject repetitively jumped on and off a 0.8-foot step. Dual US probes (Terason 15L4 linear transducer, 4-15MHz) supported by a cervical collar in fixed orientations imaged the anterior and posterior surface profiles of C4-5-6 FSUs in real time. The load applied to the axial skeleton at landing was measured by a force plate. Para-cervical muscle (SCM, upper trapezius) activity was measured by surface electromyography (EMG).

Image Processing: Subject-specific MRI scans were used to develop surface point cloud model of C4-5-6 vertebrae. Surface profiles of the vertebrae were extracted from continuous US radiofrequency (RF) data recorded during the jump test. By assuming that the vertebrae behave as rigid bodies, we created point-to-point matching between coincident ultrasound images and the bone surface model using a validated global optimal Iterative Closest Point (ICP) algorithm to calculate in-vivo FSU displacements and flexion angles.

Results/Discussion

The accuracy of the MRI-US co-registration method was validated using a cervical spine phantom model with a root-mean-square error of 0.34mm. Sequential US images of C4-5 and C5-6 portray the relative displacements and flexion angles of the FSU calculated by matching the dynamic US images to the static 3D model (Fig 1b). EMG measurement of the para-cervical muscles was correlated with dynamic FSU motion; FSU displacement during load impact was attenuated by muscle activation.

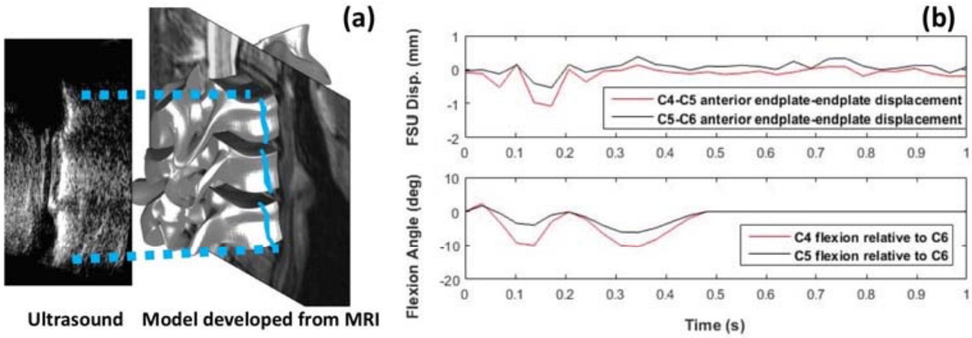

Figure 1. Cervical spine motion was tracked by Ultrasound RF data. Using the registered 3D model, translational and rotational motion were calculated. (a) Ultrasound profile was co-registered with 3D static MRI based model by minimizing the global minimum residual between the profile and the model. (b) C4-5-6 kinematics calculated from ultrasound data from a subject who jumped off an 0.8 foot high step.

P1-C9-11

Measurement of Longitudinal Wave Velocity in Articular Cartilage by Micro Brillouin Scattering

Mami Kawase[1], Mami Matsukawa[1], Hiromichi Hayashi[1], Yoshiaki Shibagaki[1], Masahiko Kawabe[1]; [1]*Doshisha University, Kyotanabe, Kyoto, Japan*

Background, Motivation and Objective

Articular cartilage is composed of cartilage cells and extracellular matrix (mainly collagen type II and proteoglycan). When stress is applied, the cartilage releases water and the stress is distributed [1]. The extra-cellular matrix structure is important to perform normal cartilaginous functions. It is then important to evaluate the elasticity and anisotropy of the cartilage, in addition to the heterogeneity. In this study, longitudinal wave velocity distribution, velocity anisotropy and the effect of water on the velocity in the cartilage were investigated using a micro-Brillouin scattering technique.

Statement of Contribution/Methods

Two thin articular cartilage specimens (8×10 mm^2) were obtained from the distal end of 31-month-old female bovine left femur. These specimens were cut normal to the anterior-posterior direction. The specimen thicknesses were approximately 150 μm. Brillouin scattering measurements were performed with a six-pass tandem Fabry-Pérot interferometer using a solid state laser with wave length of 532 nm. The system included an optical microscope. The actual spot diameter of the focused laser beam on the specimen was approximately 10 μm. The system can measure in-plane velocity anisotropy by rotating the specimen. To evaluate the effect of the water content on the cartilage, the velocities in the dry and wet specimens were also observed.

Results/Discussion

Fig.1(a) shows velocity distribution in a dry specimen. Wave propagation direction was parallel to the surface of the subchondral bone. The range of the wave velocity was 3.36-3.83×10^3 m/s, showing the heterogeneous elastic properties in the cartilage. The averaged velocity in deep layer was high, whereas they were comparatively low in the upper layer. The weak anisotropic characters were also observed as the velocity changes (Fig.1(b)), which seemed to mainly depend on the orientation of the collagen [1]. This wave velocity difference between dry and wet specimens was about 1.54×10^3 m/s. Not only the wave velocity but also the refractive index greatly changed depending on the water content in the cartilage.

[1] A.K.Jeffery, et all., J.Bone, joint Surgery, Vol. 73-B, pp. 795-801 (1991).

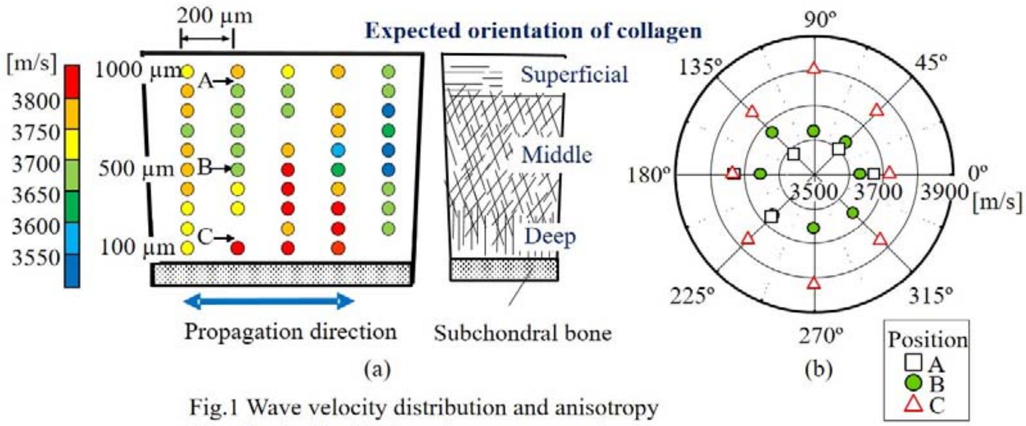

Fig.1 Wave velocity distribution and anisotropy
(a) velocity distribution of wave propagation
(b) anisotropy of velocity
0 degree indicates parallel to the surface of the subchondral bone.

P1-C10 - MTH: Ultrasound Mediated Delivery

Exhibit Hall

Saturday, September 9, 2017, 9:30 am - 4:00 pm

Chair: **Michael Oelze**
Univ. of Illinois

P1-C10-1

Ultrasound-Enhanced Drug Delivery for Treatment of Onychomycosis

Alina Kline-Schoder[1], Zung Le[2], Vesna Zderic[1]; [1]*Department of Biomedical Engineering, George Washington University, Washington, DC, USA,* [2]*Department of Podiatry, Medical Faculty Associates, Washington, DC, USA*

Background, Motivation and Objective

Onychomycosis is a fungal nail disorder that is characterized by thick and yellow nails that can be extremely painful and lead to psychosocial issues. In onychomycosis, the fungus lives on the nail bed. Current antifungal drugs are applied to the top of the nail, but due to the poor permeability of the nail, they are unable to reliably reach, and therefore treat the fungus. These drugs only have non-serious, infrequently reported side effects, but their cure rate is only 36% after 6 months of daily application. The aim of this study is to determine the efficacy and safety of using ultrasound to increase the permeability of the nail. To do this, we use low-intensity ultrasound at different parameters to perform in vitro measurements and utilize PZFlex software to perform safety modeling experiments.

Statement of Contribution/Methods

Two sets of ultrasonic experiments were performed using porcine nails: the luminosity experiments and the diffusion cell experiments. In both experiments, planar ultrasound transducers were used to sonicate nails with an intensity of 1 +/- 0.1 W/cm2, a continuous duration of 5 min and frequencies of 400 kHz, 600 kHz, 800 kHz, and 1 MHz. In the luminosity experiments, pieces of nail were placed in a 100 mL beaker, 45 mm beneath the transducer. The beaker was filled with a drug-mimicking hydrophilic blue dye and then sonicated. After sonication, the nails were cut in half and photographed. The image of the nails' cross section was analyzed using Photoshop in order to compare the average brightness - and therefore permeation of dye through each of the nails. In the diffusion cell experiments, a Franz Diffusion Cell was used; the receiving compartment below the nail was filled with saline and the donor compartment above the nail was filled with the same blue dye as was previously used. The nail was sonicated and the absorbance of the receiving compartment was measured after experimentation to quantify the permeation of dye through the nail. In the final experiment, a safety modeling experiment was performed using PZFlex software and a model of the human toe.

Results/Discussion

In both sets of in vitro experiments, a higher frequency of ultrasound was found to correlate to more dye permeation through the nail. In the luminosity experiments, the 800 kHz and 1 MHz frequencies were statistically significant ($p<0.05$) with an increase in dye delivery of up to 95% as compared to control values. The 1 MHz trial had the most diffusion through the nails with an average luminosity value of .18 compared to the average control luminosity value of .09. The diffusion cell results were statistically significant ($p<0.05$) at all four frequencies, with an increase in dye delivery of up to 70% as compared to the control. Again, the highest permeation was in the 1 MHz experiment with an average dilution of .13 g/mL as compared to the average control dilution of .077 g/mL. In the PZFlex modeling experiment a safe temperature increase of less than 1.5°C was found at all frequencies.

P1-C10-2

Antibody-Conjugated Phase-Change Nano-Droplet for Ultrasound Therapeutic Agent

Ayumu Ishijima[1], Shinya Yamahira[1], Satoshi Yamaguchi[2], Etsuko Kobayashi[1], Yoshikazu Shibasaki[2], Takashi Azuma[3], Teruyuki Nagamune[1], Ichiro Sakuma[1]; [1]*School of Engineering, The University of Tokyo, Tokyo, Japan,* [2]*Research Center for Advanced Science and Technology, The University of Tokyo, Tokyo, Japan,* [3]*School of Medicine, The University of Tokyo, Tokyo, Japan*

Background, Motivation and Objective

Nanomedicines recently gain great attention for their cancer targeting abilities and multi-functionality. Active targeting of nanoparticles with external stimuli-responsive property would improve the therapeutic efficacy and reduce harmful side effects because therapeutic effects are concentrated at the combined area of both drug and external stimuli.

Statement of Contribution/Methods

Here we developed an ultrasound-triggered therapeutic agent that employed a monoclonal antibody 9E5 conjugated to a phase-change nano-droplet (PCND). PCND is a sub-micron sized particle composed of a phospholipid shells and liquid-state perfluorocarbon that vaporises into microbubble upon ultrasound exposure. 9E5 is an anti-epiregulin (EREG) antibody that targets a receptor for epidermal growth factor. Introducing the conjugates to the inside of cancer cells via receptor-mediated endocytosis and exposing them to ultrasound can potentially induce intracellular vaporisation leading to rapid and selective disruption of cell structures.

Results/Discussion

We have succeeded in demonstrating the selective targeting and cytotoxic effects *in vitro* with direct observation of intracellular vaporisation by high-speed imaging. Results of cytotoxic efficacy measurements indicated that cell viability was reduced to 10.1 ± 1.9% ($N = 3$) for high-level EREG expression cells treated with 9E5-conjugated PCNDs and ultrasound, while there was no significant cell viability decrease for without PCNDs and without ultrasound exposure as shown in Fig. 1a. In detail, treating high EREG-expressing cells with 9E5-conjugated PCNDs for 72 h did not show decrease in viability without ultrasound exposure (95.2 ± 1.9%, $N = 3$), whereas that of ultrasound exposure to the treated cells decreased to 10.5 ± 2.0% ($N = 3$) as shown in Fig. 1 (b).

These results indicate that 9E5-conjugated PCNDs can be stable for at least 72 h in living cells and can exert their function as ultrasound-stimuli responsive therapeutic agents. Noted that any anti-cancer drugs were loaded to the particle, and it is unique that the therapeutic effects are exerted by physical actions. Thus, the present agent potentially avoids concerns about drug resistance and biological variability between cancer types. Accordingly, this approach is promising for damaging any type of cancer cell in a rapid and selective manner.

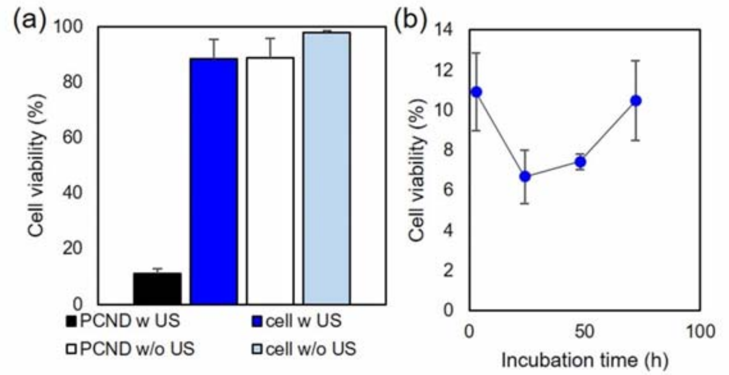

Figure 1. Cytotoxic efficacy of vaporized 9E5-conjugated PCND. (a) Flow cytometry assay of the viability of PCND-treated or non-treated cells in response to ultrasound exposure. (b) Flow cytometry assay of the viability of cells treated with PCND for 3, 24, 48 and 72 hours after ultrasound exposure. The cell viabilities were quantified by PI-staining. Each bars represent the mean ± S.D. (*N = 3*).

P1-C10-3

Transdermal Delivery of Macromolecule Using Sonophoresis with Cavitation Seed: In-Vivo Study

Hyeon Park[1], Donghee Park[1], Jongho Won[1], Jiyoung Jang[1], Bomi Hong[1], Yujin Park[1], Chulwoo Kim[1], Jongbum Seo[2]; *[1]Bioinfra Inc., Korea, Republic of, [2]Yonsei University, Korea, Republic of*

Background, Motivation and Objective

In previous studies, we have found that addition of cavitation seed such as ultrasound contrast agents (UCA) in sonophoresis accelerate and increase efficiency of transdermal drug delivery (TDD). Actively-induced cavitation with low intensity ultrasound (less than 1 MPa) on the skin causes disordering of the lipid bilayers and the formation of aqueous channels. However, commercial UCAs also have limit, because mixed UCA is uniformly positioned in the water based solution, not on the skin surface. In order to enhance the TDD, the cavitation effect of cavitation seed should be generated near skin surface. For that reason, we manufactured specialized cavitation seed for TDD, which can be sank near skin surface by gravity. In order to make sure possibility of macromolecules delivery using cavitation seed, we performed in vivo experiment using sonophoresis with specialized cavitation seed.

Statement of Contribution/Methods

FITC-labeled dextran(FD), has 150 kDa molecular weight, was used for estimation of TDD efficiency. Manufactured cavitation seed mixed again with FD solution, ratio 1:1000 (v/v). 8 weeks male Sprague-Dawley rats were shaved back hair before experiment. Ultrasound applied with specific conditions (frequency, 1.06 MHz; pulse repetition frequency, 100 msec with 3 % duty cycle; acoustic power, 2.25 W/<cm><2>). Four different experimental groups were formed to compare the efficiency of TDD (diffusion, cavitation seed only, ultrasound only, ultrasound with hexane cavitation seed).

Results/Discussion

The results of penetration depth were presented by a fluorescence microscope and total flux in region of interest was calculated using IVIS system. In results of penetration depth, the experimental groups excluding ultrasound with hexane cavitation seed, show absorption depth less than 50 µm and borderline was very clear, excluding hair pores. On the other hand, ultrasound with hexane cavitation seed group delivered to 100 µm depth under the skin. Dermis layer in rat locate at depth of 100 µm approximately. In addition, relative contrast of total flux per ROI was 6.4 fold in hexane cavitation seed group more than diffusion group. There is no significance of flux among the other three groups excluding hexane cavitation seed group. These results shows that traditional sonophoresis cannot deliver the macromolecule material, while sonophoresis with hexane cavitation seed can deliver the macromolecule materials (150kDa) into the skin. As a result, simultaneous application of cavitation seed for TDD and ultrasound demonstrated high efficiency and possibility of macromolecule delivery to dermis. We strongly believe that sonophoresis with speciallized cavitation seed has the potential for broad application including various skin diseases, vaccination, anti-aging, skin lightening, wrinkle improvement, anti-depilation.

P1-C10-4

Comparison of Single Spot and Volume Ultrasound Sonications for Efficient Nanoparticle Delivery to Glioblastoma Model in Rats.

Allegra Conti[1], Matthieu Gerstenmayer[1], Françoise Geffroy[1], Olivier Tillement[2], Francois Lux[2], Sébastien Mériaux[1], Benoit Larrat[1]; *[1]NeuroSpin, CEA, Gif-sur-Yvette, France, [2]University Lyon 1, Lyon, France*

Background, Motivation and Objective

Brain tumors therapy is limited by the Blood-Tumor Barrier (BTB) and Blood-Brain Barrier (BBB), still intact in the infiltrative areas. Low intensity Focused Ultrasound (FUS) in conjunction with microbubbles is the only method allowing the local disruption of the BTB/BBB [Hynynen et al. 2001, Zhao et al. 2015]. Proper study of the influence of acoustic scanning parameters (duty cycle, number of focal spots) on the amount of delivered nanoparticles is not available so far. Here, we compared two acoustic strategies to enhance the molecular concentration within brain tumors. The efficacy of the two methods is evaluated on the basis of absolute concentrations of delivered MR-contrast agents (CA) and on their rates of uptake/clearance by the tumors.

Statement of Contribution/Methods

9L tumors were implanted in both striatum of Fischer rats (n=8): one tumor was sonicated and the other one was used as a control. A MR-guided motorized FUS system [Magnin et al. 2016] was used to target only one of the two tumors. A single point sonication at the tumor core (n=3) and a sonication at 8 vertices of a 3D trajectory covering the whole tumor volume (n=5) were compared. Frequency, duty cycle, sonication time and estimated peak negative pressure were kept constant respectively to 1.5 MHz, 3%, 120 s and 1.2 MPa. Microbubbles administration was followed by FUS application and by the intravenous injection of a Gd-based MR-CA (AGuIX). Gd uptake and clearance inside the tumors was imaged by acquiring dynamic 3D T_1-maps within 1 hour allowing to reconstruct absolute CA-maps in the whole brain [Marty et al. 2012]. Tumors were manually segmented on T_2-weighted anatomical images co-registered to the CA-maps, in order to follow the CA concentration time courses in tumors.

Results/Discussion

Figure 1 shows the results obtained with 1 and 8 points sonications. With both methods, higher CA concentrations are delivered to sonicated tumors respect to the control ones. The single spot sonication appears to be more efficient, independently of the tumor size although not very efficient in large tumors (B). Choice of acoustic trajectory has a huge impact on drug delivery efficacy and needs to be optimized to each configuration. It seems to affect more the uptake rate than the clearance rate of the pharmacokinetics of tumors.

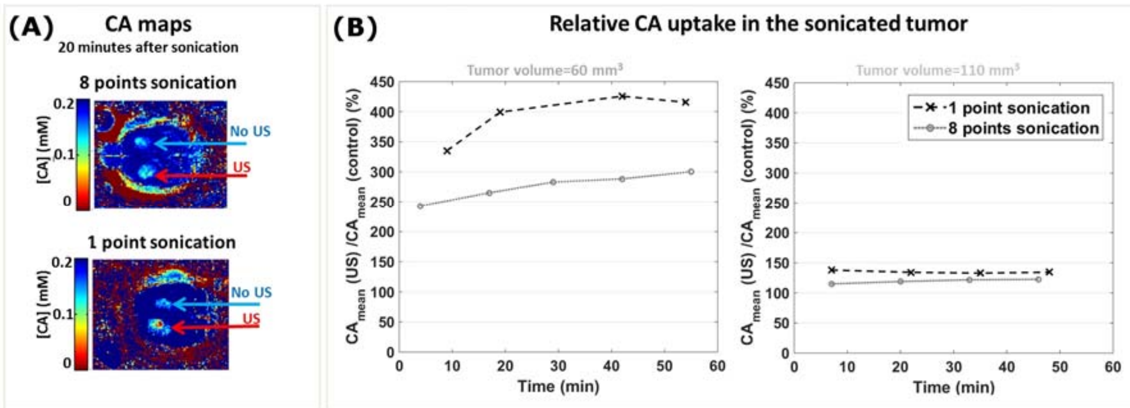

P1-C10-5

Focused Ultrasound-Facilitated Molecular Delivery to the Brain Using Drug-Loaded Nanodroplets

Shih-Ying Wu[1], Samantha Fix[2], Christopher Arena[3], Cherry Chen[1], Wenlan Zheng[1], Oluyemi Olumolade[1], Virginie Papadopoulou[3], Paul Dayton[3], Elisa Konofagou[1]; [1]*Department of Biomedical Engineering, Columbia University, USA,* [2]*Eshelman School of Pharmacy, University of North Carolina, USA,* [3]*Joint Department of Biomedical Engineering, University of North Carolina and North Carolina State University, USA*

Background, Motivation and Objective

Acoustically-activated nanodroplets facilitate localized drug delivery after vaporization with improved in vivo stability, drug payload, and minimal interference outside of the ultrasound focal zone compared with microbubbles. They are new acoustic mediators to induce blood-brain barrier (BBB) opening for drug delivery to the brain, with promising potential of extravasation to enhance targeted delivery in the extravascular space due to the nano sizes.

Statement of Contribution/Methods

In this study, low-boiling-point nanodroplets were designed to induce BBB opening and to carry fluorescent dye DiI as a model drug on the lipid shell for in vivo molecular delivery. Both octafluoropropane (OFP) and decafluorobutane (DFB) nanodroplets were used first in vitro for assessing their relative vaporization efficiency with high-speed microscopy, and then in vivo for delivering large molecules (40-kDa dextran) to the murine brain. Finally, DiI-tagged nanodroplets were used for drug delivery during and after BBB opening.

Results/Discussion

It was found that at low pressures (300-450 kPa), OFP droplets vaporized into a greater number of microbubbles compared to DFB droplets at higher pressures (750-900 kPa). Consistent with the in vitro findings, successful and safe dextran delivery was achieved with OFP droplets at 300-450 kPa using ¼ dosage compared to DFB droplets at 900 kPa where inertial cavitation caused damage. DiI-tagged OFP nanodroplets were delivered successfully to the brain for the first time after BBB opening at 450 kPa. In conclusion, low boiling-point nanodroplets can serve both as effective BBB opening mediators and drug carriers, and the amount of delivery was associated with the vaporization efficiency that can be modulated by the boiling points of nanodroplets.

(Figure 1. Fluorescence microscopy showed enhanced delivery of DiI-OFP droplets after BBB opening.)

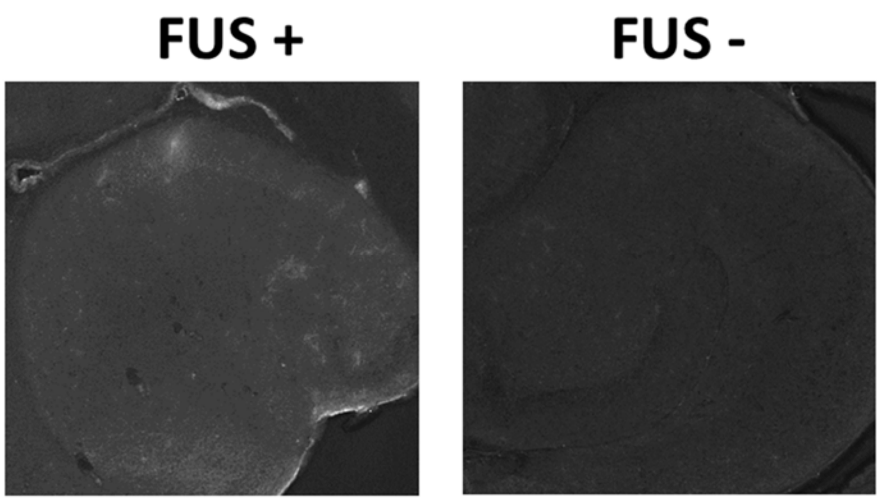

P1-C10-6

Sonodynamic therapy using protoporphyrin IX encapsulated microbubbles inhibits tumor growth

Xucai Chen[1], Bin Qin[1], Daniel Whitehurst[1], Brandon Helfield[1], Linda Lavery[1], Flordeliza S. Villanueva[1]; [1]*Center for Ultrasound Molecular Imaging and Therapeutics, University of Pittsburgh, Pittsburgh, PA, USA*

Background, Motivation and Objective

Sonodynamic therapy is a cancer treatment using drugs called "sonosensitizers" which, upon exposure to ultrasound (US), generate reactive oxygen species (ROS), thereby causing cell death. Despite the potential of sonodynamic therapy, many ideal sonosensitizers, such as protoporphyrin IX (PpIX), are hydrophobic compounds; poor water solubility limits systemic delivery and constrains clinical translation. We hypothesized that a PpIX-loaded lipid microbubble (MB) would have advantages over PpIX alone by ultimately allowing systemic delivery and also by locally concentrating US energy for greater PpIX activation. Accordingly, we developed an efficiently PpIX-loaded MB formulation and characterized its US-induced cytotoxicity *in vitro* and in an *in vivo* tumor model.

Statement of Contribution/Methods

PpIX was loaded in the hydrocarbon tail region of the lipid monolayer that forms the encapsulation shell of perfluorocarbon gas-filled MBs ("MB-PpIX"). Suspensions of MB-PpIX or PpIX alone were exposed to various US conditions (1 MHz, 1-8 W/cm^2 spatial average pulse average intensity (I_{SAPA}), 1-10% duty cycle), and ROS generation was measured with Amplex Red. MB-PpIX or equivalent amount of PpIX alone (PpIX concentration: 2.9 µM) was added to cultured squamous cell carcinoma (SCC-7) cells, followed by US treatment for 2 min and alamarBlue Assay for viability 24 hrs post US. To evaluate anti-tumor effect *in vivo*, SCC-7 tumor-bearing mice received intratumoral injection of 1×10^8 MB-PpIX (n=4), equivalent dose (18.4 µg) of PpIX only (n=5), or blank MB (no PpIX, n= 3), followed by 4 min of US treatment (1 MHz, I_{SAPA}=3 W/cm^2, 10% duty cycle). Tumor volume was serially imaged and quantified by high-resolution 3D US.

Results/Discussion

A stable MB-PpIX-formulation was achieved with high drug loading (mean MB diameter 1-2 µm; 184±49 µg PpIX per 10^9 MB). ROS was generated with MB-PpIX and PpIX solution alone, in an US- and time-dependent manner, with more ROS generated by MB-PpIX compared to PpIX alone for a given US condition. For both MB-PpIX and PpIX alone, similar US-dependent cytotoxicity was observed; e.g. for MB-PpIX, more than 90% of SCC-7 cells were killed with US at I_{SAPA}=2 or 4 W/cm^2 and 10% duty cycle. *In vivo*, MB-PpIX + US caused the greatest tumor growth inhibition, with doubling time (2.8±0.5 days) more prolonged compared to that for US-treated tumors injected with only PpIX (2.1±0.3 days; p=0.026) or blank MB (1.7±0.6 days; p=0.050). These data indicate that in conjunction with pulsed US, MB-PpIX is an effective sonodynamic therapy platform that may be superior to US + PpIX alone. Our findings set the stage for non-invasive sonodynamic therapy using systemic delivery of PpIX, whereby PpIX-carrying lipid MBs allow circulation of this otherwise insoluble compound, while also focusing and augmenting US energy for enhanced sonodynamic effect.

P1-C10-7

Ultrasound Microbubble Targeted Gemcitabine Delivery for Pancreatic Cancer Treatment

Lauren Jablonowski[1], John Eisenbrey[1], David Brown[2], Maria Stanczak[1], Ji-Bin Liu[1], Jingzhi Li[1], Flemming Forsberg[1], Margaret Wheatley[2]; [1]*Department of Radiology, Thomas Jefferson University, Philadelphia, PA, USA,* [2]*School of Biomedical Engineering, Science, and Health Systems, Drexel University, Philadelphia, PA, USA*

Background, Motivation and Objective

Pancreatic ductal adenocarcinoma (PDA) is one of the most prevalent types of cancer. Studies have shown that PDA treatment with IV administration of gemcitabine (GEM) is inhibited by excessive interstitium and connective tissue (stroma) surrounding the tumor. Ultrasound (US) irradiation combined with drug-loaded polylactic acid (PLA) microbubble contrast agents (MB) may circumvent this through targeted delivery of GEM and increased permeability of the tumor stroma, while also lodging GEM-loaded fragments into the tumor tissue for sustained release. Thus, the objective of this study was to encapsulate GEM within the shell of PLA MBs and evaluate their treatment efficacy in an *in vivo* pancreatic cancer mouse model.

Statement of Contribution/Methods

GEM-loaded PLA MBs were fabricated using an established double emulsion technique and characterized *in vitro*. The efficacy of the encapsulated GEM was tested in a xenograft MiaPaCA-2 pancreatic tumor model. GEM-loaded MB, free GEM, unmodified (blank) MB, and sterile saline were administrated to 60 nude, athymic mice (Charles River, Horsham, PA). Flash/replenishment sequences were performed with an S3000 Helx scanner with a 9L4 probe (Siemens Healthineers, Mountain View, CA) following retro-orbital bolus injection of 0.1 mL of the appropriate treatment solution. Treatments were repeated 4 times over 2 weeks. Tumor size was measured twice/week, while tumor growth and mouse survival curves were generated based on tumor progression data.

Results/Discussion

Acoustic and physical characterization suggested that GEM encapsulation does not significantly affect MB morphology, contrast activity, and inertial cavitation upon exposure to US when compared to unloaded PLA MB ($p>0.23$). *In vitro* cytotoxicity of these agents against MiPaCA-2 cells confirmed GEM release from the MBs, resulting in 100% cell death with 500nM GEM release from MBs. *In vivo*, administration of GEM MBs was well tolerated and provided substantial tumoral imaging enhancement. MB destruction within the tumor was confirmed by evaluating differences in enhancement before and after destructive pulses. However, no significant difference in mouse survival or tumor growth was observed across treatment groups ($p>0.14$). Encapsulation of GEM within the PLA shell of MBs resulted in viable drug delivery agents for pancreatic cancer treatment. However, additional efforts will be needed to increase the GEM loading within the MBs for improved drug payload and treatment efficacy at the tumor site.

P1-C10-8

Ultrasound-Stimulated Drug Delivery of Reconstituted High Density Lipoprotein Nanoparticles: Effects of Drug Concentration on Tumor Uptake

Fangyuan Xiong[1], Mouna Xiong[1], Sabnis Nirupama[2], Shashank Sirsi[1], Andras Lacko[2], Kenneth Hoyt[1]; [1]*University of Texas at Dallas, USA,* [2]*University of North Texas Health Sciences Center, USA*

Background, Motivation and Objective

The abnormal vasculature of tumor and the resulting abnormal microenvironment is a major barrier to optimal chemotherapeutic drug delivery. It is well known that ultrasound (US) can increase the permeability of the tumor vessel walls and enhance the accumulation of anticancer drugs. Reconstituted high density lipoproteins (rHDL) nanoparticles (NPs) allow selective delivery of anticancer agents to tumor cells via their overexpressed SR-B1 receptor. The goal of this study is to investigate the potential of noninvasive US therapy to further improve delivery and tumor uptake of rHDL NPs preloaded with an infrared dye (IR780), which is devoted to the establishment of a surrogate chemotherapeutic model with optical localization.

Statement of Contribution/Methods

Athymic nude mice (N = 59, Charles River Laboratories) were implanted orthotopically with one million breast cancer cells (MDA-MB-231/Luc, Cell Biolabs). Three weeks later, animals were divided into seven groups with comparable mean tumor size: control, low concentration of rHDL NPs ± US therapy, moderate concentration of rHDL NPs ± US therapy, high concentration of rHDL NPs ± US therapy (N = 7 to 11 animals per group) where low, moderate and high denote 5, 10, and 50 µg of the IR780 dye payload per rHDL NP injection, respectively. The US therapy system included a single element transducer (Olympus; 1 MHz, 1.5" diameter and 3" focus) connected in series with a function generator (Tektronix) and power amplifier (Electronics & Innovation). A custom 3D printed cone with an acoustically transparent aperture and filled with degassed water allowed delivery of focused US energy to the tumor tissue. US exposure involved a pulse sequence (N = 100 cycles with acoustic pressure = 0.45 MPa) repeated every 10 ms for a duration of 5 min. Acoustic output measurements and spatial field maps were performed using a hydrophone scanning system. Each animal in the US therapy groups received a slow bolus co-injection of MB contrast agent (Definity, Lantheus Medical Imaging) and concentrated rHDL NPs, diluted to 150 µL with saline. Animals were imaged using an optical system (Pearl Trilogy, LI-COR Biotechnology) to quantify intratumoral rHDL NP accumulation at baseline and again at 1 min, 5 min, 30 min, 24 h, and 48 h. At 48 h, all animals were euthanized and tumors were excised for ex vivo analysis.

Results/Discussion

There was a marked accumulation of IR780 dye in the tumors receiving US-stimulated drug delivery compared animals receiving rHDL NPs alone. At 48 h, the in vivo optical signal recorded in the US therapy groups revealed mean increases of 36%, 56%, and 22% when compared to animals receiving the low, moderate, and high rHDL NPs alone, respectively. Overall, the addition of US therapy considerably improved local rHDL NP accumulation in tumor tissue as verified by our ex vivo tumor tissue analysis. This study concludes that US-mediated drug delivery can facilitate tumor uptake of rHDL NPs and more research is warranted.

P1-C10-9

Enhancing Fluorescein Release from In-Situ Forming PLGA Implants Using Therapeutic Ultrasound

Peter Bielecki[1], Christopher Hernandez[1], Selva Jeganathan[1], Chawan Manaspon[1], Michael Kolios[2], Agata Exner[1,3]; [1]*Biomedical Engineering, Case Western Reserve University, Cleveland, OH, USA,* [2]*Physics, Ryerson University, Toronto, Ontario, Canada,* [3]*Radiology, University Hospitals Cleveland Medical Center, Cleveland, OH, USA*

Background, Motivation and Objective

Systemic chemotherapy has been associated with poor tumor penetration and adverse cytotoxic effects. To combat this, cancer therapy with in-situ forming implants (ISFIs) can provide continuous, high dose release of chemotherapeutic drug directly at the tumor site. However, poor drug distribution through the tumor volume has limited the effectiveness and subsequent translation of ISFIs into clinical practice. Our lab has previously demonstrated an increase in drug release and penetration from injectable, phase inverting PLGA implants in an in-vitro phantom model using low frequency ultrasound. To build on this work, in-vivo fluorescein intensity and distribution was evaluated in subcutaneous ISFIs with and without therapeutic ultrasound (TUS) exposure.

Statement of Contribution/Methods

Polymer implants were made with a 39:60:1 mass ratio of Poly(DL-lactic-co-glycolic) (PLGA), N-methyl-2-pyrrolidinone (NMP), and fluorescein. 75µL of polymer solution was subcutaneously injected into either dorsal side of BALB/c nude mice (n=3). Fluorescein intensity and distribution from the ISFIs was measured using a fluorescent imager (CSI Maestro, Caliper Life Science) with a blue excitation/emission filter (435-480 nm/515 nm). One implant on each mouse was subject to TUS exposure (Omnisound® 3000, 4 cm2 surface probe, 3 MHz frequency, 2.2 W/cm2 power, 33% duty cycle) for 5 min. Temperature was measured at the implant site using a needle thermocouple. Mice were reimaged after 24 hours. Radial profiles of fluorescein distribution were acquired using ImageJ (NIH) software.

Results/Discussion

One application of TUS after ISFI formation increased both fluorescent intensity and distribution of fluorescein after 24 hours (Fig 1a). The average fluorescent intensity at the ISFI center was 8316 (a.u.) when treated with TUS compared to 4726 (a.u.) in the untreated control (Fig 1b). At 0.5 cm from the ISFI center, the average fluorescent intensity from fluorescein was nearly 6-fold greater in the TUS group 24 hours after exposure. The temperature in the implants reached an average of 46.6 C. These results suggest that a combination of thermal and mechanical events generated by the TUS application increased the spatial penetration of fluorescein away from the implants in-vivo. The US-enhanced distribution could improve the clinical efficacy of intratumoral chemotherapy.

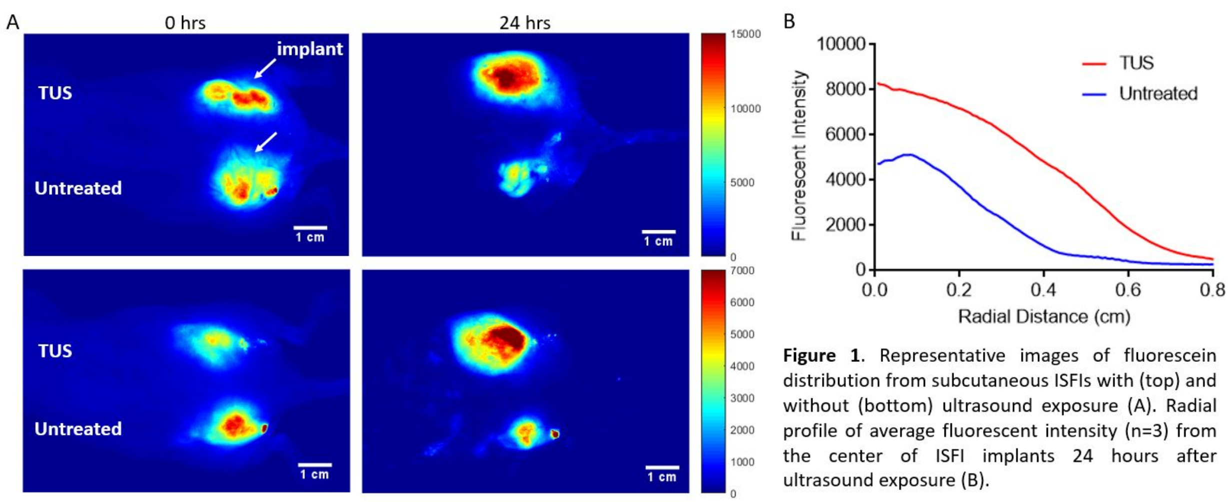

Figure 1. Representative images of fluorescein distribution from subcutaneous ISFIs with (top) and without (bottom) ultrasound exposure (A). Radial profile of average fluorescent intensity (n=3) from the center of ISFI implants 24 hours after ultrasound exposure (B).

P1-C11 - MTH: Pre-Clinical Therapeutic Ultrasound

Exhibit Hall

Saturday, September 9, 2017, 9:30 am - 4:00 pm

Chair: **David Melodelima**
INSERM

P1-C11-1

Efficient Transcranial Ultrasound Delivery via Excitation of Lamb Waves

Kamyar Firouzi[1], Pejman Ghanouni[2], Butrus T. Khuri-Yakub[1]; [1]*EE, Ginzton Lab, Stanford university, STANFORD, CA, USA,* [2]*Stanford university, STANFORD, CA, USA*

Background, Motivation and Objective

Transcranial focused ultrasound is being researched as a noninvasive means of ablating brain tumors and of increasing delivery of cancer therapeutics through the blood-brain barrier. However, the current techniques are implemented by means of a large-aperture spherical transducer. The geometric focus of these transducers limits the treatment envelope to the center of the brain, whereas the majority of cancers, especially metastases, occur along the periphery of the brain. In addition, these transducers create waves that impinge perpendicularly on the skull, which is inefficient. A normal incident transmission also sets up standing waves in the skull, which along with high attenuation leads to excess heating and a requirement for active cooling.

We have developed an array of ultrasound wedge transducers capable of efficiently delivering focused ultrasound energy into the brain with minimal heating of the skull and the ability to address regions in the brain that are close to or far from the skull.

Statement of Contribution/Methods

A wedge transducer utilizes guided Lamb waves in the skull as an efficient way of transmitting the ultrasound beam into the brain. Transmission efficiency is by virtue of a double-mode-conversion mechanism, one from the wedge into selective Lamb waves in the skull and the other from Lamb waves into the brain. Additionally, Lamb waves exhibit less attenuation than normal-incident bulk waves. The main constituents of the transducer array are wedge transducer elements arranged over a wedge ring to provide a focusing mechanism. The benefits of our approach is in improved efficiency, reduction in heating of the skull, and the ability to address regions in the brain that are close to the skull.

Results/Discussion

As a cranial phantom, we have used human skull fragments, with natural variations in thickness and porous structure. For benchmarking, we have utilized an immersion transducer to emulate both wedge and normal-incident transmissions. The field measurements are shown in Figure 1. The wedge technique exhibits around 14 dB total loss as opposed to 21 dB of the normal-incident technique. We have also fabricated wedge transducer prototypes and tested them on the skull fragments to prove the feasibility of transcranial delivery. The results demonstrate the validity of our approach both for mode-conversion and overcoming attenuation.

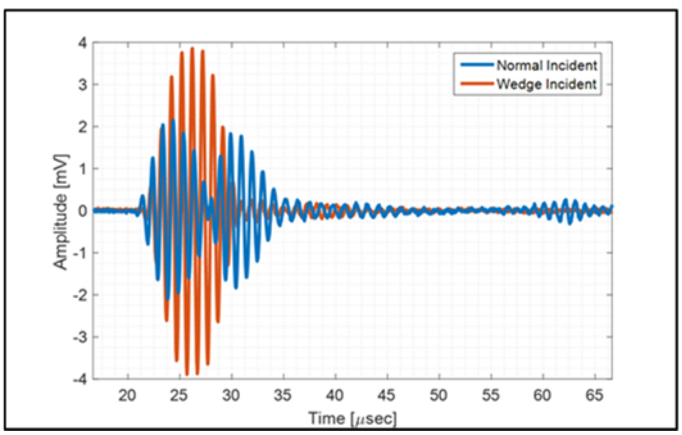

P1-C11-2

Dissolved Oxygen Scavenging by Acoustic Droplet Vaporization Using Intravascular Ultrasound

Kevin Haworth[1], Bryan Goldstein[2], Karla Mercado-Shekhar[1], Christy Holland[1], Andrew Redington[2]; [1]*Internal Medicine, University of Cincinnati, Cincinnati, Ohio, USA,* [2]*Cardiology, Cincinnati Children's Hospital Medical Center, Cincinnati, Ohio, USA*

Background, Motivation and Objective

Modification of dissolved gas content by nucleation of acoustic droplet vaporization (ADV) has been proposed for several therapeutic applications. Reducing dissolved oxygen could inhibit reactive oxygen species production during reperfusion of ischemic tissue, such as during coronary interventions to rescue myocardium. Localization of the effect may be achieved using intravascular ultrasound (IVUS), commonly used to image the coronaries in such patients. The objective of this study was to determine whether IVUS can be used to reduce dissolved oxygen by ADV.

Statement of Contribution/Methods

A perfluoropentane emulsion was created using high-speed shaking of a 4% (w/v) albumin in saline solution (0.75 mL) mixed with perfluoropentane (0.25 mL). The emulsion was infused into a coronary vessel phantom and imaged with a clinical IVUS system (40 MHz OptiCross catheter with iLabTM, Boston Scientific). Dissolved oxygen sensors were placed in the flow phantom proximal and distal to the IVUS. Duplex B-mode and passive cavitation imaging was performed using an L7-4 array (Philips) connected to a Vantage ultrasound scanner (Verasonics Inc.). Passive cavitation images (PCIs) were formed using a delay, sum, and integrate algorithm. Summation was performed over the frequency band of 2–6 MHz to map acoustic emissions.

Results/Discussion

Transverse B-mode images of the phantom and IVUS catheter with droplets infused is shown in Fig. 1A and 1B with and without IVUS acoustic output, respectively. The color map shows the location of acoustic emissions. Microbubbles are visible downstream from the IVUS transducer, indicating that ADV was nucleated. The measured dissolved oxygen for the upstream and downstream dissolved oxygen sensors are shown in Fig. 1C. A 20% decrease in dissolved oxygen was measured downstream of the IVUS transducer only when perfluoropentane droplets were infused. Modeling predicts a 20% reduction in dissolved oxygen corresponds to phase-transitioning .001% (v/v) of the infused fluid. These results demonstrate that a reduction of dissolved oxygen by ADV is feasible from a clinical IVUS system which uses a 40 MHz transmit frequency. Future studies will assess the potential therapeutic efficacy of IVUS-nucleated ADV.

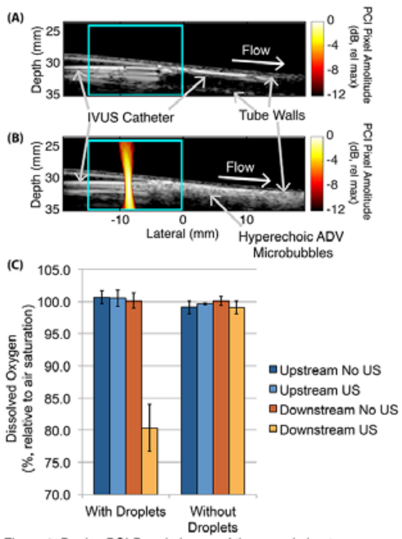

Figure 1: Duplex PCI-Bmode image of the vessel phantom containing droplets with (A) and without (B) IVUS exposure. Acoustic emissions emissions occur near -10 mm with echogenicity observed downstreamdue to ADV microbubbles (B). (C) The measured dissolved oxygen decreased downstream of the IVUS transducer when ADV was nucleated

P1-C11-3

Oxygen Microbubbles Improve Tumor Control after Radiotherapy in a Rat Fibrosarcoma Model

Samantha M. Fix[1,2], **Virginie Papadopoulou[2,3]**, Hunter Velds[4], Sandeep K. Kasoji[3], Judith N. Rivera[5], Mark A. Borden[4], Sha Chang[5], Paul A. Dayton[3]; [1]*Department of Biomedical Engineering & Eshelman School of Pharmacy, UNC Chapel Hill, USA,* [2]*These authors contributed equally to this work, USA,* [3]*Department of Biomedical Engineering, UNC Chapel Hill, USA,* [4]*Department of Mechanical Engineering, University of Colorado, USA,* [5]*Department of Radiation Oncology, UNC Chapel Hill, USA*

Background, Motivation and Objective

It is well-established that tumor hypoxia negatively impacts treatment outcome for radiation therapy (RT). In particular, tumor cell resistance to radiotherapy is increased 3-fold under anoxic conditions. Hypoxia hinders direct "oxygen radiosensitization" (increased free radical oxidative damage and formation of difficult-to-repair organic peroxides during RT), but also promotes radioresistance through biological HIF-1 complex signaling. Oxygen microbubbles (OMB) have been successfully used as an oxygen-delivery vehicle, improving the efficacy of sonodynamic therapy. Furthermore, the robust oxygen-delivery potential of OMB is demonstrated by their ability to sustain asphyxiated animals for over two hours. Here we assess whether these microbubbles can be used to relieve tumor hypoxia and thereby improve RT outcome.

Statement of Contribution/Methods

Female Fisher 344 rats were implanted with subcutaneous fibrosarcoma (FSA) tumors. Once the tumors reached approximately 1cm, animals were divided into 5 treatment groups such that their initial tumor volumes on the day of RT (day 0) were matched between groups. Treatment groups were No treatment, RT alone, OMB alone, RT + nitrogen microbubbles (NMB) and RT + OMB. RT dose prescription consisted of one single 15Gy dose of 6MV photons (field size of 2cmx2cm on the skin and 1cm bolus used) delivered using a clinical linear accelerator (Siemens Healthcare, Malvern, PA). Animals were anesthetized with medical air and 2.5% isoflurane, after induction on oxygen and 5%isoflurane for 3min. Immediately prior to RT, the tumors of animals receiving microbubbles were injected intra-tumorally (IT) with 1mL OMB or NMB. After RT, tumor volume was measured every 3 days for one month via B-mode ultrasound imaging, or until the tumor reached 2.5cm in the largest dimension. Tumor volume was calculated from Bmode ultrasound images of the largest tumor cross-section on sagittal and transverse planes.

Results/Discussion

Preliminary data with n=4 per group show a trend for IT administration of OMBs improving tumor control after RT (Fig.1) and additional experimental rounds with more animals are currently under way. If successful, IT administration could be envisaged in combination with brachytherapy towards clinical translation, where radiation sources are directly inserted into tissue.

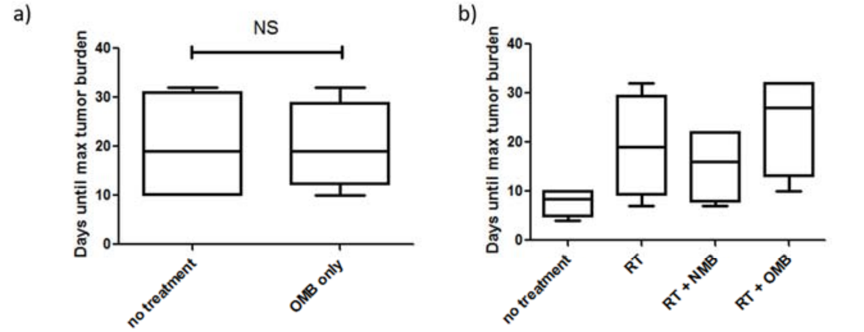

Figure 1: Preliminary data with n=4 per group showing a) No significant difference in found between animals receiving no treatment and animals receiving OMB only (no RT); b) Time (days) until maximum tumor burden is reached; Day 0 is taken as the day of RT (or day that would have been RT for animals not receiving RT); Animals below maximum tumor burden at day 31 are included as 'Day 32'; For both a) and b) respectively, groups were matched so that there was no difference in initial tumor volume

P1-C11-4

Ultrasound Modulation of the Electromechanical Function of Human Stem-Cell-Derived Cardiomyocytes

Andrew Chen[1], Aleksandra Klimas[1], Ivan Suarez Castellanos[1], Emilia Entcheva[1], Vesna Zderic[1]; [1]*Biomedical Engineering, The George Washington University, USA*

Background, Motivation and Objective

In the United States alone more than 300,000 people die suddenly every year with the cause of death being cardiac arrhythmia. The two most popular methods for cardiac function modification are electrical and chemical. It is our hypothesis that though the use of low intensity non-ablative ultrasound, we can modify cardiomyocite (CM) action in the form of activation or suppression of ion transport. Further for dyssynchronous beating we can reactivate synchrony and achieve pacing of CMs.

Statement of Contribution/Methods

To the best of our knowledge, this is the first study done on the therapeutic effects of low intensity ultrasound on human pluripotent stem-cell-derived ventricular CMs. CMs were plated in confluent monolayers. We used an in-house developed platform for all-optical cardiac electrophysiology, termed OptoDyCE, to optogenetically pace the CMs while recording optically intracellular calcium (Rhod-4) and membrane voltage (di-4-ANBDQBS) in a spectrally-optimized manner. Ultrasound probes from Sonic Concepts were combined with the OptoDyCE platform. The probes were operated at 600 and 800 kHz and 1 MHz at intensities of 0.5 and 1 W/cm2. This integrated system allowed quantification of cell behavior prior, during and after the application of the ultrasound.

Results/Discussion

We explored a range of ultrasound parameters while simultaneously monitoring the electromechanical response of the CMs. Little effect was seen at 1 MHz and 800 kHz. CM behavior was most affected by 600 kHz ultrasound at 0.5 W/cm2. As shown in the figure below, just one second of sonication with these parameters instantaneously increased the natural beat frequency of the CMs from around 0.16 Hz to 0.28 Hz. A distinctly different mechanism of pacing was observed, with partial calcium release (red arrows) preceding and likely triggering the action potentials (Vm).The ultrasound effect appears to be caused by fast onset of cellular processes rather than slower thermally mediated events. Ongoing work will focus on refining ultrasound stimulation parameters and determine the mechanism by which ultrasound modulates calcium and voltage. This work can impact the fields of stem cell biology for cardiac repair and personalized medicine. It can also inspire a new generation of ultrasound in vivo rhythm control devices.

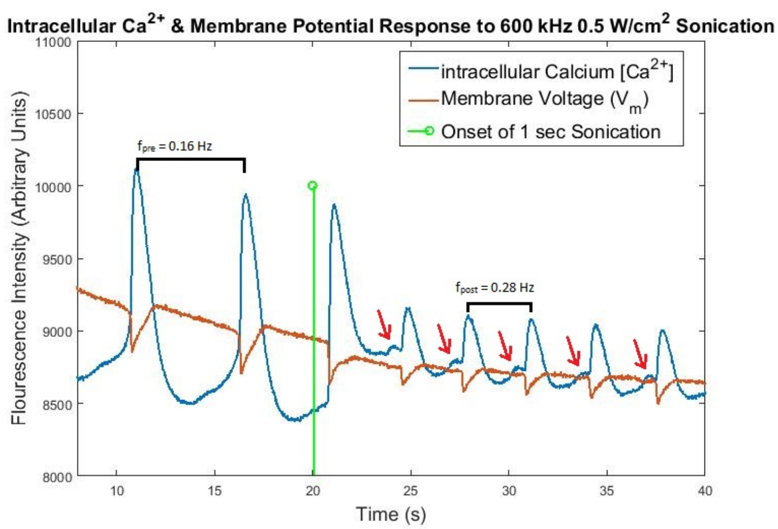

P1-C11-5

Ultrasound-Chemical Hybrid System for Manipulating Cellular Activities

Ching-Hsiang Fan[1], Yao-Shen Huang[2], Yu-Chun Lin[2], Chih-Kuang Yeh[1]; [1]*Department of Biomedical Engineering and Environmental Sciences, National Tsing Hua University, Hsinchu, Taiwan,* [2]*Institute of Molecular Medicine, National Tsing Hua University, Hsinchu, Taiwan*

Background, Motivation and Objective

Focused ultrasound (FUS) with microbubbles (MBs) can enhance delivery of impermeable materials into cells for eliminating abnormal cells or enhancing gene transfection. Very few of the existing systems can precisely control cellular physiology. Chemically-inducible dimerization (CID) system has already gained widespread popularity as a tool in cell biology and has been used to address the diverse, yet fundamental biological questions. Although remotely triggering CID system by external stimuli such as light has been developed, it is still challenging to deliver light to the tissues deeper than just 2 mm without any invasive surgical procedures. This study proposed a new ultrasound-chemical hybrid system to trigger the CID system by FUS with MBs. With FUS, membrane impermeable chemical dimerizers can be introduced into cells to spatiotemporally control cellular physiology within timescale of minutes.

Statement of Contribution/Methods

A membrane impermeable chemical dimerizers, Rapamycin-PEG6-Biotin (RPB), was used to induce the dimerization of a pair of protein binding partner: FK506 binding protein (FKBP) and the FKBP12-rapamycin binding protein (FRB). HeLa cells expressing membrane-anchored Lyn-CFP-FRB and cytosolic YFP-FKBP were incubated with Dil-labeled folate-conjugated MB and RPB. FUS sonication (energy = 0.3-0.7 MPa, duty cycle = 0.5 %, sonication = 5 sec) was applied with a 1-MHz FUS probe. The membrane permeability change and CID were confirmed by Propidium Iodide (PI) staining and FRET imaging.

Results/Discussion

FUS with MBs could enhance cellular membrane permeability since PI diffused inwards to cytosol (Fig. A). Excitation of FUS rapidly disrupted MBs and triggered the translocation of cytosolic YFP-FKBP onto plasma membrane where Lyn-CFP-FRB is localized, confirmed by FRET signal elevation (Fig. B). FUS with MBs also induced the translocation of mCherry-FKBP-Inp54p from cytosol to plasma membrane as confirmed by the decline of mCherry-FKBP-Inp54p within cytosol, suggesting our system can control cellular phosphoinositide metabolism. Our technique offers a powerful and versatile tool for using ultrasound to spatiotemporally manipulate cellular physiology in living cells, potentially valuable for extending the therapeutic applications.

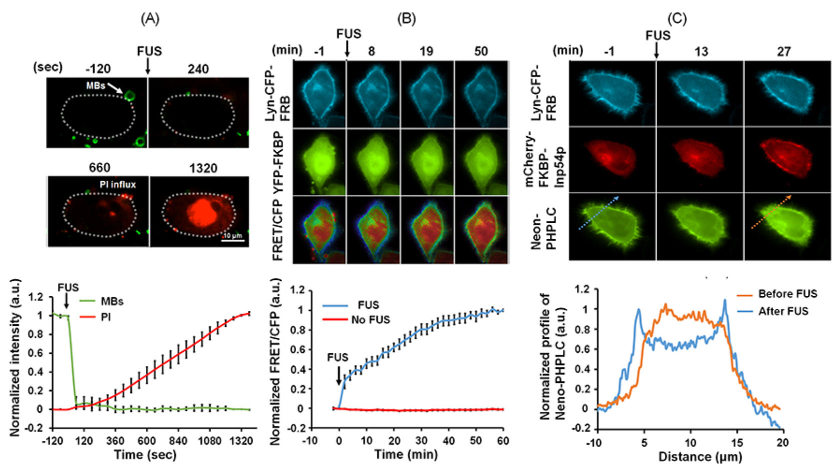

P1-C11-6

Assessment Method of Coagulation Spot Connectivity with Localized Motion Imaging to Reduce the Risk of Local Recurrence

Shun Yoshimura[1], **Takashi Azuma**[1,2], Hideki Takeuchi[1], Keisuke Fujiwara[3], Kazunori Itani[3], Shu Takagi[1]; [1]*Mechanical Engineering, The Unviersity of Tokyo, Japan,* [2]*Faculty of Medicine, The University of Tokyo, Japan,* [3]*Healthcare, Hitachi, Japan*

Background, Motivation and Objective

A real-time ultrasound (US) coagulation monitoring for coagulation based on acoustic radiation force is described. US imaging to facilitate HIFU has advantages with respect to portability, cost effectiveness and spatiotemporal resolution. Localized motion imaging (LMI) is one of the techniques based on US to detect a change of tissue mechanical properties caused by its thermal coagulation. To achieve both spatial accuracy and wide treatment area, intermittent exposure and focal shift method with sharp HIFU beam is generally used. In this paper, our purpose is to establish an assessment method of coagulation possibility between consecutive focal spots based on vibration profile caused by focal oscillation to reduce the risk of local recurrence.

Statement of Contribution/Methods

In LMI, acoustic radiation force (ARF) generated by a transducer is used as a mechanical input to deform tissue at the focus. The ARF is modulated by changing the US intensity. In this study, we focused on monitoring the expansion process of coagulated area and the merging process between the previous and current coagulated area. In our hypothesis, when two coagulated areas are merged, detected vibration profile will changes.

A prototype real-time two-dimensional LMI system was constructed using Verasonics. AM frequencies and HIFU frequency were 68 Hz and 2 MHz, respectively. The target porcine liver tissue was embedded in polyacrylamide gel. After coagulation formation in the first exposure, the focal spot moved to the next spot with distance of 1 cm in the lateral direction during pause of exposure. The vibration profile was observed during second exposure.

Results/Discussion

Fig1(a) shows a coagulated area generated by two consecutive focal spots. If dose amount or time of second spot was enough, the merged coagulation area was formed. Fig1(b,c) show vibration profile at the beginning and after exposure, respectively. While the vibration phases at the previous and current spot is different before fusion, the phase is same after fusion. Phase change was observed during these fusion processes. Respective average phase change are 17 +/-4.7 and 3.4 +/- 5.1 in the case of fusion and non-fusion.

Profile of vibration phase during fusion process of the previous and the current coagulated areas would have useful information about coagulation possibility between consecutive focal spots.

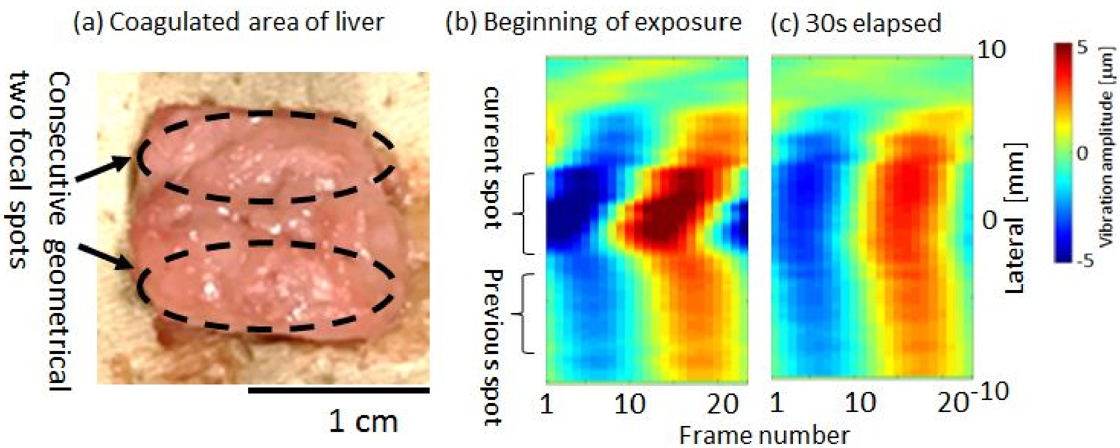

P1-C11-7

Ultrasound Characterization of Slow Precipitating Implants for Vascular Occlusion

Selva Jeganathan[1], Danielle Gilbert[1], Christopher Hernandez[1], Sidhartha Tavri[2], Agata Exner[3]; [1]*Biomedical Engineering, Case Western Reserve University, Cleveland, OH, USA,* [2]*Vascular and Interventional Radiology, University Hospitals Cleveland Medical Center, Cleveland, OH, USA,* [3]*Biomedical Engineering and Radiology, Case Western Reserve University, Cleveland, OH, USA*

Background, Motivation and Objective

A current standard clinical treatment for liver cancer patients is drug eluting bead trans-arterial chemoembolization (DEB-TACE), where doxorubicin-loaded microparticles are injected via catheter into the hepatic artery that feeds the tumor. Due to the large bead diameter (~200µm), occlusion occurs far away from the tumor creating a hypoxic region affecting both healthy and cancerous tissue. As an alternative to beads, we have developed a slow precipitating occlusion solution (sPI) which will be capable of continuous, deeper occlusion. Because the precipitation rate of the solution is critical to the penetration depth, and to the eventual success of this application, this study tested the feasibility of controlling solution precipitation by increasing polymer to solvent ratios and evaluating the occlusion distance using ultrasound imaging in a tissue-mimicking flow phantom.

Statement of Contribution/Methods

The sPI formulations consisted of 20, 30, and 40 wt. % poly(lactic-co-glycolic acid) (PLGA) dissolved in 6:1 wt.% ratio of N-Methyl-2-pyrrolidone (NMP) to benzyl benzoate (BB), followed by overnight mixing. To measure rate of precipitation, 20uL of the sPI was injected into PBS and implants were imaged using diagnostic ultrasound (Toshiba Aplio SSA-770A) at a 12 MHz (DR:60, MI:0.6, gain:80). Implant precipitation was evaluated using MATLAB processing. To measure occlusion distance, 100µL of the sPI was injected into an agarose mold with a 0.81mm channel under constant flow and imaged using the same ultrasound parameters.

Results/Discussion

Image processing allowed us to quantify the precipitated (red) and liquid (green) regions in Fig.C from the original ultrasound image (Fig.B) of the sPI. Increasing the concentration of PLGA from 20wt. % to 30wt. % shows a statistically significant difference ($p<0.05$) in total precipitated area within 15 seconds after injection shown in Fig.D. The 30wt. % PLGA formulation occluded 9.71cm away from the microcatheter (Fig.F). Other formulations are currently being tested. Altering solvent miscibility and polymer molecular weight will also play a critical role in modulating the occlusion distance, and these formulations will be tested in future studies. Injection of sPI polymer solution will allow us to occlude vessels closer to the tumor than DEB-TACE and minimize the hypoxic region to only the tumor.

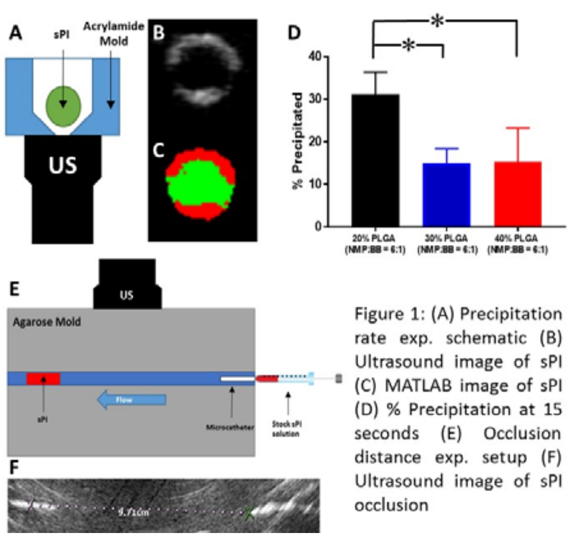

Figure 1: (A) Precipitation rate exp. schematic (B) Ultrasound image of sPI (C) MATLAB image of sPI (D) % Precipitation at 15 seconds (E) Occlusion distance exp. setup (F) Ultrasound image of sPI occlusion

P1-C11-8

Unilateral Focused Ultrasound-Induced Blood-Brain Barrier Opening Alters Spatial Profile of Hyperphosphorylated Tau in an Alzheimer's Mouse Model

Maria Eleni Karakatsani[1], Tara Kugelman[1], Shutao Wang[1], Karen Duff[2,3], Elisa Konofagou[1,4]; [1]*Biomedical Engineering, Columbia University, Manhattan, New York, USA,* [2]*Neurobiology & Behavior, Columbia University, Manhattan, New York, USA,* [3]*Taub Institute, Columbia University, Manhattan, NY, USA,* [4]*Radiology, Columbia University, Manhattan, New York, USA*

Background, Motivation and Objective

Focused ultrasound has been shown to interact with Alzheimer's pathology and particularly to trigger the reduction of the amyloid plaque load. However, a less studied interaction is that of ultrasound with the tangle formation that has been implicated in the cognitive decline of Alzheimer's patients. With the current study we investigate the interaction of unilateral focused ultrasound-induced blood-brain barrier opening with the tau distribution in an Alzheimer's mouse model.

Statement of Contribution/Methods

For this study 5 mice of the rTg4510 line (3.5 months old) were sonicated four times in the hippocampal formation and were compared to 5 control littermates. The day after the last sonication the mice were sacrificed. The brains were sectioned and counterstained for tau protein (AT8) as well as microglia activation (CD68). A customized algorithm was constructed to quantify the number of cells and the axonal distribution of the tau-marker.

Results/Discussion

Figure 1 shows two representative examples of the control and the treatment group. Following the hippocampal formation of the control brain, it can be observed that both somatodendritic and axonal tau (red) are evident. Although the cell bodies affected by tau protein are also evident in the animals that received four sonications, the axonal tau was less pronounced. Differences across hemispheres were detectable only in the treated group. In addition, the phagocytic microglia (green) seem almost absent in the control brains while they can be observed in both hemispheres of the treatment group. Quantification of the tau marker showed comparable levels of the cell body count for the two groups but significantly less axonal tau expression for the treated group. Since the cell body count was similar between groups, it can be concluded that the reduced tau protein was not transferred to other cell bodies. Finally, microglia were also significantly activated by the sonication but its relationship to tau re-distribution remains to be established.

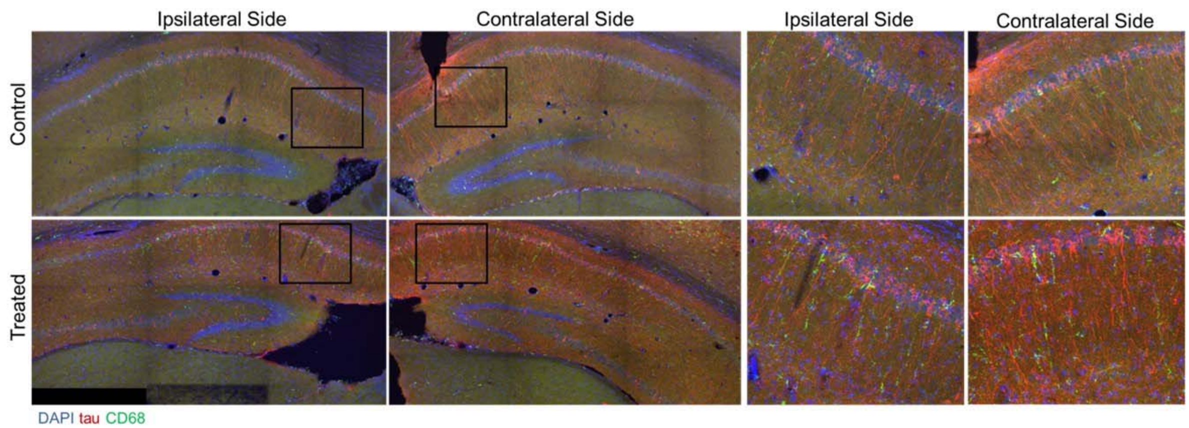

Figure: Hippocampal formation counterstained for tau protein with AT8 (red) and microglia activation with CD68 (green). The first row corresponds to the ipsilateral and contralateral side of a control brain and their magnified regions. The second row corresponds to the ipsilateral and contralateral side of a treated brain and the corresponding magnified regions.

P1-C11-9

In-Vitro Delivery of BLM into Resistant Cancer Cell Line Using Sonoporation with Low-Boiling Point Phase Change Ultrasound Contrast Agents

Samantha M. Fix[1], Anthony Novell[2], Jean-Michel Escoffre[2], James K. Tsuruta[3], Paul A. Dayton[4], Ayache Bouakaz[2]; [1]*Eshelman School of Pharmacy, University of North Carolina at Chapel Hill, Chapel Hill, North Carolina, USA,* [2]*Inserm - Imagerie et Cerveau, Université François-Rabelais, France,* [3]*Department of Pediatrics, University of North Carolina at Chapel Hill, Chapel Hill, North Carolina, USA,* [4]*Joint Department of Biomedical Engineering, University of North Carolina at Chapel Hill and North Carolina State University, Chapel Hill, North Carolina, USA*

Background, Motivation and Objective

Bleomycin (BLM) is a promising chemotherapeutic that causes oxidative damage to DNA resulting in cell death. However, this non-permeant drug is mainly internalized via receptor-mediated endocytosis. Therefore, tumors showing a poor expression of BLM-binding proteins are resistant to this therapy. This work aims to demonstrate the ability to improve the intracellular accumulation and efficacy of BLM in resistant colorectal adenocarcinoma cells (HT-29) through sonoporation with a low-boiling point formulation of phase change contrast agents (PCCAs).

Statement of Contribution/Methods

At 37°C, octafluoropropane-filled PCCAs can be converted into microbubbles (MBs) using excitation pulses with peak negative pressures (PNP) of 300 kPa [1]. In this study, these PCCAs were used for therapeutic purpose by adding them to a suspension of HT-29 cells at a ratio of 5 PCCAs: 1 cell in a plastic cuvette. This suspension was maintained at 37°C and stimulated with ultrasound at 1.0 MHz with a PNP of 400 kPa and duty cycle of 40%. Cell viability was assessed at BLM concentrations ranging from 0.01 – 10 µM using an MTT assay 48 hours post-sonoporation. Furthermore, the efficacy of drug delivery was compared using standard lipid-shelled MBs (5 MBs: 1cell) and PCCAs as sonoporation mediators.

Results/Discussion

As expected, results show that BLM alone had no effect on the viability of resistant colon cancer cells at any of the tested concentrations. However, a significant and dose-dependent decrease in cell viability was observed when BLM was delivered to the cells via either PCCA- or MB-mediated sonoporation (Fig. 1). For sonoporation, our in-vitro results suggest that PCCAs are as effective (i.e., 47% cell death at a BLM concentration of 10 µM) as regular MBs. Additionally, no significant cell death was observed when cells were exposed to the sonoporation procedure in the absence of BLM.

Future studies will be designed to investigate the in-vivo utility of PCCA-mediated BLM delivery. We believe that sonoporation with the nano-scale PCCAs will offer significant benefits over conventional MBs when used for in-vivo drug delivery; most importantly is their small size, which may allow for PCCA extravasation into solid tumors allowing for extravascular sonoporation of tumor cells.

Figure 1. Bleomycin delivered via PCCA- or microbubble-mediated sonoporation results in a dose-dependent decrease in viability.

[1] Fix, S.M., Novell, A., Yun, Y., Dayton, P.A., Arena, C.B. (2017), "An evaluation of the sonoporation potential of low-boiling point phase-change ultrasound contrast agents in vitro." J Ther Ultrasound 5: 7.

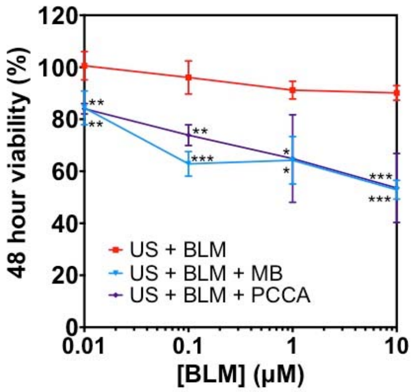

P1-C11-10

Retina Stimulation on Rat *In Vivo* with Low-frequency Ultrasound

Qiuju Jiang[1], Huixia Zhao[1], Guofeng Li[1], Lan Yue[2], Qifa Zhou[2], Mark Humayun[2], Weibao Qiu[1], Hairong Zheng[1]; [1]*Shenzhen Institutes of Advanced Technology, Chinese Academy of Sciences, China, People's Republic of,* [2]*Department of Biomedical Engineering, University of Southern California, CA, USA*

Background, Motivation and Objective

More and more researches are exploring the neurostimulation effect of ultrasound (US) on the central nervous system (e.g. brain and retina) and the peripheral nervous system (such as skin). US stimulation has been regarded as a new noninvasive neurostimulation approach by many researchers. Our previous studies had shown that the temporal response patterns of RGCs could be stimulated by US *in vitro*. In this article, we apply low-frequency (2.25 MHz) focused US stimulation to the rat retina *in vivo* to investigate the effect on the primary visual cortex.

Statement of Contribution/Methods

Experiments were conducted on adult Sprague Dawley rats (250-300 g). A 2.25 MHz focused US transducer was used to stimulate the rat eye *in vivo*. Rats were anaesthetized with urethane. Next, the rat was laid prone on an automatic heating pad at 37°C and with its head gently immobilized using a stereotaxic frame. The skin on the head was swabbed with iodine and then a local anesthetic was injected subcutaneously along the incision line. The skull was exposed and trephined in an area (4x4 mm^2) overlaying the monocular visual cortex: 6.0 mm posterior to bregma, and 3.0 mm lateral from the midline, the depth of multi-electrode arrays implantation were 300-500 µm below the pia surface. The neural activities from the primary visual cortex was amplified, filtered and digitized by Cerebus 64-Channel system.

Results/Discussion

As shown in Fig. 1a, the low-frequency focused US transducer was used to stimulate the rat left eye and a 4x4 multi-electrode array was used to record neural activities from the right primary visual cortex. Some preliminary experimental results showed that the local field potentials and the spikes recorded from the primary visual cortex were both changed by US stimulation. Fig. 1b showed the responses of local field potentials that were recorded by 13 electrodes to US stimulation. The average latency of these responses was about 250 ms, which was consistent with the previous study. The peri-stimulus time histogram (PSTH) of a single spiking unit that was sorted by Offline Sorter showed that the neuron responded to US stimulation at the offset Fig. 1c. Such influence on the neural activities in brain demonstrated that the low-frequency focused US is capable of stimulating retinas *in vivo*, which could be a novel therapy tool for ophthalmic diseases.

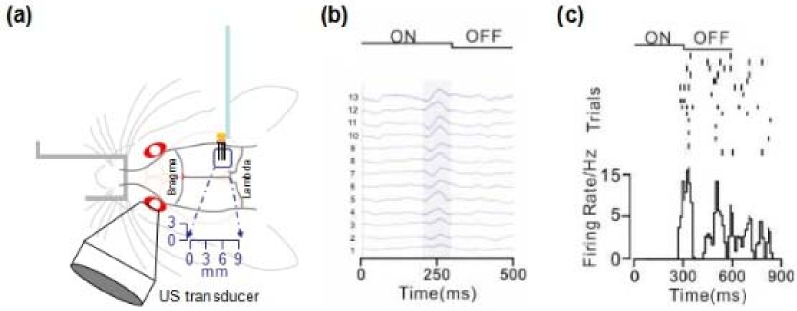

Figure 1. US influenced on the neural activities of visual cortex. (a) The experimental paradigm. US stimulation to the rat left eye and multi-electrode arrays recording from the right primary visual cortex. (b) The local field potentials responded to US stimulation. X-axis is time (ms) and Y-axis is recording channels. (c) The PSTH of a single spiking unit that was sorted by Offline Sorter. X-axis is time (ms) and Y-axis is firing rate (Hz) .

P2-C1 - Structural Health Monitoring

Exhibit Hall

Saturday, September 9, 2017, 9:30 am - 4:00 pm

Chair: **Robert Addison**
Rockwell Science Center

P2-C1-1

An Advanced Ultrasonic Method Based on Signal Modality for Structural Damage Characterization on Concrete: The Cube Problem

Alicia Carrión Garcia[1], Vicente Genovés Gómez[2], Ramón Miralles Ricós[1], Jorge Juan Payá Bernabeu[2], **Jorge Gosálbez Castillo[1]**; *[1]Instituto de Telecomunicaciones y Aplicaciones Multimedia (iTEAM), Universitat Politècnica de València, Valencia, Valencia, Spain, [2]Instituto de Ciencia y Tecnología del Hormigón (ICITECH), Universitat Politècnica de València, Valencia, Spain*

Background, Motivation and Objective

Concrete is the most important material used in the construction industry for building and civil engineering. It is a heterogeneous medium composed of different materials with different mechanical and chemical properties that complicate ultrasonic inspections. Due to the important role that concrete plays in building structures, it is necessary to develop new ultrasonic techniques that afford robust results and an accurate diagnosis. In this study, a new approach based on the signal modality of ultrasonic waves is proposed. A complex damage in concrete cube specimens under different axial loads was assessed using such new technique and comparing the results with traditional ultrasonic parameters: ultrasonic pulse velocity and attenuation.

Statement of Contribution/Methods

In the field of dynamical systems, the concept of the state space reconstruction (SSR) of a signal allows the study of the underlying system. The SSR of the ultrasonic signals is proposed in order to identify the trajectories between consecutive states characterized by the interaction of the injected wave and the nonlinear scatters present in the specimen under study. The analysis of the Recurrence Plots (RP) applied on the state space allows the signal modality characterization: the identification of different signal sources of different signal natures. Measuring the degree of predictability of the resulting signals gives information about how coherent and incoherent components are combined as a function of the inner material and, thus, about the internal damage level of the material.

Results/Discussion

Cubic concrete specimens subjected under different levels of axial loads (0%, 25%, 50%, 75% of the compressive strength) were characterized by means of ultrasonic NDT. Due to the characteristic inverted pyramidal shape of the appearing flaws, direct and indirect ultrasonic through-transmission setups were evaluated. Both the traditional measures and the brand new technique successfully identified the level of damage with direct configurations. In the case of the indirect measurements, the corresponding level of damage was accurately identified by the new proposed technique but not by the traditional ones. The degree of predictability successfully characterizes the level of damage even when many echoes are superimposed and/or the wave-front trajectory cannot be accurately estimated.

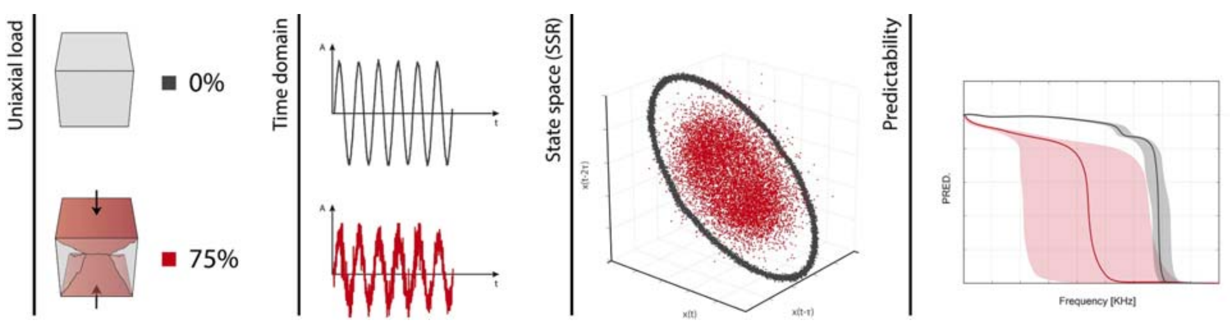

P2-C1-2

Shearography Using Wave-Defect Interactions for Crack Detection in Metallic Structures

Huajun Liu[1], Shifeng Guo[1], Yi Fan Chen[1], Hongwei Liu[1], Chin Yaw Tan[1], Karen Lin Ke[1], **Lei Zhang[1]**; *[1]Institute of Materials Research and Engineering, A*STAR, Singapore, Singapore*

Background, Motivation and Objective

Shearography is an optical non-destructive testing technique which has been used as a practical tool in industrial applications due to its suitability for large area and fast inspections. Shearography is based on the differential of two interferometric patterns obtained when the test samples are under stress loading and when the stress loading is removed. Conventional loading methods for shearography testing include loadings by vacuum, thermal and vibration excitations. Currently, shearography testing has been mainly used for detection of delamination in composite structures. For damage detection in metallic structures, it is difficult for shearography with those conventional loading methods to detect defects, especially sub-surface fatigue cracks in metals, due to the high rigidity and/or the high thermal conductivity of metals.

Statement of Contribution/Methods

In this work, we proposed a wave-based shearograhy method for crack detection in metallic structures. Piezoelectric transducers bonded on metallic structures are employed to generate acoustic waves as stress loading for shearography testing. The acoustic waves interact with defects in the metallic structures, which lead to abnormal surface deformation. The abnormal surface deformation is subsequently captured by the shearography system in a short period of time.

Results/Discussion

By using this method, we successfully detected surface fatigue cracks as short as 3 mm near rivet holes in aluminium plates. We also demonstrated the detection of sub-surface fatigue cracks as deep as 10 mm in aluminium plates. Systematic investigations on the wave-based shearography testing indicate that the optimal testing frequencies are mainly determined by the resonant frequencies of the piezoelectric transducers, which is independent of crack and sample dimensions. Finally, the minimum acoustic power required for successful crack detections in metallic structures with the wave-based shearography method is estimated. The method developed in this work allows fast and effective detection of fatigue cracks including deep sub-surface fatigue cracks in metallic structures with shearography testing, which is promising for practical industrial applications.

P2-C1-3

Experimental Setup of Continuous Ultrasonic Monitoring for Corrosion Assessment

Nutthawut Suchato[1], Steve Sharples[1], Roger Light[1], Alexander Kalashnikov[2]; [1]*Electrical and Electronic Engineering, The University of Nottingham, Nottingham, United Kingdom,* [2]*Engineering and Maths, Sheffield Hallam University, Sheffield, United Kingdom*

Background, Motivation and Objective

The progression of corrosion can be studied using continuous ultrasonic monitoring. A test rig was developed to artificially accelerate corrosion, and to ultrasonically monitor it on a real sample [1]. However, the corroded samples mostly underwent uniform corrosion, with low amounts of roughness. Non-uniform corrosion, or high surface roughness, prevents reliable ultrasonic thickness estimates. To better evaluate the influence of high surface roughness on ultrasonic thickness measurements, the test rig is further developed to generate varieties of high surface roughness, and monitor them.

Statement of Contribution/Methods

Different types of corrosion surfaces were generated using an electroplating technique. Non-uniform corrosion could be initiated by applying high electroplating current to small exposed areas, a small part of which was coated by a passive layer.

Ultrasonic waveforms, reflecting from different types of rough surfaces and different locations of the corroded sample, were continuously monitored via high accuracy ultrasonic instrumentation [2].

Results/Discussion

Fig.1 shows contour plots of four varieties of surface roughness of corroded samples carried out by accelerated corrosion. On these samples with high surface roughness, the continuous monitoring allows the application of an adaptive cross-correlation (AXC) method to mitigate under- or over-estimation of mean thickness, compared with a standard cross-correlation (XC) method, as shown in Fig.2.

[1] N. Suchato et al., International Conference for Students on Applied Engineering, Oct 2016, pp. 147–152.

[2] A. N. Kalashnikov et al., IEEE Transactions on, vol. 54, no. 8, pp. 1596–1605, 2007.

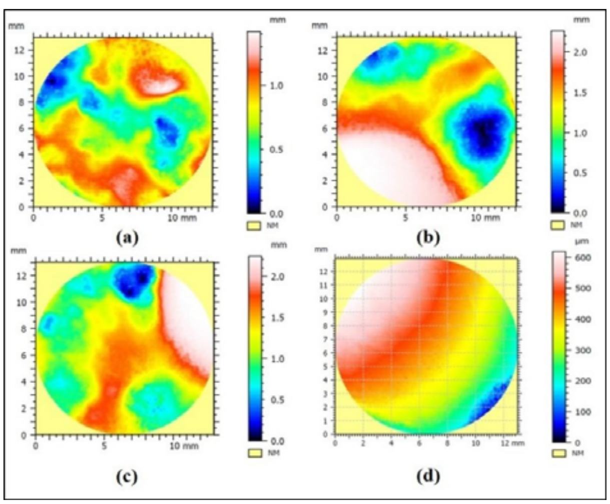

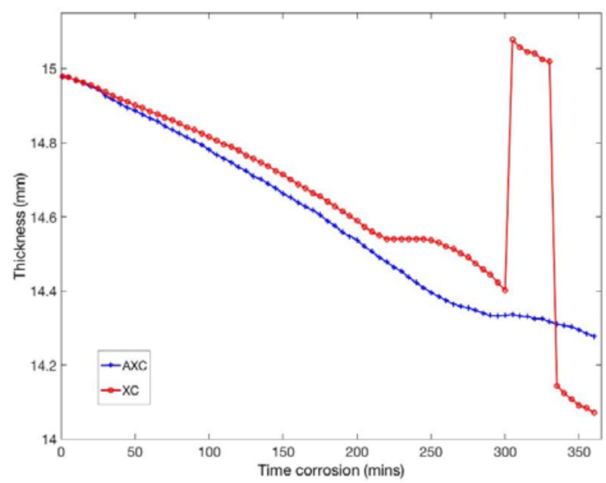

P2-C1-4

Residual Thickness Measurement Method of Corroded Steel Plate Using Ultrasonic SH Array Transducer

Tomonori Kimura[1], Akira Hosoya[2], Mitsuhiro Koike[3], Minoru Takahashi[3], Jun Murakoshi[3]; [1]*Mitsubishi Electric Corporation, Japan,* [2]*Ryoden Shonan Electrical Corporaion, Japan,* [3]*Public Works Research Institute, Japan*

Background, Motivation and Objective

Recently, the maintenance of aging structures such as steel bridge has become an important subject. For example, it is reported that corrosion occurred in a steel plate have broken the steel plate. So, development of the measurement method for residual thickness is desired.

Statement of Contribution/Methods

Several measurement methods for corrosion are reported using guided ultrasonic waves. In these methods, an echo height or a received time of an echo is used to measure a residual thickness. We have developed a measurement method that is not dependent on mere echo height or received time. In the method, the SH plate wave is transmitted in a steel plate by a SH array transducer, and a received echo by the reflection occurred due to the cut off phenomena of the plate wave is used. Furthermore, configuration of the SH array transducer suitable for the method have been studied. Ditching grooves on the surface of a protection plate of the transducer, the sensitivity and variation among array elements can be improved.

Results/Discussion

A test piece including a thin area modeled for corrosion was made of steel, and the base and residual thickness were 12mm and 8 mm, respectively. An experiment was done to verify the method using the SH array transducer with grooves. As a result, the residual thickness obtained by the method was agree well with the actual size.

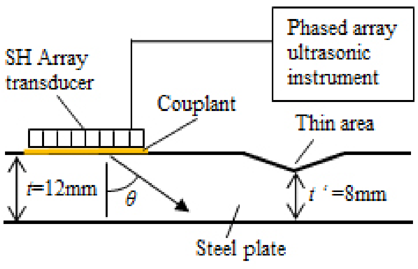

Experimental set up

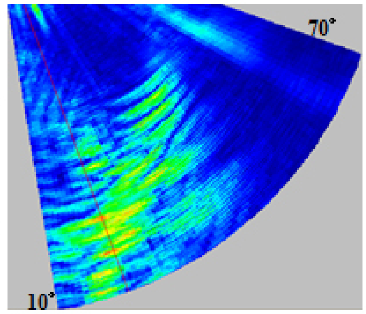

Sectorial scan image

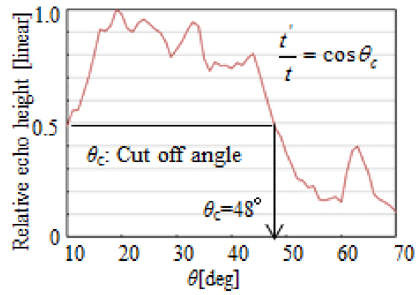

Relative echo height versus transmitting angle

P2-C1-5

Ultrasonic Detection of Spark Eroded Notches in Steel Plates

Petter Norli[1], Øyvind K.-V. Standal[2,3], Martijn Frijlink[2,3], Fabrice Prieur[3,4], Mark Tanner[5], Katharina Haakenstad[1]; [1]*Halfwave AS, Høvik, Akershus, Norway,* [2]*InPhase AS, Trondheim, Norway,* [3]*Halfwave AS, Høvik, Norway,* [4]*Department of Informatics, University of Oslo, Oslo, Norway,* [5]*Halfwave AS, Portland, United Kingdom*

Background, Motivation and Objective

A long-standing challenge in integrity management of gas pipelines is stress corrosion cracking (SCC) in the heat affected zone near girth welds. Cracks are difficult to detect, calling for a sensitive detection method with good coverage. Pipeline operators are striving to find robust and reliable methods to allow them to cost effectively manage the integrity of their pipeline infrastructure. The industry standard techniques are falling short with regards to reliability and increased cost and availability. Consequently, there is a demand for a more sensitive, precise, robust and effective ILI crack detection method. Recent advances in gas-coupled broad band ultrasound provide a potential method that is based on guided plate waves.

Statement of Contribution/Methods

The objective of this work is to describe and experimentally evaluate a method that uses guided waves and tomographic imaging principles, in order to develop a full-fledged crack detection tool, based on Halfwave's ART scan® tool. To this end, a water-immersed 12 mm-thick steel plate with crack-like, spark eroded notches (SEN) of 2 and 6 mm depth, and 10 and 20 mm lengths, respectively, at the hind side, were experimentally investigated. A broadband (0.3–1.3 MHz) piezoelectric transducer transmitted broadband pulses that were received by two transducers at different lateral distances (40-80 mm), in a pitch-catch setup. All transducers had normal incidence and a stand-off of 80-90 mm from the steel plate. 2D scans were performed using a precision motion scanner.

Results/Discussion

Significant ultrasonic energy traveling from the transmitting transducer, along the steel plate, was detected by all receiving transducers. When the ultrasonic wave passed a SEN, the received energy in a selected frequency band was 2.5 and 5.5 dB lower for the 2 and 6 mm deep SENs, respectively, compared to that of an undamaged part of the plate. The received signals combined were converted into an image (Fig. 1) featuring the 6 mm SEN using a tomographic image inversion method, showing good agreement with the actual size and location of the SEN.

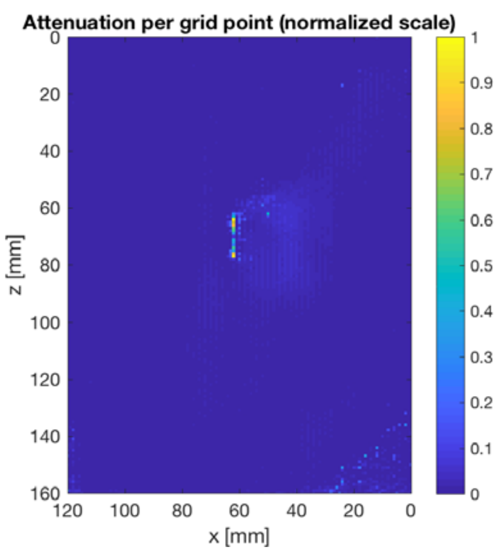

P2-C1-6

Numerical and Experimental Investigations of Nonlinear S0 Lamb Mode for Detection of Fatigue Damage

Congyun Ma[1], **Yanxun Xiang[1]**, Mingxi Deng[2], Fu-Zhen Xuan[1], Haiyan Zhang[3]; [1]*East China University of Science and Technology, China, People's Republic of,* [2]*Logistics Engineering University, China, People's Republic of,* [3]*School of Communication and Information Engineering, Shanghai University, China, People's Republic of*

Background, Motivation and Objective

Nonlinear Lamb wave has been widely acknowledged as an efficient nondestructive method for evaluating early stage of fatigue damage. The previous studies focused on the evaluation of fatigue damage using the particular mode pairs, such as S1-S2 mode pair. Recently, the nonlinear S0 Lamb mode with low-frequency was considered for its unique features of less dispersion and easy to be generated, and was indicated may as sensitive to fatigue damage as other mode pairs reported before. However, few researches were performed on experimental measurement. In this work, the S0 mode is demonstrated as an alternative for fatigue damage evaluation.

Statement of Contribution/Methods

Numerical simulations were carried out in an Al7075 plate using ABAQUS/Explicit software, in which the fatigue damage was simulated through changing the material nonlinearity. Then, experiments were performed using the S0 mode at 300 kHz. In order to produce various fatigue damage in plate-like specimens, the interrupted fatigue tests were performed under the stress-controlled mode with a stress ratio of 0.1. The maximum stress for the fatigue testing is 400Mpa, which is corresponding to 1.1 yield stress. Nonlinear ultrasonic measurements were performed at the propagation distance of 40 mm with the wedge angle of 29.5°.

Results/Discussion

The frequency of the primary Lamb wave was set as 300 kHz according to the numerical simulations, which indicates that there is an appropriate range of frequencies suitable for the detection of fatigue damage. Since at a very low frequency, it is complex for experimental measurements due to the long wavelength and small out-of-plane displacement of the Lamb mode, while at a high frequency, the increasing phase-velocity mismatching will cause a serious dispersion.

As shown in the figure below, a ″mountain-shape″ change of β with respect to loading cycle numbers was observed in experiments. A clear rise of β before about 6000 loading cycle numbers is due to the early damage happened in Al7075 plate. With a further loading, from 6000 cycles to the fracture at 12259 cycles, the β decreases monotonically as a result of micro-crack initiation. The observed tendency is in agreement with the previous results, and indicates the S0 Lamb mode is a potential alternative for the evaluation of fatigue damage in plate-like structures.

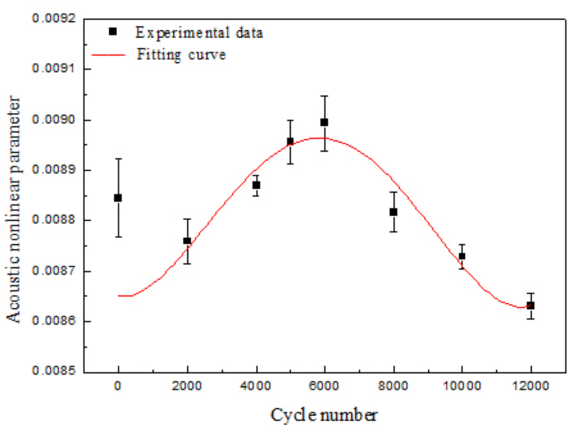

P2-C1-7

Wave and Laser Doppler Vibrometer

Ayumu Osumi[1], Youichi Ito[1]; [1]*College of Science and Technology, Nihon University, Japan*

Background, Motivation and Objective

We have been studied a nondestructive inspection of crack using high-intensity aerial ultrasonic wave and laser Doppler vibrometer(LDV).In this method, cracks are imaged from the vibration velocity distribution including the health part by non-contact measurement of the vibration velocity of the target surface excited by sound wave.Generally, in order to detect cracks, it is necessary to use a high frequency ultrasonic waves. However, there is a problem of distance attenuation.Therefore, we propose to use a high inetensity aerial ultrasonic waves and attempt to detect cracks by using higher order frequencies generated by the nonlinearity.

Statement of Contribution/Methods

Figure 1 shows a schematic view of experimental device. The experimental apparatus uses an ultrasonic sound source (frequency:40 kHz) that radiates focused sound waves and the LDV. We prepare the experimental sample (material : acrylic) which has the crack with a width of 2 mm and a length of 30 mm, and a depth of 1 mm. In the experiment, the exciting point of the sound wave is coincided with the measurement point, and the vibration velocity at that point is measured by LDV. Each frequency component is acquired from the measured value by using the band pass filter because the measured value has the same frequency component as the irradiated sound wave.

This operation is performed over the entire measurement range, and the crack is imaged from the vibration velocity distribution.

Results/Discussion

Figure 2(a),(b) show the experimental results. The experimental measurement range is 50 × 10 mm in the measurement interval of 1 mm × 0.2 mm steps.In addition, the white frame in the figure is the crack area. From the results, it is confirmed that cracks are imaged from the vibration velocity distribution as the frequency is higher.

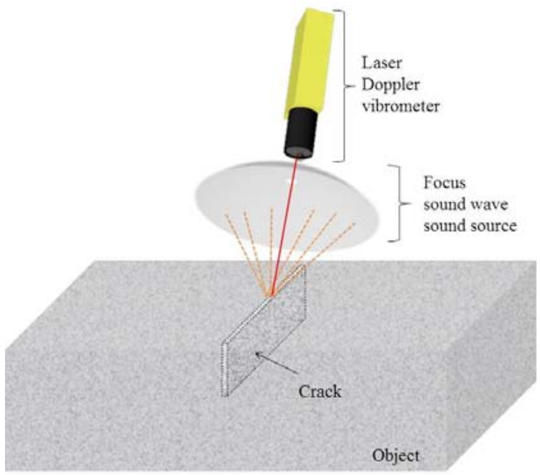

Figure 1 Schematic view of experimental device

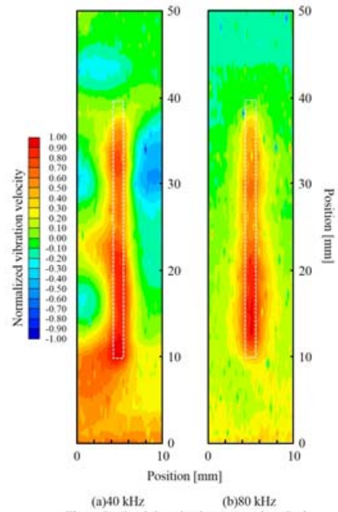

Figure 2 Crack imaging by proposed method

P2-C2 - Transducers and Industrial Measurements

Exhibit Hall

Saturday, September 9, 2017, 9:30 am - 4:00 pm

Chair: **Lawrence Kessler**
Sonoscan Inc.

P2-C2-1

High Sensitivity and Wideband Design for Impedance Matching Layer between Protection Metal and PZT

Minoru Toda[1]; [1]*Toda Microsonics Inc, Lawrenceville, New Jersey, USA*

Background, Motivation and Objective

Ultrasonic transducers for industrial applications often require front protection layer which have to be chemically inert material such as stainless steel (SS). This is particularly important for process control of semiconductor device production so as not to contaminate processing agent. It is known when metallic layer is added at front of ultrasonic transducers, boundary reflections reduce wave transmission and sensitivity is lowered. To overcome this problem, typically known method is to use very thin bonding layer between PZT and use λ/2 metallic protection layer. However, difference of thermal expansions in these materials limits operation temperature range, or otherwise causes delamination at an extreme temperature. The purpose of this work is to design optimum structure of the front protection layers and bonding layer for higher sensitivity and wider bandwidth.

Statement of Contribution/Methods

Well known acoustic wave transmission theory predicts thickness of the metallic protection layer at front of transducer should be λ/2 for highest transmissivity. Mason model analysis was conducted and proved this concept, and further revealed matching layer inserted between metallic layer and PZT layer has to be (1/4 -1/2) λ which improves bandwidth. The unique points are, (1) this matching layer is not added at outer surface, but it is in between metallic protection layer and PZT, and still plays a role of widening bandwidth. (2) The function of λ/2 SS layer is to transfer impedance of propagation medium (water) to inside without conversion, and internal matching layer works with known principle.

Results/Discussion

It is found sensitivity of λ/2 SS protection layer for 3 MHz PZT transducer improves by one order compared with 20% thinner SS layer, but this λ/2 design of SS layer has narrow bandwidth (4%). Adding matching layer of soft conductive epoxy between SS and PZT improves bandwidth wider to 8.6%. This matching layer is soft enough and absorbs thermal expansion difference and endured 40 thermal cycles between 23-155 deg. C without change of performance. Further, λ/2 SS is replaced by equivalent mass-spring-mass structure (SS-polyimide-SS) and 28% bandwidth was achieved.

The structural parameters and observed result are shown in the figure.

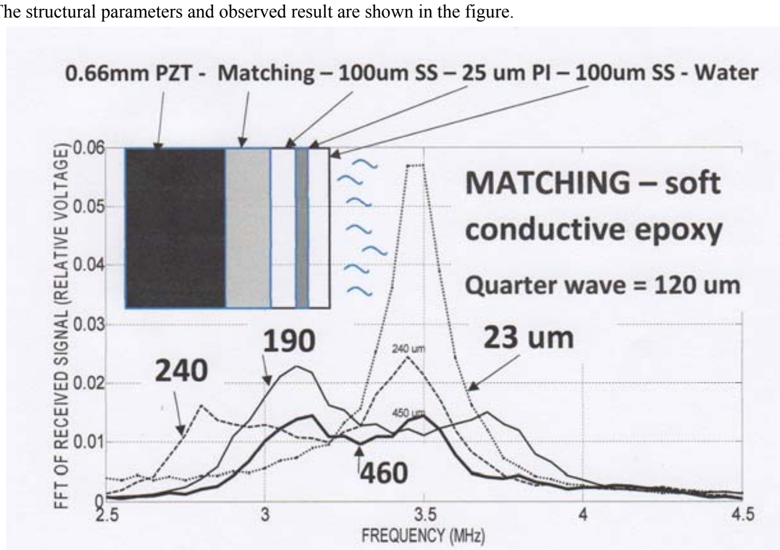

P2-C2-2

Rheological Characterization of Non-Newtonian Drilling Fluids with Non-Invasive Ultrasonic Interrogation

Morten Hansen Jondahl[1], **Håkon Viumdal**[1], Saba Mylvaganam[1], Kenneth Nonso Mozie[1]; [1]*Department of Electrical Engineering, IT and Cybernetic, University College of Southeast Norway, Porsgrunn, Norway*

Background, Motivation and Objective

The drilling process is generally costly and time consuming and prone to serious hazards. Cost-efficiency and enhanced safety measures are vital for any drilling operation. Recent studies indicate that poor reliability in the drilling process resulted in as much as 30% loss of production time. Improved sensor technology with process automation can improve process performance and safety. During drilling operations, along with the drill string, a drilling fluid, commonly very dense and viscous fluid, is circulated in a closed flow-loop. The drilling fluid, non-Newtonian in its rheological behaviour, serves three main objectives: keeping the bottom-hole pressure at an acceptable level, lubricating the drill bit and facilitating the removal of cuttings and debris from downhole. These three goals have to be kept in balance and are achieved by adjusting the density (ρ), viscosity (η) and the flow-rate (q_v) of the drilling fluid. These three drilling process parameters need to be continuously monitored for optimizing process performance and securing safety. The cuttings in the drilling fluids make it especially challenging when conventional in-line sensor systems are used due to the unavoidable erosion and maintenance costs. Non-invasive ultrasonic measurement techniques can be part of a robust and easily implementable control and monitoring system.

Statement of Contribution/Methods

In this work acoustic properties of different drilling fluids are studied. Propagational properties of different samples of drilling fluids are studied with focus on attenuation and frequency characteristics in transmission mode.

Results/Discussion

Experimental results using different sets of ultrasonic transducers with different frequencies, confirm the high attenuation of ultrasonic pulses (Figure 1). The attenuation coefficient α_s is given by Navier-Stokes equation $\alpha_s=(2\omega^2 \eta_s)/(3\rho v^3)$; where, ω is the angular frequency, η_s the shear viscosity, ρ the density, and v the speed of sound. A model is proposed to estimate the attenuation and viscosity of the drilling fluid based on acoustical and rheological parameters. This study presents results from ultrasonic interrogation of non-Newtonian fluids using different ultrasonic propagation modes with focus on their rheological properties.

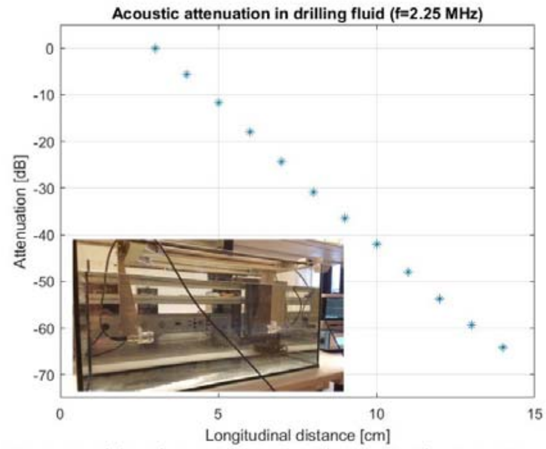

Figure 1. Graph based on experimental results, showing the attenuation characteristic by a 2,25 MHz ultrasonic immersion transducer. Inset figure displays the transmission mode measurement system.

P2-C2-3

Improvement of Compaction Rate of Radioactive Samples for Gamma Spectrometry Using High Power Ultrasound

Jungsoon Kim[1], **Jihyang Kim[2]**, Minseop Sim[2], Moojoon Kim[2]; [1]*Electrical Engineering, Tongmyong University, Busan, Korea, Republic of,* [2]*Pukyong National University, Korea, Republic of*

Background, Motivation and Objective

As interest of environmental radiation has increased, accurate analysis of the environmental radioactive sample has been demanded. The gamma ray spectroscopy is generally used to analyze the environmental radiation for solid radioactive samples such as soil compacted in a standard container. To improve the accuracy of the analysis, it is necessary to compact as much sample of the powder state as possible. Compacted amount of the sample and its density could be different depending on the force from measuring person in the case of conventional method using a compacting rod. In this study, we propose a method to improve the compacting rate with high power ultrasound for solid radioactive sample of powder state.

Statement of Contribution/Methods

Figure 1 shows a schematic of compaction system with ultrasound. Two Langevin type transducers are installed at top and bottom of the standard container filled with the powder sample, and static pressure is applied to the system during the transducers are driven. Ultrasound radiated from the transducers forms pressure distribution in the container, and it improves the compaction rate. This makes it possible to compact much sample in the same volume, thereby increasing the accuracy of radioactivity measurement such as gamma ray spectroscopy.

Results/Discussion

The compacted samples with suggested method and conventional method were analyzed with gamma ray spectroscopy, as shown in Fig. 2. The analyzed results for the same volume of samples show higher detection count in the sample compacted with ultrasound for most of radionuclides.

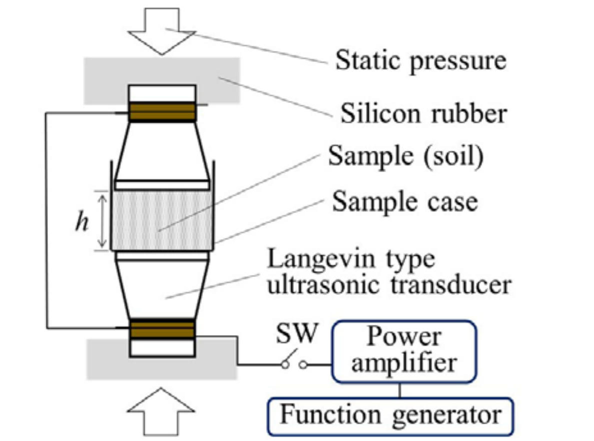

Fig. 1 Schematic of suggested compaction system

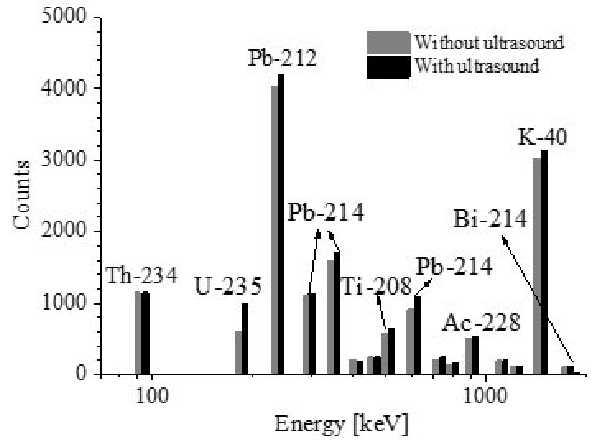

Fig. 2 Result of γ-ray spectroscopy

P2-C2-4

Multi-layer piezoelectric PVDF transducers for Nondestructive testing of concrete structures

Kamal Raj Chapagain[1], Sanat Wagle[1], Werner Bjerke[1], Terje Melandsø[1], Frank Melandsø[2]; [1]*ELOP AS, Hamar, Norway,* [2]*University of Tromsø, Norway*

Background, Motivation and Objective

Polyvinylidene fluoride (PVDF) and its copolymer (PVDF-TrFE) are known to yield lower electromechanical coupling than ceramic transducers. It is possible to increase transducer efficiency by using two or more PVDF layers with embedded electrodes by configuring the transducer layers in different ways such as folded, barker coded and switchable barker coded [Zhang *et al.*, 1997]. A multi-layer transducer can be designed in a configuration that can be electrically shielded to reduce capacitive induced currents. In this work we evaluated and compared ultrasonic field generated by single and multi-layer transducers of PVDF. The multi-layer transducers are then used to analyse the defects on the concrete structures.

Statement of Contribution/Methods

The prototypes of multi-layer transducer with circular aperture of 2 cm were made by stacking pre-polarized PVDF films of equal thicknesses by using adhesives. The ultrasonic field generated by single and multi-layer transducer prototypes were then measured using a needle hydrophone system in combination with an ultrasonic scanning system in water bath. The transducers were driven by a Ricker pulse with different central frequencies from 150-600 kHz and amplitude of ultrasonic field in the plane parallel to the transducer surface was scanned and plotted. Finally, the 8 element multi-layer transducers with backing were assembled into two-separate liquid filled rollers to build a rolling ultrasonic scanner.

Results/Discussion

The acoustic performance of single layer and multi-layer transducer is compared and it is found that the multi-layer transducer performed significantly better than the single layer. The acoustic fields generated by 1 and 8-layer transducer are shown in Fig.1. The 8-layer transducer scanner was then used to scan the concrete surface and obtained A-scans were used to form images in different planes inside the concrete. The coupling to concrete was achieved by using dry elastomer rings. SAFT (Synthetic Aperture Focusing Technique) algorithm was used for image reconstruction. For each scanning position, acoustic signal is transmitted from one element in Tx roller and is received by all 8 elements in Rx roller. The transmit element is then switched until the last element in the Tx roller has finished transmission, and the sequence is repeated to generate a 3D visualisation of the inspected concrete structure.

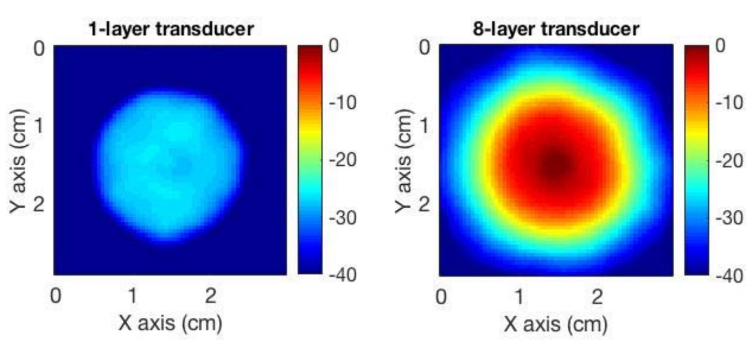

Fig.1. Acoustic fields generated by a single and 8-layer transducer at 300 kHz frequency.

P2-C2-5

Development of Dumbbell-Shape Vibration Source with Longitudinal and Torsional Transducers for Ultrasonic Metal Welding

Takuya Asami[1], Yosuke Tamada[1], Yusuke Higuchi[1], Hikaru Miura[1]; [1]*College of Science and Technology, Nihon University, Tokyo, Japan*

Background, Motivation and Objective

The ultrasonic metal welding method generally uses unidirectional vibration locus. However, this method has different weld strength depending on the direction of welding target installation. To solve this problem, we investigate ultrasonic metal welding by complex longitudinal-torsional vibration which is non-directional vibration. We study focusing on the planar vibration locus among the complex longitudinal-torsional vibration. We developed a dumbbell-shape vibration source with longitudinal and torsional transducers with excellent vibration controllability.

Statement of Contribution/Methods

Figure 1 shows the developed vibration source. The vibration source consists of a longitudinal vibration transducer, a dumbbell-shaped stepped horn, and a torsional vibration transducer. The center position of horn has the welding tip to add vibration to the welding target. We think that the vibration controllability of the vibration source is clarified by measuring the vibration loci of the welding tip. We investigate the vibration loci at each vibration resonance frequency. The both vibration displacement amplitudes were measured simultaneously with two laser Doppler vibrometer.

Results/Discussion

Figure 2 shows the vibration loci at the welding tip. When individual transducers are driven, vibration loci of welding tip corresponding to transducers are obtained. From this, we found that the vibration source can be controlled individual vibration. In addition, a planar vibration locus that is non-directional vibration locus was obtained by simultaneously driving two transducers. We found that the vibration source can be applied non-directional vibration to the welding target.

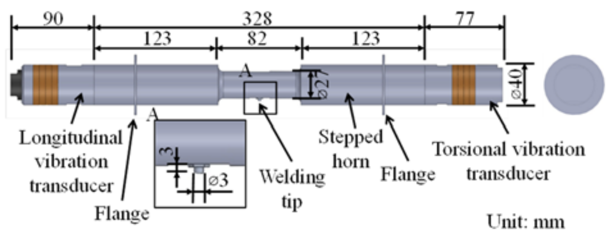

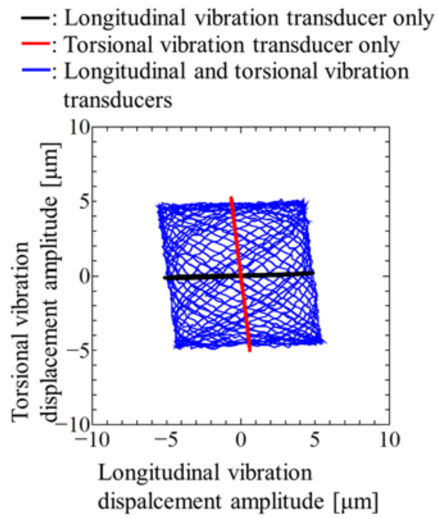

P2-C2-6

Development of Highly Efficient Piezoelectric Gas Composite Probe for Air-Coupled Ultrasonic Testing

Toshihiro Tsuji[1], Daitaro Kitahara[1], Yasuhiro Tanaka[1], Yoshikazu Ohara[2], Tsuyoshi Mihara[1]; [1]*Tohoku University, Japan,* [2]*Tohoku University, Tohoku University, Japan*

Background, Motivation and Objective

Air-coupled ultrasonic testing is required for inspection of materials where liquid acoustic coupling media cannot be applied, but transmission efficiency is a problem. Our group prototyped an ultrasonic probe fabricated using an array of piezoelectric ceramics rods by dicing a thickness-mode vibrator and the usefulness was found. However, a dicing method without rod broken was not established and unexpected frequency decrease of generated ultrasound was observed. In this study, we aim to improve the dicing method and reveal frequency-design guideline.

Statement of Contribution/Methods

PZT thickness-mode vibrator (Fujiceramics, C9, 500kHz) was bonded to Al plate (5 mm in thickness) using an epoxy adhesive and diced leaving the thickness of 0.1 mm. As a result, the fabrication of perfect array was attained [Fig.1(a)]. An aspect ratio of a rod was 5.5 [Fig. 1(b)]. The array with averaged acoustic impedances of 5.2, 9.0, and 17.3 MRayls were fabricated by changing the trench widths of 1.2, 0.77, 0.33 mm, respectively. A probe was fabricated by bonding Al plate with a thickness of 0.1 mm as a front plate using the epoxy adhesive. Prototyped probes were excited by spike signal (900V) and the vibration amplitude of polyimide film with a thickness of 5 μm was measured using a laser vibrometer[Fig. 2].

Results/Discussion

Figure 3 shows propagation waveforms at 100 mm on the center axis. In case of wide trench, narrow-band pulse with large amplitude was generated [Fig. 3(a)]. Broad-band pulses were observed, as the trench became narrow [Fig. 3(b) and (c)]. The frequency estimated from the period of the first half cycle was about 190 kHz in every case, which might be explained by a length-extensional mode of the rod.

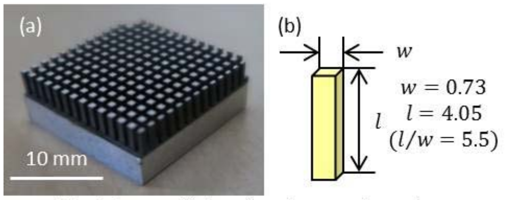

Fig. 1 Array of piezoelectric ceramics rods.
(a) Appearance. (b) Size of a rod .

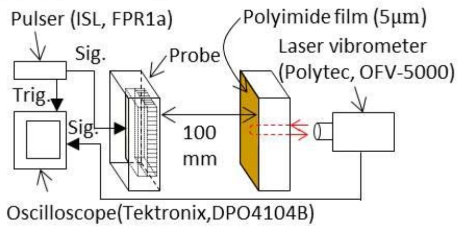

Fig. 2 Measurement setup.

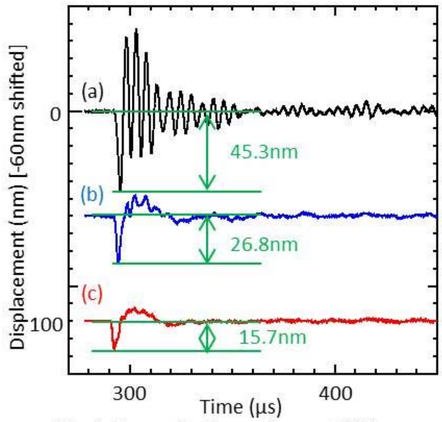

Fig. 3 Transmitted waveforms at 100 mm. Trench width of (a) 1.2 mm, (b) 0.77 mm, and (c) 0.33 mm.

P2-C2-7

Development of Hertzian Contact Ultrasonic Probe for Couplant-Free Concrete Measurement

Toshihiro Tsuji[1], Ryota Ikoma[1], Yoshikazu Ohara[1], Tsuyoshi Mihara[1]; [1]*Tohoku University, Japan*

Background, Motivation and Objective

For evaluation of aged concrete structure, it is expected to apply ultrasonic nondestructive measurement. Special coupling media with high viscosity made scanning difficult and the application to huge structure was not practical. Our group prototyped a couplant-free probe realizing strong acoustic coupling using high pressure due to Hertzian contact and found a potential to excite longitudinal wave. However, unexpected frequency decrease was observed. In this study, we aim to reveal a mechanism of frequency reduction and develop transmission-and-reception system applicable to concrete structure.

Statement of Contribution/Methods

When a thickness-mode vibrator with square cross section is not considered as a plate, lateral-mode vibration may dominate the frequency. First, we experimentally obtained frequency-designing curve depending on the vibrator width. Next, piezoelectric elements (Fujiceramics, C9) were prepared for transmission (probe A) and reception (probe B) taking large attenuation in concrete into account [Fig. 1(a)] and molded in a casing with an epoxy resin. A contact tip of alumina ceramics with a radius of 3.5 mm was fabricated so as to be the weight 1/50 less than that of the vibrator, bonded on the vibrator [Fig. 1(b) and 1(c)]. As a result, the frequencies of surface displacement vibration at the top of the tip was those of nearly expected values (probe A and B for 270 and 200 kHz, respectively).

Results/Discussion

We executed a transmission measurement using a concrete pillar of a building of Tohoku University. Schematic illustration is shown in Fig. 2. The thickness of the pillar was 300 mm. When probe A was excited using a spike signal (900V), longitudinal wave (A) was clearly observed. Therefore, it was found that this method could transmit and receive ultrasound in concrete without liquid couplant.

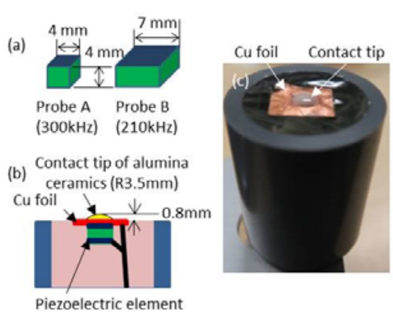

Fig. 1 Hertzian contact probe. (a) Size of piezoelectric elements, (b) structure, and (c) appearance.

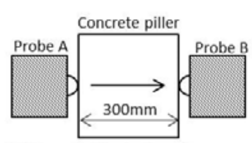

Fig. 2 Schematic illustration of measurement.

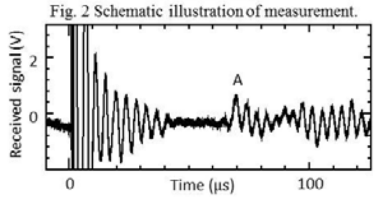

Fig. 3 Waveforms passing through a concrete pillar of the building with a thickness of 300mm received using Hertzian contact probe.

P2-C2-8

An Authentication and Identification System of Copper Containers for Spent Nuclear Fuel by means of an Ultrasonic Probe with a Beam Splitter

Chiara Clementi[1,2], Lorenzo Capineri[1], Francois Littmann[2]; [1]*Dept. of Information engineering, University of Florence, Firenze, Italy,* [2]*Nuclear Security Unit, Joint Research Centre of the European Commision, Ispra, VA, Italy*

Background, Motivation and Objective

Geological repositories are planned to be used for the long-term storage of Swedish nuclear spent fuel. Copper canisters will preserve the fuel underground for thousands of years. The IAEA (International Atomic Energy Agency) and EURATOM safeguards approaches propose to use canisters identification to support the Continuity of Knowledge (CoK) from the encapsulation plant to the final repository [1]. The external marking of canisters is not foreseen to avoid future corrosion issues then other techniques have to be used as tags for nuclear waste casks. A method for canisters labelling has been already studied by the authors [2] and this paper continues the previous studies. The aim of this work is the development of an innovative, robust and reliable tagging system based on an ultrasound beam splitter, with two different time windows to discriminate internal identification cavities on the one hand and the authentication signal of the internal welding gap filling on the other hand.

Statement of Contribution/Methods

The solution proposed envisages the use of a beam splitter to acquire two ultrasonic fingerprints: the first created by a series of inclined chamfers machined at the bottom of canisters lids (identification code) and the second related to the internal gap height between lid and tube of canisters after Friction Stir Welding (authentication signature). In accordance with the copper lid geometry, the double acquisition should be done by two probes or a single probe double focused. Our proposal involves instead the use of a mirror to split the beam of a focused transducer and then acquire echoes reflected by two different sides of the copper lid. CIVA simulations are implemented to fulfill a feasibility study on ultrasonic beam splitting on copper lids and results are compared with experimental tests.

Results/Discussion

The analysis of results revealed the possibility to realize an identification and authentication system for copper canisters based on the use of a single probe and a beam splitter. Tolerances and criticalities are discussed in the paper

.

References

[1] L. Hildingsson, C. Andersson, “Safeguards aspects Regarding a Geological Repository in Sweden”, Swedish Radiation Safety Authority, Stockholm, Sweden.

[2] C. Clementi; M. Calzolai; L. Capineri; F. Littmann, “Ultrasonic identification of copper canisters to be used for long term geological repository”, 2016 IEEE International Ultrasonics Symposium, Year: 2016, Pages: 1 - 3, DOI: 10.1109/ULTSYM.2016.7728561.

P3-C1 - PAT - Acoustic Tweezers and Particle Manipulation

Exhibit Hall

Saturday, September 9, 2017, 9:30 am - 4:00 pm

Chair: **Amit Lal**
Cornell University

P3-C1-1

Acoustic Particle Sorting by Integrated Micro-Machined Ultrasonic Transducers on Polymer-Based Microchips

Chen Yang[1], Zhangjian Li[1], Peiyang Li[1], Weiwei Shao[1], **Yaoyao Cui[1]**; [1]*Medical Acoustic Department, Suzhou Institute of Biomedical Engineering and Technology, Chinese Academy of Sciences, China, People's Republic of*

Background, Motivation and Objective

Ultrasonic standing waves (USWs) particle sorting has shown great potential to develop diverse applications in biotechnology and medical research due to its ability to offer non-contact, label-free particle manipulation. Currently, most reported on-chip acoustic particle sorters rely on high Q-value materials and elaborate geometry designs, which make these devices not easy to build and unsuited for mass fabrication. In this work, we propose a novel two-stage acoustic particle sorting strategy with the advantages of operating on low-cost polymer-based microchips and using integrated micro-machined piezoelectric transducers (PZTs).

Statement of Contribution/Methods

The schematic view of the sorter is illustrated in Fig.1(b). In order to form a three-node ultrasonic standing wave for pre-focusing of particles, a pair of 0.2-mm thick, home-made transducers were aligned parallel to the pre-focusing channel (300×150 μm) in air pockets at a distance of 5/4 wavelength at 7.5MHz. Likewise, another pair of 0.4-mm thick transducers excited at 2MHz were bonded on both sides of the separation channel (375×150 μm) using epoxy glue, allowing the resonance system working in a one-node mode. The ratio of sample inlet flow and sheath inlet flow was set to 1:6, confining the particle stream flowing in the narrow band near the side wall before entering the separation zone. Acoustic pressure fields (Fig.1(c)) and particle trajectories (Fig.1(d)) were calculated using the COMSOL software. As the pilot experiment, 3-μm fluorescent beads were injected to the microchannel to verify the feasibility of acoustic focusing by micro-machined PZTs (Fig.1(e)).

Results/Discussion

The air pockets etched throughout the bottom lid made it possible to use opposing PZTs to generate USWs in microchannels, overcoming the high acoustic attenuation caused by polymers (Fig.1(a)). According to the simulation results, when the pre-focusing US applied, particles arranged in line in the nodal plane (Fig.1(d-2)), rather than forming a narrow band (Fig.1(d-1)), which may induce clogging in experiments and disable the sorting system. By actuating the separation US, particles were separated into two streams before the bifurcation, then sorted into two outlets according to their lateral displacements (Fig.1(d-4)). Thus, successful particle sorting can be achieved on polymer-based microchips.

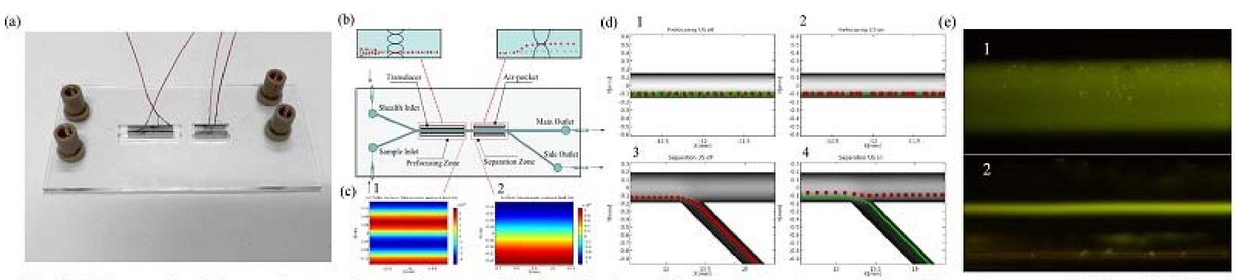

Fig 1. (a)Photograph of the on-chip acoustic particle sorter. (b)Schematic view of the experiment (not to scale). (c)Acoustic pressure field at 7.5MHz and 2MHz, respectively. The frequencies are selected to generate threee pressure nodes in pre-focusing zone and one pressure node in separation zone. The colorbar denotes the magnitude of the pressure. (d)Simulated particle trajectories of pre-focusing US off (d-1), pre-focusing US on (d-2), separation US off (d-3) and separation US on (d-4). (e)Fluorescent images of non-focused (e-1) and focused streams (e-2).

P3-C1-2

Behavior of the Oscillating Microbubble Clusters Trapped in Focused Ultrasound Field

Hironobu Matsuzaki[1], Johan Unga[2], Taichi Osaki[1], Kei Kawaguchi[1], Mitsuhisa Ichiyanagi[3], Takashi Azuma[1,4], Ryo Suzuki[2], Kazuo Maruyama[2], Shu Takagi[1]; [1]*Department of Mechanical Engineering, The University of Tokyo, Tokyo, Japan,* [2]*Department of Medical and Pharmaceutical Sciences, Teikyo University, Tokyo, Japan,* [3]*Department of Engineering and Applied Sciences, Sophia University, Tokyo, Japan,* [4]*Center for Disease Biology and Integrative Medicine, The University of Tokyo, Tokyo, Japan*

Background, Motivation and Objective

Microbubbles (MBs) are widely used in clinical site as contrast agents in ultrasound imaging due to its eminent responsiveness to several MHz band. In recent years, ultrasound drug delivery system (DDS) using MBs are widely researched to achieve selective medication to the targeted diseased part. In the condition of high number density of bubbles to enhance the performance of DDS, it is essentially important to understand interaction between bubbles and establish a control method of bubble clusters. In previous works, we can manipulate MBs using focused ultrasound, forming a bubbles cluster at the focus of the ultrasound field. The purpose of this study is to clarify scaling behavior of bubble clusters with various physical properties, since such scaling parameters is highly relating various bubble parameters which have not been measured in other methods.

Statement of Contribution/Methods

Bubbles in the ultrasound field are subjected to the primary Bjerknes force which is an acoustic radiation force represented by product of MBs f volume and gradient of acoustic pressure. From the relation between the ultrasound frequency and MBs f resonant frequency, small MBs which have higher resonant frequency can be trapped at the antinode or focus of the ultrasound field. We manipulated two types of MBs. One is Sonazoid® with average diameter of 2.6 μm and resonant frequency of about 5.2 MHz. The other is developed by Teikyo University, Japan, with average diameter of 1.5 µm measured with a coulter counter, 0.9 µm measured with DLS. Its resonant frequency is unknown. We monitored manipulation result via high-speed camera and microscope, then analyzed cluster size and behavior.

Results/Discussion

Each cluster of MBs was trapped at the antinode focal region of the ultrasound and had their own critical cluster size for each ultrasound frequency. Sonazoid formed larger clusters than MBs developed by Teikyo Univ., and Sonazoid cluster size is inversely proportional to the ultrasound frequency while the other MBs show the different scaling behavior compared to the free interface bubble cluster theory. These difference may be from diameter distribution of MBs and shell properties.

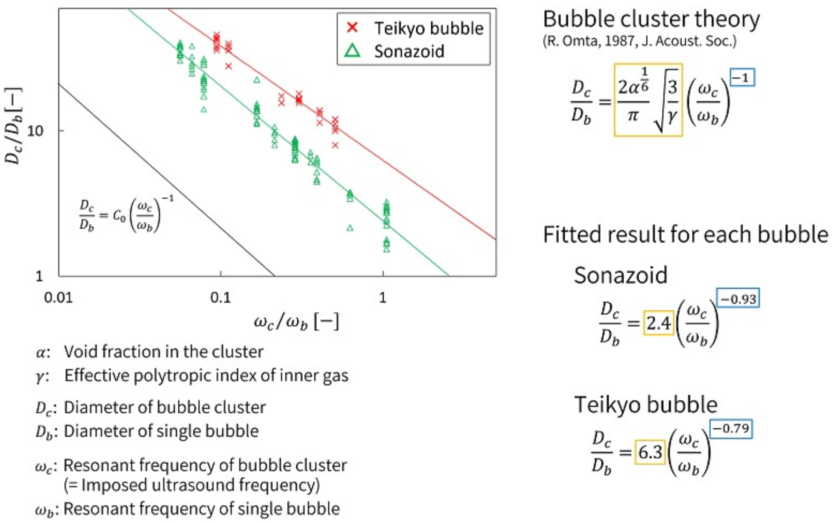

P3-C1-3

Bioparticle Manipulations Using Lamb Wave Resonator Array

Hongxiang Zhang[1], Zifan Tang[1], Zhan Wang[1], Shuting Pan[1], Chongling Sun[1], Xuexin Duan[1], Wei Pang[1]; [1]*Institution State Key Laboratory of Precision Measuring Technology and Instruments, Tianjin University, Tianjin, China, People's Republic of*

Background, Motivation and Objective

Piezoelectric transducers have been employed in trapping particles and molecules in microfluidic platform. Here we studied the acoustic streaming effect of multiple Lamb wave resonators (LWRs) in liquid. A novel device consisting of 4 LWRs was designed and fabricated. The experiment result demonstrated that the LWR array can efficiently drive multiple cylindrical vortices in liquid and trapped the particles at the center of the vortex.

Statement of Contribution/Methods

The structure of the LWR is schematic drawn in Fig. 1 (a). When the LWR is working in liquid, the Lamb wave, excited in the resonator, propagates to liquid from each side of boundaries. The acoustic wave in fluid induces flows by acoustic streaming effect. The numerical simulation results of the resonance of the LWR and the pressure of the acoustic wave in liquid are shown in Fig. 1(b). Then, the flow field is coupled by adding the body force, obtained from the vibration of the acoustic wave. The simulated acoustic streaming generated by a device consisting of 4 LWRs is demonstrated in Fig. 1 (c). An anticlockwise horizontal vortex dominates the flow in the center, accompanied by eight secondary vortices in the surrounding.

Results/Discussion

The fabricated LWR array device is employed to trigger microvortices and concentrate particles in liquid. A 40 mW, 384 MHz alternating current signal is applied to the device, and 10 ¦ÌL solution of polystyrene particles connected with human IgG antigen, is added to the device. Fig. 2(a) is the initial state of the device in liquid, and Fig. 2(b)-(f) demonstrate the process of the particles concentration from 0 s to 30 s. After 30 s, the particles are trapped in a circular area with 100 ¦Ìm diameter on the surface of the drop. It shows a great potential for biomolecular manipulations and biosensing.

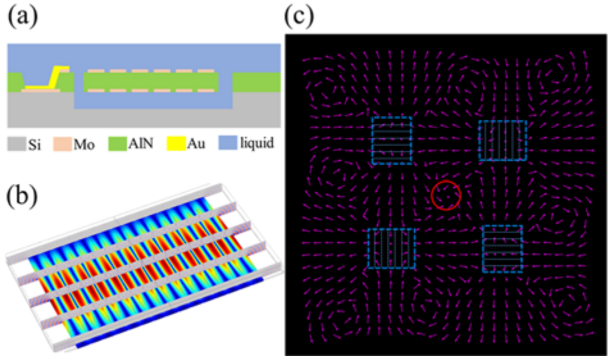

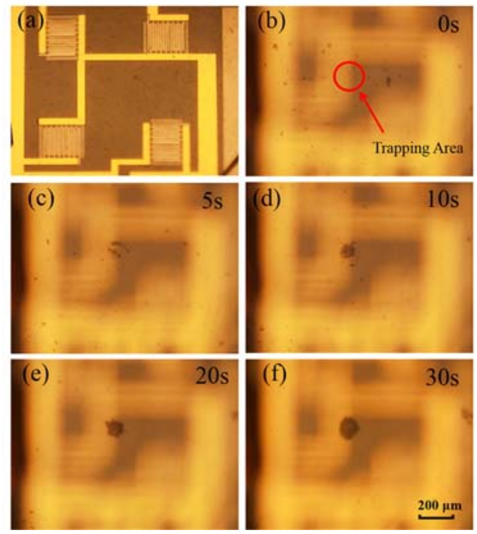

P3-C1-4

Manipulation of Microbubbles in Rabbit Blood Vessel by Using Ultrasonic Standing Wave- An In Vitro Study

Aiwei Shi[1], Xuan Du[1], Shukuan Lu[1], Lu Zhao[1], Bowen Jing[1], Lei Zhang[1], Yujin Zong[1], Mingxi Wan[1]; *[1]Xi'an Jiaotong University, China, People's Republic of*

Background, Motivation and Objective

Microbubble and its cavitation combined with ultrasound have been explored to improve the theranostics of vascular diseases. Inspiring achievements have been obtained in molecular imaging, drug delivery, and thrombolysis by using microbubbles. However, microbubbles flow along the vessel axis in the blood laminar flow, preventing the microbubbles from contacting with the targeting endothelium. Hence, transporting microbubbles to the desired site has the potential to improve the corresponding medical applications.

Statement of Contribution/Methods

In this work, manipulation of microbubbles was achieved both in a blood vessel phantom and in a rabbit abdominal aorta with a diameter of 2mm in vitro. Two transducers that located on the same side of the blood vessel phantom were employed for the manipulations in vessel. Ultrasonic standing waves were generated in the horizontal direction by the interference of two 1 MHz continuous waves with an angle of 120 degrees. Microbubbles were assembled into acoustic force potential wells in the ultrasonic standing wave. The assembled microbubbles were shifted with the acoustic potential wells by changing relative phase changes of the acoustic waves.

Results/Discussion

Firstly, manipulation of microbubbles was realized in blood vessel phantom under flow velocities ranging from 0.7 to 7 cm/s. Secondly, the microbubbles could be shifted from dozens of microns to several centimeters according to the manipulating parameters. Most important of all, manipulation of microbubbles in the rabbit abdominal aorta was realized in vitro. The microbubbles were not only assembled but also could be shifted to upstream or downstream in rabbit abdominal aorta. The future work is acoustic manipulation of microbubble in vivo.

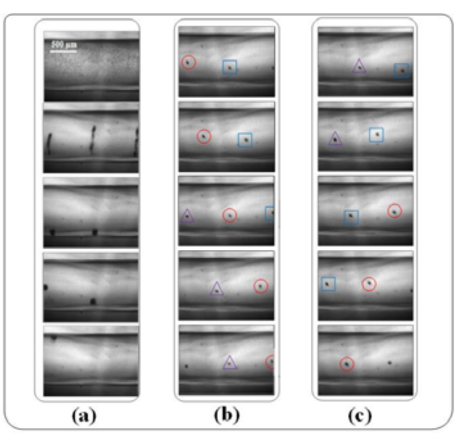

Fig.1 The optical images in (a) showed the process of microbubbles aggregation in a phantom vessel. (b) and (c) showed microbubbles were manipulated to downstream and upstream in a phantom vessel.

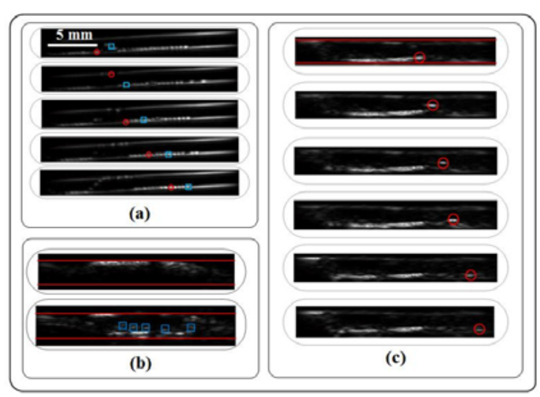

Fig.2 The ultrasonic images in (a) showed microbubbles were manipulated to downstream in a phantom vessel. (b) and (c) showed microbubbles were gathered and manipulated to downstream in rabbit abdominal aorta in vitro.

P3-C1-5

Discrimination of Minimal Residual Disease in Acute Lymphoblastic Leukemia by Using Single-Beam Acoustic Tweezer

Hsiao-Chuan Liu[1,2], Hye Na Kim[2], Enzi Jiang[2], Hae Lim[1], Ruimin Chen[1], Yong-Mi Kim[2,3], K Kirk Shung[1]; [1]*Department of Biomedical Engineering, University of Southern California, Los Angeles, California, USA,* [2]*Deptartment of Pediatrics, Division of Hematology/Oncology, Children's Hospital Los Angeles, Los Angeles, California, USA,* [3]*Pediatrics and Pathology, University of Southern California, Los Angeles, USA*

Background, Motivation and Objective

Cellular functions, for example proliferation, migration or gene expression, usually accompany a relationship with their mechanical properties. Three main methods, including atomic force microscopy (AFM), optical tweezer and magnetic tweezers, have been developed to measure cell's mechanics. However, AFM needs to contact cell resulting in prominent physical changes in elasticity and a pericellular layer of cells. Optical tweezer could damage cells by increasing the temperature generated from the applied laser. Although magnetic tweezers show an enough trapping force, the cytoplasm of a cell has to be loaded magnetic beads as the main drawback. Acoustic tweezer can provide enough trapping force and good penetration deep with a non-contact situation. Minimal residual disease (MRD) is a small number of leukemia cells which still remain in the patients after chemotherapeutical treatment. None of the tests can with an enough sensitivity be used to detect MRD cells. Single-beam acoustic tweezer was performed to generate a radiation force to study whether MRD cells can be discriminated from acute lymphoblastic leukemia cells.

Statement of Contribution/Methods

The 30MHz lithium niobate ($LiNbO_3$) ultrasound transducer with a highly focused beam was used to generate gradient force which can pull a single leukemia cell to toward a focus to be a trapping situation. Cell's concentration was allocated as approximate 0.05 e6 /ml. The transducer was sterilized by using 70% ethanol before the experiment. Five ICN24 leukemia cells before treatment and five cells after treatment by a chemotherapy drug were trapped and measured their deformability with various acoustic pressures, which were observed by an inverted microscope (IX71, Olympus, Japan) equipped with a 10X objective. The 16-bit images were recorded via a CMOS camera (C11440-10C, Hamamatsu Photonics, Japan), controlled by the software MetaMorph Version 7.7.6.0.

Results/Discussion

The preliminary result showed that the deformability of leukemia cells before treatment is slightly small than those after treatment by drugs. Single-beam acoustic tweezer is a promising technique to measure the mechanical property of acute lymphoblastic leukemia cells in a suspension condition, and could be a potential tool for discriminating leukemia between untreated cells and cells in MRD.

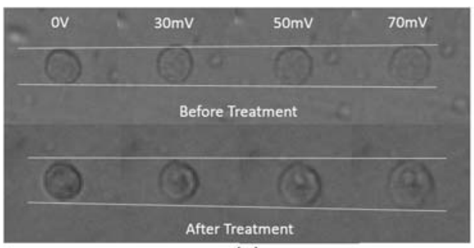

(a)

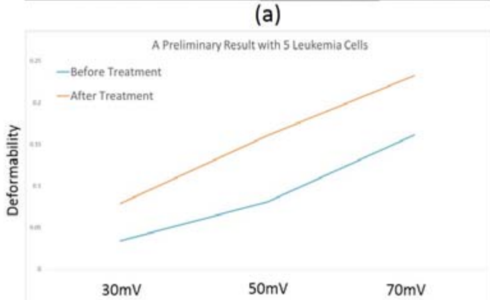

(b)

P3-C1-6

Microparticle Manipulation Using Dual-Wavelength Surface Acoustic Wave Devices

Jin-Chen Hsu[1], Chih-Hsun Hsu[1]; [1]*Department of Mechanical Engineering, National Yunlin University of Science and Technology, Douliou, Yunlin, Taiwan*

Background, Motivation and Objective

Recently, contactless manipulation of immersed objects has garnered great interest. Specifically, acoustic manipulation in microfluidic channels has emerged as a tool to control micron-sized objects in chemical, medical, and biological applications. Pure and controllable acoustic forces of the acoustic manipulation method exhibit a minor negative impact on viability and functionality of biological cells. A trend in acoustic manipulation methods involves creating a standing acoustic-wave field across a microfluidic channel and employing the resulting acoustic pressure field to trap, separate, pattern, or sort microparticles or bio-cells suspended in microfluids. Various types of acoustic-wave modes were utilized to produce desired acoustic-wave fields including ultrasonic bulk acoustic waves (BAWs), surface acoustic waves (SAWs), and Lamb waves. With respect to the design of tunable, efficient, and reproducible devices, increasing attention has been focused on SAW-based microfluidic devices.

Statement of Contribution/Methods

To explore a tunable SAW field and its acoustic effects on acoustophoresis from a systematic aspect, in this study, we propose dual-wavelength SAW devices with different transducer designs to investigate acoustic manipulation of particles in a microfluidic channel. We demonstrate the effect of spatially superimposed and separated dual-wavelength standing SAW fields and their influences on particle motion. Multi-wavelength SAW devices have immense potential in a wide range of tunable applications for microfluidic devices. However, acoustic pressure field coupled to a multi-wavelength standing SAW field traveling on a piezoelectric substrate was not investigated by previous studies. Here, we present the numerical calculations using a coupled model and experimental observations to demonstrate the design process and to comprehensively study the effects involved.

Results/Discussion

Numerical results reveal variations of acoustic pressure fields induced by the dual-wavelength standing SAWs and corresponding influences on particle motion. The acoustic radiation force in the acoustic pressure field is calculated to pinpoint zero-force positions and trace the particle motion. We fabricate dual-wavelength SAW acoustofluidic devices and experimentally demonstrate SAW field switching in sorting particles. We show that the observed particle motion and trajectories agreed well with numerical predictions, and the effects of inefficient excited SAWs on pre-actuating particles are predicted and observed. This indicated that the resulting particle trajectory variation is influenced by SAW field intensity and distributions and actuating time. The dependency of actuating response on input RF power is characterized as well. The present study enabled systematic analysis and design of multi-wavelength SAW-based microfluidic devices for tunable acoustophoresis.

P3-C1-7

Synthesized-Sound Manipulation of Microparticles: Principle and Experiments

Shuang Deng[1], Kun Jia[2], Zongwei Fan[3,4], Haoran Jin[1], Keji Yang[1]; [1]*College of mechanical engineering, Zhejiang University, Hangzhou, Zhejiang, China, People's Republic of,* [2]*School of Aerospace Engineering, Xi'an Jiaotong University, Xi'an, Shanxi, China, People's Republic of,* [3]*College of Engineering, Qufu Normal University, Rizhao, Shandong, China, People's Republic of,* [4]*School of Mechanical Engineering, Hanzghou Dianzi University, Hangzhou, Zhejiang, China, People's Republic of*

Background, Motivation and Objective

Arranging microparticles into desired pattern is of particular importance for many applications in the field of micro-electronics-mechanical system, regenerative medicine, tissue engineering and composite fabricating. A variety of techniques for patterning microparticles on the substrate have been developed in recent years based on optic, magnetic and electric field. However, each above mentioned techniques have their own potential drawbacks. The noninvasive property and little limitation of manipulating target make acoustic-based microparticle-patterning a promising alternative to the above mentioned methods. But in existing manipulations, the pattern shapes are limited and thus may hind the possible applications. In this work, we propose a method to create diverse programmable microparticle-patterns within an ultrasonic chamber. Multi-transducer based sound field synthesis technique, including mode matching and inverse filter, has been employed to design and built the trapping sound field corresponding to the desired microparticle-patterns.

Statement of Contribution/Methods

According to the Kirchhoff–Helmholtz theorem, the pressure of arbitrary point located within a source-free boundary with r radius is strictly determined by the pressure and normal velocity on the continuous boundary. In real application, finite discrete points are always used to approximate the continuous boundary. Taking spherical wave decomposition of the object acoustic field, the required pressure of these points can be calculated by mode-matching algorithm. On the other hand, the pressure of each discrete point is determined by the superposition of incident waves generated by the sources distributed on the R (R>r) radius circle. The propagation operator between the source and discrete points can be acquired using Huygens principle. Thus, the excitation signal acting on each transducer can be calculated by taking inverse filtering on the pressure of discrete points.

Results/Discussion

Figure 1(a) shows the object pattern, parallel lines, which can be traditionally realized by superposing two counter-propagating plane waves with 135 and 315 degree incident angle. The theoretical prediction of synthesized acoustic field using our methods is demonstrated in Figure 1(b). In the region marked with dashed circle, the pattern of pressure nodes and antinode accords well with the desired shape. Correspondingly, a parallel-line shape of micro-particles clusters has been realized in the ultrasoinic chamber, as shown in Figure 1(c). A hexagram pattern, shown in Figure 1(d) is selected as another object. The theoretical prediction of synthesized acoustic field and derived experimental pattern is illustrated in Figure 1(d) and (e). Except some small deviations, the experimental result shows good agreement with the designed shape.

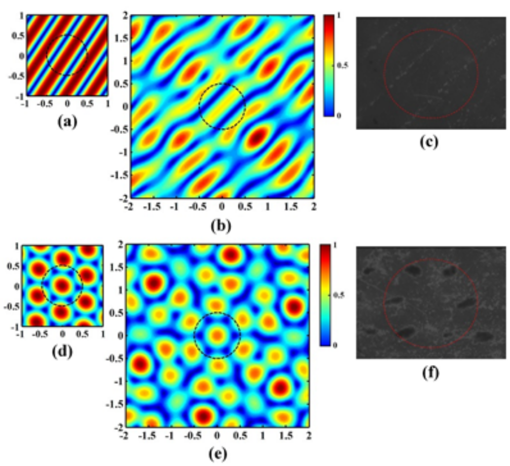

P3-C1-8

Acoustic Manipulation of Nanoparticles by Octagonal Surface Acoustic Waves

Long Meng[1], Wei Zhou[1], Lili Niu[1], Feiyan Cai[1], Fei Li[1], Hairong Zheng[1]; [1]*Shenzhen Institute of Advance Technology, Chinese Academy of Sciences, China, People's Republic of*

Background, Motivation and Objective

Nanoparticle manipulation has a variety of potential applications, from two-dimensional material fabrication to biomedical engineering. Pattern and transportation of nanoparticles has been receiving increasing attention in recent years. Ultrasound as a mechanical wave has proven to be the most effective in the manipulation of micro-objects in a non-contact and non-invasive fashion. However, due to the sharp decrease in the magnitude of the acoustic radiation force exerted on the particles from the micrometer to nanometer scale, it is difficult to manipulate the nanoparticles using acoustic method. In this paper, we established an octagonal high-frequency microfluidic device based on surface acoustic waves (SAWs) to pattern and transport the nanoparticles in a controllable manner.

Statement of Contribution/Methods

Fig. (a) shows the nanoparticles made of Au/Ag alloy with typical cubic structures. The size of the nanoparticles ranged from 60 nm to 80 nm. Four pairs of straight interdigital transducers (IDTs) was fabricated on a 128° Y-rotated, X-propagating $LiNbO_3$ substrate. The polydimethylsiloxane (PDMS) microchannel was bonded to the substrate using an oxygen plasma treatment.

Results/Discussion

Fig. (b) shows the finite element stimulation of the distribution of the acoustic filed when the adjacent three pairs of the IDTs were excited. The nanoparticles moved immediately and were trapped to the potential wells of the acoustic field, forming the corresponding pattern. We also found that the nanoparticles and the micro-sized polystyrene particles were patterned at the same location, indicating the acoustic radiation force is associated to the nanoparticle manipulation rather than the non-uniform electric field induced dielectrophoresis force. Furthermore, Fig. (c) shows a single nanoparticle could be transported precisely to write a letter 'A' using phase-shift method.In summary, we have demonstrated that the nanoparticle with special structure can be manipulated into a multi-scale pattern by the acoustic radiation force. Moreover, the single nanoparticle can be transported precisely with any arbitrary trajectory.

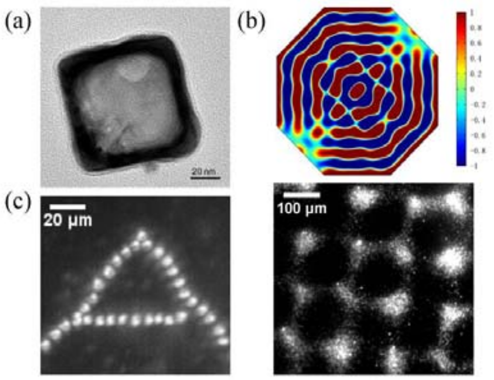

Fig. (a) The TEM photograph of the nanoparticle. (b) Stimulation of the distribution of the acoustic pressure and the patterning of the nanoparticles in the acoustic field (c) Transportation of the single nanoparticle in an arbitrary track.

P3-C1-9

2D Acoustic Focusing in a Rectangular Micro-Channel of Commercial Flow Cytometers

Li Zhangjian[1], Li Peiyang[1], Xu Jie[1], Shao Weiwei[1], Wang Ce[1], Cui Yaoyao[1]; [1]*Suzhou Institute of Biomedical Engineering and Technology, Chinese Academy of Sciences, Jiangsu, China, People's Republic of*

Background, Motivation and Objective

Flow cytometer plays a key role in cell sorting and analysis. For a higher detection precision, sheath flow is adopted to avoid the turbulent or vortex effect when the cell flowing through a capillary tube during the cell counting in many commercial cytometers. This method works well when the low flow velocity is relatively low. However, in order to have a higher analysis efficiency for clinical laboratories, a higher flow velocity is preferred, which always lead to cells siltation by using sheath flow. In this paper, to avoid this problem, an acoustic focusing method by using a pair of micro-size ultrasound transducers is proposed to help the cell flowing travel faster and smoother in a rectangular micro-channel of a commercializing flow cytometer developing by our group.

Statement of Contribution/Methods

To realize the two-dimensional acoustic focusing, two transducers are adopted to generate a stable standing wave to capture the cells in two different dimensions. By simulating and comparing the transient and frequency-domain sound field in the micro-channel generated by the couple transducers, a series of parameters are optimized and related experimental devices are designed and fabricated. The transducers are made of PZT-4, 4mm×5mm, thickness 0.4mm, working frequency range from 2MHz-4MHz; the outer diameter of the rectangular tube is 4mm×4mm; and the active module can work at different frequency, different amplitude and different phase. To verify the focused effect, an optical microscopy and a fluorescence microscope are used to track the particles' movement trail in the micro channel in different flow velocity, the particle is made of polystyrene, diameter is 3µm and the quadrate channel is 250µm×250µm. Next step, we will test the focus performance of cells which is much bigger than the particles and easier to manipulate, the flow velocity is expected to be up to 1ml/min above.

Results/Discussion

The simulation and experimental results are shown in figure 1.

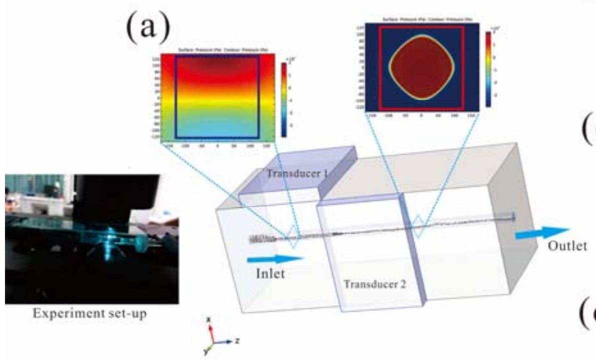

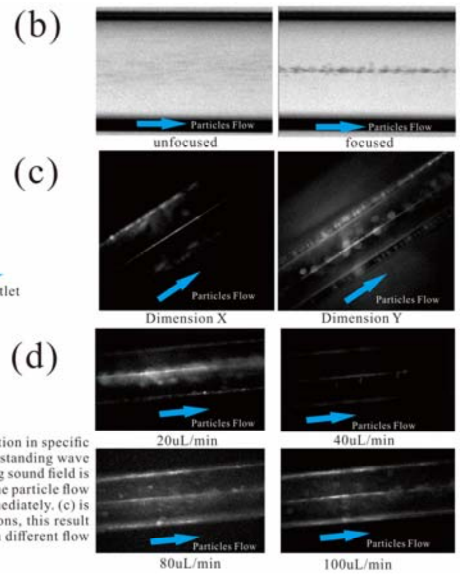

Figure 1. (a) is the structure of the micro rectangular channel and the sound field distribution in specific site is simulated, transducer 1 and transducer 2 can generate a one-dimensional focusing standing wave respectively; by combining these two transducers' sound field, a two-dimensional focusing sound field is formed. (b) shows the particles movement in the channel before and after focused; when the particle flow reach the focusing zone, all of the particles move to the center position of the channel immediately. (c) is the particle movement trails in X and Y axis; particle focusing happens in both dimensions, this result verifies that the two-dimension focused is obtained; (d) is the particle movement trails in different flow velocity; at a flow velocity of 100 μL/min, it still functions well.

P4-C1 - Design of Thin Film and Lamb Wave Devices

Exhibit Hall

Saturday, September 9, 2017, 9:30 am - 4:00 pm

Chair: **Paul Bradley**
Broadcom

P4-C1-1

High-Coupling Leaky SAWs on $LiTaO_3$ Thin Plate Bonded to Quartz Substrate

Junki Hayashi[1], Masashi Gomi[1], Masashi Suzuki[1], Shoji Kakio[1], Haruka Suzaki[2], Toshifumi Yonai[3], Kazuhito Kishida[3], Jun Mizuno[2]; [1]*University of Yamanashi, Japan,* [2]*Waseda University, Tokyo, Japan,* [3]*The Japan Steel Works, Ltd., Tokyo, Japan*

Background, Motivation and Objective

Leaky surface acoustic waves (LSAWs) and longitudinal-type LSAWs (LLSAWs) have a number of beneficial characteristics such as a larger electromechanical coupling factor K^2 and higher phase velocity than those of Rayleigh-type SAWs. However, LSAWs and LLSAWs have inherent attenuation because they lose energy by continuously radiating bulk waves into the substrate. To solve this problem, the authors previously reported that the attenuation of LSAWs and LLSAWs can be reduced by loading with an aluminum nitride (AlN) thin film with a higher phase velocity than that of the substrate [1,2]. However, K^2 is reduced owing to the small piezoelectricity of the AlN thin film. In this study, to obtain a substrate structure with a higher K^2, the propagation properties of LSAWs and LLSAWs on a $LiTaO_3$ (LT) thin plate bonded to a quartz substrate were investigated experimentally.

[1] F. Matsukura and S. Kakio, Jpn. J. Appl. Phys. 53, 07KD04 (2014).
[2] S. Kakio and K. Hosaka, Jpn. J. Appl. Phys. 55, 07KD11 (2016).

Statement of Contribution/Methods

AT-cut quartz was employed as a support substrate. 36°Y-cut X-propagating LT (36°YX-LT) and X-cut 31°Y-propagating LT (X31°Y-LT) were used as thin plates for the LSAW and LLSAW, respectively. First, the surface of a 3- or 4-inch wafer of LT and quartz with 0.2–0.8 mm thickness was activated in $Ar+O_2$ plasma after the RCA cleaning process. Next, the surfaces of LT and quartz were bonded under atmospheric pressure after ultrasonic cleaning using pure water and drying. Moreover, the bonded wafer was annealed for several hours at 100–300 °C. After dicing to a size of 20×15 mm, the surface on the LT wafer side was thinned and polished to a plate thickness h of 3.0–7.5 µm. Then, a single-electrode interdigital transducer (IDT) with a period λ of 8–20 µm and 10–30 finger pairs was fabricated on the polished surface of LT using a 1500-Å-thick Al thin film. The propagation directions of the AT-quartz were set to X for the LSAW and 60°X for the LLSAW because a higher K^2 was estimated in the theoretical calculation [3].

[3] M. Gomi, T. Kataoka, J. Hayashi, and S. Kakio, to be published in Jpn. J. Appl. Phys. 56 (2017).

Results/Discussion

The values of K^2 were determined from the measured admittance property of the IDT. For the LSAW on 36°YX-LT/ATX-quartz, K^2 of 11.8% was obtained at h/λ=0.25, while K^2 for the single LT was measured to be 5.9%. Furthermore, the admittance ratio and fractional bandwidth measured for an IDT with 30 finger pairs were increased from 22 dB and 4.5% for the single LT to 39 dB and 5.3% for the bonded structure with h/λ=0.44, respectively. For the LLSAW on X31°Y-LT/AT60°X-quartz, the value of K^2 increased from 3.2% for the single LT to 8.5% for the bonded structure with h/λ=0.25. The increases in the admittance ratio and fractional bandwidth were also observed.

P4-C1-2

The Frequency Switchable Multi-Layered BST/$BaTiO_3$ Epitaxial Film Resonator

Takahiro Shimidzu[1], Takahiko Yanagitani[1,2], Kiyotaka Wasa[3]; [1]*Waseda University, Japan,* [2]*JST PRESTO, Japan,* [3]*Yokohama City University, Japan*

Background, Motivation and Objective

The frequency switchable filters are suitable for selecting the vacant frequency bands. Usual polarity unidirectional single-layered resonators excite 1st mode whereas polarity inverted two-layered resonators excite 2nd mode. We previous reported the frequency switchable two-layered PZT/$PbTiO_3$ epitaxial film resonators[1]. However, $PbTiO_3$ films grown on PZT/$PbTiO_3$ films are difficult to obtain since Curie temperature and deposition temperature in $PbTiO_3$ are higher than those of PZT. $(Ba_x,Sr_{1-x})TiO_3$ (BST) films exhibit electrostrictive effect in paraelectric phase. In ferroelectric $BaTiO_3$, on the other hand, polarity inversion is impossible to be obtained without the application of higher than coercive electric field to films. Therefore, in this study, we considered that polarity inverted structure is easily obtained by application of less than coercive electric field of $BaTiO_3$ to two-layered $BaTiO_3$/BST epitaxial films.

[1]T. Mori, et al., Proc. IUS 2016

Statement of Contribution/Methods

First, $BaTiO_3$ epitaxial films were grown on La-$SrTiO_3$ substrate by RF magnetron sputtering with powder target. Next, $(Ba_{0.33},Sr_{0.67})TiO_3$ epitaxial films were grown on the $BaTiO_3$ films. Both the substrate temperatures were approximately 650ºC. We obtained the HBAR structure of Au/$(Ba_{0.33},Sr_{0.67})TiO_3$/$BaTiO_3$/La-$SrTiO_3$. Longitudinal wave conversion loss was measured by a network analyzer with the bias voltage.

Results/Discussion

Fig.1(a) shows experimental conversion loss curves during the application of +36 V and -36 V. Also described are the theoretical curves simulated by Mason's model including polarity inversion. 1st mode is excited at 300 MHz during the application of -36 V. On the other hand, 2nd mode is excited at 600 MHz during the application of +36 V. Fig.1(b) shows a shift of experimental conversion loss curves when the bias voltage is increased or decreased -36 V to +36 V. First, the minimum conversion loss of 1st mode decreases with decreasing the bias voltage of 0 V to -36 V. Next, the minimum conversion loss of 2nd mode decreases with increasing the bias voltage of 0 V to 36 V. These results show the two-layered BST/$BaTiO_3$ epitaxial film is frequency switchable. The lead-free resonator is promising for the environmentally friendly filters.

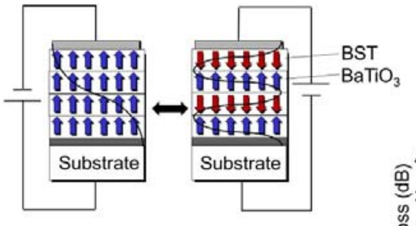

Fig.1(a) Polarity inverted structure

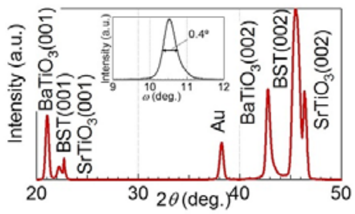

(b) 2θ–ω scan XRD pattern of $BST/BaTiO_3$

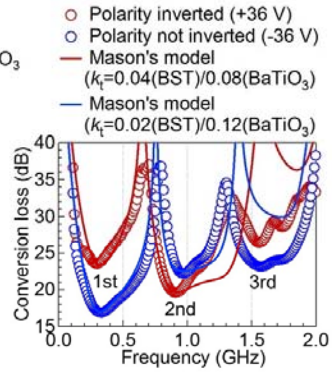

(c) Conversion loss of the longitudinal wave of HBAR when ±36 V bias voltage are applied.

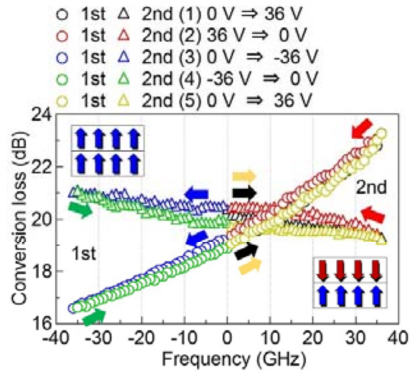

(d) Conversion loss of the longitudinal wave hysteresis in the 1st mode and 2nd mode vs bias voltage

P4-C1-3

Zero TCF Resonator based on S_0 Lamb Wave Mode in AlN Thin Plate Films

Mohammed Moutaouekkil[1,2], Abdelkrim Talbi[2], Omar Elmazria[1], El Houssaine El Boudouti[3], Philippe Pernod[2], Olivier Bou Matar[2]; [1]*Institut Jean Lamour UMR 7198, Université de Lorraine - CNRS, Nancy, France,* [2]*LIA LEMAC/LICS - IEMN UMR CNRS 8520, ECLille -USTL, PRES Université Lille Nord de France, Villeneuve d'Ascq, France,* [3]*Laboratoire de Physique de la Matière et de Rayonnements, Faculté des Sciences, Université Mohammed 1, Oujda, Morocco*

Background, Motivation and Objective

Resonator based S_0 Lamb wave mode in AlN thin films plate has drawn great attentions thanks to its high phase velocity up to 10 km/s and large electromechanical coupling coefficient (K^2). Moreover, this structure allows operation at high temperature conditions. Although several significant research efforts are ongoing to enable AlN-based piezoelectric devices for high temperature applications, an outstanding challenge in AlN-based resonators is to obtain the excellent frequency-temperature stability at operating temperatures [1]. The AlN/SiO_2 composite membrane was proposed as a solution for thermal compensation but with the counterpart of degrading K^2 and quality factor. In this work we propose an original structure leading to a better compromise between temperature coefficient of frequency (TCF) value and resonator performances.

Statement of Contribution/Methods

Several structures based on AlN membrane combined with SiO_2 layers were investigated. Different configurations were considered depending on the position, thickness and shape of SiO_2 layers, and topologies of interdigital transducers (IDT). Calculations were done thanks to implemented model on Comsol Multiphysics using general partial derivative equations interface. Dispersion curves of acoustic velocity, K^2, TCF were calculated versus AlN thickness, SiO_2 thickness of the considered configuration. An optimal structure will be selected for applications such as sensor or resonator at operating temperature.

Results/Discussion

Selection of pertinent results are shown in figure 1 for two configurations AlN/SiO_2 composite membrane (a) and AlN membrane with bridges (b) and for three IDT topologies (see in-set). In composite membrane case, the zero TCF is obtained for h_{AlN}/λ;=0.56 and related K^2 ranging from 2.4 to 2.6 % depending on the topology used and the S_0 Lamb velocity is about 7380m/s. When SiO_2 bridges are used, zero TCF could be achieved for 3 different AlN thicknesses: 0.15, 0.18 and 0.52. For h_{AlN}/λ;=0.15 we obtain K^2=3 and 3.2 respectively for topologies 1 and 2. Note that the experimental achievement of topology 2 requires complex fabrication process including double side lithography. Thus the topography 1 will be preferred due to the slight difference between obtained values of K^2. Experimental achievement of this later structure is in progress to confirm the theoretical predictions.

[1] J. Zou et al, JAP (115), 094510 (2014);

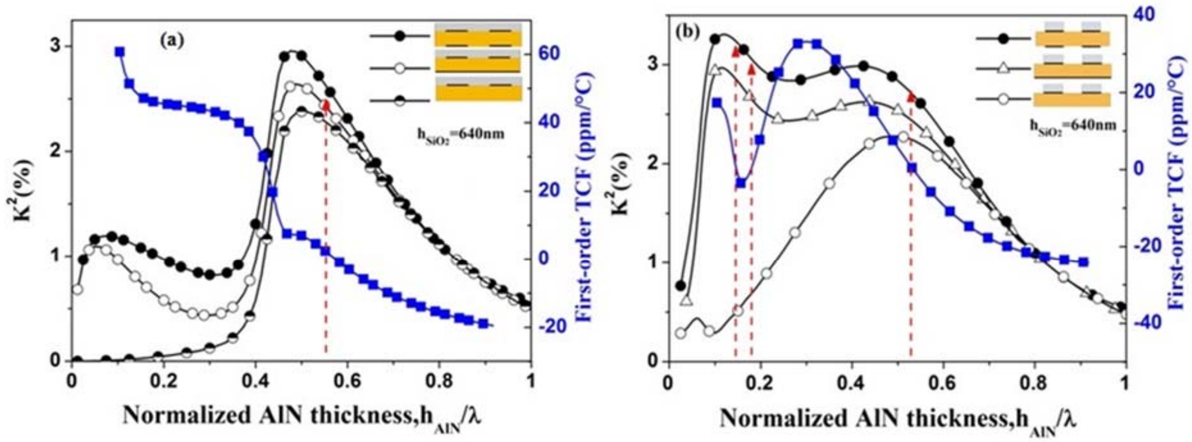

Fig. 1: Dispersive curve of K^2 and TCF calculated for AlN/SiO_2 composite membrane (a) and AlN membrane with SiO_2 bridges. SiO_2 thickness being fixe (h_{SiO2}=0.64μm).

Low Loss Delay Lines Based on Suspended Thin Film of X-Cut Lithium Niobate

Gabriel Vidal-Álvarez[1], Abhay Kochhar[1], Gianluca Piazza[1]; [1]*Electrical and Computer Engineering, Carnegie Mellon University, Pittsburgh, Pennsylvania, USA*

Background, Motivation and Objective

Analog signal processing techniques based on surface acoustic wave (SAW) devices have been commercialized in the past 50 years. Delay lines [1] and resonators [2] have been implemented for a wide range of applications [3]. The use of small scale resonators has boomed because of the continuous growth of the cell phone business, whereas components such as delay lines have been relegated to smaller markets such as base stations. Emerging applications related to the Internet of Things have brought up the need for extremely low power and high speed signal processors.

The maximum electromechanical coupling (k_t^2) of surface acoustics waves in lithium niobate ($LiNbO_3$, dubbed LN) is 5.6 % [4]. Lamb waves resonators fabricated on suspended thin films of LN have demonstrated a k_t^2 around 30 % [5]. Taking advantage of such high k_t^2 to build delay lines is extremely beneficiary. However, due to the nature of Lamb waves, which require suspended plates, achieving long delays poses an important fabrication challenge. We overcome this technological challenge in this work.

Statement of Contribution/Methods

We report on the theoretical modeling, fabrication, and experimental characterization of delay lines (length varying between 0.63 and 5.28 mm) built using LN X-cut thin films. We use a 1 µm thick LN thin film on silicon wafer prepared by NGK. The delay lines are fabricated by ion milling of LN, followed by two metals lift-off steps, and xenon difluoride (XeF_2) etching to release the structures.

Results/Discussion

We design the delay lines with an orientation of 30° with respect to the Y axis to maximize the coupling coefficient for propagation of the S0 mode. We set the pitch of the launcher and receiver to be 7.5 µm (λ = 15 µm). The launcher and receiver of the delay lines have both 32 interdigitated electrodes, and aperture of 10 λ. Different delays ranging between 0.02 µs and 0.8 µs were designed. All delay lines were successfully fabricated, with the longest one achieving a delay of 0.8 µs with an insertion loss of 11.5 dB (Fig. 1). To our knowledge, this is the first delay line with such a high delay·transmission product. The analysis of the different delay lines shows an attenuation of around -10 dB/cm.

References

[1] Tancrell, IEEE Proc, 393-409, 1971.

[2] Bell, IEEE Proc, 711-721, 1976.

[3] Morgan, 1991.

[4] Datta, 1986.

[5] Pop, IEEE MEMS, 966-969, 2017.

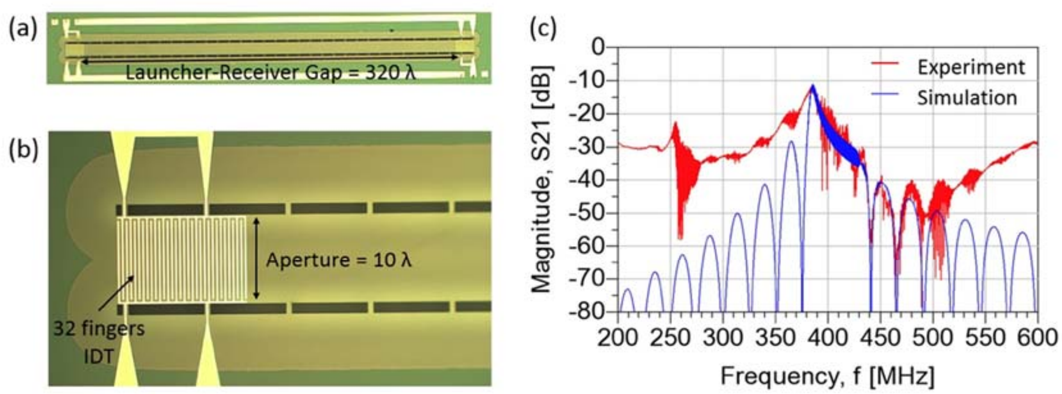

Figure 1: (a) Optical microscope picture of a delay line of length 320λ. (b) Zoom in of one of the IDTs of the delay line. (c) Experimental and theoretical transmission of the pictured delay line. The maximum transmission is 11.5 dB (with matching network added). The delay is 0.8 µs.

P4-C2 - Microacoustic Devices and System Applications

Exhibit Hall

Saturday, September 9, 2017, 9:30 am - 4:00 pm

Chair: **Karl Wagner**
RF360 Europe GmbH

P4-C2-1

Fabrication of SAW Resonators on Single-Crystal Diamonds Using Minimal-Fab Process

Satoshi Fujii[1,2], Haruki Toonoe[3], Yasunari Shiba[3]; [1]*National Institute of Technology, Okinawa College, Nago, Japan,* [2]*Dept. of Chemical Science and Engineering, Tokyo Institute of Technology, Tokyo, Japan,* [3]*Equipment Service Dept, Yokogawa Solution Service Corportation, Tachikawa, Tokyo, Japan*

Background, Motivation and Objective

Diamond has the highest sound velocity among all materials and has been applied in high frequency surface acoustic wave (SAW) devices in the gigahertz range. To date, numerous researches have reported that the SAW devices built on a diamond wafer can work in the frequency range from 2 GHz to 10 GHz. S. Fujii et al. reported that the one-port resonator with an interdigital transducer (IDT)/AlN/single crystal diamond structure has an excellent quality factor Q of 8346 at 5.2 GHz. Hashimoto et al. also reported that an SAW resonator based on the ScAlN/single crystal diamond structure exhibited resonance Q, anti-resonance Q, and K^2 values of 520, 130, and 6.1%, respectively, at 3.6 GHz. In both reports, a small size single type Ib crystal diamond with a 3 × 3 mm^2 area was employed as a substrate. However, these devices are far from becoming commercial devices because of the small substrate. Many researchers are still making an effort to realize a large diamond wafer. AIST has developed a large size single crystal diamond having a 10 × 10 mm^2 area using plasma CVD method for application in power transistors and acoustic devices.

Statement of Contribution/Methods

In general, two-inch wafers are required as the minimum size for the fabrication of devices. Nevertheless, Hara et al. has now developed a CMOS fabrication system known as the Minimal-Fab process. The Minimal-Fab process employs a half-inch size wafer and proceeds with the device process using a half-micron fine pattern lithograph without a clean room. Moreover, small size and not perfectly round shaped substrates, such as an Ib single crystal diamond, can be treated in the Minimal-Fab using a jig made of silicon. Therefore, we are making an SAW resonator on a single crystal diamond substrate using the jig.

Results/Discussion

Fig. 1 shows the jig in the minimal shuttle and the fine pattern on the diamond substrate. In this conference, we will demonstrate the fabrication and characteristics of SAW resonators on small size single crystal diamond substrates using the Minimal-Fab process.

(a) (b)

Fig. 1 (a) Ib single crystal with the jig in the minimal shuttle; minimal shuttle can be kept clean like a super clean room and the size of the jig is half inch , (b) SEM image of the fine pattern with 0.5 µm on the diamond substrate using Electron Beam lithograph

P4-C2-2

SAW Correlators on GaN

Nancy Saldanha[1], Ryan Westafer[1]; [1]*Advanced Concepts Laboratory, Georgia Tech Research Institute, Atlanta, Georgia, USA*

Background, Motivation and Objective

Conventional acoustic wave correlators are known for their small size (nearly 105 times smaller than an analogous electromagnetic correlator), zero DC power consumption, and linearity. Reconfigurable orthogonally coded correlators could be used at the front-end of a RF transmit and receive chain to provide cross-correlation properties that can aide in simultaneous transmit and receive (STAR) systems. Loss, however, has been a significant limiting factor, even on high coupling substrates. The 2-dimensional electron gas (2-DEG) hetrostructure region on a GaN wafer can be depleted to generate acoustic gain via the acoustoelectric effect, thus allowing for long correlator structures that can be easily integrated into a front GaN MMIC. In this work the feasibility of SAW correlators on GaN was investigated.

Statement of Contribution/Methods

SAW coupling and velocity for varying GaN film thicknesses on sapphire and SiC substrates were extracted via COMSOL FEM analysis. SAW delay line test structures on undoped GaN on Sapphire wafers were fabricated and measured. The SAW coupling and velocity were experimentally extracted and compared to COMSOL extracted parameters. The SAW parameters were then used in a SAW coupling of modes model to simulate coded correlator structures. The correlators were designed using a combination of M-sequence/Walsh-Hadamard PN codes for good correlation properties. The correlation properties of these devices modeled in line-of-sight (LOS) and multi-path environments were compared. For inclusion of the multi-path effect, tap weights from the COST 207 Reduced Bad Urban (RBU) model was used.

Results/Discussion

SAW coupling measured on the undoped wafers compared well to the COMSOL extracted value, however, other unexplained losses increased the insertion loss significantly. Correlator structures on GaN were modeled and can have reasonable losses if acoustic gain were applied via 2DEG depletion. The time and frequency responses of an example 255 chip correlator design on GaN are shown in Figure 1 (a) and (b), respectively. Correlators on GaN offer an integrated solution that could pave the path for future STAR radio architectures.

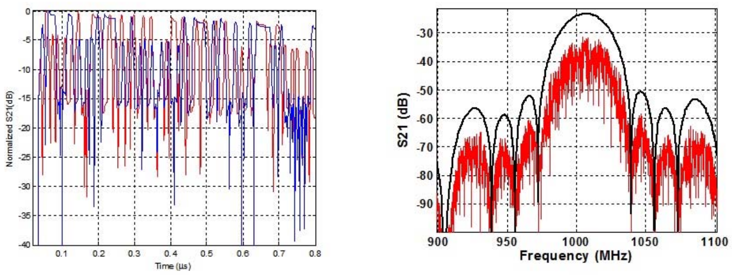

(a) (b)

Figure 1. (a) The normalized time domain responses of two orthogonal PN bi-phase M-sequence/Walsh codes; (b)Frequency response of a coded SAW correlator on GaN, assuming a coupling coefficient, k_{eff}^2 of 0.5%.

P4-C2-3

Systematic Synthesis Methodology for the Design of Acoustic Wave Stand-Alone Ladder Filters, Duplexers and Multiplexers.

Jordi Verdu[1], Iuliia Evdokimova[1], Pedro de Paco[1], Thomas Bauer[2], Karl Wagner[2]; [1]*TES, Universitat Autonoma de Barcelona, Cerdanyola del Vallès, Barcelona, Spain,* [2]*RF360 Europe GmbH, Germany*

Background, Motivation and Objective

Usually, the design of acoustic wave devices is mainly entrusted to optimization techniques due to the stringent constraints imposed by the technological feasibility of acoustic resonators and the challenging electrical specifications. A stringent transmission response and very restrictive technological factors make the designing a complex and challenging task. The objective of this work is to describe a methodology for the direct synthesis of ladder-type acoustic filters: stand-alone, duplexers or multiplexers (Carrier aggregation). The methodology is native oriented to accommodate technology, and also works with cross-couplings.

Statement of Contribution/Methods

The acoustic ladder filter can be represented, in low- and bandpass domain, as an inline configuration composed of Non-Resonant Nodes (NRN) with dangling resonators, each one contributing with a transmission zero (TZ). This common configuration exhibits characteristic similarities regarding inline prototype networks with RN and NRN: modularity, control of transmission zeros by independent resonators, and fully canonical response without a direct source load coupling. The nodal model is related to the Butterworth-Van Dyke equivalent circuit, which links electric and acoustic parameters. Then, the bandpass response is obtained by using a proper low- to bandpass frequency transformation, leading the definition of a direct synthesis methodology to obtain the bandpass electric parameters of a general RF filter based on acoustic resonators by using a coupling matrix technique.

Results/Discussion

Based on the proposed synthesis method, a LiNbO3 SAW ladder-type filter has been designed for band 28 Rx. The synthesized filter is compared with the measurement with a very high agreement between both as shown in Fig1. The output of the method is the complete electrical and acoustic characterization of each resonator in the topology, and also required external elements to accommodate the technology. This is a very fast and accurate seed to which only the electromagnetic simulation of the layout must be added to go to the last post-optimization process before fabrication. The procedure is time efficient, precise in the outcomes, provides a deep understanding of the particular interactions between technological constraints and device performance which lead to screen the best in choice topology.

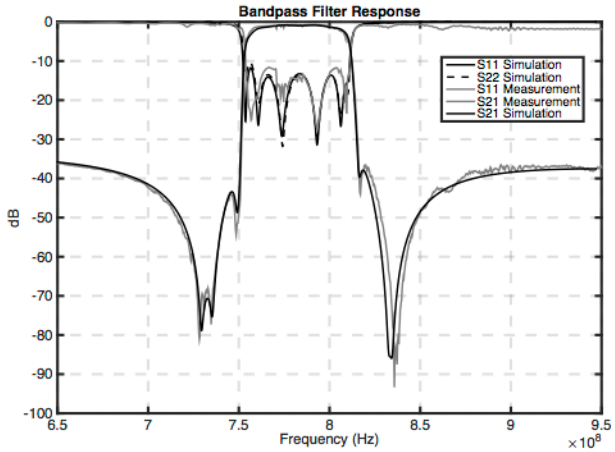

P4-C2-4

Design of RF Power Divider/Combiner based on Surface Acoustic Wave Technology

Elhadji Mansour Fall[1], Alexandre Reinhardt[2], Frédéric Domingue[1]; [1]*Laboratoire de Microsystèmes et Télécommunications, Université du Québec à Trois-Rivières, Trois-Rivières, Quebec, Canada,* [2]*CEA-LETI, Commissariat à l'énergie atomique et aux énergies alternatives, Grenoble, France*

Background, Motivation and Objective

Power dividers/combiners are used as fundamental unit for power combining/splitting in different RF/Microwave circuits such as power amplifier modules, antenna array feeds or mixers. Most common types are based on quarter wave transmission line and their miniaturization is challenging especially in frequency less than GHz range where they exhibit very large physical size that make their use impractical or impossible in portable wireless devices.

As an alternative, we propose to exploit the propagation of surface acoustic waves to implement RF signal splitting and combining functions, thus providing enhanced reduction of traditional power dividers/combiners for compact RF wireless architectures. SAW technology is well established and offer high level of miniaturization with high performance.

This paper describes an innovative power divider/combiner based on parallel connected SAW coupled resonators filter (CRF).

Statement of Contribution/Methods

Each SAW CRF of the power divider/combiner comprises three interdigital transducers (IDT) with a floating IDT and two other IDTs connected to input port and output port respectively (Figure 1). By connecting the CRFs in parallel and with proper arrangement of the distance between IDTs, RF signal splitting and combining are achieved through constructive interferences of acoustic waves at each port. Isolation between input ports is obtained by destructive interference.

The power divider/combiner is designed to combine or spilt in quadrature with 3 dB loss on YZ lithium niobate substrate. The synthesis is based on the transmission matrix method and the Mason model.

Results/Discussion

Figure 2 shows the simulated response of the SAW based power combiner/divider designed for low frequency applications and center at 87MHz. The structure exhibits a filter function with equal division of the RF signal and isolation between input ports. A simulated insertion loss of 3.2 dB is achieved with a relative bandwidth of 1%.

The total area of this designed power combined/divider is 8.4 x 4.6 mm2 which is a relative size reduction of more than 70 % in comparison to commercial power combiners at same frequency.

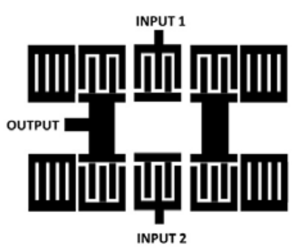

Figure 1: Schematic of the SAW based power divider/combiner

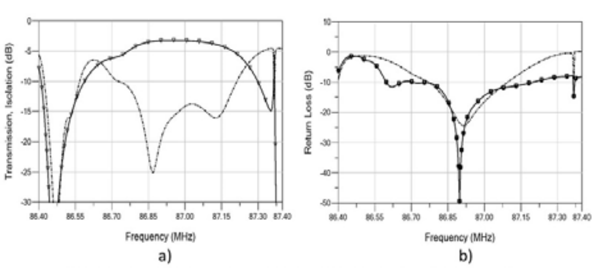

Figure 2: Simulation response of the SAW based power divider/combiner

P4-C2-5

SAW RFID with Enhanced Penetration Depth

Xupeng Zhao[1], Ruchuan Shi[1], Peng Qin[1], Xiaojun Ji[1], Yixin Ma[1], Yumei Wen[1], Ping Li[1], Tao Han[1]; [1]*Department of Instrument Science and Engineering, Shanghai Jiao Tong University, Shanghai, China, People's Republic of*

Background, Motivation and Objective

Construction of smart city has become a historical trend in the world. The management of underground pipes and the intelligent concrete are the main part of building smart city in China. Compared with the available electronic marker system, SAW-RFID system has shown excellent properties: truly passive, strong penetrating capability, long service-life, sensing and ID integration, and etc. Thus, SAW-RFID system is particularly applicable and has excellent application prospects. However, in practical implementation, the limitation of detection depth has become an obstacle on the application of SAW-RFID for the smart city in the future. Some methods to enhance penetration depth further are proposed.

Statement of Contribution/Methods

Firstly, a second harmonics single phase unidirectional transducer (SPUDT) on 128°YX-LiNbO3 substrate is designed. Different from the matching circuit for SPUDT filters, some possible matching circuits between the antenna and the SPUDT are explored and the optimal parameters are obtained based on the criterion that each reflected echo amplitude should be as high as possible. Secondly, under the criteria of enough multiple reflection suppression, the coding reflectors are designed with high reflectivity in order to decrease the reflection losses. Thirdly, the chirp interrogation signal is used to obtain 10dB signal processing gain. Finally, in the reading system, the effective center frequency range of the interrogation signal is adaptive to the center frequency shift for RFID tags due to various factors such as temperature.

Results/Discussion

In order to verify the results, the in-line SAW tag, containing second harmonics SPUDT and 5 coding reflectors on 128°YX-LiNbO3 substrate is designed. Massive subsurface materials such as dry sandy soil, moist clay-laden soil and asphalt are compared in experiments. In conclusion, the practical detective depth for dry sandy soil consequently increases to 1.5m. This demonstrates that the penetration depth of SAW-RFID is more superior than underground radar system with the same center frequency range.

P4-C2-6

Long Range Wireless SAW Passive Tag System for Vibration Monitoring

Koki Shibata[1], Eiki Takahashi[1], Hitoshi Fujiwara[1], Tamotsu Suda[1], Jun Kondoh[2], Tsuyoshi Hirose[3], Yusuke Toyota[3], Masayuki Ozaki[4]; [1]*Japan Radio Co., Ltd., Japan,* [2]*Shizuoka University, Japan,* [3]*Nippon Expressway Research Institute Company Limited, Japan,* [4]*New Japan Radio Co., Ltd., Japan*

Background, Motivation and Objective

In this paper, we describe a 920 MHz band long range wireless SAW passive tag system (WSPTS) for vibration monitoring, which achieves more than 10m reading distance. For the purpose of structural health monitoring (SHM) of aging infrastructures (e.g. bridge, building, and so forth), passive wireless sensor systems are an attractive option because they are operated battery-less and almost maintenance free. A SAW based passive tag system is suitable for the purpose; however, a conventional WSPTS is mostly limited to short range of less than 5m.

Statement of Contribution/Methods

The developed WSPTS consists of passive tags and a reader unit. The passive tag consists of a SAW device, a battery-less vibration sensor, and a patch antenna. The feature of the developed passive tag is the flexibility improved by separating the SAW device for wireless communication and the vibration sensor. Therefore, other sensing devices can be used for our WSPTS although they must be operated battery-less for realizing passive tag. The battery-less vibration sensor consists of an electricity generating device for vibration and a voltage controlled variable phase shifter for the receiving signal.

The reader unit of our WSPTS consists of a transmitter (Tx) and receiver (Rx), and Tx and Rx Yagi-antennas, both having an antenna gain of 9dBi. Our WSPTS has been achieved more than 10m reading distance by realizing a large Tx-Rx antenna isolation of the reader unit to reduce the unwanted Tx leakage signal to the Rx signal and its signal processing. The Tx-Rx isolation is achieved by utilizing polarization and directivity of the reader antennas. A frequency modulated continuous wave (FMCW) signal is used and utilized correlation processing gain. In order to meet Japanese 920 MHz band passive tag system standard specifications (ARIB STD-T108), time domain FMCW waveform is weighted by Cosine-Tukey window to reduce spectral leakage. Furthermore, each passive tag is identified by the delay time of the SAW device by correlation.

Results/Discussion

Our WSPTS has achieved more than 10m reading distance. Each reflective FMCW signal from the passive tag can be distinguished in the reader unit by realizing Tx–Rx antenna isolation of more than 40 dB and the correlation processing gain of 30dB. The transmitter FMCW signal with an antenna power of +13dBm, meets the spectrum mask of the ARIB STD-T108. Identification of the passive tag is realized by the different delay time of a multiplication interval of 1.25us. The vibration frequency is calculated from a fluctuation of the phase value of the correlation value which corresponds to the delay time of each passive tag.

P4-C2-7

Self-Healing Narrowband Filters via 3D Heterogeneous Integration of AlN MEMS and CMOS Chips

Enes Calayir[1], Jinglin Xu[1], Larry Pileggi[1], Gary K. Fedder[1], Srinivas Merugu[2], Navab Singh[2], Gianluca Piazza[1]; [1]*Electrical and Computer Engineering, Carnegie Mellon University, Pittsburgh, PA, USA,* [2]*Institute of Microelectronics, Agency for Science and Technology (A*STAR), Singapore*

Background, Motivation and Objective

AlN MEMS CMRs offer high Q and k_t^2, and a center frequency (f_0) that can be primarily set by lithography. They also have direct 50 Ω matching capability. These properties make AlN CMRs an ideal candidate to synthesize multi-frequency bandpass filters on a single chip with low insertion loss (*IL*). However, their practical implementation is hindered by fabrication induced variations. To address this challenge, we propose the use of statistical element selection (SES) technique where a subset *k* from a bank of *N* nominally identical subfilters are combinatorially selected in parallel via series CMOS switches at RF input and output in order to construct a high yield, self healing filter.

Statement of Contribution/Methods

To implement SES, we built an array of identical subfilters on the AlN MEMS chip and a switching matrix on the CMOS chip to toggle each subfilter on/off individually. Also, low loss redistribution layers (RDL) were developed on the front side of AlN MEMS chip to limit RF parasitics and use CMOS chip more efficiently. The optimum value of *k* is found to be 4 based on Monte Carlo simulations for an *N* of 12.

Results/Discussion

We demonstrated the SES technique with 1.15 GHz AlN MEMS subfilters fabricated in an 8" Si fab by A*STAR Institute of Microelectronics. The chip integration is achieved through a split fab process where the hermetically encapsulated MEMS resonators are solder bump bonded to a 28 nm CMOS chip (see Fig. 1). The SES offers 495 unique filter frequency responses with a tuning range of 150 kHz for f_0 and 250 kHz for bandwidth (*BW*). An $IL \leq 3.4$ dB and an out-of-band rejection (*OBR*) ≥ 15 dB were also achieved in the self healing filter (see Fig. 2). Thanks to RDL, we reduced parasitic capacitance by ≈20x and resistance by ≈5x compared to RF signal routing on CMOS, which, in turn, enabled a direct 50 Ω matching.

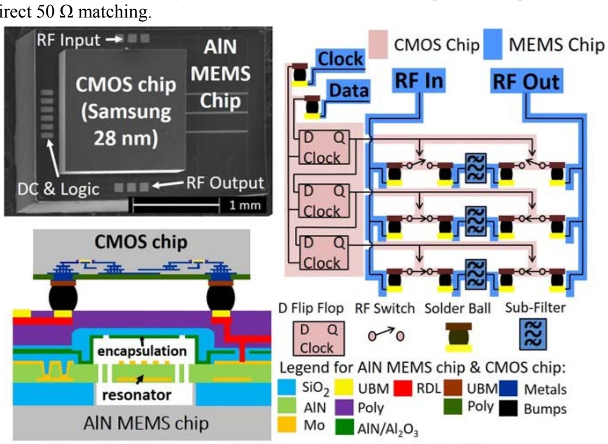

Figure 1. SEM image of 3D integrated chip stack with a cross-sectional representation (left), and its conceptual circuit diagram for SES application (right)

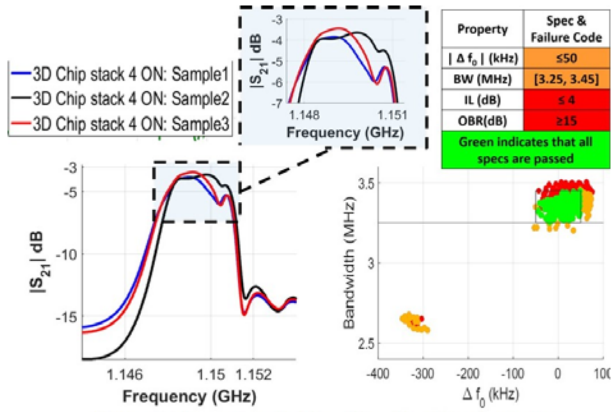

Figure 2. Three of available self healing filter frequency responses measured on a 3D integrated chip-stack (left), and center frequency offset (Δf_0) and bandwidth of each response available from the self-healing filter (right)

P4-C2-8

Electrical Characteristics of SAW Filters on $SiO_2/Al/LiNbO_3$ Structure for Inverter Multiplex Transmission Systems

Fumiya Kobayashi[1], Shoji Kakio[2], Shigeyoshi Goka[1], Keiji Wada[1]; [1]*Graduate School of Science and Engineering, Tokyo Metropolitan University, Hachioji-shi, Tokyo, Japan,* [2]*Interdisciplinary Graduate School of Medicine and Engineering, University of Yamanashi, Kohu-shi, Ymanashi, Japan*

Background, Motivation and Objective

Multilevel inverter circuits with a number of power switching devices (10–100) have been reported to generate favorable output sinusoidal waveforms and high output voltage in recent research on power electric circuits. Meanwhile, next-generation switching devices based on wide-gap semiconductors can be installed in high-temperature environments such as near a motor or in an engine room to reduce energy loss and electromagnetic interference. To address these issues, we proposed a multiplex transmission system with SAW (Surface Acoustic Wave) devices to satisfy the requirements of simple signal wiring and high heat resistance. In this paper, we show that the SAW filters on $SiO_2/Al/LiNbO_3$ structure have good electrical characteristics for the proposed system.

Statement of Contribution/Methods

Schematic of a single-phase three-level inverter with the proposed multiplex transmission system is shown in the figure below. This system can transmit multiple control signals with single coaxial line. The multiplexed signal is demultiplexed by the SAW filters with different center frequencies. In the proposed system, low temperature coefficients, high withstand voltage, and high RF power transition durability are required for the SAW filters. To satisfy these requirements, we fabricated 12-channel SAW filters on $SiO_2/Al/LiNbO_3$ structure and measured frequency temperature characteristics, withstand voltage between input and output IDTs (Interdigital transducers), electrical transmission characteristics, and RF power transmission durability.

Results/Discussion

The measured characteristics were compared with that of the conventional SAW filters on $Al/LiNbO_3$ structure. The temperature characteristics were improved from -76.5 ppm/°C to -13.1 ppm/°C. The withstand voltage was improved from 1120 V to 1351 V. The RF power transmission durability was slightly declined, however, the RF power of 2 W is sufficient value for the proposed system. These results showed that the SAW filters on $SiO_2/Al/LiNbO_3$ structure are effective for the proposed system. In addition, the single-phase three-level inverter with the fabricated the SAW filters on $SiO_2/Al/LiNbO_3$ structure was demonstrated.

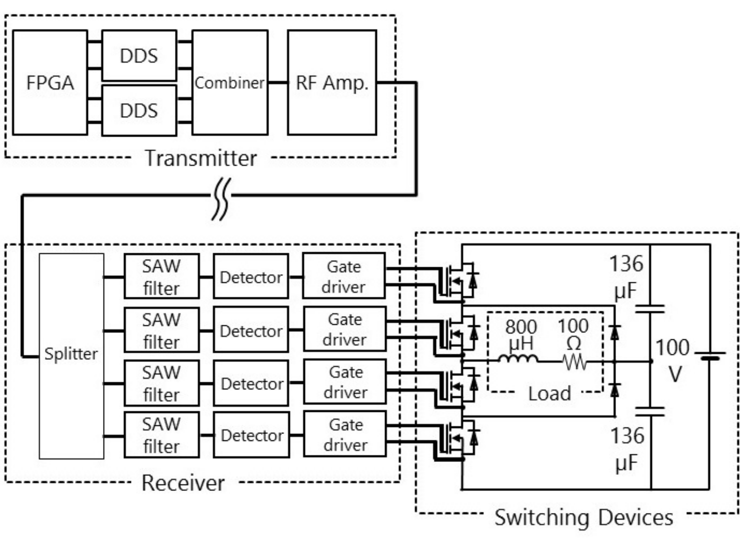

Edge Reflection Type SAW Resonators on Silicon Substrate Using ZnO Thin Films

Sai Krishna Gollapudi[1], Harsha B Nemade[2]; [1]*Electronics and Electrical Engineering, Indian Institute of Technology Guwahati, Guwahati, asssam, India,* [2]*Electronics and Electrical Engineering, Indian Institute of Technology Guwahati, Guwahati, Assam, India*

Background, Motivation and Objective

In general surface acoustic wave (SAW) devices are made on piezoelectric substrates, hence difficult to integrate with circuits made on silicon. SAW devices can be realized on a silicon substrate using a film of piezoelectric material in conjunction with interdigital transducers (IDT) facilitating monolithic integration of SAW devices with circuits. Normally, SAW resonators consist of reflector gratings with large number of fingers to form standing waves and to confine SAW, and consume significant die area. The objective of the paper is to explore implementation of edge reflection (ER) type SAW devices, which are extremely compact, on silicon substrate.

Statement of Contribution/Methods

The paper reports development of ER type SAW resonators on silicon substrate using piezoelectric ZnO film. Fig. 1 shows ZnO/IDT/Si configured ER type SAW resonators fabricated on silicon substrate. Vertical grooves are micromachined in silicon to create free edges at the device boundaries. ZnO film and IDT generate Love waves which offer total reflection at the free edges forming standing wave pattern. Dispersion characteristics of phase velocity and coupling coefficient with respect to ZnO thickness are obtained from finite element simulations of the devices. One port ER type SAW resonators with 16 µm wavelength are designed, fabricated and tested.

Results/Discussion

The S11 plot of a fabricated ER type SAW resonator obtained using network analyzer is shown in Fig. 2. Resonance frequency at 261.73 MHz with return loss of 37.19 dB is observed.

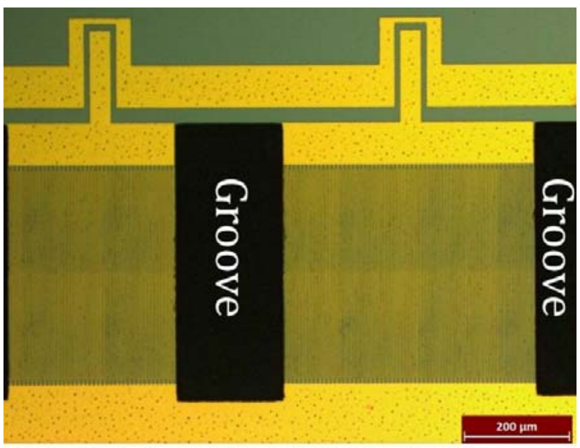

Fig. 1. Top view of ZnO/IDT/Si configured ER type one port SAW resonators fabricated on silicon substrate.

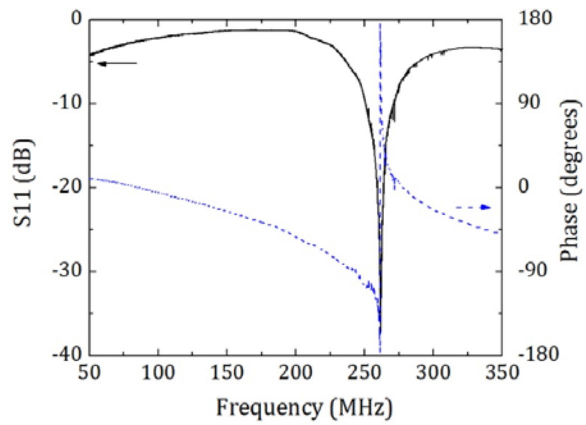

Fig. 2. Measured S11 parameters of the fabricated ER type one port SAW resonator showing resonance frequency around 260 MHz.

P5-C1 - MUT Measurement and Modelling

Exhibit Hall

Saturday, September 9, 2017, 9:30 am - 4:00 pm

Chair: **Yongrae Roh**
Kyungpook National University

P5-C1-1

Assessment of Imaging Capability of 16x16 2D Cmut Transducer Arrays

Tony Matéo[1], Cyril Meynier[1], Dominique Gross[1], Ludovic Pasquet[1], Audren Boulmé[2], Dominique Certon[2], Nicolas Sénégond[1]; *[1]Advanced Research Dpt., Vermon S.A., Tours, France, [2]GREMAN UMR-CNRS 7347, Université François Rabelais de Tours, France*

Background, Motivation and Objective

Among the different transducers technologies suitable for medical imaging, the cMUTs are known to offer an attractive alternative to conventional piezoelectric ones, with features including wider bandwidth, wider directivity, and readiness for integration with electronics. This last point is of particular interest for 2D matrix arrays. Here, we present the acoustic and imaging performances of these devices initially dedicated for external cardiac imaging (frequency range [1.5 – 4 MHz]).

Statement of Contribution/Methods

2D cMUT arrays with 256 elements (16x16) have been manufactured based on a wafer-bonding process. Two versions have been produced, a small (see Fig. 1 (a)) and a large pitch arrays, with an orthonormal pitch of 250 and 400 µm, respectively. These 16x16 chips were designed as elementary tile to be juxtaposed to form larger arrays. In this work, a single tile of each array size has been packaged into a test vehicle allowing characterization with a 256 channels Vantage echographic system (VERASONICS, Inc., Kirkland, WA, USA). All production steps (front-end wafer processing, wafer-level characterization, dicing, flip-chip assembly, test vehicle packaging) have been achieved through an industrial approach with a high yield level.

Pulse-echo measurements have been performed (see Fig. 1 (b) & (c)) to assess the intrinsic performances of both array versions (small and large pitch) and compared with model results. In a second step, hydrophone measurements were performed to evaluate precisely the transmitted ultrasound beam shape (width, side-lobe, pressure level) for various focusing depth and steering angle. Finally, B-mode imaging on a QA phantom was performed with both array sizes for different scan plan (XZ, YZ and XY).

Results/Discussion

Small and large pitch arrays have proved to be fully functional. Despite their small sizes, both 2D cMUT arrays exhibited good electroacoustic performances in agreement with modeling expectation, as well as promising imaging quality. Through the comparison of the two arrays imaging performances (spatial resolution, CNR, SNR, penetration depth, etc.), a discussion has been achieved to identify the best trade-offs (for instance the directivity vs. the sensitivity of the element) for the most performant 3D phased array imaging, especially in the case of the cMUT technology.

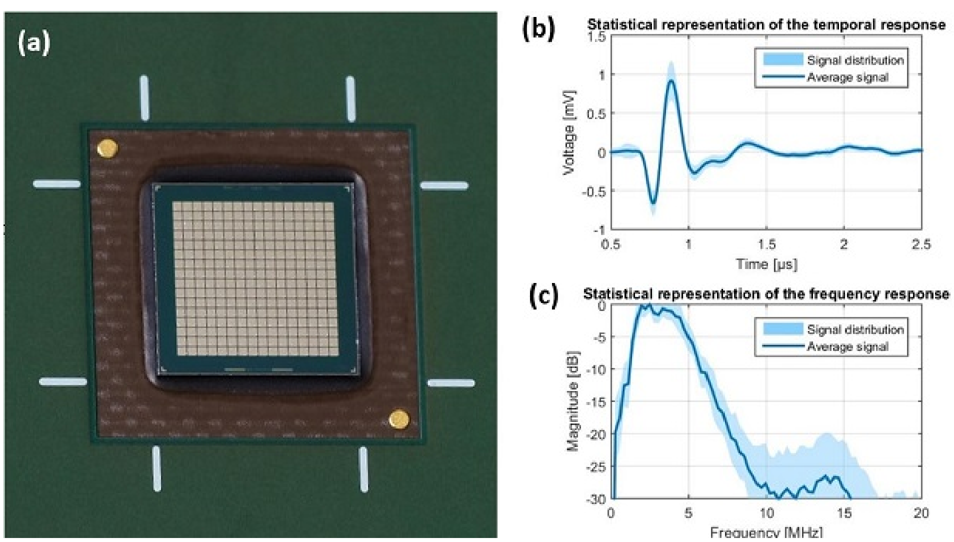

Figure 1 : Picture of the 250 µm pitch 2D CMUT array (a) together with related mean pulse echo response over all 256 matrix elements both in time (b) and frequency (c).

P5-C1-2

Simulating CMUT Arrays Using Time Domain FEA

Mathias Engholm[1], Andrew Tweedie[2], Søren E. Diederichsen[1], Gerald Harvey[3], Jørgen A. Jensen[4], Erik V. Thomsen[1]; *[1]Department of Micro and Nanotechnology, Technical University of Denmark, Kgs. Lyngby, Denmark, [2]PZFlex, Glasgow, United Kingdom, [3]PZFlex, Cupertino, USA, [4]Center For Fast Ultrasound Imaging, Technical University of Denmark, Kgs. Lyngby, Denmark*

Background, Motivation and Objective

Finite element method (FEM) has been extensively used for analyzing both static and dynamic behaviour of CMUTs. Typical parameters being evaluated include the pull-in voltage, pressure, sensitivity, bandwidth, and crosstalk. PZFlex is a commercial FEA software and has been optimized for the ultrasound industry and is commonly used to design piezo-electric ultrasound transducers. However, PZFlex is not commonly used within the CMUT research field. Nevertheless, it has an explicit modeling approach allowing large structures like CMUT arrays to be modeled and its transient analysis intrinsically supplies non-linear and broadband results from a single run. The objective is to present a multi-element CMUT array model with multiple cells per element and compare the output results to measurements of a fabricated CMUT array.

Statement of Contribution/Methods

A 128 element 1D CMUT array is fabricated and assembled in a probe. The individual CMUT cells are circular with a radius of 24.5 µm and fabricated using a LOCOS process. The plate is 2 µm silicon with 400 nm aluminum on top. The insulation oxide is 400 nm and the vacuum gap is 300 nm. The exact same CMUT cell is modeled in PZFlex using axial-symmetry. The pull-in and the spring softening effect is compared to impedance measurements. To assess the impulse response, bandwidth, output pressure and beam width a 3D CMUT linear array model is presented. The model consists of a central driven element, surrounded by passive elements, with each element containing multiple individual CMUT cells. Symmetry is applied along the elevation direction, significantly reducing model runtime while allowing crosstalk to be observed across multiple adjacent elements.

Results/Discussion

The figure to the left shows the normalized displacement as function of the normalized bias voltage. A transient and a static model is used to calculate the deflection and are compared to an analytic model. The two model agree with a relative difference less than 2% between the analytic model and the static PZFlex models. In the transient model the inertia of the plate is captured, as the plate does not snap in, predicting a 10 V higher pull-in voltage in this case. The right figure shows the resonance frequency of the transient PZFlex model compared to real measurements of a CMUT element. The model agrees with measurements with a difference of less than 3%.

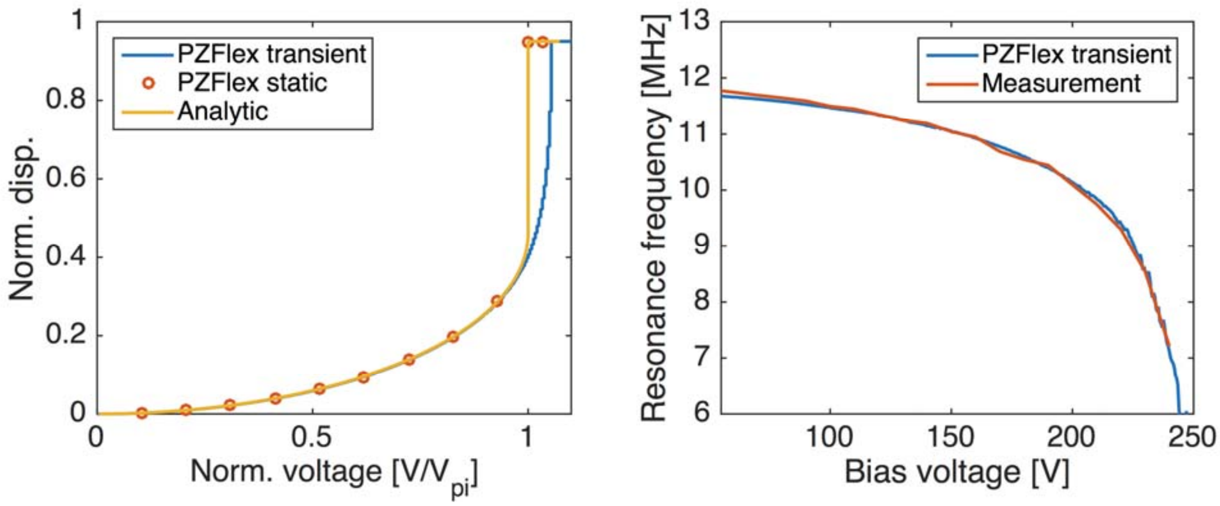

P5-C1-3

Using a Mutual Impedance Model to Improve the Time Response of PMUT Arrays

Qi Wang[1], David Horsley[1]; [1]*Mechanical and Aerospace Engineering, University of California, Davis, CA, USA*

Background, Motivation and Objective

Short pulse transmission and reception is important for piezoelectric micromachined ultrasonic transducer (PMUT) arrays to achieve high resolution. However, coupling effects cause PMUT arrays to exhibit long decay times following the transmit pulse and poor axial resolution. Here, we model the mutual acoustic impedance that couples PMUTs in an array to show that the decay behavior can be accurately predicted. This model provides a basis for improving PMUT time response and imaging resolution.

Statement of Contribution/Methods

An array model was developed which incorporates the mutual impedance between PMUTs. This model was used to simulate the frequency response of arrays with different sizes. Experiments were conducted using PMUT arrays of different sizes fabricated with ScAlN films and cavity SOI. The PMUT arrays were immersed in fluid and excited with a pulse input with the motion of a PMUT at the array center recorded using a laser Doppler vibrometer (LDV). Time-domain measurements show that the decay time increases with the size of the array. When converted to the frequency domain via FFT, the measured results agree well with the model prediction.

Results/Discussion

LDV measurements of arrays are shown in Fig. 1(a). The decay time is longer for large arrays and following the initial decay, an edge wave is visible in the response. The edge wave's time of arrival scales with the array size, Fig. 1(b). The FFT of the decay time, Fig. 1(c), shows that the smallest array has the widest bandwidth. The measured frequency response, Fig 2(a), corresponds well to the model prediction, Fig. 2(b). Both exhibit the same trends observed in the FFT of the pulse response. These demonstrate that the decay characteristics are predictable from the model, which can be used to design arrays for improved time response.

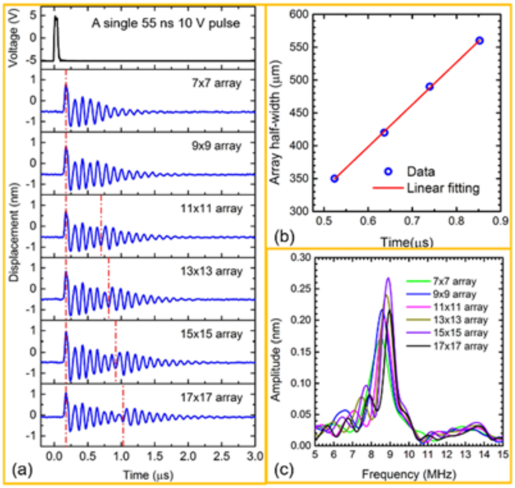

Fig. 1: (a) LDV measurement results of the center PMUT in the arrays with sizes from 7x7 to 17x17. The decay time is longer for large arrays; moreover, following the initial decay, an edge-wave, resulting from sound reflecting from the array boundary, is visible in the response. (b) The time-of-flight of the edge wave scales with the array half-width, and has a slope (643 m/s) nearly equal to the speed of sound in fluid (687 m/s), (c) FFT results of the decay time shows that the smallest array (7x7) has the widest bandwidth and that larger arrays exhibit ripples in their frequency response.

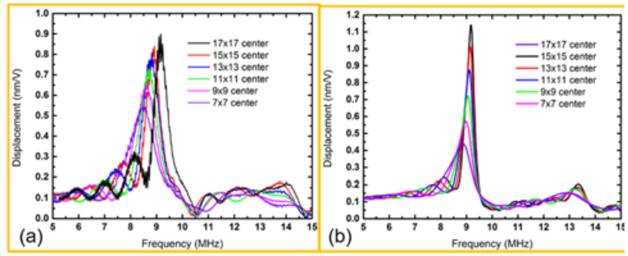

Fig. 2(a) Measured frequency response of the center PMUT in arrays from 7x7 to 17x17 using the LDV together with a network analyzer, (b) Frequency response simulated using the array model. Both (a) and (b) demonstrate the same trends observed in Fig. 1(c)

P5-C1-4

Analytical Calculation and Fabrication of FET-Embedded Capacitive Micromachined Ultrasonic Transducer

Jin Soo Park[1,2], Jung Yeon Kim[1,3], Hee-Kyoung Bae[4], Jinsik Kim[5], Kyo Seon Hwang[6], Jung Ho Park[2], Rino Choi[3], **Byung Chul Lee[1,7]**; *[1]Center for BioMicrosystems, Korea Institute of Science and Technology, Korea, Republic of, [2]Korea University, Korea, Republic of, [3]Inha University, Korea, Republic of, [4]National Nanofab Center, Korea, Republic of, [5]Dongguk University, Korea, Republic of, [6]Kyung Hee University, Korea, Republic of, [7]University of Science and Technology, Korea, Republic of*

Background, Motivation and Objective

In IUS 2016, we proposed a capacitive micromachined ultrasonic transducer embedded a field effect transistor (CMUT-FET) for 20 MHz operation. As a result, the possibility of high sensitivity in a high-frequency range was verified via a combination of two simulation tools, a 3-D finite element analysis (FEA) for the CMUT part and a technology computer aided design for the FET part. Since the results were acquired from the separate models, the exact voltage drop of the channel capacitance in the FET part was not considered into the CMUT simulation part. In this paper, we suggest a full analytic model which can simulate the whole CMUT-FET model with high accuracy and fast computation. As a consecutive work, we also report on a fabrication process of the CMUT-FET with nickel silicide source/drain contacts and low-temperature wafer bonding. Since high-temperature process on the upper CMUT during direct wafer bonding critically affects the performance of the lower FET, several low-temperature direct wafer bondings were attempted and the results were demonstrated in this paper.

Statement of Contribution/Methods

The CMUT-FET analytical model was based on Kirchhoff¡¯s plate bending theory, Poisson¡¯s equation, and an electromechanical mass-spring model. The applied voltage of the CMUT plate was iteratively calculated with consideration of the channel capacitance in the FET part. In the low-temperature direct wafer bonding process, we focused on the case of several surface activations followed by the thermal annealing around 400 °C. Several conditions of chemical and plasma activations were tested and evaluated using infrared images and focused ion beam etching.

Results/Discussion

Figure 1(a) shows analytical calculation results of the CMUT plate profiles at 20 V DC bias, which is 80% of the collapse voltage. The overlapped red and black dotted lines reveal a good agreement between the analytical and FEA simulations without taking the induced FET channel into account. Considering the FET channel capacitance gives 10% difference in the maximum displacement of the CMUT plate. After the CMUT-FET fabrication as shown in figure 1(b), tight control on the vertical direction can be achieved from the low-temperature direct wafer bonding (figure 1(c)). In addition, it is verified that the nickel silicide source/drain were unaltered during the low-temperature process.

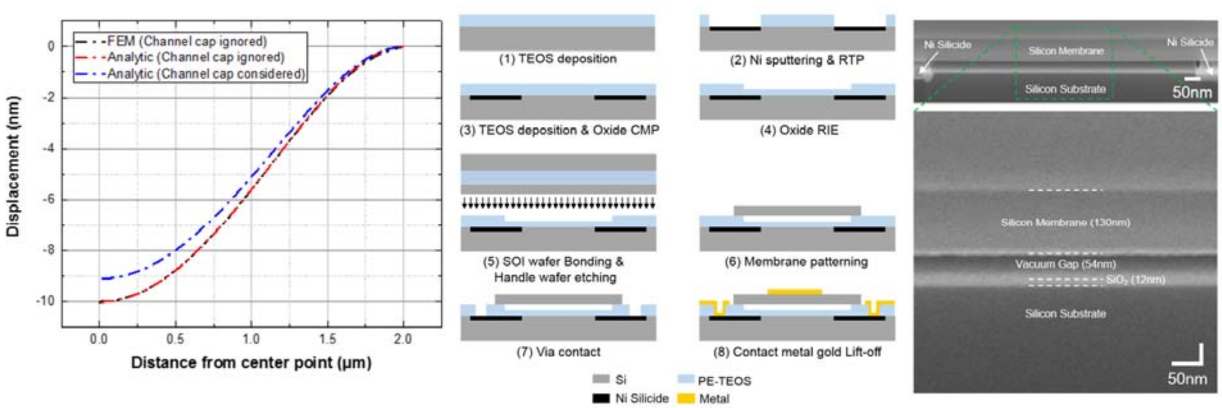

(a) (b) (c)

P5-C1-5

Multiparameter Optimization of Vented CMUTs for Airborne Applications

Bo Ma[1], Chienliu Chang[1], **Huseyin Kagan Oguz[1]**, Kamyar Firouzi[1], Butrus T. Khuri-Yakub[1]; [1]*Electrical Engineering, Stanford University, Stanford, California, USA*

Background, Motivation and Objective

Capacitive Micromachined Ultrasound Transducers (CMUTs) have become a better alternative to traditional piezoelectric transducers because of their better impedance matching characteristic and wider bandwidth. These advantages make CMUTs ideal for medical ultrasound imaging, ultrasonic flow metering, gesture sensing and other airborne applications. However conventional vacuum CMUTs have narrow bandwidth and cannot be used in pressure widely varying ambient and harsh environments. To overcome these limitations and improve CMUT′s bandwidth and sensitivity, we develop a vented CMUT and optimize its design by using multiparameter optimization method to achieve the best performance.

Statement of Contribution/Methods

The vented CMUT has been fabricated by direct fusion wafer-bonding technology. The resonance cavity is etched through the handling substrate to connect with ambient environment. Therefore, the vented CMUTs can withstand extreme pressure variations. The formed squeeze-film between the moving plate and substrate can help to enhance CMUT′s bandwidth significantly. Multiparameter optimization method has been used to improve the bandwidth and sensitivity by varying the size and gap height of the resonance cavity, and the size, location and number of perforated holes. Finally, 91 cell arrays are connected in parallel to constitute a CMUT device for greatly improving device sensitivity.

Results/Discussion

Fig. 1 shows CMUT′s profile and the impedance characteristics at different driving voltage. The measured fractional bandwidth is about 11%. Pitch-catch experimental setup is shown in Fig. 2a. Linear FM excitation and received signals are shown in Fig. 2b and 2c. The average time delay is 325µs at the distance of 10cm, and the minimum detectable velocity is 55mm/s.

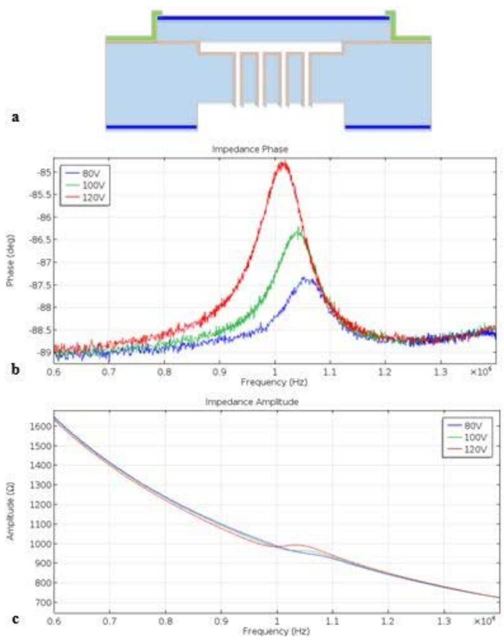

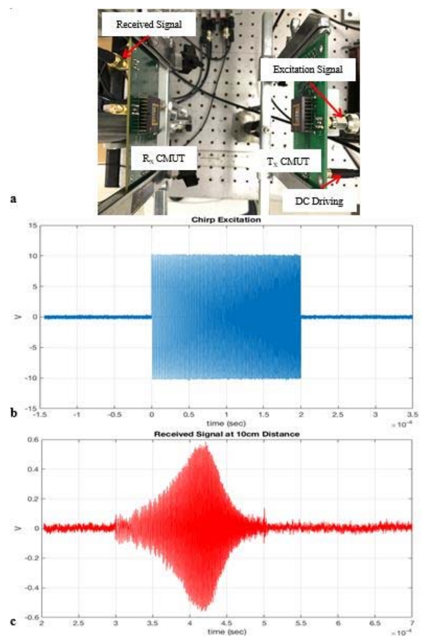

P5-C1-6

Accurate Evaluation of the Electro-Mechanical and Parasitic Parameters of CMUTs through Electrical Impedance Characterization

Alessandro Stuart Savoia[1], Barbara Mauti[1], Giosuè Caliano[1]; [1]*Roma Tre University - Department of Engineering, Roma, Italy*

Background, Motivation and Objective

Electrical impedance characterization is often used to evaluate the electro-mechanical parameters of Capacitive Micromachined Ultrasonic Transducers (CMUTs). Evaluation is achieved by fitting the measured data with simple equivalent circuit models, which do not account for many parasitic phenomena. Such parasitic phenomena may include resistive and inductive behavior of electrical interconnections, stray capacitance, and dielectric loss of the insulating materials used in CMUT microfabrication. In this paper, we propose an accurate CMUT characterization method, based on an improved equivalent circuit model, able to evaluate the electro-mechanical and parasitic parameters starting from electrical impedance measurements at several bias voltages.

Statement of Contribution/Methods

Fig.(a) shows the improved CMUT equivalent circuit in which the parasitic phenomena are modeled by connecting additional passive elements to the electrical port of the electrostatic transducer. The interconnection inductance and resistance are modeled by the Ls-Rs series, while the stray capacitance by Cp. The dielectric loss is described by three Cp-Rp series in parallel, which model the effects of the in-cavity silicon nitride passivation layers dielectric dispersion in the 1-40MHz range. The parameter evaluation of a CMUT is performed by measuring the electrical impedance at several increasing bias voltages starting from 0 V. The parasitic series and dielectric loss elements, and the unbiased CMUT electrical capacitance C0+Cp, are evaluated by fitting the equivalent circuit model impedance with the 0V-bias measured data, neglecting the mechanical parameters. Successively, the entire measured dataset is compensated for parasitic series and dielectric loss elements, and used to fit the electrostatic transducer equivalent circuit parameters as a function of the bias voltage. Finally, the mechanical resonance frequency is extrapolated and used to compute C0 and Cp.

Results/Discussion

The described method was tested on several air-coupled CMUT array elements. Results reported in fig.(b) showed excellent match between the experimental data achieved with a 7.5MHz CMUT array element and the fitted impedance curves. The method was further tested on the characterization of entire CMUT arrays, improving the accuracy of typical parameter statistical analysis [fig.(c)].

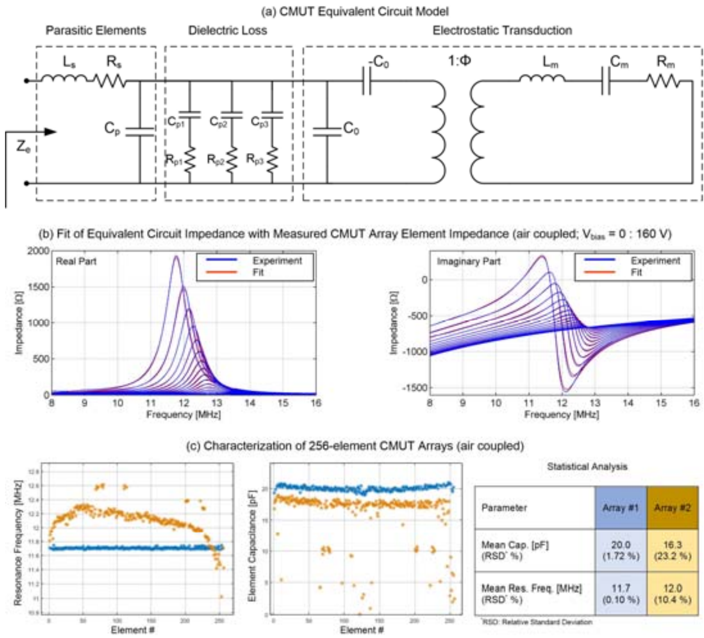

P5-C1-7

Output Pressure and Pulse-Echo Characteristics of Capacitive Micromachined Ultrasonic Transducers as Function of Plate Thickness

Søren Elmin Diederichsen[1], Jesper Mark Fly Hansen[1], Mathias Engholm[1], Jørgen Arendt Jensen[2], Erik Vilain Thomsen[1]; *[1]Department of Micro- and Nanotechnology, Technical University of Denmark, Denmark, [2]Center for Fast Ultrasound Imaging, Technical University of Denmark, Denmark*

Background, Motivation and Objective

The energy transduction of a Capacitive Micromachined Ultrasonic Transducer (CMUT) depends on the movement of a flexible plate, which has a low mechanical impedance compared to its bulky piezoelectric counterpart. Consequently, the output pressure of a CMUT is generally lower. This limits the penetration depth, and thus the visualization of deeper structures in the body, as well as non-linear imaging such as tissue harmonic imaging. The objective of this work is to investigate how the output pressure and pulse-echo signal of a CMUT scales with the (silicon) plate thickness.

Statement of Contribution/Methods

The CMUTs are fabricated using two consecutive local oxidations of silicon, followed by direct wafer fusion bonding to a silicon-on-insulator (SOI) wafer. The plate thickness is thereby determined by the SOI wafer device layer thickness. CMUTs with plate thicknesses of 2 µm, 9.3 µm, 15 µm are realized.

The cell radii and gap height resulting in an immersion frequency of 5 MHz and pull-in voltage of 200 V are designed using finite element analysis. The fabricated CMUTs are coated with PDMS and mounted in a water tank, where a hydrophone and a plane reflector, respectively, are placed in a distance of 1 cm from the CMUT surface. The two-way fractional bandwidths are measured by pulsing with a 16-period square wave at discrete frequencies using a Tektronix AGF3102C arbitrary function generator. The peak-to-peak output pressures are measured with a hydrophone by pulsing with a 5 MHz, two-period square pulse. The hydrophone and plane reflector measurements are carried out with an AC voltage of +/- 10 V and a DC voltage corresponding to 80% of the pull-in voltage.

Results/Discussion

The table shows the measured pull-in voltages, center frequencies, peak-to-peak output pressures, maximum peak-to-peak pulse-echo signals and -6 dB fractional bandwidths for the fabricated CMUTs. An optimum in both peak-to-peak output pressure and pulse-echo signal is seen for the 9.3 µm plate, which still has a moderate bandwidth of 60%. In fact, the 9.3 µm plate results in a 1.9 times higher peak-to-peak output pressure and a 3.6 times higher pulse-echo signal compared to the 2 µm plate. On the other hand, the highest bandwidth is observed for the 2 µm plate. This study shows that a higher output pressure and pulse-echo signal (evaluated at the center frequency) can be achieved by customizing the plate thickness.

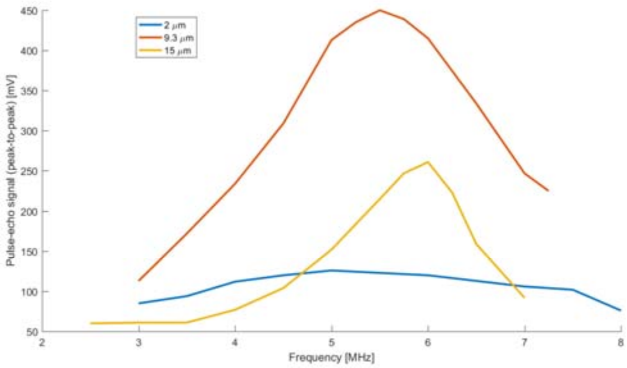

Plate thickness [μm]	Pull-in voltage [V]	Center frequency [MHz]	Peak-to-peak output pressure [kPa]	Peak-to-peak pulse-echo signal [mV]	-6 dB fractional bandwidth in %
2	210	5	203	126	> 100
9.3	200	5.5	380	450	60
15	200	6	238	261	30

P5-C1-8

Design and Measurement of a 32-Element CMUT Linear Array for Underwater Imaging

Congcong Hao[1], Changde He[1], Weijian Liang[1], Guojun Zhang[1], Binzhen Zhang[1], Wendong Zhang[1], Chenyang Xue[1]; *[1]Key Laboratory of Instrumentation Science & Dynamic Measurement, Ministry of Education, North University of China, Taiyuan, China, People's Republic of*

Background, Motivation and Objective

Ultrasonic sensor has been widely used, ranging from underwater communication to many aspects, such as medical imaging and therapy. Compared with the traditional piezoelectric sensors Capacitive micro-machined ultrasonic transducer(CMUT) have advantages of wide band, easy to integration, good consistency and low cost ,which make it a research hotspot in the field of ultrasound. As the core of the whole ultrasonic imaging system, the design and fabrication of CMUT play an important role. According to the requirements of underwater imaging, in order to improve the imaging target and the array directivity, the geometric parameters of the array are optimized.

Statement of Contribution/Methods

A 32-element optimized linear array CMUT applied underwater is designed. The shape, size, number and spacing of element to the influence of the directivity are analyzed in detail, and the optimization of parameters is realized. The spacing of element is 1.95mm. The CMUT device, fabricated by the Silicon-Silicon bonding technology, has the advantages of controllable frequency and consistency of membrane thickness.

Results/Discussion

The bandwidth test is conducted, results show that -6 dB center frequency is 430 KHz, and relative bandwidth is 148%. Directivity experiment results show that the symmetry of the line array is good, -3 dB main lobe width is 5 degrees, and no grating lobe. Three target underwater imaging experiment is completed, distance between obstacles and CMUT are 120 cm, 80 cm, and 60 cm, and distance between obstacles are 9 cm, 13 cm, and 22 cm. The imaging result is clearly visible.

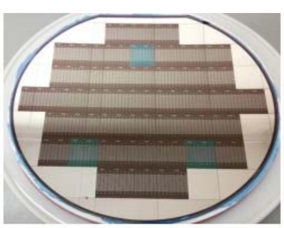

32-element CMUT linear array

packaging

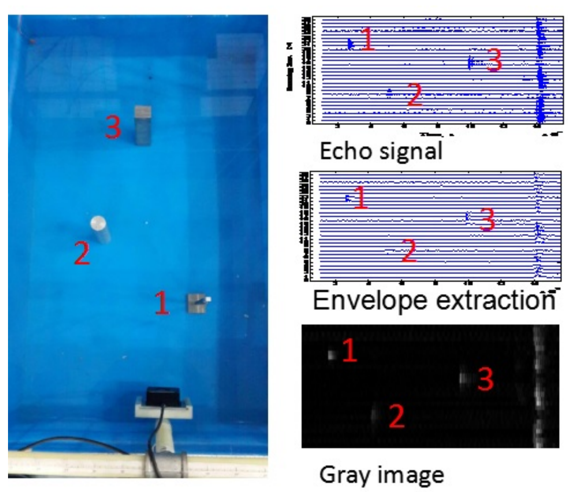

under water imaging

P5-C2 - Therapeutic Devices and Systems

Exhibit Hall

Saturday, September 9, 2017, 9:30 am - 4:00 pm

Chair: **Qifa Zhou**
University of Southern California

P5-C2-1

Analysis of CMUT Power Efficiency for Optimized Therapeutic Operation

Dominique Gross[1], Audren Boulmé[2], Nicolas Sénégond[1], Christopher Bawiec[3], W. Apoutou N'Djin[3], **Dominique Certon[2]**; [1]*Advanced Research Dpt., Vermon S.A., Tours, France,* [2]*GREMAN UMR 7347, Université François-Rabelais de Tours, Tours, France,* [3]*U1032 Labtau, Inserm, Lyon, France*

Background, Motivation and Objective

Even though the CMUT technology is currently experiencing an exciting era in the field of ultrasonic imaging, few studies have assessed the real interest of this technology for therapeutic purposes compared to the state-of-the-art technology. Moreover, CMUT transducers could benefit from their low mechanical losses to produce long burst emission without the need of a bulky external cooling device. In addition to classical acoustic considerations, the output intensity is strongly influenced by the electroacoustic efficiency of the whole system. This latter takes into account the transducer itself, but also the losses in the electronic conditioning circuitry. The proposed study is focused on the analysis of CMUT intrinsic power efficiency to better assess the maximum expected performances and the potential improvements.

Statement of Contribution/Methods

Based on a robust CMUT technology developed for high intensity ultrasound therapy using a stable industrial fabrication process, the analysis is carried out in both simulation and measurements. The accurate CMUT parameters are extracted by an inverse problem on impedance measurements, and the study is based on a simple small signal approach and classical electroacoustic circuits (Figure 1 a)). The global power efficiency, defined as the total output acoustic power dissipated in the radiation impedance (P_o) on the total input electrical power (P_i), is determined and split into several sub-efficiency formulations taking into account the different sources of loss (the series resistance R_s, the leakage resistance R_p, the parasitic capacitance C_p and the mechanical losses in R_m). The approach is then verified thanks to impedance measurements and a network analyzer coupled with a scanning hydrophone.

Results/Discussion

The results obtained from impedance measurement performed with fluid-loaded CMUT array exhibit a good matching between theory and experience (Figure 1 b)). Furthermore, the agreement between the overall experiences shows that simple impedance measurements can provide reliable information in regards with the power efficiency of the CMUT transducer. The study also gives a useful understanding of the transducer behavior and shall provide several optimization guidelines to improve the design for therapy-specific CMUT transducers.

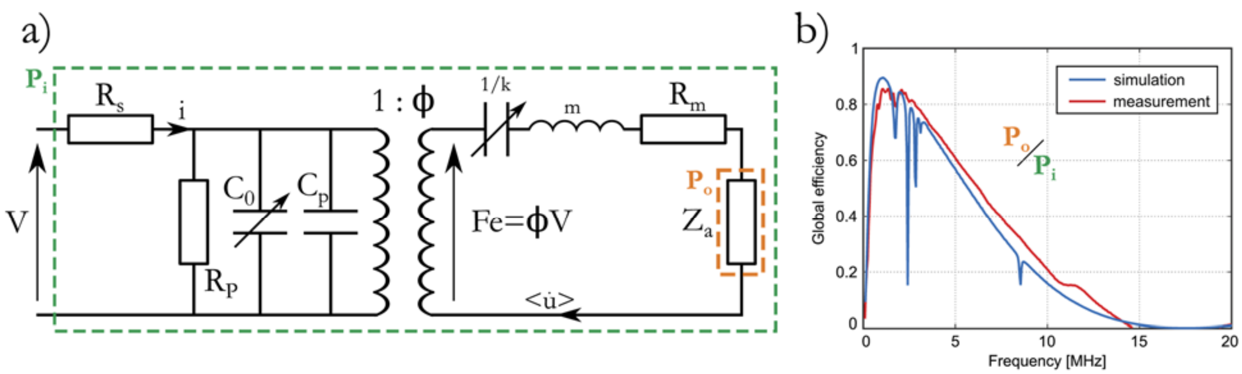

Figure 1: a) Simplified electroacoustic equivalent circuit with the different sources of loss, b) Global efficiency in measurement and simulation

P5-C2-2

A Low-Cost 10 mm Diameter Histotripsy Transducer for Tissue Ablation Guided by a Co-registered High-Frequency Endoscopic Phased Array

Jeffrey Woodacre[1], Thomas Landry[1], Jeremy Brown[1]; [1]*Biomedical Engineering, Dalhousie University, Halifax, Nova Scotia, Canada*

Background, Motivation and Objective

Combined endoscopic imaging and therapeutic tools for minimally invasive procedures may lead to increased efficacy of the procedure and reduced patient risk. Currently, our lab is investigating the use of histotripsy tissue ablation during ultrasound guided neurosurgery. In this work, we will present our progress toward the miniaturization of the histotripsy transducer for simultaneous, real-time imaging and ablation in an endoscopic form factor.

Statement of Contribution/Methods

In this work, a histotripsy transducer was created using a 5.0 MHz piezoelectric composite coupled to a 10 mm diameter, 7 mm focal length aluminum lens, where a 4 mm x 4 mm square hole was machined in the transducer for the imaging endoscope. The device used a quarter-wavelength matching layer to improve bandwidth, allowing the transducer to reach cavitation pressure in as little as one cycle, thus reducing overall power consumption. The device was driven using a custom in-house developed pulser circuit. Peak pressure developed at the transducer focus was measured for driving voltages between 15 V and 70 V using a needle hydrophone and extrapolated to estimate necessary voltage to cause cavitation in water. One-way bandwidth was measured for a single-cycle drive pulse. Measurements of the size of the cavitation region were performed in de-gassed water under a microscope for a range of driving voltages, pulse cycles, and pulse repetition rates, as-well-as ex-vivo cerebral tissue using ultrasound guidance.

Results/Discussion

The transducer one-way fractional bandwidth was 61%, and extrapolation of hydrophone measurements estimate water cavitation to initiate at a voltage of 150 V. Microscope measurements showed initial cavitation at a driving voltage of 170 V. In water, the bubble cloud diameter was tunable between 0.16 mm and 0.50 mm diameter. Cloud axial length was tunable between 0.27 mm and 2.0 mm. Ablation region size in chinchilla cerebral tissue was found to be 0.1-0.3 mm diameter when initiated inside tissue and could be easily targeted to specific sites. Ablation rate was observed to increase once an approximately 0.5 mm diameter region of liquefied tissue was carved. The tunability of bubble cloud size shows the ablation area and time are adjustable, which is especially important in surgical applications where precision may be important.

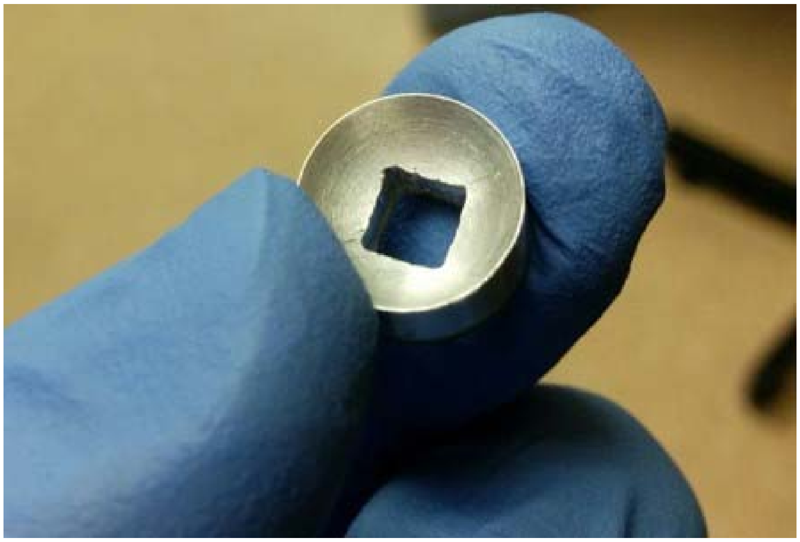

P5-C2-3

Optimal Phase on Biaxial Driven Transducers Based only on Electrical Power Measurements

Sagid Delgado[1], Laura Curiel[1,2], Oleg Rubel[3], Geovane Da Silva[4], Samuel Pichardo[1,2]; [1]*Electrical engineering, Lakehead University, Thunder Bay, ON, Canada,* [2]*Thunder Bay Regional Health Research Institute, Thunder Bay, ON, Canada,* [3]*Material Science and Engineering, McMaster University, Hamilton, ON, Canada,* [4]*Electrical Engineering, Universidade Regional de Blumenau, Blumenau, SC, Brazil*

Background, Motivation and Objective

The efficiency of a piezoelectric actuator is determined by the amount of electrical power converted into acoustic power. This efficiency can be increased using the biaxial driving technique [PloS one 10.9 (2015): e0139178] that reduces coercivity of the ferroelectric switching by applying a polarization rotation obtained dephasing two orthogonal sinusoidal electrical fields along the lateral and propagation axes of a piezoelectric actuator. In this study, we established a relationship between the electrical input power response observed on the propagation (P) and lateral (L) electrodes (top of Fig 1) from a piezoelectric actuator biaxially driven and its efficiency.

Statement of Contribution/Methods

Eight air-backed biaxial transducers (6.4 mm x 6.4 mm x 13.7 mm) fabricated with hard lead zirconate titanate were used for testing. Average of the resonant frequency on propagation and lateral modes for all transducers was 135.6 (±2.7) kHz. The effective acoustic power was measured using the radiation force method and the amount of power delivered to the L-electrode (power ratio) was a fraction of the power applied on the P-electrode. A regression analysis was executed to correlate the optimal phase shift φ relative to the P-electrode with the forward and reflected electrical powers measured on each electrode.

Results/Discussion

The results from varying φ and power (bottom of Fig 1) showed that the value φ at which the maximum power efficiency is obtained remains constant independently of the amount of power applied to the lateral electrode. The highest efficiency was observed for a power ratio between 0.1 to 0.5; which indicated that only a fraction of the energy applied to the P-electrode is required on the L-electrode to increase the efficiency. The overall baseline efficiency was 20.19 (±1.6)%, whereas the highest was for a ratio of 0.1 with an overall efficiency of 24.14 (±1.6)%. The regression analysis demonstrated that a linear relationship based on the reflected power measured on L-electrode was the best predictor overall with R^2>0.94.

The relationship of the electrical input power on both electrodes and the maximum efficiency using the biaxial method was demonstrated. This relationship will allow using only the electrical response of the transducer to determine the best driving conditions when using biaxial excitation based only on electrical response measurements.

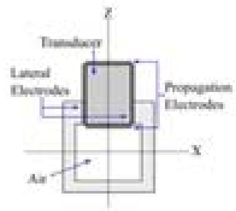

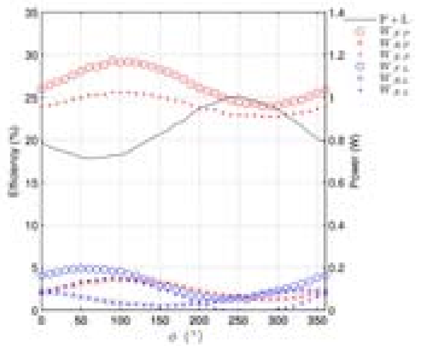

P5-C2-4

An Open Source Modular and Scalable HIFU Driver System

Huseyin Emre Ozum[1], Arif Sanli Ergun[1], Hasan Yetik[2]; [1]*Electrical and Electronics Engineering, TOBB University of Economics and Technology, Ankara, Turkey,* [2]*Center of Research for Advanced Technologies of Informatics and Information Security (BILGEM), Kocaeli, Turkey*

Background, Motivation and Objective

High-intensity focused ultrasound (HIFU) have been an attractive research topic for some time now. HIFU studies have started with single-element transducers, but using arrays provide the opportunity to scan the focal point electronically. Modular and scalable driving systems that can adapt to custom-made transducer elements to drive these arrays are needed and at the present time there are few such systems. To provide solutions for diverse HIFU applications, a reconfigurable HIFU system is designed, manufactured and tested.

Statement of Contribution/Methods

The platform consists of three main building blocks: beamformer boards, daughter boards and a main board, as shown in Fig. 1. Each beamformer board, which can be matched to the specific load, incorporate a MD2131 (Microchip) push-pull source driver along with high voltage MOSFETs (DN2625, Microchip) and offers 7.5 degree phase resolution, 256 amplitude levels and up to 230 Vpp signal output. Daughter boards utilizes LM4F120H5QR (Texas Inst.) microcontroller to control up to 8 beamformer boards. The mainboard controls the daughter boards and communicates with a PC via USB to configure any channel in the system. Output channel count can be increased in increments of 8 using additional daughter boards up to 1024 channels, and can generate bursts or CW output in a frequency range from 100 kHz to 4 MHz. The mainboard generates the HIFU signal in PWM form and feeds it to the beamformer boards. Currently the PWM frequency is limited to 4 MHz with this mainboard but can be extended to 20 MHz with a higher speed mainboard.

The driver system was tested with an MR-compatible 16-element equal area annular transducer array. The array is 5 cm in diameter, has 5 cm geometric focus, and operates around 1.25 MHz (Imasonic SAS, France). The acoustic power output and power efficiency was measured with a hydrophone (HNP-0400, Onda Corp, USA) and a scanning system.

Results/Discussion

For a 16 V high voltage DC supply, the output power was measured as a function of the amplitude level, and a maximum of 1W acoustic power per channel and 35% overall efficiency were achieved as shown in Fig. 1. Focusing and defocusing capability was also confirmed using two channels as shown in Fig. 1. A 16-channel version of the system with this annular array will be tested with MR guided ex vivo experiments.

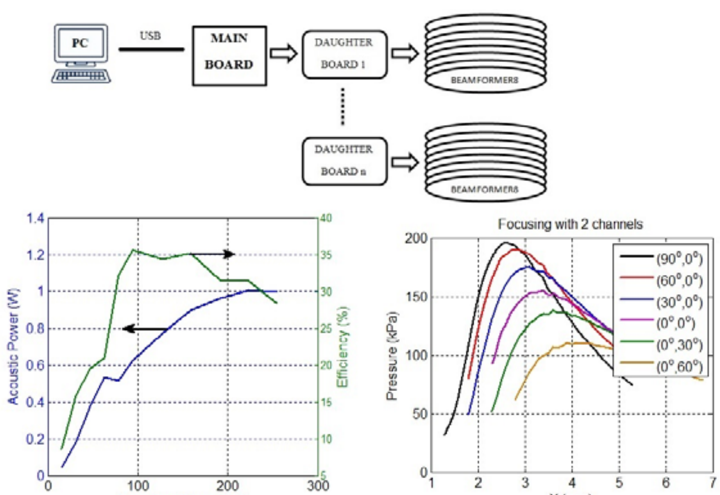

Fig. 1

P5-C3 - Transducer Materials

Exhibit Hall

Saturday, September 9, 2017, 9:30 am - 4:00 pm

Chair: **Shujun Zhang**
University of Wollongong

P5-C3-1

The Progress in the Growth of Relaxor-based Ferroelectric Single Crystals

Guisheng Xu[1], Jinfeng Liu[1], Xiu Zhu[1]; [1]*Artificial Crystal Center, Shanghai Institute of Ceramics, CAS, Shanghai, China, People's Republic of*

Background, Motivation and Objective

The relaxor-based ferroelectric single crystals have been paid great attention due to their ultrahigh piezoelectric properties, which will lead to a great breakthrough of imaging quality of medical ultrasonic probes and projective and/or receiving properties of acoustic transducers. In order to optimize the piezoelectric performance of relaxor-based ferroelectric single crystals, novel ternary system PIN-PMN-PT single crystals have been developed and first reported by our group in 2006 international ultrasonics symposium. Since then, PIN-PMN-PT single crystals have attracted a great interest and have been called ″generation two″ relaxor-based crystals. Compared with ″generation one″ relaxor-based crystals PMN-PT, PIN-PMN-PT crystals present higher Curie temperature Tc, higher phase transition temperature Trt and higher coercive field Ec, which are beneficial to the increase of temperature stability and work power of transducers. However, as PMN-PT crystals, ternary system PIN-PMN-PT crystals face great challenges, such as compositional segregation and property consistence in the process of growth due to more complicated chemical compositions. On the other hand, the mechanical quality factors are not high enough for some applications.

Statement of Contribution/Methods

In this talk, we will introduce the new progress in the growth of relaxor-based ferroelectric single crystals in our research group. PIN-PMN-PT and Mn doped Mn:PIN-PMN-PT crystals are grown by a modified Bridgman method, and their composition and property variation along growth direction and wafer diameter will be measured by composition and structure analysis and dielectric, piezoelectric and ferroelectric characterization methods.

Results/Discussion

Up to present, the PIN-PMN-PT crystals grown along [001] have been enlarged to about 4 inches and exhibit excellent and uniform piezoelectric performance, which can meet the needs of large size wafers in medical ultrasonic imaging probes. In addition, ″generation three ″relaxor-based crystals Mn:PIN-PMN-PT have also been developed in our lab. Mn:PIN-PMN-PT crystals have higher mechanic quality factors Qm as well as higher coercive field Ec than pure PIN-PMN-PT crystals, which are in favor of the increase of projective power of transducers.

P5-C3-2

Acoustical Characterisation of Carbon Nanotube-Loaded Polydimethylsiloxane Used for Optical Ultrasound Generation

Erwin J. Alles[1], Jeongmin Heo[2], Sacha Noimark[1,3], Richard J. Colchester[1], Ivan P. Parkin[3], Hyoung Won Baac[2], Adrien E. Desjardins[1]; [1]*Department of Medical Physics & Biomedical Engineering, University College London, London, United Kingdom,* [2]*School of Electronic and Electrical Engineering, Sungkyunkwan University, Seoul, Korea, Republic of,* [3]*Materials Chemistry Research Centre, Department of Chemistry, University College London, London, United Kingdom*

Background, Motivation and Objective

Optical ultrasound sources, which generate ultrasound photoacoustically, are promising alternatives to piezoelectric or capacitive transducers. Employing pulsed excitation light, high bandwidths (up to 100 MHz) and pressures (MPa range for unfocussed sources) have been achieved with materials that combine strong optical absorption with a high thermal expansion coefficient, such as carbon nanotube (CNT)-loaded polydimethylsiloxane (PDMS). However, literature suggests (Buma et al., IEEE tUFFC 50:9) that such composite materials often suffer from high acoustical attenuation, which limits the generated bandwidths and pressures. In this work, we present the broadband acoustical characterisation of both pure and CNT-loaded PDMS samples to assess the contributions of both constituents to the sound speed and attenuation coefficient.

Statement of Contribution/Methods

Pulsed excitation light (pulse energy: 5 mJ, spot diameter: 25 mm) was delivered to a CNT-PDMS coating deposited onto a glass slide to generate broadband ultrasound. Both pure PDMS samples and CNT-loaded samples (where functionalised CNTs were dispersed in PDMS with an organic solvent) were fabricated of different thicknesses, and ultrasound transmission measurements (0-35 MHz) of these homogeneous samples were performed. Arrival time differences of sound through samples of different thicknesses were used to compute the sound speed through the samples; power laws were fitted to differences in the power spectra (SNR-limited to 0-25 MHz) of different sample thicknesses to quantify the attenuation.

Results/Discussion

Pure and CNT-loaded PDMS samples (with a weight fraction of less than 1.8% CNT solution) were found to exhibit similar sound speed (pure: 956±22 m/s, CNT-loaded: 968±31 m/s) and hence a similar acoustic impedance. However, despite the small weight fraction, the presence of CNTs had a prominent effect on the attenuation: for pure samples, an attenuation of $(1.60\pm0.07) \times f^{1.47\pm0.03}$ dB/cm was obtained, with f the frequency in MHz, whereas for CNT-loaded samples a significantly higher value of $(1.17\pm0.05) \times f^{1.61\pm0.09}$ dB/cm was found (Fig. 1). While the mechanism behind this increased attenuation is presently not understood, these results can be used in numerical models to optimise optical ultrasound sources.

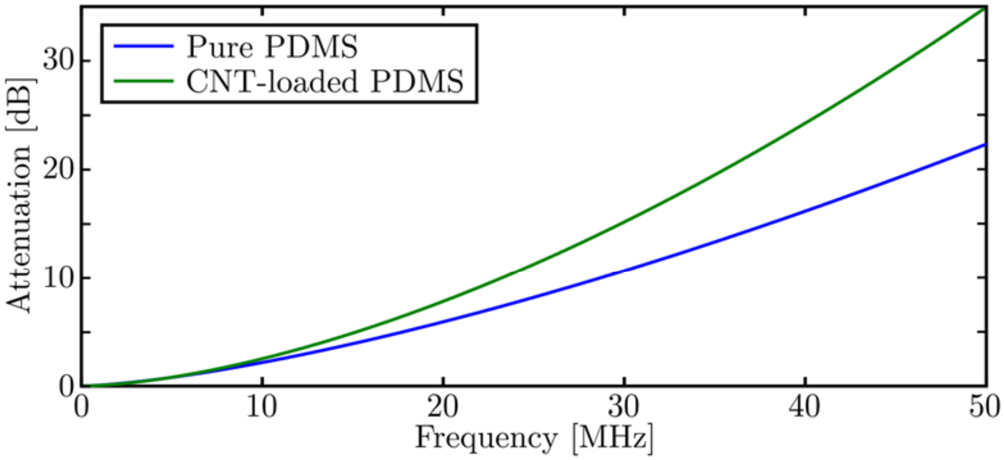

Fig. 1 - Acoustic attenuation through 500 µm thick samples of pure and CNT-loaded PDMS samples.

P5-C3-3

High-Frequency Acoustic Characterization of Porous Lead Zirconate Titanate for Backing Applications

Danjela Kuscer[1], Julien Bustillo[2], André-Pierre Abellard[3], Marc Lethiecq[2], Tina Bakaric[1], **Franck Levassort[2]**; *[1]Electronic Ceramics Department, Jozef Stefan Institute, Ljubljana, Slovenia, [2]GREMAN UMR7347 CNRS, Tours University, INSA Centre Val de Loire, Tours, France, [3]MAT-Centre des Matériaux UMR7633 CNRS, Mines-ParisTech, PSL Research University, Evry, France*

Background, Motivation and Objective

Porous piezoelectric ceramics are often integrated as constitutive elements in several devices such as ultrasound transducers. For high–frequency (HF) applications (i.e., >20 MHz), unpoled, porous lead zirconate titanate (PZT) can be used as a backing. The porosity content allows the acoustical impedance value to be adjusted but it also affects the acoustic attenuation according to the size and shape of the pores in the material. For transducer design, it is essential to know these properties. At high frequency, the corresponding experimental set-up is often difficult to implement with standard reflection or transmission method. In this work, we propose an original and easy way to measure these properties directly at the operating frequency of the transducer.

Statement of Contribution/Methods

Integrated structures composed of a porous PZT backing, bottom electrode, screen-printed piezoelectric PZT thick film and thin top electrode have been fabricated. Two backings with different pore sizes were prepared from the mixture of ceramic powder and an organic template that is then sintered. These structures with electrical interconnections can be considered as simple HF transducers. First, the electroacoustic responses of the two transducers immersed in water were measured. The porous backing characterization was performed with this return acoustic signal passing thought the piezoelectric thick film and bottom electrode toward the backing. If the porous layer is sufficiently thin, the echo from its rear face that returns to the piezoelectric thick film can be observed. The time of flight of the reflected signal is sufficiently long so it can be completely separated from the initial electrical pulse excitation. We then decrease the thickness of the porous layer step by step by machining (from 2mm to 750µm) and deduce properties such as group and phase velocities and acoustical attenuation in the bandwidth of the transducer.

Results/Discussion

The thickness coupling factors of the PZT thick films, evaluated from the electrical impedance measurements, were found to be 45 %. From electron microscopy analysis, we found that both porous backings have a porosity of 15 % but with two different mean pore sizes of 1.5 µm and 10 µm. Measured electroacoustic responses have a center frequency at 20 MHz and a fractional bandwidth (at -6 dB) of 50 %. Therefore, the parameters depending on frequency analysis are given in the 15-25 MHz range. Measured attenuations are very high with corresponding coefficients at 0.7 dB/mm/MHz and 4 dB/mm/MHz respectively for backings with 1.5 µm and 10 µm pore sizes. Our results show that attenuation is high and that it allows the thickness of the porous backing to be reduced to less than one millimeter without observing any back-wall echo, thus minimizing the size of the device. The group velocity (around 3400 m/s) ensures a good impedance matching between the PZT thick film and the backing for transducer applications.

P5-C3-4

Complete Electroelastic Set of co doped Barium Titanate for Transducer Applications

Remy Ul[1,2], Rémi Rouffaud[1], Mai Pham Thi[2], Claire Bantignies[3], Louis-Pascal Tran-Huu-Hue[1], **Franck Levassort[1]**; *[1]GREMAN UMR7347 CNRS, Tours University, INSA Centre Val de Loire, Tours, France, [2]Thales Research & Technology, Palaiseau, France, [3]Advanced Research department, VERMON SA, Tours, France*

Background, Motivation and Objective

Barium titanate (BaTiO3) is a well-known ferroelectric material which was intensively studied in the early 50's. Indeed, BaTiO3 has been rapidly substituted by lead zirconate titanate (PZT) materials, which exhibit higher piezoelectric properties. However, PZT materials contain lead and their increasing success is associated to health and environmental problems. Therefore tremendous efforts have been devoted to the development of competitive lead-free counterparts and BaTiO3 compositions comeback on center stage as promising candidates. In this work co-doped barium titanate ceramics were fabricated and characterized. Particular attention was paid to the delivery of a complete accurate set of elastic, dielectric, and piezoelectric constants. These databases are relatively rare in literature but are essential for numerical simulations of new devices integrating these piezoelectric materials.

Statement of Contribution/Methods

Barium titanate co-doped with cobalt/calcium (BTCoCa) and cobalt/niobium (BTCoNb) were prepared by conventional solid-state reaction method. Three samples with different geometries including pellets with a thickness of 0.6mm and a diameter of 13.5mm were fabricated. For the establishment of the complete set of material constants, resonance-antiresonance method was first used. In this case, measured and calculated values were mixed. This can lead to violations in the interrelations between particular groups of electromechanical and non-consistent database is provided. In this study, a method based on a genetic algorithm is used to optimize the consistency of the full set of material constants through the minimization of a defined criterion [1]. Two 1-3 piezocomposites were fabricated by the dice-and-fill method and two transducers with ceramic pellets were fabricated to evaluate these materials in operating conditions.

Results/Discussion

Full consistent database of BTCoCa was delivered with a dielectric constant at constant strain of 1250 and a thickness coupling factor (kt) of 43%. Similar properties are also measured with the BTCoNb composition. Piezocomposites with a ceramic volume fraction of 50% were successfully fabricated thanks to a dense microstructure and low grain size. Measured resonant frequencies were at 6 MHz and kt at 46% which is in accordance with the k33 values of the ceramic pellets. The two fabricated transducers, with a low backing acoustical impedance (5.2 MRa), possess a fractional bandwidth (-6dB) at 20% and a resonant frequency at 4.3 MHz. These results were in good agreement with simulated transducer behaviors using KLM scheme. They were compared with a transducer including standard PZT pellet to deliver similar sensitivities and bandwidth showing the efficiency of co-doped barium titanate for their integration of industrial process.

[1] R. Rouffaud et al., Journal of Applied Physics, vol. 116, 194106, 2014.

P5-C3-5

3D Printing of Piezoelectric Transducer/Array for Ultrasonic Imaging

Zeyu Chen[1], Xuan Song[2], Yong Chen[3], K.K Shung[4], Qifa Zhou[5]; [1]*Biomedical Engineering, University of Southern California, USA,* [2]*College of Engineering, The University of Iowa, USA,* [3]*Epstein Department of Industrial and Systems Engineering, University of Southern California, USA,* [4]*University of Southern California, USA,* [5]*Roski Eye Institute, Department of Ophthalmology and Biomedical Engineering, University of Southern California, USA*

Background, Motivation and Objective

Piezoelectric ceramics are currently of considerable interest for their capabilities of converting compressive/tensile stresses to an electric charge, or vice versa. The applications of piezoelectric devises are far reaching, ranging from acoustic imaging to energy harvesting. However, conventional manufacturing processes such as etching and dicing for piezoelectric ceramics fabrication have limited capability of achieving complex geometry. Because ceramics cannot be cast and machined easily, additive manufacturing (AM) processes (3D printing technology) are considered as a promising way in novel piezoelectric devices. This article presents piezoelectric element/array with complex geometry, fabricated by Mask-Image-Projection-based Stereolithography (MIP-SL) technology.

Statement of Contribution/Methods

This work investigated a novel 3D printing process in the fabrication of piezoelectric components using high solid loading slurry with BaTiO3 nanoparticle (1oonm). Through a specifically designed debinding and sintering process, the printed components display piezoelectric properties that can be used in ultrasonic transducer. A 6.28MHz ultrasonic scan was achieved by the transducer and shows the energy focusing and ultrasonic imaging abilities.

Results/Discussion

After a post-process, the printed ceramics shows a low dielectric loss ($\tan\delta$=0.018) and a high electromechanical coupling factor (Kt=47.4%). The density of 5.64g/cm3 was obtained, which corresponds to 93.7% of the density of bulk BaTiO3 (6.02 g/cm3). The piezoelectric constant and relative permittivity are160 pCN-1 and 1350 respectively. The axial resolution and lateral resolution of corresponding printing focused transducer are 240μm and 770μm respectively. The results indicate that the printed piezoelectric element using additive manufacturing process opens a facile and effective way toward the realization of functional ceramic assembly in three-dimensional geometry.

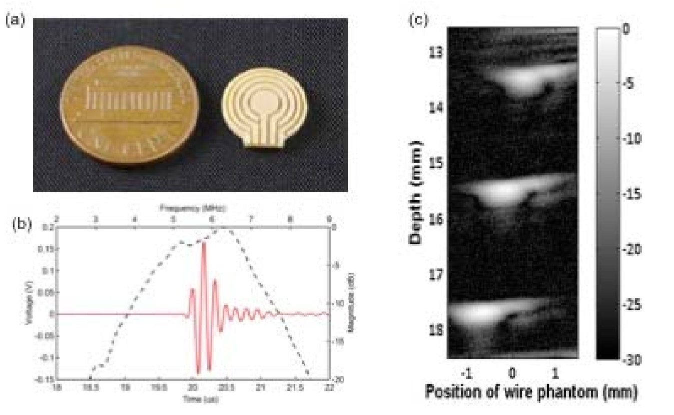

Figure 1: (a) 3D printed piezoelectric array with complex geometry. (b) Pulse-echo waveform and normalized spectrum of ultrasonic transducer with printed component. (c) Phantom imaging using the 6.28-MHz transducer.

P5-C3-6

High Sensitivity Pressure Sensors Based on Flexible Bimorph PZT/Polyimide Composites

Jiangyue Qu[1], Mohammad Gudarzi[1], Qing-Ming Wang[1]; [1]*Mechanical Engineering and Materials Science, University of Pittsburgh, Pittsburgh, PA, USA*

Background, Motivation and Objective

Real-time monitoring of pressure magnitude and ﬂ fluctuation in many systems such as water pipeline, engine combustion chambers, and respiration system of human body is very important. Flexible lead zirconate titanate think film devices due to their self-powering, fast response of highly dynamic load, and relatively simple readout circuit are appropriate candidates for pressure sensors. In this paper, a bimorph flexible PZT/Polyimide pressure sensor is designed, fabricated and experimentally calibrated in standard pressure shock tube.

Statement of Contribution/Methods

Due to friability of PZT ceramic thick films, thin polyimide layers are used as the substrate to form laminated PZT/polyimide circular diaphragm device. An edge-clamped PZT bimorph diaphragm can be deflected when a dynamic normal pressure is applied; and charge generation occurs via the transverse mode of the piezoelectric PZT thick films, Fig. 1.

With linear elastic deformation assumption, the output charge of the device should be proportional with the amplitude of applied pressure. To measure the impulse response of the pressure sensor, a shock tube is utilized and peak pressure data are compared to the ones from a standard pressure sensor.

Results/Discussion

Fig. 2 shows the voltage output versus applied pressure, for some unimorph diaphragm sensors tested on a shock tube experimental setup previously[1]. The sensor responses are almost linear in the measured range for the three sensor samples. It is expected that good linearity and higher sensitivity for the proposed bimorph flexible PZT/polyimide pressure sensors.

[1] Liang, R and Wang, Q.M., 2015. High sensitivity piezoelectric sensors using flexible PZT thick-film for shock tube pressure testing. Sensors and Actuators A: Phusical 235, pp.317-327.

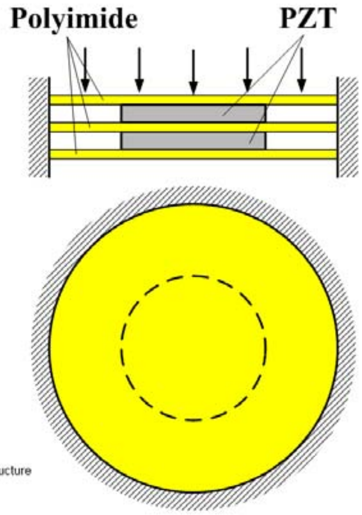

Fig. 1 Schematic of device structure

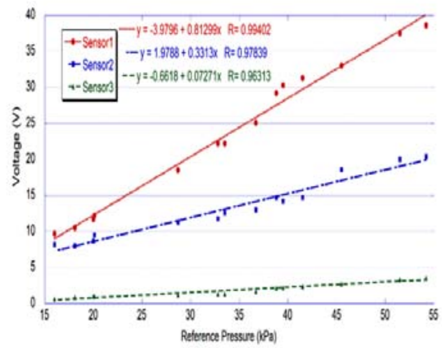

Fig. 2 Voltage output vs. Pressure for three unimorph diaphragm

P5-C3-7

High Temperature Performance of $PbTiO_3/Pb(Zr,Ti)O_3$ Thick Films Poled by Pulse Discharge at Room Temperature

Hikaru Kouyama[1], Takao Namihira[1], Makiko Kobayashi[1]; [1]*Kumamoto University, Japan*

Background, Motivation and Objective

Sol-gel composite can be useful for high temperature ultrasonic transducer applications and $PbTiO_3/Pb(Zr,Ti)O_3$ sol-gel composite is promising piezoelectric material because 100μm thick PT/PZT poled by positive DC corona discharge at high temperatures showed highest sensitivity among other sol-gel composites between room temperature and 400°C. However, high temperature poling process including cooling is time consuming. If PT/PZT can be poled at room temperature with comparable performance with PT/PZT poled at high temperature, PT/PZT will be more practical.

Statement of Contribution/Methods

100μm thick PT/PZT films were polarized by pulse discharge at room temperature. It was expected that high voltage supplied in a very short period by pulse discharge could suppress heat generation arc discharge. PT/PZT films were fabricated onto 3mm thick titanium substrate by sol-gel spray technique and then the films were poled by pulse voltage source at room temperature. The pulse repetition frequency, the output voltage, and the poling time were 100 Hz, +30 kV, and 10 min, respectively.

Results/Discussion

Ultrasonic responses were monitored in pulse echo mode. PT/PZT sample was set onto a hot plate and the results were recorded every 50°C after 5 min holding time up to 500°C by a digital oscilloscope. Measurement result at 450°C is shown in Fig. 1. Clear multiple echoes reflected from the bottom surface of the titanium substrate were confirmed. The signal amplitude was almost constant from 50°C to 400°C of hot plate temperature, dropped by ~10dB at 450°C, and significantly deteriorated at 500°C. From these results, high temperature performance was comparable with that of PT/PZT poled at high temperature and it was concluded that PT/PZT was successfully poled by pulse corona discharge at room temperature.

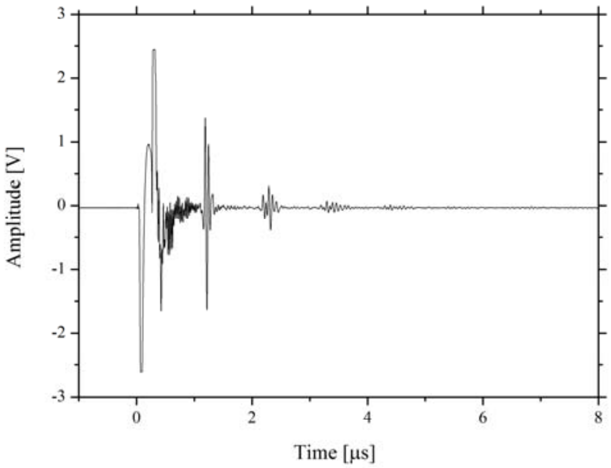

P5-C3-8

Sputter Technique for Deposition of AlN and ScAlN Thin Films in Mass Production

Valeriy Felmetsger[1]; [1]*PVD, OEM Group LLC, Gilbert, AZ, USA*

Background, Motivation and Objective

Reactively sputtered aluminum nitride (AlN) thin films are widely used in fabrication of various micro devices requiring piezoelectric actuation, such as FBAR, SMR, and Piezo MEMS. Due to recently discovered effect of scandium addition to AlN enabling enhanced electromechanical coupling coefficient, ScAlN is considered now as extremely attractive material for implementation in mass production.

In this presentation, sputter techniques for the reactive sputtering of piezo¬electric AlN and ScAlN thin films by the S-gun magnetron are described and some film properties are discussed.

Statement of Contribution/Methods

To satisfy success criteria for advanced AlN and ScAlN deposition processes suitable for mass production, it is necessary to ensure: process stability and controllability, wide process window; independent control of film properties such as thickness, uniformity, stress, texture, crystal orientation, and composition; reproducibility and homogeneity of film quality on a wafer from run to run and through a sputter target lifetime.

An earmark of the S-Gun magnetron is its dual concentric target arrangement. Due to stable and free of parasitic arcing operation and capability to deposit highly oriented AlN films without external wafer heating and biasing combined with the ability to control intrinsic stress in the films independently from other film properties, the reactive sputtering using energetic plasma of the AC (40 kHz) powered S-gun is the most effective PVD technique satisfying all these success criteria.

Results/Discussion

A novel sputter technique based on the use of pure Sc ingots embedded into the Al targets was developed to deposit ScAlN films with homogeneous properties across large size wafers (150-200 mm). With this target arrangement, a desired film composition can be attained by varying the number of the Sc pellets inserted. Composition uniformity can be also controlled by adjusting the amount of pellets in the inner and the outer targets of the S-gun.

To ensure formation of highly textured bottom electrode for AlN and ScAlN films, a thin AlN seed layer was grown prior to metal layer deposition. It was found that seed layer's orientation efficiency strongly depends on process parameters of predeposition RF plasma etch employed for cleaning and smoothening of the substrate surface.

In ScAlN films deposited with variation of AC power and intensity of ionic bombardment, Sc concentration of 7.5 at % was uniform across 150-mm wafers and did not depend on sputter process parameters. 1-ìm-thick ScAlN films deposited on Mo bottom electrodes exhibited strong c-axis orientation with X-ray rocking curve FWHM as low as 1.5°, which is comparable to crystal orientation of pure AlN films deposited by the S-gun.

The S-gun capability to reduce residual stress in AlN films to near zero level by means of redistribution of the discharge current between the targets and the internal shields of the magnetron was confirmed for ScAlN films as well.

P5-C3-9

Fabrication and Analysis of a Flexible PZT-Polymer Laminated Composite Cantilever Beam in Sensing and Actuation Modes

Zheng Min[1], Mohammad Gudarzi[1], Qing-Ming Wang[1]; [1]*Mechanical Engineering and Materials Science, University of Pittsburgh, Pittsburgh, PA, USA*

Background, Motivation and Objective

Piezoelectric lead zirconate titanate (PZT) thick films (t>10µm) with excellent electromechanical property have been considered for flexible electronics applications where precise actuation, control and sensing are desired. The main drawback of piezoelectric thick films is the fragility in device fabrication and application. To protect the PZT thick film devices from fracture, a five-layer sandwiched composite structure with three layers of polymer and two layers of PZT thick film is designed, modeled and experimentally tested in this this work. The ultimate goal of this research is to develop flexible and reliable piezoelectric thick film devices for wide range of electroemechanical applications.

Statement of Contribution/Methods

PZT thick films with thickness range from 10µm to 75µm are fabricated by tape-casting processing. After ceramic sintering, gold electrode coating, and poling process, rectangular PZT/polymer composite cantilever beams are fabricated. For the actuation mode, a sinusoidal voltage is applied to excite the mechanical vibration and the tip displacement is recoded over a frequency range. For the sensing mode, the fabricated cantilever beam is used as an accelerometer, Fig. 1. Then, the output voltage in the frequency domain is obtained by using a shaker.

Results/Discussion

In the actuation mode, natural frequencies and frequency responses of the theoretical modeling show a good agreement with the experimental results except for the frequency response near the first natural frequency which could be justified by simplification which is applied to the model. In sensing mode experiment, the accelerometer's output voltage shows a very good agreement with modeling results in the frequency domain, Fig. 2.

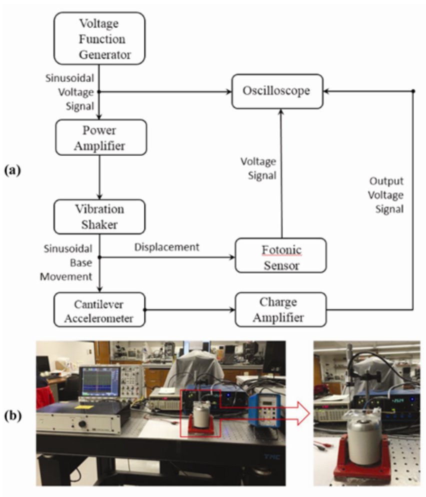

Fig 1. Experimental setup for sensory mode test

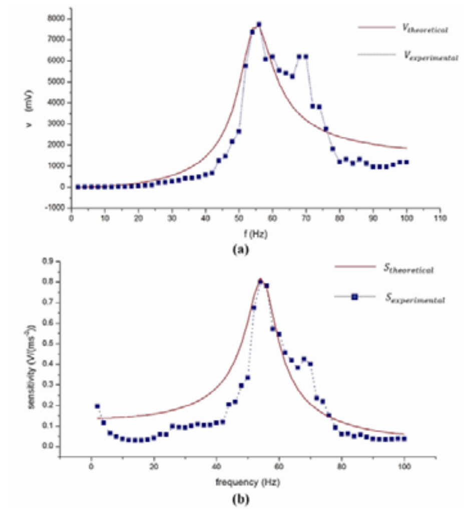

Fig 2. Accelerometer's (a) output voltage and (b) sensitivity in the frequency domain

P5-C3-10

Air-Coupled and Water Immersion Sectorized Array Transducers for Industrial and Medical Endoscopy.

Tomas Gomez Alvarez-Arenas[1], Luis Diez[1]; [1]*Institute of Physical and Information Technologies (ITEFI), Spanish National Research Council (CSIC), Madrid, Madrid, Spain*

Background, Motivation and Objective

Inspection of large or small pipes is commonly found in many different ultrasonic industrial applications. Pigs are commonly used for large pipes and inspection under working conditions. Small pipes are inspected from inside by using endoscopes, but the distance to be inspected can be limited by the pipe diameter, geometry and section variations. In medical applications, ultrasonic endoscopy are used as diagnosis tool for arteries (IVUS) and the gastrointestinal tract.

Flat transducers with conical reflectors have already been proposed for industrial and robotics applications (echolocation) but the main drawback, in the case of endoscopic applications is the need to keep the transducer aligned with the pipe axis.

Statement of Contribution/Methods

To alleviate this problem we propose a sectorized flat array transducer and either conical or parabolic cone reflectors. To proof this concept, three arrays have been produced. First, an air-coupled array, centre frequency of 400 kHz circular aperture, diameter 25 mm with 8 elements was produced. Matching to the air is designed to provide both wide band and high sensitivity and is achieved by a stack of 5 resonant and non-resonant matching layers, optimized using the frequency and impedance detuning method (see picture). Then, two water immersion arrays, frequency 3 and 4 MHz and circular aperture of 3.5 and 10 mm diameter, respectively, and 8 elements were also constructed. All the arrays are kerfless arrays made using 1-3 composites (65% ceramic volume fraction: random array of ceramic fibers in an epoxy matrix).

Two types of reflectors have been tested. First, conical reflectors that provide a non-focused beam, and then parabolic cone reflectors that provide a focused beam (see fig).

Results/Discussion

The air-coupled array was tested with a steel pipe, 12 mm thick, and diameter of 45 cm. Even considering the 2D spread of the beam, the sensitivity is high enough to provide a clear echo from the pipe wall and a SNR above 40 dB (see figure). The water coupled array was tested with an artery phantom made of a rubber pipe, 0.7 mm wall thickness and 10 mm inner radius. In both cases, the array transducer was used to measure the inner diameter and the integrity of the mesurement was checked against transducer displacement away of the pipe axis. In the case of the water coupled array, was also checked the possibility to determine phantom wall thickness

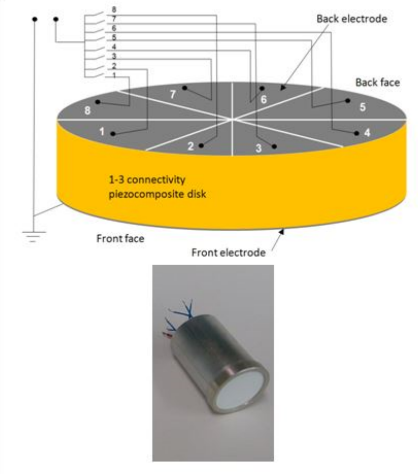

Up: schemmatic representation of the 8 elements sectorized array
Down. 400 kHz air-coupled array, 8 elements

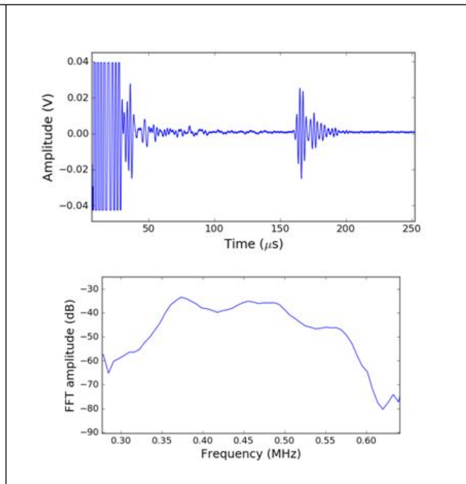

Up: Received signal in pulse echo mode using element #1, of the 400 kHz air-coupled array, conical reflector and cilindrical pipe.
Down: FFT of the echo in the previous ifigure

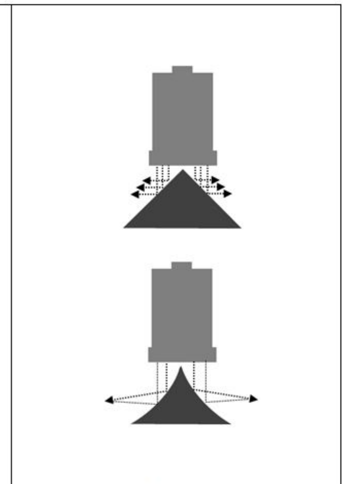

Transducer/reflector configuration:
Up: Conical reflector
Down: parabolic cone reflector

P5-C3-11

Cylindrical and Quasi-Cylindrical Focalization of Air-Coupled Single Element and Linear Array Transducers.

Tomas Gomez Alvarez-Arenas[1], Jorge Camacho[1], Luis Diez[1]; [1]*Institute of Physical and Information Technologies (ITEFI), Spanish National Research Council (CSIC), Madrid, Madrid, Spain*

Background, Motivation and Objective

The availability of better air-coupled transducers have made possible many different applications. In particular, air-coupled ultrasound is a good solution for the inspection/study of flat/plate materials than can not be wetted by working in through transmission, but experience some problems with curved surfaces. Another successful application is for the generation/reception of Lamb waves using the coincidence principle. However, this technique tunes the energy to one particular mode and is very sensitive to thickness variations, roughness of the plate, local anisotropy or when the system is subjected to vibrations. Some other times, when several modes are to be observed simultaneously (e.g. laser generation) this can also become a problem

Statement of Contribution/Methods

Several cylindrically focused 250 kHz air coupled transducer have been designed and fabricated. Use of lenses in ar-coupled transducers is problematic as they introduce a significant alteration of the impedance matching scheme which is critical in this case. The proposed design contains one flat matching layer, one cylindrical or quasi cylindrical lens and two other purely cylindrical layers. The active element is a 25 x 25 mm 1-3 piezocomposite. Linear kerfless arrays of 3-4 elements oriented normal to the axis of the cylindrical lens have also been produced to improve resolution in the non-focused direction. By this procedure we achieved a transducer with similar bandwidth and sensitivity (compared with a flat transducer), but with a 4 mm focal line at 60 mm. Measured acoustic field is shown in fig. 1. It is observed that the lens introduces an undesired apodization effect. To mitigate this problem, the possibility of using quasi cylindrical lenses is studied.

Results/Discussion

Produced transducers have been tested to generate and receive Lamb waves (A0) mode in aluminum plates. Amplitude reduction of the received signal is 9 dB, but the amplitude remains constant under variation of the angle of incidence of ± 5 degrees. On the contrary, performance improves when through transmission in a cylindrical pipe is performed. In the case of a glass fiber pipe, 4 mm thick and 30 cm diameter, the gain in the amplitude of the through transmitted signal is 3 dB. In conclusion, this specific design can be of interest when curved surfaces (better cylindrical surfaces) and/or multimode Lamb detection are required.

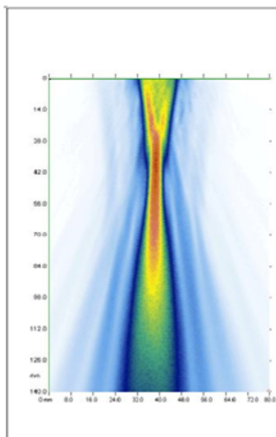

Fig1. Acoustic field of the cylindrically focused transducer

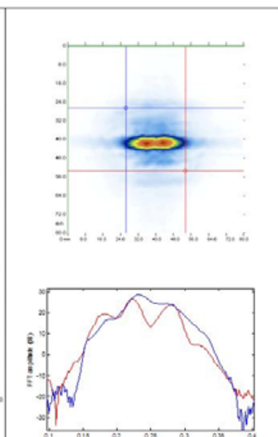

Fig 2. Up: Acoustic field in the focal plane
Down: FFT of the signal in through transmission. Blue: flat transducer, Red: cylindrically focused transducer

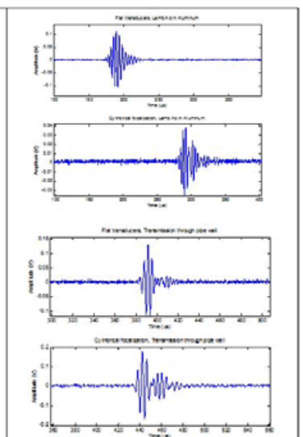

Fig. 3 Up: Comparison of Lamb wave (Ao) in Al plate generated and received with flat and with cylindrically focused transducers
Down: Comparison of signal transmitted through the wall of a cylindrical pipe using flat and cylindrically focused transducers